

# THE JOURNAL of the Acoustical Society of America

Vol. 104, No. 3, Pt. 1

September 1998

<b>EDITORIAL: ACOUSTICS RESEARCH LETTERS SECTION</b>		1129
<b>ARLO IS HERE</b>		1131
<b>SOUNDINGS SECTION</b>		
<b>ACOUSTICAL NEWS—USA</b>		1133
USA Meetings Calendar		1138
<b>ACOUSTICAL STANDARDS NEWS</b>		1142
Standards Meetings Calendar		1142
<b>BOOK REVIEWS</b>		1148
<b>REVIEWS OF ACOUSTICAL PATENTS</b>		1149
<b>SELECTED RESEARCH ARTICLES [10]</b>		
The compression wave generated by a high-speed train at a vented tunnel entrance	M. S. Howe	1158
Phantom echo generation: A new technique for investigating dolphin echolocation	Roland Aubauer, Whitlow W. L. Au	1165
<hr/>		
<b>GENERAL LINEAR ACOUSTICS [20]</b>		
Acoustical finite-difference time-domain simulations of subwavelength geometries	John De Poorter, Dick Botteldooren	1171
The radiating near-field asymptotics of a normal time-harmonic circular ultrasonic transducer in an elastic half-space	Larissa Ju. Fradkin, Aleksei P. Kiselev, Eugenia Krylova	1178
High-frequency asymptotic description of head waves and boundary layers surrounding the critical rays in an elastic half-space	Dmitri Gridin	1188
Padé approximants for the acoustical properties of rigid frame porous media with pore size distributions	K. V. Horoshenkov, Keith Attenborough, S. N. Chandler-Wilde	1198
Transient wave propagation in a circular annulus subjected to transient excitation on its outer surface	Guoli Liu, Jianmin Qu	1210
An equivalent source technique for calculating the sound field inside an enclosure containing scattering objects	M. E. Johnson, S. J. Elliott, K-H. Baek, J. Garcia-Bonito	1221
Ultrasonic interferences in polymer plates	Etienne Juliac, Jacques Arman, Daniel Harran	1232

(Continued)

## CONTENTS—Continued from preceding page

Near-field ultrasonic scattering from a cavity in steel considering the velocity amplitude on the transducer face using an error function model	Tjundewo Lawu, Makoto Tabei, Mitsuhiro Ueda	1242
On the anomalously low attenuation of the leaky Rayleigh wave in a fluid-filled cylindrical cavity	Waled Hassan, Peter B. Nagy	1246
Ultrasonic beam models: An edge element approach	Terence P. Lerch, Lester W. Schmerr, Alexander Sedov	1256
Forward projection of transient signals obtained from a fiber-optic pressure sensor	G. T. Clement, R. Liu, S. V. Letcher, P. R. Stepanishen	1266
<b>NONLINEAR ACOUSTICS, MACROSONICS [25]</b>		
Numerical simulation of the acoustic field of a phased-array medical ultrasound scanner	Mark D. Cahill, Andrew C. Baker	1274
Flow generated around particle clusters in a rotating ultrasonic waveguide	Glenn Whitworth	1284
Nonanalytic nonlinear oscillations: Christiaan Huygens, quadratic Schrödinger equations, and solitary waves	Bruce Denardo	1289
<b>AEROACOUSTICS, ATMOSPHERIC SOUND [28]</b>		
Model experiment to study sonic boom propagation through turbulence. Part II. Effect of turbulence intensity and propagation distance through turbulence	Bart Lipkens, David T. Blackstock	1301
<b>UNDERWATER SOUND [30]</b>		
On the use of stair steps to approximate bathymetry changes in ocean acoustic models	Finn B. Jensen	1310
Matched-beam processing: Application to a horizontal line array in shallow water	T. C. Yang, T. Yates	1316
Initial evaluation of the dominant mode rejection beamformer	Tina M. Redheendran, Richard A. Gramann	1331
Laboratory measurements of current flow using cross correlation on acoustic backscattering from suspended sediments	Robert F. van Unen, Peter D. Thorne, Henk Cox, Sicco D. Kamminga	1345
Nonlinear pulse propagation in shallow-water environments with attenuating and dispersive sediments	Rahul S. Kulkarni, William L. Siegmann, Michael D. Collins, B. Edward McDonald	1356
Sub-bottom scattering: A modeling approach	Charles W. Holland, Peter Neumann	1363
<b>ULTRASONICS, QUANTUM ACOUSTICS, AND PHYSICAL EFFECTS OF SOUND [35]</b>		
Application of genetic algorithms to ultrasonic tomography	P. P. Delsanto, A. Romano, M. Scalerandi, F. Moldoveanu	1374
Heterogeneous structure of modes and Kramers–Kronig relationship in anisotropic viscoelastic materials	Bernard Hosten	1382
Thermal processes in the oscillations of gas bubbles in tubes	X. M. Chen, A. Prosperetti	1389
Lamb wave assessment of fiber volume fraction in composites	Michael D. Seale, Barry T. Smith, W. H. Prosser, Joseph N. Zalameda	1399
<b>TRANSDUCTION [38]</b>		
Body waves recorded inside an elastic half-space by an embedded, wideband velocity sensor	Steven D. Glaser, Gregory G. Weiss, Lane R. Johnson	1404
The analysis and results of a continuous wave ultrasonic densitometer	Christian C. J. Smit, Edwin D. Smith	1413



**STRUCTURAL ACOUSTICS AND VIBRATION [40]**

A deconvolution method for force reconstruction in rods under axial impact	Enboa Wu, Cheng-Zorn Tsai, Ling-Hsien Tseng	1418
Thickness vibrations of rotating piezoelectric plates	J. S. Yang, H. Fang, Q. Jiang	1427
Vibration of open cylindrical shells: A three-dimensional elasticity approach	C. W. Lim, K. M. Liew, S. Kitipornchai	1436
A mixed displacement-pressure formulation for poroelastic materials	Noureddine Atalla, Raymond Panneton, Patricia Debergue	1444
A wavelet approach to the active structural acoustic control	P. Masson, A. Berry, P. Micheau	1453
Method for reducing sound radiated from structures using vibration absorbers optimized with a neural network	Kosuke Nagaya, Lianjin Li	1466

**NOISE: ITS EFFECTS AND CONTROL [50]**

Ground effect over hard rough surfaces	Patrice Boulanger, Keith Attenborough, Shahram Taherzadeh, Tim Waters-Fuller, Kai Ming Li	1474
--	--	------

**ARCHITECTURAL ACOUSTICS [55]**

Energy-time relations in a room with an electroacoustic system	U. Peter Svensson	1483
--	-------------------	------

**ACOUSTICAL MEASUREMENTS AND INSTRUMENTATION [58]**

Orthogonal acoustical factors of sound fields in a forest compared with those in a concert hall	Hiroyuki Sakai, Shin-ichi Sato, Yoichi Ando	1491
A new transducer holder mechanism for efficient generation and reception of Lamb modes in large plates	Triguna Ghosh, Tribikram Kundu	1498
Investigation of the near field of a loudspeaker using tomographic reconstruction from TV-holography measurements	Rolf Rustad, Lars Henrik Morset	1503

**PHYSIOLOGICAL ACOUSTICS [64]**

Linear and nonlinear model of the human middle ear	Jérôme Pascal, Antoine Bourgeade, Michel Lagier, Claude Legros	1509
Modeling otoacoustic emission and hearing threshold fine structures	Carrick L. Talmadge, Arnold Tubis, Glenis R. Long, Pawel Piskorski	1517
Enhancement of electrically evoked oto-acoustic emissions associated with low-frequency stimulus bias of the basilar membrane towards scala vestibuli	Desmond L. Kirk, Graeme K. Yates	1544
Changes in otoacoustic emissions in a transsexual male during treatment with estrogen	Dennis McFadden, Edward G. Pasanen, Narriman Lee Callaway	1555
Correlated amplitude fluctuations of spontaneous otoacoustic emissions in six lizard species	Pim van Dijk, Geoffrey A. Manley, Lothar Gallo	1559
The auditory evoked potential difference tone and cubic difference tone measured from the inferior colliculus of the chinchilla	Sally Arnold, Robert Burkard	1565

**PSYCHOLOGICAL ACOUSTICS [66]**

Lateralization of large interaural delays	Jennifer E. Mossop, John F. Culling	1574
Frequency-weighting functions for broadband speech as estimated by a correlational method	Christopher W. Turner, Bom Jun Kwon, Chiemi Tanaka, Jennifer Knapp, Jodi L. Hubbart, Karen A. Doherty	1580
Auditory-visual spatial integration: A new psychophysical approach using laser pointing to acoustic targets	Jörg Lewald, Walter H. Ehrenstein	1586

**SPEECH PERCEPTION [71]**

- Validity of rating scale measures of voice quality Jody Kreiman, Bruce R. Gerratt 1598

**SPEECH PROCESSING AND COMMUNICATION SYSTEMS [72]**

- Speech intelligibility assessment in a helium environment. II. The speech intelligibility index Lisa Lucks Mendel, Bruce W. Hamill, James E. Hendrix, Loring J. Crepeau, Jerry D. Pelton, Matthew D. Miley, Elizabeth E. Kadlec 1609

**MUSIC AND MUSICAL INSTRUMENTS [75]**

- Influence of a toroidal bend on wind instrument tuning Cornelis J. Nederveen 1616
- Artificial buzzing lips and brass instruments: Experimental results Joël Gilbert, Sylvie Ponthus, Jean-François Petiot 1627
- Numerical simulations of xylophones. II. Time-domain modeling of the resonator and of the radiated sound pressure Vincent Doutaut, Denis Matignon, Antoine Chaigne 1633
- Sound production by a vibrating piano soundboard: Experiment N. Giordano 1648

**BIOACOUSTICS [80]**

- Frequency and concentration dependence of the backscatter coefficient of the ultrasound contrast agent Albunex<sup>®</sup> Jon N. Marsh, Michael S. Hughes, Christopher S. Hall, Stephen H. Lewis, Rebecca L. Trousil, Gary H. Brandenburger, Harold Levene, James G. Miller 1654
- Simple methods of estimating source levels and locations of marine animal sounds Douglas H. Cato 1667
- Characterizing the graded structure of false killer whale (*Pseudorca crassidens*) vocalizations Scott O. Murray, Eduardo Mercado, Herbert L. Roitblat 1679
- The effect of spatial separation of signal and noise on masking in the free field as a function of signal frequency and age in the mouse James R. Ison, Punit Agrawal 1689
- Changes in temporal acuity with age and with hearing impairment in the mouse: A study of the acoustic startle reflex and its inhibition by brief decrements in noise level James R. Ison, Punit Agrawal, James Pak, William J. Vaughn 1696
- Focusing of therapeutic ultrasound through a human skull: A numerical study Jie Sun, Kullervo Hynynen 1705

**LETTERS TO THE EDITOR**

- Inversion of elastic waveform data in anisotropic solids using the delta-function representation of the Green's function [20] V. K. Tewary 1716
- Analysis and comparison of recent resonance scattering formulations by M. S. Choi *et al.* with earlier, traditional RST works [40] G. C. Gaunaurd 1720
- Response to "Analysis and comparison of recent resonance scattering formulations by M. S. Choi *et al.* with earlier, traditional RST work" [J. Acoust. Soc. Am. 104, 1720 (1998)] [40] Myoung-Seon Choi 1723
- Comment on "Effects of aircraft overflights on wilderness recreationists" [J. Acoust. Soc. Am. 100, 2909–2918 (1996)] [50] Susan L. Staples 1726
- Response to "Comments on 'Effects of aircraft overflights on wilderness recreationists'" [J. Acoust. Soc. Am. 104, 1726 (1998)] [50] Sanford Fidell, James Gramann, Richard Knopf, Karl Pearsons 1729
- Effects of high-frequency amplification on double-vowel identification in listeners with hearing loss [66] Kathryn Hoberg Arehart 1733

**CUMULATIVE AUTHOR INDEX**

1737

# CONTENTS

	page
Technical Program Summary .....	A8
Schedule of Technical Session Starting Times .....	A9
Map of Norfolk .....	A10
Map of Meeting Rooms .....	A12
Calendar—Technical Program .....	A14
Calendar—Other Events .....	A20
Meeting Information .....	A22
Guidelines for Presentations .....	A32
Dates of Future Meetings .....	A34
Technical Session (1a_), Monday Morning .....	1739
Technical Sessions (1p_), Monday Afternoon .....	1742
Tutorial Session (1eID), Monday Evening .....	1747
Technical Sessions (2a_), Tuesday Morning .....	1748
Technical Sessions (2p_), Tuesday Afternoon .....	1763
Technical Sessions (3a_), Wednesday Morning .....	1785
Technical Sessions (3p_), Wednesday Afternoon .....	1810
Plenary Session, Business Meeting and Awards Ceremony, Wednesday Afternoon .....	1822
Silver Medal in Animal Bioacoustics Award Encomium .....	1822
Silver Medal in Engineering Acoustics Award Encomium .....	1822
Silver Medal in Musical Acoustics Award Encomium .....	1822
von Békésy Medal Award Encomium .....	1822
Technical Sessions (4a_), Thursday Morning .....	1823
Technical Sessions (4p_), Thursday Afternoon .....	1840
Technical Sessions (5a_), Friday Morning .....	1857
Author Index to Abstracts .....	1862
Sustaining Members .....	1867
Regional Chapters .....	1869
Application Forms .....	1870
Index to Advertisers .....	1878

## Editorial: Acoustics Research Letters Section

This *Journal* will soon be adding a new section entitled “Acoustics Research Letters Online” (ARLO). It is intended to provide more rapid publication for letter-length articles about new research findings, by using a new on-line procedure for submission, reviewing, editing, and initial publication. The procedure has been developed in a two-year project jointly funded by the Acoustical Society of America (ASA) and the American Institute of Physics (AIP), conceived and administered by Prof. Robert E. Apfel of Yale University in close cooperation with the staff of the AIP Information Technology and Products Branch. Dr. Apfel will serve as the Section Editor. The features and details are outlined on pages 1131–1132 under the title “ARLO is Here.” Additional information for authors, associate editors, and reviewers is available at <http://asa.aip.org/arlo>.

ARLO letter-size articles, soon after peer reviewing and acceptance, will become available individually to on-line *Journal* subscribers and members, then will appear collectively in both printed and on-line *Journals*, and will be included in the bimonthly CD-ROM. The author-prepared copy and on-line procedure will give these articles a different appearance and their own pagination, but it is intended that they will conform to *Journal* practices and standards in all other respects, and can be cited as *Journal* articles. Many of our associate editors, who already use e-mail, will also be handling submissions through ARLO’s manuscript management system.

The ARLO section is expected to enhance the *Journal* by providing (a) more rapid publication of new research results, and (b) cumulative experience with on-line procedures which might eventually be used throughout the *Journal* as electronic publication develops further. Welcome, ARLO!

DANIEL W. MARTIN  
*Editor-in-Chief*

# ARLO IS HERE

<http://asa.aip.org/arlo>

## WHAT IS ARLO?

ARLO, Acoustics Research Letters Online, is a new additional Letters section of *The Journal of the Acoustical Society of America*, which will use a new rapid publication capability. ARLO will accept Letters (short articles up to 6 single column pages) in any area of acoustical research. However an article submitted to ARLO should represent truly novel research and not relatively minor improvements or variations on previously reported research.

ARLO will give special benefits to authors, as described below, and in return will expect authors to provide support, and to play a more active role in the manuscript preparation process.

## WHAT IS DIFFERENT ABOUT ARLO?

### **ARLO has unique online publishing capabilities.**

It will be able to display color and to include multi-media as soon as can be scheduled as part of JASA-O.

### **ARLO has a more rapid publication capability.**

It has a goal of being able to complete the review process and post individual articles online in as little as one month from the time of article submission. ARLO articles will be published individually online first, then collectively in both the printed and online journals, and included in the bi-monthly CD-ROM.

### **ARLO has a new Manuscript Management system.**

All articles will be submitted, reviewed, and processed online. Many of the regular Journal associate editors and reviewers will participate.

### **ARLO allows only one revision cycle.**

If an ARLO article requires revision, it must be acceptable after one revision (except for copy editing), or it will be withdrawn from ARLO. If withdrawn, it can continue the regular journal procedure if the Associate Editor considers it appropriate to do so.

## WHAT ARE THE AUTHORS' RESPONSIBILITIES?

In exchange for the benefits alluded to above, authors agree to the following terms:

**Authors must be able to submit articles online**, following the ARLO *Style Guidelines* and the procedures for *Postscript Submission* over the Internet. They will participate in the online review and publication process. Acoustics Research Letters will be limited to 6 single column pages including figures, tables, and references.

**Authors must pay.** There is a mandatory manuscript charge of \$350 if the manuscript is accepted after the review process. (N.B. This charge is voluntary until January of 1999, although we expect funded researchers to honor the charge in the interim period.)

## WHAT ARE THE NEW ROLES FOR AUTHORS, REVIEWERS, AND ASSOCIATE EDITORS?

The review process is carried out online. There are five entities involved:

**The American Institute of Physics (AIP):** AIP maintains the servers to which manuscripts are submitted and from which final manuscripts are published. Security is maintained at the highest industry standards by AIP, with password protection for all participating in the process.

**Manuscript Manager (MM):** Acts as the middle person for Authors, Associate Editors, and Reviewers (referees), working directly with the Editor of ARLO. All submissions first go through the MM to assure that *Style Guidelines* are met; all communications are funneled through the MM. Both automated and personal reminders are provided by MM on all manuscripts.

**Authors (A):** Register and receive appropriate i.d. and password; submit articles according to *Style Guidelines*; recommend an appropriate Associate Editor or area for review; respond to the comments of referees and associate editor; participate in the Publication Preparation process once an article is accepted for publication.

**Associate Editors (AE):** Get potential reviewers to *Register Online* for ARLO, who agree to review papers in their particular area; pick reviewers for that article; compose decisions; advise the MM of the need for copy editing in accepted manuscripts.

**Reviewers (R):** Register for Online reviewing for ARLO, identifying the research areas in which they are willing to act as reviewers; receive communications from the appropriate Associate Editor(s) by e-mail via

the MM. Reviewers will have a status screen that will list all the manuscripts they are reviewing, and will process manuscripts by choosing them from this status screen. A *Manuscript Manager* is available to assist reviewers in getting used to this process.

#### **TIMETABLES**

Authors, Reviewers, and Associate Editors have special responsibilities with respect to the timing of the submission, review, and publication process:

**Reviewers:** Since all articles will be the equivalent of six single column pages or shorter, reviewers will be asked if they agree to review a paper within TWO WEEKS. If they say yes, they will be reminded until the review is in. If a review is late, a new referee may be chosen at the discretion of the AE.

**Associate Editors:** The AE is expected to choose reviewers within 5 days, and to compose decisions within 5 days of receiving both reviews on an article.

**Authors:** Authors must compose revisions to their manuscript within one month after return for revision, or the manuscript will be withdrawn from ARLO. It can be resubmitted to JASA or another journal, but the process will have to start over.

#### **OFFICIAL LAUNCH DATE**

ARLO will be launched by the fall of 1998.

# SOUNDINGS

This front section of the *Journal* includes acoustical news, views, reviews, and general tutorial or selected research articles chosen for wide acoustical interest and written for broad acoustical readership.

## ACOUSTICAL NEWS—USA

**Elaine Moran**

Acoustical Society of America, 500 Sunnyside Boulevard, Woodbury, New York 11797

*Editor's Note: Readers of this Journal are asked to submit news items on awards, appointments, and other activities about themselves or their colleagues. Deadline dates for news items and notices are 2 months prior to publication.*

### Results of the 1998 Acoustical Society Election

The following candidates were elected Officers and Members of the Executive Council in the 1998 Acoustical Society election:

Patricia K. Kuhl, *President-Elect*

Mauro Pierucci, *Vice President-Elect*

Anthony A. Atchley, *Member of the Executive Council*

Dana S. Houglund, *Member of the Executive Council*

CHARLES E. SCHMID

*Executive Director*

### Preliminary notice: Joint ASA/EAA meeting

The joint meeting of the Acoustical Society of America and the European Acoustics Association, integrating the 25th German Acoustics DAGA Conference will be held Monday through Friday, 14–19 March 1999 at the Technical University of Berlin in Berlin, Germany.

For information about the meeting refer to the "Meetings Section" on the ASA home page at (<http://asa.aip.org/meetings.html>).

### Scientific Program

The joint ASA/EAA meeting will cover all fields of acoustics, reflecting established techniques as well as the latest developments. The technical program will consist of structured/special and regular sessions.

Technical sessions will be held from Monday to Friday, 15–19 March 1999. The conference language will be English. On Friday, national sessions may be organized by EAA member societies in their own language or by ASA. For further information please contact ASA or the national society in your own country.

An International Workshop on Active Noise and Vibration Control (IWAC) will take place on Wednesday, 17 March 1999.

A Joint ICAD/ASA/EAA Workshop on Auditory Display (ICAD) will take place on Saturday, 20 March 1999.

A satellite event, the *2nd International Conference on Voice Physiology and Biomechanics* will be held on 12–14 March 1999.

### List of Special Sessions

Short descriptions of the special sessions are listed on the meeting home page at <http://forum99-asa.tu-berlin.de>

Each session will be jointly organized by ASA and EAA. The organizers are listed in parentheses after the title of the session.

### ACOUSTICAL OCEANOGRAPHY

- **Acoustic seafloor classification** (Mayer, L.; Pouliguen, E.)
- **Acoustics in coastal ocean pollution research and monitoring** (Proni, J. R.; Zakharia, M.)
- **Theoretical and empirical innovations in fish and plankton acoustics** (Horne, J. K.; Jech, J. M.; Simmonds, E. J.)

Co-sponsored by Underwater Acoustics

- **New methods and results in acoustic tomography and thermometry** (Bjoernoe, L.; Lynch, J.; Send, U.; Spindel, R.)

### ANIMAL BIOACOUSTICS

- **Acoustics of echolocating animals** (Au, W. W. L.; Schnitzler, H.-U.)
- **Animal electrophysiological acoustics** (Jen, P.; Supin, A.)

- **Evolution in hearing and sound production** (Miller, L. A.; Popper, A.)
- **Physics of animal bioacoustics** (Au, W. W. L.; Aubauer, R.; Erbe, C.)

### ARCHITECTURAL ACOUSTICS

- **Acoustics of concert halls** (Beranek, L.; Meyer, J.)
- **Development and verification of prediction methods in building acoustics** (Gerretsen, E.; Nightingale, T.)
- **Solutions of practical problems in building acoustics** (Ljunggren, S.; Warnock, A. C. C.)

- **Sound insulation and subjective annoyance** (Campanella, A.; Rindel, J.)

Co-sponsored by Signal Processing

- **Verification of auralization and modeling programs** (Campbell, R. H.; Vorlaender, M.)

Co-sponsored by Noise

- **Modeling of noise in industrial workrooms** (Hodgson, M.; Kurze, U. J.; Probst, W.)

### BIOMEDICAL ULTRASOUND/BIORESPONSE TO VIBRATION

- **Lithotripsy** (Cleveland, R.; Delius, M.)
- **Low-intensity ultrasound for medical therapy** (Everbach, E. C.; ter Haar, G.)
- **Safety guidelines for diagnostic ultrasound** (Duck, F. A.; Nyborg, W. L.)

### EDUCATION IN ACOUSTICS

- **Acoustics education 2000** (Pompoli, R.; Raichel, D. R.)
- **European demonstrations in acoustics education** (Gaul, L.; Raju, P. K.; Revoile, S.)
- **Take fives: Five minute informal demonstrations** (Hansen, U. J.; Kohlrausch, A.)

### ENGINEERING ACOUSTICS

- **3D-loudspeaker reproduction methods** (Boone, M. M.; Shaw, N. A.; de Vries, D.)
- **Implications of recent standards** (Gottlob, D.; Nedzelnitsky, V.)
- **Recent advances in underwater transducers** (Huang, D.; Kofoed, L.)
- **SAW devices** (Hauden, D.; Robinson, H.)
- **Silicon sensors** (Busch-Vishniac, I. J.; Sessler, G.)

Co-sponsored by Signal Processing

- **Digital signal processing for hearing aids** (Doering, W. H.; Powers, J. M.; Thompson, S. C.)

### MUSICAL ACOUSTICS

- **Mapping multiple physical and perceptual attributes to musical structures** (Kendall, R. A.; McAdams, S. E.)
- **Modeling versus measurements of wind instruments** (Poster session) (Hirschberg, A.; Yoshikawa, S.)
- **Musical instruments and structural acoustics I: General time-domain models and finite element analysis** (Chaigne, A. J.; Hansen, U. J.)
- **Musical instruments and structural acoustics II: Piano and related instruments** (Bork, I.; Nakamura, I.)
- **Quality of musical instruments and human voice** (Caussé, R.; Sundberg, J. E. F.)
- **Sound production of wind instruments** (Campbell, M.; Strong, W. J.)
- **The relevance of musical instrument acoustics for the education of musicians** (Askenfelt, A.; Rossing, T. D.)

**NOISE** (see also Workshop on Active Noise and Vibration control)

- **Acoustics in towns** (Peppin, R. J.; Polack, J.-D.)
- **Aerodynamic noise from vehicles** (Barsikow, B.; Donovan, P. R.)
- **Airframe noise** (Macaraeg, M. G.; Michel, U.)
- **Community noise annoyance** (Fidell, S.; Schulte-Fortkamp, B.)
- **Computational aeroacoustics** (Tam, C. K. W.)
- **Experience with noise prediction** (Attenborough, K.; Hirsch, K.-W.)
- **Future noise policy in Europe** (Schomer, P. D.; ten Wolde, T.)
- **Harmonization of rating procedures** (Gjestland, T.; Schomer, P. D.)
- **Hearing conservation program effectiveness** (Matefi, L.; Royster, L.)
- **Hearing protection devices** (Berger, E. H.; Smoorenburg, G. F.)
- **Jet acoustics** (Fisher, M.; Morris, D.)
- **Military aircraft noise** (Berry, B. F.; Finegold, L. S.)
- **Noise at the workplace** (Schrndt, G. A.; Suter, A. H.)
- **Noise from air-conditioning, ventilating, and industrial fans** (Schlinker, R.; Turret, J.)
- **Power plant noise** (Brittain, F. H.; Gilg, J.)
- **Railway noise** (Hecht, M.; Remington, P. J.)
- **Road traffic noise** (Schumaker, R. F.; Steven, H.)
- **Rotor noise of helicopters, propellers, and wind turbines** (Dobrzynski, W.; Farrassat, F.)
- **Sleep disturbance** (Finegold, L. S.; Griefahn, B.)
- **Sound level meters** (Finke, H. O.; Marsh, A.)
- **Tribute to Henning E. von Gierke** (Gottlob, D.; McKinley, R. L.)
- **Turbomachinery noise** (Schulten, J. B. H. M.)
- **Noise emission from machinery and turbomachinery** (Campanella, A. J.; Jonasson, H. J.)

Co-sponsored by Psychological and Physiological Acoustics

- **Product sound quality** (Kohlrausch, A.; Walton, D.)

#### PHYSICAL ACOUSTICS

- **Acoustic remote sensing of the atmosphere** (Mellert, V.; Wilson, D. K.)
- **Cavitation physics and sonoluminescence** (Lauterborn, W. H.; Roy, R. A.)
- **Duct acoustics** (Eversmann, W.; Mechel, F. P.; Ronneberger, D.)
- **Elastic properties of materials** (Froehlich, H.-J.; Achenbach, J. D.)
- **Interaction of acoustic fields with suspended particles** (Apfel, R. E.; Benes, E.)
- **Measurement and evaluation of ultrasound** (Chivers, R. C.; Reibold, R.)
- **Nonlinear motion of bubbles and drops** (Holt, R. G.; Holzfuss, J.)
- **Shockwaves in liquids** (Blackstock, D. T.; Eisenmenger, W.)
- **Sonochemistry** (Reisse, J.; Suslick, K. S.)
- **Surface roughness** (Attenborough, K.; Kolaini, A.)
- **Thermoacoustics** (Herman, C.; Wetzel, M.)
- **Ultrasonic imaging: Diagnostic methods in material testing and/or medicine** (Arnold, W.; Tittmann, B. R.)

Co-sponsored by Engineering Acoustics

- **Numerical methods for computing sound radiation and scattering** (Koopmann, G. H.; Ochmann, M.)

#### PSYCHOLOGICAL AND PHYSIOLOGICAL ACOUSTICS

- **Perceptual processing of cross-spectral information** (Culling, J. F.; Kidd, G. D. Jr.)
- **Recent advances in models of auditory processing** (Dau, T.; Yost, W. A.)
- **The role of peripheral compression in hearing** (Florentine, M.; Moore, B. C. J.)

Co-sponsored by Speech Communication and Musical Acoustics

- **Honoring the contributions of Reinier Plomp in hearing, speech, and music** (Houtgast, T.; Shannon, R. V.)

Co-sponsored by Noise

- **Application of psychoacoustics in rating environmental noise** (Fastl, H.; Kalivoda, M. T.; Peppin, R. J.)

Co-sponsored by Speech Communication

- **Localization and speech perception in realistic acoustic environments** (Colburn, H. S.; Houtgast, T.; Litovsky, R. Y.)

#### SIGNAL PROCESSING IN ACOUSTICS

- **Acoustic image synthesis for arbitrary listeners** (Brammer, A. J.; Bronkhorst, A.)
- **Acoustic signal processing for systems with 2-D and 3-D arrays of sensors** (Kraus, D.; Stergiopoulos, S.)
- **Acoustics in multimedia** (Havelock, D. I.; West, J. E.)

Co-sponsored by Engineering Acoustics

- **Binaural technology** (Blauert, J.; Burkhard, M. D.)
- **Smart microphones and audio for teleconferencing** (Blauert, J.; Elko, G.; West, J. E.)

#### SPEECH COMMUNICATION

- **Cross-language and L2 phonetics** (Bohn, O.-S.; Flege, J. E.)
- **Data-based speech synthesis** (Campbell, D.; Huang, D.)
- **Fluid dynamic models for speech production** (Lofqvist, A.; Shadle, C. H.)
- **New spectral analysis techniques for speech** (Bimbot, F.; Bunnell, H. T.; Hieronymous, J. L.; Pols, L. C. W.)
- **Parameters of F0 contours** (Moebius, B.; Portele, T.)
- **Psychoacoustic methods in speech recognition** (Kollmeier, B.; Senneff, S.)
- **Speech quality in telecommunications** (Gierlich, H.-W.; Perkins)

Co-sponsored by Psychological and Physiological Acoustics

- **Models of speech processing in the auditory pathway** (Greenburg, S.; Patterson, R. D.)

#### STRUCTURAL ACOUSTICS AND VIBRATION

- **Inverse problems in structural acoustics** (Petersson, B. A.; Wu, S. F.)
- **Smart materials** (Hayek, S. I.; Varadan, V. V.)

#### UNDERWATER ACOUSTICS

- **Rapid ocean environmental assessment** (Sellschopp, J.; Wagstaff, R. A.)
- **Scattering from finite objects near boundaries** (Fawcett, J. A.; Schneider, H. G.)
- **Wave propagation: Session in honor of Leonid M. Brekhovskikh** (Dubrovsky, N.; Mikhalevsky, P.)

Co-sponsored by Acoustical Oceanography

- **Ultra low frequency (<1 Hz) ocean acoustics** (Montagner, J.-P.; Stephen, R. A.)

Co-sponsored by Acoustical Oceanography and Physical Acoustics

- **Acoustics of the comprehensive test ban treaty** (Baggeroer, A. B.; Lawrence, M.)

#### Short Course on Thermoacoustics

This short course on thermoacoustics is intended for scientists and engineers who are interested in understanding thermoacoustic phenomena and their use in engines and refrigerators. The course will include animations, demonstrations, and other material intended to convey an intuitive, phenomenological appreciation of thermoacoustics, as well as presentation of quantitative design and analysis methods and practical construction methods.

The instructor will be Greg Swift who has worked at the Los Alamos National Laboratory since 1981, and taught this well-received course at the 1996 ASA meeting in Hawaii. His review article in *The Journal of the Acoustical Society of America* (Vol. 84, page 1145, 1988) is suggestive of the style of the expected short course. The course is scheduled for Friday afternoon, 19 March, and all day Saturday, 20 March at the TU Berlin.

Further information on the course, including registration fees and how to register, may be found on ASA's home page: <http://asa.aip.org> or by contacting Elaine Moran at the ASA Office, 500 Sunnyside Blvd., Woodbury, NY 11797, USA.

#### Technical and Standards Committee Meetings

Technical Committees in all fields of acoustics will meet on Monday and Thursday evenings. All acousticians who register at the meeting are invited and encouraged to attend to learn about the latest information in their field of acoustics and to participate in the planning of future meetings. There will also be meetings of the various Standards Committees and US TAGS.

Anyone interested in Standards activities should contact:

Avril Brenig  
Standards Secretariat  
Acoustical Society of America  
120 Wall Street, 32nd Floor  
New York, NY 10005-3993, USA  
Tel: +1 212 248 0371  
e-mail: [asastds@aip.org](mailto:asastds@aip.org)



## Preprint Collection on CD-ROM

No proceedings will be published for the joint ASA/EAA meeting. In addition to the paper copy service being provided during the meeting, a CD-ROM of voluntary preprints will be produced.

The CD-ROM can be ordered together with registration or during the meeting, and will be sent after the meeting.

## Student Transportation Subsidies

A student transportation subsidies fund has been established by the ASA to provide limited funds for students from all countries to partially defray transportation expenses to meetings. Students presenting papers who propose to travel to Berlin in groups using economical transportation will be given first priority. No reimbursement is for food or lodging. The amount granted each student depends on the number of requests received. To apply for a subsidy, submit a written proposal to be received by 15 January 1999 to:

Acoustical Society of America  
Elaine Moran  
500 Sunnyside Boulevard  
Woodbury, NY 11797 USA  
Fax: +1 516 576 2377  
Tel.: +1 516 576 2360  
e-mail: asa@aip.org

The proposal should indicate your status as a student, whether you submitted an abstract, whether you are a member of the ASA, method of travel, whether you travel alone or with other students, names of those students traveling with you and approximate cost of transportation.

## Social Activities and Social Program

Berlin is the capital of Germany and its largest city. Since the fall of the Berlin Wall it has become the workshop of German unity and a gateway to the newly developing Eastern European countries. It is again becoming a metropolis of science and culture, of media and of business. The universities and research institutes, the opera houses, theatres, museums, and libraries are just as much attractions to our city as its colorful neighborhoods and the wonderful landscape of woods and lakes surrounding it. Berlin offers many possibilities for leisure and sightseeing to the visitors of the conference.

Various social and conference events are being prepared for conference delegates to the "Berlin 99" meeting (further details will be given in the final program):

- **Opening Ceremony** in the Berlin Philharmonic Hall on Monday morning. The ceremony will feature welcoming speeches by representatives of the societies responsible for the joint conference, a musical presentation and a review of the acoustics of the Berlin Philharmonic Hall which was built by the architect Hans Scharoun aided by the well known Berlin acoustician Lothar Cremer. The hall was inaugurated in 1964 and has since hosted the world's most famous orchestras and conductors.
- **Meeting Reception** on Tuesday evening. Place and further details will be given in the final program.
- **Meeting Banquet** on Wednesday evening in a medieval fortress (Zitadelle Spandau). Dating back with its main tower to the 12th century, it lies on border of the river Havel where it meets the other Berlin river, the Spree. A medieval meal will be accompanied by medieval performers and our stay at the fortress will end with fireworks. The number of spaces is limited, so please be sure to make early reservation. Tickets will cost DM 120 per person (please note this is not included in the registration fee).
- There will be a **Welcome Drink** on Sunday evening, a **Get-Together-Party** on Monday evening and a **Farewell-Drink** on Friday afternoon. All these events will take place near the conference rooms in the main building of the Technical University.

## Technical Tours

- Guided technical tours through various institutes and laboratories of and near the TU Berlin (during the meeting days)
- Guided tour on architectural acoustics through famous buildings, e.g., the Preussischer Landtag (House of the Berlin Parliament) and the Konzerthaus (Concert Hall; limited to 50 persons—first come first served). Both tours will be held on Sunday, 14 March, about midday or in the early afternoon.

## Exhibition

During the conference, an exhibition will be held from Monday afternoon to Thursday evening next to the lecture halls and poster exhibition in the main building of the TU Berlin. State-of-the art products and publications in the following fields of acoustics will be on display:

- active noise control systems and equipment
- computer based instrumentation
- sound level meters
- sound intensity systems
- signal processing systems
- devices for noise control
- acoustical materials
- measuring and computing software
- acoustical measurement tools
- microphones and vibrational instruments
- all types of analyzers
- noise prediction tools
- noise monitoring equipment

Organizations interested in exhibiting should contact:

Technische Universität Berlin  
Wissenstransfer (WTB 3)—Berlin 99  
Steinplatz 1  
10623 Berlin  
Germany  
fax: +49 30 314 24098 or 24087  
e-mail: kongresse@wtb.zuv.tu-berlin.de

## Accompanying Persons Program

Accompanying persons are welcome. A Hospitality Meeting Point will be organized near the conference rooms where information will be available on a wide variety of organized or individual cultural activities. In addition, it will be possible to make contacts with Berlin delegates and their families over a cup of coffee and you can use this opportunity to arrange some private programs for your stay in Berlin. Berlin offers plenty of sightseeing and a wealth of cultural treasures which are easily accessible with Berlin's public transport system. Many tours are available, including the beautiful surroundings of Berlin. Recommendations will be available at the Hospitality Meeting Point.

## Post Conference City Tours

Besides many other offers a selection of three destinations may be of special interest for attendees at the Joint Meeting. These three tours are being offered by a travel agency:

- (1) **Weekend tour to Dresden, the baroque city of August the Strong**
- (2) **Weekend tour to Prague, the Golden City**
- (3) **Weekend tour to Paris, the city of the French "savoir vivre"**

This is only a small selection. If you do prefer any other destinations or skiing holidays please contact the travel agency below. All tours are subject to availability.

For more information and all booking of post conference tours please contact:

Euro Lloyd Reisebuero  
Attn: Livia von Gizycki  
mail to: L.vonGizycki@EuroLloyd.de  
Fax: +49 30 3121743  
Tel.: +49 30 31109842

## Registration

Participants are kindly requested to register for the conference before 15 January 1999 using the registration form in the call for papers or on the world wide web as noted below.

## Registration Fees\*

\*Note: Payment will be in DM only. For US residents, please note that the exchange rate is about 0.55 US\$ to 1 DM.

Registration and payment **deadline 15 January 1999:**

Participant (non member).....	DM 540
Member** .....	DM 450
Student, Senior or Emeritus .....	DM 180

Registration and payment

**on/after 16 January 1999 and on-site:**

Participant (non member).....	DM 630
Member** DM .....	DM 540
Student, Senior or Emeritus .....	DM 270

Students must provide a copy of their Student ID Card or a letter of confirmation from their institution. Seniors are persons fully retired from work.

\*\*member of ASA, DEGA, EAA as well as DPG, VDI, ITG, VdT.

Registration via Internet is also possible and welcome. In that case please fax a copy of the money transfer document with clear indication of your name. When using credit card payment we kindly ask you to mail or fax the registration form with the credit card details and card holder's signature. You may find the registration form on the meeting home page at: <http://forum99-asa.tu-berlin.de>.

**Payment**

Payment must be made in German currency, the Deutsche Mark (DM), and may be made by major credit card, Eurocheque in DM, or bank transfer (free of charge to the conference). Using credit cards will automatically transfer the registrant's own currency to DM. For bank transfer please mail or fax a copy of the money transfer document together with the completed registration form.

The bank transfer must be issued to

Payee:.....	M. Moeser
Bank: .....	Grundkreditbank e.G. Berlin
Code Number:.....	101 901 00
Account #: .....	32 81 39 00 06
Reference:.....	Berlin 99
	“Name of Participant”

**Cancellation**

Cancellation of the registration received in writing by signed letter or fax on or prior to **1 March 1999** will result in a refund minus an administration fee of DM 90. Please indicate address and bank transfer number. **No refunds are possible after 1 March 1999.**

**Registration Desk**

The meeting registration desk will be located on the ground-floor hall of the main building of the TU Berlin. Turn left after entering the building from the main entrance (Strasse des 17.Juni 135) and walk through the door towards the grand lecture-hall Audi Max (H105). The desk will be open during the following hours

Sunday, March 14 .....	10:00–20:00 hours
Monday–Thursday.....	7:30–18:30 hours
Friday .....	7:30–15:00 hours

Please note that on Monday (15 March) the registration will only be at TU Berlin and not in the Berlin Philharmonic Hall. Therefore, participants should come to TU Berlin for registration prior to going to Berlin Philharmonic Hall.

**Proforma Invitation**

The Chair of the conference will be pleased to write a personal letter of invitation for an individual scientist on request. It is understood that such Proforma Invitation is provided to assist with travel arrangements (visa etc.). It cannot represent any financial commitment by the Organizing Committee nor does it imply entitlement to reduction in the regular conference fees. Mail or e-mail the request to the Berlin Conference Secretariat, Institut fuer Technische Akustik, Attn: Sigrid Baerndal, Einsteinufer 25, 10587 Berlin, Germany, email: [forum99@mach.ut.tu-berlin.de](mailto:forum99@mach.ut.tu-berlin.de)

**Accommodations**

Conference attendees may choose between the following **types of accommodations:**

- Hotels with Reduced Rates (A,B,C)
- BTM Agency (C)
- Dormitories

Rooms in categories **A** and **B** are equipped with bathrooms. Rooms in category **C** are simpler, sometimes with shared bathroom facilities. **Prices** include breakfast, taxes, and tips.

Please note that **double room** stands for double occupancy and does not necessarily mean twin beds. In case of doubt check with the hotel reception before booking. For **dormitories**, *booking is done via the Registration Form* and payment must be made together with the registration fees.

For finding a suitable hotel accommodation conference attendees may choose between **three ways of booking:**

Either

- (1) contact one of the hotels with reduced rates listed below or
- (2) Fill in the accommodation form (in the call for papers or on the World Wide Web (<http://forum99-asa.tu.berlin.de>) and send it to the Wisenstransfer Bureau of TU Berlin. If you choose method (2) note, that booking of a specific hotel other than the conference hotel can not be guaranteed.

- (3) contact Berlin Tourismus Marketing (BTM) agency directly, Tel.: +49 30 25 0025; Fax: +49 30 25 002424

While attendees may indicate a first and second hotel preference it will not always be possible to honor this request especially when booking is done late. Therefore, book as early as possible to ensure low rates and to get the hotel of your choice. **Deadline** for booking is **15 January 1999**. If you book an accommodation directly with one of the hotels, use the **booking code “Berlin 99”** to profit from the reduced rates.

**Hotels with Booking Code “Berlin 99”**

A block of rooms has been reserved at special rates for “Berlin 99” participants for various hotel categories. All hotels are within walking distance of the TUB (<30 min), some of them only 400–600 meters from the conference facilities. Prices include breakfast, taxes and tips. Please **specify code “Berlin 99”** when booking your room.

**1. Hotel Berlin (A,B)**

Luetzowplatz 17, 10785 Berlin	
Tel.: +49 30 2605-2700	
Fax: +49 30 2605 2716	
Single Room .....	DM 155
Double Room.....	DM 215

Hotel Berlin is the main conference hotel for lodging. It is a 4-Star-Plus-category hotel with excellent facilities and a high-class restaurant. It offers the largest number of rooms at low cost. Take the BVG express bus X9 (about DM 4) to get from the Airport Tegel to *Hardenbergplatz* (U- and S-Bahn station *Zoologischer Garten*), change there to bus 100 and exit at *Luetzowplatz*. To get to the TU conference site, take the same buses in opposite order and get off at *Ernst-Reuter-Platz* or walk 5 min from *Hardenbergplatz* to TU conference site (notice BVG daily and weekly rates).

**2. Savoy Hotel (A)**

Fasanenstrasse 9-10, 10623 Berlin	
Tel.: +49 30 31103 0	
Fax: +49 30 31103 333	
Single Room .....	DM 244
Double Room.....	DM 284

From Airport Tegel, take BVG express bus X9, exit at Bahnhof Zoo; 10 min walk to TU main building.

**3. Berlin Excelsior Hotel (A)**

Hardenbergstrasse 14, 10623 Berlin	
Tel.: +49 30 3155 22	
Fax: +49 30 3155 1002	
Single Room .....	DM 185
Double Room.....	DM 235

From Airport Tegel, take BVG express bus X9, exit at *Hardenbergplatz/Bahnhof Zoo*; 10 min walk to TU main building.

#### 4. Hotel Consul (B)

Knesebeckstrasse 8-9, 10623 Berlin  
Tel.: +49 30 311 06 0  
Fax: +49 30 312 2060  
Single Room .....DM 153  
Double Room.....DM 174

From Airport Tegel, take BVG express bus X9, exit at *Ernst-Reuter-Platz*; 10 min walk to TU main building.

The next two hotels are located close to the *Kurfuerstendamm*, the famous shopping boulevard of Berlin.

#### 5. Plaza Hotel (B,C)

Knesebeckstrasse 63, 10719 Berlin  
Tel.: +49 30 8841 3444  
Fax.: +49-30 8841 3754  
Single Room .....DM 150  
Double Room.....DM 190

From Airport Tegel, take BVG bus 109, exit at *Uhlandstrasse*; 15 min walking distance to TU main building.

#### 6. Berlin Mark Hotel (B,C)

Meineckestrasse 18-19, 10719 Berlin  
Tel.: +49 30 8800 2802  
Fax: +49 30 8800 2804  
Single Room .....DM 150  
Double Room.....DM 190

From Airport Tegel, take BVG bus 109, exit at *Uhlandstrasse*; 20 min walking distance to TU main building.

#### 7. Hotel Heidelberg (C)

Knesebeckstrasse 15, 10623 Berlin  
Tel.: +49 30 313 0103  
Fax: +49 30 313 5870  
Single Room .....DM 138  
Double Room.....DM 168

From Airport Tegel, take BVG express bus X9, exit at *Ernst-Reuter-Platz*; 10 min walk to TU main building.

#### 8. Econtel (C)

Soemmeringstrasse 24, 10589 Berlin  
Tel.: +49 30 3468 1147  
Fax.: +49 30 3468 1163  
Single Room .....DM 130  
Double Room.....DM 150

From Airport Tegel, take BVG express bus X9, bus stop is across the street at Econtel. To get to the TU conference site, take the same bus from Econtel and go to *Ernst-Reuter-Platz* (one stop).

#### 9. Hotel Westerland (C)

Knesebeckstrasse 10, 10623 Berlin  
Tel.: +49 30 312 1004  
Fax: +49 30 313 6489  
Single Room .....DM 125  
Double Room.....DM 165

From Airport Tegel, take BVG express bus X9, exit at *Ernst-Reuter-Platz*, 10 min walk to TU main building.

#### 10. Hotel Carmerstrasse (C)

Carmerstrasse 16, 10623 Berlin  
Tel.: +49 30 3110 0500  
Fax: +49 30 3110 0510  
Single Room .....DM 120  
Double Room.....DM 160  
Single Room.....DM 80, shared WC  
Double Room .....DM 120, shared WC

Quiet location. From Airport Tegel, take BVG express bus X9, exit at *Ernst-Reuter-Platz*; 10 min walk to TU main building.

#### BTM Agency

You may also book rooms in category C (DM 100-150 per night) or lower as well as any other accommodation through an agency. Please consult

Berlin Tourismus Marketing (BTM) GmbH  
Tel.: +49 30 25 00 25  
Fax: +49 30 25 00 24 24

Specify what price range is acceptable to you and that you want the room as close as possible to the TU Berlin. *Before* booking you should check the location. Use the URL <http://www.kulturbox.de/perl/berlininfo> to get a Berlin map on screen. Enter the street name. Some street names are used more than once, so specify the area code, too. The TUB is in 10623, the neighboring areas are 10555, 10577, 10585, 10587, 10625, 10629, 10707, 10719, 10789, and 10787.

#### Dormitories

A limited number of beds in low-cost and modest dormitory rooms (2-3 beds) are available. The price is DM 45 per person for bed & breakfast. Single occupancy is not possible! **Reservation and payment for these rooms must be made by 15 January 1999 using the Registration Form and cannot be changed after that date.** Feel free to name your roommate on the Meeting Registration Form. Notice that there will be **no refund if the reservation is cancelled after 15 January 1999.** The dormitories are located at:

#### Jugendgaestehaus der DSJ

Franz-Kuenstler-Strasse 4-10, 10969 Berlin

This is located in the Kreuzberg district, the closest underground railway station is *Prinzenstrasse*. To get from the Jugendgaestehaus to the TUB, walk north on *Alexandrinenstrasse* to *Ritterstrasse*, then turn right and go two blocks to *Prinzenstrasse* and turn right again. If the bus 140 comes by enter it for just one station. Otherwise walk south to the subway station *Prinzenstrasse*. Take the underground railway U15 (green line) and go seven stations to *Wittenbergplatz* and change to the U2 (red line). Go two stations to *Ernst-Reuter-Platz*.

#### Internet Berlin Map

Navigate through Berlin's streets at:

<http://www.kulturbox.de/perl/berlininfo>

In the field "Street," enter *Ernst-Reuter-Platz* and click OK. A partial map of Berlin will appear which shows the TUB and the subway station *Ernst-Reuter-Platz*. Put the cursor anywhere on the map and click the left mouse button. The clicked point will become the center of the next partial map.

#### General Tourist Information

For getting general tourist information you may contact:

Berlin Tourismus Marketing (BTM) GmbH  
Am Karlsbad 11, 10785 Berlin  
Tel.: +49 30 264 74 80  
Fax: +49 30 264 74 899

#### Travel Information

For all individual requests concerning travel arrangements please contact the following travel agency:

EURO LLOYD Reisebuero  
Attn. Livia von Gizycki  
Kantstr. 24, 10629 Berlin  
Tel.: +49 30 312 17 43  
Fax: +49 30 311 089 42  
e-mail: [L.vonGizycki@EuroLloyd.de](mailto:L.vonGizycki@EuroLloyd.de)

#### Weather

March temperatures in Berlin are highly variable. In average, temperatures are between 0 to +10 degrees Celsius but may achieve extreme levels such as nighttime low temperatures of -10 to -15 degrees Celsius or daytime high temperatures of +15 to +20 degrees Celsius. It may rain (or even snow) in March but normally the climate in Berlin tends more to dry

air and sunshine instead of humidity or rain. Therefore, attendees are encouraged to bring overcoats but should also carry along clothing for higher temperatures.

### International Workshop on Active Noise and Vibration Control (IWAC) (17 March 1999)

Integrated into the Joint Meeting of ASA/EAA, an International Workshop on Active Noise and Vibration Control will be held. This workshop will present and discuss recent results and advances in all areas of active control of noise and vibration. Being placed between the dedicated conferences Active 97 and Active 99 (to be held in December 1999), it will thus offer an ideal opportunity to review state of the art and developments of this wide field and its applications.

Approximately 100 technical papers, covering current aspects and latest developments of active noise and vibration control, are expected to give a broad overview of current activities and thus enable an intensive exchange of ideas, concepts and results.

To guarantee a balanced spectrum of presentations and discussions, special sessions with introductory overview lectures will be organized. These are planned to include the following topics:

- Active Noise Control in Ducts
- Active Noise Control in Enclosures
- Active Control of Structural Vibrations
- Active Control of Sound Radiation and Transmission
- Active Noise Control in Aircraft Engines
- Other Applications of Active Control
- Signal Processing and Controllers for Active Control
- Transducers for Active Noise and Vibration Control

### Joint ICAD/ASA/EAA Workshop on Auditory Display (20 March 1999)

A one-day Workshop on Auditory Display, jointly organized by the International Community for Auditory Display (ICAD), the Acoustical Society of America (ASA), and the European Acoustics Association (EAA), will be held on Saturday, March 20, 1999, also at Technische Universitaet Berlin. ICAD is a not-for-profit corporation created to support research, education and community formation in the emerging field of auditory display.

The Workshop on Auditory Display is intended to provide an open forum to bridge the gulfs between research and design, science and technology, and perception and acoustics. For more information visit (<http://www.santafe.edu/~icad>).

### 2nd International Conference on Voice Physiology and Biomechanics (12–14 March 1999)

The conference is a continuation of the former Vocal Fold Physiology Conferences. The purpose of the conference is to provide a forum for discussion of current basic research on the voice. We encourage investigators working in the following areas to attend the conference:

- Acoustics
- Aerodynamics
- Anatomy
- Biomechanics
- Muscle Physiology
- Modeling
- Neurophysiology
- Physics, and Physiology

There will be a special section devoted to animal sound production (R. Suthers agreed to give a review).

The conference will be held in the very center of Berlin:

Hotel „Albrechtshof“  
Albrechtsstrasse 8 (Mitte)  
10117 Berlin, Germany

A block of rooms is being reserved for DM165 (about \$95) (single) and DM 185 (double) incl. breakfast (for location see <http://www.kulturbox.de/perl/berlininfo>). Some rooms in the nearby guesthouse of the Humboldt University are available for less than \$50. For more details visit (<http://www.nwu.edu/csd/ICVPB/ICVPB.html>)

CHARLES E. SCHMID  
*Executive Director*

## USA Meetings Calendar

Listed below is a summary of meetings related to acoustics to be held in the U.S. in the near future. The month/year notation refers to the issue in which a complete meeting announcement appeared.

### 1998

- 13–17 Sept. American Academy of Otolaryngology—Head and Neck Surgery, San Francisco, CA [American Academy of Otolaryngology—Head and Neck Surgery, One Prince St., Alexandria, VA 22314; Tel.: 703-836-4444; Fax: 703-683-5100].
- 18–19 Sept. 6th Annual Conference on Management of the Tinnitus Patient, Iowa City, IA [Richard Tyler, Univ. of Iowa, Dept. of Otolaryngology—Head & Neck Surgery, 200 Hawkins Dr., C21GH, Iowa City, IA 52242; Tel: 319-356-2471; Fax: 319-353-6739; E-mail: rich-tyler@uiowa.edu].
- 12–16 Oct. 136th meeting of the Acoustical Society of America, Norfolk, VA [ASA, 500 Sunnyside Blvd., Woodbury, NY 11797; Tel.: 516-576-2360; Fax: 516-576-2377; E-mail: [asa@aip.org](mailto:asa@aip.org), WWW: <http://asa.aip.org>].

### 1999

- 2–4 March International Symposium on Geographic Information System (GIS) in Fishery Sciences, Seattle, WA [Fishery GIS Research Group, c/o Environmental Simulation Lab., 2F, Noble Bldg., 2-4-1 Arajuku, Kawagoe, Saitama, Japan 350-1124; Tel: 81-492-42-9262; Fax: 81-492-41-2442; E-mail: [esl@esl.co.jp](mailto:esl@esl.co.jp); WWW: [www.esl.co.jp/sympo.htm](http://www.esl.co.jp/sympo.htm)].
- 15–19 March Joint meeting: 137th meeting of the Acoustical Society of America/Forum Acusticum [Acoustical Society of America, 500 Sunnyside Blvd., Woodbury, NY 11797; Tel.: 516-576-2360; Fax: 516-576-2377; E-mail: [asa@aip.org](mailto:asa@aip.org); WWW: [asa.aip.org](http://asa.aip.org)].
- 27–30 June ASME Mechanics and Materials Conference, Blacksburg, VA [Mrs. Norma Guynn, Dept. of Engineering Science and Mechanics, Virginia Tech, Blacksburg, VA 24061-0219; Fax: 540-231-4574; E-mail: [nguynn@vt.edu](mailto:nguynn@vt.edu); WWW: <http://www.esm.vt.edu/mmconf/>]. Deadline for receipt of abstracts: 15 January 1999.
- 21–24 Oct. Second International Symposium on Middle-Ear Mechanics in Research and Otorrhinology, Boston, MA [Harvard-CME, P.O. Box 825, Boston, MA 02117-0825; Tel.: 617-432-1525; E-mail: [hms-cme@warren.med.harvard.edu](mailto:hms-cme@warren.med.harvard.edu)].

# BOOK REVIEWS

**James F. Bartram**

94 Kane Avenue, Middletown, Rhode Island 02842

*These reviews of books and other forms of information express the opinions of the individual reviewers and are not necessarily endorsed by the Editorial Board of this Journal.*

**Editorial Policy:** *If there is a negative review, the author of the book will be given a chance to respond to the review in this section of the Journal and the reviewer will be allowed to respond to the author's comments. [See "Book Reviews Editor's Note," J. Acoust. Soc. Am. **81**, 1651 (May 1987).]*

---

## Principles of Voice Production

**Ingo R. Titze**

*Prentice-Hall, Inc., Englewood Cliffs, New Jersey, 1994.  
354 pp. Price \$66.00.*

Although written primarily as a text for students and teachers of vocal production, based as much as possible on scientific principles, this book is for "anyone interested in voice." This includes all of us who speak, sing, sigh, hum, and hear. Just as the study of acoustics in general is very interdisciplinary, some of the specialized subjects within acoustics are also interdisciplinary. Voice production is a prime example.

In this book Ingo Titze has succeeded in blending knowledge drawn from research and experience in a variety of voice-related professions. Concepts, definitions, and illustrations from anatomy, physiology, physics, aerodynamics, acoustics, speech science, hearing science, and music are presented and interrelated both for normal voice production and for several types of voice disorders.

The artistic aspects of singing and the teaching of vocal technique are not neglected, but some of the related mythology has been dispelled or confirmed by knowledge gained from research that is explained, then identified by publication references at the end of each chapter.

The reader of "Principles of Voice Production" is not necessarily expected to have prior experience in any of the voice related professions. However Titze has avoided the temptation to treat subjects only qualita-

tively in the interest of easy reading. Equations are included and units are defined and used. Many graphs and illustrations are specially prepared for this book, in order to supplement figures borrowed from other published research.

Following the basics of vocal anatomy, breathing control, oscillation of the vocal folds, acoustical generation and propagation, and theoretical and spectral analyses of vowel sounds, the practical issues of voice classifications, ranges, controls, fluctuations, and disorders are explained in detail. A Glossary and five Appendices assist the reader who is unfamiliar with terminology, the metric system, decibel and musical scales, and the phonetic alphabet.

Author Titze can entertain while being instructive. Examples are (1) a picture of an "anatomically correct" four-part vocal ensemble scaled like a string quartet; (2) a picture of vocal strain by singer Mick Jagger; and (3) a limerick about fluctuations and perturbations (e.g., trills, vibrato) in vocal output.

The reviewer, with singing as a lifetime avocation (in choirs, opera, barbershop harmony), was so fascinated by this book that he read it in doctor's offices and on planes, and lost it somewhere along with accumulated notes. This very belated review followed the purchase of another copy. Any acoustician who speaks, sings (or hears) could be equally fascinated.

DANIEL W. MARTIN  
7349 Clough Pike  
Cincinnati, Ohio 45244

# REVIEWS OF ACOUSTICAL PATENTS

**Daniel W. Martin**

7349 Clough Pike, Cincinnati, Ohio 45244

The purpose of these acoustical patent reviews is to provide enough information for a Journal reader to decide whether to seek more information from the patent itself. Any opinions expressed here are those of reviewers as individuals and are not legal opinions. Printed copies of United States Patents may be ordered at \$3.00 each from the Commissioner of Patents and Trademarks, Washington, DC 20231.

## Reviewers for this issue:

GEORGE L. AUGSPURGER, Perception Incorporated, Box 39536, Los Angeles, California 90039

RONALD B. COLEMAN, BBN Acoustic Technologies, 70 Fawcett Street, Cambridge, Massachusetts 02138

HARVEY H. HUBBARD, 325 Charleston Way, Newport News, Virginia 23606

SAMUEL F. LYBARGER, 101 Oakwood Road, McMurray, Pennsylvania 15317

D. LLOYD RICE, 11222 Flatiron Drive, Lafayette, Colorado 80026

KEVIN P. SHEPHERD, M. S. 463, NASA Langley Research Center, Hampton, Virginia 23681-2199

WILLIAM THOMPSON, JR., The Pennsylvania State University, University Park, Pennsylvania 16802

ROBERT C. WAAG, University of Rochester Medical Center, 601 Elmwood Avenue, Rochester, New York 14642

5,381,386

## 43.38.Ar MEMBRANE HYDROPHONE

**P. Lum and M. Greenstein, assignors to Hewlett-Packard Company**

10 January 1995 (Class 367/163); filed 19 May 1993

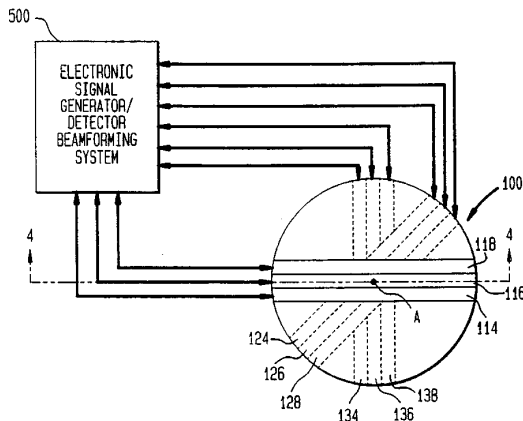
A method is discussed for fabricating an extremely small PVDF membrane hydrophone utilizing integrated circuit fabrication techniques, and including electronic components within the assembly.—WT

5,511,043

## 43.38.Fx MULTIPLE FREQUENCY STEERABLE ACOUSTIC TRANSDUCER

**J. F. Lindberg, assignor to the United States of America**  
23 April 1996 (Class 367/155); filed 6 April 1995

Transducer 100 consists of multiple layers of PVDF, disc shaped in this instance, separated from each other by insulating layers and bonded together to make an integral structure. The two electrode surfaces of each PVDF layer are cut or etched into parallel strips such as 114–118 for the top PVDF layer (only three strips, of an arbitrary number, are illustrated for each electrode layer), 124–128 for the second, 134–138 for the third, etc. The strips on both top and bottom electrode surfaces of any one PVDF layer



are parallel. The strips of alternate PVDF layers are rotated as indicated. This arrangement then allows for beam tilting perpendicular to the strips of any one PVDF layer and for rotation of the whole beam pattern structure by switching from one PVDF layer to another. The multiple frequency capa-

bility derives from the fact that a sequence of these units, each optimized for use at a different frequency, can be stacked one upon another, with a common axis through point A, to form a sandwich of sandwiches.—WT

5,736,808

## 43.38.Fx PIEZOELECTRIC SPEAKER

**Andrei Szilagyi and Michael Strugach, assignors to Aura Systems, Incorporated**

7 April 1998 (Class 310/322); filed 22 December 1995

This is a small, inexpensive loudspeaker assembly that not only generates airborne sound but propagates energy into the attachment structure. Thus, one can make musical computer keyboards and talking bicycle helmets.—GLA

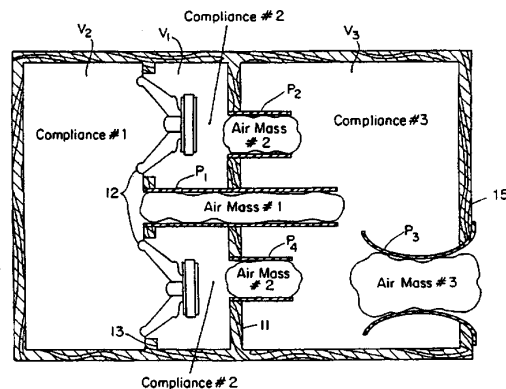
5,714,721

## 43.38.Ja PORTING

**Brian J. Gawronski and Gerald F. Caron, assignors to Bose Corporation**

3 February 1998 (Class 181/156); filed 29 October 1996

When is a vent not a vent? When it is a “Flared port tube passive radiator P3.” One little problem, of course, is that previous loudspeaker



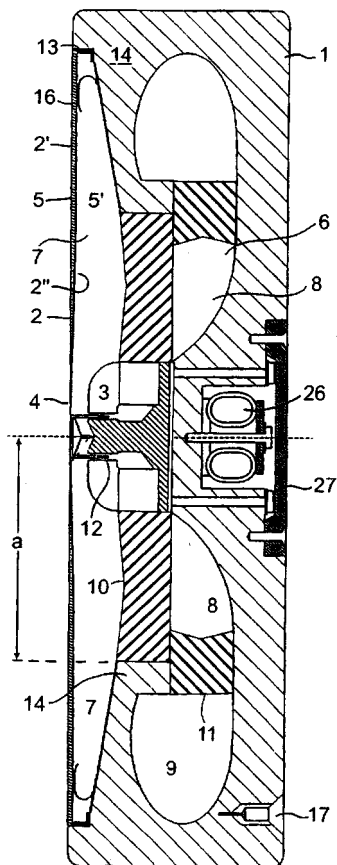
enclosure designs already include dozens of stepped, beveled, flared, and tapered vent geometries. Nonetheless, this patent is based upon “...a smoothly flared input end...and a smoothly flared output end.” Such flaring minimizes turbulence noises (see Roozen *et al.* in the October 1998 issue of this *Journal*).—GLA

5,714,722

**43.38.Ja LOUDSPEAKER**

Seppo Noponen, assignor to Transducer Valley, Incorporated  
3 February 1998 (Class 181/173); filed in Finland 25 November 1991

A generally planar diaphragm has a lightweight, flexible central area and a heavier, stiffer outer portion. The idea, which has been around for more than 50 years, is that high frequencies are reproduced by the smaller



central area whereas low frequencies are pumped out by the entire diaphragm. And intermediate frequencies? Well, that's why we have chambers 7, 8, and 9 and dampers 10 and 11. These are "...implemented in such a manner as to ensure that the various areas of the diaphragm respond in the desired manner."—GLA

5,696,521

**43.38.Si VIDEO HEADSET**

Jack D. Robinson *et al.*, assignors to Astounding Technologies  
9 December 1997 (Class 345/8); filed 22 June 1994

The patent shows the construction of a video headset provided with a headband that can be worn comfortably. A pair of horizontal LCD video displays are positioned above the level of the eyes, each with a beam-splitter positioned in front of the eyes to reflect a portion of the light from the video screens to the user. The partially transmissive beam splitters allow the user to see through to the ambient scene beyond, increasing the comfort of the user. The video screens and optics preferably set the user's convergence angle at about 8 ft. Earphones are provided for sound reception.—SFL

5,706,360

**43.38.Si HEADSET WITH SPECTACLE TEMPLE ACCOMMODATING OPENINGS**

Pramod Khandekar, Edison, NJ  
6 January 1998 (Class 381/183); filed 27 November 1995

The patent shows a headset with earphones supported by a headband. To allow eyeglasses to be worn with the headset in place, front and rear openings for the eyeglass temples are provided in the earcups.—SFL

5,724,405

**43.38.Si TEXT ENHANCED TELEPHONY**

Robert M. Engelke and Kevin Colwell, assignors to Ultratec, Incorporated  
3 March 1998 (Class 379/52); filed 24 March 1994

A system for assisting the very hard of hearing in the use of the telephone text enhanced telephony (TET) is described. In addition to the remote person's spoken voice being heard in the usual manner, the words spoken appear in written text form on a visual display. The functioning of the device is preferably based on an enhanced TDD protocol. Notch filters at 1400 and 1800 Hz separate the display signal from the voice signal.—SFL

5,729,605

**43.38.Si HEADSET WITH USER ADJUSTABLE FREQUENCY RESPONSE**

James F. Bobisuthi *et al.*, assignors to Plantronics, Incorporated  
17 March 1998 (Class 379/430); filed 19 June 1995

A headphone with user-selectable means to provide various frequency responses is shown. The acoustic elements allow adjustment of the transmission paths between a transducer element and the user's ear canal. Adjustment of the transmission path is made by selection of various ports and openings in and between various volumes in the transducer and to the ear canal.—SFL

5,729,615

**43.38.Si IN-EAR TYPE EARPHONE HAVING AN EAR HANGER**

Bill Yang, assignor to Cotron Corporation  
17 March 1998 (Class 381/183); filed 27 January 1997

The patent shows an in-ear-type earphone with its cable hanging downward. A round shaft is mounted on the top of the earphone on which a sliding sleeve can be moved that is attached to an ear hanger.—SFL

5,696,834

**43.38.Vk STEREO SYSTEM AND STEREO METHOD FOR ELECTRONIC ACOUSTICAL SYSTEM**

Hiroshi Kitagawa, assignor to Kawai Musical Instrument Manufacturing Company  
9 December 1997 (Class 381/61); filed in Japan 25 October 1991

This is a fairly elaborate method, mostly a computer program, intended to generate a stereophonic sound field from a monophonic source such as a keyboard synthesizer. "...sound data for producing stereo are synthesized, and these sound data are combined and multiplexed to produce stereo sound having a rich sense of spatiality."—GLA

5,708,719

### 43.38.Vk IN-HOME THEATER SURROUND SOUND SPEAKER SYSTEM

Hal. P. Greenberger *et al.*, assignors to REP Investment Limited Liability Company  
13 January 1998 (Class 381/18); filed 7 September 1995

The system is intended to reproduce two-channel audio in connection with a video image. A full-range front loudspeaker reproduces summed left and right channels. Signals to left and right loudspeakers are highpass filtered. A L-R difference signal is fed to a single rear ambience loudspeaker. A subwoofer is optional. More than 100 earlier patents are cited as references.—GLA

5,715,317

### 43.38.Vk APPARATUS FOR CONTROLLING LOCALIZATION OF A SOUND IMAGE

Masayuki Nakazawa, assignor to Sharp Kabushiki Kaisha  
3 February 1998 (Class 381/61); filed in Japan 27 March 1995

In a virtual reality environment having sound reproduced via earphones, the audio processing system must not only generate robust localization at any point in space but also must track head movements and adjust the synthesized sound field accordingly. These requirements can tie up sizable amounts of computer memory and processing time. One goal is to reduce computation time by "...adding sound attenuation in distance to the interpolation estimation of a head related transfer function in a three-dimensional space."—GLA

5,717,765

### 43.38.Vk THEATER SOUND SYSTEM WITH UPPER SURROUND CHANNELS

Yoshio Ozaki and Michael J. Kohut, assignors to Sony Corporation  
10 February 1998 (Class 381/18); filed 23 August 1995

One early motion picture stereo sound system used ultrasonic pilot tones to switch a sound track between different sets of loudspeakers. Now that we have dedicated surround channels, the same scheme can be used to switch among various groups of surround loudspeakers.—GLA

5,717,767

### 43.38.Vk ANGLE DETECTION APPARATUS AND AUDIO REPRODUCTION APPARATUS USING IT

Kiyofumi Inanaga and Yuji Yamada, assignors to Sony Corporation  
10 February 1998 (Class 381/25); filed in Japan 8 November 1993

The patent document is long and includes three dozen illustrations. Listener's head movements are tracked by an improved, lightweight gyroscope. This is incorporated into a more general scheme for generating a believable, three-dimensional sound field via headphones.—GLA

5,717,766

### 43.38.Vk STEREOPHONIC SOUND REPRODUCTION APPARATUS USING A PLURALITY OF LOUDSPEAKERS IN EACH CHANNEL

Alain Azoulay and Jean-Louis Queri, assignors to Alain Azoulay, Jean-Louis Queri, and Jean Rouch, all of France  
10 February 1998 (Class 381/24); filed in France 12 June 1992

Multiple pairs of loudspeakers form a large, concave array. Signals from left and right channels are "modulated" and "distributed" to appropriate groups of loudspeakers. To quote just one sentence from the patent document, "Thus, the dynamic distribution of the paths in real time over each of the quadripoles makes it possible to reinforce the natural dynamic range by a physical effect obtained by changing the emission mode, thereby making it possible to pass and send power solely to one, two, or four of the loudspeakers in each quadripole: this makes it possible to switch between a spherical wave and a cylindrical wave and then to a quasi-plane wave, using the same emitted energy at any given instant, with switching from one mode to another being performed in application of a continuous overlap relationship defined by the control and switchover thresholds, which are adjusted, in particular, so as to obtain substantially constant power per square meter for each loudspeaker." The patent style is pure Henry James.—GLA

5,740,253

### 43.38.Vk STEREOPHONIC SOUND FIELD EXPANSION DEVICE

Eiji Takeuchi, assignor to Yamaha Corporation  
14 April 1998 (Class 381/1); filed in Japan 28 April 1995

Signals from multiple delay taps are combined in such a way as to generate an expanded stereo image from two loudspeakers that can be perceived throughout a relatively large listening area. The concept is clever and the patent document contains interesting information about the field in general.—GLA

5,566,135

### 43.38.Zp DIGITAL TRANSDUCER

R. B. MacLeod, assignor to the United States of America  
15 October 1996 (Class 367/149); filed 11 July 1995

A diaphragm, on one side of which are mounted a number of optically reflective, nonplanar facets, is supported so that it will be displaced from an equilibrium position in response to an incident pressure wave. A beam of light is directed onto that reflective surface of the diaphragm. The reflected light beam is then incident upon an optical detector, containing a plurality of opto-electric transducers, which produces an electrical signal that is a function of which opto-electric transducers are illuminated. As the diaphragm vibrates, the light beam is reflected in different directions, thus illuminating the optical detector differently. The signals from the elements of the optical detector are passed to a microprocessor which then produces a digital signal corresponding to the displacement of the diaphragm.—WT

5,695,027

### 43.40.Vn ADAPTIVELY TUNED VIBRATION ABSORBER

Andreas H. von Flotow and Timothy S. Mixon, assignors to Applied Power, Incorporated  
9 December 1997 (Class 188/380); filed 15 November 1995

This patent describes an actively controlled dynamic absorber to reduce narrow-band vibrations on an aircraft fuselage. The device is attached to the vibrating structure and sensors are used to monitor the disturbance frequency of the excitation, and the resonance frequency of the absorber. A phase comparator is used to tune the resonance frequency of the absorber to match that of the disturbance. The resonance frequency of the absorber is changed by adjusting the stiffness of the spring between the structure and



the absorber mass. Details of the mechanism for altering the stiffness of the absorber are presented.—RBC

5,710,714

**43.40.Vn ELECTRONIC CONTROLLER FOR AN ADAPTIVELY TUNED VIBRATION ABSORBER**

Mathieu Mercadal *et al.*, assignors to Applied Power, Incorporated  
20 January 1998 (Class 364/508); filed 15 November 1995

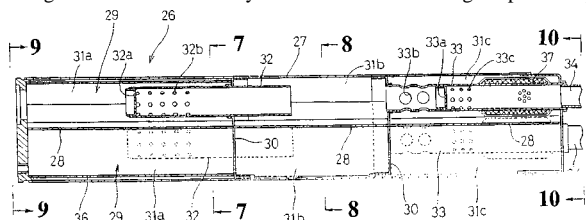
This patent describes the control circuitry for the actively controlled dynamic absorber contained in U.S. Patent 5,695,714. The controller uses two sensor inputs. The first is attached to the vibrating structure to characterize the disturbance frequency of the excitation. The second sensor is placed on the absorber proof mass to measure the resonance frequency of the dynamic absorber. A control circuit receives the signals from these sensors and produces a control signal that causes a mechanism to alter the spring stiffness of the absorber so that the spring-mass resonance frequency is maintained at the disturbance frequency. The control circuitry for this device is discussed in detail.—RBC

5,608,194

**43.50.Gf EXHAUST PIPE STRUCTURE FOR A MOTORCYCLE**

Hiroshi Okazaki *et al.*, assignors to Honda Giken Kogyo Kabushiki Kaisha  
4 March 1997 (Class 181/228); filed in Japan 13 July 1994

This patent applies particularly to the muffling of motorcycle engines. Exhaust gases from individual cylinders are carried through separate expan-



sion paths of different lengths and are exhausted separately to the atmosphere in such a manner that each cylinder can be heard.—HHH

5,670,757

**43.50.Gf EXHAUST SILENCER FOR ENGINES AND GENERATORS**

Frank E. Harris, assignor to Harco Manufacturing Company  
23 September 1997 (Class 181/264); filed 27 November 1996

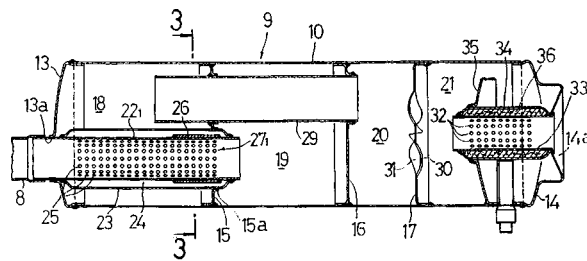
This patent relates to the reduction of exhaust noise from engines used in emergency generators and marine applications. It relates particularly to the ‘‘pancake’’ or ‘‘hockey puck’’ muffler designs which are said to have superior performance. Passive acoustical treatment consisting of 1-in.-thick fiber glass insulation retained in position and protected by a 1/2-in. 13 gauge expanded metal covering is attached to the inner reflecting surfaces.—HHH

5,708,238

**43.50.Gf EXHAUST SILENCING DEVICE**

Kosuke Asao *et al.*, assignors to Honda Giken Kogyo Kabushiki Kaisha  
13 January 1998 (Class 181/272); filed in Japan 27 July 1994

The patent describes an exhaust muffler in which ‘‘the occurrence of a whistling sound is prevented while avoiding the use of sound absorbing material.’’ The exhaust gas is led into the inner tube 22 communicating with the expansion chamber 24 through a plurality of holes 25, thereby accomplishing the deadening of exhaust noise by the expansion of the exhaust gas.



In such a construction, the occurrence of a resonance effect producing a whistling sound is unavoidable. It has been confirmed experimentally that, because of the recesses 27 on the inner surface of rear end portion of the inner tube 22, the exhaust gas flow is made turbulent to cancel the resonance effect.’’—KPS

5,712,447

**43.50.Gf VIBRATIONALLY AND ACOUSTICALLY INSULATED STRUCTURE**

Jeffrey S. Hanson, assignor to the United States of America  
27 January 1998 (Class 114/20.1); filed 14 May 1996

This patent relates to the reduction of radiated noise from the insides of underwater vehicles such as torpedoes. Passive treatments consist of an elastomeric material bonded to the interior surface of the hull plus a constraining layer of rigid segments for vibration control, plus an acoustical barrier material layer such as lightweight honeycomb, and a layer of absorption material for noise control.—HHH

5,726,397

**43.50.Gf VEHICLE EXHAUST DEVICE**

Teruaki Mukai and Satoshi Watanabe, assignors to Honda Giken Kogyo Kabushiki Kaisha  
10 March 1998 (Class 181/232); filed in Japan 19 October 1994

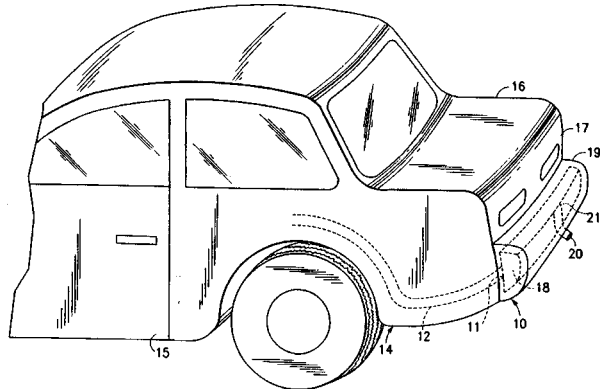
This patent describes an automobile muffler arrangement in which it is said that the placement of a large muffler close to the engine, a small one at the rear of the vehicle, and an intermediate-sized one in between results in a more efficient design with attenuation occurring close to the source and with substantially reduced length-dependent resonance of the exhaust tube.—KPS

5,726,398

**43.50.Gf AUTOMOTIVE BUMPER AND MUFFLER COMBINATION**

Wolfgang Zahn and Jon W. Harwood, assignors to AP Parts Manufacturing Company  
10 March 1998 (Class 181/282); filed 26 February 1997

This automobile exhaust muffler is incorporated directly into the rear bumper of the vehicle and extends substantially the width of the vehicle.



Thus a large, visually unobtrusive muffler is created. Various internal muffler arrangements are described.—KPS

5,692,702

#### 43.50.Ki ACTIVE CONTROL OF TONE NOISE IN ENGINE DUCTS

Anders O. Andersson, assignor to the Boeing Company  
2 December 1997 (Class 244/1 N); filed 30 April 1996

An active control scheme to reduce tonal noise radiated from a jet engine is discussed. The approach modifies the inflow to the rotor using quasi-static actuation of bleed-air nozzles or mechanical protrusions into the flow. The controller uses microphones located circumferentially in the duct to extract the amplitudes of the circumferential modes for the blade-passage frequency (BPF) and its harmonics. The output of the controller continuously adjusts the nozzle orifices or protrusion amplitudes to minimize the modal amplitudes. The number of actuators is chosen to be at least twice the largest required circumferential mode number to be controlled.—RBC

5,693,918

#### 43.50.Ki ACTIVE EXHAUST SILENCER

Cary D. Bremigan and C. Raymond Cheng, assignors to Digisonix, Incorporated  
2 December 1997 (Class 181/206); filed 29 July 1996

This patent is a continuation-in-part of U.S. Pat. No. 5,541,373 [reviewed J. Acoust. Soc. Am. 102, 2479 (1997)].—RBC

5,701,350

#### 43.50.Ki ACTIVE ACOUSTIC CONTROL IN REMOTE REGIONS

Steven R. Popovich, assignor to Digisonix, Incorporated  
23 December 1997 (Class 381/71); filed 3 June 1996

This patent describes an active control system to provide acoustic attenuation in regions other than those where error sensors are located. The approach relies on knowledge of the relationship between the response at the error sensors and the response in the region where noise suppression is desired. The controller uses a model of this relationship to filter the error signal to form a "weighted" error signal that more accurately reflects the response at the remote location. This is traditionally known as residual weighting in the controls literature.—RBC

5,702,230

#### 43.50.Ki ACTIVELY CONTROLLED ACOUSTIC TREATMENT PANEL

Robert E. Kraft, assignor to General Electric Company  
30 December 1997 (Class 415/119); filed 29 January 1996

An actively controlled acoustic treatment panel for suppressing noise in a gas turbine engine nacelle is presented. The panel includes a passive surface backed by a honeycomb of individual cells containing piezoelectric actuators and pressure sensors. The controller operates to achieve a desired acoustic impedance boundary condition at the nacelle wall. The active panel forms a continuous ring and is mounted circumferentially along the inner wall of the nacelle. The approach is said to provide noise suppression in a frequency range from 800 to approximately 8000 Hz. The control aspects of coupling between actuators in one cell to sensors in a neighboring cell are not addressed.—RBC

5,706,651

#### 43.50.Nm TURBOFAN ENGINE WITH REDUCED NOISE

Robert W. Lillibridge *et al.*, assignors to Burbank Aeronautical Corporation  
13 January 1998 (Class 60/262); filed 29 August 1995

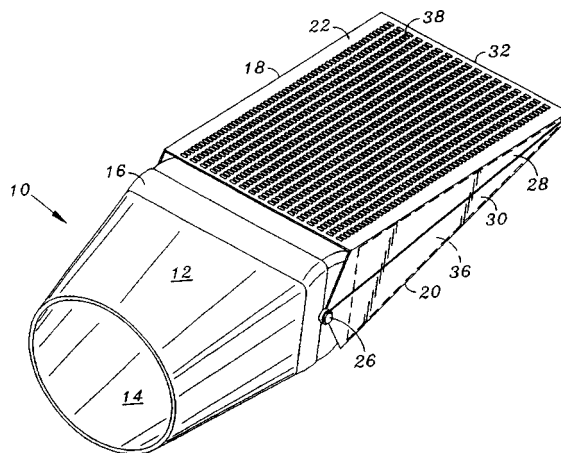
The patent describes a noise reduction (hush) kit designed for the JT3D family of engines commonly found on Boeing 707 aircraft. Major modifications to the engine consist of: replacement of the inlet center body with an acoustically treated one, forward translation of the inlet guide vanes, incorporation of an exhaust nozzle which entrains both the core and fan bypass flows, a multi-lobed exhaust mixer, and the replacement of the cascade thrust reverser with a target-type reverser. Perceived noise levels due to jet mixing noise are reduced by 3 dB with no loss of thrust.—KPS

5,717,172

#### 43.50.Nm SOUND SUPPRESSOR EXHAUST STRUCTURE

Ralph Cornelius Griffin, Jr., William David Bard, and David Brian Schein, assignors to Northrop Grumman Corporation  
10 February 1998 (Class 181/215); filed 18 October 1996

The patent describes a sound suppressor for a jet engine exhaust. The openable suppression chamber is of a clamshell-like design and is composed of two hinged structures attached to the exhaust nozzle. When closed, the



exhaust gases pass through numerous, closely spaced holes, thus providing noise suppression. When noise suppression is not required, the chamber is opened, thus allowing unimpeded exhaust flow.—KPS

5,721,402

#### 43.50.Nm NOISE SUPPRESSION SYSTEM FOR A JET ENGINE

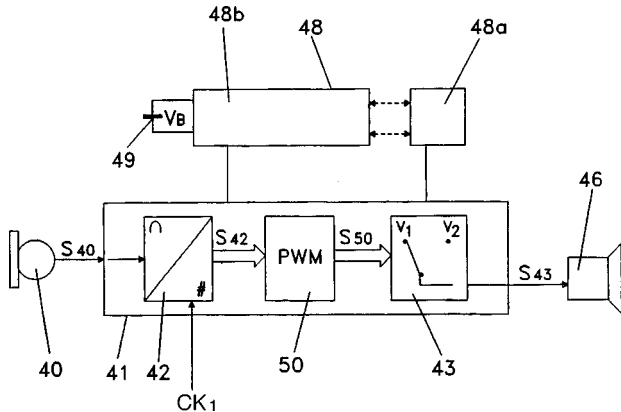
Charles A. Parente, assignor to Northrop Grumman Corporation  
24 February 1998 (Class 181/214); filed 9 September 1996

Noise produced in the inlet of a jet engine includes that due to turbulent inflow to the rotating machinery. This patent proposes the introduction of compressed air which flows into the engine intake through the acoustical (honeycomb) liner downstream of the lip of the nacelle, thus providing a layer of less turbulent, substantially laminar airflow along the surface of the engine duct.—KPS

## 43.66.Ts HEARING AID DEVICE

Erik Witthoefft Rasmussen and Enrique Marcelo Blumenkrantz, assignors to Phonak AG  
17 February 1998 (Class 330/10); filed 23 April 1996

The hearing aid described in the patent has a signal processing unit with an input operationally connected to the output of an input converter. The signal processing unit is operationally connected to the input of the

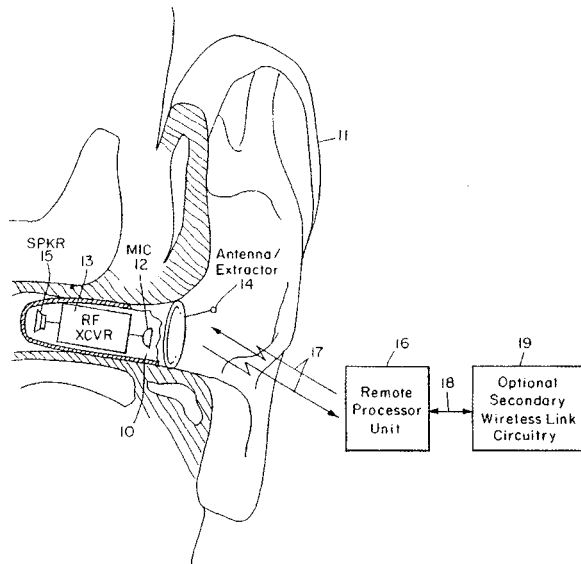


output transducer and generates an output signal switched between at least two predetermined signal levels. The signal processing unit also includes a pulse width modulator that includes a digital control input for controlling pulse-width modulation.—SFL

## 43.66.Ts HEARING AID WITH WIRELESS REMOTE PROCESSOR

James C. Anderson, Westwood, MA  
24 February 1998 (Class 381/68.6); filed 7 June 1995

The patent shows a hearing aid or audio system with an earpiece hidden in the ear canal which communicates by wireless with a remote processing unit (RPU) that enhances audio signals and can be concealed



under the clothing. User control of hearing aid parameters is accomplished using pushbuttons located on the RPU.—SFL

## 43.66.Ts HEARING-AID SYSTEM

Paul Coninx, Montreal, P.Q.  
10 March 1998 (Class 381/68.4); filed 8 October 1996

A stereophonic hearing aid is shown having gain that can be adjusted by the listener, using a hand-held remote control to give a good communication situation. A control unit having "up" and "down" buttons allows easy adjustment. The remote control is provided with a level indicator to assist in arriving at a suitable setting. The unit is stated to be particularly useful for communicating with persons who have difficulty making adjustments on a hearing aid themselves.—SFL

## 43.66.Ts HEARING AID TO BE WORN AT THE HEAD

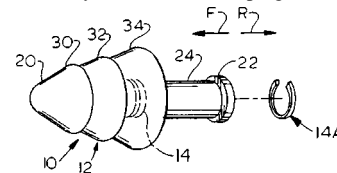
Wolfram Meyer, assignor to Siemens Audiologische Technik GmbH  
13 January 1998 (Class 381/69); filed in Germany 21 December 1993

To shield hearing aid circuitry from interference from radio frequency signals, a case consisting of two halves that are lined with conductive material is shown. When assembled, good contact between the shieldings of each half is made. Additional shielding is provided around control shafts going outside the shielded case.—SFL

## 43.66.Vt TRACKABLE EARPLUG

Howard S. Leight, assignor to Howard S. Leight and Associates  
17 March 1998 (Class 128/857); filed 20 December 1996

An earplug that is particularly useful for workers in the food or pharmaceutical industry is shown. Such industries use detectors for unwanted metallic objects, but usually cannot detect earplugs made of foam plastic or



rubber. In the earplug shown, a detectable metal ring 14A is placed firmly into one of the earplug grooves in a way that does not affect the sound attenuating property of the plug.—SFL

## 43.72.Gy METHOD DEVICE AND SYSTEM FOR AN EFFICIENT NOISE INJECTION PROCESS FOR LOW BITRATE AUDIO COMPRESSION

Davis Pan, assignor to Motorola, Incorporated  
25 November 1997 (Class 395/2.39); filed 26 October 1995

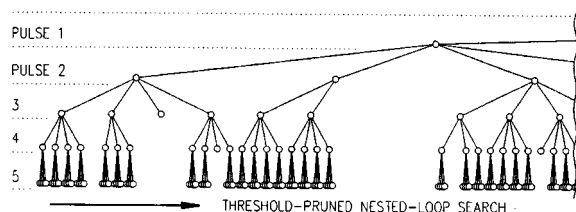
The well-known perceptual coding method of speech compression involves the reduction of coding bits such that the introduced quantization noise lies within spectral regions which are masked by the signal amplitude in those regions. By transmitting a low bitrate code along with the speech data, the improvement described in this patent allows the speech quality to be scaled to meet specific bitrate limitations.—DLR

5,701,392

### 43.72.Gy DEPTH-FIRST ALGEBRAIC-CODEBOOK SEARCH FOR FAST CODING OF SPEECH

Jean-Pierre Adoul and Claude Laflamme, assignors to Universite de Sherbrooke  
23 December 1997 (Class 395/2.28); filed in Canada 23 February 1990

This code-excited (CELP) vocoder uses a multi-level tree structure to achieve a rapid search of the excitation codebook. Excitations consist of vectors with nonzero pulses at a limited number of the 40 possible pulse



locations. The valid pulse positions can be directly computed from the codebook index, so vectors are not stored, but are generated as needed. The search strategy builds up the vector pulse by pulse, and needs only to evaluate the best location for each single new pulse.—DLR

5,704,003

### 43.72.Gy RCELP CODER

Willem Bastiaan Kleijn and Dror Nahumi, assignors to Lucent Technologies, Incorporated  
30 December 1997 (Class 395/2.29); filed 19 September 1995

A variation on code-excited (CELP) vocoders, known as relaxation CELP, involves sending excitation codes for only a single subframe of each frame. This RCELP vocoder uses a method of subframe time shifting depending on the subframe peak-to-average ratio to improve the estimates of subframe parameters.—DLR

5,710,863

### 43.72.Gy SPEECH SIGNAL QUANTIZATION USING HUMAN AUDITORY MODELS IN PREDICTIVE CODING SYSTEMS

Juin-Hwey Chen, Neshanic Station, NJ  
20 January 1998 (Class 395/2.39); filed 19 September 1995

The patented vocoder technique is referred to as a transform predictive coder (TPC). Following short-term and long-term prediction, the predictor coefficients, the gain value, and the Fourier spectrum of the residual are vector quantized for transmission. The bitrate is reduced by sending fewer bits during periods of greater perceptual masking levels.—DLR

5,699,423

### 43.72.Kb TELEPHONE SET IN WHICH AN ECHO SIGNAL IS EFFECTIVELY CANCELED IN SPIITE OF BEING PROVIDED WITH A PLURALITY OF SOUND PRODUCING UNITS

Toshio Yoshida and Michitaka Sisido, assignors to NEC Corporation  
16 December 1997 (Class 379/390); filed in Japan 18 March 1994

This telephone system uses a two-part echo canceller to provide a smoother switchover between handset mode and hands-free mode. In handset mode, a feedback loop injects a portion of the transmitted speech signal into the incoming line signal and uses that signal to preset a canceller cir-

cuit. When switching to hands-free mode, the echo cancellation easily adapts to the real echo produced by that mode.—DLR

5,706,397

### 43.72.Ne SPEECH RECOGNITION SYSTEM WITH MULTI-LEVEL PRUNING FOR ACOUSTIC MATCHING

Yen-Lu Chow, assignor to Apple Computer, Incorporated  
6 January 1998 (Class 395/2.52); filed 5 October 1995

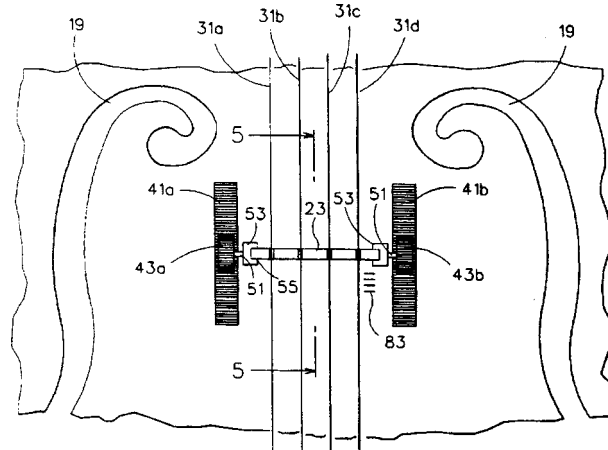
The patent describes a speech recognition system which prunes the search tree continuously during the decoding stage. During each pass through the currently active phone models, a new active list is being built. In order to qualify for the new active list, the best score for a phone model must be within a certain threshold of the global best score for that pass.—DLR

5,734,117

### 43.75.De APPARATUS AND METHOD FOR TUNING VIOLINS

Anthony J. Tanzella, Easton, PA  
31 March 1998 (Class 84/309); originally filed 3 March 1995

Violin strings 31a-31d are usually tuned by adjusting rotatable pegs to change string tension. This violin has its bridge 23, normally mounted on the top plate of the violin, supported instead on brackets 53 mounted on axle 51 passing through cogwheels 43 resting on tracks 41a and 41b which are



secured to the top plate of the violin. Tuning of the strings is intended to be accomplished by rotation of cogwheels 43a and 43b to change the tuned length of the strings by moving their termination. It is not clear to the reviewer why one would want to tune the strings as a group, rather than individually.—DWM

5,731,533

### 43.75.Tv MUSICAL TONE SIGNAL FORMING APPARATUS FOR USE IN SIMULATING A TONE OF STRING INSTRUMENT

Atsushi Hoshiai, assignor to Roland Corporation  
24 March 1998 (Class 84/661); filed 23 August 1996

The circuitry of this patent converts the musical tone signal from a single string vibration pickup on an electric guitar into a composite signal that could be formed by combining string vibration signals from several different pickups located at different positions along the same string. This is accomplished by a combination of delay circuits and comb filters in which

the delay time differences correspond to distances between the imaginary pickup locations along the string during string vibration.—DWM

5,744,743

#### **43.75.Tv PEDAL RESONANCE EFFECT SIMULATION DEVICE FOR DIGITAL PIANOS**

**Giovanni De Poli *et al.*, assignors to Generalmusic S.P.A. 28 April 1998 (Class 84/630); filed in Italy 28 April 1995**

Acoustical pianos usually have a pedal which lifts the dampers from the bass strings to provide through sympathetic vibration a reverberant tonal effect for the tones produced in the middle and treble portions of the scale. The purpose of this patent is to disclose means for producing a similar effect for digital electronic pianos. The microprocessor circuitry uses delay lines to simulate the first 18 strings in the scale and activates them when the pedal is pressed, deactivating them when the pedal is released.—DWM

5,553,035

#### **43.80.Vj METHOD OF FORMING INTEGRAL TRANSDUCER AND IMPEDANCE MATCHING LAYERS**

**M. S. Seyed-Bolorforosh *et al.*, assignors to Hewlett-Packard Company 3 September 1996 (Class 367/140); filed 21 October 1994**

For use in a diagnostic ultrasonic imaging system a slab of piezoceramic material is configured to have a set of parallel grooves cut, etched, or molded into either or both of its major faces so that an acoustic impedance matching layer or damping layer can be integrably mated to those faces. The acoustic impedance value can be controlled by the choice of groove volume fraction and filler material.—WT

5,651,365

#### **43.80.Vj PHASED ARRAY TRANSDUCER DESIGN AND METHOD FOR MANUFACTURE THEREOF**

**Amin M. Hanafy *et al.*, assignors to Acuson Corporation 29 July 1997 (Class 128/662.03); filed 7 June 1995**

In this transducer the even- and odd-numbered elements have different active widths, and the even-numbered elements are used to image in one field of interest while the odd-numbered elements are used to image in another field of interest.—RCW

5,653,234

#### **43.80.Vj METHOD AND APPARATUS FOR ADAPTIVE SPATIAL IMAGE FILTERING**

**Jin Kim *et al.*, assignors to Siemens Medical Systems, Incorporated 5 August 1997 (Class 128/660.01); filed 29 September 1995**

The spatial filter in this method and apparatus has an adjustable passband. The input of the filter is analyzed by a processor in a controller that adjusts the filter passband according to the estimated signal-to-noise ratio or the rate of change of the signal. The passband is reduced when the estimated signal-to-noise ratio decreases and the passband is increased when the signal-to-noise ratio increases. When the rate of change of the signal is used to control the passband, the passband is reduced when the rate of change of the signal increases, and the passband is increased when the rate of change of the signal decreases. The signal-to-noise ratio is estimated from the power in the signal or the variance in a measured velocity while the rate of change of the signal is computed from an estimate of the correlation distance.—RCW

5,653,235

#### **43.80.Vj SPECKLE REDUCTION IN ULTRASOUND IMAGING**

**Tat-Jin Teo, assignor to Siemens Medical Systems, Incorporated 5 August 1997 (Class 128/661.01); filed 21 December 1995**

A region of interest is illuminated by a beam from different directions and echoes from all illuminated directions are used to create an image in which echoes from different directions reduce the speckle. The beams are produced using a two-dimensional array of elements. The beam apertures are substantially the same as the aperture of a linear array of elements extending between opposite edges of the two-dimensional array.—RCW

5,653,236

#### **43.80.Vj APPARATUS FOR REAL-TIME DISTRIBUTED COMPUTATION OF BEAMFORMING DELAYS IN ULTRASOUND IMAGING SYSTEM**

**Steven C. Miller, assignor to General Electric Company 5 August 1997 (Class 128/661.01); filed 29 December 1995**

This apparatus implements an algorithm in which the required computations are separated into three groups. The first group consists of transducer array geometry computations that are beam independent. The second group consists of beam-dependent computations that are channel independent. The third group consists of channel- and beam-dependent calculations that combine the results of the first two groups. This approach reduces the required computations and takes advantage of parallel processing to reduce hardware and computational time relative to those for conventional beamformer designs.—RCW

5,655,535

#### **43.80.Vj 3-DIMENSIONAL COMPOUND ULTRASOUND FIELD OF VIEW**

**Barry H. Friemel, Lee Weng, and Tat-Jin Teo, assignors to Siemens Medical Systems, Incorporated 12 August 1997 (Class 128/660.07); filed 29 March 1996**

A compounded field of view is obtained from correlated frames of ultrasonic image data. From a manually translated ultrasonic probe, frames are processed to detect probe motion without the use of a dedicated position or motion sensor. The motion detector correlates frames for probe translation among as many as six degrees of freedom. Image registration is then accomplished using correlated portions of the images to form a large ultrasonic image.—RCW

5,655,536

#### **43.80.Vj DIAGNOSTIC ULTRASOUND IMAGING USING TWO-DIMENSIONAL TRANSDUCER ARRAY PROBE**

**Kinya Takamizawa, assignor to Kabushiki Kaisha Toshiba 12 August 1997 (Class 128/661.01); filed in Japan 22 June 1995**

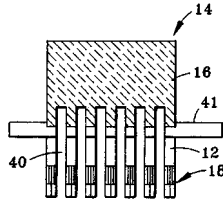
The two-dimensional array in this system is employed to scan the beam in the plane of the image and to focus the beam in the direction perpendicular to the image plane. A common driving signal is applied to elements in the direction perpendicular to the scan but echoes received on these elements are focused in this perpendicular direction using delays.—RCW

5,655,538

### 43.80.Vj ULTRASONIC PHASE ARRAY TRANSDUCER WITH AN ULTRALOW IMPEDANCE BACKFILL AND A METHOD FOR MAKING

Peter William Lorrain and Lowell Scott Smith, assignors to  
General Electric Company  
12 August 1997 (Class 128/662.03); filed 19 June 1995

This transducer **14** is backed with a material **16** that has a very low acoustic impedance. The material is either an aerogel, a carbon aerogel, an xerogel, or a carbon xerogel. A thin flexible printed circuit film **41** is bonded



to one side of the backing material. A piezoelectric ceramic material **12** and two matching layers **18** are bonded to the flexible printed circuit. Cuts **40** are used to form an array of electrically and acoustically isolated elements.—RCW

5,662,115

### 43.80.Vj METHOD FOR DETERMINING THE VELOCITY-TIME SPECTRUM OF BLOOD FLOW

Hans Torp and Kjell Kristoffersen, assignors to Vingmed Sound  
A/S  
2 September 1997 (Class 128/661.09); filed 7 June 1995

In this method, a sequence of echo signal samples is processed to obtain Doppler shift components that represent the blood velocity spectrum within a range of expected velocity values. Subsequent echo signals are sampled with an increase or decrease in delay after pulse transmission, according to the change in round-trip time of the pulses reflected from blood with a velocity corresponding to a given velocity component. The resulting samples are then processed to obtain the velocity component.—RCW

# The compression wave generated by a high-speed train at a vented tunnel entrance<sup>a)</sup>

M. S. Howe

Boston University, College of Engineering, 110 Cummington Street, Boston, Massachusetts 02215

(Received 11 May 1997; revised 10 April 1998; accepted 20 April 1998)

An analytical investigation is made of the compression wave generated when a high-speed train enters a long tunnel with distributed venting. The compression wave amplitude is determined by train speed and the area ratio of the train and tunnel, but its *rise time* depends principally on the geometry of the tunnel entrance. Vented tunnel entrance “hoods” are frequently used to increase the rise time, in order to reduce the impact of the *micro-pressure* pulse radiated from the tunnel exit when the compression wave arrives at the far end of the tunnel. Approximate calculations are performed to determine the initial rise time for a tunnel of rectangular cross section with a continuously variable vented roof near the entrance, for train Mach numbers less than about 0.2 (~150 mph). The distribution of venting apertures can be optimized to maximize rise time, and a sixfold increase is shown to be possible when the aperture distribution decreases exponentially with distance into the tunnel. The method of this paper is applicable also to more general tunnel entrance geometries, and for higher train Mach numbers. © 1998 Acoustical Society of America.

[S0001-4966(98)01408-8]

PACS numbers: 43.10.Ln, 43.28.Mw, 43.28.Py, 43.50.Lj [LCS]

## INTRODUCTION

A compression wave is generated when a train enters a tunnel. The wave propagates ahead of the train at about the speed of sound and emerges from the far end as a spherically spreading acoustic pulse, frequently called a *micro-pressure wave*.<sup>1,2</sup> Environmental problems caused by large amplitude micro-pressure waves first became apparent in 1975, in Japan. For high-speed trains (whose Mach number exceeds about 0.15) passing through a long tunnel with concrete slab tracks, nonlinear steepening of the compression wave can produce peak micro-pressure wave amplitudes of order 50 Pa ( $\approx 1$  lb/ft<sup>2</sup> or about 128 dB) in the neighborhood of the tunnel exit. The resulting disturbance is comparable in magnitude to that created on the ground by the sonic boom from a supersonic aircraft. When the track is ballasted, nonlinear steepening is opposed by dissipation of high frequency components of the compression wavefront within ballast interstices, and the micro-pressure wave is usually less important.<sup>3</sup>

The maximum amplitude of the compression wave is determined primarily by the train speed at the tunnel entrance and the cross-sectional area of the train relative to that of the tunnel. The micro-pressure wave amplitude is roughly proportional to the compression wave pressure gradient at the tunnel exit, however, and methods for reducing its intensity usually involve attempts to decrease the initial value of the pressure gradient at the tunnel entrance, because the subsequent nonlinear steepening is then smaller.<sup>3</sup> This can be done by modifying train design, either to reduce its relative cross-sectional area, or to increase the slenderness of the front of the train. In practice these approaches yield only

modest improvements. For example, reductions of about 3 dB in the peak compression wave pressure gradient are possible from optimizations of the train nose profile.<sup>4,5</sup>

Larger reductions can be achieved by changes in tunnel design. For adjacent, parallel tunnels the pressure gradient can be reduced by allowing the compression wave to “escape” through a channel joining the tunnels close to the entrance. Similar reductions occur when the wavefront passes a tunnel side-branch, which may be designed to absorb all of the entering wave energy, and a system consisting of a periodic distribution of side-branch Helmholtz resonators has been proposed.<sup>6</sup> However, the greatest attenuations are currently obtained by installing a “hood” extending 30–50 m ahead of the tunnel entrance. The compression wave begins to form as the train enters the hood, but its rise time is increased by venting high pressure air through appropriately placed “windows” in the hood walls. A fivefold increase in rise time has been achieved in this way using a hood of length 49 m.<sup>3</sup>

In this paper a theory of compression wave generation is presented for a train entering a tunnel whose walls are vented to the ambient atmosphere by a continuous distribution of openings near the tunnel entrance. Our analytical model treats the vents as a continuum, and the objective is to determine their distribution to maximize the rise time of the compression wave. Intuitive arguments suggest that this can be done by gradually decreasing the “fractional open area” of the tunnel wall with distance into the tunnel. The theory is an extension of a general method described in Ref. 7 for calculating the compression wave in terms of the geometry of the tunnel entrance. The train is represented by a distribution of sources determined by the cross-sectional variation of the train profile, and the compression wave is expressed as the convolution product of these sources and a *compact Green’s function*.<sup>8</sup> The Green’s function has vanishing normal de-

<sup>a)</sup>“Selected research articles” are ones chosen occasionally by the Editor-in-Chief that are judged (a) to have a subject of wide acoustical interest, and (b) to be written for understanding by broad acoustical readership.

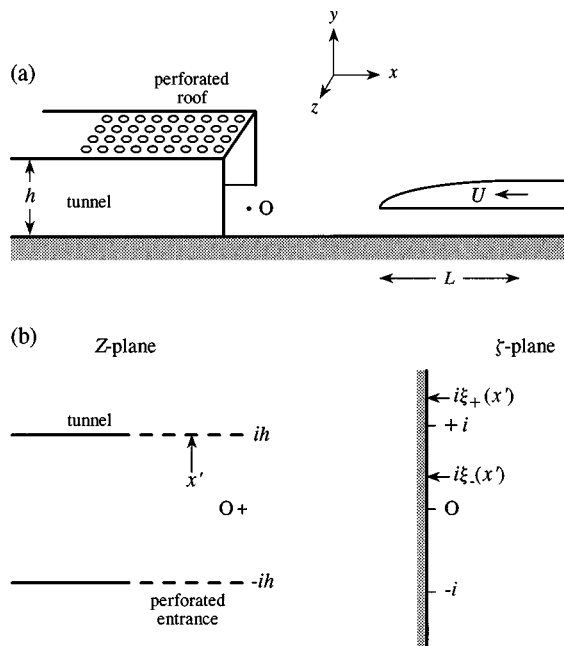


FIG. 1. (a) Tunnel entrance with vented roof. (b) Mapping the  $Z$  plane bounded by the profile of the tunnel roof and its image in the ground onto the right half of the  $\zeta$  plane.

rivative on the tunnel walls, and on any rigid structures near the entrance, and embodies all of the geometrical effects of the tunnel entrance and its environment. This approach may be contrasted, for example, with that of Vardy<sup>9,10</sup> (following Swarden and Wilson<sup>11</sup>) who used the method of characteristics for waves propagating in one dimension.

The present calculations are simplified by restricting attention to tunnels of rectangular cross-section, with the entrance vents confined to the flat roof. This permits the theory to be developed using conformal mapping. More general, three-dimensional entrance geometries will normally require Green's function to be determined numerically. The theory is formulated in Sec. I. In Sec. II the influence of roof venting on Green's function is discussed. The fractional open area of the vents is assumed to decrease in a prescribed manner with distance from the tunnel entrance, and an integral equation is derived whose solution determines the modified form of Green's function. This is solved by collocation and applied in Sec. III to investigate compression wave generation when the distribution of the vents decreases exponentially with distance into the tunnel.

## I. CALCULATION OF THE COMPRESSION WAVE

### A. Representation in terms of volume sources

Consider a train travelling at constant speed  $U$  in the negative  $x$  direction into a rigid walled, rectangular cylindrical tunnel of height  $h$  and cross-sectional area  $\mathcal{A}$ , as illustrated in Fig. 1. The tunnel extends along the negative  $x$  axis, where the origin of the rectangular axes  $(x, y, z)$  is at the point  $O$  at ground level in the plane of the tunnel entrance. The profiled nose of the train is of length  $L$ , beyond which the train cross section is constant and of area  $\mathcal{A}_0$ . The ratio  $\mathcal{A}_0/\mathcal{A}$  is assumed to be small (less than about 0.2, for the simple model described below). For the present exploratory

calculations the train Mach number  $M = U/c_0$  ( $c_0 =$  speed of sound) is assumed to be smaller than about 0.2, but this restriction can be relaxed by modification of the analysis, although this is not discussed here.

The compression wave is generated by the gross displacement of the air in the tunnel entrance by the incoming train, and for a sufficiently streamlined train the influence on this of flow separation can be ignored in a first approximation. When viscous effects at the tunnel walls are also neglected, the displacement of the air by the moving train is equivalent to that produced by a distribution of moving volume sources of constant strengths, and the unsteady motion they produce can be represented by a velocity potential  $\phi(\mathbf{x}, t)$ . The sources translate at the speed  $U$  of the train, and their distribution at time  $t$  is denoted by  $q(x + Ut, y, z)$ , where  $q(\mathbf{x})$  may be taken to be the source distribution at the instant  $t = 0$  at which the nose of the train just enters the tunnel.

The velocity potential is the solution with outgoing wave behavior of

$$\left( \frac{1}{c_0^2} \frac{\partial^2}{\partial t^2} - \nabla^2 \right) \phi = -q(x + Ut, y, z), \quad (1)$$

and must also satisfy the condition  $\partial\phi/\partial x_n = 0$  of vanishing normal velocity on the rigid surfaces  $S$ , say, comprising the tunnel walls and all solid surfaces (other than the train) outside the entrance of the tunnel. The solution can be written

$$\phi(\mathbf{x}, t) = - \int \int \mathcal{G}(\mathbf{x}, \mathbf{x}'; t - \tau) q(\mathbf{x}', \tau) d^3\mathbf{x}' d\tau,$$

where Green's function  $\mathcal{G}(\mathbf{x}, \mathbf{x}'; t - \tau)$  is the corresponding solution of (1) when the right hand side is replaced by  $\delta(\mathbf{x} - \mathbf{x}')\delta(t - \tau)$ . At typical train Mach numbers, the characteristic thickness of the compression wavefront is large compared to the tunnel diameter, and Green's function may then be approximated by<sup>7</sup>

$$G(\mathbf{x}, \mathbf{y}; t - \tau) \approx \frac{c_0}{2\mathcal{A}} \{ H(t - \tau - |\phi^*(\mathbf{x}) - \phi^*(\mathbf{y})|/c_0) - H(t - \tau + (\phi^*(\mathbf{x}) + \phi^*(\mathbf{y}))/c_0) \}, \quad (2)$$

where  $H(x) = 0, 1$  according as  $x \leq 0$  is the Heaviside step function, and  $\phi^*(x)$  is a solution of Laplace's equation describing incompressible, irrotational flow out of the tunnel entrance.  $\phi^*(x)$  is normalized such that  $\phi^*(\mathbf{x}) \approx x - \ell$ , for  $|x| \gg h$  within the tunnel and,  $\phi^*(\mathbf{x}) \sim O(1/|\mathbf{x}|)$  for  $|\mathbf{x}| \gg h$  outside the tunnel, where  $\ell \sim h$  is the tunnel end correction.<sup>12</sup> The precise functional form of  $\phi^*(\mathbf{x})$  depends on the geometry of the entrance, but  $\phi^*(\mathbf{x})$  varies continuously through the entrance, increasing from a large negative value when  $\mathbf{x}$  is far within the tunnel, to zero at  $|\mathbf{x}| = \infty$  outside. It is numerically of order  $h$  in the vicinity of the entrance, where its rate of change depends on the shape of the entrance and on the ambient environment, for example on whether or not the entrance is "flared" or opens out into an embanked channel, etc.

In a long tunnel, Eq. (1) is strictly applicable only when nonlinear steepening is ignored. In these circumstances it



predicts the initial form of the compression wave profile several tunnel diameters ahead of the entrance, where the amplitude of the unsteady motion is small, and the perturbation pressure  $p = -\rho_0 \partial \phi / \partial t$ , where  $\rho_0$  is the undisturbed air density. This initial profile is found with the aid of (2) to be given by (see Ref. 7 for details)

$$p(\mathbf{x}, t) \equiv p(x, t) \approx \frac{\rho_0 U}{\mathcal{A}} \int q(x' + U[t], y', z') \times \frac{\partial \phi^*}{\partial x'}(\mathbf{x}') d^3 \mathbf{x}', \quad \mathbf{x}' = (x', y', z'), \quad (3)$$

where the integration is taken over the region occupied by the sources, and  $[t] \approx t + x/c_0$  is the retarded time. The impulsive micro-pressure wave  $p'(\mathbf{x}, t)$ , say, that radiates from the far end of the tunnel is given in terms of the compression wave, and at large distance  $r$  from the tunnel exit at  $x = x_E$ , say, by the formula<sup>3,12,13</sup>

$$p'(\mathbf{x}, t) \approx \frac{\mathcal{A}}{\Omega c_0 r} \frac{\partial p}{\partial t}(x_E, t - r/c_0), \quad r \gg h, \quad (4)$$

where  $\Omega$  is the effective solid angle into which the wave radiates, determined by local conditions near the exit. According to Eq. (3)

$$\frac{\partial p}{\partial t}(x, t) \approx -\frac{\rho_0 U^2}{\mathcal{A}} \int q(x' + U[t], y', z') \times \frac{\partial^2 \phi^*}{\partial x'^2}(\mathbf{x}') d^3 \mathbf{x}'. \quad (5)$$

However, the actual value to be used on the right on (4) will usually be considerably different from that predicted by this formula because of nonlinear steepening of the wave in a long tunnel. Solution (3) should be regarded as defining the initial waveform for use in a one-dimensional nonlinear model of wave propagation in the tunnel. This aspect of the problem is not pursued here, where attention is restricted to the mechanism of compression wave generation.

## B. The volume source strength

Equation (3) expresses the compression wave in terms of a source distribution  $q$  that depends on the shape of the train, but is nonzero only near the nose and tail. For small values of the area ratio  $\mathcal{A}_0/\mathcal{A}$ , it was shown in Ref. 7, by comparison with the experiments of Maeda *et al.*,<sup>4</sup> that  $q$  is well approximated by the *line source*

$$q(x, y, z) = U \frac{\partial \mathcal{A}_T}{\partial x}(x) \delta(y) \delta(z - z_T), \quad (6)$$

where  $\mathcal{A}_T(x)$  is the cross-sectional area of the train at distance  $x$  measured from the nose, so that  $\mathcal{A}_T(L) \equiv \mathcal{A}_0$ , and the ground level line  $y=0, z=z_T$  lies in the vertical plane of symmetry of the train.

The integration in (3) is accordingly confined to the intervals on the  $x'$  axis where the retarded value of

$\partial \mathcal{A}_T / \partial x' \neq 0$ . For a long train, the integral becomes constant and equal to  $U \mathcal{A}_0$  just after the passage of the nose through the tunnel entrance into the region where  $\partial \phi^* / \partial x = 1$ ; this constant value is the maximum compression wave amplitude, equal approximately to  $\rho_0 U^2 \mathcal{A}_0 / \mathcal{A}$  at low Mach numbers. For a tunnel of constant cross-sectional area, or one with a ‘‘flared’’ entrance,  $\partial \phi^* / \partial x'$  decreases smoothly to zero in the direction out of the entrance along the path of the train, and the pressure rise across compression wavefront therefore tends to be monotonic.

## II. THE POTENTIAL $\phi^*(\mathbf{x})$ FOR A VENTED TUNNEL

### A. Integral formula for $\phi^*(\mathbf{x})$

Equation (5) implies that the initial rise time of the compression wavefront is governed by the behavior of  $\partial^2 \phi^*(\mathbf{x}) / \partial x^2$ , which is nonzero only in the vicinity of the tunnel entrance. The magnitude of this second derivative along the path of the train can be reduced by *moderately* flaring the tunnel entrance, thereby causing the streamlines of the hypothetical potential outflow determined by  $\phi^*$  to diverge more gradually from the entrance. A similar result is achieved by the presence of a suitable arrangement of vents near the tunnel entrance, through which a portion of the potential flow  $\phi^*$  can ‘‘escape’’ before reaching the entrance. The distribution of vents along the tunnel wall must be chosen carefully, however, since a rapid divergence of the streamlines will merely cause the tunnel to be *acoustically shorter*, and the formation of the compression wave to be delayed until the train passes from the vented to the unvented section of the tunnel entrance, with no increase in rise time.

The influence of venting will be examined by assuming the tunnel roof near the entrance to be perforated with identical apertures distributed with a number  $\mathcal{N}(\mathbf{x})$  per unit area (Fig. 1). The aperture cross section is assumed to be sufficiently large that the unsteady aperture flows produced by the passage of the train may be regarded as irrotational. This should be a good approximation during the period of wave formation, as the train enters the tunnel, since turbulence diffusion from aperture walls and from the train occurs over a much longer timescale. The aperture distribution function  $\mathcal{N}(\mathbf{x})$  is at our disposal, and can be adjusted to modify the rise time of the compression wave.

Introduce the representation

$$\phi^*(\mathbf{x}) = \phi_0^*(\mathbf{x}) + \phi_A^*(\mathbf{x}), \quad (7)$$

where  $\phi_0^*(\mathbf{x})$  is the potential function  $\phi^*$  in the absence of venting, and  $\phi_A^*(\mathbf{x})$  is the additional contribution from the presence of the vents. To determine  $\phi_A^*(\mathbf{x})$ , let  $G(\mathbf{x}, \mathbf{x}')$  denote the potential flow Green’s function that satisfies  $\nabla^2 G = \delta(\mathbf{x} - \mathbf{x}')$ , and is defined such that  $G$  has vanishing normal derivative on the *unperforated* tunnel walls, and  $\nabla G \rightarrow 0$  at large distances from the point source, both within and outside the tunnel. Then

$$\phi_A^*(\mathbf{x}) = \oint_S [G(\mathbf{x}, \mathbf{x}')]_{\mathbf{x}'} \left( \frac{\partial \phi_A^*}{\partial x'_n}(\mathbf{x}') \right)_+ dS(\mathbf{x}'), \quad (8)$$

where the integration is over the tunnel walls, and  $(\partial\phi_A^*/\partial x_n)_+$  denotes the normal velocity within an aperture directed *out* of the tunnel. The square bracket notation in this formula is defined such that, for any function  $f(\mathbf{x})$ ,  $[f(\mathbf{x})]_{\mathbf{x}}$  is the exterior minus the interior limiting values of  $f(\mathbf{x})$  as the point  $\mathbf{x}$  approaches the tunnel wall.

Now let  $\bar{Q}(\mathbf{x}_j) = \oint_{S_j} (\partial\phi_A^*/\partial x_n)_+ dS(\mathbf{x}')$  be the volume flux directed out of the tunnel through the  $j$ th aperture  $S_j$  whose centroid is at  $\mathbf{x}_j$ . When the apertures are small relative to the tunnel diameter, and the distance of the point  $\mathbf{x}$  from the nearest aperture exceeds the aperture diameter,  $G(\mathbf{x}, \mathbf{x}') \approx G(\mathbf{x}, \mathbf{x}_j)$  may be regarded as constant when performing the integration in (8) over  $S_j$ . Since the length scale of variation of  $\bar{Q}(\mathbf{x}_j)$  between neighboring apertures must be comparable to that of the potential function  $\phi_0^*$ , which may be supposed to *drive* the motion through the apertures, and there are  $\mathcal{N}$  apertures per unit area of the tunnel wall, it follows that the integrand of (8) can be approximated by  $\mathcal{N}(\mathbf{x}')\bar{Q}(\mathbf{x}') [G(\mathbf{x}, \mathbf{x}')]_{\mathbf{x}'}$ , and therefore that

$$\phi^*(\mathbf{x}) = \phi_0^*(\mathbf{x}) + \oint_S Q(\mathbf{x}') [G(\mathbf{x}, \mathbf{x}')]_{\mathbf{x}'} dS(\mathbf{x}'),$$

$$Q(\mathbf{x}') \equiv \mathcal{N}(\mathbf{x}') \bar{Q}(\mathbf{x}'). \quad (9)$$

In this formula  $Q(\mathbf{x})$  is the volume flux *per unit surface area* of the tunnel wall, and the integration is over the region where  $Q \neq 0$ .

## B. Calculation of $Q(\mathbf{x})$

The volume flux  $\bar{Q}(\mathbf{x}_j)$  through the  $j$ th aperture can be expressed in terms of the potential difference  $[\bar{\phi}^*]_{\mathbf{x}_j}$  across the aperture produced by the unperforated potential  $\phi_0^*$  and the potential generated by the volume fluxes through all of the other apertures, by means of Rayleigh's formula

$$\bar{Q}(\mathbf{x}_j) = \mathcal{H}[\bar{\phi}^*]_{\mathbf{x}_j}, \quad (10)$$

where  $\mathcal{H}$  is the *Rayleigh conductivity* of the aperture.<sup>12</sup>  $\mathcal{H}$  has the dimensions of length, and depends only on the shape and size of the aperture; it is equal to  $2R$  for a circular aperture of radius  $R$  in a thin wall, and approximately equal to  $\sqrt{\text{aperture area}/\pi}$  for a nonelongated, thin wall aperture of arbitrary shape. The potential difference  $[\bar{\phi}^*]_{\mathbf{x}_j}$  can actually be approximated by the representation (9) of  $\phi^*(\mathbf{x})$ , because, although  $[G(\mathbf{x}_j, \mathbf{x}')]_{\mathbf{x}'}$  is singular as  $\mathbf{x}' \rightarrow \mathbf{x}_j$ , the singularity is integrable, and its contribution to the surface integral from a vanishingly small region around  $\mathbf{x}' = \mathbf{x}_j$  shrinks to zero. Thus  $Q(\mathbf{x})$  satisfies the integral equation

$$Q(\mathbf{x}) = \mathcal{H}N(\mathbf{x})[\phi_0^*]_{\mathbf{x}} + \mathcal{H}N(\mathbf{x}) \oint_S Q(\mathbf{x}') \times [[G(\mathbf{x}, \mathbf{x}')]_{\mathbf{x}'}]_{\mathbf{x}} dS(\mathbf{x}'), \quad (11)$$

which can be solved by collocation when  $\phi_0^*(\mathbf{x})$  and  $\mathcal{N}(\mathbf{x})$  are prescribed.

## C. Rectangular tunnel with a vented roof

The determination of  $Q$  from (11) requires a knowledge of both the unperforated velocity potential  $\phi_0^*(\mathbf{x})$  and Green's function  $G(\mathbf{x}, \mathbf{x}')$ . Although  $\phi_0^*(\mathbf{x})$  can readily be calculated for a tunnel of circular or semi-circular cylindrical form,<sup>7</sup> a convenient analytical representation of the Green's function is not generally available. We may avoid this difficulty for the tunnel of rectangular cross section in Fig. 1 by adopting a two-dimensional approximation to the potential flow from the entrance, by assuming that the local irrotational motion in the entrance is uniform in the  $z$  direction (transverse to the direction of motion of the train). This approximation cannot give a complete description of compression wave generation, but it yields predictions that are fully consistent with analytical and numerical results obtained previously for an unvented tunnel.<sup>4,5,7,14,15</sup>

Consider the conformal transformation<sup>16</sup>

$$\frac{\pi Z}{h} - 1 = \zeta^2 + \ln \zeta^2, \quad (12)$$

which maps the  $Z = x + iy$  plane bounded by the tunnel roof and its image in the ground [Fig. 1(b)] onto the right half (Re  $\zeta > 0$ ) of the  $\zeta$  plane, with the entrance points  $Z = \pm ih$  mapping onto  $\zeta = \pm i$ , and the point at infinity within the tunnel mapping onto  $\zeta = 0$ .

The potential  $\phi_0^*$  is the real part of  $w_0 \equiv \phi_0^* + i\psi_0^* = (2h/\pi)\ln \zeta$ . The perforations are assumed to be confined to the roof of the tunnel and distributed uniformly in the  $z$  direction (out of the plane of the paper in Fig. 1), so that  $\mathcal{N} \equiv \mathcal{N}(x)$ . The complex potential of flow from the vented tunnel entrance is then given by the following analog of Eq. (9)

$$w \equiv \phi^* + i\psi^* = w_0 + \frac{1}{\pi} \int_{-\infty}^0 Q(x') \{ \ln(\zeta^2 + \xi_+^2(x')) - \ln(\zeta^2 + \xi_-^2(x')) \} dx', \quad (13)$$

where  $\zeta = i\xi_{\pm}(x')$  ( $\xi_+ > 1$ ,  $0 < \xi_- < 1$ ) are the images of the points  $Z = x' + i(h \pm 0)$  on the exterior and interior surfaces of the roof. The volume flux density  $Q$  is determined by the integral equation

$$Q(x) = 2\alpha(x) \ln \left| \frac{\xi_+(x)}{\xi_-(x)} \right| + \frac{\alpha(x)}{h} \int_{-\infty}^0 Q(x') \times \left\{ \ln \left| \frac{\xi_+^2(x') - \xi_+^2(x)}{\xi_-^2(x') - \xi_+^2(x)} \right| + \ln \left| \frac{\xi_-^2(x') - \xi_-^2(x)}{\xi_+^2(x') - \xi_-^2(x)} \right| \right\} dx', \quad (14)$$

where  $\alpha$  is the dimensionless quantity

$$\alpha(x) = \frac{h\mathcal{H}}{\pi} \mathcal{N}(x). \quad (15)$$

As indicated below, a typical maximum value of  $\alpha$  is 0.35. For circular venting apertures of diameter  $\mathcal{H} = 1$  ft and a tunnel of height  $h \approx 20$  ft, this implies that the local value of

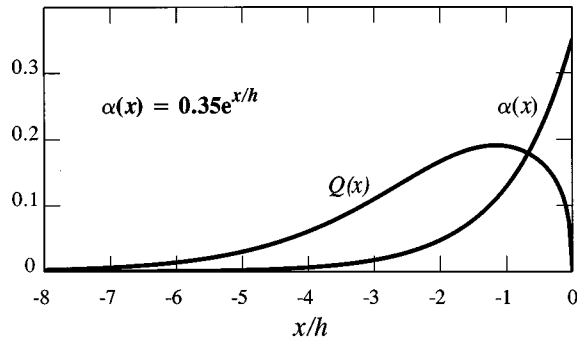


FIG. 2. Volume flux distribution function  $Q(x)$  for a vented tunnel roof with  $\alpha(x) \equiv (h\mathcal{H}/\pi)\mathcal{N}(x) = 0.35e^{x/h}$ .

the fractional open area of the roof  $\mathcal{N}\pi\mathcal{H}^2/4$  does not exceed about 5%.

#### D. Potential flow from the vented tunnel entrance

Figure 2 illustrates the variation of the predicted volume flux density  $Q$  as a function of  $x/h$  when the fractional open area of the vents decreases exponentially from the tunnel entrance according to  $\alpha(x) = 0.35e^{x/h}$ .  $Q$  vanishes at the tunnel entrance, where the potential jump across the roof is null, and attains a maximum near  $x = -h$ . The dramatic effect of these vents on the potential flow from the entrance can be calculated from (13) and is depicted in Fig. 3, in which streamlines  $\psi^*(\mathbf{x}) = \text{constant}$  are plotted for both the unvented and vented tunnel entrances. The more gradual divergence of the streamlines from the vented tunnel in the vicinity of the center line of the tunnel plus its image in the

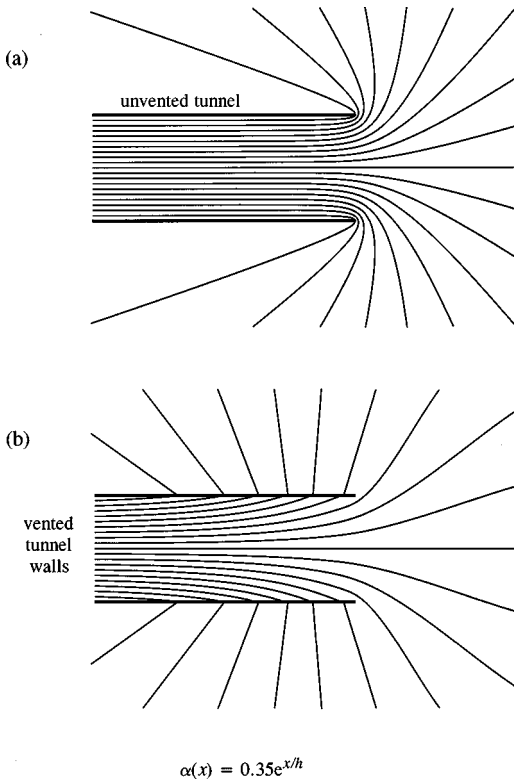


FIG. 3. Streamlines of uniform flow from the tunnel entrance defined by the velocity potential  $\phi^*(\mathbf{x})$ : (a) unvented tunnel; (b) vented roof with  $\alpha(x) \equiv (h\mathcal{H}/\pi)\mathcal{N}(x) = 0.35e^{x/h}$ .

#### Compression wave generated by a point source

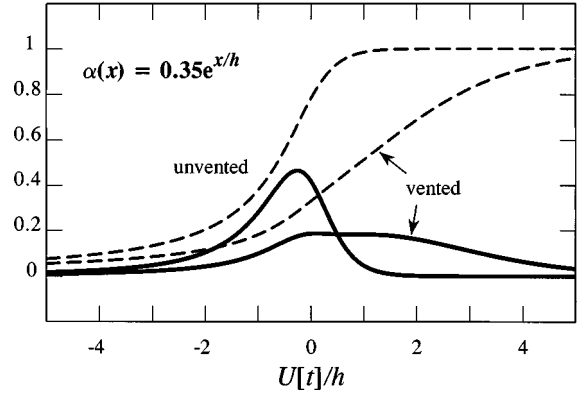


FIG. 4. Compression waves  $p/(\rho_0 U^2 \mathcal{A}_0 / h)$  (---) and pressure gradients  $(\partial p / \partial t) / (\rho_0 U^3 \mathcal{A}_0 / h)$  (—) for an unvented tunnel, and for roof venting with  $\alpha(x) = 0.35e^{x/h}$ .

ground indicates that  $\partial^2 \phi^* / \partial x^2$  will be correspondingly smaller along the train track. Equation (5) then suggests that the rise time of the compression wave will be larger for the vented tunnel.

### III. INFLUENCE OF VENTING ON COMPRESSION WAVE RISE TIME

#### A. Front of train modeled by a point source

Preliminary estimates of the influence of roof venting can be obtained by assuming that the source distribution (6) that models fluid displacement by the nose of the train is concentrated in one point, i.e., by taking

$$q(\mathbf{x}) \approx \mathcal{A}_0 U \delta(x) \delta(y) \delta(z), \quad (16)$$

where the net source strength  $\mathcal{A}_0 U = \int_0^L U(\partial \mathcal{A}_T / \partial x) dx$ , and the vertical plane of symmetry of the train is taken to coincide with  $z = 0$ . This approximation for  $q$  is formally identical to that obtained when the train is modeled by a semi-infinite cylinder of cross-sectional area  $\mathcal{A}_0$ .

Equations (3) and (5) now supply the following approximations to the pressure and pressure gradient of the compression wave generated as the train enters the tunnel,

$$p(x, t) \approx \frac{\rho_0 U^2 \mathcal{A}_0}{\mathcal{A}} \frac{\partial \Phi^*}{\partial X}(-U[t]/h, 0, 0), \quad (17)$$

$$\frac{\partial p}{\partial t}(x, t) \approx -\frac{\rho_0 U^3 \mathcal{A}_0}{h \mathcal{A}} \frac{\partial^2 \Phi^*}{\partial X^2}(-U[t]/h, 0, 0),$$

where the following dimensionless notation has been introduced:

$$X = \frac{x}{h}, \quad \Phi^*(X, y/h, z/h) = \frac{\phi^*(\mathbf{x})}{h}. \quad (18)$$

Equations (17) are applicable within the tunnel at large distances from the entrance, but before nonlinear steepening of the wavefront becomes important.

The dashed and solid curves in Fig. 4, respectively, represent the predicted pressure and pressure gradient when the behavior of  $\phi^*$  near the tunnel entrance is determined by the two-dimensional approximation (13) for (i) an unvented tun-

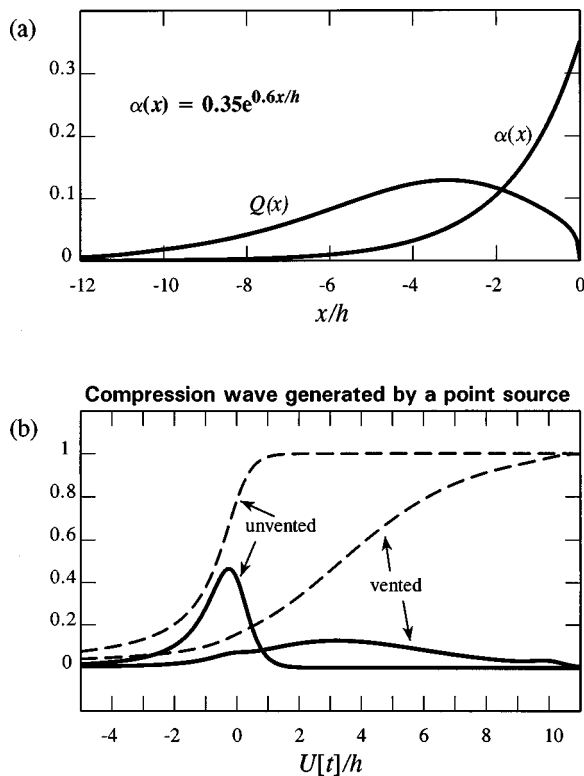


FIG. 5. (a) Volume flux distribution  $Q(x)$  for  $\alpha(x)=0.35e^{0.6x/h}$ . (b) Compression waves  $p/(\rho_0 U^2 L_0/h)$  (---) and pressure gradients  $(\partial p/\partial t)/(\rho_0 U^3 L_0/h)$  (—) for the unvented and vented tunnels.

nel, and (ii) a tunnel with the roof venting of Fig. 2 (see Sec. II D), for which  $\alpha(x) \equiv h \mathcal{N}(x)/\pi = 0.35e^{x/h}$ . Venting increases the rise time of the wave by a factor of about  $\frac{5}{2}$ , and the maximum pressure gradient is  $\frac{2}{5}$  as small. If the difference in the pressure gradients is maintained to the far end of the tunnel, the micro-pressure wave (4) radiating from the end would be reduced in intensity by about 8 dB.

The increase in compression wave rise time can be maximized by an optimal choice of the vent distribution function  $\alpha(x)$ . When the search for this optimum is restricted to exponentially varying  $\alpha(x)$ , the greatest attenuation is obtained for  $\alpha(x) = 0.35e^{0.6x/h}$ . Details for this case are depicted in Fig. 5, where the rise time is seen to experience a six-fold increase, and the maximum pressure gradient is about 27% of its value in the unvented tunnel (corresponding to a reduction in the micro-pressure wave intensity of 11.3 dB).

## B. Symmetric nose profiles

Numerical and experimental studies of compression wave generation frequently consider axisymmetric model trains projected along the axis of symmetry of a circular cylindrical tunnel. The most common nose profiles are the circular cone, and the paraboloid or ellipsoid of revolution. For the configuration of Fig. 1(a) the train would consist of the upper half of such an axisymmetric model (with its flat base lying on  $y = +0$ , just above ground level), and the analytical representation of the compression wave pressure gradient may be cast in the form

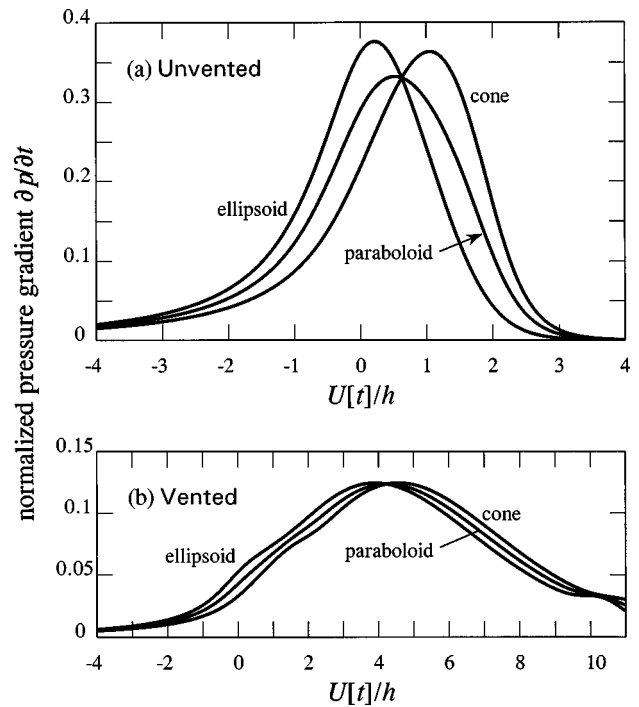


FIG. 6. Compression wave pressure gradients  $(\partial p/\partial t)/(\rho_0 U^3 L_0/h)$  for  $L/h=2$ : (a) unvented entrance; (b) vented with  $\alpha(x)=0.35e^{0.6x/h}$ .

$$\frac{\partial p}{\partial t}(x,t) \approx \frac{-2\rho_0 U^3 L_0}{L} \times \int_0^{L/h} \mathcal{F}(X,h/L) \frac{\partial^2 \Phi^*}{\partial X^2}(X-U[t]/h,0,0) dX, \quad (19)$$

where  $L$  is the length of the profiled nose, and the function  $\mathcal{F}(X,h/L)$  is given by

$$\mathcal{F}(X,h/L) = \frac{h}{L} X, \quad \frac{1}{2}, \quad 1 - \frac{h}{L} X, \quad (20)$$

respectively, for the conical, paraboloidal and ellipsoidal nose profile. The compression wave pressure gradients  $(\partial p/\partial t)/(\rho_0 U^3 L_0/h)$  generated by these profiles are plotted in Fig. 6(a) for the unvented tunnel when  $L/h=2$ . These results resemble closely both in magnitude and phase corresponding predictions for semi-circular cylindrical tunnels of radius  $h$ .<sup>3,7,14,15</sup> The corresponding profiles for the optimal case in which  $\alpha(x) = 0.35e^{0.6x/h}$  is illustrated in Fig. 6(b).

## IV. CONCLUSION

The amplitude of the compression wave produced when a high-speed train enters a long tunnel is controlled principally by train speed and the area ratio of the train and tunnel. The initial *rise time* of the wave is governed by the nose profile of the train and the geometry of the tunnel entrance and environment. Vented entrance ‘hoods’ have been used to increase the rise time and thereby reduce the impact of the micro-pressure pulse that radiates from the far end of the tunnel. The approximate calculations described in this paper

are applicable to a tunnel of rectangular cross section with a variably vented roof near the entrance, and permit the distribution of the vents to be optimized to maximize rise time. Only the very simplest case in which the aperture distribution decreases exponentially with distance into the tunnel has been considered, but our predictions indicate that at least sixfold increases in the rise time are then possible. Application of the method to tunnels with more complicated entrance geometries is straightforward in principle. This is currently being done for a tunnel of circular cylindrical cross-section, of the type frequently used in model scale tests, and which should therefore permit experimental validation of the theory.

## ACKNOWLEDGMENTS

The author expresses his gratitude to Dr. Tatsuo Maeda, Head of the Aerodynamics and Noise Reduction Group of the Railway Technical Research Institute, Tokyo, for his help and advice during the preparation of this paper.

- <sup>1</sup>S. Ozawa, Y. Morito, T. Maeda, and M. Kinoshita, "Investigation of the pressure wave radiated from a tunnel exit," Railway Technical Research Institute Rept. 1023 (in Japanese, 1976).
- <sup>2</sup>S. Ozawa, "Studies of the micro-pressure wave radiated from a tunnel exit," Railway Technical Research Institute Rept. 1121 (in Japanese, 1979).
- <sup>3</sup>S. Ozawa, T. Maeda, T. Matsumura, K. Uchida, H. Kajiyama, and K. Tanemoto, "Countermeasures to reduce micro-pressure waves radiating from exits of Shinkansen tunnels," in *Aerodynamics and Ventilation of Vehicle Tunnels* (Elsevier Science, New York, 1991), pp. 253–266.
- <sup>4</sup>T. Maeda, T. Matsumura, M. Iida, K. Nakatani, and K. Uchida, "Effect of

- shape of train nose on compression wave generated by train entering tunnel," Proceedings of the International Conference on Speedup Technology for Railway and Maglev Vehicles (Yokohama, Japan, 22–26 November 1993), pp. 315–319.
- <sup>5</sup>M. Iida, T. Matsumura, K. Nakatani, T. Fukuda, and T. Maeda, "Optimum nose shape for reducing tunnel sonic boom," Institute of Mechanical Engineers Paper C514/015/96 (1996).
- <sup>6</sup>N. Sugimoto, "Shock-free tunnel for future high-speed trains," Paper PS3-3, Proceedings of the International Conference on Speedup Technology for Railway and Maglev Vehicles (Yokohama, Japan, 22–26 November 1993).
- <sup>7</sup>M. S. Howe, "The compression wave produced by a high-speed train entering a tunnel," Proc. R. Soc. London, Ser. A **254**, 1523–1534 (1998).
- <sup>8</sup>M. S. Howe, "The generation of sound by aerodynamic sources in an inhomogeneous steady flow," J. Fluid Mech. **67**, 579–610 (1975).
- <sup>9</sup>M. C. Swarden and D. G. Wilson, "Vehicle-tunnel entry at subsonic speeds. Final Report—Part 1," Rept. No. DSR 76111-3, Engineering Projects Laboratory, Department of Mechanical Engineering, Massachusetts Institute of Technology (1970).
- <sup>10</sup>A. E. Vardy, "Ventilation approach regions for railway tunnels," Transport Engineering Journal, American Society of Civil Engineers **101**, 609–619 (1975).
- <sup>11</sup>A. E. Vardy, "Reflection of step-wavefronts from perforated and flared extensions," J. Sound Vib. **59**, 577–589 (1978).
- <sup>12</sup>Lord Rayleigh, *The Theory of Sound* (Dover, New York, 1945), Vol. 2.
- <sup>13</sup>A. D. Pierce, *Acoustics, An Introduction to its Principles and Applications* (American Institute of Physics, New York, 1989).
- <sup>14</sup>T. Ogawa and K. Fujii, "Prediction and alleviation of a booming noise created by a high-speed train moving into a tunnel," paper in *Proceedings of the European Community Conference on Computational Methods in Applied Sciences* (Wiley, New York, 1996).
- <sup>15</sup>T. Ogawa and K. Fujii, "Numerical investigation of three dimensional compressible flows induced by a train moving into a tunnel," Comput. Fluids **26**, 565–585 (1997).
- <sup>16</sup>G. K. Batchelor, *An Introduction to Fluid Dynamics* (Cambridge U.P., Cambridge, 1967).

# Phantom echo generation: A new technique for investigating dolphin echolocation<sup>a)</sup>

Roland Aubauer<sup>b)</sup> and Whitlow W. L. Au

Hawaii Institute of Marine Biology, University of Hawaii, P.O. Box 1106, Kailua, Hawaii 96734

(Received 27 May 1997; accepted for publication 28 April 1998)

In behavioral experiments where real targets are used to investigate dolphin echolocation, it is often very difficult to extract the relevant echo parameters that the animals use to discriminate or classify. The complex relationship between the physical dimensions and the reflection characteristic of real targets prevents separate control of various echo parameters of the stimuli presented in an echolocation experiment. A new echo simulation method presented in this paper avoids this problem. Dolphin echolocation sounds are transformed with the target impulse response into artificial echoes, which are played back to the animal. The phantom echo system is implemented on a digital signal processing board and gives an experimenter fully programmable control over the echo generating process and the echo structure itself. Echoes of several underwater targets were simulated to evaluate the quality of the method. A comparison of simulated echoes with the original echoes demonstrated very good agreement independent of the incident signal (cross-correlation coefficient  $>0.95$ ). The method has tremendous potential for investigating animal echolocation and understanding biosonar signal processing. © 1998 Acoustical Society of America. [S0001-4966(98)02908-7]

PACS numbers: 43.10.Ln, 43.58.Jq, 43.60.Qv, 43.80.Lb [SLE]

## INTRODUCTION

Dolphins possess a highly sophisticated echolocation system, which they use for orientation and catching prey. They emit short clicks in the ultrasonic frequency range and analyze the echoes from objects in the underwater environment. From the echoes, dolphins can gain information about the position, shape, composition, and structure of targets (Au, 1993). With these abilities, dolphins can find their way in absolute darkness or in heavily clouded water and can even find buried prey (Herzing, 1996). It is clear that the echolocation system of dolphins is superior to manmade sonar.

Many behavioral experiments have been conducted to investigate the biosonar system of dolphins, in which real targets had to be detected, discriminated, or classified by echolocation (Nachtigall and Moore, 1988; Au, 1993). Most of the targets that were used had a basic geometry (sphere, cylinder, and plate) and in each experiment only one physical dimension, such as size, material, or wall thickness was varied (for example see Dubrovskiy and Fadeyeva, 1973; Nachtigall, 1980; Hammer and Au, 1980; Au and Pawloski, 1992). Unfortunately, it has often been difficult to extract the relevant echo parameters used to discriminate between different targets, because of the complex relationship between the physical dimensions of the object and the acoustic properties of the echo it returns (Neubauer, 1986; Shirley and Diercks, 1970). The variation of only one object dimension always causes changes in several acoustic target features, so

that the reflected echo structure changes in various and sometimes subtle ways. Therefore, in order to gain a deeper understanding of how dolphins perform target discrimination, it is important to be able to vary echo parameters and to observe how these parameter affect the dolphin discrimination capabilities.

A new technique of simulating target echoes described in this paper can avoid this problem associated with real targets. The acoustic impulse response is used to reproduce realistic echoes from the emitted dolphin sounds. The method provides the experimenter with full knowledge of the stimulus and gives precise control of individual echo parameters. Ambiguity in the interpretation of echolocation experiments can thus be avoided. This phantom echo technique can be used to investigate bat echolocation as well. Compared to existing electronic target simulators used in bat echolocation research, the new phantom echo system is able not only to simulate single or multiple echo wave fronts but the whole complexity of any real target echo as well (Mogdans *et al.*, 1993; Simmons, 1973; Simmons *et al.*, 1990; Schmitt, 1992). Given this ability, new phantom echo experiments could lead to a better understanding of real target perception in echolocating animals. This paper describes the theory of acoustic echo simulation for dolphin behavioral experiments and its technical implementation.

## I. THEORY

Acoustic simulation of target echoes is one method to achieve definite and separate control of echo parameters. The acoustic impulse response  $h(t)$  of a target, which describes the backscattering process independent of the incident signal for a certain angle of incidence and reflection, can be used for phantom echo generation. The echo signal,  $e_i(t)$ , at the

<sup>a)</sup>“Selected research articles” are ones chosen occasionally by the Editor-in-Chief that are judged (a) to have a subject of wide acoustical interest, and (b) to be written for understanding by broad acoustical readership.

<sup>b)</sup>Present address: University of Erlangen, Institute of Zoology II, Staudtstrasse 5, 91058 Erlangen, Germany.

location of the target is the convolution of the target impulse response,  $h(t)$ , and the incident signal,  $s_i(t)$ :

$$e_t(t) = h(t) * s_i(t) = \int_{-\infty}^{\infty} h(\tau) \cdot s_i(t - \tau) d\tau. \quad (1)$$

In the frequency domain, the convolution becomes a multiplication and the echo spectrum is

$$E_t(\omega) = H(\omega) \cdot S_i(\omega), \quad (2)$$

where the target transfer function  $H(\omega)$  and the spectra  $E_t(\omega)$ ,  $S_i(\omega)$  are the Fourier transforms of the target impulse response, the echo, and the source signal, respectively.

The sound propagation path must be taken into consideration in order to derive the target echo at the location of the dolphin as a function of the emitted signal. The emitted signal travels two times the distance  $R$  from the dolphin to the target before it returns to the animal and is therefore delayed by  $2R/c$ , where  $c$  is the speed of sound in the propagation medium. Transmission loss along the sound propagation path consists of spreading and absorption losses. In the far field of the sound source, spreading is spherical and the source signal amplitude declines inversely proportional to the distance from the target. The amplitude of the target echo at the location of the sound source declines with  $1/R^2$ . The absorption loss in seawater is less than 0.06 dB/m for the frequency range of dolphin echolocation clicks (50–150 kHz) and can be neglected for short ranges (Fisher and Simmons, 1977). Reflections at boundaries of the sound transmitting medium (mainly at the water surface and bottom) may cause multipath propagation of the source signal and the target echo. Signal interference of the target echo with multipath signals can be minimized with a well designed experimental configuration and the use of baffles to block undesirable acoustic paths.

The echo signal,  $e_s(t)$ , at the location of the dolphin (source) for a target in the far field of the dolphin at distance  $R$  (multipath propagation and absorption loss are neglected) is

$$e_s(t) = 1/R^2 \cdot [h(t) * s_s(t - 2R/c)], \quad (3)$$

where  $s_s(t)$  is the source signal. With Eq. (3), it is possible to determine either the impulse response of a target or if the impulse response is known, to generate a phantom echo for any incident signal.

The phantom echo generation can be done either in the time or in the frequency domain. In the time domain a digital FIR filter (finite impulse response) in transversal structure directly executes the convolution of the input signal,  $s(t)$ , with the target impulse response,  $h(t)$ . The filter coefficients correspond directly to the time discrete impulse response. In the frequency domain the fast Fourier transform (FFT) is used to determine the complex spectrum of the input signal, which is then multiplied by the target transfer function  $H(\omega)$  to get the echo spectrum  $E(\omega)$ . The resulting echo spectrum is transformed back into the time domain by inverse Fourier transformation. This method is usually called “fast convolution.” Both echo generation techniques can be implemented on modern digital signal processing systems. The preference of one or the other techniques is dependent on the length of

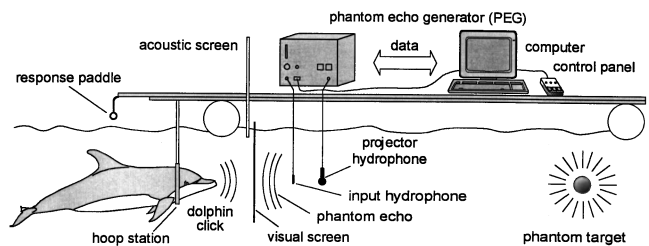


FIG. 1. Experimental setup.

the input and generated echo signal and on the signal processing system (Kammeyer and Kroschel, 1992). The complexity of the echo structure is irrelevant in making the choice of the technique. With the same processing power any phantom echo of the same duration can be generated, so that phantom echoes can be made remarkably similar to real target echoes. At the same time, the projector-hydrophone transmitting characteristic can be compensated without additional costs by pre-equalizing the target transfer function. The pre-equalized echo spectrum  $E_p(\omega)$  is

$$E_p(\omega) = E(\omega) \cdot P^{-1}(\omega), \quad (4)$$

where  $P^{-1}(\omega)$  is the inverse or reciprocal of the transfer function of the projector.

The range of the phantom target can be tuned by adjusting the time delay of the phantom echo projection. The longer the time delay the further away the phantom target appears to the dolphin.

In general, the impulse response represents a target only from one aspect and is dependent on the orientation of the target relative to the sound transmitting and receiving location. Therefore, the orientation of the test animal relative to the experimental configuration must be held relatively constant.

## II. SYSTEM DESCRIPTION

The experimental setup is presented in Fig. 1. A trained dolphin is positioned in a hoop and echolocates a phantom target. A visually opaque but acoustically transparent screen is situated permanently between the dolphin and the system hydrophones to ensure that the dolphin is using only echolocation. Between trials, an acoustically impermeable screen can be placed in front of the hoop to prevent the dolphin from echolocating on the hydrophones. Dolphin echolocation clicks are received with a Brüel & Kjaer 8103 hydrophone and fed into the phantom echo generator (PEG) for signal processing. The phantom echoes are played back to the subject with an ITC-1042 projector (International Transducer Corporation). The input and projector hydrophones are located 2 and 6 m, respectively, from the hoop at a depth of 1 m.

The dolphin's task is to identify a standard stimulus and to reject every other comparison stimulus. The PEG provides two stimulus selection modes. In the training mode, the experimenter selects either the standard or the comparison stimulus on the PEG control panel. In the double-blind mode the PEG selects the presented stimulus in a random procedure and neither the experimenter nor the test animal knows

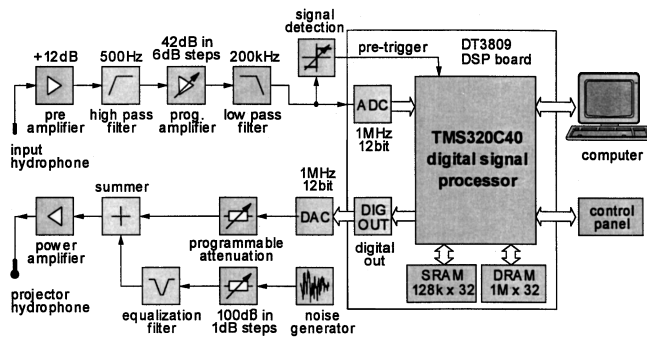


FIG. 2. Block diagram of the phantom echo generator.

which stimulus is selected. After the stimulus has been selected, optional masking white noise can be turned on and the phantom echo generating process is started. A trial starts with the dolphin swimming into the hoop. The acoustic screen is raised, signaling the animal to echolocate the phantom target. The echolocation signals are detected by the PEG and transformed into phantom echoes, which are played back with a time delay corresponding to the predetermined phantom target distance. The dolphin response to the stimulus presentation is fed by the experimenter into the PEG by depressing one of two response buttons of the external control panel. Visual and acoustic signals of the control panel then reveal the presented stimulus and indicate the correctness of the dolphin's decision to the experimenter. The results are stored on the computer connected to the PEG. The stored data include the configuration of the PEG, the selected stimuli for each task, the dolphin's response, the number, and the amplitude range of the dolphin echolocation signals. The recorded signals can also be stored. The computer automatically evaluates the data and produces a report. A feedback to the dolphin about its decision is given manually by the experimenter. In general, correct responses are indicated by an underwater reinforcement tone, followed by a fish reward for the dolphin. Incorrect responses are not rewarded.

A block diagram of the phantom echo generator is shown in Fig. 2. The signal received with the input hydrophone is amplified and filtered with high- and low-pass filters to reduce low- and high-frequency noise. The filters have a two-pole Butterworth characteristic with cutoff frequencies of 500 Hz and 250 kHz, respectively. The input gain can be adjusted in a range of 42 dB in 6-dB steps. The amplified and filtered input signal is fed into a digital signal processor (DSP) system (Fulcrum DT3809, Data Translation) and can be monitored with a digital level meter (3-dB resolution in a range of 30 dB). When the input signal exceeds the user-set threshold of the signal detection unit, an input trigger signal is generated. This trigger signal is connected to the pre-trigger input of the DSP system and is visually indicated to the experimenter. In the DSP system the analog input signal is digitized with a sampling rate of 1 MHz and 12-bit resolution. The number of points digitized is controlled by the experimenter via the computer, with 128 points (i.e., 128  $\mu$ s) being typical for an echolocating *Tursiops truncatus*. The analog/digital converter is connected to two high speed communication ports on the TMS320C40 signal processor (Texas Instruments) which are used to transfer the data via

direct memory access into the fast memory of the system. Before the input trigger signal occurs, the data stream is directed over one of the communication ports into a circular memory buffer. On a trigger event, the input data stream is switched to the second communication port and stored in a linear addressable memory buffer. The switching between the communication ports works without time delay, so none of the input signal is lost and a pre-defined number of input samples before and after signal detection can be acquired. After signal acquisition, the input data are transformed by the signal processor into the desired phantom echo. The phantom echo is pre-equalized with the inverse transfer function of the projector, so that the overall system transfer function is flat in the frequency range of 20 kHz–250 kHz within  $\pm 1$  dB. The echo samples are fed to the digital output port of the DSP system, where they are clocked out at a rate of 1 MHz when the output trigger signal occurs. The output trigger signal is synchronized with a time delay to the input trigger, where a hardware timer functions as a delay generator. This time delay between data acquisition and phantom echo output is programmable in steps of 0.5  $\mu$ s in the range of 5–32 ms, 1  $\mu$ s in the range of 32–64 ms, 2  $\mu$ s in the range of 64–128 ms, etc. The digital echo data stream is converted by a 12-bit digital/analog converter into an analog signal. The analog output signal is summed with pre-equalized white noise before going to the power amplifier. The echo signal and the masking noise can be independently attenuated over a range of 80 dB in steps of 1 dB, so that the signal-to-noise ratio can be varied and masking effects on the echolocation capability of dolphins studied. The noise pre-equalization filter consists of a notch filter that compensates for the resonance of the projector hydrophone, so that the projected noise frequency spectrum is flat in the frequency range of 10 kHz and 160 kHz within  $\pm 5$  dB.

The DSP system is connected to a host personal computer. Higher application functions, like the user interface, are performed on the host computer, whereas the DSP system executes the signal transformation. The software of the PEG system is written exclusively in the "C" computer language. The DSP program runs under the real time operating system SPOX (Spectron Microsystems), and the PC application under MS-DOS (Microsoft). Both programs run simultaneously and exchange data in a multitasking procedure.

The digital filter and fast convolution methods that transform an input signal into the desired echo were both programmed on the DSP system. For a minimum number of input samples of 128 and up to an echo length of 2048 points, the fast convolution method that generates the phantom echo in the frequency domain is at least 30% faster than the digital filter. This comparison includes the zero padding of the input signal up to the length of the echo, which is necessary for the fast convolution but not for the digital filter method. The overall signal processing time from the signal acquisition to the echo output for a 128-point input signal and a 512-point target impulse response is 2.707 ms. Echo signals up to 1024 points can fit into the fast cache memory of the signal processor and the processing time increases linearly with the echo length.



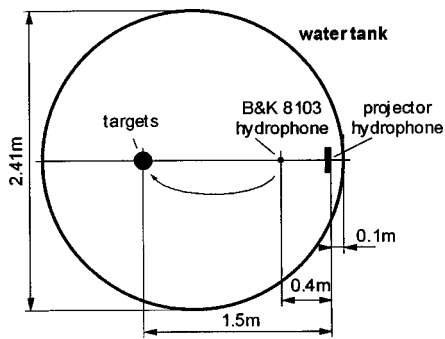


FIG. 3. Measuring setup.

### III. ECHO MODELING

Echoes of real targets were simulated to evaluate the quality of the phantom echo method. In general, the theoretical mathematical evaluation of the backscattering process of underwater targets is difficult and often needs simplifying approximations because of the presence of not only longitudinal, but also shear and surface waves in solid targets (Neubauer, 1986; Shirley and Diercks, 1970). Therefore, the impulse responses of targets were determined experimentally by measuring target echoes using broadband pulses.

The source and echo signal were measured in the far field of the source and the target. A sound projector (custom made piezoceramic multi-element array), a measuring hydrophone (B&K 8103) and the targets were placed 1 m deep along a horizontal line in a cylindrical water-tank containing 8.3 m<sup>3</sup> of seawater. The hydrophone was used to measure either the incident signal or the echoes of the targets. The measuring setup is shown in Fig. 3.

The test signals used for the echo simulation are shown in Fig. 4. A band limited delta was used to determine the impulse responses of the targets. The band limitation of delta pulse in the frequency range of 40 kHz–260 kHz was necessary in order to avoid signal distortions of the digitally pre-equalized sound projector. The bottlenosed dolphin (*Tursiops truncatus*) click was used to generate real and phantom echoes that were compared with each other.

It was necessary to enhance the signal-to-noise ratio (SNR) of the reflected target echoes because of background noise caused by multipath propagation over the tank boundaries (clutter) and statistical amplifier noise. The statistical noise was reduced by integrating the reflected signals over 2000 periods of the emitted signal (signal repetition rate: 10 Hz). The test targets were then removed and background

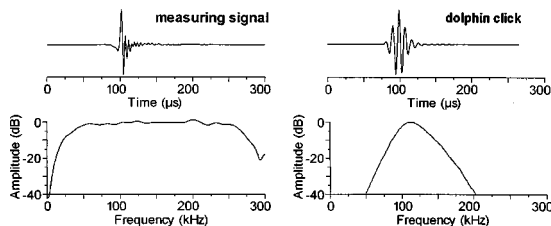


FIG. 4. Waveform and frequency spectrum of the test signals. The band limited delta pulse was used to determine the impulse responses of the targets. The dolphin click was used to generate real and phantom echoes that were compared with each other.

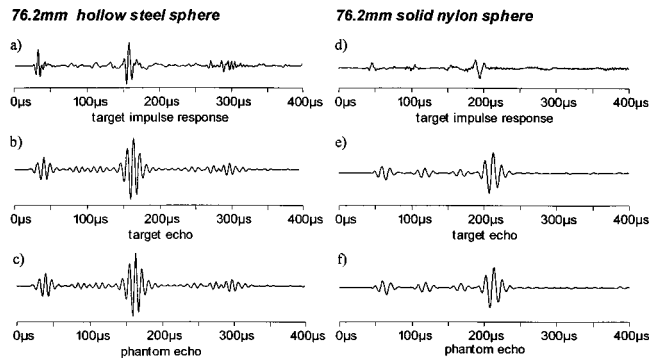


FIG. 5. (a) Target impulse response; (b), (c) comparison of real and phantom echoes of a hollow water-filled stainless steel sphere; (d) target impulse response; (e), (f) comparison of real and phantom echoes of a solid nylon sphere.

clutter was recorded in the same manner as the reflected signals. The coherent background clutter was finally subtracted from the measured echo signals. With this procedure it was possible to increase the SNR from about 19 dB to about 52 dB (depending on the specific target), which was determined by checking the signal base line just prior to the *time of arrival* of the target echo.

The target impulse response is the inverse Fourier transform,  $\mathbf{F}^{-1}$ , of the ratio of the complex spectra of the measured echo and source signals,  $e_m(t)$  and  $s_m(t)$ , respectively,

$$h(t) = \mathbf{F}^{-1} \left\{ \frac{E_m(\omega)}{S_m(\omega)} \right\}. \quad (5)$$

The acoustic impulse responses of several spheres and one cylinder were determined. The *solid* spheres all had a diameter of 76.2 mm but were made of different materials (stainless steel, brass, nylon). The single hollow sphere had a wall thickness of 1.9 mm of stainless steel and was filled with sea water. The cylinder was also hollow but of aluminum and had a diameter of 38.1 mm, a wall thickness of 6.4 mm, and a length of 178.8 mm.

The impulse response of the hollow stainless steel sphere is shown in Fig. 5(a) and was obtained by measuring the echo generated by the band limited delta pulse and applying Eq. (5). The impulse response was band limited to the frequency range of 15–250 kHz in order to minimize errors caused by low signal-to-noise ratios. The impulse response has clearly separated highlights that correspond to the wave fronts of the target echo [Fig. 5(a)–(b)]. Figure 5(c) shows the generated phantom echo of the dolphin click that matches almost perfectly with the real target echo [Fig. 5(b)]. The cross-correlation coefficient between the real and the phantom echo is 0.98.

Both solid metal spheres have relative similar echo structures and impulse responses, whereas the stainless steel sphere's echo is compressed relatively to the brass sphere because of the higher sound velocity in steel (Fig. 6). Again the phantom echoes match very well with measured real target echoes. The cross-correlation coefficient between the phantom and the corresponding target echoes are 0.97 (stainless steel) and 0.95 (brass) for the dolphin click.

Compared to the metal spheres, the nylon sphere shows a distinguishably different echo characteristic [Fig. 5(d)–(f)].

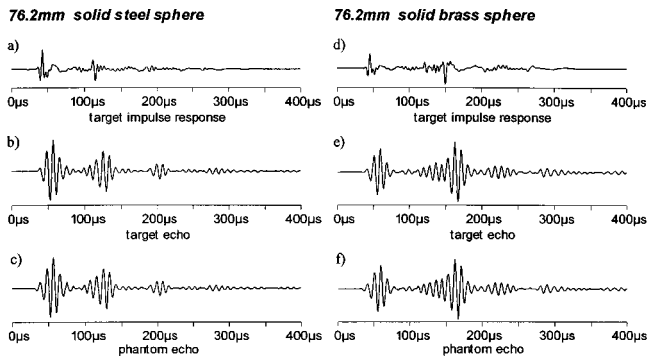


FIG. 6. (a) Target impulse response; (b), (c) comparison of real and phantom echoes of a solid stainless steel sphere; (d) target impulse response; (e), (f) comparison of real and phantom echoes of a solid brass sphere.

This is caused by the lower sound velocity in nylon (longitudinal velocity: stainless steel 5790 m/s, brass 4700 m/s, nylon 2620 m/s) and the lower specific acoustic impedance relative to the metals [characteristic impedance: stainless steel  $45.7 \times 10^6$  kg/(s m<sup>2</sup>), brass  $40.6 \times 10^6$  kg/(s m<sup>2</sup>), nylon  $2.86 \times 10^6$  kg/(s m<sup>2</sup>)] (Mason, 1958). Therefore, the front reflection of the nylon sphere is 9 dB lower than the front reflection of the steel and brass spheres. Interestingly the latest arriving echo highlight at 190  $\mu$ s has the highest amplitude level. The cross-correlation coefficient between the phantom and the real target echo for the dolphin click is 0.99.

For comparison, the impulse response of a different geometry was determined. An aluminum cylinder was used with a diameter of  $d/2$  and a length  $2.35d$ , where  $d$  is the sphere's diameter. In relation to the spheres, the impulse response of the cylinder is much shorter and all echo highlights are closer together [Fig. 7(a)–(c)]. The cross-correlation coefficient between the phantom and the real cylinder echo is 0.99.

The results from different geometries indicate that the backscattering process of an underwater target can be described precisely by the acoustic impulse response which is independent of the incident signal. Target echoes can be simulated with the PEG for any signal in high quality. The simulated phantom echoes match very well with measured target echoes of the same incident signals.

#### IV. APPLICATIONS

The phantom echo system allows the generation of a wide variety of echoes from elementary ones, consisting of only a few wavefronts, to very complex ones which simulate real targets. By changing the impulse response of a simulated target it is possible not only to modify the amplitude and the time delay but also the internal structure of an echo. This means that it is possible to change the position and amplitude of single wavefronts or portions of an echo as well as the frequency characteristic by modifying the target impulse response in the time and frequency domain. As a result relevant echo parameters that force the dolphin's decision in a target detection or discrimination experiment can be distinctly extracted from each other. The target impulse response can be modified over time to create moving targets.

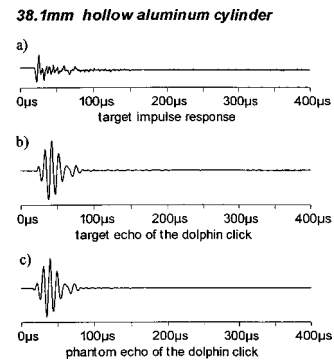


FIG. 7. (a) Target impulse response; (b), (c) comparison of real and phantom echoes of a hollow aluminum cylinder.

Not only can an approaching or departing phantom target be created, but by reproducing a target from different aspects over time, a three-dimensional representation of a target can even be produced. The number of presented phantom echoes can be controlled, so that the influence of observation time on the dolphin's decision making process can also be investigated. Finally white noise can be added to the phantom echo signal to complicate a detection or discrimination task. The PEG is currently being used in an behavioral experiment, where an echolocating dolphin has to discriminate between real target echoes and those simulated by the PEG. This first experiment will provide more information about the fidelity of the generated phantom echoes.

#### V. SUMMARY AND CONCLUSION

A new method has been presented to generate phantom targets in a dolphin behavioral experiment. Dolphin echolocation sounds are transformed into artificial echoes based on the reflection characteristics of a target. The scattering process of an underwater target for a particular angle of incidence and reflection of a signal is thereby described by the acoustic impulse response. It could be shown that the acquired impulse responses represent the reflection characteristics independent from the incident signal, so for any signals realistic phantom echoes can be produced. Comparisons of generated phantom echoes of several spheres and one cylinder with the corresponding real target echoes demonstrated very good agreement (cross-correlation coefficients close to one). The developed phantom echo system is implemented on a signal processing board and gives an experimenter full programmable control over the echo generating process and the echo structure itself. The method will allow extraction of relevant echo parameters which affect the dolphin's performance in detection and discrimination tasks, and thus will enhance understanding of the animal's outstanding sonar system.

#### ACKNOWLEDGMENTS

This work was generously supported by research grants as part of the Joint University Program III of the Federal Government of Germany provided by the German Academic Exchange Service (DAAD) and by the German Research Foundation (DFG), and in part by the Office of Naval Re-

search (Grant No. N00014-95-1-0462). At the same time, the authors would like to extend their appreciation to Dr. Paul Nachtigall, director of the Marine Mammal Research Program, Hawaii Institute of Marine Biology, for his abundant support and encouragement. This is Hawaii Institute of Marine Biology contribution No. 1037.

Au, W. L., and Pawloski, D. A. (1992). "Cylinder wall thickness difference discrimination by an echolocating Atlantic bottlenose dolphin," *J. Comp. Physiol. A* **172**, 41–47.

Au, W. L. (1993). *The Sonar of Dolphins* (Springer, New York).

Dubrovskiy, N. A., and Fadeyeva, L. M. (1973). "Discrimination of spherical targets by delphinids," *Tez. dokl. 4-y Vses. bion. konf., Moscow*, 29–34.

Fisher, F. H., and Simmons, V. P. (1977). "Sound absorption in sea water," *J. Acoust. Soc. Am.* **62**, 558–564.

Hammer, C. E., and Au, W. W. L. (1980). "Porpoise echo-recognition: an analysis of controlling target characteristics," *J. Acoust. Soc. Am.* **68**, 1285–1293.

Herzing, D. L. (1996). "Vocalization and associated underwater behavior of free-ranging Atlantic spotted dolphins, *Stenella frontalis* and bottlenose dolphins, *Tursiops truncatus*," *Aquatic Mammals* **22.2**, 61–79.

Kammeyer, K. D., and Kroschel, K. (1992). *Digitale Signalverarbeitung: Filterung und Spektralanalyse* (Stuttgart, B. G. Teubner).

Mason, W. P. (1958). *Physical Acoustics and the Properties of Solids* (van Nostrand, Princeton, NJ).

Mogdans, J., Schnitzler, H. U., and Ostwald, J. (1993). "Discrimination of two-wavefront echoes by the big brown bat, *Eptesicus fuscus*: behavioral experiments and receiver simulations," *J. Comp. Physiol. A* **172**, 309–323.

Nachtigall, P. E. (1980). "Odontocete echolocation performance on object size, shape and material," in *Animal Sonar Systems*, edited by R. G. Busnel and J. F. Fish (Plenum, New York), pp. 71–95.

Nachtigall, P. E., and Moore P. W. B. (1988). *Animal Sonar—Processes and Performance*, edited by P. E. Nachtigall and P. W. B. Moore (Plenum, New York).

Neubauer, W. G. (1986). *Acoustic Reflection from Surfaces and Shapes* (Naval Research Lab, Washington, DC).

Schmitt, S. (1992). "Perception of structured phantom targets in the echolocating bat, *Megaderma lyra*," *J. Acoust. Soc. Am.* **91**, 2203–2223.

Schusterman, R. J. (1980). "Behavioral methodology in echolocation by marine mammals," in *Animal Sonar Systems*, edited by R. G. Busnel and J. F. Fish (Plenum, New York), pp. 11–41.

Shirley, D. J., and Diercks, K. J. (1970). "Analysis of the frequency response of simple geometric targets," *J. Acoust. Soc. Am.* **48**, 1275–1282.

Simmons, J. A. (1973). "The resolution of target range by echolocating bats," *J. Acoust. Soc. Am.* **46**, 157–173.

Simmons, J. A., Ferragamo, M., Moss, C. F., Stevenson, S. B., and Altes, R. A. (1990). "Discrimination of jittered sonar echoes by the echolocating bat, *Eptesicus fuscus*: the shape of target images in echolocation," *J. Comp. Physiol. A* **167**, 587–616.

# Acoustical finite-difference time-domain simulations of subwavelength geometries

John De Poorter and Dick Botteldooren

*Department of Information Technology, University of Gent, St. Pietersnieuwstraat 41, B-9000 Gent, Belgium*

(Received 21 August 1997; accepted for publication 21 May 1998)

Accurate simulation of wave propagation around subwavelength geometries using standard finite-difference time-domain (FDTD) techniques require a fine spatial and temporal sampling resulting in high computational costs. In this paper an extension to this standard FDTD technique is proposed by means of quasi-stationary solutions on a subwavelength scale. The FDTD equations in the region near the subwavelength geometry are extended with some correction terms of which the magnitude is extracted from the quasi-stationary pressure distribution around these geometries. These pressure distributions can be calculated from the Laplace equation. Using this new technique, FDTD simulations can be based on a more coarse grid, thus reducing computational cost considerably. The accuracy of this technique is mainly determined by the accuracy of the Laplace solutions. This technique was tested with success on the simulation of resonators. It was also shown that the new FDTD equations can be extended to include viscosity effects. © 1998 *Acoustical Society of America*. [S0001-4966(98)06908-2]

PACS numbers: 43.20.Bi, 43.20.Rz [DEC]

## INTRODUCTION

Wave propagation can be effectively modeled using finite-difference time-domain (FDTD) simulation techniques.<sup>1-3</sup> This technique is based on the spatial and time discretization of the wave equation. Time-domain simulations have the advantage to allow an effective simulation of pulse responses, applicable for instance in reflectometry or scattering studies.<sup>4,5</sup> The simplicity of the FDTD equations, on the other hand, offers a great flexibility. The equations can be extended to non-Cartesian grids<sup>6</sup> and to include viscosity<sup>7</sup> and nonlinear effects.<sup>8</sup>

A limitation of all wave propagation simulation techniques is the high computational cost. For standard FDTD simulations, this cost is determined by the required fineness of the spatial discretization. A fundamental constraint concerning this discretization is that the FDTD cell size is much less (a factor of 10 to 20) than the smallest wavelength that will propagate through the investigated media. However, when special geometries smaller than this wavelength are a determining factor of the acoustical structure, the cell size has to be decreased. Some examples of possible subwavelength geometries are the mouth of a resonator determining the resonance frequency of the resonator or a rough staircase discretization of a smooth surface inducing significant errors in the results. Of course, decreasing cell size is limited by the available computer memory resources and by calculation time considerations.

Approaches to deal with this problem are presented in the literature on electromagnetics.<sup>1</sup> A possible way is to use the larger cell sizes based on wavelength considerations instead of those based on the smallest parts of the geometry, but to adapt the FDTD equations in cells close to the subwavelength geometry. The adaptation of the FDTD equations is based on known analytical solutions for simple geometries, e.g., thin wires or lumped circuit elements. More

complex configurations are solved using expansion techniques, where the feature of interest is first simulated locally in a finer grid, and these results are exported to a more coarse grid.

In this paper, a general approach to deal with subwavelength geometries in acoustical problems is described. The pressure distribution near such geometries can be calculated using a quasi-stationary approximation of the wave equations.<sup>9</sup> Correction terms for the FDTD equations in the coarse grid are extracted out of this spatial distribution. The great benefit of this approach is that almost no extra calculation time and computer memory are necessary for the FDTD simulation. Only before FDTD simulations can be performed, the quasi-stationary problem has to be solved for each subwavelength geometry of interest.

Near subwavelength geometries high pressure-field gradients may occur, resulting in significant dissipative viscosity effects in the boundary layers.<sup>10</sup> Boundary layer theory can be introduced in a general way in the FDTD simulations.<sup>7</sup> Applying the quasi-stationary approximation some simplifications can be made which allow an effective simulation of the vorticity effects near the subwavelength geometries.

## I. MATHEMATICAL MODEL

### A. Quasi-stationary approximation of linear acoustics

The linearized Euler equation in a viscous fluid relates the acoustic velocity  $\mathbf{v}$  to the acoustic pressure  $p$ ,<sup>10</sup>

$$\rho_0 \frac{\partial \mathbf{v}}{\partial t} = -\nabla p + \mu \left[ \nabla^2 \mathbf{v} + \frac{1}{3} \nabla(\nabla \cdot \mathbf{v}) \right], \quad (1)$$

where  $\rho_0$  is the equilibrium fluid density and  $\mu$  is the fluid viscosity. The linearized mass conservation equation reads

$$\frac{\partial p}{\partial t} = -\rho_0 c^2 \nabla \cdot \mathbf{v}, \quad (2)$$

where  $c$  is the speed of sound in the fluid. The combination of Eq. (1) and Eq. (2) results in the viscous wave equation.<sup>10,11</sup>

The time evolution of both acoustical velocities and pressures can be approximated as in phase in a region much smaller than the considered wavelengths. The acoustical field inside this region will be called quasi-stationary. At each instant, this field can also be regarded as a steady flow of an incompressible fluid reducing Eq. (2) to

$$\nabla \cdot \mathbf{v} \approx 0. \quad (3)$$

Combining Eq. (1) and Eq. (3) results in

$$\nabla^2 p \approx 0, \quad (4)$$

which is the Laplace equation. Notice that this stationary-flow equation remains valid when significant viscosity effects exist in the fluid.

One can conclude that within a region which is small compared to the wavelength the instantaneous pressure can be derived from the potential equation [Eq. (4)] in combination with the boundary conditions at that moment. These boundary conditions are the pressure value or the normal derivative of the pressure field at the boundary of the examined region. Due to the linearity of the potential equation, the instantaneous pressure distribution inside the region is a linear function of the instantaneous boundary condition values.

## B. FDTD formulation near subgrid geometries

For simplicity reasons, we will limit further description to a FDTD discretization in a Cartesian grid, although there are no theoretical obstacles against applying more general grids.<sup>6</sup> Also, we will initially ignore the viscosity effects. The FDTD equations in a staggered grid will first be derived by integrating the analytical wave equations over the Cartesian grid cells. The integral formulation of Eq. (2) over a closed cell volume  $V_i$  of which the surface  $S_i$  is divided in a set of subsurfaces  $S_{i,j}$  reads

$$\frac{d}{dt} \left( \frac{1}{V_i} \int_{V_i} p \, dV \right) = -\frac{\rho_0 c^2}{V_i} \sum_j S_{i,j} \left( \frac{1}{S_{i,j}} \int_{S_{i,j}} v_n \, dS \right), \quad (5)$$

where  $v_n$  is the velocity component parallel to the outer normal vector of the surfaces  $S_{i,j}$ . This equation can be interpreted in terms of the mean pressure in volume  $V_i$  and the mean normal velocity components over the surfaces  $S_{i,j}$ , which will be the unknown physical parameters in the FDTD equations. The subsurface  $S_{i,j}$  is the surface in between volume  $V_i$  and volume  $V_j$  (see Fig. 1) and is perpendicular to a coordinate axis. Adding the subsurfaces over index  $j$  results in the surface  $S_i$  enclosing the  $i$ th box with volume  $V_i$ .

A second equation describing the time derivative of the mean normal velocity components can be derived from Eq. (1) neglecting the viscosity effects,

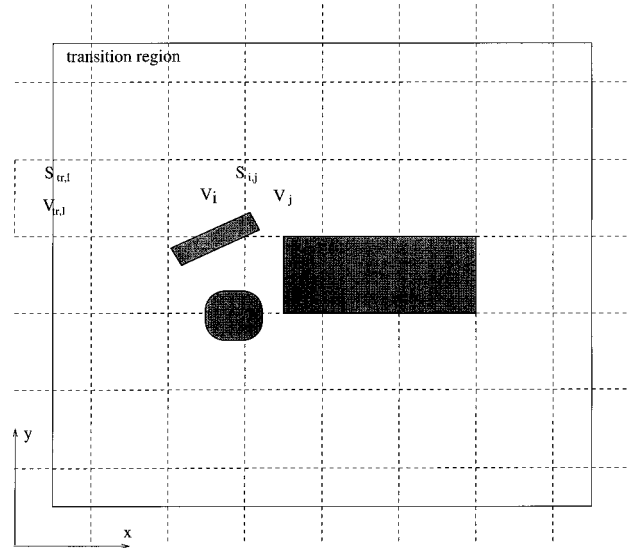


FIG. 1. Quasi-stationary region around some subwavelength geometries. The coarse Cartesian grid is insufficient to describe the geometries and the acoustical field around them. Therefore, the FDTD equations inside this region will be adapted.

$$\frac{d}{dt} \left( \frac{1}{S_{i,j}} \int_{S_{i,j}} v_n \, dS \right) = -\frac{1}{\rho_0} \left( \frac{1}{S_{i,j}} \int_{S_{i,j}} \frac{\partial p}{\partial n} \, dS \right). \quad (6)$$

To obtain a closed system of equations, the mean normal derivative of the pressure has to be estimated from the mean pressure values over the volumes  $V_i$ , which are the FDTD variables.

For a FDTD without subwavelength geometries, the mean normal derivative of the pressure of Eq. (6) is estimated by

$$\frac{1}{S_{i,j}} \int_{S_{i,j}} \frac{\partial p}{\partial n} \, dS = \left\langle \frac{\partial p}{\partial n} \right\rangle_{S_{i,j}} \approx \pm \frac{1}{dn_j} (\langle p \rangle_{V_j} - \langle p \rangle_{V_i}), \quad (7)$$

where  $dn_j$  is the cell size in the direction orthogonal to  $S_{i,j}$ ,  $\langle p \rangle_{V_j}$  and  $\langle p \rangle_{V_i}$  are the mean pressures over the volumes  $V_j$  and  $V_i$ , respectively. The sign depends on the direction of the outer normal of  $S_{i,j}$  with respect to the coordinate axes. In Eq. (7) the spatial derivative along the outer normal is approximated by the second order centered difference form. This approximation is accurate as long as third and higher order terms in  $dn_j$  of the spatial Taylor's expansion of the pressure field are negligible compared to the first and second order terms.<sup>6</sup> Combining Eqs. (6) and (7) and after time discretization of the resulting equation and Eq. (5) the standard FDTD equations can be obtained.<sup>2,6</sup> However, when subwavelength-sized structures must be modeled and the standard FDTD equations are used, one can only obtain good accuracy when the grid cell size is adapted to the dimension of these objects. This will result into a significant increase of computational costs.

Consider a subwavelength geometry with hard surfaces in a region that is discretized by a Cartesian grid (Fig. 1). The grid cell dimensions, however, are too coarse to describe the complex spatial function of the pressure field nearby this geometry or to describe the geometry itself. For this reason the right side of Eq. (7) will be a bad approximation of

$\langle \partial p / \partial n \rangle_{S_{i,j}}$ . At a certain distance of the geometry, usually several times the dimensions of the geometry, Eq. (7) will again be valid. If this region around the geometry is still small compared to the smallest wavelength, a better approximation for the pressure derivative inside this region can be calculated based on the quasi-stationary approximation described in Sec. I A. We will call this region the quasi-stationary zone. The linearity of the potential problem allows us to write the instantaneous pressure field at any point inside the quasi-stationary zone as a linear function of the pressure values at the border of this zone. As is illustrated in Fig. 1, the border surface of this quasi-stationary zone can be discretized in subsurfaces, named  $S_{tr,l}$ . The mean pressures over these surfaces  $\langle p \rangle_{S_{tr,l}}$  are the fundamental set of pressures that determine the pressures (and some derivative quantities) inside the quasi-stationary zone. This property can be applied to extend Eq. (7) for the presence of subgrid geometries resulting in

$$\begin{aligned} \left\langle \frac{\partial p}{\partial n} \right\rangle_{S_{i,j}} &\approx \pm \frac{1}{dn_j} \left( \langle p \rangle_{V_j} - \langle p \rangle_{V_i} + \sum_l a_{l,S_{i,j}} \langle p \rangle_{S_{tr,l}} \right) \\ &\approx \pm \frac{1}{dn_j} \left( \langle p \rangle_{V_j} - \langle p \rangle_{V_i} + \sum_l a_{l,S_{i,j}} \langle p \rangle_{V_{tr,l}} \right), \end{aligned} \quad (8)$$

where  $a_{l,S_{i,j}}$  is a coefficient of the linear expression, quantifying the effect of the pressure at  $S_{tr,l}$  on the correction term in surface  $S_{i,j}$ . In the FDTD calculation scheme, one only knows the mean pressure over volumes and not the mean pressures over surfaces. Therefore,  $\langle p \rangle_{S_{tr,l}}$  is approximated by  $\langle p \rangle_{V_{tr,l}}$  in Eq. (8), where  $V_{tr,l}$  encloses the surface  $S_{tr,l}$  (see Fig. 1). The coefficients  $a_{l,S_{i,j}}$  can be calculated by solving the Laplace equation in the quasi-stationary zone with boundary conditions  $\langle p \rangle_{S_l} = 1$  and  $\langle p \rangle_{S_k} = 0$  for every  $k \neq l$ . When the quasi-stationary solutions corresponding to this boundary conditions are labelled  $QS,l$ , one can derive the correction coefficients  $a_{l,S_{i,j}}$  as

$$a_{l,S_{i,j}} = \frac{\pm dn_j}{\langle p_{QS,l} \rangle_{V_{tr,l}}} \left( \left\langle \frac{\partial p_{QS,l}}{\partial n} \right\rangle_{S_{i,j}} - (\langle p_{QS,l} \rangle_{V_j} - \langle p_{QS,l} \rangle_{V_i}) \right). \quad (9)$$

For some special cases, the Laplace equation can be solved analytically, but generally numerical techniques are necessary. Many of those calculation techniques are described in the literature.<sup>12,13</sup> We preferred a finite difference calculation technique because similar grids as for FDTD could be used.

Notice that in Eq. (8) the quasi-stationary assumption is only used to calculate geometrical correction terms for  $\langle \partial p / \partial n \rangle_{S_{i,j}}$ . Another approach is to calculate  $\langle \partial p / \partial n \rangle_{S_{i,j}}$  completely out of the pressure values at the border of the quasi-stationary zone. The correction term approach, however, has the advantage that in grid cells where the correction terms are small (e.g., close to the zone borders), the wave propagation is still determined by the general FDTD algorithm instead of a quasi-stationary approximation. This improves the accuracy of the calculations.

The FDTD equations are not unconditionally stable. For a classical set of equations in a Cartesian grid the time step  $\Delta t$  has to fulfill following condition,

$$\Delta t < \frac{1}{c \sqrt{\frac{1}{\Delta x^2} + \frac{1}{\Delta y^2} + \frac{1}{\Delta z^2}}}, \quad (10)$$

with  $\Delta x$ ,  $\Delta y$ , and  $\Delta z$  the dimensions of a Cartesian grid cell in the  $x$ ,  $y$ , and  $z$  direction, respectively. Because the correction terms relate the local pressures to pressures at the border of the transition zone, it can be assumed that the quasi-stationary correction terms have no effect on this condition. No exceptions to this assumption were found experimentally.

The attenuating effects of air viscosity are most significant near rigid boundaries. The existence of a velocity boundary layer decreases the mean velocity components parallel to the boundary. An analytical expression for this effect can be derived near plane boundaries in the frequency domain.<sup>9</sup> In time domain, this expression can be transformed to a convolution between the pressure gradient along the boundary and  $t^{-1/2}$  function.<sup>11</sup> For practical applications, this convolution can be approximated by a recursion formula that is updated every time step.<sup>7</sup> In Sec. I A, it was proven that the quasi-stationary correction terms are independent of viscosity effects. Therefore, the boundary layer approach can also be applied in the velocity surfaces that are perpendicular to subwavelength rigid boundaries.

## II. EVALUATION OF HELMHOLTZ RESONATORS

### A. The quasi-stationary approach compared to finer grids

A Helmholtz resonator with volume  $V_{res}$ , area of the mouth surface  $S_{res}$ , and effective neck length  $l'_{res}$  has its resonance frequency  $f_{res}$  at

$$f_{res} = \frac{c}{2\pi} \sqrt{\frac{S_{res}}{V_{res} l'_{res}}}, \quad (11)$$

with  $c$  the speed of sound (approximated for all simulations as 340 m/s). The effective neck length is higher than the physical neck length  $l_{res}$  due to the quasi-stationary flow contraction near the resonator mouth. The difference between both lengths depends on the size of the resonators mouth. For an isolated resonator with a circular mouth with radius  $a$  this difference is equal to  $16a/2\pi$ .<sup>9,14</sup>

To prove the effectiveness of the proposed quasi-stationary correction technique, resonators with physical neck length small compared to the surface of the resonator mouth are chosen. In this way the effective neck length and the resonator frequency is completely determined by flow contraction around the resonator mouth. To model these flow contractions with a classical FDTD algorithm, the FDTD cell size should be significantly smaller than the mouth dimensions. However, the simulation space will be oversampled outside the resonator mouth region because the mouth dimensions themselves are in most cases already smaller than

TABLE I. The physical characteristics (volume  $V_{\text{res}}$ , area of resonators mouth  $S_{\text{res}}$ , physical neck length  $l_{\text{res}}$ , estimated effective neck length  $l'_{\text{res}}$ , estimated resonator frequency  $f_{\text{res}}$ , area of the tube section  $S_{\text{tube}}$ ) of the two investigated resonators.

Parameter	Mouth = square orifice	Mouth = circular orifice
$V_{\text{res}}$ (m <sup>3</sup> )	$27 \times 10^{-6}$	$18 \times 10^{-6}$
$S_{\text{res}}$ (m <sup>2</sup> )	$100 \times 10^{-6}$	$19.63 \times 10^{-6}$
$l_{\text{res}}$ (m)	0	0
$l'_{\text{res}}$ (m)	$7.6 \times 10^{-3}$	$4.24 \times 10^{-3}$
$f_{\text{res}}$ (Hz)	1195	867
$S_{\text{tube}}$ (m <sup>2</sup> )	$2500 \times 10^{-6}$	$900 \times 10^{-6}$

the wavelengths considered. In this section, the results of oversampled FDTD simulations will be compared to the quasi-stationary approach.

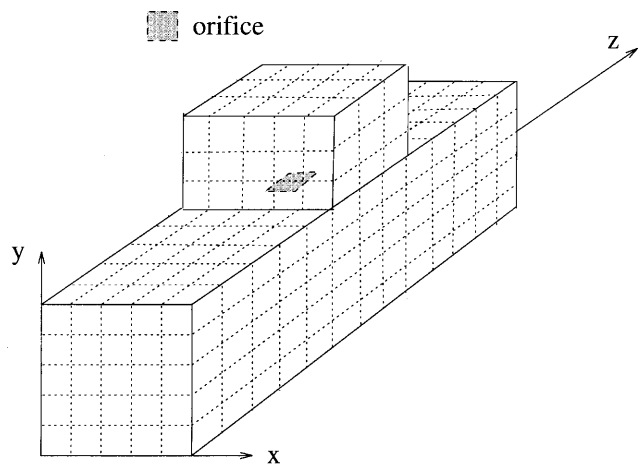
Consider a resonator with a rectangular placed on one side of a rectangular tube. The walls of the resonator and tube are considered to be acoustically hard. The characteristic dimensions of this resonator can be found in Table I. In Fig. 2(a), this resonator and tube are schematically shown in a coarse FDTD grid. Notice that the resonator mouth has the size of one grid cell surface, which is 0.01 m by 0.01 m. The effect of this resonator can be evaluated using the transmission coefficient. This coefficient is defined as the ratio of the complex pressure amplitude after the resonator at the end of the tube and the complex pressure amplitude that was injected into the tube. The frequency dependence of this coefficient characterizes the resonators effect on the zero order propagating mode of the tube. Near the resonating frequency of the resonator, the impedance of the resonator and the transmission coefficient becomes small. Away from  $f_{\text{res}}$  the resonator will have less effect on the propagating modi of the tube and the amplitude of the transmission coefficient will reach one.

The rectangular resonator tube has a length of 0.13 m. The front face and back face of the tube were modelled to have the acoustical impedance of the medium  $\rho_0 c$ . For plane waves this boundary conditions has the same effect as an outer radiation boundary condition.<sup>1</sup> At 0.015 m of the front face of the tube, a plane of transparent pressure sources parallel to this front face was placed to inject a plane wave into the tube. The transparency of the sources avoids reflection against this plane of sources. Transparent pressure sources can easily be constructed in FDTD by adding the desired time function  $p_{sc}(t)$  to Eq. (5). For this application a smooth asymmetrical impulse with a relatively broad spectrum was used,

$$p_{sc}(t) = (t - t_0) e^{-\frac{(t-t_0)^2}{\sigma}} \quad (12)$$

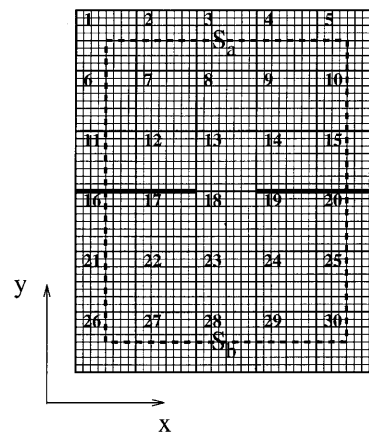
The time offset  $t_0$  was chosen to be 5 ms and  $\sigma$  was  $2.5 \times 10^{-7}$  s<sup>2</sup>. This pressure impulse gives rise to a plane wave impulse inside the tube with a frequency bandwidth between zero and  $1/\sqrt{\sigma}$ , this is 2000 Hz.

The transmission coefficient over a frequency range was calculated using the FDTD algorithm. Therefore, the signal of Eq. (12) was transmitted into the tube and the pressure response at the end of the tube was monitored during the



(a)

- border quasi-stationary zone
- FDTD grid
- grid quasi-stationary calculations



(b)

FIG. 2. (a) Scheme of a resonator inside a coarse FDTD grid. The mouth of the resonator corresponds to one FDTD cell. (b) Two-dimensional section of the grid used to calculate the quasi-stationary flow contractions around the resonator mouth.

calculations. Both time signals, the test signal, and the response are Fourier transformed and the transmission coefficient can be calculated for every frequency as the ratio of the complex signal amplitudes of response and test signal. This calculation was performed in the coarse grid and in finer FDTD grids. The finer grids had linear dimensions that were 3 times, 6 times, and 12 times smaller than the coarse FDTD grid. More details about the parameters of these calculations can be found in Table II. The time step was chosen to conform to the stability condition [see Eq. (10)]. Notice that in a first approximation the memory usage increases for each grid refinement with a third power of the one-dimensional refinement factor and the CPU time in ideal circumstances (i.e., sufficient memory resources) with the fourth power of this factor. The most accurate calculations (refinement factor = 12) are at the limit of engineering workstation possibilities as is illustrated by the figures in Table II.

The FDTD simulated transmission coefficients are

TABLE II. FDTD simulation parameters (the grid linear dimensions  $\Delta x = \Delta y = \Delta z$ , the time step  $\Delta t$ , the number of calculation steps  $N$ , number of cells that fit into the rectangular orifice  $n_{\text{orifice}}$ , memory usage, and CPU calculation time) for the simulations of the resonators with a rectangular mouth. The unit of the CPU time corresponds on a HP workstation 735/125 to 10.9 s.

Parameter	Grid 1	Grid 2	Grid 3	Grid 4
$\Delta x = \Delta y = \Delta z$ (m)	0.01	0.003 33	0.001 667	0.00083
$\Delta t$ ( $\mu\text{s}$ )	15	5	2.5	1.25
$N$	2731	8192	16 384	32 768
$n_{\text{orifice}}$	1	9	36	144
memory usage (MBy)	0.12	1.68	12.85	102.8
CPU time (a.u.)	1	81	1296	20 736

drawn in Fig. 3. The grid refinements have a significant effect on the resonating frequency (almost a doubling). This illustrates the fact that an accurate simulation of this resonator using the classical FDTD equations requires grid dimensions of  $1/340$  of the wavelength corresponding to the resonating frequency. Even if the grid refinement is only limited to a region around the resonator mouth, a significant increase in the computational efforts can be expected. It is interesting to notice that the coarse grid simulations underestimate the resonating frequency. This corresponds to an overestimation of the effective neck length [see Eq. (11)] or to an overestimation of the spatial extent of the flow contraction region around the resonator mouth.

It is clear that FDTD grid refinements are not an optimal approach to this problem. The quasi-stationary solution of this problem will now be investigated. Therefore, the potential problem in the neighborhood of the resonator mouth (i.e., a rectangular orifice) will be solved in a fine grid, schematically visualized in Fig. 2(b). The simulation grid has linear dimensions which are  $1/12$  of the coarse grid that will be used during the FDTD simulations. Following Eq. (8), every FDTD pressure in the quasi-stationary zone border will induce a correction term for every velocity point calculation inside the quasi-stationary zone. In the two-dimensional sec-

tion of Fig. 2(b), there are already 18 FDTD cells at the border of the quasi-stationary zone. However, the pressures at the border of the quasi-stationary zone around the orifice will only differ significantly before and after the orifice. At the same side of the orifice, the border pressure differences will be negligible because the border length is still small compared to the wavelength. Therefore, the number of important correction terms can be reduced to two, i.e., two correction terms for each velocity inside the quasi-stationary zone. The potential problem has only to be solved twice. For the first simulation, the pressure values at the quasi-stationary zone borders  $S_b$  before the orifice [see Fig. 2(b)] have to be put to one and pressure values at the borders  $S_a$  after the orifice to zero. For the second simulation these boundary conditions are switched. This second configuration does not have to be calculated due to the symmetry of the problem. Indeed, it can be seen that the correction term factors  $a_{b,S_{i,j}}$  and  $a_{a,S_{i,j}}$  are opposite. In conclusion, every pressure gradient inside the quasi-stationary zone can be written as

$$\left\langle \frac{\partial p}{\partial n} \right\rangle_{S_{i,j}} \approx \pm \frac{1}{dn_j} (\langle p \rangle_{V_j} - \langle p \rangle_{V_i} + a_{S_{i,j}} (\langle p \rangle_{S_a} - \langle p \rangle_{S_b})), \quad (13)$$

with  $a_{S_{i,j}} = -a_{b,S_{i,j}} = a_{a,S_{i,j}}$ . The pressures  $\langle p \rangle_{S_b}$  and  $\langle p \rangle_{S_a}$  can be approximated during the FDTD simulation by  $\langle p \rangle_{V_3}$  and  $\langle p \rangle_{V_{28}}$ , respectively.

The potential problem was solved using a finite-difference calculation technique.<sup>12</sup> In fact our standard object-oriented FDTD software was a good template for this new software package and only some minor changes had to be implemented. An overview of the correction factors for the pressure gradients from Fig. 2(b) is given in Table III.

TABLE III. Correction factors for the FDTD equations nearby a rectangular orifice with the size of an FDTD grid cell. The numbering corresponds to the notation in Fig. 2(b).

Surfaces $S_{i,j}$	Correction factor $a_{S_{i,j}}$
$S_{13,18}$	0.710
$S_{8,13}, S_{18,23}$	-0.042
$S_{12,13}, S_{18,19}$	0.157
$S_{13,14}, S_{17,18}$	-0.157
$S_{7,8}, S_{23,24}$	0.004
$S_{8,9}, S_{22,23}$	-0.004
$S_{7,12}, S_{19,24}, S_{9,14}, S_{17,22}$	-0.001

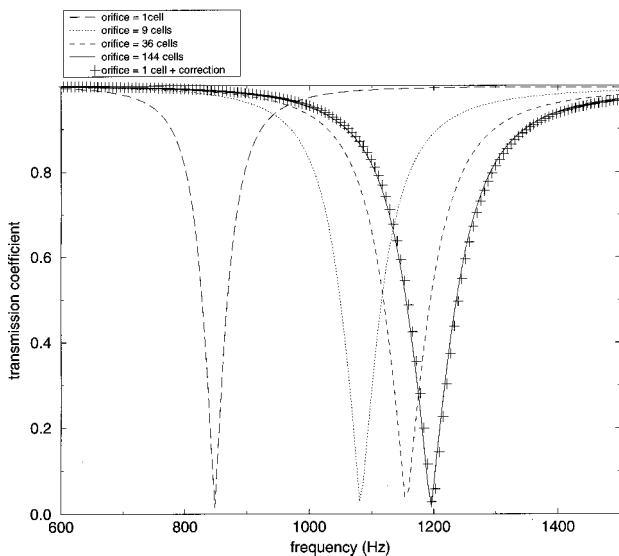


FIG. 3. Simulated frequency dependence of the transmission coefficients amplitude for the tube-resonator system. The resonator has a square resonator mouth and the effects of grid refinement is illustrated and compared to the quasi-stationary correction method.



Notice that only the velocity planes closest to the orifice and inside the orifice have a significant correction factor, the others were neglected for the FDTD calculations. The transmission coefficient, simulated with the new FDTD equations, is also printed in Fig. 3. There is a very good agreement with the results obtained using a refinement factor of 12. The quasi-stationary calculations were performed in a grid that was as fine. A similar agreement was found between the FDTD calculations performed in the grids with the other refinement factors (3 and 6) and the FDTD calculations in the coarse grid but using correction coefficients of quasi-stationary calculations in corresponding grids. These facts suggest that the error introduced by using a quasi-stationary approach can be neglected. We can therefore conclude that the accuracy of the FDTD simulations using quasi-stationary solutions is only determined by the accuracy of the quasi-stationary solution itself.

The phase variations of the transmission coefficient were also examined. The phase results in the fine grid were compared to the phase results in a coarse grid with corrected FDTD equations. The maximum phase error is around 2.9 degrees and is located near the phase jump at the resonance frequency. Taking into account the spatial sampling of the problem in the coarse grid, it can be shown that these phase errors are not related to grid dispersion.<sup>2</sup> Therefore, these phase errors are related to the quasi-stationary methodology but they are not significant for most FDTD applications.

The CPU time and computer memory of the FDTD simulations were not significantly increased by the few correction terms. Thus the FDTD simulation is done with the computer costs corresponding to the coarse grid, but with an accuracy corresponding to the accuracy of the quasi-stationary simulations. Any other FDTD simulation including square orifices with dimensions of one grid cell can be simulated using the same correction factors and with the same low computational costs.

## B. The quasi-stationary approach compared to analytical approximations

In this section we will demonstrate the potentials of the technique for the simulation of subgrid cell structures. Therefore, a resonator with a circular mouth will be examined. An advantage of this circular structure is that analytical approximations can be found describing the resonator impedance.<sup>14</sup>

A resonator configuration was studied similar to the one in Fig. 2(a). The spatial dimensions of resonator and tube can be found in Table I. The resonator mouth consisted of a circular orifice with a diameter that is equal to 0.005 m. The FDTD simulation was performed in a coarse Cartesian grid with  $\Delta x = \Delta y = \Delta z = 0.01$  m. In advance, the quasi-stationary correction terms were calculated in two finer grids with cell sizes of 0.001 m (grid 1) and 0.0005 m (grid 2), corresponding to one fifth and one tenth of the orifice diameter, respectively. The discretization of the circular orifice in these grids can be seen in Fig. 4. The most significant correction term  $S_{13,18}$  was obtained from the quasi-stationary calculations in grid 1 and grid 2, resulting in  $-0.310$  and  $-0.359$ , respectively. Notice that these correction factors are for one part determined by the field contractions around the

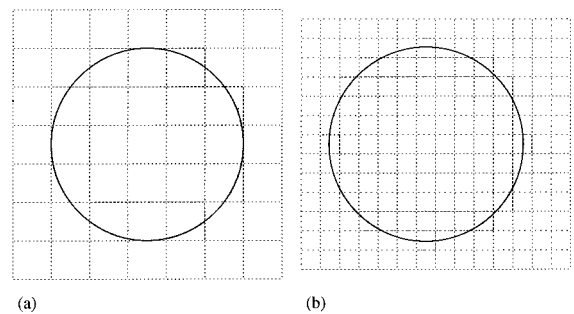


FIG. 4. Discretization of a circular orifice with a diameter equal to 0.005 m in a Cartesian grid with cell sizes of 0.001 m (a) and 0.0005 m (b).

orifice, but for another part by the fact that the pressure gradient is by definition zero for 80% of surface  $S_{13,18}$ .

The transmission coefficient obtained using the quasi-stationary based FDTD simulations in the coarse grid are compared to analytical results in Fig. 5. The resonance frequency differs by 2% for the calculation using the correction factor of grid 1 and by 0.7% for the correction factor based on grid 2. These results prove that an accurate simulation of the subwavelength circular orifice is possible using the quasi-stationary correction method. The computer resources used are minimal once the necessary correction coefficients are determined.

## C. Combination with viscosity effects

In experimental practice, acoustic energy absorption in the resonator exists mainly as a consequence of viscosity effects.<sup>9,14</sup> To illustrate that these effects can also be introduced in this quasi-stationary concept, we included viscosity effects in the circular resonator on the basis of a boundary layer formulation. The viscous attenuation will only be important near significant pressure gradients, that is, at the resonator mouth. Therefore, only the FDTD equation in the circular orifice will be compensated for viscosity effects. The

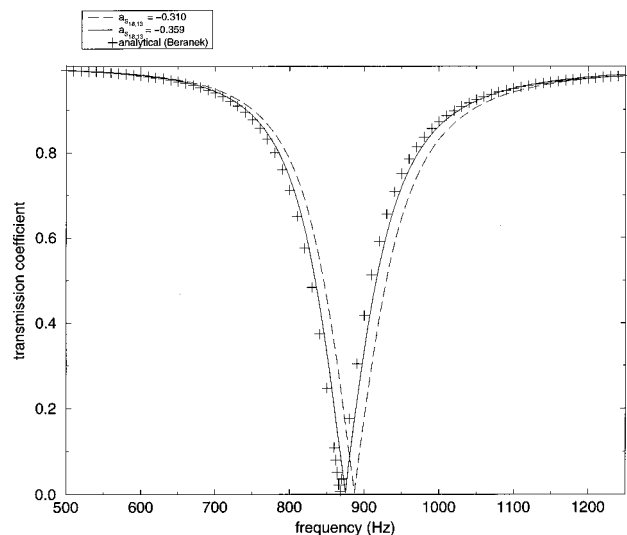


FIG. 5. Simulated frequency dependence of the transmission coefficients amplitude for the tube-resonator system with a circular orifice. The FDTD simulations based on the quasi-stationary correction terms are compared to the analytical result (Ref. 14).

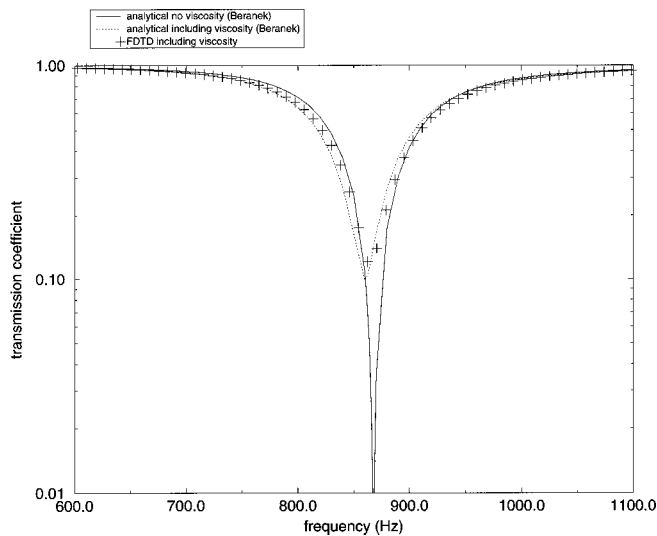


FIG. 6. Frequency dependence of the transmission coefficients amplitude for the tube-resonator system with a circular orifice including viscosity effects. The FDTD simulation is compared to the analytical results (Ref. 14).

viscous correction term [of Eq. (1)] is calculated using the results for viscous flow near an infinite plate.<sup>7</sup>

The effect on the transmission coefficient based on FDTD simulations is compared in Fig. 6 to the analytical expression that is also based on the viscous flow near an infinite-plate.<sup>14</sup> The good agreement between analytical and FDTD calculations proves that vorticity can be effectively simulated using FDTD. We must remark here that the infinite-plate boundary layer solution underestimates the viscosity effects in resonators necks that are short compared to the boundary layer thickness.<sup>15,16</sup> The viscous absorption will therefore be higher when the described resonator with very short physical neck length should be tested experimentally. However, it was not the goal of this paper to introduce a better estimation than the infinite-plate boundary layer solution. We only wanted to illustrate the possibility to combine viscosity effects with the subwavelength FDTD formalism. Viscous effects and the reliability of the used simplifications for more general configurations are now being examined in greater detail.

### III. CONCLUSIONS

The extension of the FDTD equations with correction terms in a region around subwavelength structures allows for

efficient calculation of wave propagation around such structures. Once the necessary correction terms are calculated for a specific geometry, this geometry can be included in FDTD simulations without any additional computational cost. It is considered in the FDTD equations as a subgrid object.

It was shown that the accuracy of this technique was determined by the accuracy of the correction factors, which is in turn determined by the accuracy of the Laplace solutions. The principle of using quasi-stationary solutions does not introduce significant additional error. Also, it was shown that for a specific configuration this quasi-stationary FDTD technique can be extended to include viscosity effects.

<sup>1</sup>K. Kunz and R. Luebbers, in *The Finite Difference Time Domain Method for Electromagnetics* (CRC, Boca Raton, 1993).

<sup>2</sup>D. Botteldooren, "FDTD-simulation of low frequency room acoustic problems," *J. Acoust. Soc. Am.* **98**, 3302–3308 (1995).

<sup>3</sup>J. LoVetri, D. Mardare, and G. Soulodre, "Modeling of the seat dip effect using finite-difference time-domain method," *J. Acoust. Soc. Am.* **100**, 2204–2212 (1996).

<sup>4</sup>R. Stephen, "Modeling sea surface scattering by the time-domain finite-difference method," *J. Acoust. Soc. Am.* **100**, 2070–2078 (1996).

<sup>5</sup>M. Veysoglu and C. Cooke, "Acoustic time-domain reflectometry for irregular surface recognition," *J. Acoust. Soc. Am.* **99**, 444–454 (1996).

<sup>6</sup>D. Botteldooren, "Acoustical finite-difference time-domain simulation in a quasi-Cartesian grid," *J. Acoust. Soc. Am.* **95**, 2313–2319 (1995).

<sup>7</sup>D. Botteldooren, "Vorticity and entropy boundary conditions for acoustical finite-difference time-domain simulations," *J. Acoust. Soc. Am.* **102**, 170–178 (1997).

<sup>8</sup>D. Botteldooren, "Numerical model for moderately nonlinear sound propagation in three-dimensional structures," *J. Acoust. Soc. Am.* **100**, 1357–1367 (1996).

<sup>9</sup>L. Cremer and H. A. Müller, in *Principles and Applications of Room Acoustics* (Applied Science, London, 1978), Vol. 2.

<sup>10</sup>A. Pierce, in *Acoustics, An Introduction to Its Physical Principles and Applications* (McGraw-Hill, New York, 1981).

<sup>11</sup>T. L. Szabo, "Time domain wave equations for lossy media obeying a frequency power law," *J. Acoust. Soc. Am.* **96**, 491–500 (1994).

<sup>12</sup>A. Mitchell and D. Griffiths, in *The Finite Difference Method in Partial Differential Equations* (Wiley, New York, 1990).

<sup>13</sup>C. Brebbia, J. Silva, and P. Partidge, in *Boundary Element Methods in Acoustics, Computational Formulation*, edited by R. Ciskowski and C. Brebbia (Computational Mechanics, Southampton, 1991).

<sup>14</sup>L. Beranek and I. Vér, in *Noise and Vibration Control Engineering* (Wiley, New York, 1992).

<sup>15</sup>U. Ingard, "On the theory and design of acoustic resonators," *J. Acoust. Soc. Am.* **25**, 1037–1061 (1953).

<sup>16</sup>A. Kuckes and U. Ingard, "A note on acoustic boundary dissipation due to viscosity," *J. Acoust. Soc. Am.* **25**, 798–799 (1953).

# The radiating near-field asymptotics of a normal time-harmonic circular ultrasonic transducer in an elastic half-space

Larissa Ju. Fradkin

*School of Electrical, Electronic and Information Engineering, South Bank University, 103 Borough Road, London SE1 0AA, United Kingdom*

Aleksei P. Kiselev

*Institute of Mechanical Engineering, 61 Bol'shoi Prospekt, Vassilievskii Ostrov, St. Petersburg, 199178, Russia*

Eugenia Krylova

*School of Electrical, Electronic and Information Engineering, South Bank University, 103 Borough Road, London SE1 0AA, United Kingdom*

(Received 9 December 1996; revised 6 January 1998; accepted 15 April 1998)

The modern diffraction theory is applied to analyze the radiating near zone of a normal time-harmonic circular transducer directly coupled to a homogeneous and isotropic solid. The two-tier asymptotic approach is used first to find the far-field asymptotics of a point source and then the radiating near-field asymptotics of the circular transducer. All the known ray-theoretical solutions for body waves, such as the plane  $P$  wave and the toroidal edge waves, both  $P$  and  $S$ , are obtained. The non-ray-theoretical solutions, such as the edge waves present in the axial boundary layer and the total field inside the penumbral boundary layer, are also described. The asymptotic formulas produced all have immediate physical interpretation, give explicit dependence on model parameters and involve in geometrical region elementary functions and inside boundary layers, well-known special functions. It is argued that asymptotic results may be used to write computer codes which simulate the radiating near field of the circular transducer orders of magnitude faster than the exact numerical schemes, but more accurately than other known approximations. © 1998 Acoustical Society of America. [S0001-4966(98)00109-X]

PACS numbers: 43.20.Dk, 43.20.Jr [JEG]

## INTRODUCTION

In this paper we study  $P$  (also known as longitudinal, compressional, or primary) and  $S$  (also known as transverse, shear, or secondary) wavefields in the radiating near zone of a normal time-harmonic circular transducer several millimeters in radius,  $l$ , which is directly coupled to a perfectly elastic homogeneous and isotropic solid half-space. The piston-type circular transducers are commonly employed in NDE (nondestructive evaluation) (e.g., Silk, 1984; Halmshaw, 1994), and many industrial materials, e.g., ferritic steels are homogeneous and isotropic at industrially used frequencies below 10 MHz. At these frequencies the transducers are several wavelengths,  $\lambda$ , in radius. The radiating near field of the transducers cover the depths from about one to about  $l^2/\lambda^2$  wavelengths and is of interest in NDE, since subsurface defects often occur in industrial components and the NDE technicians and expert systems are routinely trained on samples containing such defects. The propagation of pulses radiated by circular transducers have been previously studied experimentally and simulated numerically; see, e.g., Kawashima (1984), Weight (1987), Stacey and Weight (1993), Bresse and Hutchins (1989), Djelouah and Baboux (1992), and Baboux and Kažys (1992). Due to the fact that the radiated pulses are frequently wide band, the above authors all modeled the underlying physical process as the full traction boundary problem. Solving the corresponding elastodynamic equation by a finite differences/finite elements scheme or

evaluating the corresponding integral solution takes many hours of run time. Weight (1987) offered phenomenological formulas to deal with the problem. His work was taken further by Lhémery (1994) who found simple far-field approximations which give reasonable predictions of pulse shapes in the radiating near field too.

The work of Weight (1987) and Lhémery (1994) shows that away from the axis and the cylindrical surface directly underneath the transducer rim most experimental results obtained in the relative proximity of a circular transducer can be given good qualitative description in terms of plane and toroidal edge waves arriving from the nearest and farthest points on the rim, and these are ray-theoretical concepts (see, e.g., Achenbach *et al.*, 1982). It is well understood in the modern theory of diffraction (Babič and Kirpičnikova, 1975; Babič and Buldyrev, 1991; Borovikov and Kinber, 1994; Babich and Kiselev, 1989) that all the *geometrico-elastodynamic* (GE) or *ray-theoretical* solutions may be well described by using the first terms in the so-called *ray-asymptotic series*, that is, asymptotic series in inverse powers of dimensionless frequency which represent solutions of the full elastodynamic equations in the *high-frequency limit*. Experience shows that the asymptotic formulas apply even when the frequencies are only *relatively high*. Therefore, in the fields generated by ultrasonic transducers the high and intermediate frequencies dominate. This is mainly due to the fact that in most transmitted pulses the lower-frequency

modes have smaller amplitudes (see, e.g., Silk, 1984, Figs. 4.15, 4.16, 9.9, and 9.10).

In view of the above, it is beneficial to model the radiating near field of a circular transducer by concentrating on propagation of high-frequency modes, and then rely on their harmonic synthesis to describe propagation of realistic pulses. High-frequency asymptotics have been used in this context by Miller and Pursey (1954) who described the far field of a point (small) transducer, and also by Schmerr and Sedov (1989) who concentrated on the regions near to and far from the axis of a large transducer but not on the regions in between. By contrast, we carry out a consistent analysis of the *whole* radiating near field, including both the geometrical regions and the so-called *boundary layers* (also known as transition zones) in between, not only the axial region but also penumbra, where the ray-asymptotic series do not apply.

The concept of a boundary layer has been introduced by analogy with fluid dynamics first by Keller (1958) and Buchal and Keller (1960), and then developed further by Babič and Kirpičnikova (1975). Often such a layer may be described by a *boundary layer asymptotic series* involving known special functions (such as Bessel's or the Fresnel integral) of the dimensionless frequency. These functions can still be easily computed and, therefore, the approach leads to computer codes which describe the transducer field orders of magnitude faster than the nonphenomenological schemes (see another publication by Gridin and Fradkin, 1998). There are additional advantages, since unlike solutions computed with direct numerical schemes each asymptotic expression described below has an immediate physical interpretation and gives explicit dependence on model parameters. As to the phenomenological formulas of Weight (1987) and their refined version by Lhémy (1994) they lead to comparably fast computing times but according to the authors themselves, in certain cases fail to produce high accuracy, physically meaningful results or explicit parameter dependence.

The present paper is organized as follows: We start by deriving the far-field (more than a wavelength away from the source) asymptotics of the solid displacements which are due to a time-harmonic surface point source acting normally to the solid half-space. Then we integrate these asymptotics over the transducer surface and obtain asymptotic expressions for its *P* and *S* body waves valid at least for distances smaller than  $2\pi l^2/\lambda$  away from the transducer. This means that we cover most of the first Fresnel zone which extends from the transducer down to about  $l^2/\lambda^2$  wavelengths.

## I. THE MATHEMATICAL MODEL

We consider the displacement field of a time-harmonic circular normal transducer of radius  $l$  oscillating with circular frequency  $\omega$  and directly coupled to a perfectly elastic homogeneous and isotropic half-space. We introduce a Cartesian *transducer system of coordinates* ( $\mathbf{e}_x, \mathbf{e}_y, \mathbf{e}_z$ ) and the corresponding cylindrical system ( $\mathbf{e}_r, \mathbf{e}_\phi, \mathbf{e}_z$ ), with the  $z$  axis running along the axis and directed into the medium (see Fig. 1). The displacement field inside the medium ( $z > 0$ ) is described by the reduced elastodynamic equation

$$b^2 \nabla \cdot (\nabla \times \mathbf{u}) - a^2 \nabla (\nabla \cdot \mathbf{u}) - \omega^2 \mathbf{u} = \mathbf{0}, \quad (1)$$

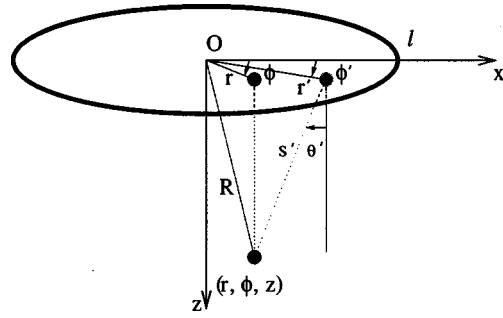


FIG. 1.  $\mathbf{R}$  is an observation point, and  $\mathbf{r}'$  is an arbitrary point on the surface of a circular transducer.

where  $a$  and  $b$  are characteristic wave speeds,  $a > b$ , and the  $\nabla$  is the nabla operator.

We seek solutions of Eq. (1) which satisfy the usual radiation condition at infinity and the normal traction boundary conditions:

$$\begin{aligned} \sigma_{zx}|_{z=0} = \sigma_{zy}|_{z=0} = 0, \\ \sigma_{zz}|_{z=0} = \begin{cases} -Q/\pi l^2, & r \leq l, \\ 0, & r > l, \end{cases} \end{aligned} \quad (2)$$

where the stress tensor components are

$$\begin{aligned} \sigma_{zx} &= \varrho b^2 (u_{z,x} + u_{x,z}), \\ \sigma_{zy} &= \varrho b^2 (u_{z,y} + u_{y,z}), \\ \sigma_{zz} &= \varrho [(a^2 - 2b^2)(u_{x,x} + u_{y,y}) + a^2 u_{z,z}]. \end{aligned} \quad (3)$$

Above, the index before the comma denotes a component and the index after the comma, the independent variable with respect to which this component is differentiated (e.g., Fung, 1965; Achenbach, 1973; Hudson, 1980).  $Q$  is the amplitude of the load which has dimension of force and can be any smooth function of  $r$  and  $\phi$ . However, for simplicity and similarly to previous authors we assume everywhere below that over the transducer surface the load is uniform, that is,  $Q$  is a constant. Our approach can be easily generalized to apodized loads.

It is based on Green's theorem and the two-tier asymptotics: We treat each point  $\mathbf{r}'$  on the transducer surface as a point source, so that the total displacement is

$$\mathbf{u}(\mathbf{R}) = \frac{1}{\pi l^2} \int_0^{2\pi} \int_0^l \mathbf{u}^{(\text{point})}(\mathbf{s}') r' dr' d\phi' \quad (4)$$

(see Fig. 1). The integrand  $\mathbf{u}^{(\text{point})}$  is the displacement at the observation point  $\mathbf{R} = (r, \phi, z)$  caused by an isolated point load situated at  $\mathbf{r}' = (r', \phi', z')$  and acting normally to the surface. Its argument  $\mathbf{s}' = \mathbf{R} - \mathbf{r}'$  (Fig. 1). Obviously,  $\mathbf{u}^{(\text{point})}$  is a Green's function, that is a solution of Eq. (1) subject to the usual radiation condition at infinity and the normal traction boundary conditions

$$\begin{aligned} \sigma_{zx}|_{z=0} = \sigma_{zy}|_{z=0} = 0, \\ \sigma_{zz}(r-r')|_{z=0} = -Q \frac{\delta(r-r')}{2\pi|r-r'|} \end{aligned} \quad (5)$$

[cf. Achenbach, 1973 (7.209)]. For simplicity of presentation we do not make the dependence of displacements on  $\omega$  ex-

plicit. We then proceed with the two-tier asymptotics: The first tier involves assuming that the frequency is high, so that we have

$$kz \gg 1, \quad (6)$$

with  $z$ , the distance from the transducer to the observation point, and  $k = \omega/a$ , the so-called compressional wave number. This allows us to evaluate the far field asymptotics of the Green's function  $\mathbf{u}^{(\text{point})}$ . As mentioned above for the asymptotics to be valid the frequencies have to be only relatively high: the  $2\pi$  factor allows Eq. (6) to be satisfied even for distances of one wavelength. The second tier relies on the assumption that we have

$$z/kl^2 \ll 1, \quad (7)$$

and thus are within the first Fresnel zone. This allows us to calculate the *radiating near-field* asymptotics of the modification of Eq. (4) which involves the far field asymptotics of the Green's function instead of the function itself. Together (6) and (7) imply that the transducer is large,  $kl \gg 1$ .

## II. THE FIRST TIER: THE FAR-FIELD ASYMPTOTICS OF THE GREEN'S FUNCTION

Let a surface point source be situated at point  $\mathbf{r}' = (r', \phi', 0)$  and act normally to a homogeneous and isotropic elastic half-space below. The resulting field is described by Eq. (1) subject to the radiation condition and boundary conditions (5). It decomposes into  $P$  and  $S$  components,

$$\mathbf{u}^{(\text{point})} = \mathbf{u}^{P(\text{point})} + \mathbf{u}^{S(\text{point})} \quad (8)$$

(e.g., Hudson, 1980). These waves are coupled on the boundary but propagate independently inside the medium,  $P$  with speed  $a$  and  $S$ ,  $b$ . Although they are more commonly known as compressional and shear, respectively, the terms can be misleading, since they describe the polarization (direction) of the leading terms in the respective ray-asymptotic series and not of the fields themselves (Fradkin and Kiselev, 1997).

In the transducer coordinates, for any observation point  $\mathbf{R}$ , the leading term of the ray-asymptotic series for  $\mathbf{u}^{P(\text{point})}$  is given by

$$\mathbf{u}_0^{P(\text{point})}(s') = -\frac{Qk}{2\pi\varrho b^2} \frac{A^P(\theta', \Delta\phi')}{ks'} e^{iks'}, \quad (9)$$

where  $\varrho$  is density of the solid,  $s'$  and  $\theta'$  are defined by

$$s' = \sqrt{z^2 + r^2 + r'^2 - 2rr' \cos \Delta\phi'},$$

$$\sin \theta' = \frac{(\mathbf{s}' \cdot \mathbf{e}_r)}{\cos \Delta\phi'}, \quad \cos \theta' = \frac{z}{s'}, \quad (10)$$

and  $\Delta\phi' = \phi' - \phi$  (see Fig. 2, where  $\Delta\phi' = 0$ ). Note that  $-\pi/2 \leq \theta' \leq \pi/2$ . This is a spherical wave with the vector amplitude

$$\mathbf{A}^P = A^P \mathbf{n}^P, \quad (11)$$

where the directivity function is

$$A^P(\theta') = \frac{2 \sin^2 \theta' - \gamma^{-2}}{R^P(\sin \theta')} \cos \theta', \quad (12)$$

$\gamma = b/a$ , Rayleigh's function is

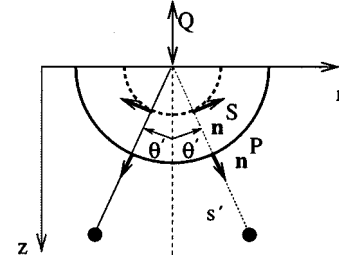


FIG. 2. The geometry of a point source acting off the  $z$  axis normally to a solid half-space. Solid line—primary front; dashed line—secondary front.

$$R^P(y) = (2y^2 - \gamma^{-2})^2 + 4y^2 \sqrt{1 - y^2} \sqrt{\gamma^{-2} - y^2}, \quad (13)$$

and the unit displacement vector,

$$\mathbf{n}^P(\theta', \Delta\phi') = \sin \theta' (\cos \Delta\phi' \mathbf{e}_r + \sin \Delta\phi' \mathbf{e}_\phi) + \cos \theta' \mathbf{e}_z \quad (14)$$

is directed from the point source to the observation point (see Fig. 2). Note that the standard form of Rayleigh's function is

$$\mathcal{R}(\xi) = (2\xi^2 - \kappa^2)^2 + 4\xi^2 \sqrt{\kappa^2 - \xi^2} \sqrt{k^2 - \xi^2}, \quad (15)$$

so that  $R^P = \mathcal{R}/k^4$  with  $y = \xi/k$ . Here  $\kappa = \omega/b$  is known as a shear wave number. For completeness, a simple method leading to this result in the local coordinates is sketched in the Appendix.

The structure of the  $S$  wavefield is more complicated and changes as  $\theta'$  crosses the critical angle defined by

$$\sin \theta_{\text{cr}} = \gamma. \quad (16)$$

For the angles  $|\theta'| < \theta_{\text{cr}}$  only a spherical  $S$  wave is present, and for the angles  $\theta_{\text{cr}} < |\theta'| < \pi/2$  there are two waves, spherical and conical (head). The boundary layer around the critical ray is described by the parabolic cylinder functions (see, e.g., Brekhovskikh, 1960; also Fradkin and Kiselev, 1997). However, this is a smaller effect and it is described in the accompanying paper (Gridin, 1998). In this paper we take into account the spherical  $S$  wave only. Hence, the leading order approximation in the ray-asymptotic series for  $\mathbf{u}^{S(\text{point})}$  is given by

$$\mathbf{u}_0^{S(\text{point})}(s') = -\frac{Q\kappa}{2\pi\varrho b^2} \frac{A^S(\theta', \Delta\phi')}{\kappa s'} e^{iks'}. \quad (17)$$

This wave has the vector amplitude

$$\mathbf{A}^S = A^S \mathbf{n}^S, \quad (18)$$

where the directivity function is

$$A^S(\theta') = \frac{2 \sin |\theta'| \sqrt{\gamma^2 - \sin^2 \theta'}}{R^S(\sin \theta')} \cos \theta', \quad (19)$$

with

$$R^S = \mathcal{R}/\kappa^4 \quad (20)$$

and the unit displacement vector (see Fig. 2)

$$\mathbf{n}^S(\theta', \Delta\phi') = \text{sign}(\theta') [\cos \theta' (\cos \Delta\phi' \mathbf{e}_r + \sin \Delta\phi' \mathbf{e}_\phi) - \sin \theta' \mathbf{e}_z]. \quad (21)$$

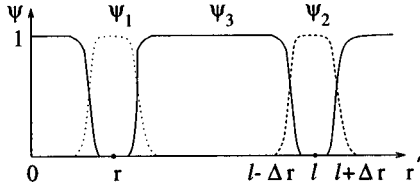


FIG. 3. A sample partition of unity for  $\phi' = \phi$  for the case of an isolated phase stationary point  $(r, \phi)$ . Dotted line— $\psi_1(r', \phi')$ ; dashed line— $\psi_2(r', \phi')$ ; solid line— $\psi_3(r', \phi')$ .

For completeness, a simple method leading to this result in the local coordinates is sketched in the Appendix. Asymptotics (9) and (17) of the 3-D Green's functions have been obtained before by Miller and Purcey (1954).

### III. THE SECOND TIER: HIGH-FREQUENCY ASYMPTOTICS OF THE RADIATING NEAR FIELD OF A CIRCULAR TRANSDUCER

We proceed by integrating the zeroth order approximations to the Green's functions (9) and (17) over the position of a point source on its surface [see Eq. (4) and Fig. 1]. All the resulting integrals are of the form

$$\mathbf{u}^\alpha(\mathbf{R}) = \int_0^l \int_0^{2\pi} \mathbf{g}^\alpha(r', \phi') e^{ikf^\alpha(r', \phi')} r' dr' d\phi', \quad (22)$$

where the superscripts  $\alpha = P$  and  $S$  correspond to the  $P$  and  $S$  waves, respectively. The corresponding integrands contain rapidly oscillating exponential factors. It is well known that apart from singularities of the amplitude function  $\mathbf{g}^\alpha$  the main contributions to the integrals of this type come from the *stationary points* of the phase functions, that is the points where  $\nabla f^\alpha = 0$  (when isolated these points are otherwise known as the critical points of the first kind; Wong, 1989, p. 424), and various types of *critical boundary points* (Wong, 1989, p. 426). We show below that in our case only one phase stationary point exists. Following the modern approach (Wong, 1989; Fedoryuk, 1977; Borovikov, 1994), we separate its contribution by introducing a partition of unity  $\{\psi_1, \psi_2, \psi_3\}$ , such that the so-called cutting functions (also known as neutralizers)  $\psi_i(r', \phi')$  are zero outside some regions of their domain known as *supp*  $\psi_i$  and maximum unity inside. All neutralizers add up to unity at each point of the integration domain, so that, at any point of the integration domain  $\sum_{i=1}^3 \psi_i = 1$ , *supp*  $\psi_1$  lies within a small neighborhood of the phase stationary point, *supp*  $\psi_2$  within a small  $\Delta r$  neighborhood of the transducer rim, and  $\psi_3 = 1 - \psi_1 - \psi_2$  (see Fig. 3). When critical points are coalescing, so that in between there are no rapid oscillations, the above considerations do not apply.

#### A. $P$ wavefield

We start our calculations with the  $P$  wavefield,

$$\mathbf{u}^P(\mathbf{R}) \equiv -\frac{Qk}{2\pi^2 l^2 \varrho b^2} \int_0^l \int_0^{2\pi} \sum_{i=1}^3 \psi_i \frac{\mathbf{A}^P(\theta', \Delta\phi')}{ks'} \times e^{iks' r'} dr' d\phi', \quad (23)$$

where  $\mathbf{A}^P$  is given by Eqs. (11)–(14) and  $s'$  by Eq. (10).

Note that using Wong [1989, Chap. VIII, Eq. (2.10)] we have

$$\begin{aligned} \mathbf{u}_3^P(\mathbf{R}) &\equiv -\frac{Qk}{2\pi^2 l^2 \varrho b^2} \int_0^l \int_0^{2\pi} \psi_3(r', \phi') \\ &\quad \times \mathbf{A}^P(\theta', \Delta\phi') \frac{e^{iks' r'}}{ks'} r' dr' d\phi' \\ &\sim \mathbf{O} \left[ \left( \frac{1}{kz} \right)^N \right], \end{aligned} \quad (24)$$

for all  $N \geq 1$ . Bold  $\mathbf{O}$  indicates a vector, and  $\sim$  means “asymptotically equal to.”

#### 1. Contribution of an isolated phase stationary point: Direct wave

It is easy to check that provided the point of observation is situated *in* the main beam there exists one isolated phase stationary point which is the projection of the point of observation onto the transducer surface,

$$(r', \phi') = (r, \phi), \quad \text{if } r \neq 0, \quad (25)$$

or

$$r' = r, \quad \text{if } r = 0. \quad (26)$$

We write this condition as

$$\sqrt{\frac{k}{2z}} (l-r) > \sqrt{\pi} \quad (27)$$

[the exact form is justified below; see arguments leading to Eq. (47)]. Using the corresponding phase stationary point formulas for multiple integrals [Wong, 1989, Chap. VIII Eqs. (3.15) and (3.16)] the isolated phase stationary point (25) or (26) gives the contribution

$$\begin{aligned} \mathbf{u}_1^P(\mathbf{R}) &\equiv -\frac{Qk}{2\pi^2 l^2 \varrho b^2} \int_0^l \int_0^{2\pi} \psi_1(r', \phi') \\ &\quad \times \frac{\mathbf{A}^P(\theta', \Delta\phi')}{ks'} e^{iks' r'} dr' d\phi' \\ &\sim \mathbf{u}^{P(\text{direct})}(\mathbf{R}), \quad \sqrt{\frac{k}{2z}} (l-r) > \sqrt{\pi}, \end{aligned} \quad (28)$$

where the leading term in the *direct ray-asymptotic series*  $\mathbf{u}^{P(\text{direct})}$  is

$$\mathbf{u}_0^{P(\text{direct})}(\mathbf{R}) = \frac{Q}{\pi \varrho a^2 k l^2} e^{i(kz + \pi/2)} \mathbf{e}_z. \quad (29)$$

It is easy to show that for the transducer of infinite radius which exerts the same pressure  $Q/\pi l^2$  as our transducer the above solution is exact. This means that when the point of observation lies well in the main beam of the transducer contribution of the phase stationary point of the first kind turns out to be the same GE plane  $P$  wave as would be radiated by the compressional uniform load of infinite extent.

If the stationary point lies well *outside* the domain of integration then its contribution is

$$\mathbf{u}_1^P(\mathbf{R}) = \frac{Qk}{2\pi^2 l^2 \rho b^2} \mathbf{O} \left[ \left( \frac{1}{kz} \right)^N \right] \sim \mathbf{0},$$

$$\sqrt{\frac{k}{2z}} (r-l) > \sqrt{\pi}, \quad (30)$$

for all  $N \geq 1$  [Wong, 1989, Chap. VIII, Eq. (2.10)]. In this case the point of observation lies well outside the main beam of the transducer, in the *geometrical shadow*, and the result is the GE solution in the exact agreement with no-load case.

## 2. Contribution of critical boundary points of the second kind: Edge waves

The contribution of critical boundary points of the second kind is usually found by integrating an inner integral by parts (Wong, 1989, Chap. V, Sec. 3). Here we consider

$$\mathbf{u}_2^P(\mathbf{R}) \equiv -\frac{Qk}{2\pi^2 l^2 \rho b^2} \int_0^l \int_0^{2\pi} \psi_2(r')$$

$$\times \mathbf{A}^P(\theta', \Delta\phi') \frac{e^{iks'}}{ks'} r' dr' d\phi' \quad (31)$$

and apply this rule to the  $r'$  integral. Using [Wong, 1989, Chap. VIII, Eq. (2.7)] we have to the leading order approximation,

$$\mathbf{u}_2^P(\mathbf{R}) \sim \frac{Qi}{2\pi^2 l^2 \rho kb^2} l \int_0^{2\pi} \frac{\mathbf{A}^P(\theta'_l, \Delta\phi')}{l-r \cos \Delta\phi'} e^{iks'_l} d\phi', \quad (32)$$

where  $s'_l$  and  $\theta'_l$  are defined by

$$s'_l = \sqrt{z^2 + r^2 + l^2 - 2rl \cos \Delta\phi'},$$

$$\sin \theta'_l = \frac{(\mathbf{s}'_l \cdot \mathbf{e}_r)}{\cos \Delta\phi'}. \quad (33)$$

By choosing  $\Delta r = 1/2|l-r|$  we assure that the pole in the double integral implicit in the RHS of Eq. (32) is neutralized.

To proceed, for any observation point off the transducer axis and off the cylindrical surface directly underneath the transducer rim [we write these respective conditions as

$$\frac{kr l}{\sqrt{z^2 + l^2}} \leq \frac{\pi}{2} \quad (34)$$

and

$$\frac{k(l-r)^2}{2z} > \pi; \quad (35)$$

see Eqs. (42) and (47) below], the phase function in Eq. (23) possesses two critical boundary points of the second kind. These are the phase stationary points of the single integral in Eq. (33),

$$\Delta\phi_{\pm} = \frac{\pi}{2} \pm \frac{\pi}{2} \quad (36)$$

(Wong, 1989, p. 246). When the observation point is  $r=0$ , that is when it lies on the axis every point on the circular boundary becomes a *degenerate* (meaning that the phase's second derivative is zero) phase stationary point of this inte-

gral. The situation does not appear to have a special name. We propose to refer to it as a *critically degenerate boundary*. When the observation point  $r=l$ , that is when it lies directly underneath the transducer rim *the critical boundary point coalesces with the phase stationary point*, and thus is again a critical point of neither first nor second kind. The boundary layers surrounding the axis and the cylindrical surface underneath the rim will be discussed separately.

First we consider the regions outside these boundary layers, so that the boundary critical points (36) are of the second kind. By applying to the integral in Eq. (32) the stationary point formulas [Wong, 1989, Chap. II, (3.2) and (3.22)], we have, to the leading order approximation,

$$\mathbf{u}_2^P(\mathbf{R}) \sim \mathbf{u}_+^P(\mathbf{R}) + \mathbf{u}_-^P(\mathbf{R}),$$

$$\frac{kr l}{\sqrt{z^2 + l^2}} > \frac{\pi}{2}, \quad \frac{k(r-l)^2}{2z} > \pi, \quad (37)$$

where the last condition applies to  $\mathbf{u}_-^P$  only, we have

$$\mathbf{u}_{\pm}^P(\mathbf{R}) \sim \mathbf{u}_{\pm}^{P(\text{edge})}(\mathbf{R})$$

$$\approx -\frac{Q}{(2\pi^3)^{1/2} \rho b^2 k l^2} \mathbf{A}^P \left( \theta_{\pm}, \frac{\pi}{2} \pm \frac{\pi}{2} \right)$$

$$\times \left( \frac{l}{r} \right)^{1/2} \left( \frac{1}{ks_{\pm}} \right)^{1/2} \frac{1}{\sin \theta_{\pm}} e^{i[k s_{\pm} + (2\mp 1)\pi/4]}$$

$$= -\frac{Q}{(2\pi^3)^{1/2} \rho b^2 k l^2} \frac{2 \sin^2 \theta_{\pm} - \gamma^{-2}}{R^P(\sin \theta_{\pm})} \left( \frac{l}{r} \right)^{1/2} \frac{\cos \theta_{\pm}}{\sin \theta_{\pm}}$$

$$\times \left( \frac{1}{ks_{\pm}} \right)^{1/2} e^{i[k s_{\pm} + (2\mp 1)\pi/4]} (\cos \theta_{\pm} \mathbf{e}_z \mp \sin \theta_{\pm} \mathbf{e}_r). \quad (38)$$

Rayleigh's function  $R^P$  is defined by Eq. (13) and  $s_{\pm}$  and  $\theta_{\pm}$  by

$$s_{\pm} = \sqrt{z^2 + (l \pm r)^2},$$

$$\sin \theta_{\pm} = \frac{r \pm l}{s_{\pm}}. \quad (39)$$

Only the leading terms in *the edge ray-asymptotic series*  $\mathbf{u}_{\pm}^{P(\text{edge})}$  are presented in Eq. (38). We can check that these waves each have a toroidal front and propagate along the two ray paths which lead from the transducer rim to the observation point and have the minimum and maximum length, respectively (see Fig. 4), as would be expected in the ray elastodynamics. The relative polarizations (displacement directions) are shown in Fig. 5. Note that the amplitude of both waves increases with  $z$  and as  $r \rightarrow 0$ . The  $-\pi/2$  shift in the phase of the far edge wave is due to the fact that it crosses the axis [see discussion after Eq. (45) below]. Note too that there is the  $\pi$  phase shift on moving the point of observation under the rim from the main beam zone into the geometrical shadow zone. These general features of the behavior of edge waves have been described before (Weight, 1987; Baboux and Kažys, 1992). However, to the best of our knowledge we are the first to present an explicit dependence of the edge waves of a circular transducer on model param-

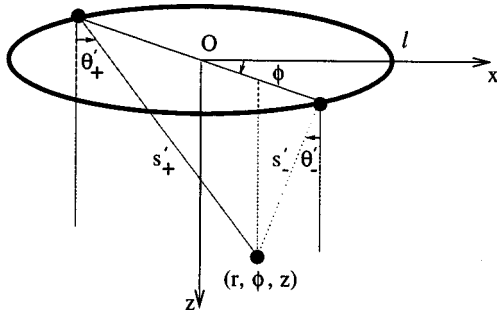


FIG. 4. The shortest and longest edge ray paths for a circular transducer acting normally to the surface of a half-space.

eters. Note that this dependence is much simpler than for the edge waves scattered by a penny-shape crack irradiated by a normal plane compressional wave (Achenbach *et al.*, 1982). The formulas have been verified against exact numerical results (see another publication by Gridin and Fradkin, 1998),

### 3. Contribution of the circular boundary close to being critically degenerate: The axial region

As we have mentioned above, inside the axial region the asymptotics (38) break down: each observation point there lies close to  $r=0$ , so that all points on the circular boundary are close to being degenerate critical points. It is easy to show that the phase difference between any two paths leading from the edge to such an observation point is approximately  $2kr \sin \theta_*$ , where  $\theta_*$  is defined by

$$s_* = \sqrt{z^2 + l^2}, \quad \sin \theta_* = \frac{l}{s_*}. \quad (40)$$

Thus it is reasonable to define this region as

$$kr \sin \theta_* \leq \frac{\pi}{2}, \quad (41)$$

so that inside this difference is no more than  $\pi$  and the exponential factor in Eq. (32) ceases to be rapidly oscillating. Condition (41) implies that the shape of the axial region is hyperbolic.

Following the modern approach (Bleistein and Handelman, 1986; Fedoryuk, 1977; Borovikov, 1994), asymptotics which are valid for this case as well may be found by introducing a new integration variable  $\Delta\psi'$ , such that the phase function in Eq. (33) may be written as

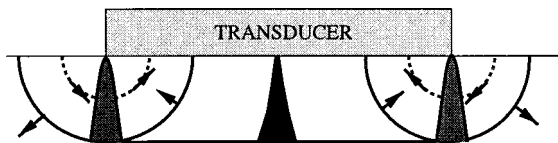


FIG. 5. The wavefronts and boundary layers underneath a circular transducer acting normally to the surface of a solid half-space. Solid line—primary fronts; dashed line—secondary front. Dark-shaded areas—penumbra (Fresnel's function); light-shaded area—the axial region (Bessel's functions).

$$\begin{aligned} s'_l &= s_* \left[ 1 + \frac{r^2}{2s_*^2} - \frac{rl \cos \Delta\psi'}{s_*^2} \right], \\ &= s_* \left[ 1 + \frac{r^2}{2s_*^2} - \frac{rl \cos \Delta\phi'}{s_*^2} \right. \\ &\quad \left. + \sum_{n=2}^{\infty} \frac{n!!}{2^n n!} \left( \frac{r^2 - 2rl \cos \Delta\phi'}{s_*^2} \right)^n \right]. \end{aligned} \quad (42)$$

The higher order terms are presented in Eq. (42) for completeness only. The variable  $\Delta\psi'$  is canonical in the sense that it allows us to represent the phase function in the form of a simplest polynomial in  $r \cos \Delta\psi'$  which for small  $r$  has the same global behavior as  $s'_l$ . It is easy to check that as a consequence  $d\Delta\phi'/d\Delta\psi'|_{r=0} = 1$  and as  $\phi'$  varies from 0 to  $2\pi$ ,  $\psi'$  also changes by  $2\pi$ . We now consider the amplitude of the integrand in Eq. (33) and expand its pre-exponential factor in the vicinity of  $r=0$ . In the leading order approximation we obtain

$$\begin{aligned} \frac{d\Delta\phi'}{d\Delta\psi'} \frac{A^P(\theta'_l, \Delta\phi')}{l - r \cos \Delta\phi'} e^{ik(s_* + r^2/2s_*)} \\ \approx \frac{1}{l} A^P(\theta_*) \{ \sin \theta_* [\cos \Delta\phi' \mathbf{e}_r + \sin \Delta\phi' \mathbf{e}_\phi] \\ + \cos \theta_* \mathbf{e}_z \} e^{iks_*}, \quad \frac{r}{l} \ll 1. \end{aligned} \quad (43)$$

Finally using Eq. (32) and the integral representation of the Bessel functions

$$i^n \pi J_n(v) = \int_0^\pi e^{iv \cos x} \cos nx \, dx, \quad (44)$$

(Gradstein and Ryzhik, 1965, Eq. [3.915(2)]) near the axis, we have

$$\begin{aligned} \mathbf{u}_2^P(\mathbf{R}) &\sim \mathbf{u}^{P(\text{axial})}(\mathbf{R}) \\ &\approx \frac{QA^P(\theta_*)}{\pi Q b^2 k l^2} e^{i(k s_* + \pi/2)} \\ &\quad \times [\cos \theta_* J_0(kr \sin \theta_*) \mathbf{e}_z + i \sin \theta_* J_1(kr \sin \theta_*) \mathbf{e}_r], \\ &\quad kr \sin \theta_* \leq \frac{\pi}{2}, \end{aligned} \quad (45)$$

where the directivity function  $A^P(\theta_*)$  is defined by Eqs. (19) and (40) [cf. Fradkin and Kiselev, 1997, Eqs. (126)–(128)]. Only the first two terms of the *axial asymptotic series*  $\mathbf{u}^{P(\text{axial})}$  are presented in Eq. (45). Note that on the axis the second component is zero, and for larger  $z$ , that is smaller  $\sin \theta_*$ , the pre-exponential factor of  $\mathbf{u}_2^P(\mathbf{R})$  is approximately the same as of  $-\mathbf{u}_0^{P(\text{direct})}$ . Evaluating asymptotics of Eq. (45) when  $kr \sin \theta_* \rightarrow \infty$  we obtain the behavior which is consistent with the expected physical picture: At any point on any side of the axis which is a focal line two rays intersect, one approaching the line and the other moving away from it. The outgoing wave has the  $-\pi/2$  phase shift. Both waves have the same form as the toroidal edge waves described by Eq. (38) [see, e.g., Kiselev, 1980; Fradkin and Kiselev, 1997, Eq. (123)].



The phase of Eq. (45) indicates that it is an edge wave as well, but its amplitude is different to any toroidal edge wave, since each point in the axial region is influenced by *all* (and not just two) points of the edge more or less equally. It is obviously not a GE solution. The fact that the behavior of edge waves changes in the axial region has been known before, and led to some controversy: Some authors (e.g., Schmerr and Sedov, 1989; Baboux and Kažys, 1992) question the relevance of the concept.

#### 4. Contribution of a phase stationary point coalescing with the boundary of the integration domain: Penumbra

The boundary layer surrounding the boundary surface separating the main beam zone from the geometrical shadow zone is known as the marginal zone or penumbra. In our case this boundary is a cylindrical surface underneath the transducer rim. As we have mentioned above, inside the penumbra the asymptotics of the edge wave  $u_{-}^{P(\text{edge})}$  [see Eq. (38)] which arrives from the nearest edge point break down, since all the corresponding phase stationary points lie close to the boundary of the integration domain. In other words, it is easy to see that inside the penumbra the phase difference between the direct and shortest edge ray is

$$k(s_{-} - z) \approx k(r - l)^2 / 2z. \quad (46)$$

Thus it is reasonable to define this region as

$$\frac{k(r - l)^2}{2z} \leq \pi, \quad (47)$$

so that inside this difference is less than  $\pi$  and the exponential factor in Eq. (23) ceases to be rapidly oscillating. Condition (47) implies that the shape of the penumbra is parabolic.

In order to produce asymptotics which are valid in this case as well, we return to Eq. (23) and apply the stationary phase formulas [Wong, 1989, Chap. II, Eqs. (3.2) and (3.22)] to the  $\phi'$  integral. Then off the transducer axis the stationary points are Eq. (36) and it follows that in the leading order approximation we have

$$\mathbf{u}_{\pm}^P(\mathbf{R}) \sim \mathbf{u}_{+}^P(\mathbf{R}) + \mathbf{u}_{-}^P(\mathbf{R}), \quad kr \sin \theta_{*} > \frac{\pi}{2}, \quad (48)$$

with

$$\begin{aligned} \mathbf{u}_{\pm}^P(\mathbf{R}) \equiv & -\frac{Q}{(2\pi^3)^{1/2} l^2 \varrho b^2} \int_0^l \psi_2(r') \mathbf{A}^P(\theta'_{\pm}, \Delta\phi') \\ & \times \left( \frac{r'}{krs'_{\pm}} \right)^{1/2} e^{i(k s'_{\pm} \mp \pi/4)} dr' \end{aligned} \quad (49)$$

and

$$\begin{aligned} s'_{\pm} &= \sqrt{z^2 + (r \pm r')^2}, \\ \sin \theta'_{\pm} &= \frac{r \pm r'}{s'_{\pm}}. \end{aligned} \quad (50)$$

On integrating by parts the leading term in the ray-asymptotic series for  $\mathbf{u}_{+,0}^P(\mathbf{R})$  is the same as given in Eq. (38). On the other hand, when the observation point is un-

derneath or almost underneath the transducer rim we return to Eq. (49) and rewrite it as

$$\begin{aligned} \mathbf{u}_{-}^P(\mathbf{R}) = & -\frac{Q}{(2\pi^3)^{1/2} l^2 \varrho b^2} \int_{-\infty}^l \psi_2(r') \mathbf{A}^P(\theta'_{-}, 0) \\ & \times \left( \frac{r'}{krs'_{-}} \right)^{1/2} e^{i(ks'_{-} + \pi/4)} dr', \end{aligned} \quad (51)$$

where an analytical continuation of the integrand has been performed for  $r' < 0$ . Following the modern approach (Bleistein and Handelsman, 1986; Fedoryuk, 1977; Borovikov, 1994), we introduce a new variable  $\xi'$ , such that the phase function in Eq. (51) may be written as

$$\begin{aligned} s'_{-} &= z \left[ 1 + \frac{\xi'^2}{2z^2} \right], \\ &= z \left[ 1 + \frac{(r' - r)^2}{2z^2} + \sum_{n=2}^{\infty} \frac{n!}{2^n n!} \left( \frac{r' - r}{z} \right)^{2n} \right]. \end{aligned} \quad (52)$$

As above the higher order terms are presented for completeness only. It follows that

$$\xi' = \pm [2z(s'_{-} - z)]^{1/2} \quad (53)$$

is a canonical variable: It allows us to represent the phase function as a simplest polynomial in  $\xi'$  which for small  $r' - r$  has the same global behavior as  $s'_{-}$ . Here and everywhere below in this section the top sign corresponds to the main beam zone ( $r < l$ ) and the bottom to the geometrical shadow zone ( $r > l$ ). By evaluating  $d\xi'/dr'$  and using L'Hôpital's rule it is easy to check that as a consequence  $dr'/d\xi'|_{r'=r} = 1$ . Also, as  $r'$  varies from  $-\infty$  to  $l$ ,  $\xi'$  varies from  $-\infty$  to  $\pm \{2z[\sqrt{z^2 + (l - r)^2} - z]\}^{1/2}$ . We now consider the amplitude of the integrand in Eq. (51) and expand the factor in front of  $\exp i\xi'^2/2z$  in the vicinity of  $r' = r$ . In the leading order approximation we obtain

$$\begin{aligned} \frac{dr'}{d\xi'} \mathbf{A}^P(\theta'_{-}, 0) \left( \frac{r'}{krs'_{-}} \right)^{1/2} e^{i(kz + \pi/4)} \\ = -\gamma^2 \left( \frac{1}{kz} \right)^{1/2} e^{i(kz + \pi/4)} \mathbf{e}_z, \quad \frac{|r' - r|}{z} \ll 1. \end{aligned} \quad (54)$$

Finally using the definition of the Fresnel integral,

$$F(x) = \left( \frac{1}{i\pi} \right)^{1/2} \int_{-\infty}^x e^{is^2} ds \quad (55)$$

(Borovikov and Kinber, 1994), we have

$$\begin{aligned} \mathbf{u}_{-}^P(\mathbf{R}) &\sim \mathbf{u}^{P(\text{penumbra})}(\mathbf{R}) \\ &\approx \frac{Q}{\pi \varrho a^2 k l^2} e^{i(kz + \pi/2)} F[\pm \sqrt{k(s_{-} - z)}] \mathbf{e}_z \\ &\approx F(\pm \sqrt{k/2z} |l - r|) \mathbf{u}_0^{P(\text{direct})}, \\ &kr \sin \theta_{*} > \frac{\pi}{2}. \end{aligned} \quad (56)$$

Only the leading term in the *penumbral asymptotic series*  $\mathbf{u}^{P(\text{penumbra})}$  is presented in Eq. (56) and the argument of the

Fresnel function in the last expression has been approximated to the leading order in  $|l-r|/z$  [Borovikov, 1994, Sec. 2.1; Wong, 1989, p. 411; Fradkin and Kiselev, 1997, Eq. (70)]. Evaluating asymptotics of (56) when  $\sqrt{k/2z}|l-r| \rightarrow \infty$  we obtain the behavior which is entirely consistent with the expected physical picture: the plane and the toroidal edge wave in the main beam zone and just a toroidal edge wave in the geometrical shadow zone [see Fradkin and Kiselev, 1997, Eq. (82)]. Note that if instead of Eq. (54) we use the first *two* terms of the Taylor series [the first order contributions are obtained by using approximations  $(r'/r)^{1/2} = 1 + \xi'/2r$  and  $\sin \theta_- = \xi'/z$ ] we obtain another term in the  $z$  component,

$$\frac{Q}{(2\pi)^{3/2} \rho a^2 k l^2} \left( \frac{z}{kr^2} \right)^{1/2} e^{i[k(l-r)^2/2z - \pi/4]} \mathbf{e}_z, \quad (57)$$

and the radial component,

$$\pm \frac{Q}{(2\pi^3)^{1/2} \rho a^2 k l^2} \left( \frac{1}{kz} \right)^{1/2} e^{i[k(z+3\pi/4)]} \mathbf{e}_r \quad (58)$$

as well. The latter is the same as the radial component of  $\mathbf{u}_-^{P(\text{edge})}$  in Eq. (38) *directly underneath the rim*. Since the direct wave has no  $r$  component this is to be expected to hold everywhere: In this direction there is no interference between the direct and edge wave [cf. Fradkin and Kiselev, 1997, Eqs. (72)–(74); Gridin and Fradkin, 1998]. However, when we move from exactly underneath the rim into the penumbra the second term in the Taylor series leads to the expression for the radial component which is a bit different to the edge wave. Similarly, outside the penumbra this term produces the  $z$  component which does not exactly coincide with the  $z$  component of the edge wave. The situation may be remedied by introducing a two-point expansion rather than Taylor, as is done to produce the so-called *uniform* asymptotics which are valid both inside and outside the boundary layer (Bleistein and Handelsman, 1986; Borovikov, 1994; see also Gridin and Fradkin, 1998).

Expression (56) is not a GE solution, but since underneath the transducer rim the fronts of the plane and edge waves are tangential to each other and thus, interference effects are present, no GE solution can be expected to be found.

## B. S wave field

The  $S$  wave field is described by

$$\mathbf{u}^S(\mathbf{R}) \approx - \frac{Q\kappa}{2\pi^2 l^2 \rho b^2} \int_0^l \int_0^{2\pi} \sum_{i=1}^3 \psi_i \frac{\mathbf{A}^S(\theta', 0)}{\kappa S'} \times e^{i\kappa S' r'} dr' d\phi', \quad (59)$$

where we have used Eq. (17). Applying the stationary point approximation for double integrals the first term in the direct ray-asymptotic series  $\mathbf{u}^{S(\text{direct})}$  is

$$\mathbf{u}_0^{S(\text{direct})} = \mathbf{0}. \quad (60)$$

As with the direct  $P$  wave, it is easy to show (and it is obvious from the GE considerations) that for the transducer of infinite radius which exerts the same uniform pressure

$Q/\pi l^2$  as our transducer the above solution is exact.

Since there is no direct wave and thus underneath the transducer rim there is no interference between the direct and edge wave the penumbral terms are zero as well. By the same token only the point sources situated on the rim give rise to the head waves. These and the vicinity of the corresponding critical rays are discussed in an accompanying paper (Gridin, 1998) and another publication (Gridin and Fradkin, 1998). The expressions for the  $S$  edge wave both off the transducer axis and inside the axial region can be obtained from Eqs. (38) and (45) by simple substitution of  $\mathbf{A}^S$  for  $\mathbf{A}^P$  and  $\kappa$  for  $k$ . They are

$$\begin{aligned} \mathbf{u}_\pm^S(\mathbf{R}) &\sim \mathbf{u}_\pm^{S(\text{edge})}(\mathbf{R}) \\ &\approx - \frac{Q}{(2\pi^3)^{1/2} \rho b^2 \kappa l^2} \mathbf{A}^S \left( \theta_\pm, \frac{\pi}{2} \pm \frac{\pi}{2} \right) \\ &\quad \times \left( \frac{l}{r} \right)^{1/2} \left( \frac{1}{\kappa S_\pm} \right)^{1/2} \frac{1}{\sin \theta_\pm} e^{i[\kappa S_\pm + (2\mp 1)\pi/4]} \\ &= - \frac{Q}{(2\pi^3)^{1/2} \rho b^2 \kappa l^2} \frac{2\sqrt{\gamma^2 - \sin^2 \theta_\pm}}{R^S(\sin \theta_\pm)} \\ &\quad \times \left( \frac{l}{r} \right)^{1/2} \left( \frac{1}{\kappa S_\pm} \right)^{1/2} \cos \theta_\pm e^{i[\kappa S_\pm + (2\mp 1)\pi/4]} \\ &\quad \times (-\sin \theta_\pm \mathbf{e}_z \mp \cos \theta_\pm \mathbf{e}_r), \quad \kappa r \sin \theta_* > \frac{\pi}{2}, \quad (61) \end{aligned}$$

and

$$\begin{aligned} \mathbf{u}_2^S(\mathbf{R}) &\sim \mathbf{u}^{S(\text{axial})}(\mathbf{R}) \approx \frac{A^S(\theta_*)}{\pi \rho b^2 \kappa l^2} e^{i(\kappa S_\pm + \pi/2)} \\ &\quad \times [-\sin \theta_* J_0(\kappa r \sin \theta_*) \mathbf{e}_z \\ &\quad + i \cos \theta_* J_1(\kappa r \sin \theta_*) \mathbf{e}_r], \\ &\quad \kappa r \sin \theta_* \leq \frac{\pi}{2}. \quad (62) \end{aligned}$$

Above,  $R^S$  is defined by Eqs. (20) and (15), the directivity function by Eqs. (18) and (40), and only the leading terms of the edge ray-asymptotic series  $\mathbf{u}_\pm^{S(\text{edge})}$  and axial asymptotic series  $\mathbf{u}^{S(\text{axial})}$  are given. The resulting wave fronts, relative polarizations and boundary layers are presented in Fig. 5. The field has a structure similar but not identical to the field scattered by a penny-shaped crack which has been irradiated by a normal plane compressional wave (Achenbach *et al.*, 1982). In particular, the edge waves exhibit a much simpler parameter dependence.

## IV. CONCLUSIONS

By using two-tier asymptotics (the first tier giving the far-field asymptotics of a point source and the second the radiating near-field asymptotics of a large transducer) we have analyzed the radiating near zone of a high-frequency time-harmonic circular normal transducer directly coupled to a perfectly elastic homogeneous and isotropic solid. We have obtained simple analytical formulas describing both its  $P$  and  $S$  wavefield: Similarly to previous authors we have identified

the plain  $P$  waves and toroidal  $P$  and  $S$  edge waves, but as a result of physical interpretation of these formulas and not after an extensive image analysis (cf. Baboux and Kažys, 1992). Our approach has allowed us to describe the boundary layers too, namely the axial and penumbral zones where diffraction effects prevail. In particular, we have sorted out the controversy surrounding the edge waves: These exhibit one type of parametric dependence outside the axial and penumbral zones and another inside (cf. Schmerr and Sedov, 1989; Baboux and Kažys, 1992). The head waves and the regions surrounding the corresponding critical ray are described in the accompanying paper (Gridin, 1998). Using high-frequency asymptotics and the harmonic synthesis principle it is possible to produce fast computer codes for modelling propagation of pulses employed in NDE, provided of course, that the low frequencies propagate with relatively low amplitudes. One such code and its evaluation are discussed in another publication (Gridin and Fradkin, 1998).

## ACKNOWLEDGMENTS

Part of this work was carried out by the second author at the South Bank University, London as an U.K. Royal Society Ex-Quota Fellow and by the third author as a South Bank Research Scholar. We are grateful to Dr. Ljepojevic for drawing our attention to the monograph by Wong and to D. Gridin for numerous useful discussions.

## APPENDIX: CALCULATION OF THE FAR FIELD OF A POINT SOURCE

**Step 1:** Consider a point source acting normally to a half-plane  $(x, z)$ . Introduce the scalar and vector potentials  $\Phi$  and  $\Psi = \Psi \mathbf{e}_y$ , which give

$$\mathbf{u}^P(\mathbf{R}) = \nabla \Phi(\mathbf{R}), \quad \mathbf{u}^P(\mathbf{R}) = \nabla \times \Psi(\mathbf{R}). \quad (\text{A1})$$

It is well known that both  $\Phi$  and  $\Psi$  satisfy the Helmholtz equation, so that we have

$$(\nabla^2 + k^2)\Phi = 0, \quad (\nabla^2 + \kappa^2)\Psi = 0. \quad (\text{A2})$$

Let a point load be applied normal to the free surface  $z = 0$ , so that we can work in the local coordinates, with the  $z$  axis running through this point. Then the boundary conditions are

$$\begin{aligned} \sigma_{zx}|_{z=0} &= \varrho b^2 \left( 2 \frac{\partial^2 \Phi}{\partial x \partial z} + \frac{\partial^2 \Psi}{\partial x^2} - \frac{\partial^2 \Psi}{\partial z^2} \right) \Bigg|_{z=0} = 0, \\ \sigma_{zz}|_{z=0} &= \varrho \left[ a^2 \left( \frac{\partial^2 \Phi}{\partial x^2} + \frac{\partial^2 \Phi}{\partial z^2} \right) \right. \\ &\quad \left. + 2b^2 \left( -\frac{\partial^2 \Phi}{\partial x^2} + \frac{\partial^2 \Psi}{\partial x \partial z} \right) \right] \Bigg|_{z=0} \\ &= -Q \delta(x). \end{aligned} \quad (\text{A3})$$

**Step 2:** Seek the Fourier modes, that is the elementary solutions of the above boundary problem in the form

$$\Phi = B^P e^{iks(\eta \cos \theta + \xi \sin \theta)}, \quad \Psi = B^S e^{iks(\eta' \cos \theta + \xi \sin \theta)}. \quad (\text{A4})$$

Similarly to Fung (1965, Sec. 8.15) it follows that we have

$$\eta = \sqrt{1 - \xi^2}, \quad \eta' = \sqrt{\gamma^{-2} - \xi^2},$$

$$B^P = -\frac{Q}{\varrho b^2 k^2} \frac{2\xi^2 - \gamma^{-2}}{R^P(\xi)}, \quad B^S = -\frac{Q}{\varrho b^2 k^2} \frac{2\xi \sqrt{1 - \xi^2}}{R^P(\xi)}. \quad (\text{A5})$$

**Step 3:** Obtain the respective formal solutions of the 2-D problem by applying the inverse Fourier transform in  $k\xi$  to  $B^P$  and  $B^S$ .

**Step 4:** Seek the high-frequency asymptotic approximation to this formal solution by applying the stationary point formulas [Wong, 1989, Chap. II, Eqs. (3.2) and (3.22)]. Note that in the inverse Fourier transform of  $B^P$  the phase stationary point is  $\xi = \sin \theta \leq 1$ , and in the inverse Fourier transform of  $B^S$  it is  $\xi = \gamma^{-2} \sin \theta \leq 1$ ,

**Step 5:** Substitute this solution into (A1) to obtain the 2-D versions of the 3-D Green's functions (11) and (20), with the  $1/2\pi s$  factor replaced by  $\sqrt{1/2\pi iks}$  and  $\sqrt{1/2\pi i\kappa s}$ , respectively.

**Step 6:** The 3-D solution (11) may be obtained in a similar manner using Hankel's transforms. Note that the 3-D Green functions differ from the 2-D ones by the conversion factors  $\sqrt{ik/2\pi s}$  and  $\sqrt{i\kappa/2\pi s}$ , respectively. These are to be expected when changing from 1-D to 2-D stationary phase method.

- Achenbach, J. D. (1973). *Wave Propagation in Elastic Solids* (North-Holland, New York).
- Achenbach, J. D., Gautesen, A. K., and McMaken, H. (1982). *Ray Methods for Waves in Elastic Solids, With Applications to Scattering by Cracks* (Pitman, Boston).
- Babič, V. M., and Buldyrev, V. S. (1991). *Short-Wavelength Diffraction Theory: Asymptotic Methods* (Springer-Verlag, Berlin).
- Babič, V. M., and Kirpičnikova, N. Ya. (1975). *The Boundary-Layer Method in Diffraction Problems* (Springer-Verlag, Berlin).
- Babich, V. M., and Kiselev, A. P. (1989). "Non-geometrical waves—are there any? An asymptotic description of some "non-geometrical" phenomena in seismic wave propagation," *Geophys. J. Int.* **99**, 415–420.
- Baboux, J. C., and Kažys, V. (1992). "Analysis of the transient ultrasonic fields radiated in solids by circular and annular sources," *J. Acoust. Soc. Am.* **92**, 2942–2951.
- Borovikov, V. A. (1994). *Uniform Stationary Phase Method* (IEE Electromagnetic Series, Stevenage), Vol. 40.
- Bleistein, N., and Handelsman, R. A. (1986). *Asymptotic Expansions of Integrals* (Dover, New-York).
- Borovikov, V. A., and Kinber, B. Ye. (1994). *Geometric Theory of Diffraction* (IEE Electromagnetic Series, Stevenage), Vol. 37.
- Brekhovskikh, L. M. (1960). *Waves in Layered Media* (Academic, New York).
- Bresse, L. F., and Hutchins, D. A. (1989). "Transient generation of elastic waves in solids by a disk-shaped normal force source," *J. Acoust. Soc. Am.* **86**, 810–817.
- Buchal, R. N., and Keller, J. B. (1960). "Boundary Layer Problems in Diffraction Theory," *Commun. Pure Appl. Math.* **13**(1), 85–114.
- Djelouah, H., and Baboux, J. C. (1992). "Transient ultrasonic field radiated by a circular transducer in a solid medium," *J. Acoust. Soc. Am.* **92**, 2932–2941.
- Fedoryuk, M. (1977). *Metod Perevala* (The Saddle Point Method) (Nauka, Moscow).
- Fradkin, L. Ju., and Kiselev, A. P. (1997). "The two-component representation of time-harmonic elastic body waves in the high and intermediate frequency regime," *J. Acoust. Soc. Am.* **101**, 52–65.
- Fung, Y. C. (1965). *Foundations of Solid Mechanics* (Prentice-Hall, Englewood Cliffs, NJ).
- Gradstein, I. S., and Ryzhik, I. M. (1965). *Table of Integrals, Series and Products* (Academic, New York).

- Gridin, D. (1998). "High-frequency asymptotic description of head waves and boundary layers surrounding the critical rays in an elastic half-space," *J. Acoust. Soc. Am.* **104**, 1188–1197.
- Gridin, D., and Fradkin, L. J. (1998). "High-frequency asymptotic description of pulses radiated by a circular normal transducer into elastic half-space," *J. Acoust. Soc. Am.* (submitted).
- Halmshaw, R. (1994). *Non-Destructive Testing* (Arnold, London).
- Hudson, J. A. (1980). *The Excitation and Propagation of Elastic Waves* (Cambridge U.P., Cambridge).
- Kawashima, K. (1984). "Quantitative calculations and measurements of longitudinal and transversal ultrasonic wave pulses in solids," *IEEE Trans. Sonics Ultrason.* **SU-31**, 83–94.
- Keller, J. B. (1958). "Geometrical theory of diffraction," *Proc. Symp. Appl. Math.* **8**, 27–52.
- Kiselev, A. P. (1980). "Focal Boundary Layer in Axisymmetric Diffraction Problems," *Izv. VUZ Radiofiz.* **13**, 333–352 [English transl.: (1980). *Radiophys. Quantum Electron.* **23**, 241–252].
- Lhémy, A. (1994). "A model for the transient ultrasonic field radiated by an arbitrary loading in a solid," *J. Acoust. Soc. Am.* **96**, 3776–3786.
- Miller, G. F., and Pursey, H. (1954). "The field and radiation impedance of mechanical radiators on the free surface of a semi-infinite isotropic solid," *Proc. R. Soc. London, Ser. A* **223**, 521–541.
- Schmer, L. W., and Sedov, A. (1989). "An elastodynamic model of compressive and shear wave transducers," *J. Acoust. Soc. Am.* **86**, 1988–1999.
- Silk, M. G. (1984). *Ultrasonic Transducers for Nondestructive Testing* (Hilger, Bristol).
- Stacey, R., and Weight, J. P. (1993). "Ultrasonic echo responses from targets in solid media using finite difference methods," *IEE Proc., Part A: Phys. Sci., Meas. Instrum., Manage. Educ.* **140**, 303.
- Weight, J. P. (1987). "A model for the propagation of short pulses of ultrasound in a solid," *J. Acoust. Soc. Am.* **81**, 815–825.
- Wong, R. (1989). *Asymptotic Approximations of Integrals* (Academic, New York).

# High-frequency asymptotic description of head waves and boundary layers surrounding the critical rays in an elastic half-space

Dmitri Gridin

School of Electrical, Electronic and Information Engineering, South Bank University, 103 Borough Road, London SE1 0AA, United Kingdom

(Received 26 May 1997; revised 20 March 1998; accepted 15 April 1998)

The high-frequency asymptotic description of head waves as well as the field inside boundary layers surrounding the critical rays are obtained for two cases: (a) a point source, and (b) a circular transducer, both acting normally on an isotropic and homogeneous elastic half-space. The edge head waves underneath a circular transducer are described by the asymptotics of a higher order compared to those of direct compressional, edge compressional, and shear waves, but are still discernible in the radiating near zone and thus might be useful in nondestructive evaluation of industrial materials. The asymptotic formulas produced involve in geometrical zones elementary functions and inside boundary layers well-known special functions. Therefore, they allow us to elucidate the physics of the problem and can be used in writing computer codes which simulate the radiating near field of a circular transducer orders of magnitude faster than full numerical schemes. The formulas have been tested against exact integral solutions evaluated numerically. © 1998 Acoustical Society of America. [S0001-4966(98)00209-4]

PACS numbers: 43.20.Bi, 43.20.Dk, 43.35.Zc [JEG]

## INTRODUCTION

The head wave is a phenomenon well-known in seismology (e.g., Brekhovskikh, 1960; Červény and Ravindra, 1971; Aki and Richardson, 1982) and in nondestructive evaluation (NDE) of industrial materials (e.g., Miller and Pursey, 1954; Ilan and Weight, 1990; Djelouah and Baboux, 1992). The existence of the head wave is due to the presence of a boundary between two media and can be explained using the generalized Huygens principle (e.g., Fung, 1965; Fradkin and Kiselev, 1997). It is well understood that the head wave may be evaluated as a contribution of branch point to the expressions for displacements which are obtained by an integral (Fourier or Hankel) transform (e.g., Miklowitz, 1978; Hudson, 1980), and that it is small compared to the compressional and shear waves (e.g., Miller and Pursey, 1954).

It has been established using full numerical schemes for solving elastodynamic equations (e.g., Djelouah and Baboux, 1992) that inside certain zones underneath a circular transducer acting normally to an isotropic and homogeneous half-space the head waves give rise to small but discernible pulses. For this reason head waves have been studied experimentally and simulated using full numerical schemes by authors interested in mathematical modeling of NDE (e.g., Ilan and Weight, 1990; Djelouah and Baboux, 1992; Baboux and Kažys, 1992). However, the full numerical schemes are extremely time consuming and do not give the explicit dependence of the field upon the problem parameters. Therefore, high-frequency asymptotics of body waves generated by a point source and a circular transducer are of interest.

It is well known that a point source (or a pointlike transducer) radiates a spherical compressional, spherical shear and conical head wave (e.g., Miklowitz, 1978, Chap. VI, and Fig. 1 below). The field radiated by a large circular normal

transducer is more complex and consists of the direct compressional, edge compressional, shear and head waves (e.g., Ilan and Weight, 1990; and Fig. 4 below). The representation of the total field as a sum of these waves is valid when the ray method is applicable and fails inside the boundary layers, such as an axial region, penumbra, and vicinity of the critical rays. The field inside the layers can be obtained using the high-frequency asymptotic theory of diffraction (e.g., Babič and Kirpichnikova, 1975; Babič and Buldyrev, 1991; Borovikov and Kinber, 1994; Borovikov, 1994). The asymptotics which are applicable in the radiating near zone of a time-harmonic circular normal transducer and give complete description of the direct compressional, edge compressional, and shear waves as well as the field inside the axial and penumbral region have been derived previously by Fradkin *et al.* (1998). The present paper is devoted to the high-frequency asymptotic description of the head waves and the boundary layers surrounding the critical rays for both a point source and a large circular transducer acting normally on a surface of an elastic half-space.

The asymptotics of the head wave are obtained as the branch point contribution to the integral expressions for displacement which have been derived using Hankel's transform. The expressions are elementary but fail inside the boundary layers surrounding the critical rays. The uniform asymptotics, that is, asymptotics which are valid both inside and outside the layers, are obtained using the uniform stationary phase method (Bleistein and Handelsman, 1986; Borovikov, 1994). These involve the well-known special functions (Bessel's and parabolic cylinder). A fast code for simulating pulse propagation based on these asymptotics is discussed in another publication (Gridin and Fradkin, 1998).

This paper is organized as follows: First, the high-frequency asymptotics of the head wave and the total field

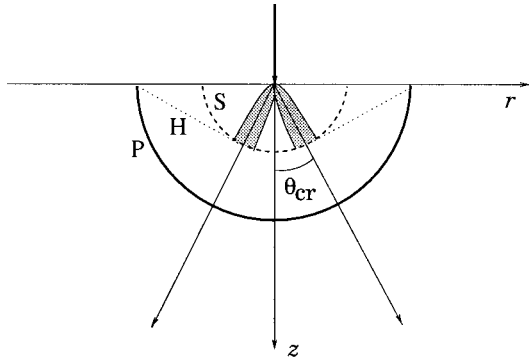


FIG. 1. Normal point source on a half-space. Solid line—front of the  $P$  wave; dashed line—front of the  $S$  wave; dotted line—front of the head wave; arrowed segments—critical rays; shaded areas—the boundary layers surrounding the critical rays.

inside the boundary layers surrounding the critical rays are derived and discussed for a normal point source (Lamb's problem). Then, similar asymptotics are obtained for a large circular normal transducer. At the end of the paper numerical results obtained by both asymptotic and exact methods are compared and discussed.

## I. THE TIME-HARMONIC NORMAL POINT LOAD

### A. The integral solution

We consider the forced time-harmonic motion of an elastic homogeneous and isotropic half-space caused by a normal point load. The displacement field  $\mathbf{u}$  inside the medium is described by the reduced elastodynamic equation

$$b^2 \nabla \times (\nabla \times \mathbf{u}) - a^2 \nabla (\nabla \cdot \mathbf{u}) - \omega^2 \mathbf{u} = \mathbf{0}, \quad (1)$$

where  $a$  is a speed of  $P$  wave and  $b$ , of  $S$  wave,  $a > b$ , and  $\omega$  is a circular frequency. The  $P$  wave is also known as compressional, longitudinal, or primary, and the  $S$  wave as shear, transverse, or secondary (Achenbach, 1973, pp. 123–124). The wave vectors of  $P$  and  $S$  waves are  $k = \omega/a$  and  $\kappa = \omega/b$ , respectively. We use the cylindrical coordinates  $(r, \varphi, z)$ , where the  $z$  axis is directed into the solid (see Fig. 1). The boundary conditions due to a normal point load are:

$$\sigma_{zr}|_{z=0} = 0, \quad (2)$$

$$\sigma_{zz}|_{z=0} = -Q \frac{\delta(r)}{2\pi r}$$

[cf. Achenbach, 1973, Eq. (7.209)], where  $\delta(r)$  is the Dirac delta function, and the components of the stress tensor are as follows:

$$\sigma_{zr} = \varrho b^2 \left( \frac{\partial u_r}{\partial z} + \frac{\partial u_z}{\partial r} \right), \quad (3)$$

$$\sigma_{zz} = \varrho a^2 \frac{\partial u_z}{\partial z} + \varrho \frac{a^2 - 2b^2}{r} \frac{\partial (ru_r)}{\partial r},$$

with  $u_r$  and  $u_z$ , the  $r$  and  $z$  components of the displacements, respectively, and  $\varrho$ , the density of the solid.

Using the Hankel transform technique and assuming the radiation condition the integral representation of the displacements is

$$u_r = \frac{Q}{2\pi\varrho b^2} \times \int_0^\infty [(2\xi^2 - \kappa^2)e^{-\alpha z} - 2\alpha\beta e^{-\beta z}] \frac{\xi}{R} J_1(\xi r) \xi d\xi, \quad (4)$$

$$u_z = \frac{Q}{2\pi\varrho b^2} \times \int_0^\infty [(2\xi^2 - \kappa^2)e^{-\alpha z} - 2\xi^2 e^{-\beta z}] \frac{\alpha}{R} J_0(\xi r) \xi d\xi,$$

where

$$\alpha = (\xi^2 - k^2)^{1/2}, \quad \beta = (\xi^2 - \kappa^2)^{1/2}, \quad (5)$$

and Rayleigh's function  $R$  is given by

$$R = (2\xi^2 - \kappa^2)^2 - 4\alpha\beta\xi^2 \quad (6)$$

[cf. Achenbach, 1973, Eqs. (7.233) and (7.234)].

### B. The far-field asymptotics

Since we are interested in the head wave phenomena we consider only the  $\exp(-\beta z)$  terms in Eq. (4): Only they are responsible for the body waves propagating with speed  $b$ , i.e., for the *total S* field which consists of the  $S$  and head waves. We start by introducing a new variable  $\eta$ , such that we have

$$\xi = \kappa \eta, \quad (7)$$

and consider the integral

$$u_z^b = -\frac{Q\kappa}{\pi\varrho b^2} \int_0^\infty \frac{\eta^3 \sqrt{\eta^2 - \gamma^2}}{R} J_0(\kappa r \eta) e^{-\kappa z \sqrt{\eta^2 - 1}} d\eta, \quad (8)$$

where

$$R(\eta) = (2\eta^2 - 1)^2 - 4\eta^2 \sqrt{\eta^2 - 1} \sqrt{\eta^2 - \gamma^2}, \quad (9)$$

and  $\gamma = k/\kappa$ .

We will derive the far-field (or high-frequency) asymptotics of Eq. (8), that is we assume that

$$\kappa z \gg 1. \quad (10)$$

Since there is no head wave near the  $z$  axis (see Fig. 1), we also assume that  $\kappa r \gg 1$ . Under these two assumptions the integrand in Eq. (8) contains a rapidly oscillating factor with mean zero. It is well known that the main contributions to the integrals of this type come from stationary points of the phase functions, limits of integration, and singular points of the amplitude functions (Wong, 1989; Fedoryuk, 1977; Borovikov, 1994). Following the traditional approach, we separate these contributions by introducing the so-called *neutralizers* (see, e.g., Erdélyi, 1956, p. 53) which cut out small neighborhoods of the critical points.

It is easy to show that the contribution of the lower limit of integration  $\eta = 0$  is asymptotically small. Therefore, we can use the large argument asymptotics of the zeroth order Bessel function,



FIG. 2. The contour of integration.

$$J_0(\kappa r \eta) \approx \frac{1}{\sqrt{2\pi\kappa r \eta}} (e^{i(\kappa r \eta - \pi/4)} + e^{-i(\kappa r \eta - \pi/4)}), \quad \kappa r \eta \gg 1 \quad (11)$$

[Abramowitz and Stegun, 1965, Eq. (9.2.1)] to represent Eq. (8) as the sum of two terms,  $u_{z,+}^b$  and  $u_{z,-}^b$ , given by

$$u_{z,\pm}^b \approx -\frac{Q\kappa}{2\pi^2 Q b^2} \sqrt{\frac{2\pi}{\kappa r}} e^{\pm i\pi/4} \times \int_0^\infty \frac{\eta^{5/2} \sqrt{\eta^2 - \gamma^2}}{R} e^{-\kappa(z\sqrt{\eta^2 - 1} \pm i\eta r)} d\eta. \quad (12)$$

The contour of integration as well as the critical points of the amplitude function in Eq. (12) are depicted in Fig. 2. There are two branch points,  $\eta = \gamma$  and  $\eta = 1$ , and the Rayleigh pole  $\eta_R$  which is a real root of the equation

$$R(\eta) = 0. \quad (13)$$

The two phase functions have one stationary point each. These lie within intervals  $(-1,0)$  and  $(0,1)$  for  $u_{z,-}^b$  and  $u_{z,+}^b$ , respectively. It may be shown that for  $\kappa z \gg 1$  the contribution of the branch point  $\eta = 1$  is asymptotically small. On the interval  $(1,\infty)$  both the integrands have only one critical point, the Rayleigh pole which gives rise to the Rayleigh surface wave. We do not consider it in this paper and instead of Eq. (12) we evaluate

$$u_{z,\pm}^b \approx -\frac{Q\kappa}{2\pi^2 Q b^2} \sqrt{\frac{2\pi}{\kappa r}} e^{\pm i\pi/4} \times \int_0^1 \frac{\eta^{5/2} \sqrt{\eta^2 - \gamma^2}}{R} e^{-i\kappa(z\sqrt{1 - \eta^2} \pm \eta r)} d\eta, \quad (14)$$

where the contour of integration passes above the branch points. Both amplitude functions have a branch point  $\eta = \gamma$ , but the phase function in  $u_{z,-}^b$  has a stationary point on the negative half-axis. Since it is to the left of  $\gamma$  the contribution of  $\gamma$  is asymptotically small (Borovikov, 1994, Secs. 1.4 and 2.4), and so is  $u_{z,-}^b$  itself. This means that in order to evaluate the  $z$  components of the total  $S$  field we have to consider only the contributions of phase stationary point  $\eta = \sin \theta$  and branch point  $\eta = \gamma$  to  $u_{z,+}^b$ . Here we have

$$s = (z^2 + r^2)^{1/2}, \quad \sin \theta = r/s. \quad (15)$$

The further mathematical treatment of the integral (14) is given in Appendix A. The first integral in Eq. (4) can be evaluated in a similar manner to obtain the  $r$  component. Let us summarize the resulting far-field asymptotics for a point source.

The stationary point  $\eta = \sin \theta$  [e.g., Wong, 1989, Chap. II, Eqs. (3.1) and (3.2)] gives rise to the  $S$  wave and the leading term of the corresponding asymptotics turns out to be

$$\mathbf{u}^S(\mathbf{s}) = -\frac{Q\kappa}{2\pi Q b^2} A^S(\theta) \mathbf{n}^S \frac{e^{-i\kappa s}}{\kappa s}, \quad (16)$$

where the unit displacement vector is given by

$$\mathbf{n}^S(\theta) = \cos \theta \mathbf{e}_r - \sin \theta \mathbf{e}_z. \quad (17)$$

This is the well-known result obtained by Miller and Pursey [1954, Eq. (117)] for a pointlike transducer (see also Fradkin *et al.*, 1998).

The branch point  $\eta = \gamma$  (Borovikov, 1994, Sec. 1.4) gives rise to the head wave, and the leading term of the corresponding asymptotics turns out to be

$$\mathbf{u}^H(\mathbf{s}) = \frac{Q\kappa}{2\pi Q b^2} \frac{A^H \mathbf{n}^H}{(\kappa r)^{1/2} (\kappa s \sin(\theta - \theta_{cr}))^{3/2}} \times e^{-i(\kappa s \cos(\theta - \theta_{cr}) - \pi/2)} H(\theta - \theta_{cr}), \quad (18)$$

where the limit displacement vector is given by

$$\mathbf{n}^H = \sqrt{1 - \gamma^2} \mathbf{e}_r - \gamma \mathbf{e}_z, \quad (19)$$

and we have

$$A^H = \frac{2\gamma^2(1 - \gamma^2)^{3/4}}{(2\gamma^2 - 1)^2}. \quad (20)$$

The critical angle is the angle between the  $z$  axis and the so-called critical ray (see Fig. 1),

$$\theta_{cr} = \arcsin \gamma. \quad (21)$$

The representation of the total  $S$  field as a sum of the  $S$  and head waves is not valid as  $\theta \rightarrow \theta_{cr}$ , i.e., inside the boundary layers surrounding the critical rays. Mathematically, this corresponds to the case of the stationary point approaching the branch points (Bleistein and Handelsman, 1986, Sec. 9.4; Borovikov, 1994, Sec. 2.4). The asymptotics of the total  $S$  field inside these layers involve the parabolic cylinder functions of the order 1/2 and 3/2,  $D_{1/2}$  and  $D_{3/2}$ , respectively [see Eq. (A23)], and the corresponding leading terms are given by

$$\begin{aligned} \mathbf{u}^b(\mathbf{s}) = & -\frac{Q\kappa}{2\pi Q b^2} \tilde{A}^S(\theta) \mathbf{n}^S \frac{e^{-i\kappa s}}{\kappa s} \\ & - \frac{Q\kappa}{2\pi Q b^2} \frac{1}{(\kappa r)^{1/2}} \frac{1}{(\kappa s)^{3/4}} e^{-i\kappa s[1 + \cos(\theta - \theta_{cr})]/2} \\ & \times \left[ \left( A_1^p D_{1/2}(\tilde{w}) + \frac{B_1^p}{\sqrt{\kappa s}} D_{3/2}(\tilde{w}) \right) \mathbf{e}_r \right. \\ & \left. + \left( A_2^p D_{1/2}(\tilde{w}) + \frac{B_2^p}{\sqrt{\kappa s}} D_{3/2}(\tilde{w}) \right) \mathbf{e}_z \right], \quad (22) \end{aligned}$$

where

$$\begin{aligned} \tilde{w} = & -(1+i)w \\ = & -(1+i) \operatorname{sgn}(\theta - \theta_{cr}) \sqrt{\kappa s(1 - \cos(\theta - \theta_{cr}))}. \quad (23) \end{aligned}$$

The coefficients  $\tilde{A}^S(\theta)$ ,  $A_i^p$ , and  $B_i^p$  are specified in Appendix B. Note that asymptotics (22) are uniform, that is, they are valid both inside and outside the boundary layers surrounding the critical rays. The leading term of the nonuni-

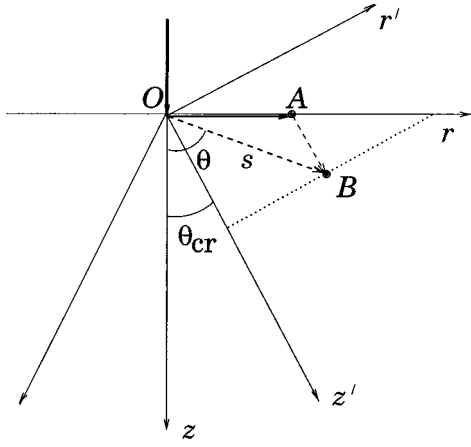


FIG. 3. The propagation of the head wave radiated by a point source. A is a surface point and B is the observation point. Dotted line is the front of the head wave.

form asymptotics (18) can be obtained from the leading term of Eq. (22) as  $w \rightarrow -\infty$  (Bleistein and Handelsman, 1986, Sec. 9.4; Borovikov, 1994, Sec. 2.4).

### C. Discussion

The fronts of the  $S$  and head waves are shown in Fig. 1. According to Eq. (16) the  $S$  wave is a spherical wave with the directivity diagram  $A^S(\theta)$ . Introducing new coordinates  $r'$  and  $z'$  (see Fig. 3), such that we have

$$r' = s \sin(\theta - \theta_{cr}), \quad z' = s \cos(\theta - \theta_{cr}), \quad (24)$$

the leading term of the asymptotics of the head wave can be rewritten as

$$\mathbf{u}^H = \frac{Q\kappa}{2\pi Qb^2} \frac{A^H}{(\kappa r')^{1/2} (\kappa r')^{3/2}} e^{-i(\kappa z' - \pi/2)} H(r') \mathbf{e}_{r'}. \quad (25)$$

Thus the front of the head wave is a frustum of a cone, and the leading term of the displacement is transverse to the critical ray. The head wave exists only for  $r' > 0$ , i.e., for  $\theta > \theta_{cr}$ .

The existence of the head wave can be understood from the generalized Huygens principle (e.g., Fung, 1965; Fradkin and Kiselev, 1997) which states that once reached by the  $P$  wave each point of the boundary (e.g., A in Fig. 3) becomes a secondary source of both  $P$  and  $S$  waves. Since the leading term of the far-field asymptotics of the  $P$  wave vanishes at the surface [e.g., Miller and Pursey, 1954, Eq. (116)] the amplitudes of these secondary waves (and consequently, of the head wave) inside the solid are smaller than those of the  $P$  and  $S$  waves. This explains why the asymptotics (18) and (25) are of a higher order than those for the  $P$  and  $S$  waves.

The ray paths of the  $S$  and head waves are depicted in Fig. 3. The  $S$  wave propagates with speed  $b$  along the straight ray  $OB$  from the source to the observation point. The head wave first propagates as the  $P$  wave along the surface ray  $OA$ , and then with speed  $b$  along the ray  $AB$  parallel to the critical ray. Thus the head wave precedes the  $S$  wave. The phase difference between the two is larger the closer the

observation point to the surface. Note that along the surface the  $P$  wave decays as  $r^{-2}$  (see Hudson, 1980, pp. 184–185; also Fradkin and Kiselev, 1997), while along  $AB$  the head wave experiences decay of the order  $r^{-1/2}$ . If the observation point moves along the front toward the critical ray the corresponding surface path  $OA$  decreases, and therefore, the amplitude of the head wave increases. This can be also seen from Eq. (25).

In the vicinity of the critical ray, i.e., inside the boundary layer surrounding this ray, expressions (18) and (25) tend to infinity. Here the fronts of the  $S$  and head waves are parallel and the waves themselves are indistinguishable. Inside the boundary layer the uniform asymptotics (22) should be used instead, where in the new coordinates the argument of the parabolic cylinder functions takes the form

$$\tilde{w} = -(1+i)w = -(1+i)\text{sgn}(r')\sqrt{\kappa(s-z')}. \quad (26)$$

The size and shape of the boundary layer surrounding the critical rays are determined by the condition that the phase difference between the  $S$  and head waves is  $\pi$ , i.e.,

$$\kappa(s-z') = \pi. \quad (27)$$

Therefore, this shape is parabolic (see Fig. 1). The boundary layer is narrower the higher the frequency.

## II. THE TIME-HARMONIC CIRCULAR NORMAL LOAD

### A. The integral solution

Let us consider the forced time-harmonic motion of an elastic half-space caused by a directly coupled circular normal transducer. The displacements are again described by Eq. (1) and in the idealized case the corresponding boundary conditions are those of the normal pressure uniformly applied over a disk of radius  $l$ . Thus we have

$$\sigma_{zr}|_{z=0} = 0, \quad (28)$$

$$\sigma_{zz}|_{z=0} = -\frac{Q}{\pi l^2} H(l-r),$$

where  $Q$  has dimension of force. The large transducer assumption is expressed as

$$\kappa l \gg 1, \quad (29)$$

that is, the radius of the transducer is assumed to be larger than the wavelength  $\lambda = 2\pi/\kappa$ .

Using the Hankel transform technique and assuming the radiation condition the integral representation of the displacements is

$$\begin{aligned} u_r &= \frac{Q}{\pi Qb^2 l} \int_0^\infty \{(2\xi^2 - \kappa^2)e^{-\alpha z} - 2\alpha\beta e^{-\beta z}\} \\ &\quad \times \frac{\xi}{R} J_1(\xi r) J_1(\xi l) d\xi, \\ u_z &= \frac{Q}{\pi Qb^2 l} \int_0^\infty \{(2\xi^2 - \kappa^2)e^{-\alpha z} - 2\xi^2 e^{-\beta z}\} \frac{\alpha}{R} \\ &\quad \times J_0(\xi r) J_1(\xi l) d\xi \end{aligned} \quad (30)$$

[e.g., Miller and Pursey, 1954, Eqs. (72) and (73)].



## B. The high-frequency asymptotics

Only the  $\exp(-\beta z)$  terms in Eq. (30) are responsible for the total  $S$  field. Let us first evaluate this term in the second integral. We introduce a new variable  $\eta$ , such that we have

$$\xi = \kappa \eta, \quad (31)$$

and obtain

$$u_z^b = -\frac{2Q}{\pi \rho b^2 l} \int_0^\infty \frac{\eta^2 \sqrt{\eta^2 - \gamma^2}}{R(\eta)} \times e^{-\kappa z \sqrt{\eta^2 - 1}} J_0(\kappa r \eta) J_1(\kappa l \eta) d\eta. \quad (32)$$

As above, we disregard the Rayleigh pole because it produces a surface wave, but concentrate on

$$u_z^b = -\frac{2Q}{\pi \rho b^2 l} \int_0^1 \frac{\eta^2 \sqrt{\eta^2 - \gamma^2}}{R(\eta)} \times e^{-i\kappa z \sqrt{1 - \eta^2}} J_0(\kappa r \eta) J_1(\kappa l \eta) d\eta, \quad (33)$$

where the contour of integration passes above the branch points. It is easy to show that the contribution of the limit of integration  $\eta=0$  is asymptotically small, and therefore it is reasonable to assume that  $\kappa l \eta \gg 1$ . Then the large argument asymptotics of the first order Bessel function are

$$J_1(\kappa l \eta) \approx \frac{1}{(2\pi \kappa l \eta)^{1/2}} \times \{e^{i(\kappa l \eta - 3\pi/4)} + e^{-i(\kappa l \eta - 3\pi/4)}\}, \quad \kappa l \eta \gg 1 \quad (34)$$

[Abramowitz and Stegun, 1965, Eq. (9.2.1)]. Substituting Eq. (34) into (33) we obtain the sum of two terms,  $u_{z,-}^b$  and  $u_{z,+}^b$ , given by

$$u_{z,\pm}^b \approx -\frac{2Q}{\rho b^2 (2\pi^3 \kappa l^3)^{1/2}} e^{\pm i3\pi/4} \times \int_0^1 \frac{\eta^{3/2} \sqrt{\eta^2 - \gamma^2}}{R(\eta)} J_0(\kappa r \eta) e^{-i\kappa(z \sqrt{1 - \eta^2} \pm l\eta)} d\eta. \quad (35)$$

These expressions may be treated similarly to Eq. (14). Note that there are two distinct regions:

- (i) Inside the axial region,  $\kappa r \leq 1$ , the amplitude function varies slowly. The resulting expressions involve the Bessel functions.
- (ii) Outside the axial region,  $\kappa r \gg 1$ , the Bessel function  $J_0(\kappa r \eta)$  can be replaced by its asymptotics. As a result we obtain two edge waves, one originating at the nearest and the other at the farthest point of the edge (see Figs. 4 and 5).

A more precise description of size and shape of the axial region is given below. The first integral in Eq. (30) can be treated in a similar manner to obtain the  $r$  component. The leading terms of the high-frequency asymptotics describing the  $S$  and head waves as well as the total  $S$  field radiated by a circular normal transducer can be summarized as follows:  
*The edge  $S$  wave inside the axial region:*

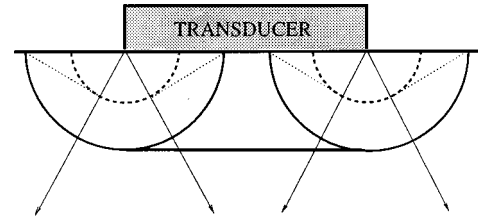


FIG. 4. A large circular transducer acting normally to the surface of a half-space. Solid line—fronts of the direct and edge  $P$  waves; dashed line—front of the edge  $S$  waves; dotted line—front of the edge head waves; arrowed segments—critical rays.

$$\mathbf{u}^{S(\text{axial})} = -\frac{Q}{\pi \rho b^2 \kappa l^2} A^S(\theta_*) e^{-i\kappa s_*} \times [\cos \theta_* J_1(\kappa r \sin \theta_*) \mathbf{e}_r - i \sin \theta_* J_0(\kappa r \sin \theta_*) \mathbf{e}_z]. \quad (36)$$

*The edge  $S$  waves outside the axial region:*

$$\mathbf{u}_{\pm}^{S(\text{edge})} = \frac{Q}{(2\pi^3)^{1/2} \rho b^2 \kappa l^2} A^S(\theta_{\pm}) \times \left[ \frac{s_{\pm}}{\kappa(l \pm r)^2} \right]^{1/2} \left( \frac{l}{r} \right)^{1/2} e^{-i(\kappa s_{\pm} + \pi/2 \mp \pi/4)} \times [\pm \cos \theta_{\pm} \mathbf{e}_r - \text{sgn}(l \pm r) \sin \theta_{\pm} \mathbf{e}_z]. \quad (37)$$

The asymptotics (36) and (37) have been obtained previously by a different method in Fradkin *et al.* (1998).

*The edge head wave inside the axial region:*

$$\mathbf{u}^{H(\text{axial})} = -\frac{Q}{\pi \rho b^2 l (\kappa l)^{1/2}} \frac{A^H}{\gamma} \frac{1}{(\kappa s_* \sin(\theta_* - \theta_{\text{cr}}))^{3/2}} \times e^{-i(\kappa s_* \cos(\theta_* - \theta_{\text{cr}}) - \pi/2)} H(\theta_* - \theta_{\text{cr}}) \times [\sqrt{1 - \gamma^2} J_1(\kappa r \gamma) \mathbf{e}_r - i \gamma J_0(\kappa r \gamma) \mathbf{e}_z]. \quad (38)$$

*The edge head waves outside the axial region:*

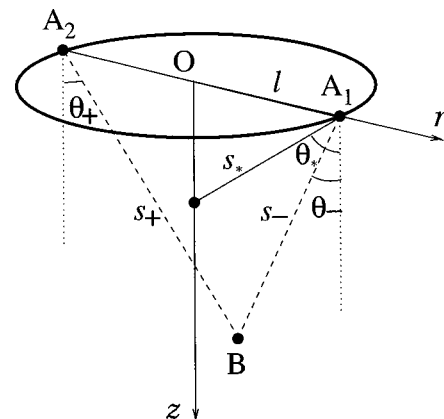


FIG. 5. The nearest ( $A_1$ ) and farthest ( $A_2$ ) edge points.  $B$  is the observation point.

$$\mathbf{u}_{\pm}^H = \frac{Q}{(2\pi^3)^{1/2} \rho b^2 \kappa l^2} \frac{A^H}{\gamma^{3/2}} \frac{1}{(\kappa s_{\pm} \sin(\theta_{\pm} - \theta_{cr}))^{3/2}} \left(\frac{l}{r}\right)^{1/2} \times e^{-i(\kappa s_{\pm} \cos(\theta_{\pm} - \theta_{cr}) \mp \pi/4)} H(\theta_{\pm} - \theta_{cr}) \times [\pm \sqrt{1 - \gamma^2} \mathbf{e}_r - \text{sgn}(l \pm r) \gamma \mathbf{e}_z]. \quad (39)$$

The total  $S$  field inside the axial region:

$$\mathbf{u}^{b(\text{axial})} = -\frac{Q}{\pi \rho b^2 l (\kappa l)^{1/2}} e^{-i\kappa s_* [1 + \cos(\theta_* - \theta_{cr})] / 2} \frac{1}{(\kappa s_*)^{3/4}} \left[ \left( A_1^t D_{1/2}(w_*) + \frac{B_1^t}{\sqrt{\kappa s_*}} D_{3/2}(w_*) \right) \mathbf{e}_r + \left( A_2^t D_{1/2}(w_*) + \frac{B_2^t}{\sqrt{\kappa s_*}} D_{3/2}(w_*) \right) \mathbf{e}_z \right] - \frac{Q}{\pi \rho b^2 \kappa l^2} \tilde{A}^S(\theta_*) e^{-i\kappa s_*} \times [\cos \theta_* J_1(\kappa r \sin \theta_*) \mathbf{e}_r - i \sin \theta_* J_0(\kappa r \sin \theta_*) \mathbf{e}_z]. \quad (40)$$

The total  $S$  field outside the axial region:

$$\mathbf{u}_{\pm}^b = -\frac{Q}{(2\pi^3)^{1/2} \rho b^2 \kappa l^2} \left(\frac{l}{r}\right)^{1/2} \left\{ e^{-i\kappa s_{\pm} [1 + \cos(\theta_{\pm} - \theta_{cr})] / 2} \frac{1}{(\kappa s_{\pm})^{3/4}} \left[ \left( A_3^t D_{1/2}(w_{\pm}) + \frac{B_3^t}{\sqrt{\kappa s_{\pm}}} D_{3/2}(w_{\pm}) \right) \mathbf{e}_r + \left( A_4^t D_{1/2}(w_{\pm}) + \frac{B_4^t}{\sqrt{\kappa s_{\pm}}} D_{3/2}(w_{\pm}) \right) \mathbf{e}_z \right] - \tilde{A}^S(\theta_{\pm}) \left[ \frac{s_{\pm}}{\kappa(l \pm r)^2} \right]^{1/2} e^{-i(\kappa s_{\pm} - \pi/2 \mp \pi/4)} [\pm \cos \theta_{\pm} \mathbf{e}_r - \text{sgn}(l \pm r) \sin \theta_{\pm} \mathbf{e}_z] \right\}. \quad (41)$$

Above, the following notations have been used:

$$s_* = (z^2 + l^2)^{1/2}, \quad \sin \theta_* = l/s_*, \quad (42)$$

$$s_{\pm} = (z^2 + (l \pm r)^2)^{1/2}, \quad \sin \theta_{\pm} = |l \pm r|/s_{\pm},$$

and

$$w_{*,\pm} = -(1+i) \text{sgn}(\theta_{*,\pm} - \theta_{cr}) \times \sqrt{\kappa s_{*,\pm} (1 - \cos(\theta_{*,\pm} - \theta_{cr}))}. \quad (43)$$

The coefficients  $A_i^t$ ,  $B_i^t$  and  $\tilde{A}^S(\theta)$  are specified in Appendix B. Note that asymptotics (40) and (41) are uniform, that is, they are valid both inside and outside the boundary layers surrounding the critical rays. All asymptotics [(36)–(41)] are valid in the radiating near field, i.e., for

$$\kappa z \gg 1, \quad \frac{z}{\kappa l^2} \ll 1 \quad (44)$$

(the latter condition is a consequence of the assumption that  $\kappa l \eta \gg 1$ ). The numerical experiments confirm more precise conditions

$$\lambda < z < l^2/\lambda, \quad (45)$$

where  $\lambda$  is a wavelength of the  $S$  wave. For a typical frequency 5 MHz and transducer radius  $l = 10$  mm this region extends in steel from about 0.5 mm to about 170 mm.

### C. Discussion and numerical results

The existence of the head waves underneath a circular normal transducer can be explained similarly to the case of a point source, only in this case both edge  $P$  waves give rise to the secondary surface sources of  $P$  and  $S$  waves. Conse-

quently, there are two edge head waves (see Figs. 4 and 5), and the overall structure of the field radiated by a circular normal source is more complex than that of a point source. All the geometrical zones and boundary layers of this field are represented in Fig. 6. Their description follows.

In geometrical zones I there are two edge head waves, one originating at the nearest and the other at the farthest edge point. The corresponding expressions are given by Eq. (39). Each is similar to that for the head wave radiated by a point source [see Eq. (19)], and hence the edge head waves exhibit similar behavior. However, the order of asymptotics (39) is  $\kappa^{3/2}$  higher than that of (19). This is due to the fact that the order of the asymptotics of the edge  $P$  waves radiated by a circular transducer is  $k^{3/2}$  higher than that of the asymptotics of the  $P$  wave of a point source (see Fradkin

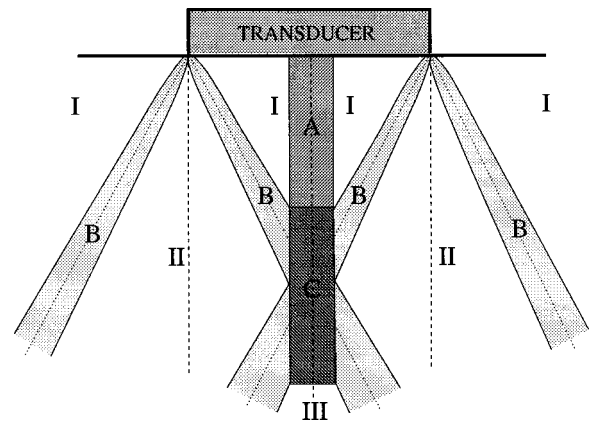


FIG. 6. Various geometrical zones (I, II, and III) and boundary layers (A, B, and C) underneath a large circular normal transducer directly coupled to an elastic half-space.

*et al.*, 1998). There is no nearest point edge head wave in zones II. Neither head wave is present in zone III. The latter is limited from above by the axis point  $z_0 = l / \tan \theta_{cr}$ .

Inside the axial region (zone A) all points of the transducer edge give rise to the head field and not just the nearest and farthest points. The corresponding description is given by Eq. (38) and involves Bessel's functions. Note that these asymptotics are of a lower order than those of the edge head waves (39). The latter focus along the axis. Both size and shape of the axial region are determined by the condition that the phase difference between the edge waves arriving from the nearest and farthest edge points is  $\pi$ . This is equivalent to the condition

$$\kappa r \gamma = \pi/2. \quad (46)$$

Therefore, the shape is cylindrical. The axial boundary layer is the narrower the higher the frequency.

The asymptotics (39) also break down in zones B, that is, inside the boundary layers surrounding the critical rays. There the total  $S$  field cannot be represented as a sum of the edge  $S$  and head waves. Equation (41) involving the parabolic cylinder functions can be used in this case. This expression shows that both the amplitude and phase of the total  $S$  field inside the boundary layers surrounding the critical rays are different to those of the  $S$  wave. For instance, the amplitude of the  $S$  wave is zero on the critical rays, but the total  $S$  field does not vanish there. The shape of these layers is parabolic just as it is for a point source.

Finally, in zone C all the critical rays from the edge intersect and the description of the field in the vicinity of the intersection point  $z_0$  is given by Eq. (40). It involves both Bessel's and the parabolic cylinder functions. The volume occupied by zone C is very small and it is the smaller the higher the frequency.

Unlike the integral solution (30) the asymptotic formulas allow us to study the time-harmonic  $S$  and head waves separately. For example, the relative magnitudes of the  $S$  and head waves near the axis of the transducer are presented in Fig. 7(a), where it is assumed that  $\gamma = 0.5$ ,  $f = 5$  MHz, and the radius of the transducer  $l = 10$  mm. For these parameters the critical angle  $\theta_{cr} = 30^\circ$  and the critical rays intersect at  $z_0 \approx 17.3$  mm. It can be seen that the magnitude of the head wave is smaller, and that both waves focus along the axis. There is a small mismatch at the transition point ( $r \approx 0.28$  mm) between the inner asymptotics (36) and (38) and the outer asymptotics (37) and (39). This mismatch can be removed by numerical smoothing. However, it is relatively small and no smoothing is required when dealing with pulses.

It is interesting to note that moving along the axis away from the transducer the amplitude of the head wave increases [see Fig. 7(b)]. This is so because the farther points of the axis are closer to the critical rays, and therefore the amplitude of the head wave is larger there (see discussion in Sec. I). The decay of the nearest edge point waves, both  $S$  and head, along the ray running from this point at the angle  $\theta_- = 60^\circ$  and directed outside the transducer is shown in Fig. 7(c). It can be seen that the head wave decays much faster.

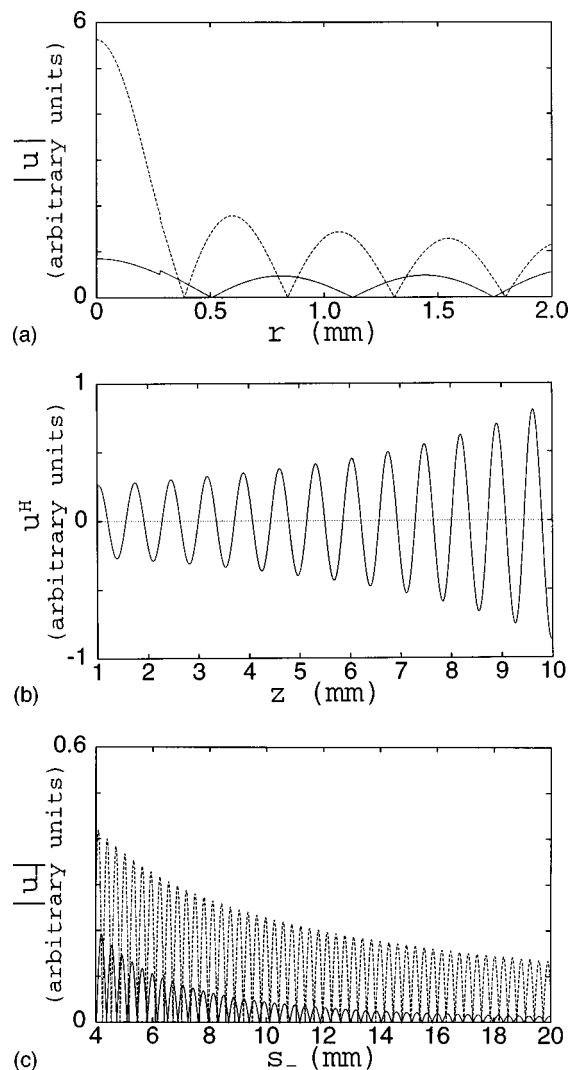


FIG. 7. The relative magnitudes of the  $S$  (dashed line) and head (solid line) waves underneath a circular transducer: (a) The waves near the axis at  $z = 10$  mm and various  $r$ ; (b) the head wave on the axis at different  $z$ ; (c) the nearest edge point waves at various  $s_-$  along the ray  $\theta_- = 60^\circ$ .

The asymptotic formulas obtained above have been validated numerically: They have been used to write a code which has been tested against another code based on exact numerical integration. The test parameters have been chosen as follows:  $\gamma = 0.4$ ,  $f = 5$  MHz, and  $l = 10$  mm, so that the critical angle  $\theta_{cr} \approx 24^\circ$ , the critical rays intersect at  $z_0 \approx 22.9$  mm, and the vertical extent of zone C is about 5 mm. The value of  $\gamma$  is realistic but larger values are possible too. However, the quality of the nonuniform asymptotics (38) and (39) and the uniform asymptotics (40) and (41) deteriorate when  $\gamma \rightarrow \gamma_*$  (see Appendix A), because in this case the complex poles of  $P(\eta)$  move close to the contour of integration and the branch point  $\eta = \gamma$ . The contribution of these poles is the smaller the higher the frequency.

The comparison of the nonuniform asymptotics to the exact numerical solution is presented in Fig. 8(a). The nonuniform asymptotics are expressed as a sum of the  $S$  and head waves as given by Eqs. (36) and (38), respectively. There is good agreement between the solutions for a wide range of  $z$ , but inside zone C the nonuniform asymptotics

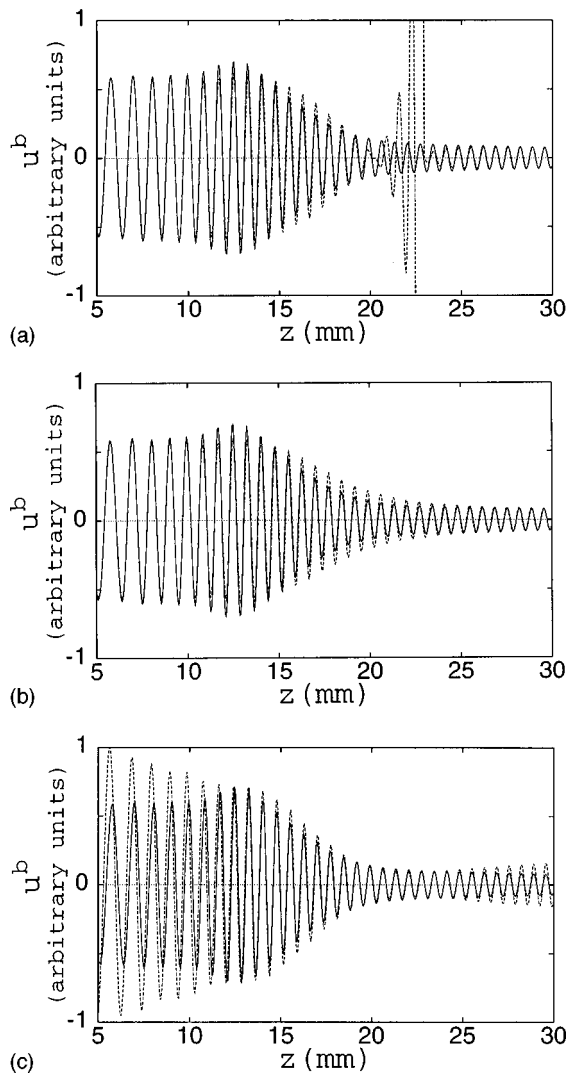


FIG. 8. The total  $S$  field on the axis of the transducer: (a) Dashed line—the nonuniform asymptotics, and solid line—the exact solution; (b) dashed line—the uniform asymptotics, and solid line—the exact solution; (c) dashed line—the leading term of the uniform asymptotics without  $D_{3/2}$  term, and solid line—the exact solution.

fail. Further comparison of the uniform asymptotics (40) with the exact solution is presented in Fig. 8(b). In this case there is good agreement for the whole range of  $z$ . In Fig. 8(c) we compare the uniform asymptotics without the  $D_{3/2}$  term to the exact solution. The agreement is good only inside zone C. It follows that although the  $D_{3/2}$  term is of a higher order than the  $D_{1/2}$  term it nevertheless makes a significant contribution. Further comparison between the asymptotic and exact solution as well as further discussion of the physics of the problem are given in another paper (Gridin and Fradkin, 1998) devoted to the propagation of pulses.

### III. CONCLUSIONS

The high-frequency asymptotics have been derived for the head wave as well as the field inside boundary layers surrounding the critical rays for (a) the far field of a point source and (b) the radiating near field of a large circular transducer, both acting normally on an isotropic and homogeneous elastic half-space. The asymptotics of the head wave

are of a higher order than those for the  $S$  wave but not entirely negligible. Inside certain zones underneath a circular transducer two edge head waves originating at the nearest and farthest edge points exist. Along the axis of the transducer the focusing of the edge head waves takes place.

The uniform asymptotics of the total  $S$  field which are valid both inside and outside the boundary layers surrounding the critical rays involve the parabolic cylinder functions  $D_{1/2}$  and  $D_{3/2}$ . The numerical results have demonstrated that the  $D_{3/2}$  terms in the uniform asymptotics are important even though they are of a higher order than the  $D_{1/2}$  terms.

The obtained asymptotics can be utilized in writing fast codes for simulating pulse propagation in the radiating near zone of a circular ultrasonic transducer. One such code is discussed in another paper (Gridin and Fradkin, 1998). The tangential loads may be treated in a similar vein.

### ACKNOWLEDGMENTS

This work was carried out by the author as a South Bank Research Scholar. He is grateful to Dr L. J. Fradkin for suggesting the problem and numerous useful discussions, and to anonymous reviewers for comments on presentation.

### APPENDIX A: THE BRANCH POINT AND COALESCING STATIONARY AND BRANCH POINTS IN INTEGRAL (14)

To find the contribution of the branch point  $\eta = \gamma$  to integral (14) let us first consider the amplitude of the integrand in  $u_{z,+}^b$ , that is

$$f(\xi) = \frac{\eta^{5/2} \sqrt{\eta^2 - \gamma^2}}{R(\eta)}. \quad (A1)$$

The branch point is present in both the numerator and denominator and (A1) can be represented in the following form:

$$f(\eta) = f_1(\eta) \sqrt{\eta - \gamma} + f_2(\eta), \quad (A2)$$

where we have

$$f_1(\eta) = \frac{\eta^{5/2} \sqrt{\eta + \gamma} (2\eta^2 - 1)^2}{P(\eta)}, \quad (A3)$$

$$f_2(\eta) = \frac{4i \eta^{9/2} \sqrt{1 - \eta^2} (\eta^2 - \gamma^2)}{P(\eta)}, \quad (A4)$$

and

$$P(\eta) = (2\eta^2 - 1)^4 - 16\eta^4(\eta^2 - 1)(\eta^2 - \gamma^2). \quad (A5)$$

The function  $P(\eta)$  possesses all the roots of  $R(\eta)$  lying on all of its Riemann sheets. Note that when  $\gamma > \gamma_* \approx 0.567$  there are two additional *real* poles; for most of materials of interest  $\gamma < \gamma_*$ . The effect produced by these poles is discussed in Sec. II (see also Hudson, 1980, Sec. 7.5).

Let us consider the integrals

$$I_1 = \int_0^1 f_1(\eta) \sqrt{\eta - \gamma} e^{-i\kappa(z\sqrt{1-\eta^2} + \eta r)} d\eta, \quad (A6)$$

and

$$I_2 = \int_0^1 f_2(\eta) e^{-i\kappa(z\sqrt{1-\eta^2} + \eta r)} d\eta \quad (\text{A7})$$

separately. The integrand in  $I_2$  has only one critical point, the phase stationary point  $\eta = \sin \theta$ . The integrand in  $I_1$  has two critical points—the stationary point  $\eta = \sin \theta$  and the branch point  $\eta = \gamma$ .

To find the contribution of the branch point (Borovikov, 1994, Secs. 1.4 and 2.4) let us first introduce a new variable  $\zeta = \eta - \gamma$  and instead of  $I_1$  in Eq. (A6) consider the integral

$$I_1 = \int_{-\gamma}^{1-\gamma} f_1(\zeta + \gamma) \sqrt{\zeta} e^{i\lambda \varphi(\zeta)} d\zeta, \quad (\text{A8})$$

where  $\lambda = \kappa s$  and we use

$$\varphi(\zeta) = -[\cos \theta \sqrt{1 - (\zeta + \gamma)^2} + \sin \theta (\zeta + \gamma)]. \quad (\text{A9})$$

Now we introduce another variable  $v$ , such that we have

$$\varphi(\zeta) - \varphi(0) = \text{sgn}(\varphi'|_0) v, \quad (\text{A10})$$

and obtain

$$I_1 = e^{-i\lambda \cos(\theta - \theta_{\text{cr}})} \int_{-\infty}^{+\infty} F(v) \sqrt{v} e^{i\lambda \text{sgn}(\varphi'|_0) v} dv, \quad (\text{A11})$$

where we have

$$F(v) \sqrt{v} = f_1(\zeta + \gamma) \sqrt{\zeta} \frac{d\zeta}{dv}, \quad (\text{A12})$$

and the limits of integration have been extended to infinity. This can be done because we are interested in the contribution of the critical point  $v=0$  only. The leading term of  $F(v)$  is

$$F_0 = F(0) = f_1(\gamma) \left( \frac{d\zeta}{dv} \Big|_0 \right)^{3/2} = \frac{f_1(\gamma)}{(|\varphi'|_0)^{3/2}}, \quad (\text{A13})$$

and therefore we have

$$I_1 \approx e^{-i\lambda \cos(\theta - \theta_{\text{cr}})} \frac{f_1(\gamma)}{(|\varphi'|_0)^{3/2}} J, \quad (\text{A14})$$

with

$$\theta_{\text{cr}} = \arcsin \gamma, \quad (\text{A15})$$

and the canonical integral

$$J = \int_{-\infty}^{+\infty} \sqrt{v} e^{i\lambda \text{sgn}(\varphi'|_0) v} dv. \quad (\text{A16})$$

It is easy to show that if  $\text{sgn}(\varphi'|_0) > 0$  we have  $J=0$ . For  $\text{sgn}(\varphi'|_0) < 0$  integral  $J$  can be expressed in terms of the Gamma function:

$$J = 2 \int_0^{+\infty} \sqrt{v} e^{-i\lambda v} dv = 2 \left( \frac{-i}{\lambda} \right)^{3/2} \Gamma(3/2) \quad (\text{A17})$$

[Borovikov, 1994, Eq. (1.14)], where  $\Gamma(3/2) = \sqrt{\pi}/2$  [Abramowitz and Stegun, 1965, Eq. (6.1.9)]. As a result we obtain

$$I_1 \approx e^{-i\lambda \cos(\theta - \theta_{\text{cr}})} \frac{\sqrt{2\pi} \gamma^3}{(2\gamma^2 - 1)^2} \frac{(1 - \gamma^2)^{3/4}}{(\lambda |\sin(\theta - \theta_{\text{cr}})|)^{3/2}} \times e^{-i3\pi/4} H(\theta - \theta_{\text{cr}}), \quad (\text{A18})$$

where  $H(\theta - \theta_{\text{cr}})$  is the Heaviside function.

The far-field asymptotics (A18) fail as  $\theta \rightarrow \theta_{\text{cr}}$ , i.e., when the stationary point approaches the branch point. To find uniform asymptotics (Bleistein and Handelsman, 1986, Sec. 9.4; Borovikov, 1994, Secs. 1.4 and 2.4) we introduce a new variable  $v$ , such that instead of Eq. (A10) we have

$$\lambda[\varphi(\zeta) - \varphi(0)] = v^2 + 2vw, \quad (\text{A19})$$

and obtain

$$I_1 = e^{-i\lambda \cos(\theta - \theta_{\text{cr}})} \int_{-\infty}^{+\infty} F(v) \sqrt{v} e^{i(v^2 + 2vw)} dv. \quad (\text{A20})$$

Expanding  $F(v)$  in the following manner:

$$F(v) = a_0 + b_0 v + v(v-w) F_1(v) \quad (\text{A21})$$

[Bleistein and Handelsman, 1986, Eq. (9.4.14)], and using the first two terms of this expansion we obtain

$$I_1 \approx e^{-i\kappa s [1 + \cos(\theta - \theta_{\text{cr}})]/2} \frac{1}{(\kappa s)^{3/4}} \times \left( \tilde{A}_0 D_{1/2}[(1+i)w] + \frac{1}{\sqrt{\kappa s}} \tilde{B}_0 D_{3/2}[(1+i)w] \right). \quad (\text{A22})$$

In the last equation  $D_{1/2}$  and  $D_{3/2}$  are the parabolic cylinder functions of the order 1/2 and 3/2, respectively,

$$D_p[(1+i)w] = \pi^{-1/2} 2^{p/2} e^{-i3\pi p/4 - i\pi/4} e^{iw^2/2} \times \int_{-\infty + i0}^{+\infty + i0} v^p e^{i(v^2 + 2vw)} dv \quad (\text{A23})$$

[Borovikov, 1994, Eq. (6.11a)],

$$w = -\text{sgn}(\theta - \theta_{\text{cr}}) \sqrt{\kappa s (1 - \cos(\theta - \theta_{\text{cr}}))}. \quad (\text{A24})$$

To obtain the total uniform asymptotics we have to add the above combined contribution of the phase stationary point and branch point to  $I_1$  to the contribution of the phase stationary point to  $I_2$ .

## APPENDIX B: THE COEFFICIENTS IN THE UNIFORM ASYMPTOTICS (22), (40), AND (41)

The coefficients  $A_i^p$ ,  $B_i^p$ ,  $A_i^t$ ,  $B_i^t$ , and  $\tilde{A}^S(\theta)$  are as follows:

$$A_1^p = 2^{5/4} e^{-i\pi/8} \sqrt{1 - \gamma^2} A^H E_1(\theta),$$

$$B_1^p = -\frac{2^{1/4} e^{-i7\pi/8}}{E_3(\theta)} \times [f_3(\sin \theta) E_2(\theta) - i\sqrt{2} \sqrt{1 - \gamma^2} A^H E_1(\theta)], \quad (\text{B1})$$

$$A_2^p = 2^{5/4} e^{i7\pi/8} \gamma A^H E_1(\theta),$$

$$B_2^p = -\frac{2^{1/4} e^{i5\pi/8}}{E_3(\theta)} [f_1(\sin \theta) E_2(\theta) - \sqrt{2} \gamma A^H E_1(\theta)], \quad (\text{B2})$$

$$A_1^i = 2^{5/4} e^{-i\pi/8} \sqrt{1-\gamma^2} \gamma^{-1} A^H J_1(\kappa r \gamma) E_1(\theta_*),$$

$$B_1^i = \frac{2^{1/4} e^{i\pi/8}}{E_3(\theta_*)} \left[ g_1(\sin \theta_*) E_2(\theta_*) \right. \\ \left. - i\sqrt{2} \frac{\sqrt{1-\gamma^2}}{\gamma} A^H J_1(\kappa r \gamma) E_1(\theta_*) \right] \quad (\text{B3})$$

$$A_2^i = 2^{5/4} e^{-i5\pi/8} A^H J_1(\kappa r \gamma) E_1(\theta_*),$$

$$B_2^i = -\frac{2^{1/4} e^{-i7\pi/8}}{E_3(\theta_*)} [g_2(\sin \theta_*) E_2(\theta_*) \\ - \sqrt{2} A^H J_0(\kappa r \gamma) E_1(\theta_*)], \quad (\text{B4})$$

$$A_3^i = 2^{5/4} e^{i(7\pi/8 \mp \pi/4)} \sqrt{1-\gamma^2} \gamma^{-3/2} A^H E_1(\theta_{\pm}),$$

$$B_3^i = \frac{2^{1/4} e^{i(9\pi/8 \mp \pi/4)}}{E_3(\theta_{\pm})} \left[ g_3(\sin \theta_{\pm}) E_2(\theta_{\pm}) \right. \\ \left. - i\sqrt{2} \frac{\sqrt{1-\gamma^2}}{\gamma^{3/2}} A^H E_1(\theta_{\pm}) \right], \quad (\text{B5})$$

$$A_4^i = -2^{5/4} e^{i(3\pi/8 \pm \pi/4)} \gamma^{-1/2} A^H E_1(\theta_{\pm}),$$

$$B_4^i = \frac{2^{1/4} e^{i(\pi/8 \pm \pi/4)}}{E_3(\theta_{\pm})} [g_4(\sin \theta_{\pm}) E_2(\theta_{\pm}) \\ - \sqrt{2} \gamma^{-1/2} A^H E_1(\theta_{\pm})], \quad (\text{B6})$$

$$\tilde{A}^s = \frac{8 \sin^3 \theta \cos^2 \theta (\sin^2 \theta - \gamma^2)}{P(\sin \theta)}, \quad (\text{B7})$$

where we have

$$E_1(\theta) = \left[ \frac{\sqrt{1-\cos(\theta-\theta_{cr})}}{|\sin(\theta-\theta_{cr})|} \right]^{3/2},$$

$$E_2(\theta) = \frac{\sqrt{|\sin \theta - \gamma|} \cos \theta}{(1-\cos(\theta-\theta_{cr}))^{1/4}},$$

$$E_3(\theta) = \text{sgn}(\theta-\theta_{cr}) \sqrt{1-\cos(\theta-\theta_{cr})},$$

$$f_3(\eta) = \frac{i \eta^{3/2} \sqrt{\eta+\gamma} \sqrt{1-\eta^2} (2\eta^2-1)^2}{P(\eta)},$$

$$g_1(\eta) = \frac{i \eta^{1/2} \sqrt{\eta+\gamma} \sqrt{1-\eta^2} (2\eta^2-1)^2}{P(\eta)} J_1(\kappa r \eta),$$

$$g_2(\eta) = \frac{\eta^{3/2} \sqrt{\eta+\gamma} (2\eta^2-1)^2}{P(\eta)} J_0(\kappa r \eta),$$

$$g_3(\eta) = \frac{i \sqrt{\eta+\gamma} \sqrt{1-\eta^2} (2\eta^2-1)^2}{P(\eta)},$$

$$g_4(\eta) = \frac{\eta \sqrt{\eta+\gamma} (2\eta^2-1)^2}{P(\eta)}. \quad (\text{B8})$$

- Abramowitz, M., and Stegun, I. A. (1965). *Handbook of Mathematical Functions* (Dover, New York).
- Achenbach, J. D. (1973). *Wave Propagation in Elastic Solids* (North-Holland, New York).
- Aki, K., and Richards, P. (1980). *Quantitative Seismology: Theory and Methods* (Freeman, San Francisco, CA).
- Babič, V. M., and Buldyrev, V. S. (1991). *Short-Wavelength Diffraction Theory: Asymptotic Methods* (Springer-Verlag, Heidelberg).
- Babič, V. M., and Kirpichnikova, N. Ya. (1975). *The Boundary-Layer Method in Diffraction Problems* (Springer-Verlag, Berlin).
- Baboux, J. C., and Kažys, R. (1992). "Analysis of the transient ultrasonic fields radiated in solids by circular and annular sources," *J. Acoust. Soc. Am.* **92**, 2942–2951.
- Bleistein, N., and Handelsman, R. A. (1986). *Asymptotic Expansions of Integrals* (Dover, New York).
- Borovikov, V. A., and Kinber, B. Ye. (1994). *Geometrical Theory of Diffraction* (IEE Electromagnetic Series, Vol. 37, London).
- Borovikov, V. A. (1994). *Uniform Stationary Phase Method* (IEE Electromagnetic Series, Vol. 40, London).
- Brekhovskikh, L. (1960). *Waves in Layered Media* (Academic, New York).
- Cervény, V., and Ravindra, R. (1971). *Theory of Seismic Head Waves* (University of Toronto Press, Toronto).
- Djelouah, H., and Baboux, J. C. (1992). "Transient ultrasonic field radiated by a circular transducer in a solid medium," *J. Acoust. Soc. Am.* **92**, 2932–2941.
- Erdélyi, A. (1956). *Asymptotic Expansions* (Dover, New York).
- Fedoryuk, M. (1977). *The Saddle Point Method* (Nauka, Moscow).
- Fradkin, L. Ju., and Kiselev, A. P. (1997). "The two-component representation of time-harmonic elastic body waves in the high and intermediate frequency regime," *J. Acoust. Soc. Am.* **101**, 52–65.
- Fradkin, L., Kiselev, A., and Krylova, E. (1998). "The radiating near field asymptotics of a time-harmonic circular normal ultrasonic transducer in an elastic half-space," *J. Acoust. Soc. Am.* **104**, 1178–1187.
- Fung, Y. C. (1965). *Foundations of Solid Mechanics* (Prentice-Hall, Englewood Cliffs, NJ).
- Gridin, D., and Fradkin, L. (1998). "High-frequency asymptotic description of pulses radiated by a circular normal transducer into an elastic half-space," *J. Acoust. Soc. Am.* (submitted).
- Hudson, J. A. (1980). *The Excitation and Propagation of Elastic Waves* (Cambridge U. P., Cambridge).
- Ilan, A., and Weight, J. P. (1990). "The propagation of short pulses of ultrasound from a circular source coupled to an isotropic solid," *J. Acoust. Soc. Am.* **88**, 1142–1151.
- Miklowitz, J. (1978). *The Theory of Elastic Waves and Waveguides* (North-Holland, Amsterdam).
- Miller, G. F., and Pursey, H. (1954). "The field and radiation impedance of mechanical radiators on the free surface of a semi-infinite isotropic solid," *Proc. R. Soc. London, Ser. A* **223**, 521–541.
- Wong, R. (1989). *Asymptotic Approximations of Integrals* (Academic, New York).

# Padé approximants for the acoustical properties of rigid frame porous media with pore size distributions

K. V. Horoshenkov

*Department of Civil and Environmental Engineering, University of Bradford, Bradford BD7 1DP, United Kingdom*

Keith Attenborough

*Faculty of Technology, Open University, Milton Keynes MK7 6AA, United Kingdom*

S. N. Chandler-Wilde

*Department of Mathematics and Statistics, Brunel University, Uxbridge UB8 3PH, United Kingdom*

(Received 21 July 1997; accepted for publication 5 June 1998)

Expressions for the viscosity correction function, and hence bulk complex impedance, density, compressibility, and propagation constant, are obtained for a rigid frame porous medium whose pores are prismatic with fixed cross-sectional shape, but of variable pore size distribution. The low- and high-frequency behavior of the viscosity correction function is derived for the particular case of a log-normal pore size distribution, in terms of coefficients which can, in general, be computed numerically, and are given here explicitly for the particular cases of pores of equilateral triangular, circular, and slitlike cross-section. Simple approximate formulae, based on two-point Padé approximants for the viscosity correction function are obtained, which avoid a requirement for numerical integration or evaluation of special functions, and their accuracy is illustrated and investigated for the three pore shapes already mentioned. © 1998 Acoustical Society of America. [S0001-4966(98)04009-0]

PACS numbers: 43.20.Bi, 43.20.Mv [DAC]

## INTRODUCTION

There have been several studies related to the theoretical description of porous granular materials that extend and augment the original analysis by Biot.<sup>1</sup> Two of the most interesting developments have been perpetrated by Stinson<sup>2</sup> and Yamamoto and Turgut<sup>3</sup> and allow for arbitrary pore shape and distributions of pore sizes, respectively. As a consequence of Stinson's work, exact analytical results for cylindrical, slitlike, triangular, and rectangular pore shapes are available. Yamamoto and Turgut concentrated on the case of a log-normal pore size distribution in sedimentary materials. Attenborough<sup>4</sup> has shown that, of the possible pore characteristics, the presence of a variable distribution of pore sizes potentially has greater effect than change in pore shape. This is of particular practical interest since pore size distribution is routinely measurable. A different type of development, but of relevance to further progress in routine calculations of acoustical properties of rigid-framed porous materials is the use of Padé approximants. These have been developed for structures consisting of uniform pores in Ref. 5. In this paper these various contributions are combined. Padé approximants for the acoustical properties of media with size distributions of variously shaped pores are derived. It is anticipated that these approximations offer a practical and efficient alternative to increasingly sophisticated models (see, for example, Ref. 4) for sound propagation in a medium with pore size distribution.

In the first section an argument is presented to justify the use of the viscosity correction function of Yamamoto and Turgut<sup>3</sup> in computing the bulk acoustic properties of rigid-frame porous media. An expression is derived for the viscos-

ity correction function in terms of a single integral involving the pore size probability density function and a single function of a complex variable,  $\bar{\psi}(z)$ , specified in terms of the pore shape. This expression is simplified further for the important case of a log-normal pore size distribution in Sec. II. Low- and high-frequency approximations to the viscosity correction function are obtained in the second section, using results on approximation of a class of integrals in the Appendix. These approximations are used to derive two-point Padé approximants for the viscosity correction function in Sec. IV, and the accuracy of these simple approximants in calculating the acoustic characteristics such as relative admittance and complex wavenumber is explored.

## I. THE VISCOSITY CORRECTION FUNCTION

The majority of porous materials are composed of pores of variable shape and size which obey a distinctive statistical distribution. For these materials we can only refer to the values of the dynamic density and complex compressibility which have been averaged over a range of realistic pore sizes identified in the material. The same argument is applicable to acoustic quantities such as the acoustic admittance and propagation constant.

To derive the general form for the viscosity correction function we consider a sample of a bulk rigid-frame porous material which is pierced through by normal to the surface prismatic (i.e., uniform with respect to cross-sectional geometry) straight pores of various sizes but the same cross-sectional shape. Let us characterize the different sizes of pore by measurement of some linear dimension  $s$  and let  $E(s)$  denote the pore size distribution function, that is,  $E(s)$  is the

fraction of the total pore volume consisting of pores of size not exceeding  $s$ . Then  $e(s) = dE(s)/ds$  is the corresponding probability density function.

Within a typical pore of size  $s$  the velocity component  $u$  in the direction of the pore axis (the  $x_3$ -direction) satisfies, for harmonic ( $e^{-i\omega t}$ ) time dependence, to a good approximation the force equation<sup>2</sup>

$$i\omega\rho_0 u + \mu\Delta u = \frac{dp}{dx_3}. \quad (1)$$

In this equation  $\rho_0$  is the equilibrium fluid density,  $\mu$  the dynamic viscosity, a Cartesian coordinate system  $Ox_1x_2x_3$  has been adopted,  $\Delta = \partial^2/\partial x_1^2 + \partial^2/\partial x_2^2$ , and  $p$  is the pressure in the fluid which depends, to a good approximation, only on  $x_3$ . The velocity  $u$  vanishes on the sides of the pore.

Similarly,<sup>2</sup> the excess temperature  $T$  satisfies that

$$\kappa\Delta T + i\rho_0\omega C_p T = i\omega p, \quad (2)$$

where  $\kappa$  is the thermal conductivity of the fluid and  $C_p$  its specific heat at constant pressure. The excess temperature is assumed to vanish on the sides of the pore.

We introduce an auxiliary function  $\psi = \psi(x_1, x_2; w)$  which is defined by a boundary value problem which it satisfies within the pore cross-section of a unit size pore of dimension  $s = 1$ . This two-dimensional boundary value problem consists of the equation

$$\Delta\psi - w^2\psi = 1 \quad (3)$$

within the pore cross-section, where  $w$  is a given constant, and the boundary condition  $\psi = 0$  around the edge of the section. The form of the function  $\psi$  depends on the value of the real or complex parameter  $w$ . We assume that  $-\pi/2 < \arg w < \pi/2$  in which case  $\psi$  is uniquely determined by these imposed conditions.

In terms of this auxiliary function  $\psi$  it is easy to see, by substitution, that the solutions of (1) and (2) which vanish on the walls of the pore are

$$u = \frac{s^2}{\mu} \frac{dp}{dz} \psi(x_1/s, x_2/s; \sqrt{-i\lambda}) \quad (4)$$

and

$$T = \frac{i\omega s^2}{\kappa} p \psi(x_1/s, x_2/s; \sqrt{-iN_{pr}^{1/2}\lambda}), \quad (5)$$

where  $N_{pr}$  is the Prandtl number and

$$\lambda = (\rho_0\omega/\mu)^{1/2}s. \quad (6)$$

For any fluid property  $\phi$  let  $\bar{\phi}$  denote the mean value over the cross-section and  $\langle\phi\rangle$  denote the mean value of  $\bar{\phi}$  over all pore sizes, i.e.,

$$\langle\phi\rangle = \int_0^\infty e(s)\bar{\phi}(s)ds. \quad (7)$$

Then, if we assume that there are sufficient interconnections between the pores of different sizes so that the dependence of  $p$  on  $x_3$  is independent of the pore size  $s$ , it follows from (1) that

$$i\omega\rho_0\langle u\rangle + \mu\langle\Delta u\rangle = \frac{dp}{dx_3}, \quad (8)$$

an equation which we can write as

$$i\omega\rho_x(\omega)\langle u\rangle = \frac{dp}{dx_3}, \quad (9)$$

where  $\rho_x(\omega)$  is an effective complex density averaged over the pore size given by

$$\rho_x(\omega) = \rho_0 + \frac{\mu\langle\Delta u\rangle}{i\omega\langle u\rangle}. \quad (10)$$

In physical terms  $\langle u\rangle$  is the mean velocity over all pores, i.e., the total volume flux through the pores divided by the total pore cross-sectional area. By Gauss' theorem,

$$\overline{\mu\Delta u} = \frac{\mu}{A} \int_P \frac{\partial u}{\partial n} ds = \frac{1}{A} \int_P \tau ds, \quad (11)$$

where  $P$  is the perimeter of the cross-section and  $\tau$  the shear stress. Thus  $\mu\langle\Delta u\rangle = \langle\tau\rangle$ , where  $\langle\tau\rangle$  denotes the total shear force in the  $x_3$ -direction per unit thickness of the sample, per unit cross-sectional area, so that

$$\rho_x(\omega) = \rho_0 + \frac{1}{i\omega} \frac{\langle\tau\rangle}{\langle u\rangle}. \quad (12)$$

In terms of the auxiliary function  $\psi$  we easily see that

$$\bar{u} = \frac{s^2}{\mu} \frac{dp}{dx_3} \bar{\psi}, \quad \overline{\Delta u} = \frac{1}{\mu} \frac{dp}{dx_3} \overline{\Delta\psi}, \quad (13)$$

where  $\bar{\psi} = \bar{\psi}(\sqrt{-i\lambda})$  and  $\overline{\Delta\psi} = \overline{\Delta\psi}(\sqrt{-i\lambda})$  are the mean values over the cross-section of the pore of size  $s = 1$  of  $\psi$  and  $\Delta\psi$ , respectively, when  $w = \sqrt{-i\lambda}$ . Clearly

$$\rho_x(\omega) = \rho_0 - \frac{R_x}{i\omega} F(\omega), \quad (14)$$

where

$$R_x = - \lim_{\omega \rightarrow 0} \frac{\langle\tau(\omega)\rangle}{\langle u(\omega)\rangle} \quad (15)$$

is an effective DC flow resistivity averaged over the pores, and

$$F(\omega) = \frac{\langle\tau(\omega)\rangle}{\langle u(\omega)\rangle} \left[ \lim_{\omega \rightarrow 0} \frac{\langle\tau(\omega)\rangle}{\langle u(\omega)\rangle} \right]^{-1} \quad (16)$$

is the viscosity correction function as utilised by Yamamoto and Turgut<sup>3</sup> and Attenborough.<sup>4</sup> In terms of the auxiliary function  $\psi$  we have that, since  $i\lambda^2\bar{\psi} + \overline{\Delta\psi} = 1$  from (3),

$$F(\omega) = - \frac{i\omega\rho_0 I(\omega)}{R_x(1 - I(\omega))}, \quad (17)$$

where

$$\begin{aligned} I(\omega) &= \int_0^\infty e(s)\overline{\Delta\psi}(\sqrt{-i\lambda})ds \\ &= 1 - \frac{i\omega\rho_0}{\mu} \int_0^\infty s^2 e(s)\bar{\psi}(\sqrt{-i\lambda})ds. \end{aligned} \quad (18)$$



In the remainder of this paper we concentrate on the problem of evaluating the viscosity correction function  $F(\omega)$ . Once  $F(\omega)$  is known we can evaluate the dynamic density  $\rho_x(\omega)$ . Further, similarly to the definition of (9), we obtain from (2) that

$$\theta(\omega)\langle T \rangle = p \quad (19)$$

with

$$\theta(\omega) = \frac{C_p \rho_0}{1 - I(N_{pr}\omega)} = C_p \rho_x(N_{pr}\omega). \quad (20)$$

From (9) and (19), the equation of continuity, and the ideal gas law, we obtain that  $p$  satisfies the usual one-dimensional Helmholtz equation with complex wave number  $k_x(\omega)$  as in Ref. 2, but with single pore size values replaced by averaged values. Precisely

$$\frac{d^2 p}{dx_3^2} + k_x^2(\omega)p = 0 \quad (21)$$

with

$$k_x^2(\omega) = \omega^2 \rho_x(\omega) C_x(\omega) \quad (22)$$

and the complex compressibility,  $C_x(\omega)$ , given by

$$C_x(\omega) = \frac{1}{P_0} - \frac{1}{T_0 \theta(\omega)} = \frac{1}{\gamma P_0} \left( \gamma - \frac{\rho_0(\gamma-1)}{\rho_x(N_{pr}\omega)} \right). \quad (23)$$

Finally, we include the effects of tortuosity and of the sample porosity  $\Omega$ . Relaxing the condition that the pores be normal to the sample surface, let  $q \geq 1$  be the ratio of pore length to sample thickness so that  $q^2$  is the tortuosity. Then  $\langle v \rangle = \Omega \langle u \rangle / q$  is the bulk velocity, the total volume flux divided by the sample cross-sectional area. Equation (9) holds with  $\langle u \rangle$  replaced by  $\langle v \rangle$  provided we replace  $\rho_x(\omega)$  by a bulk medium dynamic complex density  $\rho_b(\omega) = (q^2/\Omega)\rho_x(\omega)$ . Thus

$$\rho_b(\omega) = \frac{q^2}{\Omega} \left( \rho_0 - \frac{\Omega R_b}{i\omega q^2} F(\omega) \right), \quad (24)$$

where we have introduced the bulk flow resistivity,  $R_b = q^2 R_x / \Omega$ . Equation (21) holds with  $x_3$  replaced by  $qx_3$ , alternatively with  $k_x(\omega)$  replaced by the bulk medium wave number  $k_b(\omega) = qk_x(\omega)$ . Then Eq. (22) holds with  $\rho_x$ ,  $k_x$ ,  $C_x$  replaced by their bulk medium values, i.e.,

$$k_b^2(\omega) = \omega^2 \rho_b(\omega) C_b(\omega), \quad (25)$$

provided we define the bulk medium complex compressibility by  $C_b(\omega) = \Omega C_x(\omega)$ . Finally the complex impedance of the medium is

$$Z_b(\omega) = p / \langle v \rangle = \omega \rho_b(\omega) / k_b(\omega) = \sqrt{\rho_b(\omega) / C_b(\omega)}, \quad (26)$$

so that the bulk medium admittance relative to that of the fluid medium is

$$\beta_b(\omega) = \rho_0 k_b(\omega) / (k \rho_b(\omega)) = (q/\Omega) \beta_x(\omega), \quad (27)$$

where  $k$  is the wave number in the fluid medium and

$$\beta_x(\omega) = \rho_0 k_x(\omega) / (k \rho_x(\omega)). \quad (28)$$

## II. LOG-NORMAL PORE SIZE DISTRIBUTION

The expressions presented in the previous section are only practical if the pore size distribution  $e(s)$  in the material is known. Experimental values for the statistical distribution  $e(s)$ , which can be measured by either the water suction method<sup>6</sup> or the mercury injection technique<sup>7</sup> or recovered from acoustical experiments,<sup>8</sup> are normally replaced in Eq. (18) with an explicit expression which provides a good fit to the experimental data.

It has been found from numerous experiments in geophysics and in outdoor noise propagation that in many granular materials<sup>4,7</sup> the real pore size distribution  $e(s)$  can be closely approximated by a log-normal statistical distribution.

In the log-normal statistical distribution  $\phi = -\log_2 s$  is normally distributed with mean  $\bar{\phi} = -\log_2 \bar{s}$ , where  $\bar{s}$  is the median pore size, and standard deviation  $\sigma$ . Thus, where  $G(\phi)$  is the distribution function of  $\phi$ ,

$$E(s) = 1 - G(\phi) \quad (29)$$

so that

$$e(s) = E'(s) = -g(\phi) \frac{d\phi}{ds}, \quad (30)$$

where  $g(\phi) = G'(\phi)$  is the probability density function of  $\phi$ , i.e.,

$$g(\phi) = \frac{1}{\sqrt{2\pi}\sigma} \exp\left(-\frac{(\phi - \bar{\phi})^2}{2\sigma^2}\right). \quad (31)$$

The standard deviation  $\sigma$  is dimensionless and is a measure of the deviation of  $s$  about its median value in relative terms. Precisely, for any  $\alpha > 0$ ,

$$\Pr\left(\frac{1}{2^{\sigma\alpha}} \leq \frac{s}{\bar{s}} \leq 2^{\sigma\alpha}\right) = \Pr\left(\left|\frac{\phi - \bar{\phi}}{\sigma}\right| \leq \alpha\right) = 2\Phi(\alpha) - 1,$$

where

$$\Phi(\alpha) = \frac{1}{\sqrt{2\pi}} \int_{-\infty}^{\alpha} e^{-y^2/2} dy$$

is the distribution function of the standard normal distribution.

Recall that the viscosity correction function is given in terms of  $I(\omega)$  by (17). For a log-normal distribution, substituting  $s = 2^{-\phi}$  in (18) and noting (30), we obtain that

$$I(\omega) = 1 - \frac{i\omega\rho_0}{\mu} \int_{-\infty}^{+\infty} 2^{-2\phi} g(\phi) \bar{\psi}(\sqrt{-i\lambda}) d\phi. \quad (32)$$

Defining

$$\bar{\lambda} = \left(\frac{\rho_0\omega}{\mu}\right)^{1/2} \bar{s} \quad (33)$$

to be the median value of  $\lambda$ , noting (6) and (31), and substituting  $\phi = \bar{\phi} + \sigma t$ , we see that, for a log-normal distribution,  $I(\omega)$  depends only on the dimensionless parameter combinations  $\bar{\lambda}$  and  $\sigma$ : precisely,

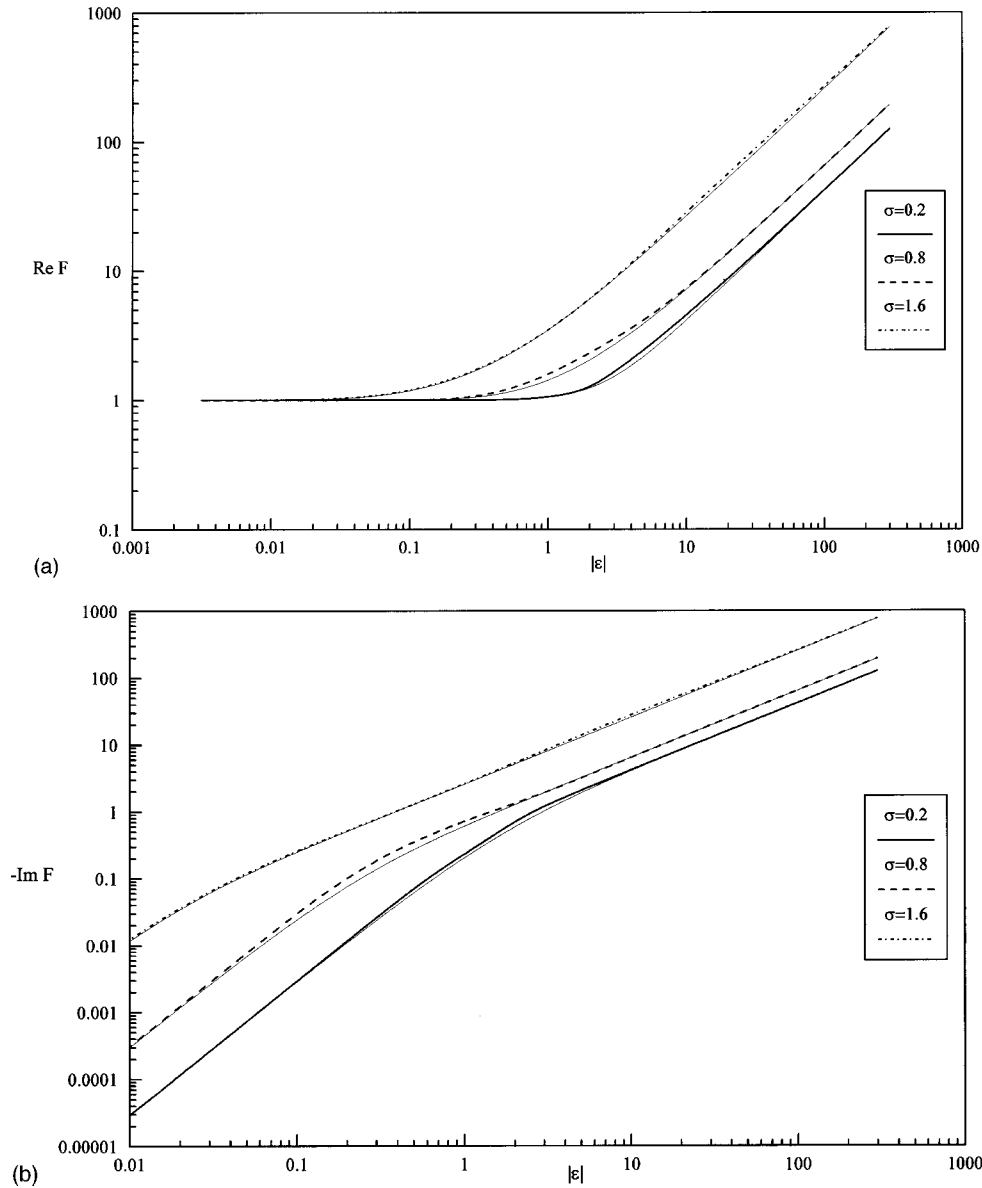


FIG. 1. (a) The real part of the viscosity correction function and its Padé approximant (thin solid lines) in the case of a material with slitlike pores. (b) The imaginary part of the viscosity correction function and its Padé approximant (thin solid lines) in the case of a material with slitlike pores.

$$\begin{aligned}
 I(\omega) &= 1 - \frac{i\bar{\lambda}^2}{\sqrt{2\pi}} \int_{-\infty}^{+\infty} 2^{-2\sigma t} e^{-t^2/2} \bar{\psi}(\sqrt{-i\bar{\lambda}} 2^{-\sigma t}) dt \\
 &= \frac{1}{\sqrt{2\pi}} \int_{-\infty}^{+\infty} \chi(\sqrt{-i\bar{\lambda}} 2^{-\sigma t}) e^{-t^2/2} dt, \quad (34)
 \end{aligned}$$

where the function  $\chi$ , which depends only on the pore shape, is defined by

$$\chi(z) = 1 + z^2 \bar{\psi}(z) \quad (35)$$

for  $-\pi/2 < \arg z < \pi/2$ . From (14) to (17) it can be seen that

$$I(\omega) = 1 - \frac{\rho_0}{\rho_x(\omega)} \quad (36)$$

and, in particular, this holds in the case  $\sigma=0$  of fixed pore size distribution  $s=\bar{s}$ . In this case (34) reduces to

$$I(\omega) = \chi(\sqrt{-i\bar{\lambda}}). \quad (37)$$

It is probably easiest to extract from the literature the form of the function  $\chi$  for various pore shapes using these last two equations (36) and (37). Using these equations, from Stinson and Champoux,<sup>2</sup> for pores which are infinite rectangular slits of half-width  $s$ , we obtain that

$$\chi(z) = \frac{\tanh z}{z}. \quad (38)$$

For circular pores of radius  $s$ , we find

$$\chi(z) = \frac{2I_1(z)}{zI_0(z)}, \quad (39)$$

where  $I_0$  and  $I_1$  are the modified Bessel functions of order one and zero, respectively. For equilateral triangular pores, with  $s$  the length of the triangle side,

$$\chi(z) = 3 \left( \frac{\coth(\sqrt{3}/4z)}{\sqrt{3}/4} - \frac{16}{3z^2} \right). \quad (40)$$

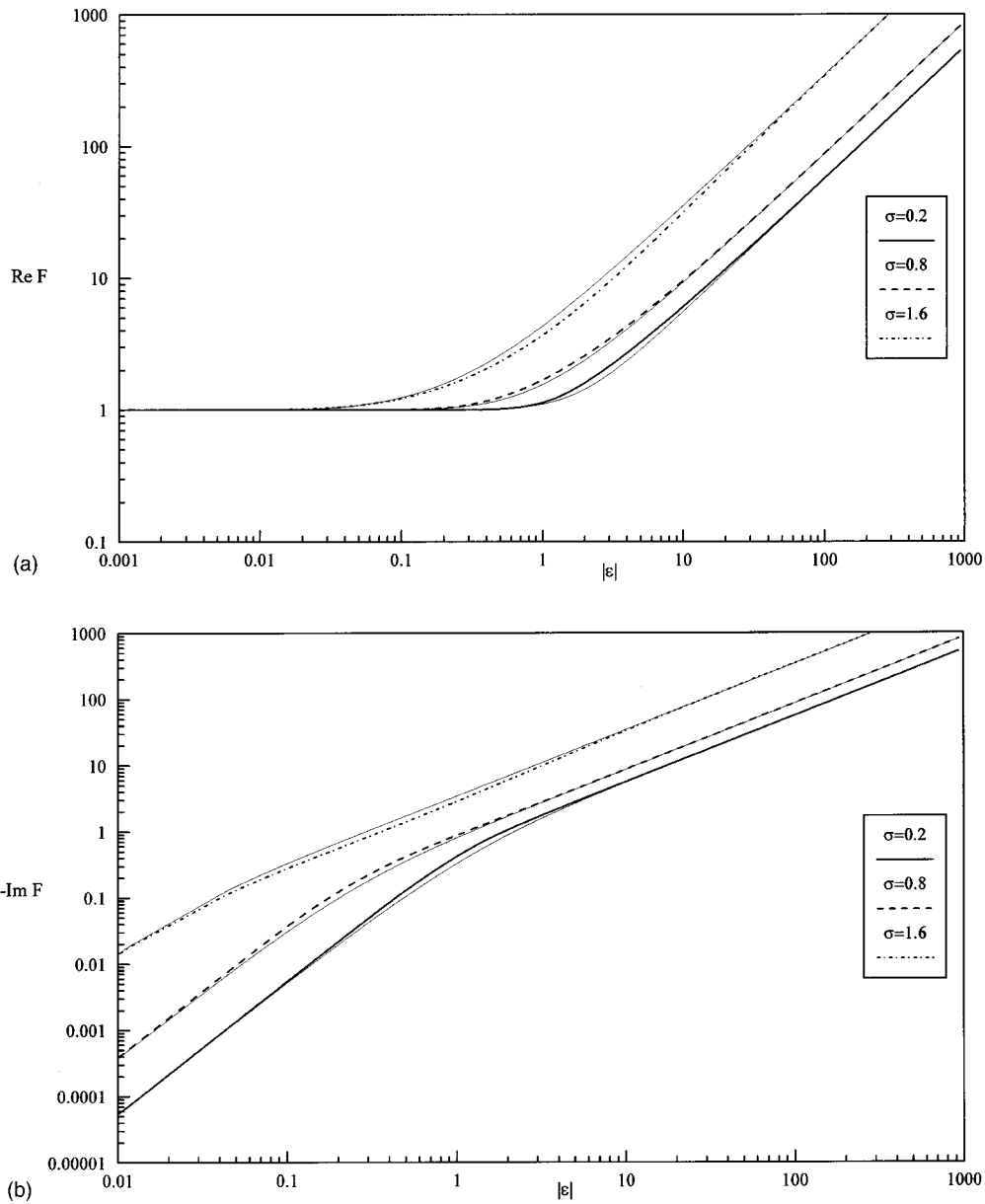


FIG. 2. (a) The real part of the viscosity correction function and its Padé approximant (thin solid lines) in the case of a material with triangular pores. (b) The imaginary part of the viscosity correction function and its Padé approximant (thin solid lines) in the case of a material with triangular pores.

### III. ASYMPTOTIC APPROXIMATIONS FOR LOW AND HIGH FREQUENCY

For none of the particular forms (38)–(40) for  $\chi(z)$  can the integral (34) be evaluated analytically, but approximations valid for low and high values of  $\bar{\lambda}$  (corresponding to low and high values of frequency  $\omega$ , with other variables fixed) can be obtained via expansions of  $\chi(z)$  for small and large  $z$ .

To obtain these approximations using results in the Appendix we write, from (34),

$$I(\omega) \equiv I(\sqrt{-i\bar{\lambda}}, d), \quad (41)$$

where, for convenience, we introduce  $d = \sigma \ln 2$  and define the function

$$I(z, d) = \frac{1}{\sqrt{2\pi}} \int_{-\infty}^{+\infty} \chi(ze^{-dt}) e^{-t^2/2} dt, \quad (42)$$

for  $-\pi/2 < \arg z < \pi/2$  and  $d \geq 0$ .

Determination of the asymptotic behavior of  $\psi = \psi(x, y; w)$  as  $w \rightarrow 0$  is a regular perturbation problem and, for any pore shape,  $\psi$  has a power series expansion in  $w^2$ , convergent for small  $w$ :

$$\psi(x, y; w) = \psi_0(x, y) + w^2 \psi_1(x, y) + w^4 \psi_2(x, y) + \dots$$

Substituting this expansion into (3) and comparing powers of  $w^2$  we find that each of the terms  $\psi_0, \psi_1, \dots$  satisfies a Poisson's equation, that is,

$$\Delta \psi_0 = 1, \quad \Delta \psi_n = \psi_{n-1}, \quad n = 1, 2, \dots \quad (43)$$

within the pore cross-section (of size  $s = 1$ ), with  $\psi_n = 0$  on the pore boundary, for  $n = 0, 1, \dots$ . From the maximum principle it follows by induction that  $\psi_n \leq 0$  for  $n$  even and that  $\psi_n \geq 0$  for  $n$  odd. Thus  $\bar{\psi}(z)$  has the power series expansion,

$$\bar{\psi}(z) = \bar{\psi}_0 + z^2 \bar{\psi}_1 + z^4 \bar{\psi}_2 + \dots, \quad (44)$$

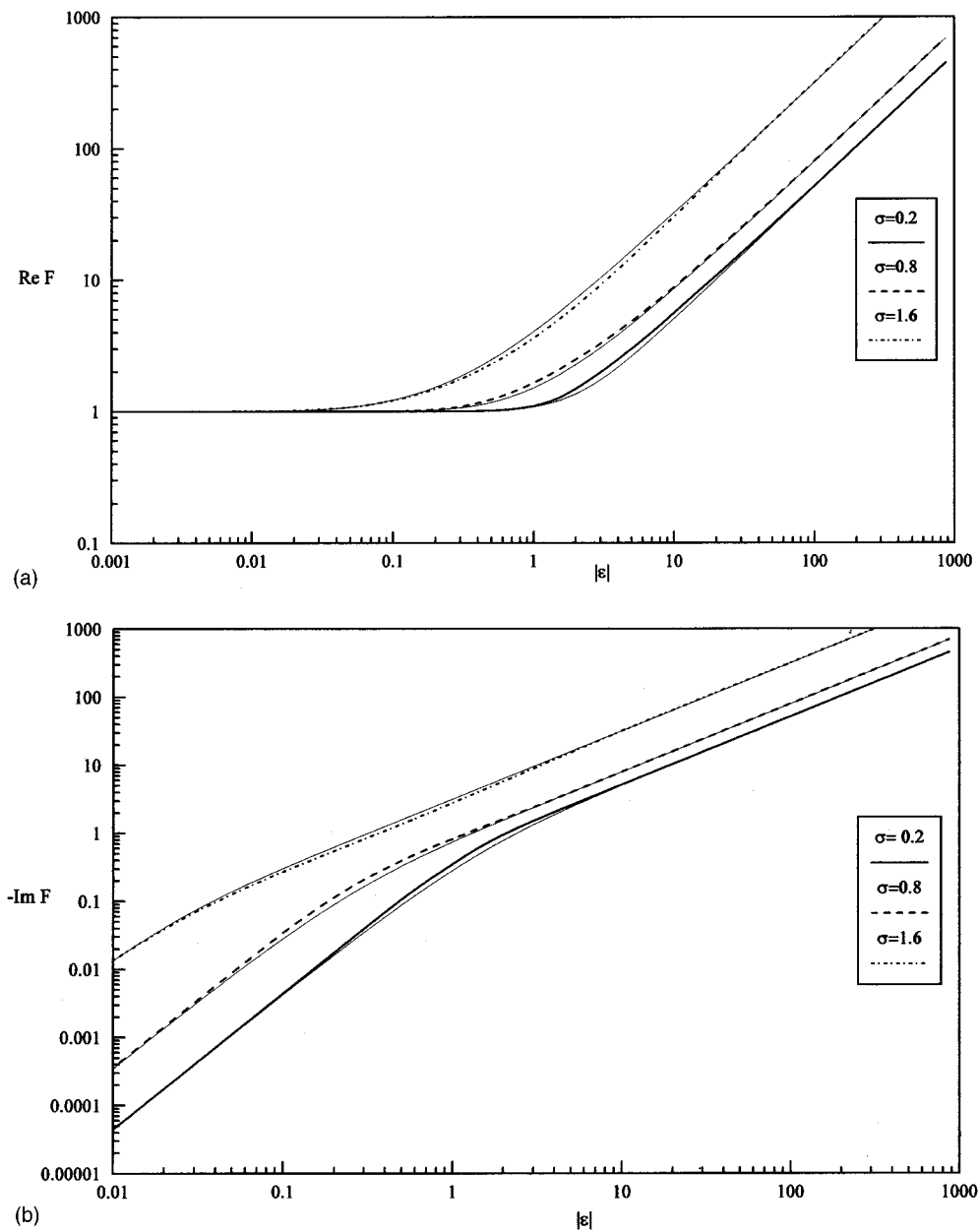


FIG. 3. (a) The real part of the viscosity correction function and its Padé approximant (thin solid lines) in the case of a material with circular cylindrical pores. (b) The imaginary part of the viscosity correction function and its Padé approximant (thin solid lines) in the case of a material with circular cylindrical pores.

convergent for small  $z$ , with  $\bar{\psi}_n$  the mean value of  $\psi_n(x, y)$  over the pore cross-section (of size  $s = 1$ ) and

$$\bar{\psi}_n < 0, \quad n = 0, 2, \dots, \quad (45)$$

$$\bar{\psi}_n > 0, \quad n = 1, 3, \dots,$$

so that, for small  $z$ ,

$$\chi(z) = 1 + z^2 \bar{\psi}_0 + z^4 \bar{\psi}_1 + \dots \quad (46)$$

It now follows from (42) and (46), and the results in the Appendix that  $I(z, p)$  has the asymptotic expansion

$$I(z, d) \sim 1 + \sum_{n=1}^{\infty} \bar{\psi}_{n-1} z^{2n} e^{2n^2 d^2} \quad (47)$$

as  $z \rightarrow 0$ , so that

$$I(\omega) \sim 1 + \sum_{n=1}^{\infty} \bar{\psi}_{n-1} (-i)^n \bar{\lambda}^{2n} e^{2n^2 d^2} \quad (48)$$

as  $\bar{\lambda} \rightarrow 0$  (the low-frequency limit).

Considering now the high-frequency limit; we note that, for  $w$  large,  $\psi \approx -1/w^2$  across the pore cross-section except within a boundary layer of width  $O(1/w)$ . A local analysis of the behavior within this boundary layer yields that (cf. Ref. 9), for a piecewise smooth boundary,

$$\begin{aligned} \psi(x, y; w) &= \frac{1}{w^2} (e^{-wr} - 1) + O\left(\frac{1}{w^2} e^{-wD}\right) \\ &+ O\left(\frac{1}{w^3} e^{-wr}\right), \quad \text{as } w \rightarrow \infty, \end{aligned} \quad (49)$$

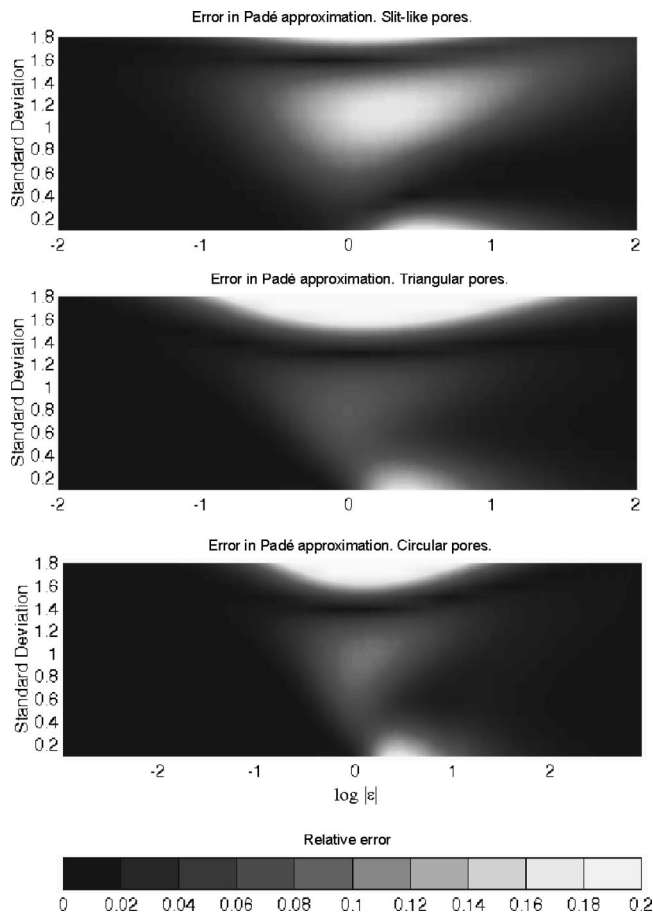


FIG. 4. Distribution of the relative error  $\Delta F$  for different values of the standard deviation and dimensionless parameter  $|\varepsilon|$ .

where  $r$  is the distance of  $(x, y)$  from the pore boundary and  $D$  is the distance to the nearest corner point.

Integrating (49) over the pore cross-section we find that

$$\bar{\psi}(z) = -\frac{1}{z^2} + \frac{A_1}{z^3} + O\left(\frac{1}{z^4}\right), \quad \text{as } z \rightarrow \infty,$$

where the pore shape factor  $A_1$  is the ratio of the length of the perimeter to the area of the cross-section for a pore of size  $s = 1$ . It follows that

$$\chi(z) = \frac{A_1}{z} + O\left(\frac{1}{z^2}\right), \quad \text{as } z \rightarrow \infty,$$

and hence, using the results in the Appendix, that

$$I(z, d) = \frac{A_1}{z} e^{d^2/2} + O\left(\frac{1}{z^2}\right), \quad \text{as } z \rightarrow \infty,$$

so that

$$I(\omega) = \frac{A_1}{\sqrt{-i\bar{\lambda}}} e^{d^2/2} + O\left(\frac{1}{\bar{\lambda}^2}\right), \quad (50)$$

as  $\bar{\lambda} \rightarrow \infty$  (the high-frequency limit).

The coefficient  $A_1$  is easily calculated for any pore cross-section. For general pore shapes the coefficients  $\bar{\psi}_0, \bar{\psi}_1, \dots$  can be obtained via a numerical solution of the Poisson's equations (43). For the particular case of slitlike, circular, and triangular pores these coefficients, which are seen in (46) to be the coefficients in the power series expansion for  $\chi(z)$ , can be obtained exactly. From (38) to (40), and the power series for  $\tanh z$  and the modified Bessel functions  $I_0(z)$  and  $I_1(z)$ ,<sup>10</sup> we have that, for slitlike pores,

$$\chi(z) = 1 - \frac{z^2}{3} + \frac{2}{15}z^4 + O(z^6), \quad z \rightarrow 0;$$

for triangular pores,

$$\chi(z) = 1 - \frac{z^2}{80} + \frac{z^4}{4480} + O(z^6), \quad z \rightarrow 0;$$

and for circular pores,

$$\chi(z) = 1 - \frac{z^2}{8} + \frac{z^4}{48} + O(z^6), \quad z \rightarrow 0.$$

Thus the coefficients  $\bar{\psi}_0, \bar{\psi}_1$  and  $A_1$  for these pore shapes are as tabulated in Table I.

For a general pore size distribution, taking the limit  $\omega \rightarrow 0$  in (18), it is found that

$$I(\omega) = 1 - \frac{i\rho_0\omega}{\mu} \bar{\psi}(0) \langle s^2 \rangle + o(\omega), \quad \text{as } \omega \rightarrow 0,$$

where  $\langle s^2 \rangle = \int_0^\infty s^2 e(s) ds$ . Thus, taking the limit  $\omega \rightarrow 0$  in (17) and noting that  $\lim_{\omega \rightarrow 0} F(\omega) = 1$  and  $\bar{\psi}(0) = \bar{\psi}_0$ , we find that

$$R_x = \frac{-\mu}{\bar{\psi}_0 \langle s^2 \rangle} = \frac{-\mu}{\bar{\psi}_0 s^2 e^{2d^2}} \quad (51)$$

in the case of a log-normal pore size distribution.

TABLE I. Values of the coefficients  $\bar{\psi}_0, \bar{\psi}_1, A_1$  and the pore shape factors  $\bar{\psi}_1/\bar{\psi}_0^2$  and  $A_1\sqrt{-\bar{\psi}_0}$ . Note that the numerical values of the coefficients  $\bar{\psi}_0, \bar{\psi}_1, A_1$ , depend on the definition of  $s$ , for each pore geometry. The values of the pore shape factors  $\bar{\psi}_1/\bar{\psi}_0^2$  and  $A_1\sqrt{-\bar{\psi}_0}$  are independent of this choice.

Pore shape	$\bar{\psi}_0$	$\bar{\psi}_1$	$A_1$	$\bar{\psi}_1/\bar{\psi}_0^2$	$A_1\sqrt{-\bar{\psi}_0}$
Slit-type	$-\frac{1}{3}$	$-\frac{2}{15}$	1	$\frac{6}{5}$	$\frac{1}{\sqrt{3}}$
Triangular	$-\frac{1}{80}$	$\frac{1}{4480}$	$4\sqrt{3}$	$\frac{10}{7}$	$\sqrt{\frac{3}{5}}$
Circular	$-\frac{1}{8}$	$-\frac{1}{48}$	2	$\frac{4}{3}$	$\frac{1}{\sqrt{2}}$

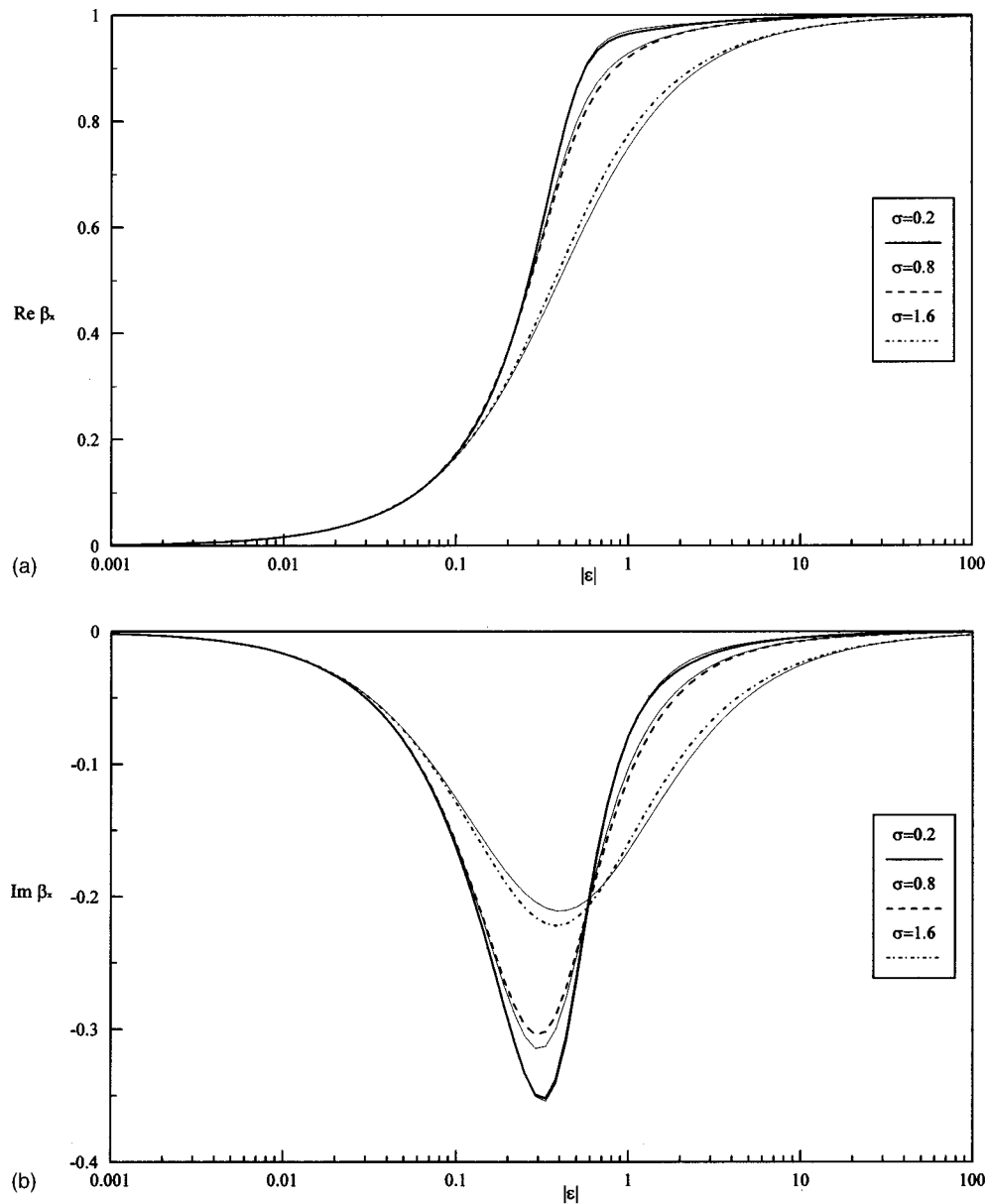


FIG. 5. (a) The real part of the relative admittance and the result obtained via Padé approximation (thin solid lines) for a material with circular cylindrical pores. (b) The imaginary part of the relative admittance and the result obtained via Padé approximation (thin solid lines) for a material with circular cylindrical pores.

Using (51), (17) and (48), it can be shown that, in the low-frequency/high flow resistivity limit  $\bar{\lambda} \rightarrow 0$ ,

$$\begin{aligned}
 F(\omega) &= 1 + i\bar{\lambda}^2 e^{2d^2} \left( \frac{\bar{\psi}_1}{\bar{\psi}_0} e^{4d^2} - \bar{\psi}_0 \right) + O(\bar{\lambda}^4) \\
 &= 1 + \theta_1 \varepsilon^2 + O(\varepsilon^4),
 \end{aligned} \tag{52}$$

where

$$\theta_1 = \frac{\bar{\psi}_1}{\bar{\psi}_0^2} e^{4d^2} - 1, \tag{53}$$

and the complex-valued, dimensionless parameter combination  $\varepsilon$  is given by

$$\varepsilon = \sqrt{\frac{-i\omega\rho_0}{R_x}} = \sqrt{-i\bar{\psi}_0} e^{d^2} \bar{\lambda}. \tag{54}$$

Similarly, using (51), (17) and (50), we find that, in the high-frequency/low flow resistivity limit  $\bar{\lambda} \rightarrow \infty$ ,

$$F(\omega) = \sqrt{-i\bar{\lambda}\bar{\psi}_0} A_1 e^{5d^2/2} + O(1) = \theta_2 \varepsilon + O(1), \tag{55}$$

where

$$\theta_2 = A_1 \sqrt{-\bar{\psi}_0} e^{3d^2/2}. \tag{56}$$

For the convenience of the reader the values of the pore shape factors  $\bar{\psi}_1/\bar{\psi}_0^2$  and  $A_1 \sqrt{-\bar{\psi}_0}$  for slit-type, triangular and circular pores are tabulated in Table I.

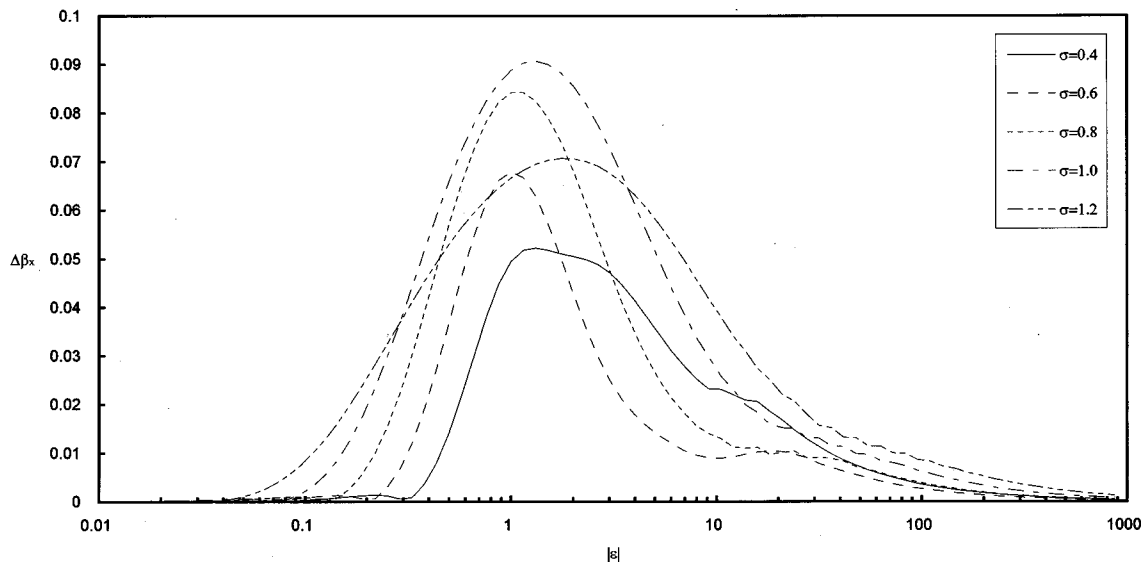


FIG. 6. The relative error in the relative admittance computed for several values of the standard deviation for a medium with circular cylindrical pores.

Utilizing these low- and high-frequency approximations for the viscosity correction function we can obtain the low- and high-frequency behavior of the complex density  $\rho_x(\omega)$ . From (14) it follows that

$$\frac{\rho_x(\omega)}{\rho_0} = 1 + \varepsilon^{-2} F(\omega)$$

so that, in the low-frequency/high flow resistivity limit,  $\varepsilon \rightarrow 0$ ,

$$\frac{\rho_x(\omega)}{\rho_0} = \frac{1}{\varepsilon^2} + 1 + \theta_1 + O(\varepsilon^2) = \frac{iR_x}{\omega\rho_0} + \frac{\bar{\psi}_1}{\bar{\psi}_0^2} e^{4d^2} + O(\varepsilon^2). \quad (57)$$

In the high-frequency/low flow resistivity limit,  $\varepsilon \rightarrow \infty$ ,

$$\begin{aligned} \frac{\rho_x(\omega)}{\rho_0} &= 1 + \frac{\theta_2}{\varepsilon} + O(\varepsilon^{-2}) \\ &= 1 + 2 \sqrt{\frac{\mu}{-i\omega\rho_0} \frac{e^{d^2/2}}{\bar{r}_h}} + O(\varepsilon^{-2}). \end{aligned} \quad (58)$$

To obtain this last equation we use expression (51) and that  $2\bar{s}/A_1 = \bar{r}_h$ , where  $\bar{r}_h$  is the median hydraulic radius, and the hydraulic radius of a pore is defined as twice the ratio of its cross-sectional area to its perimeter. Equations (57) and (58) agree with those in, e.g., Stinson and Champoux<sup>10</sup> for the case  $d=0$  of uniform pore size.

From (57) and (58) the low- and high-frequency behavior of all acoustic quantities can be deduced using relations (22), (23) and (28).

#### IV. TWO-POINT PADÉ APPROXIMANTS

Equations (52) and (55) provide good approximations to the viscosity correction function for small and large values of  $|\varepsilon| = (\rho_0\omega/R_x)^{1/2}$ , respectively. To provide an interpolation between these approximations for small and large  $|\varepsilon|$  and, hopefully, a sufficiently accurate approximation for intermediate values of  $|\varepsilon|$ , we construct a two-point Padé approxi-

mant, i.e., a rational approximant  $\tilde{F}(\omega)$  which has the same asymptotic behavior as the viscosity correction function  $F(\omega)$  at the two points  $\varepsilon \rightarrow 0$  and  $\varepsilon \rightarrow \infty$ .<sup>11</sup>

Let

$$\tilde{F}(\omega) = \frac{1 + \theta_3\varepsilon + \theta_1\varepsilon^2}{1 + \theta_3\varepsilon}, \quad (59)$$

where  $\theta_3 = \theta_1/\theta_2$  and  $\theta_1$  and  $\theta_2$  are given, by (53) and (56), in terms of  $d = \sigma \ln 2$  and the pore shape factors  $\bar{\psi}_1/\bar{\psi}_0^2$  and  $A_1\sqrt{-\bar{\psi}_0}$  (tabulated for various shapes in Table I). Then it is easy to see that  $\tilde{F}(\omega)$  has the required characteristics, i.e., that  $\tilde{F}(\omega)$  has the same asymptotic behavior, (52) and (55), for small and large  $|\varepsilon|$ , as  $F(\omega)$ : precisely

$$F(\omega) - \tilde{F}(\omega) = O(\varepsilon^4), \quad \varepsilon \rightarrow 0, \quad (60)$$

and

$$F(\omega) - \tilde{F}(\omega) = O(1), \quad \varepsilon \rightarrow \infty. \quad (61)$$

Noting that the values of  $F(\omega)$  and  $\tilde{F}(\omega)$  depend only on the pore shape and the values of the dimensionless parameter combination  $|\varepsilon|$  and the (dimensionless) standard deviation  $\sigma$ , we now investigate the accuracy of the approximation  $\tilde{F}(\omega)$  for  $F(\omega)$  for various pore shapes, various values of  $\sigma$ , and  $0 \leq |\varepsilon| < +\infty$ .

#### A. Error in the approximation of the viscosity correction function

Approximation (59) has been computed for several values of the standard deviation  $\sigma$ , for all three types of pore geometry, and has been compared with the exact viscosity correction function obtained from Eq. (17), with the integral  $I(\omega)$ , given by (34), computed by numerical integration.

The real and imaginary parts of the approximation  $\tilde{F}(\omega)$  are compared with those of the exact viscosity correction function  $F(\omega)$  in Figs. 1, 2, and 3, for slit-type, triangular, and circular pores, respectively, for  $\sigma=0.2, 0.8$ , and 1.6. As expected, in view of the asymptotic estimates (60) and (61),

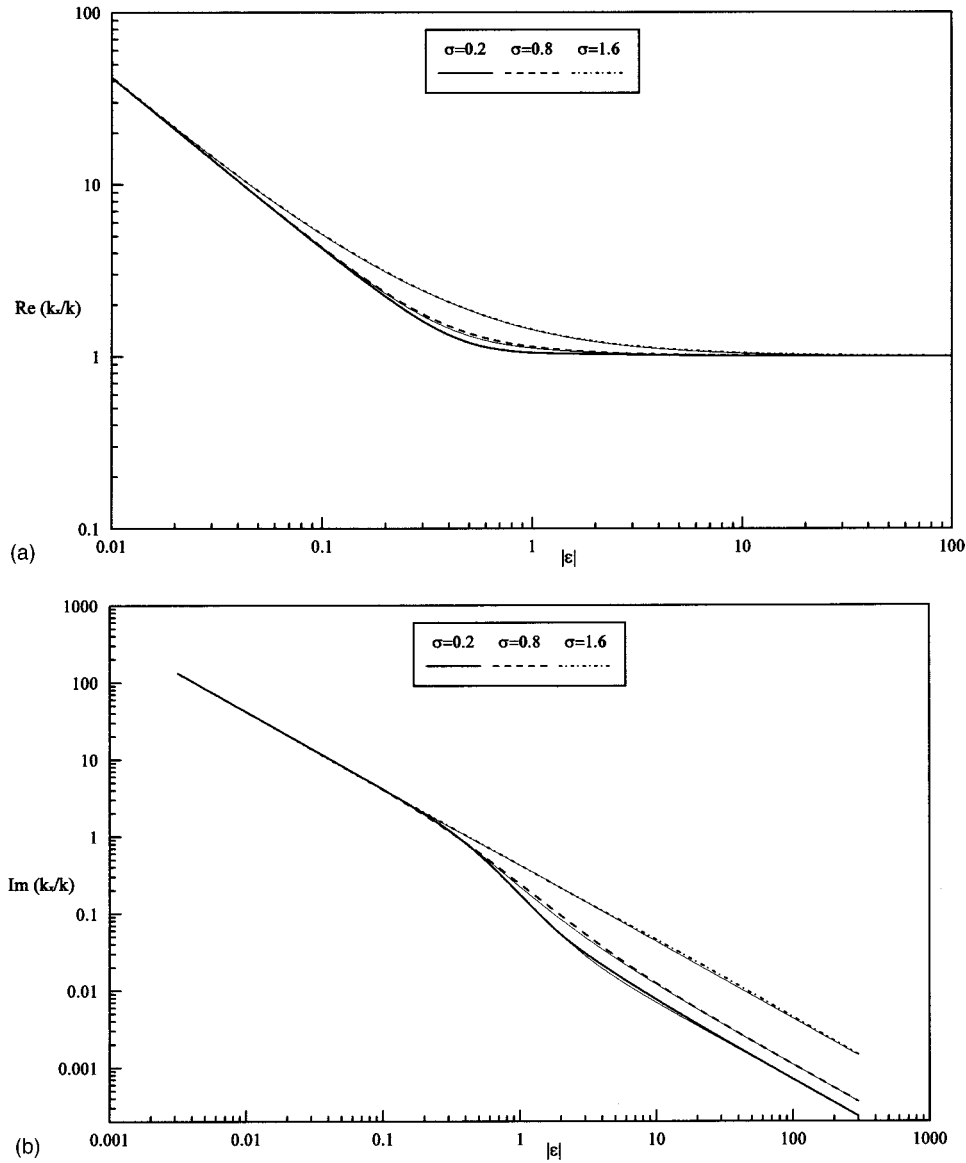


FIG. 7. (a) The real part of the complex wave number and the result obtained via Padé approximation (thin solid lines) for a material with slitlike pores. (b) The imaginary part of the complex wave number and the result obtained via Padé approximation (thin solid lines) for a material with slitlike pores.

the approximation is accurate for  $|\varepsilon| = (\rho_0 \omega / R_x)^{1/2}$  small and  $|\varepsilon|$  large. The accuracy of approximation deteriorates somewhat in the intermediate range  $0.1 < \varepsilon < 10$ .

To quantify this error more precisely, we have computed the magnitude of the relative error, i.e.,

$$\Delta F(\omega) = \left| \frac{F(\omega) - \tilde{F}(\omega)}{F(\omega)} \right|.$$

Figure 4 shows contour plots of  $\Delta F(\omega)$  as a function of  $\sigma$  and  $|\varepsilon|$  for the three pore shapes. It can be seen that the areas of maximum error are mainly concentrated in the range  $1 < |\varepsilon| < 10$  and that, as a function of  $\sigma$ , the error has two distinctive minima at around  $\sigma = 0.4$  and  $\sigma = 1.5$ . These graphs can be used for estimating the ranges of  $|\varepsilon|$  and  $\sigma$  for which  $\tilde{F}(\omega)$  satisfies given accuracy requirements.

Precise calculations indicate that the maximum relative error in the range of interest for most practical applications,

$0.2 < \sigma < 1.5$ , does not exceed 15.5% ( $\sigma = 1.1$ ) for slits, 11% ( $\sigma = 1.5$ ) for triangles, and 9% ( $\sigma = 1.0$ ) for a circular pore cross-section.

## B. Error in the approximation of other acoustic quantities

A comparison has also been made between acoustical quantities calculated approximately, by replacing  $F(\omega)$  by its approximation  $\tilde{F}(\omega)$ , and their exact values, obtained by computing  $F(\omega)$  exactly by numerical integration. Considered are the relative admittance and the complex wave number. Figures 5–8 illustrate graphically, for each of these quantities, results for the pore shape for which the approximation error is greatest.

In Fig. 5, for the case of circular cylindrical pores, the relative admittance  $\beta_x(\omega) = \beta_b(\omega)/q$ , given by (28), is plotted against  $|\varepsilon|$  for  $\sigma = 0.2, 0.8$ , and  $1.6$ , as is the approxima-



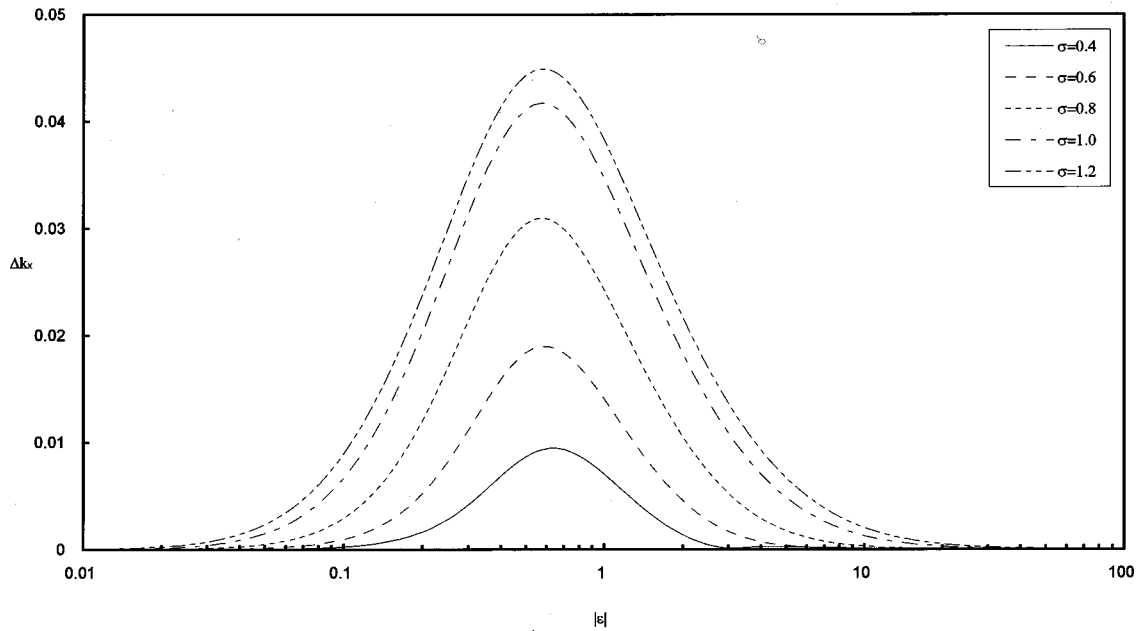


FIG. 8. The relative error in the complex wave number computed for several values of the standard deviation for a medium with slitlike pores.

tion  $\tilde{\beta}_x(\omega)$  to  $\beta_x(\omega)$  obtained by replacing  $F(\omega)$  in the computations by its Padé approximant  $\tilde{F}(\omega)$ . The agreement is good, especially for  $|\varepsilon|$  small and large, and is quantified further in Fig. 6, in which the magnitude of the relative error,

$$\Delta\beta_x(\omega) = \left| \frac{\beta_x(\omega) - \tilde{\beta}_x(\omega)}{\beta_x(\omega)} \right|$$

is plotted against  $|\varepsilon|$ , for various values of  $\sigma$ . It can be seen that the error in the derived quantity  $\beta_x(\omega)$  is less than that in the viscosity correction function, and does not exceed 9% ( $\sigma=1.0$ ,  $|\varepsilon|=1.32$ ) for circular pores. Similar calculations show that the maximum error in  $\beta_x(\omega)$  does not exceed 4% for slits ( $\sigma=1.2$ ,  $|\varepsilon|=0.44$ ), and 2.2% for triangular pores ( $\sigma=1.0$ ,  $|\varepsilon|=0.38$ ).

Analogous trends can be observed for the complex wave number. The approximation to  $k_x(\omega)$  obtained by replacing  $F(\omega)$  by  $\tilde{F}(\omega)$  is denoted by  $\tilde{k}_x(\omega)$  and  $\Delta k_x(\omega) = |(k_x(\omega) - \tilde{k}_x(\omega))/k_x(\omega)|$  is the relative error. Figure 7 plots the real and imaginary parts of  $k_x(\omega)$  and  $\tilde{k}_x(\omega)$  against  $|\varepsilon|$  for  $\sigma = 0.2, 0.8$ , and  $1.6$ , and  $\Delta k_x(\omega)$  is plotted against  $|\varepsilon|$  in Fig. 8. The agreement between both the real and imaginary parts of  $k_x(\omega)$  and  $\tilde{k}_x(\omega)$  is excellent. From Fig. 8 and similar graphs we note that the relative error  $\Delta k_x(\omega)$  does not exceed 4.5% ( $\sigma=1.2$ ,  $|\varepsilon|=0.58$ ) for slitlike pores, 3% ( $\sigma=1.0$ ,  $|\varepsilon|=0.5$ ) for circular pores and 1.4% ( $\sigma=1.2$ ,  $|\varepsilon|=0.4$ ) for triangular pores.

## V. CONCLUDING REMARKS

A theoretical justification has been given and simplified expressions presented for the form of the viscosity correction function for a porous medium with a statistically distributed pore size. This function, originally introduced by Biot<sup>1</sup> and extended by Yamamoto and Turgut<sup>3</sup> to the case of porous media with a statistically distributed pore size, describes viscous, thermal diffusion and pore size distribution effects of

sound propagation inside a porous rigid frame material. Computationally efficient and simple two-point Padé approximants for this function have been derived in this paper for various pore geometries. The resulting equations [(23)–(26) and (59)] are simple. The accuracy of the proposed approximation to the exact viscosity correction function has been investigated over the whole range of microscopic material parameters of interest. For most of this range the approximation is highly accurate and it is our belief that the accuracy established over the remaining range will be quite adequate for practical modelling of acoustical characteristics, particularly bearing in mind uncertainties in accurately identifying material parameter values and, indeed, in the accuracy of the model of acoustical characteristics in terms of viscosity correction function proposed.

The simple analytical form of the approximations means that these are likely to be of substantial practical interest for predictions of the acoustic field in the presence of a porous absorbing surface. Some preliminary and encouraging comparisons of excess attenuation predictions, using the proposed approximations for triangular pore shapes, with short range experiments over sand are reported recently in Ref. 12.

Although the most definite results are only for selected pore geometries, the general equations allow for any complex pore shape to be considered. In this case the shape factors (Table I) which relate to the asymptotic behavior of the solution of the Helmholtz equation for such particular pore shape could be obtained either numerically or experimentally. Specifically, it can be seen from the asymptotic behavior of the viscosity correction function at the lower- and higher-frequency limits [expressions (52) and (55), respectively] that the shape factors,  $\bar{\psi}_1/\bar{\psi}_0^2$  and  $\sqrt{\bar{\psi}_0}A_1$ , can be recovered from low/high-frequency acoustical experiments on the material combined with nonacoustical measurements of other parameters.

## ACKNOWLEDGMENTS

The authors would like to thank Dr. S. Taherzadeh for providing FORTRAN code for numerical evaluation of the integrals and Dr. D. C. Hothersall for his comments on this manuscript. This work was part of a project supported by the Engineering and Physical Sciences Research Council under Grant No. GR/H41966.

## APPENDIX: APPROXIMATION OF A CLASS OF INTEGRALS

Suppose that  $f(z)$  is a complex-valued function of the complex variable  $z$ , and that, for some  $\alpha$  in the range  $0 < \alpha \leq \pi$ ,  $f(z)$  is continuous in the sector of the complex plane,  $|\arg z| \leq \alpha$ ,  $|z| > 0$ . In Sec. II integrals of the form

$$I(z, d) = \frac{1}{\sqrt{2\pi}} \int_0^{+\infty} f(e^{-dt}z) e^{-t^2/2} dt \quad (\text{A1})$$

arise, for various choices of the function  $f$ .

Consider the approximation of  $f$  by a function  $\tilde{f}$  of the form

$$\tilde{f}(z) = \sum_{n=1}^N a_n z^{b_n},$$

where  $a_1, \dots, a_n, b_1, \dots, b_n$  are real coefficients, and suppose that the remainder,  $r(z) = f(z) - \tilde{f}(z)$ , satisfies, for some real constants  $c$  and  $C$  ( $C > 0$ ),

$$|r(z)| \leq C|z|^c, \quad (\text{A2})$$

for  $|\arg z| \leq \alpha$ ,  $|z| > 0$ . Let  $\tilde{I}(z, d)$  denote the corresponding approximation to  $I(z, d)$ , i.e.,

$$\begin{aligned} \tilde{I}(z, d) &= \frac{1}{\sqrt{2\pi}} \int_{-\infty}^{+\infty} \tilde{f}(e^{-dt}z) e^{-t^2/2} dt \\ &= \sum_{n=1}^N \frac{a_n z^{b_n}}{\sqrt{2\pi}} \int_{-\infty}^{+\infty} e^{-db_n t} e^{-t^2/2} dt. \end{aligned}$$

Now, for any real number  $p$ ,

$$\begin{aligned} \frac{1}{\sqrt{2\pi}} \int_{-\infty}^{+\infty} e^{-pt} e^{-t^2/2} dt &= \frac{e^{p^2/2}}{\sqrt{2\pi}} \int_{-\infty}^{+\infty} e^{-(p-t)^2/2} dt \\ &= e^{p^2/2} \end{aligned} \quad (\text{A3})$$

since

$$\frac{1}{\sqrt{2\pi}} \int_{-\infty}^{+\infty} e^{-t^2/2} dt = 1.$$

Thus

$$\tilde{I}(z, d) = \sum_{n=1}^N a_n z^{b_n} e^{d^2 b_n^2 / 2}.$$

Further, the error in this approximation satisfies

$$I(z, d) - \tilde{I}(z, d) = \frac{1}{\sqrt{2\pi}} \int_{-\infty}^{+\infty} r(e^{-dt}z) e^{-t^2/2} dt$$

and, utilizing (A2) and (A3) it follows that, for  $|\arg z| \leq \alpha$ ,

$$\begin{aligned} |I(z, d) - \tilde{I}(z, d)| &\leq \frac{C}{\sqrt{2\pi}} |z|^c \int_{-\infty}^{+\infty} e^{-cdt} e^{-t^2/2} dt \\ &= C|z|^c e^{c^2 d^2 / 2}. \end{aligned}$$

<sup>1</sup>M. A. Biot, "Theory of propagation of elastic waves in a fluid-saturated porous solid. I. Low-Frequency Range," *J. Acoust. Soc. Am.* **28**, 168–178 (1956); "II. Higher Frequency Range," *J. Acoust. Soc. Am.* **28**, 179–191 (1956).

<sup>2</sup>M. R. Stinson, "The propagation of plane sound waves in narrow and wide circular tubes, and generalisation to uniform tubes of arbitrary cross-sectional shape," *J. Acoust. Soc. Am.* **89**, 550–558 (1991).

<sup>3</sup>T. Yamamoto and A. Turgut, "Acoustic-wave propagation through porous-media with arbitrary pore-size distributions," *J. Acoust. Soc. Am.* **83**, 1744–1751 (1988).

<sup>4</sup>Keith Attenborough, "Models for the acoustical properties of air-saturated granular media," *Acta Acust. (China)* **1**, 213–226 (1993).

<sup>5</sup>S. N. Chandler-Wilde and K. V. Horoshenkov, "Padé approximants for the acoustical characteristics of rigid frame porous media," *J. Acoust. Soc. Am.* **98**, 1119–1129 (1995).

<sup>6</sup>J. M. Evans, "Measuring the pore size distribution of a model granular material using a water suction method," Working paper/Internal report, Department of Engineering Mechanics, Open University, October 1993.

<sup>7</sup>C. H. Juang and R. D. Holtz, "Fabric, pore size distribution, and permeability of sandy soils," *J. Geotechn. Eng. Am. Soc. Civil Eng.* **112**, 855–868 (1986).

<sup>8</sup>K. V. Horoshenkov, D. C. Hothersall, and K. Attenborough, "Porous materials for scale model experiments in outdoor sound propagation," *J. Sound Vib.* **194**, 685–708 (1996).

<sup>9</sup>M. R. Stinson and Y. Champoux, "Propagation of sound and the assignment of shape factors to model porous materials having simple pore shape geometries," *J. Acoust. Soc. Am.* **91**, 685–695 (1992).

<sup>10</sup>M. Abramovitz and I. A. Stegun, *Handbook of Mathematical Functions* (Dover, New York).

<sup>11</sup>G. A. Backer, *Essentials of Padé Approximants* (Academic, London, 1975).

<sup>12</sup>K. Attenborough, "Natural noise control," *Proceedings of International Congress on Noise Control Engineering*, pp. 51–73, Liverpool, England, July–August 1996.

# Transient wave propagation in a circular annulus subjected to transient excitation on its outer surface

Guoli Liu and Jianmin Qu<sup>a)</sup>

*The George W. Woodruff School of Mechanical Engineering, Georgia Institute of Technology, Atlanta, Georgia 30332-0405*

(Received 21 January 1998; accepted for publication 21 May 1998)

The objective of this work is to investigate the propagation of guided transient waves in the circumferential direction of annular structural components. For this purpose, a two-dimensional circular annulus is considered. It is assumed that the inner surface of the annulus is traction free and the outer surface of the annulus is subjected to a time-dependent transient excitation. The guided circumferential waves induced by this transient excitation are studied in detail to understand the propagation characteristics of various wave modes. The method of eigenfunction expansion is used to solve the transient wave propagation problem. To this end, the problem of time harmonic, steady-state circumferential waves is solved first as the eigenfunctions. The time-dependent response of the annulus is then obtained by superimposing all eigenfunctions over all possible frequencies. Several numerical examples are given to illustrate the method of solution and to provide some guidelines on using guided waves to detect radial cracks in annular structural components. © 1998 Acoustical Society of America. [S0001-4966(98)01709-3]

PACS numbers: 43.20.Bi [ANN]

## INTRODUCTION

Fatigue cracks have been found to initiate and grow in the radial direction in many annulus-shaped components in aging helicopters. Those include some of the most critical components such as the rotor hub, connecting links, pitch shaft, etc. At the present time, detection of such radial fatigue cracks relies mostly on visual inspection. More systematic, automated, and efficient methods to detect these cracks are needed.

Conventional ultrasonic imaging techniques can be used to detect such radial cracks. However, these techniques are impractical for real-time, integrated diagnosis. It has been proposed recently (Nagy *et al.*, 1994; Qu *et al.*, 1996) that guided ultrasonic waves might be used for the detection of radial fatigue cracks in annular structures. In the case of annulus-shaped structural components, access to the inner surface is usually unavailable. One can only generate guided waves from the outside of the annulus. Since the radial cracks are often found to initiate from the inner surface, particular wave modes must be selectively generated so that the energy is concentrated near the inner surface to increase the signal-to-noise ratio. Before such guided waves can be effectively used for this purpose, their generation and propagation must be understood. The physics and mechanics of the wave fields must be carefully examined. Although there exists a large body of literature on straight waveguides, such as bars and plates, solutions to circumferential wave propagation in annular structures are very few.

To provide the scientific foundation for the guided wave techniques for detecting radial cracks in annular structures, a two-dimensional circular annulus is considered in this paper. The outer surface of the annulus is subjected to a time-

dependent transient excitation. The guided circumferential waves induced by this transient excitation are investigated in detail. The method of eigenfunction expansion is used in this study. The steady-state, time harmonic circumferential waves are solved first as the eigenfunctions. The time-dependent response of the annulus is then obtained by superimposing all eigenfunctions over all possible frequencies. Several numerical examples are given to illustrate the method of solution and to reveal some interesting wave phenomena intrinsic to curved waveguides.

Intuitively, an annulus can be viewed as a waveguide in which elastic waves can propagate in the circumferential direction. Extensive studies have been conducted on other types of waveguides. For example, wave propagation is well understood in the axial direction of a circular cross-section bar (Mindlin and McNiven, 1960), a rectangular cross-section bar (Mindlin and Fox, 1960), a circular hollow cylinder (Gazis, 1959), and plates (Mindlin, 1960). A comprehensive review of these studies can be found in (Miklowich, 1978). A more recent work by Ditri and Rose (1992) solved the problem of transient wave propagation in the axial direction of a hollow cylinder subjected to surface tractions.

The difference between an annulus and a plate is that the annulus has a finite radius of curvature. In fact, a flat plate can be viewed as a limiting case of the annulus when the radius of the curvature of the annulus becomes infinite (Liu and Qu, 1998). Nevertheless, the finite radius of curvature does complicate the wave fields, and it generates some interesting new phenomena.

In a sense, a surface can also be viewed as a waveguide. The most familiar example of such a guided wave is the Rayleigh surface wave (Rayleigh, 1885). Later, it was observed that a Rayleigh wave may also propagate along a cylindrical surface (Cook and Valkenburg, 1954). The analytical work on Rayleigh-type waves on a cylindrical surface

<sup>a)</sup>Electronic mail: jianmin.qu@me.gatech.edu

was presented by Viktorov (1958), Grace and Goodman (1966), Keller and Karal (1960, 1964), Grimshaw (1968), Rulf (1969), and Gregory (1971). The review article by Überall (1973) gave a large amount of literature in the related subjects. It was found that unlike the Rayleigh waves on a planar surface, frequency dispersion takes place for surface waves propagating along a curved surface. In addition, in the case of a curvilinear (convex) boundary of a solid, it is also possible for other modes of surface waves to propagate, confined near the curved boundary (Brekhovskikh, 1968). These waves are sometimes called the “whispering gallery” waves. Famous examples of such whispering gallery waves include the Temple of Heaven in Beijing and the dome of St. Paul’s Cathedral in London, which was described in Rayleigh’s classic book (Rayleigh, 1945).

The dispersion of elastic waves and Rayleigh-type waves in a thin disc was investigated by Cerv (1988). The focus was to study the displacement amplitude of the various circumferential modes in a solid disc. Recently, Liu and Qu (1997) derived the dispersion equation for the time-harmonic circumferential waves in a circular annulus. In the case of an annulus, multiple reflection may take place. Consequently, a true guided wave can propagate in the circumferential direction. The guided circumferential wave consists of many different modes. It was found that, depending on the geometry of the annulus, the first and second modes correspond to the surface Rayleigh wave propagating along the outer and inner surfaces, respectively (Liu and Qu, 1998). The other higher modes are truly propagating guided waves formed by the multiple reflection from both surfaces.

The paper is arranged as follows. In Sec. II we present the fundamental governing equations and boundary conditions of transient wave motion. The initial-boundary value problem is formulated for the given loading conditions. This initial-boundary value problem is solved in Sec. III using the mode eigenfunction expansion method. Then, several numerical examples are presented in Sec. IV. A comparison of the eigenfunction expansion method with the finite-element method is given in Sec. V. Finally, the paper concludes with a summary in Sec. VI.

## I. PROBLEM STATEMENT

Consider a circular annulus of inner radius  $a$  and outer radius  $b$  as shown in Fig. 1. It is assumed that the material is linearly elastic and isotropic. For the two-dimensional deformation considered here, assume that plane strain deformation in the annulus prevails. Therefore, in the polar coordinate system  $(r, \theta)$  shown in Fig. 1, the displacement components in the annulus can be written as

$$u_r = u_r(r, \theta, t), \quad (1a)$$

$$u_\theta = u_\theta(r, \theta, t). \quad (1b)$$

For convenience, define the two-dimensional displacement vector

$$\mathbf{u} = \begin{pmatrix} u_r \\ u_\theta \end{pmatrix}. \quad (2)$$

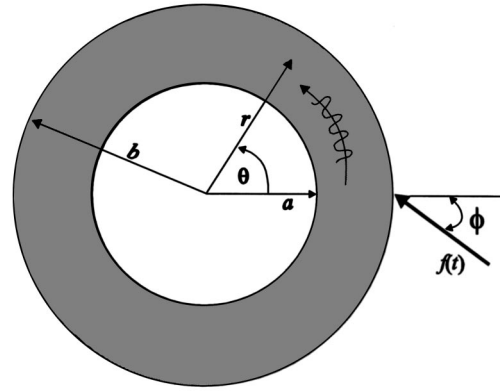


FIG. 1. A circular annulus with inner radius  $a$ , outer radius  $b$ , subjected to a time-dependent force on the outer surface.

Then, the displacement equation of motion in the absence of body force is (Achenbach, 1984)

$$L[\mathbf{u}] \equiv c_L^2 \nabla(\nabla \cdot \mathbf{u}) - c_T^2 \nabla \times \nabla \times \mathbf{u} = \frac{\partial^2 \mathbf{u}}{\partial t^2} \quad \text{in } V, \quad (3)$$

where  $V$  denotes the annulus, and  $c_L$  and  $c_T$  are the longitudinal and shear wave phase velocities, respectively. They are related to the material’s mass density,  $\rho$ , and the Lamé constants,  $\lambda$  and  $\mu$ , by

$$c_L = \sqrt{\frac{\lambda + 2\mu}{\rho}}, \quad (4a)$$

$$c_T = \sqrt{\frac{\mu}{\rho}}. \quad (4b)$$

On the boundary of  $V$ ,  $\mathbf{u}$  must satisfy the following boundary conditions (Malvern, 1969),

$$B[\mathbf{u}] \equiv \lambda(\nabla \cdot \mathbf{u}) \cdot \mathbf{n} + \mu[\nabla \mathbf{u} + (\nabla \mathbf{u})^T] \cdot \mathbf{n} = \mathbf{F} \quad \text{on } S, \quad (5)$$

where  $S$  is the boundary of  $V$ , and  $\mathbf{n}$  is the outward unit normal vector of the boundary where the traction  $\mathbf{F}$  is prescribed. Note that in (5),  $\nabla \mathbf{u}$  is the gradient of a vector, which is a dyadic. The superscript  $T$  indicates the transpose.

If the domain  $V$  is at rest before the application of  $\mathbf{F}$ ,  $\mathbf{u}$  must also satisfy the initial conditions at  $t=0$ , i.e.,

$$\mathbf{u} = \frac{\partial \mathbf{u}}{\partial t} = \mathbf{0} \quad \text{for } t \leq 0 \quad (6)$$

for all material points in  $V$ .

The above equations form a well-posed initial-boundary value problem for the displacement components  $u_r$  and  $u_\theta$ . In the subsequent sections, this initial-boundary value problem will be solved to study the time-dependent guided waves that propagate in the circumferential direction of the annulus.

## II. METHOD OF SOLUTION

Consider a body  $V$  with boundary  $S$ . Assume that when  $t \leq 0$  the body is at rest and after that the surface  $S$  is subjected to traction load  $\mathbf{F}$ . In this case, the initial-boundary value problem stated in Sec. II can be summarized as

$$L[\mathbf{u}] = \frac{\partial^2 \mathbf{u}}{\partial t^2} \text{ in } V, \quad (7a)$$

$$B[\mathbf{u}] = \mathbf{F} \text{ on } S, \quad (7b)$$

$$\mathbf{u} = \frac{\partial \mathbf{u}}{\partial t} = \mathbf{0} \text{ at } t=0. \quad (7c)$$

In this section, the above equations will be solved by the method of eigenfunction expansion (Reismann, 1967; Eringen, 1975).

For this purpose, only the wave modes that have integer wave numbers (free vibration modes) are needed for the eigenfunction expansion method. Consider the corresponding steady-state problem with homogeneous boundary conditions as stated by (A1) and (A2). It has been shown that the  $\omega_{mn}^2$  in (A1) is real and nonnegative (Love, 1944). Furthermore, the linear differential operator  $L[ \ ]$  is self-adjoint under the traction-free boundary conditions (A2) (Weaver and Pao, 1983). Under these conditions, the wave modes associated with integer wave numbers form an orthogonal set, i.e.,

$$\int_V \rho \mathbf{U}_{mn}^{(i)} \cdot \mathbf{U}_{sk}^{(j)} dV = \begin{cases} 0, & m \neq s \text{ or } n \neq k, \\ \delta_{ij} M_{mn}^{(i)}, & m = s \text{ and } n = k, \end{cases} \quad (8)$$

where  $n$  is an integer and  $\delta_{ij}$  is the Kronecker delta. These modes can be divided into two groups [see Eqs. (A3) and (A4)]. Within each group, the orthogonal relation is satisfied by the integral over  $r$  in (8). Between the two groups, the orthogonal relation is satisfied by the integral over  $\theta$  in (8). For the notation of the wave mode  $\mathbf{U}_{mn}^{(i)}$ , the first subscript is used to indicate the particular wave mode and the second subscript is to indicate the discrete wave number. For example,  $\mathbf{U}_{mn}^{(i)}$  represents the  $m$ th mode for the given wave number  $n$ . Thus, the principle of linear superposition means that the general expression of the  $m$ th mode can be obtained by summing over all integer wave numbers along that mode (the  $m$ th branch). Since  $\mathbf{U}_{mn}^{(i)}$  form a complete set, the formal solution to (7) may now be written as

$$\mathbf{u} = \mathbf{w} + \sum_{m=1}^{\infty} \sum_{i=1}^2 \sum_{n=0}^{\infty} q_{mn}^{(i)}(t) \mathbf{U}_{mn}^{(i)}, \quad (9)$$

where  $q_{mn}^{(i)}(t)$  are unknown functions of time to be determined and  $\mathbf{w}$  is the solution to the following quasistatic problem,

$$L[\mathbf{w}] = \mathbf{0} \text{ in } V, \quad (10)$$

$$B[\mathbf{w}] = \mathbf{F} \text{ on } S. \quad (11)$$

Note that although obtaining  $\mathbf{w}$  from (10) and (11) is not trivial, it will be seen later that explicit expressions of  $\mathbf{w}$  are not necessary since it can be eliminated from (9).

To determine  $q_{mn}^{(i)}(t)$ , substituting (9) into (7a) in conjunction with (A1) yields

$$\sum_{m=1}^{\infty} \sum_{i=1}^2 \sum_{n=0}^{\infty} [\ddot{q}_{mn}^{(i)}(t) + \omega_{mn}^2 q_{mn}^{(i)}(t)] \mathbf{U}_{mn}^{(i)} = -\ddot{\mathbf{w}}. \quad (12)$$

Now, multiply both sides of (12) by  $\mathbf{U}_{sk}^{(j)}$ , integrate over  $V$ , and employ (8) to obtain

$$\ddot{q}_{mn}^{(i)}(t) + \omega_{mn}^2 q_{mn}^{(i)}(t) = \frac{\ddot{P}_{mn}^{(i)}}{\omega_{mn}^2 M_{mn}^{(i)}}, \quad (13)$$

where

$$P_{mn}^{(i)} = -\omega_{mn}^2 \int_V \mathbf{w} \cdot \mathbf{U}_{mn}^{(i)} dV. \quad (14)$$

The solution to (13) with homogeneous initial conditions becomes

$$q_{mn}^{(i)}(t) = \frac{P_{mn}^{(i)}}{\omega_{mn}^2 M_{mn}^{(i)}} + \frac{Q_{mn}^{(i)}}{M_{mn}^{(i)}}, \quad (15)$$

where

$$Q_{mn}^{(i)} = \frac{1}{\omega_{mn}} \int_0^t P_{mn}^{(i)} \sin[\omega_{mn}(t-\tau)] d\tau. \quad (16)$$

Finally, substitution of (15) into (9) yields

$$\mathbf{u} = \mathbf{w} + \sum_{m=1}^{\infty} \sum_{i=1}^2 \sum_{n=0}^{\infty} \frac{P_{mn}^{(i)}}{\omega_{mn}^2 M_{mn}^{(i)}} \mathbf{U}_{mn}^{(i)} + \sum_{m=1}^{\infty} \sum_{i=1}^2 \sum_{n=0}^{\infty} \frac{Q_{mn}^{(i)}}{\omega_{mn}^2 M_{mn}^{(i)}} \mathbf{U}_{mn}^{(i)}. \quad (17)$$

In view of (14) and the orthogonal condition (8), one can easily show that the first two terms in (17) cancel each other. Therefore,

$$\mathbf{u} = \sum_{m=1}^{\infty} \mathbf{u}_m, \quad (18)$$

where

$$\mathbf{u}_m = \sum_{i=1}^2 \sum_{n=0}^{\infty} \frac{Q_{mn}^{(i)}}{M_{mn}^{(i)}} \mathbf{U}_{mn}^{(i)}. \quad (19)$$

Note that  $M_{mn}^{(i)}$  in (19) can be obtained from (8) once  $\mathbf{U}_{mn}^{(i)}$  is known from Appendix A. To further simplify  $Q_{mn}^{(i)}$ , consider (14). It follows from (A2) that

$$P_{mn}^{(i)} = - \int_V \mathbf{w} \cdot L[\mathbf{U}_{mn}^{(i)}] dV. \quad (20)$$

Making use of the divergence theorem twice in (20) in conjunction with (7) gives

$$P_{mn}^{(i)} = \int_S B[\mathbf{w}] \cdot \mathbf{U}_{mn}^{(i)} dS, \quad (21)$$

where the integral is over the entire surface of  $V$ . Subsequent substitution of (11) into (21) yields

$$P_{mn}^{(i)} = \int_S \mathbf{F} \cdot \mathbf{U}_{mn}^{(i)} dS. \quad (22)$$

To summarize the above derivation, once the corresponding steady-state problem is solved as described in Appendix A, the solution to the time-dependent initial-boundary value problem can be evaluated through (18), (16), (8) and (22). For the  $m$ th mode, the summation  $\mathbf{u}_m$  in (18) is carried out along the  $m$ th branch of the dispersion curve and called the  $m$ th mode of the transient circumferential waves.

TABLE I. Geometry and material parameters.

Inner diameter	Outer diameter	Ratio $\eta = a/b$	Poisson's ratio	L-wave speed	T-wave speed
$a = 5.08$ cm	$b = 6.28$ cm	$\eta = 0.8089$	$\nu = 0.2817$	$c_L = 5660$ m/s	$c_T = 3120$ m/s

### III. NUMERICAL EXAMPLES OF THE TIME-DEPENDENT CIRCUMFERENTIAL WAVES

In this section, some numerical results will be presented. The values of the geometry and material parameters used in the computation are given in Table I. The external load is taken to be a concentrated force on the outer surface at  $\theta = \theta_0$ , i.e.,

$$\mathbf{F} = f(t) \delta(\theta - \theta_0) \mathbf{m}/b, \tag{23}$$

where  $\delta(\theta)$  is the Dirac delta function,  $\mathbf{m}$  is the unit vector representing the direction of the force,

$$\mathbf{m} = \begin{bmatrix} -\cos \phi \\ \sin \phi \end{bmatrix}, \tag{24}$$

and the time-dependent line load amplitude  $f(t)$  is shown in Fig. 2, which was measured directly from a 0.5-MHz PZT transducer. Here, the thickness of the annulus is assumed to be unit.

Substitution of (23) into (22) yields

$$\begin{aligned} P_{mn}^{(i)}(\tau) &= \int_0^{2\pi} \mathbf{m} \cdot \mathbf{U}_{mn}^{(i)}(1, \theta) f(\tau) \delta(\theta - \theta_0) d\theta \\ &= \mathbf{m} \cdot \mathbf{U}_{mn}^{(i)}(1, \theta_0) f(\tau). \end{aligned} \tag{25}$$

Thus, it follows from (16) that

$$Q_{mn}^{(i)}(t) = \frac{1}{\omega_{mn}} \mathbf{m} \cdot \mathbf{U}_{mn}^{(i)}(1, \theta_0) \int_0^t f(\tau) \sin[(t - \tau)\omega_{mn}] d\tau. \tag{26}$$

Finally, making use of (26) in (19) yields

$$\begin{aligned} \mathbf{u}_m(r, \theta, t) &= \sum_{i=1}^2 \sum_{n=0}^{\infty} \left\{ [\mathbf{m} \cdot \mathbf{U}_{mn}^{(i)}(1, \theta_0)] \mathbf{U}_{mn}^{(i)}(\bar{r}, \theta) \right. \\ &\quad \left. \times \int_0^t f(\tau) \sin[(t - \tau)\omega_{mn}] d\tau \right\} / \omega_{mn} M_{mn}^{(i)}, \end{aligned} \tag{27}$$

where  $M_{mn}^{(i)}$  is given by (8). In the case of the annulus considered here,

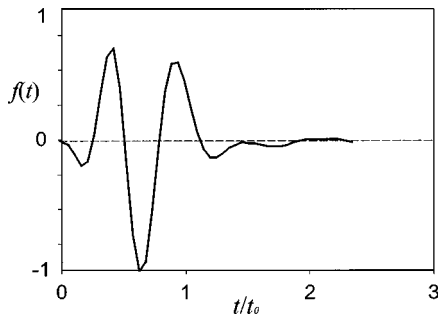


FIG. 2. Transient excitation.

$$M_{mn}^{(i)} = \rho b^2 \int_{\eta}^1 \int_0^{2\pi} \mathbf{U}_{mn}^{(i)}(\bar{r}, \theta) \cdot \mathbf{U}_{mn}^{(i)}(\bar{r}, \theta) \bar{r} d\theta d\bar{r}. \tag{28}$$

At this point, it is important to mention that the frequency  $\omega_{mn}$  appearing in the above equations is not an independent variable. Rather, it depends on  $n$  through the dispersion relationship (A7).

The numerical evaluation of (27) and (18) involves three major steps. First, the corresponding steady-state problem must be solved to obtain the individual steady-state vibration mode,  $\mathbf{U}_{mn}^{(i)}(\bar{r}, \theta)$ , as described in Appendix A. Then, the summation over the nondimensional wave number  $n$  needs to be carried out for each individual mode to obtain the time-dependent response of each mode  $\mathbf{u}_m$  as defined by (19). Finally, results for each mode should be superposed to obtain the total response,  $\mathbf{u}(r, \theta, t)$ , according to (18).

Note that the last two steps involve summation with respect to  $n$  from 0 to  $\infty$ , and summation over  $m$  from 1 to  $\infty$ , respectively. In our calculations, these processes are truncated at  $n = 300$ , and  $m = 20$ . The analysis shows that further increase of these values does not change the final results by more than 1%.

To present the data in nondimensional form, two parameters are chosen,

$$u_0 = \frac{f_0 t_0}{\rho c_T b} = 1.848 \times 10^{-5} \text{ } \mu\text{m}, \tag{29a}$$

$$t_0 = \frac{h}{c_T} = 3.846 \text{ } \mu\text{s}, \tag{29b}$$

where  $f_0 = \max\{|f(t)|\}$ . These parameters are used to normalize the displacement and time shown in the following figures.

First, consider a concentrated force at  $\theta = \theta_0 = 0$  normal to the annulus surface, i.e.,  $\phi = 0$ . The corresponding surface displacements at  $\theta = 90^\circ$  are evaluated. Their total (18) and first nine modes (27) of the radial and tangential displacement are shown in Fig. 3(a) and (b), respectively. Several observations can be made. First, for this applied load, the wave field is dominated by the first mode. All the higher modes have relatively small amplitude. Second, the arrival time of the first mode indicates that it travels at a speed slightly higher than that of the Rayleigh wave on a flat surface. This is consistent with the fact that Rayleigh waves travel slightly faster on a convex surface than on a flat surface (Viktorov, 1958). Third, comparison of the waveforms between the incident wave and the first mode indicates that the first mode is almost nondispersive. Finally, the radial and tangential displacements are almost 180 degrees out of phase, especially for lower modes. This has been observed for time-harmonic circumferential waves (Liu and Qu, 1998).

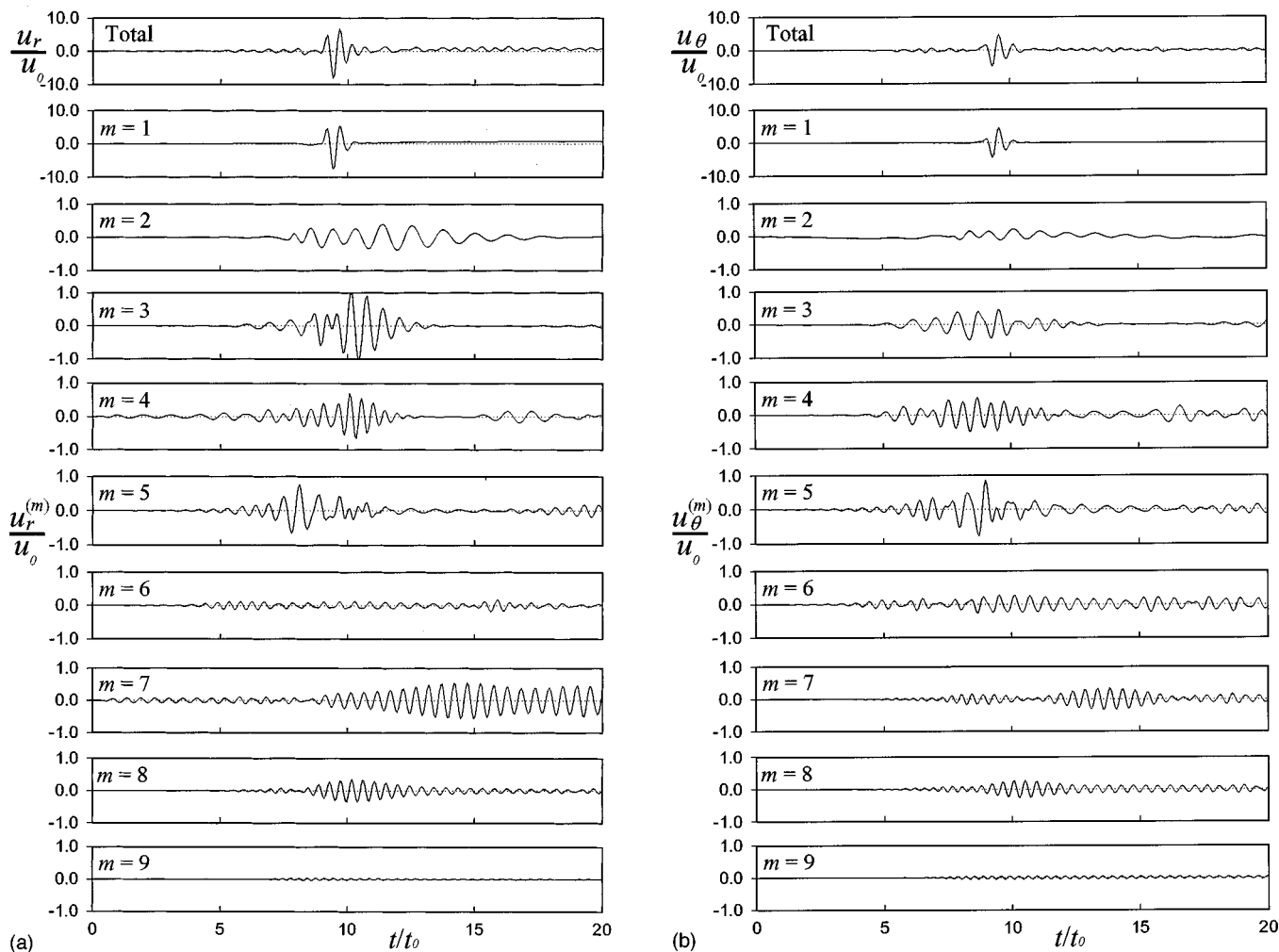


FIG. 3. (a) Radial displacement on the outer surface at  $\theta=90^\circ$  for  $\phi=0^\circ$ . (b) Circumferential displacement on the outer surface at  $\theta=90^\circ$  for  $\phi=0^\circ$ .

The next example is for a concentrated force at  $\theta=\theta_0=0$  with  $\phi=30^\circ$ . Again, the corresponding surface displacements at  $\theta=90^\circ$  are evaluated. The total and first nine modes of the radial and tangential displacement are shown in Fig. 4(a) and (b), respectively. Surprisingly, there is very little difference of the radial displacements between the normal and the inclined excitations. Not only are the wave forms the same for the lower modes, even the amplitudes of each individual mode are very similar. But for the tangential displacements, the waveform of the inclined excitation is more complicated than that of the normal excitation. Meanwhile, the amplitude of the tangential displacement for the inclined case is larger than that of the normal case, especially for the higher modes. This seems to indicate that the tangential response of displacement is more sensitive to the direction of the load than is the radial response.

To further understand the entire displacement field and the characteristics of each mode, the displacement variations across the thickness of the annulus as functions of time were studied. The radial and tangential displacements for both modes 1 and 2 are shown, respectively, in Figs. 5 and 6 for the normal excitation case.

Clearly, it is seen from these figures that the first mode is indeed a surface wave with most of the energy concentrated on the outer surface. Although the second mode has

relatively smaller amplitude, it is more “uniform” across the thickness. As mentioned in the Introduction, the guided circumferential waves may be used to detect radial cracks emitted from the inner surface of the annulus. For this purpose, a transducer must be mounted on the outer surface to induce the circumferential waves. The concentrated force considered here can be viewed as an idealization of the transducer. As the generated circumferential wave propagates, it interacts with the crack. This interaction can be measured by another transducer on a different location on the outer surface, e.g., at  $\theta=90^\circ$ . To detect the radial crack near the inner surface, wave modes that have significant energy near the inner surface are preferred. It is seen from Figs. 5 and 6 that the second mode should be chosen because of the relatively large amplitude near the inner surface. Although this mode has relatively smaller amplitude on the outer surface compared with the first mode, it is perceivable that once it encounters a radial crack, the scattered fields will transport the energy back to the outer surface to be detected by the receiving transducer. This scattering problem is being studied and the results will be reported in a separate paper.

Next, consider a distributed load generated by a PZT transducer as shown in Fig. 7(a). The two possible specimen/transducer configurations are shown in Fig. 7(b) and (c). Let the diameter of the transducer be  $d$ . Then, the total illumi-

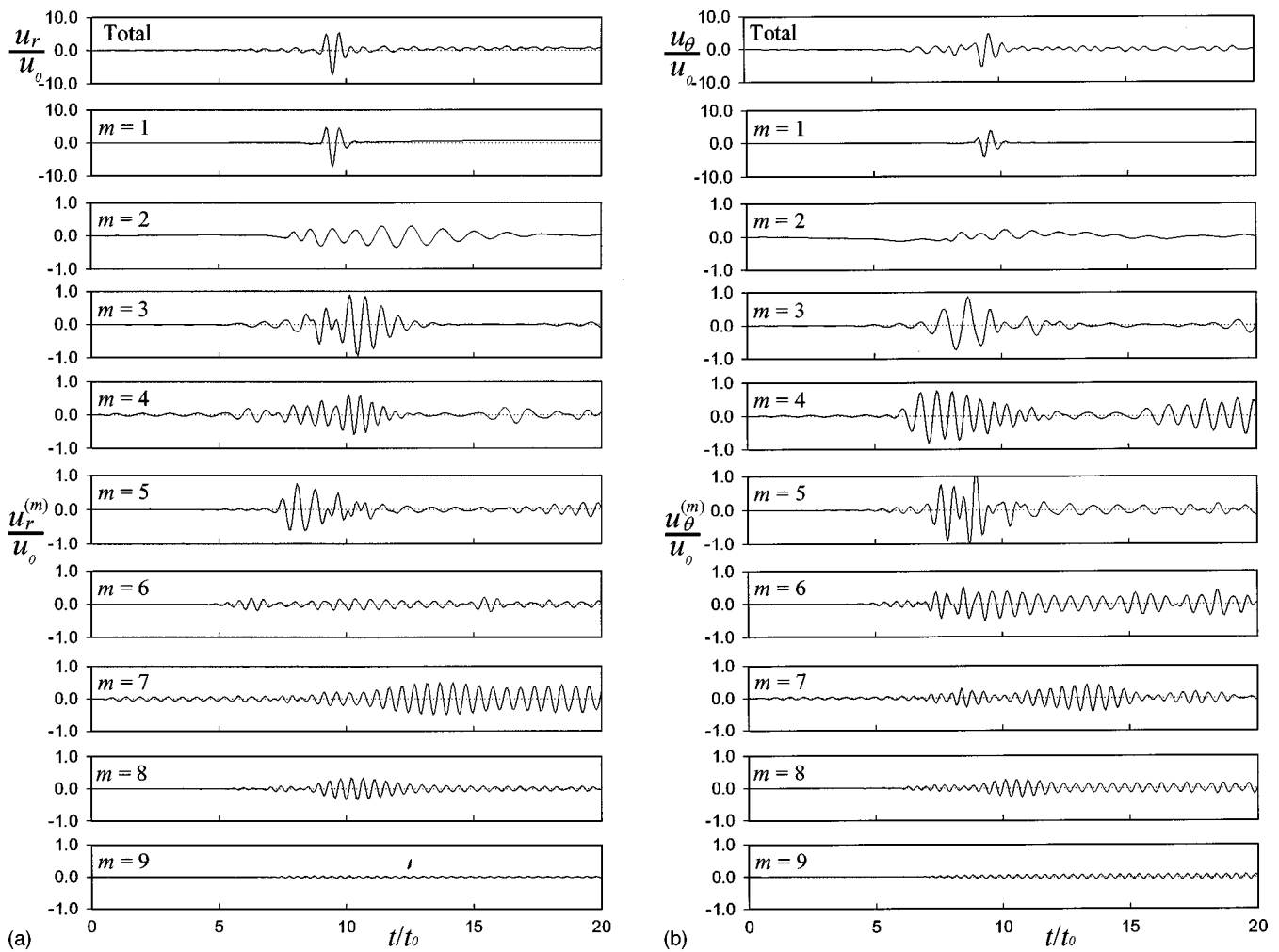


FIG. 4. (a) Radial displacement on the outer surface at  $\theta=90^\circ$  for  $\phi=30^\circ$ . (b) Circumferential displacement on the outer surface at  $\theta=90^\circ$  for  $\phi=30^\circ$ .

nated arc length on the annulus surface would be  $2\alpha b$ , where  $b=6.28$  cm is the outer radius of the annulus and  $\alpha$  is related to the incident angle  $\phi$  through

$$\sin \alpha = \frac{d}{2b \cos \phi}. \quad (30)$$

Obviously, Fig. 7(b) corresponds to the situation where  $\alpha \geq \phi$  while Fig. 7(c) corresponds to  $\alpha < \phi$ .

For simplicity, assume that the transducer generates a plane wave of uniform amplitude across its surface. This plane wave propagates through the coupling fluid and impinges upon the annulus' outer surface. Due to the different traveling distance, different rays will arrive at the annulus outer surface at different times, creating a phase delay. This makes the illuminated area a function of time. Since the coupling fluid cannot transmit shear force to the annulus, the amplitude of the traction on the annulus can be written as

$$\mathbf{F}(\theta) = -f \left[ t - t_0 + \frac{b}{c_0} \cos(\theta + \phi) \right] \times \mathbf{H}(\varphi_1 - \theta) \mathbf{H}(\varphi_2 + \theta) \mathbf{e}_r / b, \quad (31)$$

where  $\mathbf{H}(x)$  is the Heaviside step function,  $\mathbf{e}_r$  is the unit vector in the  $r$  direction, and  $c_0=1295$  m/s is the wave speed in the coupling fluid. The inclusion of a constant  $t_0$  in the

argument of  $f(t)$  is to adjust the initial time so that when  $t=0$ , the first ray arrives at the annulus' outer surface. At this initial time, the illuminated arc length is just a point. At a later time, as more rays arrive, the illuminated arc length increases to  $(\varphi_1 + \varphi_2)b$  as shown in Fig. 7. When the last ray (which travels the longest distance) arrives at the annulus' outer surface, i.e., when  $\varphi_1 = \varphi_2 = \alpha$ , the total illuminated arc length becomes  $2\alpha b$ . The expressions of  $\varphi_1$  and  $\varphi_2$  as functions of time and the constant  $t_0$  are obtained in Appendix B.

Substitution of (31) into (22) and then into (16) yields

$$Q_{mn}^{(i)} = \frac{-1}{\omega_{mn}} \int_0^t \left\{ \int_{-\varphi_1(\tau)}^{\varphi_2(\tau)} \mathbf{e}_r \cdot \mathbf{U}_{mn}^{(i)}(1, \theta) f \left[ \tau - t_0 + \frac{b}{c_0} \times \cos(\theta + \phi) \right] d\theta \right\} \sin[\omega_{mn}(t - \tau)] d\tau, \quad (32)$$

where the dependence of  $\varphi_1$  and  $\varphi_2$  on time has been explicitly indicated by its argument. Finally, the total displacement is obtained by substituting (32) into (18). Two numerical examples are given below for a 0.5-in. ( $d=1.27$  cm) transducer.



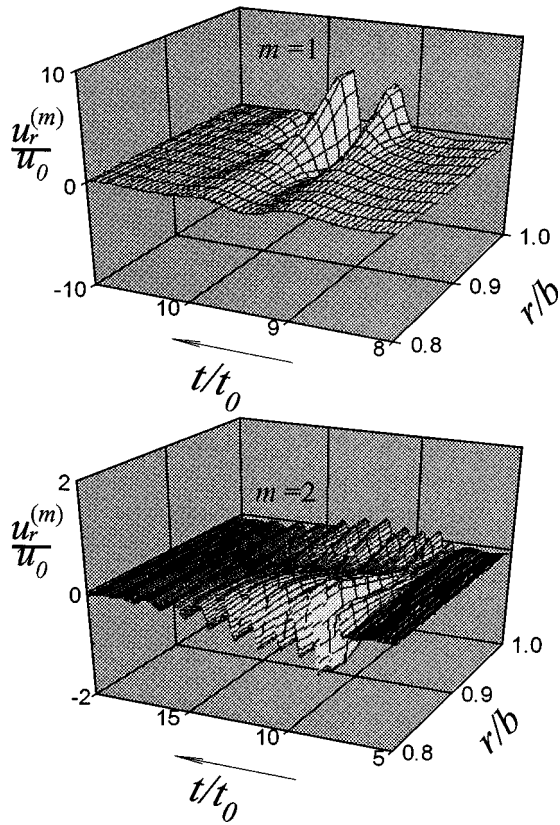


FIG. 5. Radial displacement variation across the thickness for  $\phi=0^\circ$ .

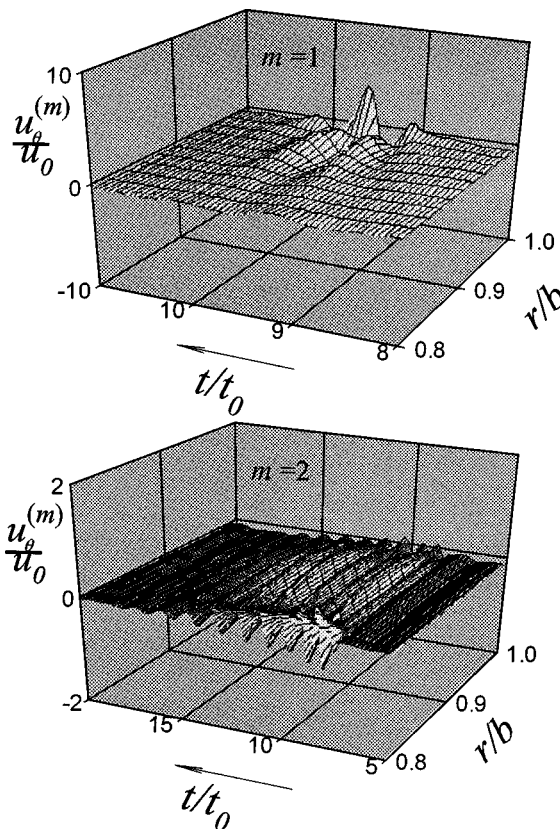


FIG. 6. Circumferential displacement variation across the thickness for  $\phi=0^\circ$ .

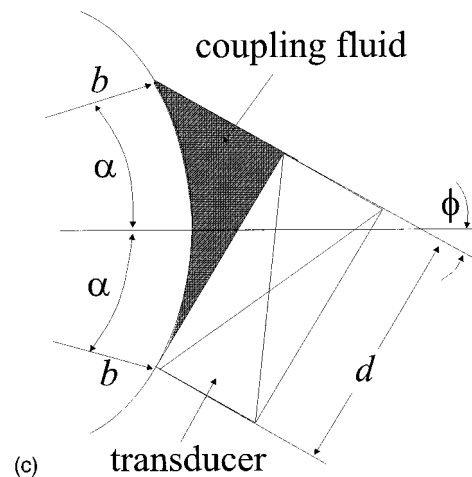
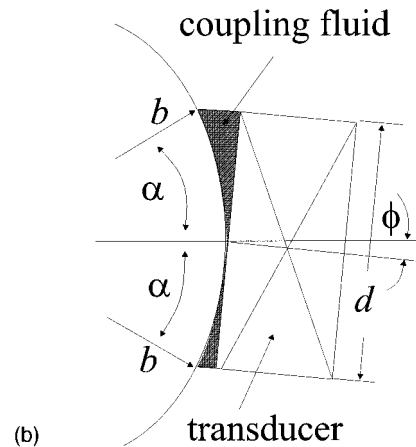
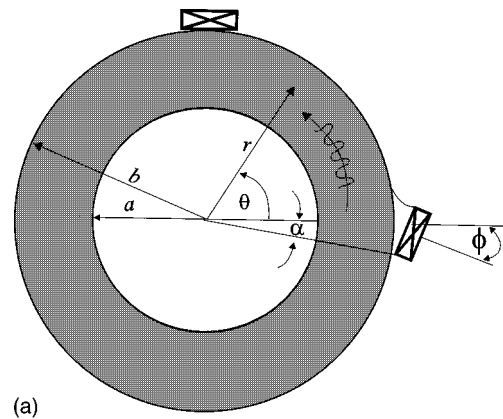


FIG. 7. (a) Annulus/transducer configurations. (b) Annulus/transducer configurations when  $\alpha \geq \phi$ . (c) Annulus/transducer configurations when  $\alpha < \phi$ .

First, consider normal incidence, i.e.,  $\phi=0$ . It then follows from (32) that  $\alpha=0.1 > \phi$ . This corresponds to case I in Appendix B. By using the appropriate  $\varphi_1$ ,  $\varphi_2$ , and  $t_0$  in (32), one can compute the total displacement. Shown in Fig. 8(a) and (b) are the total and first nine modes of the radial and tangential displacements, respectively.

The second example is for an inclined incidence,  $\phi=30^\circ$ . Again, it follows (32) that  $\alpha=0.11 < \phi$ . This corresponds to case II in Appendix B. By using the appropriate  $\varphi_1$ ,  $\varphi_2$ , and  $t_0$  in (31), one can compute the total displacement. Shown in Fig. 9(a) and (b) are the total and first nine modes of the radial and tangential displacements, respectively.

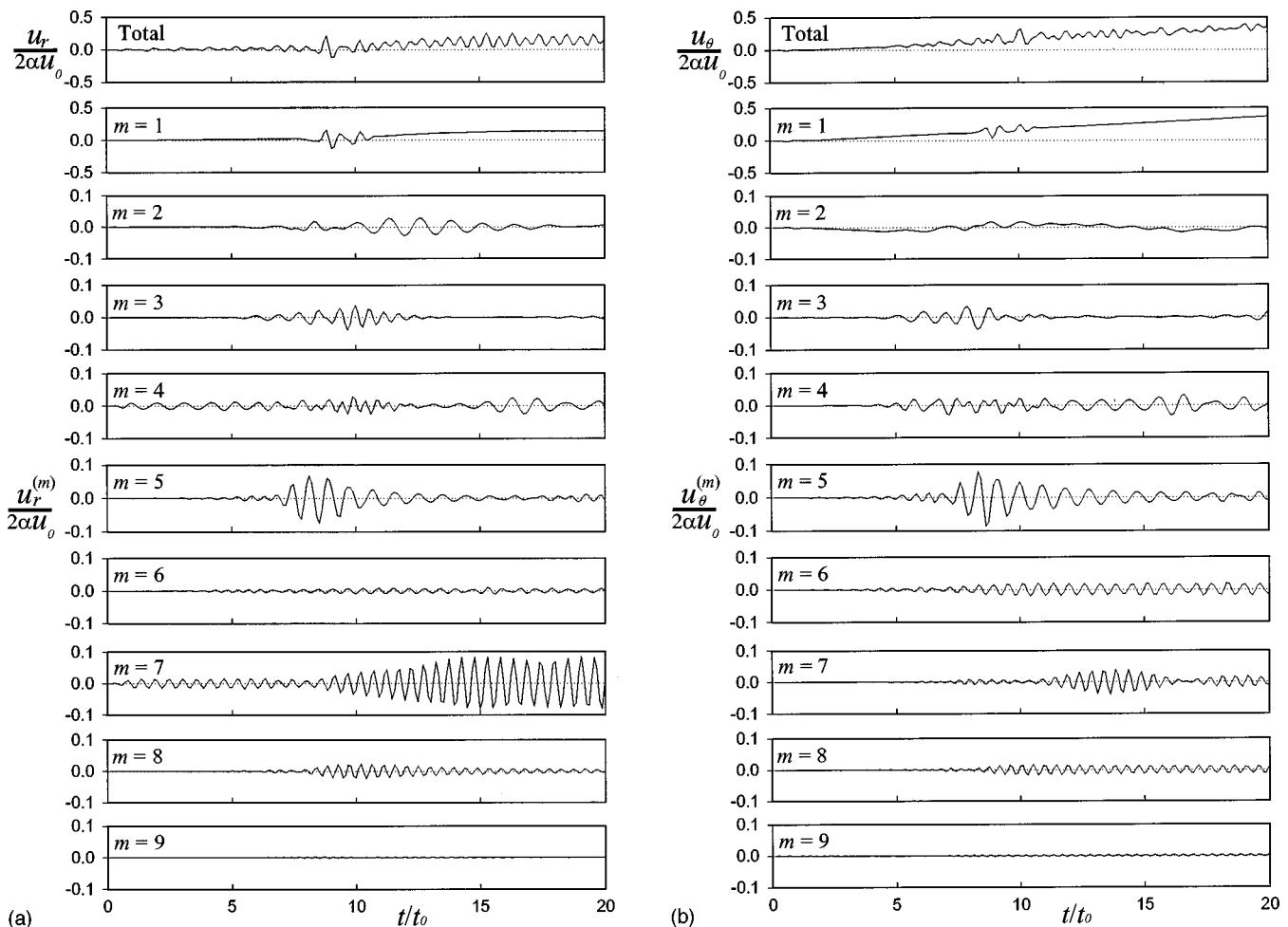


FIG. 8. (a) Radial displacement on the outer surface at  $\theta=90^\circ$  for  $\phi=0^\circ$  due to a finite transducer. (b) Circumferential displacement on the outer surface at  $\theta=90^\circ$  for  $\phi=0^\circ$  due to a finite transducer.

Several observations can be made. First of all, the signals from a concentrated force and from a finite transducer are very different. As expected, due to phase interference, a finite transducer gives rise to much more complicated wave fields. The pulse is no longer isolated in the time domain and different propagation modes are generated. Second, the amplitude of the total field becomes smaller. This, to a very large extent, is because the coupling fluid transmits only normal stress to the annulus. Therefore, inclined incident becomes very inefficient. Finally, it is seen from Figs. 8 and 9 that, unlike the case of concentrated forces, different incident angles generate very different wave fields when the source is a finite transducer. This seems to indicate that there is a potential to vary the generated wave fields by changing the angle of incidence, which is relatively easy to do experimentally.

#### IV. COMPARISON WITH FINITE-ELEMENT SOLUTION

As an independent check on the validity of the computational algorithm and the numerical results developed in this paper, a finite-element analysis was performed. The annulus was meshed into 64 000 four-noded plane strain elements. The finite-element analysis was carried out using the commercial software ABAQUS/Standard on a 200 MHz Pentium II

PC. It is found that the finite-element solutions agree very well with the numerical results obtained in this paper. As an example, both the radial and tangential displacements (total) shown in Fig. 3 are replotted in Fig. 10 together with the corresponding finite-element solutions. The dashed lines are from the finite-element solutions, while the solid lines are from the current method. One can see that they agree extremely well.

At this point, it is worth mentioning that on the same computer, the finite-element method took over 48 h to produce the results shown in Fig. 10, while the mode expansion method developed in this paper used less than 1 h to complete the calculation. The computational advantage of the eigenfunction expansion method is obvious. Furthermore, the finite-element method cannot separate the total field into individual propagating modes as shown in Figs. 3–9.

#### V. SUMMARY

In this paper, a general method of solution was described for obtaining the transient guided waves propagating in the circumferential direction of a circular annulus subjected to time-dependent surface traction. Several numerical examples were shown to illustrate the methodology. It was found that for detecting radial cracks on the inner wall, the

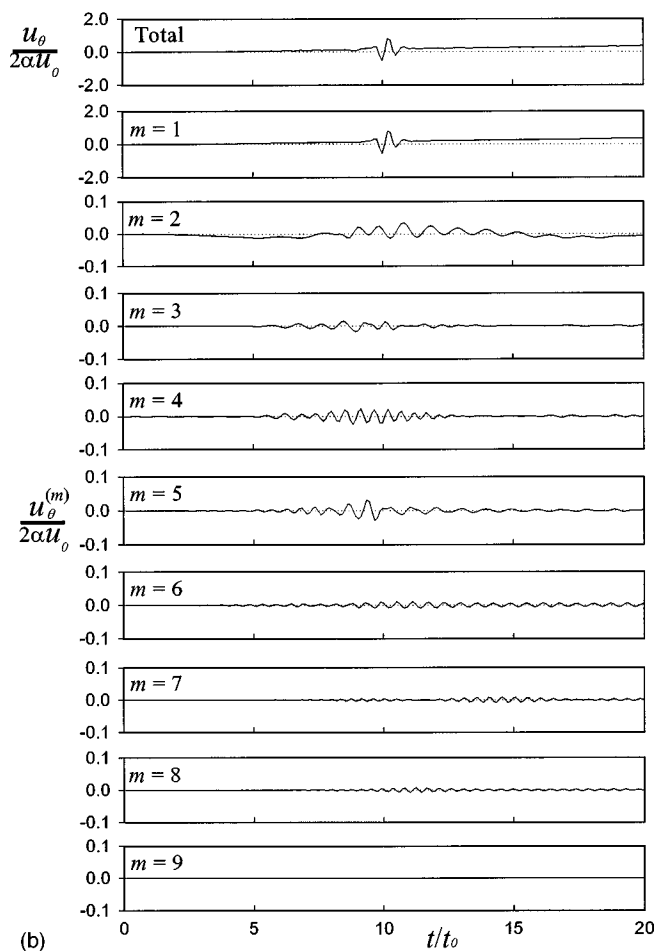
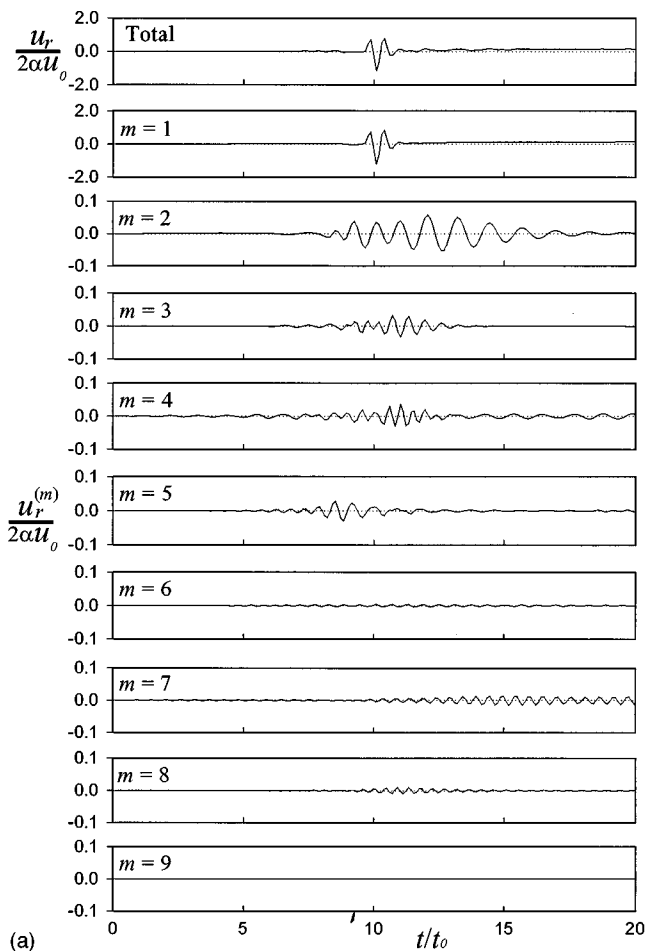


FIG. 9. (a) Radial displacement on the outer surface at  $\theta=90^\circ$  for  $\phi=30^\circ$  due to a finite transducer. (b) Circumferential displacement on the outer surface at  $\theta=90^\circ$  for  $\phi=30^\circ$  due to a finite transducer.

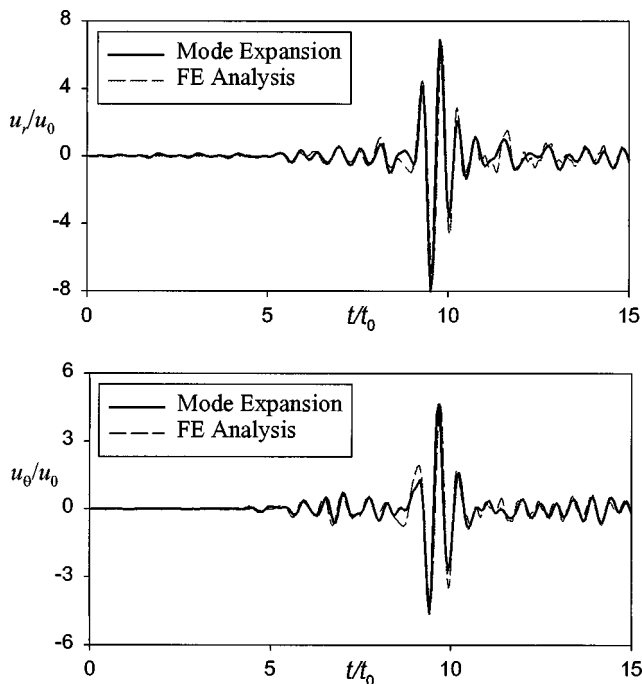


FIG. 10. Comparison of the displacement responses with the finite element method at  $\theta=90^\circ$  for  $\phi=0^\circ$ .

second and third propagating wave modes are preferred. Furthermore, variation of the incident angle of the transducer may change the wave fields significantly. Further studies are needed to understand what incident angle and frequency should be used to generate particular propagation modes.

#### ACKNOWLEDGMENTS

This work is supported by ONR through Grant No. N00014-95-1-0539. The authors would like to thank C. Valle for her help on performing the finite element computations.

#### APPENDIX A: STEADY-STATE SOLUTION

The corresponding steady state problem is governed by the following equations:

$$L[\mathbf{U}_{mn}^{(i)}] = -\omega_{mn}^2 \mathbf{U}_{mn}^{(i)} \text{ in } V, \quad (\text{A1})$$

$$B[\mathbf{U}_{mn}^{(i)}] = \mathbf{0} \text{ on } S. \quad (\text{A2})$$

The solution to this boundary value problem can be written as (Liu and Qu, 1998)

$$\mathbf{U}_{mn}^{(1)} = \begin{Bmatrix} b \cos(n\theta) & 0 \\ 0 & b \sin(n\theta) \end{Bmatrix} \cdot \mathbf{H}^{(1)}(\bar{r}, n, \hat{\omega}_{mn}) \cdot \mathbf{A}_m, \quad (\text{A3})$$

$$\mathbf{U}_{mn}^{(2)} = \begin{Bmatrix} b \sin(n\theta) & 0 \\ 0 & b \cos(n\theta) \end{Bmatrix} \cdot \mathbf{H}^{(2)}(\bar{r}, n, \hat{\omega}_{mn}) \cdot \mathbf{A}_m, \quad (\text{A4})$$

where

$$\mathbf{H}^{(i)}(\bar{r}, n, \hat{\omega}) = \frac{1}{\bar{r}} \begin{bmatrix} \frac{\hat{\omega}\bar{r}}{\kappa} J_n' \left( \frac{\hat{\omega}\bar{r}}{\kappa} \right) & \frac{\hat{\omega}\bar{r}}{\kappa} Y_n' \left( \frac{\hat{\omega}\bar{r}}{\kappa} \right) & (-1)^{i+1} n J_n(\hat{\omega}\bar{r}) & (-1)^{i+1} n Y_n(\hat{\omega}\bar{r}) \\ (-1)^i n J_n \left( \frac{\hat{\omega}\bar{r}}{\kappa} \right) & (-1)^i n Y_n \left( \frac{\hat{\omega}\bar{r}}{\kappa} \right) & -\hat{\omega}\bar{r} J_n'(\hat{\omega}\bar{r}) & -\hat{\omega}\bar{r} Y_n'(\hat{\omega}\bar{r}) \end{bmatrix}. \quad (\text{A5})$$

In the above equations,  $m$  and  $n$  are integers.  $J_n(x)$  and  $Y_n(x)$  are the  $n$ th order Bessel functions of the first and second kind, respectively. The nondimensional variables used above and in the paper are defined by

$$\bar{r} = \frac{r}{b}, \quad \hat{\omega} = \frac{\omega b}{c_T}, \quad \eta = \frac{a}{b}, \quad \kappa = \frac{c_L}{c_T} = \sqrt{\frac{2(1-\nu)}{(1-2\nu)}}, \quad (\text{A6})$$

with  $\nu$  being the Poisson's ratio.

Furthermore,  $\hat{\omega}_{mn}$  and  $\mathbf{A}_m$  must satisfy the following eigenvalue problem for each given  $n$ ,

$$\mathbf{D}^{(i)}(n, \hat{\omega}_{mn}) \mathbf{A}_m = \mathbf{0}, \quad (\text{A7})$$

where  $\mathbf{D}^{(i)}(n, \hat{\omega})$  is a  $4 \times 4$  matrix function of the wavenumber  $n$ , nondimensional frequency  $\hat{\omega}$ , and nondimensional wall thickness parameter  $\eta$ . Its components are listed below:

$$d_{11} = \frac{\hat{\omega}^2}{\kappa^2} \left[ J_{n-2} \left( \frac{\hat{\omega}}{\kappa} \right) + J_{n+2} \left( \frac{\hat{\omega}}{\kappa} \right) - 2(\kappa^2 - 1) J_n \left( \frac{\hat{\omega}}{\kappa} \right) \right],$$

$$d_{12} = \frac{\hat{\omega}^2}{\kappa^2} \left[ Y_{n-2} \left( \frac{\hat{\omega}}{\kappa} \right) + Y_{n+2} \left( \frac{\hat{\omega}}{\kappa} \right) - 2(\kappa^2 - 1) Y_n \left( \frac{\hat{\omega}}{\kappa} \right) \right],$$

$$d_{13} = (-1)^{(i+1)} \hat{\omega}^2 [J_{n-2}(\hat{\omega}) - J_{n+2}(\hat{\omega})],$$

$$d_{14} = (-1)^{(i+1)} \hat{\omega}^2 [Y_{n-2}(\hat{\omega}) - Y_{n+2}(\hat{\omega})],$$

$$d_{21} = \frac{\eta^2 \hat{\omega}^2}{\kappa^2} \left[ J_{n-2} \left( \frac{\eta \hat{\omega}}{\kappa} \right) + J_{n+2} \left( \frac{\eta \hat{\omega}}{\kappa} \right) - 2(\kappa^2 - 1) J_n \left( \frac{\eta \hat{\omega}}{\kappa} \right) \right],$$

$$d_{22} = \frac{\eta^2 \hat{\omega}^2}{\kappa^2} \left[ Y_{n-2} \left( \frac{\eta \hat{\omega}}{\kappa} \right) + Y_{n+2} \left( \frac{\eta \hat{\omega}}{\kappa} \right) - 2(\kappa^2 - 1) Y_n \left( \frac{\eta \hat{\omega}}{\kappa} \right) \right],$$

$$d_{23} = (-1)^{(i+1)} \eta^2 \hat{\omega}^2 [J_{n-2}(\eta \hat{\omega}) - J_{n+2}(\eta \hat{\omega})],$$

$$d_{24} = (-1)^{(i+1)} \eta^2 \hat{\omega}^2 [Y_{n-2}(\eta \hat{\omega}) - Y_{n+2}(\eta \hat{\omega})],$$

$$d_{31} = \frac{(-1)^i \hat{\omega}^2}{\kappa^2} \left[ J_{n-2} \left( \frac{\hat{\omega}}{\kappa} \right) - J_{n+2} \left( \frac{\hat{\omega}}{\kappa} \right) \right],$$

$$d_{32} = \frac{(-1)^i \hat{\omega}^2}{\kappa^2} \left[ Y_{n-2} \left( \frac{\hat{\omega}}{\kappa} \right) - Y_{n+2} \left( \frac{\hat{\omega}}{\kappa} \right) \right],$$

$$d_{33} = -\hat{\omega}^2 [J_{n-2}(\hat{\omega}) + J_{n+2}(\hat{\omega})],$$

$$d_{34} = -\hat{\omega}^2 [Y_{n-2}(\hat{\omega}) + Y_{n+2}(\hat{\omega})],$$

$$d_{41} = \frac{(-1)^i \eta^2 \hat{\omega}^2}{\kappa^2} \left[ J_{n-2} \left( \frac{\eta \hat{\omega}}{\kappa} \right) - J_{n+2} \left( \frac{\eta \hat{\omega}}{\kappa} \right) \right],$$

$$d_{42} = \frac{(-1)^i \eta^2 \hat{\omega}^2}{\kappa^2} \left[ Y_{n-2} \left( \frac{\eta \hat{\omega}}{\kappa} \right) - Y_{n+2} \left( \frac{\eta \hat{\omega}}{\kappa} \right) \right],$$

$$d_{43} = -\eta^2 \hat{\omega}^2 [J_{n-2}(\eta \hat{\omega}) + J_{n+2}(\eta \hat{\omega})],$$

$$d_{44} = -\eta^2 \hat{\omega}^2 [Y_{n-2}(\eta \hat{\omega}) + Y_{n+2}(\eta \hat{\omega})],$$

## APPENDIX B: TRANSDUCE CONFIGURATIONS

### 1. Case I: $\alpha \geq \phi$

In this case, the arrival point for the first ray is at  $\theta = -\phi$ , which falls within  $[-\alpha, \alpha]$ . Therefore,  $t_0$  in (46) should be replaced by  $b/c_0$ , i.e.,

$$\mathbf{F}(\theta) = -f \left[ t - \frac{b}{c_0} + \frac{b}{c_0} \cos(\theta + \phi) \right] \times \mathbf{H}(\varphi_1 \theta) \mathbf{H}(\varphi_2 + \theta) \mathbf{e}_r / b. \quad (\text{B1})$$

This way, at the initial time  $t = 0$ ,

$$\mathbf{F}(\theta) = -f(0) \delta(\theta + \phi) \mathbf{e}_r / b. \quad (\text{B2})$$

For  $0 < t \leq (b/c_0) [1 - \cos(-\alpha + \phi)]$ , a simple analysis of the geometry yield

$$\varphi_1 = \cos^{-1} \left( 1 - \frac{c_0 t}{b} \right) - \phi, \quad \varphi_2 = \cos^{-1} \left( 1 - \frac{c_0 t}{b} \right) + \phi. \quad (\text{B3})$$

For  $(b/c_0) [1 - \cos(-\alpha + \phi)] < t \leq (b/c_0) [1 - \cos(\alpha + \phi)]$ , one has

$$\varphi_1 = \cos^{-1} \left( 1 - \frac{c_0 t}{b} \right) - \phi, \quad \varphi_2 = \alpha. \quad (\text{B4})$$

The last ray arrives when  $t = (b/c_0)[1 - \cos(\alpha + \phi)]$ . After that time,  $\varphi_1 = \varphi_2 = \alpha$ .

## 2. Case II: $\alpha < \phi$

In this case, to make sure that the arrival time of the first ray is set to be the initial time  $t=0$ , the constant  $t_0$  in (46) should be chosen as  $\cos(-\alpha + \phi)b/c_0$ , i.e.,

$$\mathbf{F}(\theta) = -f \left[ t - \frac{b}{c_0} \cos(-\alpha + \phi) + \frac{b}{c_0} \cos(\theta + \phi) \right] \times \mathbf{H}(\varphi_1 - \theta) \mathbf{H}(\varphi_2 + \theta) \mathbf{e}_r / b. \quad (\text{B5})$$

Obviously, the first arrival point is at  $\theta = -\alpha$ . Therefore,  $\varphi_2 = \alpha$  for all  $t$ . As for  $\varphi_1$ ,

$$\varphi_1 = \cos^{-1} \left[ \cos(-\alpha + \phi) - \frac{c_0 t}{b} \right] - \phi$$

$$\text{for } 0 < t \leq \frac{2b}{c_0} \sin \alpha \sin \phi, \quad (\text{B6})$$

and  $\varphi_1 = \alpha$  for all  $t > (2b/c_0) \sin \alpha \sin \phi$ .

- Achenbach, J. D. (1984). *Wave Propagation in Elastic Solids* (North-Holland, New York).
- Brekhovskikh, L. M. (1968). "Surface Waves Confined to the Curvature of the Boundary in Solid," *Sov. Phys. Acoust.* **13**, 462–472.
- Červ, J. (1988). "Dispersion of Elastic Waves and Rayleigh-type Waves in a Thin Disc," *Acta Technica Csav* **89**, 89–99.
- Cook, E. G., and Valkenburg, H. E. (1954). "Surface Waves At Ultrasonic Frequencies," *ASTM Bulletin* **3**, 81–84.
- Ditri, J. J., and Rose, J. L. (1992). "Excitation of Guided Elastic Wave Modes in Hollow Cylinders by Applied Surface Traction," *J. Appl. Phys.* **72**, 2589–2597.
- Eringen, A. C., and Suhubi, E. S. (1975). *Elastodynamics* (Academic, New York), pp. 437–442.
- Gazis, D. (1959). "Three Dimensional Investigation of the Propagation of Waves in Hollow Circular Cylinders, I. Analytical Foundation, II. Numerical Results," *J. Acoust. Soc. Am.* **14**, 1869–1876.
- Grace, O. D., and Goodman, R. R. (1966). "Circumferential Waves on Solid Cylinders," *J. Acoust. Soc. Am.* **39**, 173–174.

- Gregory, R. D. (1971). "The Propagation of Rayleigh Waves over Curved Surfaces at High Frequency," *Proc. Cambridge Philos. Soc.* **70**, 103–121.
- Grimshaw, R. (1968). "Propagation of Surface Waves at High Frequency," *J. Inst. Math. Appl.* **4**, 174–193.
- Keller, J. B., and Karal, F. C. (1960). "Surface Wave Excitation and Propagation," *J. Appl. Phys.* **31**, 1039–1046.
- Keller, J. B., and Karal, F. C. (1964). "Geometrical Theory of Elastic Surface-Wave Excitation and Propagation," *J. Acoust. Soc. Am.* **36**, 32–40.
- Liu, G., and Qu, J. (1998). "Guided Circumferential Waves in a Circular Annulus," *J. Appl. Mech.* **64**, 424–430.
- Love, A. E. H. (1944). *Mathematical Theory of Elasticity* (Dover, New York), 4th ed.
- Malvern, L. E. (1969). *Introduction to the Mechanics of a Continuous Medium* (Prentice-Hall, Englewood Cliffs, NJ).
- Miklowitz, J. (1978). *The Theory of Elastic Waves and Wave Guides* (North-Holland, Amsterdam).
- Mindlin, R. D. (1960). "Waves and Vibrations in Isotropic Elastic Plates," *Structural Mechanics*, edited by J. N. Goodier and N. J. Hoff (Pergamon, New York).
- Mindlin, R. D., and Fox, E. A. (1960). "Vibrations and Waves in Elastic Bars of Rectangular Cross Section," *J. Appl. Mech.* **27**, 152–158.
- Mindlin, R. D., and McNiven, H. D. (1960). "Axially Symmetric Waves in Elastic Rods," *J. Appl. Mech.* **27**, 145–151.
- Nagy, P. B., Blodgett, M., and Gulis, M. (1994). "Weep Hole Inspection by Circumferential Creeping Waves," *NDT & E Int.* **27**, 131–142.
- Qu, J., Berthelot, Y., and Li, Z. (1996). "Dispersion of Guided Circumferential Waves in Circular Annulus," *Rev. Prog. Quant. Nondestr. Eval.* **15**, 169–176.
- Rayleigh, J. W. S. (1885). "On Waves Propagated along the Plane Surface on an Elastic Solid," *Proc. Math. Soc. London* **17**, 4–11.
- Rayleigh, J. W. S. (1945). *The Theory of Sound* (Dover, New York).
- Reismann, H. (1967). "On the Forced Motion of Elastic Solids," *Appl. Sci. Res.* **18**, 156–165.
- Rulf, B. (1969). "Rayleigh Waves on Curved Surfaces," *J. Acoust. Soc. Am.* **45**, 493–499.
- Überall, H. (1973). "Surface Waves in Acoustics," in *Physical Acoustics*, edited by W. P. Mason and R. N. Thurston (Academic, New York), Vol. 10.
- Viktorov, I. A. (1958). "Rayleigh-type Waves on a Cylindrical Surface," *Sov. Phys. Acoust.* **4**, 131–136.
- Weaver, R. L., and Pao, Y. H. (1982). "Axisymmetric Elastic Waves Excited by a Point Source in a Plate," *J. Appl. Mech.* **49**, 821–836.

# An equivalent source technique for calculating the sound field inside an enclosure containing scattering objects

M. E. Johnson, S. J. Elliott, K-H. Baek, and J. Garcia-Bonito

*Institute of Sound and Vibration Research, University of Southampton, Southampton SO17 1BJ, England*

(Received 15 August 1997; accepted for publication 24 February 1998)

The equivalent source method has previously been used to calculate the exterior sound field radiated or scattered from bodies in the free-field. In this paper the method is used to calculate the internal pressure field for an enclosure which can have arbitrary boundary conditions and may include internal objects which scatter the sound. Some of the equivalent source positions are chosen to be the same as the first order images of the source inside the enclosure, some are positioned within the scattering objects, and the remainder are positioned on a spherical surface some distance outside the enclosure. The normal velocity on the surfaces of the scattering objects and the enclosure walls is evaluated at a larger number of positions than there are equivalent sources. The sum of the squared difference between this velocity and that expected because of the admittance of the boundary, is minimized by adjusting the strengths of the equivalent sources. The convergence of the method is checked by evaluating the velocity at a larger number of monitoring positions. Example results are presented for the sound field and frequency response inside a damped rectangular enclosure, which compare very well with the conventional modal model. The effect of having rigid spheres inside the enclosure are then investigated, and it is found that the effect is significant even some distance from the spheres and at frequencies for which the size of the sphere is small compared to a wavelength. Finally the effect of a nonlocally reacting boundary condition is illustrated by assuming that one of the walls of the enclosure is an elastic plate. © 1998 Acoustical Society of America.

[S0001-4966(98)02206-1]

PACS numbers: 43.20.Fn [ANN]

## INTRODUCTION

In recent years considerable effort has been devoted to the numerical modelling of complex acoustic fields. These methods include the finite element (FE) method and the boundary element method (BEM). The finite element method is not directly suited to free-field radiation problems, since it is difficult to include infinite elements into the model, and are better suited to modelling interior problems. BEM methods are well suited to the free-field radiation problem, but suffer from singularities at the boundary and nonuniqueness in the solutions at certain critical wave numbers. The equivalent source or superposition method was suggested as an alternative to the BEM method by Koopmann *et al.*<sup>1</sup> and allows the calculation of the radiation and scattering from objects in a free-field with a reduced computational load. Other authors have built on this work to investigate the robustness of the method,<sup>2-5</sup> to develop a time domain formulation<sup>6</sup> and to use this method for investigating the active control of sound radiation.<sup>7</sup>

The equivalent source method uses an array of sources positioned inside a radiator driven to produce a normal particle velocity distribution over the surface of the radiator which matches that of the original radiator. The radiated field (external to the radiator) is then simply the field due to the set of equivalent sources. The scattering problem can be addressed in a similar way by calculating the pressure and normal particle velocities at the surface of the scattering object due to the incident field and driving the array of equivalent sources to create the desired boundary condition. The bound-

ary condition in this case is a combination of the incident field and the equivalent source field.

The equivalent source method has been used to calculate the radiation and scattering from objects in a free-field<sup>1,8</sup> and the results have been validated using an example where analytic solutions are available.<sup>9</sup> It is also important to model the behavior of scattering objects inside enclosures. The presence of objects inside an enclosure will alter the frequency response of the enclosure and this has implications for active control systems.<sup>10</sup> The equivalent source method has been considered as a solution to this modelling problem. This paper presents an equivalent source method for calculating the response of a damped enclosure with and without scattering objects inside. The equivalent sources for these examples are placed external to the boundary and the acoustic field is enclosed by the boundary. The boundary is modelled using a matrix approach which allows the boundary to be modelled as a nonlocally reacting surface such as a structure.

The equivalent source method is an alternative to the boundary element method for calculating the sound field inside an enclosure and requires relatively simple meshing elements and computation. This simplicity is achieved because the sources are placed at a distance away from the boundary (as opposed to on the boundary in the BEM) creating smooth and continuous pressure and velocity distributions at the boundary when the sources are driven. For sharp surfaces, where it may be required to place equivalent sources close to the boundary, the advantages of the equivalent source method over the BEM may not be as great.

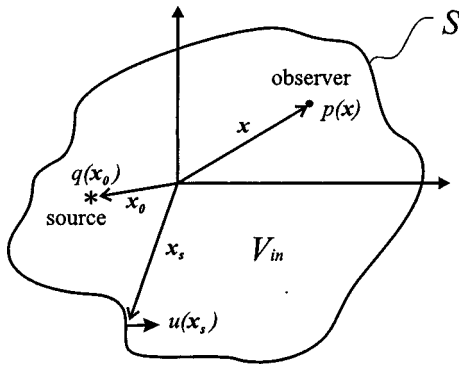


FIG. 1. The volume  $V_{in}$  enclosed by a surface  $S$  which has a normal surface velocity  $u$  and internal sources  $q$ .

## I. THEORY

### A. Kirchhoff–Helmholtz equation

The boundary element method and the equivalent source method are based on the Kirchhoff–Helmholtz integral equation which states that a sound field is completely determined by the acoustic pressure and the normal particle velocity over the bounding surfaces of the field plus any acoustic sources present within the field. Figure 1 shows a volume  $V_{in}$  which is enclosed by surface  $S$ . The pressure anywhere inside the volume can be calculated by the Kirchhoff–Helmholtz equation:

$$p(\mathbf{x}) = \int_S \left[ p(\mathbf{x}_s) \frac{\partial G(|\mathbf{x} - \mathbf{x}_s|)}{\partial n} + jkc\rho u(\mathbf{x}_s) G(|\mathbf{x} - \mathbf{x}_s|) \right] dS + jkc\rho \int_{V_{in}} q(\mathbf{x}_0) G(|\mathbf{x} - \mathbf{x}_0|) dV_{in}. \quad (1)$$

The pressure at a point  $\mathbf{x}$  inside the volume  $p(\mathbf{x})$  is due to the integral of the pressure over the surface  $p(\mathbf{x}_s)$  times the gradient of the free-field Green's function  $G$  plus the integral of the normal particle velocity over the surface  $u(\mathbf{x}_s)$  times the free-field Green's function plus the pressure due to any sources  $q(\mathbf{x}_0)$  inside the volume. The vectors  $\mathbf{x}$ ,  $\mathbf{x}_s$ , and  $\mathbf{x}_0$  denote the positions of the point where the pressure is being evaluated, the position of a point on the surface  $S$  and the position of any sources inside the volume. The wave number is  $k$  ( $k = \omega/c$ ),  $c$  is the speed of sound in the fluid, and  $\rho$  is the density of the fluid.

The free-field Green's function  $G$  is given by

$$G(\mathbf{x} - \mathbf{x}_0) = \frac{1}{4\pi|\mathbf{x} - \mathbf{x}_0|} e^{-jk|\mathbf{x} - \mathbf{x}_0|}. \quad (2)$$

The Kirchhoff–Helmholtz equation tells us that the acoustic field created inside a volume  $V_{in}$  by sources outside a boundary  $S$  [assume  $q(\mathbf{x}_0) = 0$ ] can be determined totally by the normal particle velocity and pressure at the boundary. Any set of external sources which produce the same pressure and velocity conditions at the boundary will produce the same acoustic field inside the volume. In fact the pressure at the boundary is not independent of the normal particle velocity

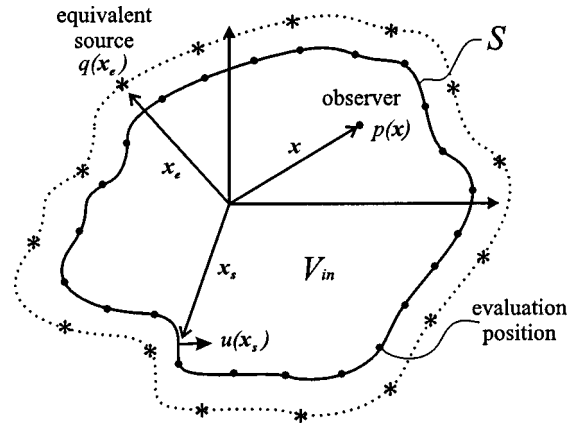


FIG. 2. The volume  $V_{in}$  enclosed by a surface  $S$ . The pressure and normal particle velocity are evaluated at a finite number of positions on the boundary ( $\bullet$ ). The equivalent sources ( $*$ ) are in the external volume  $V_{ex}$  which surrounds the surface  $S$ .

at the boundary but essentially determined by it. This can be shown by allowing the observation positions to approach the surface  $S$  (i.e.,  $\mathbf{x} \rightarrow \mathbf{x}_s$ ). In this case Eq. (1) has only two unknowns [assuming  $q(\mathbf{x}_0) = 0$ ], the pressure on  $S$  and the normal particle velocity on  $S$  and hence one can be determined from the other. Therefore, if the surface velocity of a boundary is known *a priori* then a set of sources placed on the other side of the boundary can be driven to produce a similar normal velocity at the boundary and hence a similar acoustic field. This is the basis of the equivalent source technique. The equivalent source method circumvents the direct use of the Kirchhoff–Helmholtz equation by matching the conditions at the boundary. The free-field Green's function is then used to directly calculate the acoustic field due to the internal and equivalent sources:

$$p(\mathbf{x}) = jkc\rho \left[ \int_{V_{in}} q(\mathbf{x}_0) G(|\mathbf{x} - \mathbf{x}_0|) dV_{in} + \int_{V_{ex}} q(\mathbf{x}_e) G(|\mathbf{x} - \mathbf{x}_e|) dV_{ex} \right]. \quad (3)$$

The sources are positioned at  $\mathbf{x}_0$  (internal sources) and  $\mathbf{x}_e$  (equivalent sources). The exterior volume in this case is  $V_{ex}$ .

### B. Matrix formulation of the equivalent source technique

Figure 2 shows the configuration for the equivalent source method using a finite number of monopole sources placed outside the boundary. The pressure and normal particle velocity at the boundary are calculated at a finite number of evaluation positions. If a sufficiently large number of evaluation positions on the boundary are chosen then the acoustic behavior on the boundary can be accurately described.

The pressure at the evaluation positions on the boundary, at a particular frequency, is given by a complex vector  $\mathbf{p}$  as

$$\mathbf{p} = \mathbf{p}_{int} + \mathbf{p}_{ext} = \mathbf{p}_{int} + \mathbf{Z}_e \mathbf{q}_e, \quad (4)$$

where the pressure at the boundary due to a set of sources inside the volume (internal sources) is given by  $p_{\text{int}}$  and the pressure at the boundary created by the equivalent sources (external sources) is given by  $p_{\text{ext}}$ . Given that there are a finite number of equivalent sources then the pressure due to them can be described by a matrix  $Z_e$  of complex transfer impedances and a vector of complex source strengths  $q_e$  (i.e., volume velocities) where the source strengths of the equivalent sources are chosen to create a particular condition at the boundary. The  $m$ th element of the impedance matrix  $Z_e$  is calculated using the free-field Green's function by

$$Z_{e_{mn}} = jkc\rho G(|\mathbf{x}_{s_m} - \mathbf{x}_{e_n}|), \quad (5)$$

where  $\mathbf{x}_{s_m}$  is the position of the  $m$ th evaluation point on the surface  $S$  and  $\mathbf{x}_{e_n}$  is the position of the  $n$ th equivalent source. Note that the impedance matrix  $Z_e$  has dimensions which differ from those of *specific* acoustic impedance since  $Z_e$  contains ratios of pressure to volume velocity.

The normal particle velocity  $\mathbf{u}$  at the boundary can be similarly described by

$$\mathbf{u} = \mathbf{u}_{\text{int}} + \mathbf{u}_{\text{ext}} = \mathbf{u}_{\text{int}} + \mathbf{T}_e \mathbf{q}_e. \quad (6)$$

In this case the matrix which relates the particle velocities (normal to the boundary) to the external source strengths is  $\mathbf{T}_e$  which can also be calculated using the free-field Green's function:

$$T_{e_{mn}} = \frac{\partial G(|\mathbf{x}_{s_m} - \mathbf{x}_{e_n}|)}{\partial n_m}, \quad (7)$$

where  $n_m$  is the normal to the surface  $S$  at the  $m$ th evaluation position. The pressure ( $p_{\text{int}}$ ) and the velocity ( $\mathbf{u}_{\text{int}}$ ) at the boundary due to the internal sources can be also be calculated using the free-field Green's function [Eq. (2)] if the positions and source strengths of the internal sources are known.

If the pressure (or force) and the normal particle velocity (i.e., surface velocity) at the boundary are related by an admittance (mobility) matrix  $\mathbf{Y}_b$  which characterizes the behavior of the boundary, then

$$\mathbf{u} = \mathbf{Y}_b \mathbf{p}, \quad (8)$$

where  $\mathbf{Y}_b$  is a matrix of *in vacuo* self and transfer admittance or mobility terms for every point on the boundary and takes into account the sizes of the elements and assumes the external sound field has no effect. Equations (4), (6), and (8) can be rearranged to give

$$[\mathbf{u}_{\text{int}} + \mathbf{T}_e \mathbf{q}_e] = \mathbf{Y}_b [\mathbf{p}_{\text{int}} + \mathbf{Z}_e \mathbf{q}_e]. \quad (9)$$

If there are as many equivalent sources as there are evaluation positions on the surface of the boundary then the source strengths  $q_e$  can be calculated to produce any arbitrarily chosen boundary mobility  $\mathbf{Y}_b$  by

$$\mathbf{q}_e = -[\mathbf{T}_e - \mathbf{Y}_b \mathbf{Z}_e]^{-1} [\mathbf{u}_{\text{int}} - \mathbf{Y}_b \mathbf{p}_{\text{int}}]. \quad (10)$$

If the desired boundary condition is that of a hard surface then  $\mathbf{u} = 0$  (i.e.,  $\mathbf{Y}_b \rightarrow 0$ ) and Eq. (10) simplifies to,

$$\mathbf{q}_e = -\mathbf{T}_e^{-1} \mathbf{u}_{\text{int}}. \quad (11)$$

Using a fully determined system (i.e., same number of evaluation positions on the boundary as equivalent sources) satisfies the boundary condition exactly at the evaluation positions but can cause large variations in admittance *between* the evaluation positions. To overcome this problem an overdetermined system (i.e., a larger number of evaluation positions on the boundary than equivalent sources) can be used. In these cases the term  $[\mathbf{Y}_b \mathbf{Z}_e - \mathbf{T}_e]$  [or  $\mathbf{T}_e$  in the case of Eq. (11)] is not square and the boundary condition cannot be satisfied exactly at the evaluation positions. The equivalent sources in these cases will be driven to minimize an error criterion at the boundary. The error for the example of a hard surface (i.e.,  $\mathbf{u} = 0$ ) is given by

$$E = \frac{\mathbf{u}^H \mathbf{u}}{\mathbf{u}_{\text{int}}^H \mathbf{u}_{\text{int}}}. \quad (12)$$

The error in this case is defined to be the squared normal velocity at the evaluation positions normalized such that the error when no equivalent sources are operating is unity. By substituting Eq. (6) into Eq. (12) the error becomes a quadratic function of the equivalent source strengths  $q_e$  and is minimized when

$$\mathbf{q}_e = -[\mathbf{T}_e^H \mathbf{T}_e]^{-1} \mathbf{T}_e^H \mathbf{u}_{\text{int}}, \quad (13)$$

where  $H$  denotes the conjugate transpose. For a boundary with finite admittance the error is defined to be the difference between the normal particle velocity at the evaluation positions and the expected particle velocity at the evaluation positions due to the pressure at the evaluation positions,

$$E = \frac{(\mathbf{u} - \mathbf{Y}_b \mathbf{p})^H (\mathbf{u} - \mathbf{Y}_b \mathbf{p})}{(\mathbf{u}_{\text{int}} - \mathbf{Y}_b \mathbf{p}_{\text{int}})^H (\mathbf{u}_{\text{int}} - \mathbf{Y}_b \mathbf{p}_{\text{int}})}. \quad (14)$$

The error is again a quadratic function of the equivalent source strengths and is minimized when the source strengths are set to

$$\mathbf{q}_e = -[(\mathbf{T}_e - \mathbf{Y}_b \mathbf{Z}_e)^H (\mathbf{T}_e - \mathbf{Y}_b \mathbf{Z}_e)]^{-1} \times (\mathbf{T}_e - \mathbf{Y}_b \mathbf{Z}_e)^H (\mathbf{u}_{\text{int}} - \mathbf{Y}_b \mathbf{p}_{\text{int}}). \quad (15)$$

### C. Error and convergence

With the equivalent source method one of the main issues is the convergence of the behavior of the entire boundary, i.e., between the evaluation positions. In the limit of an infinite number of evaluation positions on the boundary and an infinite number of well distributed equivalent sources the solution is an exact one. Given limited computing power and time it is important to determine the minimum number of evaluation positions and equivalent sources required to produce a reasonably accurate solution. As with all methods which approximate a continuous system using a finite number of elements the spacing of elements must be small relative to a wavelength. This implies high frequency, short wavelength problems are more difficult to solve as they require more evaluation positions and equivalent sources. The investigation of the convergence properties of the equivalent source method is complicated by the fact that there is no clearly defined way in which to add additional equivalent



sources, since a given number of equivalent sources can be arranged in a variety of positions. For the examples presented in this paper the positions of the equivalent sources are chosen on physical and intuitive grounds and the convergence is tested by adding equivalent sources in a specified physical arrangement.

For the case of a hard boundary, where the desired condition is zero velocity, the error has been defined as the residual velocity at the evaluation positions after the equivalent sources are driven to minimize this velocity [Eq. (12)]. To gain a more accurate measure of the error over the entire surface the velocity is monitored at a larger number of positions on the boundary than the number of evaluation positions used to calculate the matrices  $\mathbf{Z}_e$  and  $\mathbf{T}_e$ . This error ( $E'$ ) is defined to be the net velocity squared at the monitoring points divided by the velocity squared at the monitoring positions due to the internal sources (normalized),

$$E' = \frac{\mathbf{u}'^H \mathbf{u}'}{\mathbf{u}'_{\text{int}}{}^H \mathbf{u}'_{\text{int}}}. \quad (16)$$

$\mathbf{u}'_{\text{int}}$  is the vector of normal particle velocities at the monitoring positions due to the internal sources and  $\mathbf{u}'$  is the vector of total normal particle velocities at the monitoring positions due to the internal sources and the equivalent source field. Note that these vectors are larger than those used to calculate the source strengths of the equivalent sources and are denoted using a prime. If no equivalent sources are used then the error  $E'$  is unity. For the more general boundary condition specified by a admittance matrix  $\mathbf{Y}_b$  the error can be defined as

$$E' = \frac{(\mathbf{u}' - \mathbf{Y}'_b \mathbf{p}')^H (\mathbf{u}' - \mathbf{Y}'_b \mathbf{p}')}{(\mathbf{u}'_{\text{int}} - \mathbf{Y}'_b \mathbf{p}'_{\text{int}})^H (\mathbf{u}'_{\text{int}} - \mathbf{Y}'_b \mathbf{p}'_{\text{int}})}. \quad (17)$$

The error in this case is the difference between the normal surface velocity at the monitoring points and the expected normal velocity at the monitoring points due to the pressure at the monitoring positions. This is again normalized such that the error when no equivalent sources are operating is unity.

#### D. Damping

Most models for the acoustic behavior of enclosed spaces include some damping. Without damping the response of the enclosure becomes infinite at the resonant frequencies of the enclosure. These singularities for the interior problem are the same *critical frequencies* at which it becomes difficult to calculate the radiation from a surface (exterior problem) using the boundary element method and the equivalent source method. Damping will be introduced into this model by using a complex wave number  $k'$  in the free-field Green's function [i.e.,  $k' = k(1 - j\alpha)$ ].

The Green's function for an enclosure can be expressed as a modal summation<sup>11</sup>

$$G(\mathbf{x}, \mathbf{y}) = \sum_{n=0}^{\infty} \frac{\psi_n(\mathbf{x}) \psi_n(\mathbf{y})}{V(k_n^2 - k'^2)}, \quad (18)$$

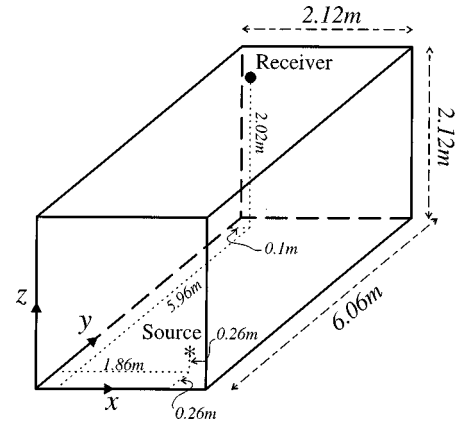


FIG. 3. The enclosure configuration used showing the position of the internal source (\*) and receiver (●).

where  $k$  is the wave number,  $k_n$  is the eigenvalue (natural frequency) for the  $n$ th mode whose shape (or eigenfunction) is given by  $\psi_n$ . Putting damping into Eq. (18) (i.e., substituting  $k'$  for  $k$ ) and assuming that  $\alpha \ll 1$  gives

$$G(\mathbf{x}, \mathbf{y}) = \sum_{n=0}^{\infty} \frac{\psi_n(\mathbf{x}) \psi_n(\mathbf{y})}{V(k_n^2 - k'^2)} \approx \sum_{n=0}^{\infty} \frac{\psi_n(\mathbf{x}) \psi_n(\mathbf{y})}{V[(k_n^2 - k^2) + 2j\alpha k^2]}. \quad (19)$$

Acoustic modal models [Eq. (A4), Appendix A] often use the modal damping ratio<sup>11</sup>  $\zeta$  which in this case is equal to  $\zeta = \alpha k_n / k$ . For low levels of damping the damping terms used in Eqs. (19) and (A4) are very similar since damping is only important near resonance (i.e., where  $k \approx k_n$ ).

## II. RESULTS: RECTANGULAR ENCLOSURE

In this section the equivalent source method will be used to model the behavior of a rectangular enclosure. A single monopole source was placed inside the enclosure and the reverberant field caused by reflections from the enclosure walls was modelled using a number of equivalent sources placed outside the enclosure. As an example the frequency response (i.e., the pressure due to unit input of volume velocity over a range of frequencies) between a source and a single receiver placed inside a rectangular enclosure will be calculated. The enclosure has dimensions  $x_0 = 2.12$  m,  $y_0 = 6.06$  m and  $z_0 = 2.12$  m, the source is positioned close to one corner of the enclosure at  $x = 1.86$  m,  $y = 0.26$  m,  $z = 0.26$  m and the receiver near the opposite corner at  $x = 0.1$  m,  $y = 5.96$  m,  $z = 2.02$  m. This configuration is shown in Fig. 3.

### A. Positioning of equivalent sources

One of the important aspects of the equivalent source technique is the placement of the equivalent sources. If, for example, the equivalent sources are arranged as a sphere in the far field around the enclosure then it is found that a large number of equivalent sources are required to accurately match the velocity at the boundary due to a monopole source inside the enclosure (i.e., to produce hard walled conditions). However, if the first order image source positions for the internal source are used, along with a sphere of far-field sources, then only relatively few equivalent sources are re-

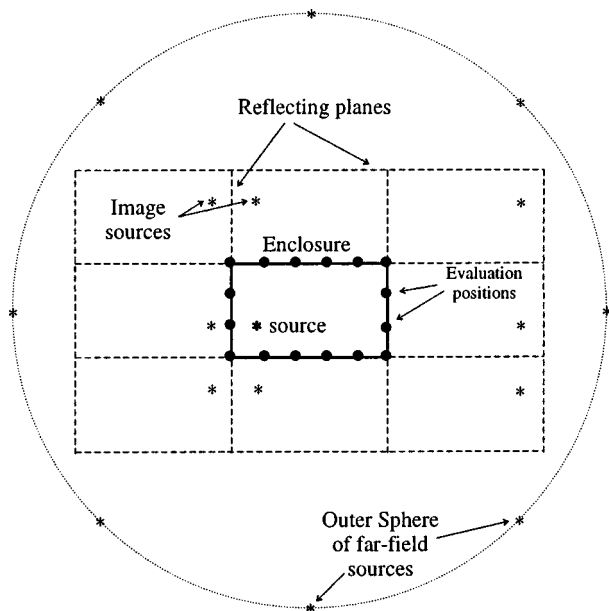


FIG. 4. The equivalent source positions used to calculate the response of a rectangular enclosure with a single monopole source.

quired to achieve good matching at the boundary. Figure 4 shows a side view of the enclosure with the equivalent sources positioned as image sources and as a sphere in the far field. The far-field sphere of equivalent sources can be thought of as efficiently compensating for all of the far-field image sources. In three dimensions there are twenty six “first order” image sources (i.e., only one reflection in any one plane).

### 1. Positioning of sources on a sphere

Different numbers of equivalent sources can be chosen on the surface of the enclosing sphere. For the examples given in this paper these positions are chosen to lie in a number of rings, or lines of latitude, around the sphere. If, for example,  $N$  rings are used then the rings are spaced with a polar angle of  $\pi/N$ . There are  $2N$  positions on the most equatorial rings with the number of positions on the other smaller rings chosen to give a similar spacing to the spacing found on the equatorial rings. The example of a sphere with eight rings is shown in Fig. 5. The side view shows the eight rings layered as lines of constant latitude. The top (polar) view shows that the smallest top ring has 4 sources with the next rings having 10, 14, and 16 sources respectively.

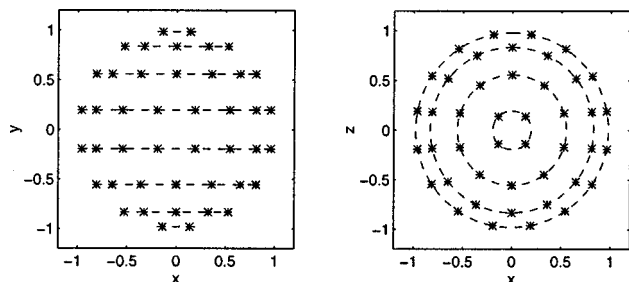


FIG. 5. The 88 monopoles for this sphere are shown from a side (left-hand figure) and top view (right-hand figure).

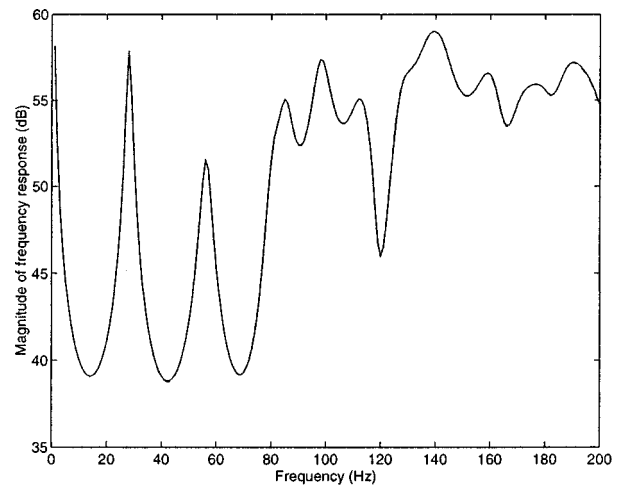


FIG. 6. The magnitude of the frequency response between the source and the receiver in the enclosure calculated using a modal model (solid line) and the equivalent source method (dashed).

Different surface geometries may require different spacing of the equivalent sources on the sphere. For surfaces with large aspect ratios it may be more effective to concentrate the far-field sources more heavily in particular regions of the sphere. This effect can also be achieved by distorting the shape of the sphere.

### B. Empty enclosure

Figure 6 shows the magnitude of the frequency response between the source and the receiver in the rectangular enclosure calculated using a modal model with 245 modes (Appendix A) and the equivalent source model. The damping in both cases is set to 0.036 (i.e., for the equivalent source method  $\alpha=0.036$  and for the modal model  $\zeta=0.036$ ). The responses calculated using these two methods match extremely well so that the two lines can barely be differentiated on this graph. This simulation confirms that the equivalent source method can be used to accurately model the behavior of an enclosure. The equivalent source method in this case used 222 equivalent sources (26 image sources plus 196 sources on a spherical surface 100 m from the center of the enclosure) and 546 evaluation positions on the boundary.

If the receiver is very close to the source then the modal model requires many more modes to converge since high wave numbers (or high order modes) need to be considered to accurately model the near field of a source. The equivalent source method calculates both the direct field from the source and the reverberant field from the boundary using the free-field Green’s function and can accurately model the behavior close to a source without convergence problems.

### 1. Convergence in an empty enclosure

This section will investigate the convergence of the surface velocity for the equivalent source method applied to an empty hardwalled rectangular enclosure (i.e.,  $Y_b=0$ ). The error is calculated [Eq. (16)] using different numbers of equivalent sources arranged on the surface of a sphere of radius 100 m (far field). In all cases the first set of image

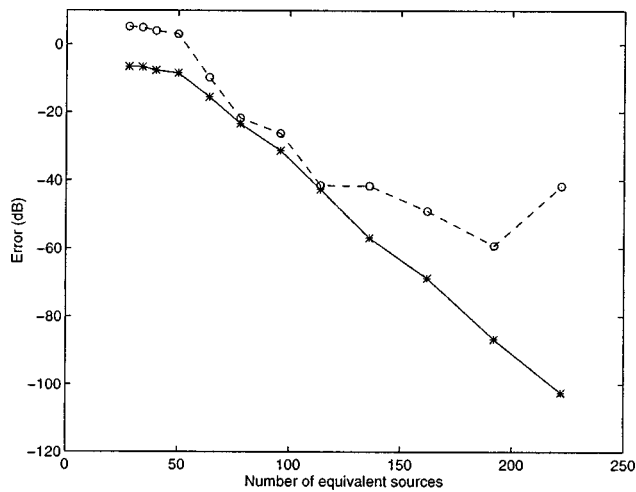


FIG. 7. The error ( $E'$ ) at the monitoring positions on the surface of the enclosure using varying numbers of equivalent sources ( $\circ$ ) and the error ( $E$ ) at the 250 evaluation positions ( $*$ ) at 88 Hz.

sources for the internal source are used [26 positions ( $3^3 - 1$ )]. The number of rings on the far-field sphere is varied from 1 to 12 which corresponds to a total of 28, 34, 40, 50, 64, 78, 96, 114, 136, 162, 192, and 222 equivalent sources being used. The source position shown in Fig. (3) is used as the internal source. The damping coefficient was  $\alpha = 0.036$ .

Figure 7 shows the error at the monitoring points  $E$  and the error at the evaluation positions  $E'$  using varying numbers of equivalent sources when the frequency is 88 Hz. There are, for this example, ten evaluation positions along the  $y$ -axis of the enclosure and five along the  $x$  and  $z$  axes, i.e.,  $2 \times [(10 \times 5) + (10 \times 5) + (5 \times 5)] = 250$  evaluation positions over the six faces of the enclosure. The error is calculated at 2250 monitoring points on the surface of the enclosure, i.e., the monitoring points are three times closer together than the evaluation positions. We would expect the error would continue to decrease as the number of equivalent sources increases. However, there is a point at around 200 equivalent sources for which additional equivalent sources causes the error at the monitoring positions to *increase* even though the velocity (or error) at the evaluation positions continues to fall. This implies that the problem is ill-conditioned and this can be shown by looking at the singular values of the matrix  $T_e$ . Figure 8 shows the magnitude of the singular values of the matrix  $T_e$  when 222 equivalent sources are used (i.e.,  $T_e$  is a 250 by 222 matrix). The first large singular values (i.e., the first 26) are “due” mainly to the action of the image sources which are closer to the surface of the enclosure and hence better coupled to it. The singular values then fall off at a relatively constant rate until around the 210th singular value where the level begins to decay rapidly. The implication is that with this number of evaluation positions the use of more than 210 equivalent sources is likely to produce a poorly conditioned result. Small singular values imply that the equivalent sources have to drive extremely hard to effect the velocity component (or eigenvector) which corresponds to that singular value. Extra equivalent sources will achieve small reductions in the error at the evaluation positions but the large source strengths required are likely to

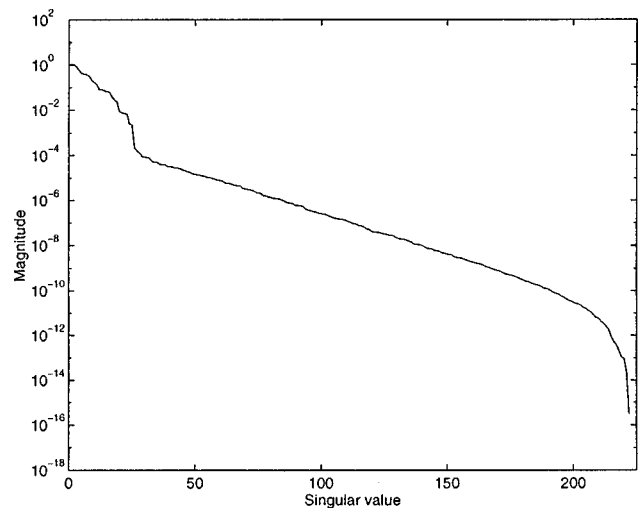


FIG. 8. The magnitude of the singular values of the matrix  $T_e$  using 222 equivalent sources and 250 evaluation positions at 88 Hz.

cause the velocity between the evaluation positions (i.e., at the monitoring points) to increase.

If the number of evaluation positions is increased then the problem becomes better conditioned. This can be shown by looking at the singular values of the matrix  $T_e$  when 546 evaluation positions are used on the surface of the enclosure (16 evaluation positions along the  $y$  axis and 7 along the  $x$  and  $z$  axes) and 222 equivalent sources are used (Fig. 9). In this case the smallest singular value is more than four orders of magnitude larger than for the case using 250 evaluation positions. The numerical stability of this arrangement is reflected in the error due to varying numbers of equivalent sources which is shown in Fig. 10 and uses 2250 monitoring positions on the boundary. It is therefore important that for a given set of evaluation positions the number of equivalent sources is chosen such that the problem is still well conditioned. If the level of error at the monitoring positions is unacceptable then potentially both the number of equivalent

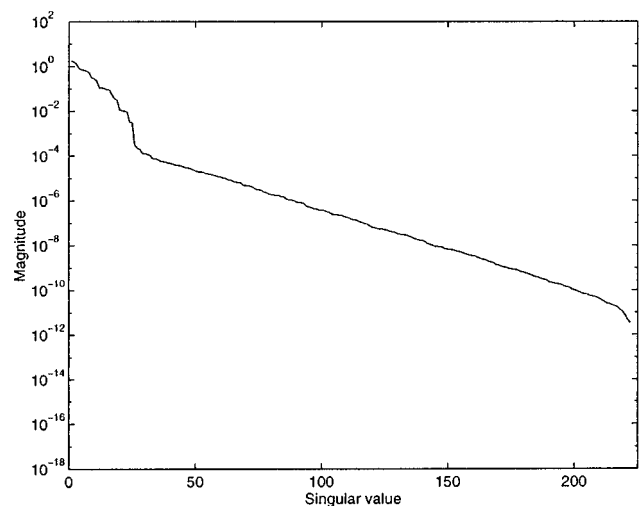


FIG. 9. The magnitude of the singular values of the matrix  $T_e$  using 222 equivalent sources and 546 evaluation positions at 88 Hz.

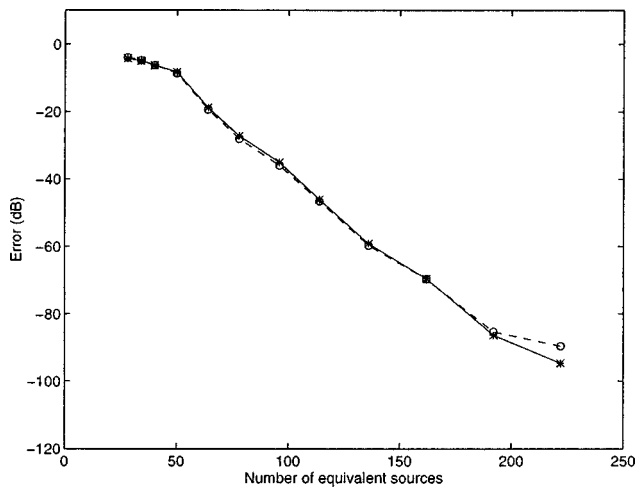


FIG. 10. The error ( $E'$ ) at the monitoring positions on the surface of the enclosure using varying numbers of equivalent sources (○) and the error ( $E$ ) at the 546 evaluation positions (\*) at 88 Hz.

sources *and* the number of evaluation positions need to be increased. Differences in the level of error at the evaluation positions and the error at the monitoring points (as shown in Fig. 7) can be due to poor sampling of the boundary as well as ill-conditioning. For example if the surface velocity is only evaluated at a few positions which are spaced at distances comparable to the size of a wavelength then the problem can be well conditioned but still produce poor results.

For higher frequencies of excitation the surface velocity is more complex and the error falls off at a slower rate with additional equivalent sources. Figure 11 shows the error as function of the number of equivalent sources for an excitation frequency of 200 Hz. For this example 546 evaluation positions are used and the internal source location is the same as for the example above. In this case the error evaluated at the monitoring positions and at the evaluation positions remains very similar and therefore there are sufficient evaluation positions and the problem is well conditioned.

To ensure that the system is converged sufficiently at

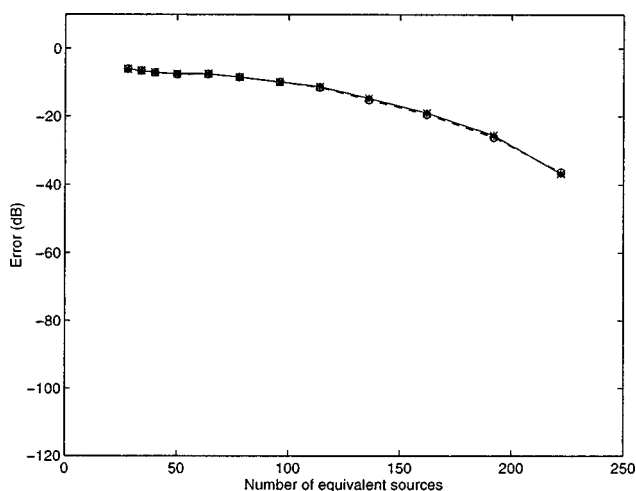


FIG. 11. The error ( $E'$ ) at the monitoring positions on the surface of the enclosure using varying numbers of equivalent sources (○) and the error ( $E$ ) at the 546 evaluation positions (\*) at 200 Hz.

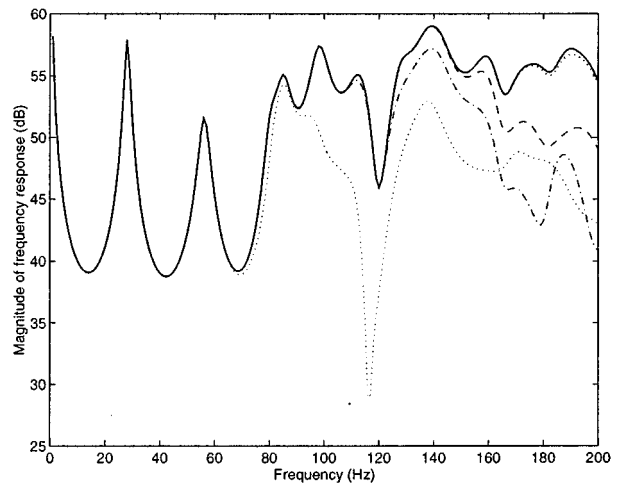


FIG. 12. The magnitude of the frequency response between the source and the receiver in the enclosure using 5 rings (dotted), 7 rings (dash dot), 9 rings (dashed), 11 rings (thick dotted), and 12 rings (solid) of equivalent sources on the far-field sphere.

below and up to the frequency of interest the frequency response between the source and the receiver was calculated using a large number of evaluation positions (546) and different numbers of equivalent sources. Frequency responses using different numbers of rings of equivalent sources on the outer sphere, namely, 5 (38 sources), 7 (70 sources), 9 (110 sources), 11 (166 sources), and 12 (196 sources) rings with an additional 26 image sources are plotted in Fig. 12. The frequency responses calculated using smaller numbers of equivalent sources becomes inaccurate at lower frequencies. The response calculated using five rings deviates from the other responses (by 1 dB) at 83 Hz where the error at the monitoring positions is  $-17.5$  dB. The response calculated using seven rings becomes inaccurate at 125 Hz and at this frequency the error at the monitoring positions is  $-16.9$  dB. The response calculated using nine rings becomes inaccurate at 158 Hz and at this frequency the error at the monitoring positions is  $-21.1$  dB. From these results it appears that when the error falls below  $-20$  dB the frequency response between this source and receiver is reasonably accurate. If the error is kept considerably below this level, for example  $-25$  dB, then we would assume that the solution is reasonably accurate.

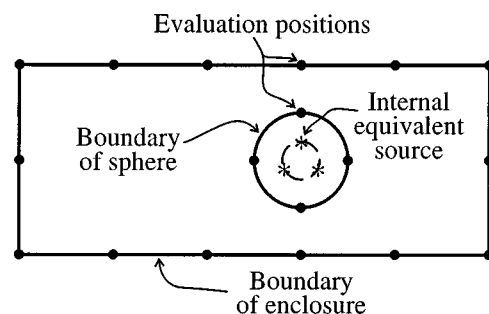


FIG. 13. The configuration used to calculate the response of an enclosure with a sphere placed inside. Evaluation positions (●) are on the surface of the enclosure and the sphere. The equivalent sources (\*) are placed outside the enclosure and inside the sphere.

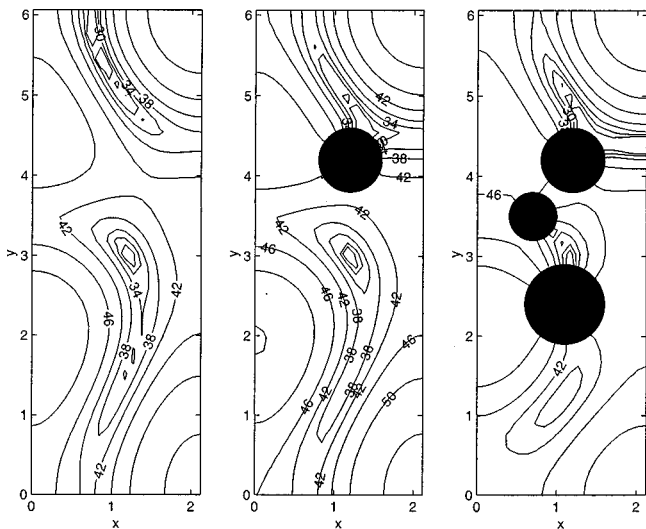


FIG. 14. A contour plot showing the pressure field at 88 Hz inside an enclosure of dimensions  $x_0=2.12$  m,  $y_0=6.06$  m, and  $z_0=2.12$  m with none, one and three scattering spheres. The contour lines are at 4 dB intervals.

### C. Rigid spheres in an enclosure

In this section the response of the enclosure is calculated with rigid spheres placed inside. Every sphere has a number evaluation positions on the surface and a small sphere of equivalent sources placed inside (Fig. 13). It is found that smaller inner spheres of sources give more accurate results than larger inner spheres of sources and this supports the findings of Song *et al.*<sup>1,2</sup> The added evaluation positions and equivalent sources are then incorporated into the calculation of the matrices  $Z_e$  and  $T_e$ .

Figure 14 is a contour plot of the pressure across the middle of the enclosure (i.e.,  $z=1.06$  m) due to the source at 88 Hz without a sphere, with one and then three spheres present in this plane. It can be noted that all of the contour lines of pressure are perpendicular to the hard surfaces on both the enclosure walls and the spheres showing that the gradient of the pressure (i.e., particle velocity) is zero. The presence of the spheres alters the sound field over the entire enclosure not just near to the surface of the spheres.

The frequency response between the source and the receiver in the enclosure will be significantly altered by the presence of a sphere as shown in Fig. 15. The sphere for this example has a radius of 0.4 m and is positioned at (1.2 m, 4.2 m, 1.06 m). This is the same sphere as shown in the second contour plot in Fig. 14.

### D. Pressure release boundary

In this section the response of the enclosure is calculated when one face of the enclosure ( $y=6.06$ ) is considered to be a pressure release boundary with all of the other faces taken to be rigid. Most of the terms in the admittance matrix  $Y_b$  are zero, as for the hard walled case, but the terms relating the velocity at a point on the pressure release boundary to the pressure at that point are set to be a large value (i.e.,  $Y_{b,ii} > 1000$  where  $i$  is an evaluation position on the pressure release boundary). This will drive the pressure at these points to small values.

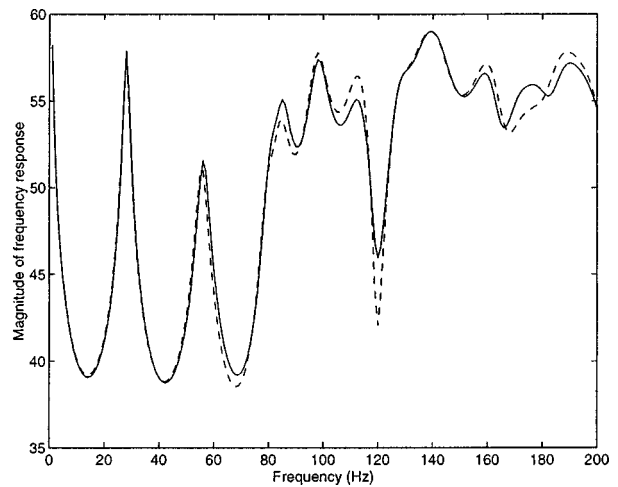


FIG. 15. The magnitude of the frequency response between the source and the receiver without (solid) and with (dashed) a 0.4 m sphere positioned at  $x=1.2$  m,  $y=4.2$  m, and  $z=1.06$  m. Damping ratio of 0.036.

Figure 16 is a contour plot of the pressure across the middle of the enclosure (i.e.,  $z=1.06$  m) due to the source at 88 Hz with hard walls, with a pressure release on the  $y=6.06$  face and with a sphere present. As expected the pressure at the  $y=6.06$  face is reduced dramatically. The third contour plot includes a hard sphere and is included to illustrate the flexibility of this method, where the shape and the behavior of each boundary can be easily altered in the same simulation.

The frequency response between the source and the receiver in the enclosure should be re-arranged to drastically altered by the pressure release surface, especially since the receiver is positioned next to this surface (Fig. 17). The overall behavior of the room changes since resonances due to wave propagation in the  $y$  direction have altered boundary conditions resulting in a drop in natural frequency. For example the first resonance is now at half the frequency of the

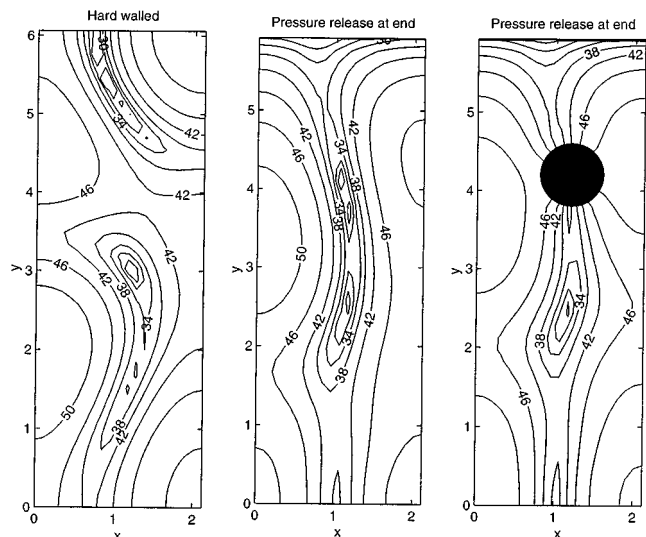


FIG. 16. A contour plot showing the pressure field at 88 Hz inside an enclosure of dimensions  $x_0=2.12$  m,  $y_0=6.06$  m and  $z_0=2.12$  m with a pressure release surface at  $y=6.06$ . The contour lines are at 4 dB intervals.

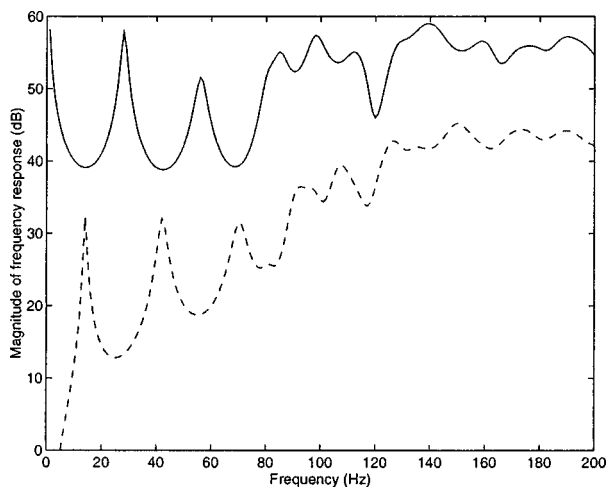


FIG. 17. The magnitude of the frequency response between a source at (1.86 m, 0.26 m, 0.26 m) and a receiver at (0.1 m, 5.96 m, 2.02 m) in an enclosure of dimensions ( $x_0=2.12$  m,  $y_0=6.06$  m and  $z_0=2.12$  m) with hard walls (solid) and with one pressure release boundary at  $y=6.06$  (dashed).

first resonance when the boundary was hard which is what would be expected from a pressure release boundary condition.

### E. Elastic plate

In this section the response of the enclosure is calculated when one face of the enclosure ( $y=6.06$ ) is considered to be a simply supported 3.2 mm thick aluminum plate with all of the other faces taken to be rigid. Most of the terms in the admittance matrix  $\mathbf{Y}_b$  are zero, as for the hard walled case, but the terms relating the velocity at a point on the plate due to the pressure (or force) at another point on the plate are given by a fully populated admittance or mobility matrix  $\mathbf{Y}_{ss}$  which is calculated from a modal model of the plate (Appendix B). The plate thus represents a nonlocally reacting surface to the enclosure. The natural frequencies of the first few modes of the plate used in the simulation are given in Table I.

Figure 18 is a contour plot of the pressure across the middle of the enclosure (i.e.,  $z=1.06$  m) due to the source at 88 Hz with hard walls, with a simply supported 3.2 mm thick aluminum plate on the  $y=6.06$  face and with the aluminum end plate and a sphere present. The response of the enclosure at this frequency is altered significantly by the presence of the flexible boundary. This change is mainly due to the fact that the frequency of excitation is close to two resonances of the plate (the  $m=1, n=2$  and the  $m=2, n=1$  modes). This

TABLE I. The natural frequencies for a simply supported 3.2 mm thick aluminum plate of dimensions 2.12 m by 2.12 m.

$m$	$n$	Natural frequency (Hz)
1	1	34.7
1	2	86.7
2	1	86.7
2	2	138.8
1	3	173.5
3	1	173.5

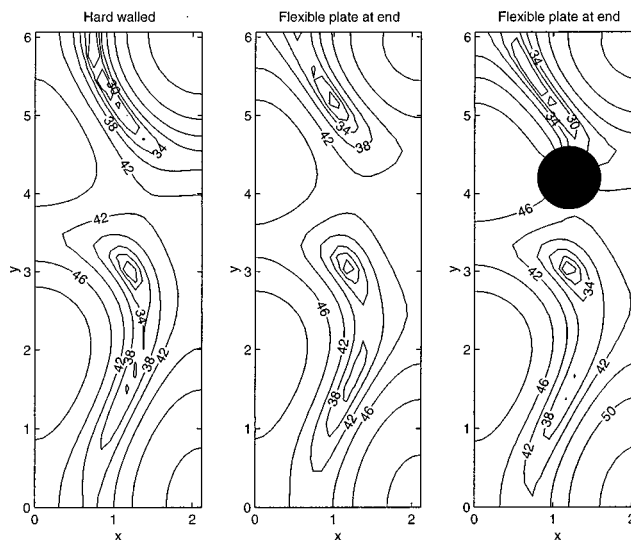


FIG. 18. A contour plot showing the pressure field at 88 Hz inside an enclosure of dimensions  $x_0=2.12$  m,  $y_0=6.06$  m, and  $z_0=2.12$  m with a 3.2 mm thick simply supported aluminum plate at  $y=6.06$ . The contour lines are at 4 dB intervals.

is illustrated by considering the frequency response between the source and receiver in the enclosure (Fig. 19) where the plate affects the acoustic response in a frequency range close to a natural frequency (i.e., the admittance is high and hence the pressure near to the boundary becomes small) but does not affect the response significantly at other frequencies.

### III. CONCLUSIONS

The equivalent boundary source method allows the acoustic pressure field in an enclosure, due to a vibrating or scattering boundary, to be calculated using a number of equivalent sources. This is a numerical technique which requires that the behavior of the boundary be evaluated at a finite number of points. The number of evaluation positions on the boundary and the number equivalent sources required

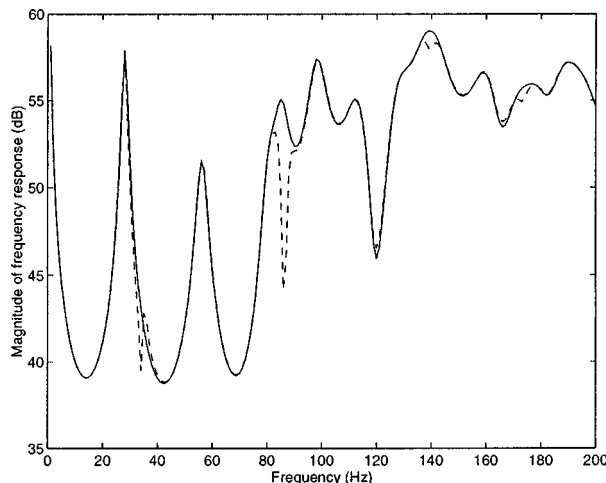


FIG. 19. The magnitude of the frequency response between a source at (1.86 m, 0.26 m, 0.26 m) and a receiver at (0.1 m, 5.96 m, 2.02 m) in an enclosure of dimensions ( $x_0=2.12$  m,  $y_0=6.06$  m and  $z_0=2.12$  m) with hard walls (solid) and with one boundary which is a simply supported 3.2 mm thick aluminum plate  $y=6.06$  (dashed).

to achieve an accurate solution is dependent on the frequency of interest and the geometry of the boundary.

A matrix formulation has been used to calculate the equivalent source strengths required to approximate the behavior of the boundary. The number of equivalent sources is chosen to be smaller than the number of evaluation positions on the boundary creating an overdetermined system. This tends to improve the conditioning of the problem and allows the behavior at the evaluation positions to be accurately modelled without causing the behavior between the evaluation positions to vary significantly. Using this approach the boundary can be modelled either as a rigid surface, as having a locally acting impedance or as a nonlocally reacting system such as an elastic body.

The example of a rectangular hard walled enclosure was used to demonstrate the equivalent source technique for the interior problem and this example was validated by comparison with a modal model. Damping was included by the use of a complex wave number and for low damping ratios this was shown to be equivalent to the modal damping ratio. The frequency response between a source and a receiver in the enclosure was shown to be very well matched to the frequency response calculated using a modal model.

To achieve accurate matching of the boundary conditions due to a source placed inside the enclosure the first set of equivalent source positions were chosen as the first order image source positions. In addition to the image source positions the equivalent sources were also placed on a large sphere surrounding the enclosure which effectively compensate for the behavior of all of the far field image sources. Inaccuracies in reproducing the boundary condition were shown to be due to the either poor sampling at the boundary or ill-conditioning of the matrices used to calculate the equivalent source strengths.

The convergence properties of this method were investigated and it has been concluded that if the normalized velocity error remains below about  $-25$  dB for the enclosure, then the calculated frequency response between a source and a receiver will generally be sufficiently converged to give an error of less than 1 dB in the predicted response. For frequencies up to 200 Hz in an enclosure of dimensions 2.12 m by 6.06 m by 2.12 m a set of 546 evaluation positions on the boundary, consisting of a 16 by 7 array on the large faces and a 7 by 7 array on the small faces, was found to be sufficient. The number of equivalent sources required is 222. For lower frequencies smaller numbers of evaluation positions and equivalent sources can be used.

The formulation was extended to include the effect of rigid spheres inside the enclosure by adding a number of equivalent sources inside the spheres and a number of velocity evaluation positions on the surface of the spheres. These spheres were shown to significantly change the global behavior of the enclosure at low frequencies even though the wavelengths were large compared to the size of the spheres. Various boundary conditions at the surface of the enclosure were also tested, including a pressure release surface and an elastic plate. Creating a pressure release boundary changed the behavior of the enclosure dramatically by changing the mode shapes and natural frequencies of the enclosure modes.

The pressure near to the simply supported plate was shown to be reduced, compared to the hard-wall case, when the frequency of excitation matched that of a plate resonance since the admittance was large at these frequencies.

The equivalent source technique was shown to be a simple alternative to the boundary element method for calculating the sound field inside an enclosure with simple scattering objects. Only the free-field Green's function and the positioning of the elements and sources are required to achieve a solution. The computations are simple and complex surface elements are not required.

## ACKNOWLEDGMENTS

The authors would like to acknowledge the support of TNO Institute of Applied Physics, The Netherlands, for funding part of this research.

## APPENDIX A: MODAL MODEL FOR THE SOUND FIELD IN A RECTANGULAR ENCLOSURE

The pressure in an enclosure can be expressed as the summation of a series of acoustic modes. For a rectangular hard walled enclosure of dimensions  $x_0, y_0, z_0$  the mode shapes take the simple form of

$$\psi_{lmn}(x, y, z) = \sqrt{\varepsilon_l \varepsilon_m \varepsilon_n} \cos\left(\frac{l\pi x}{x_0}\right) \cos\left(\frac{m\pi y}{y_0}\right) \cos\left(\frac{n\pi z}{z_0}\right), \quad (\text{A1})$$

where  $\varepsilon_l, \varepsilon_m, \varepsilon_n$  are normalization factors which are equal to one if the subscript is zero and are equal to two if the subscript is greater than zero (i.e.,  $\varepsilon_0 = 1$  and  $\varepsilon_i = 2$  if  $i > 0$ ). This equation describes the variation in pressure with spatial position  $(x, y, z)$  due to the  $lmn$ th mode. The total pressure in the enclosure at a single frequency is given by the summation,

$$p(x, y, z) = \sum_{l=0}^{\infty} \sum_{m=0}^{\infty} \sum_{n=0}^{\infty} a_{lmn} \psi_{lmn}(x, y, z), \quad (\text{A2})$$

where  $a_{lmn}$  is the complex amplitude of the  $lmn$ th mode.

The excitation of the  $lmn$ th mode, at frequency  $\omega$ , due to a monopole source positioned at  $x = x_i, y = y_i, z = z_i$  and source strength  $q_i$  is given by

$$a_{lmn}(\omega) = \frac{\rho c}{x_0 y_0 z_0} A_{lmn}(\omega) \psi_{lmn}(x_i, y_i, z_i) q_i. \quad (\text{A3})$$

The frequency dependent term  $A_{lmn}(\omega)$  is known as the complex resonance term and is given by

$$A_{lmn}(\omega) = \frac{\omega}{2\zeta_{lmn}\omega_{lmn}\omega - j(\omega_{lmn}^2 - \omega^2)}, \quad (\text{A4})$$

where  $\zeta_{lmn}$  is the damping ratio for the  $lmn$ th mode and  $\omega_{lmn}$  is the natural frequency of the  $lmn$ th mode and is given by

$$\omega_{lmn} = \pi c \left[ \left(\frac{l}{x_0}\right)^2 + \left(\frac{m}{y_0}\right)^2 + \left(\frac{n}{z_0}\right)^2 \right]^{1/2}. \quad (\text{A5})$$

It is found that as the values of  $l, m$  and  $n$  become large the contributions due to the modes become small [Eqs. (A4) and

(A5)] and good estimation of the pressure can be achieved using finite summations. Using these equations the frequency response between a source and a receiver in the enclosure can be calculated.

## APPENDIX B: CALCULATING THE MOBILITY MATRIX FOR A SIMPLY SUPPORTED PLATE

The mobility (or equivalently admittance) of a simply supported plate can be calculated using standard plate theory.<sup>12,13</sup> The vibration of a simply supported plate can be approximated using a finite modal summation. The out-of-plane velocity  $u(x,y)$  is due to flexural waves on the plate and is given by

$$u(x,y) = \sum_{m=1}^M \sum_{n=1}^N W_{mn} \psi_{mn}(x,y), \quad (\text{B1})$$

where

$$\psi_{mn}(x,y) = \sin(k_m x) \sin(k_n y). \quad (\text{B2})$$

The velocity at position  $(x,y)$  of the plate surface is calculated using a finite summation considering modes up to  $m = M$  and  $n = N$  with mode shapes  $\psi_{mn}$  and mode amplitude  $W_{mn}$ . The modal wave numbers in the  $x$  and  $y$  directions are given by  $k_m = m\pi/a$  and  $k_n = n\pi/b$  where  $a$  and  $b$  are the dimensions of the plate in the  $x$  and  $y$  directions, respectively.

The amplitude of a modes is due to the position and frequency of the force exciting the plate. A point force  $F$  acting at  $x = x_f$ ,  $y = y_f$  will excite the structure such that

$$W_{mn} = \frac{4F \psi_{mn}(x_f, y_f)}{\rho_s h a b} A_{mn}(\omega), \quad (\text{B3})$$

where  $\rho_s$  is the density of the plate material and  $h$  is the thickness of the plate.  $A_{mn}(\omega)$  is the complex resonance term and is given by

$$A_{mn}(\omega) = \frac{\omega}{2 \zeta_{mn} \omega_{mn} \omega - j(\omega_{mn}^2 - \omega^2)}, \quad (\text{B4})$$

where  $\zeta_{mn}$  is the damping ratio for the  $mn$ th mode and  $\omega_{mn}$  is the natural frequency of the  $mn$ th mode and is given by

$$\omega_{mn} = \left( \frac{EI}{\rho_s h} \right)^{1/2} [k_m^2 + k_n^2], \quad (\text{B5})$$

where for the plate  $I = h^3/[12(1 - \nu^2)]$ , where  $\nu$  is Poisson's ratio.

To calculate the admittance matrix  $Y_{ss}$  the plate is divided up equally into a number of elements which are small compared to the structural and acoustic wavelengths. It is assumed that the acoustic pressure over each element is constant such that the force over the element  $j$  is given by  $F_j = S_{el} p_j$ , where  $p_j$  is the acoustic pressure at the element  $j$  and  $S_{el}$  is the area of the elements.

The velocity at the  $i$ th element due to a pressure at the  $j$ th element is given by

$$\begin{aligned} Y_{ij}(\omega) &= \frac{u(x_i, y_i)}{p_j} \\ &= \frac{4S_{el}}{\rho_s h a b} \sum_{m=1}^M \sum_{n=1}^N A_{mn}(\omega) \psi_{mn}(x_i, y_i) \psi_{mn}(x_j, y_j), \end{aligned} \quad (\text{B6})$$

where  $(x_i, y_i)$  is the position of the  $i$ th element and  $(x_j, y_j)$  is the position of the  $j$ th element.

<sup>1</sup>G. H. Koopmann, L. Song, and J. B. Fahline, "A method for computing acoustic fields based on the principle of wave superposition," *J. Acoust. Soc. Am.* **86**, 2433–2438 (1989).

<sup>2</sup>L. Song, G. H. Koopmann, and J. B. Fahline, "Numerical errors associated with the method of superposition for computing acoustic fields," *J. Acoust. Soc. Am.* **89**, 2625–2633 (1991).

<sup>3</sup>J. B. Fahline and G. H. Koopmann, "A numerical solution for the general radiation problem based on the combined methods of superposition and singular-value decomposition," *J. Acoust. Soc. Am.* **90**, 2808–2819 (1991).

<sup>4</sup>M. Ochmann, "The source simulation technique for acoustic radiation problems," *Acustica* **81**, 512–527 (1995).

<sup>5</sup>R. Jeans and I. C. Mathews, "The wave superposition method as a robust technique for computing acoustic fields," *J. Acoust. Soc. Am.* **92**, 1156–1166 (1992).

<sup>6</sup>W. Kropp and P. U. Svensson, "Application of the time domain formulation of the method of equivalent sources to radiation and scattering problems," *Acustica* **81**, 528–543 (1995).

<sup>7</sup>L. Song, G. H. Koopmann, and J. B. Fahline, "Active control of the acoustic radiation of a vibrating structure using a superposition formulation," *J. Acoust. Soc. Am.* **89**, 2786–2792 (1991).

<sup>8</sup>J. Garcia-Bonito and S. J. Elliott, "Local active control of diffracted diffuse sound fields," *J. Acoust. Soc. Am.* **98**, 1017–1024 (1995).

<sup>9</sup>R. V. Waterhouse, "Nearfield diffraction patterns at a sphere or cylinder," *J. Acoust. Soc. Am.* **75**, 695–706 (1984).

<sup>10</sup>A. Omoto and S. J. Elliott, "The effect of structured uncertainty in multichannel feedforward control," *Proc. ICASSP 96* **2**, 965–968 (1996).

<sup>11</sup>P. A. Nelson and S. J. Elliott, *Active Control of Sound* (Academic, London, 1992).

<sup>12</sup>G. B. Warburton, "The vibration of rectangular plates," *Proc. Inst. Mech. Eng.* **168**, 371–383 (1954).

<sup>13</sup>C. R. Fuller, S. J. Elliott, and P. A. Nelson, *Active Control of Vibration* (Academic, New York, 1996).



# Ultrasonic interferences in polymer plates

Etienne Juliac, Jacques Arman, and Daniel Harran

*Université de Pau et des Pays de l'Adour, Laboratoire de Physique des Matériaux Industriels,  
E.S.A. C.N.R.S. 5067, Avenue de l'Université, 64 000 Pau, France*

(Received 26 November 1997; accepted for publication 7 May 1998)

Reflection and transmission of an ultrasonic beam by a homogeneous polymer plate (PMMA) immersed in water are studied experimentally and theoretically by the interference method. The elementary waves which emerge from the plate after 0, 1, or 2 internal reflections on the lower interface are considered individually, and their amplitude and phase shift are calculated. The interferences between these elementary waves provide the resulting waves reflected and transmitted by the plate. This method is valid because only a small number of these elementary waves have a significant amplitude when they emerge, due to the relatively high wave attenuation of polymer materials. For a 2-mm-thick PMMA plate, for example, only two internal reflections on the lower face must be taken into account for the reflection by the plate, and one for transmission. Perfect agreement with results from the classical global method confirms the validity of the interference method. This treatment enables us to better understand the physical significance of the reflection and transmission curves by the plates. Moreover, this method facilitates the calculation of accurate ultrasonic parameter values of the plate (velocities and attenuation coefficients of the longitudinal and transverse waves), by adjustment of the theoretical to the experimental reflection and transmission curves. © 1998 Acoustical Society of America. [S0001-4966(98)05308-9]

PACS numbers: 43.20.Fn, 43.35.Zc [ANN]

## INTRODUCTION

Ultrasound is commonly used for nondestructive testing, usually of metallic materials. Applied to polymers, it enables us to determine the characteristic parameters related to the longitudinal and shear moduli of these materials (i.e., the propagation velocity and the attenuation of the longitudinal and transverse waves). Knowing these moduli, the mechanical behavior of polymers in the high frequency field can be predicted.

Propagation velocity and attenuation can be measured by submitting a sample to an ultrasonic beam with normal incidence (for the longitudinal wave) or with an angle of incidence between the longitudinal and transverse critical angles of total reflection (for the transverse wave).<sup>1-4</sup> Another method consists of measuring the time interval between the echoes reflected by the two interfaces at normal incidence.<sup>5</sup> These methods do not, however, permit precise measurements. The attenuations, in particular, are given with relatively large uncertainties.

A much higher precision can be obtained by measuring ultrasonic reflection at variable frequency and constant incidence (by spectral analysis, for example<sup>4,6,7</sup>) or at variable incidence and fixed frequency.<sup>8-10</sup> The reflection curves can then be plotted theoretically and, by adjusting the experimental and theoretical curves, it is possible to solve what is called the inverse problem, that is to say, deduce the values of the ultrasonic parameters of a material from the properties of the reflected waves.<sup>11</sup>

Experimental and theoretical studies of the reflection of ultrasonic waves in a plate have been carried out for many years.<sup>12-15</sup> In the general case, the incident wave splits into a wave reflected off the first interface, and longitudinal and transverse waves which penetrate the plate. When these last

two waves reach the second interface, each of them produces three waves—a transmitted wave, a longitudinal wave and a transverse wave—which are reflected back again by the first interface and so on. It rapidly becomes very difficult to follow the incident wave and the propagation of an ultrasonic wave in a plate has therefore, to our knowledge, never been studied completely by breaking up each elementary wave and then adding up all of their components, reflected or transmitted by the plate.

This long and tedious decomposition is usually avoided by directly calculating the reflection and transmission coefficients of the plate, starting from the relationships of continuity on the two interfaces. This method can be extended for layered plates.<sup>13</sup> The advantage of this method is that it leads relatively rapidly to an exact solution, but a disadvantage is that it tends to mask the physical nature of the reflection curve. The minima and maxima observed on this curve are actually made up of the multiple reflections of the longitudinal and transverse waves within the plate. While some of them are surely caused by the longitudinal wave and others by the transverse wave, this method of calculation does not enable us to determine which.

We therefore studied ultrasonic wave propagation in a plate considering each wave individually, before combining them. In practice, this method can be used only for materials for which attenuation is great enough so that only the first ultrasonic waves have to be considered, the succeeding waves having a negligible amplitude. It lends itself very well to the study of viscoelastic materials such as polymers. These waves emerge parallel but present different phase shifts. Consequently, the composition of these waves represents a problem of interference with multiple waves. Thus the minima and the maxima on the reflection and transmis-

sion curves simply express, respectively, destructive or constructive interferences between these parallel waves.

In this article, we present results of a study of the ultrasonic wave propagation in a polymethylmethacrylate (PMMA) polymer plate immersed in a fluid. The experimental device developed in our laboratory enables us to work at fixed frequency and variable incidence. The variations of the reflection and transmission factors as functions of the angle of incidence were studied by three different methods:

- (i) the experimental method;
- (ii) the global theoretical method; and
- (iii) the method of interferences.

The global method was used only to validate the method of interferences.

## I. EXPERIMENTAL STUDY

An automated experimental device was built to determine the reflection and transmission coefficients of plane plates. The transmitter and receiver transducers are excited at a frequency of 2.12 MHz, the diameter of each transducer being  $\phi=22$  mm. In the reflection position, the receiving transducer is placed in such a way as to catch the beam reflected specularly. In the transmission position, it is laid out in the same direction as the transmitting transducer. This device will be described in more detail in a forthcoming article.

The PMMA ( $\bar{M}_w \approx 130\,000$ ) was provided by Elf AtoChem in the form of pellets. The plates, 10 cm square and 2 mm thick, were manufactured by hot compression. Water was used as the surrounding liquid.

Figure 1 shows the experimental curves  $R=f(\vartheta)$  and  $T=f(\vartheta)$ ,  $R$  and  $T$  being the amplitudes of the ultrasonic waves received by the transducer, in reflection and transmission positions, respectively,  $\vartheta$  being the angle of incidence.

## II. THEORETICAL STUDY

### A. Global method

The global method of calculation has often been used to study multilayer materials.<sup>13</sup> We used this method to verify the agreement, initially at least approximately, between the experimental and theoretical curves. It was also used as a reference to verify the results obtained by the method of interferences. Indeed, the curves determined by these two methods are identical.

The theoretical determination of the reflection and transmission coefficients of a plate immersed in a fluid requires the knowledge of the geometrical and ultrasonic characteristics of the materials used. The values of these parameters are not always available in the literature. In particular, measurement of attenuation coefficients is rather imprecise. We therefore took direct measurements beforehand, in both normal and post-critical incidences [ $\vartheta > \vartheta_{cl}$ ,  $\vartheta_{cl} = \sin^{-1}(c_0/c_l)$ ], with various plate thicknesses ( $\vartheta_{cl}$  is the critical angle of incidence for the longitudinal wave). The propagation velocity of the wave in the surrounding liquid,  $c_0$ , and the velocities of longitudinal and transverse waves in the plate,  $c_l$  and  $c_t$ , respectively, were thereby deduced. The

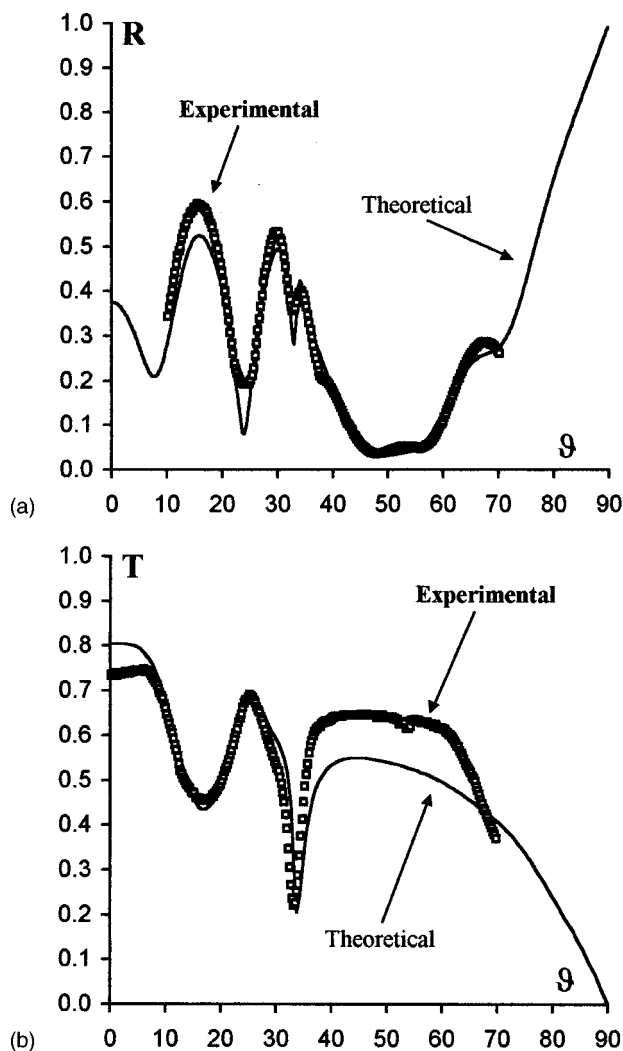


FIG. 1. Experimental and theoretical curves (global method with nonadjusted parameters): (a) Reflection curves:  $R=f(\vartheta)$ ,  $R$  is the reflection coefficient, (b) Transmission curves:  $T=f(\vartheta)$ ,  $T$  is the transmission coefficient,  $\vartheta$  is the angle of incidence (degrees).

attenuation coefficient of the longitudinal wave in the plate,  $\alpha_l$ , was measured directly. The attenuation coefficient of the transverse wave,  $\alpha_t$ , was deduced using the theoretical equation which links these two coefficients:<sup>16</sup>  $(c_l/c_t)^3 = 2(\alpha_t/\alpha_l)$ . Approximate values (Table I) were sufficient at this stage.

Because of the finite aperture of the transducer (diameter  $\phi=22$  mm), the acoustical waves are not exactly plane waves. But this effect has been already investigated and, except in the vicinity of critical angles, the approximation of using plane waves is well justified, the discrepancy between theory and experiment being negligible.<sup>17</sup> Moreover, the va-

TABLE I. Approximate values of the ultrasonic parameters used to determine the theoretical curves.  $c_0$ =propagation velocity of the waves in the liquid;  $c_l$ =propagation velocity of the longitudinal waves in polymer; and  $c_t$ =propagation velocity of the transverse waves in polymer.

$c_0$ (m/s)	$c_l$ (m/s)	$c_t$ (m/s)	$\alpha_l$ (Np/m)	$\alpha_t$ (Np/m)
1 460	2630	1350	60	220

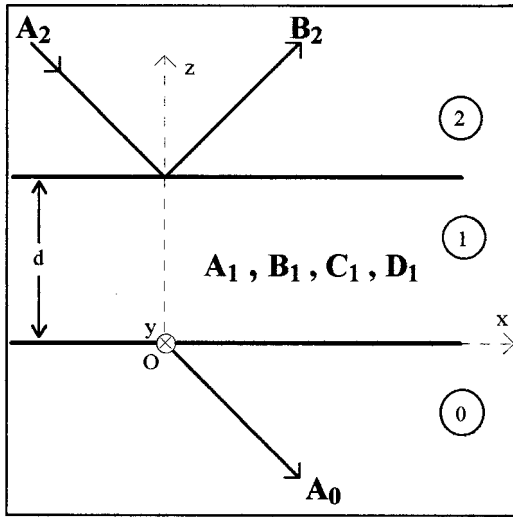


FIG. 2. Notations of the wave amplitudes and the subscripts in the three layers: A, B, C, and D are, respectively, the amplitudes of the incident longitudinal, the reflected longitudinal, the incident transverse and the reflected transverse waves.

Validity of the approximation was verified on a well-known material, aluminum.

Water being a nonabsorbing medium, the acoustical incident waves are therefore described by homogeneous plane waves. But the interface with the solid generates inhomogeneous waves inside this medium, for which the planes of constant amplitude are distinct from the planes of equal phase.<sup>18-20</sup> The inhomogeneous waves can be described by a complex wave vector. This description is equivalent, from a mathematical point of view, to the previous description by complex angles.<sup>18</sup> In this paper, we use this notation with complex angles which has the advantage of keeping the same equations below and above the critical angles. The validity of this treatment is experimentally verified by the excellent agreement between experimental and theoretical curves, at least below the longitudinal critical angle.

Thus the displacement of particles in a medium crossed by an acoustic plane wave can be expressed as a function of a scalar potential  $\varphi$  (related to the longitudinal wave) and a vectorial potential  $\psi$  (related to the transverse wave) by the equation:

$$\mathbf{u} = \text{grad } \varphi + \text{rot } \psi.$$

The reference axes of the system can be chosen so that  $\psi$  has only one component on the  $Oy$  axis (Fig. 2), that is to say  $\psi = (0, \psi, 0)$ .

Figure 2 also gives the subscripts attributed to the three layers of the solid plate immersed in a fluid.

For each layer, we can write:

$$\varphi = (Ae^{-i\beta z} + Be^{i\beta z})e^{i(\sigma x - \omega t)},$$

$$\psi = (Ce^{-i\gamma z} + De^{i\gamma z})e^{i(\sigma x - \omega t)}.$$

A and C are the amplitudes of the incident waves while B and D are the amplitudes of the reflected waves. The method of calculation is well known.<sup>13</sup>

The reflection and transmission coefficients are defined by the ratios of the amplitudes  $R = B_2/A_2$  and  $T = A_0/A_2$ , respectively.

We obtain after calculation:

$$R = \frac{M^2 - N^2 + Z_0^2}{M^2 - N^2 - Z_0^2 - 2iZ_0M} \quad (1a)$$

and

$$T = \frac{-2iZ_0N}{M^2 - N^2 - Z_0^2 - 2iZ_0M}, \quad (1b)$$

where

$$M = Z_l \cos^2 2\vartheta_t \cdot \cot p + Z_t \sin^2 2\vartheta_t \cdot \cot q$$

and

$$N = Z_l \frac{\cos^2 2\vartheta_t}{\sin p} + Z_t \frac{\sin^2 2\vartheta_t}{\sin q}.$$

Here,  $Z_l$  and  $Z_t$  are the impedances of the plate,  $Z_0$  is the impedance of the surrounding liquid,  $p = \beta_l d$ , and  $q = \gamma_l d$ .

Figure 1 shows the theoretical reflection and transmission curves for the polymer studied. Although approximate values were attributed to the ultrasonic parameters, there is a very good agreement between the angular positions of the successive signals on the experimental and theoretical curves.

The reflection curve, in particular, shows a succession of minima and maxima. These minima are associated with the resonances of the plate waves<sup>12-14</sup> and correspond to the Lamb waves.

In this method of calculation,  $B_2$  represents the total amplitude of the reflected wave. Therefore it implicitly takes into account all the waves reflected by the plate, without distinguishing between them. In the same way,  $A_0$  represents the total amplitude of the transmitted wave, without its various components appearing.

## B. Method of interferences: Principle

This method consists of calculating the characteristics of each elementary wave reflected or transmitted by the plate (amplitude and phase) separately, before superimposing them. First, their respective amplitudes must be calculated, taking into account any reflection or transmission at the two interfaces and the attenuation in the plate. All of these waves interfere at infinity since they emerge in the liquid with parallel directions. Their respective phase shifts must therefore be calculated in order to determine the amplitude of the resulting wave.

Figure 3 shows the various reflected waves after 0, 1, or 2 reflections on the lower face of the plate [0 reflection means that there was reflection on the upper face only (R1)]. The large number of waves inside the plate is due to the possibility of change of mode (longitudinal into transverse and conversely) at each internal reflection. Wave R3 is formed by the superpositioning of two elementary waves, ABE (transverse wave AB then longitudinal BE) and ACE (longitudinal then transverse) which merge at their exit. In

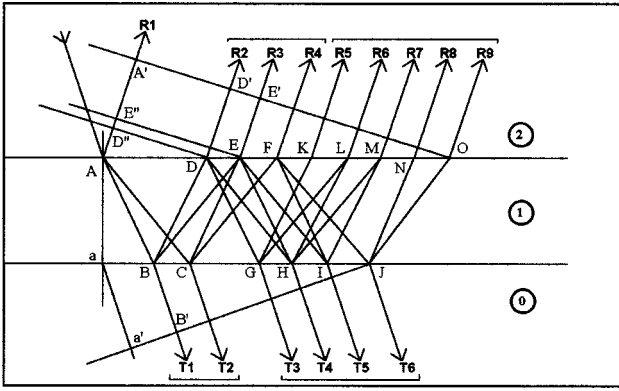


FIG. 3. Notations of elementary waves reflected and transmitted by the two interfaces.

the same way, waves R6 and R8 are formed by the superposition of four elementary waves. Wave R7 has six components. All the elementary components must be taken into account separately because their contributions are not necessarily equal.

The problem would soon become too complex to be solved by this method if the amplitude of these waves, repeatedly reflected, did not rapidly become negligible. Indeed, the amplitude of each wave decreases at each interface since each of them splits into three waves. The amplitude also decreases due to attenuation by the polymer. The interest of this method of calculation comes from the fact that, in the case of polymers, only a small number of waves are significant, those which were reflected only once or not at all by the lower face (R1 to R4). For better precision, we can take into account the waves reflected twice by the lower face (R5 to R9). The same is true for the transmitted waves.

### C. Calculation of the reflection and transmission coefficients at each interface

Three different cases of interface must be considered (Fig. 4).

The problem has already been solved in the literature and the reflection coefficient calculated.<sup>13</sup> We have also calculated the amplitudes of the transmitted longitudinal and transverse waves. The physical process is similar to that of the global method. The relationships of continuity of displacements and stresses must be expressed and applied, this time, to each individual wave and each type of interface.

#### 1. Liquid–solid interface

Let  $u_i$  be the displacements of the particles subjected to the incident wave,  $u_r$  that of the particles subjected to the reflected wave in the liquid medium, and  $u_l$  and  $u_t$  those of the longitudinal and transverse waves in the solid medium. The four displacement vectors lay in the  $Oxz$  plane. The angles which they form with the normal to the separation surface are labeled  $\vartheta$  for the incident and reflected waves,  $\vartheta_l$  and  $\vartheta_t$  for the longitudinal and transverse waves in the solid, respectively. Since the surrounding liquid is the same on both sides of the plate, we can give either the subscript 2 or

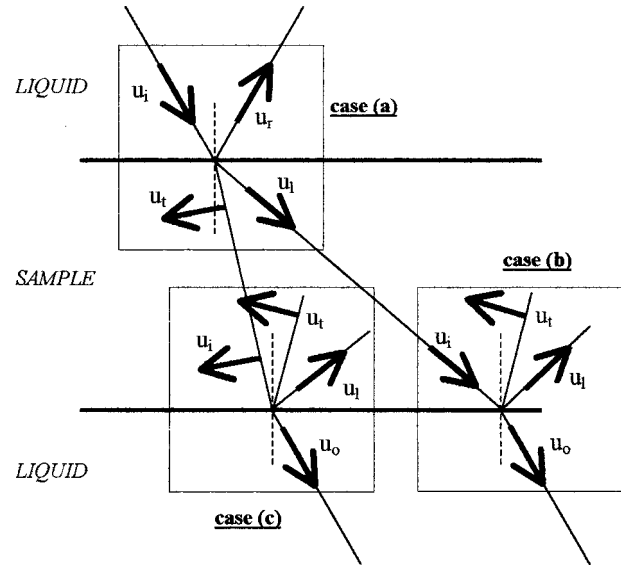


FIG. 4. Notations of the displacements of the particles on the three types of interface: (a) liquid–solid interface, (b) solid–liquid interface, longitudinal incident wave, (c) liquid–solid interface, transverse incident wave. The vectors represent the displacements of the particles subjected to the incident wave ( $u_i$ ), to the reflected wave in the liquid ( $u_r$ ), to the longitudinal ( $u_l$ ) and transverse ( $u_t$ ) waves in the solid, and to the transmitted wave in the liquid ( $u_o$ ).

0 to this medium (Fig. 2). The equations will be written with the subscript 0 in the liquid, the solid plate having subscript 1. We omit the function of time term:

$$u_i = a_i \exp\left(\frac{i\omega}{c_0}(x \sin \vartheta - z \cos \vartheta)\right),$$

$$u_r = a_r \exp\left(\frac{i\omega}{c_0}(x \sin \vartheta + z \cos \vartheta)\right),$$

$$u_l = a_l \exp\left(\frac{i\omega}{c_l}(x \sin \vartheta_l - z \cos \vartheta_l)\right),$$

$$u_t = a_t \exp\left(\frac{i\omega}{c_t}(x \sin \vartheta_t - z \cos \vartheta_t)\right).$$

The conditions of continuity on  $z=0$  can be written

$$(u_z)_0 = (u_z)_1, \quad (2a)$$

$$(\sigma_{zz})_0 = (\sigma_{zz})_1, \quad (2b)$$

$$(\sigma_{xz})_0 = (\sigma_{xz})_1. \quad (2c)$$

Equation (2a) gives

$$(-a_i + a_r) \cos \vartheta = -a_l \cos \vartheta_l - a_t \sin \vartheta_t. \quad (3)$$

The stresses are calculated from the general equation:<sup>21</sup>

$$\sigma_{ij} = 2\mu u_{ij} + \lambda u_{ll} \delta_{ij},$$

where  $\lambda$  and  $\mu$  are the Lamé coefficients ( $\mu_0=0$  in the surrounding liquid), and  $u_{ll}$  is the trace of the strain tensor.

In the liquid medium:

$$(\sigma_{zz})_0 = \lambda_0 \frac{i\omega}{c_0} (u_i + u_r),$$

$(\sigma_{xz})_0 = 0$  since there is no shear stress in the liquid.

In the solid medium:

$$(\sigma_{zz})_1 = 2\mu_1 i\omega \left( \frac{\cos^2 2\vartheta_l}{c_l} u_l + \frac{\sin \vartheta_t \cos \vartheta_t}{c_t} u_t \right) + \lambda_1 \frac{i\omega}{c_l} u_l,$$

$$(\sigma_{xz})_1 = -\mu_1 i\omega \left( \frac{\sin 2\vartheta_l}{c_l} u_l - \frac{\cos 2\vartheta_t}{c_t} u_t \right).$$

The relationships of continuity (2b) and (2c) thus give

$$\frac{\lambda_0}{c_0} (a_i + a_r) = \frac{2\mu_1 \cos^2 \vartheta_l + \lambda_1}{c_l} a_l + \frac{2\mu_1 \sin \vartheta_t \cos \vartheta_t}{c_t} a_t, \quad (4)$$

$$\frac{\sin 2\vartheta_l}{c_l} a_l = \frac{\cos 2\vartheta_t}{c_t} a_t. \quad (5)$$

The reflection and transmission coefficients are defined at the liquid–solid interface by

$$r_{00} = \frac{a_r}{a_i}, \quad t_{0l} = \frac{a_l}{a_i}, \quad t_{0t} = \frac{a_t}{a_i}.$$

With the relations  $\lambda_0 = \rho_0 c_0^2$ ,  $\lambda_1 + 2\mu_1 = \rho_1 c_l^2$ ,  $\mu_1 = \rho_1 c_t^2$ , and  $\sin \vartheta_l / c_l = \sin \vartheta_t / c_t$ , Eqs. (3)–(5) lead to a system of equations which can be put in matrix form:

$$\begin{pmatrix} \cos \vartheta & \cos \vartheta_l & \sin \vartheta_t \\ \rho_0 c_0 & -\rho_1 c_l \cos 2\vartheta_t & -\rho_1 c_t \sin 2\vartheta_t \\ 0 & \frac{\sin 2\vartheta_l}{c_l} & -\frac{\cos 2\vartheta_t}{c_t} \end{pmatrix} \begin{pmatrix} r_{00} \\ t_{0l} \\ t_{0t} \end{pmatrix} = \begin{pmatrix} \cos \vartheta \\ -\rho_0 c_0 \\ 0 \end{pmatrix}.$$

By introducing the impedances and after resolution of the system, we obtain the solutions:

$$\begin{aligned} r_{00} &= \frac{Z_l \cos^2 2\vartheta_t + Z_t \sin^2 2\vartheta_t - Z_0}{D}, \\ t_{0l} &= \frac{2\rho_0 c_0 Z_l \cos 2\vartheta_t}{\rho_1 c_l D}, \\ t_{0t} &= \frac{2\rho_0 c_0 Z_t \sin 2\vartheta_t}{\rho_1 c_t D}, \end{aligned} \quad (6)$$

with  $D = Z_l \cos^2 2\vartheta_t + Z_t \sin^2 2\vartheta_t + Z_0$ .

## 2. Solid–liquid interface, longitudinal incident wave

The calculation is similar to above. The reflection and transmission coefficients are defined at this interface by

$$r_{ll} = \frac{a_l}{a_i}, \quad r_{lt} = \frac{a_t}{a_i}, \quad t_{l0} = \frac{a_0}{a_i}.$$

We obtain the following system of equations in matrix form:

$$\begin{pmatrix} \cos \vartheta_l & \sin \vartheta_t & \cos \vartheta \\ \rho_1 c_l \cos 2\vartheta_t & \rho_1 c_t \sin 2\vartheta_t & -\rho_0 c_0 \\ \frac{\sin 2\vartheta_l}{c_l} & -\frac{\cos 2\vartheta_t}{c_t} & 0 \end{pmatrix} \begin{pmatrix} r_{ll} \\ r_{lt} \\ t_{l0} \end{pmatrix} = \begin{pmatrix} \cos \vartheta_l \\ -\rho_1 c_l \cos 2\vartheta_t \\ \frac{\sin 2\vartheta_l}{c_l} \end{pmatrix}.$$

By introducing the impedances and after resolution of the system, we obtain the solutions:

$$\begin{aligned} r_{ll} &= \frac{Z_0 + Z_t \sin^2 2\vartheta_t - Z_l \cos^2 2\vartheta_t}{D}, \\ r_{lt} &= \frac{-c_l Z_t \sin 4\vartheta_t}{c_t D}, \\ t_{l0} &= \frac{2\rho_1 c_l Z_0 \cos 2\vartheta_t}{\rho_0 c_0 D} \end{aligned} \quad (7)$$

( $D$  has the same value as previously defined).

## 3. Solid–liquid interface, transverse incident wave

The reflection and transmission coefficients are defined by

$$r_{tl} = \frac{a_l}{a_i}, \quad r_{tt} = \frac{a_t}{a_i}, \quad t_{t0} = \frac{a_0}{a_i}.$$

The same development as above gives the solutions:

$$\begin{aligned} r_{tl} &= -\frac{c_t Z_l \sin 4\vartheta_t}{c_l D}, \\ r_{tt} &= \frac{Z_2 + Z_l \cos^2 2\vartheta_t - Z_t \sin^2 2\vartheta_t}{D}, \\ t_{t0} &= \frac{2\rho_1 c_t Z_0 \sin 2\vartheta_t}{\rho_0 c_0 D}. \end{aligned} \quad (8)$$

The amplitudes of the waves reflected and transmitted by the plate depend, therefore, on the reflections and/or transmissions they underwent on the interfaces. We can now calculate, for each emergent wave, this contribution of the interfaces, without taking into account attenuation.

## D. Contribution of the interfaces to the amplitude of the emergent waves

The contribution of the interfaces is obtained simply by multiplying the amplitude of the initial wave (assumed to be 1) by each reflection and/or transmission coefficient coming into play. This calculation will be simple for the first reflected or transmitted waves R1 to R4 and T1 to T6 (Fig. 3).

Tables II and III give the contributions of the interfaces to the amplitudes of the first emergent waves reflected (Table II) or transmitted (Table III) by the plate, revealing the elementary waves which can exist.

TABLE II. Contribution of the interfaces to the amplitude of the reflected waves.

Emergent wave	Number of reflections on the lower interface	Designation of the elementary waves	Amplitude
R1	0	R1	$r_{00}$
R2	1	R2- $tt$	$t_{0l} \cdot r_{ll} \cdot t_{l0}$
R3	1	R3- $tl$ R3- $lt$	$t_{0l} \cdot r_{ll} \cdot t_{l0}$ $t_{0l} \cdot r_{ll} \cdot t_{l0}$
R4	1	R4- $ll$	$t_{0l} \cdot r_{ll} \cdot t_{l0}$

**E. Contribution of attenuation to the amplitude of the emergent waves**

The viscoelastic nature of the plate results in an exponential decrease in the amplitude related to the attenuation coefficient  $\alpha$  of the medium. We can take this attenuation into account analytically by considering a complex propagation velocity. A damped wave is represented by  $u = ae^{-\alpha x} e^{i\omega(x/c - t)}$  which can be written  $u = ae^{i\omega(x/c^* - t)}$  if  $1/c^* = (1/c) + (i\alpha/\omega)$ . For a given attenuation factor or for a given complex velocity  $c^*$ , the damping of the wave can be written:  $e^{-\alpha x} = |e^{i(\omega x/c^*)}| = |e^{i\varphi^*}|$ , where  $\varphi^*$  is the complex phase shift corresponding to the distance covered  $x$ . The phase shift undergone by each wave can therefore be calculated as a function of the angle of incidence.

The front of the receiving transducer being perpendicular to the waves, we calculated the amplitudes of the waves on a plane perpendicular to them. Initially, we arbitrarily chose the A'O plane, O being the point where the last wave reflected twice on the lower interface emerges (wave R9, Fig. 3). We therefore calculated phase shifts  $\varphi_j$  for each wave Rj between point A on the first interface, where all the waves are in phase since they merge there, and the A'O plane.

Using wave R1 as a reference, we subtracted the phase shift  $\varphi_1$  of R1 on the path AA' from each phase shift  $\varphi_j$ . This amounts to associating with wave R1 a null phase, and

TABLE III. Contribution of the interfaces to the amplitude of the transmitted waves.

Emergent wave	Number of reflections on the lower interface	Designation of the elementary waves	Amplitude
T1	0	T1- $t$	$t_{0l} \cdot t_{l0}$
T2	0	T2- $l$	$t_{0l} \cdot t_{l0}$
T3	1	T3- $ttt$	$t_{0l} \cdot (r_{ll})^2 \cdot t_{l0}$
T4	1	T4- $ttl$ T4- $ltl$ T4- $llt$	$t_{0l} \cdot r_{ll} \cdot r_{ll} \cdot t_{l0}$ $t_{0l} \cdot r_{ll} \cdot r_{ll} \cdot t_{l0}$ $t_{0l} \cdot r_{ll} \cdot r_{ll} \cdot t_{l0}$
T5	1	T5- $lll$ T5- $llt$ T5- $llt$	$t_{0l} \cdot r_{ll} \cdot r_{ll} \cdot t_{l0}$ $t_{0l} \cdot r_{ll} \cdot r_{ll} \cdot t_{l0}$ $t_{0l} \cdot r_{ll} \cdot r_{ll} \cdot t_{l0}$
T6	1	T6- $lll$	$t_{0l} \cdot (r_{ll})^2 \cdot t_{l0}$

with each other wave Rj its phase difference  $\Delta\varphi_j$  compared to R1. This phase shift is given by the sum of several terms, each corresponding to a given propagation velocity (longitudinal, transverse or in the liquid). The term of damping is then obtained by replacing the velocities in the polymer with their complex expressions ( $c_0$  and  $\varphi_1$  are real, as there is no damping in water):

$$e^{-\alpha x_j} = |e^{i(\varphi_j^* - \varphi_1)}| = |e^{i\Delta\varphi_j^*}|. \tag{9}$$

Note: A second advantage of comparing phase shifts to wave R1 is that the same phase differences  $\Delta\varphi_j = \varphi_j - \varphi_1$  will appear for the calculation of the interferences below.

We thus have for R2:

$$\begin{aligned} \Delta\varphi_2^* &= \varphi_2^* - \varphi_1 = \omega \left( \frac{AB+BD}{c_t^*} + \frac{DD'}{c_0} \right) - \omega \frac{AA'}{c_0} \\ &= \omega \left( \frac{AB+BD}{c_t^*} - \frac{AD''}{c_0} \right), \end{aligned}$$

$D''$  being the projection of point D upon AA'.

$$\begin{aligned} \Delta\varphi_2^* &= \omega \left( \frac{2d}{c_t^* \cos \vartheta_t^*} - \frac{2d \tan \vartheta_t^* \sin \vartheta}{c_0} \right) \\ &= \frac{2\omega d \cos \vartheta_t^*}{c_t^*} \end{aligned}$$

using the equation  $\sin \vartheta/c_0 = \sin \vartheta_t^*/c_t^* = \sin \vartheta_l^*/c_l^*$ . Since the propagation velocities have complex values, the angles  $\vartheta_t^*$  and  $\vartheta_l^*$  will also be expressed by complex values.

For the following waves, calculation is the same. The values of the phase shifts  $\Delta\varphi_j^*$  of the Rj waves can be written in a single formula:

$$\Delta\varphi_j^* = \varphi_j^* - \varphi_1 = \omega d \left( \frac{n_l \cos \vartheta_l^*}{c_l^*} + \frac{n_t \cos \vartheta_t^*}{c_t^*} \right) \tag{10}$$

with  $n_l$ =the number of longitudinal segments and  $n_t$ =the number of transverse segments of the path for the Rj wave in the plate (Fig. 3).

The same calculation was done for the waves transmitted by the plate. We calculated the phase shift of each wave, labeled  $\psi_j^*$ , between point A and plane B'J perpendicular to the emergent waves. Point J is the point where the last wave reflected once on each interface emerges, the following waves having negligible amplitudes.

To handle simple analytical expressions, we subtracted from each value  $\psi_j^*$  the value  $\psi_0 = (3\omega d/c_0) \tan \vartheta_l^* \sin \vartheta$ , which represents the phase shift corresponding to the imaginary path aa' in Fig. 3. We calculated for each wave transmitted by the plate:

$$e^{-\alpha x_j} = |e^{i(\psi_j^* - \psi_0^*)}| = |e^{i\Delta\psi_j^*}|.$$

The phase shifts  $\Delta\psi_j^*$  of the Tj transmitted waves can be written in a single formula as in the previous case:

$$\Delta\psi_j^* = \psi_j^* - \psi_1 = \omega d \left( \frac{n_l \cos \vartheta_l^*}{c_l^*} + \frac{n_t \cos \vartheta_t^*}{c_t^*} \right), \tag{11}$$

$n_l$  and  $n_t$  having the same significance.

## F. Amplitudes of the emergent waves

It is now possible to calculate and compare the amplitudes of the emergent waves. By adding up the contributions of the interfaces (Table II) and those of the attenuation, we have for the reflected waves:

$$\text{for R1: } |R_1| = |r_{00}|,$$

$$\text{for R2: } |R_2| = |t_{0t} \cdot r_{tt} \cdot t_{t0} \cdot e^{i\Delta\varphi_2^*}|,$$

$$\text{for R3: } |R_3| = |(t_{0t} \cdot r_{tl} \cdot t_{l0} + t_{0l} \cdot r_{lt} \cdot t_{t0}) \cdot e^{i\Delta\varphi_3^*}|, \text{ and so on.}$$

These expressions are functions of the angle of incidence.

For the transmitted waves, we have:

$$\text{for T1: } |T_1| = |t_{0t} \cdot t_{t0} \cdot e^{i\Delta\varphi_1^*}|,$$

$$\text{for T2: } |T_2| = |t_{0l} \cdot t_{l0} \cdot e^{i\Delta\varphi_2^*}|,$$

$$\text{for T3: } |T_3| = |t_{0t} \cdot (r_{tt})^2 \cdot t_{t0} \cdot e^{i\Delta\varphi_3^*}|, \text{ and so on.}$$

The variations of these amplitudes  $|R_j| = f(\vartheta)$  and  $|T_j| = f(\theta)$  are shown in the following figures for the first waves reflected or transmitted by a PMMA plate [Fig. 5(a) and (b)]. Only the waves with a significant amplitude are shown.

The reflection curve [Fig. 5(a)] shows that wave R1 is the most intense. It corresponds to the specular reflection on the plate. Then, the principal waves, in the order of decreasing amplitude, are R3=(R3-tl+R3-lt), R4-ll for the small angles, and R2-tt, especially after the critical angle ( $\vartheta_{cl}=34^\circ$ ). On the transmission curves [Fig. 5(b)], wave T2, which corresponds to a longitudinal wave in the plate (T2-l), is very intense before the longitudinal critical angle, while wave T1 is mostly present beyond this critical angle. It corresponds to a transverse wave in the plate (T1-t). Then appear, to a lesser extent, T4 (3 mixed l and t components), T5 (idem) and T3=T3-ttt. T6=T6-lll appears only for the small angles.

Indeed, few emergent waves have a significant amplitude.

## G. Reflection and transmission curves

Reflection and transmission curves were obtained by adding up the individual contributions of all the emergent waves, taking into account the phase differences between them. We therefore have for reflection:

$$R = R_1 + R_2 e^{i\Delta\varphi_2^*} + R_3 e^{i\Delta\varphi_3^*} + R_4 e^{i\Delta\varphi_4^*} + R_5 e^{i\Delta\varphi_5^*} \\ + R_6 e^{i\Delta\varphi_6^*} + \dots$$

In this equation the attenuation term is present in the complex phase shift. The  $R_j$  terms therefore represent the undamped amplitudes, which are due only to the interfaces (Table II).

The variations of  $R_1 = f(\vartheta)$  were plotted with the variations of the total reflection coefficient  $R = f(\vartheta)$  calculated using the global method [Fig. 6(a)]. They are almost identical for  $\vartheta > \vartheta_{cl}$ . Beyond the longitudinal critical angle, only transverse waves can exist in the plate, and emerge like R2-tt. However, the amplitude of this wave is small compared to  $R_1$  which explains why the latter is little disturbed by the

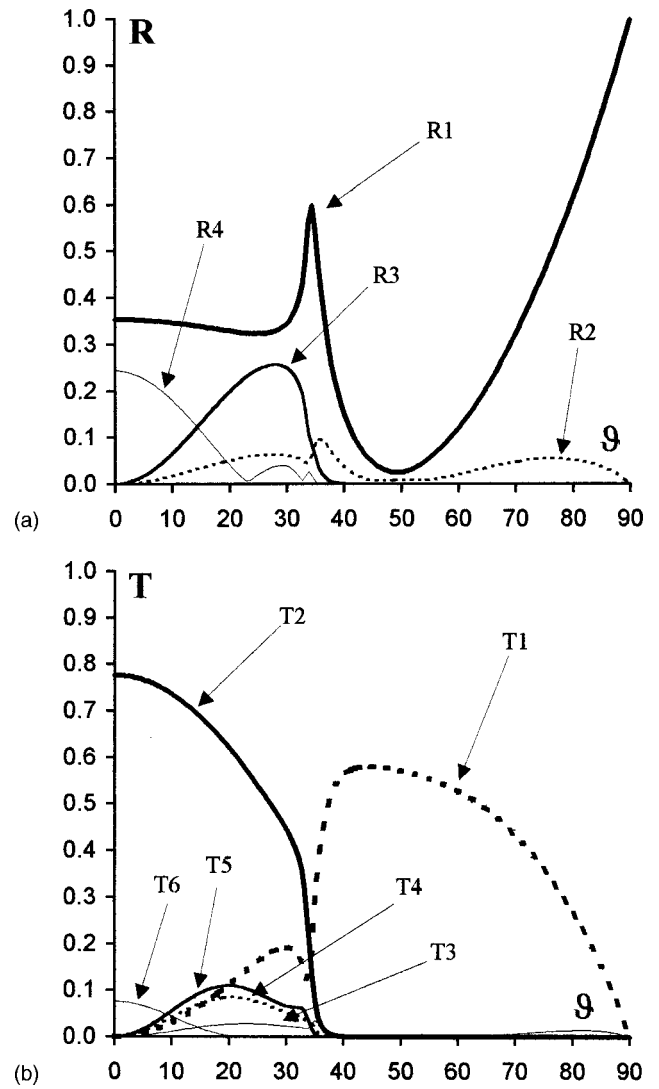


FIG. 5. Variations of the amplitudes of the elementary emergent waves: (a) Reflected waves  $|R_j| = f(\vartheta)$ , (b) transmitted waves  $|T_j| = f(\theta)$ , subscripts  $j$  are defined in Fig. 3.

interference phenomenon. For  $\vartheta < \vartheta_{cl}$ , the  $R_1 = f(\vartheta)$  curve is modulated by interferences with the other reflected waves.

The interference created by waves R1 and (R2+R3+R4) gives an excellent fit with the  $R = f(\vartheta)$  curve calculated with the global method [the curves are almost identical in Fig. 6(b)]. For a perfect fit, it is necessary to add waves R6, R7, and R9. Thus we have

$$R_{\text{PMMA}} = R_1 + R_3 e^{i\Delta\varphi_3^*} + R_2 e^{i\Delta\varphi_2^*} + R_4 e^{i\Delta\varphi_4^*} + R_9 e^{i\Delta\varphi_9^*} \\ + R_6 e^{i\Delta\varphi_6^*} + R_7 e^{i\Delta\varphi_7^*}. \quad (12)$$

For the transmission curve [Fig. 7(a)], the contribution of T1 accounts well for the  $T = f(\vartheta)$  curve above the critical angle  $\vartheta_{cl}$ . Indeed, it is the only wave and there is no interference in this angular domain. For  $\vartheta < \vartheta_{cl}$ , wave T2 is modulated by the interference with the other waves. Interference of T2 and T1 already gives an approximate agreement with the global curve [Fig. 7(b)]. For a better fit, it is necessary to add the contributions of T3, T4, T5, and T6. Thus we have

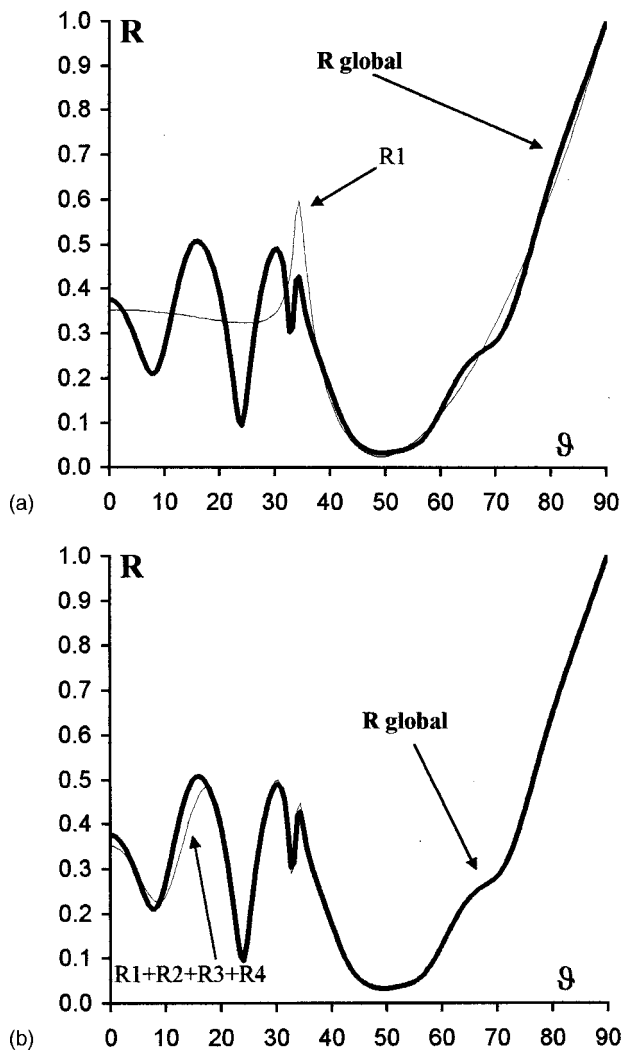


FIG. 6. Theoretical reflection curves obtained by the interferences of the first emergent waves, compared with the theoretical curve obtained by the global method: (a) thin line: R1 alone, bold line:  $R_{\text{global}}$  and  $(R1+R2+R3+R4+R6+R7+R9)$  are superimposed, (b) thin line:  $R1+R2+R3+R4$ , bold line:  $R_{\text{global}}$  and  $(R1+R2+R3+R4+R6+R7+R9)$  are superimposed.

$$T_{\text{PMMA}} = T_1 e^{i\Delta\psi_1^*} + T_2 e^{i\Delta\psi_2^*} + T_3 e^{i\Delta\psi_3^*} + T_4 e^{i\Delta\psi_4^*} + T_5 e^{i\Delta\psi_5^*} + T_6 e^{i\Delta\psi_6^*}. \quad (13)$$

Finally, it is necessary to take into account all the emergent waves which were reflected after one or, at most, two internal reflections in the plate. These results are valid for a plate thickness of  $d=2$  mm. For greater thicknesses, the weakest contributions would probably disappear and the number of terms to be taken into account would be even smaller.

### III. DISCUSSION

The excellent agreement between the theoretical reflection and transmission curves determined using the global method and those determined using the method of interferences confirms the validity of the latter. This enables us to draw the following conclusions.

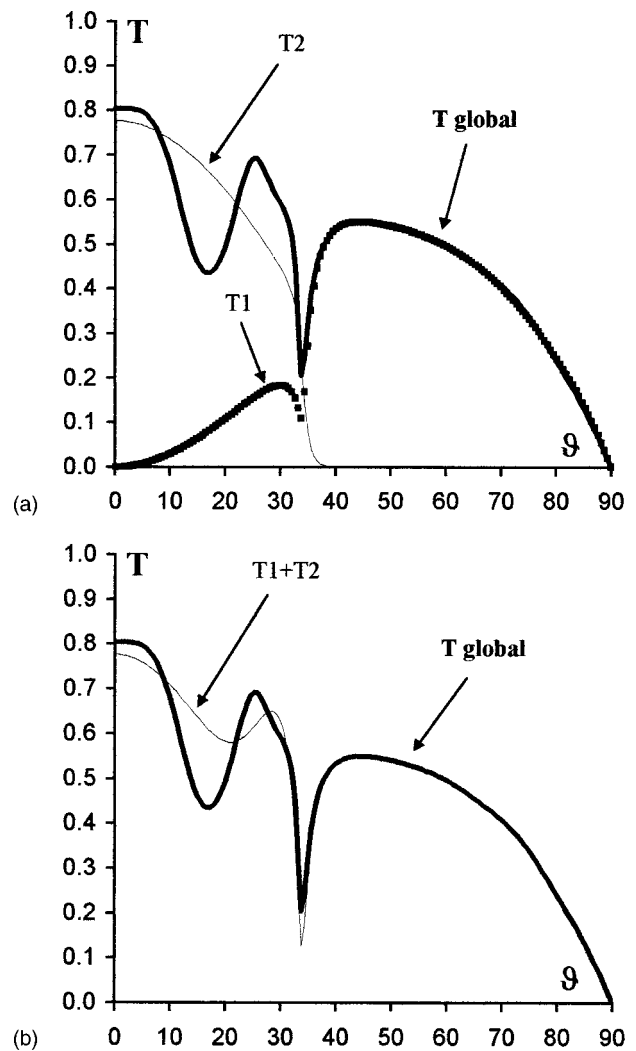


FIG. 7. Theoretical transmission curves obtained by the interferences of the first emergent waves, compared with the theoretical curve obtained by the global method: (a) thin line: T2 and T1 alone, bold line:  $T_{\text{global}}$  and  $(T1+T2+T3+T4+T5+T6)$  are superimposed, (b) thin line: T2+T1 (interferences), bold line:  $T_{\text{global}}$  and  $(T1+T2+T3+T4+T5+T6)$  are superimposed.

#### A. The meaning of the reflection and transmission curves

The reflection and transmission curves express the interferences between the first waves which emerge from the plate. As regards reflection, the specularly reflected wave (R1), which is the strongest, gives the general shape of the reflection curve. It is modulated by interferences with the other waves. In the case of transmission, wave T2 (longitudinal in the plate) gives the general shape of the resulting curve for the angles of incidence  $\vartheta < \vartheta_{cl}$ . Beyond this critical angle, the curve is given directly by wave T1 (transverse in the plate).

The maxima and minima on the curves can be easily explained by constructive or destructive interferences between the first emergent waves. For the reflection curves, R1 interferes with the other main waves R2–*tt*, R3 (of mixed nature in the plate) and R4–*ll*. For the transmission curves, the interferences between T1 and T2 alone account rather well for the global curve.



## B. Determination of ultrasonic parameters

Knowing the significance of each signal on the reflection curve, the values of the four ultrasonic parameters (propagation velocities and attenuation coefficients of longitudinal and transverse waves) can be precisely determined by adjusting the theoretical curves to fit the experimental curves.

Among the other parameters which are used in calculations, the frequency is known with good precision, the thickness of the plate is easily measured, the density of the polymer is given by the manufacturer, that of water is well known, and the attenuation factor of this liquid is negligible. A fifth parameter, the multiplying coefficient which must be applied to the experimental curves to adjust them to the theoretical curves, is not known *a priori*. Indeed, the wave amplitudes were experimentally measured with an arbitrary unit.

To determine, as precisely as possible, the values of the ultrasonic parameters, the "pure" signals on the reflection curves, if any, were selected. These "pure" signals could be the minima or maxima created by interference between R1 and the longitudinal wave R4-*ll* alone (but these signals do not exist with PMMA) or those created by interference between R1 and the transverse wave R2-*tt* alone. This last type of signal can generally be found for  $\vartheta > \vartheta_{c_l}$  if this wave has a significant amplitude, as is the case for PMMA.

The condition of phase opposition (or phase concordance) between R1 and R4-*ll* depends only on the velocity of the longitudinal waves. There is, for example, phase opposition for  $\Delta\varphi_4 = 2\omega d \cos \vartheta_l/c_l = (n + 1/2)\pi$ , *n* being an integer. In the same way, the condition of phase opposition (or concordance) between R1 and R2-*tt* depends only on the velocity of the transverse waves:  $\Delta\varphi_2 = 2\omega d \cos \vartheta_t/c_t = (n + 1/2)\pi$  for a phase opposition. The angular positions of these minima on the theoretical curves can therefore be adjusted while varying the values assigned to  $c_l$  and  $c_t$ .

Variations in amplitude between the preceding minima and the following maxima are related to wave attenuation.<sup>22,23</sup> This amplitude also depends, however, on the multiplying coefficient assigned to the experimental curves. It is therefore necessary to vary these parameters to adjust the amplitudes of the signals on the experimental and theoretical curves.

If there is no pure signal which can be assigned only to the interference of R4 with R1, adjustment is more difficult. It is then necessary to determine first the transverse parameters (for  $\vartheta > \vartheta_{c_l}$ ), and then the longitudinal parameters by considering a minimum or maximum in which R4 occurs to a great extent.

However, this means of determining ultrasonic parameters is easier when there is no interference in a portion of the reflection or transmission curves, for instance beyond the longitudinal critical angle (where no longitudinal wave can exist) if the transverse attenuation is great enough, in such a manner that only one transverse wave emerges with a significant amplitude (R2 or T1). In this case, the theoretical wave amplitude depends only on the velocity  $c_t$ , while the experimental wave amplitude depends on the multiplying coefficient which is applied to it. If the transverse velocity and

TABLE IV. Values of the ultrasonic parameters determined from the method of interferences. All these values were obtained with the following uncertainties:  $\Delta c = 10$  m/s,  $\Delta \alpha/\alpha = 20\%$ .

$c_l$ (m/s)	$c_t$ (m/s)	$\alpha_l$ (Np/m)	$\alpha_t$ (Np/m)
2 660	1 340	100	145

the attenuation coefficient have been estimated from the interference signals, adjustment of the experimental and theoretical curves in this portion enables us to deduce the value of the multiplying coefficient, and thus to better determine the ultrasonic parameters.

Table IV gives the ultrasonic parameter values obtained for PMMA. These values give an excellent agreement between the experimental reflection or transmission curves, and the theoretical curves given by the method of interferences (the global method gives the same result) [Fig. 8(a) and (b)]. This agreement confirms the validity of the description of the waves by plane waves, despite the fact that the experimental ultrasonic beam is bounded.

With the values obtained, the theoretical relationship

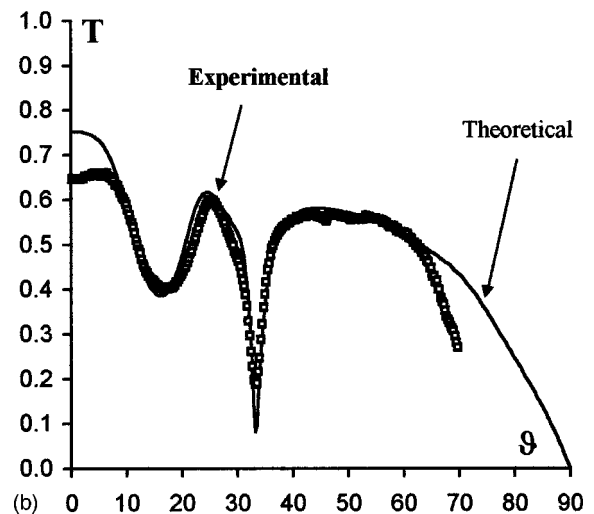
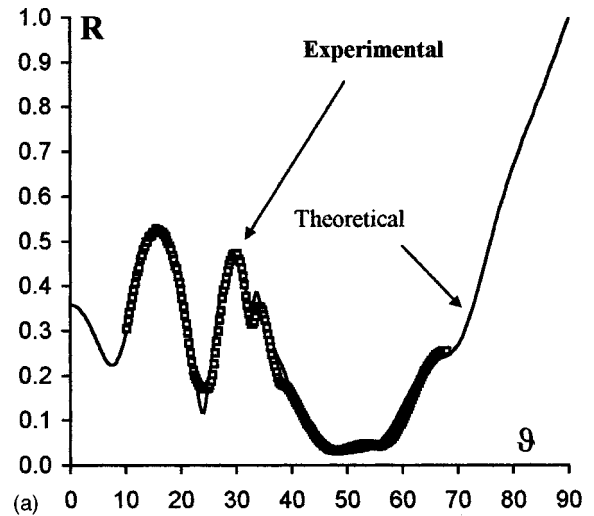


FIG. 8. Comparison of the experimental and theoretical curves (method of interferences with optimized parameters): (a) reflection curves  $R = f(\vartheta)$ , (b) transmission curves  $T = f(\vartheta)$ .

$(c_l/c_t)^3 = 2\alpha_t/\alpha_l$  (Ref. 16) between the propagation velocities and the attenuation coefficients of the longitudinal and transverse waves is not exactly respected. We have calculated a gap of 50% between the two members of the relationship, which cannot be accounted for by the uncertainties on these values. The upper relationship is, however, theoretical and supposes that the attenuation is due only to viscous mechanisms. Moreover, the available values in the literature are too rare to enable us to verify whether this relationship is valid for all the polymers.

#### IV. CONCLUSION

We developed the method of interferences to study the behavior of an ultrasonic beam reflected or transmitted by a homogeneous plate. This method is well suited to polymer plates because of the relatively high wave attenuation coefficients for these materials. Few waves emerge from the plate with a significant amplitude after internal reflection on the lower face, and need to be taken into account. For 2-mm-thick polymethylmethacrylate plates, only the waves reflected once (at most twice for better precision) by the lower interface intervene, *a fortiori* for thicker plates. The perfect agreement between the results of the classical global method and the method of interferences confirms the validity of the latter.

The first advantage of this method is that it enables us to better understand the physical significance of the experimental reflection and transmission curves. For example, the reflection curves merely express interferences between the specularly reflected wave, which is the strongest emerging wave, and the waves reflected on the lower face of the plate.

By calculating the amplitude and the phase shift of these waves, this method enables us to identify which emergent waves are responsible for the signals observed on the experimental curves. This facilitates the calculation of precise values of the ultrasonic parameters (velocity and attenuation of the longitudinal and transverse waves) by adjustment of the theoretical and experimental reflection and transmission curves. It is therefore very easy to explain the experimental curves and determine the ultrasonic parameters.

#### ACKNOWLEDGMENT

We wish to thank Elf AtoChem for supplying the polymer.

- <sup>1</sup>B. Hartman and J. Jarzynski, "Immersion apparatus for ultrasonic measurements in polymers," *J. Acoust. Soc. Am.* **56**, 1469–1477 (1974).
- <sup>2</sup>B. Hartman, "Ultrasonics measurements," in *Methods of Experimental Physics, 16-C* (Academic, New York, 1980), Chap. 12.1, pp. 59–90.
- <sup>3</sup>R. Kono, "The dynamic bulk viscosity of polystyrene and polymethyl methacrylate," *J. Phys. Soc. Jpn.* **15**, 718–725 (1960).
- <sup>4</sup>J. Laperre, W. Thys, O. Lenoir, and J. L. Izbicki, "Experimental determination of the transversal wave velocity in plates," *J. Acoust.* **5**, 161–170 (1992).
- <sup>5</sup>G. Maze, J. L. Izbicki, and J. Ripoché, "Resonances of plates and cylinders: guided waves," *J. Acoust. Soc. Am.* **77**, 1352–1357 (1985).
- <sup>6</sup>F. Leomy, M. De Billy, and G. Quentin, "Milieux en couches et ondes dispersives," *Rev. Phys. Appl.* **23**, 1547–1555 (1988).
- <sup>7</sup>Y. Tsukahara and K. Ohira, "Detection of smooth bonding of polymer coating by ultrasonic spectroscopy," *Ultrasonics* **27**, 3–7 (1989).
- <sup>8</sup>D. C. Worlton, "Experimental confirmation of Lamb waves at megacycles frequencies," *J. Appl. Phys.* **32**, 967–971 (1961).
- <sup>9</sup>G. C. Knollman and J. J. Hartog, "Shear modulus gradients in adhesive interfaces as determined by means of ultrasonic Rayleigh waves," *J. Appl. Phys.* **53**, 1516–1524 (1982).
- <sup>10</sup>D. B. Bogy and S. M. Gracewski, "On the plane-wave reflection coefficient and nonspecular reflection of bounded beams for layered half-spaces underwater," *J. Acoust. Soc. Am.* **74**, 591–599 (1983).
- <sup>11</sup>O. Lenoir, J. L. Izbicki, P. Rembert, G. Maze, and J. Ripoché, "Acoustic scattering from an immersed plane multilayer: application to the inverse problem," *J. Acoust. Soc. Am.* **91**, 601–612 (1992).
- <sup>12</sup>V. A. Schoch, "Der schalldurchgang durch platten," *Acustica* **2**, 1–17 (1952).
- <sup>13</sup>L. M. Brekhovskikh, *Waves in Layered Media* (Academic, New York, 1980).
- <sup>14</sup>I. A. Viktorov, *Rayleigh and Lamb Waves* (Plenum, New York, 1967).
- <sup>15</sup>W. T. Thomson, "Transmission of elastic waves through a stratified solid medium," *J. Appl. Phys.* **21**, 89–93 (1950).
- <sup>16</sup>W. Madigosky and R. Fiorito, "Modal resonance analysis of acoustic transmission and reflection losses in viscoelastic plates," *J. Acoust. Soc. Am.* **65**, 1105–1115 (1979).
- <sup>17</sup>P. Chevee and M. Deschamps, "Non specular effects of reflection and transmission at an immersed viscoelastic/anisotropic solid," in *Ultrasonics International Conference Proceedings* (Butterworth-Heinemann, Oxford, UK, 1991), pp. 279–282.
- <sup>18</sup>B. Hosten and M. Deschamps, "Génération d'ondes hétérogènes à l'interface liquide-solide viscoélastique. Approximation par des ondes inhomogènes," *Acustica* **59**, 193–198 (1986).
- <sup>19</sup>P. Allais, "Effets de l'atténuation sur un rayonnement quelconque dans un milieu propagatif linéaire absorbant," *C. R. Acad. Sci. Paris* **282A**, 547–549 (1976).
- <sup>20</sup>K. E.-A. Van Den Abeele, R. Briers, and O. Leroy, "Inhomogeneous plane-wave scattering and mode stimulation on periodic surfaces," *J. Acoust. Soc. Am.* **99**, 2883–2897 (1996).
- <sup>21</sup>D. Royer and E. Dieulesaint, *Ondes élastiques dans les solides* (Masson, Paris, 1996), Vol. 1.
- <sup>22</sup>R. Fiorito, W. Madigosky, and H. Überall, "Acoustic resonances and the determination of the materials parameters of a viscous fluid layer," *J. Acoust. Soc. Am.* **69**, 897–903 (1981).
- <sup>23</sup>R. Fiorito, W. Madigosky, and H. Überall, "Theory of ultrasonic resonances in a viscoelastic layer," *J. Acoust. Soc. Am.* **77**, 489–498 (1985).

# Near-field ultrasonic scattering from a cavity in steel considering the velocity amplitude on the transducer face using an error function model

Tjundewo Lawu, Makoto Tabei,<sup>a)</sup> and Mitsuhiro Ueda

*Department of International Development Engineering, Tokyo Institute of Technology, Ookayama, Meguro-ku, Tokyo 152, Japan*

(Received 25 February 1997; accepted for publication 8 May 1998)

The influence of nonuniform transducer velocity distribution in the near-field echo formation scattered from a cavity in steel is analyzed. In the present study, the velocity amplitude on the transducer face was modeled using an offset error function. Using this distribution, the echo waveforms scattered from a cylinder cavity in steel were estimated and compared with the echo estimated using uniform distribution and echo observed experimentally. The estimation accuracy of the near-field echo waveforms were improved quantitatively. © 1998 Acoustical Society of America. [S0001-4966(98)04908-X]

PACS numbers: 43.20.Fn [ANN]

## INTRODUCTION

The ultrasonic pulse-echo method has been widely used in the field of medical diagnosis and nondestructive testing of materials. Echo signals obtained from such pulse-echo systems are mainly determined by the structure of an object, but are also influenced by many factors, such as the directivity and damping characteristics of the ultrasonic transducer, and the distribution of the velocity amplitude on the surface of the transducer. These factors interact in a complicated manner, so it is difficult to analyze the effects explicitly.

The echo signals scattered by a simulated cavity in a steel block have been estimated<sup>1</sup> by assuming that the velocity amplitude on the transducer face is uniform,<sup>2-9</sup> and compared with those obtained experimentally. Good agreement was observed at the far field of the transducer; however, the estimation accuracy was degraded as the distance decreases. This might be caused by the nonuniformity of the velocity amplitude distribution on the transducer face.

This paper deals with the influence of nonuniform transducer velocity distribution in the near-field echo formation from a cavity in steel. The velocity amplitude distribution across the surface of a plane circular transducer can be characterized by the use of an angular spectrum and fast Fourier transform (FFT) techniques,<sup>10,11</sup> or by deconvolving the near-field transient radiation with the electrical characteristics of the transducer.<sup>12</sup> The angular spectrum method which characterizes the propagation of the field from one plane to another has been used as a linear filtering operation in applications such as medical imaging to give information about the acoustic properties. However, its accuracy depends on the choices of space and spatial frequency windows. In the case of a transducer placed on steel, since the time separation between the direct and edge pulse is very short, the corresponding waveforms cannot be separated well. Therefore, the latter method cannot be implemented. For this reason, the

velocity amplitude distribution is modeled using an offset error function.

## I. ECHOES SCATTERED FROM A CYLINDER CAVITY

The frequency component of the echo received by the ultrasonic transducer can be expressed as<sup>13</sup>

$$E(\omega) = j\omega\rho_0 G(\omega)F(\omega), \quad (1)$$

where  $E(\omega)$  is the Fourier transform of the echo signal  $e(t)$ ,  $\rho_0$  is the mean density of the medium, and  $G(\omega)$  is the electrical characteristics of the ultrasonic transducer.  $F(\omega)$  is the frequency response of the scattering object; that is,<sup>1</sup>

$$F(\omega) = R \int_S \Phi(\mathbf{r}, \omega) \mathbf{N} \cdot \nabla \Phi(\mathbf{r}, \omega) dS, \quad (2)$$

where  $R$  corresponds to a reflection factor of the scatterer, and  $\Phi(\mathbf{r}, \omega)$  is the velocity potential insonified by the transducer.  $S$  is the surface of the scatterer and  $\mathbf{N}$  is an outer vector normal to  $S$ . The time waveform of the echo can be obtained by taking the inverse Fourier transform of Eq. (1),

$$e(t) = \rho_0 \frac{\partial}{\partial t} [g(t) * f(t)], \quad (3)$$

or

$$e(t) = \rho_0 g(t) * \frac{\partial}{\partial t} f(t), \quad (4)$$

where the symbol  $*$  indicates the time convolution, and  $g(t)$ ,  $f(t)$  are the time dependence characteristics of the transducer and impulse response of the scattering object, respectively. For the on-axis cylinder cavity shown in Fig. 1, applying a paraxial approximation as explained in Ref. 1,  $\partial f / \partial t$  can be expressed as

$$\frac{\partial}{\partial t} f(t) \approx R \int_0^b \frac{\partial}{\partial t} \phi(z_0, r, t) * \frac{\partial}{\partial z} \phi(z_0, r, t) 2\pi r dr, \quad (5)$$

<sup>a)</sup>Present address: Ultrasound Research Laboratory, Box 648, University of Rochester, 601 Elmwood Avenue, Rochester, NY 14642.

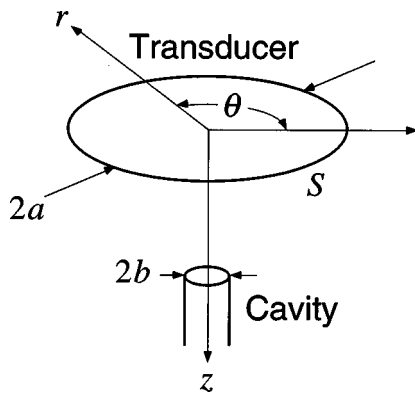


FIG. 1. Geometry of a cylinder cavity and a planar circular transducer. Radius of transducer and cavity are  $a$  and  $b$ , respectively; origin of coordinate system is set at the center of transducer.

where  $z_0$  is the distance between the transducer and the surface of the scatterer. The time dependence velocity potential is given by<sup>4</sup>

$$\phi(\mathbf{r}, t) = \frac{1}{2\pi} \int_S u(\mathbf{r}_S) \frac{\delta\left(t - \frac{|r - r_S|}{c_0}\right)}{|\mathbf{r} - \mathbf{r}_S|} dS, \quad (6)$$

where  $dS$  is the area element at position  $\mathbf{r}_S$  on the transducer surface,  $c_0$  is the velocity of propagation within the medium, and  $u(\mathbf{r}_S)$  is the normal velocity amplitude on the transducer face and is assumed to have axial symmetry.

The velocity amplitude distribution is modeled using an offset error function as

$$u(r) = 1 - G\left\{\left(\frac{r-a}{a}\right) / \sigma\right\}, \quad (7)$$

where  $a$  is the radius of the transducer,  $\sigma$  is the standard deviation of the distribution, and the Gaussian distribution function is defined as<sup>14</sup>

$$G(x) = \frac{1}{\sqrt{2\pi}} \int_{-\infty}^x \exp[-t^2/2] dt = \frac{1}{2} + \frac{1}{2} \text{erf}(x/\sqrt{2}). \quad (8)$$

Figure 2 shows the distribution of the velocity amplitude across the 10-mm radius transducer face modeled by an offset error function for  $\sigma=0.06$  compared with the uniform distribution. This value was chosen so that about 5%–95% of the expected distribution values will lie approximately  $\pm 1$

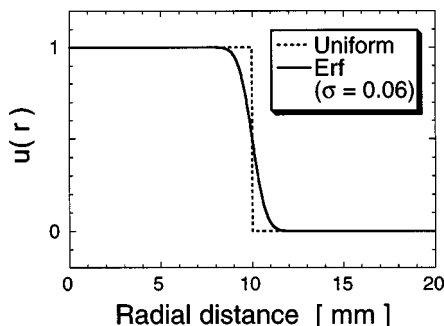


FIG. 2. Distribution of the velocity amplitude across the transducer face.

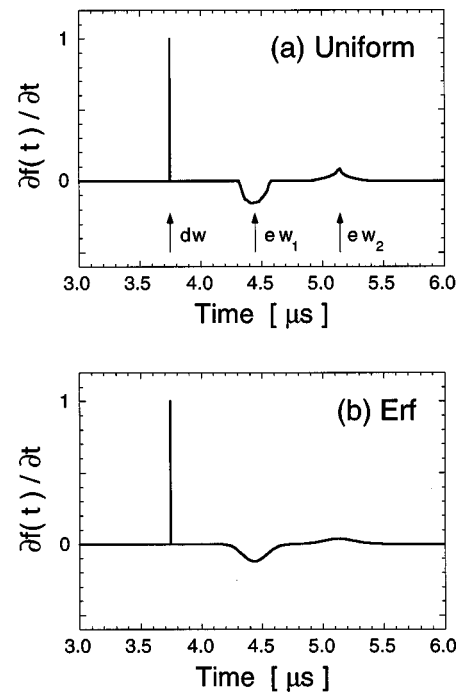


FIG. 3. On-axis impulse response for a 2-mm diameter cylinder cavity, 10 mm from the transducer; estimated using (a) uniform distribution and (b) distribution modeled by an offset error function for  $\sigma=0.06$ .

mm from the edge of the transducer, and this value was best fit the experimental results.

By considering the velocity amplitude distribution shown in Fig. 2, the estimated on-axis impulse response  $\partial f/\partial t$  for a 2-mm diameter cylinder cavity 10 mm from the transducer was calculated using Eq. (5) and the results are graphed in Fig. 3. In the case of uniform velocity amplitude over the transducer, the time dependence velocity potential in Eq. (6) was calculated using the analytic expression given in Refs. 2–5. Whereas in the case of the velocity amplitude modeled using an offset error function, the integration with respect to  $\theta$  was performed using the trapezoidal rule with a constant increment  $\Delta\theta$  of 0.5 degree. The time dependence velocity potential at each value of  $\theta$  was calculated with a sampling frequency of 240 MHz and the longitudinal sound velocity was 5950 m/s. From an exact analytic expression for the impulse response, the pulses resulting from a piston motion contain a direct wave followed by the edge waves.<sup>15,16</sup> The direct wave,  $dw$ , is the earliest pulse occurring due to direct transmission–direct reception. The first edge wave,  $ew_1$  is the direct-edge and edge-direct pulses occur simultaneously, by symmetry, to give an inverted smeared out pulse and its amplitude becomes less, and the second edge wave,  $ew_2$ , is the edge–edge pulses. By increasing the distance from the transducer, the time separation between these pulses is reduced until they eventually overlap.

## II. EXPERIMENTAL APPARATUS

Experiments were carried out to verify the theoretical results of the impulse response of wave scattered by a cylinder cavity in steel. The experimental system was a pulse-echo system used for the generation, detection, and recording of the ultrasonic pulses traversing the specimen. A 5-MHz

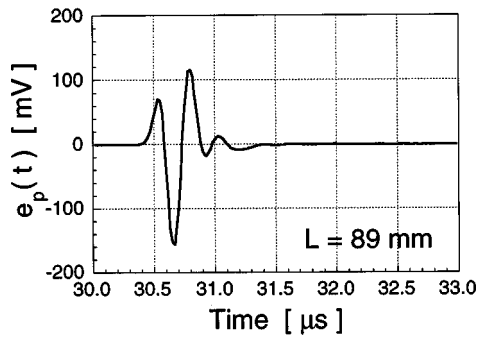


FIG. 4. Echo waveform scattered by plane reflector located at 89 mm from the planar circular transducer.

broadband planar circular transducer of 20 mm diameter (Mitsubishi Electric PB-5C20N-L) was excited by electrical pulses generated by a pulser receiver Panamatrix 5050-PR. The elastic waves were transmitted by the transducer into the specimen, and the scattered waves were then received by the same transducer. The electrical signal was displayed on the screen of an oscilloscope, and digitized using a programmable digitizer Sony-Tektronix 390-AD. Finally, after averaging the data 128 times using an average adapter RAVR-1, the output signal was transferred to the microcomputer via a GPIB interface.

As an example of a nonattenuating medium, a block of JIS G-3106 SM400B steel<sup>17</sup> was selected. To avoid wedging effects, the faces were polished so that the maximum deviation was within 3  $\mu\text{m}$ . The density of the block was 8.08 kg/m<sup>3</sup>, whereas the longitudinal sound velocity was 5950 m/s. Fabricated blocks containing a simulated cavity using an end milling process into flat bottom cylinders perpendicular to the direction of wave propagation. The diameter of the cylinders was 2 mm, and the distances between the top surface of the block and flat bottom of the cylinders were 10 and 21 mm.

The transducer was placed on the steel block, and ISO-VG10 spindle oil was used for impedance matching between the transducer and the steel block.

### III. RESULTS AND DISCUSSIONS

The echo waveforms scattered from a cavity depend critically on the response characteristics of the transducer, which include the response of the transducer element and its coupling, in addition to the loading effects resulting from the

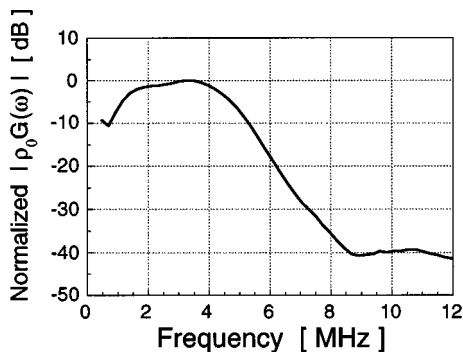


FIG. 5. The frequency characteristics of the transducer.

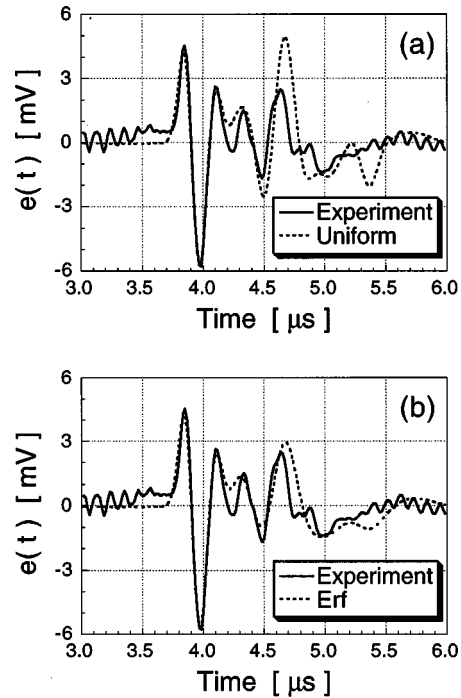


FIG. 6. On-axis echoes scattered from a 2-mm diameter cylinder cavity 10 mm from the transducer. Comparison between the experimental and estimation results calculated using (a) uniform distribution and (b) distribution modeled by an offset error function.

placing of the transducer to a specimen. The characteristics of the transducer were then determined experimentally under conditions similar to those encountered in the scattering experiments.

The circular transducer was placed on a 89-mm-thick

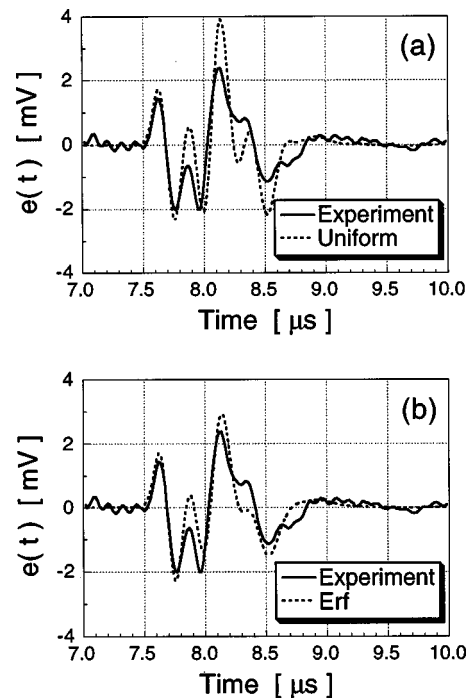


FIG. 7. On-axis echoes scattered from a 2-mm diameter cylinder cavity 21 mm from the transducer. Comparison between the experimental and estimation results calculated using (a) uniform distribution and (b) distribution modeled by an offset error function.

steel block. The flat bottom of this block was used to provide the virtual image of the transducer. The waveform observed is shown in Fig. 4. The elapsed time between the incident wave and the earliest echo returning from the plane reflector equals twice the distance from the transducer divided by the longitudinal sound velocity in the block. The frequency characteristics of the transducer were then calculated and shown in Fig. 5. These were taken as the characteristics required for the computations.

By convolving the impulse response shown in Fig. 3 with the response characteristics of the transducer, the echo scattered from a cavity can be obtained. Figures 6 and 7 show the results for 2-mm diameter cylinder cavities 10 and 21 mm from the transducer, respectively. Both of the figures show that the accuracy of the echo waveforms estimated using the velocity amplitude distribution across the surface of a transducer modeled by an offset error function were improved. It is clear from both the experiments and estimations results that by increasing the distance from the transducer, the time separation between direct and edge waves is reduced.

#### IV. CONCLUSIONS

The velocity amplitude on the transducer face was modeled using an offset error function. Using this distribution, the echo waveforms scattered from a cylinder cavity in steel were estimated and compared with the echo estimated using uniform distribution and echo observed experimentally. By considering the velocity amplitude on the transducer face, the estimation accuracy of the near-field echo waveform were improved.

<sup>1</sup>T. Lawu, M. Ueda, and M. Tabei, "Ultrasonic scattering from a simulated cavity in steel," *J. Acoust. Soc. Am.* **98**, 2809–2818 (1995).

<sup>2</sup>F. Oberhettinger, "On transient solutions of the "Baffled piston" prob-

lem," *J. Res. Natl. Bur. Stand. Sec. B* **65**, 1–6 (1961).

<sup>3</sup>J. Zemanek, "Beam behavior within the nearfield of a vibrating piston," *J. Acoust. Soc. Am.* **49**, 181–191 (1971).

<sup>4</sup>P. R. Stepanishen, "Transient radiation from pistons in an infinite planar baffle," *J. Acoust. Soc. Am.* **49**, 1629–1638 (1971).

<sup>5</sup>J. C. Lockwood and J. G. Willette, "High-speed method for computing the exact solution for the pressure variations in the nearfield of a baffled piston," *J. Acoust. Soc. Am.* **53**, 735–741 (1973).

<sup>6</sup>M. Ueda, "Fast converging series expansion for velocity potential of circular concave piston source," *J. Acoust. Soc. Jpn. (E)* **6**, 35–39 (1985).

<sup>7</sup>E. L. Madsen, T. J. Hall, J. A. Zagzebski, and M. F. Insana, "Use a Taylor series expansions for time savings in computation of accurate transducer pressure fields," *IEEE Trans. Ultrason. Ferroelectr. Freq. Control* **34**, 301–308 (1987).

<sup>8</sup>X. Chen, K. Q. Schwarz, and K. J. Parker, "Radiation pattern of a focused transducer: A numerically convergent solution," *J. Acoust. Soc. Am.* **94**, 2979–2991 (1993).

<sup>9</sup>T. Lawu, M. Tabei, and M. Ueda, "Fast converging binomial series for radiation field calculation," *J. Acoust. Soc. Am.* **98**, 2819–2824 (1995).

<sup>10</sup>R. C. Waag, J. A. Campbell, J. Ridder, and P. R. Mesdag, "Cross-sectional measurements and extrapolations of ultrasonic fields," *IEEE Trans. Sonics Ultrason.* **SU-32**, 26–35 (1985).

<sup>11</sup>M. Tabei and M. Ueda, "Two-step holographic reconstruction of an acoustic field," *Proc. Acoust. Soc. Am. and Acoust. Soc. Jpn. Third Joint Meeting*, 1349–1354 (1996).

<sup>12</sup>T. Lawu, M. Tabei, and M. Ueda, "Analysis of the near-field transient radiation considering the velocity amplitude on the transducer face," *Jpn. J. Appl. Phys.* **35**, 3236–3241 (1996).

<sup>13</sup>M. Ueda and H. Ichikawa, "Analysis on an echo signal reflected from a weakly scattering volume by a discrete model of the medium," *J. Acoust. Soc. Am.* **70**, 1768–1775 (1981); Erratum, *J. Acoust. Soc. Am.* **75**, 1012 (1984).

<sup>14</sup>See, for example, M. L. Boas, *Mathematical Methods in the Physical Sciences* (Wiley, New York, 1983), 2nd ed., Chap. 11.

<sup>15</sup>D. E. Robinson, S. Lees, and L. Bess, "Near field transient radiation patterns for circular pistons," *IEEE Trans. Acoust. Speech Signal Process.* **ASSP-22**, 395–403 (1974).

<sup>16</sup>J. P. Weight and A. J. Hayman, "Observation of the propagation of very short ultrasonic pulses and their reflection by small targets," *J. Acoust. Soc. Am.* **63**, 396–404 (1978).

<sup>17</sup>Japanese Industrial Standard, *Rolled Steels for Welded Structure JIS G 3106-1992* (Japanese Standard Association, Tokyo, 1992).

# On the anomalously low attenuation of the leaky Rayleigh wave in a fluid-filled cylindrical cavity

Waled Hassan and Peter B. Nagy

*Department of Aerospace Engineering and Engineering Mechanics, University of Cincinnati, Cincinnati, Ohio 45221-0070*

(Received 4 March 1998; accepted for publication 18 May 1998)

It is shown that the dispersive Rayleigh wave propagating around a concave cylindrical surface is substantially less attenuated by fluid loading than the corresponding wave on a flat surface. First, the analytical solution for vertically polarized shear wave scattering from a fluid-filled cylindrical cavity is formulated in the time domain, then the signal of interest is gated out and spectrum analyzed in order to numerically predict the attenuation caused by leakage into the fluid. On a concave surface the ratio of the normal and transverse displacement components produced by the circumferential creeping wave is lower than that of the ordinary Rayleigh wave propagating on a flat surface, which explains the reduced leaky attenuation caused by fluid loading. Experiments were carried out to verify these analytical predictions. The fluid-loading induced semicircumferential loss of the circumferential creeping wave around a cylindrical cavity was found to be in excellent agreement with the experimental measurements over a wide frequency range. © 1998 Acoustical Society of America. [S0001-4966(98)00609-2]

PACS numbers: 43.20.Hq [ANN]

## INTRODUCTION

The work presented in this paper was initiated by recent efforts to use circumferential creeping waves for ultrasonic nondestructive testing of inaccessible airframe structures for fatigue cracking. One particular such application of great interest in the aerospace industry is the inspection of weep holes drilled through vertical stiffeners in wet-wing structures (used as fuel tanks) of both military and civilian aircraft in order to permit remnant fuel to be evenly distributed during flight.<sup>1</sup> Unfortunately, they can become the sites from which fatigue cracks often originate. The most difficult cracks to be detected are the ones located at the upper part of the hole (12 o'clock position), away from the lower skin of the wing. The conventional ultrasonic creeping wave technique shown in Fig. 1(a) experiences a strong specular reflection from the near surface of the hole that masks the creeping wave signal that arrives later in time. Figure 1(b) shows the reflected signal from a 5-mm-diameter weep hole with and without a radial crack at 12 o'clock. This figure clearly demonstrates that the main problem with the conventional creeping wave inspection technique is the relatively low amplitude of the creeping wave signal with respect to the specular reflection which is, of course, not sensitive at all to the radial crack to be detected. In order to overcome this difficulty, a novel ultrasonic creeping wave technique was suggested.<sup>1</sup> This new split-aperture technique shown in Fig. 2(a) resulted in the specular reflection and the creeping wave echoes being approximately equal in amplitude. Figure 2(b) illustrates the improved sensitivity of the split-aperture creeping wave technique in both pitch-catch and pulse-echo modes of operation. The outstanding sensitivity of the circumferential creeping wave technique in dry weep holes was well demonstrated on both simulated and real fatigue cracks.<sup>1</sup> However, the presence of fuel or even its residues in the weep hole significantly affects the behavior of the cir-

cumferential creeping wave. It causes the creeping wave echo to split into a rather weak Rayleigh-type surface wave signal and a much stronger but somewhat slower halo signal.<sup>2</sup> In order to adapt the circumferential creeping wave inspection technique to the case of fluid-filled cavities it is important to understand the adverse effects of fluid loading on the Rayleigh-type circumferential surface wave, which is the only mode sensitive to such cracks.

The dispersion behavior of circumferential creeping waves around a fluid-filled cylindrical cavity in an infinite elastic medium was investigated in Ref. 3. Phase velocity, group velocity, as well as attenuation curves were presented. This frequency-domain analysis revealed some interesting aspects of circumferential wave propagation in a fluid-filled cylindrical cavity. However, this solution represents the overall behavior of the elastic field resulting from the interference of the two principal waves, namely the leaky Rayleigh and the halo waves, from which the propagation parameters of the leaky Rayleigh mode could not be isolated by itself. A time-domain analysis of the problem, in which the signals of the reflected field from a fluid-filled cylindrical cavity are calculated, would allow the separation of the leaky Rayleigh arrival from all other signals and would, therefore, permit an accurate study of the behavior of that specific mode.

Extensive literature is available on elastic waves propagating around solid cylinders and spheres immersed in fluid.<sup>4-6</sup> In these cases, the coupling between the fluid and the solid is relatively weak because of the usually large difference between their acoustic impedance. Of course much stronger acoustic coupling occurs when the solid rod or sphere is substituted by a thin shell. The problem of elastic waves running around air-filled elastic shells submerged in fluid has been extensively investigated by Gaunard, Werby, Überall, and others.<sup>5-11</sup> Kaduchak and Marston evaluated the

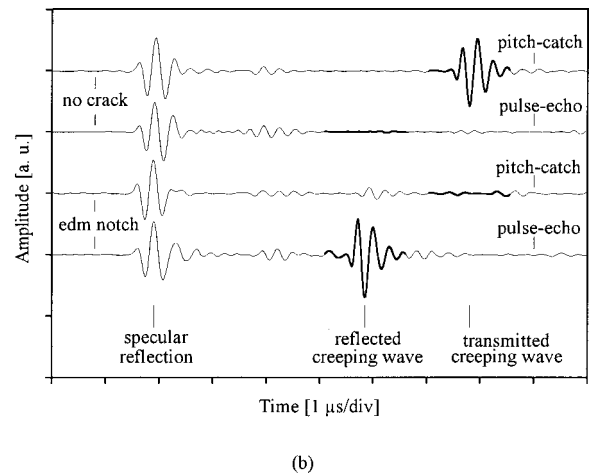
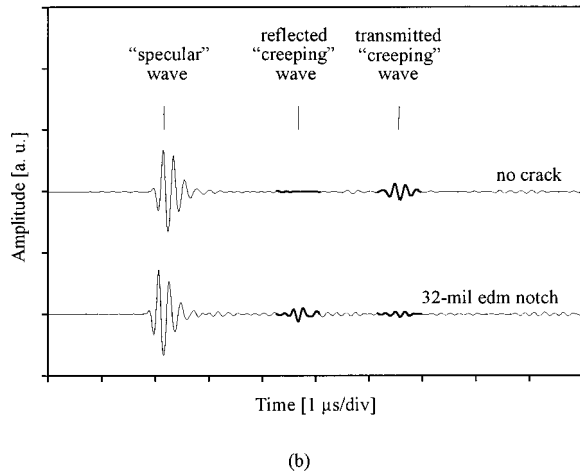
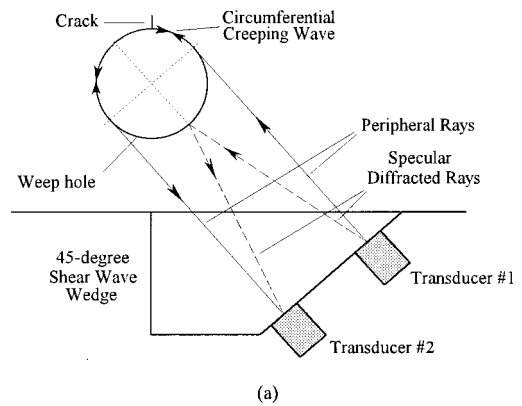
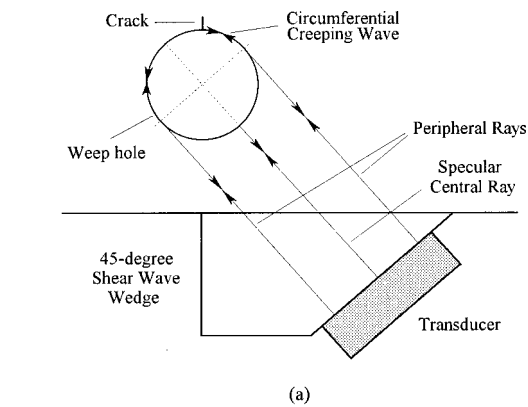


FIG. 1. (a) Schematic diagram of the conventional pulse-echo creeping wave technique and (b) the reflected signal from a 5-mm-diam weep hole with and without a radial crack at 12 o'clock (5 MHz, 45° shear wave wedge, 1/2-in.-diam transducer).

FIG. 2. (a) Schematic diagram of the split-aperture creeping wave technique and (b) the detected signals from a 1/4-in.-diam weep hole with and without a radial crack at 12 o'clock (5 MHz, 45° shear wave wedge, 1/4-in.-diam transducers).

surface displacement of a cylindrical shell insonified by plane waves perpendicular to the shell's axis of symmetry.<sup>12</sup> Optical visualization of the diffraction of a longitudinal pulse by a cylindrical cavity in an optically transparent solid was presented by Ying.<sup>13</sup> Longitudinal wave scattering from fluid-filled cylindrical holes was studied experimentally in great detail by Sachse *et al.*<sup>14-16</sup> However, in spite of the fairly strong acoustical coupling between the solid host and the fluid within the hole, their results did not show the presence of a Rayleigh-type surface mode propagating around the hole as the longitudinal mode in the solid is but very weakly coupled to this mode. We have found that vertically polarized (normal to the axis of the hole) shear waves are much more strongly coupled to the Rayleigh-type surface mode and generate relatively weaker whispering gallery modes in the fluid.<sup>2</sup> Therefore a vertically polarized incident shear wave will be used in the present analysis.

A complete analytical solution to the problem of elastic wave scattering from cylindrical cavities was first obtained by White,<sup>17</sup> whose work was later corrected by Lewis and Kraft.<sup>18</sup> Gaunard and Überall studied elastic wave scattering from fluid-filled spherical cavities.<sup>19</sup> The conventional approach to the solution of scattering problems involving simple geometries such as cylinders and spheres is to express the incident and the scattered waves in terms of a normal mode series. The expansion coefficients are determined by

solving the associated boundary value problem. The complete solution is obtained, of course, by summing over all normal modes. However, because several modes may contribute simultaneously to the total scattering amplitude at a given frequency and because of the coupling between longitudinal and shear waves at the boundary, the results are complex and difficult to interpret. Haug *et al.* showed that partial wave expansion of the incident and scattered waves can be applied advantageously to the study of scattering of incident longitudinal waves from fluid-filled cavities.<sup>20</sup> Solomon *et al.* extended the analysis of scattering from cylindrical cavities to include the case of incident shear waves.<sup>21</sup> Our analysis takes advantage of this model to formulate the amplitude of the scattered shear wave in the frequency domain and then uses the inverse Fourier transform to calculate the rf signals in the time domain.

First, the time-domain solution of the problem of vertically polarized shear wave scattering from a fluid-filled cylindrical cavity in an elastic host is reviewed. The rf signal of the scattered shear wave is calculated for the case of a 6-mm-diam water-filled cavity in aluminum. The weak leaky Rayleigh wave is gated out from the waveform and its attenuation due to fluid loading is calculated by subtracting the spectra of two signals separated by a certain propagation distance. To establish confidence in this technique and to



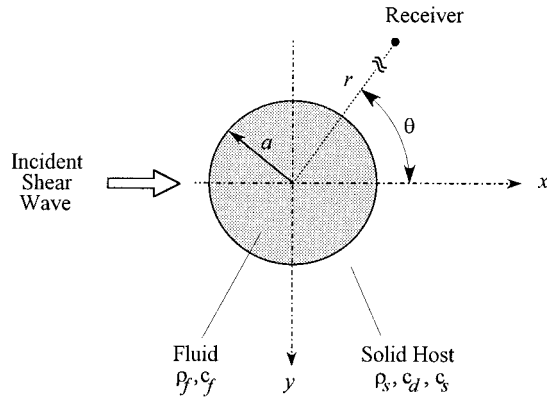


FIG. 3. Geometry of a fluid-filled cylindrical cavity in a solid host and the coordinate system.

numerically validate the results we first present attenuation calculations for two very well known cases, for which the exact solutions are readily available from the relevant dispersion equations. The two cases are (a) the case of a leaky Rayleigh wave propagating along the interface of a fluid half-space in contact with an elastic solid half-space, and (b) the case of a Rayleigh-type surface wave running around the inner surface of a free cylindrical cavity in an infinite elastic medium. Then, we calculate the attenuation of the leaky Rayleigh wave around the fluid-filled cavity and show that the leaky loss is substantially lower than expected based on the well-known leaky attenuation coefficient of the flat interface model. This anomalously low attenuation can be attributed to the fact that the aspect ratio between the normal and tangential displacement components of the elliptical surface trajectory is always smaller for the cylindrical geometry than for the frequency-independent flat case. Of course, in the high-frequency limit the aspect ratio in the curved geometry approaches that of the flat case. Finally we calculate the semicircumferential attenuation of the leaky Rayleigh wave around the fluid-filled cavity and show that the predicted result agrees very well with the experimentally measured semicircumferential attenuation.

## I. THEORETICAL BACKGROUND

The analysis of vertically polarized shear wave scattering from a fluid-filled cylindrical cavity was carried out by Solomon *et al.*<sup>21</sup> The results presented here are adapted from their paper. As shown in Fig. 3, we consider the problem of a vertically polarized shear (*SV*) wave normally incident on an infinitely long cylindrical cavity of radius  $a$ , which is aligned with the  $z$  axis. The cavity may be free or contain an inviscid fluid with density  $\rho_f$  and sound speed  $c_f$ . The elastic host is characterized by its density  $\rho_s$  and its shear and dilatational wave velocities  $c_s$  and  $c_d$ , respectively. The *SV* plane wave incident along the  $x$  axis can be expressed as a partial-wave series,

$$\psi_i = \psi_0 e^{ik_s x} = \psi_0 \sum_{n=0}^{\infty} \varepsilon_n i^n J_n(k_s r) \cos(n\theta), \quad (1)$$

where  $k_s = \omega/c_s$  is the shear wave number,  $J_n$  denotes the  $n$ th-order Bessel function of the first kind, and the Neumann

factor is  $\varepsilon_0 = 1$  and  $\varepsilon_n = 2$  for  $n \geq 1$ . For brevity, the common time factor  $e^{-i\omega t}$  has been omitted from Eq. (1) and from all subsequent equations. The scattered dilatational and shear waves in the solid host must be of the form

$$\phi_s = \sum_{n=0}^{\infty} \varepsilon_n i^n A_n H_n^{(1)}(k_d r) \sin(n\theta) \quad (2)$$

and

$$\psi_s = \sum_{n=0}^{\infty} \varepsilon_n i^n B_n H_n^{(1)}(k_s r) \cos(n\theta), \quad (3)$$

respectively, where  $k_d = \omega/c_d$  is the dilatational wave number and  $H_n^{(1)}$  denotes the  $n$ th-order Hankel function of the first kind. In addition, in a fluid-filled cavity a standing compressional wave may be excited in the form given by

$$\phi_f = \sum_{n=0}^{\infty} \varepsilon_n i^n C_n J_n(k_f r) \sin(n\theta), \quad (4)$$

where  $k_f = \omega/c_f$  is the wave number in the fluid. In Eqs. (1)–(4)  $\phi$  and  $\psi$  represent the scalar and vector displacement potentials, respectively. The expansion coefficients  $A_n$ ,  $B_n$ , and  $C_n$  can be determined from the appropriate boundary conditions.<sup>21</sup> For the fluid-filled hole these are the continuity of the normal displacement and stress and the vanishing of the shear stress at the cavity wall. In comparison, for the free hole both normal and tangential stresses must vanish at the surface.

Using the inverse Fourier transform we can write the scattered vertically polarized shear potential in the time-domain as follows:

$$\psi_s(r, \theta, t) = \int_{-\infty}^{\infty} \left( \sum_{n=0}^{\infty} \varepsilon_n i^n B_n H_n^{(1)}(k_s r) \cos(n\theta) \right) e^{-i\omega t} d\omega, \quad (5)$$

where we took the negative sign convention in the exponential for the inverse Fourier transform. A far-field approximation is obtained by substituting the high-frequency asymptote of the Hankel function of the first kind as follows

$$\psi_s(r, \theta, t) \approx \sqrt{\frac{2}{\pi}} \int_{-\infty}^{\infty} \left\{ \sqrt{\frac{c_s}{\omega r}} e^{i(\omega r/c_s - \pi/4 - \omega t)} \times \left( B_0 + 2 \sum_{n=1}^{\infty} i^n B_n e^{-n\pi/2} \cos(n\theta) \right) \right\} d\omega. \quad (6)$$

Equation (6) can be used to numerically calculate the rf waveform representing the scattered shear potential from the cylindrical cavity for both the fluid-filled and the dry cases.

## II. NUMERICAL RESULTS

In order to demonstrate how the numerically determined scattering waveforms can be further processed to obtain the attenuation coefficient of individual wave modes, we first present attenuation calculations for two very well known cases for which the exact solutions are readily available from the relevant dispersion equations. In the first example, we

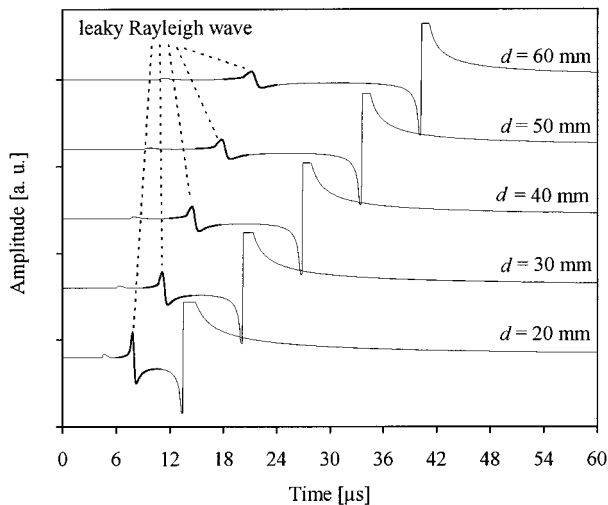


FIG. 4. Space-time Green's function for the reflected acoustic pressure in water from a water/aluminum interface as a function of time for five transmitter/receiver distances.

calculate the leaky attenuation of the Rayleigh wave propagating on a fluid-loaded solid half-space. In this case the surface wave is nondispersive and the leakage occurs into the fluid. In the second example, we calculate the leaky attenuation of the Rayleigh wave running around the inner surface of a free cylindrical cavity in an infinite elastic medium. In this case the surface wave is dispersive and the leakage occurs into the solid. Finally, we use this technique to solve the problem of main interest in this paper, i.e., to calculate the fluid-loading induced attenuation of the Rayleigh wave running around the inner surface of a fluid-filled cylindrical cavity in an infinite elastic medium. In this case the surface wave is dispersive and leaks into both the fluid and the solid. The exact attenuation of this mode cannot be directly obtained from the dispersion equation which gives the apparent attenuation of the complex interference field dominated by two principal components, namely the leaky Rayleigh and the halo modes.<sup>3</sup> To the best of our knowledge the exact attenuation of the leaky Rayleigh mode around a fluid-filled cylindrical cavity has never been calculated before and is not available in the literature. In all the numerical calculations presented below, the radius of the cylindrical cavity is taken as  $a = 3$  mm, the fluid is taken as water with density  $\rho_f = 1000$  kg/m<sup>3</sup> and sound velocity  $c_f = 1494$  m/s. The elastic solid is taken as aluminum with density  $\rho_s = 2700$  kg/m<sup>3</sup>, shear velocity  $c_s = 3140$  m/s, and longitudinal velocity  $c_d = 6380$  m/s.

### A. Fluid-loaded solid half-space

The Green's function for a system consisting of a two-dimensional, impulsive, monopole line source in a fluid/solid configuration with a plane geometry was formulated by de Hoop *et al.* using the modified Cagniard technique.<sup>22</sup> The pulse corresponding to the leaky Rayleigh mode can be readily gated out from the Green's function and spectrum analyzed. By varying the distance between the transmitter and the receiver we can compute the attenuation of the leaky Rayleigh wave propagating along the interface.

Figure 4 shows the space-time Green's function for the

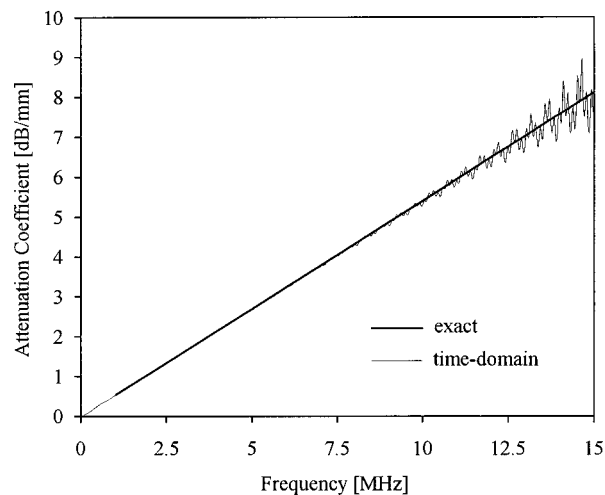


FIG. 5. Attenuation coefficient of the leaky Rayleigh wave propagating along a flat water/aluminum interface.

reflected acoustic pressure from a water/aluminum interface as a function of time for five transmitter/receiver distances,  $d$ . The transmitter and the receiver were placed infinitesimally close to the water/aluminum interface. The later arriving but very strong compressional wave was slightly clipped to better display the leaky Rayleigh pulse. All the waves present in the rf waveform for this case along with their times of arrival were positively identified and thoroughly described by de Hoop *et al.*<sup>22</sup> A flat-top window was used to isolate the leaky Rayleigh arrival from all the other modes. The attenuation coefficient was then calculated as

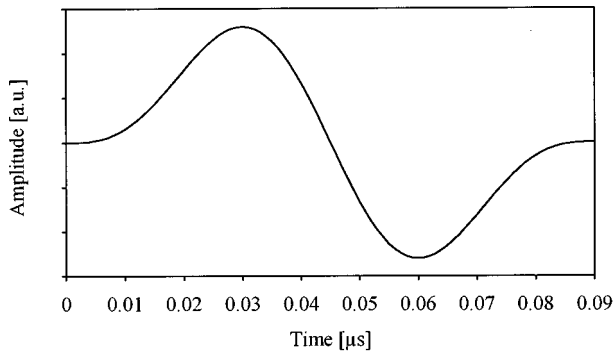
$$a^{\text{plane}} = \frac{20(\log[G_1(\omega)] - \log[G_2(\omega)])}{d_2 - d_1}, \quad (7)$$

where  $G_i(\omega)$  is the magnitude of the spectrum of the leaky Rayleigh signal at a distance  $d_i$  from the transmitter. Figure 5 shows the attenuation coefficient for the leaky Rayleigh wave along the plane water/aluminum interface as a function of frequency. The exact solution was calculated from the exact dispersion equation.<sup>23</sup> We notice that the time-domain solution is identical to the exact solution except for the numerical difficulties associated with calculating the spectrum of the time-domain signal using FFT, which cause the technique to fail at high frequencies as it is evident from the figure.

### B. Fluid-free cylindrical cavity

In order to facilitate the adaptation of our numerical technique to dispersive waves propagating on curved surfaces using Eq. (6), a bandlimited excitation was imposed to restrict the spectral components over which the integration is performed. This allowed the replacement of the integration by a finite sum. Figure 6(a) shows the bandlimited excitation used in the calculations. It is given analytically as

$$f(t) = \left[ 1 - \cos\left(2\pi\frac{t}{T}\right) \right] \sin\left(2\pi\frac{t}{T}\right), \quad (8)$$



(a)

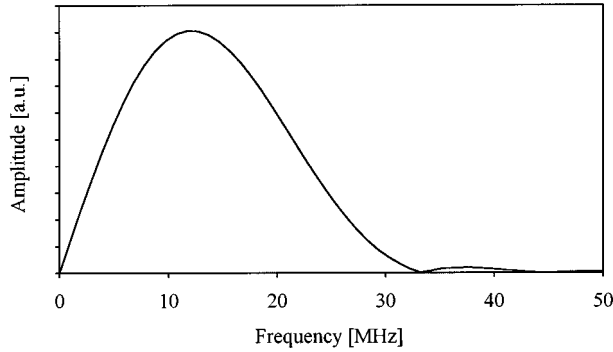


FIG. 6. (a) The single-cycle waveform of the excitation pulse used in calculating the rf signals in the cylindrical geometry and (b) its bandlimited frequency spectrum.

where  $T=0.09 \mu\text{s}$  represents the total duration of the excitation pulse. Figure 6(b) shows the band-limited frequency spectrum of the excitation signal. The center frequency and  $-3 \text{ dB}$  bandwidth are both approximately 11 MHz. It should be mentioned that the spectra of the incident and scattered signals were calculated with a relatively high resolution of 500 Hz in order to avoid folding back of the calculated waveforms up to 1 ms.

Figure 7 shows the rf signals representing the backscat-

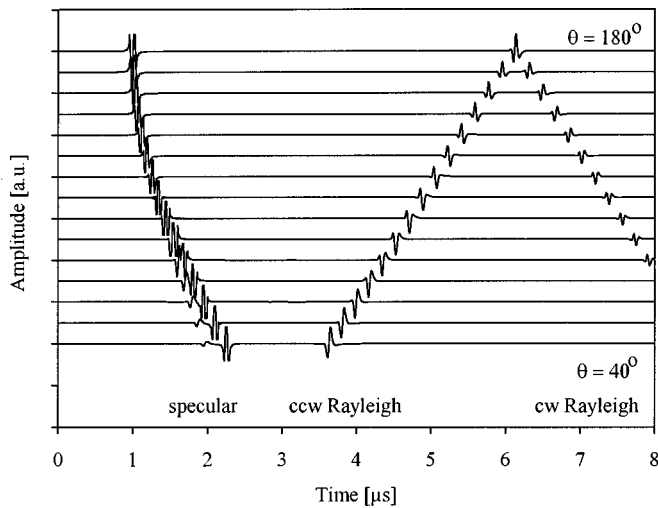


FIG. 7. The back scattered vertically polarized shear potential from a 6-mm-diameter fluid-free cylindrical cavity in an infinite aluminum host for angles between  $\theta=40^\circ$  and  $180^\circ$  calculated at every  $10^\circ$ .

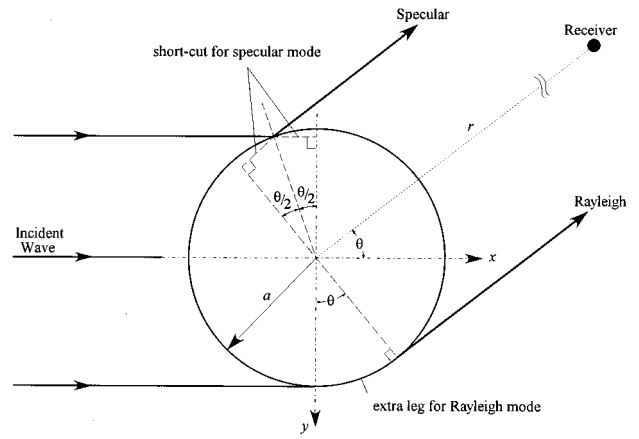


FIG. 8. Schematic diagram illustrating the first two scattered waves from a fluid-free cylindrical cavity in an infinite elastic host. Ray tracing is used to predict the times of arrival of the different signals.

tered vertically polarized shear potential from a fluid-free cylindrical cavity in an infinite aluminum host for angles between  $40^\circ$  and  $180^\circ$  degrees calculated at every  $10^\circ$  with the receiver at a distance of  $r=3a$  from the center of the cavity. It should be mentioned that Eq. (6) represents a far-field approximation of the scattered field therefore the distance of the receiver from the cavity does not affect the calculated waveform except for a  $t_r=3a/c_s$  constant time delay. These results were calculated using the same parameters mentioned previously. Again, to better display the Rayleigh arrival the stronger specular reflection was slightly clipped. The first of the three arrivals in the rf signal represents the specularly scattered shear wave, the second is the counterclockwise propagating circumferential Rayleigh wave with the shorter path and the third is the clockwise propagating circumferential Rayleigh wave with the longer path. The time of arrival of each one of these signals can be calculated from simple ray tracing considerations. Figure 8 shows a schematic diagram of the specular reflection and the earlier of the two Rayleigh arrivals. The two Rayleigh signals are generated at diametrically opposite points where the incident shear wave grazes the circumference of the cavity. The shorter-path Rayleigh arrival travels around the cavity counter-clockwise through an angle  $\theta$  equal to the azimuthal angle of the receiver, whereas the longer-path Rayleigh pulse travels clockwise through an angle of  $2\pi - \theta$ . From Fig. 8, we can write the time of arrival for each one of these signals as follows:

$$t_{\text{spec}} = t_r - \frac{2a}{c_s} \sin \frac{\theta}{2}, \quad (9a)$$

$$t_{\text{Rsp}} = t_r + \frac{a\theta}{c_R}, \quad (9b)$$

$$t_{\text{Rlp}} = t_r + \frac{a(2\pi - \theta)}{c_R}, \quad (9c)$$

where  $t_{\text{spec}}$  is the time of arrival of the specularly scattered wave, and  $t_{\text{Rsp}}$  and  $t_{\text{Rlp}}$  are the times of arrival of the short-path and long-path Rayleigh signals, respectively. For the sake of simplicity,  $c_R$  is taken as the velocity of the Rayleigh wave on the free surface of the solid half-space. The predic-

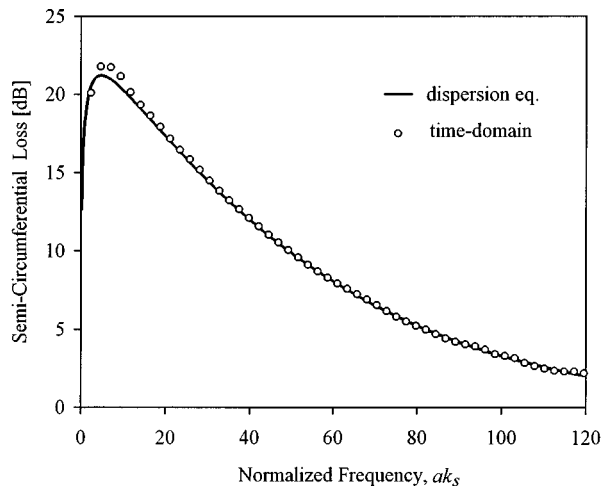


FIG. 9. The semicircumferential loss for a Rayleigh wave running around the inner surface of a fluid-free cylindrical cavity in an infinite elastic medium.

tions from Eqs. (9a)–(9c) are in very close agreement with the results obtained numerically.

The leaky attenuation caused by the curvature of the surface is measured in terms of the normalized semicircumferential loss  $L_\pi$ , which is defined as the total attenuation halfway around the cavity

$$L_\pi = 20(\log[G_1(\omega)] - \log[G_2(\omega)]) \frac{180^\circ}{\theta_2 - \theta_1}, \quad (10)$$

where  $G_i(\omega)$  is the magnitude of the spectrum of the windowed Rayleigh signal at angle  $\theta_i$ . Figure 9 shows the semicircumferential loss of the Rayleigh wave running around the inner surface of a fluid-free cylindrical cavity in an infinite solid as a function of the normalized frequency  $ak_s$ . The solid line represents the exact solution as calculated from the dispersion equation.<sup>3</sup> The circles represent the semicircumferential loss calculated from the time-domain solution. The Rayleigh arrival was gated out from the time-domain signal obtained at the two locations of  $\theta_1 = 30^\circ$  and  $\theta_2 = 60^\circ$ . A flat-top window was applied to the gated signals and the spectra of the resulting signals were calculated. Figure 9 shows that the time-domain solution is in excellent agreement with the exact solution from the dispersion equation over the normalized frequency range of 15–120. However, the time-domain solution seems to be breaking down for normalized frequencies below 15 and above 120 due to the inherent numerical difficulties involved in the calculations of the spectra at very low and very high frequencies.

### C. Fluid-filled cylindrical cavity

For the case of a fluid-filled cavity in an elastic medium, the results are obtained in a manner similar to that used in the case of the fluid-free cavity. However, the results are much more complex due to the presence of the fluid and have to be analyzed more carefully. Figure 10 shows the backscattered vertically polarized shear potential from a 6-mm-diam water-filled cylindrical cavity in an infinite aluminum host for scattering angles between  $\theta = 40^\circ$  and  $\theta = 180^\circ$  calculated at every  $10^\circ$ . Again, the receiver is placed

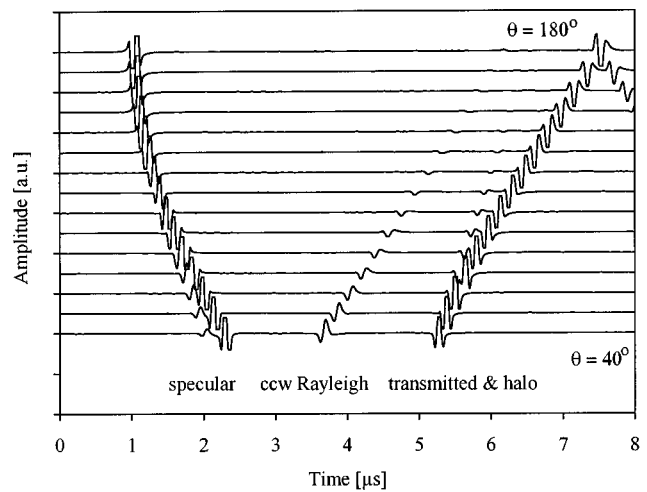


FIG. 10. The backscattered vertically polarized shear potential from a 6-mm-diam water-filled cylindrical cavity in an infinite aluminum host for angles between  $\theta = 40^\circ$  and  $180^\circ$  calculated at every  $10^\circ$ .

at a distance of  $r = 3a$  from the center of the cavity. The first arrival is the specularly scattered shear wave, followed by the weak circumferential Rayleigh-type creeping wave and a much stronger arrival through the fluid filling the cavity. The latter one is actually a combination of two modes that arrive at almost the same time. One is the direct transmission through the fluid which becomes weaker and weaker as the angle of scattering increases. For angles larger than  $\theta \approx 30^\circ$  there is a second mode, the so-called halo wave, caused by the leakage of the Rayleigh mode into the fluid.<sup>2,3</sup> According to the classical physical explanation based on ray theory, halo modes are produced by the repeated reflection of the compressional bulk wave in the fluid at the cylindrical wall. For a water/aluminum combination the signal going through the fluid is dominated by the direct transmission up to about  $\theta = 60^\circ$  while the halo mode becomes the stronger one at higher angles. It is worth mentioning that another rather weak arrival that propagates through part of its path as a dilatational skimming wave around the cavity can also appear between the leaky Rayleigh and halo waves depending on the combination of the sound velocities in the fluid and the solid. The arrival times for the specular and the leaky

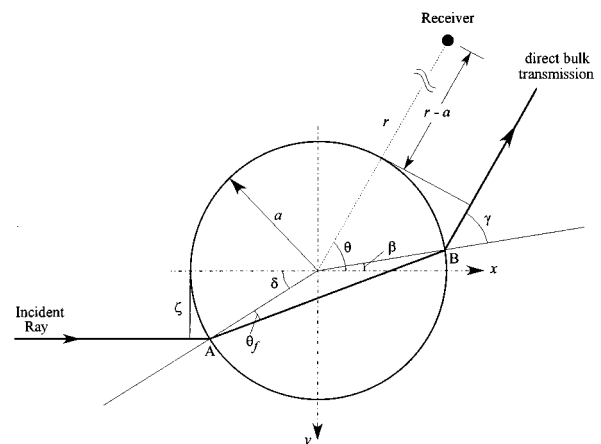


FIG. 11. Schematic diagram illustrating the path of the direct bulk transmission in a fluid-filled cylindrical cavity in an elastic medium.

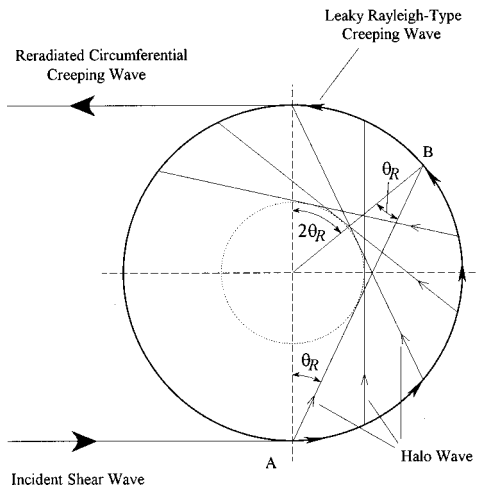


FIG. 12. Schematic diagram of the leaky Rayleigh and the halo waves propagating around a water-filled cylindrical cavity in an elastic solid.

Rayleigh modes can still be calculated from Eqs. (9a)–(9c). As for the direct bulk transmission mode, the simple ray tracing schematic diagram shown in Fig. 11 leads to the following expression for its time of arrival,

$$t_f = t_r - a \left[ \frac{\cos(\delta) + \cos(\theta - \delta + 2\theta_f)}{c_s} - \frac{2\cos(\theta_f)}{c_f} \right], \quad (11)$$

where  $\delta = \sin^{-1}(\zeta/a)$  and  $\theta_f = \sin^{-1}(c_f/c_s \sin \delta)$ . The appropriate value of  $\zeta$  for any given scattering angle  $\theta$  is obtained by requiring that the emerging ray subtends angle  $\theta$  to the incident direction. Figure 12 illustrates the path taken by the halo mode. Its arrival time can be calculated as follows:

$$t_h = t_r + a \left[ \frac{\theta - 2\theta_R}{c_R} + \frac{2\cos(\theta_R)}{c_f} \right], \quad (12)$$

where  $\theta_R = \sin^{-1}(c_f/c_R)$  is the Rayleigh angle, which is approximately  $30^\circ$  for the water/aluminum combination.

Figure 13 shows the fluid-loading induced loss of the leaky Rayleigh circumferential creeping mode around a fluid-filled cylindrical cavity for different propagation angles as a function of the normalized frequency  $ak_s$ . At a certain

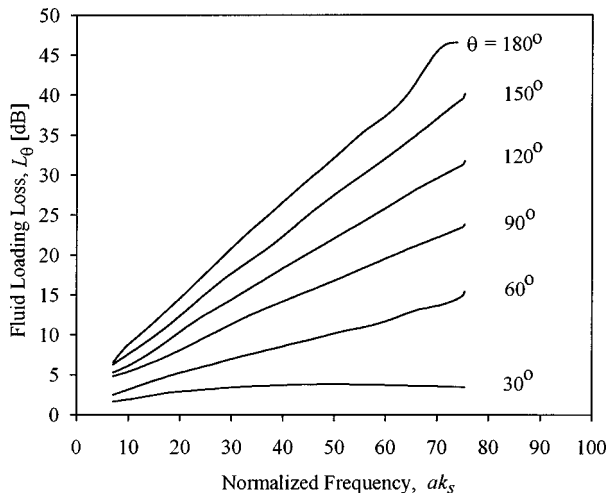


FIG. 13. Fluid-loading loss of the leaky Rayleigh wave around a water-filled cylindrical cavity in aluminum.

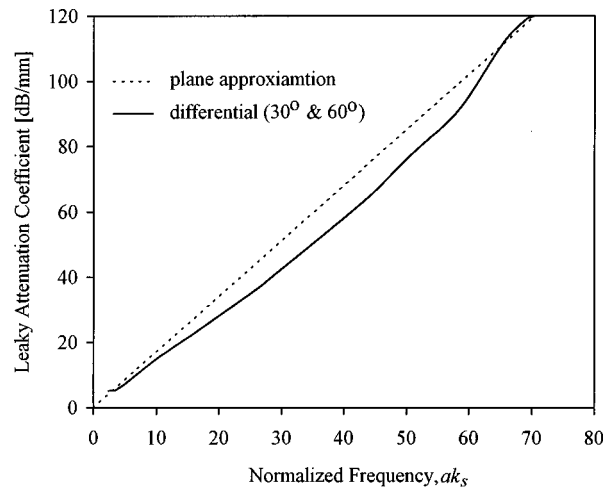


FIG. 14. The leaky attenuation coefficient of the Rayleigh circumferential creeping wave around a water-filled cylindrical cavity in aluminum. The plane approximation is shown in a dotted line for comparison purposes.

angle  $\theta$  the rf signals representing the backscattered field are computed for the cases of the water-free and water-filled cylindrical cavities in aluminum. The Rayleigh-type creeping wave is then gated out from the time-domain signals and a flat-top window is applied. Finally, the spectrum for each case is calculated and the fluid-loading induced loss is obtained as

$$L_\theta(\omega) = 20(\log[G_\theta^{\text{free}}(\omega)] - \log[G_\theta^{\text{fluid}}(\omega)]), \quad (13)$$

where  $G_\theta^{\text{fluid}}(\omega)$  and  $G_\theta^{\text{free}}(\omega)$  are, respectively, the magnitudes of the spectra of the Rayleigh wave signal with and without fluid in the cavity. It is worth noting that the change in the fluid-loading induced loss is the largest when the scattering angle is changed from  $30^\circ$  to  $60^\circ$ . As the propagation angle is increased through  $180^\circ$ , the difference becomes more uniform. This indicates that the fluid-loading loss does not change strictly linearly with the scattering angle, i.e., the propagation angle of the surface wave around the cylindrical cavity. Nevertheless, a linear approximation for the dependence of the fluid-loading loss on the propagation angle does not introduce significant error in the results and may be taken as an approximation.

Of course the dispersive leaky Rayleigh wave propagating around a fluid-free cylindrical cavity asymptotically approaches, in the high frequency limit, the true Rayleigh wave along the flat interface of an elastic half-space.<sup>24</sup> Similarly, it is expected that the “doubly-leaky” Rayleigh wave propagating around a fluid-filled cylindrical cavity also asymptotically approaches the leaky Rayleigh wave along a fluid-loaded elastic half-space. This asymptotic behavior is not obvious from Fig. 13 which shows the total fluid-loading induced loss of the Rayleigh-type surface wave over given angles of propagation rather than the leaky attenuation coefficient itself. Figure 14 shows the leaky attenuation coefficient due to fluid-loading in the two cases of flat and cylindrical geometry as a function of the normalized frequency. The dashed line represents the plane approximation whereas the solid line represents the leaky coefficient in the cylindrical

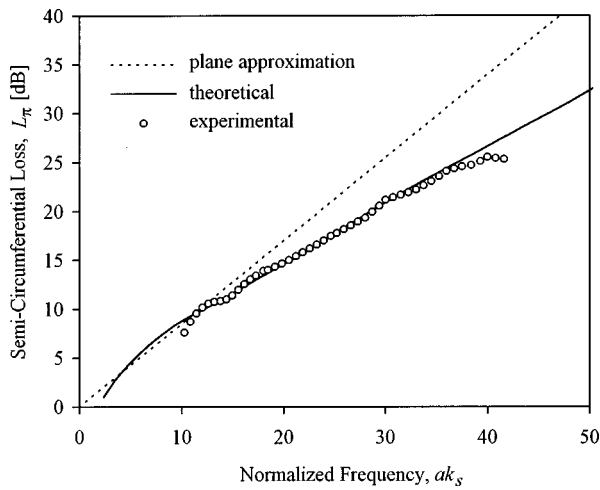


FIG. 15. Semicircumferential loss of the leaky Rayleigh mode around a water-filled cylindrical cavity in aluminum.

cal case calculated by taking the difference between the fluid-loading loss curves at  $\theta_1 = 30^\circ$  and  $\theta_2 = 60^\circ$  as follows:

$$\alpha^{\text{curved}} = \frac{L_{\theta_2}(\omega) - L_{\theta_1}(\omega)}{a(\theta_2 - \theta_1)}. \quad (14)$$

It is obvious from this figure that the leaky attenuation coefficient for the cylindrical case approaches the expected linear asymptote at high frequencies, but remains significantly below it at lower normalized frequencies of  $ak_s \approx 30$  typically used in nondestructive evaluation applications.<sup>1,2</sup>

### III. EXPERIMENTAL RESULTS AND DISCUSSION

In the previous section we presented numerical predictions showing that the Rayleigh-type surface wave is less attenuated by leakage into the fluid on curved surfaces than on flat ones. In this section we experimentally verify this somewhat unexpected prediction for the reduced attenuation of the leaky Rayleigh-type circumferential creeping mode for the case of most practical importance, namely backscattering at  $\theta = 180^\circ$ . A physical explanation of the observed behavior will also be presented.

According to the split-aperture technique described in Ref. 1, two 6.35-mm-diam, 5-MHz longitudinal transducers were mounted on a  $45^\circ$  shear wave wedge and used in a pitch catch mode to record the circumferential creeping wave around water-free and water-filled cylindrical cavities of different diameters between 5 and 10 mm in aluminum. In spite of the relatively narrow bandwidth over which sufficiently high signal-to-noise-ratio could be achieved in this configuration, it was possible to measure the fluid loading induced attenuation  $L_\pi(\omega)$  over a wider normalized frequency range of  $ak_s \approx 10$ –40 by combining the data obtained from five holes of different diameters. In order to maintain the highest possible sensitivity on different holes, the separation between the transmitting and receiving transducers, which are mounted on the same wedge, was always adjusted to match the hole diameter. The recorded signals were then used to calculate the semicircumferential loss in a manner similar to that used in constructing Fig. 13. The experimental results are shown in Fig. 15, along with the results obtained from

the plane approximation and the exact results calculated from the theoretical waveforms. The experimentally measured results are in very close agreement ( $\approx \pm 0.5$  dB) with the exact results for the cylindrical geometry and clearly verify that the Rayleigh-type surface wave is indeed less attenuated by leakage into the fluid on curved surfaces than on flat ones.

Our main experimental result which indicates that the semicircumferential loss ( $L_\pi$ ) associated with the cylindrical geometry is less than the anticipated semicircumferential loss calculated from the plane approximation ( $\alpha^{\text{plane}} a \pi$ ) can be attributed to the combined effects of two physical phenomena. First, even if the attenuation coefficients due to leakage into the fluid were the same for flat and curved surfaces, some discrepancy could exist because the mode conversion efficiency from the incident shear wave to the Rayleigh-type surface mode and vice versa is slightly affected by the presence of the fluid in the cavity. However, this conversion efficiency is not affected by the propagation distance and can be readily eliminated by subtracting the fluid-loading induced losses at two different scattering angles according to Eq. (14). The second effect, which dominates the total fluid-loading induced loss at all but very low angles, is that the leaky attenuation is actually lower on a curved surface ( $\alpha^{\text{curved}}$ ) than on a flat one ( $\alpha^{\text{plane}}$ ).

Since the leaky attenuation is solely due to the normal vibration component of the surface in contact with the fluid, it seems to be reasonable to assume that the aspect ratio of the elliptically polarized particle displacement must be lower on the curved surface than on the flat one. It is well known that a surface particle under the influence of a Rayleigh wave undergoes a counterclockwise elliptically polarized motion. For the classical Rayleigh wave propagating on the free surface of a solid half-space, this aspect ratio is a function of Poisson's ratio only. For example, in the case of aluminum with Poisson's ratio of  $\nu = 0.34$ , this ratio is approximately 1.6. For guided waves in general, e.g., for rod and plate modes, the aspect ratio is also dependent on frequency. The role of this aspect ratio in determining the degree of leakage from the surface has been recently investigated by Nagy and Kent<sup>25</sup> and Nagy and Nayfeh.<sup>26,27</sup> As this aspect ratio increases, i.e., the normal component of the displacement becomes larger compared to the tangential component, the leaky loss increases. In contrast, the leaky loss decreases as the tangential displacement component increases with respect to the normal component.

Figure 16 shows the aspect ratio of the elliptical trajectory of the particle's motion for the case of a Rayleigh wave along the free surface of an infinite elastic half-space and the case of the dispersive Rayleigh-type wave around the free surface of a cylindrical cavity in an infinite elastic solid. For the cylindrical geometry the exact aspect ratio can be readily obtained from Rulf's results.<sup>24</sup> It is clear from Fig. 16 that the aspect ratio in the cylindrical geometry is a function of frequency whereas it is frequency independent in the flat geometry. It is also clear that this aspect ratio is smaller in the cylindrical geometry than it is in the flat case, and that it approaches its high-frequency flat asymptotic limit from below. This means that the normal displacement component in

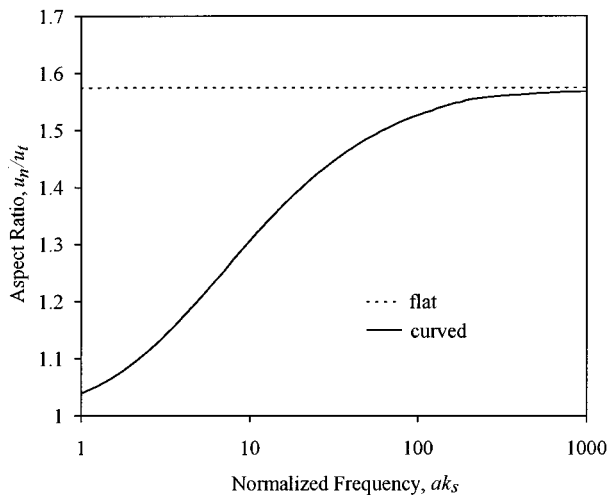


FIG. 16. The ratio of the normal and the tangential displacement components for Rayleigh-type waves propagating on the free surfaces of a solid half-space and a cylindrical cavity in an infinite elastic host.

the flat geometry is relatively larger than that in the cylindrical case, which causes the degree of leakage in the first case to be larger than in the second one. This translates into a lower leaky attenuation in the cylindrical geometry as compared to the flat case when the surface is loaded by a fluid. In summary, the lower attenuation of the leaky Rayleigh mode in the cylindrical geometry is mainly attributed to the change in the ratio of the normal to the tangential displacement components on the surface.

#### IV. CONCLUSION

The attenuation of the leaky Rayleigh wave around a fluid-filled cylindrical cavity was investigated using time-domain analysis. First, the complex waveforms representing the scattered vertically polarized shear potential from the fluid-filled cavity were calculated. Then, the principal arrivals in the rf signal were identified. The attenuation of the leaky Rayleigh mode was calculated by gating out this signal from the rest of the arrivals and spectrum analyzing it. The time-domain solutions for the attenuation of the Rayleigh wave propagating along a fluid/solid flat interface and around the free surface of a cylindrical cavity were presented and compared to the well-known exact solutions from the dispersion equations. The two methods resulted in identical solutions except for very low and very high frequencies where the time-domain calculations break down due to inherent numerical difficulties associated with the technique.

After establishing the validity of the time-domain technique, it was used to calculate the attenuation of the dispersive leaky Rayleigh wave around a fluid-filled cylindrical cavity for which the exact solution is not available from the dispersion equation. In this case the solution from the dispersion equation yields the complex wave number of the total interference field dominated by the two principal modes, namely the leaky Rayleigh and the halo waves.<sup>3</sup> The separation of the two principal modes in the frequency domain is extremely difficult, if at all possible, but due to differences in the speed and the length of the path followed by each mode they become readily separated in the time domain. The semi-

circumferential loss of the leaky Rayleigh mode was calculated theoretically and verified experimentally. It was observed that the calculated and measured semicircumferential loss was significantly less than predictions obtained from the flat interface model. The difference between the two cases can be mainly attributed to the reduced ratio of the normal and tangential surface displacement components, which represents the aspect ratio of the particle's elliptical trajectory. It was found that for a curved surface this ratio is less than the one associated with the flat case. Since the leaky attenuation is caused solely by the normal displacement component we can conclude that the leaky attenuation of the Rayleigh-type surface wave propagating on a curved surface is inherently lower than the one on a plane surface.

#### ACKNOWLEDGMENTS

This work was partially supported by the Metals, Ceramics, and NDE Division, Wright Laboratory, Wright-Patterson AFB.

- <sup>1</sup>P. B. Nagy, M. Blodgett, and M. Golis, "Weep hole inspection by circumferential creeping waves," *NDT & E Int.* **27**, 131 (1994).
- <sup>2</sup>W. Hassan and P. B. Nagy, "Feasibility of fatigue crack detection in fluid-filled cylindrical holes using circumferential creeping waves," in *Review of Progress in Quantitative Nondestructive Evaluation* (Plenum, New York, 1997), Vol. 16A, pp. 43–50.
- <sup>3</sup>W. Hassan and P. B. Nagy, "Circumferential creeping waves around a fluid-filled cylindrical cavity in an elastic solid," *J. Acoust. Soc. Am.* **101**, 2496 (1997).
- <sup>4</sup>R. D. Doolittle, H. Überall, and P. Uginčius, "Sound scattering by elastic cylinders," *J. Acoust. Soc. Am.* **43**, 1 (1968).
- <sup>5</sup>G. C. Gaunard, "Elastic and acoustic resonance wave scattering," *Appl. Mech. Rev.* **42**, 143 (1989).
- <sup>6</sup>L. R. Dragonette, "Evaluation of the relative importance of circumferential or creeping waves in acoustic scattering from rigid and elastic solid cylinders and cylindrical shell," NRL Report No. 8216, Naval Research Laboratory, Washington, DC, 1978.
- <sup>7</sup>G. C. Gaunard and M. F. Werby, "Acoustic resonance scattering by submerged elastic shells," *Appl. Mech. Rev.* **43**, 171 (1990).
- <sup>8</sup>G. C. Gaunard and H. Überall, "Relationship between creeping-wave acoustic transients and the complex-frequency poles of the singularity expansion method," *J. Acoust. Soc. Am.* **78**, 234 (1985).
- <sup>9</sup>C. W. Horton and M. V. Mechler, "Circumferential waves in a thin-walled air filled cylinder in a water medium," *J. Acoust. Soc. Am.* **51**, 295 (1972).
- <sup>10</sup>P. Smith, "Phase velocities and displacement characteristics of free waves in a thin cylindrical shell," *J. Acoust. Soc. Am.* **27**, 1065 (1955).
- <sup>11</sup>P. Uginčius, "Creeping-wave analysis of acoustic scattering by elastic cylindrical shells," Naval Weapons Laboratory Technical Report No. TR-2128, 1968.
- <sup>12</sup>G. Kaduchak and P. L. Marston, "Traveling-wave decomposition of surface displacements associated with scattering by a cylindrical shell. Numerical evaluation displaying guided forward and backward wave properties," *J. Acoust. Soc. Am.* **98**, 3501 (1995).
- <sup>13</sup>C. F. Ying, "Photoelastic visualization and theoretical analyses of scatterings of ultrasonic pulses in solids," in *Physical Acoustics* (Academic, San Diego, 1990), Vol. XIX, pp. 291–343.
- <sup>14</sup>W. Sachse, "Ultrasonic spectroscopy of a fluid-filled cavity in an elastic solid," *J. Acoust. Soc. Am.* **56**, 891 (1974).
- <sup>15</sup>W. Sachse and C. T. Chain, "Determination of the size and mechanical properties of a cylindrical fluid inclusion in an elastic solid," *Mater. Eval.* **33**, 81 (1975).
- <sup>16</sup>Y. Pao and W. Sachse, "Interpretation of the time records and power spectra of scattered ultrasonic pulses in solids," *J. Acoust. Soc. Am.* **56**, 1478 (1974).
- <sup>17</sup>R. M. White, "Elastic wave-scattering at a cylindrical discontinuity inside a solid," *J. Acoust. Soc. Am.* **30**, 771 (1958).
- <sup>18</sup>T. S. Lewis and D. W. Kraft, "Mode conversion relation for elastic waves scattered by a cylindrical obstacle," *J. Acoust. Soc. Am.* **56**, 1899 (1974).

- <sup>19</sup>G. C. Gaunard and H. J. Überall, "Theory of resonance scattering from spherical cavities in elastic and viscoelastic media," *J. Acoust. Soc. Am.* **63**, 1699 (1978).
- <sup>20</sup>A. J. Haug, S. G. Solomon, and H. J. Überall, "Resonance theory of elastic wave scattering from a cylindrical cavity," *J. Sound Vib.* **57**, 51 (1978).
- <sup>21</sup>S. G. Solomon, H. J. Überall, and K. B. Yoo, "Mode conversion and resonance scattering of elastic waves from a cylindrical fluid-filled cavity," *Acustica* **55**, 147 (1984).
- <sup>22</sup>A. T. deHoop and J. H. M. T. Van der Hijden, "Generation of acoustic waves by an impulsive line source in a fluid/solid configuration with a plane boundary," *J. Acoust. Soc. Am.* **74**, 333 (1974).
- <sup>23</sup>H. L. Bertoni and T. Tamir, "Unified theory of Rayleigh-angle phenomena for acoustic beams at liquid-solid interfaces," *Appl. Phys.* **2**, 157 (1973).
- <sup>24</sup>B. Rulf, "Rayleigh waves on curved surfaces," *J. Acoust. Soc. Am.* **45**, 493 (1969).
- <sup>25</sup>P. B. Nagy and R. M. Kent, "Ultrasonic assessment of Poisson's ratio in thin rods," *J. Acoust. Soc. Am.* **98**, 2694 (1995).
- <sup>26</sup>P. B. Nagy and A. H. Nayfeh, "Viscosity-induced attenuation of longitudinal guided waves in fluid-loaded rods," *J. Acoust. Soc. Am.* **100**, 1501 (1996).
- <sup>27</sup>P. B. Nagy and A. H. Nayfeh, "Excess attenuation of leaky Lamb waves due to viscous fluid loading," *J. Acoust. Soc. Am.* **101**, 2649 (1997).



# Ultrasonic beam models: An edge element approach

Terence P. Lerch<sup>a)</sup> and Lester W. Schmerr

Center for NDE and the Department of Aerospace Engineering and Engineering Mechanics,  
Iowa State University, Ames, Iowa 50011

Alexander Sedov

Department of Mechanical Engineering, Lakehead University, Thunder Bay, Ontario P7B 5E1, Canada

(Received 28 July 1997; accepted for publication 22 May 1998)

A new method, the edge element method, has been developed to numerically evaluate a variety of ultrasonic transducer beam models. The edge element technique divides the transducer surface into a web of sources consisting of radiating straight line elements whose individual contributions can be evaluated analytically. When all of these edge elements are summed, the wave field of the transducer can be obtained at any field point in the surrounding medium for a given ultrasonic frequency. To demonstrate the versatility of this approach, it is shown that edge elements can accurately model the wave fields radiated into a fluid by focused and unfocused transducers of circular and noncircular apertures. © 1998 Acoustical Society of America.

[S0001-4966(98)02209-7]

PACS numbers: 43.20.Ks, 43.35.Zc [ANN]

## INTRODUCTION

Modeling the fields radiated by ultrasonic nondestructive evaluation (NDE) transducers is a particularly challenging task because of the large number of possible transducer types, sizes, and configurations that are used in practice. There are, for example, circular immersion and contact transducers, rectangular shaped "paintbrush" probes, focused transducers with spherical or cylindrical focusing, etc. In all these cases, the radiated fields are usually modeled by assuming an appropriate set of sources acting over the transducer aperture. If, in particular, the sources are taken as uniform in amplitude (piston model) and the aperture is planar, then one of the most commonly used transducer models is based on the Rayleigh-Sommerfeld integral. This model represents the radiated waves by a superposition of spherical waves over the planar aperture.<sup>1</sup> Models of contact transducers also are of this same type.<sup>2</sup> Similarly, for a spherically focused piston transducer, O'Neil<sup>3</sup> approximates the radiated wave field by placing a set of spherical wave sources of uniform amplitude on a spherically shaped aperture.

In general, to directly evaluate the transducer wave fields in such models requires that a numerical two-dimensional (2-D) integration be performed over the transducer aperture, a procedure that is computationally costly to implement because of the rapid variations in the source terms. Stamnes<sup>4</sup> discusses some efficient 2-D numerical integration procedures that work well for specific planar aperture shapes, but in many instances, those methods cannot be easily extended to curved and generally shaped apertures. An expansion of the transducer wave fields in terms of Gauss-Hermite functions<sup>5</sup> is a particularly efficient method to evaluate the entire transducer wave field which only requires a simple evaluation of coefficient terms on the aperture, but

this approach uses the paraxial approximation which breaks down in the near field of the transducer's wave field and for tightly focused probes.

In some special cases, of course, the 2-D integrations can be directly evaluated. The on-axis wave fields of circular-shaped planar and spherically focused piston probes, for example, can be obtained as completely closed form analytical expressions. Explicit expressions can also be found for the far field (Fraunhofer) wave fields of planar circular and rectangular piston probes. For a number of cases the off-axis fields can be efficiently evaluated by transforming the 2-D surface integrals into two terms—an explicit "direct wave" contribution and an "edge wave" contribution that is expressed in terms of only a one-dimensional (1-D) line integral over the transducer rim.<sup>6-8</sup> Transient acoustic pressure wave fields for both planar<sup>9</sup> and spherically focused<sup>10</sup> apertures can also be evaluated with the impulse responses of the respective transducers, where these impulse responses are written in terms of direct and edge waves. For cases with cylindrical symmetry, the 2-D integrals of spherical waves can be transformed to only 1-D integrals involving cylindrical waves.<sup>1</sup>

Although many of the existing techniques described above work well for specific transducer problems, there currently does not exist a method that is capable of efficiently handling the general model case of a nonuniform distribution of sources acting over a curved (spherical, cylindrical, etc.) aperture. The finite element method<sup>11</sup> can certainly handle such source and aperture complexities, but only by also discretizing the medium into which the transducer is radiating, a procedure that is computationally very costly.

Here, we will propose a new method, called the edge element method, that can model a wide variety of the NDE transducers used in practice and can treat both nonuniform source distributions and curved aperture shapes. The edge element approach is also capable of predicting the wave fields of transducers that are radiated through interfaces,<sup>2</sup> but

<sup>a)</sup>Currently at: Materials Reliability Division, National Institute of Standards and Technology, Boulder, CO 80303.

for this discussion, we will illustrate the method for cases where the transducer is radiating into a single medium. Like many of the previous methods,<sup>4</sup> the edge element method can be considered to be a form of a boundary element method. Unlike the standard boundary element approach, however, the edge element method deals only with integration of sources over the edges of surface elements. Thus the edge element method bears a strong similarity to the edge current models used in electromagnetic scattering problems.<sup>12</sup>

The basic concept of the edge element method can be described as follows: consider a model of a transducer as a set of sources (possibly nonuniform) acting over a planar or curved aperture. If one breaks the aperture into a number of planar facets or elements that are small enough so that the source distribution amplitude can be approximated as a constant over each element, then the wave field of the entire transducer can be calculated as a superposition of the wave fields of a large number of these planar, piston transducer elements. If these elements are also sufficiently small enough so that the far field (Fraunhofer) approximation is valid for the elements themselves, then the edge element method shows that the 2-D integrals over the areas of these elements can be transformed into 1-D line integrals around the edges of the elements using Stokes' theorem. Furthermore, if the edges of the elements are taken as straight line segments, the remaining 1-D integrals themselves can be performed exactly. The end result is that the transducer wave field can be evaluated by simply summing up a series of explicit contributions from a "web" of edges of the elements that make up the aperture surface. Adding together each edge element contribution for a given element results in the Fraunhofer contribution for that element, and adding all such element contributions in the aperture gives the total transducer wave field. We should note that although the Fraunhofer approximation is assumed for each element, the same approximation need not be valid for the transducer as a whole. The field points in the surrounding medium where wave-field values are calculated by the edge element method can be located in either the near or far field of the entire transducer. The facets or elements used to divide the transducer aperture in the edge element method can be arbitrary, and differently shaped and sized elements can be mixed into the discretization of the aperture. [See Fig. 1(a) and (b).]

The individual ingredients of the edge element method are not new. The idea of dividing the aperture into a series of smaller subdomains and summing each subdomain's contribution to give the total aperture's response has been exploited by a number of authors. Hopkins,<sup>13</sup> Ludwig,<sup>14</sup> and Stamnes *et al.*<sup>15</sup> each use different combinations of approximations for both the phase and amplitude terms of each element to arrive at explicit expressions for each element's contribution to the wave field. The techniques of Hopkins and Ludwig are somewhat restrictive since both assume a fixed shape for their elements (rectangular and square, respectively). The Stamnes technique overcomes this restriction by evaluating one of the integrations with his Stamnes-Spjelkavik-Pedersen (SSP) method, and evaluating the second integration with the more familiar Gauss-Legendre

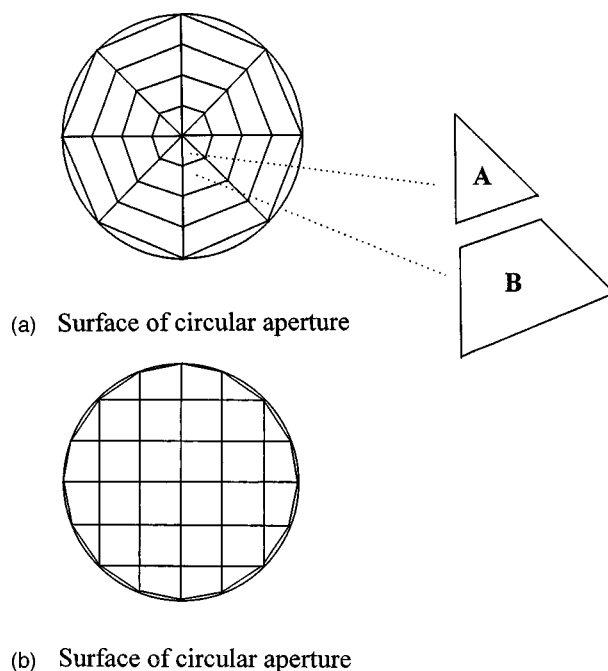


FIG. 1. (a) Simple discretization pattern of a planar, circular aperture utilizing differently shaped and sized elements, where the sum of the three edge contributions of element A represents the total contribution of element A to the radiated wave field. Likewise, the sum of the four edge contributions of element B represents its contribution to the radiated wave field. (b) More efficient discretization scheme for a planar, circular aperture.

method. See Stamnes<sup>4</sup> for computational speed and accuracy comparisons of these three techniques.

Likewise, the process that reduces the 2-D integrations over the element surface to 1-D integrals over the element edge is just an application of the same reduction process used previously in boundary diffraction wave models for entire transducers.<sup>6,7,9,16</sup> The explicit evaluation of the resulting 1-D edge integrals for straight line segments has also been used by Ganci<sup>17</sup> to evaluate the Fraunhofer radiation patterns of polygonal-shaped apertures. What is new in the edge element approach is the recognition that these reduction and evaluation steps can be generalized to nonrectangular elements in a coordinate invariant form that can then be used to construct the wave fields of general source distributions and curved aperture geometries. Although the edge element method involves very low order (i.e., constant) approximations for both the amplitude and geometry variations in each element, as a result of those approximations, no integrations need to be performed numerically so that the edge element field evaluation procedure is just a simple summation process over explicitly known terms, similar in spirit to some of the earlier techniques.<sup>13-15</sup>

In the following sections we will describe in detail the edge element approach and show its versatility and accuracy in calculating the wave fields for a variety of transducer geometries.

## I. TRANSDUCER BEAM MODELS

Consider an immersion setup where an ultrasonic transducer radiates into a fluid medium [Fig. 2(a)]. A commonly used ultrasonic beam model for this problem is the Rayleigh-

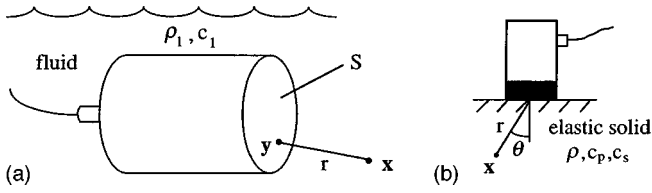


FIG. 2. (a) Baffled, planar transducer radiating into a fluid, and (b) contact, compressional wave transducer on a plane surface.

Sommerfeld integral,<sup>1</sup> which predicts the complete pressure wave field,  $p(\mathbf{x}, \omega)$ , at a point  $\mathbf{x}$  for a baffled planar piston transducer radiating at a frequency,  $\omega$ , into an infinite fluid of wave speed,  $c_1$ , as

$$p(\mathbf{x}, \omega) = \frac{-i\omega\rho_1 v_0}{2\pi} \int_S \frac{\exp(ikr)}{r} dS(\mathbf{y}), \quad (1)$$

where  $\rho_1$  is the density of the fluid,  $v_0$  is the (uniform) velocity on the face  $S$  of the transducer,  $k$  is the wave number, and  $r$  is the distance to  $\mathbf{x}$  from a general point,  $\mathbf{y}$ , on the transducer surface. The same model has been shown by O'Neil to approximate the radiation of a spherically focused piston transducer if the planar surface  $S$  is simply replaced in Eq. (1) by a curved spherical surface.<sup>3</sup> Recent studies<sup>18-20</sup> indicate that this approximation is indeed valid as long as the radiating surface is not too tightly focused. In fact, the model can be used for other types of focused transducers and aperture shapes if the surface,  $S$ , is chosen as the appropriate "active area" of the transducer.

Similar integral expressions also occur for a wide variety of problems of interest in NDE applications. For example, a high frequency model of a contact compressional wave transducer on the plane surface of a solid [Fig. 2(b)] gives, for the components of the displacement vector,  $\mathbf{u}(\mathbf{x}, \omega)$ , of the radiated bulk waves<sup>2</sup>

$$u_l(\mathbf{x}, \omega) = \frac{p_0}{\rho c_p^2} \int_S \frac{K_P(\theta) d_l^P \exp(ik_p r)}{r} dS + \frac{p_0}{\rho c_s^2} \int_S \frac{k_S(\theta) d_l^S \exp(ik_s r)}{r} dS, \quad (2)$$

where the transducer is modeled as a uniform pressure,  $p_0$ , acting on the surface area  $S$ ,  $c_\alpha$  ( $\alpha = P, S$ ) are the wave speeds of compressional and shear waves, and  $k_\alpha$  are the corresponding wave numbers,  $K_P(\theta)$  and  $K_S(\theta)$  are directivity functions for compressional and shear waves, respectively, and  $d_l^\alpha$  are components of the corresponding polarization vectors for a wave of type  $\alpha$  ( $\alpha = P, S$ ).

## II. THE EDGE ELEMENT APPROACH

The edge element method has been described in general terms in the Introduction. Here we will outline the method mathematically in more detail for problems described by models such as given in Eqs. (1) and (2). In both of these cases, the fields generated by the transducers can be represented as surface integrals of the form

$$I = \int_S f \exp(i\phi) dS, \quad (3)$$

where  $f$  is the given amplitude for a particular wave field and  $\exp(i\phi)$  is the corresponding phase term. Obtaining explicit values for these fields, therefore, requires some numerical procedure for evaluating such surface integrals.

The edge element method explicitly performs the 2-D integration, and thus retains the accuracy of that original equation by breaking up the transducer surface into  $M$  planar elements,  $\Delta S_m$  ( $m = 1, \dots, M$ ), over each of which  $f$  can be considered to be a constant. The phase term  $\exp(i\phi)$  is expanded only to first order in each element, i.e.,

$$\phi \cong \phi_{0m} + \mathbf{C}_{0m} \cdot \mathbf{y}', \quad (4)$$

where  $\mathbf{C}_{0m}$  is a constant, so that Eq. (3) becomes

$$I = \sum_{m=1}^M f_{0m} \exp(i\phi_{0m}) \int_{\Delta S_m} \exp[i(\mathbf{C}_{0m} \cdot \mathbf{y}')] dS(\mathbf{y}'). \quad (5)$$

Then, through the use of Stokes' theorem each of the surface integrals over these elements can be reduced to a line integral around the edge,  $\Delta C_m$ , of the element to give

$$I = \sum_{m=1}^M f_{0m} \exp(i\phi_{0m}) g_{0m} \int_{\Delta C_m} \exp[i(\mathbf{C}_{0m} \cdot \mathbf{y}')] dC, \quad (6)$$

where  $g_{0m}$  are known functions. However, if the edge of the element is taken as a series of  $C$  straight lines (for triangular elements  $C=3$ , etc.) the line integrals in Eq. (6) can be performed analytically, i.e.,

$$I_m \equiv \int_{\Delta C_m} \exp[i(\mathbf{C}_{0m} \cdot \mathbf{y}')] dC = \sum_{c=1}^C I_{mc}, \quad (7)$$

where the  $I_{mc}$  are known functions, and so Eq. (3) becomes, finally, an analytical sum of explicit terms given by

$$I = \sum_{m=1}^M \sum_{c=1}^C f_{0m} \exp(i\phi_{0m}) g_{0m} I_{mc}. \quad (8)$$

Since the sum in Eq. (8) is over a web of edges for all the elements used to approximate  $S$ , we have called this approach the method of edge elements. As mentioned previously, the edge element method can be considered to be the Fraunhofer approximation for a small, straight radiating edge segment and, in fact, if four such segments are combined together to form a small rectangular area element, one simply recovers the well-known Fraunhofer diffraction result for a rectangular transducer, as will be shown shortly. It should be noted that the edge element method is numerically a very simple model. Generalization to higher order expansions of both  $f$  and  $\phi$  are possible, as Roberts<sup>21</sup> has shown.

This edge element method can be used to evaluate the surface integrals appearing in the problems described previously and many others,<sup>2</sup> but here we will illustrate the method explicitly by considering only Eq. (1) for different types of transducers radiating into a fluid. To demonstrate the basic accuracy of the edge element approach, we will first show that the edge element solution for a spherically focused probe in a fluid is essentially indistinguishable from an exact solution to this problem based on a boundary diffraction wave formulation.<sup>16</sup> Then, examples will be given

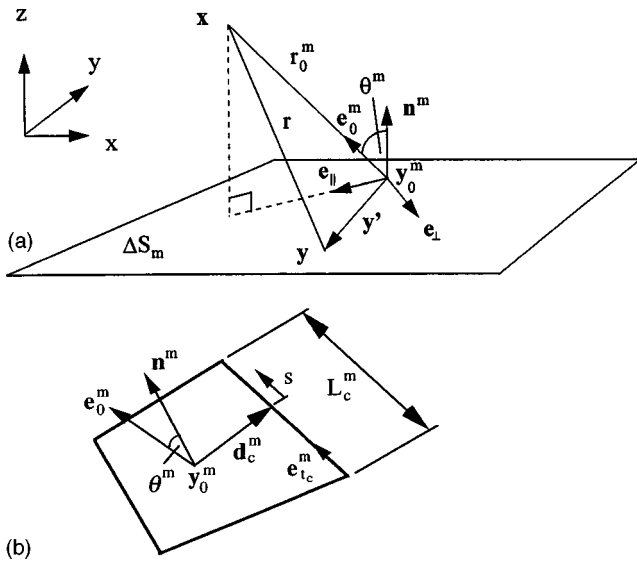


FIG. 3. (a) Small, planar area element geometry, and (b) geometry associated with an edge of a planar area element.

where edge elements are used to calculate the incident wave fields of some noncircular transducer apertures, i.e., rectangular and elliptical, with unfocused and cylindrically focused surface curvatures.

### III. AN EDGE ELEMENT MODEL

Consider a small planar element,  $\Delta S_m$ , of a transducer surface (which could be planar or curved), as shown in Fig. 3(a). If the distance  $r$  from point  $\mathbf{x}$  to  $\mathbf{y}$  is approximated, to first order, in terms of the ray from  $\mathbf{x}$  to a fixed point  $\mathbf{y}_0^m$  in  $\Delta S_m$  then we have

$$r \cong r_0^m - \mathbf{e}_0^m \cdot \mathbf{y}', \quad (9)$$

where  $\mathbf{y}' = \mathbf{y} - \mathbf{y}_0^m$  and  $\mathbf{e}_0^m$  is a unit vector for the element going from  $\mathbf{y}_0^m$  to  $\mathbf{x}$ . If the total surface,  $S$ , is broken up into  $M$  such elements, Eq. (1) then becomes

$$p(\mathbf{x}, \omega) = \frac{-i\omega\rho\nu_0}{2\pi} \sum_{m=1}^M \frac{\exp(ikr_0^m)}{r_0^m} \times \int_{\Delta S_m} \exp(-ik\mathbf{e}_0^m \cdot \mathbf{y}') dS(\mathbf{y}'). \quad (10)$$

To turn the surface integral into an integral around the element edge we note that

$$\exp(-ik\mathbf{e}_0^m \cdot \mathbf{y}') = \mathbf{n}^m \cdot [\nabla' \times \mathbf{g}^m(\mathbf{y}')], \quad (11)$$

where  $\mathbf{n}^m$  is the unit normal to the element and

$$\mathbf{g}^m(\mathbf{y}') = \frac{(\mathbf{n}^m \times \mathbf{e}_0^m) \exp[-ik(\mathbf{e}_0^m \cdot \mathbf{y}')] }{-ik[1 - (\mathbf{n}^m \cdot \mathbf{e}_0^m)^2]} \quad (12)$$

so that a direct application of Stokes' theorem gives

$$p(\mathbf{x}, \omega) = \frac{\rho c \nu_0}{2\pi} \sum_{m=1}^M \frac{\exp(ikr_0^m)}{r_0^m} I_m, \quad (13)$$

where

$$I_m = \frac{(\mathbf{n}^m \times \mathbf{e}_0^m)}{[1 - (\mathbf{n}^m \cdot \mathbf{e}_0^m)^2]} \cdot \int_{\Delta C_m} \exp(-ik\mathbf{e}_0^m \cdot \mathbf{y}') ds \quad (14)$$

is a line integral around the edge,  $\Delta C_m$ , of the element. As mentioned previously,  $I_m$  can be performed analytically if we assume the edges of the element are straight. To see this, consider the geometry of a typical element shown in Fig. 3(a). The form of the integrand in Eq. (14) can be simplified since:

$$\mathbf{n}^m \times \mathbf{e}_0^m = \sin \theta^m \mathbf{e}_\perp^m, \quad (15)$$

$$\mathbf{e}_0^m = \sin \theta^m \mathbf{e}_\parallel^m + \cos \theta^m \mathbf{n}^m, \quad (16)$$

$$\mathbf{e}_0^m \cdot \mathbf{y}' = \sin \theta^m \mathbf{e}_\parallel^m \cdot \mathbf{y}', \quad (17)$$

$$1 - (\mathbf{n}^m \cdot \mathbf{e}_0^m)^2 = 1 - \cos^2 \theta^m = \sin^2 \theta^m, \quad (18)$$

where, as shown in Fig. 3(a),  $\theta^m$  is the angle measured between the element normal,  $\mathbf{n}^m$ , and the unit vector,  $\mathbf{e}_0^m$ , pointing in the  $r_0^m$  direction,  $\mathbf{e}_\parallel^m$  is the unit vector along the projection of  $\mathbf{e}_0^m$  onto the area element,  $\mathbf{e}_\perp^m$  is the unit vector perpendicular to  $\mathbf{e}_\parallel^m$  on the transducer surface as defined by Eq. (15). The line integral,  $I_m$ , now becomes:

$$I_m = \frac{1}{\sin \theta^m} \int_{\Delta C_m} \exp[-ik \sin \theta^m (\mathbf{e}_\parallel^m \cdot \mathbf{y}')] \mathbf{e}_\perp^m \cdot ds. \quad (19)$$

For straight line elements [see Fig. 3(b)]:

$$\mathbf{y}' = \mathbf{d}_c^m + s \mathbf{e}_{t_c}^m, \quad \mathbf{L}_c^m = L_c^m \mathbf{e}_{t_c}^m, \quad (20)$$

where  $\mathbf{d}_c^m$  extends from  $\mathbf{y}_0^m$  to the centroid of the line element,  $s$  is a distance from this centroid along the line element in the direction of the unit vector,  $\mathbf{e}_{t_c}^m$ , and  $L_c^m$  is the total length of the line element. By changing the variable of integration to  $\eta = s/L_c^m$  and writing  $\mathbf{y}'$  in terms of the sum above, the integral in Eq. (19) reduces to:

$$\int_{\Delta C_m} \exp[-ik \sin \theta^m (\mathbf{e}_\parallel^m \cdot \mathbf{y}')] \mathbf{e}_\perp^m \cdot ds = \sum_{c=1}^C \left\{ L_c^m (\mathbf{e}_\perp^m \cdot \mathbf{e}_{t_c}^m) \exp[-ik \sin \theta^m (\mathbf{e}_\parallel^m \cdot \mathbf{d}_c^m)] \times \int_{-1/2}^{1/2} \exp[-ik L_c^m \sin \theta^m (\mathbf{e}_\parallel^m \cdot \mathbf{e}_{t_c}^m) \eta] d\eta \right\}, \quad (21)$$

where  $C$  is the total number of line segments enclosing an area element and the remaining integral can be evaluated explicitly. Thus we find an explicit form for the pressure wave field of the probe given by

$$p(\mathbf{x}, \omega) = \frac{\rho c \nu_0}{2\pi} \sum_{m=1}^M \sum_{c=1}^C \frac{\exp(ikr_0^m)}{r_0^m} I_{mc}, \quad (22)$$

where

$$I_{mc} = \frac{(\mathbf{n}^m \times \mathbf{e}_0^m) \cdot \mathbf{L}_c^m}{\sin^2 \theta^m} \exp[-ik \sin \theta^m (\mathbf{e}_\parallel^m \cdot \mathbf{d}_c^m)] \times \frac{\sin[k \sin \theta^m (\mathbf{e}_\parallel^m \cdot \mathbf{L}_c^m)/2]}{[k \sin \theta^m (\mathbf{e}_\parallel^m \cdot \mathbf{L}_c^m)/2]}. \quad (23)$$

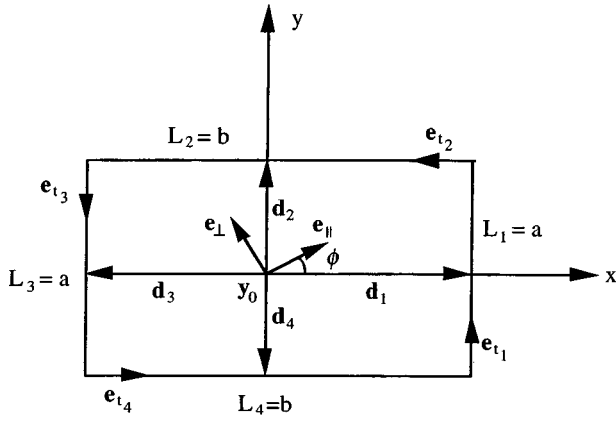


FIG. 4. Geometry associated with a single area element which represents the rectangular transducer surface.

Because of the  $\sin \theta^m$  terms in the denominator of  $I_{mc}$ , there is an apparent singularity in Eq. (23). However, as  $\theta^m \rightarrow 0$ ,

$$I_{mc} \cong \frac{\mathbf{e}_{\perp}^m \cdot \mathbf{L}_c^m}{\theta^m} - ik(\mathbf{e}_{\perp}^m \cdot \mathbf{L}_c^m)(\mathbf{e}_{\parallel}^m \cdot \mathbf{d}_c^m) + O(\theta^m), \quad (24)$$

so in adding up all such  $I_{mc}$ 's for a particular area element

$$\sum_{c=1}^C I_{mc} \cong \frac{\mathbf{e}_{\perp}^m}{\theta^m} \cdot \left\{ \sum_{c=1}^C \mathbf{L}_c^m \right\} - ik \left\{ \sum_{c=1}^C (\mathbf{e}_{\perp}^m \cdot \mathbf{L}_c^m)(\mathbf{e}_{\parallel}^m \cdot \mathbf{d}_c^m) \right\} + O(\theta^m). \quad (25)$$

The first term in brackets in Eq. (25) vanishes identically, removing the apparent singularity, and the second term in brackets can be shown to be just the area,  $\Delta S_m$ , of the  $m$ th planar element so that there is always a finite limit given by

$$\lim_{\theta^m \rightarrow 0} \sum_{c=1}^C I_{mc} = -ik \Delta S_m. \quad (26)$$

Ganci<sup>17</sup> had given expressions similar to Eq. (23) for a polygonal shaped aperture. However, Ganci's results were for a particular choice of coordinate system, while Eq. (23) is written in a more convenient coordinate independent form.

#### IV. FRAUNHOFER EXPRESSION FOR A RECTANGULAR TRANSDUCER

To connect the edge element approach with something that is considerably more familiar, consider a single rectangular element representing a transducer radiating into a fluid as shown in Fig. 4. Since we are working only with a single element, for clarity we will henceforth remove all the  $m$  superscripts in this section. For this small, rectangular transducer, Eqs. (22) and (23) give

$$p(\mathbf{x}, \omega) = \frac{\rho c v_0 \exp[ikr_0]}{2\pi r_0} \sum_{c=1}^4 \left\{ \frac{(\mathbf{n} \times \mathbf{e}_0) \cdot \mathbf{L}_c}{\sin^2 \theta} \times \exp[-ik \sin \theta (\mathbf{e}_{\parallel} \cdot \mathbf{d}_c)] \times \frac{\sin[k \sin \theta (\mathbf{e}_{\parallel} \cdot \mathbf{L}_c)/2]}{[k \sin \theta (\mathbf{e}_{\parallel} \cdot \mathbf{L}_c)/2]} \right\}. \quad (27)$$

We now focus on the sum of edge contributions for this element. Figure 4 shows the geometry of a rectangular transducer with edge lengths  $a$  and  $b$ . The dot products and cross products terms residing in the finite sum for edge elements 1 and 3 can be simplified to

$$\begin{aligned} \frac{(\mathbf{n} \times \mathbf{e}_0) \cdot \mathbf{L}_1}{\sin^2 \theta} &= \frac{\mathbf{e}_{\perp} \cdot \mathbf{L}_1}{\sin \theta} = \frac{a \cos \phi}{\sin \theta}, \\ \frac{(\mathbf{n} \times \mathbf{e}_0) \cdot \mathbf{L}_3}{\sin^2 \theta} &= \frac{\mathbf{e}_{\perp} \cdot \mathbf{L}_3}{\sin \theta} = \frac{-a \cos \phi}{\sin \theta}, \\ \mathbf{e}_{\parallel} \cdot \mathbf{L}_1 &= a \sin \phi, \quad \mathbf{e}_{\parallel} \cdot \mathbf{L}_3 = -a \sin \phi, \\ \mathbf{e}_{\parallel} \cdot \mathbf{d}_1 &= \frac{b}{2} \cos \phi, \quad \mathbf{e}_{\parallel} \cdot \mathbf{d}_3 = -\frac{b}{2} \cos \phi. \end{aligned} \quad (28)$$

Substituting these simplified terms into the finite sum expression of Eq. (27), the sum of edges 1 and 3 becomes:

$$\begin{aligned} I_1 + I_3 &= \frac{a \cos \phi \sin[A]}{\sin \theta [A]} \{ \exp[-ik(b/2) \sin \theta \cos \phi] \\ &\quad - \exp[ik(b/2) \sin \theta \cos \phi] \} \\ &= \frac{-2ia \cos \phi \sin[A]}{\sin \theta [A]} \sin[k(b/2) \sin \theta \cos \phi] \\ &= -ikab \cos^2 \phi \frac{\sin[A]}{[A]} \frac{\sin[B]}{[B]}, \end{aligned} \quad (29)$$

where

$$\begin{aligned} A &= k(a/2) \sin \theta \sin \phi, \\ B &= k(b/2) \sin \theta \cos \phi. \end{aligned} \quad (30)$$

Similar simplifications can be made for edges 2 and 4, and their sum becomes:

$$I_2 + I_4 = -ikab \sin^2 \phi \frac{\sin[A]}{[A]} \frac{\sin[B]}{[B]}. \quad (31)$$

If all four edge contributions are combined and placed into Eq. (27), we obtain the well known expression for the Fraunhofer diffraction limit of a rectangular transducer given by

$$p(\mathbf{x}, \omega) = \frac{-i\omega\rho v_0 ab \exp[ikr_0]}{2\pi r_0} \frac{\sin[A]}{[A]} \frac{\sin[B]}{[B]}. \quad (32)$$

#### V. VALIDATION OF THE EDGE ELEMENT MODEL

In this section, we will use edge elements to calculate the acoustic wave field radiated by a spherically focused transducer in a single fluid medium and compare this result to one that is found with an "exact" solution for this problem based on boundary diffraction waves.<sup>16</sup> The boundary diffraction wave (BDW) model simplifies the O'Neil surface integral for a spherically focused transducer by writing the O'Neil expression in terms of direct and edge waves. The incident pressure wave field for this particular model becomes:<sup>16</sup>

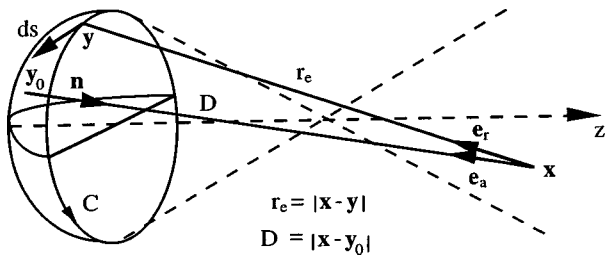


FIG. 5. The geometry associated with the boundary diffraction wave model for spherically focused transducers.

$$p(\mathbf{x}, \omega) = \frac{\rho c v_0}{q_0} \left[ \Theta \exp[ikD] - \frac{1}{2\pi} \int_C \frac{\exp[ikr_e]}{r_e} \frac{(\mathbf{e}_r \times \mathbf{e}_a) \cdot d\mathbf{s}}{[1 - (\mathbf{e}_r \cdot \mathbf{e}_a)^2]} \right], \quad (33)$$

where

$$q_0 = 1 - D/R_0, \quad (34)$$

$$\Theta = \begin{cases} 1, & \mathbf{x} \text{ inside the main beam} \\ 1/2, & \mathbf{x} \text{ on the beam edge} \\ 0, & \mathbf{x} \text{ outside the main beam} \end{cases} \quad (35)$$

and the various quantities appearing in Eq. (33) are shown in Fig. 5. This boundary diffraction wave model was chosen since it can be easily evaluated and thus used as a “standard” to test the edge element method.

The specific transducer modeled is a 1/2 in. (1.27 cm) diameter, 4 in. (10.16 cm) focal length, 5 MHz spherically focused probe, with an aperture angle of 3.6°. The incident pressure profiles are calculated in water ( $c_1 = 0.148$  cm/ $\mu$ s). For the three comparisons to be shown, the absolute magnitudes of the 5 MHz frequency component are displayed. The edge element model discretizes the transducer surface into 2048 area elements (32 radial divisions  $\times$  64 angular divisions), while the boundary diffraction wave model divides the rim of the transducer into 128 line elements for the edge wave computations. Figure 6 displays the on-axis profiles calculated by both methods. As can be seen, there are no amplitude differences between the two profiles. A cross-axis pressure profile was then taken at a distance of  $z = 10.5$  cm into the fluid medium (approximately the geo-

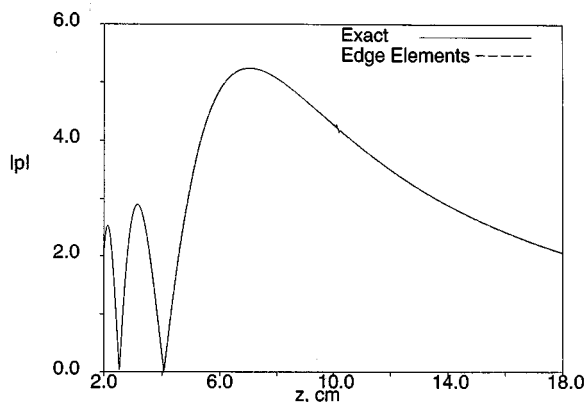


FIG. 6. The on-axis incident pressure profiles of a 1/2 in. diameter, 4 in. focal length, 5 MHz spherically focused probe.

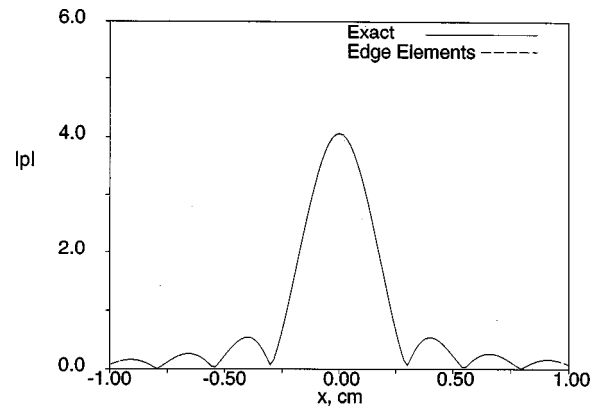


FIG. 7. The cross-axis incident pressure profiles at  $z = 10.5$  cm of a 1/2 in. diameter, 4 in. focal length, 5 MHz spherically focused probe.

metric focal length of the probe), and is displayed in Fig. 7. Again, no differences in amplitude between the two models can be seen. A second cross-axis profile was taken at a distance of  $z = 4.1$  cm into the fluid medium (approximately the last on-axis null preceding the true focus of the probe), and is displayed in Fig. 8. Only very minor differences between the relative depths of some of the nulls can be seen. Otherwise, the profiles closely agree in this case, which is well within the near field of the transducer. Based on these results and others (not shown), we conclude that the edge element model does an excellent job of predicting the full wave fields of spherically focused transducers. This same accuracy can also be expected for other problems provided that certain requirements are met. These requirements are discussed in the following section.

## VI. ACCURACY ISSUES OF THE EDGE ELEMENT MODEL

The accuracy of the wave fields predicted by the edge element model for a particular ultrasonic transducer is dependent upon a number of different geometrical and acoustical variables. These include the relative position of the field point (observation point) with respect to the transducer, the wave speed(s) of the surrounding medium, the frequency component of interest, and the size and shape of the transducer’s active area.

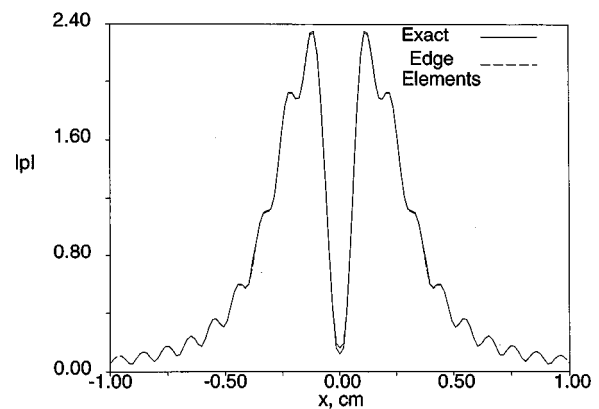


FIG. 8. The cross-axis incident pressure profiles at  $z = 4.1$  cm of a 1/2 in. diameter, 4 in. focal length, 5 MHz spherically focused probe.

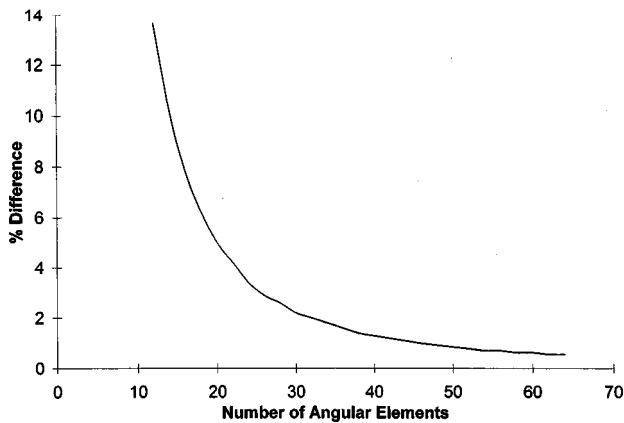


FIG. 9. The effect of increasing the size of elements used in the edge element technique. The boundary diffraction wave model prediction for this field point was used as the reference value.

Further complications arise from the fact that any number of different discretization methods can be applied to the transducer surface, each with differently shaped and sized area elements mixed together in different proportions. Obviously, for computational reasons, it is advantageous to reduce the total number of  $M$  elements representing the transducer surface to the lowest possible number. However, if too few elements are used, inaccuracies in the wave-field predictions will result, as illustrated in Fig. 9 for a single field point in the wave-field of a spherically focused probe radiating into water. In this case, a discretization method similar to the one shown in Fig. 1(a) is implemented, where the radial divisions are held constant at 24, and the angular divisions are varied. While a complete optimization algorithm that addresses these discretization issues has yet to be developed, there are some generalizations that can be made regarding this issue. As in the previous section, comparisons will be made with respect to wave-field values computed with the boundary diffraction wave model.

First, the number of  $M$  elements needed to attain a certain accuracy level is strongly dependent on the near-field length of the probe and surrounding medium, and the position of the field point with respect to the near-field length. Here, we take the near-field length to be defined as  $N = fa^2/c$ , where  $f$  is the transducer center frequency,  $a$  is the transducer radius, and  $c$  is the wave speed of the surrounding medium. For a given unfocused transducer (1/2 in. diameter, 5 MHz) radiating into water, the number of  $M$  elements required to attain a difference of 1% was recorded as the field point was moved to different on-axis locations in the wave field ( $z = N/3$  to  $z = 3N$ ). Only the sizes of the elements were varied; the shapes remained constant. We found that an approximately linear relationship seems to exist between the number of elements required and the position of the field point with respect to the near-field distance, i.e., a field point at  $z = N/3$  required three times as many elements as a field point at  $z = N$ , and a field point at  $z = 3N$  required only 1/3 as many elements as the field point at  $z = N$  (for the given accuracy level).

In another computational experiment, three different unfocused transducer-medium combinations were studied,

where each had the same near-field length. A 1/2 in. diameter, 5 MHz probe and a 1/4 in. diameter, 20 MHz probe, both radiating into water ( $c = 0.148 \text{ cm}/\mu\text{s}$ ), were studied along with a 1 in. diameter, 5 MHz probe radiating into steel ( $c = 0.592 \text{ cm}/\mu\text{s}$ ). In each case, 1344 elements (24 radial  $\times$  56 angular) were required to attain a difference of 0.5% for a field point on-axis and one near-field distance away from the transducer surface.

Recently, we have begun to use a combination of square, triangular, and quadrilateral shaped area elements in the discretization of the transducer aperture, as shown in Fig. 1(b). The bulk of the aperture is divided into square elements, while the remaining area surrounding the edge of the transducer surface is subdivided with a sparse number of triangular and quadrilateral elements. This particular discretization technique possesses two main advantages over the more conventional "spider web" technique shown in Fig. 1(a). First, the total number of elements needed to discretize the circular area of the transducer can be reduced significantly (approximately one order of magnitude) by making the size of the majority of the elements uniform. If a uniform velocity profile is assumed over the aperture plane, there is no need for a finer mesh near the center and a coarser mesh near the edges of the transducer surface, as occurs with the "spider web" technique. Second, by choosing a rectangular-type shape for the majority of the elements, the contributions from the four sides of those elements can be simultaneously evaluated using Eq. (32), further reducing the computational time needed to evaluate the predicted pressures in the wave field. The major drawback of this particular discretization method is that it becomes impractical to accurately mesh certain focused surfaces, such as a spherical or elliptical focus. In these cases and for more generally curved surfaces, the use of triangular elements is particularly convenient.

## VII. NONCIRCULAR TRANSDUCERS

Equation (22) is also directly applicable to transducers of noncircular planar and curved apertures if the elements lie on the appropriate surface area for these transducers. As long as the transducer surface area can be discretized into flat facets composed of straight edges, the edge element method can evaluate the transducer's incident wave field.

As an example, we can compare the incident wave fields radiated by rectangular shaped transducers with wave fields produced by elliptically shaped transducers of similar size. Both the rectangular and elliptical transducers can be unfocused or cylindrically focused as long as the appropriate changes are made to the area elements representing the transducer surface. While any portion of the incident wave field can be computed with the edge element technique, for our comparisons in this section we display values on a plane such as shown in Fig. 10, where the magnitude of the incident pressure was computed discretely at each point of a  $400 \times 400$  point grid to create a 2-D image.

We begin with the case of an unfocused rectangular transducer 1.0 cm long, 0.6 cm wide, and center frequency of 5 MHz radiating into water. Figure 11 shows a 2-D image of the absolute magnitudes of the incident wave field at a single frequency (in this case, 5 MHz). The transducer surface is

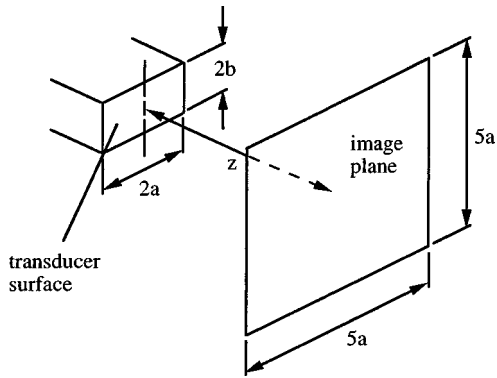


FIG. 10. Dimensions and orientation of the noncircular transducers (rectangular and elliptical) with respect to the image plane normal to the  $z$  axis.

6.75 cm ( $z$  distance in Fig. 10) away from the plane of the image, and centered about the midpoint of the image with its length parallel to the horizontal direction. The radiation pattern at this particular cross section in the wave field (which is located about one near-field distance from the transducer surface) resembles a well collimated beam with the peak magnitudes (darker shades) outlining the active transducer surface quite well. Figure 12 displays the absolute magnitudes of the incident wave field of the same transducer at the same frequency where the  $z$ -distance is now taken 27.0 cm (over 3 near-field distances) away from the transducer surface. The transducer remains oriented in the same way as the earlier figure, with its length parallel to the horizontal direction, but note that the beam is now spreading into an elliptical radiation pattern that has its major axis oriented in the vertical direction. These radiation patterns are not unexpected, since Krautkramer<sup>22</sup> has published very similar types of images previously. In both cases, the rectangular transducer surface was discretized into 240 ( $20 \times 12$ ) square area elements be-

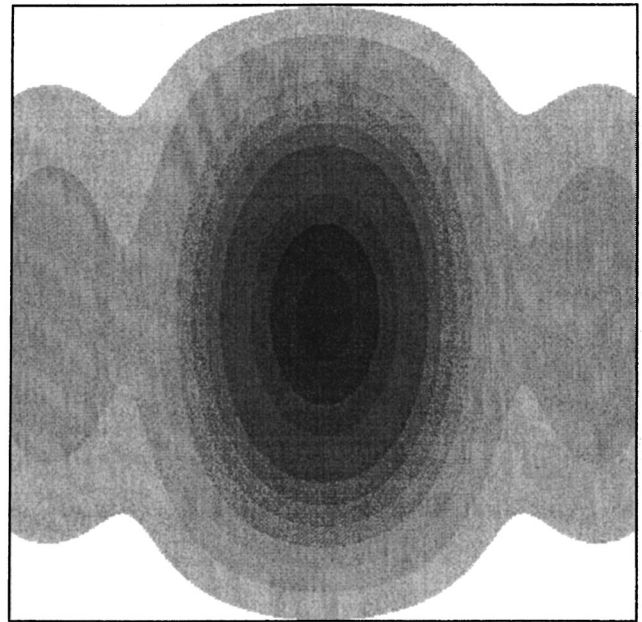


FIG. 12. 2-D image computed 27.0 cm from an unfocused rectangular transducer ( $a=0.5$  cm,  $b=0.3$  cm) with a center frequency of 5 MHz radiating into water.

fore each edge contribution of each area element was computed and summed.

If we look at the case of a cylindrically focused transducer of rectangular aperture (where the axis of symmetry for focusing runs perpendicular to the transducer's length), an entirely different wave-field structure is observed when compared to the unfocused case. Figure 13 shows a 2-D image taken a distance of 6.75 cm from the transducer surface where the transducer focal length is 25.4 cm. As expected, the effects of the focusing reduce the focal spot size in the horizontal direction, concentrating the ultrasonic en-

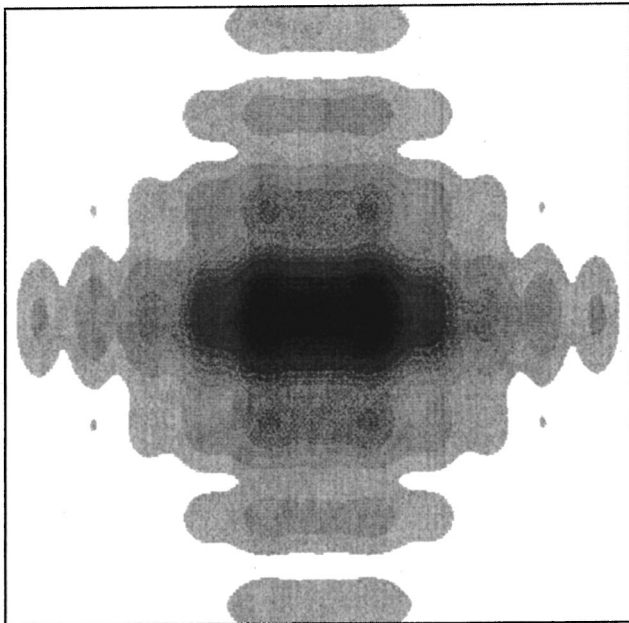


FIG. 11. 2-D image computed 6.75 cm from an unfocused rectangular transducer ( $a=0.5$  cm,  $b=0.3$  cm) with a center frequency of 5 MHz radiating into water.

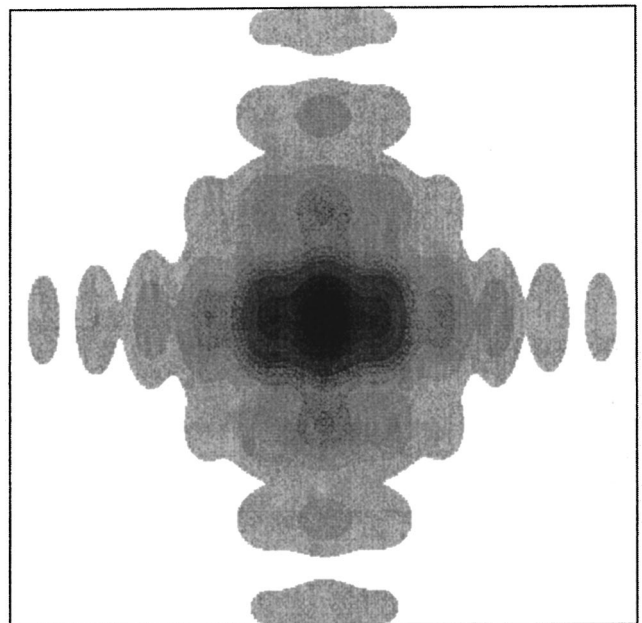


FIG. 13. 2-D image computed 6.75 cm from a cylindrically focused rectangular transducer ( $a=0.5$  cm,  $b=0.3$  cm,  $FL=25.4$  cm) with a center frequency of 5 MHz radiating into water.



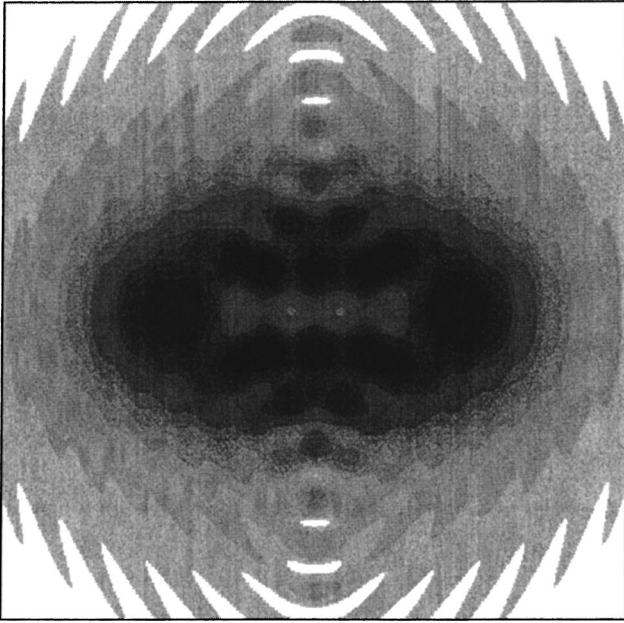


FIG. 14. 2-D image computed 6.75 cm from an unfocused elliptical transducer ( $a=0.5$  cm,  $b=0.3$  cm) with a center frequency of 5 MHz radiating into water.

ergy into a much smaller area when compared to the corresponding unfocused image. In this case, the transducer surface was also discretized using 240 ( $20 \times 12$ ) square area elements.

When the rectangular aperture is changed to an elliptical aperture, significant differences in the corresponding incident wave fields are observed. Figures 14 and 15 are the planar and focused elliptical counterparts of Figs. 11 and 13, where the major and minor axes of the elliptical probes are taken as 1.0 and 0.6 cm, respectively. The center frequency and  $z$  distance remain at 5 MHz and 6.75 cm, respectively. The

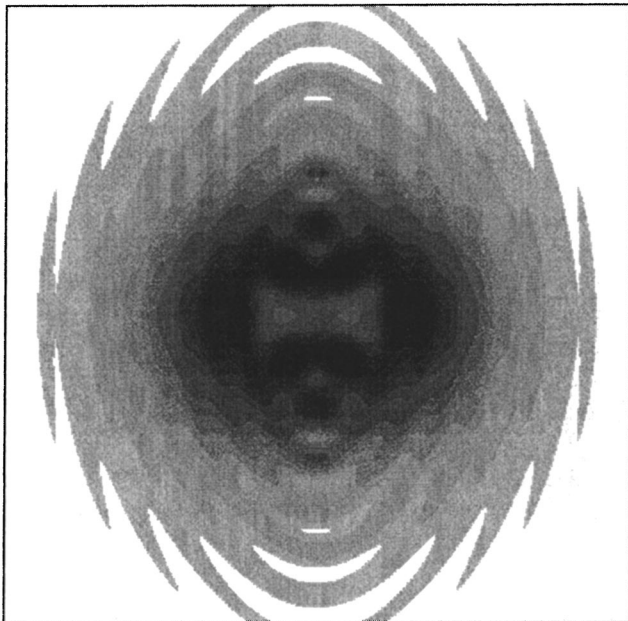


FIG. 15. 2-D image computed 6.75 cm from a cylindrically focused elliptical transducer ( $a=0.5$  cm,  $b=0.3$  cm,  $FL=25.4$  cm) with a center frequency of 5 MHz radiating into water.

focal length for the cylindrically focused case (Fig. 15) is 25.4 cm, which is the same length used in the focused rectangular probe case.

Figure 14 displays a rather structured radiation pattern for the unfocused elliptical probe, characterized by the elliptical outline of the transducer aperture. Note the peak absolute magnitudes form an elliptical ring around the central axis of the transducer, which is not unexpected when the image plane is taken close to the transducer surface. When the transducer surface becomes cylindrically focused, the resulting wave field shown in Fig. 15 behaves similarly to that observed for the rectangular case. The focal region is reduced and concentrated in the horizontal direction when compared with its elliptical, unfocused counterpart shown in Fig. 14. Both transducer surfaces were divided into 864 ( $16$  radial  $\times$   $54$  angular divisions) area elements of triangular and quadrilateral shapes.

## VIII. SUMMARY

We have introduced a new edge element approach that can be used to numerically evaluate the entire radiated wave fields of ultrasonic transducers. In general, edge elements avoid a computationally expensive and difficult to generalize 2-D numerical integration by making a linear approximation to the phase term of the integrand and employing Stokes' theorem to reduce the surface integration to an edge or line integration. The linear phase approximation further allows one to explicitly evaluate the line integrals, leading to analytical expressions that can be evaluated rapidly. When comparing the computational speed of the edge element technique to the 2-D numerical integration techniques we have examined, the edge element technique is typically five times faster and much more versatile. The possibility of making higher order approximations to the phase and amplitude terms of the integrand certainly exists, which would reduce the total number of  $M$  subdomains needed to sufficiently divide the transducer surface and be evaluated to predict the transducer's wave field. However, since these higher order approximations would entail the evaluation of more complex formulas for each element, it is presently unclear whether any increase in computational efficiency would in fact be gained.

Numerical validation of the edge element model was performed by examining the incident wave fields radiated into water by a spherically focused transducer. Excellent agreement was found between the edge element expression and the boundary diffraction wave model throughout the wave field of the spherically focused probe.

Work in progress includes applying edge elements to a wide range of other problems, such as predicting incident wave fields for transducers radiating with nonpiston behavior and evaluating wave fields through interfaces of planar and general curvature. Predicting the shape and amplitude of a time waveform response at any spatial point in the wave field is possible by repeating the evaluation technique for a number of discrete frequency components, taking the resulting spectrum, and applying an inverse FFT algorithm to it. Estimating diffraction corrections for transducers such as electromagnetic acoustic transducers (EMATs) is also possible,

as long as accurate estimation of the incident pressure profile produced by the EMAT on the surface of the material being inspected can be made.

## ACKNOWLEDGMENTS

L. W. Schmerr and T. P. Lerch were supported in this work by the Center for NDE, at Iowa State University. A. Sedov was supported by the Natural Sciences and Engineering Research Council of Canada.

- <sup>1</sup>G. R. Harris, "Review of transient field theory for a baffled planar piston," *J. Acoust. Soc. Am.* **70**, 10–20 (1981).
- <sup>2</sup>T. P. Lerch, "Ultrasonic transducer characterization and transducer beam modeling for applications in nondestructive evaluation," Ph.D. dissertation, Iowa State University, 1996.
- <sup>3</sup>H. T. O'Neil, "Theory of focusing radiators," *J. Acoust. Soc. Am.* **21**, 516–526 (1949).
- <sup>4</sup>J. J. Stamnes, *Waves in Focal Regions* (Hilger, Boston, MA, 1986).
- <sup>5</sup>B. P. Newberry and R. B. Thompson, "A paraxial theory for the propagation of ultrasonic beams in anisotropic solids," *J. Acoust. Soc. Am.* **85**, 2290–2300 (1989).
- <sup>6</sup>A. Schoch, "Betrachtungen über das schallfeld einer kolbenmembran," *Akust. Zh.* **6**, 318–326 (1941).
- <sup>7</sup>E. W. Marchand and E. Wolf, "Boundary diffraction wave in the domain of the Rayleigh-Kirchhoff diffraction theory," *J. Opt. Soc. Am.* **52**, 761–767 (1962).
- <sup>8</sup>J. A. Archer-Hall and D. Gee, "A single integral computer method for axisymmetric transducers with various boundary conditions," *NDT Int.: The Independent Journal of Non-Destructive Testing* **13**(3), 95–101 (1980).
- <sup>9</sup>P. R. Stepanishen, "Transient radiation from pistons in an infinite planar baffle," *J. Acoust. Soc. Am.* **49**, 1629–1638 (1971).
- <sup>10</sup>A. Penttinen and M. Luukkala, "The impulse response and pressure nearfield of a curved ultrasonic radiator," *J. Phys. D* **9**, 1547–1557 (1976).
- <sup>11</sup>T. Xue, W. Lord, S. Udpa, L. Udpa, and M. Mina, "Finite element modeling of transient wave phenomena at solid/fluid interfaces," *Review of Progress in ONDE*, edited by D. O. Thompson and D. E. Chimenti (Plenum, New York, 1996), Vol. 15A, pp. 299–306.
- <sup>12</sup>A. L. Maffett, *Topics for Statistical Description of Radar Cross Section* (Wiley, New York, 1989).
- <sup>13</sup>H. H. Hopkins, "The numerical evaluation of the frequency response of optical systems," *Proc. Phys. Soc. London, Sect. B* **70**, 1002–1005 (1957).
- <sup>14</sup>A. C. Ludwig, "Computation of radiation patterns involving numerical double integration," *IEEE Trans. Antennas Propag.* **AP-16**, 767–769 (1968).
- <sup>15</sup>J. J. Stamnes, B. Spjelkavik, and H. M. Pedersen, "Evaluation of diffraction integrals using local phase and amplitude approximations," *Opt. Acta* **30**, 207–222 (1983).
- <sup>16</sup>L. W. Schmerr, A. Sedov, and T. P. Lerch, "A boundary diffraction wave model for a spherically focused ultrasonic transducer," *J. Acoust. Soc. Am.* **101**, 1269–1277 (1997).
- <sup>17</sup>S. Ganci, "Simple derivation of formulas for Fraunhofer diffraction at polygonal apertures from Maggi-Rubinowicz transformation," *J. Opt. Soc. Am. A* **1**, 559–561 (1984).
- <sup>18</sup>M. F. Hamilton, "Comparison of three transient solutions for the axial pressure in a focused sound beam," *J. Acoust. Soc. Am.* **92**, 527–532 (1992).
- <sup>19</sup>F. Coulouvrat, "Continuous field radiated by a geometrically focused transducer: Numerical investigation and comparison with an approximate model," *J. Acoust. Soc. Am.* **94**, 1663–1675 (1993).
- <sup>20</sup>E. L. Madsen, M. M. Goodsitt, and J. A. Zagzebski, "Continuous waves generated by focused radiators," *J. Acoust. Soc. Am.* **70**, 1508–1517 (1981).
- <sup>21</sup>R. A. Roberts, "Aperture integral ultrasonic pulse transmission model," *Review of Progress in ONDE*, edited by D. O. Thompson and D. E. Chimenti (Plenum, New York, 1992), Vol. 11A, pp. 121–128.
- <sup>22</sup>J. Krautkramer and H. Krautkramer, *Ultrasonic Testing of Materials* (Springer-Verlag, Berlin, 1990).

# Forward projection of transient signals obtained from a fiber-optic pressure sensor

G. T. Clement, R. Liu, and S. V. Letcher

*Department of Physics, University of Rhode Island, Kingston, Rhode Island 02881*

P. R. Stepanishen

*Department of Ocean Engineering, University of Rhode Island, Kingston, Rhode Island 02881*

(Received 10 December 1996; accepted for publication 4 June 1998)

An analytical/experimental approach is presented to reconstruct the space–time pressure field in a plane and forward project the resultant space–time pressure field using tomographic and wave vector time-domain methods. Transient pressure signals from an underwater ultrasonic planar transducer are first measured using a line fiber-optic pressure sensor which is scanned across a plane at a fixed distance  $z_0$  from the transducer. The resulting spatial line integrals in the plane are time-dependent signals which are first used to reconstruct the space–time pressure field in the plane via simply implemented tomographic methods. These signals are then used to forward project the space–time pressure field to arbitrary planes employing a wave vector time-domain method. Verification of the method is first presented using synthetic signals and the impulse response approach. An experimental verification of the approach is then presented using an ultrasonic planar transducer. The results of the projected and experimental fields are compared at various distances for synthetic signals and experimental data. Good correlation is found between the calculated, projected, and experimental data. © 1998 Acoustical Society of America. [S0001-4966(98)04109-5]

PACS numbers: 43.20.Px, 43.38.Ar [JEG]

## INTRODUCTION

Several FFT algorithms have been developed that efficiently project harmonic pressure fields.<sup>1</sup> These approaches allow the time and space dependence of the acoustic pressure in a specific plane to be propagated closer to or away from a source. The use of these methods with experimental data offers a technique for global reproduction of a transducer's field from information obtained at a single plane. Experiments using these methods have been carried out, but have been limited to harmonic cases.<sup>2</sup>

In the present paper, we investigate the projection of radially symmetric acoustic space–time fields using FFT methods. The reconstruction and projection algorithm, similar to that used by Forbes *et al.*<sup>3</sup> for simulated space–time fields, is described in Sec. I. Our description optimizes the method for the particular case of axisymmetric field data obtained from an optical sensor. This symmetric field approximation is a reasonable assumption for a quality axisymmetric source and results in a significant savings in the required data and the computer reconstruction time. As a means of verifying the space–time projection algorithm, it is first applied to simulated fields in Sec. II. A previously developed impulse response method<sup>4</sup> is used to model acoustic fields from planar ultrasonic transducers that approximate those studied experimentally. Our approach is similar to our earlier studies<sup>3</sup> and is based on using the velocity of the front surface of the transducer to determine the space–time pressure field. An improved transducer model is incorporated into the present study that includes contributions from the back surface of the piezoceramic transducer.<sup>5,6</sup>

An experiment was performed to verify the use of the

space–time projection algorithm on real data obtained from a typical ultrasonic piezoelectric transducer. The experiment, described in Sec. III, consists of scanning an optical fiber along a plane parallel to the face of the transducer and obtaining an array of line integrals of the field in that plane. The space–time pressure field in the measurement plane is reconstructed from the fiber-optic measurements using tomographic methods. Fiber-optic imaging was chosen for its high sensitivity, minimal invasiveness, and its ability to easily measure a field in a fixed plane. The field data are then projected away from the measurement plane using the FFT-based method. Finally, the forward projected fields are compared with experimental data at various distances from the source in Sec. IV.

## I. RECONSTRUCTION AND PROJECTION ALGORITHM

Consider a general axisymmetric pressure field using the cylindrical coordinate system illustrated in Fig. 1, where  $p(\rho, z, t)$  denotes the space–time pressure that satisfies the usual linear wave equation, given by

$$\nabla^2 p(\rho, z, t) = \frac{1}{c^2} \frac{\partial^2 p(\rho, z, t)}{\partial t^2}. \quad (1)$$

The forward projection problem of interest is defined here as mapping the field information in a reference plane,  $p(\rho, z_0, t)$ , into another plane,  $p(\rho, z, t)$  for  $z > z_0$ .

The Hankel transform pair for the pressure is first introduced as

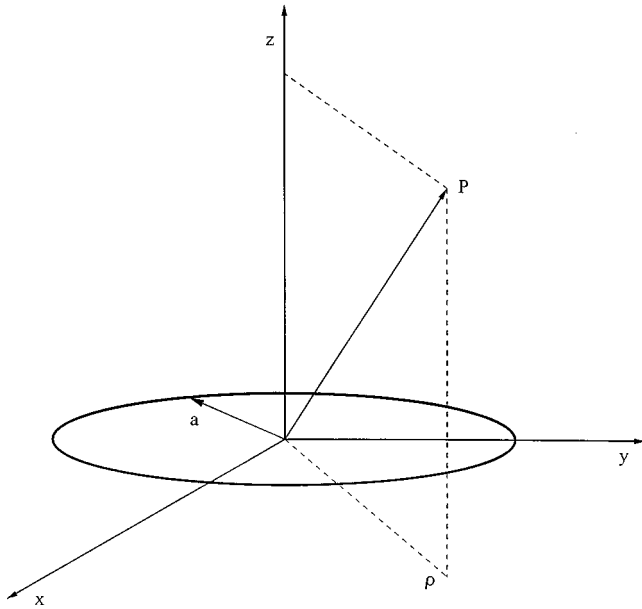


FIG. 1. Circular piston in a planar baffle.

$$P(k, z, t) = \int_0^\infty p(\rho, z, t) J_0(k\rho) \rho \, d\rho, \quad (2)$$

$$p(\rho, z, t) = \int_0^\infty P(k, z, t) J_0(k\rho) k \, dk,$$

and then the following Fourier transform pair is defined:

$$\hat{P}(k, z, \omega) = \int_{-\infty}^\infty P(k, z, t) e^{-i\omega t} \, dt, \quad (3)$$

$$P(k, z, t) = \frac{1}{2\pi} \int_{-\infty}^\infty \hat{P}(k, z, \omega) e^{i\omega t} \, d\omega.$$

The transform  $P(k, z, t)$  is in a wave vector time-space whereas  $\hat{P}(k, z, \omega)$  is in a wave vector frequency space. Ob-

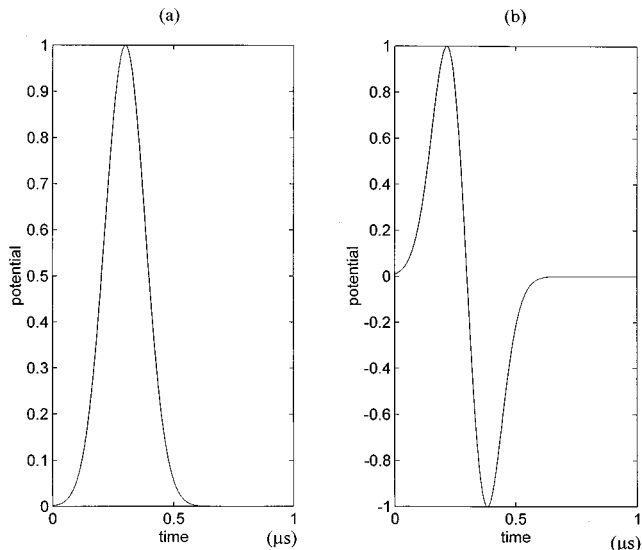


FIG. 2. Driving signal of the field. (a) Voltage applied to transducer. (b) Velocity of transducer face versus time.

viously both transforms can be combined but are separated here for later convenience.

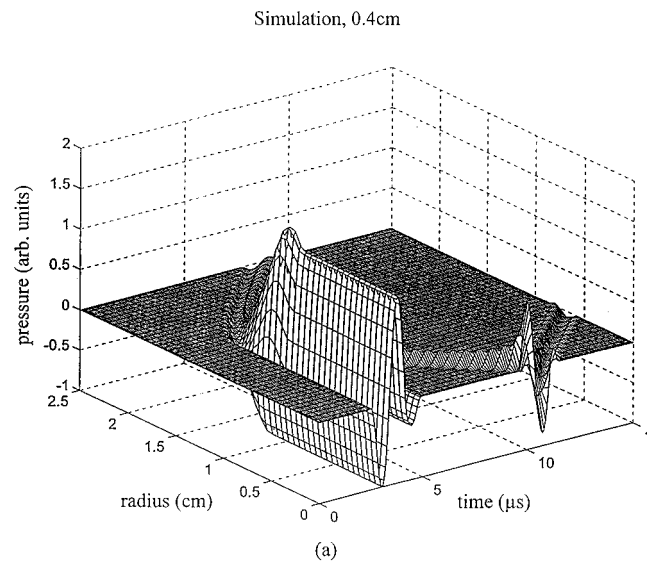
Before continuing to the forward projection problem, it is first noted that  $P(k, z_0, t)$  can also be evaluated in an indirect manner without an *a priori* knowledge of  $p(\rho, z_0, t)$ . To this end, the projection of the pressure field along the *y*-direction in Cartesian coordinates in the plane  $z = z_0$  is introduced as follows:

$$g(x, z_0, t) = \int_{-\infty}^\infty p(x, y, z_0, t) \, dy. \quad (4)$$

The Fourier transform of  $g(x, z_0, t)$  with respect to *x* is then defined as

$$\tilde{g}(k, z_0, t) = \int_{-\infty}^\infty g(x, z_0, t) e^{-ikx} \, dx. \quad (5)$$

Finally, it is noted from the projection-slice theorem of Fourier transforms that



Projection of Simulation: 0.4cm to 0.4cm

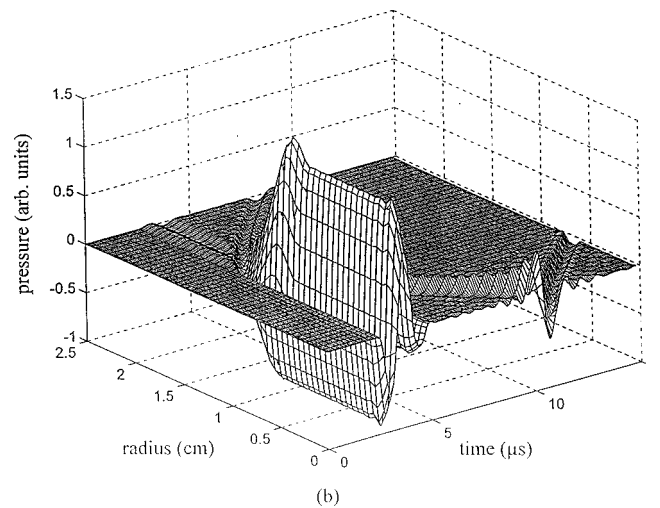


FIG. 3. Pressure field in the plane  $z = 0.4$  cm from the source. (a) Impulse response calculation as a function of radial position and time. (b) Projection from 4 mm onto itself as a function of radial position and time.

$$P(k, z_0, t) = \frac{\tilde{g}(k, z_0, t)}{2\pi}. \quad (6)$$

Although  $p(\rho, z_0, t)$  can be reconstructed from  $P(k, z_0, t)$  via the use of Eq. (2), the forward projection of the field can be accomplished directly from  $P(k, z_0, t)$  as shown in the following development.

Consider now the forward projection problem of mapping the field information in the reference plane,  $p(\rho, z_0, t)$ , into  $p(\rho, z, t)$  for  $z > z_0$ . From the Fourier–Hankel transform of Eq. (1), it is easily shown that:

$$\frac{d^2}{dz^2} \hat{P}(k, z, \omega) + \left( \frac{\omega^2}{c^2} - k^2 \right) \hat{P}(k, z, \omega) = 0. \quad (7)$$

Now Eq. (7) has the following solution for the forward projection problem:

$$\hat{P}(k, z, \omega) = \hat{P}(k, z_0, \omega) e^{-i\sqrt{\omega^2/c^2 - k^2}(z - z_0)}, \quad (8)$$

where  $\hat{P}(k, z_0, \omega)$  is to be determined. But  $\hat{P}(k, z_0, \omega)$  can be readily obtained either from the field at  $z_0$  and Eqs. (2) and (3), in which case it is given by

$$\hat{P}(k, z_0, \omega) = \int_0^\infty \int_0^\infty p(\rho, z_0, t) J_0(k\rho) e^{i\omega t} \rho \, d\rho \, dt$$

or from the lateral projection of the field and Eqs. (3) and (6), in which case it is given by

$$\hat{P}(k, z_0, \omega) = \frac{1}{2\pi} \int_{-\infty}^\infty \tilde{g}(k, z_0, t) e^{i\omega t} \, dt. \quad (9)$$

Finally, from Eqs. (2), (3), and (8), the field at  $z$  can be expressed as

$$p(\rho, z, t) = \frac{1}{2\pi} \int_0^\infty \int_{-\infty}^\infty \hat{P}(k, z_0, \omega) \times e^{-i(z - z_0)\sqrt{\omega^2/c^2 - k^2}} J_0(k\rho) e^{i\omega t} \, dk \, d\omega. \quad (10)$$

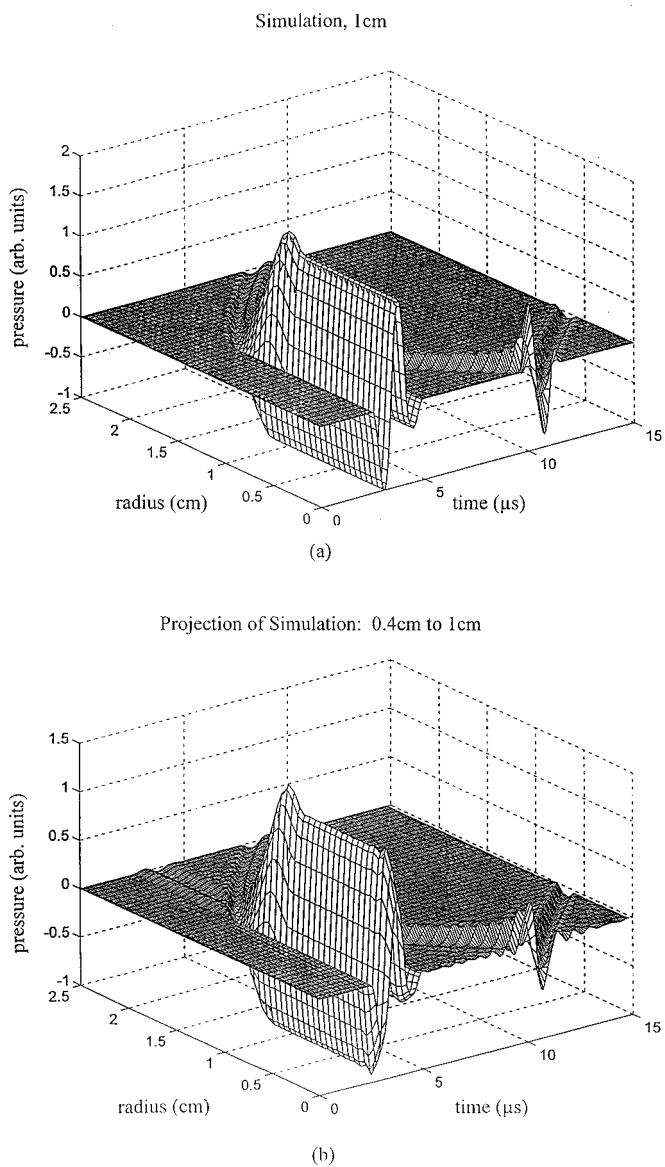


FIG. 4. Pressure field in the plane  $z=1$  cm from the source. (a) Impulse response calculation as a function of radial position and time. (b) Projection from 4 mm to 1 cm as a function of radial position and time.

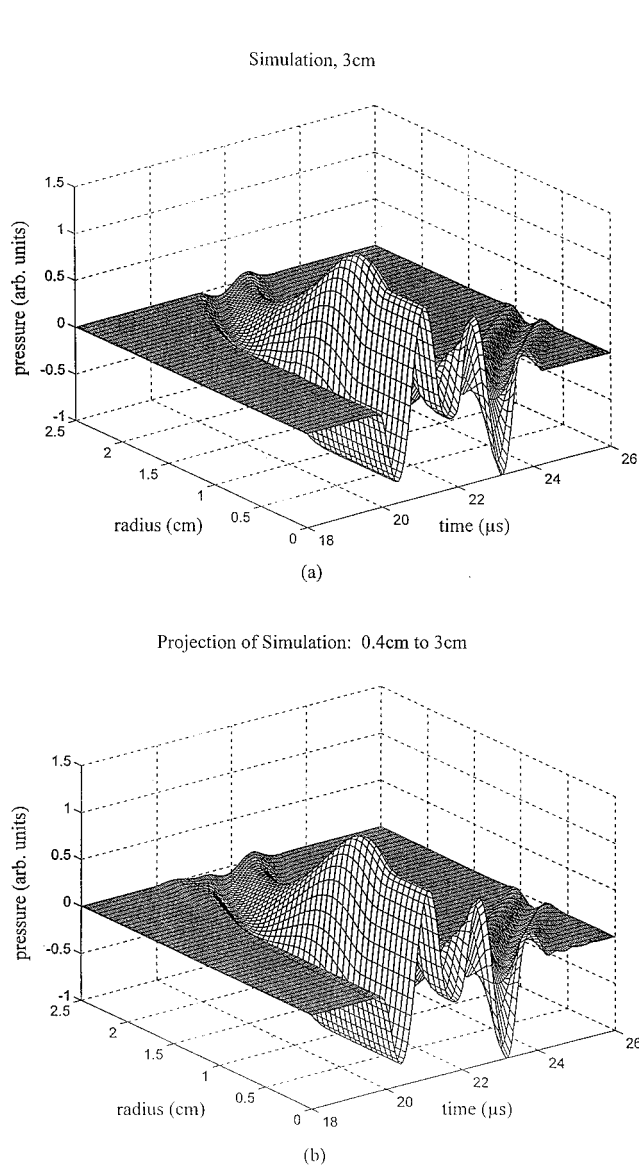


FIG. 5. Pressure field in the plane  $z=3$  cm from the source. (a) Impulse response calculation as a function of radial position and time. (b) Projection from 4 mm to 3 cm as a function of radial position and time.

## II. SIMULATED FIELD OF AN ULTRASONIC TRANSDUCER

Consider now the space-time pressure field which is generated by a circular piston-type ultrasonic transducer. It is well known that the pressure at a field point  $(\rho, z)$  may be expressed as the time derivative of the time convolution of the transducer velocity function  $v(t)$  and the impulse response function,  $h(\rho, z, t)$ ,<sup>4</sup> i.e.,

$$p(\rho, z, t) = \frac{\partial}{\partial t} [v(t) \otimes h(\rho, z, t)]. \quad (11)$$

The functional form of the impulse response function depends on whether the radial position of the field point is greater than or less than the size of the transducer.

For a circular transducer of interest, the impulse response function is given by<sup>4</sup>

$$h = \begin{cases} 0; & ct < z, \\ \rho c; & z < ct < \sqrt{z^2 + (a - \rho)^2}, \\ \frac{\rho_0 c}{\pi} \arccos\left(\frac{\rho^2 + (ct)^2 - a^2 - z^2}{2\rho\sqrt{(ct)^2 - z^2}}\right); & \sqrt{z^2 + (a - \rho)^2} < ct < \sqrt{z^2 + (a + \rho)^2}, \\ 0; & ct > \sqrt{z^2 + (a + \rho)^2}, \end{cases} \quad (12)$$

for  $\rho < a$  and by<sup>4</sup>

$$h = \begin{cases} 0; & ct < \sqrt{z^2 + (a - \rho)^2} \\ \frac{\rho_0 c}{\pi} \arccos\left(\frac{\rho^2 + (ct)^2 - a^2 - z^2}{2\rho\sqrt{(ct)^2 - z^2}}\right); & \sqrt{z^2 + (a - \rho)^2} < ct < \sqrt{z^2 + (a + \rho)^2} \\ 0; & ct > \sqrt{z^2 + (a + \rho)^2} \end{cases} \quad (13)$$

for  $\rho > a$ .

The impulse-response method was used to simulate acoustic fields from an ultrasonic transducer with the same excitation, dimensions, and characteristics as that used in the experiment described below. Since the velocity of the front surface of the transducer is required in Eq. (11),  $v(t)$  is approximated by starting with a Gaussian signal (full width at half maximum = 2  $\mu$ s) to represent the applied voltage. The initial velocity at the front surface of the transducer is then represented by the time derivative of the Gaussian. An additional contribution from the back surface of the piezoceramic is included by adding to the front surface velocity a function that has the same shape, but (i) is opposite in phase, (ii) is delayed by the time of flight from the back surface to the front, and (iii) is reduced in amplitude due to radiation into the backing of the piezoelectric disk.<sup>7</sup> Additional reverberation effects within the disk are neglected. The resultant piston velocity function that was used for the study is shown in Fig. 2(b).

A simulated field was calculated for the plane  $z = 0.4$  cm from the transducer face. This field was then propagated away from the source using the projection algorithm described in the previous section. Specifically, fields were constructed at planes 0.4, 1, 3, and 10 cm in front of the transducer. The projection to the plane at 0.4 cm is a forward

projection of 0 cm and is simply used to test the transform algorithms. Next, the impulse response method was used to calculate the field at each of the above distances. The projected and modeled fields are presented in Figs. 3–6 for the initial  $z$ -value and the four planes of projection. Except for the artifact at early  $t$  values for large  $r$  when the projection distance is short, the projected and calculated fields match very well.

Direct comparisons of the on-axis and  $r = a$  slices of the simulated and projected data are presented in Figs. 7 and 8. The on-axis plots reveal slight oscillations in the projected data for the planes close to the transducer. The edge wave amplitude is also slightly smaller in the projected data. The causes of these discrepancies are discussed below. For planes further away from the transducer and for the slice at  $r = a$  the simulated and projected fields agree closely throughout.

As a means of evaluating the effectiveness of our projection algorithm, a quantitative comparison was made between the simulated data and the corresponding projections. An rms measurement of discrepancy between the two was obtained for each distance away from the piston using the quotient

$$\left[ \frac{\sum_{i,j}^{M,N} (p_{ij} - p'_{ij})^2}{\sum_{i,j}^{M,N} (p_{ij})^2} \right]^{1/2}, \quad (14)$$

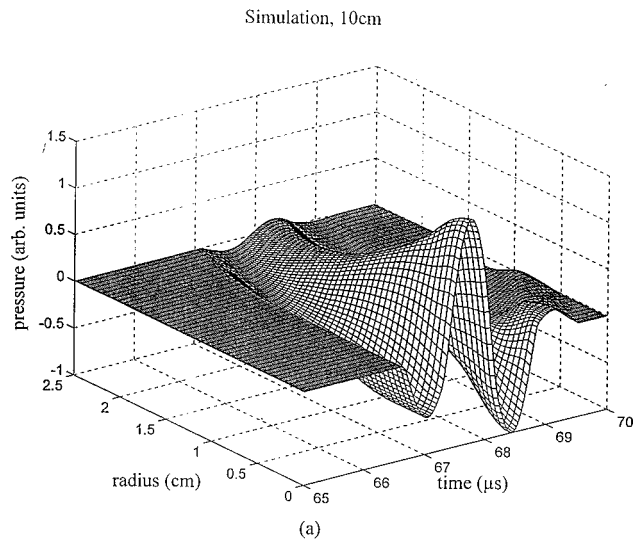
where  $p_{ij}$  is an element of the simulated data and  $p'_{ij}$  is an element of the field projection. Results range from 11% at  $z = 0.4$  cm to 4.0% at  $z = 10$  cm. The larger error close to the transducer face seems to result from the rapidly varying slopes present in the simulated field. If required, this error could be reduced by increasing the spatial resolution of the data, but at the expense of increased computation time. In addition, the projection algorithm is band limited on both the spatial and temporal axes, causing error in reconstruction of the sharply varying, broad band geometries present in the 1 cm and 4 mm simulations. The purpose of this error measurement is only to evaluate only the projection algorithm itself. Similar analysis is thus omitted for the experimental results presented in the following section.

## III. EXPERIMENT PROCEDURES AND RESULTS

### A. Apparatus

The experimental apparatus is shown in Fig. 9 to consist of a piezoelectric transducer in a water tank, a polarization-maintaining optical fiber as the sensor, a computer-controlled positioning system for the fiber, and an optical demodulation system. As indicated in the figure, the excitation to the transducer, the positioning of the fiber sensor, and the measurement of the detector output are all computer-controlled (C).

The experiments were conducted using a circular, 2.8-cm-diameter, broadband piezoceramic transducer with a peak resonance at 500 kHz. As a result of the backing, the  $Q$  of the transducer is approximately 2. The signal to the transducer (T) comes from a Real Time Systems (model 3805) arbitrary waveform generator (AWG) and an ENI power amplifier (PA). The voltage signal applied to the transducer was Gaussian with a peak voltage of 560 V and a full width at half maximum of 2  $\mu$ s. The repetition rate was 1 kHz.



Projection of Simulation: 0.4cm to 10cm

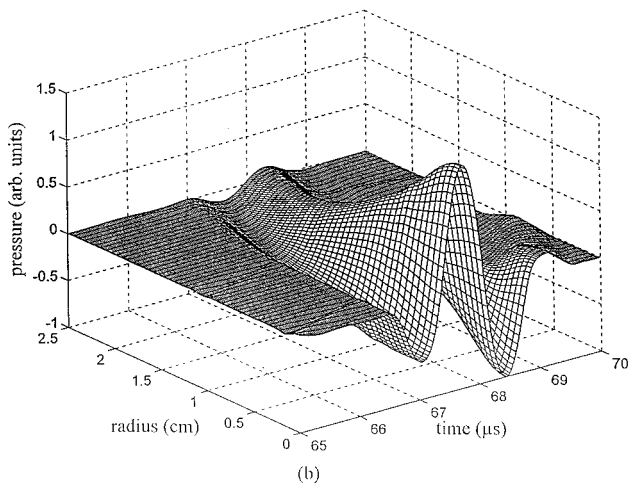


FIG. 6. Pressure field in the plane  $z=10$  cm from the source. (a) Impulse response calculation as a function of radial position and time. (b) Projection from 4 mm to 10 cm as a function of radial position and time.

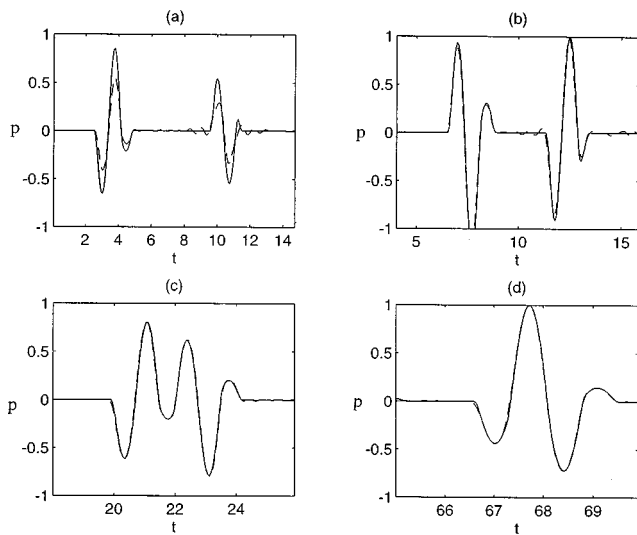


FIG. 7. On-axis pressure (solid) and its projection (dashed) from 0.4 cm. (a) 0.4 cm; (b) 1 cm; (c) 3 cm; (d) 10 cm.

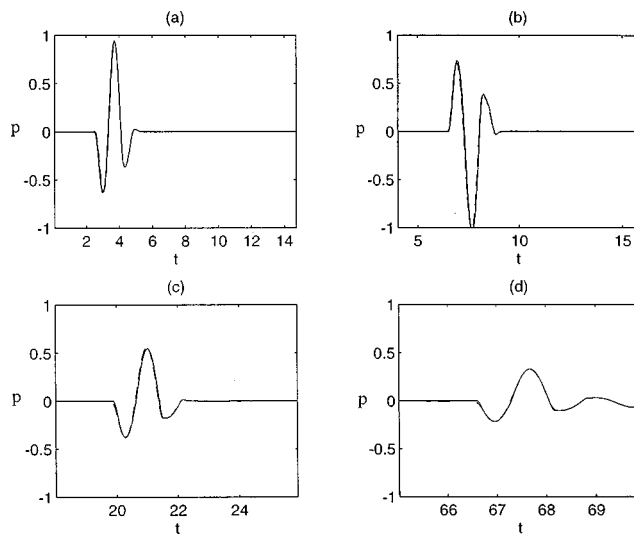


FIG. 8. Simulated pressure (solid) and its projection (dashed) from 0.4 cm along the radial position  $r=a$ . (a) 0.4 cm; (b) 1 cm; (c) 3 cm; (d) 10 cm.

The detection system is a fiber-optic polarization interferometer, similar to that described by Chiang *et al.*<sup>8</sup> The light beam from a He-Ne laser (L) passes through a polarizer (P) and a quarter-wave plate (Q) to provide circularly polarized light that is focused into the fiber core. Since the polarization-maintaining fiber is inherently birefringent, the polarization state of the light emerging from the fiber is generally elliptical and drifts due to temperature fluctuations. The strain in the fiber from the ultrasonic wave induces additional birefringence that modulates the polarization state of the emerging light beam.<sup>9,10</sup> A passive quadrature demodulation scheme was used in which the output beam is split (B) and one beam passes through a quarter-wave plate before each of them encounters an analyzing polarizer and a photodetector (D). After taking the root of the sum of the squares of the two signals, the result is independent of the ambient polarization state.

## B. Experimental procedures

At a fixed distance in front of the transducer, the fiber-optic sensor was scanned through the water in 0.15-mm increments, well below the minimum spacing permitted by the sampling theorem.<sup>11</sup> The time history of the detector output was sampled, with a sampling increment of 0.1 ms, at each

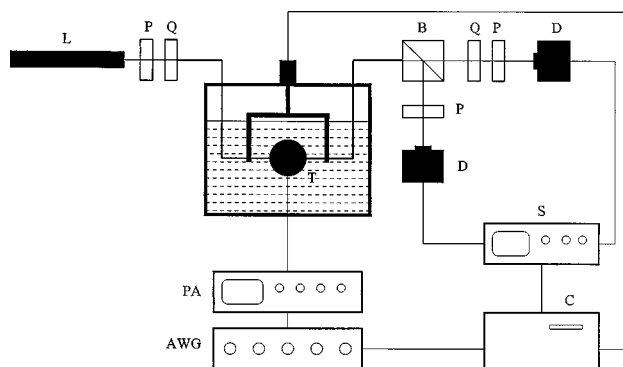


FIG. 9. Experimental setup for fiber-optic acoustic detection.

position. Due to the integrating effect of the fiber sensor, the line integral of the ultrasonic field, as expressed in Eq. (4), was measured at each position. Data from above and below the piston center were folded such that points equidistant from the axis were averaged. The data were subjected to a low-pass temporal Fourier filter before being tomographically reconstructed. The algorithm used in the reconstruction makes use of the cylindrical symmetry of the field and is expressed in the combination of Eqs. (2), (3), and (9).

### C. Projected data

Similar to the simulated case, experimental data at 0.4 cm were projected forward to planes 0.4, 1, 3, and 10 cm from the source. Since statistical error analysis of the fiberoptic sensor has not been performed, verification of the method is presented through a direct graphical comparison of

the experimental and projected results. The data were compared with experimental measurements taken at the same distances from the source. Results are presented in Figs. 10–13. The projection accurately predicts the major maxima and minima present in the experimental signals.

In Figs. 14 and 15, the time histories for radial slices on-axis and at one piston radius are given. The signals at all distances are found to be in general agreement. A notable exception occurs in the time slice 1 cm from the piston. On-axis, major peaks are reconstructed, as indicated in Fig. 14(b). However, the projection at one piston radius exhibits an apparent shift in the signal by some fraction of a microsecond. This shift may be a result of experimental error in the projection's originating data set at 0.4 cm. Similarly, the discrepancy in the profile of the projection and experiment along the radial direction at constant times (see Figs. 10–13) is seemingly a result of the combined experimental error from the data used in the projection as well as the data used for comparison at the projected distance. This discrepancy is

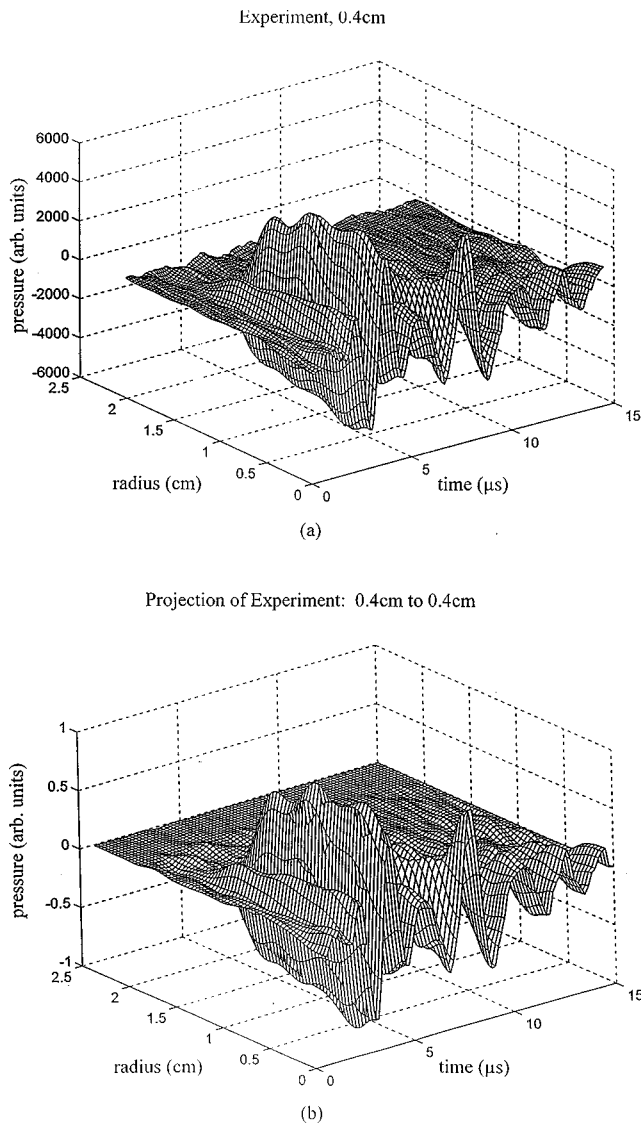


FIG. 10. Pressure field in the plane  $z=0.4$  cm from the source. (a) Experimental result as a function of radial position and time. (b) Projection of experimental result from 0.4 cm.

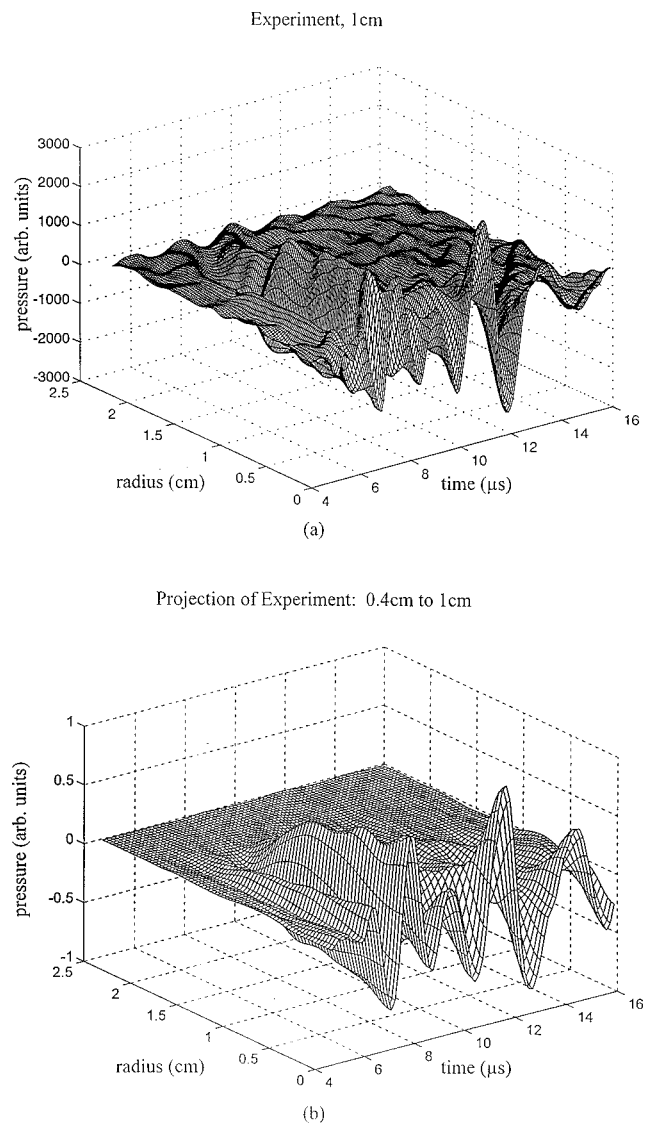


FIG. 11. Pressure field in the plane  $z=1$  cm from the source. (a) Experimental result as a function of radial position and time. (b) Projection of experimental result from 0.4 cm.



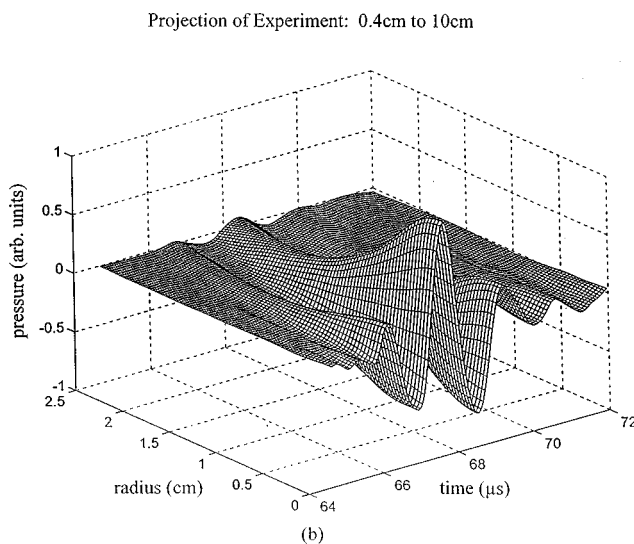
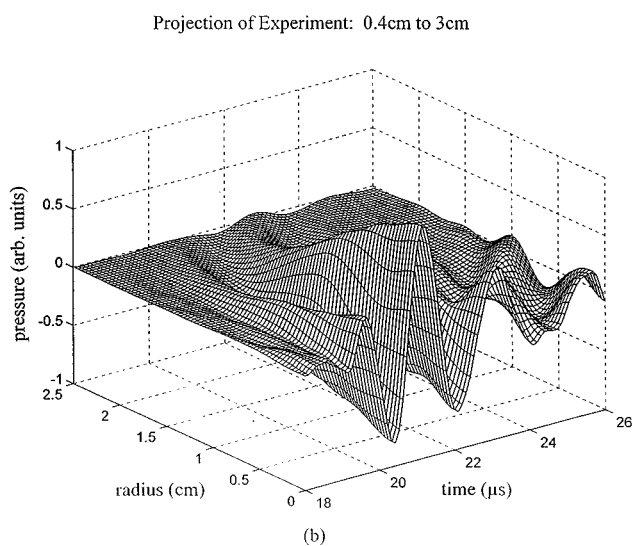
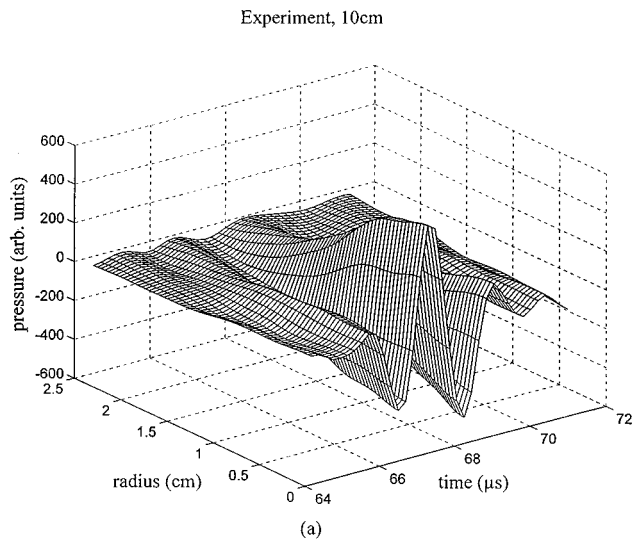
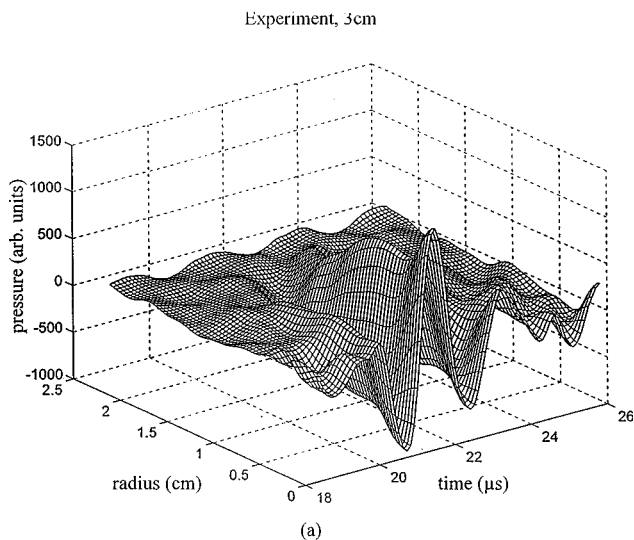


FIG. 12. Pressure field in the plane  $z=3$  cm from the source. (a) Experimental result as a function of radial position and time. (b) Projection of experimental result from 0.4 cm.

FIG. 13. Pressure field in the plane  $z=10$  cm from the source. (a) Experimental result as a function of radial position and time. (b) Projection of experimental result from 0.4 cm.

most pronounced at 3 cm (Fig. 12), the projected signal giving a smoother slope. The error is apparently a result of signal information distorted by experimental noise in the 0.4-cm experimental data. Subsequent projection to 3 cm using experimental data from 1 cm is in closer agreement with experiment. The overall shape and position of the projected signal, however, agrees with experiment throughout.

#### IV. SUMMARY

A projection algorithm is developed for efficiently propagating radially symmetric transient experimental acoustic fields forward in space. Excellent agreement between the modeled fields and their corresponding projections suggests that our projection algorithm is valid for similar experimental signals. To test the algorithm we use tomographically reconstructed data from a fiber-optic detection system. Data in a plane close to the transducer face are projected forward with the Hankel transform based algorithm. Agreement be-

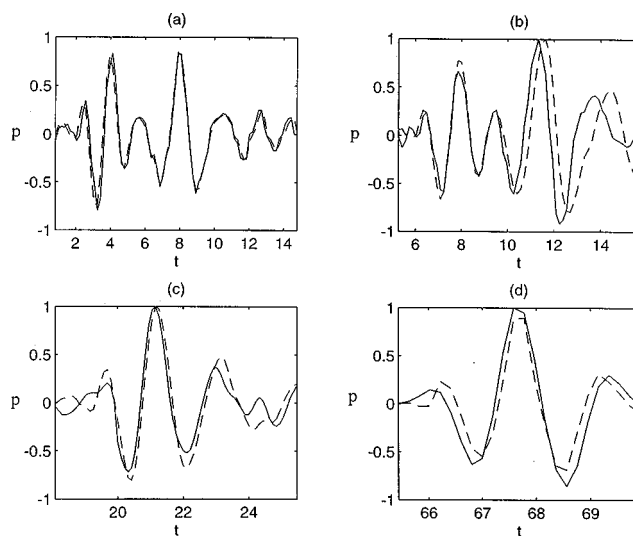


FIG. 14. On-axis experimental pressure (solid) and its projection (dashed) from 0.4 cm. (a) 0.4 cm; (b) 1 cm; (c) 3 cm; (d) 10 cm.

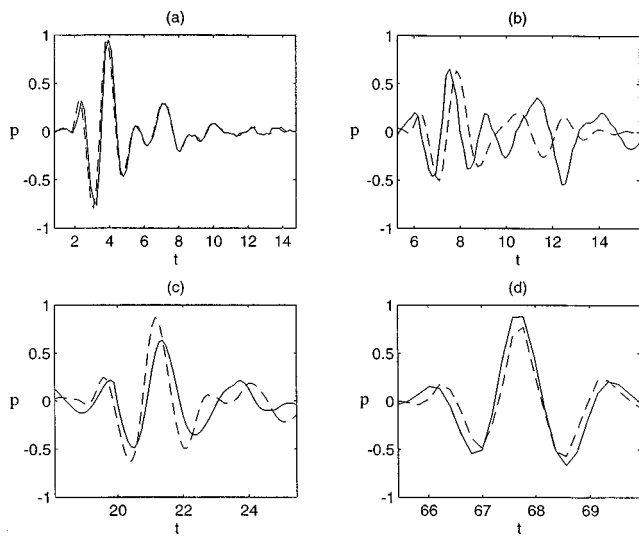


FIG. 15. Experimental pressure (solid) and its projection (dashed) from 0.4 cm along the radial position  $r = a$ . (a) 0.4 cm; (b) 1 cm; (c) 3 cm; (d) 10 cm.

tween the experimental data and the associated projected values is readily seen in Figs. 10–13, where major features present in the experimental measurements are also present in the projection, suggesting the feasibility of using the approach for full field characterization of complicated transducer signals. The algorithms employed may be modified for use with arbitrary transducer geometries by generalizing the axisymmetric arguments presented in this paper, although this generalization would entail a significant increase in the required amount of data and computation time. The theory presented is equally valid for backward projections: projecting the field toward the transducer. This technique, however,

requires a careful consideration of evanescent waves, which causes errors in the initial spectrum to increase exponentially as the field is projected backward.

## ACKNOWLEDGMENTS

This work was supported, in part, by the Ocean Technology Center at the University of Rhode Island and by the Office of Naval Research.

- <sup>1</sup>P. R. Stepanishen and K. C. Benjamin, "Forward and backward projection of acoustic fields using FFT methods," *J. Acoust. Soc. Am.* **71**, 803–812 (1982).
- <sup>2</sup>R. Reibold and F. Holzer, "Complete mapping of ultrasonic fields from optically measured data in a single cross-section," *Acustica* **58**, 11–16 (1985).
- <sup>3</sup>M. Forbes, S. V. Letcher, and P. R. Stepanishen, "A wave vector, time-domain method of forward projecting time-dependent pressure fields," *J. Acoust. Soc. Am.* **90**, 2782–93 (1991).
- <sup>4</sup>P. R. Stepanishen, "Transient radiation from pistons in an infinite planar baffle," *J. Acoust. Soc. Am.* **49**, 1629–1638 (1971).
- <sup>5</sup>P. R. Stepanishen, "Transient analysis of lumped and distributed parameter systems using an approximate  $z$ -transform technique," *J. Acoust. Soc. Am.* **52**, 270–282 (1972).
- <sup>6</sup>W. P. Mason, *Physical Acoustics* (Academic, New York, 1964), Vol. I, Part A.
- <sup>7</sup>W. P. Mason, *Electromechanical Transducers and Wave Filters* (Van Nostrand, New York, 1964).
- <sup>8</sup>K. Chiang, H. Chan, and J. Gardner, "Detection of high-frequency ultrasound with a polarization-maintaining fiber," *J. Lightwave Technol.* **8**, 1221–1226 (1990).
- <sup>9</sup>R. P. De Paula, L. Flax, J. H. Cole, and J. A. Bucaro, "Single mode fiber ultrasonic sensor," *IEEE J. Quantum Electron.* **QE-18**, 680–683 (1982).
- <sup>10</sup>R. P. De Paula, J. H. Cole, and J. A. Bucaro, "Broadband ultrasonic sensor based on induced optical phase shifts in single-mode fibers," *J. Lightwave Technol.* **LT-1**, 390–393 (1983).
- <sup>11</sup>J. W. Goodman, *Introduction to Fourier Optics* (McGraw-Hill, New York, 1968).

# Numerical simulation of the acoustic field of a phased-array medical ultrasound scanner

Mark D. Cahill and Andrew C. Baker<sup>a)</sup>

*School of Physics, University of Bath, Bath, BA2 7AY, United Kingdom*

(Received 18 November 1996; revised 17 May 1998; accepted 2 June 1998)

In order to evaluate the possible side effects of diagnostic medical ultrasound, and in particular the effects of nonlinear propagation of sound, it is necessary to characterize the scanners used. To this end, the acoustic field emitted by a phased-array Hitachi EUB-26 ultrasound scanner operating in a strongly focused mode was measured a small distance from the scanner head, and the velocity field at the surface of the head deduced. A finite difference model was then used to propagate the pressure field beyond the focus, taking into account nonlinear effects, attenuation and diffraction, and the result compared with observations in water, giving reasonable agreement out to the scanplane focus. The extrapolated field was then examined in detail, revealing those regions in which most power is lost to the medium, some of which are off-axis, and so might not be detected by normal calibration procedures. © 1998 Acoustical Society of America. [S0001-4966(98)02909-9]

PACS numbers: 43.25.Jh, 43.80.Qf [MAB]

## INTRODUCTION

This study consists of the experimental determination of the on-source field of a diagnostic ultrasound scanner, when used in a tightly focused mode, and the determination of the fine structure of the beam by numerical modeling. The predictions of the model were confirmed by comparison with experimental measurements of the beam. Detailed predictions of the model could then be used to indicate regions of the beam which might be of interest from the standpoint of safety assessments.

The non-axisymmetric Bergen code<sup>1</sup> is a finite-difference model of the propagation of acoustic beams through nonlinear media, and is capable of solving systems lacking axial symmetry. Early medical ultrasound scanners used circular transducers, and such beams have been considered by a number of authors (see, for example, Refs. 2–6), but problems lacking this symmetry require both more subtle algorithms, in order to ensure stability of the solution,<sup>7</sup> and much more computer time and memory. In this category we find both the propagation of sound from a rectangular aperture,<sup>8–10</sup> and also that from a phased array of rectangular transducers as used in modern ultrasound scanners.

Nonlinear effects are significant in determining the behavior of ultrasonic beams; this is already clear from consideration of circularly symmetric sources.<sup>11–14</sup> A previous study<sup>15</sup> by the current authors has shown that nonlinear effects due to a straight edge in the source of an ultrasonic beam can significantly affect its propagation, increasing the transfer of energy and momentum to the medium from the beam, and affecting its profile at the focus. This will be seen also to apply to the edges formed by the ends of the array elements in the scanner, although the phase difference between adjacent elements prevents any such effect in the orthogonal plane.

## I. THE NUMERICAL MODEL

The Bergen code, and the transformed beam equation (TBE) which it solves, have been described in detail elsewhere,<sup>1,7,8</sup> and it is sufficient here to note those aspects of it which affect the present study. It is based on the Khokhlov–Zabolotskaya–Kuznetsov equation,<sup>16,17</sup> which can be expressed in dimensionless terms as

$$\frac{\partial^2 p'}{\partial \sigma \partial \tau} = \alpha r_0 \frac{\partial^3 p'}{\partial \tau^3} + \frac{1}{4} \nabla_{\perp}^2 p' + \frac{r_0}{2l_d} \frac{\partial^2 p'^2}{\partial \tau^2}. \quad (1)$$

This assumes that the beam can usefully be seen as consisting of modes all propagating in approximately the same direction, taken to be the  $z$  direction, and evolving slowly in that direction (the parabolic approximation), so that the derivatives

$$\left( \frac{\partial^2}{\partial z^2} - \frac{1}{c^2} \frac{\partial^2}{\partial t^2} \right) p' \approx -2k \frac{\partial^2 p'}{\partial \tau \partial z}, \quad (2)$$

where  $\tau$  is a dimensionless retarded time

$$\tau = \omega t - kz, \quad (3)$$

and the beam is assumed to have a characteristic wavelength  $\lambda = 2\pi/k$ , frequency  $f = \omega/2\pi$ , and speed  $c$ , propagating from a source or aperture of characteristic scale  $a$ .

In the above,  $p'$  is a dimensionless acoustic pressure,

$$p' = (P - p_0)/P_0, \quad (4)$$

where  $P$  is the pressure,  $p_0$  is the ambient pressure, and  $P_0$  is a characteristic pressure of the system (e.g., the average acoustic pressure at the source). The dimensionless length  $\sigma$  is defined by

$$\sigma = \frac{z}{r_0}, \quad (5)$$

where  $r_0$  is the Rayleigh distance

$$r_0 = \frac{\pi a^2}{\lambda}, \quad (6)$$

but

<sup>a)</sup>Present address: Christian Michelsen Research AS, Fantoftvegen 38, Postboks 6031, 5020 Bergen, Norway.

$$\nabla_{\perp}^2 = a^2 \left( \frac{\partial^2}{\partial x^2} + \frac{\partial^2}{\partial y^2} \right) \quad (7)$$

represents the transverse derivatives.

The coefficients are  $\alpha$ , the attenuation coefficient, given by

$$\alpha = \alpha_0 f^2 \quad (8)$$

( $\alpha_0 = 2.5 \times 10^{-14}$  Np m<sup>-1</sup> Hz<sup>-2</sup>) in water, and  $l_d$ , the ‘‘plane wave shock formation distance,’’ which measures the nonlinearity of the medium,

$$l_d = \frac{c^2 \rho_0}{\beta k P_0}, \quad (9)$$

where  $\beta$  is the coefficient of nonlinearity (3.5 for fresh water), and  $\rho_0$  is the ambient density of the medium.

The parabolic approximation is valid (for focused sources) provided<sup>18</sup> that

$$\frac{d}{a} \gg 1 \quad (10)$$

and

$$z \gg \frac{1}{k} \left( \frac{d}{a} \right)^{4/3}, \quad (11)$$

where  $d$  is the focal length. This must be applied in each independent plane, for a source lacking axial symmetry.

The Bergen code describes  $p'$  as a truncated temporal Fourier series  $p_n(x/a, y/a, \sigma)$ , with an additional coordinate transformation to account for divergence of the beam, as described in the previous study,<sup>15</sup> which also gives approximate relations<sup>13,19</sup> for the loss of intensity by the beam per unit distance,

$$\frac{\partial I_{z,a}}{\partial z} = \frac{-P_0^2}{\rho_0 c} \sum_{n=1}^N \alpha_0 f^2 \frac{n^2}{v^2} b_n |p_n|^2 \quad (12)$$

(assumed to be converted largely into heat), and for the streaming pressure (the loss of momentum per unit volume by the beam)

$$F \approx \frac{1}{c} \frac{\partial I_{z,a}}{\partial z}. \quad (13)$$

Here  $b_n$  is an increase in the attenuation in the model at high frequencies,<sup>20</sup> which promotes convergence (the same variation was used here as in Ref. 15). The ratio, denoted by  $\nu$ , of the carrier frequency of the beam to the pulse repetition frequency (PRF) in the model (that is, the frequency of the fundamental of the Fourier series) is kept small in order to minimize the number of harmonics in the representation, and the power dissipation and streaming pressure must be reduced by the ratio of the PRF of the scanner head (3.8 kHz for that considered here) to that of the model.

## II. EXPERIMENTAL PROCEDURE

A Hitachi EUB-26 ultrasonic scanner was used, with an EZU-PL11 3.5-MHz head, which was wrapped in a double layer of thin polythene coupled by thin layers of acoustic coupling gel. This was fully immersed in deionized water, with the beam horizontal, and the long axis of the head ver-

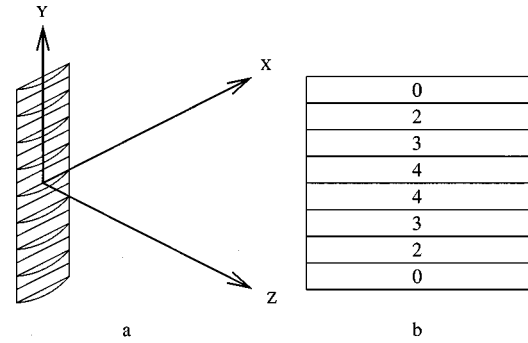


FIG. 1. (a) Illustrating the orientation of the scanner head with respect to the axes of the model. The beam propagates along the  $z$  axis. (b) Deduced phase-lag (in units of  $\frac{1}{14}$   $\mu$ s) of active array elements.

tical. Measurements were made using a 0.5-mm-diam GEC-Marconi PVDF bilaminar membrane hydrophone. The hydrophone was supported in water on a rig with stepping-motor control along the acoustic beam ( $z$  direction) and in the direction ( $x$ ) of the long axis of the array elements. Vertical ( $y$ ) positioning was via a manual vernier stage, to an accuracy of 0.3 mm. The orientation of the axes is shown in Fig. 1(a). Data were acquired by means of a LeCroy 9310 digital oscilloscope, triggered by an inductive coupling to the lead to the scanner-head, and thus by the first electronic signal in the pulse.

### A. Initial conditions

The scanner possesses a cylindrical fixed lens providing ‘‘elevation’’ focusing in the  $xz$  plane, in front of a phased array of transducer elements, which are assumed to be rectangular, providing ‘‘scanplane’’ focusing in the  $yz$  plane [see Fig. 1(a)]. While the beam can be set to scan in this plane, for the purpose of characterization the scanner was set to ‘‘ $M$ -mode,’’ which causes successive pulses to be emitted by the same group of elements, forming a beam perpendicular to the face of the head. Electronic focusing was set to the ‘‘near’’ mode, which was found to produce a scanplane focus approximately 30 mm from the front of the lens.

The coordinate system used here, shown in Fig. 1(a), has origin at the apparent center of the group of active elements, behind the lens. In order to determine the on-source field, measurements were taken 2 mm in front of the lens at intervals of 0.5 mm across its face. From the arrival times of these, the acoustic path between the array elements and the front of the lens was found to be equivalent to a water path of  $2.82 \pm 0.04$  mm, so that the front of the lens is at  $z = 2.82$  mm in our coordinates.

The effect of the lens was modeled by treating the array elements as having constant velocity amplitude and quadratically varying phase in the  $x$  direction, and arbitrarily varying amplitude and phase in the  $y$  direction. The effective length (in the  $x$  direction) of the elements was initially estimated by using a Rayleigh integral, given an assumed focal length  $d$ , and the value of  $d$  was later refined by comparing model runs with experimental data taken 30 mm from the front of the lens.

Given this model of the elevation focusing, the waveform and scanplane focusing were deduced by a deconvolu-

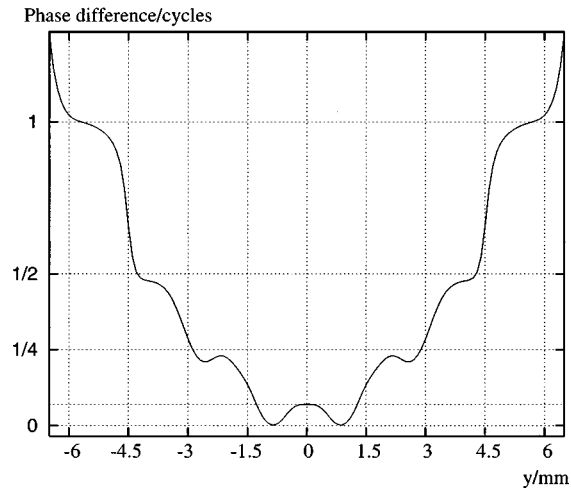


FIG. 2. Phase difference in cycles of the carrier (3.5 MHz) of the deconvolved wave as a function of  $y$  at 2.5 MHz (harmonic 5).

tion algorithm using data taken along the length of the lens. Figure 2 shows the deconvolved phase at one frequency as a function of  $y$ , evaluated at  $x=0$ ,  $z=0$ , on the apparent surface of the elements, and there are clear plateaux at 1.5-mm intervals, seeming to correspond to phase differences which are multiples of a quarter cycle of the head (which has a nominal frequency of 3.5 MHz). It is reasonable to assume that these plateaux correspond to the phase of individual array elements, each of width 1.5 mm, and this spacing is confirmed by Fig. 3, which shows the pressure amplitude of the same mode. Similar results appear at all frequencies between 2 and 6 MHz. Small uncertainties in the measured phase prevented the use of the deconvolved field for accurate modeling; however, assuming that the array elements are identical and differ only in having a phase-lag of multiples of  $1/14 \mu\text{s}$ , the Appendix shows the mean amplitude and (unwrapped) phase of each mode, derived by averaging between the centers of the middle two elements, and Fig. 4 shows the corresponding waveform.

The initial conditions used in the model, then, were that

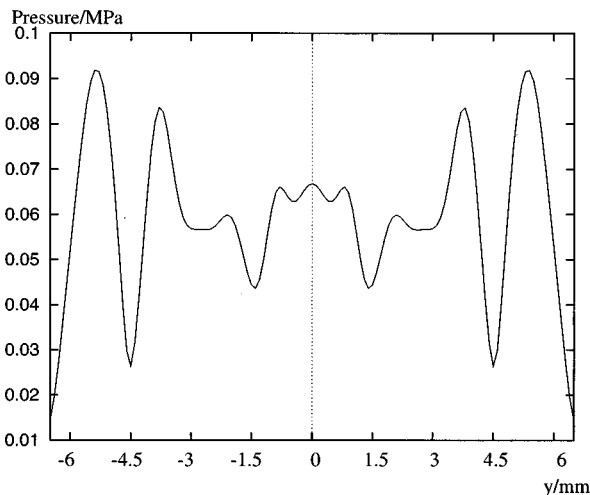


FIG. 3. Pressure amplitude in MPa of deconvolved wave as a function of  $y$  at 2.5 MHz (harmonic 5).

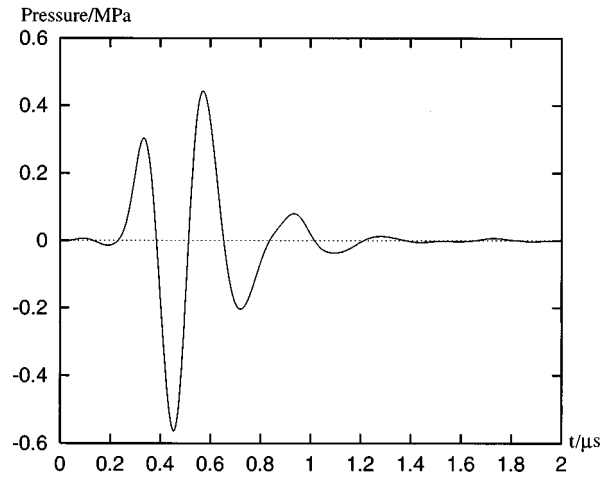


FIG. 4. Pressure waveform of deconvolved wave.

there were eight uniform rectangular elements acting as velocity sources, each with the waveform of Fig. 4, and phase varying quadratically along their length, but constant across their 1.5-mm width. These eight elements were assumed to be triggered with the relative delays shown in Fig. 1(b). Note that whereas the scanner has a PRF of 3.8 kHz, the model assumes a PRF of 0.5 MHz, corresponding to the  $2\text{-}\mu\text{s}$  window shown in Fig. 4, as mentioned in the section on the numerical model.

## B. Propagated beam

In order to improve the estimate of the focal length of the fixed lens, the numerical model was used to propagate the wave forward 33 mm from the effective position of the array, for varying focal length and displacement in the  $y$  direction, integrating it over the area of the hydrophone, and this was compared with observations of the field 30 mm in front of the lens, for varying  $x$ , at the modal frequency of 3.5 MHz. Figure 5 shows this comparison, for a fixed focal power of 9.25 dioptres, focal length 108 mm, at  $y = 0.323$  mm. Note the maximum at 2 mm. This graph shows good agreement between 2 and 4 mm from the axis, at and

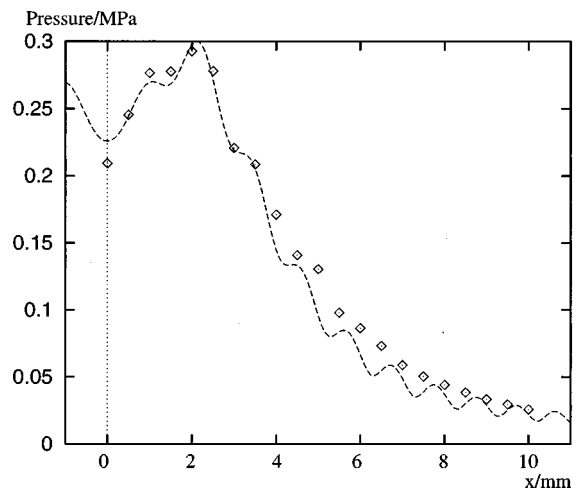


FIG. 5. Fit to observations in the  $x$  direction at 3.5 MHz.  $z = 33$  mm, offset by 0.323 mm in the  $y$  direction, fixed focal length 108 mm. Observations are diamonds, fit is a dashed line.

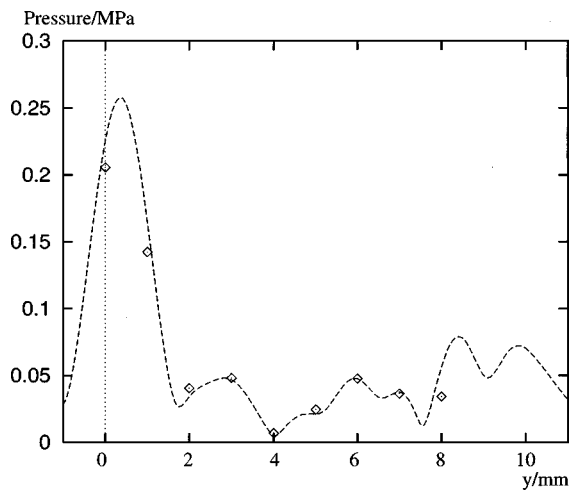


FIG. 6. Comparison of prediction with observations in the  $y$  direction at 3.5 MHz.  $z = 33$  mm. Observations are diamonds, prediction is a dashed line.

just beyond the first-order Fresnel fringe, but the experimental points imply that the real beam “fans” out more than would be expected from the model, and possesses a deeper minimum at the axis, at this frequency and distance from the scanner. Two possible reasons for this present themselves; first, the value of the field near the axis at this distance varies more rapidly in all directions than that near the first-order fringe, so that small errors in experimental alignment or in the model can have a larger effect, but also the approximation described in Sec. II A, whereby the lens was represented by a flat source with varying phase and constant amplitude in the  $x$  direction, may be at fault—for example, the lens might attenuate the beam slightly at its thickest. Unfortunately, lack of time prevented further readings being taken, once this mismatch had been noted.

Given this fit, Fig. 6 compares the observed  $y$  variation at 3.5 MHz with the numerical prediction, with excellent results. Note that at this distance from the array, the phasing has brought the beam to a sharp focus (integration over the 0.5-mm diameter of the hydrophone makes the peak seem wider), so it is not entirely surprising that the peak was missed when the data were acquired. Further confirmation of the validity of the model is supplied at other frequencies; Figs. 7 and 8 show the third harmonic of the carrier, which is almost entirely generated by nonlinear interaction in the beam, and so is very sensitive to the evolution of the beam between the array and point of observation. Figure 7 confirms the impression gained from Fig. 5, that the fit is good near the first Fresnel fringe, but either experimental misalignment or imperfections in the model make it worse both on and far off axis. Figure 8, however, is very reassuring, only the values far from the axis deviating significantly from prediction.

### III. NUMERICAL CONSIDERATIONS

In order to obtain reliable predictions (independent of the parameters of the program) it was necessary to work to quite a high spatial accuracy, in particular, the first 16 steps in the  $z$  direction were 0.04 mm long, to give the position of the peak at  $x = 2$  mm in Fig. 5, although this was then in-

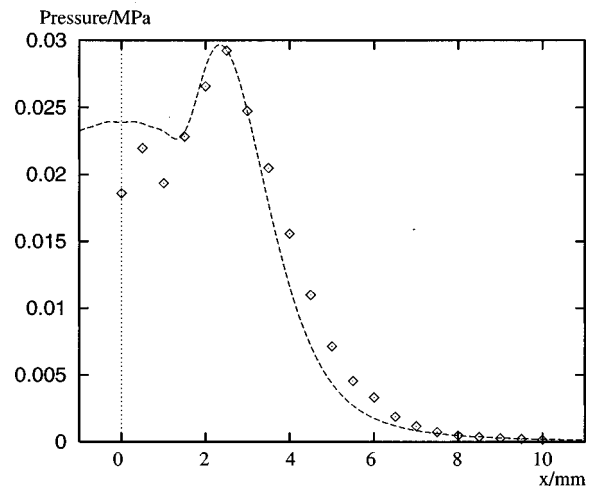


FIG. 7. Comparison of prediction with observations in the  $x$  direction at 10.5 MHz.  $z = 33$  mm. Observations are diamonds, prediction is a dashed line.

creased to 0.18 mm for the remainder of the run. (However, see below concerning power dissipation.) The transverse resolution was 362 points square, the initial grid being 27.2 mm square (comprising the quadrant  $x \geq 0, y \geq 0$ , and using symmetry for the remaining quadrants), and while the results given here are from a run with 200 harmonics (frequencies to 100 MHz), they do not differ significantly from those for 50 harmonics for frequency components less than 11 MHz.

Equations (10) and (11) define values of the parameters of the system for which the parabolic approximation can be trusted, and these must be applied in both planes,  $xz$  and  $yz$ . Taking the fixed focus first,  $d = 108$  mm, and  $a = 6.3$  mm, so that, with  $k = 14.82$  rad/mm, the two conditions are

$$17.1 \geq 1 \tag{14}$$

and

$$z \geq 2.98 \text{ mm.} \tag{15}$$

These are satisfied for all  $z$  of interest. The lowest frequency at which there is a noticeable signal is 1.5 MHz, which cor-

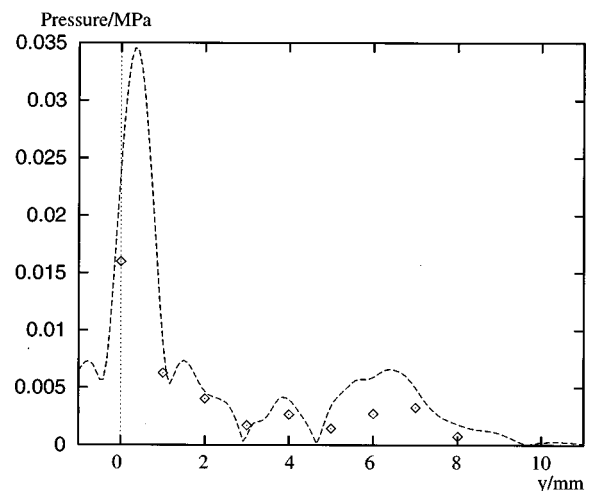


FIG. 8. Comparison of prediction with observations in the  $y$  direction at 10.5 MHz.  $z = 33$  mm. Observations are diamonds, prediction is a dashed line.

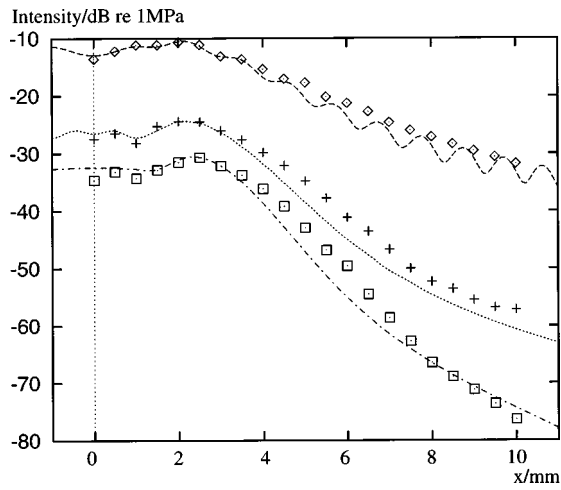


FIG. 9. Logarithmic comparison of beam profiles in the  $x$  direction at three frequencies,  $z = 33$  mm. At 3.5 MHz, observations are diamonds, prediction is a dashed line; at 7 MHz, observations are crosses, prediction is a dotted line; and at 10.5 MHz, observations are squares, prediction is a dashed-dotted line.

responds to  $k = 6.35$  rad/mm, and for which the second condition is

$$z \geq 6.96 \text{ mm}, \quad (16)$$

which again is satisfied.

Turning to the phased focusing, assuming that we can apply the same formulas, and, taking the center of the outer element, with a phase difference of one cycle from the center, as characteristic of the focusing, one obtains a focal length of 32.5 mm (this will turn out to be a reasonable estimate). The inequalities are then

$$5.42 \gg 1 \quad (17)$$

and

$$z \geq 1.50 \text{ mm}, \quad (18)$$

at 1.5 MHz. The first is within reasonable limits as shown (for circular sources) in Ref. 18, and the second is so easily satisfied that one is given pause for thought—the values of  $z$  permitted are as small as the width of the array element, which was assumed small in the approximation of the phased array by a continuously varying phase. Consider then each element of the array separately as being unfocused in the  $y$  direction, and apply the unfocused inequalities

$$1 \ll ka = 4.76 \quad (19)$$

and

$$z \geq a(ka)^{1/3} = 1.26 \text{ mm}. \quad (20)$$

These also are satisfied, so it seems that the KZK equation, and hence the TBE, can safely be applied.

#### IV. COMPARISON OF OBSERVATION AND PREDICTION

Figures 9–13 continue the comparison of observations using the 0.5-mm hydrophone with the predictions of the model, using logarithmic plots in dB *re*: 1 MPa. All plots thus refer to a spatially averaged beam which is translated slightly in the  $y$  direction to account for a small misalignment of the apparatus. Figure 9 shows the information in

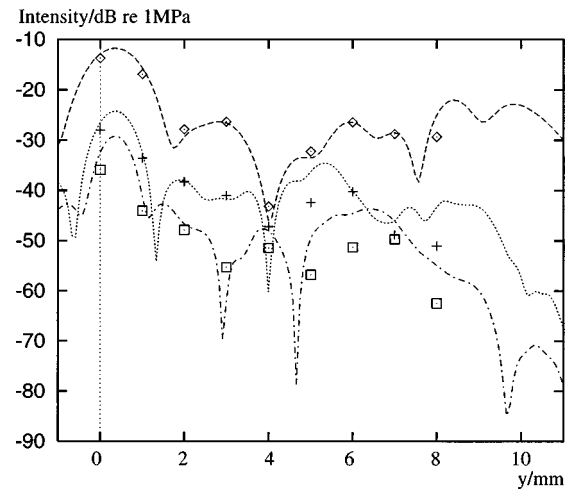


FIG. 10. Logarithmic comparison of beam profiles in the  $y$  direction at three frequencies,  $z = 33$  mm. At 3.5 MHz, observations are diamonds, prediction is a dashed line; at 7 MHz, observations are crosses, prediction is a dotted line, and at 10.5 MHz, observations are squares, prediction is a dashed-dotted line.

Figs. 5 and 7, with the addition of the intermediate frequency 7 MHz, which is the second harmonic of the nominal carrier frequency. The fit at the side peaks is less obvious in this graph, and the deviation from observation further off axis is more apparent. It may be that the predicted spatial oscillations at the carrier frequency are real, but that the hydrophone was unable to detect them (see discussion of Fig. 11 below). Certainly they are not due to reflections from the boundary of the model, because Fig. 14(a), described below, shows them radiating from the source. Figure 10, which performs the same role for Figs. 6 and 8, gives a more optimistic view of the model's predictive capabilities; all three harmonics are excellently reproduced for  $y < 5$  mm, and the carrier for all  $y$ , encouraging the suspicion that the errors in Fig. 9 are due to incorrect modeling of the properties of the lens, of which Fig. 10 is largely independent.

Figures 11 and 12 give profiles 62 mm from the source, beyond the last axial maximum of the carrier, where the

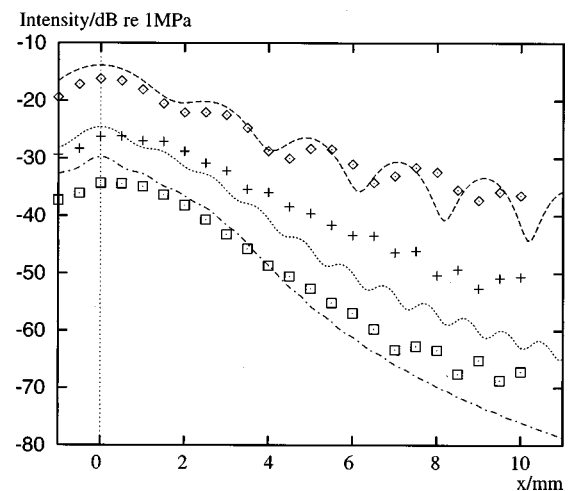


FIG. 11. Logarithmic comparison of beam profiles in the  $x$  direction at three frequencies,  $z = 62$  mm. At 3.5 MHz, observations are diamonds, prediction is a dashed line; at 7 MHz, observations are crosses, prediction is a dotted line; and at 10.5 MHz, observations are squares, prediction is a dashed-dotted line.

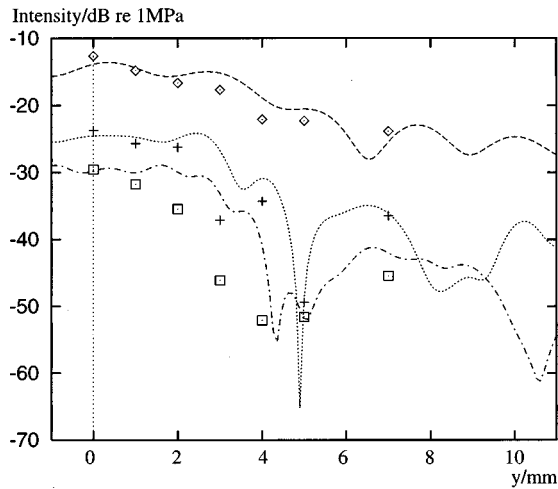


FIG. 12. Logarithmic comparison of beam profiles in the  $y$  direction at three frequencies,  $z = 62$  mm. At 3.5 MHz, observations are diamonds, prediction is a dashed line; at 7 MHz, observations are crosses, prediction is a dotted line; and at 10.5 MHz, observations are squares, prediction is a dashed-dotted line.

small errors at 33 mm seem to have compounded. There is qualitative agreement in the spatial oscillations of the carrier in Fig. 11, but the magnitude of the harmonics far-off-axis (where the field is very weak) is not so good, although the deviation in magnitude on-axis may partly be due to misalignment of the apparatus in the  $yz$  plane. In the  $y$  direction (Fig. 12), many of the observed features are predicted, although the agreement is not as good as at 33 mm. Finally, Fig. 13 shows the axial variation of the harmonics. For small  $z$  these cannot be expected to match, because of the artificial raising of the pulse repetition frequency, which causes consecutive wave packets to interfere in the model, when they would not with a more realistic PRF. Around  $z = 40$  mm the experimental observations show features not predicted by the model—in this region, the beam is so narrow in the  $yz$  plane, due to the phased focusing, that a small misalignment of the hydrophone will have caused a large error in the measurement.

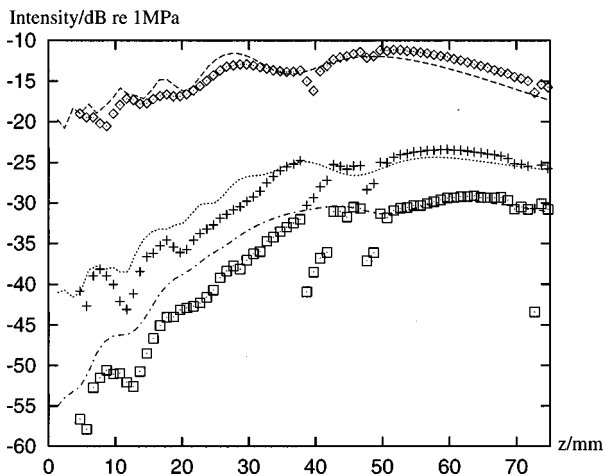


FIG. 13. Logarithmic comparison of axial intensities at three frequencies. At 3.5 MHz, observations are diamonds, prediction is a dashed line; at 7 MHz, observations are crosses, prediction is a dotted line; and at 10.5 MHz, observations are squares, prediction is a dashed-dotted line.

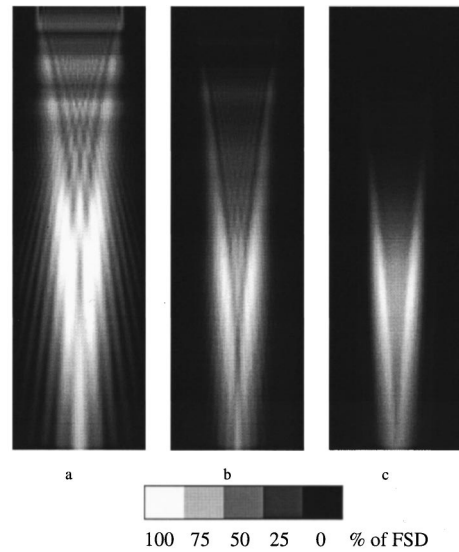


FIG. 14. Amplitude of three harmonic components of the beam, in the  $xz$  plane. The beam propagates down the page for 60 mm, with aspect ratio 1:1. (a) 3.5 MHz (the carrier), with full scale deflection (FSD) 0.3 MPa, (b) 7 MHz (second harmonic), FSD=0.1 MPa, and (c) 17.5 MHz (fifth harmonic), FSD=0.03 MPa. From the model.

## V. FORM OF THE BEAM

The beam described by the model is a complex structure, with some surprising features. In order to show its structure more clearly, Figs. 14 and 15 show the amplitudes of three harmonics in planes cutting through the central axis of the beam (in these and subsequent figures it is the raw modeled beam which is portrayed, not that averaged over the area of the hydrophone and realigned). In these plots, the brightness is proportional to the amplitude of the mode in question. Figure 14(a) shows the amplitude of the carrier at

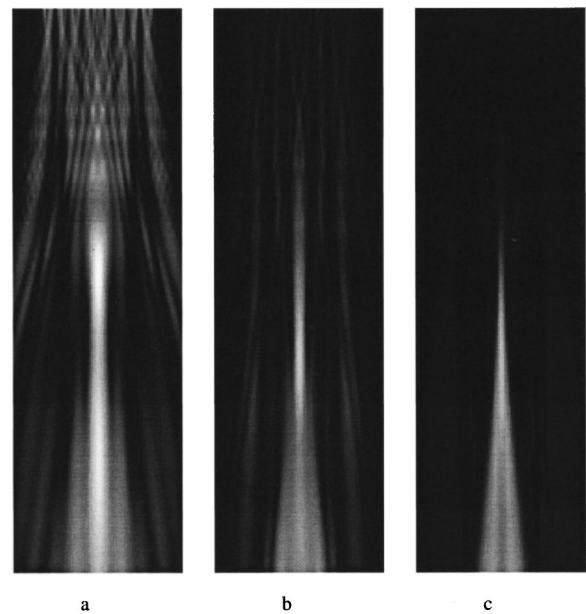


FIG. 15. Amplitude of three harmonic components of the beam, in the  $yz$  plane. The beam propagates down the page for 60 mm, with aspect ratio 1:1. (a) 3.5 MHz (the carrier), FSD=0.3 MPa; (b) 7 MHz (second harmonic), FSD=0.1 MPa; and (c) 17.5 MHz (fifth harmonic), FSD=0.03 MPa. From the model.



points over the  $xz$  plane, i.e., the plane of the fixed focus. The transducer is at the top, and the bottom of the image corresponds to  $z = 60$  mm. As noted in the previous study,<sup>15</sup> fringes emanate from the edges of the transducer, the strongest on the outside, and these finally cross at about  $z = 50$  mm. Figure 15(a), on the other hand, shows the perpendicular  $yz$  plane, in which the phased array focuses the beam. This produces a remarkably narrow beam from 25 to 45 mm in front of the array, which subsequently spreads out. Comparing the two, the hot spot at 27 mm in Fig. 15(a) corresponds to the meeting of the second-order fringes in Fig. 14(a), the horizontal bands closer to the array in Fig. 14(a) correspond to axial maxima and minima in Fig. 15(a), and the two hot spots on either side of the axis in Fig. 14(a) at 34 mm correspond to a narrow part of the beam in Fig. 15(a). By the point where the principle fringes are meeting in Fig. 14(a), the beam has become diffuse in the perpendicular plane, and so the intensity is less than one might otherwise expect. In effect, then, by combining maxima in two planes, the manufacturers have arranged that there be an unusually long stretch on the axis of high amplitude, with no severe peaks. Off-axis, however, there are two “eyes” in Fig. 14(a) of marked intensity. Turning to Figs. 14(b) and 15(b), which show the second harmonic of the carrier (7 MHz), there is some generation of this on-axis, visible in both figures, but a quite noticeable amount off-axis in the  $xz$  plane. To emphasize this, Figs. 14(c) and 15(c) show the fifth harmonic of the carrier, with sharp generation in the “eyes” in Fig. 14(c), and also in the “fan” in Fig. 15(c).

Note also that higher harmonics are produced at greater distances from the source than the maxima of the carrier—it takes a certain distance for the shock to evolve.

The appearance of off-axis maxima in this case can be attributed to the choice of strong focusing in the scanplane, which brings the location of the maxima of amplitude closer to the source than the elevation focus. It thus differs from the situation in the previous publication,<sup>15</sup> in which the beam due to a square source was unfocused, and nonlinear attenuation made the last axial maximum weaker than those off-axis.

## VI. POWER DISSIPATION

### A. Potential sources of error

It was much more difficult to obtain reliable figures for the loss of intensity of the beam than for the amplitude of the lower harmonics. Because the attenuation of sound in water varies as the square of the frequency, and the Fourier series of a shock wave varies as the inverse of the frequency (for moderate frequencies), the power dissipation of the wave is effectively constant over a wide range of frequencies, so one needs a wide spectrum to represent strongly shocked waves, and to model the evolution of high-frequency components one needs very fine axial resolution. In order to achieve this, with a reasonable run time (36 h of CPU time on a DEC 8400), it was necessary to halve the transverse resolution, compared to the runs in Figs. 14 and 15.

Figure 16 illustrates the transverse variation of power dissipation in such runs, 45 mm in front of the array, in the

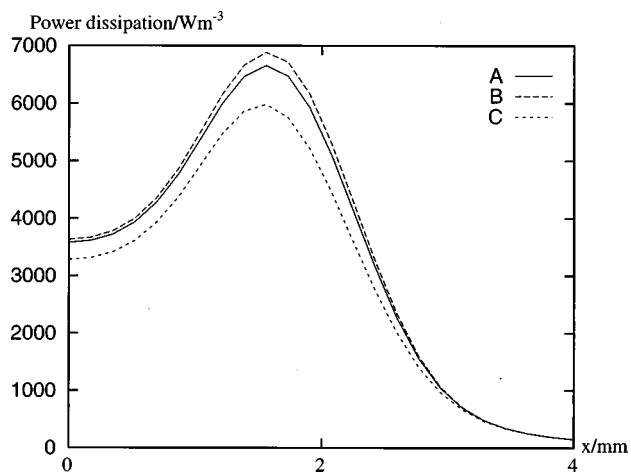


FIG. 16. Loss of power by the beam in  $\text{W m}^{-3}$  at  $z = 45$  mm,  $y = 0$ , estimated under three sets of parameters: (A) 170 harmonics,  $\delta z = 0.011$  mm, (B) 170 harmonics,  $\delta z = 0.022$  mm, and (C) 120 harmonics,  $\delta z = 0.022$  mm. From the model.

$yz$  plane, given a pulse repetition frequency of 3.8 kHz. Curve A was produced by a run with 181 points along each of the  $x$  and  $y$  axes, and 170 temporal harmonics. The resulting granularity in the transverse direction is apparent. As with all the runs in this study, the axial increment close to the source was 0.04 mm. Thereafter, the increment was 0.01 mm. Curve B shows that the effect of doubling this latter increment is to increase the estimate of the power dissipation, particularly where it is already large. Curve C shows the effect of reducing the width of the spectrum to 120 harmonics, while retaining the doubled increment—power dissipation is underestimated. The actual value of the power dissipation in this profile probably lies closest to curve A, between curves B and C, but it was not possible to refine the results further in the time available. Certainly there is significantly more loss of power by the beam away from the axis than on it.

Figure 17 shows the effect of the above variation of the model parameters on the power dissipation due to each

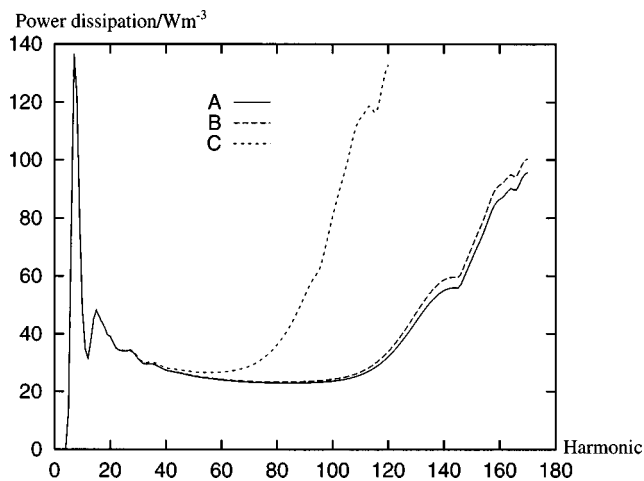


FIG. 17. Loss of power by the beam for each harmonic, in  $\text{W m}^{-3}$  per mode, at  $z = 45$  mm,  $x = 1.6$  mm,  $y = 0$ , estimated under three sets of parameters: (A) 170 harmonics,  $\delta z = 0.011$  mm, (B) 170 harmonics,  $\delta z = 0.022$  mm, and (C) 120 harmonics,  $\delta z = 0.022$  mm. Note that the value is artificially enhanced in the last 24 harmonics (see text). From the model.

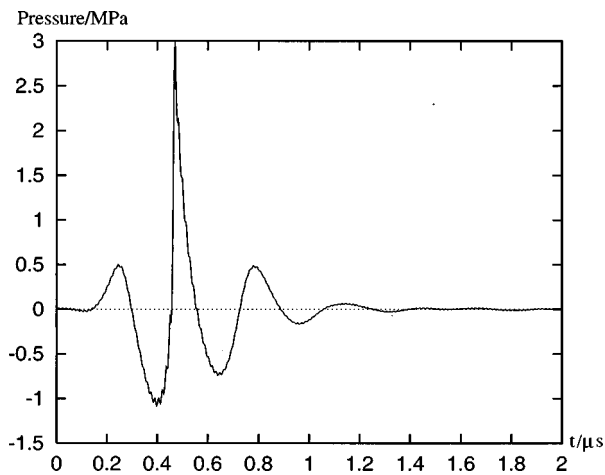


FIG. 18. Waveform at  $z=45$  mm,  $x=1.6$  mm,  $y=0$ , in MPa. From the model.

mode, at one point, near the peak of Fig. 16. At the highest frequencies there is a dramatic increase, due to the truncation of the spectrum. In the absence of the taper function  $b_n$  enhancing the attenuation [see the comments following Eq. (13)], this increase would still be seen because the amplitudes would be larger for the highest frequencies. It is seen that the effect of increasing the axial increment is to increase slightly the amplitude of the higher frequency components, while leaving the lower frequencies, which dominate the observed waveform, unaffected. The taper function  $b_n$  in Eq. (12), was included to improve convergence of the predicted power dissipation when the model uses a limited number of harmonics, and this is successful, as indicated by the similarity of the curves B and C in Fig. 16, compared with the rapid divergence of the power spectra B and C in Fig. 17.

## B. Predicted power dissipation

As stated above, curve A of Fig. 16 is a transverse profile of the predicted power dissipation in water, 45 mm from the transducer array. This is somewhat beyond the scanplane focus, but closer to the array than the elevation focus. The waveform near the maximum of this curve is shown in Fig. 18, which shows the severity of the shock in water.

To give a clearer view of the spatial distribution of power dissipation as predicted by the model, the loss of power by the beam in the  $xz$  and  $yz$  planes is depicted in Fig. 19. The “eyes” in Fig. 19(a) are saturated—as has been seen, the power dissipation reaches  $6500 \text{ W m}^{-3}$ , and the brightest parts of the image represent power dissipation of  $5000 \text{ W m}^{-3}$  or more. Note how fine the focus is in the  $yz$  plane, due to the scanplane focus, compared to that due to the elevation focus, and also that the peaks of power dissipation occur farther from the array than the maximum of the carrier in Fig. 14(a), just as did the fifth harmonic of the carrier in Fig. 14(c). The fan in Fig. 19(b), 60 mm in front of the array, appears in all runs performed, but its intensity varies such that one should not place too much reliance on it—it is also very narrow.

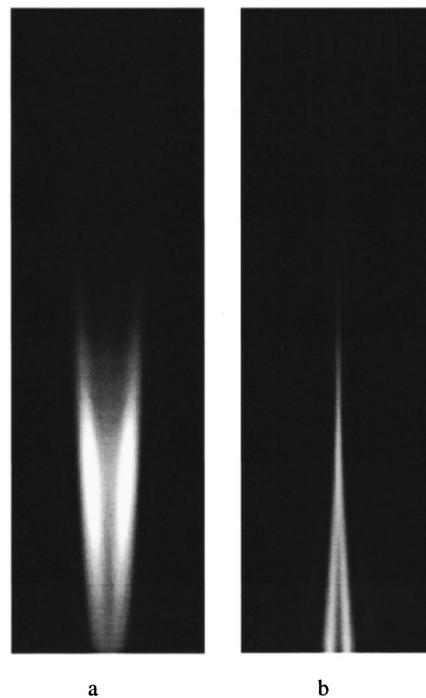


FIG. 19. Power dissipation,  $\text{FSD}=5000 \text{ W m}^{-3}$ ; (a) in the  $xz$  plane and (b) in the  $yz$  plane. The beam propagates down the page for 60 mm, with aspect ratio 1:1. From the model.

## VII. CONCLUSION

One mode of operation of a medical ultrasound scanner has been characterized to sufficient accuracy, that its behavior at frequencies less than 11 MHz out to the focus can be modeled reliably, and beyond the focal region, qualitative agreement is obtained.

It was found that, as in the previous study,<sup>15</sup> sharp discontinuities in the initial field propagated as fringes in the carrier frequency, with significantly higher amplitude than the surrounding field. In the “near” focusing mode used, the phased array produces a sharp plane of intensified sound, which, where it intersects the (off-axis) fringes in the plane of the fixed focus, creates local regions where the peak positive pressure approaches 3 MPa. As in the previous study, these generate a disproportionate intensity in higher frequency modes. Whether these off-axis hot spots are indeed more intense than those on-axis and farther from the array, as they appear to be, is not clear, both because the amount of CPU time required to produce such certainty was not available, and because the initial conditions had not been refined to the point where it was possible to be confident of the field 60 mm from the source. The greater attenuation of biological media can be expected to restrict the spectral width of the beam at the hot spots *in vivo*, so that modeling propagation through such media would be less demanding than through water. It should be noted, in particular, that most of the loss of power [and thus, by Eq. (13), of momentum] to the medium seems to be by modes with frequencies greater than 25 MHz, and small amplitude, and that normal calibration measurements are unlikely to detect these modes, even if one were to seek them off-axis.

It is worth investigating what might be the effect of

“eyes” produced in biological fluids, when they impinge on tissues, as in Ref. 20. Streaming pressure is also a consideration—the loss of momentum to more delicate tissues by beams which have gained a rich harmonic content, combined with the rapid transverse variation in that content indicated by Fig. 16, might cause significant shear stresses. In this context, it is interesting to note that a recent investigation of the related subject of Eckart streaming<sup>14</sup> has shown that at distances from the (circular) source at which the principal fringe is a few millimeters from the axis, and the (carrier) field is near a minimum on the axis, there is also a minimum in the streaming velocity, even after dynamical factors have smoothed the velocity profile over 40 s.

In conclusion, the beam structure revealed by this investigation of just one mode of one scanner head is rich in potentially interesting and biologically relevant phenomena, which are easily missed by conventional measurements. The large amount of computer power needed to obtain future detailed model runs, perhaps with the parameters of biological materials, is likely to be amply rewarded. In obtaining similar sets of initial conditions, corresponding to different sources, attention should be paid to the sensitivity of the predicted beam to the phase of the array.

## ACKNOWLEDGMENTS

The authors are grateful to Dr. F. A. Duck of the Royal United Hospital, Bath, for access to the Hitachi scanner, and to Professor J. Berntsen, Professor S. Tjøtta, and Professor J. Naze Tjøtta for the use of the Bergen code. This research was funded by Engineering and Physical Sciences Research Council grant No. GR/K28022.

## APPENDIX

Table AI gives the spectrum of the deconvolved waveform used to model Hitachi EZU-PL11 3.5-MHz scanner-head.

TABLE AI. Spectrum of the deconvolved waveform.

Frequency (MHz)	Amplitude (kPa)	Phase (rad)
0.5	6.27	1.65
1.0	6.72	0.666
1.5	7.70	0.0983
2.0	21.7	-0.268
2.5	64.2	-1.70
3.0	99.6	-3.54
3.5	101.	-5.23
4.0	87.2	-6.72
4.5	72.2	-8.20
5.0	54.2	-9.64
5.5	34.4	-11.1
6.0	20.3	-12.4
6.5	13.0	-13.6
7.0	8.74	-15.1
7.5	3.58	-16.8
8.0	0.621	-19.6
8.5	1.06	-21.6
9.0	1.57	-22.5
9.5	2.08	-24.0
10.0	2.03	-25.3
10.5	1.49	-26.6
11.0	1.02	-28.0
11.5	0.731	-29.2
12.0	0.510	-30.5
12.5	0.233	-31.7

<sup>1</sup>A. M. Berg and J. Naze Tjøtta, “Numerical Simulation of the Sound Pressure Field from Finite Amplitude, Plane or Focussing, Rectangular Apertures,” in *Proceedings of the 13th ISNA*, edited by H. Hobæk (World Scientific, Singapore, 1993), pp. 309–314.

<sup>2</sup>A. C. Baker, “Prediction of Nonlinear Propagation in Water Due to Diagnostic Medical Ultrasound Equipment,” *Phys. Med. Biol.* **36**(11), 1457–1464 (1991).

<sup>3</sup>A. C. Baker and V. F. Humphrey, “Distortion and high-frequency generation due to nonlinear propagation of short ultrasonic pulses from a plane circular piston,” *J. Acoust. Soc. Am.* **92**, 1699–1705 (1992).

<sup>4</sup>S. Nacheff, D. Cathignol, J. Naze Tjøtta, A. M. Berg, and S. Tjøtta, “Investigation of a high-intensity sound beam from a plane transducer—experimental and theoretical results,” *J. Acoust. Soc. Am.* **98**, 2303–2323 (1995).

<sup>5</sup>M. A. Averkiou and M. F. Hamilton, “Measurements of harmonic generation in a focused finite-amplitude sound beam,” *J. Acoust. Soc. Am.* **98**, 3439–3442 (1995).

<sup>6</sup>J. A. TenCate, “An experimental investigation of the nonlinear pressure field produced by a plane circular piston,” *J. Acoust. Soc. Am.* **94**, 1084–1089 (1993).

<sup>7</sup>J. Berntsen, “Numerical Calculations of Finite Amplitude Sound Beams” in *Frontiers of Nonlinear Acoustics: Proceedings of the 12th ISNA*, edited by M. F. Hamilton and D. T. Blackstock (Elsevier Science, New York, 1990), pp. 191–196.

<sup>8</sup>A. C. Baker, A. M. Berg, A. Sahin, and J. Naze Tjøtta, “The nonlinear

pressure field of plane, rectangular apertures: Experimental and theoretical results,” *J. Acoust. Soc. Am.* **97**, 3510–3517 (1995).

<sup>9</sup>T. Kamakura, M. Tani, Y. Kumamoto, and K. Ueda, “Harmonic generation in finite amplitude sound beams from a rectangular aperture source,” *J. Acoust. Soc. Am.* **91**, 3144–3151 (1992).

<sup>10</sup>T. Kamakura, M. Tani, Y. Kumamoto, and M. A. Breazeale, “Parametric Sound Radiation From a Rectangular Aperture Source,” *Acustica* **80**, 332–338 (1994).

<sup>11</sup>P. K. Verma, V. F. Humphrey, and H. C. Starritt, “Enhanced Absorption Due to Nonlinear Propagation in Diagnostic Ultrasound,” in *Proceedings of the 13th ISNA*, edited by H. Hobæk (World Scientific, Singapore, 1993), pp. 297–302.

<sup>12</sup>H. C. Starritt, F. A. Duck, and V. F. Humphrey, “Forces Acting in the Direction of Propagation in Pulsed Ultrasound Fields,” *Phys. Med. Biol.* **36**(11), 1465–1474 (1991).

<sup>13</sup>H. Mitome, T. Kozuka, and T. Tuziuti, “Effects of Nonlinearity in Development of Acoustic Streaming,” *Jpn. J. Appl. Phys., Part 1* **34**(5B), 2584–2589 (1995).

<sup>14</sup>T. Kamakura, T. Sudo, K. Matsuda, and Y. Kumamoto, “Time evolution of acoustic streaming from a planar ultrasound source,” *J. Acoust. Soc. Am.* **100**, 132–138 (1996).

<sup>15</sup>M. D. Cahill and A. C. Baker, “Increased off-axis energy deposition due to diffraction and nonlinear propagation of ultrasound from rectangular sources,” *J. Acoust. Soc. Am.* **102**, 199–203 (1997).

- <sup>16</sup>V. P. Kuznetsov, "Equations of Nonlinear Acoustics," *Sov. Phys. Acoust.* **16**, 467–470 (1971).
- <sup>17</sup>E. A. Zabolotskaya and R. V. Khokhlov, "Quasi-plane waves in the Nonlinear Acoustics of Confined Beams," *Sov. Phys. Acoust.* **15**, 35 (1969).
- <sup>18</sup>J. Naze Tjøtta, S. Tjøtta, and E. H. Vefring, "Effects of focusing on the nonlinear interaction between two collinear finite amplitude sound beams," *J. Acoust. Soc. Am.* **89**, 1017–1027 (1991).
- <sup>19</sup>J. Naze Tjøtta and S. Tjøtta, "Nonlinear equations of acoustics," in *Frontiers of Nonlinear Acoustics: Proceedings of the 12th ISNA*, edited by M. F. Hamilton and D. T. Blackstock (Elsevier Science, New York, 1990), pp. 80–97.
- <sup>20</sup>P. T. Christopher and K. J. Parker, "New approaches to nonlinear diffractive field Propagation," *J. Acoust. Soc. Am.* **90**, 488–499 (1991).

# Flow generated around particle clusters in a rotating ultrasonic waveguide

Glenn Whitworth

*P.O. Box 167, Marlborough, New Hampshire 03455*

(Received 9 February 1995; accepted for publication 18 May 1998)

A chamber cavity, which has a square cross section and pressure-release walls, is used to produce a well-defined, 160-kHz standing ultrasonic field. A suspension of latex microspheres in aqueous metrizamide fills the chamber. The chamber rotates about a horizontal axis producing the centripetal force necessary to contain the buoyant spheres in the axial region. At low particle concentrations, clusters of microspheres form at half-wavelength intervals near the axial positions of acoustic pressure amplitude ( $p_0$ ) minima, as expected because of rotational and acoustic radiation forces. At higher concentrations, additional particle distributions are often seen that suggest the presence of flow. When high concentrations of larger particles are used, small clusters also form at axial positions of  $p_0$  maxima. Theory for acoustic streaming in a rotating fluid predicts flow speeds that are too small to account for the observed flow. Reasonable agreement with observations is obtained using a theory for flow generated by the buoyant gravitational force acting on the clusters. © 1998 Acoustical Society of America. [S0001-4966(98)02109-2]

PACS numbers: 43.25.Nm [MAB]

## INTRODUCTION

Particles suspended in an acoustic field experience non-zero temporal-average radiation forces that move them to preferred regions of the field.<sup>1</sup> The first calculation of radiation force on a rigid sphere was carried out by King.<sup>2</sup> A convenient theory for the force on a small, compressible, spherical particle in an arbitrary field is given by Gor'kov.<sup>3</sup> For a dilute particle suspension in a stationary wave field, Gor'kov's theory for noninteracting particles provides a good description of the equilibrium particle distribution including the formation of particle columns.<sup>4,5</sup> However, some topics of practical interest, such as techniques for harvesting ultrasonically concentrated particles,<sup>6-12</sup> or topics of possible concern, such as the banding and stoppage of blood flow with ultrasound,<sup>13,14</sup> can involve high concentrations of particles. The present article represents the first study of the combined influence of gravitational, rotational, and acoustic radiation forces on high concentrations of particles. It is a continuation of earlier work<sup>4</sup> done at lower particle concentrations.

## I. EQUIPMENT

A detailed description of the acoustic chamber is given elsewhere.<sup>4</sup> The chamber cavity has a cross section that is 8.8 mm square and has a length of 70 mm. When filled with a particle suspension and driven at a frequency of 160 kHz, the chamber acts as a single-mode acoustic waveguide with pressure-release boundary conditions. This single mode has the amplitude

$$p_0(x, y, z) = P_0 \sin(\pi x/a) \sin(\pi y/a) \times \sin\{[(\omega/c)^2 - 2(\pi/a)^2]^{1/2} z\}, \quad (1)$$

where  $P_0$  is the spatial-peak pressure amplitude,  $a$  is the cross-sectional dimension,  $\omega$  is the acoustic angular frequency,  $c$  is the speed of sound, and the  $z$  direction is parallel

to the long axis of the chamber. The acoustic pressure varies sinusoidally in all three directions and is zero on the four side walls and on the wall opposing the transducer. In the  $x$  and  $y$  directions the pressure rises monotonically to a maximum along the axis of symmetry. In the  $z$  direction the field shows a series of equal amplitude maxima separated by cusps of zero pressure.

Aqueous metrizamide solution is used to fill the ultrasonic chamber because it has a unique combination of properties, including low viscosity and high density. The chamber rotates about a horizontal axis at 420 rpm producing the centripetal force necessary to contain the buoyant particles in the axial region.

## II. OBSERVATIONS

At low particle concentrations, clusters of microspheres form at half-wavelength intervals near the axial positions of acoustic pressure amplitude ( $p_0$ ) minima, as expected because of rotational and acoustic radiation forces.<sup>4</sup> When a greater number of particles is present, however, the particle behavior becomes more complicated. Figure 1 is a photograph showing a steady-state distribution of a large number of latex microspheres with diameter 6–14  $\mu\text{m}$ . [Approximately  $(0.08 \pm 0.02)\%$  of the chamber cavity was occupied by microspheres.] As with earlier experiments<sup>4</sup> using a small number of particles, the spheres formed clusters at half-wavelength intervals. An unexpected feature of Fig. 1 was the shell-like formations of particles between these clusters. The particle formations are sharply defined in the radial direction. This maximum radial dimension was found not to change when the spatial-peak acoustic pressure amplitude ( $P_0$ ) was varied by a factor of 5 (from 100 to 500 kPa). This observation indicates that the radial dimension of the formations is not the result of an equilibrium between a rotational force toward the chamber axis and an acoustic radiation force away from the axis.

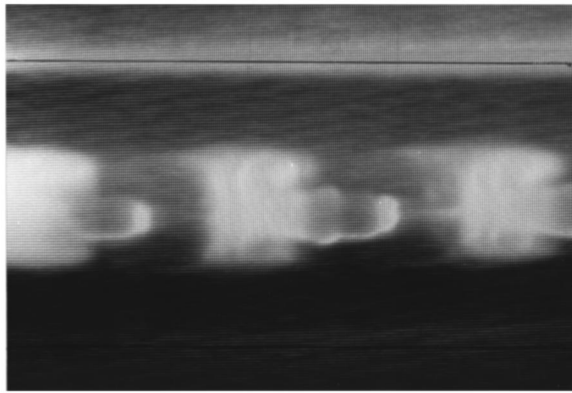


FIG. 1. A steady-state distribution of a large number of 6–14- $\mu\text{m}$  latex microspheres. The approximate positions of two of the side walls are indicated.

Different behavior was observed using larger particles. Figure 2 is a photograph showing the resulting steady-state distribution of a large number of 273- $\mu\text{m}$ -diameter latex microspheres in the acoustic chamber cavity. [The fractional volume of the chamber cavity occupied by microspheres was roughly  $(0.9 \pm 0.2)\%$ .] Again, large clusters are located along the chamber axis at the  $p_0$  minima, but an unexpected feature of Fig. 2 was the series of smaller clusters located at the  $p_0$  maxima, midway between the large clusters. These examples show that the scalar potential theory used by Whitworth and Nyborg<sup>4</sup> does not give a complete description of particle behavior when a large number of particles are present.

A clue to the reason for the unexpected particle distributions was found by observing the smaller particles before they had reached their steady-state distribution. In experiments where the ultrasound and the chamber rotation were turned on simultaneously the distributions appeared very slowly out of a cloud of particles. Although the shell-like formations had a flowing appearance, no actual particle motion could be seen. In other experiments, however, the ultrasound stayed off until the chamber had rotated long enough for the 6–14- $\mu\text{m}$  latex particles to collect in a band along the axis of rotation. After the ultrasound was then turned on, the boundary of the concentrated particles advanced into particle-free regions as a clearly visible flow. Figures 3 and 4

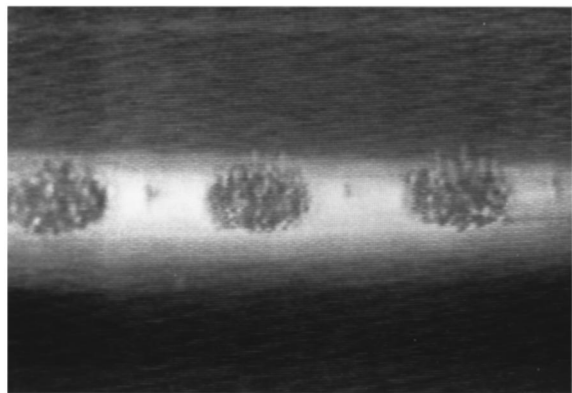


FIG. 2. When a large number of 273- $\mu\text{m}$  latex particles were present small secondary clusters could be seen at the  $p_0$  maxima in addition to the large clusters at  $p_0$  minima.

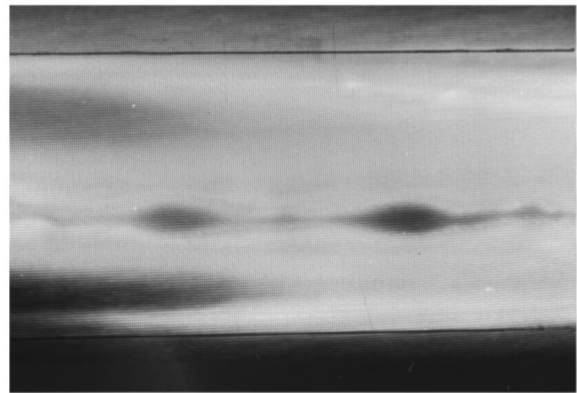


FIG. 3. A transient-state distribution of 6–14- $\mu\text{m}$  latex microspheres. Large clusters form at the  $p_0$  minima and much smaller clusters are found at the  $p_0$  maxima. The approximate positions of two of the side walls are indicated.

are in time sequence. The  $P_0$  was  $500 \pm 200$  kPa. As shown in Fig. 3 the particles initially formed spherical clusters at the  $p_0$  minima. Also, there appears to be some clustering of particles at the  $p_0$  maxima as was seen with the larger particles in Fig. 2. Particles were soon seen being dragged from the larger clusters resulting in the distribution shown in Fig. 4. The measured speed  $w_m$  at which these particles moved away from the clusters was

$$w_m = 50 \pm 10 \text{ } \mu\text{m/s.} \quad (2)$$

The formations continued to grow until the steady-state condition shown in Fig. 1 was reached.

Experiments were done to investigate the cause of flow in the chamber. The acoustic chamber cavity was filled with a rheoscopic fluid (Kalliroscope Corp., type AQ-RF) produced for the purpose of visualizing fluid motions. With the chamber rotating at 420 rpm (with no sound field present) no evidence of hydrodynamic flow could be seen. When the chamber's rotation was abruptly stopped the rheoscopic fluid came to rest within about 5 s, giving an estimate of the spin-up and spin-down times. Observations were also made of a sparse distribution of latex microspheres in a metrizamide solution chosen so as to be neutrally buoyant. Again

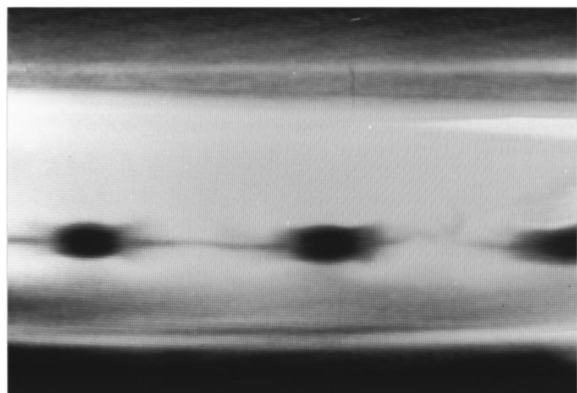


FIG. 4. The same particle clusters of Fig. 3 shown a short time later. Particles are starting to be dragged off of the clusters in the axial direction. This is the beginning stage of formation growth.

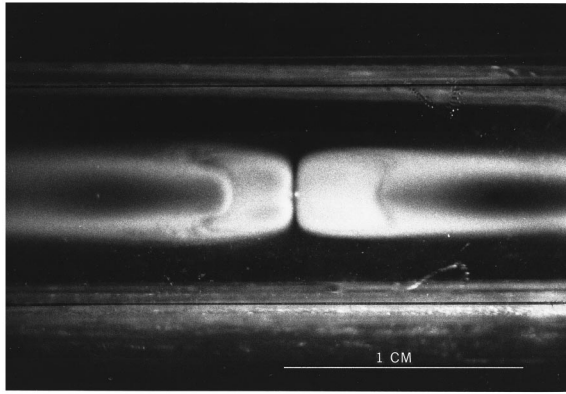


FIG. 5. The effect of a small air bubble on a dense cloud of red blood cells along the chamber axis. The “clear” region at the position of the bubble (centered in the photograph) is due to particle-free fluid being drawn inward at that location. The approximate positions of two of the side walls are indicated.

there was no evidence of a rotation-induced flow (relative to the rotating chamber) with the chamber rotating at 420 rpm and the ultrasound off.

If, however, there are inclusions that create drag on the fluid then a rotation-induced flow can be generated. An experiment was done in which an air bubble acted as an inclusion and red blood cells (RBC’s) were present to indicate flow. Figure 5 is a photograph showing the (rotating) acoustic chamber cavity containing RBC’s in a metrizamide solution and one small air bubble. The RBC’s can be seen as a dense cloud along the rotational axis of the chamber. The air bubble exerts a drag on the fluid and generates a hydrodynamic flow inward along the radial direction and outward along the chamber axis. The “clear” region at the position of the bubble is due to particle-free fluid being drawn inward at that location. [The mechanism by which a bubble resides slightly off-axis, and its drag on the fluid (equal to the  $-\Theta$  component of buoyancy) causes flow, is described in greater detail in Sec. III B.]

Particle clusters also experience drag and, therefore, have the potential for generating rotation-induced flow. With the chamber rotating at 420 rpm and the ultrasound turned on (to maintain the clusters) the stroboscopically illuminated clusters were observed by stereo-microscope. The clusters appeared to rotate backwards one revolution every 2 min (i.e., the clusters were actually rotating at 419.5 rpm while the chamber rotated at 420 rpm). Cluster rotation relative to the fluid is evidence of a small drag force on the fluid. Cluster drag will be shown to have a significant effect on flow within the chamber cavity.

Two types of hydrodynamic flow will be discussed in Sec. III. The first type of flow, called acoustic streaming, is the time-independent component of fluid motion generated by an acoustic field. The second, which will be called “rotation-induced flow” is generated by the rotation of the chamber.

### III. THEORY

#### A. Acoustic streaming

Acoustic streaming theory (for a nonrotating system) predicts that no streaming will be generated by a stationary

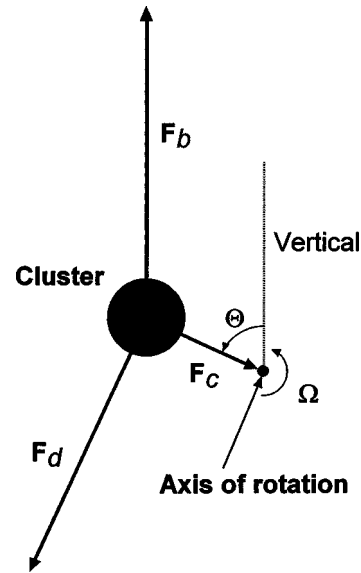


FIG. 6. The defining sketch for a stationary bubble or particle cluster in a fluid rotating with constant angular velocity.

field in a waveguide with pressure-release boundaries.<sup>5</sup> It can also be shown that if the field has a small traveling wave component (due to absorption) then a quartz-wind will develop, but it will not have a periodicity related to that of the standing wave component.<sup>15</sup>

If a nonslip boundary condition is assumed to exist at the surface of the particle clusters then the theory of Wang<sup>16</sup> for acoustic streaming generated around a sphere (in a nonrotating system) can be applied. Calculations show that the acoustic streaming speed predicted by this theory would be of marginally sufficient magnitude to account for the observed flow if the system were not rotating.<sup>15</sup> However, theory for acoustic streaming in a rotating fluid<sup>17</sup> indicates that after correcting for rotation this predicted speed becomes much too small to explain the observed flow.

#### B. Rotation-induced flow

##### 1. Estimation of cluster position

To find the flow generated by a particle cluster it is first necessary to calculate its position relative to the chamber’s axis of rotation. Figure 6 is the defining sketch for a cluster (or other buoyant inclusion such as an air bubble) in a fluid-filled rotating chamber. Three forces act on the cluster: a buoyant force  $\mathbf{F}_b$  in the vertical ( $\Theta=0$ ) direction, a centripetal force  $\mathbf{F}_c$  directed toward the axis of rotation, and a drag force  $\mathbf{F}_d$  directed tangent to the fluid flow past the cluster. These forces are given by

$$\mathbf{F}_b = Vg(\rho - \rho^*)[\cos(\Theta)\hat{r} - \sin(\Theta)\hat{\Theta}], \quad (3)$$

$$\mathbf{F}_c = -V(\rho - \rho^*)\Omega^2 r\hat{r}, \quad (4)$$

and

$$\mathbf{F}_d = D\Omega r\hat{\Theta}, \quad (5)$$

where  $V$  is the cluster volume,  $\rho$  is the fluid density,  $\rho^*$  is the cluster density,  $g$  is the gravitational field strength,  $\Omega$  is the angular speed of the fluid,  $\Theta$  is the angular position of the

cluster relative to the vertical, and  $D$  is a drag factor. An equilibrium position for the center of the cluster can be found by setting the sum of the forces in Eqs. (3)–(5) equal to zero. The resulting position is given by

$$\Theta = \tan^{-1}\{D/[\Omega V(\rho - \rho^*)]\} \quad (6)$$

and

$$r = gV(\rho - \rho^*)/\{\Omega[D^2 + [\Omega V(\rho - \rho^*)]^2]^{1/2}\}. \quad (7)$$

If it is assumed that the Stokes formula for drag on a solid sphere is approximately valid for a cluster, then the drag factor becomes

$$D = 6\pi\mu b, \quad (8)$$

where  $b$  is the cluster radius and  $\mu$  is the coefficient of shear viscosity.

The cluster is composed, in part, by latex microspheres that have a density of  $1058 \text{ kg/m}^3$ . Approximately 40% of the volume of the cluster is occupied by the microspheres. The remaining spaces between the microspheres are filled by the host medium which has a density  $\rho$  of  $1210 \text{ kg/m}^3$ . The resulting cluster density  $\rho^*$  is therefore equal to  $1150 \text{ kg/m}^3$ . The host medium has a coefficient of shear viscosity  $\mu$  equal to  $2 \text{ mPa s}$  and rotates with angular speed  $\Omega$  of  $44 \text{ rad/s}$  at positions far from the cluster. Equations (6) and (7) can be used to estimate that the center of a cluster with radius  $0.7 \text{ mm}$  will lie  $0.73 \text{ mm}$  from the axis of rotation at an angle of  $82^\circ$  from the vertical. (This distance cannot be determined directly from the figures because the angle of the camera is unspecified.)

## 2. Calculating the flow

As discussed in Sec. II, the buoyant force on an air bubble or a particle cluster can create flow within a rotating chamber. With an air bubble this flow does not require the presence of an acoustic field. With particles, an acoustic field is required only to supply the radiation forces necessary to maintain the clusters. The purpose of this section is to theoretically estimate the axial component of flow generated by a single cluster in an unbounded rotating fluid. This result is then compared with the experimental observed flow generated by clusters in the rotating chamber cavity.

An exact solution to this problem could be attempted by solving the hydrodynamic equations subject to moving boundary conditions at the surface of the off-axis cluster. (In the reference frame of the rotating fluid the cluster whirls around the axis of rotation with angular velocity  $-\Omega$ .) The time-dependent boundary conditions and the lack of axial symmetry could make solving this problem a formidable task. However, an approximate solution can be readily obtained by treating the cluster as a source of body force (its buoyant force), and replacing the cluster by an axially symmetric force distribution which is assumed to act on a homogeneous fluid. The experimental results indicate that this approximation is valid over the applied range of conditions.

The vorticity-transport equation for slow, time-independent, incompressible flow generated by a body force per unit volume  $\mathbf{G}$  in a rotating reference frame is given by Lugt.<sup>18</sup> If the Ekman number (given by  $\mu/\rho\Omega L^2$  where  $L$  is

a characteristic length)<sup>19</sup> is small then the viscous term can be omitted. If the axis of rotation is defined to be in the  $z$  direction, then the governing equation for the flow velocity  $\mathbf{u}$  becomes

$$\nabla \times \mathbf{G} = -2\rho\Omega \partial\mathbf{u}/\partial z. \quad (9)$$

The  $z$  component of Eq. (9) can be put in the form

$$u_z = (2\rho\Omega)^{-1} \int_0^z [-G_\Theta/r + \partial(-G_\Theta)/\partial r] dz, \quad (10)$$

where  $-G_\Theta$  is the body force per unit volume in the  $-\Theta$  direction and  $u_z$  is the resulting axial component of flow velocity. The cluster's body force is symmetric about the plane  $z=0$ .

It will be assumed that  $-G_\Theta$  has axial symmetry (in a time-averaged sense) and that it can be written in the form

$$-G_\Theta(r, z) = f(r)h(z), \quad (11)$$

where  $f$  is a function of  $r$  only and  $h$  is a function of  $z$  only. Equation (10) now becomes

$$u_z(r, z) = [f(r)/r + \partial f(r)/\partial r](2\rho\Omega)^{-1} \int_0^z h(z) dz. \quad (12)$$

A quantity  $B$  will be defined as the integral of  $-G_\Theta$  over volume:

$$B = \int_0^\infty 2\pi r f(r) dr \int_0^\infty 2h(z) dz. \quad (13)$$

[ $B$  is, therefore, a "known" quantity equal to the  $-\Theta$  component of  $\mathbf{F}_b$ . Substitution of values into Eq. (3) gives  $B = 0.85 \mu\text{N}$ .] The combination of Eq. (13) with Eq. (12) gives

$$u_z(r, \infty) = B[f(r)/r + \partial f(r)/\partial r] \left( 8\pi\rho\Omega \int_0^\infty r f(r) dr \right)^{-1}. \quad (14)$$

Equation (14) gives the axial component of velocity at positions which are axially distant from the cluster. It is independent of the axial force distribution  $h(z)$ . Also, Eq. (14) is dependent on the form of the radial force distribution  $f(r)$ , but not on its magnitude.

In the spirit of an order-of-magnitude approximation, a radial force distribution will be chosen so as to represent the time-averaged effect of the cluster on the fluid. The function  $f(r)$  must have a value of zero at  $r=0$ , a maximum value at some radius  $r_0$ , and approach zero at large radial positions. A function having the required form is

$$f(r) = r \exp[-(r/r_0)^2/2]. \quad (15)$$

[A number of other plausible choices for  $f(r)$  were found to predict typical flow velocities similar to those that are obtained using Eq. (15).] The combination of Eq. (15) with Eq. (14) gives the result

$$u_z(r, \infty) = 0.0317B[2 - (r/r_0)^2] \exp[-(r/r_0)^2/2] / \rho\Omega r_0^3. \quad (16)$$

The distance  $r_0$  at which the radial force distribution has its maximum value is taken to be approximately equal to the distance from the axis of rotation to the farthest point on the



cluster. Recalling that a cluster with a radius of 0.7 mm will be centered 0.73 mm from the axis of rotation, it will be assumed that  $r_0$  is equal to 1.4 mm. Equation (16) can now be evaluated at a radial position equal to  $r_0$ . The resulting flow velocity is given by

$$u_z(r_0, \infty) = 110 \text{ } \mu\text{m/s.} \quad (17)$$

This value is in fair agreement with the observed (see Sec. II) flow velocity of 50  $\mu\text{m/s}$  in the axial direction.

The particle formations shown in Fig. 1 have a sharply defined maximum radial dimension of approximately 2 mm. This type of particle distribution results from axial flow away from the cluster near the axis of rotation, and axial flow toward the cluster at larger radial positions. Flow in the axial direction must change direction at a radius less than the maximum radial dimension of the particle formation.

Equation (16) predicts a reversal of flow direction at a radial distance  $r_{\text{rev}}$  given by

$$r_{\text{rev}} = 2^{1/2} r_0. \quad (18)$$

If  $r_0$  is given by 1.4 mm then  $r_{\text{rev}}$  is equal to 2.0 mm. This is in fair agreement with the required result of  $r_{\text{rev}} < 2.0$  mm.

Equation (18) was derived under the assumption of an unbounded fluid. This reversal in axial flow direction is, therefore, not simply the result of a requirement that mass must be conserved in a closed chamber. The continuity requirements due to the additional boundaries in a closed chamber may result in a secondary flow field near the chamber walls. This secondary flow may be expected to “squeeze” the radial dimensions of the flow predicted by Eq. (16). A slightly smaller value for the reversal radius  $r_{\text{rev}}$  would produce even better agreement with observation.

### C. The effect of particle size

Figures 1 and 2 show that the smaller (6–14  $\mu\text{m}$ ) particles form diffuse shell-like formations at the  $p_0$  maxima whereas the larger (273  $\mu\text{m}$ ) particles form only clusters at these locations. Steady-state particle distributions would be expected to depend on particle size if the forces involved do not all have the same functional dependence on size. The forces due to gravity, rotation, and acoustic radiation on non-interacting particles are all linearly proportional to the particle volume.<sup>4</sup> Particles in close proximity will also experience an attractive, time-averaged, interaction force due to the difference in compressibility between the particles and the host medium. This force has its maximum effect at the positions of maximum  $p_0$ : the same region where the small clusters are found. For a pair of identical spheres, the interparticle attraction is proportional to the particle volume squared.<sup>20</sup> It is therefore consistent that larger particles should show a greater tendency to cluster at the  $p_0$  maxima.

Flow, on the other hand, tends to drag particles away from clusters. Since the Stokes drag on a particle is only proportional to the radius whereas the forces that tend to cause clusters are proportional to volume or volume squared, the flow will be relatively more successful at removing smaller particles from clusters.

## IV. CONCLUSIONS

It has been shown that a highly concentrated particle suspension in a rotating ultrasonic waveguide can behave quite differently from a suspension of lower concentration, and that this difference is due largely to the generation of flow. The acoustical mechanism of this flow generation is unusual. It is distinct from ordinary acoustic streaming and also from flow that might be generated while using a pseudostanding wave<sup>6</sup> to move particle clumps through stationary fluid. The ultrasound acts indirectly by positioning and maintaining the integrity of particle clusters. The buoyant force of those clusters can then act on the rotating fluid and cause a flow of much greater magnitude than is generated directly by acoustic streaming.

## ACKNOWLEDGMENTS

Useful discussions with Professor Wesley L. Nyborg are gratefully acknowledged. I would also like to thank the other members of my thesis committee in the Biophysics Program at the University of Virginia for their support of this project and the University of Vermont Physics department for use of their research facilities. The work was funded by NIH Grants No. GM08209 and No. CA42947.

- <sup>1</sup>W. L. Nyborg, “Physical principles of ultrasound,” in *Ultrasound: Its Applications in Medicine and Biology, Part I*, edited by F. J. Fry (Elsevier, New York, 1978), pp. 1–76.
- <sup>2</sup>L. V. King, Proc. R. Soc. London, Ser. A **147**, 212–240 (1934).
- <sup>3</sup>L. P. Gor'kov, Sov. Phys. Dokl. **6**, 773–775 (1962).
- <sup>4</sup>G. Whitworth and W. L. Nyborg, J. Acoust. Soc. Am. **90**, 2091–2096 (1991).
- <sup>5</sup>G. Whitworth and W. T. Coakley, J. Acoust. Soc. Am. **91**, 79–85 (1992).
- <sup>6</sup>G. Whitworth, M. A. Grundy, and W. T. Coakley, Ultrasonics **29**, 439–444 (1991).
- <sup>7</sup>S. Peterson, G. Perkins, and C. Baker, *IEEE/Eighth Annual Conference of the Engineering in Medicine and Biology Society* (IEEE, New York, 1986), pp. 154–156.
- <sup>8</sup>T. L. Tolt and D. L. Feke, J. Acoust. Soc. Am. **91**, 3152–3156 (1992).
- <sup>9</sup>W. T. Coakley, D. W. Bardsley, M. A. Grundy, F. Zamani, and D. J. Clarke, J. Chem. Tech. Biotechnol. **44**, 43–62 (1989).
- <sup>10</sup>D. G. Kilburn, D. J. Clarke, W. T. Coakley, and D. W. Bardsley, Biotechnol. Bioeng. **34**, 559–562 (1989).
- <sup>11</sup>G. Whitworth, “Ultrasound induced columns,” British patent application number 9005705.0.
- <sup>12</sup>C. J. Schram, “Separation of particles in a liquid medium—using varied ultrasonic wave,” European Patent 167406 (1984).
- <sup>13</sup>M. Dyson, B. Woodward, and J. B. Pond, Nature (London) **232**, 572–573 (1971).
- <sup>14</sup>M. Dyson, J. B. Pond, B. Woodward, and J. Broadbent, Ultrasound Med. Biol. **1**, 133–148 (1973).
- <sup>15</sup>G. Whitworth, Ph.D. thesis, University of Virginia, 1989, University Microfilms, Ann Arbor, Michigan.
- <sup>16</sup>C. Y. Wang, J. Sound Vib. **2**, 257–269 (1965).
- <sup>17</sup>G. Whitworth, J. Acoust. Soc. Am. **88**, 1960–1963 (1990).
- <sup>18</sup>H. J. Lugt, *Vortex Flow in Nature and Technology* (Wiley, New York, 1983).
- <sup>19</sup>H. P. Greenspan, *The Theory of Rotating Fluids* (Cambridge U. P., Cambridge, England, 1968).
- <sup>20</sup>M. A. H. Weiser, R. E. Apfel, and E. A. Neppiras, Acustica **56**, 114–119 (1984).

# Nonanalytic nonlinear oscillations: Christiaan Huygens, quadratic Schrödinger equations, and solitary waves

Bruce Denardo

*Department of Physics and Astronomy and National Center for Physical Acoustics,  
University of Mississippi, University, Mississippi 38677*

(Received 26 June 1997; revised 3 June 1998; accepted 11 June 1998)

An example of an oscillatory system with a time-reversible nonanalytic nonlinearity is shown to be a pendulum with a flexible cord sandwiched between two identical circular disks, in contrast to the analytic case of a pendulum interrupted by a single circular disk. The amplitude-dependent frequencies of both cases are perturbatively calculated, and are compared to numerical simulations over the entire range of amplitudes. The nonanalyticity causes the unusual effect of the frequency to vary *linearly* with amplitude for small amplitudes, which has also been observed in the resonant frequencies of compressional standing waves in sandstone. A general condition for a nonanalytic nonlinearity to yield this behavior is presented. The amplitude-dependent frequency for the double-interrupted pendulum allows an explanation for Huygens' surprising observation that circular interrupters were as effective as cycloidal interrupters in achieving isochronous motion. A lattice of linearly coupled double-interrupted pendulums is described near the lower and upper cutoff modes by *quadratic* nonlinear Schrödinger (NLS) equations, in contrast to cubic NLS equations which arise for analytic pendulum lattices as well as typical acoustic and surface waveguides. Solitary breather and kink solutions to the quadratic NLS equations are presented, and are compared to the known soliton solutions of the corresponding cubic NLS equations. Compressional waves in sandstone are shown to be modeled by the inclusion of a nonanalytic quadratic nonlinearity in the stress-strain relationship. Quadratic NLS breathers are predicted to occur in a waveguide of sandstone, and an analysis indicates that such an observation is feasible. © 1998 Acoustical Society of America. [S0001-4966(98)05309-0]

PACS numbers: 43.25.Ts [MAB]

## INTRODUCTION

The natural frequency of an oscillator or standing wave is typically independent of amplitude only in the limit of small amplitudes; nonlinearities cause the frequency to depend upon amplitude.<sup>1,2</sup> The standard pendulum "softens" (the frequency is a *decreasing* function of the amplitude). This character can be different in an interrupted pendulum, in which one or more obstructions alter the trajectory of the motion. The classic example is Huygens' cycloidal pendulum,<sup>3</sup> which is exactly simple harmonic and thus has an amplitude-independent frequency. In this case the softening is balanced by the "hardening" due to the shortening of the length of the pendulum. It is natural to ask how the frequency depends upon amplitude when one or two *circular* interrupters are employed (Figs. 1 and 2). Indeed, Huygens experimented with the latter arrangement and found it to be as effective as cycloidal interrupters.<sup>4</sup> An extensive search of mechanics books, monographs on nonlinear oscillations, and databases did not yield any other mention of the double circularly interrupted pendulum. Lamb<sup>5</sup> treats several limited aspects of the single-interrupted pendulum. In the first part of this article, we employ a perturbative approach to solve for the amplitude-dependent frequencies of these systems, and compare the results to numerical data. The results for the double-interrupted pendulum allow an explanation for Huygens' surprising observation. Remarkably, the results for the single-interrupted pendulum show that this system can be nearly isochronous.

A motivation for these investigations is the fact that the double-interrupted pendulum is an example of a time-reversible *nonanalytic* nonlinearity, in which a discontinuity exists in the function or any derivative of it. Nonanalytic oscillations have received little attention in the scientific literature. In contrast to our case, previous investigations have focused on either a nonlinearity that abruptly arises at a non-zero response amplitude, as in the standard case of a continuous piecewise-linear restoring force,<sup>6</sup> or on cases where linear motion does not occur even for arbitrarily small amplitudes. Examples of the latter are a force that includes a term proportional to  $x/|x|$ ,<sup>7</sup> and a force proportional to  $-|x|^{v-1}x$ , where  $0 < v < 1$ .<sup>8</sup> We generalize the results of the double-interrupted pendulum to show that a broad class of nonanalytic nonlinearities fundamentally alters the typical amplitude-dependent frequency of an oscillator or standing wave. Because recent frequency response data for plane standing compressional waves in sandstone exhibit the effect,<sup>9</sup> this system can be modeled by such a nonlinearity.

In the second part of this article, we consider lattices of single- and double-interrupted pendulums, which are representative of general lattices of analytic and nonanalytic nonlinear oscillators, respectively. Weakly nonlinear and slowly varying amplitude modulations near the lower and upper cutoff modes of the double-interrupted lattice are shown to be described by *quadratic* nonlinear Schrödinger (NLS) equations, in contrast to typical cubic NLS equations<sup>10,11</sup> which arise for the single-interrupted lattice. A motivation for in-

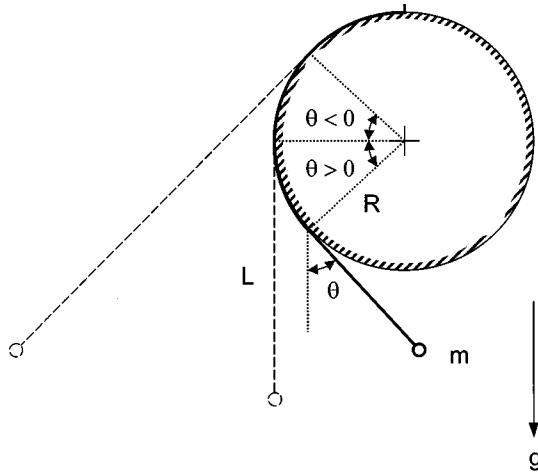


FIG. 1. Flexible pendulum with its cord wrapped around a circular interrupter. The equilibrium length of the cord is  $L$ .

investigating a lattice of single-interrupted pendulums arises from observations of cubic NLS solitons in a softening lattice of standard pendulums.<sup>10,11</sup> These solitons are of two types: lower cutoff breathers and upper cutoff kinks. A lattice of hardening oscillators has been predicted<sup>11</sup> to yield the same solitons but reversed with respect to the type of cutoff mode in which they exist. We predict that such a physical system can be obtained if a single cylindrical interrupter of sufficiently large radius is built into a flexible pendulum lattice.

Propagating breather and kink solitary wave solutions of the quadratic NLS equations are presented, and are contrasted with soliton solutions of the cubic NLS equations. A solution analogous to our breather wave arises in quantum field theory.<sup>12</sup> Algebraically (as opposed to exponentially) localized solutions of a NLS equation with both quadratic and cubic terms have recently been explored.<sup>12,13</sup> We predict that quadratic NLS solitary waves can occur in a pendulum lattice with double cylindrical interrupters, or any lattice with nonanalytic nonlinearities in the broad class mentioned above. Furthermore, because the mathematical description of a lattice of coupled oscillators near the lower cutoff mode is closely related to that of acoustic,<sup>14,15</sup> model,<sup>16</sup> and surface<sup>17-21</sup> waveguides near a cutoff mode, these solitary

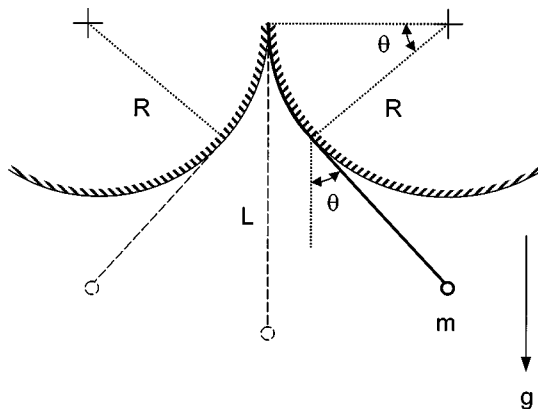


FIG. 2. Flexible pendulum with its cord sandwiched between two identical circular interrupters.

waves can occur in waveguides with similar nonanalytic nonlinearities. In particular, we show that compressional waves in sandstone can be modeled by such a softening nonanalytic nonlinearity, and that the transverse displacement in a waveguide of this medium is described by a quadratic NLS equation. Quadratic NLS breathers are thus predicted to occur, and a feasibility analysis indicates that these waves should be readily observable.

The amplitude-dependent frequencies of the single- and double-interrupted pendulums are examined in Secs. I and II, respectively. The connection of circular interrupters to Huygens' investigations is examined in Sec. III. Lattices of coupled single- and double-interrupted pendulums are considered in Sec. IV, and solitary wave solutions to the quadratic NLS equations are presented in Sec. V. Compressional waves in sandstone are considered in Sec. VI.

## I. SINGLE-INTERRUPTED PENDULUM

We assume that the cords of the circularly interrupted pendulums in Figs. 1 and 2 are massless and perfectly flexible, the bobs are point masses, and the motion is undriven and undamped. In this section, we consider the single-interrupted pendulum (Fig. 1). The kinetic energy is  $m(L - R\theta)^2(d\theta/dt)^2/2$  and potential energy is  $-mg[R \sin(\theta) + (L - R\theta)\cos(\theta)]$ . The Lagrangian approach then yields the exact equation of motion

$$\frac{d^2\theta}{dt^2} + \omega_0^2 \sin(\theta) = \rho \frac{d}{dt} \left( \theta \frac{d\theta}{dt} \right), \quad (1)$$

where the square linear frequency is  $\omega_0^2 = g/L$  and the dimensionless geometrical parameter is  $\rho = R/L$ , where  $0 \leq \rho < \infty$ . We consider oscillation amplitudes between  $\theta = 0$  and  $\theta = \theta_{\max}$ , where

$$\theta_{\max} = \min(1/\rho, \pi/2). \quad (2)$$

The first value in the parentheses of Eq. (2) corresponds to the mass striking the interrupter, while the second corresponds to vanishing tension in the pendulum cord (greater amplitudes lead to projectile motion).

It should be mentioned that an alternative to the coordinate  $\theta$  is the directed distance  $s$  along the trajectory of the mass. The differential relationship between  $\theta$  and the dimensionless coordinate  $\zeta = s/L$  is  $d\zeta = (1 - \rho\theta) d\theta$ , which yields

$$\zeta = \theta - \frac{1}{2}\rho\theta^2 \quad (3)$$

upon integration. The  $\zeta$  equation of motion can be found by equating the tangential acceleration to the tangential force per unit mass:  $d^2\zeta/dt^2 = -\omega_0^2 \sin[\theta(\zeta)]$ . Substituting  $\theta(\zeta)$  from Eq. (3) into this equation, and expanding to third order in  $\zeta$ , gives

$$\frac{d^2\zeta}{dt^2} + \omega_0^2\zeta = -\frac{1}{2}\omega_0^2\rho\zeta^2 - \frac{1}{6}\omega_0^2(3\rho^2 - 1)\zeta^3 + \dots \quad (4)$$

One can alternatively derive Eq. (4) by using Eq. (3) to transform the  $\theta$  equation of motion (1). Although the  $\zeta$  equation (4) has the conceptual advantage of possessing a simple potential energy function, we deal with the  $\theta$  equation (1) be-

cause it is exact, which is preferable in numerical simulations, and because the maximum value (2) of the  $\theta$  coordinate is more direct. All of the perturbative results in this article have been reproduced with the  $\zeta$  equation of motion (4) or its modification for the double-interrupted case (Sec. II).

Although one integration (corresponding to energy conservation) can be performed in the equation of motion (1), the second appears to be difficult to express in closed form. Regardless of such a solution for an oscillator, however, approximations are necessary when dealing with lattices and continua (Secs. IV and VI). To perturbatively determine the amplitude-dependent frequency corresponding to the equation of motion (1), we employ the method of harmonic balance.<sup>2</sup> The displacement is represented as a perturbation series of harmonics:

$$\theta = \varepsilon A \cos(\omega t) + \varepsilon^2 B \cos(2\omega t) + \varepsilon^3 C \cos(3\omega t) + \dots, \quad (5)$$

where  $\varepsilon$  is a smallness parameter which is set to unity in the final results, and where the square frequency is also expressed as a perturbation expansion:

$$\omega^2 = \omega_0^2 + \varepsilon \omega_1^2 + \varepsilon^2 \omega_2^2 + \varepsilon^3 \omega_3^2 + \dots. \quad (6)$$

The process of balancing the harmonics can be made more transparent if we define the dimensionless time variable  $\tau = \omega t$ , divide the resultant equation of motion (1) by  $\omega^2$ , and express the displacement (5) as  $\theta = \varepsilon \theta_1 + \varepsilon^2 \theta_2 + \varepsilon^3 \theta_3 + \dots$ . The equation of motion to order  $\varepsilon^2$  is then

$$\frac{d^2 \theta_2}{d\tau^2} + \theta_2 = \frac{\omega_1^2}{\omega_0^2} \theta_1 + \rho \frac{d}{d\tau} \left( \theta_1 \frac{d}{d\tau} \theta_1 \right). \quad (7)$$

We now substitute  $\theta_1 = A \cos(\tau)$  and  $\theta_2 = B \cos(2\tau)$  from the harmonic expansion (5), and express the nonlinearity in terms of  $\cos(2\tau)$ . Equating to zero the coefficient of the  $\cos(\tau)$  term yields  $\omega_1 = 0$ , while equating to zero the coefficient of the  $\cos(2\tau)$  term yields  $B = \rho A^2/3$ , which agrees with Lamb's result.<sup>5</sup> At order  $\varepsilon^3$ , the equation of motion (1) is

$$\frac{d^2 \theta_3}{d\tau^2} + \theta_3 = \frac{\omega_2^2}{\omega_0^2} \theta_1 + \frac{1}{6} \theta_1^3 + \rho \frac{d^2}{d\tau^2} (\theta_1 \theta_2). \quad (8)$$

We substitute  $\theta_1 = A \cos(\tau)$ ,  $\theta_2 = B \cos(2\tau)$ , and  $\theta_3 = C \cos(3\tau)$  from the harmonic expansion (5), and express the nonlinear terms as superpositions of  $\cos(\tau)$  and  $\cos(3\tau)$  terms. Equating to zero the coefficient of the  $\cos(\tau)$  term yields an expression for  $\omega_2^2$ . When substituted into Eq. (6), this gives the amplitude-dependent frequency relationship

$$\frac{\omega^2}{\omega_0^2} = 1 + \frac{1}{24} (4\rho^2 - 3) A^2. \quad (9)$$

Equating to zero the coefficient of the  $\cos(3\tau)$  term in Eq. (8) yields  $C = (36\rho^2 - 1)A^3/192$ . To leading order in the amplitude, the frequency shift (relative to the linear value  $\omega_0$ ) varies as the *square* of the amplitude, which is typical for nonlinear oscillators. At the next order, we find  $\omega_3 = 0$ , and so the result (9) is valid to order  $O(A^4)$  (terms of order  $A^4$  and higher are neglected). The result (9) can also be derived with the more-rigorous Lindstedt–Poincaré method of re-

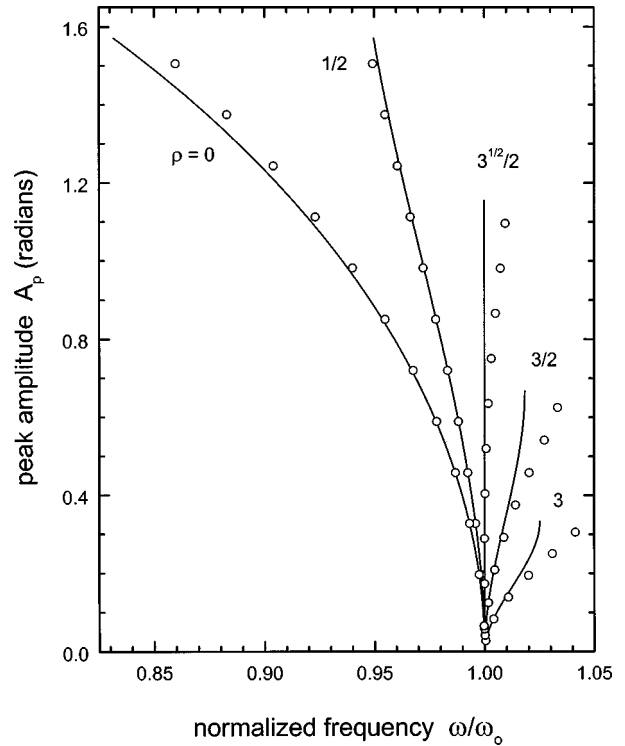


FIG. 3. Amplitude-dependent frequency of the single-interrupted pendulum in Fig. 1 for various values of  $\rho = R/L$ . The peak amplitude  $A_p$  refers to  $\theta > 0$ . The curves correspond to the perturbative theory, and the points to numerical simulations.

moving secularities.<sup>1,2</sup> In this method, no assumptions are made regarding the nature of the perturbation expansion of the displacement.

The expression (9) gives the frequency as a function of the amplitude of the *fundamental*  $A \cos(\omega t)$ . In the time domain, however, numerical and experimental results are naturally expressed in terms of the *peak* amplitude, which is different here for  $\theta > 0$  and  $\theta < 0$  due to the asymmetry of the system. To second order, the  $\theta > 0$  peak amplitude is  $A_p = A + B = A + \rho^2 A^2/3$ , in agreement with Lamb's result.<sup>5</sup> The square frequency (9), valid to order  $O(A_p^4)$ , is then

$$\frac{\omega^2}{\omega_0^2} = 1 + \frac{1}{24} (4\rho^2 - 3) A_p^2 - \frac{1}{36} \rho (4\rho^2 - 3) A_p^3. \quad (10)$$

Figure 3 shows curves of Eq. (10) for various values of  $\rho$ . The standard pendulum corresponds to the special case  $\rho = 0$ . We have plotted  $\omega$  along the abscissa and  $A_p$  along the ordinate due to the connection with frequency response curves (Sec. II). The curves in Fig. 3 are terminated at their corresponding maximum values (2). The points are essentially exact numerical results of a simple finite-difference method (Euler–Cromer method<sup>22</sup>) applied to the exact equation of motion (1). The theory is observed to be accurate for sufficiently small amplitudes, and to break down if the mass passes near the interrupter. The displacement versus time in Fig. 4 indicates that these deviations are due to the strong presence of harmonics higher than the first three, causing the theoretical displacement (5) to third order to be inadequate.

The result (10) reveals that the interrupter causes hardening, which competes with the softening caused by gravity

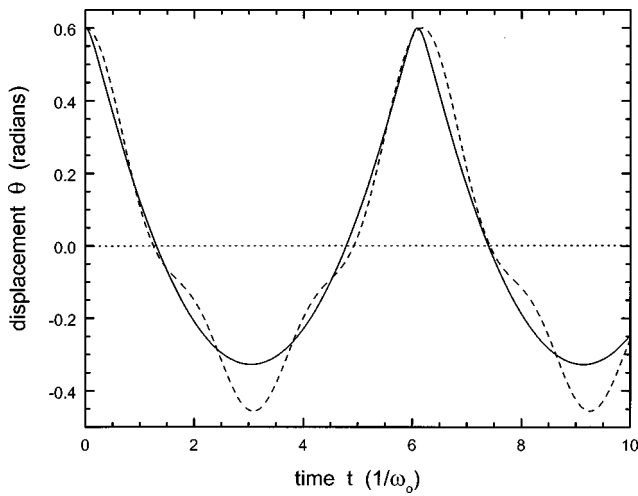


FIG. 4. Displacement versus time for the single-interrupted pendulum in Fig. 1 for  $\rho=3/2$  and  $A_p=0.6$ . The solid curves correspond to a numerical simulation, and the dashed curves to the perturbative theory.

in the absence of interruption ( $\rho=0$ ). The hardening is not obvious for a single interrupter because the pendulum length oscillates about the equilibrium value  $L$ . From Eq. (10), the hardening and softening balance when  $\rho=\sqrt{3}/2$ , which leads to motion that is linear to order  $O(A_p^4)$ . The geometry of Fig. 1 can thus yield a nearly isochronous pendulum.

## II. DOUBLE-INTERRUPTED PENDULUM

The equation of motion for the double-interrupted pendulum (Fig. 2) is given by Eq. (1) only for  $\theta \geq 0$ ; for  $\theta < 0$ , the sign of the quadratic nonlinearity must be reversed due to the symmetry of the motion. The complete equation of motion is thus

$$\frac{d^2 \theta}{dt^2} + \omega_0^2 \sin(\theta) = \rho \operatorname{sgn}(\theta) \frac{d}{dt} \left( \theta \frac{d\theta}{dt} \right), \quad (11)$$

where the sign (or signum) function is

$$\operatorname{sgn}(\theta) = \frac{\theta}{|\theta|}. \quad (12)$$

The equation of motion (11) is *nonanalytic*; in particular, the quadratic nonlinearity is discontinuous at  $\theta=0$ .

In contrast to the single-interrupted pendulum, the perturbation expansion must consist of only odd harmonics due to the symmetry of the equation of motion (11). To obtain the appropriate choice of harmonics, and as a guide in the analysis, we first express the displacement as a general perturbation expansion  $\theta = \varepsilon \theta_1 + \varepsilon^2 \theta_2 + \varepsilon^3 \theta_3 + \dots$ . As in Sec. I, we also define the dimensionless time variable  $\tau = \omega t$  and divide the resultant equation of motion (11) by  $\omega^2$  in Eq. (6). At order  $\varepsilon^2$ , the equation of motion is then

$$\frac{d^2 \theta_2}{d\tau^2} + \theta_2 = \frac{\omega_1^2}{\omega_0^2} \theta_1 + \rho \operatorname{sgn}(\theta_1) \frac{d}{d\tau} \left( \theta_1 \frac{d\theta_1}{d\tau} \right). \quad (13)$$

When the first-order solution  $\theta_1 = A \cos(\tau)$  is substituted into Eq. (3), the nonanalyticity of the nonlinearity causes the Fourier expansion to consist of all odd harmonics, rather than the

second harmonic as in the case (7) of the single-interrupted pendulum:

$$\frac{d^2 \theta_2}{d\tau^2} + \theta_2 = \frac{\omega_1^2}{\omega_0^2} \theta_1 - \rho A^2 \operatorname{sgn}[\cos(\tau)] \cos(2\tau) \quad (14a)$$

$$= \frac{\omega_1^2}{\omega_0^2} \theta_1 - \frac{4\rho A^2}{\pi} \sum_{n=0}^{\infty} \frac{(-1)^{n+1}(2n+1)}{(2n-1)(2n+3)} \times \cos[(2n+1)\tau], \quad (14b)$$

where we assume that  $A \geq 0$ . The second-order displacement thus consists of all odd harmonics, which also holds for the third-order displacement. The perturbation expansion  $\theta = \varepsilon \theta_1 + \varepsilon^2 \theta_2 + \varepsilon^3 \theta_3 + \dots$  therefore has the form

$$\theta = \varepsilon A \cos(\tau) + \varepsilon^2 \sum_{n=0}^{\infty} B_n \cos[(2n+1)\tau] + \varepsilon^3 \sum_{n=0}^{\infty} C_n \cos[(2n+1)\tau] + \dots \quad (15)$$

Substituting  $\theta_1$  and  $\theta_2$  from Eq. (15) into Eq. (14b), and equating to zero the coefficient of the  $\cos(\tau)$  term, yields  $\omega_1^2/\omega_0^2 = 4\rho A/3\pi$ . Equating to zero the coefficients of the higher harmonics yields  $B_n = \rho A^2 a_n/\pi$  for  $n \geq 1$ , where  $a_n = (-1)^{n+1}(2n+1)/n(n+1)(2n-1)(2n+3)$ . The  $B_0 \times \cos(\tau)$  term in the second-order displacement represents a homogeneous solution of Eq. (14b). The coefficient  $B_0$  therefore cannot be determined, which reflects the fact that it only serves to alter the amplitude of the first-order displacement. We thus set  $B_0=0$ .

At order  $\varepsilon^3$ , the equation of motion (11) is

$$\begin{aligned} \frac{d^2 \theta_3}{d\tau^2} + \theta_3 = & \left[ \frac{\omega_2^2}{\omega_0^2} - \left( \frac{\omega_1^2}{\omega_0^2} \right)^2 \right] \theta_1 + \frac{\omega_1^2}{\omega_0^2} \theta_2 + \frac{1}{6} \theta_1^3 \\ & + \rho \operatorname{sgn}(\theta_1) \frac{d^2}{d\tau^2} (\theta_1 \theta_2) \\ & + \rho [\operatorname{sgn}(\theta_1 + \theta_2) - \operatorname{sgn}(\theta_1)] \frac{d}{d\tau} \left( \theta_1 \frac{d\theta_1}{d\tau} \right), \end{aligned} \quad (16)$$

in contrast to Eq. (8) for the single-interrupted pendulum. Because  $\theta_2$  has zeros that are identical to  $\theta$ , and because  $|\theta_2| \ll |\theta_1|$ , the square-bracketed quantity in the final term is zero. Substituting the expressions for  $\omega_1$ ,  $\theta_1$ ,  $\theta_2$ , and  $\theta_3$  into Eq. (16), performing the Fourier decompositions, and equating to zero the coefficient of the  $\cos(\tau)$  term, we determine the second-order frequency shift  $\omega_2$ . Required in this calculation is the  $\cos(\tau)$  Fourier component of  $\operatorname{sgn}[\cos(\tau)] \cos(2n\tau)$ , for  $n=1,2,3,\dots$ , which is  $(-1)^{n+1}4/\pi(2n+1)(2n-1)$ . The result for the square frequency (6), valid to order  $O(A^3)$ , is

$$\frac{\omega_2^2}{\omega_0^2} = 1 + \frac{4}{3\pi} \rho A + \left[ \frac{16}{9\pi^2} \rho^2 \left( 1 + \frac{9}{2} \sum_{n=1}^{\infty} b_n \right) - \frac{1}{8} \right] A^2, \quad (17)$$

where  $b_n = 1/n(n+1)(2n-1)^2(2n+3)^2$ . The nonanalytic nonlinearity gives rise to an *infinite* number of contributions

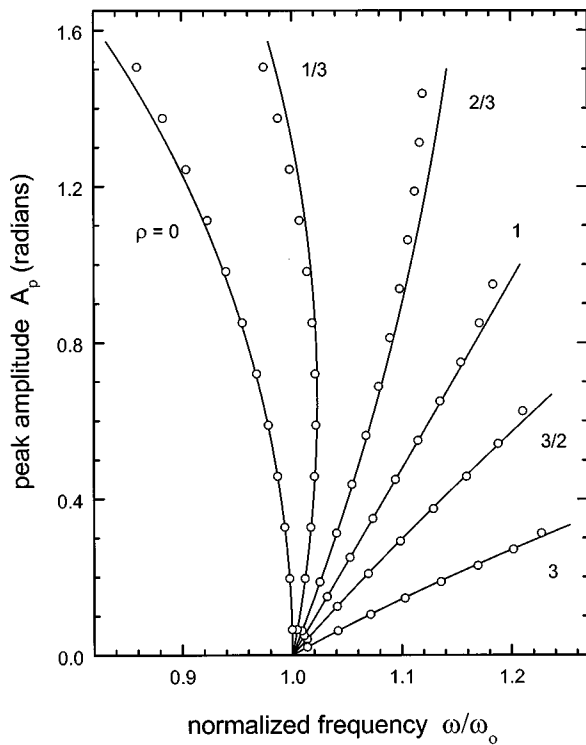


FIG. 5. Amplitude-dependent frequency of the double-interrupted pendulum in Fig. 2 for various values of  $\rho=R/L$ . The curves correspond to the perturbative theory, and the points to numerical simulations.

to the quadratic frequency shift, although the series converges rapidly. To second order, the peak amplitude is given by  $A_p = A + \sum_{n=1}^{\infty} B_n$ . The square frequency (17), valid to order  $O(A_p^3)$ , is thus

$$\frac{\omega^2}{\omega_0^2} = 1 + \frac{4}{3\pi} \rho A_p + \left\{ \frac{16}{9\pi^2} \rho^2 \left[ 1 + \frac{9}{2} \sum_{n=1}^{\infty} \left( b_n - \frac{1}{6} a_n \right) \right] - \frac{1}{8} \right\} A_p^2. \quad (18)$$

Figure 5 shows curves of Eq. (18) for various values of  $\rho$ . The frequency  $\omega$  is linear in the amplitude  $A_p$  when  $\rho$  is approximately 1.0414. As in Fig. 3, the curves are terminated at their corresponding maximum values (2), and the points are essentially exact numerical results. To leading order in the amplitude, the nonanalyticity causes the frequency shift to vary *linearly* with amplitude, in contrast to the typical case (10) where the shift is quadratic in the amplitude. Recent data for the resonant frequencies of nonlinear compressional standing waves in sandstone exhibit this behavior.<sup>9</sup>

Examination of Eqs. (14) show that this “linear bending” is a general result for any conservative oscillator that has a nonanalytic quadratic nonlinearity that gives rise to a Fourier component at the fundamental frequency when the first-order solution is substituted. The nonlinearity need not be discontinuous as in the case for the  $\theta$  equation of motion (11). For example, in the equation of motion for the path length of a double-interrupted pendulum [Eq. (4) with  $\rho$  replaced by  $\rho \operatorname{sgn}(\zeta)$ ], the nonlinearity  $|\zeta|\zeta$  is discontinuous in

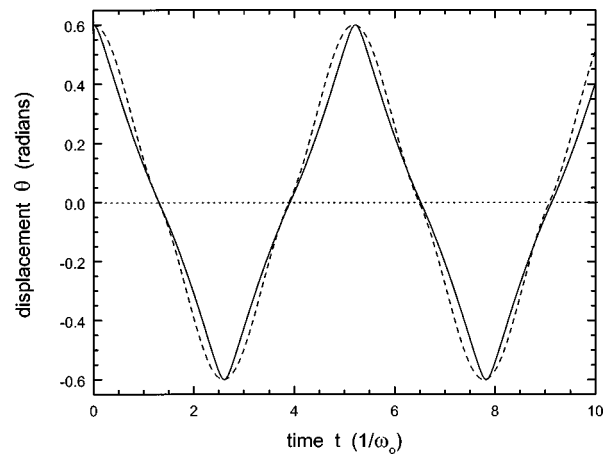


FIG. 6. Displacement versus time for the double-interrupted pendulum in Fig. 2 for  $\rho=3/2$  and  $A_p=0.6$ . The solid curves correspond to a numerical simulation, and the dashed curves to the perturbative theory.

the second derivative, but yields the linear bending identical to the  $\theta$  equation (as it must). For a nonanalytic quadratic nonlinearity to yield a Fourier component at the fundamental frequency is a weak requirement: any “glitch” that occurs at the fundamental frequency satisfies this.

The physical reason for the linear hardening in the case of the double circularly interrupted pendulum is that the cusp in the interrupting surface causes the mean length of the pendulum to be less than the equilibrium value. The nature of the cusp is important, however. The cycloidal pendulum cusp does not cause linear hardening; rather, the hardening is quadratic for small amplitudes because it cancels the quadratic gravitational softening. Both the cycloidal and circular interrupters have infinite slope at the cusp. However, the slope of the cycloidal interrupter diverges inversely as the *cube* root of the horizontal distance to the cusp, whereas the slope of the circular interrupter diverges as the *square* root of this distance. The greater sharpness of the circular cusp is responsible for the difference in the small-amplitude behavior of the two pendulums. Whereas the cycloidal path of the mass is infinitely smooth at the equilibrium point, it can be shown that the path due to the circular interrupters has a discontinuous third derivative at this point.

Comparing Figs. 3 and 5, we observe that the errors in the single-interrupter theory are typically greater than those in the double-interrupter case. The symmetry of the motion appears to be responsible for the effect. Figure 6 reveals that the theory more accurately describes the displacement of the symmetric motion than asymmetric motion (Fig. 4), even though the perturbation analysis for the displacement was carried out to third order in the asymmetric case (5) and second order in the symmetric case (15).

If drive and dissipation are included in a nonlinear oscillator, the frequency response curves (steady-state amplitude versus frequency for a fixed drive amplitude) for the primary resonance have shapes that conform to the “backbone” curve (amplitude versus frequency for undriven undamped oscillations).<sup>1,23</sup> Multivalued regions in the frequency response curves correspond to unstable equilibria and hysteresis. As a result, a backbone curve whose slope

changes sign (e.g., the  $\rho = 1/3$  curve in Fig. 5) may have two multivalued regions, and therefore two hysteresis loops.

### III. HUYGENS' INVESTIGATIONS

In his investigations on the use of the pendulum to regulate clocks, Christiaan Huygens (1629–1695) discovered in 1659 that a cycloidal path of a point mass in a uniform gravitational field yields isochronous oscillations, and that interruption of a flexible simple pendulum with double cycloids produces such a path if the height of the cycloids equals half the length of the pendulum.<sup>3</sup> These discoveries were motivated by the lack of a driving mechanism that could maintain a sufficiently constant pendulum amplitude. Huygens' work on cycloids and their application to clocks was included in his classic treatise *Horologium Oscillatorium*<sup>24</sup> of 1673. Due to the resultant improvement in accuracy of clocks, including those used at sea in an effort to determine longitude, and to the mathematical properties, Huygens considered this to be “the most fortunate finding that ever befell me.”<sup>25</sup> Indeed, much of *Horologium Oscillatorium* is devoted to proofs and developments related to the properties of cycloids.

At the other extreme, Robert Hooke (1635–1703) argued that the use of cycloidal interrupters was a “lame invention” due to drive-mechanism irregularities that cannot be obviated by isochronous oscillations, and due to the disturbance of the path resulting from bending at the point where the flexible support is attached to the pendulum rod.<sup>26</sup> One historian has stated<sup>27</sup> that the cycloidal interrupters were unsuccessful in practice due to the resultant friction and “banking,” an undefined term that probably refers to the bending described by Hooke. Regardless of these criticisms, Huygens' clocks were by far the most accurate that were available for several decades.<sup>4</sup> The use of cycloidal interrupters ceased as a result of improvements of the driving mechanism, which led to the maintenance of nearly constant pendulum amplitude. For marine pendulum clocks, cycloidal interrupters and other improvements did not sufficiently compensate for ship motion.<sup>4,24,28</sup>

Although he did not mention it in *Horologium Oscillatorium*, Huygens empirically investigated interrupted pendulums in his earliest clocks, several years before the discovery of the cycloidal properties.<sup>25,27</sup> He later found that double circular interrupters were as effective as cycloids.<sup>4</sup> The amplitude versus frequency curves in Fig. 5 appear to contradict this. In fact, as remarked in Sec. II and shown in Fig. 3, it is theoretically more accurate to employ a *single* circular interrupter, which yields nearly isochronous motion if the radius of the interrupter is  $\sqrt{3}/2$  the length of the pendulum. Huygens was apparently unaware of this.

A possible resolution of Huygens' observations and our results arises from the facts that the slope of the curves of amplitude versus frequency changes sign (“back-bends”) for values of the ratio  $\rho = R/L$  less than roughly  $1/2$ , and that isochronous motion is required only for a range of amplitudes that does not include zero. If  $\rho$  is chosen such that this range corresponds to an approximately vertical part of the curve, then the motion will be approximately isochronous. The frequency can significantly differ from the linear (small-

amplitude) value, but this is not vital because the deviation can be removed by small adjustments to the pendulum. An example in Fig. 5 occurs for  $\rho = 1/3$  and  $0.5 \text{ rad} < A_p < 0.8 \text{ rad}$ . (Reduced values of the minimum and maximum angles can be achieved with smaller values of  $\rho$ .) The corresponding deviation in frequency is roughly 0.1%, which amounts to a deviation of 1 min over a 24-h period (impressive for the mid-17th century), although the frequency deviates from the linear value by 2%.

### IV. LATTICES AND NONLINEAR SCHRÖDINGER EQUATIONS

We now consider uniform lattices of linearly coupled circularly interrupted pendulums. A possible approximate realization of this may be achieved with bifilar pendulums that oscillate transverse to the lattice, where the coupling is arranged by having the pendulums overlap and tying together the cords at the points of intersection.<sup>10,11</sup> Cylinders can be employed as interrupters. From the equation of motion (11) for one pendulum, the equation of motion for the double-interrupted lattice is

$$\begin{aligned} \frac{d^2 \theta_n}{dt^2} - \mu(\theta_{n+1} - 2\theta_n + \theta_{n-1}) + \omega_-^2 \sin(\theta_n) \\ = \rho \operatorname{sgn}(\theta_n) \frac{d}{dt} \left( \theta_n \frac{d\theta_n}{dt} \right), \end{aligned} \quad (19)$$

where  $\mu$  is the torsional coupling constant divided by the pendulum moment of inertia and  $\operatorname{sgn}$  is the sign function (12), and where it is now convenient to define  $\omega_- = \omega_0$ . The equation of motion for the single-interrupted lattice is identical to Eq. (19) with  $\operatorname{sgn}(\theta_n)$  removed.

The lattice described by Eq. (19) possesses a linear lower cutoff frequency  $\omega_-$  corresponding to the mode where the pendulums have the same amplitude and are in phase, and a linear upper cutoff frequency  $\omega_+$ , where

$$\omega_+^2 = \omega_-^2 + 4\mu, \quad (20)$$

corresponding to the mode where the pendulums have the same amplitude and are in antiphase. To describe motion near the lower-cutoff mode, we approximate Eq. (19) with its continuum limit for the continuous displacement function  $\theta_- \equiv \theta_-(x, t)$ :

$$\partial_t^2 \theta_- - c^2 \partial_x^2 \theta_- + \omega_-^2 \sin(\theta_-) = \rho \operatorname{sgn}(\theta_-) \partial_t(\theta_- \partial_t \theta_-), \quad (21)$$

where the values of the displacement function at the lattice sites are  $\theta_-(na, t) = \theta_n(t)$ , and where  $c^2 = \mu a^2$ ,  $a$  is the lattice spacing, and  $\partial_t$  and  $\partial_x$  denote  $\partial/\partial t$  and  $\partial/\partial x$ , respectively. To describe motion near the upper-cutoff mode, we define the continuous envelope function  $\theta_+ \equiv \theta_+(x, t)$  such that  $\theta_+(na, t) = (-1)^n \theta_n(t)$ , and assume that  $\theta_+(x, t)$  is spatially slowly varying over the lattice spacing  $a$ .<sup>10,11</sup> In a similar manner that leads to the lower-cutoff wave equation (21), we find

$$\begin{aligned} \partial_t^2 \theta_+ + c^2 \partial_x^2 \theta_+ + 4\mu \theta_+ + \omega_-^2 \sin(\theta_+) \\ = \rho \operatorname{sgn}(\theta_+) \partial_t(\theta_+ \partial_t \theta_+). \end{aligned} \quad (22)$$

For weakly nonlinear motion to order  $\theta_{\pm}^3$ , Eqs. (21) and (22) can be unified as

$$\begin{aligned} \partial_t^2 \theta_{\pm} \pm c^2 \partial_x^2 \theta_{\pm} + \omega_{\pm}^2 \theta_{\pm} \\ = \rho \operatorname{sgn}(\theta_{\pm}) \partial_t(\theta_{\pm} \partial_t \theta_{\pm}) + \frac{1}{6} \omega_{\pm}^2 \theta_{\pm}^3, \end{aligned} \quad (23)$$

where Eq. (20) has been employed.

The uniform lower and upper cutoff standing wave solutions of Eqs. (23) are characterized by spatially constant  $\theta_{\pm}$ , and are equivalent to a single pendulum of linear frequency  $\omega_{\pm}$ . To investigate behavior near these modes, we consider slowly varying amplitude modulations of these states. As in Secs. I and II, we employ the method of harmonic balance, extended now to the case of a standing wave mode.<sup>10,11,16</sup> The displacement functions are expressed as

$$\theta_{\pm}(x, t) = \psi_{\pm}(x, t) e^{i\omega t} + \text{c.c.} + \dots, \quad (24)$$

where  $\psi_{\pm} \equiv \psi_{\pm}(x, t)$  are complex functions that are weakly nonlinear and slowly varying in both space and time, c.c. denotes the complex conjugate, and the ellipsis denotes higher harmonic terms. The evolution equations for  $\psi_{\pm}$  are obtained by substituting Eqs. (24) into the equations of motion (23), and equating to zero the slowly varying coefficients of  $e^{i\omega t}$  and the higher harmonics.

We first consider the case of a lattice of single-interrupted pendulums, which is described by Eqs. (23) with  $\operatorname{sgn}(\theta)$  removed. If the amplitude  $\psi$  is of order  $\varepsilon$ , we show below that it is appropriate to choose  $\partial_t \psi_{\pm}$  and  $\partial_x^2 \psi_{\pm}$  to be of order  $\varepsilon^3$  or higher, and  $\omega^2 - \omega_{\pm}^2$  to be of order  $\varepsilon^2$  or higher. As in the calculation in Sec. I, the quadratic nonlinearity necessitates that the second harmonic amplitude in Eqs. (24), which we denote as  $\varphi_{\pm}(x, t)$ , first be determined as a function of the fundamental amplitude  $\psi_{\pm}(x, t)$ . Due to the slowly varying approximations, this calculation is essentially identical to that in Sec. I. When the expansions (24) are substituted into the equations of motion (23), and the slowly varying coefficient of the  $e^{2i\omega t}$  term is equated to zero at order  $\varepsilon^2$ , the result is  $\varphi_{\pm} = 2\rho\psi_{\pm}^2/3$ . At order  $\varepsilon^3$ , equating to zero the  $e^{i\omega t}$  terms then leads to the cubic nonlinear Schrödinger (NLS) equations

$$-2i\omega_{\pm} \partial_t \psi_{\pm} \mp c^2 \partial_x^2 \psi_{\pm} + (\omega^2 - \omega_{\pm}^2) \psi_{\pm} = \alpha |\psi_{\pm}|^2 \psi_{\pm}, \quad (25)$$

where the nonlinear coefficient is  $\alpha = (4\rho^2 - 3)\omega_{\pm}^2/6$ . That the nonlinear coefficient can be positive or negative, depending upon the value of the parameter  $\rho$ , is experimentally useful because the sign dictates the type of solitons that exist (Sec. V). Note that, in the special case of the uniform mode  $\partial_t \psi_{\pm} = \partial_x \psi_{\pm} = 0$ , which is equivalent to a single pendulum, Eqs. (25) yield the amplitude-dependent frequency (9) where the amplitude is  $A = 2\psi_{\pm}$  due to use of complex amplitudes in Eqs. (24). Note also that the reason for the choices of the relative smallness of the temporal and spatial variations of  $\psi_{\pm}$ , as well as the frequency shift and nonlinearity, is apparent in the NLS equations (25): Each term must be of the same order ( $\varepsilon^3$ ) for the equations to be consistent, unless the term is zero (i.e., an order higher than  $\varepsilon^3$ ).

The cubic NLS equations (25) that arise in the case of the single-interrupted pendulum lattice are very general. For

example, essentially the same equations arise in the description of modulations of transverse modes in acoustic<sup>14,15</sup> and model<sup>16</sup> waveguides, as well as surface cross modes in a channel of liquid.<sup>18-21</sup>

To determine the equations that describe the modulations (24) for the nonanalytic lattice represented by Eqs. (23), we first note that the linear terms must be identical to those in the cubic NLS equations (25). Second, because we desire only the lowest-order effect due to nonlinearities, and because the time and space variations of  $\psi_{\pm}$  are slow, these variations are negligible in the nonlinear terms in Eqs. (23). It is convenient to then temporarily express the fundamental amplitude in Eq. (24) as  $\psi_{\pm} = A e^{i\delta/2}$ , where  $A$  and  $\delta$  are real slowly varying functions, and where it is important to recognize that  $A$  may change sign due to possible slow variation. The displacement is then  $\theta = A \cos(\omega t + \delta)$ , and the Fourier decomposition of the quadratic nonlinearity in Eq. (23) proceeds as in Eqs. (14), where we must express  $A^2$  as  $|A|A$  to correctly allow for  $A < 0$ . Considering the Fourier component at frequency  $\omega$ , converting back to  $\psi_{\pm}$ , and selecting the  $e^{i\omega t}$  component, we obtain

$$-2i\omega_{\pm} \partial_t \psi_{\pm} \mp c^2 \partial_x^2 \psi_{\pm} + (\omega^2 - \omega_{\pm}^2) \psi_{\pm} = \beta |\psi_{\pm}| \psi_{\pm}, \quad (26)$$

where the nonlinear coefficient is  $\beta = 8\rho\omega_{\pm}^2/3\pi$ . The nonanalytic nonlinearity in the equation of motion gives rise to *quadratic* NLS equations for weakly nonlinear slowly varying amplitude modulations of the cutoff modes. If the amplitude  $\psi_{\pm}$  is of order  $\varepsilon$ , then Eqs. (26) are valid for  $\partial_t \psi_{\pm}$  and  $\partial_x^2 \psi_{\pm}$  of order  $\varepsilon^2$  or higher and  $\omega^2 - \omega_{\pm}^2$  of order  $\varepsilon$  or higher, in contrast to the cubic NLS equations (25) where these quantities are each one order higher. This difference affects the degree of localization of solitary waves (Sec. V). Similar to the cubic NLS equation, the uniform-mode case  $\partial_t \psi_{\pm} = \partial_x \psi_{\pm} = 0$  yields the amplitude-dependent frequency (16) to first order in  $A$ .

Although the quadratic NLS equations (26) were derived for the case of an interrupted pendulum lattice, they will arise in general when a quadratic nonanalytic nonlinearity satisfies the weak condition stated in Sec. II: upon substitution of the first-order solution, there occurs a Fourier component at the fundamental frequency.

## V. SOLITARY WAVES

A system whose motion near a cutoff mode is described by a cubic NLS equation (25) is known to possess breather or kink solitons. For  $\alpha > 0$  (hardening oscillations), the breather soliton solution of Eq. (25<sup>+</sup>) is<sup>16</sup>

$$\psi_+(x, t) = \frac{1}{2} A \operatorname{sech}[\kappa_+(x - vt - x_0)] e^{i\omega v x/c^2}, \quad (27)$$

which is an amplitude modulation of the upper cutoff mode, where  $\kappa_+^2 = \alpha A^2/8c^2$ ,  $\omega^2 = (\omega_+^2 + \alpha A^2/8)(1 + v^2/c^2)^{-1}$ , and  $v$  is the velocity of propagation. The kink soliton solution of Eq. (25<sup>-</sup>) is<sup>10,11,20</sup>

$$\psi_-(x, t) = \frac{1}{2} A \tanh[\kappa_-(x - vt - x_0)] e^{-i\omega v x/c^2}, \quad (28)$$

which is an amplitude modulation of the lower cutoff mode, where  $\kappa_- = \alpha A^2/8c^2$  and  $\omega^2 = (\omega_-^2 + \alpha A^2/4)(1 - v^2/c^2)^{-1}$ .



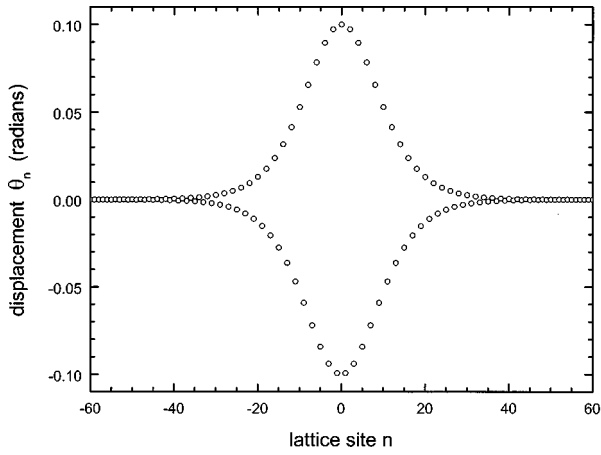


FIG. 7. Upper-cutoff breather standing wave in an infinite lattice of double-interrupted pendulums, according to Eqs. (24) and (29). The displacements are shown at a turning point of the motion. The parameters are  $\omega_0 = \mu = \rho = a = 1$ , and the peak amplitude is  $A = 0.1$ .

For  $\alpha < 0$  (softening oscillations), the breather exists in the lower cutoff mode, and the kink in the upper cutoff mode; in the solutions (27) and (28), the “+” and “-” subscripts are interchanged, and  $c^2 \rightarrow -c^2$ . The full soliton solutions to the wave equations (23) with  $\text{sgn}(\theta)$  removed are obtained by substitution of Eqs. (27) and (28) into Eq. (24). The center  $x_0$  of these solitons at  $t=0$  is arbitrary, and the values of the amplitude  $A$  and the velocity of propagation  $v$  are arbitrary as long as they do not violate the assumption of weakly nonlinear and slowly varying amplitude modulations.

Breather<sup>11</sup> and kink<sup>10,11</sup> solitons have been observed in the lower and upper cutoff modes, respectively, of an uninterrupted ( $\rho=0$ ) pendulum lattice. Both breather<sup>17,19,21</sup> and kink<sup>20</sup> solitons have been observed in surface wave cross modes of a channel of liquid, because the nonlinear coefficient changes sign with the ambient depth of the liquid. In a lattice of single-interrupted pendulums, which is described by the cubic NLS equations (25) with the nonlinear coefficient  $\alpha = (4\rho^2 - 3)\omega_0^2/6$  (Sec. IV), the oscillations harden for  $\rho > \sqrt{3}/2$ , so the breather and kink roles are *reversed* in this case: kinks are predicted to exist in the lower cutoff mode, and breathers in the upper cutoff mode.

On physical grounds,<sup>11,17,29</sup> nonpropagating breather and kink states of the upper and lower cutoff modes, respectively, are expected to exist in the lattice of nonanalytic pendulums, which is described by the quadratic NLS equations (26). Such solutions indeed exist. The nonpropagating breather solution for  $\beta > 0$  (hardening oscillations) is

$$\psi_+(x) = \frac{1}{2}A \operatorname{sech}^2[\kappa_+(x-x_0)], \quad (29)$$

where  $\kappa_+^2 = \beta A/12c^2$  and  $\omega^2 = \omega_+^2 + \beta A/3$ . An example of this solution for  $\theta_n$  is shown in Fig. 7. The nonpropagating kink solution is

$$\psi_-(x) = \frac{1}{2} \operatorname{sgn}(x-x_0)A \left\{ 1 - \frac{3}{2} \operatorname{sech}^2[\kappa_-(x-x_0)] + \chi \operatorname{sgn}(x-x_0) \right\}, \quad (30)$$

where  $\operatorname{sgn}$  is the sign function (12), and where  $\kappa_-^2 = \beta A/8c^2$ ,  $\chi = \operatorname{sech}^{-1}\sqrt{2/3}$ , and  $\omega^2 = \omega_-^2 + \beta A/2$ . An example of this solution for  $\theta_n$  is shown in Fig. 8. The solu-

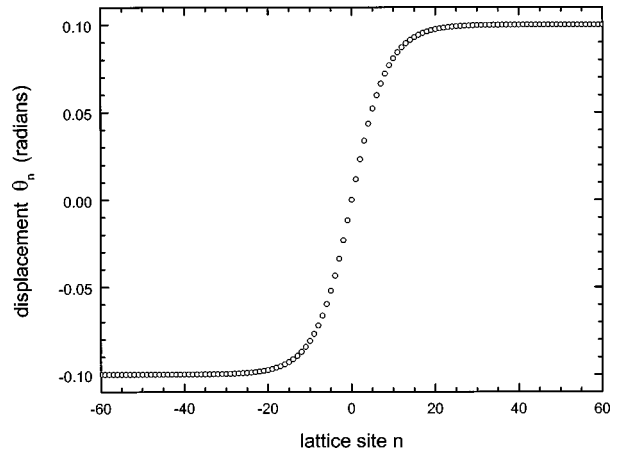


FIG. 8. Lower-cutoff kink standing wave in an infinite lattice of double-interrupted pendulums, according to Eqs. (24) and (30). The displacements are shown at a turning point of the motion. The parameters are  $\omega_0 = \mu = \rho = a = 1$ , and the peak amplitude is  $A = 0.1$ .

tions (29) and (30) are arbitrary within an overall sign, and the center  $x_0$  of the solitary wave is arbitrary. We have chosen the peak amplitude  $A$  as the arbitrary parameter. Within the context of the quadratic NLS equation (26), the amplitude  $A$  can have any positive value, but it must be sufficiently small if this equation is to accurately describe the underlying physical system. For  $\beta < 0$  (softening oscillations), as in the case of cubic NLS solitons (27) and (28), the breather exists in the lower cutoff mode and the kink in the upper cutoff mode; in the solutions (29) and (30), the “+” and “-” subscripts are interchanged, and  $c^2 \rightarrow -c^2$ .

Because it has only one sign for all  $x$ , the breather solution (29) is analytic. In contrast, the kink solution (30) changes sign at the center value  $x_0$  and consequently has a discontinuous second derivative at  $x_0$ .

The mathematical awkwardness of the kink solution (30) hides an underlying simple physics. To understand this, note that the differential equation (26) in dimensionless form is  $\partial_x^2 \psi + \psi = |\psi| \psi$  in the time-independent case, with the boundary conditions  $\psi(\pm\infty) = \pm 1$ . With the replacements  $x \rightarrow t$  and  $\psi(x) \rightarrow x(t)$ , we can consider the problem to be the determination of the position  $x$  as a function of time  $t$  of a unit-mass oscillator subject to the force  $-x + |x|x$ . By symmetry, a solution of the problem for  $x > 0$  leads to a complete solution. We thus seek a solution to  $\partial_t^2 x = -x + x^2$  with  $x(\pm\infty) = 1$ . This corresponds to the mass starting in the infinite past at rest on the top of the potential “hill” at  $x = 1$ , moving through the origin, turning around at  $x = -1/2$  (by energy conservation), and asymptotically returning to  $x = 1$ . A natural ansatz in which the turning point occurs at  $t = t_0$  is  $x(t) = 1 - (3/2)\operatorname{sech}^2[\chi(t-t_0)]$ , which is indeed found to be correct if  $\gamma = 1/2$ . (The hyperbolic secant to the first power is found not to satisfy the differential equation.) The zero crossings occur at  $t_{\pm} = t_0 \pm \chi/\gamma$ , where  $\chi = \operatorname{sech}^{-1}\sqrt{2/3}$ . A solution to the symmetric (nonanalytic) problem is found by changing the sign and translating the  $t < t_-$  solution so that the zero crossing occurs at  $t_0$ , and similarly translating the  $t > t_+$  solution. There is thus a gap of times  $t_- < t < t_+$  which are removed from the analytic motion as a step toward creating the nonanalytic solution. This is precisely what is ef-

ected by the sgn function in the square brackets in the kink solution (30). The breather solution (29) also has an oscillator analogy. In this case, the origin is a point of unstable equilibrium. The mass asymptotically begins and ends at this point, and for intermediate times it moves once through the potential well on one side.

Propagating solitary wave solutions to the quadratic NLS equations (26) can be determined in a manner<sup>16</sup> similar to that for the cubic NLS equation, by setting  $\psi_{\pm}(x,t) = \varphi_{\pm}(\xi)\exp(ibx)$ , where  $\xi = x - vt$ , and where  $v$  and  $b$  are real constants. Substituting this expression into the equation, we find that if  $b = \pm \omega v/c^2$ , then the equations for  $\varphi_{\pm}$  are equivalent to the time-independent case if  $d/dx \rightarrow d/d\xi$  and  $\omega^2 \rightarrow \omega^2(1 \pm v^2/c^2)$ . Hence, the envelopes  $\varphi_{\pm}$  are given by Eqs. (29) and (30) with these replacements. The propagating solitary breather solution to Eq. (26) is thus

$$\psi_+(x,t) = \frac{1}{2}A \operatorname{sech}^2[\kappa_+(x - vt - x_0)]e^{i\omega v x/c^2}, \quad (31)$$

where  $\kappa_+^2 = \beta A/12c^2$  and  $\omega^2 = (\omega_+^2 + \beta A/3)(1 + v^2/c^2)^{-1}$ , and the propagating solitary kink solution to Eq. (26) is

$$\psi_-(x,t) = \frac{1}{2} \operatorname{sgn}(x - vt - x_0)A \left\{ 1 - \frac{3}{2} \operatorname{sech}^2[\kappa_-(x - vt - x_0) + \chi \operatorname{sgn}(x - vt - x_0)] \right\} e^{-i\omega v x/c^2}, \quad (32)$$

where  $\kappa_-^2 = \beta A/8c^2$ ,  $\chi = \operatorname{sech}^{-1}\sqrt{2/3}$ , and  $\omega^2 = (\omega_-^2 + \beta A/2)(1 - v^2/c^2)^{-1}$ . In the solutions (31) and (32), the amplitude  $A$  and velocity  $v$  are arbitrary parameters, although these must be sufficiently small so as not to violate the slowly varying approximation that is made in the derivation of the NLS equations (26). The nonpropagating breather and kink solutions (31) and (32) are the special cases of  $v = 0$  in Eqs. (31) and (32), respectively.

The cubic and quadratic NLS breather solutions (27) and (31), as well as the kink solutions (28) and (32), have similar appearances. However, the quadratic NLS solutions are inherently more localized: If the amplitude is of order  $\varepsilon$ , then the degree of localization (given by  $\kappa_{\pm}^{-1}$  in the solitary solutions) is of order  $\varepsilon^{-2}$  in the quadratic case and of order  $\varepsilon^{-3}$  in the cubic case. This can be physically understood by considering the nonpropagating cases, which result from a balance of nonlinearity and curvature of the waveform in order to yield a monofrequency response for all  $x$ .<sup>29</sup> The greater curvature in the quadratic NLS case is thus due to the frequency varying linearly with amplitude. An additional distinction is that, whereas the cubic NLS solutions are known to be solitons (which collide elastically), it is an open question whether the quadratic NLS solitary waves are stable and, if they are, whether these states are solitons.

## VI. SANDSTONE

The resonance frequencies of compressional standing waves in sandstone exhibit the linear dependence as in Fig. 5 for  $\rho$  roughly equal to unity, but soften rather than harden.<sup>9</sup> We thus expect that these waves can be modeled with a quadratic nonanalytic nonlinearity such as that in Eq. (21) with the opposite sign. If amplitude modulations of a transverse standing wave in a long bar of sandstone are considered, analogous to acoustics in gases<sup>14,15</sup> a model wave system,<sup>16</sup> or a channel of liquid,<sup>18-21</sup> the modulations are

expected to obey a quadratic NLS equation of the form (26). As a result of the softening, a breather solitary wave of the form (31) would then exist, with an additional factor corresponding to the transverse oscillations. However, due to the existence of shear forces which couple longitudinal and transverse motion in a waveguide, and to the boundary condition that must be met, it is not immediately apparent that a quadratic NLS equation applies here, and thus whether breather solitary waves can exist in a waveguide of this medium. In this section, we show that compressional standing waves in sandstone can indeed be modeled with a quadratic nonanalytic nonlinearity. We also show that, within the approximations of the theory, a quadratic NLS equation describes the transverse motion in a waveguide of sandstone, and that the observation of a breather is feasible.

The general equation of motion for deformations of an elastic solid is<sup>30</sup>

$$\rho \ddot{u}_i = \partial_k \sigma_{ik}, \quad (33)$$

where the dots represent partial differentiation with respect to time,  $\rho$  is the ambient density of the solid,  $u_i$  is the displacement in the  $i$ th direction,  $\sigma_{ik}$  is the stress tensor, and where we employ the summation convention for a repeated index. For an isotropic solid, the stress tensor is

$$\sigma_{ik} = K u_{jj} \delta_{ik} + 2\mu(u_{ik} - \frac{1}{3}u_{jj} \delta_{ik}) + f_{ik}, \quad (34)$$

where  $K$  is the modulus of compression,  $\mu$  is the shear modulus,  $u_{ik}$  is the stress tensor  $(\partial_i u_k + \partial_k u_i)/2$ , and  $f_{ik}$  is a nonlinear function of the strain.

To model the observed amplitude-dependent resonance frequency of sandstone, we assume that the normal nonlinearities in  $f_{ik}$  are dominated by a quadratic nonanalytic nonlinearity, which must be a symmetric second rank tensor composed of the vectors  $\partial_i$  and  $u_i$ . Furthermore, if we consider the special case of one-dimensional compressional standing waves in a uniform bar whose center is defined to be the origin  $x=0$ , then the displacement is spatially described by the odd function  $\sin(kx)$  for small amplitudes. To yield the linear dependence as in Fig. 5,  $f_{ik}$  must be *even* in order that  $\partial_k f_{ik}$  have a  $\sin(kx)$  spatial component. This additional requirement drastically restricts the possible form of  $f_{ik}$ . The only simple possibility appears to be

$$f_{ik} = \Gamma u u_{ik}, \quad (35)$$

where  $u = (u_j u_j)^{1/2}$  and  $\Gamma$  is a negative constant corresponding to softening. In one dimension, the nonlinearity (35) corresponds to a spring whose force versus displacement curve softens equally for positive and negative displacements, but which has a discontinuous second derivative at zero displacement. It should be noted that our model does not include hysteresis, whereas a recent mesoscopic theory of deformations of sandstone is based upon hysteresis.<sup>31</sup>

Substituting the expressions (34) and (35) into the equation of motion (33), and utilizing the facts that the square speed of compressional (longitudinal) waves in an unbounded medium is  $c_L^2 = (3K + 4\mu)/3\rho$  and the square speed of transverse waves is  $c_T^2 = \mu/\rho$ ,<sup>30</sup> leads to the equation of motion

$$\ddot{u}_i = c_T^2 \nabla^2 u_i + (c_L^2 - c_T^2) \partial_i \partial_k u_k + \frac{\Gamma}{2\rho} \partial_k [u(\partial_i u_k + \partial_k u_i)], \quad (36)$$

subject to the boundary condition that there is no stress at any point on the surface of the solid:

$$\sigma_{ik} n_k = 0, \quad (37)$$

where  $n_k$  is a vector perpendicular to the surface at the point.

To illustrate the existence of a quadratic NLS equation and breathers in sandstone, we consider the simplest case of a two-dimensional infinite slab of thickness  $b$  in the  $y$  direction ( $-b/2 < y < b/2$ ), where the strain occurs only in the  $x$  and  $y$  directions. Similar results are expected to occur for the more complicated situation of a bar with a rectangular or circular cross section. We consider weakly nonlinear and slowly varying complex amplitude modulations of the transverse ( $y$ ) and longitudinal ( $x$ ) displacements:

$$u_y(x, y, t) = \psi(x, t) \sin(ky) e^{i\omega t} + \text{c.c.} + \dots, \quad (38a)$$

$$u_x(x, y, t) = \varphi(x, t) \cos(ky) e^{i\omega t} + \text{c.c.} + \dots, \quad (38b)$$

where the transverse wave number is  $k = \pi/b$  for the fundamental mode, and where the ellipsis denotes higher harmonics in  $y$  space and time. If  $\psi$  is of order  $\varepsilon$ , we show below that it is appropriate to consider  $\partial_x \psi$ ,  $\partial_x^2 \psi$ , and  $\dot{\psi}$  to be of order  $\varepsilon^{3/2}$ ,  $\varepsilon^2$ , and  $\varepsilon^2$  or higher, respectively,  $\varphi$ ,  $\partial_x \varphi$ ,  $\partial_x^2 \varphi$ , and  $\dot{\varphi}$  to be of order  $\varepsilon^{3/2}$ ,  $\varepsilon^2$ ,  $\varepsilon^{5/2}$ , and  $\varepsilon^{5/2}$  or higher, respectively, and  $\omega^2 - \omega_0^2$  to be of order  $\varepsilon$  or higher. (The fractional powers are due to the nonanalytic nonlinearity.) To order  $\varepsilon$ , substitution of Eqs. (38) into the equation of motion (36) for  $i=y$  yields the linear frequency  $\omega = \omega_0 = c_L k$ . To lowest nontrivial order ( $\varepsilon^{3/2}$ ), the equation of motion (36) for  $i=x$  reduces to simply  $k\varphi = -\partial_x \psi$ . Substituting this expression into the  $y$  equation of motion at order  $\varepsilon^2$  then yields

$$-2i\omega_0 \dot{\psi} + c_L^2 \partial_x^2 \psi + (\omega^2 - \omega_0^2) \psi = \frac{\Gamma}{\rho} g, \quad (39)$$

where  $g$  is the  $\sin(ky)e^{i\omega t}$  component of the nonlinear expression

$$\begin{aligned} & \partial_y [|\sin(ky)| \partial_y \sin(ky)] \times |\psi e^{i\omega t} + \psi^* e^{-i\omega t}| \\ & \times (\psi e^{i\omega t} + \psi^* e^{-i\omega t}). \end{aligned} \quad (40)$$

The first factor in Eq. (40) can be expressed as  $\partial_y^2 \{|\sin(ky)| \sin(ky)\}/2$ . When the curly bracketed term is expanded in a Fourier series of odd harmonics of  $\sin(ky)$ , the fundamental is found to have the coefficient  $8/3\pi$ . The contribution of the first factor of Eq. (40) to  $g$  is thus  $-4k^2/3\pi$ . The second factor in Eq. (40) can be handled similarly as in Sec. IV: we express  $\psi$  as  $Ae^{i\delta}/2$  where  $A$  and  $\delta$  are real slowly varying functions. As in the first factor, the fundamental component of  $|\cos(\omega t + \delta)| \cos(\omega t + \delta)$  has a coefficient  $8/3\pi$ . Converting back to  $\psi$  yields  $16|\psi|\psi/3\pi$  as the contribution of the second factor of Eq. (40) to  $g$ . Equation (39) thus becomes the quadratic NLS equation

$$-2i\omega_0 \dot{\psi} + c_L^2 \partial_x^2 \psi + (\omega^2 - \omega_0^2) \psi = \gamma |\psi| \psi, \quad (41)$$

where the nonlinear coefficient is  $\gamma = 128\Gamma/9\pi^2\rho$ . Similar to the NLS equations (25) and (26), Eq. (41) shows the reason

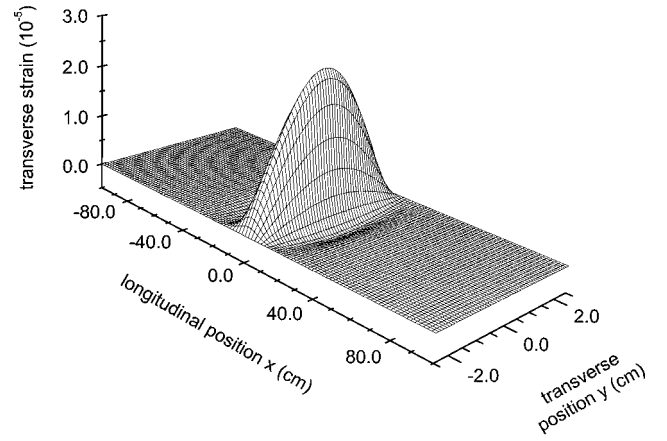


FIG. 9. Propagating quadratic NLS solitary breather wave in a slab of sandstone. The transverse strain is  $\partial u_y / \partial y$ , where  $u_y$  is given by Eq. (43) with  $t = x_0 = 0$ . The parameters are given in the feasibility estimate in Sec. VI.

for the choices of the relative smallness of the temporal and spatial variations of  $\psi$ , as well as the frequency shift and nonlinearity: Each of the terms must be of order  $\varepsilon^2$  or higher for the equation to be valid.

The boundary condition (37) is required at every point on the surface of the slab, for both  $i=x$  and  $i=y$ . A point  $P$  attached to the surface is labeled by the point's equilibrium coordinates  $(x, \pm b/2)$ , and has displacement  $(u_x, u_y)$  from equilibrium. A vector tangent to the surface at  $P$  is thus  $(\partial_x u_x, \partial_x u_y)$ , which implies that a vector normal to the surface at  $P$  is  $n = (\partial_x u_y, -\partial_x u_x)$ . The boundary condition (37) thus becomes

$$\sigma_{ix} \partial_x u_y - \partial_{iy} \partial_x u_x = 0, \quad (42)$$

for  $y = \pm b/2$ . When the stress tensor (34) and the displacements (38) are substituted into Eq. (42) and the result is evaluated for  $y = \pm b/2$ , the left side is found to be zero for  $i=x$  and of order  $\varepsilon^3$  for  $i=y$ . The boundary conditions are thus satisfied to at least the order ( $\varepsilon^2$ ) of the NLS equation (41).

Equation (41) is essentially identical to the quadratic NLS equation (26), and so has a breather solution of the form (31). Neglecting higher harmonics, the solution for the transverse displacement (38) is

$$\begin{aligned} u_y(x, y, t) = & A \sin(ky) \text{sech}^2[\kappa(x - vt - x_0)] \\ & \times \cos\left[\omega\left(t + \frac{vx}{c_L^2}\right)\right], \end{aligned} \quad (43)$$

where  $k = \pi/b$ ,  $\kappa^2 = -\gamma A/12c_L^2$ ,  $\gamma < 0$  (softening),  $\omega^2 = (\omega_0^2 + \gamma A/3)(1 - v^2/c_L^2)^{-1}$ , and  $\omega_0 = c_L k$ . The longitudinal displacement is given by Eq. (38) with  $\varphi = -\partial_x \psi/k$ . A plot of the transverse strain  $\partial u_y / \partial y$  at a definite time ( $t = 0$ ) is shown in Fig. 9.

To inquire into the feasibility of observing the quadratic NLS breather (43) in sandstone, we consider a rectangular sandstone bar of thickness  $b = 5.0$  cm. We assume that the other transverse dimension is sufficiently large that the displacements in this direction are negligible, so that the above theory applies. For longitudinal compressional waves in a thin bar, where the wavelength is large compared to trans-

verse dimensions, the wave speed is typically  $c = 2.0 \times 10^3$  m/s, the resonance quality factor is typically  $Q = 50$  which is approximately independent of frequency, and nonlinear frequency shifts of  $\delta f/f = 5\%$  corresponding to peak strains of  $9 \times 10^{-6}$  have been observed.<sup>9</sup> We assume that the values of the quality factor and nonlinear frequency shifts are also typical of transverse compressional modes of a bar. The speed  $c_L$  of compressional waves in an unbounded medium is related to the thin-bar speed  $c$  as  $c_L^2 = (1 - \sigma)(1 + \sigma)^{-1}(1 - 2\sigma)^{-1}c^2$ , where  $\sigma$  is Poisson's ratio.<sup>30</sup> Because  $\sigma$  is typically small ( $\sigma = 0.1$ ) for sandstone,<sup>32</sup> we assume  $c_L = c$ . The transverse excitation is chosen to be the fundamental mode, which has linear frequency  $f = c_L/2b = 20$  kHz. The breather will exist below this cutoff frequency, at a frequency we choose to be  $f - \delta f$ , where  $\delta f/f = 5\%$ . Comparing the solution of the NLS equation (41) for  $\psi = \text{constant}$  to the breather solution (43), we find that the peak strain  $kA$  of the breather is then triple the observed strain of  $9 \times 10^{-6}$ .

There are three criteria for the experimental feasibility of observing a breather wave in a bar of sandstone: (i) the softening dominates local variations of the cutoff frequency due to nonuniformities, (ii) the length of the breather is significantly less than the length of the bar, and (iii) the decay distance of the breather is significantly greater than the length of the breather. In regard to (i), if the variation of the local cutoff frequency is comparable to  $\delta f$ , then the breather will not remain intact. A tolerance of  $\pm 0.15$  mm in a 5.0-cm-width rod, which is readily obtainable,<sup>33</sup> implies a cutoff frequency variation of  $\pm 0.3\%$ . Because this is small compared to  $\delta f/f = 5\%$ , the criterion is met. In regard to (ii), solving for  $\kappa$  in terms of  $f = \omega/2\pi$  in the relations following Eq. (43), and assuming  $v^2/c^2$  is negligible (see below), leads to  $\kappa = \sqrt{2\delta f/f}\pi f/c = 10 \text{ m}^{-1}$ . We define the length  $L$  of the breather to correspond to a decrease in maximum amplitude by a factor of  $e$ . Solving  $\text{sech}^2(\kappa L/2) = e^{-1}$  then yields  $L = 18$  cm. Because this is significantly less than the typical 2.0-m length of sandstone bars,<sup>33</sup> the criterion is met. In regard to (iii), the distance over which the breather decays to  $e^{-1}$  of its initial amplitude is its speed multiplied by the time required for the decay:  $vQ/\pi f$ . For  $v/c = 0.20$ , this yields the decay distance 32 cm. This is roughly twice the length  $L$  of the breather, so the criterion is marginally met. One way to improve this is to dry the sandstone by placing it in vacuum, which can increase  $Q$  by roughly a factor of 3.<sup>34</sup>

The values of the parameters of the breather plotted in Fig. 9 correspond to the above feasibility estimate. Such a wave may be generated by driving a transverse mode at a frequency several percent less than the natural linear frequency of the mode. For a constant drive amplitude, the solitary waves may be spontaneously shed by a process that has been observed in a surface waveguide,<sup>19,21</sup> a magnetic lattice,<sup>35</sup> and a numerical lattice.<sup>36</sup> Alternatively, the drive amplitude can be modulated in time with a square hyperbolic secant or similar function. An experiment to generate such a solitary wave in sandstone is currently underway.

## VII. CONCLUSIONS

An example of an oscillator with a time-reversible nonanalytic nonlinearity is an undriven undamped flexible pendulum interrupted by two circular disks. This nonlinearity fundamentally alters the amplitude-dependent frequency compared to the typical analytic case, an example of which is a flexible pendulum interrupted by a single circular disk. In the typical case the frequency deviates quadratically in the amplitude for small amplitudes, whereas in the nonanalytic case the frequency varies *linearly* with amplitude. A general condition for the linear variation to occur is that the nonanalytic nonlinearity be quadratic and have a Fourier component at the fundamental frequency when the linear solution is substituted. This occurs for any quadratic nonlinearity that has a "glitch" (discontinuity in some derivative) at the fundamental frequency, for example, the nonlinearity in the equation of motion  $d^2s/dt^2 + \omega_0^2s = \alpha|s|s$ .

Huygens' observation that circular interrupters were as effective as cycloidal interrupters in achieving isochronous motion can be explained by the back bending of the amplitude-dependent frequency curves for double circular interrupters with radius equal to or less than roughly 1/2 the length of the pendulum. Along a back-bending section of the curves, the frequency is approximately independent of amplitude. Apparently unknown to Huygens was that a nearly isochronous pendulum can be obtained with a single circular interrupter if the radius of the interrupter is approximately  $\sqrt{3}/2$  the length of the pendulum.

A uniform lattice of pendulums interrupted by a single circular cylinder serves as a physical model to motivate the development of cubic NLS equations, which describe weakly nonlinear slowly varying amplitude modulations of the cutoff modes. It is also proposed as a possible physical system to observe the reversal of breathers and kinks between lower and upper cutoff modes as the nonlinear coefficient changes sign. A uniform lattice of pendulums interrupted by double circular cylinders yields *quadratic* NLS equations for amplitude modulations of the cutoff modes. These equations arise in general when a nonanalytic quadratic nonlinearity meets the above condition. The equations possess solitary breather and kink solutions that are similar to those for the cubic NLS equations but which are inherently more localized.

Compressional waves in sandstone can be modeled with a quadratic nonanalytic nonlinearity. The transverse displacement of an amplitude-modulated transverse standing wave in a slab of sandstone is approximately described by a quadratic NLS equation, and the observation of a breather solitary wave at frequencies below a cutoff frequency is feasible.

## ACKNOWLEDGMENTS

The author is grateful to Andrés Larraza for many valuable discussions, including those involving the derivations of the quadratic Schrödinger equations and the solitary wave solutions of these equations. The author is also grateful to Miguel Bernard for discussions regarding the feasibility of observing breather solitary waves in sandstone, Cecille Pemberton for assistance, and Richard Raspet for suggestions.

This research was supported by a fellowship from the American Society for Engineering Education and by a grant from the U.S. Office of Naval Research.

- <sup>1</sup>L. D. Landau and E. M. Lifshitz, *Mechanics*, vol. 1 of *Course of Theoretical Physics* (Pergamon, New York, 1976), 3rd ed., pp. 84–93.
- <sup>2</sup>A. H. Nayfeh and D. T. Mook, *Nonlinear Oscillations* (Wiley, New York, 1979), pp. 54–56.
- <sup>3</sup>A. Sommerfeld, *Mechanics, Lectures on Theoretical Physics—Vol. 1* (Academic, New York, 1952), pp. 94–96.
- <sup>4</sup>A. E. Bell, *Christian Huygens and the Development of Science in the Seventeenth Century* (Edward Arnold, London, 1947), pp. 34–40, 127–135.
- <sup>5</sup>H. Lamb, *Dynamics* (Cambridge U.P., London, 1923), 2nd ed., pp. 104–105, 113–114. See also J. B. Marion and S. T. Thornton, *Classical Dynamics of Particles and Systems* (Saunders, Fort Worth, TX, 1995), 4th ed., p. 287.
- <sup>6</sup>N. N. Bogoliubov and Y. A. Mitropolsky, *Asymptotic Methods in the Theory of Nonlinear Oscillations* (Gordon and Breach, New York, 1961), pp. 254–267; W. Weaver, Jr., S. P. Timoshenko, and D. H. Young, *Vibration Problems in Engineering* (Wiley, New York, 1990), 5th ed., pp. 143–144, 175–190.
- <sup>7</sup>W. M. Hartmann, “The dynamically shifted oscillator,” *Am. J. Phys.* **54**, 28–32 (1986). J. S. Thomsen, “A benevolent system: The dynamically shifted oscillator,” *Am. J. Phys.* **56**, 123–128 (1988); I. R. Gatland, “Theory of a nonharmonic oscillator,” *Am. J. Phys.* **59**, 155–158 (1991).
- <sup>8</sup>A. Ronveaux, “Small oscillations which are not harmonic,” *Am. J. Phys.* **52**, 618–619 (1984).
- <sup>9</sup>R. A. Guyer, K. R. McCall, P. A. Johnson, P. N. J. Rasolofosaon, and B. Zinszner, “Equation of state hysteresis and resonant bar measurements on rock,” in *Proc. of 35th U.S. Symposium on Rock Mechanics* (1995), pp. 177–181.
- <sup>10</sup>B. Denardo, B. Galvin, A. Greenfield, A. Larraza, S. Putterman, and W. Wright, “Observations of localized structures in nonlinear lattices: Domain walls and kinks,” *Phys. Rev. Lett.* **68**, 1730–1733 (1992).
- <sup>11</sup>B. Denardo, “Observations of nonpropagating oscillatory solitons,” Ph.D. dissertation, Department of Physics, University of California, Los Angeles, CA, 1990.
- <sup>12</sup>K. Hayata and M. Koshiba, “Algebraic solitary-wave solutions of a nonlinear Schrödinger equation,” *Phys. Rev. E* **51**, 1499–1502 (1995).
- <sup>13</sup>J. Fujioka and A. Espinosa, “Stability of the bright-type algebraic solitary-wave solutions of two extended versions of the nonlinear Schrödinger equation,” *J. Phys. Soc. Jpn.* **65**, 2440–2446 (1996).
- <sup>14</sup>J. A. Aranha, D. K. P. Yue, and C. C. Mei, “Nonlinear waves near a cut-off frequency in an acoustic duct—a numerical study,” *J. Fluid Mech.* **121**, 465–485 (1982).
- <sup>15</sup>A. Larraza and W. F. Coleman, “Solitons, pulse splitting, and am–fm conversion in cylindrical ducts,” *J. Acoust. Soc. Am.* **100**, 139–147 (1996).
- <sup>16</sup>A. Larraza and S. Putterman, “Theory of nonpropagating hydrodynamic solitons,” *Phys. Lett. A* **103**, 15–18 (1984).
- <sup>17</sup>J. Wu, R. Keolian, and I. Rudnick, “Observation of a nonpropagating hydrodynamic soliton,” *Phys. Rev. Lett.* **52**, 1421–1424 (1984); Junru Wu and Isadore Rudnick, “Amplitude-dependent properties of a hydrodynamic soliton,” *ibid.* **55**, 204–207 (1985).
- <sup>18</sup>A. Larraza and S. Putterman, “Theory of nonpropagating surface wave solitons,” *J. Fluid Mech.* **148**, 443–449 (1984); J. W. Miles, “Parametrically excited solitary waves,” *ibid.* **148**, 451–460 (1984).
- <sup>19</sup>E. Kit, L. Shemer, and T. Miloh, “Experimental and theoretical investigation of nonlinear sloshing waves in a rectangular channel,” *J. Fluid Mech.* **181**, 265–291 (1987).
- <sup>20</sup>B. Denardo, W. Wright, S. Putterman, and A. Larraza, “Observation of a kink soliton on the surface of a liquid,” *Phys. Rev. Lett.* **64**, 1518–1521 (1990).
- <sup>21</sup>Y. Yao, M. P. Tulin, and A. R. Kolaini, “Theoretical and experimental studies of three-dimensional wavemaking in narrow tanks, including nonlinear phenomena near resonance,” *J. Fluid Mech.* **276**, 211–232 (1994).
- <sup>22</sup>N. J. Giordano, *Computational Physics* (Prentice–Hall, Upper Saddle River, NJ, 1997), pp. 46–48, 84, 351.
- <sup>23</sup>Ref. 2, pp. 161–174.
- <sup>24</sup>R. J. Blackwell, trans., *Christiaan Huygens’ Pendulum Clock, or Geometrical Demonstrations Concerning the Motion of Pendula as Applied to Clocks* (Iowa State U.P., Ames, 1986).
- <sup>25</sup>H. J. M. Bos, in Ref. 24, pp. xii–xv.
- <sup>26</sup>R. Hooke, in Ref. 27, pp. 167–173.
- <sup>27</sup>J. Drummond Robertson, *The Evolution of Clockwork* (Cassell, London, 1931), pp. 79, 82, 120–121, 124.
- <sup>28</sup>Ref. 27, Chap. IX.
- <sup>29</sup>B. Denardo and W. B. Wright, “Structural properties of kinks and domain walls in nonlinear oscillatory lattices,” *Phys. Rev. E* **52**, 1094–1104 (1995).
- <sup>30</sup>L. D. Landau and E. M. Lifshitz, *Theory of Elasticity* (Pergamon, New York, 1986), 3rd ed., Chaps. I and III.
- <sup>31</sup>K. E-A. Van Den Abeele, P. A. Johnson, R. Guyer, and K. McCall, “On the quasi-analytic treatment of hysteretic nonlinear response in elastic wave propagation,” *J. Acoust. Soc. Am.* **101**, 1885–1898 (1997), and references therein.
- <sup>32</sup>Y. Gueguen and V. Palciauskas, *Introduction to the Physics of Rocks* (Princeton U.P., Princeton, NJ, 1994), p. 84.
- <sup>33</sup>Cleveland Quarries, Amherst, OH.
- <sup>34</sup>J. A. TenCate, K. E. A. Van Den Abeele, and T. J. Shankland, “Laboratory study of linear and nonlinear elastic pulse propagation in sandstone,” *J. Acoust. Soc. Am.* **100**, 1383–1391 (1996).
- <sup>35</sup>M. Atchley, “Observations of Solitons in a Nonlinear Lattice,” M.S. thesis, Department of Physics, Naval Postgraduate School, Monterey, CA, 1992.
- <sup>36</sup>C. Walden, *Breathers in Nonlinear Lattices*, M.S. thesis, Department of Physics, Naval Postgraduate School, Monterey, CA, 1992.

# Model experiment to study sonic boom propagation through turbulence. Part II. Effect of turbulence intensity and propagation distance through turbulence

Bart Lipkens<sup>a)</sup> and David T. Blackstock

*Applied Research Laboratories and Mechanical Engineering Department, The University of Texas at Austin, P.O. Box 8029, Austin, Texas 78713-8029*

(Received 28 July 1994; revised 11 May 1998; accepted 15 June 1998)

A model experiment was reported to be successful in simulating the propagation of sonic booms through a turbulent atmosphere [B. Lipkens and D. T. Blackstock, *J. Acoust. Soc. Am.* **103**, 148–158 (1998)]. In this study the effect on *N* wave characteristics of turbulence intensity and propagation distance through turbulence are investigated. The main parameters of interest are the rise time and the peak pressure. The effect of turbulence intensity and propagation distance is to flatten the rise time and peak pressure distributions. Rise time and peak pressure distributions always have positive skewness after propagation through turbulence. Average rise time grows with turbulence intensity and propagation distance. The scattering of rise time data is one-sided, i.e., rise times are almost always increased by turbulence. Average peak pressure decreases slowly with turbulence intensity and propagation distance. For the reported data a threefold increase in average rise time is observed and a maximum decrease of about 20% in average peak pressure. Rise times more than ten times that of the no-turbulence value are observed. At most, the maximum peak pressure doubles after propagation through turbulence, and the minimum peak pressure values are about one-half the no-turbulence values. Rounded waveforms are always more common than peaked waveforms. © 1998 Acoustical Society of America. [S0001-4966(98)05509-X]

PACS numbers: 43.28.Mw, 43.25.Cb [LCS]

## INTRODUCTION

Lipkens and Blackstock<sup>1</sup> showed that model experiments are successful in simulating the propagation of sonic booms through a turbulent atmosphere. In the model experiment electrical sparks generated the *N* waves and a plane jet produced a turbulent velocity field. A detailed description of the apparatus of the model experiment is given in Ref. 2 and summarized in Ref. 1. For the reported data, the two main results were: (1) the waveform distortion of actual sonic booms is reproduced, both in scale and in character, and (2) turbulence almost always causes the rise time to increase, and, on average, the peak pressure to decrease.

A parametric study is presented in this paper of the effect of turbulence intensity and propagation distance through turbulence on the *N* wave characteristics. Important characteristics of the *N* waves analyzed are peak pressure and rise time (time required for the pressure to increase from 10% to 90% of peak pressure), since they are all related to the loudness associated with the sonic boom when heard outdoors.<sup>3–6</sup> Half-duration, which has a minor effect on loudness, and arrival time of the *N* waves are also analyzed. The arrival time is the time at which the shock front of the spark signal arrives at the microphone. The half-duration is the time between the arrival of the shock front and the zero crossing of the *N* wave in the middle part of the signal. Experiments with spherical and plane *N* waves were performed. Our goal was to investigate to what extent the rise time and peak pres-

sure are affected by a change in turbulence intensity and propagation distance. In order to study the effect of turbulence intensity, we designed an experiment in which the turbulence intensity was progressively increased while all other characteristics were kept the same. Two experiments were done to study the effect of propagation distance. First, the receiver was positioned at various distances from the source, and at each position the above characteristics were measured with and without turbulence. Second, the source–receiver distance was kept constant, but the thickness of the turbulent layer was varied, and again the characteristics were measured for each thickness. In addition to showing figures that represent the trends observed in the data, we also provide the data in numerical form. The following symbols are used: the rise time  $\tau$  of the head shock, peak pressure  $\Delta p$ , propagation distance  $l$ , standard deviation  $\sigma$ , arrival time  $t_{ar}$ , half-duration  $T$ , and skewness  $\alpha$ .

## I. EFFECT OF TURBULENCE INTENSITY

The experiment was performed with plane waves, which were produced by a paraboloidal reflector with a spark source at its focal point. The setup of the experiment is shown in Fig. 1. The microphone and source, separated by a distance of 0.53 m, were positioned 0.515 m downstream from the rectangular nozzle of the jet which produced the turbulence along the source–receiver path. The propagation path of the *N* wave is perpendicular to the axis of the jet and parallel to the width of the nozzle. Sets of 100 *N* waves each

<sup>a)</sup>Current address: MacroSonix, 1570 East Parham Road, Richmond, VA 23228.

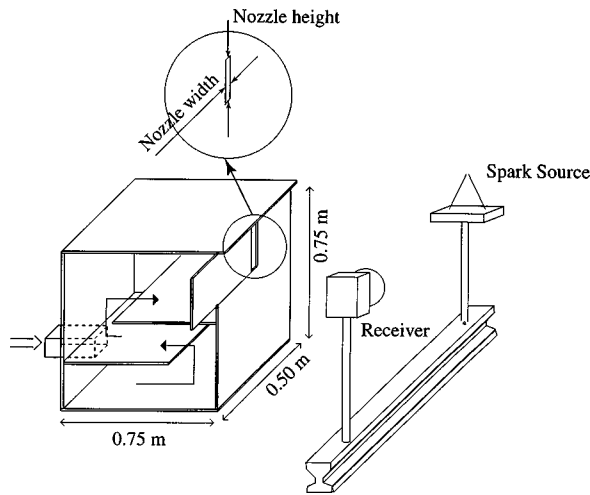


FIG. 1. The arrangement of the experiment: plane jet source, spark source (shown without the paraboloidal reflector), and receiver.

were collected by the data acquisition system at jet nozzle velocities of 0, 12.4, 18.3, 22.7, 26.6, and 31.3 m/s. The nozzle width was 25.4 mm.

The integral length scale of the jet, a representation of the large scale structures in the jet, grows linearly with distance along the axis of the jet. The Taylor microscale along the jet axis is 6 mm in the self-preservation region on the axis of the jet. The Kolmogorov length scale is about 90  $\mu\text{m}$  when the turbulence dissipation is calculated according to an isotropic turbulence assumption. Details regarding the nature of the turbulent field of the jet can be found in Ref. 2.

The streamwise turbulence intensity is defined as  $\overline{u^{2/2}}/U_M$  and the lateral turbulence intensity is  $\overline{v^{2/2}}/U_M$ , where  $u$  and  $v$  are respectively the axial and lateral component of the velocity fluctuations of the plane jet flow, and  $U_M$  is the mean axial velocity. As is shown in Ref. 2, the turbulence intensities attain a constant value of 21% (axial) and 16% (lateral) in the self-preservation region of the jet. All the measurements reported here were done in the self-preservation region of the jet. Since the axial component  $U_M$  is directly proportional to the jet nozzle velocity  $U_0$ , we will only report values of jet nozzle velocities. At 0.515 m downstream from the jet nozzle, the relationship between the jet nozzle velocity  $U_0$  and the mean axial velocity  $U_M$  is  $(U_0/U_M)^2 \approx 4$  or  $U_M \approx 0.5U_0$ . Hence, the lateral rms fluctuation velocity, which is the turbulent velocity fluctuation along the propagation direction of the  $N$  wave, is  $\overline{v^{2/2}} = 0.08U_0$ .

The results are summarized in Tables I and II. In Table I the mean and standard deviation of rise time, peak pressure, half-duration, and arrival time are given for a range of turbulence intensities or jet nozzle velocities. Table II contains the median, maximum, minimum, and skewness values of rise time and peak pressure for the same turbulence range. In Fig. 2 the mean and standard deviation of the rise time and peak pressure, mean half-duration, and mean arrival time are plotted versus jet nozzle velocities. The mean rise time  $\overline{\tau}$  and the standard deviation of the rise time  $\sigma_\tau$  grow with jet nozzle velocity. At low turbulence intensity, the increase in rise time is about 50%. At high intensity, the average rise time is three times that of the no-turbulence value. Even at low intensity, the spread in rise time is more than ten times that of rise time in quiet air. The mean peak pressure  $\overline{\Delta p}$  decays with jet speed, and the spread in peak pressure  $\sigma_{\Delta p}$  increases quickly with jet speed. At a jet speed of 31.3 m/s the decrease in average peak pressure is about 13%. For moderate to high intensities the spread in peak pressure is more than ten times that of quiet air. The mean half-duration  $\overline{T}$  remains nearly constant at first, but increases with higher nozzle velocities. The maximum increase is 10%. The mean arrival time  $\overline{t_{ar}}$  curve exhibits almost the opposite behavior of the mean half-duration. At first the arrival time is nearly constant, but eventually it decreases with nozzle velocity. The amount of decrease is essentially the same as the amount of increase for the half-duration.

The histograms of rise time and peak pressure are shown in Fig. 3. Rise time is presented in the left column, and peak pressure in the right. The bin size is 0.25  $\mu\text{s}$  for the rise time and 25 Pa for the peak pressure. The reference values (quiet air) are shown in the upper row, while the values for the different jet nozzle velocities are shown beneath it. The no-turbulence rise time data occupy the same bin, while the no-turbulence peak pressure values are distributed over three bins. With increasing jet nozzle velocity the rise time distribution becomes flatter and larger values of rise time appear. After propagation through the turbulence, only a small fraction of the waves have rise time significantly smaller than the no-turbulence values, i.e., 2%, 6%, 3%, 3%, and 3% of the waves at nozzle velocities of 12.4, 18.3, 22.7, 26.6, and 31.3 m/s, respectively. The median is always smaller than the average (see Table II). At all nozzle velocities the skewness of the rise time distribution is positive. The distributions are asymmetric and have a tail that expands out towards large rise time values. Rise times more than ten times that of the

TABLE I. Effect of turbulence intensity on the propagation of plane  $N$  waves through plane jet turbulence; mean and standard deviation for rise time ( $\tau$ ), peak pressure ( $\Delta p$ ), half-duration ( $T$ ), and arrival time ( $t_{ar}$ ).

Jet nozzle velocity (m/s)	$\overline{v^{2/2}}$ (m/s)	$\tau$ ( $\mu\text{s}$ )		$\Delta p$ (Pa)		$T$ ( $\mu\text{s}$ )		$t_{ar}$ ( $\mu\text{s}$ )	
		Mean	$\sigma$	Mean	$\sigma$	Mean	$\sigma$	Mean	$\sigma$
0	0	0.63	0.02	528.5	13.2	10.56	0.22	11.02	0.21
12.4	0.992	0.90	0.65	492.7	98.3	10.50	0.64	11.04	1.11
18.3	1.464	1.11	0.75	496.1	145.9	10.73	0.81	11.05	1.62
22.7	1.816	1.51	1.19	455.8	123.0	11.03	0.95	10.48	1.96
26.6	2.128	1.82	1.55	449.8	158.3	11.09	1.99	10.53	3.64
31.3	2.504	2.07	1.70	458.8	172.4	11.60	2.36	9.99	2.91

TABLE II. Effect of turbulence intensity on the propagation of plane  $N$  waves through plane jet turbulence; median, maximum, minimum, and skewness values for rise time ( $\tau$ ), and peak pressure ( $\Delta p$ ).

Jet nozzle velocity (m/s)	$\overline{v}^{21/2}$ (m/s)	$\tau_M$ ( $\mu$ s)	$\tau_{\max}$ ( $\mu$ s)	$\tau_{\min}$ ( $\mu$ s)	$\alpha_\tau$	$\Delta p_M$ (Pa)	$\Delta p_{\max}$ (Pa)	$\Delta p_{\min}$ (Pa)	$\alpha_{\Delta p}$
0	0	0.63	0.69	0.56	0.32	532	552	473	-1.70
12.4	0.992	0.72	3.87	0.48	2.98	467	788	285	0.46
18.3	1.464	0.80	3.96	0.41	1.63	464	946	249	0.66
22.7	1.816	0.94	5.90	0.41	1.55	445	900	245	0.76
26.6	2.128	1.18	6.80	0.44	1.49	410	1079	250	1.59
31.3	2.504	1.21	8.97	0.43	1.39	420	977	230	0.90

no-turbulence value are observed at high turbulence intensity.

The peak pressure distribution becomes wider with increasing jet nozzle velocity, and larger values occur in the distribution. The peak pressure distribution has a positive skewness at all nozzle velocities. With increasing jet speed, more rounded wave shapes are present, but concurrently some very large peak pressure values occur. The largest peak pressures observed are about twice that of the no-turbulence value, and the smallest peak pressure about half that of the no-turbulence value (see Table II).

## II. EFFECT OF PROPAGATION DISTANCE THROUGH TURBULENCE

The effect of propagation distance through the turbulent field on the  $N$  wave characteristics was investigated in two experiments with spherical waves. In experiment A, the microphone was positioned in the turbulent field at different distances from the spark. In experiment B, the distance between the spark and the microphone was fixed, but the thickness of the turbulent layer was changed.

### A. Experiment A

The general setup of the experiment is the same as in Fig. 1. A schematic sketch of the experiment is shown in Fig. 4. The shaded area in the figure represents the jet cross section. For each of seven microphone positions two sets of measurements were taken, one in quiet air and one in the

turbulent flow field. The spark source and microphone were located 0.75 m downstream from the jet nozzle. The nozzle width was 25.4 mm and the jet nozzle velocity was 31.3 m/s, which resulted in a lateral rms velocity fluctuation of 2.26 m/s. Except for the last measurement position the microphone was located inside the turbulent field. When the microphone was situated in the turbulent field, the field itself did not generate any measurable pressure fluctuation and did not interfere with the measurement of the spark signal. For each microphone position 100  $N$  waves were analyzed.

Table III summarizes the results from the experiment. At each location two rows of results are presented. The first row contains the data taken in quiet air and the second, marked with a bullet, contains the results for the turbulence. In Fig. 5(a) we show the relative change in average rise time  $(\overline{\tau}_{\text{turb}} - \overline{\tau}_{\text{no}})/\overline{\tau}_{\text{no}}$  and  $(\overline{\Delta p}_{\text{turb}} - \overline{\Delta p}_{\text{no}})/\overline{\Delta p}_{\text{no}}$ , while in Fig. 5(b) we show the normalized standard deviation of rise time  $\sigma_{\tau_{\text{turb}}}/\overline{\tau}_{\text{turb}}$  and peak pressure  $\sigma_{\Delta p_{\text{turb}}}/\overline{\Delta p}_{\text{turb}}$ , where  $\sigma_{\Delta p_{\text{turb}}}$  is the standard deviation of peak pressure in the presence of turbulence and  $\overline{\Delta p}_{\text{turb}}$  is the average peak pressure in turbulence. The relative change in average rise time increases with distance from 5% to 50% at 0.5 m. At first, the percent change in average rise time grows with propagation distance, but at larger distances the change levels off. A similar observation applies to the peak pressure data, but the change is negative, i.e., the average peak pressure after propagation through turbulence is always smaller than the no-turbulence case. The rate of decrease is relatively small, i.e., about 10%

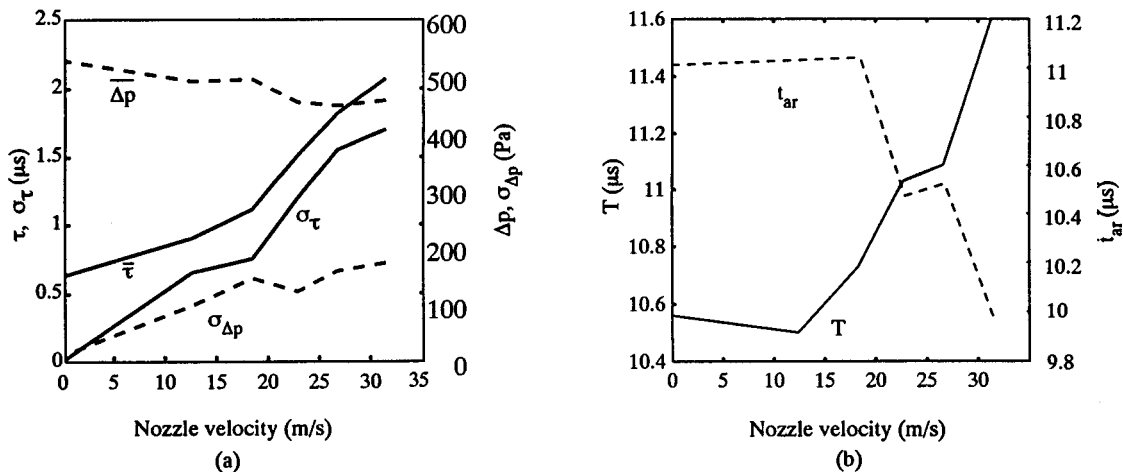


FIG. 2. The effect of increasing jet nozzle velocity on plane  $N$  waves. Graph (a) shows the effect on the mean and the standard deviation of the rise time and peak pressure. Graph (b) shows the effect on the mean half-duration and arrival time.



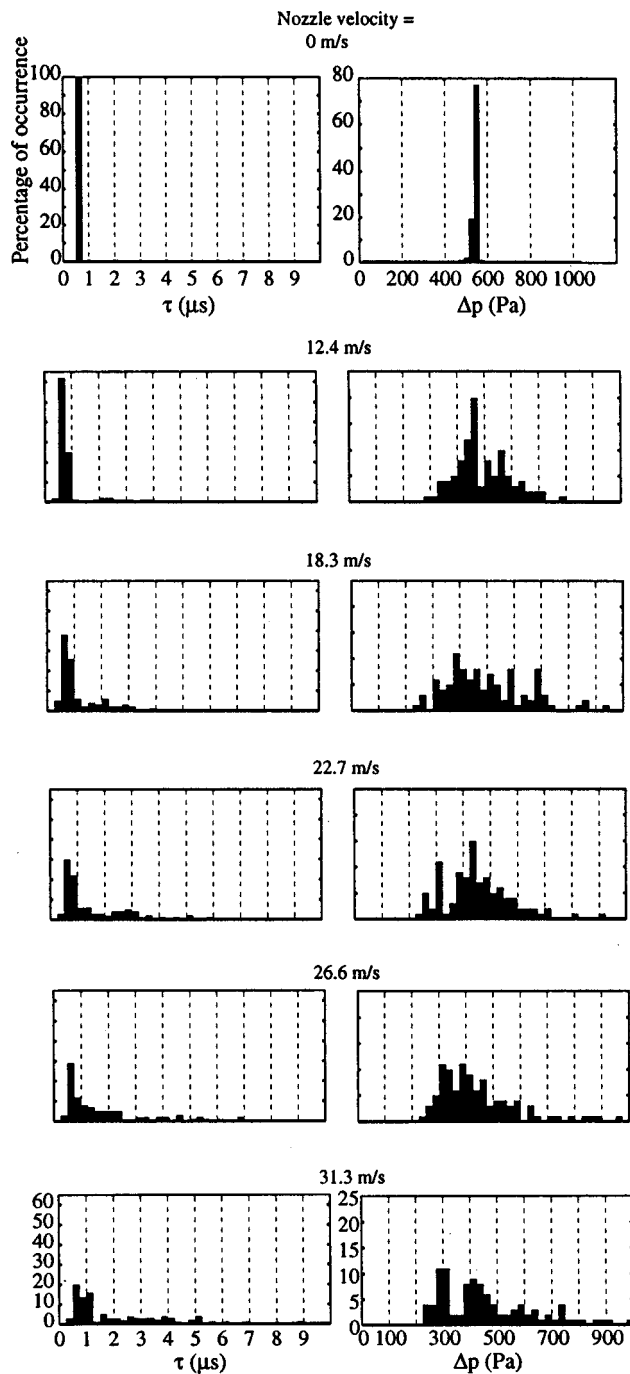


FIG. 3. Histograms of rise time and peak pressure of plane  $N$  waves as a function of jet nozzle velocities. The bin size is  $0.25 \mu\text{s}$  for the rise time and  $25 \text{ Pa}$  for the peak pressure. The first row presents the data measured in quiet air.

at a distance of  $0.5 \text{ m}$ . The normalized standard deviation of rise time increases linearly with propagation distance and reaches a maximum value of  $50\%$  at  $0.5 \text{ m}$ . The normalized standard deviation of peak pressure increases with distance at first, but eventually appears to approach a limit. The deviation is about  $0.1$  at  $0.05 \text{ m}$  and  $0.3$  at  $0.5 \text{ m}$ .

As may be observed from Table III, the average half-duration increased slightly when turbulence is present, and the average arrival time decreased when turbulence is present.

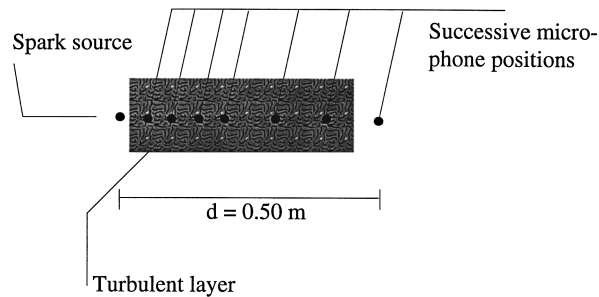


FIG. 4. Setup of experiment A: effect of propagation distance through turbulence.

## B. Experiment B

In this experiment the total distance from the spark source to the microphone was kept constant, but the thickness of the turbulent flow field traversed by the  $N$  wave was varied by varying the height of the nozzle. The waves propagated across the jet and parallel to the height of the nozzle. This was achieved by turning the settling chamber on one of its sides, as is shown in Fig. 6. A schematic view of the experiment is given in Fig. 7. The microphone was located outside the turbulent field. The distance between the spark source and the microphone was  $0.4 \text{ m}$  and spherical  $N$  waves were used. The length of the turbulent flow field was increased from  $0$  to  $0.25 \text{ m}$  in increments of  $0.025 \text{ m}$  by changing the height of the jet nozzle in similar increments. To keep the turbulence characteristics the same for all measurements, we varied the fan velocity so as to keep the nozzle Reynolds number constant as the nozzle height was changed. First, a set of  $100 N$  waves was analyzed in quiet air to establish a reference against which other results were then

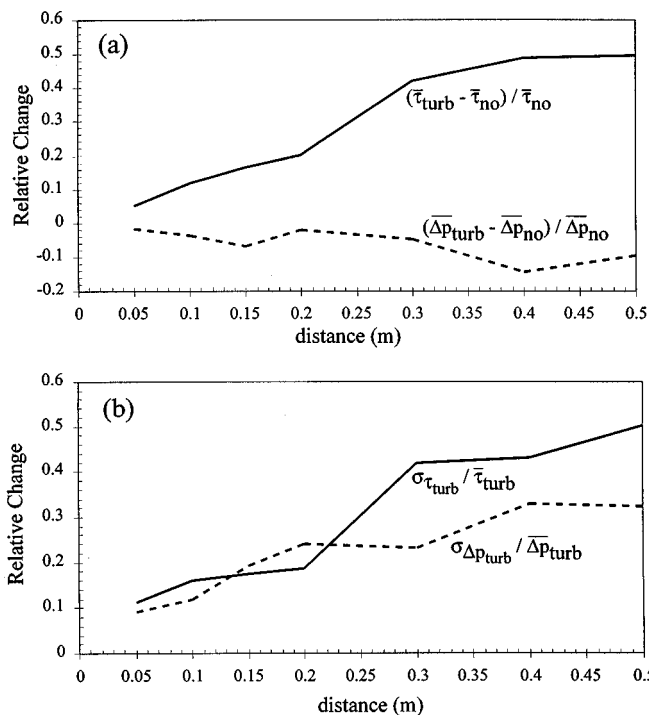


FIG. 5. Effect of propagation distance through turbulence on the rise time and peak pressure of spherical  $N$  waves.

TABLE III. Effect of propagation distance through turbulence on spherical  $N$  waves characteristics.

Propagation distance (m)	Turbulence	$\tau$ ( $\mu\text{s}$ )		$\Delta p$ (Pa)		$T$ ( $\mu\text{s}$ )		$t_{\text{ar}}$ ( $\mu\text{s}$ )	
		Mean	$\sigma$	Mean	$\sigma$	Mean	$\sigma$	Mean	$\sigma$
0.05		0.401	0.001	1772	42.1	5.794	0.220	6.465	0.143
0.05	•	0.421	0.048	1743	159	5.845	0.264	6.356	0.793
0.1		0.449	0.004	750.3	16.4	6.339	0.148	4.716	0.156
0.1	•	0.503	0.081	721.8	84.8	6.347	0.253	4.366	1.262
0.15		0.512	0.009	465.5	13.5	6.575	0.217	4.930	0.211
0.15	•	0.597	0.104	434.4	84.2	6.583	0.312	4.276	1.819
0.2		0.580	0.010	326.0	7.3	6.768	0.148	7.682	0.180
0.2	•	0.697	0.131	319.7	76.5	6.746	0.428	7.069	2.661
0.3		0.734	0.028	186.9	5.9	6.775	0.220	9.792	0.223
0.3	•	1.042	0.437	177.6	41.3	6.930	0.420	8.800	3.220
0.4		0.862	0.060	130.1	4.2	7.024	0.274	16.48	0.300
0.4	•	1.282	0.554	111.2	36.7	7.356	0.858	14.79	3.300
0.5		0.998	0.075	97.1	2.8	7.310	0.190	20.06	0.290
0.5	•	1.495	0.749	87.9	28.5	7.420	0.614	18.44	3.420

compared. For each thickness of the turbulent field 200  $N$  waves were propagated across the turbulence and captured for analysis.

The results are presented in Tables IV and V. Table IV contains the mean and standard deviation of rise time, peak pressure, half-duration, and arrival time. The median, maximum, minimum, and skewness values of peak pressure and rise time are shown in Table V. The average rise time and the standard deviation increase with propagation distance through turbulence. As is shown in Fig. 8(a), the average rise time is 0.788  $\mu\text{s}$  in quiet air and increases approximately linearly with distance. The maximum value is 2.263  $\mu\text{s}$  for a turbulence length of 0.225 m. The average peak pressure decays slowly from about 160 to 150 Pa. The standard deviation of both rise time and peak pressure grows with turbulence length. The standard deviation of rise time is ten times that of quiet air at 0.05 m and increases to 20 times at 0.25 m. The increase in standard deviation of peak pressure is from seven times the no-turbulence value at 0.05 m to ten times at 0.25 m. As is observed in Fig. 8(b), the average half-duration exhibits an increase of about 10% with propagation distance. The average arrival time has a minimum for

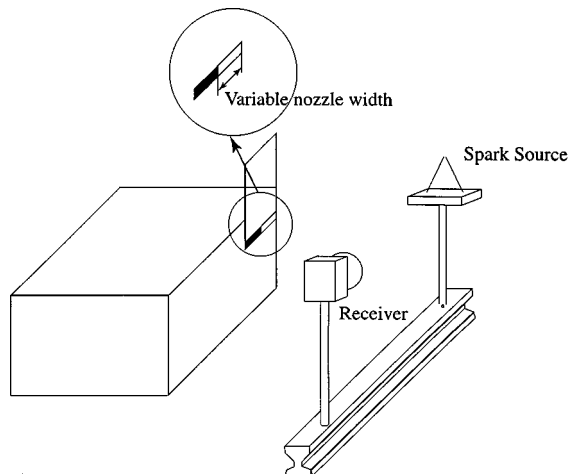


FIG. 6. Setup of experiment B: plane jet source, spark source (shown with the paraboloidal reflector), and receiver.

a propagation distance of 0.05 m and then increases to approach the value for quiet air at larger turbulence thicknesses. The maximum change is 17%.

In Fig. 9 the rise time and peak pressure histograms are displayed for each distance. Rise time is presented in the left column, and peak pressure in the right. The width of the bins in the rise time histograms is 0.25  $\mu\text{s}$ . As  $l$  increases, larger rise times appear more frequently and the distribution becomes flatter and less peaked. All distributions have positive skewness (see Table V). Turbulence almost always causes the rise time to increase. A small percentage of waves have smaller rise times than those measured in quiet air. The number of  $N$  waves that show this behavior decreases as the thickness of the turbulent field increases, i.e., ten at 0.05 m, six at 0.1 m, three at 0.15 m, one at 0.2 m, and none at 0.25 m. We noticed that in most cases the waveform of the waves with smaller rise times is in the U-shaped class or the strongly peaked one.<sup>1</sup> Higher peak pressure results in stronger nonlinear behavior and the shock is steeper than that of the reference  $N$  wave. Two examples are shown in Fig. 10. The propagation distance is 0.05 m in Fig. 10(a), and 0.1 m in Fig. 10(b). In the upper trace a reduction in rise time of 22% is observed even though the peak pressure is nearly the same as for the reference  $N$  wave. In the lower trace a 32% decrease in rise time is seen. The peak pressure is nearly twice that of the reference  $N$  wave.

The histograms for the peak pressure data are shown in the right column of Fig. 9. Each bin has a width of 10 Pa.

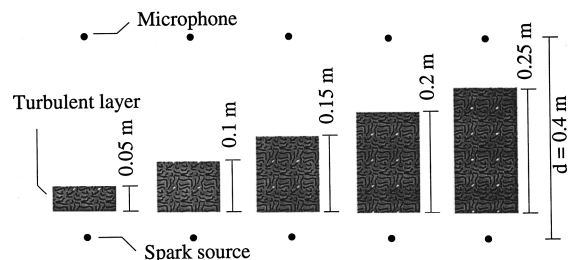


FIG. 7. Schematic setup of experiment B: effect of propagation distance through turbulence.

TABLE IV. Effect of the length of the turbulent field on the characteristics of spherical  $N$  waves: mean and standard deviation.

Length turbulence (m)	$\tau$ ( $\mu\text{s}$ )		$\Delta p$ (Pa)		$T$ ( $\mu\text{s}$ )		$t_{\text{ar}}$ ( $\mu\text{s}$ )	
	Mean	$\sigma$	Mean	$\sigma$	Mean	$\sigma$	Mean	$\sigma$
0	0.788	0.068	163.2	5.6	9.775	0.389	14.30	0.91
0.050	1.127	0.664	156.5	38.8	9.781	0.640	11.87	1.46
0.075	1.088	0.641	158.5	40.8	9.868	0.590	12.21	1.66
0.100	1.150	0.695	168.7	46.9	9.949	0.670	12.56	1.70
0.125	1.432	0.982	156.4	46.6	9.972	0.730	13.02	1.76
0.150	1.686	1.124	153.9	50.1	10.17	0.85	13.03	2.15
0.175	1.679	1.048	149.9	43.3	10.22	0.93	13.21	1.93
0.200	2.076	1.452	156.1	44.3	10.66	1.02	13.72	2.25
0.225	2.263	1.483	151.9	51.5	10.66	1.12	13.53	2.32
0.250	2.134	1.201	154.0	63.2	10.59	1.09	14.26	2.83

TABLE V. Effect of the length of the turbulent field on the characteristics of spherical  $N$  waves; median, maximum, minimum, and skewness values for rise time ( $\tau$ ), and peak pressure ( $\Delta p$ ).

Length turbulence (m)	$\tau_M$ ( $\mu\text{s}$ )	$\tau_{\text{max}}$ ( $\mu\text{s}$ )	$\tau_{\text{min}}$ ( $\mu\text{s}$ )	$\alpha_\tau$	$\Delta p_M$ (Pa)	$\Delta p_{\text{max}}$ (Pa)	$\Delta p_{\text{min}}$ (Pa)	$\alpha_{\Delta p}$
0.05	0.861	4.396	0.570	2.099	151.7	299.5	65.4	0.917
0.075	0.865	4.943	0.575	3.077	152.0	369.6	83.5	1.110
0.100	0.888	4.878	0.520	2.334	157.7	295.2	87.7	0.793
0.125	1.039	5.191	0.484	1.887	145.1	323.1	77.1	1.294
0.150	1.179	6.396	0.603	1.492	143.8	341.7	73.9	1.211
0.175	1.267	5.565	0.613	1.510	146.7	291.8	53.6	0.608
0.200	1.441	8.200	0.598	1.491	149.7	298.6	69.3	0.653
0.225	1.818	9.376	0.560	1.660	143.9	373.3	62.3	1.196
0.250	1.791	6.615	0.724	1.302	141.2	435.2	53.0	1.411

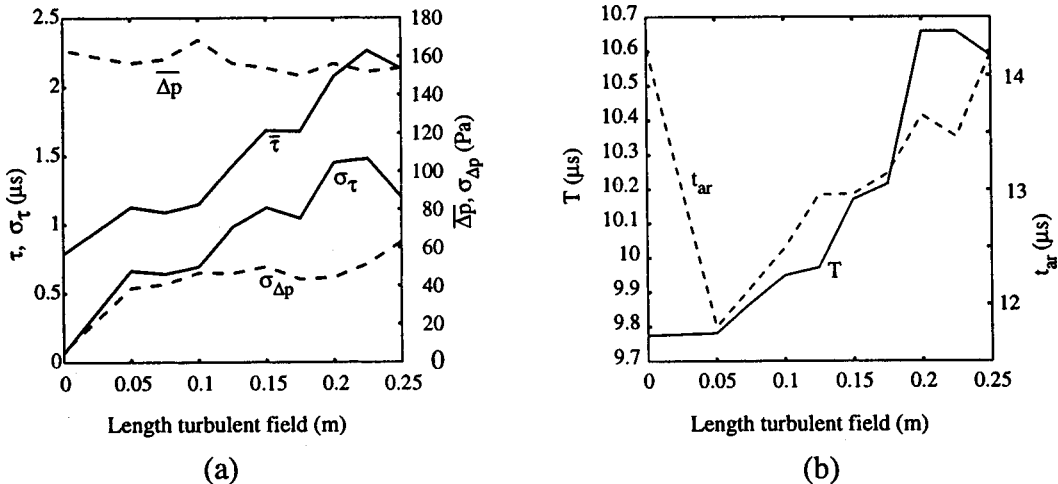


FIG. 8. Effect of thickness of the turbulent layer on spherical  $N$  waves. Graph (a) shows the effect on the mean rise time and peak pressure, and the standard deviation of the rise time and peak pressure. Graph (b) shows the effect on the mean half-duration and arrival time.

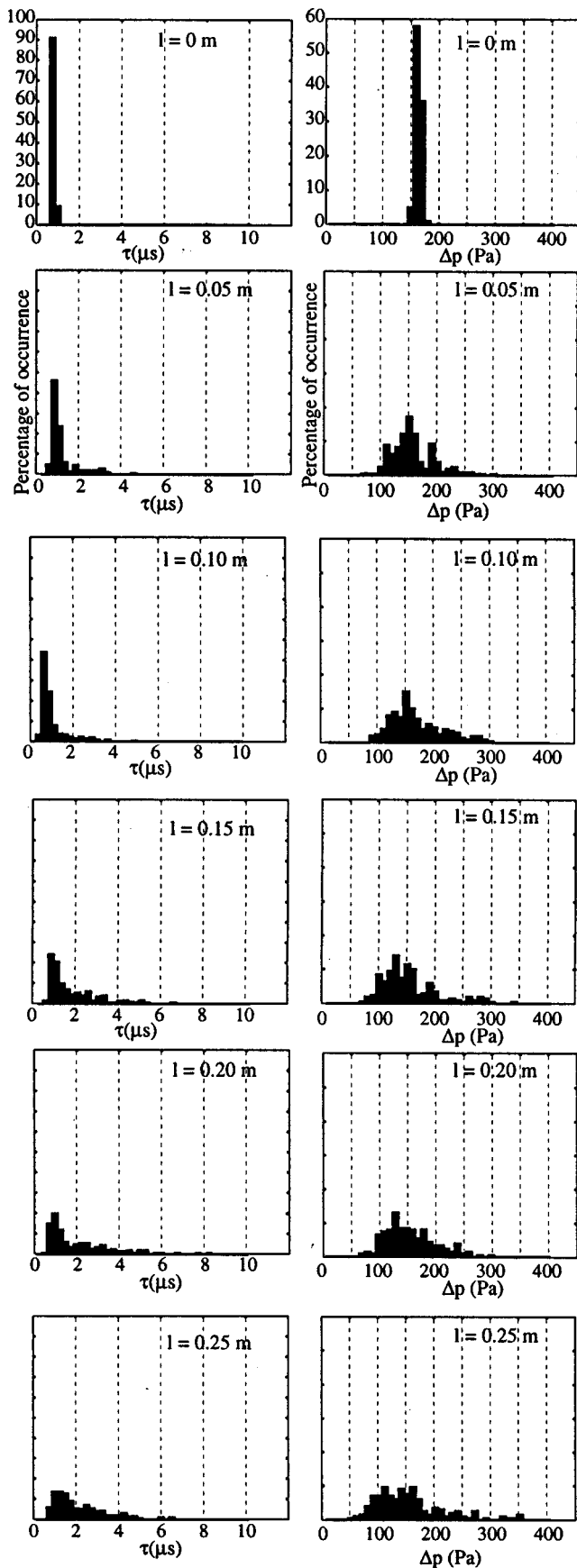


FIG. 9. Histogram of rise time and peak pressure of spherical waves: effect of thickness of the turbulent layer. The bin size is  $0.25 \mu\text{s}$  for the rise time and  $20 \text{ Pa}$  for the peak pressure.

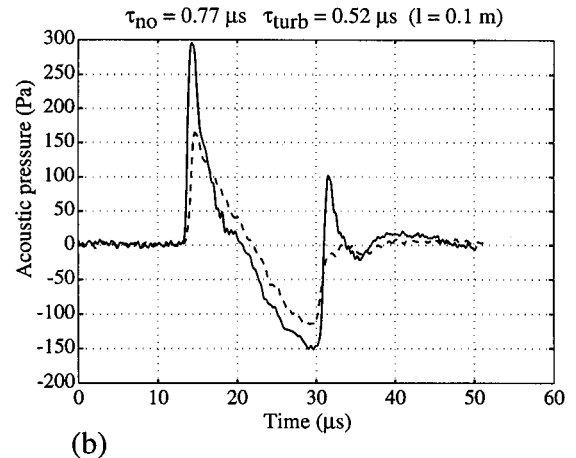
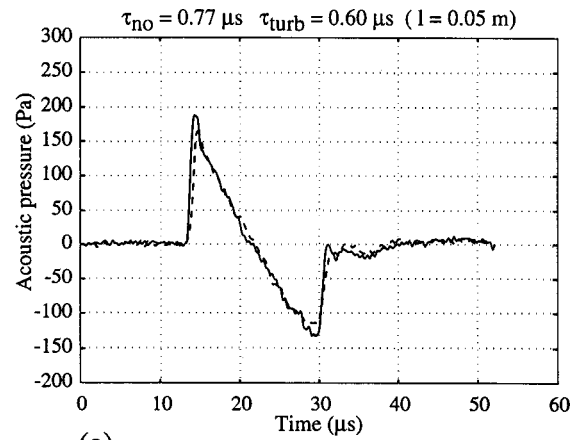


FIG. 10. Waveform examples of rise time decrease for propagation through turbulence of (a)  $0.05 \text{ m}$  and (b)  $0.1 \text{ m}$ . The solid line represents a propagation in turbulence; the dashed line is a propagation without turbulence.

With increasing distance through turbulence more outliers occur in the distribution, both very low and very high values, and the distribution becomes flatter. Again we observe positive skewness values (Table V) for all peak pressure distributions. Maximum peak pressures are about twice that of the no-turbulence value, while the minimum peak pressures are about one half the no-turbulence values.

A general conclusion of the results of this experiment is that distortion by turbulence tends to thicken the shock of the waves. Indeed, when the propagation distance through turbulence covers nearly all the distance between spark source and microphone, rise time only increases (i.e., for a propagation distance of  $0.25 \text{ m}$ ). No rise time is smaller than the rise time of the reference  $N$  waves, an indication that a possible steepening of the wavefront is destroyed by thickening of the shocks. Only for a limited propagation through turbulence and a substantial spiking of the  $N$  wave is a reduced rise time possible due to the increased steepening effect when the wave propagates through the quiet air layer before it arrives at the receiver.

### III. COMPARISON WITH SONIC BOOM DATA

Carlson and Maglieri<sup>7</sup> summarized the sonic boom data from several test programs that included five aircraft, 1625 flights, and resulted in 12 406 signature measurements. From

the cumulative probability curve of peak pressure they deduced that (1) in 99 out of every 100 occurrences the measured peak pressure value exceeds one-half the calculated value, (2) in 50 out of every 100 occurrences the measured value equals or exceeds the calculated value, and (3) in only 1 out of every 100 occurrences is the calculated value exceeded by a factor of 2 or more. Their conclusions and our experimental observations agree. However, our experiment produced more rounded wave shapes than peaked ones, and less than 50% of the waves have peak pressures that are equal to, or exceed, the no-turbulence value.

Pierce and Maglieri<sup>8</sup> presented a thorough review of the effect on sonic boom signatures of atmospheric perturbations. They used the same peak pressure data set as Carlson and Maglieri. Their analysis of the peak pressures of more restricted data sets showed that the spread in peak pressure (1) increases with lateral distance from the flight path, (2) is larger in summer than in winter, (3) decreases with increasing Mach number, and (4) varies relatively little with the type of aircraft. They noted that all of these observations are consistent with the notions that (a) the variability is caused by atmospheric perturbations, (b) the magnitude of such perturbations is greater in summer than in winter, (c) the spread in peak pressure increases with the length of the ray path between the airplane and the ground, (d) this ray path is shorter with increasing Mach number, and (e) the mechanisms causing the variations in peak pressure are primarily linear.

The observations from the model experiment data presented here corroborate the analysis by Pierce and Maglieri; namely that the spread in peak pressure data increases with increasing propagation path through the turbulence and with increasing turbulence intensity.

Pierce and Maglieri also presented relative probability curves of rise times of 638 data samples and concluded that larger rise times may be expected when the distance from the ground track, i.e., the lateral distance, increases. A larger lateral distance implies a larger propagation path through the atmospheric turbulent boundary layer. They observed that both mean rise time and the relative probability of larger rise times increase and that the relative probability curves are asymmetric with positive skewness. The effect of a lateral distance increase is to flatten the relative probability curve and more larger rise times occur. The model experiment rise time data presented here show identical behavior as a function of propagation path through turbulence.

Willshire and Devilbiss<sup>9</sup> analyzed the sonic boom data from the sonic boom propagation experiment performed at White Sands Missile Range in August 1991 as part of the NATO Joint Acoustics Propagation Experiment. They calculated rise time and peak pressure relative probability for a low (in the morning) and a moderate (in the afternoon) turbulence level. Their analysis showed that on average, peak pressure did not change appreciably, but the spread in the data increased. Both peak pressure distributions have positive skewness. The distribution at low turbulence level is more peaked than the moderate level distribution. On average, rise time increases by a factor of 4, and the rise time standard deviation is increased three times. At the moderate

turbulence level the rise time distribution is much flatter than for the low-level turbulence. Thus, their analysis of turbulence effects on peak pressure and rise time distribution for real sonic booms confirms our observations in the laboratory of the effect of turbulence intensity on peak pressure and rise time.

The rise time data measured in the model experiment strongly suggest that turbulence is a one-sided scattering mechanism, i.e., turbulence nearly always increases rise time. This conclusion is not in agreement with the results from Pierce and Kang's<sup>10</sup> numerical analysis which is based on a steady-state solution of the augmented Burgers equation. Their results show that, when compared with sonic boom data, an even scattering is predicted, i.e., some measured rise times are lower than the calculated value and others are larger in nearly the same percentages. The difference between our measurements and their analysis might be caused by their assumption that the boom front shock is always in steady state during its propagation through the atmosphere.

#### IV. CONCLUSION

Microphone measurements of plane and spherical  $N$  waves propagating through a turbulent velocity field are reported. The effect of turbulence parameters, i.e., the turbulence intensity and the propagation distance through the turbulent field, on the characteristics of the  $N$  wave is to flatten the rise time and peak pressure distributions. The increase in average rise time grows with turbulence intensity and distance traveled through the turbulence. Rise time is almost always increased by turbulence, but it is shown that in certain cases a small percentage of  $N$  waves have a smaller rise time and larger peak pressure than the incident  $N$  wave. On average, the peak pressure slowly decreases with increasing turbulence intensity or propagation distance through turbulence.

#### ACKNOWLEDGMENTS

This research was supported by a grant from NASA Langley Research Center.

<sup>1</sup>B. Lipkens and D. T. Blackstock, "Model experiment to study sonic boom propagation through turbulence. Part I. General results," *J. Acoust. Soc. Am.* **103**, 148–158 (1998).

<sup>2</sup>B. Lipkens, "Experimental and theoretical study of the propagation of  $N$  waves through a turbulent medium," Ph. D. Thesis, Mechanical Engineering Department, The University of Texas at Austin, 1993.

<sup>3</sup>A. Niedzwiecki and H. S. Ribner, "Subjective loudness of  $N$ -wave sonic booms," *J. Acoust. Soc. Am.* **64**, 1622–1626 (1978).

<sup>4</sup>A. Niedzwiecki and H. S. Ribner, "Subjective loudness of minimized sonic boom waveforms," *J. Acoust. Soc. Am.* **64**, 1617–1621 (1978).

<sup>5</sup>J. D. Leatherwood and B. M. Sullivan, "Subjective loudness response to simulated sonic booms," *Proceedings, High-Speed Research Workshop on Sonic Boom*, edited by C. M. Darden (NASA Langley Research Center, Hampton, VA, 1992), Vol. I, pp. 151–170.

<sup>6</sup>B. M. Sullivan and J. D. Leatherwood, "Experimental studies of loudness and annoyance response to sonic booms," *Proceedings, High-Speed Research Workshop on Sonic Boom*, edited by T. A. Edwards (NASA Ames Research Center, Moffet Field, CA, 1992), Vol. I, pp. 153–175.

<sup>7</sup>H. W. Carlson and D. J. Maglieri, "Review of sonic-boom generation

theory and prediction methods," J. Acoust. Soc. Am. **51**, 675–685 (1972).

<sup>8</sup>A. D. Pierce and D. J. Maglieri, "Effects of atmospheric irregularities on sonic boom propagation," J. Acoust. Soc. Am. **51**, 702–721 (1972).

<sup>9</sup>W. L. Willshire and D. W. DeVilbiss, "Preliminary results from the White Sands Missile Range sonic boom propagation experiment," *Proceedings, High-Speed Research Workshop on Sonic Boom*, edited by C.

M. Darden (NASA Langley Research Center, Hampton, VA, 1992), Vol. I, pp. 137–149.

<sup>10</sup>A. D. Pierce and J. Kang, "Molecular relaxation effects on sonic boom waveforms," in *Frontiers of Nonlinear Acoustics: Proceedings of the 12th ISNA*, edited by M. F. Hamilton and D. T. Blackstock (Elsevier Applied Science, London, 1990), pp. 165–170.

# On the use of stair steps to approximate bathymetry changes in ocean acoustic models

Finn B. Jensen

SACLANT Undersea Research Centre, 19138 La Spezia, Italy

(Received 18 November 1997; revised 27 April 1998; accepted 6 May 1998)

Stair-step discretization criteria have been established for accurately representing smoothly varying bathymetry in numerical models. It is shown that the strictest criterion applies to backscatter calculations, where the horizontal stair-step size must be a small fraction of an acoustic wavelength ( $\Delta x \leq \lambda/4$ ). The forward scatter problem—assuming that backscatter is weak—can be accurately solved with an order-of-magnitude larger step sizes. A coupled-mode approach is used to illustrate solution convergence by computing backscattering from a single bottom facet as well as backscattering in the benchmark wedge used for checking ocean acoustic models in the 1987 benchmark session of the Acoustical Society of America (ASA). Published field solutions for the ASA wedge are used to illustrate forward scatter results. [S0001-4966(98)05408-3]

PACS numbers: 43.30.Bp [SAC-B]

## INTRODUCTION

The use of small stair steps (Fig. 1) to represent smoothly varying bathymetry in ocean waveguides is common to most numerical solution techniques employed for solving range-dependent propagation and scattering problems.<sup>1</sup> It is assumed, of course, that the discrete-problem solution converges to the smooth-problem result for an increasing number of stair steps. The issue to be addressed here is how many stair steps are required to obtain a smooth-problem solution. Physically one expects that the steps must be small (in some sense) compared to the acoustic wavelength, and we would like to determine how small, and whether the same criteria apply to forward and backscattered field calculations. The issue is important since the computational effort involved in computing a full two-way field solution increases quadratically with the number of stair steps used in discretizing the bathymetry variations.

## I. PLANE-WAVE SCATTERING AT STAIR STEPS

### A. Backscattering

A simple model of the scattering process can be established by assuming that each stair step acts as a point scatterer, and that the full stair case consequently acts as an array of point scatterers. This is schematically illustrated in Fig. 2, where we consider a bottom facet with slope  $\theta$ , approximated by a number of stair steps with horizontal spacing  $\Delta x$ . The incident plane wave is taken to be horizontally propagating.

It is well known that a sparse array of point sources can have several diffraction lobes corresponding to directions of phase coherent radiation by all elements of the array. Only if the array is dense enough, i.e., element spacing less than  $\lambda/2$ , is there only one diffraction lobe, which in this case would correspond to a specular reflection of the incident plane wave in the direction  $\varphi = 180 - 2\theta$ . For large stair steps and hence large element spacing, there are several directions in which the scatterers radiate in phase.

With reference to Fig. 2, it is easy, from simple geometric considerations, to determine the directions  $\varphi_n$  for all possible diffraction lobes. We just write down the conditions for the path length difference  $\Delta x + d$  being an integer number of wavelengths, that is

$$\cos(\varphi_n + \theta) = \cos\theta \left[ \frac{n\lambda}{\Delta x} - 1 \right], \quad n = 0, 1, 2, \dots \quad (1)$$

It is clear that if we have several diffraction lobes contributing to the backscattered field, the solution is wrong. Only the fundamental lobe  $n=0$  has physical meaning for a smooth bottom facet. The criterion for having only one diffraction lobe is found from Eq. (1) to be

$$\cos\theta \left[ \frac{\lambda}{\Delta x} - 1 \right] > 1, \quad (2)$$

or

$$\Delta x < \lambda \frac{\cos\theta}{1 + \cos\theta}. \quad (3)$$

For small slope angles this criterion is seen to be equivalent to the  $\lambda/2$  element spacing of a dense array. In practice, a slightly stricter criterion must be adopted to include steeper facet slopes. The numerical results presented in Sec. II A indicate that  $\Delta x \leq \lambda/4$  is an appropriate discretization criterion for facet slopes of up to  $60^\circ$ .

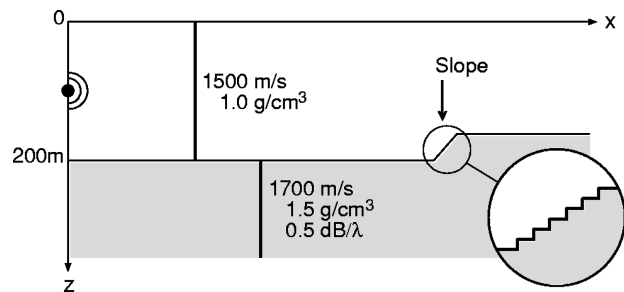


FIG. 1. Schematic of Pekeris waveguide with a single-facet protrusion on the seafloor.

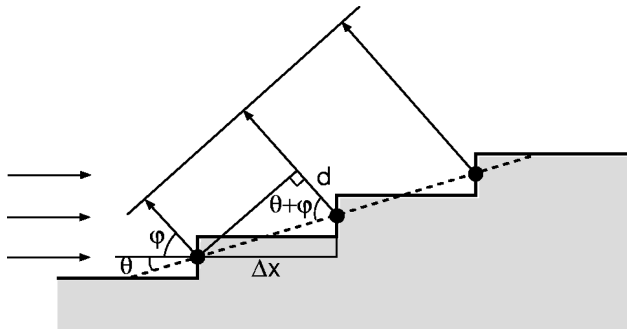


FIG. 2. Geometry for computing coherent backscatter from individual stair steps.

## B. Forward scattering

Plane-wave scattering from stair steps in the forward direction is illustrated in Fig. 3. The physical process here is quite different from the one outlined above for backscattering. Thus forward scatter is associated mainly with reflections off the horizontal interfaces of length  $\Delta x$ , whereas contributions from the vertical steps of height  $\Delta z$  can be ignored.

The mean facet slope is again  $\theta$ , and the incident plane wave is tilted downwards  $\varphi$  with respect to horizontal. Reconstructing the phase front for the reflected wave, we see that this wave is not “plane” as it would have been, had it been reflected from a smooth facet. Instead, the wavefront is “ragged” with sharp discontinuities corresponding to adjacent rays being reflected from different stair steps. Note that the propagation direction corresponding to a “mean” wavefront (dashed line in Fig. 3) forms an angle of  $\varphi + 2\theta$  with the horizontal, as would a specularly reflected plane wave from a smooth bottom facet of slope  $\theta$ .

The question is how distorted the wavefront can be before the specular reflection picture breaks down. It is reasonable to assume that the wavefront distortions must be small compared to a wavelength, or, from simple geometrical considerations,

$$\Delta z \ll \frac{\lambda}{2 \sin \varphi}. \quad (4)$$

This criterion can be written also in terms of  $\Delta x$  as

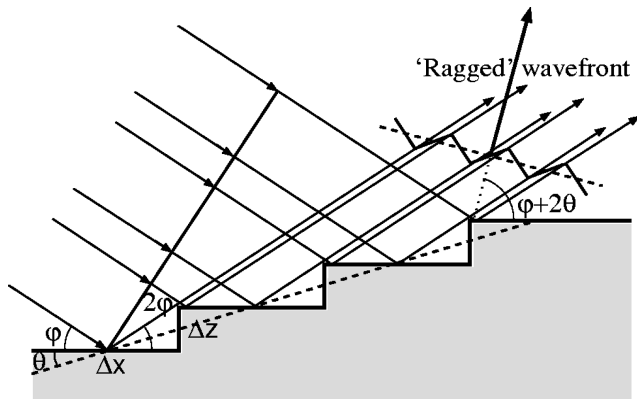


FIG. 3. Geometry for computing coherent forward scatter from individual stair steps.

$$\Delta x \ll \frac{\lambda}{2 \sin \varphi \tan \theta}. \quad (5)$$

It is easily seen that allowable step sizes for forward scatter are several wavelengths for the standard small-slope problems encountered in ocean acoustics. In Sec. II C we quantify the above discretization criterion for forward propagation in the ASA benchmark wedge, and compare to published numerical results.

## II. NUMERICAL RESULTS

The acoustics literature reporting numerical solutions for forward scatter in range-dependent ocean waveguides is abundant, and it is not difficult to find examples that illustrate the effects of coarse stair-step approximations on solution accuracy. However, when dealing with backscatter the situation is quite different. A concerted effort to generate accurate numerical solutions for backscattering in ocean waveguides due to bottom features of different shapes and heights was initiated just recently.<sup>2,3</sup> As of today few published numerical solutions are available for checking the effect of stair-step discretization on the accuracy of computed backscatter in ocean waveguides.

To generate accurate numerical solutions for backscatter in a Pekeris waveguide with a single bottom facet and with a continuous bottom slope (the ASA wedge), we employ a coupled-mode code (COUPLE) developed by Evans more than a decade ago.<sup>4</sup> This code was recently updated to include a “sponge” layer deep in the bottom,<sup>5</sup> thus improving the computational performance by a factor 20–50. COUPLE was successfully applied to a series of benchmark problems involving backscattering,<sup>2</sup> and is considered a reference code for this type of work.

### A. Backscattering from bottom facet

We consider the test problem shown in Fig. 1. The environment consists of a 200-m-deep shallow-water waveguide bounded above by a pressure-release surface and below by a penetrable, homogeneous fluid bottom. The water column is isovelocity with  $c_W = 1500$  m/s. The bottom properties are  $c_B = 1700$  m/s,  $\alpha_B = 0.5$  dB/ $\lambda$ , and  $\rho_B = 1.5$  g/cm<sup>3</sup>. We consider a two dimensional (2-D) problem with translational symmetry in the  $y$ -direction. The obstacle is a 35-m ( $7 \lambda$ ) high protrusion on the bottom placed 1.5 km down-range and having the same acoustic properties as the seabed. Thus there is only one scattering facet, namely the front-end of the protrusion. The source is a 300-Hz Gaussian beam directed towards the scattering facet. As shown in Fig. 4, this beam provides a uniform insonification of the front-end of the obstacle.

For a facet slope of  $30^\circ$  we shall investigate the effect of the stair-step discretization on the computed backscatter. A full two-way field solution from COUPLE is displayed in Fig. 4, and it is clear that energy is scattered primarily in the forward direction. This reference solution is done with 150 stair steps across the facet, i.e.,  $\Delta x = 7 \lambda / (150 \cdot \tan 30^\circ) \approx \lambda / 12$ . Hence this is an accurate sampling compared to the earlier derived discretization criterion of  $\Delta x \ll \lambda / 4$ . Additional results for scattering from a single bottom facet may



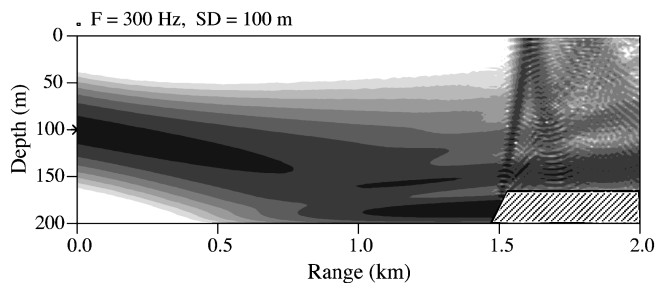


FIG. 4. Beam insonification of an obstacle placed on the bottom 1.5 km from the source. The contour levels (from black to white) are 30–60 dB in steps of 5 dB.

be found in Ref. 3, which addresses the effect of height and slope of the facet on the strength of the backscattered field.

We now turn to a display of just the backscattered field computed for the  $30^\circ$  facet discretized by an increasing number of stair steps (NSS). The first set of results are given in Fig. 5 for NSS=10, 11, 12 and 14. Thus in the upper display there are ten stair steps, and we see two backscattered beams marked  $n=1$  and  $n=2$ . If we compute the angles associated with the diffraction lobes for this case as given by Eq. (1), we find  $\varphi_0=120^\circ$  (the specularly reflected beam going forward and not seen in the display),  $\varphi_1=68.6^\circ$ , and  $\varphi_2$

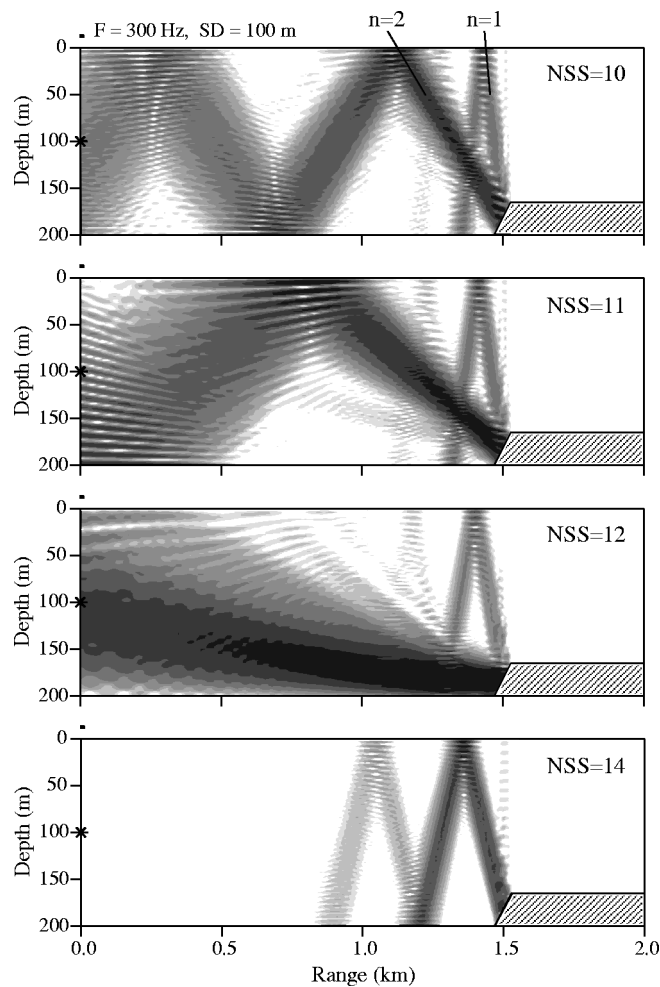


FIG. 5. Backscattered field for different number of stair steps (NSS) across the  $30^\circ$  bottom facet. The contour levels (from black to white) are 40–61 dB in steps of 3 dB.

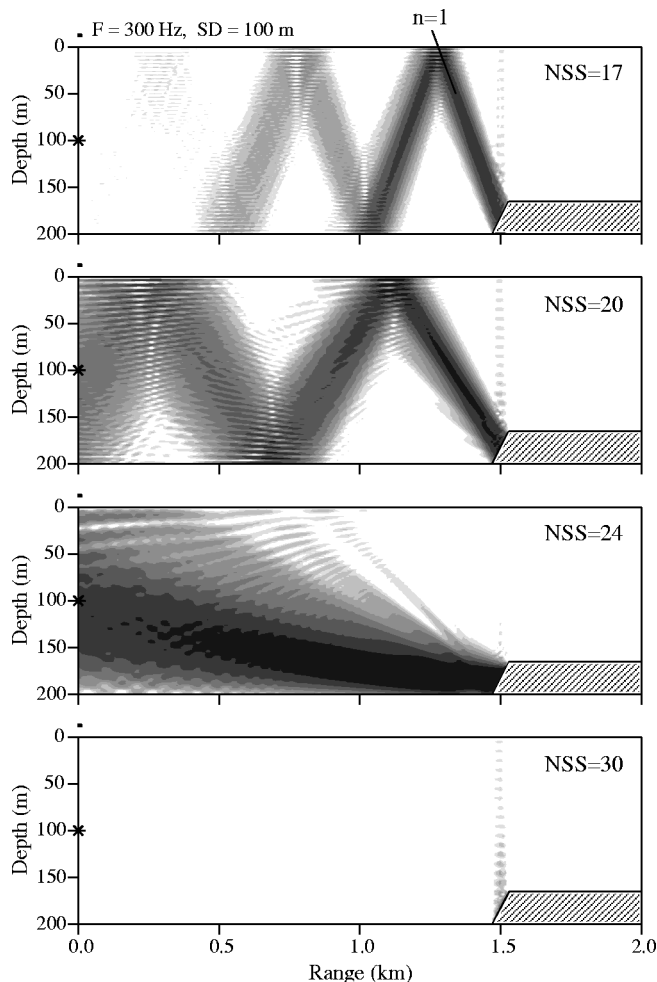


FIG. 6. Backscattered field for different number of stair steps (NSS) across the  $30^\circ$  bottom facet. The contour levels (from black to white) are 40–61 dB in steps of 3 dB.

$=25.6^\circ$ . The angles computed from our simplified scattering model are in excellent agreement with those determined from the full field display. By increasing the number of stair steps the two diffraction beams become more horizontal, and for NSS=12 the second-order beam shoots straight back at the source. In the lower graph with NSS=14, the second-order beam has disappeared (passes through lower end fire of the scattering array), and we are left with only the first-order beam. Since this beam is steeper ( $52.3^\circ$ ) than the critical angle at the bottom ( $28.1^\circ$ ), little energy is propagated back to the source.

The next series of field plots for NSS=17, 20, 24 and 30 are shown in Fig. 6. Now it is the first-order beam that moves to smaller angles and provides strong backscattering for NSS=24. Finally, when the number of stair steps is 30, also the first-order diffraction lobe disappears, and we are left with only the zeroth-order beam, which is specularly reflected in the forward direction. The very low backscatter levels seen in the lower panel is the only result here that resembles the correct solution for a smooth facet.

By computing the mean intensity over depth (0–200 m) of the backscattered field at the source range, we can summarize the convergence process for increasing number of stair steps in a single graph, see Fig. 7. Note that we gener-

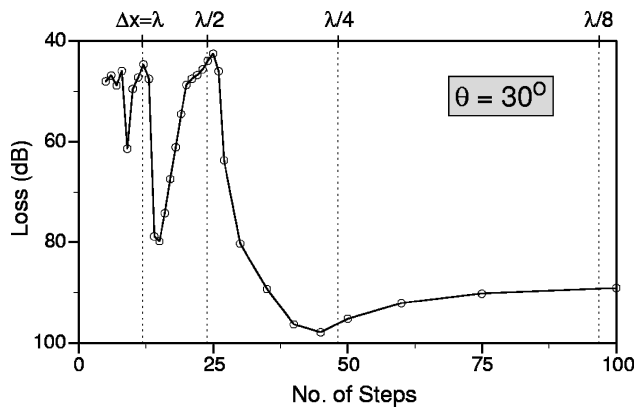


FIG. 7. Mean backscatter level as a function of the number of stair steps used for approximating the sloping bottom facet ( $\theta = 30^\circ$ ).

ally have high backscatter levels ( $\sim 45$  dB) for  $\Delta x > \lambda/2$  followed by a rapid transition to much lower levels ( $\sim 90$  dB) for  $\Delta x < \lambda/4$ . As explained earlier the high backscatter levels are caused by coherent backscatter into higher-order diffraction lobes associated with a sparse array of point scatterers. The oscillatory pattern is a critical-angle effect, and low backscatter levels are seen, for instance, for NSS=14 (Fig. 5). Clearly, the high backscatter levels is a result of using too few stair steps for representing the smooth bottom facet. The appropriate discretization criterion is  $\Delta x \leq \lambda/4$ , with a smoothly converging answer for an increasing number of stair steps. Often this criterion will provide satisfactory solution accuracy, but for benchmarking purposes even smaller steps may be required,  $\Delta x = \lambda/10$  to  $\lambda/20$ .

As a further example of solution convergence, we show in Fig. 8 the computed mean backscatter level for a facet slope of  $60^\circ$ . In this case the specularly reflected beam is in the backward direction ( $\varphi_0 = 60^\circ$ ). The facet height is again  $7\lambda$ , but since the horizontal extent of the facet is shorter, fewer stair steps are required for an accurate solution. The transition from stair-step scattering to smooth-facet scattering is again seen to occur rapidly, with a level drop of around 35 dB.

The standard approach to ensuring accurate numerical results is by increasing the number of sample points (stair steps) until the solution converges. In the present case, such an approach could lead to a completely wrong result. Thus

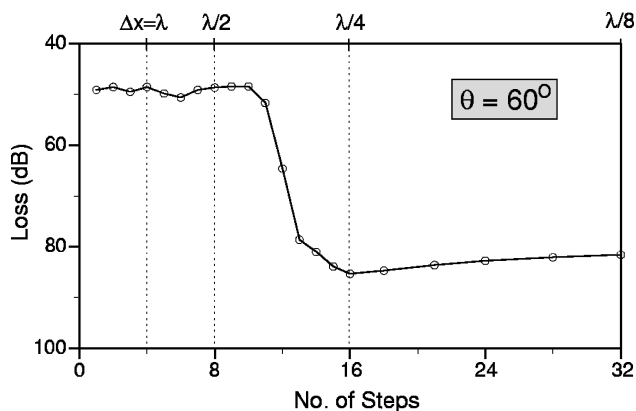


FIG. 8. Mean backscatter level as a function of the number of stair steps used for approximating the sloping bottom facet ( $\theta = 60^\circ$ ).

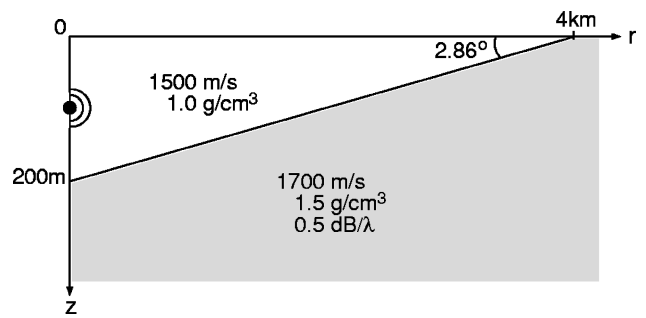


FIG. 9. Geometry of ASA benchmark wedge.

computations with NSS=2, 4 and 8 would give almost identical answers, but it is the solution to a “rough”-facet problem of some kind. The answer to the posed scattering problem involving a smooth facet is obtained by using  $\Delta x \leq \lambda/4$ .

## B. Backscattering in ASA wedge

The second test problem involves a sloping-bottom environment with the acoustic parameters given in Fig. 9. The water depth changes from 200 m at the source to 0 m at a range of 4 km. The bottom slope is  $2.86^\circ$ , and the field solution is sought for a point source of frequency 25 Hz ( $\lambda = 60$  m) located at mid water depth. This environment is the ASA benchmark wedge, for which accurate numerical forward-scatter solutions were established a few years ago.<sup>6</sup> However, so far the modeling community has not been equally successful in establishing a reference solution for the backscattered field in this geometry, but we shall prove here that stable and convergent numerical solutions can indeed be obtained for the backscattered field in the ASA wedge.

Backscattering of sound in a wedge geometry with a smooth bottom can only be explained via steepening ray paths which, after many bottom reflections, get turned around and start propagating downslope towards the source. The implication for a penetrable bottom is that backscattered energy levels are low, since bottom loss is high near vertical incidence. From a modeling point of view, the main complication is to accurately treat all spectral components from horizontal to vertical propagation.

Before proceeding to analyze the numerical convergence process, we present in Fig. 10 a loss contour of the backscattered field in the ASA wedge. Note that energy is propagating near the vertical creating a standing-wave pattern within the water column with peaks and nulls separated by  $\lambda/2$ . In the bottom the energy flow is purely downwards and near the vertical. The presence of the standing wave pattern in the vertical means that the field intensity is very low at depths that are integer multiples of  $\lambda/2$ , e.g., at 30 m. This was exactly the receiver depth chosen in the original test problem,<sup>6</sup> and this depth is clearly not a good choice for benchmarking the backscatter solution. In the following we shall be using a receiver depth of 45 m.

Compared to the beam insonification of a single facet used in Sec. II A, we consider here a much more general propagation situation with point source excitation and multiple boundary reflections for both the outgoing and the incoming field. Hence the ASA wedge is a severe check of the

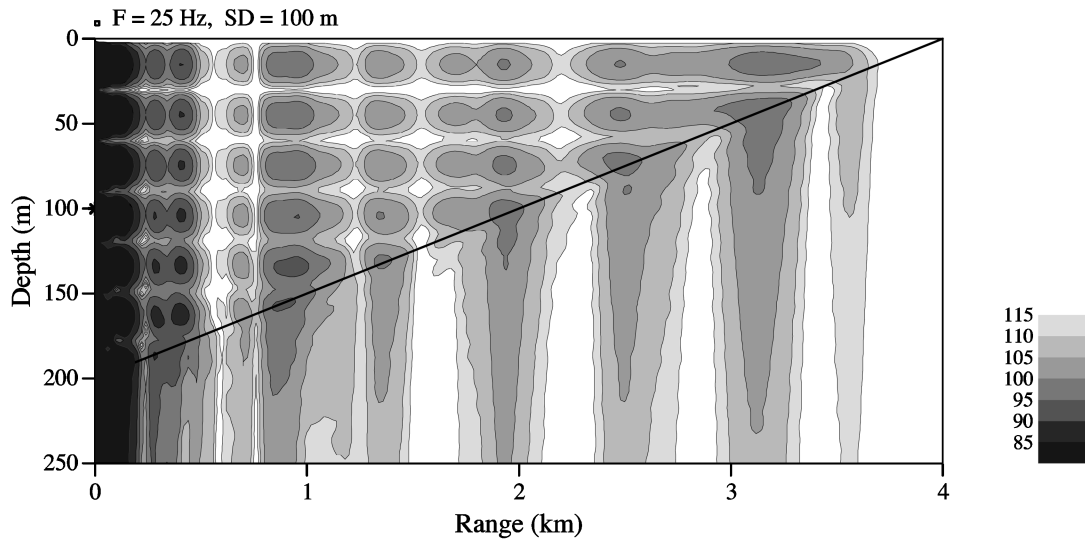


FIG. 10. Contour of backscattered field in ASA wedge.

discretization criterion derived earlier. Assuming that all other parameters (depth of computational domain, thickness of sponge layer, number of modes, etc.) affecting the numerical solution accuracy have been properly selected, we present solution convergence in Fig. 11 for an increasing number of stair steps ( $NSS=50, \dots, 1000$ ). All curves are sampled in range every 0.8 m and smoothed over 25 points to remove spikes generated at each individual stair step.

Note that the convergence behavior in Fig. 11 is quite similar to what we saw for the single facet in Figs. 7 and 8. Thus  $NSS=50$  and 100 give high backscatter levels which are not at all representative of the smooth wedge. Between 100 and 200 steps there is a rapid transition to much lower levels, and the numerical solution converges to a stable result for  $NSS=1000$ . Returning to our discretization criterion given by Eq. (3), we require  $\Delta x < \lambda/2$ , which is satisfied for  $NSS=200$  ( $\Delta x = \lambda/3$ ). In fact, this is the first solution that resembles the smooth wedge result. Generally, we would require a little higher accuracy, and we therefore may confirm the earlier result that an appropriate discretization is  $\Delta x \leq \lambda/4$ , which for this problem corresponds to  $NSS \geq 267$ . For benchmarking purposes even smaller steps are required,  $\Delta x = \lambda/10$  to  $\lambda/20$ .

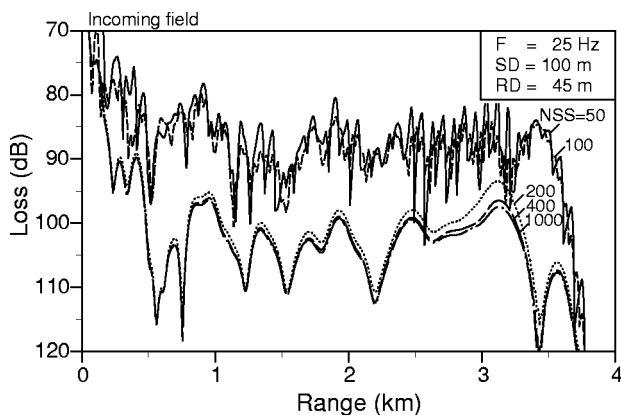


FIG. 11. Convergence of backscattered field solution for increasing number of stair steps (NSS).

For completeness we present in Fig. 12 both outgoing and incoming (backscattered) benchmark solutions for the ASA wedge. Note that the receiver depth is 45 m. The backscatter solution in Fig. 12(b) was obtained with the COUPLE code using a computational domain in depth of 800 m, with the lower 300 m being a sponge layer where the attenuation increases linearly with depth from 0.5 to 10 dB/ $\lambda$ . The number of modes included in the computation was

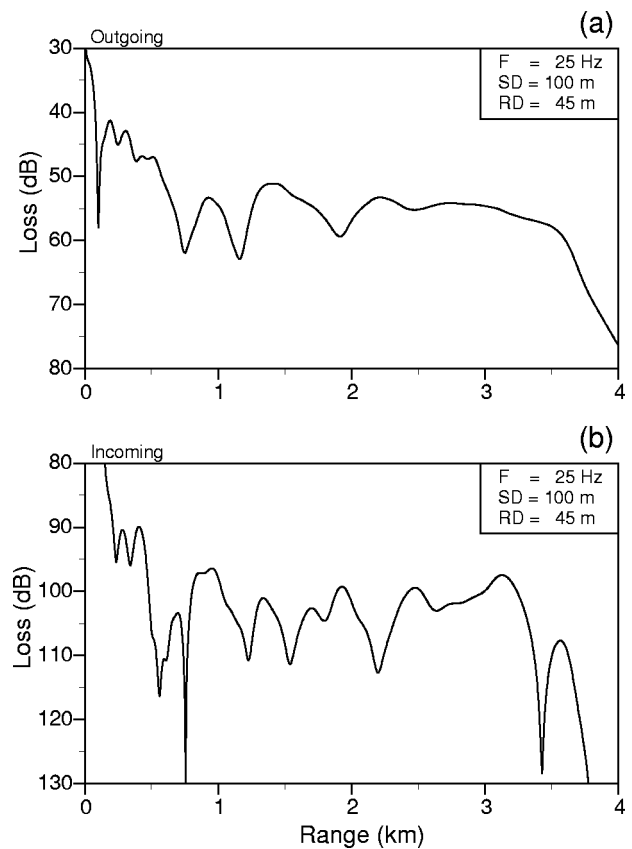


FIG. 12. Coupled-mode solutions for (a) outgoing and (b) incoming (backscattered) fields in ASA wedge. Note that the backscatter level is around 50 dB lower than the outgoing field level.

100 and the number of stair steps 1000. This problem requires approximately 30 min of CPU time on a DEC Alpha 500/500 workstation.

### C. Forward scattering in ASA wedge

If the general scattering problem due to changing bathymetry involves strong backscatter, then the full two-way field solution will require stair-step discretization according to the earlier sampling criterion, i.e.,  $\Delta x \leq \lambda/4$ . On the other hand, if we are dealing with small-slope problems where backscatter is weak, then the forward solution can be accurately computed in a single-scatter approach (backscatter neglected), and much larger stair steps are generally permissible. In Sec. I B we derived a discretization criterion, Eq. (5), which shall be tested on the ASA wedge benchmark, Fig. 9.

The original benchmark solution was generated with  $NSS=200$ , or  $\Delta x = \lambda/3$ .<sup>6</sup> Subsequently Collins<sup>7</sup> showed that very accurate forward solutions to this problem could be obtained with just 40 stair steps, or  $\Delta x = 1.67 \lambda$ . Even the double step size of  $\Delta x = 3.33 \lambda$  gave fairly good results.

Let us see if our discretization criterion for forward scattering, Eq. (5), can be reconciled with these numerical results. First of all, the angle  $\varphi$  of the incident field must be determined. Since the step length decreases with increasing angle  $\varphi$ , a conservative estimate is obtained by using for  $\varphi$  the highest propagation angle of importance in the problem, i.e., the critical angle of  $28.1^\circ$ . We find from Eq. (5) that the step size  $\Delta x$  must satisfy the criterion  $\Delta x \leq 20 \lambda$ . Assuming that it is sufficient to decrease the upper limit by an order-of-magnitude we obtain  $\Delta x \leq 2 \lambda$ , which is in agreement with the numerical results of Refs. 6 and 7. Note that forward-scatter problems generally can be done with much larger stair steps than backscatter problems, which means that forward problems are computationally easier, often by 1 to 2 orders of magnitude in CPU time.

### III. CONCLUSIONS

By using a simple plane-wave model of scattering from a series of stair steps approximating a smooth bottom slope, we established discretization criteria for accurate numerical solution of the facet scattering problem. The strictest criterion was found to apply to backscatter calculations where the horizontal step size must be smaller than  $\lambda/4$  to guarantee accurate numerical results. Actually, a completely different stair-step scattering problem is solved if the step size is larger than  $\lambda/2$ . The transition from stair-step scattering to facet scattering occurs rapidly for  $\lambda/2 > \Delta x > \lambda/4$ . For small bottom slopes where backscatter is weak, the forward problem can be solved with much larger horizontal steps, often of the order of several wavelengths. In the course of generating numerical solutions of simple waveguide scattering problems, a stable and accurate solution was established for the backscattered field in the ASA wedge. This solution is put forward here as a benchmark for future model testing.

<sup>1</sup>F. B. Jensen, W. A. Kuperman, M. B. Porter, and H. Schmidt, *Computational Ocean Acoustics* (AIP, New York, 1994).

<sup>2</sup>*R&S Workshop: Proceedings of the Reverberation and Scattering Workshop*, edited by S. A. Chin-Bing, D. B. King, J. A. Davis, and R. B. Evans (Naval Research Laboratory, Stennis Space Center, MS, 1998).

<sup>3</sup>F. B. Jensen, "Backscatter calculations in simple waveguide geometries using stepwise coupled normal modes," in *Theoretical and Computational Acoustics '95*, edited by D. Lee, Y. H. Pao, M. H. Schultz, and Y. C. Teng (World Scientific, Singapore, 1996), pp. 25–32.

<sup>4</sup>R. B. Evans, "A coupled mode solution for acoustic propagation in a waveguide with stepwise depth variations of a penetrable bottom," *J. Acoust. Soc. Am.* **74**, 188–195 (1983).

<sup>5</sup>R. B. Evans, "A reverberation calculation using stepwise coupled modes," *R&S Workshop: Proceedings of the Reverberation and Scattering Workshop* (Ref. 2).

<sup>6</sup>F. B. Jensen and C. M. Ferla, "Numerical solutions of range-dependent benchmark problems in ocean acoustics," *J. Acoust. Soc. Am.* **87**, 1499–1510 (1990).

<sup>7</sup>M. D. Collins, "A split-step Padé solution for parabolic equation methods," *J. Acoust. Soc. Am.* **93**, 1736–1742 (1993).

# Matched-beam processing: Application to a horizontal line array in shallow water

T. C. Yang<sup>a)</sup>

Naval Research Laboratory, Washington, DC 20375

T. Yates<sup>b)</sup>

Vector Research Co., 2101 Jefferson Street, Rockville, Maryland 20852

(Received 13 June 1997; accepted for publication 20 May 1998)

Matched-beam processing of a horizontal line array in a multipath shallow-water environment is presented. With conventional beamforming, the signal is split into several beams when the target is away from the broadside direction. This can result in signal gain degradation and severe bearing bias. Matched-beam processing is matched-field processing applied in the beam domain. It offers an efficient and robust approach for correcting bearing errors and signal gain degradation of horizontal line arrays in shallow water. It is based on conventional beams but extends conventional processing to incorporate full-field processing. It is applicable to existing systems where the conventional beam outputs are the only data readily available. Many of the signal processing algorithms for horizontal arrays, such as adaptive beamforming for nulling strong interferences, can be incorporated directly into matched-beam processing. Target bearing tracking and depth discrimination are illustrated using matched-beam processing for a horizontal line array. [S0001-4966(98)03009-4]

PACS numbers: 43.30.Wi, 43.60.Gk [DLB]

## INTRODUCTION

Signal processing in underwater acoustics has been centered around the problem of detecting and localizing a target or signal in an ocean waveguide. Detection and localization of a quiet target requires the use of an array of hydrophones as the array processing gain will enhance the signal-to-noise (S/N) ratio of the target. Standard array processing assumes that the signal arrives as a plane wave. Conventional beamforming uses the concept of delay and sum of received plane-wave signals to estimate the target bearing. Real life examples which use conventional beamforming include a towed or bottom-laid horizontal line array, a hull-mounted spherical array, an air-deployed vertical array which uses bottom bounced arrival to localize the source, etc. With the advent of matched field/mode processing<sup>1,2</sup> it is possible to extend the detection range by exploiting the multipath arrivals of low-frequency signals using, for example, a large aperture vertical or horizontal array. Improved signal gain is obtained because matched-field processing matches the data with signal propagation in the waveguide. (It is assumed that the acoustic environment of the ocean is known and the signal can be modeled for all source ranges and depths of interest.) Matched-field processing can also be used for source localization. The parameter estimation aspect of the method has been extensively investigated in the literature.<sup>3</sup> Target location (bearing, range, and depth) is estimated by the highest correlation point in the correlation ambiguity function. If the correlation is in terms of the mode amplitudes of the replica and data field, one has matched-mode processing.<sup>2</sup>

For a horizontal line array or spherical array, conventional beamforming has been widely used for detection and bearing estimation of a target. The signals are delayed and summed in the target look direction. The highest beam points to the target bearing if the dominant arrivals of the signal are contained in one beam, as when the target look direction is near the broadside of the horizontal array. Conventional beamforming has worked successfully in deep water.

Shallow water is a complex environment for array processing because of the many surface and bottom bounced returns of the signal. Using conventional beamforming, the multipath arrivals can split the signal in several beams and cause signal gain to be less than ideal, i.e.,  $20 \log$  of the number of sensors. Signal gain degradation reduces the detection range. In a low loss environment, many bottom bounced returns will arrive at the array at relatively high grazing angles and result in a bearing bias when the target is at a nonbroadside direction; as when the arrival angle of a dominant bottom path differs from the target bearing.

Matched-field processing applied to a horizontal (line) array would, in principle, correct the above deficiencies.<sup>4,5</sup> When applied to the real world, several factors must be considered. First, in many shallow-water environments, the bottom bathymetry and bottom properties can change substantially over a short distance. The water column sound speeds may be site dependent and can change substantially over minutes, hours, or days due to inhomogeneous oceanographic processes taking place in shallow water.<sup>6</sup> Source localization in shallow water can be sensitive to small changes in the bottom sound-speed profile.<sup>7-11</sup> This defines the mismatch problem. Second, the bearing of a target is estimated only when the target is properly localized in range and depth. This three-dimensional search procedure presents not only a heavy demand on the on-board processing power but also an

<sup>a)</sup>Electronic mail: yang@wave.nrl.navy.mil

<sup>b)</sup>Current address: Naval Surface Warfare Center, Carderock Div., West Bethesda, MD 20817.

incorrect bearing when the target is falsely localized. Last, the majority of the software in current systems is based on conventional beamforming.

Another method to correct the bearing bias in a multi-path environment is modal beamforming.<sup>12,13</sup> In terms of the normal modes, since a mode travels with a specific horizontal wave number, target bearing can be correctly estimated by beamforming the mode amplitudes (i.e., steering the mode amplitudes in different look directions) using the corresponding mode wave numbers. This requires a method to extract the individual mode amplitudes (mode decomposition) from the acoustic field data, such as when several vertical arrays are available.<sup>13</sup> (Mode decomposition is most effective with a vertical array.) For a horizontal line array, the problem is that its ability to extract the mode amplitude is very limited even in the end fire direction.<sup>5,14</sup> An effective vertical aperture can be found for a horizontal line array to judge its ability to decompose the mode amplitudes;<sup>5</sup> the effective vertical aperture is approximately  $L \tan \phi$  in the end-fire direction, where  $L$  is the array aperture and  $\phi$  is the mode grazing angle. The effective vertical aperture is usually small for a horizontal line array since the mode grazing angles in the received signal are small ( $<10^\circ\text{--}15^\circ$ ); high-order modes are attenuated.

Without effective mode decomposition, modal beamforming could produce bearing bias as when the  $n$ th mode wave number is used to steer the  $m$ th mode, and when the interference between the  $m$ th and  $n$ th modes changes the output bearing. These problems were previously discussed in depth for conventional beamforming.<sup>12,13</sup> Note that bearing estimation is influenced by the mode decomposition errors as is range estimation.<sup>5,14</sup>

To produce a high signal gain, mode amplitudes need to be combined coherently. This is done using matched-mode processing for a horizontal array.<sup>14</sup> It is shown that matched-mode processing for a horizontal line array yields identical results as that obtained with matched-field processing.<sup>14</sup> Henceforth, only matched-field processing will be referenced.

In this paper, we apply matched-beam processing<sup>15–19</sup> to a horizontal line array in shallow water. The intent is to minimize the bearing bias and signal gain degradation for a horizontal array near end-fire directions. Matched-beam processing is matched-field processing applied in the beam domain. As such, it yields the correct target bearing and theoretical signal gain. It is based on the conventional beams but extends conventional processing to incorporate full-field processing. The highlights of matched-beam processing are

(1) Matched-beam processing is an implementation of matched-field techniques to existing systems where the conventional beam outputs are often the only data readily available.

(2) Matched-beam processing is a more efficient and robust approach for correcting bearing errors and signal gain degradation of horizontal line arrays in shallow water. In certain mismatched environments, bearing may still be correctly estimated even though range estimation may be in error.

(3) Matched-beam processing is a linear transformation

(which can be used) to separate and then filter paths with high noise and/or excessive mismatch.

(4) Matched-beam processing can integrate easily with many signal processing methods previously developed to handle practical problems, such as strong interferences (adaptive beamforming), array shape corrections (for a towed array), beam domain detection statistics, and false alarm analysis. As such, matched-beam processing offers many advantages in system applications. See discussions in the next section.

This paper is organized as follows. Matched-beam processing is discussed in Sec. I. Section II presents bearing estimation for a horizontal line array in shallow water. Matched-beam processing results are compared with the conventional beamforming results in terms of bearing accuracy and signal gain degradation. Section III presents target bearing tracking results using conventional and matched-beam processing. In Sec. IV we show bearing tracking of a target in the presence of a surface clutter (ship) using depth discrimination. Bottom mismatch is discussed in Sec. V. Section VI presents a summary.

## I. MATCHED-BEAM PROCESSING

Matched-beam processing is a variation of matched-field processing conducted in the beam domain. As in matched-field processing, one assumes that the acoustic environment is given and that the signal field at the receiver array can be calculated. The receiver array can be a horizontal array, a vertical array, or an array of arbitrary shape.

Matched-beam processing (MBP) starts with conventional beamforming. It calculates (complex) beam outputs for both the data and replica field and then correlates the data and replica beams for source localization.

For a line array of  $N$  phones, the conventional beam outputs are obtained by multiplying the (narrow-band) data and replica fields by a steering vector at angle  $\theta$  (measured from the broadside of the array) and summing the products over the phones,

$$A^{\text{data}}(\theta) = \sum_j e^{-ikx_j \sin \theta} p_j^{\text{data}}, \quad (1)$$

$$A^{\text{rplc}}(\theta, s) = \sum_j e^{-ikx_j \sin \theta} p_j^{\text{rplc}}(s), \quad (2)$$

where  $x_j$  is the coordinate of the  $j$ th phone,  $k$  is the wave number used in beam-forming, and  $s$  denotes the source parameters, i.e., range, depth, and bearing.

Matched-beam ambiguity function is given by the correlation function of the data beams and replica beams,<sup>15–17</sup>

$$B(s) = \frac{|\int A^{\text{rplc}*}(\theta, s) A^{\text{data}}(\theta) d\sin \theta|^2}{[\int |A^{\text{rplc}}(\theta, s)|^2 d\sin \theta][\int |A^{\text{data}}(\theta)|^2 d\sin \theta]}. \quad (3)$$

The above expression can be generalized to other array configurations. For example, for a spherical array, one has

$$B(s) = \frac{|\int A^{\text{rplc}*}(\Omega, s) A^{\text{data}}(\Omega) d\Omega|^2}{[\int |A^{\text{rplc}}(\Omega, s)|^2 d\Omega][\int |A^{\text{data}}(\Omega)|^2 d\Omega]}, \quad (4)$$

where  $\Omega$  denotes the solid angle in the look direction.

Matched-beam processing can be shown to reduce to conventional beam-forming when the incoming signal is a plane wave. For a vertical array, matched-beam processing can be shown to reduce to matched-field processing when all beams are used. This result follows from the convolution theorem (see Appendix of Ref. 19).

For a horizontal line array, the matched-beam output can be obtained by a matrix multiplication of the conventional beam outputs. To illustrate this, we rewrite the numerator of Eq. (3) as

$$\begin{aligned}\tilde{B}(\theta_l) &= \int A^{\text{rplc}*}(\theta, \theta_l) A^{\text{data}}(\theta) d\sin \theta \\ &= \sum_i \alpha_i(\theta_l) A^{\text{data}}(\theta_i) \cos \theta_i,\end{aligned}\quad (5)$$

where  $\theta_l$  is the bearing (search) angle and

$$\alpha_i(\theta_l) = A^{\text{rplc}*}(\theta_i, \theta_l) = \sum_j e^{-ikx_j \sin \theta_i} p_j^{\text{rplc}}(s), \quad (6)$$

where  $s$  denotes the target range, depth, and bearing ( $\theta_l$ ) coordinates. Equation (5) shows that the transformation from the input beams  $A^{\text{data}}(\theta_i)$  to the output beams  $\tilde{B}(\theta_l)$  is a matrix multiplication.

Physically, we could interpret  $\alpha$  as a set of “steering vectors” which are multiplied with the data beams to form new beams. The steering vectors are composed of the replica beams which depend on the target (search) coordinates and can be precalculated under stationary conditions.

Adaptive beamforming used to null a strong interference source can be accommodated in matched-beam processing by using the adaptive beam outputs,<sup>20</sup>

$$A^{\text{data}}(\theta) = \sum_j e^{-ikx_j \sin \theta} p_j^{\text{data}} \beta_j, \quad (7)$$

$$A^{\text{rplc}}(\theta, s) = \sum_j e^{-ikx_j \sin \theta} p_j^{\text{rplc}}(s) \beta_j, \quad (8)$$

where  $\beta_j$  are the adaptive weighting coefficients which are applied to both the data and replica beams.

Equipped with the above equations, we shall illustrate below several advantages offered by matched-beam processing when dealing with practical problems. We note that as matched-beam processing can be shown to be equivalent to matched-field processing when all beams are used, there is no difference in their performance in an ideal situation (e.g., a stationary target, no clutter). For a research problem, the transformation of the phone data into beam data can be viewed as an unnecessary extra step. For a practical problem, such a transformation is advantageous to improve the robustness of target detection and tracking (bearing estimation), the processing load, and the software integration effort. For a practical system, the signal processor of choice is one that detects and tracks a target in a most effective way. The transformation to the beam domain allows us to preserve previous signal processing tools which have proven to be effective with respect to practical problems.

In the context of system applications, one finds: (Readers not interested in system issues can skip to the next section.)

(1) Matched-beam processing is an implementation of matched-field techniques to existing systems where the conventional beam outputs are the only data readily available.

With respect to existing sonar systems, matched-field processing offers the benefit of full-field (matched field) processing to existing systems without a major rewrite of the system software which is based on conventional beamforming. Matched-beam processing can be implemented as a post-processor to the existing sonar systems using conventional beams as input. [Although current systems display only the beam intensities, we assume the (analog or digital) outputs of the beamformer can be accessed.] As illustrated above, matched-beam processing can be thought of as a form of beam steering; the conventional beam outputs are multiplied by a set of steering vectors to form new beams. The steering vectors can be precalculated and stored in the post-processor.

We note that the conventional beams [Eq. (1)] are Fourier transforms of the phone data; therefore, in theory given the beam data one can retrieve the phone data. In practice, many system transfer functions are imbedded in the data processing which make the transformation of the beam data to the phone data extremely difficult if not impossible.

(2) Matched-beam processing is a more efficient or robust approach for correcting bearing errors and signal gain degradation of horizontal line arrays in shallow water.

With respect to bearing estimation and source localization, we note that for a nonvertical array matched-field processing must search for bearing, range, and depth simultaneously. As remarked above, there is the environmental mismatch problem for this application. For horizontal arrays, the conventional priority is to estimate the target bearing first. Several readings of bearings can be used to estimate target location (by triangulation) using either an array at several headings or multiple arrays.

Matched-beam processing is based on the physical principle that bearing estimation is more robust than range estimation, i.e., it is less sensitive to environmental mismatch. For a real-time detection and tracking of a target, a robust estimate of target bearing may be more useful than simultaneous estimates of range, depth, and bearing which may be questionable. Note that the arrival angle on a horizontal array can be estimated using conventional beamforming without the exact knowledge of the sound-speed profile in the water column. Arrival angles can be used to calculate the target bearing if the arriving multipaths are known. This transformation can be done by a sonar operator with a calculator. Matched-beam processing does this transformation automatically using the above algorithm which is essentially a coherent recombination of target beams. With a certain prior knowledge, matched-beam processing will be able to estimate target bearing without knowing precisely the target depth and range.

As shown below, bearing estimation can tolerate some degree of environmental mismatch. Hence for practical applications, matched-beam processing is expected to improve

the (existing) array performance in shallow water without requiring exact knowledge about the acoustic environment (as would be required by matched-field processing). With a robust estimate of the bearing, range estimate can be improved by iteration (including environmental parameters); the search space is significantly reduced compared with matched-field processing.

(3) Matched-beam processing is a linear transformation which can be used to separate and filter paths with high noise and/or excessive mismatch.

Note that signal arrivals are usually confined to a limited number of beams in the target direction. This signal arrival structure allows the rejection of undesired noise in the non-target directions. An analogy is frequency domain processing of a bandlimited signal; the out-of-the-signal-band noise is rejected most efficiently using frequency domain processing. Beam domain is the Fourier transform of phone domain as frequency domain is the Fourier transform of the time domain.

With respect to the noise, we note that matched-field processing attempts to separate the signal from noise by localizing (individual) noise sources (e.g., ships or wind-generated noise). The hope is that the target will be located in a different bearing-range-depth cell than the noise sources, and that sufficient processing gain can be obtained by bearing-range-depth differentiation. Matched-field processing requires a large bearing-range-depth volume to delineate the different noise sources and hence involves heavy computations. It requires a large three-dimensional array in order to have high resolution in bearing-range-depth. For practical arrays, we find that the sidelobes associated with the many different noise sources can contribute and raise the noise background at the target bearing-range-depth cell. It is shown in Ref. 18 that matched-field processing applied to a vertical array covering the full water column in a shallow-water environment has a limited ability to reject surface-generated noise, i.e., noise gain is higher than that of conventional beamforming. (For noise rejection using a vertical array see Ref. 18; for suppression of environmental mismatch using a beam filter see Ref. 19; for improving the sensitivity of acoustic bottom inversion using a beam filter see Refs. 16 and 17.)

For a horizontal line array, directional noise, such as noise from distant ships, can be rejected when the target is not in the noise direction, by excluding beams from the matched-beam correlation which contains the directional noise. Since only the beams in the signal direction will be used in the matched-beam correlation, the signal beams are "free" of the directional noise. The individual phone data, on the other hand, could be dominated by the noise depending on the signal-to-noise ratio; the weak target signal is picked up only after the matched-field correlation separates the target from the noise. In theory, both processors yield the same result when the signal and noise are uncorrelated. In practice, filtering the noise before correlation is more robust since the noise (data) and signal (replica) are not always uncorrelated in the matched-field correlation.

(4) Multiple targets problem. When targets are sufficiently separated in bearing, matched-beam processing re-

duces the multiple targets problem to a single target problem since only a small number of beams in the particular target direction will be used in the matched-beam correlation. In the phone domain, the data are the superposition of the acoustic fields from all targets. The replica field associated with one target location may be correlated with data from targets at other locations. In principle, the mismatch in source location will diminish the correlation, but in practice the mismatch often produces high sidelobes which are sources of false targets.

(5) Strong interference problem. The masking of a weak signal by a strong interference source (clutter) is a significant problem in practice which requires adaptive signal processing. Matched-field processing can discriminate in principle the interfering source from the target by range, depth, and bearing separation. This requires a high resolution in range-depth-bearing which can be obtained using adaptive algorithms such as the minimum variance method.<sup>3</sup> But the adaptive algorithm in the matched-field context is sensitive to environmental mismatch mentioned above. In addition, high resolution means many range-depth-bearing cells and thus extensive computations. In practice one may find that the sidelobes due to the correlation of the replica field with a strong clutter may be higher than the peak level of the correlation of the replica field with the weak signal from the target.

The conventional approach with respect to a highly directional interfering source is to use adaptive plane-wave beamforming which steers a null in the direction of the interfering source. This is a simple, effective, and robust method for interference rejection. The problem with adaptive plane-wave beamforming is that the signal energy is split over several beams which applies equally to the interfering sources. Matched-beam processing improves the performance of conventional beamforming by coherent combination of conventional beams. In doing so, it preserves the feature of adaptive nulling of interfering sources (adaptive beamforming). As shown above, adaptive beamforming can be naturally incorporated into matched-beam processing using Eqs. (7) and (8). With this algorithm, the interference source is removed (in the input beam data) before the correlation is applied to the data whereas in adaptive matched-field processing, the interference is separated only after the correlation process. This could make a big difference in practical applications.

We note that adaptive nulling of a strong interference source using adaptive match-field processing has not been demonstrated with real data nor with simulated data to the best of our knowledge. It is not expected to be robust since adaptive matched-field processing is known to be sensitive to environmental mismatch.

(6) Array shape distortion. Array shape distortion for a towed array is a source of error if it is not corrected for in the signal processing algorithm. Many algorithms have been developed in system research to deal with this problem for conventional beams. In matched-beam processing, whatever algorithm is applied to conventional beams will be applied to the replica beams in an identical way. Using matched-field processing, one must get the relative locations of the ele-



ments in order to correct for array shape distortion.

(7) Detection statistics and false alarm analysis. The statistical distributions of the signal and noise beams are well researched, and have been extensively measured from data. The probability of detection, and the probability of a false alarm can be used to determine the receiver operation curve<sup>21</sup> which is a critical element in the performance analysis of a system.

Using matched-field processing, the probability distributions of the signal and noise depend on the target range depth and the environment since matched-field processing is environment dependent. As such, a detection theory for matched-field processing has not been established. Using matched-beam processing, the signal and noise distributions at the processor output can be obtained by matrix transformation [Eq. (5)] from the well established beam signal and noise distributions at the processor input. While the matrix itself is environment dependent, the simple matrix transformation makes the detection statistics manageable.

(8) Processing load. Matched-beam processing allows the possibility of a sequential search in the order of target bearing, range, and depth. Target bearing is most robust and is searched for first. Target range is searched only at bearings near the target direction, after target bearing has been estimated. For each target depth, matched-beam processing involves  $N_b + N_r$  search steps compared with  $N_b \times N_r$  steps required for matched-field processing;  $N_b$  and  $N_r$  are, respectively, the number of bearing and range search points. Also in matched-beam processing, only replica beams in the target directions are used. The number of replica beams (e.g., ten) used is often smaller than the number of phones (e.g., 50–100) for a large aperture horizontal array. Consequently, the number of correlation calculations can be reduced by several folds. In target tracking the sequential search cues in on certain prior knowledge of the target (e.g., position, velocity) and results in orders of magnitude reduction in processing time as compared with simultaneous search in bearing, range, and depth employed in matched-field processing. This reduction in processing time could be an important consideration for a real-time system.

## II. BEARING ESTIMATION FOR A HORIZONTAL LINE ARRAY IN SHALLOW WATER

In the previous section, we have introduced matched-beam processing and pointed out various advantages of matched-beam processing for practical applications. For a stationary source with no clutter present (as is the case in many experiments), matched-beam processing yields identical results as matched-field processing; there is no need to transform the data into the beam domain. In the case of directional (shipping) noise, multiple targets, and strong interference sources (as often encountered in real world problems), beam domain processing has several advantages that have been previously demonstrated with real data using adaptive plane-wave processing algorithms. The system processing community has used and is still using, almost exclusively, the plane-wave beamforming algorithms to this day for these reasons.

The purpose of the next three sections is to demonstrate (to the system processing community) that equivalent performance of matched-field processing can be achieved in the beam domain (thus improving the performance over conventional plane-wave processing), without giving up many signal processing tools (such as adaptive beamforming) previously developed to handle practical problems. The demonstration is with simulated data using conventional beamforming without adaptive weighting.

The benefits of matched-beam processing over conventional beamforming lie in improved bearing estimation and signal gain. This will be illustrated in this section for a stationary source in a complex shallow-water environment in which signals arrive via many surface and bottom bounced returns.

Using conventional beamforming [Eq. (1)], the multipath arrivals can split the signal in several beams and cause signal gain (of conventional beamforming) to be less than ideal (i.e.,  $20 \log N$ , where  $N$  is the number of sensors). In a low loss environment, many bottom bounced returns will arrive at the array at relatively high grazing angles and result in a bearing bias using conventional beamforming for a target at a nonbroadside direction. These are well-known problems and will be illustrated using an example.

The conventional beamforming results for a horizontal array are obtained using a simulated signal. The beam outputs are normalized as follows

$$\mathbf{B}_{\text{out}}(\theta) = \frac{|A^{\text{data}}(\theta)|^2}{\sum_{j=1}^N |p_j^{\text{data}}|^2}, \quad (9)$$

which is the beam intensity [Eq. (1)] divided by the total signal level across the array. Signal gain for conventional beamforming is given by Eq. (9) times  $N^2$ . For a plane-wave arrival, signal gain is equal to  $20 \log N$  at the target direction. Equation (9) is basically the signal gain degradation for conventional beamforming.

The acoustic environment is described in Fig. 1. The horizontal array is deployed at a depth of 50 m. It contains 100 phones spaced at 1.875 m. The source (target) is at a range of 1 km at a depth of 150 m. A narrow-band signal is propagated from the source to the receiver array using the KRAKEN normal-mode code<sup>22</sup> for a band of frequencies (370–390 Hz) around the design frequency of the horizontal array. Conventional beamforming is applied to the received signals. The signal gain results are plotted in Fig. 2 as a function of target bearing for a signal frequency of 390 Hz. From Fig. 2 we observe that the signal is split in several beams with the highest beam showing a signal gain degradation of 3 and 6 dB (below the ideal gain of 40 dB) for target bearing (measured from the broadside of the array) at  $45^\circ$  and  $90^\circ$ , respectively. We also note that the highest beam shows a bearing bias of  $5^\circ$  and  $21^\circ$  from the true target bearing for targets at  $45^\circ$  and  $90^\circ$  bearing. Figure 2 also plots the signal gain as a function of bearing and frequency. We note that the bearing bias and signal gain degradation will not go away for distant targets as long as the waveguides support more than one path.

Using matched-beam processing for the horizontal array, it is next shown that the ideal signal gain will be obtained

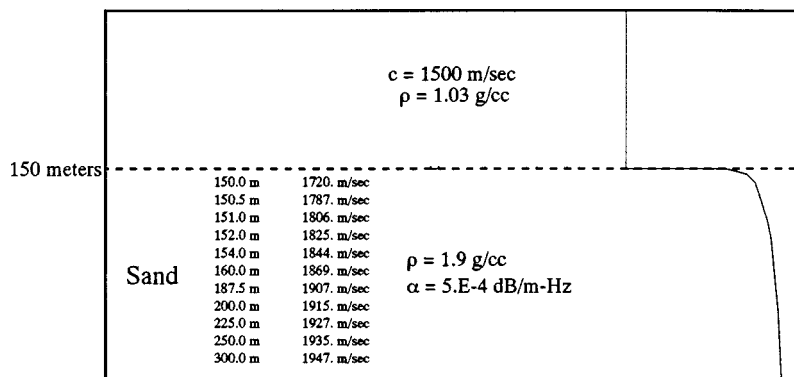


FIG. 1. Acoustic environment for a shallow-water waveguide.

and the bearing bias described above will be removed. (This result is the same as matched-field processing.) It can be shown by the convolution theorem that the matched-beam correlation [Eq. (3)] reduces to the matched-field correlation when all beams are used. The matched beam correlation is unity when the replica matched the data beams; the peak of the ambiguity surface yields 0 dB. The matched-beam signal gain is  $N^2$  times the matched-beam correlation function [Eq. (3)].

The matched-beam signal gain is plotted in Fig. 3 for the examples studied above as a function of target bearing for the frequency band of 370–390 Hz. The complex conventional beam outputs described above are used as data beams. For the replica field we assume for the moment that the target range and depth are known. The replica field is used to form replica beams using Eq. (2) for different target-search bearings. The replica beams are correlated with data beams to form new beam outputs. The matched-beam signal gain at 390 Hz is plotted as a function of the (search) bearing in Fig. 3. We see that the matched-beam correlation function (Fig. 3) peaks at the true target bearing and yields zero dB signal gain degradation.

What has happened in matched-beam processing is that the conventional beams, which pointed to the wrong target bearings, have been transformed into matched-beam outputs; the highest (output) beam points to the correct target bearing. The transformation is done by a matrix multiplication, the  $\alpha$  matrix given above in Eq. (6). This matrix multiplication can be implemented as a post processor to the existing sonar processing software.

The properties of the steering vector  $\alpha$  are illustrated below. The steering vector is a function of the beam number. We shall use the beam angle to denote the beam number. First we shall plot the magnitude of the data beams  $|A^{\text{data}}(\theta_i)|$  in Fig. 4(a) as a function of the beam angle. The target has a (true) bearing of  $45^\circ$ . Then we plot in Fig. 4(b)–(d) the replica beams at three assumed target bearings,  $\theta_l = 40^\circ, 45^\circ, \text{ and } 51^\circ$ . We note that although there are 180 elements in the steering vector ( $\theta_i$  covers  $180^\circ$ ), only these replica beams within, say,  $10^\circ$  of the (true) target bearing are important for the correlation. Thus given an approximate target direction (based on, e.g., the conventional beamforming result), the total number of replica beams used by the post-processor is not very large (e.g., ten). In contrast, the number of replica fields to be stored is  $N = 100$  using matched-field processing.

The above results showed that true target bearing is obtained when the target range and depth are known. The question is how sensitive is the bearing estimation to knowing the exact target range and depth and to knowing the exact acoustic environment. We study the first issue assuming that the target depth is known. The second issue is investigated in Sec. IV.

Assuming that the target depth is known, we investigate the matched beam ambiguity function [Eq. (3)] as a function of the target range and bearing for a narrow-band signal at 390 Hz. (Note that matched field/beam correlation is a smooth function of target depth using the Bartlett processor. Hence an approximate target depth is sufficient. Target depth can be estimated separately using a high-resolution method.<sup>23,24</sup>) We shall study three cases. For the first case, the source is in the broadside direction of the horizontal array at a range of 1.41 km. As shown in Fig. 5(a), the ambiguity surface indicates high bearing resolution and very little range resolution for a source at broadside direction. (In Fig. 5, the array sits at the origin of the  $x$ - $y$  coordinate system with the array axis oriented  $45^\circ$  from the  $x$  axis. Range and bearing can be converted from the  $x$ - $y$  coordinates.) For this case, matched-beam processing works effectively as spherical wave beamforming. The second case involves the source at  $45^\circ$  from the broadside of the array at a range of 1 km. The ambiguity surface as shown in Fig. 5(b) is narrowly peaked at the target bearing, and widely spread over range. This implies that the target bearing can be accurately estimated using matched-beam processing even for an incorrect range (used in the replica field). For this case, having estimated the target bearing accurately, one can then search for the target range by iteratively adjusting the range parameter until a maximum beam power is obtained. The third case involves a source at the end-fire direction at a range of 1.41 km. As shown in Fig. 5(c), target bearing resolution is the poorest of all three cases, but can still be fairly determined for a wide range of assumed source ranges. Range resolution is the best of all three cases. For this case, one has the best chance of searching for the target range after the bearing is established.

When the target range is not known, consistence in the bearing distribution rather than the peak of the bearing plot at a particular range should be used in the bearing estimation. For example, the mean of the bearing distribution in Fig. 5 (over many replica ranges) will be used as the target bearing. Having determined the target bearing, one can next search for the target range. The new target range can be used itera-

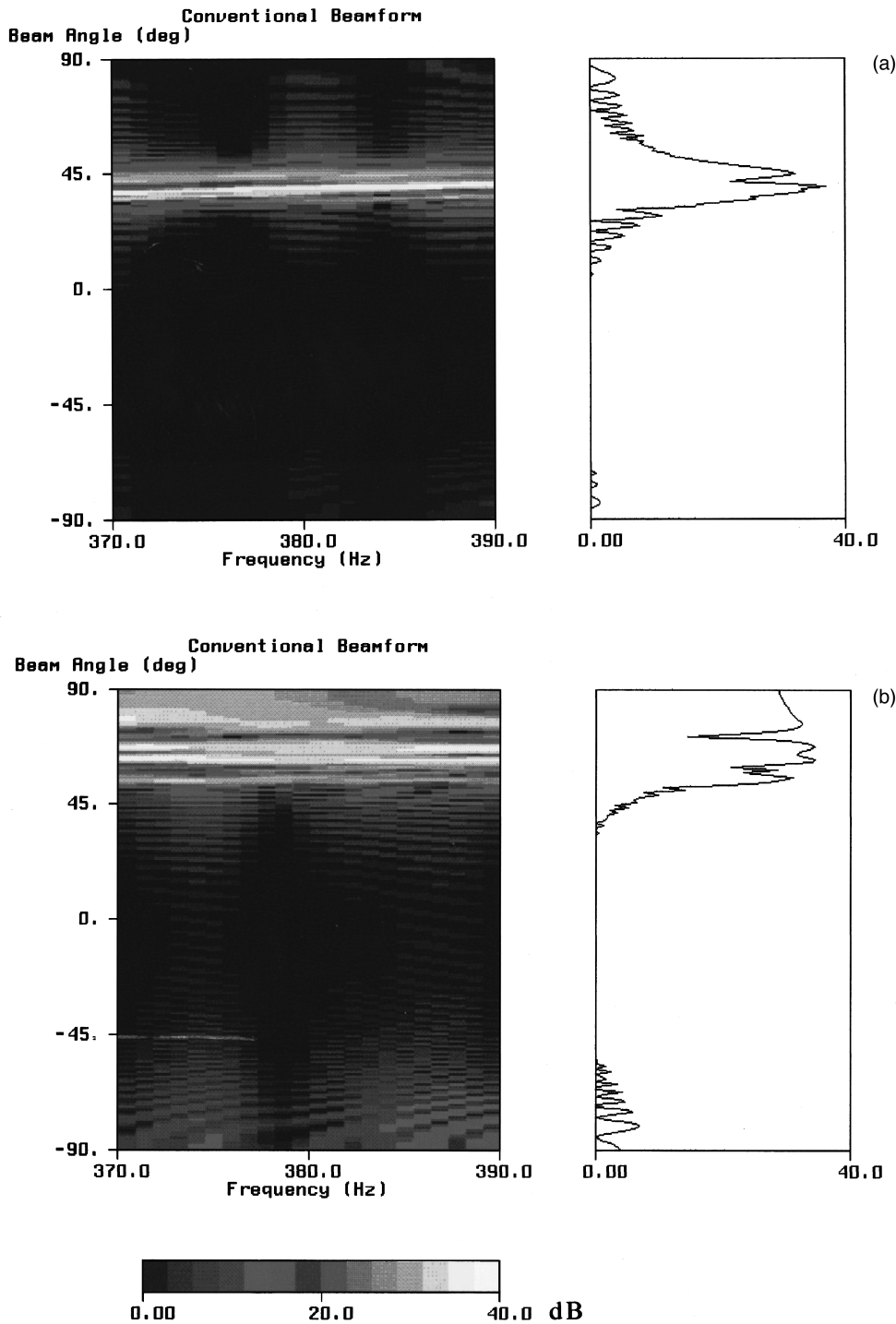


FIG. 2. Conventional beamforming signal gain for a horizontal array versus bearing for frequencies between 370 and 390 Hz: (a) target at 45° from broadside, (b) target at the end-fire direction (90°). Solid curves display intensities at 390 Hz.

tively (in a feedback loop) to improve the bearing estimation. This sequential search process involves only a limited search space in bearing and range. In contrast, matched-field processing must search for bearing and range simultaneously involving a large search space.

### III. TARGET TRACKING WITH A HORIZONTAL ARRAY

The impact of bearing bias on target bearing tracking is illustrated next. A bottom-mounted horizontal array is used and oriented in the north-east direction; the array is located at the origin in Fig. 6(a), oriented at 45° from the  $x$  axis. A near surface source at 30-m depth travels in the east direction

projecting a tone of 400 Hz. The source range is 1 km at the closest point of approach to the array. The source track is also displayed in Fig. 6(a). The array has 50 phones, spaced at 1.875 m.

Figure 6(b) shows the normalized beam outputs [Eq. (9)] using conventional beamforming as a function of bearing for each source position (labeled by its  $x$  coordinate). Bearing is measured from the broadside of the array. We note that as the source moves away from the broadside direction [the right-hand side of Fig. 6(b)], bearing tracking is discontinuous and jumps by an amount of 10°–20°. This is due to the fact that the signal energy jumps from one beam to the other

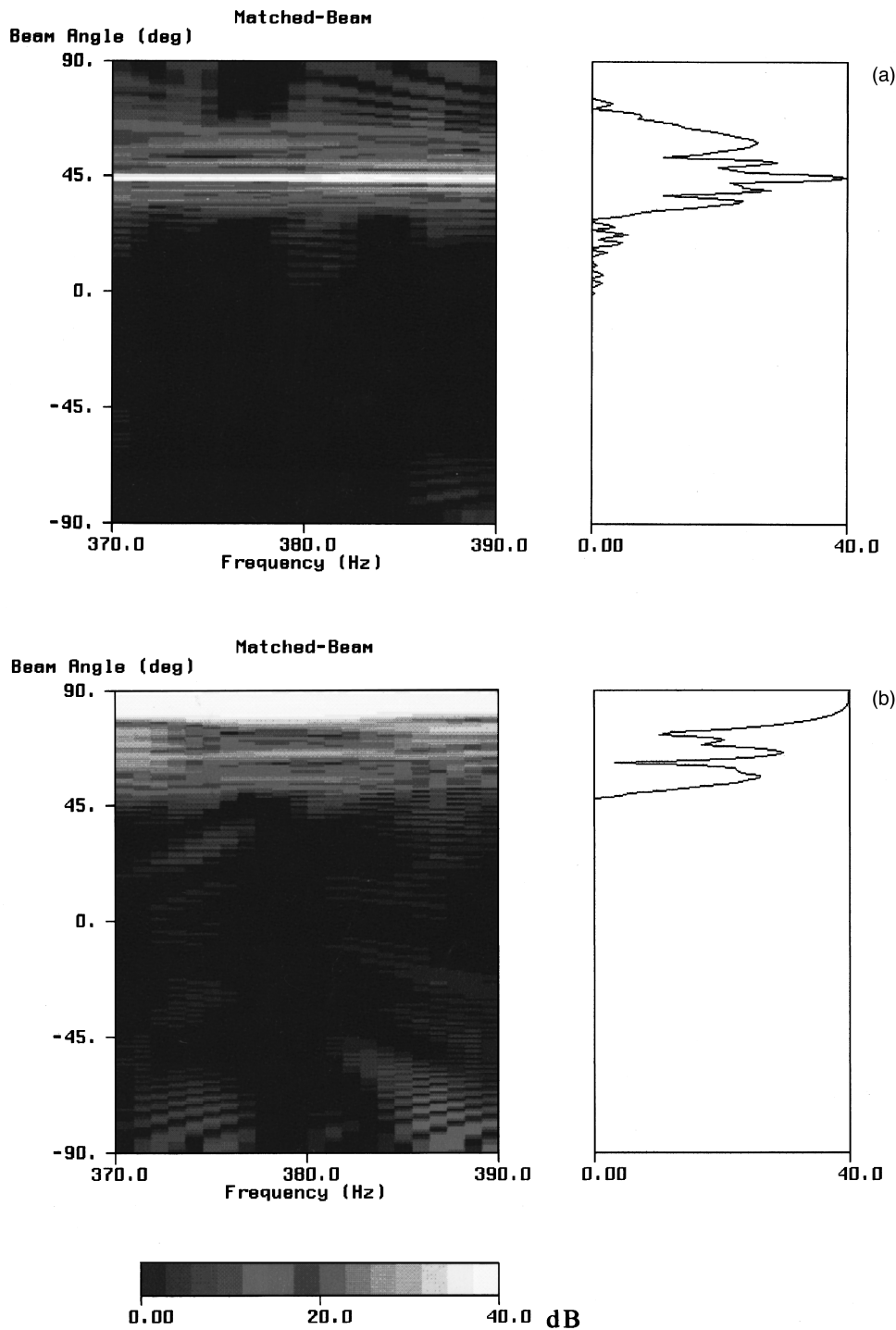


FIG. 3. Matched-beam signal gain as a function of bearing for frequencies between 370 and 390 Hz: (a) target at 45° from broadside, (b) target at end-fire direction (90°). Solid curves display intensities at 390 Hz.

as the range changes. The signal gain is 3–6 dB below theoretical. We also note that there is severe bearing bias (up to 25°).

Next we show the matched-beam bearing ambiguity function [Eq. (3)] as a function of the target position which is plotted in Fig. 6(c). Matched-beam processing yields improved performance, i.e., higher beam intensity, narrower beam width, and continuous tracking, compared with the conventional beam outputs in Fig. 6(b). In fact, the estimated bearing in Fig. 6(c) agrees with the true source bearing, since bearing bias [the right-hand side of Fig. 6(b)] has been removed. Also, the beam outputs show uniform intensity (0-dB

signal gain degradation) irrespective of the target bearing. As remarked before, for simulated data the same results can be accomplished using matched-field processing. The purpose here is to show that improved performance can be achieved with existing beamforming software by adding a post-processor.

With matched-beam processing, target tracking can be carried out efficiently using a sequential search procedure. We use continuity in target motion to guide bearing tracking. If the target position has been identified, we will use its (approximate) range estimated from current data as input to

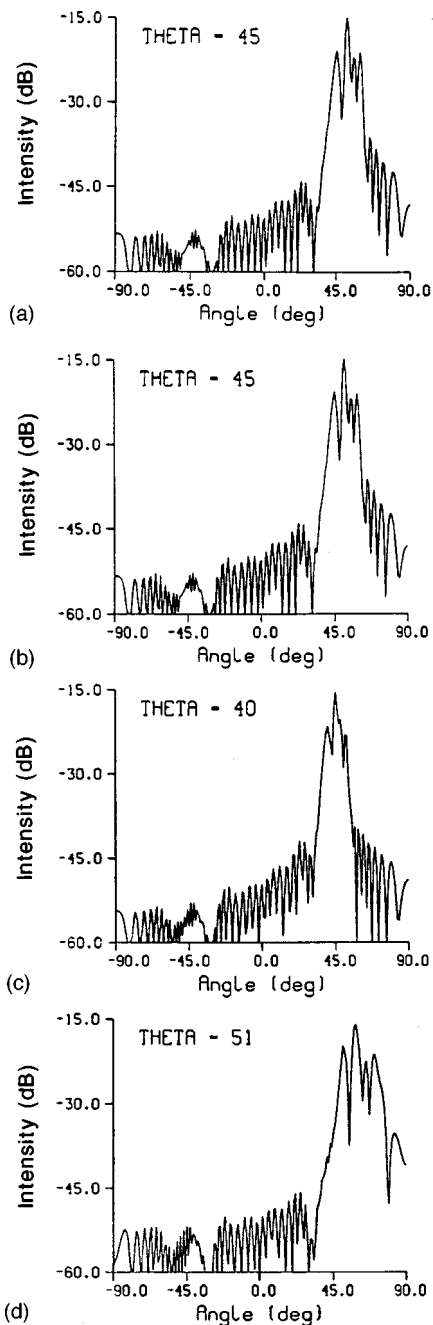


FIG. 4. The data beam intensity versus steering angle (a). The replica beam intensities versus steering angle are given in (b), (c), and (d) for target at bearing of 45°, 40°, and 51°, respectively.

create the replica field which will be used to process the immediate incoming data for estimating the new bearing of the target. As remarked above, one should be able to estimate the new bearing accurately using matched-beam processing. One can next search for the new target range in the target bearing direction. If necessary, bearing and range estimation can be refined by repeating the above process iteratively. We note that since the source movement is constrained by its speed and ability to change heading, one needs only to search the range in the neighborhood of the previous target range. This will reduce the range search space significantly.

#### IV. DEPTH DISCRIMINATION

In this section, we illustrate how matched-beam processing is used to improve tracking of a submerged target in the presence of a surface source (clutter), e.g., a surface ship.

Figure 7(a) displays the tracks of a surface source and a submerged source relative to the receiver array. The receiver is a horizontal array located at the origin of the  $x$ - $y$  coordinate system; the  $x$  axis points to the east direction and the  $y$  axis points to the north direction. The surface source travels eastbound at a depth of 30 m with the closest point of approach to (the center of) the array at 1 km. The submerged target travels south-east at a depth of 90 m with CPA at 1.41 km. The submerged source covers a distance of 2.8 km during the same period when the surface source travels 8 km eastward.

The simulated data are divided into 250 time frames. For each time frame, the acoustic field is the (coherent) summation of the fields from each source. We assume that the surface source has the same source level as the submerged source. The acoustic field containing the signals from both sources is processed using conventional beamforming for each time frame. The normalized beam intensities using Eq. (9) are plotted in Fig. 7(b) as a function of time. We note that initially, the surface and submerged sources appear at different bearings and are clearly distinguished. Later the surface and the submerged sources appear in near end-fire directions of the horizontal array. For this situation, conventional beamforming fails to estimate the true bearing of either the submerged target or the surface source. This is illustrated by the beam widening (and incorrect bearing) in Fig. 7(b) at time  $t \geq 140$ . Based on the conventional beam outputs in Fig. 7(b) one cannot tell whether there is more than one target present at  $t \geq 140$ .

To determine whether there is more than one source for the above situation using conventional beamforming, one would need another array with a different heading. When both sources are at positions which are end fire to both arrays, one needs a third array. For either case, conventional beamforming cannot tell the depth of the sources. We show below that matched-beam processing can separate the two sources in bearing with just one array and it can distinguish the submerged source from the near surface source.

The data analysis strategy is to process the data with several assumed source depths. First we process the data assuming there is a near surface source, using a source depth of 30 m. We follow the procedure described in the previous section. The matched-beam bearing tracking result using Eq. (3) is shown in Fig. 8(b). Next we process the data assuming there is a submerged source, using a source depth of 100 m. The matched-beam bearing tracking result using Eq. (3) is shown in Fig. 8(a). We could repeat this processing for other source depths. For this discussion, we shall just compare Fig. 8(a) with Fig. 8(b). We note that each figure shows a track of high intensity which is different from the track of the other figure. This suggests that there is more than one source in the data. Knowing how the data were created, we realize that the bearing of the high intensity track in Fig. 8(a) matches that of the surface source and the bearing of the high intensity track in Fig. 8(b) matches that of the submerged source. This

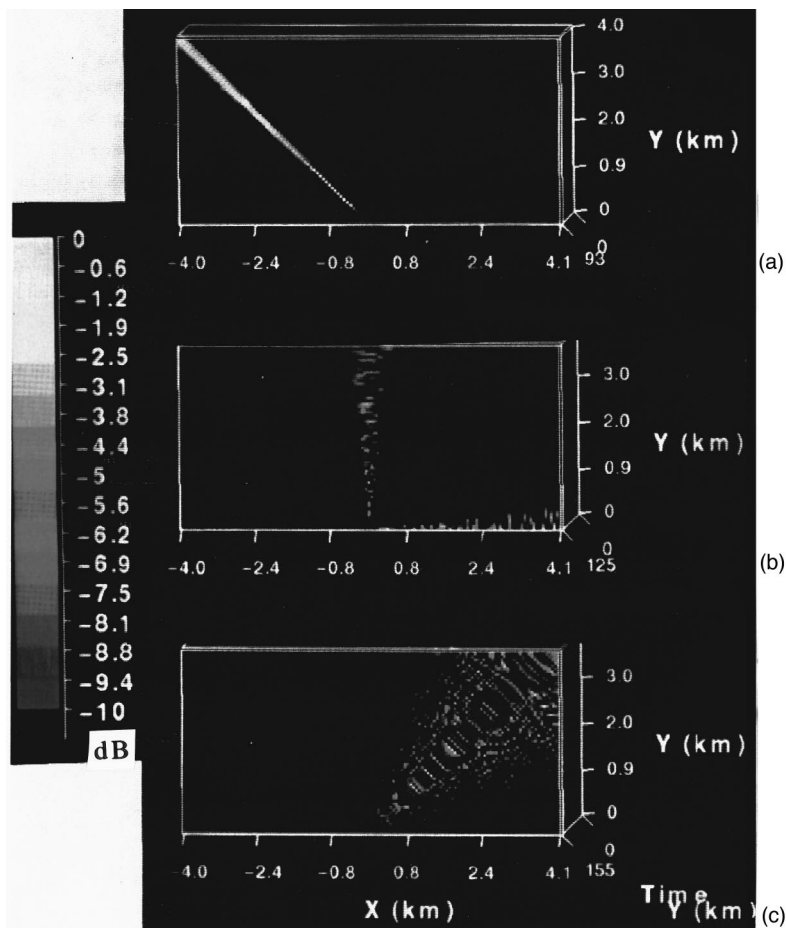


FIG. 5. Matched-beam ambiguity surface as a function of range and bearing for a signal at 390 Hz. (a) Target located at the broadside of the horizontal array at a range of 1.41 km. (b) Target located at 45° from broadside at a range of 1 km. (c) Target at the end-fire direction at a range of 1.41 km. The array sits at the origin of the  $x$ - $y$  coordinates oriented at 45° from the  $x$  axis.

shows that the bearing of the two sources can be separately tracked, which conventional beamforming fails to do (with one array). The bearings of the target and the surface source are both correctly estimated.

We also note that matched-beam processing enhances the output signal intensity of the (submerged) target more than the clutter when the source depth of the replica field matches that of the target. (We can treat either the submerged source or the near surface source as the target and the other as the clutter.) This is because the target receives a higher signal gain than the clutter when the depth of the replica field matches with that of the target.

## V. ENVIRONMENTAL MISMATCH

In the above analysis we have assumed no environmental mismatch. In this section we study the effect of bottom mismatch on the bearing estimation using matched-beam processing. We find that signal gain could be degraded if there is environmental mismatch but bearing can still be reliably estimated. We require that a general knowledge about the bottom (e.g., bottom type, silt or sand) is available, but exact sound-speed profile and depth may be uncertain.

As remarked above, we anticipate that bearing estimation is relatively robust even when the bottom sound-speed profile or bottom parameters are not exactly known. This is certainly the case when the target is in the broadside direction of the horizontal array; in this case matched-beam processing yields nearly identical results as conventional beam-

forming. Note that exact sound-speed profile or bottom parameters are not needed for conventional beamforming. In mismatched environments where range estimation may be in error, the question is whether bearing can still be estimated accurately. The ability to estimate bearing accurately (a significant improvement over conventional beamforming) is a useful thing in practical problems.

(A remark: In many shallow-water areas the general bottom type may be known but the exact sound-speed profile in the bottom is usually not well known. This database may not be good enough for matched-field processing. As reported in Refs. 10 and 11, matched-field source localization is rather sensitive to small variations in the bottom profile (e.g., sediment thickness and sound speed). For this reason, we concentrate on the bearing estimation.)

We use the sandy bottom (Fig. 1) environment and the bottom-mounted horizontal array as described above. We plot in Fig. 9 the range and bearing ambiguity surface when there is no bottom mismatch. In Fig. 9(a), the target is at a bearing 45° from the broadside direction of the horizontal array at a range of 1 km. In Fig. 9(b), the target range is at bearing 90° at a range of 1.41 km. Next, we assume that the bottom is not known. We process the data using a different bottom profile; we use a hard bottom<sup>25</sup> with a constant sound speed of 1800 m/s to generate the replica fields. The resulting range and bearing ambiguity surfaces are shown in Fig. 10. We note that while the bottom mismatch causes the range of the target to be estimated incorrectly, the target bearing

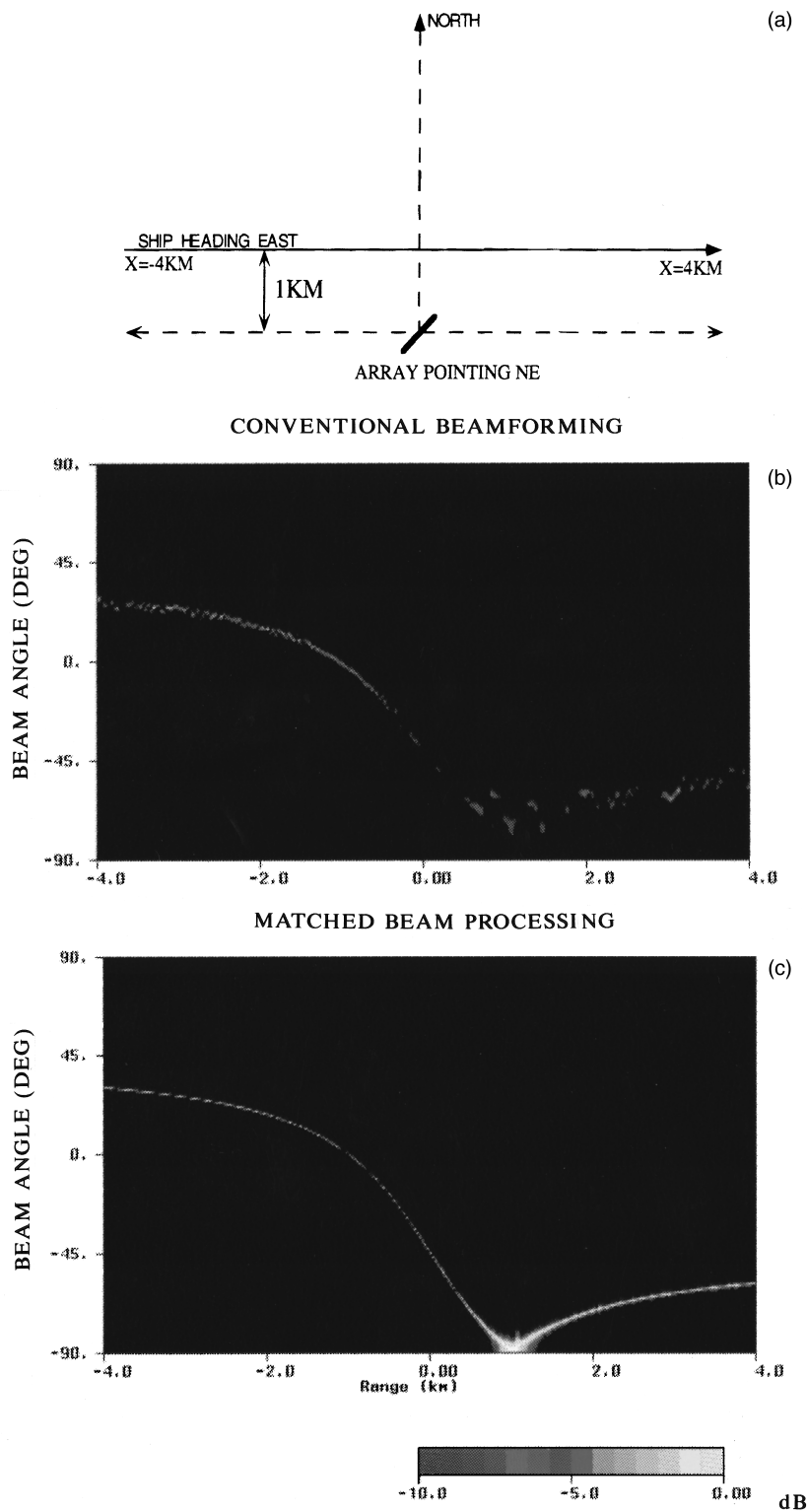


FIG. 6. (a) Tracks of a surface source relative to the receiver array located at the origin, pointing to the north-east direction. (b) Estimated bearing of the surface source using conventional beamforming. (c) Estimated bearing of the surface source using matched-beam processing. Bearing is measured from the broadside of the array;  $0^\circ$  points to north-west or south-east. Intensity scale indicates signal gain degradation.

estimation is robust. In fact, range is difficult to estimate in either case based on Figs. 9 and 10, but bearing is well indicated in both cases. Again, the consistency of the bearing distribution over many ranges (as by integrating over ranges), rather the bearing distribution at a particular range, should be used for bearing estimation.

We recall the conventional beamforming results shown

above. The target bearing is estimated at  $\sim 40^\circ$  when the true bearing is at  $45^\circ$  for the target at a range of 1 km. The target bearing is estimated at  $\sim 70^\circ$  when the true bearing is  $90^\circ$  for the target at a range of 1.41 km. (See, e.g., Fig. 2.) In comparison, the bearing estimation using matched-beam processing is much more accurate despite the bottom mismatch problem.

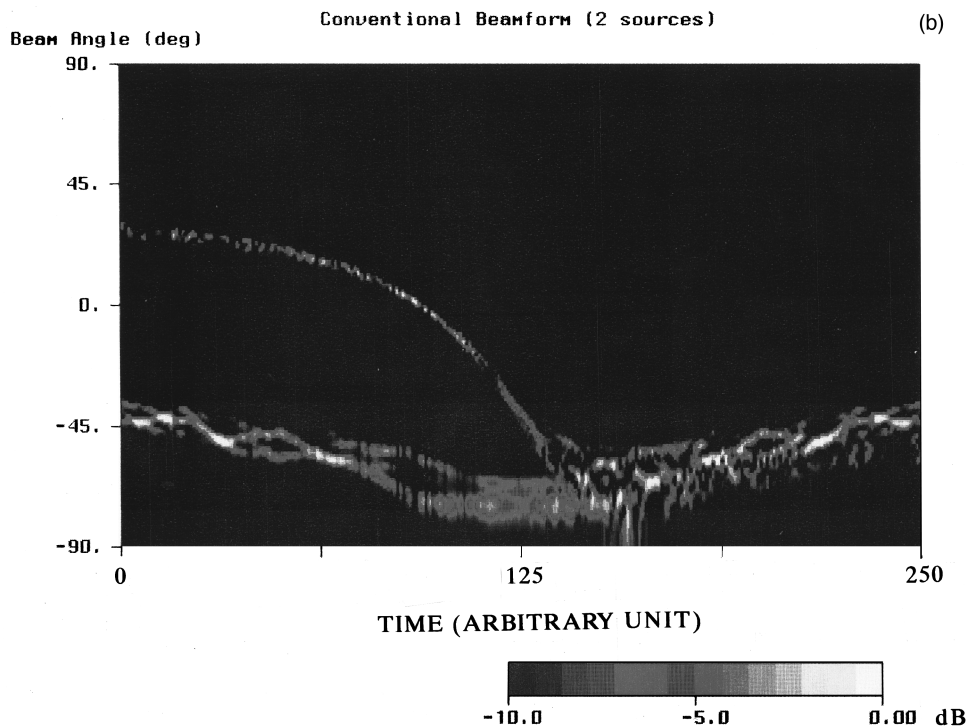
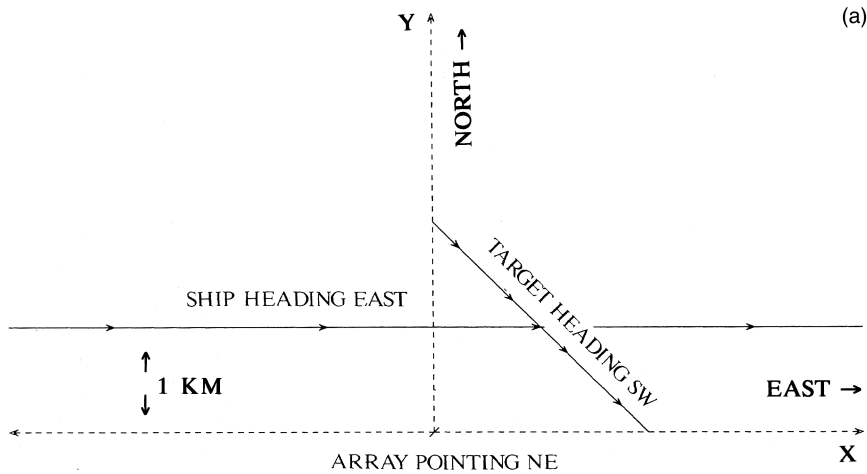


FIG. 7. (a) Tracks of a surface and a submerged source relative to the receiver array located at the origin, pointing to the north-east direction. (b) Conventional beam outputs (normalized) as a function of bearing and time. Bearing is measured from the broadside of the array;  $0^\circ$  points to north-west or south-east.

We have also investigated the effect of bottom mismatch on bearing estimation for a silty bottom<sup>25</sup> which is matched with a soft bottom<sup>26</sup> (consisting of a thin sediment layer over the bottom). We find similar conclusions regarding bearing estimation as presented above.

## VI. SUMMARY

In this paper, we apply matched-beam processing to a horizontal line array in shallow water. We showed that using conventional beamforming, the signal will be split over several beams in a multipath shallow-water environment. This results in degraded signal gain and bearing bias. Matched-beam processing yields a correct bearing and theoretical signal gain as would matched-field processing.

Matched-beam processing is matched-field processing applied in the beam domain. It is an implementation of matched-field techniques to existing systems where the conventional beam outputs are the only data readily available. For a research experiment involving a source and a fixed receiver array, the extra step of transforming the phone data into the beam data may be unnecessary. For practical applications, beam domain processing offers the advantage of removing nonsignal beams (such as strong interfering sources) before the correlation with the replica beams. This can make a significant difference in detection and tracking of a weak target.

Matched-beam processing can be implemented as a post-processor to existing system software which takes the conventional beam outputs as input. We demonstrated that



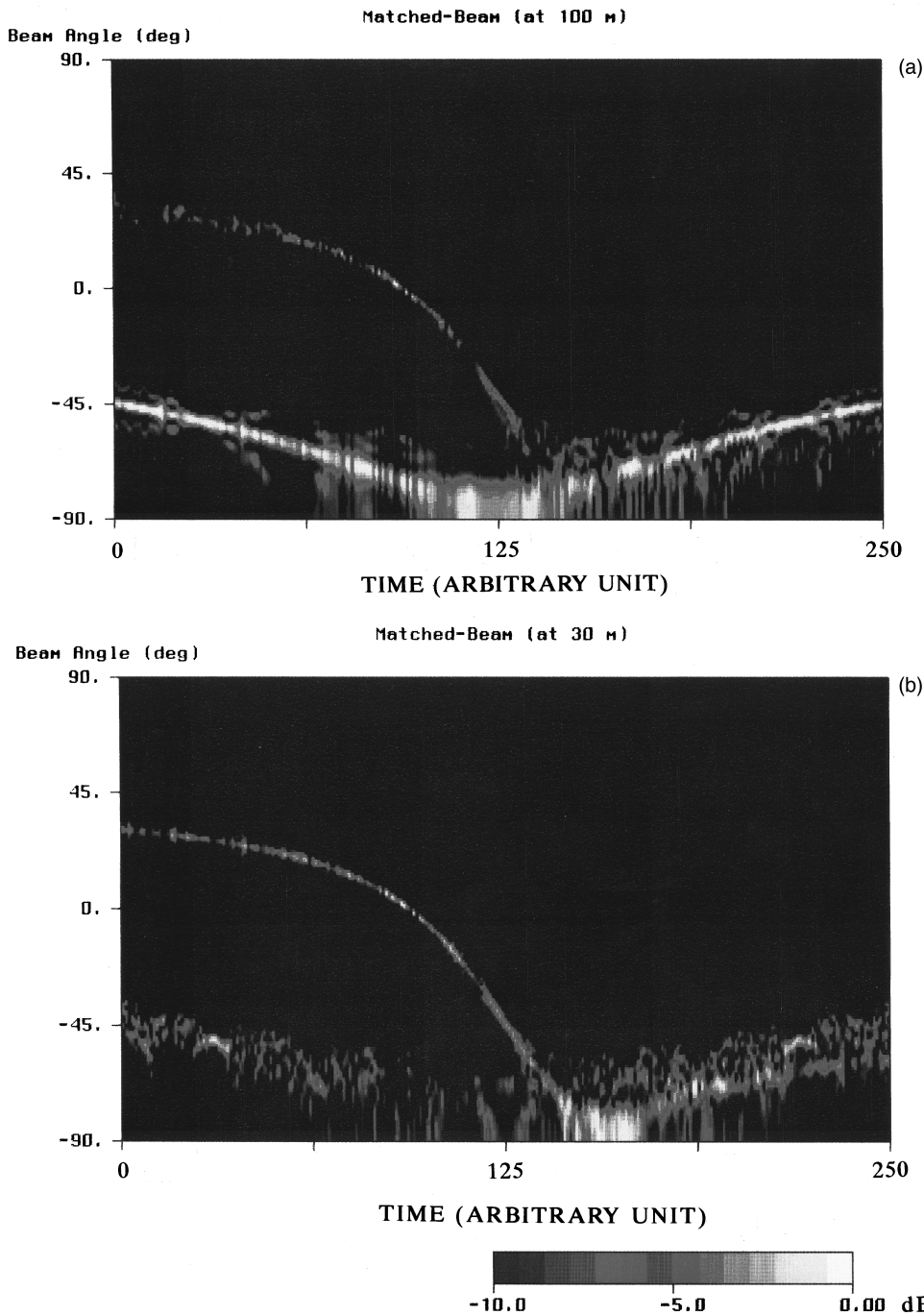


FIG. 8. Matched-beam bearing ambiguity surface as a function time when data are processed assuming source depth at (a) 100 m and (b) 30 m.

conventional beamforming can be extended (via the post-processor) to achieve the benefit of full-field (matched field) processing. Matched-beam processing can incorporate many useful (plane wave) signal processing algorithms previously developed to deal with system problems, which is not easily doable using matched-field processing.

Matched-beam processing is a more efficient or robust approach to correct bearing errors and signal gain degradation of horizontal line arrays in shallow water than matched-field processing. Range estimation based on a horizontal array is often limited and is sensitive to environmental mismatch. Accurate source localization requires exact environmental acoustic information using matched-field process-

ing. The objective of matched-beam processing is to provide robust estimation of target bearing. Bearing estimation can tolerate some degree of bottom mismatch and is more robust than range/depth estimation. Only after the bearing is (correctly) estimated, will the range be searched. Range estimation is subject to the same environmental mismatch problem as matched-field processing. In practice there are other means to improve the range estimation such as using target motion analysis and multiple contact information.

We showed target tracking using an iterative procedure in bearing and range estimation. This should reduce significantly the computation load compared with matched-field processing which searches simultaneously bearing, range,

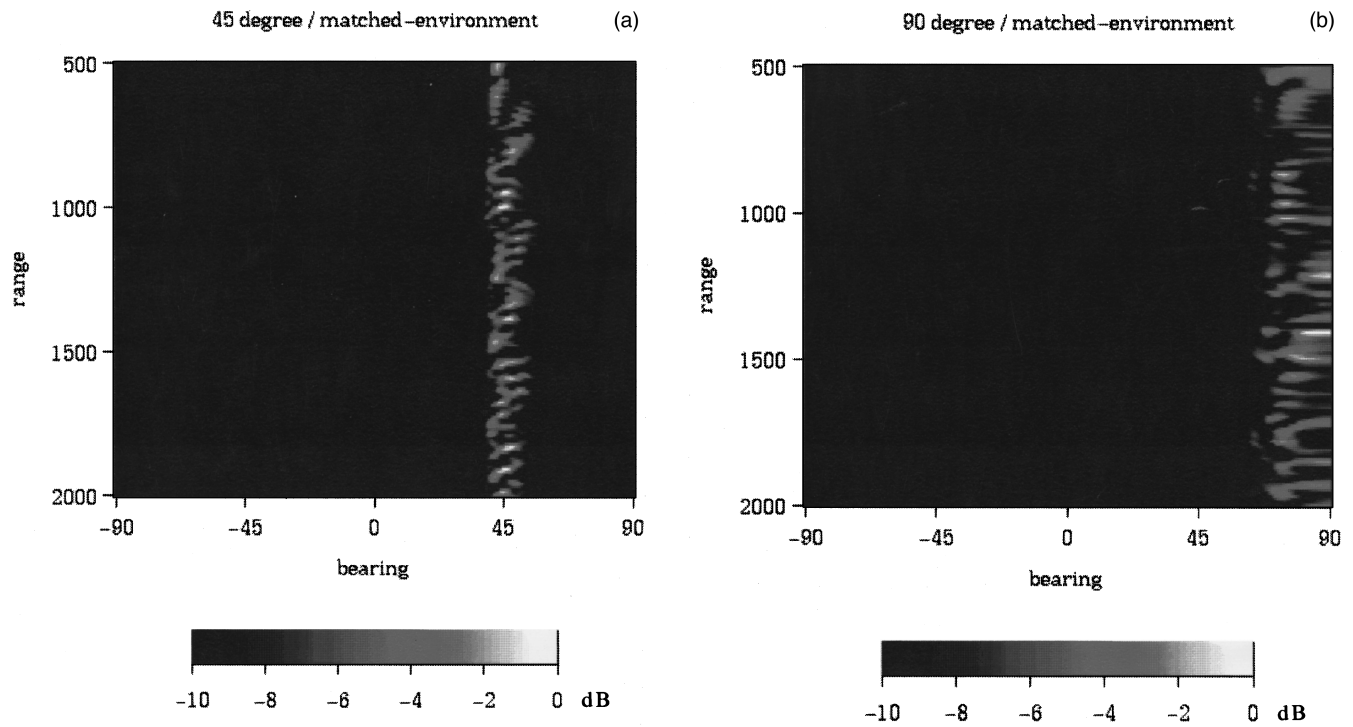


FIG. 9. The matched-beam range and bearing ambiguity surfaces with no bottom mismatch: (a) target at  $45^\circ$  from the broadside direction of the horizontal array, (b) target at the end-fire direction ( $90^\circ$ ).

and depth in a three-dimensional space. We showed that the horizontal array has some capability in discriminating a deep from a shallow target when the sources are away from the broadside direction. The deep source is enhanced by the signal gain when the depth used in the replica field matches that

of the target. The bearings of the shallow and deep sources can be separately tracked, which conventional beamforming fails to do when they are close to the end-fire direction. Bearing estimation of both sources are more accurate than conventional beamforming.

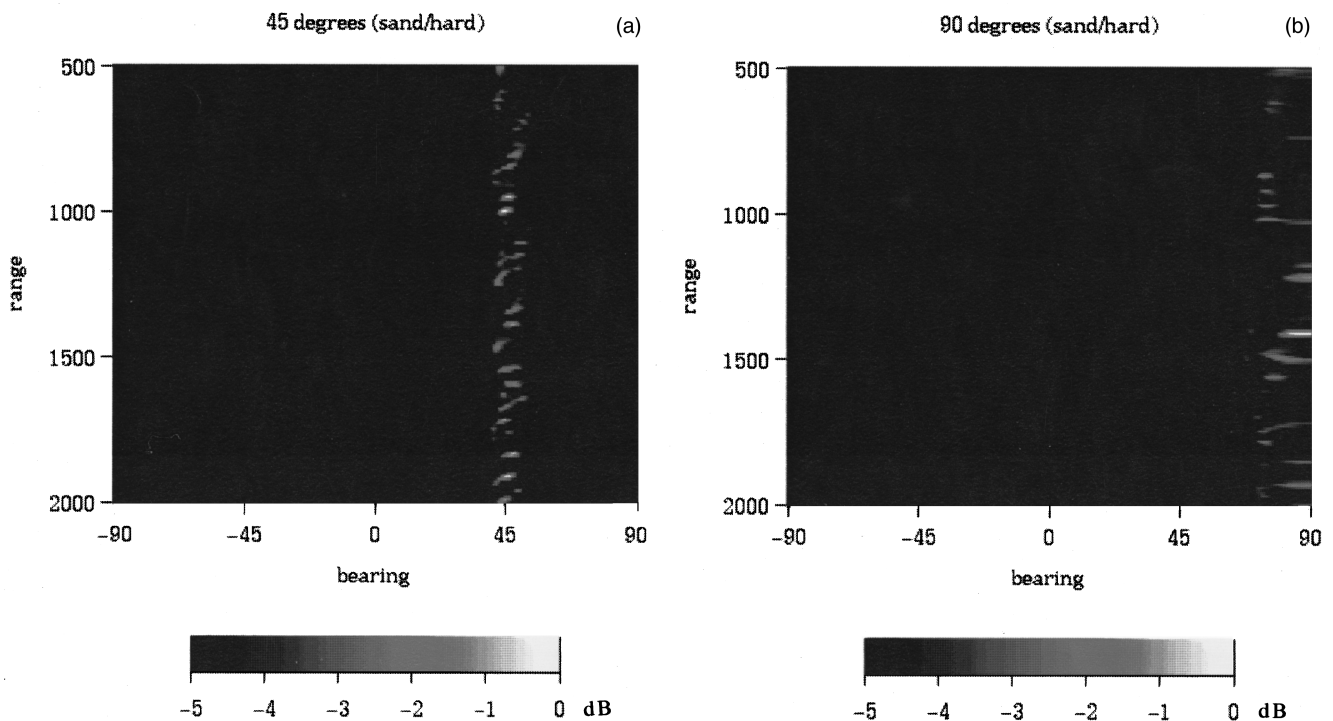


FIG. 10. Same as Fig. 9 but with bottom mismatch.

## ACKNOWLEDGMENTS

This work was supported by the Office of Naval Research. We thank the reviewers for useful comments.

- <sup>1</sup>H. P. Buckner, "Use of calculated sound fields and matched field detection to locate sound sources in shallow water," *J. Acoust. Soc. Am.* **59**, 368–373 (1976).
- <sup>2</sup>For an introduction, see T. C. Yang, "A method of range and depth estimation by modal decomposition," *J. Acoust. Soc. Am.* **82**, 1736–1745 (1987).
- <sup>3</sup>See reviews by A. B. Baggeroer and W. A. Kuperman, "Matched field processing in ocean acoustics," in *Acoustic Signal Processing for Ocean Exploration*, edited by J. M. F. Moura and I. M. G. Lourtie (Kluwer, Dordrecht, 1993), and A. Tolstoy, *Matched Field Processing for Underwater Acoustics* (World Scientific, Singapore, 1992).
- <sup>4</sup>J. M. Ozard, "Matched field processing in shallow water for range, depth and bearing determination: Results of experiment and simulation," *J. Acoust. Soc. Am.* **86**, 744–753 (1989).
- <sup>5</sup>C. W. Bogart and T. C. Yang, "Matched field localization with horizontal arrays in shallow water; spatial sampling and effective aperture," *J. Acoust. Soc. Am.* **96**, 1677–1686 (1994).
- <sup>6</sup>M. Orr and J. F. Lynch, "The New Jersey shelf shallow water random media propagation experiment," *J. Acoust. Soc. Am.* **98**, 2864 (1995).
- <sup>7</sup>D. R. Del Balzo, C. Feuillade, and M. M. Rowe, "Effects of water-depth mismatch on matched-field localization in shallow water," *J. Acoust. Soc. Am.* **83**, 2180–2185 (1988).
- <sup>8</sup>C. Feuillade, D. R. Del Balzo, and M. M. Rowe, "Environmental mismatch in shallow-water matched-field processing: Geoacoustic parameter variability," *J. Acoust. Soc. Am.* **85**, 2354–2364 (1989).
- <sup>9</sup>R. M. Hamson and R. M. Heitmeyer, "Environmental and system effects on source localization in shallow water by the matched-field processing of a vertical array," *J. Acoust. Soc. Am.* **86**, 1950–1959 (1989).
- <sup>10</sup>D. F. Gingras and P. Gerstoft, "Inversion for geometric and geoacoustic parameters in shallow water: Experimental results," *J. Acoust. Soc. Am.* **97**, 3589–3598 (1995).
- <sup>11</sup>D. P. Knobles and R. A. Koch, "A time series analysis of sound propagation in a strongly multipath shallow water environment with an adiabatic normal mode approach," *IEEE J. Ocean Eng.* **21**, 1–13 (1996).
- <sup>12</sup>C. S. Clay, "Array steering in a layered waveguide," *J. Acoust. Soc. Am.* **33**, 865–870 (1961).
- <sup>13</sup>Y. Y. Wang, C. S. Clay, and E. C. Shang, "Bearing determination in a waveguide," *J. Acoust. Soc. Am.* **82**, 233–237 (1987).
- <sup>14</sup>See Appendix B in T. C. Yang and C. W. Bogart, "Matched mode processing for sparse three-dimensional arrays," *J. Acoust. Soc. Am.* **95**, 3149–3166 (1994).
- <sup>15</sup>T. C. Yang and W. Cullop, "Source localization and tracking in a sloping littoral sea" (unpublished, 1995).
- <sup>16</sup>T. C. Yang and T. Yates, "Improving the sensitivity of full-field geoacoustic inversion for estimating bottom sound speed profiles," *Full Field Inversion in Seismic and Ocean Acoustics* (Kluwer Academic, Dordrecht, 1995), pp. 323–328.
- <sup>17</sup>T. C. Yang and T. Yates, "Acoustic inversion of bottom reflectivity and bottom sound-speed profile," *J. Oceanic Eng.* **21**, 367–376 (1996).
- <sup>18</sup>K. Yoo and T. C. Yang, "Improved vertical array performance in shallow water with a directional noise field," to appear in *J. Acoust. Soc. Am.*
- <sup>19</sup>T. C. Yang and T. Yates, "Matched beam processing: Range tracking with vertical arrays in mismatched environments," to appear in *J. Acoust. Soc. Am.*
- <sup>20</sup>See, for example, B. Widrow and S. D. Stearns, *Adaptive Signal Processing* (Prentice-Hall, Englewood Cliffs, NJ, 1985), Chap. 14.
- <sup>21</sup>See, for example, W. S. Burdick, *Underwater Acoustic System Analysis* (Prentice-Hall, Englewood Cliffs, NJ, 1991).
- <sup>22</sup>M. B. Porter and E. L. Reiss, "A numerical method for ocean acoustic normal modes," *J. Acoust. Soc. Am.* **76**, 242–252 (1984).
- <sup>23</sup>T. C. Yang, "Modal shading coefficients for high-resolution source depth localization," *J. Acoust. Soc. Am.* **87**, 668–672 (1990).
- <sup>24</sup>E. C. Shang, "An efficient high-resolution method of source localization processing in mode space," *J. Acoust. Soc. Am.* **86**, 1960–1964 (1989).
- <sup>25</sup>F. Ingenito, "Scattering from an object in a stratified medium," *J. Acoust. Soc. Am.* **82**, 2051–2059 (1987).
- <sup>26</sup>R. M. Hamson, "The theoretical responses of vertical and horizontal line arrays to wind-induced noise in shallow water," *J. Acoust. Soc. Am.* **78**, 1702–1712 (1985).

# Initial evaluation of the dominant mode rejection beamformer

Tina M. Redheendran

Motorola, Wireless Infrastructure Division, 6501 William Cannon Drive West, Austin, Texas 78735-7260

Richard A. Gramann

Applied Research Laboratories, The University of Texas at Austin, P.O. Box 8029, Austin, Texas 78713-8029

(Received 18 September 1997; revised 20 March 1998; accepted 5 May 1998)

Long integration times are needed to give accurate cross-spectral matrix (CSM) estimates; however, integration times must be short enough so that the dynamic behavior of the noise described by the CSM is captured. The dominant mode rejection (DMR) beamformer, described by Owsley and Abraham, calculates adaptive weights based on a reduced rank (CSM) estimate, where the CSM estimate is formed with a subset of the eigenvalues containing the largest eigenvalues and their eigenvectors. Thus the integration time required to obtain this CSM estimate is reduced, as the largest eigenvalue/eigenvector pairs are estimated much more rapidly than the smaller ones. The purpose of this study was to determine whether performance comparable to a fully adaptive beamformer could be achieved with the DMR beamformer, without the potential penalties associated with requiring the increased integration time for the CSM. Data acquired with bottom-mounted horizontal line arrays, in both deep- and shallow-water environments, were used to test the dominant mode rejection beamformer performance. Appropriate DMR parameters were found using the deep-water data so that the DMR performance emulated the performance of a fully adaptive beamformer with a white-noise gain constraint. Additional processing performed on the shallow-water data showed that the DMR beamformer had equivalent performance to a robust fully adaptive beamformer, but with much less output power bias at small integration times. © 1998 Acoustical Society of America. [S0001-4966(98)01109-6]

PACS numbers: 43.30.Wi, 43.60.Gk [SAC-B]

## INTRODUCTION

Many passive sonar systems rely on adaptive beamforming to provide gain against interfering signals. The adaptive beamformer places nulls in the direction of interferers and allows the gain of the array to be many times that achieved with conventional, or delay and sum, beamforming (CBF). This additional gain can be important in high noise environments, where many loud interferers are present. In particular, many shallow-water environments can be characterized as high noise, due to shipping traffic. The noise environment can also be classified as highly dynamic, due to the high bearing rates seen on many interfering traces, as the dominant interferers are generally in close proximity to the array. Thus the ability of the adaptive beamformer to adapt to this environment and suppress interferers in the sidelobe region is critical to system performance in such an environment.

In order to place nulls in the direction of the interferers, the beamformer requires information on the noise environment. The source of this information is the cross-spectral matrix (CSM). The estimate of the CSM has a specified integration time and bandwidth. Clearly, the integration time must be short enough that the dynamic behavior of the noise is captured, and the noise described by the CSM can be considered somewhat stationary. However, the bandwidth of the CSM must be small enough to avoid mismatch in the adaptive weights (due to the bandwidth being too large relative to the center frequency), and to avoid phase errors across the array. Also, at frequencies of interest, the bandwidth of the CSM must be limited to adequately describe the variation

with frequency seen in the noise field. Thus both the integration time and bandwidth must be kept to a minimum so that the dynamic noise can be adequately described.

The accuracy of the information provided to the beamforming algorithm (through the CSM) determines how well the beamformer can null out the interfering signals, and pass the desired signal without attenuation or distortion. The accuracy of the CSM estimate is directly proportional to the integration time and the CSM bandwidth. Hence an inherent conflict arises between capturing the dynamics of the noise field and obtaining an accurate estimate of the CSM.

In a previous study, Grant *et al.*<sup>1</sup> examined the bias obtained in the beamformer output power when using an estimate of the CSM that contains few samples (either time or frequency). The expression they derived, shown below, shows that the accuracy of the minimum variance distortionless response (MVDR) beamformer output power estimate is proportional to the number of samples used to calculate the CSM. The estimated MVDR beamformer output power is

$$E\{\hat{P}_o\} = \frac{N_s - N + 1}{N_s} P_o, \quad (1)$$

where  $N$  is the number of sensors described in the CSM,  $N_s$  is the number of snapshots used to calculate the CSM estimate,  $P_o$  is the output power obtained with the actual CSM, and  $\hat{P}_o$  is the MVDR output power estimated using the estimated CSM. In Grant's<sup>1</sup> terminology, a snapshot is referred to as a single-frequency bin for one FFT.

In order to keep the beam noise bias to reasonable levels for arrays with a large number of hydrophones, Eq. (1) implies that several minutes of integration time may be necessary when processed with an adaptive beamformer. Thus an alternative beamforming algorithm may be necessary for arrays with many sensors that are placed in dynamic noise environments.

The dominant mode rejection (DMR) beamformer was described by Abraham and Owsley in Ref. 2. This beamformer calculates adaptive weights based on a reduced rank CSM estimate, where the CSM estimate is formed with the  $D$  largest eigenvalues, which represent the  $D$  dominant modes in the CSM estimate. The integration time or amount of data required to obtain this CSM estimate is reduced, as the largest eigenvalue/eigenvector pairs are estimated much more rapidly than the smaller ones. Thus the weights can be calculated using less data, allowing the adaptive beamformer to adapt more rapidly to the dynamic noise environment, and possibly improving the ABF performance.

### A. Robust adaptive beamformer

The adaptive beamformer calculates a set of complex weights that, when applied to the hydrophone outputs, will give unity gain in the look direction while minimizing the output power. The output power of the beamformer is

$$P = w^H R w, \quad (2)$$

where  $w$  is the weight vector,  $R$  is the CSM, and  $H$  indicates complex conjugate, or Hermitian, transpose. The goal is to minimize the output power subject to the look direction constraint, or

$$\min(w^H R w) \text{ subject to } w^H d = 1, \quad (3)$$

where  $d$  is the look direction steering vector which describes the expected spatial properties of the desired signal. Using Lagrange multipliers gives the solution for the MVDR weights to be

$$w = \frac{R^{-1} d}{d^H R^{-1} d}. \quad (4)$$

Cox *et al.*<sup>3</sup> has described a robust adaptive beamformer. This beamformer limits the array gain against white noise (white-noise gain or  $G_w$ ) to limit signal suppression errors. Thus the white-noise gain can be used as a measure of the robustness of the beamformer.

The weights of the white-noise gain constrained beamformer are derived by minimizing the output power subject to the look direction constraint and the white-noise gain constraint, or

$$\min(w^H R w) \text{ subject to } w^H d = 1 \text{ and } G_w \geq \delta^2. \quad (5)$$

When a beamformer has unity gain in the look direction, the white-noise gain is defined as

$$G_w = \frac{1}{w^H w}. \quad (6)$$

Again, Lagrangian methods are used to find the solution

$$w = \frac{(R + \epsilon I)^{-1} d}{d^H (R + \epsilon I)^{-1} d}, \quad (7)$$

where  $\epsilon$  is the smallest positive value such that  $G_w > \delta^2$  and  $\epsilon I$  is the white noise injected into the CSM.  $G_w(\epsilon)$  is a monotonic increasing function of  $\epsilon$ , and  $G_w(\infty) = N$ , yielding the unshaded conventional beamformer. It is clear that the implementation of the white-noise gain constrained beamformer involves simply adding  $\epsilon$  to the diagonal of the CSM, which is the same as adding  $\epsilon$  to each eigenvalue of the CSM.

Gramann<sup>4</sup> discusses the implementation of the white-noise gain constrained adaptive beamformer (WNGC ABF) at ARL:UT. The white-noise gain constraint is set relative to  $10 \log N$  and, in general, the constraint is set to 3 dB below  $10 \log N$ . Thus the white-noise gain constraint equation is

$$G_w \geq 10 \log N + wnc, \quad (8)$$

where  $wnc = -3$  dB. Previous work has shown this level of the constraint provides reasonable robustness against mismatch, while not overly penalizing the ability of the beamformer to suppress interferers in directions other than the look direction.

### B. Dominant mode rejection beamformer

Abraham and Owsley developed the dominant mode rejection beamformer in Ref. 2. They rewrite the CSM in terms of its eigenvalues  $\lambda$  and eigenvectors  $m$ :

$$R = \sum_{i=1}^N \lambda_i m_i m_i^H. \quad (9)$$

The largest eigenvalues are associated with the loudest noise sources or dominant modes in the environment described by the CSM. Abraham and Owsley approximate the CSM using the  $D$  largest eigenvalues and their corresponding eigenvectors, plus a noise term. The new reduced rank CSM estimate is

$$\hat{R} = e \sum_{i=1}^D \psi_i m_i m_i^H + \sigma^2 I_N, \quad (10)$$

where  $\psi_i = \lambda_i - \sigma^2$ ,  $e$  is a scalar enhancement factor, and  $\sigma^2$  represents the uncorrelated noise power in the CSM estimate.

Replacing  $R$  with  $\hat{R}$  in the MVDR solution gives

$$\hat{w}(\theta) = \frac{d(\theta) - \sum_{i=1}^D \beta_i m_i m_i^H d(\theta)}{N - \sum_{i=1}^D \beta_i d(\theta)^H m_i m_i^H d(\theta)}, \quad (11)$$

where  $\beta = 1/[1 + (\sigma^2/e\psi)]$  and  $N$  is the number of hydrophones in the CSM.

In examining the form of Eq. (11), it is interesting to note that as  $e$  decreases to zero,  $\beta$  approaches zero, and the dominant mode rejection weights of Eq. (11) approach the unshaded conventional beamformer weights

$$w = \frac{d}{N}. \quad (12)$$

Since  $e$  is used as an ‘‘enhancement factor’’ for the eigenvalues (and thus controls emphasis of the information in

the CSM) in the weights calculation, it is logical that, as information on the noise field is removed from the weights calculation, the weights would approach the CBF solution.

Substituting the unshaded conventional beamformer weights from Eq. (12) into the white-noise gain formula in Eq. (6) shows that the unshaded conventional beamformer white-noise gain values are constant and equal to the number of hydrophones,  $N$ . As mentioned above, the dominant mode rejection weights approach the unshaded conventional beamformer weights as  $e$  decreases; therefore, as later results verify, the dominant mode rejection white-noise gain values should approach  $N$  as  $e$  decreases.

Abraham and Owsley's study used only simulated data and looked at only a few of the issues associated with the DMR beamformer. This present study expands upon Abraham and Owsley's work and looks at some of the other issues involved with the DMR beamformer. These other issues include the performance of the DMR beamformer using data from a real ocean environment and the sensitivity of the DMR beamformer to the parameters  $D$ ,  $e$ , and  $\sigma^2$ .

The purpose of this study has been to examine the performance of the dominant mode rejection beamformer in a real ocean environment and to determine whether performance comparable to a fully adaptive beamformer could be achieved. Also, a comparison of the output power bias obtained with DMR and fully adaptive ABF is provided. In order to address these issues, the DMR algorithm was coded, and a sensitivity study of its performance was conducted. Finally, data were processed from two ocean environments, and the performance of the DMR beamformer was directly compared to a fully adaptive algorithm. The following sections describe the data used for this evaluation and discuss the results of this study. Additional details are also provided in Ref. 5.

## I. ANALYSIS APPROACH

### A. Description of the data sets

Data from two experiments were chosen to evaluate the DMR beamformer's performance. Both data sets were processed at the same frequency.

#### 1. Deep-water data set (DWDS)

Data in the first experiment were acquired using a bottom-mounted horizontal line array (HLA) in a deep ocean environment in the North Atlantic. The water depth was about 1500 m. The array had eight hydrophones in a tapered design and the length of the array was 2.4 wavelengths relative to the frequency processed.

The data were acquired from the array using a data acquisition system with a 12-bit A/D converter. One minute of data was recorded every 15 min. The data were low-pass filtered at 600 Hz and sampled at around 2 kHz. FFTs were calculated using a 2 K transform length without any data overlap. Each set of FFTs was used to calculate single sample CSMs that had 1-Hz bandwidths and 1-Hz center frequency spacings; 61 single sample CSMs were then calculated, and averaged to obtain a single, 1-min CSM which was written to tape. Therefore the deep-water data set CSMs

TABLE I. Number of effective snapshots for the SWDS CSMs. Blank cells indicate the CSMs were not calculated for these combinations of time averages and bandwidths.

Number of time averages	CSM bandwidth		
	1 Hz	2 Hz	3 Hz
1	2.8	5.6	8.4
2	5.6	11.2	16.8
3	8.4	16.8	
4	11.2		
6		33.6	
7	19.6	39.2	
14	39.2	78.4	
21	58.8	117.6	

contained 61 snapshots. Approximately one week of data was processed. A preliminary examination of DMR performance was made with these data.

### 2. Shallow-water data set (SWDS)

Data from the second experiment were obtained using a bottom-mounted horizontal line array located in the Mediterranean Sea in a shallow ocean environment. In this case, the water depth was about 400 m. This array also had eight hydrophones in a tapered design and the length of the array was 3.4 wavelengths relative to the frequency processed.

The data were acquired from the array using an analog tape system and digitized at ARL:UT with a sampling rate of 800 Hz per channel. One minute of data was recorded every 10 min. The time series data were windowed using a Hanning window. The FFTs were calculated using a 4 K transform length with 50% data overlap. The CSMs were calculated with various integration times and frequency bandwidths. For integration times shorter than 1 min, only the first FFTs were used to calculate the CSMs, and the rest of the FFTs for the minute were skipped. Table I shows the number of effective snapshots for the various integration times and frequency bandwidths of the shallow-water data set CSMs. One day of data was processed.

### B. Analysis approach and methodology

The deep-water and the shallow-water data sets were processed on the ARL:UT Alliant and Sun SPARCcenter 2000 computers. First, the data sets were processed using unshaded conventional beamforming (CBF). Following the CBF processing, the data sets were processed with ARL:UT's MVDR and WNGC ABF. These results provide a baseline of results to compare to the DMR performance.

Once the baseline processing was completed, the data sets were screened by calculating the eigenvalues of the CSMs. The number of loud interferers in the environment could be determined from the eigenvalues of the CSM and then  $D$  could be chosen so that all of the loud interferers would be included in the CSM estimate. Next, DMR performance sensitivity to variations in  $e$  and  $\sigma^2$  was examined for the deep-water data set and compared to the baseline results. Initial values of  $e$  and  $\sigma^2$  were chosen that allowed the DMR beamformer performance to emulate the WNGC beamformer

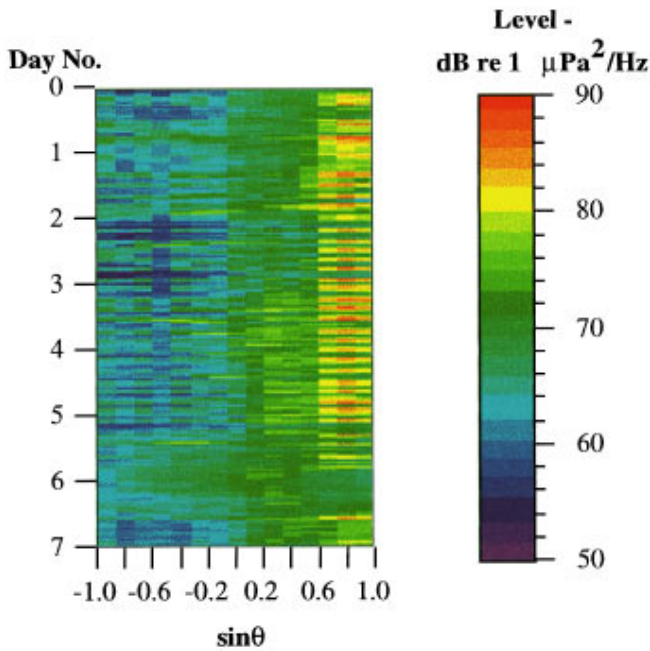


FIG. 1. DWDS CBF beam noise.

performance. Then, DMR performance was examined, with the selected values of  $e$  and  $\sigma^2$ , using CSMs from the shallow-water data set.

## II. DEEP-WATER DATA SET RESULTS

The initial studies using DMR were performed with the deep-water data set (DWDS). In this case CSMs had been calculated with a fixed integration time. Hence only limited

performance assessments could be made without reprocessing. However, the data provide a basis for determining some of the DMR parameters that were used in the shallow-water data set analysis.

Recall that one of the objectives of this study is to determine whether the DMR beamformer can provide performance equivalent to the WNGC beamformer, but use shorter CSM integration times than required by the WNGC beamformer. The WNGC is used as the standard because it has been shown to provide robust gain against interferers for a wide variety of noise fields. Thus the DWDS will be used to determine the parameter values that allow the DMR beamformer to emulate the WNGC beamformer. Then these parameter values will be tested with the shallow-water data set. If the DMR beamformer performance is close to the WNGC beamformer for the other noise environments, then the DMR parameters are satisfactory. It is possible that other settings for the DMR parameters improve the DMR performance. However, this study is interested in determining whether favorable acoustic performance is feasible using the DMR beamformer.

### A. DWDS beam noise

Figure 1 shows the beam noise for unshaded CBF, and Fig. 2 shows the beam noise for MVDR and WNGC ABF. In both figures, a seismic profiler that turns on and off at semi-regular intervals is visible at  $\sin \theta = 0.8$ . The profiler is much louder, by at least 10 dB, than any other noise source. This will influence the number of large eigenvalues in the CSM when the profiler is on.

Comparing the CBF plots (Fig. 1) with the ABF plots (Fig. 2) shows that the ABF noise levels are much quieter

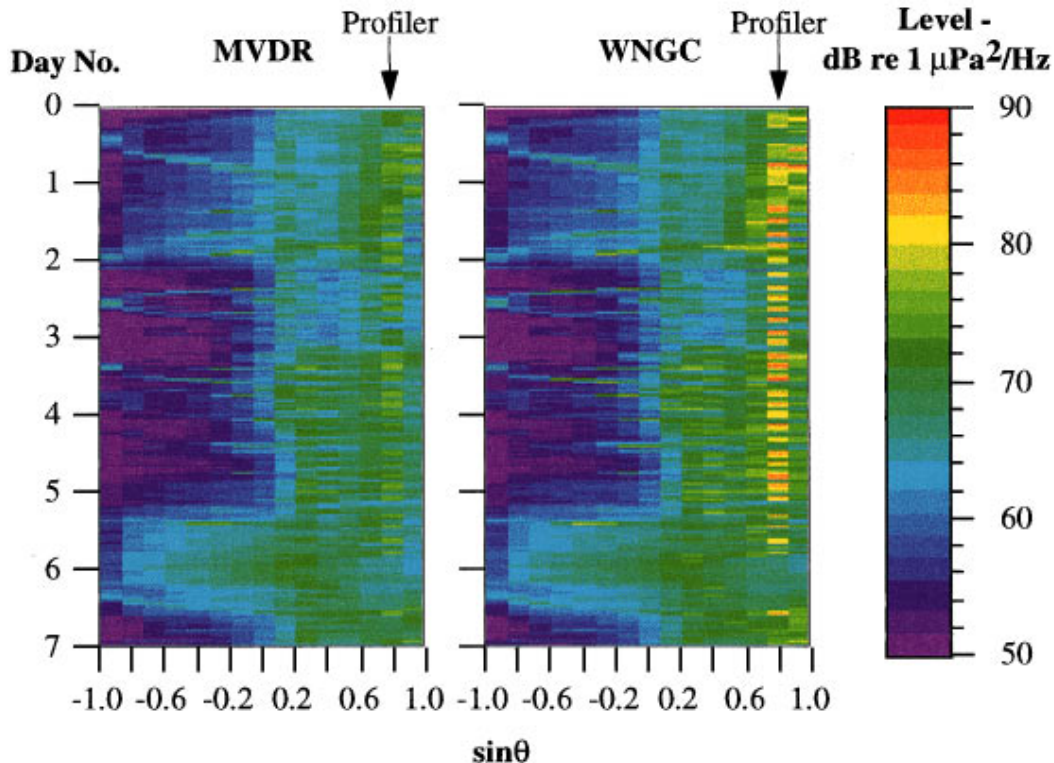


FIG. 2. DWDS WNGC ABF and MVDR beam noise.



than the CBF levels between  $\sin \theta = -1.0$  and  $\sin \theta = 0.0$ . This is because the adaptive beamformer can null out the loud source (at  $\sin \theta = 0.8$ ) when the beamformer is steered in these quiet directions. Also, the WNGC ABF levels are close to the CBF levels in the direction of the interfering source, indicating that the white-noise gain constraint is providing sufficient robustness to restrict losses due to mismatch.

The MVDR levels (Fig. 2), however, are lower than the WNGC ABF levels in the direction of the loud source (at  $\sin \theta = 0.8$ ). This is due to the lack of the white-noise gain constraint for the MVDR case. Since the loud source is not exactly in one of the look directions, the MVDR beamformer squints away from the loud source, reducing its received level. Also, multipath and other sources of mismatch contribute to the reduction in the received level. On the other hand, there is not much difference between the quiet regions in the MVDR and the WNGC ABF plots, indicating that there is very little penalty for setting the white-noise gain constraint to  $-3$  dB.

### B. DWDS eigenvalues

Figure 3 shows the eigenvalues of the DWDS CSM. All the eigenvalues are scaled by the largest eigenvalue so that the largest eigenvalue is always one. In these plots, the number of large eigenvalues varies from one large eigenvalue to three or four large eigenvalues for most time periods. This switching corresponds to the profiler seen in the beam noise plots. This is clear in Fig. 4, which shows the eigenvalues and beam noise together.

When the profiler is on, it dominates the noise field and is associated with the single eigenvalue that is significantly larger (10 dB) than the other eigenvalues (see point A). When the profiler is off, there are several significant noise sources, and consequently there are several eigenvalues of the same order of magnitude (see point B). This is consistent with the assumption that the largest eigenvalues of the CSM are associated with the loudest noise sources in the environment described by the CSM.

For most time periods, the first four eigenvalues contain the top 15–20 dB of the noise field. For this reason, a CSM based on the first four eigenvalues would contain much of the information about the spatial properties of the noise field.

### C. DWDS white-noise gain

Recall that the white-noise gain is a measure of the robustness of a beamformer. Thus in order to evaluate the robustness of the DMR beamformer one can examine the white-noise gain values from the DMR beamformer. The WNGC beamformer is known to be robust to mismatch errors; therefore the white-noise gain values of the DMR beamformer will be compared to the white-noise gain values of the WNGC beamformer. The white-noise gain constraint is set 3 dB below  $10 \log N$ , or at 6 dB, for the WNGC beamformer.

Figure 5 shows the white-noise gain percentiles for MVDR and WNGC ABF. Figure 5 illustrates that the white-noise gain values for the MVDR case can be very small ( $-20$  dB), showing this beamformer is very sensitive to mis-

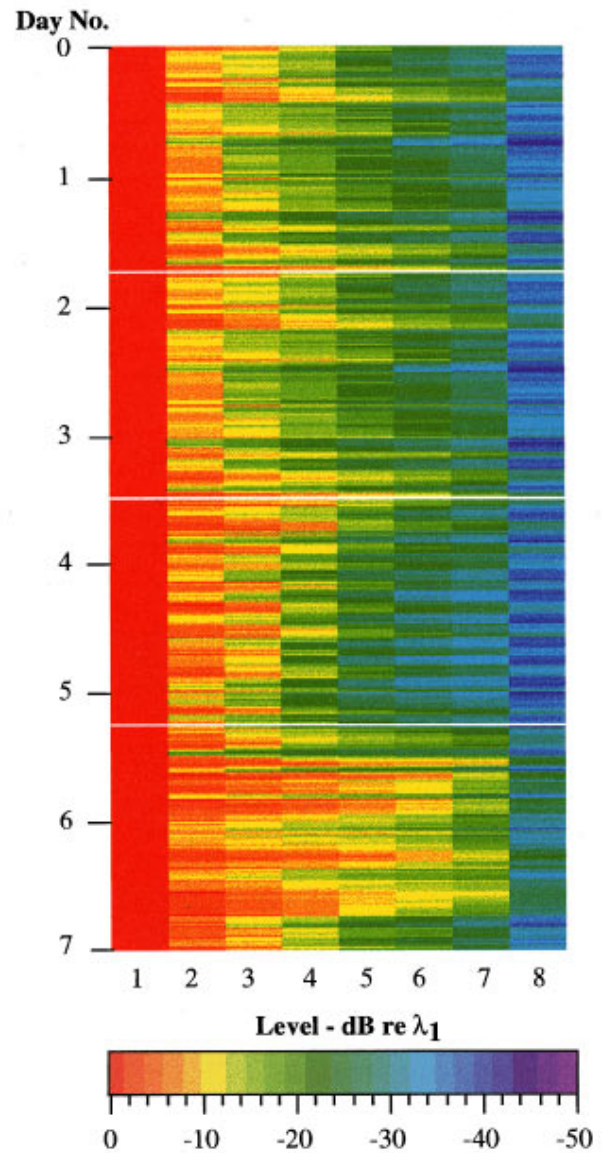


FIG. 3. DWDS eigenvalues in decibels relative to the largest eigenvalue.

match. Many of the low values are associated with times (and look directions) when the beamformer is steered near the loud interferer as seen from Fig. 2. When the white-noise gain constraint is applied, the white-noise gain never falls below 6 dB, and hence provides a guard against mismatch.

### D. Determination of appropriate $\sigma^2$ and $e$ values

As discussed earlier, values of  $e$  and  $\sigma^2$  must be chosen. Recall that  $e$  is used as an “enhancement factor” for the eigenvalues and thus controls the amount of information in the CSM that is used in calculating the weights.  $\sigma^2$  governs the amount of uncorrelated noise added to the diagonal of the CSM. This noise keeps the CSM nonsingular and forces the remainder of the environment described by the reduced rank CSM (i.e., other than the  $D$  dominant sources) to be uncorrelated noise.

In this study, the performance of the DMR beamformer is being compared directly with the fully adaptive beamformer with a white-noise gain constraint set to 3 dB below



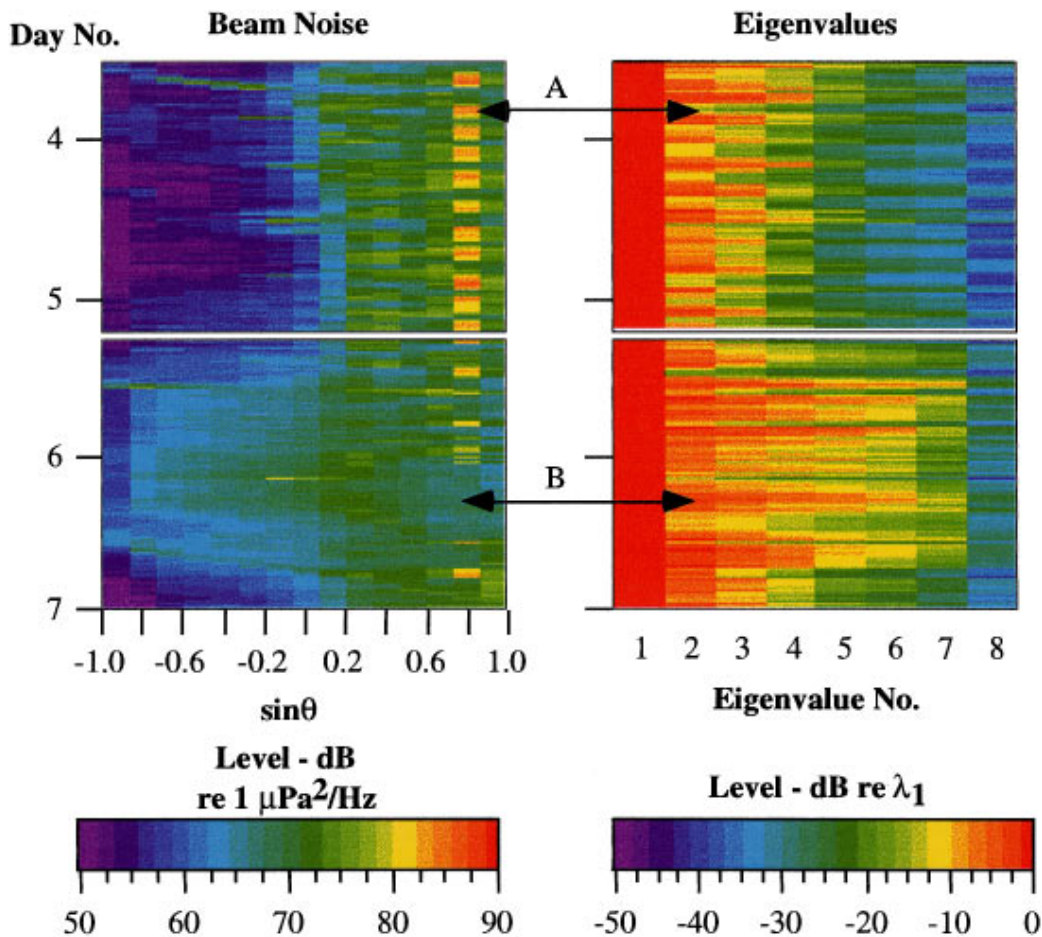


FIG. 4. DWDS beam noise and eigenvalues.

10 log  $N$ . Recall that Fig. 2 showed that this level of the constraint provides reasonable robustness against mismatch, while not penalizing the quiet sector performance. The beam noise and white-noise gain values of a beamformer were used to determine values of  $e$  and  $\sigma^2$  so that the DMR beam noise and white-noise gain values emulated the WNGC beamformer beam noise and white-noise gain values as closely as possible. This was accomplished by processing the DMR beamformer on a small part of the DWDS to examine the sensitivity of the DMR beamformer to  $e$  and  $\sigma^2$ .

### E. DMR sensitivity to $\sigma^2$

To begin the sensitivity studies,  $e$  was set to 1.0 and the DMR beamformer was run for several different values of  $\sigma^2$

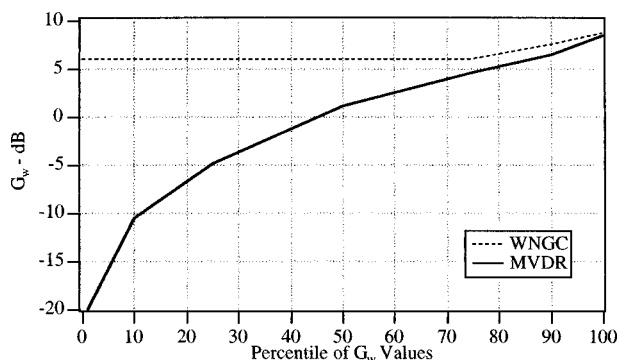


FIG. 5. DWDS MVDR and WNGC white-noise gain percentiles.

for a small amount of the DWDS data. In their work, Abraham and Owsley<sup>2</sup> used  $e$  values of 1 and 10 because they wanted a MUSIC-like angular response spectrum with sharper lobes in the look direction at the expense of the nulls in the direction of the interferers. This study, on the other hand, was more interested in nulls for the interferers than in extremely sharp look direction lobes; therefore,  $e$  values from 0 to 1 were used. For this initial study  $e$  was set to 1.0, because when  $e$  is 1.0 and  $D$  is set to the number of hydrophones in the array, so that all of the eigenvalues and eigenvectors are used to approximate the CSM, the CSM is reconstructed completely and the DMR beamformer is equivalent to the MVDR beamformer.

Figure 6 shows the beam noise for 14 sequences, or 3 h of data, where the value of  $\sigma^2$  has been varied from 0.005 to 0.5. Figure 6 also shows the WNGC ABF result for comparison. It is clear that the beam noise levels in the quiet direction ( $-1.0 \leq \sin \theta \leq 0.0$ ) are dependent on the  $\sigma^2$  selection. Larger values of  $\sigma^2$  show a penalty of increased beam noise. As  $\sigma^2$  decreases the DMR beam noise looks most like the WNGC ABF beam noise. At  $\sigma^2 = 0.005$ , the amount added to the CSM diagonal is 23 dB down from the largest eigenvalue's contribution. Since the noise data of interest (in terms of forming the weights) is contained in the top 10–20 dB, having a  $\sigma^2$  of 0.005 provides a reasonable noise floor.

Figure 7 shows the white-noise gain percentiles for the same cases. It is clear that the white-noise gain values are not

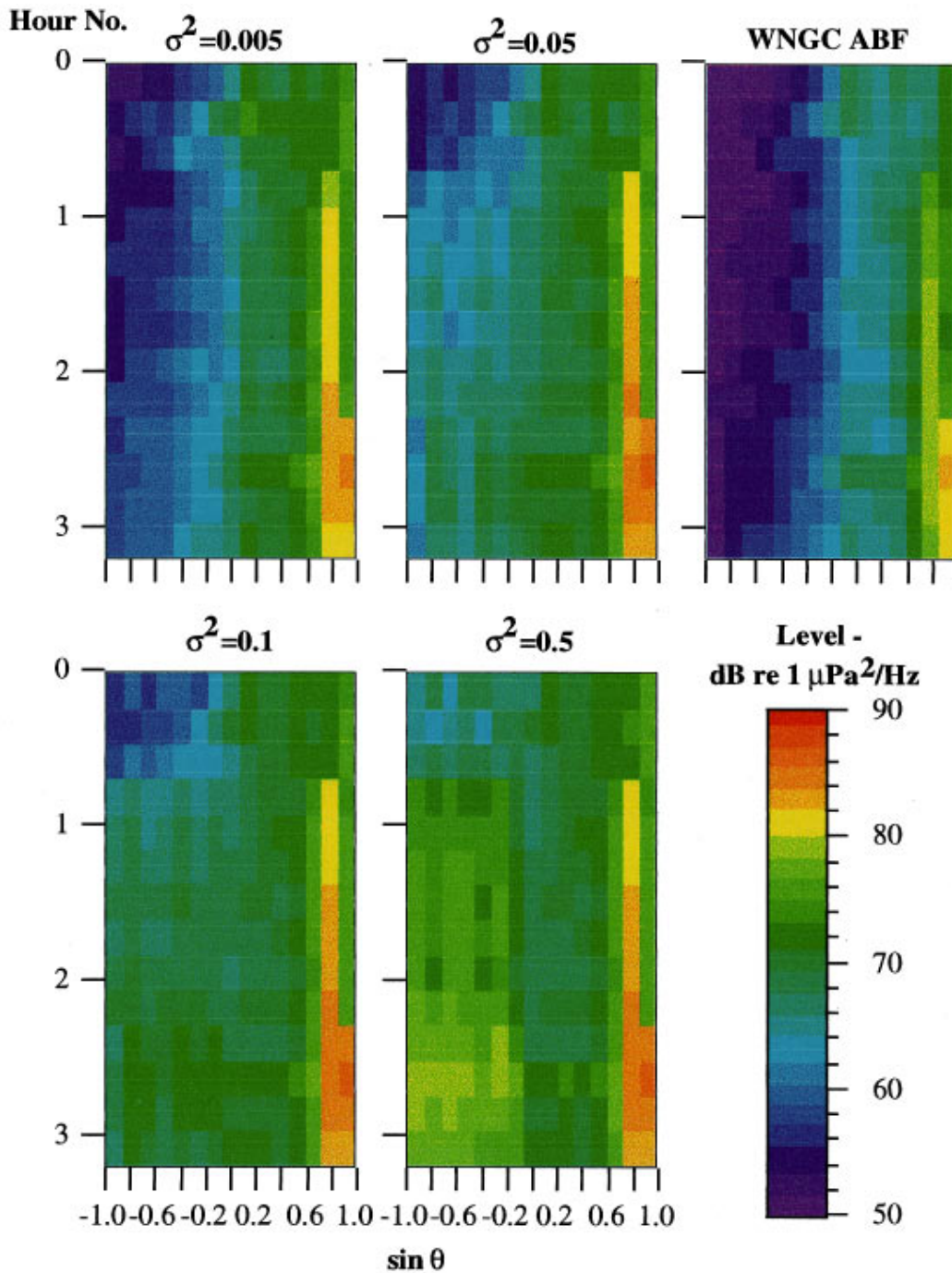


FIG. 6. DWDS DMR beam noise with  $e = 1.0$  and varying values of  $\sigma^2$ .

effected in any organized manner by the choice of  $\sigma^2$ . Thus the beam noise values were used to determine the value of  $\sigma^2$  for the DMR beamformer. Consequently,  $\sigma^2$  was chosen to be 0.005 because this value provides a reasonable noise floor, and with this value the DMR beam noise looks most like the WNGC ABF beam noise. Next,  $\sigma^2$  was set to 0.005 and the DMR beamformer was run for several different values of  $e$ .

#### F. DMR sensitivity to $e$

Figure 8 shows the beam noise for the same 3 h of data, but this time the value of  $\sigma^2$  has been set to 0.005 and the

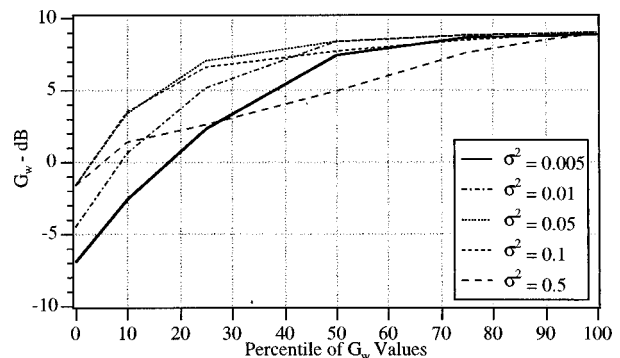


FIG. 7. DWDS DMR white-noise gain percentiles for  $e = 1.0$  and varying values of  $\sigma^2$ .

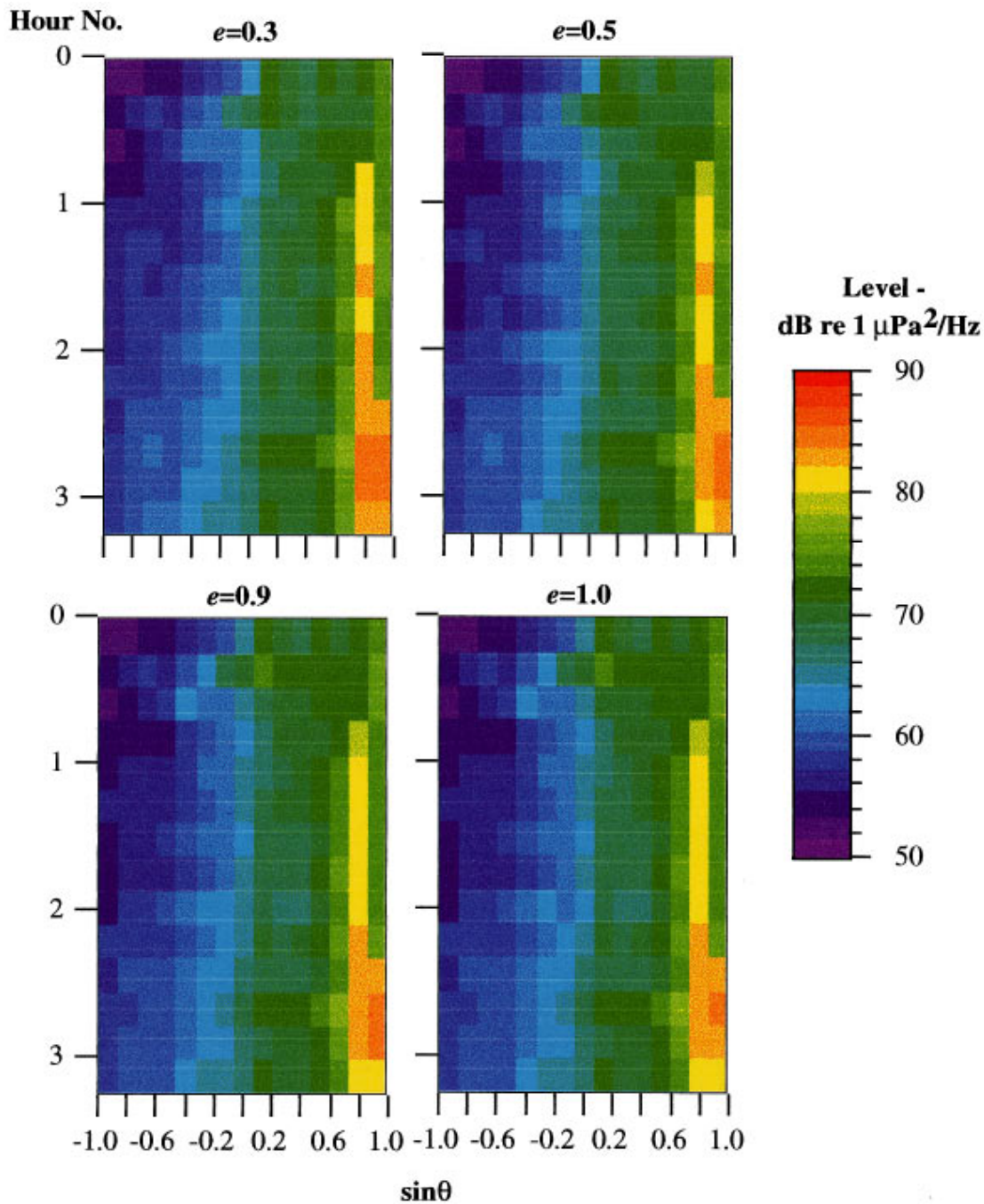


FIG. 8. DWDS beam noise with  $\sigma^2=0.005$  and varying values of  $e$ .

value of  $e$  has been varied from 0.3 to 1.0. It is clear that there is very little difference between the beam noise plots for different values of  $e$ ; hence the beam noise levels do not greatly depend on the selection of  $e$ . Thus the white-noise gain statistics were used to determine the value of  $e$  for the DMR beamformer.

Figure 9 shows the white-noise gain results for the same cases. Unlike the earlier plots with different values of  $\sigma^2$ , the white-noise gain plots are affected by the choice of  $e$ . Larger values of  $e$  show a penalty of decreased white-noise gains, which means the beamformer is more sensitive to mismatch. As  $e$  decreases, the DMR white-noise gain statistics look most like the WNGC ABF white-noise gain statistics.

The  $e=0.5$  value was chosen because the 25% point is

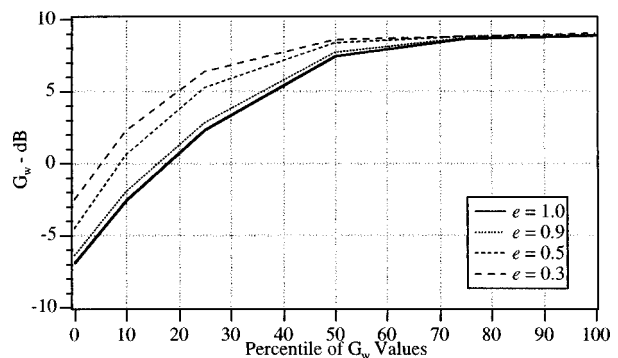


FIG. 9. DWDS DMR white-noise gain for  $\sigma^2=0.005$  and varying values of  $e$ .



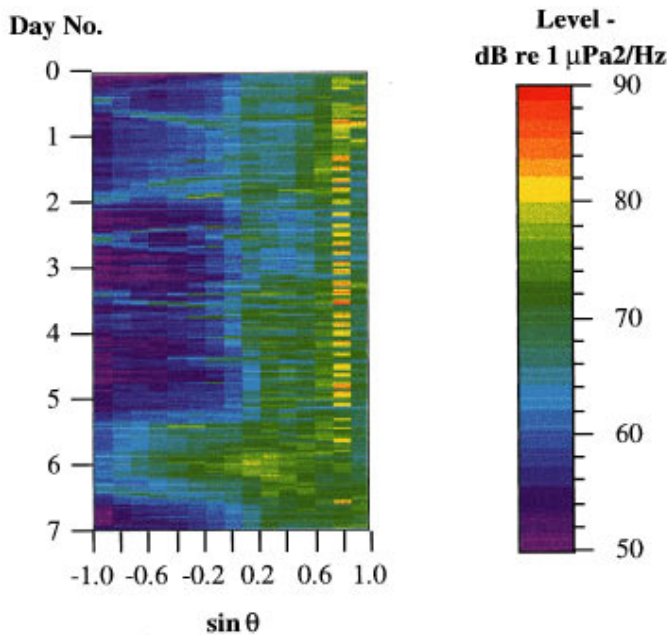


FIG. 10. DWDS DMR beam noise.

approximately 5 dB and the 10% point is above 0 dB. This means that almost 75% of the white-noise gains are above 5 dB and 90% of the white-noise gains are above 0 dB. This is to be compared with the WNGC ABF statistics where all of the white-noise gains are constrained above 6 dB. Thus almost 75% of the DMR white-noise gain values are equivalent to the WNGC white-noise gain values. Also, most of the low white-noise gain values are from times when the beamformer is pointed at the profiler, where there is less concern about signal suppression.

The final values for  $e$  and  $\sigma^2$  using the DWDS are 0.5 and 0.005, respectively. These values allow the DMR beamformer to show similar gains in the quiet directions and similar levels of robustness relative to the WNGC beamformer. These values were chosen by processing the DMR beamformer with a constant  $e$  and varying values of  $\sigma^2$  to choose a value for  $\sigma^2$ . Then, the data were processed with the DMR beamformer using the chosen value of  $\sigma^2$  and varying values of  $e$  to choose a value for  $e$ . This method is justified because  $e$  and  $\sigma^2$  have a linear relationship with respect to the reduced-rank CSM estimate from Eq. (10). Thus each variable should affect the reduced-rank CSM estimate independently. These settings were based on a small fraction of the DWDS data. Given these settings, it is important to determine how well the DMR beamformer performs for the entire data set.

### G. DWDS DMR beam noise

Figure 10 shows the beam noise from the DMR beamformer for the whole week of data with  $D=4$ ,  $e=0.5$ , and  $\sigma^2=0.005$ . Recall that the goal of the DWDS calculations was to determine the values of  $e$  and  $\sigma^2$  that caused the DMR beamformer to perform most like the WNGC beamformer. A comparison of the DMR beam noise with the CBF and ABF beam noise from Figs. 1 and 2 shows that the DMR noise levels are very similar to the WNGC ABF levels.

Between  $\sin \theta=0.0$  and  $\sin \theta=1.0$  the DMR beam noise is almost identical to the WNGC ABF beam noise. Also, the DMR beam noise levels are close to the CBF beam noise levels in the direction of the loud interferer at  $\sin \theta=0.8$ . Thus the DMR beamformer is providing sufficient robustness to restrict the losses due to mismatch. Like the WNGC ABF case, the DMR beam noise is much quieter than the CBF beam noise between  $\sin \theta=-1.0$  and  $\sin \theta=0.0$ , because the DMR beamformer nulls out the loud source at  $\sin \theta=0.8$ .

### H. DWDS summary

The DWDS analysis shows that the DMR beamformer appears to work as expected. The DMR beamformer has more parameters to adjust than the standard adaptive beamformer. The number of eigenvalues  $D$  must be chosen as well as the scalar enhancement factor  $e$  and the noise factor  $\sigma^2$ ; however,  $e=0.5$  and  $\sigma^2=0.005$  appear to work well on the DWDS data. With these values for  $e$  and  $\sigma^2$ , the DMR beamformer suitably emulates the WNGC beamformer. Thus the parameters found for this application of DMR seem reasonable. The DWDS analysis indicates that favorable acoustic performance is possible using the DMR beamformer, provided the DMR settings are not overly sensitive to the noise environment. The next section will test these settings with a different noise environment.

## III. SHALLOW-WATER DATA SET RESULTS

Only CSMs with 1-min integration times were available from the deep-water data set. Therefore the initial studies using DMR were performed on the deep-water data set and the initial values for  $D$ ,  $\sigma^2$ , and  $e$  were chosen. Following this work, additional processing was performed on a second data set that had different CSM integration times. The shallow-water data set (SWDS) was used to determine if the DMR beamformer could overcome the bias errors associated with standard adaptive beamformers with the reduced CSM integration times.

### A. SWDS beam noise

Figures 11 and 12 show the WNGC ABF and MVDR beam noise for CSMs that had 2.8, 5.6, 19.6, and 58.8 snapshots (corresponding to 2.5-, 5.1-, 17.9-, and 53.8-s integration time). These are the number of effective snapshots due to the windowing and overlapping of the SWDS FFTs. From these plots it is clear that the beam noise for the SWDS decreases as the CSM integration time decreases. Recall that the accuracy of the CSM is directly proportional to the integration time of the CSM. When the integration time is small, the CSM estimate is inaccurate and the standard adaptive beamformer will give biased results. Hence the beam noise results for the 2.8 and 5.6 snapshot CSMs for WNGC ABF and MVDR are biased low. The beam noise bias also affects the signal on boresight as well. It is important to note that work at ARL:UT<sup>6</sup> has shown that the SNR of signals on boresight decreases as the beam noise decreases. Thus the biased noise estimates do not indicate improved perfor-

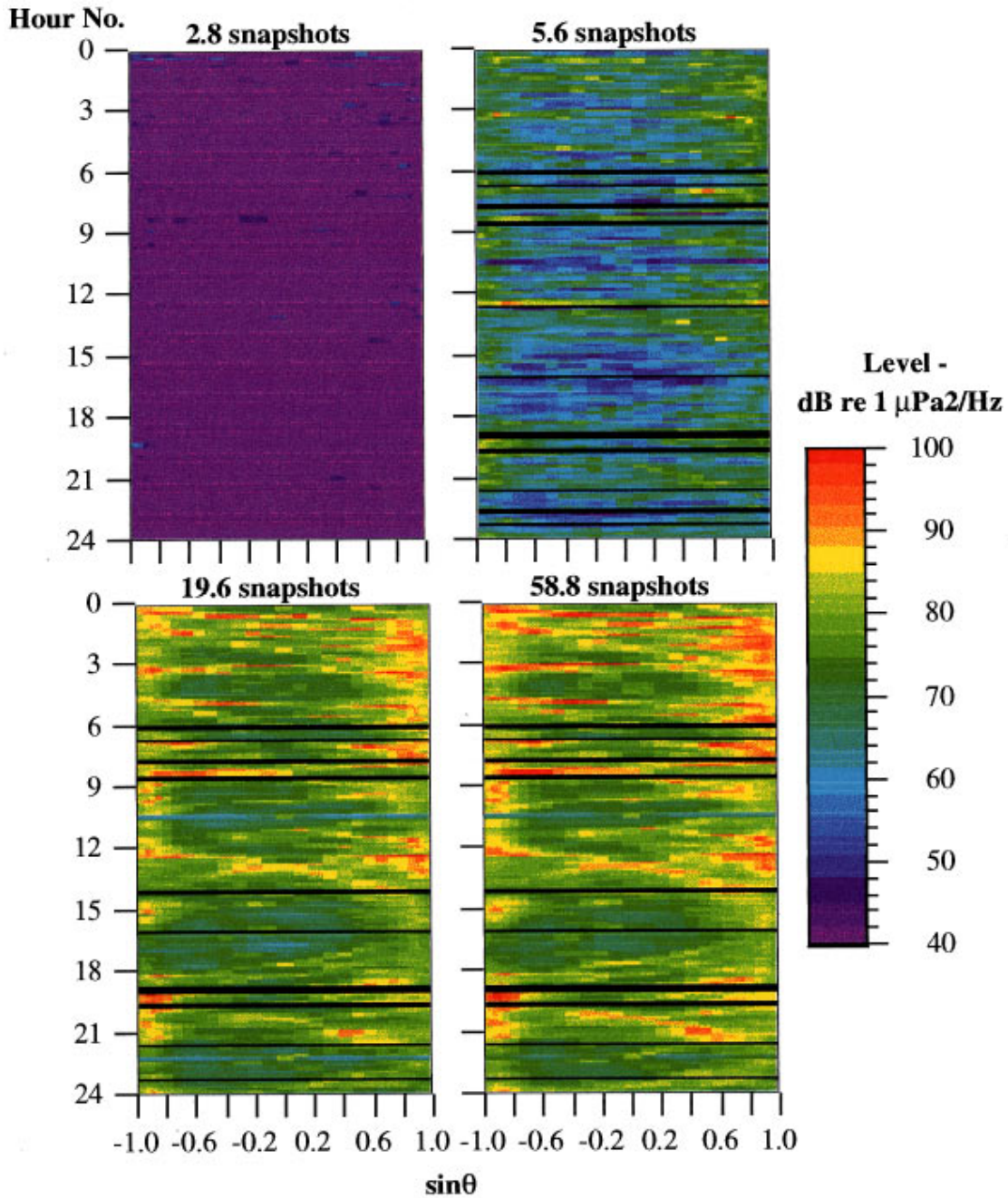


FIG. 11. SWDS MVDR beam noise. (The black bands in the data are times when the analog tape data were of insufficient quality to create time-aligned FFTs. The colorbar indicates these data, set to 0 dB, as black. In the 2.8 snapshot case, the black region in the colorbar was eliminated to prevent most of the images from being black due to its low levels.)

mance. The eigenvalues of the CSMs for this data set give some insight about why the beam noise is biased.

### B. SWDS eigenvalues

Figure 13 shows the eigenvalues of the CSM. Again, all the eigenvalues are scaled so that the largest eigenvalue is always one. Figure 13 shows that the last three eigenvalues of the CSMs made with 2.8 snapshots are extremely small. When the standard adaptive beamformer used these eigenvalues it gave the biased beam noise results seen in Figs. 11 and 12. This is because the weights are a function of the inverse of the CSM and the inverse of the CSM is inversely

proportional to the eigenvalues. Thus if one or more of the eigenvalues are very small, they will dominate the solution, and if the eigenvalues are small and wrong, the solution will also be wrong. However, the DMR beamformer only uses the  $D$  largest eigenvalues, so if  $D$  is chosen to be less than five, the DMR beamformer should give better results than the standard adaptive beamformer.

For this study  $D$  was also chosen to be four because the first four eigenvalues contain the top 15 dB of the noise field. Then the DMR beamformer was run with the values of  $\sigma^2$  and  $e$  that were found to work best with the deep-water data set and the DMR beam noise was examined.



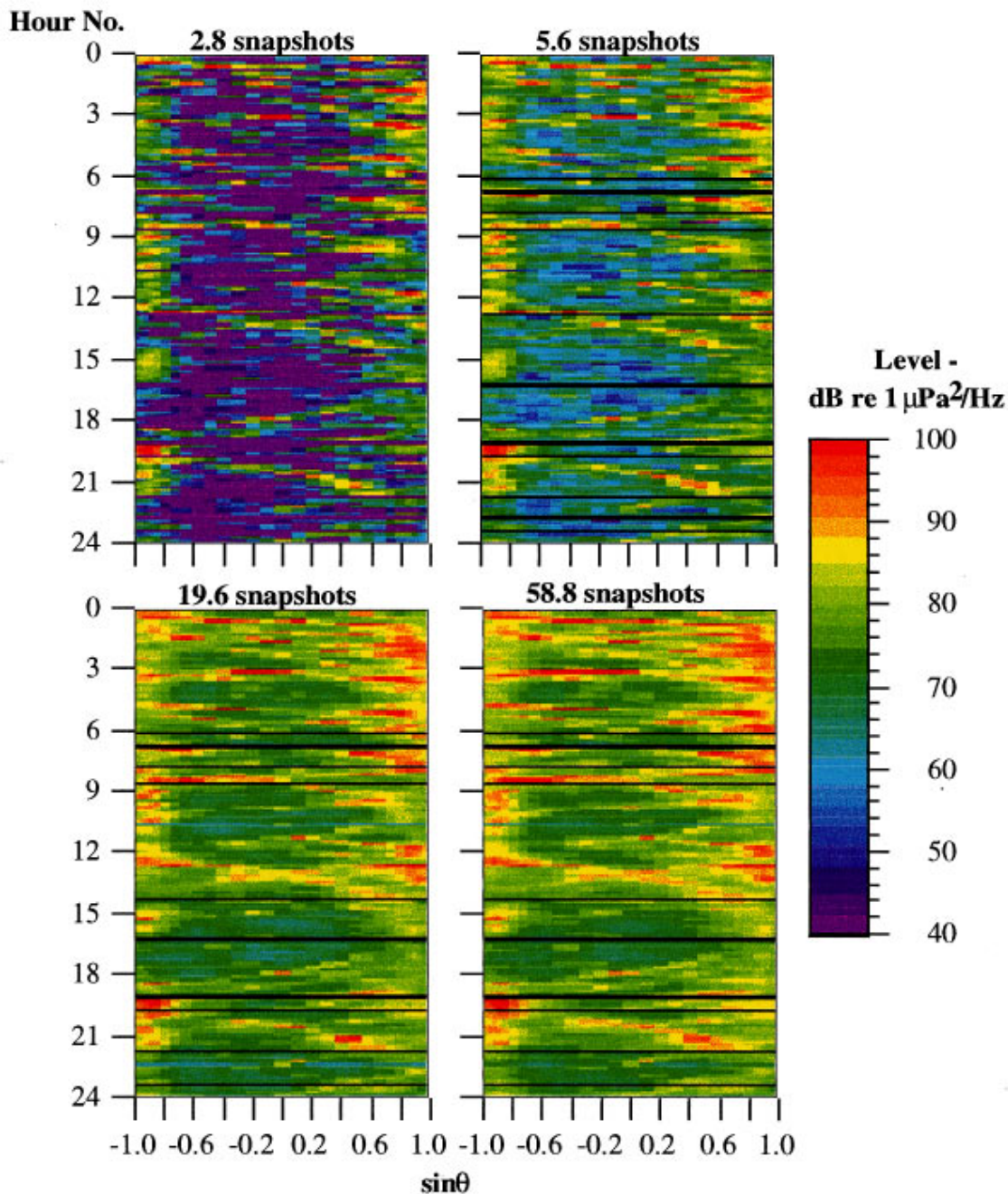


FIG. 12. SWDS WNGC ABF beam noise. (The black bands in the data are times when the analog tape data were of insufficient quality to create time-aligned FFTs. The colorbar indicates these data, set to 0 dB, as black. In the 2.8 snapshot case, the black region in the colorbar was eliminated to prevent most of the images from being black due to its low levels.)

### C. SWDS DMR beam noise

Figure 14 shows the beam noise plots for the DMR beamformer with  $D=4$ ,  $\sigma^2=0.005$ ,  $e=0.5$ . Compared to Figs. 11 and 12, the beam noise for the CSMs with the small integration times is more realistic when using the DMR beamformer. Hence the beam noise bias is reduced with the DMR beamformer. Further, the beamformer performs well with the parameter values derived from the DWDS, indicating that the DMR beamformer's performance in different noise environments is not overly sensitive to the  $\sigma^2$  and  $e$  settings.

An examination of these figures in more detail shows the

DMR beamformer beam noise based on the 2.8 and 5.6 snapshot CSMs is much closer to the 19.6 and 58.8 snapshot CSM beam noise derived using WNGC ABF. For WNGC ABF, the 2.8 snapshot CSM beam noise is 30–40 dB quieter and the 5.6 snapshot CSM beam noise is 10–20 dB quieter than the 19.6 and 58.8 snapshot CSM beam noise. In contrast, the DMR beam noise using the 5.6 snapshot CSMs is only 4 dB quieter than the WNGC 19.6 snapshot CSM beam noise.

Grant *et al.*<sup>1</sup> found that for the SWDS, the best WNGC ABF results were obtained using a CSM estimate with approximately 19.6 snapshots. That is, with 19.6 snapshots, the

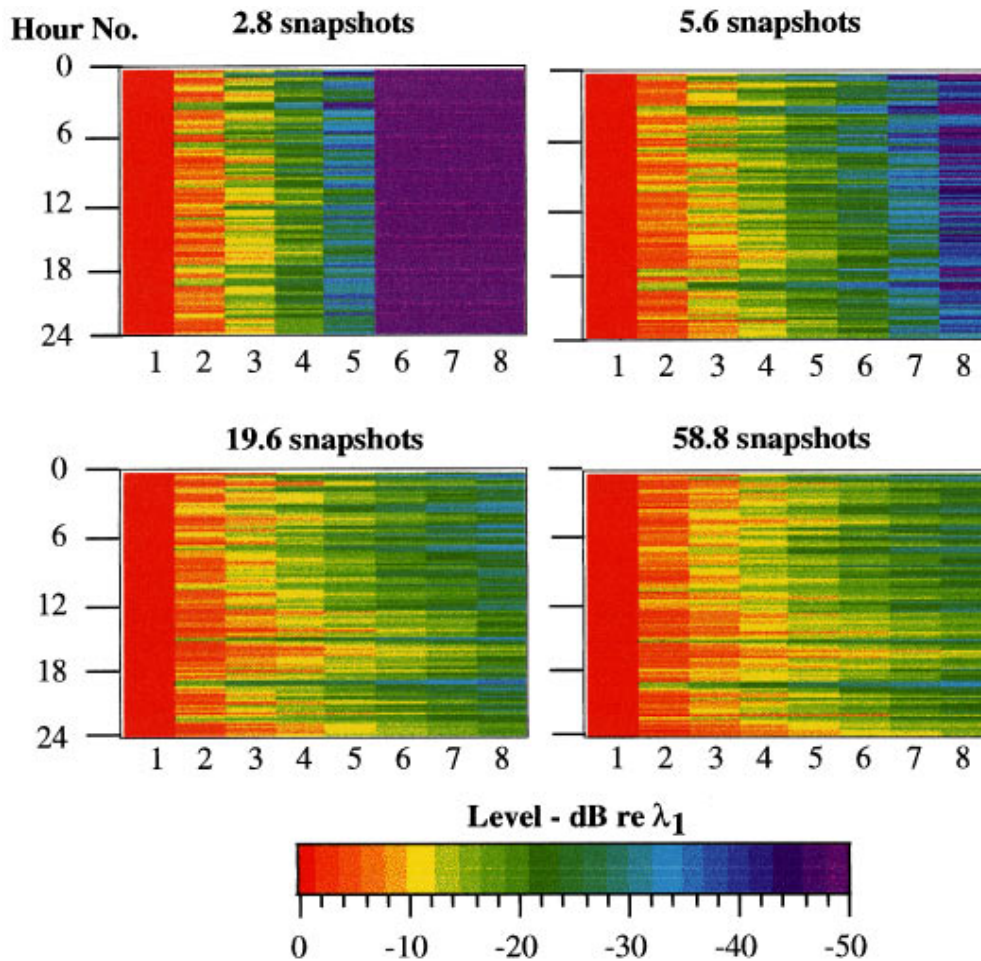


FIG. 13. SWDS eigenvalues.

integration time is sufficient to limit the noise bias to acceptable levels, and the integration time is sufficiently short to capture the dynamics of the noise. The DMR beamformer beam noise from the 5.6 snapshot CSM is close to the WNGC beamformer beam noise from the 19.6 snapshot CSM. Therefore for this data set, the DMR beamformer could be used with the 5.6 snapshot CSM, lowering the required integration time by a factor of 3.5. Given that a longer integration time can be used for the noise environment, an array with more hydrophones could be used, with the number of eigenvalues appropriately set for 19.6 snapshots. Thus additional gain might be attainable without increasing the CSM integration time.

#### D. SWDS beam noise reduction

Grant *et al.*<sup>1</sup> developed an expression of the MVDR beamformer output bias as a function of the number of snapshots. Figure 15 shows this expression assuming four and eight dominant modes in the CSM. Also plotted is the normalized median beam noise for the broadside beam from the standard adaptive beamformer and the DMR beamformer. In other words, the beam noise time series for the broadside beam for each case was extracted, and the median computed. The broadside beam was chosen because the beam noise is relatively quiet, and the beam noise bias can be clearly seen

in this area. Each noise value was normalized by the noise value for the 117.6 snapshot case, and the 117.6 snapshot cases were matched with the theoretical curve.

The results in Fig. 15 show that the ABF results fall with decreasing averages, as expected, but the DMR results are not quite as good as the theory suggests. WNGC ABF and MVDR were run using all eight eigenvalues of the CSMs, and the WNGC ABF and MVDR points follow the  $D=8$  curve. The DMR beamformer was run using  $D=4$  eigenvalues; therefore the DMR points should follow the  $D=4$  curve. However, the output power for the DMR data falls off faster than the  $D=4$  curve and is closer to the  $D=8$  curve. This mismatch may be due to the beam picked as representative of the quiet beam. Although the data corresponding to the  $D=8$  case follow the curve, this trend may have been fortuitous for this case. A more accurate measure would be to pick a representative beam (e.g., the quartile beam) at each scan, and determine the mean of these values. Still, the plot above does show that when the number of snapshots is less than 15, the DMR beamformer reduces the beam noise bias over MVDR and WNGC ABF. Also, the DMR values are much more consistent than the fully adaptive values, indicating the method is more robust to changes in the enhancement factor ( $e$ ) value.



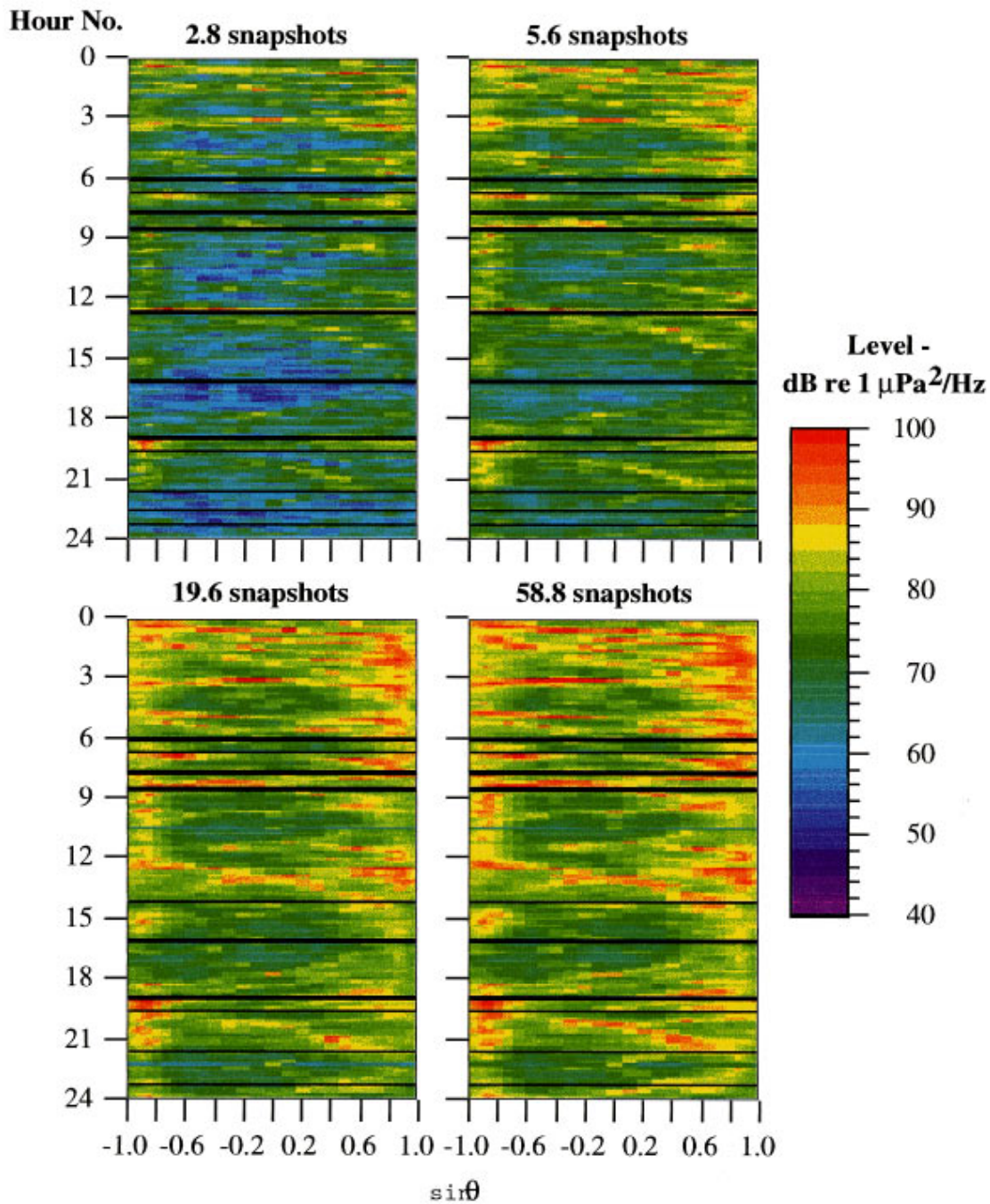


FIG. 14. SWDS DMR beam noise with  $D=4$ ,  $\sigma^2=0.005$ , and  $e=0.5$ .

### E. SWDS summary

The SWDS analysis shows that the DMR beamformer reduces the beam noise bias for CSMs with low integration times when using either  $e=1.0$  or  $0.5$ , and  $\sigma^2=0.005$ . Thus more realistic performance estimates can be made with CSMs that have reduced integration times by using the DMR beamformer. The estimated bias (based on the quiet-beam beam noise values) appears to increase faster than theory suggests for DMR; but the bias at very small CSM integration times is much smaller than that for the fully adaptive beamformer. Thus the DMR beamformer may have some attractive features for arrays with many elements that are deployed in highly dynamic noise environments, where shorter integration times may be needed.

### IV. CONCLUSIONS

The dominant mode rejection beamformer calculates adaptive weights based on a reduced rank CSM estimate, and appears to work as expected. The DWDS was used to determine initial values for the DMR parameters, and the results showed that the performance of the DMR beamformer is comparable (in terms of robustness and noise rejection) to the fully adaptive WNGC beamformer. The DMR parameter values derived using the DWDS gave DMR beamformer performance close to the WNGC beamformer when processing the SWDS. Thus it appears that these settings provide robust performance for the DMR beamformer, and that the DMR beamformer is not overly sensitive to these parameter values.



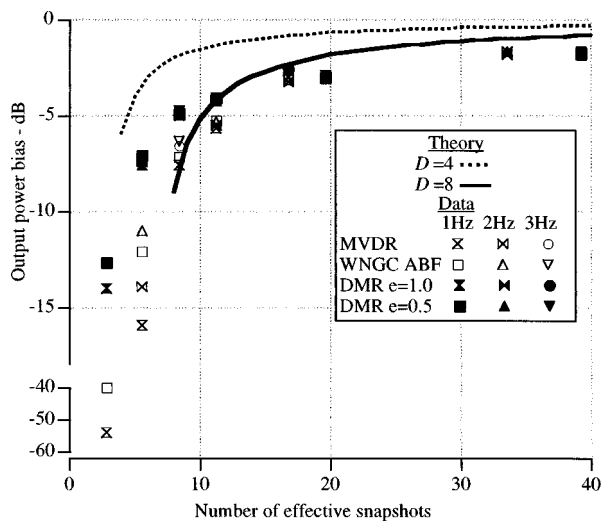


FIG. 15. SWDS beam noise loss due to CSM averaging.

The SWDS results also showed that DMR beamformer performance comparable to a fully adaptive beamformer could be achieved, without the penalties associated with the required increased integration time for the CSM. Further, the noise bias evident with the WNGC ABF and MVDR cases was noticeably reduced in the DMR results. Although the bias seen with DMR increased faster (with a reduction in

integration time) than theory predicts, the bias reduction relative to the fully adaptive solution makes DMR attractive for highly dynamic noise environments where reduced integration times may be needed.

## ACKNOWLEDGMENTS

This work was sponsored by the U.S. Navy Space and Naval Warfare Systems Command, under the technical direction of Capt. William Hatcher and Mr. J. P. Feuillet. This source of support is gratefully acknowledged.

<sup>1</sup>D. E. Grant, J. H. Gross, and M. Z. Lawrence, "Cross-spectral matrix estimation effects on adaptive beamforming," *J. Acoust. Soc. Am.* **98**, 517–524 (1995).

<sup>2</sup>D. A. Abraham and N. L. Owsley, "Beamforming with dominant mode rejection," *Oceans '90 Conference Proceedings* (1990), pp. 470–475.

<sup>3</sup>H. Cox, R. M. Zeskind, and M. M. Owen, "Robust adaptive beamforming," *IEEE Trans. Acoust., Speech, Signal Process.* **ASSP-35**, 1365–1376 (1987).

<sup>4</sup>R. A. Gramann, "ABF algorithms implemented at ARL:UT," Applied Research Laboratories Technical Report No. 92-7 (ARL-TR-92-7), Applied Research Laboratories, The University of Texas at Austin, 1992.

<sup>5</sup>T. R. Messerschmitt, "Evaluation of the dominant mode rejection beamformer for passive sonar applications," M.S. thesis, The University of Texas at Austin, 1995.

<sup>6</sup>Work at ARL:UT using correlation methods to infer SNR from the output of the beamformer have shown that along with the reduced output power, low SNR signals lose SNR as the bias increases. Thus signal power is lost faster than the noise power, resulting in lower SNR while using fewer snapshots to estimate the CSM.

# Laboratory measurements of current flow using cross correlation on acoustic backscattering from suspended sediments

Robert F. van Unen

*The Oceanographic Company of the Netherlands/OCN B.V., P.O. Box 7429, 2701 AK Zoetermeer, The Netherlands*

Peter D. Thorne

*Proudman Oceanographic Laboratory, Bidston Observatory, Birkenhead, Merseyside L43 7RA, United Kingdom*

Henk Cox and Sicco D. Kamminga<sup>a)</sup>

*National Institute for Coastal and Marine Management/RIKZ, P.O. Box 2097, 2500 EX The Hague, The Netherlands*

(Received 7 November 1997; accepted for publication 1 May 1998)

The application of acoustic backscattering, for measuring near-bed high-resolution profiles of suspended sediment concentration and particle size, has advanced substantially in recent years. To interpret these suspension observations and link them with the hydrodynamics, similarly detailed flow observations would be advantageous. In the present work backscattering from suspensions of marine sediments has been investigated to examine the potential of using the backscattered signal to also measure high-resolution near-bed vertical profiles of horizontal current flow. The approach adopted has been to attempt to utilize the temporal coherence in the suspension field, and to employ cross correlation of the backscattered signal between pairs of horizontally separated transducers to measure current profiles. To investigate this technique a series of laboratory measurements have been conducted for a variety of experimental arrangements, and the outcome from these measurements is reported in the present work. An examination of the suspension field has been conducted, and cross correlations between pairs of transducers investigated. Using cross-correlation time lags, current profiles have been calculated, and the results assessed using laser Doppler flow measurements. Comparison of the acoustic cross-correlation flow measurements with the Doppler reference measurements show a high degree of agreement, and strongly support the use of the cross-correlation approach to accurately measure vertical profiles of the mean horizontal current. © 1998 Acoustical Society of America. [S0001-4966(98)00309-9]

PACS numbers: 43.30.Ft, 43.30.Gv, 43.30.Pc, 43.30.Xm [DLB]

## INTRODUCTION

The measurement and understanding of sediment processes and transport is a central component in the prediction and management of coastal morphological change. Our capability to predict morphological evolution is limited in part by the lack of an accurate description of some of the fundamentals of sediment processes. In recent years acoustics backscattering has been applied to try and improve our capability to measure the mechanisms of near-bed suspended sediment dynamics, and this approach has been gaining increasing acceptance by the sedimentological community. The nonintrusive profiling capability, coupled with high temporal and spatial resolution, is providing new opportunities to examine the processes of how waves and currents entrain and sustain sediments in suspension. To date the near-bed application of acoustics has primarily focused on measuring suspension parameters, normally mean particle size and concentration.<sup>1-4</sup> However, there is increasing interest in developing near-bed high-resolution acoustic systems to simul-

taneously monitor the flow and the suspended sediment concentration, and hence determine sediment fluxes directly.

Although acoustic Doppler current profilers<sup>5</sup> are standard instruments for measuring currents over tens to hundreds of meters, it is only relatively recently that coherent Doppler systems with the more appropriate centimetric resolution for near-bed suspended sediment studies have been reported.<sup>6-8</sup> Vertical profiles of the horizontal current can be obtained using such systems by directing the transducer downwards at an angle to the vertical, and measuring the component of the horizontal flow along the beam. However, there are disadvantages in using a configuration that is not vertical. The interpretation of the interaction of the hydrodynamics with the suspension processes is more difficult to interpret when the profiles of the horizontal flow are not vertical, the contribution of the vertical velocity component along the beam contaminates the horizontal flow estimate, and bed echoes from sidelobes which are reflected with zero velocity can make interpretation of the very near-bed velocity estimates problematic.

In the present work<sup>9,10</sup> a complementary approach has been investigated to measure vertical profiles of the horizon-

<sup>a)</sup>Present address: P.O. Box 7435, 2701 AD Zoetermeer, The Netherlands.

tal flow. Advantage is taken of the possibility that in naturally occurring sediment transport processes there will be a degree of temporal coherence in the suspension field. It is anticipated that by using pairs of horizontally separated transducers to measure vertical profiles of the backscattered signal from sediments in suspension, it should be possible to apply cross-correlation techniques to also measure profiles of the current. Such an arrangement avoids the necessity of using a nonvertical configuration to obtain vertical profiles of the horizontal current.

The present paper reports on a series of laboratory measurements taken in a recirculating flume where a cross-correlation approach was adopted to measure mean current profiles. Although the measurements were conducted in a laboratory flume, it is indicated in the text that some of the important features of the observed suspension field have common links with those in the natural environment. Therefore it is expected that the observations should provide a useful indication of the potentiality of the present technique in the marine environment.

The aim of the work has been to explore the cross-correlation approach using suspended sediments, and to focus on mean flow averaged over records, each of which were 15 s in duration. Furthermore the present analysis is centered on rectilinear flow, and the more problematic case of high temporal resolution cross-correlation flow measurements under waves is not featured in the present work. Measurements of the backscattered signal from four transducers of varying separations, and under differing flow rates and suspended sediment concentration levels were collected. These data have been analyzed to examine the potential of the correlation technique to measure current flow. To assess the outcome of the cross-correlation approach, independent observations of the flow were obtained using a laser Doppler system. The laser data have been used as an independent benchmark with which to evaluate the cross-correlation approach.

## I. THEORY

The theoretical description of the interaction of sound with a suspension of marine sediments has developed significantly in recent years. These advances have been supported by laboratory measurements on the scattering by suspensions of spheres<sup>11</sup> and marine sands,<sup>12-14</sup> and the deployment of acoustic backscatter systems in the marine environment.<sup>15-18</sup> The result of these works shows that for incoherent scattering with suspension attenuation accounted for, but not multiple scattering, the ensemble average square backscattered pressure  $P^2$  for a piston transceiver can be written as

$$P^2 = \left\{ \frac{k_s k_t}{\psi r} \right\}^2 M e^{-4\alpha r}, \quad k_s = \frac{f}{\sqrt{\rho a_s}}, \quad (1)$$

$$k_t = P_0 r_0 \left\{ \frac{\Gamma c}{16} \right\}^{1/2} \frac{0.95}{ka_t}, \quad \alpha = \alpha_w + \frac{1}{r} \int_0^r \zeta M dr.$$

$k_s$  is a sediment dependent parameter; with  $f$  being the form function for the sediment in suspension,  $\rho$  the density of the sediment, and  $a_s$  the radius of the particles in suspension.  $k_t$

contains system-dependent parameters;  $P_0$  is the pressure at range  $r_0$  (usually 1 m),  $\Gamma$  is the transmitted pulse duration,  $c$  is the velocity of sound in water,  $k$  is the wave number of the sound in water, and  $a_t$  is the radius of the piston source.  $\alpha_w$  is the attenuation due to water, and  $\zeta$  is the sediment attenuation constant.  $M$  is the mass concentration of the sediment in suspension,  $r$  is the range from the transducer, and  $\psi$  accounts for the departure from spherical spreading of the backscattered signal within the transducer near field. The ensemble average square pressure is required to be calculated to mitigate the effects of configurational noise<sup>11,15</sup> due to the random phase distribution of the backscatter signals from the particles in theinsonified volume. It can be seen in Eq. (1) that the mean-square pressure is directly related to the suspended sediment concentration, and it is the fluctuations in the concentration field which are used in the correlation approach to measure profiles of the horizontal current flow.

Using a transceiver pair, cross-correlation analysis was conducted on the time series of the ensemble average square backscatter signal, for each range sample, to obtain a current profile. The cross-correlation function,  $R_{12}(\tau)$  at range  $r$  is given by

$$R_{12}(\tau) = \int_{-\infty}^{\infty} p_1^2(t, r) p_2^2(t + \tau, r) dt, \quad (2)$$

where  $p_1^2(t, r)$  and  $p_2^2(t, r)$  are the zero mean backscattered ensemble average square pressures from the transceiver pair,  $p_i^2(t, r) = P_i^2 - \langle P_i^2 \rangle$ ,  $i = 1$  or  $2$ ,  $\langle \rangle$  represents a time average over the record length, and  $\tau$  is the lag. In the present study the normalized cross-correlation function is used to enable comparisons to be readily made. This is written as

$$\rho_{12}(\tau) = \frac{R_{12}(\tau)}{\sqrt{R_{11}(0)R_{22}(0)}}. \quad (3)$$

The time lag at which the normalized cross-correlation function reaches its maximum value is referred to as  $\tau^*$ .

$$\rho_{12}(\tau^*) = \max(\rho_{12}(\tau)). \quad (4)$$

The cross-correlation velocity,  $v_c$ , is then simply obtained using

$$v_c = d_{12} / \tau^*, \quad (5)$$

where  $d_{12}$  is the separation distance between the transducer pair.

To obtain an estimate for the error in the cross-correlation measurements, the standard deviation in  $\tau^*$  was calculated using<sup>19</sup>

$$\sigma_{12}(\tau^*) = \left\{ \frac{0.038(2\gamma_{12})^3}{T} \left( \frac{1}{\rho_{12}^2(\tau^*)} - 1 \right) \right\}^{1/2}. \quad (6)$$

$T$  is the record length, and  $\gamma_{12}$  is the width of the cross-correlation function  $\rho_{12}(\tau)$  at  $2/\pi$  of the maximum value  $\rho_{12}(\tau^*)$ . Equation (6) is based upon the addition of bandlimited white noise being added to the signal, and represents the decorrelation in the suspension structures, as the suspension advects from one transducer to another. An error for the velocity estimate can be obtained by differentiating Eq. (5)

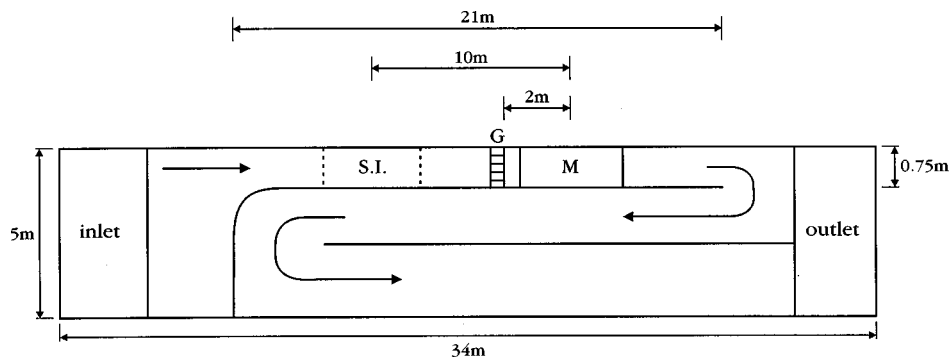


FIG. 1. Experimental arrangement in the flume: sediment injection position, S.I.; turbulent grid location, G; and the position of the transducer array and the reference measurements, M.

$$\delta v_c = \frac{\delta d_{12}}{\tau^*} - \frac{d_{12}}{\tau^{*2}} \delta \tau^* \quad (7)$$

Since the transceiver separations could be accurately measured then  $\delta d_{12} \approx 0$  is a reasonable approximation. Equating the partial derivatives with the standard deviations,  $\sigma(v_c)$  can be written as

$$\sigma(v_c) = \left| \frac{-d_{12}}{\tau^{*2}} \right| \sigma(\tau^*) \quad (8)$$

Inspection of Eqs. (6) and (8) show how the standard deviation in the velocity varies with record length, cross-correlation peak value, cross-correlation width, correlation lag, and transducer separation.

## II. EXPERIMENTAL ARRANGEMENT

The measurements were conducted in the recirculating flume shown in Fig. 1. The flume was 34 m in length, 5 m in width, and with a depth of 1.1 m. The water circulated within the flume as indicated in the figure, generating turbulent recirculating currents. The measurement region consisted of an area 21 m in length, 0.75 m in width, and with a water depth of 1 m. Acoustic backscatter measurements with no sand injected gave signal levels 20–30 dB below those with sand present. This backscattered signal level was associated with detritus in the flume. The 20–30-dB discrimination between the background levels and the returns when sediment was in suspension was considered sufficient to assume that the dominating scattering mechanism was due to the injected sediments. The sand was injected (S.I.) into the water using a hopper several meters upstream of the measurement region (M), and passed through a fine mesh grid (G) arrangement to enhance the turbulence, and thereby retain the sediment in

suspension. The suspended sediments were then advected through the measurement region, and onto the outlet. The sediment used had a mean particle radius of 80  $\mu\text{m}$ . In the study, data were collected for velocities between 0.5 and 1.5  $\text{m s}^{-1}$  with a nominal step interval of 0.25  $\text{m s}^{-1}$ . Three different types of grids to induce turbulence were employed. Measurements were taken using both single- and multi-frequency signals, although the latter frequencies only varied between  $\pm 5\%$  of the center frequency. Pulse lengths between 20 and 320  $\mu\text{s}$  were employed, and three different receiver amplifications were examined. A representative selection from these measurements is presented in the current work.

Reference velocity measurements were obtained using an Immersible Laser Doppler Flow Meter (ILDFFM). Water temperature was recorded using a thermistor. The reference instrumentation was located 0.5 m downstream of the acoustic instrumentation, and measurements were taken at 0.3 m above the bed at the midwidth of the flume.

The transducer arrangement employed is shown in Fig. 2. This consisted of four transducers mounted in a single housing at 0.8 m above the base of the flume, pointing vertically downwards and aligned along stream. The array provided transducer pair separations between 0.04 and 0.24 m. This arrangement allowed for an examination of the variation in cross-correlation functions with transducer separation, and the influence of the separation on velocity estimates. The transducers operated at 1.1 MHz with a  $-3$  dB full beamwidth of  $6.7^\circ$ . The pulse repetition frequency used in the experiments was 200 Hz, and the record duration was 15 s. The profiles of the backscattered signal from the suspended sediments were mixed down from 1.1 MHz to 100 kHz, and this signal was sampled at 400 kHz for 128 range bins. A minimum blanking time of 400  $\mu\text{s}$  was imposed before the collection of the acoustic data to provide a sampling region away from the transducer mounting, and centered at the height of the laser Doppler measurement. These acoustic profiles were collected simultaneously with the reference measurements and the data recorded. It is the analysis of the acoustic data for the various configurations described above, and the potential to obtain vertical profiles of the horizontal flow velocity using a correlation approach which are examined in the present work.

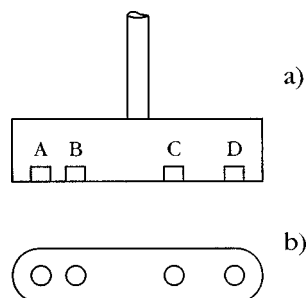


FIG. 2. Transducers array used for the measurements AB=0.04 m, BC=0.12 m, and CD=0.08 m.

## III. INTERPRETATION OF THE BACKSCATTERED DATA

As mentioned, measurements were collected for a variety of turbulence intensities obtained using different grids,

single- and multi-frequency transmits signals, differing receiver amplifications, varying pulse lengths, and a range of current velocities. The configuration of these experiments and their outcome have been documented in detailed reports,<sup>20,21</sup> and the present article summarizes the salient results with additional analysis. Here the focus is upon the results obtained for current velocities of 0.5–1.5 m s<sup>-1</sup>, for pulse lengths of 20–320 μs, using single frequency signals, with a medium turbulence grid installed and concentration levels of the order of 0.1 kg m<sup>-3</sup>. These configurations yielded results which are representative of the whole data set.

Single realizations of the backscattered signal are of limited value because of the configuration noise. To reduce this noise an averaging process needs to be employed. However, to retain the temporal structure of the signal there was the requirement to limit the number of data points averaged in the time and spatial domains. Iteratively it was determined for the flume suspension that a running average over 85 data points, 17 in the time domain and five in range, gave results which sufficiently reduced the configuration noise yet retained the suspended field structure. The running averaging retained high temporal and spatial resolution and reduced the configuration noise to 9% of the mean-square signal. The measured mean-square pressure  $P^2$  was therefore calculated using

$$P^2(t,r) = \frac{1}{(2n+1)(2m+1)} \sum_{r=-n}^n \left( \sum_{t=-m}^m \mathcal{P}^2(t,r) \right), \quad (9)$$

where  $\mathcal{P}(t,r)$  is a single instantaneous backscatter realization, at time  $t$  and range  $r$ , and as discussed above  $m=8$  and  $n=2$ . The values for  $P^2$  were then zero meaned for the correlation analysis.

In the first instance to examine the structure of the time series, sections of the data were selected and investigated for the possibility of correlation between the transducer outputs. Figure 3 illustrates the type of results obtained. The data shown in Fig. 3 were collected using transducers A and D, these had a separation of 0.24 m. The current velocity was 1.04 m s<sup>-1</sup>, a medium grid was used, and the pulse length was 40 μs. Figure 3(a) and (b), respectively, show plots of the normalized mean-square backscatter pressure  $P^2$  with range and time for transducers A and D. These visualizations of the pressure field show high backscatter levels interspersed with lower signal levels, and these observed variations are seen to be comparable in both images. The similarity of measured backscattered pressure from transducers A and D reflect a degree of temporal coherence in the suspension field which could potentially be used for velocity measurements. In Fig. 3(c) two time series records of  $P^2$ , normalized by the mean over the record, from transducers A (-) and D (···), at the 64th sample bin from the transducers are shown. The time series from transducer D has been adjusted to account for the lag associated with the time for the suspension to advect from transducer A to D. Figure 3(c) shows the detailed time series to be highly variable in form, with intermittent high values associated with high suspended sediment concentration events in the turbulent currents. Figure 3(c) clearly shows the coherence between the two time series

measurements with the high suspension events readily seen to be similar, although there is some degree of variability in the fine structure. It should be noted that even though the present observations are being collected in a flume, the structures seen in the pressure field in Fig. 3, due to the fluctuations in the concentration, have been observed in natural flows.<sup>16</sup>

To examine the dimensions of the suspension events, the temporal autocorrelation function  $\rho_{11}(\tau)$  was calculated at each bin, and multiplied by the flow velocity to give a spatial autocorrelation function. To illustrate the output obtained, the results from transducer C, for a 40-μs pulse length, at velocities of 0.54, 1.04, and 1.46 m s<sup>-1</sup> are, respectively, shown in Fig. 4(a)–(c). The three curves in each figure are associated with range bins 1 (-), 60 (···), and 120 (---). Apart from the first and 60th sample bins for the 0.54 m s<sup>-1</sup> case the spatial autocorrelation functions are nominally consistent. Taking the spatial coherence length as the  $e^{-1}$  amplitude width of the autocorrelation function, the dimension of the turbulent suspended sediment structures (neglecting the 0.54 m s<sup>-1</sup>, 1 and 60 bins) is of the order of 0.3 m. This is of the same order of magnitude as events observed in the marine environment.<sup>16</sup> A possible explanation for the somewhat anomalous results for the 0.54 m s<sup>-1</sup> case is the increasing difficulty in retaining sediments in suspension with height above the bed of the flume at the lower turbulence levels generated for the 0.54 m s<sup>-1</sup> case.

Although the autocorrelation functions give a measure of the scale of the suspension features, they do not provide information on the temporal persistence of the events as they advect downstream. To compute this the average cross-correlation peak,  $\langle \rho_{12}(\tau^*) \rangle$ , was computed for the six transducer separation distances. The 40-μs pulse length data were used for the analysis. To calculate the average cross-correlation peak, the cross-correlation functions were calculated at each range, for all six transducer pairs combinations, at the five velocities employed, and a peak value identified in each case. For each transducer pair all the correlation peak values obtained for each range and velocity were averaged to give a mean peak value. The results are presented in Fig. 5(a). These show a small reduction in mean peak cross-correlation function with separation, however, the reduction is relatively weak with only a 5% reduction as the separation increased from 0.04 to 0.24 m. A complimentary analysis was conducted on the  $e^{-1}$  widths of the cross-correlation functions for the six transducer pairs and five velocities. For each transducer pair the  $e^{-1}$  width  $\beta_{12}$  was obtained for each range bin and velocity, and averaged to give a mean value. The results for  $\langle \beta_{12} \rangle$  versus transducer pair separation are shown in Fig. 5(b). The results show little variation in  $\langle \beta_{12} \rangle$ , with a nominally uniform width of 0.36 s as the transducer pair separations increased from 0.04 to 0.24 m. Therefore although the spatial dimensions of the suspension field are of the order of 0.3 m, the integrity of the structures persists for a significantly greater distance.

Although the mean cross-correlation peaks and widths only change slowly as the transducer separation increases, the separation of the transducers can have an effect on the velocity estimates. To illustrate this, results are shown in Fig.

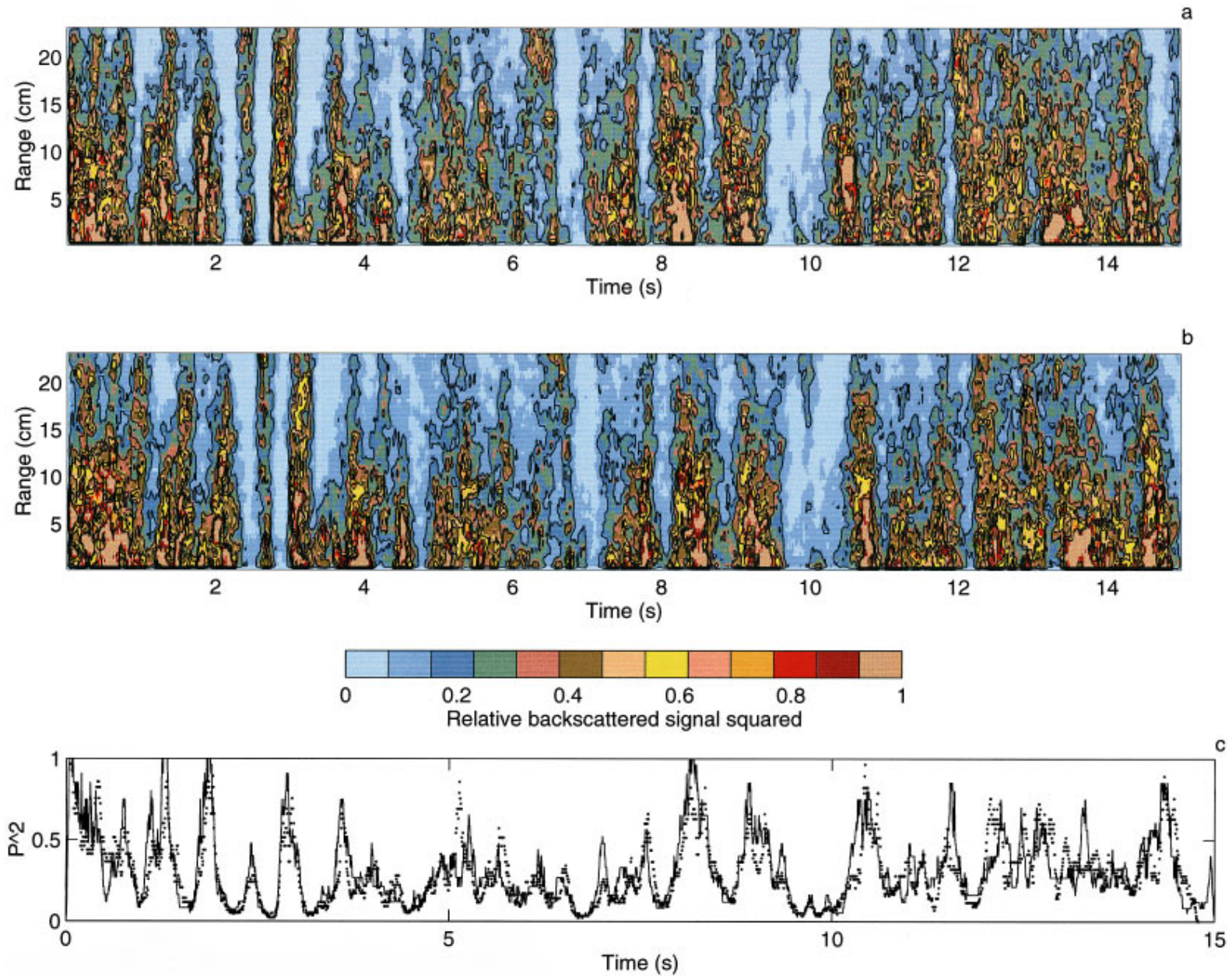


FIG. 3. (a) Plot of the normalized mean-square backscattered pressure as a function of time and range for transducer A. (b) Plot of the normalized mean-square backscatter pressure as a function of time and range for transducer D. (c) Comparison of the time series of the 64th range sample for transducers A (-) and D (....). In (c) the time series from transducer D has been adjusted to account for the time lag for the flow to advect from transducer A to D. The pulse length was  $40 \mu\text{s}$  and the current was  $1.04 \text{ ms}^{-1}$ .



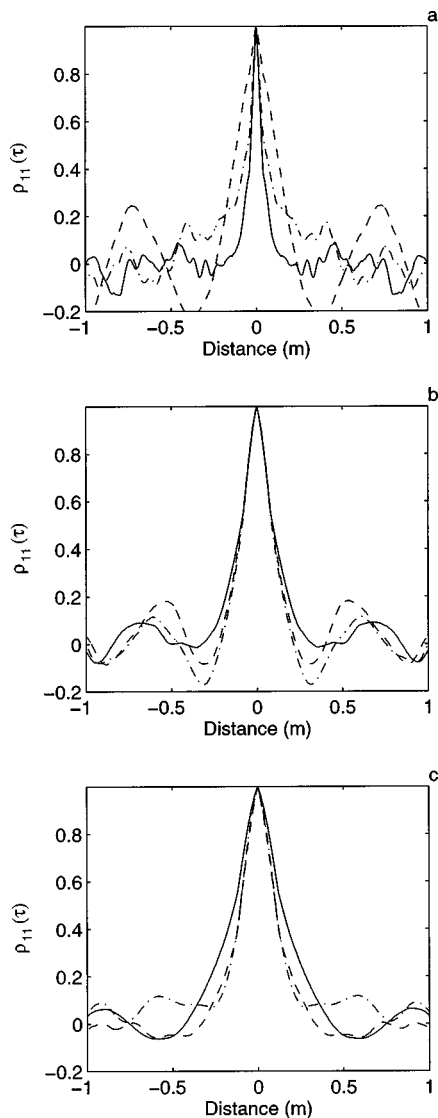


FIG. 4. Measurements of the spatial autocorrelation function  $\rho_{11}(\tau)$  for transducer C for flow velocities of (a)  $0.54 \text{ m s}^{-1}$ , (b)  $1.04 \text{ m s}^{-1}$ , and (c)  $1.46 \text{ m s}^{-1}$ . The pulse length was  $40 \mu\text{s}$ . Range bins 1 (—), 60 (---), and 120 (-·-) are shown.

6 for transducers AB and AD which had, respectively, separations of 0.04 and 0.24 m. The pulse length used was  $40 \mu\text{s}$ , and the current speed was  $0.87 \text{ m s}^{-1}$ . Figure 6(a) shows the cross-correlation peak values  $\rho_{12}(\tau^*)$  with range bin for transducers AB (○) and AD (×). These can be seen to be nominally constant with range with values close to 0.8. Figure 6(b) shows the data array locations of the cross-correlation function peak value normalized by the average location over the range bins. Previous measurements and hydraulic modeling<sup>22</sup> of the mean velocity profile had shown the profile to be uniform in the vertical over the acoustic measurement range. Hence the results presented in Fig. 6(b) should ideally be unity and constant with range. As can be seen in the figure the results for both transducers are seen to lie within 0.1% of unity for all range bins. Using these peak value locations the cross-correlation time lags  $\tau^*$  can be obtained. These lag values, normalized by the mean lag over all the range bins,  $\tau^*/\langle\tau^*\rangle$ , are shown in Fig. 6(c). Again ideally these should be unity and constant with range. This is

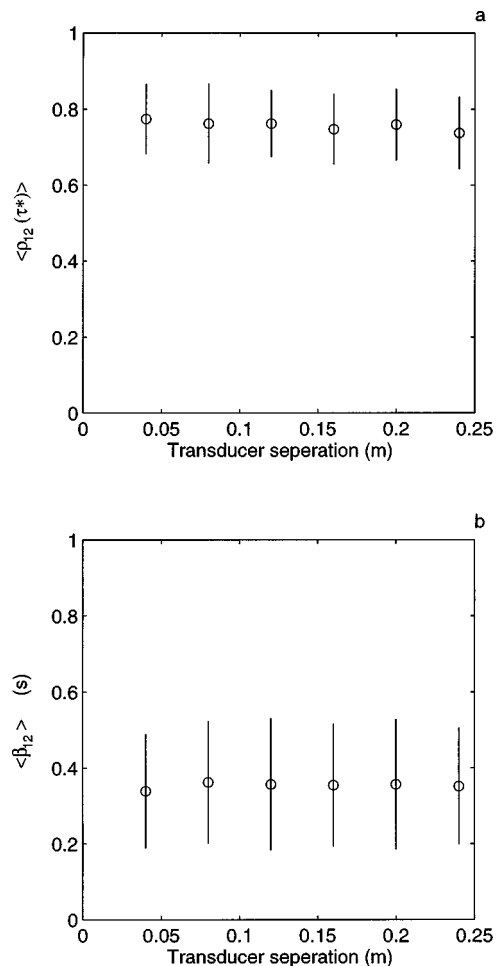


FIG. 5. (a) Variation in the mean cross-correlation peak  $\langle\rho_{12}(\tau^*)\rangle$  with transducer separation. (b) Variation in the mean cross-correlation  $e^{-1}$  width  $\langle\beta_{12}\rangle$  with transducer separation. The pulse length was  $40 \mu\text{s}$ .

the case for transducers AD, however, the values for transducers AB differ by up to 40% from unity. This is unlikely to be associated with the 5 m s digitization rate, but more probably ascribed to small variation in the location in the cross-correlation peak due to noise, having a significant effect on the cross-correlation lag for small transducer separations. This observation can be directly related to Eq. (6). Since from Fig. 5(a) and (b)  $\rho_{12}(\tau^*)$  and  $\beta_{12}$  [ $\gamma_{12}$  and  $\beta_{12}$  both measure the width of  $\rho_{12}(\tau)$ ] are nominally constant with transducer pair separation, and the record lengths  $T$  are the same,  $\sigma_{12}(\tau^*)$  is to first-order constant for transducer separations AB and AD. However, since  $\tau^*$  reduces with transducer separation,  $\sigma(\tau^*)/\tau^*$  increases, and leads to the results in Fig. 6(c). Using the lags from Fig. 6(c), the velocities were calculated with Eq. (5), and the results are shown in Fig. 6(d). The velocity profile is seen to be nominally uniform for the AD transducer pair, but has significant fluctuations for the AB case. The mean velocity averaged over all range bins for transducer pairs AB and AD, respectively, gave values of  $0.92 \pm 0.2$  and  $0.84 \pm 0.02 \text{ m s}^{-1}$ , these are consistent with the ILDFM velocity measurement of  $0.87 \pm 0.02 \text{ m s}^{-1}$ . However, for transducers AB the standard deviation is an order of magnitude larger than the AD case. As discussed above the larger standard deviation is due to small

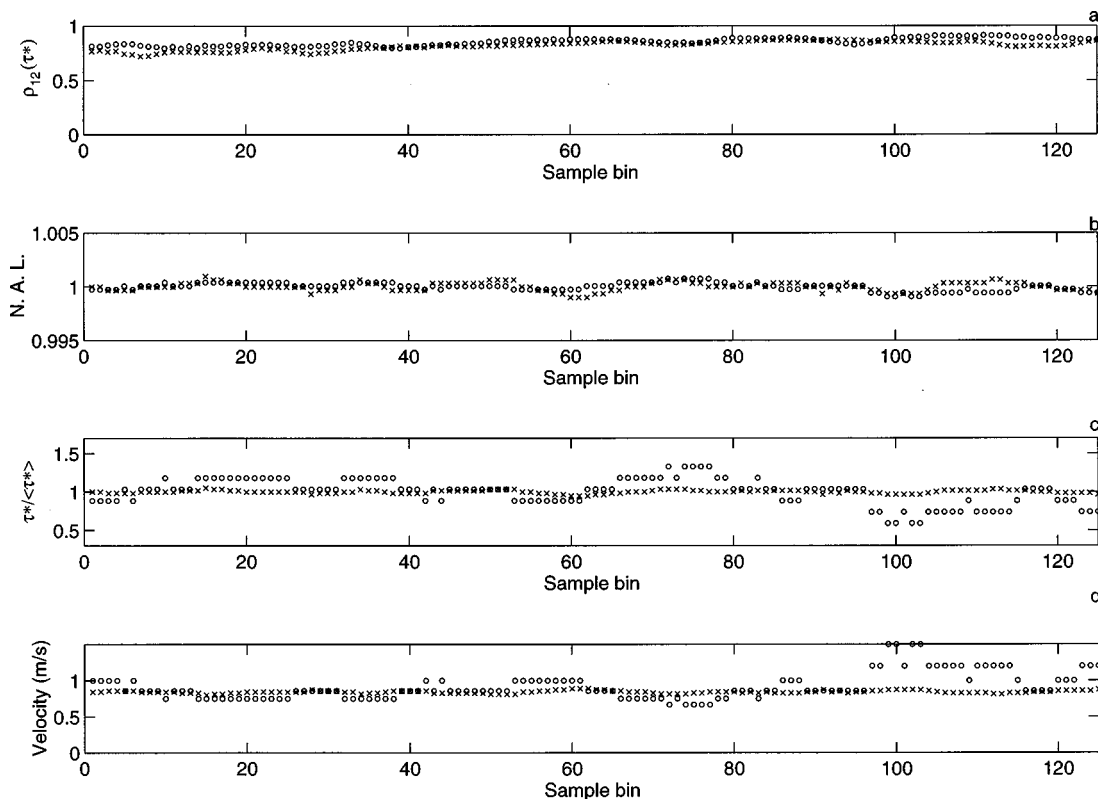


FIG. 6. Profiles of cross-correlation parameters for transducer pairs AB (O) and AD (X). (a) Cross-correlation peak values  $\rho_{12}(\tau^*)$ . (b) N.A.L.; normalized array location of the cross-correlation peak. (c) Normalized cross-correlation peak lag  $\tau^*/\langle\tau^*\rangle$ . (d) Cross-correlation velocity. The pulse length was  $40 \mu\text{s}$  and the velocity was  $0.87 \text{ m s}^{-1}$ .

variations in the location of the cross-correlation peak. Analysis of the other transducer pairs showed that separations  $0.12 \text{ m}$  and greater gave consistent velocity profiles with marginal improvement for increased separation. Therefore, for brevity, the rest of the detailed analysis only uses the AD transducer pair. Further details for other transducer pairs can be found elsewhere.<sup>20</sup>

To illustrate the cross-correlation functions observed in the present work, Fig. 7 shows plots of the cross-correlation functions with range and lag for the AD transducer pair. The pulse length was  $40 \mu\text{s}$ , and the velocities were  $0.54$ ,  $1.04$ , and  $1.47 \text{ m s}^{-1}$ . These plots clearly show readily identifiable peaks in the cross-correlation functions at all three velocities, and the peaks in the cross-correlation functions have the same lag with range, as would be expected for the nominally constant flow at midwater depth in the flume. It can be seen that for the  $0.54 \text{ m s}^{-1}$  velocity the cross-correlation peak has a value of  $0.8$  (consistent with the higher velocity cases) at the furthest range from the transducer, but this reduces to approximately  $0.4$  near the transducer. As noted above for the autocorrelations this is ascribed to increasing difficulty in retaining sediments in suspension with height above the flume bed at the low turbulence levels generated for the  $0.54 \text{ m s}^{-1}$  case. However, notwithstanding this latter difficulty, due to the experimental configuration, the salient feature of Fig. 7 is clearly identifiable peaks having a constant lag with range.

Using the cross-correlation functions, typified in Fig. 7, the cross-correlation peak lags were identified and flow velocities calculated. The output from this analysis for trans-

ducer pair AD for pulse lengths of  $40 \mu\text{s}$  (X),  $80 \mu\text{s}$  (O), and  $160 \mu\text{s}$  (+) is shown in Fig. 8. The figure shows velocity profiles in the flume for the five flow rates used. The symbols represents the acoustic measurements  $v_c$ , the dashed line shows  $\sigma(v_c)$  obtained from Eqs. (6) and (8) using the  $80\text{-}\mu\text{s}$  pulse length data, and the solid line is the ILDFM measurement. The ILDFM measurement was taken near mid-depth in the flume, and the variation of mean flow with depth about the measurement region was uniform<sup>22</sup> to within  $\pm 3\%$  of the mean. To first order it can be seen that the acoustic cross-correlation velocity profile measurements are uniform with depth, and in agreement with the ILDFM measurements. However, there are some internal differences between the acoustic measurements and between the acoustics and the ILDFM observations. The acoustic measurements for the different pulse lengths were not taken simultaneously, and therefore the internal differences are ascribed to variation of the flow in the flume from run to run. These internal acoustic velocity differences are relatively small, as illustrated using the data in Fig. 8(c). The  $40$ -,  $80$ -, and  $160\text{-}\mu\text{s}$  pulse lengths, respectively, have mean velocities averaged over the profiles of  $1.04 \pm 0.03$ ,  $1.00 \pm 0.05$ , and  $1.02 \pm 0.03 \text{ m s}^{-1}$ . The differences between the ILDFM and the acoustics are considered to be due to the assumption that the single height measurement of the ILDFM exactly represents the flow over the profile range for the  $15\text{-s}$  period, and due to the error in the cross-correlation velocity measurement. Again using the value from Fig. 8(c) the flow measured by the ILDFM over the same data period was  $1.04 \pm 0.02 \text{ m s}^{-1}$ , the acoustic values given above are very comparable with the ILDFM mea-



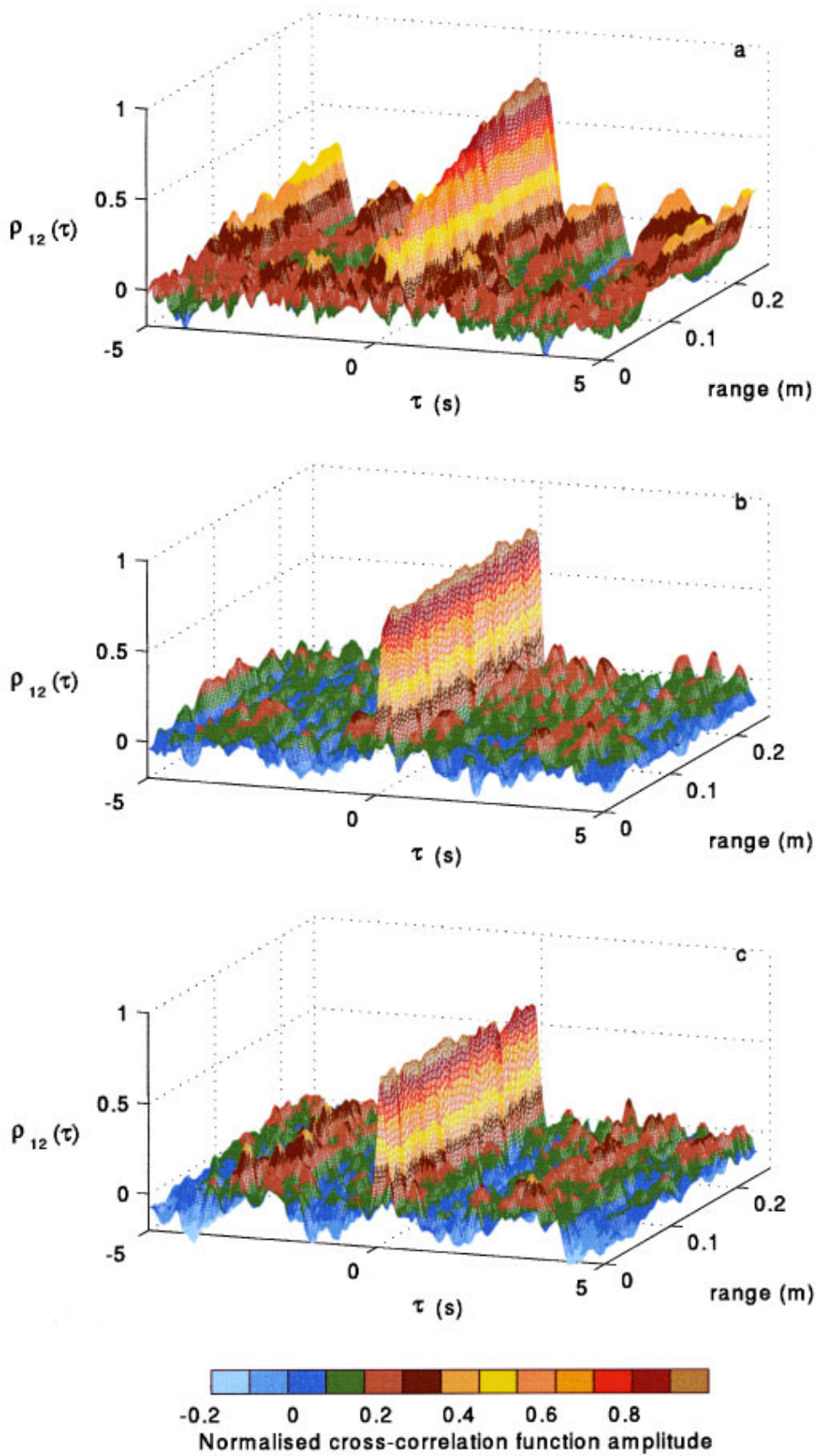


FIG. 7. Plot of the variation in the cross-correlation function  $\rho_{12}(\tau)$  with range and lag for transducer pair AD for flow velocities: (a)  $0.54 \text{ m s}^{-1}$ , (b)  $1.04 \text{ m s}^{-1}$ , (c)  $1.46 \text{ m s}^{-1}$ . The pulse length was  $40 \mu\text{s}$ .

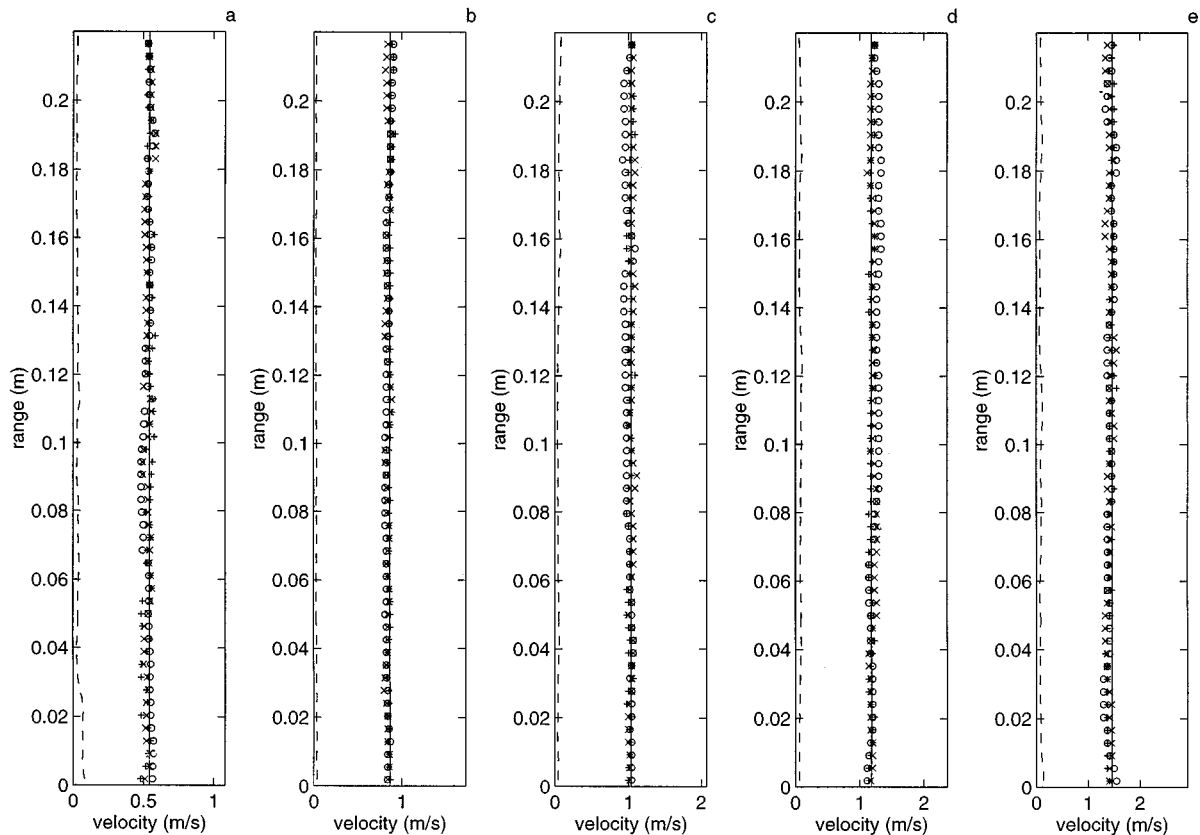


FIG. 8. Measurements of the velocity profiles for transducer pair AD for pulse lengths  $40 \mu\text{s}$  ( $\times$ ),  $80 \mu\text{s}$  ( $\circ$ ), and  $160 \mu\text{s}$  ( $+$ ) for different flow velocities. The dashed line shows the velocity error calculated from Eqs. (6) and (8). ILDFM values are given by the solid line. (a)  $0.54 \text{ m s}^{-1}$ , (b)  $0.87 \text{ m s}^{-1}$ , (c)  $1.04 \text{ m s}^{-1}$ , (d)  $1.18 \text{ m s}^{-1}$ , and (e)  $1.46 \text{ m s}^{-1}$ .

surement, and within a standard deviation, therefore there is no significant difference between the velocity estimates. If we do indeed make the assumption that the ILDFM velocity is correct over the correlation measurement range, a standard deviation can be calculated between the ILDFM velocity, and acoustic velocity at each range bin. For transducer pair AD this has been calculated for each range bin, and pulse width, at each velocity, and normalized by the ILDFM velocity measurement to give a mean normalized standard deviation. The result was  $\langle \sigma(v_c, v_l) / v_l \rangle = 0.02$ , where  $v_c$  and  $v_l$  are, respectively, the cross-correlation and ILDFM velocities. This small standard deviation over the data set illustrates the consistency between the ILDFM and acoustic correlation measurements of the flow. Further if  $\sigma(v_c)$  is calculated using Eqs. (6) and (8) for all bins, pulse widths, and velocities, for transducer pair AD, the mean normalized standard deviation gives  $\langle \sigma(v_c) / v_c \rangle = 0.05$ . This again is relatively low, and since  $\langle \sigma(v_c, v_l) \rangle / v_l = 0.02$  it may even be that Eq. (6) is overestimating the error in  $\tau^*$ .

In Fig. 9 a regression plot of the data is presented. This compares the mean acoustic profile velocities for all the pulse lengths and flow rates for the AD transducer pair with the ILDFM measurement. This figure clearly shows very good agreement between the two measurement methods. Table I shows the outcome of a regression analysis on the data sets for each of the pulse lengths. All gradients are close to unity, the intercepts are near zero, and the regression coefficients are approaching unity. Very comparable results

were obtained for transducer pairs BD and AC with transducer separations, respectively, of 0.2 and 0.16 m. For 0.12 separation and less discrepancies between the acoustic and ILDFM increased with significant variance for the 0.04-m case. Figure 10 provides an overview for all transducer pairs. Apart from the AB transducer pair which has a high degree of scatter for reasons previously discussed, consistent results

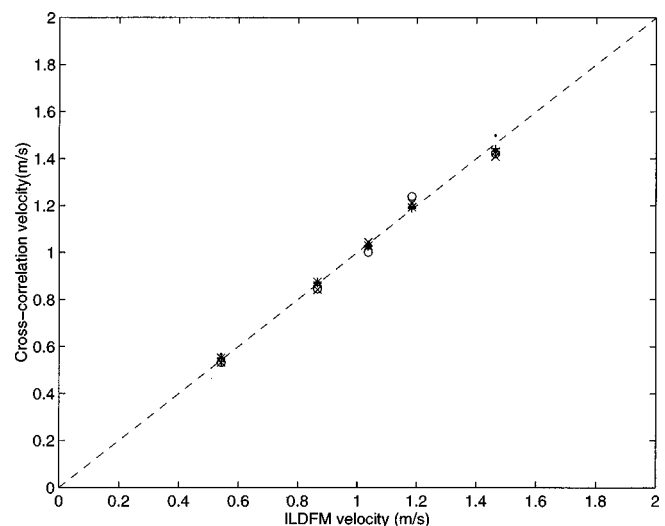


FIG. 9. Regression plot for transducer pair AD of the cross-correlation profile average velocity, and the ILDFM velocity. Pulse lengths were  $20 \mu\text{s}$  ( $\cdot$ ),  $40 \mu\text{s}$  ( $\times$ ),  $80 \mu\text{s}$  ( $\circ$ ),  $160 \mu\text{s}$  ( $+$ ), and  $320 \mu\text{s}$  ( $*$ ).

TABLE I. Regression of the cross-correlation velocity onto the ILDFM velocity,  $v_c = a + bv_1$ .

Pulse length ( $\mu\text{s}$ )	Regression coefficient	$a$ constant	$b$ gradient
20	0.999	$0.00 \pm 0.02$	$1.02 \pm 0.02$
40	0.996	$0.01 \pm 0.05$	$0.98 \pm 0.05$
80	0.993	$-0.01 \pm 0.07$	$1.00 \pm 0.07$
160	1.00	$0.01 \pm 0.02$	$0.99 \pm 0.02$
320	0.999	$0.04 \pm 0.02$	$0.96 \pm 0.02$

are obtained, and some improvement in the velocity measurements is observed as the transducer separation increased.

#### IV. CONCLUSIONS

The potential of the utilization of acoustic backscattering from suspensions of marine sediments to measure high spatial resolution measurements of mean current profiles has been investigated under laboratory conditions. The approach adopted was to take advantage of the temporal coherence in the suspension field in turbulent rectilinear currents, and use

cross correlations between transducer pairs to extract time lags, and use these lags to obtain near-bed vertical profiles of the horizontal current flow.

Data were collected for different turbulence intensities, monochromatic and multitone signals, pulse lengths between 20 and 320  $\mu\text{s}$ , differing system gains, current velocities between 0.5 and 1.5  $\text{m s}^{-1}$ , and different suspended sediment concentrations. A representative selection of these data was chosen to illustrate the general features of the whole study. To obtain backscattered signal levels that were associated with the fluctuations in the concentration field, temporal and spatial running averages were used to reduce the effects of configuration noise. The averaging selected was chosen to reduce the configuration noise to 9% of the mean value, and retain the suspension field structure. Initially to examine the form of the suspension structures autocorrelation and cross-correlation analysis were carried out on the backscattered time series signal. These indicated structural coherence lengths of the order of 0.3 m, which propagated with the flow, and persisted for greater distances.

To examine the effect of the transducer separation on the velocity estimate, transducer pairs AB and AD were exam-

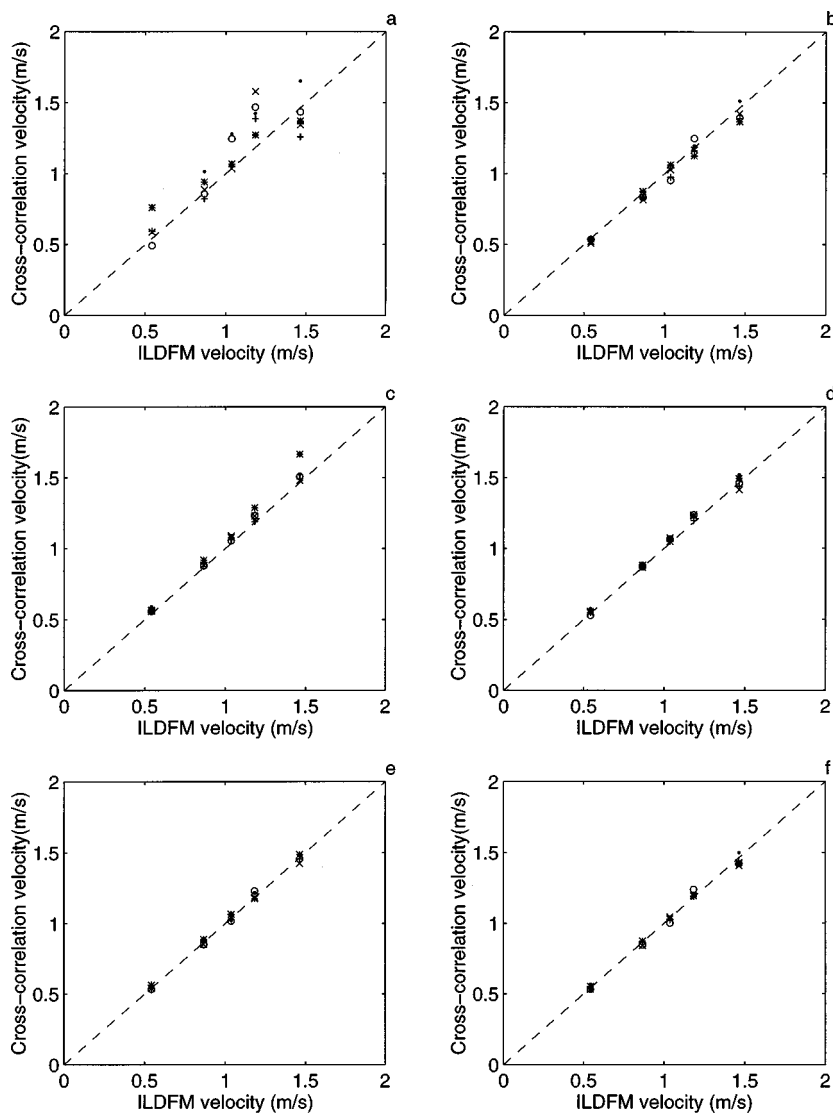


FIG. 10. Plots for all transducer pairs of the cross-correlation profile average velocity, and the ILDFM velocity. Pulse lengths were 20  $\mu\text{s}$  ( $\cdot$ ), 40  $\mu\text{s}$  ( $\times$ ), 80  $\mu\text{s}$  ( $\circ$ ), 160  $\mu\text{s}$  ( $+$ ), and 320  $\mu\text{s}$  ( $*$ ). Plots (a)–(f) are, respectively, for transducer pairs AB, CD, BC, AC, BD, AD with separations of 0.04, 0.08, 0.12, 0.16, 0.2, and 0.24 m.

ined. Both had comparable variability in the array location of the cross-correlation peak of 0.1%. However, because of the shorter lag times for the 0.04-m separation for the AB transducer pair, these fluctuations translated into greater velocity variability in the profile. Alternatively providing the back-scattered signal cross-correlation amplitude remains readily identifiable, accuracy can be improved by increasing the transducer separation.

For the transducer array used in the present work the cross-correlation peaks remained high for all transducer separations, with values typically greater than 0.75, although with some reductions in this value for the 0.54 m s<sup>-1</sup> case, which was considered to be associated with retaining the sediment in suspension with increasing distance from the bed. These peaks were readily identifiable in all cases as indicted by the characteristic example given in Fig. 7. Even for the 0.54 m s<sup>-1</sup> case velocity profiles remained consistent for the lower cross-correlation region. Internal comparisons of the velocity profiles obtained using the cross-correlation approach were conducted, and the results were shown to be ostensibly consistent. An assessment of the mean average profile velocities was carried out using an ILDFM, the results showed significant correlation with the ILDFM measurements, with an improvement for increasing transducer separation. For the AD transducer pair, where detailed profile comparisons were made with the ILDFM,  $\langle \sigma(v_c, v_l) / v_l \rangle = 0.02$ . Such a low normalized standard deviation represents a high degree of agreement between the two data sets, and demonstrates the potentiality of the cross-correlation approach to measure near-bed currents in the marine environment.

## ACKNOWLEDGMENTS

This work was partially supported by the EU through its MAST contracts VERIPASE II MAS2-CT91-007, and TRIDISMA MAS3-CT95-0017, and by RIKZ The Netherlands. P.D.T. became involved in the present study during discussions with the accompanying authors, and through an invitation to visit RIKZ for which Dr. Kees van Ruiten is thanked. Dr. Kees van Ruiten is also acknowledged for his input into the preparation of this manuscript. Dr. Jan Bosman is recognized for his support of the work.

<sup>1</sup>A. E. Hay and J. Sheng, "Vertical profiles of suspended sand concentration and size from multifrequency acoustic backscatter," *J. Geophys. Res.* **97**, 15661–15677 (1992).

<sup>2</sup>P. D. Thorne, P. J. Hardcastle, and R. L. Soulsby, "Analysis of acoustic measurements of suspended sediments," *J. Geophys. Res.* **98**, 899–910 (1993).

- <sup>3</sup>A. M. Crawford and A. E. Hay, "Determining suspended sand size and concentration from multifrequency acoustic backscatter," *J. Acoust. Soc. Am.* **94**, 3312–3324 (1993).
- <sup>4</sup>P. D. Thorne and P. J. Hardcastle, "Acoustic measurements of suspended sediments in turbulent currents and comparison with *in-situ* sampling," *J. Acoust. Soc. Am.* **101**, 2603–2614 (1997).
- <sup>5</sup>E. D. Cokelet, D. M. Dougherty, and M. L. Schall, "ADCP-Referenced geostrophic circulation in the Bering Sea Basin," *J. Phys. Oceanogr.* **26**, 1113–1128 (1996).
- <sup>6</sup>P. J. Hardcastle, "A high Resolution Coherent Acoustic Doppler Profiler for the measurement of near bed turbulent flow," *Proceedings Oceans 95 (MTS/IEEE, New York, 1995)*, pp. 1361–1366.
- <sup>7</sup>U. Lemmin and T. Rolland, "Acoustic velocity profiles for laboratory and field studies," *J. Hydraul. Eng.* **123**(12), 1089–1098 (1997).
- <sup>8</sup>L. Zedel, A. E. Hay, R. Cabrera, and A. Lohrmann, "Performance of a single-beam pulse to pulse coherent Doppler profiler," *IEEE J. Ocean Eng.* **21**, 290–297 (1996).
- <sup>9</sup>S. D. Kamminga, R. I. van Unen, and J. J. Bosman, "Acoustic experiments to test estimators for velocity," *Proceedings of the 2nd European Conference on Underwater Acoustics*, edited by L. Bjorno (The European Commission, Luxembourg, 1994), pp. 249–254.
- <sup>10</sup>R. F. van Unen, S. D. Kamminga, and D. Nijveldt, "Results of a high-resolution correlation current profiler," in *Proceedings of the Conference Oceans '97*, Halifax, Canada (MTS/IEEE, New York, 1997), Vol. 1, pp. 477–482.
- <sup>11</sup>P. D. Thorne and S. C. Campbell, "Backscattering by a suspension of spheres," *J. Acoust. Soc. Am.* **92**, 978–986 (1992).
- <sup>12</sup>J. Sheng and A. E. Hay, "An examination of the spherical scatterer approximation in aqueous suspensions of sand," *J. Acoust. Soc. Am.* **83**, 598–610 (1988).
- <sup>13</sup>A. E. Hay, "Sound scattering from a particle-laden, turbulent jet," *J. Acoust. Soc. Am.* **90**, 2055–2074 (1991).
- <sup>14</sup>A. S. Schaafsma and A. E. Hay, "Attenuation in suspensions of irregularly shaped sediment particles: A two-parameter equivalent spherical scatterer model," *J. Acoust. Soc. Am.* **102**, 1485–1502 (1997).
- <sup>15</sup>C. Libicki, K. W. Bedford, and J. F. Lynch, "The interpretation and evaluation of a 3-MHz acoustic backscatter device for measuring benthic boundary layer sediment dynamics," *J. Acoust. Soc. Am.* **85**, 1501–1511 (1989).
- <sup>16</sup>P. D. Thorne, P. J. Hardcastle, and A. Hogg, "Observations of nearbed suspended sediment turbulence structures using multifrequency acoustic backscattering," in *Coherent Flow Structures in Open Channels*, edited by P. J. Ashworth *et al.* (Wiley, London, 1996), pp. 343–358.
- <sup>17</sup>J. F. Lynch, J. D. Irish, C. R. Sherwood, and Y. C. Agrawal, "Determining suspended sediment particle size information from acoustical and optical backscatter measurements," *Cont. Shelf Res.* **14**, 1139–1165 (1994).
- <sup>18</sup>C. E. Vincent and A. Downing, "Variability of suspended sand concentration, transport and eddy diffusivity under non-breaking waves on the shoreface," *Cont. Shelf Res.* **14**, 223–250 (1994).
- <sup>19</sup>M. S. Beck and A. Plaskowski, *Cross-correlation Flow Meters—Their Design and Application* (Hilger, Bristol, 1987).
- <sup>20</sup>R. F. van Unen and G. W. Hoekstra, "Correlation estimator results, VERIPASE-II," Report prepared by OCN for RIKZ of The Netherlands, Report reference No. 684.58, p. 66 (1995).
- <sup>21</sup>R. F. van Unen, "Correlation data description document, VERIPASE-II," Report prepared by OCN for RIKZ of The Netherlands, Report reference No. 602.58, p. 94 (1994).
- <sup>22</sup>D. Nijveldt, "VERIPASE reference measurements and estimation validation," Report prepared by Delft Hydraulics of the Netherlands, Report reference No. B278, p. 63 (1995).

# Nonlinear pulse propagation in shallow-water environments with attenuating and dispersive sediments

Rahul S. Kulkarni and William L. Siegmann  
*Rensselaer Polytechnic Institute, Troy, New York 12180-3590*

Michael D. Collins and B. Edward McDonald  
*Naval Research Laboratory, Washington, DC 20375-5320*

(Received 6 June 1997; revised 15 December 1997; accepted 19 May 1998)

A hybrid treatment for wide-angle paraxial propagation that includes effects of both sediment dispersion and weak nonlinearity has been developed. A Fourier transform approach is used to combine effects of refraction, diffraction, and sediment dispersion in the frequency domain, and nonlinear effects in the time domain. A nonlinear wide-angle time-domain equation developed recently is first split into linear and nonlinear component equations. The linear equation is decomposed into its discrete frequency-domain counterparts. Sediment attenuation and dispersion are incorporated using a complex wave number along with a frequency-dependent formula for phase velocity to satisfy causality. The numerical implementation consists of first decomposing a broadband source into its frequency components and propagating them over a range step using a wide-angle parabolic equation. Fourier synthesis is used to reconstruct the signal which is then corrected to account for nonlinear effects in the time domain. Numerical examples illustrating the effects of dispersion and nonlinearity on shallow-water wide-angle propagation are presented and compared with available results. © 1998 Acoustical Society of America.  
[S0001-4966(98)00709-7]

PACS numbers: 43.30.Dr, 43.30.Lz [SAC-B]

## INTRODUCTION

The parabolic equation method<sup>1</sup> is one of the most efficient methods for simulating underwater acoustic propagation. It can successfully handle high-angle propagation in a variety of shallow-water environments.<sup>2-6</sup> Most work has relied on calculations in the frequency domain. One advantage of this approach is its simplicity, since propagation of each frequency component from a pulsed source is assumed to be independent of every other. Attenuation in the sediment can be modeled easily by using a complex wave number.<sup>7</sup> A disadvantage of frequency-domain models is that they cannot easily handle nonlinear effects, which may be significant for strong, pulsed sources.

Time-domain models can conveniently include effects of nonlinearity,<sup>8-10</sup> which were studied previously in ocean acoustics using the nonlinear progressive wave equation (NPE).<sup>11,12</sup> This time-domain model, which includes to leading order the effects of refraction, diffraction, and nonlinear steepening, is suitable for many problems in underwater acoustics. To avoid certain stability problems associated with obtaining solutions by marching in time, a related range-marching technique, implemented as the time-domain parabolic equation (TDPE),<sup>13</sup> was developed for linear, wide-angle propagation. Subsequent investigations of the TDPE involved modifications to include high-angle terms for treating refraction and diffraction in the linear case,<sup>2</sup> examinations of its stability properties,<sup>14</sup> and further extensions.<sup>15</sup> A new technique to incorporate effects of weak nonlinearity into the high-angle TDPE was recently developed.<sup>16</sup> It was demonstrated in the wide-angle case that nonlinear effects

can be significant for a strong, pulsed source in an isospeed waveguide.

One disadvantage of time-domain models is that the treatment of attenuation effects is cumbersome.<sup>13</sup> Several physical mechanisms have been proposed to explain sound absorption in sediments. Based on experimental evidence<sup>17</sup> it has been argued that attenuation in marine sediments is proportional to the sound frequency. It is known<sup>18</sup> that for plane-wave propagation, dispersion is a necessary consequence of this assumption in order to satisfy causality, regardless of the specific mechanisms involved. Futterman<sup>19</sup> and others<sup>20-22</sup> have used causality to derive Kramers-Krönig relationships between the real and imaginary parts of the wave number and, in particular for the linear proportionality, to obtain an expression for the phase velocity that varies as the logarithm of the frequency. This type of dispersive behavior has been observed experimentally.<sup>23</sup> It is therefore important to include both sediment attenuation and dispersion in propagation influenced by sediments. This is easily accomplished in frequency-domain models.

In this paper we develop a new technique which combines the advantages of both frequency-domain and time-domain parabolic equation (PE) formulations, and eliminates most of the disadvantages. The objective is to study the combined effects of sediment attenuation, dispersion, and nonlinearity. In Sec. I a hybrid approach which connects the frequency and time domains via the Fourier transform is described. Refraction and diffraction are treated in the frequency domain, whereas the nonlinearity is handled in the time domain. Section II discusses the modeling of sediment attenuation and dispersion. These effects are incorporated into the frequency-domain portion of the procedure. Section

III describes a computational procedure, based on Fourier synthesis, which combines a linear PE code<sup>24</sup> with a nonlinear implementation developed recently.<sup>16</sup> Numerical results illustrating the effects of attenuation, dispersion, and nonlinearity on wide-angle propagation are presented and discussed. They demonstrate that it may be necessary to include both sediment dispersion and nonlinearities to model pulse propagation accurately in shallow-water environments.

## I. HYBRID FREQUENCY/TIME-DOMAIN APPROACH

The starting point is a recently developed two-way nonlinear equation<sup>16</sup> for adiabatic acoustic propagation in an inviscid fluid. The mean ocean is assumed to be motionless and time independent, with spatial dependence permitted in the mean density  $\bar{\rho}$  and sound speed  $\bar{c}$ . Assuming that acoustic fluctuations are small enough to ignore cubic and higher-order terms, the pressure field  $p(\mathbf{x}, t)$  satisfies

$$\begin{aligned} \bar{\rho} \nabla \cdot \frac{1}{\bar{\rho}} \nabla p - \frac{1}{\bar{c}^2} \frac{\partial^2 p}{\partial t^2} = & - \frac{\beta}{\bar{\rho} \bar{c}^4} \frac{\partial^2 p^2}{\partial t^2} - \left[ \bar{\rho} \nabla \cdot (\mathbf{v} \cdot \nabla) \mathbf{v} - \bar{\rho} \nabla \cdot \frac{1}{\bar{\rho}^2} \right. \\ & \times \left. \left\{ \frac{1}{2\bar{c}^2} \nabla p^2 - (\nabla \bar{\rho} \cdot I \mathbf{v}) \nabla p \right\} \right] \\ & - \frac{1}{\bar{c}^2} \frac{\partial}{\partial t} \left[ \frac{\partial}{\partial t} \left\{ \frac{\bar{\rho} |\mathbf{v}|^2}{2} - \frac{p^2}{2\bar{\rho} \bar{c}^2} \right\} \right] \\ & - \frac{1}{\bar{\rho} \bar{c}^2} \{ \nabla \cdot (\bar{\rho} \bar{c}^2) \cdot I \mathbf{v} \} \frac{\partial p}{\partial t}, \end{aligned} \quad (1)$$

where  $\beta \equiv 1 + (\bar{\rho}/2\bar{c}^2)(\partial c^2/\partial \rho)(\bar{\rho}, p_0)$  is the parameter of nonlinearity.<sup>25-27</sup> Here  $\mathbf{v} = -(1/\bar{\rho})\nabla I p$  is the particle velocity, where  $I$  represents integration over time from  $t_1$  (which is before the onset of the acoustic disturbances) to  $t$ .

High-angle paraxial approximations of Eq. (1) can be obtained conveniently by using an iterative procedure combined with scaling arguments.<sup>16</sup> Equation (1) is expressed in cylindrical coordinates  $(r, \theta, z)$ , variations with  $\theta$  are ignored, and cylindrical spreading is taken into account by dividing out a factor of  $\sqrt{r}$  from pressure  $p$ . The far-field approximation<sup>1,28</sup> is made, and locally range-independent segments of the environment are treated<sup>2,3</sup> so that  $\bar{\rho} = \bar{\rho}(z)$  and  $\bar{c} = \bar{c}(z)$ . The pulse-tracking transformation  $t \rightarrow t - r/c_0$ , where  $c_0$  is an average sound speed, results in a two-way equation with first and second range derivative terms. Range variations in the acoustic field are assumed to be slow on the wavelength scale so that the second range derivative term is less important compared to the first. A narrow-angle paraxial approximation can be obtained by neglecting the second range derivative term and retaining only leading-order nonlinearities. This approximation is not sufficiently accurate for shallow waveguides with large propagation angles. A wide-angle equation is obtained by using the narrow-angle equation to approximate the second range derivative term instead of neglecting it, as explained in Ref. 16. Similarly, higher-angle paraxial equations are obtained by using the corresponding lower-angle approximations to estimate the second range derivative term in the two-way equation.

It has been demonstrated that if the source strength is small enough for effects due to propagation angle to dominate nonlinear effects, then the coupling between the two is negligible.<sup>16</sup> In the wide-angle case, this result along with an extension<sup>29</sup> of the operator splitting method<sup>30</sup> leads to the following equations to be solved at each range step:

$$\left[ \gamma \frac{\partial^2}{\partial t^2} - \frac{\bar{\rho}}{4} \frac{\partial}{\partial z} \frac{1}{\bar{\rho}} \frac{\partial}{\partial z} \right] \frac{\partial u}{\partial r} = - \frac{1}{2c_0} \left[ \left( \frac{1}{\bar{c}^2} - \frac{1}{c_0^2} \right) \frac{\partial^2}{\partial t^2} - \bar{\rho} \frac{\partial}{\partial z} \frac{1}{\bar{\rho}} \frac{\partial}{\partial z} \right] \frac{\partial u}{\partial t}, \quad (2)$$

$$\frac{\partial^2}{\partial t^2} \frac{\partial u}{\partial r} = \frac{\beta u_s}{2\bar{\rho} c_0^3 \sqrt{r}} \frac{\partial^3 u^2}{\partial t^3}, \quad (3)$$

where

$$\gamma \equiv \frac{1}{c_0^2} + \frac{1}{4} \left( \frac{1}{\bar{c}^2} - \frac{1}{c_0^2} \right), \quad (4)$$

$u(r, z, t)$  is the dimensionless far-field pressure in pulse-tracking coordinates, and  $t$  is the relative time. The significance of the nonlinearity is determined by the combination of parameters on the right side of Eq. (3), including the source strength  $u_s \equiv \delta \rho_0 c_0^2 / \sqrt{k_0}$ , where  $\delta$  determines the peak source pressure,<sup>16</sup>  $\rho_0$  is a reference density, and  $k_0$  is a reference wave number.

Loss mechanisms, which can affect shallow-water propagation significantly, are not included in Eqs. (2) and (3). In Sec. II we consider the effects of sediment attenuation, typically the most important factor contributing to energy loss in shallow waveguides. It is not convenient computationally to incorporate these effects into a time-domain model, as they require the evaluation of complicated integrals.<sup>13</sup> We therefore express the far-field pressure  $u(r, z, t)$  in terms of its frequency components  $U(r, z, \omega)$  via the Fourier transform,

$$u(r, z, t) = \int_{-\infty}^{\infty} U(r, z, \omega) e^{-i\omega t} d\omega, \quad (5)$$

$$U(r, z, \omega) = \frac{1}{2\pi} \int_{-\infty}^{\infty} u(r, z, t) e^{i\omega t} dt.$$

Equation (2) then becomes the familiar wide-angle PE,<sup>24</sup>

$$\left( 1 + \frac{1}{4} X \right) \frac{\partial U}{\partial r} = \frac{ik_0}{2} XU, \quad (6)$$

where

$$X \equiv \frac{1}{k_0^2} \left( k^2 - k_0^2 + \bar{\rho} \frac{\partial}{\partial z} \frac{1}{\bar{\rho}} \frac{\partial}{\partial z} \right), \quad (7)$$

$$k(z, \omega) = \frac{\omega}{\bar{c}(z)}, \quad k_0 = \frac{\omega_0}{c_0}. \quad (8)$$

The hybrid frequency/time-domain procedure consists of (i) decomposing a broadband source into its frequency components, (ii) propagating each component over a range step using Eq. (6), (iii) resynthesizing the signal and correcting it to account for nonlinear effects using Eq. (3), and (iv) de-

composing the corrected signal for propagation over the next range step. The next section describes modeling of the sediment attenuation and its incorporation into Eq. (6).

## II. SEDIMENT ATTENUATION AND DISPERSION

The absorption of acoustic energy in the seabed is of great interest to underwater acousticians as well as geophysicists, geologists, and seismologists. Several different mechanisms are responsible for dissipation of energy in marine sediments.<sup>31</sup> Losses due to friction between mineral grains and to relative motion between the mineral frame and pore fluid are referred to as intrinsic attenuation and are characteristics of the material of the sediment. In addition, inhomogeneities such as gas bubbles, shells, and rocks are responsible for scattering losses. Other significant sources of losses are energy conversion between compressional, shear, and interface waves, and multiple interbed reflections. The terminology of sediment attenuation in the literature refers to the total of all such losses.

Experimental evidence<sup>32</sup> has shown that attenuation depends on frequency, but the precise nature of this dependence has not yet been resolved.<sup>17</sup> Hamilton's thorough examination and analysis of experimental data (Refs. 1–17 of Ref. 32) suggest that sediment absorption is proportional to frequency over the range of frequencies from a few hertz to megahertz that are encountered in underwater acoustics. However, a theoretical treatment originally due to Biot and extended by Stoll suggests a nonlinear relationship (see, for example, Refs. 18–28 of Ref. 32). More recent studies have established that in the lower frequency range of 10–200 Hz, the total attenuation is lower than that expected by extrapolating values measured at higher frequencies.<sup>17,33,34</sup>

Sediment attenuation is usually modeled<sup>7</sup> by adding an imaginary part to the wave number. Specifically,  $k(z, \omega)$  is replaced by  $K(z, \omega) = k(z, \omega) + i\alpha(z, \omega)$ , where  $\alpha(z, \omega)$  is the attenuation in Np/m. It is known<sup>35</sup> that propagation of plane waves is causal if and only if the real and imaginary parts of  $K$  are related by a pair of Hilbert transforms. Therefore any assumed form for  $\text{Im}(K)$  unambiguously determines  $\text{Re}(K)$ . Relationships between  $\text{Re}(K)$  and  $\text{Im}(K)$  were originally derived by Kramers and Krönig for electromagnetic waves,<sup>18</sup> and were evidently first applied to acoustic propagation in homogeneous media by Ginzberg.<sup>20</sup> Subsequently Futterman<sup>19</sup> obtained simpler formulas which hold at low frequencies. More recently O'Donnell<sup>21</sup> used the Kramers–Krönig relations to derive local formulas which hold in the absence of rapid variations in frequency such as those associated with a sharp resonance. This condition should be satisfied in ocean acoustics because the change in dispersion is expected to be small over frequency ranges of interest. One such local dispersion relation in terms of the phase velocity  $c_p(\omega) \equiv \omega/\text{Re}(K(\omega))$  for homogeneous media is given as

$$\frac{dc_p(\omega)}{c_p^2(\omega)} = \frac{2}{\pi} \frac{\alpha(\omega)}{\omega^2} d\omega. \quad (9)$$

As is conventional in underwater acoustics,<sup>24</sup> it is assumed here that  $\alpha(z, \omega) = \sigma \eta(z) |k(z, \omega)|$ , where  $\sigma = (40\pi \log_{10} e)^{-1}$  and  $\eta(z)$  is the attenuation in decibels

per wavelength (dB/ $\lambda$ ). It is also assumed that the dispersion relation in Eq. (9) applies locally for ocean channels where properties vary with depth. Integration of Eq. (9) then gives

$$\frac{1}{c_p(z, \omega)} = \frac{1}{c(z)} - \frac{2\sigma \eta(z)}{\pi c(z)} \ln \left| \frac{\omega}{\omega_0} \right|, \quad (10)$$

where  $c(z) = c_p(z, \omega_0)$  and  $\omega_0$  is a very low frequency below which there is assumed to be no attenuation. Similar dispersion relations have been derived for certain special classes of inhomogeneous media that support plane waves.<sup>22</sup> The logarithmic dispersion predicted by Eq. (10) has been found to agree well with experimental measurements involving pulse propagation through Pierre Shale<sup>36</sup> and through a typical water-saturated sand.<sup>23</sup> Equation (10) has been used previously<sup>13</sup> to study shallow-water dispersive pulse propagation. In that application,  $c_p(z, \omega)$  was found to be about 40 m/s greater than  $c(z)$  over a wide range of frequencies centered at the characteristic source frequency of 100 Hz.

In summary, the effects of sediment attenuation and dispersion are included by replacing  $k(z, \omega)$  in Eq. (7) by

$$K(z, \omega) = \frac{\omega}{c_p(z, \omega)} + i\sigma \eta(z) |k(z, \omega)|. \quad (11)$$

If a nonlinear relationship<sup>37</sup> exists between attenuation and frequency, then Eq. (9) can be used to calculate the phase velocity, and Eqs. (10) and (11) can be modified appropriately. Consequently our hybrid frequency/time-domain procedure can easily handle more general forms for attenuation and the corresponding dispersion. In contrast, purely time-domain calculations, even in the case of linear attenuation, require the evaluation of complicated integrals.<sup>13</sup>

## III. NUMERICAL IMPLEMENTATION AND EXAMPLES

The frequency/time-domain procedure is handled numerically by combining a frequency-domain PE code with a recent extension<sup>16</sup> of the TDPE. A broadband source  $f(t)$  at range  $r=0$  and depth  $z=z_0$  is decomposed into frequency components  $F(\omega_j)$ ,  $j=1, \dots, m$ , where  $m$  is the number of sampled frequencies  $\omega_j$ . A PE starter<sup>7</sup> is used to initialize the complex pressure field  $U^j = U(r, z, \omega_j)$  for each  $F(\omega_j)$ . Each  $U^j$  is propagated in range by solving Eq. (6) with the PE code. The time-domain signal  $u(r + \Delta r, z, t)$  is then recovered by Fourier synthesis using an FFT<sup>38</sup> and corrected to account for nonlinear effects using Eq. (3), which is handled by an implementation of the TDPE extension. The resulting pressure field is again decomposed for propagation over the next range step, and the solution marched forward. The PE code is the implementation described in Ref. 39, and we next summarize the computational scheme used for the time-domain component.

The nonlinear Eq. (3) is first integrated twice in time using the boundary conditions  $u = \partial u / \partial t = 0$  at time  $t_1$  before the signal is detected by the observer. We emphasize that  $t$  here represents reduced time, a deviation from the average time  $r/c_0$  taken by the pulse to reach range  $r$ . The transformation  $x = 2\sqrt{r}$  is then used to express Eq. (3) in the conservation form

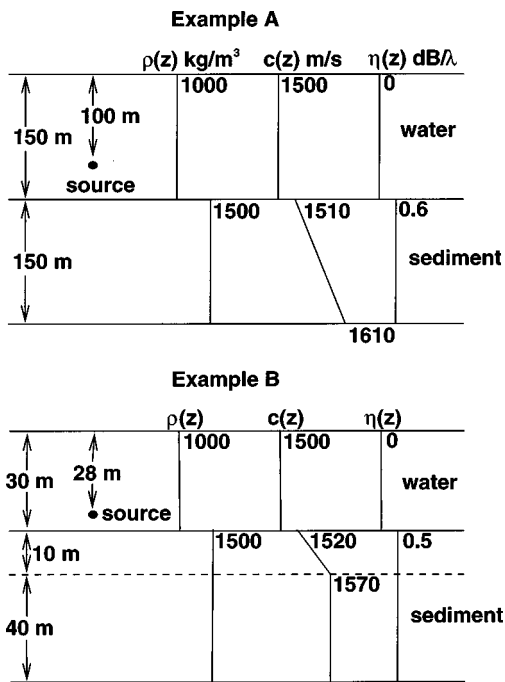


FIG. 1. Two-layer environments of examples A and B.

$$\frac{\partial u}{\partial x} + \frac{\partial}{\partial t} \phi(u), \quad (12)$$

where the flux  $\phi(u)$  is given by

$$\phi(u) = -\frac{\beta u_s}{2\bar{\rho}c_0^3} u^2. \quad (13)$$

Equation (12) is solved using a high-order upwind flux-correction method as described in Ref. 40. This approach eliminates the numerical dissipation or nonphysical dispersive ripples associated with straightforward first- or second-order accurate schemes<sup>40,41</sup> and yields a physically meaningful solution.

We first consider wide-angle propagation in a horizontally stratified shallow-water environment with a water column of 150 m over a sediment layer of the same thickness (Fig. 1, example A). The water density is  $\bar{\rho} = 1000 \text{ kg/m}^3$  and sound speed is  $\bar{c} = c_0 = 1500 \text{ m/s}$ . In the sediment,  $\bar{\rho} = 1500 \text{ kg/m}^3$  and the sound speed  $\bar{c}(z)$  is assumed to increase linearly from 1510 m/s at  $z = 150 \text{ m}$  to 1610 m/s at  $z = 300 \text{ m}$ . The attenuation  $\eta$  is assumed to be zero in the water column and 0.6 dB/λ in the sediment layer. An artificial absorbing layer of depth 300 m with a downward refracting sound-speed profile is added to the computational domain, below the sediment layer, to avoid reflections from the absolute bottom of the waveguide. The surface and absolute bottom are assumed to be pressure-release boundaries. The source is taken to be a Gaussian pulse,  $f(t) = e^{-(t/\tau)^2}$ , where  $\tau = 6.7 \text{ ms}$ , and is located at a depth of 100 m. It has a bandwidth of 132 Hz, ranging from 1 to 133 Hz, and is decomposed into 136 discrete frequencies. The source strength parameter is chosen to be  $\delta = 0.3$ , a physically reasonable value that is suitable for demonstrating effects of both nonlinearity and sediment dispersion.

Figure 2(a) and (b) illustrates effects of dispersion at

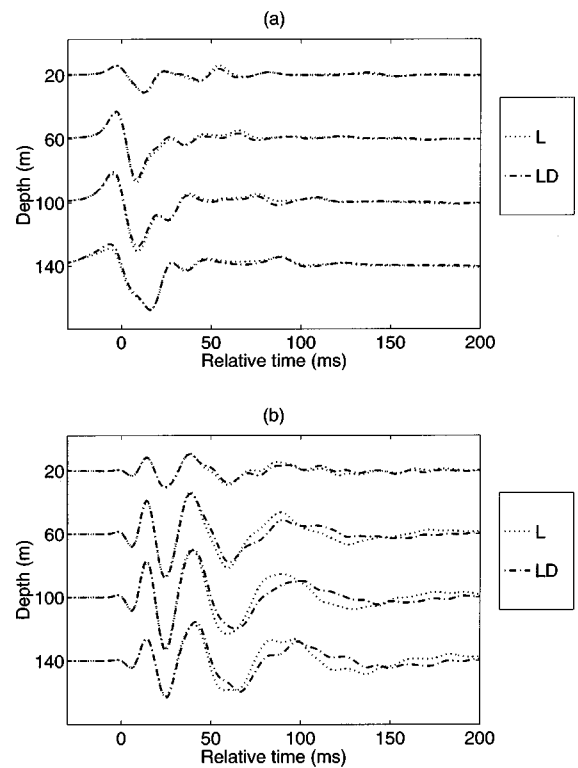


FIG. 2. Time-series waveforms of the pressure field at ranges (a) 1 km and (b) 10 km, for the two-layer environment of example A. Dash-dotted (or dotted) curves are linear solutions with (or without) sediment dispersion. Nonlinearity is not included.

ranges 1 and 10 km, respectively, caused by the attenuating sediments on linear propagation. The far-field pressure at each range is normalized by the maximum magnitude of the linear solution without dispersion at that range. Four waveforms in the water column at the depths indicated are shown as functions of relative time. Traversing each figure from left to right gives the time evolution of the pulse, where relative time zero corresponds to a reference arrival time  $r/c_0$ ; note that time intervals used for simulations were longer than those on the abscissas. The phase distortions caused by dispersion are seen to increase with range. At longer ranges they influence significantly the waterborne part of the signal and appear to be more pronounced for later arrivals, which have undergone more sediment interactions.

Figure 3(a) and (b) demonstrates nonlinear effects at the same ranges and depths as Fig. 2(a) and (b), with and without the effects of sediment dispersion. As in isospeed channel examples,<sup>16</sup> distortions caused by the nonlinearity increase with range and are strongest for earlier arrivals and less pronounced for later arrivals. When sediment dispersion is also included, the two effects appear to be roughly additive in that there is little or no interaction between them. The earlier and later arrivals are both distorted, the former predominantly due to nonlinearity and the latter predominantly due to dispersion. Nonlinear effects dominate at shorter ranges, whereas dispersion and nonlinearity are both significant at longer ranges. Thus for a strong source in a shallow waveguide, both effects may need to be included.

Next we consider wide-angle propagation in an even shallower stratified channel with a water column of 30 m



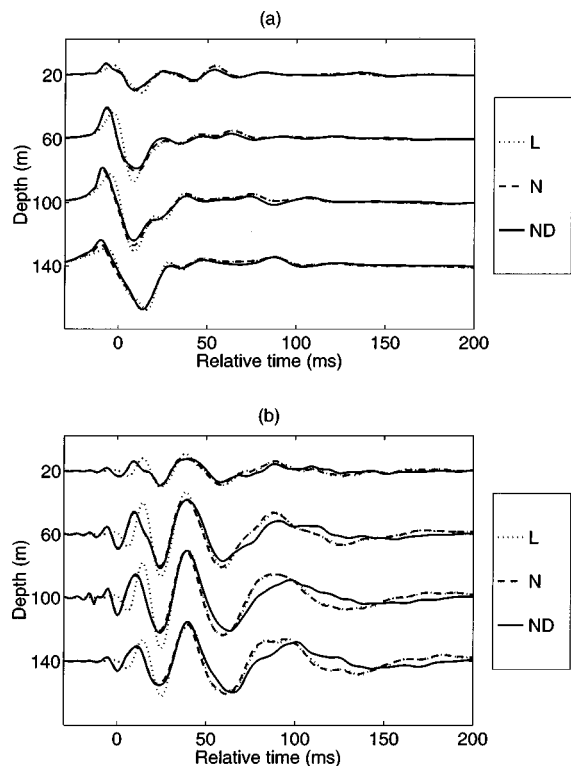


FIG. 3. Dotted curves are linear solutions without sediment dispersion, and solid (or dashed curves) are the corresponding nonlinear solutions with (or without) dispersion, for the same environment and ranges as Fig. 2.

over a sediment layer 70 m thick (Fig. 1, example B). The source is again a Gaussian pulse,  $f(t) = e^{-(t/\tau)^2}$  where  $\tau = 3.3$  ms, but with a larger bandwidth (252 Hz) than in example A and with location close to the sediment layer, at  $z = 28$  m. It is decomposed into 130 discrete frequencies ranging from 2 to 254 Hz. This example was used previously<sup>13</sup> to illustrate linear dispersive pulse propagation. The source strength parameter here is chosen to be  $\delta = 0.4$ , a magnitude we found appropriate for this environment to demonstrate the mechanisms treated in this paper. The water density and sound speed and the sediment density are taken to be the same as in example A. In the sediment,  $c(z)$  increases linearly from 1520 m/s at  $z = 30$  m to 1570 m/s at  $z = 40$  m and is constant at 1570 m/s for  $40 < z < 100$  m. The sediment attenuation is  $\eta = 0.5$  dB/ $\lambda$ .

Figure 4(a) and (b) shows effects of sediment dispersion at ranges 2 and 5 km, respectively, on linear propagation. The waveform distortion is significant at both of these ranges. As in example A, the far-field pressure at each range is normalized by the maximum magnitude of the linear solution without dispersion at that range. Results in Fig. 4(a) agree very well with those in Fig. 10(a) of Ref. 13, with minor differences that we attribute to the different starting fields in the two calculations. Figure 5(a) and (b) demonstrates nonlinear effects with and without sediment dispersion at the same ranges and depths as Fig. 4(a) and (b). In contrast with example A, nonlinear effects are seen to be significant even for the later arrivals at both ranges. Moreover, significant interaction appears to occur between nonlinearity and dispersion when the latter is included. For ex-

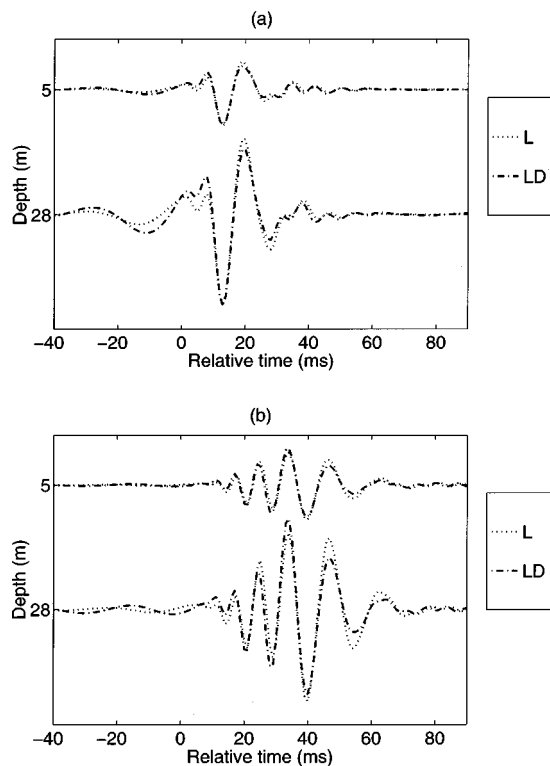


FIG. 4. Time-series waveforms of the pressure field at ranges (a) 2 km and (b) 5 km, for the two-layer environment of example B. Dash-dotted (or dotted) curves are linear solutions with (or without) sediment dispersion. Nonlinearity is not included.

ample, note the region of the waveforms between  $t = 0$  and 20 ms at  $r = 2$  km and between  $t = 20$  and 60 ms at  $r = 5$  km, where the influences of dispersion and nonlinearity are definitely not independent.

Figure 6(a)–(d) shows contour plots of the pressure field at range 2 km as a function of relative time and depth. The solid (and dashed) contours represent positive (and negative) portions of the pulse, with contour interval separations of 15% of the maximum magnitude of the linear solution without dispersion. These plots reinforce the observations made in connection with Figs. 4 and 5. They illustrate the separate and combined effects of sediment dispersion and nonlinearity at a fixed range. Distortions caused by the two separate effects, as seen in Fig. 6(b) and (c) relative to Fig. 6(a), are substantially different for earlier as well as later arrivals. Characteristic changes with depth are apparent. Their combined effects in Fig. 6(d) indicate significant coupling between them, visible most conspicuously in the region between  $t = -10$  and 20 ms.

We note that dispersive effects as seen in the waveforms of Figs. 2 and 4 are in qualitative agreement with those observed in an experimental study of pulse propagation in Pierre Shale<sup>36</sup> and with more recent measurements of dispersion in a typical water-saturated sand.<sup>23</sup>

#### IV. SUMMARY

A new procedure based on successive Fourier decomposition and synthesis is introduced to handle wide-angle pulse propagation that includes effects of sediment attenuation and dispersion in addition to weak nonlinearity. A nonlinear

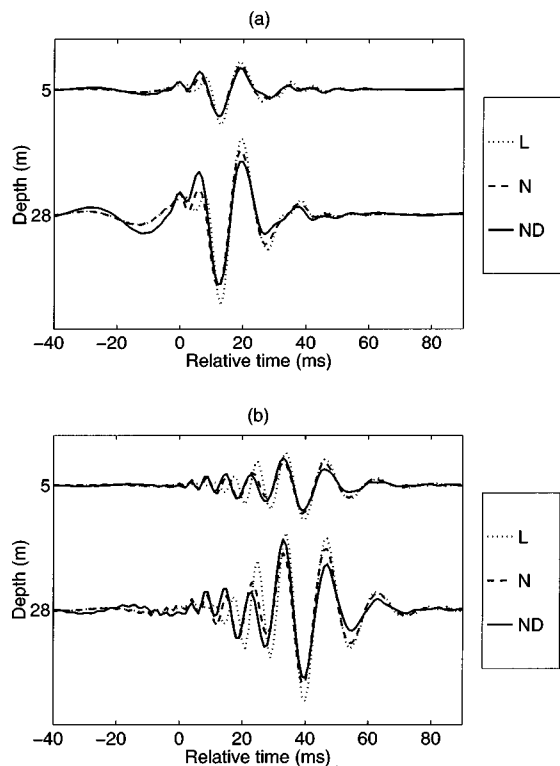


FIG. 5. Dotted curves are linear solutions without sediment dispersion, and solid (or dashed) curves are the corresponding nonlinear solutions with (or without) dispersion, for the same environment and ranges as Fig. 4.

wide-angle time-domain equation is first split into linear and nonlinear component equations. The linear equation is Fourier transformed to obtain a frequency-domain wide-angle PE. The nonlinear equation is expressed in conservation form to make the numerical implementation tractable. The implementation consists of first decomposing a pulse source into component frequencies using the FFT. Each component is propagated over a range step using the FEPE code to solve

the wide-angle PE. The pulse is then resynthesized, corrected to account for nonlinearities in the time domain using a high-order upwind flux correction method, and decomposed for propagation over the next range step.

Sediment attenuation is incorporated into the linear PE as the imaginary part of a complex wave number. It is known that pulse propagation is causal if and only if the real and imaginary parts of the wave number are related through the Kramers–Krönig relations. Any assumed functional form for attenuation unambiguously determines the real part, which in turn determines the dispersion relation for the phase velocity. We emphasize that the method developed in this paper does not depend on a particular choice for frequency dependence of the attenuation. In the examples treated here, attenuation is assumed to depend linearly on frequency, in accord with most literature in underwater acoustics, and the corresponding phase velocity varies with the logarithm of the frequency.

Numerical results for idealized shallow-water environments are presented and discussed. They demonstrate that effects of both sediment dispersion and nonlinearity can be substantial at all ranges. In summary, we have developed a method to treat simultaneously the effects of weak nonlinearity, sediment attenuation, and dispersion, and have constructed an implementation of it. Computational results show that it can be necessary to include effects of both sediment dispersion and nonlinearity to model accurately pulse propagation from strong sources in shallow channels.

## ACKNOWLEDGMENTS

This work was supported by Grant No. N00014-J-91-1033 from Code 3243, Office of Naval Research. It is part of a thesis submitted by Rahul S. Kulkarni in partial fulfillment of the requirements for the degree of Doctor of Philosophy in the Department of Mathematical Sciences at Rensselaer Polytechnic Institute.

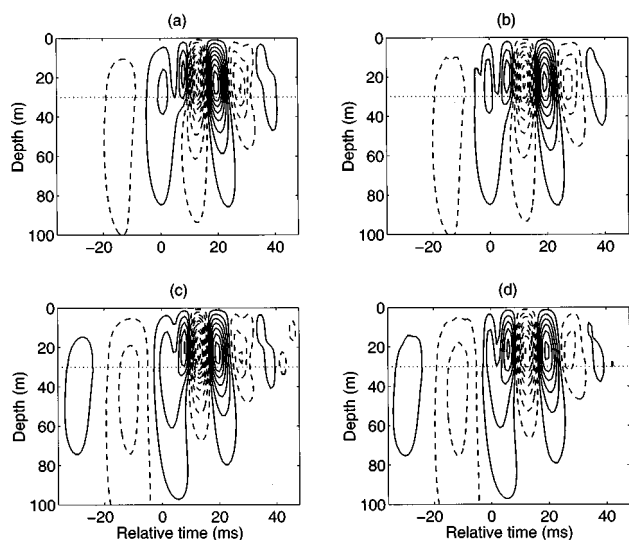


FIG. 6. Contour plots of solutions versus relative time and depth at range 5 km for the environment of example B: (a) linear solution without sediment dispersion; (b) nonlinear solution without dispersion; (c) linear solution with dispersion; (d) nonlinear solution with dispersion. Dotted line shows water-sediment interface.

<sup>1</sup>F. D. Tappert, “The parabolic approximation method,” in *Wave Propagation in Underwater Acoustics*, edited by J. B. Keller and J. S. Papadakis (Springer-Verlag, New York, 1977), pp. 224–287.

<sup>2</sup>M. D. Collins, “Applications and time-domain solution of higher-order parabolic equations in underwater acoustics,” *J. Acoust. Soc. Am.* **86**, 1097–1102 (1989).

<sup>3</sup>M. D. Collins, “A higher-order parabolic equation for wave propagation in an ocean overlying an elastic bottom,” *J. Acoust. Soc. Am.* **86**, 1459–1464 (1989).

<sup>4</sup>M. D. Collins, “An energy-conserving parabolic equation for elastic media,” *J. Acoust. Soc. Am.* **94**, 975–982 (1993).

<sup>5</sup>M. D. Collins and R. B. Evans, “A two-way parabolic equation for acoustic backscattering in the ocean,” *J. Acoust. Soc. Am.* **91**, 1357–1368 (1992).

<sup>6</sup>M. D. Collins, W. L. Siegmund, and W. A. Kuperman, “A parabolic equation for poro-elastic media,” *J. Acoust. Soc. Am.* **98**, 1645–1656 (1995).

<sup>7</sup>F. B. Jensen, W. A. Kuperman, M. B. Porter, and H. Schmidt, *Computational Ocean Acoustics* (AIP, New York, 1994).

<sup>8</sup>M. F. Hamilton, “Fundamentals and applications of nonlinear acoustics,” in *Nonlinear Wave Propagation in Mechanics*, edited by T. W. Wright (American Society of Mechanical Engineers, New York, 1986).

<sup>9</sup>D. T. Blackstock, “History of nonlinear acoustics and a survey of Burgers’ and related equations,” in *Nonlinear Acoustics, Proceedings of the Symposium held at Applied Research Laboratories*, edited by T. G. Muir (University of Texas at Austin, Austin, 1969), pp. 1–27.

<sup>10</sup>J. N. Tjøtta and S. Tjøtta, “Nonlinear equations of acoustics,” in *Fron-*

- ters of *Nonlinear Acoustics: Proceedings of 12th ISNA*, edited by M. F. Hamilton and D. T. Blackstock (Elsevier, London, 1990), pp. 80–97.
- <sup>11</sup> B. E. McDonald and W. A. Kuperman, “Time domain formulation for pulse propagation including nonlinear behavior at a caustic,” *J. Acoust. Soc. Am.* **81**, 1406–1417 (1987).
- <sup>12</sup> J. J. Ambrosiano, D. R. Plante, B. E. McDonald, and W. A. Kuperman, “Nonlinear propagation in an ocean acoustic waveguide,” *J. Acoust. Soc. Am.* **87**, 1473–1481 (1990).
- <sup>13</sup> M. D. Collins, “The time-domain solution of the wide-angle parabolic equation including the effects of sediment dispersion,” *J. Acoust. Soc. Am.* **84**, 2114–2125 (1988).
- <sup>14</sup> B. J. Orchard, W. L. Siegmann, G. J. Habetler, and M. J. Jacobson, “Stability analysis of higher-order time-domain paraxial equations,” *J. Acoust. Soc. Am.* **93**, 1335–1346 (1992).
- <sup>15</sup> B. J. Orchard, W. L. Siegmann, and M. J. Jacobson, “Three-dimensional time-domain paraxial approximations for ocean acoustic wave propagation,” *J. Acoust. Soc. Am.* **91**, 788–801 (1991).
- <sup>16</sup> R. S. Kulkarni, W. L. Siegmann, and M. D. Collins, “Nonlinear wide-angle paraxial acoustic propagation in shallow-water channels,” *J. Acoust. Soc. Am.* **102**, 224–232 (1997).
- <sup>17</sup> E. L. Hamilton, “Acoustic properties of sediments,” in *Acoustics and the Ocean Bottom*, edited by A. Lara-Saenz, C. R. Cuierra, and C. Carbo-Fité (Consejo Superior de Investigaciones Científicas, Madrid, 1987), pp. 3–58.
- <sup>18</sup> H. M. Nussenzveig, *Causality and Dispersion Relations* (Academic, New York, 1972).
- <sup>19</sup> W. I. Futterman, “Dispersive body waves,” *J. Geophys. Res.* **67**, 5279–5291 (1962).
- <sup>20</sup> V. L. Ginzberg, “Concerning the general relationship between absorption and dispersion of sound waves,” *Sov. Phys. Acoust.* **1**, 32–41 (1955).
- <sup>21</sup> M. O’Donnell, E. T. Jaynes, and J. G. Miller, “Kramers-Krönig relationship between ultrasonic attenuation and phase velocity,” *J. Acoust. Soc. Am.* **69**, 696–701 (1981).
- <sup>22</sup> R. L. Weaver and Y.-H. Pao, “Dispersion relations for linear wave propagation in homogeneous and inhomogeneous media,” *J. Math. Phys.* **22**, 1909–1918 (1980).
- <sup>23</sup> D. J. Wingham, “The dispersion of sound in sediment,” *J. Acoust. Soc. Am.* **78**, 1757–1760 (1985).
- <sup>24</sup> M. D. Collins, “Benchmark calculations for higher-order parabolic equations,” *J. Acoust. Soc. Am.* **87**, 1535–1538 (1990).
- <sup>25</sup> R. T. Beyer, “Nonlinear acoustics in fluids,” in *Benchmark Papers in Acoustics, Vol. 18* (Van Nostrand Reinhold, New York, 1984).
- <sup>26</sup> B. K. Novikov, O. V. Rudenko, and V. L. Timoshenko, *Nonlinear Underwater Acoustics* (Sudostroenie, Leningrad, 1981).
- <sup>27</sup> R. T. Beyer, “Parameter of nonlinearity of fluids,” *J. Acoust. Soc. Am.* **32**, 719–721 (1960).
- <sup>28</sup> W. L. Siegmann, G. A. Kriegsmann, and D. Lee, “A wide-angle three-dimensional parabolic wave equation,” *J. Acoust. Soc. Am.* **78**, 659–664 (1985).
- <sup>29</sup> N. N. Yanenko, *The Method of Fractional Steps* (Springer-Verlag, New York, 1971).
- <sup>30</sup> M. D. Collins, “Time-domain solution of higher-order parabolic equations,” in *Computational Acoustics*, edited by D. Lee, A. Cakmak, and R. Vichnevetsky (Elsevier, Amsterdam, 1990), pp. 261–273.
- <sup>31</sup> A. C. Kibblewhite, “Attenuation of sound in marine sediments: A review with emphasis on new low-frequency data,” *J. Acoust. Soc. Am.* **86**, 716–738 (1989).
- <sup>32</sup> L. D. Hampton, “Acoustic properties of sediments: An update,” *Rev. Geophys.* **23**, 49–60 (1985).
- <sup>33</sup> J.-X. Zhou, X.-Z. Zhang, and P. H. Rogers, “Effect of frequency dependence of sea-bottom attenuation on the optimum frequency for acoustic propagation in shallow water,” *J. Acoust. Soc. Am.* **82**, 287–291 (1987).
- <sup>34</sup> J.-X. Zhou, X.-Z. Zhang, P. H. Rogers, and J. Jarynski, “Geoacoustic parameters in a stratified sea bottom from shallow water acoustic propagation,” *J. Acoust. Soc. Am.* **82**, 2068–2074 (1987).
- <sup>35</sup> J. S. Toll, “Causality and the dispersion relation: Logical foundations,” *Phys. Rev.* **104**, 1760–1770 (1956).
- <sup>36</sup> P. C. Wuenschel, “Dispersive body waves—an experimental study,” *Geophysics* **37**, 539–551 (1965).
- <sup>37</sup> C. W. Horton, Sr., “Dispersion relationships in sediments and sea water,” *J. Acoust. Soc. Am.* **55**, 547–549 (1974).
- <sup>38</sup> W. H. Press, S. A. Teukolski, W. T. Vetterling, and B. P. Flannery, *Numerical Recipes in FORTRAN: The Art of Scientific Computing* (Cambridge U.P., Cambridge, England, 1992), 2nd ed.
- <sup>39</sup> M. D. Collins, “FEPE user’s guide,” NORDA Technical Note 365, Naval Research Laboratory, Stennis Space Center, MS, 1988.
- <sup>40</sup> B. E. McDonald and J. Ambrosiano, “High-order upwind flux correction methods for hyperbolic conservation laws,” *J. Comput. Phys.* **56**, 448–460 (1984).
- <sup>41</sup> C. Hirsch, *Numerical Computation of Internal and External Flows* (Wiley, New York, 1988), Vol. 2.

# Sub-bottom scattering: A modeling approach

Charles W. Holland<sup>a)</sup> and Peter Neumann

Planning Systems, Inc., 7923 Jones Branch Drive, McLean, Virginia 22102

(Received 3 July 1997; accepted for publication 28 April 1998)

Bottom scatter strength data exhibit artifacts when the sub-bottom plays a role in the scattering process. The artifacts arise from the classical assumption in the data processing that the scattering process occurs at the water–sediment interface. Many of the current bottom scattering models, even those that explicitly treat sub-bottom scattering, do not address these artifacts. A new bottom scatter modeling approach is proposed. The essence of the approach is to (1) employ a geoacoustic model capable of predicting the sub-bottom insonified field, (2) avoid the usual plane-wave assumption, and (3) compute the received level in the time domain. The first condition suggests the analysis of bottom loss data concurrent with bottom scatter data and leads naturally to the idea of a self-consistent geoacoustic basis. The model is employed to analyze a data set that showed surprising discrepancies between low angle ( $<20^\circ$ ) and intermediate angle ( $28^\circ$ – $50^\circ$ ) bottom scattering strength. The proposed acoustic model predicts this discrepancy, which arises from the fact that the two angular regimes are controlled by entirely different scattering mechanisms. The difference in mechanisms suggests caution in the current and common practice of extrapolation from survey (intermediate angle) measurements to the low angles of interest for system performance prediction. © 1998 Acoustical Society of America. [S0001-4966(98)05208-4]

PACS numbers: 43.30.Ma, 43.20.Fn [DLB]

## INTRODUCTION

Scattering from the seafloor can be considered to arise from two mechanisms: interface scattering and sub-bottom scattering. The sub-bottom scattering can further be subdivided into a sediment volume and a sub-bottom horizons component. In this paper, the problem of low frequency (100–1000 Hz) scattering from sub-bottom inhomogeneities and sub-bottom horizons is addressed. While various sub-bottom volume scattering models have been developed [e.g., Ivakin (1981), Tang and Frisk (1992), Mourad and Jackson (1993)] there is still much that is not understood about the physical mechanisms that control sub-bottom scattering and the requirements for modeling such phenomena.

Recent data collected by the Critical Sea Test (CST) program provide a valuable basis for beginning to identify and model these mechanisms. A data set from the Messina Cone was selected for this study because: the data were in an area where sub-bottom scattering was the probable mechanism; there were collocated bottom scatter measurements at both low (less than  $20^\circ$ ) and intermediate angles ( $28^\circ$ – $50^\circ$ ); there were bottom loss data (which provided an opportunity to test the self-consistent geoacoustic model concept); and there were good supporting environmental and geoacoustic data.

Figure 1 indicates the location of the bottom scatter measurements and also the location of the supporting acoustic and geophysical data. The seafloor on this region of the Messina Cone is relatively flat. The sub-bottom is characterized by a soft silt-clay material with interspersed thin silt layers arising from slump, debris, and turbidite flows. The unconsolidated sediments are about 300 m thick, below

which is a rough horizon composed of an evaporite sequence of dolomitic mudstone and gypsum layers hereafter termed the “basement.”

The low angle bottom scatter data were collected by Reilly and Sundvik (1992) using a vertical line array (VLA) source steered down  $25^\circ$ , and a towed horizontal line array (HLA). Source and receiver depths are nominally 150 and 140 m, respectively. Figure 2 shows the beam pattern of the VLA and the HLA (the  $138^\circ$  aft beam) mapped onto the bottom.<sup>1</sup> The VLA beam pattern is not symmetrical down range because the array tilts aft about  $4^\circ$  when towed. The received level data are gated in time to produce bottom scattering as a function of grazing angle along the intersection of the VLA and HLA beam pattern. The intermediate angle bottom scatter data were collected by Ogden (1992) using signals, underwater sound (SUS) (540-m detonation depth) and the HLA (140-m depth). There is a left-right ambiguity in both data sets, that is each data point actually is averaged over two illuminated areas separated by roughly 5–10 nmi. Seismic, bathymetry, and core data all suggest that the measurements were conducted over a single physiographic province, i.e., illuminated areas were subject to the same scattering mechanisms. Cores 25–30 were at ranges coincident with bottom scatter at grazing angles of  $10^\circ$ – $20^\circ$ .

The majority of the low-frequency bottom scatter measurements to date (using omnidirectional sources and receivers) sample only intermediate grazing angles. Typically these measurements are extrapolated to low grazing angles using Lambert’s rule.<sup>2</sup> Thus the collocated low and intermediate angle data sets also provide an opportunity to examine this common extrapolation procedure.

The low<sup>3</sup> and intermediate angle bottom scatter data are shown in Fig. 3. The traditional extrapolations from the intermediate angle data are also shown. It is clear that low

<sup>a)</sup>Presently at SACLANT Centre, Viale S. Bartolomeo, 400, 19138 La Spezia, Italy.

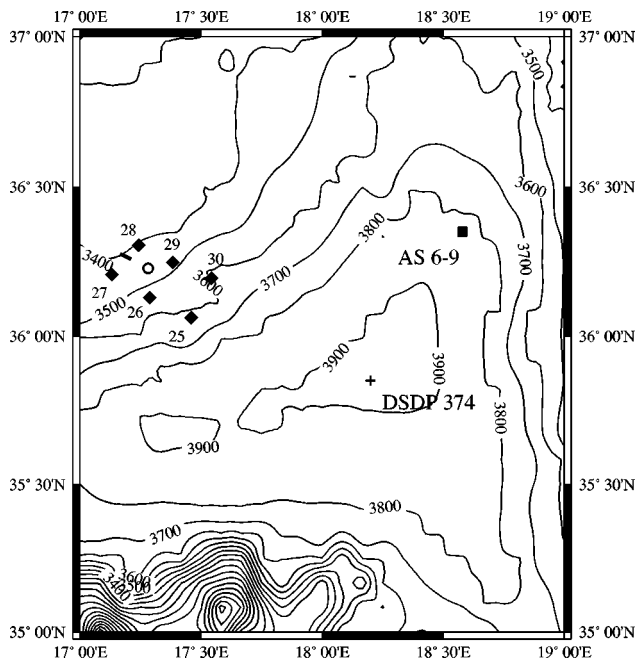


FIG. 1. Bottom scatter experiment locations: low angle measurements (solid line) and intermediate angle measurements (circle). Core locations are marked as 25–30 (gravity cores), AS-9 (piston core), and DSDP 374 (Deep Sea Drilling Project Hole).

angle bottom scattering strength is *not* predicted from the intermediate angles in this environment. For example, the frequency dependence associated with the intermediate angles is quite different than at low angles. The scattering strength at intermediate angles decreases by more than 10 dB from 225 to 930 Hz, in contrast to the 2 to 3-dB decrease in

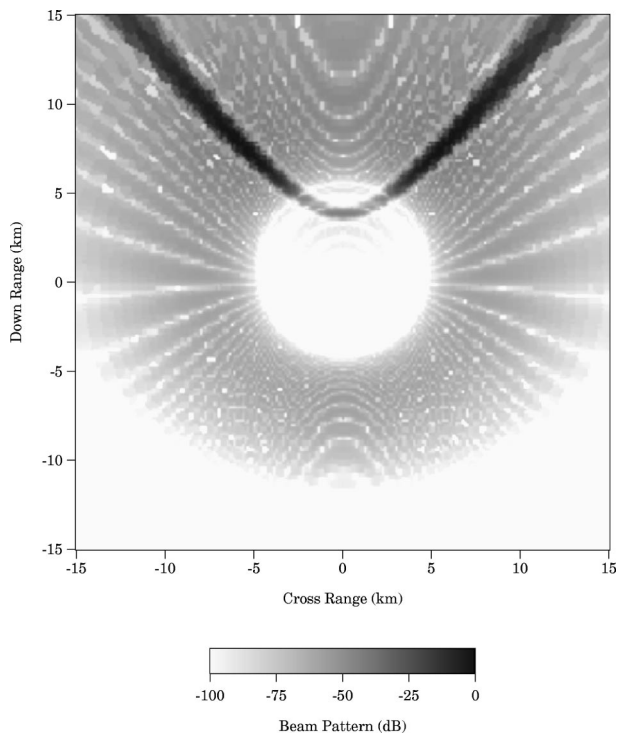


FIG. 2. Projected product of VLA and HLA beam patterns on the bottom at 930 Hz. The VLA is steered at 25° down and the HLA is steered at 138° (aft).

the low angle data. These results are disturbing inasmuch as intermediate angle data are routinely extrapolated down to lower grazing angles. This disparity between low and intermediate angle bottom scatter has also been observed for other data sets where both angular regimes were probed with a coherent source. Thus it is believed that the disparity observed in Fig. 3 is not due to the difference in source types.

The primary objective of this research was to identify and model the scattering mechanism(s) in order to predict the angle and frequency dependence of the bottom scatter. The secondary objective was to demonstrate a self-consistency in the geoacoustic model. That is, to develop a model capable of predicting both forward loss as well as back scatter. Generally, there is a lack of geoacoustic consistency in the treatment of bottom loss and bottom scatter. For example, a geoacoustic approach is often employed for bottom loss, while Lambert's rule (or another empirical or semiempirical approach) is usually employed for bottom scattering. This fragmented approach is largely due to the lack of knowledge of the processes that control bottom scattering.

The approach taken here consists of the development of three linked models: (1) a geoacoustic model, (2) a scattering kernel, and (3) a bottom scatter prediction model. The geoacoustic model defines all of the physical properties of the sub-bottom that are believed to control propagation and scattering. The scattering kernel predicts scattering from individual sediment volume inhomogeneities. The bottom scatter prediction model incorporates the geoacoustic model and the scattering kernel with all of the experimental parameters (e.g., frequency, pulse length, beam patterns, and source and receiver geometry) to simulate a received level versus time. In the final step, the simulated received level data are processed to obtain a bottom scattering strength using the same assumptions that were applied to the measured received level data.

The details of each model are presented in the following sections. Measured received levels are compared with modeled received levels to determine the success of the modeling approach. Then, measured bottom scatter data are compared with modeled bottom scatter. Artifacts that arise in the data because of assumptions in the bottom scatter processing are explored in some detail. Results are discussed and summarized in the final section.

## I. THE GEOACOUSTIC MODEL

The first major step in creating a geoacoustic model is to define the parameters. The parameter set is a statement (more usually a guess) of which physical mechanisms control propagation and scattering. The second and more difficult step is to provide each parameter a reasonable and consistent value. This is accomplished here by employing a combination of geophysical (core) data and acoustic (bottom loss) data. Each step is detailed below.

### A. Parameter definition

The first task in defining the parameter set is to identify the physical mechanism(s) causing the scattering. This is most easily accomplished by ruling out mechanisms one by one. The first mechanism to be examined is scattering at the

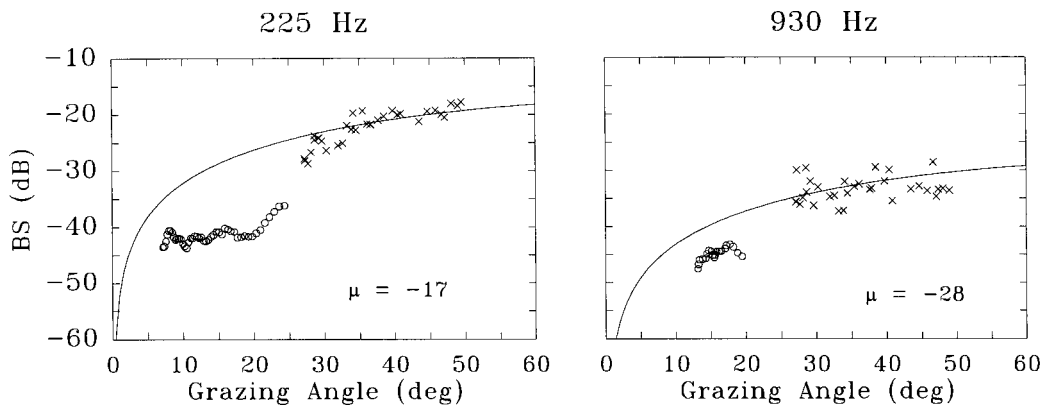


FIG. 3. Comparison of measured low angle (O) and intermediate angle (X) bottom scatter data and Lambert's rule (solid line).

water-sediment interface. Predicted bottom scatter from interface roughness using perturbation theory (Mourad and Jackson, 1993) is several tens of dB lower than that observed in the data. The predicted scattering strength is small (as expected) because the impedance contrast at the water-sediment interface is small and because the roughness is also small. Since the measured scattering strength is so much greater than that predicted from interface scattering we assume that the scattering is due to some sub-bottom scattering mechanism. The sub-bottom scattering mechanism for the low angle data is considered first.

### 1. Parameter definition for low angles

Scattering from a sub-bottom rough horizon (in this case, the evaporite sequence) is considered as an alternative mechanism. Figure 4, however, shows theinsonified field in the sub-bottom from the VLA source. Note that the evaporite sequence at 300 m sub-bottom (or depth of -3750 m) is not insonified. Having ruled out interface scattering at the evaporite sequence and the water-sediment interface we deduce that the scattering mechanism must arise from sub-bottom volume inhomogeneities.

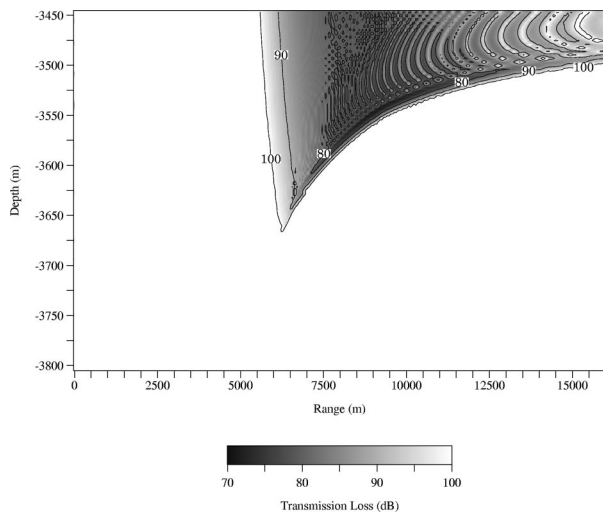


FIG. 4. Transmission loss in the sub-bottom at 930 Hz along the VLA-HLA intersecting beams of Fig. 1. The water-sediment interface is at 3447 m. Vertical exaggeration is a factor 30.

What kind of inhomogeneities could cause the observed scattering? The most apparent and prevalent geologic feature in this area is fine-scale layering. Core data in Fig. 5 show the properties associated with such layering. The higher speed layers are the terrigenous layers (silt in this case) and the host material is a pelagic silty clay. Our hypothesis is that lateral discontinuities in the layering gives rise to the scattering. That is, the terrigenous layers are finite in lateral extent and diffraction from their edges produce the observed scattering. The processes that control this lateral heterogeneity are complex and poorly understood but research on land-based slump and debris flows (Cook, 1979) suggests lateral dimensions on the order of tens to a few hundred meters. Lateral heterogeneity on a larger spatial scale (hundreds to thousands of meters) is due to faulting which is seen extensively in seismic data across this region.

In order to keep the model as simple as possible, these layer discontinuities are idealized as oblate spheroids, i.e., thin disks or lenses (see Fig. 6). The geoacoustic properties required for the lenses are given by a density and velocity. The rationale for the lens parametrization will be discussed in Sec. II.

Having defined the scattering mechanism and its parametrization, we turn to the remainder of the geoacoustic model. One of the authors (Holland and Muncill, 1993) has

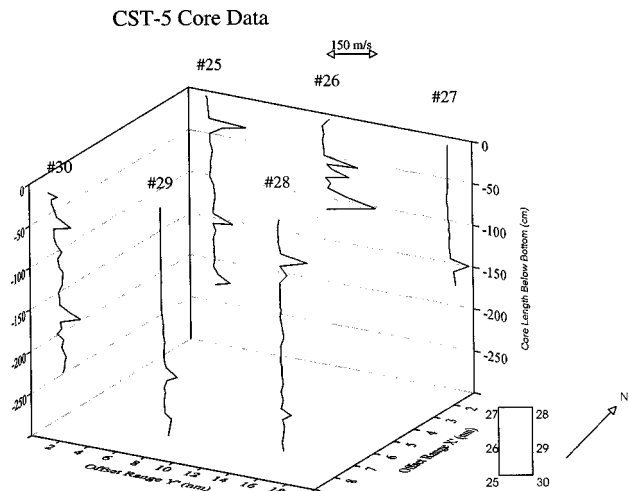


FIG. 5. Gravity core data around the measurement locations.

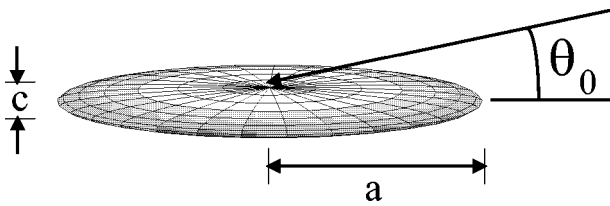


FIG. 6. Idealized sediment lens parametrized by radial length and thickness  $a$  and  $c$ , respectively.

developed a geoacoustic model for treating bottom loss from a stochastic layered medium. The distribution of lenses can be incorporated in that geoacoustic model by adding two parameters: aspect ratio (lateral/vertical radius) and the lens population density. The lateral probability density function for the lens principal radius  $a$  is assumed to be

$$W(a) = \frac{ae^{-a/g}}{g^2}, \quad (1)$$

where  $2g$  is the mean and the standard deviation is  $2^{1/2}g$ .

## 2. Parameter definition for intermediate angles

The sub-bottom scattering mechanism dominating the intermediate angle data is now considered. At intermediate grazing angles, the field *does* interact with the basement horizon. Thus at intermediate angles the scattering mechanism is a combination of both basement scattering and sediment volume scattering. Which mechanism dominates will be explored later in the paper.

The basement horizon exhibited a significant amount of roughness in the seismic data. In addition, core data from the Deep Sea Drilling Project (DSDP) Site 374 showed that the basement consisted of interbedded mudstone and gypsum. The gypsum layers are expected to be laterally heterogeneous so that the scattering from this assemblage is probably a function of the basement volume heterogeneities as well as roughness.

## B. Parameter value specification

The technique for determining parameter values for the Messina Cone environment relies upon both geophysical and acoustic data. The geophysical data consists of core data (density and velocity as a function of depth in the core) and seismic data. Bottom loss data are used to extract attenuation and to provide a check on the sound-speed gradient, and the vertical length scales of the layering as well as basement properties. The parameter specification for the sediment volume is discussed first.

### 1. Sediment volume properties

Core data that were available in the region included six gravity cores (#25–30) collected by the Naval Oceanographic Office and DSDP data. The location of these data in relation to the bottom scatter site are shown in Fig. 1. Sound speed (see Fig. 5) and density were measured on the gravity cores. Observed lithologic changes governed the measurement sampling frequency (which varied from about 2.5 to 10 cm) on each core. The lateral separation of the cores was about 8 nmi. Even though the lateral separation is much too

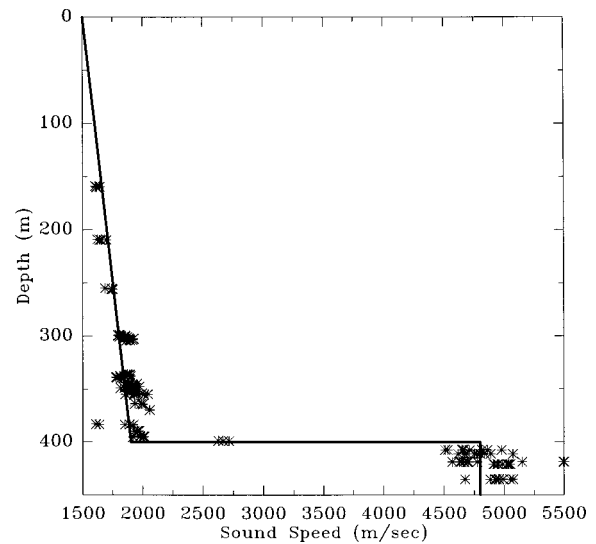


FIG. 7. Modeled sediment sound-speed profile (solid line) with DSDP data (\*). For clarity, layering is not shown in the solid line.

large to permit an estimate of the lateral length scale of individual layers, the core data are invaluable in that: (1) they demonstrate that individual layers are discontinuous (i.e., lenslike); (2) they provide the required density, velocity, and thickness in the host and scatterers (see Table I); and (3) they indicate that the bottom and sub-bottom environment are consistent in gross features across the measurement area. The DSDP data provided the velocity profile for the unconsolidated sediment column as shown in Fig. 7. Hamilton's (1980) empirical sound-speed gradient for turbidites ( $1.3 \text{ s}^{-1}$ ) seems to fit quite well.

Bottom loss (BL) data in this environment will be sensitive to all of the parameters in the geoacoustic model with the exception of the lateral length scale. Thus measured bottom loss data can be an extremely useful way to determine or check nearly all of the sub-bottom parameters required for predicting sub-bottom volume scattering. For example, the data provide a check on the sediment sound-speed profile extrapolation from DSDP sites to the area where the bottom scatter data were acquired. The bottom loss data also provide a check on the implicit extrapolation of the intercalating layers in the core data in range and depth. One of the most important functions of the bottom loss data was to provide an independent estimate of attenuation in the upper sediment column. The bottom loss modeling approach of Holland and Muncill (1993) is employed in the following analysis.

In order to examine the effects of the layering on bottom loss, modeling is performed both with and without the layers. Figure 8 compares the bottom loss data and the predictions without the layers. At low frequencies (50–200 Hz) the paths that interact with the evaporite horizon are apparent starting at about  $30^\circ$ . Since the low angle bottom scatter data are not sensitive to this horizon (see Fig. 5) we only show paths that refract above this horizon. At low grazing angles and low frequencies the slope of the BL versus angle is quite sensitive to the sediment attenuation because the BL is dominated by arrivals which refract through the sediment. The dashed line is a prediction using the "host" properties derived from the core data (see Table I) and an attenuation of 0.08 dB/m/

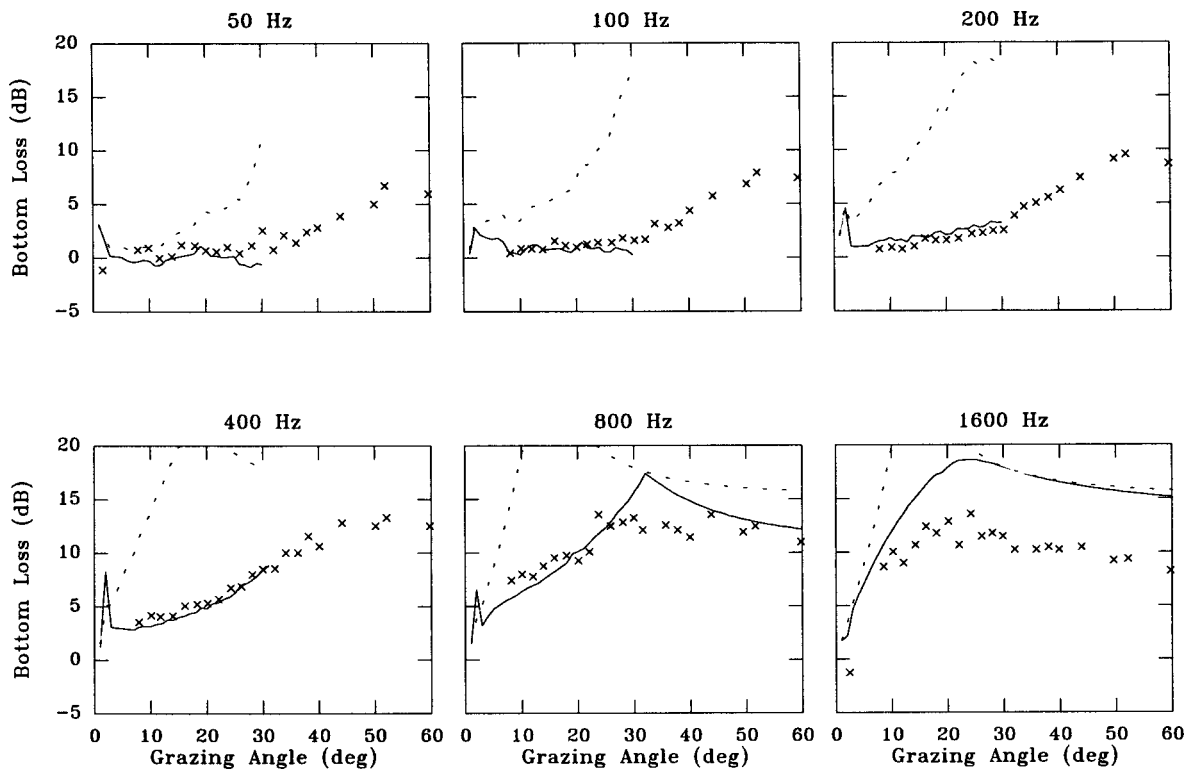


FIG. 8. Bottom loss data (×) and model predictions using an attenuation of 0.08 dB/m/kHz (dashed line) and an attenuation of 0.01 dB/m/kHz (solid line).

kHz, as given by Hamilton (1980) for this sediment type. It is clear that this attenuation is much too large because the slope of the data is much smaller than that of the predictions. Using the slope of the low grazing angle BL, we estimate a value of 0.01 dB/m/kHz. The improved fit is shown in Fig. 8 as the solid line. In Fig. 9, the effect of the fine-scale layering is shown. The dashed line is the prediction without the layering and the solid line is predictions with the layering (see Table I). As frequency increases, the bottom loss becomes increasingly sensitive to smaller sedimentary length scales. It is important to note that the length scales and properties of the layering from the core data are sufficient to predict the correct frequency and angle dependence of the bottom loss.

In order to complete the geoacoustic model for the sediment volume, the aspect ratio and number of lenses per unit volume are required. Neither parameter was measured. However, both of the unknown parameters only control the overall level of the bottom scatter results. Thus the angular and frequency dependence of the bottom scatter predictions (and hence the conclusions) do not hinge on knowing the precise

distribution of the sub-bottom scatterers. A 100:1 aspect ratio was selected as a reasonable estimate. The number of scatterers per unit volume was chosen based on the number of intercalating layers per unit depth (roughly 0.8 per meter) and a percent coverage of each layer. A 40% coverage of each layer was chosen as an initial estimate.

## 2. Basement properties

Core data indicates that the basement consisted of a complex interlayering of mudstone and gypsum (note the basement compressional sound-speed variability in Fig. 7). Densities in the basement were also highly variable and ranged from between 2.1 and 2.5 g/cc.

## II. THE SCATTERING MODEL

Having now developed the geoacoustic model, the next step is to develop scattering kernels for both the sediment volume and the basement. Sediment volume scattering is treated first.

### A. Sediment volume scatter model

It was postulated that the dominant scattering mechanism in this environment is discontinuous layering. These discontinuities are idealized as thin oblate spheroids (lenses). The lens model offers the possibility of studying interaction from a single “idealized” scatterer. Scattering from such a sedimentary structure is treated in this section with the goal of understanding the angle and frequency dependence of the scattering process. In particular, the importance of shear waves in the scattering process and the validity of the Born approximation are examined.

TABLE I. Geoacoustic model.

Parameter	Units	Host	Scatterers
	unconsolidated sediment column		
Interface sound-speed ratio	...	0.969	0.996
Sound-speed gradient	1/s	1.3	1.3
Density	g/cc	1.45	1.6
Attenuation	dB/m/kHz	0.01	0.05
Mean layer thickness	m	1	0.2
Layer aspect ratio ( $a/c$ )	...	...	100:1
Total sediment thickness	m	300	



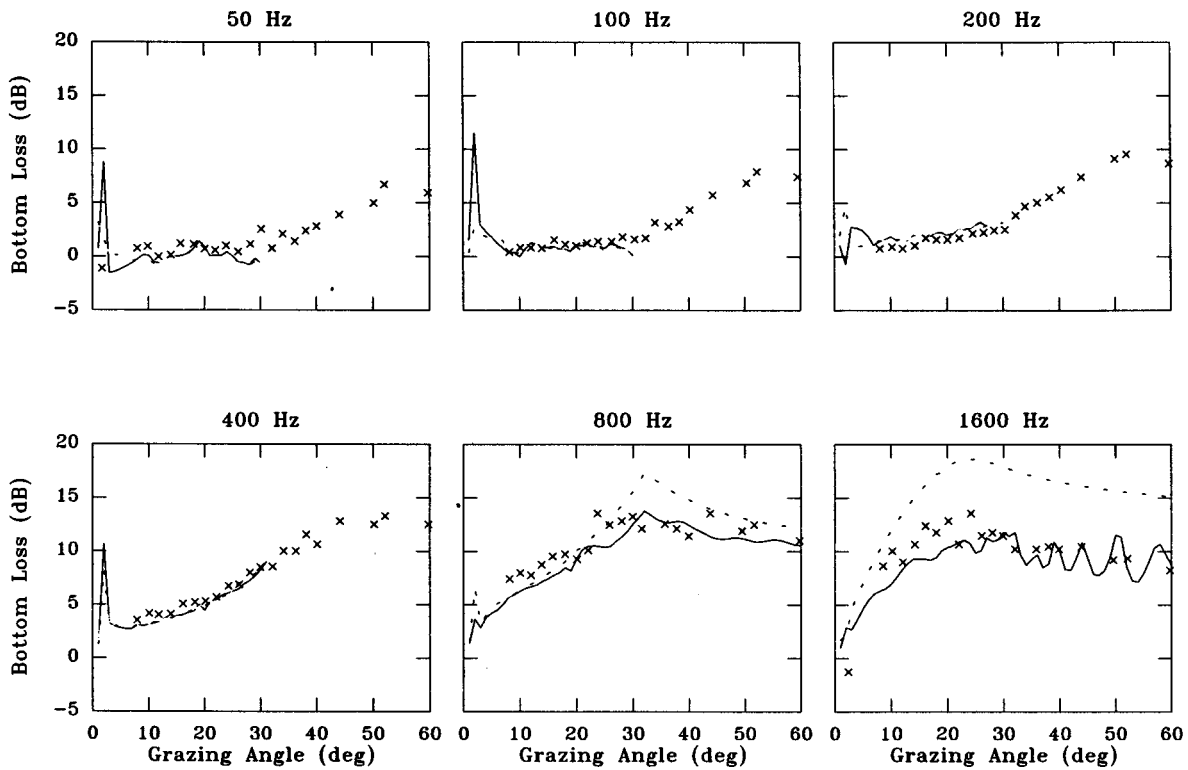


FIG. 9. Bottom loss data (×) and model predictions with layering (solid line) and without layering (dashed line).

Calculation of scattering from a thin oblate spheroid is a formidable problem. Solutions for low or high frequencies or for pressure release or rigid boundary conditions have been developed [e.g., Achenbach *et al.* (1978), Kristensson and Waterman (1982)] but the full solution requires spheroidal functions which are difficult numerically or spherical functions which are convergent only outside a sphere defined by the lens radius. Instead, an approximate solution is employed (Simons, 1980) that neglects multiple scattering within the spheroid.

The backscattered differential cross section for a silt lens embedded in an infinite silty clay host is shown in Fig. 10. The material parameters are those appropriate for the geoacoustic model developed in the previous section (see Table I). The modeled shear speeds in the silty clay host and silt lens are 80 and 120 m/s, respectively. The observed interference pattern in angle is simply the interference between the diffracted contribution from the front and back edge of the

lens. Assuming that scattering from a random distribution of lenses smoothes over the interference effects, the envelope of the predicted scattering below  $20^\circ$  is nearly independent of angle and frequency.

In Fig. 10 scattering from an elastic lens in an elastic host medium and scattering from a fluid lens in a fluid medium are shown. Differences between the two predictions are less than a line width. Thus shear wave coupling for these kinds of sedimentary parameters is negligible. By neglecting shear waves in both the scatterer and the host material the far-field differential scattering cross section ( $dP/d\Omega$ ) can be written as:

$$\frac{dP}{d\Omega}(\theta_0) \cong \left[ c \left( \frac{\partial \rho}{\rho} + \frac{\partial \lambda}{\lambda} \right) \left( \frac{\sin(2a\alpha \cos \theta_0)}{2a\alpha \cos \theta_0} - \cos(2a\alpha \cos \theta_0) \right) / 4 \cos^2 \theta_0 \right]^2, \quad (2)$$

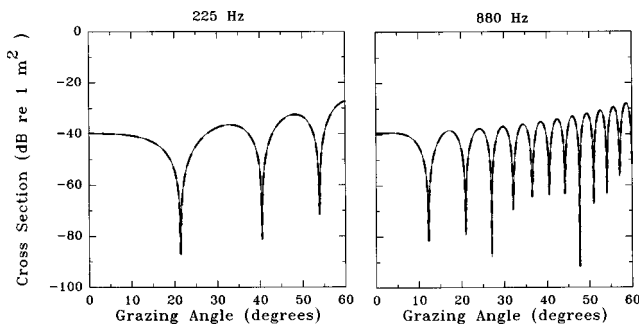


FIG. 10. Differential scattering cross section from a silt lens. The aspect ratio is 100:1, and the lens thickness is 20 cm. The predictions with shear (solid line) and without shear (dashed line) are nearly identical.

where  $\rho$  and  $\lambda$  are the Lamé parameters for the host medium,  $\partial \rho$  and  $\partial \lambda$  are the differences in Lamé parameters between the host and scatterer,  $\alpha$  is the compressional wave number,  $a$  is the lens principal radius,  $c$  is the lens radial thickness (see Fig. 6), and  $\theta_0$  is the grazing angle. Note that scattering is proportional to the lens thickness and the velocity and density difference between the host and scatterer. The overall level of the backscatter is insensitive to the lateral radius.

In Fig. 11, the validity of the Born approximation is compared with Simons expression. The Born approximation appears to be reasonably good which is not surprising given the small impedance contrast.

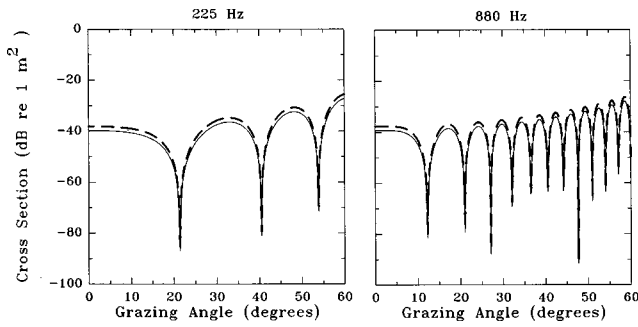


FIG. 11. Differential scattering cross section from a silt lens. Aspect ratio is 100:1, and the lens thickness is 20 cm. The Born approximation (dashed line) compares favorably with Eq. (2) (solid line).

### B. Basement scatter model

Scattering at the basement is complicated by the fact that: (1) both basement interface and basement volume scattering are expected to be significant and (2) the impedance contrast between gypsum and dolomitic mudstone layers precludes the use of the Born approximation. In order to obviate these difficulties, a Lambert scattering kernel with coefficient  $\mu_b$  is employed at the sediment–basement interface.

### III. THE ACOUSTIC BOTTOM SCATTER MODEL

In order to understand the measured bottom scatter data, the data processing assumptions must be considered. The underlying assumption is that the scattering process occurs at the water–sediment interface. Thus the classical equation for computing bottom scatter is

$$BS(\theta_k) = \langle RL(t; \theta_k) \rangle - SL + TL_s + TL_r - 10 \log(A(t, \tau)), \quad (3)$$

where SL is the source level,  $\langle RL \rangle$  is the ensemble averaged reverberation level,  $\theta_k$  is the angle at water–sediment interface defined by the ray at the center of an interface patch illuminated by the pulse at time  $t$ ,  $TL_s$  and  $TL_r$  are the transmission losses (including beam pattern losses) from source to the center of the scattering area and from scattering area to the receiver, respectively, and  $A$  is the insonified area at the water–sediment interface as a function of time and pulse length  $\tau$ . The last three terms in Eq. (3) constitute a quantity known as the “effective area.” The effective area was calculated by a numerical integration over the water–sediment interface, i.e., by summing the product of the two-way transmission loss and the cell area over discrete cells. CAPARAY (Westwood and Vidmar, 1987) was used to compute the TL terms, travel times, and angles for the effective area calculation.

What happens in the case where the scattering process does not depend upon area (at the sediment interface) but upon the sub-bottom volume or sub-bottom interfaces? The data in Fig. 3 (and essentially all other bottom scatter data sets) are processed with the assumption that the scattering process occurs at the water–sediment interface. But since these data are governed not by interface but by sub-bottom scattering what artifacts might be expected?

Figure 4 shows the sub-bottom field at 930 Hz as insonified by the VLA and a long cw pulse. The caustic<sup>4</sup> defines the lower bound of acoustic penetration. Thus the depth di-

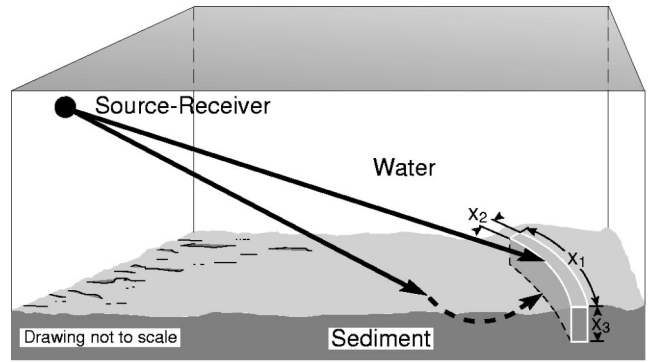


FIG. 12. Three-dimensional cartoon of a pulse in the sub-bottom.

mension of the insonified volume is controlled entirely by the sound-speed profile in the bottom. A cartoon of the pulse in three dimensions is shown in Fig. 12, where the cross range dimension  $x_1$  is controlled by the beam pattern of the HLA, the down range dimension  $x_2$  is controlled by the pulse length, and the vertical dimension  $x_3$  is controlled by the sound-speed profile in the sub-bottom.

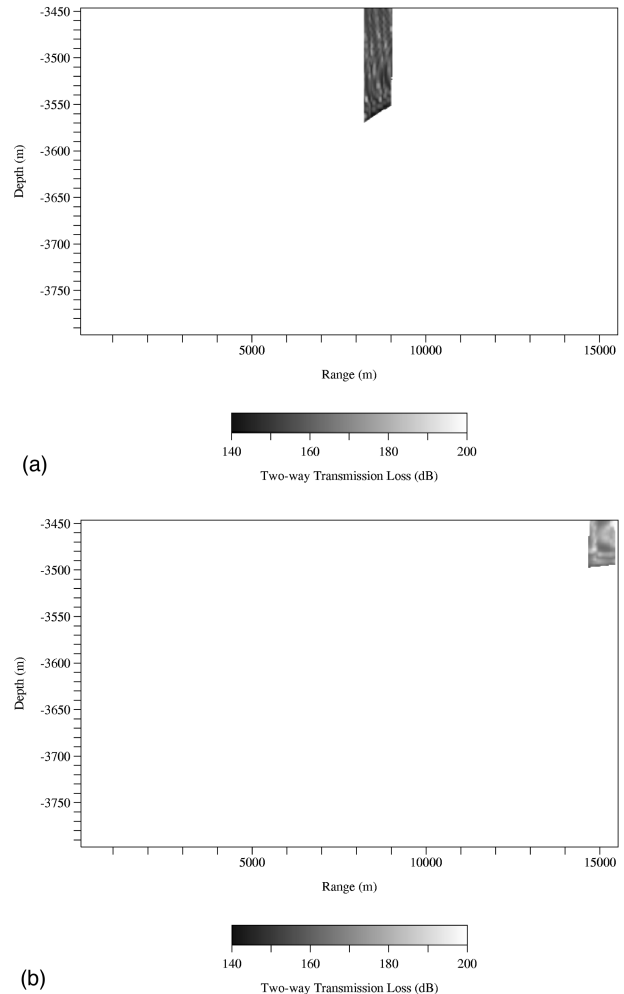


FIG. 13. Two-dimensional cross-sectional view of the pulse in the sediment at 930 Hz. The time is (a) 12 s corresponding to a reference angle of 18° and (b) 20 s corresponding to an angle of 7.5° at the water–sediment interface. Source and receiver beam patterns are included in the calculation. Vertical exaggeration is 30:1.

In Fig. 13, a 1-s pulse at two different times (or grazing angles) is displayed in two dimensions. What is apparent here and displayed in Fig. 14 is that when bottom scatter is controlled by sub-bottom volume scattering, the range of angles is greater than that for interface scattering (as assumed in the data processing). Figure 14 shows the range of vertical angles insonified for volume scattering and the narrower range applicable for interface scattering. For example, at a reference angle of 20°, the angles at the water-sediment interface are 18°–22°, but the actual angles involved in the sub-bottom volume scattering process range from 18° to 30°. The beam pattern at 930 Hz in Fig. 14 is shown for reference as the dashed line. The miss-assignment of angles for a given time in the data processing can cause anomalies in the data interpretation and will be discussed in the next section.

The foregoing indicates several important considerations in modeling the sub-bottom volume scattering. First, the gross sound-speed profile in the sediment plays a crucial role in the scattering process because it delimits one dimension of the insonified volume (see Fig. 4). Thus sub-bottom volume scattering is a function of both the scattering process and the amount of volume that is illuminated. Just as importantly, the sediment sound-speed profile controls what mechanism(s) is illuminated. For example, ray paths above 27° in this environment interact with a very rough and inhomogeneous, evaporite sequence. Thus the intermediate angle bottom scatter data in Fig. 3 are controlled by an entirely different mechanism than the low angle data.

A second important consideration is that measured bottom scattering strength may or may not be a plane-wave quantity. Bottom scatter data are not plane-wave quantities when the scattering function, transmission loss, or the source/receiver beam patterns are not constant at a given time (or reference angle). The bottom scatter data set considered here clearly does not represent a plane-wave measure-

ment (e.g., note the nonconstant beam pattern at 20° reference angle in Fig. 14).

Most of the bottom scatter models in the community do not adequately address these sub-bottom scattering issues. For example, bottom scatter models typically ignore sediment sound-speed gradients [e.g., Ivakin (1981), Tang and Frisk (1992)] that seem to be critical in identifying the mechanism and defining the appropriate volume. Mourad and Jackson (1993) use an unusual form of the sound-speed gradient that may not be appropriate at low frequencies. In addition, almost all current models [excepting Tang and Frisk (1992)] make the plane-wave assumption.

Early on in the data interpretation it became clear that plane methods would be inadequate and that the complexities of the experiment geometry needed to be included to understand the measured data. This was accomplished by modeling the received level in the time domain and then calculating bottom scatter in the same fashion as the data were processed (i.e., with the usual interface scattering assumptions). Assuming that the scattering is incoherent, and invoking the Born approximation, the received level from a single ping can be written as a sum of delayed, scaled, replicas of the transmit source intensity  $S(t)$ :

$$RL(t; \theta_k) = 10 \log \left[ \sum_{i=1}^N S(t-t_i) 10^{TL_i^1/10} 10^{TL_i^2/10} \times \frac{dP}{d\Omega}(\theta_i, z_i) \right], \quad (4)$$

where  $TL_i^1$  and  $TL_i^2$  are the transmission losses (including the beam pattern) from the source to scattering element  $i$  and from element  $i$  back to the receiver, respectively. For sub-bottom volume scattering  $dP/d\Omega$  is the differential scattering cross section of the lens  $i$  at depth  $z$  and  $N$  is the number

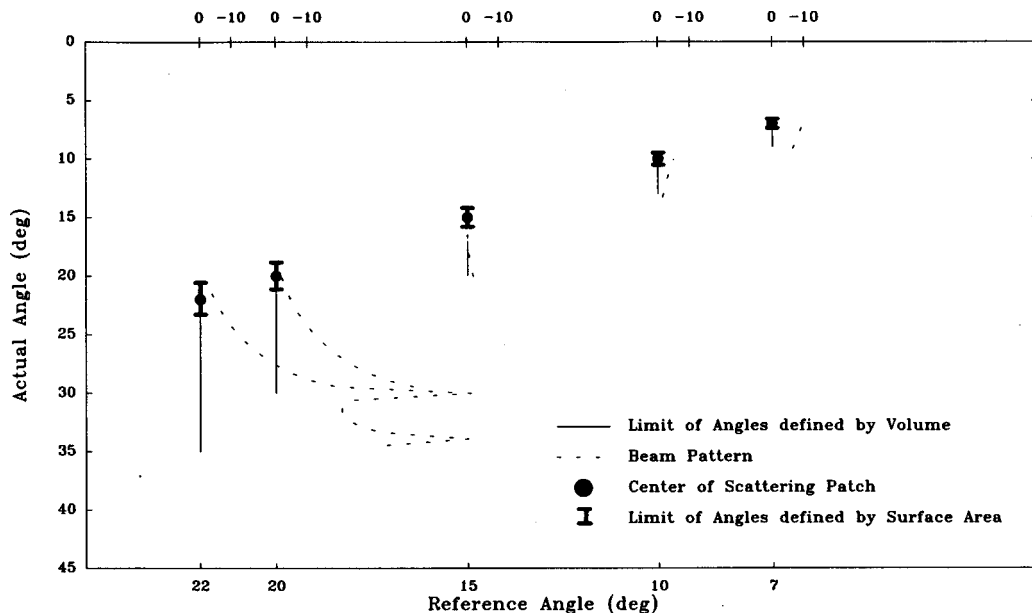


FIG. 14. Angle spreads associated with a volume scattering process for a 1-s pulse. The reference angle is the angle assigned at the water-sediment interface for bottom scatter. The circle represents the center of the scattering patch. The error bars show the range of angles insonified at the water-sediment interface, the solid line represents the range of angles insonified in the sediment volume. The dashed line represents the 930-Hz beam pattern in the sediment normalized to 0 dB along the array maximum response axis: 10-dB tic marks are given at the top of the plot.

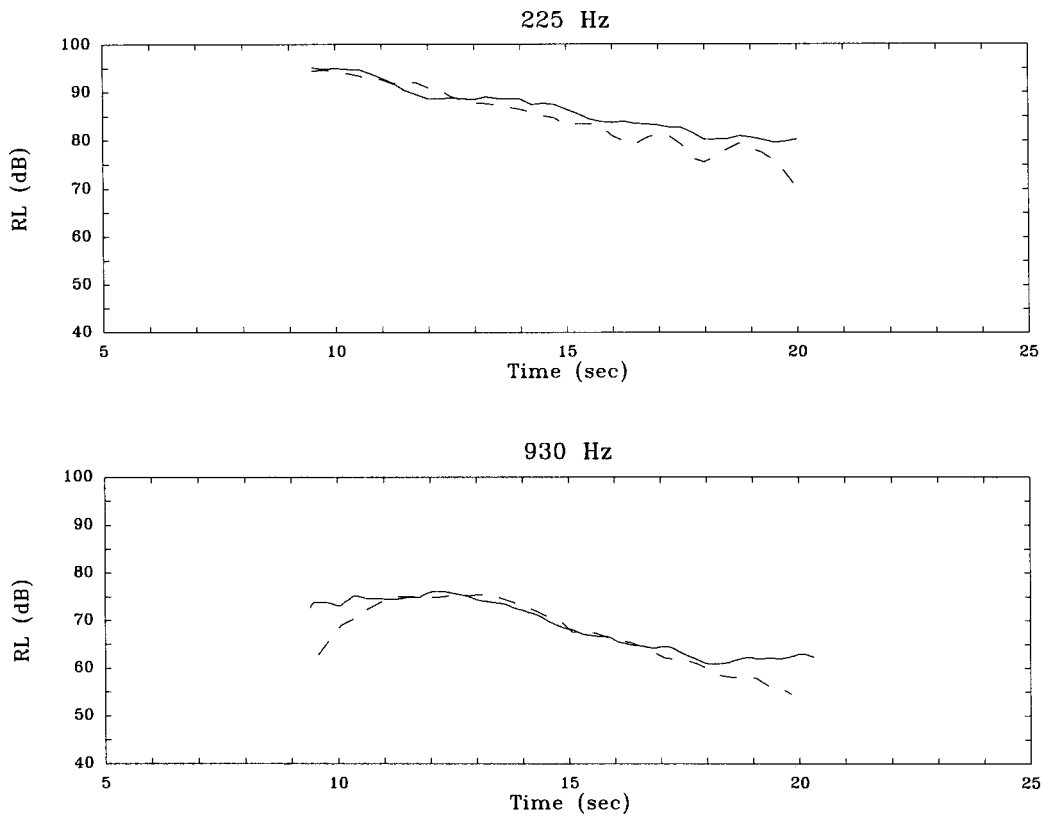


FIG. 15. Measured (solid) and modeled (dashed) bottom reverberation at (a) 225 Hz and (b) 930 Hz.

of lenses. For the basement scattering contribution, the basement interface is discretized into  $N$  cells and  $dP/d\Omega$  is simply the Lambert scattering kernel at cell  $i$  multiplied by the cell area. SAFARI (Schmidt, 1988) was used to compute the TL terms in the cw approximation. SAFARI treats the vertical source array beam pattern explicitly, the HLA beam pattern was approximated by wave-number filtering. CAPARAY was used to compute travel times  $t_i$  and angles  $\theta_i$ .

The number of pings used in the low angle data processing varied from 5 to 19. In the modeling, the lenses are randomly distributed for each ping, and the received level is ensemble averaged. The relatively small source and receiver offsets<sup>5</sup> are explicitly modeled though the results are nearly identical with a monostatic assumption.

The “apparent bottom scatter” for both the low and intermediate angle data is then calculated using Eq. (3). It is crucial to note that the correction for TL as well as angles in Eq. (3) are to the water–sediment interface, whereas the TL and angles in Eq. (4) are to the volume scatterer or basement interface.<sup>6</sup> Thus the model attempts to treat all of the effects of the experiment geometry as well as the artifacts introduced by the assumptions in the data processing.

#### IV. BOTTOM SCATTER MODEL TO DATA COMPARISONS

The acoustic model of Sec. III is now applied to the data with the geoaoustic model of Table I as inputs. The form of the scattering kernel was given in Sec. II. Model-to-data comparisons are first shown for the low angle data.

#### A. Low angle bottom scatter

Comparisons between the measured and modeled  $\langle RL \rangle$  at low angles are shown in Fig. 15. Processing the modeled time series using Eq. (3) yields the bottom scattering predictions shown in Fig. 16. The model predicts the measured

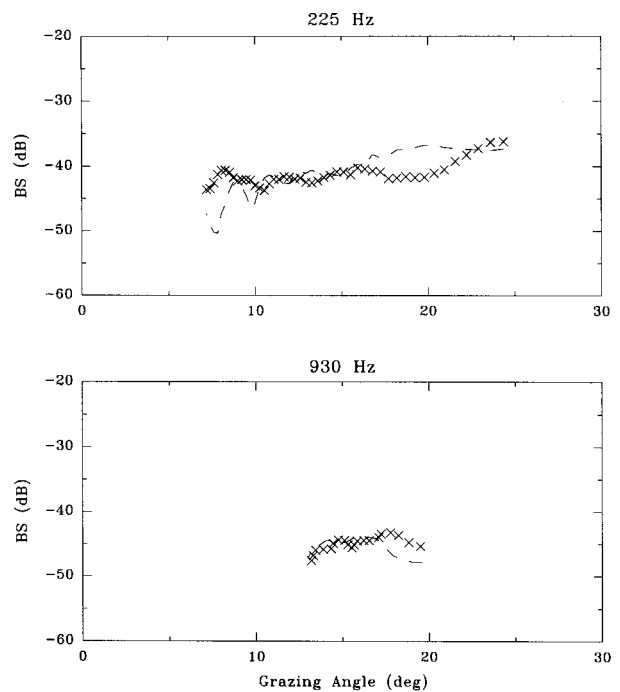


FIG. 16. Measured ( $\times$ ) and modeled (dashed) bottom scatter at: (a) 225 Hz and (b) 930 Hz.

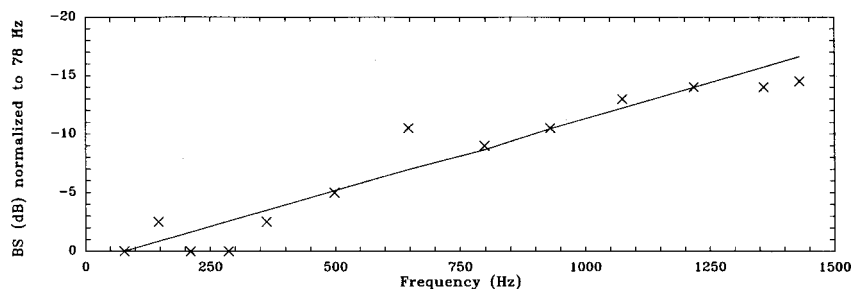


FIG. 17. Measured ( $\times$ ) and modeled (solid line) intermediate angle data at  $40^\circ$ .

data quite well. Recall that the overall level of the predictions is a function of two unknown parameters: the number of lenses per unit volume and aspect ratio. However, the fact that the model predicts the frequency and angular dependence observed in the data suggests that the geoacoustics and scattering kernel are reasonably accurate. Thus the hypothesis that the low angle data are controlled by sub-bottom volume scattering seems to be borne out.

An interesting feature observed both in the measured and modeled scattering is worth noting. From  $18^\circ$  to  $20^\circ$  the bottom scattering at 930 Hz appears to decrease. This turns out to be an artifact of the interface scattering assumption. Figure 14 shows that for a sub-bottom volume scattering process, a nominal  $20^\circ$  angle at the water-sediment interface actually corresponds to angles between  $18^\circ$  and  $30^\circ$ . Most of that angular range is poorly insonified by the beam pattern as shown by the dashed line. Thus the processing assumes high insonification (the beam pattern is referenced to the water-sediment interface at  $20^\circ$ ), while the actual insonification is small which leads to erroneously small scattering levels.

This artifact, though small, is reflected in both the data and model and further demonstrates that: (1) this data set is dominated by sub-bottom volume scattering effects, and (2) that modeling must account for the non-plane-wave nature of such a phenomenon.

### B. Intermediate angle bottom scatter

Sediment volume scatter predictions at intermediate angles are on the order of 10 dB lower than the measured data. Thus basement scattering must be the dominant scattering mechanism. Figure 17 shows the frequency dependence of the measured data at about  $30^\circ$  grazing angle and the model predictions with a constant scattering coefficient  $10 \log \mu_b = -18.5$  dB. Changing  $\mu_b$  to another value would shift the curve up or down without changing the slope of the prediction. Thus the frequency dependence of the intermedi-

ate angle data appears to be solely due to the sediment attenuation. The fact that this was the same attenuation used in the bottom loss (see Fig. 9) and in the low angle predictions (see Fig. 16) adds substantial weight to the geoacoustic model. Therefore the basement scattering kernel appears to be independent of frequency. The volume scattering component was not included in the intermediate angle predictions because it contributes negligibly to the overall scattering strength.

Figure 18 shows both the low and intermediate angle data along with the predictions. The hypothesis that the low angle data are governed by sediment volume inhomogeneities and that the intermediate angle data are governed by the basement appears to be confirmed.

## V. DISCUSSION AND SUMMARY

Bottom scatter strength data exhibit artifacts when the sub-bottom plays a role in the scattering process. The artifacts arise from the classical assumption in the data processing that the scattering process occurs at the water-sediment interface. Many of the current bottom scattering models, even those that explicitly treat sub-bottom scattering, do not address these artifacts. A new bottom scatter modeling approach was proposed, implemented, and employed to analyze a bottom interaction data set. The development of the model and the subsequent model-to-data comparisons yielded a number of insights into bottom scatter measurement and interpretation issues:

- (1) A self-consistent geoacoustic basis was demonstrated that predicted not only the angular and frequency dependence of the low and intermediate angle bottom scatter data but also the bottom loss. Both kinds of data (bottom loss and bottom scatter) were seen to be largely controlled by the sediment sound-speed profile and the attenuation.
- (2) The self-consistent geoacoustic basis provided the clue to unraveling the disparity between the low and the

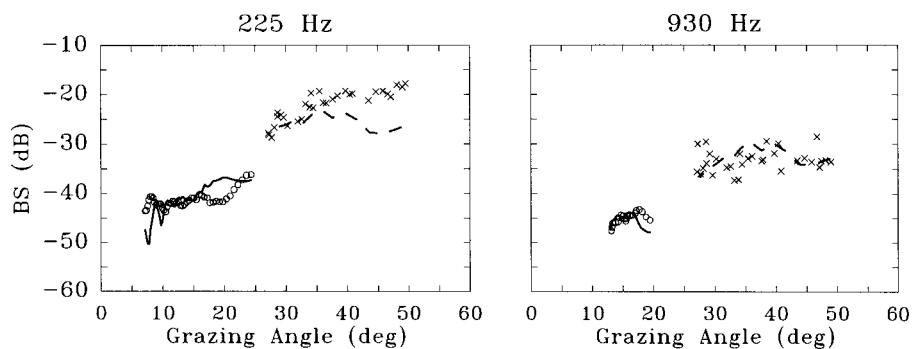


FIG. 18. Measured low angle ( $\circ$ ) and intermediate angle ( $\times$ ) bottom scatter data and model predictions at low angles (solid line) and intermediate angles (dashed line).

intermediate angle bottom scatter data. It appears that the two data sets are controlled by two entirely different mechanisms. The low angle data is controlled by sub-bottom volume scattering while the intermediate angle data appear to be controlled by the rough evaporite horizon. The disparity in bottom scatter between low and intermediate angles has been observed in at least two other sites.

(3) Caution should be exercised in the current and common practice of extrapolation from intermediate angle measurements (such as those collected by the survey community) to low angles. The ability to extrapolate between intermediate and low angles requires knowledge of the sediment properties (including sediment thicknesses, sound-speed profile, and attenuation). If these are known, the model can provide predictions about regions where direct extrapolation is feasible.

(4) Our approach demonstrates the usefulness of bottom loss in developing an understanding of the mechanisms and parameters that also control bottom scattering. For example, the bottom loss data enabled a good estimate of sediment attenuation and was useful in verifying the vertical length scales of the layering obtained from the core data. Bottom loss measurements can be a valuable adjunct to direct path bottom scatter measurements.

(5) The results demonstrate that when the sub-bottom is involved in the scattering process, the measured bottom scatter contains artifacts which are a function of both sub-bottom propagation and experimental geometry. These artifacts are commensurate with well-known artifacts in bottom loss and arise in both kinds of data because of the classical assumption in the data processing that the reflection or scattering phenomenon occurs at the water-sediment interface.

- (a) These artifacts can obscure the effects of the scattering mechanism itself. As an example, the roll-off of the 930-Hz bottom scatter data at 20° can be attributed to artifacts associated with the beam pattern coupled with the sub-bottom sound-speed profile. This dictates caution in attributing the angular or frequency dependence of bottom scatter data to the angular or frequency dependence of the scattering mechanism.
- (b) The existence of artifacts in the measured data also suggests caution in applying plane-wave models to the bottom scattering problem since for sub-bottom scattering there can be a substantial spread in angles for a given time or reference angle. Thus, contrary to common practice, plane-wave models may be inappropriate when sub-bottom scattering dominates.

## ACKNOWLEDGMENTS

This work was sponsored by Dr. Edward Estalote of the Office of Naval Research METOC Models Databases and

Simulation Program and Mr. Charles Bohman of the Space and Naval Warfare Systems Command, PMW-182. We also gratefully acknowledge helpful conversations with Mr. Sean Reilly (Naval Undersea Warfare Center), Dr. Peter Ogden, and Dr. Roger Gauss (Naval Research Lab) regarding details of the data processing.

<sup>1</sup>In practice, the source and receive arrays together gave on the order of 50–60-dB rejection of normal incident reflections. Modeling indicated that this was sufficient to eliminate multipaths.

<sup>2</sup>Lambert's rule predicts a grazing angle dependence of  $\sin \theta_i \sin \theta_s$  where  $\theta_i$  is the incident grazing angle and  $\theta_s$  is the scattered angle.

<sup>3</sup>1- and 0.25-s pulse lengths were employed for the 225 and 930 Hz data, respectively. That the bottom scatter is independent of pulse length was shown by Henyey *et al.* (1995).

<sup>4</sup>Note that the levels at the caustic exceed those at the water-sediment interface even at 930 Hz. Since the levels are high at the caustic it may seem possible that the backscattered field is controlled by the scattering at the caustic. However, for scattering elements distributed throughout the sediment column, the volume contained within the caustic is so much smaller than the volume contained outside the caustic that the caustic actually plays a fairly minor role, at least for this frequency and environment.

<sup>5</sup>Source-receiver offsets were about 850 m for the low angle data and 50 m for the intermediate angle data.

<sup>6</sup>This leads to a shift and stretch of the disk or Lambert angular dependence.

Achenbach, J. D., Gautesen, A. K., and McMaken, H. (1978). "Diffraction of point source signals by a circular crack," *Bull. Seismol. Soc. Am.* **68**, 889–905.

Cook, H. E. (1979). "Ancient continental slope sequences and their value in understanding modern slope development," *Soc. Econ. Pal. and Min. Special Publication No. 27*, pp. 287–305.

Hamilton, E. L. (1980). "Geoacoustic modeling of the seafloor," *J. Acoust. Soc. Am.* **68**, 1313–1339.

Henyey, F. S., Thorsos, E. I., and Nathwani, K. M. (1995). "Scattering strength cannot depend on the length of the pulse," *J. Acoust. Soc. Am.* **98**, 2986–2987.

Holland, C. W., and Muncill, G. (1993). "Acoustic reflection from quasi-periodic sedimentary sequences," *J. Acoust. Soc. Am.* **94**, 1609–1620.

Ivakin, A. N., and Lysanov, Yu. P. (1981). "Theory of underwater sound scattering by random inhomogeneities of the bottom," *Sov. Phys. Acoust.* **27**, 61–64.

Kristensson, G., and Waterman, P. C. (1982). "The *T* matrix for acoustic and electromagnetic scattering for circular disks," *J. Acoust. Soc. Am.* **72**, 1612–1625.

Mourad, P. D., and Jackson, D. R. (1993). "A model/data comparison for low-frequency bottom backscatter," *J. Acoust. Soc. Am.* **94**, 344–358.

Ogden, P. M. (1992). "Low frequency bottom and surface scattering measurements using SUS charges in the Ionian Sea during CST-5," Naval Research Laboratory, Washington, DC 20375, 30 April 1992.

Reilly, S., and Sundvik, M. (1992). "CST-5 direct path, active waveform bottom reverberation analysis," TRACOR Doc No. T92-95-1013-U.

Schmidt, H. (1988). "SAFARI: Seismo-Acoustic Fast Field Algorithm for Range Independent Environments," Report No. SR-113, SACLANT Undersea Research Centre, La Spezia, Italy.

Simons, D. A. (1980). "Scattering of elastic waves by thin inclusions," *J. Appl. Phys.* **51**, 934–940.

Tang, D. J., and Frisk, G. (1992). "Spectral parameterization of scattering from a random ocean bottom," *J. Acoust. Soc. Am.* **92**, 2792–2799.

Westwood, E., and Vidmar, P. (1987). "Eigenray finding and time series simulation in a layered-bottom ocean," *J. Acoust. Soc. Am.* **81**, 912–924.

# Application of genetic algorithms to ultrasonic tomography

P. P. Delsanto, A. Romano, and M. Scalerandi

*INFN, Dip. di Fisica del Politecnico di Torino, C.so Duca degli Abruzzi 24, Torino, Italy*

F. Moldoveanu

*Universitatea Politecnica Bucuresti, Splaiul Independentei 313, Bucuresti, Romania*

(Received 25 June 1997; accepted for publication 8 April 1998)

A new method for ultrasonic tomography based on genetic algorithms is proposed for the prediction of the geometry of an inclusion of known physical properties in a given specimen. New inversion operators are introduced in order to take full advantage of the physical properties of the system investigated. The efficiency of the proposed method is tested through a comparison with other existing techniques for the solution of the inverse problem. The accuracy of the procedure is verified by using a variety of sets of synthetic data. Good and fast convergence is obtained even in the case of complex geometries if parallel processing is adopted. © 1998 Acoustical Society of America. [S0001-4966(98)00108-8]

PACS numbers: 43.35.Cg, 43.35.Wa [HEB]

## INTRODUCTION

Ultrasonic tomography (UT) has the potential for becoming a basic tool both for industrial and medical applications, particularly when it is desirable to avoid the use of radiation or when a propagation velocity map is more meaningful than an attenuation map (such as provided by x-ray tomography). In UT, however, the refraction of the acoustic paths poses an additional complication. In fact, unless the impedance mismatch is very small, the assumption of straight rays is no longer valid, and it becomes necessary to predict not only the physical properties of the specimen, but also the ray paths between each transmitter and each receiver. Therefore the selection of an efficient algorithm for the tomographic reconstruction becomes of paramount importance.<sup>1,2</sup>

Tomographic reconstruction techniques may be classified in two major categories. The first one, based on the projection-slice theorem, includes such methods as filtered backprojection and direct Fourier transform algorithms.<sup>3,4</sup> These methods are extremely fast, but usually restricted to data acquired on sets of straight ray paths called projections. The second class is based on iterative procedures to reconstruct the image and includes methods such as the algebraic reconstruction technique (ART)<sup>2,5,6</sup> and the simultaneous iterative reconstruction technique (SIRT).<sup>7</sup> They are much slower, but they may be used with irregular sampling geometries and may take into account the ray bending. The method presented here falls into the category of ray tomography (i.e., the ray bending may be considered), but exploits an efficient algorithm for the inversion based not solely on iterative procedures.

The goal of a reliable multiparameter reconstruction technique for a general tomographic problem is difficult to achieve and very costly (in terms of CPU time). Current techniques, although in principle capable of solving the general problem, have not delivered a reasonably economic solution. However, special tomographic problems, e.g., when some *a priori* information about the specimen is available, can be addressed successfully.

The purpose of the present contribution is to propose an alternative method based on genetic algorithms (GA),<sup>8,9</sup> for a special purpose UT. We assume that the specimen is homogeneous, except for a homogeneous inclusion (or cavity) of arbitrary shape. The physical properties of both the specimen and the inclusion are assumed to be known. The goal is to predict the geometry of the inclusion. We wish to show that the GA method is more efficient than other techniques in taking advantage of the *a priori* information. While we recognize that the above assumptions are rather restrictive, we can easily think of many important medical or NDE applications in which the nature of the inclusion(s) is well known. For example, the inclusion may represent a cancerous growth surrounded by healthy tissue or a defect in a structural component.

GA's, developed by Holland in 1975,<sup>8</sup> are search algorithms based on the dynamics of natural selection and genetics.<sup>9</sup> They represent the evolution of a given population in the parameter space towards an optimal configuration, the only one able to "survive" in relation with the given experimental data. GA's have been widely applied in geophysics,<sup>10</sup> but, never, to our knowledge, to UT.<sup>11</sup> The growing interest in GA's is due to their computational simplicity and their capability of detecting also local minima. Moreover, the technique does not require mathematical conditions, which limit the search space.

In order to point out the advantages of GA based UT with respect to other techniques, we perform here a comparison between GA and ART in the solution of a specific mathematical problem. In fact, a very elementary model describing the propagation of ultrasonic pulses has been chosen, in which times of flight (TOF) are computed using Snell's law, rather than a full-field simulation, such as provided by the local interaction simulation approach (LISA).<sup>12-15</sup> Even in its simplicity, our model allows us to reach the following goals:

- (a) the GA and ART techniques are treated under the same conditions;
- (b) the inversion can be performed very quickly, so that

many data can be accumulated for a comprehensive comparison of the two methods.

A more realistic model based on LISA is not expected to affect the convergence properties of the inversion technique.

Even though the method appears to be more efficient than others, the CPU time required on conventional architectures remains very large, especially in the case of complex geometries. However, an optimal speed-up may be obtained by using parallel supercomputers,<sup>16,17</sup> since the method can be easily parallelized.

In Sec. I, the problem under consideration is presented and the misfit function defined. In Sec. II, after a brief introduction and description of the classic GA operators, the multistep procedure and the intelligent mutation are introduced as “special purpose” operators for UT. Section III addresses the problem of parallelization and implementation on different parallel architectures [single instruction multiple data (SIMD) and multiple instruction multiple data (MIMD) machines]. Section IV reports some numerical results, which demonstrate the efficiency and convergence of the proposed technique. The optimization in the choice of free GA parameters and the effect of special purpose operators are also briefly described. Some future developments are discussed in the Conclusion.

## I. THE ULTRASONIC TOMOGRAPHY ALGORITHM

A simple UT experiment can be realized as follows.  $N$  transmitters and  $M$  receivers are located along the border of a given specimen, providing  $N \times M$  pieces of information, i.e., the times of flight (TOF's) of an ultrasonic pulse from each transmitter to each receiver. Since each material has a characteristic (longitudinal or shear) phase velocity, the set of  $M \times N$  TOF's may be used for reconstructing the physical properties and geometry of the specimen and its inclusion.

Three components are required for the tomographic algorithm: a model for ray tracing, an algorithm for the calculation of TOF's, and a technique for the tomographic inversion.

### A. Ray tracing

In order to obtain a numerical algorithm, the specimen is discretized as an  $m \times n$  grid, assuming each grid cell to be homogeneous. To simulate the propagation of the wavefront, a ray tracing technique, based on Snell's law, is used.

A large number of rays (about 100) is generated from each transmitter and covers the whole solid angle in the specimen. The path of each ray is then followed separately. The ray intersections with cell borders are determined and the new propagation angle in the adjacent cell is determined by the incident angle and the slowness ratio of the two cells. Reflected rays are neglected. This intersection procedure is then repeated until the ray intersects the border of the specimen. The intersection points are stored in a vector and used for the calculation of TOF's. The time of flight of each ray from the transmitter to the border is calculated as

$$t = \sum_{i,j} \frac{l_{ij}}{v_{ij}}, \quad (1)$$

where  $(i,j)$  are the grid coordinates of all the cells traversed by the ray,  $l_{ij}$  is the path length inside the cell  $(i,j)$ , and  $v_{ij}$  the phase velocity of the medium inside.

### B. Times-of-flight calculation

For each transmitter ( $i$ ) and each receiver ( $j$ ), the two rays intersecting the border closest to the receiver on each side of it are selected. The TOF  $t_{ij}$  is then calculated by a linear interpolation of the TOF's corresponding to the two rays (stored in the ray tracing algorithm):

$$t_{ij} = \frac{t_{Rj} - t_{Lj}}{p_{Rj} - p_{Lj}} (p_j - p_{Rj}) + t_{Rj}, \quad (2)$$

where  $p_j$  is the position of the receiver along the border and  $t_{Rj}$  and  $t_{Lj}$  are the TOF's of the two rays intersecting the border at the positions  $p_{Rj}$  and  $p_{Lj}$ , respectively. If no ray intersects the border close enough to the receiver (e.g., within a given number of cells), the corresponding TOF is not used for the inversion, since it is assumed that the pulse reaches the receiver through multiple reflections which are not included in the model.

### C. The inverse problem

By using the GA technique described in the next section, the tomographic inversion algorithm modifies the slowness' distribution in the specimen until the estimated TOF's match the measured ones. The agreement between estimated and experimental results is evaluated through the so-called misfit function  $\Phi$ , defined as

$$\Phi = \sum_{i=1}^N \sum_{j=1}^M \frac{(t_{ij} - \tilde{t}_{ij})^2}{t_{ij} \tilde{t}_{ij}}, \quad (3)$$

where  $t_{ij}$  and  $\tilde{t}_{ij}$  are the experimental and estimated TOF's from transmitter  $i$  to receiver  $j$ , respectively.

A few assumptions are introduced to simplify the procedure.

- (1) A binary code may be used for representing the slowness in each cell. In fact, since grid cells belong only to the surrounding material (specimen) or to the inclusion, both of fixed and known physical properties, we assign a “value” of 0 to the former and 1 to the latter.
- (2) The cells on the border of the specimen cannot belong to the inclusion.
- (3) Along paths for which the experimental TOF's match exactly with TOF's calculated as belonging entirely to the specimen, all cells are forced to remain specimen cells during the whole inversion procedure and are assigned a value of 2.

## II. GENETIC ALGORITHMS

GA techniques differ from other inversion methods in the following respects:

- (i) GA's do not directly act on the parameters, but on the coding of the parameters set.



- (ii) GA searches start from a large population of elements and not from one or a few elements, thus avoiding the pitfall of converging to local minima (typical of gradient methods).
- (iii) GA's exploit directly all the information from the fitness function and therefore do not require specific assumptions about the parameter space (such as continuity or derivability).
- (iv) GA's are not a deterministic method, yet they are not a simple random walk, since the search in the parameter space is guided by an efficient use of previously achieved information.

The GA technique is based on three fundamental operators: selection, crossover, and mutation. Many other operators (e.g., inversion, elitism, gradient-bit search, etc.) may also be added to accelerate and/or guarantee convergence. In our particular UT application some of these operators have been modified in order to best accommodate the problem under investigation.

### A. Basic operators

The basic idea of GA's stems directly from genetic evolution theory. All the physical parameters are coded into one string or matrix, whose genetic counterpart is a chromosome, consisting of a series of genes. The survival of the string is related to its capability of adapting to the environment, in our case the matching of the data obtained by the parameters included in the string with the experimental data. An initial population of  $N$  strings or matrices is then randomly generated and allowed to evolve.

The evolution is governed by a few operators, which are briefly illustrated here.

**Selection.** The elements of the population are sampled in order to generate  $N/2$  couples (parents). We note that each element may be chosen more than once and that the probability of being selected for each element is related to its survival probability.

**Crossover.** Two children are generated from each pair of parents, by swapping substrings or submatrices. The size and location of the components to be interchanged are selected completely at random (see, e.g., Fig. 1).

**Mutation.** A single element of the generated string or matrix (child) is mutated (e.g., a 1 becomes 0) with a given mutation probability. This operator increases the amount of diversity in the population.

From the  $2N$  available elements ( $N$  parents and  $N$  children), the  $N$  with the highest survival probability are kept and used for starting a new cycle (selection-crossover-mutation). The procedure is repeated until convergence. Additional operators may be required, either to guarantee a larger diversity in the population and avoid local minima or to speed up the convergence.

### B. The multistep procedure

In our specific UT problem the number of possible configurations in the parameters space is extremely large and increases dramatically with the grid dimension. On a grid  $20 \times 20$  we already have  $2^{400}$  possible configurations.<sup>18</sup> From

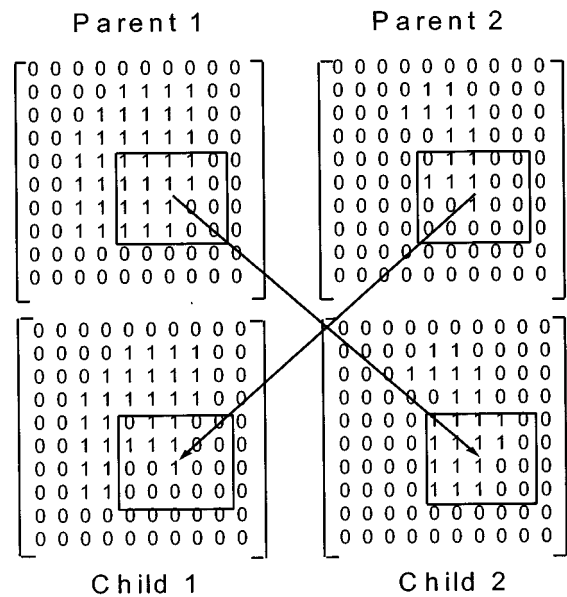


FIG. 1. Crossover between two parent matrices.

a mathematical analysis we know that the dimension of the initial population required for convergence is related to the number of possible configurations. But, a larger initial population requires a correspondingly larger CPU time. Therefore a method for reducing the possible configurations is essential for a practical applicability of GA's to UT.

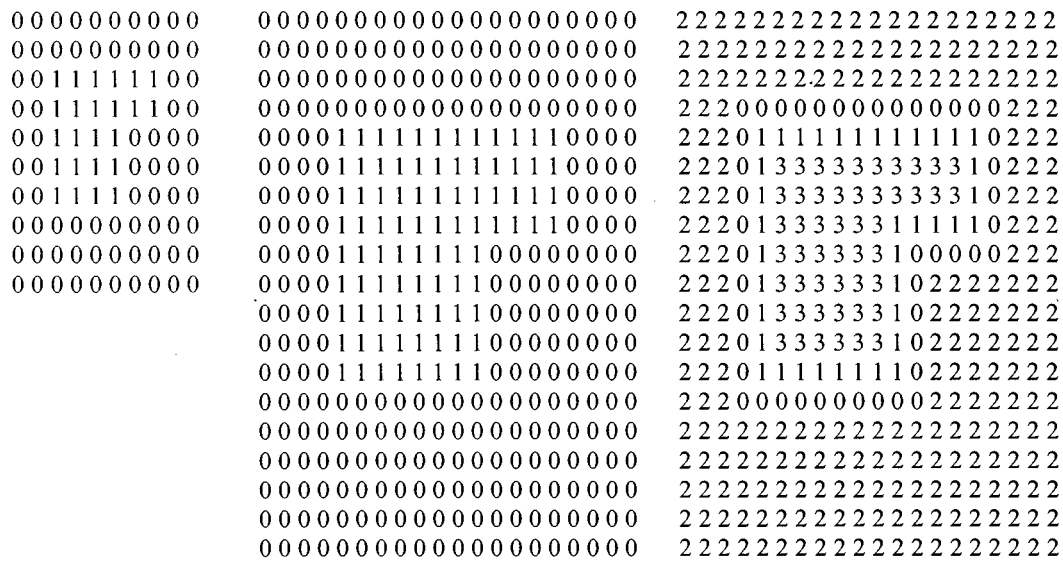
The number of configurations is related to the number of "schemata." A schema is a similarity template describing a subset of strings (or matrices) with similarities at certain positions. Solving the problem on a coarser grid should give us the large scale structure of the inclusion, suggesting a schema to which all the strings in the finer grid must belong. For example, since inclusions are usually rather compact, a strongly compact block obtained on the coarser grid should be "frozen" in its core (with an assigned value of 3) during the iterations on the finer grid. Thus the number of configurations in the finer grid is strongly reduced.

The numerical implementation of the multistep scheme proceeds as follows. At first the problem is solved on a coarse grid (e.g.,  $10 \times 10$ ). The result is then used for generating the population for the next step on a twice finer grid ( $20 \times 20$ ) in the following way (see Fig. 2):

- (1) split: the specimen obtained from the  $10 \times 10$  grid is fitted on a  $20 \times 20$  grid splitting each cell into four;
- (2) freeze: each cell completely surrounded by similar cells is frozen. If the frozen cell is a specimen cell, its value is set to 2, otherwise to 3;
- (3) generation: the first element of the population on the finer grid is kept as the result of item 2. The other elements are generated by assigning at random the value 0 or 1 to the unfrozen cells.

The procedure is repeated, each time doubling the dimension of the grid, up to when the desired resolution is achieved.

The numerical experiments have confirmed that it is not possible to obtain convergence in a reasonable CPU time without using the multistep procedure. However, we must



10 x 10  
Best Result

Split  
on a 20 x 20 grid

Freeze

FIG. 2. Example of the application of the multistep procedure.

remark that this scheme does not guarantee the resolution of shapes with a size smaller than a cell of the coarsest grid. An intelligent mutation may partly eliminate this difficulty.

**C. Intelligent mutations**

In order to favor even further more compact configurations, the mutation operator, which was almost useless in its original format, has been modified as follows:

- (1) a cell is randomly selected;
- (2) the cell and its nearest neighbors (a block of nine cells) are assigned to be either all inclusion or all specimen cells, according to what the majority of the block cells are.

The procedure is repeated for a certain number of cells, which increases with the size of the grid. Implicit in this "intelligent mutation" is a second advantage. In fact, some frozen cells may defrost (i.e., two or three became zero or one, respectively), if the mutation is efficient (i.e., reduces the misfit function). This defrosting capability is very useful, since it can compensate for the risk of excessive freezing in the multistep procedure.

**D. Controlled selection**

The procedure described up to now is very efficient in finding the bulk structure of the inclusion, but not in defining precisely its borders. In fact, the randomness of the method implies a larger amount of selection and mutation on cells inside the specimen than on the border.

In order to avoid this bias, a controlled selection may be introduced to force selections and mutations including cells on the border. Numerical experiments have shown that the best results are obtained if normal and controlled selection iterations are alternated.

**III. PARALLEL IMPLEMENTATION**

The proposed technique is extremely suitable for parallel implementation. In fact, the misfit function is calculated for all the elements of the population in a way, which is homogeneous, since the model is always the same, albeit with different parameters, and almost synchronous, since the ray paths differ slightly from specimen to specimen inside the population. Therefore the speed-up is optimal.

The coding for parallelization is strongly dependent on the parallel architecture, i.e., whether multiple instruction multiple data (MIMD) or single instruction multiple data (SIMD) is used. In the first case, the parallelization is simpler. In fact, since the number of processors is of the same order as the number of elements in the population, an easy one-to-one correspondence between processors and elements may be implemented. The speed up is then approximately equivalent to the number of elements in the initial population.

The implementation on SIMD architectures is a little more complex. If, as it is usually the case, the number of processors  $P$  is larger than the number of population elements  $Q$ , a second level of parallelization should be carried on in order to take full advantage of the parallel architecture. A partition of the processors in  $Q$  groups is defined, each one containing  $T$  processors, where  $T$  is the number of transmitters. If the product  $Q \times T$  is larger than  $P$ , then virtual processors are used. The GA operators are performed on the  $Q$  leading processors of each group, while the ray paths for each transmitter are evaluated in parallel from the  $T$  processors inside each group. An optimal speed-up is expected to be of the order of  $Q \times T$ . Of course, due to the lack of synchronization and use of virtual processors, the real speed-up may be considerably less.

The calculations presented in the next section have been

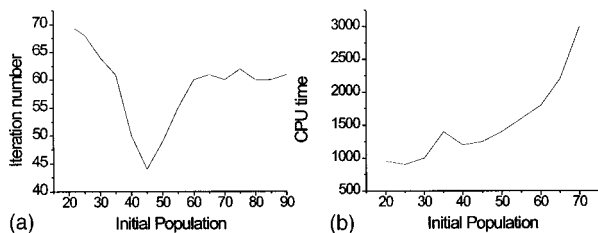


FIG. 3. Influence of the size of the initial population  $N$  on the number of iterations (a) and on the CPU time (b) required for convergence.

partly performed on a Connection Machine CM-5 with 512 processing elements (SIMD architecture).

## IV. RESULTS AND DISCUSSION

### A. Optimization of the procedure

Preliminary calculations have been performed to test the effect of parameters, such as the dimension of the initial population and the ratio between the number of transmitters and receivers, on the convergence of the algorithm. The importance of the size of the initial population has been investigated in detail (see Fig. 3). Using a simplified model, which does not take into account the ray bending (straight rays model), a problem on a  $20 \times 20$  grid has been solved varying the number  $N$  of elements in the initial population. The result has been that a minimum of about 20 elements is necessary to guarantee convergence. For fewer elements, convergence is reached only occasionally, due to the stochasticity of GA's. The minimum number of iterations is obtained for  $N \approx 45$ . However, as Fig. 3(b) shows, the best choice of  $N$  for minimizing the CPU time is right above the threshold  $N = 20$ . Since the number of possible configurations increases dramatically with the grid size,  $N$  must also increase correspondingly. However, in order to limit the CPU time within a reasonable amount, features such as the multistep procedure must be introduced in order to reduce its increase. As a consequence, on a  $160 \times 160$  grid, a population between 60 and 100 is a good choice for convergence.

We can summarize the other results concerning the optimization of the parameters as follows.

(1) Without intelligent mutations it is very difficult to obtain convergence and the decreasing of the misfit function is considerably slower (see Fig. 4). We observe long plateaus between successive improvements of the misfit function, leading to a large number of wasteful iterations.

(2) Convergence may also be obtained without the multistep procedure, but only at the price of a large number of

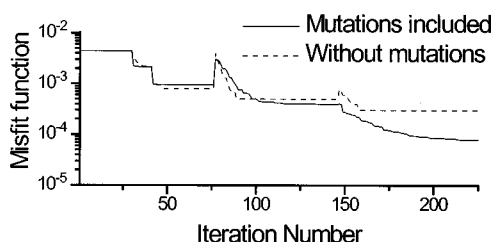


FIG. 4. Misfit function with and without intelligent mutations.

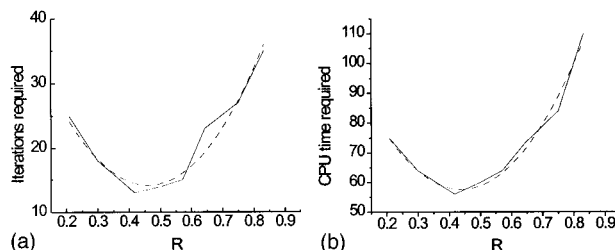


FIG. 5. Number of iterations (a) and CPU time (b) required for convergence versus the ratio  $R$  between the number of transmitters and of receivers.

iterations and elements in the initial population. Correspondingly, the required memory and CPU time are at least 20 times higher.

(3) The procedure may be optimized also by a proper choice of the ratio  $R$  between the number of transmitters and of receivers. Figure 5 shows an almost parabolic behavior for both the number of required iterations and CPU time versus  $R$  with a minimum for  $R \approx 0.4$ .

### B. ART-GA comparison

To test the efficiency of the proposed algorithm, a comparison has been performed with other reconstruction techniques. The GA method seems to be most suitable for problems in which the only unknown is the geometry of the inclusion. In this situation, it seems to be working well even in the case of irregularities, holes, and noncompact shapes. By contrast ART requires, in such cases, a strong increase in the number of transmitters.<sup>1</sup>

A comparison between the results obtained by using GA and ART is reported in Fig. 6. Synthetic data obtained for two specimens discretized on a grid  $20 \times 20$  have been used. The two specimens and the results of the inversion by means of GA and ART are reported. Only the tomograms produced by GA are perfectly convergent, even though the ART tomograms are very close. The CPU times required on a PC-Pentium 100 MHz, 16 MB RAM, have been 1 and 2 h for the first specimen and 2 and 6 h for the second specimen for GA and ART, respectively.

For more complex inclusion geometries or larger grids, the advantage of GA over ART becomes even larger. Al-

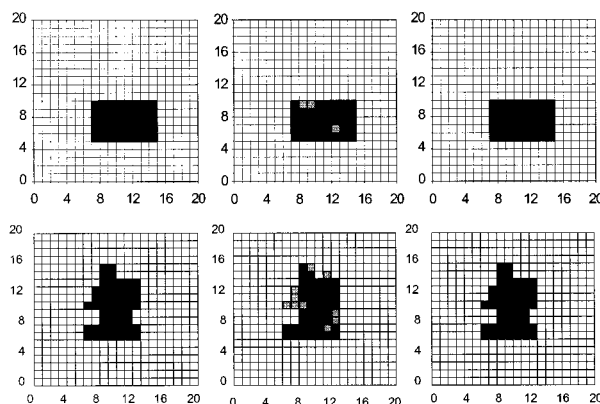


FIG. 6. Comparison between tomograms obtained by GA and ART. Left plots: original specimens, center plots: ART tomograms, right plots: GA tomograms.

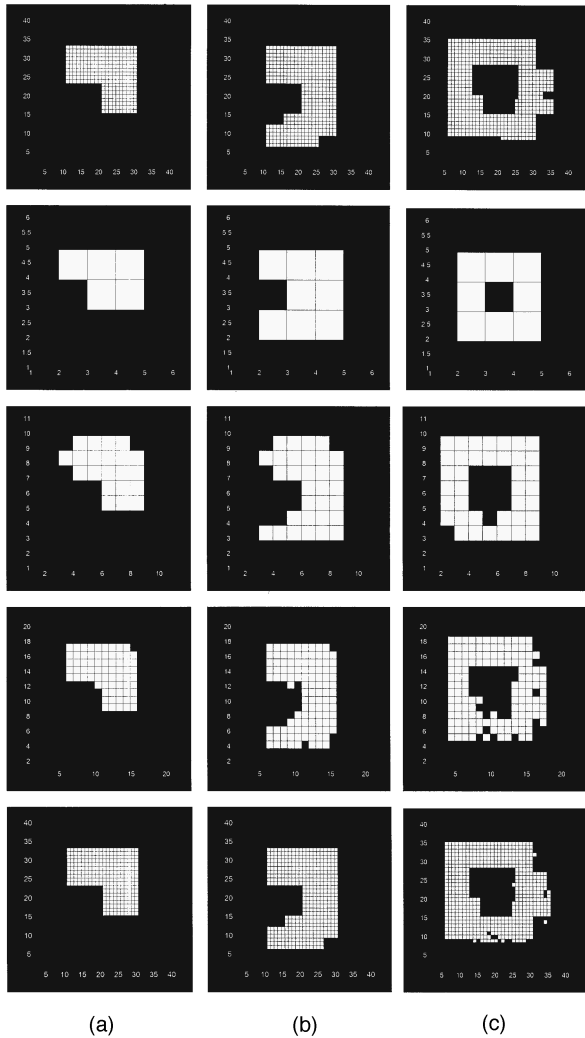


FIG. 7. Multistep results for the inversion procedure for three specimens (a), (b), and (c) (in the three columns). From top to bottom are shown the original specimen and the tomograms at progressively finer grids.

ready for a grid  $40 \times 40$  the CPU time required by ART becomes unaffordable with a PC. It must be recalled, however, that the present comparison is restricted to the particular case, in which it is known *a priori* that the physical properties of each cell may be of only two kinds (matrix and inclusion). Although the GA method can be easily extended to cases in which the physical parameters vary with continuity, it is clear that in the process it will become both more cumbersome and time consuming.

### C. Numerical experiments

The convergence of the solution of the inverse problem by means of the proposed GA technique has been tested numerically by considering various phantoms on grids of different dimensions. The synthetic data corresponding to the phantoms have been calculated numerically to simulate experimental data, by using the model described in Sec. II for the solution of the direct problem.

Figure 7 shows the convergence towards the solution for three rather complex specimens (with a concavity or a hole). In order to illustrate the multistep procedure, intermediate tomograms (at grids  $5 \times 5$ ,  $10 \times 10$ ,  $20 \times 20$ ) are also shown.

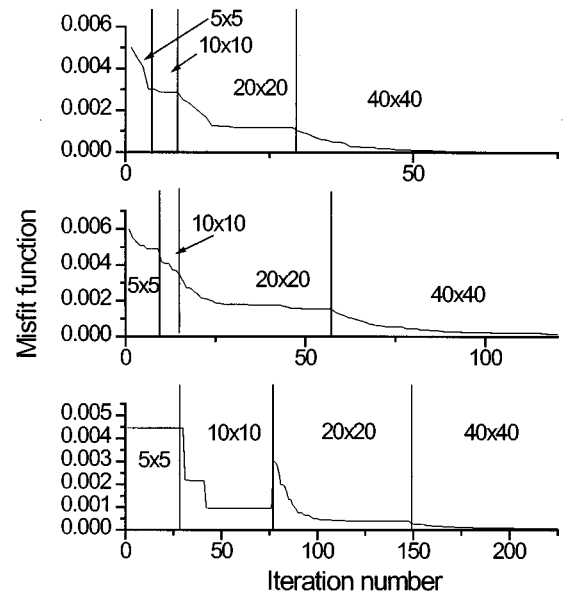


FIG. 8. Misfit function versus number of iterations in the inversion procedure for the three specimens shown in Fig. 7.

The behavior of the misfit function versus the number of iterations for the three cases is reported in Fig. 8. The vertical lines represent the transition from one grid to the next in the multistep procedure. The plots show that at each step the convergence of the misfit function is quickly saturated and starts improving again only when a finer grid is introduced.

Figure 9 shows the tomograms obtained on a  $160 \times 160$  grid for three phantom specimens: (a) with a circular inclusion, (b) with two rectangular inclusions, (c) with an inclusion having both a hole and concavities. The results are quite satisfactory, particularly for the circular shape. The corresponding plots for the misfit function are shown in Fig. 10. As already remarked, concavities and holes represent considerable difficulties for the inversion procedures, as it can be appreciated by the slow decrease of the misfit function in the case of specimen (c).

The results presented here have been obtained by using both a sequential machine (SUN Ultral, peak performance 109M Flops, 64 MB main memory) and a parallel machine (Connection Machine CM-5 with 512 Processing Elements). In Table I the CPU times required for performing the inversion on both machines are reported. The CPU times on a CRAY T3D (256 Dec Alpha processors, peak performance of 40 GFlops and 16 GB main memory) and on a Quadrics machine APE 100 (1024 processors, peak performance of 51.2 GFlops) are expected to be similar to the corresponding times on the CM-5.

The effect of an experimental noise on the inversion procedure has also been considered. The synthetic TOFs have been perturbed with an external noise of up to 5%. The results for the inversion on a grid  $160 \times 160$  are reported in Fig. 11. The final tomogram is still very satisfactory, implying a small effect of the experimental errors on the convergence. This conclusion is, however, valid only for relatively small rates of experimental errors: in fact, we have found that increasing them up to 10%, convergence is no longer obtained and quite different tomograms are generated.

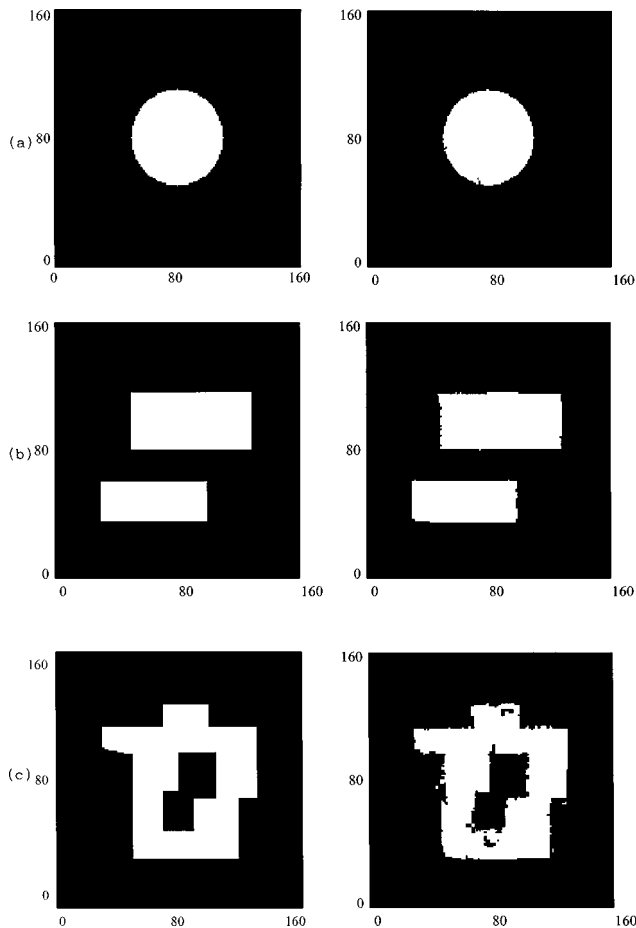


FIG. 9. Results of the GA inversion for three specimens [(a), (b), and (c)] on a  $160 \times 160$  grid. Left plots: original specimens. Right plots: tomograms.

## V. CONCLUSIONS

A new technique for ultrasonic tomographic reconstruction has been proposed. We have considered the problem of predicting the geometry of an inclusion of known physical properties embedded in a given specimen. This assumption is exploited in an optimal way by a genetic algorithm technique. In order to adapt the GA's to ultrasonic tomography, some special purpose operators have been introduced, with a bias towards compact structures.

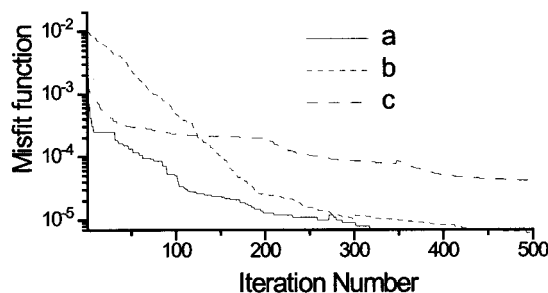


FIG. 10. Misfit function versus number of iterations in the inversion procedure for the three specimens shown in Fig. 9.

TABLE I. CPU times required for the reconstruction procedure for various specimens using sequential or parallel processing.

Specimen	Grid	SUN	CM-5
Figure 7(a)	$40 \times 40$	3 h 10 min	1.5 min
Figure 7(b)	$40 \times 40$	4 h 15 min	2 min
Figure 7(c)	$40 \times 40$	6 h 45 min	3.1 min
Figure 9(a)	$160 \times 160$	35 h 45 min	15 min
Figure 9(b)	$160 \times 160$	55 h 13 min	25 min
Figure 9(c)	$160 \times 160$	62 h 27 min	30 min

The method has been compared with other techniques, such as ART (algebraic reconstruction technique). In the two materials (matrix plus inclusion) assumption considered, the GA method has been found far more efficient, both for the accuracy of the results and for the CPU time required. In fact, convergence is reached both for compact and noncompact inclusions in a relatively small number of iterations, with a difference between final tomograms and original phantoms of at most a few grid cells. The efficiency of the method is furthermore increased by an easily achieved parallel implementation.

Many phantoms with synthetic data have been considered in order to test the technique in a variety of nontrivial cases, e.g., with concave, noncompact, nonsimply connected inclusions and large grids. Good convergence has been obtained up to a  $160 \times 160$  grid, corresponding to  $2^{25\,600}$  different possible configurations. Also the impact of experimental errors in the TOF data has been considered, with the conclusion that their effect is negligible, provided that the errors are not too large (up to about 5%).

The technique, as proposed in the present contribution, may be applied to several problems of quantitative nondestructive (or noninvasive) evaluation in the medical or industrial fields. It can also be extended to problems in which several inclusions or components of different physical properties are present, or even to the determination of the physical properties themselves, after a proper digitization depending on the required accuracy.

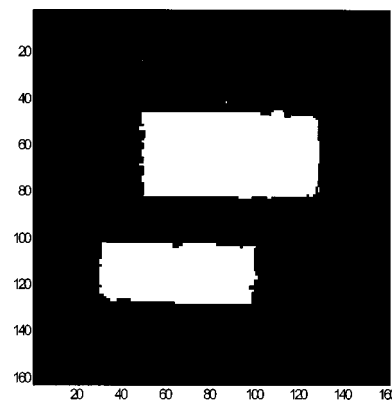


FIG. 11. Final tomogram for the specimen shown in Fig. 9(b) with the experimental data affected by a 5% error.

## ACKNOWLEDGMENTS

This work has been partly supported by the EC Program Copernicus No. ERBCI-PACT940132.

- <sup>1</sup>C. Sullivan, R. Kline, R. B. Mignogna, and P. P. Delsanto, "A parallel processing approach to acoustic tomography," *J. Acoust. Soc. Am.* **99**, 2142 (1996).
- <sup>2</sup>R. S. Schechter, R. B. Mignogna, and P. P. Delsanto, "Ultrasonic tomography using curved ray-paths obtained by wave propagation simulations on a massively parallel computer," *J. Acoust. Soc. Am.* **100**, 2103 (1996).
- <sup>3</sup>R. M. Lewitt, "Reconstruction algorithms: transform methods," *Proc. IEEE* **71**, 390 (1983).
- <sup>4</sup>A. C. Kak, "Computerized tomography with x-ray and ultrasonic sources," *Proc. IEEE* **67**, 1245 (1979).
- <sup>5</sup>R. Gordon, R. Bender, and G. T. Herman, "Algebraic Reconstruction Techniques (ART) for three-dimensional electron microscopy and X-ray photography," *J. Theor. Biol.* **29**, 471 (1970).
- <sup>6</sup>R. Gordon, "A Tutorial on ART," *IEEE Trans. Nucl. Sci.* **21**, 78 (1994).
- <sup>7</sup>P. Gilbert, "Iterative methods for the three-dimensional reconstruction of an object from projections," *J. Theor. Biol.* **29**, 105 (1972).
- <sup>8</sup>J. H. Holland, *Adaptation in Natural and Artificial Systems* (The University of Michigan Press, Ann Arbor, 1975).
- <sup>9</sup>D. Goldberg, *Genetic Algorithms in Search, Optimization and Machine Learning* (Addison-Wesley, Reading, MA, 1989).
- <sup>10</sup>M. Sanbridge and G. Drijkoningen, "Genetic algorithm in seismic waveform inversion," *Geophys. J. Int.* **109**, 323 (1992).
- <sup>11</sup>P. P. Delsanto, F. Moldoveanu, and M. Scalerandi, "A Genetic Algorithm Technique for Acoustic Tomography," in *Proceedings of the Conference on Physics Computing*, edited by P. Borchards *et al.* (Cyfronet, Krakow, 1996), p. 301.
- <sup>12</sup>P. P. Delsanto, R. S. Schechter, H. H. Chaskelis, R. B. Mignogna, and R. Kline, "Connection machine simulation of ultrasonic wave propagation in materials II: the two-dimensional case," *Wave Motion* **20**, 295 (1994).
- <sup>13</sup>P. P. Delsanto, R. S. Schechter, H. H. Chaskelis, and R. B. Mignogna, "Real-time parallel computation and visualization of ultrasonic pulses in solids," *Science* **295**, 1188 (1994).
- <sup>14</sup>P. P. Delsanto, R. S. Schechter, and R. B. Mignogna, "Connection machine simulation of ultrasonic wave propagation in materials III: the three-dimensional case," *Wave Motion* **26**, 329 (1997).
- <sup>15</sup>P. P. Delsanto, R. B. Mignogna, R. S. Schechter, and M. Scalerandi, "Simulation of ultrasonic wave propagation in complex media," in *New Perspectives on Problems in Classical and Quantum Physics*, edited by P. P. Delsanto and A. W. Saenz (Gordon and Breach, New York, 1998), p. 51.
- <sup>16</sup>W. D. Hillis, *The Connection Machine* (MIT, Cambridge, MA, 1985).
- <sup>17</sup>D. P. Bertsekas and J. N. Tsitsiklis, *Parallel and Distributed Computation. Numerical Methods* (Prentice-Hall, Englewood Cliffs, NJ, 1989).
- <sup>18</sup>J. E. Whitesitt, *Boolean Algebra and its Applications* (Dover, New York, 1995).

# Heterogeneous structure of modes and Kramers–Kronig relationship in anisotropic viscoelastic materials

Bernard Hosten<sup>a)</sup>

Laboratoire de Mécanique Physique, Université de Bordeaux I, URA C.N.R.S. N° 867. 351,  
Cours de la Libération, 33405-Talence Cedex, France

(Received 6 February 1998; accepted for publication 26 May 1998)

Composite materials made of fibers and a viscoelastic matrix, exhibit an orthotropic viscoelastic behavior that is described by a tensor with nine independent complex viscoelastic moduli. This tensor makes it possible to compute the velocity and attenuation of heterogeneous or homogeneous modes in any direction. In experiments, the immersion method of a plate shaped sample insonified by plane ultrasonic waves is used to measure this complex tensor. The liquid/solid interface generates heterogeneous quasilongitudinal and quasishear bulk modes that propagate through the plate with velocities and attenuations that depend on the frequency. In a viscoelastic material, velocity and attenuation are linked by the Kramers–Kronig relations. For heterogeneous modes, the attenuation that needs to be used is the projection of the damping vector on the wave vector. This paper shows that these relations limited to a “local” frequency band can be experimentally verified and permit one to link anisotropic velocity and attenuation dispersion of quasilongitudinal and quasishear modes only if their heterogeneous structure is taken into account. The extrapolation of the material properties determined by ultrasonic measurements, towards low frequencies, relies on this feature in combination with a model of the attenuation evolution versus frequency. © 1998 Acoustical Society of America. [S0001-4966(98)02409-6]

PACS numbers: 43.35.Cg, 43.35.Mr [HEB]

## INTRODUCTION

Measuring elastic constants ( $C'_{ij}$ ) of composite materials from ultrasonic velocities, using the propagation of bulk modes generated at the fluid–solid interface, is a very well known technique.<sup>1,2</sup> There is still a question about the validity of these measurements at lower frequencies or for static stress fields. Composite materials are often composed of a viscoelastic matrix and fibers that introduce anisotropy. Hence the attenuation is also anisotropic. In addition, the propagation of waves in an absorbing medium is dispersive: the phase velocity depends on the frequency. Attenuation and velocity are linked through the Kramers–Kronig relations, deduced from the principle of causality.<sup>3</sup>

One way to validate  $C'_{ij}$  measurements in the static domain is to extrapolate their variation toward lower frequencies. This paper presents a preliminary approach to this problem: the connection between anisotropic attenuation and anisotropic phase velocity as a function of frequency. The “classical” way to model the propagation in a viscoelastic material is to use complex velocities and wave vectors with complex modulus. In such a case, the structure of the waves is homogeneous. It will be shown in this paper that this representation is not adequate when the material is anisotropic and that the heterogeneous structure of the modes has to be taken into account when using the immersion method and Kramers–Kronig relations.

In the first paragraph, the immersion method is recalled. Then, the local Kramers–Kronig relationships are extended to heterogeneous modes. In the third paragraph, four empiri-

cal models are compared to fit the dependence of attenuation on frequency. The models are used to predict the evolution of the velocities over a large frequency band. In the fourth paragraph, the comparison with experimental velocity measurements shows good agreement for the two most elaborate models. At the same time, one model has predictive capability for  $C'_{ij}$  measurements at low frequencies.

## I. APPARATUS AND VISCOELASTIC MODULI MEASUREMENT

The axis convention and viscoelasticity tensor notation ( $C_{ij}$ ) are introduced in Fig. 1. In orthotropic materials, there are three planes of symmetry.<sup>4</sup> For unidirectional fiber composites, the plane  $P_{12}$  perpendicular to the fibers, is almost isotropic. The plane  $P_{13}$  contains the fibers and is the most anisotropic plane. The plane  $P_{23}$  is similar to the plane  $P_{13}$  and not usable in the immersion method (Fig. 2).

### A. Immersion method

Essentially, the plane wave through-transmission method uses a goniometer to suspend the sample between two ultrasonic transducers, imposing an incident angle  $\theta$  (Fig. 2). Transducers (bandwidth  $\approx 0.7$ –3 MHz, in this work) and sample are immersed in water.

A plane wave incident from the liquid generates three modes in an anisotropic material at a liquid–solid interface.<sup>5</sup> When the sample is thick enough and the emitted pulse is short, the internal multiple reflections can be separated in time to study the first bulk transmitted mode.

Each of these modes is heterogeneous<sup>6,7</sup> and the correspondent displacement field  $U$  can be represented by the expression:

<sup>a)</sup>Electronic mail: hosten@lmp.u-bordeaux.fr

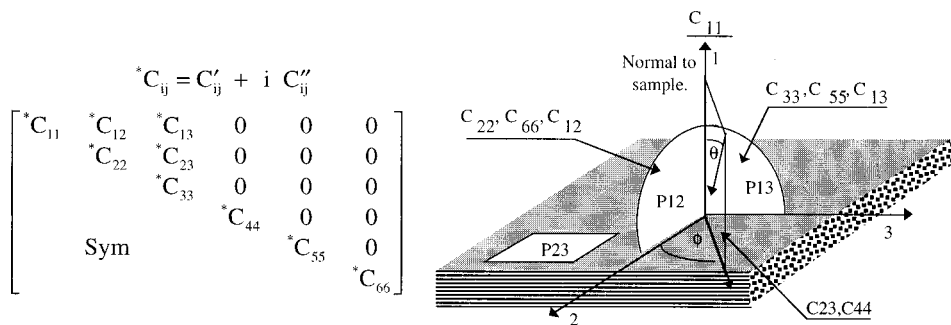


FIG. 1. Axis and planes of symmetry in long fiber composite materials.

$$\mathbf{U} = \mathbf{P} \exp(+i(2\pi\nu(t - \mathbf{S} \cdot \mathbf{M}))), \quad (1)$$

in which  $\mathbf{P}$  is the polarization vector,  $\nu$  the frequency and  $\mathbf{M}$  the position vector.

The complex slowness vector  $^*\mathbf{S}$ , is composed of the  $\mathbf{S}'$  propagation vector and the  $\mathbf{S}''$  damping vector, such that:  $^*\mathbf{S} = \mathbf{S}' - i\mathbf{S}''$ .

At interfaces between nonabsorbing and absorbing medium, an incident homogeneous wave is converted in a heterogeneous wave [Fig. 2(a)]. According the Snell's laws, the damping vector  $\mathbf{S}''$  in the absorbing medium must be perpendicular to the interface.<sup>6-8</sup> The equiamplitude planes are parallel to the interface and their angle with the equiphase planes is the refraction angle  $\theta_r$ . In the frequency domain used in this paper, the attenuation in water was always found negligible in comparison with the attenuation in composite. Then the heterogeneous structure of the modes must be taken into account when one wants to measure the attenuation using the immersion method.<sup>6,7</sup>

The incident wave amplitude  $A_r(\nu)$  is defined by the Fourier transform of the acquired waveform resulting from the propagation between transmitter and receiver when the sample is not present. The amplitude of the first through-transmitted waveform  $A_s(\nu)$  is normalized by  $A_r(\nu)$  to get the transfer function of the two interfaces and the propagation through the solid. This normalized amplitude  $A(\nu) = A_s(\nu)/A_r(\nu)$  corresponds to the amplitude of the first transmitted heterogeneous bulk mode.

The delay introduced by the propagation of the wave from one interface to the other is given by:

$$\tau(\nu) = \frac{\varphi(\nu)}{2\pi\nu} = \frac{e}{\cos(\theta_r)} S', \quad (2)$$

where  $\varphi(\nu)$  is the phase of the complex amplitude  $A(\nu)$ ,  $\theta_r$  the refraction angle and  $e$  the thickness of the sample. It is straightforward to deduce the evolution of the phase velocity ( $1/S'$ ) versus frequency from the  $S'$  measurement. It will be shown later in this paper (Figs. 8 and 9) that, in the frequency range used to measure the  $C'_{ij}$  values, the phase velocities can be assumed almost constant, and therefore  $C'_{ij}$  can be considered frequency independent, in that range.

In order to satisfy the plane wave condition and correctly measure the transmitted amplitudes, it is important to translate the receiver over a lateral distance in accordance to the Snell's law (Fig. 2). Doing so, the modulus of the normalized complex amplitude permits one to compute from the formula:

$$|A(\nu)| = T \exp(-2\pi\nu S'' e). \quad (3)$$

Here  $T$  is the transmission coefficient of both interfaces, computed from the real part of  $^*C_{ij}$ .<sup>6,7</sup> It is assumed frequency independent as the velocity dispersion is small.

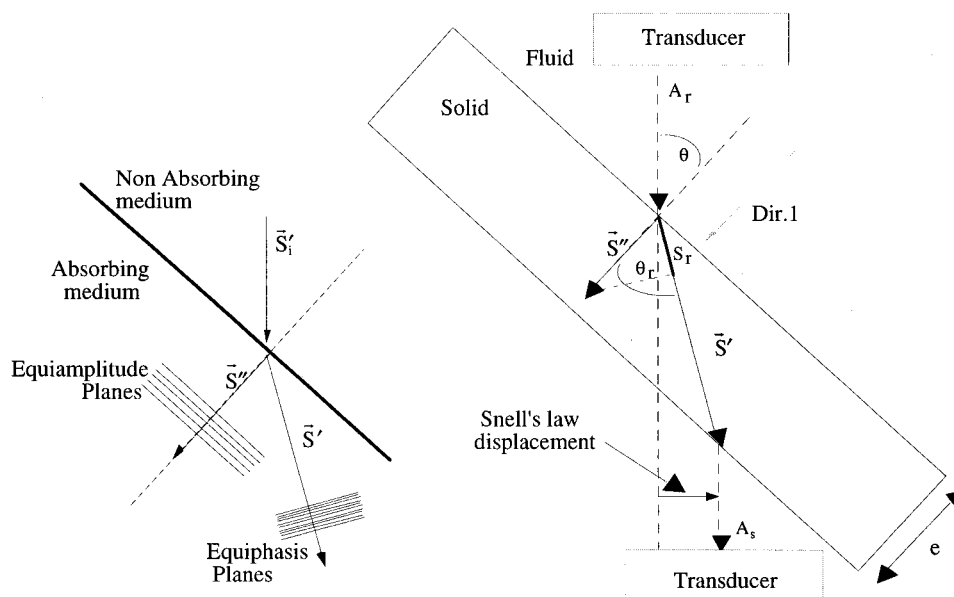


FIG. 2. (a) Heterogeneous wave generation at the interface between nonabsorbing and absorbing medium. (b) Experimental configuration of immersion method.



TABLE I.  $*C_{ij}$  values identified from the planes  $P_{12}$ ,  $P_{13}$ , and  $\varphi=45^\circ$  (in GPa at 1.5 MHz).

$C'_{22}$	$C'_{66}$	$C'_{12}$
14.1 ( $\pm 0.3$ ) + $i0.56$ ( $\pm 0.05$ )	3.6 ( $\pm 0.2$ ) + $i0.20$ ( $\pm 0.03$ )	7.1 ( $\pm 0.2$ ) + $i0.1$ ( $\pm 0.03$ )
$C'_{33}$	$C'_{55}$	$C'_{13}$
38.7 ( $\pm 0.5$ ) + $i1.0$ ( $\pm 0.3$ )	39 ( $\pm 0.06$ ) + $i0.25$ ( $\pm 0.02$ )	7.0 ( $\pm 0.1$ ) + $i0.19$ ( $\pm 0.07$ )
$C'_{11}$	$C'_{44}$	$C'_{23}$
14.4 ( $\pm 1$ ) + $i0.53$ ( $\pm 0.04$ )	2.9 ( $\pm 0.4$ ) + $i0.08$ ( $\pm 0.05$ )	7.3 ( $\pm 0.6$ ) + $i0.5$ ( $\pm 0.2$ )

## B. Procedure of $*C_{ij}$ identification

In an infinite anisotropic material only three modes can propagate. The Christoffel's equations  $|\Gamma'_{ij}(C'_{ij}, S'_j) - \rho \delta_{ij}| = 0$  provide the link between the slowness vectors and the properties of materials.<sup>5</sup> Classically for nonviscous media the Christoffel's tensor  $\Gamma'_{ij}$  is built up from the elasticity moduli  $C'_{ij}$  and the direction of propagation.<sup>5</sup>  $\rho$  is the density.

In viscoelastic media, the Christoffel's tensor is modified by replacing  $C'_{ij}$  with complex valued viscoelasticity moduli  $*C_{ij}$  and by introducing the complex valued slowness vector representation  $*\mathbf{S}$  for an attenuated homogeneous or heterogeneous mode  $|\Gamma_{ij}(*C_{ij}, *S_j) - \rho \delta_{ij}| = 0$ . The solutions of these equations resolve the forward problem of computing the complex wave vector from  $*C_{ij}$ .<sup>6,7</sup>

As it is difficult to identify nine complex coefficients (18 real coefficients), the  $C'_{ij}$  are first identified individually from measurements of the real part  $S'$  of the slowness vector.  $C'_{11}$  is measured in direction 1 (normal to the sample).  $C'_{22}$ ,  $C'_{66}$ ,  $C'_{12}$  and  $C'_{33}$ ,  $C'_{55}$ ,  $C'_{13}$  are, respectively, identified from the velocity measurements in the  $P_{12}$  and  $P_{13}$  planes of symmetry (Fig. 1). For an orthotropic material, the two other constants,  $C'_{44}$ ,  $C'_{23}$ , can be identified<sup>7</sup> from a nonprincipal plane ( $\varphi=45^\circ$  for instance).

The attenuation is supposed to be small. The imaginary parts of the viscoelasticity tensor are identified by a similar procedure as the one used for the real parts. The experimental values are the imaginary component  $S''$  of the slowness, perpendicular to the interface.  $C''_{11}$  can be identified from a measurement in direction 1,  $C''_{22}$ ,  $C''_{66}$ ,  $C''_{12}$  in the plane  $P_{12}$ ,  $C''_{33}$ ,  $C''_{55}$ ,  $C''_{13}$  in the plane  $P_{13}$  and  $C''_{44}$ ,  $C''_{23}$  in the plane  $\varphi=45^\circ$ . We will show later (Sec. III) that  $S''$  is slightly dependent on frequency, and consequently, the coefficients  $C''_{ij}$  are also slightly frequency dependent. For a complete determination of these parameters, it is necessary to introduce a model of variation versus frequency. This aspect is out of the scope of this paper.

Table I gives the results of  $*C_{ij}$  measurements for a 32 plies, unidirectional epoxy matrix glass fiber composite ( $\rho = 1.8 \text{ g/cm}^3$ ), at 1.5 MHz frequency. The size of the samples used in this work was  $5.8 \times 70 \times 70 \text{ mm}$ .

The upper bounds of the relative errors for each of those parameters are estimated from the insensitivity matrix de-

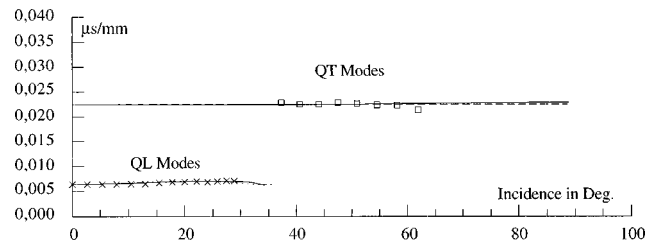


FIG. 3.  $S_r$  versus angle of incidence for quasilongitudinal and quasishear modes in the plane  $P_{12}$ .  $\times$ : Experimental data; —:  $S_r$  for heterogeneous mode; ---:  $S''$  for homogeneous mode.

finied in Ref. 9. The precision is best in normal incidence and in the planes of symmetry. In this paper we focus on the propagation in the most anisotropic plane. The Kramers–Kronig relationship for heterogeneous modes will be compared to experimental data in the  $P_{13}$  plane of symmetry.

## C. Comparison between homogeneous and heterogeneous wave attenuation

Let  $S_r$  denote the projection of the damping vector onto the propagation vector (Fig. 2), i.e.,  $S_r = \mathbf{S}'' \cdot \mathbf{S}' / |\mathbf{S}'|$ . In Fig. 3, the experimental data of  $S_r$  in the  $P_{12}$  plane and the values of  $S_r$  computed from the  $*C_{ij}$  values (Table I) for heterogeneous modes are plotted as a function of the angle of incidence. As expected, this plane looks almost isotropic. This is one convenient way to check the transverse isotropy property of a viscoelastic unidirectional composite.

From the  $*C_{ij}$  values, and the Christoffel's equations, it is possible to compute the values of  $S''$  for homogeneous modes. For comparison, these values are also shown in Fig. 3 for homogeneous modes propagating in the same direction as the heterogeneous modes. Because, in general, homogeneous modes cannot be generated at the fluid/viscoelastic interface, the term ‘‘incidence angle’’ has no physical meaning; it is calculated from the direction of propagation applying Snell's laws. As proved in an earlier paper,<sup>8</sup> if the attenuation is small, the value of  $S_r$  for heterogeneous modes in an isotropic plane is close to the value of  $S''$  for homogeneous modes.

If the plane is anisotropic (Fig. 4), there is a noticeable difference between the computed homogeneous and heterogeneous mode attenuation. The comparison with experimental data confirms the heterogeneous structure of the modes and clearly indicates that the projected component of the damping vector on the propagation direction has to be used in the Kramers-Kronig relations.

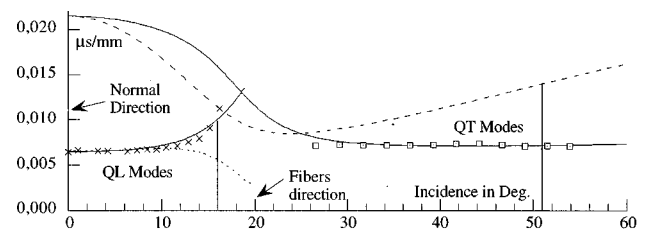


FIG. 4.  $S_r$  versus incidence for quasilongitudinal and quasishear modes in the plane  $P_{13}$ .  $\times$ : Experimental data; —:  $S_r$  for heterogeneous mode; ---:  $S''$  for homogeneous mode.

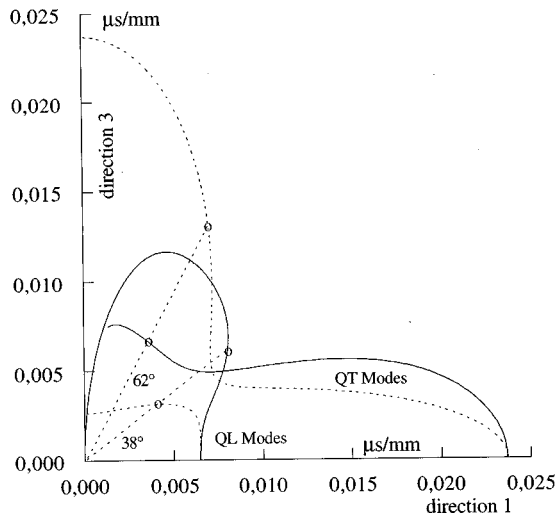


FIG. 5. Imaginary part of slowness vector of the quasilongitudinal and quasishear modes in the plane  $P_{13}$ . —:  $S_r$  for heterogeneous mode; ----:  $S''$  for homogeneous mode.

Solving the complex Christoffel's equations, one can study the imaginary part of the slowness vector as a function of the direction of propagation inside the composite. Figure 5 presents the solution for quasilongitudinal and quasishear modes when heterogeneous or homogeneous behavior of the wave is considered. The larger attenuation factor of quasilongitudinal heterogeneous waves is confirmed by comparing the curves of  $S_r$  for the heterogeneous mode and  $S''$  for the homogeneous mode. The difference between these two quantities at  $\theta_r = 38^\circ$  (corresponding to an incidence angle  $\theta = 16^\circ$  in Fig. 4) is much larger than the errors attributed to the imprecision of the  $*C_{ij}$  measurements.

Also in Fig. 5, attenuation of homogeneous and heterogeneous modes is plotted for quasishear modes. Note that there is a refraction limit angle for the heterogeneous mode, because the phase velocity of the incident mode becomes larger than the refracted one. This figure also illustrates that the attenuation factor for heterogeneous waves is not always larger than the corresponding factor for homogeneous modes. For directions closer to the normal to the sample, the attenuation of the heterogeneous mode is larger. For larger angles of incidence, the attenuation of the heterogeneous mode becomes smaller.

## II. KRAMERS-KRONIG RELATIONSHIP FOR HETEROGENEOUS MODES

In a viscoelastic material, the dispersion relation for any modulus like Young's or Coulomb's modulus, viscoelastic moduli  $*C_{ij}$  in an axis of symmetry, etc., is given by:<sup>3</sup>

$$*G(\nu) = G_1(\nu) + iG_2(\nu) = \frac{\rho}{*S \cdot *S} \quad (4)$$

In the general case of an arbitrary direction of propagation in an infinite medium, three heterogeneous modes are the solutions of the complex Christoffel's equations  $|* \Gamma_{ij}(*C_{ij}, *S_j) - \rho \delta_{ij}| = 0$ . The damping vector is assumed to be much smaller than the wave vector. This is essential if one wants to propagate waves through materials in order to measure their properties. Indeed, if the signal attenuation is too large, no signal can be transmitted through the sample. Taking into account the hypothesis of small attenuation, the complex Christoffel's equations can be decomposed in the real part and the imaginary part following procedures similar to that described in Refs. 6 and 7.

Under this assumption:

$$G_1(\nu) = \frac{\rho}{S'^2} \quad \text{and} \quad G_2(\nu) = 2 \frac{\rho S' \cdot S''}{S'^4} \quad (5)$$

The principle of causality imposes that  $G_1$  and  $G_2$  are Hilbert transforms from one to the other. The Fourier transform property of the real temporal representation  $g(t)$  lead to the classical Kramers-Kronig relations,<sup>3</sup> for homogeneous waves in a viscous medium:

$$G_1(\nu) = -\frac{2}{\pi} \int_0^{+\infty} \frac{u G_2(u)}{u^2 - \nu^2} du$$

and (6)

$$G_2(\nu) = \frac{2\nu}{\pi} \int_0^{+\infty} \frac{G_1(u)}{u^2 - \nu^2} du.$$

In the case of heterogeneous waves generated at the liquid-solid interface, the damping vector  $S''$  can be decomposed in a part parallel to the propagation direction and a part perpendicular to it. The relationships between real and imaginary parts of the slowness vector then become:

TABLE II. Four empirical models to fit the attenuation evolution versus frequency.

Models	Incidence in $P_{13}$			Standard deviation
$M_0 \alpha = a_0 + a_1 \nu$	$0^\circ$	$a_0 = -0.029 \text{ 1/mm}$	$a_1 = 0.061 \text{ } \mu\text{S/mm}$	5.3%
$M_1 \alpha = a_1 \nu$	$0^\circ$		$a_1 = 0.048 \text{ } \mu\text{S/mm}$	18%
$M_2 \alpha = a_1 \nu + a_2 \nu^2$	$0^\circ$	$a_1 = 0.027 \text{ } \mu\text{S/mm}$	$a_2 = 0.009 \text{ } \mu\text{S}^2/\text{mm}$	6%
$M_3 \alpha = a_1 \nu^{a_2}$	$0^\circ$	$a_1 = 0.034 \text{ } \mu\text{S/mm}$	$a_2 = 1.40$	4%
$M_2 \alpha = a_1 \nu + a_2 \nu^2$	$16^\circ$	$a_1 = 0.071 \text{ } \mu\text{S/mm}$	$a_2 = 0.0002 \text{ } \mu\text{S}^2/\text{mm}$	1.5%
$M_3 \alpha = a_1 \nu^{a_2}$	$16^\circ$	$a_1 = 0.071 \text{ } \mu\text{S/mm}$	$a_2 = 1.002$	1.4%
$M_2 \alpha = a_1 \nu + a_2 \nu^2$	$51^\circ$	$a_1 = 0.038 \text{ } \mu\text{S/mm}$	$a_2 = 0.005 \text{ } \mu\text{S}^2/\text{mm}$	1.2%
$M_3 \alpha = a_1 \nu^{a_2}$	$51^\circ$	$a_1 = 0.042 \text{ } \mu\text{S/mm}$	$a_2 = 1.19$	1.6%

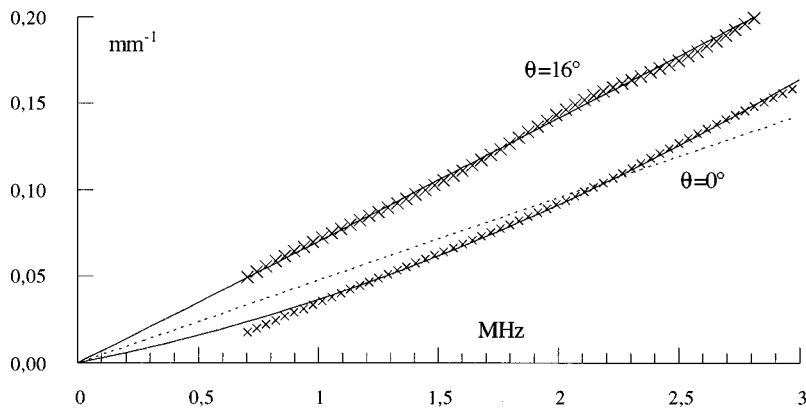


FIG. 6. Attenuation factor  $\alpha=2\pi\nu S_r$  versus frequency of the quasilongitudinal mode in the plane  $P_{13}$  for  $\theta=0^\circ$  and  $\theta=16^\circ$  (×: experiment, solid line: models  $M_2$  or  $M_3$ ). (Dashed line: fit for  $\theta=0^\circ$  with  $M_1$ .)

$$\frac{1}{S'^2} = \frac{4}{\pi} \int_0^{+\infty} \frac{S_r}{S'^3} \frac{u}{u^2 - \nu^2} du, \quad (7)$$

$$\frac{S_r}{S'^3} = \frac{\nu}{\pi} \int_0^{+\infty} \frac{1}{S'^2(u^2 - \nu^2)} du.$$

Donnell *et al.*<sup>10</sup> proved that these relations can be written in a ‘local’ form, i.e., over a limited frequency bandwidth  $[\nu_0, \nu]$ , as follows:

$$S' = S'_0 - \frac{2}{\pi} \int_{\nu_0}^{\nu} \frac{S_r}{u} du \quad \text{where} \quad S'_0 = \frac{1}{C(\nu_0)} = \frac{1}{C_0}. \quad (8)$$

### III. EMPIRICAL MODELS FOR ATTENUATION EVOLUTION VERSUS FREQUENCY

In the present work, only the attenuation due to the viscoelastic behavior of materials is taken into account. The diffraction effects appear when the size of the structure elements of the material is comparable with the wavelength. For composite materials the stacking sequence and the ply thickness can have a large influence on the ultrasonic attenuation. Unidirectional composites permit one to minimize the diffraction influence, since the fibers diameter ( $\approx 10\text{--}50 \mu\text{m}$ ) is much smaller than the wavelengths ( $\approx 1\text{--}5 \text{mm}$ ) used for the present experimental investigation.

As mentioned in many papers,<sup>11–14</sup> the attenuation factor  $\alpha=2\pi\nu S_r$  of polymeric materials or a composite made of polymeric matrix can be assumed to be linearly dependent on frequency in the ultrasonic frequency range.

The slope of the curve is defined as  $a_1$ . This classical model that will be referred to as  $M_0$ , where  $\alpha=a_0+a_1\nu$ , is

simple because it implies that the coefficients  $C''_{ij}$  are constant.<sup>11</sup> However, the linear fit of the experimental data introduces a nonzero value at the origin. For instance, the best linear fit of the attenuation in normal incidence with  $M_0$  leads to a good fitting, but the value of the coefficient  $a_0$  (Table II) is not acceptable since the viscoelastic effects must disappear at zero frequency. This model is not appropriate to reach realistic values of  $*C_{ij}$ , especially at low frequencies.

To avoid this mistake, the model must be constrained to pass through the origin. In Fig. 6, the best linear fit given by model  $M_1$  ( $\alpha=a_1\nu$ ) is shown for the case of normal incidence. By increasing the degree of the polynomial, the model can be still constrained to pass through to the origin, with a smaller standard deviation. In normal incidence, the use of the model  $M_2$  ( $\alpha=a_1\nu+a_2\nu^2$ ) reduces the standard deviation by a factor of 3. Finally, the model,  $M_3$  ( $\alpha=a_1\nu+a_2\nu^2$ ), gives the same good fitting as the model  $M_2$  (Table II). As a conclusion, even in a limited frequency bandwidth, there is more structure in the data than what can be explained by classical models  $M_0$  and  $M_1$ . Therefore one should use  $M_2$  or  $M_3$ .

In the isotropic plane  $P_{12}$ , as expected, the best values for  $a_1$  and  $a_2$  were found to be nearly independent of the direction of propagation, with an equivalent standard deviation. In the anisotropic plane  $P_{13}$ , when the direction of propagation deviates from normal incidence, the quasilongitudinal mode attenuation tends to be almost linear in frequency (see Fig. 6 and Table II).

To identify the moduli  $C''_{ij}$  (cf. Sec. I), the value of  $S''$ , for any direction, is given by the formula  $S''\cos(\theta_r) = M_i(\nu_1)/2\pi\nu_1$  where  $M_i$  is the selected model and  $\nu_1$  is a

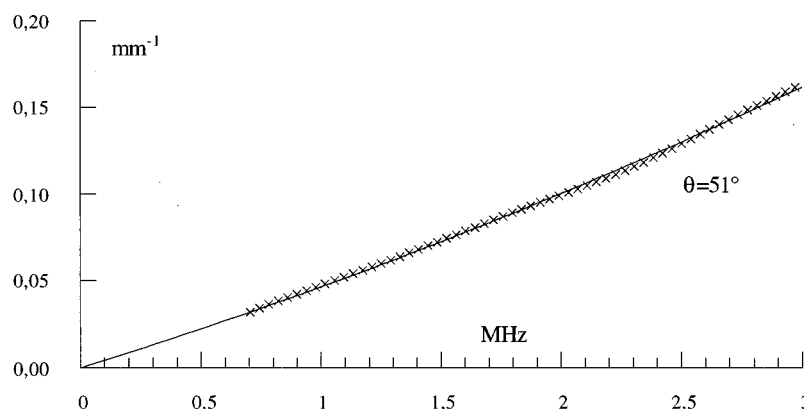


FIG. 7. Attenuation factor  $\alpha=2\pi\nu S_r$  versus frequency of the quasishear mode in the plane  $P_{13}$  for  $\theta=51^\circ$  (×: experiment, solid line: models  $M_2$  or  $M_3$ ).

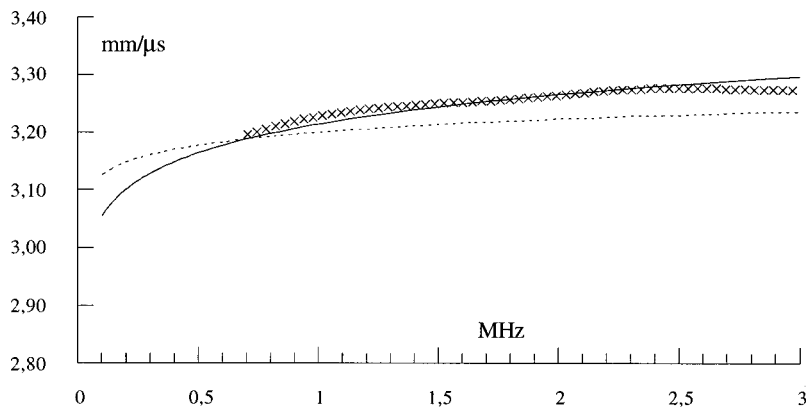


FIG. 8. Velocity versus frequency of the quasilongitudinal mode in the plane  $P_{13}$  for  $\theta=16^\circ$ .  $\times$ : Experimental velocities; —: velocities computed from heterogeneous wave attenuation; ---: velocities computed from homogeneous wave attenuation.

specific frequency (1.5 MHz in Table I). The coefficients  $a_i$  are identified by a Newton-Raphson's procedure to get the best fit between the model and the attenuation measurements, in any direction.

The attenuation factor for the quasishear mode exhibits the same evolution versus frequency as the quasilongitudinal mode. For any direction of propagation,  $M_2$  and  $M_3$  both gave the same good fitting (standard deviation  $\approx 5\%$ ). Figure 7 illustrates the frequency dependence of the shear attenuation factor and its fit for an incidence angle of  $51^\circ$  corresponding to a mode propagation in the direction  $\theta_r=62^\circ$ .

#### IV. VELOCITY MEASUREMENT AND PREDICTION VERSUS FREQUENCY

Following Eq. (8), the slowness dispersion can be easily calculated from the attenuation using model  $M_2$ , by the formula:

$$S' = S'_0 - \frac{a_1}{\pi^2} \ln\left(\frac{\nu}{\nu_0}\right) - \frac{a_2}{\pi^2} (\nu - \nu_0) \quad (9)$$

and using model  $M_3$ , by the formula:

$$S' = S'_0 + \frac{a_1}{\pi^2(a_2 - 1)} \nu_0^{(a_2 - 1)} - \frac{a_1}{\pi^2(a_2 - 1)} \nu^{(a_2 - 1)}. \quad (10)$$

Thus the phase velocity can be predicted from the values of  $a_1$  and  $a_2$  which result from the fit of the attenuation data. The frequency  $\nu_0$  is the lower frequency in the bandwidth.  $S'_0$  is the value of the slowness at this frequency which is

estimated from the experimental slowness measurements by a Newton-Raphson's procedure.

Although the two models  $M_2$  and  $M_3$  lead to similar standard deviations, the second one seems better when applied to predict the low frequency limit. As a matter of fact, formula (9) is not defined for the zero frequency, whereas formula (10) gives the static value of the slowness.

From Fig. 4, one can notice that the attenuation factor for a quasilongitudinal heterogeneous mode in the anisotropic plane  $P_{13}$  is larger when the direction of propagation approaches the fiber direction and that the attenuation factor is larger for heterogeneous waves than for homogeneous waves propagating in the same direction. These results can be substantiated by the measured and predicted velocity dependence on frequency which is shown in Fig. 8 for the quasilongitudinal heterogeneous mode propagating in the direction  $\theta_r=38^\circ$  (angle of incidence  $\theta=16^\circ$ ) in the frequency range of 0.7–3 MHz.

The good agreement between measured and computed velocities, when using the  $M_2$  or  $M_3$  models, validates the local Kramers-Kronig relations between the velocity and attenuation factor for heterogeneous waves. The same accurate fitting was observed in any other direction. In Fig. 8 the dispersion curve computed from values of  $S''$  for homogeneous waves propagating in the same direction is also plotted. The smaller attenuation factor leads to a smaller velocity dispersion. The difference is much larger than the velocity variation induced by errors of typically a few percent in the coefficients  $a_1$  and  $a_2$ . This proves the need to take into account the wave heterogeneity.

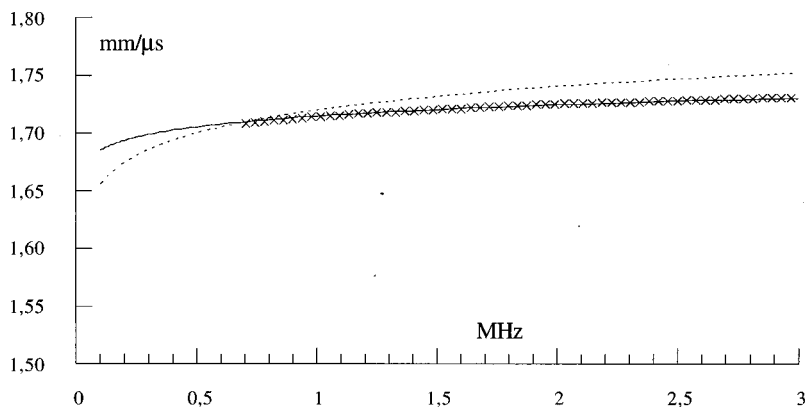


FIG. 9. Velocity versus frequency of the quasishear mode in the plane  $P_{13}$  for  $\theta=51^\circ$ .  $\times$ : Experimental velocities; —: velocities computed from heterogeneous wave attenuation; ---: velocities computed from homogeneous wave attenuation.

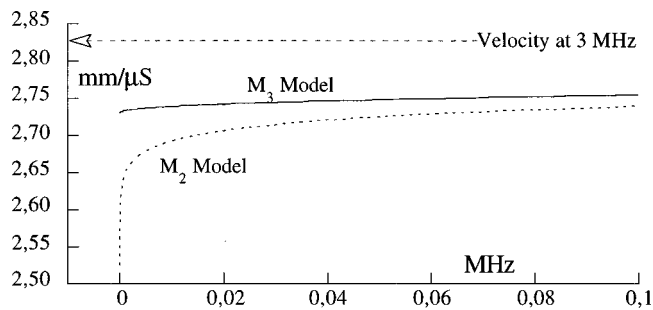


FIG. 10. Comparison between models  $M_2$  and  $M_3$  at low frequency ( $\theta = 0^\circ$ ).

As shown in Figs. 4 and 5 and contrary to the quasilongitudinal mode, the attenuation for the homogeneous quasi-shear mode is larger than its equivalent for the heterogeneous mode propagating in the direction  $\theta_r = 62^\circ$ . This results in a larger velocity dispersion for a quasi-shear homogeneous mode (Fig. 9).

Finally in Fig. 10, the dispersion of the wave velocity for normal incidence is computed with models  $M_2$  and  $M_3$  and compared for lower frequency. It is clear that the difference between both models appears only for very low frequencies and the most appropriate model cannot be distinguished from the ultrasonic frequency domain. Measurements at lower frequency are needed to validate one of these models. Only then, they could be used to predict the static values of moduli. Until now, it is still doubtful that the static values of viscoelastic moduli can be predicted only from the ultrasonic frequency domain.

## V. CONCLUSIONS

The through-transmission immersion method is well adapted to measure the viscoelastic anisotropic behavior of composite materials made of polymer matrix. The measurements of the complex viscoelastic moduli are precise enough to be used in the investigation of the attenuation in composite materials and its dependence on direction of propagation, nature of the mode, frequency, temperature, matrix-fiber proportion, etc.

In this paper it was shown that the local Kramers–Kronig relations between attenuation and velocity in an anisotropic medium are satisfied, as in the case of isotropic media, if the heterogeneity of the quasilongitudinal and quasi-shear modes is taken into account.

This is an important feature in view of the extrapolation of composite material properties towards low frequencies, based on ultrasonic measurements. A way to reach this goal could be the use of two models. One is the Kramers–Kronig relations deduced from the dependence of matrix properties on frequency. The second predicts the viscoelastic properties of composite material from its components. The question of how far the models can be extended towards lower frequencies using these relations is still pending. Other measurements at lower frequencies are underway.

- <sup>1</sup>M. F. Markham, "Measurement of the elastic constants of fiber composites by ultrasonics," *Composites* **1**, 145–149 (1970).
- <sup>2</sup>Y. C. Chu and S. I. Rokhlin, "Comparative analysis of through-transmission ultrasonic bulk wave methods for phase velocity measurements in anisotropic materials," *J. Acoust. Soc. Am.* **95**, 3204–3212 (1994).
- <sup>3</sup>M. Ward, *Mechanical Properties of Polymers* (Wiley-Interscience, New York, 1971).
- <sup>4</sup>M. J. P. Musgrave, "On an elastodynamic classification of orthorhombic media," *Proc. R. Soc. London, Ser. A* **374**, 401–429 (1981).
- <sup>5</sup>B. A. Auld, *Acoustic Fields and Waves in Solids* (Wiley-Interscience, New York, 1973), Vol. I.
- <sup>6</sup>B. Hosten, M. Deschamps, and B. R. Tittmann, "Inhomogeneous wave generation and propagation in lossy anisotropic solids. Application to the viscoelastic characterization of composite materials," *J. Acoust. Soc. Am.* **82**, 1763–1770 (1987).
- <sup>7</sup>B. Hosten, "Reflection and transmission of acoustic plane waves on an immersed orthotropic and viscoelastic solid layer," *J. Acoust. Soc. Am.* **89**, 2745–2752 (1991).
- <sup>8</sup>B. Hosten and M. Deschamps, "Génération d'ondes hétérogènes à l'interface liquide-solide viscoélastique. Approximation par des ondes inhomogènes," *Acustica* **59**, 193–198 (1986).
- <sup>9</sup>S. Baudouin and B. Hosten, "Comparison between prediction and measurement of viscoelastic moduli in composite materials versus temperature using ultrasonic immersion technique with oil," *J. Acoust. Soc. Am.* **102**, 3450–3457 (1997).
- <sup>10</sup>M. O. Donnell, E. T. Jaynes, and J. G. Miller, "Kramers-Kronig relationship between ultrasonic attenuation and phase velocity," *J. Acoust. Soc. Am.* **69**, 696–701 (1981).
- <sup>11</sup>B. Hosten and M. Castaings, "Transfer matrix of multilayered absorbing and anisotropic media. Measurements and simulations of ultrasonic wave propagation through composite 1 materials," *J. Acoust. Soc. Am.* **94**, 1488–1495 (1993).
- <sup>12</sup>B. F. Pouet and N. J. P. Rasolofosan, "Measurement of broadband intrinsic ultrasonic attenuation and dispersion in solids with laser techniques," *J. Acoust. Soc. Am.* **93**, 1286–1292 (1993).
- <sup>13</sup>H. A. Huang, C. E. Bakis, and H. T. Hahn, "Prediction of ultrasonic wave attenuation in fiber reinforced composite laminates," *Rev. Prog. Quant. Nondestr. Eval.* **13**, 1181–1188 (1994).
- <sup>14</sup>D. Zhou, L. Peirlinckx, and L. V. Biesen, "Identification of parametric models for ultrasonic double transmission experiments on viscoelastic plates," *J. Acoust. Soc. Am.* **99**, 1446–1458 (1996).

# Thermal processes in the oscillations of gas bubbles in tubes

X. M. Chen and A. Prosperetti

Department of Mechanical Engineering, The Johns Hopkins University, Baltimore, Maryland 21218

(Received 31 October 1997; accepted for publication 14 April 1998)

The forced oscillations of a system consisting of two finite liquid columns in a duct separated by a gas bubble are studied in the linear approximation. It is found that thermal processes in the gas induce a very significant damping in the system, which can exceed viscous damping even in capillaries with a submillimeter diameter. The study is motivated by the possibility of using gas bubbles as actuators in microdevices. © 1998 Acoustical Society of America.

[S0001-4966(98)00608-0]

PACS numbers: 43.35.Ud [HEB]

## INTRODUCTION

It is well known that a gas bubble pulsating in a large liquid mass loses energy by viscosity, acoustic radiation, and thermal conduction (see, e.g., Apfel, 1981; Prosperetti, 1984, 1991). The additional dissipation due to gas diffusion is essentially always negligible, while thermal effects due to phase change are insignificant for a liquid like water at normal temperature. Over a wide range of bubble radii and frequencies, thermal conduction is by far the most significant dissipative mechanism. In addition to energy dissipation, thermal processes also influence the stiffness of the bubble the behavior of which, in general, will be intermediate between isothermal and adiabatic. The corresponding processes for bubbles pulsating in a duct have not been studied, and they constitute the object of this paper.

The motivation for this work lies in the possibility to use pulsating bubbles as actuators in small fluid-handling devices such as those made possible by recent progress in silicon manufacturing techniques (see e.g., Fujita and Gabriel, 1991; Lin and Pisano, 1991; Gravesen *et al.*, 1993). Of course, energy dissipation is important as it determines the width of the resonance and the magnitude of the response under forced oscillation. The stiffness of the bubble determines the resonance frequency.

## I. FORMULATION

Since this is the first study devoted to the problem, we feel justified in introducing some approximations that will, on the one hand, simplify the analysis and, on the other, facilitate a comparison with the established results for a spherical bubble.

In the first place, and just as in the case of a spherical bubble, we assume the wavelength in the gas to be much larger than both the lateral dimensions of the channel and the axial length of the bubble, so that the gas pressure can be considered spatially uniform and only a function of time (see, e.g., Prosperetti, 1991). Another approximation in common with the standard analyses for spherical bubbles is the neglect of the vapor contribution to the bubble internal pressure and of phase change processes, both approximations being motivated by the consideration of only relatively ‘cold’ liquids (see, e.g., Plesset and Prosperetti, 1977).

In the case of bubbles in large liquid masses a substantial simplification arises from the assumption of spherical shape. Here we introduce a parallel assumption on the shape of the bubble: since our interest lies in channels with a diameter of the order of 1 mm or less, we take the bubble to occupy an entire section of the channel, ignoring the problems associated with contact angles and the detailed shape of the gas-liquid interface (Fig. 1). The gas volume is therefore assumed to be bounded by two flat liquid surfaces orthogonal to the axis of the channel, and by the surface of the channel comprised between these two surfaces. The amplitude of the oscillations is taken to be so small that the problem can be linearized, and the liquid surfaces bounding the gas volume are supposed to move remaining flat and orthogonal to the channel walls; the complexities associated with the motion of the gas-liquid-solid contact line are therefore ignored. This approximation has the consequence of rendering it impossible to account for a velocity profile in the liquid. Energy dissipation due to liquid viscosity will be reintroduced in an approximate way later (Sec. V). In spite of the relative crudeness of this model, one may expect the results to be a valid first estimate of the quantitative effects of the physical processes involved.

Let  $x_1(t)$  and  $x_2(t)$  denote the time-dependent positions of the two gas-liquid interfaces, both measured from the midpoint of the undisturbed bubble, and define

$$x_2 - x_1 = 2L_B[1 + X(t)], \quad (1)$$

where  $2L_B$  is the undisturbed length of the bubble. We shall only consider the steady-state problem in which the time dependence of all disturbances is proportional to  $\exp i\omega t$ .

Due to the translational invariance of the channel and to the fact that, in a linear problem, the perturbation of any quantity is proportional to that of any other, one may write without loss of generality the gas pressure in the form

$$p(t) = p_0[1 - \Phi X(t)], \quad (2)$$

where  $p_0$  is the equilibrium value and  $\Phi$  is a complex constant. It will be noted that this relation may be considered as the linearization of a relation of the type  $pV^\Phi = \text{const}$  (where  $V$  is the bubble volume), so that  $\Phi$  may be regarded as a (complex, frequency dependent) polytropic index.

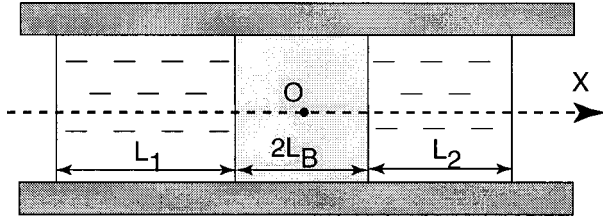


FIG. 1. The physical model simulated in this study: a duct contains two liquid columns separated by a gas bubble.

If the length of the liquid columns bounded by the surface  $x_j$ ,  $j=1,2$ , is denoted by  $L_j$ , and if the pressure acting on the free end of each column is

$$p_j(t) = p_0[1 + P_j(t)], \quad (3)$$

the equations of motion for the columns are

$$L_1 \rho \ddot{x}_1 = p_0[P_1 + \Phi X], \quad (4)$$

$$L_2 \rho \ddot{x}_2 = -p_0[P_2 + \Phi X], \quad (5)$$

where  $\rho$  is the liquid density. Define the abscissa of the center of mass of the liquid by

$$\xi = \frac{L_1 x_1 + L_2 x_2}{L_1 + L_2} + \frac{1}{2}(L_2 - L_1). \quad (6)$$

Then the two equations can be combined to give equations of motion for  $\xi$  and  $X$ :

$$\rho(L_1 + L_2)\ddot{\xi} = p_0(P_1 - P_2), \quad (7)$$

$$\ddot{X} = -\frac{p_0}{2L_B \rho} \left[ \frac{1}{L_2}(P_2 + \Phi X) + \frac{1}{L_1}(P_1 + \Phi X) \right]. \quad (8)$$

Upon noting that  $iX = \dot{X}/\omega$ , the second equation may be rewritten as

$$\begin{aligned} \ddot{X} + \frac{p_0}{2L_B \rho \omega} (\text{Im } \Phi) \left[ \frac{1}{L_1} + \frac{1}{L_2} \right] \dot{X} + \frac{p_0}{2L_B \rho} (\text{Re } \Phi) \left[ \frac{1}{L_1} + \frac{1}{L_2} \right] X \\ = -\frac{p_0}{2L_B \rho} \left[ \frac{P_1}{L_1} + \frac{P_2}{L_2} \right]. \end{aligned} \quad (9)$$

The equation for  $\xi$  describes the overall motion of the system. In particular, if  $P_1 = P_2$  and the initial velocity vanishes,  $\xi$  is independent of time irrespective of the behavior of the bubble. Thermal effects only affect the second equation (8) through  $\Phi$ , and it is on this quantity that we now focus. It is obvious from (9) that the real part of this quantity governs the natural frequency of the system, while the imaginary part is responsible for thermal dissipation.

The determination of  $\Phi$  requires a consideration of the energy equation. For a perfect gas with spatially uniform pressure  $p$ , in the linear approximation, this is

$$\rho_G c_p \frac{\partial T}{\partial t} - \dot{p} = k \nabla^2 T, \quad (10)$$

where  $T$  is the gas temperature,  $\rho_G$  is its density,  $c_p$  is the specific heat at constant pressure, and  $k$  is the thermal conductivity. By combining with the equation of continuity and using the relation  $c_p \rho_G T_0 = \gamma p_0 / (\gamma - 1)$  valid for perfect

gases (with  $\gamma$  the ratio of specific heats), this equation becomes

$$\dot{p} - \gamma p \nabla \cdot \mathbf{u} = k \nabla^2 T, \quad (11)$$

where  $\mathbf{u}$  is the gas velocity. When this equation is integrated over the surface of the gas volume  $V$  one finds an equation for the gas pressure in the form

$$V \dot{p} = -\gamma p \dot{V} - (\gamma - 1) Q, \quad (12)$$

where

$$Q = - \oint_A k \frac{\partial T}{\partial n} dA \quad (13)$$

is the total heat flow rate out of the surface  $A$  bounding the bubble. The calculation of the gas pressure presupposes a knowledge of  $Q$ , and hence of the gas temperature field, to which we now turn.

## II. THE THERMAL PROBLEM

By virtue of the assumed exponential time dependence, the energy equation (10) may be written

$$\left( \nabla_{\perp}^2 + \frac{\partial^2}{\partial x^2} \right) T - i \frac{\omega}{D} (T - T_0) = i \frac{\gamma - 1}{\gamma} \frac{\omega}{D} T_0 \Phi X, \quad (14)$$

where  $D = k / \rho_G c_p$  is the gas thermal diffusivity,  $T_0$  is the undisturbed temperature of the system, and  $\nabla_{\perp}^2$  denotes the two-dimensional Laplacian over the cross section of the channel, the shape of which for the moment we do not need to specify. At this point we introduce another assumption which is also standard for a gas bubble in a large mass of liquid, namely that the surface delimiting the gas remains at the undisturbed temperature  $T_0$ . The justification for this assumption lies in the large heat capacity *per unit volume* of most solids and liquids, which far exceeds that of gases. Amounts of heat sufficient to cause significant temperature changes in the gas are therefore too small to cause any appreciable temperature disturbance in the materials surrounding the bubble. On this basis, we seek a solution of (14) subject to the condition  $T = T_0$  on the boundary of the gas volume.

We determine this solution by expanding  $T$  over a set of eigenfunctions of  $\nabla_{\perp}^2$ . Specifically, consider the eigenfunction, eigenvalue pairs  $(v_n, \lambda_n)$  satisfying

$$\nabla_{\perp}^2 v_n = -\frac{\lambda_n^2}{l^2} v_n, \quad (15)$$

over the cross section of the channel, subject to the boundary condition  $v_n = 0$  on the perimeter of the cross section. Depending on the shape of the cross section, the index  $n$  may actually stand for a pair of indices, as in one of the examples of Sec. IV below. In (15) we have made the eigenvalues dimensionless in terms of a characteristic length  $l$  defined as the ratio of the bubble volume to its surface:

$$l = \frac{L_B S}{S + \mathcal{P} L_B}, \quad (16)$$

where  $S$  is the area of the cross section and  $\mathcal{P}$  is its perimeter. The reason for this definition is the fact that, when one

of the lengths characterizing the geometry of the bubble (e.g., its extension in the axial direction, or the size of the channel cross section) is much smaller than the others,  $l$  is close to this length. Thus,  $l$  is a measure of the shortest distance between the bubble “core” and the fixed-temperature boundaries that enclose the gas. The physical relevance of this distance will be apparent shortly.

It is easy to see, by use of Green’s identity, that the eigenfunctions satisfying (15) are orthogonal to each other (see the Appendix). We thus write

$$T = T_0 \left[ 1 + \sum_n A_n(x, t) v_n(y, z) \right], \quad (17)$$

substitute into (14), and exploit the orthogonality of the eigenfunctions to find

$$\frac{\partial^2 A_n}{\partial x^2} - \frac{k_n^2}{l^2} A_n = i \frac{\gamma - 1}{\gamma} \frac{\omega \sqrt{S}}{D} \sigma_n \Phi X, \quad (18)$$

where

$$k_n = \sqrt{\lambda_n^2 + i\Omega}, \quad \Omega = \frac{\omega l^2}{D}, \quad (19)$$

$$\sigma_n = \frac{1}{\sqrt{S}} \int_S v_n dS. \quad (20)$$

Due to linearization, the boundary conditions are  $A_n = 0$  at the undisturbed positions  $x_{i0} = \mp L_B$ ,  $i = 1, 2$ , of the liquid surfaces bounding the bubble. The solution is readily found to be

$$A_n = i \frac{\gamma - 1}{\gamma} \frac{\omega l^2 \sqrt{S}}{D} \frac{\sigma_n}{k_n^2} \left[ \frac{\cosh k_n x / l}{\cosh k_n L_B / l} - 1 \right] \Phi X, \quad (21)$$

where it will be recalled that the coordinate  $x$  is measured from the midpoint of the undisturbed bubble.

With this result the heat flow rate  $Q$  can be calculated from (13). We break up the integral into the contribution  $Q_s$  of the liquid surface and the contribution  $Q_w$  of the tube wall,  $Q = Q_s + Q_w$ . For the former we have

$$\begin{aligned} Q_s &= -2k \int_S \frac{\partial T}{\partial x} \Big|_{x=L_B} dS \\ &= i\omega(p - p_0) V \sum_n \sigma_n^2 \frac{\tanh k_n \mathcal{A}}{k_n \mathcal{A}}, \end{aligned} \quad (22)$$

where  $\mathcal{A}$  is the *aspect ratio* of the bubble defined by

$$\mathcal{A} \equiv \frac{L_B}{l} = 1 + \frac{4L_B}{\mathcal{D}}, \quad (23)$$

with  $\mathcal{D} = 4S/\mathcal{P}$  the hydraulic diameter of the tube. For the second component we have, noting that  $\mathbf{n} \cdot \nabla = \mathbf{n} \cdot \nabla_{\perp}$ ,

$$\begin{aligned} Q_w &= -2kT_0 \sum_n \int_0^{L_B} A_n dx \int_{\mathcal{P}} d\mathcal{P} \mathbf{n} \cdot \nabla_{\perp} v_n \\ &= -2kT_0 \sum_n \int_0^{L_B} A_n dx \int_S dS \nabla_{\perp}^2 v_n \\ &= -2kT_0 \sum_n \int_0^{L_B} A_n dx \int_S dS \left( -\frac{\lambda_n^2}{l^2} \right) v_n \\ &= i\omega(p - p_0) V \sum_n \frac{\sigma_n^2 \lambda_n^2}{k_n^2} \left( 1 - \frac{\tanh k_n \mathcal{A}}{k_n \mathcal{A}} \right), \end{aligned} \quad (24)$$

where in the first step we have used the divergence theorem to convert the line integral over the perimeter of the cross section into a surface integral over the cross section, and in the following steps the eigenvalue equation (15) and the definition (20) of  $\sigma_n$ . Upon combining the two contributions (22) and (24) we then find

$$Q = i\omega(p - p_0) V G, \quad (25)$$

where

$$G = \sum_n \frac{\sigma_n^2}{k_n^2} \left[ \lambda_n^2 + i\Omega \frac{\tanh k_n \mathcal{A}}{k_n \mathcal{A}} \right]. \quad (26)$$

Upon substitution of (25) into the pressure equation (12) we find, comparing with (2),

$$\Phi = \frac{\gamma}{1 + (\gamma - 1)G}. \quad (27)$$

In the framework of the present model, the function  $G$  describes the effect of the thermal processes occurring in the bubble on the gas pressure. An alternative form for this quantity may be derived by using the identity

$$\sum_n \sigma_n^2 = 1, \quad (28)$$

proven in the Appendix, to obtain

$$G = 1 + i\Omega \sum_n \left( \frac{\sigma_n}{k_n} \right)^2 \left[ \frac{\tanh k_n \mathcal{A}}{k_n \mathcal{A}} - 1 \right]. \quad (29)$$

Since  $G$  is complex, Eq. (25) shows that the heat transfer rate has components in phase and in quadrature with the pressure disturbance. The former one is proportional to  $\text{Im } G$ , and is responsible for the thermal losses of the system. Although it might seem that  $G$  depends explicitly only on  $\Omega$  and  $\mathcal{A}$ , there may be an additional dependence on other dimensionless parameters characterizing the shape of the tube cross section through the eigenvalues  $\lambda_n$ .

### III. ASYMPTOTIC BEHAVIOR

Before looking at numerical results for some specific examples, it is useful to consider two limit cases of the previous results (26) and (27) that are applicable to channels of arbitrary cross section.

We start with the low-frequency limit or, more precisely, with frequencies such that the corresponding thermal penetration length is much larger than the smallest bubble dimension:



$$\sqrt{\frac{D}{\omega}} \gg l. \quad (30)$$

In these conditions the parameter  $\Omega$ , defined in (19), is small, and one would expect nearly isothermal behavior to prevail. To confirm this expectation we approximate the expression (19) for  $k_n$  and the hyperbolic tangent in (29) by a Taylor series and find

$$G = 1 + \Omega^2 \sum_n \frac{\sigma_n^2}{\lambda_n^4} \left[ \frac{3}{2} \frac{\tanh \lambda_n \mathcal{A}}{\lambda_n \mathcal{A}} - \frac{1}{2 \cosh^2 \lambda_n \mathcal{A}} - 1 \right] + i\Omega \sum_n \frac{\sigma_n^2}{\lambda_n^2} \left( \frac{\tanh \lambda_n \mathcal{A}}{\lambda_n \mathcal{A}} - 1 \right), \quad (31)$$

from which

$$\text{Re } \Phi = 1 + \frac{\gamma-1}{\gamma} \Omega^2 \sum_n \frac{\sigma_n^2}{\lambda_n^4} \left[ \frac{3}{2} \frac{\tanh \lambda_n \mathcal{A}}{\lambda_n \mathcal{A}} - \frac{1}{2 \cosh^2 \lambda_n \mathcal{A}} - 1 + \dots \right], \quad (32)$$

$$\text{Im } \Phi = \frac{\gamma-1}{\gamma} \Omega \sum_n \frac{\sigma_n^2}{\lambda_n^2} \left[ 1 - \frac{\tanh \lambda_n \mathcal{A}}{\lambda_n \mathcal{A}} + \dots \right]. \quad (33)$$

These formulas simplify if  $\mathcal{A} = L_B/l \gg 1$ , i.e., for a relatively long bubble. In this case they become

$$\text{Re } \Phi \approx 1 + \frac{\gamma-1}{\gamma} \Omega^2 \sum_n \frac{\sigma_n^2}{\lambda_n^4} \left[ \frac{3}{2} \frac{1}{\lambda_n \mathcal{A}} - 1 \right], \quad (34)$$

$$\text{Im } \Phi \approx \frac{\gamma-1}{\gamma} \Omega \sum_n \frac{\sigma_n^2}{\lambda_n^2} \left[ 1 - \frac{1}{\lambda_n \mathcal{A}} \right]. \quad (35)$$

A parallel analysis of the opposite limit of large  $\Omega$  is complicated mathematically although, of course, one expects an adiabatic behavior for which  $\Phi \rightarrow \gamma$ . Rather than starting from the explicit representations (26) or (29), it is simpler to proceed as follows. Consider a one-dimensional problem in which a constant-temperature plane surface is exposed to a gas environment of infinite extent, the pressure of which fluctuates in time. One readily finds the following result for the heat flux out of the gas volume:

$$q = -(p - p_0) \sqrt{i\omega D}. \quad (36)$$

In the high-frequency limit, when the thermal penetration layer in the gas is much smaller than the geometric dimensions of the bubble, each point at the bubble surface is subject to this heat flux, so that the total heat transfer rate out of the gas volume must become, for  $\omega \rightarrow \infty$ ,

$$Q \approx 2(L_B \mathcal{P} + S)(p - p_0) \sqrt{i\omega D}. \quad (37)$$

Upon equating to the previous general result (25) for  $Q$ , we find

$$G \rightarrow \frac{1-i}{\sqrt{2\Omega}} \quad \text{for } \Omega \rightarrow \infty, \quad (38)$$

from which we have the following asymptotic limits:

$$\text{Re } \Phi \rightarrow \gamma \left[ 1 + \frac{\gamma-1}{\sqrt{2\Omega}} \right], \quad \text{Im } \Phi \rightarrow \frac{\gamma(\gamma-1)}{\sqrt{2\Omega}}. \quad (39)$$

It will be observed that these results are independent of the aspect ratio  $\mathcal{A}$ , a result that it would be quite difficult to establish directly from (26) or (29).

By following a similar line of approach we can deduce approximate results valid for very short bubbles,  $\mathcal{A} - 1 \ll 1$ , and very long bubbles,  $\mathcal{A} \gg 1$ . In the former case most of the heat exchange occurs with the liquid and one can ignore the directions orthogonal to the duct axis. Upon dropping the operator  $\nabla_{\perp}^2$  in the energy equation (14) we find

$$T - T_0 = \frac{D}{k} (p - p_0) \left( 1 - \frac{\cosh \sqrt{i\omega/D} x}{\cosh \sqrt{i\omega/D} L_B} \right), \quad (40)$$

from which the total heat flow rate into the liquid is readily found as

$$Q = 2S(p - p_0) \sqrt{i\omega D} \tanh(\sqrt{i\Omega} \mathcal{A}). \quad (41)$$

Upon comparison with (25) we thus have

$$G \approx \frac{\tanh(\mathcal{A} \sqrt{i\Omega})}{\mathcal{A} \sqrt{i\Omega}}, \quad \mathcal{A} \rightarrow 1. \quad (42)$$

It is readily checked that this result agrees with (31) for small  $\Omega$  and, noting that  $\mathcal{A} \approx 1$ , with (38) for large  $\Omega$ . The real and imaginary parts of  $\Phi$  evaluated using  $G$  given by (42) are plotted in Fig. 2(a) and (b) as functions of  $\Omega \mathcal{A}^2$ . These results are valid whatever the shape of the cross section of the duct.

For the opposite limit of a long bubble, heat exchange occurs mostly with the wall of the tube and the  $x$  derivative in (14) can be dropped. The temperature field can be solved by using the same expansion (17) as before in which, however, the coefficients  $A_n$  are constants. Other than this change, the calculation is therefore the same as the general one outlined in the previous section and one finds

$$G \approx \sum_n \frac{\sigma_n^2 \lambda_n^2}{\lambda_n^2 + i\Omega}. \quad (43)$$

It will be observed that this is just the first summation in (26). For  $\Omega$  small we recover (31) to first order.

## IV. SPECIFIC EXAMPLES

The limits considered in the previous section appear to be the only ones for which results valid for arbitrary cross sections can be derived. For intermediate values of the frequency, we need to consider specific geometries. As noted before, for each specific shape of the cross section of the tube, the result (26) depends on the dimensionless frequency  $\Omega$  defined by (19), the aspect ratio  $\mathcal{A}$  defined by (23), and possibly other dimensionless parameters characterizing the shape of the cross section.

### A. Circular tube

For a circular tube of radius  $R$ , the characteristic length  $l$  defined by (16) is given by

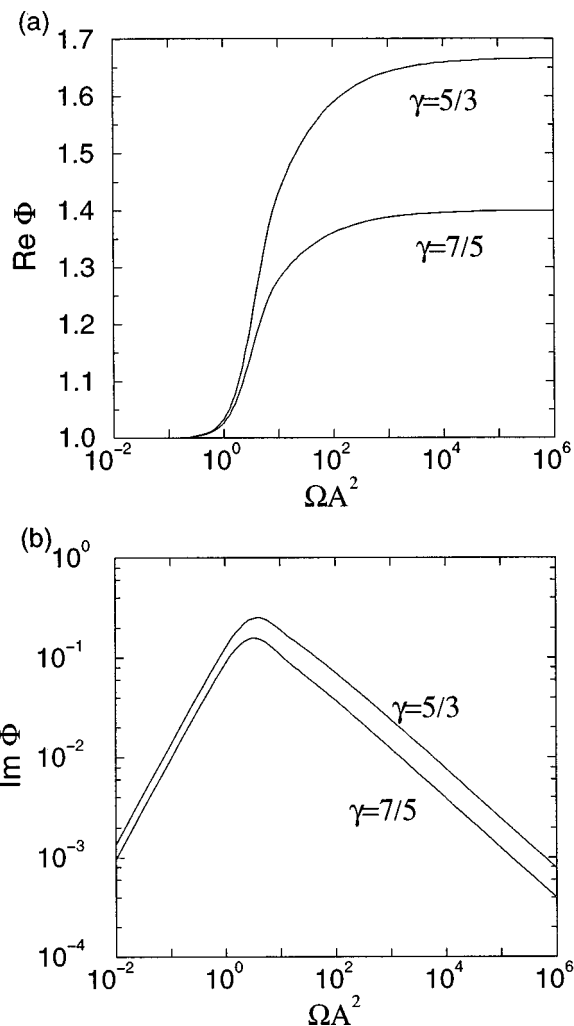


FIG. 2. The real (a) and imaginary (b) parts of  $\Phi$  evaluated using the approximate result (42) valid for short bubbles as functions of the  $\Omega \mathcal{A}^2$ , where  $\Omega$  is the dimensionless frequency given by (19) and  $\mathcal{A}$  is the aspect ratio (23). These results are valid for any shape of the cross section of the duct.

$$l = \frac{RL_B}{R + 2L_B}, \quad (44)$$

so that the aspect ratio is

$$\mathcal{A} = 1 + \frac{2L_B}{R}. \quad (45)$$

The eigenfunctions, normalized according to (A4) of the Appendix, are given by

$$v_n = \frac{1}{\sqrt{\pi R}} \frac{J_0(\alpha_n r/R)}{J_1(\alpha_n)}, \quad (46)$$

where  $r$  is the radial distance from the tube axis, the  $J$ 's are Bessel functions, and the  $\alpha_n$ 's are the zeros of  $J_0' = -J_1$ . The eigenvalues  $\lambda_n$  are given by

$$\lambda_n = \alpha_n \frac{l}{R} = \alpha_n \frac{\mathcal{A} - 1}{2\mathcal{A}}, \quad (47)$$

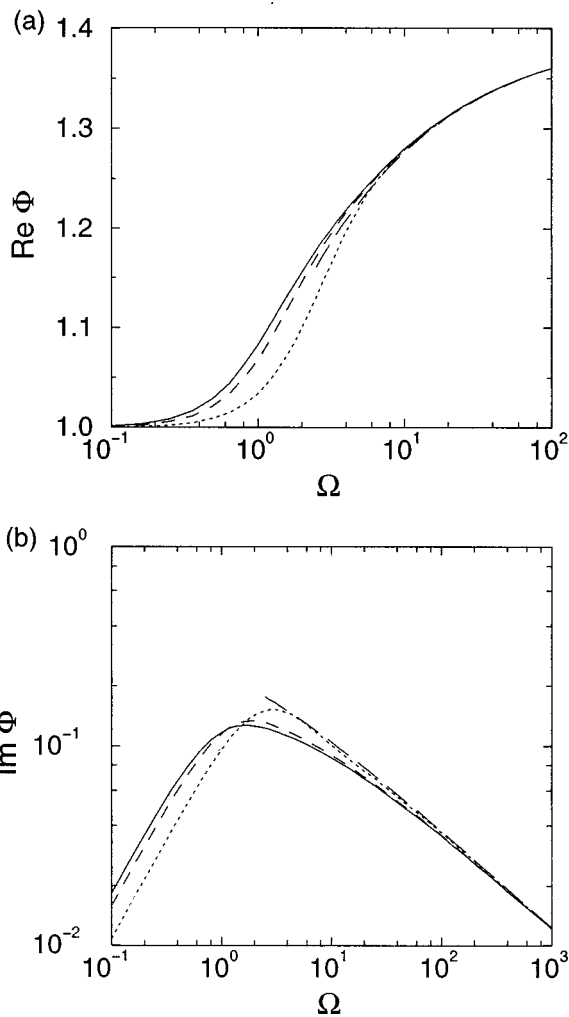


FIG. 3. The real (a) and imaginary (b) parts of  $\Phi$  as functions of the dimensionless frequency  $\Omega$  defined in (19) for  $\gamma=7/5$  for a cylindrical cross section. The three lines correspond to  $\mathcal{A}=1.1$  (dotted), 2 (solid), and 11 (dashes), i.e., to  $2L_B/R=0.1, 1,$  and  $10$ , respectively. The interrupted line marked with long dashes is the asymptotic approximation (39) valid at high frequencies.

which shows that, for this geometry, the function  $G$  only depends on  $\mathcal{A}$  and  $\Omega$ . The constants  $\sigma_n$  defined in (20) are readily calculated and they are

$$\sigma_n = \frac{2}{\alpha_n}. \quad (48)$$

With these results, the function  $\Phi$  can be calculated explicitly as a function of the parameters of the problem. We show in Fig. 3 the real and imaginary parts of  $\Phi$  as functions of the dimensionless frequency  $\Omega$  for  $\gamma=7/5$ . The three lines correspond to  $\mathcal{A}=1.1$  (dotted), 2 (solid), and 11 (dashed), i.e., to  $2L_B/R=0.1, 1,$  and  $10$ , respectively. The asymptotic trends for small and large frequencies are in precise agreement with the deductions of the previous section. The lines for  $\mathcal{A}=1.1$  are nearly identical to the approximation shown in Fig. 2.

The figures also show that the results are close to each other, and their variation with the parameter  $\mathcal{A}$  is not systematic. Both features indicate that the characteristic length  $l$

defined in (16) is effective in achieving an approximate scaling for  $\Phi$ .

## B. Rectangular channel

For a rectangular cross section of sides  $a$  and  $b$  the eigenfunctions are labelled by a pair of indices and are given by

$$v_{nm} = \frac{2}{\sqrt{ab}} \sin \frac{m\pi y}{a} \sin \frac{n\pi z}{b}. \quad (49)$$

The characteristic length  $l$  of (16) and aspect ratio  $\mathcal{A}$  of (23) are

$$l = \frac{abL_B}{ab + 2(a+b)L_B}, \quad \mathcal{A} = 1 + \frac{2L_B(a+b)}{ab}, \quad (50)$$

the eigenvalues are

$$\frac{\lambda_{nm}}{l} = \pi \left[ \left( \frac{m}{a} \right)^2 + \left( \frac{n}{b} \right)^2 \right]^{1/2}, \quad (51)$$

and

$$\sigma_{nm} = \frac{8}{mn\pi^2}, \quad (52)$$

when  $m$  and  $n$  are both odd, while  $\sigma_{nm} = 0$  otherwise. In addition to  $\mathcal{A}$ , the result (51) for the eigenvalues depends on the ratio  $a/b$ . This is an example of a feature of the result anticipated at the end of Sec. II.

Results for  $\text{Re } \Phi$  and  $\text{Im } \Phi$  for this geometry are shown in Figs. 4–7 for  $\gamma = 7/5$  and for  $\mathcal{A} = 1.1, 2$ , and 11 and  $a/b = 0.1$  and 1. The results for  $\mathcal{A}$  close to 1 coincide with those given in Fig. 2. Notice also that the formulas are invariant under an interchange of  $a$  and  $b$ , so that it is sufficient to consider  $a \leq b$ .

The graphs are similar to those of the previous case and the same comments apply.

## V. VISCOUS DISSIPATION

For a spherical bubble in an unbounded liquid, viscosity only affects the condition of balance of normal stresses and is usually of little importance unless the bubble radius is small. The present situation is different due to the viscous dissipation of energy in the course of the motion of the two liquid columns bounding the bubble. The effect can be estimated as follows (Öguz and Prosperetti, 1998).

With the approximation of parallel flow, the viscous energy dissipation per period for the  $j$ th liquid column ( $j = 1, 2$ ) is

$$\mathcal{E}_j = \frac{\nu m_j}{S} \int_0^{2\pi/\omega} dt \int_S dS \left( \frac{\partial u}{\partial r} \right)^2, \quad (53)$$

where  $\nu$  is the kinematic viscosity coefficient,  $m_j = \rho S L_j$  is the mass of liquid constituting the column, and  $u$  is the axial velocity. For a harmonic oscillator with velocity  $\dot{x}_j$  and damping parameter  $\beta_{vj}$ , the energy dissipated in a cycle is

$$\mathcal{E}_{dj} = 2\beta_{vj} \int_0^{2\pi/\omega} \dot{x}_j^2 dt. \quad (54)$$

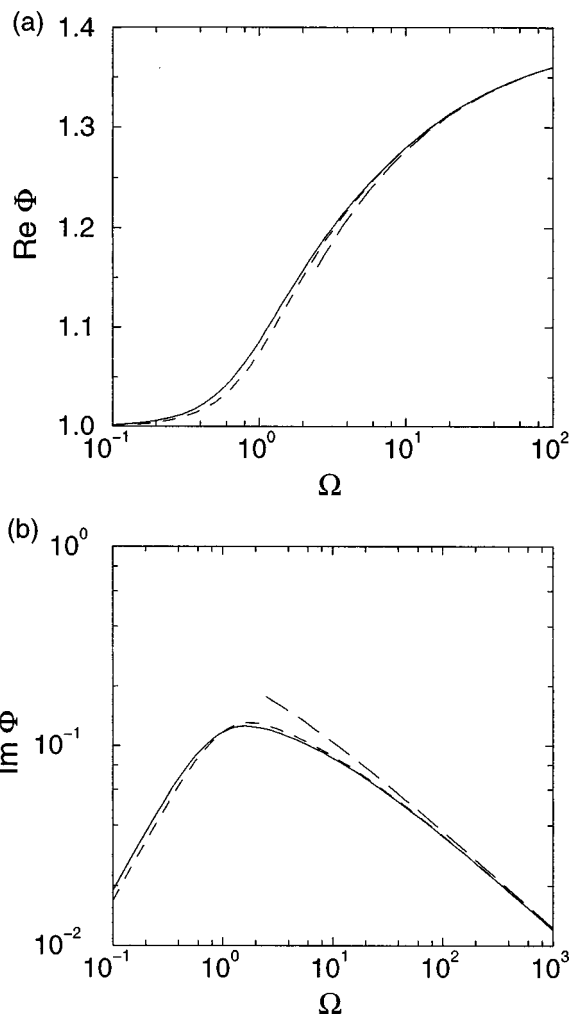


FIG. 4. The real (a) and imaginary (b) parts of  $\Phi$  as functions of the dimensionless frequency  $\Omega$  defined in (19) for  $\gamma = 7/5$  for a rectangular cross section. The bubble aspect ratio  $\mathcal{A}$  is 2 and the lines are for  $a/b = 1$  (solid) and 0.1 (dashes). The interrupted line marked with long dashes is the asymptotic approximation (39) valid at high frequencies.

Upon equating (53) and (54) one can define an equivalent viscous damping parameter by

$$\beta_{vj} = \frac{\omega \nu m_j}{2\pi S} \int_0^{2\pi/\omega} dt \int_S dS \left[ \frac{\partial}{\partial r} \left( \frac{u}{\dot{x}_j} \right) \right]^2. \quad (55)$$

A relation between  $u$  and  $\dot{x}_j$  can be established by equating the volume flow rates:

$$S \dot{x}_j = \int_S u dS. \quad (56)$$

From the linearity of this relation it is clear that the integral in (55) will be independent of  $\dot{x}_j$ . Note that, from (55), we see that

$$b_v = \frac{\beta_{v1}}{m_1} = \frac{\beta_{v2}}{m_2}. \quad (57)$$

An exact solution of the Navier–Stokes equation for parallel oscillatory flow in an infinitely long circular tube is available (see, e.g., Leal, 1992), but it is expressed in terms of Bessel functions and the integral in (55) cannot be evalu-

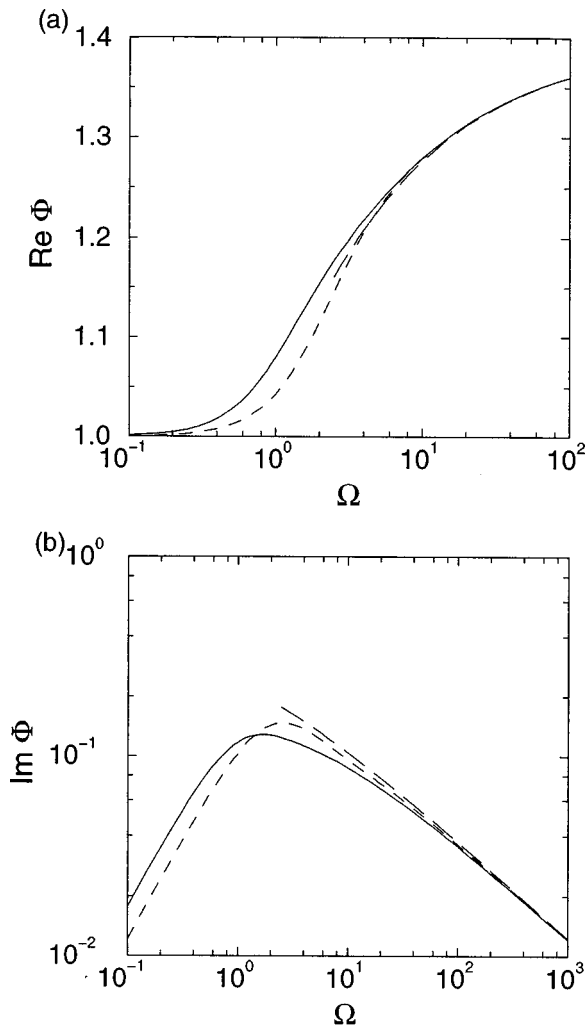


FIG. 5. The real (a) and imaginary (b) parts of  $\Phi$  as functions of the dimensionless frequency  $\Omega$  defined in (19) for  $\gamma=7/5$  for a rectangular cross section. The bubble aspect ratio  $\mathcal{A}$  is 11 and the lines are for  $a/b=1$  (solid) and 0.1 (dashes). The interrupted line marked with long dashes is the asymptotic approximation (39) valid at high frequencies.

ated in closed form. By using the well-known result for Poiseuille flow one has the approximation

$$b_v = 4 \frac{\nu}{R^2}, \quad (58)$$

as also follows from the exact result (55) in the limit  $\sqrt{\nu/\omega} \gg R$ . In the opposite limit,  $\sqrt{\nu/\omega} \ll R$ , viscosity is only significant in a thin boundary layer at the tube wall and the corresponding result is

$$b_v = \sqrt{\frac{\pi \nu \omega}{2S}}. \quad (59)$$

The result has been written in this way to stress its applicability to tubes of arbitrary cross section, provided the viscous boundary layer thickness  $\sqrt{\nu/\omega}$  is small compared with the shortest dimension of the cross section. In Fig. 8 we show the dimensionless viscous damping

$$\tilde{b}_v = \frac{R^2 b_v}{4\nu} \quad (60)$$

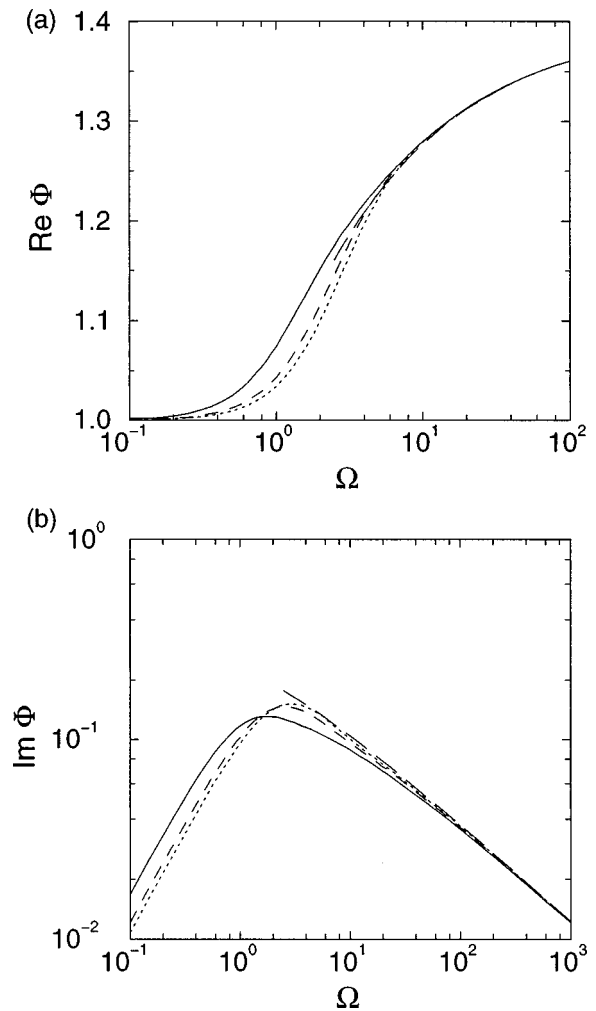


FIG. 6. The real (a) and imaginary (b) parts of  $\Phi$  as functions of the dimensionless frequency  $\Omega$  defined in (19) for  $\gamma=7/5$  for a rectangular cross section with  $a/b=0.1$ . The bubble aspect ratio  $\mathcal{A}$  is 1.1 (dotted), 2 (solid), and 11 (short dashes). The interrupted line marked with long dashes is the asymptotic approximation (39) valid at high frequencies.

as a function of the Womersley number  $Wo = \omega R^2/\nu$  evaluated by numerical integration of the exact result (55), and we compare it with the two asymptotic limits (58) and (59) (dashed lines).

Upon introducing an equivalent damping in the equations of motion (4) and (5) along the lines outlined before, and again separating the real and imaginary parts of  $\Phi$  as done in connection with Eq. (9), we have

$$m_1 \ddot{x}_1 + 2\beta_{v1} \dot{x}_1 - Sp_0 \Phi X = Sp_0 P_1, \quad (61)$$

$$m_2 \ddot{x}_2 + 2\beta_{v2} \dot{x}_2 + Sp_0 \Phi X = -Sp_0 P_2. \quad (62)$$

The steady solution of this system is given by

$$\frac{x_1 - x_{10}}{2L_B} = \frac{p_0}{2L_B \rho \Delta} \times \left[ \frac{P_1}{L_1} - \frac{P_1 - P_2}{L_1 + L_2} \frac{\omega_0^2}{\omega^2} \frac{1 + i \text{Im } \Phi / \text{Re } \Phi}{1 - 2ib_v/\omega} \right], \quad (63)$$

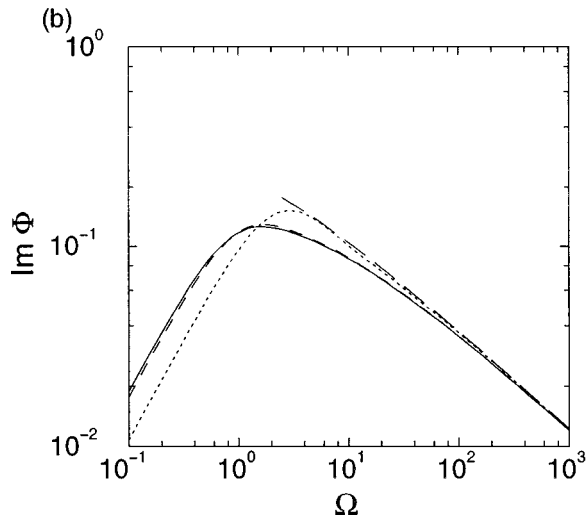
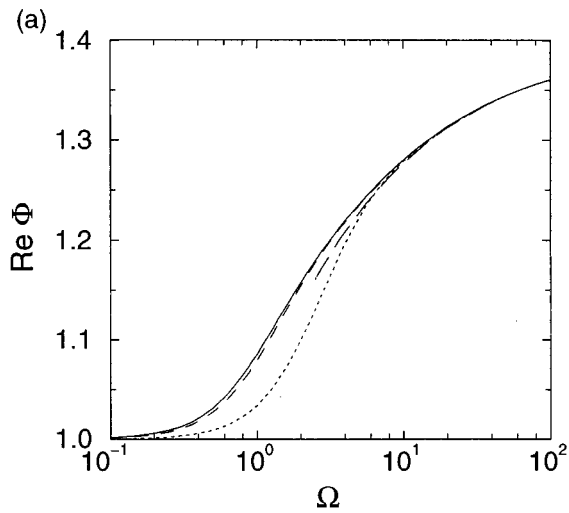


FIG. 7. The real (a) and imaginary (b) parts of  $\Phi$  as functions of the dimensionless frequency  $\Omega$  defined in (19) for  $\gamma=7/5$  for a square cross section,  $a/b=1$ . The bubble aspect ratio  $\mathcal{A}$  is 1.1 (dotted), 2 (solid), and 11 (short dashes). The interrupted line marked with long dashes is the asymptotic approximation (39) valid at high frequencies.

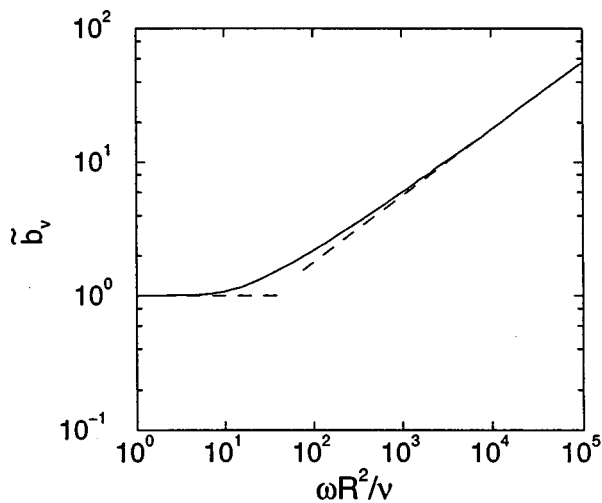


FIG. 8. The dimensionless viscous damping  $\bar{b}_v$  defined by (60) for a cylindrical tube according to the approximate procedure of Sec. V as a function of the Womersley number  $Wo=\omega R^2/\nu$ .

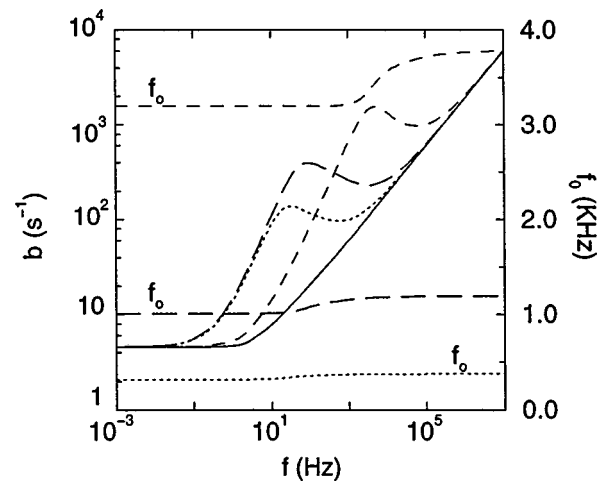


FIG. 9. Viscous and total damping (left scale) and resonance frequency  $f_0$  (right scale) for an air bubble in a cylindrical tube with  $R=1$  mm and  $L_1=L_2=5$  mm as functions of the driving frequency  $f$ . The solid line is the viscous contribution to the damping. The dotted lines are for  $2L_B=10$  mm ( $\mathcal{A}=11$ ), the lines marked with long dashes for  $2L_B=1$  mm ( $\mathcal{A}=2$ ), and those with short dashes for  $2L_B=0.1$  mm ( $\mathcal{A}=1.1$ ). The liquid is water, the temperature  $20^\circ\text{C}$ , and the undisturbed pressure atmospheric.

$$\frac{x_2-x_{20}}{2L_B} = \frac{p_0}{2L_B\rho\Delta} \left[ -\frac{P_2}{L_2} - \frac{P_1-P_2}{L_1+L_2} \frac{\omega_0^2}{\omega^2} \frac{1+i \text{Im } \Phi/\text{Re } \Phi}{1-2ib_v/\omega} \right], \quad (64)$$

from which, according to (1),

$$X = \frac{x_2-x_{20}}{2L_B} - \frac{x_1-x_{10}}{2L_B} = -\frac{p_0}{2L_B\rho\Delta} \left( \frac{P_1}{L_1} + \frac{P_2}{L_2} \right). \quad (65)$$

In these equations  $b_v$  is defined in (57),

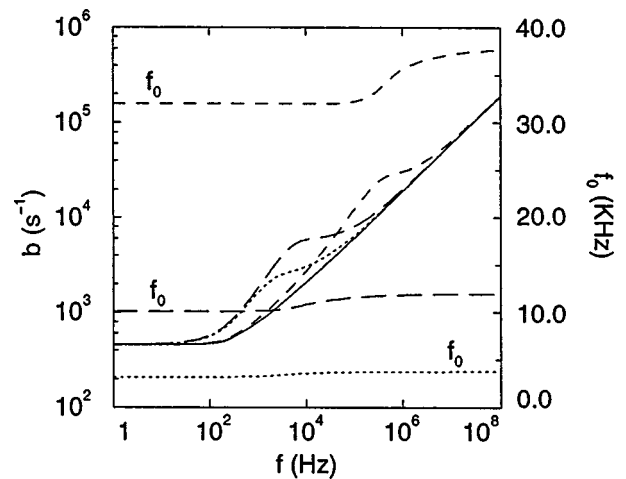


FIG. 10. Viscous and total damping (left scale) and resonance frequency  $f_0$  (right scale) for an air bubble in a cylindrical tube with  $R=0.1$  mm and  $L_1=L_2=0.5$  mm as functions of the driving frequency  $f$ . The solid line is the viscous contribution to the damping. The dotted lines are for  $2L_B=1$  mm ( $\mathcal{A}=11$ ), the lines marked with long dashes for  $2L_B=0.1$  mm ( $\mathcal{A}=2$ ), and those with short dashes for  $2L_B=0.01$  mm ( $\mathcal{A}=1.1$ ). The liquid is water, the temperature  $20^\circ\text{C}$ , and the undisturbed pressure atmospheric.

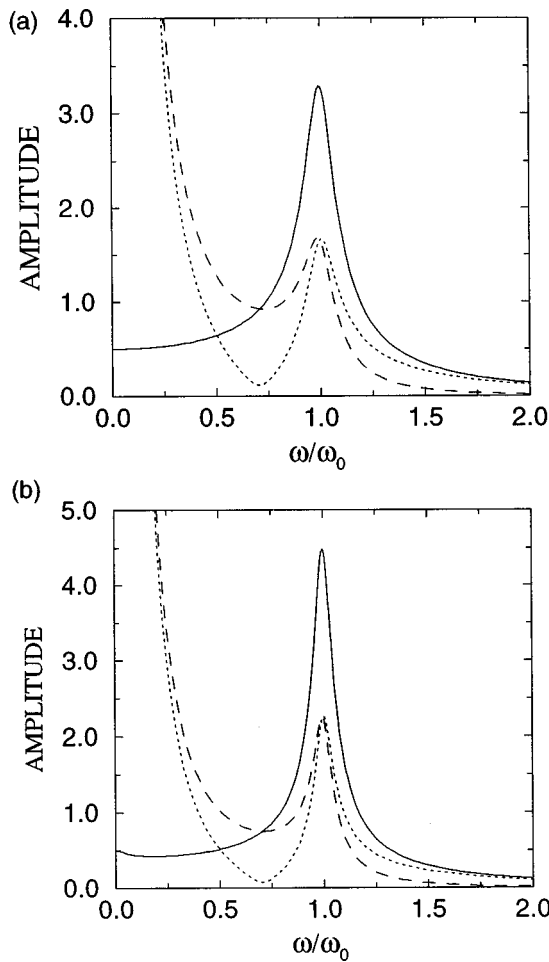


FIG. 11. Dimensionless amplitudes of oscillation of the left liquid surface  $|(x_1 - x_{10})/2L_B P_1|$  [dotted line, Eq. (63)], of the right surface  $|(x_2 - x_{20})/2L_B P_1|$  [dashes, Eq. (64)], and of the bubble length  $|X/P_1|$ , given by (65), as a function of the excitation frequency normalized by the resonance frequency. The bubble oscillation is driven by a pressure disturbance applied to the left liquid column. The tube radius is  $R=1$  mm and the common length of the liquid columns 5 mm. Part (a) is for  $2L_B=0.1$  mm ( $\mathcal{N}=1.1$ ); this is the case shown by the line marked with short dashes in Fig. 9. Part (b) is for  $2L_B=10$  mm ( $\mathcal{N}=11$ ), which is the dotted line in Fig. 9. The gas is air, the liquid water, the temperature 20 °C, and the undisturbed pressure atmospheric.

$$\Delta = -\omega^2 + 2i \left( b_v + \frac{\omega_0^2}{2\omega} \frac{\text{Im } \Phi}{\text{Re } \Phi} \right) \omega + \omega_0^2, \quad (66)$$

and

$$\omega_0^2 = \frac{p_0}{2L_B \rho} \left( \frac{1}{L_1} + \frac{1}{L_2} \right) \text{Re } \Phi. \quad (67)$$

Since the present system has two degrees of freedom, we expect two characteristic frequencies. One corresponds to the center-of-mass motion which is subject to no restoring force. Resonance therefore occurs for  $\omega=0$ , as shown by the denominators in the last terms of (63) and (64). The resonance structure of the other mode is embodied in the quantity  $\Delta$  defined in (66), from which we see that  $\omega_0$  is the resonant frequency while the total damping  $b$ , consisting of a viscous and a thermal part, is given by

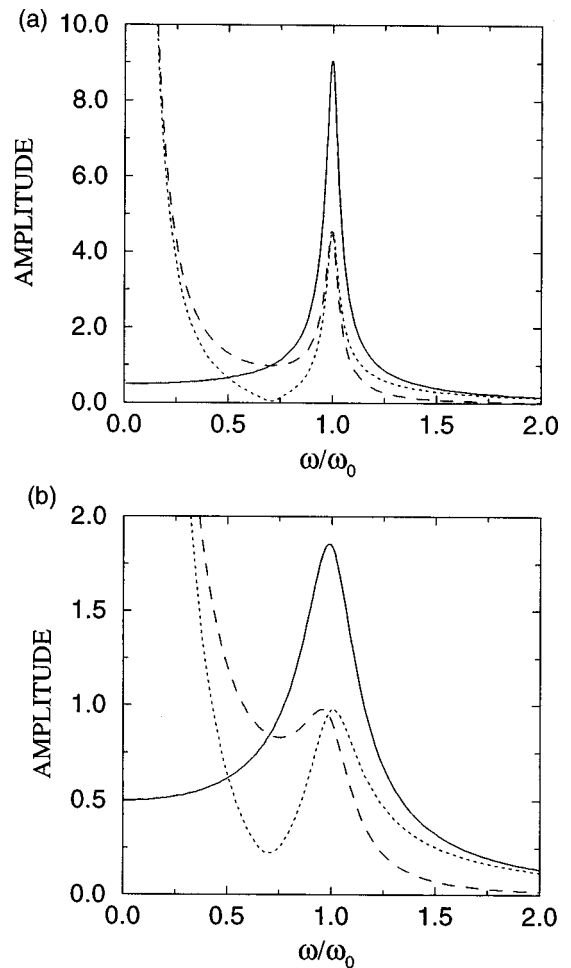


FIG. 12. Dimensionless amplitudes of oscillation of the left liquid surfaces  $|(x_1 - x_{10})/2L_B P_1|$  [dotted line, Eq. (63)], of the right surface  $|(x_2 - x_{20})/2L_B P_1|$  [dashes, Eq. (64)], and of the bubble length  $|X/P_1|$ , given by (65), as a function of the excitation frequency normalized by the resonance frequency. The bubble oscillation is driven by a pressure disturbance applied to the left liquid column. The tube radius is  $R=0.1$  mm and the common length of the liquid columns 0.5 mm. Part (a) is for  $2L_B=0.01$  mm ( $\mathcal{N}=1.1$ ); this is the case shown by the line marked with short dashes in Fig. 10. Part (b) is for  $2L_B=1$  mm ( $\mathcal{N}=11$ ), which is the dotted line in Fig. 10. The gas is air, the liquid water, the temperature 20 °C, and the undisturbed pressure atmospheric.

$$b = b_v + \frac{\omega_0^2}{2\omega} \frac{\text{Im } \Phi}{\text{Re } \Phi}. \quad (68)$$

Figures 9 and 10 show graphs of  $b$  (left scale) and  $f_0 = \omega_0/2\pi$  (right scale) as functions of the driving frequency  $f = \omega/2\pi$  for several cases. The solid line is the viscous contribution (57). It is seen that thermal dissipation has a marked effect over a broad frequency range encompassing the resonant frequency.

In order to illustrate the nature of the solutions (63)–(65) we consider a situation in which the bubble is excited only on the left by a pressure  $P_1$ , while  $P_2=0$ . Figures 11 and 12 show  $|(x_1 - x_{10})/2L_B P_1|$ ,  $|(x_2 - x_{20})/2L_B P_1|$ , and  $|X/P_1|$ , for several cases of Figs. 9 and 10. At very low frequencies the displacements of the two liquid columns are large, corresponding to the resonance at zero frequency mentioned before. The amplitude of oscillation of the bubble length, on the other hand, remains relatively small. As the

true resonance frequency is approached, the relative phase of the motion of the two liquid surfaces changes sign and, at resonance, the bubble elongation equals approximately twice the amplitude of oscillation of each surface. The sharpness of the resonance peak depends in a complex way on the values of the parameters. In general, it is found that, for a fixed bubble length and liquid columns of equal length, the peak becomes sharper the shorter the liquid column. When the left column is taken progressively longer than the right one, the peak decreases while the opposite trend is observed when the right column becomes progressively longer than the left one.

## VI. SUMMARY AND CONCLUSIONS

We have studied the forced oscillations of a system composed of a gas bubble bounded by two liquid columns in a duct. It has been found that, while the natural frequency of the system is only weakly dependent on the thermal processes occurring in the gas, the damping parameter is very sensitive to the energy exchange between the gas and the surrounding surfaces. Even for tubes with a radius as small as 1 mm or less, thermal damping can be more significant than viscous damping over a broad frequency range.

The situation considered here is that of a bubble large enough to fill the cross section of the duct. Results for the resonance frequencies of smaller bubbles (without consideration, however, of thermal effects) are given in Oğuz and Prosperetti (1998).

## ACKNOWLEDGMENTS

We wish to thank Dr. He Yuan for some helpful comments. This study has been supported by AFOSR under Grant No. F49620-96-1-0386.

## APPENDIX

Consider two eigenfunctions  $v_m, v_n$  satisfying (15) and homogeneous Dirichlet boundary conditions:

$$\nabla_{\perp}^2 v_m = -\frac{\lambda_m^2}{l^2} v_m, \quad \nabla_{\perp}^2 v_n = -\frac{\lambda_n^2}{l^2} v_n. \quad (\text{A1})$$

Without loss of generality we take the eigenfunctions to be real. Multiply the first equation by  $v_n$  and the second one by  $v_m$ , subtract, and integrate over the cross section of the channel. The result is

$$\int (v_n \nabla_{\perp}^2 v_m - v_m \nabla_{\perp}^2 v_n) dS = -\frac{\lambda_m^2 - \lambda_n^2}{l^2} \int v_m v_n dS. \quad (\text{A2})$$

By use of Green's identity and Stokes' theorem, it is readily shown that the left-hand side vanishes due to the vanishing of  $v_{m,n}$  on the boundary. If the eigenvalues are distinct, this relation then implies that the integral on the right-hand side vanishes for  $m \neq n$ , i.e., that the eigenfunctions are orthogonal. If the eigenvalue is degenerate, the eigenfunctions spanning the corresponding eigenspace can be rendered orthogonal, e.g., by the Gram-Schmidt procedure. Hence we can assume that the eigenfunctions constitute an orthogonal system.

In order to prove (28), note that, as is readily verified, the  $\sigma_n$ 's are exactly the coefficients of the expansion of the constant  $1/\sqrt{S}$  over the basis of the  $v_n$ 's:

$$\frac{1}{\sqrt{S}} = \sum_n \sigma_n v_n, \quad (\text{A3})$$

provided the eigenfunctions are normalized to 1:

$$\int v_n^2 dS = 1. \quad (\text{A4})$$

Squaring (A3) and integrating over the cross section, by the orthogonality and normalization of the  $v_n$ 's, we have

$$1 = \int_S \left( \frac{1}{\sqrt{S}} \right)^2 dS = \sum_n \sum_m \sigma_n \sigma_m \int_S v_n v_m dS = \sum_n \sigma_n^2. \quad (\text{A5})$$

- Apfel, R. E. (1981). "Acoustic cavitation," in *Methods of Experimental Physics*, edited by P. D. Edmonds (Academic, New York), Vol. 19, pp. 355–411.
- Fujita, H., and Gabriel, K. J. (1991). "New opportunities for micro actuators," in *Transducers '91* (IEEE, New York), pp. 14–20.
- Graveson, P., Branebjerg, J., and Jensen, O. S. (1993). "Microfluidics—A review," *J. Micromech. Microeng.* **3**, 168–182.
- Leal, L. G. (1992). *Laminar Flow and Convective Transport Processes* (Butterworth-Heinemann, Boston).
- Lin, L., and Pisano, A. P. (1991). "Bubble forming on a micro line heater," in *Micromechanical Sensors, Actuators, and Systems* (ASME, New York), Vol. DSC-32, pp. 147–163.
- Oğuz, H. N., and Prosperetti, A. (1998). "The natural frequency of oscillation of gas bubbles in tubes," *J. Acoust. Soc. Am.* **103**, 3301–3308.
- Plesset, M. S., and Prosperetti, A. (1977). "Bubble dynamics and cavitation," *Annu. Rev. Fluid Mech.* **9**, 145–185.
- Prosperetti, A. (1984). "Bubble phenomena in sound fields: part one," *Ultrasonics* **22**, 69–77.
- Prosperetti, A. (1991). "The thermal behaviour of oscillating gas bubbles," *J. Fluid Mech.* **222**, 587–616.

# Lamb wave assessment of fiber volume fraction in composites

Michael D. Seale<sup>a)</sup>

*Department of Physics, The College of William and Mary, Williamsburg, Virginia 23187*

Barry T. Smith

*Norfolk Academy, 1585 Wesleyan Drive, Norfolk, Virginia 23502*

W. H. Prosser and Joseph N. Zalameda<sup>b)</sup>

*NASA Langley Research Center, Mail Stop 231, Hampton, Virginia 23681*

(Received 12 December 1997; accepted for publication 6 June 1998)

Among the various techniques available, ultrasonic Lamb waves offer a convenient method of examining composite materials. Since the Lamb wave velocity depends on the elastic properties of a material, an effective tool exists to evaluate composites by measuring the velocity of these waves. Lamb waves can propagate over long distances and are sensitive to the desired in-plane elastic properties of the material. This paper discusses a study in which Lamb waves were used to examine fiber volume fraction variations of approximately 0.40–0.70 in composites. The Lamb wave measurements were compared to fiber volume fractions obtained from acid digestion tests. Additionally, a model to predict the fiber volume fraction from Lamb wave velocity values was evaluated. © 1998 Acoustical Society of America. [S0001-4966(98)03809-0]

PACS numbers: 43.35.Zc [HEB]

## INTRODUCTION

Manufacturing anomalies such as porosity, fiber misalignment, and low fiber volume fraction can all degrade the performance of composite materials. Mechanical testing by Ghiorse<sup>1</sup> and Olster<sup>2</sup> have shown that the strength and modulus of composites exhibit a significant decrease due to porosity. The most widely used procedure for determining the fiber volume fraction and porosity content of a composite is chemical digestion. This method is destructive, only provides a local measurement, and produces toxic waste which requires disposal. Thus developing a nondestructive means of characterizing composites in order to assure the quality of the product being produced would be useful.

In past studies, thermal diffusivity measurements have shown some promise in determining porosity<sup>3,4</sup> and fiber volume fraction.<sup>4,5</sup> Eddy current measurements<sup>6</sup> have been used to measure fiber volume fraction in metal matrix composites and radiography<sup>7</sup> has been used in an effort to measure porosity. Although these techniques show promise, ultrasonics is one of the most widely accepted nondestructive techniques used to measure fiber volume fraction and porosity. Ultrasonic attenuation measurements have been used to measure porosity<sup>3,8</sup> and fiber volume fraction<sup>9</sup> and the variation of ultrasonic velocity (longitudinal and/or transverse) with both porosity<sup>4,10–13</sup> and fiber volume fraction<sup>9,11–13</sup> has been examined.

Ultrasonic Lamb waves have also been used to investigate porosity<sup>14–16</sup> as well as fiber volume fraction.<sup>14,16</sup> Lamb waves offer a convenient method of evaluating these composite materials. Since the Lamb wave velocity depends on the material properties of a structure, an effective tool exists

to monitor composites by measuring the velocity of these waves. Additionally, Lamb wave measurements are better than conventional through-the-thickness ultrasonic measurements because they can propagate over long distances and are sensitive to the desired in-plane elastic properties of the material.

The following sections describe an experimental study which uses Lamb waves to nondestructively assess fiber volume fraction in composites. Previous studies by Balasubramaniam and Rose<sup>16</sup> successfully used higher order Lamb modes to investigate both porosity and fiber volume fraction. In this work, the velocity of the extensional mode is measured for composite samples with various fiber volume fractions. The results are also related to a model and the model is used to predict the fiber volume fraction from the velocity measurements.

## I. SAMPLES

The composite samples studied were T300/934 carbon/epoxy with stacking sequences of  $[0/90]_{4S}$  and  $[0/90]_{8S}$ . The fiber volume fractions had values ranging from approximately 0.40 to 0.70. The samples were cured in a mechanical press in an attempt to achieve consistent thickness. In order to attain 0.65 and 0.70 fiber volume fractions, the plies for these samples were prebled prior to final curing. The samples were cut from a 30.5-cm  $\times$  30.5-cm plate and had dimensions of 15.2 cm by 15.2 cm. The thicknesses, obtained by averaging ten measurements for each sample, decreased with increasing fiber volume fraction. Specimens were taken in three different areas of the large plate and chemical digestion tests were done to determine the average fiber volume fraction. According to ASTM standards,<sup>17</sup> the values for fiber volume fraction obtained from digestion testing are accurate to within 2%. The results for the destructive tests are shown in Table I.

<sup>a)</sup>Current address: NASA Langley Research Center, Mail Stop 231, Hampton, VA 23681.

<sup>b)</sup>Army Research Lab, Vehicle Technology Center.



TABLE I. Destructive test results to determine fiber volume fraction (FVF).

Sample	Layers	Target FVF	Destructive FVF	Thickness (mm)
40-1	16	0.40	0.380	2.00
50-1	16	0.50	0.529	1.78
60-1	16	0.60	0.590	1.57
65-1	16	0.65	0.659	1.35
70-1	16	0.70	0.690	1.35
40-2	32	0.40	0.395	3.84
50-2	32	0.50	0.518	3.40
60-2	32	0.60	0.580	3.40
65-2	32	0.65	0.660	2.72
70-2	32	0.70	0.690	2.72

## II. LAMB WAVE MODEL

For a laminated composite with the 1-axis defined as the fiber direction, the 2-axis transverse to the fibers, and the 3-axis being out of the plane of the plate, the stress-strain relationship in an individual lamina is given by<sup>18</sup>

$$\begin{bmatrix} \sigma_1 \\ \sigma_2 \\ \tau_6 \end{bmatrix} = \begin{bmatrix} Q_{11} & Q_{12} & 0 \\ Q_{12} & Q_{22} & 0 \\ 0 & 0 & Q_{66} \end{bmatrix} \begin{bmatrix} \epsilon_1 \\ \epsilon_2 \\ \gamma_6 \end{bmatrix}, \quad (1)$$

where  $\sigma$  and  $\tau$  represent the normal and shear stresses, respectively, and  $\epsilon$  and  $\gamma$  represent the normal and shear strains, respectively. The  $Q_{ij}$  are the reduced stiffness components and are defined in terms of the engineering parameters as<sup>18</sup>

$$\begin{aligned} Q_{11} &= E_1 / (1 - \nu_{12}\nu_{21}), \\ Q_{22} &= E_2 / (1 - \nu_{12}\nu_{21}), \\ Q_{12} &= \nu_{12}E_1 / (1 - \nu_{12}\nu_{21}), \end{aligned} \quad (2)$$

where  $E_1$  and  $E_2$  are the Young's moduli in the longitudinal and transverse directions, respectively, and  $\nu_{12}$  and  $\nu_{21}$  are the major and minor Poisson's ratios, respectively. The Poisson's ratios in Eq. (2) are not independent quantities and are related to each other by<sup>18</sup>

$$\nu_{21} = \frac{E_2}{E_1} \nu_{12}. \quad (3)$$

The in-plane stiffnesses for the entire plate,  $A_{11}$  and  $A_{22}$ , are obtained by integrating the  $Q_{ij}$  through the thickness of the plate. These stiffness values are defined as<sup>19</sup>

$$A_{ij} = \int_{-h/2}^{h/2} (Q'_{ij})_k dz, \quad i, j = 1, 2, \quad (4)$$

where  $h$  is the plate thickness and the subscript  $k$  represents each lamina. The  $Q'_{ij}$  are the transformed stiffness coefficients which take into account the orientation of each ply with respect to the wave propagation direction and are defined as<sup>18</sup>

$$\begin{aligned} Q'_{11} &= m^4 Q_{11} + n^4 Q_{22} + 2m^2 n^2 Q_{12} + 4m^2 n^2 Q_{66}, \\ Q'_{22} &= n^4 Q_{11} + m^4 Q_{22} + 2m^2 n^2 Q_{12} + 4m^2 n^2 Q_{66}, \\ Q'_{12} &= m^2 n^2 Q_{11} + m^2 n^2 Q_{22} + (m^4 + n^4) Q_{12} - 4m^2 n^2 Q_{66}, \end{aligned} \quad (5)$$

where  $m = \cos(\theta)$  and  $n = \sin(\theta)$ . The angle  $\theta$  is defined as positive for a counterclockwise rotation from the primed (laminated) axes to the unprimed (individual lamina) axes. From Eq. (5), the  $Q'_{ij}$  for the  $0^\circ$  and  $90^\circ$  laminas are given by

$$\begin{aligned} (Q'_{11})_{0 \text{ deg}} &= Q_{11}, & (Q'_{11})_{90 \text{ deg}} &= Q_{22}, \\ (Q'_{22})_{0 \text{ deg}} &= Q_{22}, & (Q'_{22})_{90 \text{ deg}} &= Q_{11}, \\ (Q'_{12})_{0 \text{ deg}} &= Q_{12}, & (Q'_{12})_{90 \text{ deg}} &= Q_{12}. \end{aligned} \quad (6)$$

The velocity of the extensional plate mode can be related to the in-plane stiffness of a composite.<sup>19</sup> For propagation in the  $0^\circ$  and  $90^\circ$  directions, these stiffnesses are  $A_{11}$  and  $A_{22}$ , respectively. The extensional plate mode velocity is related to the stiffness by<sup>19</sup>

$$v_1 = \sqrt{\frac{A_{11}}{\rho h}} \quad (7)$$

for propagation in the  $0^\circ$  direction and by

$$v_2 = \sqrt{\frac{A_{22}}{\rho h}} \quad (8)$$

for propagation in the  $90^\circ$  direction. The values for the in-plane stiffnesses  $A_{11}$  and  $A_{22}$  can be calculated using Eqs. (2)–(6) if the engineering stiffnesses of the composite are known. If the density,  $\rho$ , and overall thickness of the plate,  $h$ , are known as well, then the extensional mode velocity in the  $0^\circ$  and  $90^\circ$  directions can be computed using Eqs. (7) and (8).

The effect of fiber volume fraction on composite lamina parameters can be derived from a simple rule of mixtures approach. The density takes the form<sup>20</sup>

$$\rho = \rho_f V_f + \rho_m V_m \quad (9)$$

and the elastic constants are given by<sup>18</sup>

$$E_1 = E_{1f} V_f + E_m V_m, \quad (10)$$

$$E_2 = \frac{E_m E_{2f}}{E_{2f} V_m + E_m V_f}, \quad (11)$$

$$\nu_{12} = \nu_{12f} V_f + \nu_m V_m, \quad (12)$$

where  $\rho$  is the density,  $E_1$  and  $E_2$  are the longitudinal and transverse moduli, respectively,  $\nu_{12}$  is Poisson's ratio,  $V_f$  is the fiber fraction, and  $V_m$  is the matrix fraction. The  $f$  and  $m$  subscripts represent the constituent properties of the fiber and matrix, respectively, and quantities without subscripts represent the composite lamina properties.

In order to predict the composite properties as a function of fiber volume, the properties of the fiber and matrix must be obtained. The elastic modulus of the matrix was obtained from the manufacturer<sup>21</sup> and the density and Poisson's ratio were estimated using common matrix values found in

TABLE II. Composite material properties.

Material	$\rho$ (kg/m <sup>3</sup> )	$E_1$ (GPa)	$E_2$ (GPa)	$\nu_{12}$
Matrix	1220 <sup>a</sup>	4.14 <sup>b</sup>	4.14 <sup>b</sup>	0.35 <sup>a</sup>
Fiber <sup>c</sup>	1770	220.6	13.79	0.20

<sup>a</sup>Estimated from common matrix values found in Ref. 20.

<sup>b</sup>Reference 21.

<sup>c</sup>Reference 20.

Chamis.<sup>20</sup> The fiber properties were obtained from Chamis.<sup>20</sup> The various values used in the model are compiled in Table II.

The material parameters as a function of fiber volume fraction were calculated using Eqs. (9)–(12) and the values listed in Table II. From these values, the reduced stiffnesses for an individual lamina,  $Q_{ij}$ , were calculated using Eqs. (2)–(3). The in-plane stiffnesses for the laminate,  $A_{11}$  and  $A_{22}$ , were then computed using Eqs. (4)–(6). Finally, the extensional mode velocity as a function of fiber volume fraction was determined from Eqs. (7) to (8). Due to the architecture of the laminates, the velocity in the 90° direction is identical to the velocity in the 0° direction. Also, since the in-plane stiffness,  $A_{ij}$ , is dependent on the thickness of the sample, the Lamb wave velocity is independent of sample thickness because the thickness term is canceled by the factor of  $h$  in the denominator of Eqs. (7)–(8). Therefore, the calculated velocity as a function of fiber volume fraction is representative for both the 16-ply and 32-ply samples as well as for propagation in the 0° and 90° directions.

### III. LAMB WAVE MEASUREMENTS

A 0.5-mm pencil lead break (Hsu-Neilsen source) on the edge of the samples was used to excite Lamb modes in the sample over a broad range of frequencies. Breaking the lead on the edge of the plate will tend to excite extensional mode ( $S_0$ ) due to the fact that this mode is dominated by in-plane motion.<sup>19</sup> A typical signal for a lead break on the edge of a composite is shown in Fig. 1. As can be seen from the figure, the first arrival is the faster, nondispersive extensional mode, followed by the slower, dispersive flexural mode.

The signals were received by two Panametrics model V103 1.3-cm-diam transducers with a nominal center frequency of 1.0 MHz. The transducers were placed at distances of 5.1 cm and 10.2 cm from the lead break and a coupling gel was used between the transducers and the plate. The

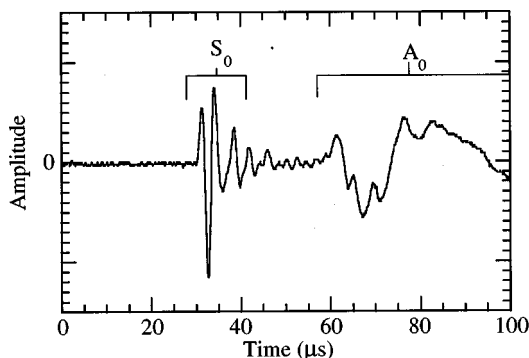


FIG. 1. Signal produced by a pencil lead break on the edge of a composite.

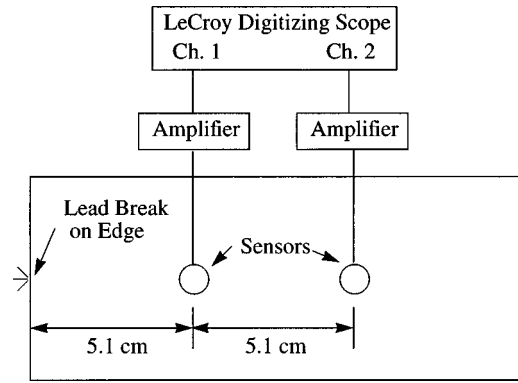


FIG. 2. Schematic showing source and receiver locations.

signals from the transducers were amplified with Tektronix AM 502 differential amplifiers and recorded on a LeCroy model 9420 digital oscilloscope. A schematic of the experimental setup is shown in Fig. 2.

The time differences were measured by imposing a delay on the first signal to overlap the signal received at a greater distance. The small thickness of the plates combined with the low-frequency Lamb wave yielded frequency-thickness products between 0.3 and 0.7 MHz-mm. In this region, only the  $S_0$  and  $A_0$  modes propagate (see Fig. 1). The leading part of the wave was identified as the extensional wave, which is not very dispersive. The trailing portion of the signals contained the dispersive flexural wave which was clearly separated from the extensional mode. The separation distance between the two receiving transducers was measured using a ruler and held fixed at 5.1 cm. Using the distance and time values, the velocity of the  $S_0$  mode was measured in both the 0° and 90° directions. The final value for the velocity in each direction was obtained from the average of three measurements.

The results of the Lamb wave velocity measurements for the 16-layer samples are plotted as a function of the destructively obtained fiber volume fraction in Fig. 3. Also shown in the figure is the predicted Lamb wave velocity as a function of fiber volume fraction obtained from the model. The results for the 32-layer samples are shown in Fig. 4. The error bars represent the variation in the velocity measurements for each sample. The standard deviation for most of the specimens

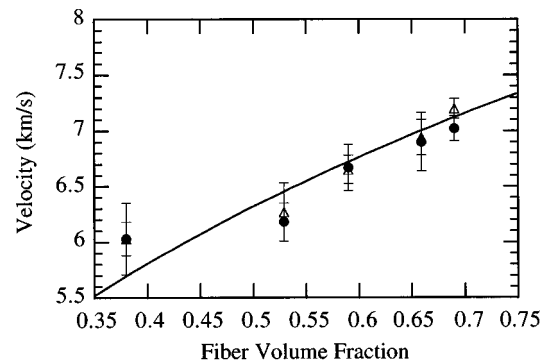


FIG. 3. Lamb wave velocity measurements in the 0° (solid circles) and 90° (open triangles) directions for the 16-layer samples. Also shown is the numerically predicted  $S_0$  mode velocity (solid line).

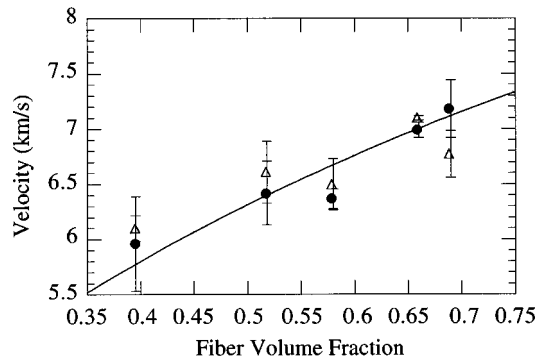


FIG. 4. Lamb wave velocity measurements in the  $0^\circ$  (solid circles) and  $90^\circ$  (open triangles) directions for the 32-layer samples. Also shown is the numerically predicted  $S_0$  mode velocity (solid line).

was less than 4% from the average of the three measurements.

Several interesting features are seen in the figures. First, the increase of the Lamb wave velocity with fiber volume fraction for both the 16-layer and 32-layer samples is quite dramatic. The increase in velocity from the 0.40 fiber volume fraction sample to the 0.70 fiber volume fraction sample is on the order of 15%. Second, due to the geometry of the samples, the velocity in the  $0^\circ$  and  $90^\circ$  directions are very similar. This is expected because the model predicts the velocities to be identical. Finally, the experimental velocities are very close to those predicted by the model. The discrepancies are probably due to the fact that the material properties used in the model were values taken from the literature. As properties of composites may vary significantly depending on cure conditions and variations in resin chemistry, the discrepancy between the actual material parameters of the manufactured composite and nominal values obtained from literature is not unexpected. Additionally, as stated earlier, there is up to a 2% error associated with the determination of fiber volume fraction from chemical digestion.<sup>17</sup> Therefore, the destructively obtained fiber volume fraction reported here may have some inaccuracies due to the measurement technique.

An alternate way of presenting the Lamb wave data is to use the velocity measurements to predict the fiber volume fraction. If the velocity is known, the in-plane stiffness can

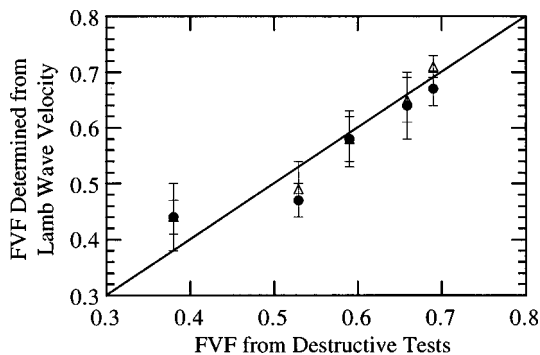


FIG. 5. Fiber volume fraction predicted using Lamb wave velocity measurements in the  $0^\circ$  (solid circles) and  $90^\circ$  (open triangles) directions compared to destructively obtained fiber volume fraction. Data are for 16-layer samples and the solid line represents an exact fit.

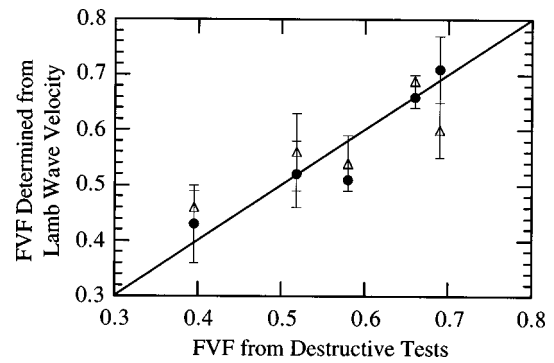


FIG. 6. Fiber volume fraction predicted using Lamb wave velocity measurements in the  $0^\circ$  (solid circles) and  $90^\circ$  (open triangles) directions compared to destructively obtained fiber volume fraction. Data are for 32-layer samples and the solid line represents an exact fit.

be calculated using Eqs. (7)–(8). From the values of  $A_{11}$  and  $A_{22}$ , the fiber volume fraction can be backed out using Eqs. (2)–(6) and Eqs. (9)–(12). The results for the 16-layer samples are shown in Fig. 5 and the results for the 32-layer samples are shown in Fig. 6. The fiber volume fraction predicted by the Lamb wave velocity measurements correlates well with the values obtained from the destructive tests. As mentioned above, the deviations seen are probably due to estimating the material properties of the system as well as manufacturing variations in the measured samples.

In addition to the Lamb wave velocity measurements, the frequency content of the  $S_0$  mode was also examined as a function of fiber volume fraction. The average frequency from four measurements is shown in Fig. 7 for both the 16-layer and the 32-layer samples. The frequency of propagation is higher for the thin plates and the frequency increases with increasing fiber volume fraction for both the thick and the thin plates. This shift toward higher frequencies with increasing fiber fraction was demonstrated by Balasubramaniam and Rose<sup>16</sup> for higher order Lamb modes. Thus the frequency content as well as the Lamb wave velocity can provide useful information in characterizing the fiber volume fraction of composites.

#### IV. CONCLUSION

The Lamb wave velocity measurements in this study were conducted at long wavelengths. This was done for several reasons. First, if the wavelength is large compared to the

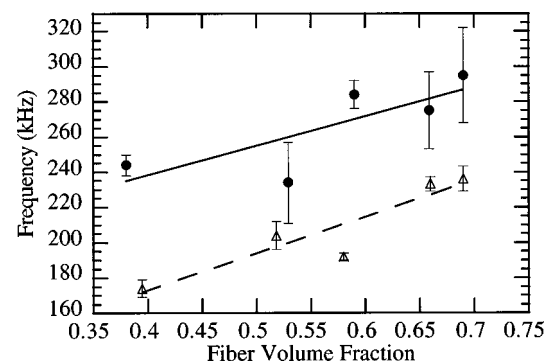


FIG. 7. Frequency versus fiber volume fraction for the 16-layer (solid circles) and 32-layer (open triangles) samples.

diameter of the fibers, composites can be treated as homogeneous. Second, only the lowest order modes propagate in the frequency range where the contact measurements were conducted. Finally, the effective elastic properties of the material can be measured because local anomalies, which scatter high frequency waves, will not be observed at long wavelengths.

Lamb waves offer a useful technique for characterizing the material properties in composite materials. Lamb wave velocity measurements are better than conventional ultrasonic measurement schemes (i.e., through-the-thickness measurements) because they can propagate over long distances and are sensitive to the desired in-plane elastic properties of the material. The propagation of Lamb waves depends on a variety of material properties: elastic stiffness constants, density, and thickness. As manufacturing abnormalities (porosity, fiber misalignment, and low fiber volume fraction) are introduced into a composite, one or more of these material properties are altered. Since the Lamb wave velocity is directly related to these parameters, a convenient method exists to monitor composites by measuring the velocity of these waves.

The Lamb wave velocity is a quantitative measurement and it has been shown by this work to be an effective tool in evaluating fiber volume fraction in composites. Thus the Lamb wave method can be used to verify the integrity of a composite after it is manufactured. This is an important measurement for flight qualified composite materials that may be used in extreme conditions. With the continued development of assessment techniques such as the Lamb wave method, the safety of such structures can be assured.

<sup>1</sup>S. R. Ghiorse, "Effect of void content on the mechanical properties of carbon/epoxy laminates," *SAMPE Quarterly* **24**, 54–59 (1993).

<sup>2</sup>E. F. Olster, "Effect of voids on graphite fiber reinforced composites," AVCO Corporation Systems Division, Final Report for U.S. Naval Air Systems Command, 1973.

<sup>3</sup>P. H. Johnston, W. P. Winfree, E. R. Long, Jr., S. M. Kullerd, N. Nathan, and R. D. Partos, "Thermal and ultrasonic evaluation of porosity in composite laminates," in *Review of Progress in Quantitative Nondestructive Evaluation*, edited by D. O. Thompson and D. E. Chimenti (Plenum, New York, 1992), Vol. 11, pp. 1555–1562.

<sup>4</sup>J. N. Zalameda, "Full field nondestructive techniques for imaging composite fiber volume fraction," Master's thesis, The College of William and Mary, 1996.

<sup>5</sup>J. N. Zalameda and W. P. Winfree, "Quantitative thermal diffusivity measurements on composite fiber volume fraction (FVF) samples," in *Review of Progress in Quantitative Nondestructive Evaluation*, edited by D. O. Thompson and D. E. Chimenti (Plenum, New York, 1993), Vol. 12, pp. 1289–1295.

<sup>6</sup>R. E. Beissner, G. L. Burkhardt, and J. L. Fisher, "Eddy current measurement of fiber volume fraction in metal matrix composites," in *Review of Progress in Quantitative Nondestructive Evaluation*, edited by D. O. Thompson and D. E. Chimenti (Plenum, New York, 1993), Vol. 12, pp. 1321–1328.

<sup>7</sup>B. E. Shull and J. N. Gray, "X-Ray measurement of material properties in composites," in *Review of Progress in Quantitative Nondestructive Evaluation*, edited by D. O. Thompson and D. E. Chimenti (Plenum, New York, 1990), Vol. 9, pp. 1465–1471.

<sup>8</sup>D. K. Hsu, "Ultrasonic measurements of porosity in woven graphite polyimide composites," in *Review of Progress in Quantitative Nondestructive Evaluation*, edited by D. O. Thompson and D. E. Chimenti (Plenum, New York, 1988), Vol. 7, pp. 1063–1068.

<sup>9</sup>H. C. Kim and J. M. Park, "Ultrasonic wave propagation in carbon fibre-reinforced plastics," *J. Mater. Sci.* **22**, 4536–4540 (1987).

<sup>10</sup>D. K. Hsu and H. Jeong, "Ultrasonic velocity change and dispersion due to porosity in composite laminates," in *Review of Progress in Quantitative Nondestructive Evaluation*, edited by D. O. Thompson and D. E. Chimenti (Plenum, New York, 1989), Vol. 8, pp. 1567–1573.

<sup>11</sup>K. Balasubramaniam, C. A. Issa, and S. Alluri, "Ultrasonic wave propagation studies in anisotropic plates with built-in material degradation," in *Review of Progress in Quantitative Nondestructive Evaluation*, edited by D. O. Thompson and D. E. Chimenti (Plenum, New York, 1993), Vol. 12, pp. 1375–1382.

<sup>12</sup>B. G. Martin, "Ultrasonic wave propagation in fiber-reinforced solids containing voids," *J. Appl. Phys.* **48**, 3368–3373 (1977).

<sup>13</sup>W. N. Reynolds and S. J. Wilkinson, "The analysis of fibre-reinforced porous composite materials by the measurement of ultrasonic wave velocities," *Ultrasonics* **16**, 159–163 (1978).

<sup>14</sup>J. L. Rose, K. Balasubramaniam, J. Ditri, and A. Pilarski, "The utility of guided waves in the ultrasonic NDE of composite materials," in *Non-Destructive Testing*, Proceedings of the Twelfth World Conference, Amsterdam, Netherlands, 23–28 Apr. 1989 (A91-18526 05-38) (Elsevier Science, New York, 1989), Vol. 2, pp. 1567–1572.

<sup>15</sup>Y. Bar-Cohen and D. E. Chimenti, "NDE of defects in composites using leaky lamb waves," in *Symposium on Nondestructive Evaluation*, 15th, San Antonio, TX, 23–25 April 1985, Proceedings (A86-47129 22-38) (Nondestructive Testing Information Analysis Center, San Antonio, TX, 1986), pp. 202–208.

<sup>16</sup>K. Balasubramaniam and J. L. Rose, "Guided plate wave potential for damage analysis of composite materials," in *Review of Progress in Quantitative Nondestructive Evaluation*, edited by D. O. Thompson and D. E. Chimenti (Plenum, New York, 1990), Vol. 9, pp. 1505–1512.

<sup>17</sup>D 3171-76 (Reapproved 1990) Standard Test Method for Fiber Content of Resin-Matrix Composites by Matrix Digestion, *Annual Book of ASTM Standards*, Vol. 08.01, pp. 128–130.

<sup>18</sup>I. M. Daniel and O. Ishai, *Engineering Mechanics of Composite Materials* (Oxford U.P., New York, 1994), pp. 3–76.

<sup>19</sup>W. H. Prosser, "The propagation characteristics of the plate modes of acoustic emission waves in thin aluminum plates and thin graphite/epoxy composite plates and tubes," NASA Technical Memorandum 104187 (November, 1991).

<sup>20</sup>C. C. Chamis, "Simplified composite micromechanics equations for hygral, thermal, and mechanical properties," *SAMPE Quarterly* **15**, 14–23 (1984).

<sup>21</sup>Private communication, Tom Triplett, Fiberite®, Inc.

# Body waves recorded inside an elastic half-space by an embedded, wideband velocity sensor

Steven D. Glaser

*Department of Civil and Environmental Engineering, University of California, Berkeley, California 94720-1710*

Gregory G. Weiss

*Lockheed/Martin Astronautics, P.O. Box 179, MS T500, Denver, Colorado 80201*

Lane R. Johnson

*Department of Geology, University of California, Berkeley, California 94720-1710*

(Received 10 October 1997; accepted for publication 18 May 1998)

This paper presents a unique embeddible acoustic emission sensor. Comparison with theoretically calculated waveforms for the embedded sensor, surface step force Lamb's problem prove the sensor to be an accurate transducer of particle velocity, with sensitivity of 2.34 V output per mm/s. Calibration as a surface sensor by the National Institute of Standards and Technology (NIST) show the sensor to be an accurate transducer of surface displacement with a sensitivity of 2.8 V/nm. The paper presents details about the design and construction of the sensor as well as calibration and verification. Unique design elements include the use of a lead-alloy backing masses, soft elastomer shear-spring isolation and mounting, and embedment. The sensor is based on the NIST conical lead zirconate-titanate (PZT) element and has a finished length of 38 mm and a diameter of 16 mm. The sensor is robust enough to work under 1 MPa of brine pressure. © 1998 Acoustical Society of America. [S0001-4966(98)01409-X]

PACS numbers: 43.38.Ar, 43.40.Le, 43.38.Fx [SLE]

## INTRODUCTION

Traditionally, acoustic emission (AE) studies are conducted by placing an array of sensors on the surface of the specimen being tested. Unfortunately the physical constraints of many practical testing geometries preclude surface placement of sensors. A simple solution to this problem is to place the sensors inside the body to be monitored, but to date no such sensors have been available. This paper introduces a unique, embeddible, high-fidelity particle velocity transducer, including design parameters and National Institute of Standards and Technology (NIST) calibration. The design yields sensitivity equal to commercial resonant devices while maintaining the high fidelity of the NIST displacement sensors. The embeddible high-fidelity sensor discussed here for the first time allows experimental verification of Lamb's problem of body motions due to a surface excitation. Validation of the performance of the sensors is provided by a parametric study of recorded and theoretical waveforms for Lamb's problem, buried transducer, surface source.

Using embedded sensors has several advantages over surface mounted sensors, including: (i) mode conversion is avoided so the measured waveforms are simpler and easier to interpret; (ii) a greater length of signal can be recorded before being contaminated by surface reflections/mode conversions; (iii) the sensor(s) can be located closer to the area of crack growth; (iv) embedded sensors may be less susceptible to accidental movement or damage; (v) embedded sensors are the only option when free surfaces are not accessible (Glaser, 1991).

Most acoustic emission studies use resonant sensors because they provide greater sensitivity near the resonance fre-

quency. Unfortunately, resonant devices lack the bandwidth needed to analyze incoming waveforms with the rigor with which seismologists study earthquake waveforms (e.g., Aki and Richards, 1980). Resonant sensors provide a reasonably accurate estimate of the AE time of arrival, but beyond the direction of first motion the received signal is more a function of the sensor than of the kinematics at the crack tip (e.g., Pao, 1978; Hamstad and Fortunko, 1995). An acoustic emission study using resonant sensors "is empirical, relies on correlations, and suffers from a very thin causal science basis" (Eitzen *et al.*, 1981).

By using a wideband sensor having a flat frequency response over several octaves, the recorded signal is equivalent to the actual kinetics at the receiver location, enabling researchers to determine not only the time of first arrival, but also the arrival times of the *P* wave, *S* wave, and boundary reflections, as well as their relative magnitudes (e.g., Glaser and Nelson, 1992b; Kishi, 1985). It has been shown that by using a high-fidelity sensor, the inverse problem of determining the source function from remote measurements can be achieved (e.g., Eisenblatter, 1980; Eitzen *et al.*, 1981; Kim and Sachse, 1986). Full waveform signals also allow the use of forward modeling to evaluate source kinematics (e.g., Aizawa *et al.*, 1987).

## I. BACKGROUND AND THEORY

### A. Lamb's problem

Wave propagation problems involving an elastic half-space have come to be known as Lamb's problems due to the early work in the field by Horace Lamb (1904). Lamb looked

TABLE I. Mechanical properties of the dolostone test block.

Young's modulus, $E$ (GPa)	Shear modulus, $G$ (GPa)	Bulk modulus, $K$ (GPa)	Poisson's ratio, $\sigma$	Density, ( $\text{kg}/\text{m}^3$ )	$v_p$ ( $\text{mm}/\mu\text{s}$ )	$Q_p$	$v_s$ ( $\text{mm}/\mu\text{s}$ )	$Q_s$
95.4	39.4	107.3	0.21	2660	6.35	50	3.37	50

at surface response due to a surface excitation by integrating Rayleigh's (1887) discovery of the surface wave. Both researchers were attempting to understand surface response to earthquake excitation. Lamb noted that the  $P$ - and  $S$ -wave history (minor tremors) was a function of the time derivative of the source function while the surface wave (major tremor) history was a direct function of the source kinematics (Lamb, 1904).

The first partial solution to the more complicated half-space problem, internal motions due to surface excitation, was published by Miller and Pursey (1954). Miller and Pursey derived integral representations of the internal motions due to simple harmonic motions normal to the surface of the half-space. Pekeris provided a full solution for the motion of the half-space surface due to a buried Heaviside pulse in terms of a single integral (Pekeris and Lifson, 1957). Five years later Cherry (1962) published a solution for body and surface wave propagation due to a horizontal motion on the surface of the half-space.

Johnson (1974) presented a complete solution for the three-dimensional Lamb's problem in the form of a Green's function and spacial derivatives for an elastic, uniform half-space. Ohtsu and Ono (1984) published a computer program simplifying Johnson's numerical procedure for the surface receiver-interior source case. Using ray theory, Pao and Gajewski (1977) provided general solutions for transient waves generated by a multitude of sources for layered solids, with more detailed solutions derived by Mal (e.g., Mal *et al.*, 1982). Application of these solutions to decoding acoustic emission source events include work by Wadley (e.g., Wadley and Hill, 1983) and Michaels (Michaels *et al.*, 1981).

## B. Solution of Lamb's problem

Using the viscoelastic propagator method introduced by Kennett (1983), synthetic seismograms were generated for a uniform half-space having the elastic properties listed in Table I. The attenuation properties of the rock half-space were modeled with the quality factors  $Q_p = Q_s = 50$ , and the constant  $Q$  model of Kjartansson (1979) was used for the dispersion relationship. These synthetic seismograms are an appropriate solution for our problem: a unit step function in force acting on the free surface, a receiver that records vertical motion at a depth of 152 mm within the half-space, and at a range of horizontal offsets from the source position. The calculations were performed for a buried source and surface receiver and then reciprocity was used to obtain the results for the experimental geometry.

## II. DESIGN OF THE EMBEDDED HIGH-FIDELITY ACOUSTIC EMISSION SENSOR

A cutaway schematic of the sensor as built is shown in Fig. 1. The following sections explain how the sensor is

constructed, with further details in Weiss and Glaser (1998).

### A. Sensor element

The embedded sensor uses a 2.5-mm-tall truncated cone of PZT-5a (a lead-zirconate-titanate composition), with an aperture diameter of 1.5 mm and a base diameter of 6.5 mm. This geometric design of piezoelectric cone was developed by the National Institute of Standards and Technology (NIST) for use in wideband acoustic emission sensors (e.g., Eitzen *et al.*, 1981; Proctor, 1982a, b). The conical design eliminates the aperture effect by keeping the contact area small, is sensitive to only one parameter (motion in line with the cone axis), and reduces the degeneracies of the normal modes of the usual piezoelectric disk element (Proctor, 1982b; Greenspan, 1987). The element has a high piezoelectric coupling constant and a mechanical stiffness estimated to be  $1.1 \times 10^8 \text{ N/m}$  at a minimum (Hamstad and Fortunko, 1995).

### B. Electronics system

Only a small fraction of the energy released from an acoustic emission event ever reaches a sensor. Furthermore, a piezoelectric sensor converts only a fraction of the received energy into an electrical signal. Unless this signal is amplified at the crystal, it will be corrupted by electromagnetic noise and capacitive loading from the cable between the sen-

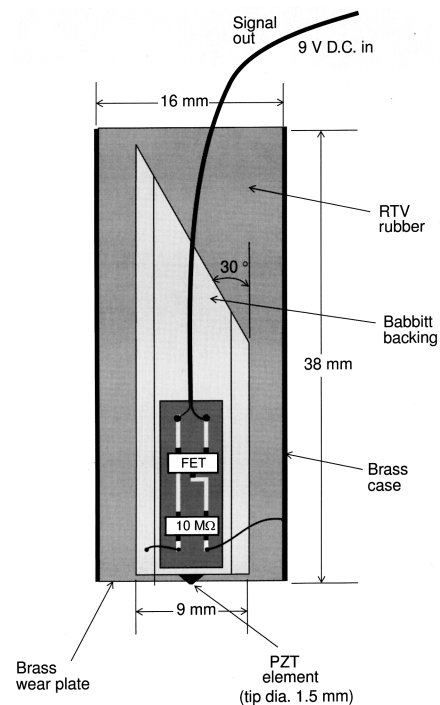


FIG. 1. Cutaway schematic drawing of the embeddible sensor.

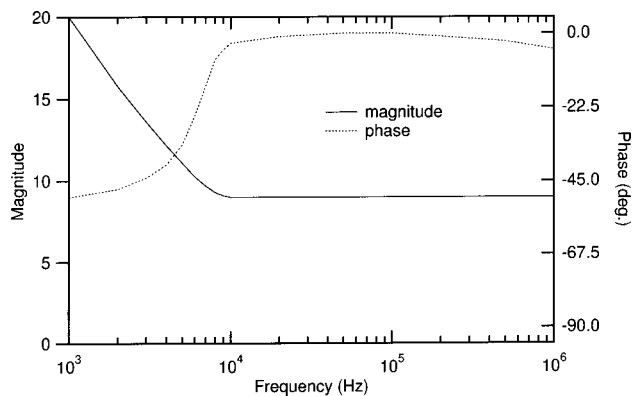


FIG. 2. Frequency response of the FET-based preamplifier.

sensor and the A/D converter. The capacitance of 50  $\Omega$  coaxial cables are approximately 95 pF/m, while the conical element output impedance is “in the tens of pF range” (Fortunko *et al.*, 1992). The amplification system used for the embedded sensor, originally developed by Shiwa *et al.* (1992), includes a small field emission transistor (FET)-based (Sanyo 2SK715W) preamplifier internal to the sensor casing to improve impedance matching. The internal preamplifier also reduces noise pickup in the signal cable, and minimizes the signal losses from capacitive loading in the cable between the conical element and the external amplifier. The circuitry has been optimized to more closely match the characteristics of the smaller conical piezoelectric element (Fortunko *et al.*, 1992). Figure 2 shows the frequency response of the FET preamplifier. Note that the phase and magnitude are virtually flat from 10 kHz to 1 MHz.

### C. Backing mass

Previous research (Proctor, 1982a, 1986) has shown that the geometry of the backing mass is the single most important element of wideband acoustic emission sensor design. In general, a larger backing mass will have fewer resonances and will give a more satisfactory performance at lower frequencies. A unique problem was presented since the embedded sensor was not supposed to affect the passing wavetrain. Thus the backing mass has been carefully designed to be as compact as possible, while reducing resonances and maximizing the total mass. The feasible choices were tungsten and lead, lead having never before used as an AE sensor backing material. Of the two, lead has a much lower  $Q$ , thereby minimizing possible resonance. Lead proved difficult to machine and solder so a lead-based babbitt metal (95% lead, 4% antimony, 1% tin) was used, yielding a final backing mass of 20 g. This alloy has a specific acoustic impedance of 25 MPa·s/m compared to 34 MPa·s/m for the PZT conical element. Brass, a common backing material with specific acoustic impedance very close to that of the piezoelectric element was tried, but exhibited spurious resonances.

The backing mass was machined from 9.5-mm round stock, with a 7-mm flat milled along the axis to reduce cylindrical resonances and to provide a mounting point for the FET board. The back end of the mass is cutoff at an angle of 30° to the long axis to reduce symmetry in the design and to prevent direct reflections from reaching the piezoelectric el-

ement (Proctor, 1986). The babbitt metal backing mass is soldered to the piezoelectric crystal using a low melting temperature indium-based solder. Insuring a continuous and uniform bond between crystal and backing is the single most critical aspect of sensor assembly, and a repeatable and dependable construction technique was developed after a long trial and error process. A poor joint is detected during calibration as an anomalous response between 714 and 755 kHz. In this frequency range the phase angle shifts by several multiples of  $2\pi$ , accompanied by a strong antiresonance.

### D. Casing and acoustic isolation

A unique sensor casing was designed so that the sensor would accommodate strain and deformation of the host material, and operate in a brine pore fluid environment under pressure approaching 1 MPa. This has been achieved by pouring a soft (Shore-A hardness=9), moldable room temperature vulcanizing (RTV) rubber between the tubular brass sensor casing and the internals. The RTV rubber provides longitudinal compliance between the sensor casing and internals to maintain intimate contact between sensor tip and specimen (i.e., shear spring). The casing constrains the rubber from expanding laterally when a coupling force is applied to the rear of the sensor, allowing the sensor to be placed in a hole just slightly larger than the casing without significant traction forces. RTV rubber has a high Poisson’s ratio (0.498), and is relatively insensitive to hydrostatic pressure. Increasing surrounding fluid pressure actually causes the rubber to seal more tightly against water infiltration, whereas pressure proofing a rigid casing would be much more problematic. The surfaces of the sensor internal components are coated with a primer to provide strong adhesion with the rubber, further preventing fluid infiltration. Unfortunately the rubber did not provide acoustic isolation between the host specimen and the sensor internals, resulting in coupling between the backing mass/PZT tip and specimen.

## III. EXPERIMENTAL METHODS

### A. Sensor calibration methods

Laboratory development of the sensor was guided by frequent calibration. Calibrations were performed on a large 50-mm-thick steel plate, with the signal being measured and the top surface, 76 mm from the source, also input on the plate top (Hsu and Breckenridge, 1981). Both capillary and 0.3-mm mechanical pencil lead breaks were used as calibration sources per standard AE practice (e.g., Breckenridge *et al.*, 1990). Although the pencil lead source only approaches a true step impulse, it is convenient to use, very repeatable, and makes for easy comparison with the work of most AE researchers who use this source exclusively. Figure 3 shows a comparison of impulse response of the embeddible sensor to the theoretical infinite plate solution of the same geometry and loading (Hsu, 1985). The sensor response differs little from the theoretical, with most of the difference due to the lack of 0–12 kHz energy that the piezoelectric device cannot sense. The functional difference is the overshoot on the initial spike arrival rebound shown by the sensor. During design and assembly the embeddible sensor re-

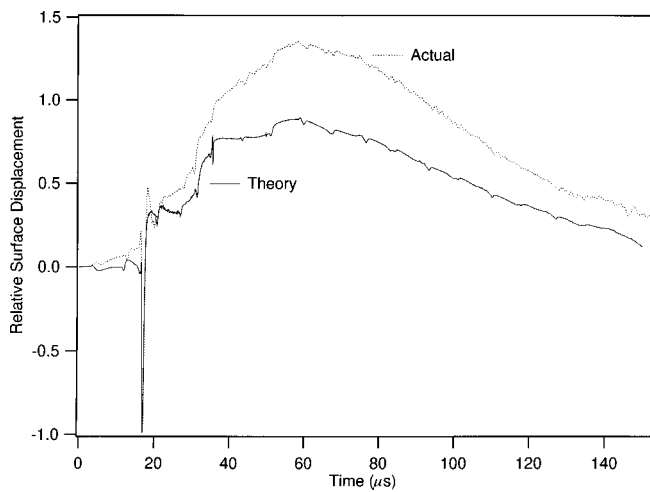


FIG. 3. Comparison of actual sensor output with results for the same problem solved by ray theory.

sponse was also directly compared to the output of a large, brass-backed conical sensor, built and calibrated to NIST Standard Reference Material (SRM) specifications (Glaser and Nelson, 1992a).

Final absolute surface calibration of the embeddible sensor was done by the Ultrasonics Standards Group, National Institute of Standards and Technology, Gaithersburg, MD (Fick, 1996). Figure 4 shows the actual displacement spike measured by the NIST capacitive standard transducer compared with the response of our sensor. Here too, as seen in Fig. 3, there is overshoot on the rebound for the embeddible sensor. The results of NIST calibration of the surface-mounted embeddible sensor is shown in Fig. 5 as frequency magnitude and phase in terms of absolute displacement compared to the frequency response of the NIST SRM conical sensor. Note that the response of our sensor is virtually flat from 12 to 960 kHz, with an absolute sensitivity between 28 and 30 V output per nm displacement. For the phase response, the statistical uncertainty of the measurement is greater than the induced phase shift. This calibration shows that the sensor gives an accurate time measure of very small surface displacements over a broad bandwidth.

### B. Experimental verification of Lamb's problem

In order to verify the embedded behavior of the sensor, a set of experiments was run to measure the *in situ* body wave

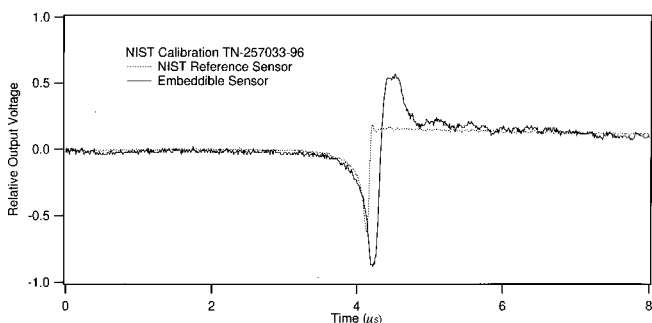


FIG. 4. Impulse response of the embeddible sensor compared to the NIST reference, NIST Calibration TN-257033-96.

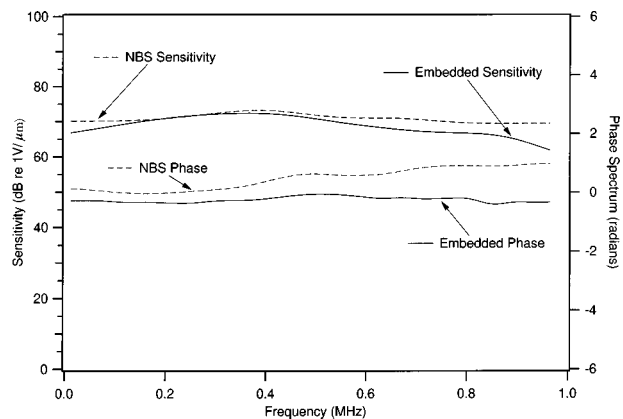


FIG. 5. Magnitude and phase spectra for the NIST-calibrated embeddible sensor compared with the NIST SRM conical sensor.

response for the buried sensor–surface force Lamb's problem. A sketch of the experimental geometry is shown in Fig. 6. A large (0.33-m cube) dolostone block was used as the "half-space." The block is homogeneous and isotropic for the scale of the test (Nelson and Glaser, 1992), and material properties are given in Table I.

The sensor itself was cemented into a 20-mm-diameter borehole 152 mm beneath the horizontal surface upon which the source acted. A hole was bored into the bottom of the block with a flat-end diamond tool, and the bottom hand-ground flat. The sensor is then inserted tip-down into the hole, with the tip resting on the bottom, and the annulus filled with very low viscosity epoxy. Downward pressure on the casing before and during curing results in 1.5-mm axial deformation of the casing relative to the sensor tip. This displacement forces the sensor tip into intimate contact with the rock by the shear-spring action of the RTV rubber in the annular space between the brass casing tube (now part of the specimen) and the sensing element. The beauty of our design is that the shear spring insures that intimate contact is maintained after cure shrinkage of the epoxy, and specimen deformation. The entire open volume between the sensor and rock is filled so that there is no free surface near the sensing element.

The step source used for this experiment was a glass

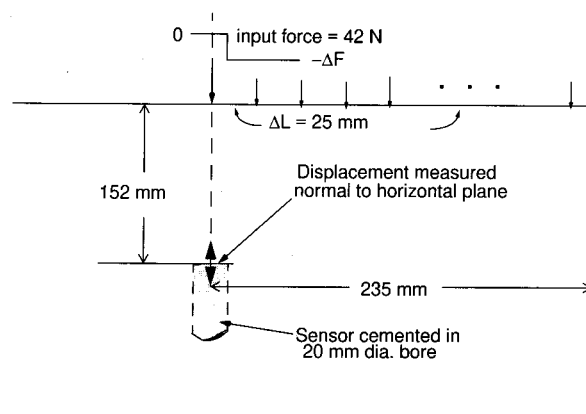


FIG. 6. Geometry of Lamb's problem experiment. Note that step force drop was input at epicenter, and every 25 mm up to 152 mm from epicenter.



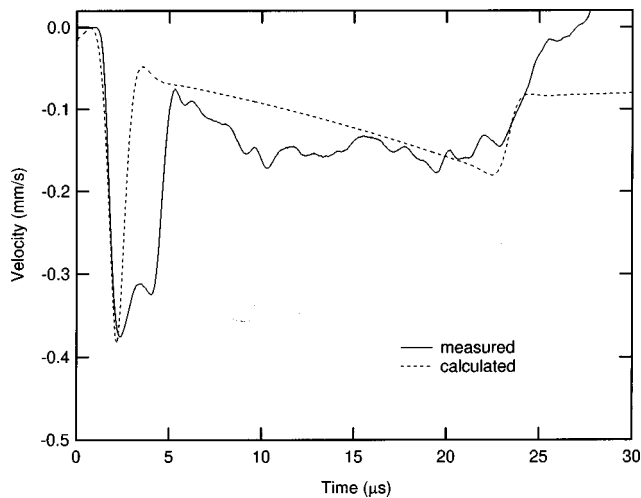


FIG. 7. Comparison of measured and calculated epicentral surface step force of 42 N. The sensor is embedded 152 mm below epicenter and is sensitive to particle velocity normal to the top surface.

capillary break rather than pencil lead since the capillary source imparts significantly more force, and better approaches a true step force impulse. For the upper frequency bound of interest to us, 1 MHz, the capillary source yields a near-perfect step drop normal to the horizontal surface (Breckenridge *et al.*, 1990). NIST typically uses a 0.12-mm o.d. capillary source, yielding a 4-N force step with a 0.25- $\mu$ s rise time. For our experiment the source pulse must penetrate through more than 215 mm of attenuative and dispersive rock and still have an amplitude well above the noise floor. Therefore 0.5-mm o.d. capillaries were used, yielding a 42-N force, and an estimated rise time of 1.1  $\mu$ s.

The first signal was recorded with the step-source in the epicentral position on top of the rock block, 152 mm above the sensor face. The 42-N step force was input on the surface at six successive 25-mm horizontal steps from epicenter (Fig. 6). Normalizing linear dimensions by the 152-mm embedment depth,  $D$ , the step source was input at  $0.167D$ ,  $0.333D$ ,  $0.5D$ ,  $0.667D$ ,  $0.833D$ , and  $D$ . All experimental signals were recorded at 14-bit resolution and a digitization rate of 10 mega samples/second. Only the initial portion of each event waveform was used for analysis, from the initial arrival of event energy with the  $P$  wave to just after the arrival of the  $S$  wave. The use of only the initial, uncontaminated segment of the waveform insured that the analysis would be free from the effects of sample size and shape, and modal analysis would not need to be undertaken. The signals analyzed were effectively from an infinite half-space.

#### IV. VERIFICATION OF SENSOR PERFORMANCE

##### A. Epicentral results, experiment and theory

A rigorous verification process was undertaken to calibrate the embedded sensor to the theoretical particle velocity time histories for the given geometry. The epicentral geometry was used as the fundamental calibration case. The sensor response to a 42-N step force (capillary break) input normal to the top surface directly above the center-line of the embedded sensor is shown in Fig. 7, with output given as ab-

solute particle velocity time history. For comparison, the theoretical particle velocity time history for this scenario is also shown in Fig. 7. The segments of signals shown covers the period from just before the  $P$ -wave arrival to just after the  $S$ -wave arrival.

Numerous experiments had shown that the dispersive rock effectively filters out frequencies above 450 kHz for travel paths much over 50 mm (Nelson and Glaser, 1992), so the only processing of the theoretical waveform was 450-kHz low-pass filtering (single-pole bidirectional Butterworth) that mimics the dispersive attenuation of the rock half-space. The experimental time history is presented without signal processing, scaled to theoretical peak first-arrival  $P$ -wave velocity.

##### B. Results from various geometries, experiment and theory

The embedded sensor is designed to be sensitive strictly to motion in-line with the sensor axis. To verify the design, step forces were input on the horizontal top of the test block at various off-epicentral locations (hence azimuths) relative to the sensor axis (Fig. 6). Given a point source-point receiver, the radiation pattern for both  $S$ - and  $P$ -wave motions will have significant energy normal to the plane being monitored. The experimental results were then compared to the theoretical waveforms for the same off-epicentral locations. The comparisons are shown in Fig. 8(a)–(f). The capillary source step force results for offsets of 25 to 152 mm are shown for verification.

##### C. Evolution of the head wave

In an elastic half-space there exists (for some geometries) a refracted shear-wave referred to as a head wave (e.g., Pao and Gajewski, 1977; Cerveny and Ravindra, 1971). The high fidelity of our sensors was further tested by recording waveforms at source offsets of 107, 112, 117, and 122 mm. Theoretical velocity time histories were also calculated for these geometries. Results of theory and experiment are compared in Fig. 9. Again, the figure shows the waveform from pre- $P$ -wave to post- $S$ -wave arrival, before mechanical resonances of the specimen and source contaminate the waveform.

#### V. DISCUSSION OF RESULTS

##### A. Discussion of sensor epicentral performance and calibration from theory

Figure 7 presents the epicentral particle motion time history from the initial arrival of the longitudinal wave ( $P$  wave) to just after the arrival of the shear wave ( $S$  wave). The rise time of the initial arrival of  $P$ -wave energy as measured by the sensor matches the theoretical solution for particle velocity exactly. The behavior at the arrival of the  $S$  wave is also in congruence, as is the gradual downward slope between the  $P$ - and  $S$ -wave arrivals.

After extensive theoretical modeling and comparison to the recorded signals, it was decided that the sensor measures particle velocity when embedded, in contrast to its being a

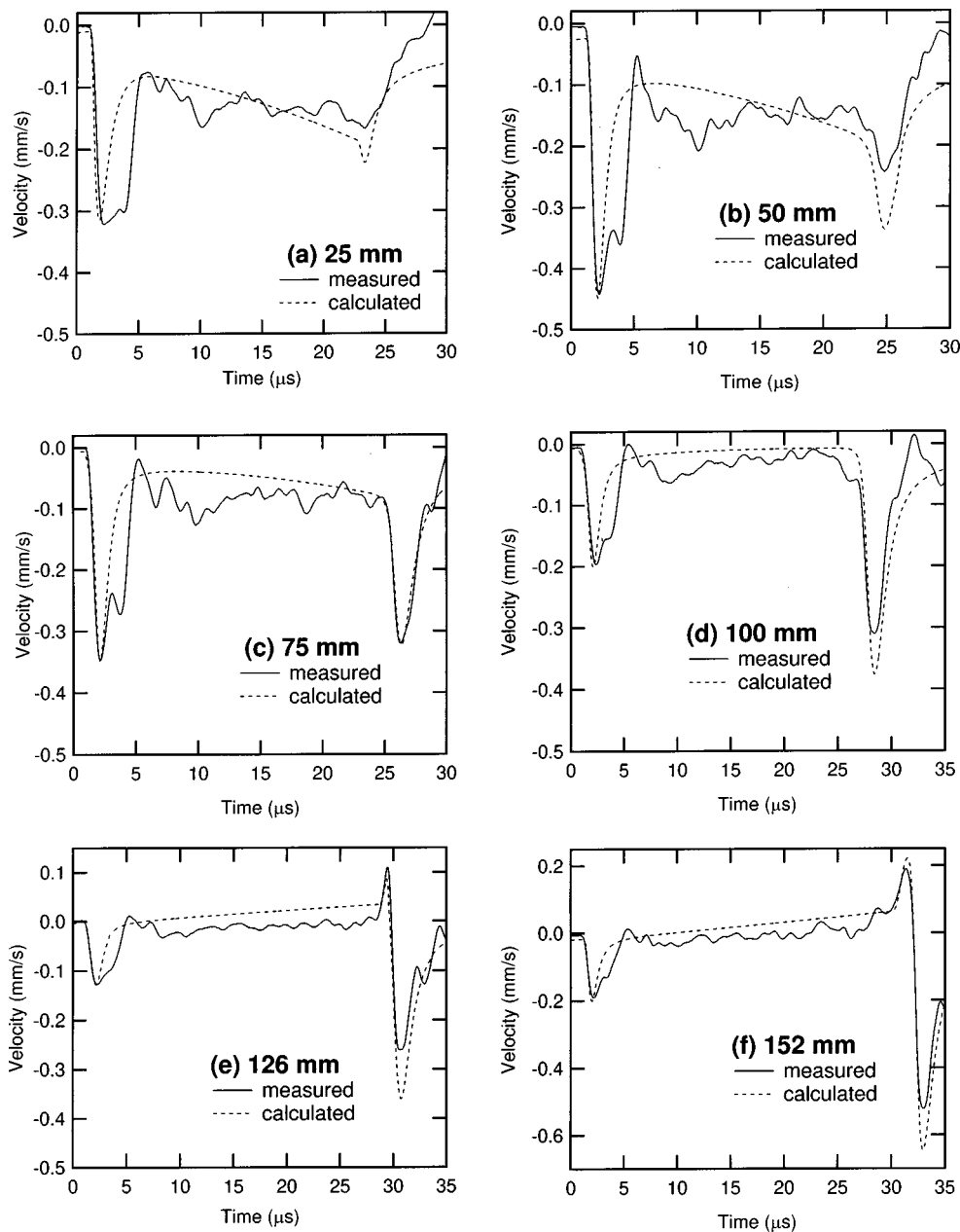


FIG. 8. Comparison of measured and calculated waveforms due to surface step force. The sensor is embedded 152 mm below the surface. Source located on the surface at (a) 25 mm, (b) 50 mm, (c) 75 mm, (d) 100 mm, (e) 126 mm, (f) 152 mm.

particle displacement transducer when surface mounted. When surface mounted, the sensor casing is physically isolated from the half-space. When embedded, it was initially assumed that the soft RTV rubber potting would serve to isolate the active sensor elements from the host motions. However, it was found that silicon rubber has a glass transition frequency at about 10 kHz. For example, the Young's modulus of a soft RTV-141 rubber increases almost three orders of magnitude in the 10-kHz frequency range resulting in a high-frequency stiffness of 5 GPa (Bosc and Mauguen, 1990). We are currently evaluating a urethane elastomer which is quite acoustically isolating at high frequencies (Selfridge, 1998).

The congruence between the measured and calculated particle velocity time histories gives credence to the calibration of the sensor from the Kennett propagator theoretical solution, which accounts for the source kinematics and geometry of the capillary break. Since this is the first time

experimental waveforms for the embedded sensor geometry have been recorded, the sensor must be calibrated by comparing experimental sensitivity to the theoretical wave field. Comparison of theoretical particle velocity history and sensor output voltage at the initial *P*-wave peak yields a particle velocity sensitivity of 2.34 V output per mm/s. The calculation was checked against an independent solution based on a modified Cagniard technique (Ruitenbeek *et al.*, 1991), which yields the same calibration factor.

The major difference between theory and experiment is the extra downward pulse output by our sensor following the initial peak. Forward modeling could only duplicate this artifact by including a thin, very slow, surface layer underneath the source. Continued improvements in sensor design should eliminate this artifact. The other minor wiggles are assumed due to "imperfections of reality," such as finite extent of the source, imperfect material, etc., and do not interfere with interpretation of the recorded signal. The "double-pulse"

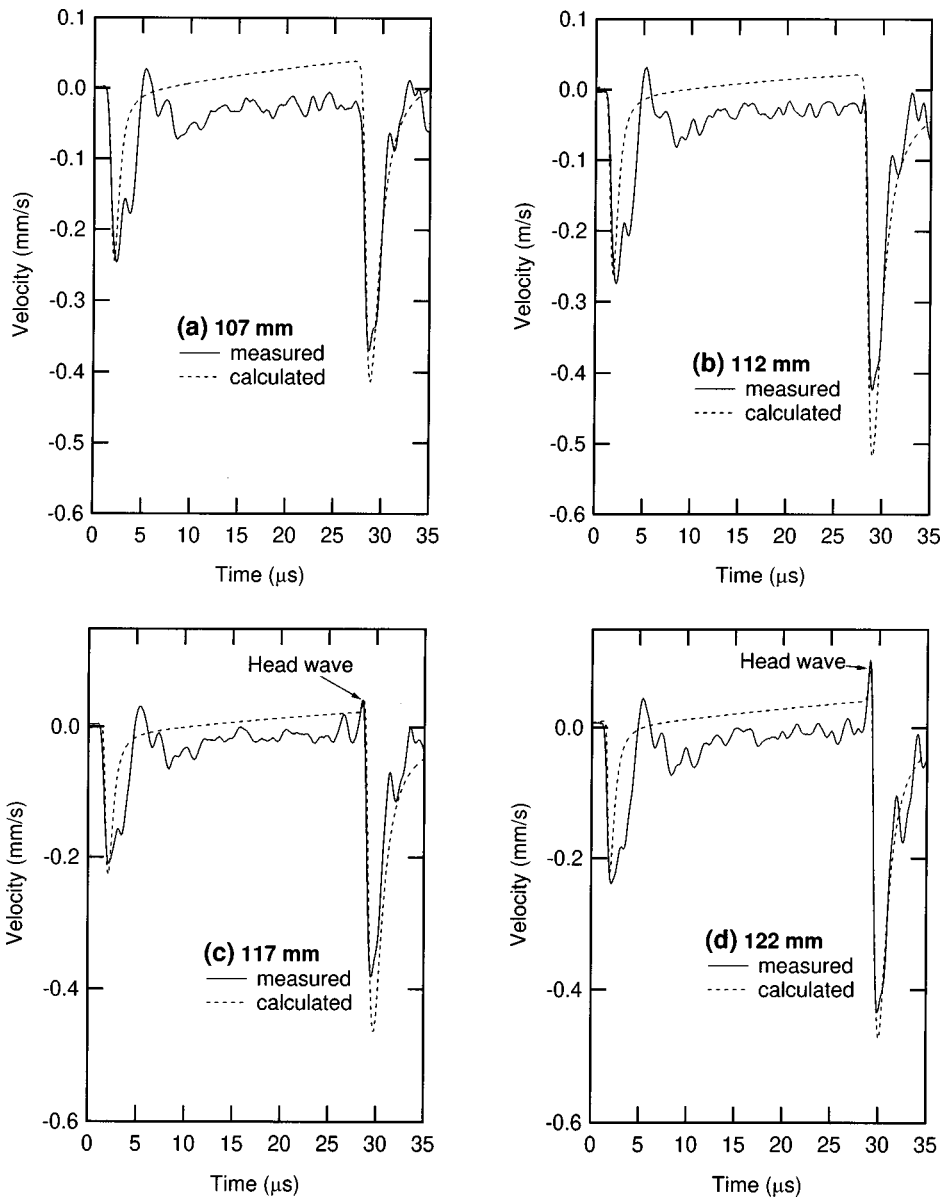


FIG. 9. Evolution of the head wave, experiment versus theory. The sensor is embedded 152 mm below the surface. Source position on surface (a) 107 mm; (b) 112 mm; (c) 117 mm; (d) 122 mm from epicenter.

should not interfere with quantitative interpretation of source kinematics because it can easily be accounted for through deconvolution. Since the “double-pulse” appears after the initial rise starts falling, the principle parameters for moment tensor inversion such as polarity of initial *P*- and *S*-wave arrival, rise time, and peak amplitude are not distorted.

### B. Discussion of theoretical and recorded off-epicentral waveforms

A comparison of measured and calculated particle velocity time histories for a variety of source–receiver geometries is shown in Fig. 8. The sensor was buried in a constant position 152 mm below the horizontal surface, monitoring motions parallel to this exposed surface. A step force was input by capillary breaks every 25 mm from epicenter, from 25 to 152 mm. These six positions correspond to azimuths of 9.5°, 18.5°, 26.5°, 33.7°, 40°, and 45°. As the azimuthal angle increases, more energy is partitioned from the *P* wave to the *S* wave, as is evidenced by the changing ratio of *P*- and *S*-wave peak amplitudes.

For all signals recorded, the rise times and the ratios of *P*-wave to *S*-wave amplitude are very similar for theory and experiment. The fit of the *S* wave is exact for the 75-mm [Fig. 8(c)] offset and within 76% for the 100-, 126-, and 152-mm offsets [Fig. 8(d)–(f)]. For the epicenter and the 25- and 50-mm offsets the Green’s function method (Johnson, 1974) provided a better fit than the viscous model (Kennett, 1983). The quality of these results leads to the conclusion that our sensor provides a quantitative time history of the particle motion inside the test block.

### C. Evolution of the head wave

For the geometry used in this experiment, the head wave should appear when the angle between source and receiver was greater than or equal to the critical angle  $\gamma_c$  (Pao and Gajewski, 1977; Cervený and Ravindra, 1971)

$$\gamma_c = \sin^{-1} \left( \frac{v_s}{v_p} \right). \quad (1)$$

As a test of the accuracy of modeling assumptions made in this paper, a step force was input at four offsets bracketing the expected initial arrival offset. These signals are shown in Fig. 9(a)–(d) compared with the actual particle velocity time histories recorded within the test block. For the host material used for this experiment  $\gamma_c = 37.3^\circ$ , and the head wave should start to appear at a source offset of 116 mm. The headwave first appears at the 117-mm offset compared to the 116-mm offset expected from theory. Note that for both the 117 [Fig. 9(c)] and 122 mm [Fig. 9(d)] offsets the duration and amplitude of the headwave is identical for theory and experiment.

## VI. APPLICATION OF THE EMBEDDED SENSOR

We are working in conjunction with Shell Exploration and Production Research Company, to conduct laboratory-scale experiments of hydraulic fracture propagation (Dudley *et al.*, 1995). To gain a better understanding of the fracture mechanisms occurring, the test samples are being monitored with an array of acoustic emission and active imaging sensors. Sandstone samples are loaded into a polyaxial load frame located at Shell E&P in Houston, TX, so that independent confining stresses can be applied to the sample in the principle directions, pore water pressure can be controlled, and fluid can be injected into the sample to induce fracture. In this application, the driving consideration for using embedded sensors is the inaccessibility of the specimen surface.

During hydrofracture testing at Shell E&P the embedded sensor was subjected to difficult environmental conditions. The test specimen was subjected to confining effective pressures of about 3.5 MPa, and could be saturated with brine with a pore pressure of 1 MPa. Embeddible sensors have been glued inside several specimens which were then loaded to failure and the sensors retrieved by overcoring. The only damage to the retrieved sensors was some tearing of the brass film wearplate.

The embedded sensor is an ideal laboratory tool for material science investigations. Potential applications for embedded sensors include: monitoring of concrete dams and highway bridges, monitoring of mines, tunnels, or other geologic structures, and monitoring and basic research on the performance of new polymer and composite structures.

Various improvements to the sensor containment are being investigated. The stiffness of the PZT ceramic leads to an impedance matching problem when it is used to monitor relatively low stiffness materials. We are currently investigating other soft elastomers such as urethanes which will not exhibit glass transition at frequencies of interest.

## VII. CONCLUSIONS

Construction details of the embeddible sensor have been presented to give the reader insight into the device. The sensor is based on the NIST conical piezoelectric element, measures particle velocity at a point, and is sensitive only to motion parallel to the sensor long axis. The device is small, 38 mm long and 16 mm in diameter, which allows convenient mounting both inside or on a specimen.

This paper presents a unique view of motion inside a solid. For the first time, particle velocity time histories inside a body due to external forces have been accurately recorded. Comparison with theory shows that the sensor is an extremely faithful transducer of particle motion. When embedded the output is proportional to particle velocity and gives a sensitivity of 2.34 V per mm/s. Comparison with theory and NIST calibration prove the sensor to be an excellent transducer of surface displacement with a calibrated sensitivity of 2.8 V per nm.

## ACKNOWLEDGMENTS

Funding was provided by the Gas Research Institute (Contract No. 5093-221-2611), Shell Exploration and Production Co., and the National Science Foundation Young Investigator Program (Grant No. CMS-9727002). Many of the manufacturing procedures used to build the embeddible sensor were developed by staff at the National Institute of Standards and Technology, Materials Reliability Division, Boulder, CO. The authors wish to thank all these organizations, and more importantly, the individuals we worked with, for both technical assistance and support.

- Aizawa, T., Kishi, T., and Mudry, F. (1987). "Acoustic emission wave characterization: a numerical simulation of the experiments on cracked and uncracked specimens," *J. Acoust. Emiss.* **6**, 85–92.
- Aki, K., and Richards, P. G. (1980). *Quantitative Seismology* (Freeman, San Francisco).
- Bosc, D., and Mauguen, P. (1990). "Acoustic properties of transparent polysiloxanes," *J. Appl. Polym. Sci.* **40**, 135–142.
- Breckenridge, F. R. (1982). "Acoustic emission transducer calibration by means of the seismic surface pulse," *J. Acoust. Emiss.* **1**, 87–94.
- Breckenridge, F. R., Proctor, T. M., Hsu, N. N., Fick, S. E., and Eitzen, D. G. (1990). "Transient sources for acoustic emission work," in *Progress in Acoustic Emission, V, Proc. 10th International Acoustic Emission Symposium*, edited by K. Yamaguchi, H. Takakashi, and H. Niitsuma (Japanese Society for Non-Destructive Inspection, Tokyo), pp. 20–37.
- Cerveny, V., and Ravindra, R. (1971). *Theory of Seismic Head Waves* (Univ. of Toronto, Toronto).
- Cherry, Jr., J. T. (1962). "The azimuthal and polar radiation patterns obtained from a horizontal stress applied at the surface of an elastic half-space," *Bull. Seismol. Soc. Am.* **52**, 27–36.
- Dudley II, J. W., Shlyapobersky, J., Stanbury, R. B., Chudnovsky, A., Gorelik, M., Wen, Z., Glaser, S., Hand, M., and Weiss, G. (1995). "Laboratory investigation of fracturing processes in hydraulic fracturing," GRI-95/0355, annual report to the Gas Research Institute: Chicago.
- Eisenblatter, J. (1980). "The origin of acoustic emission—Mechanisms and models," *Acoustical Emission* (Deutsche Gesellschaft für Metallkunde e. V.), pp. 189–204.
- Eitzen, D. G., Breckenridge, F. R., Clough, R. B., Fuller, E. R., Hsu, N. N., and Simmons, J. A. (1981). "Fundamental developments for quantitative acoustic emission measurements," Interim Report NP-2089, prepared for Electric Power Research Institute.
- Fick, S. E. (1996). *Report of Test of Transducers 96130 and 96131* (NIST, Gaithersburg, MD).
- Fortunko, C. M., Hamstad, M. A., and Fitting, D. W. (1992). "High-fidelity acoustic-emission sensor/preamplifier subsystems: modeling and experiments," *IEEE 1992 Ultrasonics Symposium Proceedings*, 20–23 October 1992, Tucson, Arizona, edited by B. R. McAvoy (IEEE, New York), Vol. 1, pp. 327–332.
- Glaser, S. D. (1991). "Development of a high-fidelity, embedded displacement transducer," *Proc., 4th World Meet. Acoust. Emission* (ASNT, Columbus).
- Glaser, S. D., and Nelson, P. P. (1992a). "High-fidelity waveform detection for acoustic emissions from rock," *Mater. Eval.* **50**, 354–366.

- Glaser, S. D., and Nelson, P. P. (1992b). "Acoustic emissions produced by discrete fracture in rock-Part 2: kinematics of crack growth during controlled Mode I and Mode II loading of rock," *Int. J. Rock Mech.* **29**, 253–265.
- Greenspan, M. (1987). "The NBS conical transducer: Analysis," *J. Acoust. Soc. Am.* **81**, 173–183.
- Hamstad, M. A., and Fortunko, C. M. (1995). "Development of practical wideband high-fidelity acoustic emission sensors," in *Proceedings of SPIE Conference on Nondestructive Evaluation of Aging Infrastructure 1995* (SPIE, Philadelphia), Vol. 2456, pp. 281–288.
- Hsu, N. N. (1985). "Dynamic Green's functions of an infinite plate-A computer program," NB-SIR 85-3234 (NIST, Gaithersburg, MD).
- Hsu, N. N., and Breckenridge, F. R. (1981). "Characterization and calibration of acoustic emission sensors," *Mater. Eval.* **39**, 60–68.
- Johnson, L. R. (1974). "Green's function for Lamb's problem," *Geophys. J. R. Astron. Soc.* **37**, 99–131.
- Kennett, B. L. N. (1983). *Seismic Wave Propagation in Stratified Media* (Cambridge U.P., Cambridge, England).
- Kim, K. Y., and Sachse, W. (1986). "Acoustic emissions from penny-shaped cracks in glass," *J. Appl. Phys.* **59**(8), 2711–2715.
- Kishi, T. (1985). "Acoustic Emission Source Characterization and Its Application to Micro-Cracking," *Z. Metallkd.* **76**(7), 512–518.
- Kjartansson, E. (1979). "Constant  $Q$  wave propagation and attenuation," *J. Geophys. Res.* **84**, 4737–4748.
- Lamb, H. (1904). "On the propagation of tremors over the surface of an elastic solid," *Philos. Trans. R. Soc. London, Ser. A* **203**, 1–42.
- Mal, A. K., Kundu, T., and Xu, P.-C. (1982). "Ground motion calculations," ASME Symposium on Earthquake Ground Motion and its Effect on Structures **AMD-53**, 21–40.
- Michaels, J. E., Michaels, T. E., and Sachse, W. (1981). "Application of deconvolution to acoustic emission signal analysis," *Mater. Eval.* **39**, 1032–1036.
- Miller, G. F., and Pursey, H. (1954). "The field and radiation impedance of mechanical radiators on the free surface of a semi-infinite isotropic solid," *Proc. R. Soc. London, Ser. A* **223**, 521–541.
- Nelson, P. P., and Glaser, S. D. (1992). "Acoustic emissions produced by discrete fracture in rock," *Int. J. Rock Mech.* **29**, 237–251.
- Ohtsu, M., and Ono, K. (1984). "A generalized theory of acoustic emission and Green's functions in a half space," *J. Acoust. Emiss.* **3**, 27–40.
- Pao, Y.-H. (1978). "Theory of acoustic emission," *Elastic Waves and Non-destructive Testing of Materials, AMD*, edited by Y.-H. Pao (ASME, New York) Vol. 29, pp. 85–106.
- Pao, Y.-H., and Gajewski, R. R. (1977). "The generalized ray theory and transient responses of layered elastic solids," *Physical Acoustics XIII*, edited by W. P. Mason and R. N. Thurston (Academic, New York), pp. 183–265.
- Pekeris, C. L., and Lifson, H. (1957). "Motion of the surface of a uniform elastic half-space produced by a buried pulse," *J. Acoust. Soc. Am.* **29**, 1233–1238.
- Proctor, T. M. (1982a). "An improved piezoelectric acoustic emission transducer," *J. Acoust. Soc. Am.* **71**, 1163–1168.
- Proctor, T. M. (1982b). "Some details on the NBS conical transducer," *J. Acoust. Emiss.* **1**, 173–178.
- Proctor, T. M. (1986). "More-recent improvements on the NBS conical transducer," *J. Acoust. Emiss.* **5**, 134–142.
- Rayleigh, Lord (1887). "On waves propagated along the plane surface of an elastic solid," *Proceedings of the London Mathematical Society* **17**, 4–11.
- Ruitenbeek, J. C., Berni, A. J., and de Hoop, M. V. (1991). "Non-far-field vibroseis deconvolution," Publication 1072, Koninklijke/Shell Exp. and Prod. Lab., Rijswijk, the Netherlands.
- Selfridge, A. (1998). "Acoustic material property tables," <http://www.ultrasonic.com/tables/index.htm>.
- Shiwa, M., Inaba, S. H., Carpenter, S. H., and Kishi, T. (1992). "Development of high-sensitivity and low-noise integrated acoustic emission sensor," *Mater. Eval.* **51**, 868–874.
- Wadley, H. N. G., and Hill, J. J. (1983). "Dynamic elastic displacements at the surface of an elastic half-space due to defect sources," *J. Phys. D* **16**, 1069–1083.
- Weiss, G. G., and Glaser, S. D. (1998). "Internal measurement of picometer-scale dynamic displacements inside rock," in *Transportation Research Record* (Trans. Research Board, National Research Council (NAS/NAE), Washington, DC).

# The analysis and results of a continuous wave ultrasonic densitometer

Christian C. J. Smit and Edwin D. Smith

Department of Electrical and Electronic Engineering, University of Pretoria, Pretoria, South Africa

(Received 25 July 1997; accepted for publication 11 March 1998)

This paper investigates an ultrasonic densitometer capable of measuring the densities of liquids. Lynnworth originally proposed an ultrasonic densitometer operating in pulse-echo mode. This instrument makes use of the phase velocity of a torsional elastic wave pulse traveling in a noncircular waveguide immersed in a liquid to indicate the density of the liquid under investigation. In this paper a second mode of operation is proposed by making use of a continuously excited torsional wave to reveal liquid density. An important advantage of this mode of operation is the larger cross-sectional dimensions possible without sacrificing performance degradation which might result from wave dispersion. The theory of this mode of operation is described and used to construct a densitometer. Densities of a few liquids are measured and compared to the theoretical values. © 1998 Acoustical Society of America. [S0001-4966(98)05806-8]

PACS numbers: 43.38.Ar, 43.38.Fx, 43.35.Yb [SLE]

## INTRODUCTION

Lynnworth showed that the phase velocity of a torsional wave propagating in a waveguide of noncircular cross section is a function of the liquid density in which the waveguide is immersed.<sup>1</sup> Generally, the speed of any elastic or sound wave is proportional to the square root of a stiffness term divided by an inertia term. For the application described here the inertia is the sum of the waveguide and liquid-induced inertia. A larger liquid-induced inertia results in a lower torsional wave velocity. The torsional wave velocity is therefore a function of the liquid density surrounding the waveguide.

Torsional forces can be excited by means of a torsional transducer. A voltage pulse applied to the terminals of the piezoelectric transducer results in a torsional pulse propagating along a waveguide as illustrated in Fig. 1. The first echo received by the transducer is due to the interface indicated by A as shown in Fig. 1. The second echo originates from the reflection of the surface designated by B. It is during the wave's propagation in waveguide 2 that its velocity is a function of the surrounding fluid's density.

Other researchers have worked in this field to optimize the performance of this instrument. Bau<sup>2</sup> gave a first-order approach to the operation of the instrument, and also derived an equation for the phase velocity of the wave under the above-mentioned conditions. Various other authors published results measured with this instrument.<sup>3-6</sup> Kim *et al.* analyzed waveguides with various types of cross sections in order to optimize the performance of the instrument.<sup>7</sup>

This paper investigates three performance parameters of Lynnworth's proposed ultrasonic densitometer operating in a pulse-echo (PE) mode. These parameters are sensitivity, viscosity, and wave dispersion. This is then used as a basis to derive the theory of a similar instrument operating in a continuous wave (cw) mode. The theory is subsequently used to point out that the dimensions of the cw mode-operated instrument is more practical than the PE mode-operated instru-

ment. The paper concludes with the measured results of a constructed densitometer operating in the cw mode.

## I. PE MODE OPERATION

### A. Sensitivity

Sensitivity of the instrument operating in a PE mode is defined as  $dt_s/d\rho_f$ , where  $t_s$  is the total traveling time of the wave in waveguide 2 (see Fig. 1) of the probe, and  $\rho_f$  is the fluid density surrounding the waveguide. Bau has shown that the phase velocity of the torsional wave traveling in waveguide 2 can be approximated by<sup>2</sup>

$$c_s \approx K_{nc} \sqrt{\frac{\mu_s}{\rho_s}} \left( 1 + \frac{J_f \rho_f}{J_s \rho_s} \right)^{-1/2}, \quad (1)$$

where  $K_{nc}$  is a factor indicating the ratio of the speed of a torsional wave in a waveguide with noncircular cross section to that of a torsional wave in a waveguide with circular cross section. Here  $J_s$  is the polar second moment of area of waveguide 2 with respect to its axial length,  $J_f$  is the same polar moment, but originates because of the interaction between the waveguide and surrounding fluid,  $\mu_s$  is the waveguide's shear modulus, and  $\rho_s$  and  $\rho_f$  are the waveguide and liquid densities, respectively. The traveling time of the wave in waveguide 2 is given by

$$t_s = \frac{2l_s}{c_s}, \quad (2)$$

where  $l_s$  is the length of the waveguide. Substituting this into Eq. (1) gives

$$t_s = \frac{2l_s}{K_{nc} \sqrt{\mu_s/\rho_s} (1 + J_f \rho_f / J_s \rho_s)^{-1/2}} \quad (3)$$

In the case where  $\rho_f/\rho_s \ll 1$ ,  $(1 + J_f \rho_f / J_s \rho_s)^{1/2}$  can be approximated by  $\frac{1}{2}(J_f \rho_f / J_s \rho_s) + 1$ , which changes Eq. (3) to

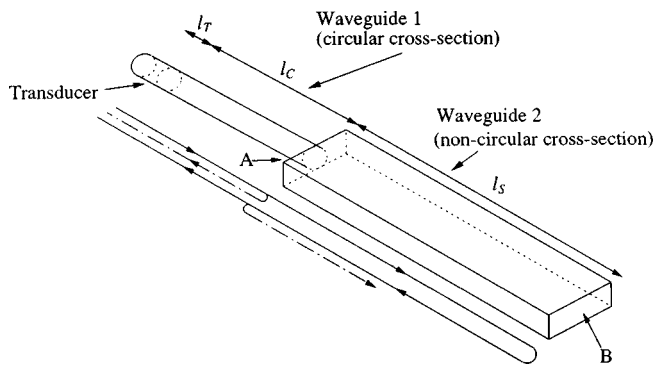


FIG. 1. Densitometer configuration.

$$t_s \approx \frac{2l_s(1/2(J_f\rho_f/J_s\rho_s)+1)}{K_{nc}\sqrt{\mu_s/\rho_s}} = \left(\frac{J_f l_s}{K_{nc} J_s \sqrt{\mu_s \rho_s}}\right) \rho_f + \frac{2l_s}{K_{nc} \sqrt{\mu_s/\rho_s}}. \quad (4)$$

The first term of Eq. (4) gives the relationship between fluid density and resulting propagation delay. The second term is a constant value and is the propagation time of the wave in waveguide 2 in vacuum (or for practical purposes air). For a zero fluid density, the first term is zero and the propagation time is that due to the waveguide in a vacuum. As the fluid density increases, the propagation time also increases linearly. Sensitivity can now be defined as

$$\frac{dt_s}{d\rho_f} = \frac{J_f l_s}{K_{nc} J_s \sqrt{\mu_s \rho_s}}. \quad (5)$$

The design parameters for sensitivity are therefore  $J_s$ ,  $J_f$ ,  $K_{nc}$ ,  $l_s$ ,  $\mu_s$ , and  $\rho_s$ . Kim *et al.* showed that the ratio  $J_f/J_s$  and the factor  $K_{nc}$  are both functions of the aspect ratio of the geometry of the waveguide's cross section.<sup>7</sup> Figures 2 and 3 show the relationship between these parameters and the geometries of various cross sections.

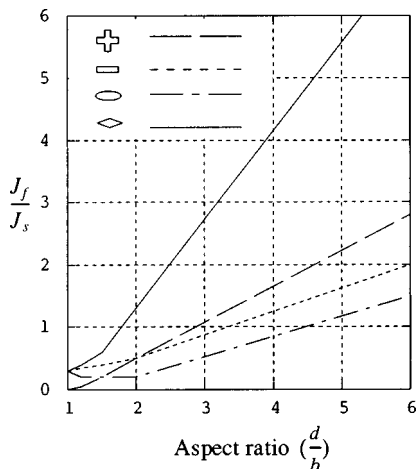


FIG. 2.  $J_f/J_s$  as a function of aspect ratio ( $d/b$ ). See also Ref. 7.

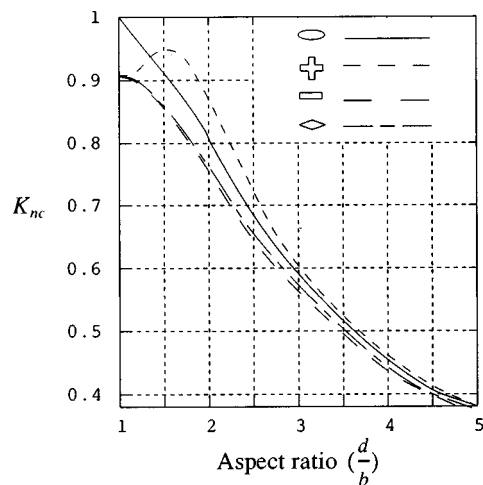


FIG. 3.  $K_{nc}$  as a function of aspect ratio ( $d/b$ ). See also Ref. 7.

## B. Viscosity

For densitometer application the effects of viscosity are undesirable. It can be neutralized by either determining the viscosity of the fluid and then compensating for it, or by designing the probe in such a way that the effect of viscosity can be ignored. Bau has indicated that viscosity can be ignored if the viscous boundary layer surrounding the probe is much smaller than the larger dimension of the probe's cross section.<sup>7</sup> The order of the viscous boundary layer can be approximated by

$$d_v \sim (\nu\lambda)^{1/2}, \quad (6)$$

where  $\lambda$  is the wave's wavelength and  $\nu$  is the kinematic viscosity. Viscosity can be ignored if

$$d \gg (\nu\lambda)^{1/2}, \quad (7)$$

where  $d$  is the larger dimension of the probe's cross section. Usually the effects of viscosity are not considered a problem since the viscous boundary layer is on the order of  $10^{-1}$ – $10^{-2}$  mm for waveguides operating at frequencies of 50–150 kHz.<sup>2,7</sup>

## C. Wave dispersion

Wave dispersion causes different frequency components of a wave to travel at different speeds. It too has therefore an undesirable effect on the performance of the proposed instrument. Until now, no analytical equation has been determined to quantify wave dispersion for this application. Lynnworth has, however, shown that dispersion can be ignored if<sup>1</sup>

$$d < \frac{\lambda}{10}. \quad (8)$$

## II. CW MODE OPERATION

### A. Principle of operation

One drawback of the proposed densitometer operating in PE mode is the small cross-sectional dimensions of the probe as governed by the sensitivity, the effects of viscosity, and wave dispersion. In order to maximize sensitivity,  $J_f/J_s$  should be maximized which results in a large aspect ratio as

shown in Fig. 2. Wave dispersion, on the other hand, demands that  $d$  should be small for a fixed wavelength [see Eq. (8)]. An increase in  $d$  can be accommodated, but this means that the wave's wavelength must be increased. A longer wavelength means a lower operating frequency which results in a lower measuring resolution. Kim *et al.* used a probe made of stainless steel with an axial length of 300 mm, an operating frequency of around 60–80 kHz, and cross-sectional dimensions of 2.58 mm by 0.73 mm.<sup>7</sup> Lynnworth used similar cross-sectional dimensions for his experiments.<sup>1</sup> These probes can be difficult to manufacture, especially for the geometries as proposed by Kim *et al.* (see Figs. 2 and 3).

Larger cross-sectional dimensions are possible by making use of a cw mode operation. The principle of operation makes use of the fact that the resonance frequency of a structure is a function of the phase velocity of the wave in the structure. The fundamental resonating frequency of an unloaded structure is given by

$$f_{(1/2)\lambda} = \frac{c}{2l}, \quad (9)$$

where  $l$  is the length of the structure. Equation (1) shows that  $c$  is a function of  $\rho_f$ . If only waveguide 2 of Fig. 1 is considered, it can be stated that the resonance frequency of the structure will be a function of the liquid's density surrounding it, as described by Eqs. (1) and (9).

The resonance wavelength of this system is given by  $2l$ . The maximum dimension of the cross section can be obtained by substituting  $2l$  into  $\lambda$  in Eq. (8):

$$d < \frac{2l}{10}. \quad (10)$$

A waveguide with an axial length of 100 mm can therefore have a  $d$  of 20 mm. If the cross section has an aspect ratio of 4, the smaller dimension of the cross section would be 5 mm. Both these dimensions can be practically implemented.

An important issue is the sensitivity of the instrument operating in the cw mode. Another issue concerns the generation of the torsional wave in the probe. A transducer needs to be attached to the probe in order to excite the torsional wave. This complicates matters since the structure becomes composite in nature.

## B. Analysis

The configuration of the instrument operating in the cw mode is similar to that of the PE mode (see Fig. 1). For the general case a mechanism of coupling is needed to couple the transducer to the probe. Depending on the application, it might not be desirable to attach the transducer directly to the probe, in which case waveguide 1 is used as shown in Fig. 1.

To simplify the sensitivity analysis, only waveguide 2 will be considered. The effect of the transducer and coupling piece on the resonating frequency of the structure will be investigated later. The sensitivity analysis commences by rewriting Eq. (2) as

$$c_s = \frac{2l_s}{t_s}. \quad (11)$$

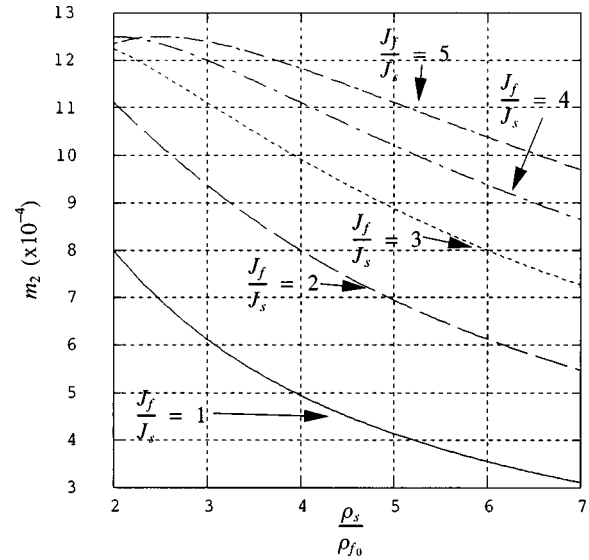


FIG. 4.  $m_2$  for various  $J_f/J_s$  and  $\rho_s/\rho_{f0}$ .

Substituting this into Eq. (9) leaves

$$f_s = \frac{1}{t_s}, \quad (12)$$

where  $f_s$  is the fundamental resonance frequency of the structure.  $f_s$  as a function of  $\rho_f$  can be obtained by substituting Eq. (4) into Eq. (12). This results in

$$f_s(\rho_f) = \frac{K_{nc} J_s \mu_s}{J_f l_s \sqrt{\mu_s / \rho_s} \rho_f + 2l_s \sqrt{\mu_s \rho_s} J_s}. \quad (13)$$

The sensitivity is obtained by differentiating  $f_s$  with respect to  $\rho_f$ :

$$\frac{df_s}{d\rho_f} = \frac{-K_{nc} \sqrt{\mu_s / \rho_s}}{l_s} \left[ \left( \frac{J_f \rho_f}{J_s \rho_s} + 4 \frac{\rho_s J_s}{\rho_f J_f} + 4 \right) \rho_f \right]^{-1}. \quad (14)$$

From this equation it is clear that  $df_s/d\rho_f$  is not constant and therefore the system will not be linear. It is shown later that the system is quasi-linear, which allows one to approximate a constant sensitivity. The sensitivity can be determined at the average density (designated by  $\rho_{f0}$ ) of the total density range of interest. Sensitivity can now be written as

$$\frac{df_s}{d\rho_f}(\rho_{f0}) = \frac{-K_{nc} \sqrt{\mu_s / \rho_s}}{l_s} \left[ \left( \frac{J_f \rho_{f0}}{J_s \rho_s} + 4 \frac{\rho_s J_s}{\rho_{f0} J_f} + 4 \right) \rho_{f0} \right]^{-1}. \quad (15)$$

Equation (15) can be written as  $m_1 \cdot m_2$  where

$$m_1 = \frac{-k_{nc} \sqrt{\mu_s / \rho_s}}{l_s} \quad (16)$$

and

$$m_2 = \left[ \left( \frac{J_f \rho_{f0}}{J_s \rho_s} + 4 \frac{\rho_s J_s}{\rho_{f0} J_f} + 4 \right) \rho_{f0} \right]^{-1}. \quad (17)$$

The term in Eq. (16) states that  $df_s/d\rho_f$  is proportional to the phase velocity of the torsional wave in the probe, and inversely proportional to the length of the probe. This is the inverse of the PE method's sensitivity equation. The term in



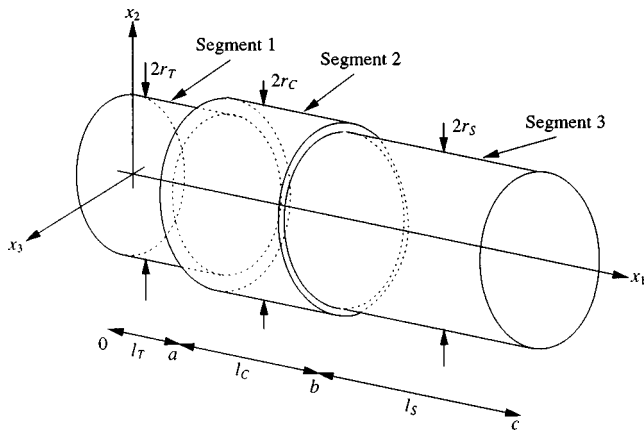


FIG. 5. Simplified presentation of a CW mode.

Eq. (17) can be interpreted by making use of a graph. Figure 4 shows  $m_2$  for various values of  $J_f/J_s$  and  $(\rho_s/\rho_{f0}) \rho_{f0}$  was chosen to be  $1000 \text{ kg/m}^3$ , which is the density of water at  $4^\circ\text{C}$ . According to Fig. 4, the sensitivity of the cw mode has the same trend as that of the PE mode. For both cases an increase in  $\rho_s$  leads to a decrease in sensitivity, while an increase in  $J_f/J_s$  leads to an increase in sensitivity. For the PE mode case sensitivity is a linear function of  $J_f/J_s$  [as evident from Eq. (4)]. For the cw mode sensitivity seems to converge to a limit for an increasing  $J_f/J_s$ . Figure 4 shows that spacing between successive  $m_2$  values decreases for an increase in  $J_f/J_s$  and a particular value of  $\rho_s/\rho_{f0}$ .

A practical instrument operating in the cw mode typically consists of a three-piece system similar to that of the PE mode (see Fig. 1). The purpose of the following theory is to determine the frequency at which the composite structure resonates. To perform this analysis, the frequency equation of the composite structure will be solved. To simplify the derivation, a three-piece structure, of which the cross section of each piece is circular, will be analyzed (see Fig. 5). The final frequency equation can be converted to make provision for the noncircular cross section (segment 3 of Fig. 5). For each segment a frequency equation can be obtained. They are for segments 1, 2, and 3, respectively,

$$\frac{(-G \tan(k_C l_T) - H \tan(k_T l_T)) \tan(k_C (l_T + l_C)) + (G - H \tan(k_T l_T) / \tan(k_C l_T))}{G \tan(k_C l_T) - H \tan(k_T l_T) + \tan(k_C (l_T + l_C)) (G - H \tan(k_T l_T) / \tan(k_C l_T))} = \frac{1}{G} \tan(k_S l_S), \quad (27)$$

where  $G = \mu_C r_C^4 k_C$ ,  $H = \mu_T r_T^4 k_T$ ,  $I = \mu_S r_S^4 k_S$ ,  $l_T = a$ ,  $l_C = b - a$ , and  $l_S = c - b$ . This is the frequency equation for the torsional mode of vibration and its roots designate the frequencies at which the structure shall resonate. Equation (27) is valid for the structure shown in Fig. 5 of which the radii, material type, and length of each piece differ. According to Kilpatrick *et al.* the error introduced to the frequency equation of a torsional system is small if one of the segments does not have a circular cross section.<sup>8</sup> Here  $G$ ,  $H$ , and  $I$  are proportional to  $r^4$ , which is in turn proportional to the par-

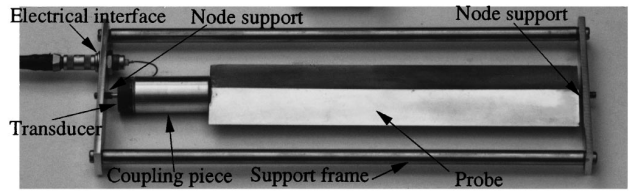


FIG. 6. Construction of the CW densitometer.

$$\theta_T = A \cos(k_T x_1) + B \sin(k_T x_1), \quad (18)$$

$$\theta_C = C \cos(k_C x_1) + D \sin(k_C x_1), \quad (19)$$

$$\theta_S = E \cos(k_S x_1) + F \sin(k_S x_1), \quad (20)$$

where  $k_T$ ,  $k_C$ , and  $k_S$  are the wave numbers of segments 1, 2, and 3, respectively.  $A$ ,  $B$ ,  $C$ ,  $D$ ,  $E$ , and  $F$  are obtained by evaluating the boundary conditions of the structure and interfaces between segments. Six boundary conditions are therefore needed to solve Eqs. (18)–(20). The boundary equations are (see Fig. 5)

$$\frac{d\theta_T}{dx_1} = 0 \quad \text{at } x_1 = 0, \quad (21)$$

$$\frac{d\theta_S}{dx_1} = 0 \quad \text{at } x_1 = c, \quad (22)$$

$$\theta_T(a) = \theta_C(a), \quad (23)$$

$$\theta_C(b) = \theta_S(b), \quad (24)$$

$$\mu_T r_T^4 \frac{d\theta_T}{dx_1} = \mu_C r_C^4 \frac{d\theta_C}{dx_1} \quad \text{at } x_1 = a, \quad (25)$$

$$\mu_C r_C^4 \frac{d\theta_C}{dx_1} = \mu_S r_S^4 \frac{d\theta_S}{dx_1} \quad \text{at } x_1 = b, \quad (26)$$

where  $\theta_T$ ,  $\theta_C$ , and  $\theta_S$  are the angular displacements of segments 1, 2, and 3, respectively. Substituting the boundary equation into Eqs. (18)–(20) leaves

ticular segment's polar moment. The  $r^4$  part of  $G$ ,  $H$ , and  $I$  can therefore be replaced with their respective polar moment equivalents. The polar moment of a waveguide with circular cross section is given by

$$J = \frac{\pi r_0^4}{2}. \quad (28)$$

For the densitometer application segments 1 and 2 are circular in cross section. This leaves  $G = \mu_C J_C k_C$ ,  $H = \mu_T J_T k_T$ , and  $I = \mu_S J_S k_S$ . The polar moment of segment 3 depends on

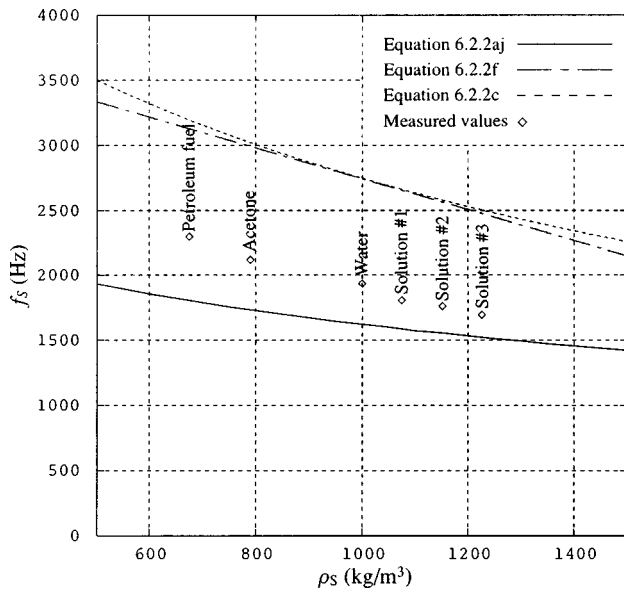


FIG. 7. Calculated and measured results.

the geometry of its cross section.  $J_S$  of a diamond-shaped geometry, for example, has a polar moment of

$$J_S = \frac{1}{48}(ab)(a^2 + b^2). \quad (29)$$

### III. THEORETICAL AND MEASURED RESULTS

A probe was constructed in order to test the validity of the derived theory. The probe was designed to be as sensitive as possible without sacrificing performance due to viscosity and wave dispersion. The probe was made from aluminium and is shown in Fig. 6. A diamond-shaped cross section was chosen which allowed for high sensitivity (see Fig. 2). The dimensions of the diamond-shaped cross section are 32 mm by 8 mm. The total length of the probe is 336.5 mm. The transducer used to excite the torsional waves is similar to that used in torsional-longitudinal ultrasonic motors. It is made of lead zirconate-titanate (PZT4) material and has a fundamental resonant frequency of 135.7 kHz. The complete structure is supported at its torsional vibrational nodes in order not to suppress the torsional motion. The structural resonance frequency for each case was obtained by measuring the impedance frequency response (magnitude and phase) over the frequency range of interest. A vector impedance meter was connected to the terminals of the transducer to obtain these measurements. From the frequency response readings, the resonance frequency of the structure could be determined.

The theoretical and measured results of the probe are shown in Fig. 7. Two theoretical curves are shown. They are

due to Eqs. (13) and (27). Equation (13) neglects the effects of the transducer and coupling piece on the resonance frequency of the structure. The effective axial length of the structure is therefore shorter, resulting in larger structural resonance frequencies. The second curve is due to Eq. (27), which gives the resonance frequency of the composite structure. This equation is the more complete theoretical model for the cw densitometer. It is therefore expected that the measured results should agree best with this curve.

Figure 7 also gives the measured results of six liquids with various densities. Solutions 1, 2, and 3 were prepared by varying the concentration of calcium chloride in water. The result of these measurements is a curve of which the gradient is approximately the same as for the theoretical predictions.

### IV. CONCLUSION

This paper investigates a densitometer which makes use of the properties of torsional waves to reveal liquid density. The instrument is operated in a cw mode in which the probe is continuously excited in a torsional mode. The theory for the cw mode is derived and the measured results are within 22% of the measurements made. This compares well to the 20% deviation of the measured and theoretical predictions as reported by Bau.<sup>2</sup> Although Bau conducted his experiments for the PE mode the 20% deviation is also relevant to that of the cw mode, since both the theoretical performance of the cw and PE mode of operation is based on Eq. (1). One should keep in mind that Eq. (1) is only a first-order prediction derived from a two-dimensional model. Better theoretical predictions can be obtained by employing three-dimensional fluid dynamic theory.

<sup>1</sup>L. C. Lynnworth, "Slow torsional wave sensors," Ultrasonics Symposium Proceedings, IEEE catalogue #77CH1264-ISU (1977), pp. 29-34.

<sup>2</sup>H. H. Bau, "Torsional wave sensor—A theory," J. Appl. Mech. **53**, 846-848 (1986).

<sup>3</sup>W. B. Dress, "A high resolution ultrasonic densitometer," Ultrasonics Symposium Proceedings, IEEE catalogue #0090-5607/83/0000-0287 (1983), pp. 287-290.

<sup>4</sup>A. E. Arave, "Ultrasonic densitometer development," Ultrasonics Symposium Proceedings, IEEE catalogue CH1482-9/79/0000-0370\$00.75 (1979), pp. 370-375.

<sup>5</sup>S. A. Jacobson, J. M. Korba, L. C. Lynnworth, T. H. Nguten, G. F. Orton, and A. J. Oraziotti, "Low-gravity sensing of liquid/vapor interface and transient liquid flow," IEEE Trans. Ultrason. Ferroelectr. Freq. Control **UF34**(2), 212-223 (1987).

<sup>6</sup>W. B. Dress, "Torsional ultrasonic technique for LWR (Light Water Reactor) liquid level measurement," Prepared for the US Nuclear Regulatory Research under interagency agreements DOE 40-551-75 and 40-552-75, Oak Ridge National Laboratory (1983).

<sup>7</sup>J. O. Kim and H. H. Bau, "On line realtime densimeter—Theory and optimization," J. Acoust. Soc. Am. **85**, 432-439 (1989).

<sup>8</sup>M. F. Kilpatrick and J. E. Kilpatrick, "Torsional vibrations of coupled cylinders," J. Acoust. Soc. Am. **22**, 224-230 (1950).

# A deconvolution method for force reconstruction in rods under axial impact

Enboa Wu, Cheng-Zorn Tsai, and Ling-Hsien Tseng

*Institute of Applied Mechanics, National Taiwan University, Taipei, Taiwan 106, Republic of China*

(Received 22 August 1997; accepted for publication 16 May 1998)

A deconvolution method to extract the force history exerted axially on one end of a rod using the responses recorded remotely from the impact location is presented in this paper. The traditional Green's function is completely eliminated in the solution process. To apply the developed method, another set of force and response data, at the same locations as in the impact event in which the force is to be reconstructed, needs to be obtained either from measurement or from a theoretical/numerical solution. The latter was adopted in bar impact events due to the fact that the signals have very wide frequency bands, and the theoretical responses were calculated separately using the Love theory and the Pochhammer–Chree equation. Using optimization algorithms to search for the force from the input signals that were recorded by multiple gauges and were contaminated with noises, the method has been demonstrated to be robust. Further, to show that the developed method is general, an example for extracting the impact force exerted on a complicated sandwich structure using the recorded strain signals as the input data are also presented. This further demonstrates that the method can be applied to an impact event in which the Green's function is very difficult to construct. © 1998 Acoustical Society of America. [S0001-4966(98)06408-X]

PACS numbers: 43.40.Cw [CBB]

## INTRODUCTION

Distortion of wide-band wave signals when they travel along a structure is a well-known phenomenon. Numerous results have been published for dispersion of stress waves in rods, beams, plates, etc.,<sup>1-5</sup> which have shown that the phase velocity of each harmonic component of the waves varies and that the level of variation depends on both the structure and its frequency. The problem of stress waves traveling along a rod is probably one of the most interesting problems, partly due to introduction of the split-Hopkinson bar technique, which is still the most frequently used method for testing of material properties at high strain rates.<sup>6</sup> In 1948, Davies<sup>1</sup> showed the dispersion characteristic of a nearly rectangular wave when it travels a finite distance away from the impact end of a rod. The famous bar impact test was conducted by Oliver<sup>7</sup> using a 19 ft long rod, which demonstrated propagation of several groups of waves each arriving at the sensor locations at different times.

Thus, signals received in a bar-to-bar impact test have been distorted from the force pulse which is exerted at the bar end. This is because sensors are usually located at finite distances away from the impact end. Therefore, the recorded signals cannot be directly treated as the impact force. Further, the dispersed phenomenon becomes significant as the velocity of the striker bar increases. On one hand, bars of smaller diameter have usually been employed and signals closer to the impact end have been recorded to remedy this annoying problem. On the other hand, methods have been developed to trace the received signal backward to obtain the force history. Among them, the phase shift method has been used and expressed in different forms,<sup>8-13</sup> some of which have adopted the solution from the Pochhammer-Chree frequency equation.<sup>1,14</sup> Although this exact two-dimensional so-

lution was employed, it was found in this study that a direct correction of the phase of impact-induced dispersive waves may not give a reasonable result. This is due to noise and the imperfect experimental configuration which always exist in impact test runs. The latter, in turn, results from the combined effects of the location and orientation of the mounted gauges, the imperfection of the rods, equipment limitation, etc.

In this study we developed a deconvolution method to extract the force from the signals recorded remotely from the impact end of a struck bar without using the traditional Green's function. This method is considered to be general and, in principle, can detect the impact force exerted on a waveguide or a structure of an arbitrary configuration as long as the responses of the waveguide/structure by another impact force, both at the same locations as in the impact event in which the force is to be extracted, are either calculated using a theoretical/numerical model or measured. In this paper, a theoretical deconvolution method is implemented for bar impact problems. Both the Love theory<sup>1</sup> and the Pochhammer–Chree frequency equation will be used to construct the solution in the needed reference impact run. The result of this deconvolution method will be verified both numerically and experimentally, and will further be compared with the solution obtained by directly using the phase shift method. This developed deconvolution method has also been applied to the measurement of the material stress–strain relationship at high strain rates using the direct impact technique.<sup>15,16</sup> On the other hand, the impact force exerted on a complicated sandwich structure is extracted, under which conditions the Green's function is considered to be very difficult to construct, to show that the developed method is general.

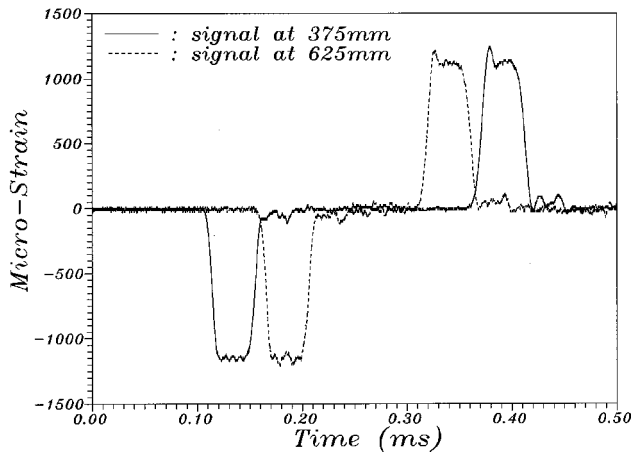


FIG. 1. Two sets of recorded strain signals on a pressure bar struck by a 100 mm blunt projectile at an initial velocity of 10.91 m/s. The compressive and tensile signals represent incoming and reflected waves, respectively.

### I. WAVES INDUCED BY IMPACT ON RODS

Figure 1 illustrates typically recorded strain signals when a 100-mm-long blunt projectile (striker bar) strikes a stationary pressure bar 1 m long at an initial velocity of 10.91 m/s. Both the projectile and the bar were made of Ti6Al4V and were 12.7 mm in diameter. Two gauge sets were mounted on the bar, each composed of two strain gauges 180° opposite to each other in the bar cross section, to remove the effect of bending waves. Their distances from the impact end were 375 and 625 mm. Both the incoming waves and waves reflected from the free end are plotted in Fig. 1, in which the former were in compression. These waves are found to be distorted mainly due to lateral motion of the bar as the waves traveled through it. This dispersion phenomenon was more significant in the reflected waves because the distance traveled was longer, as expected. Further, there existed rise times whose periods were longer than 16  $\mu$ s in the two incoming waves and were longer than 20  $\mu$ s for the two reflected waves. This also evidences the fact that dispersion is more significant when waves travel a longer distance.

In order to illustrate this phenomenon in more detail, two analytical methods, one of which was the simpler one-dimensional Love's theory while the other used the two-dimensional Pochhammer frequency equation, were employed to forward calculate the stress waves from a given impact force with a very short rise time. The derivation process of both analyses will be described later in this paper; Fig. 2 shows the result when a trapezoidal wave with only 1  $\mu$ s rise time travelled 375 mm from the impact end of a titanium alloy bar 12.7 mm in diameter. The effect of wave dispersion due to lateral motion of the bar can clearly be observed, especially at the upper corner of the rising part and the lower corner of the falling part of the signals. This is because the signals in these regions had the widest frequency spectrum. Thus, the dispersion phenomenon was more significant in these regions. On the other hand, the deviation between the two analytical solutions was not significant, especially for the slopes in the rising and falling parts of the signals.

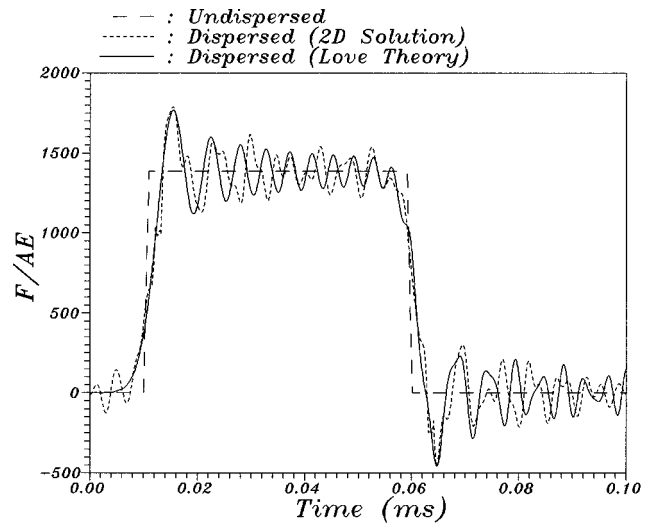


FIG. 2. A trapezoidal pulse with a 1- $\mu$ s rise time traveling a distance of 375 mm down a 12.7 mm bar.

Distortion between the force acting on the bar and the wave signals traveling along the bar is also affected by the duration of the rise time of the original force pulse. Figure 3 illustrates another typical example, in which the rise time of the original force pulse was set to be 5  $\mu$ s. The correlation between the two analytical methods is found to be generally better than that in Fig. 2. Further, the propagating waves were also oscillating less except for at the upper left and lower right corners of the pulse where the frequency contents were still rich. On the other hand, although the slope of the rising part between the original force and the propagating wave was approximately the same, the actual value of the rise time still differed significantly due to distortion of the waves at the two corners in the rising part. Thus, even though the rise time is long, the effect of wave dispersion on propagation of stress waves is still significant. This effect is always observed in the high strain rate test of material in

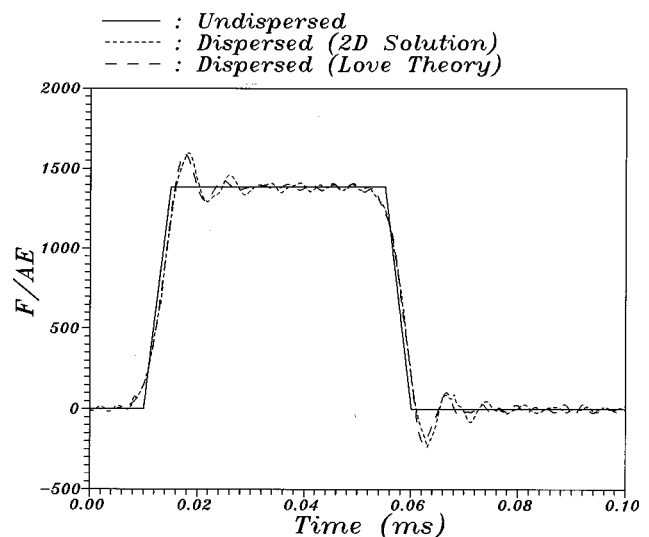


FIG. 3. A trapezoidal pulse with a 5- $\mu$ s rise time traveling a distance of 375 mm down a 12.7 mm bar.

which the split-Hopkinson bar technique is the most frequently used.

## II. DECONVOLUTION OF STRESS WAVES

### A. Convolution relationship

The general relationship between an impact force,  $F$ , and the corresponding recorded signals, such as the strain,  $\epsilon$ , in a waveguide or a structure is

$$\epsilon = G * F, \quad (1)$$

where  $*$  represents convolution integral and  $G$  is the Green's function. This relationship cannot only be applied to any bar impact problems, such as that mentioned in the above section, but also to finding the force and response relationship for waveguides/structure having arbitrary configurations, as long as the Green's function can be constructed. This idea has been successfully incorporated to detecting both locations and forces on a plate when it is subjected to low velocity impact.<sup>17-21</sup> However, the Green's function in many problems is difficult to construct due to either complicated geometry or materials composed of a waveguide/structure. Thus, this may limit application of Eq. (1) in solving a more general problem. In a later part of the paper, i.e., in Sec. IV D, an example for impact on a sandwich panel will be demonstrated in which the Green's function is very difficult to construct. To further broaden the application of the method, we will herein present a convolution relationship which essentially eliminates use of the Green's function in an impact/wave propagation event.

Because a Green's function only depends on the geometry, material properties and the locations of the force and response on a waveguide/structure, the Green's function remains the same if these parameters are fixed. Thus, for a known impact force,  $F^0$ , and the corresponding response,  $\epsilon^0$ , acting on the same locations as those of  $F$  and  $\epsilon$ , respectively, in Eq. (1), the following equation holds:

$$\epsilon^0 = G * F^0. \quad (2)$$

Combining Eqs. (1) and (2) and noting that convolution sequence is commutable, one obtains

$$\epsilon * F^0 = \epsilon^0 * F. \quad (3)$$

Letting  $R = \epsilon * F^0$  and  $G' = \epsilon^0$ , Eq. (3) becomes

$$R = G' * F. \quad (4)$$

Thus, the original Green's function,  $G$ , is eliminated from the convolution relationship in Eq. (4).

The merit of Eq. (4) is that one only needs to obtain the impact force,  $F^0$ , and the corresponding response of a waveguide, such as  $\epsilon^0$ , from a reference impact either by calculation or by experiment. Then, the impact force,  $F$ , from any other elastic impact at the same location can always be determined as long as the corresponding response signal, such as  $\epsilon$ , is recorded. Thus, no traditional Green's function is involved. Note also that whereas the Green's function is usually difficult to construct in a general impact event, the target response to an impact force can usually be obtained much easier by using experimental methods or numerical methods

such as traditional finite element or finite difference schemes. This is because one only needs the excitation force and the corresponding responses of the target in using the developed method, but not the Green's function. Thus, this developed method can easily be applied to impact problems involving complicated geometries and materials. Also, the response of the waveguide/structure can be any of strain, displacement, velocity, acceleration, etc. On the other hand, the requirement for using the developed method is that the frequency bands of  $\epsilon^0$  and  $F^0$  in the reference impact event should not be narrower than the bands corresponding to  $\epsilon$  and  $F$ , as will also be described in later parts of the paper.

### B. Deconvolution method

In principle, the impact force in Eq. (4) can be obtained directly by means of conventional numerical methods, such as the Gauss elimination method. However, since deconvolution of Eq. (4) represents an ill-posed problem, a trivial error, such as noise from measurement or an insignificant deviation between the theoretical and the physical models in an experiment, always propagates and results in a divergent solution.<sup>22</sup>

Thus, Eq. (4) will be solved in this study using an optimization algorithm. The objective function is constructed by using a quadratic function:

$$E = \frac{1}{2} \left\| \sum_{k=1}^l (R_k - G'_k F) \right\|^2, \quad (5)$$

where  $l$  is the number of the sensors used, and  $\|\cdot\|$  is the Euclidean norm. Use of multiple sensors in the search process usually gives a more reliable solution.<sup>17-21</sup> To further improve the quality of the optimally searched solution, a unilateral constraint

$$F(t) \geq 0, \quad t \geq 0 \quad (6)$$

is employed, which reflects the physical situation that the force must not be in tension during impact. Thus, the problem of detecting the impact force on a bar from the recorded signals remote from source location is converted into a constrained optimization problem. The gradient projection method is then employed to search for the optimal impact force.<sup>23</sup> Further, since  $G'^T G'$  is positive definite, there must be only one extreme value. Thus, the searched solution, except for the effect of the induced numerical errors and the experimentally induced noises and imperfection, must be unique.

Since iteration is needed in the search process of the optimal solution, the optimal iteration number must also be determined. The criterion selected in this study is similar to that reported previously by Wu *et al.*<sup>17</sup> A detailed description of the algorithm for the optimal convergence criterion can also be found in this reference. Because the noise level in a reference impact test in a laboratory is generally a very small fraction of that of the signals, the solution, which in this study is the impact force acting on the bar end, is found to

remain essentially unchanged even if the iteration step used in the search process was a few thousandths more than the optimal iteration number.

### III. FORWARD SOLUTION FOR IMPACT ON A BAR

Although the developed method can be employed to detect impact force exerted on a waveguide/structure of arbitrary geometries from the recorded signals remote from the impact location, the main goal of this study was to apply this method to bar-to-bar impact problems. On the other hand, although the most direct routine seems to be one that measures  $F^0$  and  $\epsilon^0$  directly in an actual impact test run, this direct approach is generally not feasible. This is because the impact force in either bar-to-bar or Hopkinson bar types of experiments always has a wide frequency band due to its sharp rising pattern and short duration, as typically shown in Fig. 1. Thus, the force and the response in a reference impact, i.e.,  $F^0$  and  $\epsilon^0$  in Eq. (3), must also have a compatible wide frequency band. Due to the resonance limitation of conventional contact type of force sensors, such as a force transducer embedded in an instrumented hammer or an accelerometer, the recorded force history,  $F^0$ , does not usually have a wide enough frequency band. Thus, the process of using measured signals to retrieve the force in plate impact problems, in which the frequency bands of both the force and responses are much narrower,<sup>21</sup> cannot be applied to the present bar impact problems.

Therefore, an alternate approach using a theoretical method or finite element/difference programs to model the bar impact problem must be employed. In this study, the former was employed, and the problem of impact-induced wave traveling along a rod was modeled using either the simpler one-dimensional Love theory,<sup>24</sup> or the more complicated two-dimensional theory of Pochhammer and Chree.<sup>1</sup> These two theories were employed in this study for two reasons. First, the applicability of these two analytical solutions to the developed deconvolution method will be evaluated. Second, the developed deconvolution process will be compared with the previously reported phase-shift method,<sup>8,10,13</sup> which, in turn, uses the first mode of the Pochhammer-Chree solution.

#### A. Solution by Love theory

In the Love theory, the radial motion of a rod was postulated by a simple relation with the axial motion as<sup>1,24</sup>

$$v = -\nu r \frac{\partial u(x,t)}{\partial x}, \quad (7)$$

where  $u$  and  $v$  are the displacements of the rod in the axial and radial directions, respectively,  $\nu$  is the Poisson's ratio, and  $x$  and  $r$  are the coordinates in the axial and radial directions of the rod, respectively. For a rod of length  $L$  subjected to impact force,  $F^0(t)$ , at its one end exerted by a striker bar, the governing equation, boundary conditions, and initial conditions, respectively, are<sup>25</sup>

$$\frac{\partial^2 u}{\partial x^2} + \frac{\nu^2 k^2}{c_0^2} \frac{\partial^4 u}{\partial x^2 \partial t^2} = \frac{1}{c_0^2} \frac{\partial^2 u}{\partial t^2}, \quad 0 \leq x \leq L, \quad t \geq 0, \quad (8a)$$

$$\rho \left( \nu^2 k^2 \frac{\partial^3 u}{\partial t^2 \partial x} + c_0^2 \frac{\partial u}{\partial x} \right) = 0, \quad x=0, \quad (8b)$$

$$\rho \left( \nu^2 k^2 \frac{\partial^3 u}{\partial t^2 \partial x} + c_0^2 \frac{\partial u}{\partial x} \right) = \frac{F^0(t)}{A}, \quad x=L, \quad (8c)$$

$$u(x,0) = 0, \quad (8d)$$

$$\frac{\partial u(x,0)}{\partial t} = v_0, \quad (8e)$$

where  $c_0 = \sqrt{E/\rho}$  is the one-dimensional wave velocity;  $k^2 = (1/A) \int_A r^2 dA$  is the polar radius of gyration of the bar cross section,  $A$ ; and  $v_0$  is the initial velocity of the striker bar. Let  $h^2 = \nu^2 k^2$ ,  $p = n\pi/L$ , and  $\alpha = pc_0/(\sqrt{1+p^2 h^2})$ . By imposing the initial and boundary conditions, the displacement history at any locations down the impact end of the bar can be expressed in terms of Fourier series as

$$u(x,t) = v_0 t + \frac{1}{\rho A L} \int_0^t F^0(\tau)(t-\tau) d\tau + \frac{2}{\rho A L} \sum_{n=1}^{\infty} \frac{(-1)^n}{(1+p^2 h^2)} \frac{1}{\alpha} \cos\left(\frac{n\pi x}{L}\right) \times \int_0^t F^0(\tau) \sin \alpha(t-\tau) d\tau. \quad (9)$$

Since strain gauges were employed in this study to record the wave motion of the rod due to impact at one end, the strain history was obtained by taking the derivative with respect to  $x$  as

$$\epsilon(x,t) = \frac{2}{\rho A L} \sum_{n=1}^{\infty} \frac{(-1)^{n+1}}{(1+p^2 h^2)} \frac{n\pi}{\alpha L} \sin\left(\frac{n\pi x}{L}\right) \times \int_0^t F^0(\tau) \sin \alpha(t-\tau) d\tau. \quad (10)$$

Discretizing Eq. (10) using equal time intervals and treating the force history within each time interval to be uniform, the discrete strain signal at  $t=t_j$  becomes

$$\epsilon(x,t_j) = \frac{2}{\rho A L} \sum_{n=1}^{\infty} \frac{(-1)^{n+1}}{(1+p^2 h^2)} \frac{n\pi}{\alpha L} \sin\left(\frac{n\pi x}{L}\right) \times \sum_{k=1}^j F^0_k (\cos \alpha(k-1)\Delta t - \cos \alpha k \Delta t), \quad (11)$$

where  $n$  is the number of the modes used. Throughout this study,  $n=400$  was used, reflecting a cutoff frequency of 2 MHz. This was considered to be sufficient to obtain accurate solutions for the bar-to-bar impact problems performed in this study. The time step used was  $0.1 \mu\text{s}$ . Figures 2 to 3 illustrate typical propagating results using the Love theory for a bar struck by trapezoidal pulses with  $1 \mu\text{s}$  and  $5 \mu\text{s}$  rise times, respectively, at one end of the bar.

## B. Solution by two-dimensional method

The impact force of an arbitrary shape can always be constructed using a finite number of harmonic components as

$$F^0(t) = \sum_n [A_n \cos(2n\pi\omega t) + B_n \sin(2n\pi\omega t)], \quad (12)$$

where  $F^0(t)$  is the impact force,  $\omega$  is the fundamental frequency, and  $n$  is the number of harmonic components. Based on the first mode of the Pochhammer and Chree solution, the phase of each harmonic component, after travelling a fixed distance in a rod-type wave guide, can be expressed as<sup>14</sup>

$$\phi(\omega) = 2n\pi\omega x \left( \frac{1}{c_0} - \frac{1}{c_n} \right), \quad (13)$$

where  $c_n$  is the phase velocity of the  $n$ th harmonic wave and is calculated from linear interpolation of the data in Bancroft,<sup>14</sup> and  $x$  is the traveling distance along the bar. The waves after travelling 375 mm from the bar end are also plotted in Figs. 2 and 3 for trapezoidal pulses with 1  $\mu$ s and 5  $\mu$ s rise times, respectively. The following equations were used for the calculation:

$$\begin{aligned} F^0(t) &= \sum_n [A_n \cos(2n\pi\omega t + \phi) + B_n \sin(2n\pi\omega t + \phi)] \\ &= \sum_n [A'_n \cos(2n\pi\omega t) + B'_n \sin(2n\pi\omega t)], \end{aligned} \quad (14)$$

where

$$\begin{aligned} A'_n &= A_n \cos(\phi) + B_n \sin(\phi), \\ B'_n &= B_n \cos(\phi) - A_n \sin(\phi). \end{aligned} \quad (15)$$

In all the calculations in this study involving the two-dimensional method, the value of  $n$  was also taken to be 400.

## IV. DISCUSSION AND APPLICATIONS

### A. Noise effect

In order to extract the impact force from the recorded strain data using the developed deconvolution method, the force,  $F^0$ , in the reference impact run was taken as the original trapezoidal pulse shown in Fig. 3. On the other hand, both the Love theory and the two-dimensional method using the first mode of the Pochhammer-Chree solution were employed to forward calculate the strain histories  $\epsilon^0$  from the impact force  $F^0$ , shown by the dotted curves in Fig. 3. In order to more realistically simulate bar-to-bar impact test conditions, 10% noise was added on  $\epsilon_0$  in Fig. 3 to form  $\epsilon$ . For purposes of illustration, only the forward solution using the two-dimensional method is plotted in Fig. 4. The noise was randomly generated, and the signal-to-noise ratio (SNR) is

$$\text{SNR ratio} = \frac{S_{\max} - S_{\min}}{N_{\max} - N_{\min}}, \quad (16)$$

where  $S_{\max}$  and  $S_{\min}$  are the maximum and the minimum wave signals, and  $N_{\max}$  and  $N_{\min}$  are the noise of the maxi-

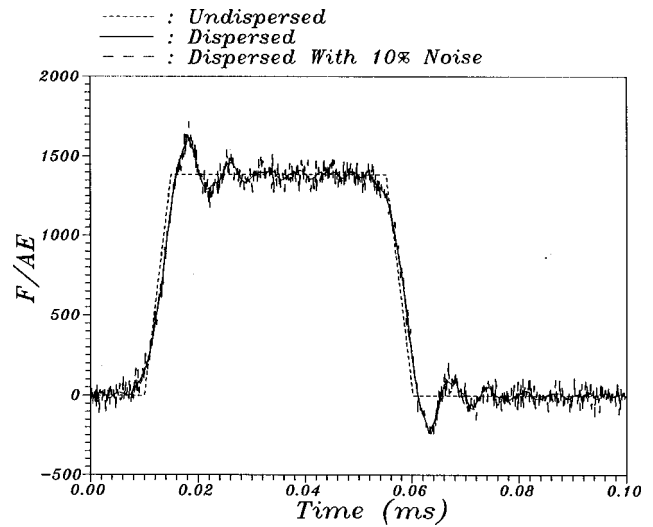


FIG. 4. A trapezoidal pulse with a 5- $\mu$ s rise time, the corresponding dispersed wave after travelling 375 mm, and the dispersed signal with 10% noise added.

mum and the minimum values, respectively. The noise was generated randomly in a Gaussian distribution with 0 and 1 for the mean and the standard deviation, respectively. The strain histories,  $\epsilon$ , were constructed by adding the noise to the original signals, as shown in Fig. 4. The forces extracted using the developed deconvolution method are shown in Fig. 5, in which the noise-contaminated input signals,  $\epsilon$ , were originally formed using the Love theory and the two-dimensional method. On the other hand, the force and the corresponding strain in the reference impact event,  $F^0$  and  $\epsilon^0$ , although not necessarily required, were taken to be noise free. The two extracted forces differ negligibly and both agree very well with the original trapezoidal force. The slight deviation between the original and deconvoluted forces at the corners was considered to be due to use of finite modes in Eqs. (11) and (14). In this study, the cutoff frequency was 2 MHz because 400 modes were employed. Although not shown in this paper, it has been found that the forces detected using multiple gauges generally have even better cor-

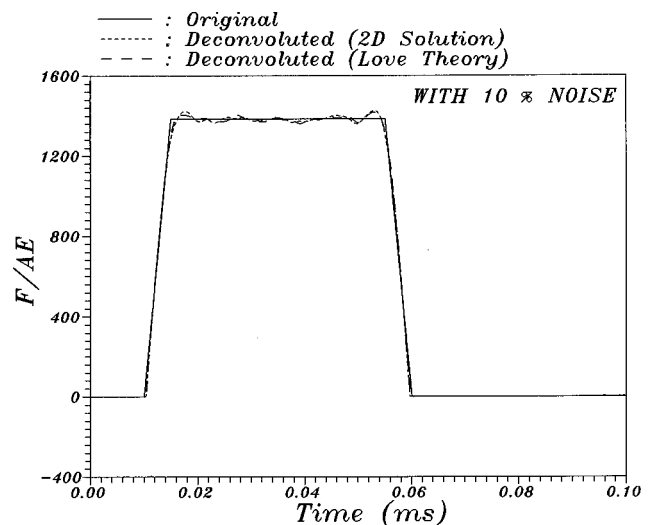


FIG. 5. A trapezoidal pulse with a 5- $\mu$ s rise time and the results deconvoluted from the noise contaminated dispersed wave in Fig. 4.

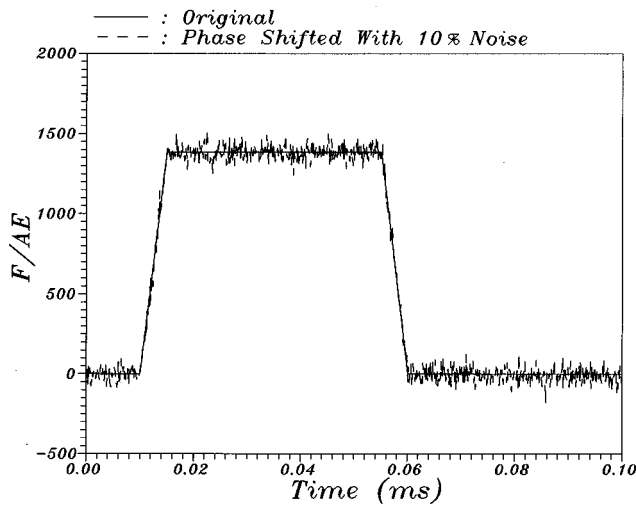


FIG. 6. A trapezoidal pulse with a 5- $\mu$ s rise time and the result obtained using the phase shift method and the noise contaminated dispersed wave in Fig. 4.

relation with the original force.<sup>15,16</sup> Further, similarly good agreement was obtained between the original and the deconvoluted force pulses when  $F^0$  with a 1  $\mu$ s rise time (Fig. 2) was employed.

On the other hand, the phase shift method was adopted by other researchers to obtain impact force from the recorded strain history. The idea was to have a negative sign in  $x$  in Eq. (13) and to recover the force by using Eq. (14). Because the phase-shift method simply shifts the phase angle of the propagated signals in the discrete Fourier domain, the detected impact force reflects the patterns of the noise on top of the original force pulse. Figure 6 exemplifies this situation. The randomly generated noise in the propagated wave signals are completely observed in this figure.

## B. Verification using experimental data

Although it is random in nature, numerically generated noise is still not able to reflect effects from all sources such as those due to imperfection and slight misalignment of sensors, limited resolution of equipment, deviation between the mathematical model and the physical experimental configuration, etc. Thus, the developed method had to be verified using experimental data. As a typical example, the recorded signals in Fig. 1 were employed as the  $\epsilon$  in Eq. (3), and the undispersed trapezoidal pulse and the calculated disperse waves in Fig. 3 were treated as  $F^0$  and  $\epsilon^0$ , respectively, in the evaluation process. The deconvoluted force histories are illustrated in Fig. 7(a) and (b) as dotted curves. In this calculation, the value of  $l$  was equal to 2 in the search process using Eq. (5). That is, the compressive strains from both sets of strain gauges 375 and 625 mm from the impact end of the bar in Fig. 1 were employed as the input data,  $\epsilon$ . Thus, the two dotted curves obtained by using the developed deconvolution method are identical in Fig. 7(a) and (b). Further, since the difference in the results obtained using the Love theory and the two-dimensional method is insignificant, as has been shown in Fig. 5, only the Love theory was employed in the developed deconvolution method to reconstruct the force in

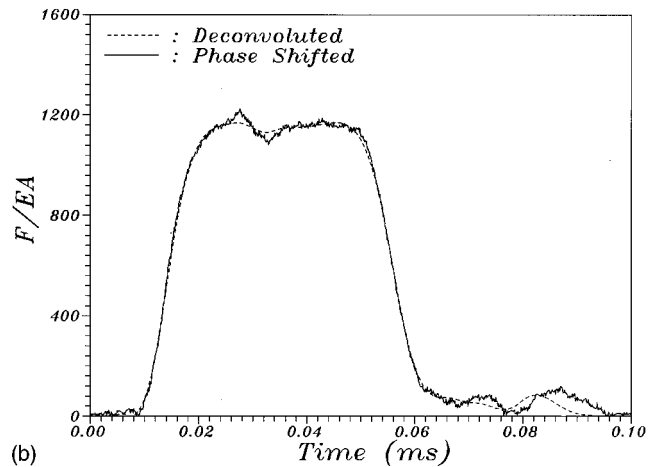
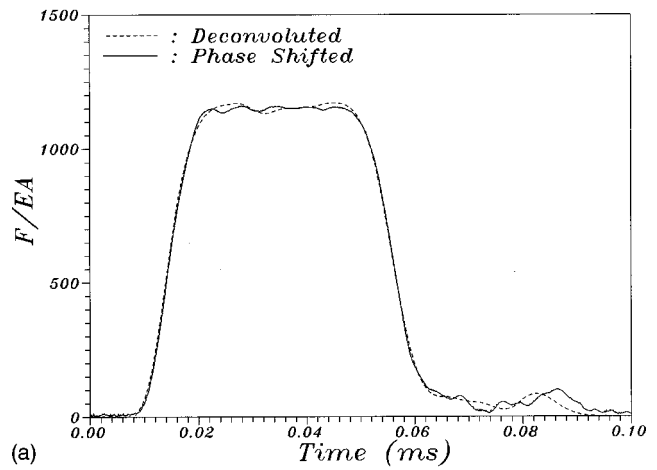


FIG. 7. Pulse at the impact end obtained using the deconvolution method (dotted curves) and the phase shift method. Two sets of compressive strains in Fig. 1 were employed in using the deconvolution method. The solid curves were obtained using the phase shift method with the (a) first and (b) second sets of strains.

this example. In Fig. 7(a) and (b), essentially no oscillation is found in the deconvoluted force pulse, as expected.

On the other hand, in the phase-shift method, the results obtained using the signals recorded by the first and the second sets of the strain gauges in Fig. 1 are separately plotted in Fig. 7(a) and (b), respectively, as solid curves. Comparing the two extracted force pulses shown in Fig. 7(a) and (b), the correlation between the results obtained using the present deconvolution and the previous phase-shift methods is excellent in Fig. 7(a) while a significant deviation is found in Fig. 7(b). Since the detected force in an impact event must have the same value no matter what input data were used, this unsatisfactorily detected force history obtained using the phase-shift method once more reveals the fact that this method is strongly dependent upon the quality of the recorded signals. On the other hand, due to employment of two sets of strains as the input data in the developed deconvolution method, the adverse effect from one of the sensors is much suppressed. Thus, the developed method is considered to be more robust in terms of extracting impact force from the recorded signals in a bar impact event.

It is also worthwhile pointing out that the rise time of the detected force pulses was approximately 10  $\mu$ s. This is much



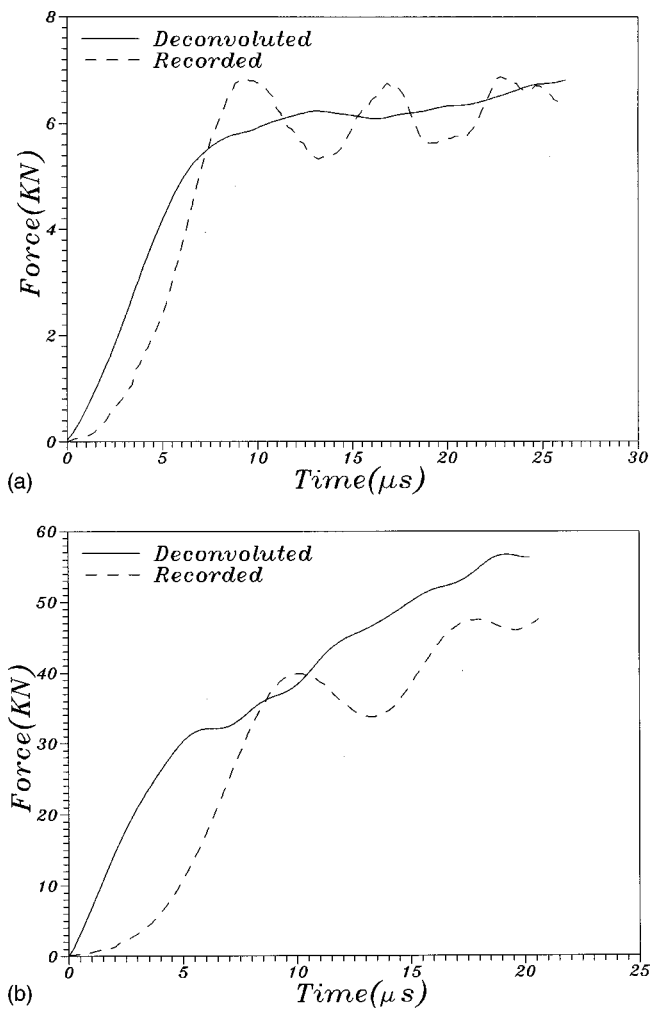


FIG. 8. The recorded force obtained from strain gauges and the deconvoluted force for testing of (a) 6061-T6 aluminum and (b) 1020 steel at constant strain rates of 8000 1/s and 35 000 1/s, respectively.

shorter than the rise time in both the incoming and the reflected waves in Fig. 1. This once more demonstrates the importance of correcting the dispersion effect in the force reconstruction process in bar-to-bar impact events. On the other hand, employment of the data in Fig. 3 for force  $F^0$  and response  $\epsilon^0$  in the deconvolution process is justified because the rise time of 5  $\mu s$  in  $F^0$  is only half of the rise time of the deconvoluted forces in Fig. 7(a) and (b). Thus, the frequency band for  $F^0$  is wider than that for  $F$  in Fig. 7.

### C. Applications to high strain rate test of materials

As mentioned above, waves recorded by the strain gauges remote from the impact end of a bar are dispersed. This situation inevitably occurs in high strain rate tests of material properties, either using the traditional split-Hopkinson bar apparatus or the direct impact method.<sup>15,16,26,27</sup> Thus, the effect of dispersion has to be properly considered before the recorded signals can be treated as the impact force. Figure 8(a) and (b) illustrate typical examples for aluminum 6061-T6 and 1020 steel specimens tested at constant strain rates of 8000  $s^{-1}$  and 35 000  $s^{-1}$ , respectively, using the direct impact method.<sup>27</sup> Details of the achievement of constant strain rate conditions

during high strain rate test of materials can be found in our recently completed work.<sup>15,16</sup> Both the blunt projectile and the stationary pressure bar were 12.7 mm in diameter and were also made of titanium alloy. The aluminum specimen was 4 mm in both height and diameter and was struck at 34.0 m/s by a 65 mm long projectile. The steel specimen was 1 mm in height and 6.35 mm in diameter and was struck at 75.8 m/s by a 50 mm long projectile. Both the “uncorrected forces” and the forces deconvoluted using the developed deconvolution method are plotted in Fig. 8(a) and (b), in which the “uncorrected forces” are the recorded strains multiplied directly by the Young’s modulus and the cross sectional area of the pressure bar. In each uncorrected force the effect of dispersion is clearly observed because it oscillates drastically. On the other hand, employment of the developed deconvolution method for dispersion correction of the force pulse not only gives a much sharper rise time, but the oscillation in the force is also much suppressed.

As shown in Fig. 8(a), even when the impact speed is lower and the specimen has greater height, the corrected force pulse still shows a much steeper slope in the rising part of the force. As the specimen moves into the plastic stage, the force pulse becomes much more flat. In this stage, the corrected force pulse is found to pass the mean of the oscillated signals. This is evidence that the developed method is very effective in correcting for the dispersion of propagated waves when the testing strain rate is as high as at several thousands  $s^{-1}$ .

When the impact speed is higher and the specimen is shorter in height, the cushion effect due to the existence of the specimen becomes much more reduced. In such a situation, the impact force should be much larger and the original dispersed signal is found to be completely out of phase when it is compared with the force pulse obtained by using the deconvolution method, as illustrated in Fig. 8(b). Thus, the developed method is considered to be essential for obtaining the actual impact force history when the test strain rate is in the range of several tens of thousands  $s^{-1}$ . In our recently completed work,<sup>15</sup> it was also shown that a meaningful stress-strain relationship can only be constructed when the force pulse is obtained by taking the dispersion effect into consideration.

### D. Applications to other impact events

As described in Sec. II, the developed method was claimed to be general. In order to demonstrate that the method can be applied to other impact conditions, another test run, which was to extract the impact force history exerted on a honeycomb-cored sandwich panel, is illustrated. Figure 9 shows the dimensions of the panel and locations of strain gauges. The panel was square with 302 mm in sides, the thickness was 14 mm, and the strain gauges were mounted on the impact side of the face plate at coordinates of  $G\#1:(30,0)$  mm,  $G\#2:(80,0)$  mm, and  $G\#3:(0,70)$  mm. These gauges were oriented in the  $x$ ,  $x$ , and  $y$  directions, respectively. The face plates were made of Fiberite 1076E T300/976 Graphite/epoxy laminates of  $[0/45/90/-45]_{2S}$  in the stacking sequence. The material properties of each lamina are:<sup>19</sup>

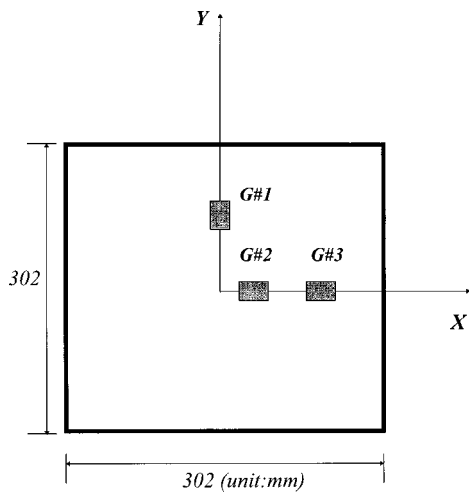


FIG. 9. Dimensions and strain gauge locations of a honeycomb-cored sandwich panel.

$$\begin{aligned}
 E_1 &= 121.6 \text{ Gpa}, & E_2 &= E_3 = 9.17 \text{ Gpa}, \\
 G_{12} &= G_{13} = 5.21 \text{ Gpa}, & G_{23} &= 3.22 \text{ Gpa}, \\
 \nu_{12} &= \nu_{13} = 0.29, & \nu_{23} &= 0.42, \\
 \rho &= 1553 \text{ Kg/m}^3,
 \end{aligned}
 \tag{17}$$

and the core was made of Hexcel CRIII-3.17-5052-0.0381-97.909-10.0 honeycomb.<sup>28</sup> These numerical numbers are cell size, aluminum type, thickness of the honeycomb wall, density, and the height of the core. The adhesive used to bond the face plates and the core was the Cyanamid epoxy type FM300K. This specimen was cured in an autoclave according to the manufacturer's fabrication procedure.

Figure 10(a) is the impact force,  $F^0$ , that was applied at (3,1) mm and was recorded using a PCB 086B01 SN6445 instrumented hammer. The corresponding strain responses,  $\epsilon^0$ , are plotted in Fig. 10(b) to (d) for gauge 1 to gauge 3, respectively. In order to extract the impact force,  $F$ , plotted in Fig. 11(a) and applied at the same location as the force shown in Fig. 10(a), the corresponding recorded strain signals are plotted in Fig. 11(b) to (d). Thus, in this example  $l$  is equal to 3 in using Eq. (5). The extracted impact force using the method developed in this study is also plotted in Fig. 11(a) as the darker curve. The agreement is considered to be very satisfactory. Because the Green's function for such a complicated structure is very difficult, if not impossible, to construct, the developed method is considered to be more general than the traditional Green's function method. Also, it is worthwhile noting that the strain signals recorded in Figs. 10 and 11 are both quite noisy. This further demonstrates that the developed method is applicable even when noises of a significant magnitude exist in the recorded signals.

## V. CONCLUSIONS

A deconvolution method has been successfully developed in this paper to retrieve impact force history from the corresponding responses of a waveguide or a structure having arbitrary configurations. In using this method, the traditional Green's function is essentially excluded in the formulation. Use of this developed method requires only a set of

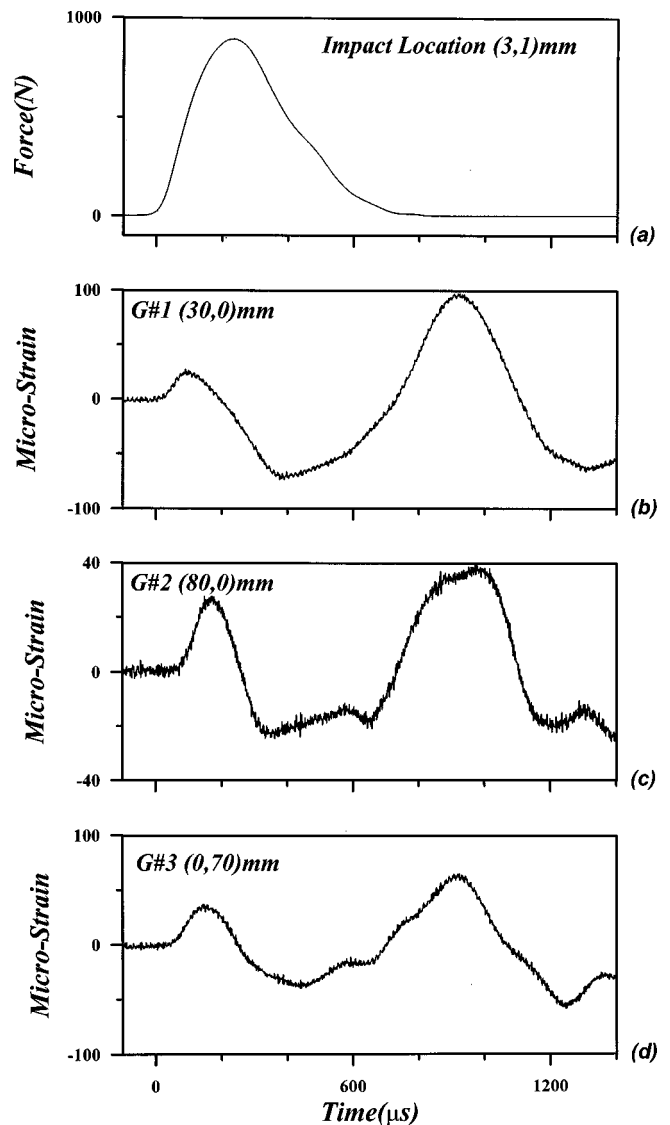


FIG. 10. The recorded (a) impact force ( $F^0$ ), and strain data ( $\epsilon^0$ ) at (b) gauge 1, (c) gauge 2, and (d) gauge 3 in a reference impact event.

known data from a reference impact run that includes impact force and the corresponding responses of the waveguides/structure. These are at the same locations as in the impact event in which the force is to be reconstructed. This set of known data can be obtained either from experiment or calculation as long as they have a wider frequency band than that of the impact force to be reconstructed. In this paper, the main applications has been to retrieve the impact force in a bar-to-bar impact event using the signals which are remote from the impact end. Due to experimental difficulties in recording the impact force with a wide enough frequency band, the response of an artificial force with a very short rise time has been obtained from theoretical calculation. Both the Love theory and the first mode of the Pochhammer-Chree frequency equation were employed to obtain the forward solution for axial impact of a bar. The forward solution obtained by using these two methods has been found to have a very good correlation even though the force pulse has a rise time on the order of  $1 \mu\text{s}$ .

A constrained optimization algorithm has been employed to bypass the annoying ill-posed problem in the de-

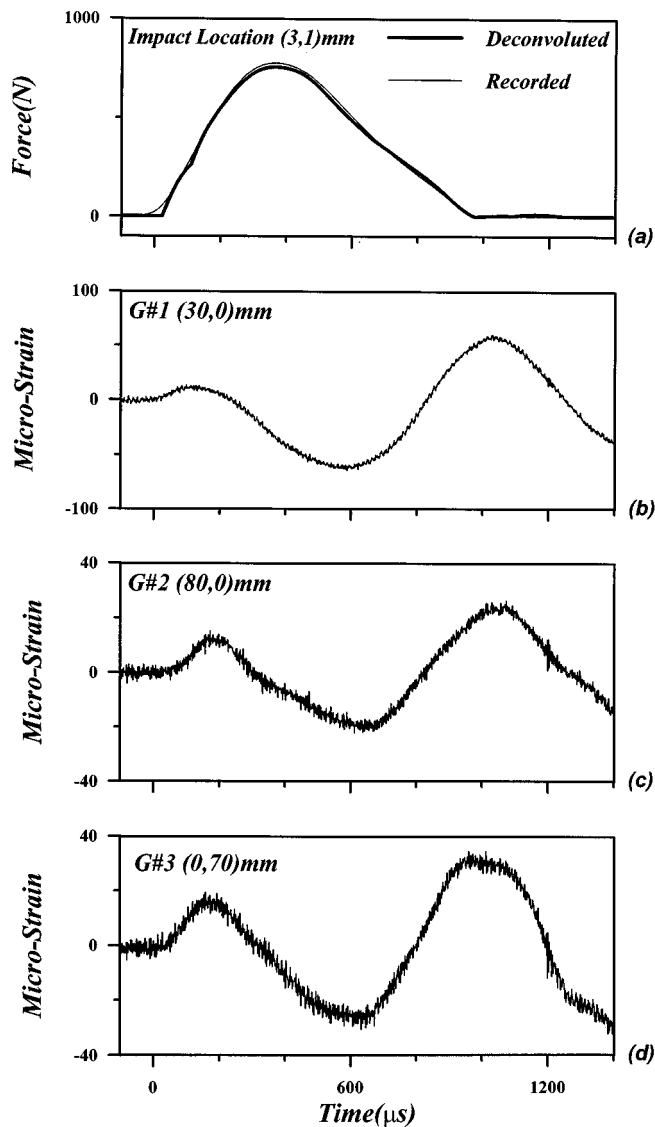


FIG. 11. (a) The recorded and the deconvoluted impact force ( $F$ ) using the data in Fig. 10 and the strain signals recorded from (b) gauge 1, (c) gauge 2, and (d) gauge 3 as the input data.

convolution process to search for the optimal force history. This developed deconvolution method has been verified both numerically and experimentally for impact of a slender bar at its one end, and the reconstructed force is found to be more reliable than the previously reported phase shift method in that the developed method is much less affected by noises when signals from multiple gauges are employed. The method has also been applied to high strain rate testing of materials. The force extracted from the distorted signals recorded remotely from the impact end of a pressure bar has a much shorter rise time and does not show the erroneous oscillation, as expected.

To demonstrate that the presented method is general, another example to determine the impact force acting on a honeycomb-cored sandwich panel using measured strain signals, instead of the calculated ones as in the bar impact problems, has also been illustrated. The agreement between the recorded and the deconvoluted impact force histories is considered to be very satisfactory. Because a theoretical Green's function is essentially impossible to construct in this impact

event due to the complicated geometry and material properties of the sandwich panel, the developed method is considered to be able to extract impact forces under general impact conditions.

## ACKNOWLEDGMENTS

This work was supported by the National Science Council of Taiwan, the Republic of China, under Contract Nos. NSC 85-2623-D-002-013 and NSC 86-2212-E-002-087.

- <sup>1</sup>R. M. Davies, "A critical study of the Hopkinson pressure bar," *Philos. Trans. R. Soc. London, Ser. A* **204**, 375–457 (1948).
- <sup>2</sup>Y. H. Pao and R. D. Mindlin, "Dispersion of flexural waves in an elastic, circular cylinder," *ASME J. Appl. Mech.* **27**, 513–520 (1960).
- <sup>3</sup>H. Kolsky, *Stress Wave in Solids* (Dover, New York, 1963).
- <sup>4</sup>K. F. Graff, *Wave Motions in Elastic Solids* (Dover, New York, 1975).
- <sup>5</sup>J. D. Achenbach, *Wave Propagation in Elastic Solids* (North-Holland, New York, 1973).
- <sup>6</sup>J. A. Zukas, T. Nicholas, H. F. Swift, L. B. Greszczuk, and D. Curran, *Impact Dynamics* (Wiley, New York, 1982), Chap. 8.
- <sup>7</sup>J. Oliver, "Elastic wave dispersion in a cylindrical rod by a wide-band short duration pulse technique," *J. Acoust. Soc. Am.* **29**, 189–194 (1957).
- <sup>8</sup>C. H. Yew and C. S. Chen, "Experimental study of dispersive waves in beam and rod using FFT," *ASME J. Appl. Mech.* **45**, 940–942 (1978).
- <sup>9</sup>P. S. Follansbee and C. Frantz, "Wave propagation in the split Hopkinson pressure bar," *ASME J. Eng. Mater. Technol.* **105**, 61–66 (1983).
- <sup>10</sup>D. A. Gorham, "A numerical method for the correction of dispersion in pressure bar signals," *J. Phys. E* **16**, 477–479 (1983).
- <sup>11</sup>J. C. Gong, L. E. Malvern, and D. A. Jenkins, "Dispersion investigation in the split Hopkinson pressure bar," *ASME J. Eng. Mater. Technol.* **112**, 309–314 (1990).
- <sup>12</sup>C. K. B. Lee and R. C. Crawford, "A new method for analyzing dispersed bar gauge data," *Meas. Sci. Technol.* **4**, 931–937 (1993).
- <sup>13</sup>J. M. Lifshitz and H. Leber, "Data processing in the split Hopkinson pressure bar tests," *Int. J. Impact Eng.* **15**, 723–733 (1994).
- <sup>14</sup>D. Bancroft, "The velocity of longitudinal wave in cylindrical bars," *Phys. Rev.* **59**, 588–593 (1941).
- <sup>15</sup>L.-H. Tseng, "An improved method for testing of material properties at higher strain rates," MS thesis, Institute of Applied Mechanics, National Taiwan University, Taiwan, ROC, 1995 (in Chinese).
- <sup>16</sup>K. B. Lin, "Testing of fracture strength of composites at higher strain rates," MS thesis, Institute of Applied Mechanics, National Taiwan University, Taiwan, ROC, 1996 (in Chinese).
- <sup>17</sup>E. Wu, J. C. Yeh, and C. S. Yen, "Impact on composite laminated plates: An inverse method," *Int. J. Impact Eng.* **14**, 417–433 (1994).
- <sup>18</sup>C. S. Yen and E. Wu, "On the inverse problems of rectangular plates subjected to elastic impact, Part 1: Method development and numerical verification," *ASME J. Appl. Mech.* **62**, 692–698 (1995).
- <sup>19</sup>C. S. Yen and E. Wu, "On the inverse problems of rectangular plates subjected to elastic impact, Part 2: Experimental verification and further applications," *ASME J. Appl. Mech.* **62**, 699–705 (1995).
- <sup>20</sup>E. Wu, J. C. Yeh, and C. S. Yen, "Identification of impact forces at multiple locations on laminated plates," *AIAA J.* **32**, 2433–2439 (1994).
- <sup>21</sup>E. Wu, T. D. Tsai, and C. S. Yen, "Two methods for determining impact force history on elastic plates," *Exp. Mech.* **35**, 11–18 (1995).
- <sup>22</sup>H. Inoue, K. Kishimoto, T. Shibuya, and T. Koizumi, "Estimation of impact load by inverse analysis," *JSME, Int. J. Series I* **35**, 420–427 (1992).
- <sup>23</sup>E. J. Haug and J. S. Arora, *Applied Optimal Design* (Wiley, New York, 1979).
- <sup>24</sup>A. E. H. Love, *A Treatise on the Mathematical Theory of Elasticity* (Dover, New York, 1944).
- <sup>25</sup>H. D. Conway and M. Jakubowski, "Axial impact of short cylindrical bars," *ASME J. Appl. Mech.* **36**, 809–813 (1969).
- <sup>26</sup>C. K. H. Dharan and F. E. Hauser, "Determination of stress-strain characteristics at very high strain rates," *Exp. Mech.* **10**, 370–376 (1970).
- <sup>27</sup>D. A. Gorham, P. H. Pope, and J. E. Field, "An improved method for compressive stress-strain measurement at very high strain rates," *Proc. R. Soc. London, Ser. A* **438**, 153–170 (1992).
- <sup>28</sup>E. Wu and W. S. Jiang, "Axial crush of metallic honeycombs," *Int. J. Impact Eng.* **19**, 439–456 (1997).

# Thickness vibrations of rotating piezoelectric plates

J. S. Yang and H. Fang

*Department of Engineering Mechanics University of Nebraska, Lincoln, Nebraska 68588*

Q. Jiang

*Department of Mechanical Engineering University of California, Riverside, California 92521*

(Received 17 April 1997; accepted for publication 29 May 1998)

Thickness vibrations of a piezoelectric plate rotating at a constant angular velocity about its normal are studied using the equations of linear piezoelectricity. The transcendental equation that determines the resonant frequencies is derived for materials with general anisotropy and solved for specific materials of polarized ceramics and rotated Y-cut quartz. The results are useful in the understanding and analysis of plate piezoelectric gyroscopes. © 1998 Acoustical Society of America. [S0001-4966(98)02609-5]

PACS numbers: 43.40.Dx, 43.38.Fx [CBB]

## INTRODUCTION

Piezoelectric materials can be used to make gyroscopes (angular rate sensors)<sup>1,2</sup> to measure the angular velocity of a rotating body. Piezoelectric gyroscopes make use of two modes of a vibrating piezoelectric body. In these two working modes material particles must move in perpendicular directions so that they are coupled by Coriolis force when the body is rotating. The natural frequencies of the two modes must be very close for the gyroscope to work at resonant conditions with optimal sensitivity. Examples include flexural vibrations of beams,<sup>3-6</sup> torsional and radial vibrations of circular cylindrical shells,<sup>7</sup> and thickness-shear vibrations of plates.<sup>8,9</sup> The analysis of piezoelectric gyroscopes is based on the dynamics of a linear piezoelectric body in a rotating frame. The equations for a piezoelectric body in a rotating frame can be obtained by adding Coriolis and centrifugal forces to the equations of linear piezoelectricity in an inertial frame. Then numerical analyses and analytical methods can be used to solve these equations. A rotated Y-cut quartz plate piezoelectric gyroscope is proposed in Ref. 8, which works with thickness-shear modes and is analyzed by finite element method. A ceramic plate thickness-shear piezoelectric gyroscope is suggested in Ref. 9 and is studied using Mindlin's two-dimensional equations for piezoelectric plates<sup>10</sup> in conjunction with a perturbation method. The perturbation method simplifies the analysis and clearly reveals the mechanism of piezoelectric gyroscopes. The analysis in Ref. 8 is numerical and that in Ref. 9 is analytical with an approximate and qualitative nature. For a better understanding of plate thickness-shear piezoelectric gyroscopes and an accurate prediction of their behavior, it is purposeful to study thickness vibrations of a rotating piezoelectric plate from the three-dimensional equations of linear piezoelectricity. Thickness vibrations of a stationary piezoelectric plate have been thoroughly studied<sup>11,12</sup> because of their important applications in piezoelectric resonators and filters. In this paper, thickness vibrations of a piezoelectric plate rotating at a constant angular velocity about its normal are studied using the equations of linear piezoelectricity. The solutions are useful in the understanding and design of plate piezoelectric gyroscopes. The transcendental equation that determines the reso-

nant frequencies is derived for materials with general anisotropy and is solved either analytically or numerically for polarized ceramics and rotated Y-cut quartz plates.

## I. PROPAGATION OF PLANE WAVES IN A ROTATING PIEZOELECTRIC BODY

For some basic understanding of the behavior of waves and vibrations of a rotating piezoelectric body we first consider the propagation of plane waves in such a body. The results will also be useful later in the study of thickness vibrations of rotating piezoelectric plates. Let a piezoelectric body be rotating about a fixed axis at a constant angular rate  $\Omega$ . Without loss of generality we orient the  $x_3$  axis of our Cartesian coordinate system along the rotation axis. Then the angular velocity vector has only one nontrivial component  $(0,0,\Omega)$ . The coordinate system is fixed to the body and is rotating together with it. We consider small vibrations of the body in the rotating frame. Let  $u_i$  be the mechanical displacement of the piezoelectric body,  $\rho$  the mass density,  $T_{ij}$  the stress tensor, and  $D_i$  the electric displacement vector. All quantities are with respect to the rotating frame. Cartesian tensor notation, the summation convention for repeated tensor indices and the convention that a comma followed by an index denotes partial differentiation with respect to the coordinate associated with the index are used. A superimposed dot represents time derivative. The equations of motion and the electrostatic equation for a linear piezoelectric body rotating about the  $x_3$  axis can be written as

$$\begin{aligned} T_{j1,j} &= \rho(\ddot{u}_1 - 2\Omega\dot{u}_2), & T_{j2,j} &= \rho(\ddot{u}_2 + 2\Omega\dot{u}_1), \\ T_{j3,j} &= \rho\ddot{u}_3, & D_{i,i} &= 0, \end{aligned} \quad (1)$$

where we have included the Coriolis force but neglected the centrifugal force. This is because piezoelectric gyroscopes are very small devices with sizes in the order of 1–2 cm and resonant frequencies of 10 k–100 kHz. The angular velocity  $\Omega$  to be measured is much smaller than the resonant frequencies of the working modes of the gyroscopes. In this situation the Coriolis force which is linear in  $\Omega$  is responsible for the sensing mechanism of the gyroscopes but the centrifugal force which is quadratic in  $\Omega$  is very small and can be ne-

glected. We note that the Coriolis force terms are linear in velocity, which resembles damping terms but in fact the system is not dissipative because Coriolis force is always perpendicular to velocity and does not do work in the motion. For (1) we have the following constitutive relations<sup>12</sup>

$$T_{ij} = c_{ijkl} S_{kl} - e_{kij} E_k, \quad D_i = e_{ijk} S_{jk} + \epsilon_{ij} E_j, \quad (2)$$

where

$$S_{ij} = \frac{1}{2}(u_{i,j} + u_{j,i}), \quad E_i = -\phi_{,i}. \quad (3)$$

In (2)–(3)  $S_{ij}$  is the strain tensor,  $E_i$  the electric field vector, and  $\phi$  the electric potential.  $c_{ijkl}$ ,  $e_{kij}$ , and  $\epsilon_{ij}$  are the elastic, piezoelectric, and dielectric tensors which are material properties. With the compressed matrix notation,<sup>12</sup> the material constants in the most general case can be represented by the following matrices

$$\begin{pmatrix} c_{11} & c_{12} & c_{13} & c_{14} & c_{15} & c_{16} \\ c_{21} & c_{22} & c_{23} & c_{24} & c_{25} & c_{26} \\ c_{31} & c_{32} & c_{33} & c_{34} & c_{35} & c_{36} \\ c_{41} & c_{42} & c_{43} & c_{44} & c_{45} & c_{46} \\ c_{51} & c_{52} & c_{53} & c_{54} & c_{55} & c_{56} \\ c_{61} & c_{62} & c_{63} & c_{64} & c_{65} & c_{66} \end{pmatrix}, \begin{pmatrix} e_{11} & e_{21} & e_{31} \\ e_{12} & e_{22} & e_{32} \\ e_{13} & e_{23} & e_{33} \\ e_{14} & e_{24} & e_{34} \\ e_{15} & e_{25} & e_{35} \\ e_{16} & e_{26} & e_{36} \end{pmatrix}, \quad (4)$$

$$\begin{pmatrix} \epsilon_{11} & \epsilon_{12} & \epsilon_{13} \\ \epsilon_{21} & \epsilon_{22} & \epsilon_{23} \\ \epsilon_{31} & \epsilon_{32} & \epsilon_{33} \end{pmatrix},$$

where the elastic and dielectric matrices are symmetric. For the special purpose of this work on plate piezoelectric gyroscopes, we consider plane waves propagating in the  $x_3$  direction with  $\partial_1 = \partial_2 = 0$ . Then from (1)<sub>4</sub>, with the related equations in (2)–(4), we obtain

$$D_{3,3} = (e_{33}u_{3,3} + e_{34}u_{2,3} + e_{35}u_{1,3} - \epsilon_{33}\phi_{,3})_{,3} = 0, \quad (5)$$

which implies

$$D_3 = e_{33}u_{3,3} + e_{34}u_{2,3} + e_{35}u_{1,3} - \epsilon_{33}\phi_{,3} = -\epsilon_{33}L_1, \quad (6)$$

where  $L_1$  is an integration constant which may depend on time  $t$ . Integrating (6) once more we have

$$\phi = \frac{e_{35}}{\epsilon_{33}} u_1 + \frac{e_{34}}{\epsilon_{33}} u_2 + \frac{e_{33}}{\epsilon_{33}} u_3 + L_1 x_3 + L_2, \quad (7)$$

where  $L_2$  is another integration constant. Substituting (7) into the relevant equations in (2)–(4) we obtain

$$\begin{aligned} T_{31} &= \bar{c}_{55}u_{1,3} + \bar{c}_{54}u_{2,3} + \bar{c}_{53}u_{3,3} + e_{35}L_1, \\ T_{32} &= \bar{c}_{45}u_{1,3} + \bar{c}_{44}u_{2,3} + \bar{c}_{43}u_{3,3} + e_{34}L_1, \\ T_{33} &= \bar{c}_{35}u_{1,3} + \bar{c}_{34}u_{2,3} + \bar{c}_{33}u_{3,3} + e_{33}L_1, \end{aligned} \quad (8)$$

where

$$\begin{aligned} \bar{c}_{33} &= c_{33} + e_{33}e_{33}/\epsilon_{33}, & \bar{c}_{34} &= c_{34} + e_{33}e_{34}/\epsilon_{33}, \\ \bar{c}_{35} &= c_{35} + e_{33}e_{35}/\epsilon_{33}, & \bar{c}_{44} &= c_{44} + e_{34}e_{34}/\epsilon_{33}, \\ \bar{c}_{45} &= c_{45} + e_{34}e_{35}/\epsilon_{33}, & \bar{c}_{55} &= c_{55} + e_{35}e_{35}/\epsilon_{33}, \end{aligned} \quad (9)$$

are the piezoelectrically stiffened elastic constants. The substitution of (8) into (1)<sub>1–3</sub> yields the displacement equations of motion

$$\begin{aligned} \bar{c}_{55}u_{1,33} + \bar{c}_{54}u_{2,33} + \bar{c}_{53}u_{3,33} &= \rho(\ddot{u}_1 - 2\Omega\dot{u}_2), \\ \bar{c}_{45}u_{1,33} + \bar{c}_{44}u_{2,33} + \bar{c}_{43}u_{3,33} &= \rho(\ddot{u}_2 + 2\Omega\dot{u}_1), \\ \bar{c}_{35}u_{1,33} + \bar{c}_{34}u_{2,33} + \bar{c}_{33}u_{3,33} &= \rho\ddot{u}_3. \end{aligned} \quad (10)$$

We consider the following plane wave solution

$$u_i = A_i e^{i(kx_3 + \omega t)}, \quad (11)$$

where  $A_i$  are constants which may be complex but we consider the case when  $k$  and  $\omega$  are both real. Substitution of (11) into (10) results in the following homogeneous system of linear algebraic equations for  $A_i$

$$\begin{aligned} (\rho\omega^2 - \bar{c}_{55}k^2)A_1 + (2i\rho\omega\Omega - \bar{c}_{45}k^2)A_2 - \bar{c}_{35}k^2A_3 &= 0, \\ (-2i\rho\omega\Omega - \bar{c}_{45}k^2)A_1 + (\rho\omega^2 - \bar{c}_{44}k^2)A_2 - \bar{c}_{34}k^2A_3 &= 0, \\ -\bar{c}_{35}k^2A_1 - \bar{c}_{34}k^2A_2 + (\rho\omega^2 - \bar{c}_{33}k^2)A_3 &= 0. \end{aligned} \quad (12)$$

For nontrivial solutions the determinant of the coefficient matrix of the above system of linear equations must vanish. This leads to the following dispersion relation

$$\begin{aligned} (\rho\omega^2 - \bar{c}_{33}k^2)(\rho\omega^2 - \bar{c}_{44}k^2)(\rho\omega^2 - \bar{c}_{55}k^2) - 2\bar{c}_{34}\bar{c}_{35}\bar{c}_{45}k^6 \\ - \bar{c}_{45}^2k^4(\rho\omega^2 - \bar{c}_{33}k^2) - \bar{c}_{35}^2k^4(\rho\omega^2 - \bar{c}_{44}k^2) \\ - \bar{c}_{34}^2k^4(\rho\omega^2 - \bar{c}_{55}k^2) \\ = 4\rho^2\omega^2\Omega^2(\rho\omega^2 - \bar{c}_{33}k^2). \end{aligned} \quad (13)$$

The term on the right-hand side of (13) is due to the rotation of the body. When the body is not rotating, this term is not present and (13) yields three real positive roots  $\omega = \omega(k)$  or  $k = k(\omega)$  which are linear and homogeneous functions. Hence the waves are not dispersive.<sup>12</sup> The three roots represent a quasi-longitudinal wave for which  $\bar{c}_{33}$  is the major elastic constant and two quasi-transverse waves for which  $\bar{c}_{44}$  and  $\bar{c}_{55}$  are important. When the body is rotating, for the quasi-longitudinal wave material particles move mainly in the  $x_3$  direction and do not cause much Coriolis force. The two quasi-transverse waves are directly coupled by the Coriolis force, in addition to possible couplings by elastic constants. It can be expected that (13) will still have three real positive roots when  $\Omega$  is very small. However, because of the right-hand side term in (13) the waves are clearly dispersive now. The left-hand side of (13) is a polynomial of degree six while the right-hand side of degree four. For very large  $\omega$ , the right-hand side term in (13) has little contribution and the behavior of the dispersion relations is like those of a nonrotating body. We can obtain an approximate expression of the dispersion relations when  $\Omega \ll \omega$ . Denoting the three wave speeds when the piezoelectric body is not rotating by  $v_1$ ,  $v_2$ , and  $v_3$ , also denoting  $v = \omega/k$  and  $v_{30}^2 = \bar{c}_{33}/\rho$ , then (13) can be written as

$$(v^2 - v_1^2)(v^2 - v_2^2)(v^2 - v_3^2) = 4 \frac{\Omega^2}{k^2} v^2 (v^2 - v_{30}^2). \quad (14)$$

Since  $\Omega$  is very small, the dispersion relations when the piezoelectric body is not rotating are perturbed by small quantities. For example, denoting  $\nu^2 - \nu_1^2 = \Delta$  where  $\Delta$  is a small quantity compared to  $\nu^2$ , substituting  $\nu^2 = \nu_1^2 + \Delta$  into (14) and keeping the lowest order terms, we can determine  $\Delta$  and obtain an approximation of the dispersion relation when the piezoelectric body is rotating. Similarly, we can obtain approximations for the other two branches of the dispersion relations. The results are

$$\begin{aligned}\omega^2 &\approx \nu_1^2 k^2 + 4\Omega^2 \frac{\nu_1^2(\nu_1^2 - \nu_{30}^2)}{(\nu_1^2 - \nu_2^2)(\nu_1^2 - \nu_3^2)}, \\ \omega^2 &\approx \nu_2^2 k^2 + 4\Omega^2 \frac{\nu_2^2(\nu_2^2 - \nu_{30}^2)}{(\nu_2^2 - \nu_1^2)(\nu_2^2 - \nu_3^2)}, \\ \omega^2 &\approx \nu_3^2 k^2 + 4\Omega^2 \frac{\nu_3^2(\nu_3^2 - \nu_{30}^2)}{(\nu_3^2 - \nu_1^2)(\nu_3^2 - \nu_2^2)},\end{aligned}\quad (15)$$

which are clearly dispersive. Equations (15) represent hyperbolas with the dispersion curves of the nonrotating body as asymptotes.

For each specific root of (13), the normalized amplitude ratios can be obtained from (12) and are denoted by

$$(A_1^{(i)} : A_2^{(i)} : A_3^{(i)}) = (\beta_1^{(i)} : \beta_2^{(i)} : \beta_3^{(i)}), \quad i = 1, 2, 3. \quad (16)$$

Then the following general wave type functions are also solutions to (10)

$$\begin{aligned}u_j &= \sum_{i=1}^3 B^{(i)} \beta_j^{(i)} e^{i(k^{(i)}x_3 + \omega t)}, \\ \phi &= \sum_{i=1}^3 B^{(i)} \alpha^{(i)} e^{i(k^{(i)}x_3 + \omega t)} + L_1 x_3 e^{i\omega t} + L_2 e^{i\omega t},\end{aligned}\quad (17)$$

where  $B^{(i)}$  are arbitrary constants,  $k^{(i)}(\omega)$  is the  $i$ th of the three roots of (13), and

$$\alpha^{(i)} = \frac{e_{35}}{\epsilon_{33}} \beta_1^{(i)} + \frac{e_{34}}{\epsilon_{33}} \beta_2^{(i)} + \frac{e_{33}}{\epsilon_{33}} \beta_3^{(i)}. \quad (18)$$

The integration constants in (17) differ from those in (7) in that the time dependence is explicitly harmonic. We note that there can also be waves with  $e^{i(-kx_3 + \omega t)}$  dependence.

## II. THICKNESS VIBRATIONS OF ROTATING PIEZOELECTRIC PLATES

We now study the free vibration of a rotating piezoelectric plate bounded by two major surfaces at  $x_3 = \pm h$ . By thickness vibration we mean that the vibration depends on the plate thickness coordinate  $x_3$  and time  $t$  only, and is independent of the in-plane coordinates  $x_1$  and  $x_2$ . Thickness vibrations are related to plane waves traveling between the two major surfaces of the plate. Corresponding to the one quasi-longitudinal wave and two quasi-transverse waves, there are three types of modes for thickness vibrations. One is an essentially thickness-stretch vibration and the other two are essentially thickness-shear vibrations. We consider traction-free mechanical boundary conditions  $T_{3j}(\pm h) = 0$ .

We will discuss several cases of electrical boundary conditions, which will become clear later. First we consider the anti-symmetric free vibration modes

$$u_i = A_i \sin kx_3 e^{i\omega t}. \quad (19)$$

Then in a procedure similar to (11)–(17) we have the following solutions to (10)

$$\begin{aligned}u_j &= \sum_{i=1}^3 B^{(i)} \beta_j^{(i)} \sin k^{(i)} x_3 e^{i\omega t}, \\ \phi &= \sum_{i=1}^3 B^{(i)} \alpha^{(i)} \sin k^{(i)} x_3 e^{i\omega t} + L_1 x_3 e^{i\omega t} + L_2 e^{i\omega t}.\end{aligned}\quad (20)$$

For plates, (20) still needs to satisfy appropriate boundary conditions. To apply boundary conditions we need, from (6), (8), and (20)<sub>1</sub>, the following expressions

$$\begin{aligned}D_3 &= -\epsilon_{33} L_1 e^{i\omega t}, \\ T_{31} &= \sum_{i=1}^3 B^{(i)} \gamma_1^{(i)} k^{(i)} \cos k^{(i)} x_3 e^{i\omega t} + e_{35} L_1 e^{i\omega t}, \\ T_{32} &= \sum_{i=1}^3 B^{(i)} \gamma_2^{(i)} k^{(i)} \cos k^{(i)} x_3 e^{i\omega t} + e_{34} L_1 e^{i\omega t}, \\ T_{33} &= \sum_{i=1}^3 B^{(i)} \gamma_3^{(i)} k^{(i)} \cos k^{(i)} x_3 e^{i\omega t} + e_{33} L_1 e^{i\omega t},\end{aligned}\quad (21)$$

where

$$\begin{aligned}\gamma_1^{(i)} &= \bar{c}_{55} \beta_1^{(i)} + \bar{c}_{45} \beta_2^{(i)} + \bar{c}_{35} \beta_3^{(i)}, \\ \gamma_2^{(i)} &= \bar{c}_{45} \beta_1^{(i)} + \bar{c}_{44} \beta_2^{(i)} + \bar{c}_{34} \beta_3^{(i)}, \\ \gamma_3^{(i)} &= \bar{c}_{35} \beta_1^{(i)} + \bar{c}_{34} \beta_2^{(i)} + \bar{c}_{33} \beta_3^{(i)}.\end{aligned}\quad (22)$$

There is a similar set of symmetric solutions to (10) with

$$\begin{aligned}u_j &= \sum_{i=1}^3 B^{(i)} \beta_j^{(i)} \cos k^{(i)} x_3 e^{i\omega t}, \\ \phi &= \sum_{i=1}^3 B^{(i)} \alpha^{(i)} \cos k^{(i)} x_3 e^{i\omega t} + L_1 x_3 + L_2,\end{aligned}\quad (23)$$

and stress, electric displacement components as

$$\begin{aligned}D_3 &= -\epsilon_{33} L_1 e^{i\omega t}, \\ T_{31} &= \sum_{i=1}^3 -B^{(i)} \gamma_1^{(i)} k^{(i)} \sin k^{(i)} x_3 e^{i\omega t} + e_{35} L_1 e^{i\omega t}, \\ T_{32} &= \sum_{i=1}^3 -B^{(i)} \gamma_2^{(i)} k^{(i)} \sin k^{(i)} x_3 e^{i\omega t} + e_{34} L_1 e^{i\omega t}, \\ T_{33} &= \sum_{i=1}^3 -B^{(i)} \gamma_3^{(i)} k^{(i)} \sin k^{(i)} x_3 e^{i\omega t} + e_{33} L_1 e^{i\omega t}.\end{aligned}\quad (24)$$

### A. Unelectroded plates or plates with open electrodes

First we consider the cases when the two major surfaces of the plate are both unelectroded or with open electrodes. In all these cases the electrical boundary condition requires  $D_3(\pm h) = 0$  which implies  $L_1 = 0$  from (6). For anti-

symmetric modes from (21) it can be seen that when  $L_1 = 0$  the traction-free boundary conditions require

$$\begin{aligned} \sum_{i=1}^3 B^{(i)} \gamma_1^{(i)} k^{(i)} \cos k^{(i)} h &= 0, \\ \sum_{i=1}^3 B^{(i)} \gamma_2^{(i)} k^{(i)} \cos k^{(i)} h &= 0, \\ \sum_{i=1}^3 B^{(i)} \gamma_3^{(i)} k^{(i)} \cos k^{(i)} h &= 0. \end{aligned} \quad (25)$$

For nontrivial solutions of  $B^{(i)}$  the determinant of the coefficient matrix must vanish which is equivalent to

$$\cos k^{(1)} h \cos k^{(2)} h \cos k^{(3)} h = 0, \quad (26)$$

or

$$k_{(n)}^{(i)} h = \frac{n\pi}{2}, \quad n = 1, 3, 5, \dots, \quad (27)$$

which is the frequency equation for the anti-symmetric modes. Similarly, for symmetric modes from (24) we have

$$\sin k^{(1)} h \sin k^{(2)} h \sin k^{(3)} h = 0,$$

$$k_{(n)}^{(i)} h = \frac{n\pi}{2}, \quad n = 2, 4, 6, \dots \quad (28)$$

## B. Plates with shorted electrodes

We now consider the case when the two major surfaces of the plate are electroded and shorted with  $\phi(h) = \phi(-h)$ . For anti-symmetric modes from (20)<sub>2</sub> and (21)<sub>2-4</sub> we have

$$\begin{aligned} \sum_{i=1}^3 B^{(i)} \gamma_1^{(i)} k^{(i)} \cos k^{(i)} h + e_{35} L_1 &= 0, \\ \sum_{i=1}^3 B^{(i)} \gamma_2^{(i)} k^{(i)} \cos k^{(i)} h + e_{34} L_1 &= 0, \\ \sum_{i=1}^3 B^{(i)} \gamma_3^{(i)} k^{(i)} \cos k^{(i)} h + e_{33} L_1 &= 0, \\ \sum_{i=1}^3 B^{(i)} \alpha^{(i)} \sin k^{(i)} h + L_1 h &= 0. \end{aligned} \quad (29)$$

For nontrivial solutions of  $B^{(i)}$  and/or  $L_1$  we must have

$$\begin{vmatrix} \gamma_1^{(1)} k^{(1)} \cos k^{(1)} h & \gamma_1^{(2)} k^{(2)} \cos k^{(2)} h & \gamma_1^{(3)} k^{(3)} \cos k^{(3)} h & e_{35} \\ \gamma_2^{(1)} k^{(1)} \cos k^{(1)} h & \gamma_2^{(2)} k^{(2)} \cos k^{(2)} h & \gamma_2^{(3)} k^{(3)} \cos k^{(3)} h & e_{34} \\ \gamma_3^{(1)} k^{(1)} \cos k^{(1)} h & \gamma_3^{(2)} k^{(2)} \cos k^{(2)} h & \gamma_3^{(3)} k^{(3)} \cos k^{(3)} h & e_{33} \\ \alpha^{(1)} \sin k^{(1)} h & \alpha^{(2)} \sin k^{(2)} h & \alpha^{(3)} \sin k^{(3)} h & h \end{vmatrix} = 0, \quad (30)$$

which is the frequency equation for the anti-symmetric modes. For symmetric modes, from (23) and (24) the frequency equation is found to be exactly the same as (28).

## III. PLATES OF POLARIZED CERAMICS

We now consider a ceramic plate poled in the  $x_3$  direction. The material matrices are<sup>12</sup>

$$\begin{pmatrix} c_{11} & c_{12} & c_{13} & 0 & 0 & 0 \\ c_{21} & c_{11} & c_{13} & 0 & 0 & 0 \\ c_{31} & c_{31} & c_{33} & 0 & 0 & 0 \\ 0 & 0 & 0 & c_{44} & 0 & 0 \\ 0 & 0 & 0 & 0 & c_{44} & 0 \\ 0 & 0 & 0 & 0 & 0 & c_{66} \end{pmatrix}, \begin{pmatrix} 0 & 0 & e_{31} \\ 0 & 0 & e_{31} \\ 0 & 0 & e_{33} \\ 0 & e_{15} & 0 \\ e_{15} & 0 & 0 \\ 0 & 0 & 0 \end{pmatrix}, \begin{pmatrix} \epsilon_{11} & 0 & 0 \\ 0 & \epsilon_{11} & 0 \\ 0 & 0 & \epsilon_{33} \end{pmatrix}. \quad (31)$$

Equations (6)–(8) and (10) reduce to the following two sets of uncoupled equations of thickness-stretch

$$\begin{aligned} \bar{c}_{33} u_{3,33} &= \rho \ddot{u}_3, \quad T_{33} = \bar{c}_{33} u_{3,3} + e_{33} L_1, \\ \phi &= \frac{e_{33}}{\epsilon_{33}} u_3 + L_1 x_3 + L_2, \end{aligned} \quad (32)$$

$$D_3 = e_{33} u_{3,3} - \epsilon_{33} \phi_{,3} = -\epsilon_{33} L_1,$$

and thickness-shear

$$\begin{aligned} c_{44} u_{1,33} &= \rho (\ddot{u}_1 - 2\Omega \dot{u}_2), \\ c_{44} u_{2,33} &= \rho (\ddot{u}_2 + 2\Omega \dot{u}_1), \\ T_{31} &= c_{44} u_{1,3}, \quad T_{32} = c_{44} u_{2,3}. \end{aligned} \quad (33)$$

The dispersion relation (13) now takes the following factored form

$$(\rho \omega^2 - \bar{c}_{33} k^2)(\rho \omega^2 - c_{44} k^2)^2 = 4\rho^2 \omega^2 \Omega^2 (\rho \omega^2 - \bar{c}_{33} k^2). \quad (34)$$

Equations (32)–(34) show that there exist two uncoupled types of vibrations. One is the thickness-stretch motion of  $u_3$  and  $\phi$ , the other is the thickness-shear motion of  $u_1$  and  $u_2$ . The common factor of both sides of (34) is the longitudinal or thickness-stretch branch of the dispersion relation

$$\omega = \sqrt{\frac{\bar{c}_{33}}{\rho}} k, \quad (35)$$

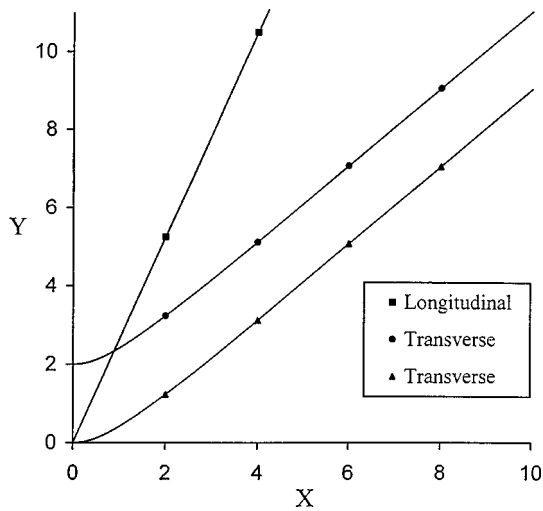


FIG. 1. Dispersion curves of plane waves in a rotating ceramic body from (37).  $X = \sqrt{c_{44}/\rho}k/\Omega$ ,  $Y = \omega/\Omega$ .

which can also be obtained from (32) directly. This branch is nondispersive. From (32) it can be seen that thickness-stretch is coupled to the electric field  $E_3 = -\phi_{,3}$  but it is not affected by the rotation of the plate. The other two branches are the transverse or thickness-shear branches, which can be found from (34) or (33) as

$$\omega = \sqrt{\frac{c_{44}}{\rho}k^2 + \Omega^2} \mp \Omega. \quad (36)$$

From (33) we see that thickness-shears are not coupled to the normal electric field  $E_3$ . However, they can be excited by lateral electric fields  $E_1$  or  $E_2$  and can be used as the working modes of plate piezoelectric gyroscopes.<sup>9</sup> These two thickness-shear branches are clearly dispersive and are affected by the rotation of the plate. The procedure used in obtaining (15) from (13) leads to the exact dispersion relations (36) in this special case. The dispersion relations (35)–(36) can be written in the following dimensionless form

$$Y = \sqrt{\frac{c_{33}}{c_{44}}}X, \quad Y = \sqrt{1+X^2} - 1, \quad Y = \sqrt{1+X^2} + 1, \quad (37)$$

$$X = \sqrt{\frac{c_{44}}{\rho}}\frac{k}{\Omega}, \quad Y = \frac{\omega}{\Omega}.$$

As an example, for PZT-5H, we have<sup>13</sup>

$$\begin{aligned} c_{11} &= 12.6, & c_{33} &= 11.7, & c_{44} &= 2.30, \\ c_{12} &= 7.95, & c_{13} &= 8.41 \times 10^{10} \text{ N/m}^2, \\ c_{66} &= (c_{11} - c_{12})/2, \\ e_{15} &= 17.0, & e_{31} &= -6.5, & e_{33} &= 23.3 \text{ C/m}^2, \\ \epsilon_{11} &= 1700\epsilon_0, & \epsilon_{33} &= 1470\epsilon_0, \\ \epsilon_0 &= 8.854 \times 10^{-12} \text{ farads/m}, \\ \bar{c}_{33} &= 15.87, & \sqrt{\bar{c}_{33}/c_{44}} &= 2.63, & \rho &= 7500 \text{ kg/m}^3. \end{aligned} \quad (38)$$

Therefore for PZT-5H the thickness-stretch dispersion relation (37)<sub>1</sub> becomes  $Y = 2.63X$ .

Dispersion relations from (37) are plotted in Fig. 1. The

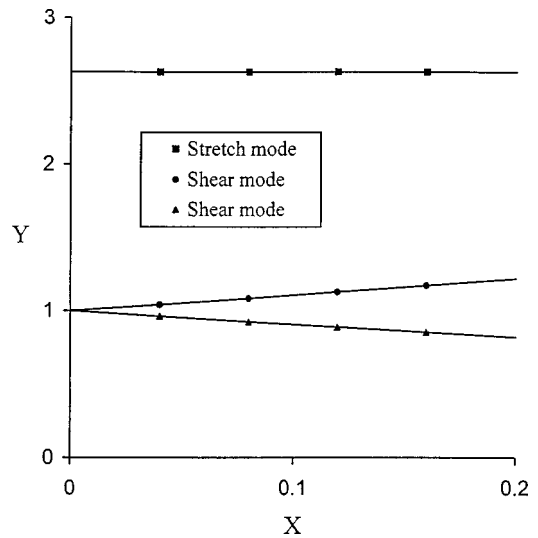


FIG. 2. Lowest thickness vibration frequencies of a rotating ceramic plate from (42) for  $n=1$  and from (50).  $X = \Omega/\omega_1$ ,  $Y = \omega/\omega_1$ .

dispersion due to rotation and the large  $\omega$  behavior can be seen clearly. We note that for small  $\omega$  the assumption that  $\omega \gg \Omega$  is not true. Therefore an accurate prediction of the behavior of the dispersion curves for small  $\omega$  requires the consideration of the centrifugal force. This is not relevant to the particular application of piezoelectric gyroscopes considered in this paper.

### A. Thickness-shear modes

Corresponding to the two dispersion relations in (36), the following two sets of anti-symmetric thickness-shear modes can be found from (33), respectively

$$u_1 = \sin kx_3 \sin \omega t, \quad u_2 = -\sin kx_3 \cos \omega t, \quad (39)$$

and

$$u_1 = \sin kx_3 \sin \omega t, \quad u_2 = \sin kx_3 \cos \omega t, \quad (40)$$

with the frequency equation

$$\cos kh = 0, \quad k_{(n)}h = \frac{n\pi}{2}, \quad n = 1, 3, 5, \dots \quad (41)$$

The frequencies of the two modes given by (39) and (40) are determined from the two dispersion relations in (36), respectively. Hence the two modes have different frequencies for the same  $k$

$$\omega_{(n)} = \sqrt{\omega_n^2 + \Omega^2} \mp \Omega, \quad n = 1, 3, 5, \dots, \quad (42)$$

$$\omega_n^2 = \frac{c_{44}\pi^2}{4\rho h^2} n^2,$$

where  $\omega_n$  are the thickness-shear resonant frequencies of a nonrotating plate.

Frequencies predicted by (42) are plotted in Fig. 2 for small values of  $\Omega$  and  $n=1$ , where  $\omega_{(1)}$  and  $\Omega$  are normalized by the fundamental thickness-shear frequency  $\omega_1$  of a nonrotating plate. It is seen that  $\Omega$  causes the two shear frequencies to split. The  $\Omega$  dependence of the shear mode frequencies is important in gyroscope design where the fre-



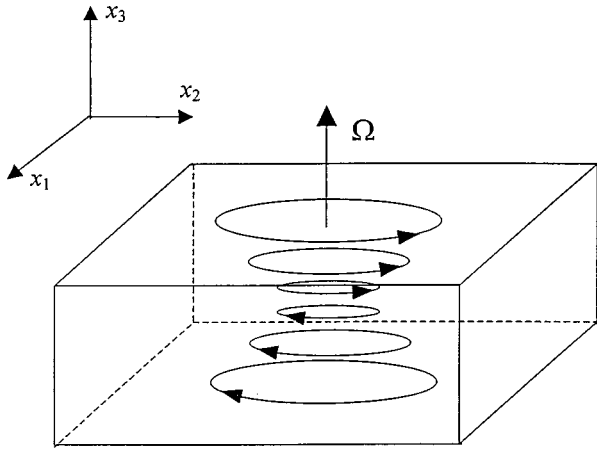


FIG. 3. Mode shape of a rotating ceramic plate in thickness-shear vibration from (39).

quencies of the lowest two shear modes have to be predicted accurately and tuned very close to each other so that the gyroscope will work at resonant conditions with maximum sensitivity. The dependence of resonant frequencies on  $\Omega$  was neglected in the approximate analysis in Ref. 9.

Different from the case when the plate is not rotating where the two thickness-shear modes in the  $x_1$  and  $x_2$  directions are not coupled and material particles move in straight lines, now the shears in both directions are coupled as a result of the Coriolis force and material particles now move in planar circles with radii depending on  $x_3$  (Fig. 3). The middle plane of the plate is also the nodal plane of this shear mode where material particles do not move. This suggests that for plate thickness-shear gyroscopes the finite vibrating plate can be mounted at the edges near the middle plane so that the shear vibration of the plate will not be affected. We note that for the modes described by (39) and (40) material particles are moving in opposite directions, counterclockwise in one type of modes and clockwise in the other when looked from the positive  $x_3$  direction.

Similarly, there exist two sets of symmetric modes of (33) corresponding to the two branches of dispersion relations in (36)

$$u_1 = \cos kx_3 \sin \omega t, \quad u_2 = -\cos kx_3 \cos \omega t, \quad (43)$$

and

$$u_1 = \cos kx_3 \sin \omega t, \quad u_2 = \cos kx_3 \cos \omega t, \quad (44)$$

with the frequency equation

$$\sin kh = 0, \quad k_{(n)}h = \frac{n\pi}{2}, \quad n = 2, 4, 6, \dots \quad (45)$$

The frequencies have the same expression as (42) except that  $n$  assumes even numbers now.

As a comparison, we now compute the frequency of the fundamental thickness-shear mode from the two-dimensional plate equations by Mindlin<sup>10</sup> which assume the following form when Coriolis force is included

$$-3b^{-2}\kappa^2 c_{44}u_1^{(1)} = \rho\ddot{u}_1^{(1)} - 2\rho\Omega\dot{u}_2^{(1)}, \quad (46)$$

$$-3b^{-2}\kappa^2 c_{44}u_2^{(1)} = \rho\ddot{u}_2^{(1)} + 2\rho\Omega\dot{u}_1^{(1)},$$

where  $\kappa^2 = \pi^2/12$  is the shear correction factor. We seek solutions in the form

$$u_1^{(1)} = Ae^{i\omega t}, \quad u_2^{(1)} = Be^{i\omega t}. \quad (47)$$

Substitution of (47) into (46) results in two linear homogeneous equations for  $A$  and  $B$ . For nontrivial solutions the determinant of the coefficient matrix must vanish, which leads to a frequency equation whose solution is exactly (42) for  $n=1$ . Thus for the fundamental thickness-shear mode, the three-dimensional equations and the two-dimensional plate equations yield the same frequency. It is well known that Mindlin's plate equations can predict correct shear frequencies for a nonrotating plate with the help of shear correction factors. The above shows that the plate equation can also yield correct shear frequencies when the plate is rotating.

### B. Thickness-stretch modes

As it is seen from (32), the thickness-stretch modes are electrically coupled but are not affected by the rotation of the plate. Material particles are in linear motion in the  $x_3$  direction. This case was treated in Ref. 11. For completeness we summarize the results below.

When the plate is unelectroded or with open electrodes, from (32) we have the following anti-symmetric and symmetric modes

$$u_3 = \sin kx_3 e^{i\omega t}, \quad k_{(n)}h = \frac{n\pi}{2}, \quad n = 1, 3, 5, \dots, \quad (48)$$

and

$$u_3 = \cos kx_3 e^{i\omega t}, \quad k_{(n)}h = \frac{n\pi}{2}, \quad n = 2, 4, 6, \dots, \quad (49)$$

with  $\omega$  determined from (35).

When the major surfaces of the plate are electroded and shorted, from (32) we have, for the anti-symmetric modes

$$u_3 = \sin kx_3 e^{i\omega t}, \quad \tan kh = \frac{e_{33}^2}{\epsilon_{33}c_{33}} kh. \quad (50)$$

For symmetric modes from (32) we have

$$u_3 = \cos kx_3 e^{i\omega t}, \quad k_{(n)}h = \frac{n\pi}{2}, \quad n = 2, 4, 6, \dots \quad (51)$$

The lowest thickness-stretch frequency predicted by (50) is plotted in Fig. 2 which, in this special case, is unaffected by rotation and remains a horizontal straight line.

## IV. PLATES OF ROTATED Y-CUT QUARTZ

For plates made of rotated Y-cut quartz, following Refs. 10–12 we orient the  $x_2$  axis along the normal of the plates and the material matrices are<sup>12</sup>

$$\begin{pmatrix} c_{11} & c_{12} & c_{13} & c_{14} & 0 & 0 \\ c_{21} & c_{22} & c_{23} & c_{24} & 0 & 0 \\ c_{31} & c_{32} & c_{33} & c_{34} & 0 & 0 \\ c_{41} & c_{42} & c_{43} & c_{44} & 0 & 0 \\ 0 & 0 & 0 & 0 & c_{55} & c_{56} \\ 0 & 0 & 0 & 0 & c_{65} & c_{66} \end{pmatrix}, \begin{pmatrix} e_{11} & 0 & 0 \\ e_{12} & 0 & 0 \\ e_{13} & 0 & 0 \\ e_{14} & 0 & 0 \\ 0 & e_{25} & e_{35} \\ 0 & e_{26} & e_{36} \end{pmatrix}, \begin{pmatrix} \epsilon_{11} & 0 & 0 \\ 0 & \epsilon_{22} & \epsilon_{23} \\ 0 & \epsilon_{32} & \epsilon_{33} \end{pmatrix}. \quad (52)$$

Values of the material constants can be found in Ref. 12. For thickness vibrations with  $\partial_1 = \partial_3 = 0$  we have the following equations:

$$\begin{aligned} \bar{c}_{66}u_{1,22} &= \rho(\ddot{u}_1 + 2\Omega\dot{u}_3), \\ c_{22}u_{2,22} + c_{24}u_{3,22} &= \rho\ddot{u}_2, \\ c_{24}u_{2,22} + c_{44}u_{3,22} &= \rho(\ddot{u}_3 - 2\Omega\dot{u}_1), \end{aligned} \quad (53)$$

with

$$\begin{aligned} T_{21} &= \bar{c}_{66}u_{1,2} + e_{26}L_1, \quad T_{22} = c_{22}u_{2,2} + c_{24}u_{3,2}, \\ T_{23} &= c_{24}u_{2,2} + c_{44}u_{3,2}, \\ D_2 &= -\epsilon_{22}L_1, \quad \phi = \frac{e_{26}}{\epsilon_{22}}u_1 + L_1x_2 + L_2, \\ \bar{c}_{66} &= c_{66} + e_{26}^2/\epsilon_{22}. \end{aligned} \quad (54)$$

From Ref. 11 we know that for a nonrotating rotated Y-cut quartz plate there are two uncoupled groups of modes. In the first group the thickness-shear motion  $u_1$  is electrically coupled to  $\phi$ , and in the second group the thickness-shear motion  $u_3$  is coupled to the flexure  $u_2$  but they are not electrically coupled. From (53) it can be seen that when the plate is rotating all these modes are coupled together because of Coriolis force. If a solution similar to (11) (depending on  $x_2$  now, rather than  $x_3$ ) is substituted into (53), we obtain

$$\begin{aligned} (\rho\omega^2 - \bar{c}_{66}k^2)A_1 - 2i\rho\omega\Omega A_3 &= 0, \\ (\rho\omega^2 - c_{22}k^2)A_2 - c_{24}k^2A_3 &= 0, \\ 2i\rho\omega\Omega A_1 - c_{24}k^2A_2 + (\rho\omega^2 - c_{44}k^2)A_3 &= 0. \end{aligned} \quad (55)$$

From (55) we obtain the dispersion relation as

$$\begin{aligned} (\rho\omega^2 - \bar{c}_{66}k^2)[(\rho\omega^2 - c_{22}k^2)(\rho\omega^2 - c_{44}k^2) - c_{24}^2k^4] \\ = (\rho\omega^2 - c_{22}k^2)4\rho^2\Omega^2\omega^2. \end{aligned} \quad (56)$$

For the large  $\omega$  approximation like (15), under small  $\Omega$  we have

$$\begin{aligned} \omega^2 &\approx \nu_1^2k^2 + 4\Omega^2 \frac{\nu_1^2(\nu_1^2 - \nu_{20}^2)}{(\nu_1^2 - \nu_2^2)(\nu_1^2 - \nu_3^2)}, \\ \omega^2 &\approx \nu_2^2k^2 + 4\Omega^2 \frac{\nu_2^2(\nu_2^2 - \nu_{20}^2)}{(\nu_2^2 - \nu_1^2)(\nu_2^2 - \nu_3^2)}, \\ \omega^2 &\approx \nu_3^2k^2 + 4\Omega^2 \frac{\nu_3^2(\nu_3^2 - \nu_{20}^2)}{(\nu_3^2 - \nu_1^2)(\nu_3^2 - \nu_2^2)}, \end{aligned} \quad (57)$$

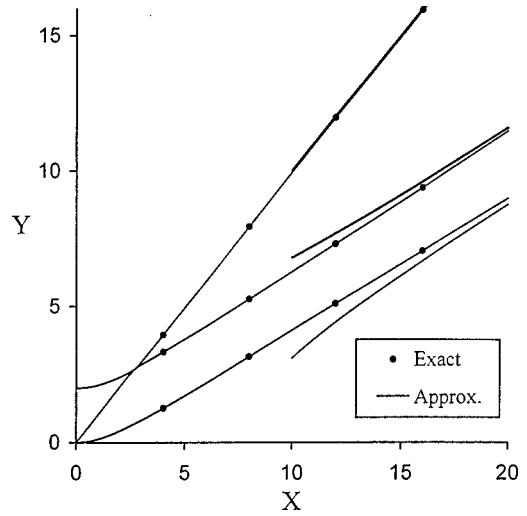


FIG. 4. Dispersion curves from (56) and their approximations from (57) for plane waves in a rotating quartz body.  $X = \sqrt{c_{22}/\rho}k/\Omega$ ,  $Y = \omega/\Omega$ .

where

$$\begin{aligned} \nu_1^2 &= \frac{\bar{c}_{66}}{\rho}, \\ \nu_2^2 &= \frac{1}{2\rho} [c_{22} + c_{44} + \sqrt{(c_{22} - c_{44})^2 + 4c_{24}^2}], \\ \nu_3^2 &= \frac{1}{2\rho} [c_{22} + c_{44} - \sqrt{(c_{22} - c_{44})^2 + 4c_{24}^2}], \\ \nu_{20}^2 &= \frac{c_{22}}{\rho}. \end{aligned} \quad (58)$$

Dispersion relations determined by (56) are obtained numerically and plotted in Fig. 4, along with their large  $\omega$  approximation (57). It can be seen that for larger  $\omega$  the approximation gets better. The behavior of small  $\omega$  requires the consideration of the centrifugal force.

Amplitude ratios like (16) can be obtained from (55) as

$$\begin{aligned} \beta_1^{(i)} &= 2i\rho\omega\Omega/(\rho\omega^2 - \bar{c}_{66}k^2), \\ \beta_2^{(i)} &= c_{24}k^2/(\rho\omega^2 - c_{22}k^2), \quad \beta_3^{(i)} = 1, \end{aligned} \quad (59)$$

where the superscript  $i$  means that the  $i$ th of the three dispersion relations  $k = k^{(i)}(\omega)$  determined from (56) is to be substituted into the right-hand side of (59). These amplitude ratios have been normalized with  $\beta_3^{(i)}$  being equal to one. We have the following anti-symmetric solutions to (53)

$$\begin{aligned} u_j &= \sum_{i=1}^3 B^{(i)}\beta_j^{(i)} \sin k^{(i)}x_2 e^{i\omega t}, \\ \phi &= \sum_{i=1}^3 B^{(i)}\alpha^{(i)} \sin k^{(i)}x_2 e^{i\omega t} + L_1x_2 e^{i\omega t} + L_2 e^{i\omega t}, \\ \alpha^{(i)} &= \frac{e_{26}}{\epsilon_{22}}\beta_1^{(i)}, \end{aligned} \quad (60)$$

with

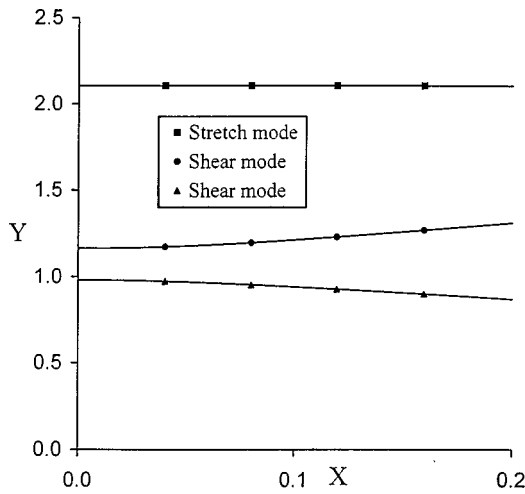


FIG. 5. Lowest thickness vibration frequencies of a rotating quartz plate from (64).  $X = \Omega/\omega_1$ ,  $Y = \omega/\omega_1$ .

$$\begin{aligned}
 D_2 &= -\epsilon_{22}L_1 e^{i\omega t}, \\
 T_{21} &= \sum_{i=1}^3 B^{(i)} \gamma_1^{(i)} k^{(i)} \cos k^{(i)} x_2 e^{i\omega t} + e_{26}L_1 e^{i\omega t}, \\
 T_{22} &= \sum_{i=1}^3 B^{(i)} \gamma_2^{(i)} k^{(i)} \cos k^{(i)} x_2 e^{i\omega t}, \\
 T_{23} &= \sum_{i=1}^3 B^{(i)} \gamma_3^{(i)} k^{(i)} \cos k^{(i)} x_2 e^{i\omega t}, \\
 \gamma_1^{(i)} &= \bar{c}_{66} \beta_1^{(i)}, \quad \gamma_2^{(i)} = c_{22} \beta_2^{(i)} + c_{24} \beta_3^{(i)}, \\
 \gamma_3^{(i)} &= c_{24} \beta_2^{(i)} + c_{44} \beta_3^{(i)}.
 \end{aligned} \tag{61}$$

The symmetric solutions to (53) are

$$u_j = \sum_{i=1}^3 B^{(i)} \beta_j^{(i)} \cos k^{(i)} x_2 e^{i\omega t}, \tag{62}$$

$$\phi = \sum_{i=1}^3 B^{(i)} \alpha^{(i)} \cos k^{(i)} x_2 e^{i\omega t} + L_1 x_2 e^{i\omega t} + L_2 e^{i\omega t},$$

with

$$D_2 = -\epsilon_{22}L_1 e^{i\omega t},$$

$$T_{21} = \sum_{i=1}^3 -B^{(i)} \gamma_1^{(i)} k^{(i)} \sin k^{(i)} x_2 e^{i\omega t} + e_{26}L_1 e^{i\omega t}, \tag{63}$$

$$T_{22} = \sum_{i=1}^3 -B^{(i)} \gamma_2^{(i)} k^{(i)} \sin k^{(i)} x_2 e^{i\omega t},$$

$$T_{23} = \sum_{i=1}^3 -B^{(i)} \gamma_3^{(i)} k^{(i)} \sin k^{(i)} x_2 e^{i\omega t}.$$

For unelectroded plates or plates with open electrode, the frequency equations are exactly the same as (26)–(28).

For plate with shorted electrodes, the symmetric modes have a frequency equation the same as (28). For anti-symmetric modes we have the following frequency equation

$$\begin{vmatrix}
 \gamma_1^{(1)} k^{(1)} \cos k^{(1)} h & \gamma_1^{(2)} k^{(2)} \cos k^{(2)} h & \gamma_1^{(3)} k^{(3)} \cos k^{(3)} h & e_{26} \\
 \gamma_2^{(1)} k^{(1)} \cos k^{(1)} h & \gamma_2^{(2)} k^{(2)} \cos k^{(2)} h & \gamma_2^{(3)} k^{(3)} \cos k^{(3)} h & 0 \\
 \gamma_3^{(1)} k^{(1)} \cos k^{(1)} h & \gamma_3^{(2)} k^{(2)} \cos k^{(2)} h & \gamma_3^{(3)} k^{(3)} \cos k^{(3)} h & 0 \\
 \alpha^{(1)} \sin k^{(1)} h & \alpha^{(2)} \sin k^{(2)} h & \alpha^{(3)} \sin k^{(3)} h & h
 \end{vmatrix} = 0. \tag{64}$$

Equation (64) is solved numerically with results plotted in Fig. 5 for the lowest thickness-shear and thickness-stretch frequencies, where the frequencies are normalized by the fundamental thickness-shear frequency in the  $x_1$  direction of a nonrotating plate

$$\omega_1 = \sqrt{\frac{\bar{c}_{66} \pi^2}{4\rho h^2}}, \quad \bar{c}_{66} = c_{66} + \frac{e_{26}^2}{\epsilon_{22}}. \tag{65}$$

In Fig. 5, the essentially thickness-stretch mode is affected little by rotation and its frequency remains an almost horizontal line. The other two are essentially thickness-shear modes which are affected more by rotation.

## V. CONCLUSION

Propagation of plane waves in a rotating piezoelectric body is studied which shows they are generally dispersive due to the effect of Coriolis force. Analytical solutions to the problem of thickness vibrations of an infinite piezoelectric plate rotating at a constant angular velocity about its normal are obtained for plates with materials of general anisotropy. Transcendental equation that determines the resonant frequencies is derived and solved for specific materials. When the solutions are specialized to polarized ceramic plates and rotated Y-cut quartz plates, it is shown that modes originally uncoupled when the plate is not rotating are now coupled.

The results are useful in the understanding and analysis of plate piezoelectric gyroscopes.

## ACKNOWLEDGMENT

The support from the Office of Naval Research under Contract No. ONR N00014-94-1-0053 is gratefully acknowledged.

- <sup>1</sup>W. D. Gates, "Vibrating angular rate sensor may threaten the gyroscope," *Electronics* **41**, 130–134 (1968).
- <sup>2</sup>J. Soderkvist, "Micromachined gyroscopes," *Sens. Actuators A* **43**, 65–71 (1994).
- <sup>3</sup>C. S. Chou, J. W. Yang, Y. C. Hwang, and H. J. Yang, "Analysis on vibrating piezoelectric beam gyroscope," *Int. J. Appl. Electromagn. Mater.* **2**, 227–241 (1991).
- <sup>4</sup>S. Kudo, M. Konno, S. Sugawara, and T. Yoshida, "Consideration on equivalent mechanical circuits for vibratory gyroscope," *Proc. IEEE Ultrasonics Symposium*, 397–400 (1994).

- <sup>5</sup>I. A. Ulitko, "Mathematical theory of the fork-type wave gyroscope," *Proc. IEEE Frequency Control Symposium*, 786–793 (1995).
- <sup>6</sup>J. Soderkvist, "Piezoelectric beams and vibrating angular rate sensors," *IEEE Trans. Ultrason. Ferroelectr. Freq. Control* **38**, 271–276 (1991).
- <sup>7</sup>J. S. Yang, "A circular cylindrical shell piezoelectric gyroscope," *Int. J. Appl. Electromagn. Mech.* **8**, 259–271 (1997).
- <sup>8</sup>G. M. Reese, E. L. Marek, and D. W. Lobitz, "Three dimensional finite element calculations of an experimental quartz rotation sensor," *Proc. IEEE Ultrasonics Symposium*, 419–422 (1989).
- <sup>9</sup>J. S. Yang, "Analysis of ceramic thickness shear piezoelectric gyroscopes," *J. Acoust. Soc. Am.* **102**, 3542–3548 (1996).
- <sup>10</sup>R. D. Mindlin, "High frequency vibrations of piezoelectric crystal plates," *Int. J. Solids Struct.* **8**, 895–906 (1972).
- <sup>11</sup>H. F. Tiersten, "Thickness vibrations of piezoelectric plates," *J. Acoust. Soc. Am.* **35**, 53–58 (1963).
- <sup>12</sup>H. F. Tiersten, *Linear Piezoelectric Plate Vibrations* (Plenum, New York, 1969).
- <sup>13</sup>B. A. Auld, *Acoustic Fields and Waves in Solids* (Wiley, New York, 1973), Vol. 1, pp. 357–382.

# Vibration of open cylindrical shells: A three-dimensional elasticity approach

C. W. Lim<sup>a)</sup>

*Department of Civil Engineering, The University of Queensland, Brisbane, Queensland 4072, Australia*

K. M. Liew

*Division of Engineering Mechanics, School of Mechanical and Production Engineering, Nanyang Technological University, Singapore 639798*

S. Kitipornchai

*Department of Civil Engineering, The University of Queensland, Brisbane, Queensland 4072, Australia*

(Received 14 October 1997; revised 8 May 1998; accepted 20 May 1998)

The three-dimensional elastic analysis of the vibration of open cylindrical shells are presented. Transverse normal stress usually neglected in plate and shell higher-order theories has been considered. The natural frequencies and vibration mode shapes have been obtained via a three-dimensional displacement-based extremum energy principle. Excessive requirements for memory and computational effort have been overcome, without sacrificing numerical accuracy, by (i) decoupling the three-dimensional displacements into the product of a set of beam and shell shape functions; and (ii) classifying the vibration modes. The effects of subtended angle and aspect ratio have been concluded for shells with various boundary conditions. Typical vibration mode shapes demonstrating the dependence of vibration characteristics on boundary constraints are presented.

© 1998 Acoustical Society of America. [S0001-4966(98)01609-9]

PACS numbers: 43.40.Ey [CBB]

## INTRODUCTION

Despite the practical importance of elastic vibration solutions to engineering design of thick structures, particularly in armed vehicles and nuclear power plants, direct three-dimensional elasticity theory has rarely been exploited in numerical vibration analysis. This is because three-dimensional numerical analysis of thick plates and shells requires huge computational memory and long execution hours.

The vibration of thick plates and shells has conventionally been solved using the first-order<sup>1,2</sup> and higher-order theories.<sup>3</sup> Solutions to the vibration of thick shallow shells have been presented by Lim and Liew<sup>4,5</sup> and Liew and Lim<sup>6</sup> for singly curved and doubly curved shells with arbitrary boundary conditions. Three-dimensional elastic solutions are particularly scarce and almost all investigations have been concerned with rods and beams,<sup>7-9</sup> parallelepipeds,<sup>10-16</sup> cylinders,<sup>17-20</sup> and hollow cones.<sup>21</sup> To the authors' knowledge, only closed shells or hollow cylinders<sup>18-20</sup> and cones<sup>21</sup> have been investigated. Numerical studies for thick, open cylindrical shells have received relatively little attention despite their common applications in the armament industry and nuclear storage designs such as protective tank walls and thick cylindrical covers.

The closed shells, being bodies of revolution, permit one to assume whole periodic wave numbers ( $\sin n\theta$  and  $\cos n\theta$ ) in representing displacement variations in the circumferential direction, yielding the proper periodicity in  $\theta$ . This also permits one to separate out the modes by respective circumferential wave numbers ( $n$ ), reducing the mathematical com-

plexity to a set of two-dimensional analyses. For open shells, the assumption of whole periodic wave numbers in the circumferential direction is inappropriate and a set of complete three-dimensional analysis is required. This forms a major deterrent so that analyses of open shells have not been widely available.

In view of the lack of analytical solutions, this paper presents an endeavor to investigate the free vibration characteristics of thick and open shells using a three-dimensional displacement-based extremum energy principle. The strain energy integral considers transverse normal stress which is usually neglected in first-order and higher-order theories. The solutions are therefore exact so far as the energy expression is concerned. A Ritz energy functional is defined and minimized to derive a governing eigenvalue equation. The three-dimensional displacement field is characterized by a cylindrical coordinate system with orthogonal displacement components. Although the analysis is completely three-dimensional, excessive requirements for memory and computational effort have been overcome, without sacrificing numerical accuracy, by (i) decoupling the three-dimensional displacements into the product of a set of  $p$ -Ritz beam and shell shape functions, and (ii) classifying the vibration modes into various symmetry classes. One- and two-dimensional (1-D and 2-D)  $p$ -Ritz functions are formulated to describe the thickness deformation and the midsurface deformation, respectively. By classifying the vibration modes, memory requirements and execution time can be tremendously reduced while maintaining the same level of numerical accuracy. The effects of subtended angle and aspect ratio have been investigated for shells with various boundary conditions. Typical vibration mode shapes demonstrating the de-

<sup>a)</sup>Present address: Department of Mechanical Engineering, The University of Hong Kong, Pokfulam Road, Hong Kong.

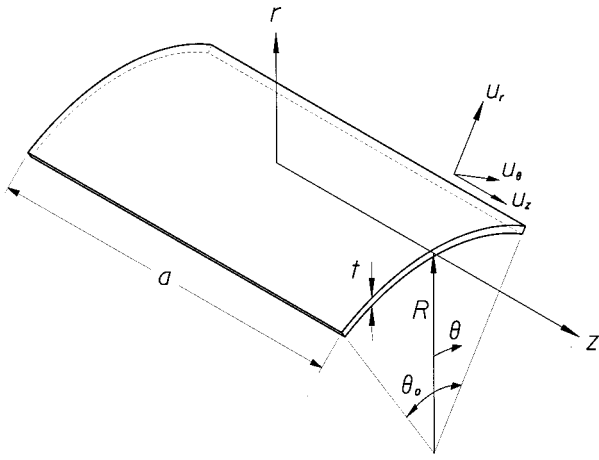


FIG. 1. Geometry of a thick cylindrical shell.

pendence of vibration characteristics on boundary constraints have been presented.

## I. THEORY AND FORMULATION

### A. Basic definition and cylindrical coordinate system

Consider an isotropic, open and thick cylindrical shell with length  $a$ , midsurface radius  $R$ , subtended angle  $\theta_0$ , thickness  $t$  as shown in Fig. 1. The circumferential arc length is  $b = R\theta_0$ . An orthogonal cylindrical coordinate system  $(r, \theta, z)$  is defined with  $r$  the radial coordinate,  $\theta$  the angular coordinate, and  $z$  parallel to the axis of cylindrical shell. For brevity and generality, a dimensionless coordinate system,

$$\bar{r} = \frac{r}{R}, \quad (1a)$$

$$\bar{\theta} = \frac{\theta}{\theta_0}, \quad (1b)$$

$$\bar{z} = \frac{z}{a}, \quad (1c)$$

is defined such that the shell is bounded by  $1 - t/2R \leq \bar{r} \leq 1 + t/2R$ ,  $-0.5 \leq \bar{\theta} \leq 0.5$ , and  $-0.5 \leq \bar{z} \leq 0.5$ . The midsurface is defined as  $\bar{r} = 1$ . The orthogonal displacement components are  $u_r$ ,  $u_\theta$ , and  $u_z$ .

### B. Three-dimensional strain and kinetic energy expressions

For linear and elastic free vibration, the strain energy of a three-dimensional solid is

$$U = \frac{1}{2} \int \int \int_V [(\Delta + 2G)(\epsilon_{rr}^2 + \epsilon_{\theta\theta}^2 + \epsilon_{zz}^2) + 2\Delta(\epsilon_{rr}\epsilon_{\theta\theta} + \epsilon_{\theta\theta}\epsilon_{zz} + \epsilon_{zz}\epsilon_{rr}) + G(\gamma_{\theta z}^2 + \gamma_{zr}^2 + \gamma_{r\theta}^2)] r dr d\theta dz, \quad (2)$$

where  $V$  is the volume,  $G$  is the shear modulus, and

$$\Delta = \frac{\nu E}{(1 + \nu)(1 - 2\nu)}, \quad (3a)$$

$$G = \frac{E}{2(1 + \nu)}, \quad (3b)$$

in which  $E$  is the Young's modulus.

The normal and shear strain-displacement relations are

$$\epsilon_{rr} = \frac{\partial u_r}{\partial r}, \quad (4a)$$

$$\epsilon_{\theta\theta} = \frac{1}{r} \frac{\partial u_\theta}{\partial \theta} + \frac{u_r}{r}, \quad (4b)$$

$$\epsilon_{zz} = \frac{\partial u_z}{\partial z}, \quad (4c)$$

$$\gamma_{\theta z} = \frac{\partial u_\theta}{\partial z} + \frac{1}{r} \frac{\partial u_z}{\partial \theta}, \quad (4d)$$

$$\gamma_{zr} = \frac{\partial u_z}{\partial r} + \frac{\partial u_r}{\partial z}, \quad (4e)$$

$$\gamma_{\theta z} = \frac{1}{r} \frac{\partial u_r}{\partial \theta} + \frac{\partial u_\theta}{\partial r} - \frac{u_\theta}{r}. \quad (4f)$$

The kinetic energy is

$$T = \frac{\rho}{2} \int_V \left[ \left( \frac{\partial u_r}{\partial t} \right)^2 + \left( \frac{\partial u_\theta}{\partial t} \right)^2 + \left( \frac{\partial u_z}{\partial t} \right)^2 \right] dV, \quad (5)$$

where  $\rho$  is the mass density per unit volume.

For linear, small deformation vibration, the displacement components assume temporal simple harmonic functions in the forms

$$u_r(\bar{r}, \bar{\theta}, \bar{z}, t) = U_r(\bar{r}, \bar{\theta}, \bar{z}) \sin \omega t, \quad (6a)$$

$$u_\theta(\bar{r}, \bar{\theta}, \bar{z}, t) = U_\theta(\bar{r}, \bar{\theta}, \bar{z}) \sin \omega t, \quad (6b)$$

$$u_z(\bar{r}, \bar{\theta}, \bar{z}, t) = U_z(\bar{r}, \bar{\theta}, \bar{z}) \sin \omega t, \quad (6c)$$

where  $U_r$ ,  $U_\theta$ ,  $U_z$  are the displacement amplitude functions and  $\omega$  is the angular frequency of vibration.

The maximum strain and kinetic energy integral expressions  $U_{\max}$  and  $T_{\max}$  can be derived easily by substituting Eqs. (6a)–(6c) into Eqs. (2) and (5) and determining the extremum with respect to time  $t$ .

### C. Elastic energy functional and eigenvalue equation

The displacement amplitude functions for a vibrating thick cylindrical shell can be expressed by a set of three-dimensional (3-D)  $p$ -Ritz functions. These functions are the products of 2-D  $p$ -Ritz functions  $\phi_r(\bar{\theta}, \bar{z})$ ,  $\phi_\theta(\bar{\theta}, \bar{z})$ ,  $\phi_z(\bar{\theta}, \bar{z})$

for midsurface deformation and 1-D  $p$ -Ritz functions  $\psi_r(\bar{r})$ ,  $\psi_\theta(\bar{r})$ ,  $\psi_z(\bar{r})$  for thickness deformation. The displacement amplitude functions are

$$U_r(\bar{r}, \bar{\theta}, \bar{z}) = \sum_{i=1}^m \sum_{j=1}^n c_r^{ij} \phi_r^i(\bar{\theta}, \bar{z}) \psi_r^j(\bar{r}), \quad (7a)$$

$$U_\theta(\bar{r}, \bar{\theta}, \bar{z}) = \sum_{i=1}^m \sum_{j=1}^n c_\theta^{ij} \phi_\theta^i(\bar{\theta}, \bar{z}) \psi_\theta^j(\bar{r}), \quad (7b)$$

$$U_z(\bar{r}, \bar{\theta}, \bar{z}) = \sum_{i=1}^m \sum_{j=1}^n c_z^{ij} \phi_z^i(\bar{\theta}, \bar{z}) \psi_z^j(\bar{r}), \quad (7c)$$

in which  $c_r^{ij}$ ,  $c_\theta^{ij}$ ,  $c_z^{ij}$  are unknown coefficients.

An energy functional is defined as the difference of the maximum strain and kinetic energy components

$$\Pi = U_{\max} - T_{\max}. \quad (8)$$

Numerical frequency solutions can be obtained by minimizing this energy functional with respect to the coefficients in accordance with the Ritz procedure

$$\frac{\partial \Pi}{\partial c_\alpha^{ij}} = 0, \quad \alpha = r, \theta, \text{ and } z, \quad (9)$$

which leads to the governing eigenvalue equation

$$(\mathbf{K} - \Lambda^2 \mathbf{M})\{\mathbf{C}\} = \{\mathbf{0}\}, \quad (10)$$

where

$$\Lambda = \frac{\lambda}{\theta_0}, \quad (11a)$$

$$\lambda = \omega b \sqrt{\frac{\rho}{E}} \quad (11b)$$

are the dimensionless frequency parameters in which  $b = R\theta_0$  is the circumferential arc length.

The stiffness and mass matrices are

$$\mathbf{K} = \begin{bmatrix} \mathbf{k}_{rr} & \mathbf{k}_{r\theta} & \mathbf{k}_{rz} \\ & \mathbf{k}_{\theta\theta} & \mathbf{k}_{\theta z} \\ \text{sym} & & \mathbf{k}_{zz} \end{bmatrix}, \quad (12)$$

$$\mathbf{M} = \begin{bmatrix} \mathbf{m}_{rr} & [0] & [0] \\ & \mathbf{m}_{\theta\theta} & [0] \\ \text{sym} & & \mathbf{m}_{zz} \end{bmatrix}, \quad (13)$$

and the vector of unknown coefficients is

$$\mathbf{C} = \left\{ \begin{matrix} \{\mathbf{c}_r\} \\ \{\mathbf{c}_\theta\} \\ \{\mathbf{c}_z\} \end{matrix} \right\}. \quad (14)$$

The elements in the stiffness submatrix are

$$k_{rr}^{ijkl} = \frac{\Delta + 2G}{E} [I_{\phi_{rr}^{ik}\psi_{rr}^{jl}}^{0000,11(1)} + I_{\phi_{rr}^{ik}\psi_{rr}^{jl}}^{0000,00(-1)}] + \frac{\Delta}{E} [I_{\phi_{rr}^{ik}\psi_{rr}^{jl}}^{0000,10(0)} + I_{\phi_{rr}^{ik}\psi_{rr}^{jl}}^{0000,01(0)}] + \frac{G}{E} \left[ \frac{R^2}{a^2} I_{\phi_{rr}^{ik}\psi_{rr}^{jl}}^{0101,00(1)} + \frac{1}{\theta_0^2} I_{\phi_{rr}^{ik}\psi_{rr}^{jl}}^{1010,00(-1)} \right], \quad (15a)$$

$$k_{r\theta}^{ijkl} = \frac{\Delta + 2G}{E\theta_0} I_{\phi_{r\theta}^{ik}\psi_{r\theta}^{jl}}^{0010,00(-1)} + \frac{\Delta}{E\theta_0} I_{\phi_{r\theta}^{ik}\psi_{r\theta}^{jl}}^{0010,10(0)} + \frac{G}{E\theta_0} [I_{\phi_{r\theta}^{ik}\psi_{r\theta}^{jl}}^{1000,01(0)} - I_{\phi_{r\theta}^{ik}\psi_{r\theta}^{jl}}^{1000,00(-1)}], \quad (15b)$$

$$k_{rz}^{ijkl} = \frac{\Delta R}{Ea} [I_{\phi_{rz}^{ik}\psi_{rz}^{jl}}^{0001,00(0)} + I_{\phi_{rz}^{ik}\psi_{rz}^{jl}}^{0001,10(1)}] + \frac{GR}{Ea} I_{\phi_{rz}^{ik}\psi_{rz}^{jl}}^{0100,01(1)}, \quad (15c)$$

$$k_{\theta\theta}^{ijkl} = \frac{\Delta + 2G}{E\theta_0} I_{\phi_{\theta\theta}^{ik}\psi_{\theta\theta}^{jl}}^{1010,00(-1)} + \frac{G}{E} \left[ \frac{R^2}{a^2} I_{\phi_{\theta\theta}^{ik}\psi_{\theta\theta}^{jl}}^{0101,00(1)} + I_{\phi_{\theta\theta}^{ik}\psi_{\theta\theta}^{jl}}^{0000,11(1)} + I_{\phi_{\theta\theta}^{ik}\psi_{\theta\theta}^{jl}}^{0000,00(-1)} - I_{\phi_{\theta\theta}^{ik}\psi_{\theta\theta}^{jl}}^{0000,10(0)} - I_{\phi_{\theta\theta}^{ik}\psi_{\theta\theta}^{jl}}^{0000,01(0)} \right], \quad (15d)$$

$$k_{\theta z}^{ijkl} = \frac{R}{a\theta_0} \left[ \frac{\Delta}{E} I_{\phi_{\theta z}^{ik}\psi_{\theta z}^{jl}}^{1001,00(0)} + \frac{G}{E} I_{\phi_{\theta z}^{ik}\psi_{\theta z}^{jl}}^{0110,00(0)} \right], \quad (15e)$$

$$k_{zz}^{ijkl} = \frac{(\Delta + 2G)R^2}{Ea^2} I_{\phi_{zz}^{ik}\psi_{zz}^{jl}}^{0101,00(1)} + \frac{G}{E} \left[ \frac{1}{\theta_0^2} I_{\phi_{zz}^{ik}\psi_{zz}^{jl}}^{1010,00(-1)} + I_{\phi_{zz}^{ik}\psi_{zz}^{jl}}^{0000,11(1)} \right], \quad (15f)$$

and the elements in the mass submatrix are

$$m_{rr}^{ijkl} = I_{\phi_{rr}^{ik}\psi_{rr}^{jl}}^{0000,00(1)}, \quad (16a)$$

$$m_{\theta\theta}^{ijkl} = I_{\phi_{\theta\theta}^{ik}\psi_{\theta\theta}^{jl}}^{0000,00(1)}, \quad (16b)$$

$$m_{zz}^{ijkl} = I_{\phi_{zz}^{ik}\psi_{zz}^{jl}}^{0000,00(1)}, \quad (16c)$$

in which

$$I_{\phi_{\alpha\beta}^{ik}\psi_{\alpha\beta}^{jl}}^{abcde,ef(g)} = \int \int_{\bar{A}} \frac{\partial^{a+b} \phi_\alpha^i(\bar{\theta}, \bar{z})}{\partial \bar{\theta}^a \partial \bar{z}^b} \frac{\partial^{c+d} \phi_\beta^k(\bar{\theta}, \bar{z})}{\partial \bar{\theta}^c \partial \bar{z}^d} d\bar{\theta} d\bar{z} \times \int_{\bar{r}} \frac{\partial^e \psi_\alpha^j(\bar{r})}{\partial \bar{r}^e} \frac{\partial^f \psi_\beta^l(\bar{r})}{\partial \bar{r}^f} \bar{r}^g d\bar{r}, \quad (17)$$

where  $\alpha, \beta = r, \theta, z$ ;  $i, j, k, l = 1, 2, \dots, m$ , and  $m$  is the total number of terms employed in the  $p$ -Ritz shape functions. The normalized midsurface area is denoted as  $\bar{A}$  and the normalized thickness is  $\bar{t}$ .

TABLE I. Convergence of  $\lambda = \omega b \sqrt{\rho/E}$  for a thick cylindrical shell with  $\nu=0.3$ ,  $a/b=2$ ,  $t/b=0.2$ , and  $\theta_0 = 180^\circ$ .

B.C.	$p_{\theta_z} \times p_r$	Mode sequence number			
		S-1	S-2	A-1	A-2
CFFF	8×2	0.093 645	0.49 279	0.15 593	0.26 904
	9×2	0.093 542	0.49 237	0.15 580	0.26 873
	10×2	0.093 479	0.49 207	0.15 572	0.26 851
	10×3	0.093 425	0.49 122	0.15 509	0.26 772
	10×4	0.093 421	0.49 119	0.15 507	0.26 769
		SS-1	SA-1	AS-1	AA-1
CFCF	6×2	0.48 287	0.46 806	1.1378	1.0451
	8×2	0.48 134	0.45 980	1.0838	1.0196
	10×2	0.48 068	0.45 868	1.0805	1.0168
	10×3	0.47 935	0.45 416	1.0754	1.0040
	10×4	0.47 927	0.45 403	1.0752	1.0035
CCCC	6×2	2.6317	1.8671	2.5180	2.2833
	8×2	2.6314	1.8630	2.5165	2.2778
	10×2	2.6313	1.8620	2.5160	2.2768
	10×3	2.6034	1.8174	2.5144	2.2341
	10×4	2.5993	1.8113	2.5142	2.2285

#### D. The 1-D and 2-D $p$ -Ritz admissible functions

The midsurface and thickness displacements denoted by  $u_r(\bar{r}, \bar{\theta}, \bar{z})$ ,  $u_\theta(\bar{r}, \bar{\theta}, \bar{z})$ , and  $u_z(\bar{r}, \bar{\theta}, \bar{z})$  are truncated finite series given in Eqs. (6a)–(6c). The midsurface deformation admissible functions are sets of geometrically compliant 2-D polynomials  $\phi_r(\bar{\theta}, \bar{z})$ ,  $\phi_\theta(\bar{\theta}, \bar{z})$ , and  $\phi_z(\bar{\theta}, \bar{z})$  derived such that the geometric boundary conditions are satisfied at the outset. They are composed of the product of a series of simple two-dimensional polynomials (degree of polynomial  $p_{\theta_z}$ ) and boundary-compliant basic functions  $\phi_r^b(\bar{\theta}, \bar{z})$ ,  $\phi_\theta^b(\bar{\theta}, \bar{z})$ , and  $\phi_z^b(\bar{\theta}, \bar{z})$ . The latter are geometric expressions of the cylindrical shell boundary raised to an appropriate basic power in accordance with various boundary constraints. These 2-D  $p$ -Ritz admissible functions have been developed and formulated<sup>4–6</sup> for shallow shell studies using a higher-order shell theory. Similarly, the 1-D thickness admissible functions  $\psi_r(r)$ ,  $\psi_\theta(r)$ , and  $\psi_z(r)$  are the products of sets of 1-D polynomials (degree of polynomial  $p_r$ ) and appropriate basic functions  $\psi_r^b(r)$ ,  $\psi_\theta^b(r)$ , and  $\psi_z^b(r)$ .

Classification of vibration modes is possible by grouping terms with odd and even powers in  $\phi_r(\bar{\theta}, \bar{z})$ ,  $\phi_\theta(\bar{\theta}, \bar{z})$ , and  $\phi_z(\bar{\theta}, \bar{z})$ .<sup>4,5</sup> This tremendously reduces the number of terms in each series and thus the determinant size of the eigenvalue equation is considerably smaller. Huge computational effort can be saved as discussed in detail in the next section.

## II. RESULTS AND DISCUSSION

### A. Convergence and comparison of eigenvalues

The convergence characteristics of the dimensionless frequency parameter  $\lambda$  are presented in Table I for CFFF (cantilevered), CFCF, and CCCC shells. In these cases, C denotes a clamped edge and F denotes a free edge with sequence from  $\bar{z} = -0.5$  going anticlockwise (see Fig. 1). The vibration modes are classified into various symmetry classes. A CFFF shell has two symmetry classes while CFCF and

CCCC shells have four symmetry classes. The degrees of 2-D and 1-D polynomial,  $p_{\theta_z}$  and  $p_r$ , are related to the number of terms in each series by  $m_{\theta_z} = (p_{\theta_z} + 1)(p_{\theta_z} + 2)/2$  and  $m_r = p_r + 1$ . Classification of modes has a significant effect on the efficiency of algorithm as the determinant size of the eigenvalue problem can be greatly reduced and tremendous numerical computation can be saved while maintaining the same level of numerical accuracy.

It can be observed in Table I that good convergence of  $\lambda$  has been achieved for admissible functions with  $p_{\theta_z} \times p_r = 10 \times 4$ . These degrees of polynomial have been adopted for all subsequent calculation unless stated otherwise. All the eigenvalues converge downwards as expected because the Ritz method overestimates stiffness and vibration frequency and underestimates displacement. The determinant size is  $792 \times 792$  without mode classification. With mode classification, it is only  $432 \times 432$  for the symmetric class (S) and  $360 \times 360$  for the antisymmetric class (A) for CFFF shell. For CFCF and CCCC shells, the determinant sizes are  $252 \times 252$  for the SS class and  $180 \times 180$  for the SA, AS, and AA classes. Details of vibration mode classification have been addressed in Lim *et al.*<sup>14,15</sup>

A comparison of frequency parameters with finite-element solutions (FEM) is presented in Table II. The FEM solutions are obtained using LUSAS, a commercial finite element package, with two different elements. The QTS8 elements,<sup>22</sup> are eight-node thick shell elements for the analysis of arbitrarily curved shell geometries. These elements take account of membrane, shear, and flexural deformations. The HX8M elements<sup>22</sup> are eight-node three-dimensional isoparametric solid elements where the variation of stresses within an element is regarded as linear.

As observed in Table II, the  $p$ -Ritz solutions agree well with the FEM solutions and agreement is excellent with the solutions using HX8M elements. This is expected as the HX8M elements are 3-D elements which consider transverse normal stress similar to the present analysis. Convergence of



TABLE II. Comparison of  $\lambda = \omega b \sqrt{\rho/E}$  for a thick cylindrical shell with  $\nu=0.3$ ,  $t/b=0.2$ , and  $\theta_0 = 180^\circ$ .

B.C.	$a/b$	Sources	Mode sequence number				
			S-1	S-2	A-1	A-2	
CFFF	1	FEM <sup>a</sup>	0.34079	1.1483	0.40619	0.69750	
		FEM <sup>b</sup>	0.34295	1.1476	0.40706	0.70120	
		3-D	0.34299	1.1347	0.40676	0.70092	
	2	FEM <sup>a</sup>	0.093042	0.48893	0.15497	0.26706	
		FEM <sup>b</sup>	0.093433	0.49583	0.15507	0.26792	
		3-D	0.093425	0.49122	0.15509	0.26772	
				SS-1	SA-1	AS-1	AA-1
	CFCF	1	FEM <sup>a</sup>	1.3101	1.1981	2.6625	2.5794
			FEM <sup>b</sup>	1.3386	1.2269	2.7589	2.6855
3-D			1.3235	1.2141	2.7000	2.6257	
2		FEM <sup>a</sup>	0.47587	0.45196	1.0668	0.99628	
		FEM <sup>b</sup>	0.48591	0.45796	1.1029	1.0281	
		3-D	0.47935	0.45416	1.0754	1.0040	
CCCC	1	FEM <sup>a</sup>	2.8071	2.2988	3.6263	3.5733	
		FEM <sup>b</sup>	2.9055	2.3672	3.6855	3.6826	
		3-D	2.8696	2.3383	3.6567	3.6346	
	2	FEM <sup>a</sup>	2.5140	1.7504	2.5110	2.1692	
		FEM <sup>b</sup>	2.6422	1.8477	2.5243	2.2680	
		3-D	2.6034	1.8174	2.5144	2.2341	

<sup>a</sup>LUSAS solutions with 30×30 QTS8 thick shell elements (Ref. 22).

<sup>b</sup>LUSAS solutions with 15×15×6 HX8M 3-D isoparametric solid elements (Ref. 22).

the FEM solutions for 30×30 QTS8 elements and 15×15×6 HX8M elements used in the computation have been checked. It is emphasized here that it takes 1.5–4 h to obtain a converged FEM solution using LUSAS while it takes less than a minute to obtain equally accurate solutions using the  $p$ -Ritz approach with mode symmetry classification. Noting that some of the finite-element solutions are higher than the 3-D Ritz solutions and keeping in mind that solutions from the Ritz approach are always upper-bounded, the 3-D Ritz solutions presented in Table II not only require considerably less time than the finite-element method, but are also more accurate.

### B. Vibration frequency and mode shapes

A set of new results for the free vibration of CFFF cylindrical shells with aspect ratio  $a/b$  varying from 1 to 2, where  $a$  and  $b$  are the length and arc of the open shell, is presented in Figs. 2 and 3. The corresponding results for CFCF and CCCC cylindrical shells are presented in Figs. 4 and 5, and 6 and 7. The subtended angle  $\theta_0$  ranges from 10° to 180°. Because the aspect ratio is constant, the open shell radius varies while  $\theta_0$  is changed, keeping the thickness  $t$  constant. The idea or initiative of the authors is to investigate the effects of subtended angle while the deepness of an open shell is changed by bending a given plate with fixed length  $a$  and width  $b$ .

In the figures, most of the frequencies have been computed using  $p_{\theta z} \times p_r = 10 \times 4$  while lower polynomial degrees have been employed for small  $\theta_0$  as indicated in the figures because the matrix becomes ill conditioned. The fundamental mode for a CFFF shell is the S-1 mode while for CFCF

and CCCC shells the fundamental mode switches from the SS-1 mode to the SA-1 mode. The threshold of  $\theta_0$  at which switching of fundamental mode occurs varies depending on  $a/b$  and boundary conditions as indicated by the intersections of the SS-1 and SA-1 curves in Figs. 4–7, which are, respectively, 120°, 160°, 130°, and 120°, approximately. It

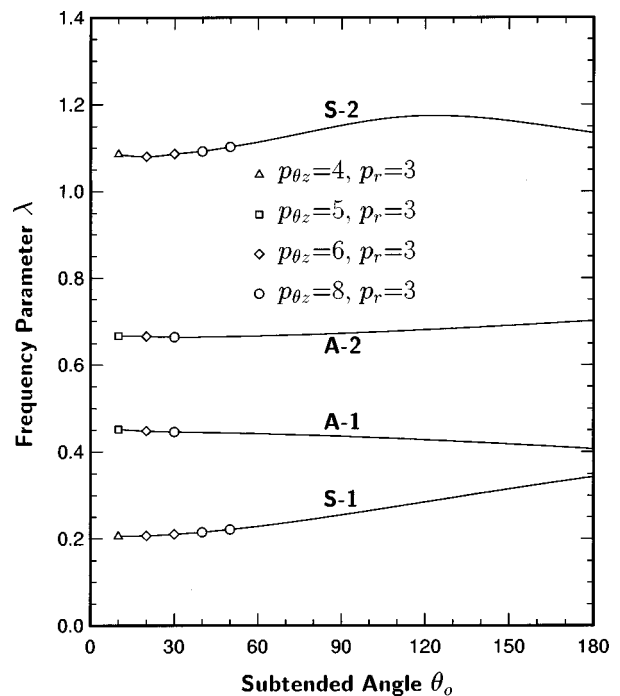


FIG. 2. Effect of subtended angle (degree) on frequency for a thick cylindrical shell (CFFF) with  $\nu=0.3$ ,  $t/b=0.2$ , and  $a/b=1$ .

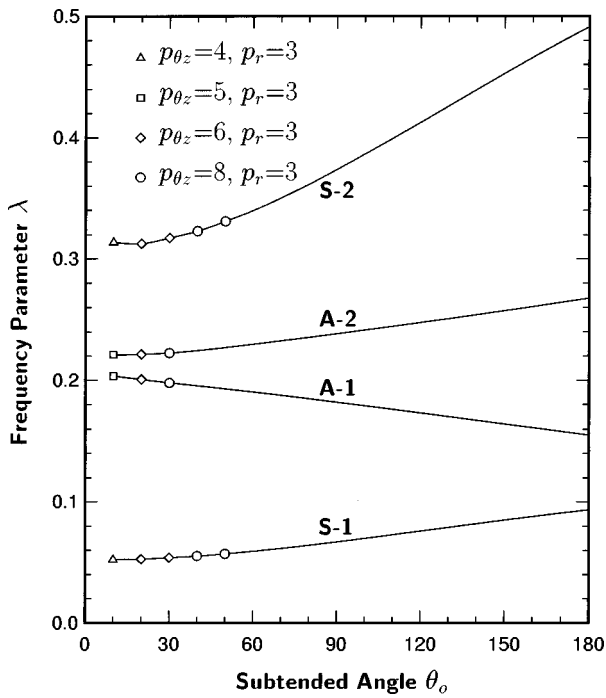


FIG. 3. Effect of subtended angle (degree) on frequency for a thick cylindrical shell (CFFF) with  $\nu=0.3$ ,  $t/b=0.2$ , and  $a/b=2$ .

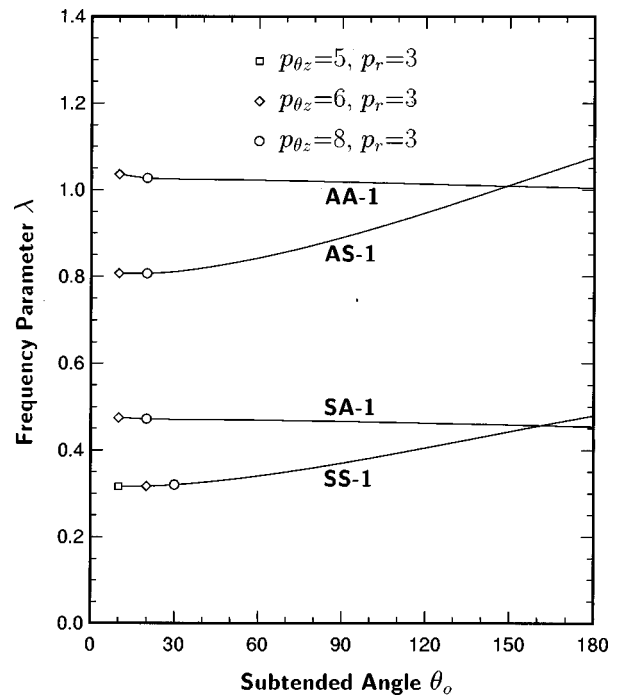


FIG. 5. Effect of subtended angle (degree) on frequency for a thick cylindrical shell (CFCF) with  $\nu=0.3$ ,  $t/b=0.2$ , and  $a/b=2$ .

should be emphasized that the curves do not actually cross. If these curves were to cross, then, for some subtended angles, two different vibration modes would exist at the same frequency, which is indeed a violation of the uniqueness of a vibration mode. In this respect, computations have been conducted at very small intervals of  $\theta_0$  and it is realized that the frequency curves belonging to different modes approach each other but they never coalesce. In fact, after the "coalescence," the frequency curves interchange their corre-

sponding types. This almost coalescence is not novel and it occurs in many problems whether in structural dynamics, acoustics, or fluid mechanics.

For a CFFF shell with  $a/b=1$  and 2, the S-1 and A-2 frequencies increase with increasing  $\theta_0$  while the A-1 frequency decreases. The S-2 frequency demonstrates irregular tendency with respect to  $\theta_0$ . For CFCF and CCCC shells, the SS-1 and AS-1 frequencies increase while the SA-1 and AA-1 frequencies decrease for shells with larger  $\theta_0$ . The

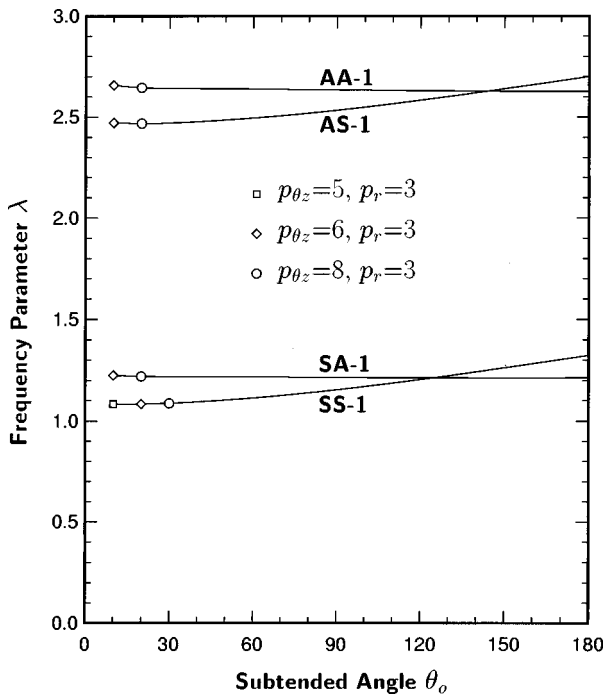


FIG. 4. Effect of subtended angle (degree) on frequency for a thick cylindrical shell (CFCF) with  $\nu=0.3$ ,  $t/b=0.2$ , and  $a/b=1$ .

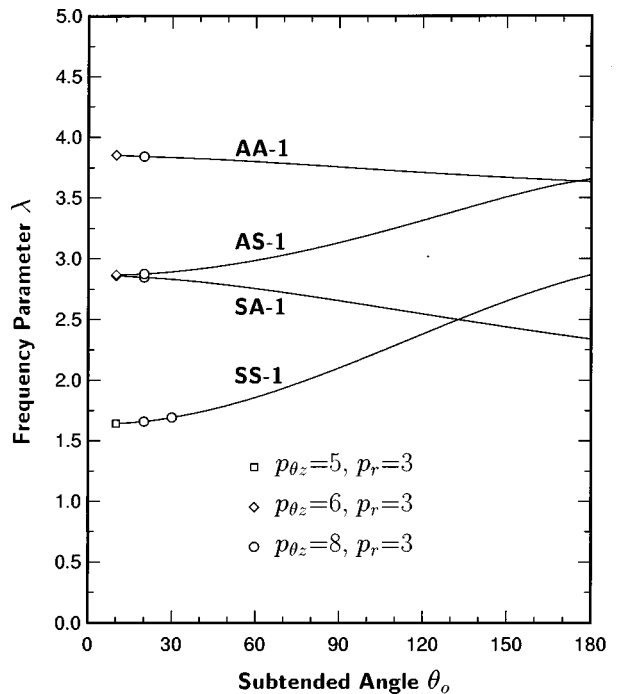


FIG. 6. Effect of subtended angle (degree) on frequency for a thick cylindrical shell (CCCC) with  $\nu=0.3$ ,  $t/b=0.2$ , and  $a/b=1$ .

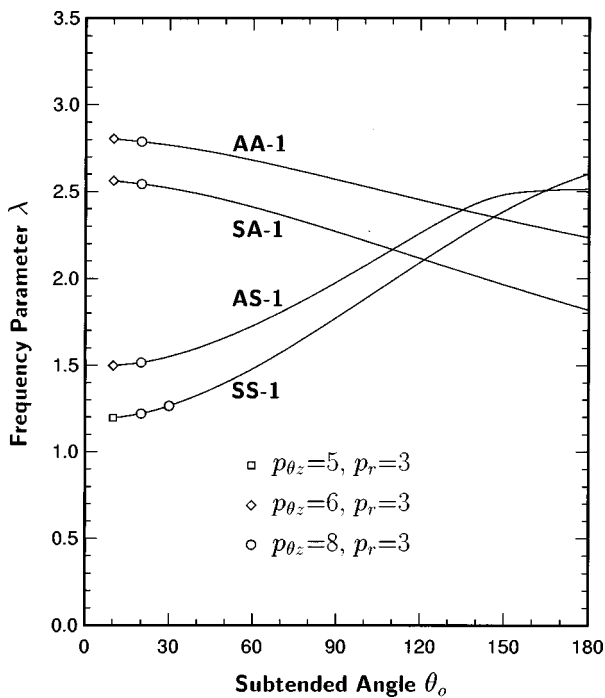


FIG. 7. Effect of subtended angle (degree) on frequency for a thick cylindrical shell (CCCC) with  $\nu=0.3$ ,  $t/b=0.2$ , and  $a/b=2$ .

increasing rate of AS-1 frequency for a CCCC shell with  $a/b=2$  (Fig. 7) decreases rapidly as  $\theta_0$  approaches  $150^\circ$  and onwards. In all these shell configurations, the frequency is smaller for longer shells (higher  $a/b$ ) but it is larger for shells with stronger boundary constraints (from CFFF, CFCF to CCCC).

New vibration mode shapes for the CFFF, CFCF, and CCCC shells are depicted in three-dimensional displacement meshes in Fig. 8. Various vibration modes can be observed from these figures, for instance, the S-1 and S-2 modes are the first and second flapwise bending modes. The A-1 and A-2 modes look alike but they are in fact the first twisting mode and the first in-surface mode in the circumferential direction, respectively. The free end of the A-1 mode is twisted while the free end of the A-2 mode is displaced in a circumferential direction. Because the cylinders are thick, not all lower frequency modes have the normal component,  $U_r$ , as the predominant component. For instance, the A-2 mode is circumferential dominant. The dependence of vibratory characteristics on boundary conditions are illustrated in these figures. The frequencies of a CFFF shell are lower than the CFCF and CCCC shells while the frequencies of a CCCC shell are the highest.

### III. CONCLUSIONS

A new analysis method using a three-dimensional elasticity approach for free vibration of thick, open cylindrical shells has been developed. The spatial integrals for strain, with transverse normal stress, and kinetic energy components have been formulated. An energy functional has been defined and its extremum determined to arrive at a governing eigenvalue equation. The two-dimensional  $p$ -Ritz admissible functions previously used in thick shallow shell studies have

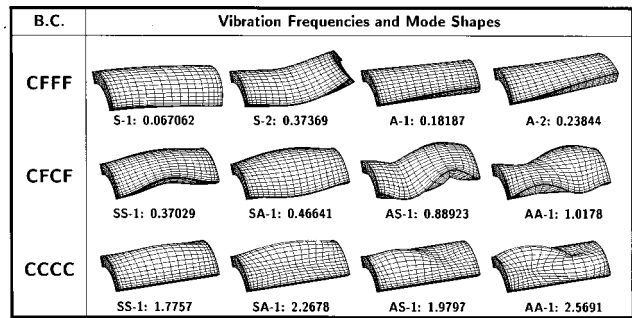


FIG. 8. Vibration frequencies  $\lambda$  and mode shapes for a thick cylindrical shell with  $\nu=0.3$ ,  $t/b=0.2$ ,  $a/b=2$ , and  $\theta_0=90^\circ$ .

been generalized to three-dimensional functions by associating the two-dimensional functions with a one-dimensional  $p$ -Ritz admissible function.

Convergence of vibration frequencies has been examined and excellent comparison with finite-element solutions has been recorded. Classification of vibration modes by grouping terms in the  $p$ -Ritz functions tremendously reduces the matrix determinant size and thus much computation effort can be saved while maintaining the same level of accuracy. The algorithm developed here requires less than a minute to obtain accurate solutions which take hours for a finite-element package to compute. Most of the frequencies show consistent tendency with respect to increasing subtended angle. The frequency decreases for longer shells and shells with weaker boundary constraints. New three-dimensional mode shapes have been presented.

### ACKNOWLEDGMENT

The authors are grateful to anonymous reviewers for their valuable comments which helped improve the quality of this paper.

- <sup>1</sup>E. Reissner, "The effect of transverse shear deformation on the bending of elastic plates," Trans. ASME, J. Appl. Mech. **12**, A69–A77 (1945).
- <sup>2</sup>R. D. Mindlin, "Influence of rotatory inertia and shear on flexural motions of isotropic, elastic plates," Trans. ASME, J. Appl. Mech. **18**, 31–38 (1951).
- <sup>3</sup>C. W. Lim and K. M. Liew, "Vibration of moderately thick cylindrical shallow shells," J. Acoust. Soc. Am. **100**(6), 3665–3673 (1996).
- <sup>4</sup>J. N. Reddy and C. F. Liu, "A higher-order shear deformation theory of laminated elastic shells," Int. J. Eng. Sci. **23**, 319–330 (1985).
- <sup>5</sup>C. W. Lim and K. M. Liew, "A higher order theory for vibration of shear deformable cylindrical shallow shells," Int. J. Mech. Sci. **37**(3), 277–295 (1995).
- <sup>6</sup>K. M. Liew and C. W. Lim, "A higher-order theory for vibration of doubly-curved shallow shells," Trans. ASME, J. Appl. Mech. **63**(3), 587–593 (1996).
- <sup>7</sup>J. R. Hutchinson, "Axisymmetric vibration of a free finite-length rod," J. Acoust. Soc. Am. **51**, 233–240 (1971).
- <sup>8</sup>J. R. Hutchinson, "Transverse vibration of beams: Exact versus approximate solutions," Trans. ASME, J. Appl. Mech. **48**, 923–928 (1981).
- <sup>9</sup>A. W. Leissa and J. So, "Comparisons of vibration frequencies for rods and beams from one-dimensional and three-dimensional analyses," J. Acoust. Soc. Am. **98**, 2122–2135 (1995).
- <sup>10</sup>J. A. Fromme and A. W. Leissa, "Free vibration of the rectangular parallelepiped," J. Acoust. Soc. Am. **48**, 290–298 (1970).
- <sup>11</sup>S. Srinivas, C. V. Rao, and A. K. Rao, "An exact analysis for vibration of simply supported homogeneous and laminated thick rectangular plates," J. Sound Vib. **12**, 187–199 (1970).
- <sup>12</sup>J. R. Hutchinson and S. D. Zillmer, "Vibration of a free rectangular parallelepiped," Trans. ASME, J. Appl. Mech. **50**, 123–130 (1983).

- <sup>13</sup>A. W. Leissa and Z. D. Zhang, "On the three-dimensional vibrations of the cantilevered rectangular parallelepiped," *J. Acoust. Soc. Am.* **73**, 2013–2021 (1983).
- <sup>14</sup>C. W. Lim, K. H. Liew, and S. Kitipornchai, "Numerical aspects for free vibration of thick plates. Part I: Formulation and verification," *Comput. Methods Appl. Mech. Eng.* **156**(1–4), 15–29 (1998).
- <sup>15</sup>C. W. Lim, S. Kitipornchai, and K. M. Liew, "Numerical aspects for free vibration of thick plates. Part II: Numerical efficiency and vibration frequencies," *Comput. Methods Appl. Mech. Eng.* **156**(1–4), 31–44 (1998).
- <sup>16</sup>K. M. Liew, K. C. Hung, and M. K. Lim, "Free vibration studies on stress-free three-dimensional elastic solids," *Trans. ASME, J. Appl. Mech.* **62**(1), 159–165 (1995).
- <sup>17</sup>J. R. Hutchinson, "Vibrations of solid cylinders," *Trans. ASME, J. Appl. Mech.* **47**, 901–907 (1980).
- <sup>18</sup>K. M. Liew, K. C. Hung, and M. K. Lim, "Vibration of stress-free hollow cylinders of arbitrary cross section," *Trans. ASME, J. Appl. Mech.* **62**(3), 718–724 (1995).
- <sup>19</sup>A. W. Leissa and J. So, "Accurate vibration frequencies of circular cylinders from three-dimensional analysis," *J. Acoust. Soc. Am.* **98**(4), 2136–2141 (1995).
- <sup>20</sup>J. So and A. W. Leissa, "Free vibrations of thick hollow circular cylinders from three-dimensional analysis," *Trans. ASME, J. Vib. Acoust.* **119**, 89–95 (1997).
- <sup>21</sup>A. W. Leissa and J. So, "Three-dimensional vibrations of truncated hollow cones," *J. Vib. Control* **1**, 145–158 (1995).
- <sup>22</sup>LUSAS Manual, Version II, *Finite Element Library* (FEA Ltd., Surrey, United Kingdom), pp. 134–138, 183–190.

# A mixed displacement-pressure formulation for poroelastic materials

Noureddine Atalla, Raymond Panneton, and Patricia Debergue  
*GAUS, Mech. Eng., Univ. de Sherbrooke, Sherbrooke, Québec J1K 2R1, Canada*

(Received 26 January 1998; accepted for publication 10 May 1998)

Recently, finite element models based on Biot's displacement ( $\underline{u}, U$ ) formulation for poroelastic materials have been extensively used to predict the acoustical and structural behavior of multilayer structures. These models while accurate lead to large frequency dependent matrices for three-dimensional problems necessitating important setup time, computer storage and solution time. In this paper, a novel exact mixed displacement pressure ( $\underline{u}, p$ ) formulation is presented. The formulation derives directly from Biot's poroelasticity equations. It has the form of a classical coupled fluid-structure problem involving the dynamic equations of the skeleton *in vacuo* and the equivalent fluid in the rigid skeleton limit. The governing ( $\underline{u}, p$ ) equations and their weak integral form are given together with the coupling conditions with acoustic media. The numerical implementation of the presented approach in a finite element code is discussed. Examples are presented to show the accuracy and effectiveness of the presented formulation. © 1998 Acoustical Society of America. [S0001-4966(98)06008-1]

PACS numbers: 43.40.Rj, 43.50.Gf, 43.20.Gp, 43.55.Rg [CBB]

## INTRODUCTION

The vibroacoustic performance of finite multilayer systems containing poroelastic materials is of utmost importance for noise control in automobiles, aircraft and several other engineering applications. In the absence of absorbing materials, the vibroacoustic response of complex multilayer structures are classically modeled using the finite element and the boundary element methods. To account for absorbing media, finite element formulations for sound absorbing materials have been developed. They range from simple approaches (impedance techniques: Beranek and Ver, 1992; equivalent fluid models: Craggs, 1978; Panneton *et al.*, 1995) to sophisticated approaches based on the Biot theory (Kang and Bolton, 1995; Johansen *et al.*, 1995; Coyette and Wynendaele, 1995; Panneton and Atalla, 1996, 1997a). For the general case of multilayer systems containing poroelastic media, the use of the sophisticated approaches becomes necessary. These approaches are mainly based on the classical displacement ( $\underline{u}, U$ ) formulation of Biot's poroelasticity equations (Biot, 1956). However, it has been shown that while accurate the ( $\underline{u}, U$ ) formulation has the disadvantage of requiring cumbersome calculations for large finite element models and spectral analyses (Panneton, 1996; Panneton and Atalla, 1996, 1997a). To alleviate these difficulties, a mixed formulation using the solid phase displacement and the interstitial fluid pressure as variables seems more suitable for large size finite element models since it requires only four degrees of freedom per node. However, few efforts have been devoted to this idea. Lately, a simplified mixed ( $\underline{u}, p$ ) formulation was proposed by Göransson (1995). However, in his formulation, Göransson neglected the strain couplings between the fluid and solid phases of the porous material. He solved the one-dimensional wave propagation in porous media using a weighted residual formulation based on Galerkin's method. In geomechanics, several authors have investigated mixed formulations (see Simon and Zienkiewicz,

1986 for references). However, all these formulations are based on assumptions that neglect inertia coupling, which is not acceptable for vibroacoustic applications. Based on these investigations, it is widely believed in acoustics that a ( $\underline{u}, p$ ) formulation is not possible without limiting assumptions.

In this paper, an exact ( $\underline{u}, p$ ) formulation recently developed by the authors is presented (Atalla *et al.*, 1996). In this new formulation, the classical Biot-Allard equations are rewritten in terms of the solid phase macroscopic displacement vector and the interstitial fluid phase macroscopic pressure. The new coupled equations have the advantage of recasting the poroelasticity equations in the classical form of a fluid-structure coupled problem wherein the coupling is between an equivalent elastodynamic equation for the skeleton *in vacuo* and an equivalent Helmholtz equation for the fluid in the limit of a rigid skeleton. In the first part of the paper, the classical formulation is recalled. Next, the new formulation is derived followed by its numerical implementation. The coupling conditions between the presented formulation and acoustic formulation are given. Finally, examples demonstrating the accuracy and efficiency of the approach are presented.

## I. THEORY

The problem of interest deals with the prediction of the vibroacoustic response (dynamic and acoustic response) of multilayer structures made up of elastic, poroelastic and acoustic media. The poroelastic material may be bonded or unbonded to the structure. The classical assumptions concerning linear acoustic, elastic, and poroelastic wave propagation are assumed (Allard, 1993). Also, the air contained in the porous medium is initially at rest.

### A. The Biot's displacement formulation

The modeling of the poroelastic material is based on the Biot's poroelasticity equations (Biot, 1956; Allard, 1993):

$$\operatorname{div} \underline{\underline{\sigma}}^s = \rho_{11} \ddot{\underline{u}} + \rho_{12} \ddot{\underline{U}} + \tilde{b}(\dot{\underline{u}} - \dot{\underline{U}}) \quad (1)$$

$$\operatorname{div} \underline{\underline{\sigma}}^f = \rho_{22} \ddot{\underline{U}} + \rho_{12} \ddot{\underline{u}} - \tilde{b}(\dot{\underline{u}} - \dot{\underline{U}}),$$

where the tilde symbol indicates that the associated physical property is complex and frequency dependent. In Eq. (1),  $\underline{u}$  and  $\underline{U}$  denote the solid and fluid macroscopic displacement vectors, respectively. These displacements are average values in the sense of the Biot theory, i.e., the average volume displacements per unit area cross section. Densities  $\rho_{11}$  and  $\rho_{22}$  are mass coefficients which take into account the fact that the relative flow through the pores is not uniform. They are related to the mass density of the material from which the skeleton is made,  $\rho_s$ , and to the mass density of the interstitial fluid,  $\rho_0$ , by :

$$\rho_{11} = (1-h)\rho_s - \rho_{12}, \quad \rho_{22} = h\rho_0 - \rho_{12}, \quad (2)$$

where  $h$  is the porosity of the poroelastic material. The coefficient  $\rho_{12}$  accounts for the interaction between the inertia forces of the solid and fluid phases; it is function of the tortuosity of the material (Allard, 1993).  $\underline{\underline{\sigma}}^s$  and  $\underline{\underline{\sigma}}^f$  denote the partial stress tensors associated with the skeleton particle and the macroscopic fluid particle, respectively. Tensor  $\underline{\underline{\sigma}}^f$  is related to the averaged pressure prevailing in the saturating fluid by  $\underline{\underline{\sigma}}^f = -hp\underline{\underline{1}}$ , while tensor  $\underline{\underline{\sigma}}^s$  is given by  $(1-h)$  times the averaged stress tensor prevailing in the matrix of the poroelastic material. Note that  $\underline{\underline{\sigma}}^s$  and  $\underline{\underline{\sigma}}^f$  are linearly related to the partial strain tensors  $\underline{\underline{\epsilon}}^s$  and  $\underline{\underline{\epsilon}}^f$  prevailing in the skeleton and the interstitial fluid, respectively. These relations define the stiffness coupling between the solid and the fluid phases and account for dissipation due to thermal exchanges between both phases in the material. Also, they include the structural damping associated with the frame. Finally,  $\tilde{b}$  is a frequency dependent viscous damping coefficient accounting for viscous interaction forces. It can be related to the macroscopic flow resistivity of the porous material (Allard, 1993). A detailed discussion about the field quantities occurring in the Biot theory may be found in De Vries (1989) and Geerits (1996, 1997).

Using the solid and fluid displacement vectors  $(\underline{u}, \underline{U})$  as primary variables and assuming harmonic oscillations  $(e^{j\omega t})$ , the weak integral form of the poroelasticity equations, Eq. (1), reads (Panneton and Atalla, 1996):

$$\begin{aligned} & \int_{\Omega_p} (\underline{\underline{\sigma}}^s(\underline{u}, \underline{U}) : \underline{\underline{\epsilon}}^s(\delta \underline{u}) - \rho_{11} \omega^2 \underline{u} \cdot \delta \underline{u} - \rho_{12} \omega^2 \underline{U} \cdot \delta \underline{u} \\ & + j\omega \tilde{b}(\underline{u} - \underline{U}) \cdot \delta \underline{u}) d\Omega \\ & - \int_{\partial\Omega_p} \delta \underline{u} \cdot [\underline{\underline{\sigma}}^s(\underline{u}, \underline{U}) \cdot \underline{n}] dS = 0, \\ & \int_{\Omega_p} (\underline{\underline{\sigma}}^f(\underline{u}, \underline{U}) : \underline{\underline{\epsilon}}^f(\delta \underline{U}) - \rho_{22} \omega^2 \underline{U} \cdot \delta \underline{U} - \rho_{12} \omega^2 \underline{u} \cdot \delta \underline{U} \\ & - j\omega \tilde{b}(\underline{u} - \underline{U}) \cdot \delta \underline{U}) d\Omega \\ & - \int_{\partial\Omega_p} \delta \underline{U} \cdot [\underline{\underline{\sigma}}^f(\underline{u}, \underline{U}) \cdot \underline{n}] dS = 0, \quad \forall (\delta \underline{u}, \delta \underline{U}), \end{aligned} \quad (3)$$

where  $\delta \underline{u}$  and  $\delta \underline{U}$  denote admissible variations of  $\underline{u}$  and  $\underline{U}$ ,

respectively, and where  $\Omega_p$  and  $\partial\Omega_p$  denote the medium domain and its boundary.

For the finite element implementation of Eq. (1), an analogy with the three-dimensional elastic solid elements is used; however, this time, six degrees of freedom per node are used. They account for three displacement components of the solid phase and three displacement components of the fluid phase. However, because of the viscous and thermal dissipation mechanisms, the system's matrices are frequency dependent. In consequence, for large 3D multilayer structures, this formulation has the disadvantage of requiring cumbersome calculations for large finite element models and spectral analyses. To alleviate these difficulties, a mixed displacement pressure formulation is presented.

## B. The mixed displacement pressure formulation

In the following, an exact mixed formulation valid for harmonic motion is given. It derives directly from Biot poroelasticity equations, Eq. (1). The developments assume that the porous material properties are homogeneous. Note that a more general time domain formulation valid for anisotropic materials is given by Gorog *et al.* (1997).

For harmonic motion  $(e^{j\omega t})$ , introducing the effective densities

$$\begin{aligned} \tilde{\rho}_{11} &= \rho_{11} + \frac{\tilde{b}}{j\omega} \\ \tilde{\rho}_{22} &= \rho_{22} + \frac{\tilde{b}}{j\omega} \\ \tilde{\rho}_{12} &= \rho_{12} - \frac{\tilde{b}}{j\omega}, \end{aligned} \quad (4)$$

system (1) is rewritten:

$$\begin{aligned} \omega^2 \tilde{\rho}_{11} \underline{u} + \omega^2 \tilde{\rho}_{12} \underline{U} + \operatorname{div} \underline{\underline{\sigma}}^s &= 0 \\ \omega^2 \tilde{\rho}_{22} \underline{U} + \omega^2 \tilde{\rho}_{12} \underline{u} - h \nabla p &= 0. \end{aligned} \quad (5)$$

Using the second equation in (5), the displacement vector of the fluid phase  $\underline{U}$  is expressed in terms of the pressure  $p$  in the pores and in terms of the displacement vector of the solid phase particle  $\underline{u}$ :

$$\underline{U} = \frac{h}{\tilde{\rho}_{22} \omega^2} \nabla p - \frac{\tilde{\rho}_{12}}{\tilde{\rho}_{22}} \underline{u}. \quad (6)$$

This last equation will be used to express system (5) in terms of the  $(\underline{u}, p)$  variables.

### 1. The solid phase equation in terms of $(\underline{u}, p)$ variables

Using Eq. (6), the first equation in (5) transforms into:

$$\omega^2 \tilde{\rho} \underline{u} + h \frac{\tilde{\rho}_{12}}{\tilde{\rho}_{22}} \nabla p + \operatorname{div} \underline{\underline{\sigma}}^s = 0, \quad (7)$$

where the following effective density has been introduced:

$$\tilde{\rho} = \tilde{\rho}_{11} - \frac{(\tilde{\rho}_{12})^2}{\tilde{\rho}_{22}}. \quad (8)$$

Equation (7) is still dependent on the fluid phase displacement vector  $\underline{U}$  because of the dependency  $\underline{\sigma}^s = \underline{\sigma}^s(\underline{u}, \underline{U})$ . Indeed, the stress-strain relations in the Biot theory are given by (Allard, 1993):

$$\begin{aligned} \underline{\sigma}^s(\underline{u}, \underline{U}) &= \tilde{A} \operatorname{div} \underline{u} \underline{1} + 2N \underline{\epsilon}^s + \tilde{Q} \operatorname{div} \underline{U} \underline{1} \\ -hp \underline{1} &= \tilde{R} \operatorname{div} \underline{U} \underline{1} + \tilde{Q} \operatorname{div} \underline{u} \underline{1}, \end{aligned} \quad (9)$$

in which  $\underline{1}$  denotes the identity tensor, the elastic coefficients  $\tilde{A}$  and  $N$  correspond to the Lamé coefficients for elastic solids,  $\tilde{Q}$  is a coupling coefficient between the dilatation and stress of the two phases, and  $\tilde{R}$  may be interpreted as the bulk modulus of the air occupying a fraction  $h$  of a unit volume of aggregate.  $\tilde{R}$  is related to the bulk modulus  $\tilde{K}_f$  of the air in the pores by the scale factor  $h$ :  $\tilde{R} = h\tilde{K}_f$ . The elastic coefficients  $\tilde{A}$ ,  $\tilde{Q}$  and  $\tilde{R}$  are related to  $K_b$ , the bulk modulus of the skeleton *in vacuo*, to  $K_s$ , the bulk modulus of the elastic solid from which the skeleton is made and to  $\tilde{K}_f$ , the bulk modulus of the air in the pores by (Allard, 1993):

$$\tilde{A} = \frac{(1-h)[1-h-K_b/K_s]K_s + h(K_s/\tilde{K}_f)K_b}{1-h-K_b/K_s+hK_s/\tilde{K}_f} - \frac{2}{3}N, \quad (10)$$

$$\tilde{Q} = \frac{[1-h-K_b/K_s]hK_s}{1-h-K_b/K_s+hK_s/\tilde{K}_f}, \quad (11)$$

$$\tilde{R} = \frac{h^2K_s}{1-h-K_b/K_s+hK_s/\tilde{K}_f}, \quad (12)$$

where  $N$  is the complex *in vacuo* shear modulus of the skeleton taking into account structural damping. Since  $\tilde{K}_f$  takes into account the thermal effects in the pore, it has a frequency dependent complex amplitude, and so do the elasticity tensors. In consequence, in the numerical implementation of the  $(\underline{u}, \underline{U})$  formulation, the stiffness matrix associated to the frame is frequency dependent, which limits the computational efficiency of this formulation (the corresponding matrix should be reconstructed at each computational frequency).

To eliminate the dependency  $\underline{\sigma}^s = \underline{\sigma}^s(\underline{u}, \underline{U})$ , the first and second equation in Eq. (9) are combined to obtain:

$$\underline{\sigma}^s(\underline{u}, \underline{U}) = \left( \tilde{A} - \frac{\tilde{Q}^2}{\tilde{R}} \right) \operatorname{div} \underline{u} \underline{1} + 2N \underline{\epsilon}^s - h \frac{\tilde{Q}}{\tilde{R}} p \underline{1}. \quad (13)$$

Next, introducing the tensor  $\hat{\underline{\sigma}}^s$  defined by

$$\hat{\underline{\sigma}}^s(\underline{u}) = \left( \tilde{A} - \frac{\tilde{Q}^2}{\tilde{R}} \right) \operatorname{div} \underline{u} \underline{1} + 2N \underline{\epsilon}^s, \quad (14)$$

the solid phase stress tensor writes:

$$\underline{\sigma}^s(\underline{u}, \underline{U}) = \hat{\underline{\sigma}}^s(\underline{u}) - h \frac{\tilde{Q}}{\tilde{R}} p \underline{1}. \quad (15)$$

Since tensor  $\hat{\underline{\sigma}}^s$  depends only on the solid phase displacement vector, Eq. (15) may be used to eliminate the dependency  $\underline{\sigma}^s = \underline{\sigma}^s(\underline{u}, \underline{U})$  in Eq. (7). Substituting (15) into (7), the

solid phase equation is obtained in terms of the  $(\underline{u}, p)$  variables:

$$\operatorname{div} \hat{\underline{\sigma}}^s(\underline{u}) + \tilde{\rho} \omega^2 \underline{u} + \tilde{\gamma} \nabla p = 0, \quad (16)$$

where the following notation is used:

$$\tilde{\gamma} = h \left( \frac{\tilde{\rho}_{12}}{\tilde{\rho}_{22}} - \frac{\tilde{Q}}{\tilde{R}} \right). \quad (17)$$

To grasp the physical meaning of Eq. (16), note from Eqs. (10) to (12) that the expression (14) for  $\hat{\underline{\sigma}}^s$  is equivalent to:

$$\hat{\underline{\sigma}}^s(\underline{u}) = (K_b - \frac{2}{3}N) \operatorname{div} \underline{u} \underline{1} + 2N \underline{\epsilon}^s, \quad (18)$$

which is the classical stress-strain relation for an elastic solid. Moreover, since  $K_b$  and  $N$  denote the bulk modulus and the shear modulus of the skeleton *in vacuo*, respectively, tensor  $\hat{\underline{\sigma}}^s$  is the stress tensor of the material *in vacuo*. In other words,  $\hat{\underline{\sigma}}^s$  represents the stress tensor prevailing in the poroelastic material when the fluid is totally drained off. In consequence, the first two terms of Eq. (16) represent the elastodynamic equation of the material *in vacuo*. One valuable feature is that  $\hat{\underline{\sigma}}^s$  is independent of the bulk modulus of the air and hence does not depend on frequency thus increasing the efficiency of the numerical implementation.

## 2. The fluid phase equation in terms of $(\underline{u}, p)$ variables

Next, to derive the fluid phase equation in terms of  $(\underline{u}, p)$  variables, the divergence of Eq. (6) is taken and gives:

$$\operatorname{div} \underline{U} = \frac{h}{\omega^2 \tilde{\rho}_{22}} \Delta p - \frac{\tilde{\rho}_{12}}{\tilde{\rho}_{22}} \operatorname{div} \underline{u}. \quad (19)$$

Combining this equation with the second equation in (9), the fluid phase equation is obtained in terms of the  $(\underline{u}, p)$  variables:

$$\Delta p + \frac{\tilde{\rho}_{22}}{\tilde{R}} \omega^2 p + \frac{\tilde{\rho}_{22}}{h^2} \tilde{\gamma} \omega^2 \operatorname{div} \underline{u} = 0, \quad (20)$$

where  $\tilde{\gamma}$  is defined in (17).

Note that Eq. (20) is exactly the classical equivalent fluid equation for absorbing media with a source term (Allard, 1993; Panneton *et al.*, 1995). The first two terms of this equation may be obtained directly from Biot's equations in the limit of a rigid skeleton. Those two terms represent the dynamic behavior of the material when its frame is supposed motionless. It is well known that Eq. (20) models correctly the behavior of rigid porous materials and/or situations in which the material is not mechanically excited or directly bonded to a vibrating structure and that for frequencies higher than the decoupling frequency (Panneton and Atalla, 1996).

## 3. Poroelasticity equations in terms of $(\underline{u}, p)$ variables

Grouping Eqs. (16) and (20), the Biot poroelasticity equations in terms of  $(\underline{u}, p)$  variables are given by:

$$\operatorname{div} \hat{\underline{\underline{\sigma}}}^s(\underline{u}) + w^2 \tilde{\rho} \underline{u} + \tilde{\gamma} \nabla p = 0 \quad (21)$$

$$\Delta p + \omega^2 \frac{\tilde{\rho}_{22}}{\tilde{R}} p - \omega^2 \frac{\tilde{\rho}_{22}}{h^2} \tilde{\gamma} \operatorname{div} \underline{u} = 0.$$

This system exhibits the classical form of a fluid-structure coupled equation. However, the coupling is of a volume nature since the poroelastic material is a superposition in space and time of the elastic and fluid phases. The first two terms of the structure equation represent the dynamic behavior of the material *in vacuo* while the first two terms of the fluid equation represent the dynamic behavior of the fluid when the frame is supposed motionless. The third terms in both equations couple the dynamics of the two phases.

The next section discusses the implementation of this formulation in a finite element code. It will be shown that this formulation is symmetric. One obvious advantage of the presented formulation is that four degrees of freedom are needed rather than 6 for the classical  $(\underline{u}, \underline{U})$  formulation.

### C. The weak integral formulation

Let  $\delta u$  and  $\delta p$  be two admissible variations of the displacement field  $u$  and the pressure field  $p$ , respectively. Then, using Galerkin's procedure (Reddy, 1991), the following symmetric  $(\underline{u}, p)$  coupled weak integral formulation is obtained after few algebraic manipulations:

$$\begin{aligned} & \int_{\Omega_p} \hat{\underline{\underline{\sigma}}}^s(\underline{u}) : \underline{\underline{\varepsilon}}^s(\delta \underline{u}) d\Omega - \omega^2 \int_{\partial\Omega_p} \tilde{\rho} \underline{u} \cdot \delta \underline{u} d\Omega \\ & - \int_{\Omega_p} \tilde{\gamma} \nabla p \cdot \delta \underline{u} d\Omega - \int_{\partial\Omega_p} [\hat{\underline{\underline{\sigma}}}^s \cdot \underline{n}] \cdot \delta \underline{u} dS = 0, \quad (22) \\ & \int_{\Omega_p} \left[ \frac{h^2}{\omega^2 \tilde{\rho}_{22}} \nabla p \cdot \nabla \delta p - \frac{h^2}{\tilde{R}} p \delta p \right] d\Omega - \int_{\Omega_p} \tilde{\gamma} \nabla \delta p \cdot \underline{u} d\Omega \\ & + \int_{\partial\Omega_p} \left[ \tilde{\gamma} u_n - \frac{h^2}{\tilde{\rho}_{22} \omega^2} \frac{\partial p}{\partial n} \right] \delta p dS = 0, \quad \forall (\delta \underline{u}, \delta p), \end{aligned}$$

where  $\Omega_p$  and  $\partial\Omega_p$  denote the poroelastic domain and its boundary. Note from Eq. (22) the volume nature of the symmetric coupling between the two phases.

Equation (22) exhibits several advantages of the presented formulation over the  $(\underline{u}, \underline{U})$  formulation. First, the stiffness matrix associated with the solid phase is frequency independent. Second, it accounts naturally for poroelastic-poroelastic interfaces; no essential boundary conditions are needed. Indeed, let indices 1 and 2 denote the two interfacing poroelastic media, respectively. The continuity equations are given by (Panneton and Atalla, 1996):

$$\begin{aligned} \underline{u}_1 &= \underline{u}_2 \\ h_1(u_{1n} - U_{1n}) &= h_2(u_{2n} - U_{2n}) \\ p_1 &= p_2 \\ \underline{\underline{\sigma}}_1^s \cdot \underline{n} &= \underline{\underline{\sigma}}_2^s \cdot \underline{n}, \end{aligned} \quad (23)$$

where the first condition ensures the continuity of the solid phase displacement vector. The second equation ensures the continuity of the relative mass flux across the boundary. The

two last equations ensure the continuity of the total normal stresses and the interstitial fluid pressure, respectively. Note that the total stress tensor  $\underline{\underline{\sigma}}^t$  is the total stress tensor given by:

$$\underline{\underline{\sigma}}^t(\underline{u}, \underline{U}) = \underline{\underline{\sigma}}^s(\underline{u}, \underline{U}) + \underline{\underline{\sigma}}^f(\underline{u}, \underline{U}) = \underline{\underline{\sigma}}^s(\underline{u}, \underline{U}) - h p \underline{\underline{1}}, \quad (24)$$

which may be written in terms of the in-vacuo stress tensor  $\hat{\underline{\underline{\sigma}}}^s$  using Eq. (15):

$$\underline{\underline{\sigma}}^t(\underline{u}, \underline{U}) = \hat{\underline{\underline{\sigma}}}^s(\underline{u}, \underline{U}) - h \left[ 1 + \frac{\tilde{Q}}{\tilde{R}} \right] p \underline{\underline{1}}. \quad (25)$$

Using the following two relations, derived easily from Eqs. (6), (16) and (17):

$$\begin{aligned} (1-h) \underline{u} \cdot \underline{n} + h \underline{U} \cdot \underline{n} &= \left[ 1 - h - h \frac{\tilde{Q}}{\tilde{R}} \right] \underline{u} \cdot \underline{n} \\ &- \left[ \tilde{\gamma} \underline{u} \cdot \underline{n} - \frac{h^2}{\tilde{\rho}_{22} \omega^2} \frac{\partial p}{\partial n} \right], \quad (26) \end{aligned}$$

$$h(\underline{u} - \underline{U}) \cdot \underline{n} = \left[ \tilde{\gamma} \underline{u} \cdot \underline{n} - \frac{h^2}{\tilde{\rho}_{22} \omega^2} \frac{\partial p}{\partial n} \right] + h \left[ 1 + \frac{\tilde{Q}}{\tilde{R}} \right] \underline{u} \cdot \underline{n}, \quad (27)$$

the coupling conditions given by Eq. (23) may be written in terms of the  $(\underline{u}, p)$  variables as follows

$$\begin{aligned} \underline{u}_1 &= \underline{u}_2 \\ \left[ \tilde{\gamma}_1 u_{1n} - \frac{h_1^2}{\tilde{\rho}_{22} \omega^2} \frac{\partial p_1}{\partial n} \right] + h \left[ 1 + \frac{\tilde{Q}_1}{\tilde{R}_1} \right] u_{1n} \\ &= \left[ \tilde{\gamma}_2 u_{2n} - \frac{h_2^2}{\tilde{\rho}_{22} \omega^2} \frac{\partial p_2}{\partial n} \right] + h \left[ 1 + \frac{\tilde{Q}_2}{\tilde{R}_2} \right] u_{2n} \end{aligned} \quad (28)$$

$$p_1 = p_2$$

$$\hat{\underline{\underline{\sigma}}}_1^s \cdot \underline{n} - h \left[ 1 + \frac{\tilde{Q}_1}{\tilde{R}_1} \right] u_{1n} = \hat{\underline{\underline{\sigma}}}_2^s \cdot \underline{n} - h \left[ 1 + \frac{\tilde{Q}_2}{\tilde{R}_2} \right] u_{2n}.$$

Using the fourth relation, the first boundary integrals in Eq. (22) related to the interface  $\partial\Omega_p$  between the two coupled domains reads:

$$\begin{aligned} I_1 &= - \int_{\partial\Omega_p} h_1 \left( 1 + \frac{\tilde{Q}_1}{\tilde{R}_1} \right) p_1 \delta u_{1n} dS \\ &+ \int_{\partial\Omega_p} h_2 \left( 1 + \frac{\tilde{Q}_2}{\tilde{R}_2} \right) p_2 \delta u_{2n} dS. \end{aligned} \quad (29)$$

Similarly, using the second and fourth relations of Eq. (28), the second boundary integral of Eq. (22) reduces to

$$\begin{aligned} I_2 &= - \int_{\partial\Omega_p} h_1 \left( 1 + \frac{\tilde{Q}_1}{\tilde{R}_1} \right) u_{1n} \delta p_1 dS \\ &+ \int_{\partial\Omega_p} h_2 \left( 1 + \frac{\tilde{Q}_2}{\tilde{R}_2} \right) u_{2n} \delta p_2 dS. \end{aligned} \quad (30)$$

The signs in both equations account for the direction of the normal vector which is assumed to be directed from medium



1 toward medium 2. Equations (29) and (30) show that the two poroelastic media will be coupled through symmetrical coupling terms. This coupling occurs naturally between the solid phase normal displacement of one medium and the interstitial fluid pressure of the other medium. In addition to these surface coupling terms, the kinematic relation  $\underline{u}_1 = \underline{u}_2$  and  $p_1 = p_2$  will have to be explicitly applied on  $\partial\Omega_p$ .

For the majority of poroelastic media used in acoustics  $K_b/K_s \ll 1$  (Allard, 1993). Thus since [see Eqs. (11) and (12)]:

$$h \frac{\tilde{Q}}{R} = 1 - h - \frac{K_b}{K_s}, \quad (31)$$

we have:

$$h \left( 1 + \frac{\tilde{Q}}{R} \right) \cong 1. \quad (32)$$

In this case, both integrals  $I_1$  and  $I_2$  fall to zero and only the kinematic relations have to be applied. These conditions are taken into account through assembling. This is in contrast with the  $(u, U)$  formulation which involves the imposition of the second boundary condition in (23) through kinematic relations.

Another advantage of the presented  $(u, p)$  formulation over the  $(u, U)$  formulation lies in its coupling with air media. Indeed, denoting by  $p^a$  the pressure in the air layer, the continuity equations are given by (Panneton and Atalla, 1996):

$$\begin{aligned} \frac{1}{\rho_0 \omega^2} \frac{\partial p^a}{\partial n} &= (1-h)u_n + hU_n \\ \underline{\underline{\sigma}}^t \cdot \underline{\underline{n}} &= -p^a \underline{\underline{1}} \cdot \underline{\underline{n}} \\ \underline{\underline{\sigma}}^s \cdot \underline{\underline{n}} &= -(1-h)p^a \underline{\underline{1}} \cdot \underline{\underline{n}}; \quad \underline{\underline{\sigma}}^f \cdot \underline{\underline{n}} = -hp^a \underline{\underline{1}} \cdot \underline{\underline{n}}. \end{aligned} \quad (33)$$

The first equation ensures the continuity of the normal volume velocity (modified Euler's equation due to the porosity), while the second and third equations ensure the continuity of the normal stresses. Using Eqs. (25) and (26), the coupling conditions in Eq. (33) are proved to be equivalent to:

$$\begin{aligned} \left[ 1 - h - h \frac{\tilde{Q}}{R} \right] u_n - \left[ \tilde{\gamma} u_n - \frac{h^2}{\tilde{\rho}_{22} \omega^2} \frac{\partial p}{\partial n} \right] &= \frac{1}{\rho_0 \omega^2} \frac{\partial p^a}{\partial n} \\ p &= p^a \end{aligned} \quad (34)$$

$$\underline{\underline{\hat{\sigma}}}^s \cdot \underline{\underline{n}} = \left[ h \frac{\tilde{Q}}{R} - (1-h) \right] p \underline{\underline{n}}.$$

Note that the first and third conditions in (34) lead to symmetric coupling terms of the form [see Eq. (22)]:

$$I_1 = \int_{\partial\Omega_p} \left( 1 - h - \frac{\tilde{Q}}{R} \right) p \delta u_n dS \quad (35)$$

and

$$I_2 = \int_{\partial\Omega_p} \left( 1 - h - \frac{\tilde{Q}}{R} \right) u_n \delta p dS, \quad (36)$$

where  $\partial\Omega_p$  denotes the poroelastic-air interface. Once again for the majority of porous materials used in acoustics, the approximation given by Eq. (32) applies and these coupling terms vanish. Thus, only the continuity of the pressure at the poroelastic-air interface should be accounted for. In this case, contrary to the  $(\underline{u}, U)$  formulation, no coupling matrix is needed. This represents another advantage and time saving feature of the presented formulation.

Finally, it is worth mentioning that a detailed description of the boundary, support and loading conditions of the presented  $(\underline{u}, p)$  formulation together with corresponding validation examples will be presented in a sequel paper (Debergue *et al.*, 1998).

## II. NUMERICAL IMPLEMENTATION

In the presented work, the weak formulation [Eq. (22)] has been discretized using linear volume elements with four degrees of freedom per node: the three solid macroscopic displacements  $\underline{u}$  and the pressure  $p$  in the interstitial fluid. Two finite volume elements have been implemented: a six node wedge element and an eight node brick element. Accordingly, within a finite element, it is assumed that the solid phase displacement vector and the pressure can be represented in matrix form following

$$\underline{u}^e = [N_s] \{u_n\}^e \quad \text{and} \quad p^e = [N_f] \{p_n\}^e, \quad (37)$$

where  $[N_s]$  and  $[N_f]$  are the element's shape functions used to approximate the solid phase displacement vector and the interstitial pressure within element "e."  $\{u_n\}^e$  and  $\{p_n\}^e$  are respectively the nodal displacement and the nodal pressure variables.

Since the solid phase governing equation is similar to a 3D elastodynamic equation, an analogy with solid elements is used. Similarly, since the fluid phase equation is similar to the Helmholtz's equation, an analogy with acoustic finite elements is used.

Substituting Eq. (37) into Eq. (22), the following matrices are obtained:

$$\int_{\Omega_p} \underline{\underline{\hat{\sigma}}}^s(\underline{u}) : \underline{\underline{\epsilon}}^s(\delta \underline{u}) d\Omega \Rightarrow \langle \delta u_n \rangle [K] \{u_n\}, \quad (38)$$

$$\int_{\Omega_p} \tilde{\rho} \underline{u} \cdot \delta \underline{u} d\Omega \Rightarrow \langle \delta u_n \rangle [\tilde{M}] \{u_n\}, \quad (39)$$

$$\int_{\Omega_p} \tilde{\gamma} \nabla p \cdot \delta \underline{u} dS \Rightarrow \langle \delta u_n \rangle [\tilde{C}] \{p_n\}, \quad (40)$$

$$\int_{\Omega_p} \frac{h^2}{\tilde{\rho}_{22}} (\nabla p \cdot \nabla \delta p) d\Omega \Rightarrow \langle \delta p_n \rangle [\tilde{H}] \{p_n\}, \quad (41)$$

$$\int_{\Omega_p} \frac{h^2}{R} p \cdot \delta p d\Omega \Rightarrow \langle \delta p_n \rangle [\tilde{Q}] \{p_n\}, \quad (42)$$

$$\int_{\Omega_p} \tilde{\gamma} \underline{u} \cdot \nabla \delta p dS \Rightarrow \langle \delta p_n \rangle [\tilde{C}]^T \{u_n\}, \quad (43)$$

where  $\{u_n\}$  and  $\{p_n\}$  represent the solid phase and the fluid phase global nodal variables, respectively.  $[\tilde{M}]$  and  $[K]$  represent equivalent mass and stiffness matrices for the solid

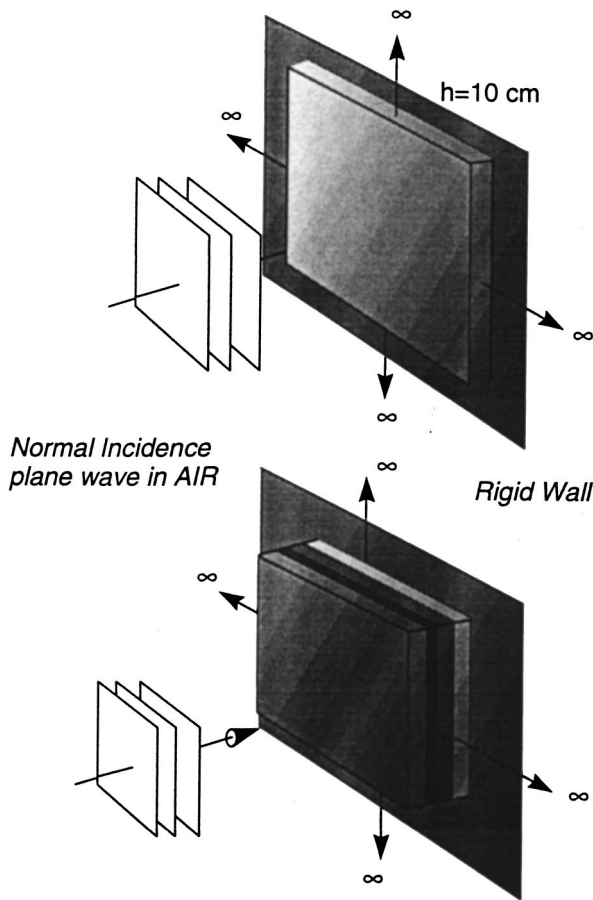


FIG. 1. Geometry of the surface impedance problem. (a) Single poroelastic layer; and (b) multilayered poroelastic material.

phase, respectively.  $[\tilde{H}]$  and  $[\tilde{Q}]$  represent equivalent kinetic and compression energy matrices for the fluid phase, respectively. Finally,  $[\tilde{C}]$  is a volume coupling matrix between the solid phase displacement variables and the fluid phase pressure variable. Note that contrary to a classical fluid-structure coupling problem, the coupling within a poroelastic system is of a volume nature. The numerical evaluation of the different matrices is classical and will not be detailed in this paper. Note finally that the discretization of the interface integrals depends on the boundary conditions of the system (= loading conditions).

Substituting Eqs. (38) to (43) into Eq. (22), the following coupled system is formed:

$$\begin{pmatrix} [K] - \omega^2[\tilde{M}] & -[\tilde{C}] \\ -\omega^2[\tilde{C}]^T & [\tilde{H}] - \omega^2[\tilde{Q}] \end{pmatrix} \begin{Bmatrix} u_n \\ p_n \end{Bmatrix} = \begin{Bmatrix} F_s \\ F_p \end{Bmatrix}, \quad (44)$$

where  $\{F_p\}$  denotes the loading vector for the poroelastic medium (these vectors depends on the nature of the excitation; they are not detailed here). Solution of system (44) leads simultaneously to the nodal displacements of the solid phase and to the nodal pressures of the fluid phase. Once more, note that system (44) exhibits the classical form of a fluid structure coupled system. This system is smaller compared to the corresponding system in the classical  $(u, U)$  formulation since four degrees of freedom are used rather

than six. Moreover, for a homogeneous poroelastic medium, all the frequency dependency in matrices (38) to (43) show up as multiplication coefficients that may be taken out of the integrals. Thus, the matrices may be calculated and assembled, once for all, for a given mesh. The spectra of the frequency dependent coefficient are accounted for during the formation of the global system (44). This is in contrast with the  $(u, U)$  formulation where the frequency dependence of the stiffness matrix is implicit in the stress-strain relations, thus necessitating recalculation of the matrix at each frequency.

Moreover, it is worth mentioning that the presented formulation while improving significantly the performances of the numerical solutions of the Biot's poroelasticity equations still suffers from the necessity of using a spectral approach necessitated by the nonlinearity of the frequency dependence of the final matrix system. At this stage of the research, two potential solutions may be mentioned. The first is the use of a set of acceptable approximations that lead to a linearisation of the matrix system (see Panneton and Atalla, 1997b). The second is to use the selective modal reduction technique developed by Sgard *et al.* (1997).

Finally, recall from the previous section that coupling conditions are accounted for naturally in the presented formulation compared to the  $(u, U)$  formulation. The above mentioned features of the presented approach lead to important savings in setup and solution time as it will be demonstrated in the following numerical examples.

### III. NUMERICAL EXAMPLES

In the following, the presented  $(u, p)$  formulation is validated by comparisons with the  $(u, U)$  formulation for both two-dimensional and three-dimensional problems. Note that detailed validation examples for the  $(u, U)$  formulation and its interface with elastic and poroelastic media have been presented elsewhere (Panneton and Atalla, 1996, 1997a).

#### A. Surface impedance for a single poroelastic layer

As a first example, the surface impedance of laterally infinite poroelastic materials predicted by the presented  $(u, p)$  finite element Biot model of Eq. (21) is compared with the prediction of the  $(u, U)$  formulation. The configuration under study is depicted in Fig. 1(a). A laterally infinite glass wool layer, described in Table I, is bonded onto a rigid impervious wall. A normal incidence plane wave of unit amplitude excites the absorbing material. To simulate the laterally infinite extent with the finite element model, only the axial macroscopic displacements are considered, i.e., the lateral displacements are set to zero. For both formulations, the poroelastic domain is meshed using an eight node linear brick element. A mesh of  $7 \times 7 \times 5$  elements was used. The normal incidence surface impedance is calculated using the axial nodal solid and fluid components,  $u_n$  and  $U_n$  respectively, at the input surface for the unit acoustic pressure excitation by the following equation:

$$Z_n = \frac{1}{j\omega(hU_n + (1-h)u_n)}. \quad (45)$$

TABLE I. Physical properties and dimensions of the poroelastic materials.

	$k_s$	$\rho_l$ (kg/m <sup>3</sup> )	$\sigma$ (Ns/m <sup>4</sup> )	$h$	$N$ (kPa)	$\nu$	$\Lambda$ (m)	$\Lambda'$ (m)	Thickness (cm)
Glass wool	1.06	130	40 000	0.94	2200 (1+j0.1)	0	$0.56 \times 10^{-4}$	$1.10 \times 10^{-4}$	10
Blanket	1.18	41	34 000	0.98	110(1+j0.015)	0.3	$0.60 \times 10^{-4}$	$0.87 \times 10^{-4}$	0.4
Screen	2.56	125	$320 \times 10^4$	0.80	1000 (1+j0.1)	0.3	$0.06 \times 10^{-4}$	$0.24 \times 10^{-4}$	0.08
Foam A	2.52	31	87 000	0.97	55 (1+j0.055)	0.3	$0.37 \times 10^{-4}$	$1.19 \times 10^{-4}$	0.5
Foam B	1.98	16	65 000	0.99	18 (1+j0.1)	0.3	$0.37 \times 10^{-4}$	$1.21 \times 10^{-4}$	1.6
Fiberglass	1.4	30	25 000	0.95	21 (1+j0.05)	0.0	$0.93 \times 10^{-4}$	$0.93 \times 10^{-4}$	7.62

For the formulation, the normal displacement of the fluid phase  $U_n$  is calculated using Eq. (6). This equation necessitates the evaluation of the nodal values of the pressure gradient. The classical procedure relying on evaluation of the pressure gradients at Gauss integration points followed by a least-square procedure in order to get nodal values is used. Note that the results of the  $(u, U)$  finite element Biot model have been validated by comparison with an exact analytical calculation (Allard, 1993). Figure 2 presents the real and imaginary parts of the surface impedance predicted by both models. An excellent agreement is observed. For this simple problem, the  $(u, p)$  formulation took approximately one-fifth of the time needed for the  $(u, U)$  formulation.

### B. Surface impedance for a multilayer poroelastic material

To show the efficiency of the approach, the surface impedance of a laterally infinite multilayer poroelastic material is calculated. The configuration under study is depicted in Fig. 1(b). A laterally infinite multilayer poroelastic material is bonded onto a rigid impervious wall. From the front face to the rear face, the multilayer consists of a blanket, a screen, foam A, and foam B. The material properties are listed in Table I. A normal incidence plane wave of unit amplitude excites the absorbing material. To simulate the laterally infi-

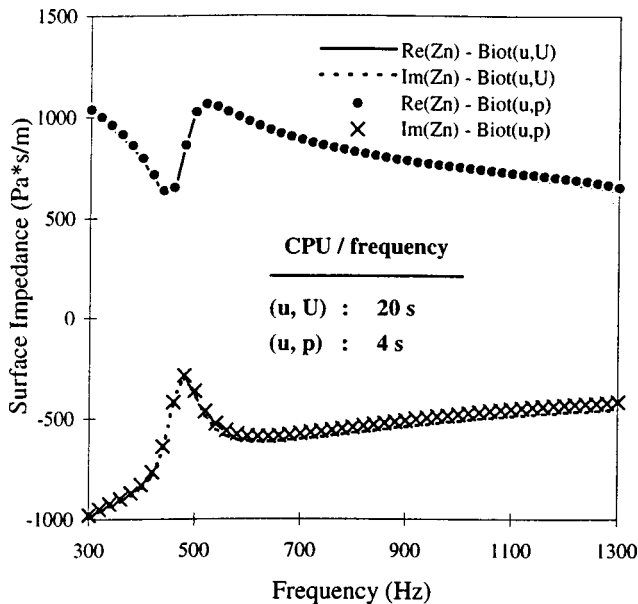


FIG. 2. Comparison of the surface impedance calculated with the  $(u, U)$  and the  $(u, p)$  Biot finite element models for the laterally infinite glass wool layer of Table I.

nite extent with the finite element model, only the axial macroscopic displacements are considered, i.e., the lateral displacements are set to zero. Identical meshes using eight node linear brick elements are used for both formulations. The cross section of the material was meshed using  $7 \times 7$  elements. The blanket, the screen, foam A and foam B were meshed using five elements. Note that this problem has been validated elsewhere by comparison with an analytical calculation (Allard, 1993). Figure 3 compares the real and imaginary parts of the surface impedance predicted by both models. A perfect agreement is observed. For this problem, the  $(u, p)$  formulation took approximately one-fourth the time needed for the  $(u, U)$  formulation.

### C. A rigid cavity with surface absorption

Next, a coupled acoustic-poroelastic problem is considered. The geometry of the problem is depicted in Fig. 4. A wall of a rigid cavity (dimensions:  $0.35 \text{ m} \times 0.22 \text{ m} \times 0.01 \text{ m}$ ) is treated with 10 cm of the fiberglass of Table I. The fiberglass is totally bonded to the rigid wall. The system is excited with a point source positioned at a corner of the rigid cavity. The quadratic pressure in the cavity is calculated using the  $(u, U)$  and the  $(u, p)$  formulations. Identical meshes are used for both formulations. The cavity is discretized using six-node linear pentahedron acoustic elements with one

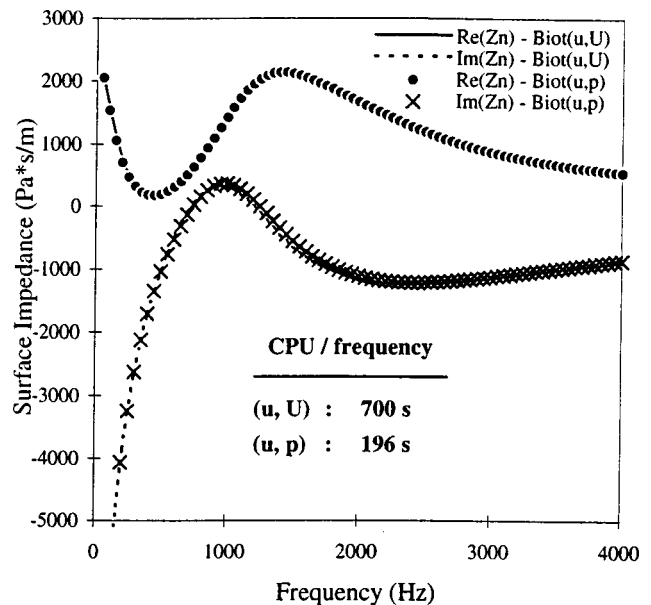


FIG. 3. Comparison of the surface impedance between the  $(u, U)$  and the  $(u, p)$  Biot finite element models for the laterally infinite multilayer.

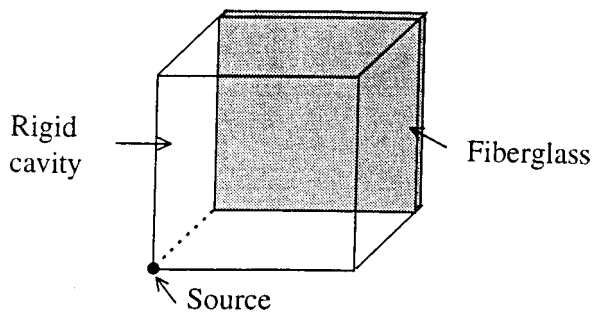


FIG. 4. Geometry of the acoustic-poroelastic problem.

degree-of-freedom per node: the acoustic pressure. A  $7 \times 7 \times 7$  mesh is used for the cavity. For the poroelastic domain, a  $7 \times 7 \times 3$  mesh is used. Note that this problem has been validated elsewhere by comparison with an impedance model for the poroelastic material (Atalla and Panneton, 1996). The results of the calculation are given in Fig. 5. Once again, excellent agreement is found between the two approaches. The  $(u, p)$  formulation took approximately one-twelfth of the time needed with the  $(u, U)$  formulation. This is mostly due to the reduction of the number of degrees of freedom for the problem and the more natural way of accounting for the coupling between the poroelastic and the acoustic domain.

#### IV. CONCLUSION

The presented mixed  $(u, p)$  formulation for poroelastic materials has several features:

- (1) It is exact, in the sense that no new assumptions are introduced beyond those governing Biot's poroelastic equations.
- (2) It leads to a classical coupled fluid-structure problem involving the dynamic equations of the skeleton *in vacuo* and the equivalent fluid in the rigid skeleton limit.

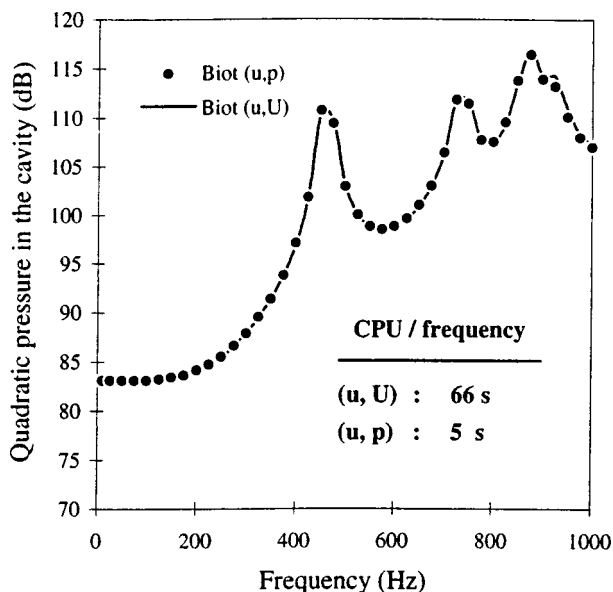


FIG. 5. Comparison of the quadratic velocity at the poroelastic surface calculated with the  $(u, U)$  and the  $(u, p)$  Biot finite element models for the cavity problem of Fig. 4.

- (3) It handles naturally coupling conditions with acoustic and other pyroelastic media.
- (4) It involves four degrees of freedom per node element compared to six for the classical  $(u, U)$  formulation; important savings in computer storage and solution time are achieved.
- (5) The physical nature of its coupled equations and its variables allows for efficient numerical implementation; important savings in setup and solution time are achieved.
- (6) For the presented numerical simulations, the  $(u, p)$  was shown to be 5 to 12 times faster than the  $(u, U)$  formulation with identical accuracy.

#### ACKNOWLEDGMENTS

The authors thank Professors Jean-François Allard and M. A. Hamdi for various stimulating discussions during this work. Thanks are also expressed to Bombardier Inc. Canada, N.S.E.R.C. and F.C.A.R. for their financial support.

Allard, J.-F. (1993). *Propagation of Sound in Porous Media: Modeling Sound Absorbing Materials* (Elsevier, New York).

Atalla, N., and Panneton, R. (1996). "The effects of multilayer sound-absorbing treatments on the noise field inside a plate backed cavity," *Noise Control Eng. J.* **44**, 235–243.

Atalla, N., Panneton, R., Debergue, P., and Allard, J.-F. (1996). "A mixed displacement pressure formulation for Biot's poroelasticity equations," 131st meeting of the A.S.A., Indianapolis.

Beranek, I. I., and Vér, I. L. (1992). *Noise and Vibration Control Engineering. Principles and Application* (Wiley, New York).

Biot, M. A. (1956). "The theory of propagation of elastic waves in a fluid-saturated porous solid," *J. Acoust. Soc. Am.* **28**, 168–191.

Coyette, J. P., and Wynendaele, H. (1995). "A finite element model for predicting the acoustic transmission characteristics of layered structures," *Proceedings of INTER-NOISE 95*, 1279–1282.

Craggs, A. (1978). "A finite element for rigid porous absorbing materials," *J. Sound Vib.* **61**, 101–111.

Geerits, T. W. (1996). "Acoustic wave propagation through porous media, revisits," *J. Acoust. Soc. Am.* **100**, 2949–2959.

Geerits, T. W. (1997). "Acoustic wave propagation through porous media: Theory and experiments," *J. Acoust. Soc. Am.* **102**, 2495–2510.

Debergue P., Panneton, R., and Atalla, N. (1998). "Boundary conditions for the weak formulation of the mixed  $(u, p)$  poroelasticity problem," *J. Acoust. Soc. Am.* (submitted for publication).

De Vries, S. M. (1989). "Propagation of transient acoustic waves in porous media," Ph.D. thesis, Delft University of Technology.

Göransson, P. (1995). "A weighted residual formulation of the acoustic wave propagation through a flexible porous material and comparison with a limp material model," *J. Sound Vib.* **182**, 479–494.

Gorog, S., Panneton, R., and Atalla, N. (1997). "Mixed displacement-pressure formulation for acoustic anisotropic open porous media," *J. Appl. Phys.* **82**, 4192–4196.

Johansen, T. F., Allard, J.-F., and Brouard, B. (1995). "Finite element method for predicting the acoustical properties of porous samples," *Acta Acust.* (submitted for publication).

Kang, Y. J., and Bolton, J. S. (1995). "Finite element modeling of isotropic elastic porous materials coupled with acoustical finite elements," *J. Acoust. Soc. Am.* **98**, 635–643.

Panneton, R. (1996). "Modélisation numérique par éléments finis des structures complexes absorbantes," Ph. D. thesis, Univ. de Sherbrooke, Québec, Canada.

Panneton, R., and Atalla, N. (1996). "Numerical prediction of sound transmission through multilayer systems with isotropic poroelastic materials," *J. Acoust. Soc. Am.* **100**, 346–354.

Panneton, R., and Atalla, N. (1997a). "An efficient finite element scheme for solving the three-dimensional poroelasticity problem in acoustics," *J. Acoust. Soc. Am.* **101**, 3287–3298.

- Panneton, R., and Atalla, N. (1997b). "Low-frequency approximations for acoustic porous materials: Linearization of the poroelasticity eigenvalue problem," *Trans. CSME* **21**, 401–413.
- Panneton, R., Atalla, N., and Charron, F. (1995). "A finite element formulation for the vibro-acoustic behaviour of double plate structures with cavity absorption," *Can Aero. Space J.* **41**, 5–12.
- Reddy, J. N. (1991). *Applied Functional Analysis and Variational Methods in Engineering* (Krieger, Malabar, FL).
- Sgard, F., Atalla, N., and Panneton, R. (1997). "A model reduction technique for the finite-element formulation of Biot's poroelasticity equations in acoustics," 134th Meeting ASA, San Diego, December 1997.
- Simon, B. R., Wu, J. S. S., Zienkiewicz, O. C., and Paul, D. K. (1986). "Evaluation of  $u-w$  and  $u-\pi$  finite element formulation for the dynamic response of saturated porous media using one-dimensional models," *Int. J. Numer. Anal. Methods Geomech.* **10**, 461–482.

# A wavelet approach to the active structural acoustic control

P. Masson, A. Berry, and P. Micheau

*G.A.U.S., Mechanical Engineering Department, Université de Sherbrooke, Sherbrooke, Québec J1K 2R1, Canada*

(Received 24 February 1997; accepted for publication 24 April 1998)

This paper presents a new cost function to be used in active control strategies, approximating the radiated acoustic power from a planar structure by a wavelet transform. This cost function is defined to be global, i.e., in terms of energy, and in the wave number domain to exploit the fact that only wave number components located in the supersonic region contribute to sound power radiation. It is shown that the wavelet transform of the transverse displacement field can provide an energy localization both in the supersonic region and spatially on the structure. Thus, the new cost function is defined as being representative of the radiated acoustic power and is obtained from a wavelet transform which depends solely on a scale parameter which is directly related to the frequency so that this representation extends over a broadband frequency range without requiring more than a single step, i.e., the wavelet transformation. The wavelet approach is compared to the radiated acoustic power from simply supported beams of finite and infinite width and very good agreement is obtained. Optimal control simulations are performed to validate the use of the wavelet transform as the cost function in an active control strategy. The performance obtained using the wavelet approach as the cost function compares advantageously with the performance obtained using the radiated acoustic power. © 1998 Acoustical Society of America. [S0001-4966(98)01108-4]

PACS numbers: 43.40.Rj, 43.60.Gk, 43.50.Ki, 43.40.At [CBB]

## INTRODUCTION

Active noise control (ANC)<sup>1</sup> and active structural acoustic control (ASAC)<sup>2</sup> techniques have been used in low-frequency noise reduction, where passive methods are inefficient. While active noise control requires the use of actuators located in the acoustic field, i.e., loudspeakers, the active structural acoustic control allows for the integration of both the error sensors and the actuators in the structure itself, following the trend towards smart materials. Moreover, it has been shown that, most of the time, ASAC has a lower requirement on the number of secondary sources needed to perform the control as compared to ANC.

In the context of ASAC, error sensors like accelerometers<sup>3-5</sup> have been employed to measure acceleration or velocity, while embedded error sensors like PVDF films<sup>6</sup> and fiber optic sensors<sup>7,8</sup> have been proposed to measure strain. Actuators can be implemented as point forces or piezoelectric transducer (PZT) patches.<sup>9</sup> The information given by the error sensors was used in the definition of cost functions based either on the far-field pressure in prescribed directions,<sup>3</sup> the volume velocity,<sup>10,11</sup> or the radiated acoustic power.<sup>8,12</sup> The latter appears to be very promising as it ensures global control and, working in the wave number domain,<sup>13,14</sup> allows for proper concentration of the control effort in the supersonic region of the structural displacement wave number spectrum, where the radiating wave number components are located.

The control strategy based on the radiated acoustic power and defined in the wave number domain first requires the wave number transformation of the displacement (or acceleration) field of the structure. The supersonic (radiating) components of the spectrum can then be identified and minimized. The restriction to the supersonic region can be per-

formed using an assumed model with discrete sensors,<sup>15</sup> thus requiring, in addition to the wave number transformation, an additional step. Avoiding this step and in order to restrict the spatial aliasing inherent to the use of discrete sensors, an interesting alternative is to use a low-pass spatial wave number filtering approach with shaped PVDF sensors.<sup>14,16,17</sup> The shape of the sensors is then dependent on the extent of the supersonic region, which means that it depends directly on the acoustic frequency. For broadband excitation, one can use either multi-shaped sensors, each shape corresponding to a given resonance frequency of the structure to be controlled, or single-shaped sensors corresponding to the highest resonance frequency to be controlled.<sup>17</sup> This approach, however, is inappropriate for two-dimensional displacement fields because the PVDF sensor cannot distinguish between the components of the strain, leading to inadequate filtering. In all of these approaches, the estimation of the radiated acoustic power would require an additional step, i.e., the integration of the supersonic components of the spectrum.

This paper is therefore concerned with the definition of a global cost function in the wave number domain, requiring one or very few space-wave-number transformations (no extra filtering or costly integration) and using discrete error sensors. To perform efficient restriction to the supersonic region using a single space-wave-number transformation, the wavelet transform is chosen in this paper. It is known that the wavelet transform has the property of localizing the energy both in a given region of the wave number spectrum and spatially on the structure. The approach presented in this paper thus benefits from the wavelet framework, even if the analysis is mostly herein restricted to the wave number localization in order to simplify the illustration of the approach. The use of the spatial localization property could

allow the development of a control strategy adapted to spatial variation of vibratory phenomena. The approach could then be well suited for controlling the acoustic power radiated from planar structures vibrating below the critical frequency where it is known that the structures radiate through corner and edge modes (regions of uncanceled volume velocity).<sup>18</sup> Another interesting application of the spatial localization property of the wavelet transform is the far-field radiation of spatially local, highly irregular scatterers on planar structures (rivets, joints,...).<sup>19</sup>

While the spatial localization is not fully exploited in this paper, the localization of the wavelet transform in the wave number domain is herein specified in order to follow the variation of the extent of the supersonic region with the frequency.<sup>20</sup> The cost function defined in terms of wavelet transforms is valid over a broad frequency range and is defined as a representative quantity of the radiated acoustic power. This cost function is first validated through a comparison with the radiated acoustic power and both the wavelet-based and the radiated acoustic-power-based approaches are used within an optimal control situation so that the performance of the wavelet approach can be evaluated. For simplicity, the wavelet approach is herein presented for a one-dimensional case.

Some fundamentals of the wavelet analysis are first presented. The radiated acoustic power and the wavelet approaches are then compared and assessed in the context of optimal control. The acoustic radiation from a baffled rectangular thin beam in a fluid is considered in this work.

## I. WAVELET THEORY

The use of wavelets in the definition of a cost function requires a basic knowledge of the wavelet theory. This section thus presents some fundamentals in wavelet transformation, followed by a description of the wavelet basis and its appropriate representation for the calculation of the transform.

### A. Wavelet analysis

The well-known Fourier transform decomposes a function into mutually orthogonal exponential components. For a piecewise continuous function  $f$  of the space ( $x$ ) domain, this transform is defined in the wave number domain ( $\kappa$ ) by

$$\tilde{f}(\kappa) = \int_{-\infty}^{\infty} f(x) e^{-i\kappa x} dx. \quad (1)$$

Thus, in order to study the  $\kappa$  spectral behavior of a function  $f(x)$  from its Fourier transform, full knowledge of the function in the  $x$  domain is required. A single value of the transform in the  $\kappa$  domain is related to the entire  $x$  domain and, conversely, a single value in the  $x$  domain is related to the entire  $\kappa$  domain. Hence, the Fourier transform is not appropriate for localization in the space-wave-number domain. The short-time Fourier transform was proposed<sup>21</sup> to overcome this difficulty and provide a two-dimensional representation ( $x, \kappa$ ) of a function  $f(x)$ , where the resolution is *fixed* over the entire space-wave-number plane. Presented as an alternative to the short-time Fourier transform, the wavelet

transform<sup>22</sup> uses short spatial windows at high wave numbers and long spatial windows at low wave numbers. This transform is then attractive because the space and wave number resolutions are varied over the space-wave-number plane. The continuous (or integral) wavelet transform (CWT) of a function  $f(x)$  is defined as<sup>20</sup>

$$(W_{\psi} f)(b, a) = \frac{1}{\sqrt{|a|}} \int_{-\infty}^{\infty} f(x) \overline{\psi\left(\frac{x-b}{a}\right)} dx, \quad (2)$$

where  $\psi(x)$  is called the mother wavelet from which all the other wavelets are generated using a *translation* parameter  $b$  and a *dilation* parameter  $a$ . The overbar indicates the complex conjugate. As  $b$  and  $a$  define the *scaling* of the wavelet, the function  $f(x)$  is then mapped into a *space-scale* plane.

It can be shown<sup>20</sup> that the wavelet transform gives localized information on a function  $f(x)$  within space and wave number windows which can be defined in the root mean square sense, consequently leading to a localization which is also expressed in the mean square sense. The information is then localized with a *space window* given by

$$[b + ax^* - a\Delta_{\psi}, \quad b + ax^* + a\Delta_{\psi}], \quad (3)$$

where  $x^*$  is the center and  $\Delta_{\psi}$  is the root mean square (rms) extent (or radius) of the mother wavelet, as given by

$$x^* = \frac{1}{\|\psi\|_2^2} \int_{-\infty}^{\infty} x |\psi(x)|^2 dx, \quad (4)$$

$$\Delta_{\psi} = \frac{1}{\|\psi\|_2} \left\{ \int_{-\infty}^{\infty} (x - x^*)^2 |\psi(x)|^2 dx \right\}^{1/2}, \quad (5)$$

where the norm  $\|f(x)\|_2$  of a function  $f(x)$  is defined as the square root of its energy:

$$\|f\|_2 = \left\{ \int_{-\infty}^{\infty} |f(x)|^2 dx \right\}^{1/2}. \quad (6)$$

In a similar way, the wavelet transform is seen to give localized information in the wave number domain with the exception of a multiplying factor and a linear phase shift:<sup>20</sup>

$$(W_{\psi} f)(b, a) = \frac{\sqrt{|a|}}{2\pi} \int_{-\infty}^{\infty} \tilde{f}(\kappa) e^{ib\kappa} \overline{\tilde{\psi}(a\kappa)} d\kappa \quad (7)$$

within a *wave number window* given by

$$\left[ \frac{\kappa^* - \Delta_{\tilde{\psi}}}{a}, \frac{\kappa^* + \Delta_{\tilde{\psi}}}{a} \right], \quad (8)$$

where  $\tilde{\psi}(\kappa)$  is the Fourier transform of the mother wavelet and, as before,  $\kappa^*$  is the center and  $\Delta_{\tilde{\psi}}$  is the root mean square (rms) bandwidth (or radius) of the Fourier transform of this mother wavelet given by

$$\kappa^* = \frac{1}{\|\tilde{\psi}\|_2^2} \int_{-\infty}^{\infty} \kappa |\tilde{\psi}(\kappa)|^2 d\kappa, \quad (9)$$

$$\Delta_{\tilde{\psi}} = \frac{1}{\|\tilde{\psi}\|_2} \left\{ \int_{-\infty}^{\infty} (\kappa - \kappa^*)^2 |\tilde{\psi}(\kappa)|^2 d\kappa \right\}^{1/2}. \quad (10)$$

As mentioned, the space and wave number windows presented in Eqs. (3) and (8) are defined in the mean square

sense and the space-wave-number localization will be obtained correspondingly in the mean square sense. The quantities  $\Delta_\psi$  and  $\Delta_{\tilde{\psi}}$  also define space and wave number resolutions associated with a particular wavelet. These resolutions satisfy the uncertainty principle:<sup>20</sup>

$$\Delta_\psi \Delta_{\tilde{\psi}} \geq \frac{1}{2}. \quad (11)$$

## B. Energy considerations

The squared norm of the Fourier transform [see Eq. (1)] given by  $|f(\kappa)|^2$  is known to lead to a continuous representation of the energy density distribution of  $f(x)$  in the wave number domain, known as a *spectrogram*. The energy density is thus obtained only as a function of  $\kappa$ . To obtain an energy density distribution of the signal all over the space-wave-number plane, a similar quantity can be defined in the case of the wavelet transform as the squared norm of Eq. (2) and given by

$$|(W_{\psi f})(b, a)|^2, \quad (12)$$

and this quantity can be referred to as a *scalogram*.<sup>23</sup> The resolution capabilities of the scalogram depend on the analyzed wave number, as presented in Sec. I A. The shape of the wavelet  $\psi$  and of its Fourier transform  $\tilde{\psi}$  obviously determines a weighting for the localization obtained in both domains. Following Eqs. (3) and (8), the energy is distributed into space and wave number windows in the mean square sense depending on the parameters  $b$  and  $a$ . The integration of the squared norm of the wavelet transform over  $b$  is equal to the weighted integration of the squared norm of the spectral components of  $f(x)$ :

$$\begin{aligned} & \int_{-\infty}^{\infty} |(W_{\psi f})(b, a)|^2 db \\ &= \frac{a}{2\pi} \int_{-\infty}^{\infty} |\tilde{f}(\kappa)|^2 |\tilde{\psi}(a\kappa)|^2 d\kappa. \end{aligned} \quad (13)$$

Moreover, if the wavelet respects the following admissibility condition

$$\int_{-\infty}^{\infty} \frac{|\tilde{\psi}(\kappa)|^2}{|\kappa|} d\kappa < \infty, \quad (14)$$

then the total energy of  $f(x)$  is obtained by integrating the distribution of energy density over the parameters  $b$  and  $a$  of the wavelet transform:<sup>22,23</sup>

$$\begin{aligned} & \int_{-\infty}^{\infty} \int_{-\infty}^{\infty} |(W_{\psi f})(b, a)|^2 \frac{db da}{a^2} \\ &= \|f(x)\|_2^2 \equiv \text{energy of } f(x). \end{aligned} \quad (15)$$

Equation (15) thus shows that the wavelet transform preserves energy.

## C. Description of the wavelet

Many functions  $\psi(x)$  can be used as mother wavelets; Haar, Daubechies, Coifman, and Meyer wavelets are among the most frequently used as mother wavelets.<sup>22,24</sup> In the fol-

lowing, due to its simplicity, the mother wavelet will be chosen as the Morlet wavelet even if, rigorously, this wavelet is only numerically admissible, i.e., only numerical reconstruction of  $f(x)$  from its wavelet transform is possible. The use of the Morlet wavelet as mother wavelet, however, is justified as the real and imaginary parts of a specific Morlet wavelet are seen to match almost exactly with cubic and quadratic  $B$ -spline wavelets,<sup>20</sup> respectively, which are very well-known admissible wavelets.

The mother wavelet to be used in the following is based on the modulated Gaussian window defined as<sup>20</sup>

$$G_{\beta, \zeta}^\alpha(x) = \frac{1}{2\sqrt{\pi\alpha}} e^{-i\zeta x} e^{-(x-\beta)^2/4\alpha}. \quad (16)$$

The Morlet wavelet is defined as the modulated Gaussian window centered at  $x=0$  with  $\beta=3.5$  and  $\zeta=2\pi$ :

$$\psi_G(x) := G_{3.5, 2\pi}^\alpha(x+3.5) = \frac{1}{2\sqrt{\pi\alpha}} e^{-i2\pi(x+3.5)} e^{-x^2/4\alpha}, \quad (17)$$

where  $\alpha$  will be chosen in order to meet special requirements, as shown later. The Morlet wavelet defined with these parameters, together with a given  $\alpha$ , corresponds almost exactly to a cubic spline wavelet.

The relation between the Morlet wavelet and the  $B$ -spline wavelets is worth mentioning because the latter are generated using cardinal  $B$ -splines which can be used as scaling functions in a multiresolution analysis,<sup>25</sup> allowing for efficient filter bank implementation.<sup>26</sup> It should also be noticed that  $B$ -spline wavelets have an explicit representation, are compactly supported and, moreover, have the smallest possible support among the known wavelets. A wavelet  $\psi(x)$  is said to be *compactly supported* within  $[A, B]$  if  $\psi(x)=0$  for  $x < A$  or  $x > B$ , which is not to be confused with the rms extent of the Morlet wavelet used in Eqs. (3) and (8). Also worth mentioning is that for space-wave-number localization, the equality in the uncertainty principle holds if and only if  $\psi$  is a Morlet wavelet, and it was shown<sup>20</sup> that  $B$ -spline wavelets are close to being optimal, i.e.,  $\Delta_\psi \Delta_{\tilde{\psi}} \geq \frac{1}{2}$ .

Figures 1 and 2 present, respectively, the real (symmetric) and imaginary (antisymmetric) parts of the Morlet wavelet for  $\alpha=0.2925$ . Figure 3 presents the wavenumber Fourier transform of this wavelet over the range  $[-15, 15]$ . The non-symmetric wave number Fourier transform of the Morlet wavelet arises from the summation of the wave number Fourier transform of its real (symmetric) part and of the wave number Fourier transform of its imaginary (antisymmetric) part. The following centers and radii are easily obtained for the Morlet wavelet  $\psi_G(x)$ :

$$x^* = 0, \quad (18)$$

$$\Delta_\psi = \sqrt{\alpha}, \quad (19)$$

$$\kappa^* = -2\pi, \quad (20)$$

$$\Delta_{\tilde{\psi}} = \frac{1}{2\sqrt{\alpha}}. \quad (21)$$



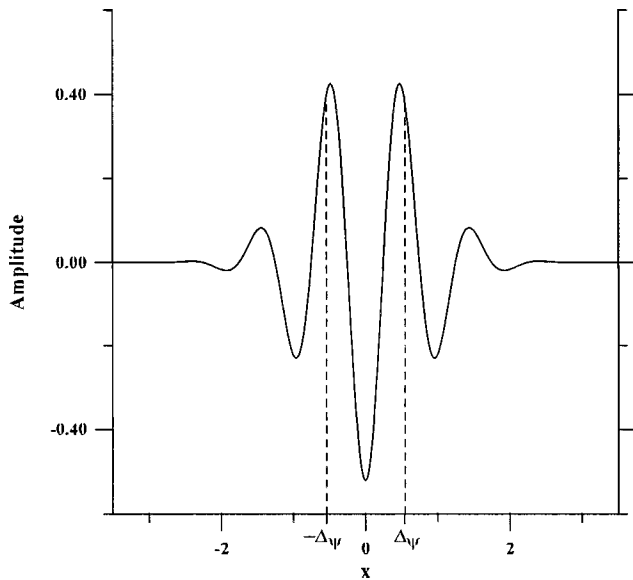


FIG. 1. Real part of the Morlet wavelet  $\psi_G(x)$ ,  $\alpha=0.2925$  and  $\Delta_\psi=0.5408$ .

## II. WAVELET TRANSFORM AND ACOUSTIC RADIATION

In this section, the acoustic power radiated from a flexural beam is derived and compared to an approximation of the acoustic power based on an appropriate wavelet transform of the structural displacement. The two setups used for the simulation are shown in Figs. 4 and 5. The first setup consist of a beam of half-width  $l_y=0.012$  m while the second setup consist of a beam which is assumed to be infinite in the  $y$  direction. In both cases, the beam is assumed to be thin, baffled, simply supported on the edges parallel to the  $y$  axis, and made of steel with half-length  $l_x=0.4$  m, Young's modulus  $E=210$  GPa, thickness  $h=3$  mm, Poisson's ratio  $\nu=0.29$ , density  $\rho=7850$  kg/m<sup>3</sup>, and loss factor  $\eta=1\%$ . The beam of finite width has free boundary conditions on the

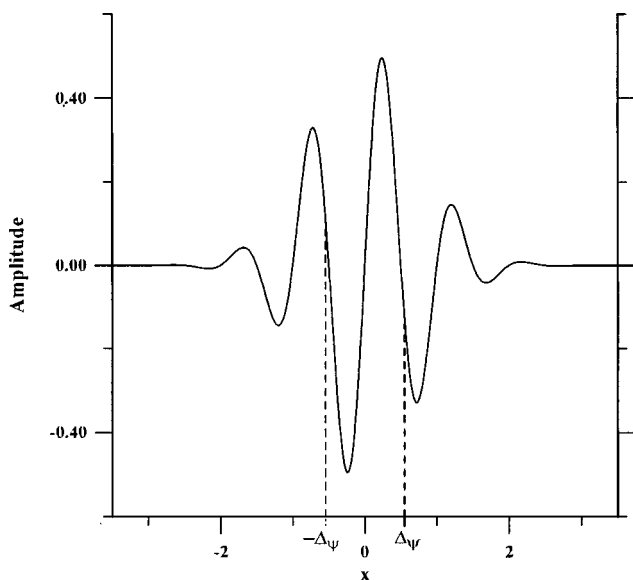


FIG. 2. Imaginary part of the Morlet wavelet  $\psi_G(x)$ ,  $\alpha=0.2925$  and  $\Delta_\psi=0.5408$ .

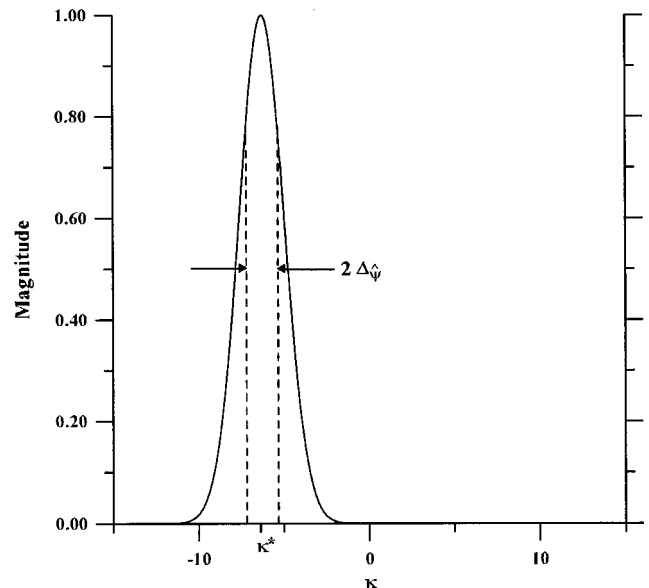


FIG. 3. Wave number Fourier transform of the Morlet wavelet  $\tilde{\psi}_G(\kappa)$ ,  $\alpha=0.2925$  and  $\Delta_{\tilde{\psi}}=0.9245$ .

edges parallel to the  $x$  axis and is excited by a point force disturbance of amplitude  $F=1$  N and frequency  $\omega_0$ , located at  $(\hat{x}, \hat{y})=(0.232, 0)$  m while the beam of infinite width is excited by a line force of amplitude  $f=1$  N/m located at the same position.

The modal expansion for the displacement  $W(x, t)$  used to numerically simulate the beam's response to the disturbance can be written as

$$W(x, t) = \sum_m a_m \hat{w}_m(x) e^{i\omega_0 t}, \quad m=1, 2, \dots, \quad (22)$$

where the  $a_m$  are the modal coefficients, and  $\hat{w}_m(x)$  are the eigenfunctions given, in the case of a simply supported beam, by

$$\hat{w}_m(x) = \sin\left(\frac{m\pi(x+l_x)}{2l_x}\right). \quad (23)$$

The modal coefficients are given by

$$a_m = -\frac{f\hat{w}_m(\hat{x})}{2\rho h l_x (\omega_0^2 - \omega_m^2 - i\eta\omega_m^2)}, \quad (24)$$

where  $f$  is the line force for the beam of infinite width and  $f=F/l_y$  for the beam of finite width, and where  $\rho$  is the mass density of the beam and  $\omega_m$  is the modal frequency given by

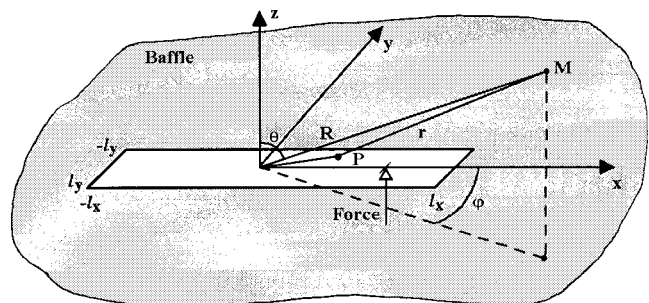


FIG. 4. Coordinate system for the finite beam.

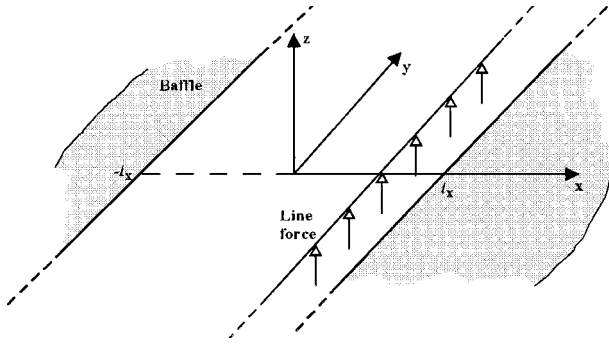


FIG. 5. Coordinate system for the infinite beam.

$$\omega_m = \sqrt{\frac{Eh^2}{12\rho}} \sigma_m^2, \quad (25)$$

where

$$\sigma_m = \frac{m\pi}{2l_x}. \quad (26)$$

The modal frequencies of the beam are presented in Table I.

### A. Radiated acoustic power

This section presents the derivation of the radiated acoustic power in the wave number domain, as presented in previous works.<sup>8,13,17</sup> This approach can be applied to any planar structure.

#### 1. Acoustic radiation for the beam of finite width

The acoustic pressure  $p(M)$  radiated to a point  $M$  from a baffled beam can be expressed by the Rayleigh's integral:

$$p(M) = \frac{\rho_0}{2\pi} \int_A \ddot{W}(P) \frac{e^{-ikr}}{r} dA, \quad (27)$$

where  $\rho_0$  is the mass density of the fluid,  $\ddot{W}(P)$  is the beam transverse acceleration at a point  $P$ ,  $k$  is the acoustic wave number in the fluid,  $r$  is the distance between  $P$  and  $M$ , and  $A$  is the surface of the beam. Assuming harmonic and constant displacement along the  $y$  direction, such that  $W(P, t) = w(x)e^{i\omega_0 t}$ , the previous equation can be used to obtain a far-field approximation of the radiated acoustic pressure for a beam of finite width:<sup>27</sup>

$$p(R, \lambda, \mu) = -\frac{\omega_0^2 \rho_0}{2\pi} \frac{e^{-ikR}}{R} \tilde{w}(\lambda, \mu), \quad (28)$$

where

$$\lambda = k \sin \theta \cos \varphi, \quad (29)$$

$$\mu = k \sin \theta \sin \varphi, \quad (30)$$

and where  $R$ ,  $\theta$ , and  $\varphi$  are the spherical coordinates of the point  $M$  (see Fig. 4),  $\tilde{w}(\lambda, \mu)$  is the double wave number transform of the beam displacement, analogous to the inverse Fourier transform, defined as<sup>10</sup>

$$\tilde{w}(k_x, k_y) = \frac{2 \sin k_y l_y}{k_y} \int_{-l_x}^{l_x} w(x) e^{ik_x x} dx \quad (31)$$

TABLE I. Beam modal frequencies.

Mode	Modal frequency (Hz)
1	11
2	44
3	99
4	176
5	275
6	396
7	539
8	704

$$= \frac{2 \sin k_y l_y}{k_y} \tilde{w}(k_x), \quad (32)$$

and  $k_x$  and  $k_y$  are respectively the  $x$  and  $y$  components of the structural wave number.

The acoustic power  $\Pi$  radiated from the beam can be expressed as the integral over a hemisphere of the mean square of the sound pressure in the far field:

$$\Pi = \frac{1}{2\rho_0 c} \int_S |p(R, \theta, \varphi)|^2 dS, \quad (33)$$

where  $S$  is the surface of the hemisphere and  $c$  is the speed of sound in the fluid.

In order to exploit the physical mechanisms of structural radiation, the radiated acoustic power is expressed in the wave number domain.<sup>13,17,28</sup> The radiated acoustic power in the wavenumber domain is obtained by substituting Eq. (28) into Eq. (33):

$$\Pi = \frac{\rho_0 \omega_0^3}{8\pi^2} \int_{-k}^k \int_{-\sqrt{k^2-\lambda^2}}^{\sqrt{k^2-\lambda^2}} \frac{|\tilde{w}(\lambda, \mu)|^2}{\sqrt{k^2-\lambda^2-\mu^2}} d\mu d\lambda. \quad (34)$$

In Eq. (34), the integration is performed over the supersonic region of the structural wave number spectrum (i.e., the region where the acoustic wave number  $k$  is larger than the structural wave number given by  $\sqrt{\lambda^2 + \mu^2}$ ), which shows that only supersonic structural waves radiate sound in the far field. The minimization of the displacement wave number spectrum (weighted by  $1/\sqrt{k^2-\lambda^2-\mu^2}$ ) in the supersonic region will then minimize the radiated acoustic power. Equation (34) relates the wave number transform of the structural displacement to the radiated acoustic power and will be used as the reference approach.

For a narrow beam (for which  $|k_y l_y| \ll 1$ ) and using Eqs. (28) and (32), Eq. (34) reduces to the following form:

$$\Pi_{\text{finite}} = \frac{\rho_0 \omega_0^3 l_y^2}{2\pi} \int_{-k}^k |\tilde{w}(\lambda)|^2 d\lambda. \quad (35)$$

#### 2. Acoustic radiation for the beam of infinite width

In the more general case of a beam of infinite width ( $l_y \rightarrow \infty$ ), it can be shown<sup>18</sup> that the radiated acoustic power per unit width is given by the following expression:

$$\Pi_{\text{infinite}} = \frac{\rho_0 \omega_0^3}{4\pi} \int_{-k}^k \frac{|\tilde{w}(\lambda)|^2}{\sqrt{k^2-\lambda^2}} d\lambda. \quad (36)$$

## B. Wavelet-based approximation of the radiated acoustic power

In the preceding approach, the radiated acoustic power was related to the weighted integration, in the supersonic region of the wave number domain, of the squared norm of the spectral components (corresponding to energy density) of the displacement field, as it appears in Eqs. (35) and (36). On the other hand, as presented in Secs. I A and I B, for particular scale  $a$  and location  $b$ , the squared norm of the wavelet transform  $|(W_{\psi f})(b, a)|^2$  gives an energy density information which is localized both in the space and wave number domains according to wavelet rms supports given by Eqs. (3) and (8) and the integration of the squared norm of the wavelet transform over  $b$  is given by Eq. (13).

Considering the above, it is first proposed in this section that the squared norm of the wavelet transform of the beam displacement field  $|(W_{\psi w})(b, a)|^2$  can observe the contribution of this local displacement field to the total vibratory energy. It is next proposed that the quantity given by

$$\omega_0^3 \left| \frac{2\pi}{\sqrt{|a|}} (W_{\psi w})(b, a) \right|^2 \quad (37)$$

can be used to represent the acoustic power radiated by the beam if the parameter  $a$  is chosen such that the wavelet transform gives localized energy information in the supersonic region of the wave number spectrum. In this case, Eq. (13) takes the form

$$\begin{aligned} & \int_{-\infty}^{\infty} \omega_0^3 \left| \frac{2\pi}{\sqrt{|a|}} (W_{\psi w})(b, a) \right|^2 db \\ &= 2\pi\omega_0^3 \int_{-\infty}^{\infty} |\tilde{w}(\kappa)|^2 |\tilde{\psi}(a\kappa)|^2 d\kappa. \end{aligned} \quad (38)$$

For an appropriate choice of the mother wavelet and of the scale parameter  $a$ , the weighted integration in the wave number domain presented in Eq. (38) could therefore approximate the radiated acoustic power given by Eqs. (35) or (36). However, such a choice for the wavelet leads, rigorously, to a nonadmissible wavelet, in the sense presented in Eq. (14). An alternative to this approach is only to represent the energy in the supersonic region of the wave number domain and not to match exactly the weighted integration in Eqs. (35) or (36) anymore. In this way, it will be assumed that a single vibratory energy density component in the  $b$  axis is representative of the total energy contained in the supersonic region of the wave number domain, and thus, of the radiated acoustic power of the beam. This implies that the emphasis is herein put on the wavelet capability to observe the local contribution to the radiated acoustic power. Thus, a *single* spatial window which covers at least the length of the beam and which is centered on it can be employed to obtain a proper representation. Hence, in most cases presented in this paper, the parameter  $b$  will be set to 0, thereby restricting the center of the *space window* [Eq. (3)] to  $x=0$ . As mentioned, another approach would be to allow the exploration of many areas in the space domain by varying the parameter  $b$  in order to study the spatial variation of vibratory phenomena, but this approach is only partially investigated in this paper.

Even if the Morlet wavelet is not, strictly speaking, compactly supported, the wavelet transform in Eq. (37) can be considered to be spatially confined and rewritten, with  $b=0$ , as a definite integral if it is observed that the mother wavelet has negligible values outside a region  $[-\Lambda, \Lambda]$ :

$$\Pi^{\text{wavelets}} \approx \omega_0^3 \left| \frac{2\pi}{a} \int_{-\Lambda a}^{\Lambda a} w(x) \overline{\psi_G\left(\frac{x}{a}\right)} dx \right|^2. \quad (39)$$

In practice, however, the integration is performed over the entire length of the beam since  $w(x)=0$  on the baffle surrounding the beam. Equation (39) presents the proposed approximation of the radiated acoustic power by a wavelet transform.

### 1. Formulation for the beam of infinite width

In order to bring to the fore the localization properties of the wavelet transform, a formulation to estimate the radiated acoustic power from a beam which is assumed to have an *infinite* width will be considered first [Eq. (36)]. A line force is used for the disturbance. Considering the modal expansion used in the following for a simply supported beam [Eq. (22)], the wave number spectrum of the displacement is either symmetric or antisymmetric and, therefore, the localization may be performed only for negative wave numbers in the spectrum using the wave number spectrum of the wavelet presented in Fig. 3.

Following the discussion in Sec. II B, the energy contained in the supersonic region of the wave number domain is to be represented by a single component of the wavelet transform with  $b=0$ . The localization in the supersonic region therefore dictates a design criterion  $\alpha$  for the Morlet wavelet, as mentioned in Sec. I C. The design is accomplished through two steps. As a first step, referring to Eq. (8), the position of the center of the window in the supersonic region of the wave number domain can be specified using a parameter  $\gamma$  by

$$\frac{\kappa^*}{a} = \gamma k = \gamma \frac{\omega_0}{c} = \gamma \frac{2\pi}{\lambda_{\text{acoustic}}}, \quad (40)$$

where  $c$  is the speed of sound in the fluid and  $\lambda_{\text{acoustic}}$  is the acoustic wavelength while, as a second step, the width of the window can be specified using

$$\frac{\Delta_{\tilde{\psi}}}{a} = (1 - \gamma)k \quad (41)$$

with  $0.5 \leq \gamma \leq 1$  to ensure that, considering the center specified for the window, its width will not cause the window to exceed the supersonic region. It should be noticed that the specification of the position of the center of the window also leads to a relation between the parameter  $a$  and the frequency  $\omega_0$ :

$$a = \frac{c}{\omega_0} \frac{\kappa^*}{\gamma}. \quad (42)$$

The combination of Eqs. (40) and (41) implies the following relation between the center and the bandwidth of the Fourier transform of the mother wavelet,

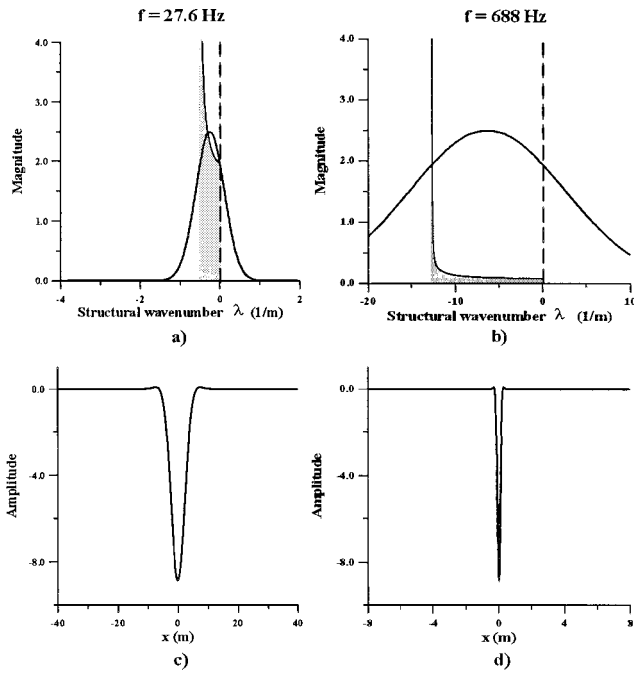


FIG. 6. Wave number and space (real part) localization using the centered approach ( $\gamma=0.5$ ). The shaded area is upper bounded by the weighting factor  $1/\sqrt{k^2-\lambda^2}$  introduced in the calculation of the radiated acoustic power for a beam of infinite width. Half of the (symmetrical) supersonic region in the wave number domain is shown.  $\alpha=1/16\pi^2$ . (a) and (c):  $f=27.6$  Hz,  $k=0.5041$  m $^{-1}$ , and  $a=25$ ; (b) and (d):  $f=688$  Hz,  $k=12.57$  m $^{-1}$ , and  $a=1$ . The wavelet is scaled by a factor of 2.5 for the purpose of the presentation.

$$\Delta_{\tilde{\psi}} = \kappa^* \frac{1-\gamma}{\gamma}, \quad (43)$$

and, substituting the values of the center and bandwidth of the Fourier transform of the Morlet wavelet [Eqs. (20) and (21)] in Eq. (43), the following design criterion  $\alpha$  which defines the shape of the mother wavelet can be determined:

$$\alpha = \frac{1}{16\pi^2} \frac{\gamma^2}{(1-\gamma)^2}. \quad (44)$$

Based on these expressions, two distinct approaches are proposed in order to estimate the radiated acoustic power from the beam of infinite width. In the first approach, the *wave number window* is forced to cover entirely the supersonic region, i.e.,  $\Delta_{\tilde{\psi}}/a = k/2$ . This approach will be called the *centered* approach. The obvious choice for  $\gamma$  in this case is then  $\gamma=0.5$ , leading to the following value of  $\alpha$  for the Morlet wavelet:

$$\alpha = \frac{1}{16\pi^2}. \quad (45)$$

Figure 6 presents the wave number and space representations of the wavelet for two scales  $a$  or, equivalently, for two frequencies. The wave number representation of the wavelet is presented in Fig. 6(a) and (b) while the space representation is presented in Fig. 6(c) and (d). The shaded regions present the extent of the supersonic region in the wave number domain at these two frequencies. The weighting factor  $1/\sqrt{k^2-\lambda^2}$  introduced in the calculation of the

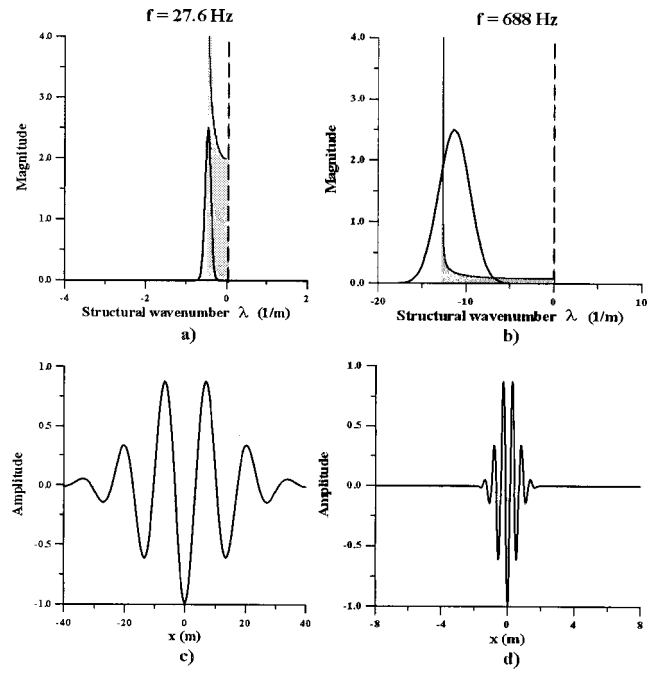


FIG. 7. Wave number and space (real part) localization using the off-center approach, with  $\gamma=0.9$ . The shaded area is upper bounded by the weighting factor  $1/\sqrt{k^2-\lambda^2}$  introduced in the calculation of the radiated acoustic power for a beam of infinite width. Half of the (symmetrical) supersonic region in the wave number domain is shown.  $\alpha=81/16\pi^2$ . (a) and (c):  $f=27.6$  Hz,  $k=0.5041$  m $^{-1}$ , and  $a=13.84$ ; (b) and (d):  $f=688$  Hz,  $k=12.57$  m $^{-1}$ , and  $a=0.5554$ . The wavelet is scaled by a factor of 2.5 for the purpose of the presentation.

radiated acoustic power for a beam of infinite width is represented as an upper bound for the shaded regions. As seen in Fig. 6(a), the centered approach gives adequate representation of the energy over the entire supersonic region when the acoustic wave number is relatively low (low frequency). As the acoustic wave number increases, the weighting  $1/\sqrt{k^2-\lambda^2}$  introduced in the calculation of the radiated acoustic power using Eq. (36) relatively favors the energy components localized in a narrower band, close to the acoustic wave number, as shown in Fig. 6(b). A reconstruction of the energy over the entire supersonic region using the weighting introduced by the Fourier transform of the mother wavelet is therefore no longer appropriate, as the weighting introduced in Eq. (36) should be taken into account if one wants to estimate properly the radiated acoustic power. Moreover, as the acoustic wave number increases [compare Fig. 6(c) and (d)], the *space window* introduced by the wavelet reduces its extent so that the energy is taken only on a small spatial extent of the beam.

An alternative approach would therefore be to obtain a representation of the energy in a smaller band, close to the acoustic wave number, as shown in Fig. 7. To obtain this *off center* representation,  $\gamma$  is chosen close to 1, with  $\gamma=0.9$  being chosen in Fig. 7, leading to the following design criterion:

$$\alpha = \frac{81}{16\pi^2}. \quad (46)$$

Referring to Fig. 7(b) in this case, the energy represen-

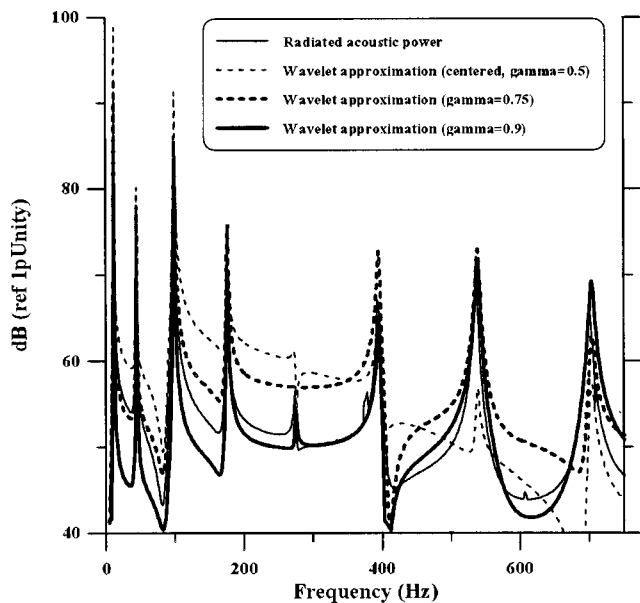


FIG. 8. Validation of the wavelet-based approximation using the formulation for the beam of infinite width.

tation for high acoustic wave numbers appears to be more appropriate with  $\gamma$  close to 1, but, apparently, this is done to the detriment of poor representation at low acoustic wave numbers, as shown in Fig. 7(a).

With the parameter  $a$  specified as in Eq. (42), the squared norm of the wavelet transform is thus seen to represent the energy of the displacement field over the selected subregion (according to  $\gamma$ ) of the supersonic region of the wave number spectrum and over the corresponding space region, according to the windows given by Eqs. (3) and (8) in the mean square sense. This localization is obtained through the use of a weighting by the wavelet itself for the space localization and by the Fourier transform of this wavelet for the wave number localization. Such a choice for the parameter  $a$  will ensure that the desired localization will follow the variation in the extent of the supersonic region, as the acoustic wave number and, hence, the frequency varies. A representation of the energy in the supersonic region and, therefore, of the radiated acoustic power is thus obtained through one wavelet transform as a function of the parameter  $a$  or, equivalently by Eq. (42), as an inverse function of  $\omega_0$ . As seen in Fig. 7, the amplitude of the weighting  $1/\sqrt{k^2 - \lambda^2}$  introduced in the calculation of the radiated acoustic power [Eq. (36)] is an inverse function of  $\omega_0$ ; an additional factor of  $k$  then has to be introduced in the wavelet representation to compensate for its constant wave number amplitude weighting over  $\omega_0$ . It should be noticed that the wavelet wave number and space representations shown in Figs. 6 and 7 are independent of the beam.

The radiated acoustic power is compared to the wavelet approximation using the formulation for a beam of infinite width with an approximation of the radiated acoustic power given by Eq. (39). Results obtained for the radiated acoustic power and wavelet approximation are shown in Fig. 8 where the wavelet approach using the centered wavelet ( $\gamma=0.5$ ) is first compared to the radiated acoustic power. The agreement is quite good at low frequencies, as expected from the dis-

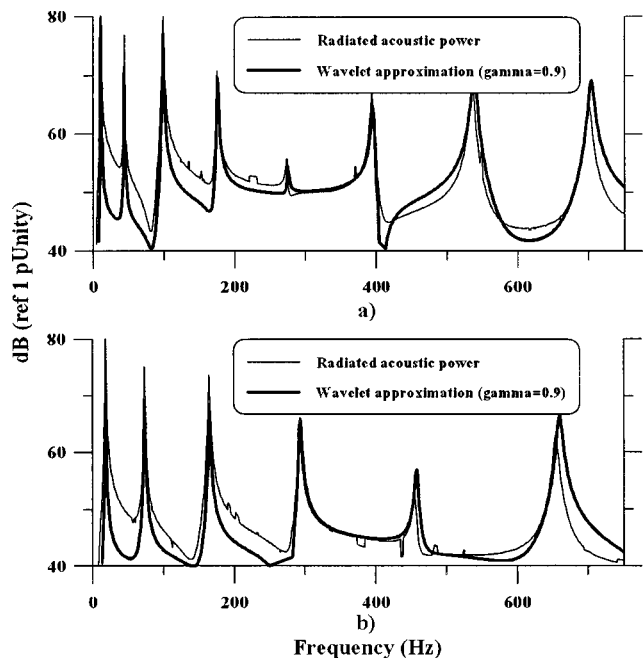


FIG. 9. Validation of the wavelet-based approximation for two beams of different thicknesses using the formulation for the beam of infinite width: (a)  $h = 3$  mm and (b)  $h = 5$  mm.

cussion in Sec. II B but, as seen in Fig. 6(b), an increase in the frequency leads to poor energy representation using the centered wavelet. As also presented in Fig. 8, much better agreement is obtained at high frequencies, and even at low frequencies, when the value of  $\gamma$  is increased, using the off-center approach presented in Fig. 7, especially with  $\gamma=0.9$ . From these results, it can be observed that the wavelet approach, with an appropriate choice for  $\gamma$  in Eqs. (40) and (41), provides a suitable representation for the radiated acoustic power over an extended frequency range, the latter being related to  $\gamma$ . The robustness of the wavelet approximation to a variation of the parameters of the structure is illustrated in Fig. 9 where the wavelet approximation is compared to the radiated acoustic power for beams of different thicknesses. These results therefore show the ability of the wavelet approach to localize the energy in a given region of the wave number spectrum.

Assuming that the transverse velocity or acceleration is measured at discrete points on the structure, the evaluation of the radiated acoustic power [Eq. (36)] would require the Fourier transform of these measurements and, for each frequency  $\omega_0$ , a different integral must be evaluated over the resulting components. On the other hand, the proposed approximation of the radiated acoustic power only requires *one* wavelet transform [Eq. (39)] to approximate the radiated acoustic power as a function of the frequency. Indeed, the resulting components are expressed in terms of the parameter  $a$  and a mapping to the frequency domain ( $\omega_0$ ) exists and is given by Eq. (42). The net computational gain obtained using the wavelet approximation over the Fourier approach is thus dependent on the number of frequency components where the radiated acoustic power is to be evaluated. Assuming that the computational burden involved in both Fourier and wavelet transforms is comparable, the evaluation of the radi-

ated acoustic power at a single frequency component using the wavelet approximation already has lower requirements in CPU time as no extra integration is required. For the evaluation of the radiated acoustic power over an extended region in frequency, the computational gain can be significant using the wavelet approximation, as only one wavelet transform is necessary.

## 2. Formulation for the beam of finite width

In order to estimate the radiated acoustic power from a more realistic beam of *finite* width, a slightly different strategy must be adopted, based on multiple wavelet transforms. Indeed, as the weighting introduced in the calculation of the radiated acoustic power [Eq. (35)] is now constant over the supersonic region, the *wave number window* should entirely cover the supersonic region, as for the centered approach presented in Sec. II B 1. However, as discussed in Sec. II B 1 [see Fig. 6(d)], increasing the wave number extent of the window reduces its spatial extent. Therefore, in order to avoid the problem that the energy is taken only over a small spatial extent of the beam, two approaches can be used. The first approach, based on Eq. (38), consists in using many wavelets in the space domain by varying the parameter  $b$  but, consequently, this approach no longer allows one to highlight the wavelet capability to observe the local contribution to the radiated acoustic power. The second approach which will be used in the following consists in using many wavelet transforms and thus, many wavelets in the wave number domain, each of them having  $b=0$  and each of them taking care of the energy in a given subregion of the supersonic region, and then summing all these contributions. By doing so, the *wave number window* of each wavelet is of limited extent and, therefore, the corresponding spatial extent is larger and then more appropriate to cover the entire beam. The wavelet transforms are performed on the same displacement field but using different mother wavelets, each of them using a different relation between the parameter  $a$  and the acoustic frequency [Eq. (42)] and, consequently, a different design criterion  $\alpha$  [Eq. (44)]. The approximation using these multiple wavelet transforms then takes the form

$$\Pi^{\text{wavelets}} \approx \omega_0^3 \sum_{i=1}^n \left| \frac{2\pi}{a_i} \int_{-\Lambda a_i}^{\Lambda a_i} w(x) \overline{\psi_{G_i}\left(\frac{x}{a_i}\right)} dx \right|^2, \quad (47)$$

where  $a_i$  and  $\psi_{G_i}$  are associated with the  $i$ th wavelet transform. In this case, Eq. (13) takes the form

$$\begin{aligned} & \int_{-\infty}^{\infty} \omega_0^3 \sum_{i=1}^n \left| \frac{2\pi}{\sqrt{|a_i|}} (W_{\psi_i} w)(b, a_i) \right|^2 db \\ &= 2\pi \omega_0^3 \int_{-\infty}^{\infty} |\tilde{w}(\kappa)|^2 \left( \sum_{i=1}^n |\tilde{\psi}_i(a_i \kappa)|^2 \right) d\kappa. \end{aligned} \quad (48)$$

The multiple mother wavelets can be designed as a *mother* uniform filter bank covering the entire supersonic region and consisting of  $n$  filters, each of them behaving like a wavelet in the manner presented before. It is also observed that increasing the number of filters (or wavelets) in the filter bank leads to increased selectivity of the global filter bank. In consequence and based on Eq. (40), a parameter  $\gamma_i$  can be

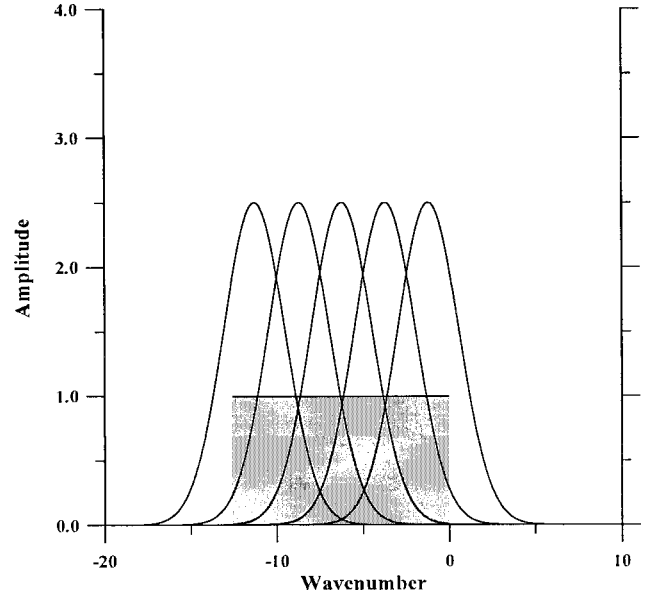


FIG. 10. Multiple wavelet approach for the beam of finite width. Five wavelets with  $f=688$  Hz;  $k=12.57$  m $^{-1}$ ;  $a_1=5.0$ ,  $a_2=1.666$ ,  $a_3=1.0$ ,  $a_4=0.7141$ , and  $a_5=0.5554$ ; and  $\alpha_1=1/16\pi^2$ ,  $\alpha_2=3/16\pi^2$ ,  $\alpha_3=5/16\pi^2$ ,  $\alpha_4=7/16\pi^2$ , and  $\alpha_5=9/16\pi^2$ . The wavelet is scaled by a factor of 2.5 for the purpose of the presentation.

defined for each wavelet  $i$  in the bank in order to specify its centering:

$$\gamma_i = \frac{2i-1}{2n}, \quad i=1, \dots, n, \quad (49)$$

where  $n$  is the number of mother wavelets (or wavelet transforms), so that, based on Eq. (42), a different relation between the acoustic frequency and the scale parameter  $a_i$  associated with each wavelet transform is obtained:

$$a_i = \frac{c}{\omega_0} \frac{2n}{2i-1} \kappa^*, \quad i=1, \dots, n. \quad (50)$$

In this case, the width of the *wave number window* is common to all the wavelet transforms and is given in terms of the number of wavelet transforms  $n$  as

$$\frac{\Delta_{\tilde{\psi}}}{a_i} = \frac{k}{2n}. \quad (51)$$

Combining Eqs. (50) and (51), a design criterion  $\alpha_i$  for each mother wavelet is given by

$$\alpha_i = \frac{(2i-1)^2}{16\pi^2}, \quad i=1, \dots, n. \quad (52)$$

Figure 10 presents the particular case of five wavelets covering the supersonic region. The number  $n$  of wavelet transforms to be used can be determined from Eqs. (3), (19), (50), and (52) by requiring that the rms extent of the spatial window be at least equal to the length of the beam at a given maximum analysis frequency  $\omega_{\max}$ , leading to  $n \geq (\omega_{\max}/c)l_x$ .

Comparison between the radiated power and the wavelet approximation in the case of a beam of finite width using Eq. (47) is shown in Fig. 11. Remembering that only one component of the wavelet transform is employed here ( $b=0$ ), it

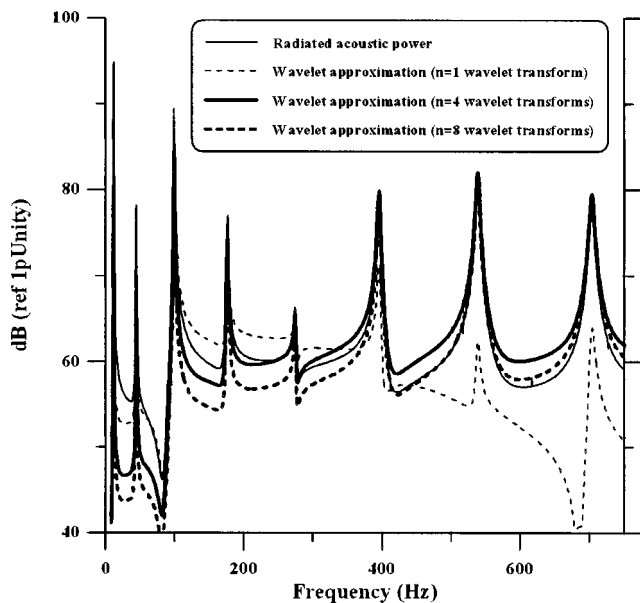


FIG. 11. Validation of the wavelet-based approximation using few wavelet transforms for the beam of finite width.

appears that one wavelet transform ( $n = 1$ ) does not provide an adequate representation of the radiated acoustic power at high frequencies for this beam, where the spatial extent of the wavelet does not cover the entire beam. The radiated acoustic power is only represented locally in this case. As can be seen in Fig. 11, increasing the number of wavelet transforms ( $n = 4$  and  $n = 8$ ) leads to a better representation up to a certain point where the selectivity of the wavelet filters seems to put the representation at low frequencies at a relative disadvantage. While ensuring that the condition given by  $n \geq (\omega_{\max}/c)l_x$  is met, a low number of wavelet transforms should be used.

In order to give some indication on the ability of the wavelet approach to localize the energy in the space domain, the effect of the translation parameter  $b$  is briefly investigated here. Figure 12 presents a comparison of two wavelet approximations using four spatially centered wavelets ( $b = 0$  m) and four wavelets centered on one edge of the beam ( $b = -0.4$  m). According to the given criterion, four spatially centered wavelets allow a maximum analysis frequency of 546 Hz because of the limited extent of the wavelets in the space domain. The robustness of the wavelet approximation in relation with this limited extent is illustrated in Fig. 12 by revealing that using wavelets of limited spatial extent but centered differently still provides a good representation of the radiated acoustic power.

In summary, this approach involves only  $n$  wavelet transforms [Eq. (47)] and the summation of the resulting components while the exact evaluation of the radiated acoustic power requires a Fourier transform and the evaluation of a different integral for each frequency  $\omega_0$  [Eq. (35)]. It therefore appears again that the proposed approximation requires less and less operations than the exact evaluation of the radiated acoustic power as the number of frequency components where the radiated acoustic power is to be evaluated is increased.

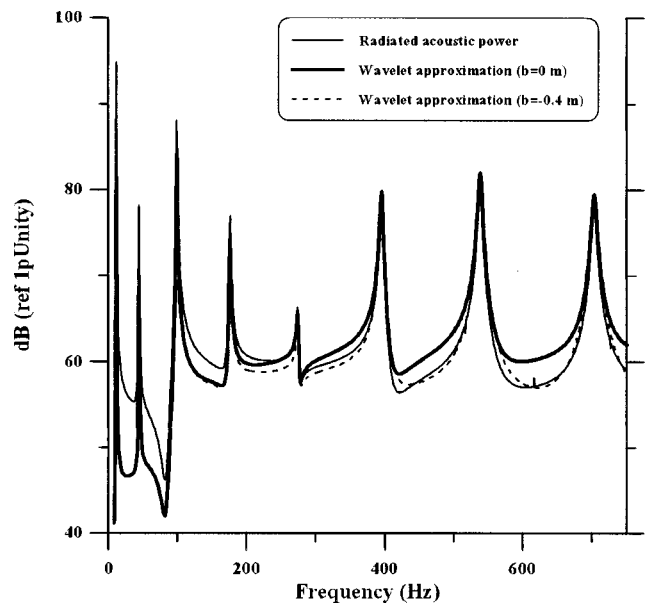


FIG. 12. Validation of the wavelet-based approximation using  $n = 4$  wavelet transforms and two different values of the translation parameter  $b$  for the beam of finite width.

### III. OPTIMAL CONTROL RESULTS

Optimal control simulations are conducted to compare the active control of the sound radiation using the exact sound power as the cost function, or using the wavelet approximation of the sound power as the cost function. The setup for the simulation is described and cost function minimization results are briefly presented using both proposed control strategies. The case of a beam of finite width is considered here.

#### A. Optimal control

In the context of active control, the total structural displacement field is the sum of a primary displacement field (labeled  $p$ ) created by a disturbance, i.e., a point force, and secondary displacement fields (labeled  $s$ ) originating from  $n$  actuators exciting the structure. Actuators can be implemented as point forces or piezoelectric elements (PZT).<sup>29</sup> The total displacement field of the beam is given by

$$w(x) = w_p(x) + \mathbf{w}_s(x) \cdot \mathbf{V}_s, \quad (53)$$

where  $w_p$  is the primary displacement,  $\mathbf{w}_s$  is an  $n$ -dimensional line vector defined as

$$\mathbf{w}_s(x) = [\cdots w_s^i(x) \cdots], \quad (54)$$

where the  $i$ th element represents the displacement field resulting from the  $i$ th actuator ( $i = 1, \dots, n$ ) and  $\mathbf{V}_s$  is the dimension  $n$  row vector of the control variable, to be adjusted so as to minimize the radiated power:

$$\mathbf{V}_s = \begin{bmatrix} \vdots \\ V_s^i \\ \vdots \end{bmatrix}. \quad (55)$$

Upon substitution of the total displacement field in Eq. (35) or (47), a quadratic function  $\Pi$  of  $\mathbf{V}_s$  is obtained and this function has only one minimum.<sup>1</sup> The optimal control solution for this function is thus found by differentiating, at a single frequency, the cost function with respect to the real and imaginary parts of the control variable and setting them to zero.<sup>14</sup> This can be expressed as

$$\frac{\partial \Pi}{\partial \mathbf{V}_s} = 0. \quad (56)$$

### 1. Radiated power-based approach

For the first approach, upon substitution of Eq. (53) in the expression of the radiated acoustic power from a beam of finite width [Eq. (35)], the cost function has the form

$$\Pi^{\text{finite}} = \frac{\rho_0 \omega_0^3 l_y^2}{2\pi} [\alpha_{pp*} + \mathbf{V}_s^H \alpha_{ps*} + \alpha_{ps*} \mathbf{V}_s + \mathbf{V}_s^H \alpha_{ss*} \mathbf{V}_s], \quad (57)$$

where

$$\alpha_{pp*} = \int_{-k}^k \tilde{w}_p(\lambda) \tilde{w}_p^*(\lambda) d\lambda, \quad (58)$$

$$\alpha_{ps*} = \int_{-k}^k \tilde{w}_p(\lambda) \tilde{\mathbf{w}}_s^H(\lambda) d\lambda, \quad (59)$$

$$\alpha_{ps*} = \int_{-k}^k \tilde{w}_p^*(\lambda) \tilde{\mathbf{w}}_s(\lambda) d\lambda, \quad (60)$$

$$\alpha_{ss*} = \int_{-k}^k \tilde{\mathbf{w}}_s^H(\lambda) \tilde{\mathbf{w}}_s(\lambda) d\lambda, \quad (61)$$

where  $\alpha_{ps*}$  is a column vector,  $\alpha_{ps*}$  is a row vector,  $\alpha_{ss*}$  is a matrix, and <sup>H</sup> denotes the Hermitian transpose. The minimization of this cost function takes the following form.<sup>8</sup>

$$\frac{\partial \Pi^{\text{finite}}}{\partial \mathbf{V}_s} = \frac{\rho_0 \omega_0^3 l_y^2}{2\pi} [2\alpha_{ps*} + 2\alpha_{ss*} \mathbf{V}_s] = 0. \quad (62)$$

Optimal control will then be achieved if  $\mathbf{V}_s$  is chosen such that

$$\mathbf{V}_s = -\alpha_{ss*}^{-1} \alpha_{ps*}. \quad (63)$$

### 2. Wavelet-based approach

For the second approach, the cost function is based on Eq. (47). As presented, for the case of the beam of finite width, the cost function to be used is thus given in terms of multiple wavelet transforms, each one having its own relation between  $a_i$  and the acoustic frequency. The cost function therefore has the following form,

$$\Pi^{\text{wavelets}} = \omega_0^3 \sum_{i=1}^n \left| \frac{2\pi}{a_i} \int_{-\Lambda a_i}^{\Lambda a_i} (w_p + \mathbf{w}_s \mathbf{V}_s) \psi_{G_i} \left( \frac{x}{a_i} \right) dx \right|^2 \quad (64)$$

$$= \omega_0^3 \sum_{i=1}^n \left| \frac{2\pi}{a_i} \int_{-\Lambda a_i}^{\Lambda a_i} w_p \psi_{G_i} \left( \frac{x}{a_i} \right) dx + \frac{2\pi}{a_i} \int_{-\Lambda a_i}^{\Lambda a_i} \mathbf{w}_s \psi_{G_i} \left( \frac{x}{a_i} \right) dx \mathbf{V}_s \right|^2, \quad (65)$$

and with the change of variable,

$$\xi_{p_i} = \frac{2\pi}{a_i} \int_{-\Lambda a_i}^{\Lambda a_i} w_p \psi_{G_i} \left( \frac{x}{a_i} \right) dx, \quad (66)$$

$$\xi_{s_i} = \frac{2\pi}{a_i} \int_{-\Lambda a_i}^{\Lambda a_i} \mathbf{w}_s \psi_{G_i} \left( \frac{x}{a_i} \right) dx, \quad (67)$$

the following expression is obtained:

$$\Pi^{\text{wavelets}} = \omega_0^3 \sum_{i=1}^n |\xi_{p_i} + \xi_{s_i} \mathbf{V}_s|^2 \quad (68)$$

$$= \omega_0^3 \sum_{i=1}^n [|\xi_{p_i}|^2 + \xi_{p_i} \mathbf{V}_s^H \xi_{s_i}^H + \bar{\xi}_{p_i} \xi_{s_i} \mathbf{V}_s + \mathbf{V}_s^H \xi_{s_i}^H \xi_{s_i} \mathbf{V}_s]. \quad (69)$$

The minimization takes the following form:

$$\frac{\partial \Pi^{\text{wavelets}}}{\partial \mathbf{V}_s} = \omega_0^3 \sum_{i=1}^n [2\xi_{s_i}^H \xi_{p_i} + 2\xi_{s_i}^H \xi_{s_i} \mathbf{V}_s] = 0. \quad (70)$$

The control variable  $\mathbf{V}_s$  minimizing the cost function is then obtained by solving

$$\sum_{i=1}^n [\xi_{s_i}^H \xi_{s_i}] \mathbf{V}_s = - \sum_{i=1}^n [\xi_{s_i}^H \xi_{p_i}]. \quad (71)$$

### B. Setup

The control setup used for the simulation consists, in addition to the setup presented in Sec. II, of one PZT patch (PSI-5A-S2) with dimensions  $6 \times 2.4 \text{ cm}^2$  centered at  $x = -0.15 \text{ m}$ . The Poisson's ratio, Young's modulus, and thickness of the piezoelectric material are respectively  $\nu_{pe} = 0.29$ ,  $E_{pe} = 61 \text{ GPa}$ , and  $h_{pe} = 0.2 \text{ mm}$ , while the piezoelectric strain constant is  $d_{31} = 1.71 \times 10^{-10} \text{ m/V}$ . Control results are presented for a spanning of the excitation frequency between 0 and 750 Hz. The control is then performed at a single frequency by solving either Eq. (63) (sound power minimization) or Eq. (71) (wavelet approximation).

### C. Actuators equations

A modal expansion similar to the one presented in Eq. (22) is also used to simulate the beam's response to the actuator:

$$W_s(x, t) = \sum_m a_m^s \hat{w}_m(x) e^{i\omega_0 t}, \quad m = 1, 2, \dots \quad (72)$$

For a piezoelectric patch (PZT) extending from  $x_1$  to  $x_2$  and from  $y_1$  to  $y_2$ , the modal coefficients are calculated as follows<sup>29</sup> for a simply supported beam:



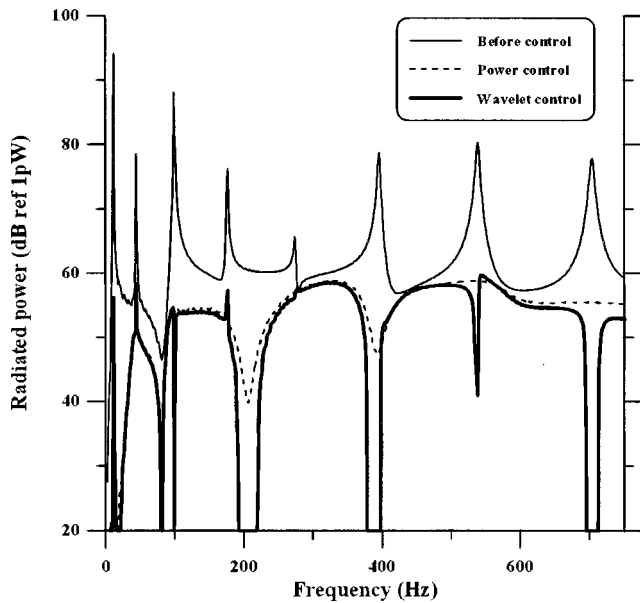


FIG. 13. Wavelet- versus radiated-power-based approaches in optimal control of the acoustic power radiated from a beam of finite width. Four wavelet transforms are used ( $n=4$ ). Discretization using 16 measurement points.

$$a_m^s = \frac{C_0 \epsilon_{pe} (y_2 - y_1)}{2 \rho h l_x l_y (\omega_0^2 - \omega_m^2 - i \eta \omega_m^2)} \sigma_m [\cos \sigma_m (x_1 + l_x) - \cos \sigma_m (x_2 + l_x)], \quad (73)$$

where  $\omega_m$  and  $\sigma_m$  are given respectively by Eqs. (25) and (26) and

$$C_0 = -E \frac{2P}{3(1-P)} \frac{h^2}{4}, \quad (74)$$

$$P = -\frac{E_{pe}}{E} K, \quad (75)$$

$$K = \frac{3 h h_{pe} (h + h_{pe})}{4 (h^3/8 + h_{pe}^3) + \frac{3}{2} h h_{pe}^2}, \quad (76)$$

$$\epsilon_{pe} = \frac{d_{31}}{h_{pe}} V, \quad (77)$$

where  $V$  is the voltage applied to the PZT. This voltage is the control variable and corresponds to an element of  $\mathbf{V}_s$  in Eq. (53).

#### D. Comparison of the approaches

Optimal control results are presented in Fig. 13. The integrals in both approaches [Eqs. (58)–(61) and (66) and (67)] are discretized using 16 points on the structure, thereby simulating measurement points for the displacement. The optimal control variable is obtained at each frequency by solving Eq. (63) or (71) and substituting into Eq. (57) to obtain the radiated acoustic power after control for both approaches. It is seen that the approach using the wavelet transform (with  $n=4$  wavelet transforms) as the cost function provides a similar behavior to that obtained using the radiated acoustic power as the cost function, after the control has been applied.

Using the wavelet approach as the cost function would therefore lead to control results similar to those obtained using the radiated acoustic power as the cost function.

#### IV. CONCLUSIONS

A new approximation of the radiated acoustic power was proposed using the wavelet transform. This approximation has been applied to a simply supported beam and it was shown that a single local component of the wavelet transform can represent the vibratory energy in a given region of the structural wave number spectrum. Adjusting the scale parameter of the wavelet allows energy localization over the supersonic region of the structural wave number spectrum and, hence, leads to an approximation of the radiated acoustic power.

The Morlet wavelet was presented and it was shown that the wavelet transform of the displacement field can provide, in one or very few steps, a representation of the energy in the supersonic region as a function of the frequency, as opposed to the multi-step approach consisting of a wave number transform (Fourier) of the displacement field and integration of the components over the supersonic region. Such an approximation is thus very attractive in the context of ASAC since the cost function in this case requires lower computational load. It was shown that this representation is obtained from a wavelet transform which depends solely on a scale parameter that is directly related to the frequency.

The wavelet approximation was validated through comparison with the exact radiated acoustic power and very good agreement was obtained. Optimal control results were also presented in order to assess the use of the wavelet approach in an active control context. It was shown that the sound attenuation similar to the one obtained using the radiated acoustic power can be achieved using the wavelet transform as the cost function.

The wavelet approach presented in this paper mostly restricts the analysis to a given region centered at  $x=0$  through the use of  $b=0$  in the wavelet transform. As briefly explored in this paper, another approach would be to allow the exploration of many areas in the space domain by varying the parameter  $b$ . By doing so, the acoustic radiation of complex planar structures could be studied by positioning the wavelets on significant radiating areas. The vibratory energy in the supersonic region associated with each area would then be summed.

Because it requires a single step, the proposed approach is therefore expected to be more efficient in practical implementation than other multi-step approaches for the estimation of the acoustic power radiated from a planar structure, especially if broadband control is required. Fast algorithms (involving filter banks) for the wavelet transform can be used. Because it uses discrete sensors, the approach can be extended to two-dimensional planar structures, preserving the distinction between  $k_x$  and  $k_y$  components of the wave number spectrum and, therefore, still allowing for a wave number approach. A two-dimensional wavelet transform would then have to be used. Work is currently in progress on these topics as well as on the application of the approach to beams with other boundary conditions.

## ACKNOWLEDGMENTS

This work was supported by the Fonds pour la formation de Chercheurs et Aide à la Recherche (FCAR), Québec, Canada. The authors would like to thank the reviewers for their constructive comments.

- <sup>1</sup>S. J. Elliott and P. A. Nelson, "Active noise control," *IEEE Signal Process. Mag.* 12–35 (1993).
- <sup>2</sup>C. R. Fuller, "Active control of sound transmission/radiation from elastic plates by vibration inputs: I. Analysis," *J. Sound Vib.* **136**(1), 1–15 (1990).
- <sup>3</sup>J. P. Maillard and C. R. Fuller, "Advanced time domain wave-number sensing for structural acoustic systems. Part I. Theory and design," *J. Acoust. Soc. Am.* **95**, 3252–3261 (1994).
- <sup>4</sup>J. P. Maillard and C. R. Fuller, "Advanced time domain wave-number sensing for structural acoustic systems. Part II. Active radiation control of a simply supported beam," *J. Acoust. Soc. Am.* **95**, 3262–3272 (1994).
- <sup>5</sup>J. P. Maillard and C. R. Fuller, "Advanced time domain wave-number sensing for structural acoustic systems. Part III. Experiments on active broadband radiation control of a simply supported plate," *J. Acoust. Soc. Am.* **98**, 2613–2621 (1995).
- <sup>6</sup>R. L. Clark and C. R. Fuller, "Modal sensing of efficient acoustic radiators with polyvinylidene fluoride distributed sensors in active structural acoustic control approaches," *J. Acoust. Soc. Am.* **91**, 3321–3329 (1992).
- <sup>7</sup>R. L. Clark, C. R. Fuller, B. R. Fogg, W. V. Miller, A. M. Vengsarkar, and R. O. Claus, "Active structural acoustic control using fiber sensors and piezoelectric actuators," In Proceedings of the ADPA/AIAA/ASME/SPIE Conference on Active Materials and Adaptive Structures, pp. 547–552 (1992).
- <sup>8</sup>P. Masson, A. Berry, and J. Nicolas, "Active structural acoustic control using strain sensing," *J. Acoust. Soc. Am.* **102**, 1588–1599 (1997).
- <sup>9</sup>E. F. Crawley, "Use of piezoelectric actuators as elements of intelligent structures," *AIAA J.* **25**(10), 1373–1385 (1987).
- <sup>10</sup>C. Guigou, A. Berry, F. Charette, and J. Nicolas, "Active control of finite beam volume velocity using shaped PVDF sensor," *Acust. Acta Acust.* **82**(5), 772–783 (1996).
- <sup>11</sup>C. Guigou, A. Berry, and F. Charette, "Active control of plate volume velocity using shaped PVDF sensor," in Proceedings of the 1994 ASME Winter Annual Meeting, Chicago, pp. 247–255 (1994).
- <sup>12</sup>Y. Gu and C. R. Fuller, "Active control of sound radiation from a fluid-loaded rectangular uniform plate," *J. Acoust. Soc. Am.* **93**, 337–345 (1993).
- <sup>13</sup>C. R. Fuller and R. A. Burdisso, "A wavenumber domain approach to the active control of structure-borne sound," *J. Sound Vib.* **148**(2), 355–360 (1991).
- <sup>14</sup>S. D. Sommerfeldt, "Active wavenumber control of acoustic radiation from a plate," in Proceedings of the Second Conference on Recent Advances in Active Control of Sound and Vibration, pp. 929–940 (1993).
- <sup>15</sup>R. L. Clark and C. R. Fuller, "A model reference approach for implementing active structural acoustic control," *J. Acoust. Soc. Am.* **92**, 1534–1544 (1992).
- <sup>16</sup>S. D. Sommerfeldt and B. L. Scott, "Wavenumber sensors for active control of acoustic radiation," in Proceedings of the 1993 North American Conference on Smart Structures and Materials, Vol. 1917 (1993).
- <sup>17</sup>S. D. Sommerfeldt and B. L. Scott, "Estimating acoustic radiation using wavenumber sensors," in Proc. Noise-Con 94, pp. 279–284 (1994).
- <sup>18</sup>F. Fahy, *Sound and Structural Vibration. Radiation, Transmission and Response* (Academic, New York, 1985).
- <sup>19</sup>B. Z. Steinberg and J. J. McCoy, "Toward local effective parameter theories using multiresolution decomposition," *J. Acoust. Soc. Am.* **96**, 1130–1143 (1994).
- <sup>20</sup>C. K. Chui, *An Introduction to Wavelets*, Series on Wavelet Analysis and its Applications (Academic, New York, 1992).
- <sup>21</sup>M. R. Portnoff, "Time-frequency representation of digital signals and systems based on short-time Fourier analysis," *IEEE Trans. Acoust., Speech, Signal Process.* **ASSP-28**(1), 55–69 (1980).
- <sup>22</sup>O. Rioul and M. Vetterli, "Wavelets and signal processing," *IEEE Signal Process. Mag.* 14–37 (1991).
- <sup>23</sup>O. Rioul and P. Flandrin, "Time-scale energy distributions: A general class extending wavelet transforms," *IEEE Trans. Signal Proc.* 1746–1757 (1992).
- <sup>24</sup>I. Daubechies, *Ten Lectures on Wavelets*, CBMS-NSF regional conference series in applied mathematics (Society for Industrial and Applied Mathematics, Philadelphia, PA, 1992).
- <sup>25</sup>C. K. Chui and J.-Z. Wang, "A cardinal spline approach to wavelets," *Proc. Am. Math. Soc.* **113**(3), 785–792 (1991).
- <sup>26</sup>S. G. Mallat, "A theory for multiresolution signal decomposition: The wavelet representation," *IEEE Trans. Pattern. Anal. Mach. Intell.* **11**(7), 674–693 (1989).
- <sup>27</sup>A. Berry, J. L. Guyader, and J. Nicolas, "A general formulation for the sound radiation from rectangular, baffled plates with arbitrary boundary conditions," *J. Acoust. Soc. Am.* **88**, 2792–2802 (1990).
- <sup>28</sup>R. L. Clark and C. R. Fuller, "Active structural acoustic control with adaptive structures including wavenumber considerations," in Proceedings of the Conference Recent Advances in Active Control of Sound and Vibration, pp. 507–524 (1991).
- <sup>29</sup>E. K. Dimitriadis, "Piezoelectric actuators for distributed vibration excitation of thin plates," *ASME J. Vib. Acoust.* **113**, 100–107 (1991).

# Method for reducing sound radiated from structures using vibration absorbers optimized with a neural network

Kosuke Nagaya and Lianjin Li

Department of Mechanical Engineering, Gunma University, Kiryu, Gunma 376, Japan

(Received 30 September 1997; accepted for publication 11 May 1998)

The usual design methods for the vibration absorbers are applicable to suppress vibrations of machines and structures, but they are invalid for reducing sounds. This study discusses a method for reducing sound radiated from structures by the use of vibration absorbers. In the current study, the peaks of sound power in the frequency domain are considered to be cost functions. Hence the equations for obtaining optimal parameters of the absorbers become nonlinear expressions. In order to have the optimal parameters, a neural network procedure is applied. Since it is difficult to give appropriate initial values in the usual neural network procedure which gives rapid convergence of the solution, a method for accelerating the neural network is discussed. Numerical calculations were conducted for a plate-type cantilever beam with a large width, and experimental tests were also performed for the same beam. It is proven that the present method is valid for reducing noises radiated from structures. In the usual design method for the vibration absorbers, a modal analysis has been used, so the number of absorbers should be the same as that of control modes, on the other hand the present method can treat nonlinear problems, hence there is no restriction between the number of absorbers and the modal number. © 1998 Acoustical Society of America.

[S0001-4966(98)00409-3]

PACS numbers: 43.40.Vm [PJR]

## LIST OF SYMBOLS

$I_{c,k}$  input to the neuron  $k$  of the output layer  $C$   
 $I_{bj}$  input to the neuron  $i$  of the middle layer  $B$   
 $I_{a,i}$  input to the neuron  $i$  of the input layer  $A$   
 $O_{c,k}$  output from the neuron  $k$  of the output layer  $C$   
 $O_{bj}$  output from the neuron  $j$  of the middle layer  $B$   
 $O_{a,i}$  output from the neuron  $i$  of the input layer  $A$   
 $W_{bc,jk}$  weight between the neuron  $j$  of the layer  $B$  and the neuron  $k$  of the layer  $C$   
 $W_{ab,ij}$  weight between the neuron  $i$  of the layer  $A$  and the neuron  $j$  of the layer  $B$   
 $X_i$  input to the unit  $i$  of the layer  $A$  which corresponds to the  $i$ th parameters of the absorbers  
 $J_{n,k}$  cost function for the neuron  $k$  of the output layer  $C$ , where  $k$  corresponds to the  $k$ th peak of sound power in the frequency domain  
 $T_{n,k}$  output from the neuron  $k$  of the output layer  $C$   
 $E_n$  errors between the cost function and the output of the neural network for the  $n$ th iteration  
 $U_{a,i}$  gradient of the output function  $g$  of the neuron  $i$  for the input layer  $A$

$U_{bj}$  gradient of the output function  $g$  of the unit  $j$  for the middle layer  $B$   
 $U_{c,k}$  gradient of the output function  $g$  of the unit  $k$  for the output layer  $C$   
 $k_2$  spring constant of the vibration absorber  
 $c_2$  damping coefficient of the vibration absorber  
 $M_2$  mass of the absorber  
 $u$  displacement of the absorber  
 $EI$  flexural rigidity of the beam  
 $\omega$  forced angular frequency  
 $m_j$  mass of the  $j$ th beam element  
 $a_1, a_2$  location of the absorbers measured from the built-in end  
 $a_3$  location of the forcing point measured from the built-in end  
 $L_j$  beam element length  
 $y$  amplitude of displacement of the beam  
 $\phi$  amplitude of bending slope of the beam  
 $T$  amplitude of bending moment of the beam  
 $Q$  amplitude of shearing force of the beam  
 $F_0$  amplitude of external sinusoidal force  
 $v$  velocity of the beam

## INTRODUCTION

Vibration absorbers have been utilized to reduce vibrations of machines and structures, and a number of studies concerning the methods for tuning absorbers have been described.<sup>1,2</sup> The tuning of the absorbers as previously mentioned are made based on the usual concept of minimizing vibration amplitudes. However, the optimal values of absorbers will be different from those with minimizing sound powers. Fuller *et al.* presented a method using active forces in

conjunction with a radiated sound cost function to minimize radiated sound (the technique is called ASAC).<sup>3</sup> For the vibration absorbers, Fuller *et al.*<sup>4</sup> and the current authors have introduced the method for tuning based on ASAC at almost the same time (Ref. 4 in July 1995, and the current study in April 1995). In Ref. 4, an interesting method has been introduced for reducing sound power in a cylindrical shell by the use of vibration absorbers, but there was no experimental check.

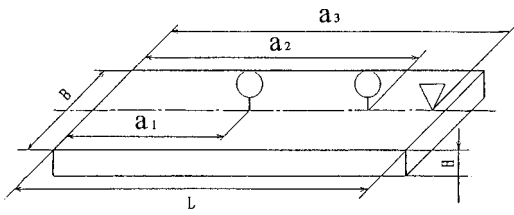


FIG. 1. Geometry of plate-type beams.

The current study discusses a method for tuning vibration absorbers based on the ASAC technique for reducing sound radiated from structures. Although the principle of using the cost function in terms of the sound power is the same as that in Ref. 4, the method is quite different. In Ref. 4, the mass, locations of the absorbers, and the value  $Q$  ( $=M\omega_r/c$ ) were not included in the tuning parameters, so only the frequency ratio was tuned for a target frequency based on Sequential Quadratic Programming techniques. Since the problem is complex, the parameters as mentioned above have been determined by considering mode shapes as given in Ref. 4, but the parameters do not give correct optimal values. The current study chooses all physical values of the absorbers such as the masses, spring constants, damping coefficients, and locations, as the tuning parameters of the absorbers. Structures are excited, in general, by mechanical vibrations involving various frequency components, so it is important to reduce peak values of response curves in a frequency domain. This is a possibility to reduce vibrations for impulse response<sup>1</sup> having various frequency components. Then, the current study chooses the square of peak values of the sound power as a cost function, hence the equation for obtaining tuning parameters becomes nonlinear. Since a number of parameters have to be obtained from the nonlinear equations, the current study applies the neural network procedure. However, the calculation time becomes significantly large or the calculation often diverges when invalid initial values are used in the usual neural network procedure, so a method of acceleration of the neural network is discussed. Numerical calculations were conducted for a beam-type plate. To validate the method and analysis, experimental tests are also conducted.

## I. ANALYTICAL MODEL

### A. Response of a plate-type beam with vibration absorbers

Consider sound control problems of a cantilever plate-type beam with vibration absorbers as shown in Fig. 1. The vibration load  $f=F_0e^{i\omega t}$  ( $i=\sqrt{-1}$ ) locates at  $a_3$  from the built-in end, and vibration absorbers at  $a_1$  and  $a_2$ , respectively. The beam is divided into a number of beam elements without mass and concentrated masses. The mass is numbered 1,2,3,... from the built-in end (left end).

#### 1. Transfer matrices for the beam

The field transfer matrix of the beam element between the left side  $L$  of mass  $j$  and the right side  $R$  of mass  $j-1$  is

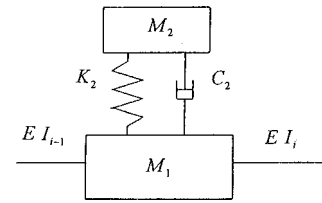


FIG. 2. A beam element with the absorber.

$$\begin{Bmatrix} y \\ \phi \\ T \\ Q \\ 1 \end{Bmatrix}_L = \begin{bmatrix} 1 & -L_j & L_j^2/(2EI_j) & L_j^3/(6EI_j) & 0 \\ 0 & 1 & -L_j/(EI_j) & -L_j^2/(2EI_j) & 0 \\ 0 & 0 & 1 & L_j & 0 \\ 0 & 0 & 0 & 1 & 0 \\ 0 & 0 & 0 & 0 & 1 \end{bmatrix} \times \begin{Bmatrix} y \\ \phi \\ T \\ Q \\ 1 \end{Bmatrix}_R, \quad (1)$$

where  $y$  is the bending displacement,  $\phi$  the bending slope,  $T$  the bending moment,  $Q$  the shearing force,  $L_j$  the length of the beam element, and  $EI_j$  the flexural rigidity. Equation (1) is given using the vector as

$$V_j^L = F_j V_{j-1}^R, \quad j=1,2,3,\dots,N, \quad (2)$$

where  $N$  is the number of division of the beam which also denotes the point number of the right end. The point transfer matrix between the left side  $L$  and the right side  $R$  of the mass  $j$  is

$$\begin{Bmatrix} y \\ \phi \\ T \\ Q \\ 1 \end{Bmatrix}_R = \begin{bmatrix} 1 & 0 & 0 & 0 & 0 \\ 0 & 1 & 0 & 0 & 0 \\ 0 & 0 & 1 & 0 & 0 \\ m_j\omega^2 & 0 & 0 & 1 & F_0 \\ 0 & 0 & 0 & 1 & 0 \end{bmatrix} \begin{Bmatrix} y \\ \phi \\ T \\ Q \\ 1 \end{Bmatrix}_L, \quad (3)$$

where  $F_0$  is the amplitude of external force which acts on the mass  $j$ . If  $j$  is not the exciting point,  $F_0$  is zero of course. Equation (3) is also written as

$$V_j^R = P_j V_j^L, \quad (4)$$

where  $V=(y \ \phi \ T \ Q \ 1)^T$  is the state vector,  $F_j$  the field transfer matrix [see Eq. (1)],  $P_j$  the point transfer matrix [see Eq. (3)],  $m_j$  the element mass, and  $\omega$  the forced angular frequency.

#### 2. Point transfer matrix at the absorber

Let the absorber lie at the point  $S(j=S)$  in the beam. Figure 2 shows a geometry of the absorber connected to the beam, in which  $M_1 (=m_s)$  is the element mass of the beam,  $M_2$  the mass of the absorber,  $k_2$  the spring constant, and  $c_2$  the damping coefficient. The equation of motion of the absorber is

$$M_2 \frac{d^2u}{dt^2} + c_2 \left( \frac{du}{dt} - \frac{dy}{dt} \right) + k_2(u-y) = 0, \quad (5)$$

where  $u$  is the displacement of the absorber. Substituting  $y = Y_0 e^{i\omega t}$  and  $u = A_0 e^{i\omega t}$  into Eq. (5) yields

$$A_0 = \frac{p^2 + 2\mu(i\omega)}{p^2 - \omega^2 + 2\mu(i\omega)} Y_0, \quad (6)$$

where  $2\mu = c_2/M_2$ ,  $p^2 = k_2/M_2$ , and  $i = \sqrt{-1}$ . Hence the force  $Q$  acting on the point  $S$  is

$$Q = c_2 \left( \frac{du}{dt} - \frac{dy}{dt} \right) + k_2(u - y) \\ = \frac{p^2 + 2\mu(i\omega)}{p^2 - \omega^2 + 2\mu(i\omega)} M_2 \omega^2 Y_0 = B(\omega) M_2 \omega^2 Y_0. \quad (7)$$

Using the above equations, the point transfer matrix at the absorber becomes

$$\begin{Bmatrix} y \\ \phi \\ T \\ Q \\ 1 \end{Bmatrix}_j^R = \begin{bmatrix} 1 & 0 & 0 & 0 & 0 \\ 0 & 1 & 0 & 0 & 0 \\ 0 & 0 & 1 & 0 & 0 \\ (M_1 + BM_2)\omega^2 & 0 & 0 & 1 & 0 \\ 0 & 0 & 0 & 0 & 1 \end{bmatrix} \begin{Bmatrix} y \\ \phi \\ T \\ Q \\ 1 \end{Bmatrix}_j^L \quad (8)$$

or

$$V_j^R = P_j V_j^L. \quad (9)$$

When the point transfer matrix given in Eq. (4) for the element without absorbers or that in Eq. (9) where the absorber is applied, one obtains the transfer matrix in the whole range of the beam. The state vector at the right side on an arbitrary point  $n$  is obtained by multiplying the point transfer matrix and the field transfer matrix. When the symbol  $R$  is omitted, the equation yields

$$V_n = P_n F_n \cdots P_j F_j \cdots P_1 F_1 V_0, \quad (10)$$

where  $V_0$  is the state vector at the built-in end (left end in Fig. 1) of the beam (point 0). Substituting the boundary conditions at the built-in end ( $Y_0 = 0$ ,  $\Phi_0 = 0$ ) and the free end ( $T_N = 0$ ,  $Q_N = 0$ ), the state variables at the built-in end are obtained as

$$Y_0 = 0, \quad \phi_0 = 0, \\ T_0 = (a_{34}a_{45} - a_{35}a_{44}) / (a_{33}a_{44} - a_{34}a_{43}), \quad (11) \\ Q_0 = (a_{43}a_{35} - a_{33}a_{45}) / (a_{33}a_{44} - a_{34}a_{43}),$$

where  $a_{mn}$  is the element of the  $m$ th row and  $n$ th column for the transfer matrix  $V_n = P_n F_n, \dots, P_1 F_1$ . Substituting Eq. (11) into Eq. (10) gives the state vector at the  $n$ th point in the beam.

## B. Relationship between sound power and vibrations of structures

### 1. Sound pressure due to a plate moving like pistons

When a plate vibrates, a complex sound field is generated in front of the plate. Consider a small square element with an area  $ds$  in a plate vibrating like a piston. The sound

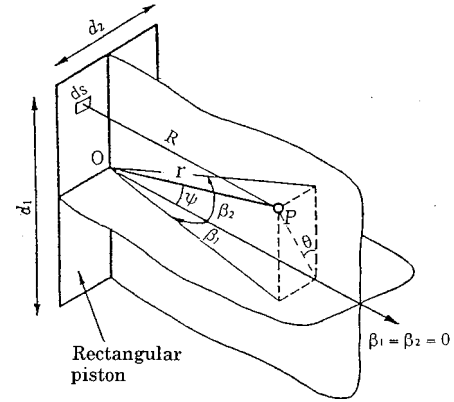


FIG. 3. A rectangular piston model.

pressure can be obtained by integrating the pressure  $dp$  due to a piston motion of the structure in the whole area  $S$  of the plate.<sup>5,6</sup> Hence

$$p_m = i\rho f \int_s \frac{v(x)e^{-i\omega t}}{R} \prod_{l=1}^2 \frac{\sin \alpha_l}{\alpha_l} ds, \quad (12)$$

$$\alpha_l = \frac{\pi d_l}{\lambda} \sin \beta_l,$$

where  $p_m$  is the sound pressure at the point  $P$ ,  $f (= \omega/2\pi)$  the frequency of the piston motion which corresponds to the frequency of the plate,  $\rho$  the density of the air,  $v (= i\omega y)$  the piston speed which corresponds to the velocity of the plate,  $d_1 (= L)$  the length and  $d_2 (= B)$  the width of the rectangular plate,  $\lambda$  the wavelength,  $R$  the length from the center of the small element to the point, and  $r$  is the length measured from the origin to point  $P$  in a space (see Fig. 3). The symbol  $\beta_1$  is the angle as shown in Fig. 3. When the plate is divided into  $N$  pieces, Eq. (12) is written as

$$p_m = i\rho f \sum_{j=1}^N \left\{ \frac{v_j e^{-i\omega t}}{R_j} \left[ \prod_{l=1}^2 \frac{\sin \alpha_{lj}}{\alpha_{lj}} \right] \Delta S_j \right\}, \quad (13)$$

where subscript  $j$  denotes the  $j$ th square element.

### 2. Sound powers due to vibrating plates

In the current study, steady-state vibrations are discussed. Let the sound pressure be  $p_m(r, \theta, \psi)$  at point  $P$  whose coordinate is  $(r, \theta, \psi)$ . The sound power  $P_w$  is<sup>7,8</sup>

$$P_w = \frac{r^2}{\rho c} \int_0^{2\pi} \int_0^\pi p_m^2(r, \theta, \psi) \sin \theta d\theta d\psi. \quad (14)$$

Substituting Eq. (13) into Eq. (14), one obtains<sup>8</sup>

$$P_w = \frac{\rho r^2 f^2}{c} \int_0^{2\pi} \int_0^\pi \left| \sum_{j=1}^N \left\{ \frac{v_j e^{-i\omega t}}{R_j} \left[ \prod_{l=1}^2 \frac{\sin \alpha_{lj}}{\alpha_{lj}} \right] \Delta S_j \right\} \right|^2 \\ \times \sin \theta d\theta d\psi. \quad (15)$$

The velocity of the surface of the plate is obtained by Eq. (10), so the sound power is calculated by substituting the velocity  $v_j$  into Eq. (15).

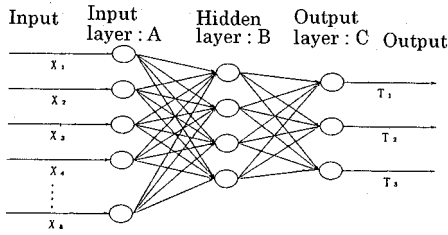


FIG. 4. Three layered neural network used in this analysis.

## II. METHOD OF ABSORBERS DESIGN FOR REDUCING SOUND BY USING THE NEURAL NETWORK

A number of studies discussed optimization problems.<sup>9-13</sup> The neural network procedure is straightforward to solve nonlinear problems like the current system because the neural network can be used to simultaneously approximate the optimal cost function and to compute the variation in the absorber parameters. Then, consider a three layered neural network system with an input layer (layer A), middle layer (layer B), and output layer (layer C). The signals flow from the input layer to the output layer as shown in Fig. 4. The output function  $g(X,U)$  is shown in Eq. (16), where the range is taken as  $0 < g(x) < 1$ .

The vibration absorber behaves like a fluid damper because of the existence of a damper. Since higher-mode vibrations damp due to the small amount of damping, it also absorbs vibrations for higher modes due to "fluid damper effect," but the effect of the damper is small for low-frequency vibrations because the damping force due to the damper is small in the low-frequency region. Hence in the present article, low-frequency vibrations are suppressed by the optimal vibration absorber, and vibrations for higher modes are suppressed by the effects of the fluid damper.

In the experiment as mentioned below, three peaks in the frequency region are significant in this system, so the higher modes more than the third mode will be suppressed to almost zero due to the fluid damper effect. Hence three peaks are suppressed by the vibration absorbers. Two vibration absorbers give sufficient effects to suppress three peaks when using our design method as mentioned below.

When one considers two vibration absorbers and three peaks, the number of units for the neural network becomes as follows: eight for layer A, four for layer B, and three for layer C [see Eq. (19)]. The relationship between an input and an output for each unit is

$$\begin{aligned}
 I_{a,i} &= X_i, & O_{a,i} &= g(I_{a,i}U_{a,i}), \\
 I_{b,j} &= \sum_{i=1}^8 w_{ab,ij} O_{a,i}, & O_{b,j} &= g(I_{b,j}U_{b,j}), \\
 I_{c,k} &= \sum_{j=1}^4 w_{bc,jk} O_{b,j}, & O_{c,k} &= g(I_{c,k}U_{c,k}), \\
 g(X,U) &= 1/(1 + e^{-XU}),
 \end{aligned}
 \tag{16}$$

where  $U$  is the gradient of the output function  $g(X,U)$  which differs in each neuron in the current study as stated below,  $w_{ab,ij}$  denotes the weight between neuron  $i$  of layer A and

neuron  $j$  of layer B. The subscripts  $a,b,c$  denote layers A, B, and C, and  $i,j$  denote neurons  $i$  and  $j$ , respectively.

### A. Geometry of the neural network

The design method of vibration absorbers for structures were given in previous works, in which the number of vibration absorbers had to be equal to the number of control modes in the design. The design was made by using the vibration modes of the structure. As mentioned below, the intensity of the sound power does not always correspond to the vibration amplitude, so that the vibration absorbers for reducing sound should be designed by using sound power. From this situation, this study introduces a method of design for vibration absorbers to reduce sound, in which the parameters are decided by using the sound powers, and the higher modes more than the number of absorbers can be included. Let us assume the number of absorbers is two and the control modes are three. The parameters of the absorbers are the location of the absorbers  $a_1, a_2$ , masses, spring constants, and damping coefficients. Hence the number of parameters is eight.

### B. Cost function

Structures are excited, in general, by mechanical vibrations involving various frequency components, so it is important to suppress peak values in a frequency domain. This is a possibility to reduce vibrations of impulsive response (which has various frequency components). The following function is considered as a cost function:

$$J_k = \max\{P_{w,f}(r, \theta, \psi, f)\}, \quad k=1,2,3, \tag{17}$$

where  $\max\{\}$  depicts the value of the  $k$ th peak of the sound pressure in the frequency domain. When Eq. (17) becomes minimum for all  $k$ 's simultaneously, the parameters of the absorbers yield optimum. For the optimal control problems, the cost function is obtained in the time domain, so that the well-known Ricatti equation is applicable. In the current study, the nonlinear cost function is considered in a frequency domain from a vibration engineering point of view, the linear control theory as mentioned above is not applicable. Hence the neural network method is developed and is applicable to autotuning mechanisms. Equation (17) is written as

$$\begin{aligned}
 P_w &= \max \left\langle \sum_f \frac{\rho r^2 f^2}{c} \right. \\
 &\times \sum_{\Psi} \sum_{\theta} \left| \sum_{j=1}^N \left\{ \frac{v_j e^{-i\omega t}}{R_j} \prod_{l=1}^2 \frac{\sin \alpha_{lj}}{\alpha_{lj}} \Delta S_j \right\} \right|^2 \\
 &\times \sin \theta \Delta \theta \Delta \psi \left. \right\rangle, \quad k=1,2,3.
 \end{aligned}
 \tag{18}$$

In the calculation of Eq. (18), a half of a spherical region with radius  $r$  which covers the plate is considered and half of the sphere is divided into nine sections in  $\theta$ , and 12 sections in  $\psi$  directions. Equation (18) is calculated by using areas  $r\Delta\theta$  and  $r\Delta\psi$ .

### C. Method of improvement of input functions

The parameters for two vibration absorbers are

$$\mathbf{X} = (X_1, X_2, \dots, X_8)^T = (k_1, c_1, m_1, a_1, k_2, c_2, m_2, a_2)^T. \quad (19)$$

Let the output from neuron  $k$  of layer C for the  $n$ th iteration be  $T_{n,k}$  (see Fig. 4). The error between the cost function  $J_{n,k}$  and the output  $T_{n,k}$  of the neural network, then the error is written as

$$E_n = \sum_{k=1}^3 (J_{n,k} - T_{n,k})^2 / 2, \quad (20)$$

where  $n$  denotes the iteration number. By using the neural network,  $T_{n,k}$  becomes a minimum value, so that when  $E_n$  becomes minimum, the cost function yields minimum. The derivation of  $E_n$  with respect to the input variable  $X_i$  is

$$\frac{\partial E_n}{\partial X_i} = \sum_{k=1}^3 (J_{n,k} - T_{n,k}) \left( \frac{\partial J_{n,k}}{\partial X_i} - \frac{\partial T_{n,k}}{\partial X_i} \right). \quad (21)$$

Equation (21) is shown by using the three point formula as

$$\frac{\partial J_{n,k}}{\partial X_i} = \frac{3J_{n,k} - 4J_{n-1,k} + J_{n-2,k}}{2(X_{i,n} - X_{i,n-1})}. \quad (22)$$

For the output  $T_{n,k}$  of the neural network for the  $k$ th peak, one obtains

$$\frac{\partial T_{n,k}}{\partial X_i} = U_{c,k} O_{c,k} (1 - O_{c,k}) \left[ \sum_{j=1}^4 U_{b,j} w_{bc,jk} O_{b,j} (1 - O_{b,j}) \times U_{a,i} w_{ab,ij} O_{a,i} (1 - O_{a,i}) \right]. \quad (23)$$

Substituting Eqs. (22) and (23) into Eq. (21) yields

$$\frac{\partial E_n}{\partial X_i} = \sum_{k=1}^3 (J_{n,k} - T_{n,k}) \left\{ \frac{3J_{n,k} - 4J_{n-1,k} + J_{n-2,k}}{2(X_{i,n} - X_{i,n-1})} - U_{c,k} O_{c,k} (1 - O_{c,k}) \left[ \sum_{j=1}^4 U_{b,j} w_{bc,jk} O_{b,j} (1 - O_{b,j}) \times U_{a,i} w_{ab,ij} O_{a,i} (1 - O_{a,i}) \right] \right\}. \quad (24)$$

If the value  $\Delta \mathbf{x} = \eta (\partial E_n / \partial \mathbf{x}_i)$  is taken as a variation vector, the relationship between the vector of  $n$ th iteration and  $n+1$ th iteration becomes

$$X_{i,n+1} = X_{i,n} + \eta \frac{\partial E_n}{\partial X_i} \quad (i = 1, 2, 3, \dots, 8). \quad (25)$$

### III. METHOD OF ACCELERATION OF THE NEURAL NETWORK

The result as mentioned above is obtained based on the usual neural network procedure. The solution converges and one obtains the optimal values of the absorber when appropriate initial values are reached. However, if the initial values are not appropriate, the convergence becomes significantly

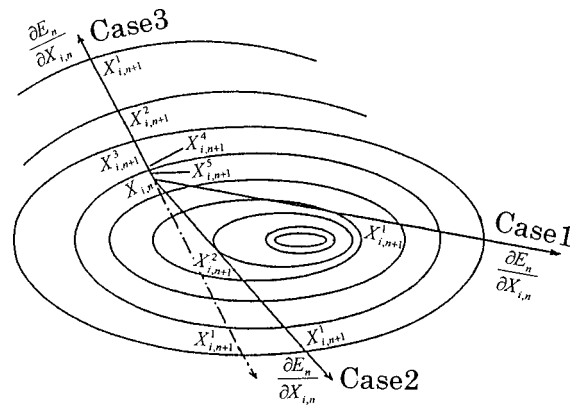


FIG. 5. Geometry of the accelerated neural network.

cantly slow or the solution often diverges. In order to have rapid convergence, the current study researches a method of acceleration of the neural network.

#### A. Improvement of $\eta$

There are some cases for the convergence of the cost function in the calculation of optimal values of the absorber. Hence the variation of the cost function is researched along the directions  $\partial E_n / \partial X_{i,n}$  as shown in Fig. 5, in which the closed loop shows the line having the same value of  $J_n^2 = \sum_{k=1}^3 J_{n,k}^2$ , and it decreases in the direction of the small closed loop. Take, for instance, case 1, since the cost function  $J_{n+1}^2$  decreases in comparison with  $J_n^2$  as shown in Fig. 5, the usual iteration is performed as written in Eq. (25). If the value  $J_{n+1}^2$  for  $X_{i,n+1}$  becomes larger than that for  $n$  as shown in case 3 in Fig. 5

$$J_{n+1}^2(X_{i,n+1}^1) > J_n^2(X_{i,n}),$$

$X_{i,n+1}^1$  is invalid. Then value  $\eta$  is varied to  $\eta/2$ , and the value of  $X_{i,n+1}$  is obtained. This calculation is performed  $M$  times. Hence the expression becomes

$$X_{i,n+1}^s = X_{i,n} + \frac{\eta}{2^s} \frac{\partial E_n}{\partial X_{i,n}}, \quad s = 1, 2, \dots, M.$$

For case 2 in Fig. 5, the absolute values of  $J_{n+1}^2$  are also greater than  $J_n^2$ , but the direction of  $\partial E_n / \partial X_{i,n}$  is opposite, so

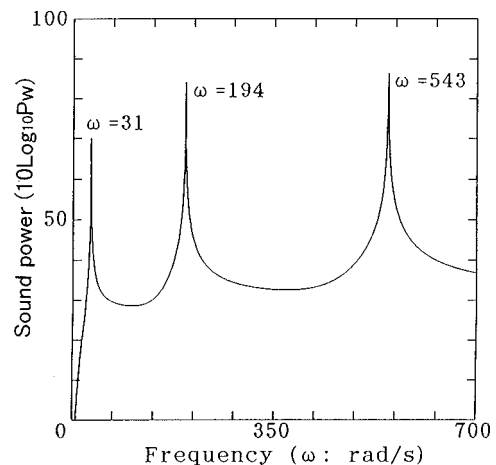


FIG. 6. Sound power level ( $10 \log_{10} P_w$ ) in the case of without absorbers.

TABLE I. Optimal parameters of absorbers by the author's method.

Method	Parameter			
	$K$ N/cm	$C$ N/cm	$M$ kg	$L$ cm
Dynamic absorbers (1)	$8.474 \times 10$	1.379	$2.697 \times 10^{-2}$	34.2
Dynamic absorbers (2)	$6.437 \times 10$	$5.288 \times 10^{-3}$	$9.156 \times 10^{-1}$	47.2

the sign becomes negative. In the calculation, when the cost function does not decrease until  $M$  iterations, the sign is changed. When the initial value of  $\eta$  is assumed to be 0.1 and  $M$  is assumed to be 5, we can use the following equations

$$\eta = \eta_0 = 0.1 \quad \text{for } n=1 \text{ initial value,}$$

$$\eta = 0.1 \quad \text{for } \sum_{k=1}^3 J_{n,k}^2 < \sum_{k=1}^3 J_{n-1,k}^2,$$

$$\eta = \eta_0 / 2^s \quad (s=2,3,\dots,5) \quad \text{for } \sum_{k=1}^3 J_{n,k}^2 > \sum_{k=1}^3 J_{n-1,k}^2,$$

$$\eta = -0.1 \quad \text{when } \eta \leq \eta_0 / 32 \quad \text{and} \quad \sum_{k=1}^3 J_{n,k}^2 > \sum_{k=1}^3 J_{n-1,k}^2.$$

**B. Improvement of weight  $w$  with consideration of the appropriate gradient of the output function**

The improvement of the weight in the back propagation algorithm is<sup>12</sup>

$$\mathbf{w}(n+1) = \mathbf{w}(n) - \epsilon \Delta \mathbf{w}(n), \tag{26}$$

where  $\epsilon$  is the coefficient of convergence. The variation of the weight for the general layer  $m$  is

$$\Delta w_{m-1,m,i,j}(n) = \delta_j^m(n) O_{m,i}(n). \tag{27}$$

Hence for layer C,  $\delta_j^m(n)$  becomes

$$\delta_k^c(n) = (J_{n,k} - T_{n,k}) O_{c,k}(1 - O_{c,k}). \tag{28}$$

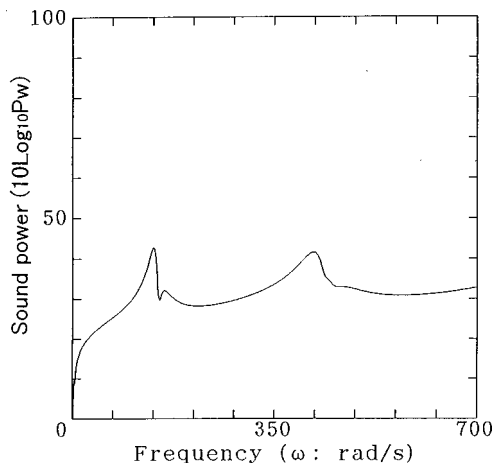


FIG. 7. Sound power level ( $10 \log_{10} P_w$ ) by the author's method.

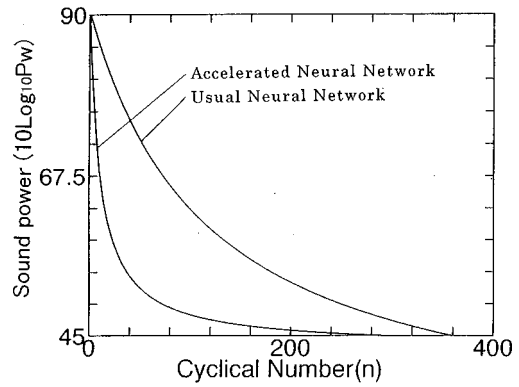


FIG. 8. Speed of convergence.

$\delta_j^m(n)$  for layer B is

$$\delta_j^b(n) = \left[ \sum_{k=1}^3 w_{bc,jk} \delta_k^c(n) \right] O_{b,j}(1 - O_{b,j}). \tag{29}$$

Equation (16) indicates a function  $g(X,U)$ . The slope  $U$  in the function  $g(X,U)$  is constant in general neural network procedures. But, gradient  $U$  also affects the convergence. After a number of calculations, the appropriate values are obtained as  $|X_n U_{mi}| \leq 2.2$  in this calculation.

**IV. NUMERICAL EXAMPLES**

Numerical calculations have been conducted for a cantilever beam with the length measuring 51 cm, width 15 cm, thickness 0.15 cm, in which the load  $P = 0.2 \sin(\omega t)[N]$  acts on the location 1.7 cm from the free end. The beam is divided into 30 elements, and the divided points are numbered from 1 to 31. Hence the point at the load is No. 30.

Figure 6 depicts the sound power for the beam without vibration absorbers. There are three peaks at  $\omega_1 = 31$  rad/s,  $\omega_2 = 194$  rad/s, and  $\omega_3 = 543$  rad/s in the range from  $\omega = 0$  to 700 rad/s. Those frequencies correspond to resonant frequencies of the beam. The locations at the peaks coincide with those for the resonant peaks of vibration. In the numerical calculation, the reason for the above is the beam with two vibration absorbers.

The optimal parameters (location, mass, spring constant, and damping coefficient) of the vibration absorbers were calculated by using the neural network procedure as mentioned above. In the calculation, the gradients of the output function were chosen as  $U_{a,i} = 0.5/X_i$  for layer A,  $U_{b,j} = 0.5$  for layer B, and  $U_{c,k} = 0.5$  for layer C. For the neural network system,

TABLE II. Optimal parameters of absorbers by the Seto *et al.* method.

Method	Parameter			
	$K$ N/cm	$C$ N/cm	$M$ kg	$L$ cm
Dynamic absorbers (1)	$1.510 \times 10$	$3.145 \times 10^{-2}$	$4.806 \times 10^{-2}$	23.8
Dynamic absorbers (2)	0.3326	$6.249 \times 10^{-3}$	$4.902 \times 10^{-2}$	49.3



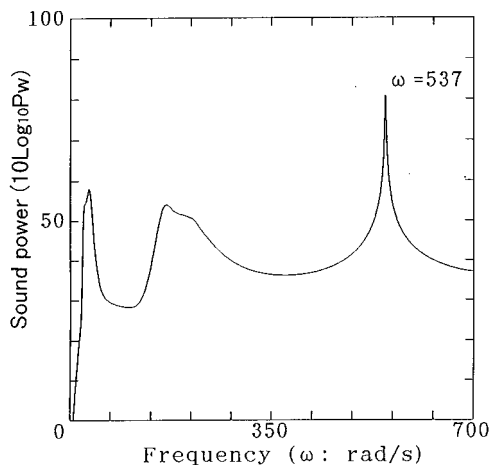


FIG. 9. Sound power level ( $10 \log_{10} P_w$ ) by the Seto *et al.* method.

the calculated result is often reduced to a local minimum value which is different from the minimum value. Hence the calculations were performed for various initial values. In the current calculation, the results are reduced to the same minimum value, so the optimal values can be obtained. Table I depicts the optimal parameters obtained for the vibration absorbers. By using the table, the sound power was calculated as shown in Fig. 7. It can be observed that the peaks for the curve in Fig. 7 are significantly smaller than those in Fig. 6. The decreased values are 27.1 dB for the first peak, 44.1 dB for the second, and 44.3 dB for the third.

The same results will be obtained by use of the usual neural network procedure, but the convergence is slow as compared to the current accelerated neural network procedure. Figure 8 shows a comparison between them. The result by the current method converges until  $n=250$ , while it converges  $n=360$  for the usual neural network procedure with  $\eta=0.1$ .

A design method of vibration absorbers for structures has been described by Seto *et al.*<sup>1</sup> They used the modal analysis, and designed the absorber for each vibration mode. Table II depicts the optimal parameters obtained by the Seto *et al.* method, and Fig. 9 depicts the result for the sound power level. The results of our method are depicted in Fig. 7. The optimal values in Table II by Seto *et al.* are significantly different from ours (Table I). Only first and second peaks are suppressed in Fig. 9 because of the use of two absorbers, while all peaks are suppressed in our results (Fig. 7). In Seto's method, the number of absorbers should be the same as that of control modes, so it requires three absorbers to control up to three peaks, while our method can control three peaks by using two absorbers. The design in Seto's method is based on vibration amplitudes, so that some values remain

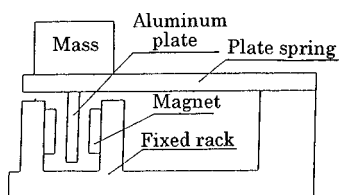


FIG. 10. Geometry of a magnetic vibration absorber.

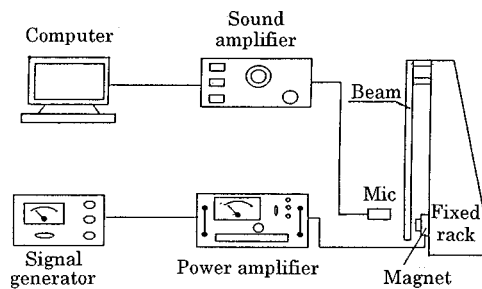


FIG. 11. Geometry of an experimental apparatus.

even in the first two peaks. This implies that the absorbers design for sound is different from that for vibrations. Based on these discussions, it can be shown that our method is superior to their method.

## V. EXPERIMENT

To validate the current method, experimental tests have been conducted. Magnetic vibration absorbers, as shown in Fig. 10, were used in the experiment. The spring constant of the absorber varies with the length of the plate spring, and the damping coefficient also varies with the gaps between the permanent magnets and the conductor (aluminum plate). As a result, the absorbers with the optimal values shown in Table I can be constructed. Figure 11 illustrates an experimental apparatus in which the sinusoidal exciting force is generated by an electromagnet, and sound pressures are detected by a microphone. The experiments were conducted in a noise absorbing box. In the experiment, sound pressures at a number of points are measured by moving the microphone in the box. Since the exciting force is sinusoidal, the sound pressures reach steady state, so the method of measurement as previously mentioned gives appropriate values. The measured sound pressures are stored in the memory of a micro-computer, and the sound powers were calculated by using a program for analyzing acoustic problems given by A&D Co. Ltd. Figure 12 depicts the sound power obtained by the experiment for the beam without absorbers. Although the beam in the experiment did not satisfy the baffled condition perfectly, the theoretical results coincide with the experimental data.

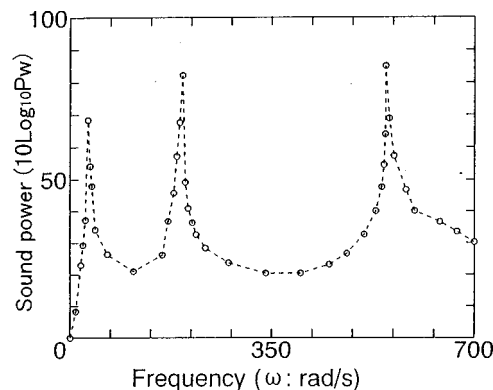


FIG. 12. Sound power level ( $10 \log_{10} P_w$ ) obtained by the experiment without absorbers.

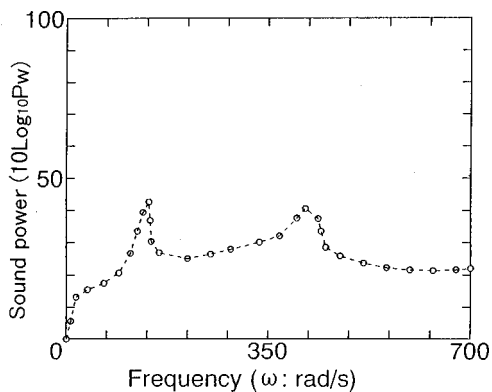


FIG. 13. Sound power level ( $10 \log_{10} P_w$ ) obtained by the experiment with the absorbers.

Figure 13 shows the sound power for the beam with the absorbers designed as previously mentioned. The figures show that the vibration absorbers give significant effects for suppressing sound powers. The curve in Fig. 13 also coincides with that in Fig. 7, so the analysis developed in the current study seems to be valid from a design engineering point of view.

## VI. CONCLUSION

This study discusses a method for reducing sound radiated from structures by use of vibration absorbers. The results are summarized as follows:

(1) A design method of vibration absorbers for reducing sound radiated from structures was introduced. In the method, significant peak values of sound powers in the frequency domain were used as cost functions, and the optimal parameters were obtained by making use of the improved neural network procedure given in the current study. Hence higher modes can be included in the design of absorbers whose number is less than that of control modes. However, an appropriate number of absorbers are required to have sufficient effects of absorbers of course. In the current case, two absorbers are appropriate.

(2) The current analysis does not require a special method such as the modal analysis. The sound pressures or sound powers can be obtained directly when the response of structures are calculated analytically or numerically. Numerical calculations were conducted for a plate-type cantilever beam with a large width. It is determined that the effect of the absorbers designed by the current method is significantly large for suppressing sounds.

(3) To validate the method and analysis, experimental tests have been conducted. The experimental data coincided with the theoretical results.

(4) An accelerated neural network procedure has been introduced which will be able to handle nonlinear systems. The method has been applied to the optimal design of vibration absorbers to reduce sounds radiated from structures. The convergence of the cost function in the current accelerated neural network is better than that in the usual neural network procedures

## ACKNOWLEDGMENTS

The authors express their heartfelt thanks to the reviewers for their useful comments.

- <sup>1</sup>K. Seto, K. Iwanami, and Y. Takita, "Vibration control of multi-degree-of-freedom system by dynamic absorbers," *Trans. Jpn. Soc. Mech. Eng., Ser. C* **50**, 1962–1969 (1983).
- <sup>2</sup>A. H. von Flotow, A. Beard, and D. Bailey, "Adaptive tuned vibration absorbers: Tuning laws, tracking agility, sizing and physical implementations," *Proceedings of Noise-Con 94*, Ft. Lauderdale, FL (1994), pp. 437–454.
- <sup>3</sup>C. R. Fuller and R. J. Silcox, "Active structural acoustic control," *J. Acoust. Soc. Am.* **91**, 519 (1992).
- <sup>4</sup>C. R. Fuller, J. P. Maillard, M. Mercadal, and A. H. von Flotow, "Control of aircraft interior noise using globally detuned vibration absorbers," *Proceedings of the First Joint CEAS/AIAA Aeroacoustics Conference*, Munich (1995), pp. 615–624 (AIAA paper no. 95-082).
- <sup>5</sup>K. Wakasa, N. Iwatsuki, and I. Hayashi, "The equation of total loss factor of plate with a damping foil and its application to the estimation of radiated sound power," *Proc of Asia-Pacific Vibration Conference'93*, 4(Japan) (1993), pp. 753–758.
- <sup>6</sup>C. E. Wallace, "Radiation resistance of a rectangular panel," *J. Acoust. Soc. Am.* **51**, 946–952 (1972).
- <sup>7</sup>Cyril M. Harris and E. Charler, *Shock and Vibration Handbook* (McGraw-Hill, New York, 1976), pp. 2.7–2.12.
- <sup>8</sup>E. G. Williams, "A series expansion of the acoustic power radiated from planar sources," *J. Acoust. Soc. Am.* **73**, 1520–1524 (1983).
- <sup>9</sup>T. Yamada and T. Yabuta, "Dynamic system identification using neural network," *IEEE Trans. Syst. Man Cybern.* **23**, 204–211 (1993).
- <sup>10</sup>K. Worden, G. R. Tomlinson, and W. Lim, "Modeling and classification of non-linear systems using neural network," *Mech. Syst. Signal Process* **8**, 395–419 (1994).
- <sup>11</sup>C. I. Chen, M. R. Napolitano, and J. E. Smith, "Active vibration control with piezoelectric actuators using the modified independent modal space control algorithm and neural network as state estimators," *Proc. Conf. Recent. Adapt. Aens. Mater. Their. Appl'92* (1992), pp. 633–649.
- <sup>12</sup>L. O. Chua and Y. Lin, "Cellular neural network," *IEEE Trans. Circuits Syst.* **35**, 1257–1272 (1988).
- <sup>13</sup>D. Germund and B. Ake, *Numerical Methods* (Prentice-Hall, Englewood Cliffs, NJ, 1974), pp. 2–12.

# Ground effect over hard rough surfaces

Patrice Boulanger, Keith Attenborough,<sup>a)</sup> Shahram Taherzadeh, Tim Waters-Fuller,  
and Kai Ming Li

*Engineering Mechanics Discipline, Faculty of Technology, The Open University, Milton Keynes  
MK7 6AA, England*

(Received 20 October 1997; accepted for publication 19 May 1998)

Laboratory and outdoor measurements are reported of the relative sound pressure level spectrum over hard surfaces containing either random or periodically spaced arrays of 2-D roughnesses. The resulting data have been compared with predictions obtained analytically and with numerical predictions of a boundary element code. Effective impedances of the rough surfaces have been calculated from the boss theory developed by Twersky. A classical asymptotic approximation for propagation near grazing incidence from a point source over an impedance boundary has been modified, heuristically, to allow for diffraction grating effects. The resulting predictions are found to be in tolerable agreement with the data except for close and random packing. The boundary element code is found to give superior results for larger roughnesses, but computational restrictions on element size reduce its usefulness for roughnesses with small width or height. © 1998 Acoustical Society of America. [S0001-4966(98)01809-8]

PACS numbers: 43.50.Vt, 43.28.Fp [MRS]

## INTRODUCTION

Surface roughness of characteristic dimensions that are small compared with audio-frequency wavelengths is known to have significant influence on near-grazing sound especially if the surface material is acoustically hard. Several measurements have been made of the sound pressure level (SPL) spectra, relative to free field, above rough surfaces, where the roughness height and spacing are small compared to the wavelengths of interest.<sup>1-5</sup> These data have been compared with predictions of models derived by Attenborough and Taherzadeh<sup>1</sup> from a boss theory by Tolstoy.<sup>6,7</sup> The models predict that a rough boundary has an effective admittance located at the smooth imbedding plane which produces a distinct ground effect<sup>8</sup> at lower frequencies than correspond to the interference effect due to path length difference alone that would occur at a smooth boundary for a given source-receiver geometry. Specifically, the presence of roughness reduces the frequencies of the main ground effect maximum (sound level minimum). This suggests that deliberate roughening of otherwise acoustically hard surfaces may assist in the passive control of noise from outdoor sources.

Rough surface ground effect has been calculated by means of boss models for the effective admittance of the rough surface and a classical analytical approximation for the field due to a point source above an impedance plane. However, some difficulties have been encountered in reconciling data and predictions. Attenborough and Taherzadeh<sup>1</sup> found it necessary to adjust the impedance of the scatterers and imbedding plane to obtain good agreement between predictions based on the Tolstoy boss theory and the data. Tolstoy's effective admittance models<sup>6,7</sup> predict that a surface wave is generated at grazing incidence above a hard rough boundary and that the effective admittance above a hard rough boundary is purely imaginary. However, comparison of data with

Tolstoy-based predictions indicate that the surface wave component is overestimated, especially at grazing incidence,<sup>2</sup> and that it is necessary to include an attenuation term due to incoherent scatter to obtain a good fit with these data.<sup>3</sup> Poor agreement between laboratory measurements of propagation over rough convex surfaces and predictions based on the Tolstoy effective admittance formulation has been found<sup>4</sup> and it has been suggested that the absence of a real part of admittance corresponding to incoherent scatter effects might be responsible for this. In other comparisons of predictions and data,<sup>5</sup> the assumed location of the effective admittance plane has been adjusted to improve agreement with data at higher frequencies.

In this paper we outline analytical results derived from the more complete semi-cylindrical boss theory by Twersky *et al.*<sup>9-12</sup> that includes the influences of incoherent scatter, interaction between scatterers, and correlation in scatterer distributions. Twersky's results lead to the introduction of a real part term to the admittance of the nonperiodically rough hard surface due to incoherent scattering. Generalizations of Twersky's results are suggested on the basis of analogous formulations for specialized cases deduced by Tolstoy. The resulting predictions are compared with experimental data obtained over hard surfaces containing periodic and randomly spaced two-dimensional (2-D) roughnesses of various shapes in the laboratory and outdoors. Data for periodic and pseudo-random spacing are distinguished. The classical analytical approximation for propagation from a point source over an impedance plane near grazing incidence is extended heuristically to include diffraction grating effects, and resulting predictions are shown to be consistent with the data obtained over periodic roughnesses. It is found possible to obtain reasonable agreement between predictions and data without attributing nonzero admittances to the scatterers and imbedding plane or adjusting the assumed location of the impedance plane as before.

<sup>a)</sup>Please address correspondence to Keith Attenborough.

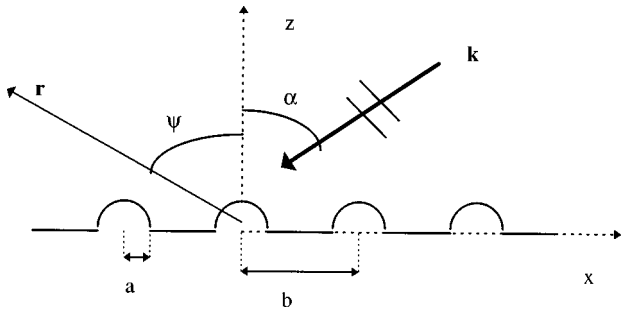


FIG. 1. The 2-D representation of a plane wave incident on a surface containing a regularly spaced grating of semi-cylindrical bosses.

In addition, predictions of a boundary element code developed by Chandler-Wilde and Hothersall<sup>13</sup> are compared with those resulting from the analytical models and with the data. This boundary element code may be used to predict propagation of sound over surfaces containing 2-D roughnesses of any shape. It calculates the pressure due to a line source at a receiver above a rough locally reacting boundary numerically by a standard numerical technique involving discretization of the rough boundary according to constraints that are discussed later.

In Sec. I Twersky's effective impedance formulations for semi-cylindrical scatterers distributed on an acoustically hard plane are outlined, a proposal for their generalization to arbitrary scatterer shapes near grazing incidence is made, and a heuristic method of including diffraction grating effects in the predicted field due to a point source above a rough hard surface is suggested. Experiments over artificially roughened acoustically hard surfaces are described in Sec. II. Data and predictions are compared in Sec. III. Concluding remarks are stated in Sec. IV.

## I. ANALYTICAL FORMULATIONS

### A. Twersky's semi-cylindrical boss model

Twersky has developed a boss model<sup>9-12</sup> to describe coherent reflection from a hard surface containing semi-cylindrical roughnesses in which the contributions of the scatterers are summed to obtain the total scattered field. Sparse and closely packed distributions of bosses have been considered and interaction between neighbor scatterers has been included. His results lead to a real part of the effective admittance of the rough hard surface which may be attributed to incoherent scattering. Consider a plane wave incident on an array of semi-cylinders of radius  $a$  and mean center-to-center spacing  $b$  on an otherwise plane hard boundary (Figs. 1 and 2). Denoting the angle of incidence with respect to the normal by  $\alpha$ , the azimuthal angle between the wave vector and the roughness axes by  $\varphi$ , Twersky's results for the effective relative admittance  $\beta$  of a rough hard surface containing nonperiodically spaced 2-D circular semi-cylinders are

$$\beta = \eta - i\xi. \quad (1)$$

where

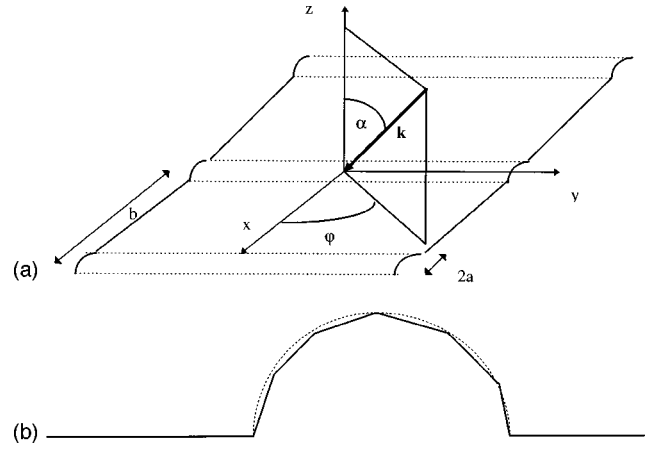


FIG. 2. (a) The 3-D representation of a plane wave incident on a surface containing a regularly spaced grating of semi-cylindrical bosses. (b) Example discretization of a semi-cylindrical rod section for use in the BEM.

$$\xi(\alpha, \varphi) \approx kV[-1 + (\delta \cos^2(\varphi) + \sin^2(\varphi)\sin^2(\alpha))] + O(k^3), \quad (2)$$

$$\eta(\alpha, \varphi) \approx \frac{nk^3\pi^2a^4}{8}(1-W^2) \left\{ (1 - \sin^2\alpha \sin^2\varphi) \times \left[ 1 + \left( \frac{\delta^2}{2} \cos^2\varphi - \sin^2\varphi \right) \sin^2\alpha \right] \right\} + O(k^5), \quad (3)$$

$V = n\pi a^2/2$  is the raised cross-sectional area per unit length,  $n$  is the number of semi-cylinders per unit length ( $=1/b$ ),  $\delta = 2/(1+I)$  is a measure of the dipole coupling between the semi-cylinders,  $I = (a^2/b^2)I_2$  where

$$I_2 \cong 2W(1 + 0.307W + 0.137W^2), \quad \text{for } W < 0.8,$$

$$I_2 \cong \frac{\pi^2}{3} \left[ 1 - \frac{2(1-W)}{W} \right] + 6 \frac{(1-W)^2}{W^2} \left[ \frac{\pi^2}{6} + 1.202 \right], \quad \text{for } W \geq 0.8$$

$$I \cong \frac{(\pi a)^2}{3b^2}, \quad \text{for } W = 1 \text{ (periodic),}$$

$(1-W)^2$  is a packing factor introduced for random distributions,  $W = nb^* = b^*/b$ ,  $b^*$  is the minimum (center to center) separation between two cylinders, and  $k$  is the wave number.

The real part  $\eta$  of the admittance (the incoherent scattering loss term) is zero only for periodic distributions of bosses. For grazing incidence normal to the cylinder axes,  $\alpha = \pi/2$ , and azimuthal angle  $\varphi = 0$  we obtain

$$\beta = \frac{na^2k}{2} \left( (1-W^2) \frac{(1 + \delta^2/2)k^2\pi^2a^2}{4} - i\pi(\delta - 1) \right). \quad (4)$$

According to Lucas and Twersky,<sup>12</sup> for semi-elliptical cylinders with eccentricity  $K$ , so that  $V = n\pi a^2K/2$ ,

$$\delta = \frac{1+K}{1+I[K(1+K)/2]}. \quad (5)$$

## B. Heuristic generalization of Twersky's cylindrical boss theory

Twersky's cylindrical boss theory may be generalized to scatterers of arbitrary shape by comparison with equivalent results from Tolstoy's work. Equations (1)–(3) may be contrasted with the equivalent results from Tolstoy's boss theory<sup>3</sup> for the effective admittance of a surface containing 2-D roughnesses of arbitrary shape, after correcting his expression for a missing coefficient  $\sigma$ : According to Tolstoy,<sup>3</sup>

$$\beta = -ik\varepsilon (\cos^2 \varphi - \sigma \cos^2 \alpha), \quad (6)$$

where

$$\varepsilon = V \left( \frac{2s_2}{\nu_2} - 1 \right), \quad \sigma = \left( \frac{2s_2}{\nu_2} - 1 \right)^{-1}, \quad (7)$$

$s_2 = \frac{1}{2}(1+K)$  is a shape factor,  $K$  is a hydrodynamic factor depending on steady flow around a scatterer,  $\nu_2 = 1 + 2\pi V s_2 / 3b$  is a scatterer interaction factor, and  $V$  is the cross-sectional scatterer area above the plane per unit length. Values of  $K$  are known for various shapes.<sup>1</sup> For semi-elliptical cylinders  $K = a'/b'$ , where  $a'$  is the height and  $b'$  is the semi base. For a scatterer having an isosceles triangular section with side  $u$  and height  $h$ ,  $K = 1.05(h/u) + 0.14(h/u)^2$ . For semi-cylinders the expressions for  $\varepsilon$  and  $\sigma$  can be simplified to obtain

$$\varepsilon = \frac{\pi a^2}{2b} \left( \frac{2}{1 + (\pi^2/3)(a/b)^2} - 1 \right) \quad (8)$$

and

$$\sigma = \frac{1}{\left( \frac{2}{1 + (\pi^2/3)(a/b)^2} - 1 \right)}. \quad (9)$$

Equation (2) can be rewritten as

$$\xi(\alpha, \varphi) \approx kV [(\delta - 1) \cos^2(\varphi) - \cos^2(\alpha)(1 + (\delta - 1) \cos^2(\varphi))]. \quad (10)$$

Comparison of Eqs. (6) and (10) suggests that Twersky's and Tolstoy's expressions for the imaginary part of the effective admittance are equivalent for circular semi-cylinders if  $\delta$  is replaced by  $\varepsilon/V + 1 = 2s_2/\nu_2$ . Moreover, Twersky's result [Eq. (5)] for elliptical semi-cylinders shows the same dependence on  $K$ , the eccentricity, as can be obtained from Tolstoy's<sup>3</sup>  $\delta = (1+K)/[1+IK(1+K)/2]$ . This more general expression for  $\delta$  gives a dependence on the hydrodynamic factor  $K$  (through  $\varepsilon$ ) and thus on the shape of the scatterer. Therefore, we suggest that generalized forms for the real and imaginary parts of effective admittance may be obtained from Eqs. (1), (2), and (5) and the following form:

$$\eta(\alpha, \varphi) \approx \frac{k^3 b V^2}{2} (1 - W^2) \left\{ (1 - \sin^2 \alpha \sin^2 \varphi) \times \left[ 1 + \left( \frac{\delta^2}{2} \cos^2 \varphi - \sin^2 \varphi \right) \sin^2 \alpha \right] \right\} + O(k^5), \quad (11)$$

TABLE I. Admittance and hydrodynamic factors used in Twersky's model.

Roughness shape	$\eta = \text{Re}(\beta)$	$\xi = \text{Im}(\beta)$	$K$
Semi-cylindrical	(3)	(2)	1
Semi-elliptical and rectangular	(11)	(2)	$a'/b'$
Triangular	(11)	(2)	$1.05(h/u) + 0.14(h/u)^2$
Slats	(11)	(2)	1

where  $V$  represents the scatterer volume per unit area (raised area per unit length in two dimensions). Data for propagation over thin wooden slats is presented later. To deduce  $K$  for such scatterers, we assume that each slat affects the fluid flow as if it were a lamina.<sup>14</sup> The expression for the virtual mass of a lamina of width  $2a$  is identical to the one for a cylinder of radius  $a$ , i.e.,  $K = 1$ . Table I summarizes the relations for the effective admittance and the value of the hydrodynamic factor used for the various roughness shapes.

## C. Heuristic treatment of diffraction grating effects

The sound pressure level relative to the free field (henceforth called relative SPL), from a point source over an impedance plane, is obtained from

$$\text{rel. SPL} = 20 \log \left| \frac{P}{P_1} \right|, \quad (12)$$

where

$$P = P_0 \frac{e^{ikR_1}}{R_1} + Q P_0 \frac{e^{ikR_2}}{R_2} \quad (13)$$

is the total pressure at the receiver due to a point source above a homogeneous impedance plane and

$$P_1 = P_0 \frac{e^{ikR_1}}{R_1} \quad (14)$$

is the pressure due to the direct wave from the source [using  $\exp(-i\omega t)$  for the time dependence]. Here  $Q$  is the spherical wave reflection coefficient,  $R_1$  is the direct path length from source to receiver,  $R_2$  is the path length through the specular reflection point (see Fig. 1), and  $P_0$  is a constant. It should be noted that the expression for the imaginary part of the admittance [Eq. (2)] is quadratic in the roughness period  $b$  and predicts, for example, the same frequencies of the first relative SPL minima for scatterers packing densities (percentage of distance between source and receiver occupied by roughness) of 25% and 80%.

To model the diffraction grating effect, we postulate an additional term proportional to the area occupied by the elements of the diffracting array. The total wave reaching the receiver is considered to consist of a direct wave, a reflected wave from the rough surface based on the spherical wave reflection from the effective admittance at the imbedding plane, and a third component reflected coherently by the "grating" of roughnesses. The additional wave component is considered to have an extra path length  $\Delta = pb \sin \alpha$ , where  $p$  is an integer depending on the order of the interference effect, and is expressed by

$$P' = P_0 \frac{e^{ik(R_2 + \Delta)}}{(R_2 + \Delta)}. \quad (15)$$

The relative SPL is obtained using relation (12) with  $P$  replaced by

$$P_d = W_a P + W_b P', \quad (16)$$

where  $W_b$  is the proportion of the ground between source and receiver that is covered by the roughnesses and  $W_a = 1 - W_b$ .

#### D. The boundary element model

Chandler-Wilde and Hothersall<sup>13</sup> have developed a boundary integral equation method to evaluate the pressure at the receiver. A solution for the Helmholtz equation for the pressure at the receiver can be solved numerically for a locally reacting ground by a standard boundary element technique. An equivalent two-dimensional problem can be solved in order to save computation time. Source, receiver, and specular point are assumed to be in a vertical plane perpendicular to the roughness axis, and a line integral is solved instead of a surface integral. It is necessary to input node coordinates that discretize the various roughness shapes used in the study. Thus the discretization of a rough boundary is finer than would be employed for a plane boundary. It is necessary to use boundary element lengths that are smaller than the smallest segment that gives a reasonable discretization of the shape of the roughness. An example of seven-node discretization for a semi-cylindrical rod section is shown in Fig. 2(b). However, to discretize the semi-circular or the semi-elliptical cross sections used in the subsequent experiments with better accuracy, the model used 11 nodes instead of the 7 shown in the figure. A second constraint for an accurate use of the boundary element technique is that one needs to choose boundary element lengths no more than one-fifth of the wave length. The first and second constraints govern computation times at low frequencies and high frequencies, respectively.

## II. EXPERIMENTS

A Tannoy driver, fitted with a 1-m long tube having 3-cm internal diameter was used as a point source in both the laboratory and outdoor measurements. The receiver was a Bruel & Kjaer type 4311  $\frac{1}{2}$ -in.-diam condenser microphone fitted with a preamplifier. Signal processing and signal generation were carried out using a maximum length sequence system analyzer. Background noise effects were reduced by analyzing with respect to the known output sequence. For the relative SPL reference, a measurement was made with source and receiver at the maximum possible height of 2 m above the floor of the anechoic chamber. Varnished halves of 1-m-long large and small radius wooden dowel rods were taped on to the boards to act as cylindrical two-dimensional roughnesses. The smaller rods have semi-elliptical cross sections with major axis (base) of 0.0135 m and semi-minor axis

(height) of 0.005 m. The larger rods are more semicircular in cross section and have been modeled as perfectly semicircular with radius 0.02 m.

The point source and receiver were suspended 0.1 m above the board surface and 1 m apart. Periodically spaced distributions included close-packed and packing densities of 50% and 25%. Only 30 of the smaller rods were used for the close packing. The resulting array was centered on the specular reflection point halfway between source and receiver but covered only 40% of the ground between source and receiver. Fifteen of the larger rods (radius 0.02 m) were used for close packing. The resulting array was centered on the specular reflection point but covered only 60% of the ground between source and receiver. However, it should be noted by reference to Fig. 4 from Boulanger *et al.*<sup>15</sup> that, for the geometry used in our work and for frequencies between 3800 and 1900 Hz, respectively, the relevant Fresnel zone covers only 40% and 60% of the ground between source and receiver. Since the frequency of the main ground effect (lowest frequency minimum in the relative SPL spectrum) found in this work is greater than the above values (corresponding to a smaller Fresnel zone area), it can be argued that the partial ground coverage in cases of 100% packing should not affect the measured results. The 50% packing densities were obtained by removing every other rod from the close-packed array and replacing them at the ends of the array to cover as much of the source-receiver distance as possible. Further removal of every other rod produced the 25% packing densities.

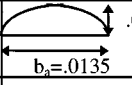

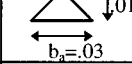

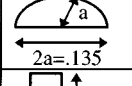
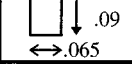
Anechoic laboratory measurements have been made also over periodic arrays of isosceles triangular cross section wooden rods (0.03 m base and 0.015 m high) with close 75% and 50% packing. Twenty of the triangular rods were used for the close packing. The resulting array was centered on the specular reflection point but covered only 60% of the source-receiver distance.

As well as periodically spaced distributions, random distributions were studied for all types of rods using, in turn, 20 small semi-cylindrical rods corresponding to 27% packing, 12 large semi-cylindrical rods corresponding to 48% packing, and 15 triangular rods corresponding to 50% packing. The positions of the rods were determined by using random number tables.

The final series of anechoic laboratory measurements have been carried out over periodically spaced thin wooden slats having a rectangular cross section. The slat section was 0.02 m high and 0.002 m wide and the slat length roughly 1 m. Two center-to-center spacings  $b = 0.05$  m and  $b = 0.098$  m were studied.

Outdoor measurements of relative SPL spectra have been performed over an asphalt-covered ground (parking lot) on which were placed rows of semicircular cylindrical tiles (diameter  $2a = 0.135$  m) and rows of bricks (dimensions  $0.2 \times 0.09 \times 0.065$  m<sup>3</sup>). Source and receiver were located 2.5 m apart and a reference measurement was made with source and receiver at a height of 1 m. Over the tiles, the source and receiver heights were 0.25 and 0.3 m, respectively. Consecutive rows were periodically spaced at a center-to-center distance  $b = 0.235$  m. Over the bricks, the source and receiver

TABLE II. The experimental geometries and roughness characteristics.

	source height (m)	receiver height (m)	source-receiver distance (m)	radius/size (m)	% packing in periodic case	period	% packing for random distributions
small semi-cylindrical rods	0.1	0.1	1	 .05 $b_s = .0135$	100 50 25	$b_a$ $2 b_a$ $4 b_a$	27
large semi-cylindrical rods	0.1	0.1	1	 $a = .02$	100 50 25	$2a$ $4a$ $8a$	48
triangular rods	0.1	0.1	1	 $.015$ $b_s = .03$	100 75 50	$b_a$ $1.3 b_a$ $2 b_a$	50
slats	0.1	0.1	1	 $.02$ $\phi = .002$	4 2	$0.05m$ $0.098m$	—
semi-cylindrical tiles	0.25	0.3	2.5	 $a$ $2a = .135$	56	$0.235m$	—
bricks	0.2	0.2	2.5	 $.09$ $\leftrightarrow .065$	50	$0.125m$	—

heights were both 0.2 m. The bricks were resting on their longer edges such that the rows were 0.065 m wide, 0.09 m high, and about 2 m long. Rows of bricks were spaced regularly at a center-to-center distance  $b = 0.125$  m. Table II summarizes the various experimental conditions.

### III. COMPARISONS BETWEEN DATA AND PREDICTIONS

#### A. Laboratory data

Example results of the measurements (solid line) and predictions (dotted, dot-dash, and dash lines) using the boundary element method (BEM) and Eqs. (1) and (2) for nominally periodic spacing (center-to-center =  $4a$ ) and close packing of semi-cylindrical rods are shown in Figs. 3 and 4. The predictions used Eq. (3) in Figs. 3(b) and 4(b) where the rod sections are modeled as perfectly semi-cylindrical, and the predictions used Eqs. (5) and (11) in Figs. 3(a) and 4(a) where the rod sections are modeled as semi-elliptical. Twersky's effective admittance model is subject to the approximation  $ka \leq 1$  which is valid up to 8000 Hz for the smaller rods ( $a = 0.007$  m) and 3000 Hz for the larger rods ( $a = 0.02$  m). Some improvement in the prediction [dotted line in Fig. 3(a)], based on the Twersky admittance model (semi-elliptical rod section), of the main ground effect magnitude (i.e., dip in relative SPL with greatest magnitude and lowest frequency), over the regular array of the smaller rods with center-to-center spacing ( $b = 0.027$  m approximately twice the rod diameter), results from assuming that the rod array was slightly nonperiodic, i.e.,  $b^* (= 0.026 \text{ m}) < b$  (dot-dash line). The relative SPL predictions resulting from Twersky's admittance formulation [Eqs. (1)–(3) and semi-cylindrical rod section] for the close-packed rod arrays of both sizes and the spaced array of larger rods are poor. No significant improvements in agreement between data and theory resulted from including diffraction grating effects for these cases. The BEM predictions for the small rods [dashed lines in Figs. 3(a) and 4(a)] are relatively poor. Allowing for an elliptical

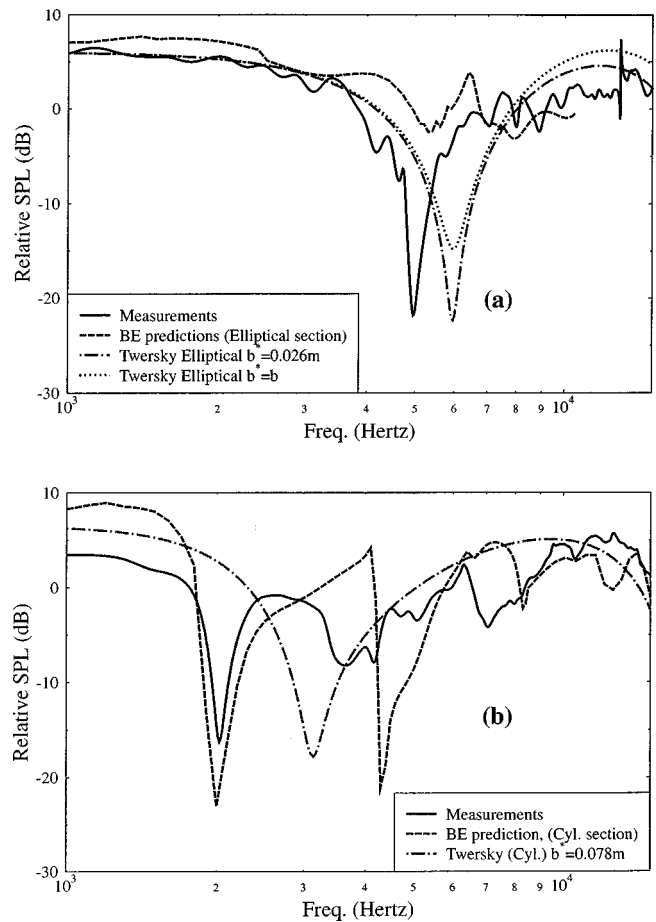


FIG. 3. (a) Relative SPL data (solid line) obtained over a surface containing 15 small semi-elliptical rods (base 0.0135 m, height 0.005 m) symmetrically distributed about the central point between source and receiver separated by 1 m and at a height of 0.1 m. Predictions shown are calculated from (i) BEM code assuming semi-elliptical boss cross sections, (ii) Eqs. (1)–(3), (5), and (12)–(16) with  $b^* = 0.026$  m, and (iii) as for (ii) but with  $b^* = b$ . (b) Relative SPL data (solid lines) obtained over a surface containing eight semi-circular rods (radius 0.02 m) symmetrically distributed about the central point between source and receiver separated by 1 m and at a height of 0.1 m. Predictions shown are calculated from (i) BEM code, and (ii) Eqs. (1)–(3) and (12)–(16) with  $b^* = 0.078$  m.

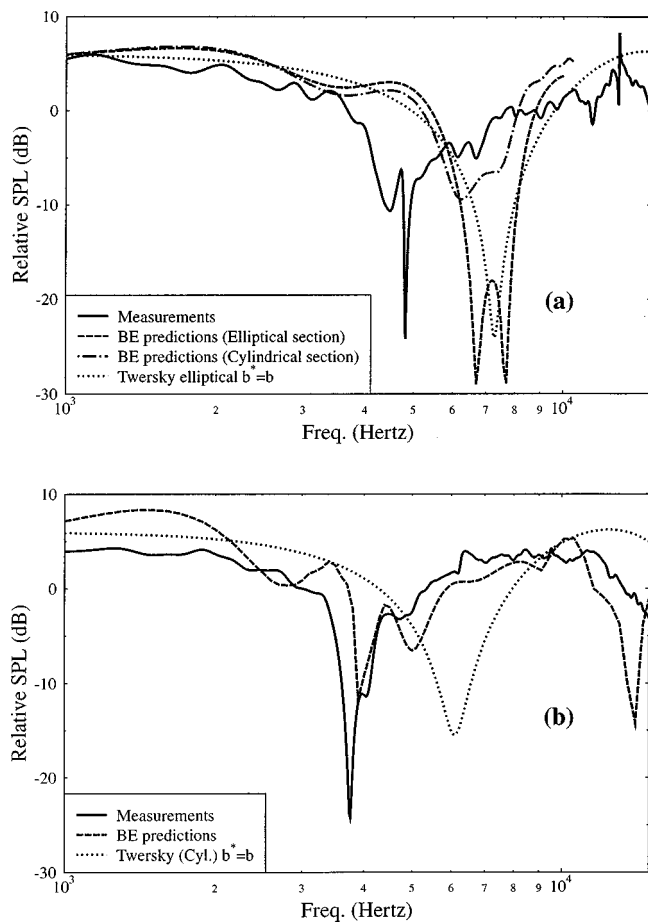


FIG. 4. (a) Relative SPL data (solid line) obtained over a surface containing 30 small semi-elliptical rods (base 0.0135 m, height 0.005 m) in a close-packed array distributed between source and receiver separated by 1 m and at a height of 0.1 m. Predictions shown are calculated from (i) BEM code assuming semi-elliptical boss cross sections, (ii) BEM code assuming semi-circular boss cross sections (radius 0.007 m) and 100% area coverage, and (iii) Eqs. (1)–(3) and (5). (b) Relative SPL data (solid lines) obtained over a surface containing 15 close-packed semi-circular rods (radius 0.02 m) symmetrically distributed about the central point between source and receiver separated by 1 m and at a height of 0.1 m. Predictions shown are calculated from (i) BEM code and (ii) Eqs. (1)–(3).

shape of the scatterers increases the magnitude of the predicted dip but does not improve the correspondence between the measured and predicted frequency position [Fig. 4(a)]. Additional BEM calculations taking into account the lack of total ground coverage by the roughness in the 100% packing density cases show no improvement to the predictions, as is expected from Fresnel zone considerations. On the other hand, the BEM predictions for the larger rods [dashed lines in Figs. 3(b) and 4(b)] are in reasonable agreement with data. In Fig. 3(b) the measured data and the BEM calculations of relative SPL display additional dips near 4000 Hz that cannot be reconciled with a path length difference between direct and reflected wave, and thus are most likely due to diffraction grating effects.

Measurements over the randomly spaced distributions of rods [solid line in Fig. 5(a) and (b)] show a range of ground effects, none of which are predicted by using Twersky's effective admittance model [Eqs. (1)–(3)] assuming a random distribution [dashed line in Fig. 5(a) and (b)]. It should be noted that the parameter introducing randomness in Twersky's

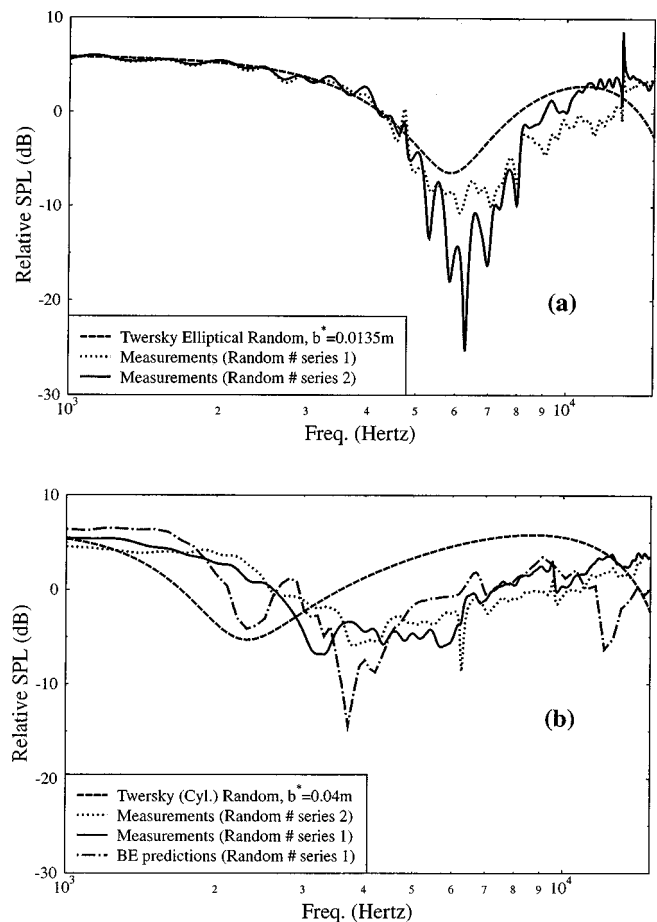


FIG. 5. (a) Relative SPL data (solid line) obtained over a surface containing 15 small semi-elliptical rods (base 0.0135 m, height 0.005 m) in two different random distributions between source and receiver (geometry as for Figs. 3 and 4). Predictions shown are calculated from Eqs. (1)–(3) and (5) for a random distribution with  $b^* = 0.0135$  m. (b) Relative SPL data (solid lines) obtained over a surface containing 12 semi-circular rods (radius 0.02 m) in two different random distributions between source and receiver. Predictions shown are calculated from (i) Eqs. (1)–(3) and (12)–(16) with  $b^* = 0.04$  m and (ii) BEM code assuming one random distribution.

theory is the minimum (center-to-center) separation between two rods  $b^*$ . Additional calculations not displayed here have shown that a decrease in the distance  $b^*$  to small values produces a continuous decrease in the predicted magnitude of the ground effect. The series of random numbers used to generate the position of the rods always included a spacing smaller than the rod diameter. For such cases two of the rods were assumed to be adjacent and hence the minimum (center-to-center) separation between two rods was assumed to be  $b^* = 2a$ . Consequently, for each type of rod, only one prediction can be computed using Twersky's theory. The BEM predictions for the random arrays of large rods [dash-dot line in Fig. 5(b)] are more successful.

Example results from measurements over triangular rods (solid line), predictions using Twersky's effective admittance theory modified for scatterers with triangular cross section and for diffraction grating effects [Eqs. (11)–(16)] (dot-dash lines) and Twersky's without diffraction grating (dotted line) as well as predictions of the BEM code (dashed line), are shown in Fig. 6(a) and (b). The measured data for relative SPL display additional dips near 8000 and 10 000 Hz in Fig.



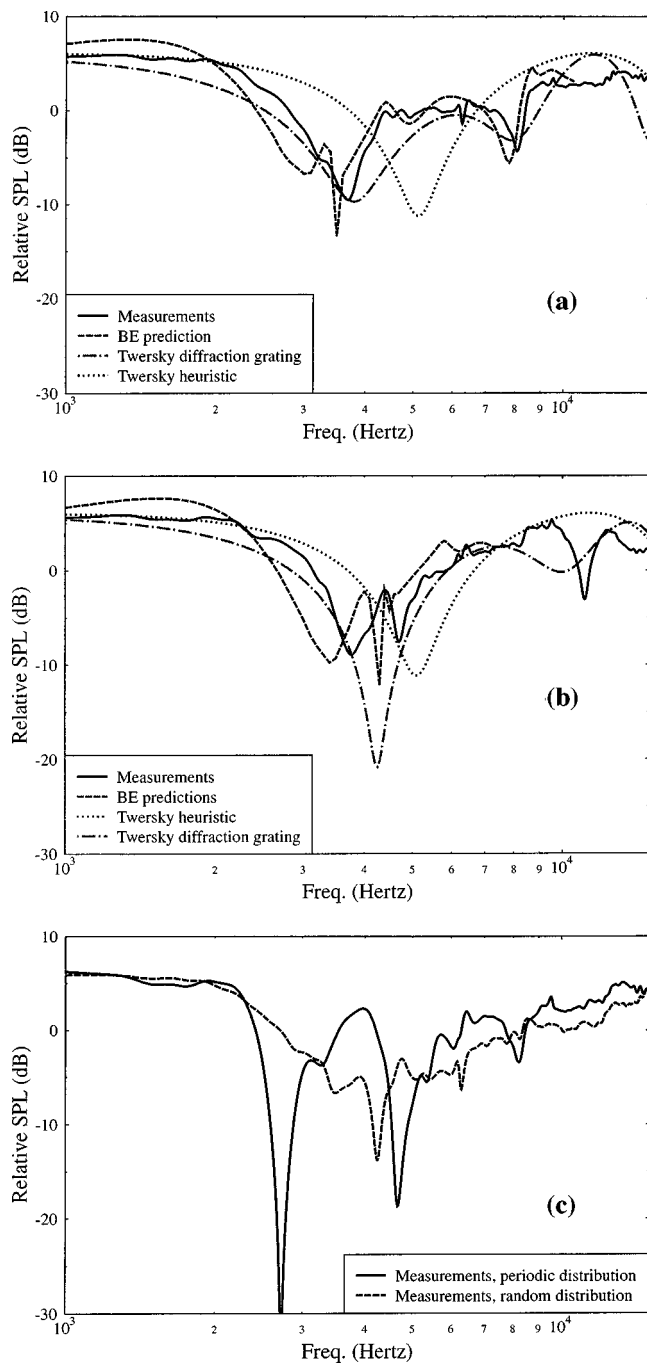


FIG. 6. (a) Relative SPL data (solid lines) obtained over a surface containing 15 regularly spaced triangular cross section rods (base 0.035 m, height 0.015 m) with and without a rod at the point of specular reflection between source and receiver separated by 1 m and at a height of 0.1 m. Predictions shown are calculated from (i) BEM code (ii) Eqs. (1)–(3), (5), and (12)–(16), and (iii) as for (ii) but without the diffraction grating effects. (b) Relative SPL data (solid lines) obtained over a surface containing 20 close-packed triangular cross section rods (base 0.035 m, height 0.015 m) between source and receiver separated by 1 m and at a height of 0.1 m. Predictions shown are calculated from (i) BEM code, (ii) Eqs. (1)–(3), (5), and (12)–(16) with  $p=1$ , and (iii) as for (ii) but without the diffraction grating effects. (c) Relative SPL data obtained over a surface containing 15 randomly spaced (dashed line) and periodically spaced (solid line) triangular cross section rods (base 0.035 m, height 0.015 m) between source and receiver separated by 1 m and at a height of 0.1 m.

6(a) and (b), respectively, that can be explained by diffraction grating effects. The numerical predictions provided by the BEM code are good for both packing densities although its computational demands have restricted predictions to a maximum frequency of 7000 Hz in Fig. 6(b). Twersky's effective admittance model is subject to the approximation  $ka \leq 1$  which is valid up to 3600 Hz for the triangular rods assuming that the characteristic dimension of the roughness is the height  $a=0.015$ . The best analytical predictions (dot-dash lines) use  $\Delta=b \sin(\alpha)$ ,  $b^*=b$ , and  $W_b=0.5$ , although the packing density is 75%. In this and subsequent examples  $W_b$  has been used as an adjustable parameter. Figure 6(c) shows the measured data for a 50% packing density of periodically spaced triangular rods (solid line) and the measured data for a 50% packing density of randomly spaced triangular rods (dashed line). Comparisons between the measured data for these cases and between data obtained over 50% packing density of large semi-cylindrical rods in periodic and random distributions [Figs. 3(b) and 5(b)] show considerable differences in the magnitudes and frequency locations of the ground effects. These and additional measurements not reported here support the conclusion that larger ground effect dips are found over periodic arrays than over random arrays.

Example results from measurements over thin wooden slats (solid lines), boundary element predictions (dashed lines), and predictions based on Eqs. (2), (3), and (13)–(16) using the heuristic Twersky diffraction grating model (dot-dash lines) are shown in Fig. 7(a) and (b) for packing densities of 4% and 2%, respectively. The measurements show multiple dips due to diffraction grating effects. Predictions using the heuristic Twersky diffraction grating model are based on  $K=1$  (lamina hypothesis),  $b^*=b$  (0.05 m), and  $\Delta=2b \sin(\alpha)$ , and  $W_b=0.3$  has been used again in this case as an adjustable parameter. Although this fitted value of 30% packing is much greater than the actual 2% or 4% packing density in plan area, it is consistent with the larger surface area of the slats that is brought into play near grazing. The approximation  $ka \leq 1$  included in Twersky's effective admittance model is valid up to 2700 Hz for the slats assuming that the characteristic dimension of the roughness is the height  $a=0.02$  m. However, agreement with the measured data over the sparser packing is good in the range 1500–10 000 Hz. The boundary element code is difficult to implement for the slat roughnesses because of their small width. Typically the boundary element model gives tolerable predictions for the frequencies of the multiple ground-effect dips, but tends to overpredict their magnitudes. In the second case, it also predicts a low-frequency dip (1500 Hz) that is not present in the measured data.

## B. Outdoor data

The relative SPL spectrum measured over inverted glazed ceramic tiles placed on flat asphalt is shown by the solid line in Fig. 8. The tile cross sections are close to perfectly semi-circular with only 2% difference between the semi-width and the height. The main ground effect is found at a frequency of 800 Hz which is considerably less than the value 3000 Hz expected for an acoustically hard flat

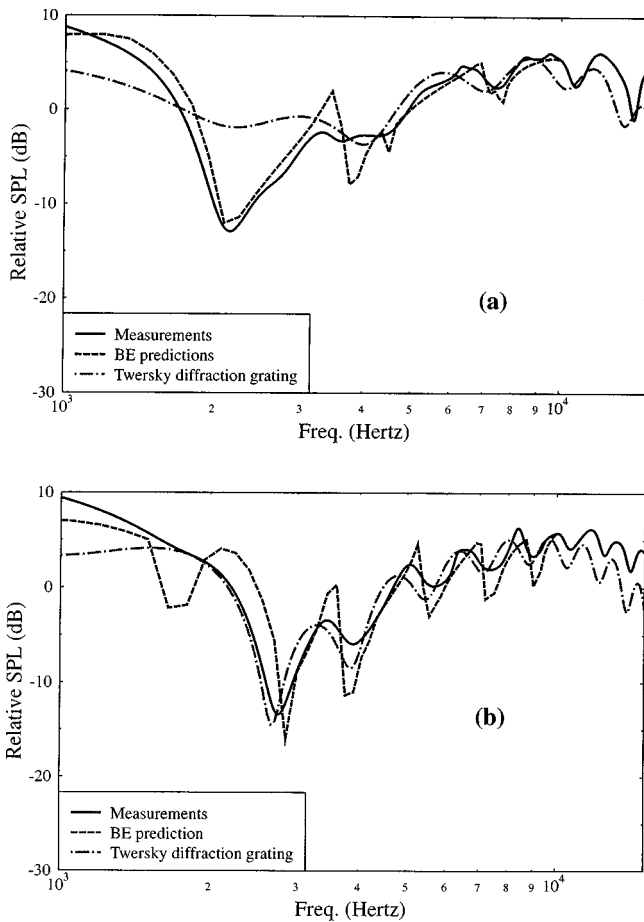


FIG. 7. Relative SPL data (solid line) obtained over 0.002-m-thick and 0.02-m-high wooden slats on a hard wooden surface (solid lines): (a) center-to-center spacing 0.05 m and (b) center-to-center spacing 0.098 m. Predictions shown in each case are obtained with (i) the BEM code and (ii) Eqs. (1)–(3), (5), and (12)–(16) with  $p=2$ .

surface located at the base of the tiles. The measured data show a secondary relative SPL maximum at 2000 Hz.

The boundary element predictions are shown as the dashed lines and predictions derived from generalized Twersky admittance and including diffraction grating effects are represented by dash-dot lines. The analytical model is com-

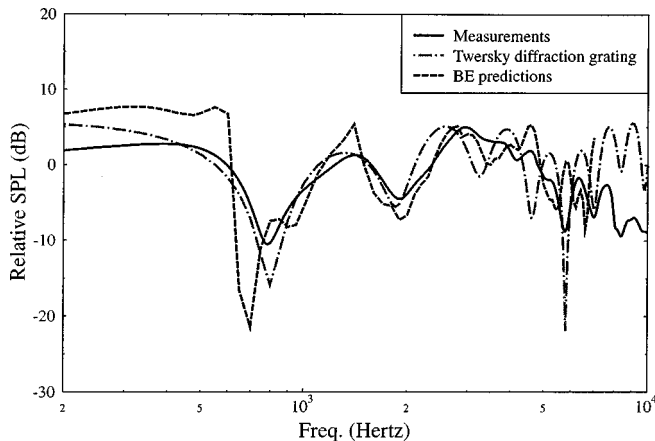


FIG. 8. Relative SPL data (solid line) obtained outdoors over glazed ceramic tiles compared with BEM code predictions and predictions obtained with Eqs. (1)–(3) and (12)–(16) with  $p=2$ .

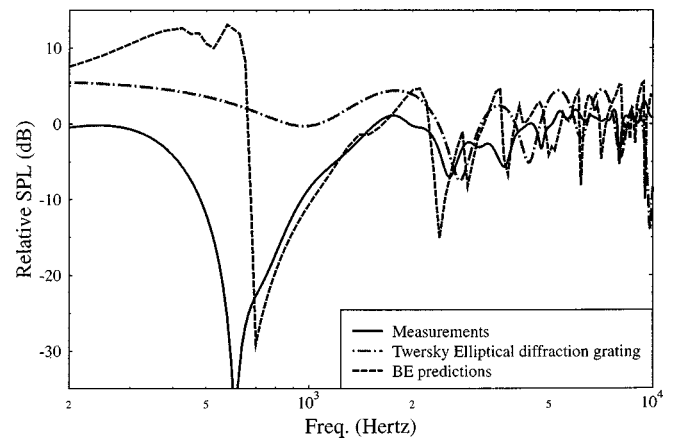


FIG. 9. Relative SPL data (solid line) obtained outdoors over parallel rows of bricks compared with BEM code predictions and predictions obtained with Eqs. (1)–(3), (5), and (12)–(16) assuming semi-elliptical cross sections and with  $p=1.23$ .

puted using  $b=0.235$  m,  $b^*=0.23$  m,  $\Delta=2b \sin(\alpha)$ , and  $W_b=0.56$  (since only 56% of the ground between source and receiver was covered with tiles). The condition  $ka \leq 1$  and the radius  $a=0.067$  m implies that the Twersky boss model should be valid only up to 800 Hz. Nevertheless, the model predicts the frequency position and the magnitude of both the first and second measured relative SPL minima. The boundary element model predictions agree with the data also being within 3 dB in the range 800–5000 Hz. However, the BEM overpredicts the magnitude of the ground effect.

The relative SPL spectrum measured over rows of bricks on asphalt is represented by the solid line in Fig. 9. The main ground effect (dip in relative SPL with largest magnitude) is found at a frequency of 600 Hz which is considerably less than the value 3000 Hz expected for an acoustically hard flat surface and even lower than the one found with the rows of tiles for the same geometry. The measured data show also secondary relative SPL minima of smaller magnitude at 2600, 3700, and 4800 Hz. These secondary maxima are obtained repeatedly for various geometries but could not be predicted with the diffraction grating theory. Predictions of the model based on modified Twersky admittance and including diffraction grating effects are shown as the dash-dot line and are obtained after approximating the rectangular section of a brick by a semi-ellipse. The computations use the semi base  $b'=0.043$  m, the height  $a'=0.09$  m,  $b=0.125$  m,  $b^*=0.115$  m, and  $\Delta=1.3b \sin(\alpha)$ . Because about 50% of the ground between source and receiver was covered with bricks, the value  $W_b=0.5$  was chosen. Note that the value of  $\Delta$  giving the best prediction of the first two relative SPL minima is not an integer multiple of  $b \sin(\alpha)$ . This may be a consequence of approximating the rectangular cross sections by ellipses. The condition  $ka \leq 1$  and the semi base  $b'=0.043$  m implies that the Twersky boss model should be valid only up to 1300 Hz. The analytical model including diffraction overpredicts the frequency position of the first relative SPL maximum by 200 Hz and underpredicts its magnitude by 20 dB. The agreement is satisfactory in the range 800–3000 Hz and the second maximum is predicted correctly. However, discrepancies arise above 3000 Hz.

TABLE III. Agreement between the models predictions and the measured data.

	Small rods		Large rods		Triangular rods		Slats		Cylindrical tiles		Bricks	
	Periodic	Random	Periodic	Random	Periodic	Periodic	Periodic	Periodic	Periodic	Periodic		
Packing density (periodic)/random	50	100	27	50	100	50	75	100	2	4	56	50
Figure no.	3(a)	4(a)	5(a)	3(b)	4(b)	5(b)	6(a)	6(b)	7(a)	7(b)	8	9
Twersky semi-cylindrical	...	...	...	P	P	P	...	...	...	...	...	...
Twersky semi-elliptical	P	P	T	...	...	...	...	...	...	...	...	...
Twersky triangular	...	...	...	...	...	...	P	P	...	...	...	...
Twersky triangular + diffraction grating	...	...	...	...	...	...	G	T	...	...	...	...
Twersky semi-cylindrical + diffraction grating	...	...	...	...	...	...	...	...	...	...	G	...
Twersky lamina + diffraction grating	...	...	...	...	...	...	...	...	G	G	...	...
Twersky semi-elliptical + diffraction grating	...	...	...	...	...	...	...	...	...	...	...	P
Boundary element model	P	P	...	T	T	T	T	T	G	G	G	T

The boundary element predictions (dashed line) underpredict the first measured relative SPL maximum at 700 Hz by 10 dB. The agreement is good between 700 and 2000 Hz and the predictions are within approximately 6 dB of the measured spectrum for frequencies over 2500 Hz. Table III summarizes the comparisons between predictions and data and indicates the corresponding figure. The agreement between data and predictions is indicated qualitatively by P for ‘‘Poor,’’ a T for ‘‘Tolerable,’’ and a G for ‘‘Good.’’

#### IV. CONCLUSIONS

As noted previously,<sup>1,2</sup> relative SPL spectra measured over acoustically hard rough surfaces show a shift in ground effect to lower frequency than would be expected for a smooth acoustically hard surface. The measurements reported here have shown that there are considerable differences between the ground effects caused by periodically and randomly spaced roughnesses with the same packing density. Periodically spaced roughnesses yield additional diffraction grating effects and give greater relative SPL minima. Predictions of ground effect due to regularly spaced roughnesses based on an extended Twersky effective admittance model are sensitive to small deviations from exactly periodic spacing. Incoherent scattering plays an important role for the source-receiver geometries and roughness sizes studied in this work.

The Twersky effective admittance model has been generalized for arbitrary scatterer shape. Diffraction grating effects have been predicted both by the boundary element model and by a heuristic modification of the classical analytical approximation for propagation from a point source near to an impedance boundary. The resulting approximation gives some good predictions of propagation over wooden

slats and triangular wooden rods on a flat hard surface. However, for all of the larger scatterers considered, the boundary element code gives better predictions.

- <sup>1</sup>K. Attenborough and S. Taherzadeh, ‘‘Propagation from a point source over a rough finite impedance boundary,’’ *J. Acoust. Soc. Am.* **98**, 1717–1722 (1995).
- <sup>2</sup>J. P. Chambers, R. Raspet, and J. M. Sabatier, ‘‘Incorporating the effects of roughness in outdoor sound propagation models,’’ *Noise Con 1996*.
- <sup>3</sup>Y. Berthelot and J. P. Chambers, ‘‘On the analogy between sound propagation over a rough surface and sound propagation over a smooth surface with modified surface impedance,’’ *Seventh International Symposium on Long-Range Sound Propagation*, Lyon, France, 1996.
- <sup>4</sup>J. P. Chambers and Y. H. Berthelot, ‘‘An experimental investigation of the propagation of sound over a curved rough, rigid surface,’’ *J. Acoust. Soc. Am.* **102**, 707–714 (1997).
- <sup>5</sup>J. P. Chambers, J. M. Sabatier, and R. Raspet, ‘‘Grazing incidence propagation over a soft rough surface,’’ *J. Acoust. Soc. Am.* **102**, 55–59 (1997).
- <sup>6</sup>I. Tolstoy, ‘‘Coherent sound scatter from a rough interface between arbitrary fluids with particular reference to roughness element shapes and corrugated surfaces,’’ *J. Acoust. Soc. Am.* **72**, 960–972 (1982).
- <sup>7</sup>I. Tolstoy, ‘‘Smoothed boundary conditions, coherent low-frequency scatter, and boundary modes,’’ *J. Acoust. Soc. Am.* **75**, 1–22 (1984).
- <sup>8</sup>K. Attenborough, ‘‘Review of Ground Effects on Outdoor Sound Propagation from Continuous Broadband Sources,’’ *Appl. Acoust.* **24**, 289–319 (1988).
- <sup>9</sup>V. Twersky, ‘‘Scattering and reflection by elliptically striated surfaces,’’ *J. Acoust. Soc. Am.* **40**, 883–895 (1966).
- <sup>10</sup>V. Twersky, ‘‘Multiple scattering of sound by correlated monolayers,’’ *J. Acoust. Soc. Am.* **73**, 68–84 (1983).
- <sup>11</sup>V. Twersky, ‘‘Reflection and scattering of sound by correlated rough surfaces,’’ *J. Acoust. Soc. Am.* **73**, 85–94 (1983).
- <sup>12</sup>R. J. Lucas and V. Twersky, ‘‘Coherent response to a point source irradiating a rough plane,’’ *J. Acoust. Soc. Am.* **76**, 1847–1863 (1984).
- <sup>13</sup>S. N. Chandler-Wilde and D. C. Hothersall, ‘‘Sound propagation above an inhomogeneous impedance plane,’’ *J. Sound Vib.* **98**, 475–491 (1985).
- <sup>14</sup>H. Lamb, *Hydrodynamics* (Dover, New York, 1945), p. 85.
- <sup>15</sup>P. Boulanger, T. Waters-Fuller, K. Attenborough, and K. Ming Li, ‘‘Models and measurements of sound propagation from a point source over mixed impedance ground,’’ *J. Acoust. Soc. Am.* **102**, 1432–1442 (1997).

# Energy-time relations in a room with an electroacoustic system

U. Peter Svensson<sup>a)</sup>

Department of Applied Acoustics, Chalmers University of Technology, S-412 96 Gothenburg, Sweden

(Received 17 October 1997; revised 7 April 1998; accepted 28 April 1998)

This paper presents an extended diffuse field model for estimating the energy-time relationships in a room with an electroacoustic system. Discrete-time room impulse responses are used with a direct sound pulse and an exponentially weighted white-noise sequence modeling the reverberation tail. Transducer directivities and electronic finite impulse response (FIR) filters are included as model parameters. It is shown that the convolution of two exponentially weighted noise sequences is expressed as  $\sqrt{t} \exp(-\delta t)$ . Early and total energy levels can easily be estimated and it is demonstrated that when direct sound components are omitted, this impulse response model results in the classical value of total energy supplied to a room by an electroacoustic system with feedback. Comparisons of such estimates with measurements in an auditorium with a single electroacoustic channel are presented. Four configurations were examined, including close and far microphone positions, combined with a single electronic delay or an FIR filter pattern. In the 500-Hz and 1-kHz octave bands, the early energy contribution from the electroacoustic channel spanned a 15-dB range. Predictions were reasonable, coming within 2 dB of the measured values for all four configurations.  
© 1998 Acoustical Society of America. [S0001-4966(98)04308-2]

PACS numbers: 43.55.Jz [JDQ]

## INTRODUCTION

Electroacoustic systems in auditoria are, among other purposes, used for sound reinforcement and reverberation enhancement. Studies of such systems usually apply either a sophisticated direct sound analysis, for sound reinforcement systems, or simplified diffuse field analysis, for reverberation enhancement systems. With access to either measured or predicted room impulse responses (RIRs) for all transducers of such a system, the total sound field of a room with a multi-channel system can be calculated, as long as the electronic impulse responses (IRs) are time invariant.<sup>1</sup> Time-varying electronic filters are, however, often employed to control feedback in reverberation enhancement systems.<sup>2-4</sup> If the filters are periodically time varying, more elaborate analysis methods can be used.<sup>5</sup> As a complement to accurate prediction methods, simplified estimates of how the early and late energy levels are affected by the number of channels, transducer distances and directivities, and electronic reverberation, might be useful for basic system planning. Diffuse-field relations are useful for estimates of acoustic parameters in a room,<sup>6</sup> and it is the purpose of this paper to apply diffuse-field models, augmented by direct sound components, to rooms with electroacoustic systems. Systems for reverberation enhancement are the primary object of this study, but since even systems for sound reinforcement have to encounter the reverberation in rooms, the results would be applicable to many kinds of electroacoustic systems.

Electroacoustical systems introduce convolutions of RIRs. Vogel and de Vries examined this by modeling the RIRs as sequences of Dirac pulses with increasing density but their approach did not permit an explicit derivation of the convolved IR.<sup>7</sup> In the current paper, a discrete-time impulse response model is used instead to facilitate such derivations.

By this method, estimates of, for example, early energy levels supplied by an electroacoustic system can be studied. By including regeneration effects, the total energy supplied by a system can be predicted as well. Since only basic parameters, such as room volume, reverberation time, transducer distances, and directivities are included, studies of both sound reinforcement systems and reverberation enhancement systems can be analyzed using this unified approach.

## I. IMPULSE RESPONSE MODEL

A discrete-time RIR model is used, with the aim of implementing the relationship for the spatially averaged squared-rms sound pressure,  $\bar{p}^2$ , in a room, with a direct sound and a reverberation component, as suggested by Barron and Lee.<sup>6</sup> Their model predicts a reverberation level which decreases as the distance from the source increases, as effected by the factor  $\exp(-2\delta r/c)$  in

$$\bar{p}^2 = W\rho c \left[ \frac{\Gamma}{4\pi r^2} + \frac{4}{A'} \exp\left(-\frac{2\delta r}{c}\right) \right], \quad (1)$$

where  $W$  indicates the output power of the source,  $\rho$  and  $c$  are the density and sound speed of the air, respectively,  $r$  is the distance from the source to the receiver, and  $\Gamma$  is the directivity factor from the source to the receiver.  $A'$  is the total absorption area in the room, which equals  $8V\delta/c$ , where  $V$  is the room volume,  $\delta$  is the decay constant which is  $3 \ln(10)/T$ , and  $T$  is the reverberation time. The directivity factor  $\Gamma$  is the ratio between the free-field sound intensity in a certain direction, and the intensity averaged over radiation angles. This model was justified by Barron and Lee by the observed decrease in reverberation level as the distance increases in many large rooms. Recently, Vorländer presented another modified reverberation level expression which did not depend on distance, as is the case in the model used here.<sup>8</sup> That study was, however, aimed at smaller rooms such

<sup>a)</sup>Electronic mail: peter@ta.chalmers.se

as reverberation chambers. As a basis for defining IRs, we introduce the relative sound-pressure amplitude,  $\tilde{p}_{\text{rel}}$ , relating the sound pressure to the direct sound pressure in a reference position (e.g., 1 m in front of the source), if the source had been omnidirectional with the same output power, denoted  $\tilde{p}_{\text{dir,ref}}$ . From Eq. (1) the relative sound-pressure amplitude for the direct sound component,  $\tilde{p}_{\text{dir}}$ , would be

$$\tilde{p}_{\text{dir,rel}} = \frac{\tilde{p}_{\text{dir}}}{\tilde{p}_{\text{dir,ref}}} = r_{\text{ref}} \frac{\Gamma^{1/2}}{r}, \quad (2)$$

where  $r_{\text{ref}}$  is the reference distance, and for the reverberation component,  $\tilde{p}_{\text{rev}}$ ,

$$\tilde{p}_{\text{rev,rel}} = \frac{\tilde{p}_{\text{rev}}}{\tilde{p}_{\text{dir,ref}}} = r_{\text{ref}} \left( \frac{2\pi c}{V\delta} \right)^{1/2} \exp\left(-\frac{\delta r}{c}\right). \quad (3)$$

These two components can be expressed as discrete-time IRs with a direct sound component  $h_{\text{dir}}(i)$  such as

$$h_{\text{dir}}(i) = r_{\text{ref}} \left( \frac{\Gamma^{1/2}}{r} \right) \Delta\left(i - \left\lfloor \frac{f_s r}{c} \right\rfloor\right), \quad (4)$$

where  $i$  is the discrete-time index  $[0, \infty]$ ,  $\Delta(i)$  is a unit impulse of amplitude 1 for  $i=1$ , and otherwise it is zero.  $\lfloor x \rfloor$  is the largest integer which is smaller than the real number  $x$ ,  $f_s$  is the sampling frequency, and other parameters are as defined for Eq. (1). Note that the delay indicates that the time is related to the position of the source and not the reference position. The reverberation component  $h_{\text{rev}}(i)$  can be modeled as a white-noise sequence, weighted by an exponentially decaying function<sup>9</sup> given as

$$h_{\text{rev}}(i) = r_{\text{ref}} \left( \frac{4\pi c}{Vf_s} \right)^{1/2} \exp\left(-\frac{\delta i}{f_s}\right) \xi_i \theta\left(i - \left\lfloor \frac{f_s r}{c} \right\rfloor\right), \quad (5)$$

where  $\theta(i)$  is a unit step function of amplitude 1 for  $i \geq 0$  and otherwise it is zero.  $\xi_i$  is a white-noise sequence (i.e., independent samples of a normal distributed random variable, RV) with  $\mu=0$  and  $\sigma=1$ , denoted below as  $N(0;1)$ . Other parameters are as defined for Eq. (1). Whenever an IR consists of an RV multiplied by a weighting function, this weighting function will be called the envelope function furtheron. The total impulse response  $h(i)$  is

$$h(i) = h_{\text{dir}}(i) + h_{\text{rev}}(i), \quad (6)$$

and Fig. 1 shows an example of such an IR. The electronic IR of the electroacoustic system is consequently defined as relating the sound pressure 1 m in front of the loudspeaker, if the loudspeaker had been radiating the same power omnidirectionally, to the sound pressure at the microphone, with a gain factor of  $K_{\text{ML}}$  which includes the sensitivities of the transducers. This can be described with an IR such as

$$g_{\text{ML}}(i) = K_{\text{ML}} \Delta(i - \lfloor f_s \tau_{\text{aux}} \rfloor), \quad (7)$$

where  $\tau_{\text{aux}}$  is the electronic delay. Note that to be consistent with the time reference mentioned in conjunction with Eq. (4), the 1-m delay is not present in Eq. (7) either. All the IRs presented above are dimensionless because they are discrete-time IRs relating two identical quantities. For the sake of fluency the rounding off to integers, indicated by  $\lfloor \cdot \rfloor$ , will be left out below. The primary quantity of interest here is the energy of the IR, which is denoted  $E[h]$ , and it is defined as

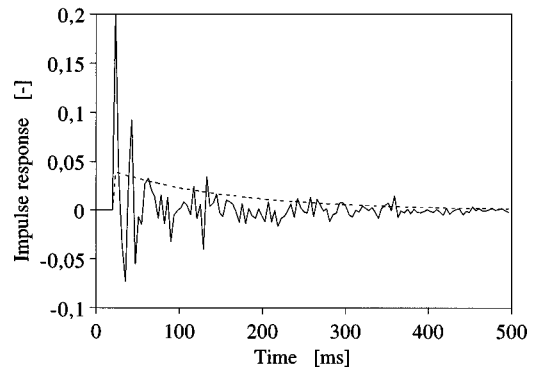


FIG. 1. An example of a room impulse response with the presented model. The direct sound component is visible as a pulse and it is followed by a random tail where the exponential envelope is indicated. The impulse response is plotted as a continuous-time impulse response but should represent a discrete-time impulse response.

$$E[h(i)] = \left\langle \sum_{i=i_1}^{i_2} h^2(i) \right\rangle = \sum_{i=i_1}^{i_2} \langle h^2(i) \rangle, \quad (8)$$

where we have assumed that all samples are independent samples of an RV. The energy can be studied over any desired time range, represented by the sample numbers  $i_1$  and  $i_2$ . If we thus calculate the total energy  $E_t$  of a reverberation IR as given by Eq. (5), and assume that  $2\delta/f_s$  is  $\ll 1$ , the result is

$$\begin{aligned} E_t[h_{\text{rev}}(i)] &= r_{\text{ref}}^2 \frac{4\pi c}{Vf_s} \sum_{i=f_s r/c}^{\infty} \exp\left(-\frac{2\delta i}{f_s}\right) \langle \xi_i^2 \rangle \\ &= r_{\text{ref}}^2 \frac{4\pi c}{Vf_s} \frac{\exp(-2\delta r/c)}{1 - \exp(-2\delta/f_s)} \\ &\approx r_{\text{ref}}^2 \frac{4\pi c}{Vf_s} \exp\left(-\frac{2\delta r}{c}\right) \frac{f_s}{2\delta} \\ &= r_{\text{ref}}^2 \frac{2\pi c}{V\delta} \exp\left(-\frac{2\delta r}{c}\right), \end{aligned} \quad (9)$$

which corresponds to the known reverberation field expression in Eq. (3).

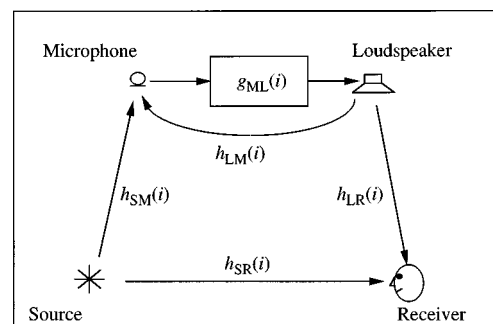


FIG. 2. A single electroacoustic channel in a room illustrating the designations for the involved impulse responses.

## II. ENERGY SUPPLIED BY THE ELECTROACOUSTIC SYSTEM

### A. A single-channel system

In Fig. 2 it can be seen that the total RIR from the source to the receiver is a sum of two components, the natural RIR,  $h_{SR}$ , and the electroacoustic RIR, denoted  $h_{EA}$ . For a single-channel system  $h_{EA}$  can be described by an equivalent infinite series description,

$$h_{EA} = h_{EA,0} + h_{EA,1} + h_{EA,2} + \dots, \quad (10)$$

where

$$h_{EA,0} = h_{SM} * g_{ML} * h_{LR},$$

$$h_{EA,1} = h_{SM} * g_{ML} * h_{LM} * g_{ML} * h_{LR}, \dots,$$

and the asterisk indicates a convolution. In the following derivations of the early energy of  $h_{EA}$  it is assumed that only the component  $h_{EA,0}$  contributes early energy to any significant extent. This is justified by the involved delays that make every new loop's contribution start at a later instant than the previous loop. If interconnected microphones and loudspeakers are placed far apart in order to minimize feedback, long

acoustic delays result. For systems with closely positioned transducers higher-order loops have to be taken into account and this is also necessary if a later time division than, for example, 80 ms is chosen for the early energy. The convolutions of  $h_{EA,0}$  in Eq. (10), using the expressions from Eqs. (4)–(6), are straightforward, except for the convolution of the two exponential reverberation processes which is detailed in Appendix A. It should be noted that the convolution of the two exponential reverberation tails cannot be studied by means of a convolution of two exponential envelopes, as is demonstrated in Appendix A. This fact was also mentioned by Poletti but the convolution of two exponential envelopes was still studied as an approximation of the true convolved decay.<sup>10</sup> The approach used here is equivalent to energy based studies, and leads to similar results for the convolution of two exponential responses, as were found in classical studies of coupled rooms.<sup>11</sup> Poletti also used the analogy of coupled rooms but only for reverberant fields.<sup>10</sup>

An explicit expression for the IR  $h_{EA,0}$  can be formulated using the expression derived in Appendix A. The initial delay time  $\tau_{0,EA} = \tau_{aux} + (r_{SM} + r_{LR})/c$ , as given in Table I, is also introduced so that  $h_{EA,0}(i)$  can be written

$$\begin{aligned} h_{EA,0}(i) &= [h_{SM,dir}(i) + h_{SM,rev}(i)] * g_{ML}(i) * [h_{LR,dir}(i) + h_{LR,rev}(i)] \\ &= K_{ML} r_{ref}^2 \frac{(\Gamma_{SM} \Gamma_{LR})^{1/2}}{r_{SM} r_{LR}} \Delta(i - f_s \tau_{0,EA}) + K_{ML} r_{ref}^2 \exp\left[-\frac{\delta(i - f_s \tau_{0,EA})}{f_s}\right] \theta(i - f_s \tau_{0,EA}) \\ &\quad \times \left\{ \left( \frac{4\pi c}{V f_s} \right)^{1/2} \left[ \frac{\Gamma_{SM}^{1/2}}{r_{SM}} \exp\left(-\frac{\delta r_{LR}}{c}\right) \psi_i + \frac{\Gamma_{LR}^{1/2}}{r_{LR}} \exp\left(-\frac{\delta r_{SM}}{c}\right) \xi_i \right] \right. \\ &\quad \left. + \frac{4\pi c}{V f_s} \exp\left[-\frac{\delta(r_{SM} + r_{LR})}{c}\right] (i - f_s \tau_{0,EA})^{1/2} \gamma_i \right\}, \end{aligned} \quad (11)$$

where  $\xi$ ,  $\psi$ , and  $\gamma$  are RVs which are  $N(0;1)$ . As pointed out in Appendix A the RV  $\gamma$  should not, for low values of  $i - f_s \tau_{0,EA}$ , have a normal distribution. However, for the purpose of calculating the energy, only  $\mu$  and  $\sigma$  of the RV matter, and consequently, the use of a normal distributed RV introduces no errors. Finally,  $h_{EA,0}(i)$  can be written somewhat more compactly as

$$\begin{aligned} h_{EA,0}(i) &= K_{ML} r_{ref}^2 \frac{(\Gamma_{SM} \Gamma_{LR})^{1/2}}{r_{SM} r_{LR}} \Delta(i - f_s \tau_{0,EA}) + K_{ML} r_{ref}^2 \\ &\quad \times \exp\left[-\frac{\delta(i - f_s \tau_{0,EA})}{f_s}\right] \theta(i - f_s \tau_{0,EA}) \\ &\quad \times \left\{ \left( \frac{4\pi c}{V f_s} \right)^{1/2} \left[ \frac{\Gamma_{SM}}{r_{SM}^2} \exp\left(-\frac{2\delta r_{LR}}{c}\right) \right. \right. \\ &\quad \left. \left. + \frac{\Gamma_{LR}}{r_{LR}^2} \exp\left(-\frac{2\delta r_{SM}}{c}\right) \right]^{1/2} \eta_i + \frac{4\pi c}{V f_s} \right\} \end{aligned}$$

$$\times \exp\left[-\frac{\delta(r_{SM} + r_{LR})}{c}\right] (i - f_s \tau_{0,EA})^{1/2} \gamma_i, \quad (12)$$

where  $\eta$  is  $N(0;1)$ . Equation (12) has three terms: one unit pulse term, one exponential term, and one nonexponential term which results from convolving the two exponential reverberation components. This last term, denoted  $h_{EA,0,nonexp}$ , is plotted in Fig. 3 which illustrates the nonexponential envelope. To derive the energy of the IR in Eq. (12), the squared IR must be summed. After squaring  $h_{EA,0}(i)$ , only the three terms in Eq. (12) multiplied with themselves need to be considered since all cross terms will have a mean which is zero. For the term in Eq. (12) which contains an exponentially weighted RV it is straightforward to calculate the early energy portion.<sup>6</sup> The derivation of the energy of  $h_{EA,0,nonexp}$  is described in Appendix B. Calculating the early energy means summing all terms up to the index which corresponds to a time  $\tau_e$  which is, for example, 80 ms after the direct sound of the natural impulse response (i.e.,  $\tau_e = 0.080 + r_{SR}/c$ , as in Table I). Using the result from Ap-

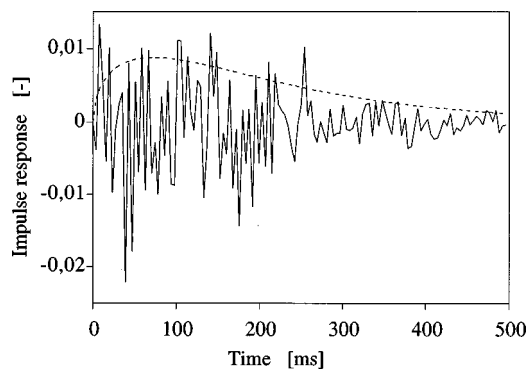


FIG. 3. The result of a convolution of two exponential impulse responses without direct sound components. The envelope has the shape  $\sqrt{t} \exp(-\delta t)$ , as indicated in Eq. (12) by the factor  $\sqrt{i-f_s \tau_{0,EA}} \exp[-\delta i - f_s \tau_{0,EA} / f_s]$ .

pendix B, the early energy  $E_e$  of the IR  $h_{EA,0}$  can be calculated as

$$E_e[h_{EA,0}] = K_{ML}^2 r_{ref}^4 \left\{ \frac{\Gamma_{SM} \Gamma_{LR}}{r_{SM}^2 r_{LR}^2} + \frac{2\pi c}{V\delta} \left[ \frac{\Gamma_{SM}}{r_{SM}^2} \exp\left(-\frac{2\delta r_{LR}}{c}\right) + \frac{\Gamma_{LR}}{r_{LR}^2} \exp\left(-\frac{2\delta r_{SM}}{c}\right) \right] [1 - \exp(-2\delta\tau_{e,EA})] + \left(\frac{2\pi c}{V\delta}\right)^2 \exp\left[-\frac{2\delta(r_{SM}+r_{LR})}{c}\right] \times [1 - (1 + 2\delta\tau_{e,EA}) \exp(-2\delta\tau_{e,EA})] \right\}, \quad (13)$$

where  $\tau_{e,EA} = \tau_e - \tau_{0,EA}$ , as defined in Table I. If this early energy measure should be expressed as the early strength index  $G_{80}$ ,  $r_{ref}$  should be given the value 10 m.<sup>12</sup> Often, it is not necessary to include all terms in Eq. (13). The direct sound components from the loudspeakers to the listeners are usually insignificant unless highly directional loudspeakers are used, or the loudspeakers are positioned close to the listeners. Microphones are more often placed at shorter distances (from the source) and can thus give a significant direct sound component.

$$E_t[\hat{h}_{EA}] = r_{ref}^4 K_{ML}^2 \frac{[\Gamma_{SM}/r_{SM}^2 + (2\pi c/V\delta)\exp(-2\delta r_{SM}/c)][\Gamma_{LR}/r_{LR}^2 + (2\pi c/V\delta)\exp(-2\delta r_{LR}/c)]}{1 - r_{ref}^2 K_{ML}^2 (2\pi c/V\delta)\exp(-2\delta r_{LM}/c)}. \quad (17)$$

At this stage it is practical to introduce the mean power loop gain  $B$ ,

$$B = r_{ref}^2 K_{ML}^2 \frac{2\pi c}{V\delta} \exp\left(-\frac{2\delta r_{LM}}{c}\right), \quad (18)$$

and write the total energy as

$$E_t[\hat{h}_{EA}] = r_{ref}^4 K_{ML}^2 \frac{1}{1-B}$$

## B. Effects of regeneration

In the derivations of early energy described above, no regenerated components were included. If all such higher-order components are included, the system's total energy can be calculated by summing the energy contributions from all components. Rather than carrying this out using the RIR expressions, a much more straightforward approach is to calculate the total energy in the frequency domain, since no information is needed about the temporal distributions. Accordingly, the total transfer function for the single-channel feedback loop in Fig. 1 can be written

$$\hat{h}_{EA}(\omega) = \hat{h}_{SM}(\omega) \frac{\hat{g}_{ML}(\omega)}{1 - \hat{g}_{ML}(\omega)\hat{h}_{LM}(\omega)} \hat{h}_{LR}(\omega), \quad (14)$$

where  $\hat{g}$  and  $\hat{h}$  are the Fourier transforms of the corresponding RIRs. The total energy is the same for the RIR and for the transfer function, for which the energy is given by

$$E_t[h_{EA}] = E_t[\hat{h}_{EA}] = \overline{|\hat{h}_{EA}(\omega)|^2}, \quad (15)$$

where  $\overline{|\hat{h}_{EA}(\omega)|^2}$  is the mean of the squared magnitude averaged over the frequency range of interest. Under the assumption used by Franssen for multichannel reverberation enhancement systems that the regenerated components add uncorrelated,<sup>13</sup> this total energy can be written as

$$E_t[\hat{h}_{EA}] = \overline{|\hat{h}_{SM}(\omega)|^2} \frac{\overline{|\hat{g}_{ML}(\omega)|^2}}{1 - \overline{|\hat{g}_{ML}(\omega)|^2} \overline{|\hat{h}_{LM}(\omega)|^2}} \overline{|\hat{h}_{LR}(\omega)|^2}. \quad (16)$$

This assumption of uncorrelated addition is valid as long as the degree of regeneration is low; that is, a small number of regenerated terms contribute to the total energy. The total energies for  $\hat{h}_{SM}$  and  $\hat{h}_{LR}$  are directly available from Eqs. (2) and (3). As for  $\hat{h}_{LM}$ , it is reasonable to assume that the direct sound is negligible. Furthermore,  $\overline{|\hat{g}_{ML}(\omega)|^2}$  is simply  $K_{ML}^2$ , so that

$$\begin{aligned} & \times \left[ \frac{\Gamma_{SM}}{r_{SM}^2} + B \exp\left(-\frac{2\delta(r_{SM}-r_{LM})}{c}\right) \right] \\ & \times \left[ \frac{\Gamma_{LR}}{r_{LR}^2} + B \exp\left(-\frac{2\delta(r_{LR}-r_{LM})}{c}\right) \right]. \quad (19) \end{aligned}$$

In Eq. (19) the classic relationship for a reverberation system's contribution to a hall is directly identifiable by, first, assuming that the direct sound components are negligible by setting  $\Gamma_{SM} = \Gamma_{LR} = 0$  and, second, assuming that the dis-

TABLE I. The various time constants used in the text.

$\tau_0$	$r_{SR}/c$
$\tau_{0,EA}$	$\tau_{aux} + (r_{SM} + r_{LR})/c$
$\tau_e$	$r_{SR}/c + 0.080$
$\tau_{e,EA}$	$r_{SR}/c + 0.080 - \tau_{aux} - (r_{SM} + r_{LR})/c$

tances  $r_{LR} = r_{SM} = r_{LM} = 0$ . These simplifications result in

$$E_t[\hat{h}_{EA}] = \frac{1}{K_{ML}^2} \frac{B_0^2}{1 - B_0}, \quad (20)$$

with

$$B_0 = r_{ref}^2 K_{ML}^2 \frac{2\pi c}{V\delta}. \quad (21)$$

The natural sound field, under the same assumption of negligible direct sound, and with  $r_{SR} = 0$ , has a total energy of

$$E_t[\hat{h}_{SR}] = r_{ref}^2 \frac{2\pi c}{V\delta} = \frac{B_0}{K_{ML}^2}, \quad (22)$$

and if the electroacoustic energy in Eq. (20) is expressed relative to the natural energy of the room in Eq. (22), the result is

$$\frac{E_t[\hat{h}_{EA}]}{E_t[\hat{h}_{SR}]} = \frac{B_0}{1 - B_0}, \quad (23)$$

which is the classic expression in Ref. 13. Having access to the total energy, Eq. (17), and the early energy, Eq. (13), it is possible to derive the early-to-late and early-to-total energy ratios, both for the total sound field and for the electroacoustic sound field only.

### C. Effects of electronic reverberation and multiple channels

Many electroacoustic systems use electronic units such as delays, equalizers, or reverberation units. Reverberation units have the effect of convolving the electroacoustic IR with the unit's own IR. This can have the form of a sparse finite impulse response (FIR) filter with a few taps or a long simulated RIR from a reverberation unit. Vogel and de Vries argued that the electronic IR preferably should be chosen to give a desired shape of the final electroacoustic IR (e.g., exponential instead of the "balloon" shape indicated in Fig. 3).<sup>7</sup> All electronic IRs affect the parameters significantly by distributing the energy towards later times. For a filter of the sparse FIR type, each tap could be treated as an independent delay which permits a summing of the individual components. Such an approximation might be adequate if the transfer function of the FIR filter yields the energy-based magnitude average over the studied bandwidth. For certain FIR filters, interference effects could be significant over the studied bandwidth and would have to be considered. The expressions derived above are for a single-channel system. For a multichannel system with individual channels, such as the classical multiple channels of reverberation (MCR),<sup>14</sup> the different channels' contributions to the early energy are simply added.

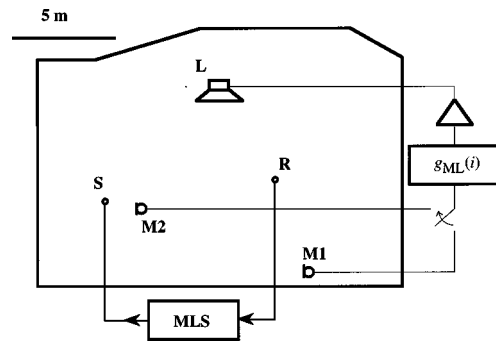


FIG. 4. Sketch of the small auditorium used for the measurements, from a top view. The source, receiver, loudspeaker, and the two microphone positions are marked by S, R, L, M<sub>1</sub>, and M<sub>2</sub> respectively. MLS indicates an impulse response measurement system based on maximum-length sequences.

In a system that uses a single microphone connected to several loudspeakers, every sound path involved could be seen as a separate channel. This should be valid for the early energy contributions (i.e., before regeneration needs to be considered) as long as the loudspeakers are placed at least a few wavelengths apart. When a loudspeaker receives signals from more than one microphone, all cross combinations can be treated as separate sound paths when calculating the early energy. For some systems that do not employ reverberation units, separate microphones are intended for separate source positions, which means that it could be viewed as a system using a single microphone connected to several loudspeakers. Whenever direct sound components are non-negligible in multichannel systems, interference effects might need to be taken into account.

### III. COMPARISONS WITH MEASUREMENTS

A single electroacoustic channel was set up in a small auditorium in order to compare estimated and measured values of early energy supplied by the channel. The hall had a seating capacity of 300 persons, a volume of 1600 m<sup>3</sup> and a reverberation time of 1.1 s in the studied 500-Hz and 1-kHz octave bands. Only one source and one receiver position were studied and the electroacoustic channel used one loudspeaker position and two different microphone positions. Figure 4 shows a sketch of the room, from a top-view, with the relevant positions marked. Two different electronic filters

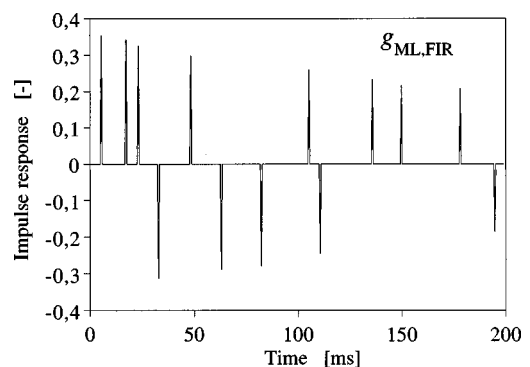


FIG. 5. The electronic impulse response of the FIR filter setting, consisting of 13 taps using a standard program on a Yamaha DSP-1.



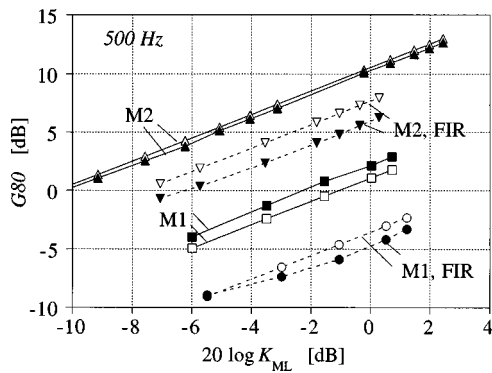


FIG. 6. Measured and predicted values of the electroacoustic system's contribution to early energy,  $G_{80}$ , at 500 Hz in the hall presented in Fig. 4, for the four different configurations described in Sec. III. The curves with empty markers ( $\square$  $\square$  $\nabla$  $\triangle$ ) show the calculated values, and those with filled markers ( $\bullet$  $\blacktriangledown$  $\blacktriangle$ ) show the measured values.

were tested using a Yamaha DSP-1 unit; a single delay of 10 ms, and a sparse FIR filter pattern, illustrated in Fig. 5. Small two-way loudspeakers, Yamaha NS10, were used both as source and system loudspeakers and all microphones were omnidirectional. For the four combinations of microphone positions and electronic filters, the impulse response from the source to the receiver was measured for a number of electronic gain settings, using a measurement system based on maximum-length sequences (MLS). By subtracting the energy of the hall's natural impulse response from the energies of all measured impulse responses, the system's contribution could be determined. The high signal-to-noise ratio that is possible with MLS based measurements was necessary to extract the weak contributions of the system at low gain settings.

Figures 6 and 7 present the early energy contribution by the electroacoustic channel, expressed as  $G_{80}$ , for the two octave bands 500 Hz and 1 kHz. Measured and predicted values are presented for the four combinations of microphone position and electronic filter type, denoted by M1, M1, FIR, M2, and M2, FIR, respectively, and at different gain settings. The completely linear relationship between  $G_{80}$  and the gain,  $20 \log K_{ML}$ , indicates that regeneration is not significant for this part of the impulse response. The gain

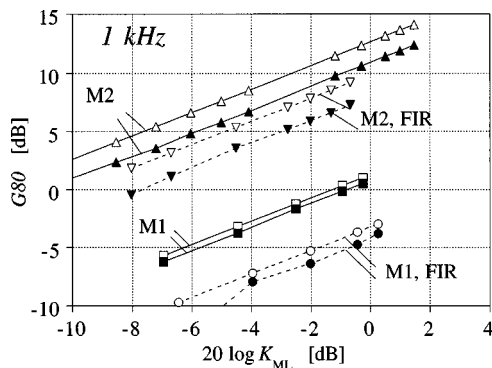


FIG. 7. Measured and predicted values of the electroacoustic system's contribution to early energy,  $G_{80}$  at 1 kHz in the hall in Fig. 4, for the four different configurations described in Sec. III. The curves with empty markers ( $\square$  $\square$  $\nabla$  $\triangle$ ) show the calculated values, and those with filled markers ( $\bullet$  $\blacktriangledown$  $\blacktriangle$ ) show the measured values.

$K_{ML}$  was found by fitting the late energy contribution of the system to the expression given in Eq. (19). The late parts of the impulse responses followed the (modified) diffuse field values well in this hall. Furthermore, the individual directivity factors were estimated from the measured impulse responses. The first 3 ms were cut out and that part was considered to be the direct sound. This was compared to the late part of the impulse response, which was assumed to follow Barron and Lee's model, and thus the directivity factor could be calculated with knowledge of the hall's volume and reverberation time. The agreement between predicted and measured values is within about 2 dB, both at 500 Hz and 1 kHz. This agreement could be viewed as acceptable, since it has been shown that the total level is quite easy to predict in rooms, even with simple models, but early energy estimates are more difficult.<sup>15</sup> The method does well at predicting the variations caused by close or far microphone position, or the use of an FIR filter. The four different settings give values of  $G_{80}$  that span over a range of 15 dB, indicating the differences to expect when using such different microphone positions as those used here. The values of  $G_{80}$  in Figs. 6 and 7 could be compared with the values for the hall itself. At 500 Hz, the hall itself had a value of  $G_{80}=9.7$  dB, measured in the receiver position without including the direct sound, whereas the predicted value was 10.0 dB according to the model by Barron and Lee. At 1 kHz, the measured value for the hall itself was 8.1 dB and the predicted value was 9.8 dB. A reason for omitting the direct sound when comparing measured and predicted values is that the direct sound should basically be correctly predicted and consequently mask differences in the early energy which are caused by the reflected sound. It is obvious that compared to the hall itself, the electroacoustic system's early energy contribution is rather low unless FIR filters are avoided and close microphone positions are used.

#### IV. DISCUSSION AND CONCLUSIONS

The presented method applies diffuse field RIR models to rooms with electroacoustic sound fields. It has been shown that explicit expressions result for the convolution of exponential RIRs, and these expressions permit calculations of early energy levels. It has also been demonstrated that the energy calculated by this IR method corresponds to the one in classical studies as long as the RIRs have negligible direct sound and the reverberation field has the classical constant value throughout the room.

The inclusion of direct sound components, transducer directivities, and initial-time delays, is a natural extension which gives more reasonable estimates of early energy contributions. In the derivations, the reverberation level suggested by Barron and Lee has been used, but the method is not dependent on it. Furthermore, in this study no regenerated components were included in the calculation of the early energy contributions but it is possible to derive and add any number of higher-order contributions using the same methodology as here.

Since it is based on a (modified) diffuse field model, this method will give less accurate estimates in halls which de-

viate from (modified) diffuse field conditions. In a hall with a multichannel system, however, the large number of involved sound paths could average out detail errors that occur when the individual impulse responses are modeled with the extended diffuse field model.

The 1 to 2-dB difference between estimates and measurements for the early energy contribution by the electroacoustic channel could be seen as reasonable since the tested setups gave early energy levels which varied within a range of 15 dB and since early energy typically is more dependent on the details in rooms than the total energy is.

It can be argued that the use of a sharp time limit such as, for example, 80 ms, for the early energy measures could be even more questioned here than for ordinary exponential RIRs. Due to the nonexponential shape of the electroacoustic RIR, the system's early energy capability increases quite rapidly if a later time division is chosen. A system's flexibility increases if its early energy capability increases but the more early energy that is supplied by the system, the higher the risk of subjective localization of the loudspeakers will be. Increasing the transducer directivities and decreasing the transducer distances is then only possible for the microphone end of the system. Advanced solutions, such as arrays, with the potential for correctly perceived source localization, might be the only choice for the loudspeaker end.

## ACKNOWLEDGMENTS

The author wishes to thank his colleagues in the Room Acoustics Group at Chalmers, Professor Mendel Kleiner and Dr. Bengt-Inge Dalenbäck and Dr. Johan Ludvig Nielsen. Contributions to the project were given by the Swedish Natural Science Research Council and the Johnson foundation. Valuable suggestions to the structure of the paper were given by one anonymous reviewer.

## APPENDIX A: CONVOLUTION OF EXPONENTIALLY WEIGHTED WHITE-NOISE SEQUENCES

Assume two impulse responses,  $h_1(i)$  and  $h_2(i)$ , which are both white-noise sequences that are weighted by the same exponential function, and with two different starting points,

$$h_1(i) = A \exp\left(-\frac{\delta i}{f_s}\right) \xi_i \theta(i - i_{01}), \quad (\text{A1})$$

$$h_2(i) = A \exp\left(-\frac{\delta i}{f_s}\right) \psi_i \theta(i - i_{02}),$$

where  $\delta$ ,  $f_s$ , and  $\theta(i)$  are as used in Eq. (5),  $i = [0, \infty]$ , and  $\xi_i$  and  $\psi_i$  are independent samples of normal distributed RVs with  $\mu = 0$  and  $\sigma = 1$  [i.e., they are  $N(0; 1)$ ]. A convolution of the two IRs in Eq. (A1) is

$$\begin{aligned} h_{\text{conv}}(i) &= h_1(i) * h_2(i) \\ &= \sum_{j=0}^i h_1(j) h_2(i-j) \\ &= A^2 \exp\left(-\frac{\delta i}{f_s}\right) \theta(i - i_{01} - i_{02}) \sum_{j=i_{01}}^{i-i_{02}} \xi_j \psi_{i-j}. \end{aligned} \quad (\text{A2})$$

In this last sum, each term is a product of two independent samples of RVs which are  $N(0; 1)$ . Such a product is a new RV,  $y = \xi \psi$ , which does not have a normal distribution, but with  $\mu = 0$  and  $\sigma = 1$ . Furthermore, the sum of  $n$  samples of the RV  $y$  forms another RV which does not have a normal distribution but which has  $\mu = 0$  and  $\sigma = \sqrt{n}$ . This sum will, for large  $n$ , have a normal distribution. The sum can, for our purposes, safely be replaced by  $\Lambda_n = \sqrt{n} \gamma_n$  where  $\gamma_n$  is  $N(0; 1)$ , since for energy calculations it is only  $\mu$  and  $\sigma$  that matters, not the actual distribution. Using  $\gamma_n$ ,  $h_{\text{conv}}(i)$  can be written

$$\begin{aligned} h_{\text{conv}}(i) &= A^2 (i - i_{01} - i_{02})^{1/2} \\ &\times \exp\left(-\frac{\delta i}{f_s}\right) \gamma_i \theta(i - i_{01} - i_{02}). \end{aligned} \quad (\text{A3})$$

This result should be compared to what results when the two envelope functions are convolved,

$$\begin{aligned} h_{\text{conv,env}}(i) &= A^2 \sum_{j=0}^i \exp\left(-\frac{\delta j}{f_s}\right) \theta(j - i_{01}) \\ &\times \exp\left(-\frac{\delta(i-j)}{f_s}\right) \theta(i - j - i_{02}) \\ &= A^2 \exp\left(-\frac{\delta i}{f_s}\right) \theta(i - i_{01} - i_{02}) \sum_{j=i_0}^{i-i_{02}} 1 \\ &= A^2 (i - i_{01} - i_{02}) \exp\left(-\frac{\delta i}{f_s}\right) \theta(i - i_{01} - i_{02}). \end{aligned} \quad (\text{A4})$$

The difference between the expressions in Eqs. (A3) and (A4) is that the envelope functions have the factors  $(i - i_{01} - i_{02})^{1/2}$  and  $(i - i_{01} - i_{02})$ , respectively. For regenerated IR components, the above derived convolved IR must be convolved with yet another exponentially weighted white-noise sequence, which can be carried out using the same methodology as here.

It should be pointed out here that the convolution of two, or more, exponential impulse responses results in a nonexponential impulse response. As such, its reverberation time is not defined and attempts to determine an effective reverberation time will depend on which time range of the impulse response is used for the calculations.

## APPENDIX B: THE EARLY ENERGY OF $h_{\text{EA},0}$

The early energy of  $h_{\text{EA},0}$  has three components, as indicated by the three terms in Eq. (12). One of these terms, which we call  $h_{\text{conv}}(i)$  here, is a convolution of two exponentially weighted RVs, as derived in Appendix A, and also a further convolution with the electronic IR,

$$\begin{aligned} h_{\text{conv}}(i) &= K_{\text{ML}} r_{\text{ref}}^2 \frac{4\pi c}{V f_s} \exp\left[-\frac{\delta(r_{\text{SM}} + r_{\text{LR}})}{c}\right] (i - f_s \tau_{0,\text{EA}})^{1/2} \\ &\times \exp\left[-\frac{\delta(i - f_s \tau_{0,\text{EA}})}{f_s}\right] \gamma_i \theta(i - f_s \tau_{0,\text{EA}}), \end{aligned} \quad (\text{B1})$$

where the parameters are as used in Eq. (12). The calculation of the early energy portion of  $h_{\text{conv}}(i)$  means finding the expected value of the sum of the squared impulse response, where the sum should go up to the index  $i = f_s \tau_e$ ,

$$\begin{aligned}
E_e[h_{\text{conv}}(i)] &= \left\langle \sum_{i=f_s\tau_{0,\text{EA}}}^{f_s\tau_e} h_{\text{conv}}^2(i) \right\rangle = K_{\text{ML}}^2 r_{\text{ref}}^4 \left( \frac{4\pi c}{V f_s} \right)^2 \exp \left[ -\frac{2\delta(r_{\text{SM}}+r_{\text{LR}})}{c} \right] \sum_{i=f_s\tau_{0,\text{EA}}}^{f_s\tau_e} (i-f_s\tau_{0,\text{EA}}) \exp \left[ -\frac{2\delta(i-f_s\tau_{0,\text{EA}})}{f_s} \right] \langle \gamma_i^2 \rangle \\
&= K_{\text{ML}}^2 r_{\text{ref}}^4 \left( \frac{4\pi c}{V f_s} \right)^2 \exp \left[ -\frac{2\delta(r_{\text{SM}}+r_{\text{LR}})}{c} \right] \sum_{i'=0}^{f_s\tau_{e,\text{EA}}} i' \exp \left( -\frac{2\delta i'}{f_s} \right) \\
&= K_{\text{ML}}^2 r_{\text{ref}}^4 \left( \frac{4\pi c}{V f_s} \right)^2 \exp \left[ -\frac{2\delta(r_{\text{SM}}+r_{\text{LR}})}{c} \right] S_N,
\end{aligned} \tag{B2}$$

where  $\tau_{e,\text{EA}} = \tau_e - f_s\tau_{0,\text{EA}}$ , and  $N = f_s\tau_{e,\text{EA}}$ . The sum  $S_N$  is found via partial summation

$$\begin{aligned}
S_N &= \sum_{i'=1}^N i' \exp \left( -\frac{2\delta i'}{f_s} \right) = \sum_{i'=1}^N \exp \left( -\frac{2\delta i'}{f_s} \right) + \sum_{i'=2}^N (i'-1) \exp \left( -\frac{2\delta i'}{f_s} \right) \\
&= \sum_{i'=1}^N \exp \left( -\frac{2\delta i'}{f_s} \right) + \exp \left( -\frac{2\delta}{f_s} \right) \sum_{j'=1}^{N-1} j' \exp \left( -\frac{2\delta j'}{f_s} \right) \\
&= \exp \left( -\frac{2\delta}{f_s} \right) \sum_{i'=0}^{N-1} \exp \left( -\frac{2\delta i'}{f_s} \right) + \exp \left( -\frac{2\delta}{f_s} \right) \left[ S_N - N \exp \left( -\frac{2\delta N}{f_s} \right) \right] \\
&\Rightarrow S_N \left[ \exp \left( \frac{2\delta}{f_s} \right) - 1 \right] \\
&= \frac{1 - \exp(-2\delta N/f_s)}{1 - \exp(-2\delta/f_s)} - N \exp \left( -\frac{2\delta N}{f_s} \right) \\
&\Rightarrow S_N \frac{2\delta}{f_s} \\
&\approx \frac{f_s}{2\delta} \left[ 1 - \exp \left( -\frac{2\delta N}{f_s} \right) \right] - N \exp \left( -\frac{2\delta N}{f_s} \right) \Rightarrow S_N = \left( \frac{f_s}{2\delta} \right)^2 \left[ 1 - \left( 1 + \frac{2\delta N}{f_s} \right) \exp \left( -\frac{2\delta N}{f_s} \right) \right],
\end{aligned} \tag{B3}$$

and if this is inserted in Eq. (B2), together with the expression for  $N$ , the early energy  $E_e[h_{\text{conv}}(i)]$  is

$$E_e[h_{\text{conv}}(i)] = K_{\text{ML}}^2 r_{\text{ref}}^4 \left( \frac{2\pi c}{V\delta} \right)^2 \exp \left[ -\frac{2\delta(r_{\text{SM}}+r_{\text{LR}})}{c} \right] \left[ 1 - \left( 1 + 2\delta\tau_{e,\text{EA}} \right) \exp(-2\delta\tau_{e,\text{EA}}) \right]. \tag{B4}$$

<sup>1</sup>P. U. Svensson, "Influence of electroacoustic parameters on the performance of reverberation enhancement systems," *J. Acoust. Soc. Am.* **94**, 162–171 (1993).

<sup>2</sup>A. J. Berkhout, "A holographic approach to acoustic control," *J. Aud. Eng. Soc.* **36**, 977–995 (1988).

<sup>3</sup>D. Griesinger, "Improving room acoustics through time-variant synthetic reverberation," *J. Aud. Eng. Soc.* **39**, 380 (1991).

<sup>4</sup>W. C. J. M. Prinssen and M. Holden, "System for improved acoustic performance," *Proc. Inst. Acoust.* **14**(2), 93–101 (1992).

<sup>5</sup>P. U. Svensson, "Computer simulations of periodically time-varying filters for acoustic feedback control," *J. Aud. Eng. Soc.* **43**, 667–677 (1995).

<sup>6</sup>M. Barron and L. J. Lee, "Energy relations in concert auditoriums," *J. Acoust. Soc. Am.* **84**, 618–628 (1988).

<sup>7</sup>P. Vogel and D. de Vries, "Electroacoustic system response in a hall: A convolution of impulse sequences," *J. Aud. Eng. Soc.* **42**, 684–690 (1994).

<sup>8</sup>M. Vorländer, "Revised relation between the sound power and the aver-

age sound pressure level in rooms and consequences for acoustic measurements," *Acustica* **81**, 332–343 (1995).

<sup>9</sup>J. L. Nielsen and U. P. Svensson, "Verification of a simple stochastic room impulse response model suitable for computer simulations" (in preparation).

<sup>10</sup>M. A. Poletti, "On controlling the apparent absorption and volume in assisted reverberation systems," *Acustica* **78**, 61–73 (1993).

<sup>11</sup>A. P. Hill, "Combined reverberation time of electrically coupled rooms," *J. Acoust. Soc. Am.* **4**, 63–68 (1932).

<sup>12</sup>J. S. Bradley, "A comparison of three classical concert halls," *J. Acoust. Soc. Am.* **89**, 1176–1192 (1991).

<sup>13</sup>N. V. Franssen, "Sur l'amplification des champs acoustiques," *Acustica* **20**, 315–323 (1968).

<sup>14</sup>A. Krokstad, "Electroacoustic means of controlling auditorium acoustics," *Appl. Acoust.* **24**, 275–288 (1988).

<sup>15</sup>M. Vorländer, "International round robin on room acoustical compute simulations," *Proceedings of the 15th International Congress on Acoustics, Trondheim, Norway, 1995* (1995), pp. 689–692.

# Orthogonal acoustical factors of sound fields in a forest compared with those in a concert hall

Hiroyuki Sakai, Shin-ichi Sato, and Yoichi Ando

Graduate School of Science and Technology, Kobe University, Rokkodai, Nada, Kobe 657-8501, Japan

(Received 10 October 1997; accepted for publication 13 May 1998)

In order to discuss acoustical quality of sound fields in a forest, measurements were carried out obtaining four orthogonal factors [Y. Ando, *J. Acoust. Soc. Am.* **74**, 873–887 (1983)]. Results were compared with those in a concert hall. In the forest, for example, the subsequent reverberation time,  $T_{\text{sub}}$  was 1.66 s (500 Hz), and the interaural cross correlation (IACC) was 0.44 (1 kHz) at a point 40 m from the source. Such an outdoor space has specific acoustic properties being blended for certain sound sources involving the middle and higher frequency ranges. It was found that the value of the width of the interaural cross-correlation function,  $W_{\text{IACC}}$ , which is related to the apparent source width (ASW) of sound fields in the forest, was smaller than that in the concert hall. © 1998 Acoustical Society of America. [S0001-4966(98)01309-5]

PACS numbers: 43.58.Gn, 43.55.Br [SLE]

## INTRODUCTION

The original acoustic space for humans might well have been a sound field in a forest. Since then we have experientially determined that such an outdoor space has excellent acoustic properties. A forest consists of various randomly distributed trees of different diameters. Obviously, it is difficult to calculate impulse response at present, because complicated reflections are scattered from the trunks of trees. In this paper, measurements were made to determine the acoustic properties of sound fields in a forest as well as those in a concert hall.

A number of acoustical measurements in outdoor fields that involved a forest have been carried out (for example, Eyring, 1946; Embleton, 1963; Price *et al.*, 1988). In a recent study, the reverberation time and the SPL attenuation as a function of the distance in a forest were reported (Huisman and Attenborough, 1991). In designing sound fields, however, both temporal and spatial factors must be simultaneously satisfied to achieve a total preference maximum (Ando, 1983).

In order to compare the qualities of these sound fields, measurements were undertaken to obtain the following orthogonal factors (Ando, 1983, 1985):

- (1) sound pressure level (SPL);
- (2) IACC (interaural cross correlation);
- (3) initial time delay gap ( $\Delta t_1$ ); and
- (4) subsequent reverberation time ( $T_{\text{sub}}$ ).

In addition, the value of  $A$  which indicates the total amplitude of reflections, the value of  $\tau_{\text{IACC}}$  which is a factor in relation to sound localization or image shift, and  $W_{\text{IACC}}$  as a factor of the apparent source width (ASW) (Sato and Ando, unpublished) were also analyzed, namely,

- (5) total amplitude of reflections ( $A$ );
- (6) interaural time delay ( $\tau_{\text{IACC}}$ ); and
- (7) the width of the interaural cross-correlation function ( $W_{\text{IACC}}$ ).

In these measurements, values for  $\Delta t_1$  could not be identified

in the forest other than for reflection from the ground, because of weak scattered reflections from the trees. The  $\Delta t_1$  as a orthogonal factor is defined as a time interval between a direct sound and a first reflection from a side wall except a reflection from a floor. Hence the first reflections coming from the ground were neglected in accordance with the definition.

In order to obtain the impulse response of sound fields clearly, a method using a maximum-length sequence (MLS) signal (Alrutz, 1981; Alrutz and Schroeder, 1983; Borish and Angell, 1983) was applied.

## I. PROCEDURE

### A. Forest investigated

The acoustical measurements were performed in a forest owned by Kirishima Shrine in Kagoshima, Japan. The diameters of trees which consisted mainly of deciduous trees and various shrubs were classified into three categories; i.e., 0.3, 0.6, and 1.0 m as shown in Fig. 1. The heights of all trees were about 18.5 m. In the center of the forest, there was a 5-m-wide path made of asphalt where the loudspeaker and receivers were placed.

Wind was not present during the measurements in the forest. The humidity and temperature near the ground were almost constant for about 20-min measurements. A waveguide from the upper portion of the forest (Embleton, 1996) was not considered, because the measurements were conducted so far as 40 m from the source.

Sound fields obtained in the Kirishima International Concert Hall, Kagoshima, Japan were compared with results obtained in the forest. The location of the sound source and measuring points indicated by the gray seats are illustrated in Fig. 2.

### B. Measurement setup

An omnidirectional dodecahedron loudspeaker,  $S$ , and receiving points were arranged as shown in Figs. 1 and 2. The height of the center of  $S$  was 1.5 m above the ground

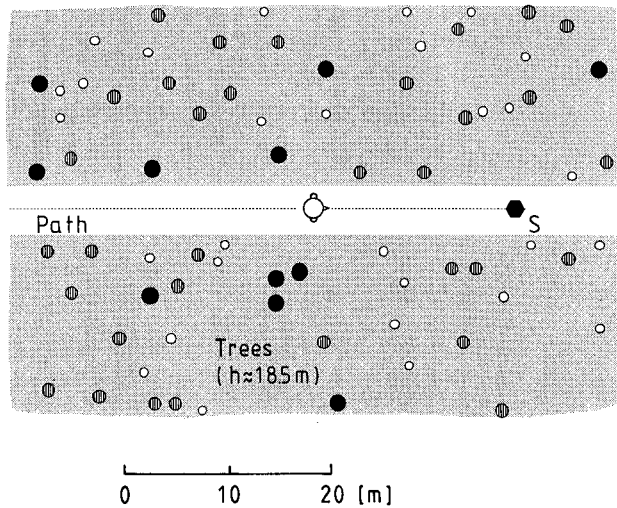


FIG. 1. The main path of the forest investigated over a total area of about 200 000 m<sup>2</sup>. The symbols indicate different diameters; ●: 1.0; ⊙: 0.6; ○: 0.3 [m]. A loudspeaker was set as a sound source *S*. The person with two condenser microphones placed at ear-entrances was applied to each receiving point.

surface or the stage floor. The heights of the receiving points were 1.7±0.05 m (in the forest, standing) or 1.15±0.05 m (in the concert hall, sitting), respectively.

The measurement setup is illustrated in Fig. 3. The MLS signal radiated from the sound source *S*. The A-weighted SPL was about 100 dB at the 5-m-reference point. Two microphones were placed at the ears of a person who faced the loudspeaker during measurement. The microphones were of the 1/2-in. condenser type.

The four physical factors and three additional factors previously mentioned were analyzed using binaural-impulse responses. In order to obtain impulse responses, first of all, signals after A/D conversion into microphones were analyzed using a fast Hadamard transform (FHT). After obtaining binaural-impulse responses, physical factors were calculated for each 1/1 octave-band center frequency between 125 Hz and 4 kHz. The signal's duration was 2.7 s, and the sampling frequency was 48 kHz. In order to improve the

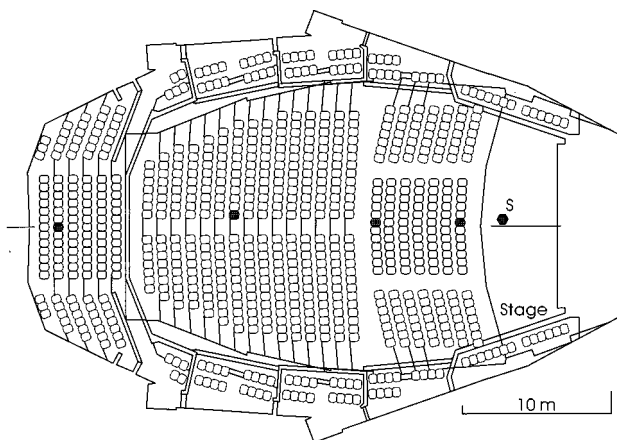


FIG. 2. Concert hall measured for comparison. It has a volume of 8475 m<sup>3</sup> and 770 seats. The loudspeaker was set on the stage as a sound source *S*. The receiving point was set at the height of 1.15±0.05 m above the seating floor.

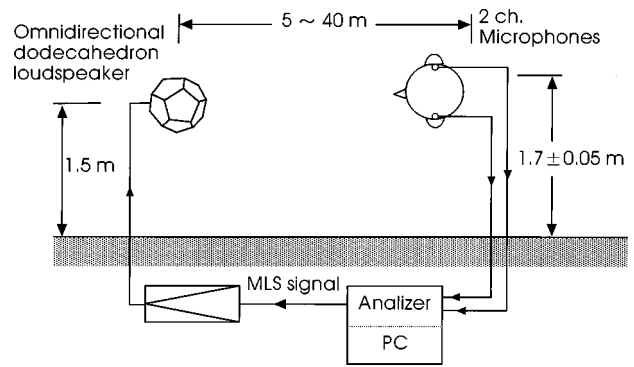


FIG. 3. Schematic illustration of measurement with a dodecahedron loudspeaker and the real head.

signal-to-noise ratio, the sequenced signals were repeated eight times.

### C. Measuring method for binaural-impulse response

The impulse responses can be analyzed by applying a MLS signal to the Hadamard-matrix-conversion technique through only an adding operation without any multiplication (Alrutz, 1981; Alrutz and Schroeder, 1983). The impulse responses are obtained by the cross-correlation function between the input and output signals in a linear system.

By applying the method, binaural-impulse responses,  $h_l(t)$  and  $h_r(t)$  at both ears, were able to analyze each sound field. The indexes *l* and *r* represent the left ear and right ear, respectively.

### D. MLS signal

The MLS signal used during this measurement is called pseudorandom white noise. This signal is generated by a system with the shift registers shown in Fig. 4 and it has the following characteristics (Davies, 1966a, b, c).

The MLS consists of binary digits of +1 and -1. This sequence is repetitive with the largest possible period  $L = 2^n - 1$ . The number of *n* are stages of shift register as shown in Fig. 4. The autocorrelation function given by the following equation is *L* at the origin, and -1, otherwise, so that:

$$\Phi_l = \sum_{j=0}^{L-1} m_j m_{j+L} = \begin{cases} L, & \text{for } l=0_{\text{modulo } L}, \\ -1, & \text{otherwise.} \end{cases} \quad (1)$$

This is where *j* indicates the number of sequence elements. The sum of each element of the sequence becomes -1:

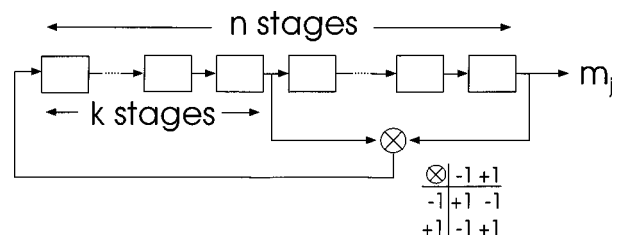


FIG. 4. Shift registers for generating the MLS signal.

$$\sum_{j=0}^{L-1} m_j = -1. \quad (2)$$

## E. Method of analyzing acoustical factors

Each acoustical factor previously mentioned was calculated by binaural-impulse responses,  $h_{jl}$  and  $h_{jr}$  (Osaki and Ando, 1983). The index  $j$  indicates the sampled elements of MLS with time interval  $\sigma$  ( $j=0,1,\dots,L-1$ ).

### 1. Relative SPL and total amplitude of reflections (A)

The relative SPL at the listening position was obtained relative to the SPL of the reference point.

The SPL at each ear is given by the autocorrelation function  $\Phi_{ll,rr}(\tau)$  at  $\tau=0$  of the impulse responses  $h_{jl,r}$ , so that

$$\Phi_{ll,rr}(0) = \sum_{j=0}^{L-1} h_{jl,r}^2. \quad (3)$$

The relative SPL is defined by

$$\text{SPL} = 10 \log_{10} \frac{\sqrt{\Phi_{ll}(0)\Phi_{rr}(0)}}{\Phi^{(\text{ref})}(0)} \quad \text{if } h_{jl,r} \neq 0, \quad (4)$$

where

$$\Phi^{(\text{ref})}(0) = \sqrt{\Phi_{ll}^{(\text{ref})}(0)\Phi_{rr}^{(\text{ref})}(0)}. \quad (5)$$

Here,  $\Phi^{(\text{ref})}(0)$  is the geometrical mean of the autocorrelation functions of binaural-impulse responses at  $\tau=0$  at the reference point as indicated by Eq. (5).

The value of total amplitude of reflections,  $A$ , is calculated after obtaining impulse responses,  $h_{jl,r}$ , as the energy ratio between the direct sound and early-plus-subsequent reverberation by

$$A = \sqrt{\frac{\sum_{\epsilon}^{L-1} h_j^2}{\sum_0^{\epsilon} h_j^2}}, \quad (6)$$

where the value  $\epsilon$  is the short delay time for the duration of direct sound. The value  $A$  is obtained by averaging both ears.

### 2. Subsequent reverberation time ( $T_{\text{sub}}$ )

The decay curve is obtained by the square and integration of impulse responses (Schroeder, 1965). The subsequent reverberation time,  $T_{\text{sub}}$ , was obtained by fitting the regression line of the curves for initial 10-dB decay after the arrival of direct sound. Examples of the decay curves for this measurement are in Fig. 10. The results of  $T_{\text{sub}}$  are represented as an average value for both ears. The value of  $T_{\text{sub}}$  is defined by the time interval for 60-dB attenuation for this regression line, so that

$$T_{\text{sub}} = k\sigma, \quad (7)$$

where  $\sigma$  is the time duration for a sampled element and  $k$  is the number of sampled data until 60-dB decay is presented by the regression line.

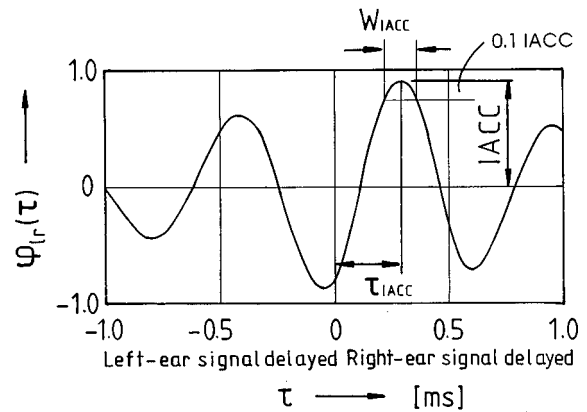


FIG. 5. Definition of spatial acoustic factors, IACC,  $\tau_{\text{IACC}}$ , and  $W_{\text{IACC}}$  in the normalized interaural cross-correlation function.

### 3. Factors of the interaural cross-correlation function (IACC, $\tau_{\text{IACC}}$ , and $W_{\text{IACC}}$ )

The definitions of IACC,  $\tau_{\text{IACC}}$ , and  $W_{\text{IACC}}$  as representatives of the interaural cross-correlation function are illustrated in Fig. 5.

The normalized interaural cross-correlation function is defined by

$$\phi_{lr}(j\sigma) = \frac{\Phi_{lr}(j\sigma)}{\sqrt{\Phi_{ll}(0)\Phi_{rr}(0)}}, \quad (8)$$

where the values of  $\Phi_{ll}(0)$  and  $\Phi_{rr}(0)$  represent the autocorrelation functions ( $\tau=0$ ) of impulse responses at both ears, respectively. The denominator means the geometrical mean of the sound energies arriving at two ears. The  $\Phi_{lr}(j\sigma)$  is the cross-correlation of impulse responses at both ears. These three factors are expressed as follows:

(1) The magnitude of the interaural cross-correlation function is defined by

$$\text{IACC} = |\phi_{lr}(\tau)|_{\text{max}}, \quad |\tau| \leq 1 \text{ ms}. \quad (9)$$

This quantity is a significant factor in determining the degree of subjective diffuseness as well as subjective preference in the sound field (Ando, 1983). It represents the degree of similarity in incident sound waves between both ears.

(2) The interaural delay time, at which the IACC is decided as shown in Fig. 5, is the  $\tau_{\text{IACC}}$ . When  $\tau_{\text{IACC}}$  is zero, then usually the frontal-sound-source image and a well-balanced-sound field may be perceived.

(3) The width of the interaural cross-correlation function  $W_{\text{IACC}}$  is defined by the interval of delay time at a value 10% below the orthogonalized IACC as shown in Fig. 5. The factor  $W_{\text{IACC}}$  is a significant factor related to the apparent source width (ASW). It is worth noticing that the ASW can be evaluated by IACC and  $W_{\text{IACC}}$  (Sato and Ando, 1996; Sato and Ando, unpublished).

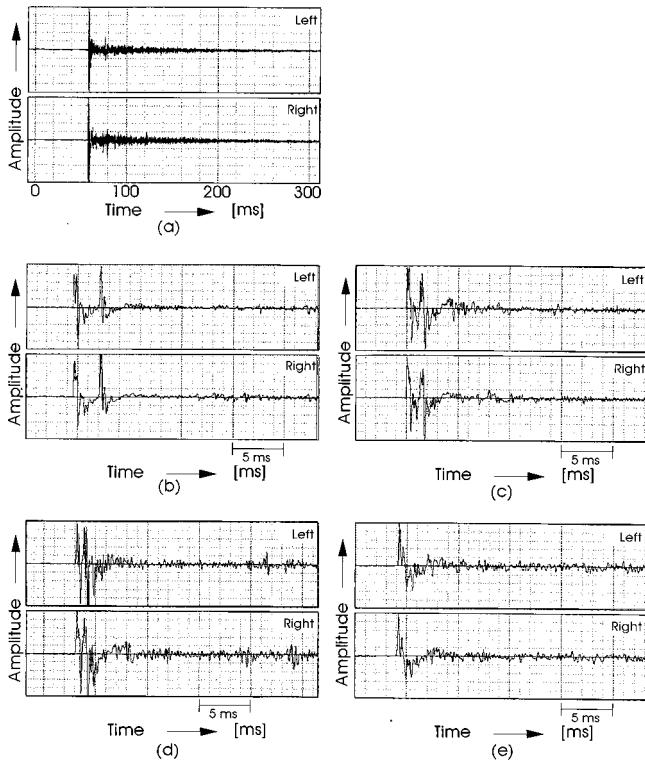


FIG. 6. Normalized impulse responses analyzed in the forest. Binaural-impulse responses at 20 m from the source point for (a) 0–300 ms; (b) initial binaural impulse responses at 5 m for 0–30 ms; (c) at 10 m; (d) at 20 m; (e) at 40 m.

## II. RESULTS

### A. SPL and $A$

Binaural-impulse responses obtained at a distance 20 m in the forest are shown in Fig. 6(a). The initial 30 ms of impulse responses at each receiving point are illustrated in Fig. 6(b)–(e).

The measured relative SPLs for 1/1 octave band frequencies between 125 Hz and 4 kHz are shown in Fig. 7, as

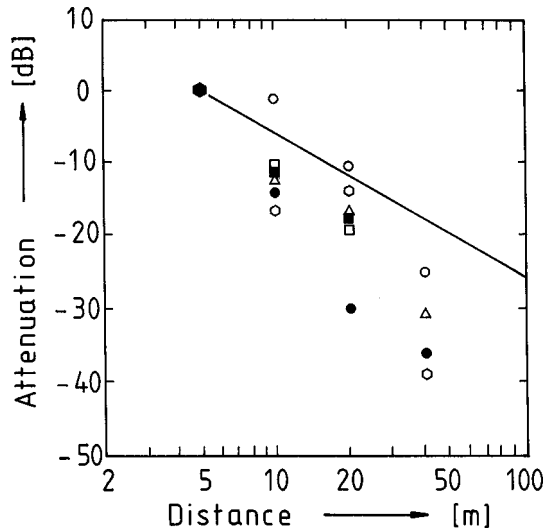


FIG. 7. SPL attenuations in the forest measured as a function of the distance.  $\circ$ : 125 Hz;  $\triangle$ : 250 Hz;  $\bullet$ : 500 Hz;  $\square$ : 1 kHz;  $\blacksquare$ : 2 kHz;  $\circ$ : 4 kHz of 1/1-octave-band center frequency, —: inverse square law.

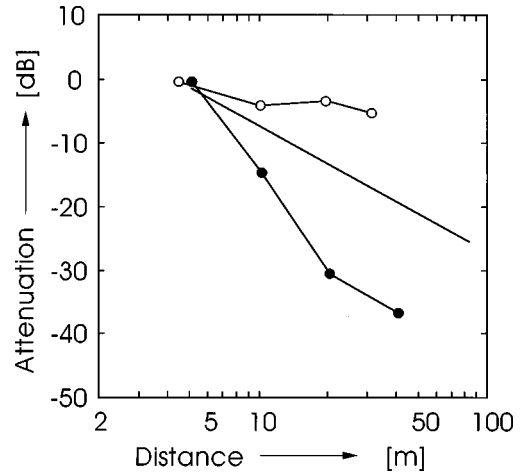


FIG. 8. Comparison of SPL attenuations in the forest with those in the concert hall at 500 Hz.  $\bullet$ : in the forest;  $\circ$ : in the hall; —: inverse square law.

a function of the distance. In general, SPL attenuates according to the inverse-square law in a free sound field as shown by the straight line in Fig. 7. However, the SPL in the forest decreased much more than the SPL for the inverse-square law except for 125 Hz.

The results of SPL at 500 Hz are compared with those in the concert hall as shown in Fig. 8. In the sound field of the hall the SPL was remarkably higher than the inverse square law due to the multiple reflections of walls and ceilings.

Figure 9 shows values of total reflections  $A$  in the forest and the hall. The longer the distance between the sound source and the receiver is, the greater the values of  $A$  are in both cases. The room radius defined by  $A=1$  which means there is equal energy between direct sound and early reflection-plus-subsequent reverberation, is found near 40 m in the forest, while that in the room is about 4 m.

### B. $T_{\text{sub}}$

Figure 10 shows examples of the decay curves of reverberation in the forest and in the concert hall. Figure 10(c) and (d) shows examples of the decay curves at 500 Hz and 1

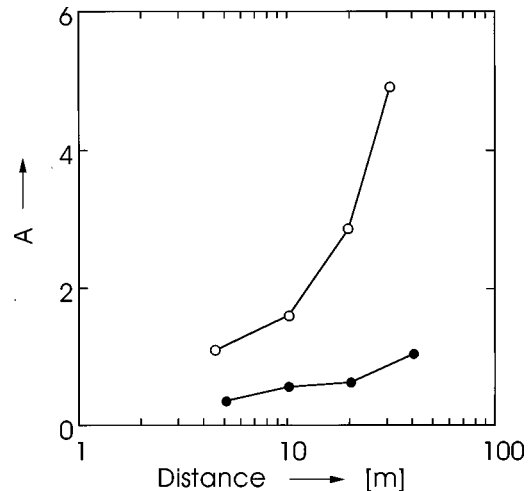


FIG. 9. Comparison of total amplitudes of reflections in the forest with those in the concert hall.  $\bullet$ : in the forest;  $\circ$ : in the hall.

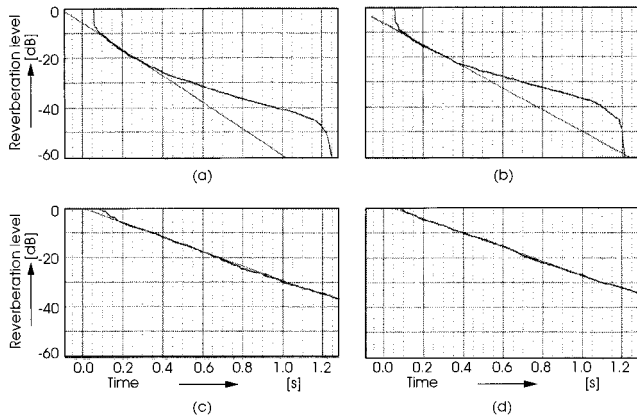


FIG. 10. Comparisons of decay curves for reverberation at the left ear 20 m in the forest obtained by Schroeder's method. (a) Forest, 500 Hz; (b) forest, 1 kHz; (c) concert hall, 500 Hz; (d) concert hall, 1 kHz.

kHz at a point 19.1 m from the source in the concert hall (Sato *et al.*, 1994). As shown in Fig. 10, the decay curve in the decibel scale decreased almost linearly in the concert hall. However, in the forest, the curves were not linear, maintaining their level after 0.4 s [Fig. 10(a) and (b)].

The results of measured  $T_{sub}$  in the forest are shown in Fig. 11. It is remarkable that the values of  $T_{sub}$  at 250 Hz are the shortest of those of the other frequencies measured. The maxima of  $T_{sub}$  appeared near the frequency band around 500 Hz particularly at distances longer than 10 m; i.e., 1.66 s at 500 Hz and 1.60 s at 1 kHz at the 40-m point.

### C. IACC, $\tau_{IACC}$ and $W_{IACC}$

The normalized interaural cross-correlation functions ( $-1 \leq \tau \leq 1$  ms) at each receiving point in the forest are shown in Fig. 12. The values of  $\tau_{IACC}$  and  $W_{IACC}$  were obtained from them. The results of measured IACC are shown in Fig. 13. Here it is interesting that the IACC is small at distances further than 20 m for higher frequency ranges

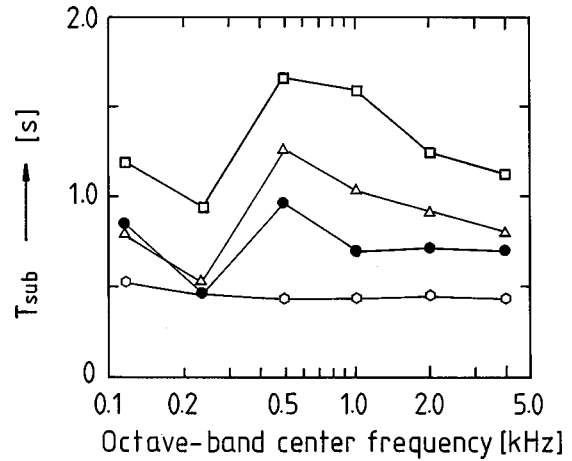


FIG. 11. Subsequent reverberation time as a factor of the center frequency of the 1/1 octave band obtained by the 0–10-dB curve after the direct sound in the forest.  $\circ$ : 5;  $\bullet$ : 10;  $\triangle$ : 20;  $\square$ : 40 [m].

above 500 Hz, for example, 0.53 (2 kHz, 20 m), and 0.44 (1 kHz, 40 m). At low frequency below 250 Hz, the IACCs are around 0.95.

The values for  $\tau_{IACC}$  at all measuring points nearly equal zero in the forest as shown in Fig. 12. This means that a frontal direction for the sound source can be perceived. Figure 14 compares the  $W_{IACC}$  between the forest and the hall at the allpass band as a parameter of distance. The  $W_{IACC}$  in the forest is always smaller than that of the room. The  $W_{IACC}$  gradually increases further away from the sound source in both cases. This indicates that the ASW should be perceived to be wider at far-field points.

### III. DISCUSSION

The results obtained here may be related to the diameters of trunks of trees (Sakai *et al.*, unpublished). The lack

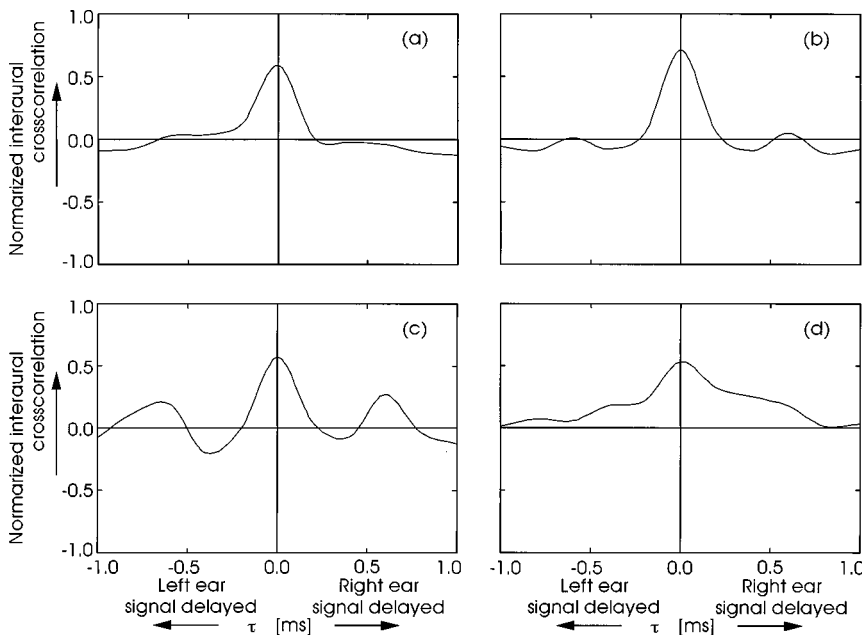


FIG. 12. Normalized interaural cross-correlation function at each receiving point in the forest. (a) 5; (b) 10; (c) 20; (d) 40 [m].



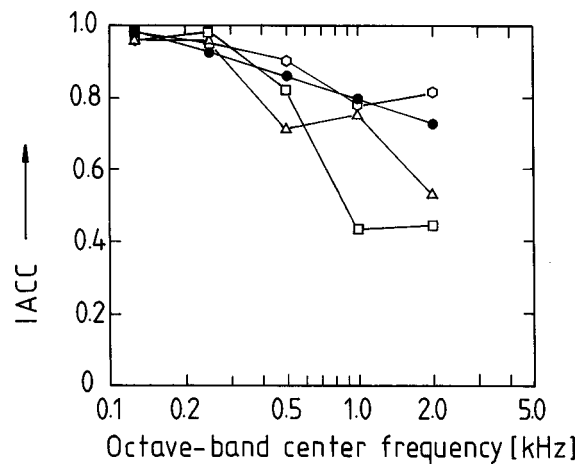


FIG. 13. IACC as a function of frequency, and as a parameter of the distance in the forest. ○: 5; ●: 10; △: 20; □: 40 [m].

of exponential decay curves shown in Fig. 10(a) and (b) is considered to be caused by effects of multiple scattering from trees.

About 10 dB of attenuation was found in the initial 50 ms after the direct sound arrived, and subsequent components consistently compared with linear attenuation in a concert hall. These characteristics were found in all decay curves in the forest.

Generally, a person prefers a condition where there are dissimilar sound signals at both ears (a small IACC value). Figure 13 shows that IACCs are small at longer distance and higher frequency. It is interesting that the IACC is as small as about 0.4 at 40 m (1 and 2 kHz) in the forest, although the initial reflections are weak as indicated by the impulse responses in Fig. 6.

The  $W_{IACC}$  was almost constant around 0.10–0.12 until it reached 20 m and there was an immediate increase at 40 m in the forest. The  $W_{IACC}$  of the room was larger than that of the forest in each measuring point. Regarding the rapid increase at the furthest point (40 m) in the forest, this may be due to the direct sound becoming weaker and coherent multiple-scattering reflections.

If music with an effective duration of ACF  $\tau_e$  values centered on 70 ms (Ando, 1985) is played, then the most preferred value of  $T_{sub}$  approaches 1.66 s ( $23 \tau_e$ ,  $\tau_e = 72$  ms) at a frequency of 500 Hz. This condition is realized at a distance of 40 m in the forest. At 40 m, the IACC is also small. For instance, the forest would be a fine sound field for string and wind instruments involving higher frequency ranges. It is found that the forest has excellent acoustic properties, especially for factors of subsequent reverberation time ( $T_{sub}$ ) and IACC. Music may be better at further points relative to this sound field for large  $T_{sub}$  and small IACC.

The excess attenuation by the interference of the direct sound and reflection over the asphalt surface with a high impedance is occurred in the higher frequency range in the forest (Embleton, 1996). But, this interference is not as effective for the result of the SPL than the multiple-scattering effects by trunks of trees. The SPL at 125 Hz in the forest at 10 and 20 m was greater than that of the inverse-square law

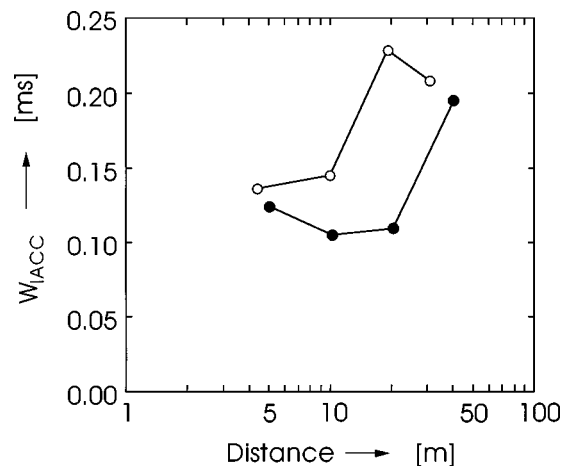


FIG. 14. The comparison of measured values for  $W_{IACC}$  as a function of the distance. ●: in the forest; ○: in the concert hall.

as shown in Fig. 7. This is caused by the interference of the direct sound and reflection arriving at the receiver in phase.

#### IV. CONCLUSION

In the forest, it is found that the forest has excellent acoustic properties, especially for factors of subsequent reverberation time ( $T_{sub}$ ) and IACC. The value of  $T_{sub}$  was 1.66 s (500 Hz), and IACC was 0.44 (1 kHz) at a point 40 m from the source. Also, it is found that the value of the width of the interaural cross-correlation function,  $W_{IACC}$ , was smaller than that in the concert hall.

#### ACKNOWLEDGMENTS

The author wishes to thank Dr. Tatsumi Nakajima for his cooperation and assistance with measurements.

- Alrutz, H. (1981). "Ein Neuer Algorithmus zur Auswertung von Messungen mit Pseudoranschsignalen," *Fortschritte der Akustik DAGA* **81**, 525–528.
- Alrutz, H., and Schroeder, M. R. (1983). "A fast hadamard transform method for the evaluation of measurements using pseudorandom test signals," *Proc. of 11th Intern. Congr. Acoust.*, Paris, Lyon-Toulouse (Ecole Nationale des Travaux Publics de l'Etat, Paris), pp. 235–238.
- Ando, Y. (1983). "Calculation of subjective preference at each seat in a concert hall," *J. Acoust. Soc. Am.* **74**, 873–887.
- Ando, Y. (1985) *Concert Hall Acoustics* (Springer-Verlag, New York).
- Borish, J., and Angell, J. B. (1983). "An efficient algorithm for measuring the impulse response using pseudorandom noise," *J. Audio Eng. Soc.* **31**, 478–488.
- Davies, W. D. T. (1966a). "Generation and properties of maximum-length sequences," *Control* **10**, 302–304.
- Davies, W. D. T. (1966b). "Generation and properties of maximum-length sequences, Part 2," *Control* **10**, 364–365.
- Davies, W. D. T. (1966c). "Generation and properties of maximum-length sequences, Part 3," *Control* **10**, 431–433.
- Eyring, C. F. (1946). "Jungle acoustics," *J. Acoust. Soc. Am.* **18**, 257–270.
- Embleton, T. F. W. (1963). "Sound propagation in homogeneous deciduous and evergreen woods," *J. Acoust. Soc. Am.* **35**, 1119–1125.
- Embleton, T. F. W. (1996). "Tutorial on sound propagation outdoors," *J. Acoust. Soc. Am.* **100**, 31–48.
- Huisman, W. H. T., and Attenborough, K. (1991). "Reverberation and attenuation in a pine forest," *J. Acoust. Soc. Am.* **90**, 2664–2677.
- Osaki, S., and Ando, Y. (1983). "A fast method of analyzing the acoustical parameters for sound fields in existing auditoria," *Proc. 4th Comp. Environ. Eng. Build.*, Tokyo, pp. 441–445.
- Price, M. A., Attenborough, K., and Heap, N. W. (1988). "Sound attenuation through trees: Measurements and models," *J. Acoust. Soc. Am.* **84**, 1836–1844.

- Schroeder, M. R. (1965). "New method of measuring reverberation time," J. Acoust. Soc. Am. **37**, 409–412.
- Sakai, H., Doge, K., Shibata, S., and Ando, Y. (unpublished). "Orthogonal acoustical factors of sound fields in bamboo forest."
- Sato, S., Ando, Y., Nakajima, T., Merthayasa, I. G. N., Chen, C. G., Sakai, H., Sumioka, T., Furuichi, H., Nishio, K., and Shoda, T. (1994). "Architectural acoustical measurement of Kirishima International Concert Hall," Report of the Meeting of the Acoustical Society of Japan, October, the Acoustical Society of Japan, 1994, pp. 1003 and 1004, in Japanese.
- Sato, S., and Ando, Y. (1996). "Effect of interaural cross-correlation function on subjective attributes," J. Acoust. Soc. Am. **100**, 2592A.
- Sato, S., and Ando, Y. (unpublished). "On the apparent source width (ASW) relation to the width of the interaural crosscorrelation function ( $W_{IACC}$ ) as well as the IACC."

# A new transducer holder mechanism for efficient generation and reception of Lamb modes in large plates

Triguna Ghosh and Tribikram Kundu

*Department of Civil Engineering and Engineering Mechanics, University of Arizona, Tucson, Arizona 85721*

(Received 20 January 1998; accepted for publication 9 June 1998)

A new transducer holder mechanism is described in this paper. This mechanism is very useful for inspecting large plates by Lamb waves. The new mechanism allows water coupling between the ultrasonic transducers and the specimen but requires neither a water jet nor a big water tank for immersing the specimen into it. This mechanism allows the transducers to rotate for changing the angle of strike of the incident beam and avoids undesirable multiply-reflected signals between the transducer and the specimen. An aluminum plate with fabricated internal defects has been inspected by the Lamb wave technique using the new transducer holder mechanism. The experimental results clearly show the superiority of the new design when compared with the conventional designs available today. © 1998 Acoustical Society of America. [S0001-4966(98)04609-8]

PACS numbers: 43.58.Vb, 43.35.Zc [SLE]

## INTRODUCTION

Ultrasonic inspections are carried out by several well-established techniques using low-, medium-, and high-frequency ultrasonic transducers and modest to very sophisticated signal processing techniques. The ultrasonic inspection of small specimens (a few centimeters or millimeters in dimension) is typically carried out in the frequency range 1–100 MHz. These specimens are immersed in a coupling fluid that transmits the ultrasonic waves from the transducer to the specimen. The techniques involving large specimens (several meters in dimension) typically use contact transducers and low-frequency (50–500 kHz) ultrasound, such as the pulse velocity technique and the impact echo technique. Owing to the large wavelength of ultrasound used in these techniques, small defects cannot be detected by the conventional C-scan technique that uses low-frequency signals. The C-scan technique is not very efficient for inspecting large structures, because it overlooks small defects and takes a long time to scan a large specimen. Lamb waves, because of the nature of their interaction with defects and their propagation mechanism, have shown tremendous potential for detecting relatively small defects in large structures.

Earlier works which involve interaction of Lamb waves with defective and defect-free plates have been carried out by Dayal and Kinra (1991), Mal *et al.* (1991), Chimenti and Martin (1991), Alleyne and Cawley (1992), Ditri *et al.* (1992), Kundu *et al.* (1996), Maslov and Kundu (1997), and Yang and Kundu (1998), among others. In these studies the plate specimens are small, typically a few centimeters in length and width, and a few millimeters in thickness. Recent attempts to extend the Lamb wave inspection technique to large specimens require the specimen to be immersed in a large water tank or use of direct-contact or air-coupled transducers (Castaings and Hosten, 1997). Disadvantages of these conventional methods are described below, followed by a section describing the development of a new experimental setup for generating and receiving Lamb waves at low frequencies for inspecting large structures.

## I. DIFFICULTIES ASSOCIATED WITH THE LARGE SPECIMEN INSPECTION

For inspecting large plates one needs to use a relatively low-frequency signal so that the signal can propagate through a long distance along the plate without being attenuated quickly. However, the low-attenuation property of low-frequency signals can also give rise to some difficulties. When the plate is immersed in the coupling fluid in a tank and the transmitter and receiver are positioned above the specimen as shown in Fig. 1(a), then the signal received by the receiver is composed of several signals or waves. These are the Lamb waves propagating along the specimen [signal 1 in Fig. 1(a)] and longitudinal waves—signals 2 and 3. Signal 2 is multiply reflected between the top surface of the specimen and the free surface of the liquid and signal 3 is multiply reflected between the specimen and the bottom surface of the tank. Naturally, a small disturbance of the water surface affects the received signal significantly. Figure 1(b) shows four different received signals generated under the same transducer–receiver–specimen orientation but when the free water surface is slightly disturbed by the finger. As a result, these four signals correspond to the four different free water surface geometries. The four signals are shown on the same plot with different vertical shifts so that they do not overlap one another. It is very difficult to obtain consistent results with low-frequency signals with this arrangement since the received signal is very sensitive to any disturbance of the free surface of the coupling fluid (typically water). This problem does not arise when high-frequency signals are used because the high-frequency signal is highly attenuative in water and signals of types 2 and 3 of Fig. 1(a) do not reach the receiver.

Direct contact between transducers and the specimen avoids the use of a water tank. However, in this case one cannot generate a specific Lamb mode by easily changing the angle of inclination of the transducers relative to the specimen as was done by Kundu *et al.* (1996). Wedge-shaped inserts should be placed between the transducers and the specimen to change the striking angle. As a result, it is very

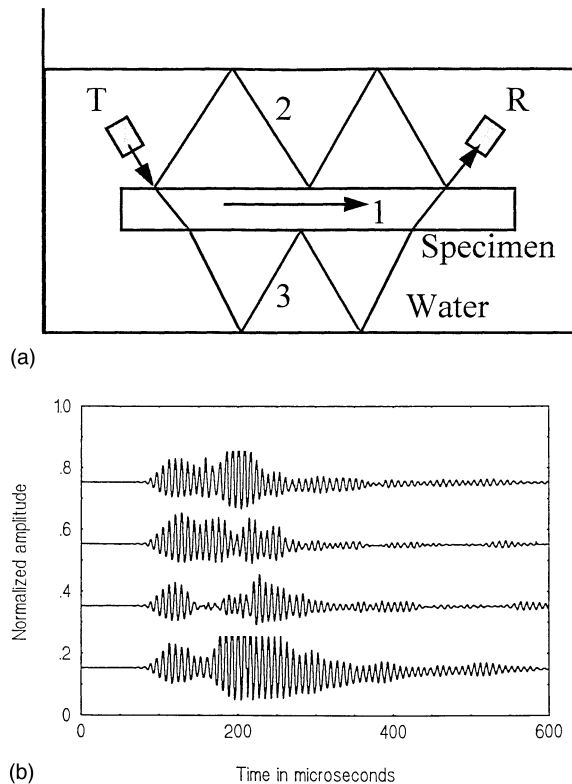


FIG. 1. (a) Three different signals 1, 2, and 3 can reach the receiver for low-frequency excitation when the specimen is immersed in water. (b) Four different received signals obtained during four different experiments for the same specimen-transducer arrangement immersed in water.

difficult to continuously change the incident angle by inserting a fixed number of wedge-shaped inserts. Another disadvantage of the direct-contact arrangement is that the received signal varies significantly with the contact pressure between the transducers and the specimen.

Air-coupled transducers (Castaings and Hosten, 1997) are also being used for inspecting large plates with low-frequency ultrasound. However, in this case the signal-to-noise ratio is low and the received signal is very weak; as a result expensive amplifiers as well as transducers and sophisticated signal processing techniques are required for extracting reliable information from the weak noisy signals. Since air-coupled transducers are still in their developing stage, the question regarding the consistency and repeatability of the

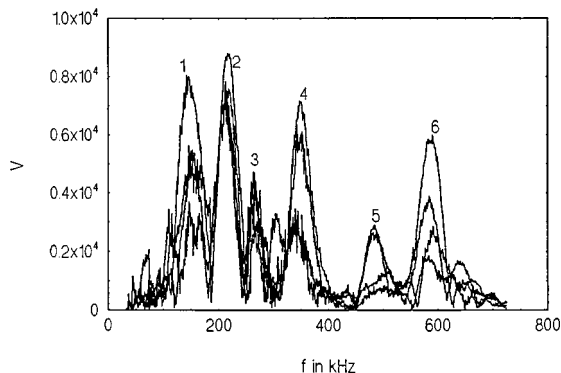


FIG. 2. Four  $V(f)$  curves generated by transducers contained in tubes and placed over the defect free region.

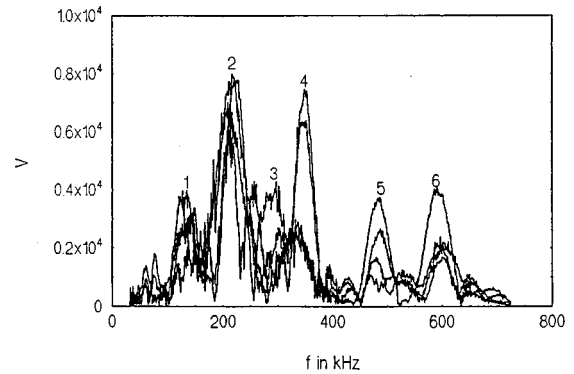


FIG. 3. Four  $V(f)$  curves generated by transducers contained in tubes and placed over the defective region.

experimental results obtained by air-coupled transducers has not been fully resolved yet.

## II. EVOLUTION OF THE NEW DESIGN AND EXPERIMENTAL RESULTS

To overcome the problems described above, several alternative orientations of the transmitter and the receiver with respect to the specimen have been tried out. The first attempt was to replace the big water tank with two small water pools placed directly over the plate specimen. This arrangement allows only the Lamb wave to reach the receiver and eliminates the longitudinal waves [signals of types 2 and 3 in Fig. 1(a)]. As a result, with this arrangement the signal should be comparatively more stable. It also allows the transmitter and the receiver to be easily inclined relative to the specimen, and thus different Lamb modes can be generated. Thus, in principle, this arrangement should enjoy the positive qualities of both conventional arrangements, fully immersed and direct contact, and avoid their negative qualities. With this arrangement, although detectable signals could be received by the receiver, the consistency of the signal was still not acceptable. This was attributed to the multiple reflections of the signal within the water pool between the water free surface and the specimen.

### A. Water columns

From the above experiments one can conclude that a good transducer holder mechanism must not allow reflected waves from the top surface of the water to reach the transducer face. With this requirement in mind, a holder was envisioned as a narrow column of water, slightly larger than the transducer diameter. Water fills the space between the transducer face and the specimen. Such a water column was made by cutting short-length copper tubes to hold the transducers inside. Copper tubes were chosen for ease of availability.

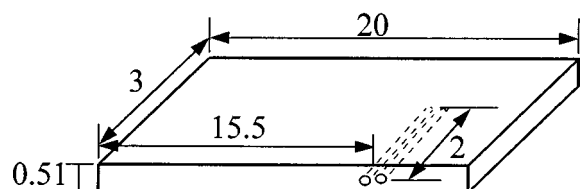


FIG. 4. Geometry of the aluminum specimen; all dimensions are in inches.

TABLE I. Amplitudes of different peaks of the  $V(f)$  curve in the absence of any defect (Fig. 2).

	Peak 1	Peak 2	Peak 3	Peak 4	Peak 5	Peak 6
High	7598	8630	4229	6912	2780	5753
Low	2845	6941	2386	2435	724	1751
Range/Average	0.98	0.22	0.58	1.0	1.28	1.19
Average	4851	7636	3179	4457	1605	3375

When one end of a tube was cut to a certain angle and placed on the specimen, the transducer would be inclined to the specimen at that angle when it is inserted inside the tube. Alleyne and Cawley (1992) used a similar setup. They drilled two holes of opposite inclinations in a solid block, filled those by coupling fluid, and placed the transmitter and the receiver into those two holes. The inclined tube arrangement improved the signal consistency slightly; however, it was still not very good, as one can see in Figs. 2 and 3. Four curves in each of these figures were obtained under the same conditions during four different experiments. Before analyzing these results, the experimental setup that generated the  $V(f)$  curves of Figs. 2 and 3 is first described below.

## B. Experimental setup

A personal-computer-based data acquisition software controls a model 395 Wavetech arbitrary waveform generator, which sends out tone-burst signals in the sweeping frequency mode, continuously varying from a lowest frequency to the highest frequency. The signal from this generator is amplified by a model 310 Matec broadband gated amplifier and then used to excite the transmitting transducer, inclined at an angle of 26 degrees. The receiving transducer is located at a distance of 12 in. (304.8 mm) from the transmitter and inclined at the same angle (26 degrees), but in the opposite direction. The received signal is amplified by a Tektronix TM 506 amplifier and is routed back to the computer through an interface. The software processes the signals and produces the received voltage versus the signal frequency or the  $V(f)$  curve which can be displayed on the screen or can be stored in a file for future analysis.

The  $V(f)$  curves generated by the method, described above, are shown in Figs. 2 and 3. Each of these two figures show four  $V(f)$  curves. Four curves are the results of four separate experiments with a 0.51 in. (13-mm)-thick aluminum plate over nondefective (Fig. 2) and defective (Fig. 3) regions of the plate respectively. Geometry of the specimen

TABLE II. Amplitudes of different peaks of the  $V(f)$  curve in the presence of the defect (Fig. 3).

	Peak 1	Peak 2	Peak 3	Peak 4	Peak 5	Peak 6
High	3629	7421	3866	7212	3591	3917
Low	1525	5664	1007	2075	760	1591
Range/Average	0.81	0.26	1.48	1.22	1.38	0.98
Average	2587	6736	1931	4211	2053	2375
% Change due to defect	-46.7	-11.8	-39.3	-5.5	+27.9	-29.6

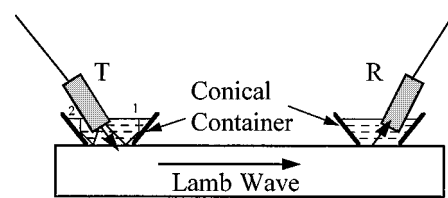


FIG. 5. Transducers in conical containers. Signals of types 1 and 2 cannot strike the specimen after being reflected by the container wall.

is shown in Fig. 4. It has two holes of same size, 2 in. (50.8 mm) deep and 1/8 in. (3.175 mm) in diameter, located side by side at the central plane of the plate.

Experiments were repeated over defective and nondefective zones to test the consistency of the experimental results. Relevant data from the  $V(f)$  curves of Figs. 2 and 3 are summarized in Tables I and II, respectively. For the six peaks at six frequencies, the “high” for each frequency refers to the value of the tallest peak at that frequency and “low” refers to the shortest peak. “Range/Average” is the difference between the “high” and “low” values divided by the “average” value corresponding to a particular frequency. “Range/Average” gives a measure of the scatter in the experimental data. The “average” is computed by the least squares error minimization technique for each of the six frequencies. Numbers 1–6 in Figs. 3 and 4 mark the six peaks in each figure. It will be shown later that only three (second, fourth, and sixth) of the six peaks correspond to the three Lamb modes and the other three peaks do not.

In the last row of Table II, one can see that the defects change the average values of the peaks numbered 1, 2, 3, 4, 5, and 6 by -46.7%, -11.8%, -39.3%, -5.5%, +27.9%, and -29.6%, respectively. The first peak shows the highest percentage change (-46.7%). However, the “range/average” ratio in Tables I and II for this peak are 0.98 (in absence of defects) and 0.81 (in presence of defects), respectively. These high values indicate that there is a considerable amount of scatter in the experimental values and the “low” peak value (2845) in absence of the defect comes out to be lower than the “high” peak value (3629) in presence of the defect. In other words, the consistency of the results and the repeatability of the experiments are not satisfactory. The same conclusion can be drawn from third to sixth peaks, the “range/average” ratios, in the absence of the defects, for

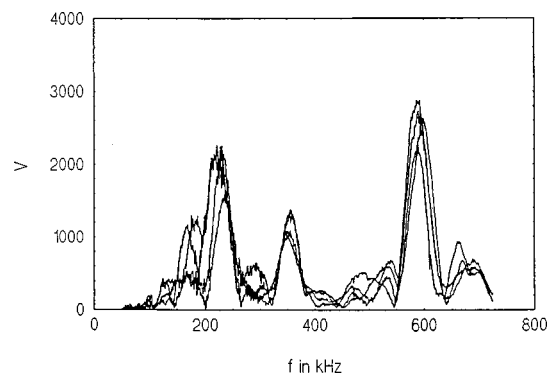


FIG. 6. Four  $V(f)$  curves generated by the setup of Fig. 5 over the defect-free region.

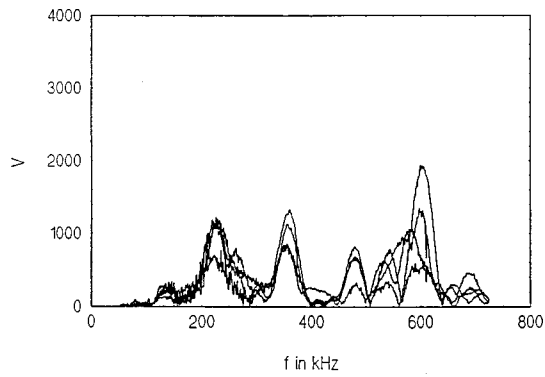


FIG. 7. Four  $V(f)$  curves generated by the setup of Fig. 5 over the defective region.

peaks 3, 4, 5, and 6 are 0.58, 1.0, 1.28 and 1.19, respectively; these values increase further in presence of the defects. Only the second peak shows small scattering; range/average ratios for this peak are 0.22 and 0.26 in the absence and presence of the defects, respectively. However, the peak amplitude change for the second peak is only  $-11.8\%$  due to the defect and the low peak value (6941) in the absence of the defect still comes out to be lower than the high peak value (7421) in the presence of the defect. To produce more consistent experimental values it is therefore necessary to prevent the multiply-reflected waves, from the inner walls of the tubes, from reaching the receiver. A conical water pool, described in the following section, is designed to achieve this goal.

Another disadvantage of the inclined tube arrangement is that one pair of tubes is good for only one angle of incidence. A pair of new tubes has to be cut for every angle the experiment is to be conducted at.

### C. Conical container

If the water container shape is made conical, then reflected waves from the container wall do not reach the transducer face (see rays 1 and 2 in Fig. 5). The transducer can be held by a holder at the larger end of the container facing the smaller end, as shown in Fig. 5. The added advantage of this setup is that transducers can be inclined at any desired angle inside the conical container, unlike a transducer fitted inside a tube or in a hole. As a result, the transducer inclination angle between experiments can be changed easily and quickly. While conducting experiments with this setup it was noted that, as expected, disturbing the water of the conical container did not affect the received signal and the  $V(f)$  curve. Experiments carried out with this arrangement showed consistent results.

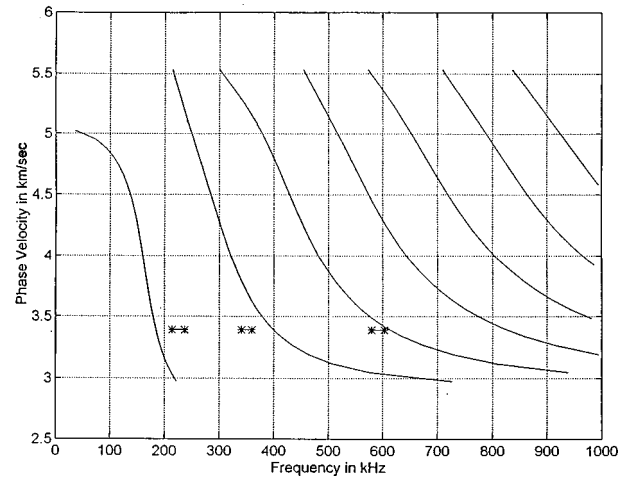


FIG. 8. Theoretical dispersion curves for a 0.51-in. (13-mm) thick aluminum plate (P wave speed 5.9 km/s, S wave speed 2.9 km/s, and density 2.7 g/cc). Frequency values at which three peaks are observed in Fig. 6 are shown by stars (\*). Two stars connected by a straight line near 200, 350, and 600 kHz show the extent of experimental scatter at the three peak positions in Fig. 6.

Experimental results with the new setup are shown in Figs. 6 and 7 for the same aluminum specimen when the transducers are inclined at 26 degrees. A comparison between Figs. 2 and 3 and Figs. 6 and 7 show the superiority of the new setup. In Fig. 6 one can see only three distinct peaks near 230, 350, and 590 kHz frequencies. Theoretical dispersion curves generated for the aluminum specimen (P-wave speed 5.9 km/s, S-wave speed 2.9 km/s, and density 2.7 g/cc) are shown in Fig. 8.

From these dispersion curves one can see that the three main peaks of Fig. 6 correspond to the zeroth-order symmetric (S0), first-order antisymmetric (A1) and first-order symmetric (S1) modes at 3.39 km/s phase velocity. From Snell's law,

$$c = \frac{c_f}{\sin \theta}, \quad (1)$$

where  $c$  is the phase velocity,  $c_f$  is the P-wave speed in water (1.49 km/s), and  $\theta$  is the incident angle, one can show that 26 degree angle of incidence ( $\theta$ ) corresponds to the 3.39 km/s phase velocity ( $c$ ). Stars in Fig. 8 show the frequency values corresponding to the three peaks of Figs. 6 and 7.

Quantitative comparisons between the appropriate peaks of the  $V(f)$  curves generated by the tube container and the conical container are shown in Tables III and IV.

Out of the six peaks of Figs. 2 and 3, only three peaks (second, fourth, and sixth) correspond to the Lamb modes;

TABLE III. Comparison of the three Lamb mode peaks in the absence of any defect (Figs. 2 and 6).

	S0 Mode (230 kHz)		A1 Mode (350 kHz)		S1 Mode (590 kHz)	
	Peak 1 (conical)	Peak 2 (tube)	Peak 2 (conical)	Peak 4 (tube)	Peak 3 (conical)	Peak 6 (tube)
High	2124	8630	1328	6912	2794	5753
Low	1519	6941	984	2435	2173	1751
Range/Average	0.33	0.22	0.30	1.0	0.25	1.19
Average	1820	7636	1164	4457	2500	3375

TABLE IV. Comparison of the three Lamb mode peaks in presence of the defects (Figs. 3 and 7).

	S0 Mode (230 kHz)		A1 Mode (350 kHz)		S1 Mode (590 kHz)	
	Peak 1 (conical)	Peak 2 (tube)	Peak 2 (conical)	Peak 4 (tube)	Peak 3 (conical)	Peak 6 (tube)
High	1172	7421	1295	7212	1896	3917
Low	700	5664	771	2075	506	1591
Range/Average	0.47	0.26	0.55	1.22	1.31	0.98
Average	1008	6736	949	4211	1063	2375
% Change due to defect	-44.6	-11.8	-18.5	-5.5	-57.5	-29.6

the other three peaks (first, third, and fifth) are the results of the interference between different waves interacting inside the water tube. As a result, it is difficult to distinguish the Lamb wave peaks from the other peaks in the  $V(f)$  curves generated by the transducers placed in tubes. However, one can see in Fig. 6 that only three peaks corresponding to the three Lamb modes (S0, A1, and S1) are prominent in the  $V(f)$  curves generated by the new setup with the conical water containers. As a result, the identification of Lamb wave peaks become easier with the new setup. In Table III we see that the “Range/Average” values are small for all three peaks generated by the new setup, but two of these values (corresponding to the A1 and S1 modes) are large for the old setup. With the conical container S0 and S1 modes show large change (-44.6% and -57.5%) in their “average” peak amplitude values in the presence of the defect and do not have any overlap region. In other words, all four peaks in the defect-free region for each of these two modes come out to be higher than the four peaks in the defective region. This was not the case when the tubes were used. It can be also noticed that the  $V(f)$  curves generated by the new setup are more sensitive to defects. The S0, A1, and S1 modes show a change of -44.6%, -18.5%, and -57.5%, respectively, as opposed to the -11.8%, -5.5%, and -29.6%, respectively, obtained with the previous setup.

### III. CONCLUDING REMARKS

A new setup with conical water containers is presented in this paper. It is shown that this setup is very effective for generating and receiving different Lamb modes in a large plate. Since it does not need the entire specimen to be immersed in a water tank, the specimen can be fairly large. It

allows the transducers to be oriented at any angle and does not allow the diverging beams to strike the specimen; as a result, a specific Lamb mode can be generated in the plate. Superiority of the conical water containers in comparison to the tubes and other ordinary water containers has been verified by carrying out experiments with an aluminum specimen using new and old types of water containers.

- Alleyne, D. N., and Cawley, P. (1992). “The Interaction of Lamb Waves with Defects,” *IEEE Trans. Ultrason. Ferroelectr. Freq. Control* **39**, 381–396.
- Castaigns, M., and Hosten, B. (1997). “The Use of Electrostatic, Ultrasonic, Air-Coupled Transducers to Measure the Elastic and Damping Properties of Anisotropic Material and to Generate and Receive Lamb Wave Modes in Composite Plates,” in *Proceedings of the 17th International Conference of Ultrasonics International '97*, 2–4 July 1997 (Elsevier Science, Delft, The Netherlands).
- Chimenti, D. E., and Martin, R. W. (1991). “Nondestructive Evaluation of Composite Laminates by Leaky Lamb Waves,” *Ultrasonics* **29**, 13–21.
- Dayal, V., and Kinra, V. K. (1991). “Leaky Lamb waves in an anisotropic plate. II: Nondestructive evaluation of matrix cracks in fiber-reinforced composites,” *J. Acoust. Soc. Am.* **89**, 1590–1598.
- Ditri, J. J., Rose, J. L., and Chen, G. (1992). “Mode Selection Criteria for Defect Detection Optimization Using Lamb Waves,” *Rev. Prog. Quant. Nondestr. Eval.* **11**, 2109–2115.
- Kundu, T., Maslov, K., Karpur, P., Matikas, T., and Nicolaou, P. (1996). “A Lamb Wave Scanning Approach for Mapping Defects in [0/90] Titanium Matrix Composites,” *Ultrasonics* **34**, 43–49.
- Mal, A. K., Yin, C. C., and Bar-Cohen, Y. (1991). “Ultrasonic Nondestructive Evaluation of Cracked Composite Laminate,” *Composites Eng.* **1**, 85–101.
- Maslov, K. I., and Kundu, T. (1997). “Selection of Lamb Modes for Detecting Internal Defects in Composite Laminates,” *Ultrasonics* **35**, 141–150.
- Yang, W., and Kundu, T. (1998). “Guided Waves in Multilayered Anisotropic Plates and its Use in Internal Defect Detection,” *ASCE Journal of Engineering Mechanics* **124**(3), 311–318.

# Investigation of the near field of a loudspeaker using tomographic reconstruction from TV-holography measurements

Rolf Rustad<sup>a)</sup> and Lars Henrik Morset

*Applied Optics Group, Institute of Physics, Norwegian University of Science and Technology, N-7034 Trondheim, Norway*

(Received 21 January 1998; accepted for publication 26 May 1998)

It has previously been shown that a three-dimensional mapping of an acoustic field's amplitude and phase may be calculated from a set of TV-holography measurements by use of tomographic techniques. In this paper a thorough mathematical description of this measuring technique is given. An increased number of measured projections improves the tomographic reconstructions significantly. Techniques for obtaining quantitative data for the pressure amplitude of the acoustic field are implemented. The technique is demonstrated by measurements of the near field of a loudspeaker and these measurements are shown to agree well with measurements obtained with a microphone. © 1998 Acoustical Society of America. [S0001-4966(98)02309-1]

PACS numbers: 43.58.Vb, 43.38.Ja, 43.35.Sx, 43.60.Sx [SLE]

## INTRODUCTION

Many techniques are used to obtain experimental data on the spatial structure of acoustic fields. They usually rely on microphones either being scanned through the field or formed into arrays which are placed into the field. TV holography<sup>1</sup> offers a noninvasive alternative to these techniques. The probe in TV-holography measurements of acoustic fields is an expanded laser beam. The technique is sensitive to the harmonic variations in optical refractive index which are produced by the acoustic field. These variations cause a harmonic modulation of the phase of the light passing through the acoustic field. Phase modulated TV holography allows us to determine both the phase and the magnitude of this modulation with great accuracy.<sup>2</sup> Each pixel in a TV-holography recording measures the integrated modulation along the path the light traverses on its way from source to detector. The two-dimensional distribution of such measurements in a TV frame is a projection of the acoustic field's amplitude and phase. From a set of projections obtained from different viewing angles, a tomographic reconstruction of the amplitude and the phase of the acoustic field may be computed.

It has previously been shown qualitatively that this technique works.<sup>1</sup> In this paper we give a detailed mathematical description of the measuring procedure. Improvements in the measuring setup have resulted in tomographic reconstructions of high spatial resolution with calibrated values for the pressure amplitude of the acoustic field. We present measurements of the near field of a loudspeaker. These measurements are compared with measurements obtained with a scanning microphone.

## I. THEORY

### A. Light propagation in acoustic fields

A light ray of wave number  $k$  traversing an acoustic field of frequency  $\Omega$  along a path  $S$  is subject to a modulation of its optical phase equal to

$$\begin{aligned}\psi(t) &= k \int_S \mu(\mathbf{r}) \cos(\Omega t + \Phi(\mathbf{r})) ds \\ &= k p_{\text{op}} \int_S P(\mathbf{r}) \cos(\Omega t + \Phi(\mathbf{r})) ds,\end{aligned}\quad (1)$$

$\mu(\mathbf{r})$  is the maximal change in refractive index at a given location. It is related to the pressure amplitude  $P(\mathbf{r})$  through the piezo-optic constant  $p_{\text{op}} = \partial n / \partial P$ .  $\Phi(\mathbf{r})$  is the phase of the acoustic field.

Our goal is to recover the acoustic field's pressure amplitude  $P(\mathbf{r})$  and phase  $\Phi(\mathbf{r})$  with high spatial resolution from a series of TV-holography measurements of the modulation  $\psi(t)$  by using tomographic reconstruction.

Equation (1) may be written in the form

$$\begin{aligned}\psi(t) &= k p_{\text{op}} \left[ \cos(\Omega t) \int_S P(\mathbf{r}) \cos(\Phi(\mathbf{r})) ds \right. \\ &\quad \left. - \sin(\Omega t) \int_S P(\mathbf{r}) \sin(\Phi(\mathbf{r})) ds \right] \\ &\equiv k p_{\text{op}} \left[ \cos(\Omega t) \int_S P_{\text{Re}}(\mathbf{r}) ds \right. \\ &\quad \left. - \sin(\Omega t) \int_S P_{\text{Im}}(\mathbf{r}) ds \right].\end{aligned}\quad (2)$$

The two integrals are the integrals of the real and imaginary parts of the  $\mathbf{P}$  phasor along the path  $S$ . Figure 1 illustrates the relationship between the phasor  $\mathbf{P}$  and its real and imaginary parts. We define

<sup>a)</sup>Electronic mail: rustad@phys.unit.no



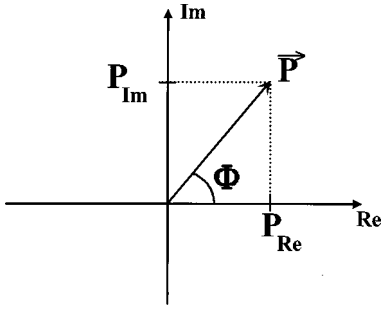


FIG. 1. A pressure phasor  $\mathbf{P}$  of magnitude  $P$  and phase  $\Phi$ , and its real and imaginary parts  $P_{\text{Re}}$  and  $P_{\text{Im}}$ .

$$\Pi_{\text{Re}} = \int_s P_{\text{Re}}(\mathbf{r}) ds, \quad \Pi_{\text{Im}} = \int_s P_{\text{Im}}(\mathbf{r}) ds. \quad (3)$$

The modulation  $\psi(t)$  may now be characterized by a phasor  $\mathbf{a}_\psi$  of magnitude  $a_\psi$  and phase  $\phi$  given by

$$a_\psi = p_{\text{op}} \sqrt{\Pi_{\text{Re}}^2 + \Pi_{\text{Im}}^2}, \quad (4)$$

$$\phi = \tan^{-1} \left( \frac{\Pi_{\text{Im}}}{\Pi_{\text{Re}}} \right) \bmod 2\pi,$$

so that  $\psi(t) = ka_\psi \cos(\Omega t + \phi)$ . Figure 2 illustrates the relationship between the modulation phasor  $\mathbf{a}_\psi$  and the integrals  $\Pi_{\text{Re}}$  and  $\Pi_{\text{Im}}$ .

## B. TV holography

$\psi(t)$  is measured by phase modulated time-average TV holography, as described elsewhere.<sup>1,2</sup> The exposure time of the TV camera is long compared to the modulation period, and the intensity at a given location,  $I(x, y)$ , is proportional to the squared zero-order Bessel function of the first kind  $J_0^2(x)$ .<sup>3</sup> The argument of this function is given by the vector difference between the modulation phasor  $\mathbf{a}_\psi(x, y)$  and the phasor describing the modulation of the reference arm of the interferometer,  $\mathbf{a}_r$ .<sup>4</sup>

$$I(x, y) \propto J_0^2(k|\mathbf{a}_r - \mathbf{a}_\psi(x, y)|)$$

$$= J_0^2(k\sqrt{a_r^2 + a_\psi^2(x, y) - 2a_\psi(x, y)a_r \cos(\phi(x, y) - \theta)}). \quad (5)$$

$\theta$  is the phase of the modulation of the reference arm of the interferometer.  $a_r$  is chosen so that we work on the linear

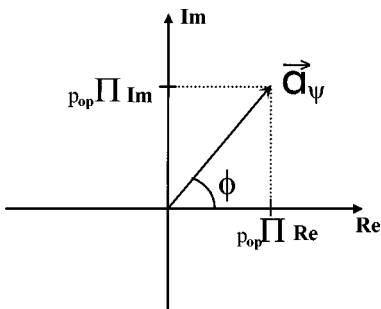


FIG. 2. A modulation phasor  $\mathbf{a}_\psi$  of magnitude  $a_\psi$  and phase  $\phi$ , and its real and imaginary parts, the integrals  $\Pi_{\text{Re}}$  and  $\Pi_{\text{Im}}$  multiplied by the piezo-optic constant  $p_{\text{op}}$ .

part of the first lobe of the Bessel function,<sup>5</sup> and provided  $a_\psi \ll a_r$  we may do the approximation:

$$I(x, y) \propto J_0^2(k\sqrt{a_\psi^2(x, y) + a_r^2 - 2a_\psi(x, y)a_r \cos(\phi(x, y) - \theta)})$$

$$\approx I_b(x, y) - c(x, y)a_\psi(x, y)\cos(\phi(x, y) - \theta). \quad (6)$$

$I_b$  and  $c$  are pixel dependent constants. To determine  $a_\psi$  and  $\phi$ , four measurement frames are recorded.  $\theta$  is shifted by  $90^\circ$  between consecutive frames, and we get the four intensity distributions:

$$I_{\theta=0}(x, y) = I_b(x, y) - c(x, y)a_\psi(x, y)\cos(\phi(x, y)),$$

$$I_{\theta=90}(x, y) = I_b(x, y) - c(x, y)a_\psi(x, y)\cos(\phi(x, y) - 90)$$

$$= I_b(x, y) + c(x, y)a_\psi(x, y)\sin(\phi(x, y)), \quad (7)$$

$$I_{\theta=180}(x, y) = I_b(x, y) - c(x, y)a_\psi(x, y)\cos(\phi(x, y) - 180)$$

$$= I_b(x, y) + c(x, y)a_\psi(x, y)\cos(\phi(x, y)),$$

$$I_{\theta=270}(x, y) = I_b(x, y) - c(x, y)a_\psi(x, y)\cos(\phi(x, y) - 270)$$

$$= I_b(x, y) - c(x, y)a_\psi(x, y)\sin(\phi(x, y)).$$

The integrals  $\Pi_{\text{Re}}$  and  $\Pi_{\text{Im}}$  may now be found from

$$\Pi_{\text{Re}}(x, y) = \frac{I_{\theta=180}(x, y) - I_{\theta=0}(x, y)}{2p_{\text{op}}c(x, y)}$$

$$= \frac{a_\psi(x, y)}{p_{\text{op}}} \cos(\phi(x, y)), \quad (8)$$

$$\Pi_{\text{Im}}(x, y) = \frac{I_{\theta=90}(x, y) - I_{\theta=270}(x, y)}{2p_{\text{op}}c(x, y)}$$

$$= \frac{a_\psi(x, y)}{p_{\text{op}}} \sin(\phi(x, y)).$$

The constant  $c(x, y)$  is determined from calibration frames, as described in Ref. 2. The piezo-optic constant of air,  $p_{\text{op}}$  is given by Ref. 6 as  $2.7 \cdot 10^{-9} \text{ Pa}^{-1}$ .

## C. Tomography

Tomography is well known from a large number of applications in medicine, research, and industry.<sup>7</sup> Tomographic techniques have also been applied to optical measurements of ultrasonic fields in water.<sup>8</sup> The aim of tomography is to reconstruct a function in two or three dimensions from its projections. We intend to reconstruct the pressure amplitude and the phase of an acoustic field in a plane perpendicular to the TV target of our interferometer, i.e., a plane that is spanned by the set of rays which strike a horizontal line of pixels on our TV target. We now let  $x$  and  $y$  be coordinates in this plane, and  $t$  be the position along a line being imaged onto the TV target. The TV target is at an angle  $\theta$  to the  $x$  axis, so that

$$t = x \cos(\theta) + y \sin(\theta). \quad (9)$$

For each viewing angle  $\theta$  we may write the integrals in Eq. (3) on the form

$$\Pi_{\text{Re}, \theta}(t) = \int_{-\infty}^{\infty} \int_{-\infty}^{\infty} P_{\text{Re}}(x, y)$$

$$\begin{aligned} & \times \delta(x \cos(\theta) + y \sin(\theta) - t) dx dy, \\ \Pi_{\text{Im},\theta}(t) &= \int_{-\infty}^{\infty} \int_{-\infty}^{\infty} P_{\text{Im}}(x,y) \\ & \times \delta(x \cos(\theta) + y \sin(\theta) - t) dx dy. \end{aligned} \quad (10)$$

These are the Radon transforms<sup>9</sup> of the real and imaginary part of the pressure phasor.

Several techniques are available for reconstructing a function from its Radon transforms.<sup>7,10</sup> We use the technique of filtered backprojection (FBP) as described in Ref. 7, and we apply the algorithm to the real and imaginary components separately. FBP has proved particularly attractive for performing tomographic reconstructions from TV-holography measurements, provided the number of measured projections is sufficiently high. This is because the Fourier filtering step in the FBP reconstruction process may be used to reduce the high-frequency noise present in the projections. The choice of filter parameters is a balance between the wish for high spatial resolution in the reconstructions and the need to filter out noise in the measurements.

The output of the tomographic reconstruction algorithm is a matrix with a discrete representation of the reconstructed function. For the real and imaginary parts of the pressure phasor we have the two matrixes  $P_{\text{Re}}$  and  $P_{\text{Im}}$ . Each matrix element represents a contribution to the integrals in Eqs. (3) and (10), so that

$$P_{\text{Re}}(i,j) = P \cos(\Phi) 2d, \quad (11)$$

$$P_{\text{Im}}(i,j) = P \sin(\Phi) 2d.$$

$d$  is the width of the matrix elements and is equal to the distance between points in the reconstruction plane imaged onto adjacent pixels in a line of the TV target. In the measuring configuration used in this work, the light passes through the acoustic field twice (Sec. II), hence the factor 2 in front of the  $d$ . The matrix elements are small, so  $P$  and  $\Phi$  are assumed to be constant for each element. We may now compute the pressure and phase at any position in the reconstruction plane from the corresponding matrix elements by

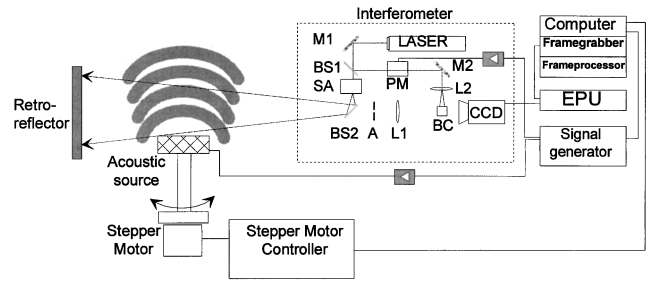


FIG. 3. Experimental setup for measuring acoustic fields with TV holography. M1 and M2 are mirrors, L1 and L2 are lenses, BS1 and BS2 are beam splitters, A is an aperture, SA is a speckle averaging unit, PM a phase modulator, and BC a beam combiner.

$$\begin{aligned} P(x,y) &= \frac{1}{2d} \sqrt{P_{\text{Re}}^2(i,j) + P_{\text{Im}}^2(i,j)}, \\ \Phi(x,y) &= \tan^{-1} \frac{P_{\text{Im}}(i,j)}{P_{\text{Re}}(i,j)} \bmod 2\pi. \end{aligned} \quad (12)$$

If necessary, interpolation or averaging over several matrix elements may be applied. The reconstruction process is repeated for all the lines in the TV image. This produces reconstructions in parallel planes, one on top of the other, resulting in a full-field, three-dimensional, reconstruction of the acoustic field.

## II. EXPERIMENTAL

### A. Setup and procedure

Measurements for tomographic reconstructions of acoustic fields are recorded with a TV-holography interferometer as shown in Fig. 3. The light source is a 5-mW HeNe laser operating at 632.8 nm. The measuring arm of the interferometer is expanded and directed out of the interferometer by a beam splitter (BS2) which is placed in the line of view of the CCD camera. The light traverses the acoustic field under investigation and illuminates a massive wall coated with retroreflective tape. The retroreflective tape causes the light to be reflected back along the same path through the

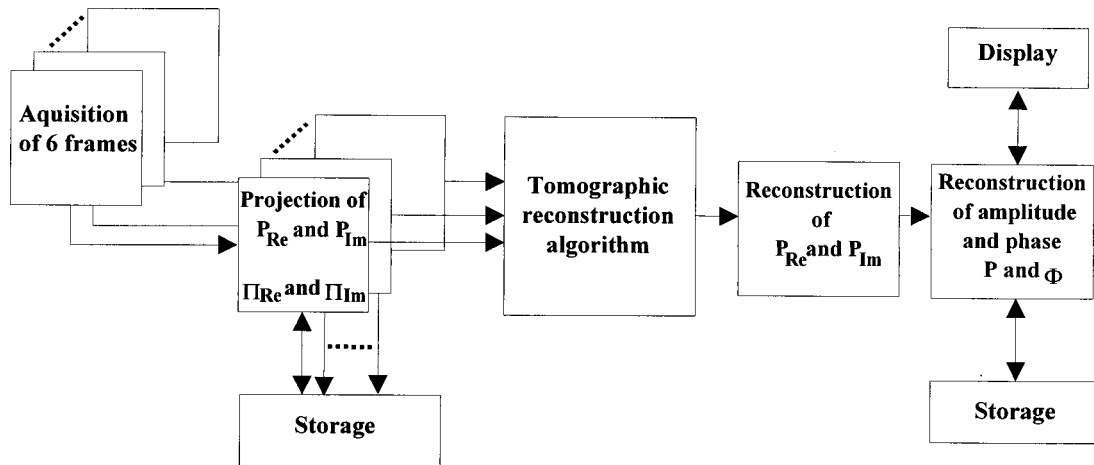


FIG. 4. Data flow from acquisition to reconstruction.

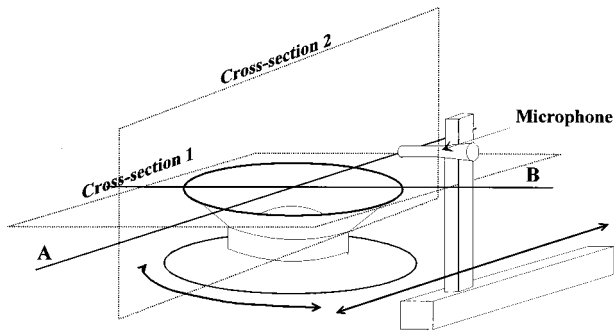


FIG. 5. A tomographic reconstruction of an acoustic field produced by an electrodynamic loudspeaker has been computed. Two cross sections through this reconstruction are presented. The first is placed parallel to and immediately above the opening of the loudspeaker. The second is placed perpendicularly to the first and intersects the center of the loudspeaker. Measurements with a scanning microphone are performed along the lines **A** and **B** in the figure.

acoustic field a second time. The resulting speckle field is imaged through a lens system and interferes with the reference arm of the interferometer in a beam combiner (BC) before hitting the target of a CCD camera. A mirror mounted on a piezoelectric crystal in the reference arm (PM) allows modulation of the phase of the light in the reference arm.

The interferogram is recorded by the CCD camera, and the TV signal is high-pass filtered and square rectified in an analog electronic processing unit<sup>11</sup> (EPU) before it is digitized by a frame grabber for storage and subsequent processing on a personal computer (PC). The PC also controls a two-channel signal generator which provides the drive signals for the acoustic source and the phase modulator in the reference arm of the interferometer.

The acoustic source is mounted on a support connected to a stepper motor drive with an angular resolution of  $1.5^\circ$ . The stepper motor drive is controlled by the same PC. This allows for full automation of the recording process.

As described in Sec. I, six frames must be recorded to determine the values of the two integrals  $\Pi_{Re}$  and  $\Pi_{Im}$  for each angular position of the acoustic field. Two of these frames are needed for calibration, while the other four are interferograms of the acoustic field with the phase of the modulation of the reference arm shifted by  $90^\circ$  between each of the frames. From these six frames, calibrated values for  $\Pi_{Re}$  and  $\Pi_{Im}$  are computed and stored before the acoustic source is rotated and the procedure is repeated for as many times as there are projections to record.

The projection data are available as floating point matrixes of dimensions  $128 \times 128$ . We see this as 128 separate measurements in the form of horizontal lines, each 128 elements long. For  $M$  projections, the tomographic reconstruction algorithm is applied to  $M$  such lines. The result is a reconstruction on a matrix with  $128 \times 128$  elements. The reconstruction is then a sampling of the acoustic field in the plane, or slice, determined by the  $M$  lines. To obtain a three-dimensional mapping we stack many such slices one on top of the other to form a three-dimensional matrix. Figure 4 shows the process from recording to reconstruction.

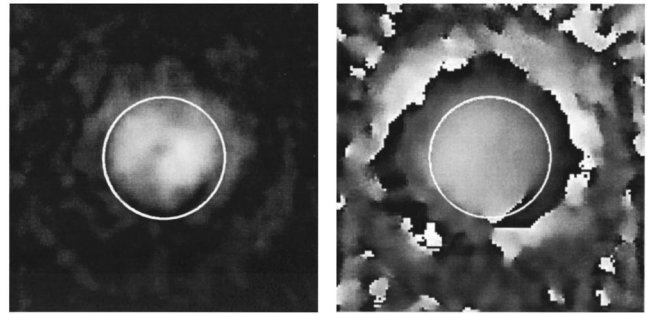


FIG. 6. The amplitude, left, and the phase of the acoustic field produced by an electrodynamic loudspeaker at 4500 Hz in cross section 1. The amplitude is presented in a grayscale plot where brighter intensity corresponds to higher amplitude. White corresponds to a pressure amplitude of 35 Pa. The phase is wrapped and presented in a grayscale plot so that black corresponds to a phase of  $-\pi$  and white to a phase of  $\pi$ . The white circle indicates the rim of the loudspeaker.

### B. Measurement example

We mounted an electrodynamic loudspeaker<sup>12</sup> with a membrane diameter of 125 mm in a wooden box measuring  $200 \times 200 \times 100$  mm. The box was filled with sound-absorbing material and was attached to the rotary support of the measuring setup. The loudspeaker was excited at 4500 Hz and 120 projections with an angular separation of  $1.5^\circ$  were recorded. A  $3 \times 3$  running window median filter was applied to the recorded data prior to the tomographic reconstruction process. From this data set a reconstruction of the acoustic field of the loudspeaker was computed for a cylindrical volume with a diameter of approximately 225 mm and a height of 175 mm. Two cross sections through the reconstruction are presented in Figs. 6 and 7. The cross sections are placed as indicated in Fig. 5.

To verify the validity of the tomographic reconstructions, they were compared with microphone recordings of the same acoustic field. A condenser microphone with a diameter of 3 mm was mounted on a support which allowed it to be placed anywhere in a volume in front of the loudspeaker. The microphone signal and the drive signal for the loudspeaker were digitized with the help of a two-channel audio board in a PC. The pressure amplitude of the acoustic field and the phase difference between the two signals were found through Fourier analysis.

The microphone was scanned along straight lines in 128 steps of 2 mm. Two of these scans are presented in the plots in Figs. 8 and 9 together with the corresponding values from the tomographic reconstruction. The filtering operation in the

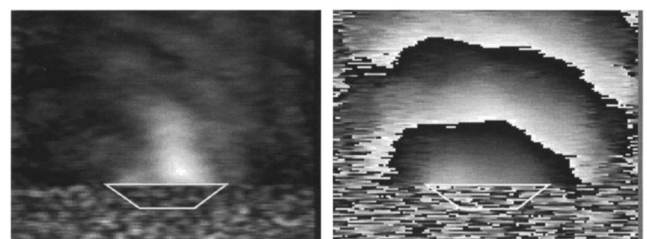


FIG. 7. The amplitude and phase of the same acoustic field in cross section 2, presented in the same manner as in Fig. 6. The white polygon indicates the perimeter of the loudspeaker.

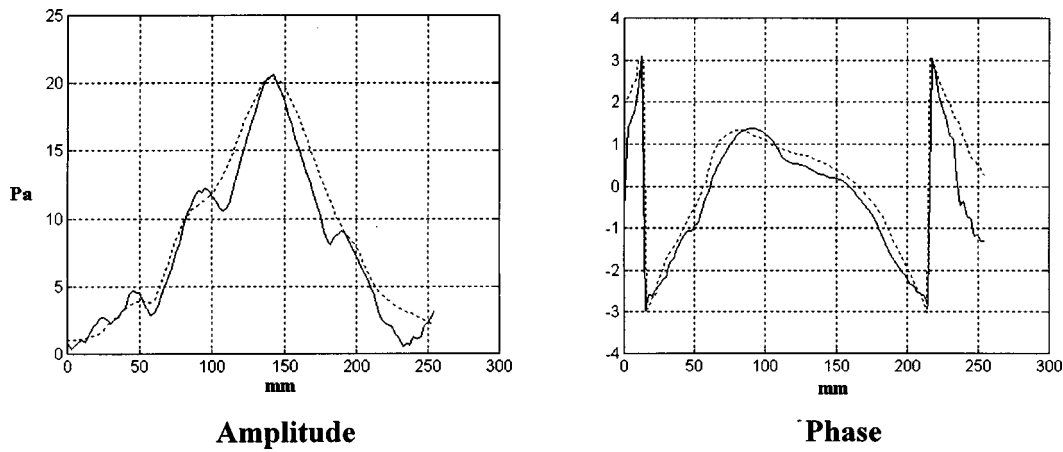


FIG. 8. Plots of the amplitude, in pascal, and the phase of the acoustic field along line **A** in Fig. 5. The abscissa is in millimeters. The solid lines are the tomographic reconstruction, while the dashed lines are the microphone recording.

FBP algorithm was combined with a low-pass filter to produce a reconstruction with a spatial resolution comparable to that of the microphone measurements.

### III. DISCUSSION

The plots in Figs. 8 and 9 show that there is good overall agreement between the tomographic reconstructions of the acoustic field and the microphone measurements of the same field. The sound intensities recorded here are rather high, with peak pressure amplitudes on the order of 35 Pa. Towards the edges of the tomographic reconstruction area, where the sound pressure is lower, the TV-holographic measurements have a poor signal-to-noise ratio. This results in less reliable reconstruction data in these parts of the reconstructions.

The lower detection limit for time-average TV holography of vibrations with a HeNe laser is on the order of 1 nm. For acoustic fields in air this corresponds to a pressure amplitude of approximately 0.4 Pa/m, meaning that if the path of the light through the acoustic field is 1 m long, the average pressure amplitude along the path must be at least 0.4 Pa. Even at significantly higher pressure amplitudes, the signal-to-noise ratio of the TV-holography system is rather poor, and it is necessary to average a large number of measure-

ments to obtain satisfactory results. The need for high sound intensities in combination with averaging of many measurements, and hence long recording sequences, to get an acceptable signal-to-noise ratio remains the most important limitation for this technique.

Another limiting factor is that tomography requires the function that is to be reconstructed to be equal to zero outside the area viewed by the TV camera. This means that the acoustic field must have a finite width at the reconstruction plane. In addition, the TV-holography instrument must have an imaging system and a detector capable of measuring fields of this width with sufficient spatial resolution. It is very difficult to produce acoustic fields of finite width at audible frequencies. But, in our experience, good tomographic reconstructions may be produced even if this requirement is not rigorously met, as long as the pressure amplitudes outside the reconstruction area are small compared with those inside the area.

The amplitude measurements show good agreement regarding the overall magnitude of the sound pressure, but the tomographic reconstructions seem to contain more details, and these details are not always in agreement with the microphone measurements. In our opinion, this can be due to the lower spatial resolution of the microphone recordings, or

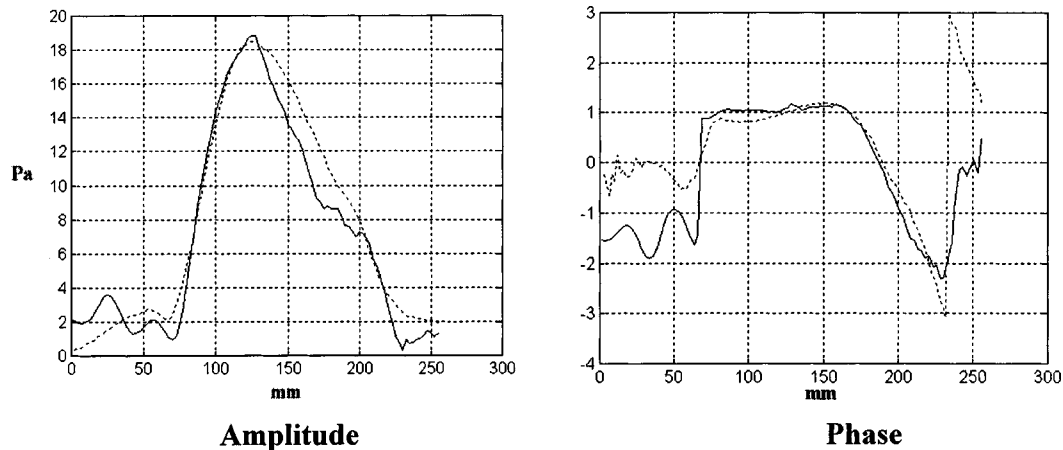


FIG. 9. Same as Fig. 8, but this time along line **B** in Fig. 5.

to errors in the tomographic reconstructions caused by noise in the TV-holography measurements. The TV-holography interferometer employed in this work has been used as is, and has not been optimized for recording acoustic fields. It is very likely that even better results may be obtained with an optimized setup.

The sensitivity of the technique is independent of frequency, and there are no theoretical limits to the bandwidth. The exposure time of the TV camera and the stability of the system will set a lower limit for the frequencies that may be measured. The technique has been successfully applied to ultrasonic fields in water with frequencies as high as 4 MHz, and it is reasonable to assume that it may be used to measure any high-frequency acoustic field in air, provided that it has a sufficient acoustic intensity.

#### IV. CONCLUSION

We have described the theory and application of tomographic reconstructions of acoustic fields from TV-holography measurements. The technique has been demonstrated through measurements of the near field of a loudspeaker. These measurements were compared to measurements obtained with a scanning microphone. There was good agreement between the measurements of both the amplitude and the phase of the acoustic field obtained by the two methods.

It has been documented that tomographic reconstruction from TV-holography measurements give reliable quantitative data for the spatial structure of acoustic fields. This technique offers a noninvasive alternative to microphone recordings, combining high spatial resolution with a very large number of measurement points in three dimensions.

#### ACKNOWLEDGMENT

We would like to thank our supervisor, Professor Ole Johan Løkberg, for his help with the preparation of this manuscript.

- <sup>1</sup>M. Espeland, O. J. Løkberg, and R. Rustad, "Full field tomographic reconstruction of sound fields using TV-holography," *J. Acoust. Soc. Am.* **98**, 280–287 (1995).
- <sup>2</sup>S. Ellingsrud and G. O. Rosvold, "Analysis of data-based TV-holography system used to measure small vibration amplitudes," *J. Opt. Soc. Am. A* **9**, 237–251 (1992).
- <sup>3</sup>H. Osterberg, "An interferometer method for studying the vibrations of an oscillating quartz plate," *J. Opt. Soc. Am.* **22**, 19–35 (1932).
- <sup>4</sup>C. C. Aleksoff, "Time averaged holography extended," *Appl. Phys. Lett.* **14**, 23 (1969).
- <sup>5</sup>K. Høgmoen and O. J. Løkberg, "Detection and measurement of small vibrations using electronic speckle pattern interferometry," *Appl. Opt.* **16**, 1869–1875 (1977).
- <sup>6</sup>H. Barell and J. E. Sears, "The refraction and dispersion of air for the visible spectrum," *Philos. Trans. R. Soc. London, Ser. A* **238**, 1–64 (1939).
- <sup>7</sup>A. C. Kak and M. Slaney, *Principles of Computerized Tomographic Imaging* (IEEE, New York, 1988).
- <sup>8</sup>R. Reibold and W. Molkenstruck, "Light diffraction tomography applied to the investigation of ultrasonic fields. I: Continuous waves," *Acustica* **56**, 180–192 (1984).
- <sup>9</sup>J. Radon, "Über die bestimmung von Funktionen durch ihre Intergralwerte längs gewisser Mannigfaltigkeiten," *Ber. Verh. Saechs. Akad. Wiss. Leipzig, Math. Phys., Kl.69* (1917).
- <sup>10</sup>G. T. Herman, *Image Reconstruction From Projections* (Academic, New York, 1980).
- <sup>11</sup>K. Høgmoen and H. M. Pedersen, "Measurement of small vibrations using electronic speckle pattern interferometry: Theory," *J. Opt. Soc. Am.* **67**, 1578–1583 (1977).
- <sup>12</sup>Vifa C17WH-27 4Ω loudspeaker element.

# Linear and nonlinear model of the human middle ear

Jérôme Pascal and Antoine Bourgeade

CEA-Centre d'Etudes Scientifiques et Techniques d'Aquitaine, BP 2, 33114 Le Barp, France

Michel Lagier

Thomson-Marconi sonar 525 route des Dolines, BP 157, 06903 Sophia-Antipolis Cedex, France

Claude Legros

Laboratoire d'Acoustique de l'Université Toulouse-le Mirail, 5 allées Antonio Machado, 31058 Toulouse Cedex, France

(Received 26 January 1998; accepted for publication 3 June 1998)

The measurement of the middle ear transfer function usually requires invasive methods. An equivalent analog equivalent model enables us to evaluate its characteristics without damaging any part of the ear. A linear and a nonlinear model of the middle ear have been developed to predict intracochlear pressure and the stapes volume velocity for various sound pressure levels (SPL). The linear model results have been compared with human eardrum impedance and middle ear transfer function data. The nonlinear phenomena due to the contraction of the stapedius muscle over 80 dB and to the stapes clipping displacement above 120 dB are represented by a set of variable electrical components. The model of the acoustic reflex is based on experimental observations. The study of the annular ligament behavior was performed on cats and extrapolated to humans with some hypothetical restrictions. These approximations provide information on the middle ear transfer function and enable us to better understand the nonlinear middle ear mechanisms in an intense acoustic field. © 1998 Acoustical Society of America. [S0001-4966(98)03309-8]

PACS numbers: 43.64.Bt, 43.64.Ha [BLM]

## INTRODUCTION

The behavior of the middle ear in an intense acoustic field differs from normal behavior. For a sound pressure level (SPL) of between 80 and 120 dB, the stapedius muscle contracts and modifies the propagation of the acoustic wave. Beyond that sound level, another mechanism appears: The stapes displacement is bounded by the annular ligament. This nonlinear phenomenon modifies the propagation of the acoustic wave through the middle ear. We propose here a model to evaluate the amplitude and the phase of the acoustic pressure.

The study of these nonlinear phenomena requires considerable experimental means. The methods used to measure the pressure in the cochlea and the stapes displacement are invasive and therefore require destruction of part of the ear. They have been performed on human cadavers (Puria *et al.*, 1993) and on animals, especially on cats (Guinan and Peake, 1967). These experiments will be used to design and validate the model.

The main purpose of this study is to represent the linear and nonlinear behaviors of the ear. Flanagan (1962) and Møller (1963) proposed mathematical functions to evaluate the middle ear transfer function. They are, however, bounded at low frequencies and fail to describe the action of each auditory organ, thus providing only a global view of their actions.

Our electroacoustic analogy allows us to consider all the physical phenomena during the propagation of the acoustic wave through the middle ear. The viscous losses, the heat conduction, the mass of the organs and their elasticity can be represented by means of electrical components. The sound

pressure and volume velocity flowing through a section of the acoustic system are analogous to electrical voltage and current sources.

Various middle ear models have used this electroacoustic analogy in the past (Onchi, 1961; Zwislocki, 1962; Lutman and Martin, 1979; Kringlebotn, 1988; Giguère and Woodland, 1994; Rosowski and Merchant, 1995). Based on these studies, we developed an electrical analog model of the middle ear to describe its linear and nonlinear behavior. The cgs unit system is used because the calculated values of physical elements correspond to the values of usual electric components. We first validated the linear model with recent data (Puria *et al.*, 1993). The end of the circuit is modified in order to better understand the operating mechanism of the middle ear and especially of the stapes, the annular ligament, and the inner ear.

The behavior of the acoustic reflex and of the stapes motion are next introduced into the model. The lack of results on human beings is important, requiring certain approximations on the operational mechanisms of the nonlinearities. The acoustic reflex and the effects of the annular ligament are represented by variable capacitance and resistance. The values of the component vary with the SPL. A brief discussion on the limitations of our model concludes this paper.

## I. LINEAR MODEL

### A. Electrical circuit

Zwislocki (1962) proposed an electrical model of the middle ear divided into five blocks. The first block represents middle ear cavities, the second the eardrum losses. The ear-

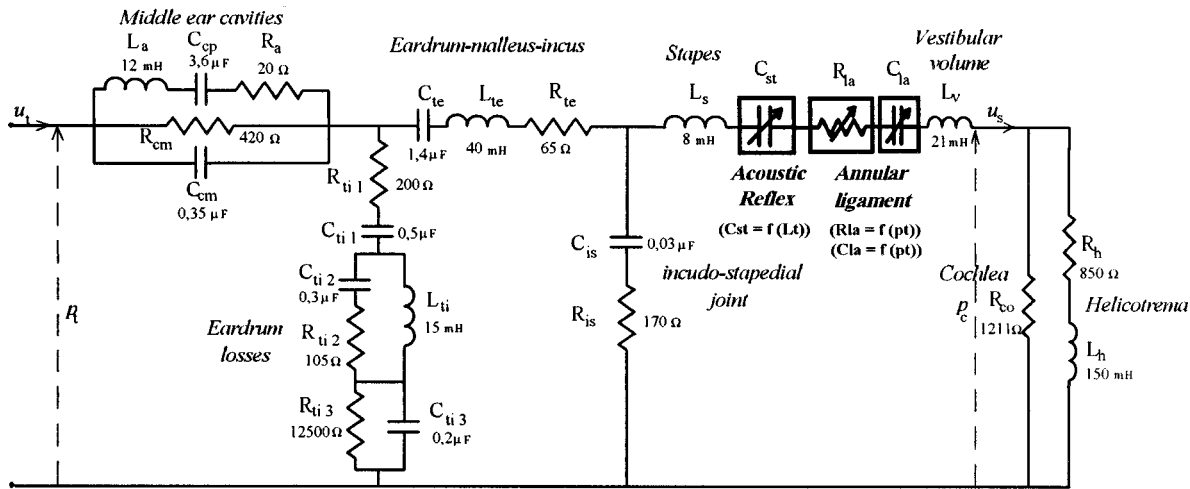


FIG. 1. Electrical model of the human middle ear [adapted from Zwislocki (1962)].

drum in fact vibrates in several segments. The part of the eardrum that moves in phase with the ossicular structure is represented by the third block. Block number four deals with the energy loss of the incudo-stapedial joint due to the elastic junction between these two ossicles. The fifth block is analogous to the action of the stapes and to the cochlear impedance. For a better comparison between the experimental and theoretical results, the last block can be divided into two parts: The stapes, the annular ligament, and the vestibular volume are isolated to study the acoustic reflex and the annular ligament effects; the cochlea and the helicotrema are considered simply as a load impedance.

The electrical element values are calculated from anatomical data and from impedance and transfer function measurements. Knowledge of the auditory organs masses and volumes allows us to determine the electrical components, as well as the inductance and the capacitance. The resistance and the capacitance representing the organ's elasticity are estimated using a minimization algorithm (Nelder and Mead, 1965). The model and all the values are given in Fig. 1.

The impedance match between the eardrum and the cochlea can be symbolized by an electrical transformer. This influence is not represented in Fig. 1 but must be considered in the computation. The lever ratio can be considered as being close to 1 (Dancer and Franke, 1995). The gain of the sound transmission to the inner ear is the result of the area ratio ( $A_t/A_f$ ). The transformer ratio ( $T_r$ ), between the eardrum and the stapedius footplate, is close to 17 [Eq. (1)].

$$T_r = (\text{lever ratio}) \cdot (\text{area ratio}). \quad (1)$$

The total volume of the cavities ( $V_c$ ) was estimated by Zwislocki (1962) to be at most equal to  $8 \text{ cm}^3$ , but this result seems to be over-rated. We will consider the total volume to be equal to  $5.5 \text{ cm}^3$ , which is consistent with the data of Dancer and Franke (1995). The air volumes of the antrum and the pneumatic cells thus have an approximate value of  $5 \text{ cm}^3$  (Table I). We can compute the capacitances equivalent to these air volumes, assuming normal atmospheric pressure and normal middle ear temperature, using Eq. (2).

$$C = \frac{V}{\rho_a c^2}. \quad (2)$$

## B. Modification of the last part of the circuit

The last part of the circuit is modified in comparison with Zwislocki's model (1962). The stapes mass ( $m_s$ ) is equal to 2.5 mg. The acoustic mass ( $m_{as} = m_s/A_f^2$ ) is then  $2.44 \text{ g cm}^{-4}$ . With the transformer ratio ( $T_r$ ), the electrical inductance  $L_s$  is equal to 8 mH. In the same way, the inductance  $L_v$  representing the vestibular volume is calculated, considering that its mass is near 6.4 mg. The form of the cochlear model is defined before testing many solutions and seems to be the same as the model developed by Lynch *et al.* (1982) in cats. The acoustic impedance of the cochlea is resistive and equal to  $0.35 \text{ N s m}^{-5}$  (Zwislocki, 1975). Thus the electrical resistance  $R_{co}$ , taking into account the transformer ratio ( $T_r$ ), is estimated to be  $1211 \Omega$ . The other components are determined with the Simplex minimization algorithm. The number of parameters is very high, so the analysis is complex. The values of the resistance, capacitance, and inductance are determined with respect to anatomical considerations. This minimization is realized with the results of only one subject, but it is not necessary to fit the data more precisely, because we do not want to limit this model to a particular case. We could do the same analysis with a more complete study of the transfer function of the human middle ear.

TABLE I. Anatomical data of the human middle ear.

Volume of the cavities $V_c$ ( $\text{cm}^3$ )	2–6.8	Effective eardrum area $A_t$ ( $\text{mm}^2$ )	55
Volume of the tympanic cavity $V_{ic}$ ( $\text{cm}^3$ )	0.5	Footplate area $A_f$ ( $\text{mm}^2$ )	3.2
Air density $\rho_a$ ( $\text{g cm}^{-3}$ )	$1.15 \times 10^{-3}$	lever ratio	1
Sound celerity $c$ ( $\text{cm s}^{-1}$ )	$3.5 \times 10^4$	area ratio	17

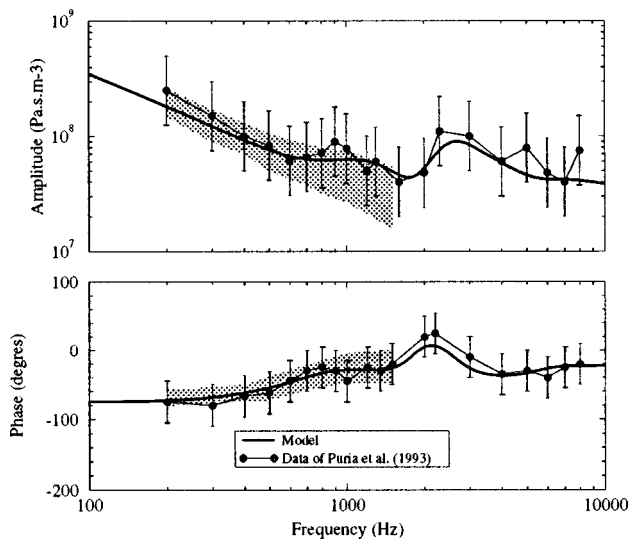


FIG. 2. Middle ear input impedance  $z_e(p_e/u_e)$  compared with measurement of Puria *et al.* (1993).

### C. Validation of our model

The amplitude and phase input impedance of the middle ear are represented in Fig. 2. Our results fit very well with the experimental data measured on human cadavers (Puria *et al.*, 1993). Rosowski *et al.* (1990) have shown that the auditory apparatus behavior on human cadavers is similar to that of a living human for high sound levels below 5 kHz. A slight difference appears at low frequencies, but these results are in agreement with the data from Zwislocki and Feldman (1970) on 33 living subjects with normal hearing (shaded area of Fig. 2). Our analog model gives a good estimation of the eardrum impedance.

The middle ear transfer function  $H(f)$  (ratio of cochlear pressure to eardrum pressure) has not been measured in human ears. It is not possible to make any pressure measurements in the inner ear without destroying the auditory apparatus. However, Puria *et al.* (1993, 1997) measured the amplitude and the angle of the middle ear pressure gain on human cadavers. Above 5 kHz, the apparatus disturbs the measure, and data are less precise. These experimental results allow us to fit our model with the input impedance of the middle ear and also with the transfer function (Fig. 3). The model is in good agreement with these data. The slight difference between the experimental data and simulation can result from the difficulties in measuring acoustic pressure at high frequencies, or can be explained by the fact that above 2.5 kHz the incudomalleal joint introduces a phase angle (Buser and Imbert, 1987). We consider in this study that this junction is stiff. There is a great similarity between the transfer functions in cats and humans. The electrical model gives a good description of the human middle ear behavior up to 80 dB SPL.

## II. NONLINEAR MODEL

We will now study the acoustic reflex action and the influence of the annular ligament to include them in our equivalent model. The behaviors of these nonlinear mecha-

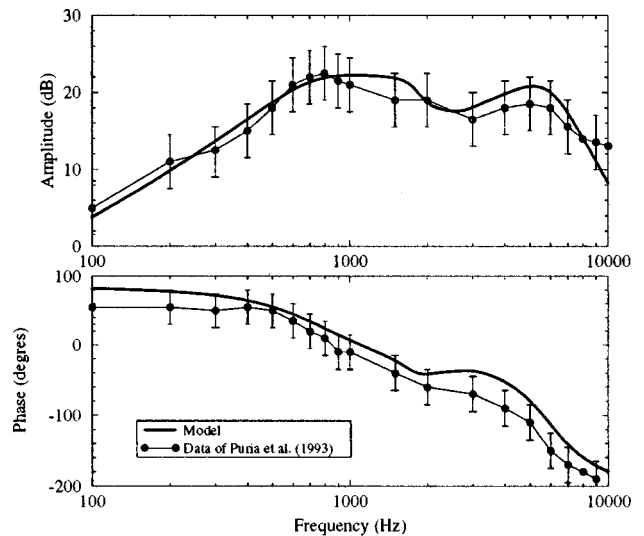


FIG. 3. Transfer function of the middle ear  $H(f)$   $[20 \log(p_c/p_e)]$  compared to data of Puria *et al.* (1993).

nisms are represented by electrical components the properties of which may vary with the sound pressure.

### A. Acoustic reflex

Muscular contraction is induced by the high sound level reaching the cochlea. The intensity of the contraction depends on the amplitude of the stimulation. The acoustic reflex acts as a feedback loop (Dallos, 1973), to decrease the sound pressure.

The acoustic reflex can be characterized by its threshold, its latency, and its effects on sound transmission through the middle ear. The acoustic reflex threshold (ART) is dependent on both stimulus duration and frequency (Moller, 1974). For wideband noise, the ART is close to 80 dB SPL, considerably lower than for pure tones (Dallos, 1964). For pure tones, the ART is between 90 and 100 dB, depending on the frequency (Peterson and Lidèn, 1972). The ART increases with the stimulus duration for each frequency. The steady state of the ART is reached when the acoustic wave duration is greater than 500 ms (Weiss *et al.*, 1963). The contraction of the muscles of the middle ear appears after a latent period. The latency of the acoustic reflex mainly depends on the sound-pressure level but also on the stimulus duration and frequency. The latency decreases as the amplitude of the acoustic stimulation increases (Metz, 1951). There is a great discrepancy in all data, but latency is considered to vary between 150 ms from the ART and to 25–35 ms for the maximum intensity, around 120 dB (Moller, 1974). In an initial approximation, we will consider the effect of a wideband noise on the middle ear and the stimulus duration is assumed to be greater than 500 ms.

The sound transmission through the auditory apparatus is modified by the contraction of the middle ear muscles, which can be considered in an initial approximation to be proportional to the middle ear input impedance variation (Moller, 1962; Borg, 1972), even if Moller (1974) showed that the two variations are not exactly the same. The modification of the human eardrum impedance observed is mainly due to the stapedius muscle, the tensor tympani plays no



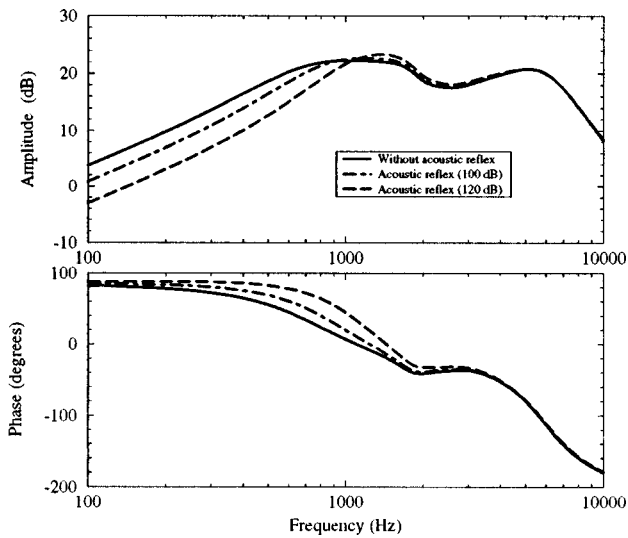


FIG. 4. Transfer function of the middle ear  $H(f)$  [ $20 \log(p_c/p_t)$ ] with and without acoustic reflex.

significant part (Moller, 1958). The stapedius muscle reduces the middle ear sound transmission at frequencies below the resonance frequency, situated around 1 kHz, for human beings (Borg, 1968). Between 1 and 3 kHz, there is a slight amplification due to muscular contraction (Moller, 1974). The acoustic reflex modifies the stiffness of the ossicular chain and can then be symbolized by a variable capacitance  $C_{st}$  (Lutman, 1976). The value of this capacitance depends on the sound-pressure level. Using the value of Lutman and Martin (1979) and the experimental data of Lutman (1976), we inferred a mathematical relation [Eq. (3)] to evaluate its values as a function of the sound-pressure level above the ART.

$$\frac{1}{C_{st}} = t_1 L_{ts}^2 + t_2 L_{ts}. \quad (3)$$

This equation gives the capacitance  $C_{st}$  (in Farad) at between 80 and 120 dB SPL.  $L_{ts}$  is the eardrum SPL above the reflex threshold [ $L_{ts} = 20 \log(p_t/p_{ts})$  with  $p_{ts} = 0.2$  Pa]. The coefficients  $t_1$  and  $t_2$  are, respectively, equal to  $1675 \text{ dB}^{-2} \text{ F}^{-1}$  and  $33\,000 \text{ dB}^{-1} \text{ F}^{-1}$ . The capacitance is infinite for no reflex response, equal to  $0.75 \mu\text{F}$  for moderate contraction (100 dB) and to  $0.25 \mu\text{F}$  near the maximum contraction (120 dB).

Figure 4 shows the middle ear transfer function  $H(f)$  with and without the acoustic reflex. The attenuation due to the stapedius muscle contraction increases with the SPL, to reach a maximum value around 120 dB SPL. Up to 1 kHz the intracochlear pressure  $p_c$  is reduced. Above this frequency, we can see that there is a slight increase. These results are in good agreement with available experimental observations. The model shows that the acoustic reflex introduces a shift between 500 and 2000 Hz, but the lack of experimental data prevents us from validating the phase of our transfer function. Taking individual variability into account, this model seems to give a good average estimation of the acoustic reflex behavior.

## B. Annular ligament

Above the maximum activity of the stapedius muscle (120 dB SPL), another phenomenon disturbs the incident acoustic wave. At high intensities, the annular ligament limits the stapes displacement and the behavior of the middle ear becomes nonlinear. The intracochlear pressure is therefore modified. Price and Kalb (1991) proposed a mathematical model to explain the Guinan and Peake (1967) measurements, made on a cat's ear. There is a great lack of data on the behavior of the annular ligament in humans. We use here data from cats to better understand the mechanism. Assuming that the human ear is similar, we will transfer, with some modest adaptations, the operational principles in our model to evaluate the stapes displacement in an intense acoustic field.

### 1. Study of the behavior of the annular ligament in the cat

The various studies made on an impulse noise exposure are based on empirical criteria. Price and Kalb (1991) proposed a more theoretical insight. The physiological and acoustic values are best known for the cat. They therefore developed an electrical circuit representing the behavior of the cat's ear. This model allows us to take into account the effects of all the elements between free-field pressure and intracochlear pressure. The transformer ratio ( $T_r$ ) is represented by an electrical transformer between the eardrum and the incus. We calculated its values based on some anatomical data. In the case of the cat, the effective area of the eardrum is  $0.40 \text{ cm}^2$  and the footplate area is  $0.0126 \text{ cm}^2$ . The area ratio, multiplied by the lever ratio  $l$ , which is near 1.15 (Dancer and Franke, 1995), gives us a transformer ratio ( $T_r$ ) equal to 36.5.

We modified those two values for a better fit with the transfer characteristic. The resistance  $R_h$  and the capacitance  $C_{al}$  (Price and Kalb, 1991) are, respectively,  $15 \Omega$  and  $1.3 \times 10^{-10} \text{ F}$ .

$$\frac{x_{lin}}{p_t} = \frac{H(f)}{j2\pi f z_{co} A_f}, \quad (4)$$

$x_{lin}$  is the linear stapes displacement,  $p_t$  is the eardrum pressure,  $z_{co}$  is the complex input acoustic impedance of the cochlea, and  $A_f$  is the footplate area. Equation (4) is deduced from the definition of the acoustic impedance

The model results are in good agreement with the data of Guinan and Peake (1967) (Fig. 5). The slight difference between both numerical and experimental analysis derives from the correction of the open bulla measurements. These measurements depend on the size of the opening. Near the resonance frequency of the middle ear cavities (around 4 kHz for the cat), the correction is hard to establish precisely.

The previous model only represented the linear behavior. We will now study the nonlinearity elicited by the presence of the annular ligament. The stapes motion above 120 dB was measured by Guinan and Peake (1967) at various frequencies. By using these data, Kalb and Price (1987) proposed a mathematical model for a stimulus frequency of 315

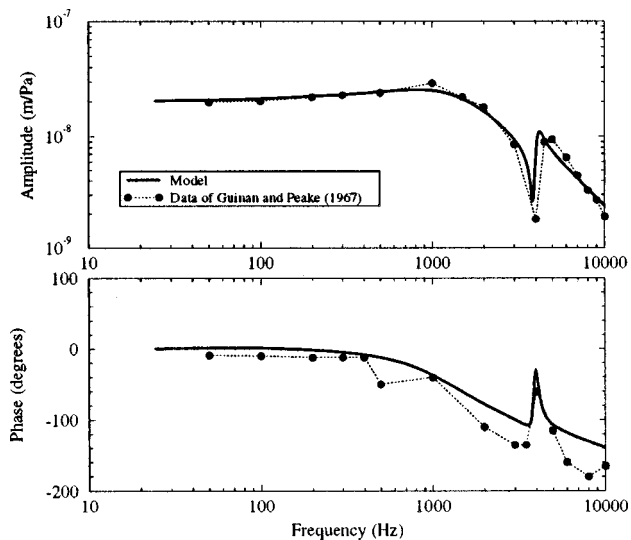


FIG. 5. Middle ear transfer characteristic ( $x_{lin}/p_t$ ) versus frequency compared with measurements of Guinan and Peake (1967).

Hz. This empirical formula, used for converting the linear solution for the stapes motion into a nonlinear solution, is given by Eq. (5).

$$x_{nl} = \frac{x_{lin}}{1 + |x_{lin}/x_{max}|} \quad (5)$$

$x_{nl}$  is the nonlinear stapes displacement. In the case of a low-frequency tone  $x_{lin} = p_t^* A_{lf}$  [ $A_{lf} = 0.142 \times 10^{-6} \text{ cm}^3/\text{dyn}$ , Table II in Guinan and Peake (1967)]  $x_{max}$  (20  $\mu\text{m}$ ) is the maximum stapes displacement extrapolated from experimental data (Kalb and Price, 1987).

Considering that the linear displacement can be calculated with the analog model, we can deduce the nonlinear displacement for all frequencies [Eqs. (4) and (5)]. Figure 6 shows the results of the electrical model compared to experimental data for three frequencies. We can see a slight difference between the results for a stimulus frequency of 3350 Hz. This is due to the fact that the model is validated using

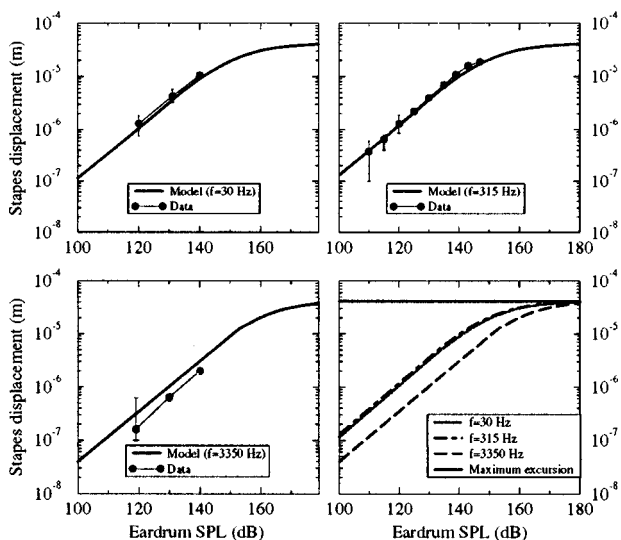


FIG. 6. Peak-to-peak stapes displacement versus SPL compared with measurements of Guinan and Peake (1967).

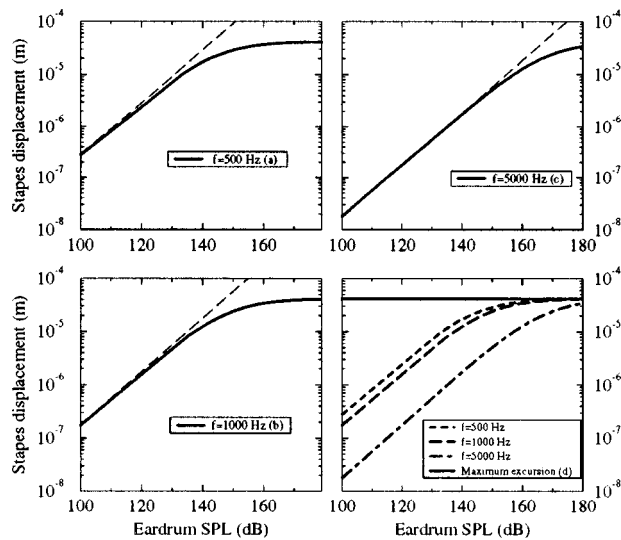


FIG. 7. Peak-to-peak stapes displacement versus eardrum SPL in humans.

an average, while the experimental data were measured on only one subject. The work of Nedzelnsky (1980) shows that the middle ear is linear between 20 and 140 dB and that the transfer function depends on frequency. Our results are in the same range as the measurements and give a good estimation of the peak-to-peak stapes displacements. Using these observations, we can study the human ear behavior in a high acoustic field.

## 2. Extension to the behavior of the annular ligament behavior in humans

There is a great lack of data on the maximum stapes displacement in humans. Yamamoto (1953) found an absolute limit to stapes displacement at about 30  $\mu\text{m}$ . In a rough approximation, we can consider that the behavior of the human annular ligament is similar to that of the cat. We assume an absolute peak-to-peak displacement of 40  $\mu\text{m}$ . Figure 7 gives the theoretical stapes displacements at three frequencies: 500, 1000, and 5000 Hz. The dotted line gives the linear displacement with no annular ligament. The limitation of the displacement depends on the SPL and on the frequency. It is smaller at high frequencies, because the clipping model becomes more significant at low frequencies if SPL is greater than 140 dB. The limitation does not act for high frequencies up to 150–160 dB SPL.

Equation (5) enables us to evaluate the amplitude of the intracochlear pressure, but gives no information on the phase of the acoustical signal. The electrical components symbolize the mechanical behavior of the human middle ear (elasticity, mass, resistance). The annular ligament properties are modified during intense stimulation, with the result that the values of the electrical resistance and capacitance representing the annular ligament vary with the SPL. Comparing the result of the equation and the variation of the values of the components, we can infer some simple empirical equations which give the values of the component as functions of the eardrum sound pressure  $p_t$ .

$$R_{la} = r_1 \alpha_t^{re} + r_2 \alpha_1 + r_3, \quad (6)$$

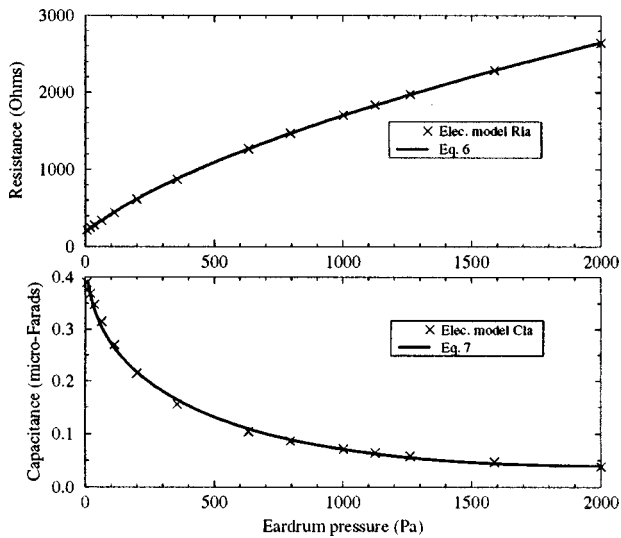


FIG. 8. Determination of  $R_{1a}$  and  $C_{1a}$ .

$$C_{1a} = c_1 \exp(\alpha_t^{ce}) + c_2 \alpha_1 + c_3. \quad (7)$$

The equation coefficients are found with a Simplex minimization algorithm.  $\alpha_t$  represents the tympanic pressure normalize by 1 Pa ( $\alpha_t = p_t/1$ ). So for Eq. (6) the values are  $r_1 = 72 \Omega$ ,  $r_2 = -251 \Omega$ ,  $r_3 = 442 \Omega$ , and  $r_e = 0.266$ . For Eq. (7) the computed values are  $c_1 = -3.33 \times 10^{-2}$  F,  $c_2 = 4.64 \times 10^{-4}$  F,  $c_3 = 0.54$  F, and  $c_e = 0.174$ .

Using the mathematical relation [Eq. (5)], we calculated, with a Simplex algorithm, electrical variables values of  $R_{1a}$  and  $C_{1a}$  versus the eardrum pressure (Fig. 8). Equations (6) and (7) introduced in our electrical model (Fig. 1) allow us to evaluate the middle ear transfer function for different SPL values (Fig. 9). There is a good agreement between both data, except at high frequencies, but taking into account our hypothesis and approximations, the 2 dB difference at high frequencies is small compared to the total results.

The amplitude of the transfer function  $H(f)$  is attenuated at frequencies lower than 2 kHz. As we can see in Fig. 9, the attenuation changes the transfer function at high fre-

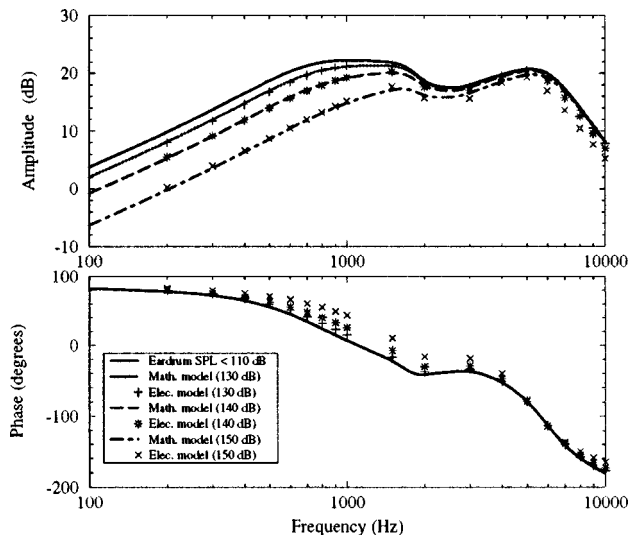


FIG. 9. Middle ear transfer function with annular ligament for high SPL.

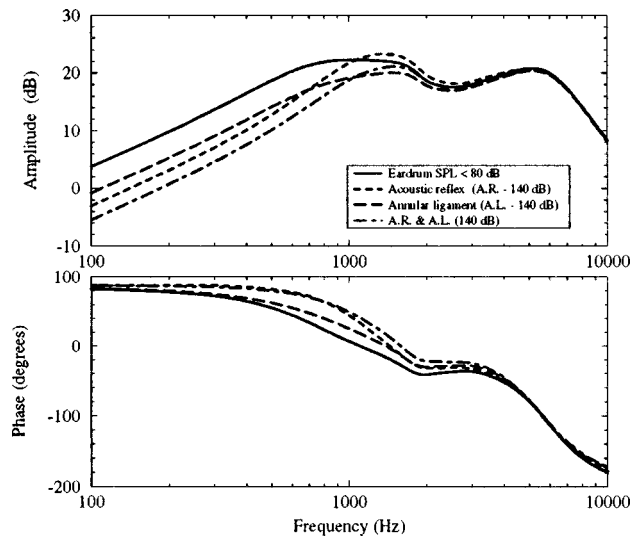


FIG. 10. Middle ear transfer function with annular ligament for a 140 dB SPL.

quencies only above 140 dB SPL. The biggest phase lag appears between 500 and 4000 Hz. We can see a  $40^\circ$  phase difference due to the stapes limitation in the oval window. Our nonlinear model seems to give a good approximation of the behavior of the annular ligament between 100 and 160 dB.

### C. Acoustic reflex and annular ligament

From 80 to 120 dB, the main nonlinearity is due to the acoustic reflex. Above 120 dB, the two nonlinearities combine and disturb the middle ear transfer function, mainly at low frequencies. Considering the circuit of Fig. 1 and Eqs. (3), (6), and (7), we can evaluate the intracochlear pressure and the stapes volume velocity. For a 140 dB SPL, the stapedius muscle contraction introduces an attenuation greater than the stapes limitation (Fig. 10). The combined effect of both mechanisms diminishes the gain by about 10 dB for low frequencies, below the cavities resonance frequency. The phase is mainly modified by the acoustic reflex. However, the stapedius muscle works by stretching the annular ligament, thus decreasing the middle ear pressure, especially at low frequency, such that the behavior of the annular ligament is modified by the acoustic reflex. But the two nonlinearities act in two different dynamic ranges (80–120 dB for the acoustic reflex and over 140 dB for the annular ligament). Their behavior as a function of the acoustic pressure seems to be slightly coupled and can be represented by series components.

The transfer function is plotted for different SPL values in Fig. 11. We can see that the attenuation increases with the incident pressure. The high attenuation at low frequencies is due to the muscular contraction, while above 1 kHz it depends more on the stapes limitation. The acoustic reflex elicits the modification of the transfer function phase up to 1 kHz. Above this frequency, the modification combines both phenomena.

Our theoretical model gives the maximum SPL reaching the cochlea. Figure 12 shows the intracochlear SPL as a

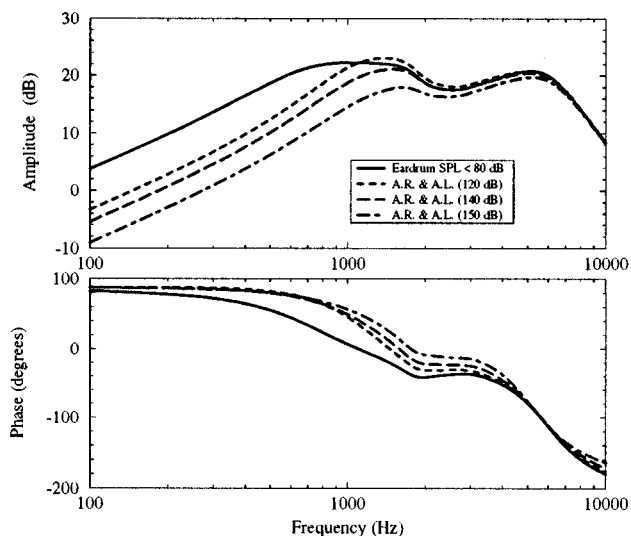


FIG. 11. Middle ear transfer function with acoustic reflex and annular ligament.

function of the eardrum SPL. We can infer that at 500 Hz the SPL reaches a maximum value at around 160 dB SPL. For a 1-kHz frequency, the acoustic reflex introduces no attenuation, so only the annular ligament limits the acoustic wave near 170 dB. At higher frequencies, the maximum value is higher, but the rupture of the eardrum occurs around 180 dB SPL. The model does not enable the prediction of the intracochlear pressure  $p_c$  over 180 dB SPL, because the behavior of the tympanic membrane changes.

### III. DISCUSSION

The enormous difficulties involved in performing measurements in the cochlea in human beings have led us to propose an analog electrical circuit of the middle ear. The physical phenomena are then represented by electrical components. The last part of our circuit is different from that of Zwislocki (1962) and our results are in agreement with experimental data for the input impedance  $z_i$  and for the transfer function  $H(f)$  of the middle ear.

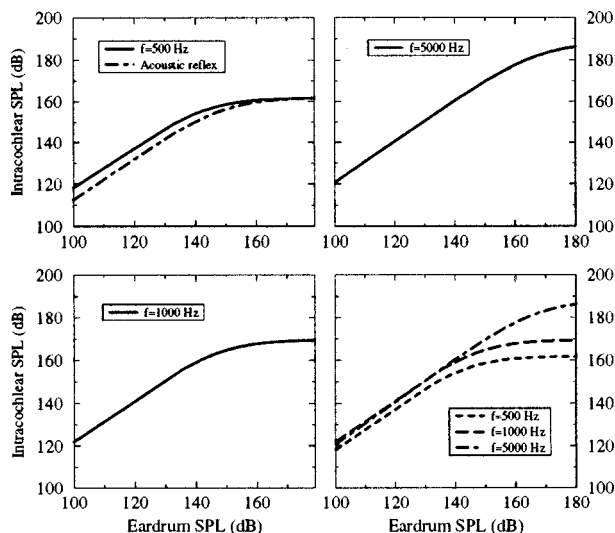


FIG. 12. Intracochlear SPL versus eardrum SPL.

The properties of the auditory organs vary for a SPL over 80 dB. The values of the components must also vary to take account of the modified behavior of the organs concerned. The nonlinear phenomena developed in the middle ear for high sound levels can be represented by variable electrical components:  $C_{st}$ ,  $C_{la}$ ,  $R_{la}$ . They represent the modified properties of the human ear, due to muscular contraction and annular ligament distortion.

The first nonlinearity that we observe is due to the acoustic reflex. The stapedius muscle contraction alters the middle ear stiffness measured on the eardrum. The resistance of the eardrum remains constant and its reactance increases with the stimulation amplitude (Lutman, 1976). The acoustic reflex attenuates the low frequencies, such that the effect of muscular contraction can be represented by a nonlinear capacitance  $C_{st}$  (Lutman and Martin, 1979), computed using Eq. (3). The equation coefficients are determined by comparing Lutman data and the mathematical relation with a minimization algorithm. The results closely match the experimental data. To complete this work, however, eardrum impedance measurements as a function of SPL are required to confirm our hypothesis.

The second nonlinear phenomenon arises from the stapes displacement. The footplate advance is limited by the presence of the annular ligament. Its behavior is represented by a resistance  $R_{la}$  and a capacitance  $C_{la}$  which vary with the eardrum sound pressure  $p_t$  [Eqs. (6) and (7)]. Their values are calculated by comparing the results of Kalb and Price (1987) on cats and by supposing that the operational mechanisms are similar to those in humans. The maximum stapes displacement, which corresponds to the maximum stretching of the annular ligament, is unknown in humans. This lack of information forces us to consider that the peak-to-peak stapes displacement is the same as in cats. Measurements of this value would enable us to predict the intracochlear pressure and the stapes volume velocity in an intense acoustic field.

Taking account of the lack of experimental data, this model seems to give a good evaluation of the transfer function and of the middle ear input impedance for eardrum SPL between 80 and 160 dB. Our electrical model gives a complete description of the human auditory apparatus and allows us to better understand the nonlinear mechanisms of the middle ear. This model is limited by the eardrum behavior in the high acoustic field, but enables us to evaluate the amplitude and the phase at all points of the middle ear below 160 dB SPL.

Measurements of the eardrum impedance and evaluation of the middle ear acoustic transmission, when the acoustic reflex triggers the maximum displacement of the annular ligament in humans, are needed to improve our knowledge of the propagation of the acoustic wave through the ear.

### ACKNOWLEDGMENTS

The authors wish to acknowledge and thank CEA-CESTA and Thomson Marconi sonar for their support during the period of this research.

- Borg, E. (1968). "A quantitative study of the effect of the acoustic stapedius reflex on sound transmission through the middle ear of man," *Acta Oto-Laryngol.* **66**, 461–472.
- Borg, E. (1972). "On the change in the acoustic impedance of the ear as a measure of middle ear muscle activity," *Acta Oto-Laryngol.* **74**, 163–171.
- Buser, P., and Imbert, M. (1987). *Audition* (Collection Méthodes, Hermann, Paris), pp. 95–137.
- Dallos, P. J. (1964). "Dynamics of the acoustical reflex: phenomenological aspects," *J. Acoust. Soc. Am.* **36**, 2175–2183.
- Dallos, P. J. (1973). *The Auditory Periphery, Biophysics and Physiology* (Academic, New York), pp. 465–510.
- Dancer, A., and Franke, R. (1995). "Biomécanique de l'oreille moyenne," *Rev. Laryng. Otol. Rhinol.* **116**, 5–12.
- Flanagan, J. L. (1962). "Models for approximating basilar membrane displacement," *Bell Syst. Tech. J.* **41**, 959–1009.
- Giguère, C., and Wooland, P. C. (1994). "A computational model of the auditory periphery for speech and hearing research. I. Ascending path," *J. Acoust. Soc. Am.* **95**, 331–342.
- Guinan, J. J., and Peake, W. T. (1967). "Middle-ear characteristics of anesthetized cats," *J. Acoust. Soc. Am.* **41**, 1237–1261.
- Kalb, J. T., and Price, R. (1987). "Mathematical model of the ears's response to weapons impulses," in *Proceedings of the Third Conference on Weapon Launch Noise Blast Overpressure*, Special Publication BRL-SP-66 (U.S. Army Ballistics Research Lab, Aberdeen Proving Ground, MD).
- Kringelbotn, M. (1988). "Network model for the human middle ear," *Scand. Audiol.* **17**, 75–85.
- Lutman, M. E. (1976). "The protective action of the acoustic reflex," Ph. D. thesis, University of Southampton.
- Lutman, M. E., and Martin, A. (1979). "Development of an electroacoustic analogue model of the middle ear and acoustic reflex," *J. Sound Vib.* **64**, 133–157.
- Lynch, T. J., Nedzelnitsky, V., and Peake, W. T. (1982). "Input impedance of the cochlea in cat," *J. Acoust. Soc. Am.* **72**, 108–130.
- Metz, O. (1951). "Studies on the contraction of the tympanic muscles as indicated by changes in the impedance of the ear," *Acta Oto-Laryngol.* **39**, 397–405.
- Møller, A. R. (1958). "Intra-aural muscle contraction in man examined by measuring acoustic impedance of the ear," *Laryngoscope* **68**, 48–62.
- Møller, A. R. (1962). "The sensitivity of contraction of the tympanic muscles in man," *Ann. Otol. Rhinol. Laryngol.* **71**, 86–95.
- Møller, A. R. (1963). "Transfer function of the middle ear," *J. Acoust. Soc. Am.* **35**, 1526–1534.
- Møller, A. R. (1974). "The acoustic middle ear muscle reflex," in *Auditory System*, edited by W. D. Keidel and W. D. Neff (Springer-Verlag, Berlin), pp. 520–544.
- Nedzelnitsky, V. (1980). "Sound pressures in the basal turn of the cat cochlea," *J. Acoust. Soc. Am.* **68**, 1676–1689.
- Nelder, J. D., and Mead, R. (1965). "A simplex method for function minimization," *Comput. J., Technometrics* **7**, 308–313.
- Onchi, Y. (1961). "Mechanism of the middle ear," *J. Acoust. Soc. Am.* **33**, 794–805.
- Peterson, J. L., and Lidén, G. (1972). "Some static characteristics of stapedial muscle reflex," *Audiology* **11**, 97–116.
- Price, G. R., and Kalb, J. T. (1991). "Insights into hazard from intense impulses from a mathematical model of the ear," *J. Acoust. Soc. Am.* **90**, 219–227.
- Puria, S., Peake, W. T., and Rosowski, J. J. (1997). "Sound-pressure measurements in cochlear vestibule of human-cadaver ears," *J. Acoust. Soc. Am.* **101**, 2754–2770.
- Puria, S., Rosowski, J. J., and Peake, W. T. (1993). "Middle-ear pressure gain in humans: preliminary results," Symposium on Biophysics of Hair Cell Sensory Systems (unpublished), pp. 345–351.
- Rosowski, J. J., Davis, P. J., Donahue, K. M., Merchant, S. N., and Coltrera, M. D. (1990). "Cadaver middle ears as models for living ears: comparisons of middle ear input immittance," *Ann. Otol. Rhinol. Laryngol.* **99**, 403–412.
- Rosowski, J. J., and Merchant, S. N. (1995). "Mechanical and acoustic analysis of the middle ear reconstruction," *Am. J. Otolaryngol.* **16**, 486–497.
- Weiss, H. S., Mundie, J. R., Cashin, J. L., and Shinabarger, E. W. (1963). "The normal human intra-aural muscle reflex in response to sound," *Acta Oto-Laryngol.* **55**, 505–515.
- Yamamoto, S. (1953). "Supplement to the physiology of conduction apparatus of rabbits. The maximal value of the movement of the stapedial basis," *Hiroshima J. Med. Sci.* **2**, 259–273.
- Zwislocki, J. (1975). "The role of the external and middle ear in sound transmission," in *The Nervous System, Human Communication and its Disorders*, edited by D. B. Tower (Raven, New York), Vol. 3, pp. 45–53.
- Zwislocki, J. J. (1962). "Analysis of the middle-ear function. Part I: Input impedance," *J. Acoust. Soc. Am.* **34**, 1514–1523.
- Zwislocki, J. J., and Feldman, A. S. (1970). "Acoustic impedance of pathological ears," *ASHA Monogr.* **15**.

# Modeling otoacoustic emission and hearing threshold fine structures

Carrick L. Talmadge and Arnold Tubis

*Department of Physics, Purdue University, West Lafayette, Indiana 47907*

Glenis R. Long

*Department of Audiology and Speech Sciences, Purdue University, West Lafayette, Indiana 47907*

Pawel Piskorski

*Boys Town National Institute, Omaha, Nebraska 68131*

(Received 21 January 1998; accepted for publication 18 May 1998)

A class of cochlear models which account for much of the characteristic variation with frequency of human otoacoustic emissions and hearing threshold microstructure is presented. The models are based upon wave reflections via distributed spatial cochlear inhomogeneities and tall and broad cochlear activity patterns, as suggested by Zweig and Shera [J. Acoust. Soc. Am. **98**, 2018–2047 (1995)]. They successfully describe in particular the following features: (1) the characteristic quasiperiodic frequency variations (fine structures) of the hearing threshold, synchronous and click-evoked emissions, distortion-product emissions, and spontaneous emissions; (2) the relationships between these fine structures; and (3) the distortion product emission filter shape. All of the characteristic frequency spacings are approximately the same (0.4 bark) and are mainly determined by the phase behavior of the apical reflection function. The frequency spacings for spontaneous emissions and threshold microstructure are predicted to be the same, but some deviations from these values are predicted for synchronous and click-evoked and distortion-product emissions. The analysis of models is aided considerably by the use of the solutions of apical, and basal, moving solutions (basis functions) of the cochlear wave equation in the absence of inhomogeneities. © 1998 Acoustical Society of America. [S0001-4966(98)01509-4]

PACS numbers: 43.64.Bt, 43.64.Ha, 43.64.Jb [BLM]

## INTRODUCTION

When estimates of the lowest level of sound needed for detection 50% of the time (absolute threshold) are determined in small frequency increments, consistent quasiperiodic patterns of threshold change with frequency (threshold microstructure) are obtained. Regions of relatively stable good sensitivity (threshold maxima) are separated by narrow regions of higher sensitivity (threshold minima). This pattern is reminiscent of those seen with standing waves and is known as threshold microstructure. Isolated investigations (Elliot, 1958; Van den Brink, 1970; Thomas, 1975) of this phenomena which appeared in the literature prior to 1979 indicated that the frequency spacing of the threshold fine structure is approximately a constant fraction of estimates of the frequency resolution capacity of the ear (the critical band). In 1979, Kemp suggested that the capacity of the healthy ear to generate sounds (known as otoacoustic emissions) could be due to the same mechanisms as those responsible for the threshold microstructure (Kemp, 1979b; Kemp, 1997).

The majority of normal hearing ears generate narrow-band signals even in the absence of any external acoustic stimulation [spontaneous otoacoustic emissions or SOAEs, reviewed in Bright (1997)], and all normal hearing ears generate sounds in response to external stimuli [evoked otoacoustic emissions or EOAEs; see, e.g., Norton and Stover (1994)]. These OAEs are believed to be generated by the same processes responsible for the remarkable sensitivity of

the human ear and even small amounts of hearing loss will correlate with the significant reduction of the levels of SOAEs and EOAEs. Different types of acoustic stimuli are used to generate EOAEs and the resulting OAEs differ somewhat in their characteristics. Transient otoacoustic emissions (TEOAEs) are generated by clicks, tone bursts, or chirps and appear as transient echolike responses to these stimuli. The temporal and frequency characteristics of the TEOAEs are unique to each ear [reviewed in Glatcke and Robinette (1997)]. EOAEs can also be generated in response to longer duration single tones. These are somewhat harder to study because the resulting synchronous evoked otoacoustic emissions (SEOAEs) or stimulus frequency otoacoustic emissions (SFOAEs) occur at the same time and at the same frequency as the evoking stimulus (e.g., Kemp and Chum, 1980; Brass and Kemp, 1993; Stover and Norton, 1993). OAEs are also generated in response to multitone stimuli such as intermodulation distortion products (DPOAEs). The most commonly investigated response of this type is the generation of distortion at the  $2f_1 - f_2$  frequency, which is produced when two tones of frequencies  $f_1$  and  $f_2$  (where  $f_2 > f_1$ ) are introduced to the ear (reviewed in Lonsbury-Martin *et al.*, 1997). DPOAEs are stable acoustic stimuli at predictable frequencies that are clearly separable from the acoustic stimuli used to generate them.

All types of OAEs in humans are characterized by strikingly similar fine structures in the frequency domain. In the case of click-evoked emissions (CEOAEs) (reviewed in

Zwicker and Peisl, 1990), synchronous evoked emissions (SEOAEs) (e.g., Zweig and Shera, 1995), and distortion product emissions (DPOAEs) (e.g., He and Schmiedt, 1993; Talmadge *et al.*, 1996), there are consistent patterns of amplitude maxima and minima in the frequency dependence of the OAEs. The frequency spacing of the adjacent maxima or minima of the different types of EOAEs is very similar to the frequency spacing of neighboring spontaneous otoacoustic emissions (SOAEs) (e.g., Zwicker and Peisl, 1990; Talmadge *et al.*, 1993). The variations of OAEs with frequency are collectively referred to as *otoacoustic emission fine structure* (e.g., He and Schmiedt, 1993; Talmadge *et al.*, 1996). An alternative designation is *otoacoustic emission microstructure*. Similarly *threshold microstructure* may be called *threshold fine structure*. The characteristic frequency spacings of the threshold microstructure (Kemp, 1979b) are very similar to those of otoacoustic emission fine structure.

When DPOAEs are measured under conditions in which one of the primaries is fixed in frequency and the other varied, the fine-structure paralleling the other OAE and threshold fine structures exhibits a “bandpass” characteristic such that the DPOAE amplitude reaches a maximum when the ratio of the primary frequencies ( $f_2/f_1$ ) is approximately 1.225 (reviewed in Brown *et al.*, 1992; van Hengel and Duifhuis, unpublished). This approximate “bandpass” structure has commonly been proposed as evidence for a second mechanical filter (e.g., Brown *et al.*, 1992; Allen and Fahey, 1993). However, a number of studies (Matthews and Molnar, 1986; Neely and Stover, 1997; van Hengel and Duifhuis, unpublished; see also Sec. V E of this paper) have demonstrated that this bandpass shape can arise naturally in models that do not contain a second filter.

Kemp's (1979a) discovery of the connection between threshold microstructure and OAEs stimulated increased interest in threshold microstructure (Schloth, 1983; Long, 1984; Zwicker and Schloth, 1984; Long and Tubis, 1988a, b; Furst *et al.*, 1992). Threshold minima occur at frequencies near those of SOAEs or large EOAEs. Changes in the frequencies of the emissions are associated with changes in the frequencies of the threshold minima (Long and Tubis, 1988a; Furst *et al.*, 1992; He, 1990). The frequency dependences of some suprathreshold psychoacoustic phenomena have also been investigated and found to vary with the threshold microstructure. These phenomena include the perceived loudness of low-sensation-level tones (Kemp, 1979b), temporal integration (Cohen, 1982), masked thresholds (Long, 1984), amplitude-modulation detection of low level signals (Zwicker, 1986; Long *et al.*, 1993a), and binaural diplacusis (Van den Brink, 1970, 1980). At higher signal levels, the phase of the psychoacoustic microstructure may change (Long, 1984). The patterns of cochlear fine structures have been found to move down in frequency with little change in frequency spacing when the overall stimulus level increases. This feature has been specifically investigated for TEOAEs (e.g., Wilson *et al.*, 1986), SEOAEs (e.g., Kemp and Chum, 1980; Wilson *et al.*, 1986; Norton and Stover, 1994), and for DPOAEs (He and Schmiedt, 1993; Heitmann *et al.*, 1996; Mauermann *et al.*, 1997).

The frequency separations of threshold microstructure

and cochlear emission fine structure appear to be about 2/5 the average critical band (frequency resolution) estimates for human subjects, which correspond to a 0.4-mm tonotopic displacement along the basilar membrane with respect to Greenwood's estimate (Greenwood, 1990) of the cochlear map (reviewed in Zwicker and Peisl, 1990; He and Schmiedt, 1993, 1996; Sun *et al.*, 1994a, b; Talmadge *et al.*, 1996). Fine structures in nonprimate ears do not seem to be as pronounced as they are in humans (Long *et al.*, 1993b). The similarities of the spacings of the fine structures of SEOAEs and DPOAEs, of the spectral peaks of SOAEs and CEOAEs, and of the threshold microstructure maxima, suggest a common cochlear origin for these features.

The pseudoperiodicity of OAEs and hearing thresholds has been interpreted as evidence for quasiperiodic spatial variations of cochlear partition properties (reviewed in Zweig and Shera, 1995). However, the same pattern can be generated in a cochlear model by introducing spatially random inhomogeneities (roughness) in the mechanics of the cochlear partition (Shera and Zweig, 1993b; Talmadge and Tubis, 1993; Zweig and Shera, 1995). Small closely spaced irregularities may cause reflections of the apically traveling wave. If these reflections are generated in a cochlea whose traveling wave activity pattern has a large enough tip-to-tail ratio and a peak broad enough to contain at least two wavelengths of the traveling wave, then the coherent reflection of cochlear waves around the activity maximum may be large enough to be detected in the ear canal as otoacoustic emissions. Since the tip-to-tail ratio of the traveling wave decreases with stimulus level, the relative magnitude of the reflected cochlear wave component at the stapes, and thus in the ear canal, will decrease with increasing stimulus level.

One of the key assumptions of the model of Zweig and Shera is that the spatial activity pattern of the traveling wave is both “tall and broad.” The traveling wave has to be tall enough in this model to produce significant reflection from a very small level of cochlear inhomogeneities, and the activity pattern peak region has to be broad enough to contain 1 to 2 wavelengths of the traveling wave, a requirement for coherency of the cochlear reflections.

The assumption of a tall–broad activity pattern was suggested by basilar membrane data such as that obtained from squirrel monkeys by Rhode (e.g., 1971). These data are supported by measurements on other species such as cats, guinea pigs, and chinchillas (reviewed in Patuzzi *et al.*, 1996). Basilar membrane response data are usually obtained as a function of frequency at a fixed cochlear location. However, if it is assumed that the response function is approximately scale invariant [i.e., it is only a function of the frequency divided by the place frequency, see for example Zweig (1991)], then this data can be reinterpreted in terms of the spatial cochlear activity pattern at a fixed frequency.

Tall–broad activity patterns are obtained in Zweig's cochlear model (Zweig, 1991) by the introduction of time-delayed stiffness. The increased complexity of Zweig's model is a result of the observation by Kim *et al.* (1980) that simply adding distributed negative resistance on the basilar membrane as an energy source generates activity patterns that are tall but unphysiologically narrow. Kim *et al.* were

able to demonstrate it was sufficient to assume that the amplifier resided in a region basal to the activity pattern peak in order to obtain tall–broad activity patterns. It has since been argued by de Boer (reviewed in de Boer, 1995) using increasingly general and more sophisticated models that placing the cochlear amplifier basal to the activity pattern peak is a necessary condition for obtaining tall–broad activity patterns.

Distortion product (DP) otoacoustic emissions are generated in the region of maximum overlap between the primaries (reviewed in Kummer *et al.*, 1995). One component of the DP-generated wave travels towards the cochlear base and the middle ear, and in the case of the DP tonotopic site being apical to the generation region, the other component travels apically to the DP site, and is amplified on route. Some of this wave is reflected and travels back along the basilar membrane and through the middle ear. The DPOAE detected in the ear canal is associated with the sum of these two components (Kummer *et al.*, 1995; Brown *et al.*, 1996; Talmadge *et al.*, 1997; Heitmann *et al.*, 1998). The relative amplitudes of these components depend on the levels of the primaries and the size of the reflection from the DP site. The relative phase of the two components is mainly determined by the phase of the apical reflectance function. This phase is related to the round-trip group delay for waves traveling from the generation region to the DP place, and will thus depend on the frequency separation between the two primaries (Talmadge *et al.*, 1997; Mauermann, 1997), especially for narrower frequency ratios of the two primaries.

In this paper, a unified nonlinear time-domain cochlear model approach to the spacings between neighboring SOAEs and the fine structure of the auditory threshold and of evoked emissions is presented. Preliminary reports on the model have been given by Talmadge and Tubis (Talmadge and Tubis, 1993; Talmadge *et al.*, 1997). The essential features of the model are tall–broad activity patterns given by the linear-active component of the cochlear mechanics, and a random inhomogeneity in cochlear properties (Zweig and Shera, 1995). Spontaneous emissions may arise and are associated with instability modes of the linear-active component of the cochlear mechanics. The cochlear nonlinearity provides the requisite stabilization for converting the instabilities into limit-cycle oscillations corresponding to actual SOAEs. Any cochlear model whose linear-active component gives similar features for the primary traveling wave patterns (reviewed by de Boer, 1995) will give similar results for the fine structure of emissions when nonlinearity and random inhomogeneities are incorporated into the models, as long as these models have sufficiently “tall and broad” activity patterns, and have a physiologically reasonable wavelength for the traveling wave in the region of the activity pattern peak. The model leads to specific predictions for the relative frequency spacings of the micro/fine structures determined psychophysically and from the different OAE paradigms. In particular, it predicts that psychoacoustic and SOAE/SEOAE/TEOAE fine structure spacings should be similar, but that the DPOAE spacings should be wider.

It should be noted that Kemp (1980) was the first to suggest that if there were internal reflections in the cochlea

both at some positions on the basilar membrane as well as at the stapes, the cochlea would then exhibit a resonance phenomenon when driven by external acoustical stimulation. He used this observation to construct a model of SEOAEs and discussed in particular the roles of ear canal acoustics, the forward and reverse transfer functions of the middle ear, apical and basal cochlear wave reflections, and some of the conditions for the existence of SOAEs. Kemp did not use a detailed cochlear model or a specific apical reflection mechanism. As was just mentioned, such a mechanism is proposed in this paper in the context of a specific class of cochlear models, and the analysis of fine structure is generalized to all types of otoacoustic emissions and to the microstructure of the hearing threshold in order to obtain testable implications concerning the relationships among all of the fine structures.

For the purpose of clarity of presentation, the interpretative model used in this paper is based on a one-dimensional macromechanical model using time-delayed stiffness of the form suggested by Zweig (1991), and simplified models of the middle and outer ears. However, the essential features of this approach are expected to carry over to more elaborate and realistic models. In Sec. I, the formal details of the interpretative model are summarized, and a short discussion is given of the basis function formalism and its application to studying cochlear models with internal reflection. A more comprehensive presentation of these topics will be deferred to future publications.

This formalism is applied in Sec. II to the study of SEOAEs and their spacings. The relationship between SEOAEs and TEOAEs is also discussed in this section. The auditory threshold and its associated threshold microstructure and microstructure spacings are studied in Sec. III. In Sec. IV the relationship between the resonant TEOAE amplitude and SOAE frequency spacings is determined. The theory of DPOAEs of two external primaries is examined in Sec. V in the limit of weak nonlinearity, for the two classes of cubic DPOAEs (apical DPOAEs, whose frequency is less than those of the primaries, and basal DPOAEs, whose frequency is greater than those of the primaries). The effect of an extended generator region is included in this theory, and it is shown, in confirmation of an earlier study of van Hengel and Duifhuis (van Hengel and Duifhuis, unpublished), that the so-called “bandpass filter shape” of DPOAEs can be explained in terms of an interference phenomenon. A detailed treatment of the predictions of this formalism for the various DPOAE experimental paradigms is, however, deferred to a future publication. Finally the issues of the generality of this formalism, the inter-relationships of the various cochlear fine structures, the treatment of larger scale nonlinearity, possible experimental tests suggested by this formalism, and the clinical significance of an improved understanding of cochlear fine structure are addressed in the Discussion (Sec. VI). A List of Symbols used in this study is included as an appendix.

## I. COCHLEAR MODEL

### A. Time-domain model

In the analysis which follows, only one-dimensional cochlear models with constant cross-sectional areas and basilar



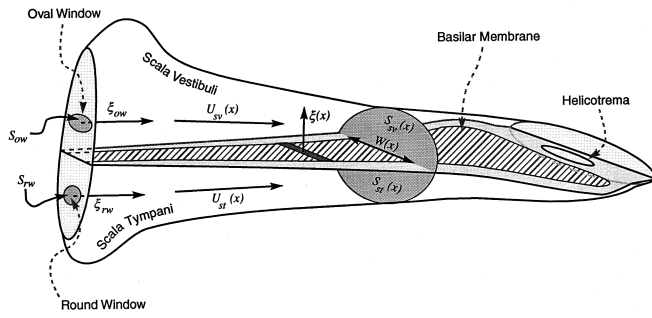


FIG. 1. Schematic diagram of cochlear model and notation used. The model displayed here includes variable scalae cross sections and basilar membrane widths. However, as is discussed in the text, these variables are normally replaced by their mean values since allowing them to vary in our one-dimensional model does not significantly affect our results.

membrane width will be considered (see Fig. 1). For such models, the equations of motion are given by (see Table I for specific parameter choices)

$$\frac{\partial^2 P_d(x,t)}{\partial x^2} = k_0^2 \sigma_{\text{bm}} \ddot{\xi}(x,t), \quad (1)$$

$$\begin{aligned} \ddot{\xi}(x,t) + \gamma_{\text{bm}}(x, \xi, \dot{\xi}) \dot{\xi}(x,t) + \omega_{\text{bm}}^2(x, \xi, \dot{\xi}) \xi(x,t) \\ = \frac{P_d(x,t)}{\sigma_{\text{bm}}}, \end{aligned} \quad (2)$$

$$\gamma_{\text{bm}}(x, \xi, \dot{\xi}) = \gamma_0(x) + \gamma_2(x) \xi^2(x,t), \quad (3)$$

$$\begin{aligned} \omega_{\text{bm}}^2(x, \xi, \dot{\xi}) \xi(x,t) = \omega_0^2(x) \xi(x,t) + \kappa_f(x) \xi(x,t - \tau_f(x)) \\ + \kappa_s(x) \xi(x,t - \tau_s(x)), \end{aligned} \quad (4)$$

$$\omega_0(x) \equiv \omega_0 e^{-k_\omega x} + \omega_1, \quad (5)$$

$$k_0 = \sqrt{\frac{2\rho W_{\text{bm}}}{\sigma_{\text{bm}} S_{\text{avg}}}}, \quad (6)$$

where  $P_d(x,t)$  is the differential pressure between the scala tympani and scala vestibuli,  $\xi(x,t)$  is the upward displacement of the basilar membrane (considered positive if it is towards the scala vestibuli), and  $x$  is the distance along the basilar membrane from the basal end. Other parameters of this model are defined in Table I, and a description of the notation used in this study may be found in the Appendix.

TABLE I. Table of cochlear and middle ear parameters. In most cases, numerical values listed represent typical values chosen for our numerical studies. For many parameters, a range of values was used in the calculations. See also the List of Symbols for a full list of parameter definitions. The parameters for the frequency map come from Greenwood (1990), the values for  $\rho_s$  and  $\psi_s$  are from Zweig (1991), and we use the value for the bulk modulus for air quoted in Rosowski (1995).

Parameter	Value/Definition	Description
$a_d$	$(S_{\text{avg}} P_0 / 2\rho V_e) G_{\text{me}} \approx 1.7 \times 10^5 \text{ cm s}^{-2}$	parameter coupling $P_e$ to $(1/\omega^2) \partial P_d / \partial x$
$\Gamma_{mi}$	1.4	lever ratio of incus
$\gamma_0(x)$	$\gamma_0 e^{-k_\gamma x} + \gamma_1$	passive linear damping
$\gamma_0$	$5035 \text{ s}^{-1}$	damping exponential coefficient
$\gamma_1$	$100 \text{ s}^{-1}$	damping additive constant
$\gamma_2(x)$	$\gamma_0(x) / b_{\text{nl}}^2$	nonlinear damping
$b_{\text{nl}}$	$1.4 \times 10^{-7} \text{ cm}$	Scale for nonlinear saturation
$\gamma_{\text{ow}}$	$500 \text{ s}^{-1}$	middle ear damping constant
$G_{\text{me}}$	$S_{\text{ty}} / S_{\text{ow}} \Gamma_{mi} = 21.4$	mechanical gain of ossicles
$\kappa_f(x)$	$\rho_f \omega_0^2(x), \rho_f = 0.16$	‘fast feedback’ stiffness
$\kappa_s(x)$	$\rho_s \omega_0^2(x), \rho_s = 0.1416$	‘slow feedback’ stiffness
$\hat{k}$	$k(\hat{x}, \omega) \approx 75 \text{ cm}^{-1}$	wave number at activity pattern maximum
$k_\omega$	$1.382 \text{ cm}^{-1}$	frequency map exponential constant
$k_0$	$\sqrt{2\rho W_{\text{bm}} / \rho_{\text{bm}} S_{\text{avg}}} \approx 31 \text{ cm}^{-1}$	geometrical wave number of cochlea
$k_{\text{ow},0}$	$2\rho S_{\text{ow}} / \sigma_{\text{bm}} S_{\text{avg}} \approx 1100 \text{ cm}^{-1}$	coupling of oval window to perilymph
$L_{\text{bm}}$	3.5 cm	length of basilar membrane
$m_{\text{ow}}$	0.059 g	effective mass of oval window+ossicles
$\sigma_{\text{bm}}$	0.0055 g cm <sup>-2</sup>	areal density of basilar membrane
$\sigma_{\text{ow}}$	$m_{\text{ow}} / S_{\text{ow}} \approx 1.85 \text{ g cm}^{-2}$	areal density of oval window
$P^a$	$\rho_a c_a^2 = 1.42 \times 10^6 \text{ dyn cm}^{-2}$	adiabatic bulk modulus of air
$\rho$	1.0 g cm <sup>-3</sup>	density of perilymph
$S_{\text{avg}}$	0.011 cm <sup>2</sup>	reciprocal average cross-sectional area of cochlear scalae
$S_{\text{ow}}$	0.032 cm <sup>2</sup>	area of oval window
$S_{\text{ty}}$	0.49 cm <sup>2</sup>	effective area of tympanic membrane
$\tau_f(x)$	$\psi_f / \omega_0(x), \psi_f = 0.24 \cdot 2\pi$	delay of ‘fast feedback’
$\tau_s(x)$	$\psi_s / \omega_0(x), \psi_s = 1.742 \cdot 2\pi$	delay of ‘slow feedback’
$V_{\text{tc}}$	2.0 cm <sup>3</sup>	volume of tympanic cavity
$\omega_0(x)$	$\omega_0 e^{-k_\omega x} + \omega_1$	place-frequency map
$\omega_0$	20 800 Hz $\times 2\pi$	frequency map exponential coefficient
$\omega_1$	-145.5 Hz $\times 2\pi$	frequency map additive constant
$\omega_{\text{ow}}$	1500 Hz $\times 2\pi$	middle ear frequency
$W_{\text{bm}}$	0.029 cm	average width of basilar membrane

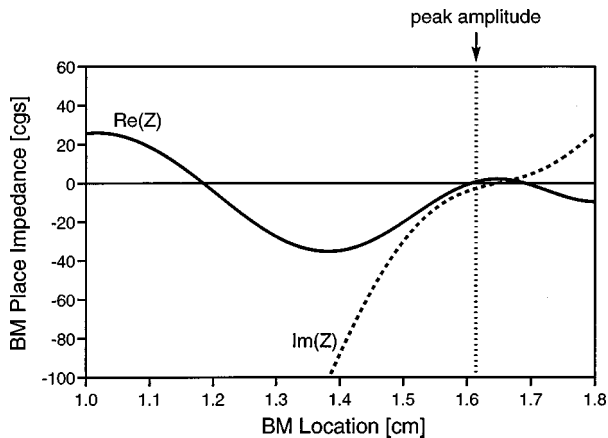


FIG. 2. Real (black) and imaginary (dashed) components of the place impedance of the traveling wave for the model described in Table I.

As shown in Table I, the cochlear model incorporates a frequency map of the form suggested by Greenwood (1990), in which the usual assumption of an exponentially varying frequency map is violated by the inclusion of an additive constant  $\omega_1$ . In addition, the  $Q$  of the basilar membrane response to an external tone is allowed to vary from  $\sim 15$  near the base, to  $\sim 5$  near the apex in keeping with estimates of cochlear tuning in humans (Moore, 1978). The inclusion of these assumptions into the cochlear model will manifestly violate the usual assumption of scale invariance (i.e., tuning is constant along the cochlea; see, e.g., Zweig, 1991). The inclusion of a tuned middle ear that interfaces between the external auditory canal and the cochlea will also lead to a lack of scale invariance in the response of the cochlea to external stimuli.

The cochlear nonlinearity is modeled as a quadratic, or ‘‘Van der Pol’’-type, nonlinear damping function (i.e., the nonlinearity is the  $\gamma_2(x)\xi(x,t)^2$  contribution from the full Van der Pol damping). Also, the slow- and fast-feedback time-delayed stiffness contributions are of the form suggested by Zweig (1991). Here the fast-feedback time-delayed stiffness effectively behaves as a source of negative-damping for stationary signals, whereas the slow-feedback time-delayed stiffness helps create ‘‘tall and broad’’ activity patterns on the basilar membrane. A sufficient condition for obtaining tall and broad activity patterns, as first pointed out by Kim *et al.* (1980) (see also de Boer, 1983), is that the real part of the local impedance  $Z_{bm} = P_d(x,t)/i\omega\xi(x,t)$  must be *negative* in a region slightly apical to traveling wave peak. As shown in Fig. 2, the impedance function implied by Eqs. (1) and (2) satisfies this requirement [compare with Fig. 3 in de Boer (1983)].

In Eq. (6), the parameter  $k_0$  depends not only on  $W_{bm}$  and  $S_{avg}$ , for which significant anatomical data exists, but also on  $\sigma_{bm}$ , which is a phenomenological parameter. In our calculations, the value  $\sigma_{bm} \cong 0.0053 \text{ g cm}^{-2}$  was chosen to give a total number of wavelengths,  $N_\lambda \cong k_0/4k_\omega$ , from the cochlear base to the activity maximum in the range  $N_\lambda = 3-5$ .

Equations (1) and (2) are assumed to be supplemented by the boundary conditions,

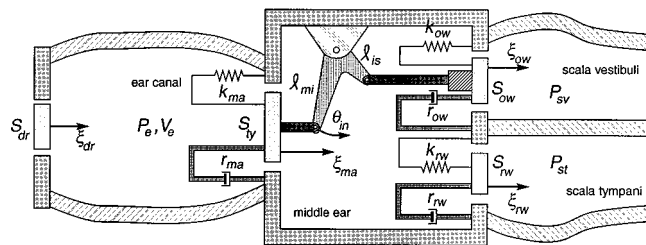


FIG. 3. Simple middle ear model and notation used. Note that this model is based on a single-piston representation of the tympanic membrane, and a noncompliant incudostapedial joint.

$$\frac{1}{\sigma_{bm}} \frac{\partial P_d(0,t)}{\partial x} = k_{ow,0} \ddot{\xi}_{ow}(t), \quad (7)$$

$$P_d(L_{bm}, t) = 0, \quad (8)$$

$$k_{ow,0} = \frac{2\rho S_{ow}}{\sigma_{bm} S_{avg}}, \quad (9)$$

where Eq. (8) is the so-called short-circuit condition, and Eq. (7) arises from the usual hydrodynamic considerations near the stapes.

The mechanics of the middle ear and outer ear are based on a simple mechanical model which treats the tympanic membrane as a single piston and has a fixed incudo-stapedial joint (see Fig. 3). The ear canal is assumed to be capped by a driver/microphone assembly, and it is further assumed that the length of the canal between this assembly and the tympanic membrane is small relative to the sound wavelength. Thus the pressure  $P_e(t)$  in the ear canal may be considered to be uniform. It is also assumed that all air pressure changes occur adiabatically (occurring without loss or gain of heat), so that the model of Fig. 3 gives rise to a single oscillator equation of the form,

$$\begin{aligned} \ddot{\xi}_{ow}(t) + \gamma_{ow} \dot{\xi}_{ow}(t) + \omega_{ow,e}^2 \xi_{ow}(t) \\ = \frac{1}{\sigma_{ow}} [P_d(0,t) + G_{me} P_e(t)], \end{aligned} \quad (10)$$

where

$$G_{me} \equiv \frac{S_{ty}}{S_{ow}} \Gamma_{mi}, \quad (11)$$

and where the parameters  $\sigma_{ow}$ ,  $\gamma_{ow}$ , and  $\Gamma_{mi}$  are phenomenological constants defined in the Appendix and in Table I. As discussed in the Appendix,  $\omega_{ow,e}^2$  is understood to be the ratio of the effective mechanical stiffness of the middle ear to its effective mass. Because Eq. (10) originates from a more detailed middle ear model,  $\sigma_{ow}$  is highly constrained. The middle ear frequency  $\omega_{ow,e}$  can be related to the mechanical frequency of the ossicles  $\omega_{ow,mech}$  via the relationship,

$$\omega_{ow,e}^2 = \omega_{ow,mech}^2 + \frac{P_{tc}^a S_{ty}^2 \Gamma_{mi}^2}{m_{ow} V_{tc}}, \quad (12)$$

where the term,  $P_{tc}^a S_{ty}^2 \Gamma_{mi}^2 / m_{ow} V_{tc} \approx (2\pi \times 945 \text{ Hz})^2$ , gives the contribution to the square of the middle ear frequency from the tympanic cavity. Also  $P_{tc}^a = \gamma_{air} P_0^{tc}$ , where  $\gamma_{air}$

$\cong 1.4$  is the ratio of specific heats of air, and  $P_0^{\text{tc}}$  is the ambient pressure in the tympanic cavity.

Equation (10) relates the displacement of the oval window  $\xi_{\text{ow}}(t)$  to a fixed pressure  $P_e(t)$  in the ear canal. For most experimental setups, however, the pressure  $P_e(t)$  is an observable rather than a fixed experimental input. Instead, the experimental input is the ‘‘calibrated ear canal pressure,’’  $P_{\text{dr}}(t)$ , which is the pressure in the ear canal in the case of a rigid ear drum. With the assumption of adiabatic compression/expansion, the relation between  $P_{\text{dr}}(t)$  and  $P_e(t)$  is

$$P_{\text{dr}}(t) = P_e(t) + \frac{P_e^a S_{\text{ty}} \Gamma_{\text{mi}}}{V_e} \xi_{\text{ow}}(t), \quad (13)$$

where  $P_e^a = \gamma_{\text{air}} P_e^0$ , and  $P_e^0$  is the ambient pressure of the air in the ear canal. Combining Eqs. (10), (12), and (13) gives

$$\begin{aligned} & \ddot{\xi}_{\text{ow}}(t) + \gamma_{\text{ow}} \dot{\xi}_{\text{ow}}(t) + \omega_{\text{ow}}^2 \xi_{\text{ow}}(t) \\ &= \frac{1}{\sigma_{\text{ow}}} [P_d(0, t) + G_{\text{me}} P_{\text{dr}}(t)], \end{aligned} \quad (14)$$

where

$$\omega_{\text{ow}}^2 \equiv \omega_{\text{ow,dr}}^2 = \omega_{\text{ow,mech}}^2 + \frac{S_{\text{ty}}^2 \Gamma_{\text{mi}}^2}{m_{\text{ow}}} \left[ \frac{P_{\text{tc}}^a}{V_{\text{tc}}} + \frac{P_e^a}{V_e} \right]. \quad (15)$$

The term  $P_e^a S_{\text{ty}}^2 \Gamma_{\text{mi}}^2 / m_{\text{ow}} V_e \approx (2\pi \times 1340 \text{ Hz})^2$  represents the ear canal volume contribution to  $\omega_{\text{ow}}^2$ . When matching Eq. (15) to experimentally measured quantities, it is important to note that

$$\omega_{\text{ow}}^2[\text{resonance}] = \omega_{\text{ow}}^2 - \gamma_{\text{ow}}^2/2, \quad (16)$$

where  $\omega_{\text{ow}}[\text{resonance}]$  is the resonant frequency of the middle ear coupled to the ear canal.

Equations (1)–(9) together with Eq. (14) represent the complete system of equations for the full cochlear model used in this analysis. An important extension of this model, as suggested by Shera and Zweig (1993a) and Zweig and Shera (1995), is the inclusion of small random inhomogeneities (‘‘roughness’’) along the basilar membrane in the parameters of the cochlear model. In these models, it is sufficient for the present study to apply roughness only to the place-frequency map  $\omega_0(x)$ . The presence of a sufficiently tall and broad traveling wave will give rise to a coherent basal reflection from the peak region of the traveling wave, which leads to the generation of various OAE and hearing threshold fine structures.

Stiffness-feedback models, such as those of Zweig (1991); Shera and Zweig (1993a); Zweig and Shera (1995), have been criticized (van Hengel, 1993) because formally these models lead to a negative real part of the input impedance for frequencies outside of the valid range of the basilar membrane place frequency map, and lead to SOAEs with frequencies corresponding to basilar membrane place frequencies of the cochlear base and the apex. As was pointed out in a response to this comment (Talmadge and Tubis, 1993), the feedback parameters near these end points in the

cochlea can be chosen so that the behavior in these regions is passive and would not give rise to (possibly unphysical) SOAEs.

The cochlear equations are solved in the time domain using a combination of the method of finite differences to solve for  $P_d(x, t)$  at a given time, and the standard fourth-order Runge–Kutta method to integrate each basilar membrane dynamical equation forward in time. The ease of obtaining a numerical solution to these equations is mainly due to the facts that there are no terms in the equations involving spatial derivatives of  $\xi(x, t)$  and no explicit time derivatives of  $P_d(x, t)$ . Nevertheless, as a consequence of the ‘‘tall and broad’’ activity pattern, the system of equations is highly sensitive to relatively small spatial discretizations. In practice, it is necessary to use at least 1024 spatial elements in the finite difference solutions. For the simulations used in this paper, at least 4096 elements were used.

Although an objection to a discretization finer than 4096 elements might be raised on the basis that there are less than 4000 rows of hair cells on the basilar membrane, it should be understood that the purpose of a fine spatial discretization is to accurately integrate Eq. (1). Reducing the number of elements in the finite element approximation of this equation is equivalent to adding a significant number of higher-order derivatives to  $\partial^2 P_d(x, t) / \partial x^2$  (see, e.g., Press *et al.*, 1992). The modification to the underlying dynamics which is introduced by too crude an approximation of Eq. (1) has a far different effect than that produced by setting a ‘‘grain size’’ to the basilar membrane parameters. The latter is associated with adding small inhomogeneities in the basilar membrane along the entire cochlea.

## B. Frequency-domain formulation

A frequency domain version of the ‘‘full’’ cochlear model described above can be easily obtained in the linearized approximation of Eq. (2). In order to do so, all time varying parameters  $A(x, t)$  are written as

$$A(x, t) = A(x, \omega) e^{i\omega t} + \text{complex conjugate}. \quad (17)$$

The frequency-domain model can then be expressed as

$$P_d''(x, \omega) + k^2(x, \omega) P_d(x, \omega) = 0, \quad (18)$$

$$\xi(x, \omega) = \frac{1}{\sigma_{\text{bm}} \Delta(x, \omega)} P_d(x, \omega), \quad (19)$$

$$k(x, \omega) = \frac{k_0 \omega}{\sqrt{\Delta(x, \omega)}}, \quad (20)$$

$$\begin{aligned} \Delta(x, \omega) = & \omega_0^2(x) - \omega^2 + i\omega \gamma_0(x) + \rho_f \omega_0(x) e^{-i\psi_f \omega / \omega_0(x)} \\ & + \rho_s \omega_0(x) e^{-i\psi_s \omega / \omega_0(x)}, \end{aligned} \quad (21)$$

where  $\rho_f = \kappa_f(x) / \omega_0(x)^2$ ,  $\rho_s = \kappa_s(x) / \omega_0(x)^2$ ,  $\psi_f = \tau_f(x) \times \omega_0(x)$ , and  $\psi_s = \tau_s(x) \omega_0(x)$ . The boundary conditions for these equations are

$$P_d'(0, \omega) + k_{\text{ow}}(\omega) P_d(0, \omega) = -G_{\text{me}}(\omega) k_{\text{ow}}(\omega) P_{\text{dr}}(\omega), \quad (22)$$

$$\xi_{ow}(\omega) = \frac{1}{\sigma_{ow}\Delta_{ow}(\omega)} [P_d(0,\omega) + G_{me}(\omega)P_{dr}(\omega)], \quad (23)$$

$$k_{ow}(\omega) = \frac{\sigma_{bm}k_{ow,0}\omega^2}{\sigma_{ow}\Delta_{ow}(\omega)}, \quad (24)$$

$$\Delta_{ow}(\omega) = \omega_{ow}^2 - \omega^2 + i\omega\gamma_{ow}, \quad (25)$$

$$P_d(L_{bm}, \omega) = 0. \quad (26)$$

Here  $G_{me}(\omega) = G_{me} = \text{constant}$  in the simple middle ear model used in this study. It can be shown, however, that under the assumptions of incompressible perilymph and constant pressure within the tympanic cavity, that the forms given by Eqs. (22) and (23) still hold. However, the forms of  $k_{ow}(\omega)$  and  $G_{me}(\omega)$  become much more complex. In order to be applicable to this more general class of middle ear models, the mechanical gain of the middle ear  $G_{me}$  will be written as a function of  $\omega$  throughout the rest of this paper. The pressure in the ear canal is given by

$$P_e(\omega) = P_{dr}(\omega) - \frac{P_e^a S_{ty} \Gamma_{mi}}{V_e} \xi_{ow}(\omega), \quad (27)$$

which follows from Eq. (13). It should be noted that  $\xi_{ow}(\omega)$  can be related to  $P'_d(0,\omega)$  by using Eqs. (7) and (9) to obtain

$$P'_d(0,\omega) = -\frac{2\rho S_{ow}}{S_{avg}} \omega^2 \xi_{ow}(\omega). \quad (28)$$

Combining this equation with Eq. (27) gives

$$P_e(\omega) = T_{dr}(\omega)P_{dr}(\omega) + T_{pd}(\omega)P'_d(0,\omega), \quad (29)$$

$$T_{dr}(\omega) = 1, \quad T_{pd}(\omega) = \frac{a_d}{\omega^2}, \quad (30)$$

$$a_d = \frac{S_{avg} P_e^a}{2\rho V_e} G_{me}. \quad (31)$$

Equations (27) and (29) relate  $P_e(\omega)$  to only the calibrated ear canal pressure  $P_{dr}(\omega)$ , and the derivative of the pressure difference  $P_d(0,\omega)$  or equivalently the volume velocity at the base of the cochlea. For the more complex classes of middle ear models mentioned above, the form of Eq. (29) is retained; however, the definitions of  $T_{dr}(\omega)$  and  $T_{pd}(\omega)$  would again become more complex. The relationship given by Eq. (29) indicates that the middle ear acts as an ear canal pressure-to-volume velocity transformer.

## C. Basis function formalism

### 1. Determining the basis functions

Equation (18) is known as the cochlear pressure-wave equation and characterizes the propagation of traveling waves throughout the cochlea. Since this equation is of second order, it has two linearly independent solutions, which will be referred to as  $\psi_1(x,\omega)$  and  $\psi_2(x,\omega)$ . The general solution  $P_d(x,\omega)$  of Eq. (18) can be expressed as a linear combination of these two solutions; that is,

$$P_d(x,\omega) = a_1(\omega)\psi_1(x,\omega) + a_2(\omega)\psi_2(x,\omega), \quad (32)$$

where  $a_1(\omega)$  and  $a_2(\omega)$  are constant with respect to  $x$ . Since any solution of Eq. (18) can be composed of a combination of  $\psi_1(x,\omega)$  and  $\psi_2(x,\omega)$ , these solutions are referred to in this analysis as basis functions.

If the cochlear model gives a wave-number function,  $k(x,\omega)$ , which is sufficiently smoothly varying with  $x$  so that it satisfies the validity condition for the Wentzel–Kramers–Brillouin (WKB) approximation (e.g., Zweig *et al.*, 1976; de Boer and Viergever, 1982; de Boer and Viergever, 1984; Mathews and Walker, 1964),

$$\left| \frac{(\partial/\partial x)k(x,\omega)}{k^2(x,\omega)} \right| \ll \frac{1}{2\pi}, \quad (33)$$

and also the condition,

$$\frac{\partial \text{Re}[k(x,\omega)]}{\partial \omega} > 0 \quad (\text{for all } x), \quad (34)$$

where “Re” returns the real part of its argument, it can be shown that the  $\psi_{1,2}(x,\omega)$  solutions may be associated with purely “right” or apically moving and “left” or basally moving waves. These will be labeled, respectively, as  $\psi_r(x,\omega)$  and  $\psi_l(x,\omega)$ . Since these “pure” basis functions have a simple physical interpretation, significant insight into the behavior of a cochlear model may be obtained by expressing general solutions in terms of these specific ones. The function  $\psi_r(x,\omega)$  can be obtained in a “smooth” cochlear model by driving the cochlea at the base. In the absence of internal reflection, this model response will correspond (with appropriate normalization) to a purely right or apically moving solution. Similarly, by driving the cochlear model at the apex and eliminating basal reflections, the model response will correspond to a purely left or basally moving solution.

Cochlear models which do not satisfy the criteria necessary to produce pure apically or basally traveling waves can still be studied using the  $\psi_r(x,\omega)$  and  $\psi_l(x,\omega)$  basis functions by relating these cochlear models to an underlying (smooth) model with a wave-number function that satisfies Eqs. (33) and (34) and thus gives rise to purely right and left moving basis functions. This is done by relating the deviation of a given cochlear model from the underlying smooth model to an additional source term. For instance, if  $k_{sm}(x,\omega)$  is the wave-number function associated with the underlying cochlear model that gives rise to pure  $\psi_{r,l}(x,\omega)$  solutions, then the total wave number may be written as

$$k^2(x,\omega) = k_{sm}^2(x,\omega) + \delta k^2(x,\omega), \quad (35)$$

where  $\delta k^2(x,\omega)$  now characterizes the deviation of a particular cochlear model from the underlying “smooth” model due, e.g., to a quasisinusoidal spatial modulation of the cochlear parameters (as suggested, e.g., by Strube, 1989), to distributed spatial cochlear inhomogeneities (roughness) (e.g., Shera and Zweig, 1993a; Zweig and Shera, 1995), or to the presence of a weak nonlinearity. Equation (18) can then be written as

$$P''_d(x,\omega) + k_{sm}^2(x,\omega)P_d(x,\omega) = -\delta k^2(x,\omega)P_d(x,\omega). \quad (36)$$

In Sec. V B it will be shown that in a perturbative analysis of the effect of cochlear nonlinearity, there will be an additional inhomogeneous term on the right-hand side of Eq. (36) for cochlear wave components with frequencies of various intermodulation distortion products. Any terms on the right-hand side of Eq. (36) will be referred to collectively as “source terms” in the present discussion.

In the absence of source terms,  $\psi_r(x, \omega)$  and  $\psi_l(x, \omega)$  will be the solutions of the homogeneous form of Eq. (36), and have the interpretations of purely right and left moving waves of the underlying model, respectively. Also, by convention, the normalization,

$$\psi_r(0, \omega) = \psi_l(0, \omega) \equiv 1, \quad (37)$$

is chosen. It is easily shown that the Wronskian  $W_0(\omega)$  of the basis functions, given by

$$W_0(\omega) = \psi_l'(x, \omega)\psi_r(x, \omega) - \psi_l(x, \omega)\psi_r'(x, \omega), \quad (38)$$

is independent of  $x$ . From Eqs. (36) and (38), it follows that

$$W_0(\omega) = k_l(0, \omega) - k_r(0, \omega), \quad (39)$$

where the “wave-number” functions  $k_{r,l}(x, \omega)$  are given by

$$k_r(x, \omega) \equiv \frac{\psi_r'(x, \omega)}{\psi_r(x, \omega)}, \quad k_l(x, \omega) \equiv \frac{\psi_l'(x, \omega)}{\psi_l(x, \omega)}. \quad (40)$$

It can also be shown that to a good approximation in most cases,

$$\psi_l'(0, \omega) \equiv (\psi_r'(0, \omega))^*, \quad (41)$$

and hence, from Eqs. (37)–(41), that  $W_0(\omega)$  can be approximately expressed in terms of  $\psi_r(x, \omega)$ :

$$W_0(\omega) \equiv (k_r(0, \omega))^* - k_r(0, \omega) = -2i \operatorname{Im}[k_r(0, \omega)], \quad (42)$$

where “Im” returns the imaginary part of its argument.

The solution  $P_d(x, \omega)$  of Eq. (36) may also be written in terms of right and left going components:

$$P_d(x, \omega) = P_r(x, \omega) + P_l(x, \omega). \quad (43)$$

However,  $P_r(x, \omega)$  and  $P_l(x, \omega)$  are not in general solutions to the homogeneous form of Eq. (36).  $P_{r,l}(x, \omega)$  may be formally related to the basis functions  $\psi_{r,l}(x, \omega)$  by writing

$$P_r(x, \omega) = a_r(x, \omega)\psi_r(x, \omega), \quad (44)$$

$$P_l(x, \omega) = a_l(x, \omega)\psi_l(x, \omega), \quad (45)$$

where the coefficients  $a_{r,l}(x, \omega)$  carry the units of pressure, so that the  $\psi_{r,l}(x, \omega)$  basis functions are dimensionless. Combining Eqs. (43) with Eqs. (44) and (45) gives

$$P_d(x, \omega) = a_r(x, \omega)\psi_r(x, \omega) + a_l(x, \omega)\psi_l(x, \omega). \quad (46)$$

Equation (46) is a direct analog of Eq. (32), except that the coefficients are now allowed to vary with  $x$ .

It should be noted that  $\psi_{r,l}(x, \omega)$  depend only on the cochlear model in the absence of any basilar membrane sources, and therefore are independent of these sources. The traveling wave amplitudes  $a_{r,l}(x, \omega)$  vary only in regions of the basilar membrane which contain source terms, and are

constant otherwise. The basis functions  $\psi_{r,l}(x, \omega)$  describe how the effects of these local sources are propagated throughout the cochlea.

Since  $a_{r,l}(x, \omega)$  are underspecified, the additional derivative condition,

$$P_d'(x) = a_r(x)\psi_r'(x) + a_l(x)\psi_l'(x), \quad (47)$$

can be imposed. This implies the auxiliary constraint (e.g., Shera and Zweig, 1991),

$$a_r'(x, \omega)\psi_r(x, \omega) + a_l'(x, \omega)\psi_l(x, \omega) = 0. \quad (48)$$

The approximate solutions of the pressure difference equation in the presence of sources is discussed in Sec. I D.

## 2. Basilar membrane basis functions

The basilar membrane displacement can be obtained from  $P_d(x, \omega)$  in Eq. (46) by combining Eq. (46) with Eq. (19) to obtain

$$\xi(x, \omega) = a_r(x, \omega) \frac{\psi_r(x, \omega)}{\sigma_{\text{bm}}\Delta(x, \omega)} + a_l(x, \omega) \frac{\psi_l(x, \omega)}{\sigma_{\text{bm}}\Delta(x, \omega)}. \quad (49)$$

In general  $\Delta(x, \omega)$  will contain “source” term contributions, so that the identification of  $\psi_{r,l}(x, \omega)/\Delta(x, \omega)$  with basilar membrane basis functions would be inappropriate. Just as in the case of  $k^2(x, \omega)$  in Eq. (35), the source component  $\delta\Delta(x, \omega)$  of  $\Delta(x, \omega)$  can be separated out from the underlying smooth component  $\Delta_{\text{sm}}(x, \omega)$ :

$$\Delta(x, \omega) = \Delta_{\text{sm}}(x, \omega) + \delta\Delta(x, \omega). \quad (50)$$

This allows the definitions,

$$\xi(x, \omega) = b_r(x, \omega)\chi_r(x, \omega) + b_l(x, \omega)\chi_l(x, \omega), \quad (51)$$

$$\chi_{r,l}(x, \omega) = \frac{\Delta_{\text{sm}}(0, \omega)}{\Delta_{\text{sm}}(x, \omega)} \psi_{r,l}(x, \omega), \quad (52)$$

$$b_{r,l}(x, \omega) = \frac{1}{\sigma_{\text{bm}}\Delta_{\text{sm}}(0, \omega)} \frac{\Delta_{\text{sm}}(x, \omega)}{\Delta(x, \omega)} a_{r,l}(x, \omega). \quad (53)$$

As defined in Eq. (52), the  $\chi_{r,l}(x, \omega)$  functions describe apical and basal traveling waves on the basilar membrane for an underlying smooth cochlea. The basilar membrane amplitudes  $b_{r,l}(x, \omega)$  are constant except in regions where sources are present. Also, the normalizations of  $\chi_{r,l}(x, \omega)$  have been chosen so that

$$\chi_r(0, \omega) = \chi_l(0, \omega) = 1. \quad (54)$$

## 3. WKB approximation

An approximate representation of the cochlear basis functions may be obtained using the Wentzel–Kramers–Brillouin (WKB) approximation (e.g., Mathews and Walker, 1964; Zweig *et al.*, 1976). This approximation, which is valid in the “long-wave” region (i.e., from the base to near the peak activity region), yields

$$\psi_r(x, \omega) = \sqrt{\frac{k(0, \omega)}{k(x, \omega)}} \exp\left\{-i \int_0^x k(x', \omega) dx'\right\}, \quad (55)$$

$$\psi_l(x, \omega) = \sqrt{\frac{k(0, \omega)}{k(x, \omega)}} \exp\left\{ +i \int_0^x k(x', \omega) dx' \right\}. \quad (56)$$

Note that these equations satisfy the normalization conditions of Eq. (37).

In most cases, Eqs. (55) and (56) give a fairly accurate description of the behaviors of  $\psi_r(x, \omega)$  and  $\psi_l(x, \omega)$  and thus provide very useful tools in the prediction of cochlear model behavior. One application of the WKB approximation is in the estimation of the Wronskian,  $W_0(\omega)$ . Substitution of Eqs. (55) and (56) into (38) gives

$$W_0(\omega) \cong 2ik(0, \omega) \approx \frac{2ik_0\omega}{\omega_0}, \quad (57)$$

where the approximation for  $k(0, \omega)$  holds for  $\omega \ll \omega_0$ .

An approximate evaluation of Eqs. (55) and (56) is obtained by using Eq. (20) under the approximation that the resistive component of the impedance may be neglected, and that  $\omega_0(x) = \omega_0 e^{-k_\omega x}$  (i.e., the Greenwood scale-invariance breaking term  $\omega_1$  may be neglected). In this case,

$$k(x, \omega) \approx \frac{k_0\omega}{\sqrt{\omega_0^2 e^{-2k_\omega x} - \omega^2}}, \quad (58)$$

and Eqs. (55) and (56) give

$$\psi_r(x, \omega) = \left[ \frac{\omega_0^2 e^{-2k_\omega x} - \omega^2}{\omega_0^2 - \omega^2} \right]^{1/4} e^{-i\varphi(x, \omega)}, \quad (59)$$

$$\psi_l(x, \omega) = \left[ \frac{\omega_0^2 e^{-2k_\omega x} - \omega^2}{\omega_0^2 - \omega^2} \right]^{1/4} e^{+i\varphi(x, \omega)}, \quad (60)$$

$$\begin{aligned} \varphi(x, \omega) &= \int_0^x k(x', \omega) dx' \\ &\cong \frac{k_0}{k_\omega} \left\{ \arcsin\left[ \frac{\omega}{\omega_0(x)} \right] - \arcsin\left[ \frac{\omega}{\omega_0(0)} \right] \right\}. \end{aligned} \quad (61)$$

An interesting result can be obtained from Eq. (61) by noting that at resonance the total phase from the base to the activity pattern maximum is

$$\hat{\varphi} = \varphi(\hat{x}) \approx \frac{\pi k_0}{2k_\omega}. \quad (62)$$

This implies that the total number of wavelengths of the activity pattern from the cochlear base to the point of maximum basilar membrane displacement is approximately  $N_\lambda = k_0/4k_\omega$ .

#### 4. Numerical solutions

The typical behaviors of  $\psi_{r,l}(x, \omega)$  are shown in Fig. 4. The WKB solutions for these basis functions are given for two different cochlear models, one in which the Zweig feedback contributions are present (and correspond to an active cochlear model), and the other in which these contributions are turned off (a passive cochlear model). The numerical solutions obtained for the full cochlear model are not shown, since they would be indistinguishable from the WKB solutions if they were displayed in the figure.

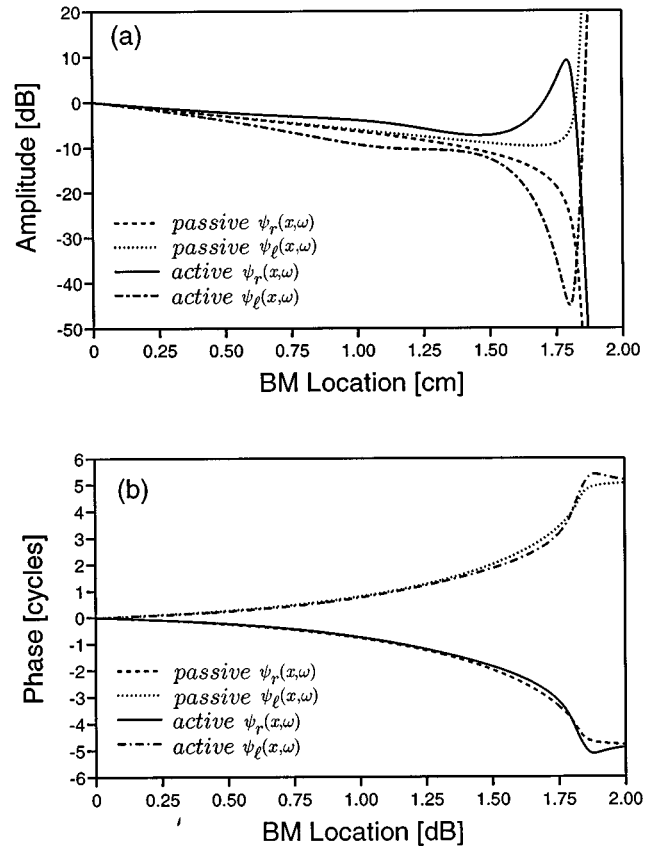


FIG. 4. Amplitude (a) and phase (b) of the basis functions for a passive model and of an active model incorporating stiffness feedback. All of the parameter values of the models are listed in Table I, except for the case of the passive model, in which the stiffness feedback amplitudes  $\rho_f$  and  $\rho_s$  are set to zero. The basis functions shown are for a frequency  $f=1500$  Hz, and are the solutions obtained using the WKB method (see text). The numerical solutions are not shown since they would be almost indistinguishable from the WKB solutions.

For the active model, an enhancement of the pressure traveling wave is observed for a right-moving wave, and a reduction of the wave is observed for a left-moving wave. No such effects are observed for the passive model. Although these results were obtained from a model with Zweig feedback, the relationship between  $\psi_{r,l}(x, \omega)$  and  $k(x, \omega)$  makes it clear that these results generalize to any cochlear model that has a cochlear wave-number function  $k(x, \omega)$  that is consistent with that of Fig. 2. The issue of the asymmetry in the left/right traveling waves for active cochlear models will be addressed in greater detail in a future publication.

The basilar membrane traveling wave basis functions  $\chi_{r,l}(x, \omega)$  are shown in Fig. 5. In this case the apically traveling wave for the active cochlear model shows a significant enhancement of more than 40 dB over that of the passive model, while the basally traveling wave shows a slight reduction of about -10 dB. The fact that  $|\chi_r(x, \omega)| \gg |\chi_l(x, \omega)|$  near  $\hat{x}(\omega)$  will be shown to have important consequences in the study of cochlear fine structure.

#### D. Solutions to the pressure wave equation

The formalism discussed in Sec. I C can be used to obtain solutions to the pressure wave equation in the presence of sources,  $\rho_{\text{source}}(x, \omega)$ :

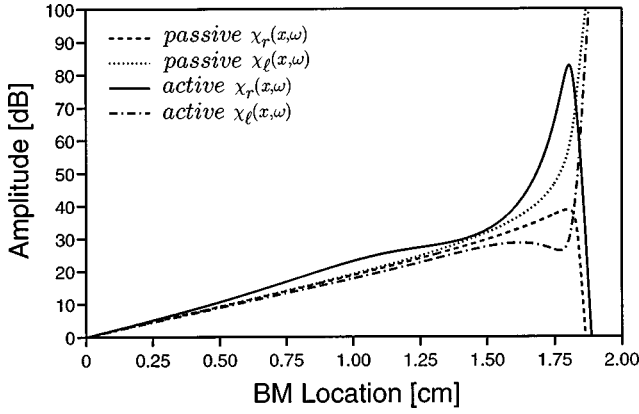


FIG. 5. Basilar membrane basis functions for active model incorporating stiffness feedback for a frequency of  $f=2000$  Hz. All of the parameter values of these models are listed in Table I.

$$P_d''(x, \omega) + k_{sm}^2(x, \omega)P_d(x, \omega) = \rho_{source}(x, \omega). \quad (63)$$

In Eq. (63),  $k_{sm}^2(x, \omega)$  again denotes the square of the wave number for a “smooth” cochlea, and the effects of roughness and nonlinearity are contained in the source term. Using Eqs. (38), (46), (47), and (48), as well as the fact that  $\psi_{r,l}(x, \omega)$  are solutions to the homogeneous pressure wave equation [Eq. (63) with  $\rho_{source}(x, \omega) = 0$ ], an explicit solution for  $P_d(x, \omega)$  can be obtained in terms of basis functions:

$$\begin{aligned} P_d(x, \omega) = & \left[ a_l(0, \omega) + \frac{1}{W_0(\omega)} \right. \\ & \times \left. \int_0^x \rho_{source}(x', \omega) \psi_r(x', \omega) dx' \right] \psi_l(x, \omega) \\ & + \left[ a_r(0, \omega) - \frac{1}{W_0(\omega)} \right. \\ & \times \left. \int_0^x \rho_{source}(x', \omega) \psi_l(x', \omega) dx' \right] \psi_r(x, \omega). \end{aligned} \quad (64)$$

This result is now applied to the calculation of the effects of scattering by inhomogeneities along the basilar membrane. The square of the total wave number is expressed as

$$\tilde{k}^2(x, \omega) = k_{sm}^2(x, \omega) + \delta\tilde{k}^2(x, \omega), \quad (65)$$

where any quantity “A” that contains inhomogeneities is denoted by “ $\tilde{A}$ .” The definition  $\delta\tilde{A} = \tilde{A} - A_{sm}$  signifies the change in the quantity  $A_{sm}$  resulting from the presence of the inhomogeneities. It is assumed that  $\delta\tilde{A} \ll A_{sm}$ .

For the studies that follow, distributed inhomogeneities (roughness) in the basilar membrane place frequency is assumed (although random spatial variations of almost any cochlear parameter will give rise to similar effects), so that

$$\tilde{\omega}_0(x) = \omega_0(x) + \delta\tilde{\omega}(x), \quad (66)$$

$$\delta\tilde{\omega}(x) = \omega_0(x)r_0(x)\tilde{r}(x), \quad (67)$$

where  $\tilde{r}(x)$  is a function that gives a pseudorandom Gaussian number with  $\sigma=1$ , and the amplitude of basilar membrane

roughness is parametrized by  $r_0(x)$  with  $r_0(x) \ll 1$  (all  $x$ ). In this case

$$\delta\tilde{k}^2(x, \omega) \equiv - \frac{2k_0^2\omega^2\omega_0^2(x)r_0(x)\tilde{r}(x)}{\Delta_{sm}^2(x, \omega)}. \quad (68)$$

Inserting Eq. (65) into Eq. (18) gives

$$P_d''(x, \omega) + k_{sm}^2(x, \omega)P_d(x, \omega) = -\delta\tilde{k}^2(x, \omega)P_d(x, \omega). \quad (69)$$

This equation can be solved perturbatively by assuming that  $\delta\tilde{k}^2(x, \omega) \ll 1$ , so that given a solution,

$$P_{0d}(x, \omega) = a_{0r}(\omega)\psi_r(x, \omega) + a_{0l}(\omega)\psi_l(x, \omega), \quad (70)$$

of the “smooth” cochlea,  $P_{1d}(x, \omega)$ , the first-order “scattered pressure wave” correction to  $P_d(x, \omega)$  is determined by the wave equation,

$$\begin{aligned} P_{1d}''(x, \omega) + k_{sm}^2(x, \omega)P_{1d}(x, \omega) = & -\delta\tilde{k}^2(x, \omega)P_{0d}(x, \omega) \\ \equiv & \tilde{\rho}_{scat}(x, \omega). \end{aligned} \quad (71)$$

Equation (71) has a general solution of the form given by Eq. (64), with  $\rho_{source}(x, \omega) = \tilde{\rho}_{scat}(x, \omega)$ , and  $a_r(0, \omega) = a_l(0, \omega) = 0$ . For ease of physical interpretation, Eq. (71) is solved separately for the cochlear activity resulting from an initially right-moving wave (as would be the case, e.g., for an external tone in the ear canal) and for an initially left-moving wave (as would be the case for a pressure wave generated within the cochlea). For an initially right-moving wave,

$$P_{0d}(x, \omega) = a_{0r}(\omega)\psi_r(x, \omega), \quad (72)$$

where  $a_{0r}(\omega)$  is understood to be the amplitude of the (unperturbed) traveling wave evaluated at  $x=0$ . Applying Eq. (72) to Eq. (71) gives a scattering density of the form,

$$\tilde{\rho}_{scat}(x, \omega) = -a_{0r}(\omega)\delta\tilde{k}^2(x, \omega)\psi_r(x, \omega). \quad (73)$$

Thus  $P_d(x, \omega) (= P_{0d}(x, \omega) + P_{1d}(x, \omega))$  is given to first order in  $\delta\tilde{k}^2(x, \omega)$  by

$$\begin{aligned} P_d(x, \omega) \equiv & \left[ \frac{1}{W_0(\omega)} \int_x^\infty \delta\tilde{k}^2(x', \omega)\psi_r^2(x', \omega) dx' \right] \\ & \times a_{0r}(\omega)\psi_l(x, \omega) + \left[ 1 + \frac{1}{W_0(\omega)} \right. \\ & \times \left. \int_0^x \delta\tilde{k}^2(x', \omega)\psi_r(x', \omega)\psi_l(x', \omega) dx' \right] \\ & \times a_{0r}(\omega)\psi_r(x, \omega), \end{aligned} \quad (74)$$

where Eqs. (73) and (64) have been used to obtain this result. Although it will not be directly relevant for practical calculations, it is instructive to consider an initially left-moving wave in the absence of reflections from the stapes:

$$P_{0d}(x, \omega) = a_{0l}(\omega)\psi_l(x, \omega), \quad (75)$$

where  $a_{0l}(\omega)$  is understood to be the amplitude of the (unperturbed) traveling wave evaluated at  $x=L_{bm}$ . Following the same procedure used for the right-moving wave solution gives

$$\begin{aligned}
P_d(x, \omega) \equiv & \left[ 1 + \frac{1}{W_0(\omega)} \int_x^\infty \delta \tilde{k}^2(x', \omega) \psi_r(x', \omega) \right. \\
& \times \psi_l(x', \omega) dx' \left. \right] a_{0l}(\omega) \psi_l(x, \omega) \\
& - \left[ \frac{1}{W_0(\omega)} \int_0^x \delta \tilde{k}^2(x', \omega) \psi_l^2(x', \omega) dx' \right] \\
& \times a_{0l}(\omega) \psi_r(x, \omega). \tag{76}
\end{aligned}$$

## E. Cochlear reflection

### 1. Definition and interpretation

For an initially apically or right-moving wave, the ratio,

$$R_a(x, \omega) = \frac{P_l(x, \omega)}{P_r(x, \omega)}, \tag{77}$$

where  $P_l(x, \omega)$  and  $P_r(x, \omega)$  are, respectively, given by Eqs. (45) and (44), is a measure of the first-order effects of the inhomogeneities apical to the position  $x$ . Similarly the ratio

$$R_b(x, \omega) = \frac{P_r(x, \omega)}{P_l(x, \omega)} \tag{78}$$

is a measure of the first-order reflective effects of the inhomogeneities basal to the position  $x$  for an initially left-moving wave. Note that  $R_a(x, \omega)$  and  $R_b(x, \omega)$  generally vary with  $x$  even outside of the source regions. On the other hand, the ratios of traveling wave amplitudes,

$$r_a(x, \omega) = \frac{a_l(x, \omega)}{a_r(x, \omega)}, \quad r_b(x, \omega) = \frac{a_r(x, \omega)}{a_l(x, \omega)}, \tag{79}$$

will be constant outside the source regions. This statement will obviously be true for general solutions of Eq. (63). In terms of the ratios of traveling waves, Eqs. (77) and (78) become

$$R_a(x, \omega) = r_a(x, \omega) \mathcal{R}_a(x, \omega); \tag{80}$$

$$\mathcal{R}_a(x, \omega) \equiv \psi_l(x, \omega) / \psi_r(x, \omega),$$

$$R_b(x, \omega) = r_b(x, \omega) \mathcal{R}_b(x, \omega); \tag{81}$$

$$\mathcal{R}_b(x, \omega) \equiv \psi_r(x, \omega) / \psi_l(x, \omega).$$

In general, the reflectance at the base,

$$R_b(\omega) \equiv R_b(0, \omega), \tag{82}$$

represents the traveling wave reflectance resulting from the cochlea–middle ear interface as measured at the base of the cochlea in the absence of external driving (see Fig. 6). As a consequence of the normalizations of the basis function [Eq. (37)],  $\mathcal{R}_b(0, \omega) \equiv 1$ , and therefore  $R_b(\omega) \equiv R_b(0, \omega) = r_b(0, \omega)$ . Here  $R_b(\omega)$  is understood to be the basal reflectance at the stapes due to a cochlea driven from a more apical location, with  $P_{dr}(\omega) = 0$ .

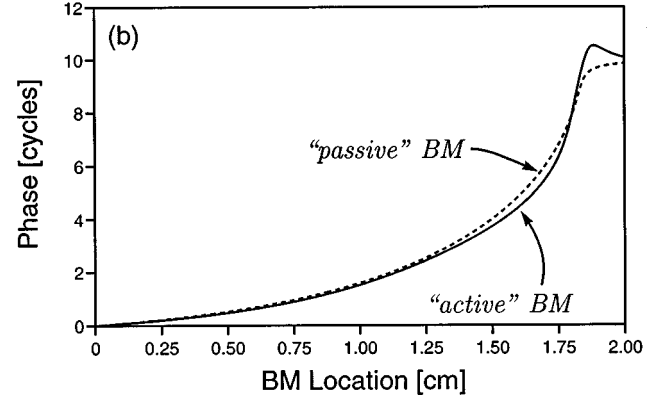
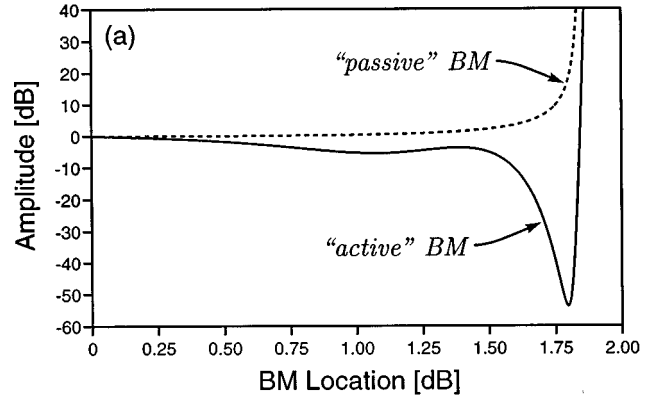


FIG. 6. Comparison of amplitudes (a) and phases (b) of the ratio  $\mathcal{R}_a(x, \omega) = \psi_l(x, \omega) / \psi_r(x, \omega)$  for an input frequency of 1500 Hz. The curves labeled “passive” basilar membrane refer to a passive cochlea, and the “active” basilar membrane curve refers to an active model incorporating stiffness feedback.

### 2. Evaluation of the basal reflectance at the stapes

$R_b(\omega)$  can be determined by evaluating the reflection from the stapes of a left-moving wave  $P_l(0, \omega) = a_l(0, \omega) \psi_l(0, \omega)$  with the condition,  $P_{dr} = 0$ , in the ear canal and using Eq. (22):

$$P_d(0, \omega) = a_l(0, \omega) [1 + R_b(\omega)], \tag{83}$$

$$\begin{aligned}
P'_d(0, \omega) &= a_l(0, \omega) [\psi'_l(0, \omega) + R_b(\omega) \psi'_r(0, \omega)] \\
&= -k_{ow}(\omega) P_d(0, \omega). \tag{84}
\end{aligned}$$

By forming the ratio  $P_d(0, \omega) / P'_d(0, \omega)$  the arbitrary constant  $a_l(0, \omega)$  can be eliminated. After simplification, this procedure yields

$$R_b(\omega) = - \frac{k_{ow}(\omega) + k_l(0, \omega)}{k_{ow}(\omega) + k_r(0, \omega)}. \tag{85}$$

A different form of this equation can be found by using Eq. (39) evaluated at the stapes:

$$k_l(0, \omega) = k_r(0, \omega) + W_0(\omega). \tag{86}$$

Combining Eqs. (85) and (86) gives

$$R_b(\omega) = -1 - \frac{W_0(\omega)}{k_{ow}(\omega) + k_r(0, \omega)}. \tag{87}$$



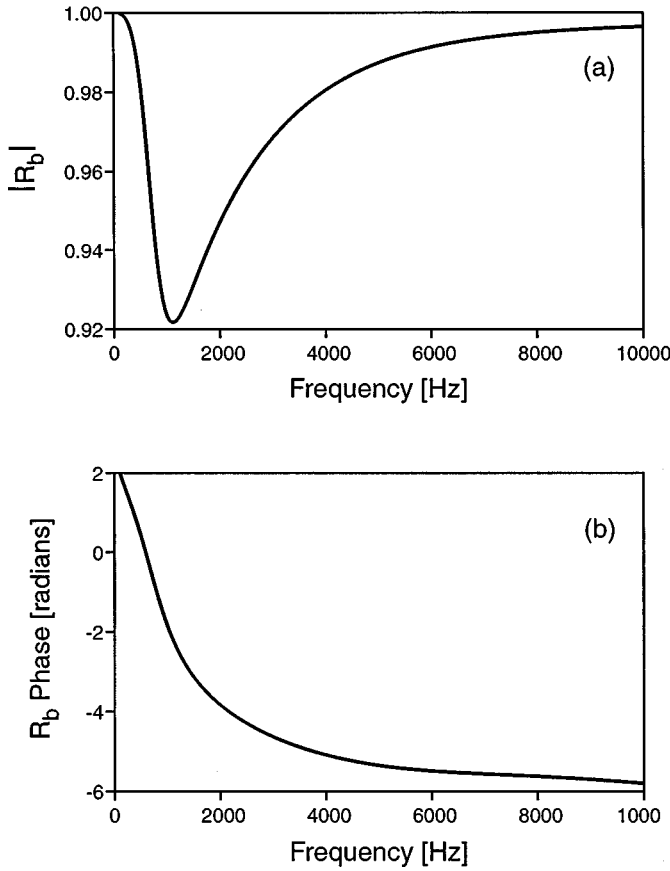


FIG. 7. Amplitude (a) and phase (b) of the reflectance  $R_b(\omega)$  evaluated at the base of the cochlea.

Typical results for  $R_b$  are displayed in Fig. 7. As is expected,  $|R_b|$  has a minimum near the middle ear resonance.

### 3. Reflectance due to roughness

The reflectance due to inhomogeneities for a “tall and broad” activity pattern was first considered by Zweig and Shera (1995). As discussed in Sec. III B, these inhomogeneities are modeled in this study as a small “roughness” in stiffness, as parametrized by Eqs. (66) and (67). The change in  $k_{sm}^2(x, \omega)$  from the presence of these inhomogeneities is given by Eq. (68). For an initially apically traveling wave, Eqs. (52), (67), and (74) give

$$r_a(x, \omega) \cong - \frac{2r_0 k_0^2 \omega^2}{W_0(\omega) \Delta_{sm}^2(0, \omega)} \int_x^\infty \omega_0^2(x') \chi_r^2(x', \omega) \times \tilde{r}(x') dx', \quad (88)$$

where it is assumed that the roughness is approximately constant over the region of interest, so that  $r_0(x) \approx r_0 = \text{constant}$ . Under the assumption of a tall and broad activity pattern,  $\chi_r(x, \omega)$  is given approximately by

$$\chi_r(x, \omega) = |\hat{\chi}_r| e^{-2\pi i N_\lambda} e^{-i\hat{k}[x - \hat{x}(\omega)]} e^{-[x - \hat{x}(\omega)]^2 / 2\sigma_x^2}, \quad (89)$$

where  $\hat{k} = \text{Re}[k(\hat{x}(\omega), \omega)]$ ,  $\hat{\chi}_r = \chi_r(\hat{x}(\omega), \omega) = |\hat{\chi}_r| e^{-2\pi i N_\lambda}$  and  $\sigma_x$  is the full width at half maximum of the activity pattern. Substitution of Eq. (89) into Eq. (88) gives

$$r_a(x, \omega) \cong - \frac{2\sqrt{\pi} r_0 k_0^2 \omega^4 \sigma_x |\hat{\chi}_r|^2}{W_0(\omega) \omega_0^4} e^{-4\pi i N_\lambda} e^{k_0^2 \sigma_x^2} e^{2i\hat{k}\hat{x}(\omega)} \times \tilde{r}_f(\hat{x}(\omega) + k_0 \sigma_x^2), \quad (90)$$

which holds for  $x \ll \hat{x} - 2\sigma_x$ . In obtaining Eq. (90), the approximation  $\Delta_{sm}^2(0, \omega) \cong \omega_0^4$  has also been used. Also  $\tilde{r}_f(x, \omega)$  is the basilar membrane roughness which has been filtered around the spatial frequency region centered at twice the spatial wave number ( $2\hat{k}$ ), where

$$\tilde{r}_f(x) = \int_{-\infty}^{+\infty} \tilde{r}(k_1 + 2\hat{k}) e^{-k_1^2 \sigma_x^2 / 4} e^{ik_1 x} dk_1. \quad (91)$$

The consequence of the  $\tilde{r}_f(x)$  term is that the magnitude of  $r_a(x, \omega)$  fluctuates in the manner of narrow-band filtered noise, with a correlation length of  $\sigma_x$ . It should also be noted that since scale-invariance is an approximate symmetry of the human cochlea,  $\hat{k}$ ,  $|\chi_r|$ , and  $\sigma_x$  are all approximately constant. It can be further demonstrated that

$$r_a(\hat{x}(\omega), \omega) \cong r_a(0, \omega) / 2. \quad (92)$$

The magnitude of the reflectance arising from distributed inhomogeneities depends on the factor  $\sigma_x |\chi_r|^2$ . Consequently the taller and broader the activity pattern, the more sensitive a right-moving traveling wave will be to inhomogeneities on the basilar membrane. Unlike the case for nonlinearity-induced reflectance, however, the phase for roughness-induced reflectance is strongly dependent on frequency through the term,

$$e^{2i\hat{k}\hat{x}(\omega)} \cong e^{-i(2\hat{k}/k_0) \log(\omega/\omega_0)} = e^{-i\varphi_0 \log(\omega/\omega_0)}. \quad (93)$$

As will be shown in the subsequent sections, this phase dependence of the roughness-induced reflectance is responsible for the observed cochlear periodicities in humans, as was emphasized originally by Zweig and Shera (1995) for the case of SEOAEs.

### 4. Response to an external tone of a cochlea with internal apical reflection

The effects of apical cochlear reflection on the cochlear response to an external tone can be considered by assuming that  $r_a(x, \omega)$  has a constant value  $r_a(0, \omega)$  near the base. Then,

$$R_a(\omega) \equiv R_a(0, \omega) = r_a(0, \omega), \quad (94)$$

where  $R_a(\omega)$  is understood to be the apical reflectance evaluated at the base due to cochlear reflections at more apical locations (e.g.,  $x > 0$ ) of an initially apically moving traveling wave, and  $r_a(0, \omega)$  is given by Eq. (90) evaluated at  $x = 0$ .

As before, the analysis proceeds with the evaluation of  $P_d(0, \omega)$  and  $P_d'(0, \omega)$ :

$$P_d(0, \omega) = a_r(0, \omega) [1 + R_a(\omega)], \quad (95)$$

$$P_d'(0, \omega) = a_r(0, \omega) [k_r(0, \omega) + R_a(\omega) k_l(0, \omega)], \quad (96)$$

where Eq. (95) follows from Eqs. (37) and (46), and again Eq. (96) follows directly from Eq. (47). The response of the cochlea to the external tone is determined by combining Eqs.

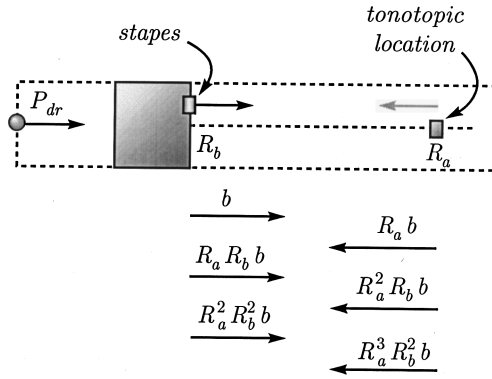


FIG. 8. Geometrical interpretation of the cochlear response to an external stimulus. The pressure wave  $b$  and its multiple-reflection contributions are labeled by the apically pointing arrows, and the initially reflected wave  $R_a b$  and its multiple-reflection contributions by the basally pointing arrows. The initial wave  $b$ , its first reflection  $R_a b$ , and all further internal reflections sum together to give the expansion given in Eq. (100).

(85), (95), and (96) with Eq. (22) and simplifying. This gives

$$a_r(0, \omega) = - \frac{G_{me}(\omega) k_{ow}(\omega)}{k_r(0, \omega) + k_{ow}(\omega)} \frac{1}{1 - R_a(\omega) R_b(\omega)} P_{dr}(\omega). \quad (97)$$

Some physical insight into the implications of Eq. (97) can be obtained by noting that the resulting pressure difference at the base,  $P_d(0, \omega)$ , is then given by

$$P_d(0, \omega) = b(\omega) \frac{1 + R_a(\omega)}{1 - R_a(\omega) R_b(\omega)}, \quad (98)$$

$$b(\omega) = - \frac{G_{me}(\omega) P_{dr}(\omega) k_{ow}(\omega)}{k_r(0, \omega) + k_{ow}(\omega)}. \quad (99)$$

If  $|R_a(\omega)| \ll 1$ , Eq. (98) can be expanded as

$$P_d(0, \omega) = b(\omega) + R_a(\omega) b(\omega) + R_a(\omega) R_b(\omega) b(\omega) + R_a(\omega)^2 R_b(\omega)^2 b(\omega) + R_a(\omega)^3 R_b(\omega)^2 b(\omega) + \dots \quad (100)$$

As illustrated in Fig. 8,  $P_d(0, \omega)$  is comprised of a sum of terms having simple geometric interpretations. The first term,  $b(\omega)$ , is simply the amplitude of the initial apically moving wave; the second term,  $R_b(\omega) b(\omega)$ , is that of the initial basally moving reflected wave; the third term,  $R_a(\omega) R_b(\omega) b(\omega)$ , is that of the reflections from the stapes of the initial basally moving wave, and so on. It is interesting to note that multiple internal reflections of the pressure traveling wave is not an assumption about the dynamics of the pressure wave, but rather is a straightforward consequence of the boundary conditions at the base of the cochlea.

## II. SYNCHRONOUS EVOKED AND TRANSIENT OTOACOUSTIC EMISSIONS

Synchronous emissions can be obtained by calculating the ear canal pressure  $P_e$  resulting from a tone injected into the ear canal of level  $P_{dr}$ .  $P_e$  can be easily determined by using Eq. (29), which relates  $P_e$  to  $P_{dr}$  and  $P'_d(0, \omega)$ . In terms of basis functions,  $P'_d(0, \omega)$  is given by

$$P'_d(0, \omega) = a_r(0, \omega) [\psi'_r(0, \omega) + R_a(\omega) \psi'_l(0, \omega)] = a_r(0, \omega) k_r(0, \omega) [1 + R_a(\omega) \mathcal{R}_s(\omega)], \quad (101)$$

$$\mathcal{R}_s(x, \omega) \equiv \frac{k_l(x, \omega)}{k_r(x, \omega)}, \quad \mathcal{R}_s(\omega) \equiv \mathcal{R}_s(0, \omega). \quad (102)$$

Also, the value of  $a_r(0, \omega)$  due to an external tone of level  $P_{dr}$ , for the case of cochlear reflection, is given by Eq. (97), so that Eq. (101) becomes

$$P'_d(0, \omega) = - \frac{G_{me}(\omega) k_r(0, \omega) k_{ow}(\omega)}{k_r(0, \omega) + k_{ow}(\omega)} \frac{1 + R_a(\omega) \mathcal{R}_s(\omega)}{1 - R_a(\omega) R_b(\omega)} \times P_{dr}(\omega). \quad (103)$$

Inserting Eq. (103) into Eq. (29) gives the relationship between  $P_e$  and  $P_{dr}$ :

$$P_e(\omega) = \left[ T_{dr}(\omega) - G_{me}(\omega) T_{pd}(\omega) \times \frac{k_r(0, \omega) k_{ow}(\omega)}{k_r(0, \omega) + k_{ow}(\omega)} \frac{1 + R_a(\omega) \mathcal{R}_s(\omega)}{1 - R_a(\omega) R_b(\omega)} \right] P_{dr}(\omega). \quad (104)$$

As was mentioned in the previous section, the SEOAE fine structure arises in Eq. (104) from the interference associated with the phase variations of the various terms in square brackets "[ ]". Thus in analyzing the consequences of this equation, it is important to understand the frequency dependence of the second term in brackets. In order to make definite predictions, it is necessary to choose a specific model for  $R_a$ , since the phase dependence of this factor is different for different models of cochlear reflection. For specificity, it will be initially assumed in this discussion that  $R_a$  arises from distributed inhomogeneities, so that according to Eq. (90),  $R_a(\omega)$  has a phase variation with frequency given mainly by the factor  $e^{2ik\hat{x}(\omega)}$ .

Because  $\psi_l(x, \omega) \cong \psi_r^*(x, \omega)$  for  $x \ll \hat{x}(\omega)$ , it follows that  $\psi'_l(x, \omega) \cong [\psi'_r(x, \omega)]^*$ . Also, the phase of the quantities  $\mathcal{R}_s(\omega)$ ,  $k_{ow}(\omega)$ ,  $k_r(0, \omega)$ , and  $R_b(\omega)$  are all slowly varying with frequency in comparison to  $R_a(\omega)$ . Hence the dominant phase behavior will arise from the terms involving  $R_a(\omega)$ , which are

$$\frac{1 + R_a(\omega) \mathcal{R}_s(\omega)}{1 - R_a(\omega) R_b(\omega)} \cong 1 + R_a(\omega) [\mathcal{R}_s(\omega) + R_b(\omega)] + \dots, \quad (105)$$

where the right-hand side of Eq. (105) holds for  $R_a(\omega) \ll 1$ , since  $|R_b(\omega)| \leq 1$ . This equation implies that  $P_e(\omega)$  will fluctuate with a frequency spacing between successive maxima or minima corresponding to a tonotopic displacement of  $\Delta \hat{x}(\omega)$  along the basilar membrane given approximately by  $\Delta \arg(R_a) \cong 2\hat{k} \Delta \hat{x}(\omega) = 2\pi$ , or  $\Delta \hat{x} = \pi/\hat{k}$ . Studies of spacings between SEOAE maxima suggest a value for  $\Delta \hat{x}(\omega) \cong 0.042$  cm for humans, which further implies  $\hat{k} \cong 75$  cm<sup>-1</sup>. This separation can be recast in terms of a frequency separation by noting that

$$\frac{\Delta \omega}{\omega} \cong k_{ow} \Delta \hat{x} \cong 1.382 \text{ cm}^{-1} \cdot 0.042 \text{ cm} \cong \frac{1}{17}. \quad (106)$$

Equation (104) also provides a description of the spectra of transient evoked otoacoustic emissions (TEOAEs). For simplicity, it is assumed that the calibrated driving pressure  $P_{dr}$ , is proportional to a unit impulse,

$$P_{dr}(t) = P_0 \delta(t) = \frac{P_0}{2\pi} \int_{-\infty}^{+\infty} d\omega e^{i\omega t}. \quad (107)$$

If the auditory periphery response function is assumed to be linear, causal, and time-invariant, the resulting ear-canal incremental pressure is then (e.g., Koshigoe and Tubis, 1982),

$$P_e(t) = \frac{P_0}{2\pi} \int_{-\infty}^{+\infty} d\omega \left[ \frac{P_e(\omega)}{P_{dr}(\omega)} \right] e^{i\omega t}, \quad (108)$$

where  $[P_e(\omega)/P_{dr}(\omega)]$  is given by Eq. (104).

The TEOAE is identified with the delayed response [associated with the  $R_a(\omega)$  terms]. If the  $[P_e(\omega)/P_{dr}(\omega)]$  term for  $R_a(\omega) = 0$  is sufficiently slowly varying with  $\omega$ , the early response is

$$P_e(t)|_{\text{early}} = \frac{P_0}{2\pi} \int_{-\infty}^{+\infty} d\omega \left[ T_{dr}(\omega) - G_{me}(\omega) T_{pd}(\omega) \frac{k_r(0, \omega) k_{ow}(\omega)}{k_r(0, \omega) + k_{ow}(\omega)} \right] e^{i\omega t}, \quad (109)$$

and the TEOAE is therefore

$$P_{\text{TEOAE}}(t) \equiv P_e(t) - P_e(t)|_{\text{early}} = -\frac{P_0}{2\pi} \int_{-\infty}^{+\infty} d\omega G_{me}(\omega) T_{pd}(\omega) \times \frac{k_r(0, \omega) k_{ow}(\omega)}{k_r(0, \omega) + k_{ow}(\omega)} \times \frac{R_a(\omega) [\mathcal{R}_s(\omega) + R_b(\omega)]}{1 - R_a(\omega) R_b(\omega)} e^{i\omega t}. \quad (110)$$

Equation (110) implies that the fine structure of the TEOAE amplitude spectrum will be mainly determined by  $|1/(1 - R_a(\omega) R_b(\omega))|$  (for  $|R_{a,b}| \ll 1$ ) so that the peak separations will correspond to  $\Delta \arg(R_a) \approx 2\pi$ , just as in the case of SEOAEs. However, it is interesting to note that in the absence of basal reflectance ( $R_b = 0$ ), there will still be fine structure in the SEOAE amplitude spectrum, but not in the TEOAE spectrum.

The connection between resonant TEOAE modes [corresponding to  $R_a(\omega) R_b(\omega) \approx 1$ ] and SOAEs will be discussed in Sec. IV.

### III. THRESHOLD MICROSTRUCTURE

The hearing threshold is modeled by assuming that the detection threshold occurs at the level where the BM motion is above a minimum detectable BM amplitude,  $\xi_{th}(\omega)$ , for a given frequency  $\omega$ . The hearing threshold curve then gives the ear canal driving level  $P_{dr}(\omega) = P_{th}(\omega)$  necessary to generate a basilar membrane amplitude of strength  $\xi_{th}(\omega)$ . For simplicity, it is assumed that  $\xi_{th} \approx \text{constant}$ . Morphological deviations are known to occur along the cochlea from its

base to its apex both specifically for inner hair cells as well as generally for the entire organ of Corti. These deviations are likely to lead to a variation in threshold sensitivity with frequency  $\omega$ . However, these deviations are expected to vary much less rapidly with frequency than does  $R_a(\omega)$ , and can be neglected for the present considerations.

From Eqs. (51)–(53), the displacement at the traveling wave maximum is

$$\begin{aligned} \hat{\xi} &= b_r(0, \omega) [\hat{\chi}_r + R_a(\omega) \hat{\chi}_l / 2], \\ &\equiv \frac{a_r(0, \omega)}{\sigma_{bm} \omega_0^2} \hat{\chi}_r. \end{aligned} \quad (111)$$

In obtaining this expression, the previously discussed result from Eq. (92) that  $r_a(\hat{x}, \omega) \equiv R_a(\omega)/2$  was used, in addition to the observation that  $\hat{\chi}_l \ll \hat{\chi}_r$  for an active cochlea. Equations (97) and (111) then give

$$\begin{aligned} \xi_{th}(\omega) &= \left| \frac{k_{ow}(\omega)}{k_r(0, \omega) + k_{ow}(\omega)} \frac{1}{1 - R_a(\omega) R_b(\omega)} \right. \\ &\quad \left. \times G_{me}(\omega) \hat{\chi}_r \frac{P_{th}(\omega)}{\sigma_{bm} \omega_0^2} \right|. \end{aligned} \quad (112)$$

Finally, solving for the driving pressure at threshold,  $P_{th}(\omega)$ , gives

$$P_{th}(\omega) = \left| \frac{k_r(0, \omega) + k_{ow}(\omega)}{k_{ow}(\omega)} \cdot [1 - R_a(\omega) R_b(\omega)] \cdot \frac{\sigma_{bm} \omega_0^2 \xi_{th}(\omega)}{G_{me}(\omega) \hat{\chi}_r} \right|. \quad (113)$$

Equation (113) connects the basilar membrane sensitivity,  $\xi_{th}(\omega)$ , to the minimum audible pressure in the ear canal,  $P_{th}(\omega)$ . It also parametrizes the efficiency of the middle ear transformer through  $G_{me}(\omega)$  as well as the strength of the cochlear amplifier via  $\hat{\chi}_r$ . If either the middle ear's ability to transmit sound is compromised [in which case  $G_{me}(\omega)$  is reduced] or the cochlear amplifier in a given basilar membrane region is damaged (in which case  $\hat{\chi}_r$  is reduced), then the minimum audible pressure is increased.

A further effect is the presence of a ‘‘ripple’’ in the auditory threshold arising from the factor  $1 - R_a(\omega) R_b(\omega)$ , which corresponds to threshold microstructure. In audiograms,  $1/P_{th}(\omega)$  is plotted versus frequency, so that the interference term takes the form  $1/[1 - R_a(\omega) R_b(\omega)]$ . Consequently, threshold microstructure from audiograms is expected to have characteristics similar to SEOAE and TEOAE fine structures. This point will be explored further in the Discussion section.

It is also interesting to explore the effects of damage to the inner ear on the microstructure. If the effect of the damage is to introduce a larger roughness, but does not seriously affect the cochlear amplifier, then an increased microstructure is expected. On the other hand, if the cochlear amplifier is damaged,  $R_a(\omega)$ , and consequently the threshold microstructure, will be reduced.

#### IV. SPACINGS OF RESONANT TRANSIENT EVOKED AND SPONTANEOUS OTOACOUSTIC EMISSIONS

Transient evoked otoacoustic emissions that have a slow decay (“resonant” TEOAEs) will appear as amplitude maxima in TEOAE spectra. Such TEOAEs, along with SOAEs, correspond to natural resonance modes of the cochlea. In mathematical terms, they may be identified with homogeneous ( $P_{dr}=0$ ) solutions of the linearized cochlear equations. From Eq. (104) it is seen that they have the harmonic time dependence  $e^{i\omega t}$ , where  $\omega$  is complex and has discrete values  $\omega_n$  ( $n=1,2,3,\dots$ ) determined from the relation,

$$R_a(\omega_n)R_b(\omega_n) = 1, \quad (114)$$

$$\omega_n = \omega_{R,n} + i\omega_{I,n}. \quad (115)$$

Modes with  $\omega_{I,n} > 0$  will be decaying and will correspond to TEOAEs. On the other hand, modes with  $\omega_{I,n} < 0$  will be unstable and will correspond to SOAEs (after the inclusion of a stabilizing nonlinearity). For these complex frequencies, the traveling wave ratio at the cochlear base, as determined by the dynamics of the cochlear base, and the middle and outer ear, when  $P_{dr} = 0$ .

Equation (114) can be solved approximately by assuming that for  $\omega \approx \omega_n$ ,

$$R_a(\omega) \cong |R_a| e^{-i\varphi_0 \log(\omega/\omega_0) + \varphi_a}, \quad (116)$$

$$R_b(\omega) \cong |R_b| e^{-i\omega\tau_b + \varphi_b}, \quad (117)$$

$$\tau_b = -\frac{d}{d\omega} \arg(R_b), \quad (118)$$

where  $\varphi_a$  and  $\varphi_b$  are real constants, and  $|R_a|$ ,  $|R_b|$ , and  $\tau_b$  refer to the values of these quantities for real  $\omega \approx \omega_{R,n}$ . For the auditory peripheral models used in this study,  $\tau_b \approx 1-4$  ms over the frequency range of interest so that the phase of  $R_b$  is slowly varying compared to that of  $R_a$ . Substituting Eqs. (116) and (117) into Eq. (114) gives

$$\varphi_0 \log\left(\frac{|\omega_n|}{\omega_0}\right) + \omega_{R,n}\tau_b + \varphi_a + \varphi_b = 2\pi n, \quad (119)$$

$$\varphi_0 \tan^{-1}\left(\frac{\omega_{I,n}}{\omega_{R,n}}\right) + \omega_{I,n}\tau_b = -\log(|R_a(\omega_n)||R_b(\omega_n)|). \quad (120)$$

Equation (119) can be used to estimate the spacing between adjacent modes by writing  $\Delta\omega_n = \omega_{n+1} - \omega_n \ll \omega_n$ , and assuming  $\omega_{I,n}/\omega_{R,n} \ll 1$ :

$$\frac{\Delta\omega_n}{\omega_{R,n}} \cong \frac{2\pi}{\varphi_0 + \omega_{R,n}\tau_b}. \quad (121)$$

Equation (121) predicts that the separation between adjacent SOAEs will be comparable to that for SEOAEs. The imaginary component of  $\omega_n$  can also be determined by again assuming that  $\omega_{I,n}/\omega_{R,n} \ll 1$ :

$$\omega_{I,n} \cong -\frac{\omega_{R,n}}{\varphi_0 + \omega_{R,n}\tau_b} \log(|R_a(\omega_{R,n})||R_b(\omega_{R,n})|). \quad (122)$$

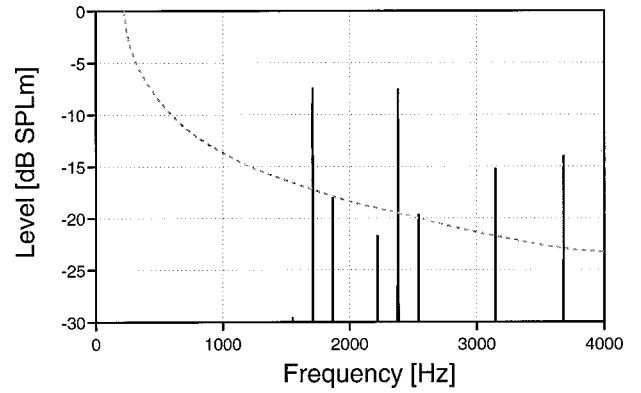


FIG. 9. Results of model calculation showing SOAEs generated in a time-domain nonlinear cochlear model with stiffness feedback and distributed basilar membrane roughness. The dashed line indicates the approximate noise floor of microphone recording systems.

Since  $|R_b(\omega_{R,n})| < 1$ ,  $\omega_{I,n}$  will be positive only if  $|R_a(\omega_{R,n})| |R_b(\omega_{R,n})| > 1$ . Equation (122) thus predicts that SOAEs will occur only in frequency ranges for which  $|R_a(\omega)| > 1$ .

Shown in Fig. 9 are SOAEs from a typical time-domain simulation of the cochlear model described in Sec. I A. In this case the observable SOAEs (those above the denoted noise floor of typical microphone recording systems) are of fairly, but not unrealistically, low level. In this particular simulation, basilar membrane roughness was distributed over a tonotopic range from about 1000 to 4000 Hz. As is typical in these models, the number, frequencies, and levels of the model SOAEs cannot be predicted before running the simulation. Consequently, the frequency spacings of the model SOAEs are the result of the tall and broad activity patterns plus distributed roughness, rather than being due to the *ad hoc* frequency placement of the SOAEs, as would be the case, e.g., for embedded Van der Pol models.

#### V. DISTORTION PRODUCT OTOACOUSTIC EMISSION FINE STRUCTURE

##### A. Introduction

Distortion product otoacoustic emissions (DPOAEs) (Kemp, 1979b) are generated in the cochlea via the nonlinear interaction of the excitations produced by two primary tones of frequencies  $\omega_1$  and  $\omega_2 (> \omega_1)$ . Their initial production is in the region of strong overlap of the  $\omega_1$  and  $\omega_2$  activity patterns, which is around the  $\omega_2$  tonotopic site (e.g., Hall, 1974; Kemp and Brown, 1983). From the generation region, DPOAE components propagate both basally and apically [reviewed in O’Mahoney and Kemp (1995); Kummer *et al.* (1995); Stover *et al.* (1996); Engdahl and Kemp (1996)]. In humans the most prominent DPOAEs are those arising from odd-order distortion, for which the DPOAE frequency  $\omega_{dp}$  is related to its primaries by  $\omega_{dp} = \omega_1 + n(\omega_2 - \omega_1)$ , where  $n = \dots, -3, -2, -1, 2, 3, 4 \dots$ .

A portion of the basally traveling distortion product (DP) component will be transmitted through the middle ear to the ear canal and detected as a DPOAE. The remaining signal will be reflected back into the cochlea. The component traveling apically can be detected psychoacoustically, in the

response of the auditory nerve and on the basilar membrane [reviewed in Robles *et al.* (1997)]. The DP cochlear wave reaching the DP tonotopic place will be partially reflected by small irregularities in the cochlear properties. A tall and broad DP activity peak will allow coherent scattering from many reflectors to give a large basalward reflection of the cochlear traveling wave. Some part of this reflected wave will also be seen in the ear canal otoacoustic emission and some will be reflected back into the cochlea (Talmadge *et al.*, 1997).

The components of the DP traveling waves that enter the ear canal from the generation region and from the DP tonotopic site will combine together in the ear canal to produce the observable DPOAE. In general these two components will not arrive in phase. The relative phase difference between them will mainly depend on the DP frequency [through the phase behavior of the apical reflectance  $R_a(\omega_{dp})$ ] and the resulting interference will give an observable fine structure as a function of the DP frequency.

It will be shown below that the above description of the production of DPOAEs is not an assumption but is a specific prediction of nonlinear cochlear models which incorporate a tall and broad activity pattern and distributed basilar membrane roughness. In the derivation, it is assumed that the nonlinearities responsible for generating the DP and the levels of the primaries are small enough to justify the use of perturbative solutions of the traveling wave equations. This will allow for the modeling of the DP generator, which in turn will permit the calculation of the response of the cochlear model to the presence of the DP generator. Problems associated with higher stimulation levels such as self-suppression and two-tone suppression (e.g., Kanis and de Boer, 1993, 1994) are not addressed in this paper.

In analyzing the cochlear response, it is important to distinguish the cases where  $\omega_{dp} < \omega_1 < \omega_2$ , for which the DP tonotopic site is apical to the generation region, and where  $\omega_{dp} > \omega_2 > \omega_1$ , for which the DP tonotopic site is basal to the generation region. Consequently the two cases, ‘‘apical DPOAEs’’ and ‘‘basal DPOAEs,’’ will be considered separately.

## B. Modeling the DP generator

It is assumed that the nonlinearity is of the form given by Eq. (3), which is expected to be valid for low level basilar membrane excitations. For primaries of sufficiently low level and large enough peak activity pattern separation on the basilar membrane, the nonlinear modifications of the activity patterns of the two primaries and the modification of the activity pattern of the DP by the primaries can be neglected. Under these circumstances, the dominant nonlinear effect will be the generation of the cubic distortion products  $2\omega_1 - \omega_2$  and  $2\omega_2 - \omega_1$ .

### 1. DP generator function for $\omega_{dp} = 2\omega_1 - \omega_2$

A frequency representation of the pressure wave equation can be obtained by writing for the basilar membrane solution:

$$\xi(x, t) \cong \xi_1(x, t) + \xi_2(x, t) + \xi_{dp}(x, t), \quad (123)$$

where the subscripts ‘‘1,’’ ‘‘2,’’ and ‘‘dp’’ refer to the frequency components of physical quantities corresponding, respectively, to  $\omega_1$ ,  $\omega_2$ , and  $\omega_{dp}$ , and where the magnitudes of  $\xi_{dp}(x, t)$  and  $\gamma_2(x)\xi(x, t)^2\xi(x, t)$  are assumed to be small compared to those of  $\xi_1(x, t)$  and  $\xi_2(x, t)$ .

If the complex representation of Eq. (17) is used for real quantities, and only the  $\omega_{dp}$  frequency component is retained for terms such as  $\xi^2(x, t)\xi(x, t)$ , it is easily verified that,

$$\begin{aligned} \xi^2(x, t)\dot{\xi}(x, t) &\cong i\omega_{dp}\xi_1^2(x, \omega_1)\xi_2^*(x, \omega_2)e^{i\omega_{dp}t} \\ &+ \text{complex conjugate.} \end{aligned} \quad (124)$$

This gives rise to the dynamical equation,

$$\begin{aligned} \Delta(x, \omega_{dp})\xi_{dp}(x, \omega_{dp}) &= \frac{1}{\sigma_{bm}} P_{dp}(x, \omega_{dp}) \\ &- i\omega_{dp}\gamma_2(x)\xi_1^2(x, \omega_1)\xi_2^*(x, \omega_2), \end{aligned} \quad (125)$$

where  $\Delta(x, \omega_{dp})$  is the quantity given by Eq. (21) evaluated at  $\omega_{dp}$ . This equation gives rise to the traveling wave equation for the DP,

$$P''_{dp}(x, \omega_{dp}) + k^2(x, \omega_{dp})P_{dp}(x, \omega_{dp}) = \rho_{dp}(x), \quad (126)$$

$$\rho_{dp}(x) = \frac{i\sigma_{bm}\gamma_2(x)k_0^2\omega_{dp}^3\xi_1^2(x, \omega_1)\xi_2^*(x, \omega_2)}{\Delta(x, \omega_{dp})}. \quad (127)$$

Equation (127) can be simplified by letting  $\gamma_2(x, \omega) = \epsilon\omega_0(x)/b_{nl}^2$  as before. Since the nonlinearity is assumed to be weak,  $\xi_1(x, \omega_1) \cong b_r(\omega_1)\chi_r(x, \omega_1)$  and  $\xi_2(x, \omega_2) \cong b_r(\omega_2)\chi_r(x, \omega_2)$ , where  $b_r(\omega_1)$  and  $b_r(\omega_2)$  are the basilar membrane amplitudes given by Eq. (53) in response to driving pressures of  $P_{dr1}$  and  $P_{dr2}$ , respectively. Using these assumptions, Eq. (127) becomes

$$\rho_{dp}(x) = \rho_0(\omega_1, \omega_2) \frac{\omega_0(x)\chi_r^2(x, \omega_1)\chi_r^*(x, \omega_2)}{\Delta(x, \omega_{dp})}, \quad (128)$$

$$\rho_0(\omega_1, \omega_2) = \frac{i\sigma_{bm}\epsilon k_0^2\omega_{dp}^3 b_r^2(\omega_1)b_r^*(\omega_2)}{b_{nl}^2}. \quad (129)$$

Substituting Eq. (128) into Eq. (64) gives

$$\begin{aligned} P_{dp}(x, \omega_{dp}) &= \left[ a_l(0, \omega_{dp}) + \frac{\rho_0(\omega_1, \omega_2)}{\Delta(0, \omega_{dp})W_0(\omega_{dp})} \right. \\ &\quad \times I_r(x, \omega_1, \omega_2) \left. \right] \psi_l(x, \omega_{dp}) + \left[ a_r(0, \omega_{dp}) \right. \\ &\quad \left. - \frac{\rho_0(\omega_1, \omega_2)}{\Delta(0, \omega_{dp})W_0(\omega_{dp})} I_l(x, \omega_1, \omega_2) \right] \\ &\quad \times \psi_r(x, \omega_{dp}), \end{aligned} \quad (130)$$

$$\begin{aligned} I_{r,l}(x, \omega_1, \omega_2) &= \int_0^x \omega_0(x')\chi_r^2(x', \omega_1)\chi_r^*(x', \omega_2) \\ &\quad \times \chi_{r,l}(x', \omega_{dp}) dx', \end{aligned} \quad (131)$$

where  $\hat{x}_2 = x(\omega_2)$ . The integrals  $I_{r,l}(x, \omega_1, \omega_2)$  can be evaluated with the usual assumptions of a ‘‘tall and broad’’ activity pattern for  $\chi_r(x, \omega)$ . Furthermore, since  $\chi_r(x, \omega) \rightarrow 0$  for

$x \gg \hat{x}_2$ , the integrands in  $I_{r,l}(x, \omega_1, \omega_2)$  will be sharply peaked about  $\hat{x}_2$ . Consequently the various terms in the integrands can be written as

$$\chi_r(x, \omega_1) \cong \chi_r(\hat{x}_2, \omega_1) e^{-ik_1(x-\hat{x}_2)}, \quad k_1 = k(\hat{x}_2, \omega_1), \quad (132)$$

$$\chi_r(x, 2\omega_1 - \omega_2) \cong \chi_r(\hat{x}_2, 2\omega_1 - \omega_2) e^{-ik_{dp}(x-\hat{x}_2)}, \quad k_{dp} \cong k(\hat{x}_2, \omega_{dp}), \quad (133)$$

$$\chi_l(x, 2\omega_1 - \omega_2) \cong \chi_l(\hat{x}_2, 2\omega_1 - \omega_2) e^{+ik_{dp}(x-\hat{x}_2)}, \quad (134)$$

$$\chi_r^*(x, \omega_2) \cong |\hat{\chi}_r| e^{+2\pi i N_\lambda} e^{ik(x-\hat{x}_2)} e^{-(x-\hat{x}_2)^2/2\sigma_x^2}, \quad (135)$$

$$\omega_0(x) \approx \omega_2 e^{-k_\omega(x-\hat{x}_2)}. \quad (136)$$

Using these approximations, Eq. (131) reduces to

$$I_{r,l}(x, \omega_1, \omega_2) = \begin{cases} 0, & x \ll \hat{x}_2 - \sigma_x, \\ \gamma_{r,l}(\omega_1, \omega_2) \chi_{r,l}(\hat{x}_2, 2\omega_1 - \omega_2), & x \gg \hat{x}_2 + \sigma_x, \end{cases} \quad (137)$$

$$\begin{aligned} \gamma_r(\omega_1, \omega_2) &= \sqrt{2\pi} \omega_2 \sigma_x |\hat{\chi}_r| \chi_r^2(\hat{x}_2, \omega_1) \\ &\times e^{-[(\hat{k}-2k_1-k_{dp})^2 - k_\omega^2] \sigma_x^2/2} e^{-ik_\omega(\hat{k}-2k_1-k_{dp})\sigma_x^2} \\ &\times e^{+2\pi i N_\lambda}, \end{aligned} \quad (138)$$

$$\begin{aligned} \gamma_l(\omega_1, \omega_2) &= \sqrt{2\pi} \omega_2 \sigma_x |\hat{\chi}_r| \chi_r^2(\hat{x}_2, \omega_1) \\ &\times e^{-[(\hat{k}-2k_1+k_{dp})^2 - k_\omega^2] \sigma_x^2/2} e^{-ik_\omega(\hat{k}-2k_1+k_{dp})\sigma_x^2} \\ &\times e^{+2\pi i N_\lambda}. \end{aligned} \quad (139)$$

For this analysis, it is not necessary to obtain an estimate of  $I_{r,l}(x, \omega_1, \omega_2)$  for intermediate values of  $x$ .

Combining Eqs. (130), (137), (138), and (139) gives

$$P_{dp}(x, \omega_{dp}) = \begin{cases} a_{rI} \psi_r(x, \omega_{dp}) + a_{lI} \psi_l(x, \omega_{dp}), & 0 \leq x \leq \hat{x}_2 - \sigma_x, \\ a_{rII} \psi_r(x, \omega_{dp}) + a_{lII} \psi_l(x, \omega_{dp}), & x \geq \hat{x}_2 + \sigma_x, \end{cases} \quad (140)$$

$$a_{lII} = a_{lI} + \frac{\Gamma_r(\omega_1, \omega_2) \psi_r(\hat{x}_2, \omega_{dp})}{W_0(\omega_{dp})}, \quad (141)$$

$$a_{rII} = a_{rI} - \frac{\Gamma_l(\omega_1, \omega_2) \psi_l(\hat{x}_2, \omega_{dp})}{W_0(\omega_{dp})}, \quad (142)$$

$$\Gamma_{r,l}(\omega_1, \omega_2) = \frac{\rho_0(\omega_1, \omega_2) \gamma_{r,l}(\omega_1, \omega_2)}{\Delta(\hat{x}_2, 2\omega_1 - \omega_2)}, \quad (143)$$

where ‘‘I’’ and ‘‘II,’’ respectively, label the regions with  $0 \leq x \leq \hat{x}_2 - \sigma_x$  and  $x \geq \hat{x}_2 + \sigma_x$ . It is interesting to note that Eqs. (140)–(142) may also be obtained by initially assuming the source density (Talmadge *et al.*, 1997),

$$\rho_{dp}(x; \omega_1, \omega_2) = \Gamma_s(\omega_1, \omega_2) \delta(x - \hat{x}_2), \quad (144)$$

where  $\Gamma_s(\omega_1, \omega_2) \approx \Gamma_r(\omega_1, \omega_2) \approx \Gamma_l(\omega_1, \omega_2)$ . This ‘‘short cut’’ does not lead to any specific prediction for either the amplitude, frequency, or the phase dependence of  $\Gamma_s$  on the two primaries. The more extended model considered here also addresses the criticism concerning the effects of an ex-

tended interaction region of the traveling waves of the two primaries, at least in the limit of tall and broad activity patterns.

## 2. DP generator function for $\omega_{dp} = 2\omega_2 - \omega_1$

Following the procedure described above, it can be shown that the traveling wave for this DP is given by

$$P''_{dp}(x, \omega_{dp'}) + k^2(x, \omega_{dp'}) P_{dp'}(x, \omega_{dp'}) = \rho_{dp'}(x), \quad (145)$$

$$\rho_{dp'}(x) = \frac{i\sigma_{bm} \gamma_2(x) k_0^2 \omega_{dp'}^3 \xi_1^*(x, \omega_1) \xi_2^2(x, \omega_2)}{\Delta(x, \omega_{dp'})}. \quad (146)$$

Substituting Eq. (146) into Eq. (64) gives

$$P_{dp'}(x, \omega'_{dp}) = \left[ a_l(0, \omega'_{dp}) + \frac{\rho_0(\omega_1, \omega_2)}{\Delta(0, \omega'_{dp}) W_0(\omega_{dp'})} I_r(x, \omega_1, \omega_2) \right] \times \psi_l(x, \omega_{dp'}) + \left[ a_r(0, \omega_{dp'}) - \frac{\rho_0(\omega_1, \omega_2)}{\Delta(0, \omega'_{dp}) W_0(\omega_{dp'})} I_l(x, \omega_1, \omega_2) \right] \times \psi_r(x, \omega_{dp'}), \quad (147)$$

$$I'_{r,l}(x, \omega_1, \omega_2) = \int_0^x \omega_0(x') \chi_r^*(x', \omega_1) \chi_r^2(x', \omega_2) \times \chi_{r,l}(x', \omega_{dp'}) dx'. \quad (148)$$

Because  $|\chi_r(x, \omega_2)|$  has its maximum in a region apical to that of the maximum for  $|\chi_r(x, \omega_{dp'})|$ , the evaluation of the integrals  $I'_{r,l}(x, \omega_1, \omega_2)$  is problematic. The reason for this is the rapid falloff of the  $\chi_r(x, \omega_{dp'})$  basis function in the region apical to its maximum (see Fig. 5). For narrower primary frequency ratios, the dominant contribution to the integrals will come from around the  $\omega_2$  tonotopic location, and the integrals for this case can be evaluated as before, to give

$$P_{dp'}(x, \omega_{dp'}) = \begin{cases} a_{rI} \psi_r(x, \omega_{dp'}) + a_{lI} \psi_l(x, \omega_{dp'}), & 0 \leq x \leq \hat{x}_2 - \sigma_x, \\ a_{rII} \psi_r(x, \omega_{dp'}) + a_{lII} \psi_l(x, \omega_{dp'}), & x \geq \hat{x}_2 + \sigma_x, \end{cases} \quad (149)$$

$$a_{lII} = a_{lI} + \frac{\Gamma_r(\omega_1, \omega_2) \psi_r(\hat{x}_2, \omega_{dp'})}{W_0(\omega_{dp'})}, \quad (150)$$

$$a_{rII} = a_{rI} - \frac{\Gamma_l(\omega_1, \omega_2) \psi_l(\hat{x}_2, \omega_{dp'})}{W_0(\omega_{dp'})}, \quad (151)$$

$$\Gamma'_{r,l}(\omega_1, \omega_2) = \frac{\rho'_0(\omega_1, \omega_2) \gamma'_{r,l}(\omega_1, \omega_2)}{\Delta(\hat{x}_2, 2\omega_2 - \omega_1)}, \quad (152)$$

$$\begin{aligned} \gamma'_r(\omega_1, \omega_2) &= \sqrt{2\pi} \omega_2 \sigma_x |\hat{\chi}_r| \chi_r^2(\hat{x}_2, \omega_1) \\ &\times e^{-[(2\hat{k}-k_1+k_{dp'})^2 - k_\omega^2] \sigma_x^2/2} e^{+ik_\omega(2\hat{k}-k_1+k_{dp'})\sigma_x^2} \\ &\times e^{-2\pi i N_\lambda}, \end{aligned} \quad (153)$$

$$\begin{aligned} \gamma'_l(\omega_1, \omega_2) &= \sqrt{2\pi}\omega_2\sigma_x|\hat{\chi}_r|\chi_r^2(\hat{x}_2, \omega_1) \\ &\times e^{-[(2\hat{k}-k_1-k_{dp'})^2-k_\omega^2]\sigma_x^2/2}e^{+ik_\omega(2\hat{k}-k_1-k_{dp'})\sigma_x^2} \\ &\times e^{-2\pi iN\lambda}, \end{aligned} \quad (154)$$

$$\rho'_0(\omega_1, \omega_2) = \frac{i\sigma_{bm}\epsilon k_0^2\omega_{dp}^3 b_r^*(\omega_1)b_r^2(\omega_2)}{b_{nl}^2}. \quad (155)$$

Because of the increased complexity of the problem for wide ratios, the complete treatment of the production of basal distortion products is deferred to a future publication.

### C. Modeling apical DPOAE fine structure

For apical DPOAEs,  $0 < \hat{x}_2 < \hat{x}(\omega_{dp})$ , i.e., the DP tonotopic site is apical to the DP generating region. Consequently, the additional relationships,

$$R_a(\omega_{dp}) = \frac{a_{III}}{a_{rII}}, \quad (156)$$

$$R_b(\omega_{dp}) = \frac{a_{rI}}{a_{II}}, \quad (157)$$

hold, where  $R_a(\omega_{dp})$  and  $R_b(\omega_{dp})$  are defined as usual. Combining Eqs. (141), (142), (156), and (157), gives

$$a_{II} = -\frac{\Gamma_r(\omega_1, \omega_2)\psi_r(\hat{x}_2, \omega_{dp})}{W_0(\omega_{dp})} \frac{1 + R_a(\omega_{dp})\mathcal{R}_d(\hat{x}_2, \omega_1)}{1 - R_a(\omega_{dp})R_b(\omega_{dp})}, \quad (158)$$

$$\begin{aligned} \mathcal{R}_d(\hat{x}_2, \omega_1) &\equiv \frac{\Gamma_l(\omega_1, \omega_2)\psi_l(\hat{x}_2, \omega_{dp})}{\Gamma_r(\omega_1, \omega_2)\psi_r(\hat{x}_2, \omega_{dp})} \\ &= \mathcal{R}_a(\hat{x}_2, \omega_{dp})e^{-2k_{dp}(\hat{k}-2k_1)\sigma_x^2}e^{2ik_\omega k_{dp}\sigma_x^2}. \end{aligned} \quad (159)$$

Finally the pressure in the ear canal  $P_e(\omega_{dp})$  can be related to the traveling wave amplitudes using Eq. (27), with  $P_{dr}=0$ , and Eq. (47):

$$\begin{aligned} P_e(\omega_{dp}) &= T_{pd}(\omega_{dp})P'_d(0, \omega_{dp}) \\ &= T_{pd}(\omega_{dp})[R_b(\omega_{dp})k_r(0, \omega_{dp}) + k_l(0, \omega_{dp})]a_{II}. \end{aligned} \quad (160)$$

Using Eqs. (37), (40), (85), and (86), this becomes

$$P_e(\omega_{dp}) = T_{pd}(\omega_{dp}) \frac{k_{ow}(\omega_{dp})W_0(\omega_{dp})}{k_r(0, \omega_{dp}) + k_l(0, \omega_{dp})} a_{II}. \quad (161)$$

Combining Eqs. (158) and (161) gives,

$$\begin{aligned} P_e(\omega_{dp}) &= -T_{pd}(\omega_{dp}) \frac{k_{ow}(\omega_{dp})}{k_{ow}(\omega_{dp}) + k_r(0, \omega_{dp})} \\ &\times \frac{1 + R_a(\omega_{dp})\mathcal{R}_d(\hat{x}_2, \omega_1)}{1 - R_a(\omega_{dp})R_b(\omega_{dp})} \Gamma_r(\omega_1, \omega_2) \\ &\times \psi_r(\hat{x}_2, \omega_{dp}). \end{aligned} \quad (162)$$

Equation (162) gives the relationship between the frequencies, phases, and levels of the primaries used to generate the  $\omega_{dp}$  DP, and the level and phase of the DP as measured in the ear canal. As in the case for SEOAEs, the dominant phase

behavior will arise from terms involving  $R_a(\omega_{dp})$ , which are

$$\begin{aligned} \frac{1 + R_a(\omega_{dp})\mathcal{R}_d(\hat{x}_2, \omega_1)}{1 - R_a(\omega_{dp})R_b(\omega_{dp})} &\cong 1 + R_a(\omega_{dp})[\mathcal{R}_d(\hat{x}_2, \omega_1) \\ &+ R_b(\omega_{dp})], \end{aligned} \quad (163)$$

where again the assumption has been made that  $|R_a(\omega_{dp})| \ll 1$ .

### D. Modeling basal DPOAE fine structure

For basal DPOAEs,  $0 < \hat{x}(\omega_{dp'}) < \hat{x}_2$ , i.e., the DP tonotopic site is basal to the DP generating region. For this case, the regions  $0 < x < \hat{x}(\omega_{dp'})$ ,  $\hat{x}(\omega_{dp'}) < x < \hat{x}(\omega_2)$ , and  $\hat{x}(\omega_2) < x < L_{bm}$  are, respectively, labeled regions I, II, and III. The equations analogous to Eqs. (141) and (142) are then

$$a_{III} = a_{III} + \frac{\Gamma'_r(\omega_1, \omega_2)\psi_r(\hat{x}_2, \omega_{dp'})}{W_0(\omega_{dp'})}, \quad (164)$$

$$a_{rIII} = a_{rII} - \frac{\Gamma'_l(\omega_1, \omega_2)\psi_l(\hat{x}_2, \omega_{dp'})}{W_0(\omega_{dp'})}, \quad (165)$$

where Eqs. (164) and (165) were adapted directly from Eqs. (150) and (151). Since no internal source of reflection exists apical to  $\hat{x}_2$ , it also follows that  $a_{III} = 0$ .

In modeling the relationships between  $a_{II}$  and  $a_{rI}$ , and  $a_{III}$  and  $a_{rII}$ , it should be noted that  $|r_b(\hat{x})| \ll |r_a(\hat{x})|$ , which follows from the fact that  $\chi_l(x, \omega)$  rather than  $\chi_r(x, \omega)$  enters in the calculation of the reflectance of a basally traveling wave due to distributed roughness [compare Eqs. (74) and (76)]. Since  $|\hat{\chi}_l| \ll |\hat{\chi}_r|$ , it follows that  $r_b$  is negligible. In a similar manner it can be shown that the effect on both the apically and basally traveling waves transmitted through the  $\hat{x}_{dp'}$  region is also negligible.

In addition, the following relationships hold:

$$R_a(\omega_{dp'}) = \frac{a_{II} - a_{III}}{a_{rI}}, \quad (166)$$

$$R_b(\omega_{dp'}) = \frac{a_{rI}}{a_{II}}. \quad (167)$$

Equation (166) comes from assuming a basal-ward traveling pressure wave “driving” the cochlea from a position  $x > \hat{x}_{dp'}$ . Equations (164)–(167) give

$$a_{II} = -\frac{1}{1 - R_a(\omega_{dp'})R_b(\omega_{dp'})} \frac{\Gamma'_r(\omega_1, \omega_2)\psi_r(\hat{x}_2, \omega_{dp'})}{W_0(\omega_{dp'})}. \quad (168)$$

Finally, the ear canal pressure is

$$\begin{aligned} P_e(\omega_{dp'}) &= -T_{pd}(\omega_{dp'}) \frac{k_{ow}(\omega_{dp'})}{k_{ow}(\omega_{dp'}) + k_r(0, \omega_{dp'})} \\ &\times \frac{1}{1 - R_a(\omega_{dp'})R_b(\omega_{dp'})} \Gamma'_r(\omega_1, \omega_2) \\ &\times \psi_r(\hat{x}_2, \omega_{dp'}), \end{aligned} \quad (169)$$

which differs in form from Eq. (162) only in the missing factor  $1 - R_a(\omega_{dr})\mathcal{P}_d(\hat{x}_2, \omega_1)$ . As noted above, Eq. (169) is expected to hold only for narrower frequency ratios. Since basal distortion products are not normally observable for wide frequency ratios except for very high-level primaries (which violate the assumptions used in this derivation), this restriction is not a severe one.

From Eq. (169) it can be seen that the predicted spacing between fine structure maxima for basal DPOAEs should be identical to the spacings for threshold microstructure. However, the presense of the  $\psi_r(\hat{x}_2, \omega_{dp'})$  term heavily suppresses any basal DPOAEs due to the rapid falloff in  $|\psi_r(x, \omega)|$  for  $x$  apical to  $\hat{x}(\omega)$  (see Fig. 4). Only for very small ratios of  $\omega_2/\omega_1$  would significant basal DPOAEs be expected to be observed. In this case, however, the  $\omega_2$  primary would suppress the DPOAE basis function at  $\hat{x}_{dp'}$  [causing  $r_a(\omega_{dp'}) \rightarrow 0$ ], and hence suppress any fine structure

for these DPOAEs. This topic will be considered in greater detail in a future publication.

### E. Modeling higher-order DPOAEs

The two distortion products that have been considered so far are  $\omega_{dp} \equiv \omega_{dp21} = 2\omega_1 - \omega_2$  and  $\omega_{dp'} \equiv \omega_{dp12} = 2\omega_2 - \omega_1$ . In practice, many higher-order DPs are observable in DPOAE measurements in humans (e.g., Brown *et al.*, 1992), such as  $\omega_{dp32} = 3\omega_1 - 2\omega_2$ ,  $\omega_{dp43} = 4\omega_1 - 3\omega_2$ , etc. These higher-order DPs are also present in a cochlear model with a pure cubic nonlinearity [e.g., Eq. (3)], but the full treatment of these DPs lies outside the scope of the present paper.

Some insight about the behavior of the higher-order apical DPs can be obtained by considering their leading nonzero source density contributions:

$$\rho_{dp32}(x) = \frac{i(3\omega_1 - 2\omega_2)^3 \sigma_{bm} \gamma_2(x) k_0^2 \xi_1(x, \omega_1) \xi_{dp21}(x, 2\omega_1 - \omega_2) \xi_2^*(x, \omega_2)}{\Delta(x, 3\omega_1 - 2\omega_2)}, \quad (170)$$

$$\rho_{dp43}(x) = \frac{i(4\omega_1 - 3\omega_2)^3 \sigma_{bm} \gamma_2(x) k_0^2 \xi_1(x, \omega_1) \xi_{dp32}(x, 3\omega_1 - 2\omega_2) \xi_2^*(x, \omega_2)}{\Delta(x, 4\omega_1 - 3\omega_2)}, \quad (171)$$

$$\rho_{dp54}(x) = \frac{i(5\omega_1 - 4\omega_2)^3 \sigma_{bm} \gamma_2(x) k_0^2 \xi_{dp21}(x, 2\omega_1 - \omega_2) \xi_{dp32}(x, 3\omega_1 - 2\omega_2) \xi_2^*(x, \omega_2)}{\Delta(x, 5\omega_1 - 4\omega_2)}. \quad (172)$$

Since all of these source densities contain a  $\xi_2^*(x, \omega_2)$  term, the resulting integrands will all be peaked about  $\hat{x}_2$ , as before. This means that the main features of the two-source model of DPOAEs, namely a contribution to the ear canal signal coming from around the  $\hat{x}_2$  place and a separate component coming from around the DP tonotopic site, generalizes to higher-order DPOAEs even for the case of a pure cubic nonlinearity. As a consequence, the higher-order apical DPOAEs will correspond to equations of the same form as Eqs. (141), (142), and (162) where  $\Gamma_r(\omega_1, \omega_2)$  and  $\Gamma_l(\omega_1, \omega_2)$  are replaced by increasingly complex functions. Thus the fine structures of apical DPOAEs, regardless of order, will be controlled by the factor given in Eq. (163). An important implication of this result is that when the  $\omega_2$  primary is held constant in frequency while sweeping the  $\omega_1$  primary in frequency, the resulting DPOAEs have fine structures whose minima and maxima will approximately line up.

The higher-order basal DPs can be studied in a similar fashion. For instance, the leading nonzero source density contribution for  $\omega_{dp23} = 3\omega_2 - 2\omega_1$  is

$$\rho_{dp23}(x) = \frac{i(3\omega_2 - 2\omega_1)^3 \sigma_{bm} \gamma_2(x) k_0^2 \xi_2(x, \omega_2)^2 \xi_{dp21}^*(x, 2\omega_1 - \omega_2)}{\Delta(x, 3\omega_2 - 2\omega_1)}. \quad (173)$$

This source density will lead to an equation for the ear canal pressure for the  $3\omega_2 - 2\omega_1$  DPOAE which is proportional to  $\psi_r(\hat{x}_2, 3\omega_2 - 2\omega_1)$ , with  $\hat{x}(3\omega_2 - 2\omega_1) < \hat{x}_2$ , in analogy to

Eq. (169). Since  $|\psi_r(\hat{x}_2, 3\omega_2 - 2\omega_1)| \ll 1$  under these conditions, the resulting basal DPOAE will be negligible except for very small primary frequency ratios and/or very high primary levels.

### F. Modeling the “bandpass” character of apical and basal DPOAEs

It is well documented (e.g., Brown *et al.*, 1992) that the  $2\omega_1 - \omega_2$  DPOAE in humans has a maximum near  $\omega_2/\omega_1 \approx 1.225$ . For DPOAE measurements with  $\omega_2$  held fixed, the DPOAE level rapidly decreases as the ratio of  $\omega_2/\omega_1$  is moved away from this optimal ratio. This approximately “bandpass” structure has commonly been referred to as evidence for a second mechanical filter (e.g., Brown *et al.*, 1992; Allen and Fahey, 1993). However, a number of studies (Matthews and Molnar, 1986; Neely and Stover, 1997; van Hengel and Duifhuis, unpublished) have demonstrated that this bandpass shape arises naturally in models that do not contain a second filter. It has also been argued by van Hengel and Duifhuis that the bandpass shape is due to an interference between different components of the generated  $2\omega_1 - \omega_2$  DP wave in the cochlea.

This argument can be tested in the current model, in which the bandpass structure would be related to the presence of a maximum in  $\Gamma_r(\omega_1, \omega_2)$  for  $\omega_2/\omega_1 = 1.225$ . In order to simplify the discussion, the only case considered is that for which no roughness is present (so that  $R_a \rightarrow 0$ ). Then



the  $2\omega_1 - \omega_2$  DPOAE will have a maximum (for fixed  $\omega_2$ ) when  $(\partial/\partial\omega_1)\Gamma_r(\omega_1, \omega_2) = 0$ , which approximately occurs when

$$\hat{k} - 2k_1 - k_{dp} = 0. \quad (174)$$

For  $\omega_2/\omega_1$  sufficiently large, it can be shown that

$$k_1 \approx \frac{k_0\omega_1}{\sqrt{\omega_2^2 - \omega_1^2}}, \quad (175)$$

$$k_{dp} \approx \frac{k_0(2\omega_1 - \omega_2)}{\sqrt{\omega_1(\omega_2 - \omega_1)}}. \quad (176)$$

Consequently the extremum condition Eq. (174) becomes

$$\frac{\hat{k}}{k_0} = \frac{2}{\sqrt{(\omega_2/\omega_1)^2 - 1}} + \frac{2 - \omega_2/\omega_1}{2\sqrt{\omega_2/\omega_1 - 1}}. \quad (177)$$

If it is assumed that the  $2\omega_1 - \omega_2$  DPOAE maximum occurs when  $\omega_2/\omega_1 \cong 1.225$ , Eq. (177) then gives the relation

$$\hat{k} \cong 3.6k_0. \quad (178)$$

Since  $\hat{k} \cong 78 \text{ cm}^{-1}$  from fine structure measurements, this gives the prediction  $k_0 \cong 22 \text{ cm}^{-1}$ , which in turn implies that  $N_\lambda \cong 3.9$  [see Eq. (62)].

A criticism that has been raised about these models is that the bandpass structure does not roll-off rapidly enough. This criticism is answered in the context of the current model by requiring that the basilar membrane activity pattern be sufficiently tall and broad so that  $\chi_r(\hat{x}_2, \omega_{dp})$  in  $\Gamma_r(\omega_1, \omega_2)$  decreases rapidly for  $\omega_2/\omega_1 \gg 1.225$ . Since the models of the previous studies did not exhibit tall-broad activity patterns, it is not surprising that these models were unable to reproduce the observed rapid roll-off.

The observation of van Hengel and Duifhuis (unpublished) that the bandpass shape is related to interference effects can be addressed in this formalism by letting  $k_1, k_{dp} \rightarrow 0$  in Eq. (138). Doing so removes the phase dependence of  $\chi_r(x, \omega_1)$  and  $\chi_r(x, \omega_{dp})$ , and changes the expression for  $\gamma_r(\omega_1, \omega_2)$  to

$$\gamma_r(\omega_1, \omega_2) = \sqrt{2\pi}\omega_2\sigma_x |\hat{\chi}_r| \chi_r^2(\hat{x}_2, \omega_1) \times e^{-[\hat{k}^2 - k_0^2]\sigma_x^2/2} e^{-ik_0\hat{k}\sigma_x} e^{+2\pi i N_\lambda}. \quad (179)$$

For this case,  $\Gamma_r(\omega_1, \omega_2)$  becomes peaked at  $\omega_1 = \omega_2$ , confirming that the phenomenon arises as from the interference. However, unlike the study of van Hengel and Duifhuis, the current model suggests that the interference is due to both the  $\omega_1$  and  $2\omega_1 - \omega_2$  travel waves, rather than just the  $2\omega_1 - \omega_2$  traveling wave as suggested by their paper.

For basal DPOAEs, it can be shown that the ratio of  $\omega_2/\omega_1$  for which the DPOAE is maximum occurs at a ratio much closer to one. From Eq. (153), we have the approximate condition for a minimum to be

$$2\hat{k} - k_1 + k_{dp} = 0, \quad (180)$$

which gives

$$2\frac{\hat{k}}{k_0} - \frac{1}{\sqrt{(\omega_2/\omega_1)^2 - 1}} + \frac{2 - \omega_2/\omega_1}{2\sqrt{\omega_2/\omega_1 - 1}} = 0. \quad (181)$$

For  $\hat{k}/k_0 \cong 3.6$ , this implies that  $\omega_2/\omega_1 \cong 1.0008$ , so that no ‘‘bandpass’’ filter shape is expected for basal DPOAEs. Since this value of  $\omega_2/\omega_1$  clearly violates the assumption that the maximum occurs at a wide ratio, what can actually be concluded from this analysis is that if a maximum in  $\Gamma_r'$  is present, it must be for a much more narrow ratio of  $\omega_2/\omega_1$ .

Equations (170)–(172), when integrated to give their source functions, also give rise to ‘‘bandpass’’ filtered responses. The equivalent expressions to Eq. (174) for the location of the maximum value of the generator functions for these higher orders is

$$\hat{k} - k(\hat{x}_2, \omega_1) - k(\hat{x}_2, 2\omega_1 - \omega_2) - k(\hat{x}_2, 3\omega_1 - 2\omega_2) = 0, \quad (\omega_{dp} = 3\omega_1 - 2\omega_2), \quad (182)$$

$$\hat{k} - k(\hat{x}_2, \omega_1) - k(\hat{x}_2, 3\omega_1 - 2\omega_2) - k(\hat{x}_2, 4\omega_1 - 3\omega_2) = 0, \quad (\omega_{dp} = 4\omega_1 - 3\omega_2), \quad (183)$$

$$\hat{k} - k(\hat{x}_2, 2\omega_1 - \omega_2) - k(\hat{x}_2, 3\omega_1 - 2\omega_2) - k(\hat{x}_2, 5\omega_1 - 4\omega_2) = 0, \quad (\omega_{dp} = 5\omega_1 - 4\omega_2). \quad (184)$$

Using the value of  $\hat{k}/k_0$  given by Eq. (178), these equations all give  $\omega_{dp}/\omega_2 \approx 0.70$  for the maximum value of the generator function, for all of the orders considered above. The maximum variation between all orders was approximately 10% (higher orders tended to have their peak at a slightly higher DP frequency). The experimental question of the degree to which the bandpass maxima line up with frequency has not been well explored, and its testing is complicated by the presence of fine structure in humans.

## VI. DISCUSSION

### A. Generality of the results

In obtaining the results of the previous sections, a number of assumptions have been made which might appear to reduce the generality of the results. These assumptions were made in order to obtain specific tests for the validity of the analysis, and for the most part do not influence the general form of the cochlear fine structures that were obtained.

In particular, a specific cochlear model which gives rise to tall and broad activity patterns was described in Sec. I. The advantage of this model is that it allows one to make specific predictions regarding various modeling assumptions (e.g., the effect of nonlinearity or distributed roughness), as well as to directly test in a time-domain cochlear model the predictions of the theoretical framework laid out in this paper. It is useful to note that the formal theory of fine structure presented here does not depend on the particular cochlear model described in this paper, although it does depend on the assumption of a one-dimensional cochlea.

It is also suggested by the results that even the inclusion of the higher cochlear dimensions in the analysis may not significantly alter the results reported here. This is because the quantities that relate the effects of roughness on the basilar membrane, etc., are mainly connected with a description of the dynamics of the basilar membrane. Thus including the full dimensionality of the cochlea into the model will modify

the form of the basilar membrane wave functions  $\chi_r(x, \omega)$  and  $\chi_l(x, \omega)$ , but should not otherwise influence the description of the generation of cochlear fine structure given in this study.

## B. Influence of nonlinearity

For simplicity, it has been assumed in this analysis that the nonlinearity originates solely from a Van der Pol type cubic nonlinearity in damping. It is likely that the actual form of the nonlinearity in the cochlea takes on a more complicated form (e.g., Van den Raadt and Duifhuis, 1990). However, in the limit of weak nonlinearity (small displacements), it can be shown that the cubic contribution is dominant in the generation of the  $2\omega_1 - \omega_2$  and  $2\omega_2 - \omega_1$  DPOAEs as long as the functional form of the nonlinearity is analytic at zero displacement.

Several effects of nonlinearity that were neglected in this analysis would have modified the formal results presented in this paper. The first is the effect of the nonlinearity on the place-frequency map. At higher levels of stimulation, the frequency that evokes maximal response at a given basilar membrane position decreases (reviewed in Ruggero *et al.*, 1997), and this will influence the positions of the maxima and minima of OAE fine structure when they are plotted against the emission frequency. Since threshold microstructure is not obtained at constant external tone level, the variation in tone level can in principle affect the locations of the maxima/minima. Finally, since SOAEs are not of equal level, the nonlinearity can affect the frequency spacings of large SOAEs relative to those of smaller SOAEs.

Other neglected nonlinear effects are those of self-suppression and two-tone suppression (reviewed in Kanis and de Boer, 1993, 1994). Self-suppression, in which the activity pattern of a traveling wave becomes progressively broader and less tall with the peak of the activity pattern shifting basally as the amplitude of the traveling wave increases, would be expected to manifest itself in, e.g., the fine structure of SEOAEs, the auditory threshold, and TEOAEs. As the height of the activity pattern (parametrized by  $\hat{\chi}_r$ ) decreases, the peak-to-peak height of the fine structure is expected to decrease. Because the nonlinearity does not have a strong effect on either the phase of the traveling wave in these models or in actual basilar membrane data (e.g., Ruggero *et al.*, 1997), nonlinearity is not expected to have a large effect on the wavelength of the traveling wave at the activity pattern peak (parametrized by  $\hat{k}$ ) and therefore should not have a large effect on the spacings of the fine structure. Two-tone suppression, in which one (larger) tone suppresses the activity pattern of a second tone, would be expected to manifest itself, e.g., in DPOAE phenomena. Some of the expected effects of two-tone suppression were discussed in Sec. V D. A very important effect described in that section was the suppression of the apical reflectance  $R_a(\omega_{dp})$  at the distortion product frequency  $\omega_{dp}$  by the external tones.

Full treatment of the nonlinear effects discussed above lies outside the scope of the present paper. The current study suffices to establish the connection among the OAE and threshold fine structures for low level stimuli. A more com-

plete treatment of the effects of nonlinearity on cochlear fine structure will be the subject of a future publication.

## C. Relationship among fine structures

The strong experimental evidence that the frequency spacing characteristics of SOAEs and SEOAEs, DPOAEs, and threshold microstructure are very similar suggests a close connection between the underlying mechanisms that give rise to these phenomena. This connection has a natural explanation in terms of cochlear reflections of traveling waves.

The main determinant of the frequency spacings in all of these measures is the rapid phase variation with frequency of  $R_a(\omega)$ , or equivalently the time of travel of a narrow-band cochlear wave packet from the base to the location of the activity pattern peak,  $\hat{x}(\omega)$ . This equivalence follows from the comparison of twice the group delay (relative to the signal at the base) of a narrow-band signal of center frequency  $\omega$  at  $x = \hat{x}(\omega)$  and the round-trip [from  $x = 0$  to  $x = \hat{x}(\omega)$ ] group delay associated with the phase variation with frequency of  $R_a(\omega)$ . The former is given by [see Eq. (55) and, e.g., Lighthill, 1978]

$$\tau_{\pi}(\omega) = 2 \int_0^{\hat{x}(\omega)} \frac{\partial k}{\partial \omega}(x, \omega) dx. \quad (185)$$

If scale invariance of the form

$$k(x, \omega) = k_{\text{scale inv.}} \left( \frac{\omega}{\omega_0 e^{-k\omega x}} \right) \quad (186)$$

is assumed, it follows that

$$\frac{\partial k(x, \omega)}{\partial \omega} = \frac{1}{\omega k_{\omega}} \frac{\partial k(x, \omega)}{\partial x}, \quad (187)$$

and hence that

$$\begin{aligned} \tau_{\pi}(\omega) &= \frac{2}{\omega k_{\omega}} \int_0^{\hat{x}(\omega)} \frac{\partial k(x, \omega)}{\partial x} dx \\ &= \frac{2}{\omega k_{\omega}} [k(\hat{x}(\omega), \omega) - k(0, \omega)] \approx \frac{2\hat{k}}{\omega k_{\omega}}, \end{aligned} \quad (188)$$

where  $\hat{k}$  is the wave number at the activity peak. The group delay coming from the phase variation of  $R_a(\omega)$  is given by [see Eqs. (90) and (93)]

$$\begin{aligned} \tau_a(\omega) &\equiv - \frac{\partial}{\partial \omega} [2\hat{k}\hat{x}(\omega)] \cong - \frac{\partial}{\partial \omega} \left[ \frac{2\hat{k}}{k_{\omega}} \log \left( \frac{\omega_0}{\omega} \right) \right] \\ &\approx \frac{2\hat{k}}{\omega k_{\omega}}, \end{aligned} \quad (189)$$

which is in agreement with Eq. (188). This equivalence was originally pointed out by Zweig and Shera (private communication).

Typical group delays range from approximately 10 ms for a 1500-Hz tone to 3 ms for a 5000-Hz tone. The delays coming from the other experimental parameters such as  $R_b(\omega)$  are generally much smaller, and are typically no larger than 0.5 ms. For the experimental measures considered above, it is only necessary to consider the contributions

arising from terms involving  $R_a$ . Assuming  $|R_a| \ll 1$ , the dominant phase dependences arise from the contributions,

$$\frac{1 + R_a \mathcal{R}_s}{1 - R_a R_b} \cong 1 + R_a (R_b + \mathcal{R}_s) \quad (\text{SEOAEs}), \quad (190)$$

$$\frac{1 + R_a \mathcal{R}_d}{1 - R_a R_b} \cong 1 + R_a (R_b + \mathcal{R}_d) \quad (\text{DPOAEs}), \quad (191)$$

$$\frac{1}{1 - R_a R_b} \cong 1 + R_a R_b \quad (\text{SOAEs, TEOAEs, threshold}). \quad (192)$$

The frequency spacings of the fine structure maxima/minima for these various phenomena can be obtained by noting that the phases of the coefficients of  $R_a$  in the three expressions all vary much more slowly than the phase of  $R_a$ . The effects of the slowly varying coefficients can be parametrized by writing

$$\left( \frac{\Delta \omega}{\omega} \right)_{\text{SEOAE}} = \frac{2\pi}{\phi_0 + \omega \tau_s},$$

$$\tau_s = \frac{d}{d\omega} \arg(R_b + \mathcal{R}_s) \quad (\text{SEOAEs}), \quad (193)$$

$$\left( \frac{\Delta \omega}{\omega} \right)_{\text{DPOAE}} = \frac{2\pi}{\phi_0 + \omega \tau_d},$$

$$\tau_d = \frac{d}{d\omega} \arg(R_b + \mathcal{R}_d) \quad (\text{DPOAEs}), \quad (194)$$

$$\left( \frac{\Delta \omega}{\omega} \right)_{\text{SOAE}} = \frac{2\pi}{\phi_0 + \omega \tau_b},$$

$$\tau_b = \frac{d}{d\omega} \arg(R_b) \quad (\text{SOAEs, TEOAEs, threshold}). \quad (195)$$

There are a number of qualitative predictions that can be made from Eqs. (190)–(195). First of all,  $\phi_0 \cong 30\pi \gg \omega \tau_s, \omega \tau_d, \omega \tau_b$ , so that qualitatively  $\Delta\omega/\omega$  is expected to be approximately equal for each type of fine structure phenomena.

The frequency spacings for SOAEs and threshold microstructure are predicted to be equal, but a deviation is expected from these for the spacings of both SEOAEs and DPOAEs. However, the sign of the shift in  $\Delta\omega/\omega$  for SEOAEs and DPOAEs depends sensitively on the underlying model, and possibly on the frequency of the OAE, since the shift arises from the addition of two slowly varying terms.

It is interesting to note that, from Eqs. (110) and (113), the frequencies of high level TEOAEs and SOAEs [for which the condition of Eq. (114) is approximately satisfied] should correspond to minima of the threshold microstructure. This implication of the model is in agreement with experimental data (e.g., Long, 1984; Zwicker and Schloth, 1984; Long and Tubis, 1988a).

## D. Asymmetry of the forward- and reverse-traveling waves

A surprising effect that was uncovered in this study is the asymmetric effect of the cochlear amplifier on the forward- [parametrized by  $\chi_f(x, \omega)$ ] and reverse- [parametrized by  $\chi_r(x, \omega)$ ] traveling waves. This asymmetry is easily observed in Fig. 5, and is manifested by a 40–60-dB enhancement of the forward-traveling wave compared to a 20–30-dB reduction in the reverse-traveling wave.

The upward amplitude shift in the forward-traveling wave for the active compared to passive case has an immediate interpretation in terms of cochlear amplification of acoustical energy. On the other hand, the reduction in the amplitude of the reverse-traveling wave does not imply that the reverse-traveling wave is not amplified. The reason for this is that the reverse-traveling wave starts at an apical point and moves basally. Thus to “fairly” compare the active versus passive models, one must set the two  $\chi_l(x, \omega)$  curves in Fig. 5 to the same initial amplitude (rather than final amplitude, as is done for purposes of mathematical convenience). When the two curves are set equal, e.g., at the position of the maximum amplitude for the forward-traveling wave  $\chi_f(x, \omega)$ , one finds that in fact the reverse-traveling wave for the active case is enhanced by the 20–30-dB factor mentioned above relative to the passive case. It should also be noted that significant amplification effects occur for both forward- and reverse-traveling waves only near the traveling wave’s tonotopic location.

A second result is the lack of a peaked reverse-traveling wave as predicted by this study. An important implication of this result is that forward-traveling waves should be more readily affected by suppression by external tones than reverse-traveling waves. Consequently, the relative strengths of the two DPOAE sources can be influenced, e.g., by the placement of a suppressor tone near in frequency to the DPOAE (see Heitmann *et al.*, 1998). Another prediction is that only the forward-traveling wave should be significantly influenced by inhomogeneities on the basilar membrane. Also, coherent reflections will only be possible for the forward-traveling wave.

## E. Comparison of apical to basal DPOAEs

As discussed in Secs. V C and V D, important differences in the phenomenology are expected for apical versus basal DPOAEs. These differences arise because apical DPOAEs are generated in the so-called stiffness-dominated region, where the propagating traveling wave is only slightly attenuated, whereas basal DPOAEs are generated in the so-called mass-dominated region where the propagating traveling wave is highly attenuated. As a result of this large attenuation, basal DPOAEs are generally not observed except at narrow primary-frequency ratios, or when the levels of the primaries are very large ( $L \geq 65$  dB SPL). It is expected in this model that basal DPOAEs would be observed at a significant level for higher-level primaries because of the expected broadening of the traveling wave, which results in a greater overlap of the traveling waves of the primaries. Since the traveling wave becomes broader at smaller primary frequencies, an increase in the levels of the basal DPOAEs will

also be expected for lower frequency primaries. Both of these effects are observed experimentally (e.g., Piskorski, 1997; Martin *et al.*, 1998).

The existence of a “bandpass” structure for apical DPOAEs has been widely reported in the literature (e.g., Brown *et al.*, 1992). This bandpass structure appears to be missing in the basal DPOAEs (e.g., Piskorski, 1997). Both results are accounted for in this study (see Sec. V F) by differences in the DPOAE generator functions for the two cases. The bandpass structure of apical DPOAEs was shown to originate from an interference phenomenon involving the primaries and the DPOAE traveling waves.

## F. Experimental tests

In spite of the generality of the formalism, a number of relationships exist among the cochlear fine structures that allow for very specific predictions. As discussed above, one of the strongest predictions is that the fine structure spacings are approximately equal. This prediction is in agreement with the many studies of the various fine structures which were summarized in the Introduction.

The data on the fine structure of DPOAEs provides one of the strongest tests of the formalism presented in this study. However, because of the diverse nature of DPOAE phenomena, the inclusion of the complete analysis of DPOAE fine structure in the present paper would make it prohibitively long. A complete treatment of the phenomenology of DPOAEs as it relates to the “two source” model given in this paper, along with the corroborating evidence, will be the subject of future publications. Some of the salient features of this study are now summarized.

An important prediction of the formalism is that the source region for DP reflection is around the DP tonotopic place. Because of the strong phase dependence of the apical reflectance  $R_a(\omega_{dp})$  on the DP frequency, the fine structure of DPOAEs is rooted in the tonotopic location of the DP and not in the interaction region of the primaries as suggested by He, Schmiedt, and colleagues (He and Schmiedt, 1993, 1996; Sun *et al.*, 1994a, 1994b). This implies that DPOAE fine structure will have similar spacing (but not necessarily the same phase of oscillation), independent of the experimental paradigm (e.g., fixed ratio, fixed  $f_1$ , or fixed  $f_2$ ) and independent of DP order for ratios  $f_2/f_1 \geq 1.05$ , when the DPOAE level is plotted versus DP frequency. However, if instead the DPOAE level is plotted versus either  $f_1$  or  $f_2$ , a strong dependence of the frequency spacing on the paradigm used and DP order can be observed. An exception to this result occurs in the case of the fixed ratio paradigm, for which the fine structure spacing remains independent of DPOAE order regardless of whether the level is plotted versus  $f_{dp}$ ,  $f_1$ , or  $f_2$ . This result is a consequence of the approximately exponential scaling of the place-frequency map. Also, the fine structure spacing will become somewhat dependent on the individual primary frequencies in the case of small ratios ( $f_2/f_1 \cong 1.05$ ) of the primaries. This follows from a careful analysis of  $\mathcal{R}_d(\hat{x}_2, \omega_1)$  in Eq. (159) when  $\hat{x}_2$  is in the short wave region of the DP waves. This interesting point will be explored experimentally and theoretically in another paper.

The model of this paper may give important insight concerning the effect of cochlear damage on OAE fine structure and threshold microstructure. As is shown in Fig. 5, there is a large difference in the relative magnitudes of the basis functions,  $\chi_r(x, \omega)$  and  $\chi_l(x, \omega)$ , for passive and active cochlea. This may result, e.g., in a decrease of  $R_a$  and an increase in  $\mathcal{R}_d(\hat{x}_2, \omega_1, \omega_2) (\approx \chi_l(\omega_{dp})/\chi_r(\omega_{dp}, \hat{x}_2))$  in Eq. (162) for a passive (or damaged) cochlea versus a healthy (active) one. A number of our results are based on the assumption that the magnitude of the ratio  $\chi_l(x, \omega_{dp})/\chi_r(x, \omega_{dp})$  is very small for  $x \approx \hat{x}(\omega_{dp})$ , implying that these results may have to be modified for the case of damaged cochleae. Also, according to Eqs. (104) and (162), there may still be a substantial level of DPOAE fine structure in damaged ears even though the level of the SEOAE fine structure is considerably reduced. A detailed study of tests of the model for damaged ears will be given in a future study.

## VII. SUMMARY AND CONCLUSIONS

A class of nonlinear-active cochlear models has been shown to successfully describe a broad body of data on the quasi-periodic (approximately 0.4 bark) variation with frequency of otoacoustic emission fine structure and the microstructure of the hearing threshold. The key elements of the models are (1) tall/broad cochlear traveling wave activity patterns (as discussed in Secs. I A, I B, and I C and plotted in Figs. 4 and 5; (2) cochlear wave reflections at the base of the cochlea (Sec. I E 2) and around the tonotopic place of the traveling wave, with the latter being due to distributed cochlear inhomogeneities in conjunction with the tall/broad activity pattern (Sec. I E 3); and (3) distributed nonlinear cochlear response (Secs. I A, V). In order to obtain approximate analytic expressions for the various fine structures, it is convenient to introduce cochlear basis functions, i.e., right- and left-moving solutions of the linear-active cochlear wave equation in the frequency domain (Sec. I C). The analytic expressions so obtained are extremely useful for providing insight into the relationships among the OAE and hearing threshold fine structures.

The fine structures for SEOAEs [Eq. (104)], TEOAEs [Eq. (110)], threshold microstructure [Eq. (113)], DPOAEs [Eqs. (162) and (169)], and the frequency spacing of neighboring spontaneous emissions [Eqs. (114) and (121)] are mainly determined by the parameters for basal reflectance ( $R_b$ ), apical reflectance around the tonotopic place ( $R_a$ ), and the ratio of the standard basis functions and their spatial derivatives. The various relationships between the fine structures are concisely summarized in Sec. VI C [Eqs. (193)–(195) and the text following them]. The models also account for the bandpass character of DPOAEs as discussed in Sec. V F.

## ACKNOWLEDGMENTS

We wish to thank Jont Allen, Egbert de Boer, Paul Fahy, Peter van Hengel, Douglas Keefe, Christopher Shera, Hero Wit, and George Zweig for many stimulating discussions concerning mechanisms for generation of cochlear fine structure. We also wish to thank Chris Tong for reading this

manuscript. We would also like to acknowledge the careful reviews by Rick Schmiedt and an anonymous reviewer, which helped to make this a better paper. This research was supported in part by NIH/NIDCD Grants No. R01 DC00307 and No. R29 DC03094.

## APPENDIX: FREQUENTLY USED SYMBOLS AND THEIR MEANING

Frequently used mathematical symbols used in this study and their meaning are summarized below. In the cases for which the symbol has a defining equation, its corresponding equation number is also included. The organization of this Appendix is loosely based on that of Zweig and Shera (1995).

### Operators

$\text{Re}(z)$	real part of $z$
$\text{Im}(z)$	imaginary part of $z$
$\arg(z)$	phase of $z$
$ z $	magnitude of $z$
$\hat{A}$	denotes that the quantity $A$ contains a random component
$\delta A$	denotes the difference $A - A_{\text{sm}}$ , where $A_{\text{sm}}$ is the value of the underlying quantity for a smooth linear cochlea

### Independent variables

$f$	frequency
$k$	wave number ( $2\pi/\lambda$ ), also used to signify quantities with units of inverse length
$P$	pressure
$t$	time
$x$	position along basilar membrane ( $x=0$ corresponds to base)
$\lambda$	wavelength
$\omega$	angular frequency ( $2\pi \times f$ )
$\xi$	linear displacement

### Physical quantities (cochlea)

$b_{\text{nl}}$	scale for nonlinear saturation, assumed independent of $x$ (see Table I)
$\hat{k}$	real value of wave number at activity pattern maximum ( $\hat{k}$ is assumed independent of frequency)
$k_0$	geometric wave number of cochlea [Eq. (6)]
$k_\omega$	exponential constant of frequency map
$k(x, \omega)$	complex wave number [Eq. (20)]
$k_{r,l}(x, \omega)$	wave-number basis functions [Eq. (40)]
$k_{\text{sm}}(x, \omega)$	smooth component of wave number [Eq. (65)]
$L_{\text{bm}}$	length of basilar membrane (see Table I)
$P_d(x, t)$	instantaneous pressure difference between scala tympani and scala vestibuli [Eq. (1)]
$P_d(x, \omega)$	complex amplitude of basilar membrane motion [Eq. (18)]
$S_{\text{avg}}$	reciprocal average of cross-sectional areas of cochlear scalae (see Table I)
$W_{\text{bm}}$	average width of basilar membrane (see Table I)

$\hat{\chi}(\omega)$	tonotopic location of traveling wave of frequency $\omega$
$\hat{\chi}_{r,l}$	level of right, left basilar membrane basis functions at tonotopic frequency of traveling wave ( $\hat{\chi}_{r,l}$ is assumed independent of frequency)
$\gamma_{\text{bm}}(x, \xi, \dot{\xi})$	total basilar membrane damping function
$\gamma_0(x)$	linear (with displacement) basilar membrane damping function ( $\gamma_0 e^{-k_r x} + \gamma_1$ ) (see Table I)
$\gamma_2(x)$	nonlinear (with displacement) basilar membrane damping function [ $\gamma_2(x) = \gamma_0(x)/b_{\text{nl}}^2$ ]
$\kappa_{f,s}(x)$	“fast, slow” feedback coupling strength [Eq. (4)]
$\omega_{\text{bm}}(x, \xi, \dot{\xi})$	total basilar membrane frequency map of cochlea [Eq. (4)]
$\omega_0(x)$	linear (with displacement) component of basilar membrane frequency map [Eq. (5)]
$\omega_0$	value of linear basilar membrane frequency map at base [ $\omega_0 = \omega_0(0)$ , see also Table I]
$\rho$	density of the perilymph
$\rho_{f,s}$	“fast,slow” feedback coupling strength coefficients [ $\kappa_{f,s}(x)/\omega_0(x)$ ]
$\psi_{f,s}$	“fast,slow” feedback constant [ $\tau_{f,s}(x)/\omega_0(x)$ ]
$\sigma_{\text{bm}}$	effective mass per unit area of basilar membrane
$\tau_{f,s}(x)$	“fast,slow” feedback delay function [Eq. (4)]
$\xi(x, t)$	instantaneous displacement of basilar membrane [Eq. (2)]
$\xi(x, \omega)$	complex amplitude of basilar membrane motion [Eq. (19)]

### Derived quantities (cochlea)

$a_{r,l}$	right, left pressure wave basis function amplitudes [Eqs. (44) and (45)]
$b_{r,l}$	right, left basilar membrane basis function amplitudes [Eq. (53)]
$N_\lambda$	number of wavelengths of traveling wave from base to activity maximum ( $N_\lambda \cong k_0/4k_\omega$ , see also Table I)
$r_{a,b}(x, \omega)$	ratios of pressure wave amplitudes [Eq. (79)]
$R_a(x, \omega)$	ratio of basal to apical traveling waves [Eq. (77)]
$R_b(x, \omega)$	ratio of apical to basal traveling waves [Eq. (78)]
$R_a(\omega)$	reflectance function at the base for an initially apically moving wave [Eq. (94)]
$R_b(\omega)$	reflectance function at the base for an initially basally moving wave [Eq. (82)]
$\mathcal{R}_a(x, \omega)$	ratio of basal to apical traveling basis functions [Eq. (81)]
$\mathcal{R}_b(x, \omega)$	ratio of apical to basal traveling basis functions [Eq. (81)]
$\mathcal{R}_d(x_2, \omega_1)$	ratio of DP sources $\Gamma_l/\Gamma_r$ [Eq. (159)]
$\mathcal{R}_s(x_2, \omega_1)$	ratio of derivatives of basis function $\psi'_l(x, \omega)/\psi'_r(x, \omega)$ [Eq. (102)]
$W_0(\omega)$	Wronskian [Eq. (38)]
$\chi_{r,l}(x, \omega)$	right, left basilar membrane basis functions [Eq. (51)]

$\Delta(x, \omega)$	denominator of wave number [Eq. (21)]	$T_{pd}(\omega)$	transfer function relating $P'_d(0, \omega)$ to $P_e(\omega)$ [Eq. (30)]
$\delta k^2(x, \omega)$	deviation of a particular cochlear model from underlying "smooth" model [Eq. (35)]	$V_{tc}$	volume of tympanic cavities
$\rho_{scat}(x, \omega)$	scattering density due to distributed inhomogeneities on basilar membrane [Eq. (71)]	$\Delta_{ow}$	denominator of middle ear wave-number function [Eq. (25)]
$\rho_{source}(x, \omega)$	cochlear pressure source density [Eq. (63)]	$\Gamma_{mi}$	incus level ratio (see Table I)
$\psi_{r,l}(x, \omega)$	right, left pressure wave basis functions [Eqs. (44) and (45)]	$S_{ty}$	effective area of tympanic membrane (see Table I)
<b>Derived quantities (fine structures)</b>			
$P_{th}$	minimum detectable driving pressure threshold	$S_{ow}$	effective area of oval window (see Table I)
$\varphi_0$	phase constant relating phase behavior of $R_a$ with frequency [Eq. (93)]	$\gamma_{ow}$	damping constant for middle ear (see Table I)
$\mathcal{R}_s(\omega)$	ratio of apical to basal wave-number functions [Eq. (102)]	$\sigma_{ow}$	effective areal density of oval window ( $S_{ow}/m_{ow}$ , see also Table I)
$\Delta x$	tonotopic spacing between adjacent fine structure maxima [Eq. (106)]	$\omega_{ow,mech}$	mechanical frequency of middle ear [square root of mechanical (nonacoustic) stiffness divided by mass]
$\Delta \omega$	frequency spacing between adjacent fine structure maxima [Eq. (106)]	$\omega_{ow,e}$	frequency of middle ear corrected for loading of tympanic cavity [Eq. (12)]
$\Gamma_{r,l}(\omega_1, \omega_2)$	source function for the $2\omega_1 - \omega_2$ DP [Eq. (143)]	$\omega_{ow}$	frequency of middle ear, corrected for loading of tympanic and ear canal cavities [Eq. (15)]
$\Gamma'_{r,l}(\omega_1, \omega_2)$	source function for the $2\omega_2 - \omega_1$ DP [Eq. (152)]	$\xi_{ow}(x, t)$	instantaneous displacement of oval window [Eq. (10)]
$\rho_{dp}(x)$	source density function for $2\omega_1 - \omega_2$ DPOAE [Eq. (127)]	$\xi_{ow}(x, \omega)$	complex amplitude of oval window [Eq. (23)]
$\rho_{dp'}(x)$	source density function for $2\omega_2 - \omega_1$ DPOAE [Eq. (127)]		
$\tau_a$	group delay associated with the apical reflectance function $R_a(\omega)$ [Eq. (189)]		
$\tau_b$	group delay associated with the basal reflectance function $R_b(\omega)$ [Eq. (118)]		
$\tau_{rt}(\omega)$	round-trip travel time of a traveling wave of frequency $\omega$ [Eq. (185)]		
$\xi_{th}$	basilar membrane displacement detection threshold		
<b>Physical and derived quantities (middle/outer ear)</b>			
$a_d$	parameter coupling $P_e$ to $(1/\omega^2)\partial P_d/\partial x$ [Eq. (31)]		
$G_{me}$	mechanical gain of ossicles [Eq. (11)]		
$G_{me}(\omega)$	generalized mechanical gain of ossicles for general middle ear models [Eq. (22), see also Table I]		
$k_{ow}(\omega)$	wave-number function of middle ear [Eq. (24), see also Table I]		
$k_{ow,0}$	geometrical constant relating pressure in ear canal to pressure difference at base [Eq. (9), see also Table I]		
$P_e(x, t)$	instantaneous pressure in ear canal		
$P_e(x, \omega)$	complex pressure amplitude in ear canal		
$P_{dr}(t)$	"calibrated driving pressure" [Eq. (13)]		
$P_{dr}(\omega)$	complex "calibrated driving pressure" amplitude		
$P_e^a$	adiabatic bulk modulus of air in ear canal		
$P_{tc}^a$	adiabatic bulk modulus of air in tympanic cavities		
$T_{dr}(\omega)$	transfer function relating $P_{dr}(\omega)$ to $P_e(\omega)$ [Eq. (30)]		
<p>Allen, J. B., and Fahey, P. F. (1993). "A second cochlear-frequency map that correlates distortion product and neural tuning measurements," <i>J. Acoust. Soc. Am.</i> <b>94</b>, 809–816.</p> <p>Brass, D., and Kemp, D. T. (1993). "Suppression of stimulus frequency otoacoustic emissions," <i>J. Acoust. Soc. Am.</i> <b>93</b>, 920–939.</p> <p>Bright, K. E. (1997). "Spontaneous otoacoustic emissions," in <i>Otoacoustic Emissions: Clinical Applications</i>, edited by M. Robinette and T. J. Glatke (Theime, New York), pp. 46–62.</p> <p>Brown, A. M., Gaskill, S. A., and Williams, D. M. (1992). "Mechanical filtering of sound in the inner ear," <i>Proc. R. Soc. London, Ser. B</i> <b>250</b>, 29–34.</p> <p>Brown, A. M., Harris, F. P., and Beveridge, H. A. (1996). "Two sources of acoustic distortion products from the human cochlea," <i>J. Acoust. Soc. Am.</i> <b>100</b>, 3260–3267.</p> <p>Cohen, M. F. (1982). "Detection threshold microstructure and its effect on temporal integration data," <i>J. Acoust. Soc. Am.</i> <b>71</b>, 1719–1733.</p> <p>de Boer, E. (1983). "No sharpening? A challenge for cochlear mechanics," <i>J. Acoust. Soc. Am.</i> <b>73</b>, 567–573.</p> <p>de Boer, E. (1995). "On equivalence of locally active models of the cochlea," <i>J. Acoust. Soc. Am.</i> <b>98</b>, 1400–1409.</p> <p>de Boer, E., and Viergever, M. A. (1982). "Wave propagation and dispersion in the cochlea," <i>Hearing Res.</i> <b>13</b>, 101–112.</p> <p>de Boer, E., and Viergever, M. A. (1984). "Validity of the Liouville–Green (or WKB) method for cochlear mechanics," <i>Hearing Res.</i> <b>8</b>, 131–155.</p> <p>Elliot, E. (1958). "A ripple effect in the audiogram," <i>Nature (London)</i> <b>81</b>, 1076.</p> <p>Engdahl, B., and Kemp, D. T. (1996). "The effect of noise exposure on the details of the distortion product emissions in humans," <i>J. Acoust. Soc. Am.</i> <b>99</b>, 1573–1588.</p> <p>Furst, M., Reshef, I., and Attias, J. (1992). "Manifestations of intense noise stimulation of spontaneous otoacoustic emissions and threshold microstructure: Experiment and model," <i>J. Acoust. Soc. Am.</i> <b>91</b>, 1003–1014.</p> <p>Glatke, T. J., and Robinette, M. (1997). "Transient evoked otoacoustic emissions," in <i>Otoacoustic Emissions: Clinical Applications</i>, edited by M. Robinette and T. J. Glatke (Theime, New York), pp. 63–82.</p> <p>Greenwood, D. D. (1990). "A cochlear frequency position function for several species—29 years later," <i>J. Acoust. Soc. Am.</i> <b>87</b>, 2592–2605.</p> <p>Hall, J. L. (1974). "Two-tone distortion products in a nonlinear model of the basilar membrane," <i>J. Acoust. Soc. Am.</i> <b>56</b>, 1818–1828.</p> <p>He, N.-J. (1990). "Frequency shift in spontaneous otoacoustic emission and threshold fine structure," Ph.D. thesis, University of Iowa.</p> <p>He, N.-J., and Schmiedt, R. A. (1993). "Fine structure of the <math>2f_1 - f_2</math> acoustic distortion product: Changes with primary level," <i>J. Acoust. Soc. Am.</i> <b>94</b>, 2659–2669.</p>			

- He, N.-J., and Schmiedt, R. A. (1996). "Effects of aging on the fine structure of the  $2f(1)-f(2)$  acoustic distortion product," *J. Acoust. Soc. Am.* **99**, 1012–1015.
- Heitmann, J., Waldmann, B., and Plinkert, P. K. (1996). "Limitations in the use of distortion product otoacoustic emissions in objective audiometry as the result of fine structure," *European Archives of Otolaryngology* **253**, 167–171.
- Heitmann, J., Waldmann, B., Schnitzler, H.-U., Plinkert, P. K., and Zenner, H.-P. (1998). "Suppression of distortion production otoacoustic emissions (DPOAE) near  $2f_1-f_2$  removes dp-gram fine structure—Evidence for a secondary generator," *J. Acoust. Soc. Am.* **103**, 1527–1531.
- Kanis, L. J., and de Boer, E. (1993). "Self-suppression in a locally active nonlinear model of the cochlea: A quasi-linear approach," *J. Acoust. Soc. Am.* **94**, 3199–3206.
- Kanis, L. J., and de Boer, E. (1994). "Two-tone suppression in a locally active nonlinear model of the cochlea," *J. Acoust. Soc. Am.* **96**, 2156–2165.
- Kemp, D. T. (1979a). "Evidence of nonlinearity and frequency selective wave amplification in the cochlea," *Archives of Otorhinolaryngology* **224**, 37–45.
- Kemp, D. T. (1979b). "The evoked cochlear mechanical response and auditory microstructure - evidence for a new element in cochlear mechanics," *Scandinavian Audiology Supplement* **9**, 35–47.
- Kemp, D. T. (1980). "Towards a model for the origin of cochlear echoes," *Hearing Res.* **2**, 533–548.
- Kemp, D. T. (1997). "Otoacoustic emissions in perspective," in *Otoacoustic Emissions: Clinical Applications*, edited by M. Robinette and T. J. Glatke (Theime, New York), pp. 1–21.
- Kemp, D. T., and Brown, A. M. (1983). "An integrated view of the cochlear mechanical nonlinearities observable in the ear canal," in *Mechanics of Hearing*, edited by E. de Boer and M. A. Viergever (Martinus Nijhoff, The Hague, The Netherlands), pp. 75–82.
- Kemp, D. T., and Chum, R. (1980). "Properties of the generator of stimulated acoustic emissions," *Hearing Res.* **2**, 213–232.
- Kim, D. O., Neely, S. T., Molnar, C. E., and Matthews, J. W. (1980). "An active cochlear model with negative damping in the partition: Comparison with Rhode's ante- and post-mortem observations," in *Psychophysical and Behavioral Studies in Hearing*, edited by G. V. d. Brink and F. A. Bilsen (Delft U.P., Delft), pp. 7–14.
- Koshigoe, S., and Tubis, A. (1982). "Implications of causality, time-translation invariance, linearity, and minimum-phase behavior for basilar membrane response functions," *J. Acoust. Soc. Am.* **71**, 1194–1200.
- Kummer, P., Janssen, T., and Arnold, W. (1995). "Suppression tuning characteristics of the  $2f_1-f_2$  distortion product otoacoustic emission in humans," *J. Acoust. Soc. Am.* **98**, 197–210.
- Lighthill, J. (1978). *Waves in Fluids* (Cambridge U.P., Cambridge, England).
- Long, G. R. (1984). "The microstructure of quiet and masked thresholds," *Hearing Res.* **15**, 73–87.
- Long, G. R., Sun, C., and Talmadge, C. (1993a). "Interactions between spontaneous emissions and external tones: Suppression, frequency shifting and distortion product generation," in *Biophysics of Hair Cell Sensory Systems*, edited by H. Duifhuis, J. W. Horst, P. van Dijk, and S. M. van Netten (World Scientific, Singapore), pp. 40–46.
- Long, G. R., Sun, C., and Talmadge, C. L. (1993b). "Interactions between spontaneous emissions and external tones: Suppression, frequency shifting and distortion product generation," in *Biophysics of Hair Cell Sensory Systems*, edited by H. Duifhuis, J. W. Horst, P. van Dijk, and S. M. van Netten (World Scientific, Singapore), pp. 40–46.
- Long, G. R., and Tubis, A. (1988a). "Investigations into the nature of the association between threshold microstructure and otoacoustic emissions," *J. Acoust. Soc. Am.* **84**, 1343–1353.
- Long, G. R., and Tubis, A. (1988b). "Modification of spontaneous and evoked otoacoustic emissions and associated psychoacoustic microstructure by aspirin consumption," *J. Acoust. Soc. Am.* **84**, 1343–1353.
- Lonsbury-Martin, B. L., Martin, G. K., and Whitehead, M. L. (1997). "Distortion product otoacoustic emissions," in *Otoacoustic Emissions: Clinical Applications*, edited by M. Robinette and T. J. Glatke (Theime, New York), pp. 83–109.
- Martin, G. K., Jassir, D., Stagner, B. B., Whitehead, M. L., and Lonsbury-Martin, B. L. (1998). "Locus of generation for the  $2f_1-f_2$  vs  $2f_2-f_1$  distortion-product otoacoustic emissions in normal-hearing humans revealed by suppression tuning, onset latencies, and amplitude correlations," *J. Acoust. Soc. Am.* **103**, 1957–1971.
- Mathews, J., and Walker, R. (1964). *Mathematical Methods of Physics* (Benjamin, New York).
- Matthews, J. W., and Molnar, C. E. (1986). "Modeling intracochlear and ear canal distortion product ( $2f_1-f_2$ )," in *Peripheral Auditory Mechanisms*, edited by J. B. Allen, A. Hubbard, S. T. Neely, and A. Tubis (Springer-Verlag, Berlin), pp. 258–265.
- Mauermann, M. S. (1997). "Analyse von otoakustischen Emissionen und ihr Zusammenhang sur Psychoakustik," Master's thesis, Carl von Ossietzky Universitat Oldenburg.
- Mauermann, M. S., Uppenkamp, S., and Kollmeier, B. (1997). "Periodiztaet und pegelabhaengigkeit der spektralen feinstruktur von verzerrungsprodukt-emissionen," *Audiol. Akustik* **36**, 92–104.
- Moore, B. C. J. (1978). "Psychophysical tuning curves measured in simultaneous and forward masking," *J. Acoust. Soc. Am.* **63**, 524–532.
- Neely, S. T., and Stover, L. J. (1997). "A generation of distortion products in a model of cochlear mechanics," in *Diversity in Auditory Mechanics*, edited by E. Lewis, G. Long, R. Lyon, P. Narins, and C. Steele (World Scientific, Singapore), pp. 434–440.
- Norton, S. J., and Stover, L. J. (1994). "Otoacoustic emissions: An emerging clinical tool," in *Handbook of Clinical Audiology*, edited by J. Katz (Williams and Wilkins, Maryland), pp. 448–462.
- O'Mahoney, C. F., and Kemp, D. (1995). "Distortion product otoacoustic emission delay measurement in humans," *J. Acoust. Soc. Am.* **97**, 3721–3735.
- Patuzzi, R. (1996). "Cochlear micromechanics and macromechanics," in *Springer Handbook of Auditory Research, Volume 8: The Cochlea*, edited by P. Dallos, A. N. Popper, and R. R. Fay (Springer-Verlag, New York), pp. 186–257.
- Piskorski, P. (1997). "The origin of the distortion product otoacoustic emission fine structure," Ph.D. thesis, Purdue University.
- Press, W. H., Teukolsky, S. A., Vetterling, W. T., and Flannery, B. P. (1992). *Numerical Recipes in C* (Cambridge U.P., Cambridge, England), 2nd ed.
- Rhode, W. S. (1971). "Observations of the vibration of the basilar membrane in squirrel monkeys using the Mössbauer technique," *J. Acoust. Soc. Am.* **49**, 1218–1231.
- Robles, L., Ruggero, M. A., and Rich, N. C. (1997). "Two-tone distortion on the basilar membrane of the chinchilla cochlea," *J. Neurophysiol.* **77**, 2385–2399.
- Rosowski, J. R. (1995). "Models of external- and middle-ear function," in *Springer Handbook of Auditory Research, Volume 6: Auditory Computation*, edited by H. L. Hawkins, T. A. McMullen, A. N. Popper, and R. R. Fay (Springer-Verlag, New York), pp. 15–61.
- Ruggero, M. A., Rich, N. C., Recio, A., and Narayan, S. S. (1997). "Basilar-membrane responses to tones at the base of the chinchilla cochlea," *J. Acoust. Soc. Am.* **101**, 2151–2163.
- Schloth, E. (1983). "Spectral content of spontaneous otoacoustic emissions and fine structure of the threshold in quiet," *Acustica* **53**, 250–256.
- Shera, C. A., and Zweig, G. (1991). "Reflection of retrograde waves within the cochlea and at the stapes," *J. Acoust. Soc. Am.* **89**, 1290–1305.
- Shera, C. A., and Zweig, G. (1993a). "Dynamic symmetry creation: The origin of spectral periodicity in evoked otoacoustic emissions," in *Biophysics of Hair Cell Sensory Systems*, edited by H. Duifhuis, J. W. Horst, P. van Dijk, and S. M. van Netten (World Scientific, Singapore), pp. 54–63.
- Shera, C. A., and Zweig, G. (1993b). "Noninvasive measurements of the cochlear traveling wave ratio," *J. Acoust. Soc. Am.* **93**, 3333–3352.
- Stover, L. J., Neely, S. T., and Gorga, M. P. (1996). "Latency and multiple sources of distortion product emissions," *J. Acoust. Soc. Am.* **99**, 1016–1024.
- Stover, L. J., and Norton, S. J. (1993). "The effects of aging on otoacoustic emissions," *J. Acoust. Soc. Am.* **94**, 2670–2681.
- Strube, H. W. (1989). "Evoked otoacoustic emission as cochlear Bragg reflections," *Hearing Res.* **38**, 35–46.
- Sun, X. M., Schmiedt, R. A., He, N.-J., and Lam, C. F. (1994a). "Modeling the fine structure of the  $2f(1)-f(2)$  acoustic distortion product. 1. Model development," *J. Acoust. Soc. Am.* **96**, 2166–2174.
- Sun, X. M., Schmiedt, R. A., He, N.-J., and Lam, C. F. (1994b). "Modeling the fine structure of the  $2f(1)-f(2)$  acoustic distortion product. 2. Model evaluation," *J. Acoust. Soc. Am.* **96**, 2175–2183.
- Talmadge, C., Long, G. R., and Tubis, A. (1993). "New off-line method for detecting spontaneous otoacoustic emissions in human subjects," *Hearing Res.* **71**, 170–182.
- Talmadge, C., and Tubis, A. (1993). "On modeling the connection between

- spontaneous and evoked otoacoustic emissions,” in *Biophysics of Hair Cell Sensory Systems*, edited by H. Duifhuis, J. W. Horst, P. van Dijk, and S. M. van Netten (World Scientific, Singapore), pp. 25–32.
- Talmadge, C. L., Tubis, A., Long, G. R., and Piskorski, P. (1996). “Evidence for multiple spatial origins of the fine structure of distortion product otoacoustic emissions in humans, and its implications: Experimental and modeling results,” in Abstracts of the Nineteenth Midwinter Research Meeting of the Association for Research in Otolaryngology, edited by D. J. Lim (unpublished), p. 94, Abstract.
- Talmadge, C., Tubis, A., Piskorski, P., and Long, G. R. (1997). “Modeling otoacoustic emission fine structure,” in *Diversity in Auditory Mechanics*, edited by E. Lewis, G. Long, R. Lyon, P. Narins, and C. Steele (World Scientific, Singapore), pp. 462–471.
- Thomas I. B. (1975). “Microstructure of the pure tone threshold,” *J. Acoust. Soc. Am.* pp. S26 and S27, abstract.
- Van den Brink, G. (1970). “Experiments on binaural diplacusis and tone perception,” in *Frequency Analysis and Periodicity Detection in Hearing*, edited by R. Plomp and G. F. Smoorenburg (Sijthoff, Leiden), pp. 362–374.
- Van den Brink, G. (1980). “Cochlear mechanics as the possible cause of binaural diplacusis,” in *Psychological, Physiological and Behavioural Studies in Hearing*, edited by G. van den Brink and F. Bilsen (Delft U.P., Delft), pp. 64–67.
- Van den Raadt, M. P. M. G., and Duifhuis, H. (1990). “A generalized Van der Pol-oscillator cochlea model,” in *Mechanics and Biophysics of Hearing*, edited by P. Dallos, C. D. Geisler, J. W. Matthews, M. Ruggero, and C. R. Steele (Springer-Verlag, New York), pp. 227–234.
- van Hengel, P. (1993). “Comment on ‘periodicity in otoacoustic emissions’,” in *Biophysics of Hair Cell Sensory Systems*, edited by H. Duifhuis, J. W. Horst, P. van Dijk, and S. M. van Netten (World Scientific, Singapore), p. 62.
- van Hengel, P. W., and Duifhuis, H. (unpublished). “Is there a second filter in the cochlea?”
- Wilson, J. P., Baker, R. J., and Whitehead, M. L. (1986). “Level dependence of frequency tuning in human ears,” in *Basic Issues in Hearing*, edited by J. W. H. H. Duifhuis and H. P. Wit (Academic, London), pp. 80–87.
- Zweig, G. (1991). “Finding the impedance of the organ of Corti,” *J. Acoust. Soc. Am.* **89**, 1229–1254.
- Zweig, G., Lipes, R., and Pierce, J. R. (1976). “The cochlear compromise,” *J. Acoust. Soc. Am.* **59**, 975–982.
- Zweig, G., and Shera, C. A. (1995). “The origins of periodicity in the spectrum of evoked otoacoustic emissions,” *J. Acoust. Soc. Am.* **98**, 2018–2047.
- Zweig, G., and Shera, C. A. (private communication).
- Zwicker, E. (1986). “Spontaneous oto-acoustic emissions, threshold in quiet, and just noticeable amplitude modulation at low levels,” in *Auditory Frequency Selectivity*, edited by B. C. J. Moore and R. D. Patterson (Plenum, New York), pp. 49–59.
- Zwicker, E., and Peisl, W. (1990). “Cochlear processing in analog models, in digital models, and in human inner ear,” *Hearing Res.* **44**, 206–216.
- Zwicker, E., and Schloth, E. (1984). “Interrelation of different oto-acoustic emissions,” *J. Acoust. Soc. Am.* **75**, 1148–1154.



# Enhancement of electrically evoked oto-acoustic emissions associated with low-frequency stimulus bias of the basilar membrane towards scala vestibuli

Desmond L. Kirk and Graeme K. Yates

*The Auditory Laboratory, The Department of Physiology, The University of Western Australia, Nedlands, W.A. 6907, Australia*

(Received 20 January 1998; accepted for publication 10 June 1998)

Electrically evoked oto-acoustic emissions (EEOAEs) are sounds present in the ear canal when ac current is passed into the cochlea. EEOAEs are attributed to the activation of fast electromotile responses in outer hair cells (OHCs). An interesting property of EEOAEs is the phenomenon of “acoustic enhancement,” where the emission amplitude is increased by moderate-level sound [D. C. Mountain and A. E. Hubbard, *Hear. Res.* **42**, 195–202 (1989)]. In this report a form of enhancement is described which occurs with displacements of the basilar membrane toward scala vestibuli, during amplitude modulation of the EEOAE waveform by low-frequency tones. This “SV-bias enhancement” possibly consists of two components: (i) a low-level component induced by sound at levels which produce nonlinear growth of the cochlear microphonic and which may be equivalent to the “acoustic enhancement” described previously, and (ii) a high-level component which occurs at sound levels well above those which cause saturation of the cochlear microphonic. The low-level component could be explained by either an increased access of the extrinsically applied current to a membrane-based source of OHC motility, perhaps coupled with a reduction in negative feedback, or an increase in electromotile output during scala vestibuli displacements, but the origin of the high-level component is obscure. © 1998 Acoustical Society of America. [S0001-4966(98)05209-6]

PACS numbers: 43.64.Jb, 43.64.Ld, 43.64.Bt, 43.64.Kc [BLM]

## INTRODUCTION

An ac stimulation of the cochlea produces sound in the ear canal at the frequency of the electrical stimulus (Hubbard and Mountain, 1983; Mountain and Hubbard, 1989; Murata *et al.*, 1993; Nakajima *et al.*, 1994; Kirk and Yates, 1996). These electrically evoked oto-acoustic emissions (EEOAEs) occur together with displacements of the basilar membrane (Xue *et al.*, 1996) and are attributed to fast electromotile responses (Ashmore, 1987; Dallos and Evans, 1995) in the outer hair cells (OHCs). They are assumed to be the output, propagated through the middle ear, of the sensitivity enhancing “active process” or “cochlear amplifier” (Davis, 1983; Patuzzi and Robertson, 1988; Dallos, 1992).

An interesting property of EEOAEs is the phenomenon of acoustic enhancement (Mountain and Hubbard, 1989). When a tonal acoustical stimulus of moderate intensity (60–80 dB SPL) is applied together with the injected current the emissions are increased in amplitude. Acoustic enhancement of EEOAEs presumably reflects some influence of the acoustical stimulus on either or both of the generation or the mechanical propagation of OHC motility. Mountain and Hubbard (1989) and Xue *et al.* (1993) have explained acoustic enhancement as being due to the saturation of forward (mechanical to electrical) transduction in OHCs by the enhancing tone. They suggested the saturation of forward transduction released the EEOAE from a tonic suppression by reducing negative feedback; essentially lowering the loop gain. Predictions of this hypothesis have been realized in the gerbil cochlea (Hubbard and Mountain, 1990; Roddy *et al.*,

1994; Nakajima *et al.*, 1996) but were contradicted in the guinea pig (Kirk and Yates, 1996).

In this report we describe a form of enhancement of EEOAEs which occurs at relatively high sound levels when the emission amplitude is modulated in phase with a low-frequency biasing tone. During low-frequency stimulus bias, EEOAE amplitude increases with displacements of the basilar membrane to scala vestibuli and decreases with scala tympani displacements. In a separate report (Yates and Kirk, 1998) we have attributed these amplitude modulations, which grow in proportion to the extracellular cochlear microphonic (CM) evoked by the biasing tone, to the mechanical gating of transduction channels in the OHC stereocilia.

We show here that, as the level of the low-frequency biasing tone is increased above about 80–90 dB SPL, the amplitude of the emission during the scala vestibuli phase continues to grow, well beyond the sound level at which the CM is saturated. The overall result of the growth in amplitude during the scala vestibuli phase is a net enhancement of the emission, by up to 20 dB at sound levels above 100 dB SPL. A preliminary account of this work has appeared in abstract form (Kirk and Yates, 1997).

## I. METHODS

Experiments were performed on pigmented guinea pigs (250–350 g) according to protocols approved by the National Health and Medical Research Council of Australia and the Experimental Ethics Committee of the University of Western Australia. The animals were anaesthetized with

Nembutal (40 mg/kg i.p. initially; 20 mg/kg after 3 h) and Leptan (Fentanyl citrate/Droperidol; 1.5 ml/kg i.m. repeated at 45 min intervals). They were paralyzed (Alloferin 0.3 ml/kg i.m.) during data collection to prevent middle ear movements. In unparalyzed animals the anaesthetic regime induced continuous deep anaesthesia, evidenced by lack of withdrawal response and absence of spontaneous respiration. During paralysis potentially noxious stimulation produced no change in heart rate.

The basic surgical procedures and methods of stimulation and recording were as described in Kirk and Yates (1996), except that in the present experiments the electrical and acoustical stimuli were generated and the responses recorded by a desktop computer using a multi-media sound card (Crystal CDB4231) and custom software. EEOAE and CM waveforms were stored to disk for analysis after experiments. The electrical stimulation system delivered a constant voltage. The current passing through the electrode was measured as described previously (Kirk and Yates, 1996) and was monitored on an oscilloscope to verify it remained constant throughout the experiment.

Electrical stimulation of scala media, mainly in turn 2 but also in turns 1 and 3, was paired with sound stimulation at a frequency ( $f_a$ ; usually 86 Hz) well below and phase-locked to the electrical frequency ( $f_e$ ; 1076–4091 Hz). Samples of the ear canal sound pressure, which comprised the EEOAE and the low-frequency sound were taken over 2 complete cycles of the acoustical stimulus, generally averaged over 2–4 s. The output from the microphone (Bruel and Kjaer 4133) recording the ear canal sound pressure was electronically filtered, stored to disk, and then processed numerically (see Yates and Kirk, 1998) to remove residual contamination by the acoustical stimulus and high-level harmonic distortion. This procedure extracted from the recording only those components which were related to the electrical stimulus. Briefly, it involved calculation of the Fourier spectrum of the raw waveform, setting to zero all components other than the fundamental of the electrical frequency and the intermodulation frequencies and then inverse-Fourier transforming back to the time domain.

The CM evoked by the low-frequency acoustical stimulus was recorded through the scala media pipette without ac stimulation. CM samples for 2 cycles of the low-frequency tone were taken over a range of sound levels. The acoustical stimulus at each sound level was then presented together with the phase-locked electrical stimulus, and the EEOAE was recorded during two cycles of the tone.

Each CM record was superimposed on the corresponding EEOAE waveform acquired during sound stimulation at the same SPL. A close fit was obtained between a CM envelope (described by the actual CM and its inverted mirror image) and the EEOAE modulation envelope (see Fig. 1). The fitting procedure incorporated (i) shifting the CM in the time domain to compensate for the delay between the instantaneously recorded electrical CM and the modulations of the EEOAE which were recorded after propagation to the stapes and through the middle ear, and (ii) scaling the CM amplitude to match the depth of modulation of the EEOAE and

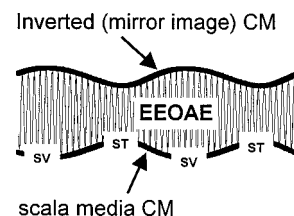


FIG. 1. The CM recorded from scala media was fitted over the modulated EEOAE waveform to match the modulation envelope. Both the recorded CM (lower trace) and its inverted mirror image (upper trace) were scaled numerically to match the depth of modulation of the EEOAE, and a dc offset was applied to match the EEOAE amplitude. Scaling factors were constant for all sound levels. As indicated, negative voltage deflections in the scala media CM correspond to displacements of the basilar membrane to scala vestibuli, positive deflections to scala tympani. The CM was shifted along the time axis by  $570 \mu\text{s}$  to compensate for the propagation delay of modulations in the EEOAE envelope. In this example from the second turn, the electrical frequency was 2024 Hz and the acoustic biasing stimulus was 86 Hz at 70 dB SPL.

applying a vertical offset to match the EEOAE amplitude. For more details see Yates and Kirk (1998).

The condition of the cochlea was monitored throughout experiments using the compound action potential (CAP) as described in Kirk and Yates (1996).

## II. RESULTS

### A. Enhancement associated with scala vestibuli bias

Examples of EEOAE waveforms modulated by 86 Hz tones ( $f_a$ ) over a range of sound levels can be seen in Figs. 2 and 3. The data are from two preparations in which ac stimulation was applied to scala media in the second cochlear turn. The electrical stimulus frequencies ( $f_e$ ) were 3402 Hz (Fig.

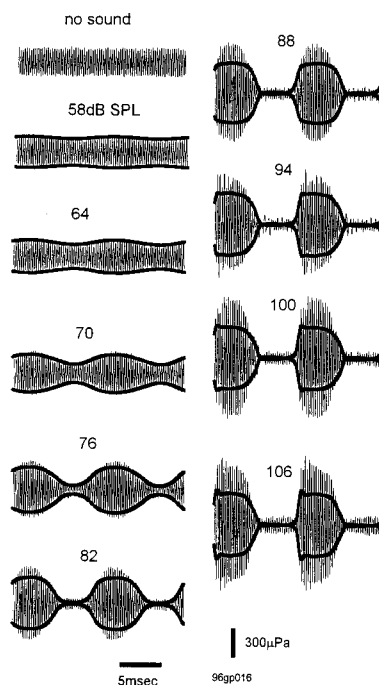


FIG. 2. An EEOAE generated by  $10 \mu\text{A}$  ac at 3402 Hz applied in the second cochlear turn was modulated by a tone at 86 Hz at the indicated sound pressure levels (SPL). The thick lines show the actual and inverted waveform of the extracellular CM in scala media evoked by the 86 Hz tone. The CM has been shifted by  $400 \mu\text{s}$  (see Fig. 1 for explanation).

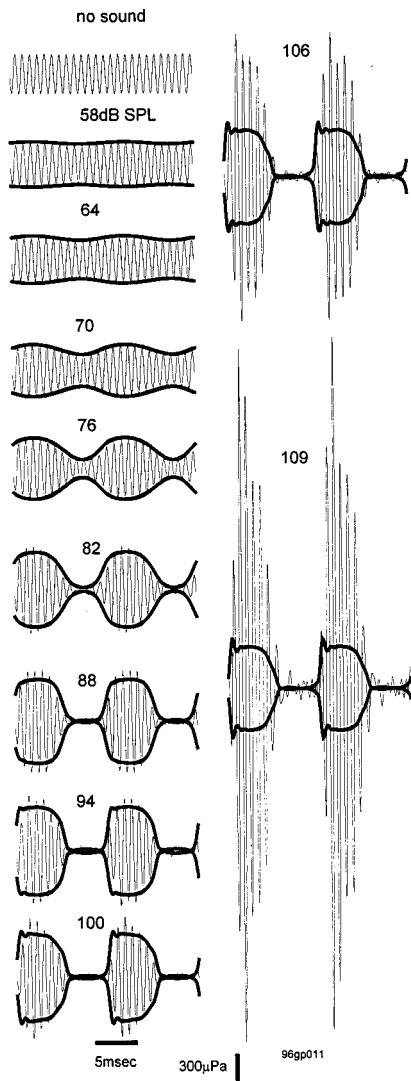


FIG. 3. Modulation of an EEOAE from the second turn ( $f_e = 1076$  Hz,  $10 \mu\text{A}$ ) by 86 Hz tones. The CM has been shifted by  $520 \mu\text{s}$ .

2) and 1076 Hz (Fig. 3). In each set of data the waveform of the CM response to the 86 Hz tone (scaled and adjusted in phase as described in Sec. I) and an inverted (mirror image) CM waveform have been drawn over the modulated EEOAE waveform acquired at the same sound level. This produces a “CM envelope” (see Fig. 1) which expands during its negative-going scala vestibuli phase (SV) and contracts during its positive-going scala tympani phase (ST).

During the negative (SV) phase of the CM the EEOAE amplitude increased, during the positive (ST) phase it decreased. We (Yates and Kirk, 1998) have attributed these amplitude changes to the modulation of the OHC apical transducer conductance which produces the CM. At the lower sound levels modulation of the EEOAEs in Figs. 2 and 3 was proportional to the CM voltage, and the CM waveform envelopes matched the EEOAE modulation envelopes very closely, up to 70 dB SPL in Fig. 2 and up to 82 dB SPL in Fig. 3. However, at higher stimulus levels the proportionality between the CM and EEOAE modulation broke down. While the reduction of the amplitude of the EEOAE during the positive CM phase approached asymptote, effectively reaching zero amplitude in Fig. 3, the increase in amplitude during

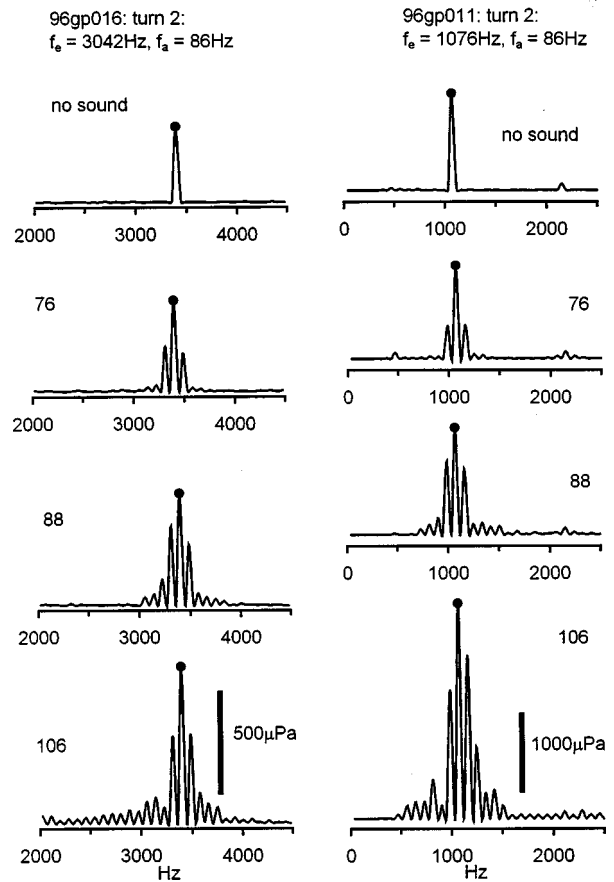


FIG. 4. Spectral composition of selected waveforms from Figs. 2 and 3 showing generation of intermodulation sidebands.

the negative CM phase overshoot the CM envelope, and continued to grow with sound level well after the CM amplitude had saturated. This disproportionate expansion of the EEOAE during displacements of the BM to scala vestibuli resulted in a net increase in the amplitude of the EEOAE, as described below (Figs. 4, 5, 6).

Modulation of the EEOAE was accompanied by the generation of intermodulation sidebands, as shown in Fig. 4. These sidebands (at frequencies  $f_e \pm n f_a$ ) grew in number and magnitude with increasing sound level. The primary spectral component at  $f_e$  also increased with sound level; that is, there was a net enhancement of both the total rms level of the EEOAE waveform ( $f_e +$  sidebands) and of the primary spectral component at the electrical stimulation frequency.

The progressive enhancement with increasing sound level, for the two sets of data in the preceding three figures, has been plotted in Fig. 5, along with the intensity functions of the respective 86 Hz CM. In 96gp016 [3402 Hz EEOAE, Fig. 5(a)] enhancement of both the total rms amplitude of the EEOAE and the primary spectral component at  $f_e$  began at 76 dB SPL and roughly followed the growth of the CM up to 88 dB SPL (note that the modulation of this EEOAE overshoot the CM envelope at 70–76 dB SPL). Enhancement continued to increase with sound level after saturation of the CM, with a small change of slope or dip in the curve at 94 dB SPL. Nonmonotonic growth of enhancement, that is a range of sound levels over which the slope of the curve be-

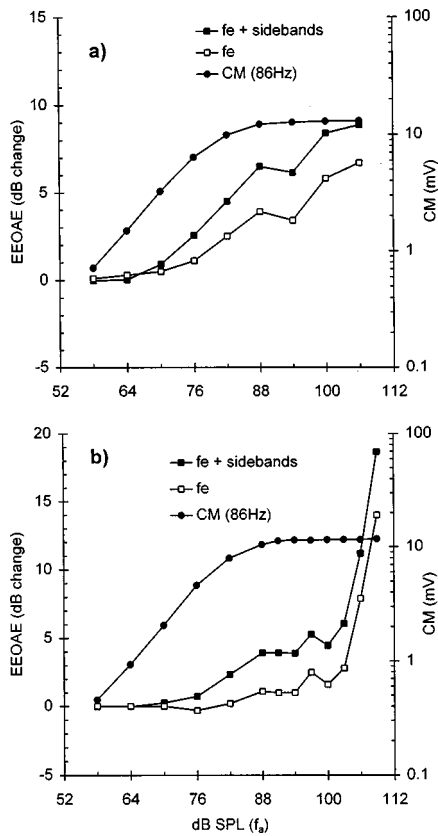


FIG. 5. EEOAE enhancement and CM growth functions from waveforms in Fig. 1(a) and Fig. 2(b). The  $f_e$  + sidebands data refer to the total rms amplitude of the emission,  $f_e$  data to the amplitude of the primary spectral component at the electrical stimulation frequency.

came negative, even to such a degree that there was net suppression of the EEOAE, was present in other enhancement curves (see below and Figs. 6 and 8).

In 96gp011 [1076 Hz EEOAE, Fig. 5(b)] there was relatively little enhancement until the acoustical stimulus was 15 dB above the level at which the CM had saturated. Then the emission amplitude increased steeply by approximately 12 dB over a 6 dB increase in sound level.

## B. Enhancement in different cochlear turns

While we collected most of our data (5 preparations) from the second cochlear turn, we also took measurements from the third turn (2 preparations) and the first turn (3 preparations). Enhancement associated with scala vestibuli bias was present in all turns but, for any given set of stimulus parameters it varied from turn to turn, being generally greater in the apical cochlea than in the basal turn. This is illustrated in Fig. 6. We made successive electrode placements in turns 1, 2 and 3 in a single cochlea, and recorded modulated EEOAEs using the same stimulus frequencies ( $f_e = 1421$  Hz,  $f_a = 86$  Hz) in each turn. CAP thresholds were maintained to within 3 dB below 10 kHz and to within 8 dB from 10 to 20 kHz throughout this procedure, and the EE-OAE tuning functions in all turns were unchanged when the penetration sequence was reversed to verify there had been no progressive degeneration which might have produced order effects. In the third turn [Fig. 6(a)] enhancement grew

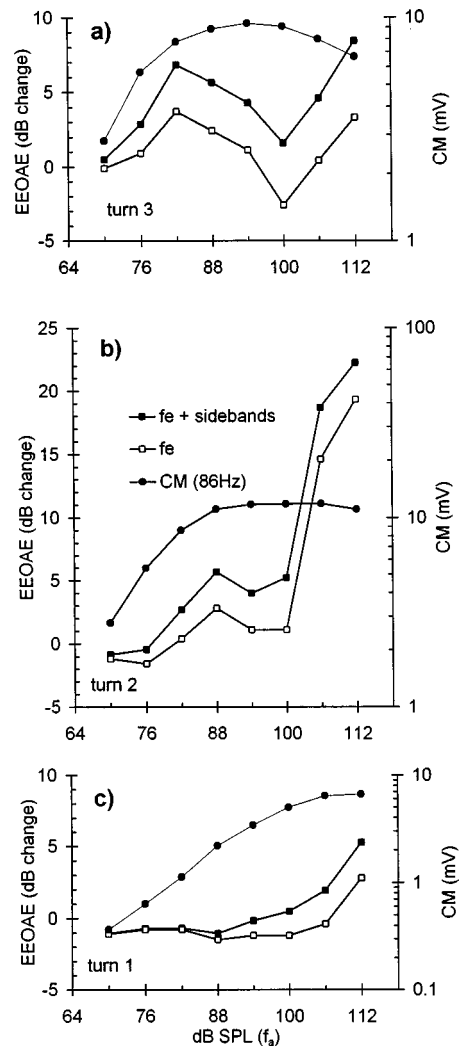


FIG. 6. EEOAE enhancement and CM growth functions obtained in three cochlear turns in the same preparation (96GP021). Stimulus parameters were  $f_e = 1421$  Hz;  $f_a = 86$  Hz.

approximately in line with the CM amplitude between 70 and 82 dB SPL. Between 82 dB SPL and 100 dB SPL the slope of the enhancement curve became negative and there was a net suppression, by 2.6 dB, of the primary EEOAE at 100 dB SPL. Above 100 dB SPL the slope again became positive yielding a net enhancement by 3.3 dB at 112 dB SPL. Net suppression of the emission was also seen in other preparations and appeared to depend to some extent on the electrical stimulation frequency (Sec. C below). The modulated waveforms from which the data in Fig. 6(a) were obtained can be seen in Fig. 7. The net suppression at 100 dB SPL is apparent as the sharp reduction in the amplitude of the emission at the center of the negative phase of the CM.

In the second turn [Fig. 6(b)] the nonmonotonic part of the enhancement function was narrower than in the third turn and there was no net suppression. At 112 dB SPL the primary emission at  $f_e$  was enhanced by 19 dB.

In the first turn of this cochlea [Fig. 6(c)] the rate of increase of enhancement with sound level was relatively slow, with the primary emission at  $f_e$  showing no enhancement at all until 112 dB SPL. This may have been because the low-frequency acoustical stimulus was mechanically less

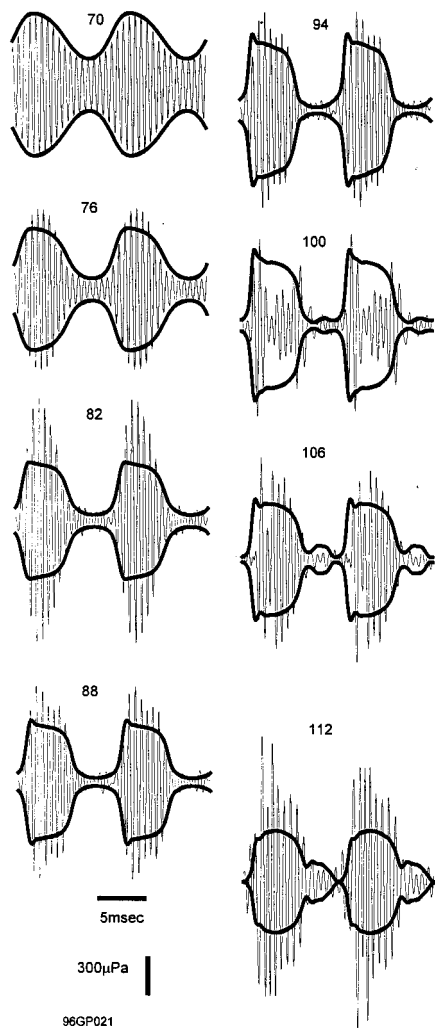


FIG. 7. Modulated EEOAE waveforms from turn 3 [corresponding to data plotted in Fig. 6(a)] showing net suppression at 100 dB SPL.

effective in the basal cochlea, where the growth function of the CM saturated at higher sound levels than in the apex. We noted in an earlier report that EEOAEs from the first turn sometimes exhibit complex modulation patterns at multiples of the acoustical frequency, with no obvious dependence on the stimulus parameters (Yates and Kirk, 1998). In the three first turn preparations we examined in this study, enhancement associated with scala vestibuli bias was relatively poor or absent at all tested emission frequencies and irrespective of whether the modulation pattern was simple or complex.

A significant point of the data in Fig. 6 is that, for fixed electrical and acoustical frequencies, the effect of the biasing stimulus depends on where in the cochlea the EEOAE is generated. This is clear evidence that the phenomena we see are not the result of low-frequency modulation of transmission through the middle ear, which should be independent of the site of generation of the emission.

### C. Stimulus frequency

For a fixed acoustical frequency at the highest sound levels, maximum enhancement was generally observed at

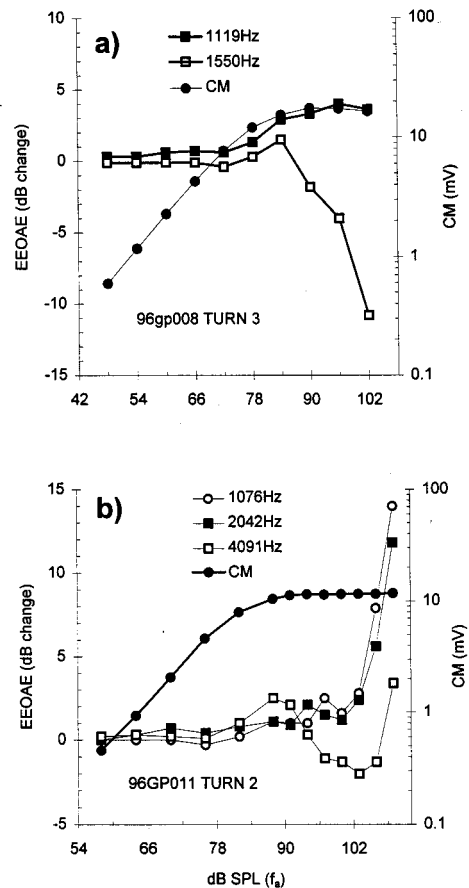


FIG. 8. Enhancement and CM growth functions from turn 3 (a) and turn 2 (b) showing stronger enhancement at lower electrical frequencies. Stimulus parameters were  $f_a = 86$  Hz;  $f_e$  as indicated.

lower electrical frequencies. Figure 8 shows examples from a turn 3 preparation (a) and a turn 2 preparation (b). The acoustical frequencies were 172 Hz (a) and 86 Hz (b).

In the third turn [Fig. 8(a)] an emission at 1119 Hz was enhanced by 4 dB when the acoustical stimulus was 96 dB SPL. However, at 1550 Hz, the approximate characteristic frequency (CF) of the turn 3 stimulation site (Kirk and Yates, 1996), the effect of the acoustical stimulus was predominantly suppression.

In turn 2 [Fig. 8(b)] a 2042 Hz EEOAE was enhanced by 12 dB at 109 dB SPL whereas the 4091 Hz EEOAE (approximate second turn CF) showed a mix of suppression and enhancement with a maximum amplitude increase of only 3.5 dB.

Most of the EEOAE modulation data were obtained with the low-frequency acoustical stimulus at 86 Hz but tones as high as 699 Hz were also used. Although only limited observations were made at higher acoustical frequencies, there did not appear to be any difference in the modulation and enhancement effects obtained, but the CM waveform was less distorted at lower frequencies and would also be less liable to contamination by out of phase components from remote sources (Patuzzi *et al.*, 1989). It was also easier to filter the acoustical fundamental electronically and prevent overload in the recording system with tone frequencies several octaves below the electrical frequencies.

### III. DISCUSSION

#### A. “SV-bias enhancement” and “acoustic enhancement”

We have demonstrated here an amplitude enhancement of EEOAEs associated with bias of the basilar membrane to scala vestibuli, during modulation of the EEOAE waveform by low-frequency tones. For the purposes of discussion we will call this phenomenon “SV-bias enhancement” to distinguish it from the “acoustic enhancement” described previously (Mountain and Hubbard, 1989; Hubbard and Mountain, 1990; Xue *et al.*, 1993; Roddy *et al.*, 1994; Kirk and Yates, 1996; Nakajima *et al.*, 1996). We are not certain if SV-bias enhancement is indeed a distinct phenomenon, but it does have apparently unique characteristics which might suggest so. Apart from its association specifically with one phase of the modulated EEOAE waveform, SV bias enhancement required relatively high sound levels. While there was, in some instances [e.g., Fig. 5(a)], a few dB of enhancement when the biasing tone was less than 90 dB SPL, the most pronounced effects were not seen unless the tones were in excess of 100 dB SPL, well above the level at which growth of the low-frequency CM saturated. Acoustic enhancement was produced with sound levels as low as 50–60 dB SPL (Mountain and Hubbard, 1989) in the gerbil and 60–75 dB SPL in the guinea pig (Kirk and Yates, 1996).

The relatively high-level dependence of SV-bias enhancement may reflect the low frequencies of the acoustical stimuli used to modulate the EEOAE waveforms. Acoustic enhancement presumably depends on the magnitude of the basilar membrane displacements. It follows the basilar membrane tuning and is best when the acoustical frequency is near the characteristic frequency (CF) of the site of generation of the EEOAE (Xue *et al.*, 1993; Kirk and Yates, 1996). A stimulus well below CF, say 3–4 octaves below (on the extreme tail of the basilar membrane tuning curve) would be 20–40 dB less effective in displacing the basilar membrane than a stimulus near CF (Sellick *et al.*, 1982).

A striking feature of SV-bias enhancement was its very steep growth at the highest sound levels, for example the 19 dB increase in enhancement over a 12 dB sound-intensity range above 100 dB SPL [Fig. 6(b)]. Over an intermediate range of sound levels (90–100 dB SPL) near CM saturation there was often a dip in the curve, even leading to net suppression of the emission. At lower sound levels, SV-bias enhancement grew by less than 5 dB over a 20–30 dB intensity range, comparable with the rates of growth of acoustic enhancement (Mountain and Hubbard, 1989; Kirk and Yates, 1996). These relatively small amounts of SV-bias enhancement we observed below 80–90 dB SPL [e.g., Figs. 5(a), 6(a),(b)] may be no different from acoustic enhancement, but the high-level effect, and perhaps the intermediate suppression, could reflect some genuinely distinct influence of an intense, low-frequency sound on either the generation of motility or its propagation, selectively during basilar membrane displacement to scala vestibuli. Hubbard and Mountain (1983) described what may be essentially the same phenomenon. They measured intermodulation sideband emissions generated by simultaneous acoustical and electrical stimuli.

At higher acoustical frequencies, near the CF of the electrical stimulation site, the amplitude of the sidebands increased with sound level in parallel with the growth of the CM. However, at acoustical frequencies well below the CF of the stimulation site the growth of the sidebands resembled the growth of SV-bias enhancement, with a leveling-off at intermediate sound levels and rapid growth at the highest levels after the CM had begun to saturate.

#### B. Possible sources of SV-bias enhancement

##### 1. Increased current drive during SV displacement

We (Yates and Kirk, 1998) have attributed the amplitude modulation of EEOAEs by low-frequency sound to transitions between open and closed states of the mechano-electrical transduction (MET) channels in OHC stereocilia. We proposed, as one possible basis of the phenomenon, that the EEOAE generating current gains access to a cell-based motility source through the MET channels and is modulated along with the channel conductance by low-frequency sound. In this context we would interpret the virtually complete suppression during scala tympani displacement, of the 1076 Hz emission in Fig. 3, as due to complete elimination of the electrical drive to OHC motility. The incomplete suppression of the 3402 Hz EEOAE in Fig. 2 may reflect a small portion of current entering through the OHC apical capacitance at this higher electrical frequency (Yates and Kirk, 1998).

Net enhancement of emissions during low-frequency modulation of MET channels could arise if the increase in current drive during SV displacement was significantly greater than the decrease during ST displacement. This would depend on the extent to which the OHC mechano-electrical operating point was offset towards scala tympani; that is, how much closer it was to saturation in the hyperpolarizing direction than in the depolarizing direction. The net emission amplitude would be determined by the ratio of the areas under the negative (SV) and positive (ST) phases of the scala media CM waveform, and would require a 2:1 difference to produce 6 dB of enhancement. This is a fairly extreme and unlikely degree of asymmetry. We would not expect more than 2 dB or so of enhancement to be directly associated with the asymmetry of the CMs we have recorded. Furthermore, the modulation envelope of an EEOAE enhanced in such a manner should coincide with the CM envelope. However, where we measured enhancement of EEOAEs at nonsaturating sound levels (Figs. 2, 7), and most obviously with the large effects at the highest sound levels, this was not the case. Enhancement was associated with disproportionate growth, relative to the CM amplitude, of the emission during SV displacements.

We have assumed that the instantaneous voltage of the low-frequency CM is a reliable index of the distribution of open and closed MET channels in OHCs near the recording/stimulation site (Patuzzi *et al.*, 1989). If this assumption is correct, then the breakdown in proportionality between the CM and the EEOAE modulation envelope indicates that factors additional to the open or closed status of the MET channels influence the EEOAE amplitude during scala vestibuli displacements.

This is most certainly the case when the emission is enhanced by 10–20 dB by tones around 100 dB SPL and above, but perhaps less so in respect of modulation at the lower sound levels, where only a few dB of enhancement was produced. The CM as shown here was recorded without electrical stimulation, and may not have reflected precisely how the MET conductance followed the low-frequency tone in the presence of the high-frequency electrical stimulus. Small changes in the CM generation are known to occur in the presence of ac stimulation (Hubbard *et al.*, 1979). Also, dc length changes in OHCs, associated with the ac stimulus (Evans *et al.*, 1991), could shift the mechano-electrical operating point even to relatively extreme positions.

## 2. Change in electromotile sensitivity

In isolated OHCs the relationship between intracellular voltage change and motility (length change) is sigmoidal. The transfer curve is asymmetrical about the resting membrane potential, with the mean slope being steeper ( $\approx 15$  nm/mV) in the depolarizing direction than in the hyperpolarizing direction ( $\approx 2$  nm/mV; Santos-Sacchi, 1989, 1991). The depolarization induced by the SV-displacement phase of the low-frequency tone might have shifted the operating bias of electromotility to a more sensitive region. Indeed, the difference between the hyperpolarizing and depolarizing slopes of the voltage-to-motion transfer function is sufficient to account for the amount of SV-bias enhancement (up to 20 dB) we observed. However, the voltage range covered by the transfer curve, as demonstrated in isolated OHCs, is extreme. It extends from  $-150$  mV to  $+30$  mV about a resting intracellular potential of  $-70$  mV (Santos-Sacchi, 1989, 1991), whereas the intracellular voltage fluctuations induced by physiological stimulation are small, less than  $\pm 10$  mV (Dallos, 1986; Russell *et al.*, 1986). Over this physiological range the asymmetry in the transfer function is minimal. While there are no available data showing the electromotile characteristics of OHCs *in vivo*, the demonstrated asymmetry in the isolated OHC, if present *in vivo*, may not be of great significance over the physiological operating range, perhaps accounting for only a few dB of sensitivity change (Roddy *et al.*, 1994).

More significantly, enhancement grew most rapidly at sound levels well above those at which the growth of the CM had saturated. Presumably, over this intensity range, there would be no level-dependent increase in depolarizing intracellular currents during SV displacements.

Thus two considerations argue against intracellular voltage changes causing SV-bias enhancement. First, the changes induced by the biasing tones might not alter the electromotile sensitivity of the OHCs sufficiently to induce up to 20 dB of enhancement, and second, intracellular currents would probably saturate at sound levels below those at which most of the enhancement occurred.

It is feasible though, that at sound levels where the CM amplitude was still increasing and where there was only a few dB of enhancement, an increased electro-motile gain could have contributed. (See also the comment regarding membrane tension in Sec. C below.)

## 3. Saturation of forward transduction and reduction in negative feedback

Mountain and Hubbard (1989) and Xue *et al.* (1993) have proposed that EEOAEs are enhanced when the forward-transduction mechanism begins to saturate with increasing levels of the acoustical stimulus. In their model, the saturation of forward transduction releases the basilar membrane vibration from a tonic suppression imposed by negative feedback (Mountain *et al.*, 1983; Mountain, 1986). In an earlier report (Kirk and Yates, 1996) we argued against this explanation of acoustic enhancement, primarily because we found enhancement and not suppression at emission frequencies near CF where, according to the negative feedback model, the feedback should switch phase and become positive. However, other studies (Hubbard and Mountain, 1990; Roddy *et al.*, 1994) are in favor of the saturation hypothesis, and recently Nakajima *et al.* (1996) have put forward evidence that feedback may indeed switch polarity at CF in the gerbil cochlea. Indeed, the data in Fig. 8 of the present report show enhancement at frequencies below CF and a mix of enhancement and suppression near CF. Could there be a ‘‘reduced negative feedback’’ contribution to SV-bias enhancement?

We have modeled a system (see the Appendix) where the response to a constant ac stimulus input is subject to negative feedback. The feedback is modulated, through a nonlinear (Boltzmann type) transfer characteristic (Holton and Hudspeth, 1986; Patuzzi and Rajan, 1990), by a low-frequency sinusoid.

The nonlinear component represents OHC mechano-electrical transduction and generates a CM. The model was designed to mimic the effects on OHC electromotility of (i) reductions in the gain of a suppressive negative feedback with saturation of forward transduction and (ii) modulation of the electrical drive to the motility mechanism by changes in the input resistance (MET channel state).

Figure 9 shows how the model modulated an EEOAE waveform envelope under two conditions.

In the first example (a) tonic suppression of the EEOAE was reduced by partial saturation of forward transduction. The status of the MET channels had no effect, in this simulation, on the electrical drive to the EEOAE generator. The only action of MET modulation was to open partially the negative feedback loop (Xue *et al.*, 1993). The simulation predicts that, under these conditions, the EEOAE would be increased in amplitude during both positive and negative phases of the CM. This is because deflection of the stereocilia (MET modulation) in *either* direction would drive forward transduction toward saturation and reduce the negative feedback. Increases in the amplitude of the EEOAE would thus occur at double the frequency of the biasing stimulus. Clearly, this does not match our experimental observations.

In the second case (b) the simulation incorporated, as well as displacement-sensitive negative feedback, a displacement-sensitive input-resistance to the electrical input, which mimicked a modulation of the drive to EEOAE generators by the MET channels. The electrical drive was increased with displacements in one direction and decreased in the other. The modeled envelope from this simulation was

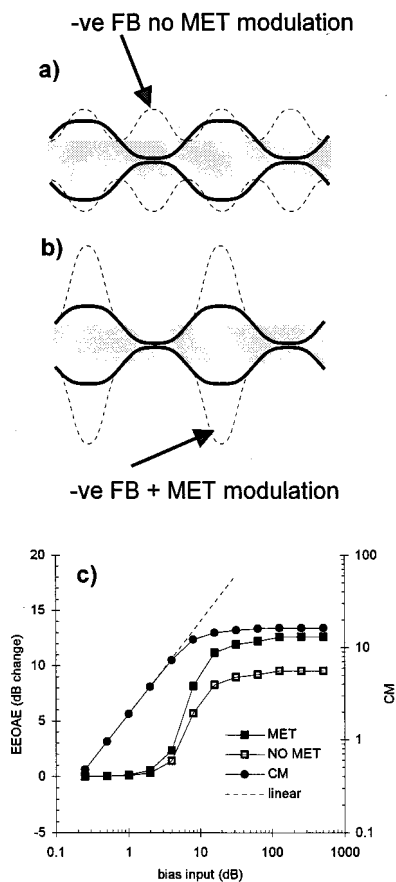


FIG. 9. Results of a simulation of the "saturation of negative feedback" model of Mountain and Hubbard (1989). The line traces in (a) and (b) represent the scala media CM and its inverted mirror image (thick lines) and the outline of the EEOAE modulation envelope (lighter dashed lines) as in Figs. 1, 2, and 3. The shaded area represents the unmodulated EEOAE waveform. (a) is the predicted effect of saturation of negative feedback without modulation of MET channels. (b) is the result of saturation and MET modulation. (c) shows the growth of EEOAE enhancement produced by conditions (a) and (b) and the nonlinear saturating growth of the CM.

virtually identical to those observed experimentally (Figs. 2 and 3). Note that without the inclusion of a negative feedback component, and its reduction during saturating deflections, there would be no overshoot of the EEOAE during SV displacement, the EEOAE modulation would be proportional to the CM at all sound levels.

The clear resemblance between the results from the model and the observations suggests that a reduction in negative feedback, combined with modulation of the driving current by MET channels, might underlie SV-bias enhancement. However, there is a discrepancy, once again associated with the enhancement at high sound levels.

The model predicted that enhancement would begin when the growth of the CM became nonlinear; that is, when the nonlinear forward transduction mechanism was driven into partial saturation (Mountain and Hubbard, 1989). Enhancement then grew until the CM was fully saturated, at which point it leveled off [Fig. 9(c)]. Clearly, when forward transduction is completely saturated there can be no further reduction in negative feedback. We again face the problem of the dramatic growth of SV-bias enhancement well after saturation of the CM. In addition, the observed enhancement

growth functions characteristically were nonmonotonic to varying degrees. The slopes of the curves became negative at about where the CM growth reached saturation, sometimes to the extent that there was a region of net suppression of the EEOAE. These two features of the data are not consistent with the simple monotonic growth of enhancement over a limited range of sound intensities predicted by the model. While our simulated data suggest that a reduction in negative feedback might account for enhancement of the EEOAE over the range of sound levels where the CM amplitude was growing [e.g., in Figs. 5(a), 6(a), and (b)], the discrepancies at higher sound levels complicate this interpretation.

### C. Is there a single cause of enhancement of EEOAEs?

Neither of the three options discussed in the last section appears to be a satisfactory, complete explanation for SV-bias enhancement. Although either might plausibly account for part of the phenomenon at the lower sound levels, the expectation that all effects should asymptote when the intensity-dependent growth of the CM saturates, leaves the higher-level phenomenon unexplained. Of course, saturation of the low-frequency CM (at around 90 dB SPL in the second turn) does not mean that increasing sound levels have no further effect in the cochlea. For example, the basilar membrane displacement continues to increase with sound level after the CM has saturated (Sellick *et al.*, 1982; Patuzzi, 1987). In the present report, while the CM waveforms in Figs. 2, 3, and 7 do not increase in amplitude over the range of SPLs where most of the EEOAE enhancement occurred, they do show increasing amounts of asymmetrical distortion. This distortion may reflect mechanical events which could also influence some aspect of EEOAE generation or propagation. It has been shown, for instance, that the voltage-dependent asymmetry of the OHC motility-function is sensitive to the cell's membrane tension; increasing intracellular pressure increased the electromotile gain (Takehata and Santos-Sacchi, 1995). If extreme displacements of the basilar membrane to scala vestibuli were to stress the OHC membrane more than scala tympani displacements then a differential increase in electromotile gain might result.

The dc summing potential (SP) also continues to grow with sound level after saturation of the CM (Honrubia and Ward, 1969). In our experience (unpublished data) intense low-frequency stimuli generate complex SP responses in scala media with a negative component which continues to grow in amplitude with increasing sound level up to at least 20 dB or so beyond CM saturation. The SP is a poorly understood phenomenon, but at relatively high sound levels in the apical turns it is probably produced mainly by the outer hair cells as a consequence of the asymmetry of their mechano-electrical transfer characteristic (Cheatham and Dallos, 1994). Negative dc potentials in scala media indicate an increase in the conductance across the partition, as does the scala vestibuli phase of the CM, and this may contribute to enhancement of EEOAEs at sound levels above CM saturation. It is not clear, however, how there could be a substantial increase in dc conductance after saturation of the ac modulation of the MET conductance. If the higher-level



stimulation opened other conductance pathways through OHCs (e.g., Raybould and Housley, 1997) one would expect this to show up in the CM, assuming such pathways were mechanically sensitive on a cycle by cycle basis. If the increasing negativity of the SP were due to current through other (e.g., inner hair cell) resistance pathways it is hard to see how this would influence the EEOAE.

The SP warrants further consideration though, in relation to the moderate-level acoustic enhancement described in earlier studies (Mountain and Hubbard, 1989; Xue *et al.*, 1993; Kirk and Yates, 1996). There are several published accounts of one explanation of this phenomenon (Mountain and Hubbard, 1989; Xue *et al.*, 1993; Roddy *et al.*, 1994; Nakajima *et al.*, 1996), and in an earlier report (Kirk and Yates, 1996) we have discussed another. We would like now to raise the possibility that acoustic enhancement of EEOAEs by moderate-level sound at frequencies near to or above the emission frequency could be contributed to by an increase in dc conductance associated with SP generation. This suggestion is prompted by our basic observation here and elsewhere (Yates and Kirk, 1998), that EEOAE amplitude follows low-frequency modulations in the MET conductance, perhaps in consequence of modulation of the electrical drive to the OHC motor. If a high-frequency acoustical stimulus produced asymmetrical deflection of the stereocilia, in consequence of a noncentral mechano-electrical operating point, then enhancement could result from a rectification toward scala vestibuli generating a dc increase in the apical conductance (negative SP in scala media). It is known that the polarity of the SP follows the basilar membrane tuning and changes from positive to negative as the stimulus frequency approaches the CF of the recording site (Honrubia and Ward, 1969; Dallos *et al.*, 1972). This could underlie the greater effectiveness of enhancing tones at frequencies near the CF of the stimulation site (Xue *et al.*, 1993; Kirk and Yates, 1996). Also, at a given stimulus frequency, SP increases in negativity and, at frequencies below CF, changes from positive to negative with increasing stimulus level. Acoustic enhancement increases with sound level (Mountain and Hubbard, 1989; Xue *et al.*, 1993; Kirk and Yates, 1996). If acoustic enhancement were related to the SP-producing rectification in OHCs then this may explain why we (Kirk and Yates, 1996) found little enhancement of EEOAEs generated from the basal turn, as indeed we did in the present study. OHCs in the basal cochlea have relatively symmetrical transfer functions and do not rectify to the same degree as do apical OHCs (Russell *et al.*, 1986).

Discussion so far has been based on the commonly accepted premise (Dallos and Evans, 1995) that a baso-lateral membrane motor underlies OHC motility. However, an alternative motility source in the stereocilia, associated with the transduction channels themselves, has been proposed as a potential contributor (Benser *et al.*, 1996; Hudspeth, 1997; Hudspeth and Gillespie, 1994; Manley and Gallo, 1997). We have suggested elsewhere that the output of such a motor might be influenced by the mechanical status of the channels (Yates and Kirk, 1998). Conceivably, some mechanical effect of extreme displacements to scala vestibuli, where a saturated CM indicated saturation of the assumed driving

voltage, could enhance the output of a stereocilia motor. However, there is no real evidence that an effective channel-based motility source exists in mammalian OHCs, let alone what its properties would be.

#### IV. SUMMARY AND CONCLUSIONS

EEOAEs were amplitude-modulated by low-frequency tones, and at high sound levels were enhanced in amplitude by up to 20 dB. The enhancement occurred as an extension of the amplitude increase during the scala vestibuli phase of the waveform modulation. The amount of enhancement grew most steeply, with increasing intensity of the acoustical stimulus, over a range of SPLs well above the level at which growth of the CM had saturated.

“SV-bias enhancement” may consist of two components, which characterize its growth function and which are often separated by a region of negative slope or suppression. One, induced at lower intensities of the acoustical stimulus, could be essentially similar to the “acoustic enhancement” described previously (Mountain and Hubbard, 1989) and would be consistent with any of the following: (i) an increase in electrical drive to OHC motility during displacements to scala vestibuli coupled with an asymmetrical mechano-electrical operating point (not evident in the CM recorded in the absence of the electrical stimulus); (ii) an increased electromotile sensitivity during OHC depolarization; or (iii) saturation of negative feedback coupled with modulation of MET conductance. Another, possibly distinct component is characterized by rapid growth over a range of sound levels well above those at which growth of the CM and, presumably, the potential causes of the low-level enhancement saturates. Its origin is uncertain.

#### ACKNOWLEDGMENTS

This research was supported by grants from the National Health and Medical Research Council of Australia (Project Grant No. 960566) and from the University of Western Australia. The authors are grateful to D. Robertson and to two anonymous reviewers for helpful criticism of earlier versions of the manuscript.

#### APPENDIX: A SIMPLE FEEDBACK MODEL FOR EEOAE PRODUCTION

This simple model of the cochlear amplifier (Fig. A1) is a modification of one originally proposed by Mountain *et al.* (1983), in which a feedback loop controls the vibration amplitude of the basilar membrane. It is based around a block (**A**) representing the basilar membrane response to pressure difference between scala vestibuli and scala tympani. The input to the block,  $V_a$ , represents the pressure difference while the output,  $V_{out}$ , represents basilar membrane displacement.  $V_{out}$  also drives a saturating nonlinearity (**B**) representing the MET process in the OHC stereocilia, in series with the OHC motor.  $V_{feedback}$  represents the pressure fluctuations across the basilar membrane generated by the motor, and is fed back to the summing junction. Summation therefore represents the mixing of the pressure from the sound stimulus and the reverse transduction. Since the reverse

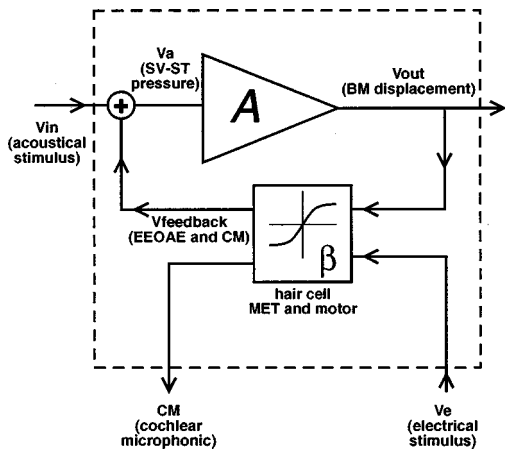


FIG. A1. Model for the calculation of modulation patterns of electrically evoked emissions.

transduction stage is assumed linear, the feedback signal  $V_{\text{feedback}}$  can also be taken to represent the cochlear microphonic in scala media (with a reversal of sign). Hence, when a voltage representing an acoustical stimulus is applied to the circuit input, the output may be taken as basilar membrane displacement and the feedback voltage as either CM or a measure of the active process and hence of the otoacoustic emission. The feedback phase is chosen so as to make the feedback voltage of opposite phase to the input, so the circuit acts as a negative feedback amplifier (Mountain *et al.*, 1983).

Electrically evoked emissions are generated in the model by injecting current into the nonlinearity block  $\beta$ , representing direct stimulation of the reverse transduction process through the top of the hair cells. Two cases are considered in this paper. In the first case the current is assumed to enter the cell independently of the forward transduction channels, presumably through the apical capacitance of the cell (Dallos and Evans, 1995). In the second, the current is assumed to pass through the MET channels so that the amount of current activating the reverse transduction depends upon the percentage of channels open (Yates and Kirk, 1998). The magnitude of electrical stimulation is assumed to be small, so that operation of the feedback loop is unaffected by the presence of the injected current. Solutions are found numerically in a spreadsheet program (Microsoft Excel) using the bisection method to solve the nonlinear equations. A full cycle of the low-frequency acoustical input stimulus is calculated and, at each time increment, the response to injected current is calculated as if it were a dc current. This latter simplification is permissible because of the assumption that the electrical current is small and no frequency-dependencies are considered. Emission magnitudes for Fig. 9(c) were then calculated by averaging the emission amplitude across the entire cycle of the acoustical stimulus.

Equations for the model:

For acoustical stimulation:

$$V_{\text{out}} = \frac{V_{\text{in}}\beta A}{1 - \beta A}; \quad \beta < 0, \quad (\text{A1})$$

$$V_a = V_{\text{in}} + V_{\text{feedback}}, \quad (\text{A2})$$

$$V_{\text{feedback}} = 2 \left( \frac{e^{V_{\text{out}}}}{1 + e^{V_{\text{out}}}} \right) - 1, \quad (\text{A3})$$

and for simultaneous acoustical and electrical stimulation:

$$V_{\text{feedback,electrical}} = \frac{1}{2} V_e \left( \frac{e^{V_{\text{out}}}}{1 + e^{V_{\text{out}}}} \right); \quad V_{\text{out}} = \frac{V_{\text{in}}\beta A}{1 - \beta A}. \quad (\text{A4})$$

- Aschmore, J.F. (1987). "A fast motile response in guinea pig outer hair cell: The cellular basis of the cochlear amplifier," *J. Physiol. (London)* **388**, 323–347.
- Benser, M.E., Marquis, R.E., and Hudspeth, A.J. (1996). "Rapid, active hair bundle movements in hair cells in the bullfrog's sacculus," *J. Neurosci.* **16**, 5629–5643.
- Cheatham, M.A., and Dallos, P. (1994). "Stimulus biasing: A comparison between cochlear hair cell and organ of Corti response patterns," *Hearing Res.* **75**, 103–113.
- Dallos, P. (1986). "Neurobiology of cochlear inner and outer hair cells: Intracellular recordings," *Hearing Res.* **22**, 185–198.
- Dallos, P. (1992). "The active cochlea," *J. Neurosci.* **12**, 4575–4585.
- Dallos, P., and Evans, B.N. (1995). "High-frequency motility of outer hair cells and the cochlear amplifier," *Science* **267**, 2006–2009.
- Dallos, P., Schoeny, Z.G., and Cheatham, M.A. (1972). "Cochlear summating potentials: Descriptive aspects," *Acta Oto-Laryngol. Suppl.* **302**, 1–46.
- Davis, H. (1983). "An active process in cochlear mechanics," *Hearing Res.* **9**, 79–90.
- Evans, B.N., Hallworth, R., and Dallos, P. (1991). "Outer hair cell electromotility: The sensitivity and vulnerability of the dc component," *Hearing Res.* **52**, 288–304.
- Holton, T., and Hudspeth, A.J. (1986). "The transduction channel of hair cells from the bull-frog characterized by noise analysis," *J. Physiol. (London)* **375**, 195–227.
- Honrubia, V., and Ward, P.H. (1969). "Properties of the summing potential of the guinea pig's cochlea," *J. Acoust. Soc. Am.* **45**, 1443–1449.
- Hudspeth, A.J. (1997). "Mechanical amplification of stimuli by hair cells," *Curr. Opin. Neurobiol.* **7**, 480–486.
- Hudspeth, A.J., and Gillespie, P.G. (1994). "Pulling strings to tune transduction: Adaptation by hair cells," *Neuron* **12**, 1–9.
- Hubbard, A.E., and Mountain, D.C. (1983). "Alternating current delivered into the scala media alters sound pressure at the eardrum," *Science* **222**, 510–512.
- Hubbard, A.E., and Mountain, D.C. (1990). "Haircell forward and reverse transduction: Differential suppression and enhancement," *Hearing Res.* **43**, 269–272.
- Hubbard, A.E., Geisler, C.D., and Mountain, D.C. (1979). "Comparison of the spectra of the cochlear microphonic and of the sound-elicited electrical impedance changes measured in scala media of the guinea pig," *J. Acoust. Soc. Am.* **66**, 431–445.
- Kakehata, S., and Santos-Sacchi, J. (1995). "Membrane tension directly shifts voltage dependence of outer hair cell motility and associated gating charge," *Biophys. J.* **68**, 2190–2197.
- Kirk, D.L., and Yates, G.K. (1996). "Frequency tuning and acoustic enhancement of electrically evoked otoacoustic emissions in the guinea pig cochlea," *J. Acoust. Soc. Am.* **100**, 3714–3725.
- Kirk, D.L., and Yates, G.K. (1997). "Enhancement of electrically evoked otoacoustic emissions in the guinea pig with displacements of the basilar membrane towards scala vestibuli," *Abstracts XXth Midwinter Research Meeting, Assoc. Res. Otolaryngol., St. Petersburg*, p. 123.
- Manley, G.A., and Gallo, L. (1997). "Otoacoustic emissions, hair cells and myosin motors," *J. Acoust. Soc. Am.* **102**, 1049–1055.
- Mountain, D.C., and Hubbard, A.E. (1989). "Rapid force production in the cochlea," *Hearing Res.* **42**, 195–202.
- Mountain, D.C. (1986). "Electromechanical properties of hair cells," in *Neurobiology of Hearing: The Cochlea*, edited by R.A. Altschuler, D.W. Hoffman, and R.P. Bobbin (Raven, New York), pp. 77–90.
- Mountain, D.C., Hubbard, A.E., and McMullen, T.A. (1983). "Electromechanical processes in the cochlea," in *Mechanics of Hearing*, edited by E. de Boer and M.A. Viergever (Martinus Nijhoff, Delft U. P., The Hague), pp. 119–126.

- Murata, K., Moriyama, T., Hosokawa, Y., and Minami, S. (1991). "Alternating current induced otoacoustic emissions in the guinea pig," *Hearing Res.* **55**, 201–214.
- Nakajima, H.H., Olson, E.S., Mountain, D.C., and Hubbard, A.E. (1994). "Electrically evoked otoacoustic emissions from the apical turns of the gerbil cochlea," *J. Acoust. Soc. Am.* **96**, 786–794.
- Nakajima, H.N., Olson, E.S., Mountain, D.C., and Hubbard, A.E. (1996). "Acoustic overstimulation enhances low-frequency electrically-evoked oto-acoustic emissions and reduces high-frequency emissions," *Aud. Neurosci.* **3**, 79–99.
- Patuzzi, R.B. (1987). "A model of the generation of the cochlear microphonic with nonlinear hair cell transduction and nonlinear basilar membrane mechanics," *Hearing Res.* **30**, 73–82.
- Patuzzi, R.B., and Rajan, R. (1990). "Does electrical stimulation of the crossed olivo-cochlear bundle produce movement of the organ of corti?" *Hearing Res.* **45**, 15–32.
- Patuzzi, R.B., and Robertson, D. (1988). "Tuning in the mammalian cochlea," *Physiol. Rev.* **68**, 1009–1082.
- Patuzzi, R.B., Yates, G.K., and Johnstone, B.M. (1989). "The origin of the low-frequency microphonic in the first cochlear turn of guinea-pig," *Hearing Res.* **39**, 177–188.
- Raybould, N.P., and Housley, G.D. (1997). "Variation in expression of the outer hair cell P2X receptor conductance along the guinea-pig cochlea," *J. Physiol. (London)* **498**, 717–727.
- Roddy, J., Hubbard, A.E., Mountain, D.C., and Xue, S. (1994). "Effects of electrical biasing on electrically evoked otoacoustic emission," *Hearing Res.* **73**, 148–154.
- Russell, I.J., Cody, A.R., and Richardson, G.P. (1986). "The response of inner and outer hair cells in the basal turn of the guinea pig cochlea and in the mouse cochlea grown *in vitro*," *Hearing Res.* **22**, 199–216.
- Santos-Sacchi, J. (1989). "Asymmetry in voltage-dependent movements of isolated outer hair cells from the organ of Corti," *J. Neurosci.* **9**, 2954–2962.
- Santos-Sacchi, J. (1991). "Reversible inhibition of voltage-dependent outer hair cell motility and capacitance," *J. Neurosci.* **11**, 3096–3110.
- Sellick, P.M., Patuzzi, R., and Johnstone, B.M. (1982). "Measurement of basilar membrane motion in the guinea pig using the Mossbauer technique," *J. Acoust. Soc. Am.* **72**, 131–141.
- Xue, S.W., Mountain, D.C., and Hubbard, A.E. (1993). "Acoustic enhancement of electrically evoked otoacoustic emissions reflects basilar membrane tuning—Experiment results," *Hearing Res.* **70**, 121–126.
- Xue, S., Mountain, D.C., and Hubbard, D.C. (1996). "Electrically-evoked otoacoustic emissions: Direct comparisons with basilar membrane motion," *Aud. Neurosci.* **2**, 301–308.
- Yates, G.K., and Kirk, D.L. (1998). "Cochlear electrically evoked emissions modulated by mechanical transduction channels," *J. Neurosci.* **18**, 1996–2003.

# Changes in otoacoustic emissions in a transsexual male during treatment with estrogen

Dennis McFadden,<sup>a)</sup> Edward G. Pasanen, and Narriman Lee Callaway

*Department of Psychology and Institute for Neuroscience, Mezes Hall 330, University of Texas, Austin, Texas 78712*

(Received 20 December 1997; revised 1 June 1998; accepted 5 June 1998)

Otoacoustic emissions (OAEs) were monitored in two human males undergoing estrogen treatment prior to sex-reversal surgery. In one subject, multiple spontaneous emissions (SOAEs) appeared where none had been evident previously. One reasonable interpretation is that (in this male, at least) androgens normally produced a suppressive effect on the cochlear mechanisms responsible for SOAEs, and that the decline in androgen levels produced by the estrogenic drug led to a reduction in that suppression. © 1998 Acoustical Society of America. [S0001-4966(98)03209-3]

PACS numbers: 43.64.Jb, 43.64.Kc [BLM]

## INTRODUCTION

This is an interim report on an on-going study of a special population of subjects. Most case studies have weaknesses that good experimental research does not have, and this study is no exception. Nevertheless, we believe that the outcomes to date are worth bringing to the attention of others interested in otoacoustic emissions (OAEs) [see Probst *et al.* (1991) for a review] and sex differences in the auditory system [see McFadden (1998) for a review].

Females have more spontaneous otoacoustic emissions (SOAEs) and stronger click-evoked otoacoustic emissions (CEOAEs) than do males (Talmadge *et al.*, 1993; McFadden *et al.*, 1996), and this difference exists in infants as well as adults (Burns *et al.*, 1992; Norton, 1992). In recent times, this laboratory has been interested in the origin of this and other auditory sex differences. We have shown that females having male co-twins (opposite-sex dizygotic or OSDZ twins) have OAEs that are more like those of males than those of other females (McFadden, 1993; McFadden *et al.*, 1996). Further, the CEOAEs of homosexual females are significantly weaker (the male direction) than those of heterosexual females (McFadden and Pasanen, 1998). Our working hypothesis is that prenatal exposure to high levels of androgens leads to weaker cochlear amplifiers (Davis, 1983), and thus to fewer SOAEs and weaker CEOAEs.

Transsexuals taking sex hormones to alter their bodily appearance present an opportunity to study further the effects of hormones on the auditory system. Two such subjects have been recruited to date. Both are genetic and phenotypic males who are taking estrogenic hormones prior to undergoing sex-reversal surgery.

## I. METHOD

Both subjects were recruited by referrals from local psychologists and physicians who oversee the pre-surgical treatment of such patients. Attempts to recruit additional subjects continue.

One subject, JF, was 34 years old at the onset of testing. He was married to women twice, and is the father of one child. Unfortunately, subject JF had already started hormone therapy several months prior to our first measurement session, so no true pre-drug baseline exists for him.

Of primary interest here is the other subject, DJ, who was 50 years old at the onset of testing. He has been married to three women for 4, 11, and 15 years each, but fathered no children because of a low sperm count. One test session was completed for subject DJ prior to his beginning drug treatment. He began taking estropipate (crystalline estrone sulfate stabilized with piperazine) in mid-August 1996 at a dose of 0.75 mg daily. The dose was doubled in November 1996 and doubled again in June 1997. [In early July 1997, 50 mg daily of spironolactone (Aldactone) was added, and that dose was doubled in mid-August 1997, when 5 mg daily of medroxyprogesterone was also added.] Throughout the test series, subject DJ was taking 2.5 mg of glyburide twice daily for diabetes. Subject DJ's serum testosterone level was 340 ng/dl prior to beginning estrogen therapy and it had fallen to 289 ng/dl in June 1997 (normal range for males is 241–826 ng/dl). With treatment, subject DJ noted decreased speed of growth of body hair, softer skin, development of the breasts, and increased hip size. Also, subject DJ has recently experienced a strong attraction to a male for the first time in his life. A hearing screening test conducted prior to his beginning estropipate revealed hearing losses of about 25, 45, and 65 dB at 3, 4, and 6 kHz, respectively, in the left ear, and losses of about 25 and 45 dB at 4 and 6 kHz, respectively, in the right ear.

Experimental sessions were approximately 2 h in length. SOAEs and CEOAEs were measured in both ears during each test session. For SOAEs, four to eight 30-s digital recordings were obtained of the acoustic waveform in the external ear canal. Sampling was 16-bit at 22.05 kHz. The rms level was calculated for 185.8-ms time segments whose onsets were delayed successively by increments of 46.4 ms (75% overlap). The quietest 500 of these time segments were shaped with a Hanning window function and then used to calculate 4k-point FFTs. The resulting squared magnitudes were summed to create the spectra shown in Fig. 1. For

<sup>a)</sup>Electronic mail: mcfadden@psy.utexas.edu

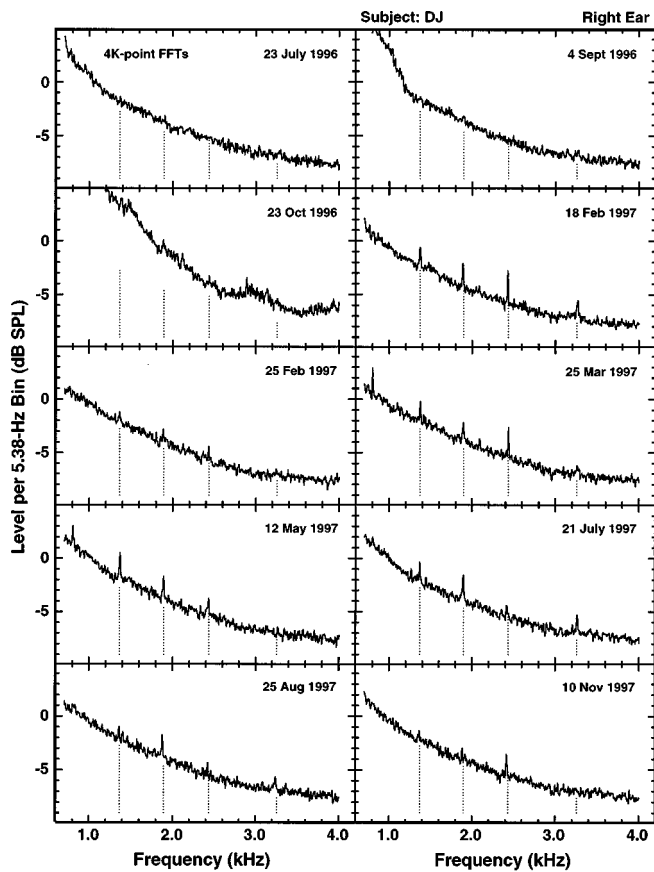


FIG. 1. Spectra obtained from ear-canal recordings on successive test sessions from the right ear of subject DJ. Perpendicular dotted lines have been added at the frequencies of the emergent SOAEs to aid in comparisons across panels. Each spectrum was based upon the most quiet five-hundred 186-ms time samples from 2 to 4 min of acoustic waveform recorded from the external ear canal.

CEOAEs, data were collected for four click levels ranging from 57 to 75 dB peak equivalent SPL (see McFadden and Pasanen, 1998) in 6-dB steps. At each level, the responses to 250 clicks were averaged. The presentation rate of the clicks was nominally ten per second, but the sound level in the canal was monitored continually and no click was presented until the noise level was below a criterion value. Thus the presentation rate varied, depending upon the noisiness of the subject (for additional detail see McFadden and Pasanen, 1998).

## II. RESULTS

The OAEs of subject JF, for whom no pre-drug baseline existed, never exhibited SOAEs and showed no changes in his CEOAEs over the course of 13 months of repeated testing. Consequently, no data are shown for this subject.

For subject DJ, some changes did appear, but as noted at the outset, the data are not without flaws. Figure 1 shows the spectra obtained from the time samples collected from the right ear for successive test sessions. The most recent data are shown at the bottom of these figures, where the SOAEs have been marked with perpendicular dotted lines. Those same dotted lines have been added to the other panels in each figure to facilitate comparisons.

Medroxyprogesterone (mg)	none		5	
Spirolactone (mg)	none		50	100
Estropiate (mg)	none	0.75	1.50	3.00

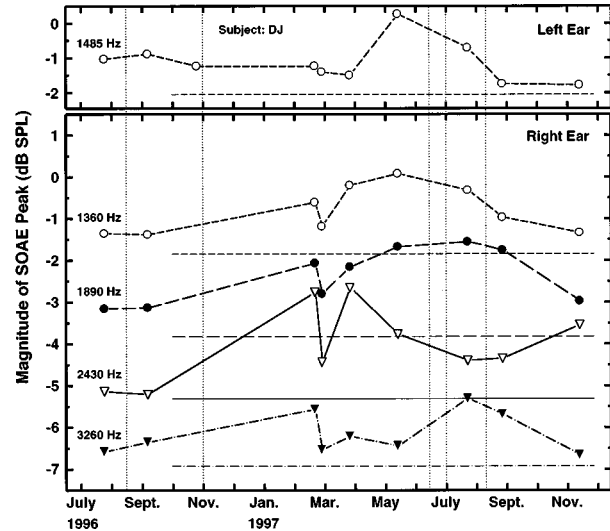


FIG. 2. Peak levels for each of five SOAE frequencies in the two ears of subject DJ as a function of test session. The horizontal lines represent the best estimates of the noise floor at each of the five SOAE frequencies; they were obtained by smoothing the spectra in the local vicinity of the SOAEs in the data collected in July and September 1996. At the top of the figure, the time course is noted for each daily dose level for each drug. No values were plotted for the right ear from the especially noisy session in October 1996 (see Fig. 1).

Figure 1 shows that the right ear contained easily identifiable SOAEs in later sessions where none had been clearly evident in the earliest sessions. As noted, subject DJ began estrogen therapy in mid-August 1996, and the dose was doubled in November 1996 and doubled again in June 1997. Thus both of the test sessions at the top of Fig. 1 can be used for comparison with the later sessions; the first was truly pre-drug and the second was measured soon after a low dose of the drug was begun. A parallel series of spectra for the left ear revealed generally similar effects. A single weak SOAE was present in the baseline measures, and its level increased slightly after the beginning of estrogen administration.

Some of the problems with these data arise from the fact that the waveforms collected from some test sessions were quite noisy. As a consequence, those spectra were elevated to an extent that obscured any SOAEs that might have existed. In one case, the entire spectrum was elevated (23 October 1996, right ear), rendering it totally useless for our purposes. In other cases, however, the problem existed only for frequencies below about 1400 Hz. Above about 1400 Hz, the measured background noise levels were about the same across test sessions. When only the regions above about 1400 Hz are considered, it is easier to accept the conclusion that SOAEs were emerging in the right ear where none existed in the earliest records. (Whether the apparent SOAE at 797 Hz in the March and May 1997 data was present at the time of the baseline measurements is difficult to know because of the great variability in the low-frequency noise floor across test sessions.)

The data of Fig. 1 are presented differently at the bottom of Fig. 2, where the peak level at each of the four SOAE

frequencies is plotted as a function of test session. This figure shows that, generally, these SOAEs grew in level up through the middle of 1997, and then declined. The onset of the decline was associated with the highest dose of estropipate administered and also with the addition of spironolactone and medroxyprogesterone to the drug regimen. Thus there are multiple possible explanations for the decline, but the obvious tests cannot be performed. Peak levels for the single identifiable SOAE in the left ear are also shown in Fig. 2; again, a maximum occurred just prior to the estrogen dose being raised to its highest value. (SOAE frequencies can drift slightly from session to session. All the peak levels shown in Fig. 2 are the largest values obtained within  $\pm 2$  frequency bins of the nominal frequency of the SOAE. Each frequency bin was 5.38 Hz in width.)

Some of the variability in level seen across test sessions in these SOAEs is to be expected for such weak SOAEs (Probst *et al.*, 1991). In addition, some of the variability may have resulted from variation in the concentration of the estrogenic drugs in the cochlea; SOAE intermittency has been seen in experiments involving other drugs that are active in the cochlea (e.g., McFadden and Plattsmier, 1984; McFadden and Pasanen, 1994). While the OAE measurements were always made in the early evening, different amounts of time had elapsed since the last dose of one drug or another, and the effects of these differences are unknown.

The CEOAEs obtained from subject DJ showed no substantial change in overall level across test sessions. However, several frequency bands containing a (new) SOAE did increase, presumably because the SOAEs were being synchronized by the click trains (Probst *et al.*, 1991). Some peaks in the CEOAE spectrum having no associated SOAEs also increased in level across test sessions. We remind the reader that this subject had considerable hearing loss in both ears.

Two tests of cognitive ability that show marked sex differences (Hampson and Kimura, 1992) were administered during each test session, but the results were inconclusive. Performance on a mental-rotation task showed small improvement (not the decline that might be expected to accompany demasculinization), but this may have been a general practice effect, even though care was taken not to reuse the same items for each test. There was also an improvement in a word-production task (the expected direction of effect to accompany feminization for this task), but the improvements were too small to be definitive.

### III. DISCUSSION

There are multiple possible interpretations of these data. One parsimonious interpretation is that the SOAEs seen in the right ear after February 1997 are in fact *new* SOAEs, whose emergence is attributable to the estrogen treatment. Estrogen is administered to subjects of this sort both to reduce the androgen levels and to increase the estrogen levels in their bodies. The emergence of softer skin and larger breasts, the decrease in growth rate of body hair, and the loss of muscle mass in subject DJ is testimony to the effectiveness of this treatment. Previously, we have attributed the sex differences in the expression of OAEs to a suppressive action of androgens acting prenatally on the cochlear amplifiers

(McFadden, 1993, 1998), although the actual mechanisms of this suppressive action are still unknown. In accord with this prenatal hormonal explanation is the fact that the patterns of sex and ear differences in OAEs are the same in infants and children as in adults (Burns *et al.*, 1992; Norton, 1992) even though the sex differences in androgen levels are minimal, both at birth and again from about six months of age until the onset of puberty (see Smail *et al.*, 1981).

If these *are* new SOAEs that are attributable to the estrogen treatment, it would be desirable to know exactly what aspect of that treatment led to their emergence. One possibility [that is in accord with our previous suggestion about the suppressive effects of androgens (McFadden, 1993, 1998)] is that androgens act suppressively on SOAEs *both* prenatally and in adulthood, and that the reduction in androgen levels experienced by subject DJ allowed those cochlear amplifiers having a tendency toward instability to go into oscillation, thereby giving rise to new SOAEs. (Said differently, androgens may act both organizationally and activationally to suppress SOAEs.) A weakness with this interpretation is that subject DJ's serum testosterone level fell only modestly during the time the SOAEs emerged, from 340 ng/dl prior to beginning estrogen therapy to 289 ng/dl in June 1997 (the normal range for males is 241–826 ng/dl). Currently, there is no evidence whether a change of that magnitude would be adequate to alter SOAEs. An alternative possibility is that the higher estrogen levels themselves were responsible for the emergence of these new SOAEs. The problem with this interpretation is that past research suggests that increases in estrogen level do not greatly affect SOAEs. Estrogen levels change through the menstrual cycle with little effect on SOAEs (Bell, 1992; Haggerty *et al.*, 1993; Penner, 1995), and estrogen levels increase dramatically through the course of pregnancy also with minimal apparent effect on SOAEs (Burns *et al.*, 1993). Of course, the effects of androgens and estrogens may be different in adult male and female cochleas, making these facts misleading, but they do constitute current knowledge. At this time, it appears impossible to know whether the emergence of new SOAEs in our adult male subject is best attributable to the reduction in his androgen levels or the increase in his estrogen levels, but parsimony suggests the former.

A completely opposing interpretation is that the SOAEs seen in the right ear after February 1997 were *not* new, and only appeared to be new because of problems with the baseline data. SOAEs are affected by exposure to intense sounds (Norton *et al.*, 1989; Penner, 1996), various common drugs (e.g., McFadden and Plattsmier, 1984; McFadden and Pasanen, 1994), and other agents (Probst *et al.*, 1991). Thus it is logically possible that the absence of SOAEs from the baseline data in Fig. 1 was temporary, and attributable to some unknown, short-term effect(s) that dissipated by February 1997, allowing the SOAEs to reassert themselves, quite independent of any contribution from estrogen. Interpretations of this sort are common with case studies because adequate tests are often impossible to conduct, as is the case here. While it is currently impossible to know whether the SOAEs observed were new or not, we are presenting the data publicly now, in part because of our considerable uncertainty

about whether, and when, another subject of this sort will become available to us for study.

Whether or not the SOAEs in subject DJ's right ear are new and were produced by the estrogen treatment, various facts about sex differences in OAEs suggest that high levels of androgens contribute to a male-like auditory periphery, both prenatally and in adulthood. Consequently, an important next step is to investigate the structural and functional effects of androgens and estrogens on the relevant cochlear structures during both prenatal and adult stages of life.

## ACKNOWLEDGMENTS

This research was supported by Research Grant No. R01 DC 00153 from the National Institute on Deafness and Other Communication Disorders. We greatly appreciate the cooperation of subjects JF and DJ during this experiment.

- Bell, A. (1992). "Circadian and menstrual rhythms in frequency variations of spontaneous otoacoustic emissions from human ears," *Hearing Res.* **58**, 91–100.
- Burns, E. M., Arehart, K. H., and Campbell, S. L. (1992). "Prevalence of spontaneous otoacoustic emissions in neonates," *J. Acoust. Soc. Am.* **91**, 1571–1575.
- Burns, E. M., Campbell, S. L., Arehart, K. H., and Keefe, D. H. (1993). "Long-term stability of spontaneous otoacoustic emissions," *Abstr. Assoc. Res. Otolaryngol.* **16**, 98.
- Davis, H. (1983). "An active process in cochlear mechanics," *Hearing Res.* **9**, 79–90.
- Haggerty, H. S., Lusted, H. S., and Morton, S. C. (1993). "Statistical quantification of 24-hour and monthly variabilities of spontaneous otoacoustic emission frequency in humans," *Hearing Res.* **70**, 31–49.
- Hampson, E., and Kimura, D. (1992). "Sex differences and hormonal influences on cognitive function in humans," in *Behavioral Endocrinology*, edited by J. B. Becker, S. M. Breedlove, and D. Crews (Bradford, Cambridge, MA), pp. 357–398.
- McFadden, D. (1993). "A masculinizing effect on the auditory systems of human females having male co-twins," *Proc. Natl. Acad. Sci. USA* **90**, 11900–11904.
- McFadden, D. (1998). "Sex differences in the auditory system," *Devel. Neuropsych.* (in press).
- McFadden, D., Loehlin, J. C., and Pasanen, E. G. (1996). "Additional findings on heritability and prenatal masculinization of cochlear mechanisms: Click-evoked otoacoustic emissions," *Hearing Res.* **97**, 102–119.
- McFadden, D., and Pasanen, E. G. (1994). "Otoacoustic emissions and quinine sulfate," *J. Acoust. Soc. Am.* **95**, 3460–3474.
- McFadden, D., and Pasanen, E. G. (1998). "Comparison of the auditory systems of heterosexuals and homosexuals: Click-evoked otoacoustic emissions," *Proc. Natl. Acad. Sci. USA* **95**, 2709–2713.
- McFadden, D., and Plattsmier, H. S. (1984). "Aspirin abolishes spontaneous otoacoustic emissions," *J. Acoust. Soc. Am.* **76**, 443–448.
- Norton, S. J. (1992). "The effects of being a newborn on otoacoustic emissions," *J. Acoust. Soc. Am.* **91**, 2409(A).
- Norton, S. J., Mott, J. B., and Champlin, C. A. (1989). "Behavior of spontaneous otoacoustic emissions following intense acoustic stimulation," *Hearing Res.* **38**, 243–258.
- Penner, M. J. (1995). "Frequency variation of spontaneous otoacoustic emissions during a naturally occurring menstrual cycle, amenorrhea, and oral contraception: A brief report," *Ear. Hear.* **16**, 428–432.
- Penner, M. J. (1996). "The emergence and disappearance of one subject's spontaneous otoacoustic emissions," *Ear. Hear.* **17**, 116–119.
- Probst, R., Lonsbury-Martin, B. L., and Martin, G. K. (1991). "A review of otoacoustic emissions," *J. Acoust. Soc. Am.* **89**, 2027–2067.
- Smail, P. J., Reyes, F. I., Winter, J. S. D., and Faiman, C. (1981). "The fetal hormonal environment and its effect on the morphogenesis of the genital system," in *Pediatric Andrology*, edited by S. J. Kogan and E. S. E. Hafez (Martinus Nijhoff, The Hague), pp. 9–19.
- Talmadge, C. L., Long, G. R., Murphy, W. J., and Tubis, A. (1993). "New off-line method for detecting spontaneous otoacoustic emissions in human subjects," *Hearing Res.* **71**, 170–182.

# Correlated amplitude fluctuations of spontaneous otoacoustic emissions in six lizard species

Pim van Dijk<sup>a)</sup>

Department of Otorhinolaryngology, University Hospital Groningen, P.O. Box 30.001, 9700 RB Groningen, The Netherlands

Geoffrey A. Manley and Lothar Gallo

Institut für Zoologie, Technische Universität München, Lichtenbergstr. 4, 85748 Garching, Germany

(Received 12 March 1998; accepted for publication 5 June 1998)

Spontaneous otoacoustic emissions were recorded from 17 lizard ears (six species: *Gerrhosaurus major*, *Iguana iguana*, *Basiliscus vittatus*, *Tupinambis teguixin*, *Varanus exanthematicus*, and *Cordylus tropidosternum*). The spectrum of each recording contained multiple spectral peaks. For each peak, the envelope cross-correlation  $R(\tau)$  with all other peaks from the same ear was computed. Of the total of 346 emission peak pairs, 58 (17%) showed a significant correlation. Thus like in humans, multiple emission peaks in lizards frequently interact. In the lizards, the cross-correlation was positive in 30 cases, and negative in 28 cases. The cross-correlation function peaked at either a positive ( $\tau_{\text{peak}} > 0$ ) or a negative ( $\tau_{\text{peak}} < 0$ ) delay time. Peak delays ranged from  $-3.7$  ms to  $6.2$  ms with an average  $0.2$  ms (s.d.  $1.8$  ms). The range of observed peak delay values differs from that in human [average  $\tau_{\text{peak}} = 11.0$  ms (s.d.  $22.1$  ms)]. © 1998 Acoustical Society of America. [S0001-4966(98)04209-X]

PACS numbers: 43.64.Jb, 43.64.Kc [BLM]

## INTRODUCTION

Spontaneous otoacoustic emissions (SOAE) have been recorded in a wide variety of species (reviewed by Köppl, 1995). In both mammalian and nonmammalian species, an individual ear may emit several SOAEs as evidenced by the presence of multiple narrow peaks in the emission frequency spectrum. The number of emissions per ear varies across species. In humans, Talmadge *et al.* (1993) describe one subject with 32 emissions in one ear, while the median number across subjects was 5.0. In frogs, it appears that each ear may potentially have four emission peaks, although at a particular body temperature only 2 or 3 peaks are present (Long *et al.*, 1996). In lizards, the SOAE spectra show a wide variety across species, with the number of emission peaks being correlated to the morphology of the tectorial membrane (Manley, 1997). In some species, the tectorium consists of a cascade of subunits, termed “sallets.” In these species up to 15 SOAE peaks may be observed in the SOAE spectrum. The spectrum is similar in species where the relevant hair-cell area lacks a tectorial membrane. In contrast, species having a continuous tectorial membrane typically display only 2 or 3 emission peaks.

In humans, the SOAEs in an individual ear display interactions. These interactions are evidenced by correlated amplitude variations (Burns *et al.*, 1984; Long, 1993; Van Dijk and Wit, 1998a) and phase correlations (Van Dijk and Wit, 1998b). In this paper, we describe amplitude correlations in SOAE recordings from lizard ears. We applied the analysis technique developed by Van Dijk and Wit (1998a), and found a number of correlated emission peaks. We will

discuss similarities and differences between the emission interactions observed in human and lizard ears.

## I. MATERIAL AND METHODS

For the measurements of SOAE, which were carried out in a sound-attenuating chamber, the animals were lightly anaesthetized using i.p. doses of sodium pentobarbital (“Narcoren;” 25–35 mg/kg bodyweight). This anaesthetic dose was effective for between one and four hours. The animals breathed unaided and recovered completely within a few hours following the measurements. The animals were placed on a heating pad lying on a vibration-isolation table inside the chamber. Body temperature was monitored using a small temperature sensor, which had been calibrated against a mercury thermometer, in the animal’s mouth. *Gerrhosaurus* did not tolerate the sensor in its mouth, so the temperature in this species was monitored in a skin fold behind the ear; these measurements were then corrected using a difference measurement to the mouth temperature at the end of the experiment. The temperature was held constant at a species-specific level (between 28 and 32 °C) by regulating the heating pad.

The tip of a metal cone enclosing the condenser microphone (Brüel and Kjær, 4166) was brought close to the external ear opening and sealed to the skin using vaseline. Microphone signals were amplified (B&K 2660, +20 dB) and fed through an amplifying filter (Tektronix TM503 or Grass P15) with a gain of 1000 and a passband between 300 or 1000 Hz and 10 kHz (3-dB roll-off) either via an instrumentation tape recorder (Bell & Howell System TI) or directly into a Silicon Graphics workstation. The tape recordings (*Iguana iguana*, *Cordylus tropidosternum*, and *Varanus ex-*

<sup>a)</sup>Electronic mail: P.van.Dijk@med.rug.nl



TABLE I. Summary of subjects and results. Per lizards species (column 1) (2) family, (3) tectorial structure covering the papillar frequency area above 1 kHz, (4) number of subjects tested, (5) number of ears tested, (6) number of emission peaks included in the study, (7) number of pairs of emission peaks included in the study, (8) number of correlated pairs.

(1) Species	(2) Family	(3) TM Structure	(4) Lizards tested	(5) Ears tested	(6) Number of SOAEs analyzed	(7) Number of SOAE pairs analyzed	(8) Number of correlated SOAE pairs
<i>Iguana iguana</i>	Iguanidae	none	1	2	9	18	1
<i>Basiliscus vittatus</i>	Iguanidae	none	2	3	14	34	11
<i>Gerrhosaurus major</i>	Gerrhosauridae	sallets	4	6	60	263	29
<i>Cordylus tropidosternum</i>	Cordylidae	sallets	1	1	11	55	2
<i>Tupinambis teguixin</i>	Teeidae	continuous	3	6	30	65	14
<i>Varanus exanthematicus</i>	Varanidae	continuous	1	1	2	1	1
Total			14	17	126	346 (100%)	58 (17%)

*anthematicus*, see Table I) were digitalized offline with a workstation (sampling rate 44.1 kHz), while the emissions of *Tupinambis teguixin*, *Basiliscus vittatus*, and *Gerrhosaurus major* were directly fed into the workstation and digitalized online (sampling rate 44.1 kHz).

All further analysis was performed on the digitized recordings. For each recording, an emission spectrum was computed. For each peak in the spectrum, the envelope cross-correlation function was computed with all other emission peaks in the spectrum, respectively. The cross-correlation analysis is described in detail by Van Dijk and Wit (1998a). They describe the following steps in detail, which are applied to each pair of peaks present in the emission spectra: (1) the two emission frequencies of interest were isolated by (digital) bandpass filtering of the recording; (2) for each filtered signal, the corresponding envelope signal was computed, using the Hilbert transformation; and finally (3) the cross-correlation function of both envelope signals was computed. The statistical significance level  $p$  of the computed cross-correlation was determined with the method described by Van Dijk and Wit (1998a) where  $p < 0.01$  was considered evidence for a significant correlation.

In lizards, emission peaks are usually of smaller peak amplitude and broader (full width at half maximum ( $\Delta f_{\text{SOAE}} = 10\text{--}170$  Hz; Köppl and Manley, 1993; Manley *et al.*, 1996) than in human data ( $\Delta f_{\text{SOAE}} = 0.15\text{--}50$  Hz; Van Dijk and Wit, 1990; Talmadge *et al.*, 1993). Peaks broader than 150 Hz were not included in the correlation analysis. The bandpass filters used to isolate individual emission peaks must be rather broad in order to include the entire emission peak. On the other hand, if the bandpass filters applied are too broad, their pass bands overlap, and artificial envelope correlation will be observed (Van Dijk and Wit, 1998a). We chose the filter width ( $\Delta f_{\text{filter}}$ ) as broad as possible, but usually no broader than five times the full width at half maximum ( $\Delta f_{\text{SOAE}}$ ) of the emission under study. If this resulted in overlapping bandpass filters, we narrowed the filter such that its width plus the width of the filter used for a neighboring emission peak would be smaller than the frequency separation of both filter center frequencies. The filter widths used ranged from  $\Delta f_{\text{filter}} = 10$  Hz–400 Hz. The relative filter width  $\Delta f_{\text{filter}}/\Delta f_{\text{SOAE}}$  ranged from 0.9 to 14.6, with an average of 3.2 (s.d. 2.4). Thus we often used filters which

are too narrow (e.g.,  $\Delta f_{\text{filter}}/\Delta f_{\text{SOAE}} < 5$ ) to include the entire emission peak. The consequences of this procedure for the interpretation of our data will be discussed below.

All the work described here was carried out in accordance with German animal-protection law.

## II. RESULTS

Figure 1(a) shows a correlation function computed for the envelopes of two emissions at 2052 Hz and 2326 Hz, respectively, in *Tupinambis teguixin*. Figure 1(b) shows the corresponding phase spectrum. The cross-correlation function in Fig. 1(a) is typical in that it contains a single extre-

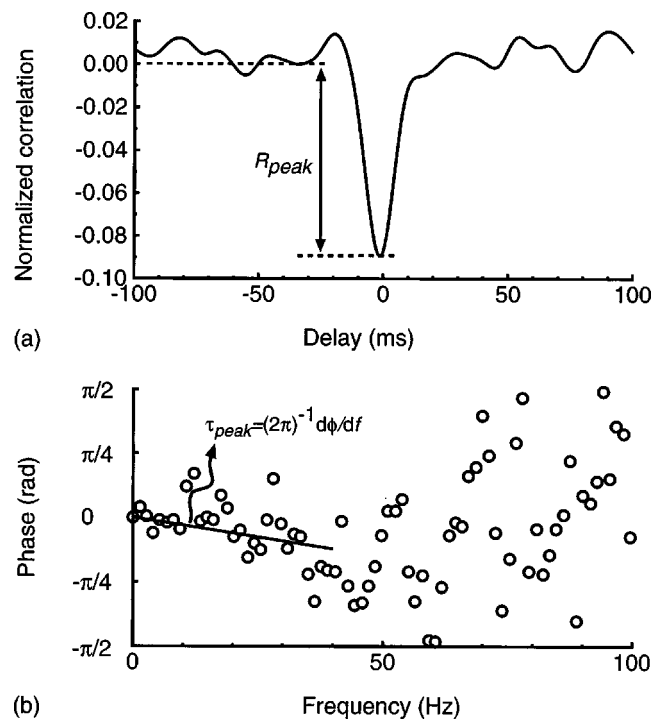


FIG. 1. (a) Envelope cross-correlation function of two emission peaks at 2052 Hz and 2326 Hz in *Tupinambis teguixin*. The peak correlation is  $R_{\text{peak}} = -0.09$ . (b) Phase spectrum corresponding to the function in panel (a). The line is a linear fit to the data points. The negative slope of the phase spectrum emphasizes the fact that the peak in panel (a) is slightly to the left of  $\tau = 0$  ms. From the slope of the phase spectrum it follows that  $\tau_{\text{peak}} = -1.5(\pm 0.3)$  ms.

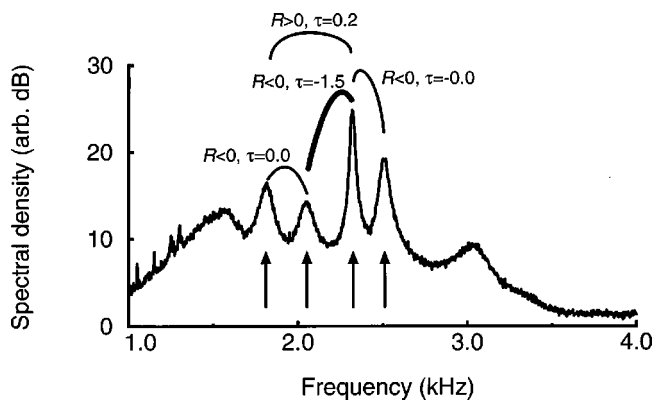


FIG. 2. Spectral density of the spontaneous otoacoustic emission signal in the lizard *Tupinambis teguixin*. For each ‘narrow’ peak ( $\Delta f_{\text{SOAE}} < 150$  Hz, arrows) the envelope cross-correlation with all other narrow peaks in the spectrum was computed. The arches connect emission pairs for which the envelopes were significantly correlated. For each arch, the sign of the peak correlation ( $R=$ ), and the peak delay in milliseconds ( $\tau=$ ) is indicated. The amplitude cross-correlation between the peaks at 2052 Hz and 2326 Hz (thick arch) is illustrated in Fig. 1.

mum  $R_{\text{peak}}$  at a particular time delay  $\tau_{\text{peak}}$ . In this case  $R_{\text{peak}} = -0.09$  and  $\tau_{\text{peak}} = -1.5 (\pm 0.3)$  ms. The peak delay is determined from a straight line fit to the phase spectrum, where only data points up to the 3-dB cutoff frequency of the amplitude spectrum (not shown) were included (see Van Dijk and Wit, 1998a).

Figure 2 displays the emission spectrum in the same subject. The arches in the figure connect emission-peak pairs for which a significant envelope correlation was observed.

Seventeen spontaneous otoacoustic emission spectra from 14 lizards of 6 species (*Gerrhosaurus major*, *Iguana iguana*, *Basiliscus vittatus*, *Tupinambis teguixin*, *Varanus exanthematicus*, and *Cordylus tropidosternum*, see Table I) were included in the correlation analysis. Record lengths ranged from 60 to 300 s. A total of 126 emission peaks were analyzed, from which 346 pairs of peaks could be formed. For 58 pairs (17%) a significant envelope cross-correlation was observed. The frequency ratio of the investigated emission pairs ranged up to 5.8, but was smaller than 1.6 for the correlated pairs (Fig. 3).

We separately considered triplets of SOAE peaks, equally spaced in the frequency spectrum. Triplets (with center frequencies  $f_1$ ,  $f_2$ , and  $f_3$ ) were classified as ‘equally spaced’ if the frequency separations  $f_2 - f_1$  and  $f_3 - f_2$  differed by less than 3 Hz. Across the 17 recordings, 6 triplets were identified. For such triplets, one of the SOAE peaks is possibly a cubic distortion product of the other emissions, which may account for amplitude correlations of such SOAEs. For all but one triplet, the mid-frequency peak had the largest full width at half maximum. According to Van Dijk and Wit (1998a), this makes it very unlikely that cubic distortion is involved in generation of one of the peaks. For the other triplet (in *Iguana iguana*) the SOAE peaks did not exhibit correlated amplitude fluctuations.

Table I gives detailed results per lizard species. No evident differences were observed between lizard species, except that in *Tupinambis teguixin* 11 out of the 14 correlated emission pairs showed negative correlation, while in *Basilis-*

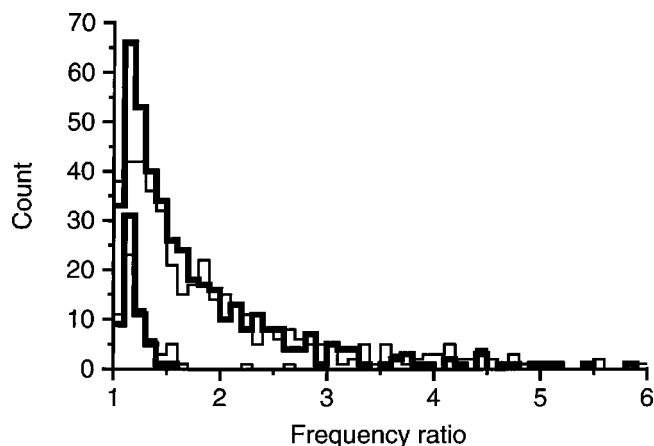


FIG. 3. Histogram of the frequency ratio of (1) all emission pairs investigated (upper black curve) and (2) emission pairs with a significant envelope cross correlation (lower black curve). For comparison, the figure also displays the distribution of frequency ratios in human (thin upper and lower curves; Van Dijk and Wit, 1998a).

*cus vittatus* 10 out of 11 correlated pairs showed positive correlation. Combining results of all investigated lizards showed that the peak correlation  $R_{\text{peak}}$  ranged from  $-0.22$  to  $+0.13$  and was positive in 30 cases and negative in 28 cases.

Across subjects, both positive and negative delay values  $\tau_{\text{peak}}$  were observed. A positive (negative) delay indicates that fluctuation of the lower frequency emission in a pair tends to lag (precede) fluctuation of the higher frequency emission. The peak delays  $\tau_{\text{peak}}$  ranged from  $-3.7$  ms to  $6.2$  ms, and were distributed around the average value  $0.2$  ms (s.d.  $1.8$  ms). Figure 4 displays a histogram of delay values (shaded columns).

### III. DISCUSSION

Before discussing our results in relation to similar data on human emissions, we will first discuss the limitations of our technique.

As mentioned in Sec. I, the bandwidth of the analysis filters we used was often too narrow to include the entire width of the emission peaks under study. In principle, the filters could have been chosen more broadly, but then filters used for neighboring peaks would be overlapping. The use of a too-narrow filter may, however, influence the results of our

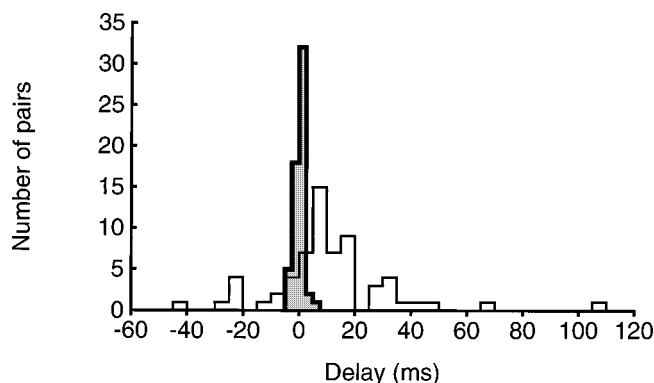


FIG. 4. Histogram of peak delay values  $\tau_{\text{peak}}$  (solid curve, filled). For comparison, the distribution of peak delay values in human is also shown (thin curve, open; Van Dijk and Wit, 1998a).

correlation analysis. The spectral broadening of an emission peak results from frequency fluctuation of the corresponding emission component (for lizard data see Köppl and Manley, 1993; Manley *et al.*, 1996), and this fluctuation may cause the emission component to move out of the filter passband. This will cause a drop of the computed envelope of the filtered signal. Such a drop of the envelope may influence the computed cross-correlation in two ways.

First, if two emission peaks have correlated frequency fluctuations, and they both move out of their respective analysis filter simultaneously, the envelopes of both filtered signals will drop simultaneously. Such an event will result in a significant positive envelope cross-correlation, even if the actual emission envelopes are uncorrelated. Since the filters only excluded a small portion of the bandwidth (e.g., Köppl and Manley, 1993), the chance of such simultaneous events is small and will thus not greatly influence the present data.

Second, if two emission peaks have uncorrelated frequency fluctuations, a drop of one of the filtered signals will not be correlated with an envelope change of the other filtered signal. This will reduce the envelope cross-correlation revealed by our analysis.

Combining these two points, we conclude that (1) a small proportion of the positive envelope correlations we found may result from frequency rather than amplitude fluctuations, and (2) there is a chance that some emission pairs with correlated envelopes may not have been identified as such by our analysis. In addition, note that the presence of microphone noise in the analysis filters may mask the envelope correlation (Van Dijk and Wit, 1998a). In the following, we will not explicitly refer to these limitations of the analysis technique, but their effect should be kept in mind.

The outcome of the correlation analysis depends in a nonlinear fashion on the microphone noise in the analysis filter (Middleton, 1987). As Van Dijk and Wit (1998a), we do not attempt to correct for the effect of microphone noise, but merely remark that for each pair of SOAEs, the observed peak correlation  $|R_{\text{peak}}|$  should be considered as lower limits to the actual correlation.

An order of magnitude of the effect can, however, be given. Consider two strong emissions, which are isolated by the bandpass filtering procedure described above. If, (1) each filtered emission has an (emission)signal-to-(microphone)noise-ratio of about 10 dB, (2) their relative spontaneous amplitude fluctuation is about 20% (a typical value; Van Dijk *et al.*, 1996), and (3) the envelopes of both emission peaks are perfectly correlated, then it can be shown that the measured cross-correlation is only about  $|R_{\text{peak}}| \approx 0.4$ . If the signal-to-noise ratios were poorer, a smaller peak correlation would be observed. Examples of two (for lizards) “strong” emissions are both large peaks in Fig. 2. There, the peak correlation was only  $-0.08$  (Fig. 1), which implies that the amplitude fluctuations were not perfectly correlated.

The characteristics of the envelope correlations we describe in lizard SOAEs are to a remarkable degree similar to those in humans (Van Dijk and Wit, 1998a) in the following respects: (1) the occurrence of correlation is comparable (17% of SOAE pairs in lizards, Table I; 14% in humans; Van Dijk and Wit, 1998a); (2) the shape of the correlation func-

tions is similar; (3) the number of positively correlated pairs is approximately equal to the number of negatively correlated peaks; and (4) the distribution of the frequency ratios of interacting emissions (Fig. 3) is virtually identical. These similarities between lizard and human SOAEs are confirmed by other evidence (for a review of lizard SOAE, see Köppl, 1995), such as: (1) they are all physiologically vulnerable; (2) each ear shows a specific pattern of peak frequencies that is maintained over long periods of time; (3) the statistical characteristics of the amplitude distributions indicates an origin in a sinusoidal oscillator (Van Dijk *et al.*, 1996); (4) they are suppressible in a frequency-selective fashion, whereby the form of the suppression tuning curves strongly resembles that of threshold tuning of primary auditory nerve fibres; and (5) the SOAE center frequency is temperature dependent. These data thus suggest that there are broad and important similarities between the spontaneous-emission phenomena in mammals and lizards.

The only conspicuous difference between the human and the lizard amplitude correlation data is the distribution of the peak delay value  $\tau_{\text{peak}}$  (see Fig. 4). In humans the average peak delay 11.0 ms (s.d. 22.1 ms) differs significantly from 0 ms (*t*-test: one-sided significance  $p = 0.0001$ ). In contrast, for the lizards, the delays were distributed around an average of 0.2 ms (s.d. 1.8 ms), and the average does not differ significantly from 0 ms (*t*-test:  $p = 0.22$ ).

In principle, amplitude correlation of two emission peaks can be described by a model system of two coupled self-sustained oscillators (Wit, 1990; Murphy *et al.*, 1995a). In such a system, the peak delay  $\tau_{\text{peak}}$  is a function of (1) the parameters of the individual oscillators, and (2) the coupling strength which describes the interaction between the oscillators. For example, if both oscillators are identical except for a different oscillation frequency, and the coupling is symmetrical, then the peak correlation will be at  $\tau_{\text{peak}} = 0$  ms. In contrast, if oscillator 1 influences oscillator 2, but the reverse interaction is absent, amplitude changes in oscillator 1 will precede amplitude changes of oscillator 2, and  $\tau_{\text{peak}} \neq 0$ . The latter situation was described in detail by Murphy *et al.* (1995a).

Caution is necessary when interpreting emission–emission interactions as resulting from the same mechanisms as tone-emission interactions, especially in lizards. While emissions are usually suppressed by external tones in both lizards and mammals, in lizards, but not in mammals, facilitation by external tones is a common phenomenon (Köppl and Manley, 1994; Manley *et al.*, 1996). Emission–emission interactions, however, occur as mutual suppression ( $R_{\text{peak}} < 0$ ) or as mutual facilitation ( $R_{\text{peak}} > 0$ ) in approximately the same number of emission pairs in both lizards (this work) and humans (Van Dijk and Wit, 1998a).

Even though lizard and mammals SOAE are very similar in most respects, some of the subtle differences we see may be traceable to micromechanical phenomena in the hearing epithelia of these two groups. In mammals, the basilar-membrane is an integral part of the frequency-tuning complex, as is demonstrated by its frequency specific response. In contrast, the lizard basilar membrane is not selectively tuned. Instead, the basilar-membrane seems to operate

as a broadly tuned driver affecting all hair cells similarly, which themselves respond in a narrow frequency range (Manley, 1990).

As is demonstrated by suppression of a SOAE by an external tone, the external tone interacts with the emission generator. The asymmetry of suppression tuning curves (STC; steep high-frequency slope versus shallower low-frequency slope), strongly resembles the asymmetry measured in primary neural tuning curves (Köppl and Manley, 1994; Manley *et al.*, 1996). This suggests that the factors that determine the hair-cell responses that lead to an increased discharge of primary auditory neurons have the same frequency-tuning characteristics as the factors that lead to suppression of spontaneous hair-cell motion.

The asymmetry of the STCs implies that a high-frequency suppressor is less effective than a low-frequency suppressor. Consequently, we would expect that a low-frequency emission couples stronger to a higher-frequency emission than vice versa, e.g., that the low-frequency emission drives the high-frequency emission. As discussed above, such an asymmetrical coupling of two oscillators results in a lag of amplitude fluctuations of the high-frequency oscillator relative to the low-frequency emissions. This conclusion does not match the data: (1) in humans amplitude fluctuations of higher-frequency SOAE mostly precede fluctuations of lower-frequency SOAE, e.g., high-frequency emissions mostly drive low-frequency emissions (Van Dijk and Wit, 1998a), and (2) in lizards on average there is no lag (delay values distribute around  $\tau=0$ ), despite the fact that the suppression tuning curves are asymmetrical (Köppl and Manley, 1994; Manley *et al.*, 1996), similar to those in humans. Again, this shows that the assumption that emission-emission interactions are similar to tone-emission interaction is incorrect.

The asymmetrical interaction in humans may be related to the asymmetrical spatial distribution of the excitation pattern typical of mammals. If we assume that (1) an SOAE generates an excitation pattern on the basilar membrane, similar to that of an external tone of the same frequency, and (2) the interaction between two emissions takes place in the overlap region of their respective excitation patterns (Fig. 5), then the asymmetry in the interaction in humans may result from the fact that in the overlap region, emission  $f_2$  has a larger amplitude than  $f_1$ . In contrast, in lizards, the basilar membrane is broadly tuned, and consequently, the excitation pattern of an SOAE may be fairly broad. Then, in the overlap region of the excitation patterns of two SOAEs, they will be of similar amplitude (see Fig. 5), which results in a symmetrical interaction.

Another way to look at the same mechanisms is as follows. While the excitation patterns in lizard papillae are not known, it is known that there is no traveling wave along the basilar membrane (Manley *et al.*, 1988, 1989; Peake and Ling, 1980). Due to the lack of tuning on the lizard basilar membrane, a spontaneous oscillation generated in the hair cells may set up a broad excitation pattern in the hair-cell epithelium that travels in both basal and (in contrast to the mammalian case) apical directions (see Fig. 5), which eventually results in the symmetrical interactions in lizards.

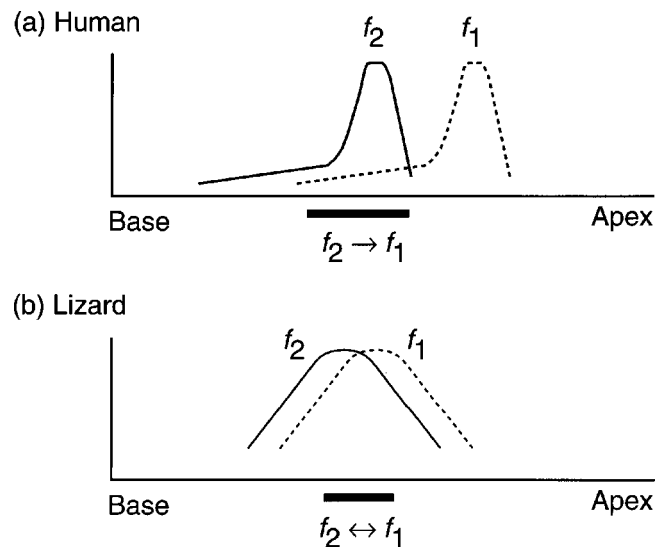


FIG. 5. Hypothetical basilar membrane excitation patterns during SOAE activity at two frequencies in (a) human, and (b) lizard. The interaction between both emissions is assumed to take place in the overlap region of the excitation patterns (see the bars below the horizontal axes). In the lizard the excitation patterns are assumed to be spatially symmetrical and more overlapping. This may result in a symmetrical interaction between both emission frequencies (see Sec. III).

In humans, the delay shows a considerable variation across emission pairs (Van Dijk and Wit, 1998a; Fig. 4). This indicates that there is a considerable variation of the bidirectional coupling strength across emission pairs. If the coupling for a particular pair is entirely unidirectional, then the amplitude fluctuation of one of the emissions will follow fluctuations of the other emission, as was discussed above for a pair of theoretical oscillators. The observed delay  $\tau_{\text{peak}}$  will be of the order of magnitude of the relaxation time constants for amplitude fluctuations. Consequently, the range of delay values, observed across emission pairs, must be similar to the range of amplitude relaxation time constants of SOAEs.

For humans, amplitude relaxation time constants follow from both spontaneous random amplitude fluctuations (Bialek and Wit, 1984; Van Dijk and Wit, 1990; Van Dijk *et al.*, 1994) and from suppression relaxation experiments (Schloth and Zwicker, 1983; Murphy *et al.*, 1995b). The observed values are between 2 and 92 ms, which corresponds well with the range of emission-interaction delay values  $\tau_{\text{peak}}$  reported by Van Dijk and Wit (1998a), with its rather broad distribution (Fig. 4, thin line). In lizards, the distribution of delay values extends over a much smaller range than for humans (Fig. 4). Unfortunately, no amplitude relaxation data are available for the lizards. Our data suggest that relaxation time constants will be shorter for lizards than for humans.

Due to the lack of sufficient data on (micro)mechanics of the lizard ear, our discussion on the difference between human and lizards SOAE must remain speculative. Nevertheless, we think that the interesting differences, including the symmetry of the effects, in which higher-frequency emissions in mammals tend to “drive” lower-frequency emissions, rather than vice versa, is presumably related to differences between cochlear and papillar mechanics. A more

comprehensive understanding of mechanical models for the mammalian and lizard inner ear and the respective emission-generation mechanisms will be needed to explain the differences and similarities between the lizard and human emission data more fully.

## ACKNOWLEDGMENTS

The recording work was supported by a grant to GAM from the Deutsche Forschungsgemeinschaft within the programme of the SFB 204 (Gehör). The analysis work was supported by an Academy-fellowship to PvD from The Royal Netherlands Academy of Sciences and Arts. The work of PvD is part of the research program of the Groningen Department: Communication through Hearing and Speech. This program is incorporated in the Sensory Systems Group of the Groningen Graduate School for Behavioral and Cognitive Neurosciences (BCN) and is supported by the Heinius Houbolt Fund.

- Bialek, W., and Wit, H. P. (1984). "Quantum limits to oscillator stability: theory and experiments on acoustic emissions from the human ear," *Phys. Lett. A* **104**, 173–178.
- Burns, E. M., Strickland, E. A., Tubis, A., and Jones, K. (1984). "Interactions among spontaneous otoacoustic emissions. I. Distortion products and linked emissions," *Hearing Res.* **16**, 271–278.
- Köppl, C. (1995). "Otoacoustic emissions as an indicator for active cochlear mechanics: a primitive property of vertebrate auditory organs," in *Advances in Hearing Research*, edited by G. A. Manley, G. M. Klump, C. Köppl, H. Fastl, and H. Oeckinghaus (World Scientific, Singapore), pp. 207–216.
- Köppl, C., and Manley, G. A. (1993). "Spontaneous otoacoustic emissions in the bobtail lizard. I: General characteristics," *Hearing Res.* **71**, 157–169.
- Köppl, C., and Manley, G. A. (1994). "Spontaneous otoacoustic emissions in the bobtail lizard. II: Interactions with external tones," *Hearing Res.* **72**, 159–170.
- Long, G. R. (1993). "Interactions between spontaneous emissions and external tones: Suppression, frequency shifting and distortion product generation," in *Biophysics of Hair Cell Sensory Systems*, edited by H. Duifhuis, J. W. Horst, P. van Dijk, and S. M. van Netten (World Scientific, Singapore), pp. 40–46.
- Long, G. R., Van Dijk, P., and Wit, H. P. (1996). "Temperature dependence of spontaneous otoacoustic emissions in the edible frog (*Rana esculenta*)," *Hearing Res.* **98**, 22–28.
- Manley, G. A. (1990). *Peripheral Hearing Mechanisms in Reptiles and Birds* (Springer, Berlin).
- Manley, G. A. (1997). "Diversity in hearing-organ structure and the characteristics of spontaneous otoacoustic emissions in lizards," in *Diversity in Auditory Mechanics*, edited by E. R. Lewis, G. R. Long, R. F. Lyon, P. M. Narins, C. R. Steele, and E. Hecht-Poinar (World Scientific, Singapore), pp. 32–38.
- Manley, G. A., Gallo, L., and Köppl, C. (1996). "Spontaneous otoacoustic emissions in two gecko species, *Gekko gecko* and *Eublepharis macularius*," *J. Acoust. Soc. Am.* **99**, 1588–1603.
- Manley, G. A., Yates, G., and Köppl, C. (1988). "Auditory peripheral tuning: Evidence for a simple resonance phenomenon in the lizard *Tiliqua*," *Hearing Res.* **33**, 181–190.
- Manley, G. A., Yates, G., and Köppl, C. (1989). "Micromechanical basis of high-frequency tuning in the bobtail lizard," in *Cochlear Mechanics*, edited by J. Wilson and D. Kemp (Plenum, New York), pp. 143–150.
- Middleton, D. (1987). *Introduction to Statistical Communication Theory* (Peninsula, Los Altos, CA).
- Murphy, W. J., Talmadge, C. L., Tubis, A., and Long, G. R. (1995a). "Relaxation dynamics of spontaneous otoacoustic emissions perturbed by external tones. II. Suppression of interacting emissions," *J. Acoust. Soc. Am.* **97**, 3711–3720.
- Murphy, W. J., Talmadge, C. L., Tubis, A., and Long, G. R. (1995b). "Relaxation dynamics of spontaneous otoacoustic emissions perturbed by external tones. I. Response to pulsed single-tone suppressors," *J. Acoust. Soc. Am.* **97**, 3702–3710.
- Peake, W. T., and Ling, A. (1980). "Basilar-membrane motion in the alligator lizard: Its relation to tonotopic organization and frequency selectivity," *J. Acoust. Soc. Am.* **67**, 1736–1745.
- Schlöth, E., and Zwicker, E. (1983). "Mechanical and acoustical influences on otoacoustic emissions," *Hearing Res.* **11**, 285–293.
- Talmadge, C., Long, G., Murphy, W., and Tubis, A. (1993). "New off-line method for detecting spontaneous otoacoustic emissions in human subjects," *Hearing Res.* **71**, 170–182.
- Van Dijk, P., Manley, G. A., Gallo, L., and Pavusa, A. (1996). "Statistical properties of spontaneous otoacoustic emissions in one bird and three lizard species," *J. Acoust. Soc. Am.* **100**, 2220–2227.
- Van Dijk, P., and Wit, H. P. (1990). "Amplitude and frequency fluctuations of spontaneous otoacoustic emissions," *J. Acoust. Soc. Am.* **88**, 1779–1793.
- Van Dijk, P., and Wit, H. P. (1998a). "Correlated amplitude fluctuations of spontaneous otoacoustic emissions," *J. Acoust. Soc. Am.* **104**, 336–343.
- Van Dijk, P., and Wit, H. P. (1998b). "Synchronization of cubic distortion spontaneous otoacoustic emissions," *J. Acoust. Soc. Am.* **104**, 591–594.
- Van Dijk, P., Wit, H. P., Tubis, A., Talmadge, C. L., and Long, G. R. (1994). "Correlation between amplitude and frequency fluctuations of spontaneous otoacoustic emissions," *J. Acoust. Soc. Am.* **96**, 163–169.
- Wit, H. P. (1990). "Spontaneous otoacoustic emission generators behave like coupled oscillators," in *The Mechanics and Biophysics of Hearing*, edited by P. Dallos, C. Geisler, J. Matthews, M. Ruggero, and C. Steele (Springer, Berlin), pp. 259–266.

# The auditory evoked potential difference tone and cubic difference tone measured from the inferior colliculus of the chinchilla

Sally Arnold

Department of Speech Language Pathology, Buffalo State College, Buffalo, New York  
and Center for Hearing and Deafness, State University of New York at Buffalo, Buffalo, New York 14214

Robert Burkard<sup>a)</sup>

Center for Hearing and Deafness, and Department of Communicative Disorders and Sciences,  
and Department of Otolaryngology, State University of New York at Buffalo, Buffalo,  
New York 14214-3007

(Received 17 November 1997; revised 29 April 1998; accepted 16 June 1998)

The auditory evoked potential  $f_2 - f_1$  difference tone (DT) and the  $2f_1 - f_2$  cubic difference tone (CDT) were recorded from electrodes implanted in the inferior colliculus in a group of chinchillas. The purpose of this study was to measure normative aspects of AEP distortion products in awake chinchillas, by comparing the DT and CDT under a variety of stimulus conditions. For experiment 1,  $f_1$  was held constant at 1998 Hz, while the  $f_2/f_1$  ratio was varied from 1.05 to 1.50. Input-output functions were measured over a range of primary tone levels up to 80 dB SPL. The amplitude of the DT was greatest for the smallest  $f_2/f_1$  ratio, and decreased systematically as  $f_2/f_1$  ratio increased. DT amplitude was greater than CDT amplitude for all primary tone pairs. Experiment 2 was conducted to determine the effect of  $f_1$  frequency upon the DT and CDT for a constant  $f_1 - f_2$  difference frequency of 102 Hz ( $f_1 = 999, 1998, 4999, \text{ and } 9998$  Hz). The DT input-output functions were overlapping for all  $f_1$  frequencies. For the CDT, amplitude decreased with increasing  $f_1$  frequency, which corresponded to an increase in CDT frequency. In experiment 3, the relationship between ear of stimulation and inferior colliculus recorded from was investigated. DT input-output functions ( $f_1 = 1998$  Hz, DT = 102 Hz) were measured for monaural contralateral, monaural ipsilateral, and dichotic stimulus conditions. DT amplitude was largest for the contralateral condition, followed by the ipsilateral condition. A smaller, dichotic component to the DT was observed as well. © 1998 Acoustical Society of America. [S0001-4966(98)06309-7]

PACS numbers: 43.64.Qh, 43.64.Ri [RDF]

## INTRODUCTION

Auditory system nonlinearities are manifested when the ear is stimulated simultaneously by two frequencies,  $f_1$  and  $f_2$ . These nonlinearities produce additional frequencies at the output of the system. Commonly studied distortion products include the  $f_2 - f_1$  difference tone (DT) and the  $2f_1 - f_2$  cubic difference tone (CDT). These nonlinearities have become increasingly important in recent years in the evaluation of auditory system integrity. A notable example of this is in otoacoustic emission (OAE) distortion product measurement, in which the CDT is the predominant component, being larger than the DT (Kim, 1980; Brown, 1993).

Distortion products have also been measured using scalp-recorded auditory evoked potentials (AEPs) in guinea pigs (Chertoff and Hecox, 1990; Chertoff *et al.*, 1992), Mongolian gerbils (Dolphin *et al.*, 1994), and humans (Chertoff and Hecox, 1990; Rickman *et al.*, 1991). In contrast to otoacoustic emissions, for AEP measurements the DT is larger than the CDT (Rickman *et al.*, 1991; Chertoff *et al.*, 1992).

The AEP DT is sometimes referred to as the envelope following response (EFR) (Dolphin *et al.*, 1994), because the frequency of the DT ( $f_2 - f_1$ ) corresponds to the periodicity

of the stimulus envelope. The EFR has also been measured using sinusoidally amplitude-modulated (SAM) tones or noise, in which the response occurs at the modulation frequency (Rodenburg *et al.*, 1972; Rickards and Clark, 1984; Kuwada *et al.*, 1986; Rees *et al.*, 1986; Picton *et al.*, 1987; Cohen *et al.*, 1991; Dolphin and Mountain, 1992; Levi *et al.*, 1993; Lins *et al.*, 1995). Dolphin *et al.* (1994) have shown that the EFR to two-tone stimuli and SAM stimuli behave similarly, and are probably manifestations of the same auditory nonlinearity. For modulation frequencies below 80 Hz, the scalp-recorded EFR to SAM stimuli is dependent on subject state (Cohen *et al.*, 1991; Levi *et al.*, 1993).

Our approach to the study of nonlinearities in the AEP was to use near-field recordings, from electrodes placed in the inferior colliculus of chinchillas, rather than scalp recordings. The predominant generator is thus known, and the resulting response is larger than would be obtained from the scalp. Animals were tested unanesthetized, to reduce variability due to subject state. We chose to use two-tone stimuli, rather than SAM tones, in order to simultaneously measure and compare the DT and CDT. The goal of these experiments was to quantify the effects of various stimulus manipulations upon the DT and CDT, as measured from a known location within the auditory nervous system (the IC)

<sup>a)</sup>Electronic mail: RFB@ACSU.BUFFALO.EDU

in the unanesthetized chinchilla. Our goal is to establish normative data for AEP distortion products in awake chinchillas, for future studies evaluating the effects of hearing loss upon auditory system nonlinearities.

Another aim of this study was to determine whether the DT could be elicited with dichotic stimulation, and if so, to compare the amplitude of the DT for ipsilateral, contralateral, and dichotic conditions. Hink *et al.* (1980) investigated dichotic interaction in the scalp-recorded human frequency following response. When stimulating dichotically with two tones differing slightly in frequency, the waveform of the response showed amplitude fluctuations whose “beating” corresponded to the frequency difference between the two tones. Thus it appears useful to examine this phenomenon further, with the goal of establishing a metric of dichotic processing for future studies involving degeneration of inputs into the central auditory nervous system.

## I. METHODS

### A. Subjects

A total of 11 young adult chinchillas (5 males, 6 females, weight 430–607 gms) were used, 5 for experiment 1, and the remaining 6 for both experiments 2 and 3. For evoked response recording, chronic electrodes were implanted in one or both inferior colliculi. For the implantation surgery, the animals were anesthetized with a mixture of ketamine (35 mg/kg) and acepromazine (0.5 mg/kg). The recording electrode(s) were then stereotaxically implanted into the left IC (experiments 1 and 2) or both IC (experiment 3), with a ground electrode implanted 1–2 cm anteriorly in the dura. The electrodes were advanced to the region of the IC, while acoustically stimulating the contralateral ear with a toneburst. The presence of a large amplitude diphasic or triphasic response was taken as evidence of appropriate electrode placement. Although electrode impedances were not specifically measured for the animals used in the present investigation, electrode impedances were measured in a separate group of eight animals in which electrodes were implanted in both the right IC and left IC. For these 16 electrodes, electrode impedance was measured between the IC and the anterior electrode using a Grass EZM electrode impedance meter. Electrode impedance ranged from 24 to 90 k $\Omega$ , with a mean of 43.4 k $\Omega$  and a standard deviation of 20.3 k $\Omega$ . Following the surgery, animals were allowed to recover for a period of at least one week before testing.

### B. Stimuli

Stimuli were two tones,  $f_1$  and  $f_2$ , presented simultaneously ( $f_2 > f_1$ ). The two tones were generated using the D/A converters (16 bits, 62 kHz) on two signal processing boards (Spectrum Signal Processing # TMS320C25), located in a Prism N8 Portable PC. The output of each D/A converter was low-pass filtered and led to a custom-built, computer controlled attenuator (127.5 dB, 0.5-dB steps), buffer amplifier, and sound source (Etymotic ER2 insert earphone). The two-tone stimuli were presented for a duration of 232 ms, with approximately 30 ms between repetitions.

For experiments 1 and 2,  $f_1$  and  $f_2$  were presented through two separate ER2 earphones whose outputs were routed to the right ear canal. For experiment 3, each ear had a pair of ER2 earphones, and four different stimulus presentation modes were used:  $f_1$  and  $f_2$  to right ear;  $f_1$  and  $f_2$  to left ear;  $f_1$  to right ear and  $f_2$  to left ear;  $f_2$  to right ear and  $f_1$  to left ear. For all conditions, primary tone sound pressure level was measured in the ear canal using a probe microphone. For experiments 1 and 2, the insert earphones were routed through the housing of an Etymotic ER10B microphone, which was coupled to an impedance probe tip and inserted into the ear canal. Tone pairs were presented through the appropriate transducers, the microphone output was routed to the analog-to-digital converter of the Spectrum Signal Processing DSP board, and primary tone magnitude was determined by estimating the Fourier coefficients at the probe tone frequencies. Once the voltage magnitude at each primary tone was determined, sound pressure level was determined by use of the sensitivity specification of the microphone (1  $\mu$ V=20  $\mu$ Pa). For experiment 3, this procedure was modified such that an Etymotic ER7C probe microphone was threaded through a foam insert in each ear canal, the outputs of the microphones were electrically mixed and input to the analog-to-digital converter of the DSP board, and the Fourier coefficients for each primary tone were determined and used in the sound pressure level calculations.

### C. Electrophysiologic recording

For evoked response recording, animals were placed in a chinchilla restraint device (Snyder and Salvi, 1994) inside a single-walled IAC booth. For experiments 1 and 2, electrical activity was recorded in a monopolar fashion from the left IC, with the frontal electrode serving as ground. For experiment 3, a two-channel recording paradigm was utilized, to simultaneously measure the response from the right and left IC electrodes, again with frontal electrode as ground. Response collection began 100 ms after stimulus onset, to eliminate onset potentials, and continued for 132 ms (232 ms total stimulus duration). The elimination of the first 100 ms, combined with the brief time between tone-pair presentations (approximately 30 ms) ensured that the observed response was primarily a steady-state response, with minimal effects of any onset response. Electrical activity was amplified 10 000 times and bandpass filtered (30–10 000 Hz for experiments 1 and 2, 30–3000 Hz for experiment 3) by Grass P511 bioamplifier(s). Responses to 50 stimuli were averaged in the time domain prior to spectral calculations.

### D. Analysis

The amplified and filtered electrical activity was fed to the A/D converter on the Spectrum Signal Processing board, and digitized at a sampling rate of 31 kHz, for a 132-ms time period, initiated 100 ms following the onset of the stimulus. For the two-channel recording in experiment 3, A/D converters on two separate signal processing boards were used. The responses to 50 stimulus presentations were averaged and the

TABLE I. Value of  $F1$  and  $F2$ ,  $F2/F1$  ratio, and the corresponding DT and CDT components for each of the eight two-tone stimulus pairs in experiment 1.

Component	Frequency (Hz)							
$F1$	1998	1998	1998	1998	1998	1998	1998	1998
$F2$	2100	2199	2301	2399	2501	2600	2800	3001
$F2/F1$	1.05	1.10	1.15	1.20	1.25	1.30	1.40	1.50
$F2 - F1$	102	201	303	401	503	602	802	1003
$2F1 - F2$	1896	1797	1695	1597	1495	1396	1196	995

evoked potential amplitude of the primary tones, DT, and CDT were obtained by computing the Fourier coefficients at these frequencies.

## E. Procedures

### 1. Experiment 1

The purpose of this experiment was to explore the characteristics of the DT and the CDT, and to determine the effect of  $f2/f1$  ratio on these responses. Responses were obtained from five animals. In all animals, the two-tone stimulus was presented to the right ear, and electrophysiological responses were recorded from the left IC. The frequency of  $f1$  was held constant at 1998 Hz, while the  $f2/f1$  ratio was varied from 1.05 to 1.50 in eight steps. The specific stimulus pairs were chosen to cover a wide range of  $f2 - f1$  differences, within software constraints which required that  $f2/f1$  be an integer percentage ratio. Table I shows the  $f1$  and  $f2$  values for each of the eight ratios, as well as the value of the DT and the CDT. For all stimuli, the level of  $f1$  was equal to that of  $f2$ . Input/output functions were measured for DT and CDT for each of the eight stimulus pairs, with primary tone levels increasing from 0 to 80 dB SPL in 10-dB steps. One response was obtained for each stimulus condition.

### 2. Experiment 2

Six animals were used as subjects for experiment 2. The purpose of this experiment was to determine the effect of  $f1$  frequency on the DT and CDT, for a constant  $f1 - f2$  difference frequency of 102 Hz. The following four stimulus pairs were used:  $f1 = 999$  Hz,  $f2 = 1101$  Hz;  $f1 = 1998$ ,  $f2 = 2100$  Hz;  $f1 = 4999$  Hz,  $f2 = 5101$  Hz;  $f1 = 9998$  Hz,  $f2 = 10100$  Hz. The  $f2/f1$  ratio and the frequency value of the DT and CDT are shown in Table II for each stimulus pair. Input/output functions were measured from  $-20$  to 80 dB SPL, in 10-dB steps, for all stimulus conditions except the 1998/2100 Hz data, for which stimulus level varied in level

TABLE II. Value of  $F1$  and  $F2$ ,  $F2/F1$  ratio, and the corresponding DT and CDT components for each of the four two-tone stimulus pairs in experiment 2.

Component	Frequency (Hz)			
$F1$	999	1998	4999	9998
$F2$	1101	2100	5101	10100
$F2/F1$	1.10	1.05	1.02	1.01
$F2 - F1$	102	102	102	102
$2F1 - F2$	897	1896	4897	9896

from 0 to 80 dB SPL. The data used as the 1998/2100 Hz condition were taken from experiment 3 (see below). As in experiment 1, the right ear was stimulated and recordings were obtained from the left IC. One response was obtained for each stimulus condition, with the exception of the 1998/2100 Hz condition, for which two responses were obtained.

### 3. Experiment 3

The purpose of experiment 3 was to compare the amplitude of the DT for ipsilateral, contralateral, and dichotic stimulation. The same six subjects from experiment 2 were used. A two-channel recording configuration was utilized to record simultaneously from the left and right IC. Input/output functions were measured for a single stimulus pair ( $f1 = 1998$  Hz,  $f2 = 2100$  Hz), presented in the following modes: 1. Monaural left ear; 2. Monaural right ear; 3. Dichotic,  $f1$  to right ear,  $f2$  to left ear; 4. Dichotic,  $f2$  to right ear,  $f1$  to left ear. Each mode was repeated twice in each subject. The order of stimulus presentation modes was randomized across animals.

### 4. Acoustic distortion measures

To measure the degree of distortion in the stimulus delivery system, the level of the noise floor/distortion at the DT and CDT frequencies was recorded by placing the acoustic assembly used in experiments 1 and 2 into a 0.5-cc volume, and evaluating the stimulus conditions used in experiments 1 and 2. The output of the microphone was digitized and converted to SPL in the same manner as described for acoustic calibration. For primary-tone levels of 60 dB SPL and less, all estimates of acoustic distortion at the DT and CDT frequencies were less than 1 dB SPL. The measures of acoustic distortion obtained with the 80 dB SPL primary tones are shown in Table III. For all stimulus pairs, the amplitude of the distortion is less than 16 dB SPL. The magnitude of distortion for 70 dB SPL primaries is not shown, but was less than 3 dB SPL in all cases. These low levels of acoustic distortion at the DT and CDT frequency suggest that the responses we observed were not the result of distortion in the acoustic system.

## II. RESULTS

### A. Experiment 1

The purpose of this experiment was to compare the DT and CDT measured simultaneously, and to determine the effect of  $f2/f1$  ratio on the amplitudes of these distortion components.



TABLE III. Acoustic distortion at DT and CDT frequency, measured using 80 dB SPL primary tones at the frequencies used for experiments 1 and 2.

	$F1$ (Hz)	$F2$ (Hz)	DT (dB SPL)	CDT (dB SPL)
Experiment 1	1998	2100	13.9	-12.0
	1998	2199	14.3	-10.5
	1998	2301	15.7	0.1
	1998	2399	14.8	-6.6
	1998	2501	14.6	-11.3
	1998	2600	13.9	-4.7
	1998	2800	12.9	-8.5
	1998	3001	13.0	2.3
Experiment 2	999	1101	6.6	-3.6
	4999	5101	3.2	-4.1
	9998	10100	5.1	-19.4

### 1. DT amplitude

The mean input-output functions for the DT are shown in Fig. 1 for each of the eight  $f2/f1$  ratios. DT amplitude increases with increasing stimulus intensity, with mean DT values of greater than  $10 \mu\text{V}$  seen for the 102-Hz DT frequency at higher primary-tone levels. The amplitude of the DT is greatest at 102 Hz, and decreases as DT frequency increases. For high primary-tone levels, the DT amplitude drops from  $>10 \mu\text{V}$  to slightly above  $1 \mu\text{V}$  for DT frequency increases from 102 to 401 Hz. For larger DT frequencies, DT amplitude is less than  $1 \mu\text{V}$ , even for the 80 dB SPL condition.

### 2. CDT amplitude

The corresponding input-output functions for the CDT are shown in Fig. 2. In contrast to the DT, the amplitude of the CDT is very small. The input-output functions remain flat until about 50 dB SPL, then rise slightly at higher stimulus levels. The small amplitude of these responses precludes visualizing any clear relationship between  $f2/f1$  ratio and

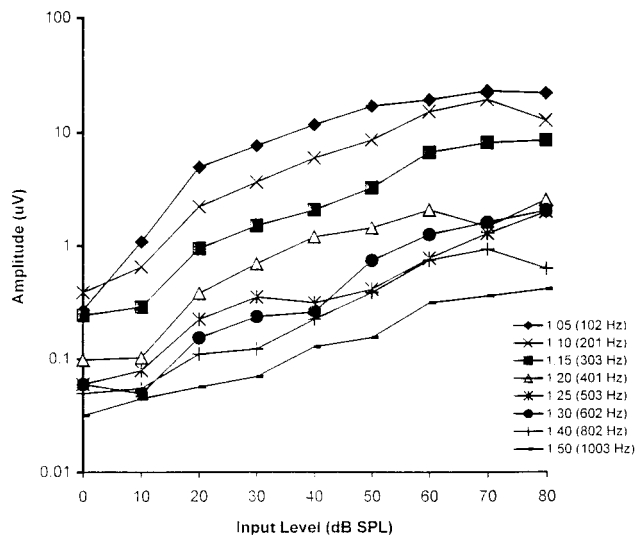


FIG. 1. Amplitude of the difference tone ( $f2 - f1$ ) as a function of stimulus level for  $f1 = 1998$  Hz, for each of the eight  $f2/f1$  ratios. Each curve represents mean data from five chinchillas. The symbol legend shows the  $f2/f1$  ratio and the corresponding frequency value of the DT for each curve.

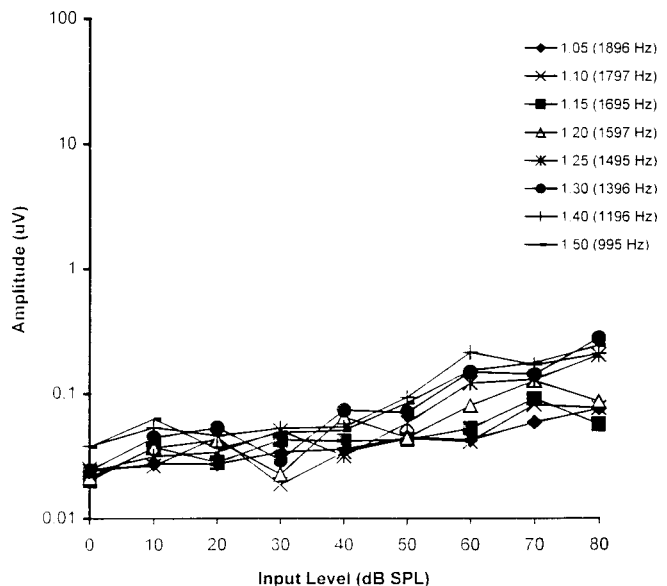


FIG. 2. This figure shows the cubic difference tone ( $2f1 - f2$ ) data obtained for each of the eight stimulus pairs. The symbol legend shows the  $f2/f1$  ratio and the corresponding value of the CDT.

CDT, although at high primary-tone levels it appears that responses to large  $f2/f1$  ratios show the largest amplitude.

### 3. Comparison of DT and CDT amplitude

When comparing Figs. 1 and 2, it is apparent that the DT is greater than the CDT for all  $f2/f1$  ratios, often by several orders of magnitude. This is further illustrated in Fig. 3(a)–(d), in which the DT and CDT input-output functions are plotted together, for four of the eight stimulus pairs. It can be seen that the amplitude of the DT is larger than the CDT in all cases. For the ratio shown in Fig. 3(a) (1.05), the DT ( $=102$  Hz) is  $>10 \mu\text{V}$  at high stimulus levels, while the CDT ( $=1898$  Hz) is  $<0.1 \mu\text{V}$ . Increasing  $f2/f1$  ratio shows a convergence of the DT and CDT functions. This is primarily due to the large decrease in DT amplitude with increasing  $f2/f1$  ratio. At high stimulus levels, DT amplitude drops from  $>10 \mu\text{V}$  at  $f2/f1$  ratio of 1.05 (DT= $102$  Hz) to just  $>1.0 \mu\text{V}$  at a ratio of 1.2 (DT= $401$  Hz). At  $f2/f1$  ratios of 1.4 and 1.5 (DT= $802$  Hz and  $1003$  Hz, respectively), DT amplitude is less than  $1.0 \mu\text{V}$  at high primary-tone levels. In contrast, there appears to be a trend toward larger CDT amplitude with increasing  $f2/f1$  ratios. CDT amplitude exceeds  $0.1 \mu\text{V}$  at high primary-tone levels for an  $f2/f1$  ratio of 1.5 (CDT= $995$  Hz), while its maximum mean amplitude never exceeds  $0.1 \mu\text{V}$  for the  $f2/f1$  ratio of 1.05 (CDT= $1896$  Hz). It is interesting to note, then, that response amplitudes appear to increase with decreasing CDT and DT frequency. However, even when DT frequency is greater than CDT frequency (only for the  $f2/f1$  ratio of 1.50, DT= $1003$  Hz, CDT= $995$  Hz), the mean amplitude of DT is still somewhat larger than that of CDT [see Fig. 3(d)].

## B. Experiment 2

In this experiment, the DT and CDT were measured for  $f1$  frequencies of 999, 1998, 4999, and 9998 Hz, and a constant  $f2 - f1$  difference of 102 Hz.

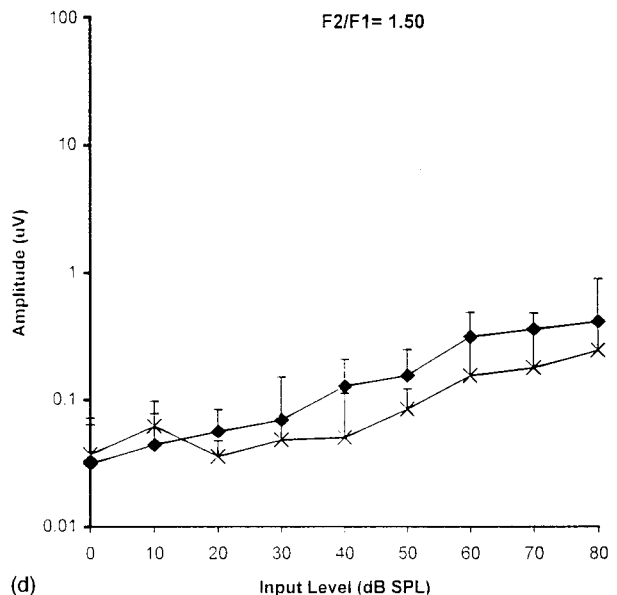
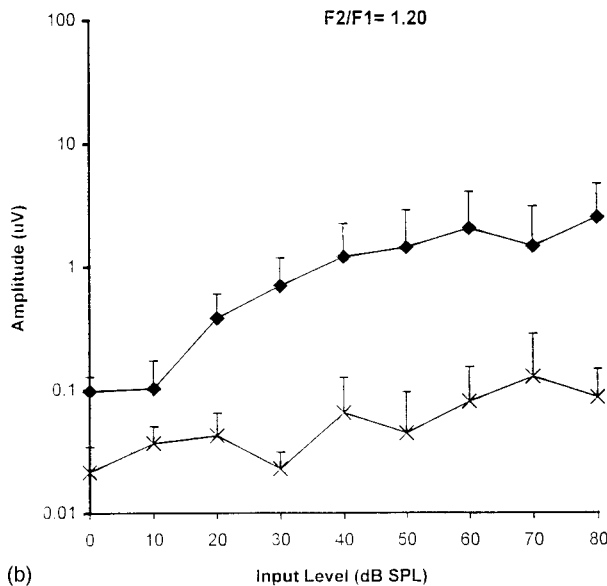
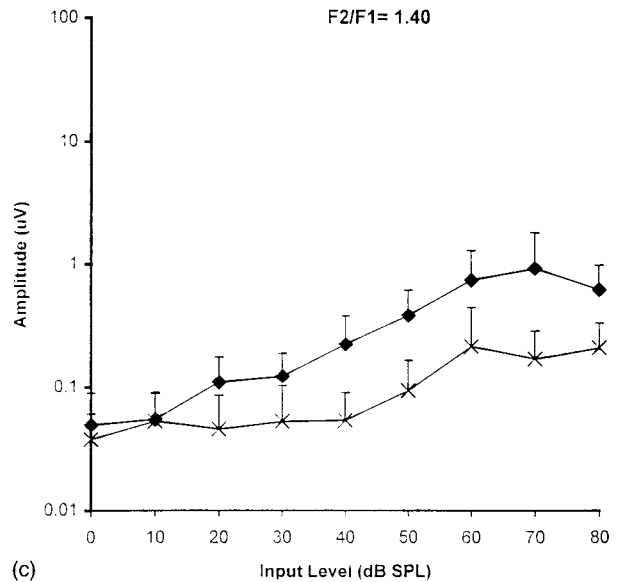
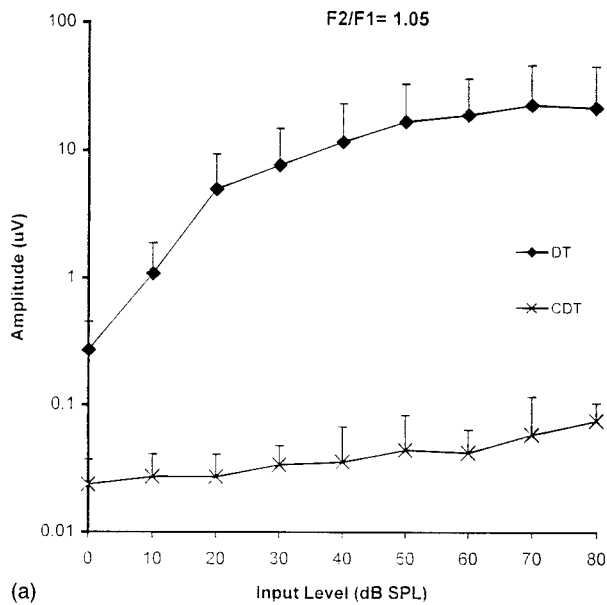


FIG. 3. (a)–(d) The DT and CDT data from Figs. 1 and 2 are plotted here for  $f_2/f_1$  ratios of 1.05, 1.20, 1.40, and 1.50. Error bars represent +1 standard error.

### 1. DT amplitude

Figure 4 shows the input–output functions for the DT for the four  $f_1$  frequencies tested. It can be seen that the DT is present for all  $f_1$  frequencies, and that the input–output functions are virtually overlapping. Responses appear to start growing for primary-tone levels exceeding 0–10 dB SPL, and plateau at mean response amplitudes of roughly 10  $\mu$ V.

### 2. CDT amplitude

The corresponding CDT data are shown in Fig. 5. Here, the input–output function amplitudes appear to be inversely related to  $f_1$  frequency, which corresponds to an increase in CDT frequency. For  $f_1 = 999$  Hz, the CDT is 897 Hz and at high primary-tone levels, CDT amplitude exceeds 1.0  $\mu$ V. For  $f_1 = 1998$  Hz, the CDT is 1896 Hz, and the largest mean CDT amplitude never exceeds 0.1  $\mu$ V. Finally, for  $f_1 = 4999$  Hz and 9998 Hz (CDTs of 4897 Hz and 9896 Hz, respectively), there is no evidence of a CDT response, even

at high primary-tone levels. That is, the response does not grow with increasing primary tone level, and the response amplitude of 2–3 nanovolts appears to represent the recording noise floor.

### C. Experiment 3

This experiment compared the amplitude of the DT for ipsilateral, contralateral, and binaural (dichotic) stimulation, while simultaneously recording from the left and right IC. A single stimulus pair ( $f_1 = 1998$  Hz,  $f_2 = 2100$  Hz) was used for all conditions.

Figure 6(a) and (b) shows the data from the right and left IC, respectively. A few observations are apparent. Regardless of recording site, the largest responses are seen for conditions where the primary tones are presented to the same ear. Comparing the right and left IC, a symmetrical pattern of responses is seen. In both figures, the largest DT amplitude is seen for the monaural, contralateral condition (left ear

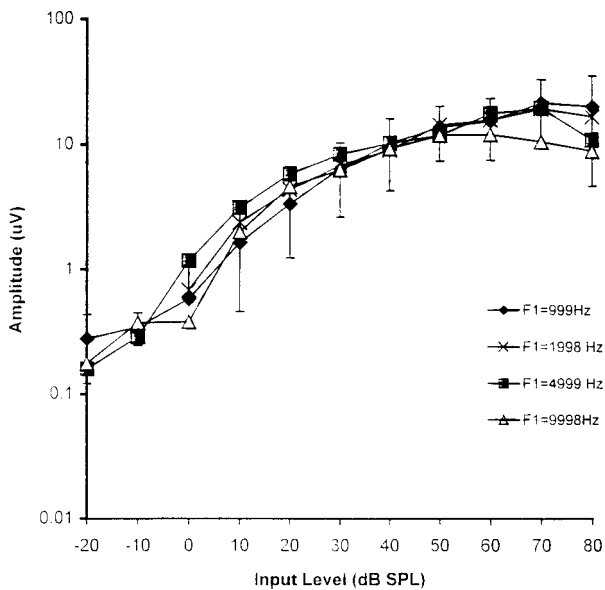


FIG. 4. DT input-output functions for four  $f_1$  frequencies and a constant  $f_2 - f_1$  difference of 102 Hz. Mean data from six chinchillas. Error bars represent the standard error for the  $f_1 = 999$  Hz data.

monaural stimulation for the right IC, right ear monaural stimulation for the left IC), with mean amplitudes of  $>10 \mu\text{V}$  at high primary-tone levels. The next largest response is seen for the monaural, ipsilateral conditions (right ear monaural for right IC, left ear monaural for left IC), with mean response amplitudes of  $5.0\text{--}8.0 \mu\text{V}$  at high primary-tone levels. Figure 6 shows that there is a small, low level dichotic component to the DT as well. That is, when the stimulus tones are presented one to each ear, a small DT can still be measured from the IC electrode. For each IC, the curves for the two dichotic stimulus conditions ( $f_1$  to right ear- $f_2$  to left ear, and vice versa) are similar, with DT amplitudes slightly greater than  $1 \mu\text{V}$  at high primary-tone levels.

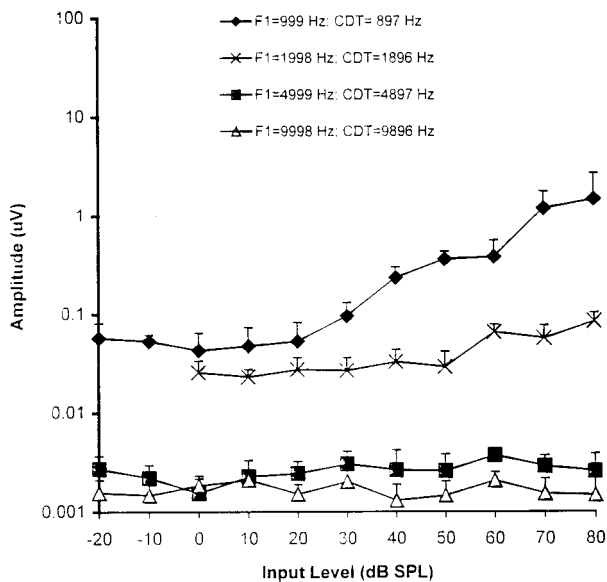


FIG. 5. CDT input-output functions obtained for experiment 2 are shown. The parameter is  $f_1$  frequency.

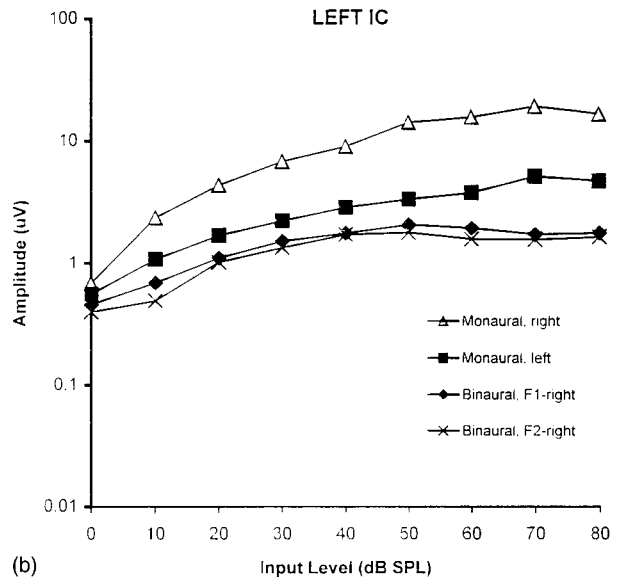
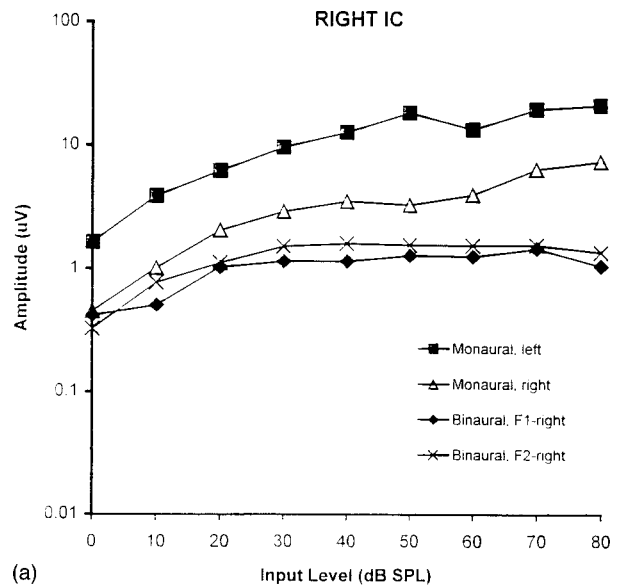


FIG. 6. (a) shows DT data collected from the right IC. (b) shows DT data collected from the left IC. Each figure compares input-output functions recorded from the IC under four stimulus presentation modes: 1: monaural, left ear stimulation; 2: monaural, right ear stimulation; 3: binaural,  $f_1$  to right ear,  $f_2$  to left ear; and 4: binaural,  $f_2$  to right ear,  $f_1$  to left ear. A single stimulus pair ( $f_1 = 1998$  Hz,  $f_2 = 2100$  Hz) was used for all recordings. Curves represent mean data from six animals.

### III. DISCUSSION

#### A. Characteristics of the $f_2 - f_1$ difference tone (DT)

We found that, for a constant  $f_1$  frequency (1998 Hz), the amplitude of the DT decreased as the  $f_2/f_1$  ratio increased from 1.05 to 1.50. A similar effect was reported by Chertoff *et al.* (1992), recording from the scalp in guinea pigs. They found decreasing DT amplitude for increasing  $f_2/f_1$  ratios, for  $f_1$  frequencies between 500 and 2000 Hz. Dolphin *et al.* (1994), using far-field recording from the scalp in anesthetized gerbils, found that the amplitude of the DT response first decreased, then increased, as  $f_2 - f_1$  difference increased, creating a “notchlike” pattern. They speculated that the notch was due to two different generators contributing to the response—a brainstem generator for high

$f_2 - f_1$  differences, and a cortical generator for lower  $f_2 - f_1$  differences—which are out of phase at the notch frequency. The fact that we did not observe such a notching pattern in our data when recording from a single brainstem location tends to support their hypothesis, but does not explain the absence of such notching in the Chertoff *et al.* (1992) data.

The largest DT values occurred for the 102-Hz DT condition, which was the lowest DT frequency used herein. We do not know the amplitude of the DT for smaller DT frequencies, and hence do not know whether the response amplitude gets larger, smaller or stays the same for lower DT frequencies. Rees and Moller (1983) investigated the responses of IC neurons to sinusoidally amplitude modulated tones in urethane-anesthetized rats. They found that IC units typically showed a bandpass modulation-rate transfer function, and that in all cases the most effective modulation frequency was below 120 Hz. In light of the Rees and Moller (1983) data, it seems likely that the amplitude of our IC DT response would remain constant or increase with decreasing DT frequency, until some cutoff value is reached, and then drop substantially in amplitude. However, this is purely conjecture, and a conclusive answer to the shape of the DT function for DT frequencies below 102 Hz awaits the collection of suitable empirical data.

Another finding of the present study was that, for  $f_1$  frequencies of 999, 1998, 4999, and 9998 Hz, and a constant  $f_2 - f_1$  difference of 102 Hz, the DT input/output curves were virtually overlapping. Chertoff *et al.* (1992) found that DT amplitude **decreased** with increasing  $f_1$  frequency, but since the same  $f_2/f_1$  ratios were used for all  $f_1$  frequencies, the absolute frequency of the DT increased as  $f_1$  increased. They speculated that DT amplitude is dependent upon the absolute frequency of the DT rather than the primary frequencies or ratios. Our data are in good agreement with this speculation.

## B. Characteristics of CDT

When measured with the same stimulus pairs, the CDT was smaller in all cases than the DT. This finding is similar to the results found by Chertoff *et al.* (1992) for  $f_1$  frequencies between 500 and 2000 Hz, and by Rickman *et al.* (1991) for  $f_1$  frequencies of 510 and 800 Hz.

In contrast to DT amplitude, which was independent of  $f_1$  frequency for a constant DT frequency, CDT amplitude decreased as  $f_1$  frequency increased. In fact, CDT was not present above the noise floor for high frequency primaries ( $f_1 = 4999$  and 9998 Hz). However, in experiment 2, we held DT constant while varying primary-tone frequencies, which produced an increase in CDT frequency with increasing primary-tone frequencies. It thus appears that the most parsimonious interpretation of these data is that there is a decrease in CDT amplitude with increasing CDT frequency.

## C. Relation to single-unit studies

Single unit studies using two-tone stimulus pairs in the auditory nerve (Goldstein and Kiang, 1968; Kim, 1980) and the anteroventral cochlear nucleus (Smooenburg *et al.*,

1976) have shown that some neurons fire at a rate corresponding to the frequency of the DT and/or the CDT. Since we are measuring distortion products by spectral analysis of the evoked potential at the distortion product frequency, detection of a response depends upon synchronous firing of a population of IC neurons at the frequency of the distortion component. The ability to measure these distortion components in the evoked potential, then, would be limited by the upper frequency limit of phase locking of these neurons.

While phase locking in the mammalian auditory nerve occurs up to about 4000–5000 Hz (Kiang *et al.*, 1965; Rose *et al.*, 1967; Palmer and Russell, 1986), the upper limit of phase locking is lower for neurons in the IC. Kuwada *et al.* (1984) reported that, in the cat IC, the majority of units that exhibited phase locking did so to frequencies at or below 600 Hz. There was a decline in units showing phase locking at higher frequencies, up to a maximum limit of about 1200 Hz. Therefore we would not expect to obtain distortion products in the evoked potential at frequencies much higher than this. A number of aspects of the behavior of the evoked potential distortion products in our data correlate with the phase-locking ability of neurons in the IC. Specifically, the decrease in amplitude of DT with increasing DT frequency may be explained by a decrease in the number of neurons responding synchronously to the stimulus envelope. Similarly, the finding that the CDT was smaller than the DT for all stimulus pairs may be due to the fact that the frequency value of the CDT was typically higher than the DT for a given stimulus pair. However, in experiment 1, the  $f_2/f_1$  ratio of 1.5 produced a DT whose frequency was slightly higher than the CDT. Interestingly, CDT amplitude was still smaller than that of DT. Thus distortion product frequency appears to contribute to distortion product magnitude, but this cannot be the sole factor determining response magnitude. The absence of the CDT at  $f_1$  frequencies of 4999 and 9998 Hz is likely due to the fact that the frequency value of the CDT (4897 and 9896 Hz, respectively) is too high to allow for phase locking.

## D. Comparison to distortion product otoacoustic emissions

Our results for the evoked potential distortion products differ markedly from otoacoustic emission (OAE) distortion products. For OAE measurement, the CDT is the predominant distortion component seen, being larger than the DT measured with identical stimulus pairs (Kim, 1980; Brown, 1993). In our data, the DT was always larger than the CDT, even at  $f_2/f_1$  ratios between 1.2 and 1.3, which are optimal for CDT generation in the OAE (Kemp and Brown, 1984; Lonsbury-Martin *et al.*, 1987). Also, while we were not able to measure AEP CDTs for  $f_1$  frequencies above 2000 Hz, the OAE CDT has been recorded in the chinchilla with  $f_1$  frequencies as high as 8000 Hz (Trautwein *et al.*, 1996). These differences can be explained by the fact that the presumed generator of the OAE's is the outer hair cells in the cochlea. Since OAE's are generated pre-synaptically, then phase-locking ability of neurons is not a limiting factor in the ability to record distortion products in the OAE, as it is for the AEP.

## E. Relation of DT to studies using sinusoidally amplitude modulated (SAM) tones

Dolphin *et al.* (1994) measured evoked potentials from the scalp in Mongolian gerbils, using both two-tone stimulus complexes and sinusoidally amplitude modulated (SAM) tones. They showed that the waveform envelopes of these two types of stimuli are similar, showing amplitude fluctuations at the difference frequency (for two-tone stimuli) or the modulation frequency (for SAM stimuli). The component in the evoked response that follows the stimulus envelope has been termed the envelope-following-response (EFR) (Dolphin and Mountain, 1992). Dolphin *et al.* (1994) noted that the EFR to two-tone and SAM stimuli appear to be quite similar when the frequency difference between the two tones is equal to the modulation frequency of the SAM stimulus. They speculated that the two are manifestations of the same nonlinear phenomenon. The scalp-recorded EFR has been studied extensively, both in animals (Dolphin and Mountain, 1992; Dolphin *et al.*, 1994) and in humans (Rodenburg *et al.*, 1972; Rickards and Clark, 1984; Kuwada *et al.*, 1986; Rees *et al.*, 1986; Picton *et al.*, 1987; Cohen *et al.*, 1991; Griffiths and Chambers, 1991; Levi *et al.*, 1993; Lins *et al.*, 1995).

Based upon lesion studies (Kiren *et al.*, 1994), the origin of the scalp-recorded EFR to SAM stimuli is theorized to be the IC, for modulation frequencies between 20 and 200 Hz. Studies of single unit responses to SAM stimuli have shown that IC neurons respond best to modulation frequencies below 100 Hz (Langner and Schreiner, 1988; Batra *et al.*, 1989; Rees and Palmer, 1989) but will respond to a lesser extent at higher modulation frequencies, up to about 1000 Hz (Langner and Schreiner, 1988). Therefore, our measurements of the DT from the IC probably reflect the same phenomenon as the EFR to SAM stimuli. We chose to use the two-tone stimulus pair in order to simultaneously measure the DT and CDT, and to allow for use of the dichotic paradigm.

## F. DT to dichotic stimuli

We found that, at high stimulus levels, when  $f_1$  was presented to one ear, and  $f_2$  to the other ear, a small response was measured at the  $f_2 - f_1$  difference frequency. This dichotic stimulus paradigm is reminiscent of human psychophysical binaural beat studies (Licklider *et al.*, 1950; Perrott and Musicant, 1977), in which two tones of slightly differing frequency are presented to either ear, and listeners report a perception of beating or amplitude fluctuation, up to a difference frequency of about 60 Hz.

There have been other physiological studies related to the binaural beat phenomenon. Hink *et al.* (1980), measuring the scalp-recorded frequency following response from human subjects, used a dichotic stimulus in which a 500-Hz toneburst was presented to one ear and a 540-Hz toneburst was presented to the opposite ear. The authors noted amplitude fluctuations in the waveform of the response corresponding to the frequency difference between the two stimuli, i.e., 40 Hz.

Kuwada and colleagues (Kuwada *et al.*, 1979; Yin and Kuwada, 1983) have used a binaural beat stimulus to study binaural properties of single auditory neurons in the cat IC.

They noted that some cells exhibit a discharge pattern that is phase locked to the difference, or beat, frequency. Such synchronization has been noted up to a beat frequency of 80 Hz, using primary frequencies as high as 2800 Hz.

In our study, we saw a dichotic response to a difference frequency of 102 Hz, which is somewhat higher than has been reported previously in psychoacoustic or physiological studies. Whether this discrepancy is due to species differences, lack of anesthesia, or some other factor, is unclear.

It is possible that the response observed to dichotic stimulation may be due to stimulus crossover between ears, and hence is really a response to monaural stimulation with an amplitude difference between primary tones. Unpublished measurements from our laboratory show that interaural attenuation of sounds between the right and left ear in one chinchilla was about 25 dB at 2000 Hz. If the DT can be elicited with unequal level primaries, then it may be that the response seen in the dichotic stimulus condition reflects monaural interaction at the cochlear level. Nevertheless, if the dichotic response proves to be real, the ability to measure a dichotic DT response from the IC holds promise as a method of studying dichotic processing in an awake animal model.

## ACKNOWLEDGMENTS

This research was supported in part by Grant No. R01DC00166-13 from the National Institute on Deafness and Other Communicative Disorders, National Institutes of Health. The authors wish to thank Mark Chertoff for his comments on an earlier draft of this manuscript. Sandra McFadden is acknowledged for her input to this project.

- Batra, R., Kuwada, S., and Stanford, T. R. (1989). "Temporal coding of envelopes and their interaural delays in the inferior colliculus of the unanesthetized rabbit," *J. Neurophysiol.* **61**, 257-268.
- Brown, A. M. (1993). "Distortion in the cochlea: Acoustic  $f_2 - f_1$  at low stimulus levels," *Hearing Res.* **70**, 160-166.
- Chertoff, M. E., and Hecox, K. E. (1990). "Auditory nonlinearities measured with auditory-evoked potentials," *J. Acoust. Soc. Am.* **87**, 1248-1254.
- Chertoff, M. E., Hecox, K. E., and Goldstein, R. (1992). "Auditory distortion products measured with averaged auditory evoked potentials," *J. Speech Hear. Res.* **35**, 157-166.
- Cohen, L. T., Rickards, F. W., and Clark, G. M. (1991). "A comparison of steady-state evoked potentials to modulated tones in awake and sleeping humans," *J. Acoust. Soc. Am.* **90**, 2467-2479.
- Dolphin, W. F., and Mountain, D. D. (1992). "The envelope following response: Scalp potentials elicited in the mongolian gerbil using sinusoidally AM acoustic signals," *Hearing Res.* **58**, 70-78.
- Dolphin, W. F., Chertoff, M. E., and Burkard, B. (1994). "Comparison of the envelope following response in the Mongolian gerbil using two-tone and sinusoidally amplitude-modulated tones," *J. Acoust. Soc. Am.* **96**, 2225-2234.
- Goldstein, J. L., and Kiang, N. Y. S. (1968). "Neural correlates of the aural combination tone  $2f_1 - f_2$ ," *Proc. IEEE* **56**, 981-992.
- Griffiths, S. K., and Chambers, R. D. (1991). "The amplitude modulation-following response as an audiometric tool," *Ear and Hearing* **12**, 235-241.
- Hink, R. F., Kodera, K., Yamada, O., Kaga, K., and Suzuki, J. (1980). "Binaural interaction of a beating frequency-following response," *Audiology* **19**, 36-43.
- Kemp, D. T., and Brown, A. M. (1984). "Ear canal acoustic and round window electrical correlates of  $2f_1 - f_2$  distortion generated in the cochlea," *Hearing Res.* **13**, 39-46.

- Kiang, N. Y. S., Watanabe, T., Thomas, E. D., and Clark, L. F. (1965). *Discharge Patterns of Single Fibers in the Cat's Auditory Nerve* (MIT Press, Cambridge, MA).
- Kim, D. O. (1980). "Cochlear mechanics: implications of electrophysiological and acoustical observations," *Hearing Res.* **2**, 297–317.
- Kiren, T., Aoyagi, M., Furuse, H., and Koike, Y. (1994). "An experimental study on the generator of amplitude-modulation following response," *Acta Oto-Laryngol. Suppl.* **511**, 28–33.
- Kuwada, S., Yin, T. C., and Wickesberg, R. E. (1979). "Response of cat inferior colliculus neurons to binaural beat stimuli: Possible mechanisms for sound localization," *Science* **206**, 586–588.
- Kuwada, S., Yin, T. C., Syka, J., Buunen, T. J., and Wickesberg, R. E. (1984). "Binaural interaction in low-frequency neurons in inferior colliculus of the cat. IV. Comparison of monaural and binaural response properties," *J. Neurophysiol.* **51**, 1306–1325.
- Kuwada, S., Batra, R., and Maher, V. L. (1986). "Scalp potentials of normal and hearing-impaired subjects in response to sinusoidally amplitude-modulated tones," *Hearing Res.* **21**, 179–192.
- Langner, G., and Schreiner, C. E. (1988). "Periodicity coding in the inferior colliculus of the cat. I. Neuronal mechanisms," *J. Neurophysiol.* **60**, 1799–1822.
- Levi, E. C., Folsom, R. C., and Dobie, R. A. (1993). "Amplitude-modulation following response (AMFR): Effects of modulation rate, carrier frequency, age, and state," *Hearing Res.* **68**, 42–52.
- Licklider, J. C. R., Webster, J. C., and Hedlun, J. M. (1950). "On the frequency limits of binaural beats," *J. Acoust. Soc. Am.* **22**, 468–473.
- Lins, O. G., Picton, P. E., Picton, T. W., Champagne, S. C., and Durieux-Smith, A. (1995). "Auditory steady-state responses to tones amplitude-modulated at 80–110 Hz," *J. Acoust. Soc. Am.* **97**, 3051–3063.
- Lonsbury-Martin, B. L., Martin, G. K., Probst, R., and Coats, A. C. (1987). "Acoustic distortion product in rabbit ear canal. I. Basic features and physiological vulnerability," *Hearing Res.* **28**, 173–189.
- Palmer, A. R., and Russell, I. J. (1986). "Phase-locking in the cochlear nerve of the guinea-pig and its relation to the receptor potential of inner hair-cells," *Hearing Res.* **24**, 1–15.
- Perrott, D. R., and Musicant, A. D. (1977). "Rotating tones and binaural beats," *J. Acoust. Soc. Am.* **61**, 1288–1292.
- Picton, T. W., Skinner, C. R., Champagne, S. C., Kellett, A. J. C., and Maiste, A. C. (1987). "Potentials evoked by the sinusoidal modulation of the amplitude or frequency of a tone," *J. Acoust. Soc. Am.* **82**, 165–178.
- Rees, A., and Moller, A. (1983). "Response of neurons in the inferior colliculus of the rat to AM and FM tones," *Hearing Res.* **10**, 301–330.
- Rees, A., and Palmer, A. R. (1989). "Neuronal responses to amplitude-modulated and pure-tone stimuli in the guinea pig inferior colliculus, and their modification by broadband noise," *J. Acoust. Soc. Am.* **85**, 1978–1994.
- Rees, A., Green, G. G. R., and Kay, R. H. (1986). "Steady-state evoked responses to sinusoidally amplitude-modulated sounds recorded in man," *Hearing Res.* **23**, 123–133.
- Rickards, F. W., and Clark, G. M. (1984). "Steady-state evoked potentials to amplitude-modulated tones," in *Evoked Potentials II. The Second International Evoked Potentials Symposium*, edited by R. H. Nodar and C. Barber (Butterworth, Boston), pp. 163–168.
- Rickman, M. D., Chertoff, M. E., and Hecox, K. E. (1991). "Electrophysiological evidence of nonlinear distortion products to two-tone stimuli," *J. Acoust. Soc. Am.* **89**, 2818–2826.
- Rodenburg, M., Verweij, C., and van den Brink, G. (1972). "Analysis of evoked responses in man elicited by sinusoidally modulated noise," *Audiology* **11**, 283–293.
- Rose, J. E., Brugge, J. L., Anderson, D. J., and Hind, J. E. (1967). "Phase-locked response to low-frequency tones in single auditory nerve fibers of the squirrel monkey," *J. Neurophysiol.* **30**, 769–793.
- Smoorenburg, G. F., Gibson, M. M., Kitzel, L. M., Rose, J. E., and Hind, J. E. (1976). "Correlates of combination tones observed in the response of neurons in the anteroventral cochlear nucleus of the cat," *J. Acoust. Soc. Am.* **59**, 945–962.
- Snyder, D. L., and Salvi, R. J. (1994). "A novel chinchilla restraint device," *Laboratory Animal* **23**, 42–44.
- Trautwein, P., Hofstetter, P., Wang, J., Salvi, R., and Nostrand, A. (1996). "Selective inner hair cell loss does not alter distortion product otoacoustic emissions," *Hearing Res.* **96**, 71–82.
- Yin, T. C., and Kuwada, S. (1983). "Binaural interaction in low-frequency neurons in inferior colliculus of the cat. II. Effects of changing rate and direction of interaural phase," *J. Neurophysiol.* **50**, 1000–1019.

# Lateralization of large interaural delays

Jennifer E. Mossop and John F. Culling

University Laboratory of Physiology, Parks Road, Oxford OX1 3PT, United Kingdom

(Received 11 April 1997; revised 7 May 1998; accepted 28 May 1998)

Two experiments explored the limits of listeners' abilities to interpret large interaural time delays (ITDs) in terms of laterality. In experiment 1, just-noticeable differences (jnd's) were measured, using an adaptive procedure, for various reference ITDs of Gaussian noise between 0 and 3000  $\mu$ s. The jnd's increased gradually with reference ITD for reference ITDs between 0  $\mu$ s and 700  $\mu$ s, then rose sharply to plateau at much higher jnd's for the remainder of the standard ITDs tested (1000–3000  $\mu$ s). The second experiment tested left/right discrimination of Gaussian noise that was interaurally delayed up to 10 000  $\mu$ s, and high-pass filtered to cutoff frequencies between 0 Hz (broadband) and 3000 Hz. There was good discrimination (62%; significantly above chance,  $p < 0.05$ ) for broadband and 500-Hz high-pass cutoff stimuli for all ITDs up to 10 000  $\mu$ s, and for ITDs up to at least 3000  $\mu$ s for higher high-pass cutoff frequencies. These results indicate that laterality cues are discriminable at much larger ITDs than are experienced in free-field listening, even in the absence of energy below 3 kHz. © 1998 Acoustical Society of America. [S0001-4966(98)02709-X]

PACS numbers: 43.66.Ba, 43.66.Qp, 43.66.Pn [RHD]

## INTRODUCTION

The size of the human head creates maximum interaural time delays (ITDs) of approximately 600  $\mu$ s, depending on the frequency components of the sound (Kuhn, 1977). ITDs of broadband noise stimuli within this range and up to about 1 ms, presented through headphones, produce images that are described as fused and lateralized to some intracranial position (for a review, see Durlach and Colburn, 1978). As ITDs are increased beyond the physiological range, the sound image of continuous broadband noise remains at the leading ear but gradually becomes more diffuse until the image either appears at both ears or fills the head entirely and the perception of laterality is abolished (Blodgett *et al.*, 1956). It is well known that the perception of laterality persists for ITDs much greater than those experienced ecologically, but there is relatively little data on the limits of this ability. It is important to establish such limits as they may give insights into binaural mechanisms. They may, for instance, have particular relevance to estimates of the range of lengths of the delay lines which are widely believed to underlie binaural processing (Jeffress, 1948; Colburn, 1996).

From a variety of studies, Durlach and Colburn (1978) estimate that this loss of laterality occurs, for continuous wide-band signals, between 10 and 30 ms of ITD. In a more recent review Colburn (1996, p. 340) suggests a figure of about 15 ms. Blodgett *et al.* (1956) used an adjustable head on a magnetic tape recorder to create large noise delays and asked listeners to reduce the ITD until the noise could be lateralized. Delays up to about 13 ms were perceived as directional for broadband noise. Blodgett *et al.* observed that this estimate of the maximum lateralizable delay was probably conservative, since the listeners were invariably correct in their lateralization judgment once they had reduced the delay to one that they perceived as lateralized. In a second experiment they measured a mean threshold of 14.0 ms for low-frequency bands of noise (106–212 Hz). Higher-

frequency bands of noise (2400–4800 Hz) had large thresholds at large delays (mean 8.0 ms). At larger ITDs beyond 15–20 ms or so, the percept is of a diffuse noise, indistinguishable from uncorrelated noise, but at even longer ITDs (on the order of hundreds of milliseconds) the presence of an ITD is detectable once again as a subtle echo percept with no lateralization (Warren *et al.*, 1981).

Some studies have reported just noticeable difference (jnd) measurements for ITDs against reference ITDs other than 0  $\mu$ s. For 500-Hz pure-tone stimuli, Domnitz (1973) found consistently low jnd's (9  $\mu$ s) for 0-, 200-, and 400- $\mu$ s reference ITDs, and higher jnd's (26  $\mu$ s) at 700- $\mu$ s reference ITD. Domnitz and Colburn (1977) found similar trends with more intersubject variability in a virtually identical experiment which also included 1000- $\mu$ s reference ITDs, at which jnd's were, on average, 62  $\mu$ s. Hershkowitz and Durlach (1969), also using a 500-Hz pure tone, found jnd's which were less than 20  $\mu$ s for reference ITDs of 200 and 400  $\mu$ s, but that, above 600- $\mu$ s reference ITD, subjects could not perform a jnd task reliably and reported changes in subjective cues. These changes included cue reversals, where stimuli with a larger time lead in the left ear produced a percept to the right of a stimulus that had a smaller time lead in the left ear. These cue reversals may have been associated with ambiguity about which ear receives the leading signal for pure tones with large ITDs. Hershkowitz and Durlach noted, however, that for three of four subjects the reversals occurred at a reference ITD of only 750  $\mu$ s, somewhat less than the half-period of the signal (1000  $\mu$ s). Kohenke *et al.* (1995) have reported jnd's for 1/3-octave bandpass noise centered around 500 Hz and 4000 Hz at 0, 300, and 600  $\mu$ s of ITD. They found that jnd's for reference ITDs of noise with a center frequency of 500 Hz were between 20 and 40  $\mu$ s for reference ITDs of 0 and  $\pm 300$   $\mu$ s and around 70  $\mu$ s for  $\pm 600$ - $\mu$ s reference ITDs. For stimuli with a center frequency of 4000 Hz, jnd's were higher; around 60  $\mu$ s for 0

and  $\pm 300 \mu\text{s}$  and near  $250 \mu\text{s}$  for  $\pm 600\text{-}\mu\text{s}$  reference ITDs.

Using sinusoidal stimuli at large ITDs creates phase ambiguity when the ITD is equivalent to half a period of the sinusoid. This ambiguity can be removed by using broadband noise stimuli, rather than tones or narrow-band noise. However, no experiments to our knowledge have systematically studied the ability to perceive laterality of broadband noise at increasingly large ITDs, or have extensively examined jnd's for ITDs greater than  $0 \mu\text{s}$ . Here, we present two experiments designed to obtain objective measurements of the limits of human performance in discriminating differences between large ITDs.

Experiment 1 examines jnd's in relation to reference ITDs from 0 to  $3000 \mu\text{s}$  with the purpose of exploring the transition from ITDs experienced in everyday life ( $\pm 600 \mu\text{s}$ ) to larger, supra-ecological ITDs. Experiment 2 involves left/right discriminations of noise with even larger ITDs (from 0.5 to 10 ms) and a range of high-pass cutoffs (from broadband to 3000-Hz high-pass cutoff). The second experiment was designed to examine the extent to which a lateralizable perception is evoked by large ITDs, and also the effect of eliminating low-frequency components upon this lateralization ability. The high-pass filtered stimuli were used in order to explore the importance of low frequencies to the correct lateralization of large ITDs, by determining whether large ITDs could still be lateralized when the low frequencies were absent.

## I. EXPERIMENT 1

The purpose of experiment 1 was to determine jnd's for ITD at a range of ITDs from 0 to  $3000 \mu\text{s}$ .

### A. Subjects

Four adult subjects including the first author participated in experiment 1. Three had prior experience in binaural experiments. The subjects had no known hearing deficits.

### B. Stimuli

The stimuli were broadband 8192-sample Gaussian noises, generated digitally (20-kHz sampling rate; 16-bit quantization) using a TDT II AP2 array processor, and duplicated for stereo channels. One channel was then transformed into the frequency domain, delayed by a given amount (by modifying the phase spectrum), and transformed back into the time domain. Application of a delay in the frequency domain meant that the delays did not change the onset time of the noise<sup>1</sup> and that the delays could be specified precisely rather than being quantized to the nearest sampling period. Channels were gated on and off simultaneously with a 50-ms rise/fall time, for a total stimulus duration of 409.6 ms, including the rise/fall ramps. Thus each stimulus had an ongoing ITD, but not an onset or offset ITD. All ITDs had the left channel lagging the right. The stimuli were converted to analog waveforms and amplified (using the Tucker-Davis DD1 digital-to-analog converter, FT5-9 reconstruction filter with 10-kHz cutoff, PA4 digitally controlled attenuators and HB6 headphone amplifier), before being fed into a double-walled sound-attenuating chamber, and presented to a sub-

ject through Sennheiser HD414 headphones. Sound level output was calibrated using a Bruel & Kjaer artificial ear and 4130 half-inch microphone. Sounds were presented at equal A-weighted levels to each ear at 76 dB.

## C. Procedure

A two-down/one-up adaptive method was used to determine jnd's (Levitt, 1971). We employed a three-interval, two-alternative forced-choice task where the first of the three intervals was a noise with a set ITD (the "reference" stimulus). The second and third intervals were, in random order, the reference ITD again and noise with a larger ITD (the "test" stimulus). All noise bursts were generated from fresh noise samples.

Subjects indicated, by button press on a computer terminal whether the second or the third interval of the set appeared to be located in a different intracranial position than the first interval. The adaptive procedure adjusted the difference in ITD between the test stimulus and the reference stimuli on a logarithmic scale, as recommended by Saberi (1995), using a step size of 12.2% increase/decrease in ITD, until 14 reversals had taken place. The jnd values were determined from the geometric average of the microsecond values of the final ten reversals in direction. This procedure estimates the value of ITD yielding 70.7% correct performance.

Subjects attended a series of one-hour sessions during which they usually performed one adaptive run at each of 16 reference ITDs that ranged from  $0 \mu\text{s}$  to  $3000 \mu\text{s}$ . Subjects were trained until they were judged to be giving consistent performance across trials at each reference ITD value. This training took between 3 and 12 sessions depending on the subject. Sometimes during training, different subsets of the stimuli were interleaved to give subjects more practice on stimulus conditions that they found more difficult. At reference ITDs greater than about  $800 \mu\text{s}$ , subjects required more training in order to achieve consistency of performance comparable to that obtained at lower reference ITDs. Once relatively consistent performance was achieved for all reference ITD magnitudes, 8 adaptive thresholds at each reference ITD were taken as the results.

## D. Results

Figure 1 shows the mean jnd's from 8 recorded thresholds with standard error bars for the 4 individual subjects at each of 16 reference ITDs. The reference ITDs tested were 0– $800 \mu\text{s}$  in  $100\text{-}\mu\text{s}$  steps, and 1000, 1200, 1400, 1600, 2000, 2500, and  $3000 \mu\text{s}$ .

The magnitudes of the jnd values in Fig. 1 vary from subject to subject, with subject JM notably lower than the rest at large reference ITDs. However, the shape of each curve is similar across subjects. All curves begin, at  $0\text{-}\mu\text{s}$  reference ITD, with low jnd values ranging from  $12.3 \mu\text{s}$  (subject MT) to  $62.2 \mu\text{s}$  (subject EH). From 0 to  $700 \mu\text{s}$ , jnds became gradually larger for each subject, but remain generally low, usually below  $100 \mu\text{s}$ . Between  $700 \mu\text{s}$  and  $1000 \mu\text{s}$ , all subjects show a sharp increase in jnd. Above about  $1000 \mu\text{s}$ , the jnd's become more variable, and do not con-



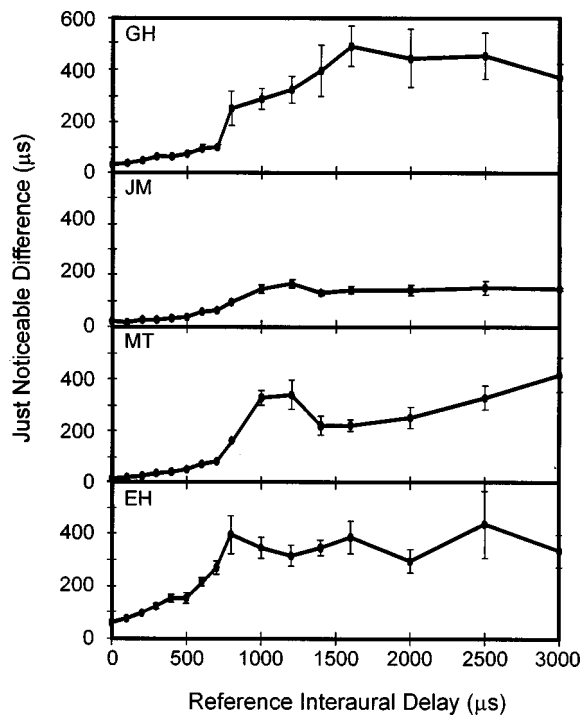


FIG. 1. Mean jnd's of eight trials each for the four subjects in experiment 1, as a function of reference ITD, with standard error bars.

tinue to increase in a systematic manner but remain roughly constant. For all subjects, the standard error bars are greater for larger reference ITDs than smaller ITDs. Three of four subjects reported (informally) that their judgments were based on intracranial position alone, even at the largest ITDs. One subject reported occasionally noticing a spreading out of the images at large ITDs, but said judgments were mainly based on intracranial position.

## E. Discussion

The jnd's at zero reference ITD are higher than Klumpp and Eady's (1956) measurement of  $10 \mu\text{s}$  for 75% correct detection of ITD of broadband noise. The present study used a relatively small amount of training, involved 409.6-ms stimuli which had no interaural onset-time differences, employed no response feedback, and used a 70.7% jnd criterion (Levitt, 1971). Klumpp and Eady used longer duration stimuli (about 1700 ms) which had onset as well as ongoing ITDs. They did not report listener training or feedback, but the differences between the stimuli used, and perhaps in listener training, may account for the differences between the present jnd's at  $0 \mu\text{s}$  and Klumpp and Eady's values. In experiment 1, the smallest thresholds obtained were more typical of naive, than of well-trained listeners (Colburn, 1996).

The reference ITD at which jnd's increase for all subjects (about  $700 \mu\text{s}$ ) corresponds approximately to the ITD at which sounds exceed the ecological range (about  $\pm 600 \mu\text{s}$ ). This is unsurprising considering listener's everyday experience.

Listeners' performance at supra-ecological ITDs was also examined here. In designing this experiment, it was anticipated that there may be a shift in the available cues, as the

ITD increased. At some point beyond the ecological range, it was anticipated that the lateral position cue may be superseded by a diffuseness cue. As ITD increases from zero, the image would be perceived further and further to the right, but with even larger ITDs the image would also become more diffuse, and perhaps spread back towards the midline. Thus for large reference ITDs, the target interval may be discriminable on the basis of having a more diffuse image than the two reference intervals. However, as noted in Sec. II D, only one listener occasionally reported using cues which seemed consistent with this expectation. All four listeners described the dominant percept as being intracranial position.

The experimental design does not distinguish directly between the cues (intracranial position or diffuseness) that the listeners were actually using. Although the listener's comments were obtained informally, they give some insight into the possible cues that they were using. The dominance of an intracranial location cue over a diffuseness cue has some precedent in the work of Jeffress *et al.* (1962) and of Pollack and Trittipoe (1959). Jeffress *et al.* measured the precision with which listeners could adjust the ITD of a partially correlated noise in order to center it within the head (i.e., find zero ITD using purely auditory feedback). They found that listeners could center the noise almost as accurately when it had a correlation of only 0.2 as when it was perfectly correlated. Thus it appears that the binaural system is very sensitive to small movements in an auditory image even when that image is very diffuse. On the other hand, Pollack and Trittipoe (1959) showed that listeners are poor at discriminating the interaural correlation of two noises when both have small interaural correlations (see Durlach *et al.*, 1986, Table III). To correctly discriminate (75% accuracy) a second noise from a reference noise with a cross correlation of 0.2, their listeners required an increment in interaural correlation of 0.38. For higher reference correlations listeners were much more sensitive. For a reference correlation of 0.93 listeners only needed an increment of 0.06 to achieve 75% accuracy. Hence, listeners have relatively coarse abilities to discriminate differences between diffuse noises. At the large interaural delays used in experiment 1, the image of the reference noise is already somewhat diffuse, perhaps explaining why listeners reported continued use of intracranial position rather than diffuseness of the sound image at large ITDs.

The results for the nonecological ITD stimuli ( $>700 \mu\text{s}$ ) presented in experiment 1 show that subjects can discriminate differences in the perceived position of sounds with supra-ecological ITDs to some extent. In this experiment, jnd's increased by about an order of magnitude for ITDs greater than  $700 \mu\text{s}$ .

## II. EXPERIMENT 2

Experiment 2 was designed to test whether subjects could assign a sidedness (left or right) to broadband signals with various high-pass cutoff frequencies that had large ITDs of up to 10 ms.

## A. Subjects

Five subjects participated; the four subjects from experiment 1 and one other subject with normal hearing and previous experience in binaural experiments.

## B. Stimuli

The stimuli were Gaussian noises generated digitally using |WAVE software (Culling, 1996). As in experiment 1, the noises were filtered in the frequency domain. In this experiment, the amplitude spectrum was also manipulated to create a range of high-pass cutoffs. The high-pass cutoff frequencies used were 0 (broadband), 500, 1000, 1500, 2000, 2500, and 3000 Hz. The noises were then duplicated for two channels. One channel was interaurally delayed or advanced by between 500  $\mu$ s and 10 ms (in 500- $\mu$ s steps) in order to create an ongoing ITD. The two channels were gated simultaneously with a rise/fall time of 50 ms. Each stimulus was 409.6 ms in total duration.

The delayed and filtered noise was added to a 24-dB-less-intense interaurally uncorrelated broadband noise (0–10 kHz) which was used to prevent listeners from using any low-frequency lateralization cues that may be reintroduced by distortion products or by spread of excitation.

The complete set of 280 individual stimuli consisted of one exemplar of each of 140 conditions delayed to the left and right sides. The conditions were 7 high-pass cutoff frequencies  $\times$  20 ITDs. The A-weighted stimuli were presented at between 76 and 79 dB, depending on the particular high-pass cutoff. The stimulus set was periodically regenerated in order to prevent the characteristics of individual noise bursts from influencing the results.

## C. Procedure

The task was single-interval forced choice, where the subjects heard each of the 280 stimuli in a random sequence. After each stimulus, they were asked to choose by button press on a computer terminal whether the sound was located on the left or the right of the midline. No feedback was provided.

Subjects attended eighteen half-hour sessions in which they did four blocks of the complete stimulus set, for a total of 72 responses for each stimulus condition. Subjects received no training in this task. Their responses at the first of 18 sessions were the very similar to the last.

## D. Results

Figure 2 shows results matrices for each of the five subjects from experiment 2 in the form of a grid, where ITD is represented on the ordinate axis and high-pass cutoff frequency on the abscissa. The gray scale shade at each vertex of the grid represents the percent of trials (72 per vertex) in which the subject was able to correctly discriminate whether the stimulus at that particular combination of ITD and high-pass cutoff frequency was delayed to the right or left. The shaded contours were bilinearly interpolated. In Fig. 2, the white area indicates performance that is not significantly above chance (below 62%: binomial probability,  $p < 0.05$ ).

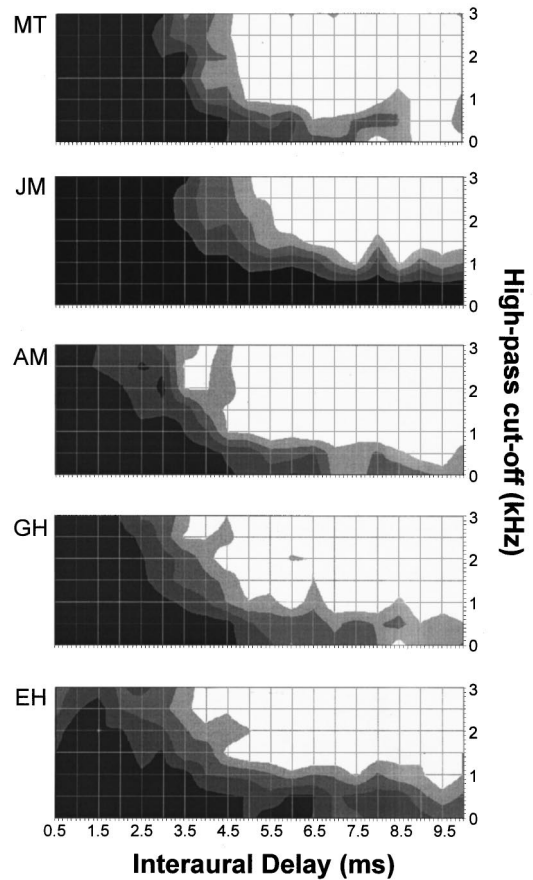


FIG. 2. Pattern of results from experiment 2. For each of the five subjects, the gray scale shades represent percent correct left/right discrimination, where each vertex is one high-pass cutoff frequency and ITD combination. Black is 92%–100% correct, dark gray 82%–92%, medium gray 72%–82%, light gray 62%–72% and white below 62% (not significantly above chance).

The top right edge of the lightest gray band indicates the boundary between chance performance and performance that is significantly above chance. The lightest gray indicates 62%–72% correct, medium gray 72%–82%, dark gray 82%–92%, and black 92%–100%.

The most accurate subject (JM) was able to correctly discriminate left from right above chance as indicated by the lightest gray band, for all ITDs tested, up to and including 10 ms at high-pass frequency cutoffs of up to 1000 Hz. At higher cutoff frequencies, JM discriminated correctly to at least 5.0 ms. Subjects EH, AM, and GH performed significantly above chance for broadband (0-Hz high-pass cutoff) stimuli to 10 ms. MT was able to correctly discriminate up to 8 ms for broadband and 500-Hz cutoff stimuli.

All subjects were able to perform above chance at all cutoff frequencies to at least 3.5-ms delay.

## E. Discussion

The data from experiment 2 confirm and extend those of Blodgett *et al.* (1952). Listeners are able to lateralize broadband noises at very large ITDs, at least 15 times larger than those which are experienced in free-field listening. The results also support Blodgett *et al.*'s finding that a greater range of delays can be lateralized when low frequencies are

present, than when only high frequencies are available. The present results show the relationship between the maximum lateralizable ITD and the high-pass cutoff frequency. The function has the general form of a reciprocal relationship, which may be explained in at least three different ways.

The maximum lateralizable ITD might be related to the period of the cutoff frequency. However, at each cutoff frequency the maximum lateralizable ITD is many times this period, and a closer inspection of the relationship shows that the ratio between the maximum lateralizable ITD and the period of the cutoff frequency varies considerably. In particular, at high cutoff frequencies ( $\geq 1500$  Hz) the maximum lateralizable ITD becomes relatively constant at around 3.5 ms; about five times the maximum ecological delay.

The maximum lateralizable ITD may alternatively be related to the bandwidth of the lowest available frequency channel. The cross correlation of a frequency band is a cyclic function of ITD. This function has a maximum correlation near to the true ITD of the stimulus. The wider the frequency band, the more sharply the correlation declines away from this ITD (i.e., the envelope of the cross-correlation function is narrow). The short-term interaural correlation of the noise within the channel consequently declines sharply at high frequencies, where frequency channels are wider. Likewise, at lower frequencies where frequency channels are narrower, the envelope of the cross-correlation function is broader. So, for stimuli with various different cutoff frequencies such as in experiment 2, the short-term interaural correlation of the lowest available channel will have a narrow or broad envelope, depending on the high-pass cutoff of the stimulus. If the binaural system has a fixed range of ITDs over which its delay lines are capable of detecting interaural correlation, then a stimulus which has an ITD greater than that fixed internal range might only be detected if the edge of the cross-correlation function's envelope in the lowest available frequency band overlaps with the fixed internal range of ITD processing. Thus for large ITDs (i.e., greater than 3.5 ms) the presence of low frequencies, with broad cross-correlation envelopes at those large ITDs, might explain the subjects' abilities to lateralize correctly at broadband and 500-Hz cutoffs, but not at higher-pass cutoffs.

Finally, at high-pass cutoffs between 1.0 and 1.5 kHz the maximum lateralizable delay changes from 10+ ms to around 3.5 ms. This is the same frequency region over which binaural processing is thought to shift from exploiting the fine structure of the stimulus waveform to exploiting its envelope, so it is also possible that peripheral nonlinearities, which filter out the fine structure, play a role in this shift in maximum lateralizable delay with frequency cutoff.

### III. GENERAL DISCUSSION

The purpose of the present investigation was to explore the limits of listeners abilities to interpret large ITDs in terms of laterality. It is hoped that these data will provide insight into the mechanisms underlying binaural processing and help to shed light on the issue of the lengths of delay lines in the binaural system.

Experiment 1 has shown that listeners are able to discriminate differences between ITDs much more acutely at

ecological delays than at supra-ecological delays (above 600  $\mu$ s), and that this acute discrimination falls off rapidly as ITDs are increased past 700  $\mu$ s. However, listeners are still able to make location-based judgments at supra-ecological ITDs, but have much higher thresholds, indicating that there is at least some degree of perceptible spatial information in these large ITDs. Experiment 2 shows that even larger ITDs up to at least 10 ms, especially with the presence of low-frequency information, are perceived as having some spatial location (left versus right).

These data, showing that listeners are able to lateralize large ITDs, may have implications for centrally weighted models of sound lateralization like those of Stern and Colburn (1978), Shackleton *et al.* (1992), and Stern *et al.* (1988), which all emphasize ITDs near zero. However, the fact that listeners are able to lateralize large ITDs and discriminate one large ITD from another does not directly imply that the system contains delay lines which apply delays of magnitudes comparable to the range over which lateralization and discrimination can be measured, since a number of other factors come into play. These factors include peripheral nonlinearities, the specificity with which coincidence detectors respond to stimuli with one particular ITD and no other (especially stimuli with longer ITDs), the way in which lateralization information is integrated across frequency channels, and the way that the information is then transformed into a lateral position percept. It is probably the case that any single set of data may be explained by manipulating different parameters of the same model. The present study provides two new forms of data which may provide useful constraints on such models.

### ACKNOWLEDGMENTS

We would like to thank Dennis Phillips, whose supervisory role in a previous project led directly to this one. Steve Colburn and Trevor Shackleton and two anonymous reviewers provided helpful comments on an earlier version of this manuscript. This work was supported by a Natural Sciences and Engineering Research Council (Canada) postgraduate scholarship, an Oxford McDonnell-Pew award, and an Overseas Research Studentship to JEM, and a Medical Research Council postdoctoral fellowship to JFC.

<sup>1</sup>Since the analysis buffer was completely filled with noise, the waveform wrapped around when a delay was applied, so that the tail end of the waveform appeared at the front, preventing a delay in the onset time. Generating noise in the time domain and then filtering it in the frequency domain is considerably more computationally efficient than generating arrays of Rayleigh-distributed amplitude values and rectangularly distributed phase values and then generating and summing sine waves with those parameters. In a sense, a Fourier transform of Gaussian noise is an efficient means of generating an appropriate set of amplitude and phase values for Gaussian noise, while an inverse Fourier transform is an efficient way of generating and summing sine waves.

Blodgett, H. C., Wilbanks, W. A., and Jeffress, L. A. (1956). "Effect of large interaural time differences upon the judgment of sidedness," *J. Acoust. Soc. Am.* **28**, 639–643.

Colburn, H. S. (1996). "Computational models of binaural processing," in *Springer Handbook of Auditory Research, Vol. VI: Auditory Computation*, edited by H. L. Hawkins, T. A. McMullen, A. N. Popper, and R. R. Fay (Springer-Verlag, New York).

- Culling, J. F. (1996). "Signal-processing software for teaching and research in psychoacoustics under UNIX and X-windows," *Behav. Res. Methods Instrum. Comput.* **28**, 376–382.
- Domnitz, R. H. (1973). "The interaural time jnd as a simultaneous function of interaural time and interaural amplitude," *J. Acoust. Soc. Am.* **53**, 1549–1552.
- Domnitz, R. H., and Colburn, H. S. (1977). "Lateral position and interaural discrimination," *J. Acoust. Soc. Am.* **61**, 1586–1598.
- Durlach, N. I., and Colburn, H. S. (1978). "Binaural phenomena," in *Handbook of Perception*, edited by E. C. Carterette and M. P. Friedman (Academic, New York), Vol. 4, pp. 360–466.
- Durlach, N. I., Gabriel, K. J., Colburn, H. S., and Trahiotis, C. (1986). "Interaural correlation discrimination: II. Relation to binaural unmasking," *J. Acoust. Soc. Am.* **79**, 1548–1557.
- Hershkowitz, R. M., and Durlach, N. I. (1969). "Interaural time and amplitude jnds for a 500-Hz tone," *J. Acoust. Soc. Am.* **46**, 1464–1467.
- Jeffress, L. A. (1948). "A place theory of sounds localization," *J. Comp. Physiol. Psychol.* **41**, 35–39.
- Jeffress, L. A., Blodgett, H. C., and Deatherage, B. H. (1962). "Effect of interaural correlation on the precision of centering a noise," *J. Acoust. Soc. Am.* **34**, 1122–1123.
- Klumpp, R. G., and Eady, H. R. (1956). "Some measurements of interaural time difference thresholds," *J. Acoust. Soc. Am.* **28**, 859–860.
- Kohenke, J., Culotta, C. P., Hawley, M. L., and Colburn, H. S. (1995). "Effects of reference interaural time and intensity differences in listeners with normal and impaired hearing," *Ear and Hearing* **16**, 331–353.
- Kuhn, G. F. (1977). "Model of the interaural differences in the azimuthal plane," *J. Acoust. Soc. Am.* **62**, 157–167.
- Levitt, H. (1971). "Transformed up-down methods in psychoacoustics," *J. Acoust. Soc. Am.* **49**, 467–477.
- Pollack, I., and Trittipoe, W. J. (1959). "Binaural listening and interaural noise cross correlation," *J. Acoust. Soc. Am.* **31**, 1250–1252.
- Saberi, K. (1995). "Some considerations on the use of adaptive methods for estimating interaural-delay thresholds," *J. Acoust. Soc. Am.* **98**, 1803–1806.
- Shackleton, T. M., Meddis, R., and Hewitt, M. J. (1992). "Across frequency integration in a model of lateralization," *J. Acoust. Soc. Am.* **91**, 2276–2279.
- Stern, R. M., Zeiberg, A. S., and Trahiotis, C. (1988). "Lateralization of complex binaural stimuli: A weighted-image model," *J. Acoust. Soc. Am.* **84**, 156–165.
- Stern, R. M., and Colburn, H. S. (1978). "Theory of binaural interaction based on auditory nerve data. IV. A model for subjective lateral position," *J. Acoust. Soc. Am.* **64**, 127–140.
- Warren, R. M., Bashford, J. A., and Wrightson, J. M. (1981). "Detection of long interaural delays for broadband noise," *J. Acoust. Soc. Am.* **69**, 1510–1514.

# Frequency-weighting functions for broadband speech as estimated by a correlational method

Christopher W. Turner, Bom Jun Kwon, Chiemi Tanaka, Jennifer Knapp,  
and Jodi L. Hubbartt

*Department of Speech Pathology and Audiology, University of Iowa, Iowa City, Iowa 52241*

Karen A. Doherty

*Program in Communication Sciences and Disorders, Syracuse University, Syracuse, New York 13244*

(Received 10 November 1997; accepted for publication 20 May 1998)

The relative contributions of various regions of the frequency spectrum to speech recognition were assessed with a correlational method [K. A. Doherty and C. W. Turner, *J. Acoust. Soc. Am.* **100**, 3769–3773 (1996)]. The speech materials employed were the 258-item set of the Nonsense Syllable Test. The speech was filtered into four frequency bands and a random level of noise was added to each band on each trial. A point biserial correlation was computed between the signal-to-noise ratio in each band on the trials and the listener's responses, and these correlations were then taken as estimates of the relative weights for each frequency band. When the four bands were presented separately, the correlations for each band were approximately equal; however, when the four bands were presented in combination, the correlations were quite different from one another, implying that in the broadband case listeners relied much more on some bands than on others. It is hypothesized that these differences reflect the way in which listeners combine and attend to speech information across various frequency regions. The frequency-weighting functions as determined by this method were highly similar across all subjects, suggesting that normal-hearing listeners use similar frequency-weighting strategies in recognizing speech. © 1998 Acoustical Society of America. [S0001-4966(98)07108-2]

PACS numbers: 43.66.Ba, 43.66.Lj, 43.66.Ts, 43.71.Gv [RVS]

## INTRODUCTION

Speech recognition is generally dependent upon cues that exist across a broad range of frequencies. Different types of speech sounds are associated with characteristic spectral shapes and changes in those spectral shapes across time (e.g., Kewley-Port, 1983); thus persons listening to speech often have to attend to a wide range of frequencies, especially if the possible responses encompass a broad range of speech sounds. Specific speech features such as voicing, place, or manner may have distinguishing acoustic characteristics in several frequency regions at the same time. This redundancy of information in the frequency domain is one aspect of speech that contributes to its robust nature as a communication form. How do listeners use and combine information across frequency regions when understanding speech? One way of addressing this issue comes from the Articulation Index (AI) (e.g., ANSI, 1969; French and Steinberg, 1947; Fletcher and Galt, 1950). The experiments described in this paper use an alternative approach, one based upon a correlational procedure as applied to speech recognition (Doherty and Turner, 1996). A major purpose of the present paper is to compare the results obtained from the two different procedures.

Articulation Index (AI) is a quantity between zero and one that describes the proportion of total speech information available to a listener. The AI is based upon frequency-importance functions that have been determined by conducting speech recognition experiments under high- and low-pass filtering conditions. "Importance" here is used in the sense

of the proportional contribution a discrete band of speech makes to the total Articulation Index (French and Steinberg, 1947). By systematically removing either low- or high-frequency parts of the frequency spectrum and measuring recognition scores, the relative importance of the various frequency bands is determined. The total Articulation Index is then a sum of the proportions of the audible parts of each frequency band weighted by each band's importance.

In a previous article, Doherty and Turner (1996) demonstrated the feasibility of a correlational method to determine the "frequency-weighting" functions for speech materials. In this approach, the entire frequency range of speech is available to the listener and an estimate is obtained for the contribution of individual frequency bands to recognition. The term "frequency-weighting" function will be used in this paper for results obtained using this correlational method, to distinguish it from the more traditional "frequency-importance" function obtained from the AI procedure described above. The general correlational method is described in detail by Richards and Zhu (1994) and Lutfi (1995). In Doherty and Turner (1996), speech signals were divided into three frequency bands, and the information in each band was independently and randomly degraded by a given amount on each trial by the addition of noise. The trial-by-trial data were then analyzed by calculating a point-biserial correlation between the amount of degradation in each band and the subject's performance to provide an estimate of the "weight" the subject places upon each band. The correlations are then presented as "relative weights" for each band by normalizing the absolute values of the raw

correlations across the bands to yield a sum of one. Thus each band's relative weight represents the proportion that band's correlation contributed to the total.

In the filtering (AI) experiments, subjects are asked to identify speech sounds under conditions of restricted frequency ranges. Thus the frequency-importance functions from the AI method can specify the amount of speech information that is potentially available to a subject within a specified frequency band. In contrast, the present study's correlational method uses a broadband listening condition. This difference in experimental procedure suggests at least two reasons why results from the correlational method may differ from those of Articulation Index methods.

First, it may not be necessary for subjects to attend to all the information available within each frequency band when redundant cues are available to them in other frequency regions. Since accurate recognition of most speech materials does not require an AI of 1.0, listeners may derive adequate recognition information even while not attending to redundant information in some bands. Second, listeners might combine speech information from frequency regions that are separated substantially in the frequency domain. A recent study by Lippman (1996), showed that when speech is presented with frequencies between 800 and 4000 Hz removed, listeners could still attain nearly 90% correct phoneme identification. This high level of performance when the so-called "important" frequency regions of speech were absent is presumably due to the ability of listeners to combine speech cues across disparate frequency regions. This "synergistic" combination of speech information from widely separated frequency bands is not accounted for by traditional Articulation Theory. For these reasons, the broadband listening conditions of the correlational method may yield different estimates of the "weighting" of various frequency regions than the AI importance function. The present experiment reports a comparison of the frequency-importance functions (as previously obtained by AI methods) with frequency-weighting functions (as obtained by the correlational method) for the same speech materials. The purpose is to investigate possible differences between the ways listeners' use information in speech under restricted-bandwidth listening conditions as compared to wider, unrestricted-bandwidth listening conditions.

A second issue addressed in the present experiment is to determine the degree to which frequency-weighting functions differ across individual listeners. Some previous studies on frequency-weighting functions in normal-hearing listeners suggest that considerable variation exists in the way listeners use various frequency regions. In Doherty and Lutfi (1996), normal-hearing listeners' weighting functions for level discrimination of tonal complexes were quite different from one another. Similarly in Doherty and Turner (1996), the speech recognition weighting functions of normal-hearing subjects were somewhat different from each other. However, Doherty and Turner's (1996) study used speech materials consisting of only three alternatives, in which individual listeners may have learned during practice sessions to use specific cues to distinguish between the members of this limited stimulus set. In the present study we examine if individual normal-hearing

listeners also use dissimilar listening strategies in perceiving speech, when the speech materials employed contain a much larger number of possible responses (i.e., presumably more like real-world speech recognition).

## I. EXPERIMENT 1

The purposes of the first experiment were to (1) compare the frequency-weighting functions for speech bands presented in isolation to those obtained in a broadband listening condition, and (2) to measure frequency-weighting functions in a group of normal-hearing listeners.

### A. Methods

#### 1. Subjects

This experiment employed 13 normal-hearing listeners, ranging in age from 22 to 45. Each had audiometric thresholds of 20 dB HL or better at octave test frequencies from 250 to 8000 Hz. Only one ear was tested in each listener.

#### 2. Speech materials

To facilitate a comparison between the two methods (AI versus correlational method) in terms of their resulting frequency-importance (or weighting) functions, we have chosen to use a well-known and standardized set of speech materials for which the AI frequency-importance functions have already been carefully determined. The UCLA version of the Nonsense Syllable Test (NST) and its corresponding frequency-importance function has been used in numerous speech recognition studies (e.g., Dubno and Schaefer, 1992; Dubno and Ahlstrom, 1995). A detailed 1/3 octave-band frequency-importance function for these materials has been previously determined (Dirks *et al.*, 1990a, 1990b) and was provided to us by Professor Don Dirks (personal communication). When compared to other speech materials, the UCLA NST materials give a greater emphasis upon speech cues in the higher frequencies, with a crossover frequency dividing the AI frequency-importance function into equal halves of approximately 2200 Hz. These speech materials are therefore well suited to investigating frequency-weighting functions across a wide frequency range.

The UCLA version of the NST consists of six lists of Consonant-Vowel (CV) and six lists of Vowel-Consonant (VC) syllables. The vowels used are /a, i, or u/ and they are paired with either 21 or 22 different consonants. Six lists are spoken by a female talker and six are spoken by a male talker for a total of 258 items. For our experiment, the stimuli were digitally filtered into four frequency bands using FIR filter algorithms with 1 dB of passband ripple and 40 dB for the stopband attenuation. The cutoff frequencies were chosen on the basis of the AI frequency-importance function for these materials to yield four bands of speech, each having an importance value of approximately 0.25. Band 1 was 1120 Hz and below, band 2 was 1120–2250 Hz, band 3 was 2250–3500 Hz, and band 4 was 3500–10 000 Hz.

#### 3. Procedures

The correlational method for estimating speech weighting functions requires that each frequency band of speech be

degraded by a random amount on each trial to produce some errors in recognition. The amount of degradation within each frequency band is then correlated with the recognition performance (correct versus incorrect) on individual trials. As in Doherty and Turner (1996), we used the addition of a speech spectrum noise, bandpass filtered to correspond to the speech bands, as the method for degrading the information in each band. On each trial the signal-to-noise ratio chosen for each frequency band was independent of the noise levels chosen for the other three bands. For each of the 258 stimuli, the rms level of the speech stimulus within each of the four bands was calculated. The noise level added to each band was specified as the signal-to-noise ratio (in dB) relative to this rms level of the individual speech token within that band. On any given trial a signal-to-noise ratio was randomly chosen from a uniform distribution with a 24-dB range (in 2-dB steps) with respect to the rms level of the speech band presented on that trial. The midpoint of this 24-dB range was determined separately for each subject (either  $-3$ ,  $-1$ , or  $0$  dB), on the basis of pilot data to determine a signal-to-noise midpoint that yielded recognition performance of approximately 60%-correct. In the broadband listening conditions (bands-together) the four bands were then recombined and presented to the subject. In a separate bands-alone condition, recognition was tested for the four speech bands presented individually.

Stimulus generation and experiment control was accomplished by either a Macintosh IIX or Macintosh PC 9500 computer. The onset of the noise preceded the onset of the speech by approximately 10 ms. The stimulus was then presented via a Digital-to-Analog 16-bit converter (DigiDesign) at a sampling rate of 44.1 kHz (anti-aliasing filter set at 20 kHz), attenuated and amplified (Crown D-75) prior to monaural presentation via a Sennheiser HD-25 SP supra-aural headphone. The speech level of the NST materials was fixed at the nominal level of 70 dB SPL (corresponding to the long-term average speech level calibration tone supplied with the UCLA NST speech materials) as developed in a 6-cc coupler (B & K artificial ear).

A pilot experiment was also conducted in which one subject was tested with each of the bands presented alone. This was done, in part, to insure that the chosen range of noise levels to each band served to degrade the information within that band. Speech recognition was measured for each of the four bands presented alone across a range of S/N ratios for the entire 258-item NST materials. Twenty-four hundred trials were obtained for each band with a randomly chosen level of added noise, chosen from a 24-dB range centered about the  $-1$  dB signal-to-noise ratio (*re*: the rms level of each individual stimulus band). A visual inspection of the resulting psychometric functions (plotting percent correct as function of S/N ratio) revealed that this 24-dB range did produce a monotonic function across the entire S/N range for each of the four bands, indicating that the 24-dB range did serve to adequately degrade each band.

Subjects listened to each stimulus presentation, then indicated their choice for the consonant heard by pressing response buttons. Subjects were required to respond with one of the 21 or 22 consonant alternatives on every trial. In all

previous published work with the correlational method, trial-by-trial feedback has been provided to the subjects. For our first 11 subjects, trial-by-trial feedback in the form of lights on the response box was provided. On the other hand, such trial-by-trial feedback is rarely provided for subjects in typical speech recognition experiments. As a simple test of the possible influences of providing feedback, the remaining two subjects were provided trial-by-trial feedback only for the first few practice sessions to acquaint them with the stimuli, thereafter no individual-trial feedback was provided. Verbal feedback was provided to all listeners following each run to inform them of the overall percentage correct on each run. Approximately 4 s was provided following the subject's response before another trial was begun.

Each subject initially completed recognition of all 12 lists in a random ordering (100 trials per list) presented at a midpoint signal-to-noise ratio of +30 dB to allow the listener to become familiar with the consonant alternatives and the use of the response buttons. After the first few lists, all listeners scored over 90% correct on these lists. Then the midpoint of the signal-to-noise ratio was decreased to +10 dB for several 100-trial lists to acquaint the subject with the randomized noise bands added to the speech. Each subject was then tested for several lists (100 trials per list) at several S/N midpoints between 0 and  $-3$  dB, to determine the midpoint S/N ratio to be used for that subject's final data collection. The S/N ratio that the experimenter estimated would yield a score of approximately 60%-correct for each particular individual was used for final data collection. The analyzed data consisted of results for the entire 258-item UCLA NST speech materials with 200 trials on each of the 12 lists. Each band's point-biserial correlation was therefore based upon a total of 2400 trials.

## B. Results

### 1. Speech bands presented alone

From the data of the pilot experiment, in which one subject was tested with each of four the speech bands presented alone, a point-biserial correlation was calculated between the signal-to-noise ratios in the band on each of the trials and the listener's response on the corresponding trials. This was done for each of the four speech bands (2400 trials per band). In Fig. 1 the solid line displays the relative weights of the four bands when presented alone (obtained by normalizing the raw correlations to yield a sum of 1.0) for this subject. The relative weights are similar, ranging from 0.21 for band 4 to 0.30 for band 2. That the relative weights for the four speech bands when presented in isolation are approximately equal shows that each band was affected by the noise in a similar fashion. In the next section of this paper, we compare performance for the case of the four bands presented together to the case where the bands were presented alone.

### 2. Speech bands presented together

For comparison, the dashed line of Fig. 1 displays the relative weights of the four bands when they were presented together for this same subject (2400 trials). The band weights

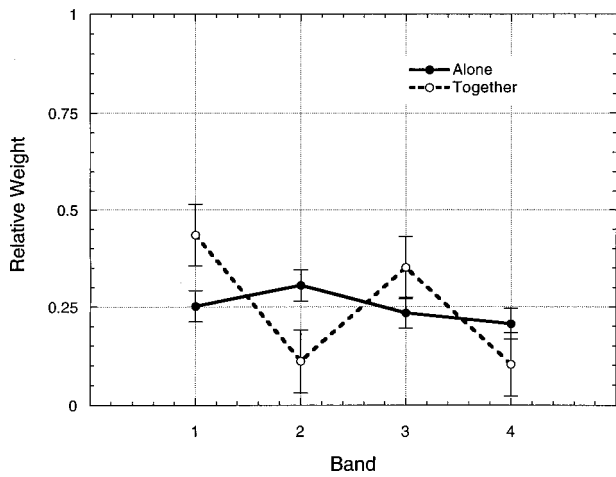


FIG. 1. Frequency-weighting functions (relative weights) for the four bands of speech for the condition of bands presented alone (solid line) and bands presented together (dashed line). The data are from one subject listening to the entire 12 lists of NST materials. Each data point is based upon 2400 trials. The error bars represent 95%-confidence intervals on the relative weights, which were derived from the 95%-confidence intervals of the raw correlations.

in this case were calculated in the same manner as before, by normalizing the raw correlation values and expressing them as relative weights. Recall that in this experiment, the other three bands are available to the listener, at various randomly chosen S/N ratios in each band. Here the relative weights of the four bands are quite different from that of the previous band-alone case. Highest relative weight is placed upon bands 1 and 3 (0.44 and 0.35, respectively). This suggests that the listener primarily used the information in bands 1 and 3 to recognize the speech tokens and did not attend highly to the information in bands 2 and 4. Figure 1 demonstrates that the information potentially available to a listener in a single speech band may not always correspond to the information actually used by the listener in a broadband listening condition.

### 3. Group data

The full group of 13 normal-hearing listeners were tested with the four bands presented together. Subjects A

through K received trial-by-trial feedback throughout the testing, whereas subjects L and M did not. The raw correlations for the 13 subjects are shown in Table I. Of the 52 correlations (13 subjects  $\times$  4 bands), 44 were significantly greater than zero at the 0.05 level of probability in a one-tailed test, as indicated by the bold entries in Table I. Seven of the eight nonsignificant correlations occurred for band 4. These nonsignificant correlations suggest that those bands had no contribution to the listener's recognition performance, in that degrading the information contained in that band had no significant effect upon speech recognition. Also listed in Table I are the midpoint S/N ratios used for each subject, along with the overall percent-correct scores obtained for the testing at that midpoint S/N ratio. In addition, for each subject the partial correlations for each band were also computed to check for possible influences of the S/N ratios in other bands. The raw correlations were not significantly different from the partial correlations in each case, indicating that the noise bands degraded performance in their corresponding speech bands independently of the other bands.

### 4. Frequency-weighting functions

The raw correlations of Table I were then used to estimate the relative weighting function for each of the 13 listeners, which are summarized in Fig. 2. The relative weights for each listener are based upon the final data for each listener, consisting of 2400 total trials across all 12 lists of the NST. The data of the first 11 listeners (A thru K) are shown by the solid line representing the average value of their relative weights, along with the standard deviation of the data. The relative weights of the remaining two subjects (L and M), who did not receive trial-by-trial feedback, are shown by the dashed lines. The relative weighting functions for all 13 listeners are remarkably similar. All functions show the same qualitative pattern, with bands 1 and 3 receiving high relative weights and bands 2 and 4 showing low relative weights. In addition, the relative weighting functions of the subjects who did receive trial-by-trial feedback were not consistently different from those who did not.

TABLE I. The point biserial correlation coefficients for the four bands of speech for the 13 individual normal-hearing listeners. The signal-to-noise ratio in each band was correlated with the listener's responses (correct versus incorrect) from the trial-by-trial experimental record. The bold numbered entries indicate correlations that are significantly different from zero ( $p < 0.05$ ) in a one-tailed test. Also listed are the midpoint S/N ratios employed for final data collection for each subject, as well as each subjects' overall percent correct score for the final data collected at that S/N ratio. Subjects A thru K received trial-by-trial feedback during the data collection. Subjects L and M (indicated by "nF" following their entries) did not receive trial-by-trial feedback.

Subject	Midpoint	Ave %-correct	Band #1	Band #2	Band #3	Band #4
A	-1	67%	<b>0.2102</b>	<b>0.5484</b>	<b>0.1489</b>	-0.0046
B	-1	61%	<b>0.2083</b>	<b>0.0600</b>	<b>0.0857</b>	<b>0.0487</b>
C	-3	64%	<b>0.2293</b>	<b>0.0623</b>	<b>0.1774</b>	<b>0.0463</b>
D	-3	64%	<b>0.2129</b>	<b>0.0729</b>	<b>0.1603</b>	0.0227
E	-1	60%	<b>0.1987</b>	<b>0.0351</b>	<b>0.1395</b>	<b>0.0384</b>
F	-3	57%	<b>0.1908</b>	<b>0.0714</b>	<b>0.1382</b>	0.0121
G	-1	64%	<b>0.2061</b>	<b>0.0560</b>	<b>0.1377</b>	0.0266
H	-3	62%	<b>0.2494</b>	<b>0.0395</b>	<b>0.1464</b>	0.0157
I	-1	62%	<b>0.1856</b>	<b>0.0473</b>	<b>0.1498</b>	<b>0.0440</b>
J	-1	60%	<b>0.1912</b>	0.0306	<b>0.1472</b>	<b>0.0366</b>
K	-3	61%	<b>0.1717</b>	<b>0.0624</b>	<b>0.1503</b>	0.0037
L (nF)	0	55%	<b>0.1691</b>	<b>0.0734</b>	<b>0.1079</b>	0.0213
M (nF)	-1	60%	<b>0.2132</b>	<b>0.0635</b>	<b>0.1066</b>	<b>0.0348</b>



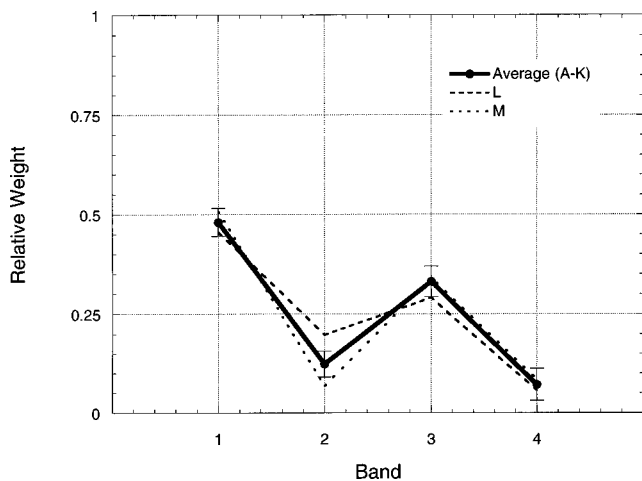


FIG. 2. The frequency-weighting functions (relative weights) of the four speech bands for the group of 13 normal-hearing listeners for the entire 12 lists of the NST speech materials. The first 11 listeners (A thru K) received trial-by-trial feedback during the testing and their mean data is shown by the heavy solid line along with the standard deviations of the relative weights across subjects. The final two listeners (L and M) did not receive trial-by-trial feedback and their individual data is shown by the dashed lines.

## II. EXPERIMENT 2

It is possible that the shape of the frequency-weighting functions of Fig. 2 are due to the specific level of performance (i.e., midpoint of S/N ratio) that was chosen for the correlational procedure. Recall that the midpoint of the signal-to-noise ratio for each subject in experiment 1 was individually chosen to yield a percent-correct score near 60%. The purpose of the second experiment was to examine the effects of a more systematic manipulation of the midpoints of the signal-to-noise ratio in a new subject group. Each subject was tested using two different signal-to-noise midpoints.

### A. Subjects and methods

Three normal-hearing subjects were recruited (none were participants in experiment 1). The methods were the same as described for the group of normal-hearing listeners of experiment 1, with the exception that two pre-specified conditions of signal-to-noise ratio were completed (+1 and -3 dB). For each condition, 2400 trials of final data for the correlational procedure were gathered in the same manner as described above. All three subjects were provided with trial-by-trial feedback.

### B. Results

The group mean frequency-weighting functions for the two signal-to-noise midpoint ratios are shown in Fig. 3. The percent-correct level of performance for under the two conditions was, as expected, different between the two conditions. For the -3 dB condition, the average level of performance was 52% correct, whereas for the +1 dB condition, it was 75% correct. In general, the two functions are very similar, showing that changing the midpoint of the signal-to-noise ratios for the correlational procedure makes little or no difference in the obtained frequency-weighting functions, at least for this range of performance. Although it would cer-

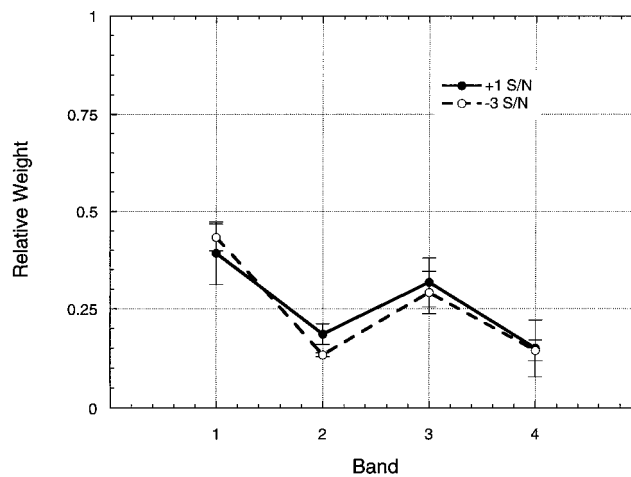


FIG. 3. The frequency-weighting functions (relative weights) of the four bands of speech obtained under two different levels of difficulty. The level of difficulty was determined by the midpoint of the S/N ratio (+1 or -3 dB). The data shown are the average and standard deviations across three subjects.

tainly be of interest to obtain frequency-weighting functions in these normal-hearing subjects for even higher levels of performance (more favorable signal-to-noise ratios), the correlational method is limited in this respect. Since the correlational method is dependent upon correlating the listener's errors with noise levels in each band, if the overall level of performance becomes too high, the strength of the raw correlations begin to decrease and approach zero.

## III. DISCUSSION

### A. Consistency across subjects

In view of the redundant nature of speech across frequency, there should be more ways than one to achieve a particular speech recognition score when the entire signal is available to a listener. The correlational method could provide an insight into the particular speech listening strategy a listener chooses. However, one of the more interesting findings of the present study is that the frequency-weighting functions were similar across all of our subjects, suggesting that normal-hearing listeners employ very similar strategies in using redundant speech information in a wideband listening condition. This consistency across normal-hearing listeners implies that a valid "normal" weighting function could be defined, and it would be very possible to determine, in individual listeners (both normal hearing and hearing impaired), if they deviate from this pattern. It would also be of interest in future research to determine if such deviations from a "normal" pattern are related to listener's percent-correct recognition performance in quiet.

### B. Comparison between correlational method and AI method

Our choice for the frequency ranges of the four speech bands was based upon the AI frequency-importance for which each band contained approximately equal amounts of speech information according to the derivation procedure for AI based upon filtering experiments. If the correlational

method of the present study measured the same quantity as the frequency-importance functions from AI methods, then the relative weights for bands presented together should be equal. This was not the case, however. Instead bands 1 and 3 showed higher relative weights and bands 2 and 4 were lower.

The most likely explanation for the difference in results between the two methods arises from the fact that the correlational method measures frequency weights in a broadband listening condition. As mentioned in the introduction, the results of Lippman (1996) have shown that subjects can combine information across widely separated frequency bands. Therefore, one interpretation of the present results is that the higher weights for bands 1 and 3 when presented together versus presented alone is that listeners combine the information in bands 1 and 3 to yield a sum greater than the parts. In addition, speech information may be redundant across frequency regions, and listeners have the opportunity to obtain information from a particular frequency region and ignore redundant information in another band. For example, it has been shown that some information on the distinctive features of voicing and manner is present in low-, mid-, and high-frequency regions of the speech spectrum (Grant and Walden, 1996). Indeed the articulation function for these NST materials reaches its asymptotic maximum recognition score when the AI value is approximately 0.7 to 0.8 (Dirks *et al.*, 1990a, 1990b; Hogan and Turner, 1998). Thus further increases in audibility beyond 0.8 AI do not provide an increase in recognition score, even as speech information is being increased for the listener. The speech materials of the present study were presented at an average level of 70 dB SPL, which would (in quiet) provide an AI of essentially 1.0 for each of the normal-hearing listeners, indicating that redundant information was potentially available to the listeners when the S/N ratios were favorable in the correlational procedure.

The possibility exists that the noise added to some bands could have influenced the detectability of neighboring bands. In particular, the noise levels in some bands may have produced upward spread of masking on some trials, for example, leading to the lower weights for bands 2 and 4. However, as mentioned in the Results section of experiment 1, we calculated the partial correlations for the various bands (i.e., correcting for the possible influence of the noise in another band upon the correlation for the band in question; see Lutfi, 1995), and no such influences were observed. Thus the masking noises in each band operated independently from one another and we can rule out the possible contaminating effects of neighboring noise bands upon the relative weights due to spread of masking. However, it is possible that the

natural shape of the speech spectrum itself leads to upward spread of masking (or self-masking) of the speech. This may be one contributing factor to the obtained results, and may be an additional reason why the correlational method more realistically describes how speech is naturally used by listeners in a typical broadband listening situation.

## ACKNOWLEDGMENTS

This work was supported by a grant from the National Institute on Deafness and other Communicative Disorders (DC 00377). Helpful suggestions on conducting these experiments were provided by participants in a lively discussion at the 1996 conference "Issues in Advanced Hearing Aid Research" at Lake Arrowhead, California. That conference was sponsored by the House Ear Institute and the Acoustical Society of America. Helpful suggestions on an earlier draft of this paper were provided by Dr. Fan-Gang Zeng.

- ANSI (1969). ANSI S3.5-1969, "American National Standards Methods for the Calculation of the Articulation Index" (ANSI, New York).
- Dirks, D.D., Dubno, J.R., Ahlstrom, J.B., and Schaefer, A.B. (1990). "Articulation index importance and transfer functions for several speech materials," *ASHA* **32**, 91.
- Dirks, D.D., Dubno, J.R., and Bell, T.S. (1990b). "Problems in the prediction of speech recognition among normal-hearing and hearing-impaired listeners," *J. Acoust. Soc. Am. Suppl.* **1** **88**, S32.
- Doherty, K.A., and Lutfi, R.A. (1996). "Spectral weights for overall level discrimination in listeners with sensorineural hearing loss," *J. Acoust. Soc. Am.* **99**, 1053-1058.
- Doherty, K.A., and Turner, C.W. (1996). "Use of a correlational method to estimate a listener's weighting function for speech," *J. Acoust. Soc. Am.* **100**, 3769-3773.
- Dubno, J.R., and Schaefer, A.B. (1992). "Comparison of frequency selectivity and consonant recognition among hearing-impaired and masked normal-listeners," *J. Acoust. Soc. Am.* **91**, 210-2121.
- Dubno, J.R., and Schaefer, A.B. (1995). "Frequency selectivity and consonant recognition for hearing-impaired and normal-hearing listeners with equivalent masked thresholds," *J. Acoust. Soc. Am.* **97**, 1165-1174.
- Fletcher, H., and Galt, R.H. (1950). "The perception of speech and its relation to telephony," *J. Acoust. Soc. Am.* **22**, 89-150.
- French, N.R., and Steinberg, J.C. (1947). "Factors governing the intelligibility of speech sounds," *J. Acoust. Soc. Am.* **19**, 90-119.
- Grant, K.W., and Walden, B.E. (1996). "Evaluating the articulation index for auditory-visual consonant recognition," *J. Acoust. Soc. Am.* **100**, 2415-2424.
- Hogan, C., and Turner, C.W. (1998). "High-frequency audibility: Benefits for hearing-impaired listeners," *J. Acoust. Soc. Am.* **104**, 432-441.
- Kewley-Port, D. (1983). "Time-varying features as correlates of place of articulation in stop consonants," *J. Acoust. Soc. Am.* **73**, 322-335.
- Lippman, R.P. (1996). "Accurate consonant perception without mid-frequency speech energy," *IEEE Trans. Speech Audio Process.* **4**, 66-69.
- Lutfi, R.A. (1995). "Correlation coefficients and correlation ratios as estimates of observer weights in multiple-observation tasks," *J. Acoust. Soc. Am.* **97**, 1333-1334.
- Richards, V.M., and Zhu, S. (1994). "Relative estimates of combination weights, decision criteria, and internal noise based upon correlational coefficients," *J. Acoust. Soc. Am.* **95**, 423-424.

# Auditory-visual spatial integration: A new psychophysical approach using laser pointing to acoustic targets

Jörg Lewald<sup>a)</sup>

Ruhr-Universität, Kognitions- und Umweltpsychologie, D-44780 Bochum, Germany

Walter H. Ehrenstein

Institut für Arbeitsphysiologie, Sinnes- und Neurophysiologie, Ardeystrasse 67, D-44139 Dortmund, Germany

(Received 27 March 1997; accepted for publication 12 May 1998)

The alignment of auditory and visual spatial perception was investigated in four experiments, employing a method of laser pointing toward acoustic targets in combination with various tasks of visual fixation in six subjects. Subjects had to fixate either a target LED or a laser spot projected on a screen in a dark, anechoic room and, while doing so, direct the laser beam toward the perceived azimuthal position of the sound stimulus (bandpass-filtered noise; bandwidth 1–3 kHz; 70 dB sound pressure level, duration 10 s). The sound was produced by one of nine loudspeakers, located behind the acoustically transparent screen between 22° to the left and 22° to the right of straight ahead. Systematic divergences between sound azimuth and laser adjustment were found, depending on the instructions given to the subjects. The eccentricity of acoustic targets was generally overestimated by up to 10.4° with an only slight influence of gaze direction on this effect. When the sound source was straight ahead, gaze direction had a substantial influence in that the laser adjustments deviated by up to 5.6° from sound azimuth, toward the side to which the gaze was directed. This effect of eye position decreased with increasing eccentricity of the sound. These results can be explained by the interactive effects of four distinct factors: the lateral overestimation of the auditory eccentricity, the effect of eye position on sound localization, the effect of the retinal eccentricity on visual localization, and the extraretinal effect of eye position on visual localization. © 1998 Acoustical Society of America. [S0001-4966(98)06308-5]

PACS numbers: 43.66.Qp, 43.66.Pn [RHD]

## INTRODUCTION

### A. General objectives

A primary function of auditory localization is to direct the eyes to the source of the sound (Heffner and Heffner, 1992). Accurate performance requires that the coordinates of auditory and visual spatial perception are in exact alignment. In fact, humans usually perform such a task with sufficient accuracy; i.e., a sound is linked to a visual location in space without any noticeable mislocalizations. Contrary to this everyday experience, recent psychophysical studies show that, under certain experimental conditions, significant divergences between auditory and visual localization occur (Lewald and Ehrenstein, 1996b; Lewald, 1997, 1998). Although small, these effects are quite replicable and may reflect the functional organization of neuronal mechanisms that integrate auditory and visual space perception. As will be outlined in the two following sections, the present work attempts to extend our previous experimental studies on auditory-visual spatial divergences by a subtle analysis of the several distinct effects, which possibly interact in a complex manner.

### B. Neurobiological aspects

From a neurobiological viewpoint, the central nervous system has to solve a number of problems as it is to integrate

auditory and visual localization into a coherent spatial perception. These problems are due to the substantial differences in the physical properties of sound and light, in the peripheral mechanisms of sensory reception, and in the further central processing of different stimulus information.

Starting from the premise that both auditory and visual localization are based on the neural encoding of spatial cues within topographical representations of sensory space, these neural maps should have defined spatial relations to each other. Brain maps of visual space are, however, “projectional maps” (i.e., the receptor epithelia of the retinae are topographically mapped), whereas auditory space maps are “centrally synthesized maps,” which are created by neuronal circuits processing the interaural time and level differences, as well as spectral cues (Konishi, 1986). As a consequence, the auditory system encodes sound location primarily within a craniocentric frame of reference, defined by the position of the ears and the acoustical properties of the head and the pinnae. In contrast, the retinotopical representations of visual space are within an oculocentric frame of reference so that movements of the eyes in their orbits produce shifts of these maps with respect to the extrapersonal space.

The finding of multimodal areas, containing superimposed auditory and visual maps (for a review, see Sparks and Nelson, 1987), implies neural transformations of the spatial coordinates such that the two representations remain in register when the eyes move (Pöppel, 1973). Such a transforma-

<sup>a)</sup>To whom correspondence should be sent.

tion of auditory coordinates from the originally craniocentric to an oculocentric frame of reference has been indicated by neurophysiological recordings in combination with fixation tasks in the superior colliculus (SC) of the monkey and cat midbrain (Jay and Sparks, 1984, 1987; Hartline *et al.*, 1995; Peck *et al.*, 1995). However, the quantitative data have suggested that this coordinate transformation is incomplete, and the two maps still diverge when the eyes deviate from straight ahead (Jay and Sparks, 1987). In addition to this problem of eye position, further divergences in the auditory and visual representations of space may be due to the fact that in contrast to auditory space, the visual space is restricted to the frontal range of the head with a strongly magnified representation of the foveal area.

Almost all recent knowledge on this topic is related to the SC, the primary function of which may be to control sensorily guided motor responses rather than to provide conscious representation of space (see Sparks and Nelson, 1987; Brainard, 1994). On the one hand, one cannot exclude the possibility that the SC might influence the perception of stimulus location. But on the other hand, the posterior parietal cortex (area LIP) of the monkey has recently been found to contain spatially tuned bimodal neurons, responding to both auditory and visual stimuli (Mazzoni *et al.*, 1996; Stricanne *et al.*, 1996). When the monkey performed saccades to remembered sound locations, some of these neurons showed auditory-triggered discharges in an eye-centered manner, which suggests that such neurons provide a modality-independent code for stimulus location in space, used for oculomotor control (Stricanne *et al.*, 1996). Furthermore, one should take into account that several cortical brain areas have been found where visual space is represented within a craniocentric or egocentric frame of reference (see, e.g., Gentilucci *et al.*, 1983; Andersen *et al.*, 1985, 1990; Galletti *et al.*, 1993; Fogassi *et al.*, 1992; Weyand and Malpeli, 1993). Even though auditory topographic representations of space have not been demonstrated thus far in the cortex, it is possible that those coordinate transformations also occur for the auditory modality and are reflected by perceptual phenomena (cf. Mazzoni *et al.*, 1996; Stricanne *et al.*, 1996). In any case, one may expect that systematic deviations of perceived auditory and visual directions will occur, depending both on stimulus position with respect to the head and the position of the eyes in the orbits. The aim of the present study is to measure such deviations and their interactions in localization psychophysically.

### C. Previous psychophysical studies

Auditory-visual interactions in localization have been investigated in many earlier studies (see, e.g., Klemm, 1910; Thomas, 1941; Witkin *et al.*, 1952; Jackson, 1953; Welch and Warren, 1980; Perrott *et al.*, 1991; Lueck *et al.*, 1990; Perrott, 1993; Stein *et al.*, 1996; Ehrenstein and Reinhardt-Rutland, 1996a,b). Those experiments have focused either on mutual interferences of spatially disparate or coincident auditory and visual stimuli, or on more complex, perceptual and cognitive phenomena such as the spatial association of a sound and a visual target rather than deviations in the perceived directions. Few other studies have tried to demon-

strate specific effects of eye position on sound localization (Pierce, 1901; Goldstein and Rosenthal-Veit, 1926; Weerts and Thurlow, 1971; Ryan and Schehr, 1941; Bohlander, 1984; Cullen *et al.*, 1992), but with the only exception of Weerts and Thurlow (1971) their results were either merely qualitative, statistically insignificant, or contradictory for different subjects (for further details, see Lewald and Ehrenstein, 1996a).

Because of the inconsistency in the previous literature, we have recently made a new, straightforward approach to this problem by a series of detailed studies, employing several different psychophysical methods (Lewald and Ehrenstein, 1996a, b; Lewald, 1997, 1998). Our studies have so far demonstrated the interaction of two different perceptual effects in auditory-visual spatial integration:

- (1) A shift of the perceived azimuthal sound direction as a function of horizontal eye position. This shift is opposite to the direction of eccentric gaze (Lewald and Ehrenstein, 1996a; Lewald, 1998).
- (2) A slight shift in perceived sound direction toward the direction of gaze with respect to a visual target (Lewald and Ehrenstein, 1996b; Lewald, 1997, 1998). This effect results from a shift of the visual direction opposite to the direction of eccentric gaze that is larger than that of the auditory direction. Thus an auditory and a visual target physically located at the same position are perceived as spatially dissociated when the eyes deviate from straight ahead.

These previous studies have, however, been restricted to the localization of target positions within or near the median plane of the head. They do not refer to eccentric targets, for which different effects might be expected. The present experiments were designed to fill this gap by using a laser-pointing method in combination with different visual fixation tasks and sound stimuli distributed over the frontal azimuthal range up to 22° to either side with respect to the median plane.

## I. METHODS

### A. Subjects

Six subjects (three female and three male; mean age 28.0, range 24–36 years) participated in each of the four experiments as volunteers. They all had no hearing deficiencies as determined by an audiometric test. All subjects were right-handed as assessed by a subscale of a questionnaire (Coren, 1993; German adaptation by Ehrenstein and Arnold-Schulz-Gahmen, 1993). In four subjects the right eye and in two subjects the left eye was the dominant eye as assessed by another subscale of Coren's (1993) questionnaire and by the pointing test (Walls, 1951). All subjects had normal or corrected-to-normal vision. Three of the subjects were experienced in previous auditory-visual localization studies; the others had never participated in psychophysical experiments before. Except for one subject (one of the authors), subjects were undergraduate students to whom only general information on the purpose of the experiments was provided, i.e., that it was to study relations of auditory and visual localiza-

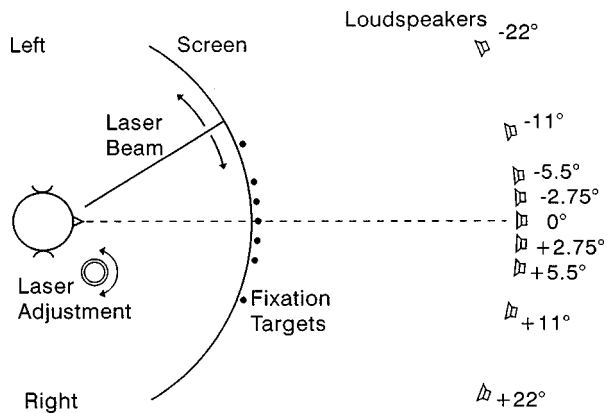


FIG. 1. Experimental setup. By turning the knob, the subject could control the direction of a laser beam and thus adjust the position of a light spot projected on the translucent, acoustically transparent screen. Seven light-emitting diodes, arranged behind the screen, served as fixation targets, and nine loudspeakers were used to produce sound stimuli from different azimuthal directions.

tion. For each experiment, one initial practice session was conducted to familiarize the subjects with the experimental setup, the specific task, and the instructions.

## B. Sound stimuli

The basic experimental setup was similar to that used in preceding studies (Lewald and Ehrenstein, 1996b; Lewald, 1997, 1998). All experiments were conducted within an absolutely dark soundproof, anechoic room (5.4×4.4×2.1 m; ambient noise around 30 dB sound pressure level; for details, see Guski, 1990). The subject sat on a chair with the head fixed by a framework with stabilizing rests for the chin, forehead, and occiput (see Lewald, 1997).

Acoustic stimuli were presented from a horizontal array of nine broadband loudspeakers (∅ 13 cm; Visaton FRWS 13) which were mounted along the arc of a circle centered at the subject's head at eye level (distance 3.4 m; see Fig. 1). One of the loudspeakers was straight ahead in the subject's median plane, four were on the left, and four on the right, with angular distances of 2.75°, 5.5°, 11°, and 22° with respect to the central loudspeaker (0°). In experiments 1 and 2, all nine loudspeakers were used; in experiment 3 only the central one; and in experiment 4 the central loudspeaker and those at 11° and 22° on either side.

The sound stimulus was bandpass-filtered noise (center frequency 2 kHz, bandwidth 2 kHz), generated by a custom-made noise generator connected to a bandpass filter (24 dB/octave, Rockland 432), and shaped by a modified envelope generator (Burchard Akustischer Stimulator II; rise and fall time 20 ms; plateau time 10 s). Sound pressure level was calibrated to 70 dB *re*: 20  $\mu$ Pa, using a 1-in. microphone (Brüel & Kjær 4145) in conjunction with a measuring amplifier (Brüel & Kjær 2603). We used this stimulus as standard since it proved easy to localize in preceding studies on eye-position effects and allowed a direct comparison of the present with the previous results (Lewald and Ehrenstein, 1996a, b; Lewald, 1997, 1998). The frequency range of the stimulus is within the range of the lowest interaural intensity difference thresholds (around 1.5–3 kHz; see Grantham,

1984; Yost and Dye, 1988) as well as that of the lowest just noticeable differences in interaural time (around 1 kHz; Klumpp and Eady, 1956; Zwislocki and Feldman, 1956). In addition, its broad bandwidth provides high-frequency ongoing time differences for localization (McFadden and Pasanen, 1976).

If not stated otherwise, the stimulus described above was employed, except for a part of the measurements of experiment 1, in which a narrow-band noise with several center frequencies (0.5, 1, 2, 4, 8 kHz) was used, generated by a one-third octave bandpass filter (Wandel & Goltermann TB-1). These narrow-band stimuli were employed to demonstrate effects of sound frequency on auditory-visual divergence.

## C. Fixation targets

Seven green light-emitting diodes (LEDs; 0.2 mcd, ∅ 1.8 mm) served as fixation targets. They were arranged in the azimuthal plane at a distance of 1.5 m from the subject's head (Fig. 1). One LED was located in the median plane of the head (0°) and the others at eccentricities of 5.5°, 11°, and 22° to either side. The LEDs were arranged along the arc of a circle around the center of the subject's head at the same level as the loudspeakers, such that each LED was exactly in front of the center of a loudspeaker at the corresponding azimuthal position.

## D. The laser-pointing method

The spatial arrangement of both the LEDs and the loudspeakers was hidden by a smooth curtain of white, thin fabric that was acoustically transparent, so that the sound field was not measurably disturbed by it. The curtain was arranged along the arc of a circle around the center of the subject's head, covering a frontal azimuthal range of about 135° and almost the full height of the room (1.9 m). It was translucent and mounted very close (less than 1 cm) in front of the LEDs, the light of which was neither substantially attenuated nor blurred (Fig. 1). The curtain served as a surface on which a red light spot (∅ ca. 3 mm; ca. 5 mcd) was projected by a laser beam. For this purpose, a compact laser-diode system was mounted on the head restraint above the subject's head (about 30 cm above eye level). The laser diode could be rotated horizontally by a galvanometer (G330, General Scanning), the angular range of which was enlarged to about 90° by a custom-made gear system. The axis of rotation coincided with the vertical axis intersecting the midpoint of the line joining the centers of rotation of the subject's eyes. The subject could control the azimuthal position of the laser spot by adjusting the knob of a ten-turn potentiometer that varied the input voltage of the amplifier driving the galvanometer (AX-200, General Scanning). Each full rotation of the knob resulted in a horizontal shift of the light spot by about 10°. Clockwise rotation resulted in a shift to the right, counterclockwise rotation to the left. The potentiometer was in a small case, so that the subject could hold it in one hand while turning the knob with the other hand. The elevation at which

the light spot was displayed on the screen was approximately the same as that of the loudspeaker, but about 1 cm above the LEDs so as not to interfere with them.

## E. Procedures

The basic task was the same in all four experiments: the subject was instructed to adjust the position of the laser spot toward the perceived azimuthal direction of the sound. The experiments essentially differed with respect to the conditions of fixation and the presentation of the acoustic stimulus.

In experiment 1, each trial began with the onset of both the acoustic stimulus (produced by the loudspeaker) and the laser spot, both presented for 10 s. Within this period, the subject had to simultaneously obey two main instructions: (1) the laser spot had to be fixated with the gaze for as long as it was present; (2) the position of the laser spot had to be adjusted by turning the knob of the potentiometer, such that the perceived direction of the laser spot coincided with the perceived direction of the sound. For this purpose, at each trial onset, the subject had to first turn the knob several times alternately to the left and right, so that the laser spot was moved to the left and right of the perceived sound azimuth, and converge by slow movements, becoming smaller, to the final position. When this position was reached, the subject released the knob. Performing this task usually took the subject 5–8 s. The azimuthal position of the laser was measured by the potentiometer linked to the axis rotating the laser, and the angle was recorded automatically by the computer program at stimulus offset. The adjustments of the subject were monitored on line by the experimenter. Four seconds after stimulus offset the next trial began. Each session comprised 270 trials, i.e., 30 trials for each of the nine loudspeakers the position of which was varied in a pseudo-random order. One session was subdivided into four blocks of equal durations; after each block, the subject was allowed to rest for 5–10 min. Data of two subsequent sessions (540 trials), conducted on different days, were combined for analysis. No systematic practice effects were found in a comparison of the data of the first and the second session.

Experiment 2 differed from experiment 1 only in that 2 s before the onset of the sound stimulus and the laser the central fixation target ( $0^\circ$ ) was presented, which remained illuminated until the end of the sound. The subject was instructed to fixate the LED and to maintain fixation for as long as it was present. While fixating straight ahead, the subject had to direct the laser beam toward the perceived sound in the same manner as described for the first experiment.

In experiment 3, fixation was directed to one out of seven possible target LEDs, but only one loudspeaker, at straight ahead ( $0^\circ$ ), was used. The fixation directions varied in a pseudo-random order. One session comprised 210 trials, and three rests were taken.

Experiment 4 combined the conditions of the experiments 2 and 3 by using all seven fixation targets and five of the loudspeakers, the positions of which varied in a pseudo-random order. The number of trials was 210 for each of the

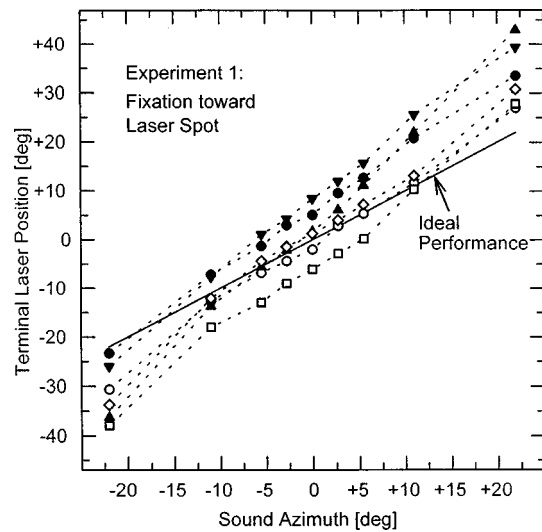


FIG. 2. Terminal positions of the laser beam adjusted to the perceived azimuthal position of the sound stimulus (experiment 1). Datapoints represent median values measured in each of six subjects and are plotted as a function of sound azimuth (bandpass-filtered noise, center frequency 2 kHz, bandwidth 2 kHz). Subjects are indicated by different symbols. The solid line indicates ideal performance.

two sessions conducted, so that each LED/loudspeaker combination was presented 12 times. Three rests were taken during each session.

## F. Data analysis

First, for each subject median values of the adjustments were computed for each LED/loudspeaker combination. To pool the results of different subjects the resulting azimuthal angles were normalized such that each subject's adjustment with both gaze and sound direction toward straight ahead ( $0^\circ$ ) was assigned  $0^\circ$ . As in our previous studies (see Lewald and Ehrenstein, 1996a,b; Lewald, 1997, 1998), the normalization served to cancel variations due to individual asymmetries, e.g., in the sensitivity of the ears, or small differences in the straight ahead calibration of the head position. Then, mean values and standard errors for all subjects were calculated, and the azimuthal deviations of the subjects' adjustments from the actual stimulus azimuths were plotted either as a function of gaze direction or sound azimuth. Negative angles indicate directions to the left, positive angles to the right.

## II. RESULTS

### A. Experiment 1

This experiment required the subjects to direct the laser beam toward the perceived direction of the sound, while following its projection on the screen with their gaze. In Fig. 2, the median terminal positions of the laser beam are plotted as a function of sound azimuth for each of the six subjects tested. The individual datapoints are typically scattered over a range of about  $15^\circ$ , but the curves for different subjects show, at least for sound directions around straight ahead, approximately the same slope; i.e., each subject showed an almost constant individual bias in the adjustments to either-

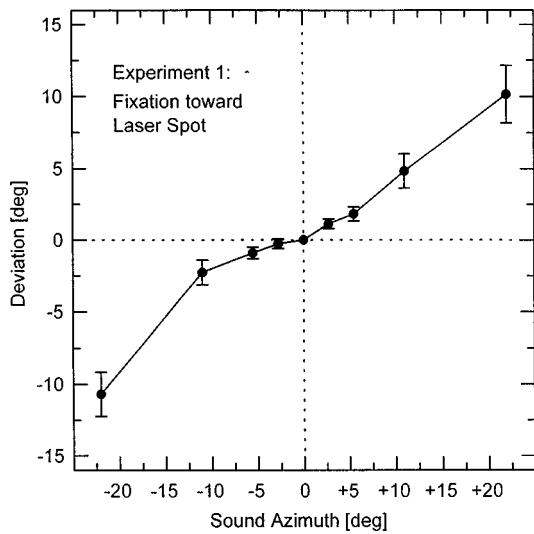


FIG. 3. Deviation of the laser adjustments from the actual sound azimuth with fixation toward the laser spot projected on the screen (experiment 1). Datapoints and error bars represent normalized means and standard errors (for six subjects) and are plotted as a function of the stimulus azimuth (bandpass-filtered noise, center frequency 2 kHz, bandwidth 2 kHz).

the left or right. There was no clearcut relation of the directions of these biases to the eye dominances assessed in the subjects. For further analysis all data were normalized such that each subject's adjustment with both gaze and sound direction toward straight ahead was assigned  $0^\circ$ .

The normalized mean deviations of the laser position from the physical sound azimuth, for the six subjects tested, are plotted as a function of sound azimuth in Fig. 3. The deviations were significantly correlated with sound direction (Spearman's rank correlation coefficient  $r_s = 0.76$ ;  $p < 0.001$ ). The negative deviations from the sound directions on the left of the median plane ( $0^\circ$ ) and the positive deviations on the right indicate that in both cases the position of the laser spot was more eccentric than the actual sound azimuth; i.e., the eccentricity of the sound was overestimated. The magnitudes of these deviations were almost identical on both sides; for the most eccentric sound azimuths tested ( $22^\circ$ ), the mean deviation was  $10.4^\circ$  to either side. The curve is not a linear function, but it is steeper at more eccentric sound directions than around straight ahead.

Additional measurements were made using the same methods as for the main experiment, but by employing a one-third octave bandpass noise with various center frequencies (0.5, 1, 2, 4, 8 kHz) as the acoustic stimulus. Figure 4 shows the individual data for two subjects. The trends of the curves are clearly positive for frequency bands of 0.5, 2, 4, and 8 kHz, indicating an overestimation of the lateral angle of sound azimuth. The shape of the curve is approximately linear at 0.5 kHz, whereas the functions seem to become more complex toward higher frequencies above 1 kHz. Considerable deviations between the two subjects occur only at 8 kHz. As shown by the plot of the mean deviations measured with  $\pm 22^\circ$  sound eccentricity as a function of the center frequency of the narrow-band noise in Fig. 5, the magnitude of the overestimation effect depends on frequency in a systematic manner with an only slight deviation ( $2.2^\circ$ ) for 1 kHz, a maximum ( $13.9^\circ$ ) for 4 kHz, and intermediate devia-

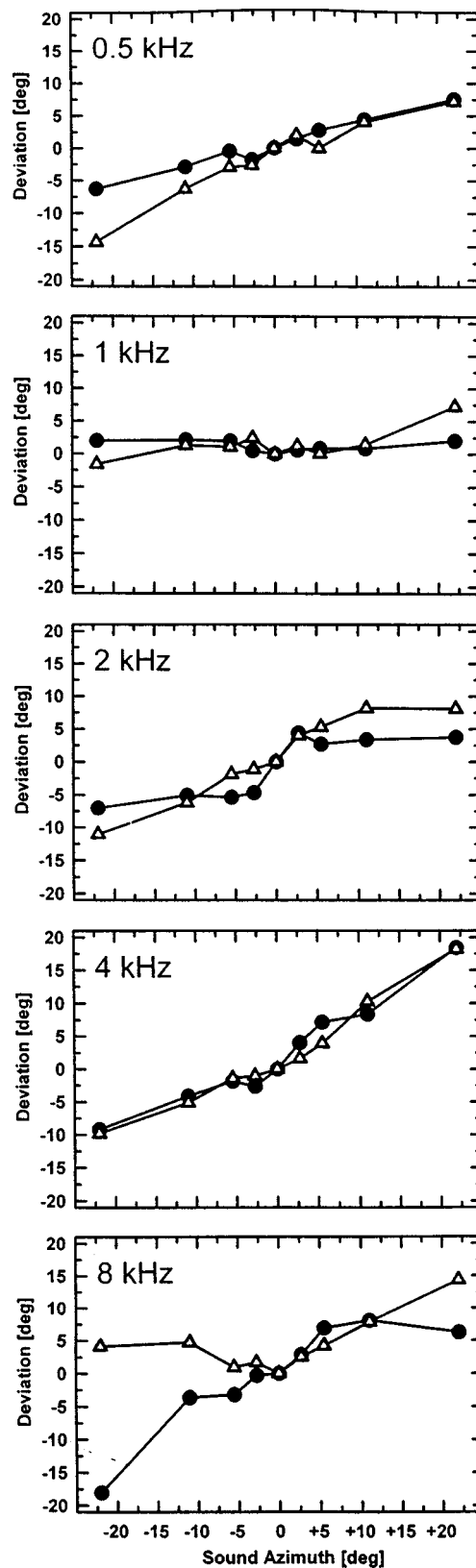


FIG. 4. Deviation of the laser adjustments from sound azimuth with fixation toward the laser spot for one-third octave bandpass noise (center frequencies 0.5, 1, 2, 4, and 8 kHz). Datapoints represent individual results from two subjects, indicated by different symbols.

tions of approximately equal magnitude ( $7.5^\circ$ – $8.8^\circ$ ) for 0.5, 2, and 8 kHz. Each of the latter three values differed significantly from both the 1-kHz minimum and the 4-kHz maximum deviation (Mann-Whitney U-test;  $p < 0.001$ ). The

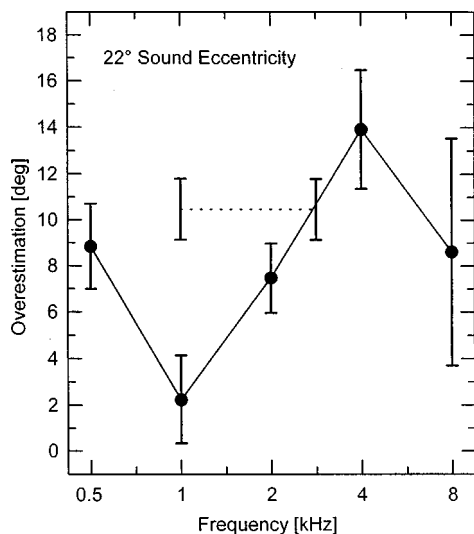


FIG. 5. Dependence of the overestimation effect, found with fixation toward the laser spot for 22° eccentric sound azimuth, on the center frequency of one-third octave bandpass noise (smooth line). The dashed line indicates the deviation for noise of 1–3 kHz bandwidth. Mean values and standard errors are calculated from overestimations to the left and right for two subjects (same data as in Figs. 3 and 4).

mean magnitude of the overestimations found with noise of 1–3 kHz bandwidth in the same subjects (10.5°) falls between the deviations for 0.5, 2, and 8 kHz and the maximum at 4 kHz. Except for the 8-kHz value ( $p > 0.4$ ), each of the deviations obtained with narrow-band noise differed significantly from that measured with 1–3 kHz bandwidth ( $p < 0.001$ ).

### B. Experiment 2

In this experiment, the subjects had to adjust the direction of the laser beam toward the sound direction while simultaneously fixating a visual target (LED) at straight ahead (0°). As shown in Fig. 6, the deviations of the light spot from

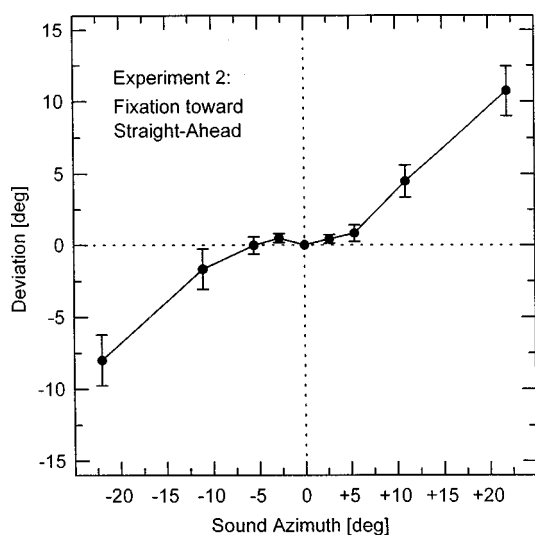


FIG. 6. Deviation of the laser adjustments from the actual sound azimuth with fixation toward a target LED located in the median plane of the head (experiment 2:). Datapoints and bars represent normalized means and standard errors (six subjects) and are plotted as a function of the stimulus azimuth.

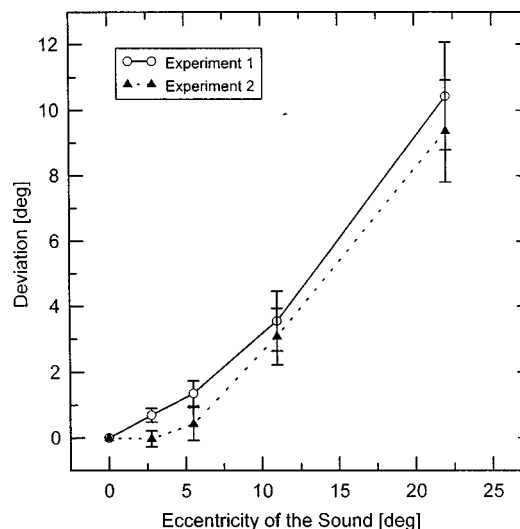


FIG. 7. Comparison of the results of experiments 1 and 2. The deviations of the laser adjustments from the actual sound azimuth with fixation toward the laser spot (experiment 1, open symbols) and toward a target LED located in the median plane of the head (experiment 2, closed symbols) are plotted as a function of stimulus eccentricity with respect to the median plane (0°). The data were averaged for stimuli to the left and right (normalized means and standard errors for six subjects). The differences between the two curves are significant (Mann-Whitney U-test;  $p < 0.002$ ).

the actual azimuths of the loudspeakers vary as a function of sound direction in a manner quite similar to that in experiment 1, indicating an overestimation of the eccentricity of the sound source. For the six subjects, the normalized deviations were significantly correlated with sound azimuth ( $r_s = 0.59$ ;  $p < 0.001$ ). The mean magnitude of the deviations was 9.4° for a sound eccentricity of 22°.

Figure 7 allows a more detailed comparison between the results of experiment 1 and 2. It shows the mean magnitudes of the deviations measured in both experiments as a function of sound eccentricity (mean values from the deviations on the left and right). The courses of the two functions are approximately parallel, with a consistently stronger deviation for experiment 1 (gaze toward laser spot) than for experiment 2 (gaze toward straight ahead). The differences between the two measurements are slight (mean 0.8°) but statistically significant for all subjects (Mann-Whitney U-test;  $p < 0.002$ ), and they are fairly constant over the range of eccentric sound directions tested.

### C. Experiment 3

In this experiment, the sound azimuth remained at a constant straight ahead position, while the position of the fixation targets varied. As in experiment 2, the subjects had to adjust the laser toward the perceived sound azimuth, while fixating a visual target. The normalized adjustments for all subjects were significantly correlated with gaze direction ( $r_s = 0.71$ ;  $p < 0.001$ ). As shown by the curve of the mean data in Fig. 8, the adjustments shift as a function of gaze direction with a positive trend; i.e., they deviate to the left when the gaze is to the left, and to the right when gaze is to the right. The magnitude of the deviations is more pronounced with gaze to the right (+8.2° at +22°) than with



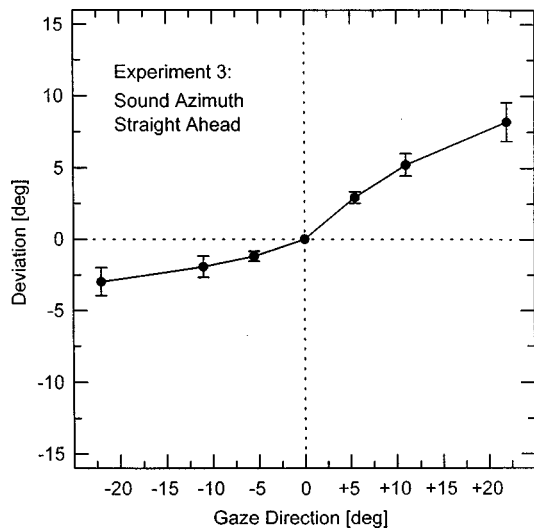


FIG. 8. Deviation of the laser adjustments from sound azimuth, actually located in the median plane, plotted as a function of horizontal fixation direction (experiment 3; normalized means and standard errors for six subjects).

gaze to the left ( $-3.0^\circ$  at  $-22^\circ$ ; mean  $5.6^\circ$  to either side). The adjustments do not follow a linear function of gaze direction, but change more strongly with gaze around straight ahead than with eccentric gaze.

#### D. Experiment 4

The fourth experiment was designed to demonstrate interactions between the effects of eye position and sound eccentricity. Figure 9 shows the deviations of the subjects' adjustments from five different sound azimuths as functions of gaze direction. The curves for the central sound directions exhibit positive trends; the correlations were statistically significant for  $-11^\circ$  ( $r_s=0.54$ ;  $p<0.001$ ) and  $0^\circ$  sound azimuth ( $r_s=0.61$ ;  $p<0.001$ ). The deviations from the two

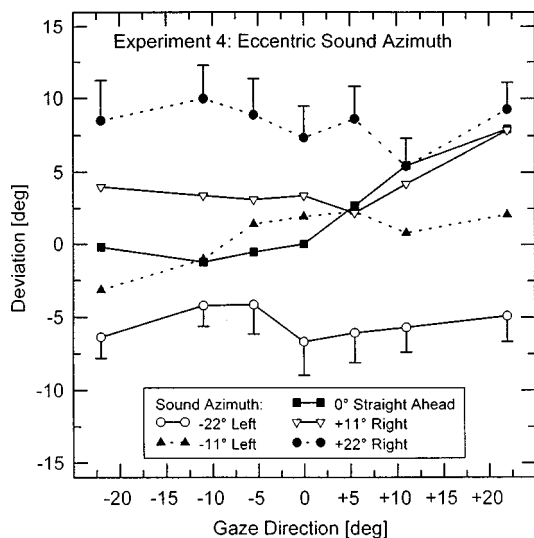


FIG. 9. Deviations of the laser adjustments from actual sound azimuth plotted as functions of gaze direction for five different stimulus directions (indicated by different symbols) from  $-22^\circ$  to the left and  $+22^\circ$  to the right of the median plane (experiment 4). Datapoints represent normalized means for six subjects; standard errors are given only for the most eccentric sound azimuths.

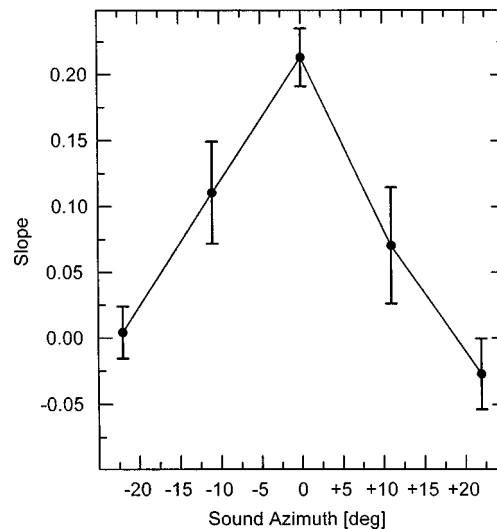


FIG. 10. Quantitative analysis of the eye-position effect. The slopes of the regression lines, calculated from the data shown in Fig. 9, are plotted as a function of stimulus azimuth. Datapoints represent the mean angular shifts of the deviations of the laser adjustments from the actual sound azimuths (in degrees) when the gaze changes by one degree (means and standard errors for six subjects). Negative slopes represent shifts in deviation opposite to the direction of the shift in eye position; positive slopes represent shifts toward the shift in eye position.

most eccentric acoustic targets ( $-22^\circ$  and  $+22^\circ$ ) were approximately constant with variation of gaze direction ( $|r_s|<0.08$ ;  $p>0.10$ ). The correlations of the auditory-visual deviations with sound azimuth were significant for all fixation directions ( $r_s>0.40$ ;  $p<0.025$ ). Compared to those measurements of experiments 1–3 that were made under the same conditions of visual fixation, the deviations found in experiment 4 were generally slightly smaller. This may be due to the greater variability of both the fixation targets and the sound directions presented to the subject.

Summing up, the plot of Fig. 9 indicates that the position of the eyes in the orbits has a significant influence on the adjustments measured only in case the sound source is located within the azimuthal range close to the median plane. In contrast, deviations are of an approximately constant magnitude with different gaze directions for more eccentric sound positions. Due to the interaction of these two factors, the variation of the auditory-visual deviation as a function of sound azimuth is, generally, the smallest when gaze direction and sound are in the same angular range, even though the absolute deviations can be substantial.

The relation of the effects of eye position and sound eccentricity is analyzed in more detail in Fig. 10. For this purpose, linear regression analysis was carried out for the data shown by the five curves of Fig. 9. The slopes of the resulting regression lines were used as measures of the magnitudes of the eye-position effect and are plotted as a function of sound azimuth in Fig. 10. The curve in Fig. 10 shows a pronounced maximum at straight ahead sound ( $0^\circ$ ) with a mean change of the deviations by 0.21 degrees per one degree change in gaze direction. The magnitude of the eye-position effect decreases with increasing eccentricity of the sound almost symmetrically toward the left and right, until it

levels off with sound at 22° eccentricity. The differences of the slopes for sound from straight ahead (0°) and those for sound at 22° to the side were statistically significant for all subjects (Mann-Whitney U-test;  $p < 0.01$ ).

### III. DISCUSSION

The experiments described here demonstrate systematic deviations in auditory and visual spatial perception. In the following, we suggest a comprehensive hypothesis to explain this mismatch by the complex interaction of four main factors that influence the spatial alignment of the perceived auditory and visual azimuthal directions: (1) a general tendency to overestimate auditory eccentricity; (2) an effect of the retinal eccentricity of a visual stimulus (with respect to the fovea) on the perceived stimulus location; (3) an effect of eye position on visual localization, depending on extraretinal information; and (4) a nonvisual effect of eye position on sound localization.

#### A. Overestimation of sound eccentricity

The results of the experiments 1 and 2 indicate that the eccentricity of a sound source (with respect to the median plane) is generally overestimated with laser pointing, almost irrespective of the position of the eyes in the orbits. This effect may be related to the well-known (but rarely investigated) phenomenon that the subjective auditory left/right axis is shifted toward straight ahead by about 10°–15° compared to the geometrical line intersecting both ears (e.g., Matsumoto, 1897; Pierce, 1901; Preibisch-Effenberger, 1966). Our data suggest that this overestimation effect is not only relevant for sound directions near 90° to the side, but it becomes rather significant already close to the median plane, with a deviation as large as 10° or more for a sound eccentricity of 22°.

This result is in qualitative agreement with that of Oldfield and Parker (1984, Fig. 6) who measured smaller deviations of about 6° within a corresponding azimuthal range, using a hand-pointing method. By verbally reporting the apparent spatial coordinates of the sound source, most of the subjects of Wightman and Kistler (1989, Figs. 2–9) also showed overestimations of sound eccentricity, but in contrast to the present study, only for sound azimuths of more than about 40° to the side. This discrepancy may be due to the method used by Wightman and Kistler (1989). Compared to our pointing method, verbal reports require a higher-level cognitive remapping and thus may be less accurate (cf. Oldfield and Parker, 1984). Similarly, the study of Gilkey and Anderson (1995), whose subjects indicated the perceived locations of the sound stimuli by pointing on a small globe, relies on higher cognitive spatial representations. This might explain why they failed to show consistent deviations in the range of azimuths tested here. In contrast to those studies, the method employed here enables the subject to subtly indicate the sound location by continuously adjusting the laser beam during stimulus presentation over a prolonged period and correcting its position under visual control. Thus it may represent a more direct and accurate method to investigate

the relatively slight systematic deviations focused by the present study.

The present results also appear to contradict other studies on sound localization that showed no systematic deviations or rather a tendency to *underestimate* sound eccentricity. While the subjects' head was fixed in present study, in those experiments the subjects either were allowed to freely move their head during stimulus presentation (Rakerd and Hartmann, 1985) or were explicitly instructed to turn the head and face the sound source during (Perrott *et al.*, 1987; Makous and Middlebrooks, 1990, closed-loop condition) or after stimulus presentation (Makous and Middlebrooks, 1990, open-loop condition). Consequently, in the first case, the subjects localized the sound while the median plane of their head was in an undefined, variable position with respect to the sound source; and in the second case, the (active or remembered) sound source was approximately within the median plane of the head when the subjects indicated the position of the stimulus by facing it. Thus those data may not allow conclusions about the localization of eccentric sound with respect to a head-centered coordinate system. The deviations observed by those studies may rather reflect effects of head-to-trunk position on localization (see Lewald and Ehrenstein, 1998). Furthermore, in comparing the results of previous studies with the present data, one should realize that the former reflect absolute sound localization, whereas the method of laser adjustment measured auditory *relative* to visual localization. The response therefore involves visual and oculomotor information in addition to auditory cues (see below).

The overestimation effect clearly depends on sound frequency when narrow-band signals are used. This fact suggests that the effect is based on *physical* factors (i.e., directional properties of the external ears and interaural transfer functions) rather than central-nervous processes. The frequency dependence of auditory-visual misalignment found here may partially be based on the effect, reported first by von Hornbostel (1926), that the perceived location of a stationary eccentric (pure-tone or narrow-band) sound source changes depending on its frequency (Sandel *et al.*, 1955; Boerger, 1965; for review, see Blauert, 1974). For example, Boerger (1965) found an overestimation of the eccentricity of high-frequency narrow-band sound with a maximum of about 15° at 4-kHz center frequency and a clear underestimation around 1 kHz, with broadband sound at 40° eccentricity taken as the reference (see also Blauert, 1974, Fig. 22). Assuming that the eccentricity of the broadband reference stimulus was also overestimated, those results may correspond to the deviations plotted in Fig. 5 which showed a maximal overestimation effect at 4 kHz and a minimum at 1 kHz.

In any case, the central-nervous system seems to be unable to compensate for the resulting auditory-visual divergence, neither for that found with sound of broader bandwidth nor for the frequency-specific changes with narrow-band signals. However, more detailed experiments are needed, using a larger variety of sound stimuli, to substantiate this view.

## B. Relevance of visual effects to the results

Since we used positioning of a light spot with visual feedback as a method for indicating sound direction, possible influences of the eccentricity of the visual stimulus (i.e., the laser spot) on its perceived direction have to be taken into account in addition to auditory effects. Previous studies on visual localization suggest an interaction of two distinct components: (1) an underestimation of eccentric eye position by up to about  $2^\circ$  which increases with the eccentricity of the gaze; and (2) an overestimation of retinal eccentricity of a visual stimulus with respect to the fovea, which is approximately constant (about  $2^\circ$ – $4^\circ$ ) with stimuli presented to the extrafoveal peripheral range of the retina (Morgan, 1978; Bock, 1986). Consequently, in experiment 2 (gaze direction always straight ahead) the overestimation of the auditory eccentricity should interact exclusively with the visual overestimation of the retinal eccentricity with respect to the fovea. Both the auditory and the visual effect are in the same direction, thus partially cancelling each other. In experiment 1 (gaze toward the laser spot), the overestimation of the auditory eccentricity should interact with the effect of the underestimation of eccentric eye position. The latter, extraretinal, effect results in an underestimation of the eccentricity of the visual target, fixated with the gaze, with respect to the median plane. Consequently, one should expect that the auditory-visual deviation measured is larger under these conditions, and the difference should be precisely equal to the sum of the extraretinal and the retinal effects on visual localization. The former prediction is, in fact, confirmed by the comparison shown in Fig. 7. However, the differences between the two curves are very slight (about  $1^\circ$ ), compared with the data of Morgan (1978) and Lewald (1998) that demonstrated significantly greater shifts of visual direction by about  $4^\circ$ – $6^\circ$  when the gaze eccentricity was  $22^\circ$ .

## C. Effect of eye position on sound localization

In addition to the overestimation of sound eccentricity and the visual effects described above, a further factor must be included here. Our previous studies (Lewald and Ehrenstein, 1996a; Lewald, 1998) have clearly shown that eccentric eye position influences not only visual localization but also the perceived auditory direction: near the median plane, sound localization can shift by about  $2^\circ$  opposite to the direction of eccentric gaze which is  $22^\circ$  to the side (Lewald, 1998). This type of effect has not yet been investigated with eccentric acoustic targets. If it were also present under these conditions, one should expect a partial compensation for the effect of overestimation of the auditory eccentricity; i.e., in the present experiments the deviation should be less with gaze toward the target compared to straight ahead fixation, if only these two auditory effects are taken into account. However, as discussed above, the influence of visual effects needs to be considered in addition. In experiment 1, the extraretinal eye-position effect may shift the perceived visual direction of the laser spot in a manner that counteracts the eye-position effect on perceived sound direction. On the basis of the data of Morgan (1978) and Lewald (1998), one can assume that the extraretinal component of the visual eye-position effect

and the eye-position effect on auditory localization are of approximately the same magnitude. Thus they may compensate for each other when the gaze is directed toward an auditory/visual target deviating from the median plane in azimuth (as performed in experiment 1), so that only the lateral-overestimation effect remains as the source of the observed auditory-visual deviation. When the eyes are straight ahead and the two kinds of eye-position effects are thus absent (experiment 2), only the retinal effect, that is partially compensating for the general lateral-overestimation effect in sound localization, should determine the overall result; hence, in experiment 2 a smaller deviation should occur than in experiment 1.

This hypothesis presents an alternative explanation for the differences between the two curves shown in Fig. 7. Two points make this hypothesis more likely than that mentioned in the previous section. First, the differences between the results of experiments 1 and 2 are approximately constant, as has been shown for the retinal effect (Morgan, 1978; Bock, 1986, 1993). Second, their magnitude (about  $1^\circ$ ) differs less from the magnitude suggested for the retinal effect (about  $2^\circ$ – $4^\circ$ , Morgan, 1978; Bock, 1986). The remaining slight discrepancy may reside on either different psychophysical methods used or on the fact that magnitudes of the extraretinal eye-position effect and the auditory eye-position effect differ slightly.

Since the present method uses visual localization, unequivocal conclusions regarding a pure eye-position effect on auditory localization can not be drawn from these experiments. Experiments 3 and 4 give, however, some hints supporting the involvement of the effect of eye position on sound localization in auditory-visual spatial integration. Experiment 3 demonstrated a highly significant effect of eccentric eye position on the auditory-visual spatial alignment for an acoustic target located straight ahead. As shown recently (Lewald, 1998), the deviation measured here may result from the shift of the perceived sound direction opposite to eccentric gaze and the sum of the extraretinal and the retinal effect, both of which shift the perceived visual location in the same direction as the shift of the sound, but by an angle that is about twice the auditory shift. Our present data are in agreement with the previous data, even though the deviations measured (about  $6^\circ$  for a gaze eccentricity of  $22^\circ$ ) were of a somewhat greater magnitude than expected, which may possibly be due to the specific method used.

In contrast to this clear effect with an acoustic target located straight ahead, experiment 4 shows that the eye-position effect disappears with increasing eccentricity of the sound (see Fig. 9). Thus the effect seems to be of a relevant magnitude only when (1) the gaze deviates substantially from the sound source and (2) the sound direction is within the frontal azimuthal range near the median plane. This result is in agreement with the hypothesis proposed above: that the extraretinal effect of eccentric eye position on the localization of a visual target compensates for the eye-position effect on the localization of a sound in the same azimuthal position, when the gaze is directed toward them. If one assumes that the retinal overestimation effect is constant for perifoveal visual stimuli, its influence on the overall

auditory-visual deviation effect should likewise be constant, as long as the stimulus is, with respect to the median plane, more eccentric than the gaze direction. Consequently, no significant variation of the deviation as a function of eye position should result, as was demonstrated by the two curves for  $\pm 22^\circ$  sound azimuth in experiment 4 (see Figs. 9 and 10). Only when the auditory target was kept straight ahead (experiment 3), the interaction of the retinal and extraretinal effects on visual localization together with the effect of eye eccentricity on sound localization produced a significant auditory-visual divergence, the magnitude of which varied as a function of gaze direction (see Fig. 8).

#### D. Functional aspects

In the present study, the subjects indicated the sound azimuth by positioning a light spot so that it was perceived as being congruent with the direction of the sound source. Consequently, the geometrical deviations of the auditory and the visual stimulus found here describe, on the one hand, a substantial mismatch between the space perceptions in the two sensory modalities with eccentric sound sources. On the other hand, these deviations do not result in noticeable mislocalizations with normal orientation. This apparent contradiction may be resolved if one considers the fact that localizing an acoustic target of significance usually means to direct the eyes, the head, and/or the body toward it in a coordinated manner, and then to identify it by further visual analysis. This implies that the motor programs involved in this process may either compensate for the sensory mismatch, or the apparent sensory mismatch may compensate for insufficiencies of the motor system. In both cases, their interaction seems to provide an appropriate accuracy of performance.

The eyes usually do not deviate so much from a straight ahead position that the effect of eccentric gaze on the auditory-visual alignment exceeds the general range of acuity of sound localization; thus, it may play no crucial role in most natural situations. The present data rather suggest that the lateral overestimation of sound eccentricity is the most prominent source of an auditory-visual divergence, since it seems to be only partly compensated by the retinal-eccentricity effect. Furthermore, it depends markedly on the frequency of the sound, if its bandwidth is narrow. In an open-loop condition, such an overestimation should result in overshooting movements of the eyes and/or the head directed toward the sound source. However, previous experiments on this topic have rather suggested an undershooting (Zahn *et al.*, 1978; Whittington *et al.*, 1981; Zambarbieri *et al.*, 1981, 1982; Jay and Sparks, 1989; Yao and Peck, 1997). Possibly this paradox reflects a complex interaction between the sensory and the motor system.

#### E. Relation to neurophysiological results

Our results show that auditory space is perceived, with respect to visual space, in a distorted manner and that this distortion is additionally modulated by gaze direction. These phenomena found psychophysically may be related to brain maps of auditory space that are in approximate spatial align-

ment to visual maps. Neurophysiological investigations on the accuracy of auditory-visual alignment in the SC maps of several nonprimate species demonstrated auditory receptive fields lying slightly more eccentrically compared to the positions of visual receptive fields (Knudsen, 1982; King and Palmer, 1983; Middlebrooks and Knudsen, 1984; King and Hutchings, 1987; Withington *et al.*, 1995). These results seem to be in contrast to our psychophysical data showing overestimations of auditory eccentricity with respect to visual position. At times, one cannot decide whether this obvious contradiction is due to interspecies differences or whether those divergences in the auditory and visual SC maps are not relevant to the overestimation effect reported here.

One source of auditory-visual misalignment found here is the effect of eye position. As already discussed elsewhere in detail (Lewald and Ehrenstein, 1996a; Lewald, 1997, 1998), this phenomenon can be related to neurophysiological results in the monkey SC that indicate a transformation of the auditory spatial coordinates from the originally cranio-centric frame of reference into an oculocentric one, such that both maps remain in register when the eyes move in their orbits (Jay and Sparks, 1984, 1987). Since this neural coordinate transformation is obviously incomplete (Jay and Sparks, 1987), a relative shift in auditory and visual coordinates should occur: when the eyes are in an eccentric position and both the auditory and the visual stimulus are straight ahead, the locus of neural excitation evoked by the sound will be shifted, within the SC maps, toward the direction of eccentric gaze (with respect to the visually evoked excitation). To bring them into alignment, the visual stimulus must, consequently, be positioned more toward the fixation direction, as was the result of experiment 3. In contrast to that, no neurophysiological data are available at present that could be related to the psychophysical finding of experiment 4: that the effect of eye position disappeared with increasing eccentricity of the sound azimuth.

#### ACKNOWLEDGMENTS

We are especially grateful to R. Guski for his generous support and to K.P. Dillmann for preparing the software and parts of the electronic equipment. We furthermore thank C. R. Cavonius, G. J. Dörrscheidt, and A. Ehrenstein for critical discussion of the results and valuable comments on the manuscript. This research was supported by the Deutsche Forschungsgemeinschaft (Gu 261/7-1).

- Andersen, R. A., Essick, G. K., and Siegel, R. M. (1985). "Encoding of spatial location by posterior parietal neurons," *Nature (London)* **230**, 456-458.
- Andersen, R. A., Bracewell, R. M., Barash, S., Gnadt, J. W., and Fogassi, L. (1990). "Eye position effects on visual, memory, and saccade-related activity in areas LIP and 7a of macaque," *J. Neurosci.* **10**, 1176-1196.
- Blauert, J. (1974). *Räumliches Hören* (Hirzel, Stuttgart).
- Bock, O. (1986). "Contribution of retinal versus extraretinal signals toward visual localization in goal-directed movements," *Exp. Brain Res.* **64**, 476-482.
- Bock, O. (1993). "Localization of objects in the peripheral visual field," *Behav. Brain Res.* **56**, 77-84.
- Boerger, G. (1965). "Die Lokalisation von Gaußtönen," dissertation, Technische Universität, Berlin.

- Bohlander, R. W. (1984). "Eye position and visual attention influence perceived auditory direction," *Percept. Motor Skills* **59**, 483–510.
- Brainard, M. S. (1994). "Neural substrates of sound localization," *Curr. Opin. Neurobiol.* **4**, 557–562.
- Coren, S. (1993). "The lateral preference inventory for measurement of handedness, footedness, eyedness, and earedness: Norms for young adults," *Bull. Psychonom. Soc.* **31**, 1–3.
- Cullen, Jr., J. K., Collins, M. J., Dobie, T. G., Rappold, P. W. (1992). "The effects of perceived motion on sound-source lateralization," *Aviat., Space Environ. Med.* **63**, 498–504.
- Ehrenstein, W. H., and Arnold-Schulz-Gahmen, B. E. (1993). "Fragebogen zur Bevorzugung von Auge, Ohr, Hand und Fuß: German adaptation of Coren's (1993) inventory," Institute's Report of the Institut für Arbeitsphysiologie an der Universität Dortmund.
- Ehrenstein, W. H., and Reinhardt-Rutland, A. H. (1996a). "A cross-modal aftereffect: Auditory displacement following adaptation to visual motion," *Percept. Motor Skills* **82**, 23–26.
- Ehrenstein, W. H., and Reinhardt-Rutland, A. H. (1996b). "Adaptation to auditory motion in the free-field: Aftereffects depend on carrier frequency," *Pflügers Arch.* **432**, R136.
- Fogassi, L., Gallese, V., di Pellegrino, G., Fadiga, L., Gentilucci, M., Lupino, G., Matelli, M., Pedotti, A., and Rizzolatti, G. (1992). "Space coding by premotor cortex," *Exp. Brain Res.* **89**, 686–690.
- Galletti, C., Battaglini, P. P., and Fattori, P. (1993). "Parietal neurons encoding spatial locations in craniotopic coordinates," *Exp. Brain Res.* **96**, 221–229.
- Gentilucci, M., Scandolara, C., Pigarev, I. N., and Rizzolatti, G. (1983). "Visual responses in the postarcuate cortex (area 6) of the monkey that are independent of eye position," *Exp. Brain Res.* **50**, 464–468.
- Gilkey, R. H., and Anderson, T. R. (1995). "The accuracy of absolute localization judgments for speech stimuli," *J. Vestib. Res.* **5**, 487–497.
- Goldstein, K., and Rosenthal-Veit, O. (1926). "Über akustische Lokalisation und deren Beeinflussbarkeit durch andere Sinnesreize," *Psychol. Forsch.* **8**, 318–335.
- Grantham, D. W. (1984). "Interaural intensity discrimination: Insensitivity at 1000 Hz," *J. Acoust. Soc. Am.* **75**, 1191–1194.
- Guski, R. (1990). "Auditory localization: Effects of reflecting surfaces," *Perception* **19**, 819–830.
- Hartline, P. H., Pandey Vimal, R. L., King, A. J., Kurylo, D. D., and Northmore, D. P. M. (1995). "Effects of eye position on auditory localization and neural representation of space in superior colliculus of cats," *Exp. Brain Res.* **104**, 402–408.
- Heffner, R. S., and Heffner, H. E. (1992). "Visual factors in sound localization in mammals," *J. Comp. Neurol.* **317**, 219–232.
- Hornbostel, E. M. von (1926). "Das räumliche Hören," in *Handbuch der normalen und pathologischen Physiologie*, edited by A. Bethe (Springer-Verlag, Berlin), Vol. 11, pp. 601–618.
- Jackson, C. V. (1953). "Visual factors in auditory localization," *Q. J. Exp. Psych.* **5**, 52–65.
- Jay, M. F., and Sparks, D. L. (1984). "Auditory receptive fields in primate superior colliculus shift with changes in eye position," *Nature (London)* **309**, 345–347.
- Jay, M. F., and Sparks, D. L. (1987). "Sensorimotor integration in the primate superior colliculus. II. Coordinates of auditory signals," *J. Neurophysiol.* **57**, 35–55.
- Jay, M. F., and Sparks, D. L. (1989). "Localization of auditory and visual targets for the initiation of saccadic eye movements," in *Comparative Perception*, edited by M. A. Berkley and W. C. Stebbins (Wiley, New York), Vol. 1, pp. 351–374.
- King, A. J., and Hutchings, M. E. (1987). "Spatial response properties of acoustically responsive neurons in the superior colliculus of the ferret: a map of auditory space," *J. Neurophysiol.* **57**, 596–624.
- King, A. J., and Palmer, A. R. (1983). "Cells responsive to free-field auditory stimuli in guinea-pig superior colliculus: Distribution and response properties," *J. Physiol. (London)* **342**, 361–383.
- Klemm, O. (1910). "Lokalisation von Sinneseindrücken bei disparaten Nebenreizen," *Psychologische Studien* **5**, 73–162.
- Klump, R. G., and Eady, H. R. (1956). "Some measurements of interaural time difference thresholds," *J. Acoust. Soc. Am.* **28**, 859–864.
- Knudsen, E. I. (1982). "Auditory and visual maps of space in the optic tectum of the owl," *J. Neurosci.* **2**, 1177–1194.
- Konishi, M. (1986). "Centrally synthesized maps of sensory space," *Trends Neurosci.* **9**, 163–168.
- Lewald, J. (1997). "Eye-position effects in directional hearing," *Behav. Brain Res.* **87**, 35–48.
- Lewald, J. (1998). "The effect of gaze eccentricity on perceived sound direction and its relation to visual localization," *Hearing Res.* **115**, 206–216.
- Lewald, J., and Ehrenstein, W. H. (1996a). "The effect of eye position on auditory lateralization," *Exp. Brain Res.* **108**, 473–485; **110**, 322 (Erratum).
- Lewald, J., and Ehrenstein, W. H. (1996b). "Auditory-visual shift in localization depending on gaze direction," *NeuroReport* **7**, 1929–1932.
- Lewald, J., and Ehrenstein, W. H. (1998). "Influence of head-to-trunk position on sound lateralization," *Exp. Brain Res.* (in press).
- Lueck, C. J., Crawford, T. J., Savage, C. J., and Kennard, C. (1990). "Auditory-visual interaction in the generation of saccades in man," *Exp. Brain Res.* **82**, 149–157.
- Makous, J. C., and Middlebrooks, J. C. (1990). "Two-dimensional sound localization by human listeners," *J. Acoust. Soc. Am.* **87**, 2188–2200.
- Matsumoto, M. (1997). "Researches on acoustic space," *Yale Psychol. Lab. Studies* **5**, 1–75.
- Mazzoni, P., Bracewell, M., Barash, S., and Andersen, R. A. (1996). "Spatially tuned auditory responses in area LIP of Macaques performing delayed memory saccades to acoustic targets," *J. Neurophysiol.* **75**, 1233–1241.
- McFadden, D., and Pasanen, E. G. (1976). "Lateralization at high frequencies based on interaural time differences," *J. Acoust. Soc. Am.* **59**, 634–639.
- Middlebrooks, J. C., and Knudsen, E. I. (1984). "A neural code for auditory space in the cat's superior colliculus," *J. Neurosci.* **4**, 2621–2634.
- Morgan, C. L. (1978). "Constancy of egocentric visual direction," *Percept. Psychophys.* **23**, 61–68.
- Oldfield, S. R., and Parker, S. P. A. (1984). "Acuity of sound localisation: A topography of auditory space. I. Normal hearing conditions," *Perception* **13**, 581–600.
- Peck, C. K., Baro, J. A., and Warder, S. M. (1995). "Effects of eye position on saccadic eye movements and on the neuronal responses to auditory and visual stimuli in cat superior colliculus," *Exp. Brain Res.* **103**, 227–242.
- Perrott, D. R. (1993). "Auditory and visual localization: Two modalities, one world," in *Proc. AES 12th International Conference* (Snekkersten, Copenhagen), pp. 221–231.
- Perrott, D. R., Ambarsoom, H., and Tucker, J. (1987). "Changes in head position as a measure of auditory localization performance: Auditory psychomotor coordination under monaural and binaural listening conditions," *J. Acoust. Soc. Am.* **82**, 1637–1645.
- Perrott, D. R., Sadralodabai, T., Saberi, K., and Strybel, T. Z. (1991). "Aurally aided visual search in the central visual field: Effects of visual load and visual enhancement of the target," *Hum. Factors* **33**, 389–400.
- Pierce, A. H. (1901). *Studies in Auditory and Visual Space Perception* (Longmans, New York), Chap. 6, pp. 130–144.
- Pöppel, E. (1973). "Comment on 'Visual system's view of acoustic space'," *Nature (London)* **243**, 231.
- Preibisch-Effenberger, R. (1966). *Die Schalllokalisationsfähigkeit des Menschen und ihre audiomeirische Verwendbarkeit zur klinischen Diagnostik* (Habilitationsschrift, Medizinische Akademie, Dresden).
- Rakerd, B., and Hartmann, W. M. (1985). "Localization of sound in rooms, II: The effects of a single reflecting surface," *J. Acoust. Soc. Am.* **78**, 524–533.
- Ryan, T. A., and Schehr, F. (1941). "The influence of eye movement and position on auditory localization," *Am. J. Psychol.* **54**, 243–252.
- Sandel, T. T., Teas, D. C., Feddersen, W. E., and Jeffress, L. A. (1955). "Localization of sound from single and paired sources," *J. Acoust. Soc. Am.* **27**, 842–852.
- Sparks, D. L., and Nelson, J. S. (1987). "Sensory and motor maps in the mammalian superior colliculus," *Trends Neurosci.* **10**, 312–317.
- Stein, B. E., London, N., Wilkinson, L. K., and Price, D. D. (1996). "Enhancement of perceived visual intensity by auditory stimuli: A psychophysical analysis," *J. Cogn. Neurosci.* **8**, 497–506.
- Stricanne, B., Andersen, R. A., and Mazzoni, P. (1996). "Eye-centered, head-centered, and intermediate coding of remembered sound locations in area LIP," *J. Neurophysiol.* **76**, 2071–2077.
- Thomas, G. J. (1941). "Experimental study of the influence of vision on sound localization," *J. Exp. Psychol.* **28**, 163–177.
- Walls, G. L. (1951). "A theory of ocular dominance," *A.M.A. Arch. Ophthalmol.* **45**, 387–412.
- Weerts, T. C., and Thurlow, W. R. (1971). "The effects of eye position and

- expectation on sound localization," *Percept. Psychophys.* **9**, 35–39.
- Welch, R. B., and Warren, D. H. (1980). "Immediate perceptual response to intersensory discrepancy," *Psychol. Bull.* **88**, 638–667.
- Weyand, T. G., and Malpeli, J. G. (1993). "Responses of neurons in primary visual cortex are modulated by eye position," *J. Neurophysiol.* **69**, 2258–2260.
- Whittington, D. A., Hepp-Reymond, M.-C., and Flood, W. (1981). "Eye and head movements to auditory targets," *Exp. Brain Res.* **41**, 358–363.
- Wightman, F. L., and Kistler, D. J. (1989). "Headphone simulation of free-field listening. II: Psychophysical validation," *J. Acoust. Soc. Am.* **85**, 868–878.
- Withington, D. J., Mark, R. F., Thornton, S. K., Liu, G. B., and Hill, K. G. (1995). "Neural responses to free-field auditory stimulation in the superior colliculus of the wallaby (*Macropus eugenii*)," *Exp. Brain Res.* **105**, 233–240.
- Witkin, H. A., Wapner, S., and Leventhal, T. (1952). "Sound localization with conflicting visual and auditory cues," *J. Exp. Psychol.* **43**, 58–67.
- Yao, L., and Peck, C. K. (1997). "Saccadic eye movements to visual and auditory targets," *Exp. Brain Res.* **115**, 25–34.
- Yost, W. A., and Dye, Jr., R. H. (1988). "Discrimination of interaural differences of level as a function of frequency," *J. Acoust. Soc. Am.* **83**, 1846–1851.
- Zahn, J. R., Abel, L. A., and Dell'Osso, L. F. (1978). "Audio-ocular response characteristics," *Sens. Processes* **2**, 32–37.
- Zambarbieri, D., Schmid, R., Prablanc, C., and Magenes, G. (1981). "Characteristics of eye movements evoked by the presentation of acoustic targets," in *Progress in Oculomotor Research*, edited by A. F. Fuchs and W. Becker (Elsevier, New York), pp. 559–566.
- Zambarbieri, D., Schmid, R., Magenes, G., and Prablanc, C. (1982). "Saccadic responses evoked by presentation of visual and auditory targets," *Exp. Brain Res.* **47**, 417–427.
- Zwislocki, J., and Feldman, R. S. (1956). "Just noticeable differences in dichotic phase," *J. Acoust. Soc. Am.* **28**, 860–864.

# Validity of rating scale measures of voice quality

Jody Kreiman<sup>a)</sup> and Bruce R. Gerratt

Division of Head and Neck Surgery, UCLA School of Medicine, 31-24 Rehab Center, Los Angeles, California 90095-1794

(Received 2 June 1997; revised 10 March 1998; accepted 5 May 1998)

The validity of perceptual measures of vocal quality has been neglected in studies of voice, which focus more commonly on rater reliability. Validity depends in part on reliability, because an unreliable test does not measure what it is intended to measure. However, traditional measures of rating reliability only partially represent interrater agreement, because they cannot reflect variations or patterns of agreement for specific voice samples. In this paper the likelihood that two raters would agree in their ratings of a single voice is examined, for each voice in five previously gathered data sets. Results do not support the continued assumption that traditional rating procedures produce useful indices of listeners' perceptions. Listeners agreed very poorly in the midrange of scales for breathiness and roughness, and mean ratings in the midrange of such scales did not represent the extent to which a voice possesses a quality, but served only to indicate that listeners disagreed. Techniques like analysis by synthesis or judgment of similarity avoid decomposing quality into constituent dimensions, and do not require a listener to compare an external stimulus to an unstable internal representation, thus decreasing the error in measures of quality. Modeling individual differences in perception can increase the variance accounted for in models of quality, further reducing the error in perceptual measures. Thus such techniques may provide valid alternatives to current approaches. © 1998 Acoustical Society of America. [S0001-4966(98)04708-0]

PACS numbers: 43.71.Bp, 43.71.Gv [WS]

## INTRODUCTION

Measurement validity—the extent to which a scale or instrument measures what it is intended to measure—is a central concern in the development and evaluation of any measurement system. Measures that are weakly or variably related to a concept are not useful indices of that concept (e.g., Kerlinger, 1973; Carmines and Zeller, 1979; Crocker and Algina, 1986). This paper examines the validity of traditional rating protocols that use scales like breathiness, roughness, hoarseness, or harshness as measures of vocal quality. Although a few authors have expressed doubt about the validity of such scales (Jensen, 1965; Perkins, 1971), issues of the validity of perceptual measures are typically neglected in studies of voice, which focus more commonly on rater reliability (see Kreiman *et al.*, 1993; Kreiman and Gerratt, 1998a, for review).

The validity of traditional protocols for rating vocal quality is important in part because perceptual methods are often used clinically to evaluate vocal disorders (Gerratt *et al.*, 1991). Perceptual ratings are also used to validate acoustic and other instrumental or “objective” measures of voice (e.g., Fritzell *et al.*, 1986; Hillenbrand *et al.*, 1994; de Krom, 1995; Martin *et al.*, 1995; Sodersten *et al.*, 1995). Voice quality is an interaction between an acoustic voice stimulus and a listener; the acoustic signal itself does not possess vocal quality, it evokes it in the listener. For this reason, acoustic measures are meaningful primarily to the extent that they correspond to what listeners hear (Gerratt and Kreiman, 1995; Kreiman and Gerratt, 1996).

Finally, validity is important because measurement pro-

ocols imply a model of the construct being measured. Therefore studies of the validity of rating scales for voice also serve to test the adequacy of the implied model of vocal quality. Because vocal quality is a perceptual response to an acoustic signal, rating protocols for vocal quality comprise a set of claims about both signals and listeners. When vocal quality is measured by means of ratings on scales for particular aspects of quality, this implies that the overall impression a listener receives from a voice can be decomposed into several perceptually distinct aspects corresponding to various terms such as breathiness and roughness. It is assumed that individual listeners can focus their attention on these different aspects of the stimuli, and can make the judgments required. Finally, and crucially, it is assumed that characteristics of the measurement tool remain constant across listeners and voices, so that different listeners use the scales in the same way and measurements of different voices can be meaningfully compared. This implies that quality is fairly constant across listeners, so that voice quality may be treated as an attribute of the voice signal itself, rather than as the product of a listener's perception. That is, traditional protocols for assessing voice quality necessarily treat individual differences in perception as noise, and do not model them explicitly. Because voice signals provide listeners with large amounts of information (for example, about the identity and physical, mental, and emotional state of the speaker; see Kreiman, 1997, for review), such claims about the perceptual process have interest beyond their clinical applications, and the validity or invalidity of voice assessment protocols has important implications for models of auditory pattern recognition and perception of complex signals in general.

<sup>a)</sup>Electronic mail: jkreiman@ucla.edu

## A. Approaches to the study of scale validity

Quality is traditionally defined as “that attribute of auditory sensation in terms of which a listener can judge that two sounds similarly presented and having the same loudness and pitch are dissimilar” (ANSI Standard S1.1.12.9, p. 45, 1960; cf. Helmholtz, 1885). However, most authors avoid studying overall vocal quality, preferring instead to focus on single dimensions or specific aspects (for example, breathiness, harshness, or strain). One way to motivate scales for specific aspects of quality is with reference to overall quality: Individual scales or sets of scales may be valid to the extent that as a group they measure overall quality. For example, studies using multidimensional scaling (Murry *et al.*, 1977; Kreiman *et al.*, 1990, 1992, 1994; Kempster *et al.*, 1991; Kreiman and Gerratt, 1996) attempt to identify the perceptual dimensions that underlie listeners’ judgments of the overall similarity of pairs of voices. Unfortunately, traditional scales have not generally emerged as perceptual dimensions from these studies, which in consequence provide little support for the validity of such scales as measures of overall vocal quality.

However, for clinical purposes, it may not be necessary to model overall quality in detail. Instead, it may be adequate to focus quality assessment on a limited number of clinically significant perceptual dimensions, while neglecting other irrelevant aspects of vocal quality. In this case, motivating and defining individual scales remain critical aspects of scale development, to specify what is being measured, to justify why those aspects of voice (and not others) are of interest, and to clarify the relationship among different scales. Few studies have investigated these issues. Individual scales are typically validated by appeals to consensual or face validity (Silverman, 1977; Allen and Yen, 1979), or by reference to their association with purported acoustic, aerodynamic, and/or physiological correlates. However, because appeals to face or consensual validity do not involve empirical examination of evidence or reference to theory, they are of little use in the assessment of measurement systems. Thus the literature on pathologic voice quality does not provide convincing or consistent evidence for the validity of traditional scales for vocal quality. (See, e.g., Colton and Estill, 1981; Kreiman and Gerratt, 1998a, for extensive review of these issues.)

## B. Reliability as a tool for assessing validity

Although the validity of traditional scales for voice quality has never been formally established, little evidence exists that such scales are invalid, largely due to lack of research. However, because the validity of perceptual measures depends on characteristics of both listeners and stimuli, validity is partially determined by reliability. That is, because quality is a function of both listeners and stimuli, an unreliable test cannot be a valid measure of quality, because it does not model listener behavior accurately (e.g., Young and Downs, 1968; Cone, 1977; Ventry and Schiavetti, 1980; Suen and Ary, 1989). Thus evidence about patterns of agreement and disagreement among listeners in their use of quality scales can provide evidence for or against the validity of the scales. If listeners cannot agree when making the required judg-

ments, the critical assumption of listener equivalence is violated, and the validity of traditional protocols for quality assessment is not supported.

In this study we combined traditional approaches to reliability with new analyses designed to examine patterns of agreement and disagreement among listeners that bear upon issues of measurement validity. Conventional statistical analyses of reliability do not provide enough information to answer questions about scale validity. Such analyses produce a single number representing the overall reliability of a set of ratings, across all the voices and listeners in a study. This conventional approach derives from the literature on psychological test construction (Allen and Yen, 1979; Crocker and Algina, 1986), with listeners substituted for test items and voices substituted for examinees or subjects. Errors are assumed to be random in this model, so averaging together scores from a large number of raters will give the best estimate of the “true” score for a voice on a scale, and the mean rating approaches the true score as the number of raters increases. Thus reliability in classic theory is a function of both the average interrater correlation and the number of raters in a study.

In this traditional framework, reliability implies that another sample of listeners would produce the same mean ratings for the same test voices, but does not necessarily inform us of how the subjects would agree in their ratings of a new set of voices. Conventional reliability statistics are not informative about many other important aspects of listener performance. For example, they cannot indicate agreement for specific voice samples (Young and Downs, 1968), and they cannot capture information about systematic variations in reliability or agreement across raters or parts of the rating scale. Patterns of agreement and disagreement among listeners may provide evidence about the perceptual processes that underlie judgments of vocal quality. Such evidence may be helpful in establishing the validity of different scales for vocal quality, and may help determine why measurement protocols may fail. Finally, because the validity of measurement systems ultimately depends on the success of the underlying perceptual model, such detailed knowledge about listener agreement may guide the design of future protocols for quality assessment.

## I. METHOD

To determine if patterns of rater agreement support rating scale validity, we reevaluated existing data from experiments using unidimensional scales for different traditional vocal qualities or ratings of the similarity of pairs of voices. Data were drawn from four previously published studies (Kreiman *et al.*, 1993; Kreiman *et al.*, 1994; Rabinov *et al.*, 1995; Kreiman and Gerratt, 1996) and one unpublished study (Chhetri, 1997). Two of these studies (Kreiman *et al.*, 1993; Rabinov *et al.*, 1995) were specifically concerned with issues of rating reliability. Listeners in these studies judged the roughness of samples of pathologic voices, and recorded their responses on equal-appearing interval (EAI) or visual analog (VA) scales.

Three other studies (Kreiman *et al.*, 1994; Kreiman and Gerratt, 1996; Chhetri, 1997) used EAI scales to address



TABLE I. Characteristics of the data sets.<sup>a</sup>

Study	Raters	Speakers	Scale(s)	Rating task
Kreiman <i>et al.</i> (1993)	30 expert <sup>b</sup>	30 (22 disordered, 8 normal)	seven-point EAI 100 mm VA	Judgments of roughness Judgments of roughness
Kreiman <i>et al.</i> (1994)	5 expert	18 disordered	seven-point EAI	Paired comparison: Dissimilarity of pairs of voices with respect to breathiness
			seven-point EAI	Paired comparison: Dissimilarity of pairs of voices with respect to roughness
Rabinov <i>et al.</i> (1995)	8 expert	18 disordered 18 disordered	seven-point EAI	Judgments of breathiness
			seven-point EAI	Judgments of roughness
Kreiman and Gerratt (1996)	8 expert	80 disordered (males)	seven-point EAI	Paired comparison: Overall dissimilarity of pairs of voices
Chhetri (1997)	9 expert	32 disordered (pre/post operative)	seven-point EAI	Paired comparison: Overall dissimilarity of pairs of voices
			seven-point EAI	Judgments of severity of pathology

<sup>a</sup>EAI=equal-appearing interval scale; VA=visual analog scale.

<sup>b</sup>Data from experiments 1 and 2 have been combined.

more general issues of the perception of pathologic voice quality. Two groups of raters participated in the studies reported in Kreiman *et al.* (1994). The first group judged the similarity of pairs of voices with respect to breathiness or roughness. The second directly rated the breathiness or roughness of the individual voices. Raters in Kreiman and Gerratt (1996) judged the overall similarity of pairs of voices. Raters in Chhetri (1997) rated the severity of vocal pathology for samples of voices gathered pre- and post-operatively. Further details are given in Table I.

For our current purposes, we calculated several traditional measures of overall intra- and interrater reliability and agreement for each data set. We also examined an additional measure, the empirical likelihood that two raters would agree in their ratings of a specific voice, for each voice in the data sets. These finer-grained analyses assessed how likely it was that individual raters would agree with one another for specific voice stimuli, rather than how well the population of raters agreed on average or how well the averaged data estimated the “true mean rating.” This approach also allowed us to capture detailed information about variations in agreement across voices and parts of the rating scale. Similar analyses of intrarater agreement were undertaken, comparing the first and second rating of a voice by a single listener, to determine whether individuals were more self-consistent for some voices than for others.

To simplify comparisons among studies using VA and EAI scales, differences between pairs of ratings on the VA scale were converted from mm to “scale value equivalents.” For example, a 100-mm VA scale was divided into seven intervals of 14.3 mm each, analogous to a seven point EAI scale. Pairs of ratings within 7.2 mm of each other were

considered to agree exactly; ratings that differed by 21.5 mm (7.2+14.3) were considered to be within 1 scale value of each other, and so on. For the 75-mm VA scale, a scale interval was defined as 10.7 mm. Thus ratings differing by 5.4 mm or less were considered to agree exactly, and ratings differing by 16.1 mm or less were considered within 1 scale value of each other. Differences in mm and in scale value equivalents were highly correlated (data from Kreiman *et al.*, 1993:  $r=0.98$ ; data from Rabinov *et al.*, 1995:  $r=0.98$ ).

## II. RESULTS

### A. Intrarater agreement: How self-consistent were listeners?

Traditional analyses of intrarater agreement examine overall levels of listener self-consistency, summed across voices. In contrast, Table II shows the likelihood that a given voice would be rerated consistently, calculated across listeners. Numbers in this table represent the likelihood that a single rerating of a single voice would agree with the first rating by some amount (for example, exactly or within one scale value).

Listeners produced the same value when rerating a stimulus for 32%–50% of trials, depending on the study. Pooled across studies, a second rating agreed exactly with the first for 38.6% of repeated trials, and 76.8% of repeated ratings agreed with the first within 1 scale value. In comparison, across studies traditional test–retest agreement (calculated across voices for each listener, and then averaged across listeners) ranged from 72.5%–92.0% of ratings within  $\pm 1$  scale value.

TABLE II. Likelihood that a single rerating of a single voice would differ from the first rating by a given amount.<sup>a</sup>

Study/Scale	N <sup>b</sup>	Ratings differ			
		Exact agreement	by 1 scale value	by 2 scale values	by 3 or more scale values
Kreiman <i>et al.</i> (1993) (EAI/Roughness)	900	44.9%	38.6%	12.0%	4.6%
Kreiman <i>et al.</i> (1993) (VA/Roughness)	900	48.8%	33.6%	11.8%	5.9%
Kreiman <i>et al.</i> (1994) (EAI/Roughness)	144	38.9%	43.8%	11.1%	6.3%
Kreiman <i>et al.</i> (1994) (EAI/Breathiness)	144	47.2%	38.2%	11.1%	3.5%
Kreiman <i>et al.</i> (1994) (Dissimilarity/Roughness)	765	36.5%	36.9%	15.3%	11.4%
Kreiman <i>et al.</i> (1994) (Dissimilarity/Breathiness)	765	32.0%	40.5%	16.3%	11.1%
Rabinov <i>et al.</i> (1995) (VA/Roughness)	500	44.2%	35.4%	13.8%	6.6%
Kreiman and Gerratt (1996) (Dissimilarity/Male voices)	5056	36.6%	38.1%	16.4%	9.0%
Kreiman and Gerratt (1996) (Dissimilarity/Female voices)	5056	38.4%	38.9%	15.7%	7.0%
Chhetri (1997) (EAI/Severity)	66	50.0%	42.4%	6.1%	1.5%
Pooled data	14 296	38.6%	38.2%	15.3%	7.8%

<sup>a</sup>EAI=equal-appearing interval scale; VA=visual analog scale.

<sup>b</sup>N=(number of listeners)×(number of repeated trials/listener). Differences between VA ratings were converted to scale equivalents, as described in the text.

Figure 1 shows how test–retest agreement varied across listeners and voices for EAI ratings of roughness [Fig. 1(a); Kreiman *et al.*, 1993], VA ratings of roughness [Fig. 1(b); Rabinov *et al.*, 1995], and ratings of overall similarity of pairs of voices [Fig 1(c); Kreiman and Gerratt, 1996]. In this figure, each point represents a single stimulus presented to a single rater; the difference between the first and second rating that voice received from that rater is plotted against the mean of that individual’s two ratings for that voice. Because agreement is plotted against the mean rating for a given voice, the probability of agreement must be high when mean ratings are near scale end points. However, agreement in the midrange of a scale may be high (if a listener consistently rates voices as moderately pathologic) or low (if a listener responds with a large scale value on one occasion and a small value on another occasion).

As Fig. 1 shows, for all three tasks individual listeners were often self-consistent in their use of these rating scales. In particular, individual listeners appeared to maintain stable standards for the midrange of a scale, so that many voices received ratings of 3, 4, or 5 both times they were rated.

Figure 2 summarizes the data from Fig. 1(a) and (b) (Kreiman *et al.*, 1993) by showing the overall probability of test-retest agreement for individual voices. Levels of self-consistency for individual stimuli were quite high overall, with most values above 0.8. This suggests that individual listeners are able to make reasonably consistent judgments of traditional vocal qualities.

## B. Pairwise agreement among raters

### 1. Overall likelihood of interrater agreement

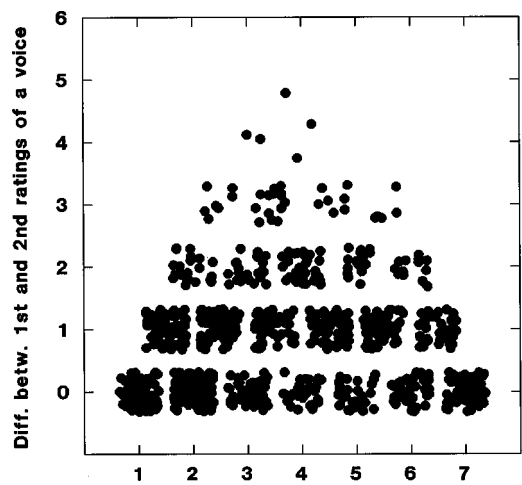
Measures of interrater agreement, like measures of intrarater agreement, usually sum across voices to provide a single measure of rater concordance. In contrast, the present analyses sum across listeners to provide a measure of the likelihood that two raters will agree in their ratings of indi-

vidual stimuli. Table III lists the overall likelihood of raters agreeing exactly, within one scale value, and so on, in their ratings of a single voice or pair of voices. Across studies, pairs of listeners agreed exactly for 26.7% of trials (versus 38.6% test–retest agreement). Ratings differed by 1 scale value or less for 63.7% of trials (versus 76.8% test–retest agreement). Gross disagreements (ratings differing by 3 or more scale values on a seven-point scale) occurred for a total of 15.6% of trials (cf. Mackey *et al.*, 1997, who reported similar values for ratings of speech naturalness).

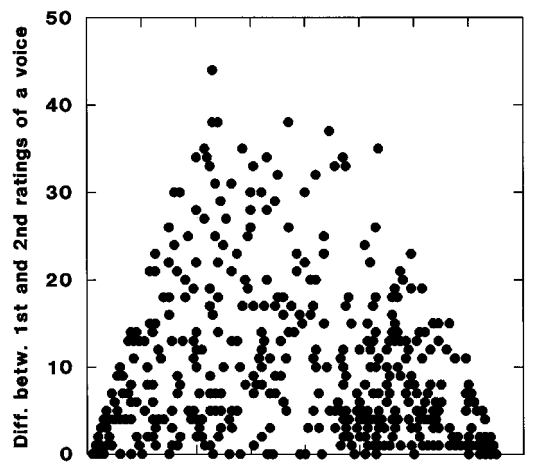
### 2. Patterns of interrater agreement for traditional rating scales

Patterns of interrater agreement depended on the listening task. For ratings of breathiness, roughness, and severity, interrater agreement levels were consistently poor in the midrange of the rating scales. Figure 3 shows the likelihood of two raters agreeing exactly [Fig. 3(a) and (c)] or within 1 scale value [Fig. 3(b) and (d)] for each voice in two representative data sets. Because we were interested in the extent to which mean ratings represent the underlying raw data, the probability of agreement is plotted against the group mean rating for each voice. As above, agreement near scale end points must be high in these plots, because average values can only approach scale end points when listeners agree. However, average values away from scale end points can result from agreement that voices are moderately pathologic, or from disagreement about the extent of pathology.

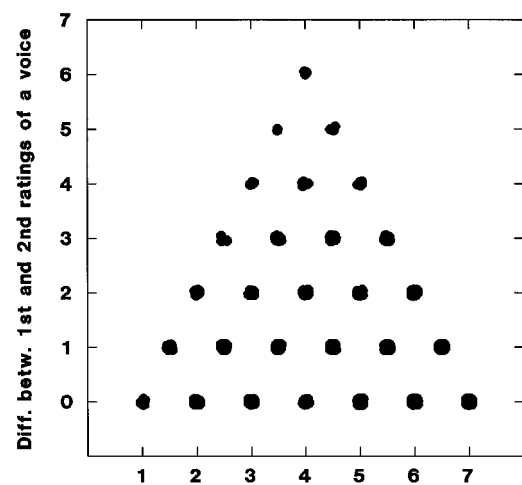
In the present data, the likelihood that two raters would agree exactly for voices with mean ratings between 2.5 and 5.5 on a seven-point EAI scale averaged 0.21 (range = 0.19–0.24; chance agreement for independent ratings on a seven-point scale=0.14), despite the fact that individual listeners were self-consistent in the same scale range. The likelihood of agreement within 1 scale value averaged 0.57 (range=0.50–0.61; chance=0.39). Although these values



(a) Individual's mean rating for that voice

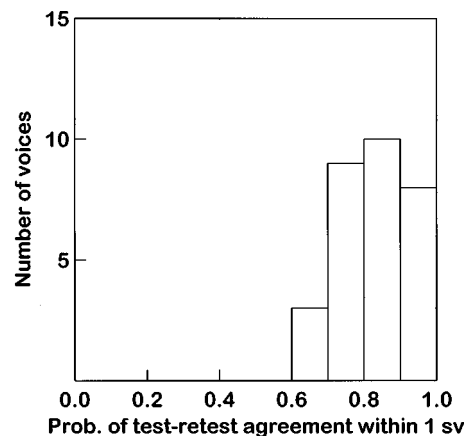


(b) Individual's mean rating for that voice

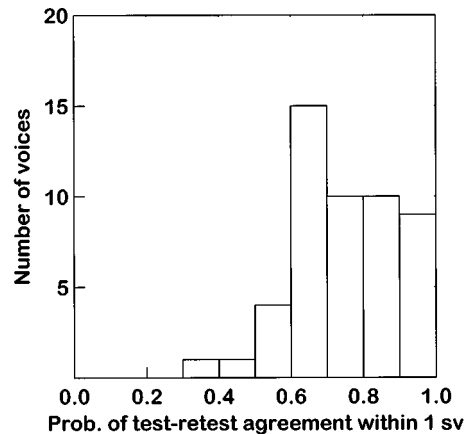


(c) Individual's mean rating for that voice

FIG. 1. Test-retest agreement for individual stimuli. A value of 0 on the y axis indicates that a rater gave that voice the same score both times it was rated (i.e., the difference between the first and second ratings was 0); a value of 1 indicates that the first and second ratings differed by 1; and so on. Values on the x axis represent the mean of a single individual's two ratings of that stimulus. Points have been jittered slightly to show overlapping values. (a) Test-retest agreement for EAI ratings of roughness (Kreiman *et al.*, 1993). (b) Test-retest agreement for visual analog ratings of roughness (Rabinov *et al.*, 1995). (c) Test-retest agreement for similarity ratings (Kreiman and Gerratt, 1996).



(a)



(b)

FIG. 2. The probability of observing test-retest agreement within one scale value (or scale value equivalent) for individual voices. Each column shows the number of voices for which overall test-retest agreement occurred with the given likelihood. (a) EAI ratings of roughness (Kreiman *et al.*, 1993). (b) Visual analog ratings of roughness (Rabinov *et al.*, 1995).

significantly exceed chance levels of agreement (one-sample  $t$  tests;  $p < 0.05$ ), they are very low. Further, across all the data examined here, we did not find a single voice that listeners consistently agreed was moderately deviant in quality. Thus the present data suggest that mean ratings in the midrange of the scale do not arise from a consensus among raters that the voice is moderately deviant, but indicate instead that raters disagreed about the extent of deviation on that scale.

Because a significant statistical result does not necessarily indicate the size of the effect (especially when  $n$  is large, as it is here), we also calculated the amount of variance in quality ratings that is attributable to differences among voices. Variance accounted for was estimated by one-way analyses of variance for the different sets of ratings (e.g., Young, 1993). The independent variable in these analyses was the voice being rated, and the dependent variable was the rating received; the error term reflects all other sources of variability in quality ratings, including (but not limited to) interrater variability and random error. Because agreement near scale end points is in part artifactual, analyses included only voices with mean ratings between 2.5 and 5.5 (inclusive).

Results are given in Table IV. Differences among voices

TABLE III. Pairwise agreement among raters.<sup>a</sup>

Study/Scale	N <sup>b</sup>	Exact agreement	Ratings differ by 1 scale value	Ratings differ by 2 scale values	Ratings differ by 3 or more scale values
Kreiman <i>et al.</i> (1993) (EAI/Roughness)	26 100	31.7%	40.2%	17.7%	10.4%
Kreiman <i>et al.</i> (1994) (EAI/Roughness)	1008	20.7%	35.5%	22.2%	21.5%
Kreiman <i>et al.</i> (1994) (EAI/Breathiness)	1008	25.4%	41.7%	21.0%	11.9%
Kreiman <i>et al.</i> (1994) (Dissimilarity/Roughness)	3060	24.4%	34.9%	21.3%	19.3%
Kreiman <i>et al.</i> (1994) (Dissimilarity/Breathiness)	3060	20.9%	31.7%	20.4%	27.0%
Kreiman and Gerratt (1996) (Dissimilarity/Male voices)	88 480	24.9%	35.2%	21.4%	18.5%
Kreiman and Gerratt (1996) (Dissimilarity/Female voices)	88 480	26.2%	39.0%	21.5%	13.3%
Kreiman <i>et al.</i> (1993) (VA/Roughness)	26 100	30.6%	33.3%	18.7%	17.4%
Rabinov <i>et al.</i> (1995) (VA/Roughness)	4500	27.0%	37.9%	17.6%	17.4%
Chhetri (1997) (EAI/Severity)	1152	32.2%	35.3%	22.3%	10.2%
Pooled data	242 948	26.7%	37.0%	20.7%	15.6%

<sup>a</sup>EAI=equal-appearing interval scale; VA=visual analog scale.

<sup>b</sup>N=(number of possible pairs of listeners)×(number of stimuli). Differences between VA ratings were converted to scale value equivalents, as described in the text.

with average ratings in the “moderately pathologic” range accounted for an average of 32% of the variance in ratings (range=22%–42%). In other words, for the midrange of the scales examined here, on average more than 60% (and as much as 78%) of the variance in ratings of voices was due to factors other than differences among voices in the quality being rated.

### 3. Patterns of interrater agreement for similarity ratings

The pattern of pairwise agreement among listeners for ratings of the similarity of pairs of voices was different than that for ratings of roughness, breathiness, and severity. Although agreement levels varied substantially across voice pairs, perfect or near-perfect agreement among raters was more common for ratings of overall similarity [Kreiman and Gerratt, 1996; Fig. 4(a) and (b)] than for ratings of traditional qualities (where the likelihood of two raters agreeing perfectly never exceeded 0.8). Good agreement occurred across the entire scale. In particular, listeners did agree that some pairs of voices were moderately similar.

Patterns of agreement for ratings of the similarity of voices with respect to specific vocal qualities [Fig. 4(c) and (d); Kreiman *et al.*, 1994] shared characteristics of both similarity ratings and ratings of specific qualities. Although levels of agreement were lower than for ratings of overall similarity, listeners did consistently agree in their ratings of at least some voices in the midrange of the scale.

#### C. Conventional measures of rater reliability

Conventional measures of rating reliability, such as Cronbach’s alpha (Cronbach, 1951) and the intraclass correlation for the reliability of mean ratings (Ebel, 1951; Berk, 1979; Shrout and Fleiss, 1979), do not reflect the variability that occurs in interrater agreement, because they cannot represent patterns of agreement among raters and they cannot indicate agreement for specific voice samples (Young and Downs, 1968). Table V lists values of these statistics for the

data in Figs. 3 and 4. Summary reliability statistics were high overall, ranging from 0.68–0.99 across studies. Thus these data met conventional standards for reliability (see Kreiman *et al.*, 1993, for review), despite the great variability that appeared when agreement levels for specific voices were examined. In particular, values were very high for data sets where the likelihood of listener agreement was poor (Kreiman *et al.*, 1993) or variable (Kreiman and Gerratt, 1996), but *n* was large.

## III. DISCUSSION

The experimental tasks examined here—ratings of breathiness, roughness and severity; similarity ratings; and ratings of similarity with respect to breathiness and roughness—showed varying patterns of agreement among listeners. For ratings of traditional vocal qualities (Kreiman *et al.*, 1993, 1994; Rabinov *et al.*, 1995; Chhetri, 1997), individual listeners were self-consistent in their use of EAI scales. However, there were relatively few voices about which listeners as a group consistently agreed. In particular, consistent agreement *never* occurred for voices with mean ratings in the midrange of a scale. In fact, only about 30% of the variance in quality ratings was related to differences among voices when average ratings were between 2.5 and 5.5 on a seven-point scale.

For ratings of the overall similarity of pairs of voices (Kreiman and Gerratt, 1996), listeners as a group did agree that some voices were moderately similar. Patterns of agreement for ratings of similarity with respect to breathiness or roughness (Kreiman *et al.*, 1994) shared characteristics of both traditional breathiness/roughness ratings and ratings of the overall similarity of pairs of voices. Unlike ratings of breathiness and roughness, listeners sometimes agreed in their ratings for voices with mean ratings in the midrange of the scale, but overall reliability was lower than for ratings of overall similarity.

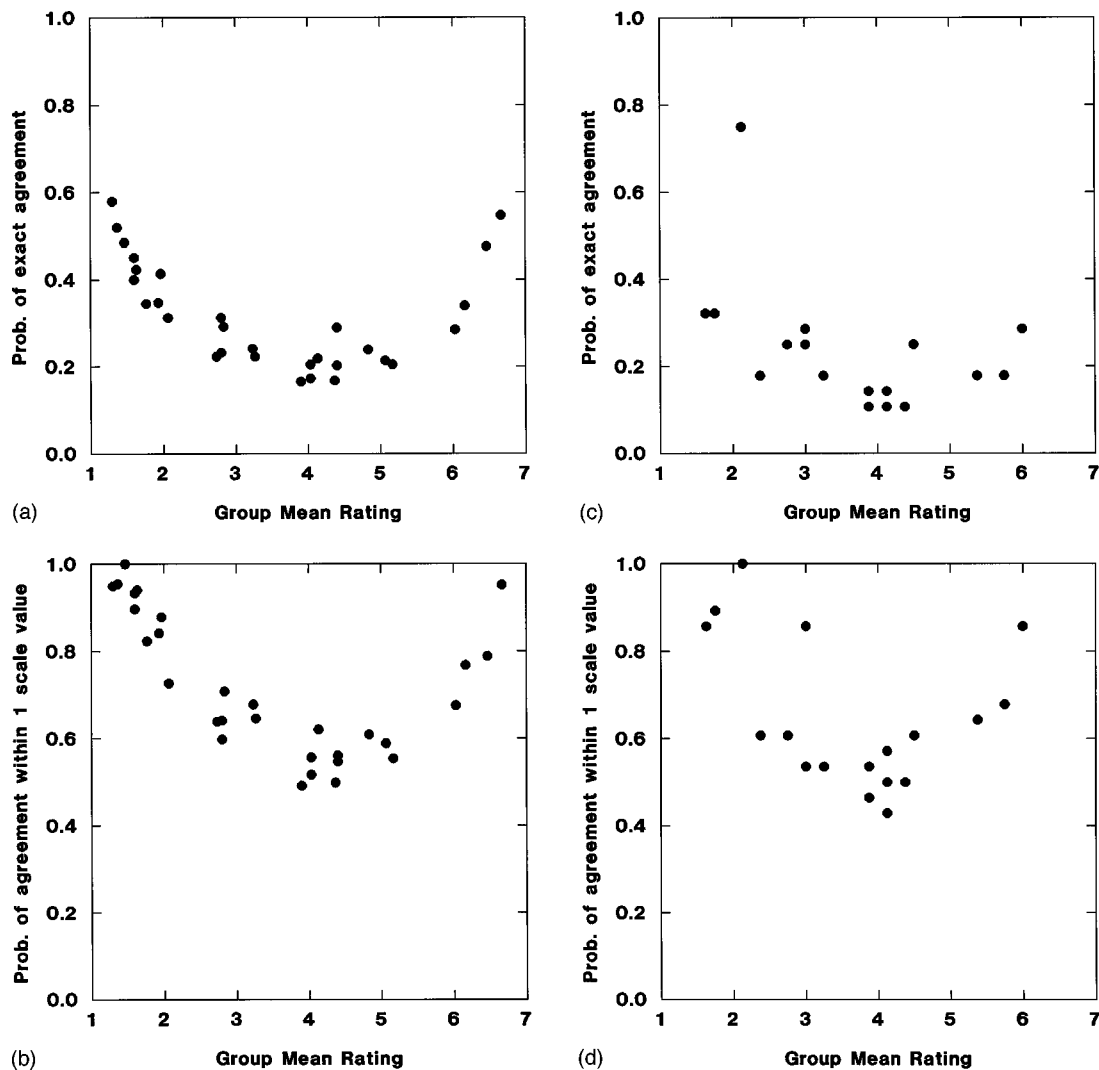


FIG. 3. For each voice in a data set, the probability that two raters agreed in their ratings of that voice, versus the overall mean rating for that voice. Results reflect only the first rating given each voice by each rater; the second rating was discarded. (a) The likelihood of exact agreement for EAI ratings of roughness; data from Kreiman *et al.* (1993). (b) The likelihood of agreement within 1 scale value for the same data. (c) The likelihood of exact agreement for EAI ratings of breathiness; data from Kreiman *et al.* (1994). (d) The likelihood of agreement within 1 scale value for the same data.

Several broad issues emerge from the patterns of agreement observed, and from observed differences among tasks. First, are patterns of results consistent with the assumption that traditional voice rating protocols provide valid measures of vocal quality? If these protocols are not sufficiently valid, how should vocal quality be measured? Finally, what mea-

asures of rating reliability are appropriate for evaluating data in studies of vocal quality?

### A. Validity of rating scale protocols

Paradigms for assessing vocal quality on traditional unidimensional scales like breathiness and roughness require the assumption that individual differences among listeners in ratings are noise or error, so that the “true score” for a voice on a scale is solely a function of the voice itself. Average ratings provide meaningful measures of quality only if this assumption holds. The present results are inconsistent with this assumption, and thus provide evidence against the validity of many protocols for assessing voice quality. Although listeners agreed at above-chance levels, most of the variance in quality ratings was due to factors other than differences among voices. The extent of variability in ratings received by voices away from scale end points indicates that mean ratings in the midrange of such scales poorly represent the

TABLE IV. Variance in voice ratings accounted for by differences among voices with mean ratings in the midrange of a scale.<sup>a</sup>

Study/Scale	$R^2$
Kreiman <i>et al.</i> (1993) (EAI/Roughness)	0.30
Kreiman <i>et al.</i> (1993) (VA/Roughness)	0.37
Kreiman <i>et al.</i> (1994) (EAI/Breathiness)	0.29
Kreiman <i>et al.</i> (1994) (EAI/Roughness)	0.22
Rabinov <i>et al.</i> (1995) (VA/Roughness)	0.42
Chhetri (1997) (EAI/Severity)	0.34

<sup>a</sup>EAI=equal-appearing interval scale; VA=visual analog scale. Midrange of a seven-point EAI scale is defined as the segment between 2.5 and 5.5, inclusive; VA scales were truncated proportionally.

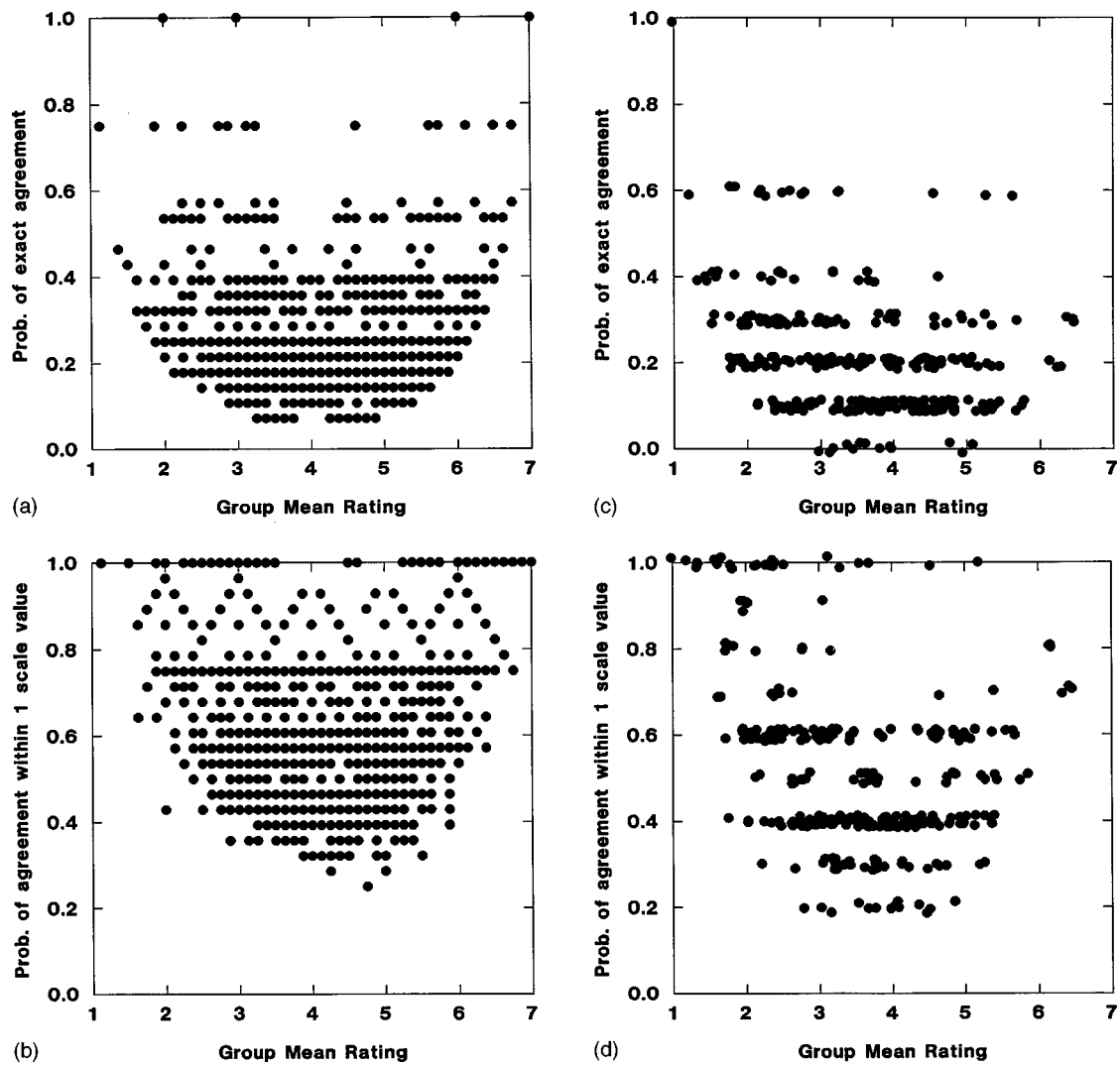


FIG. 4. For each pair of voices in a data set, the probability that two raters agreed in their ratings of the similarity of that pair of voices, versus the overall mean rating for that voice. Points have been jittered slightly to show overlapping values. (a) The likelihood of exact agreement for ratings of the similarity of pairs of female voices; data from Kreiman and Gerratt (1996). (b) The likelihood of agreement within 1 scale value for the same data. (c) The likelihood of exact agreement for ratings of the similarity of pairs of voices with respect to breathiness; data from Kreiman *et al.* (1994). (d) The likelihood of agreement within 1 scale value for the same data.

extent to which a voice possesses a quality. Instead, ironically, mean ratings in the middle of a scale serve primarily to indicate that listeners disagreed. If differences among voices are not consistently reflected by differences in ratings, then

traditional rating scale protocols do not measure what they are intended to measure, and their validity is not supported.

Although traditional rating protocols do not appear to provide valid measures of the quality of a given voice, scalar

TABLE V. Traditional measures of rating reliability.<sup>a</sup>

Study	Quality judged	Interrater agreement/reliability
Kreiman <i>et al.</i> (1993)	Roughness (EAI scale)	Reliability of mean rating (ICC)=0.99 Cronbach's alpha=0.99
Kreiman <i>et al.</i> (1994)	Dissimilarity of pairs of voices with respect to breathiness (EAI scale)	Reliability of mean rating (ICC)=0.68 Cronbach's alpha=0.74
	Breathiness (EAI scale)	Reliability of mean rating (ICC)=0.93 Cronbach's alpha=0.97
Kreiman and Gerratt (1996)	Dissimilarity of pairs of female voices (EAI scale)	Reliability of mean rating (ICC)=0.89 Cronbach's alpha=0.90

<sup>a</sup>ICC=intraclass correlation coefficient; EAI=equal-appearing interval scale.

ratings may still provide valuable information, if used to evaluate individual differences in perceptual strategy. For example, differences in patterns of disagreement that emerged from different rating tasks may provide insight into the mechanisms underlying the observed disagreements. Both traditional ratings of specific qualities and judgments of similarity with respect to specific qualities require listeners to compare observed voice stimuli to mental representations for the selected levels of that quality. This external-to-internal comparison introduces several sources of rating variability, including short- and long-term changes in mental representations, differences across listeners in how they define a quality or in standards for particular scale values, and variations in the importance of a cue in the context of variations in other cues (e.g., Kreiman *et al.*, 1992, 1993). In contrast, similarity rating tasks require listeners to compare stimuli globally and directly, without the need to refer to mental standards or assess particular attributes. Thus such tasks are not subject to error related to internal representations of a quality or drift in standards for particular levels of that quality. However, all tasks are subject to errors due to individual differences, perceptual biases, influences of perceptual context, mistakes, and changes over time in attention to these complex multidimensional stimuli.

Hypotheses regarding the effects of unstable internal standards for nonextreme levels of a quality are supported by data from a rating protocol using explicit anchors for each scale point (Gerratt *et al.*, 1993). When listeners made their ratings with reference to external “anchor” stimuli (instead of presumed internal criteria), good agreement occurred when stimuli were identical to the anchors. However, agreement dropped sharply between anchors, again suggesting that listeners cannot maintain internal standards for different levels of traditional vocal qualities. These results also demonstrate the major weakness of anchored protocols. The increase in agreement gained by including an external anchor was limited to the stimuli identical to the anchor, and listener agreement quickly decreased when stimuli fell between anchors. These data indicate that unless a protocol includes a large number of anchors spaced closely together, reference stimuli will not solve the problem of listener disagreements in ratings of particular voices. Further, providing anchors for a traditional quality scale circumvents the issue of the scale’s validity, which must be established by some other means.

It remains possible that listener training may provide a partial solution to these difficulties. Although short-term training has not been shown to consistently improve overall listener agreement (see Kreiman *et al.*, 1993 for review), with extensive training listeners may learn to focus selectively on different aspects of complex auditory stimuli. Whether this is in fact the case, and whether the effects of training persist after training ceases, remain as issues for future research. In any case, the scales and stimuli with which listeners are trained must be viewed as arbitrarily chosen, unless independent evidence supports their validity.

## **B. How should vocal quality be measured?**

If traditional unidimensional rating scales are abandoned, a large gap in the conventional approach to clinical

voice assessment will result. Obviously, much study is necessary to evaluate alternative strategies. Novel approaches to quality assessment should address the problems that appear to underlie listener disagreements. First, the present findings are consistent with the view that listener disagreements result in part from comparing external stimuli to idiosyncratic and/or unstable internal standards when attempting to use traditional rating scales. Second, it appears that listeners are unable to selectively attend to individual elements or dimensions of quality, as required by traditional voice assessment paradigms.

Measurement of overall vocal quality offers an alternative to traditional unidimensional ratings of specific vocal qualities. Many approaches to measurement of overall quality are possible. Techniques using analysis by synthesis and/or similarity ratings have long histories in psychometric research, and issues of their validity have been addressed in some detail (e.g., Gregson, 1975). Such tasks involve explicit comparisons between stimuli, rather than mappings between stimuli and internal standards, and they do not require listeners to focus attention on single dimensions of quality. Thus, in theory, they should eliminate the two causes of listener disagreement described above.

We have previously suggested that analysis by synthesis could be used to determine how listeners manipulate acoustic or other parameters to construct a synthetic token that matches the quality of a natural voice of interest (Kreiman and Gerratt, 1996). The values of these parameters would then directly represent a listener’s perceptual response, rather than only having a statistical association with that response as in current correlative approaches. Although synthesizer parameters are manipulated individually, listeners still judge quality as a whole when evaluating the success of the synthesis. Thus analysis by synthesis combines unidimensional and overall approaches to quality.

Further, with the addition of multivariate or multidimensional statistical techniques, analysis by synthesis may allow development and testing of specific hypotheses about the nature and direction of changes in quality. For example, single acoustic parameters can be manipulated systematically and the resulting quality changes evaluated with similarity judgments. If the acoustic parameter in question predicts patterns of perceived similarity, a strong case for its importance to perception can be made. Note that this approach allows hypotheses about perceptual dimensions and their correlates to be investigated without the use of traditional scales for single qualities.

## **C. Reliability and the measurement of vocal quality**

Although the minimum “acceptable” level for listener agreement and reliability varies from study to study, a consensus exists that for most statistics, a value above 0.7 (or 49% variance in common) is “good” to “excellent,” but that a value above 0.5 is adequate (e.g., Kazdin, 1977; Fleiss, 1981; Hammarberg and Gauffin, 1995; de Bodt *et al.*, 1997). The present results highlight several difficulties with this view. Measures of overall reliability (such as intraclass correlations and Cronbach’s alpha) can mask large and predictable differences in agreement levels for different voices. For

example, a data set for which Cronbach's alpha equals 0.9 or better may include individual voices for which agreement levels do not exceed chance. The presence or absence of normal and/or extremely severely pathologic voices in the stimulus set inflates or deflates these statistics (Kearns and Simmons, 1988). For example, ratings of roughness in the present data were more reliable overall for studies that included normal voices (Kreiman *et al.*, 1993) than for studies that did not (Rabinov *et al.*, 1995; Kreiman *et al.*, 1994). The number of raters in a study also affects overall reliability. For example, a mean interrater correlation of 0.4 will produce Cronbach's alpha of 0.87, given an *n* of only ten raters (Carmines and Zeller, 1979). Thus such measures depend on differences in experimental design as well as differences in ratings.

If averaging ratings is inappropriate, as argued above, it follows that unaveraged data must be analyzed. In other words, individual differences in quality perception must be modeled (Kreiman and Gerratt, 1996). With individual differences models of perception there is no expectation that listeners will agree, so mean ratings are without interest. In this case, the reliability of the mean rating and the extent to which listeners agree in their ratings become moot points. Measures of variance accounted for may provide an alternative method of assessing the usefulness of a set of listener judgments. Such measures are particularly useful because they make explicit the factors being used to predict variance in ratings. In this way, the statistical model (and its fit to the data) are precisely specified, rather than implied (as they have been in the past).

For example, in the present data, overall reliability was slightly lower for similarity ratings than for ratings of traditional qualities. However, multidimensional scaling analyses accounted for much of this increased variability by quantifying the contributions of presentation order and/or individual differences in perceptual strategy to rating variability (Kreiman *et al.*, 1994; Kreiman and Gerratt, 1996). The  $r^2$  values for individual listeners' data in Kreiman and Gerratt (1996) ranged from 0.56 to 0.83;  $r^2$  due to differences between voices in the unidimensional rating tasks reviewed here ranged from 0.22 to 0.42.

Finally, patterns of listener agreement provide information not available from measures of overall reliability, and thus may serve as a useful supplement to measures of total variance accounted for. For example, understanding which voices listeners consistently agree about, and which they cannot agree about, may provide clues to the factors underlying judgments of vocal quality [see Kreiman and Gerratt (1998b) for an example of this kind of analysis].

#### IV. CONCLUSIONS

Accurate modeling of voice perception is essential to the success of many endeavors, including development of instrumental measures of voice, refinement of speech synthesizers, and evaluation of the effectiveness of treatments for voice disorders. The low levels of listener agreement reported here indicate that traditional protocols for assessing qualities like breathiness and roughness are not useful for measuring perceived vocal quality. More detailed analyses of listeners'

performance in voice evaluation tasks, and better quantification of the adequacy of models of voice perception, will contribute to improved measurement of voice quality.

#### ACKNOWLEDGMENTS

We thank Ted Bell, James Hillenbrand, and Don Dirks for discussions of many statistical and nonstatistical aspects of this work. Dinesh Chhetri generously provided his severity rating data. Winifred Strange, Thomas Baer, and one anonymous reviewer provided many helpful comments on an earlier version of the manuscript. This research was supported by Grant No. DC01797 from the National Institute on Deafness and Other Communication Disorders. Please address correspondence to Jody Kreiman, Division of Head and Neck Surgery, UCLA School of Medicine, 31-24 Rehab Center, Los Angeles, CA 90095-1794 (Electronic mail: jkreiman@ucla.edu).

- Allen, M. J., and Yen, W. M. (1979). *Introduction to Measurement Theory* (Brooks/Cole, Monterey, CA).
- ANSI (1960). ANSI S1.1-1960, "Acoustical Terminology" (American National Standards Institute, New York).
- Berk, R. (1979). "Generalizability of behavioral observations: A clarification of interobserver agreement and interobserver reliability," *Am. J. Mental Deficiency* **83**, 460-472.
- Carmines, E. G., and Zeller, R. A. (1979). *Reliability and Validity Assessment*, Sage University Paper series on Quantitative Applications in the Social Sciences, 07-017 (Sage, Newbury Park, CA).
- Chhetri, D. K. (1997). "Treatment of voice disorders related to unilateral paralysis of the vocal cord," unpublished senior medical student thesis, University of California, Los Angeles.
- Colton, R. H., and Estill, J. A. (1981). "Elements of voice quality: Perceptual, acoustic, and physiologic aspects," in *Speech and Language: Advances in Basic Research and Practice*, edited by N. J. Lass (Academic, New York), Vol. 5, pp. 311-403.
- Cone, J. D. (1977). "The relevance of reliability and validity for behavioral assessment," *Behav. Therapy* **8**, 411-426.
- Crocker, L., and Algina, J. (1986). *Introduction to Classical and Modern Test Theory* (Holt, Rinehart and Winston, New York).
- Cronbach, L. J. (1951). "Coefficient alpha and the internal structure of tests," *Psychometrika* **16**, 297-334.
- de Bodt, M. S., Wuyts, F. L., Van de Heyning, P. H., and Croux, C. (1997). "Test-retest study of the GRBAS scale: Influence of experience and professional background on perceptual rating of voice quality," *J. Voice* **11**, 74-80.
- de Krom, G. (1995). "Some spectral correlates of pathological breathy and rough voice quality for different types of vowel fragments," *J. Speech Hear. Res.* **38**, 794-811.
- Ebel, R. (1951). "Estimation of the reliability of ratings," *Psychometrika* **16**, 407-424.
- Fleiss, J. L. (1981). *Statistical Methods for Rates and Proportions* (Wiley, New York).
- Fritzell, B., Hammarberg, B., Gauffin, J., Karlsson, I., and Sundberg, J. (1986). "Breathiness and insufficient vocal fold closure," *J. Phon.* **14**, 549-553.
- Gerratt, B. R., and Kreiman, J. (1995). "The utility of acoustic voice measures," in *Proceedings of the Workshop on Standardization in Acoustic Voice Analysis*, edited by D. Wong (National Center for Voice and Speech, Denver), pp. GER1-GER7.
- Gerratt, B. R., Kreiman, J., Antonanzas-Barroso, N., and Berke, G. S. (1993). "Comparing internal and external standards in voice quality judgments," *J. Speech Hear. Res.* **36**, 14-20.
- Gerratt, B. R., Till, J., Rosenbek, J. C., Wertz, R. T., and Boysen, A. E. (1991). "Use and perceived value of perceptual and instrumental measures in dysarthria management," in *Dysarthria and Apraxia of Speech*, edited by C. A. Moore, K. M. Yorkston, and D. R. Beukelman (Brookes, Baltimore), pp. 77-93.
- Gregson, R. A. (1975). *Psychometrics of Similarity* (Academic, New York).



- Hammarberg, B., and Gauffin, J. (1995). "Perceptual and acoustic characteristics of quality differences in pathological voices as related to physiological aspects," in *Vocal Fold Physiology: Voice Quality Control*, edited by O. Fujimura and M. Hirano (Singular, San Diego), pp. 283–303.
- Helmholtz, H. (1885; reprinted 1954). *On the Sensations of Tone* (Dover, New York).
- Hillenbrand, J., Cleveland, R. A., and Erickson, R. L. (1994). "Acoustic correlates of breathy vocal quality," *J. Speech Hear. Res.* **37**, 769–778.
- Jensen, P. J. (1965). "Adequacy of terminology for clinical judgment of voice quality deviation," *The Eye, Ear, Nose and Throat Monthly* **44**, 77–82.
- Kazdin, A. (1977). "Artifact, bias, and complexity of assessment: The ABCs of reliability," *J. Appl. Behav. Anal.* **10**, 141–150.
- Kearns, K., and Simmons, N. (1988). "Interobserver reliability and perceptual ratings: More than meets the ear," *J. Speech Hear. Res.* **31**, 131–136.
- Kempster, G. B., Kistler, D., and Hillenbrand, J. (1991). "Multidimensional scaling analysis of dysphonia in two speaker groups," *J. Speech Hear. Res.* **34**, 534–543.
- Kerlinger, F. N. (1973). *Foundations of Behavioral Research* (Holt, Rinehart, and Winston, New York), 2nd ed.
- Kreiman, J. (1997). "Listening to voices: Theory and practice in voice perception research," in *Talker Variability in Speech Processing*, edited by K. Johnson and J. W. Mullennix (Academic, San Diego), pp. 85–108.
- Kreiman, J., and Gerratt, B. R. (1996). "The perceptual structure of pathologic voice quality," *J. Acoust. Soc. Am.* **100**, 1787–1795.
- Kreiman, J., and Gerratt, B. R. (1998a). "Measuring vocal quality," to appear in *Handbook of Voice Quality Measurement*, edited by R. Kent and M. J. Ball (Singular, San Diego).
- Kreiman, J., and Gerratt, B. R. (1998b). "Sources of listener disagreement in voice quality assessment" (in preparation).
- Kreiman, J., Gerratt, B. R., and Berke, G. S. (1994). "The multidimensional nature of pathologic vocal quality," *J. Acoust. Soc. Am.* **96**, 1291–1302.
- Kreiman, J., Gerratt, B. R., Kempster, G. B., Erman, A., and Berke, G. S. (1993). "Perceptual evaluation of voice quality: Review, tutorial, and a framework for future research," *J. Speech Hear. Res.* **36**, 21–40.
- Kreiman, J., Gerratt, B. R., and Precoda, K. (1990). "Listener experience and perception of voice quality," *J. Speech Hear. Res.* **33**, 103–115.
- Kreiman, J., Gerratt, B. R., Precoda, K., and Berke, G. S. (1992). "Individual differences in voice quality perception," *J. Speech Hear. Res.* **35**, 512–520.
- Mackey, L. S., Finn, P., and Ingham, R. J. (1997). "Effect of speech dialect on speech naturalness ratings: A systematic replication of Martin, Haroldson, and Triden (1984)," *J. Speech Lang. Hear. Res.* **40**, 349–360.
- Martin, D., Fitch, J., and Wolfe, V. (1995). "Pathologic voice type and the acoustic prediction of severity," *J. Speech Hear. Res.* **38**, 765–771.
- Murry, T., Singh, S., and Sargent, M. (1977). "Multidimensional classification of abnormal voice qualities," *J. Acoust. Soc. Am.* **61**, 1630–1635.
- Perkins, W. (1971). "Vocal function: A behavioral analysis," in *Handbook of Speech Pathology and Audiology*, edited by L. Travis (Appleton Century Croft, New York), pp. 481–504.
- Rabinov, C. R., Kreiman, J., Gerratt, B. R., and Bielamowicz, S. (1995). "Comparing reliability of perceptual ratings of roughness and acoustic measures of jitter," *J. Speech Hear. Res.* **38**, 26–32.
- Shrout, P., and Fleiss, J. (1979). "Intraclass correlations: Uses in assessing rater reliability," *Psychol. Bull.* **86**, 420–428.
- Silverman, F. H. (1977). *Research Design in Speech Pathology and Audiology* (Prentice-Hall, Englewood Cliffs, NJ).
- Sodersten, M., Hertegard, S., and Hammarberg, B. (1995). "Glottal closure, transglottal airflow, and voice quality in healthy middle-aged women," *J. Voice* **9**, 182–204.
- Suen, H. K., and Ary, D. (1989). *Analyzing Quantitative Behavioral Observation Data* (Erlbaum, Hillsdale, NJ).
- Ventry, I. M., and Schiavetti, N. (1980). *Evaluating Research in Speech Pathology and Audiology* (Addison-Wesley, Reading, MA).
- Young, M. A. (1993). "Supplementing tests of statistical significance: Variation accounted for," *J. Speech Hear. Res.* **36**, 644–656.
- Young, M. A., and Downs, T. D. (1968). "Testing the significance of the agreement among observers," *J. Speech Hear. Res.* **11**, 5–17.

# Speech intelligibility assessment in a helium environment. II. The speech intelligibility index

Lisa Lucks Mendel<sup>a)</sup>

*Center for Speech and Hearing Research, Department of Communicative Disorders,  
University of Mississippi, University, Mississippi 38677*

Bruce W. Hamill

*The Johns Hopkins University, Applied Physics Laboratory, Laurel, Maryland 20723-6099*

James E. Hendrix

*Oxford Signal Processing, Oxford, Mississippi 38655*

Loring J. Crepeau and Jerry D. Pelton

*Navy Experimental Diving Unit, Panama City, Florida 32407-7015*

Matthew D. Miley

*X<sup>N</sup> Technologies, Cheney, Washington 99004*

Elizabeth E. Kadlec

*University of Georgia, Athens, Georgia 30602*

(Received 13 September 1997; accepted for publication 29 May 1998)

The Speech Intelligibility Index (SII) was measured for Navy divers participating in two saturation deep dives and for a group of nondivers to test different communication systems and their components. These SIIs were validated using the Speech Perception in Noise (SPIN) test and the Griffiths version of the Modified Rhyme Test (GMRT). Our goal was to determine if either of these assessments was sensitive enough to provide an objective measure of speech intelligibility when speech was processed through different helmets and helium speech unscramblers (HSUs). Results indicated that SII values and percent intelligibility decreased incrementally as background noise level increased. SIIs were very reliable across the different groups of subjects indicating that the SII was a strong measurement for predicting speech intelligibility to compare linear system components such as helmets. The SII was not useful in measuring intelligibility through nonlinear devices such as HSUs. The speech intelligibility scores on the GMRT and SPIN tests were useful when the system component being compared had a large measurable difference, such as in helmet type. However, when the differences were more subtle, such as differences in HSUs, neither the SPIN nor the GMRT appeared sensitive enough to make such distinctions. These results have theoretical as well as practical value for measuring the quality and intelligibility of helium speech enhancement systems. © 1998 Acoustical Society of America. [S0001-4966(98)03109-9]

PACS numbers: 43.72.Kb, 43.72.Ew, 43.71.Gv, 43.70.Dn [JLH]

## INTRODUCTION

Accurate assessment of speech intelligibility is important for determining the effectiveness of different communication systems used with Navy divers who are exposed to high noise levels in their work environments. Further, these divers work under hyperbaric conditions at depths of several hundred feet of seawater (FSW) in a helium–oxygen (heliox) environment. These conditions affect the acoustical properties of the speech they produce making it significantly different from typical discourse and difficult to understand.

Helium speech unscramblers (HSUs) attempt to convert the frequency spectra of helium speech into a frequency range that is closer to average conversational speech, making it more intelligible to listeners and thus improving communication among divers (Belcher and Andersen, 1983; Copel, 1966; Giordano *et al.*, 1973; Stover, 1967). While such de-

vices provide significant improvement to intelligibility, the effects of noise, pressure, and helium still contribute significantly to poor speech understanding among divers. Thus refinements continue to be made in diver communication systems by using state-of-the-art technology to improve speech intelligibility. Our work has focused on evaluating the effectiveness of different speech intelligibility assessment tools for providing accurate estimations of speech understanding in order to test these system refinements.

Traditional speech recognition tests such as Griffiths (1967) version (GMRT) of the Modified Rhyme Test (House *et al.*, 1965) and the Speech Perception in Noise (SPIN) test (Kalikow *et al.*, 1977) have been used extensively for measuring helium speech intelligibility in Navy divers, but have not proven to be sensitive enough to measure small but noticeable intelligibility differences. Mendel *et al.* (1995) showed that GMRT and SPIN scores do not reflect divers' subjective impressions of the performance of different HSUs. In that investigation, the GMRT and SPIN produced almost

<sup>a)</sup>Electronic mail: cdmendel@olemiss.edu

identical test scores for two types of HSU, suggesting that neither test was more sensitive than the other, at least in a dry chamber. Thus these traditional speech recognition assessment tools proved to be ineffective methods of determining accurate measures of speech understanding in a dry chamber helium environment.

The Speech Intelligibility Index (SII) is a different assessment tool that is based on the audibility of the speech signal and is calculated as the sum of a number of contiguous frequency bands that are each weighted according to their contribution to speech understanding (ANSI, 1995; Pavlovic, 1991). The SII is an updated version of the standard for the Articulation Index (AI, ANSI, 1970) which defines a method for computing an objective, physical measure that is closely correlated with the intelligibility of speech when measured by standard perceptually based speech intelligibility tests under a variety of adverse listening conditions. This objective SII measure appeared to have significant application to predicting speech understanding in a helium environment.

The purposes of the studies presented here were to: (1) investigate the effectiveness of the GMRT and SPIN tests in assessing the intelligibility of divers' helium speech using different HSUs and helmets during two in-water saturation deep dives (Deep Dive 1995, DD 95, and Deep Dive 1996, DD 96) conducted in the Ocean Simulation Facility (OSF) at the Navy Experimental Diving Unit (NEDU) in Panama City, FL, and (2) determine the effectiveness of the SII in assessing speech understanding in dry and wet chambers during the same saturation deep dives.

## I. SPEECH INTELLIGIBILITY INDEX MEASUREMENTS

### A. Manikin testing

Initial measurements using two acoustic manikins were taken prior to the saturation deep dives. Digital audio tape (DAT) recordings from earlier deep dives conducted at NEDU were analyzed, and specific segments of these tapes were dubbed and edited for use during manikin and human subject testing. The SII measurement method we used required separate measurements of *speech without noise* and *noise without speech*. Therefore noise recorded on DAT from the helmet of a diver in the water at 850 FSW was used for the *noise without speech*, and speech segments taken from topside-to-diver communications of previous deep dives were used as the *speech without noise*.

A spectrum analysis of each of the measures of *speech without noise* and *noise without speech* was obtained using a Hewlett-Packard Dynamic Signal Analyzer (HP 35665A). Once the spectra and the SPLs of these segments were obtained at the desired overall levels, the data were written to ASCII files suitable for input to the SII critical band calculation program provided with the ANSI SII standard (ANSI, 1995).

### B. Human subject testing

#### 1. Subjects

In order to validate the SII calculations obtained on the manikins, human subject testing was conducted prior to the saturation deep dives. The goal of this testing was to deter-

mine how the SII calculations compared to typical speech recognition performance. A group of normally hearing non-divers ( $N=14$ ; ages 18–44) and two groups of normally hearing divers (DD 95:  $N=8$ ; ages 24–43; DD 96:  $N=8$ ; ages 26–38) participated in the studies.

## 2. Procedure

The GMRT and the SPIN test lists were used in this study. A complete description of each test can be found in Mendel *et al.* (1995). Lists No. 8 of both the GMRT and SPIN tests were edited to sound like continuous discourse so they could be used as the *speech without noise* stimuli for the SII measurements.

*a. Nondivers.* All speech stimuli were presented at 68 dB SPL corresponding to the raised standard speech level. The *noise without speech* measurement consisted of seven different overall noise levels of the same "helmet noise" used in the manikin measurements (i.e., 50, 56, 62, 68, 74, 80, and 86 dB SPL). After a hearing screening, power spectral density (PSD) curves of the spectra of the edited (compressed) GMRT and SPIN lists and the spectra of each noise level were obtained for each subject and stored for later calculation of the SII. Each subject then listened to either three GMRT and SPIN lists at three different noise levels of four GMRT and SPIN lists at four different noise levels. To avoid learning effects, subjects were paired so that no subject heard the same randomized list pair from either test. Subjects provided written responses to the stimuli heard.

*b. Divers.* The same DAT tapes used with the nondivers were used to measure SII for the Navy divers participating in DD 95 and DD 96. Two identical equipment configurations were used to test two divers at a time in a dry living chamber (Alpha Chamber) with background noise reduced as much as possible. Each diver wore a headset on his better ear, and the DAT recordings of *speech without noise* and *noise without speech* were presented to that ear.

For DD 95, SII were measured at four different noise levels (i.e., 78, 84, 90, and 96 dB SPL); the chamber noise floor was 68 dB SPL. DAT recordings of the compressed GMRT and SPIN stimuli (*speech without noise*) were each presented at 90 dB SPL, and a PSD curve for each was measured and stored. For DD 96, SII were measured using noise levels at 106, 111, 116, and 121 dB SPL. Overall the noise levels were higher than those used in DD 95 because we were attempting to measure SII and speech intelligibility performance in more adverse listening conditions than had been measured previously. DAT recordings of the compressed GMRT and SPIN stimuli were each presented at 65 dB SPL, instead of 90 dB SPL, and a spectrum for each was measured and stored. Once the spectra and the SPLs of *speech without noise* and *noise without speech* were obtained and stored at the desired overall levels, SII calculations were made using the procedures described earlier.

After the SII measurements were obtained on the divers, speech intelligibility testing was conducted to determine how the SII calculations compared to typical speech recognition performance. Each diver heard one 50-item GMRT and one 50-item SPIN list at each noise level through the headset on his better ear. The lists were presented to each diver so that

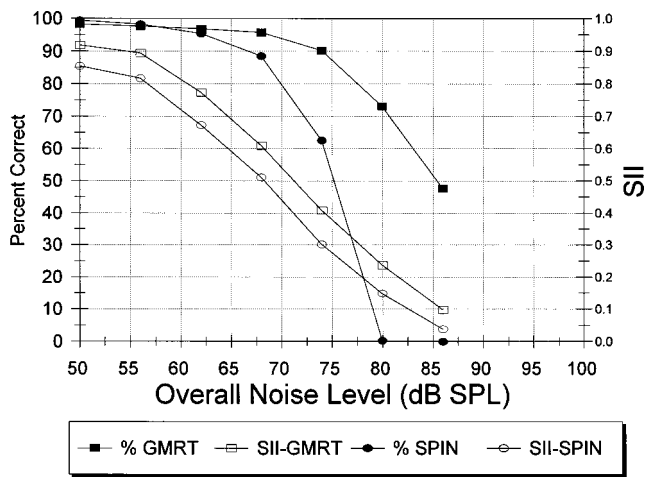


FIG. 1. Nondivers' mean percent correct GMRT and SPIN scores and Speech Intelligibility Index (SII) values for compressed GMRT and SPIN stimuli as a function of noise level for DD 95.

no subject heard the same randomized list pair from either test. Subjects provided written responses to the stimuli heard.

For DD 96, SII values were also measured while divers were in the wet chamber. DAT recordings of the compressed GMRT and SPIN stimuli were presented to each diver immediately before he entered the water. A PSD measurement was then taken and stored on a diskette. The helmet was then placed on the diver and he entered the water. Once the diver was quiet and in the water, a spectrum measurement was taken of the background noise level in the helmet and stored on a diskette. This measure of actual helmet noise served as the *noise without speech* measurement needed for the SII calculation.

### C. Results

#### 1. Nondivers

Figure 1 plots the mean GMRT and SPIN percent correct scores and SII values as a function of noise level for the nondivers. GMRT and SPIN percent correct scores and SII values remained high for the lower noise levels even though SII values decreased more rapidly than percent correct scores. GMRT intelligibility scores of 90%–98% were comparable to SII values ranging from 0.41 at 90% intelligibility to 0.92 at 98% intelligibility. SPIN intelligibility scores of 88%–99% were comparable to SII values ranging from 0.51 at 88% to 0.85 at 99%. Both SII values decreased appropriately as the level of noise increased for both the GMRT and SPIN.

#### 2. Divers

The average results of the SII calculations and intelligibility performance for the divers are plotted as a function of noise level in Fig. 2 (DD 95) and Fig. 3 (DD 96). As seen with the nondivers, SII values decreased appropriately as the level of noise increased for both the GMRT and SPIN stimuli; intelligibility and SII values generally were lower for the SPIN than for the GMRT. Overall GMRT percent correct performance was better than SPIN performance which may be a reflection of the open-set nature of the SPIN test versus the closed-set nature of the GMRT. Also, Figs. 2

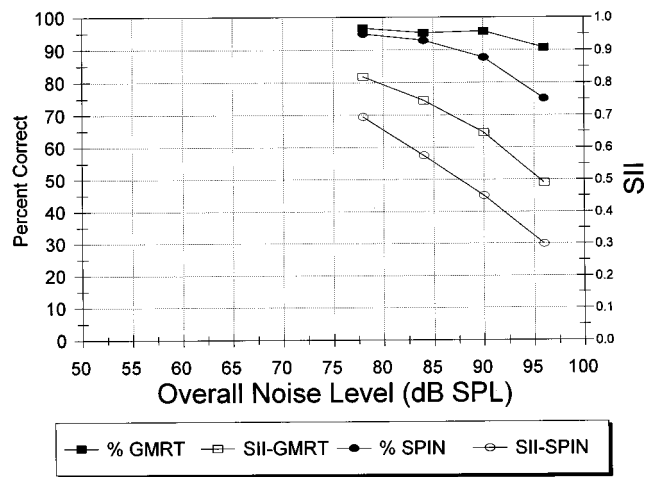


FIG. 2. Divers' mean percent correct GMRT and SPIN scores and Speech Intelligibility Index (SII) values for compressed GMRT and SPIN stimuli as a function of noise level for DD 95.

and 3 show that SPIN performance drops more rapidly at the higher noise levels than does GMRT performance.

Figure 4 plots the dry chamber data for both nondivers and divers collected during DD 95 and DD 96. In this figure, GMRT and SPIN percent correct intelligibility scores are plotted as a function of the SII in three conditions: (a) nondivers tested at one atmosphere in 1994 (M/000; S/000); (b) divers tested in dry chambers at 850 FSW in DD 95 (M/850/95; S/850/95); and (c) divers tested in dry chambers at 850 FSW in DD 96 (M/850/96; S/850/96). All GMRT points are represented by rectangles and all SPIN points are ovals. Examination of this figure suggests that the data collected in DD 96 were quite similar to those collected in the laboratory situation and in DD 95 and that SII values decreased as percent intelligibility decreased. Note that the two unaveraged points on the curve reflect the GMRT and SPIN scores for the one diver who was exposed to the highest noise level. Even though these points are not averaged, they do fall appropriately on the curve and line up well with the other data.

Figures 5 and 6 show plots of the GMRT and SPIN

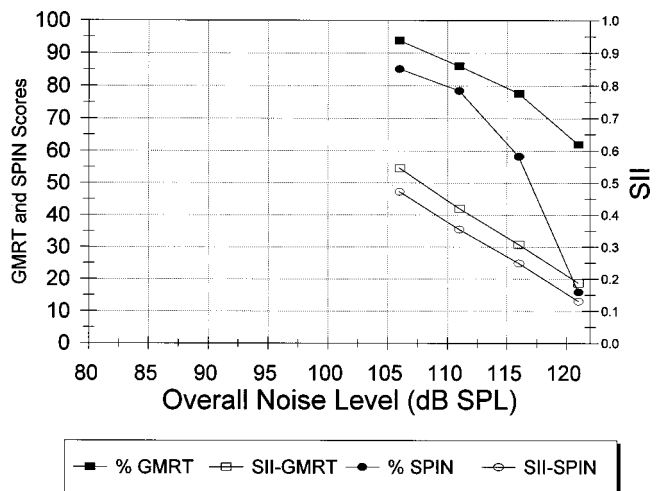


FIG. 3. Divers' mean percent correct GMRT and SPIN scores and Speech Intelligibility Index (SII) values for compressed GMRT and SPIN stimuli as a function of noise level in the dry chamber for DD 96.

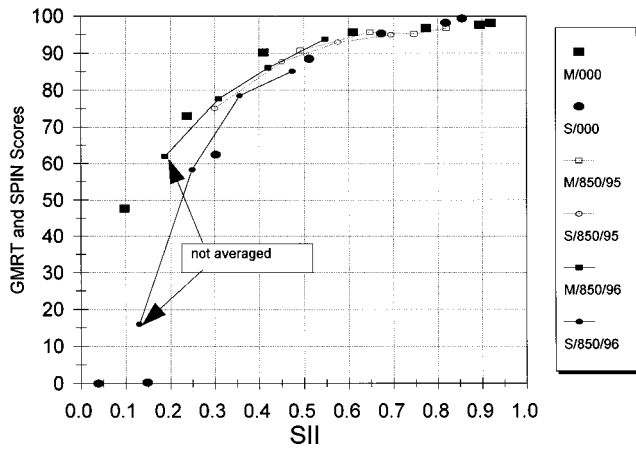


FIG. 4. GMRT and SPIN mean percent correct performance as a function of Speech Intelligibility Index (SII) in the dry chamber for three studies: (a) nondivers in laboratory environment, (b) divers in DD 95, and (c) divers in DD 96. (*M/000*=GMRT scores at one atmosphere; *S/000*=SPIN scores at one atmosphere; *M/850/95*=DD 95 GMRT scores at 850 FSW; *S/850/95*=DD 95 SPIN scores at 850 FSW; *M/850/96*=DD 96 GMRT scores at 850 FSW; *S/850/96*=DD 96 SPIN scores at 850 FSW.)

intelligibility performance, respectively, as a function of SII for all dry and wet chamber data taken to date. The wet chamber data are shown as large open squares or ovals and are not averaged or connected because the noise levels in the water could not be controlled. Thus these data are not grouped into distinct noise levels as they were in the dry chamber measurements. The data points for the SPIN do not line up quite as well as they do for the GMRT, but there is still a clear pattern in the results. There was considerably more scatter in the SPIN wet chamber intelligibility data than in the GMRT intelligibility data which is probably a reflection of the open-set nature of the SPIN test. The SPIN scores also appeared to be more affected by the adverse noisy conditions in the water than the GMRT.

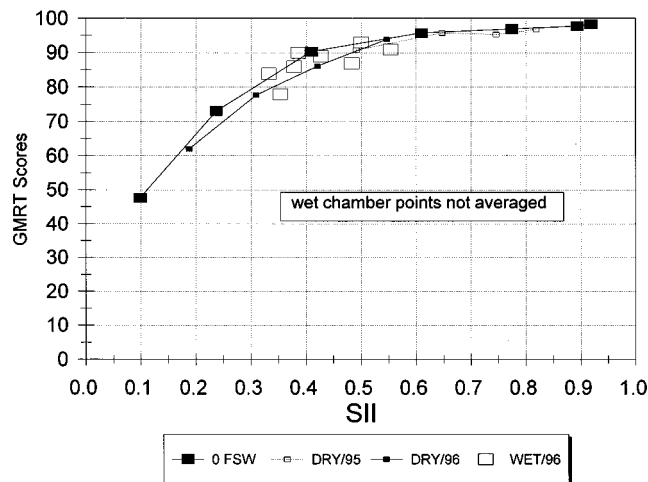


FIG. 5. GMRT mean percent correct performance as a function of Speech Intelligibility Index (SII) in the dry and wet chambers for three studies: (a) nondivers in laboratory environment, (b) divers in DD 95, and (c) divers in DD 96. (*O FSW*=GMRT scores at one atmosphere; *DRY/95*=DD 95 GMRT scores at 850 FSW; *DRY/96*=DD 96 GMRT scores at 850 FSW; *WET/96*=DD 96 GMRT scores at 850 FSW.)

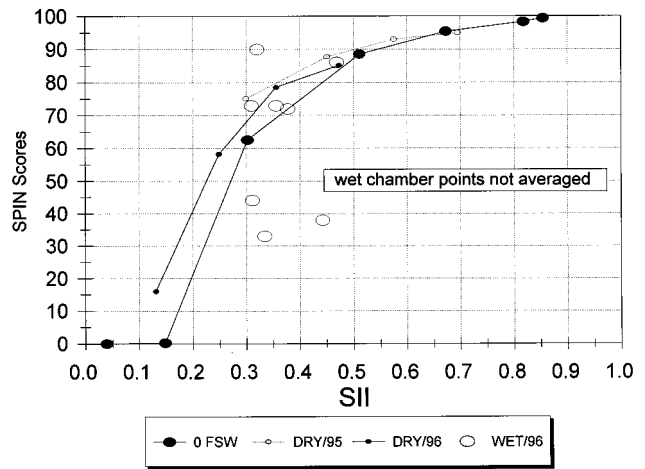


FIG. 6. SPIN mean percent correct performance as a function of Speech Intelligibility Index (SII) in the dry and wet chambers for three studies: (a) nondivers in laboratory environment, (b) divers in DD 95, and (c) divers in DD 96. (*O FSW*=SPIN scores at one atmosphere (laboratory environment); *DRY/95*=DD 95 SPIN scores at 850 FSW; *DRY/96*=DD 96 SPIN scores at 850 FSW; *WET/96*=DD 96 SPIN scores at 850 FSW.)

## II. IN-WATER GMRT AND SPIN TESTING AT 850 FSW

### A. Subjects

The same two groups of Navy divers from DD 95 and DD 96 served as subjects during the in-water test phase.

### B. Stimuli and instrumentation

A tethered diver communications system (TDCS) was used to enable divers to communicate with each other and support personnel in the OSF control room. Two different helmets were used during all dives: a standard helmet and a modified helmet which had no supply valve and was reported to be much quieter than the standard helmet. Also, two different HSUs were employed during the dives. HSU1 used a 16-bit processor which performed sampling, compression, and reconstruction in the time domain using a speech signal processing algorithm and A/D converter (Dildy, 1992). HSU2 used a high-speed, floating point digital signal processor to provide improved synchronization over the entire dynamic range of the signal, smooth transitions in the waveforms, and overlapping of waveforms (Hendrix, 1996).

The same GMRT and SPIN lists used in the dry chamber SII measurement and validation were used in this portion of the experiment. DAT recordings and helium live-voice presentations of eight lists each of the GMRT and SPIN tests were used. The DAT recordings of the stimuli were presented via a Panasonic DAT deck (model SV-3700).

### C. Procedure

During DD 95 and DD 96, all divers were tested in pairs while in the water. Each diver heard four lists of stimuli: one DAT-recorded SPIN and GMRT list presented from topside (topside-diver) and a randomization of both lists presented live-voice (using helium speech) from the paired diver (diver-diver). In all cases, the diver heard the stimuli from a particular list before he read them to his paired diver to avoid

TABLE I. Overall mean percent intelligibility scores and standard deviations (s.d.s) for the GMRT and SPIN in the wet chamber across condition (topside–diver versus diver–diver). All GMRT scores were corrected to account for the closed-set nature of the test. The formula used to correct the scores was  $2 \times [\text{No. right} - (\text{No. wrong}/4)]$ . Starred values (\*) indicate significant differences.

Dive	Condition	Helmet	GMRT mean	GMRT s.d.	SPIN mean	SPIN s.d.
DD 95	topside–diver	NA	78*	12.6	66*	29.5
	diver–diver	NA	32	16.5	27	19.3
DD 96	topside–diver	NA	84*	6.3	63*	21.6
	diver–diver	NA	41	16.3	36	19.7
	topside–diver	standard	81	4.9	47	16.4
		<i>n</i> = 8				
		modified	87*	6.4	81*	9.0
		<i>n</i> = 8				
	diver–diver	standard				
		( <i>n</i> = 8)	34	11.4	27	16.3
		HSU 1 ( <i>n</i> = 4)	31	13.3	33	21.6
		HSU 2 ( <i>n</i> = 4)	38	10.1	21	7.9
	Modified					
	( <i>n</i> = 8)	48	13.1	46	18.7	
	HSU 1 ( <i>n</i> = 4)	50	18.1	38	12.3	
	HSU 2 ( <i>n</i> = 4)	46	8.1	54	22.5	

learning effects within a listener. All stimuli were presented at comfortable listening levels, and all diver responses were written on answer sheets.

## D. Results

### 1. In-water GMRT and SPIN intelligibility scores

The overall mean percent correct scores and standard deviations for DD 95 and DD 96 on the GMRT and SPIN for the two listening conditions (taped, topside–diver and live-voice, diver–diver) are provided in Table I. All GMRT scores were corrected to account for the closed-set nature of the test using the formula:  $2 \times [\text{No. right} - (\text{No. wrong}/4)]$ . Analyses of variance (ANOVAs) conducted on the means of the two intelligibility scores for each diver’s GMRT and SPIN tests in the water revealed a significant main effect favoring topside–diver presentation of test lists over diver–diver presentation [DD 95:  $F(1,7) = 77.29$ ,  $p < 0.0001$ ; DD 96:  $F(1,6) = 55.03$ ,  $p < 0.0005$ ], and a significant main effect of overall higher test scores for the GMRT than for the SPIN in both conditions [DD 95:  $F(1,7) = 39.82$ ,  $p < 0.0005$ ; DD 96:  $F(1,6) = 16.62$ ,  $p < 0.01$ ]. No interaction effects were observed.

An item analysis of the divers’ responses to the stimuli on the SPIN and GMRT showed that divers made considerably more errors on the SPIN than on the GMRT. More SPIN errors were made on low-predictability (noncontextual) items than on high-predictability items.

The data in Table I also show DD 96 pooled GMRT and SPIN mean percent intelligibility scores and standard deviations across both helmet types along with a breakdown of the scores as a function of helmet type. An ANOVA conducted on the means of the two intelligibility scores for each diver’s GMRT and SPIN tests in the water revealed a significant main effect for helmet [standard versus modified,  $F(1,6) = 8.12$ ,  $p < 0.05$ ] revealing higher test scores measured in the modified helmet compared to the standard helmet. A signifi-

cant two-way interaction between tests and helmets,  $F(1,6) = 6.93$ ,  $p < 0.05$ , revealed that GMRT scores obtained using the modified helmet were higher than SPIN scores in the standard helmet. The significant two-way interaction between conditions and tests,  $F(1,6) = 27.96$ ,  $p < 0.005$ , indicated that diver–diver scores on both tests were lower than topside–diver SPIN scores, which, in turn, were lower than topside–diver GMRT scores. There was also a significant three-way interaction.

Also shown in Table I are the mean percent intelligibility scores and standard deviations for the GMRT and SPIN as a function of the type of HSU used during the diver–diver presentations in the water during DD 96. An ANOVA conducted on these GMRT and SPIN test scores revealed no significant effects across HSUs for either the modified or the standard helmet.

### 2. Comparison of SIIs and intelligibility scores for DD 96

Correlations were computed to examine the relationship between the GMRT and SPIN percent intelligibility scores and their corresponding SII values obtained during DD 96. Four general relationships were examined: (a) GMRT score and the SII value using the GMRT stimuli (SII-GMRT), (b) SPIN score and the SII value using the SPIN stimuli (SII-SPIN), (c) GMRT and SPIN scores, and (d) SII-GMRT and SII-SPIN. Each subject heard two different GMRT and SPIN lists, and correlations were computed in two ways: (1) on the overall means of the scores by test list and (2) on the individual lists heard by divers as a function of helmet. The correlations are shown in Table II.

The correlations measured were considerably higher for the modified helmet than for the standard helmet, which is consistent with the main effect for helmets found in the ANOVA. This finding indicates that, except for the GMRT-SPIN percent correct correlation, intelligibility test data and

TABLE II. Correlations examining the relationship between speech intelligibility scores and Speech Intelligibility Index (SII) values. Correlations were computed using scores by individual test lists per subject and means of scores for two test lists per subject.

Correlations by test list	Overall (df=14)	Standard helmet (df=6)	Modified helmet (df=6)
GMRT×SII-GMRT	0.602 <sup>b</sup>	0.373	0.668 <sup>d</sup>
SPIN×SII-SPIN	0.007	-0.086	0.324
GMRT×SPIN	0.708 <sup>a</sup>	0.511	0.770 <sup>c</sup>
SII-GMRT×SII-SPIN	0.261	0.103	0.616
Correlations by mean scores	Overall (df=6)	Standard helmet (df=2)	Modified helmet (df=2)
GMRT×SII-GMRT	0.706 <sup>c</sup>	0.474	0.833
SPIN×SII-SPIN	0.076	0.076	0.331
GMRT×SPIN	0.755 <sup>c</sup>	0.529	0.906 <sup>d</sup>
SII-GMRT×SII-SPIN	0.252	-0.161	0.624

Significance levels: <sup>a</sup> $p < 0.01$ ; <sup>b</sup> $p < 0.02$ ; <sup>c</sup> $p < 0.05$ ; <sup>d</sup> $p < 0.10$ .

SIIs collected from divers wearing the standard helmet do not correlate as well as might be expected. One interesting finding was that the SPIN percent score correlates fairly well with the GMRT percent score, but does not correlate with the SII-SPIN.

### III. DISCUSSION

#### A. SII assessments

The combined dry chamber data from our laboratory work, DD 95, and DD 96 shown in Fig. 4 reveal that SII values and percent intelligibility for the GMRT and SPIN stimuli decreased incrementally as the background noise level increased. These findings agree with earlier studies by Kryter (1962a, b) on the original Articulation Index, which produces calculations of speech audibility similar to those of the SII. Low SII values agreed with low GMRT and SPIN intelligibility scores, suggesting that little speech information was available to the listener when the background noise level was high. Likewise, higher SII values corresponded to higher percent correct scores when the noise levels were low, indicating that more speech information was available, contributing to enhanced intelligibility. Despite differences in the environments where we employed the SII for the nondiver and diver portions of DD 95 and DD 96, there was a very close match at all points along the curves. The data collected in DD 96 contributed to the lower portion of the curve showing performance in the most adverse noise conditions. The similarity of these results across the three different experiments and varying conditions lends support to the strength of the SII measurement for predicting speech intelligibility.

A consistent finding observed across all studies we performed using both the GMRT and SPIN has shown that SPIN scores were generally lower than the GMRT scores. This difference is possibly a result of the difference in response format across the two tests. The closed-set nature of the GMRT allows for a guessing floor, while the open-set format of the SPIN makes responses more difficult. However, even when GMRT scores were corrected to compensate for its closed-set nature, this disparity in scores still existed.

Also, the majority of SPIN errors were on the low-predictability stimulus items where context could not be used to help determine an appropriate response.

Overall, the SII data collected in DD 96 confirm our findings from DD 95 suggesting that it can be used as a speech intelligibility assessment tool to compare linear system components in a diving environment. Ultimately, we wanted to be able to use the SII as an objective tool for speech intelligibility assessment that could test different communication systems, including HSUs, without the use of Navy divers.

Unfortunately, we have recently ascertained that the SII may not to be an appropriate tool for intelligibility measurements of speech processed through inherently nonlinear devices, such as HSUs. Fundamentally, the SII only measures the audibility of a signal above the background noise level, and its calculations are based on long-term average spectra of normal, intelligible speech. The speech coming into an HSU is distorted, that is, not within the normal frequency range of speech, and it is often unintelligible. Because of the nature of the signal processing performed by HSU technology, it is not appropriate to use the SII to compare such devices since the SII will only provide information about how well noise is suppressed through the HSU, not how intelligible the speech is. However, based on our findings during DD 95 and DD 96, the SII remains a promising tool for testing other diver communication system components, especially helmets, within a helium environment.

#### B. GMRT and SPIN assessments

The purpose of the in-water intelligibility testing using the SPIN and GMRT was to expand our previous findings by using these tests in a noisy, in-water environment with well controlled variables. We wanted to determine whether either test was sufficiently sensitive to accurately measure small changes in the communication systems when in a high level of background noise. The significant main effects observed for test condition (i.e., topside-diver scores higher than diver-diver scores) and for type of test (i.e., GMRT scores higher than SPIN scores) were found across both studies. Interestingly, this significant difference in test scores for the GMRT and SPIN was not found during DD 92 (Mendel *et al.*, 1995) which measured intelligibility only in a dry chamber. Most likely, the results obtained during DD 92 in the dry chamber were ceiling effects which contributed significantly to the inability of either the GMRT or SPIN tests to be more sensitive than the other in a less adverse environment. Thus these findings suggest that the GMRT may be more useful under noisier conditions such as when used in the water.

In DD 96, we were able to isolate the variable of helmet type and HSU to determine if either the SPIN or GMRT could measure differences in such system components. The significant ANOVA findings suggest that when the system component being compared has a large measurable difference, such as in helmet type, the SPIN and GMRT can be used as accurate speech intelligibility assessment tools. However, when the differences are more subtle, such as with differences in HSUs, neither the SPIN nor GMRT appears

sensitive enough to make such distinctions. The two types of HSU used in this study were either too similar for differences to be measured, or the subtle differences in the HSUs may not have affected intelligibility enough for the GMRT or SPIN to assess those differences.

Stimulus context continued to enhance intelligibility in the SPIN test, as the lowest percent of error occurred among the high-predictability items that had semantic context imbedded in them. Also, although the GMRT scores were significantly higher than the SPIN scores, the overall mean scores were quite low, especially in the diver–diver condition. These low overall scores provide more justification for our assertion that these tests lack the sensitivity needed to measure small but noticeable intelligibility differences. Therefore the findings from the in-water testing generally agree with our earlier work and suggest that the traditional speech intelligibility tests we have studied (GMRT and SPIN) are inadequate tools for determining the true effectiveness of varied aspects of diver communication systems under adverse listening conditions.

#### IV. CONCLUSION

The results from Deep Dives 1995 and 1996 along with our laboratory work suggest that the SII holds some promise as a speech intelligibility assessment tool in a helium environment. The robust relationship between SII values and speech intelligibility performance measured here lends strong justification for the use of SIIs for some speech intelligibility assessments. The results of the studies presented here suggest that the GMRT may be more useful than the SPIN in assessing speech intelligibility in a noisy helium environment like the in-water conditions. It should be noted that the GMRT is a tool that is designed to measure the intelligibility of speech content through all the communication system components whereas the SII can only measure the noise masking effects on speech. Nonetheless, SII measurements may be preferred for some components since they can be performed using a manikin and would alleviate the need and expense of testing divers under difficult in-water conditions.

#### ACKNOWLEDGMENTS

The authors thank the Navy Experimental Diving Unit in Panama City, Florida for the use of their facilities and personnel during the collection of the data obtained from the Navy divers. Special appreciation is expressed to Jeff McDonell and Larry Gibbs for their work on the SII data collection. We also thank the anonymous reviewers for their constructive comments on earlier versions of this manuscript. This work was supported by the Naval Sea Systems Command.

- ANSI (1970). ANSI S3.5-1970, "American National Standard Methods for the Calculation of the Articulation Index" (American National Standards Institute, New York).
- ANSI (1995). ANSI S3.5-1995, "American National Standard Methods for the Calculation of the Speech Intelligibility Index-Draft V4.0" (American National Standards Institute, New York).
- Belcher, E. O., and Andersen, K. (1983). "Helium speech enhancement by frequency-domain processing," in *Proceedings of the IEEE International Conference on Acoustics, Speech, and Signal Processing*, Boston, MA (IEEE, New York), pp. 1160–1163.
- Copel, M. (1966). "Helium voice unscrambling," *IEEE Trans. Audio Electroacoust.* **AU-14**, 122–126.
- Dildy, C. (1992). *A Helium Speech Unscrambler—Version 2.0* (Panama City, Florida; Copyright-All Rights Reserved).
- Giordano, T. A., Rothman, H. B., and Hollien, H. (1973). "Helium speech unscramblers—A critical review of the state of the art," *IEEE Trans. Audio Electroacoust.* **AU-21**, 436–444.
- Griffiths, J. D. (1967). "Rhyming minimal contrasts: A simplified diagnostic articulation test," *J. Acoust. Soc. Am.* **42**, 236–241.
- Hendrix, J. E. (1996). Personal communication.
- House, A. S., Williams, C. E., Hecker, M. H. L., and Kryter, K. D. (1965). "Articulation testing methods: Consonantal differentiation with a closed response set," *J. Acoust. Soc. Am.* **37**, 158–166.
- Kalikow, D. N., Stevens, K. N., and Elliott, L. L. (1977). "Development of a test of speech intelligibility in noise using sentence materials with controlled word predictability," *J. Acoust. Soc. Am.* **61**, 1337–1351.
- Kryter, K. D. (1962a). "Methods for the calculation and use of the articulation index," *J. Acoust. Soc. Am.* **34**, 1689–1697.
- Kryter, K. D. (1962b). "Validation of the articulation index," *J. Acoust. Soc. Am.* **34**, 1698–1702.
- Mendel, L. L., Hamill, B. W., Crepeau, L. J., and Fallon, E. (1995). "Speech intelligibility assessment in a helium environment," *J. Acoust. Soc. Am.* **97**, 628–636.
- Pavlovic, C. V. (1991). "Speech recognition and five articulation indexes," *Hearing Instrum.* **42** (4), 20–23.
- Stover, W. R. (1967). "Technique for correcting helium speech distortion," *J. Acoust. Soc. Am.* **41**, 70–74.



# Influence of a toroidal bend on wind instrument tuning

Cornelis J. Nederveen

Acaciaaan 20, 2641 AC Pijnacker, The Netherlands

(Received 14 October 1997; revised 5 May 1998; accepted 26 May 1998)

In a toroidal bend in a cylindrical wind instrument, with the same cross section as the cylindrical part, the inertance for longitudinal waves is reduced. This induces a change in the resonance frequency. The magnitude of this change depends on the length and the sharpness of the bend and on its position in the sound field. A transition to a cylinder gives an additional inertance correction. The present study compares known results from literature and adds new facts, employing analytical and numerical methods. Possible causes of the discrepancies between measurements and theory as reported in the literature are considered. The theory was verified by measurements on some toroidal bends in between cylindrical tube pieces. Corrections were applied for diameter differences between the torus and the rest of the pipe system. Within experimental uncertainty, a satisfactory correspondence with theory was found. The results obtained in the present study determine which diameter reduction in the bend can compensate the effects of the bend on the tuning. © 1998 Acoustical Society of America. [S0001-4966(98)02509-0]

PACS numbers: 43.75.Ef, 43.75.Fg [WJS]

## LIST OF SYMBOLS

$a$	ratio of inner and outer radii of a bend= $(1+b)/(1-b)$	$T$	temperature, °C
$b$	parameter indicating (local) bend sharpness= $y/R_0$	$u$	particle velocity, m/s
$B$	bend sharpness for a toroidal bend= $r_0/R_0$	$V$	volume, m <sup>3</sup>
$c$	sound speed, m/s	$x$	position coordinate, m
$d$	diameter, m	$y$	half-width of curved rectangular duct, m
$f$	frequency, s <sup>-1</sup>	$Z$	acoustic impedance, kg/m <sup>4</sup> s
$h$	mesh size of finite difference grid, m	$\alpha$	wall damping term
$k$	wave number, m <sup>-1</sup>	$\epsilon$	geometrically determined factor
$K$	bulk modulus of air, Pa	$\vartheta$	tangential coordinate in circular section
$L$	tube length, m	$\nu$	angular wave number
$M$	inertance, kg/m <sup>4</sup> s	$\rho$	density of air, kg/m <sup>3</sup>
$p$	acoustic pressure, Pa	$\rho_B$	apparent air density in bend, kg/m <sup>3</sup>
$Q$	resonator quality	$\varphi$	(i) angle coordinate in bend, (ii) geometrically determined factor
$r$	radial coordinate in bore, m	$\Phi$	total angle of bend
$r_0$	radius of bore, m	$\xi$	length of torus measured along the center line, m
$R_0$	radius of curvature of center line of a bend, m	$\psi$	phase angle
$S$	cross-sectional area of bore, m <sup>2</sup>	$\omega$	angular frequency= $2\pi f$ , s <sup>-1</sup>
		$\zeta$	$z/r_0$

## INTRODUCTION

Bends help to keep long wind musical instruments compact. Usually such a bend closely resembles a torus, i.e., the center line of the tube lies on a circle and the tube cross section is circular everywhere. At least for low notes, the diameter and the length of a bend are small as compared to the wavelength. In a musical instrument the mode of paramount interest is the longitudinal one. To a first approximation, the sound field in a torus can be assumed to be the same as in a cylindrical (“substitution”) tube of the same cross section and of a length equal to the length measured along the center line. However, this is only a good approximation for the compressibility. The inertance of the bend is smaller than that of the substitution cylinder since the flow takes a kind of shortcut, as can be seen from Fig. 1. This figure was obtained with the Schwarz-Christoffel conformal transforma-

tion package from MATLAB. The circular boundaries are approximated by polygons, but at least visually, the flow is not very much affected by this approximation. The reduced inertance in the bend causes changes in the tuning, which are different for different harmonics.

Various authors have studied the effects of a bend. Nederveen (1969) calculated the inertance reduction for a bend with a circular cross section. Rostafinski (1972, 1974, 1991) and Cummings (1974), investigated a bend of rectangular cross section and considered effects due to the attachment to a straight tube. These calculations are also applicable to bends no longer short with respect to the wavelength. Brindley (1973) performed measurements on a tube with a bend. Keefe and Benade (1983) considered circularly shaped bends and called attention to the existence of a transition correction where the bend joins the straight tube. They also performed

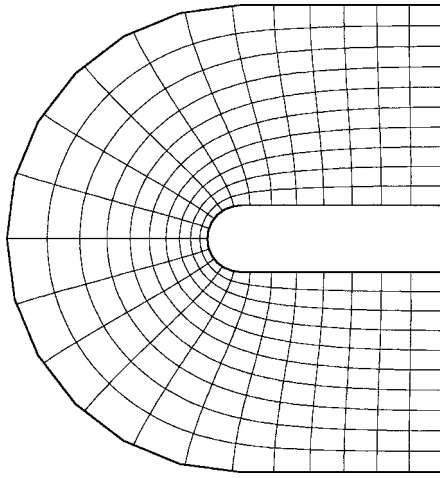


FIG. 1. Flow and potential lines in a curved duct, at both ends connected to a straight duct.

measurements of the bend inductance and of the transition correction. Other aspects of curved tubes were studied by Fuller and Bies (1978), Cabelli (1980), Cabelli and Shepherd (1984), Firth and Fahy (1984), and Ting and Miksis (1983).

### I. THEORY

In the normal playing range, the cross dimensions of the air column in a woodwind instrument are small with respect to the wavelength so that the only propagating modes are longitudinal; modes in the cross dimensions are evanescent. In many cases, the length of bends is also small with respect to the wavelength. Then the acoustic pressure  $p$  in the bend is adequately described by the Laplace equation  $\nabla^2 p = 0$ . To start with, and for simplicity, the properties of bends will first be studied based on this presumption.

A bend constitutes a perturbation in an otherwise straight tube. Its effects can be described in the same way as those for a local diameter perturbation in a straight bore; for example, a closed side hole. The effect of a closed side hole on the tuning was studied by Nederveen and Van Wulfften Palthe (1963), Nederveen (1969), Keefe (1982), Kergomard and Meynial (1988), and Nederveen *et al.* (1998). Figure 2 shows a circuit representation of the perturbed tube where, between the impedances of the regular tube pieces, are added an additional shunt compliance of  $-j(\rho c/S)/(\varphi k \Delta V/S)$  and an additional series inductance (divided in two halves flanking the shunt) of  $-j(\rho c/S)(\epsilon k \Delta V/S)$  at the position of the perturbation, where  $\rho$  is the air density,  $c$  the sound speed,  $\Delta V$  the excess volume of the perturbation over the

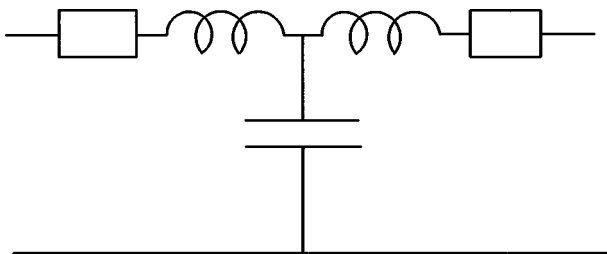


FIG. 2. Substitution circuit for a tube showing extra impedances due to a local perturbation.

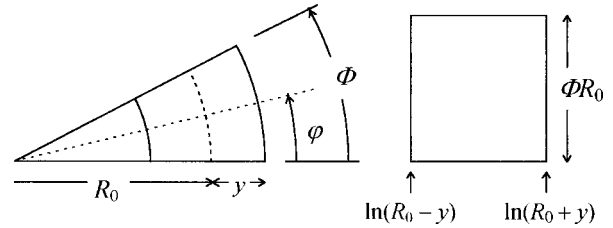


FIG. 3. Conformal transformation of a curved duct into a rectangular one.

bore with cross section  $S$ ,  $k = \omega/c$  the wave number,  $\omega$  the angular frequency, and  $\varphi$  and  $\epsilon$  factors determined by the geometry. The effect of a closed side hole on the resonance frequency can be expressed as a length correction  $\Delta L$

$$\Delta L = (\varphi \sin^2 kx - \epsilon \cos^2 kx) \Delta V/S, \quad (1)$$

where  $x$  is the distance to the open end or a velocity antinode (Nederveen *et al.*, 1998). For a very smooth perturbation,  $\varphi = \epsilon = 1$  and the expression becomes equal to that of Rayleigh for a smooth bore perturbation (1878, page 67, section 265), derived by considering changes in potential and kinetic energy density in the tube. For a short cylindrical side hole,  $\varphi$  remains equal to unity, but  $\epsilon < 1$ .

A similar description can be used for other types of perturbations, for example, a thin diaphragm in the bore. In that case still  $\varphi = 1$ , but  $\epsilon$  takes on other values (Pierce, 1989, page 324; Morse and Ingard, 1986, page 480).

For a description of the effects of a bend it is convenient to use Eq. (1), although in a bend (at least in the one we consider first, namely one with the same diameter as the rest of the tube) there is no volume change as compared to the substitution cylinder. Since there is no change in the potential energy, the compliance remains the same, which means that  $\varphi = 0$  in Eq. (1). There is no plausible reason to assume a change in compliance in a bend, as was suggested by Keefe and Benade (1983) to explain their measurement results. However, the kinetic energy in the bend is not the same as in the substitution cylinder. Its inductance change can be characterized by assigning a certain value to the product  $\epsilon \Delta V/S$ . This value determines the effects of the bend on the sound field.

For a rectangular duct of the same cross dimensions everywhere the problem is two dimensional, for which analytical solutions are available, for example, using conformal transformations in the complex plane. The acoustic flow at low frequencies is governed by the Laplace equation which also describes potential flow. The flow resistance and the inductance are essentially the same. A quantity is obtained from the transformation, which is sometimes called the conformal modulus; it defines the dimensions of a rectangular duct with the same flow resistance as the curved one (Morse and Ingard, 1986, page 483).

Figure 3 shows the nomenclature used for a curved duct of width  $2y$  and unit thickness. An annular region bounded by  $R_0 + y$  and  $R_0 - y$  and encompassing an angle of  $\Phi$  radians can be conformally transformed into a rectangle of length  $\Phi R_0$  and width  $\ln(R_0 + y) - \ln(R_0 - y)$ . Its conformal modulus is equal to its inductance  $M_B = \Phi / \ln a$ , where  $a$

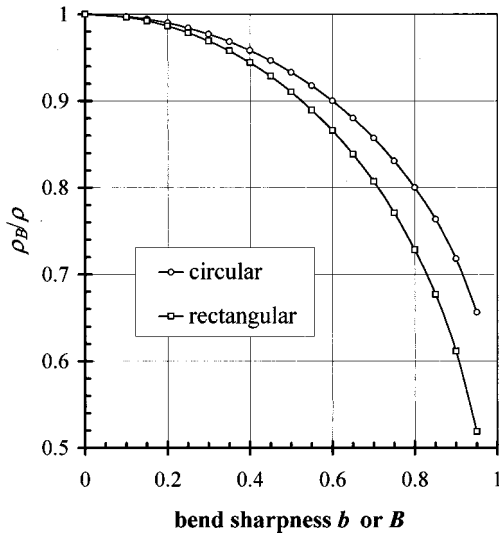


FIG. 4. Relative apparent density  $\rho_B/\rho$  in bends of rectangular and circular cross section.

$= (1+b)/(1-b)$  and  $b$  is a parameter indicating the sharpness of the bend:

$$b = y/R_0. \quad (2)$$

The inertance of the bend is different from that of a “substitution” rectangle, the latter defined as having the same area (volume) as the bend. Its length is  $\Phi R_0$ , its cross-section  $2y$ , so its inertance is  $M = \Phi R_0/2y$ . Introducing this quantity, the real (apparent) inertance of the bend becomes  $M_B = M(2b/\ln a)$ . Correspondingly, the apparent density  $\rho_{B2}$  for longitudinal waves in the 2-D bend is

$$\rho_{B2} = \rho(2b/\ln a). \quad (3)$$

In Fig. 4 the relative apparent density  $\rho_B/\rho$  is plotted as a function of  $b$  (squares).

Rostafinski (1972) carried out calculations on a rectangular bend, by modal decomposition, fitting Bessel functions in it. He calculated the argument of the wave function, or “angular wave number”  $\nu_0$  of the lowest tangential mode, which is given by his Eq. (5):

$$\nu_0^2 = \frac{2(a^2 - 1)/\ln a}{4(kR_1)^{-2} + a^2 + 1 + (a^2 - 1)/\ln a}, \quad (4)$$

where  $R_1$  is the inner radius of curvature of the bend. For long wavelengths,  $kR_1$  is small and the expression reduces to  $\nu_0^2 = (kR_1)^2(a^2 - 1)/2 \ln a$ . Inserting  $R_1 = 2R_0/(a + 1)$  we obtain  $\nu_0^2 = (kR_0)^2(2b/\ln a)$ . Since the wave number is proportional to the square root of the density, this expression is essentially identical to Eq. (3). This conclusion differs from that by Keefe and Benade (1983) who concluded that Rostafinski’s calculation was incorrect since it should predict an increase instead of a decrease in the wave impedance. This, however, does not appear from the present results.

Similar calculations by Cummings (1974) on ducts with rectangular cross section gave identical results.

The apparent density of a three-dimensional torus was analytically calculated by Nederveen (1969, page 60). Toroidal coordinates are used, where  $R$  = the distance to the axis

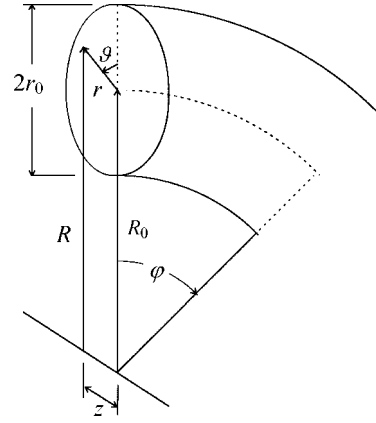


FIG. 5. Coordinates in a torus.

of curvature and  $\varphi$  = the angular coordinate in tangential direction (Fig. 5). Substituting  $x = R\varphi$  in the equation of motion  $u = (-1/j\omega\rho)(\partial p/\partial x)$  for an air particle at a distance  $R$  from the center of the torus gives

$$u = (-1/j\omega\rho R)(\partial p/\partial\varphi). \quad (5)$$

Pressure  $p$  is the same over the cross section, the mean velocity  $u_{\text{mean}}$  over the cross section  $S$  of the tube is found from

$$u_{\text{mean}} = (1/\pi r_0^2) \int u \, dS, \quad (6)$$

where  $r_0$  = tube radius. Inserting Eq. (5) into Eq. (6) and introducing  $R = R_0 + r \cos \vartheta$ ,  $z = r \sin \vartheta$ , we find

$$\begin{aligned} u_{\text{mean}} &= \frac{-2\partial p/\partial\varphi}{j\omega\rho\pi r_0^2} \int_0^{r_0} \int_0^\pi \frac{r \, dr \, d\vartheta}{R_0 + r \cos \vartheta} \\ &= \frac{-2}{j\omega\rho r_0^2} [R_0 - \sqrt{R_0^2 - r_0^2}] \frac{\partial p}{\partial\varphi}. \end{aligned} \quad (7)$$

From this result the “apparent” density of the bend,  $\rho_{B3}$ , can be determined. Introducing the longitudinal position parameter  $x = R\varphi$  and replacing  $u_{\text{mean}}$  by  $u$ , Eq. (7) is rewritten as

$$u = (-1/j\omega\rho_{B3})(\partial p/\partial x), \quad (8)$$

where

$$\rho_{B3} = \rho \frac{B^2/2}{1 - \sqrt{1 - B^2}} < \rho \quad (9)$$

and where  $B = r_0/R_0$  is a parameter indicating the bend sharpness. In Fig. 4 the relative apparent density for a torus is plotted as a function of  $B$  (circles).

The effects of the inertance change in the bend can be described as a change in the input impedance of the bend. It will be related to the input impedance  $Z = p/Su$  of a straight cylinder with cross section  $S$  and length  $\xi$  which can be written as follows (Nederveen, 1969, page 8):

$$\begin{aligned} Z &= -j(\rho c/S)\tan(\omega\xi/c + \psi) \\ &= -jS^{-1}(K\rho)^{1/2} \tan[\omega\xi(\rho/K)^{1/2} + \psi], \end{aligned} \quad (10)$$

where  $K = \rho c^2$  is the bulk modulus of air and  $\psi$  is a constant determined by the boundary condition at  $\xi = 0$ . Writing the

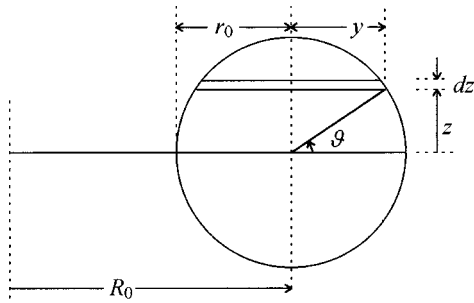


FIG. 6. Nomenclature for a slice cut from a torus.

input impedance of a toroidal tube of length  $\xi$  as

$$Z = -jS^{-1}(K\rho_B)^{1/2} \tan[\omega\xi(\rho_B/K)^{1/2} + \psi], \quad (11)$$

the bend's wave (or characteristic) impedance  $Z_{B,ch}$  and its phase velocity  $c_B$  are

$$Z_{B,ch} = Z_{ch} \sqrt{\rho_B/\rho}, \quad (12)$$

$$c_B = c \sqrt{\rho/\rho_B}, \quad (13)$$

where  $Z_{ch} = \rho c/S$ . Alternatively, the impedance can be written as that of a cylinder with area  $S_B$  and a length  $\xi_B$ :

$$Z = -jS_B^{-1}(K\rho)^{1/2} \tan[\omega\xi_B(\rho/K)^{1/2} + \psi], \quad (14)$$

$$S_B = S \sqrt{\rho/\rho_B}, \quad (15)$$

$$\xi_B = \xi \sqrt{\rho_B/\rho}. \quad (16)$$

This "apparent" cylinder is wider and shorter than the torus as measured along its center line. For example, for  $B = 0.75$ ,  $S/S_B = \xi_B/\xi = \sqrt{0.83} = 0.91$ , or a change of 9%. Note that these changes reduce the inertance of the tube piece but do not affect its compressibility. To compensate for the effect on the inertance, cross section, and length of the bend can be changed opposite to the changes given by Eqs. (15) and (16). When the bend is part of a conical tube (and conical itself) this can have consequences for the continuity of the conicity of the tube piece after the bend (Nederveen, 1969, page 62).

Another way of calculating the inertance change in a 3-D torus is (see Fig. 6) integrating the reciprocal inertance of parallel thin layers over the thickness (Keefe and Benade, 1983). A slice of thickness  $dz$  at a distance  $z$  from the center plane has a half-width

$$y = (r_0^2 - z^2)^{1/2}. \quad (17)$$

The local bend parameter  $b$  of this slice is related to the total bend parameter  $B = r_0/R_0$  by

$$b = B(1 - \zeta^2)^{1/2}, \quad (18)$$

where  $\zeta = z/r_0$ . The reciprocal inertance of a slice of  $\Phi$  radians and of thickness  $dz$  is

$$d(1/M_B) = [(\ln a)/\Phi] dz. \quad (19)$$

Integration over  $z$  gives the reciprocal inertance of the bend. The inertance of a cylinder with radius  $r_0$  and length  $\Phi R_0$  is  $M = \Phi R_0/\pi r_0^2$ . Changing to the variable  $\zeta$ , the apparent density of the torus is obtained from

$$\rho_{B3} = \rho_B \pi \left[ \int_{-1}^1 \ln \frac{1 + B\sqrt{1 - \zeta^2}}{1 - B\sqrt{1 - \zeta^2}} d\zeta \right]^{-1}. \quad (20)$$

When substituting  $\zeta = \sin \theta$  this expression becomes identical to the one derived by Keefe and Benade (1983). After numerical integration they found the results to be equal to the exact results of the present algebraic expression, Eq. (9). This should be no surprise, since it can be shown that both results are analytically identical (Nilsson, 1995).

Cummings (1974) gave results for a torus by applying the formulae for a rectangular bend to a circular tube with the same cross-sectional area. This means that his corrections to the density are too large, as appears from Fig. 4.

## II. THE TRANSITION CORRECTION

As appears from Fig. 1, a distortion of the wavefronts occurs at the junction of bend and straight tube, which diminishes away from the junction and disappears at a distance of about the diameter of the tube. The effect of these distortions can be described as a local inertance increase, as Keefe and Benade (1983) proposed. This is equivalent to a positive length correction, which reduces the magnitude of the (negative) torus length correction. Rostafinski's 1972 article mentions the distortion of the wavefronts at the transition, but not a correction to the angular wave number due to this.

Modeling the curved boundaries as polygons, the Schwarz-Christoffel conformal transformation can be used to investigate various aspects of this correction by composing various combinations of curved and straight portions. The conformal modulus found from this transformation is proportional to the inertance (flow resistance) of the polygon. Some results for  $b = 0.75$  are given in Table I. To obtain an impression of the magnitude of the error when approximating the boundaries by polygons, conformal moduli of a bend without straight portions are compared with the exact theoretical values from Eq. (3). In Table I the exact solutions are given in column 2, the polygonal approximation in column 4, for three angles of  $\Phi$ , in rows 2, 5, and 8. The magnitude of the adjacent angles is given in column 3. The relative errors in the polygonal approximation appear to be less than  $2 \times 10^{-4}$ .

To obtain the transition correction  $L_T$ , the values for a curved tube,  $L_B$ , and of a straight tube,  $L_C$ , are subtracted from the inertance (apparent length) of the combined tube,  $L_{BC}$ . The last column of Table I shows the results. The tubes should be of sufficient length to be outside the near field of the junction, but not too long, to avoid inaccuracies due to subtracting two large numbers. An indication of the sensitivity for the length can be obtained by doubling the length of the straight piece  $L_C$  from 1 to 2. As can be seen, this changes the correction by less than  $10^{-4}$ . A similar effect occurs when the curved portion becomes too short; then the transition correction is no longer independent of the bend length. This can be seen in Table I from observing the magnitude of  $L_T$  as a function of the angle  $\Phi$  of the curved part. Decreasing it from  $\pi$  to  $\pi/2$  only gives a slight decrease, but for  $\pi/4$  the transition correction changes more than 10%. This effect increases for increasing bend sharpness. For  $b$

TABLE I. Calculated inertance (or apparent length) for curved rectangular ducts. Inertances of a duct of unit width are expressed in units of length (of duct width), for various compositions of bends of various apparent lengths  $L_B$  (angular lengths  $\Phi$ ), connected to straight tubes of length  $L_C$ , giving a tube of apparent length  $L_{BC}$ . From these results, the transition correction  $L_T$  is calculated. Sharpness parameter of the bend is  $b=0.75$ .

$\Phi$	Exact solution	Polygon angle	$L_B$	$L_C$	$L_{BC}$	$L_T=L_{BC}-L_B-L_C$
$\pi$	1.614 46	$\pi/12$	1.614 75	0		
$\pi$		$\pi/12$		1	2.662 58	0.047 83
$\pi$		$\pi/12$		2	3.662 66	0.047 91
$\pi/2$	0.807 22	$\pi/12$	0.807 37	0		
$\pi/2$		$\pi/12$		1	1.854 91	0.047 54
$\pi/2$		$\pi/12$		2	2.854 99	0.047 62
$\pi/4$	0.403 61	$\pi/24$	0.403 62	0		
$\pi/4$		$\pi/24$		1	1.446 58	0.042 96
$\pi/4$		$\pi/24$		2	2.446 65	0.043 03

$>0.85$  the dependence of  $L_T$  on the angle of the bend for  $\Phi \leq \pi$  becomes larger than 2% of its value. Since bends of these sharpnesses are not found on musical instruments, we took  $b=0.85$  as the upper limit of the investigations. For a low bend sharpness, the correction becomes very small and no longer small compared to the error of the polygonal approximation. As a practical lower limit  $b=0.1$  was chosen. Results between these upper and lower limits are plotted as squares in Fig. 7, where it should be noted that the values are referred to the half-width (radius in the figure), whereas those in Table I are referred to the full width. After some trial and error it was found that the results can be represented by the following formula (the line through the squares in the diagram):

$$L_{T2}/y = 0.13b^2/(1 - 0.71b^4). \quad (21)$$

The 2-D result can be used to obtain an estimate for the 3-D case by assuming the flow to stay in planes parallel to the plane through the center line of the bend. The inertance in this case is obtained by integration of the reciprocal inertance in the direction perpendicular to the plane through the center line (here called the thickness). Since in reality the inertances along these slices will vary, there will be cross

flow between them, causing a lowering of the inertance of the tube (Pierce, 1989, page 343). So the inertance obtained in this way will be an upper limit. Analogous to Eq. (19), the reciprocal inertance of a slice of thickness  $dz$  is

$$d(1/M_B) = (\Phi/\ln a + L_{T2}/2y)^{-1} dz. \quad (22)$$

Performing the integration gives a corrected inertance, from which the transition correction can be derived. Direct integration of Eq. (22) leads to division by zero near the boundaries. To circumvent this, the term with the transition correction is first brought to the numerator, and after integration back to the denominator, using  $(1 - \epsilon) \approx 1/(1 + \epsilon)$  for small  $\epsilon$ . The following expression is obtained

$$\frac{L_{T3}}{r_0} = \left(\frac{\rho_{B3}}{\rho}\right)^2 \frac{1}{B^2 \pi} \int_{-1}^1 \frac{L_{T2}}{2y} (\ln a)^2 d\xi. \quad (23)$$

The integral was numerically determined; results are shown with triangles in Fig. 7.

Keefe and Benade experimentally investigated the transitional corrections by comparing the difference of two curved sections, made from U-turns, one a helical tube of 2.5 full turns and another one a sinuous tube of five 180-degree turns. They assumed the correction at a reversal of the curvature to be twice that of an adaptation to a straight tube. So a helix between two straight pipes should have two transitional corrections, a sinuous system with 5 S-turns between two straight pieces  $2 + 4 \times 2 = 10$ . To verify this assumption we calculated the conformal modulus of a pipe system with a reversed turn (Fig. 8) and deduced the transition corrections at the junctions with the straight ducts. The results for the curvature reversal correction for values of  $b$  between 0.3 and 0.75 are shown in Fig. 7 with crosses. The values are between 3.7 and 4 times as large as the transitional correction of a single transition from curved to straight tube. This number appears not to be very dependent on the bend sharpness, so it may be assumed that the factor for a curvature reversal in a torus will be about the same, in other words, being nearly twice as large as Keefe and Benade assumed.

### III. THE FINITE DIFFERENCE METHOD

To find the magnitude of the transition correction in three dimensions without systematic errors, a finite differ-

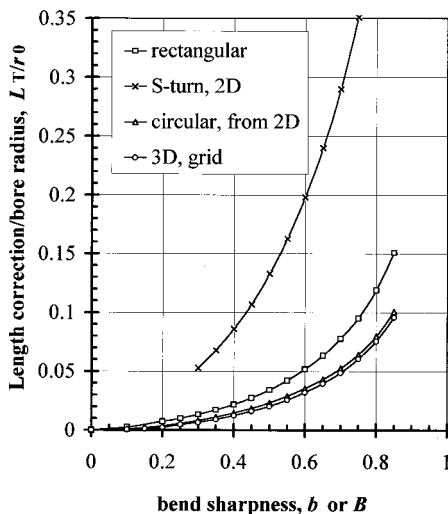


FIG. 7. Transition correction bend-to-cylinder,  $L_T/r_0$ , as a function of the bend sharpness  $b$  or  $B=r_0/R_0$ .

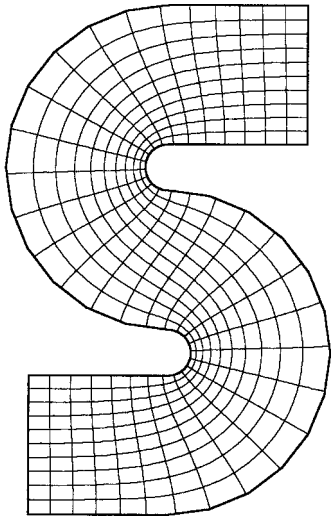


FIG. 8. Flow and potential lines in a duct with an S-turn.

ence method can be applied. The accuracy obtained is determined by the number of points of the grid. A Cartesian grid is fitted in the cylindrical part. In the torus a grid is used based on cylindrical polar coordinates following the curvature. The Laplace equation for the pressure  $p$  in cylindrical coordinates is

$$\frac{1}{r} \frac{\partial}{\partial r} \left( r \frac{\partial p}{\partial r} \right) + \frac{1}{r^2} \frac{\partial^2 p}{\partial \varphi^2} + \frac{\partial^2 p}{\partial z^2} = 0. \quad (24)$$

Figure 9 shows the 3-D discretization grid. The central point  $C$  is surrounded by points to the north ( $N$ ), the south ( $S$ ), the west ( $W$ ), and the east ( $E$ ), and perpendicular to the plane through the center line, to the top ( $T$ ) and the bottom ( $B$ ) (Patankar, 1980). In the cylindrical part the mesh is Cartesian with a mesh size  $h$ . In the torus,  $r$  is the local radius of curvature,  $R_0$  the radius of curvature of the center line, at which radius the mesh size is taken equal to that of the connecting cylinder, so  $\Delta \varphi = h/R_0$ . The discretization equations for the three terms of Eq. (24) are as follows

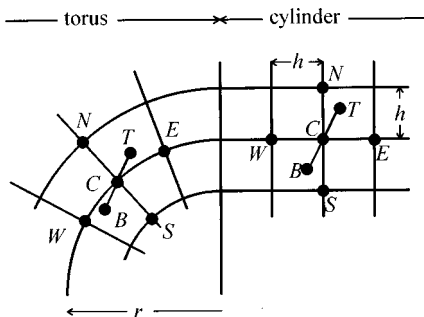


FIG. 9. Grid layout for the numerical solution in a torus connected to a cylinder.

$$\begin{aligned} \frac{1}{r} \frac{\partial}{\partial r} \left( r \frac{\partial p}{\partial r} \right) &= \frac{1}{r} \left( \frac{(r+h/2)(p_N-p_C)/h - (r-h/2)(p_C-p_S)/h}{h} \right), \\ \frac{1}{r^2} \frac{\partial^2 p}{\partial \varphi^2} &= \frac{1}{r^2} \left( \frac{p_E - 2p_C + p_W}{(\Delta \varphi)^2} \right) = \frac{R_0^2}{r^2 h^2} (p_E - 2p_C + p_W), \end{aligned} \quad (25)$$

$$\frac{\partial^2 p}{\partial z^2} = \frac{p_T - 2p_C + p_B}{h^2}.$$

The condition for the cylindrical part is the common one; it follows from that for the torus by leaving out  $h/2$  and setting  $R_0 = r$ . Then the conditions for the connection of the two areas (where torus, west, and cylinder, east, are joining) are specified:  $(R_0/r)(p_C - p_W) = p_E - p_C$ . At those boundaries where the flow is parallel to the boundary, the pressures of virtual points just outside the boundary are set equal to those of the inner mirror points. The values of the pressures at the end faces are specified. This leads to a set of equations for all grid points, which can be solved on a computer. From the gradients of the end faces the inertance is calculated. Finally, the correction is obtained from a comparison with the unperturbed case.

A Cartesian grid does not exactly fit the curved boundary. Although it is possible to adapt the mesh sizes of the grid and the discretization equation at the curved boundaries, for simplicity it was preferred to keep the mesh sizes the same everywhere. The resulting ragged boundaries cause fluctuations in the cross-sectional area, which results in fluctuations in the quantities calculated. At a sufficiently large number of points the errors become small. To get an impression of the possible errors, the earlier obtained values for a pure torus as well as those for a 2-D transition correction were compared with results from the finite difference method. At 90 points over the width (6000 over the cross section) an accuracy of  $10^{-3}$  to  $10^{-4}$  was obtained. At 30 points, results were better than 1%. This corresponds with results of finite difference calculations of Cabelli and Shepherd (1984) where a leveling of the errors above 17 points was found. Since the transition correction is the difference between two larger numbers its relative error is larger. The available computer capacity limited the 3-D calculations for the transition correction to about 40 points over the width, resulting in an uncertainty in the results for the transition correction of  $\pm 5\%$ . Results, referred to the radius, are plotted as circles in Fig. 7. No error bars were inserted for clarity. The upper error limit approximately coincides with the values obtained with the parallel-flow approximation (triangles). The 3-D values are somewhat lower than those obtained with this approximation, conform the expectations (see remark in the previous section). As with the 2-D calculations, results above  $B = 0.85$  were discarded since they were dependent on the length of the curved part if this encompassed less than 180 degrees. As remarked above, such sharp bends are not found in wind instruments so they were not investigated further.

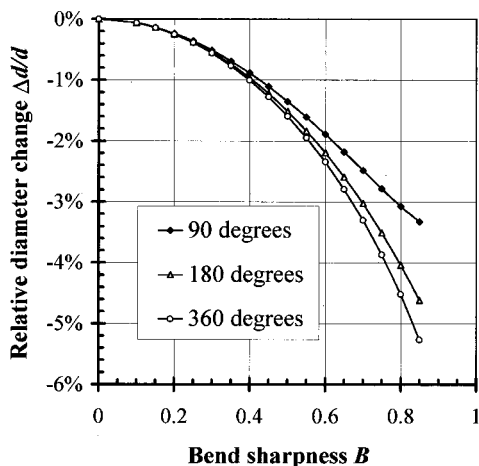


FIG. 10. Recommended diameter reduction in 90-, 180-, and 360-degree toroidal bends.

#### IV. OVERVIEW OF THEORETICAL RESULTS

For a bend short with respect to the wavelength, the inertance change as given by Eq. (9) and that due to the transition can be added. Leaving out 3 in the subscript we find for the modified inertance of a bend of length  $\Phi R_0$  with apparent density  $\rho_B$

$$(\rho_B/\rho)' = \rho_B/\rho + nL_T/\Phi R_0. \quad (26)$$

When the bend is connected to straight cylinders, the number of transitions from curved to straight,  $n$ , is equal to 2. When the bend also has a reversal of the curvature,  $n = 2 + 3.85 \pm 0.15$ .

Analogous to Eq. (1), the effect of the change in inertance can be expressed as a length correction. For a bend in a straight tube located at a distance  $x$  to an open end or to a velocity antinode, we find

$$\Delta L_B = \Phi R_0 [(\rho_B/\rho)' - 1] \cos^2 kx. \quad (27)$$

Since  $\cos kx$  is position and frequency dependent, different vibrational modes are affected differently.

When the bend diameter is not the same as the rest of the bore, for instance  $\Delta d$  larger than the bore diameter  $d$ , Eq. (1) can provide a correction. Taking  $\varphi = \epsilon = 1$  and  $\Delta V/S \approx \Phi R_0(2\Delta d/d)$ , and using  $\sin^2 kx + \cos^2 kx = 1$ , Eq. (27) is extended as

$$\Delta L'_B = [\Phi R_0(\rho_B/\rho - 1 - 4\Delta d/d) + nL_T] \cos^2 kx + 2\Phi R_0 \Delta d/d. \quad (28)$$

From this expression it can be seen what bore change in the bend has to be applied to compensate the (frequency-dependent) effects of the bend: the term between square brackets must be zero. This gives

$$\Delta d/d = 0.25(\rho_B/\rho - 1 + nL_T/\Phi R_0). \quad (29)$$

Figure 10 shows the magnitude of the diameter reduction, calculated with Eq. (29), for 90, 180 and 360 degree bends ( $n = 2$ ).

When the bend is not short with respect to the wavelength, Eq. (28) must be integrated over the length of the

bend, from  $x_1$  to  $x_2$ , where it is to be noted that the transition corrections are located at the ends of the bend:

$$\Delta L'_B = \int_{x_1}^{x_2} \left[ \left( \frac{\rho_B}{\rho} - 1 - \frac{4\Delta d}{d} \right) \cos^2 kx + \frac{2\Delta d}{d} \right] dx + \frac{nL_T}{2} (\cos^2 kx_1 + \cos^2 kx_2). \quad (30)$$

In the experiments to be described in the next section the center of the bend is either located in a node or in an antinode. When in a velocity antinode, the integration limits are  $-\xi/2$  and  $+\xi/2$ , where  $\xi = \Phi R_0$ . When the bend is in a velocity node, the influence is found by integration between the same limits, only with  $\cos$  replaced by  $\sin$  in Eq. (30). Carrying out both integrations and labeling the effects from antinode and node with  $A$  and  $N$ , respectively, gives the following expression

$$\Delta L_B^* = \Delta L'_{BA} - \Delta L'_{BN} = (\rho_B/\rho - 1 - 4\Delta d/d)k^{-1} \sin k\xi + nL_T \cos k\xi. \quad (31)$$

Expanding the trigonometric functions in series and retaining only the first two terms gives a formula applicable for the present investigations:

$$\Delta L_B^* = \xi(\rho_B/\rho - 1 - 4\Delta d/d)[1 - (k\xi)^2/6] + nL_T[1 - (k\xi)^2/2]. \quad (32)$$

Note that  $k = m\pi/L$  and  $m$  is the mode number. For an S-shaped tube a term  $nL_T$  is added, where  $n = 3.85$  (there is no wavelength influence: the reversal of curvature is exactly in the middle of the bend).

#### V. EXPERIMENTS

Experiments are reported in the literature. Cummings (1974) found good agreement between experiments and theory for tube systems with rectangular cross section. Brindley (1973) and Keefe and Benade (1983) performed experiments on tubes with circular cross section. Brindley found inertance changes to be larger than theoretically expected, he did not offer an explanation. Keefe and Benade found changes lower than expected, with the extra complication that the impedance changes were different from the phase velocity changes. As an explanation, they proposed a compliance shift or increased shearing losses in the bend, but found no decisive evidence for this. None of the authors considered possible influences of differences in internal diameters of bend and cylinder. These effects can be important as will appear below, consequently, they were considered in the present experiments.

Instrument builders and repair shops helped us to find suitable U bends and matching straight tubes with nominal internal diameters of 11.8 mm and 16.5 mm. Some of the 16.5 mm bends were soldered into a helical turn of 360 degrees and an S-turn of two times 180 degrees. Sleeves were attached to the ends for convenient connection to the cylinders. Pipe systems were built with the curved sections located in the center (see Fig. 11).

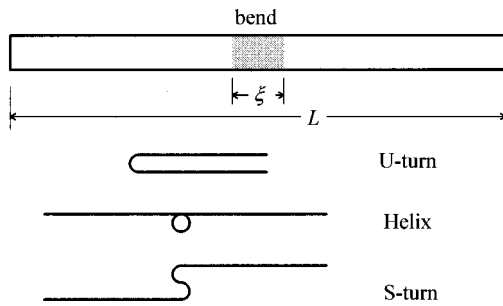


FIG. 11. Survey of tube combinations measured.

By sawing one of the 16.5-mm bends in slices it was found that the inner diameter varied between 16.5 and 16.8 mm, or approximately 0.15 mm more than the connecting cylinders. The bore was elliptical and position dependent. Since the wall thickness varied substantially across the circumference, the inner diameter could not be measured from the outside. A nondestructive method of measuring the diameter was preferred, but nothing commercially available could be found. So a simple tool was made consisting of two cap nuts on a piece of threaded rod, fixed with counter nuts and attached to an adjustable handle enabling maneuvering it in the bend (see Fig. 12). The distance between the cap nuts was measured with a caliber. Varying the distance between the cap nuts and comparing with readings in the cylindrical tubes resulted in numbers with estimated accuracies of  $\pm 0.05$  mm.

Table II gives an overview of dimensions and results for the present investigations and those of Brindley and of Keefe and Benade. In the present investigations, three U-turn bends were employed, one 360-degree helix and one S-turn. Brindley's two bends were distinguished by BI and BII. KB stands for the experiments of Keefe and Benade. Brindley located the bend at one third of the tube length  $L$ , closing one end and leaving the other open. By alternating the end closure, either a node or an antinode was situated in the bend. He measured three vibrational modes, where subsequently 3, 9, and 15 quarter-wavelengths fitted in the tube. Keefe and Benade's one-sided open tube was a quarter wavelength long.

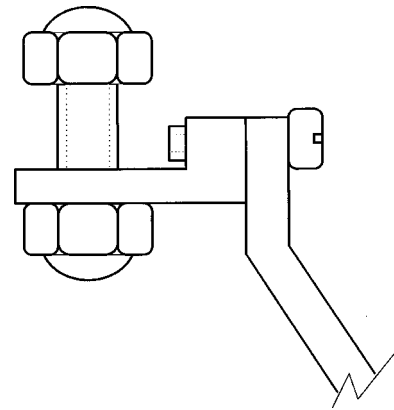


FIG. 12. Tool for measuring internal diameter in a bend.

For the present investigations and those of Brindley, the theoretically expected relative frequency shift  $D = \Delta f/f = -\Delta L/L$  was calculated with Eq. (32) and expressed in cent (0.0595%). The magnitude of the various terms is separately shown in Table II. The first order approximation for a "short" bend, the terms with  $(\rho_B/\rho - 1)$ , is  $D_1$ . The next term, the effect of the diameter deviation is given as  $D_{dia}$ . The transitional correction  $D_T$  is the term with  $nL_T$ . The magnitude of the higher order effects, the terms with  $(k\xi)^2$ , is designated by  $D_2$ . The sum of all contributions is the total theoretical frequency shift  $D_{th}$ . This is transformed into a relative apparent density with

$$(\rho_B/\rho) = 1 - (L/\xi)(0.0595D/100) \quad (33)$$

and listed in the table. Keefe and Benade used various pipe combinations with relatively large toroidal portions and took wavelength dependencies into account. From their measurements they derived changes in wave impedance of  $-6.3\%$  and in phase velocity of  $+4.7\%$ . These values can be transformed into density using Eqs. (12) and (13). Both numbers are listed in Table II, together with the theoretical value given by Eq. (9).

For the present acoustical measurements, one of the closed ends was connected to the impedance measuring head

TABLE II. Survey of dimensions and results of pipe systems investigated. Part of the symbols are explained in Figs. 5 and 11.  $d (=2r) =$  measured internal diameter of cylindrical tubes (cyl) or torus (bend).  $B = r_0/R_0 =$  bend sharpness parameter.  $D = \Delta f/f$  is tuning difference at the second mode in cent ( $=0.01$  semitone) between even and odd modes. Indices: 1 = only first order, dia = diameter change in bend,  $T =$  transition correction, 2 = second order term, th = total theoretical, exp = experimental. BI, BII = Brindley investigations for bend types I and II. KB = Keefe/Benade investigations.

Type	$d_{cyl}$ mm	$2r_0 = d_{bend}$ mm	$2R_0$ mm	$B = r_0/R_0$	$\xi$ mm	$L$ mm	$D_1$ cent	$D_{dia}$ cent	$D_T$ cent	$D_2$ cent	$D_{th}$ cent	$\rho_B/\rho$ theory	$D_{exp}$ cent	$\rho_B/\rho$ exp
U1	11.8	11.75	19.6	0.600	30.8	527	9.8	-1.6	-1.2	-0.1	6.9	0.930	6.8	0.931
U2a	16.5	16.65	29.4	0.565	46.2	856	7.9	+3.3	-0.9	-0.1	10.2	0.888	9.1	0.900
U2b	16.5	16.65	29.4	0.565	46.2	856	7.9	+3.3	-0.9	-0.1	10.2	0.888	10.1	0.888
Helix	16.5	16.65	29.4	0.565	92.4	902	15.1	+6.2	-0.8	-1.4	19.1	0.889	20.7	0.880
S-turn	16.5	16.65	29.4	0.565	92.4	902	15.1	+6.2	-2.4	-1.4	17.5	0.899	17.8	0.896
BI	9.5	9.5	13	0.731	20.4	1100	4.9		-0.8	0	4.1	0.868	11.1	0.645
BI	9.5	9.5	13	0.731	20.4	1100	4.9		-0.8	0	4.1	0.869	10.5	0.664
BI	9.5	9.5	13	0.731	20.4	1100	4.9		-0.8	-0.1	4.0	0.871	7.0	0.775
BII	9.5	9.5	45	0.211	70.7	1151	1.2		0	-0.1	1.1	0.989	3.8	0.964
BII	9.5	9.5	45	0.211	70.7	1151	1.2		0	-0.2	1.0	0.990	3.0	0.971
BII	9.5	9.5	45	0.211	70.7	1151	1.2		0	-0.4	0.8	0.992	2.6	0.974
KB	18.5	18.5	25.4	0.728	269.5	550						0.843		0.878
KB	18.5	18.5	25.4	0.728	269.5	550						0.843		0.912



TABLE III. Survey of some experimental and theoretical results. Measured resonance frequencies  $f$  in Hz for five tube combinations and four modes. Temperature  $T$  in degrees Celcius (C).  $f_\infty$ =hypothetical resonance frequency of first mode for zero damping and no bend effect.

Type of bend	Experimental							Theoretical	
	$T$	$f_1$	$f_2$	$f_3$	$f_4$	$f_{\infty, \text{exp}}$	$\alpha_{\text{exp}}$	$f_{\infty, \text{th}}$	$\alpha_{\text{th}}$
U1	19.8	321.99	645.23	974.34	1296.5	327.7	0.0158	326.2	0.0146
U2a	20.2	197.52	395.32	597.79	793.63	200.2	0.0129	201.0	0.0133
U2b	20.4	197.69	395.14	597.70	793.54	200.4	0.0143	201.1	0.0133
Helix	20.1	188.97	375.25	571.07	754.13	190.8	0.0169	190.7	0.0136
S-turn	20.2	188.71	375.60	570.82	754.64	190.8	0.0160	190.7	0.0136

of the Acoustics Department of the University of Le Mans, France (Dalmont and Herzog, 1993). The measurements were performed in an anechoic room, after temperature equilibrium, which usually took one hour. The tube was excited in the first four modes. Measured were temperature, resonance frequency, and resonator quality  $Q$ . The first two quantities are listed in Table III.

The sound speed at temperature  $T$  [°C] is calculated from

$$c = 331.45(1 + T/546.32 + 0.16 r_{\text{wv}}) \text{m/s}, \quad (34)$$

where  $r_{\text{wv}}$  is the fractional pressure of water vapor, in this case taken as 0.007 (Hardy *et al.*, 1942; Nederveen, 1969; Kinsler *et al.*, 1982; Caussé *et al.*, 1984; Pierce, 1989). The frequency in the absence of damping then is calculated from  $f_{\infty, \text{th}} = c/2L$ , where  $L$  is the tube length specified in Table II, and given in Table III.

Wall damping adds a frequency-dependent term to the sound speed. According to theory, the wave number in a cylinder with radius  $r$  becomes  $k = k_\infty(1 + \alpha_{\text{th}})$ , where  $\alpha_{\text{th}} = 0.00021r^{-1}k^{-0.5}$ ; experiments have confirmed this (Fay, 1940; Nederveen, 1969; Caussé *et al.*, 1984; Pierce, 1989). Values calculated for the corresponding  $f_{\infty, \text{th}}$  are given in Table III.

Due to this wall damping influence, the measured resonance frequencies divided by the mode number,  $f/m$ , will lie on a straight line when plotted against  $1/\sqrt{f}$ . Such a plot is shown in Fig. 13. For every pipe combination two straight lines are found, one for even and one for odd modes. Extrapolation of the even-mode line (the lower one) to the vertical axis gives  $f_{\infty, \text{exp}}$ , and the damping term is obtained from  $\alpha_{\text{exp}} = 2f_{\infty, \text{exp}}/f_2 - 1$ . Both values are listed in Table III.

From Table III it appears that experimental and theoretical values are not exactly the same. There are some possible causes for the discrepancies. The diameter deviation in the bends as compared to the rest of the system gives a small frequency shift which can be calculated with the term  $2\Phi R_0 \Delta d/d$  in Eq. (28), but the shifts are too small to explain the discrepancies. Higher order effects at higher modes slightly change the slopes of the lines to be extrapolated to  $f_{\infty, \text{exp}}$ . But these slopes are also effected by increased losses in the bend and due to dirt and some spurious leakage. Besides, unknown diameter and temperature uncertainties influence the results as well. There is little evidence for large increases in losses in the bend, a suggestion of Keefe and Benade (1983) for which they also did not found evidence. An independent estimate of the damping values is obtained

from the measured resonator qualities  $Q$  (not reported here), related to the damping by  $Q = 1/2\alpha$ , but there were fluctuations in these values too, although in general the correspondence was reasonable. There are too many uncertainties to explain the small errors in the absolute values. However, it can be concluded that the absolute values of the measurements are sufficiently consistent with theoretical expectations to give credibility to the experimental setup. There is no evidence for a compliance change in a bend as suggested by Keefe and Benade (1983). Their effects are most likely caused by (undetected) diameter changes.

From the vertical distances of the even- and odd-mode lines in Fig. 13 at the second mode, the frequency shift was obtained after division by the frequency. Results are listed in Table II as  $D_{\text{exp}}$ , together with the relative apparent density obtained from Eq. (33).

The values for  $\rho_B/\rho$  obtained from the measurements

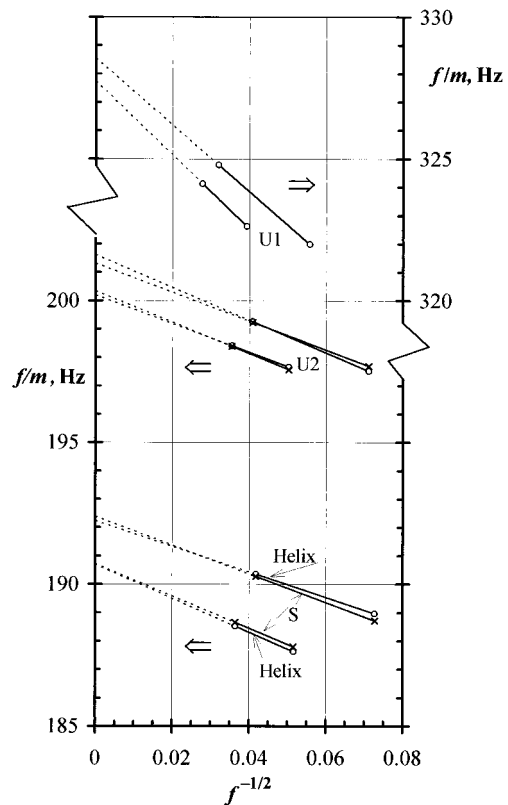


FIG. 13. Frequency  $f$ , divided by the mode number  $m$ , plotted versus the reciprocal square root of frequency.

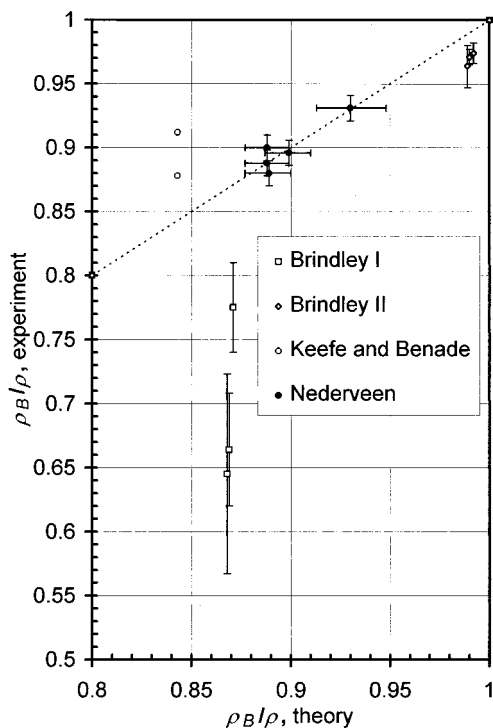


FIG. 14. Plot of measured versus calculated relative apparent densities in toroidal bends obtained from various sources.

were plotted versus those of the theory in Fig. 14. The horizontal error bars correspond to a diameter uncertainty of  $\pm 0.05$  mm. The vertical error bars correspond to an estimated measurement error of  $\pm 1$  cent. The correspondence between theory and experiment is satisfactory.

The measurement results of Brindley and of Keefe and Benade are also plotted in Fig. 14. Error estimates as given by Brindley are indicated by error bars. Keefe and Benade did not give error estimates.

The magnitude of the transition correction in a reversed turn appears from the difference between the helix and the S-turn. From Table II it can be found that theory predicts a difference of  $19.1 - 17.5 = 1.6$  cent, whereas experiment gives  $20.7 - 17.8 = 2.9$  cent. The discrepancy can be due to diameter variations and inaccurate soldering of the bends.

With the present tubes it is not possible to verify the theory more accurately. For an accurate analysis, the diameters in tubes and bend have to be the same and perfectly circular everywhere, to avoid complicating corrections. The diameter would need to be exactly known, say within 0.02 mm. This would reduce the lengths of the horizontal error bars in Fig. 14 to those of the vertical bars.

## VI. CONCLUSIONS

A bend causes a reduction of the local inertance of a magnitude determined by its sharpness. Theoretical predictions of various authors and those of the present author appear to be the same. The present study extends these studies with "transition" corrections at positions where a bend joins a straight tube. Numerical values of this transition correction were obtained by approximative calculations. The results are

sufficiently accurate for practical applications, since the transition correction is of the order of 20% of the total inertance correction in a bend.

Measurements reported in the literature on influences of a bend on the resonance frequency deviate from the predictions. As a possible cause the present author suggests influences of small diameter deviations in the bend. In the present experiments, this effect was taken into account, resulting in a reasonable correspondence with theory.

The tuning changes due to a sharp bend are sufficiently large to be detectable in practice on a woodwind instrument. From Table II it can be seen that for bends common on wind instruments the effects can be between 10 and 20 cents (0.1–0.2 of a semitone), which is substantial in musical instruments. Since the effects are mode dependent the tuning changes are uneven. To compensate for this the diameter in a bend can be reduced in an amount shown in Fig. 10.

## ACKNOWLEDGMENTS

I am grateful for the help of the Dutch instrument builders who provided and soldered bends: Paul van Bebber, Ruud Pfeiffer, and Hans Smit. The measurements were carried out during a stay at the Acoustical Laboratory of the University of Le Mans, France. With Jean Kergomard I had fruitful discussions on the torus problem, Jean-Pierre Dalmont gave me crucial help with the measurements. Jos Jansen of the Eindhoven University of Technology, The Netherlands, helped with the setup of the numerical calculations.

- Brindley, G. S. (1973). "Speed of sound in bent tubes and the design of wind instruments," *Nature* (London) **246**, 479–480.
- Cabelli, A. (1980). "The acoustic characteristics of duct bends," *J. Sound Vib.* **68**, 369–388.
- Cabelli, A., and Shepherd, I. C. (1984). "Duct acoustics—A numerical technique for the higher order mode solution of three-dimensional problems with rigid walls and no flow," *J. Sound Vib.* **92**, 419–426.
- Caussé, R., Kergomard, J., and Lurton, X. (1984). "Input impedance of brass musical instruments—Comparison between experimental and numerical models," *J. Acoust. Soc. Am.* **75**, 241–254.
- Cummings, A. (1974). "Sound transmission in curved duct bends," *J. Sound Vib.* **35**, 451–477.
- Dalmont, J.-P., and Herzog, Ph. (1993). "Improved analysis of impedance measurements," *Proc. of the Institute of Acoustics* **15**, 681–688.
- Fay, R. D. (1940). "Attenuation of sound in tubes," *J. Acoust. Soc. Am.* **12**, 62–67.
- Firth, D., and Fay, F. J. (1984). "Acoustic characteristics of circular bends in pipes," *J. Sound Vib.* **97**, 287–303.
- Fuller, C. R., and Bies, D. A. (1978). "Propagation of sound in a curved bend containing a curved axial partition," *J. Acoust. Soc. Am.* **63**, 681–686.
- Hardy, H. C., Telfain, D., and Pielemeier, W. H. (1942). "The velocity of sound in air," *J. Acoust. Soc. Am.* **13**, 226–233.
- Keefe, D. H. (1982). "Theory of the single woodwind tone hole," *J. Acoust. Soc. Am.* **72**, 676–687.
- Keefe, D. H., and Benade, A. H. (1983). "Wave propagation in strongly curved ducts," *J. Acoust. Soc. Am.* **74**, 320–332.
- Kergomard, J., and Meynial, X. (1988). "Systèmes micro-intervalles pour les instruments de musique à vent avec trous latéraux," *J. Acoust.* **1**, 255–270.
- Kinsler, L. E., Frey, A. R., Coppens, A. B., and Sanders, J. V. (1982). *Fundamentals of Acoustics* (Wiley, New York), 3rd ed.
- Morse, M. M., and Ingard, K. U. (1986). *Theoretical Acoustics* (Princeton U.P., Princeton, NJ).
- Nederveen, C. J. (1969). *Acoustical Aspects of Woodwind Instruments*, 1st ed. (Knuf, Amsterdam), 2nd ed. in preparation at Northern Illinois U.P., DeKalb, IL.

- Nederveen, C. J., and Van Wulfften Palthe, D. W. (1963). "Resonance frequency of a gas in a tube with a short closed side-tube," *Acustica* **13**, 65–70.
- Nederveen, C. J., Jansen, J. K. M., and Van Hassel, R. R. (1998). "Corrections for woodwind tone-hole calculations," to be published in *Acustica/Acta Acustica*.
- Nilsson, B. E. (1995). Private communication.
- Patankar, S. V. (1980). *Numerical Heat Transfer and Fluid Flow* (Taylor and Francis, London).
- Pierce, A. D. (1989). *Acoustics. An Introduction to its Physical Principles and Applications* (Acoustical Society of America, New York).
- Rayleigh, J. W. S. (1878). *The Theory of Sound* (Reprint Dover, New York, 1945), Vol. 2, p. 67.
- Rostafinski, W. (1972). "On propagation of long waves in curved ducts," *J. Acoust. Soc. Am.* **52**, 1411–1420.
- Rostafinski, W. (1974). "Analysis of propagation of waves of acoustic frequencies in curved ducts," *J. Acoust. Soc. Am.* **56**, 11–15.
- Rostafinski, W. (1991). "Monograph on propagation of sound waves in curved ducts," NASA reference publication 1248.
- Ting, L., and Miksis, M. J. (1983). "Wave propagation through a slender curved tube," *J. Acoust. Soc. Am.* **74**, 631–639.

# Artificial buzzing lips and brass instruments: Experimental results

Joël Gilbert and Sylvie Ponthus

*Institut d'Acoustique et de Mécanique de l'Université du Maine, Laboratoire d'Acoustique—UMR CNRS 6613, Avenue Olivier Messiaen, 72085 Le Mans Cedex 9, France*

Jean-François Petiot

*Institut de Recherche en Cybernétique de Nantes, UMR CNRS 6597—Equipe CMAO Productique, 1 rue de la Noë, BP 92101, 44321 Nantes Cedex 3, France*

(Received 21 January 1998; revised 12 May 1998; accepted 13 May 1998)

Experimental results of a special artificial trombone player are presented: A mechanical device is a substitute for the musician. Wind instruments, and particularly the brass, are self-sustained oscillators. The oscillations are induced by a mechanical oscillator (the lips of the player) acting as a valve which modulates the flow. Measured mechanical parameters of the artificial buzzing lips for different “embouchures of the player” are presented, and analyzed in connection with the played frequencies obtained for the same “embouchures.” The results are obtained with two resonator systems (a mouthpiece alone and a trombone with its mouthpiece). © 1998 Acoustical Society of America. [S0001-4966(98)00509-8]

PACS numbers: 43.75.Fg [WJS]

## INTRODUCTION

Oscillations of wind instruments, and particularly lip-driven wind instruments (the brass), are driven by self-sustained oscillations of an air flow. These oscillations are induced by a mechanical oscillator (the lips of the player), acting as a valve which modulates the flow. The destabilization of the mechanical element is the result of a complex aeroelastic coupling among (1) the lips, (2) the air flow entering the instrument as a result of the static overpressure in the mouth of the musician, and (3) the resonant acoustic field in the instrument itself. The brass instruments have been extensively studied (see, for example, Backus, 1976; Pratt *et al.*, 1977; Elliot *et al.*, 1982; Causse *et al.*, 1984). A global study including the player behavior has been proposed by Elliot and Bowsher (1982). In the last 10 years, time-domain simulations based on this kind of model have been proposed (Strong and Dudley, 1993; Dietz and Amir, 1995; Adachi and Sato, 1996; Rodet and Vergez, 1996; Juin, 1996; Msallam *et al.*, 1997). Due to the essential nonlinearity of the governing equations describing the mechanical behavior of the lips coupled with the air flow entering the instrument, it is important to focus our attention on this part of the system. Some experimental results focused on the human lip oscillations have been obtained: Martin (1942); Elliot and Bowsher (1982); Saneyoshi *et al.* (1987); Yoshikawa (1995); Bailliet *et al.* (1995); Chen and Weinreich (1996); Copley and Strong (1996). One of the major difficulties of this kind of experimental study on vibrating lips is the human player. In order to avoid this major difficulty, we have decided to develop an artificial mouth for brass using artificial buzzing lips.

Previous studies on reed musical instruments (Backus, 1963; Wilson and Beavers, 1974; Meynial, 1987; Gilbert, 1991; Idogawa *et al.*, 1993; Gazengel, 1994; Dalmont *et al.*, 1995) have demonstrated the usefulness of a mechanical de-

vice as a substitute for the musician. This substitution allows stable mouth controls and makes it possible to take extensive measurements during stable playing conditions and to compare these with characteristic features of the instrument. We will present here comparisons of the playing frequency near the threshold of oscillations, the acoustical passive resonance frequency of the instrument and the mechanical passive resonance frequency of the lips. After a first artificial mouth for brass instruments (Gilbert and Petiot, 1997a, b) was developed in order to measure the effect of nonlinear propagation in the instrument (Beauchamp, 1980; Hirschberg *et al.*, 1996), a second one (Piau, 1997) has been constructed with improved control of the embouchure, and the latter has been used in the experiments described in this paper.

The present paper is divided into three parts. After this brief Introduction, we present the experimental setups in Sec. I: the artificial mouth setup, the input impedance measurement, and the artificial lips' mechanical characterization are described successively. Different frequencies are obtained from these setups (Sec. II): the acoustical resonance frequency ( $F_{res}$ ) from the input impedance measurement, the lips' eigenfrequencies ( $F_{lip}$ ) from the mechanical characterization, and the played frequencies ( $F_{play}$ ) by playing the instrument with the artificial mouth. By controlling the “embouchure” of the artificial mouth, the lips' frequencies and the played frequencies are slightly modified. The measurements are reported twice: first with a mouthpiece alone, second with the entire trombone including its mouthpiece. Finally the experimental results are analyzed.

## I. EXPERIMENTAL SETUPS AND PROCEDURES

### A. Artificial mouth and buzzing lips

The artificial mouth (Fig. 1) consists of a hermetically sealed box (volume 1500 cm<sup>3</sup>) fed by a high-pressure (5-bar maximum) air supply. The mouth pressure in the box is con-

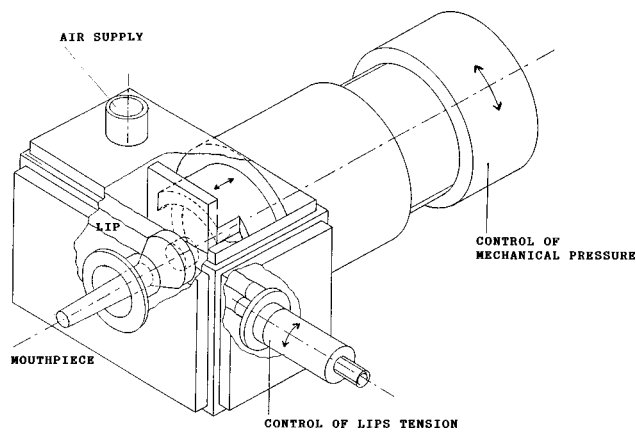


FIG. 1. The artificial mouth for brass instruments.

trolled by a pressure regulator. A 1 m long tube of 1 cm diameter connects the regulating valve to the artificial mouth. The “artificial lip” is a latex tube filled with water. The lip is 150 mm long, with a diameter of 16 mm, and a wall thickness of 0.6 mm. It is constrained by an “artificial jaw” consisting of a plate with a circular hole of 2 cm diameter (Fig. 1). The lip is pressed by the mouthpiece against the “jaw.” There are two mechanical control parameters for the embouchure: a control of the lip tension, and a control of the position of the mouthpiece relative to the lip. Thus the “embouchure,” the way the mouthpiece and lips interact, is controlled by the intrinsic parameters of the lips such as the tension of the latex tubes, the mass of water inside, and the position of the mouthpiece relative to the lips. The last is the only parameter used to vary the embouchure for experiments presented in Sec. II.

There are minor differences with respect to the first version of the artificial mouth described in Gilbert and Petiot (1997a, b). The mechanical system of the embouchure is moved from the front to the back of the mouth; the mouthpiece is clamped and remains fixed. Therefore it is possible to replace one brass instrument with another without perturbation of the embouchure. In the experiments described here, to have a mechanical system as simple as possible, only one latex lip is installed, the other being replaced by a solid plate. The artificial mouth has a realistic playing performance, as judged by listening to the sound produced by the system. Notice that such a single lip drive has already been used by Gokhstein (1981) for observations on human lip oscillations.

## B. Resonator input impedance

### 1. Input impedance measurement

The air resonator system, a mouthpiece alone or a trombone with its mouthpiece, is characterized by its input impedance (complex quotient of the acoustical pressure and volume velocity in the input of the resonator in forced oscillations). The input impedances are measured by the apparatus described in Dalmont and Bruneau (1991). The apparatus is a simple plane support for three microphones (including one microphone acting as source) and the object to be measured. In practice, an adaptor needs to be custom-made to fix the object to the support. Within the measuring probe an

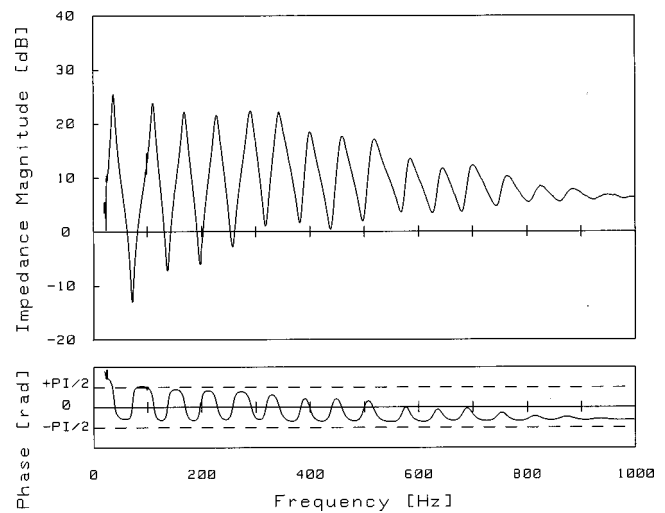


FIG. 2. The measured input impedance of the trombone (Courtois model 149) with its mouthpiece (Bach model Megatone 6<sup>1/2</sup> AM). The value of the impedance magnitude (decibel representation) is expressed in units of  $\rho c/S$  (the characteristic impedance of the air in the pressure-volume velocity analogy,  $S$  is the input cross-sectional area of the mouthpiece). The value of the impedance phase is expressed in radian.

electrostatic transducer (1/2-in electrostatic microphone cartridge B&K) is used as a source and two electret microphones (electret microphone cartridges, Sennheiser KE4) are used as receivers. The two receivers are placed in the same plane as the emitter on either side and diametrically opposite each other. Notice that for our application we only use one of the two receiving microphones. The second one is useful when measurements of the first helical mode are performed (Dalmont and Bruneau, 1991). Our impedance measurements are done below the first cut-off frequency, so that the plane-wave propagation approximation is accurate.

The impedance measurements shown below are made with a harmonic source. The transfer function (microphone signal over excitation signal) is obtained by a dual-phase-lock-in technique. The frequency range of the swept sine is typically 20–1000 Hz. Before the measurements we use a method of calibration based on preliminary measurements with a set of closed cylindrical tubes [for further details, see Dalmont and Bruneau (1991)].

## 2. Results

Figure 2 shows the measured input impedance of the trombone (Courtois model 149) with its mouthpiece (Bach model Megatone 6<sup>1/2</sup> AM). The impedance curve is comparable with, among others, the experimental results of Elliot and Bowsher (1982). The parameters (frequency, quality factor, magnitude) of the eight first resonances are given in Table I. Moreover the input impedance of the trombone mouthpiece alone has been measured. As expected, the mouthpiece has only one resonance frequency (frequency corresponding to a magnitude maximum and a zero phase of the input impedance): the resonance frequency is  $F_m = 545.6$  Hz, and the quality factor of this resonance is 19.9.

We will use in our further discussion the following resonance frequencies for comparison with the other frequencies: the resonance frequency  $F_m$  of the mouthpiece ( $F_m$

TABLE I. Frequency (Hz), quality factor (dimensionless), and magnitude (dB) of the eight first resonances of the trombone (Courtois model 149) with its mouthpiece (Bach model Megatone 6<sup>1/2</sup> AM).

Resonance number	Frequency (Hz)	Quality factor	Magnitude (dB)
1	38.1	8.4	25.5
2	111.3	18.1	23.9
3	169.1	19.8	22.2
4	228.2	24.6	21.6
5	290.8	24.9	22.4
6	343.3	34.6	22.1
7	399.2	31.1	18.4
8	458.1	28.0	17.5

=545.6 Hz), and the resonance frequencies number 3, 4, 5 of the trombone ( $Ft3 = 169.1$  Hz,  $Ft4 = 228.2$  Hz,  $Ft5 = 290.8$  Hz).

### C. Artificial lip mechanical response

#### 1. Mechanical response measurement

The aim of the experimental setup described below is to allow a mechanical characterization of the embouchure (the lip and its boundary conditions imposed by the position of the mouthpiece). The mechanical response of the lip is obtained by simultaneous measurement of lip vibration (using a laser vibrometer Polytec OFV 3000) and the acoustic pressure in the mouth behind the lip and the jaw (using an electret microphone cartridge, Sennheiser KE4). The lip is excited in forced oscillation by a sound source (a compression loudspeaker driver, JBL model TRS001). The mechanical response (vibrometer displacement signal over mouth pressure signal) is obtained by means of a dual-phase-lock-in technique (Fig. 3). The frequency range of the swept sine is typically 50 to 500 Hz.

The source is positioned behind the lip; we assume that the pressure there is locally uniform, and representative of

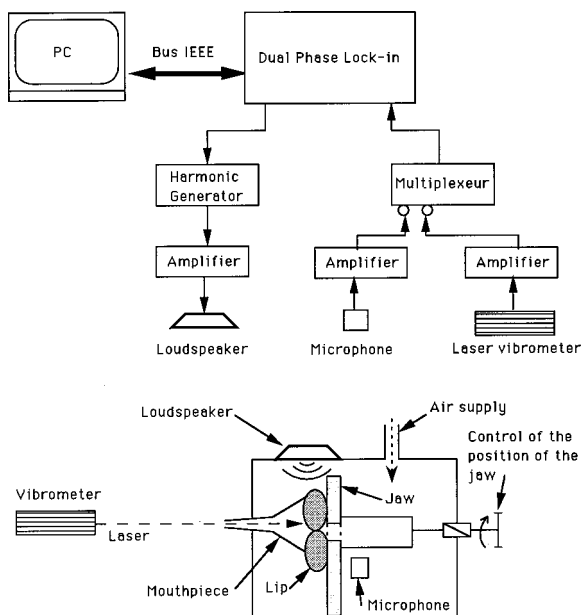


FIG. 3. The mechanical response measurement setup.

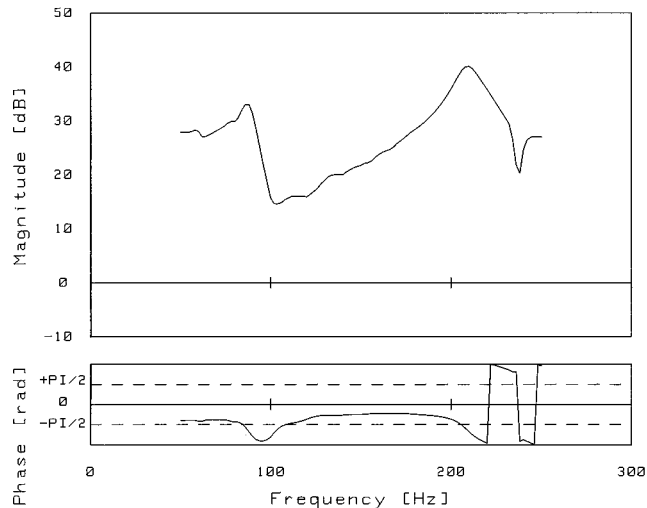


FIG. 4. A measured mechanical response of the lips. The value of the mechanical response magnitude (decibel representation) is expressed in arbitrary units. The value of the phase is expressed in radian.

the force applied to the lip. Because of the construction of the artificial mouth and to keep the embouchure constant during the measurement, the mouthpiece remains in position during the measurement. The frequency range used is below the resonance frequency of the mouthpiece ( $Fm = 545.6$  Hz). We assume that the latter does not influence too much the mechanical response measurement of the lip. To avoid degradation of the vibrometer signal through absorption in the transparent box wall, the laser is focused on the lip through the mouthpiece tube. The vibrometer detects the velocity of the vibration of the lip along the axis of the laser, which is the axis of the mouthpiece in our case (longitudinal vibration). In order to derive the mechanical response as defined below, we need the lip displacement. Thus after the experiments the velocity measurements are divided by  $j\omega$  to obtain the displacement results.

#### 2. Results

The mechanical response of the lip is the response of the longitudinal lip displacement (in the flow direction) to the driving pressure as a function of the frequency. On the curve presented in Fig. 4 we choose the lip frequency  $Flip$  (210 Hz) as the frequency where we have the most pronounced resonance (highest magnitude) with a phase equal to  $-\pi/2$ . Incidentally, a phase equal to  $-\pi/2$  at the resonance corresponds to the “outward beating reed” behavior according to the model of Elliot and Bowsler (1982).

Testing the artificial mouth, we have observed that the most efficient parameter to control the embouchure is the position of the mouthpiece relative to the lip. This parameter controlling the geometric boundary conditions of the lip is more effective and accurate than the control parameter of the lip tension. Mechanical responses of the lip have been measured for different settings of the embouchure. For an increase of the static pressure of the mouthpiece on the lips, we observe an increase of the lip frequency  $Flip$  from 120 to 260

Hz. These frequencies are compared with playing frequencies following an experimental procedure described in the next section.

## II. COMPARISON OF TUBE RESONANCE, LIP RESONANCE, AND PLAYING FREQUENCIES

### A. Experimental procedure

Once the mouthpiece is fixed in position, for a particular setting of the embouchure, the experimental procedure is carried out as follows:

(1) We generate a stable sound with the mouthpiece alone. This is done by a slow increase of the supply pressure until stable buzzing of the lip is achieved. We measure the corresponding fundamental oscillation frequency (the played frequency  $F_{play1}$  corresponding to the mouthpiece alone).

(2) We place the trombone on the mouthpiece. We repeat the procedure described in (1) and we measure the fundamental oscillation frequency (the played frequency  $F_{play2}$  corresponding to the trombone and the mouthpiece).

(3) The air supply is switched off, the trombone is dismantled, and the source of sound (the loudspeaker) is switched on. We perform the mechanical response measurement on the lips. The mechanical resonance frequency of the lip is measured (the lip frequency  $Flip$ ).

(4) We repeat the operation (1) to ensure that the embouchure has remained constant during the entire procedure. We then modify the embouchure and repeat the complete procedure.

Notice that we have performed the mechanical response measurement of the lip with the air supply switched off to have a direct characterization of the mechanical behavior of the embouchure, assumed uncoupled to the acoustic resonator in this case. To do the same kind of measurement with nonzero mean flow could be an interesting and useful extension of the results described in this paper. In this way, we could see how the coupling between the mechanical oscillator (the lip) and the acoustical oscillator (the mouthpiece, for example) due to the airflow at the lip orifice, modifies the eigenfrequencies of the coupled system, and consequently modifies the  $Flip$  estimated from the vibrometer measurement of lip vibration.

### B. Results and discussion

We have measured three frequencies for each embouchure: the played frequencies  $F_{play1}$  and  $F_{play2}$ , and the lip frequency  $Flip$ . It is useful to present the played frequencies as functions of the lip frequency. The results with two kinds of acoustical resonators are presented, respectively: the mouthpiece alone (Fig. 5), and the trombone with its mouthpiece (Fig. 6). Please note again that we have simplified the artificial lips using only one lip: the second half of the mouthpiece entrance, corresponding to the removed lip, is closed with a plate.

Figure 5 plots the frequency of the self-excited sound  $F_{play}$  against the lip eigenfrequency  $Flip$ . As expected from the case of buzzing lips, the sound frequency increases with the lip frequency. Some of the results are, however, unexpected. The playing frequency is always below the resonance

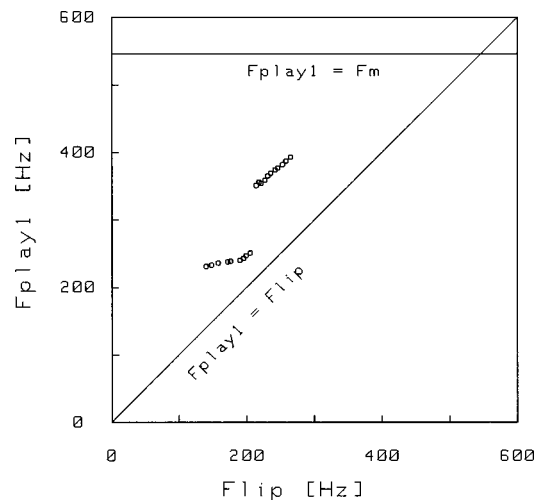


FIG. 5. The played frequency  $F_{play1}$  as a function of the lip frequency  $Flip$ . The resonator is the mouthpiece alone (Bach model Megatone 6<sup>1/2</sup> AM), its resonance frequency is  $F_m = 545.6$  Hz.

frequency of the mouthpiece and always above the lip frequency. At first sight this is inconsistent with results of the classic one mass model: according to the “inward beating reed” behavior, the playing frequency should be below both the resonance frequency and the lip frequency. According to the “outward beating reed” behavior, the playing frequency should be above both the resonance frequency and the lip frequency (Fletcher, 1979). Moreover we found with the artificial mouth a second oscillation regime (see in Fig. 5 the bifurcation between the two regimes near the frequency lip value of 210 Hz) which is not predicted by a single mass model. This might be a second vibrating mode of the lip. Such a second lip mode could be a second longitudinal mode observed in the measured mechanical response (see the second mechanical resonance around 80 Hz in Fig. 4). It could also be a transverse mode invisible in our measurements because of the particular position of the vibrometer which measures the lip vibration only along the axis of the mouthpiece.

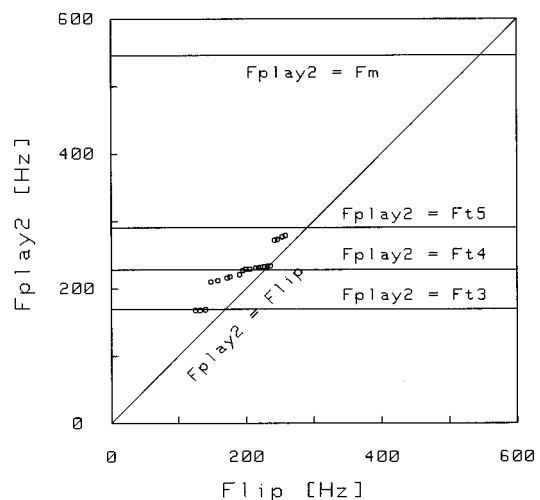


FIG. 6. The played frequency  $F_{play2}$  as a function of the lip frequency  $Flip$ . The resonator is the trombone (Courtois model 149) with its mouthpiece (Bach model Megatone 6<sup>1/2</sup> AM), the useful resonance frequencies are  $F_{t3} = 169.1$  Hz,  $F_{t4} = 228.2$  Hz, and  $F_{t5} = 290.8$  Hz.

At the moment such hypotheses remain unconfirmed. In view of the existence of these two buzzing regimes, using a two mass model for the lip becomes attractive.

During the experimental procedure, for each embouchure we have placed the trombone on the mouthpiece. For a variation of the lip frequency from 120 to 260 Hz, we have obtained three notes corresponding to the resonance frequencies number 3, 4, and 5 of the trombone. The three notes played are F3, Bflat3, and D4. Figure 6 plots the frequency of the self-sustained sound  $F_{\text{play}}$  against the lip eigenfrequency  $F_{\text{lip}}$  with the resonance frequencies number 3, 4, and 5 of the trombone (the horizontal straight lines in the figure). The bisection line where  $F_{\text{play}}$  is equal to  $F_{\text{lip}}$  is also drawn. Between adjacent resonance modes, frequency gaps that represent the mode transitions between two adjacent notes are found. But in each resonance mode, the playing frequency  $F_{\text{play}}$  does not take a constant value. Instead, there is a frequency range of  $F_{\text{play}}$  where a self-oscillation is possible and where  $F_{\text{play}}$  gradually ascends with an increase in  $F_{\text{lip}}$ . This behavior of the artificial mouth is quite similar to that observed for a human trombone player. Is it possible to draw a conclusion about the lip model from these experimental results? Again, the results are not compatible with the basic one-mass model: the played frequencies are sometimes below and sometimes above the resonance frequencies.

Even if these experimental results on artificial buzzing lip cannot be directly linked with the simplified one-mass or two-mass models, it is interesting to perform a qualitative comparison with previous experimental results obtained for real brass players. As observed by Chen and Weinreich (1996), brass players are able to pull the pitch of the played note both well above and well below the resonant frequency of the instrument (bend technique); we have observed the same kind of results with the artificial buzzing lip coupled with a trombone (Fig. 6). This confirms that the simple one-mass model (outward or inward beating) does not suffice. But we should note that a one-mass model such as that proposed by Elliot and Bowsher (1982) can predict both an inward and an outward behavior: As remarked by Campbell and Greated (1987), the two forces acting on the mechanical oscillator with one degree of freedom have opposite signs, so by making one or the other force dominate, the desired type of behavior can be obtained. The two forces are the pressure difference between the mouth and the mouthpiece and the Bernoulli pressure at the lip orifice. In the same way, the one-mass model of Elliot and Bowsher is compatible with the observations of Yoshikawa (1995) of the transition from the outward-striking oscillation in low modes to the upward-striking oscillations in high modes. On the other hand, the experimental results obtained with the artificial buzzing lip coupled with a mouthpiece alone (Fig. 5) seem not to be easily compatible with a one-mass model, because of the existence of two different buzzing regimes. In this case, to describe the essential features of the oscillatory behavior of the lips, it seems that we need a two-mass model similar to that used to describe vocal fold motion (Ishizaka and Flanagan, 1972; Pelorson *et al.*, 1994) or snoring (Auregan and Depollier, 1995). Direct visualizations have already highlighted two degrees of freedom (Martin, 1942; Jorno, 1996;

Copley and Strong, 1996), and Gokhshtein (1981), using a subtle and interesting visualization technique, observed that in the low register the human lips execute a wavelike motion. Moreover this two-mass model is attractive from the viewpoint of the trombone player: it could explain the ability to generate self-sustained lip oscillations over a large range of frequencies without the mouthpiece and the instrument (the “buzz technique”). We are convinced that additional experiments on other artificial mouths in progress (Vergez and Rodet, 1997; Cullen *et al.*, 1998) will in the near future provide a better understanding of the buzzing lips behavior. Incidentally such experiments will supply parameter values for the time simulations of brass instruments.

## ACKNOWLEDGMENTS

We would like to acknowledge D. M. Campbell, J. Cullen, J. P. Dalmont, A. Hirschberg, and R. Msallam for helpful discussions about acoustics of brass instruments and for comments on this work.

- Adachi, S., and Sato, M. (1996). “Trumpet sound simulation using a two-dimensional lip vibration model.” *J. Acoust. Soc. Am.* **99**, 1200–1209.
- Aurégan, Y., and Depollier, C. (1995). “Snoring: linear stability analysis and in-vitro experiments.” *J. Sound Vib.* **188**, 39–54.
- Backus, J. (1963). “Small-vibration theory of the clarinet.” *J. Acoust. Soc. Am.* **35**, 305–313.
- Backus, J. (1976). “Input impedance curves for the brass instruments.” *J. Acoust. Soc. Am.* **60**, 470–480.
- Bailliet, H., Pelorson, X., Richardson, B., and Lallouache, T. (1995). “Lip vibration and pressure recordings during french horn playing,” in *Proceedings of the International Symposium on Musical Acoustics*, Dourdan, France (Société Française d’Acoustique, Paris), pp. 23–28.
- Beauchamp, J. W. (1980). “Analysis of simultaneous mouthpiece and output waveforms,” Audio Engineering Society, preprint No. 1626, pp. 1–11.
- Campbell, D. M., and Greated, C. (1987). *The Musician’s Guide to Acoustics* (Dent, London).
- Caussé, R., Kergomard, J., and Lurton, X. (1984). “Input impedance of brass musical instruments—Comparison between experiment and numerical models,” *J. Acoust. Soc. Am.* **75**, 241–254.
- Chen, F. C., and Weinreich, G. (1996). “Nature of the lip reed,” *J. Acoust. Soc. Am.* **99**, 1227–1233.
- Copley, D. C., and Strong, W. J. (1996). “A stroboscopic study of lip vibrations in a trombone,” *J. Acoust. Soc. Am.* **99**, 1219–1226.
- Cullen, J., Gilbert, J., Campbell, D. M., and Greated, C. A. (1998). “Acoustical measurements in resonators driven by an artificial mouth, oscillation threshold behavior,” in *Proceeding of the International Symposium on Musical Acoustics*, Seattle (Acoustical Society of America and Catgut Acoustical Society), pp. 141–146.
- Dalmont, J. P., and Bruneau, A. M. (1991). “Acoustic impedance measurement: plane-wave mode and first helical-mode contributions,” *J. Acoust. Soc. Am.* **91**, 3026–3033.
- Dalmont, J. P., Gazengel, B., Gilbert, J., and Kergomard, J. (1995). “Some aspects of tuning an clean intonation in reed instruments,” *Appl. Acoust.* **46**, 19–60.
- Dietz, P., and Amir, N. (1995). “Synthesis of trumpet tones by physical modeling,” in *Proceedings of the International Symposium on Musical Acoustics* (Société Française d’Acoustique, Paris), pp. 471–477.
- Elliot, S. J., and Bowsher, J. M. (1982). “Regeneration in brass wind instruments,” *J. Sound Vib.* **83**, 181–217.
- Elliot, S. J., Bowsher, J., and Watkinson, P. (1982). “Input and transfer response of brass wind instruments,” *J. Acoust. Soc. Am.* **72**, 1747–1760.
- Fletcher, N. H. (1979). “Excitation mechanisms in woodwind and brass instruments,” *Acustica* **43**, 63–72.
- Gazengel, B. (1994). “Caractérisation objective de la qualité de justesse, de timbre et d’émission des instruments à vent à anche simple” (text in french), Doctoral thesis, Université du Maine, Le Mans, France.
- Gilbert, J. (1991). “Etude des instruments de musique à anche simple: extension de la méthode de l’équilibrage harmonique, rôle de l’inharmonicité



- des résonances, mesure des grandeurs d'entrée" (text in french), Doctoral thesis, Université du Maine, Le Mans, France.
- Gilbert, J., and Petiot, J. F. (1997a). "Non-linéarités dans les instruments à vent de type cuivre" (text in french), *Actes du 4ième Congrès Français d'Acoustique*, Marseille (Société Française d'Acoustique, Paris), Vol. 1, pp. 641–644.
- Gilbert, J., and Petiot, J. F. (1997b). "Brass instruments, some theoretical and experimental results," *Proceedings of the International Symposium on Musical Acoustics* (Institute of Acoustics, London), Vol. 19, pp. 391–400.
- Gokhshtein, A. Y. (1981). "Role of airflow modulator in the excitation of sound in wind instruments," *Sov. Phys. Dokl.* **25**, 954–956.
- Hirschberg, A., Gilbert, J., Msallam, R., and Wijnands, A. P. J. (1996). "Shock waves in trombones," *J. Acoust. Soc. Am.* **99**, 1754–1758.
- Idogawa, T., Kobata, T., Komuro, K., and Iwaki, M. (1993). "Nonlinear vibrations in the air column of a clarinet artificially blown," *J. Acoust. Soc. Am.* **93**, 540–551.
- Ishizaka, K., and Flanagan, J. (1972). "Synthesis of voiced sounds from a two-mass model of the vocal cords," *Bell Syst. Tech. J.* **51**, 1233–1268.
- Jorno, D. (1996). "Etude théorique et expérimentale de l'auto-oscillation des lèvres en présence d'un couplage acoustique" (text in french), Rapport du DEA ATIAM, Institut de la Communication Parlée, Grenoble, France.
- Juin, F. (1996). "Simulations numériques d'instruments à vent de type cuivre" (text in french), Rapport du DEA d'Acoustique Appliquée, Université du Maine, Le Mans, France.
- Martin, D. W. (1942). "Lip vibrations in a cornet mouthpiece," *J. Acoust. Soc. Am.* **13**, 305–308.
- Meynial, X. (1987). "Systèmes micro-intervalles pour instruments à vent à trous latéraux; Oscillation d'une anche simple couplée à un résonateur de forme simple" (text in french), Doctoral thesis, Université du Maine, Le Mans, France.
- Msallam, R., Dequidt, S., Tassart, S., and Caussé, R. (1997). "Physical model of the trombone including non-linear propagation effects," *Proceedings of International Symposium on Musical Acoustics* (Institute of Acoustics, London), Vol. 19, pp. 419–424.
- Pelorson, X., Hirschberg, A., Van Hassel, R. R., Wijnands, A. P. J., and Auregan, Y. (1994). "Theoretical and experimental study of quasisteady-flow separation within the glottis during phonation. Application to a modified two-mass model," *J. Acoust. Soc. Am.* **96**, 3416–3431.
- Piau, L. (1997). "Etude expérimentale du comportement d'instruments de musique en situation de jeu, Bouche artificielle version 2" (text in french), Rapport de recherche, Ecole Centrale de Nantes, France.
- Pratt, R. L., Elliott, S. J., and Bowsher, J. M. (1977). "The measurement of the acoustic impedance of brass instruments," *Acustica* **38**, 236–246.
- Rodet, X., and Vergez, C. (1996). "Physical models of trumpet-like instruments detailed behavior and model improvements," *Proceedings of ICMC96, Honk-Kong* (unpublished).
- Saneyoshi, J., Teramura, H., and Yoshikawa, S. (1987). "Feedback oscillations in reed woodwind and brasswind instruments," *Acustica* **62**, 194–210.
- Strong, W. J., and Dudley, J. D. (1993). "Simulation of a player-trumpet system," *Proceedings of the Stockholm Music Acoustics Conference* (Royal Swedish Academy of Music, Stockholm), No. 79, pp. 520–524.
- Vergez, C., and Rodet, X. (1997). "Model of the trumpet functioning: real time simulation and experiments with an artificial mouth," *Proceedings of International Symposium on Musical Acoustics* (Institute of Acoustics, London), Vol. 19, pp. 425–432.
- Wilson, T. A., and Beavers, G. S. (1974). "Operating modes of the clarinet," *J. Acoust. Soc. Am.* **56**, 653–658.
- Yoshikawa, S. (1995). "Acoustical behavior of brass player's lips," *J. Acoust. Soc. Am.* **97**, 1929–1939.

# Numerical simulations of xylophones. II. Time-domain modeling of the resonator and of the radiated sound pressure

Vincent Doutaut, Denis Maignon, and Antoine Chaigne<sup>a)</sup>

*Ecole Nationale Supérieure des Télécommunications, Département Signal, CNRS URA 820,  
46 Rue Barrault, 75634 Paris Cedex 13, France*

(Received 26 November 1997; revised 22 May 1998; accepted 2 June 1998)

This paper presents a time-domain modeling for the sound pressure radiated by a xylophone and, more generally, by mallet percussion instruments such as the marimba and vibraphone, using finite difference methods. The time-domain model used for the one-dimensional (1-D) flexural vibrations of a nonuniform bar has been described in a previous paper by Chaigne and Doutaut [J. Acoust. Soc. Am. **101**, 539–557 (1997)] and is now extended to the modeling of the sound-pressure field radiated by the bar coupled with a 1-D tubular resonator. The bar is viewed as a linear array of equivalent oscillating spheres. A fraction of the bar field excites the tubular resonator which, in turn, radiates sound with a certain delay. In the present model, the open end of the resonator is represented by an equivalent pulsating sphere. The total sound field is obtained by summing the respective contributions of the bar and tube. Particular care is given for defining a valid approximation of the radiation impedance, both in continuous and discrete time domain, on the basis of Kreiss's theory. The model is successful in reproducing the main features of real instruments: sharp attack, tuning of the bar, directivity, tone color, and aftersound due to the bar-resonator coupling. © 1998 Acoustical Society of America. [S0001-4966(98)03409-2]

PACS numbers: 43.75.Kk [WJS]

## INTRODUCTION

A discrete time-domain formulation of the system of equations that govern the transverse bending motion of a xylophone bar excited by the blow of a mallet has been obtained in the past with the use of finite differences. This model yields both the time history and spatial distribution of the bar velocity, among other results.<sup>1</sup>

This paper is now dealing with the time-domain calculation of the sound-pressure field radiated by mallet percussive instruments, in direct continuity with the previous work. The contribution of the bar to the pressure field is computed from its velocity, by summing together, at each time step, the pressure radiated by each discrete segment of the bar. Following Junger, it is assumed that the bar can be viewed as a linear array of dipoles.<sup>2</sup> This radiation model accounts for the use of the instrument without resonators. However, in most musical situations, a tubular resonator is placed under the bar. In the time domain, under the assumption of free space, the physical phenomena can be then summarized as follows: In the half-space above the bar, the radiated sound pressure propagates without any modification. At the same time, a pressure wavefront propagates below the bar and reaches the open end of the tube shortly after the blow of the mallet. Thus a fraction of the bar acoustic field is transformed into stationary waves inside the tube. A part of the internal energy of the tube is then reemitted to the free space through its open end, due to the radiation impedance. The total sound field is the sum of both contributions of the bar and tube.

In this paper, it will be assumed that the lower end of the

tube is closed and perfectly rigid. As a consequence, the spectrum of the sound radiated by the tube is made of frequencies nearly equal to the odd harmonics of the fundamental frequency, the wavelength corresponding to this fundamental being closely equal to four times the length  $l_T$  of the tube. It is also assumed that the open end of the tubular resonator behaves like a monopole, which is in accordance with observations made by other authors, and modeled here as an equivalent pulsating sphere.<sup>3</sup> The continuous model of the instrument is presented in Sec. I.

In Sec. II, the numerical formulation of the problem, based on finite differences, is presented. Emphasis is put on the resonator with special considerations on the time-domain modeling of the radiation impedance. Based on Kreiss's theory,<sup>4</sup> it is shown that the approximation used for this impedance must fulfill specific criteria in order to ensure the stability of the resonator model. Detailed mathematical derivations of these criteria can be found in Appendixes A and B.

The results of the model are presented in Sec. III. First, the numerical scheme of the tube is validated by a comparison between analytical and numerical solutions. In a second step, it is shown to what extent the model is efficient in reproducing the main musical qualities of real instruments. Comparisons between measured and simulated xylophone sounds contribute to illustrate the capabilities and the limits of the method.

## I. PHYSICAL MODELING

### A. Radiation of the bar

The transverse motion of a free-free bar with a variable section is described by the classical one-dimensional Euler–

<sup>a)</sup>Electronic mail: chaigne@sig.enst.fr

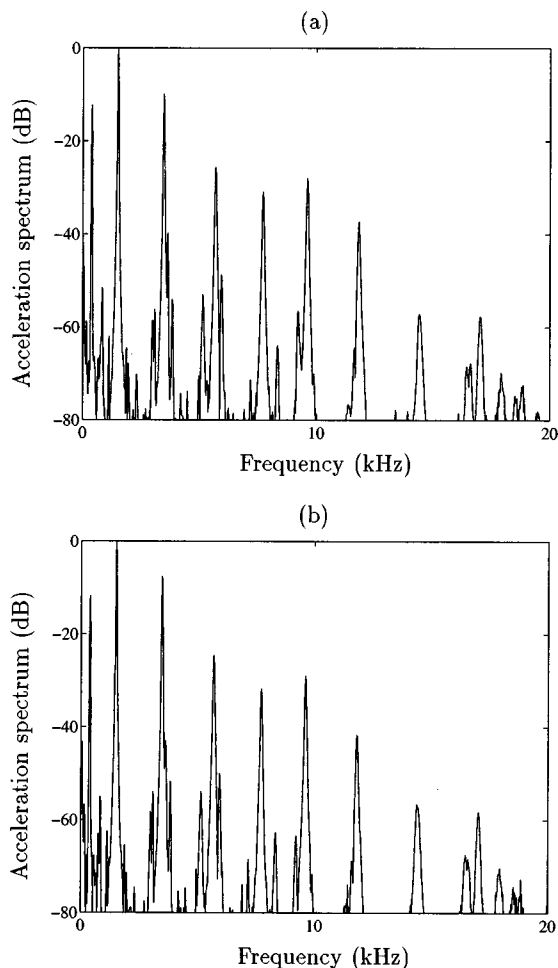


FIG. 1. Acceleration spectrum at a given point of the bar. (a) Without resonator; (b) with resonator. The spectra are identical showing the negligible influence of the tube on bar vibration.

Bernoulli partial differential equation. This equation has been slightly modified in order to account for the losses and for the restoring force of the suspending cord. The action of the mallet against the bar is described by Hertz's law. The model also includes a differential equation that governs the motion of the mallet. This vibratory model has been extensively described in a previous paper and will not be discussed further here.<sup>1</sup> The system of equations is solved in the time domain by means of finite-difference methods. The results can be alternatively expressed in terms of displacement, velocity, or acceleration of the bar.

In this section, the model used for calculating the sound pressure resulting from the bar displacement is presented. The basic assumption is that the reaction of the radiated field on the vibrating bar is negligible, even in the case where a tubular resonator is situated close to it. This assumption is justified by a series of experiments which have been conducted in order to investigate the influence of the resonator on the vibration of the bars. Figure 1 shows, for example, a comparison between the acceleration spectrum at a given point of a  $F_4^{\#}$  bar without a resonator [Fig. 1(a)], and with a resonator placed under the bar [Fig. 1(b)]. No significant differences can be detectable between these two spectra. As a

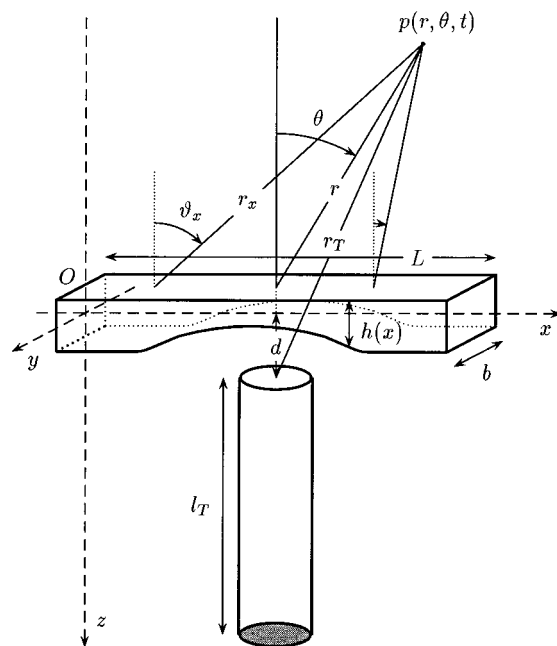


FIG. 2. Geometry and notations for the xylophone bar and tube.

consequence, the influence of the pressure radiated by the tube on the motion of the bar will be neglected.

According to Junger, the far field radiated by the flexural vibrations of an un baffled beam can be approximated, in the low-frequency range, by modeling the bar as a distribution of dipole sources. This assumption is valid if the thickness of the bar  $h(x)$  is small compared to the acoustic wavelength.<sup>2</sup> In mallet percussion instruments the bar thickness is generally less than 2 cm, which corresponds to acoustic wavelengths for frequencies above 17 kHz. The Junger approximation is thus justified.

In order to apply this result to the sound radiated by a xylophone bar, the acoustic source is viewed as a linear array of equivalent oscillating spheres, where the volume  $\Delta V(x)$  of each sphere is equal to the volume of one spatial element of the beam of length  $\Delta x$ . This approach is similar to the one adopted by Akay *et al.* for beams and can also be related to the work by Ochmann where vibrating structures are represented by equivalent distributions of multipoles.<sup>5,6</sup> The following mathematical derivations are restricted to the plane of symmetry  $xOz$  of the system composed by the xylophone bar and the resonator and the radiation problem is expressed in polar coordinates (see Fig. 2).

Each element  $\Delta x$  of the bar is viewed as an oscillating sphere of equivalent volume:

$$\Delta V(x) = \frac{4}{3}\pi a^3(x) = bh(x)\Delta x, \quad (1)$$

where  $a(x)$  is the radius of the sphere. This approximation is valid in the low-frequency range, which means that we must fulfill the condition

$$\forall x \in [0; L], \quad ka(x) \ll 1, \quad (2)$$

where  $L$  is the length of the bar and  $k$  is the acoustic wave number.

Under the additional geometrical assumption of far field [ $a(x) \ll r$ ], the contribution of each oscillating sphere at po-

sition  $x_i = i\Delta x$  on the bar to the sound pressure at a point of observation  $M(r, \theta)$  in free space, in the time domain, is given by<sup>7</sup>

$$\Delta p_i(r_{x_i}, \vartheta_{x_i}, t) = \frac{3}{8\pi} \rho_0 \Delta V(x_i) \cos(\vartheta_{x_i}) \left( \frac{1}{r_{x_i}^2} \frac{\partial^2 w}{\partial t^2}(x_i, t - r_{x_i}/c_0) + \frac{1}{r_{x_i} c_0} \frac{\partial^3 w}{\partial t^3}(x_i, t - r_{x_i}/c_0) \right), \quad (3)$$

where  $w(x_{i,t})$  represents the transverse displacement of the bar,<sup>1</sup>  $\rho_0$  is the density of air, and  $c_0$  is the speed of sound in air. By applying the principle of superposition, the sound-pressure field radiated by the discrete bar is written

$$p_B(r, \theta, t) = \sum_{i=1}^N \Delta p_i(r_{x_i}, \vartheta_{x_i}, t), \quad (4)$$

where  $N = L/\Delta x$  is the number of discrete elements of the bar. If the resonator is removed, Eq. (4) is sufficient for calculating the sound radiated by the instrument. However, it is necessary to take the contribution of the resonator into account in order to obtain a more general model. Therefore in the next paragraph, the resonator is assumed to be excited by the bar pressure field  $p_B(d, \pi, t)$ . At this point it must be said that the geometrical far-field assumption may be not fully justified in this case since the distance  $d$  corresponding to the position of the open end of the resonator below the bar is usually equal to a few centimeters only, which is not significantly larger than the dimensions of the bar elements. This assumption may explain some of the discrepancies between predicted and measured pressure.

## B. Resonator model

In order to account for the radiation of the resonator, the model must include a time-domain formulation for both the wave propagation in the tube and the radiation impedance at its open end. This section deals with the continuous formulation of the problem, which has to be mathematically well-posed in order to be physically relevant in the space-time domain and to allow the stability of the inferred numerical schemes.

Most resonators of bar percussion instruments are cylindrical, with a radius  $a_T$  significantly smaller than the length  $l_T$ . The sound wave inside the tube can be considered to consist of one-dimensional plane waves below the cutoff frequency given by<sup>8</sup>

$$f_c = \frac{1.8411}{2\pi} \frac{c_0}{a_T} = 0.2930 \frac{c_0}{a_T}. \quad (5)$$

At this frequency, the wavelength is  $\approx 1.7$  times the diameter of the opening. With  $c_0 = 340$  m/s and a radius of 2.0 cm (which is a typical order of magnitude for a xylophone), Eq. (5) yields a lower limit of  $f_c$  equal to 4980 Hz. In comparison, the fundamental frequency of the highest note ( $C_8$ ) in xylophones is nearly equal to 4284 Hz. As a consequence, it is justified to describe the propagation in the pipe by the plane-wave equation

$$\frac{\partial^2 p}{\partial t^2}(z, t) - c_0^2 \frac{\partial^2 p}{\partial z^2}(z, t) = 0, \quad (6)$$

where  $p(z, t)$  is the acoustic pressure in the resonator. However, Eq. (6) may be invalid for some marimba or vibraphone resonators having a relatively larger cross section.

The resonators of bar-mallet percussion instruments are metallic with perfect rigid walls. The losses are essentially localized near the walls due to viscothermal effects. Thus the speed of sound in the pipe and the damping factor of the wave become frequency dependent:<sup>8</sup>

$$c(\omega) = c_0 \left( 1 - \frac{\epsilon_{vt}}{a_T \sqrt{2}} \sqrt{\frac{c_0}{\omega}} \right), \quad \alpha(\omega) = \frac{\epsilon_{vt}}{a_T \sqrt{2}} \sqrt{\frac{\omega}{c_0}} \quad (7)$$

with  $\omega$  the radian frequency,  $\epsilon_{vt} = \sqrt{l_v} + (\gamma - 1)\sqrt{l_h}$ ,  $l_v \approx 4 \times 10^{-8}$  m and  $l_h \approx 5.6 \times 10^{-8}$  m are the characteristic lengths of viscous and heat propagation effects, respectively, and  $\gamma = C_p/C_v$ .

Equation (7) can be transposed to the time domain,<sup>9</sup> but cannot be easily solved because of the dependence of both terms with the square root of frequency.<sup>10</sup> However, the problem can be greatly simplified if one considers that the fundamental frequency  $f_1 = \omega_1/2\pi$  of the resonator is generally tuned to the fundamental of the bar and that the upper partials of the bar will generally not match one of the upper eigenfrequencies of the tube. As it is currently observed in practice, the spectrum of the wave reemitted by the tube is thus very similar to the one of a pure tone. Therefore the losses in the tube can be taken into account by adding a fluid-damping term independent of frequency in Eq. (6) which yields

$$\frac{\partial^2 p}{\partial t^2}(z, t) + \gamma_T \frac{\partial p}{\partial t}(z, t) - c^2 \frac{\partial^2 p}{\partial z^2}(z, t) = 0 \quad (8)$$

with

$$c = c_0 \left( 1 - \frac{\epsilon_{vt}}{a_T \sqrt{2}} \sqrt{\frac{c_0}{\omega_1}} \right), \quad \gamma_T = \epsilon_{vt} \frac{c}{a_T} \sqrt{\frac{2\omega_1}{c_0}}. \quad (9)$$

Equation (8) has been used for the modeling of the wave propagation inside the tube. This propagation equation needs now to be complemented by boundary conditions, i.e., by a time-domain modeling of the radiation impedance.

The general idea behind this step of the modeling is to find a suitable time-domain approximation of the radiation impedance, starting from its continuous expression in the frequency domain. Therefore some of the most significant and well-known results, with regard to the radiation impedances of tubes, are first briefly reviewed.

Neglecting the edge effects, let us first assume that the open end of the tube acts like a baffled planar piston radiating in free space. Following Rayleigh, the radiation impedance is then given by<sup>8</sup>

TABLE I. Values of the coefficients  $\alpha_i$  and  $\beta_i$  for the approximate radiation impedance.

Coefficients	$\beta_0$	$\beta_1$	$\beta_2$	$\alpha_0$	$\alpha_1$	$\alpha_2$
Rayleigh (first order)	0.0000	0.8488	0.0000	1.0000	0.8488	0.0000
Rayleigh (second order)	0.0000	0.8488	0.4000	1.0000	1.0186	0.4000
Levine–Schwinger (second order)	0.0000	0.6133	0.2100	1.0000	0.7000	0.2100

$$Z_r(ka_T) = Z_0 \left( 1 - \frac{J_1(2ka_T)}{ka_T} + j \frac{S_1(2ka_T)}{ka_T} \right)$$

with  $Z_0 = \frac{\rho_0 c_0}{S_T}$  and  $k = \frac{\omega}{c_0}$ , (10)

where  $Z_0$  is the characteristic impedance of the tube with section  $S_T$ , and where  $J_1$  and  $S_1$  are the Bessel function and the Struve function of first order. In the low-frequency range ( $ka_T \ll 1$ ), Eq. (10) reduces to

$$Z_r^{LF}(ka_T) \approx Z_0 \left( \frac{1}{2} (ka_T)^2 + j \frac{8}{3\pi} ka_T \right)$$

$$= Z_0 \left( \frac{1}{2} (ka_T)^2 + j 0.8488 ka_T \right). \quad (11)$$

The Rayleigh impedance has been used as a benchmark for comparing numerical and analytical solutions for the isolated tube (see Sec. III A). However, it turns out that an unbaffled model yields simulations closer to experimental results for mallet percussion instruments (see Sec. III B). Therefore the calculation of the radiation impedance carried out by Levine and Schwinger is more appropriate.<sup>11</sup> Due to the usual frequency range of the instruments, the following approximations were used:<sup>12</sup>

For  $ka_T < 1.5$ :

$$\frac{Z_r(ka_T)}{Z_0} = \frac{(ka_T)^2}{4} + 0.0127(ka_T)^4$$

$$+ 0.082(ka_T)^4 \ln ka_T - 0.023(ka_T)^6$$

$$+ j(0.6133ka_T - 0.036(ka_T)^3$$

$$+ 0.034(ka_T)^3 \ln ka_T - 0.0187(ka_T)^5). \quad (12)$$

For  $1.5 \leq ka_T < 3.5$ :

$$\frac{Z_r(ka_T)}{Z_0} = j \tan \left( k\Delta l + \frac{1}{2} \ln R \right),$$

where

$$R = e^{-ka_T} \sqrt{\pi ka_T} [1 + (3/32)(1/(ka_T)^2)]$$

and

$$\frac{\Delta l}{a_T} = 0.634 - 0.1102ka_T + 0.0018(ka_T)^2$$

$$- 0.00005(ka_T)^{4.9}.$$

In the low-frequency range ( $ka_T \ll 1$ ), Eq. (12) reduces to

$$Z_r^{LF}(ka_T) \approx Z_0 \left( \frac{1}{4} (ka_T)^2 + j 0.6133ka_T \right). \quad (13)$$

In order to allow transposition to the time domain, the radiation impedance is approximated by a fraction of second-order polynomials:

$$\tilde{\xi}_r(jka_T) = \frac{\tilde{Z}_r(ka_T)}{Z_0} = \frac{B_r(jka_T)}{A_r(jka_T)}$$

$$= \frac{\beta_0 + \beta_1 jka_T + \beta_2 (jka_T)^2}{\alpha_0 + \alpha_1 jka_T + \alpha_2 (jka_T)^2}, \quad (14)$$

where  $\tilde{\xi}_r(jka_T)$  denotes the normalized approximated radiation impedance.

The selection of the six coefficients ( $\alpha_i, \beta_i$ ) is based on the minimization of the least-squares error between the Rayleigh (respectively, Levine–Schwinger) expression and Eq. (14), with the constraints of convergence to Eq. (11) [respectively, Eq. (13)] as the frequency tends to zero, and to  $Z_0$  as the frequency tends to infinity. As a consequence of these last conditions we get:

$$\alpha_0 = 1, \quad \beta_0 = 0, \quad \alpha_2 = \beta_2$$

and (15)

$$\beta_1 = 0.8488 \text{ (Rayleigh) or}$$

$$\beta_1 = 0.6133 \text{ (Levine–Schwinger).}$$

In addition, the transposition to the time domain (i.e., the replacement of  $j\omega$  by the time-derivative operator  $\partial/\partial t$ ) requires that  $\tilde{\xi}_r$  must fulfill the Kreiss’s stability criterion which states that<sup>4</sup>

$$\forall s \in \mathbb{C} \quad \text{with } \Re(s) > 0, \quad \Re(\tilde{\xi}_r(s)) > 0, \quad (16)$$

where  $s$  is the Laplace transform variable.

It is interesting to point out here that the condition (16) corresponds exactly to the definition of positive real functions which have been widely investigated in the past in the context of electrical network synthesis, as mentioned by Smith.<sup>13</sup> This criterion yields the following sufficient conditions (see Appendix A):

$$\alpha_1, \alpha_2 > 0 \quad \text{and} \quad \alpha_1 \beta_1 > \alpha_2. \quad (17)$$

Table I gives the values obtained for the coefficients  $\alpha_i$  and  $\beta_i$ . This second-order approximation yields a mean error of nearly 1% for the radiation impedance in the complete register of the instrument ( $f \leq 4.5$  kHz, i.e.,  $ka_T \leq 1.5$  for  $a_T \approx 1.8$  cm) (see Figs. 3 and 4). A higher-order approximation does not seem to be required in view of this obtained degree of accuracy.

It is possible to derive another stable approximation of the impedance  $\tilde{\xi}_r$ , using a fraction of first-order polynomials, instead of second-order polynomials. The results, for the Rayleigh impedance only, are shown in Table I. As expected, the first-order approximation is less accurate than the second-order one because of the reduced number of “degrees of freedom.” It can be seen in Fig. 3 that the first-order approximation leads to a systematic overestimation of the

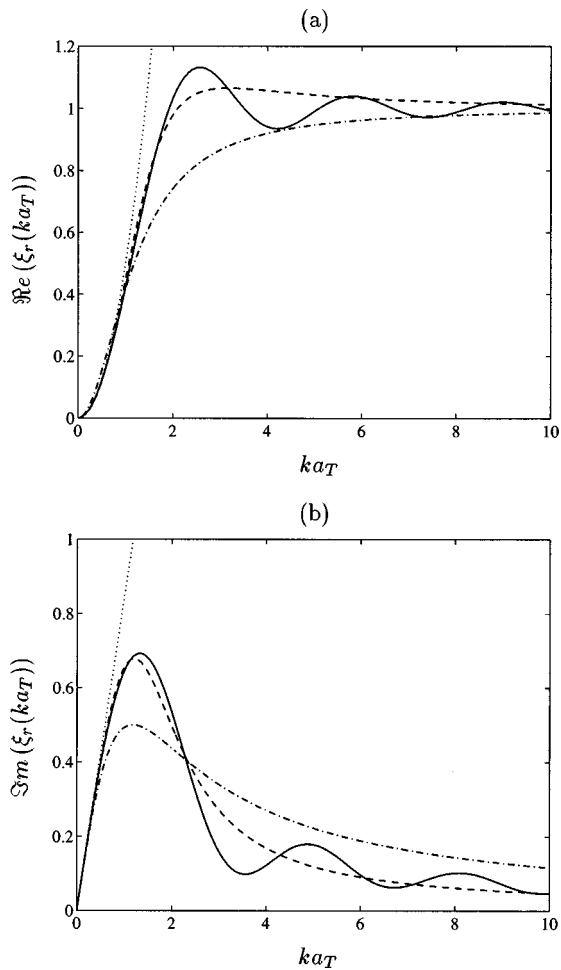


FIG. 3. Rayleigh radiation impedance. (a) Real part; (b) imaginary part. Solid line: Rayleigh formula. Dotted line: low-frequency approximation of Rayleigh formula. Dashed line: second-order approximation. Dash-dotted line: first-order approximation.

imaginary part of the impedance for  $ka_T \gg 1$  and to a systematic overestimation of the real part of the impedance for  $ka_T \ll 1$ .

Finally, it is important to remark that the direct transposition of the low-frequency approximation of the radiation impedance to the time-domain shown in Eqs. (11) and (13) leads to an ill-posed problem since, in this case, one has  $\beta_2 = -0.5$  which is not compatible with the conditions expressed in Eq. (17). In practice, such an approximation does not ensure the stability of the continuous system of equations which means that some solutions may increase exponentially with time.

The time-domain formulation of the boundary condition at the open end of the tube is now derived from Eq. (14). It is assumed that the resonator is excited at its open end by the total pressure  $p_B(d, \pi, t)$  radiated by the bar [see Eq. (4)]. For the sake of convenience, the input pressure will now be denoted  $p_B(t)$  and the open end of the tube, located at a distance  $d$  below the bar, will be taken as the new origin of the  $z$  axis (see Fig. 2).

Through application of the superposition theorem, the total sound pressure at  $z=0$  is obtained by summing the pressure radiated by the resonator and the bar pressure  $p_B(t)$ , which yields in the frequency domain

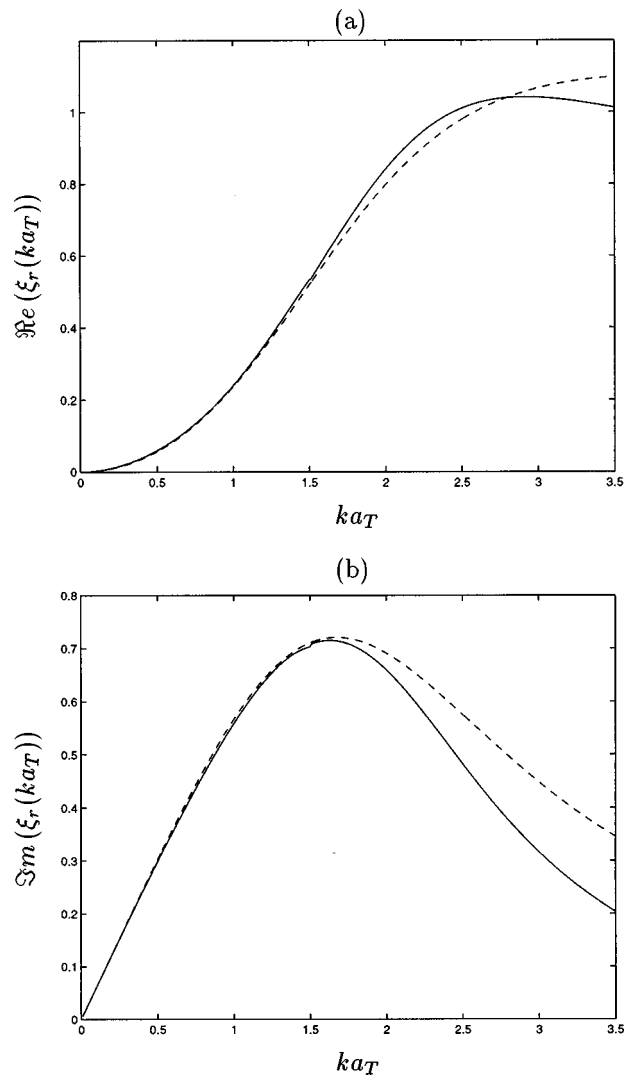


FIG. 4. Levine-Schwinger radiation impedance. (a) Real part; (b) imaginary part. Solid line: analytical approximation [Eq. (12)] by Causse *et al.* (Ref. 12). Dashed line: second-order approximation.

$$p(0, j\omega) = -Z_r(j\omega)S_T u(0, j\omega) + p_B(j\omega), \quad (18)$$

where  $u(z, t)$  is the acoustic velocity. By combining Euler's equation with the approximate expression of  $Z_r(j\omega)$ , one obtains

$$j\omega p(0, j\omega) - c_0 \tilde{\xi}_r \left( j\omega \frac{a_T}{c_0} \right) \frac{\partial p}{\partial z}(0, j\omega) = j\omega p_B(j\omega). \quad (19)$$

In the time domain, Eq. (19) becomes

$$\mathbf{A}_r \left( \frac{a_T}{c_0} \partial_t \right) \frac{dp_B}{dt}(t) = \mathbf{A}_r \left( \frac{a_T}{c_0} \partial_t \right) \frac{\partial p}{\partial z}(0, t) - c_0 \mathbf{B}_r \left( \frac{a_T}{c_0} \partial_t \right) \frac{\partial p}{\partial z}(0, t), \quad (20)$$

where the differential operators  $\mathbf{A}_r$  and  $\mathbf{B}_r$  are given by

$$\mathbf{A}_r \left( \frac{a_T}{c_0} \partial_t \right) = \alpha_0 + \alpha_1 \frac{a_T}{c_0} \frac{\partial}{\partial t} + \alpha_2 \left( \frac{a_T}{c_0} \right)^2 \frac{\partial^2}{\partial t^2},$$

$$\mathbf{B}_r \left( \frac{a_T}{c_0} \partial_t \right) = \beta_0 + \beta_1 \frac{a_T}{c_0} \frac{\partial}{\partial t} + \beta_2 \left( \frac{a_T}{c_0} \right)^2 \frac{\partial^2}{\partial t^2}.$$

At the closed end of the tube ( $z=l_T$ ), the acoustic velocity is equal to zero (the condition for a perfect rigid wall), and the boundary condition can be written

$$\frac{\partial p}{\partial z}(l_T, t) = 0. \quad (21)$$

In summary, Eqs. (8), (9), (20), and (21) form the continuous time-domain model used in this study for the tubular resonator of mallet percussion instrument. The numerical formulation of these equations will be now examined together with the numerical model used for the calculation of the total sound pressure radiated by the instrument.

## II. NUMERICAL FORMULATION

### A. A finite difference formulation for the resonator

A uniform grid of  $N_T$  segments is considered for the discrete resonator. Let  $\Delta z = l_T/N_T$  and  $\Delta t = 1/f_s$  be the spatial step and the time step, respectively, the sampling frequency being  $f_s$ . Approximating Eq. (8) with central difference derivatives of second order in time and space, one obtains the following explicit formulation for the inner mesh points:

$$\begin{aligned} \forall i \in [1; N_T - 1], \\ (1 + \gamma_T \Delta t / 2) p_i^{n+1} &= 2p_i^n - (1 - \gamma_T \Delta t / 2) p_i^{n-1} \\ &+ c^2 \frac{\Delta t^2}{\Delta z^2} (p_{i+1}^n - 2p_i^n + p_{i-1}^n), \end{aligned} \quad (22)$$

where  $i$  and  $n$  are the spatial and times indices, respectively.  $p_i^n$  denotes the calculated value of the acoustic pressure at position  $z_i = i\Delta z$ , and time  $t_n = n\Delta t$ . In the undamped case ( $\gamma_T = 0$ ), the scheme remains stable under the condition

$$r_{\text{CFL}} = c \frac{\Delta t}{\Delta z} \leq 1, \quad (23)$$

where  $r_{\text{CFL}}$  represents the so-called Courant–Friedrichs–Levy number. It can be shown that the introduction of the fluid damping term  $\gamma_T$  tends to stabilize the scheme.<sup>14,15</sup> Another remarkable and well-known property of this 2-2 explicit scheme for the one-dimensional wave equation is that no numerical dispersion occurs if  $r_{\text{CFL}} = 1$ . Under this condition, the eigenfrequencies of the discretized simulation are equal to those of the continuous boundary value problem. Therefore the time and spatial steps were selected in accordance with the equality  $c\Delta t = \Delta z$  for the tube model.

If no loss of energy occurs at the boundaries, one can use the method of images, which guarantees both the stability and second-order precision of the entire scheme, in order to obtain an appropriate numerical formulation of the boundary condition.<sup>14,15</sup> This is applied here to the closed end of the pipe, which yields

$$\frac{\partial p}{\partial z}(l_T, t) \approx \frac{p_{N_T+1}^n - p_{N_T-1}^n}{\Delta z^2} = 0 \Rightarrow p_{N_T+1}^n = p_{N_T-1}^n. \quad (24)$$

Thus for  $i = N_T$  and with  $r_{\text{CFL}} = 1$ , the difference equation becomes

$$p_{N_T+1}^{n+1} = 2p_{N_T-1}^n - p_{N_T}^{n-1}. \quad (25)$$

If an absorbing boundary condition is introduced, as it is the case for the radiation impedance, the stability is not guaranteed unless a thorough analysis of the numerical scheme is conducted on the basis of the Kreiss criterion.<sup>4</sup> This criterion leads here to the following sufficient condition in terms of time step (see Appendix B):

$$\Delta t < \frac{a_T}{c_0} \frac{2\beta_1(\alpha_1 - \beta_1)}{2\beta_1 - \alpha_1}. \quad (26)$$

With the second-order approximation of the radiation impedance (see Table I),  $a_T = 2$  cm and  $c_0 = 340$  m/s, Eq. (26) yields  $\Delta t_{\text{max}} = 2.5 \times 10^{-5}$  s (Rayleigh), or  $\Delta t_{\text{max}} = 1.2 \times 10^{-5}$  s (Levine–Schwinger), which means that the sampling frequency must be greater than 40 (respectively, 84) kHz. In practice a sampling frequency of 192 kHz has been selected in order to guarantee the fine tuning of the bar (see Ref. 1), which fulfills the condition expressed in (26) for both the baffled and unbaffled radiation impedance. Thus under the assumption that both the continuous and discrete stability condition are fulfilled, these conditions are being expressed in terms of the coefficients of the approximate impedance ( $\alpha_i$  and  $\beta_i$ ) and of the time step  $\Delta t$ , respectively, the second-order finite difference formulation of Eq. (20) for the open end of the resonator, i.e., for  $i = 0$ , is written

$$\begin{aligned} (1 + a_1 + b_1 + 2a_2) p_0^{n+1} &= (a_1 + 3a_2) p_0^n - a_2 p_0^{n-1} + (b_1 \\ &+ a_2) p_1^{n+1} - a_2 p_1^n + (1 + a_1 \\ &+ a_2) p_B^{n+1} - (a_1 + 2a_2) p_B^n \\ &+ a_2 p_B^{n-1}, \end{aligned} \quad (27)$$

where

$$a_1 = \frac{\alpha_1 a_T}{\Delta t c_0}, \quad b_1 = \frac{\beta_1 a_T}{\Delta t c_0}, \quad \text{and} \quad a_2 = \alpha_2 \left( \frac{a_T}{c_0 \Delta t} \right)^2. \quad (28)$$

Equation (27) yields explicitly the radiated sound pressure  $p_0$  at the open end of the tube as a function of both the internal pressure  $p_1$  at position  $z_1 = \Delta z$  and pressure  $p_B$  radiated by the bar.

### B. Total sound pressure radiated by the instrument

The numerical formulation of the acoustic pressure due to the bar derives from the continuous model presented in Sec. I. At each time step, the finite difference scheme used in Ref. 1 for the vibrating bar yields the velocity

$$v_i(n\Delta t) = (w_i^{n+1} - w_i^{n-1}) / (2\Delta t). \quad (29)$$

Thus Eqs. (3) and (4) become

$$\Delta p_i(r_i, \vartheta_i, n\Delta t) = \frac{3}{8\pi} \rho_0 \Delta V_i \cos(\vartheta_i) \left[ \frac{1}{r_i^2} \dot{v}_i(n\Delta t - r_i/c_0) + \frac{1}{r_i c_0} \ddot{v}_i(n\Delta t - r_i/c_0) \right] \quad (30)$$

and

$$p_B(r, \theta, n\Delta t) = \sum_{i=1}^N \Delta p_i(r_i, \vartheta_i, n\Delta t), \quad (31)$$

where  $\dot{v}_i$  and  $\ddot{v}_i$  represent the numerical time derivatives of velocity and acceleration. Under the assumption of an un-baffled tube, the open end of the resonator can be viewed as a pulsating sphere. Using the time-domain expression of the acoustic field radiated by such an elementary source,<sup>7</sup> with the system of coordinates shown in Fig. 2, one obtains

$$p_T(r_T, n\Delta t) = -\frac{\rho_0 S_T}{4\pi r_T} \frac{\partial u}{\partial t}(0, n\Delta t - r_T/c_0). \quad (32)$$

By combining Eq. (32) with Euler's equation, one obtains

$$p_T(r_T, n\Delta t) = \frac{S_T}{4\pi r_T} \frac{\partial p}{\partial z}(0, n\Delta t - r_T/c_0) \quad (33)$$

which, in numerical form, becomes

$$p_T(r_T, n\Delta t) = \frac{S_T}{4\pi r_T} \frac{p(1, n\Delta t - r_T/c_0) - p(0, n\Delta t - r_T/c_0)}{\Delta z}. \quad (34)$$

This simplified radiation model is valid in the low-frequency range ( $ka_T \ll 1$ ) and yields an acceptable model for the radiation of bar-mallet percussion instruments. Finally, the total pressure field of the bar-resonator system is obtained by adding the two contributions:

$$p(r, \theta, n\Delta t) = p_B(r, \theta, n\Delta t) + p_T(r_T, n\Delta t). \quad (35)$$

Equation (35) illustrates one interesting feature of the time-domain modeling, which allows independent control of the bar and tube contributions in the total sound radiated by the instrument. The model can be easily transposed to the case of a baffled tube. In this case, one should represent the open end by a half-pulsating sphere, rather than a com-

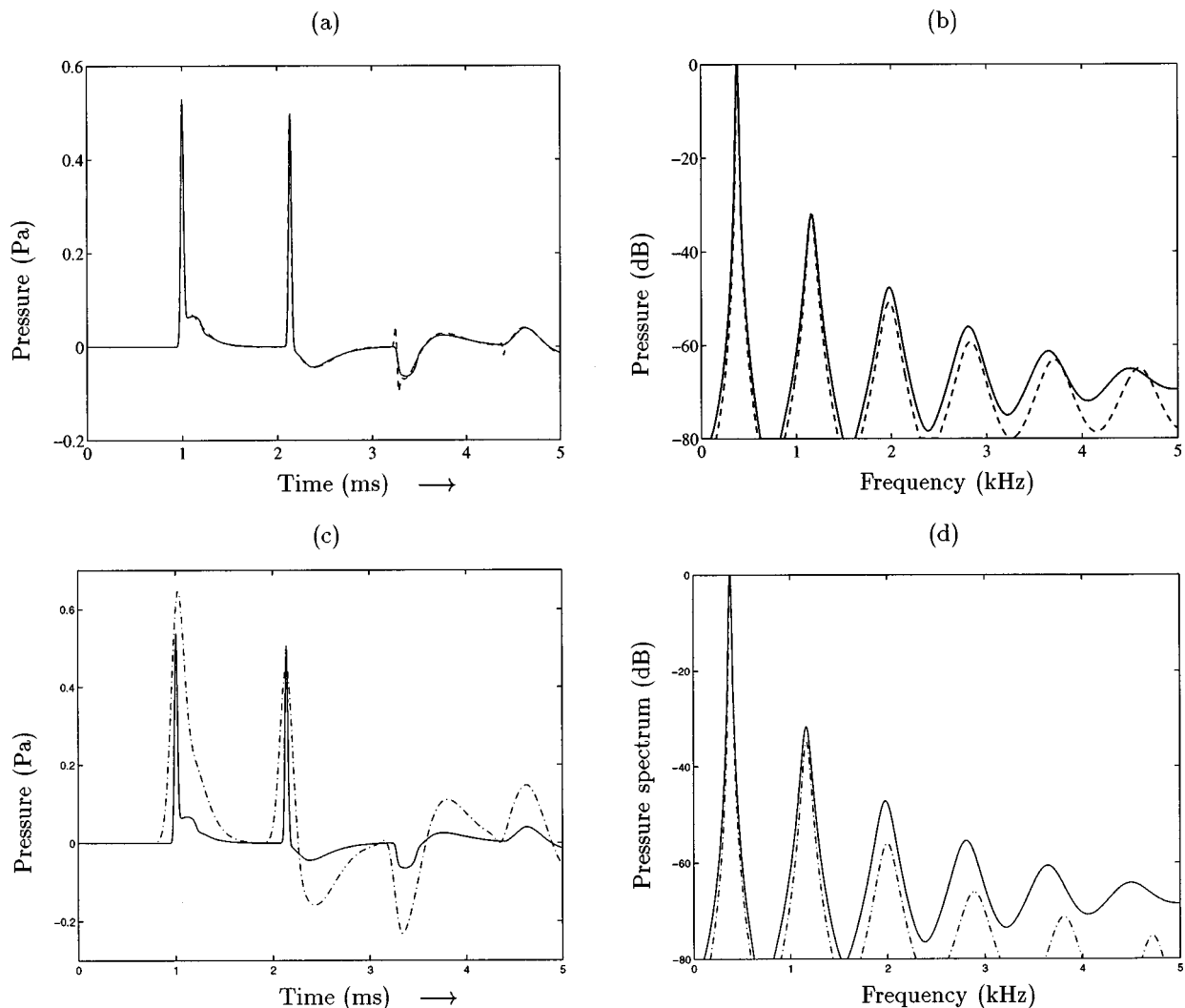


FIG. 5. Comparison between analytical and numerical impulse response of a baffled tube of length  $l_T=19.3$  cm and radius  $a_T=1.85$  cm closed at one end. (a) Pressure waveform at the open end; (b) pressure spectrum. Solid line: analytical solution with Rayleigh radiation impedance at the open end. Dashed line: second-order approximation with sampling rate  $f_s=192$  kHz. (c) Pressure waveform at the open end; (d) pressure spectrum. Solid line: analytical solution with Rayleigh radiation impedance at the open end. Dash-dotted line: second-order approximation with sampling rate  $f_s=44.1$  kHz.



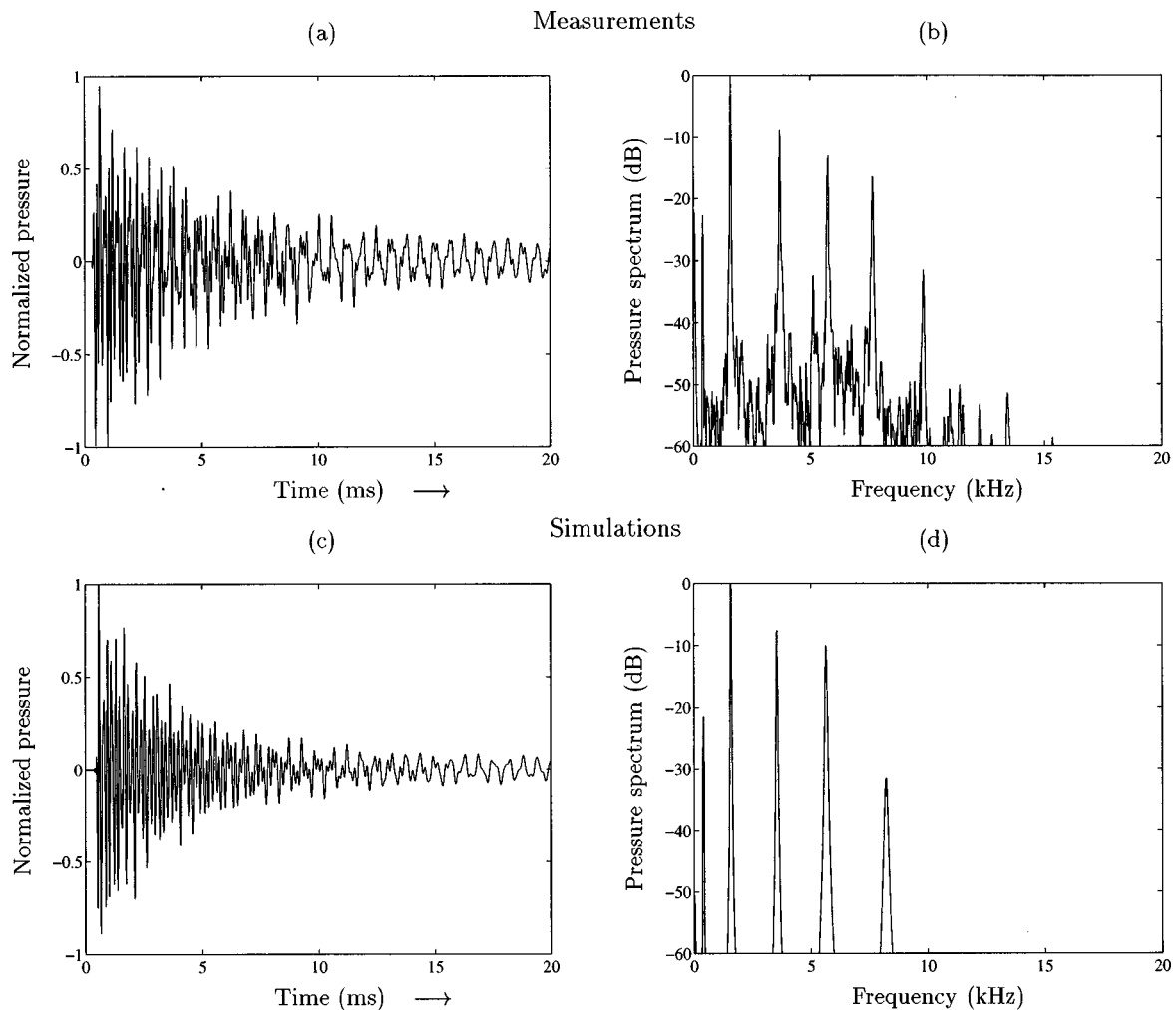


FIG. 6. Bar radiation. Comparison between measurements and simulations of the sound radiated by a xylophone  $G_4$  bar (without resonator) struck by a boxwood mallet. (a) Sound pressure recorded at  $r=0.8$  m,  $\theta=\pi/6$ ; (b) measured pressure spectrum; (c) simulated pressure; (d) simulated pressure spectrum.

plete sphere, and the right-hand side of Eqs. (32)–(34) should be consequently multiplied by a factor of 2.

### III. EXPERIMENTS AND SIMULATIONS

From a musical point of view, a xylophone model should be able to reproduce the following main relevant qualities of a real instrument: initial sharp attack, tuning, directivity, tone color, and aftersound due to the tubular resonator. The control of the tuning and of the initial sharp attack are mainly dependent on exciter and bar properties. These two points have been widely investigated in a previous paper and will not be discussed further here.<sup>1</sup>

The reproduction of the directivity pattern of the instrument is directly related to the above-presented linear array of dipoles model used for the bar and to the pulsating sphere model used for the tube. The ability of the model to account for the directivity measured on a real instrument is presented in Fig. 8. In addition, it is shown to what extent variations of the tube diameter in the model can change the balance between “bar” sound and “tube” sound (see Fig. 10).

During the initial transient, the tone color of the instrument is essentially due to the interaction between bar and mallet. However, after a short delay, the magnitude of the

tube contribution becomes predominant and the spectrum of the tone is clearly altered. Thus it is essential to examine whether the model is adequate for controlling the delay, magnitude, and spectrum of this aftersound. The capability of the model for reproducing the characteristic beats observed when the bar and the tube are detuned will be presented in Fig. 11.

#### A. Comparison between numerical and analytical solution for the isolated tube

The resonator model to be validated is composed of two parts: the acoustic wave propagation in the tube and the radiation impedance. The 2-2 explicit scheme used for the internal wave is standard and gives no difficulty. It yields no dispersion, in particular, since it is used with the condition  $r_{\text{CFL}}=1$  [see Eq. (23)]. As a consequence, the validation test for the resonator model has been essentially conducted in order to check the efficiency of the radiation impedance approximation.

The reference solution has been obtained using the analytical formulation of the Rayleigh radiation impedance shown in Eq. (10) for a baffled tube. From this equation, the transfer function  $\mathcal{H}_T(j\omega)$  between the resulting sound pressure at the open end  $p_0$  and the incoming bar pressure  $p_B$  at

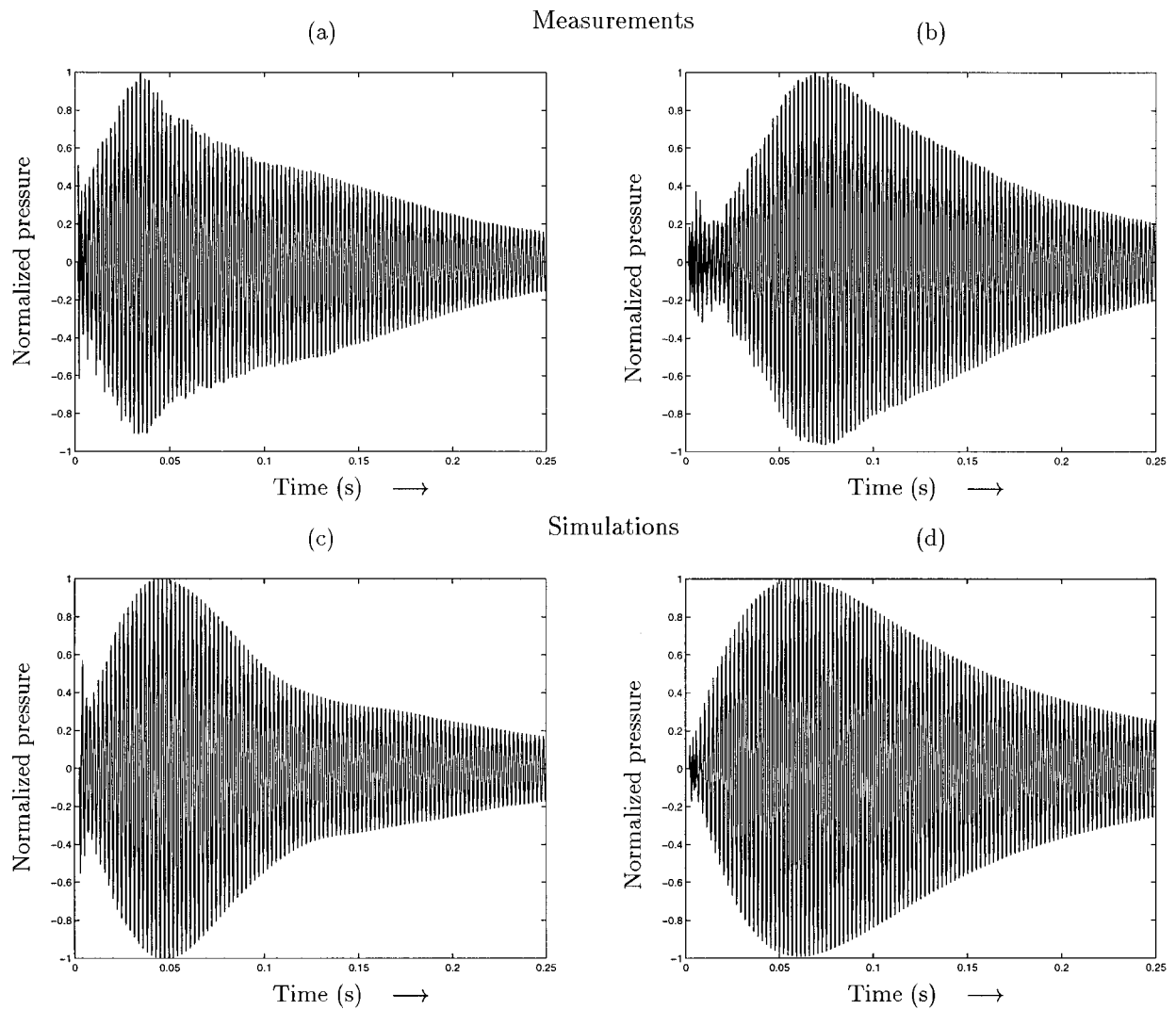


FIG. 7. Directivity. Comparison between measurements and simulations of sound pressure radiated by a xylophone  $A_4$  bar (with resonator) struck by a rubber mallet near the center. (a) Measured pressure with  $r=0.8$  m,  $\theta=0$ ; (b)  $r=0.8$  m,  $\theta=80^\circ$ . (c) Simulated pressure  $r=0.8$  m,  $\theta=0$ ; (d)  $r=0.8$  m,  $\theta=80^\circ$ .

this point has been calculated (see Appendix A). The corresponding impulse response of the tube  $h_T(t)$  is obtained by inverse Fourier transform. The pressure  $p_0$  radiated by the tube is calculated by convolving  $h_T(t)$  with a Gaussian pulse:

$$p_B(t) = \exp\left(-\frac{t-t_0}{2\Delta\tau}\right)^2. \quad (36)$$

The duration of the Gaussian pulse  $2\Delta\tau$  is taken equal to  $10 \mu\text{s}$  in order to be significantly lower than the propagation time in the tube. The reference solution is compared with the radiated pressure obtained by means of the numerical model presented in Sec. II.

Figure 5(a) shows the comparison between analytical and numerical time responses for an ideal lossless ( $\gamma_T=0$ )  $A_4$  resonator of length  $l_T=19.3$  cm with fundamental  $f_1=440$  Hz, closed at one end. The radiation at the open end is modeled by the second-order approximation of the Rayleigh impedance presented in the previous section. The calculations have been made at a sampling frequency  $f_s=192$  kHz, i.e.,  $\Delta z=c_0\Delta t=1.8$  mm, for a radius  $a_T=1.85$  cm. The relative error with the analytical solution is

equal to 0.03% for the first 100 ms of the signal. Figure 5(b) shows the frequency responses of these two waveforms, obtained by means of a FFT analysis. The agreement is excellent below 1 kHz and is equal to a few dB between 1 and 4 kHz with a slight deviation of the maxima.

In comparison, Fig. 5(c) and (d) show how the model performs at  $f_s=44.1$  kHz, which is the most commonly used audio sampling rate. In this case, the simulated waveform shows significant artifacts and the agreement between theoretical and simulated spectra is restricted to frequencies smaller than 1.5 kHz. Therefore for audio applications where a high degree of accuracy for the radiation impedance would be requested, the simulation should be made first at nearly four times the audio sampling rate and followed by a decimation with a factor of 4 before digital-to-analog conversion.

## B. Radiation of the bar: Comparison between simulation and experiments

In a first step, only the bar radiation is investigated. Figure 6 shows the comparison between measurements and

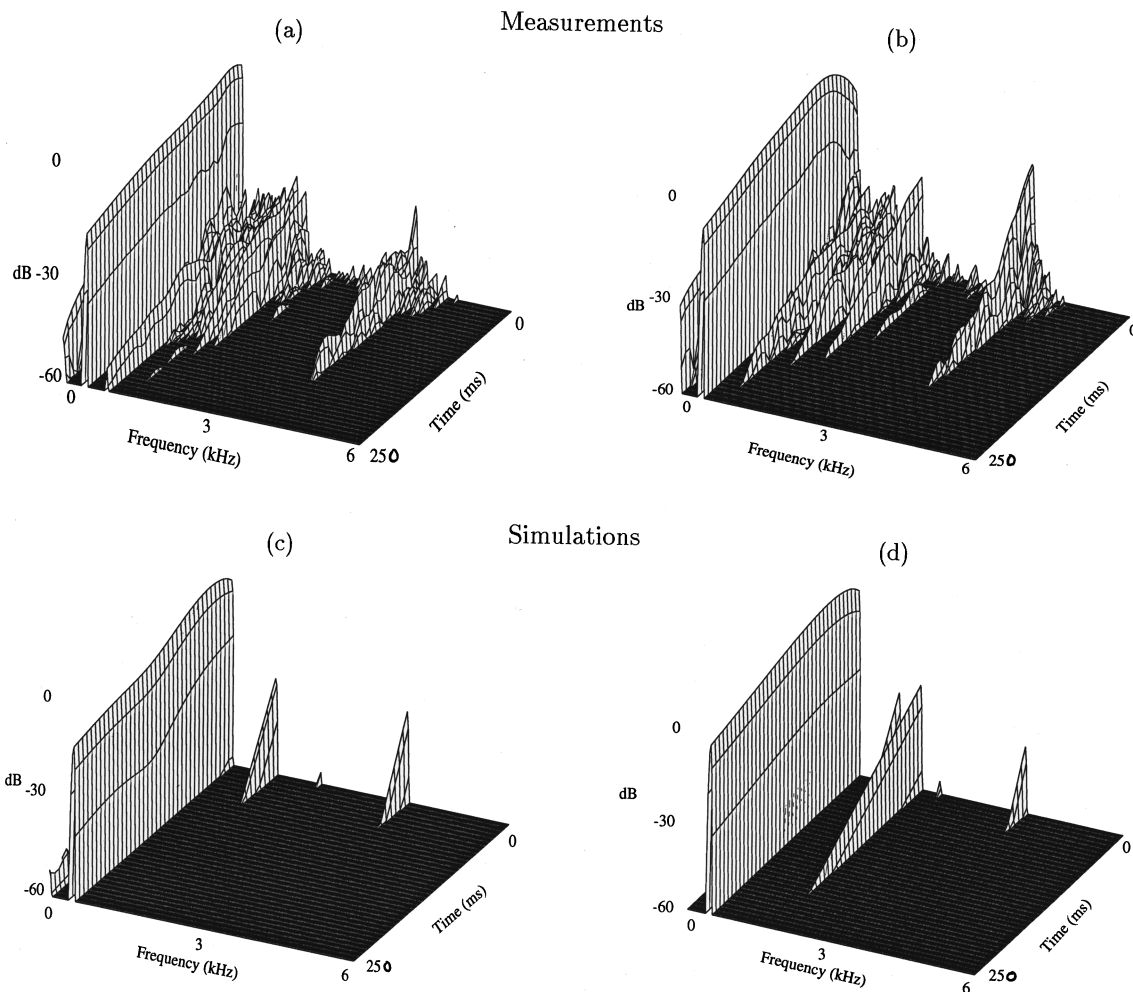


FIG. 8. Directivity (spectral plots). Comparison between measurements and simulations of sound pressure radiated by a xylophone  $A_4$  bar (with resonator) struck by a rubber mallet near the center. (a) Measured pressure with  $r=0.8$  m,  $\theta=0$ ; (b)  $r=0.8$  m,  $\theta=80^\circ$ . (c) Simulated pressure  $r=0.8$  m,  $\theta=0$ ; (d)  $r=0.8$  m,  $\theta=80^\circ$ .

simulations both in the time and frequency domains. The recording position for the comparisons between measured and simulated sound pressure has been taken at a point corresponding roughly to the location of the player's ear ( $r=0.8$  m,  $\theta=\pi/6$ ). The sound pressure has been measured with a microphone Schœps CMC3-D and the output signals were recorded on a Digital Audio Tape Sony TCD10-Pro. The comparisons were made for the  $G_4$  note ( $f_1=396$  Hz) of a xylophone Concorde X 4001, played with a boxwood mallet at the third of the bar length. A good agreement can be observed in the results. The general shape of the pressure waveforms are similar, except during the first few milliseconds. This discrepancy is mainly a consequence of the phase shift due to dispersion in the rapidly damped high-frequency range ( $f>5$  kHz). The spectra of the measured and simulated sound pressure show a large degree of similarity, at least for the first three partials where the observed discrepancies are less than 3 dB. For higher partials, the differences can be explained by the model used for the bending vibration of the bar, which takes neither torsional waves nor shear and rotary inertia effects into account.<sup>1</sup>

### C. Simulation of total sound field: Function of the resonator

Figure 7 illustrates the capability of the model to account for the directivity of the instrument. In these numerical experiments, the resonator is tuned to a frequency close to the fundamental frequency of the bar. The waveform envelope is very sensitive to small variations of the tuning. Temperature and humidity changes during the experiments may alter these waveforms significantly. These differences are more clearly seen in the time domain than in the frequency domain. Figure 7(a) and (c) corresponds to the case  $\theta=0$  whereas Fig. 7(b) and (d) corresponds to the case  $\theta=80^\circ$ . For  $\theta=0$  the bar contribution is relatively significant whereas this contribution is largely reduced for  $\theta=80^\circ$ . During the first 10 ms of the sound, the radiativity is of dipole type. The pressure signal reaches its maximum 40–60 ms after the impact. Systematic simulations show that this delay primarily depends on the bar-tube tuning and, more generally, on the coupling parameters: bar-tube distance, tube radius, and tube length. Notice that this delay is much larger than the time needed for the sound wave below the bar to reach the resonator before being reemitted, which would

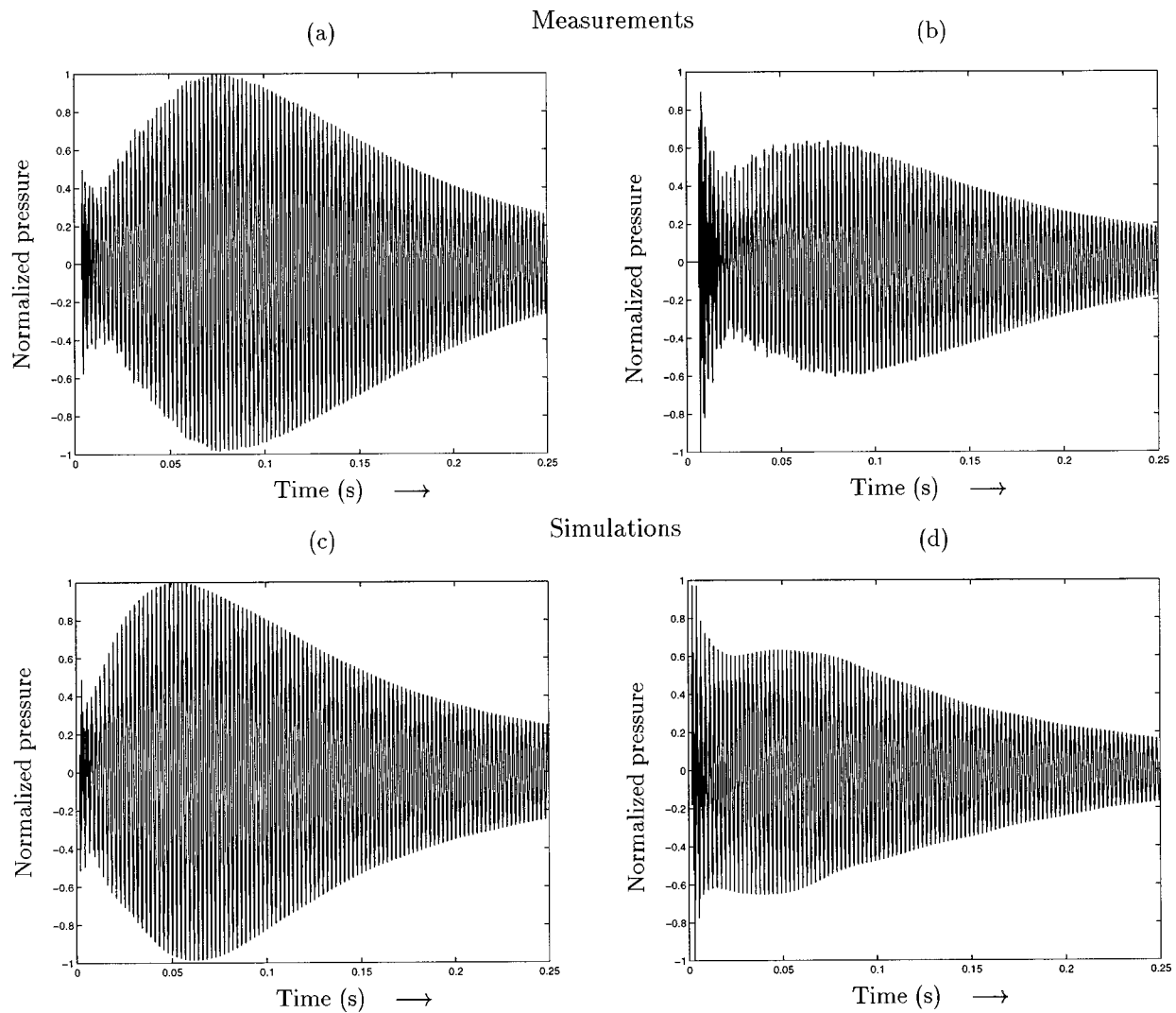


FIG. 9. Effect of tube radius. Comparison between measurements and simulations of sound pressure radiated by a xylophone  $A_4$  bar (with resonator) struck by a rubber mallet near the center. (a) Measured pressure with  $r=0.8$  m,  $\theta=45^\circ$ ,  $a_T=1.85$  cm; (b)  $r=0.8$  m,  $\theta=45^\circ$ ,  $a_T=1.1$  cm. (c) Simulated pressure  $r=0.8$  m,  $\theta=45^\circ$ ;  $a_T=1.85$  cm; (d)  $r=0.8$  m,  $\theta=45^\circ$ ,  $a_T=1.1$  cm.

yield a delay equal to  $2(d+l_T)/c_0=1.2$  ms, a confusion which is frequently encountered. Between typically 10 and 50 ms, the directivity pattern of the instrument changes gradually from dipole to monopole type. These results confirm previous experiments made by other authors on a vibraphone.<sup>16</sup> The model is able to reproduce the main features of the measured sounds although some differences can be seen for  $\theta=80^\circ$  where the magnitude of the measured waveform is about twice the simulated waveform during the attack.

Figure 8 shows the spectral plots corresponding to the waveforms displayed in Fig. 7. These plots were obtained from short-time Fourier transform using a window length of 40 ms and a step size of 5 ms. It is confirmed from these plots that the tube contribution is prominent and that the bar contributes to the sound essentially during the first 50 ms. The model is able to reproduce the time-envelope of the main spectral peaks.

Figure 9 shows variations of simulated sound pressure with tube radius. The recording point here is such that  $\theta=45^\circ$  and  $r_T=60$  cm. On the left-hand side of the figure, the

tube radius  $a_T=18.5$  mm whereas  $a_T=11$  mm on the right-hand side. As expected, the magnitude of the tube field becomes larger as the radius increases. In the experiments, the length of the tube has been slightly readjusted in order to compensate the consecutive small variations of the fundamental frequency. Both measurements and simulations clearly show the dramatic changes in bar-tube balance and sharpness of the attack due to modification of the tube radius.

The spectral plots corresponding to these sounds are shown in Fig. 10. It can be seen that, with the smaller radius, the initial magnitude of the bar components are of the same order of magnitude than the fundamental of the tube whereas, with the larger radius, these components are nearly 20 dB lower than the main tube component. Here again, the simulated time-envelopes of the main peaks agree well with the experiments.

Finally, Fig. 11 shows the simulated pressure waveforms obtained when the resonator is not tuned to the fundamental frequency of the bar. In order to illustrate this point, a  $B_4$  resonator of length  $l_T=159$  mm is placed under a  $A_4$  bar. Here the main effect of the tube is to produce the character-

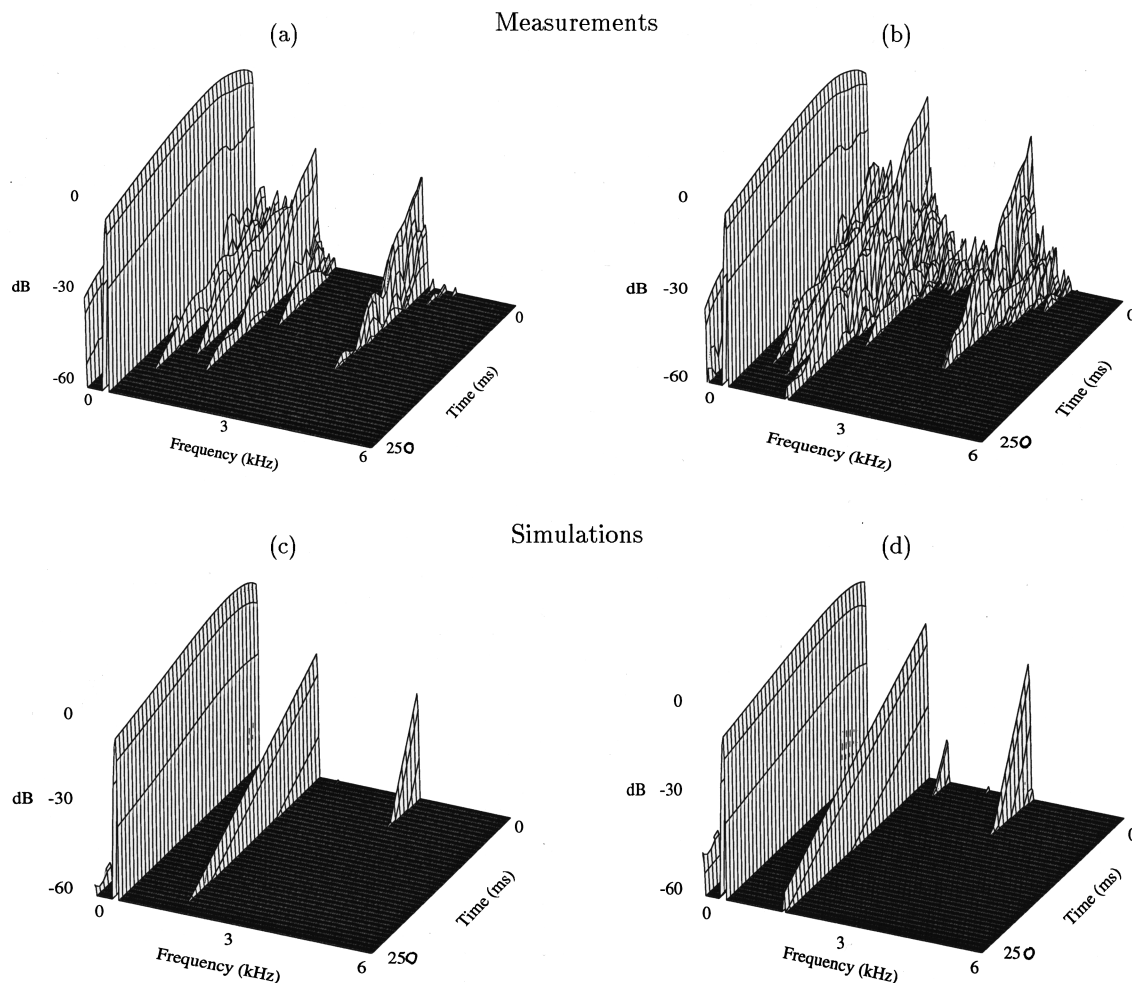


FIG. 10. Effect of tube radius (spectral plots). Comparison between measurements and simulations of sound pressure radiated by a xylophone  $A_4$  bar (with resonator) struck by a rubber mallet near the center. (a) Measured pressure with  $r=0.8$  m,  $\theta=45^\circ$ ,  $a_T=1.85$  cm; (b)  $r=0.8$  m,  $\theta=45^\circ$ ,  $a_T=1.1$  cm. (c) Simulated pressure  $r=0.8$  m,  $\theta=45^\circ$ ;  $a_T=1.85$  cm; (d)  $r=0.8$  m,  $\theta=45^\circ$ ,  $a_T=1.1$  cm.

istic beats which can be clearly heard on real instruments.

It has been also observed experimentally that the fundamental frequency of the tube decreases slightly with the bar-tube distance  $d$ . This phenomenon becomes significant if  $d$  is typically smaller than 3 cm and is due to the fact that the bar is an inertial obstacle to the sound field emitted by the open end which, in turn, modifies the radiation impedance.<sup>17</sup> In our model, this detuning can be compensated by adjusting the imaginary part of the simulated radiation impedance.

#### IV. CONCLUSION

A theoretical model has been developed which accounts for the sound field radiated by mallet percussion instruments. This time-domain modeling is based on the one-dimensional Euler–Bernoulli equation for the flexural vibrations of the bar coupled with the one-dimensional wave equation in the resonator under appropriate boundary conditions. Particular attention has been paid to the time-domain modeling of the radiation impedance of the tube, in order to guarantee that the problem is well-posed. Simulation of real instruments tones are obtained as a result of the numerical formulation of the problem. These simulations are based on finite difference approximations of the complete system of equations. Here

again, a thorough numerical analysis is conducted in order to ensure stability and sufficient precision of the numerical algorithms in the audio range. From a practical point of view, the computing time is not significantly longer for a complete instrument than for the bar equation only (typically  $10^3$  s for 1 s of sound on a Sun-Sparc10 workstation). The most time-consuming part of the model is due to the necessary fine tuning of the bar (see Ref. 1).

Various types of measurements and simulations have been conducted. First, it has been checked experimentally on wooden xylophone bars that the tube sound field has no appreciable influence on both eigenfrequencies and decay times of the bar vibrations, which confirms one of the basic assumptions of the model. This negligible influence of the tube is due first to the fact that, for wooden xylophone bars, the coupling with the tube is relatively weak and, second, to the relatively high internal losses compared to the radiation losses. However, this assumption is not justified for marimbas and vibraphones in the low-frequency range since these instruments exhibit a stronger bar-tube coupling and a lower internal damping in the bars. As a consequence, differences in the decay times, with and without the tube, are clearly seen.<sup>18</sup> In order to take this coupling into account, the present

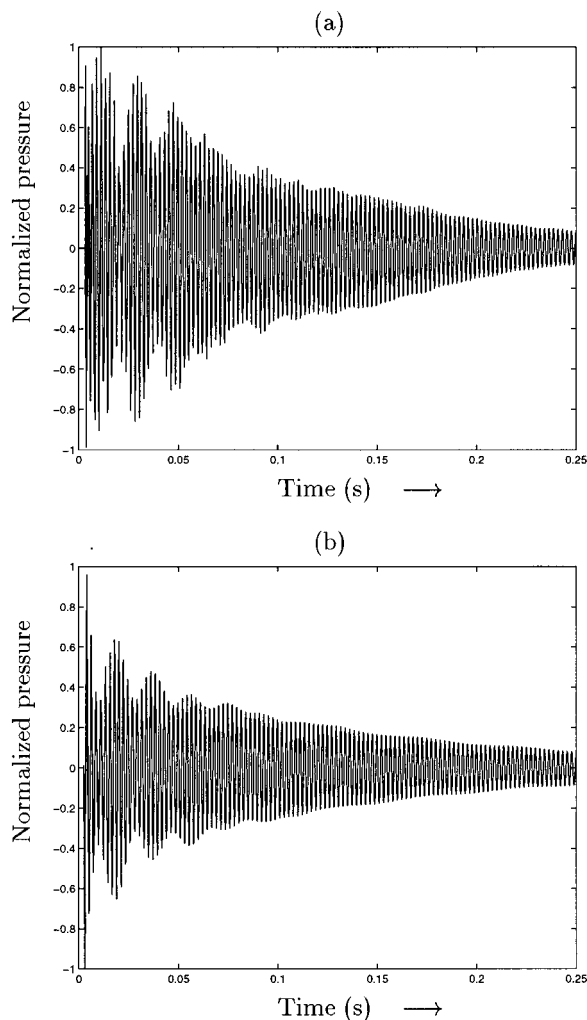


FIG. 11. Effect of tube length. Sound pressure radiated by a xylophone A<sub>4</sub> bar (with resonator) struck by a rubber mallet near the center:  $r=0.8$  m,  $\theta=0$ ,  $l_r=159$  mm (B<sub>4</sub> tube). (a) Measured; (b) simulated.

model should be modified in future versions by adding a tube pressure term in the vibrating bar equation.<sup>1</sup>

The tube model has been validated by comparisons between the numerical results and an analytical solution based on Rayleigh radiation impedance. In a third series of experiments, it has been shown to what extent the numerical model is able to reproduce the main features of real instruments, with regard to the balance between bar and tube contributions and to the directivity pattern of the instrument. The influence of tube length and bar-tube distance were also investigated. With the present one-dimensional model of the resonator, it is not yet possible to investigate with great detail the influence of the geometry of the tube on the sound field. However, the general structure of the model has proven to be valid and a number of problems of interest for makers could be solved in the future through the generalization of the acoustic wave equation in Eq. (6) to higher dimensions.

This time-domain approach yields a better understanding of the physics of mallet percussion instruments which complements previous works conducted in the frequency domain.<sup>3</sup> The results are currently of use for the design of

real instruments and for psychoacoustical studies. Sequences of simulated tones sound very realistic and can be used in the context of musical sound synthesis.

## APPENDIX A: STABILITY OF THE CONTINUOUS RESONATOR MODEL

The following derivations are based on Kreiss's theory, which has been developed in order to analyze whether a boundary value problem is well-posed or not. In practice, the boundary conditions must fulfill a number of conditions in order to ensure that no waves of increasing magnitude with time can be the solution of the problem.<sup>4</sup> This theorem applies to problems where the boundary conditions are complex impedances. In the Laplace domain, the specific impedances are then written in the form of a ratio of two polynomials:

$$\xi(s) = \frac{B(s)}{A(s)}, \quad (\text{A1})$$

where  $s$  is the Laplace transform variable. It can be shown that the problem is well-posed in the sense of Kreiss theory, providing that<sup>14</sup>

$$\forall s \in \mathbb{C} \quad \text{with } \Re(s) \geq 0, \quad \Re(\xi(s)) = \Re\left(\frac{B(s)}{A(s)}\right) > 0. \quad (\text{A2})$$

One can equivalently write the condition (A2) in terms of the reflection coefficient  $R(s)$  as follows:

$$\forall s \in \mathbb{C} \quad \text{with } \Re(s) \geq 0, \quad |R(s)| < 1. \quad (\text{A3})$$

From a physical point of view, Eq. (A3) implies energy losses at the boundary.

### The resonator model

The previous criterion is applied to a quarter-wavelength lossless tube, excited at its open end ( $z=0$ ) by the pressure signal  $p_B(t)$  generated by the bar. The total pressure at this end is written  $p(0,t)$ . In the Laplace domain, the transfer function  $\mathcal{H}_T(s)$  of the tube is written

$$\mathcal{H}_T(s) = \frac{p(0,s)}{p_B(s)} = \frac{1-R_0(s)}{2} \frac{1+e^{-2\Gamma(s)l}}{1-R_0(s)e^{-2\Gamma(s)l}}, \quad (\text{A4})$$

where  $\Gamma(s)=s/c_0$ , and  $R_0(s)=R(0,s)$  is the reflection coefficient at the open end:

$$R_0(s) = \frac{\tilde{\xi}_r(s)-1}{\tilde{\xi}_r(s)+1} \Leftrightarrow \tilde{\xi}_r = \frac{1+R_0(s)}{1-R_0(s)}. \quad (\text{A5})$$

A sufficient condition for ensuring the stability of the system represented by the transfer function  $\mathcal{H}_T(s)$  is given by  $|R_0(s)| < 1$ . A direct consequence of this condition is that  $\tilde{\xi}_r$  must have no poles with a non-negative real part. In our case, the specific radiation impedance is given by the second-order approximation:

$$\tilde{\xi}_r(s) = \frac{a_T}{c_0} \frac{\beta_1 s + \alpha_2 (a_T/c_0) s^2}{1 + \alpha_1 (a_T/c_0) s + \alpha_2 (a_T/c_0)^2 s^2}. \quad (\text{A6})$$

The condition of no poles with a non-negative real part for  $\tilde{\xi}_r$  implies first:

$$\alpha_1 > 0 \quad \text{and} \quad \alpha_2 > 0. \quad (\text{A7})$$

Second, it turns out that the condition (A2) needs to be checked on the imaginary axis  $s = j\omega$  only, through application of the maximum modulus principle to the function  $R_0(s)$  which must be analytic in the right-half complex plane. It is easy to establish in our case that

$$\begin{aligned} \Re e(\tilde{\xi}_r(j\omega)) &= \left(\frac{a_T}{c_0}\right)^2 [(-\alpha_2\omega^2)(1-\alpha_2\omega^2) + \omega^2\alpha_1\beta_1] \\ &> 0 \Leftrightarrow \alpha_1\beta_1 > \alpha_2. \end{aligned} \quad (\text{A8})$$

In summary, Eqs. (A7) and (A8) yield the stability conditions for the continuous system:

$$\alpha_1, \alpha_2 > 0 \quad \text{and} \quad \alpha_1\beta_1 > \alpha_2. \quad (\text{A9})$$

## APPENDIX B: STABILITY OF THE DISCRETE RESONATOR MODEL

For the numerical formulation of the problem, the approach for investigating the stability conditions is similar to the one presented in Appendix A, apart from the fact that the partial derivatives are now approximated by finite differences. It has been shown in another context that a good strategy consists in approximating the partial differential operators by the following expressions:<sup>19</sup>

$$\begin{aligned} \frac{\partial p}{\partial t} &\approx (\delta_t^- p)_i^{n+1} = \frac{p_i^{n+1} - p_i^n}{\Delta t}, \\ \frac{\partial^2 p}{\partial t^2} &\approx (\delta_t^2 p)_i^n = \frac{p_i^{n+1} - 2p_i^n + p_i^{n-1}}{\Delta t^2}, \\ \frac{\partial p}{\partial z} &\approx (\delta_z^+ p)_i^{n+1} = \frac{p_{i+1}^{n+1} - p_i^{n+1}}{\Delta z}. \end{aligned} \quad (\text{B1})$$

With these notations, the discrete wave equations in the isolated tube are written

$$(\delta_t^2 p)_i^n - c_0^2 (\delta_z^2 p)_i^n = 0 \quad \text{for } z \neq 0 \quad (\text{B2})$$

and

$$\begin{aligned} \mathbf{A}_r(\delta_t^-)[(\delta_t^-)p_0^{n+1}] - c_0 \mathbf{B}_r(\delta_t^-)[(\delta_z^+)p_0^{n+1}] &= 0 \\ \text{for } z = 0. \end{aligned} \quad (\text{B3})$$

Solutions to the problem of the form

$$p_i^n = \zeta^n \kappa^i \quad \text{with } |\zeta| \geq 1, |\kappa| \leq 1, \quad (\text{B4})$$

where the case  $\zeta = \kappa = 1$  corresponds to the particular case of harmonic waves, are not allowed to propagate in the system since their magnitudes are increasing with time. With (B4), Eqs. (B2) and (B3) become

$$\begin{aligned} (\zeta - 2 + \zeta^{-1}) - r_{\text{CFL}}^2 (\kappa - 2 + \kappa^{-1}) &= 0, \\ (1 - \zeta^{-1}) \mathbf{A}_r \left( \frac{1 - \zeta^{-1}}{\Delta t} \right) - r_{\text{CFL}} (\kappa - 1) \mathbf{B}_r \left( \frac{1 - \zeta^{-1}}{\Delta t} \right) &= 0. \end{aligned} \quad (\text{B5})$$

With the second-order radiation impedance Eq. (A6) and the finite difference approximations (B1), Eq. (B3) becomes

$$\begin{aligned} 1 + \frac{\alpha_1 a_T}{\Delta t c_0} (1 - \zeta^{-1}) + \frac{\alpha_2}{\Delta t^2} \left( \frac{a_T}{c_0} \right)^2 (1 - \zeta^{-1})^2 \\ - \frac{a_T}{\Delta z} (\kappa - 1) \left[ \beta_1 + \frac{\alpha_2 a_T}{\Delta t c_0} (1 - \zeta^{-1}) \right] &= 0. \end{aligned} \quad (\text{B6})$$

The stability theory in the discretized case is essentially the same as in the continuous case. It implies here that  $|\kappa| > 1$  in Eq. (B6), which yields

$$2\alpha_2\alpha_1\sigma + \alpha_1^2 - 2\alpha_2(1 + \beta_1\sigma) > 0 \quad (\text{B7})$$

with  $\sigma = a_T/c_0\Delta t$ . Taking further the stability condition of the continuous problem (A9) into account, Eq. (B7) is written finally in terms of the time step:

$$\Delta t < \frac{a_T}{c_0} \frac{2\beta_1(\alpha_1 - \beta_1)}{2\beta_1 - \alpha_1}. \quad (\text{B8})$$

Notice that, in order to ensure the positivity of  $\Delta t$ , we must have in addition

$$\beta_1 < \alpha_1 < 2\beta_1. \quad (\text{B9})$$

- <sup>1</sup>A. Chaigne and V. Doutaut, "Numerical simulation of xylophones. I: Time-domain modeling of the vibrating bars," *J. Acoust. Soc. Am.* **101**, 539–557 (1997).
- <sup>2</sup>M. C. Junger, "Sound radiation by resonances of free-free beams," *J. Acoust. Soc. Am.* **52**, 332–334 (1972).
- <sup>3</sup>I. Bork, "Zur Abstimmung und Kopplung von schwingenden Stäben und Hohlraumresonatoren," Ph.D. thesis, Technische Universität Carolo-Wilhelmina, Braunschweig, 1983.
- <sup>4</sup>H. O. Kreiss, "Stability theory of difference approximations for mixed initial boundary value problems," *Math. Comput.* **22**, 703–714 (1968).
- <sup>5</sup>A. Akay, M. T. Bengisu, and M. Latcha, "Transient acoustic radiation from impacted beam-like structures," *J. Sound Vib.* **91**, 135–145 (1983).
- <sup>6</sup>M. Ochmann, "Die Multipolstrahlersynthese—Ein effektives Verfahren zur Berechnung der Schallabstrahlung von schwingenden Strukturen beliebiger Oberflächengestalt," *Acustica* **72**, 233–246 (1990).
- <sup>7</sup>A. D. Pierce, *Acoustics. An Introduction to its Physical Principles and Applications* (Acoustical Society of America, New York, 1989), 2nd ed.
- <sup>8</sup>P. M. Morse and K. U. Ingard, *Theoretical Acoustics* (McGraw-Hill, New York, 1968).
- <sup>9</sup>J. D. Polack, "Time domain solution of Kirchhoff's equation for sound propagation in viscothermal gases: a diffusion process," *J. Acoust.* **4**, 47–67 (1991).
- <sup>10</sup>D. Matignon and B. d'Andrea Novel, "Spectral and time-domain consequences of an integrodifferential perturbation of the wave PDE," in *Proceedings of the 3rd International Conference on Mathematical and Numerical Aspects of Wave Propagation* (SIAM-INRIA, Philadelphia, 1995), pp. 769–771.
- <sup>11</sup>H. Levine and J. Schwinger, "On the radiation of sound from an unflanged circular pipe," *Phys. Rev.* **73**, 383–406 (1948).
- <sup>12</sup>R. Caussé, J. Kergomard, and X. Lurton, "Input impedance of brass musical instruments. Comparison between experiment and numerical models," *J. Acoust. Soc. Am.* **75**, 241–254 (1984).
- <sup>13</sup>J. O. Smith, "Techniques for digital filter design and system identification with application to the violin," Ph.D. thesis, CCRMA Department of Music, Stanford University, Stanford, California, 1983, Report No. STAN-M-14.
- <sup>14</sup>R. D. Richtmyer and K. W. Morton, *Difference Methods for Initial-value Problems* (Interscience, New York, 1967), 1st ed.
- <sup>15</sup>W. F. Ames, *Numerical Methods for Partial Differential Equations* (Academic, London, 1992), 3rd ed.
- <sup>16</sup>B. C. Tuttle and C. B. Burroughs, "The effects of a resonator tube on the timbre and directivity of sound radiation from a vibraphone bar," in *Proceedings of the Institute of Acoustics—ISMA '97* (1997), Vol. 19(5), pp. 207–211.
- <sup>17</sup>V. Doutaut, A. Chaigne, and G. Bedrane, "Time-domain simulation of the

sound pressure radiated by mallet percussion instruments,” in *Proceedings of the International Symposium on Musical Acoustics*, Dourdan (1995), pp. 518–524.

<sup>18</sup> N. H. Fletcher and Th. D. Rossing, *Physics of Musical Instruments*

(Springer-Verlag, New York, 1991).

<sup>19</sup> P. Joly and J. E. Roberts, “Approximation of the surface impedance for a stratified medium,” in *Geophysical Inversion*, edited by J. B. Bednar *et al.* (SIAM, Philadelphia, 1992), Chap. 10, pp. 245–276.



# Sound production by a vibrating piano soundboard: Experiment

N. Giordano

*Department of Physics, 1396 Physics Building, Purdue University, West Lafayette, Indiana 47907-1396*

(Received 9 March 1998; revised 4 June 1998; accepted 5 June 1998)

The generation of sound by a piano soundboard is investigated experimentally, through measurements of the sound pressure,  $p$ , and the soundboard velocity,  $v_b$ , produced in response to a force applied at the bridge. Results for the ratio  $p/v_b$  as a function of frequency, for forces applied perpendicular to the soundboard at different locations (i.e., driving points) on the bridge, are presented. At all locations,  $p/v_b$  is largest at frequencies of order  $\sim 1$  kHz, and falls off below a few hundred Hz and above  $\sim 5$  kHz. A few results obtained with the force applied along the string direction (i.e., parallel to the plane of the soundboard) are also described. These results are compared and contrasted with previous experiments, and with theoretical expectations. © 1998 *Acoustical Society of America*. [S0001-4966(98)04409-9]

PACS numbers: 43.75.Mn [WJS]

## INTRODUCTION

Pianos have been the subject of many experimental and theoretical investigations.<sup>1,2</sup> Much of this work has been concerned with string vibrations, the hammer string interaction, and, of course, the spectrum of a piano tone and its variation with time. Relatively little attention has been paid to soundboard vibrations and how these produce sound.

A convenient way to characterize sound production by a vibrating soundboard is the ratio  $p/v_b$ , where  $p$  is the sound pressure and  $v$  is the velocity of the soundboard. Of course, both  $p$  and  $v_b$  will depend on the position at which they are measured, and on where the force is applied. It is perhaps most informative to apply the driving force to the bridge, since this is where the force from a string is applied. It is then natural to measure  $v_b$  at the same point on the bridge. As for  $p$ , while its magnitude will certainly vary with position, this will presumably not greatly affect the general variation of  $p/v_b$  with frequency.

So far as we know, there have been only two experimental investigations of  $p/v_b$ . Wogram<sup>3,4</sup> studied this quantity for an upright piano. He reported that it exhibits a maximum at a frequency near or below 1 kHz, and that it falls sharply at frequencies below about 100 Hz, and above about 1 kHz. In particular, he found that it falls by typically a factor of 10 as the frequency is varied from 1 to 5 kHz. In later experiments, Suzuki<sup>5</sup> investigated the integrated (with respect to area above the soundboard) sound produced by a grand piano. While he did not show results over a wide frequency range for any one location of either the driving force or measurement area, his results imply that integrated sound intensity normalized by the input power is approximately constant from 200 Hz up to 5 kHz. Hence, these two experiments, even though they measure slightly different quantities, do not appear to agree. One motivation for the present experiment was to resolve this discrepancy. Another was to provide systematic results for  $p/v_b$  for a representative choice of driving points. Such results are central for our ongoing effort<sup>6</sup> to construct a full, numerical model of piano sound production. Our intent is to use the new experimental results for  $p/v_b$  reported in this paper to guide and test numerical models of

soundboard vibrations and sound production which are now under development.

In this paper we report studies of  $p/v_b$  using two techniques. One involved a “frequency domain” measurement, similar to that used previously,<sup>3,5</sup> in which a force was applied to the soundboard using a shaker. The other method was a “time domain” approach, in which the force from a vibrating string was employed. Results obtained with these two methods are in agreement, and they are consistent with those reported by Suzuki.

For most of our measurements the force was applied perpendicular to the plane of the soundboard. However, we also investigated the sound produced by a force parallel to the string direction. The aim here was to better understand how longitudinal string vibrations<sup>2,7</sup> give rise to sound.

## I. EXPERIMENTAL SETUP

The experiments were carried out with two soundboards. One was in an intact (fully assembled) piano,<sup>8</sup> while the other had been removed from an instrument<sup>9</sup> (both of the pianos were upright models). We will refer to the latter as the “free-standing” soundboard. However, its edges were attached to rigid metal braces, using closely spaced ( $\approx 10$  cm) screws. The intent was to approximate the boundary conditions found in an assembled piano. The bridge motion was measured with miniature accelerometers<sup>10</sup> attached with either a screw mounting or with wax. In previous work<sup>11</sup> we have established that both mounting schemes are satisfactory in the frequency range studied here. The sound pressure was measured using a microphone<sup>12</sup> positioned 30 cm from the center of the back of the soundboard. The results for other microphone positions were explored (as discussed some below), and the results at this position were representative. The measurements were performed in an ordinary laboratory, with no special acoustical material on the walls or ceiling. The acoustic environment was somewhat (but in our subjective opinion, not excessively) “livelier” than might be found in a living room. We do not believe that the measurements were sufficiently sensitive for this to have a significant effect.

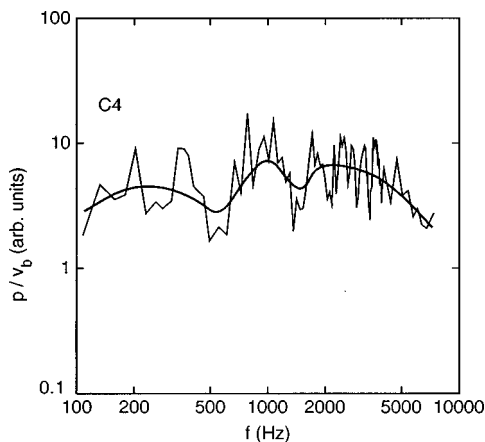


FIG. 1. Results for  $p/v_b$  as a function of frequency for the free-standing soundboard. The force was applied using the shaker at the point where the strings for the note C4 cross the bridge. The microphone was 30 cm from the center of the back of the soundboard. The heavy solid line here, and in the next two figures, is drawn as a guide to the eye, to emphasize the "average" behavior.

Two different measurement schemes were employed. (1) A sinusoidal force was applied to the bridge using a shaker,<sup>13</sup> with the accelerometer located as close as possible (typically within 1 cm) to the point where the force was applied. The rms acceleration and sound pressure were then recorded as the frequency was swept over the desired range. This type of measurement was most convenient with the free-standing soundboard, since all locations on both the treble and bass bridges were readily accessible. For the intact piano, only a limited region on the treble bridge was accessible, so it was not possible to study in this way the behavior for driving points on the bridge above the note G3 (~192 Hz). (2) We also measured  $p/v_b$  using the force from the strings to drive the soundboard. In this approach we recorded the accelerometer and microphone signals as functions of time just after a key was struck. These signals were then Fourier analyzed to obtain the relative strengths at the frequencies of the various partials. The ratio  $p/v_b$  at these frequencies could then be derived. While this approach only allows one to measure  $p/v_b$  at selected frequencies, these are the frequencies of most interest.

## II. RESULTS

### A. Swept frequency measurements

Figure 1 shows results for  $p/v_b$  for the free-standing soundboard with the force applied at the bridge point for middle C. (Note: in order to make comparisons easiest, we have used similar scales for the axes in Figs. 1–3, 5, 7, and 8. In addition, the arbitrary units for  $p/v_b$  are the same in all of these figures, so that the values of  $p/v_b$  may be compared directly.) These results, which are representative for notes on the treble bridge, exhibit several features. (1) There are rapid fluctuations of  $p/v_b$  with frequency. Fluctuations of order of a factor of  $\pm 3$  are common, even for changes in frequency much less than the spacing between different partials, which in this case is ~262 Hz.<sup>14</sup> It is tempting to attribute these fluctuations to variations of the mechanical impedance,  $Z$ , of the soundboard as one moves from one vibrational mode to

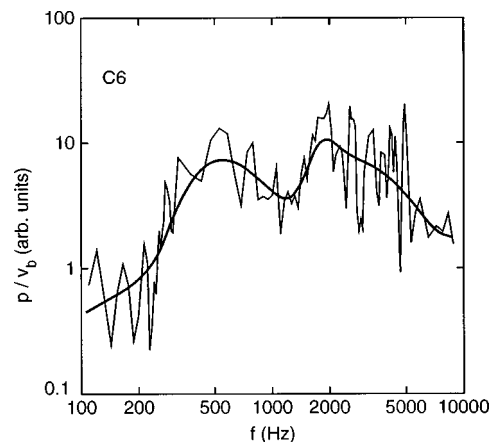


FIG. 2. Same as Fig. 1, but the force was applied at the bridge point for the note C6.

another.<sup>11</sup> Since the driving force in our experiments,  $F$ , varied smoothly with frequency (this was known from previous experiments with the same shaker<sup>11</sup>), fluctuations in  $Z$  will cause corresponding fluctuations in  $v_b \equiv F/Z$ . However, the results in Fig. 1 are for the ratio  $p/v_b$ , so the effect of fluctuations in  $v_b$  alone are removed. Hence, the fluctuations seen in Fig. 1 are not due simply (or solely) to fluctuations of the mechanical impedance. They are due instead to "modal" effects. That is, the various soundboard normal modes will have nodal lines at different locations. As the frequency is varied, the positions of the nodal lines will vary with respect to the driving point, and this will affect  $v_b$ . In addition, different modes will radiate with different directionalities, and this will affect  $p$ . We will return to these points below. (2) The "average" value of  $p/v_b$ , illustrated qualitatively by the heavy solid line in Fig. 1, exhibits slow fluctuations, which are of order  $\sim \pm 2$ . The largest values of  $p/v_b$  are found near 1 kHz, and the "average" value begins to fall substantially only above about 5 kHz.

This behavior is very different from that described by Wogram, who reported that the average value (in the sense just defined) of  $p/v_b$  falls by a factor of 10 or more in going from 1 to 5 kHz. The reason for this discrepancy is probably linked to difficulties in his measurement of  $v_b$ , as has been discussed elsewhere.<sup>11,15</sup> Our results are quite consistent with the related measurements of Suzuki.

Figure 2 shows the results when the force is applied, and  $v_b$  is measured, at the bridge point corresponding to the note C6 (fundamental ~1048 Hz). The major difference between this result and the behavior at C4 is that  $p/v_b$  begins its low-frequency falloff at approximately 300 Hz, which is about a factor of 2 higher than is the case for C4. Note that we again observe sizable fluctuations in  $p/v_b$ , whose magnitude is similar to that seen at C4. The behavior is basically similar for forces applied to the bass bridge, Fig. 3, except that the falloff at high frequencies begins somewhat sooner, here at about 3 kHz.

### B. Fourier transform results for $p/v_b$

To investigate the behavior of our intact piano we employed the Fourier transform approach described briefly in

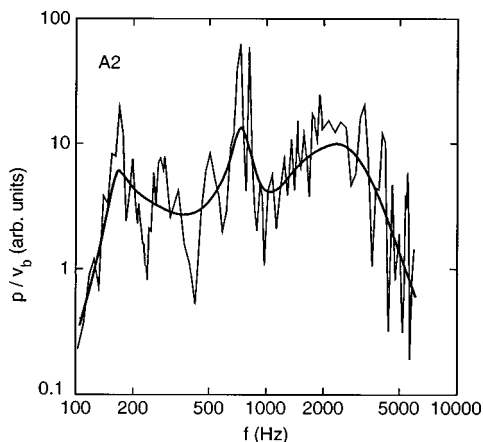


FIG. 3. Same as Fig. 1, but the force was applied at the bridge point for the note A2.

Sec. II. In our particular experiments, the accelerometer and microphone signals were recorded simultaneously at a sampling rate of 22.05 kHz. Typical examples are given in Fig. 4, which shows the sound pressure just after the onset of sound, and the bridge acceleration just after the transverse string displacement pulse reaches the bridge, for the note C4. Since the bridge point for this note was, as noted above, not accessible (due to the bass strings, along with the action), for this measurement the accelerometer was positioned on the back of the soundboard (directly opposite the location where this string crosses the bridge), rather than on the bridge. The horizontal arrows in the figure show the period of the fundamental, and it can be seen that the high-order partials of both signals are quite substantial.

These signals were Fourier analyzed to obtain the power spectra. For this calculation, 2048 digitized points were used, starting from the onset of the signal in Fig. 4. This corresponds to approximately 0.093 s of real time. Similar results for  $p/v_b$  were obtained if later portions of the signal were used instead (portions as late as 1 s after the onset were analyzed for comparison, and gave essentially identical results; the windowing used in the Fourier analysis was also found to not affect the results). We next normalized the ac-

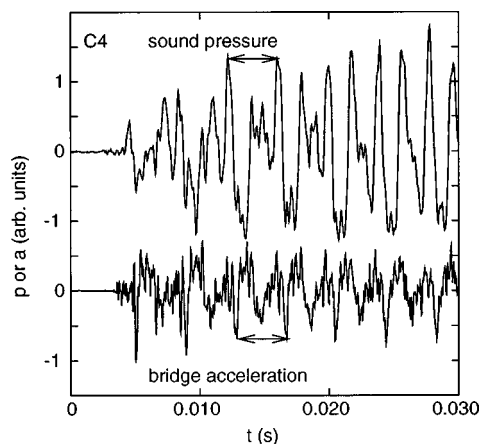


FIG. 4. Sound pressure (top) and bridge acceleration (bottom) just after the strings for the note C4 (middle C) were set into motion by a hammer blow. The horizontal arrows show the period of C4.

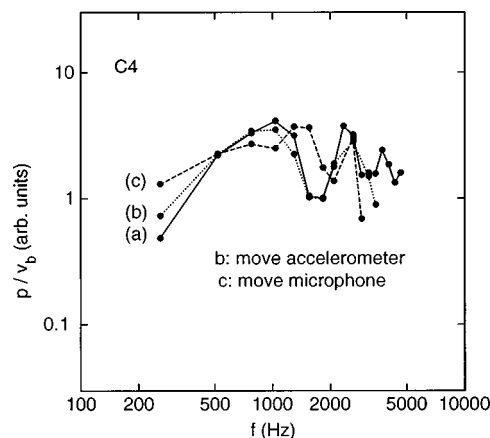


FIG. 5. Fourier transform results for  $p/v_b$  for the note C4 of our intact piano. The results labeled (a) were derived from the data in Fig. 4.

celeration spectrum by the square of the frequency to obtain the velocity power spectrum. The values of the power for the different partials were then extracted, and the ratio of the pressure power spectrum to the velocity power spectrum, at the frequency of each partial, was obtained. This yielded  $(p/v_b)^2$  at each of these frequencies.

Some results for  $p/v_b$  obtained from the signals in Fig. 4, and for several other measurements with the note C4, are shown in Fig. 5. These results show fluctuations in  $p/v_b$  as the frequency is varied from partial to partial, similar to what was observed above in the swept frequency measurements. To investigate the source of these fluctuations, data set (b) in Fig. 5 shows the effect of moving the accelerometer approximately 1 cm from its position in measurement (a). For both measurements the microphone position was kept fixed, approximately 40 cm from the back of the center of the soundboard, a location which placed it between two back posts. While moving the accelerometer this relatively small amount does change  $p/v_b$  somewhat; the major fluctuations, including the large dip near 1.5 kHz, are essentially unchanged. Result (c) in Fig. 5 shows the effect of moving the microphone 22 cm towards the bass end of the piano (it was again between posts). This is seen to have a much larger effect on  $p/v_b$ , and indicates that the fluctuations in  $p/v_b$  are due largely to the interference of sound emitted from different parts of the soundboard. This is not surprising, since the wavelength of sound at the fundamental is  $\sim 1.3$  m, which is comparable to the soundboard (and other relevant) dimensions. The change found in moving the accelerometer a small amount [data sets (a) and (b) in Fig. 5], while smaller than the change found in moving the microphone, is also significant. We believe that it is due to the different amounts of sound generated by the different normal modes of the soundboard, together with the effect of their nodal lines on the value of  $v_b$  (as mentioned above). At any given frequency, several normal modes can be excited; these will have different sound generation efficiencies, and make contributions to  $v_b$  whose sizes vary with position on the board.

Figure 6 shows Fourier transform results for several different notes. In addition to the fluctuations noted in connection with the results for C4, two other features can be seen. First, the overall or “average” value of  $p/v_b$  is approxi-

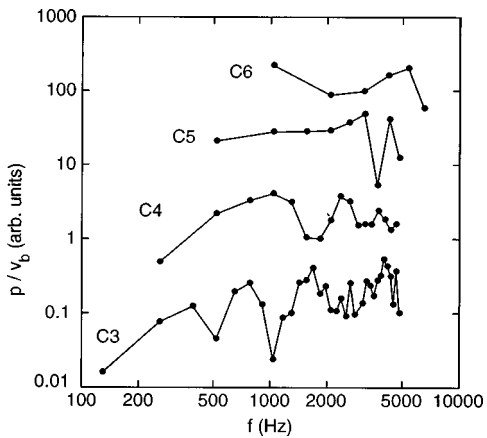


FIG. 6. Fourier transform results for  $p/v_b$  for several notes of our intact piano. The units on the vertical axis are arbitrary, and the results for each data set are displaced vertically for clarity.

mately constant over the range 500–5000 Hz. In considering the “average” behavior, we are attempting to separate the fluctuations (which have been discussed above) from the “overall” or background behavior (which we have attempted to indicate by the smooth curve). While this background behavior certainly does appear to vary somewhat over the range considered in Fig. 6, it varies by only about a factor of 2 or so over the range 500–5000 Hz. This is in sharp contrast to the results of Ref. 3, where it is reported that the background value of  $p/v_b$  fell by more than an order of magnitude in going from 1000 to 5000 Hz. Second, we observe from Fig. 6 that  $p/v_b$  falls somewhat below about 300 Hz. This is especially clear from the results for C3, and can also be seen for C4. These two features are consistent with the swept frequency results for the free-standing soundboard (Figs. 1–3).

In order to more directly compare the two types of measurements, we show results for the note G3 for our intact piano in Fig. 7. The bridge position for this note was directly accessible, so here we were able to mount the accelerometer directly on the bridge. The force from the shaker was also

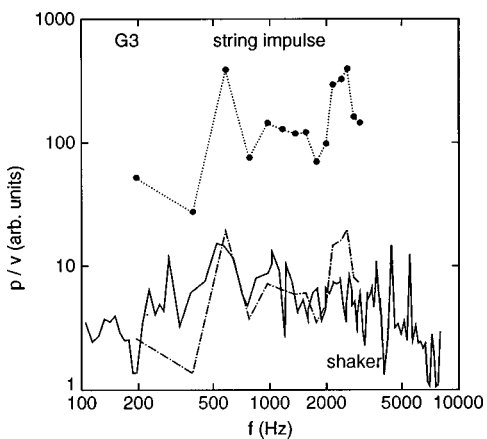


FIG. 7. Fourier transform (dotted curve) and swept frequency (force applied with the shaker) results (solid curve) for  $p/v_b$  for the note G3 of our intact piano. The units on the vertical axis are arbitrary, and the results for the two data sets are displaced vertically for clarity. The dot-dashed curve shows the impulse results shifted so that they approximately overlap the swept frequency measurements.

applied to the bridge. Hence, in this case we can directly compare the two types of measurements (since the microphone and accelerometer positions were the same), although we have not attempted to determine the absolute magnitudes of  $p/v_b$ . The results here, as in the earlier figures, only give the relative values. Thus there is an undetermined overall scale factor for the two data sets in Fig. 7. To compare the two we have simply shifted the Fourier transform results by a constant factor (the dashed curve), and the results from the two rather different measurements are seen to be in fairly good agreement. An interesting difference is near 2000 Hz, where the Fourier transform results appear to be somewhat larger than the swept frequency measurements. This difference may simply be due to uncertainties in the Fourier transform results; at these high frequencies the Fourier amplitudes are quite small, making it difficult to extract accurate values of  $p/v_b$ . However, it is also possible that another effect is becoming important, and that effect is the subject of the next section.

### III. SOUND PRODUCTION BY AN IN-PLANE FORCE ON THE BRIDGE

It is well known that the blow of a piano hammer excites both transverse and longitudinal vibrations of the string.<sup>2,7</sup> The transverse vibration leads to a force on the bridge which is directed perpendicular to the soundboard, and thus to sound, and this sound generation has been the main subject of the present work. Longitudinal string vibrations will yield a force on the bridge which is along the string direction, i.e., parallel to the plane of the soundboard. This force will also drive soundboard vibrations which can produce sound, although one might expect that the amount of sound generated by this mechanism will be small. To the best of our knowledge, generation of sound via this mechanism has not previously been studied.

Longitudinal string forces might have an impact on our Fourier transform measurements for the following reason. This measurement uses the force from a string to drive the bridge. Since the string force will have components which are both perpendicular and parallel to the soundboard, this measurement will detect sound from both sources. This is in contrast to the shaker measurements, in which the force is applied (by the shaker) purely perpendicular to the soundboard. Indeed, one might now wonder why the two types of measurements should ever agree (as we have already observed above). One reason is that the longitudinal string vibrations have a much higher frequency than the transverse ones. The longitudinal wave speed is about an order of magnitude higher than the transverse speed,<sup>2,7</sup> making the corresponding frequencies higher by the same factor. Experiments have shown that the longitudinal vibrations have most of their strength near 2–4 kHz, so the sound they produce would not interfere with most of the measurements presented above. However, they might be the cause of the small peak in  $p/v_b$  seen in the Fourier transform measurements in Fig. 7.

To investigate this question, we have used a shaker to apply a force along the string direction for the free-standing soundboard, and measured  $p/v_b$  for this configuration. Note

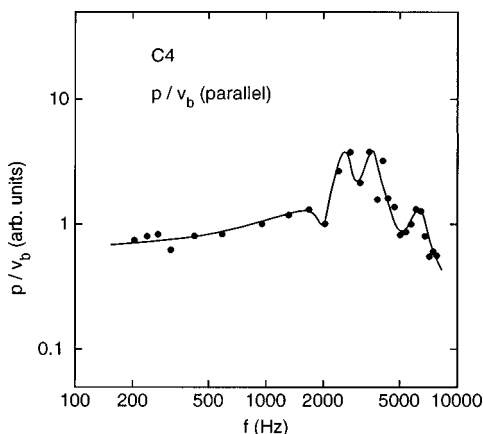


FIG. 8. Results for  $p/v_b$  (parallel) for the free-standing soundboard, obtained with the force applied parallel to the string direction. The smooth curve is a guide to the eye.

that here  $v_b$  is the bridge velocity *along the string direction*. This measurement was performed by aligning the axis of the shaker along the string direction, and using a long (22-cm) stinger rod, so that the force could be applied at the top edge of the bridge, at the same point at which the force from the string would be applied. This is important, since such an in-plane force will exert a substantial torque on the bridge. Presumably, the resulting twisting motion of the bridge is the mechanism by which the soundboard is excited and sound is produced.<sup>16</sup> The accelerometer was oriented so as to detect motion parallel to the string direction, and was mounted on the edge of the bridge very close (within 1 cm) to where the stinger made contact. Some results are shown in Fig. 8. In all of our previous results in this paper we have considered the bridge velocity in the direction perpendicular to the plane of the soundboard. Here, however, we are considering  $v_b$  along the string direction, and in Fig. 8 we have plotted  $p/v_b$ (parallel). We have also measured  $v_b$ (perpendicular) as produced by a parallel force, and found that for a parallel force of the same size, these two velocities are *very* similar in magnitude at all frequencies studied. The reason why  $v_b$ (parallel)  $\approx v_b$ (perpendicular) is not clear to us at present, but it does mean that the semi-quantitative behavior of  $p/v_b$  does not depend on which velocity component is considered.

Returning to Fig. 8, we see that the ratio  $p/v_b$ (parallel) is largest near 3 kHz, which is also the frequency range where the longitudinal vibrations are largest.<sup>7</sup> It is also worthwhile to compare the  $p/v_b$ (parallel) as measured here to  $p/v_b$ (perpendicular) as found with the force applied perpendicular to the soundboard (Fig. 1). We find that under similar conditions, i.e., the same microphone location, for the bridge position for the (same) note C4,  $p/v_b$ (perpendicular) measured with a perpendicular driving force is approximately *equal* to  $p/v_b$ (parallel) measured with a driving force parallel to the string direction. That is, the “arbitrary units” used in Figs. 1 and 8 were the same, from which we see that near a frequency of 3 kHz,  $p/v_b$  was approximately the same in the two cases. This comparison is made difficult by the fluctuating nature of  $p/v_b$ , so there is perhaps a factor of 2 or 3 uncertainty involved. Nevertheless, we find that  $p/v_b$ (parallel) is surprising large.

## IV. DISCUSSION

In this paper we have presented new results for the production of sound by a piano soundboard. The measurements were carried out with two different techniques, which yielded similar results for a free-standing soundboard and an intact piano. Our results are consistent with the earlier results of Suzuki,<sup>5</sup> but are in sharp disagreement with those reported by Wogram.<sup>3,4</sup>

Several features of our results can be readily understood, at least qualitatively. The fluctuations with frequency seem due largely due to interference effects, and are a strong function of the position of the microphone (i.e., the listener). These fluctuations can be quite substantial; for example, for the note G3 with our intact piano,  $p/v_b$  for the third partial can be nearly a factor of 10 larger than the first or second partial. We also find that  $p/v_b$  falls at low frequencies, a result that is probably caused the wavelength becoming larger than the size of the source.

We have also presented the first measurements of the sound produced by a force applied parallel to the string direction. In this case  $p/v_b$ (parallel) is surprisingly large, implying that longitudinal string vibrations produce sound with a (relatively) high efficiency. This result should be essential in understanding the importance of longitudinal string vibrations in tone production.

To the best of our knowledge, there have not yet been any quantitative calculations to which we can compare our experimental results. In recent work with a simple numerical soundboard model,<sup>6</sup> we calculated  $p/v_b$  using two extremely crude approximations. One of the results is actually consistent with the measurements we have reported here, but that agreement is likely accidental. A quantitative numerical calculation of the sound pressure in the vicinity of a vibrating soundboard seems feasible. We hope to report on such a calculation in the near future.

## ACKNOWLEDGMENTS

We are grateful to P. F. Muzikar for useful comments, especially concerning the manuscript, and to B. Martin for kindly providing the free-standing soundboard, and for her advice and enthusiasm. This work was supported in part by the NSF through Grant No. PHY-9722031.

<sup>1</sup>H. Suzuki and I. Nakamura, “Acoustics of pianos,” *Appl. Acoust.* **30**, 147 (1990).

<sup>2</sup>H. A. Conklin, Jr., “Design and tone in the mechanoacoustic piano. Part I. Piano hammers and tonal effects,” *J. Acoust. Soc. Am.* **99**, 3286 (1996); “Design and tone in the mechanoacoustic piano. Part II. Piano structure,” *J. Acoust. Soc. Am.* **100**, 695 (1996); “Design and tone in the mechanoacoustic piano. Part III. Piano strings and scale design,” *J. Acoust. Soc. Am.* **100**, 1286 (1996).

<sup>3</sup>K. Wogram, “Acoustical research on pianos. Part I: Vibrational characteristics of the soundboard,” *Das Musikinstrument* **24**, 694 (1980); *ibid.* pp. 776 and 872.

<sup>4</sup>K. Wogram, in *The Acoustics of the Piano*, Royal Swedish Academy of Music Publication No. 64, edited by A. Askenfelt (Stockholm, 1990), p. 83.

<sup>5</sup>H. Suzuki, “Vibration and sound radiation of a piano soundboard,” *J. Acoust. Soc. Am.* **80**, 1573 (1986).

<sup>6</sup>N. Giordano, “Modeling a piano soundboard: Some observations and a simple model,” *J. Acoust. Soc. Am.* **102**, 1159 (1997).

<sup>7</sup>See, for example, N. Giordano and A. J. Korty, “Motion of a piano string:

Longitudinal vibrations and the role of the bridge," J. Acoust. Soc. Am. **100**, 3899 (1996).

<sup>8</sup>The piano was an upright made by the Charles Fredrich Stein Company in approximately 1935.

<sup>9</sup>The free-standing soundboard was taken from an Estey spinet piano.

<sup>10</sup>Two different accelerometers, both obtained from PCB Piezotronics, were used. One (model 352B68) had a mass of 2.0 g, while the other (model 352A10) had a mass of 0.7 g.

<sup>11</sup>N. Giordano, "Mechanical impedance of a piano soundboard," J. Acoust. Soc. Am. **103**, 2128 (1998).

<sup>12</sup>The microphone was a model 130A10 from The Modal Shop, Inc.

<sup>13</sup>The shaker was a model V102 from Ling Dynamical Systems.

<sup>14</sup>To accurately measure or characterize the magnitude of such rapidly varying fluctuations, it is useful to be aware of the effective resolution in frequency. That is, the results for  $p/v_b$  are effectively averaged over a range of  $f$ ; the use of a larger averaging interval in frequency can reduce the magnitude of the fluctuations in  $p/v_b$ . In order to facilitate compari-

sons, we used approximately the same frequency resolution in Figs. 1–3 and 7. This resolution varied smoothly from  $\sim 12$  Hz at the lowest frequencies, to  $\sim 50$  Hz near 1 kHz, to  $\sim 300$  Hz at the highest frequencies. The frequency resolution was much wider for the measurements in Fig. 8 (as evidenced by the spacing between the data points), and was near 100 Hz at the lowest frequencies, and 300 Hz near 1 kHz. For this reason, the fluctuations appear smaller in Fig. 8.

<sup>15</sup>As discussed in Ref. 11, it appears that the magnitude of  $v_b$  was underestimated in Refs. 3 and 4, due to a mechanical decoupling of the accelerometer from the soundboard.

<sup>16</sup>A more complete discussion of this mechanism would require a measurement of the bridge velocity in the parallel direction produced by a measured parallel force; i.e., the corresponding mechanical impedance. We will report on such measurements in the near future. For the purposes of the present paper, where our emphasis is on  $p/v_b$ , impedance measurements are not required for the analysis.

# Frequency and concentration dependence of the backscatter coefficient of the ultrasound contrast agent Albunex<sup>®</sup>

Jon N. Marsh

*Laboratory for Ultrasonics, Department of Physics, Washington University, St. Louis, Missouri 63130*

Michael S. Hughes

*Mallinckrodt Inc., 675 McDonnell Boulevard, Hazelwood, Missouri 63042*

Christopher S. Hall, Stephen H. Lewis, and Rebecca L. Trousil

*Laboratory for Ultrasonics, Department of Physics, Washington University, St. Louis, Missouri 63130*

Gary H. Brandenburger

*Mallinckrodt Inc., 675 McDonnell Boulevard, Hazelwood, Missouri 63042*

Harold Levene

*Molecular Biosystems, Inc., 10030 Barnes Canyon Road, San Diego, California 92121*

James G. Miller

*Laboratory for Ultrasonics, Department of Physics, Washington University, St. Louis, Missouri 63130*

(Received 1 December 1997; revised manuscript received 19 February 1998; accepted 7 May 1998)

A broadband ultrasonic measurement system has been utilized to characterize the concentration and frequency dependence of *in vitro* suspensions of Albunex<sup>®</sup> microspheres at concentrations ranging from  $1.7 \times 10^5$  to  $2.1 \times 10^7$  microspheres/mL and over a bandwidth of 1–16 MHz. The apparent backscattered power (not compensated for effects due to attenuation) was shown to increase with dose for lower concentrations of microspheres, but then to decrease rapidly with increasing concentration where attenuation effects become significant. Measurements of signal loss demonstrated that the attenuation grew exponentially with increasing concentration, so that a doubling of the number of microspheres led to a doubling of the value of the attenuation coefficient measured in dB/cm. This relationship was demonstrated over the entire system bandwidth. Compensation of the apparent backscattered power for the attenuation yielded the backscatter transfer function. This quantity was shown to be linearly proportional to concentration, so that a doubling of the number of microspheres led to a 3-dB increase in the backscatter transfer function. A broadband data reduction technique was used to further reduce the data to backscatter coefficient, an absolute parameter describing the intrinsic scattering efficiency of the Albunex<sup>®</sup> microsphere suspensions. The backscatter coefficient was shown to be linearly proportional to microsphere concentration at all concentrations investigated and over all the usable bandwidth. This suggests that, with appropriate compensation for attenuation and equipment parameters, perfusion or flow quantification techniques which assume a linear dependence of backscatter with contrast agent concentration should be applicable. The backscatter coefficient exhibits a rapid rise with frequency below 3 MHz, and appears to approach a frequency independent limit above 3 MHz. The relationships of the attenuation coefficient and backscatter transfer function to concentration were generally consistent with predictions from a simple scattering model. These relationships appear to be valid within the usable bandwidth of our measurement system for all concentrations investigated.

© 1998 Acoustical Society of America. [S0001-4966(98)05508-8]

PACS numbers: 43.80.Ev, 43.80.Jz, 43.80.Qf, 43.80.Vj [FD]

## INTRODUCTION

Development of enhanced next-generation ultrasonic contrast agents may require detailed and reliable characterization of the agents' ultrasonic properties and physical behavior. Knowledge of these properties over a broad range of interrogating frequencies will also become essential when these agents are used in conjunction with advanced clinical imaging systems, which may employ higher frequency transducers or detect higher harmonic emissions of the injected contrast. It is necessary to understand the dependence of

backscatter, attenuation, and phase velocity of the contrast agent on both frequency and concentration in order to better interpret the results obtained using these advanced tools. Recently, radio-frequency (RF) analysis techniques have been investigated in order to detect and quantify myocardial perfusion.<sup>1-4</sup> In these techniques, parameters such as integrated backscatter and centroid frequency are measured in the myocardium before and after injection of contrast. Changes in these parameters may indicate the arrival of contrast agent in the tissue. Determination of the concentration in a region of tissue may then permit the quantitative assess-

ment of regional myocardial perfusion. It is typically assumed (and predicted by simple scattering models) that the backscatter intensity for suspensions of contrast agent particles is linearly proportional to concentration. At low concentrations, this relationship has been validated.<sup>5-8</sup> However, at higher concentrations, the attenuation of contrast within and overlying the scattering volume of interest may substantially alter this behavior<sup>4,9</sup> and mask the true relationship between backscattered intensity and concentration. In standard echocardiographic imaging, the attenuation effect is manifested as acoustic shadowing. Common techniques utilizing contrast (e.g., measurements of videointensity versus time as an estimation of blood flow), which assume a linear relationship between microsphere concentration and backscatter, must compensate for the effects of attenuation, especially at higher doses.<sup>10,11</sup>

In this study we delineate the effects of attenuation and backscatter in suspensions of the contrast agent Alunex<sup>®</sup>, in order to clarify the concentration- and frequency-dependent behavior of scattering and acoustic shadowing in contrast-enhanced echocardiography. The Washington University Laboratory for Ultrasonics has worked in conjunction with Mallinckrodt Inc. to develop an *in vitro* measurement system for performing reliable, high-precision, broadband measurements of many of the physical properties of ultrasonic contrast agents.<sup>12-14</sup> Results obtained from quantitative measurements of the concentration and frequency dependence of attenuation and backscatter for specific concentrations of Alunex<sup>®</sup> microspheres utilizing this system will be presented. Empirical knowledge of the attenuation permits compensation for its effects on backscatter and allows determination of the backscatter coefficient, an absolute, equipment-independent parameter describing intrinsic scattering efficiency. These measurements illustrate a fundamental difference in the dependence of attenuation and backscatter on concentration, a difference which is predicted by simple scattering models: backscatter is linearly proportional to concentration, but attenuation exhibits exponential dependence on concentration. Our results, obtained using one single-element transducer pair, also considerably extend the range of frequencies and concentrations reported in the literature over which the ultrasonic backscatter properties of Alunex<sup>®</sup> have been measured.

## I. THEORY

The theoretical predictions of scattering and attenuation for Alunex<sup>®</sup> are derived from a linear scattering model for homogeneously and randomly distributed scatterers. The scattering cross section  $\sigma_s(r, f)$  at frequency  $f$  for a scatterer of radius  $r$  is defined as the total power scattered by the object per unit incident intensity at the frequency  $f$ . Assuming there is no multiple scattering, the total scattering cross section for a large number  $N$  of randomly distributed identical scatterers is given by  $N\sigma_s(r, f)$ .<sup>15</sup> Similarly, the total scattering cross section per unit volume for a cloud of various-sized scatterers is given by  $\sum_r n(r)\sigma_s(r, f)$  where  $n(r)$  is the number of scatterers of radius  $r$  per unit volume. For scatterers such as microbubbles that are small compared to a wavelength and whose scattering behavior is predomi-

nantly isotropic,<sup>16</sup> the theoretical differential scattering cross section per unit volume (or differential volumetric scattering cross section<sup>17</sup>) is then given by

$$\eta(f) = \frac{\sum_r n(r)\sigma_s(r, f)}{4\pi}, \quad (1)$$

where  $\eta$  is in units of (cm sr<sup>-1</sup>). This quantity is also known as the backscatter coefficient.<sup>18</sup>

The attenuation through a layer of scatterers is derived in a similar fashion. After traveling through a layer of thickness  $x$  (and assuming again there is no multiple scattering), the intensity of a plane wave of initial intensity  $I_0$  is given by<sup>19</sup>

$$I = I_0 \exp\left[-\left(\sum_r n(r)\sigma_e(r, f)\right)x\right] = I_0 \exp[-\alpha_I x], \quad (2)$$

where  $\alpha_I$  is the theoretical attenuation coefficient for intensity and  $\sigma_e(r, f)$  is the extinction cross section of a scatterer of radius  $r$ , which is defined as the total power extinguished by the scatterer per unit incident intensity at frequency  $f$ . The quantity  $\alpha_I$  is then given by the total extinction cross section,  $\sum_r n(r)\sigma_e(r, f)$ , in units of Np/cm. It should be noted that the intensity attenuation coefficient  $\alpha_I$  shown here differs from the theoretical linear amplitude attenuation coefficient  $\alpha_A$  by a factor of 2. The amplitude attenuation coefficient is typically included in the expression for a propagating plane wave as part of the complex wave number:  $\tilde{k} = k + i\alpha_A$ . The complex pressure amplitude for a plane wave is given by

$$\begin{aligned} A(x, t) &= A_0 \exp[i(\tilde{k}x - \omega t)] \\ &= A_0 \exp[-\alpha_A x] \exp[i(kx - \omega t)]. \end{aligned} \quad (3)$$

Because the intensity of such a wave is proportional to the square of the pressure amplitude, the intensity after propagating through a distance  $x$  is then

$$I = I_0 \exp[-2\alpha_A x]. \quad (4)$$

Thus from Eqs. (2) and (4),

$$\alpha_I = 2\alpha_A. \quad (5)$$

To clarify the notation, we note that the attenuation coefficient expressed in dB/cm,  $\alpha_{dB}$ , is given by

$$\begin{aligned} \alpha_{dB}(f) &= [20 \log(A_0/A)]/x = \{20 \log[\exp(\alpha_A x)]\}/x \\ &= \alpha_A(20 \log e) = 8.69\alpha_A. \end{aligned}$$

Expressed in terms of the attenuation coefficient for intensity, the previous expression becomes

$$\begin{aligned} \alpha_{dB}(f) &= [10 \log(I_0/I)]/x = \{10 \log[\exp(\alpha_I x)]\}/x \\ &= \alpha_I(10 \log e) = 4.34\alpha_I. \end{aligned}$$

From this and Eq. (2), we note that



$$\alpha_I = \sum_r n(r) \sigma_e(r),$$

$$\alpha_A = 0.5 \sum_r n(r) \sigma_e(r), \quad (6)$$

$$\alpha_{dB} = 4.34 \sum_r n(r) \sigma_e(r).$$

Equations (1) and (6) indicate the theoretical dependence of backscatter and attenuation on scatterer concentration, respectively (in the single scattering approximation). Although the expressions appear similar, it is important to note that the predicted backscattered power scales linearly with concentration, whereas the relative amount of power lost from the incident wave due to the scatterers increases exponentially with concentration. This fundamental difference is reflected in the units describing these quantities: the backscatter coefficient is typically measured in linear terms, but the attenuation coefficient  $\alpha_{dB}$  is measured on a logarithmic basis in dB/cm. Thus a doubling of the concentration of microspheres in a given volume should result in a doubling of the linear value of the backscatter coefficient, i.e., an increase of approximately 3 dB. However, there will be an exponential decrease in the strength of the signal passing through this same volume. These effects compete: the backscattered signal strength grows linearly with increasing dose until the attenuation, which increases much more rapidly, becomes the dominant factor. After this point the backscattered signal strength decreases rapidly. This effect has been predicted in simulations<sup>9,20</sup> and may be one of the main sources of contrast-induced acoustic shadowing observed in clinical images. It should also be noted that both the attenuation and backscatter of bubble-based contrast agents can be highly frequency dependent due to bubble resonances, so that the shadowing effect will be more pronounced in frequency ranges where the attenuation is greatest.

## II. DATA REDUCTION

Reduction of the experimentally determined backscatter data to absolute backscatter coefficient entails compensation of the returned ultrasonic signal for the electromechanical response of the measurement system, beam diffraction, and the effects of attenuation and interfaces. We briefly review here some of the methods proposed for calculating the backscatter coefficient. These methods typically differ most significantly in the calculation of the beam diffraction correction. Sigelmann and Reid<sup>21</sup> described a technique in which the sample is insonified with narrow-band sine wave bursts from a planar transducer in the far field. The effective beam volume (i.e., the volume of scatterers which contribute significantly to the backscattered signal of interest) is determined laterally by the 3-dB beamwidth, and axially by time gating. In this approximation the field is taken to be constant everywhere within the cylindrical volume imposed by the time gates and 3-dB beamwidth. This approach was adopted by O'Donnell and Miller<sup>22</sup> and modified for the case of focused transducers and broadband insonifying pulses, and was applied to samples situated in the focal region of focused

transducers and in the far field of planar transducers. Campbell and Waag<sup>23</sup> described a more complete and general method applicable to the case of a two-transducer scattering system. They attempted to account rigorously for the effects of the convolution of time-domain gating as well as for effects of beam diffraction in the case of transducers having Gaussian beam sensitivity patterns. Subsequently, Madsen *et al.*<sup>24</sup> proposed an approach for determination of backscatter coefficient in which the diffraction pattern is calculated exactly from knowledge of the shape of the transducer face, in order to account for variations in beam sensitivity both laterally and axially with respect to the insonified volume. In work performed at the Laboratory for Ultrasonics in St. Louis, Wear *et al.*<sup>25</sup> combined several of the simplifications of the earlier methods with the more demanding calculations of the Madsen *et al.* approach; in this case, the variation in lateral pressure amplitude in the scattering volume due to diffraction was accounted for, whereas both the axial variation in beam intensity and the convolution of the sinc function introduced by time gating were ignored.

Of the treatments mentioned here, those that attempt to accurately model the transducer's beam function typically require the evaluation of integrals of the pressure field across the face of the transducer and/or over the volume occupied by the scatterers in order to compensate for diffraction effects; the time required for numerical computation of these quantities may be considerable. The treatment of O'Donnell and Miller<sup>22</sup> compromises by introducing various approximations which act to reduce the amount of computation involved (often by several orders of magnitude<sup>26</sup>), though at the expense of complete determination of the beam function. A benefit of this simpler approach, however, is that the formulation for reducing the data to backscatter coefficient can be written in an intuitive form as a product of separate terms individually describing the compensation for electromechanical effects, diffraction effects, and attenuation and interface losses. The Wear *et al.*<sup>25</sup> formulation also offers this feature and employs more accurate diffraction modeling, though this requires computation of some integrals involving the complex pressure field.

We have chosen in the present study to use a technique for determining the backscatter coefficient recently described by Chen *et al.*<sup>27</sup> Following their example, we apply this method to the specific case of a spherically focused transducer insonifying an ensemble of scatterers positioned at the transducer's geometrical focus with a reference measurement acquired from a flat reflector placed in the focal plane of the transducer. For this case, the authors are able to reduce complicated integrals of the diffraction coefficients over the surface of the transmitting transducer and over the volume that the scatterers occupy to simple function evaluations, thereby substantially decreasing the amount of computation involved while still accurately calculating terms associated with beam diffraction effects. We note that two significant approximations employed in this technique are similar to those used by Wear *et al.*,<sup>25</sup> namely that the diffraction correction is roughly constant along the length of the gated volume, and that the effect of the convolution of the time gate with the backscattered signal is negligible.

TABLE I. Definitions of terms and symbols used in reduction of backscatter and attenuation data to backscatter coefficient.

Symbol	Definition
$\langle  V_s(f) ^2 \rangle$	average measured power spectrum of the backscatter from the sample
$ V_{\text{ref}}(f) ^2$	power spectrum returned from the reflector placed in the focal plane of the transducer
$\langle  S(f) ^2 \rangle_{\text{apparent}}$	apparent backscatter transfer function of sample (dimensionless quantity)
$\langle  S(f) ^2 \rangle_{\text{compensated}}$	backscatter transfer function compensated for effects due to attenuation (dimensionless quantity)
$D_{\text{ref}}(f)$	acoustic coupling function (Ref. 27) defined in Eq. (8) (dimensionless quantity)
$R$	intensity reflection coefficient (dimensionless quantity)
$T_s^2$	two-way intensity transmission coefficient across the medium-sample interface (dimensionless quantity)
$T_{\text{ref}}^2$	two-way intensity transmission coefficient across any interface overlying the reflector (dimensionless quantity)
$A_s$	attenuation compensation factor (dimensionless quantity)
$r_0$	transducer's focal length (cm)
$a$	transducer's radius (cm)
$\alpha_A(f)$	measured amplitude attenuation coefficient of the sample (Np/cm)
$x_0$	distance between front surface of sample and front surface of scattering volume of interest (cm)
$l = c\tau/2$	length of the insonified volume (cm), $\tau$ = gate duration (s), $c$ = speed of sound in sample (cm/s).
$E_\infty$	0.46 [see Chen <i>et al.</i> (Ref. 27) for details on the determination of this dimensionless constant]
Other symbols	see text

The experimentally determined backscatter coefficient,  $\eta(f)$ , is then given by

$$\eta(f) = \underbrace{\left\{ \frac{\langle |V_s(f)|^2 \rangle}{|V_{\text{ref}}(f)|^2} \right\}}_{\text{backscatter measurement and electromechanical compensation}} \underbrace{\left\{ \frac{r_0^2}{\pi a^2 l E_\infty} |D_{\text{ref}}(f)|^2 \right\}}_{\text{diffraction compensation}} \times \underbrace{\left\{ \frac{1}{A_s(\alpha_A(f), l, x_0)} \right\}}_{\text{attenuation compensation}} \underbrace{\left\{ R \frac{T_{\text{ref}}^2}{T_s^2} \right\}}_{\text{interface loss compensation}}, \quad (7)$$

where many of the symbols and definitions of the terms of this equation are given in Table I. The remaining factors require more detailed descriptions.  $D_{\text{ref}}(f)$  is the acoustic coupling function, given by

$$D_{\text{ref}}(f) = -\{1 - \exp(-iG_p)[J_0(G_p) + iJ_1(G_p)]\}, \quad (8)$$

$$G_p = ka^2/2r_0,$$

where  $J_n$  is the Bessel function of the first kind of order  $n$ , and  $k$  is the wave number. The attenuation correction factor  $A_s$  is given in terms of the experimentally determined attenuation coefficient  $\alpha_A(f)$ :

$$A_s(\alpha_A(f), l, x_0) = \exp[-4\alpha_A(f)x_0] \cdot \exp[-2\alpha_A(f)l] \times \frac{\exp[2\alpha_A(f)l] - \exp[-2\alpha_A(f)l]}{4\alpha_A(f)l}, \quad (9)$$

which is equivalent to the attenuation correction factor given by Sigelmann and Reid<sup>21</sup> for insonifying pulses much shorter than the time gate selecting the scattering volume.  $A_s$  is also equivalent to the reciprocal of the term  $F$  employed in previous formulations by our laboratory.<sup>22,25,28</sup> The attenuation of water is assumed to be zero in this study. The quotient  $\langle |V_s(f)|^2 \rangle / |V_{\text{ref}}(f)|^2$  in the expression for backscatter coefficient is often labeled the average apparent backscatter transfer function,  $\langle |S(f)|^2 \rangle_{\text{apparent}}$ .<sup>22</sup> The term  $R$  represents the intensity reflection coefficient for the reference reflector; this term was added to the formula for  $\eta(f)$  to account for the fact that we were not able to use a perfectly reflecting surface for the reference measurement. We also incorporated the term  $T_{\text{ref}}^2$  into the formula to account for the fact that our reference measurement was obtained from a reflector placed behind the specimen chamber front wall.

Computationally, this method of determining the backscatter coefficient is less demanding than other approaches requiring evaluations of integrals. Physically, Eq. (7) provides a rational basis for understanding the behavior of the backscatter coefficient by separating it into terms describing apparent scattering strength, diffraction correction for the effective beam volume, attenuation correction, and interface losses.

### III. METHODS

#### A. Specimen chamber and material handling procedure

Most of the techniques, material handling procedures, and fixtures employed in this study have been described in detail in our previous work.<sup>12-14</sup> Briefly, the contrast agent was contained within a specimen chamber having flat, parallel walls of Saran Wrap<sup>®</sup> (set approximately 0.25 cm apart) which served as acoustic windows. A schematic of the specimen chamber is shown in Fig. 1(a). A calibrated pipette was used to deliver 8.5 mL of degassed Isoton<sup>®</sup>, preheated to 37 °C, into the chamber for each measurement. A micropipette was used to continuously mix the suspension in the chamber during each measurement in order to ensure a different random, homogeneous distribution of microspheres for each waveform acquisition. The mixing technique for the measurements in this study was modified slightly from our previous work: the specimen chamber was left unplugged, and the pipette tip itself was inserted several millimeters into the chamber. This protocol modification resulted in enhanced mixing, and the omission of the chamber plug decreased the chance of creating any slight overpressure in the chamber. Care was taken at all times to prevent formation of extraneous bubbles in the chamber. All measurements were performed in a waterbath maintained at 37 °C. The chamber was emptied and rinsed thoroughly with slightly chilled water between each data run; the lower temperature of the rinsing water enhanced destruction of any Albnex<sup>®</sup> microspheres

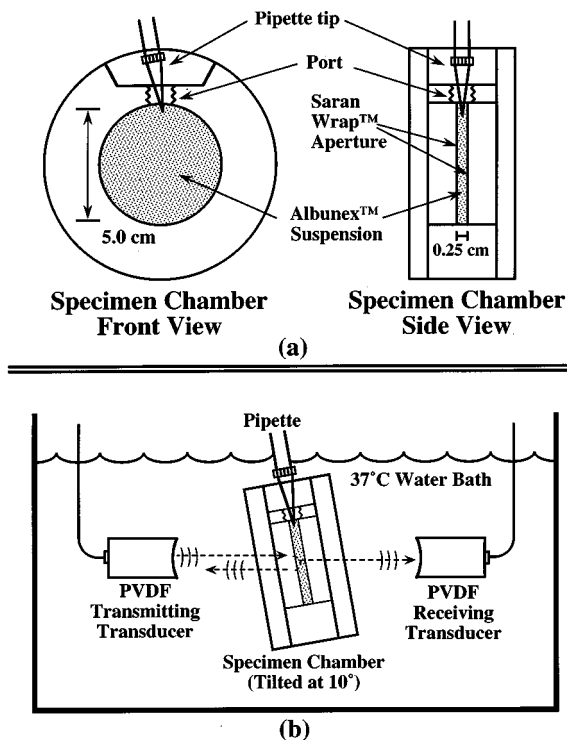


FIG. 1. (a) Schematic of the specimen chamber used for both through-transmission and pulse-echo measurements. (b) Diagram illustrating position and orientation of specimen chamber and transducers in the 37°C waterbath. The center of the specimen chamber is positioned at the focal zone of both transducers.

remaining in the chamber. A Coulter Multisizer<sup>®</sup> (Coulter Corporation, Hialeah, FL) was used to provide size distribution information about the Albnex<sup>®</sup> microspheres.

Because Albnex<sup>®</sup> microspheres outside of the vial tend to deteriorate over time, certain precautions were taken to minimize destruction of the microspheres during each measurement. For example, the total amount of time that any individual sample was exposed to the insonifying field was kept to a minimum through use of rapid data acquisition rates: each backscatter measurement took approximately 20 s to complete, while each through-transmission measurement lasted less than 10 s. The total amount of time from initially opening the vial to the completion of the entire set of through-transmission and backscatter measurements was approximately 1 h. The amplitude and duration of the insonifying pulse used in all the measurements (described below) were also minimized, since it is known that large-amplitude interrogating pulses can destroy the microspheres. Mixing the suspension during data acquisition provided constant circulation of microspheres and so prevented any particular group of microspheres from remaining in the focal region of the transmitting transducer for very long. Both the backscatter and through-transmission measurements exhibited very little change over the course of each measurement. Although it is possible that some microspheres may have been destroyed over the time period of a typical measurement, the stability of the acquired RF traces suggested that any microsphere destruction which may have occurred was insignificant.

Eight different concentrations of Albnex<sup>®</sup> (Lot number

003597) were investigated in this manner; from lowest to highest, these were:  $0.17 \times 10^6$ ,  $0.34 \times 10^6$ ,  $0.69 \times 10^6$ ,  $1.4 \times 10^6$ ,  $2.7 \times 10^6$ ,  $5.5 \times 10^6$ ,  $11 \times 10^6$ , and  $21 \times 10^6$  microspheres/mL. These concentrations represented a series of doublings of the number of Albnex<sup>®</sup> microspheres in the chamber, and were chosen to span a range which might be encountered *in vivo*. The manufacturer recommends intravenously administered doses of approximately 5–15 mL for a 70-kg patient. Given a typical total blood volume of 5 L, such doses represent Albnex<sup>®</sup> concentrations of  $0.73 \times 10^6$  to  $2.2 \times 10^6$  microspheres/mL, assuming uniform distribution throughout the entire blood volume. The actual *in vivo* concentration at any particular point and time may be quite different, however: the initial bolus may have a concentration of  $25 \times 10^6$  microspheres/mL,<sup>29</sup> yet the concentration and size distribution of Albnex<sup>®</sup> actually reaching the myocardium could be substantially altered through a variety of mechanisms (e.g., filtration by the lungs, bubble destruction by overpressure in the ventricles or by the acoustic pressure of the imaging transducer, etc.). The impact of changes in size distribution on the acoustic properties of Albnex<sup>®</sup> is addressed in the Discussion section below.

## B. Experimental setup and acquisition

Two sets of measurements were acquired: first, backscatter measurements were performed for the entire range of concentrations; then through-transmission measurements were performed on an identical set of concentrations extracted from the same vial of Albnex<sup>®</sup>. The total time needed to perform both data runs was approximately 1 h.

The backscatter measurements were performed using a single broadband immersion PVDF (polyvinylidene fluoride) transducer (0.4-in. diameter, 3.25-in. focal length, model ZF3002-SU, Panametrics, Waltham, MA). The benefits of using a broadband single transducer system have been elucidated in a previous study.<sup>13</sup> The transducer was excited using a dc voltage step. The pulser system was composed of a function generator (model 8116A, Hewlett-Packard, Palo Alto, CA), a high voltage power supply (model PS310, Stanford Research Systems, Inc., Sunnyvale, CA), and a power MOSFET switch (model GRX-1.5K-E, Directed Energy, Inc., Ft. Collins, CO). This system produced square pulse trains whose duty cycle and amplitude could be precisely controlled. For the measurements described here, the transducer was excited on the downward sloping edge of a 50-V amplitude square pulse (1-kHz pulse repetition frequency), which yielded a broadband (0.8–16 MHz at –20-dB level) ultrasonic pulse. The subsequent upward sloping edge of the exciting square pulse occurred 40  $\mu$ s later. The chamber's apparent back wall echo occurred less than 5  $\mu$ s after the front wall echo, so that results of the second transducer excitation occurred significantly later, and were excluded from acquisition. A diplexer (model RDX2, Ritec, Inc., Warwick, RI) was placed in line between the pulser and transducer for impedance matching and to protect the receiver input from the high-voltage electronic excitation pulse.

The sample chamber was positioned so that the central portion of the Saran Wrap<sup>®</sup> front surface was at the focal distance of the transducer. The specimen chamber was

placed on a tilted platform angled at  $10^\circ$  relative to the axis of the transducer [see Fig. 1(b)], in order to minimize effects from internal reflections and to minimize the relatively large specular reflection from the water/Saran Wrap<sup>®</sup> interface. The suspension was pipette-mixed continuously during the course of each of these measurements. The backscattered ultrasonic signal was received by the transducer, and a broadband receiver (model BR640, Ritec, Inc.) set to 1-M $\Omega$  input impedance provided amplification prior to digitization. A digital delay generator (model DG353, Stanford Research Systems, Sunnyvale, CA) with maximum jitter of 50 ps was used to trigger the digitizer to start acquiring the waveform after a delay of 108  $\mu$ s relative to the initial excitation of the transducer; this delay corresponded to the ultrasonic travel time for a backscattered echo to be received by the transducer. The radio-frequency waveform was sampled at 250 megasamples per second by an 8-bit digitizer (Compuscope 2125, Gage Applied Sciences, Inc., Montreal, Canada). Five hundred RF traces (each 2048 points long) were acquired at a rate of 30 traces per second for each concentration of Albnex<sup>®</sup> in the chamber. This acquisition rate was selected based on the approximate mixing frequency, so that each trace was acquired from a different independent spatial distribution of the microspheres. A PC (166 MHz Pentium, Gage Applied Sciences, Inc.) was used to control acquisition and to store data to disk. Reference measurements for backscatter were obtained using a custom-made stainless steel reflector. The reflector could be mounted inside the Isoton-filled specimen chamber, directly behind the Saran Wrap<sup>®</sup> front window. The front surface of the reflector was ground at a  $10^\circ$  angle, such that the reflector's face was normal to the axis of the transducer while the Saran Wrap<sup>®</sup> interface was at a constant  $10^\circ$ , i.e., the same geometry as in the data acquisition measurements. 500 reference traces were acquired using this specular reflection, and the mean power spectrum was calculated for the purposes of normalization (described in the Analysis section below).

In the through-transmission measurements, a second, identical transducer was coaxially positioned 6.5 in. away from the transmitting transducer and was used to receive the ultrasonic signal after it had passed through the contrast agent suspension. The signal from the receiving transducer was then amplified by 10 dB by a high input impedance preamplifier (Ritec, Inc.). The pulse repetition rate was set to 1 kHz for rapid data acquisition. The through-transmitted signal was time-averaged in sets of 1000 traces in order to enhance dynamic range and reduce effects from random noise.<sup>12</sup> Five time-averaged sample traces were acquired in this manner for each concentration investigated. Immediately after each data run, the sample path length was determined ultrasonically by measuring the time interval between the through-transmitted signal and the signal from the first round-trip reverberation. This measurement was performed in order to account for small variations in the distance between the chamber walls. The chamber was maintained at its original  $10^\circ$  angle during the path length measurement, in order to account for the small increase in distance (caused by the tilt) relative to the actual chamber thickness. The signal for this measurement was amplified by an additional 10–20

dB, and then filtered with a 10-MHz high-pass filter (12 pole Butterworth) before digitization in order to define more sharply the front and back wall echoes. Measurements<sup>14</sup> and simulations<sup>30</sup> of phase velocity of Albnex<sup>®</sup> also show that there is relatively little dispersion (i.e., change of speed of sound with frequency) above 10 MHz, and that the phase velocity appears to approach an asymptotic value near that of the host medium. The chamber thickness was determined using the delay time between the echoes from chamber windows and assuming the phase velocity was equal to that of water at 37 °C. The thickness determined in this manner varied between 0.23 and 0.30 cm for the measurements in this study. A reference trace was acquired in the same fashion as for the sample traces, using a specimen chamber filled only with Isoton. The instrumentation setup and data acquisition process were identical in all other respects to those used in the backscatter measurements.

### C. Analysis

Reduction of the data to backscatter coefficient was accomplished in a multistep process. First, the backscatter waveforms for a particular concentration were time gated using a 2.56- $\mu$ s rectangular gate applied at a specific delay time after the chamber's front wall echo. The power spectra (in linear, rather than logarithmic, units) of the gated portions of the 500 sample traces were computed and averaged together in the frequency domain. The mean power spectrum was then divided by the power spectrum of the reference waveform (also in linear, rather than logarithmic, units) obtained from the steel plate specular reflection to compensate for the electromechanical conversion factor of the transducer and the instrumentation. This yielded the average power spectrum of the apparent backscatter transfer function,  $\langle |S(f)|^2 \rangle_{\text{apparent}}$ . This procedure was repeated for each concentration investigated.

Signal loss was determined using the through-transmission data. The log spectral power of each of the time-domain-averaged RF traces was subtracted from the log spectral power of the time-domain-averaged through-transmission reference, yielding signal loss in decibels. These signal loss results were then divided by the sample path length to yield the intensity attenuation coefficient in dB/cm. The resulting five attenuation curves were averaged and their standard errors determined. This procedure was repeated for each concentration investigated.

The apparent backscatter transfer functions were then compensated for effects due to attenuation of Albnex<sup>®</sup> overlying and within the gated volume. The quantity  $A_s[\alpha_A(f), l, x_0]$  was calculated from the experimentally determined attenuation coefficient. Division of the apparent backscatter transfer function,  $\langle |S(f)|^2 \rangle_{\text{apparent}}$ , by  $A_s$  yielded the attenuation-compensated backscatter transfer function,  $\langle |S(f)|^2 \rangle_{\text{compensated}}$  (that is, the backscatter compensated for effects due only to attenuation of material overlying and within the scattering volume of interest).

The intensity reflection coefficient  $R$  for the steel plate reflector was calculated from

TABLE II. Values of diffraction correction term at specific frequencies for the transducer used in backscatter measurements.

	2.5 MHz	5 MHz	7.5 MHz	10 MHz
$ D_{\text{ref}}(f) ^2 =$	0.423	0.561	0.597	0.650

$$R = \frac{[Z_{\text{reflector}} - Z_{\text{Isoton}}]^2}{[Z_{\text{reflector}} + Z_{\text{Isoton}}]^2} = 0.88. \quad (10)$$

The two-way intensity transmission coefficients,  $T_s^2$  and  $T_{\text{ref}}^2$ , correspond to round-trip transmission across interfaces of water/Saran Wrap®/Isoton-diluted-Albunex®, and water/Saran Wrap®/Isoton, respectively. The ratio  $T_{\text{ref}}^2/T_s^2$  was negligibly different from 1.0 for all the data presented below.

The diffraction correction term  $|D_{\text{ref}}(f)|^2$  was calculated for our particular transducer and experimental setup at all frequencies within the experimental bandwidth. Determination of  $|D_{\text{ref}}(f)|^2$  and the parameters listed above permitted reduction of the data to backscatter coefficient  $\eta(f)$ . Specific values of  $|D_{\text{ref}}(f)|^2$  at 2.5, 5, 7.5, and 10 MHz are given in Table II.

As an independent means of validating this approach for determining backscatter coefficient, we performed measurements (in a separate experiment) of the backscatter coefficient of a suspension of well-characterized solid polymer microspheres and compared the results with theoretical predictions based on the work of Faran.<sup>31</sup> The microspheres were obtained from Duke Scientific Corporation (Palo Alto, CA). These microspheres are manufactured for use in calibrating particle sizing systems. Although size distribution information was provided by the manufacturer, an optical particle sizer (Accusizer™ 770 with 512 channels from 1.5 to 400  $\mu\text{m}$ , Particle Sizing Systems, Inc., Santa Barbara, CA) was used to obtain independent measurement of the distribution of the microsphere suspension. The mean diameter measured in this way was found to be 101.6  $\mu\text{m}$ , with a standard deviation of 7.0  $\mu\text{m}$ . The number density was  $1.8 \times 10^4$  microspheres/mL, so that the suspension was about 1% solids by volume. We utilized the same sample chamber, mixing technique, transducers, and gate length as employed in the Albunex® measurements; however, a different pulser and receiver were used in order to obtain enhanced sensitivity at higher frequencies. The attenuation coefficient and apparent backscatter transfer function were measured for the microspheres, and the backscatter coefficient was determined using the procedure described above. Theoretical predictions for the backscatter coefficient were obtained using an expression for the scattered pressure field from an elastic, solid sphere suspended in an inviscid liquid when insonified by plane waves.<sup>31,32</sup> Using this theory, we calculated the theoretical differential scattering cross section at 180° (i.e., backscatter) for each microsphere size present in the measured size distribution. These quantities were multiplied by the respective measured number density of microspheres for each size, and the results were summed (on the assumption of single scattering) to obtain the total predicted backscatter coefficient for the suspension.

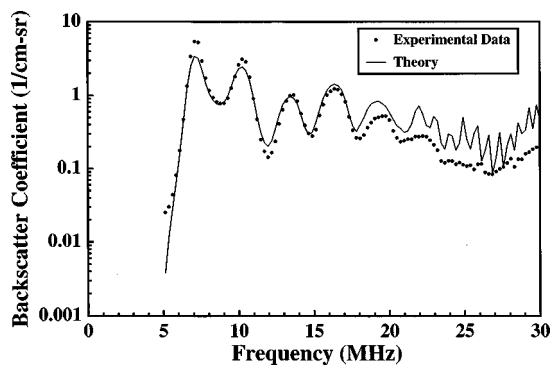


FIG. 2. Backscatter coefficient for a suspension of 100- $\mu\text{m}$ -diam. solid polymer microspheres. The data points represent experimentally measured values, and the solid line represents theoretical predictions from an elastic scattering model. This data set was used to validate the data reduction scheme which was used in the Albunex® measurements.

#### IV. RESULTS

We compare in Fig. 2 the experimental and theoretical backscatter coefficient for the suspension of 100- $\mu\text{m}$  solid polymer microspheres. The data points represent the measured results, and the solid line represents the theoretical predictions for the suspension. The many maxima and minima present in the data are associated with the acoustic resonances that the microspheres exhibit due to their geometry. The measured and theoretical results for backscatter coefficient exhibit very good agreement across the bandwidth, suggesting that the diffraction, attenuation, and interface losses present in the experiment have been properly accounted for.

Figure 3 shows the results of the through-transmission measurements of the attenuation coefficient for the eight different Albunex® concentrations which were investigated. These concentrations were:  $0.17 \times 10^6$ ,  $0.34 \times 10^6$ ,  $0.69 \times 10^6$ ,  $1.4 \times 10^6$ ,  $2.7 \times 10^6$ ,  $5.5 \times 10^6$ ,  $11 \times 10^6$ , and  $21 \times 10^6$  microspheres/mL. The attenuation coefficient is given in units of dB/cm as a function of frequency in MHz. The error bars overlying each curve represent the standard error of five time-averaged measurements of attenuation of a

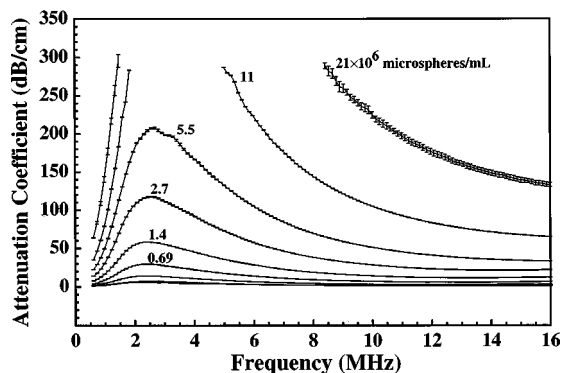


FIG. 3. Attenuation coefficient plotted versus frequency for specific concentrations of Albunex® microspheres diluted in Isoton at 37 °C. Each curve represents the attenuation coefficient (mean of five time-averaged measurements of a single sample) of Albunex at a specific concentration:  $0.17 \times 10^6$ ,  $0.34 \times 10^6$ ,  $0.69 \times 10^6$ ,  $1.4 \times 10^6$ ,  $2.7 \times 10^6$ ,  $5.5 \times 10^6$ ,  $11 \times 10^6$ , and  $21 \times 10^6$  microspheres/mL. Error bars represent the standard error of 5 measurements.

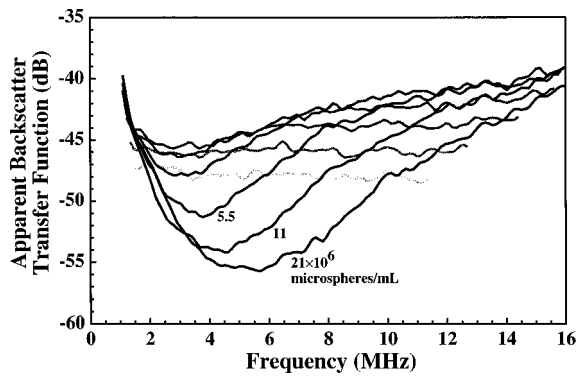


FIG. 4. Apparent backscatter transfer function (i.e., uncompensated for effects due to attenuation) plotted versus frequency for specific concentrations of Albunex<sup>®</sup> microspheres diluted in Isoton at 37 °C. Each curve represents the backscatter transfer function (mean of 500 measurements of a single sample) of Albunex<sup>®</sup> at a specific concentration:  $0.17 \times 10^6$ ,  $0.34 \times 10^6$ ,  $0.69 \times 10^6$ ,  $1.4 \times 10^6$ ,  $2.7 \times 10^6$ ,  $5.5 \times 10^6$ ,  $11 \times 10^6$ , and  $21 \times 10^6$  microspheres/mL. The curves drawn in lighter shades of gray correspond to the lower concentrations.

single sample. The curves for the two highest concentrations are truncated in the region of the attenuation peak, since these large doses attenuated the incoming pulse to such an extent that no meaningful signal could be observed in this frequency range.

The spectral power of the apparent backscatter transfer functions for the same concentrations are displayed in Fig. 4, in units of dB (relative to the steel plate reflector). The curves drawn in lighter shades of gray correspond to lower concentrations. Each curve represents the mean of 500 measurements of the apparent backscatter transfer function of a single sample of Albunex<sup>®</sup>. Error bars have been excluded from this graph in order to more easily distinguish the curves from each other; values for the standard error were typically about 0.2 dB. The gated region used in the backscatter analysis to produce this graph began  $0.75 \mu\text{s}$  (approximately 0.6 mm) after the front wall echo. The results are truncated to display data only in frequency ranges where there was an adequate signal-to-noise ratio. In order to illustrate the magnitude of the effect of overlying contrast agent on the amount of energy backscattered, the apparent backscatter transfer function for a single concentration,  $2.7 \times 10^6$  microspheres/mL, is shown as a function of gate depth in Fig. 5. Each curve represents the mean apparent backscatter transfer function obtained from the same data set (consisting of 500 traces acquired from a single sample), using a  $2.56\text{-}\mu\text{s}$  gate, as the gate is shifted down from the front wall echo in increments of  $0.5 \mu\text{s}$ . The error bars overlying each curve represent the standard error of the mean. Note that the backscatter decreases with increasing amounts of overlying contrast agent.

The corresponding spectral power (in units of decibels) of the backscatter transfer functions, compensated for the effects of attenuation, is shown in Fig. 6. The results shown in this figure were calculated with the time gate placed immediately behind the front wall echo; this was done because the signal-to-noise ratio of the backscatter was greatest immediately after the front wall echo and decreased rapidly with increasing depth due to attenuation of overlying contrast agent. Note that there are no data displayed in the re-

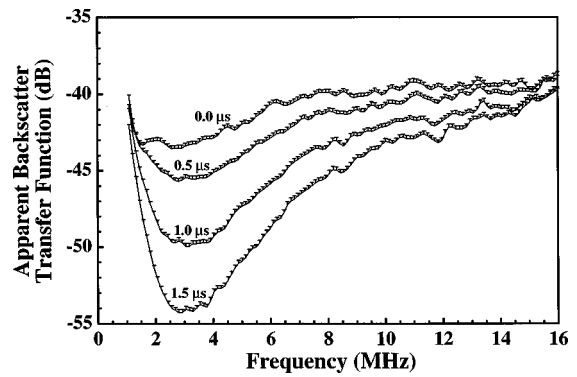


FIG. 5. Apparent backscatter transfer function plotted versus frequency for  $2.7 \times 10^6$  microspheres/mL Albunex<sup>®</sup> concentration. The curves represent the ‘‘apparent’’ backscatter (mean of 500 measurements) from a  $2.56\text{-}\mu\text{s}$  gated region beginning at specific time delays of 0.0, 0.5, 1.0, and  $1.5 \mu\text{s}$  after the chamber’s front wall echo. Standard errors of the 500 measurements are shown as error bars overlying the curves.

gions where attenuation information was unavailable for compensation. The error bars represent the uncertainties in the values, determined by propagation of errors from the measurements of apparent backscatter transfer function and attenuation described above.

To aid the discussion which follows, we show graphs of the attenuation and backscatter measured at specific frequencies and as functions of concentration. The values of the attenuation coefficient (in dB/cm), the apparent backscatter transfer function (in dB), and the attenuation-compensated backscatter transfer function (in dB) measured at 5 MHz are displayed as functions of concentration in Fig. 7(a) and (b). The microsphere concentrations are given in microspheres/mL ( $\times 10^6$ ). The apparent and compensated backscatter transfer functions are shown together in Fig. 7(b) to facilitate comparison.

The backscatter coefficients are shown in Fig. 8(a) in units of  $(\text{cm sr})^{-1}$ . Note again that there are no data displayed in the regions where attenuation information was unavailable for compensation. The error bars represent the uncertainties in the values, determined by propagation of errors from the apparent backscatter transfer function and attenua-

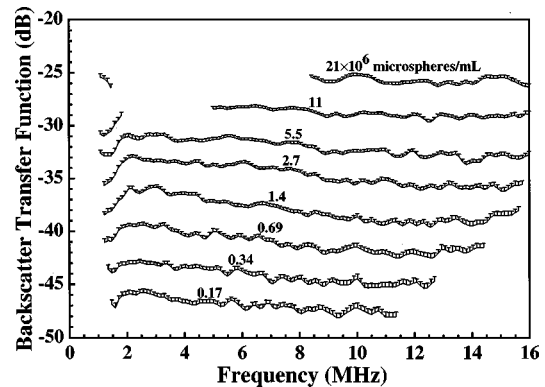


FIG. 6. Attenuation-compensated backscatter transfer function plotted versus frequency for specific concentrations of Albunex<sup>®</sup> microspheres diluted in Isoton at 37 °C. Here we have compensated for the effects due to attenuation of material overlying and within the scattering volume of interest. Error bars represent uncertainties determined by propagation of errors from attenuation and apparent backscatter transfer function measurements.

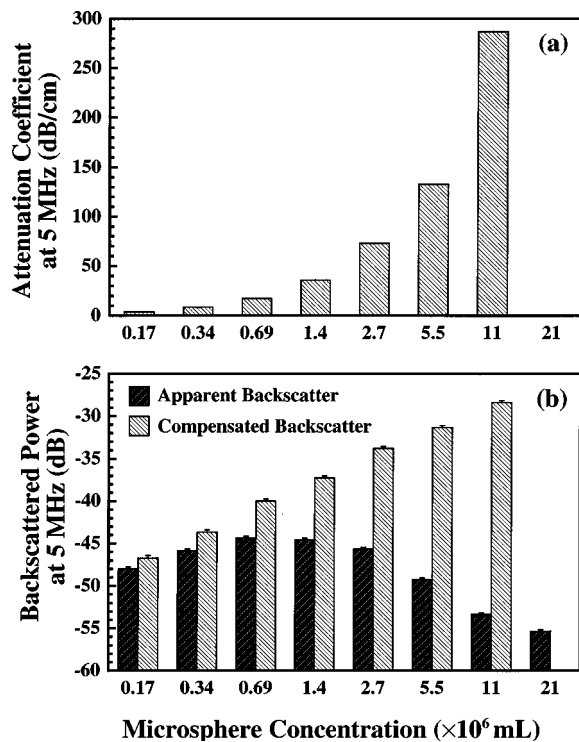


FIG. 7. (a) Attenuation coefficient at 5 MHz as a function of Alunex<sup>®</sup> concentration. (b) Apparent and compensated backscatter transfer functions as a function of Alunex<sup>®</sup> concentration. Apparent backscatter is represented by the darker cross-hatched bars, and the corresponding backscatter compensated for attenuation is represented by the lighter cross-hatched bars.

tion. Theoretical predictions of the backscatter coefficient for the same concentrations of Alunex<sup>®</sup> microspheres are shown for comparison in Fig. 8(b). The theory used to generate the data for this figure is given in the Discussion section below.

In Fig. 9(a), we show plots of the attenuation coefficient measured at 2, 5, 7.5, and 10 MHz as functions of Alunex<sup>®</sup> concentration. The vertical axis represents the attenuation coefficient in dB/cm, and the horizontal axis represents Alunex<sup>®</sup> concentration in microspheres/mL ( $\times 10^6$ ). Measured values are shown as data points, and the solid lines represent fits to the data of the form  $\alpha_{dB}(n) = bn^r$ , where  $n$  is total particle concentration and  $b$  and  $r$  are adjustable parameters. Values for  $r$  are shown in Table III. In a similar fashion, plots of the backscatter coefficient [in units of  $(\text{cm sr})^{-1}$ ] as a function of microsphere concentration, measured at 2, 5, 7.5, and 10 MHz, are shown in Fig. 9(b). Power law fits are shown as solid lines overlying the measured data points, with corresponding values for  $r$  shown in Table III. The horizontal and vertical axes of Fig. 9 are displayed using logarithmic scales.

## V. DISCUSSION

All of the parameters investigated in this study show strong dependences on both concentration and frequency. The attenuation data in Fig. 3 corroborate previously reported characteristics for Alunex<sup>®</sup> suspensions. The attenuation measured in dB/cm increases linearly with increasing concentration and has a pronounced peak in the range between 2 and 3 MHz. The peak is due to microsphere reso-

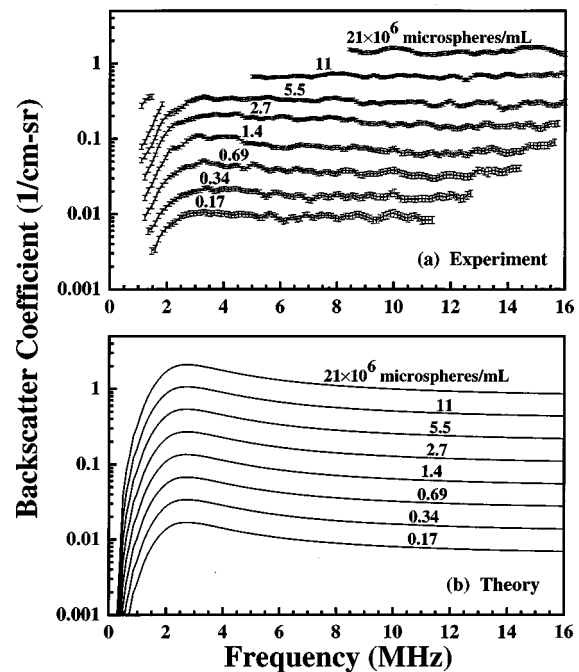


FIG. 8. (a) Experimentally determined backscatter coefficient plotted versus frequency for specific concentrations of Alunex<sup>®</sup> microspheres diluted in Isoton at 37 °C. Error bars represent uncertainties in the values determined by propagation of errors from attenuation and apparent backscatter transfer function measurements. (b) Theoretical predictions for backscatter coefficient for encapsulated microspheres for the same concentrations as in (a). The model used was that described by de Jong *et al.* with shell elasticity parameter  $S_p = 7500$  dyn/cm and shell friction parameter  $S_f = 0.0025$  dyn s/cm.

nance, and its position is determined primarily by the size distribution and shell characteristics of the microspheres.<sup>5,8,20,30,33</sup> The measured attenuation coefficient at 2.5, 5, 7.5, and 10 MHz is displayed as a function of microsphere concentration in Fig. 9(a). Power law fits of the form  $\alpha_{dB}(n) = bn^r$ , where  $n$  is microsphere concentration, are shown overlaying the data points. A value for  $r$  of 1 indicates direct linear proportionality. The values of  $r$  for the frequencies 2.5, 5, 7.5, and 10 MHz were 0.99, 1.02, 1.03, and 1.02 (see also Table III), respectively, indicating an essentially linear dependence of  $\alpha_{dB}$  on concentration at each frequency. Note that this concentration dependence is consistent with the theoretical expression in Eq. (6).

The quantity most directly related to image pixel brightness on a clinical imaging system is the apparent backscatter transfer function. This quantity has not been compensated for the effects of attenuation or diffraction. The graph of the apparent backscatter transfer function for all concentrations (Fig. 4) appears fairly complex, but it illustrates some important effects. At low concentrations, the apparent backscattered power from the Alunex<sup>®</sup> increases uniformly at all frequencies with increasing concentration. After a certain point, however, the apparent backscatter begins to decrease with increasing dose, as noted previously in the literature.<sup>4,9</sup> This is due to the attenuation of the Alunex<sup>®</sup> overlying and within the sample volume. The transition is frequency dependent, and occurs at lower concentrations for some frequencies than others. The effect is most prominent where the Alunex<sup>®</sup> attenuation is highest. This corresponds to the

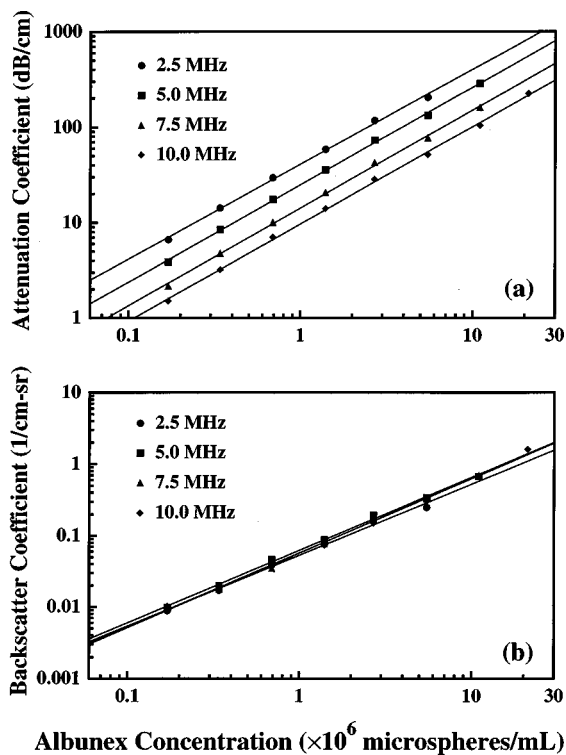


FIG. 9. (a) Attenuation coefficient at specific frequencies as a function of Albunex<sup>®</sup> concentration. Power law fits of the form  $\alpha_{dB}(n) = bn^r$  are shown as solid lines overlying the data points. (b) Backscatter coefficient at specific frequencies as a function of Albunex<sup>®</sup> concentration. Power law fits of the form  $\eta(n) = bn^r$  are shown as solid lines overlying the data points.

clinical (low MHz) range for cardiac imaging. It should be noted that there was less than 1 mm of Albunex<sup>®</sup> suspension overlying theinsonified volume, so the concentration of unfiltered microspheres required to produce shadowing need not be very large. In this case, significant attenuation begins to appear near 3 MHz at concentrations of  $0.69 \times 10^6$  microspheres/mL; for a typical patient blood volume of 5 L, this concentration would roughly correspond to a uniformly distributed *in vivo* dose of 5 mL of Albunex<sup>®</sup>, although the concentration of the initial injected bolus may be much higher.

Increasing the amount of overlying contrast agent exacerbates shadowing effects. Figure 5 displays the apparent backscatter transfer function for a single concentration of microspheres ( $2.7 \times 10^6$  microspheres/mL) as a function of gate position relative to the apparent front wall echo. The position of the gate is delayed in increments of  $0.5 \mu s$ , which corresponds to approximately 0.4-mm steps. We note that the attenuation of the overlying Albunex<sup>®</sup> affects not only the overall magnitude of the apparent backscatter, but also its frequency dependence: increasing the gate depth by approxi-

TABLE III. Values of the exponent  $r$  from power law fits of the form  $y = bn^r$  to experimentally determined attenuation and backscatter coefficients, where  $n$  = microsphere concentration.

	2.5 MHz	5 MHz	7.5 MHz	10 MHz
$\alpha_{dB}(n) = bn^r$ :	$r=0.99$	$r=1.02$	$r=1.03$	$r=1.02$
$\eta(n) = bn^r$ :	$r=0.99$	$r=1.02$	$r=1.05$	$r=1.04$

mately 1.2 mm causes the apparent backscatter at 3 MHz to fall more than 10 dB, while the apparent backscatter at 10 MHz decreases by less than 3.5 dB.

The attenuation-compensated backscatter transfer function shown in Fig. 6 exhibits an approximately 3-dB increase across the bandwidth for each doubling of concentration. Thus the compensated backscatter appears to be linearly related to concentration for each dose investigated here. Again, this should be compared with the much faster growth of the attenuation with concentration, as shown in Fig. 7(a). The bar graph of Fig. 7(b) plots the apparent and compensated backscatter at 5 MHz side by side for comparison.

Further compensation of the backscatter data for diffraction effects yields the backscatter coefficient shown in Fig. 8. The diffraction compensation is frequency dependent, but independent of concentration, and thus affects the slope and overall magnitude of each of the curves equally. The magnitude of this compensation was typically smaller than the attenuation compensation for the higher doses. The backscatter coefficient at specific frequencies is displayed as a function of microsphere concentration in Fig. 9(b). Power-law fits of the form  $\eta(n) = bn^r$ , where  $n$  is microsphere concentration, are shown overlaying the data points. The values of  $r$  for the frequencies 2.5, 5, 7.5, and 10 MHz were 0.99, 1.02, 1.05, and 1.04 (see also Table III), respectively, indicating an essentially linear dependence of  $\eta$  on concentration at each frequency. The backscatter coefficient rises rapidly at low frequencies, and then rolls over at approximately 2.5 MHz.  $\eta$  changes little with frequency above 3 MHz, which is consistent with previously published broadband data.<sup>8</sup> It is important to note that there is no significant peak in the backscatter coefficient, in marked contrast to the behavior of the attenuation coefficient. Individual microspheres are expected to exhibit pronounced peaks both in extinction and scattering cross sections due to resonance, but this effect is significantly blunted when considering the combined contributions of the broad distribution of microspheres sizes present in Albunex<sup>®</sup>. Contrast agents with narrower size distributions may display more pronounced resonant behavior in backscatter. The fact that above 3 MHz the backscatter coefficient is relatively flat while the attenuation coefficient is decreasing suggests that Albunex<sup>®</sup> may have enhanced utility at higher frequencies due to decreased potential for shadowing.

One might expect the Albunex<sup>®</sup> microspheres to exhibit significant multiple-scattering effects, considering that the measured backscatter coefficients of Albunex<sup>®</sup> suspensions (at the higher doses examined here) are several orders of magnitude larger than for typical biological soft tissues. The measured data, however, exhibit concentration dependence consistent with single scattering. In order to demonstrate this, let us assume that the attenuation and backscatter coefficients are given by their single scattering forms, as shown in Eqs. (1) and (6). Upon rearranging terms in Eq. (7), we can see more clearly how the apparent backscatter transfer function would depend on the concentration of scatterers:



$$\langle |S(f)|^2 \rangle_{\text{apparent}} = \frac{T_s^2}{RT_{\text{ref}}^2} \cdot \frac{\pi a^2 l E_\infty}{r_0^2 |D_{\text{ref}}(f)|^2} \cdot A_s \left[ \underbrace{\alpha_A(f), l, x_0}_{\frac{\sum_r n \sigma_e}{2}} \cdot \underbrace{\eta(f)}_{\frac{\sum_r n \sigma_s}{4\pi}} \right]. \quad (11)$$

We obtain the backscatter transfer function by dividing through by the attenuation correction factor  $A_s$ :

$$\langle |S|^2 \rangle_{\text{compensated}} = \frac{\langle |S|^2 \rangle_{\text{apparent}}}{A_s} \propto \sum_r n(r) \sigma_s(r). \quad (12)$$

Thus in the single-scattering approximation, both the backscatter coefficient and the attenuation-compensated backscatter transfer function should display a 3-dB increase with each doubling of scatterer concentration. The experimental results shown in Figs. 6–9 appear to corroborate this behavior.

Contrast agent microbubbles have been demonstrated to behave nonlinearly with respect to the insonifying acoustic pressure level by promoting energy from the fundamental frequency to higher harmonics.<sup>30,34,35</sup> This effect could under some conditions lead to “nonideal” scaling of backscatter and attenuation with respect to concentration: as the incident acoustic pressure field passes through the microbubble suspension, the pressure field’s amplitude and frequency content may be altered due to both attenuation and higher harmonic generation. Unlike the fundamental scattering cross section (and the theoretical backscatter coefficient described here), the higher harmonic scattering cross sections depend explicitly on the incident pressure level. Thus it may be more difficult to implement quantitative measurements of myocardial perfusion based on backscattered higher-harmonic signals, as it would require knowledge of the absolute pressure field at all depths and more sophisticated compensation for attenuation and equipment-related effects in order to determine the concentration-dependence of higher-harmonic backscatter. Here we have attempted to employ relatively low acoustic

pressures in order to reduce harmonic generation. A calibrated, 0.4-mm-diam PVDF hydrophone (model PVDFZ44-0400, Specialty Engineering Associates, Soquel, CA) was used to measure the pressure field in the focal zone of the transmitting transducer. The peak positive and negative pressures were 180 and  $-110$  kPa, respectively, as determined from the RF time trace (these levels were much lower than the  $\sim 1$ -MPa peak output of typical transthoracic cardiac imaging systems). The duration of the RF pulse was also quite short ( $\leq 200$  ns). We have performed additional measurements at lower pressure levels and found the results to be generally consistent with those given here, suggesting we are operating in a regime where any nonlinear effects (which scale with applied acoustic pressure) are rather small. We have shown here that under these specific experimental conditions both attenuation and backscatter are directly proportional to concentration over the entire experimental bandwidth, consistent with the first-order linear scattering theory described above.

The potential for nonlinearity in microbubble measurements makes direct comparison of published results difficult. In our previously published measurements of the attenuation of Alunex<sup>®</sup> suspensions,<sup>12</sup> the microspheres were exposed to a pressure field whose magnitude was approximately twice as large as that used in the present study. Because second harmonic effects scale with the square of the pressure magnitude,<sup>30</sup> the lowest-order nonlinear terms would grow by factor of 4. This may partially explain the apparent discrepancy in position of the attenuation peak in the two data sets (a difference of approximately 0.5 MHz). This difference is manifested when fitting an empirical, linear, lumped-parameter model described by de Jong and Hoff<sup>8</sup> to the attenuation data in each case. The essential equations in the de Jong *et al.* formulation are given below:

$$\sigma_e(r, \omega) = \sigma_s(r, \omega) \frac{[\delta_{\text{rad}} + \delta_{\text{vis}} + \delta_{\text{therm}} + (S_f/m_{\text{eff}}\omega)]}{\delta_{\text{rad}}}, \quad (13)$$

$$\sigma_s(r, \omega) = \frac{4\pi r^2}{((\omega_{rg}^2 + (8\pi S_p/m_{\text{eff}})/\omega^2) - 1)^2 + (\delta_{\text{rad}} + \delta_{\text{vis}} + \delta_{\text{therm}} + (S_f/m_{\text{eff}}\omega))^2}, \quad (14)$$

where  $\sigma_e(r, \omega)$  is the extinction cross section at angular frequency  $\omega$  for a bubble of radius  $r$ ,  $\sigma_s(r, \omega)$  is the scattering cross section at angular frequency  $\omega$  for a bubble of radius  $r$ , and  $\omega_{rg}$  is the resonance frequency for a bubble without a shell. The attenuation and backscatter coefficient can be derived by inserting Eqs. (13) and (14) into Eqs. (1) and (6). The terms corresponding to radiative, viscous, and thermal damping ( $\delta_{\text{rad}}$ ,  $\delta_{\text{vis}}$ , and  $\delta_{\text{therm}}$ , respectively) and the effective mass  $m_{\text{eff}}$  of the system are described in the work by de Jong *et al.*<sup>8,33</sup> The two adjustable parameters  $S_p$  and  $S_f$  describe the relative elasticity and friction, respectively, contributed by the microspheres’ encapsulating shells. The shell parameters are very sensitive to changes in the attenuation

peak frequency and magnitude, as well as microsphere size distribution. Our earlier attenuation data was described by an average elasticity parameter equal to 4200 dyn/cm and average friction parameter equal to 0.0054 dyn s/cm, as compared with values of 7500 dyn/cm and 0.0025 dyn s/cm for the present measurements. These differences confirm the fact that the attenuation peak has shifted somewhat in position and height.

The same model can be used to predict the scattering behavior of contrast agent suspensions. Calculations of backscatter coefficient predicted using this model are shown in Fig. 8(b) and correspond to the same concentrations as measured in this study. The calculations were run using input

TABLE IV. Values of physical constants [at a temperature of 37 °C] used in the theoretical calculations of backscatter coefficient shown in Fig. 8(b).

	Physical quantity	Numerical value
Gas (air)	Density	$1.139 \times 10^{-3}$ g/mL
	Thermal conductivity	$2.69 \times 10^3$ erg/s cm K
	Specific heat at constant pressure	$1.01 \times 10^7$ erg/g K
	Ratio of specific heats	1.4
Liquid (water)	Density	1.00 g/mL
	Speed of sound	$1.524 \times 10^5$ cm/s
	Shear viscosity	0.0069 g/cm s
	Surface tension	70 dyn/cm
Albunex shell	Elasticity parameter $S_p$	7500 dyn/cm
	Friction parameter $S_f$	0.0025 dyn s/cm
General	Ambient pressure	$1.013 \times 10^6$ dyn/cm <sup>2</sup>

values for shell elasticity of 7500 dyn/cm and shell friction of 0.0025 dyn s/cm, as determined from the attenuation data, and using actual size distributions as measured with the Coulter Multisizer (using a different vial of commercial-grade Albunex<sup>®</sup>). Other physical constants used in the simulation are listed in Table IV. The Multisizer was used to perform two measurements of the Albunex<sup>®</sup> separated by approximately 1 h, in order to account for any degradation which might occur over the span of the measurement; the average of these two size distribution measurements was used as the input to the model. There is good semiquantitative agreement between the experimental data and theoretical predictions, both of which show a rapid rise with frequency below 3 MHz, and level off at higher frequencies to approximately the same asymptotic value. However, the theory predicts a modest peak in the backscatter between 2 and 3 MHz that is not evident in the actual data.

Most of the current literature pertaining to simulation and measurement of gas-based contrast agents has asserted or assumed that the microbubbles scatter spherically symmetrically. This assumption permits the simple connection between total scattering cross section and backscatter coefficient outlined in the Theory section above. However, it has recently been suggested that the scattering from Albunex<sup>®</sup> microbubbles may not always be omnidirectional, but that for larger microbubbles or at higher frequencies the scattering may become anisotropic.<sup>36</sup> Scattering behavior such as this would affect determination of differential scattering cross section, and would require a multiangle, two-transducer system for complete determination of the total scattering cross section. However, the main concern in this study was experimental determination of backscatter coefficient, for which the assumption of isotropic scattering is not necessary and thus does not change the fundamental experimental result that the backscattered power (compensated for attenuation effects) is linearly proportional to the number of scatterers.

It should be noted that we have used the Albunex<sup>®</sup> microspheres as both the scattering medium and the intervening attenuating medium. In a clinical imaging scenario, the region of interest might instead be a segment of contrast-perfused myocardium situated below a contrast-filled cham-

ber and other myocardial tissue. The frequency-dependent attenuation effects of the overlying tissue, the scattering effects of the perfused myocardium, the distribution of contrast agent, and the system response would need to be determined in order to calculate the compensated backscatter and perform quantitative RF analysis. Nevertheless, certain effects can be anticipated based on the results of the present work. It is clear from the plots presented above for apparent backscattered power that both the integrated backscatter and frequency centroid of a region of interest situated behind a contrast-filled area may change dramatically with agent concentration, region depth, imaging system bandwidth, and transducer center frequency. In an *in vivo* study performed by Wang *et al.*,<sup>4</sup> it was found that the RF signals backscattered from contrast-perfused myocardial cavities and tissue were significantly affected by the presence of contrast agent in the path between the transducer and the region of interest and exhibited either an upward or a downward shift of the frequency centroid. Holm *et al.*<sup>9</sup> used a mathematical model for predicting changes in the backscattered spectrum after passing through human tissue and Albunex<sup>®</sup> microspheres. It was demonstrated that the amount and direction of changes in both the frequency centroid and backscattered intensity were highly dependent upon microsphere size distribution, the concentration of microspheres in the path between the transducer and the region of interest, and the instrumentation bandwidth. We have shown experimentally that it is possible under carefully controlled conditions to compensate for effects from attenuation, region of interest length and position, and measurement system response, and thus demonstrate that there is a linear relationship of backscatter coefficient to contrast agent concentration. We have also shown that the linear relationship exists between backscattered power and concentration even when there is no compensation for beam diffraction. This relationship appears to hold (within the usable bandwidth) for all the concentrations of Albunex<sup>®</sup> used in this study. It is this linear relationship which may aid in enabling quantitative measurements of myocardial perfusion from RF analysis. The fact that the microsphere size distribution might be substantially altered *in vivo* (due to filtering by the lungs, gas diffusion into or out of the microspheres, dilution of the bolus in the blood, etc.) would alter the frequency dependence of the attenuation and backscatter from the agent,<sup>8,9,33,37</sup> but would presumably not affect the linear backscatter-concentration relationship.

<sup>1</sup>M. J. Monaghan, J. M. Metcalfe, S. Odunlami, and D. E. Jewitt, "Myocardial contrast echocardiography: Applications of digital ultrasound data acquisition and processing," *Am. J. Card. Imaging* **5**, 237–249 (1991).

<sup>2</sup>M. J. Monaghan, J. M. Metcalfe, S. Odunlami, A. Waaler, and D. E. Jewitt, "Digital radiofrequency echocardiography in the detection of myocardial contrast following intravenous administration of Albunex<sup>®</sup>," *European Heart Journal* **14**, 1200–1209 (1993).

<sup>3</sup>B. Wilson, K. K. Shung, B. Hete, H. Levene, and J. L. Barnhart, "A feasibility study on quantitating myocardial perfusion with Albunex<sup>®</sup>, an ultrasonic contrast agent," *Ultrasound Med. Biol.* **19**, 181–191 (1993).

<sup>4</sup>S. H. Wang, P. H. Chang, K. K. Shung, and H. B. Levene, "Some considerations on the measurements of mean frequency shift and integrated backscatter following administration of Albunex<sup>®</sup>," *Ultrasound Med. Biol.* **22**, 441–451 (1996).

<sup>5</sup>H. J. Bleeker, K. K. Shung, and J. L. Barnhart, "Ultrasonic characteriza-

- tion of Albunex<sup>®</sup>, a new contrast agent," J. Acoust. Soc. Am. **87**, 1792–1797 (1990).
- <sup>6</sup>H. J. Bleeker, K. K. Shung, and J. L. Barnhart, "On the application of ultrasonic contrast agents for blood flowmetry and assessment of cardiac perfusion," J. Ultrasound Med. **9**, 461–471 (1990).
- <sup>7</sup>P. H. Chang and K. K. Shung, "Attenuation and backscatter measurements on Albunex," *IEEE Ultrasonics Symposium Proceedings*, Baltimore, MD, 1993 (IEEE, New York, 1993), 93CH3301-9, pp. 913–916.
- <sup>8</sup>N. de Jong and L. Hoff, "Ultrasound scattering properties of Albunex microspheres," *Ultrasonics* **31**, 175–181 (1993).
- <sup>9</sup>S. Holm, M. Myhrum, and L. Hoff, "Modelling of the ultrasound return from Albunex microspheres," *Ultrasonics* **32**, 123–130 (1994).
- <sup>10</sup>P. A. Heidenreich, J. G. Wienczek, J. G. Zaroff, S. Aronson, L. J. Segil, P. V. Harper, and S. B. Feinstein, "In Vitro Calculation of Flow by Use of Contrast Ultrasonography," *Journal of the American Society of Echocardiography* **6**, 51–61 (1993).
- <sup>11</sup>C. M. Seghal and P. H. Arger, "Mathematical modeling of the dilution curves for ultrasonographic contrast agents," J. Ultrasound Med. **16**, 471–479 (1997).
- <sup>12</sup>J. N. Marsh, C. S. Hall, M. S. Hughes, J. Mobley, J. G. Miller, and G. H. Brandenburger, "Broadband through-transmission signal loss measurements of Albunex<sup>®</sup> at concentrations approaching in vivo doses," J. Acoust. Soc. Am. **101**, 1155–1161 (1997).
- <sup>13</sup>C. S. Hall, J. N. Marsh, M. S. Hughes, J. Mobley, K. D. Wallace, J. G. Miller, and G. H. Brandenburger, "Broadband measurements of the attenuation coefficient and backscatter coefficient for suspensions: A potential calibration tool," J. Acoust. Soc. Am. **101**, 1162–1171 (1997).
- <sup>14</sup>J. Mobley, M. S. Hughes, J. N. Marsh, C. S. Hall, G. H. Brandenburger, and J. G. Miller, "Broadband measurements of phase velocity in Albunex<sup>®</sup> suspensions," J. Acoust. Soc. Am. **103**, 2145–2153 (1998).
- <sup>15</sup>E. Merzbacher, J. M. Feagin, and T.-H. Wu, "Superposition of the radiation from  $N$  independent sources and the problem of random flights," Am. J. Phys. **45**, 964–969 (1977).
- <sup>16</sup>H. Medwin, "Counting bubbles acoustically: a review," *Ultrasonics* **15**, 7–13 (1977).
- <sup>17</sup>K. K. Shung, "Ultrasonic propagation in tissues" in *Ultrasonic Scattering in Biological Tissues*, edited by K. K. Shung and G. A. Thieme (CRC, Boca Raton, FL, 1993), pp. 1–17.
- <sup>18</sup>M. F. Insana and D. G. Brown, "Acoustic scattering theory applied to soft biological tissues" in *Ultrasonic Scattering In Biological Tissues*, edited by K. K. Shung and G. A. Thieme (CRC, Boca Raton, FL, 1993), pp. 75–124.
- <sup>19</sup>P. M. Morse and K. U. Ingard, *Theoretical Acoustics* (Princeton U. P., Princeton, NJ, 1968), Chap. 8.
- <sup>20</sup>N. de Jong, F. J. T. Cate, C. T. Lancée, J. R. T. C. Roelandt, and N. Bom, "Principles and recent developments in ultrasound contrast agents," *Ultrasonics* **29**, 324–330 (1991).
- <sup>21</sup>R. A. Sigelmann and J. M. Reid, "Analysis and measurement of ultrasound backscattering from an ensemble of scatterers excited by sine-wave bursts," J. Acoust. Soc. Am. **53**, 1351–1355 (1973).
- <sup>22</sup>M. O'Donnell and J. G. Miller, "Quantitative broadband ultrasonic backscatter: An approach to nondestructive evaluation in acoustically inhomogeneous materials," J. Appl. Phys. **52**, 1056–1065 (1981).
- <sup>23</sup>J. A. Campbell and R. C. Waag, "Normalization of ultrasonic scattering measurements to obtain average differential scattering cross-sections for tissues," J. Acoust. Soc. Am. **74**, 393–399 (1983).
- <sup>24</sup>E. L. Madsen, M. F. Insana, and J. A. Zagzebski, "Method of data reduction for accurate determination of acoustic backscatter coefficients," J. Acoust. Soc. Am. **76**, 913–923 (1984).
- <sup>25</sup>K. A. Wear, M. R. Milunski, S. A. Wickline, J. E. Perez, B. E. Sobel, and J. G. Miller, "Differentiation between acutely ischemic myocardium and zones of completed infarction in dogs on the basis of frequency-dependent backscatter," J. Acoust. Soc. Am. **85**, 2634–2641 (1989).
- <sup>26</sup>C. S. Hall, "Measurements of ultrasonic backscatter coefficient and attenuation coefficient for anisotropic inhomogeneous media and suspensions of solid and gaseous microspheres," Ph.D. thesis, Washington University, St. Louis, MO, 1996.
- <sup>27</sup>X. Chen, D. Phillips, K. Q. Schwarz, J. G. Mottley, and K. J. Parker, "The Measurement of Backscatter Coefficient from a Broadband Pulse-Echo System: A New Formulation," *IEEE Trans. Ultrason. Ferroelectr. Freq. Control* **44**, 515–525 (1997).
- <sup>28</sup>S. L. Bridal, K. D. Wallace, R. L. Trousil, S. A. Wickline, and J. G. Miller, "Frequency dependence of acoustic backscatter from 5 to 65 MHz ( $0.06 < ka < 4.0$ ) of polystyrene beads in agarose," J. Acoust. Soc. Am. **100**, 1841–1848 (1996).
- <sup>29</sup>M. W. Miller, M. Azadniv, Y. Doida, and A. A. Brayman, "Effect of a stabilized microbubble contrast agent on CW ultrasound induced red blood cell lysis in vitro," *Echocardiography* **12**, 1–11 (1995).
- <sup>30</sup>C. C. Church, "The effects of an elastic solid surface layer on the radial pulsations of gas bubbles," J. Acoust. Soc. Am. **97**, 1510–1521 (1995).
- <sup>31</sup>J. J. Faran, "Sound scattering by solid cylinders and spheres," J. Acoust. Soc. Am. **23**, 405–418 (1951).
- <sup>32</sup>A. E. Hay and D. G. Mercer, "On the theory of sound scattering and viscous absorption in aqueous suspensions at medium and short wavelengths," J. Acoust. Soc. Am. **78**, 1761–1771 (1985).
- <sup>33</sup>N. de Jong, L. Hoff, T. Skotland, and N. Bom, "Absorption and scatter of encapsulated gas filled microspheres: theoretical considerations and some measurements," *Ultrasonics* **30**, 95–103 (1992).
- <sup>34</sup>N. de Jong, R. Cornet, and C. T. Lancée, "Higher harmonics of vibrating gas-filled microspheres. Part one: simulations," *Ultrasonics* **32**, 447–453 (1994).
- <sup>35</sup>N. de Jong, R. Cornet, and C. T. Lancée, "Higher harmonics of vibrating gas-filled microspheres. Part two: measurements," *Ultrasonics* **32**, 455–459 (1994).
- <sup>36</sup>Z. Ye, "On sound scattering and attenuation of Albunex<sup>®</sup> microbubbles," J. Acoust. Soc. Am. **100**, 2011–2028 (1996).
- <sup>37</sup>L. Hoff, C. Christiansen, and T. Skotland, "Consideration about the contribution to acoustic backscatter from albunex microspheres with different sizes," J. Ultrasound Med. **13**, 181–182 (1994).

# Simple methods of estimating source levels and locations of marine animal sounds

Douglas H. Cato

Defence Science and Technology Organisation, P. O. Box 44, Pyrmont, NSW 2009, Australia

(Received 12 June 1995; accepted for publication 21 May 1998)

This paper describes three relatively simple methods of estimating source levels of marine animal sounds by estimating the source distance acoustically, using one or two hydrophones. The methods are logistically simpler than using arrays of hydrophones of known positions but are accurate over a smaller range of distances. One method makes use of the differences in the arrival times and levels of the signals received at two hydrophones from the same sound emission. No knowledge of the positions of the hydrophones is required, however, if these are known the position of the source can be determined, with left–right ambiguity. The second method uses the difference in received levels only, but requires the hydrophone spacing to be known. Adequate accuracy requires the source to be significantly closer to one hydrophone than to the other. Third, if the direct and surface reflected arrivals can be separated, the source level can be determined with a single hydrophone. The methods require accurately calibrated hydrophones. © 1998 Acoustical Society of America.

[S0001-4966(98)03509-7]

PACS numbers: 43.80.Ka, 43.30.Sf [FD]

## INTRODUCTION

Marine animals inhabit a medium in which visual and olfactory senses have limited effectiveness except in special circumstances or environments. Consequently, they make extensive use of sound which is an important component of their behavior and contributes substantially to the ambient noise of the ocean. The source levels of individual sounds determine the distance over which the sounds are likely to be detectable and effective, both in influencing the behavior of other individuals and in contributing to the ambient noise. These factors may be of significance in assessing the impact on marine animals of noise from human activities (Richardson *et al.*, 1995) and knowledge of source levels is needed for passive acoustic assessment of stocks. There are, however, considerable difficulties in estimating source levels and as a consequence, the amount of source level data available in the literature is limited. Very few estimates have been made for fish and invertebrates. Estimates are available for most species of the great whales and for some of the smaller species, but usually only a small number of estimates per species, and it would be useful to obtain estimates for a wider range of behavioral conditions. For example, where a number of measurements have been made, significant variation in source level has been observed for bowhead whales (Cummings and Holliday, 1987) and for finback whales (Watkins *et al.*, 1987).

Source level is usually defined as the level at unit distance from a point source which produces the same level at any distance in the far field as the real source does at that same distance (see discussions by Urick, 1983, and Richardson *et al.*, 1995). This definition allows the properties of the source to be separated from the variable effects of the propagation of sound in the ocean. Determination of source level thus requires an estimate of the source distance and the propagation loss for that distance. The thrust of this paper is concerned with determining the source distance since there is a substantial amount of information available about propaga-

tion loss. However, the effects of propagation loss are also considered, and methods of checking this in the field are discussed. The inherent uncertainties of measurements in the ocean warrant an estimate of the errors involved. A detailed discussion is provided of the errors associated with the methods presented.

The difficulty in estimating source levels of marine animal sounds usually lies in estimating the distance of the source from the hydrophone. The source is submerged and often not visible. Even when fish and invertebrates are visible in clear water there are usually many individuals producing sounds and it is difficult to determine just which individuals are responsible for the particular signals recorded. Whales can be located visually when they surface to breathe, but the sound radiated by a near surface source is significantly attenuated by the interference between the direct and surface reflected paths, making estimates of source level difficult and unreliable. When a whale dives it may change position. If there is more than one whale present, there is usually no visual indication of which animal is vocalizing. The closest whale is not necessarily the source because apparently loud sounds can come from distant whales.

It is possible in some conditions to relate behavior to vocalization. For example, Winn and Winn (1978) found that singing humpback whales surfaced to blow at a particular part of the song. Tyack (1981) used this and the reduction in received sound level to locate singers. This method requires suitable conditions and may not be possible with other species. Estimating source levels using visual estimates of distance may result in substantial errors because of the uncertainty in identifying the source and determining its distance. Furthermore, the magnitude of these errors may not be known.

Acoustical methods of locating the sources of underwater sounds are well established, and have been used to locate whales. These are generally based on measurement of differences in the times of arrival of the sounds at two or more

hydrophones. A measurement of arrival time difference between two receivers is very suitable for determining the direction of a source (except when its distance is much less than the hydrophone separation) but provides no indication of its distance. Many applications, therefore, have made use of measurements of source direction in combination with visual information to locate sources. For example, Winn and Winn (1978) used a ship mounted sonar array to determine the direction of singing humpback whales so that they could be approached and then located visually. Clark (1980) described a compact three hydrophone system and associated processing which provided a real time estimate of source direction to identify sources in a study of right whale behavior.

The actual position of the source can be determined from arrival time differences alone, if there are sufficient combinations of hydrophones to provide intersecting cross bearings. This requires at least three accurately placed hydrophones with adequate baseline dimensions. Walker (1963) used three hydrophones to track sources of 20-Hz pulses (apparently from whales). Cummings *et al.* (1964) used arrival time differences on three hydrophones at the corners of an equilateral triangle to determine the locations and source levels of sounds from fish and invertebrates. Watkins and Schevill (1972) describe a three-dimensional array of four hydrophones which they have used successfully to track whales. Cummings and Holliday (1985, 1987) located and tracked bowhead whales using a nearly linear array of three widely spaced sonobuoys, and Freitag and Tyack (1993) used up to six hydrophones to track dolphins over short ranges. Sophisticated acoustic tracking systems have also been used to locate whales (Cummings and Thompson, 1994; Clark *et al.*, 1994; Stafford *et al.*, 1994).

Determination of the source distance, however, requires less information than determination of its position, so simpler methods of estimating source levels should be possible. Since the received level of a sound changes significantly with distance from a source, the difference in level between two hydrophones provides information about relative source distances. This paper describes three simple methods of using received differences in level and arrival times between two hydrophones to estimate source distances. The source levels can then be determined from absolute received levels and knowledge of the propagation loss. The results are accurate over a smaller range of distances than those determined by conventional acoustic methods involving precise positioning of several hydrophones. The value lies in the logistic simplicity, since recordings obtained without accurate positioning of the hydrophones can provide estimates of acceptable accuracy. The first method uses both the differences in level and arrival times. The distance to the source can be determined without knowing the positions of the hydrophones. If these are known, however, the position of the source can also be determined with the usual left-right ambiguity that arises from measurement of arrival time differences between two receivers. The uncertainty in the estimate becomes unacceptably large as the source approaches a position equi-distant from the two hydrophones (where differences in arrival times and levels approach zero). The second

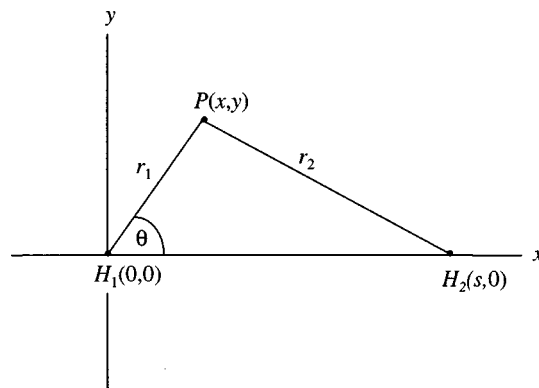


FIG. 1. Geometry of the model. The hydrophones are at  $H_1$  and  $H_2$ , and the source at  $P$ .

method uses only the difference in level to determine the distance to the source, and adequate accuracy is obtained if the difference in level is significant. The hydrophone spacing must be known. Third, if the direct and surface reflected arrivals can be separated, these methods can be used with a single hydrophone, the surface reflected arrival providing the equivalent of an arrival on a virtual or image receiver vertically above the hydrophone. Cummings *et al.* (1968) determined the locations and source levels of gray whale sounds by a method similar to the first method. The second method has been used to determine source levels of various fish sounds (Cato, 1980). As in any measurement of source level, these methods require accurately calibrated hydrophones.

## I. THEORY

### A. Introduction

There are two hydrophones on the  $x$  axis, one at  $H_1(0,0)$  and one at  $H_2(s,0)$ , as shown in Fig. 1. The source is at position  $P(x,y)$ , distance  $r_1$  from  $H_1$  and  $r_2$  from  $H_2$ . Let  $k=r_2/r_1$  and choose  $r_2>r_1$  so that the source is closer to hydrophone  $H_1$ . Let the received intensity at  $H_1$  and  $H_2$  for the same sound emission from the source be  $I_1$  and  $I_2$ , respectively. We assume that propagation loss is proportional to  $ar^n$  so that the received intensity at  $H_1$  is

$$I_1 = I_0 / (ar_1^n), \quad (1)$$

where  $I_0$  is the source strength (intensity at unit distance). Absorption attenuation has been ignored since it would be negligible for most frequencies and propagation distances of interest here. The source level is then given by

$$SL = 10 \log_{10} I_0 = 10 \log_{10}(I_1 ar_1^n) \quad (2)$$

and

$$k = (I_1/I_2)^{1/n} = (p_1/p_2)^{2/n}, \quad (3)$$

where  $p_1$  and  $p_2$  are the received pressures at  $H_1$  and  $H_2$ , respectively. The difference in received level DL at the two hydrophones is

$$DL = 10 \log_{10}(I_1/I_2) = 10n \log_{10}(r_2/r_1) = 10n \log_{10} k. \quad (4)$$

When  $a=1$  and  $n=2$ , propagation loss is according to spherical spreading. For many conditions of interest,  $n=2$

will be an acceptable approximation. The significance of propagation loss in determining source levels is discussed in Sec. II A.

### B. Method 1, using the differences in the received levels and arrival times

The following derivation uses the measured difference in the levels DL and the difference in arrival times  $\tau$  of the signals received at the hydrophones from the same sound emission from the source. Now

$$\tau = (r_2 - r_1) / c_0, \quad (5)$$

where  $c_0$  is the speed of sound which can be assumed to be constant for the purpose of this calculation. Substituting  $r_2 = r_1 k$  in Eq. (5) gives

$$r_1 = c_0 \tau / (k - 1). \quad (6)$$

This simple expression for the distance of the source from the closer hydrophone is useful so long as the source is significantly closer to one hydrophone than the other. This can be seen by noting that

$$\partial r_1 / \partial \tau = c_0 / (k - 1) = r_1 / \tau, \quad \rightarrow \infty \text{ as } \tau \rightarrow 0$$

and

$$\partial r_1 / \partial k = -c_0 \tau / (k - 1)^2 = -r_1 / (k - 1), \quad \rightarrow -\infty \text{ as } k \rightarrow 1$$

so that  $r_1$  changes very rapidly as  $\tau \rightarrow 0$  or  $k \rightarrow 1$  and small errors in either  $\tau$  or  $k$  would result in large errors in the estimate of  $r_1$ . These conditions arise as the source approaches the plane bisecting (at right angles) the line between the hydrophones. When  $\tau = 0$ ,  $k = 1$ , the source lies on this plane and Eq. (6) is indeterminate. This is the only condition for which  $\tau \rightarrow 0$ , but  $k \rightarrow 1$  also where the distance to the source is much larger than the hydrophone separation. The significance and magnitude of these errors, and ways of reducing them, are discussed in detail in Sec. II B. For square law propagation,  $k = 10^{DL/20}$  and substituting this into Eq. (6) gives a result similar to that presented by Cummings (1968).

From Eqs. (2) and (6), the source level is

$$SL = 10 \log_{10} \{ I_1 a (c_0 \tau)^n / (k - 1)^n \}, \quad (7)$$

where  $k = 10^{DL/10n}$ . For square law propagation (spherical spreading),  $k = 10^{DL/20}$  and the expression for source level becomes

$$SL = RL + 10 \log_{10} \{ a (c_0 \tau)^2 / (k - 1)^2 \}, \quad (8)$$

where  $RL = 10 \log_{10} I_1$  is the received level at hydrophone  $H_1$ . Note that RL and SL are in the same units and measure the same property of the sound signal, e.g., broadband level, spectrum level at a particular frequency, or peak level, etc.

Note that evaluation of Eqs. (6)–(8) does not require knowledge of the positions of the hydrophones or their separation. The accuracy of the result, however, will tend to improve as the hydrophone separation increases (Sec. II B). Evaluation of the source distance  $r_1$  requires the value of  $n$  to be known [Eq. (4)] but only for propagation over distances from  $r_1$  to  $r_2$ . This can be seen by noting that  $k$  is deter-

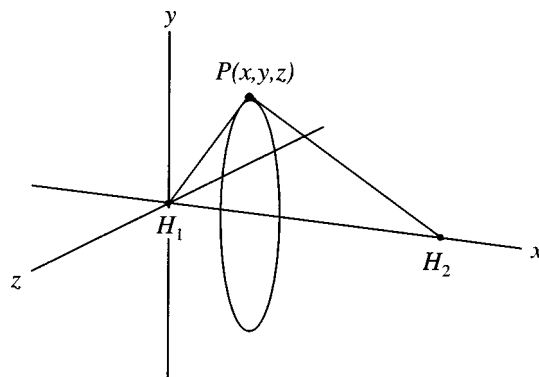


FIG. 2. Diagrammatic representation of the locus of the position  $P$  of the source in three dimensions, determined from differences in levels and arrival times (method 1).  $P$  lies on the circumference of a circle normal to the plane containing  $P$ ,  $H_1$ , and  $H_2$ .

mined from DL which depends on the propagation loss at  $r_1$  relative to that at  $r_2$ . Evaluation of Eq. (7) requires  $n$  to be known for all distances up to  $r_2$ .

### 1. Determination of the source position

If the positions of the two hydrophones are known, the position of the source can be estimated, with the usual left–right ambiguity that arises when arrival time differences are used on a linear array. From Fig. 1,

$$k^2 r_1^2 = r_2^2 = (s - x)^2 + y^2 \quad (9)$$

and

$$\cos \theta = x / r_1, \quad (10)$$

where  $\theta$  is the angle between the line  $H_1 P$  and the  $x$  axis (Fig. 1). Expanding Eq. (9) and substituting  $r_1^2 = x^2 + y^2$  leads to

$$x = s/2 - r_1^2 (k^2 - 1) / (2s) \quad (11)$$

and

$$\cos \theta = \{ s^2 - (k^2 - 1) r_1^2 \} / (2r_1 s). \quad (12)$$

Equations (6) and (12) provide the range of the source from hydrophone  $H_1$ , and the angle of the source direction relative to the line through the hydrophones, respectively. Rotation of the plane containing  $P$ ,  $H_1$ , and  $H_2$  about the  $x$  axis (the line through the hydrophones) does not change the above results. Then  $P$  sweeps out a circle in a plane normal to the  $x, y$  plane, as shown diagrammatically in Fig. 2. The three-dimensional locus of the source position,  $P(x, y, z)$ , therefore lies on the circumference of this circle which has its center at  $(x, 0, 0)$  and a radius of  $\sqrt{y^2 + z^2}$ . It intersects the  $x, y$  plane at points  $P(x, y, 0)$  and  $P'(x, y', 0)$ , where  $y' = -y$ . This type of uncertainty in determining the source position is usual in estimates using arrival time differences. It is partially resolved if distances are significantly greater than the water depth, or there is some other reason to assume that the source and receivers are constrained vertically. If the differences in depths of the source and the hydrophones are much less than their separations, the angle  $\theta$  is approximately the azimuthal bearing of the source relative to the line

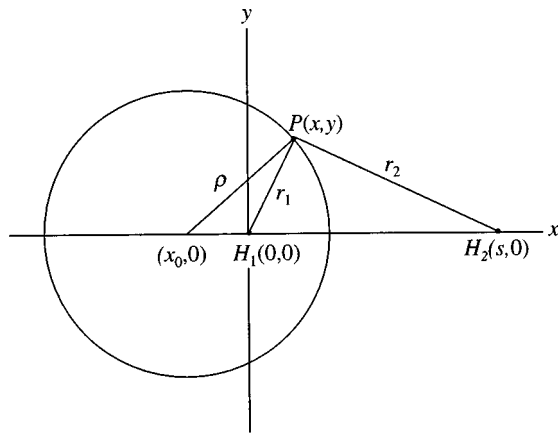


FIG. 3. Circle showing the locus of the source position  $P$  in the plane of the paper, determined from the differences in received levels only (method 2). The three-dimensional locus of  $P$  is the spherical surface swept out by rotation of the circle about the line  $H_1H_2$ .

through the hydrophones. It is not possible, however, to determine if  $\theta$  in Fig. 1 is positive or negative (since  $\cos \theta = \cos -\theta$ ) so that the source can be either side of the line through the hydrophones, providing the left-right ambiguity relative to this line.

### C. Method 2, using the difference in the received levels only

Manipulation of Eq. (9) gives

$$(k^2 - 1)x^2 + (k^2 - 1)y^2 - s^2 + 2sx = 0$$

which leads to

$$(x - x_0)^2 + y^2 - \rho^2 = 0, \quad (13)$$

where

$$x_0 = -s/(k^2 - 1) \quad (14)$$

and

$$\rho = sk/(k^2 - 1). \quad (15)$$

Equation (13) is the equation of a circle with radius  $\rho$ , and center at the point  $(x_0, 0)$ . It is the locus of the point  $P(x, y)$  for fixed values of  $k$  and  $s$ , as shown in Fig. 3. The circle lies in the plane containing the points  $P$ ,  $H_1$ , and  $H_2$  (the plane of the paper). Since rotation of this plane about the  $x$  axis does not change the above result, the three-dimensional locus of the source position,  $P(x, y, z)$ , is the surface of the sphere swept out by rotation of the circle about the line  $H_1$  and  $H_2$ . Thus we have determined that the source lies on the surface of a sphere of radius  $\rho$  centered at the point  $(x_0, 0, 0)$ .

Rearranging Eq. (11) gives

$$r_1^2 = s(s - 2x)/(k^2 - 1). \quad (16)$$

Without further information, we cannot determine the values of  $x$  or  $r_1$  in Eq. (16) apart from noting that they are constrained by the locus of  $P$ . Equation (16) shows that, within this constraint,  $r_{\min}$ , the minimum value of  $r_1$ , occurs when  $x$  is maximum, and the maximum value,  $r_{\max}$ , when  $x$  is minimum. It is apparent in Fig. 3 that these values occur where the circle crosses the  $x$  axis so that

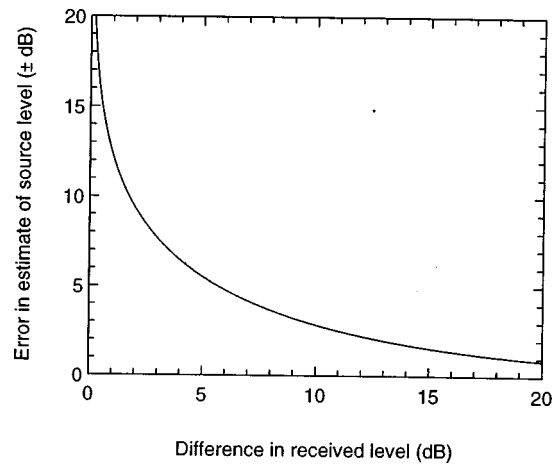


FIG. 4. Uncertainty in estimating the source level for method 2, which uses the difference in levels only, for square law propagation, expressed as the error about the mean source level [from Eq. (22)].

$$r_{\min} = \rho + x_0 = s/(k + 1) \quad (17)$$

and

$$r_{\max} = \rho - x_0 = s/(k - 1), \quad (18)$$

so that

$$\frac{r_{\max}}{r_{\min}} = \frac{k + 1}{k - 1}. \quad (19)$$

These values of  $r_{\max}$  and  $r_{\min}$  can be substituted into Eq. (2) to provide an upper and lower limit, respectively, in the estimate of the source level, giving a range of uncertainty in the estimate of  $10n \log_{10}((k + 1)/(k - 1))$  [from Eq. (19)]. The mean value of the source level is obtained by using the geometrical mean of  $r_{\min}$  and  $r_{\max}$  as our estimate of  $r_1$ , i.e.,

$$r_1 \cong s/\sqrt{k^2 - 1} \quad (20)$$

so that the source level estimate is

$$\begin{aligned} \text{SL} &= 10 \log_{10}\{I_1 a s^n / (k^2 - 1)^{n/2}\} \\ &\pm 10(n/2) \log_{10}\{(k + 1)/(k - 1)\}; \end{aligned} \quad (21)$$

for square law propagation this reduces to

$$\begin{aligned} \text{SL} &= \text{RL} + 10 \log_{10}\{a s^2 / (k^2 - 1)\} \\ &\pm 10 \log_{10}\{(k + 1)/(k - 1)\}, \end{aligned} \quad (22)$$

where  $k = 10^{\text{DL}/20}$ .

The range of uncertainty decreases as the value of  $k$  increases [Eq. (21)]. In other words, the error in the estimate decreases as the difference in level received on the two hydrophones increases. This method is therefore useful where the difference in the received level is adequate to provide an acceptably small error. Figure 4 shows the error in the source level estimate of Eq. (22) as a function of the difference in level. This method does not determine the position of the source other than that it lies on the surface of a sphere defined by the circle of Eq. (13).

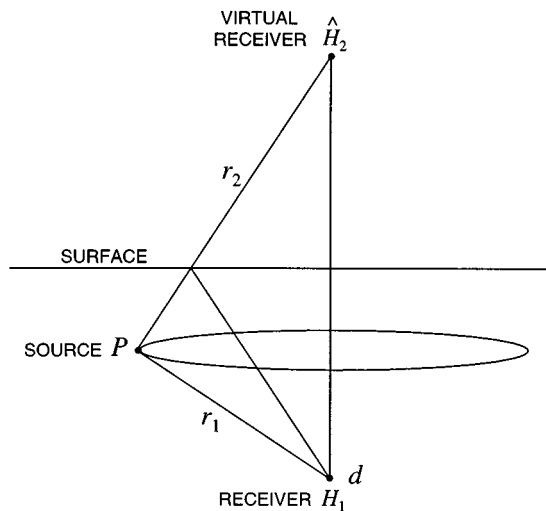


FIG. 5. Geometry for method 3, using the direct and surface reflected arrivals at a single hydrophone  $H_1$ .

### D. Method 3, using direct and surface reflected arrivals to one hydrophone

If the direct and surface reflected arrivals can be separated in time from each other and from the bottom reflected arrivals, then the above methods can be applied to the direct and surface reflected arrivals at a single hydrophone. It is assumed here that reflection from the sea surface occurs with negligible loss. This is an acceptable assumption except at high frequencies and high sea states, so will apply to most conditions of interest. Figure 5 shows the geometry. The hydrophone is at  $H_1$ , depth  $d$ . The surface reflected arrival at  $H_1$  is the same, apart from the reversal of phase, as would be received at an image or virtual hydrophone at  $\hat{H}_2$  distance  $2d$  vertically above  $H_1$  in a medium with the acoustical properties of water. Thus the geometry of Fig. 1 applies with  $\hat{H}_2$  replacing  $H_2$  and with  $s = 2d$ , and the above methods can be used, so long as the measurements take account of the reversal of phase in the surface reflected arrival (the phase reversal will, in fact, be useful in identifying the surface reflected arrival). An estimate based on the differences in levels and arrival times determines that the source is on the circumference of a circle like the one shown.

Note that no knowledge of either the source depth or the hydrophone depth is required for the source level estimate. If the receiver depth is known, the locus of the source position can be estimated using the method described in Sec. I B 1. The angle  $\theta$  [Eq. (12)] is now the angle to the vertical of the source from the receiver. The depth of the source,  $d_s$ , can be determined from the expression for  $x$  in Eq. (11), noting that  $x = d - d_s$ :

$$d_s = d - x = r_1^2(k^2 - 1)/(4d). \quad (23)$$

The need to separate in time the direct, surface and bottom reflected arrivals limits the application of this method to short duration signals, although these separations can be increased by changing the source-receiver geometry. Reducing the distance between the source and receiver will increase the arrival time difference between direct and surface reflected paths. This difference also increases as source and

receiver depths increase, but this reduces the time difference between surface and bottom reflections. Source and receiver depths need to be significantly less than half the water depth to ensure that there is adequate separation between surface and bottom reflected arrivals.

Use of a second hydrophone (of known position relative to the first) would provide a cross bearing to reduce the ambiguity in source position, by locating the source on the circle of Fig. 5.

If the direct and surface reflected arrivals overlap but there is sufficient delay in the reflected arrival to measure the amplitude relative to that of the direct arrival, then the method using the difference in received levels can be used.

### E. Graphical representation

A fixed difference in level constrains the source to lie on the surface of a sphere as described in Sec. I C. It is well known that a fixed difference in the arrival times constrains the source to lie on the surface of the conical section swept out by the rotation of a hyperbola about the line through the hydrophones. The expression for the hyperbola is obtained by the following procedure. From Eq. (5),

$$c_0\tau + r_1 = r_2.$$

Squaring both sides and substituting  $r_1^2 = x^2 + y^2$  and  $r_2^2 = (s - x)^2 + y^2$  gives

$$2c_0\tau\sqrt{x^2 + y^2} = s(s - 2x) - c_0^2\tau^2. \quad (24)$$

Squaring both sides and some manipulation leads to

$$\frac{\hat{x}^2}{a^2} - \frac{y^2}{b^2} = 1, \quad (25)$$

where  $a^2 = c_0^2\tau^2/4$ ,  $b^2 = (s^2 - c_0^2\tau^2)/4$ , and  $\hat{x} = x - s/2$ . This is the equation of a hyperbola which is symmetrical about the  $x$  axis and has asymptotes crossing the  $x$  axis at  $x = \hat{x}$ , the point midway between the hydrophones.

Thus in the plane containing the source and the receivers, the source must lie on the circle determined from received differences in level and the hyperbola determined by the difference in the arrival times. Its position, therefore, is one of the two points of intersection of the circle and the hyperbola. Figure 6 shows the circles for various values of DL for square law propagation [from Eq. (13)] and the hyperbolas for various values of  $\tau$ . It is apparent that the arrival time difference is an effective indication of the direction of the source, except where the source is very close to  $H_1$ , but gives no indication of source distance. The difference in level, on the other hand, is an effective indicator of the relative distance of the source, but gives no indication of its direction. Together they provide both range and bearing of the source relative to the receiver positions. As the source approaches the plane bisecting the line  $H_1H_2$  at right angles, the circles and hyperbolas intersect at decreasingly small angles so that small changes in DL or  $\tau$  result in large changes in the points of intersection and thus the position of the source. This shows graphically how the uncertainties in the estimates increase as  $\tau \rightarrow 0$  and  $DL \rightarrow 0$ , ( $k \rightarrow 1$ ). In the



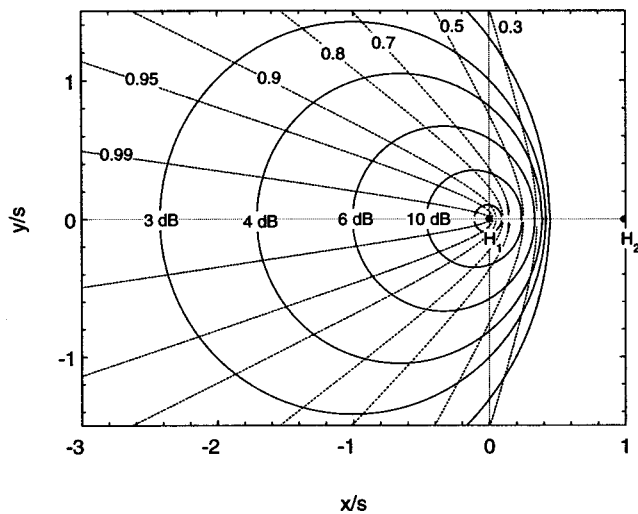


FIG. 6. Graphical representation of the methods described. The circumference of each circle is the locus of the position of the source for the received difference in level shown, for square law propagation [from Eq. (13)]. Each hyperbola is the locus of the source position for the arrival time difference shown, expressed as a proportion of the maximum time difference, i.e., as the value of  $c_0\tau/s$  [from Eq. (25)]. Hydrophone spacing has been normalised to unity. These sets of curves are effectively contours of differences in level and arrival time differences.

limit, the source position becomes indeterminate as the circle and hyperbola merge with the plane intersecting  $H_1H_2$ .

Figure 6 suggests that, in general, a most effective way of locating a source would be to use the arrival time difference to determine its direction and the difference in level to determine its distance. This would be true in a uniform, non-refracting ocean and where source and receivers are far enough from boundaries that reflections are not important. The real ocean environment causes significant perturbation of the intensity of sound as it propagates, due to fluctuations in microstructure, refraction, and interference with boundary reflections, so that the precision in measuring and modeling propagation loss and thus the difference in received level is limited. This limits the precision with which the source distance can be estimated. By comparison, transmission time suffers little perturbation and allows significantly higher precision in estimating source directions, so it might be expected that greater precision in locating a source would generally be achieved using cross bearings from arrival time differences on pairs of hydrophones. The only exception might be where the source is much closer to one hydrophone than to the others, so that its direction departs substantially from the asymptotes of the hyperbolas and the solution becomes more complicated, and resolution of ambiguities more difficult. This, of course, is the region where the methods presented here are most accurate.

## II. APPLICATION

### A. Propagation effects

Estimation of source level requires a knowledge of the propagation loss from unit distance to the distance of the source, whatever method is used to determine the source distance. Estimation of the source distance using the methods of Sec. I requires the relative propagation loss to be known

between ranges  $r_1$  and  $r_2$ . Propagation in the ocean is very variable and this section discusses the conditions for which the propagation model of Eq. (1) is likely to give reliable results, and methods of checking the model with measured data.

If the signal arriving by direct path is adequately separated in time from the surface and bottom reflected arrivals to allow the direct arrival to be measured, then it is reasonable to assume that the propagation loss is by spherical spreading over the range of distances likely to be used for source level measurements. Then  $a=1$  and  $n=2$ . This would apply for short transient signals (e.g., some stridulatory sounds of fish or invertebrates, or cetacean clicks) where source-to-receiver distances are not much larger than the distances to the boundaries.

If it is not possible to separate the arrivals, significant enhancement or reduction in the signal due to interference between the arrivals may occur for very narrow-band (i.e., tonal) signals for certain values of source and receiver depths and separations. Propagation loss varies widely under these conditions, and changes significantly for small changes in the source-receiver geometry. Then no method of determining source levels will give reliable results, unless the geometry is accurately known and an accurate propagation model is available for the area. Under these conditions, the methods of Sec. I will not provide a reliable estimate of the source range. When interference is confined to direct and surface reflected paths, the resulting propagation is described by the Lloyd's Mirror Effect (Urlick, 1983). Even moderate broadening of the bandwidth will significantly reduce these effects.

Propagation loss for broader band signals is less likely to show rapid fluctuations with range due to interference effects. The methods described here can be used so long as propagation loss can be modeled by Eq. (1). For example, the semi-empirical expressions for propagation loss presented by Marsh and Schulkin (1962), based on a large number of measurements in shallow water, follow this form with  $n=2$ , for distances up to their "skip distance"  $H$ . Examples of minimum skip distances (no isothermal layer) are 1.9 km for a water depth of 10 m and 5.9 km for a depth of 100 m. These results apply for water depths of more than four wavelengths and for frequencies 100 Hz to 10 kHz. The value of  $a$  in Eq. (1) is given by their "near field anomaly"  $k_L = -10 \log_{10} a$ .

Relative propagation loss at a site can be measured using vessels as sources if their ranges are known. Fitting a straight line to a plot of received level (in the appropriate frequency band) as a function of the logarithm of distance, will provide an estimate of the value of  $n$ , the slope of the line being  $10n$  dB per decade change in distance, or  $3n$  dB per doubling of distance. In practice, measurements would need to be made over a range of distances of at least a factor of 2 if a trend in the slope is to be detectable. Running a boat directly toward or away from a hydrophone at constant speed will provide a continuous record over a wide range of distances. Only data for which the boat noise exceed the background noise by at least 8 dB should be used unless a correction for the contribution of the background noise is made, otherwise the result will underestimate the value of  $n$ . A maximum useable dis-

tance of a few kilometers should be possible under conditions of low background noise (e.g., low wind speeds, no nearby vessels). This maximum distance will decrease substantially as the background noise rises. A factor to be considered in these measurements is that propagation loss can vary significantly with time and with horizontal direction.

Estimates of source level can be used to check the relative propagation loss over the range of distances for which the estimates were obtained. This requires the source level to be constant for these estimates, so it might be useful if a ship is available as a source, but its distance is not known. The basis for this is given in Appendix A and applies to both methods 1 and 2 in Sec. I. The procedure is to plot the estimated values of source level (in decibels) as a function of the logarithm of the estimates of  $r_2$  (the distance of source from the further hydrophone), and fit a straight line to the data points. The slope of the line in decibels per decade of distance divided by 10 (or per distance doubled divided by 3) will give the difference between the assumed value of  $n$  and the true value. The slope will be positive if the true value of  $n$  is less than the assumed value. The results can then be recalculated using this measured value of  $n$ . For example, if a line fitted to the data (estimated assuming  $n=2$ ) increases by 10 dB per decade increase in distance, we would estimate the true value as  $n=1$ . In practice, it would be difficult to see a trend in the data unless the measured distances varied by more than a factor of 2. Also, the results apply only for the range of distances given by the minimum value of  $r_1$  and the maximum value of  $r_2$ . If the source level varies for these measurements, a trend with distance may be evident if there are sufficient data points over a wide enough range in values of  $r_2$ .

## B. Errors in estimation and ways of minimizing them

The accuracy of the methods depends on adequate accuracy in measuring time of arrival differences and differences in received level. In the first method (Sec. I B), the error in the estimate of the source level due to the error in measuring the arrival time difference is, from Eq. (7), for square law propagation,

$$\epsilon_{SL} = 20 \log_{10}(\hat{\tau}/\tau), \quad (26)$$

where  $\epsilon_{SL}$  is the error in the estimate of the source level (in decibels), while  $\hat{\tau}$  and  $\tau$  are the estimated and true values, respectively, of the arrival time difference. The result is fairly insensitive to errors in arrival time difference. For example, the error in the source level estimate varies from 1 to 3 dB as the error in time difference varies from 12% to 40%. The magnitudes of arrival time differences are likely to be of the order of milliseconds for many situations of interest. For example, for a hydrophone spacing of 10 m, the maximum possible arrival time difference, which occurs when the source is on the line through the hydrophones (but not between them), is about 7 ms. Adequate resolution in the measurement of arrival time differences of this magnitude would normally require that the signals from the two hydrophones are fed directly to the analysis equipment or recorded on the same tape recorder. Increasing the hydrophone separation re-

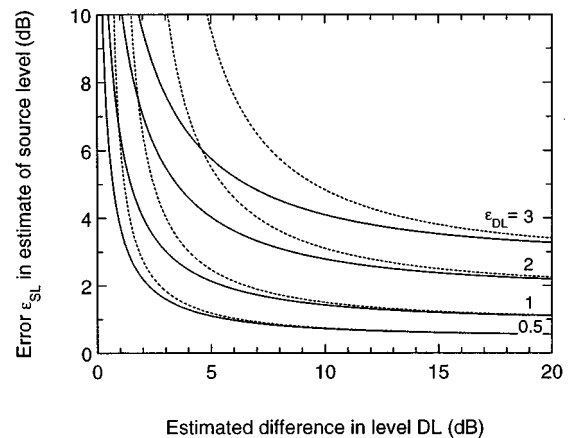


FIG. 7. Magnitude of the error in estimating the source level due to an error  $\epsilon_{DL}$  in the difference in level, for method 1 (differences in arrival times and received levels), for square law propagation [from Eq. (B3)]. Dashed lines are for positive values of  $\epsilon_{DL}$  (overestimates) and solid lines for negative values of the magnitudes shown on the curves. The sign of the error in the source level is opposite to the sign of  $\epsilon_{DL}$ .

duces the time resolution required to obtain a certain accuracy in the estimate of the source level.

The main factor determining the accuracy of the calculated source level will be the errors in estimating the received difference in level. This is evident in Fig. 6, which shows that a change in the difference in level has a much greater effect on the estimate of the source distance than a change in the arrival time difference. The errors in estimating source levels resulting from errors in measuring the differences in levels are calculated in Appendix B for square law propagation, and some examples are shown in Fig. 7 for method 1, which uses differences in both arrival times and levels (Sec. I B) and in Fig. 8 for method 2, which uses differences in level only (Sec. I C). Figures 7 and 8 can also be used to determine the errors as a function of the true difference in level DL, by using the dashed curves for negative errors and the continuous curves for positive errors [see Eqs. (B4) and (B7)]. Errors are defined to be positive if the estimated level

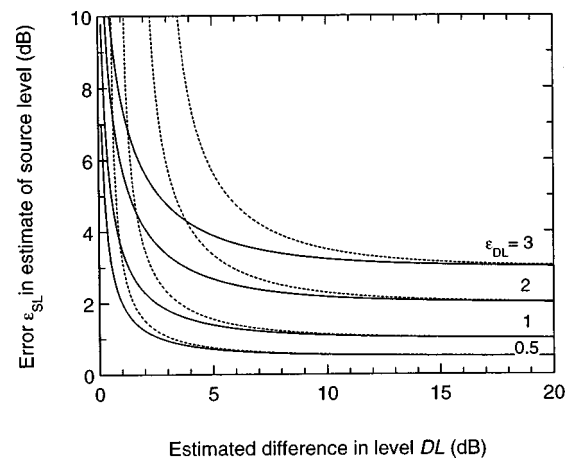


FIG. 8. Magnitude of the error in estimating the mean source level due to an error  $\epsilon_{DL}$  in the difference in level for method 2 (difference in received levels only), for square law propagation [from Eq. (B6)]. Dashed lines are for positive values of  $\epsilon_{DL}$  (overestimates) and solid lines for negative values, of the magnitudes shown on the curves. The sign of the error in the source level is opposite to the sign of  $\epsilon_{DL}$ .

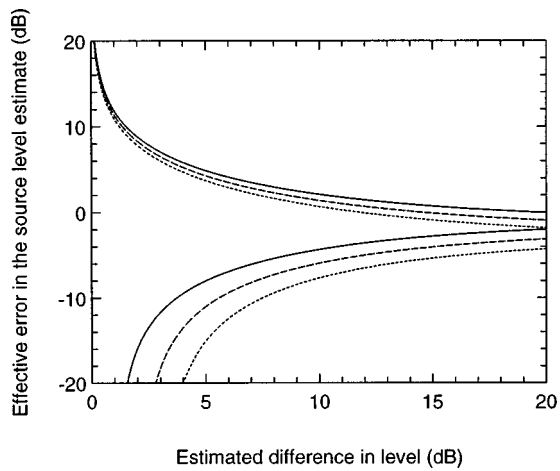


FIG. 9. Uncertainty in estimating the source level for method 2 (difference in level only), for positive errors  $\epsilon_{DL}$  in the difference in level, and for square law propagation, expressed as the error about the estimated mean source level [from Eqs. (B8) and (B9)]. Values of  $\epsilon_{DL}$  are: solid lines, 1 dB; dashed lines, 2 dB; dotted lines, 3 dB.

exceeds the true level. Thus the best estimate of the range in source level is obtained by subtracting the errors (taking account of their signs) from the estimated level.

For significant differences in level between the two hydrophones, the error in the estimate of the source level is comparable in magnitude (but opposite in sign) to the error in measuring the difference in level, and increases as the difference in level decreases. Measurements of differences in level require the sensitivity of the two hydrophones and the channel gains to be known and it is difficult to achieve this for an error of much less than 1 dB. Changing the sign of the error in the difference in level changes the sign of the error in the source level, so errors will be partially cancelled by averaging source level estimates for the source closer to one hydrophone with those for the source closer to the other (if there is little change in source level between samples). Comparison of the magnitudes of the dashed and continuous curves in Figs. 7 and 8 will show the extent to which the errors will cancel. For the larger differences in level, the errors will substantially cancel.

For method 2, which uses the difference in level only, an error in DL will affect the range of uncertainty of the estimate in source level shown in Fig. 4 as well as providing an error in the estimate of the mean source level. These two effects are combined and expressed as an effective error about the estimated mean source level in Eqs. (B8) and (B9), and shown in Figs. 9 and 10 for positive and negative errors, respectively, in DL. The effective errors should be subtracted (taking account of the sign of the errors) from the estimated source level to determine the best estimate of the range of uncertainty in the source level.

An idea of the range of distances over which the methods are likely to give acceptable results can be obtained from Fig. 6 for the value of DL corresponding to the maximum acceptable error in the source level. This value of DL is obtained from Figs. 7 or 9 and 10, as appropriate, for the maximum acceptable error in source level and the likely error in DL. For example, an error of about  $\pm 3$  dB in source

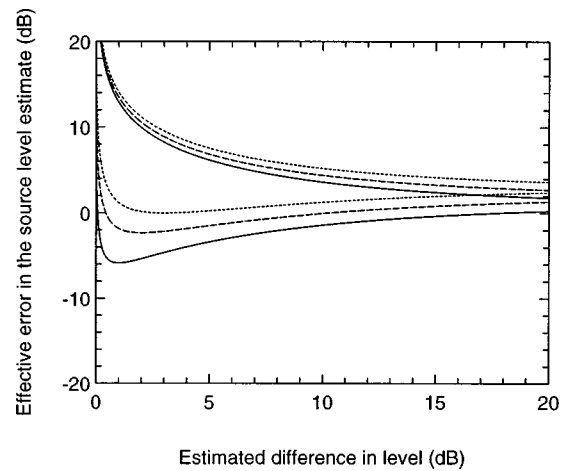


FIG. 10. Uncertainty in estimating the source level for method 2 (difference in level only), for negative errors  $\epsilon_{DL}$  in the difference in level, and for square law propagation, expressed as the error about the estimated mean source level [from Eqs. (B8) and (B9)]. Values of  $\epsilon_{DL}$  are: solid lines, 1 dB; dashed lines, 2 dB; dotted lines, 3 dB.

level estimated using method 1 (differences in arrival times and levels), corresponds to  $DL \approx 3.5$  for an error  $\epsilon_{DL} = 1$  (Fig. 7). Figure 6 shows that the maximum distance of the source from the closer hydrophone for which this accuracy is possible is about twice the hydrophone spacing when the source is on the negative  $x$  axis, and less than this elsewhere (for example, it is slightly less than the hydrophone spacing if the source is on the  $y$  axis). These distances are approximately doubled for an error in the source strength estimate of  $\pm 6$  dB. Where the estimate is made from the difference in level only (method 2), the range of distances is significantly less.

By comparison, Watkins and Schevill (1972) considered that their system of four accurately positioned hydrophones gave good estimates of source locations from arrival time differences to ranges of about ten times the array dimensions under good conditions, although usually they were confident of locations only within three or four times the array dimensions. Since they were interested in determining the source position, they may have required smaller errors in distance than would be acceptable in estimating source levels. Cummings and Holliday (1985, 1987) plotted sources up to distances of more than about four times the array base line length of 2.46 km.

The error in estimating the position of the source using Eqs. (6) and (12) will depend mainly on the error in estimating the distance  $r_1$ , which in turn will depend mainly on the error in measuring the difference in level. The error in  $r_1$  due to the error in DL is given by the ratio of estimated to true values  $\hat{r}_1/r_1 = 10^{\epsilon_{SL}/20}$  [Eq. (B5)].

Figures 4 and 7–10 show that accuracy improves as the value of DL, and thus the value of  $k$ , increases. Increasing the value of  $\tau$  also improves accuracy, because, for a fixed error in measuring  $\tau$ , the resolution will be improved [ $\hat{\tau}/\tau$  in Eq. (26) will be reduced]. From Eq. (16),

$$k^2 = (s/r_1^2)(s - 2x) + 1$$

so that  $k$  can be increased by increasing  $s$  or reducing  $r_1$ . For fixed values of  $s$  and  $r_1$ ,  $k$  is maximum when  $s - 2x$  is maxi-

imum, i.e., when  $x$  takes the largest negative value such that  $r_1 = \sqrt{x^2 + y^2}$  is constant, which occurs when  $y = 0$ . From Eq. (6),  $\tau$  increases as  $k$  increases for a fixed value of  $r_1$ , so that  $\tau$  also increases as  $s$  increases or as  $y \rightarrow 0$ . These effects can be seen in Fig. 6. For a fixed value of  $r_1$ , the source lies on the circumference of a circle centered on  $H_1$ . Moving around the circumference towards the  $x$  axis for negative values of  $x$  increases the values of DL and  $c_0\tau/s$ . Also, for any point in Fig. 6,  $\tau$  increases as  $s$  increases. Thus accuracy will generally be improved by increasing  $s$ , reducing  $r_1$ , and aligning the hydrophones so that the source is near the negative  $x$  axis. As the source approaches the axis, the circle of ambiguity in source position in Fig. 2 collapses to a point.

The implications of the above for the experimental design can be summarized as follows. In general, accuracy will improve as the hydrophone spacing increases. The limitations will be logistic ones and ensuring that there is adequate signal-to-noise ratio for the signal received on the hydrophone further from the source. If some idea of the source position is already known, the line of the hydrophones should point in the direction of the source, with the closer hydrophone placed as close as possible to the source. Both hydrophones should be on the same side of the source. As the source approaches the line through the hydrophones, the ambiguity in the estimate of its position decreases. Variation of the positions of the hydrophones (and the direction of the line through the hydrophones) will provide some variation in the relative received levels so that the results with the largest differences in level and thus smallest errors can be used to calculate the source level. Careful calibration of the receiving systems to minimize the error in the relative sensitivities will significantly improve accuracy (see Figs. 7 and 8).

In applying this to the use of direct and surface reflected arrivals on a single hydrophone (method 3, Sec. I D), note that for a particular geometry of Fig. 5, interchanging the source and receiver positions does not change the values of  $r_1$ ,  $r_2$ , or, therefore, DL or  $\tau$ , so that errors are also unchanged. From Eq. (23),

$$k^2 = 1 + 2d_s(\cos \theta + d_s/r_1)/r_1, \quad (27)$$

so that the value of  $k$ , and thus of DL, increases as the value of  $\theta$  increases or the value of  $r_1$  decreases. The value of  $\theta$  is maximum when the source and receiver are at the same depth, but the main factor affecting the accuracy is the value of  $r_1$ . Thus accuracy will be improved by reducing the distance between source and receiver. This also has the advantage of increasing the time difference between the direct and surface reflected arrivals, improving their separation. Using Eq. (27) and Fig. 7, it can be shown that acceptable accuracy requires the distance between source and receiver to be less than about three times the source depth.

Using the direct and surface reflected arrivals on the same hydrophone avoids the error of relative sensitivities between two hydrophones, so that this method is intrinsically more accurate (at frequencies where surface scattering loss is low), although more limited under the range of conditions under which it can be used.

When there are many sources distributed over some area, as is often the case with fish and invertebrates, the

relative distances from the hydrophones will vary significantly from source to source and so will the differences in level. It will then be a matter of choosing the received signals that satisfy conditions of low errors.

Differences in level can be measured with two separated systems, for example on different boats, as a means of improving the flexibility of the measurement procedure and obtaining a wider hydrophone separation. Arrival time differences measured between signals recorded on separate systems will generally not be useful unless the timing of the two systems can be coordinated to a precision of the order of milliseconds, or tenths of milliseconds. Such precision would not normally be feasible, so that estimates of source level using separate recording systems would normally be limited to methods using differences in level only (method 2, Sec. I C). Sonobuoys, however, can be used to provide widely separated hydrophones while still retaining accurate measurements of time of arrival differences at the point of reception of the radio transmissions (Cummings and Holliday, 1985).

The signal received on a hydrophone is the sum of the signal from the source and the background noise. If the received level of the signal plus noise is at least 10 dB above the background noise level, then ignoring the contribution of the background noise will result in a tolerable error of less than 0.5 dB. If the level of the signal plus noise exceeds the noise level by less than 10 dB, a correction should be made by converting levels to intensities and subtracting the noise intensity from the intensity of the received signal plus noise, and converting the resulting signal intensity to received signal level.

In any measurements of the type described here, the most effective way of checking the accuracy and verifying the results is by calibrating the system and the procedures *in situ*, using a known source at a known position relative to the hydrophones.

### III. SUMMARY

This paper describes methods of estimating source levels of marine animal sounds that are simple to execute logistically. Equation (8) gives the source level in terms of the measured differences in levels and arrival times on two hydrophones (method 1) for square law dependent propagation, and requires no knowledge of the positions of the hydrophones. The results can be applied to other propagation conditions using Eq. (7), if the propagation can be modeled by Eq. (1). The error in the source level estimate due to the error in the difference in level is given in Fig. 7. With well calibrated systems, it should be possible to obtain reasonably accurate results at distances of the source from the closer hydrophone up to about twice the hydrophone separation. The accuracy decreases with increasing distance although useful results may be possible for distances up to about four times the separation. The exception is where the source approaches the plane bisecting at right angles the line between the hydrophones, where the differences in levels and arrival times approach zero and the errors increase rapidly, the result becoming indeterminate when the source is on this plane.

The location of the source can be determined (with ambiguity) if the positions of the hydrophones are known. Equations (6) and (12) give the distance to the source from the closer hydrophone and the angle of the source from the line through the hydrophones, respectively, with the usual left–right ambiguity that arises from arrival time differences on a linear array. Figure 2 shows diagrammatically the locus of the source position in three dimensions.

If arrival time differences cannot be measured accurately, then the source level can be estimated using only the received difference in level, if the hydrophone spacing is known [method 2, Eqs. (21) or (22)]. This method is less accurate and there is an uncertainty in the estimate given by Fig. 4. This uncertainty and the errors due to the errors in the difference in level are combined to provide an effective error in Figs. 9 and 10.

If the direct and surface reflected arrivals can be separated, the above results can be determined using the differences in levels and times of the direct and surface reflected arrivals to a single hydrophone (method 3). The effective hydrophone spacing is twice the hydrophone depth, which need not be known to determine the source level. If the depth is known, the depth of the source and the angle to the vertical of the source from the hydrophone can be determined. This method is intrinsically more accurate than the others but more limited in the range of conditions for which it can be used.

In general, accuracy improves as the received difference in level increases, so that better accuracy results from increasing the hydrophone spacing and decreasing the distance of the closer hydrophone from the source. Accuracy also improves by pointing the line through the hydrophones in the direction of the source.

Some insight into the methods is given by Fig. 6 which shows the locus of the source position in the plane containing the source and receivers for various arrival time differences (the hyperbolas) and for various differences in level (the circles). The arrival time difference gives the source direction but no indication of its distance. The difference in level gives the relative source distance but no indication of its direction. The precision of these methods in locating a source is limited by the significant limitations in the precision of measuring and modeling the difference in level, due to the perturbations by the ocean environment in the intensity of a propagating signal. Because travel time is far less perturbed by the environment, greater precision is generally to be expected in locating a source using cross bearings from arrival time differences on accurately placed arrays of hydrophones, except perhaps where the source is much closer to one hydrophone than to the others, where the above methods are likely to be more accurate. Such systems are more complex than those required for the methods described here.

## ACKNOWLEDGMENTS

Thanks are due to Mike Bell for useful comments on the manuscript and to Rob McCauley for trying out method 3 on a single hydrophone in the measurement of source levels of

fish sounds. Thanks are also due to Dr. W. C. Cummings for many useful comments on the revised version of the manuscript.

## APPENDIX A: USING SOURCE LEVEL ESTIMATES TO CHECK THE PROPAGATION MODEL

The following shows that if the value of  $n$  in Eq. (1) is incorrect, the estimates of source level will vary as a function of the estimated distance of measurement, if the actual source level is constant. This can be inverted to estimate the correct value of  $n$ . The result is more accurate if  $r_2$ , the distance of the source from the further hydrophone, is used in preference to  $r_1$ .

From Eq. (2), an estimate of source level from the received intensity  $I_2$  at  $r_2$  is

$$\hat{S}L = 10 \log_{10}(\hat{a}\hat{r}_2^m I_2) = 10 \log_{10}\{\hat{a}\hat{r}_2^m I_0 / (ar_2^n)\}, \quad (\text{A1})$$

where  $\hat{a}$ ,  $\hat{r}_2$  are estimated values and  $a$ ,  $r_2$  true values, respectively, and  $m$  is the assumed value of  $n$ . For the first method, from Eq. (6),  $r_2 = c_0 \tau k_n / (k_n - 1)$ , where  $k_n = 10^{\text{DL}/10n}$ . Dividing by a similar expression for  $\hat{r}_2$ , in which  $m$  and  $k_m$  replace  $n$  and  $k_n$ , gives

$$r_2 = \frac{1 - k_m^{-1}}{1 - k_n^{-1}} \hat{r}_2. \quad (\text{A2})$$

Substituting in Eq. (A1) and rearranging gives

$$\hat{S}L = 10 \log_{10}(\hat{a}I_0/a) + 10(m-n)\log_{10}\hat{r}_2 - 10n \log_{10}\{(1 - k_m^{-1})/(1 - k_n^{-1})\}. \quad (\text{A3})$$

The first term of Eq. (A3) is constant. Evaluation of the third term shows that it varies by less than 2.4 dB as DL varies from 5 to 20 dB, for any particular value of  $n$  between 1 and 3, and  $m=2$ . Since this covers most of the likely range of  $n$ , the third term can be considered to be approximately constant. Then Eq. (A3) can be written

$$\hat{S}L \cong \text{constant} + 10(m-n)\log_{10}\hat{r}_2. \quad (\text{A4})$$

Thus a plot of  $\hat{S}L$  as a function of  $\log \hat{r}_2$  should show a tendency for the data points to cluster about a straight line with a slope of  $10(m-n)$ . Fitting a straight line to the data will thus provide an estimate of  $m-n$ , leading to an estimate of  $n$ .

For the second method, from Eq. (20),

$$r_2 = k_n s / \sqrt{k_n^2 - 1}. \quad (\text{A5})$$

Dividing by a similar expression for  $\hat{r}_2$  gives

$$r_2 = \frac{k_n \sqrt{k_m^2 - 1}}{k_m \sqrt{k_n^2 - 1}} \hat{r}_2. \quad (\text{A6})$$

Substituting in Eq. (A1) and rearranging gives

$$\hat{S}L = 10 \log_{10}(\hat{a}I_0/a) + 10(m-n)\log_{10}\hat{r}_2 - 5n \log_{10}\{(1 - k_m^{-2})/(1 - k_n^{-2})\}. \quad (\text{A7})$$

As above, the first term of Eq. (A7) is constant, and evaluation of the third term shows that it varies by less than 1.4 dB as DL varies from 5 to 20 dB, for any particular value of  $n$

between 1 and 3, and  $m=2$ . Thus Eq. (A4) and the dependence of  $\hat{S}L$  on  $\log \hat{r}_2$  also applies to this method.

## APPENDIX B: CALCULATION OF THE ERRORS IN ESTIMATING SOURCE LEVELS DUE TO THE ERRORS IN DIFFERENCES IN LEVEL

### 1. Method 1 using differences in both arrival times and levels (Sec. 1 B)

From Eq. (7), for square law propagation, the error  $\epsilon_{SL}$  (in decibels) in the estimate of the source level due to the error in the estimate of the difference in level only, is

$$\epsilon_{SL} = 20 \log_{10}\{(k-1)/(\hat{k}-1)\}, \quad (B1)$$

where  $\hat{k}$  and  $k$  are the estimated and true values, respectively, of  $k$ . From this we obtain

$$\epsilon_{SL} = 20 \log_{10}\{(k/\hat{k}-\hat{k}^{-1})/(1-\hat{k}^{-1})\}, \quad (B2)$$

$$= 20 \log_{10}\{(10^{-\epsilon_{DL}/20} - 10^{-\hat{DL}/20})/(1 - 10^{-\hat{DL}/20})\}, \quad (B3)$$

where  $\epsilon_{DL} = 20 \log_{10} \hat{k} - 20 \log_{10} k$  is the error in estimating the difference in level (in decibels), and  $\hat{DL}$  is the estimate of DL. Note that the sign of the error in the source level estimate is opposite to that of the error in the estimate of the difference in level. Figure 7 is a plot of Eq. (B3). By substituting  $DL + \epsilon_{DL}$  for  $\hat{DL}$ , this result can also be expressed in terms of the true difference in level DL:

$$\epsilon_{SL} = -20 \log_{10}\{(10^{\epsilon_{DL}/20} - 10^{-DL/20})/(1 - 10^{-DL/20})\}, \quad (B4)$$

which is of the same form as Eq. (B3) with a change of sign.

Using the above procedure with Eq. (6) provides the error in estimating the source distance  $r_1$  due to the error in DL. The result [with reference to Eqs. (B2) and (B3)] is

$$\hat{r}_1/r_1 = (k/\hat{k}-\hat{k}^{-1})/(1-\hat{k}^{-1}) = 10^{\epsilon_{SL}/20}, \quad (B5)$$

where  $\hat{r}_1$  and  $r_1$  are the estimated and true values, respectively, of  $r_1$ .

### 2. Method 2, using differences in levels only (Sec. 1 C)

From Eq. (21) for square law propagation, the error in the mean source level estimate is

$$\epsilon_{SL} = 10 \log_{10}\{(k^2-1)/(\hat{k}^2-1)\}, \\ = 10 \log_{10}\{(10^{-\epsilon_{DL}/10} - 10^{-\hat{DL}/10})/(1 - 10^{-\hat{DL}/10})\}, \quad (B6)$$

using the same procedure as in obtaining Eqs. (B2) and (B3). Again the signs of the error in the source level and the error in the difference in level are opposite. Figure 8 is a plot of Eq. (B6). Equation (B6) can also be expressed in terms of the true difference in level DL:

$$\epsilon_{SL} = -10 \log_{10}\{(10^{\epsilon_{DL}/10} - 10^{-DL/10})/(1 - 10^{-DL/10})\}. \quad (B7)$$

An error in DL also affects the range of uncertainty in the source level estimate of Eqs. (21) and (22). The upper limit in the range of uncertainty of the source level is, from Eqs. (2) and (18),

$$SL_{\max} = 10 \log_{10}\{I_1 a s^2 / (k-1)^2\} \\ = 10 \log_{10}\{I_1 a s^2 / (10^{(\hat{DL}-\epsilon_{DL})/20} - 1)^2\}.$$

Similarly, from Eqs. (2) and (17), the lower limit is

$$SL_{\min} = 10 \log_{10}\{I_1 a s^2 / (10^{(\hat{DL}-\epsilon_{DL})/20} + 1)^2\}.$$

The differences between these values and the estimated mean source level of Eq. (22) are

$$\hat{S}L - SL_{\min} = 10 \log_{10}\{(10^{(\hat{DL}-\epsilon_{DL})/20} + 1)^2 / (10^{\hat{DL}/10} - 1)\} \quad (B8)$$

and

$$\hat{S}L - SL_{\max} = 10 \log_{10}\{(10^{(\hat{DL}-\epsilon_{DL})/20} - 1)^2 / (10^{\hat{DL}/10} - 1)\}, \quad (B9)$$

where  $\hat{S}L$  is the estimated value of the mean source level [Eq. (22)]. Equations (B8) and (B9) may be considered to be the effective errors  $\epsilon_{SL}$  about the mean in estimating the source level, incorporating both the range of uncertainty and the effect of errors in estimating the difference in level. Figure 9 is a plot of Eq. (B8) and Fig. 10 a plot of Eq. (B9) for various values of  $\epsilon_{DL}$ .

- Cato, D. H. (1980). "Some unusual sounds of apparent biological origin responsible for sustained background noise in the Timor Sea," J. Acoust. Soc. Am. **68**, 1056-1060.
- Clark, W. C. (1980). "A real-time direction finding device for determining the bearing to the underwater sounds of Southern Right Whales, *Eubalaena australis*," J. Acoust. Soc. Am. **68**, 508-511.
- Clark, D. S., Flattery, J., Gisiner, R., Schilling, J., Sledzinski, T., and Trueblood, R. (1994). "MMATS: Acoustic localization of whales in real time over large areas," J. Acoust. Soc. Am. **96**, 3250(A).
- Cummings, W. C. (1968). "Requirements of a method for locating underwater bio-acoustic sources," Technical Note NUWC TN 150, Naval Undersea Warfare Center (now SPAWARSCEN), San Diego (unpublished).
- Cummings, W. C., and Holliday, D. V. (1985). "Passive acoustic location of bowhead whales in a population census off Point Barrow, Alaska," J. Acoust. Soc. Am. **78**, 1163-1169.
- Cummings, W. C., and Holliday, D. V. (1987). "Sound and source levels from bowhead whales off Point Barrow, Alaska," J. Acoust. Soc. Am. **82**, 814-821.
- Cummings, W. C., Brahy, B. D., and Herrkind, W. F. (1964). "The occurrence of underwater sounds of biological origin off the west coast of Bimini, Bahamas," in *Marine BioAcoustics*, edited by W. N. Tavolga (Pergamon, New York), pp. 27-43.
- Cummings, W. C., and Thompson, P. O. (1994). "Characteristics and seasons of blue and finback whales along the U.S. west coast as recorded at SOSUS stations," J. Acoust. Soc. Am. **95**, 2853(A).
- Cummings, W. C., Thompson, P. O., and Cook, R. (1968). "Underwater sounds of migrating gray whales, *Eschrichtius glaucus* (Cope)," J. Acoust. Soc. Am. **44**, 1278-1282.
- Freitag, L. E., and Tyack, P. L. (1993). "Passive acoustic localization of the Atlantic bottlenose dolphin using whistles and echo location clicks," J. Acoust. Soc. Am. **93**, 2197-2205.
- Marsh, H. W., and Schulkin, M. (1962). "Shallow water transmission," J. Acoust. Soc. Am. **34**, 863-864 (also reported in Urick, 1983, pp. 177-179).
- Richardson, W. J., Greene, Jr., C. R., Malme, C. I., and Thomson, D. H. (1995). *Marine Mammals and Noise* (Academic, San Diego).
- Stafford, K. M., Fox, C. G., and Mate, B. R. (1994). "Acoustic detection and location of blue whales (*Balaenoptera musculus*) from SOSUS data by matched filtering," J. Acoust. Soc. Am. **96**, 3250(A).
- Tyack, P. (1981). "Interactions between singing Hawaiian humpback whales and conspecifics nearby," Behav. Ecol. Sociobiol. **8**, 105-116.
- Urick, R. J. (1983). *Principles of Underwater Sound* (McGraw-Hill, New York), pp. 131-133.

- Walker, R. A. (1963). "Some intense, low-frequency, underwater sounds of wide geographic distribution, apparently of biological origin," J. Acoust. Soc. Am. **35**, 1816–1824.
- Watkins, W. A., and Schevill, W. E. (1972). "Sound source location by arrival-times on a non-rigid three-dimensional hydrophone array," Deep-Sea Res. **19**, 691–706.
- Watkins, W. A., Tyack, P., and Moore, K. E. (1987). "The 20-Hz signals of finback whales (*Balaenoptera physalus*)," J. Acoust. Soc. Am. **82**, 1901–1912.
- Winn, H. E., and Winn, L. K. (1978). "The song of the humpback whale *Megaptera novaeangliae* in the West Indies," Mar. Biol. **47**, 97–114.

# Characterizing the graded structure of false killer whale (*Pseudorca crassidens*) vocalizations

Scott O. Murray<sup>a)</sup>

Center for Neuroscience, University of California, Davis, Davis, California 95616

Eduardo Mercado and Herbert L. Roitblat

Department of Psychology, 2430 Campus Road, University of Hawaii, Honolulu, Hawaii 96822

(Received 30 October 1997; revised 30 April 1998; accepted 5 June 1998)

The vocalizations from two, captive false killer whales (*Pseudorca crassidens*) were analyzed. The structure of the vocalizations was best modeled as lying along a continuum with trains of discrete, exponentially damped sinusoidal pulses at one end and continuous sinusoidal signals at the other end. Pulse trains were graded as a function of the interval between pulses where the minimum interval between pulses could be zero milliseconds. The transition from a pulse train with no inter-pulse interval to a whistle could be modeled by gradations in the degree of damping. There were many examples of vocalizations that were gradually modulated from pulse trains to whistles. There were also vocalizations that showed rapid shifts in signal type—for example, switching immediately from a whistle to a pulse train. These data have implications when considering both the possible function(s) of the vocalizations and the potential sound production mechanism(s). A short-time duty cycle measure was developed to characterize the graded structure of the vocalizations. A random sample of 500 vocalizations was characterized by combining the duty cycle measure with peak frequency measurements. The analysis method proved to be an effective metric for describing the graded structure of false killer whale vocalizations. © 1998 Acoustical Society of America. [S0001-4966(98)03609-1]

PACS numbers: 43.80.Ka [FD]

## INTRODUCTION

One of the most remarkable characteristics of dolphin (*Delphinidae*) behavior is the diversity and apparent complexity of their vocalizations. Most descriptions of dolphin vocalizations have used aural analysis and/or visual analysis of spectrograms (e.g., Caldwell and Caldwell, 1968; Dahlheim and Awbrey, 1982; Evans and Prescott, 1962; Ford, 1989; Herzing, 1996; Kaznadzei *et al.*, 1976; Lilly and Miller, 1961; McCowan and Reiss, 1995; Sjare and Smith, 1986; Tyack, 1986). As a result of such studies, dolphin vocalizations have been classified traditionally into three distinct signal types: (1) click trains; (2) burst-pulse sounds; and (3) whistles. Click trains and burst-pulse sounds are collapsed sometimes into a single category: pulsed sounds/pulse trains (e.g., Herman and Tavolga, 1980).

Click trains are comprised of a sequence of brief acoustical pulses spaced over time. The pulses can be described as exponentially damped sine waves and range in duration from approximately 40  $\mu$ s in bottlenosed dolphins (Au, 1993) to over 10 ms in killer whales (Steiner *et al.*, 1979). Because their durations are short, pulses have a wide frequency bandwidth, making them sound clicklike. Their peak frequencies can vary tremendously, from 5 kHz (Steiner *et al.*, 1979) to over 150 kHz in some species (Au, 1993). The repetition rate of pulses within a click train range from a pulse every 1–2 s to hundreds of pulses per second (Ford and Fisher, 1978; Dawson, 1991); pulse rate can also change over the course of

a “train.” Click trains can contain a few to hundreds of clicks.

When the interval between pulses in a pulse train is sufficiently brief (around 5 ms or less), human perception can no longer separate the pulses in time and the vocalization is perceived as a continuous tonal sound. Although such pulse trains may be structurally identical to click trains, to the human ear they sound very different and are given a different name: burst-pulse sounds, which sound subjectively like screams, squeals, or moans (Caldwell and Caldwell, 1967; Dahlheim and Awbrey, 1982; Dawson and Thorpe, 1990; Schevill and Watkins, 1966). The peak frequencies of burst-pulse sounds vary between species. For example, killer whales produce burst-pulse sounds with peak frequencies below 20 kHz (Ford, 1989). Hector’s dolphins (Dawson and Thorpe, 1990) and Commerson’s dolphins (Evans *et al.*, 1988), however, produce burst-pulsed sounds with peak frequencies above 100 kHz. Burst-pulse sounds range in duration from tens of milliseconds to several seconds (Ford, 1989; Overstrom, 1983). Finally, whistles are narrow-band, tonal sounds that are usually frequency modulated. Most species of dolphins produce whistles between 5 and 20 kHz with ranges in duration similar to burst-pulse sounds (Caldwell *et al.*, 1990; Richardson *et al.*, 1996). While all dolphin species produce pulsed sounds, some species may not produce whistles (Herman and Tavolga, 1980).

### A. Traditional analysis

Determining the *type* of vocalization (e.g., whistle, burst-pulse, click train) has often been the first step in past analyses of dolphin vocalizations. As previously mentioned,

<sup>a)</sup>Electronic mail: smurray@braindev.uoregon.edu



most characterizations of dolphin vocalizations have been based on aural impressions and visual inspections of spectrograms. Through aural analysis, labels such as “whistles,” “squawks,” “screams,” “clicks,” etc. are derived. Signals may be reliably classified by individual researchers using such labels, but such classifications are highly subjective and generalize poorly across researchers. Additionally, these categories are highly dependent upon the perceptual capabilities of humans. We may be incapable of distinguishing or recognizing subtle differences in the underlying acoustic structure and, consequently may be forming categories that are irrelevant for dolphins.

Researchers have also analyzed spectrographic representations of dolphin vocalizations in attempts to describe their structure. These analyses have relied on the notion that different signal types yield visually discriminable spectrograms. For example, because clicks are short, broadband signals, click trains are represented on a spectrogram by a series of vertical lines with intervals between lines corresponding to the intervals between clicks. A whistle, on the other hand, appears as one or more horizontal lines with the bottom line usually representing the fundamental frequency of the signal and lines above it representing harmonics.

Forming categories based on visual inspection of spectrograms can be problematic. The determination of whether one whistle or burst-pulse sound looks different from another is highly subjective and thus may generalize poorly between investigators. Additionally, spectrograms are subject to a time versus frequency resolution tradeoff. A gain in time resolution results in a loss in frequency resolution, and vice versa. Therefore, the choice of the analysis bandwidth can dramatically affect the visual representation of the signal. It is possible to arrive at similar looking spectrograms through quite different underlying waveforms. For example, what may appear to look like a whistle (a line on a spectrogram with many harmonics) can be created by pulsing a signal faster than can be resolved by the analysis window of a spectrogram (Davis, 1964; Watkins, 1967). Simply decreasing the size of the analysis window will resolve the pulsed signal into what appears to be a click train. In other words, with one signal and two window sizes, you can arrive at two very different looking spectrograms.

## B. Graded signals

The traditional model for classifying dolphin vocalizations assumes that their repertoires consist of acoustically discrete signal types (e.g., whistles, burst-pulse sounds, and click trains). However, click trains and whistles may be at opposite ends of a continuum (with burst-pulse sounds being intermediate). This continuum may have been previously unrecognized because subjective analyses and single window size spectral analyses have been the norm.

Determining whether the structure of dolphin vocalizations lie along a continuum or occupy discrete categories is important when considering the potential function(s) of the signals. For example, if the structure is graded, with no clear acoustic demarcations, some function(s) of the signals may not be discrete. One possible function of a graded structure may be to communicate arousal level or behavioral state. If,

however, the acoustic structure of the signals is comprised of discrete categories, it would suggest that the various signal types may serve unique functions.

The existence of a graded acoustic structure would also have implications for possible sound producing mechanisms. One of the questions regarding dolphin vocalizations<sup>1</sup> is the mechanism(s) responsible for producing sound. Many theories have been suggested; the two most commonly suggested sources being the larynx (e.g., Purves and Pilleri, 1983) and the nasal sac system (e.g., Cranford *et al.*, 1996). It is sometimes assumed that there is a generator for echolocation pulses and a separate site for whistles (e.g., Evans and Prescott, 1962). This assumption is partly due to the fact that whistles and clicks are regularly produced simultaneously, suggesting that there are two distinct mechanisms. If the vocal structure is shown to be graded, however, another possibility may be that the same mechanism produces both pulsed sounds and whistle-like vocalizations. The occurrence of simultaneous clicks and whistles could be the result of twin mechanisms each capable of producing whistles and clicks as well as all gradations in between.

## C. Study goals

False killer whales (*Pseudorca crassidens*) are an extremely vocal delphinid species and have a diverse repertoire. They produce sounds that meet the “traditional” categories described above (clicks, burst-pulse, and whistles) as well as many other sounds that appear to be “intermediate” between categories (e.g., have both pulsed and continuous-wave characteristics). This diversity provides a unique opportunity to analyze the acoustic similarities between what have traditionally been considered distinct categories.

The determination of whether the structure of false killer whale vocalizations is graded or consists of discrete categories should be based on acoustic structure and not on human perception, which may introduce arbitrary groupings. Given the difficulties in describing signal type (e.g., pulsed versus continuous) through traditional methods such as aural analysis or visual inspection of spectrograms, this study developed an alternative measure of signal type based on a short-time duty cycle calculation. The advantage to this new technique was that it eliminated human judgment and subjected all vocalizations to the same measure. The signal type measure was combined with peak frequency measurements. Each vocalization, consequently, was characterized by simultaneous changes in signal type and peak frequency.

## I. DATA COLLECTION

Recordings were made of two false killer whales, one male and one female, located at Sea Life Park, Oahu. They were approximately 3 years old when captured and approximately 9 years old when the recordings were made. At the time of recording, the male was 3.9 m and weighed approximately 600 kilograms and the female was 3.7 m and weighed about 450 kilograms. The two animals had been housed together since capture.

Recordings were made by moving each animal to a distant portion of its tank. The other animal remained behind a

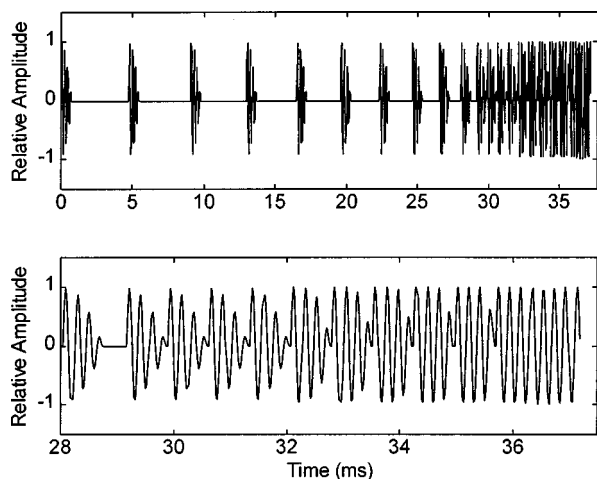


FIG. 1. A simulated signal representing the graded structure of the vocalizations. The bottom panel is a close-up view between 28 and 37 ms. From 0 to 29 ms, the signal is comprised of discrete, exponentially damped pulses and the inter-pulse interval is gradually reduced to 0.0 ms. From 29 ms to 36 ms the damping function is gradually reduced until a continuous sinusoid remains.

gate in another portion of the tank. The minimum distance between the animal being recorded and the other animal behind the gate was approximately 30 m. The trainer turned the animal on its back in order to get the melon (forehead region of the animal from which it is believed sound emanates) underwater and positioned the animal so that its head was about 1–2 m away from the hydrophone. Because the amplitude of the signals was higher in this upside down position, this procedure ensured very high signal-to-noise ratios as well as confidence concerning the identity of the animal making the sounds.

All sounds were recorded with a Sony Digital Audio Tape-recorder (DAT), TCD-D8, which uses a sampling rate of 44.1 kHz, for a frequency bandwidth to 22 kHz. A custom built hydrophone (W. Au) with a sensitivity of  $-185$  dB and a bandwidth to 200 kHz was used for all recordings. Using a quasi-random procedure, 500 vocalizations were chosen for analysis and digitized onto a PC computer using a Sound-Blaster 32 sound card.

*Pseudorca* produce ultrasonic vocalizations (Au *et al.*, 1995; Kamminga and van Velden, 1987; Thomas *et al.*, 1988). To test whether higher-frequency signals were missed due to the relatively low bandwidth of the DAT recorder, broader band recordings were made using a RACAL reel-to-reel recorder at a tape speed of 30-in.-per-second, resulting in a bandwidth of 170 kHz. One additional recording session was made with this equipment.

## II. GRADED MODEL

Through visual inspection of the waveforms, the following model was developed to describe how the structure of the vocalizations is graded. Clicks and burst-pulse vocalizations can be modeled as exponentially damped, brief sinusoidal pulses spaced over time. Figure 1 shows a computer generated signal that is comprised of exponentially damped, 5-kHz pulses. The figure begins arbitrarily with 5 ms between each pulse. The time interval between each pulse is reduced

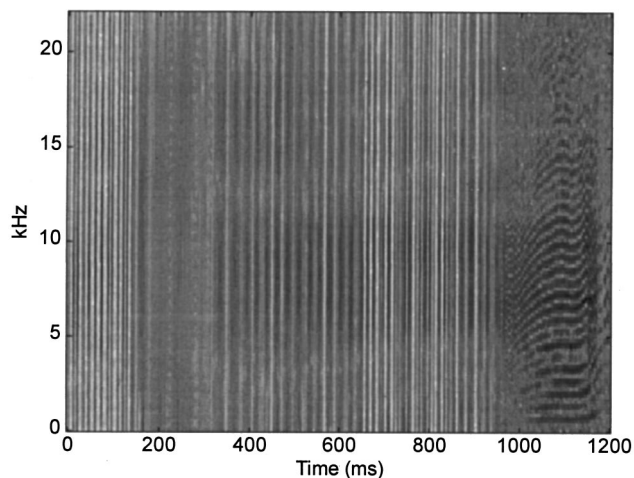


FIG. 2. The 256-point spectrogram of example 1 showing a vocalization grade from a click train to a burst-pulse sound. The horizontal banding between 1000 and 1200 ms is characteristic of rapidly pulsed signals.

gradually until there is no interval between the pulses (see Fig. 1, bottom panel). The signal is graded as a function of time between pulses, where the minimum interval between pulses is zero milliseconds. At an interval of zero milliseconds, the signal is pulsed in that it consists of damped sinusoids that regularly oscillate. It is continuous in that there is no interval in the vocalization without energy. From there, the signal grades into a “whistle” (i.e., continuous sinusoid) as a function of the degree of damping on the sinusoid, eventually reaching a continuous, nondamped sinusoid.

Visual examination of the waveforms of the false killer whale vocalizations revealed that there were vocalizations that represent each stage of the model. Moreover, some vocalizations gradually modulated through each stage of the model. Examples of such vocalizations are described below.

### A. Example 1

The 256 point spectrogram of the first example is shown in Fig. 2. This example demonstrates the grading that occurs from pulses that are spaced apart to pulses that have no inter-pulse interval. This vocalization covers the traditional categories of click trains and burst-pulse sounds. The beginning of the vocalization is characterized by pulses with a maximum inter-pulse interval of 12 ms. The intervals gradually reduce in length. At 900 ms into the vocalization the pulses are approximately 5 ms apart. At 1000 ms they are about 2 ms apart and at 1100 ms there is no inter-pulse interval (see Fig. 3). The aural and spectrographic appearance of the vocalization changes dramatically from the beginning to the end. However, the only change in the waveform is the time between each pulse.

### B. Example 2

This example of a pulse train (Fig. 4) demonstrates how the degree of damping changes on the pulses as they begin to approximate a sine wave. The waveform at 420 ms shows that the vocalization has approximately 2 ms between each pulse. At 1330 ms there is no interval between the pulses and at 1460 ms the damping function reduces and the waveform

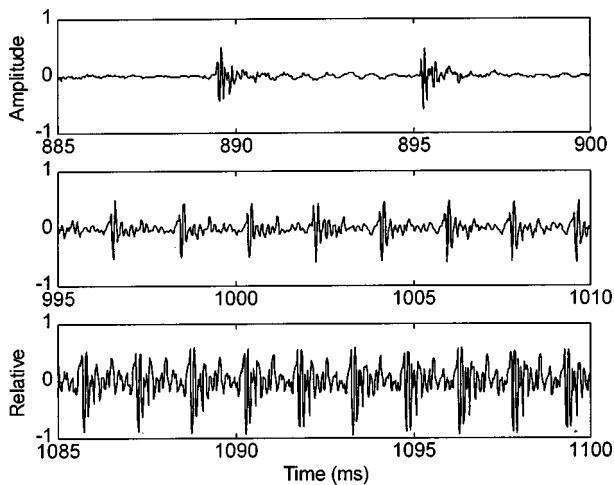


FIG. 3. Close-ups of the waveform of example 1 at three different locations in the vocalization. The three panels show the inter-pulse interval gradually reduce from approximately 5 ms in the top panel to 0.0 ms in the bottom panel.

begins to approximate a sinusoid. This vocalization resembles the model (Fig. 1) between 28 ms and 35 ms.

### C. Example 3

The final example is a vocalization that appears aurally and spectrographically to be a whistle (see Fig. 5, top panel). In general, the spectrograms of false killer whale whistles look similar to whistles produced by other odontocete species (e.g., Herzing, 1996; Sjare and Smith, 1986; Sayigh *et al.*, 1990; Tyack, 1986). The peak frequency of the vocalization ascends from approximately 4 kHz to 7 kHz. The 128 point spectrogram shows a relatively narrow-band signal. A close examination of the waveform (Fig. 5, bottom panel) of the whistle, however, reveals that it has pulsed components. Between 8 and 16 ms the whistle is comprised of a series of

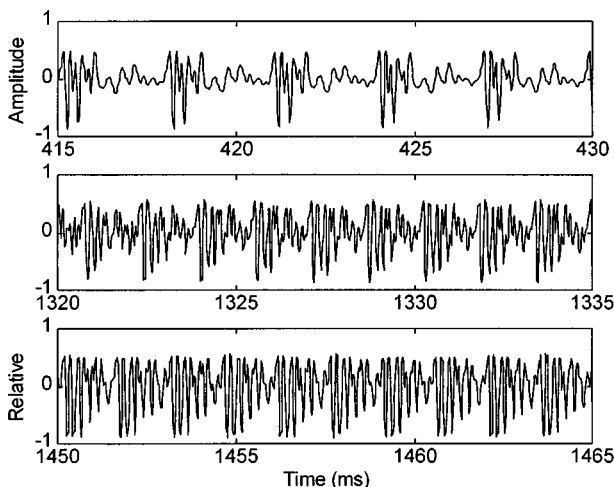


FIG. 4. The waveform of example 2 at three different locations. The top panel shows discrete pulses with an inter-pulse interval of approximately 3 ms. In the middle panel the inter-pulse interval is 0.0 ms. The damping reduces in the bottom panel and the signal is beginning to approximate a continuous sinusoid.

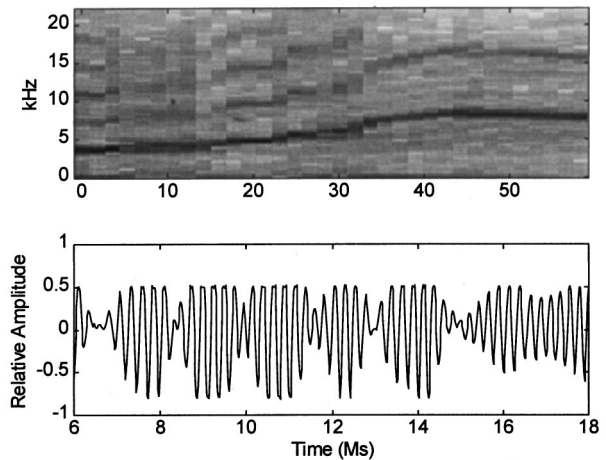


FIG. 5. The 128-point spectrogram (top panel) and a close-up of the waveform of example 3. There is a pulsed component to the signal between 6 and 16 ms shown in the bottom panel.

nondamped sinusoidal pulses (i.e., regular oscillations in amplitude) and looks very similar to the waveform of the model at 34 ms (see Fig. 1).

## III. ANALYSIS PROCEDURE

### A. Duty cycle

In order to describe the structure of the vocalizations with respect to the above model, a short-time duty cycle measure was developed in an attempt to characterize the shape of the waveforms and thus characterize changes in signal type. Duty cycle refers to the percentage of time that a signal is “on” versus the total length of the signal. At one end of the extreme are vocalizations comprised of widely spaced pulses (e.g., a click train) corresponding to a low duty cycle. That is, the pulses are very brief as compared to the interval between pulses. As the interval between pulses decreases, duty cycle increases until there is no interval between pulses: the vocalizations begin to approximate a constant sine wave and correspondingly have a high duty cycle. At this end of the extreme, the vocalizations sound whistle-like.

All signals were compared to a nonamplitude modulated sine wave. The duty cycle measure was calculated by taking the rectified digital waveform and converting each point to a percentage of the maximum value in 512-point “windows” (about 11 ms for a 44.1-kHz sampled signal). The average of these percentages was calculated and normalized to a sine wave value for the calculation. Therefore, if the signal was an unmodulated sine wave (“tonal”), it received a value very close to 1.0. A threshold was used such that windows that did not surpass the threshold received a value of 0.0. In this way it was possible to represent inter-pulse intervals that were longer than 512 points.

The duty cycle measurement took into account the degree to which the waveform of a signal deviated from an unmodulated sine wave. Signals received values between 1.0 (unmodulated sine wave—a “perfect” whistle) and 0.0 (no signal). Values between 1.0 and 0.0 reflected the degree of

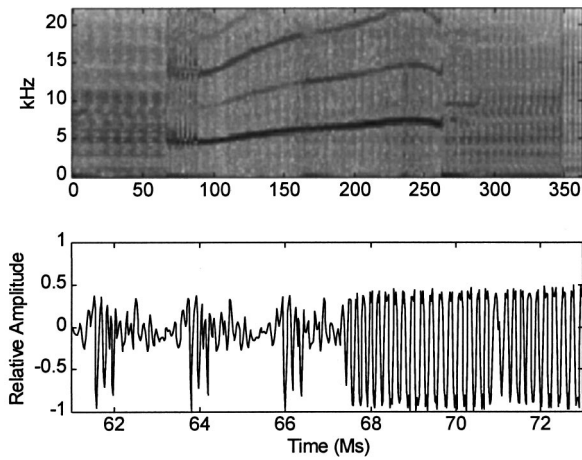


FIG. 6. The 128-point spectrogram of the first example (top) and a close-up view of the transition between the pulses and the whistle occurring at approximately 67 ms.

pulsing. For example, a typical click train might have a value of approximately 0.05, a typical burst-pulse signal between 0.3 and 0.6, and a typical whistle-like signal may have a value of 0.8 or greater.

There were additional circumstances in which values less than 1.00 could have arisen. For example, if the duty cycle measure was applied to a continuous sine wave that changed amplitude, values less than 1.00 would occur. Each point of the signal was expressed as a percentage of the maximum of the signal. The measure assumed that the overall amplitude of the signal was not changing. For this reason, choosing an appropriate window size was important. The 512-point window size was chosen after analyzing the waveforms of many vocalizations with changes in amplitude. In general, the overall amplitude of the vocalizations changed little in the 512-point window.

## B. Peak frequency

Signals were also analyzed for peak frequency (i.e., the frequency with peak energy). A 512-point window was used (to correspond to the duty cycle window) and peak frequency was calculated. Thus each vocalization was characterized by changes in duty cycle and peak frequency.

## IV. RESULTS

### A. Analysis procedure

The following examples demonstrate how various vocalization types were represented by the analysis procedure. Vocalizations that changed waveform structure were common. The first vocalization has multiple sound types (whistle and burst-pulse) and is included to demonstrate how the duty cycle measure is able to represent changes in signal type over time. The second example is a click train. The examples are not meant to represent all of the observed signal types; the emphasis of the demonstration is on the performance of the analysis procedure.

#### 1. Example 1

The first example (Fig. 6) is a whistle preceded and fol-

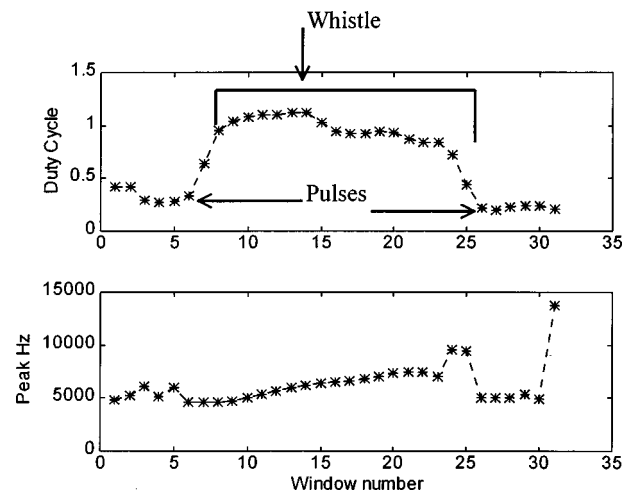


FIG. 7. Plots of the characterization vectors for the vocalization shown in Fig. 6. Duty cycle is shown in the top panel and peak frequency in the bottom panel. The initial and final duty cycle values are approximately 0.35, corresponding to the pulse trains. The values of close to 1.00 correspond to the whistle portion of the vocalization.

lowed by pulsed sounds. The inter-pulse intervals of the pulsed components vary but are approximately 2–3 ms. The pulsed portion of the vocalization (top panel) extends from approximately 0 to 65 ms and from 260 to 360 ms. The whistle shows as the series of dark lines beginning at approximately 65 ms. The bottom line represents the fundamental frequency of the whistle and the lines above it represent harmonics. Before and after the whistle are the pulse trains.

Although the vocalization is comprised of several sound types, it is treated as a single vocalization because there are no “breaks”—the transition between sound types is immediate. Figure 6, bottom panel, is a close-up view of the waveform showing the transition from a pulse train to a whistle that occurs at approximately 67 ms.

Figure 7 shows the measurement values for this vocalization. The top panel represents duty cycle values. The x-axis represents each analysis window and the y-axis represents duty cycle value. Visual examination of these values gives an easily interpretable representation of how signal type is changing over time. The whistle is clearly seen as values approaching 1.0. The pulse trains before and after the whistle are represented by the lower duty cycle values of approximately 0.35. The bottom panel of Fig. 7 represents peak frequency as it changed throughout the vocalization.

#### 2. Example 2

The second example is a pulse train that is approximately 900 ms long. In the spectrogram display, each click is clearly visible as a vertical line (see Fig. 8). The duty cycle display, in Fig. 9, shows the relatively low values (less than 0.10). The zeros result from windows that did not exceed the threshold and represent inter-pulse intervals.

### B. High-frequency recordings

Pseudorca also produce ultrasonic vocalizations (e.g., Au *et al.*, 1995). The ultrasonic vocalizations observed by Au *et al.* (1995) were produced in an echolocation task in

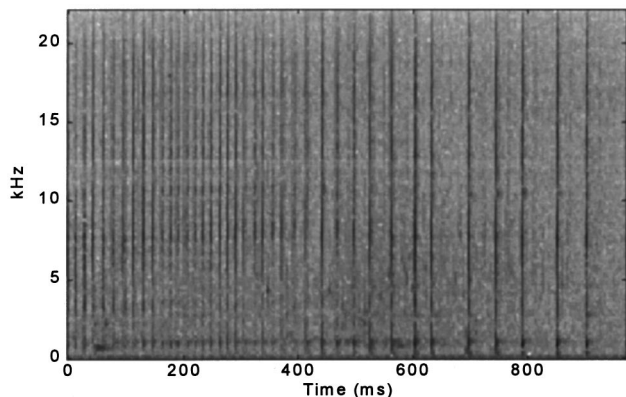


FIG. 8. The 256-point spectrogram of example 2 showing the inter-pulse interval gradually increasing.

which the animal had to detect small differences in the wall thickness of a target. The maximum peak frequency observed in that experiment was approximately 100 kHz. The DAT recorder used in this study has a bandwidth limited to 22.05 kHz. Therefore, it was necessary to evaluate whether higher-frequency vocalizations were being missed with the DAT recorder.

A total of 5 min of recordings made with the RACAL reel-to-reel recorder (bandwidth to 170 kHz) were analyzed for peak frequency. The analysis did not consider frequencies below 3.5 kHz in order to reduce tank noise. Each vocalization was analyzed in 512 point windows and the maximum value of the power spectrum was calculated. A total of 1% of peak frequencies were outside the 22-kHz range of the DAT recorder (see Fig. 10). The maximum peak frequency recorded with the RACAL was 50 kHz and was a pulse in a click train. Additionally, vocalizations with peak frequencies below 22 kHz often had ultrasonic harmonic components, and these components changed in parallel with the sonic peak frequencies. It appears that in this context ultrasonic vocalizations are rare. The observance of few vocalizations having peak frequencies above the limit of the DAT recorder suggests that the following discussion of peak frequency is valid.

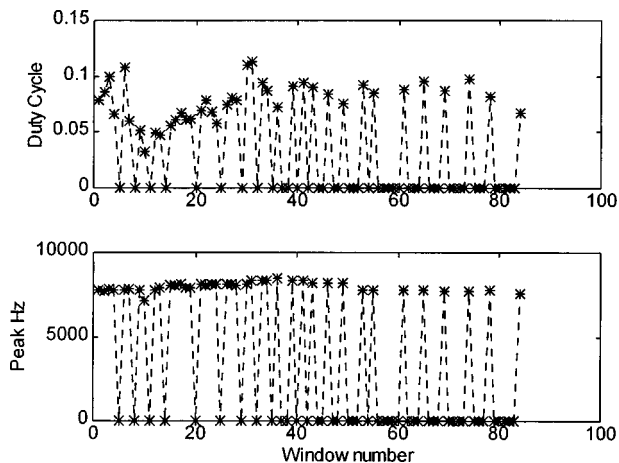


FIG. 9. The duty cycle (top panel) and peak frequency values for example 2. The zeros correspond to inter-pulse intervals.

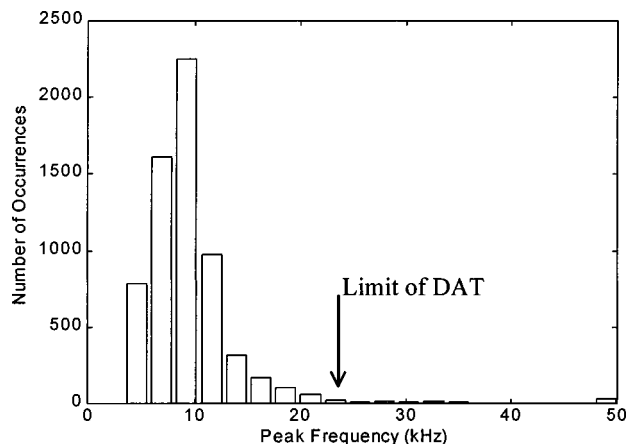


FIG. 10. The distribution of peak frequencies recorded with the RACAL reel-to-reel recorder (bandwidth to 170 kHz). Very few (1%) of the values are above the limit of the DAT recorder.

### C. Peak frequency

Peak frequencies ranged from a low of 3 kHz (the minimum frequency considered in the analysis) to a maximum of 22 kHz (the frequency limit of the DAT). The average starting peak frequency for all 500 vocalizations was 6212 Hz (s.d.=2651 Hz). The average ending frequency was 7834 Hz (s.d.=2843 Hz). A two-sample *t*-test comparing the average starting and ending frequency revealed a significant difference,  $t(499) = -10.59$ ,  $p < 0.0001$ . The trend for the vocalizations to begin at a low frequency and end at a higher frequency may have resulted from the frequent occurrence of short duration, ascending whistle vocalizations. Although whistles showed a variety of frequency modulations, the most common was an ascending whistle.

### D. Duty cycle

Values on the duty cycle measure ranged from a minimum of 0.0 (inter-pulse intervals) to a maximum value of 1.31. Values above a score of 1.00, the theoretical limit of the scale, were not expected. A total of 3% of the values were above 1.00. Upon closer inspection, values greater than 1.00 seemed to result from distorted signals (possibly due to one of the recording instruments being overdriven).

A significant negative correlation ( $-0.49$ ,  $p < 0.0001$ , see Fig. 11) was found between the average peak frequency for each vocalization and the average value on the duty cycle measure (removing duty cycle values greater than 1.00 resulted in a correlation of  $-0.48$ ). Low duty cycle vocalizations such as click trains tended to be higher in peak frequency than higher duty cycle vocalizations such as whistles. Whistles tend to be lower in frequency than pulses (e.g., Au, 1993; Popper, 1980). Employing the duty cycle measure revealed a direct linear relationship between waveform structure and peak frequency; peak frequencies drop as the vocalizations shift from pulse trains to whistles. Models of odontocete sound production must take this finding into account.

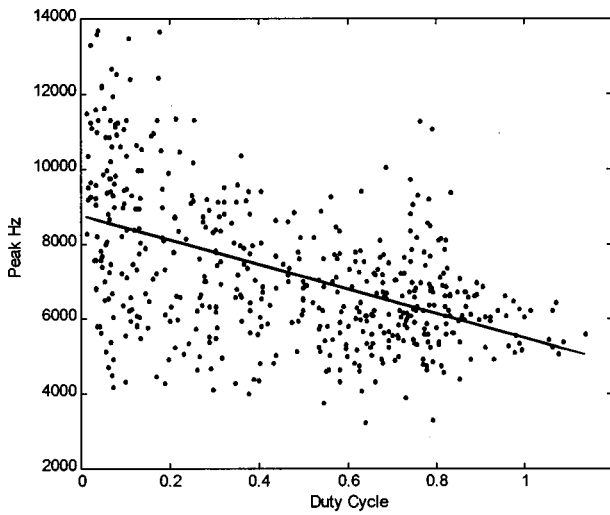


FIG. 11. The distribution and regression line ( $r = -0.49$ ) of the relationship between average duty cycle and average peak frequency showing that as duty cycle increases peak frequency tends to decrease.

### E. Duration

The duration of each vocalization was measured to the nearest millisecond. The average duration was 506 ms (s.d.=761 ms). Longer duration vocalizations tended to be pulse trains, evident in a significant negative correlation between the average duty cycle for each vocalization and duration ( $-0.37$   $p < 0.0001$ , see Fig. 12). This means that as duty cycle was lower, the average duration was longer, implying that there may be a limited air supply for each vocalization. This supply can be released to drive the production mechanism gradually, over a longer time in the form of pulse trains or more quickly in the form of whistles.

### F. Graded signals

#### 1. Distribution of duty cycle values

One way to examine whether the vocalizations are graded is to observe the frequency distribution of duty cycle

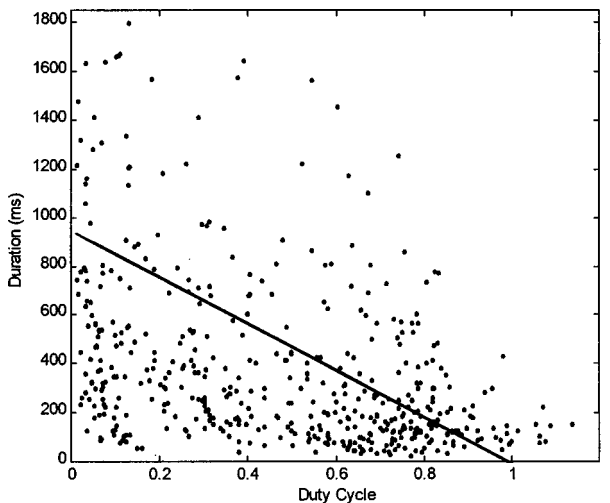


FIG. 12. The distribution and regression line ( $r = -0.37$ ) of the relationship between duration and average duty cycle showing that the duration of the vocalizations tends to decrease with increasing duty cycle values.

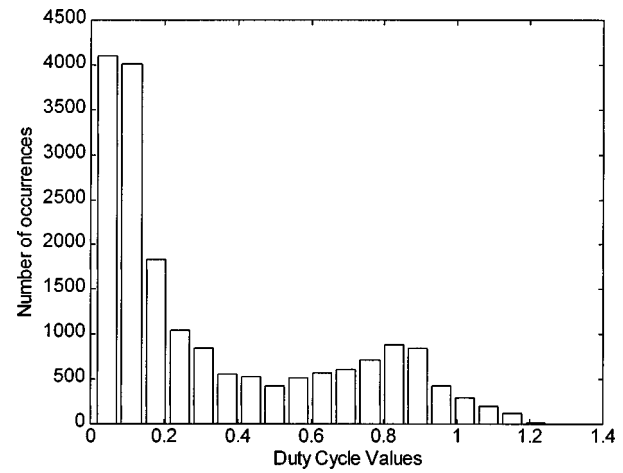


FIG. 13. The distribution of nonzero duty cycle values. There are many low values corresponding to pulse trains. The values above 1.0 appeared to result from distorted signals.

values. The values on this measure reflect signal *type* (e.g., click train, burst-pulse, whistle) by comparing each vocalization to a sine wave. If discrete signal types exist, they should be reflected as discontinuities in the values obtained on this measure.

The total of 18 515 nonzero duty cycle values were distributed throughout the entire range of possible values, indicating a graded structure with whistles and clicks being at opposite ends of a continuum (see Fig. 13). The distribution of duty cycle scores shows many (53%) low values ( $< 0.20$ ) and many (14%) high values ( $> 0.80$ ). These values roughly correspond to pulse trains and whistles, respectively.

### G. Maintaining peak frequency

Many vocalizations contained more than one signal type. For example, a vocalization could begin as a whistle and switch to a pulse train. Approximately 10% of the vocalizations were whistles that switched suddenly to a pulse train. The peak frequency of many of these vocalizations was maintained across this switch in signal type (see Fig. 14). The spectrogram clearly shows the whistle ending and the pulse train beginning at approximately 100 ms. Figure 14 (bottom panel) also shows a plot of peak frequency where the line represents the peak frequency of the whistle and the asterisks represent peak frequency of the pulses. The peak frequency of the end of the whistle is 6.1 kHz and peak frequency of the first pulse is 6.0 kHz. A two sample  $t$ -test comparing the mean frequency of the whistle ( $M = 5.32$  kHz, s.d.=0.18) and the mean frequency for the pulses ( $M = 5.52$  kHz, s.d.=0.09) revealed no significant difference,  $t(9) = -0.46$ ,  $p < 0.33$ . In other words, there was no change in peak frequency when switching from the whistle to the pulses.

Figure 15 shows the waveform of a transition between a whistle and a pulse train. The first pulse starts at the end of and is “attached” to the whistle waveform. The maintenance of peak frequency across changes in signal type, when considered along with the evidence of a graded vocal structure, strongly suggests that a single mechanism is the source of both pulsed and continuous signals.

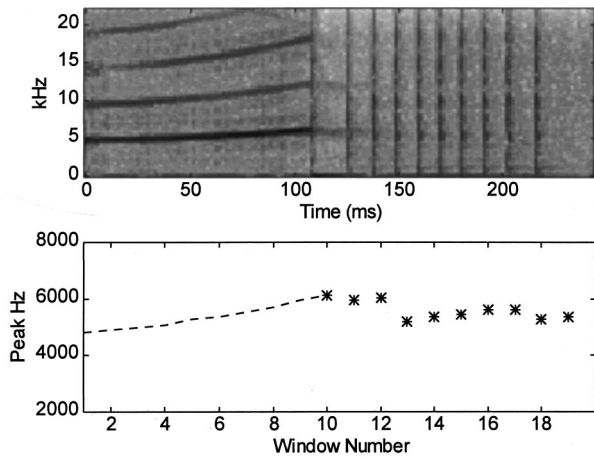


FIG. 14. The 128-point spectrogram (top) and a graph of peak frequency (bottom) of a vocalization switching from a whistle to a click train. The line represents peak frequency of the whistle and the asterisks represent peak frequency of the pulses in the click train. Peak frequency is maintained across the change in signal type.

### H. Independent/simultaneous signals

The available evidence suggests that a single mechanism is able to produce both pulsed and continuous waveforms. However, there appear to be vocalizations comprised of “independent” and simultaneous signal types. There are numerous reports of other dolphin species producing simultaneous whistles and clicks (e.g., Lilly and Miller, 1961) and it appears that pseudorca do the same. Figure 16 shows an example of a concurrently produced whistle and pulse train. On the spectrogram (top panel), the whistle and pulses begin at different times. The bottom panel shows a disparity in amplitude between the two signal types with the lower amplitude portion of the waveform corresponding to the whistle; a higher amplitude pulse occurs at approximately 301 ms. It is difficult to explain the co-occurrences in signal type without the attribution of two production mechanisms, given that many of these co-produced vocalizations begin and end at different times and often have different amplitudes. We discuss this apparent contradiction later.

### V. GENERAL DISCUSSION

The two false killer whales recorded in this study vocalized often and produced a wide variety of sounds. Most of

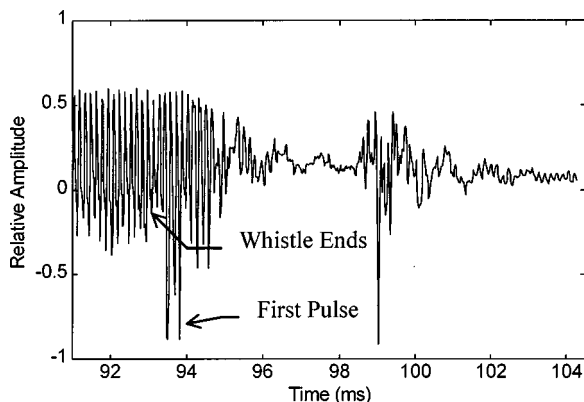


FIG. 15. An example of a whistle to click transition. The first pulse occurs at the very end of the whistle (approx. 93 ms).

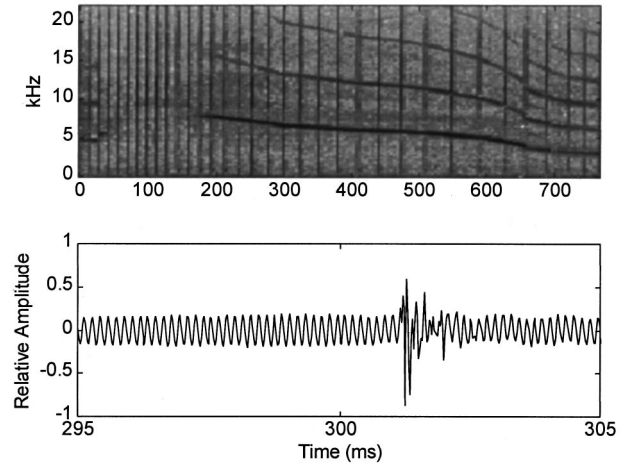


FIG. 16. The 256-point spectrogram (top) and a close-up of the waveform around 300 ms of a click produced simultaneously with a whistle. The click train and whistle begin at different times and have different amplitudes.

the vocalizations fit into the traditional categories of whistles, burst-pulse sounds, and click trains. However, based on detailed visual analyses of the waveforms, a better model does not recognize discrete categorical differences in signal (i.e., waveform) type. The vocalizations are graded; that is, they lie along a continuum with trains of discrete, exponentially damped sinusoidal pulses at one end, and continuous sinusoidal signals at the opposite end. Therefore, the traditional categories (e.g., pulse trains, burst-pulse sounds, whistles) should not be viewed as distinct, but instead, should be viewed as occupying locations along a continuum from widely spaced pulses to a continuous sinusoid.

Pulse trains are graded as a function of the interval between pulses where the minimum interval between pulses is 0.0 ms. The transition from pulse trains with no inter-pulse interval to a whistle can be modeled by gradations in the degree of damping. There were many examples of vocalizations that were gradually modulated from pulse trains to whistles, encompassing the entire continuum. There were also vocalizations that showed sudden shifts in signal type—for example, switching immediately from a whistle to a pulse train.

Because of the changes in signal type, it was important to have a measure that could objectively represent the location of a vocalization along the continuum. The short-time duty cycle measure seemed to be effective in this capacity. Values on the duty cycle measure occupied the entire range from zero to one, which seems to reflect the graded structure of the vocalizations. It was possible, however, to identify modal duty cycle values. The majority of values (53%) were below 0.20. These vocalizations subjectively sounded like click trains. There were also many duty cycle values (14%) above 0.70, which subjectively sounded like whistles.

Correlations between behavioral state and vocalizations have often been noted in both wild and captive animals and in a variety of dolphin species (e.g., Ford, 1989; Herzing, 1996; Morton *et al.*, 1986; Norris *et al.*, 1994). Describing the behavior of Hawaiian spinner dolphins, Norris *et al.* (1994) remarked, “One hears a quiet ‘muttering of clicks’ during (rest)...” (p. 179). They observed that as activity level

increased, the number of whistles and burst-pulse signals increased. There may be a strong correlation between the duty cycle values of the vocalizations and the activity level of the Hawaiian spinner dolphin. Anecdotally, a similar trend was observed with the false killer whales used in this study. At the beginning of each recording session, they were generally much more active and produced many whistles and rapidly pulsed vocalizations. Toward the end of each recording session, after resting on their back for 20–30 mins, the animals were much quieter and generally emitted only widely spaced clicks.

All of the recordings for this study were made in a single behavioral context: the animals were resting on their backs. It may be that modal duty cycle values shift as a function of behavioral state. For example, if the animal were highly active/aroused, the proportion of high duty cycle values might increase. If the animals were at rest, possibly at night, there would likely be many more low value signals.

Although the acoustic structure of the vocalizations is best modeled as lying along a continuum, this does not mean that the animals are perceiving them as such. In human speech perception, for example, continuous changes in voice-onset time are perceived discontinuously (e.g., Cutting and Rosner, 1974). Dolphins, in general, have a hearing system that is adapted for higher frequencies and greater time resolution than humans (Ketten, 1992). While false killer whales probably do not perceive their own vocalizations as humans do, categorical perceptual processes may be occurring.

The observation of the entire continuum (click train to whistle) in single vocalizations suggests that a single production mechanism can potentially produce all of the observed signal types. Additionally, the maintenance of peak frequency in single vocalizations across abrupt changes in signal type (e.g., whistle → click train) is further evidence for a single mechanism. However, seemingly independent signal types such as whistles and clicks commonly occur simultaneously. The two signal types would often begin and end at different times and exhibit differential changes in amplitude. Such occurrences are difficult to explain without invoking at least two production mechanisms.

The conflict between the likelihood that a single production mechanism can produce everything from click trains to whistles and the apparent need to posit two mechanisms may be resolvable. The sound production system in dolphins may be analogous to that found in birds in that there may be two production sites. The syrinx, the sound-producing organ in birds, is located at the junction of the two bronchi. This means that there are two potential sound sources, one in each bronchus (Catchpole and Slater, 1995). In some species (e.g., canaries) there is considerable lateralization where one side of the syrinx produces the majority of sounds (Nottebohm, 1971). In other species (e.g., catbirds), both sides contribute equally, each producing its own unique repertoire of sounds (Suthers, 1990).

Odontocetes have two separate nasal passages. Possibly there is a sound producing mechanism in each of them. Cranford *et al.* (1996) proposed that the likely mechanism for click generation is an oscillator driven by an air stream mov-

ing through the nasal passage. The air stream apparently passes between the so-called monkey lip/dorsal bursa (MLDB) region and causes the monkey lips to open and slap together. Cranford *et al.* suggest that pulse repetition rate could be regulated by such factors as air pressure and/or muscle tension on vibratory elements. Once muscle tension reaches a critical value, the monkey lips might operate harmonically and produce whistle-like sounds. There is a pair of monkey lips in each nasal passage, meaning that there are two potential sound producing mechanisms (Cranford *et al.*, 1996). Additionally, delphinids have moderately asymmetric MLDBs, suggesting that one side may be favored for high-frequency vocalizations and the other for low-frequency vocalizations: "...if the duration of the vibratory event and the event location (along the length of the monkey lips) are under voluntary control of the dolphin, then a rich variety of possible combinations could help explain the varied repertoire of signals recorded from delphinids" (Cranford *et al.*, 1996, p. 275).

## ACKNOWLEDGMENTS

This study was conducted as part of an M.A. program at the University of Hawaii, and was made possible through the support of Marlee Breese, formerly of Sea Life Park, Oahu. Many thanks to Dr. Paul Nachtigall, to Dr. Whitlow Au for providing equipment and technical assistance, and to Molly Lucas for help with data collection.

<sup>1</sup>The use of the term "vocalization" in this paper is not meant to imply that vocal folds are necessarily the mechanism producing the sounds. It is used as a general term for dolphin sounds that are internally generated via air flow in the head region.

- Au, W. W. L. (1993). *The Sonar of Dolphins* (Springer-Verlag, New York).
- Au, W. W. L., Pawloski, J. L., Nachtigall, P. E., Blonz, M., and Gisinger, R. C. (1995). "Echolocation signals and transmission beam pattern of a false killer whale (*Pseudorca crassidens*)," *J. Acoust. Soc. Am.* **98**, 51–59.
- Caldwell, M. C., and Caldwell, D. K. (1967). "Intra-specific transfer of information via pulsed sound in captive odontocete cetaceans," in *Animal Sonar Systems*, edited by R. G. Busnel (Laboratoire de Physiologie Acoustique, Jouy-en-Josas, France), pp. 879–836.
- Caldwell, M. C., and Caldwell, D. K. (1968). "Vocalization of naive captive dolphins in small groups," *Science* **159**, 1121–1123.
- Caldwell, M. C., Caldwell, D. K., and Tyack, P. L. (1990). "Review of the signature-whistle hypothesis for the Atlantic bottlenose dolphin," in *The Bottlenose Dolphin*, edited by S. Leatherwood and R. R. Reeves (Academic, San Diego), pp. 199–235.
- Catchpole, C. K., and Slater, P. J. B. (1995). *Bird Song* (Cambridge U.P., Cambridge).
- Cranford, T. W., Amundin, M., and Norris, K. S. (1996). "Functional morphology and homology in the odontocete nasal complex: Implications for sound generation," *J. Morphol.* **228**, 223–285.
- Cutting, J. E., and Rosner, B. S. (1974). "Categories and boundaries in speech and music," *Percept. Psychophys.* **16**, 564–570.
- Dahlheim, M. E., and Awbrey, F. T. (1982). "A classification and comparison of vocalizations of captive killer whales," *J. Acoust. Soc. Am.* **72**, 661–670.
- Davis, L. I. (1964). "Biological acoustics and the use of the sound spectrograph," *The Southwestern Naturalist* **9**, 118–145.
- Dawson, S. M., and Thorpe, C. W. (1990). "A quantitative analysis of the sounds of Hector's dolphin," *Ethology* **86**, 131–145.
- Dawson, S. M. (1991). "Clicks and communication: The behavioural and social contexts of Hector's dolphin vocalizations," *Ethology* **84**, 265–276.
- Evans, W. E., Awbrey, F. T., and Hackbarth, H. (1988). "High frequency pulses produced by free-ranging Commerson's dolphin (*Cephalorhynchus commersonii*) compared to those of phocoenids," in *Reports of the Inter-*



- national Whaling Commission (Special Issue 9). Biology of the genus Cephalorhynchus*, edited by R. L. Brownell and G. P. Donovan (International Whaling Commission, Cambridge), pp. 173–181.
- Evans, W. E., and Prescott, J. H. (1962). "Observations of the sound production capabilities of the bottlenosed porpoise: A study of whistles and clicks," *Zoologica* **47**, 121–128.
- Ford, J. K. B., and Fisher, H. D. (1978). "Underwater acoustic signals of the narwhal (*Monodon monoceros*)," *Can. J. Zool.* **56**, 552–560.
- Ford, J. K. B. (1989). "Acoustic behaviour of resident killer whales off Vancouver Island, British Columbia," *Can. J. Zool.* **67**, 727–745.
- Herman, L. M., and Tavolga, W. N. (1980). "The communication systems of cetaceans," in *Cetacean Behavior: Mechanisms and Functions*, edited by L. M. Herman (Wiley-Interscience, New York), pp. 149–209.
- Herzing, D. (1996). "Vocalizations and associated underwater behavior of free-ranging Atlantic spotted dolphin, *Stenella frontalis*, and bottlenose dolphins, *Tursiops truncatus*," *Aquatic Mammals* **22**, 61–79.
- Kamminga, C., and van Velden, J. G. (1987). "Sonar signals of *Pseudorca crassidens* in comparison with *Tursiops truncatus*," *Aquatic Mammals* **13**, 43–49.
- Kaznadzei, V. V., Krechi, S. A., and Khakhalkina, E. N. (1976). "Types of dolphin communication signals and their organization," *Sov. Phys. Acoust.* **22**, 484–488.
- Ketten, D. R. (1992). "The cetacean ear: form, frequency, and evolution," in *Marine Mammal Sensory Systems*, edited by J. A. Thomas, R. A. Kastelein, and A. Y. Supin (Plenum, New York), pp. 53–76.
- Lilly, J. C., and Miller, A. M. (1961). "Sounds emitted by the bottlenose dolphin," *Science* **133**, 1689–1693.
- McCowan, B., and Reiss, D. (1995). "Maternal aggressive contact vocalizations in captive bottlenose dolphins (*Tursiops truncatus*): Wide-band, low-frequency signals during mother/aunt-infant interactions," *Zoo Biol.* **14**, 293–309.
- Morton, A. B., Gale, J. D., and Prince, R. C. (1986). "Sound and behavioral correlations in captive *Orcinus orca*," in *Behavioral Biology of Killer Whales*, edited by B. C. Kirkeveld and J. S. Lockard (Alan R. Liss, New York), pp. 303–333.
- Norris, K. S., Wursig, B., Wells, R. S., and Wursig, M., with Brownlee, S. M., Johnson, C. M., and Solow, J. (1994). *The Hawaiian Spinner Dolphin* (University of California Press, Berkeley).
- Nottebohm, F. (1971). "Neural lateralization of vocal control in passerine bird song," *J. Exp. Zool.* **177**, 229–262.
- Overstrom, N. A. (1983). "Association between burst-pulsed sounds and aggressive behavior in captive Atlantic bottlenosed dolphins," *Zoo Biol.* **2**, 93–103.
- Popper, A. N. (1980). "Sound emission and detection by delphinids," in *Cetacean Behavior: Mechanisms and Functions*, edited by L. M. Herman (Wiley-Interscience, New York), pp. 1–52.
- Purves, P. E., and Pilleri, G. (1983). *Echolocation in Whales and Dolphins* (Academic, London).
- Richardson, W. J., Greene, C. R., Malme, C. I., and Thomson, D. H. (1995). *Marine Mammals and Noise* (Academic, San Diego).
- Sayigh, L. S., Tyack, P. L., Wells, R. S., and Scott, M. D. (1990). "Signature whistles of free-ranging bottlenose dolphins *Tursiops truncatus*: Stability and mother-offspring comparisons," *Behav. Ecol. Sociobiol.* **26**, 247–260.
- Schevill, W. E., and Watkins, W. A. (1966). "Sound structure and directionality in *Orcinus* (killer whale)," *Zoologica* **51**, 71–76.
- Sjare, B. L., and Smith, T. G. (1986). "The vocal repertoire of white whales, *Delphinapterus leucas*, summering in Cunningham Inlet, Northwest Territories," *Can. J. Zool.* **64**, 407–415.
- Steiner, W. W., Hain, J. H., Winn, H. E., and Perkins, P. J. (1979). "Vocalizations and feeding behavior of the killer whale (*Orcinus Orca*)," *J. Mammal.* **60**, 823–827.
- Suthers, R. A. (1990). "Contributions to birdsong from the left and right sides of the intact syrinx," *Nature (London)* **327**, 473–477.
- Thomas, J., Stoermer, M., Bowers, C., Anderson, L., and Garver, A. (1988). "Detection abilities and signal characteristics of echolocating false killer whales (*Pseudorca crassidens*)," in *Animal Sonar: Processes and Performance*, edited by P. E. Nachtigall and P. W. B. Moore (Plenum, New York), pp. 323–328.
- Tyack, P. L. (1986). "Whistle repertoires of two bottlenosed dolphins, *Tursiops truncatus*: Mimicry of signature whistles?," *Behav. Ecol. Sociobiol.* **18**, 251–257.
- Watkins, W. A. (1967). "The harmonic interval: Fact or artifact in spectral analysis of pulse trains," in *Marine Bio-acoustics, Vol. 2*, edited by W. N. Tavolga (Pergamon, New York), pp. 15–42.

# The effect of spatial separation of signal and noise on masking in the free field as a function of signal frequency and age in the mouse

James R. Ison and Punit Agrawal

*Department of Brain and Cognitive Sciences, Meliora Hall, University of Rochester, Rochester, New York 14627*

(Received 2 October 1997; accepted for publication 22 May 1998)

Masking of low- (4 kHz) and high-frequency (25 kHz) signals by one-octave bandpass maskers either spatially coincident with the signal or contralateral to it was examined in mice, 4–6 and 20–22 months of age, in the free field. Signals were presented 120 ms prior to a startle stimulus and differences in their inhibition of the startle reflex, relative to startle stimulus alone trials, were used to measure the severity of masking. Inhibition was reduced or eliminated by spatially coincident noise for weak but not for relatively intense signals, providing the type of “loudness recruitment” effect characteristic of human listeners in similar stimulus conditions. The spatial separation of the signal and its masker relieved this maskinglike effect for the high-frequency pair in both young and old mice. In contrast there was no beneficial effect of the shift in spatial location for the low-frequency pair at either age. This finding of masking release for high- but not low-frequency stimuli supports the hypothesis that the sound shadow provided by the head and pinna would yield a favorable signal-to-noise level difference for a contralateral masker and an ipsilateral signal only at very high frequencies in the mouse. The presence of masking release in these old mice, a first generation hybrid strain with near-normal high-frequency hearing in ABR measures, agrees with reports that the masking release resulting from a similar manipulation in aged human listeners with minimal high-frequency hearing loss is the equal of that obtained in the young listener. © 1998 Acoustical Society of America. [S0001-4966(98)07008-8]

PACS numbers: 43.80.Lb, 43.66.Sr, 43.66.Gf, 43.66.Mk [FD]

## INTRODUCTION

The purpose of the present experiment was to determine whether the masking of a tonal signal by noise would be relieved by their spatial separation in mice, and whether either the degree of masking or the degree of masking relief afforded by the shift in location would be affected by the frequency of the signal or by the age of the mouse. The experiment was performed under free field conditions using the methods of reflex modification audiometry (Young and Fechter, 1983). These methods have been used in human listeners, both those with normal hearing and the hearing impaired, to provide objective behavioral evidence for the masking of weak signals by noise, and for loudness recruitment at high signal levels under masking conditions (Reiter and Ison, 1979) and they are readily adapted to study similar problems in laboratory animals (Hoffman and Ison, 1991). One rationale for examining this sensory phenomenon in the mouse follows from the observation that the many inbred strains of mice and their hybrid offspring provide animal models that capture various types of age-related hearing loss [see especially Willott (1996) for a recent review of this work and its implications]. The neural substrates of age-related hearing loss as well as the genetics of hearing loss are being vigorously investigated in the C57BL/6J strain, often contrasted with the CBA strain. In the present research we used the first generation (*F1*) hybrid mouse of a C57×CBA pairing, which yields offspring with minimal individual differences within a group and a relative minor hearing loss

with age, as the first generation hybrid offspring have better hearing than either of the parent strains (for example, Erway *et al.*, 1993; Henry and Chole, 1980; Li and Borg, 1991). The study of masking and masking release in this mouse may provide a useful vehicle for subsequent physiological analyses, and add to our general understanding of these phenomena as they appear in different groups of human listeners.

There are many studies of the beneficial effects for stimulus detection of varying the spatial location (or laterality) of signals and maskers in human listeners, with the general outcome that the hearing impaired and the elderly profit less from the spatial separation of signal and masker in either the free field (Colburn *et al.*, 1982; Duquesnoy, 1983; Warren *et al.*, 1978) or under earphones (Grose *et al.*, 1994; Pichora-Fuller and Schneider, 1991). These findings are consistent with other data showing the elderly to be less successful in sound localization than young normal listeners (Colburn, 1982; Colburn *et al.*, 1987; Tønning, 1975). However, some data indicate that the benefit of spatial separation of signals from maskers is lost not with age alone, but only when age is combined with hearing impairment, so that, e.g., the advantage provided by this manipulation for elderly listeners with minimal hearing impairment is the same as that seen in young listeners under free field conditions, both groups doing better than aged listeners with severe mid- and high-frequency hearing loss (Gelfand *et al.*, 1988). This last report indicates that the critical cues which the elderly human listeners use in this task are those provided by high-

frequency components of the signal and the masker: An important implication of this finding is that the elderly listener must perform this task on the basis of interaural level differences.

As far as we can determine, there are no published behavioral analyses of sensory processing in laboratory animals that have examined the relationship between auditory masking and the relative locations of signals and their maskers with age or with hearing impairment. Heffner and Donnell (1993) have studied the related problem of auditory spatial location in the C57 strain, finding that old mice were less sensitive to differences in spatial location than younger mice. The authors attributed this deficit to the age-related high-frequency hearing loss that is characteristic of this strain, and they provided supportive evidence for their conclusion in their demonstration that the young mice performed like old mice when the critical high-frequency components of the signals were filtered out. An examination of auditory spatial discrimination by the mouse, as provided by Heffner and Donnell, and the study of masking release with shifts in spatial location, as provided here, are both of particular interest for the comparative study of auditory ability, because in contrast to the dual mechanisms for interaural time differences and for interaural level differences available to human listeners, the mouse must apparently rely solely on the interaural changes in level that accompany shifts in location. The region of maximum sensitivity to tonal input in the mouse audiogram is about two octaves above that of the human (see Fay, 1988, p. 367), and the mouse has minimal sensitivity to the frequencies especially useful in providing masking release in human listeners when interaural level differences are controlled (that is, those frequencies below about 2 kHz at which phase locking is prominent and interaural temporal differences would be most apparent: Hirsh, 1948). As Heffner and Donnell (1993) have described, an interaural level difference can be present in the mouse only for very high-frequency signals, above, e.g., 20 kHz, because, given the small size of the mouse, only these frequencies would create an effective sound shadow contralateral to the sound source.

One semantic question of some theoretical consequence is whether "masking release," which is classically defined as a binaural phenomenon, is appropriate for describing the auditory performance of any species which has an audiogram restricted to the very high frequencies, and for which changes in signal location must be coded by interaural differences in signal level. (And this question is also relevant for the human listener when level differences are manipulated independently of temporal differences under artificial earphone conditions.) The conceptual problem is that as a high-frequency signal moves away from the spatial location of the noise masker then it necessarily moves away from one ear and toward the other. Depending in detail on the head-related transfer function across frequency (Shaw, 1974, for humans; McFadden and Willott, 1994a, for mice), then it can be expected that the level of the signal must increase at one ear and decrease at the other; and if the masker is fixed in position, then the signal-to-noise ratio must necessarily increase at one ear and must necessarily decrease at the other. Thus when relative signal-to-noise interaural level differ-

ences are provided by shifts in the relative locations of signal and noise any beneficial effect this might have on the severity of masking is "binaural" only in the sense that the binaural listener has one ear for which the signal-to-noise ratio has necessarily improved; and the listener must differentially weight this ear over the other.

For this reason, a demonstration in the mouse that the severity of masking is reduced when a signal is moved away from a masker is an instance of "binaural unmasking" only in the sense that the data demand that the mouse can differentiate between the inputs at the two ears and be more responsive to the ear that provides the better signal-to-noise ratio. (This analysis for the mouse is exactly that proposed for the human listener by Bronkhorst and Plomp, 1988, when isolated level differences were used to indicate the spatial locations of signals and maskers. Listeners with asymmetric high-frequency hearing losses were shown not to benefit from shifts in spatial location when the more favorable signal-to-noise ratio was presented to the impaired ear.) It is of considerable interest that McFadden and Willott (1994b) have recently provided electrophysiological evidence for "location unmasking" of this sort in young anesthetized C57 mice. Tone-evoked single unit activity in the inferior colliculus contralateral to the signal increased when a masker was moved away from the signal, showing thus a physiological analogue of the binaural masking level difference. This unmaskinglike effect was not evident in older mice with a high-frequency hearing loss, which is consistent with the deficit in spatial location ability described by Heffner and Donnell (1993). However, the physiological effects provided by McFadden and Willott do not necessarily imply that a similar unmasking phenomenon can be demonstrated in a behavioral analysis. In their experiment the experimenters (not surprisingly) chose to measure activity in the inferior colliculus contralateral to the signal; but if they had measured activity on the side ipsilateral to the signal they would have surely found more masking, not less masking, as the masker was moved away from the signal, because the masker would then be moving to the more favorable contralateral position. In order for a similar unmasking effect to appear in a behavioral experiment, we must assume that the mouse is also able to selectively use just that part of the central auditory system contralateral to the signal that provides the better signal-to-noise ratio.

In the present experiment we masked high (25 kHz) and low (4 kHz) tonal signals in one-octave bandpass noise centered on the signal, with masker and noise either spatially coincident or separated by 180 degrees, left and right. The subjects were first generation offspring of C57BL/6J and CBA/CaJ mice. They have the typical high-frequency hearing of mice and show "hybrid vigor" compared to their parents, having minimal high-frequency hearing loss with age (Erway *et al.*, 1993). Two independent hypotheses were tested. First, if release from masking does occur in the mouse, then it should be evident only for the high-frequency signal. Second, if the older mice have no high-frequency hearing impairment, then they should also have no age-related decline in the strength of masking release that is

found following a shift in the relative spatial locations of signal and masker in young mice.

## I. METHOD

### A. Subjects

The subjects were 12 male mice, the *F1* hybrid offspring of CBA/CaJ males and C57BL/6J females. The original breeding stock was obtained from Jackson Laboratories. Six mice were 4 months of age at the beginning of testing, and 6 were 20 months of age. They were group housed in the University of Rochester vivarium under constant climate control and a 12/12 hour normal light/dark cycle, and tested in the daylight hours. Food and water were available *ad libitum*.

### B. Apparatus

The subject was confined for testing in a movable frame made up of six pairs of vertical wire rods (0.125 cm diameter, 1 cm apart), which were brought up lightly alongside the torso from the hind end to just short of the ears. The subject's head was fixed in place by cementing a wooden Q-tip to the skin on the top of the head, this projecting slightly downward from a fastener to run along the back of the mouse. The head was not held absolutely rigid by this device, but in the lightly tranquilized mouse any movement of the head was minimal. The holding apparatus was secured on top of a suspended acrylic platform that had been covered with a sound absorbent material, and was mounted directly over an attached accelerometer (model SA-2-300, Statham Laboratories, Beverly Hills, CA). This assembly was placed in a double walled sound-attenuating room (inside dimensions approximately 2 m on a side), constructed by the Industrial Acoustics Company, Bronx, NY. White noise that was used for the startle stimulus was provided by a white noise generator, then shaped by an electronic switch and attenuated by a programmable attenuator, all constructed at the University of Rochester. This stimulus was amplified on one channel of a wide band stereo amplifier then delivered through a high-frequency speaker (model 075-105C, JBL Sound Inc., Los Angeles, CA), placed vertically directly over the subject's head, at a distance of 32 cm. The startle stimulus was 25 ms in duration, with 5-ms rise/decay times, and was set at 115 dB (SPL, linear scale). On a Bruel & Kjaer sound-level meter (model 2203, Naerum, Denmark) the startle stimulus varied by no more than  $\pm 3$  dB at octave bands centered at 4–16 kHz, dropping by 10 dB at 32 kHz.

Thirty cm and 90 degrees off the midline to the left and to the right of the subject were two Sony MDR-004 head phone speakers, 180 degrees apart. The left speaker was used to present a sinusoidal prepulse of 4 kHz or 25 kHz which had a total duration of 40 ms including 15-ms rise/decay times. This signal was generated by a Krohn-Hite model 4400A function generator, gated through a electronic switch, then amplified. Its level was set by a second programmable attenuator constructed at the University of Rochester, and varied between 30 and 80 dB SPL, in 10-dB steps. Bandpass noise was presented on some trials, with the noise source passed through a 1-octave bandpass filter centered at the sig-

nal frequency, and then to an attenuator to create the two 50-dB bandpass maskers, 1-octave wide. The masker was either mixed with the signal and presented through the left speaker, or was directed to the right hand speaker. Signal and masker levels were measured using the external filter of the B&K sound level meter and a  $\frac{1}{4}$ -in. microphone.

On the recording side of the experiment, the force of the animal's response to the intense noise burst was detected by the accelerometer. The output of the accelerometer was passed through a bridge amplifier and integrated over a 100-ms period beginning with the onset of the startle stimulus. Stimulus presentation and response recording were under computer control.

### C. Procedure

In this experiment it was important that the head of the animal be fixed in place so that the stimuli would be presented at a consistent spatial location. For this reason the subjects were lightly sedated for testing, using chlorprothixene ("Taracten"), a neuroleptic dopamine antagonist that at higher doses is in common use to tranquilize awake animals for electrophysiological experiments (e.g., Walton *et al.*, 1997). The dose was titrated across animals and across days to be sufficient to maintain the animal in a quiet posture during testing, without eliminating startle behavior. Initially the animals were injected with about 0.3 mg/kg (IM) and the dose was progressively increased by as much as 0.1 mg/kg as the subjects developed higher levels of tolerance over the course of the experiment. The subjects were placed in a quiet environment for 45 min after the injection to allow the drug to take effect, and sometimes a supplementary dose was given at the end of this rest period. If the startle reflex was strongly depressed or if the animal began to move then testing was discontinued for that day.

The mice received trials in which the startle stimulus was delivered alone or preceded by the tonal prepulse, presented at a lead time of 120 ms (signal onset to startle onset), with the signal variously set at 30, 40, 50, 60, 70, or 80 dB SPL. Trials were given in blocks of eight trials, each block containing two control startle alone trials and one each of the signal levels, these given in random order. There were six different types of blocks, resulting from the  $2 \times 3$  factorial design of two types of signal (4 kHz and 25 kHz, presented on the left) and three masking conditions (no masker, masker on left, and masker on right). On every day of testing the subjects were presented at least once with all six test conditions in random order, allowing for their even representation at a subject's level of sedation across all conditions. If sedation continued after running the first set of conditions, the subject continued to be tested through another set of testing conditions. If the sedation wore off before completing a full set either the mouse received additional sedative and was retested on all conditions in that set, or was allowed to rest and started at the beginning of that set of test conditions on the next scheduled test day. This experiment was carried out over a course of 2 months, with at least 2 full days between test days. A total of nine sets of each blocked condition was completed for each subject.

The analysis of these data used a relative response transformation of the response amplitude scores. For each block of trials the amplitude score (in voltage units) for each condition was normalized, that is, expressed as a proportion of the total amount of responding in that block, in order to equate the contribution of each block of trials to the total, as the amplitude of the reflex across days may have been affected variously by the levels of drug effective at the time. Then a mean for each condition was taken from the nine sets of normalized scores, and then the mean of each of the prepulse conditions was expressed as a proportion relative to the mean of the control condition. This proportion was then subtracted from 1.0 to give the value of the strength of reflex inhibition provided by each prepulse level, relative to the size of the control response. These resulting data were subjected to repeated measures analyses of variance (ANOVA). The probability values associated with the *F*-values were calculated using the Huynh–Feldt adjustments for degrees of freedom.

At the end of the behavioral experiment the hearing of the two groups of mice was tested using standard brain stem evoked response audiometry (see Ison *et al.*, 1997, for procedural details). ABR audiograms were provided using tone bursts presented at 11/s having 5-ms durations, 1-ms cosine shaped rise–fall times (10%–90%), and center frequencies of 4, 8, 10, 12, 16, 24, and 36 kHz. Each averaged response was comprised of 300–500 stimulus presentations, with the ABR recorded over a time epoch of 10 ms. The stimulus level was lowered in 10 dB SPL and then 5-dB steps to below the threshold of the most prominent wave, typically wave 4/5, appearing at about 5 ms. The data were analyzed by repeated measures ANOVA, again using the Huynh–Feldt adjustments.

## II. RESULTS

### A. Masking and the effects of spatial location

Figure 1 displays the mean inhibitory effects of the high- and low-frequency signals on the acoustic startle reflex under the several masking conditions, the younger mice in the upper portion of the figure, the older mice in the lower. Increasing the level of the signal increased its inhibitory effect (as seen in the open symbols), which is a basic finding in experiments on reflex inhibition (see Hoffman and Ison, 1980). The overall effect of the noise on reflex inhibition was identical to those seen previously in human subjects run under similar conditions (Reiter and Ison, 1979) in that the masking effect of the noise was maximal with weak signals and then declined and finally disappeared with stronger signals (as seen in the comparison of solid and open symbols). In both subject populations, humans and mice, increasing the level of the signal provided a “recruitment” type of effect on reflex inhibition similar to that shown for loudness judgments in the psychophysical data presented in the classic report of Steinberg and Gardner (1937). The degree of masking was reduced when the 25-kHz signal and its high-frequency masker were presented from different locations, the signal on the left and the masker moved 180 degrees to the right (seen in the comparison of the two sets of solid symbols at the

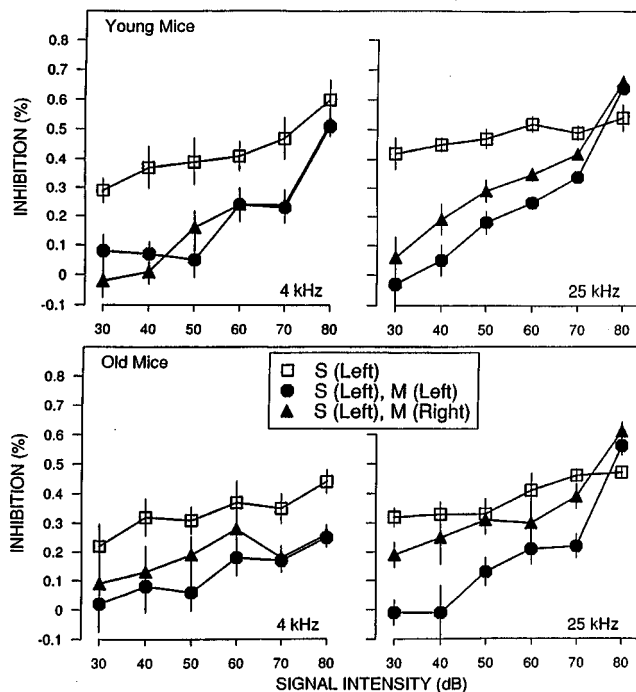


FIG. 1. Relative strength of reflex inhibition ( $\pm 1$  SEM) for signals of 4 and 25 kHz, presented in isolation 120 ms before the startle stimulus (open square), or against a background of 1-octave band noise from the same location (solid circle) or from the contralateral location (solid triangle). Data from young mice (4 months old at the beginning of testing) are at the top, data from old mice (20 months old) at the bottom.

right of Fig. 1), while there was no systematic difference between the two locations of the low-frequency masker for the 4-kHz signals (seen on the left side the figure). To the extent that age effects were present in the data depicted in Fig. 1, they were seen as a slight overall decrement in inhibition in older mice, and, if anything, as a slight increase in “release from masking” provided by the shift in the location of the high-frequency masker.

The increase in reflex inhibition provided by the increase in signal level led to a significant main effect in the ANOVA: for signal level,  $F(6/60)=127.70$ ,  $p<0.01$ ; and the decrement in reflex inhibition in the presence of the masking noise led to a second significant main effect: for masking condition:  $F(2/20)=60.56$ ,  $p<0.01$ . This effect of masking condition interacted with signal frequency,  $F(2/20)=6.72$ ,  $p<0.01$ , with signal level,  $F(12/120)=16.48$ , and with their interaction, for  $MC \times SF \times SL$ ,  $F(12/120)=6.11$ ,  $p<0.01$ . The older mice were less inhibited than the younger mice overall,  $F(1/10)=12.84$ ,  $p<0.01$ , and this effect of age interacted with the interaction of frequency level and signal level,  $F(6/60)=2.89$ ,  $p=0.02$ , but not with masking condition ( $p>0.30$ ).

A subsequent ANOVA compared the inhibitory effects of the nonmasked signal against that of the masked signal with the masker at the same location. The deleterious effect of the masker on the signal was significant,  $F(1/10)=101.63$ ,  $p<0.01$ , but this masking effect was reduced at the higher signal levels, for the  $MC \times SL$  interaction,  $F(6/60)=21.87$ ,  $p<0.01$ . It is noteworthy that this masking effect of the noise did not vary with age or with signal fre-

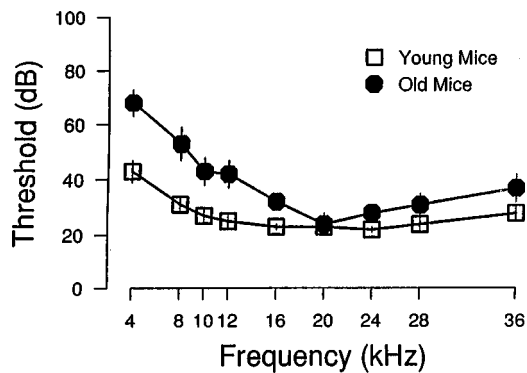


FIG. 2. Mean thresholds ( $\pm 1$  SEM) for frequencies ranging from 4 to 36 kHz measured with ABR methods, in young and old mice (8 months vs 22 months old at the time of testing).

quency,  $F_s < 0.01$ . Other ANOVA examined the effect that shifting the location of the masking noise had on the severity of masking, in comparisons of the two masked functions having solid symbols in Fig. 1. Here the most important outcome was that the reduction in the masking effect produced by changing the location of the masker depended on the frequency of the signal, for the masker location by SF interaction,  $F(1/10) = 11.00$ ,  $p < 0.01$ ; and separate ANOVA for each frequency alone showed that the relief from masking provided by shifting the location of the masker contralateral to the signal was significant for the high-frequency signal,  $F(1/10) = 31.10$ ,  $p < 0.01$ , but not for the low-frequency signal,  $p > 0.25$ . In general there was no significant effect of age on either the severity of masking or on the degree of masking release in this set of comparisons, for interactions of  $A \times L$ , all  $p > 0.10$ . Age effects were apparent only in their interaction with signal level for the 4-kHz signal, for  $A \times SL$ ,  $F(6/60) = 7.19$ ,  $p < 0.01$ , perhaps reflecting the observation that older mice appeared to show less inhibition than the young mice for the highest signal level, at 80 dB,  $F(1/10) = 16.66$ ,  $p < 0.01$ , but were not different at lower signal levels,  $F < 1$ .

### B. ABR measures of threshold in young and old mice

Figure 2 provides the mean thresholds from 4 kHz to 36 kHz in the two groups of mice. The old mice had higher thresholds than the younger mice, but their loss occurred primarily at the lower frequencies, below 16 kHz. The ANOVA of these data showed an age effect,  $F(1/10) = 9.38$ ,  $p < 0.02$ , which interacted with the significant frequency effect,  $F(8/80) = 4.84$ ,  $p < 0.01$ . Subsequent ANOVA showed that there was no significant age effect for 24 kHz and above ( $p = 0.1$ ), whereas there was significant loss of sensitivity for frequencies in the older mice below 16 kHz,  $F(1/10) = 12.54$ ,  $p < 0.01$ . These data are unusual as most age-related hearing loss in the mouse is apparent first for high-frequency signals, as in the C57BL/6J parent, or is a relatively flat loss, as in the CBA parent, for example. However, the findings are consistent with those reported by Erway *et al.* (1993) for this particular hybrid mouse. In the ABR data provided by Erway *et al.* the hybrid offspring of the C57 and CBA strains showed no loss in click thresholds from 12 months of age at least up to 23 months, indicating

that they must have a substantial band of frequencies for which there was no loss in hearing; but their 23 month old mice had a significant greater loss at low frequencies coupled with significant greater sensitivity at high frequencies in comparison to the old CBA parent. It will be noted that in the data of Erway *et al.* and in the present data the age-related loss of threshold sensitivity in the ABR was greatest for the 4-kHz frequency. This is the signal condition in the behavioral data showing less inhibition in the old mice compared to the young mice, although they were not significantly different in the severity of masking at either frequency.

### III. DISCUSSION

In this experiment the graded reduction in reflex inhibition obtained by presenting the signals at varying levels against a noise background shown here in the mouse is the same as that seen in a similar behavioral experiment with human subjects (Reiter and Ison, 1979), and both sets of data capture the characteristic "loudness recruitment" effect found for masked tones varying in level in psychophysical measures of loudness (Steinberg and Gardner, 1937). Our older mice had a modest impairment in threshold sensitivity as measured in the ABR, particularly at the lower frequency, and a similar slight decrement in reflex inhibition. We did not find that overall the masking effect of the noise background was more severe in our older mice, whereas this is the typical finding in the older human listener (Patterson *et al.*, 1982). We do note, however, that the age-related difference in masking is relatively small in listeners with minimal hearing impairment (Gelfand *et al.*, 1988), and perhaps the present experiment did not have sufficient power to detect what might be expected to be a small effect. It is also possible that the failure to find an increase in masking with age is in part a result of the age-related loss of inhibition for the less intense nonmasked signals apparent in Fig. 1. The level of inhibition for the unmasked signals provides the baseline against which masking is assessed, and the lower baseline in the older mice, plus the fact that masking was very strong even in young mice at the low and moderate signal levels, may have resulted in a "floor effect" for masking at these levels. There is some hint that masking was more severe in the older mice for higher signal levels, at which not only did the older mice show reasonably high levels of baseline inhibition but, also, masking was reduced for the young mice. For these values, at 70 dB and 80 dB, the greater difference for old compared to young animals between the inhibition scores provided by the unmasked signal and those provided by the signal coincident with the masker was of marginal significance,  $t(10) = 2.05$ ,  $p < 0.05$ , 1-tail.

There is a very small but consistent literature on changes in the ability to locate sound objects in space in aged or in hearing impaired laboratory animals. Brown (1984) and Harrison (1981) both found a loss of discrimination between spatial locations in aged rats, and Heffner and Donnal (1993) showing a similar effect in the C57BL mouse. The data of Heffner and Donnal (1993) must clearly be attributed to age-related hearing impairment rather than age alone, but the meaning of the effects obtained with aged rats is not certain as they may be more heterogeneous in their sensory impair-

ments than the inbred strains of mice. The one study of the changes in neural activity in the inferior colliculus that varied the spatial location of masker and signal (McFadden and Willott, 1994b) provided neurophysiological data generally consistent with the findings of Heffner and Donnal in their showing that the "masking release" associated with a change in the relative location of the masker was greater in the young C57BL mouse compared to the old mouse, although they also report evidence for masking release with relatively low-frequency signals that would not be expected to provide significant interaural level differences. It is generally thought that only interaural intensity differences are available to very small mammals such as mice (e.g., Brown, 1994), because the small interaural distance across their heads, approximately 3 cm, provides only slight interaural timing cues at onset, and the phase locking that provides interaural phase differences for larger mammals with low-frequency hearing are therefore not available to them. Indeed, the brain stem nuclei presumed to be sensitive to interaural phase relations in large mammals are poorly represented in small mammals (Heffner and Masterton, 1990). The behavioral data provided in the present experiment are consistent with this line of reasoning in their showing that moving the masker away from the signal reduced the severity of masking for the high-frequency but not the low-frequency masker, which, by hypothesis, could not provide interaural differences in signal versus masker level: but the data of McFadden and Willott raise the interesting possibility that under some conditions the mouse may have a second cue to spatial location.

The beneficial effect of shifting the masker away from the high-frequency signal was at least as powerful in our old mice as it was in the young mice. If the ability to detect changes in the location of a sound source is assumed to be related to the "unmasking" provided by a relative shift in spatial location, then this finding appears contrary to the various reports showing age-related decrements in spatial localization in rats and mice. There are several possible explanations for this apparent conflict. One is that we had a single extreme measure of the effects of shifting spatial location, by 180 degrees, and perhaps smaller shifts in the angle between the masker and the signal would have revealed more subtle changes: but on the other hand, the loss of spatial discrimination noted in rats was obtained with just two locations 180 degrees apart. A second possibility is that this hybrid mouse represents an example of hybrid vigor along several auditory dimensions, including not only a resistance against age-related changes in threshold sensitivity as measured in the ABR, but also against deterioration at those central auditory sites important for computing the spatial location of sound objects. This is an interesting hypothesis to test in future research with the homozygous C57BL/6J and CBA parent strains. The third explanation depends on the reasonable assumption that the one essential acoustic cue associated with the change in the relative locations of the signal and the masker for these mice is the resulting interaural difference in their relative levels, a cue that can be present only for high frequencies but would be available in old mice with good high-frequency hearing. A relative reduction in the level of

the high-frequency components of the now contralateral masker would be provided by the shadowing effect of the head and pinna at the ear ipsilateral to the signal, which would thus increase the signal-to-noise ratio at this ear, though, to be sure, the change in location would also result in an equivalent reduction in the signal-to-noise ratio at the ear contralateral to the signal. Assuming also that an old mouse, like the young mouse, is able to selectively respond to the ear with the better signal-to-noise ratio then the present results can be expected. The present outcome is very similar of that Gelfand *et al.* (1988), showing that aged human listeners with good high-frequency hearing benefit from the separation of signal and noise as much as do young listeners, and the acoustic cues available to our aged mice are likely to be those also available to the aged human.

#### IV. CONCLUDING REMARKS

The data on masking release presented here are not substantially different from those obtained under the more complicated conditions possible with aged human listeners, at least with the understanding that young human listeners use both temporal cues and level cues for determining spatial location, while the mouse has only the level cue. In humans the beneficial effect of shifts in spatial location are studied most often using earphone presentation of the stimuli, which, although they may assume configurations never obtained in the free field, allow complete control over both the temporal and the intensity cues that are important for humans in the free field. Pichora-Fuller and Schneider (1991) found no effects of age in "normal hearing" elderly versus young listeners when they compared masked thresholds for low-frequency tones in diotic masking conditions, but found that the elderly listeners showed less benefit from dichotic presentation, when the phase of either the noise or of the tonal signal was shifted by 180 degrees. Analogous effects were observed by Grose *et al.* (1994) for spondee recognition, again under earphone conditions with 180 degree shifts in the phase of the signal. These effects obtained in "normal hearing" aged humans seem different to those obtained in our "normal hearing" aged mouse, but the single cue to stimulus location in the human experiments was a difference in phase. These data strongly suggest that even "normal hearing" elderly humans have some difficulty in spatially locating the signal and the masker when only the temporal cue is available. Support for this idea is further provided in the data of Gelfand *et al.* (1988) who found no impairment in the benefit provided by a shift in the location of the signal relative to the masker in aged listeners with normal hearing in the free field, while they found a clear deficit in aged listeners with impaired hearing: the free field, in contrast to earphones, provides relative level information for signals and maskers at the two ears. These data, and our data as well, agree also with the report by Herman *et al.* (1977) that the ability to detect shifts in earphone lateralization for interaural level differences does not deteriorate with age. For the signals used in the present experiment, which had relatively long rise times so as to avoid a click at their onset, yet durations too brief to allow any orientation and subsequent "homing-in" on the signal as would be possible under com-

pletely natural conditions (for example, Ehret and Dreyer, 1984), only interaural differences in the relative levels of signal and masker could provide the cues to the changed location of the masker. We may hypothesize that in a similar behavioral experiment that used the hearing impaired C57BL/6J mouse as a subject the masking release attendant on the ability to separate masker and signal in space would diminish with age, unlike the persistence of this ability in their old F1 hybrid offspring, but in agreement with the perceptual effects shown by the impaired elderly listeners in the experiment of Gelfand *et al.* (1988): and, indeed, in agreement with the physiological data provided by McFadden and Willott (1994b).

## ACKNOWLEDGMENTS

This research was supported by USPHS Research Grant No. AG09524, a Center Support Grant to the Center for Visual Science, EY01319, and by the Rochester International Center for Hearing and Speech Research.

- Bronkhorst, A. W., and Plomp, R. (1988). "The effect of head-induced interaural time and level differences on speech intelligibility in noise," *J. Acoust. Soc. Am.* **83**, 1508–1516.
- Brown, C. H. (1984). "Directional hearing in aging rats," *Exp. Aging Res.* **10**, 35–38.
- Brown, C. H. (1994). "Sound localization," in *Comparative Hearing: Mammals*, edited by R. R. Fay and A. N. Popper (Springer-Verlag, New York), Chap. 4, pp. 57–96.
- Colburn, H. S. (1982). "Binaural interaction and localization with various hearing impairments," *Scand. Audiol. Suppl.* **15**, 27–45.
- Colburn, H. S., Barker, M. A., and Milner, P. (1982). "Free-field tests of hearing-impaired listeners: Early results," *Scand. Audiol. Suppl.* **15**, 123–133.
- Colburn, H. S., Zurek, P. M., and Durlach, N. I. (1987). "Binaural directional hearing—Impairments and aids," in *Directional Hearing*, edited by W. A. Yost and G. Gourevitch (Springer-Verlag, New York), pp. 261–278.
- Duquesnoy, A. J. (1983). "Effect of a single interfering noise or speech source upon the binaural sentence intelligibility of aged persons," *J. Acoust. Soc. Am.* **74**, 739–743.
- Ehret, G., and Dreyer, A. (1984). "Localization of tones and noise in the horizontal plane by unrestrained house mice (*Mus musculus*)," *J. Exp. Biol.* **109**, 163–174.
- Erway, L. C., Willott, J. F., Archer, J. R., and Harrison, D. E. (1993). "Genetics of age-related hearing loss in mice: I. Inbred and F1 hybrid strains," *Hearing Res.* **65**, 125–132.
- Fay, R. R. (1988). *Hearing in Vertebrates: A Psychophysics Databook* (Hill-Fay Associates, Winnetka, IL).
- Gelfand, S. A., Ross, L., and Miller, S. (1988). "Sentence reception in noise from one versus two sources: Effects of aging and hearing loss," *J. Acoust. Soc. Am.* **83**, 248–256.
- Grose, J. H., Poth, E. A., and Peters, R. W. (1994). "Masking level differences for tones and speech in elderly listeners with relatively normal audiograms," *J. Speech Hear. Res.* **37**, 422–428.
- Harrison, J. M. (1981). "Effects of age on acquisition and maintenance of a location discrimination in rats," *Exp. Aging Res.* **7**, 467–476.
- Heffner, R. S., and Masterton, B. (1990). "Sound localization in mammals: Brainstem mechanisms," in *Comparative Perception, Vol. I*, edited by M. A. Berkley and W. C. Stebbins (Wiley, New York), pp. 285–314.
- Heffner, R. S., and Donnal, T. (1993). "Effect of high frequency hearing loss on sound localization in mice (C57BL/6J)," *Abstr. Assn. Res. Otolaryngol.* **16**, 49.
- Henry, K. R., and Chole, R. A. (1980). "Genotypic differences in behavioral, physiological and anatomical expressions of age-related hearing loss in the laboratory mouse," *Audiology* **19**, 369–383.
- Herman, G. E., Warren, L. R., and Wagener, J. W. (1977). "Auditory lateralization: Age differences in sensitivity to dichotic time and amplitude cues," *J. Gerontol.* **32**, 187–191.
- Hirsh, I. J. (1948). "The influence of interaural phase on summation and inhibition," *J. Acoust. Soc. Am.* **20**, 536–544.
- Hoffman, H. S., and Ison, J. R. (1980). "Principles of reflex modification in the domain of startle: I. Some empirical findings and their implications for the interpretation of how the nervous system processes sensory input," *Psychol. Rev.* **87**, 175–189.
- Hoffman, H. S., and Ison, J. R. (1991). "The application of reflex modification to the analysis of sensory processing in developmental and comparative research," in *Attention and information processing in infants and adults: Perspectives from human and animal research*, edited by B. A. Campbell, H. Hayne, and R. Richardson (Erlbaum, Hillsdale, NJ), pp. 83–111.
- Ison, J. R., Payman, G. H., Palmer, M. J., and Walton, J. P. (1997). "Nimodipine at a dose that slows ABR latencies does not protect the ear against noise," *Hearing Res.* **106**, 179–183.
- Li, H. S., and Borg, E. (1991). "Age-related loss of auditory sensitivity in two mouse genotypes," *Acta Oto-Laryngol.* **111**, 827–834.
- McFadden, S. L., and Willott, J. F. (1994a). "Responses of inferior colliculus neurons in C57BL/6J mice with and without sensorineural hearing loss: Effects of changing the azimuthal location of an unmasked pure-tone stimulus," *Hearing Res.* **78**, 115–131.
- McFadden, S. L., and Willott, J. F. (1994b). "Responses of inferior colliculus neurons in C57BL/6J mice with and without sensorineural hearing loss: Effects of changing the azimuthal location of a continuous noise masker on responses to contralateral tones," *Hearing Res.* **78**, 132–148.
- Patterson, R. D., Nimmo-Smith, I., Weber, D. L., and Milroy, R. (1982). "The deterioration of hearing with age: Frequency selectivity, the critical ratio, the audiogram, and speech threshold," *J. Acoust. Soc. Am.* **72**, 1788–1803.
- Pichora-Fuller, M. K., and Schneider, B. A. (1991). "Masking-level differences in the elderly: A comparison of antiphasic and time-delay dichotic conditions," *J. Speech Hear. Res.* **34**, 1410–1422.
- Reiter, L. A., and Ison, J. R. (1979). "Reflex modulation and loudness recruitment," *J. Aud. Res.* **19**, 201–207.
- Shaw, E. A. G. (1974). "Transformation of sound pressure level from the free field to the eardrum in the horizontal plane," *J. Acoust. Soc. Am.* **56**, 1848–1861.
- Steinberg, J. C., and Gardner, M. B. (1937). "The dependence of hearing impairment on sound intensity," *J. Acoust. Soc. Am.* **9**, 11–23.
- Tonning, F. M. (1975). "Auditory localization and its clinical applications," *Audiology* **14**, 368–380.
- Walton, J. P., Frisina, R. D., Ison, J. R., and O'Neill, W. E. (1997). "Neural correlates of behavioral gap detection in the inferior colliculus of the young CBA mouse," *J. Comp. Physiol. A* **181**, 161–176.
- Warren, L. R., Wagener, J. W., and Herman, G. E. (1978). "Binaural analysis in the aging auditory system," *J. Gerontol.* **33**, 731–736.
- Willott, J. F. (1996). "Anatomic and physiologic aging: a behavioral neuroscience perspective," *J. Am. Acad. Audiol.* **7**, 141–151.
- Young, J. S., and Fechter, L. D. (1983). "Reflex inhibition procedures for animal audiometry: A technique for assessing ototoxicity," *J. Acoust. Soc. Am.* **73**, 1686–1693.



# Changes in temporal acuity with age and with hearing impairment in the mouse: A study of the acoustic startle reflex and its inhibition by brief decrements in noise level

James R. Ison, Punit Agrawal, James Pak, and William J. Vaughn

Department of Brain and Cognitive Sciences, Meliora Hall, University of Rochester, Rochester, New York 14627

(Received 8 August 1997; accepted for publication 28 April 1998)

Temporal acuity for brief gaps in noise was studied in mice of different ages (1–36 months) from strains with differing susceptibility to age-related hearing loss, using reflex modification audiometry. Prepulse inhibition of the acoustic startle reflex (ASR) increased with gap depth (GD: 10–40 dB in 70 dB SPL noise) and lead time (LT: 1–15 ms). The increase in inhibition with LT followed an exponential function in which the two parameters, asymptotic inhibition (AINH) and the time constant ( $\tau$ ), were both affected by GD. AINH rapidly declined from 1 to 6 and then to 18 months of age in C57BL/6J mice with progressively severe hearing loss, but first increased with maturation and then gradually declined beyond 6–12 months of age in CBA/CaJ and CBA×C57BL F1-hybrid mice, which show no apparent change in sensory function at these ages. In contrast,  $\tau$  was unaffected by hearing loss or by age, this suggesting that age-related changes in this form of temporal acuity occur because of a reduction in the efficiency with which gaps are centrally processed, not from any reduced ability to follow their rapid shift in noise level. © 1998 Acoustical Society of America. [S0001-4966(98)03608-X]

PACS numbers: 43.80.Lb, 43.66.Sr, 43.66.Mk [FD]

## INTRODUCTION

The objective of this research was to describe developmental changes in temporal acuity in auditory processing in the mouse over the life span, from early maturation to late senescence. Temporal acuity was measured by a variant of the “gap detection” paradigm, which is assumed to measure the sensory persistence of a stimulus after its physical offset (Plomp, 1964). The behavioral method of reflex modification audiometry (Young and Fechter, 1983) was used in the present work to exploit the observation that the offset of a background noise inhibits the acoustic startle reflex (ASR) if it is presented immediately before the noise burst that normally elicits the reflex (Stitt *et al.*, 1973). One strain of mice, the C57BL/6J, was chosen for its well-characterized age-related hearing loss, and two others, the CBA/CaJ and the F1 hybrid of a C57 and the CBA, because of their minimal expression of hearing loss with age (see Henry and Chole, 1980; Li and Borg, 1993; Mikaelian, 1979; and especially Willott, 1996).

Gap detection thresholds improve with age in children (for example, Davis and McCroskey, 1980; Irwin *et al.*, 1985; and others) and rat pups (Kellogg *et al.*, 1983; Dean *et al.*, 1990), and are then raised in aged compared to young adult humans (McCroskey and Davis, 1976, cited in McCroskey and Kasten, 1982; Schneider *et al.*, 1994; Snell, 1997), and also in aged mice compared to young mice (Ison *et al.*, 1993). Threshold changes are seen especially in aged listeners with sensorineural hearing loss (for example, Lutman, 1990; Moore *et al.*, 1992), which also increases gap detection thresholds in young humans (for example, Fitzgibbons and Wightman, 1982; Buss and Florentine, 1985; and

others), and young chinchillas (Giraudi-Perry *et al.*, 1982; Salvi and Arehole, 1985).

Gap detection, which is accepted as a simple and convenient measure of temporal acuity, has been shown to correlate with measures of speech perception in humans (Tyler *et al.*, 1982), and it is therefore encouraging that the alteration of gap thresholds with age and hearing loss seen in humans, described above, can be captured in animal models that afford the possibility of studying its physiological bases (Walton *et al.*, 1997). In this latter pursuit, it is of considerable interest to determine if these observed changes in gap detection thresholds are necessarily best understood as an effect of age and/or hearing loss on an intrinsic temporal characteristic of auditory function, or whether, instead, the effects might be better interpreted as a change in the overall “efficiency” of a central detection mechanism. This theoretical distinction was introduced by Patterson *et al.* (1982) in an abstract model intended to account for the effects of age on the critical ratio and masking in human listeners, and it was subsequently extended to gap detection by Plack and Moore (1990). Hall and Grose (1994) found that the improvement in temporal acuity seen in children (not using gap detection, but temporal modulation transfer functions to measure temporal acuity) resulted from an increase in the efficiency of a central processor in detecting a shift in the level of its afferent input, rather than to a change in ability to follow and encode the temporal course of the amplitude modulated stimulus. Given these data we were then concerned to see if a similar account might be appropriate for gap detection obtained under various conditions in the mouse.

In our previous work we have shown that noise offset is in fact inhibitory, that is, it reduces the ASR below that

obtained when the reflex is elicited in the absence of the background noise (Ison, 1982). Further, for gaps of the same sized decrement but beginning at different background levels, neither the rate of development of inhibition nor its asymptote varies with noise level, but larger decrements result in different asymptotic levels of inhibition; further, explicit variation in decay time at the beginning of the gap alters the rate of development of inhibition (Ison *et al.*, 1996): the implications of these findings are that in the present experiment reflex inhibition should be little affected by at least moderate shifts in the audibility of the noise carrier (as is true also for psychophysical experiments with human listeners: Buss and Florentine, 1985); that a change in the “internal” signal-to-noise ratio of the neural representation of gaps, which would be expected from a change in processing efficiency, should be evident in a change in the asymptotic level of inhibition; and a change in its “internal” decay time indicative of a change in an intrinsic temporal process should be apparent in the time course of inhibition rather than in its asymptotic level.

## I. METHOD

### A. Subjects

The subjects were 156 mice (92 male and 64 female), 24 acquired as breeding stock from the Jackson Laboratories and Harlan Sprague Dawley, and 132 born and raised in the vivarium at the University of Rochester. The strains and nominal ages at testing were as follows: the C57BL/6J at 1 month of age ( $n=6$ ), 3 months ( $n=6$ ), 6 months ( $n=15$ ), 1 year ( $n=10$ ), and 18 months ( $n=9$ ); the CBA/CaJ at 1 month of age ( $n=7$ ), 3 months ( $n=6$ ), 6 months ( $n=6$ ), 1 year ( $n=10$ ), 18 months ( $n=12$ ), and 2 years ( $n=9$ ); and the F1-hybrid cross of a CBA male and a C57BL female at 1 month of age ( $n=8$ ), 2 months ( $n=9$ ), 3 months ( $n=13$ ), 6 months ( $n=8$ ), 1 year ( $n=6$ , all of which had been tested at 6 months of age), 2 years ( $n=19$ , three previously tested at 6 months of age), and 3 years ( $n=10$ , four of which had been tested at 2 years of age). The actual ages varied slightly from those listed above because of limitations in the availability of subjects of specified ages and because the testing time varied from 7 days to about 14 days across different cohorts. The actual mean ages for the groups are given in the results section. The mice were maintained generally in group cages, rarely in single cages because of fighting, under conditions of constant temperature and humidity, with a 12-12 h light-dark cycle (lights on at 6 a.m.). Food and water were available at all times. Tests were run from about 9 a.m. to 5 p.m.

### B. Apparatus

The subjects were confined for testing in a cage made of acrylic plastic (7 cm long, 5 cm wide, and 4 cm high) with slotted sides and roof for free sound penetration, which could be mounted on a suspended acrylic platform directly over an attached accelerometer (model SA-2-300, Statham Laboratories, Beverly Hills, CA). The platform was placed in an anechoic chamber (inside dimensions  $84 \times 84 \times 84$  cm, manufactured by the Eckel Corp., Cambridge MA). The acceler-

ometer was sensitive to the vertical force exerted in the startle reflex, and its output was amplified and then integrated over a 100-ms interval beginning with the startle stimulus. The startle stimulus was a noise burst provided by a wideband noise generator that was gated through an electronic switch, amplified, then delivered through a high-frequency speaker. It was presented at 115 dB SPL, and was 20 ms in duration with near instantaneous rise and fall times. The subjects were run in a noise background at 70 dB SPL, provided by the same noise generator but delivered through a Panasonic high-frequency leaf tweeter. The level of the background noise was controlled by programmable attenuators with near instantaneous response times. The spectrum of the startle stimulus varied by no more than  $\pm 2$  dB over a range of octave bands centered at 1–32 kHz, while the noise background varied by no more than  $\pm 6$  dB over a range of 2–100 kHz. (These were measured with a 1/4-in. Bruel & Kjaer microphone, model 4135, connecting to a measuring amplifier, Bruel & Kjaer, model 2610.) Stimulus presentation and response recording were under computer control.

### C. Procedure

The subjects received trials on which the startle stimulus was delivered alone in the noise background and trials on which the startle stimulus was preceded by the partial offset of the noise, to noise floors of 30, 40, 50, or 60 dB (gap decrements (GD) of 40, 30, 20, and 10). These decrements led the onset of the startle stimulus by 1, 2, 4, 6, 8, 10, or 15 ms. The experiment was continued over 4 test days, each 2–4 days apart. On any one test day only one level within the gap was used but all of the gap intervals were presented in random order within blocks of trials. Each block consisted of three control trials (with startle stimuli not preceded by a gap, in order to provide the baseline startle response), and one each of the gap conditions, for a total of ten trials within each block. Eleven blocks were presented on each day with a mean interval between trials of 20 s. The order of testing for the different floor levels was random.

### D. Data analysis

Two indices of response strength were used for the primary statistical analyses. For the first, mean integrated response amplitudes (in units that are linearly related to volts) were calculated within subjects for each stimulus condition. This measure for the baseline control response was useful for assessing the effects of age and strain on the average force exerted in the startle reflex, that is, for showing the effect of maturation, senescence, and hearing loss on the baseline acoustic reflex response. The second measure provided the fundamental index of reflex inhibition, and was based on the ratio formed by dividing the inhibited response amplitude score for each condition for each mouse by the baseline control response for that subject in that particular floor condition (that is,  $1 - \text{mean prestimulus condition}/\text{mean control}$ ). This relative inhibition measure provided the metric on which the temporal course of inhibition ( $\tau$  values) and the asymptotic levels of inhibition (AINH values) were determined from the formula

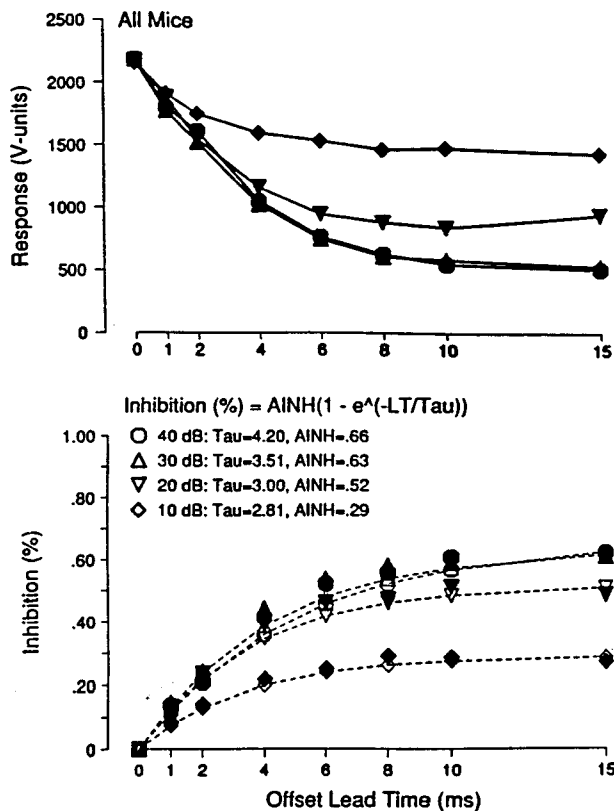


FIG. 1. (Top) Mean amplitudes of the acoustic startle reflex on control trials (at 0 ms) and on trials when the startle stimulus was preceded by a decrement in a 70-dB background noise of 10–40 dB, at lead intervals of 1–15 ms, for all subjects. (Bottom) Mean relative inhibition of the startle response for these same stimulus conditions, obtained data in the solid symbols, and calculated values derived from an exponential growth function in open symbols connected by broken lines. The inset gives the parameter values for each noise decrement, as the time constant ( $\tau$ ) and the asymptotic value for inhibition (AINH).

$$\text{Relative inhibition} = AINH(1 - e^{-LT/\tau})$$

with LT as the lead time of noise offset. Both response measures were analyzed by mixed design analyses of variance (ANOVA) in which strain and age were the between-*S* variables and gap duration and floor level were the within-*S* variables. Degrees of freedom for repeated measures were adjusted for nonhomogeneity of between cell correlations by the Hunyh–Feldt procedure.

## II. RESULTS

### A. Overall analysis of LT and GD at noise offset

Figure 1 presents the mean values for the two major response indices, ASR amplitude in the upper portion and relative inhibition in the lower, as they varied with the lead time and the depth of the noise decrement, this taken across all groups. Inhibition increased with LT towards an asymptotic limit determined by GD, but it may be noted that even the smallest decrement (10 dB) at the smallest LT (1 ms) significantly reduced the ASR,  $F(1/150) = 29.90$ ,  $p < 0.01$ , and there was also a small but significant difference between the noise floors at this interval,  $F(3/450) = 4.63$ ,  $p < 0.01$ . The solid symbols in the lower portion of Fig. 1 give the observed data points for relative inhibition across the

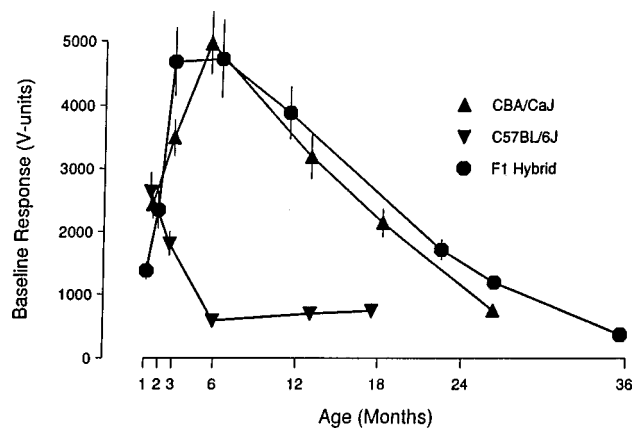


FIG. 2. Mean amplitudes for the baseline control reflex ( $\pm 1$  SEM) for each of three strains of mice at each age.

entire set of subjects, and the open symbols are the predicted values provided by the best fitting exponential function, these values being highly correlated,  $r = +0.994$ . The two parameters of this function for each of the noise floors are given in the upper left corner in this figure. The size of the noise decrement affected both parameters, a greater decrement resulting in a slower growth rate of inhibition but also a greater asymptotic level of inhibition. The inferential analysis of these parameters was complicated because while grouped data were stable and suitable for curve fitting, the data provided by individual subjects often had random irregularities, particularly for the lower GD, which could not be reasonably fit with an exponential function. For this reason the analysis of the differences in AINH described in Fig. 1 used the obtained values for relative inhibition for each subject at the 10- and 15-ms intervals as the surrogates for the predicted values. This analysis of variance showed an overall significant effect for GD,  $F(3/504) = 96.86$ ,  $p < 0.01$ , large and significant differences between the adjacent 10- vs 20-dB and the 20- vs 30-dB decrements ( $p < 0.01$ ), and a small but significant difference between the 30- vs 40-dB decrements ( $p < 0.05$ ). A second surrogate measure was devised to analyze the growth rates, in which the values of inhibition for each subject became proportions of maximum inhibition in that particular condition (for example, the data for a subject with 30% inhibition at 2 ms and 60% at 15 ms would be converted to scores of 50% at 2 ms and 100% at 15 ms). These relative growth values were analyzed by a nonparametric test of proportions, with the values for each adjacent noise floor subtracted from each other for each lead time. This analysis showed that the relative growth of inhibition was greater for the 10-dB vs the 20-dB decrement at 1 ms ( $p = 0.056$ ); for the 20-dB vs the 30-dB decrement at 2, 4, 6, and 10 ms; and for the 30-dB vs 40-dB decrement at 2 ms (all  $p < 0.05$ ), indicating that the inhibitory effect of the smaller noise decrement was approaching its (smaller) asymptotic level at a faster relative rate than the adjacent greater decrement.

### B. Startle response baseline

Figure 2 presents the mean ASR control values for each age and strain. The age-related patterns in ASR amplitudes

for the CBA and the F1 mice were similar, with an increase from 1 to 3 or to 6 months of age (maturation) followed by a steady decline in response amplitudes (senescence). In contrast, the C57 mouse responded most vigorously at 1 month of age, with substantial decrements to 3 and then to 6 months, and a constant but low level of responding apparent from 6 to 18 months of age. The overall analyses of the effects of age within each strain were all significant ( $p < 0.01$ ). Within the C57BL strain, analyses of adjacent ages showed that the drop from 1 to 3 months was significant,  $F(1/10) = 5.29$ ,  $p < 0.05$ , as was that from 3 to 6 months,  $F(1/19) = 88.56$ ,  $p < 0.01$ , while ASR values at 6, 12, and 18 months were not different ( $p > 0.20$ ). Within the CBA strain ASR increases from 1 to 3 months and from 3 to 6 months were both significant,  $F(1/11) = 8.87$ ,  $F(1/10) = 7.09$ ,  $p < 0.05$ , as were the subsequent declines from 6 to 12 months of age, from 12 to 18 months of age, and from 18 to 26 months of age:  $F(1/14) = 9.52$ ,  $p < 0.01$ ;  $F(1/20) = 6.97$ ,  $p < 0.05$ ;  $F(1/19) = 29.31$ ,  $p < 0.01$ . Within the F1-hybrid strain the increases from 1 to 2 months of age and from 2 to 3 months of age were both significant,  $F(1/15) = 11.51$ ,  $F(1/20) = 16.50$ ,  $p < 0.01$ ; as were the decrements in response from 12 to 22 months,  $F(1/17) = 42.04$ ,  $p < 0.01$ , from 22 to 26 months,  $F(1/17) = 6.96$ ,  $p < 0.05$ , and from 26 to 36 months,  $F(1/22) = 234.39$ ,  $p < 0.01$ . Comparing across the three strains, for young mice averaging 6 weeks of age there was no difference in the ASR,  $p > 0.05$ , while at 3 months of age the C57BL strain responded less than the CBA and F1-hybrid strains,  $F(2/30) = 13.41$ ,  $p < 0.01$ . ASR amplitudes for the CBA and the hybrid F1 strains were significantly different only at 26 months of age,  $F(1/13) = 40.86$ ,  $p < 0.01$ . The 3-year-old F1 mice responded less vigorously (mean ASR=355) than the 2-year-old CBA mice (ASR=737) and the 18-month-old C57BL mice (ASR=730),  $F(2/25) = 10.28$ ,  $p < 0.01$ , which were not different from each other,  $p > 0.2$ . The mean ASR of each of these groups save the 3-year-old F1 hybrids was significantly higher than would be expected on the basis of spontaneous activity in the absence of a startle stimulus, which in other experiments typically has had a median value of 200–250 V units.

### C. Effects of age and hearing loss on the parameter values for relative inhibition

Eight  $\tau$  values are missing because the obtained group means for those conditions could not be fitted successfully with the exponential formula, six of them because the level of inhibition was zero at 10 and 15 ms. For these six scores the AINH value was taken as 0.

#### 1. Asymptotic levels of inhibition (AINH)

Figure 3 presents the calculated AINF values at each GD for each age and each strain, the C57BL at the top, the CBA in the center, and the F1-hybrid mouse at the bottom. The effect of hearing loss, which must be entirely responsible for the early changes seen in the C57BL data, but was confounded with senescence in the oldest group of this strain, was to substantially reduce AINH, especially for the higher GD. This change was apparent at 3 months, and while noise

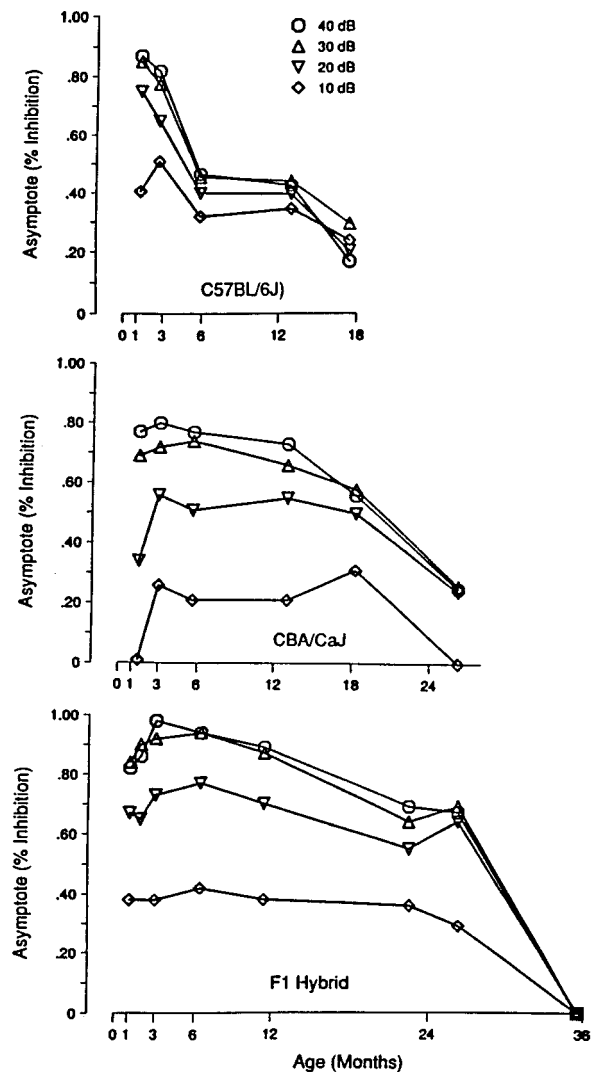


FIG. 3. Calculated values for asymptotic levels of inhibition, provided for each group on the basis of the data included in Fig. 1 (bottom), for each of the three strains and the four stimulus conditions, at each age.

decrements still provided significant inhibition at 18 months ( $p < 0.01$ ), there was no differential effect of GD at this age. There were two effects of age in the CBA and F1-hybrid strains: a modest maturational effect of increasing inhibition that lasted up to 3 or 6 months of age, followed by a senescence effect beginning at 6 or 12 months of age, possibly confounded with an increasing degree of hearing loss beyond 18 months of age. The analysis of variance of all three strains through 12 months of age (in which the two earliest F1 groups were combined, their mean age approximating that of the CBA and C57BL strains, at 1.5 months) provided significant effects for strain,  $F(2/98) = 24.07$ ,  $p < 0.01$ ; for age,  $F(3/98) = 7.96$ ,  $p < 0.01$ ; and for their interaction,  $F(6/98) = 9.72$ ,  $p < 0.01$ . All of these effects interacted with GD (beyond  $p < 0.01$ ), which attests to the reliability of the data showing that the decremental effects of hearing loss and senescence were both more pronounced when there was a greater noise decrement. In the young mice below 3 months of age, the C57BL mouse and the F1-hybrid mice did not differ from each other, but both showed greater inhibition than the comparable CBA mouse. In contrast, at 6 and 12

months of age the C57BL mice showed less inhibition than the CBA, a difference to be understood as some consequence of hearing loss in the C57BL strain, while the difference favoring the F1-hybrid over the CBA strain remained. An analysis of the data at 1.5 vs 6 months in the hybrid and the CBA mice showed that the overall increase in inhibition between these ages was significant,  $F(1/36)$ ,  $p < 0.05$ , supporting the reliability of the graphic indication that the processes responsible for the detection of the noise decrements or for their inhibitory effects matured with age. In contrast, the C57BL mouse showed a significant overall decline in inhibition over this same period,  $F(1/19) = 29.66$ ,  $p < 0.01$ , which can be again attributed to its early onset hearing loss. In fact, in the C57BL mouse the decrement in inhibition was significant for the greater noise decrements in the comparison of the 1 vs 3 month data,  $F(1/10) = 5.90$ ,  $p < 0.05$ . Across all three strains combined, there were no significant age differences in inhibition between the ages of 6 and 12 months. However, it is interesting that even with its evident substantial hearing loss at 6 and 12 months of age the inhibitory effect of the 10-dB decrement was greater in the C57BL than in the CBA,  $F(1/37) = 4.11$ ,  $p < 0.05$ , and equal in strength to that of its F1-hybrid offspring.

The inhibitory effect of the noise decrements diminished beyond 12 months of age in each strain. For the C57BL there was a significant and general decrement in inhibition at 18 months compared to the apparent plateau of 6 and 12 months,  $F(1/32) = 7.65$ ,  $p < 0.01$ , even in the absence of changes in the control ASR baseline. For the CBA mouse at 18 compared to 12 months there was a selective loss of inhibition for the higher noise decrements, this was apparent in an interaction between age and GD,  $F(3/60) = 4.36$ ,  $p < 0.05$ ; and at 26 compared to 18 months of age there was a general loss of inhibition across all of the stimulus conditions including the smallest decrements,  $F(1/19) = 73.19$ ,  $p < 0.01$ . In the F1 mouse at 22 compared to 12 months of age there was a significant loss of inhibition with age,  $F(1/17) = 8.00$ ,  $p < 0.01$ , and a marginal age  $\times$  GD interaction,  $F(1/17) = 3.46$ ,  $p = 0.08$ , resulting because there was no change with age with the 10-dB decrement,  $F < 1$ , but a loss for the larger decrements,  $F(1/17) = 8.84$ ,  $p < 0.01$ . The 22 month group did not differ from the 26-month-old mice, but from 26 to 36 months there was a total loss of inhibition. However, the interpretation of this observation is confounded by the particularly low level of the startle baseline obtained in the most aged mice.

## 2. The time constant for the development of inhibition ( $\tau$ )

Figure 4 presents the  $\tau$  values for each of the groups. The median  $\tau$  value was 3.37 ms, the interquartile range 2.66–4.09 ms. The  $\tau$  values showed the same modest effect of GD seen in the overall analysis, above, being in general greater for large compared to small decrements in noise (thus, 14 of the 18 groups had lower  $\tau$  values for their lowest compared to their highest decrement,  $p < 0.05$ ). No systematic effect of age or hearing loss on the growth rates for inhibition is evident in Fig. 4: thus for the C57BL, going across all stimulus conditions from one age to the next there

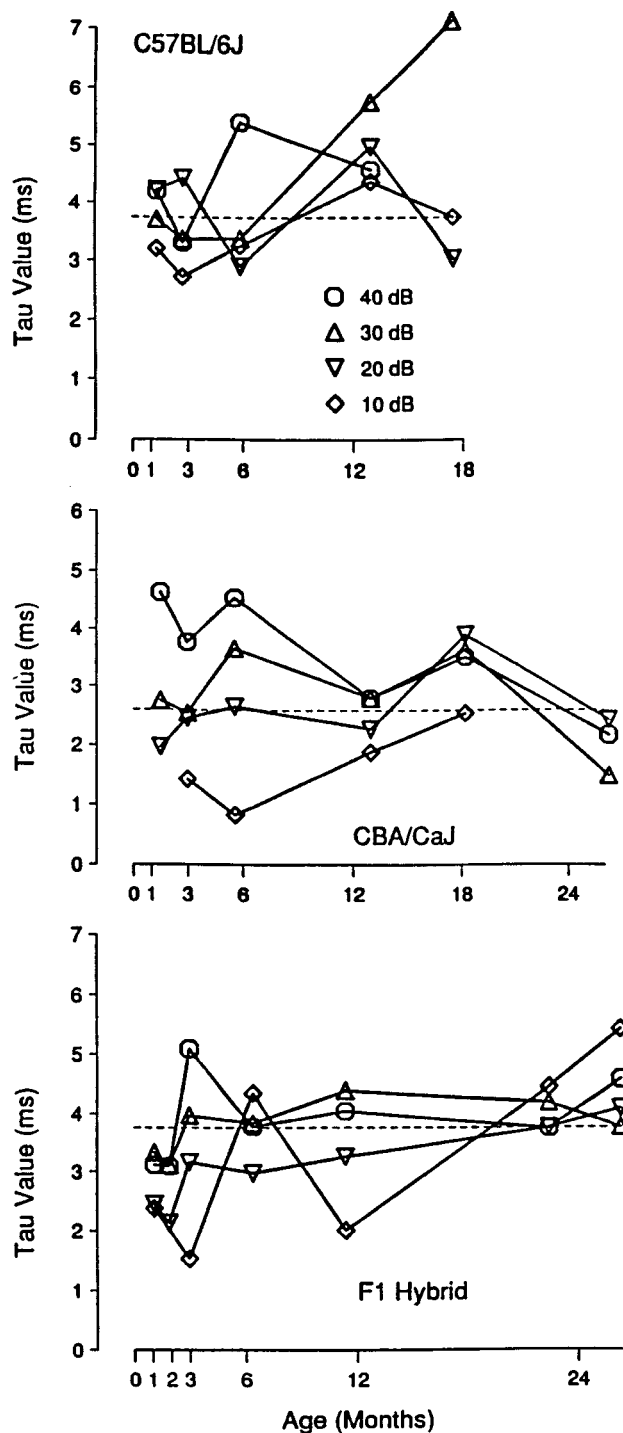


FIG. 4. Calculated values for the time constant  $\tau$ , provided for each group on the basis of the data included in Fig. 1 (bottom), for each of the three strains and the four stimulus conditions, at each age. Eight data points are not included, six because the stimulus did not inhibit the response, and two because the obtained functions were too irregular.

were eight increments in  $\tau$  and seven decrements; for the CBA, nine increments and nine decrements; and for the F1-hybrid, 12 increments and nine decrements; and across all three strains, looking just at changes in  $\tau$  beyond 12 months of age, there was a total of ten increments and eight decrements. The null hypothesis that the time course for the development of inhibition does not change with age or with hearing impairment seems to be strongly suggested in these

data, especially in comparison to their large significant systematic consequences for asymptotic levels of inhibition.

### III. DISCUSSION

#### A. Changes in ASR amplitudes with age and hearing impairment

The ASR increases in the first month of life in C57BL mice (Shnerson and Willott, 1980), in parallel with the development of auditory function seen in compound action potentials (Shnerson and Pujol, 1981). Parham and Willott (1988) reported that ASR levels progressively decline in the middle aged C57BL mice, 6 and 10 months of age, while older CBA mice show relatively small but progressive decrements at 12 and then 18 months. Our findings generally agree with this report, save that we found that CBA mice, like the F1 hybrid offspring, were most reactive in middle age, with smaller reactions at and beyond 12 months of age and below 2 to 3 months of age. A similar nonmonotone age effect is apparent in humans. Ornitz *et al.* (1986) showed an ASR increase in children at least up to 8 years of age, and Ford *et al.* (1995) showed a ASR decrement in aged compared to young adults (mean ages 69 vs 22 years). While the early ASR decrement in the C57BL must be a consequence, either primary or secondary, of its rapidly developing hearing loss, in general ASR age effects seem not best attributed to changes in auditory function, at least as auditory function is captured in detection thresholds. Profound changes in muscle mass and muscle composition are apparent during early development (Wirtz *et al.*, 1983) and in late senescence (Einseidel and Luff, 1992), and these must account for some of the age-related changes in the ASR. But Krauter *et al.* (1981) showed that the startlelike reflex elicited by a cutaneous stimulus was affected by age much less than was the ASR, suggesting that some change in the auditory system is important for the age effect on the ASR. Willott and Bross (1990) found age-related changes in the numbers, density, and dendritic arborization of octopus cells of the ventral cochlear nucleus, particularly in the first year of life in the C57BL and in the second year in the CBA. These periods coincide with the substantial loss in the vigor of the ASR even in mice that typically have no evident signs of hair cell pathology. Although it is not certain that octopus cells contribute to the startle reflex arc, they are large cells with a fast onset response across wide frequency bands, characteristics that would be favorable for the ASR. It may be that in early maturation and later senescence changes in large onset cells in the cochlear nucleus contribute to the age-related modification of the ASR that has been noted in both humans and in rodents.

#### B. The physiology of acoustic startle, and a model for its inhibition by noise offset

The ASR pathway begins with the haircells, then the auditory nerve and cells in the ventral cochlear nucleus (or possibly the cochlear root nucleus, Lee *et al.*, 1996); thence passing into the caudal pontine nucleus at the head of the reticulospinal tract (Wu *et al.*, 1988; Lingenhohl and Friauf, 1992); and terminating in the spinal motor neurons that in-

nervate the flexor and extensor muscles. Consistent with this depiction of perhaps no more than three central synapses, EMG measures of the ASR appear with a latency as rapid as 5 ms and a duration of only about 10 to 20 ms in rodents (Ison *et al.*, 1973; Wu, 1987). The physiological basis of ASR inhibition by noise offset is uncertain, but because of its temporal characteristics some reasonable hypotheses can be considered. First, because background noise may facilitate the startle reflex (in the rat: Davis, 1974; Hoffman and Searle, 1965; Ison and Hammond, 1971; and in the mouse, Ison *et al.*, 1996), it might be that depression at noise offset results simply because a stimulus condition that is favorable for ASR expression has been removed. But noise produced facilitation of the ASR depends on the integrity of forebrain mechanisms (Davis and Gendleman, 1977). It seems impossible that a signal for noise offset could reach the forebrain, turn off the arousal mechanism, and then have its effect register back in the brainstem, when the delay between noise offset and startle stimulus onset is just 1 ms, and when even the delay between offset and EMG activity is only 6 or 7 ms. Further problems with the "defacilitation" hypothesis arise first, because the optimal noise level depends on the level of the startle stimulus, and there is little if any facilitation apparent with a 115-dB startle stimulus in the presence of a 70-dB background (Ison *et al.*, 1996: the optimal noise level would be 50 dB); and second, because noise decrements depress the ASR considerably below the level obtained in the long-term absence of background noise (Ison, 1982). This latter observation means that noise offsets provide active inhibition of the ASR rather than passive "defacilitation."

A second possible explanation is that noise offset inhibition is a consequence of auditory adaptation resulting from the prior noise exposure. Thus classic reports (Kiang *et al.*, 1965; Young and Sachs, 1973a) show that if an auditory-nerve fiber is driven by a prolonged stimulus there is an initial fast rate of firing at stimulus onset and a subsequent decline to a steady state, followed, as in the present data, by a transient depression at noise offset below the spontaneous rate. Similar effects are apparent in psychophysical judgements (Young and Sachs, 1973b). Clearly, the ASR does not agree with the time course of these latter measures of either adaptation or of detection thresholds, both of which are most depressed immediately at stimulus offset and then recover in strength with an increasing delay between noise offset and the startle stimulus. The data contradict the hypothesis that sensory adaptation is critical for ASR inhibition.

A third possibility is that inhibition at noise offset results from a relatively complex form of forward masking. The typical forward masking effect, like the "neural adaptation" effects studied by Young and Sachs, is a simple continuation of simultaneous masking, and declines in strength with a delay between the masker and the test stimulus. But while the physiology of the auditory nerve may not allow for increasing inhibitory or masking effects over a delay period, masking studies in the cochlear nucleus do yield such functions (Kaltenbach *et al.*, 1993). For some cells in the dorsal cochlear nucleus forward masking is not immediately apparent at noise offset but increases in strength as a probe tone is separated from the masking tone, over a range of some 5–10

ms or even more. The relevant observation of Kaltenbach *et al.* is that forward masking occurs only to the extent that there is a distinguishable gap between the signal and the masker: we find this critically interesting, because it mirrors the effect seen in our behavioral data. Given this observation and the inadequacies of other hypotheses, we suggest that ASR inhibition at noise offset is a form of behavioral “gap detection” that depends on active inhibitory circuits present in the lower brainstem.

## C. The inhibitory effect of noise offset

### 1. Asymptotic levels of inhibition

The asymptotic inhibitory effect of a noise decrement was (a) greater the larger the decrement; (b) progressively reduced by hearing loss in early middle aged C57BL mice; and (c) first increased with maturation and then declined in middle age in CBA and F1-hybrid mice with minimal hearing loss. Where direct comparisons are available, these results agree with those for psychophysical measures of temporal acuity in humans and with other behavioral measures of gap detection in animals: thus, human gap detection (a) is related to the depth of the gap (e.g., Forrest and Green, 1987); (b) is reduced with hearing impairment (e.g., Fitzgibbons and Wightman, 1982); and (c) is increased with maturation in childhood and then degraded with advancing age (e.g., Davis and McCroskey, 1980; Snell, 1997). These similarities support the assumption that inhibition of the ASR shares with these other measures of temporal acuity a common dependence on underlying sensory and integrative neural mechanisms.

One difference between the present data and those obtained in the more usual study of gap thresholds is that here a continuous behavioral function is obtained across the range of gap durations, including evident suprathreshold gap values. The most evident special outcome in the present data is that almost all of the effects are captured as differences in the mean level of reflex inhibition at asymptote, and thus can be attributed to differences in the inhibitory strength of “forward-masking-type” neural circuits presumed to be activated at the offset of the noise. How might activity in such hypothetical inhibitory circuits be modulated by these variables? One way is to change the level of their input, so that, as was seen, the greater the noise decrement then the greater the level of inhibition. A similar effect might be responsible for changes in inhibition in the middle aged C57BL mouse with sensorineural hearing loss, because as the higher frequency components of the noise background are progressively lost, they obviously could not contribute to the inhibitory effect at noise offset. In fact, providing a background masker of variable bandwidth to eliminate the contribution of particular frequencies to noise offset does reduce its inhibitory effect, and thus appears to simulate the effect of high-frequency hearing loss in the C57BL mouse (work in preparation). Other work has shown that reductions of 10 dB off noise levels ranging from 40 to 80 dB yields constant levels of ASR inhibition, and these data suggest that a hearing loss for particular components of the background noise would reduce the levels of ASR inhibition only if the loss

was substantial, i.e., beyond 40 dB. The hearing loss of the 6-month-old C57BL mouse might approach this value for frequencies above about 20 kHz, and the 18-month-old C57BL mouse would have a loss approaching this magnitude across the frequency spectrum (Li and Borg, 1993). That in these mice the strength of inhibition was no different for decrements of 10–40 dB suggests that noise levels of less than 60 dB (that is, floor levels that were more than 10 dB below the 70-dB carrier level) may have all been below their hearing threshold, and so could not differentially affect behavior. Perhaps the most surprising effects seen in these old C57BL mice is that they did provide both reliable ASR values on the control trials and then reliable inhibition with a small decrement in the background level.

It is unlikely that either the CBA or the F1-hybrid mice had a peripheral hearing loss so serious as to render significant components of the background noise inaudible, and for these mice it is more reasonable to suggest that central changes in auditory function were responsible for the steady losses in asymptotic inhibition that are apparent in their data beyond 6 or 12 months of age. For most groups the age-related loss of inhibition was apparent primarily for the greater noise decrements, suggesting that the fundamental problem was that of not being able to generate a substantial degree of inhibition (only two groups, the youngest and the oldest of the CBA mice, were particularly insensitive to small decrements while being responsive to larger decrements). It is then interesting that Raza *et al.* (1994) and Milbrandt and Caspary (1995) report age-related declines in the numbers of glycine receptors and in the production of GABA in the brainstem of the rat. Either of these effects, if present in aged mice, could account for the obtained age-related changes in sensitivity and asymptotic levels of behavioral inhibition.

### 2. The time constant for inhibition

The relative growth of inhibition was most rapid with the smallest decrement of 10 dB, and overall was negatively related to the asymptotic level of inhibition provided by each offset condition (though it was not at all related to age-related differences in asymptotic inhibition). It is possible that this change in the time constant for the development of inhibition resulted either in the “afferent” task of detecting the change in stimulus input or in the “efferent” task of generating its inhibitory consequence. This could happen on the afferent side because the decay in neural excitation per unit time immediately after the noise decrement is to some extent independent of the size of the decrement, or on the efferent side because the generation of inhibition proceeds with the same inhibitory output per unit time more or less independently of the asymptotic level of inhibition generated in that particular stimulus condition. Thus the afferent processing necessary for a small decrement in neural excitation would be completed more swiftly as would the task of generating a small amount of neural inhibition: and in either case, the time course of development for the inhibitory effect of a small decrement in noise level must necessarily have a smaller time constant. But in the present experiment the most interesting outcome is that the rate of development of inhi-

bition was not systematically different across groups varying in their age or in their degree of hearing loss. The primary effect of each of these variables was to change the asymptotic level of inhibition, but not to change its temporal rate of development. This outcome suggests that increasing age or increasing hearing loss must reduce the amount of inhibition that can be generated per unit time just as it reduces the asymptotic level of potential inhibition: that is, there may be no age-related change in the relative growth rate of inhibition, but there must be an age-related change in the absolute growth rate of inhibition. This suggestion is entirely consistent with the hypothesis that the underlying neural effect underlying the developmental and age-related effects seen in the present experiment is a change in the amount of neurotransmitter release at noise offset, and/or a decrease in the number of receptors sensitive to that release, because both of these effects would change the absolute growth of inhibition per unit time in tandem with the asymptotic level of inhibition.

#### D. Concluding comments

The present experiment provided parallels to outcomes apparent in studies of gap detection in human listeners in showing that compared to young adult mice, very young and very old mice and hearing impaired middle aged mice are all deficient in responding to gaps in noise. These deficits in responsiveness to brief gaps in noise are particularly interesting in that they are attributable entirely to changes in asymptotic levels of inhibition, and not in the relative rate of development of inhibition. In light of the model for gap detection presented by Plack and Moore (1990), it could be argued, therefore, that the deficits in temporal acuity are not due to the inability of these mice to follow the temporal envelope of the noise decrement, but to a loss in the efficiency of more central parts of the auditory system that are responsible for responding to rapid shifts in afferent input and then moderating the level of the startle reflex. It is of great interest that Hall and Grose (1994) found in their study of children that age effects on temporal acuity were also restricted entirely to differences in sensitivity at asymptote for high levels of modulation depth, with no effects apparent in the time constants of the modulation contrast functions. The similarity of the findings, even to the point that the time constants presented by Hall and Grose approximate those found in the present work, suggests that this conclusion has a considerable degree of generality.

#### ACKNOWLEDGMENTS

This research was supported by USPHS Research Grant No. AG09524, a Center Support Grant to the Center for Visual Science, EY01319, and by the Rochester International Center for Hearing and Speech Research.

Buus, S., and Florentine, M. (1985). "Gap detection in normal and impaired listeners: The effect of level and frequency," *Time Resolution in Auditory Systems*, edited by A. Michelsen (Springer-Verlag, Berlin), pp. 159–179.  
 Davis, M. (1974). "Signal-to-noise ratio as a predictor of startle amplitude and habituation in the rat," *J. Comp. Physiol. Psychol.* **86**, 812–825.

Davis, M., and Gendleman, P. M. (1977). "Plasticity of the acoustic startle reflex in acutely decerebrate rats," *J. Comp. Physiol. Psychol.* **91**, 549–563.  
 Davis, S. M., and McCroskey, R. L. (1980). "Auditory fusion in children," *Child Dev.* **51**, 75–80.  
 Dean, K. F., Sheets, L. P., Crofton, K. M., and Reiter, L. W. (1990). "The effect of age and experience on inhibition of the acoustic startle response by gaps in background noise," *Psychobiology* **18**, 89–95.  
 Einsiedel, L. J., and Luff, A. R. (1992). "Alterations in the contractile properties of motor units within the ageing rat medial gastrocnemius," *J. Neurol. Sci.* **112**, 170–177.  
 Fitzgibbons, P. J., and Wightman, F. L. (1982). "Gap detection in normal and hearing-impaired listeners," *J. Acoust. Soc. Am.* **72**, 761–765.  
 Ford, J. M., Roth, W. T., Isaacks, B. G., White, P. M., Hood, S. H., and Pfefferbaum, A. (1995). "Elderly men and women are less responsive to startling noises: N1, P3 and blink evidence," *Biol. Psychol.* **39**, 57–80.  
 Forrest, T. G., and Green, D. M. (1987). "Detection of partially filled gaps in noise and the temporal modulation transfer function," *J. Acoust. Soc. Am.* **82**, 1933–1943.  
 Giraudi-Perry, D. M., Salvi, R. J., and Henderson, D. (1982). "Gap detection in hearing-impaired chinchillas," *J. Acoust. Soc. Am.* **72**, 1387–1393.  
 Hall, J. W., and Grose, J. H. (1994). "Development of temporal resolution in children as measured by the temporal modulation transfer function," *J. Acoust. Soc. Am.* **96**, 150–154.  
 Henry, K. R., and Chole, R. A. (1980). "Genotypic differences in behavioral, physiological, and anatomical expressions of age-related hearing loss in the laboratory mouse," *Audiology* **19**, 369–383.  
 Hoffman, H. S., and Searle, J. L. (1965). "Acoustic variables in the modification of the startle reaction in the rat," *J. Comp. Physiol. Psychol.* **60**, 53–58.  
 Irwin, R. J., Ball, A., Kay, N., Stillman, J., and Rosser, J. (1985). "The development of auditory temporal acuity in children," *Child Dev.* **56**, 614–620.  
 Ison, J. R. (1982). "Temporal acuity in auditory function in the rat: Reflex inhibition by brief gaps in noise," *J. Comp. Physiol. Psychol.* **96**, 945–954.  
 Ison, J. R., Bowen, G. P., Barlow, J. A., Taylor, M., and Walton, J. P. (1993). "Diminished response to acoustic transients in aged rodents," *J. Acoust. Soc. Am.* **93**, 2409.  
 Ison, J. R., Gutierrez, E., Agawal, P., Pak, J., and Vaughn, W. (1996). "Reflex inhibition by partially filled gaps in developing and aged mice: Ontogenetic changes in processing efficiency not temporal ability of audibility," *Soc. Neurosci. Abstr.* **22**, 1822.  
 Ison, J. R., and Hammond, G. R. (1971). "Modification of the startle reflex in the rat by changes in the auditory and visual environments," *J. Comp. Physiol. Psychol.* **75**, 435–452.  
 Ison, J. R., McAdam, D. W., and Hammond, G. R. (1973). "Latency and amplitude changes in the acoustic startle reflex of the rat produced by variations in auditory prestimulation," *Physiol. Beh.* **10**, 1035–1039.  
 Kaltenbach, J. A., Meleca, R. J., Falzarano, P. R., Myers, S. F., and Simpson, T. H. (1993). "Forward masking properties of neurons in the dorsal cochlear nucleus: possible role in the process of echo suppression," *Hearing Res.* **67**, 35–44.  
 Kellogg, C., Ison, J. R., and Miller, R. K. (1983). "Prenatal diazepam exposure: Effects on auditory temporal resolution in rats," *Psychopharmacol.* **79**, 332–337.  
 Kiang, N. Y. S., Watanabe, T., Thomas, A. C., and Clark, L. F. (1965). *Discharge Patterns of Single Fibers in the Cat's Auditory Nerve* (MIT, Cambridge, MA).  
 Krauter, E. E., Wallace, J. E., and Campbell, B. A. (1981). "Sensory-motor function in the aging rat," *Beh. & Neural Biol.* **31**, 367–392.  
 Lee, Y., Lopez, D. E., Meloni, E. G., and Davis, M. (1996). "A primary acoustic startle pathway: Obligatory role of cochlear root neurons and the nucleus reticularis pontis caudalis," *J. Neurosci.* **16**, 3775–3789.  
 Li, H.-S., and Borg, E. (1993). "Auditory degeneration after acoustic trauma in two genotypes of mice," *Hearing Res.* **68**, 19–27.  
 Lingenhohl, K., and Friauf, E. (1992). "Giant neurons in the caudal pontine reticular formation receive short latency acoustic input: an intracellular recording and HRP-study in the rat," *J. Comp. Neurol.* **325**, 473–492.  
 Lutman, M. E. (1990). "Degradations in frequency and temporal resolution with age and their impact on speech identification," *Acta Oto-Laryngol. Suppl.* **476**, 120–125.  
 McCroskey, R. L., and Davis, S. M. (1976). "Auditory function: develop-



- mental trends," Convention of American Speech and Hearing Association, Houston, Texas (unpublished).
- McCroskey, R. L., and Kasten, R. N. (1982). "Temporal factors and the aging auditory system," *Ear Hear.* **3**, 124–127.
- Mikaelian, D. O. (1979). "Development and degeneration of hearing in the C57/b16 mouse: relation of electrophysiologic responses from the round window and cochlear nucleus to cochlear anatomy and behavioral responses," *Laryngoscope* **89**, 1–15.
- Milbrandt, J. C., and Caspary, D. M. (1995). "Age-related reduction of [3H]strychnine binding sites in the cochlear nucleus of the Fischer 344 rat," *Neuroscience* **67**, 713–719.
- Moore, B. C., Peters, R. W., and Glasberg, B. R. (1992). "Detection of temporal gaps in sinusoids by elderly subjects with and without hearing loss," *J. Acoust. Soc. Am.* **92**, 1923–1932.
- Ornitz, E. M., Guthrie, D., Kaplan, A. R., Lane, S. J., and Norman, R. J. (1986). "Maturation of startle modulation," *Psychophysiology* **23**, 624–634.
- Parham, K., and Willott, J. F. (1988). "Acoustic startle response in young and aging C57BL/6J and CBA/J mice," *Behav. Neurosci.* **102**, 881–886.
- Patterson, R. D., Nimmo-Smith, I., Weber, D. L., and Milroy, R. (1982). "The deterioration of hearing with age: frequency selectivity, the critical ratio, the audiogram, and speech threshold," *J. Acoust. Soc. Am.* **72**, 1788–1803.
- Plack, C. J., and Moore, B. C. J. (1990). "Temporal window shape as a function of frequency and level," *J. Acoust. Soc. Am.* **87**, 2178–2187.
- Plomp, R. (1964). "Rate of decay of auditory sensation," *J. Acoust. Soc. Am.* **36**, 277–282.
- Raza, A., Milbrandt, J. C., Arneric, S. P., and Caspary, D. M. (1994). "Age-related changes in brainstem auditory neurotransmitters: measures of GABA and acetylcholine function," *Hearing Res.* **77**, 221–230.
- Salvi, R. J., and Arehole, S. (1985). "Gap detection in chinchillas with temporary high-frequency hearing loss," *J. Acoust. Soc. Am.* **77**, 1173–1177.
- Schneider, B. A., Pichora-Fuller, M. K., Kowalchuk, D., and Lamb, M. (1994). "Gap detection and the precedence effect in young and old adults," *J. Acoust. Soc. Am.* **95**, 980–991.
- Shnerson, A., and Pujol, R. (1981). "Age-related changes in the C57BL/6J mouse cochlea. I. Physiological findings," *Brain Res.* **254**, 65–75.
- Shnerson, A., and Willott, J. F. (1980). "Ontogeny of the acoustic startle response in C57BL/6J mouse pups," *J. Comp. Physiol. Psychol.* **94**, 36–40.
- Snell, K. B. (1997). "Age-related changes in temporal gap detection," *J. Acoust. Soc. Am.* **101**, 2214–2220.
- Stitt, C. L., Hoffman, H. S., and Marsh, R. (1973). "Modification of the rat's startle reaction by termination of antecedent acoustic signals," *J. Comp. Physiol. Psychol.* **84**, 207–215.
- Tyler, R. S., Summerfield, Q., Wood, E., and Fernandes, M. (1982). "Psychoacoustic and phonetic temporal processing in normal and hearing impaired listeners," *J. Acoust. Soc. Am.* **72**, 740–752.
- Walton, J. P., Frisina, R. D., Ison, J. R., and O'Neill, W. E. (1997). "Neural correlates of behavioral gap detection in the inferior colliculus of the young CBA mouse," *J. Comp. Physiol. A* **181**, 161–176.
- Willott, J. F. (1996). "Anatomic and physiologic aging: a behavioral neuroscience perspective," *J. Am. Acad. Audiol.* **7**, 141–151.
- Willott, J. F., and Bross, L. S. (1990). "Morphology of the octopus cell area of the cochlear nucleus in young and aging C57BL/6J and CBA/J mice," *J. Comp. Neurol.* **300**, 61–81.
- Wirtz, P., Loermans, H. M., Peer, P. G., and Reintjes, A. G. (1983). "Postnatal growth and differentiation of muscle fibres in the mouse. II. A histochemical and morphometrical investigation of dystrophic muscle," *J. Anat.* **137**, 127–142.
- Wu, M.-F. (1987). "Effect of prestimuli, background noise, and noise-offset on the acoustic pinna reflex: the relationships between emg and multiple-unit responses in the inferior colliculus of spinally transected rats," Doctoral dissertation, Department of Psychology, University of Rochester, pp. 1–159.
- Wu, M. F., Suzuki, S. S., and Siegel, J. M. (1988). "Anatomical distribution and response patterns of reticular neurons active in relation to acoustic startle," *Brain Res.* **457**, 399–406.
- Young, E., and Sachs, M. B. (1973a). "Recovery from sound exposure in auditory-nerve fibers," *J. Acoust. Soc. Am.* **54**, 1535–1543.
- Young, E., and Sachs, M. B. (1973b). "Recovery of detection probability following sound exposure: Comparison of physiology and psychophysics," *J. Acoust. Soc. Am.* **54**, 1544–1553.
- Young, J., and Fechter, L. D. (1983). "Reflex inhibition procedures for animal audiometry: A technique for assessing ototoxicity," *J. Acoust. Soc. Am.* **73**, 1686–1693.

# Focusing of therapeutic ultrasound through a human skull: A numerical study

Jie Sun and Kullervo Hynynen

Division of MRI/Department of Radiology, Brigham and Women's Hospital, Harvard Medical School,  
Boston, Massachusetts 02115

(Received 15 December 1997; revised 7 May 1998; accepted 2 June 1998)

A numerical model was developed which can use digitized layer interfaces to calculate ultrasound wave absorption, diffraction, reflection, and refraction. This model was used to evaluate the feasibility of ultrasound therapy and surgery through a human skull. A digitized human skull profile was obtained from magnetic resonance (MR) images and used to calculate the ultrasound field in the brain of a volunteer from a spherically curved phased array. With no phase correction, the focus of the array was shifted and defocused. The phased array technique was used to correct focal shift, reduce side lobes, and enhance focal amplitude. The optimum source element width was estimated for each frequency to obtain a near optimum focus, and an appropriate frequency range for transskull ultrasound therapy and surgery was determined. Acoustic pressure amplitude on the skull surfaces was examined, and it was shown that the skull heating problem could be overcome. Despite high attenuation, complex interface shape, and nonuniform thickness of a human skull, a sharply focused transskull ultrasound field can be generated for noninvasive ultrasound therapy and surgery in the brain. © 1998 Acoustical Society of America. [S0001-4966(98)03709-6]

PACS numbers: 43.80.Sh, 43.35.Wa [FD]

## INTRODUCTION

It has long been sought to use focused ultrasound to treat brain tumor,<sup>1-11</sup> and the skull has always been the biggest obstacle in the way. Until now, in order to use focused ultrasound for brain treatment, generally a piece of the skull has to be removed first. The removal of a piece of the skull is invasive, which significantly complicates the whole procedure. It is desirable to apply focused ultrasound through the intact skull; however, due to the skull's high sound speed (~2700 m/s), irregular shape and nonuniform thickness, it is practically impossible to obtain a sharp transskull focus at 1.0 MHz and above;<sup>3,4,6,12</sup> also due to skull's high attenuation, it is difficult to achieve enough focal amplitude without simultaneously overheating the skull.<sup>3,11</sup>

Phased arrays have been extensively studied and widely used in diagnostic medical ultrasound for several decades. By manipulating either or both amplitude and phase of the normal velocity specified at each source element, phased arrays can be used not only for conventional beam steering and spatial shading, but also for correction of ultrasonic beam degradation due to its propagation through inhomogeneous media. Smith *et al.* introduced this technique to ultrasound diagnostic imaging in order to correct the beam degradation due to the presence of intervening bone.<sup>13,14</sup> Thomas and Fink proposed to use this technique in therapeutic ultrasound, but only the results from a one-dimensional small element array were obtained.<sup>15</sup> Recently, it was demonstrated experimentally that it is practical to use two-dimensional large phased arrays for transskull ultrasound therapy and surgery.<sup>12</sup> In this experiment, a piece of formaldehyde fixed human skull was used, and through which sonications were performed and tissue destruction was induced in the exposed rabbit brain, *in vivo*.

Contingent with the experimental study,<sup>12</sup> it is the intent

of this paper to evaluate theoretically the feasibility of generating a sharply focused ultrasound field through a human skull for therapeutic purposes. A numerical model was developed and used to study the appropriate frequency range and the optimum phased array element size. In order to evaluate the skull heating problem, the pressure gains (ratios of the focal pressure amplitudes compare to those on the skull surfaces) and the specific absorption rate (SAR) gains (ratios of the focal SARs compare to those on the skull surfaces) are studied, and methods to increase them are explored. With the development of a clinical MRI guided and monitored ultrasound system<sup>16</sup> which makes it possible to accurately deposit ultrasound energy deep in tissues, the stage has been set to further examine the possibility of totally noninvasive ultrasound therapy and surgery in the brain.

## I. THEORY

The problem of interest is shown in Fig. 1. [The file MAMM002B.GIF for the skull diagram is obtained from: <ftp://cnephia.bio.uottawa.ca/ftp/BIODIAC/ZOO/VERTEBRA/DIAGBW/>.] Consider a spherically curved phased array that is in contact with multilayer media; the basic problem of interest is to evaluate the acoustic pressure field in the tissue layers in front of the array due to its specified normal velocity distribution. To address this problem, a numerical model has been developed. This model is based on techniques developed by Fan and Hynynen<sup>17,18</sup> that allows the irregular tissue layer interface to be taken into account in the simulation.

The pressure radiated by an arbitrary source, whose characteristic dimension is small in terms of the acoustic wavelength, is determined by its surface-averaged acceleration, or its volume acceleration, i.e., the surface integral of the normal acceleration. A source small in terms of the

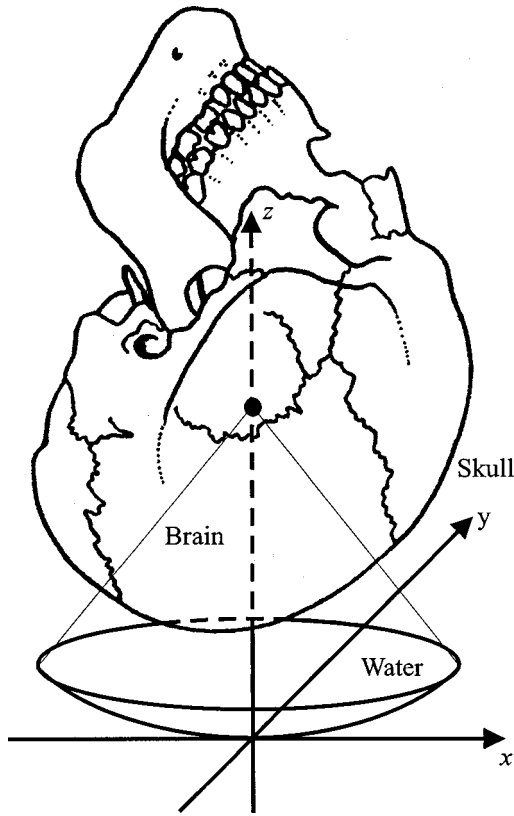


FIG. 1. The problem of interest.

acoustic wavelength can therefore be replaced by a point source (a simple source) embodying the same volume acceleration, regardless of the source geometry or of the local acceleration distribution over the source.<sup>19</sup>

### A. Building block

Consider a small vibrating surface (area  $ds_1$ ) in a medium. Its normal velocity  $u_1$  can be specified if, e.g., it is on the surface of a transmitting transducer or caused by acoustic wave propagation. If the dimension of  $ds_1$  is small enough compared with the acoustic wavelength, a simple source can be defined for the vibrating surface<sup>19</sup> with its source strength being denoted as  $u_1 ds_1$ .

Assuming the simple source location is at  $(x_1, y_1, z_1)$ , due to its baffled harmonic radiation, the corresponding acoustic pressure  $p$  at  $(x, y, z)$  can be written as<sup>19,17</sup>

$$p(x, y, z) = \frac{jk_{c_1} \rho_1 c_1}{2\pi} \frac{e^{-jk_{c_1} R}}{R} (u_1 ds_1), \quad (1)$$

where  $k_{c_1} = k - j\alpha_1$  is the complex wave number of the medium with  $\alpha_1$  being the attenuation coefficient,  $\rho_1$  and  $c_1$  are density and sound speed of the medium, respectively, and  $R = \sqrt{(x-x_1)^2 + (y-y_1)^2 + (z-z_1)^2}$ . Equation (1) is an alternative form of the classical Rayleigh–Sommerfeld integral for a single simple source.

Now consider a small surface (area  $ds_2$ ) at  $(x_2, y_2, z_2)$ , and on different sides of which there are different media, i.e.,  $\rho_1$  and  $c_1$  are density and sound speed of the first medium on one side, and  $\rho_2$  and  $c_2$  are density and sound speed of the

second medium on the other side. The normal velocity of the surface due to the simple source  $u_1 ds_1$  can be written as<sup>20,17</sup>

$$u_2 = \frac{jk_{c_1}}{2\pi} (u_1 ds_1) \frac{e^{-jk_{c_1} R_{12}}}{R_{12}} \times \left( 1 - j \frac{1}{k_{c_1} R_{12}} \right) T_{v_2} \cos(\theta_{2i}), \quad (2)$$

where

$$R_{12} = \sqrt{(x_1 - x_2)^2 + (y_1 - y_2)^2 + (z_1 - z_2)^2},$$

$$T_{v_2} = \frac{2}{(\rho_2 c_2 / \rho_1 c_2) + [\cos(\theta_{2i}) / \cos(\theta_{1i})]},$$

and  $\theta_{2i}$ ,  $\theta_{1i}$  satisfy the Snell's law, i.e.,  $(\sin \theta_{2i} / \sin \theta_{1i}) = c_2 / c_1$ . The effects of acoustic wave reflection and refraction are included in Eq. (2). Clearly, a new simple source can be defined at  $(x_2, y_2, z_2)$  with its source strength being denoted as  $u_2 ds_2$ .

For a small vibrating surface, the pressure at the source location can be related to its normal velocity by a factor of the characteristic impedance of the medium right in front of the source,<sup>21</sup> e.g., for the sources above, the pressure at  $(x_l, y_l, z_l)$  can be approximated to be

$$p(x_l, y_l, z_l) = (\rho_l c_l) u_l, \quad (3)$$

where  $l=1,2$ . Equation (3) has been referred to as the impedance relation for linear plane waves.<sup>22</sup>

The equation relating the specific absorption rate (SAR) which is a descriptor of tissue heating and the pressure amplitude is also presented here for future reference,

$$\text{SAR} = \alpha \frac{|p|^2}{\rho c}, \quad (4)$$

where  $|p|$  is the pressure amplitude,  $\alpha$  is the pressure attenuation coefficient,  $\rho$  and  $c$  are density and sound speed of the medium, respectively.

### B. A multilayer problem

For a multilayer problem, an interface between adjacent layers will be divided into small pieces, and each piece will be treated as a simple source. A section of the layer interface which contains many simple sources can be considered as a secondary source.<sup>20,17,23,24,18</sup> Equation (2) can be used to relate the simple sources on one interface (which can be the transducer surface) to those on the next one, while Eq. (1) can be used to evaluate the acoustic pressure field in the last layer from the simple sources defined on the last layer interface. As stated before, the acoustic wave reflection and refraction at the layer interface are taken into account, but not the multiple reflection and reverberation in each layer.

Assuming  $(M-1)$  tissue layers plus a layer (usually water) that is in direct contact with the transducer, the interface between layer  $l$  and  $l+1$  is denoted the  $(l+1)$ th interface, while the first interface is actually the transmitting transducer surface. Subscript (or subsubscript)  $l$  will be used to denote the parameters on the  $l$ th interface, while index (or

subscript)  $i$  will be used to denote the  $i$ th simple source, e.g., on the  $i$ th interface, there are  $N_i$  simple sources and the  $i$ th simple source, etc.

As an example, the equation for a two-layer problem is first presented. By combining Eqs. (1) and (2), the acoustic pressure in the second layer can be expressed as

$$\begin{aligned}
 p &= \sum_{i_2=1}^{N_2} \frac{jk_{c_2}\rho_2c_2}{2\pi} \frac{e^{-jk_{c_2}R_{i_2}}}{R_{i_2}} (u_{i_2} ds_{i_2}) \\
 &= \sum_{i_1=1}^{N_1} \sum_{i_2=1}^{N_2} \left[ \frac{jk_{c_1}}{2\pi} \frac{e^{-jk_{c_1}R_{i_1,i_2}}}{R_{i_1,i_2}} \left( 1 - j \frac{1}{k_{c_1}R_{i_1,i_2}} \right) \right. \\
 &\quad \left. \times T_{v_{i_2}} \cos(\theta_{i_2,t}) \right] \left[ \frac{jk_{c_2}\rho_2c_2}{2\pi} \frac{e^{-jk_{c_2}R_{i_2}}}{R_{i_2}} \right] u_{i_1} (ds_{i_1} ds_{i_2}), \tag{5}
 \end{aligned}$$

where  $k_{c_1} = k - j\alpha_1$ ,  $k_{c_2} = k - j\alpha_2$  are the complex wave numbers of the first and second layer, respectively, with  $\alpha_1$  and  $\alpha_2$  being the corresponding attenuation coefficients.  $(x_{i_1}, y_{i_1}, z_{i_1})$  is used to denote the location of a simple source on the transducer, while  $(x_{i_2}, y_{i_2}, z_{i_2})$  is used to denote the location of a simple source on the layer interface between the first and second layers.

$$R_{i_1,i_2} = \sqrt{(x_{i_1} - x_{i_2})^2 + (y_{i_1} - y_{i_2})^2 + (z_{i_1} - z_{i_2})^2}$$

and

$$R_{i_2} = \sqrt{(x - x_{i_2})^2 + (y - y_{i_2})^2 + (z - z_{i_2})^2}.$$

Apparently, summation over all the simple sources is an equivalent representation to integration over the transducer surface and the secondary source surface.

It is noted that

- (1) In Eq. (5), the summations over the transducer surface and the secondary source surface are interchangeable, i.e.,
  - (a) By summing over the transducer surface first, the normal particle velocity at each simple source on the layer interface due to the whole transducer can first be obtained, then by summing over the whole secondary source surface, the total acoustic pressure can be obtained; or
  - (b) By summing over the secondary source surface first, the acoustic pressure due to each simple source on the transducer can first be obtained, then by summing up the acoustic pressure due to each simple source on the transducer, the total acoustic pressure can be obtained.
- (2) Equation (5) can easily be extended to a multilayer problem by cascading layers using Eq. (2), e.g., for an  $M$ -layer problem, the pressure in the  $M$ th layer can be expressed as

$$\begin{aligned}
 p &= \sum_{i_1=1}^{N_1} \cdots \sum_{i_M=1}^{N_M} \prod_{l=1}^{M-1} \left[ \frac{jk_{c_l}}{2\pi} \frac{e^{-jk_{c_l}R_{i_l,i_{l+1}}}}{R_{i_l,i_{l+1}}} \right. \\
 &\quad \left. \times \left( 1 - j \frac{1}{k_{c_l}R_{i_l,i_{l+1}}} \right) T_{v_{i_{l+1}}} \cos(\theta_{i_{l+1},t}) \right] \\
 &\quad \times \left[ \frac{jk_{c_M}\rho_Mc_M}{2\pi} \frac{e^{-jk_{c_M}R_{i_M}}}{R_{i_M}} \right] u_{i_1} \left( \prod_{l=1}^M ds_{i_l} \right). \tag{6}
 \end{aligned}$$

It is well known that the classical Rayleigh–Sommerfeld integral is an expression of Huygen’s principle which characterizes diffractive propagation as that of the linear sum of a field’s constituent point sources;<sup>25</sup> obviously, Eq. (6) can be considered as an extended form of the Rayleigh–Sommerfeld integral for a multilayer case.

- (3) It is important to determine an effective secondary source area on the layer interface, so that outside this area, the simple source strength diminishes, i.e., the amplitude of normal particle velocity sharply decays at or inside the edge of the defined secondary source on the layer interface. Contrary to many other acoustic propagation problems, due to its narrow main beam, a secondary source area in front of a focused transducer can easily be determined to be confined in a reasonably small area.
- (4) For the frequency range and typical transducer size of interest, the amount of the simple sources either on the transducer surface or on the secondary sources could be overwhelmingly large.

### C. Digitized interface

For real human anatomies, e.g., a human skull, the layer interface has to come in the form of digitized data profiles. The numerical model is designed such that a data file with  $z$  coordinates over an equispaced rectangular  $x$ - $y$  grid can be read in to specify the layer interface. Assuming the layer interface is continuous and so is its first order derivative, it is important to be able to calculate accurately the normal direction and area of a small piece on the layer interface which will be treated as a simple source.

A nine-point grid for  $[x_{i-1}, x_i, x_{i+1}]$  and  $[y_{j-1}, y_j, y_{j+1}]$  is extracted from the digitized layer interface which will be used to define a simple source at  $(x_i, y_j)$  in terms of its normal direction and area. Assuming the nine-point data are on a continuous surface specified by  $z = f(x, y)$ , for a tangential plane at  $(x_i, y_j, f(x_i, y_j))$ , its normal direction can be represented as  $(f'_x(x_i, y_j), f'_y(x_i, y_j), -1)$ , where  $f'_x(x_i, y_j)$  and  $f'_y(x_i, y_j)$  can be obtained approximately using the following Lagrange formula,

$$\begin{aligned}
 f'_x(x_i, y_j) &= \frac{f(x_{i+1}, y_j) - f(x_{i-1}, y_j)}{x_{i+1} - x_{i-1}}; x_{i+1} > x_i > x_{i-1} \\
 f'_y(x_i, y_j) &= \frac{f(x_i, y_{j+1}) - f(x_i, y_{j-1})}{y_{j+1} - y_{j-1}}; y_{j+1} > y_j > y_{j-1}. \tag{7}
 \end{aligned}$$

Here,  $f(x, y_j)$  is assumed to be continuous in  $[x_{i-1}, x_{i+1}]$  and  $f(x_i, y)$  is assumed to be continuous in  $[y_{j-1}, y_{j+1}]$ . This type of calculation is carried out for all the simple sources on a layer interface by simply moving the nine-point grid except at the edge of the layer interface profile where extrapolations are needed.

Assuming equal square area ( $dA$ ) for the  $x$ - $y$  plane projection of each simple source on the layer interface, the surface area for the simple source at  $(x_i, y_j)$  can be obtained as

$$ds = \frac{dA}{[\sqrt{(f'_x(x_i, y_j))^2 + (f'_y(x_i, y_j))^2}]^{-1}}, \quad (8)$$

where the denominator is actually the corresponding directional cosine with respect to the  $z$  axis.

#### D. Phase correction

In a phased array architecture, the purpose of phase correction is to introduce extra phase offset to each source element so that the acoustic wave radiated from each source element will add up coherently at a desired focal point. The optimum case is that the radiated acoustic wave from each source element should arrive at the desired focal point with the same phase.

In the forward problem of evaluating the acoustic field radiated from a transducer, instead of integrating over the whole transducer surface at once, one can integrate over one element first and obtain its corresponding complex pressure at a desired focal point. With the complex pressure obtained, a phase delay can be calculated for the source element. Hence, phase delays can be obtained for all the source elements on a phased array, which will then be fed into the second iteration of the forward problem to obtain the acoustic field. If the integration in Eq. (6) is still performed for each source element separately, the complex pressure obtained at the desired focal point due to each source element should have the same phase. On the other hand, the phase-corrected acoustic field can be obtained by integrating over the whole transducer surface at once after feeding back the phase delay information for each source element.

When there are large amount of phased array elements, the procedure described above for calculating the phase delay for each source element can be a prohibitively tedious process. A second approach, the reversed problem, is devised. In the reversed problem, a point source is radiating at the desired focal point, and the complex pressure at each source element location on the transducer can be evaluated all at once, which will then be fed in to the forward problem.

## II. SIMULATIONS

The numerical model was extensively tested before actually being used to evaluate the focused ultrasound field through a human skull.<sup>26</sup> A digitized human skull profile was built from MR images. Figure 2 shows the 3-D skull traces at different MR image slices for the skull's outer and inner surfaces, respectively. The benchmark configuration for our investigation is that a spherically curved transducer driven at 1.0 MHz; the transducer has a curvature radius of 10 cm and

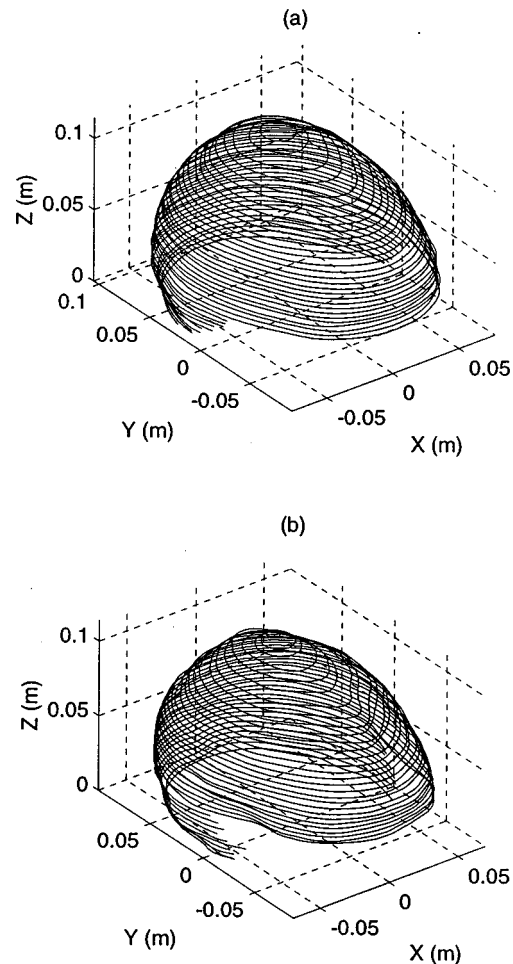


FIG. 2. A digitized human skull profile. Contours: (a) outer surface; (b) inner surface.

a diameter of also 10 cm ( $F$  number is 1.0); the transducer was positioned towards the skull such that the focal depth inside the skull was around 6 cm.

The phased array architecture is shown in Fig. 3 which is a two-dimensional diagram of the projection of an  $M \times M$  element transducer (a  $16 \times 16$  element transducer is shown in the figure, where  $M$  is chosen to be 16) in order to show how the phased array elements are divided. The projection is in the base plane of the transducer, i.e., in the  $x$ - $y$

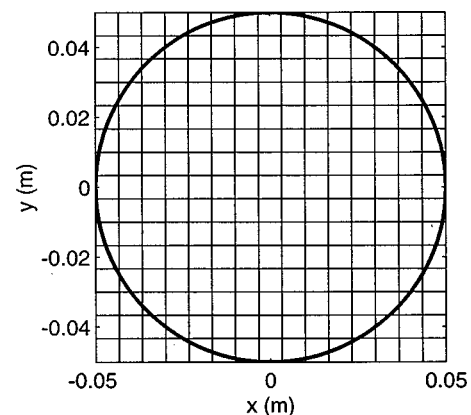


FIG. 3. Projection in the transducer base plane for the configuration of a  $16 \times 16$  element phased array.

TABLE I. The properties of the three layers: the water–skull–brain layers in front of the transducer.

	Density (kg/m <sup>3</sup> )	Sound speed (m/s)	Attenuation (nep/m)								
			Frequency (MHz)								
			0.5	0.625	0.75	0.875	1.0	1.125	1.25	1.375	1.5
Water	998.0	1500					0.0				
Skull	1796.6	2652.6	50	50	85	137	179	223	315	390	464
Brain	1030.0	1545.0				4.0×frequency					

plane where  $z=0.0$ , clearly, the projection of each element has an equal square area, which will simply be referred to as a square element later on. It was shown that not all the  $M \times M$  elements fall onto the transducer surface, some elements were outside the circular area of the transducer, hence the total number of source elements on the transducer was less than  $M \times M$ . However, for simplicity, if the width of a square element is obtained from dividing the diameter of the transducer by  $M$ , the corresponding phased array will still be referred as an  $M \times M$  element transducer. The frequency range under investigation was from 0.5 to 1.5 MHz, with more details were presented for the 0.5-, 1.0-, and 1.5-MHz frequency cases. At 1.0 MHz, the effects of changing focal depth inside the skull from 1.0 to 8.0 cm were investigated, and a transducer with the same curvature radius but increased diameter of 13.625 cm ( $F$  number is 0.734) was also considered. The total acoustic power into the transducer was 1 W, so the following results can be interpreted as normalized quantities with a reference of 1-W total acoustic power, and the pressure and the normal velocity of interest due to some other total acoustic power can be scaled accordingly. The effects of nonlinear propagation can be ignored with this focused transducer as was shown by *in vivo* measurements.<sup>27</sup>

Although the skull is generally considered as bone, more detailed skull acoustic properties have to be taken into consideration. The acoustic properties of the human skull used in this paper are mainly derived according to a paper published by Fry and Barger.<sup>4</sup> The density and the sound speed of the skull were obtained by weighted averages combining inner table, diploe, and outer table. In the numerical model, the reflection loss has been taken into account, so the attenuation loss can be estimated by subtracting the reflection loss from the insertion loss. It has been shown that, in the human skull, the absorption loss is linearly proportional to the frequency, while the scattering loss is much more frequency dependent. Within the frequency range of 0.5–1.5 MHz, the scattering loss is a more dominant factor, particularly in diploe.<sup>4</sup> Table I shows the layer properties. A three-layer model was considered in front of the transducer, more specifically, water outside the skull, skull, and brain inside the skull. In the brain tissue, the attenuation is linearly related to the frequency, while in the skull, the attenuation is strongly dependent on the acoustic wave frequency.

The emphasis is on transskull ultrasonic field in the focal plane, while the axial ultrasonic field inside the brain is presented only for some examples. In order to have a better view of the acoustic field pattern, both surface and contour

plots are presented, and the contour lines are drawn with the interval of 10% of the peak value.

### III. RESULTS

Figure 4 shows the transskull ultrasonic field in the focal plane at 1.0 MHz. The  $1 \times 1$  element case is presented as a reference, which is the uniform phased case with a single element.  $4 \times 4$ ,  $8 \times 8$ , and  $16 \times 16$  element cases are presented as examples to show the effects of phase correction. For  $1 \times 1$  and  $16 \times 16$  element cases, Fig. 5 shows the axial ultrasonic field in the brain also at 1.0 MHz, and the axial ultrasonic field is presented in the  $x$ - $z$  and  $y$ - $z$  planes that contain the focal point. Figure 6 shows the transskull ultrasonic field in the focal plane, for  $1 \times 1$  and  $16 \times 16$  element cases, at 0.5 and 1.5 MHz, respectively.

Figure 7 summarizes the change of the normalized focal amplitude versus the phased array element sizes (numbers). The ideal focal amplitudes were obtained with the  $256 \times 256$  element phased array (total number of simple sources equals total number of source elements) which were used as normalization references. Three driving frequencies of 0.5, 1.0, and 1.5 MHz were considered. The focal amplitude increased with the increase of transducer element number (the decrease of the element size) at all frequencies. The focal amplitude approached the ideal value asymptotically and reached above 90% of the ideal value with element width of about 15 mm at 0.5 MHz, 10 mm at 1.0 MHz, and 6.7 mm at 1.5 MHz, respectively.

For real transskull therapy and surgery without skull overheating,<sup>6,8,11</sup> it is important to examine the relative pressure amplitude on the surface of and inside the skull compared with that at the focal point. As shown in Eq. (3), the pressure on the skull surfaces can be directly related to the normal velocity at the same point approximately. For the  $F=1.0$  transducer, Fig. 8 shows the acoustic pressure amplitude on both the outer and inner surfaces of the skull for the  $16 \times 16$  element case at 1.0 MHz. The acoustic pressure amplitude on the skull surface is presented in the coordinates that correspond to the  $x$ - $y$  plane projection of the skull surface. From Fig. 8 and other simulations (not shown), it is clear that the pressure amplitude on the outer skull surface is larger than that on the inner skull surface. Table II summarizes the relative peak pressure amplitude on the skull surfaces compared with that at the focal point. A pressure gain is introduced as the ratio of the peak pressure amplitude at the focal point to that on the outer skull surface ( $\zeta_o$ ). In

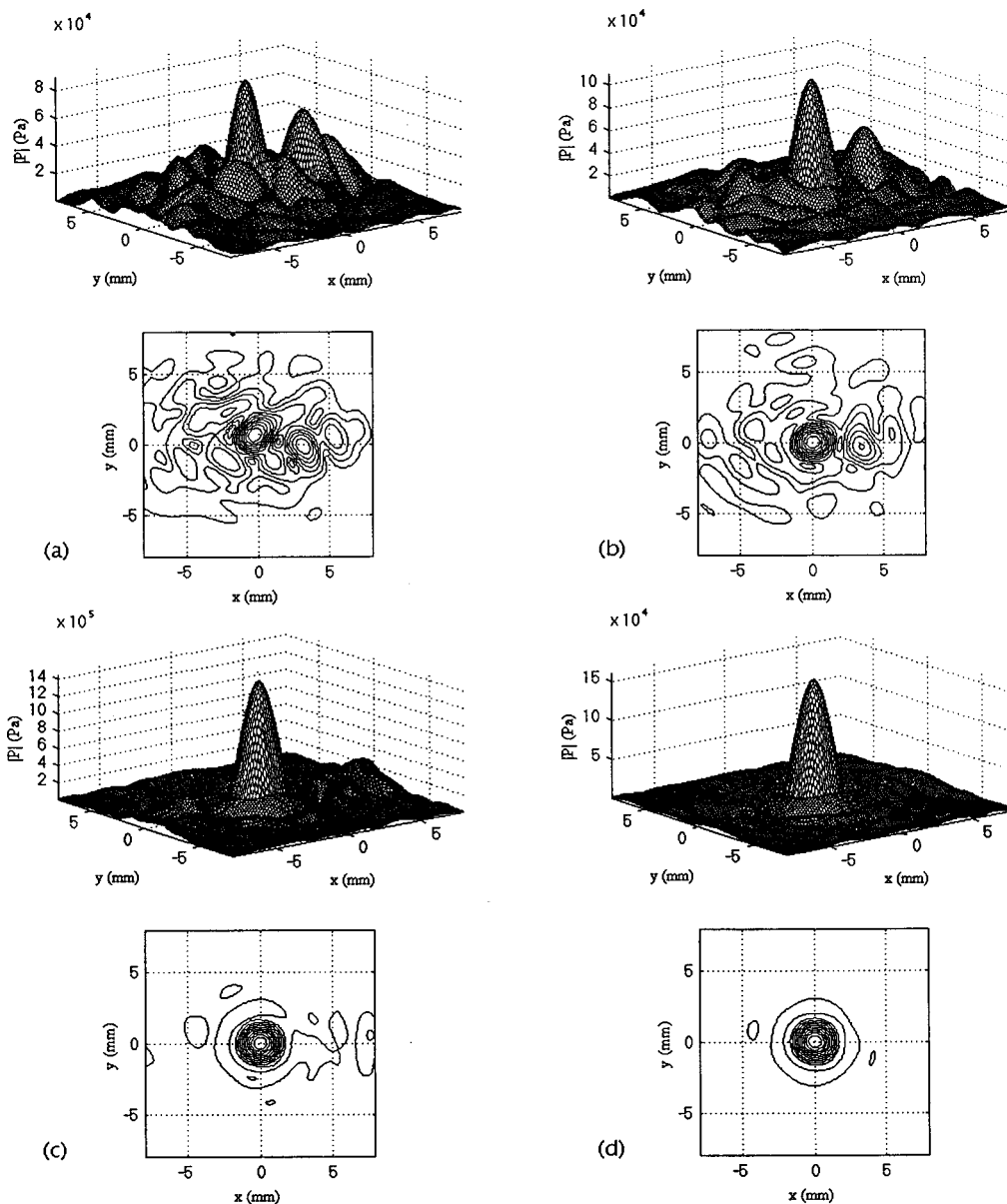


FIG. 4. The transskull ultrasonic field in the focal plane at 1.0 MHz: (a)  $1 \times 1$ ; (b)  $4 \times 4$ ; (c)  $8 \times 8$ ; (d)  $16 \times 16$ .

order to ensure that no immediate skull heating adjacent to the brain which is a much worse case, the pressure gain of the peak pressure amplitude at the focal point compare to that on the inner skull surface ( $\zeta_i$ ) is also examined. Clearly, SAR gains can be similarly defined. To further investigate the frequency dependency of the pressure and SAR gains, a set of simulations were performed. Figure 9 shows both pressure and SAR gains as a function of frequency for the  $16 \times 16$  element case. The pressure gain curve peaks at 0.60–0.65 MHz above which the value decays slowly and drops below 1.0 at about 1.25 MHz. The SAR gain curve shows very high value at low frequencies and quickly drops below 1.0 at about 0.85 MHz.

The influence of the focal depth inside the skull was also investigated, and the pressure and SAR gains are plotted in Fig. 10 for the  $16 \times 16$  element case at 1.0 MHz. Both gains increase with the increase of focal depth.

#### IV. DISCUSSION

The simulation shows that it is possible to obtain a sharp focus through a human skull at a low frequency, or by using a phased array with phase correction. The pressure and SAR gains achieved show that transskull ultrasound therapy and surgery should be feasible with a single element spherically curved transducer at frequencies around 0.5 MHz, and with a phased array at frequencies up to 1.0 MHz. This agrees with the earlier experimental results.<sup>12</sup>

By using a single-element, spherically curved transducer, a sharp focus can be generated through the skull at frequencies up to 1.0 MHz, and the focus is destroyed by the phase shifts cause by the bone at higher frequencies. This agrees with many earlier works on single-element, spherically curved transducers.<sup>3,6,12</sup> By using a phased array with phase correction, the destroyed focus can be restored and a sharp focus can be generated through the skull. This is in

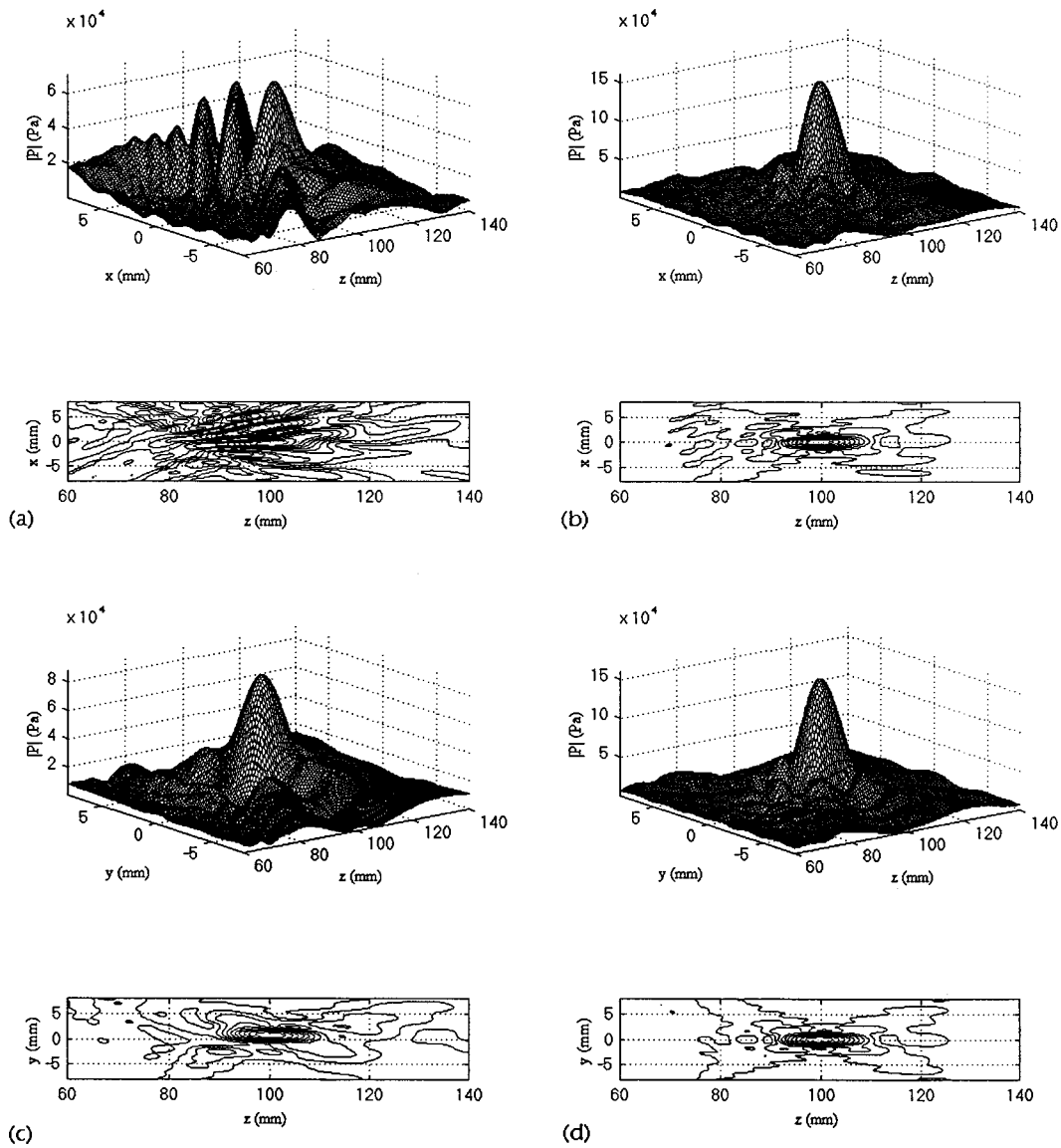


FIG. 5. The axial ultrasonic field in the brain at 1.0 MHz: (a)  $1 \times 1$ —in the axial  $x$ - $z$  plane; (b)  $16 \times 16$ —in the axial  $x$ - $z$  plane; (c)  $1 \times 1$ —in the axial  $y$ - $z$  plane; (d)  $16 \times 16$ —in the axial  $y$ - $z$  plane.

agreement with the one-dimensional array experiments<sup>15</sup> and the two-dimensional large array experiments.<sup>12</sup>

Both the single element and the phased array simulated field distribution show qualitatively the same fields as were detected experimentally,<sup>12</sup> which indicates that the numerical model is accurate enough for investigating the major physical parameters influencing the beam propagation through the skull.

At 1.0 MHz, without phase correction, the focus was shifted and the side lobes were unacceptable. The focal shift can be mostly corrected by using a  $4 \times 4$  element phased array. The side lobes were further reduced and the focal amplitude was further enhanced by using more source elements. At 0.5 MHz, there was a clear dominant main lobe even without phase correction; the defocusing effect was not obvious, but the focus was clearly shifted. With a phased array, no significant increase of focal amplitude was observed, and the focal shift can be corrected by a  $4 \times 4$  or more element phased array. At 1.5 MHz, the focus was totally destroyed

without phase correction. With a  $4 \times 4$  element phased array, the focus was restored at the desired location, but the side lobes were unacceptable. With more source elements, significant focal amplitude enhancement was achieved.

It is obvious that enhanced focal amplitude can be achieved by dividing the transducer into smaller elements (more elements); however, there is a limit, and a near optimum focus can be defined when the element is already small, in essence that there will be little or no focal amplitude improvement by using a smaller element size. From a practical point of view, smaller element size means more source elements and their corresponding hardware. The trade-off between the focal amplitude and the element size (number) has to be made. In Fig. 7, at 1.0 MHz (wavelength in water 1.5 mm), it is shown that an optimum focus can be obtained with a  $10 \times 10$  element phased array (square element width 10.0 mm), i.e., when more source elements were used, little focal amplitude enhancement was achieved. Similarly, at 0.5 MHz (wavelength in water 3.0 mm), an optimum focus can be



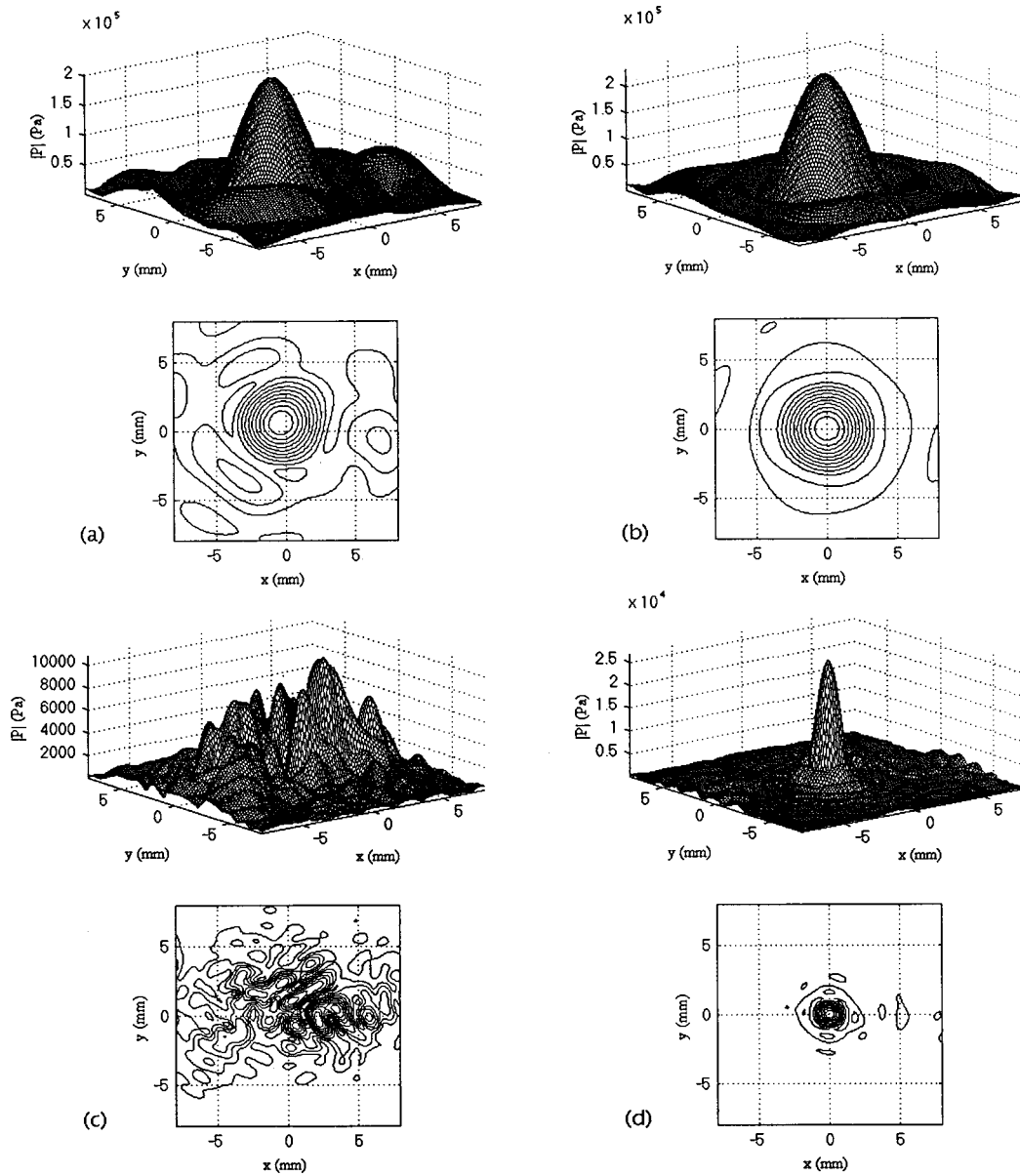


FIG. 6. The transskull ultrasonic field in the focal plane: (a)  $1 \times 1$  at 0.5 MHz; (b)  $16 \times 16$  at 0.5 MHz; (c)  $1 \times 1$  at 1.5 MHz; (d)  $16 \times 16$  at 1.5 MHz.

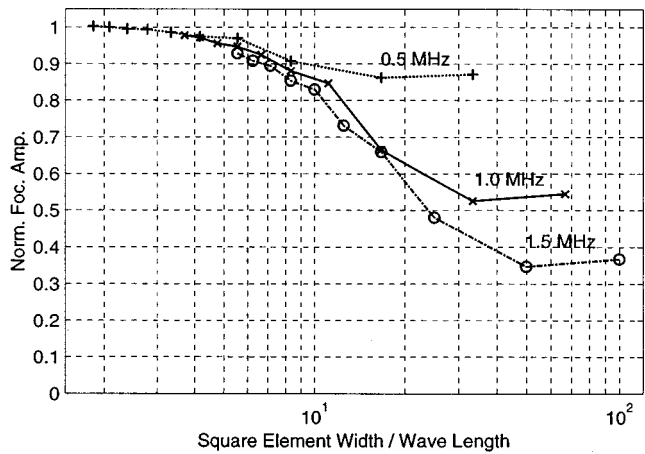


FIG. 7. Pressure/SAR gains versus the phased array element size.

obtained with a  $6 \times 6$  element phased array (the square element width of  $\sim 16.7$  mm), and at 1.5 MHz (wavelength in water 1.0 mm), an optimum focus can be obtained with a  $14 \times 14$  element phased array (the square element width of  $\sim 7.1$  mm). As a rule of thumb, in order to achieve a near optimum focus, the square element width should be less than 5–6 times the acoustic wavelength.

In Fig. 9, the pressure gain of as high as 4.5 has been observed, with the maximum observed SAR gain being about 3.1. It is apparent that, in order to deliver a predetermined amount of power deposition in the brain, the power flux through a unit area on the skull surface should be inversely proportional to penetration area. For the  $F=1.0$  transducer, only about 1/6 of the available skull surface area is utilized. If the total available skull surface area were to be utilized, the peak pressure amplitude on the skull surfaces could be reduced by  $1/\sqrt{6}$  assuming the same focal amplitude is maintained, hence the pressure gains could increase

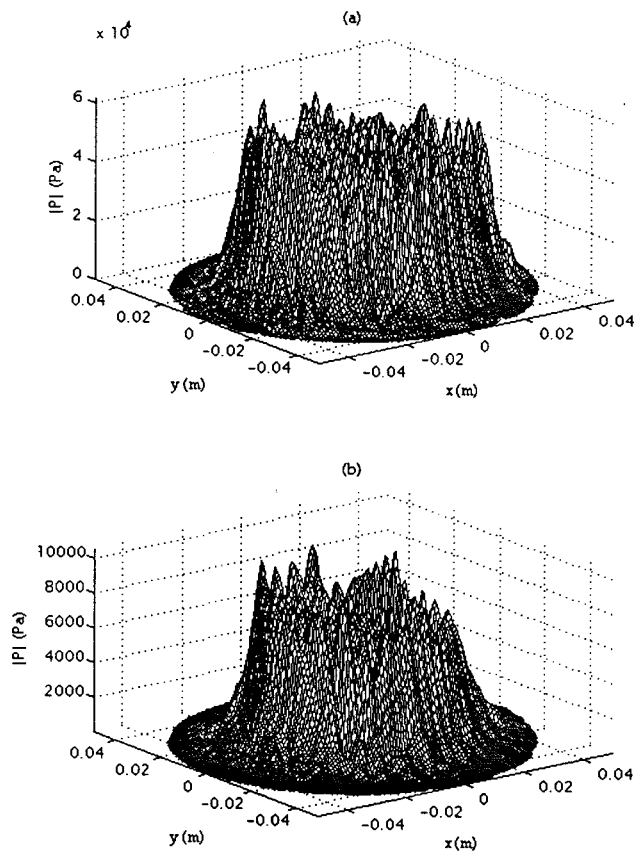


FIG. 8. The acoustic pressure amplitude on the skull surfaces for the  $16 \times 16$  element case at 1.0 MHz: (a) outer surface; (b) inner surface.

by  $\sim \sqrt{6}$ . The SAR gains could increase by 6.0, because the absorbed power is proportional to the pressure amplitude square. In order to avoid skull overheating, the SAR gains between the focal point and on the skull has to be larger than 1.0.<sup>12</sup> At 0.5–1.0 MHz, it might be possible to induce thermal effects in the brain for therapeutic purposes, and on the other hand, it has been demonstrated recently<sup>12</sup> that the cavitation effects might be another option, particularly for fre-

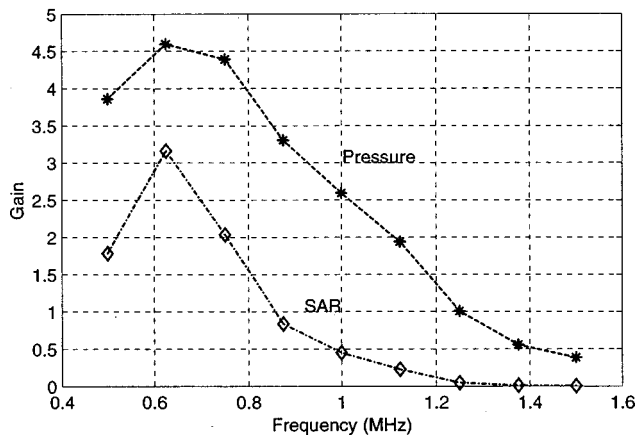


FIG. 9. Pressure/SAR gains versus frequency.

quencies with only marginal achievable SAR gains. Although single location pulsed sonication appears to be controllable,<sup>28</sup> it is not known if the generated microbubbles would distort the power deposition when larger volumes are covered with multiple sonications. Clearly, much more works are needed before the cavitation mechanism can be used for brain therapy and surgery.

From Fig. 10, it is shown that the pressure gains are adequate only for relatively deep targets. If pressure gain of 1.5 is used as a guideline, the targets have to be deeper than 30.0 mm in the brain. On the other hand, it may be possible reach even more superficial targets when the whole skull surface is used for the transmission of the ultrasound beam. Similarly, it may be possible to treat superficial targets from the opposite side through the brain. However, this was not simulated here.

Despite the distortion caused by the presence of the skull, and the phase correction applied to correct and restore the focus, the linear relationship<sup>29</sup> between the focal volume (in terms of transverse focal width  $D_t$ , axial focal length  $D_a$ ) and the acoustic wave frequency remains intact (Table II). Clearly, the focal volume is the largest at 0.5 MHz, and the

TABLE II. The peak acoustic pressure amplitude on the skull surface compared with that at the focal point.

	Frequency (MHz)	Peak pressure amplitude (Pa $\times 10^3$ )			Pressure gain		Focal dimensions (mm)	
		Focal point	Outer skull surface	Inner skull surface	$\zeta_o$	$\zeta_i$	$D_t$	$D_a$
1 $\times$ 1	0.5	202.8	55.2	27.2	3.7	7.5	3.0	20.0
	1.0	89.8	55.6	12.9	1.6	7.0	N/A	N/A
	1.0 (F=1.0)	102.8	38.1	12.2	2.7	8.4	N/A	N/A
	1.5 (F=0.734)	10.8	54.0	3.0	0.20	7.0	N/A	N/A
16 $\times$ 16	0.5	232.7	60.3	24.4	3.9	9.5	3.0	20.0
	1.0	160.0	61.7	10.5	2.6	15.2	1.5	10.0
	1.0 (F=1.0)	199.8	51.6	12.4	3.9	16.2	1.1	5.0
	1.5 (F=0.734)	26.7	69.2	3.1	0.39	8.6	1.0	6.5

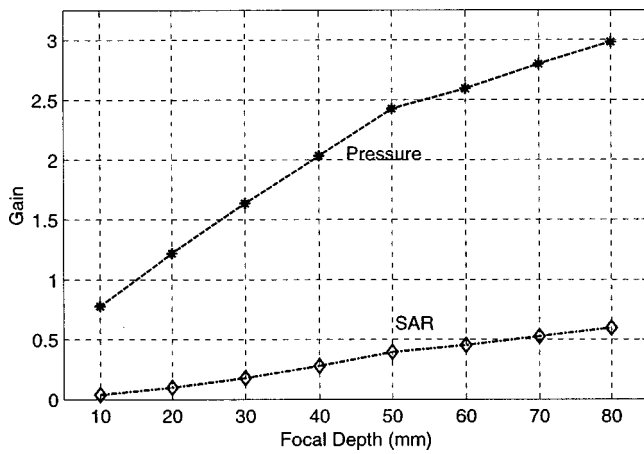


FIG. 10. Pressure/SAR gains versus the focal depth inside the skull.

smallest at 1.5 MHz. Although a lower-frequency enjoys many advantages like lower attenuation in the skull, etc., its applicability is limited by its focal volume size, which calls for a trade-off in practical use.

## V. CONCLUSIONS

A numerical model was developed to evaluate acoustic field in multiple layers with irregular layer interface shapes from a spherically curved phased array. This method was applied to evaluating the transskull ultrasound field in the brain. A digitized human skull profile was obtained from MR images which was then used to specify the layer interfaces in the numerical simulations.

Without phase correction, a single transskull focus could be obtained for frequencies below 1.0 MHz, but not for higher frequencies. The phased array technique could be used to restore the destroyed focus, correct focal shift, reduce side lobes, and enhance focal amplitude at all frequencies. The optimum element width for a phased array in order to achieved the near optimum focus was determined to be less 5–6 times the acoustic wavelength. However, due to inevitable skull overheating, frequencies above 1.0 MHz are deemed to be not appropriate for transskull therapy and surgery. The appropriate frequency range for transskull therapy and surgery is below 1.0 MHz which confirms the results previously obtained.<sup>3,4,12</sup> By increasing the skull penetration area, both the pressure and SAR gains can be increased.

Despite high attenuation, complex interface shape, and nonuniform thickness of a human skull, sharply focused transskull ultrasound fields can be generated for noninvasive ultrasound therapy and surgery in the brain.

## ACKNOWLEDGMENTS

This research was supported by PHS Grant No. CA 46627 awarded by NCI/NIH, PHHS. The authors would like to thank the reviewers for their comments on the potential difficulties in applying cavitation effects for brain therapy and surgery.

<sup>1</sup>J. G. Lynn, R. L. Zwemer, A. J. Chick, and A. E. Miller, "A new method for the generation and use of focused ultrasound in experimental biology," *J. Gen. Physiol.* **26**, 179–193 (1942).

- <sup>2</sup>W. J. Fry, J. W. Barnard, F. J. Fry, R. F. Kruminis, and J. F. Brennan, "Ultrasonic lesions in the mammalian central nervous system," *Science* **122**, 517–518 (1955).
- <sup>3</sup>F. J. Fry, "Transskull transmission of an intense focused ultrasonic beam," *Ultrasound Med. Biol.* **3**, 179–184 (1977).
- <sup>4</sup>F. J. Fry and J. E. Barger, "Acoustical properties of the human skull," *J. Acoust. Soc. Am.* **63**, 1576–1590 (1978).
- <sup>5</sup>J. B. Marmor and G. M. Hahn, "Ultrasound heating in previously irradiated sites," *Int. Journal of Radiation Oncology and Biological Physics* **4**, 1029–1032 (1978).
- <sup>6</sup>F. J. Fry and S. A. Goss, "Further studies of the transskull transmission of an intense focused ultrasonic beam: Lesion production at 500 kHz," *Ultrasound Med. Biol.* **6**, 33–38 (1980).
- <sup>7</sup>P. M. Corry, B. Barlogie, E. J. Tilchen, and E. P. Armour, "Fundamental results concerning integral representation in acoustical radiation," *Int. Journal of Radiation Oncology and Biological Physics* **8**, 1225–1229 (1982).
- <sup>8</sup>F. J. Fry, N. T. Sanghvi, R. F. Morris, S. Smithson, L. Atkinson, K. Dines, T. Franklin, and J. Hastings, "A focused ultrasound system for tissue volume ablation in deep seated brain sites," *Proceedings of IEEE 1986 Ultrasonics Symposium* **2**, 1001–1004 (1986).
- <sup>9</sup>A. N. Guthkelch, L. P. Carter, J. R. Cassady, K. Hynynen, K. Iacono, R. P. Johnson, P. C. Obbens, E. A. Roemer, R. B. Seeger, J. F. Shimm, and B. Stea, "Treatment of malignant brain tumors with focussed ultrasound hyperthermia and radiation: Results of a phase I trial," *Journal of Neuro-Oncology* **10**, 271–284 (1991).
- <sup>10</sup>E. B. Hutchinson, M. T. Buchanan, and K. Hynynen, "Design and optimization of an aperiodic ultrasound phased array for intracavitary prostate thermal therapies," *Med. Phys.* **23**, 767–776 (1996).
- <sup>11</sup>K. M. Quan, D. J. Watmough, and J. R. Mallard, "Theoretical considerations in relation to the treatment of brain tumours by means of local hyperthermia generated by ultrasound fields," *European Journal of Surgical Oncology* **17**, 454–465 (1991).
- <sup>12</sup>K. Hynynen and F. Jolesz, "Demonstration of noninvasive ultrasound brain therapy through an intact skull," *Ultrasound Med. Biol.* **24**, 275–283 (1998).
- <sup>13</sup>S. W. Smith, D. J. Phillips, O. T. von Ramm, and F. L. Thurstone, "Some advances in acoustic imaging through skull," in *Symposium on Biological Effects and Characterizations of Ultrasound Sources*, edited by D. G. Hazzard and M. L. Litz, pp. 37–52 (HEW, Rockville, MD, 1977).
- <sup>14</sup>S. W. Smith, G. E. Trahey, and O. T. von Ramm, "Phased array ultrasound imaging through planar tissue layers," *Ultrasound Med. Biol.* **12**, 229–243 (1986).
- <sup>15</sup>J.-L. Thomas and M. A. Fink, "Ultrasonic beam focusing through tissue inhomogeneities with a time reversal mirror: Application to transskull therapy," *IEEE Trans. Ultrason. Ferroelectr. Freq. Control* **43**, 1122–1129 (1996).
- <sup>16</sup>K. Hynynen, A. Chung, T. Fjield, M. Buchanan, D. Daum, V. Colucci, P. Lopath, and F. A. Jolesz, "Feasibility of using ultrasound phased arrays for MRI monitored noninvasive surgery," *IEEE Trans. Ultrason. Ferroelectr. Freq. Control* **43**, 1043–1052 (1996).
- <sup>17</sup>X. Fan and K. Hynynen, "The effects of curved tissue layers on the power deposition patterns of therapeutic ultrasound beams," *Med. Phys.* **21**, 25–34 (1994).
- <sup>18</sup>X. Fan, "Noninvasive Ultrasound Surgery using Spherically Curved Phased Arrays," Ph.D. thesis, Department of Electrical and Computer Engineering, University of Arizona, 1995.
- <sup>19</sup>M. C. Junger and D. Feit, *Sound, Structures, and Their Interaction* (Acoustical Society of America, Woodbury, NY, 1993).
- <sup>20</sup>X. Fan and K. Hynynen, "The effects of wave reflection and refraction at soft tissue interfaces during ultrasound hyperthermia treatments," *J. Acoust. Soc. Am.* **91**, 1727–1736 (1992).
- <sup>21</sup>M. F. Hamilton, "Comparison of three transient solutions for the axial pressure in a focused sound beam," *J. Acoust. Soc. Am.* **92**, 527–532 (1992).
- <sup>22</sup>K. E. Frøysa, J. N. Tjøtta, and S. Tjøtta, "Linear propagation of a pulsed sound beam from a plane or focusing source," *J. Acoust. Soc. Am.* **93**, 80–92 (1993).
- <sup>23</sup>X. Fan and K. Hynynen, "A study of various parameters of spherically curved phased array for noninvasive ultrasound surgery," *Phys. Med. Biol.* **41**, 591–608 (1996).
- <sup>24</sup>X. Fan and K. Hynynen, "Ultrasound surgery using multiple sonications—Treatment time considerations," *Ultrasound Med. Biol.* **22**, 471–482 (1996).

- <sup>25</sup>P. T. Christopher and K. J. Parker, "New approaches to the linear propagation of acoustic fields," *J. Acoust. Soc. Am.* **90**, 507–521 (1991).
- <sup>26</sup>X. Fan and K. Hynynen, "Control of the necrosed tissue volume during noninvasive ultrasound surgery using a 16-element phased array," *Med. Phys.* **22**, 297–306 (1995).
- <sup>27</sup>K. Hynynen, "The role of nonlinear ultrasound propagation during hyperthermia treatments," *Med. Phys.* **18**, 1156–1163 (1991).
- <sup>28</sup>N. I. Vykhodtseva, K. Hynynen, and C. Damianou, "Histologic effects of high intensity pulsed ultrasound exposure with subharmonic emission in rabbit brain *in vivo*," *Ultrasound Med. Biol.* **21**, 969–979 (1995).
- <sup>29</sup>F. J. Fry, "Intense focused ultrasound in medicine," *European Urology* **23**, 2–7 (1993).

# LETTERS TO THE EDITOR

*This Letters section is for publishing (a) brief acoustical research or applied acoustical reports, (b) comments on articles or letters previously published in this Journal, and (c) a reply by the article author to criticism by the Letter author in (b). Extensive reports should be submitted as articles, not in a letter series. Letters are peer-reviewed on the same basis as articles, but usually require less review time before acceptance. Letters cannot exceed four printed pages (approximately 3000–4000 words) including figures, tables, references, and a required abstract of about 100 words.*

---

## **Inversion of elastic waveform data in anisotropic solids using the delta-function representation of the Green's function**

V. K. Tewary

*Materials Reliability Division, National Institute of Standards and Technology, Boulder, Colorado 80303*

(Received 20 November 1996; accepted for publication 5 June 1998)

A method for inversion of measured data on elastic waveforms in anisotropic solids is proposed, using the delta-function representation of the Green's function. The method requires integration over a closed 2-D (two-dimensional) space. In contrast, inversion using the traditional Fourier representation requires integration over an infinite 4-D space. The method can be used to determine the Green's function for imaging applications and elastic constants for materials characterization. The method is illustrated by applying it to determine all six elastic constants of a model graphite fiber composite assuming a tetragonal structure and using simulated data. © 1998 Acoustical Society of America. [S0001-4966(98)04509-3]

PACS numbers: 43.20.Gp, 43.20.Jr, 43.35.Cg, 43.35.Pt [DEC]

### **INTRODUCTION**

We describe a new method for the inversion of measured data on transient elastic waveforms in anisotropic solids by using the delta-function representation of the Green's function.<sup>1,2</sup> The inversion of the waveform data is required for determining the elastodynamic Green's function for applications such as imaging in elastic and acoustic scattering problems, characterization of the source in acoustic emissions, measurement of elastic constants, and materials characterization.

Traditionally, inversion<sup>3</sup> of waveform data is done by using the Fourier representation of the Green's function. The exact inversion would require measurement of waveforms over the infinite Fourier space (wave vector and frequency). Since that is not possible in practice, special techniques have been developed for processing of data in the Fourier space. However, that is subject to sampling errors and statistical uncertainties. The use of delta-function representation reduces these uncertainties.

We have shown earlier<sup>1,2</sup> that the delta-function representation is computationally very efficient for forward calculations. Now we show that it is particularly suitable for the inversion problem. The inversion formula using delta-function representation requires integration over a closed 2-D (two-dimensional) space of the surface of a unit sphere. In contrast, the Fourier inversion formula requires integration over the 4-D infinite space of frequency and wave vectors. The main characteristic of the delta-function representation is that it uses a variable that is a linear combination of the space and time variables and maps the Green's function

in the slowness space. In the Fourier representation, the space and time variables are treated separately and are mapped into the corresponding frequency and wave vector space.

Full inversion leading to the determination of the whole Green's function is needed only for imaging applications. The elastic constants of isotropic solids have been traditionally determined by measuring the transit time or the ultrasonic phase velocities and interpreting the data using Fourier representation.<sup>3</sup> This technique does not work very well for anisotropic solids, because of uncertainties due to energy flux deviation and path length variations.<sup>4–6</sup>

Experimentally,<sup>7</sup> it is possible to measure the waveforms at a large number of points over the surface of a hemisphere with a transient point source at its center, or over the surface of a semicylinder with a transient line source at its axis. The waveforms can then be analyzed in terms of the Green's function that accounts for the response of the whole solid and therefore does not suffer from the uncertainties like path length. The delta-function representation provides an efficient inverse relationship for determination of elastic constants by such measurements.

We show here how to use the inversion formula of the delta-function representation to obtain the elastodynamic Green's function and elastic constants of anisotropic solids from the transient waveforms measured over a closed space. To illustrate our method, we use simulated data to determine all the six elastic constants of graphite-fiber composite assuming a tetragonal model. We calculate the waveforms using known elastic constants over a finite set of points on the

surface of a hemisphere. We treat the calculated values as the “measured values.” We then apply our method to determine the elastic constants of the solid by using these “measured values.” We find an excellent agreement between the original and the derived values of the elastic constants.

## I. GREEN'S FUNCTION REPRESENTATION AND INVERSION OF WAVEFORMS

We use the same notation and frame of reference as in Ref. 2. For a step function pulse, the elastodynamic Green's function is written as<sup>1,2</sup>

$$\mathbf{G}(\mathbf{x}, t) = \frac{1}{4\pi^3} \int \mathbf{g}(\mathbf{q}) \delta(t - \mathbf{q} \cdot \mathbf{x}) d\mathbf{q}, \quad (1)$$

where  $\mathbf{g}(\mathbf{q})$ , the Green's function in slowness space, is given by

$$\mathbf{g}(\mathbf{q}) = \text{Im}[\Lambda(\mathbf{q}) - (1 - i\varepsilon)\mathbf{I}]^{-1}, \quad (2)$$

$$\Lambda_{ij}(\mathbf{q}) = c_{ikjl}q_kq_l, \quad (3)$$

$\mathbf{I}$  is the unit matrix,  $c$  is the elastic constant tensor,  $\mathbf{q}$  is a vector in the slowness space,  $\mathbf{x}$  and  $t$  are the 3-D space and time variables, respectively,  $\Lambda$  is the Christoffel matrix, and  $\varepsilon = +0$  in the limit. The integration in Eq. (1) is over the entire vector space of  $\mathbf{q}$ . The function  $\mathbf{g}(\mathbf{q})$ , defined as the imaginary part of  $[\Lambda(\mathbf{q}) - (1 - i\varepsilon)\mathbf{I}]^{-1}$  in Eq. (2), has delta-function type resonances.<sup>1,2</sup> The real and imaginary parts of  $\mathbf{g}(\mathbf{q})$  are related due to causality. Equation (1) is the Radon representation of the Green's function.<sup>8</sup> Using the inversion formula<sup>8</sup> for the Radon transform yields

$$\mathbf{g}(\mathbf{Q}) = \frac{1}{4\pi^3} \int_{x=1} \mathbf{G}''(\mathbf{x}, t = \mathbf{Q} \cdot \mathbf{x}) d\mathbf{x}, \quad (4)$$

where the primes denote the second derivative with respect to time and the integration in Eq. (4) is over the surface of a unit sphere.

Equation (4) provides a prescription for experimentally determining  $\mathbf{g}(\mathbf{Q})$  for any vector  $\mathbf{Q}$  in the slowness space. Take a hemispherical sample. Choose units such that the radius of the hemisphere is 1. Apply a localized step-function force at the center. Measure the waveforms as function of time at various points on the surface of the sample. At each point on the surface, extract the second derivative of the displacement field at  $t = \mathbf{Q} \cdot \mathbf{x}$  for a selected value of  $\mathbf{Q}$ . Integrate over the surface by summing over all values of  $\mathbf{x}$  in accordance with Eq. (4). This would give  $\mathbf{g}(\mathbf{Q})$  if the force is known, or the force if  $\mathbf{g}(\mathbf{Q})$  is known.

Our present objective is to determine only the elastic constants of a solid. It would be sufficient to measure the location of resonances in the elements of  $\mathbf{g}(\mathbf{Q})$ . If the applied force is a point force, and if the density of the solid is uniform, the position of the resonance would depend only upon the eigenvalues of the Christoffel matrix. The eigenvalues are simple functions of the elastic constants of the solid for  $\mathbf{Q}$  in symmetry directions. Thus, by choosing suitable values of  $\mathbf{Q}$ , we can determine the elastic constants by locating the resonances in the elements of  $\mathbf{g}(\mathbf{Q})$ .

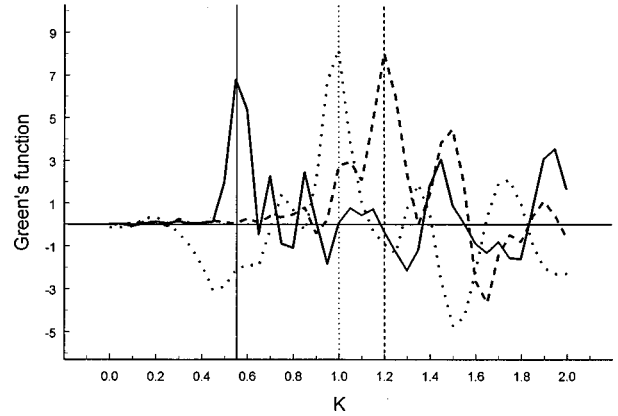


FIG. 1. Green's function determined from the simulated measurements, plotted against  $K$ , a component of the slowness vector  $\mathbf{Q}$ . Solid line— $G_{11}(\mathbf{Q})$ , dotted— $G_{22}(\mathbf{Q})$ , dashes— $G_{33}(\mathbf{Q})$ , where  $\mathbf{Q} = (K, 0, 0)$ . The vertical lines are locations of resonance.

## II. APPLICATION TO SIMULATED DATA

To test our method, we use simulated data for a model tetragonal solid assuming uniform density. We assume that we have the specimen in the form of a hemisphere as used by Hurley *et al.*<sup>7</sup> We further assume that the transient elastic waves are generated by a step-function-type point source at the center of the hemisphere and we measure the first derivative of the velocity field at various points on the curved surface of the hemisphere. We also assume that all six components of the Green's function can be obtained by measuring the three components of the displacement field for each direction of the force.

The chosen values of the elastic constants for a model<sup>2</sup> graphite-fiber composite are given below in units of  $c_{44}$ :

$$c_{11} = 3.1, \quad c_{33} = 54.6, \quad c_{44} = 1,$$

$$c_{66} = 0.7, \quad c_{12} = 1.2, \quad c_{13} = 1.9.$$

We calculate the second derivative of the displacement field at  $t = \mathbf{Q} \cdot \mathbf{x}$  for selected values of  $\mathbf{Q}$  and  $\mathbf{x}$  by using Eqs. (1)–(3). We treat these calculated values as the experimental data. We assume units such that the density of the solid, the radius of the hemisphere, and  $c_{44}$  are all equal to 1. We choose 561 points over the surface of the sphere—17 points for  $0 \leq \theta \leq \pi$  and 33 points for  $0 \leq \phi \leq 2\pi$ , where  $\theta$  and  $\phi$  are, respectively, the polar and the azimuthal angles. We choose  $\mathbf{Q}$  in the symmetry directions given below. It is experimentally possible<sup>7</sup> to make measurements over a few thousand points on the surface of the hemisphere.

We integrate the measured values of  $\mathbf{G}''(\mathbf{x}, t = \mathbf{Q} \cdot \mathbf{x})$  numerically over the 561 integration points on the surface of the sphere. The number of integration points can be reduced by exploiting the symmetry of the configuration depending upon the direction of  $\mathbf{Q}$ . Figures 1–4 show plots of the different components of  $\mathbf{G}(\mathbf{Q})$  for  $\mathbf{Q}$  in the symmetry directions. The curves have resonances (peaks) at those values of  $Q$  where the delta-function singularities are located in the Green's function in Eq. (1). This is because we compute the integral in Eq. (4) by summing over a discrete set of finite points. The finite sum smoothens out the delta functions in the Green's function.

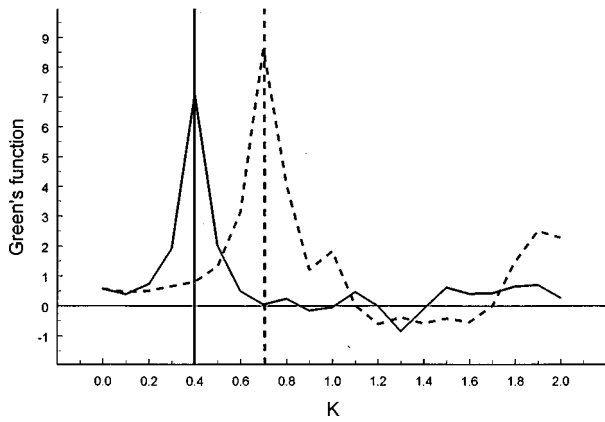


FIG. 2. Same as Fig. 1 for  $\mathbf{Q}=(K,K,0)$ . Solid line— $G_{11}(\mathbf{Q})+G_{12}(\mathbf{Q})$ , dashes— $G_{11}(\mathbf{Q})-G_{12}(\mathbf{Q})$ .

We determine the elastic constants from the position of the resonances, obtained by equating to unity the eigenvalues of the Christoffel matrix given in Eq. (3). We write  $\mathbf{Q}$  in the form  $(\alpha K, \beta K, \gamma K)$  where  $\alpha$ ,  $\beta$ , and  $\gamma$  are constants and  $K$  is a scalar variable. The predicted values are obtained by using the elastic constants given earlier. The observed values are obtained from the position of the vertical lines in Figs. 1–4. The predicted and observed locations of resonances in the chosen symmetry directions are given below.

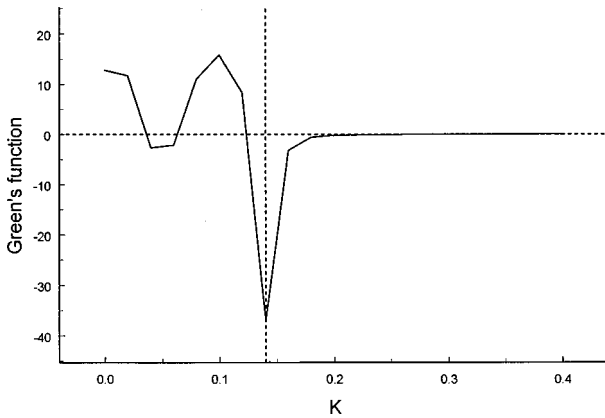


FIG. 3. Same as Fig. 1 for  $\mathbf{Q}=(0,0,K)$ . Solid line— $G_{33}(\mathbf{Q})$ .

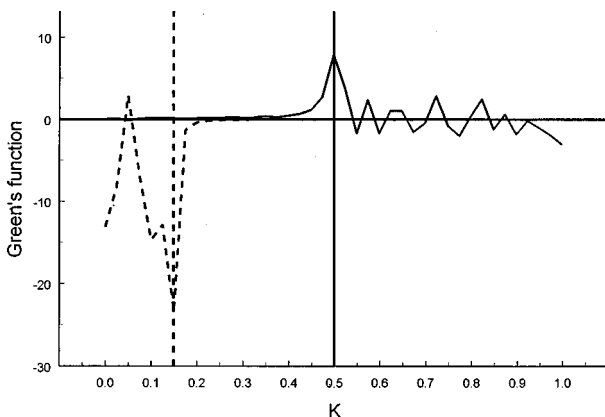


FIG. 4. Same as Fig. 1 for  $\mathbf{Q}=(0,K,K)$ . Solid line— $G_{33}(\mathbf{Q})$ , dashes— $G_{22}(\mathbf{Q})$ .

- (i)  $\mathbf{Q}=(K,0,0)$ ; gives  $c_{11}$ ,  $c_{44}$ , and  $c_{66}$ .  $G_{11}(K)$ —resonance at  $[1/c_{11}]^{1/2}$ , predicted—0.57, observed—0.57.  $G_{22}(K)$ —resonance at  $[1/c_{66}]^{1/2}$ , predicted—1.2, observed—1.2.  $G_{33}(K)$ —resonance at  $[1/c_{44}]^{1/2}$ , predicted—1.0, observed—1.0.
- (ii)  $\mathbf{Q}=(K,K,0)$ ; gives  $c_{12}$ .  $G_{11}(K)+G_{22}(K)$ : resonance at  $[1/(c_{11}+c_{12}+2c_{66})]^{1/2}$ , predicted—0.42, observed—0.4.  $G_{11}(K)-G_{22}(K)$ : resonance at  $[1/(c_{11}-c_{12})]^{1/2}$ , predicted—0.72, observed—0.7.
- (iii)  $\mathbf{Q}=(0,0,K)$ ; gives  $c_{33}$ .  $G_{33}(K)$ —resonance at  $[1/c_{33}]^{1/2}$ , predicted—0.14, observed—0.14.
- (iv)  $\mathbf{Q}=(0,K,K)$ ; gives  $c_{13}$ .  $G_{22}(K)$  and  $G_{33}(K)$ : two resonances at  $[B \pm (B^2 - A)^{1/2}]/A$ , where  $2B = c_{11} + c_{33} + 2c_{44}$  and  $A = (c_{11} + c_{44})(c_{33} + c_{44}) - (c_{11} + c_{13})^2$ ; predicted—0.5 and 0.14, observed—0.5 and 0.15.

The predicted and the observed locations of the resonances agree almost exactly. Hence the estimated values of the elastic constant come out to be the same as the original values.

The excellent agreement between the actual and the estimated values of the elastic constants is partly due to the fact that we have used simulated data. Such an agreement is unlikely with real data. However, it should provide an incentive to make measurements of the elastic waveforms in slowness space. The present calculation proves the feasibility of our method. It gives the very useful result that it suffices to make measurements over a finite set of points for the purpose of inversion of elastic waveforms. This is due to the fact that our inversion formula scans a closed 2-D space unlike those based upon the Fourier representation that scan an infinite 4-D space.

### III. DISCUSSION

The main advantages of our method are the following.

- (1) Measurements are needed over a closed 2-D space. The main source of mathematical error is due to integration over a discrete set of points. This error should be small because, unlike the Fourier transform, the integrand is not singular or oscillatory. This advantage should be particularly significant if the whole Green's function needs to be measured such as in imaging applications. Inversion using the Fourier representation would require a much larger amount of data over an infinite 4-D space, which introduces statistical sampling errors and numerical errors due to poor convergence.
- (2) The method includes the total response of the solid and not the response in just a few directions. This makes the method particularly suitable for anisotropic solids.
- (3) The magnitude of the applied force does not need to be measured. The locations of the resonances are not very sensitive to the space–time behavior of the applied force. However, if the whole Green's function has to be determined, then a detailed knowledge of the force function would be necessary.
- (4) The method does not suffer from the difficulties in the conventional methods associated with the fluctuations in measurements made at different frequencies and uncer-

tainties due to energy flux deviation and path length variations.

The main disadvantages of our method are as follows.

- (1) The effect of free surface boundary conditions has not been included. The appropriate surface boundary conditions are essential to account for other waves in the solid such as the head waves and Rayleigh waves. These waves are slower than the bulk waves. They will not affect the location of the resonances arising from the bulk waves which occur at smaller values of  $Q$ . If the contribution of these waves is included in the inversion of the radon transform, they will give additional resonances in  $G(Q)$  vs  $Q$  plots. These resonances will occur at larger values of  $Q$ , and, therefore, can be identified experimentally. The values of the elastic constants are determined only from the location of the bulk resonances which are independent of the contribution of the other waves. Efficient methods for including the effect of free surfaces on elastic waves already exist in the literature and can be used if experimental results are available. The additional resonances may be used to extract information about their sources such as surfaces and interfaces in solids.
- (2) We have neglected the contribution of the reflected waves. These waves will arrive at the observation point much later than the directly propagating bulk waves. Hence, for reasons discussed above, they will not affect the location of the bulk wave resonances.
- (3) The hemispherical test specimens of anisotropic composite materials are difficult to make. However, methods<sup>7</sup> have been developed for the preparation of hemispherical samples and ultrasonic velocity measurements in such samples of composite materials.
- (4) Measurements need to be made at a large number of points, including those in nonsymmetry directions and all components of the displacement need to be measured. However, even in the conventional methods,<sup>7</sup> it seems to be necessary because of the angular dependence of the ultrasonic velocity in anisotropic solids. Hurley *et al.*<sup>7</sup> have used a hemispherical test sample and made measurements at 5040 data points. In our calculation we have shown that even 561 points can yield a reliable set of values of the elastic constants. The number of measurements that is needed may be reduced by exploiting the symmetry of the solid if known. In this paper, in order to test the numerical convergence of our method, we have not exploited the symmetry of the solid.
- (5) A major source of error is the numerical evaluation of the second derivatives of measured displacements with respect to time. This error may introduce spurious peaks in the curves and may flatten the real delta-function peaks in the Green's function. The error may be reduced by measuring the displacement field at a large number of time points. The error may be further reduced by mea-

suring the velocity field or even the acceleration field rather than the displacement field by using appropriate transducers.

- (6) Some spurious peaks may be obtained as in Figs. 1–4. We have chosen the sharpest and the largest peaks. If the measurements were available at infinite number of points and the integration in Eq. (4) could be done exactly, the plots in Figs. 1–4 would have the perfect delta-function singularities. The evaluation of this integration as a discrete sum smooths out the delta-function singularities and introduces spurious peaks in the Green's function. The spurious peaks may be reduced by making measurements at a larger number of points on the sphere and at smaller time steps. Hurley *et al.*<sup>7</sup> have measured the waveforms at 5040 space points and 2048 time points at each space point.
- (7) The numerical stability of the algorithm has not been established.

#### IV. CONCLUSION

To summarize, the proposed method has a strong potential for application to inversion of elastic waveforms data for anisotropic solids because it requires scanning over a closed 2-D space, in contrast to the conventional methods of inversion based upon the use of Fourier transforms that requires scanning of infinite 4-D space. The method can be used for measurement of elastic constants of anisotropic materials as well as ultrasonic imaging. The method is potentially most attractive for imaging applications for anisotropic solids where the whole Green's function is required because of various numerical and statistical uncertainties in the alternative method of inversion using Fourier transforms over a 4-D space.

#### ACKNOWLEDGMENTS

The author thanks Dr. Donna Hurley, Dr. Dale Fitting, and Dr. Chris Fortunko for useful suggestions.

<sup>1</sup>V. K. Tewary, "Computationally efficient representation for elastodynamic and elastostatic Green's functions for anisotropic solids," *Phys. Rev. B* **51**, 15 695 (1995).

<sup>2</sup>V. K. Tewary and C. M. Fortunko, "Surface waves in three-dimensional half-space tetragonal solids," *J. Acoust. Soc. Am.* **100**, 86 (1996).

<sup>3</sup>F. Santosa, Y. Pao, W. W. Symes, and C. Holland, *Inverse Problems of Acoustics and Elastic Waves* (SIAM, Philadelphia, 1984).

<sup>4</sup>H. Ledbetter, C. Fortunko, and P. Heyliger, "Orthorhombic elastic constants of boron-aluminum fiber-reinforced composite: an ultrasonic resonance spectroscopy study," *J. Appl. Phys.* **78**, 1352 (1995).

<sup>5</sup>E. P. Papadakis, T. Patton, Y. M. Tsai, and D. O. Thomson, "The elastic moduli of thick composites," *Rev. Prog. Quant. Nondestr. Eval.* **9**, 1387 (1990).

<sup>6</sup>E. S. Boltz, "Waveform-based ultrasonics for characterization of elastodynamic anisotropy and acoustic emission sources in thick plates: theory and experiment," Ph.D. thesis, The Johns Hopkins University, Baltimore, 1996.

<sup>7</sup>D. C. Hurley, D. W. Fitting, and R. Y. Chiao, "Angularly-dependent ultrasonic velocity and attenuation measurements in an anisotropic material," *Rev. Prog. Quant. Nondestr. Eval.* **14B**, 1585 (1995).

<sup>8</sup>C. Y. Wang and J. D. Achenbach, "A new method to obtain 3-D Green's functions for anisotropic solids," *Wave Motion* **18**, 273 (1993).



# Analysis and comparison of recent resonance scattering formulations by M. S. Choi *et al.* with earlier, traditional RST works

G. C. Gaunaurd<sup>a)</sup>

Naval Surface Warfare Center, Carderock Division—Code 684, 9500 MacArthur Boulevard, West Bethesda, Maryland 20817-5700

(Received 10 November 1997; accepted for publication 11 May 1998)

Some comparisons are studied between several recent (1997 and 1998) formulations of acoustic resonance scattering, by M. S. Choi *et al.* and other earlier, traditional ones. In the *practical* cases here analyzed, the recent formulations are: (a) more complicated; (b) of purely formal character; (c) make use of information not known or available *a priori*; (d) eventually reduce to the traditional ones; and (e) seem to offer little new practical advantages. Finally, none of these formulations has been used for target identification purposes, which is the essential underlying reason for these investigations. [S0001-4966(98)05608-2]

PACS numbers: 43.40.Ey, 43.20.Fn [CBB]

## ANALYSIS AND COMPARISONS

In reference to the findings of the resonance scattering theory<sup>1</sup> it has been recently stated<sup>2</sup> that the background coefficients suitable to isolate the resonance features contained in the form function of an empty spherical shell in a fluid medium are more appropriately given by:

$$R_n^{(b)} = - \frac{j_n'(x_1) - [F_n(0^+)/x_1]j_n(x_1)}{h_n^{(1)'}(x_1) - [F_n(0^+)/x_1]h_n^{(1)}(x_1)}, \quad (1)$$

where

$$\frac{F_n(0^+)}{x_1} = - \frac{\rho_1}{\rho_2 h x_1} \left[ h^* \frac{n + (n+1)(1-h)^{2n+1}}{1 - (1-h)^{2n+1}} \right], \quad (2)$$

and  $x_1 \equiv k_1 a$ ,  $h = (a-b)/a$ ,  $k_1$  is the wave number in the (outer) fluid,  $a$  and  $b$  are the outer/inner shell radius, and  $\rho_1$  and  $\rho_2$  are the mass densities of the outer fluid and the shell material, respectively.

Another earlier<sup>3,4</sup> expression for the background coefficients of thin shells was found to be:

$$R_n^{(b)} = - \frac{j_n'(x_1) - \eta_0 j_n(x_1)}{h_n^{(1)}(x_1) - \eta_0 h_n^{(1)}(x_1)}, \quad (3)$$

where  $\eta_0$ , using Eq. (31) of Ref. 3, was

$$\eta_0 = \frac{\rho_1}{\rho_2 h x_1} * \frac{1}{1 + x_1^{-2}}. \quad (4)$$

Reference 3 assumed high frequencies (i.e.,  $x_1 \gg 1$ ) in the derivation of the  $R_n^{(b)}$  in Eq. (3), which was called  $A_n$  there. For naval applications, submerged shells thicker than  $h \approx 5\%$  are not practical, and this justifies the use of thin shells in Refs. 3 and 4. [Note also that Eq. (4) does not depend on the partial wave order  $n$ .]

It is easily verified that for thin shells, both approaches above [i.e., Eqs. (2) and (4)] yield the same result, viz.,

$$\eta_0 = \frac{F_n(0^+)}{x_1} = \frac{\rho_1}{\rho_2 h x_1} \equiv \frac{\Omega}{x_1}, \quad (5)$$

and then Eqs. (1) and (3) coincide. Equation (5) also defines the fluid-loading parameter,  $\Omega$ , introduced by Norris and his associates.<sup>5,6</sup>

For thick shells, a situation still formally included within the formulation of Refs. 3 and 4, it follows from Eq. (4) that at high frequencies (i.e.,  $x_1 \gg \Omega$ ), one has  $\eta_0 \rightarrow 0$ . Then Eqs. (1) and (3) again coincide, and they both reduce to the conventional “rigid background” case. On the other hand, if  $x_1 \ll \Omega$ , then Eq. (4) yields  $\eta_0 \rightarrow \infty$ . In this case Eqs. (1) and (3) again coincide, and they both reduce to the traditional “soft background” case. The apparent advantage of Eqs. (1) and (2) is their higher accuracy for the larger shell thicknesses (i.e., for  $h > 5\%$ ), provided that the shell has no fillers, it is not layered, and it lacks losses or structural damping. The discrepancy between this approach and that resulting from the use of Eqs. (3) and (4), even in these thicker shell cases, seems to manifest itself only slightly in the first few partial waves. Some disadvantages of Eqs. (1) and (2) rest in their greater complexity and on that  $F_n(0^+)$  depends on the partial-wave order  $n$ , and that dependence is not known *a priori*.

The proposition that (Ref. 2, p. 2084, top) “after removing all the resonances from the partial waves  $R_n$ , the remainder can be used as the background coefficients,” seems to follow a backward line of reasoning. The background coefficients are removed or subtracted in order to isolate the otherwise veiled resonances, not the other way around. The isolated resonances are not known *a priori* (i.e., prior to the effect).

The analysis presented for the cylindrical shell case<sup>7</sup> is identical to that for the spherical case<sup>2</sup> even in the wording of the paragraphs. The final result given for the “inherent background” coefficients  $R_n^{(b)}$  is like Eq. (1), but with the spherical Bessel functions replaced by Bessel functions, and a slightly different  $F_n(0^+)$ , viz.,

<sup>a)</sup>Electronic mail: Gaunaurd@oasys.dt.navy.mil

$$F_n(0^+) = \frac{\rho_1}{\rho_2 h} * n h * \frac{1 + (1-h)^{2n}}{1 - (1-h)^{2n}}, \quad n \geq 1. \quad (6)$$

For a solid cylinder (i.e.,  $h=1$ ) Eq. (6) reduces to  $n\rho_1/\rho_2$ . All comments made above for the spherical case also hold for the cylindrical. Multilayered shells are discussed below.

In Ref. 8, an expression for the resonances in each partial wave was found to be:

$$R_n^{(\text{reso})} = i \frac{\text{Im} \left( \frac{1}{z_n^{(1)}} \right)}{\frac{1}{z_n^{(1)}} - \frac{1}{F_n}}, \quad (7)$$

where

$$\bar{z}_n^{(1)} = \frac{x_1 h_n^{(1)'}(x_1)}{h_n^{(1)}(x_1)} - \Omega_n, \quad (8a)$$

$$\bar{F}_n = -\frac{\rho_1}{\rho_2} x_T^2 \frac{D_n^{11}}{D_n^{21}} - \Omega_n, \quad (8b)$$

and

$$\Omega_n \equiv F_n(0^+) = \text{See Eq. (2)} \\ = \frac{\rho_1}{\rho_2} \frac{n + (n+1)(1-h)^{2n+1}}{1 - (1-h)^{2n+1}}. \quad (8c)$$

The  $\Omega_n$  in Eqs. (8) is not to be confused with the fluid-loading parameter:  $\Omega = \rho_1/(\rho_2 h)$ . Equation (7) holds because, as the authors of Ref. 8 later state, one has:

$$|R_n - R_n^{(b)}| = |R_n^{(\text{reso})}|, \quad (9)$$

with the  $R_n^{(b)}$  in Eq. (1). The authors<sup>8</sup> conclude that the resonances can be found “without having to subtract any background.” This is a circular argument because the information and parameters required to obtain  $|R_n^{(\text{reso})}|$ , in Eq. (7), are the same as those required to obtain  $R_n^{(b)}$ , and thus,  $|R_n - R_n^{(b)}|$ . Hence, this formal result introduces no true advantage. Furthermore, the case described in the Numerical Analysis (Sec. II) of Ref. 8 pertains to a steel spherical shell with a minute hole (i.e.,  $h=99\%$ , or a 1% hole). These results are practically indistinguishable from those obtained with the traditional rigid background. In this case,

$$\frac{F_n(0^+)}{x_1} = \frac{n\Omega}{x_1} \rightarrow 0 \quad (\text{since } x_1 \gg n\Omega) \quad (10)$$

and thus,

$$R_n^{(b)} = -\frac{j_n'(x_1)}{h_n^{(1)'}(x_1)} \quad (\text{rigid}). \quad (11)$$

This conclusion also emerges from the analysis given in Ref. 2.

Classical scattering by submerged multilayered cylindrical shells with  $n$ -layers was first studied by Akay.<sup>9</sup> The traditional RST formulation, including resonance/background

separation, for the double-layered ( $j=2$ ), cylindrical, fluid-filled, shell was first analyzed and computed in Ref. 10. This work was re-done in a recent (1998) paper, Ref. 11, which introduced a modified set of background coefficients denoted the “inherent background.” These coefficients used  $[F_n(0^+)]_j$ -values given by:

$$[F_n(0^+)]_j = n \frac{\rho_{j+1}}{\rho_j} \cdot \frac{n + \frac{1 + (1-h_j)^{2n}}{1 - (1-h_j)^{2n}} \cdot [F_n(0^+)]_{j-1}}{n \cdot \frac{1 + (1-h_j)^{2n}}{1 - (1-h_j)^{2n}} + [F_n(0^+)]_{j-1}}. \quad (12)$$

For the innermost shell layer ( $j=1$ ) Eq. (12) reduces to Eq. (6) for the case of the single shell. Now  $\rho_1$  and  $\rho_2$  are interchanged in view of a notational change introduced in Ref. 11. The solid cylinder case ( $j=0$ ) simplifies as stated after Eq. (6). Reference 11 only discusses and evaluates the *double-layered* case ( $j=2$ ), and the formulation is the same as in the earlier Ref. 10 except for the use of the modified (“inherent”) background coefficients. We note that the evaluations in Ref. 11 are computed for layers made out of different metals (i.e., Al and WC), a hypothetical situation of little practical value. In any case, as in the single-layer shell [cf. Eq. (6)], at high frequencies (i.e.,  $x_1 \gg \Omega$ ) Eq. (12) yields  $[F_n(0^+)]_j/x_1 \rightarrow 0$ . This means that the “inherent” coefficients reduce to the earlier rigid ones [cf. Eq. (11)]. Analogously, for low frequencies one has,  $[F_n(0^+)]_j/x_1 \rightarrow \infty$ , and the inherent coefficients reduce to the earlier “soft” ones. Therefore, again, all comments and comparisons made for the single-shell case (cylindrical or spherical) also hold for multilayered shells.

## I. CONCLUSIONS

For thin shells, and also for thick ones in the limit of solid (metal) objects, the newly proposed approach gives results that are practically indistinguishable from the traditional ones, and in view of its complexity, it offers no practical advantage. We note that an approximate but quite simple way to isolate the resonance features “without any background subtraction” was described in Refs. 12 and 13, in some cases that included *bistatic* situations. We remark in closing that the whole point of isolating resonance features in a cross section (or form function) is to use them for target-identification purposes.<sup>13</sup> The real goal is to identify targets from “resonances” in their echoes, and this important point is nowhere addressed in Refs. 2, 7, 8, and/or 11. With regard to the recent reformulation for the multilayered shell, the outcome reduces to that in Refs. 9 and 10. Finally, from the analytical point-of-view, the modifications introduced in these works are relatively minor to present them as a “new formulation of the RST.”<sup>8</sup>

## ACKNOWLEDGMENTS

The author thanks the Independent Research Program of the NSWC-CD for support.

- <sup>1</sup>L. Flax, G. C. Gaunard, and H. Uberall, "The theory of resonance scattering," in *Physical Acoustics* (Academic, New York, 1981), Vol. 15, pp. 191–294.
- <sup>2</sup>M. S. Choi and Y. S. Joo, "Theory of the background amplitudes in acoustic resonance scattering," *J. Acoust. Soc. Am.* **101**, 2083–2087 (1997).
- <sup>3</sup>G. C. Gaunard, "Hybrid background coefficients to isolate the resonance 'spectrograms' of submerged shells," *J. Acoust. Soc. Am.* **92**, 1981–1984 (1992).
- <sup>4</sup>G. C. Gaunard and M. Werby, "Sound scattering by resonantly-excited, fluid-loaded, elastic spherical shells," *J. Acoust. Soc. Am.* **90**, 2536–2550 (1991).
- <sup>5</sup>A. N. Norris and N. Vasudevan, "Acoustic wave scattering from thin shell structures," *J. Acoust. Soc. Am.* **92**, 3320–3336 (1992).
- <sup>6</sup>A. N. Norris and D. A. Rebinsky, "Acoustic coupling to membrane waves on elastic shells," *J. Acoust. Soc. Am.* **95**, 1809–1829 (1994).
- <sup>7</sup>M. S. Choi, Y. S. Joo, and J. P. Lee, "Inherent background coefficients for submerged cylindrical shells," *J. Acoust. Soc. Am.* **101**, 1743–1745 (1997).
- <sup>8</sup>M. S. Choi, "New formulation of the resonance scattering theory," *J. Acoust. Soc. Am.* **101**, 2491–2495 (1997).
- <sup>9</sup>A. Akay, "Scattering of sound from concentric cylindrical shells," *J. Acoust. Soc. Am.* **89**, 1572–1578 (1991).
- <sup>10</sup>A. Akay, S. Sener, and G. C. Gaunard, "Acoustic scattering from fluid-filled, concentric, submerged, cylindrical, elastic shells," *J. Acoust. Soc. Am.* **94**, 3277–3294 (1993).
- <sup>11</sup>J. S. Joo, J. G. Ih, and M. S. Choi, "Inherent background coefficients for acoustic resonance scattering from submerged, multilayered, cylindrical structures," *J. Acoust. Soc. Am.* **103**, 900–910 (1998).
- <sup>12</sup>G. C. Gaunard and A. Akay, "Isolation of the spectrograms and 'rosettes' of insonified sets of submerged concentric thin shells," *ASME J. Vib. Acoust.* **116**, 573–577 (1994).
- <sup>13</sup>G. C. Gaunard and H. C. Strifors, "Transient resonance scattering and target identification," *Appl. Mech. Rev.* **50**, 131–149 (1997). (See references therein.)

# Response to “Analysis and comparison of recent resonance scattering formulations by M. S. Choi *et al.* with earlier, traditional RST work” [J. Acoust. Soc. Am. 104, 1720 (1998)]

Myoung-Seon Choi

Department of Physics, Yeungnam University, Kyongsan 712-749, Korea

(Received 12 January 1998; revised 14 March 1998; accepted 11 May 1998)

In the letter by Gaunaurd, there were some comments on recent resonance scattering formulations by the author and his colleagues. Replies to the comments are made here. To clarify the discussion, brief reviews on the recent formulations and more traditional ones are included. It is shown that the recent approaches are based on much more robust physical concepts and approximations than the traditional ones, so that they are sufficient to be presented as novel tools for target identification purposes. © 1998 Acoustical Society of America. [S0001-4966(98)05708-7]

PACS numbers: 43.40.Ey, 43.20.Fn [CBB]

## INTRODUCTION

In two recent papers by the author and his colleagues,<sup>1,2</sup> the so-called “inherent background coefficient” had been formulated to describe the background amplitude correctly in acoustic scattering from a submerged, empty, elastic shell. The magnitude of the resonance spectra, which were obtained by using the traditional RST<sup>3</sup> (i.e., by subtracting the inherent background from the scattered field), represented the pure resonances of the shell, but the phase seems to be inaccurate. The latter motivated a new formulation of the RST.<sup>4</sup> In another paper,<sup>5</sup> the approach to the inherent background coefficient was extended to concentrically multilayered cylindrical shells.

In a recent letter by Gaunaurd,<sup>6</sup> there were some comments on the inherent background and the new RST formulation. Replies to the comments are made here. To clarify the discussion, brief reviews on the backgrounds and the resonance scattering theories are also included.

## I. DISCUSSION ON THE ANALYSIS AND COMPARISON

The scattering coefficient for the spherical shell is given as

$$R_n = - \frac{x_1 j_n'(x_1) - F_n j_n(x_1)}{x_1 h_n^{(1)'}(x_1) - F_n h_n^{(1)}(x_1)}, \quad (1)$$

where  $x_1 = k_1 a$ ,  $k_1$  is the wave number in the (outer) fluid, and  $a$  are the outer radius of the shell.<sup>1</sup> The elastic properties of the shell are relative only to the surface admittance function  $F_n$ . The scattering coefficient for a perfectly rigid sphere is given as the rigid one  $R_n^{(r)} = -j_n'(x)/h_n^{(1)'}(x)$  and the admittance function becomes zero, while the scattering coefficient for an ideally soft sphere is given as the soft one  $R_n^{(s)} = -j_n(x)/h_n^{(1)}(x)$  and the admittance function becomes infinity.

It is well known that with increasing frequencies, the background coefficient  $R_n^{(b)}$  for the elastic shell should undergo a transition from the soft to the rigid one, and be expressed in the form

$$R_n^{(b)} = - \frac{x_1 j_n'(x_1) - \Omega_n j_n(x_1)}{x_1 h_n^{(1)'}(x_1) - \Omega_n h_n^{(1)}(x_1)}, \quad (2)$$

where  $\Omega_n$  is a dimensionless frequency characterizing the transition. If such an expression can be based on some statement of a physical approximation, then the expression will give us physical insight, and it will be more likely to work over a wide range of physical parameters.

Gaunaurd<sup>7</sup> and Werby<sup>8</sup> formulated the so-called “hybrid background coefficient” by developing a masslike description of the shell, which seems to be based on the mass law that substitutes a mass barrier for the shell. The transition frequency was given by

$$\Omega_n = \Omega_* / (1 + x_1^{-2}), \quad (3)$$

where  $\Omega_* = \rho_1 / (\rho_2 h)$ ,  $\rho_1$  is the density of the (outer) fluid,  $\rho_2$  is the density of the shell,  $h = (a - b)/a$ , and  $b$  is the inner radius of the shell. In obtaining the background expression, they assumed that the modal mass may be approximated by the physical mass (i.e., the volume times the density) of the shell. This approximation seems to be appropriate only for thin shells (i.e.,  $h \ll 1$ ), since it is obvious that physical masses of thick shells should not be concentrated on the outer surfaces. They also assumed high frequencies (i.e.,  $x_1 \gg 1$ ). Therefore, we can say that the transition frequency in Eq. (3) should be used only for thin shells at high frequencies, where it is actually equal to the fluid-loading parameter  $\Omega_*$ , introduced by Norris and Vasudevan.<sup>9</sup> In the letter,<sup>6</sup> Gaunaurd stated that “for naval applications, submerged shells thicker than  $h \approx 5\%$  are not practical, and this justifies the use of thin shells.” However, the author believes that there may be ever so many other applications (for example,<sup>10</sup>

nondestructive evaluation of nuclear fuel rods) where thick shells are involved and the thin-shell approximation is no longer appropriate.

In the paper<sup>1</sup> developing the theory of the inherent background with a discussion of increasing the material damping in the shell, the author demonstrated that the admittance function  $F_n$  in Eq. (1) consists of the constant component and the resonance component. The constant component corresponding to the inherent background could be extracted from the zero-frequency limit of the admittance function for the analogous liquid shell,  $F_n^{(L)}(0^+)$ , as follows:

$$\Omega_n = F_n^{(L)}(0^+) = \Omega_* h \frac{n + (n+1)(1-h)^{2n+1}}{1 - (1-h)^{2n+1}}. \quad (4)$$

It was proven that the inherent background can be used with no limitation in applicability to shell thickness, material property, frequency, and partial-wave order. For thin shells, the transition frequency also led to the fluid-loading parameter  $\Omega_*$  (see Fig. 2 in Ref. 1). In the letter,<sup>6</sup> Gaunaud made the following comment on the inherent background: “some disadvantages of Eq. (4) rest in its complexity and on that it depends on the partial-wave order  $n$ , and that dependence is not known *a priori*.” The author thinks that the added computational effect associated with slight complexity in form should be of no concern. In calculating the background coefficient of Eq. (2) for a given partial wave, the use of Eq. (4) is more effective rather than the use of Eq. (3), since Eq. (4) does not depend on the frequency of the incident wave so that in a given frequency range, it is sufficient to calculate it once. The  $n$  dependence of Eq. (4) was derived in Sec. II of Ref. 1.

Gaunaud’s comment on the sentence in Ref. 1, “after removing all the resonances from...” seems to be due to his misunderstanding on the physical concept of the inherent background. The sentence means that the background coefficient may be obtained by increasing the material damping such that all resonances are damped out, not by subtracting the unknown resonances from the scattering coefficient.

The traditional RST postulates that the scattering coefficient of Eq. (1) consists of two components, the background and resonance components, and the resonance component can be obtained by subtracting the background component from the scattering coefficients. Contrary to this postulation, in a new formulation of the RST,<sup>4</sup> it was shown that there is another component representing the mutual interaction between the background and the resonance component, and the scattering coefficient is given by  $R_n = R_n^{(b)} + R_n^{(\text{reso})} + 2R_n^{(\text{reso})}R_n^{(b)}$ , where

$$R_n^{(\text{reso})} = \frac{-i \operatorname{Im}(1/\bar{z}_n^{(1)})}{1/\bar{z}_n^{(1)} - 1/\bar{F}_n}, \quad (5)$$

$\bar{F}_n = F_n - \Omega_n$  and  $\bar{z}_n^{(1)} = x_1 h_n^{(1)'}(x_1)/h_n^{(1)}(x_1) - \Omega_n$ . This indicates that the new RST formulation provides a means of calculating the resonance coefficient  $R_n^{(\text{reso})}$  directly such that the sum of the inherent background and resonance coefficients and their mutual interaction agrees exactly with the first principle calculation  $R_n$ . It was also proven that the magnitude of the resonance coefficient is exactly equal to

that of the residual coefficient used in the traditional RST, i.e.,  $|R_n^{(\text{reso})}| = |R_n - R_n^{(b)}|$ . Furthermore, as shown in Fig. 1 of Ref. 4, the resonance coefficient generated the pure phase spectra showing the exact  $\pi$ -phase shift through resonances and at anti-resonances, which have never been obtained using the traditional RST. It can therefore be said that the new RST formulation is based on the physically correct statement: the scattering  $S$ -function should be expanded in the product of the background and resonance functions, not in their sum that has been implicitly assumed in the traditional RST. Even in the viewpoint of reducing the computation time, the direct use of the resonance coefficient is much more effective than the use of the residual coefficient.

In the letter, Gaunaud also stated that “for thick shells, these results are practically indistinguishable from those obtained with the traditional rigid background.” This is true at the high-frequency limit of  $x_1 \gg n\Omega_n$  as indicated in his Eq. (10), but even for the 99% thick shell it is false at low and middle frequencies (see Fig. 2 of Ref. 2).

There seems to be no paper reporting that the hybrid background approach could be used for submerged multilayered cylindrical shells. In our recent study, the inherent background coefficients for the shells were proposed and their validation was successfully demonstrated.<sup>5</sup> The transition frequency  $\Omega_n$  could be obtained by a recursion relation. The new RST formulation was not used there to focus our attention on the extension of the inherent background.

## II. CONCLUSIONS

The hybrid background based on the rough approximation of the modal mass should be used for thin shells at high frequencies. On the other hand, the inherent background based on the replacement of the surface admittance function with the zero-frequency limit of the admittance function for the analogous liquid shell can be used with no limitation in applicability to shell thickness, material property, frequency, and partial-wave order. Furthermore, the physical approximation for the inherent background is applicable to multilayered shells. The new RST formulation provides a means of calculating the pure (in both magnitude and phase) resonance coefficient directly such that the sum of the inherent background and resonance coefficients and their mutual interaction agrees exactly with the scattering coefficient. Therefore, the recent resonance scattering formulations are sufficient to be presented as novel tools for the real goal of target identification.

## ACKNOWLEDGMENT

The author is very grateful to Dr. Y.-M. Cheong for his helpful discussion in preparing this response.

<sup>1</sup>M.-S. Choi and Y.-S. Joo, “Theory of the background amplitudes in acoustic resonance scattering,” *J. Acoust. Soc. Am.* **101**, 2083–2087 (1997).

<sup>2</sup>M.-S. Choi, Y.-S. Joo, and J.-P. Lee, “Inherent background coefficients for submerged cylindrical shells,” *J. Acoust. Soc. Am.* **101**, 1743–1745 (1997).

- <sup>3</sup>L. Flax, L. R. Dragonette, and H. Überall, "Theory of elastic resonance excitation by sound scattering," *J. Acoust. Soc. Am.* **63**, 723–731 (1978).
- <sup>4</sup>M.-S. Choi, "New formulation of the resonance scattering theory," *J. Acoust. Soc. Am.* **101**, 2491–2495 (1997).
- <sup>5</sup>Y.-S. Joo, J.-G. Ih, and M.-S. Choi, "Inherent background coefficients for acoustic resonance scattering from submerged, multilayered, cylindrical structures," *J. Acoust. Soc. Am.* **103**, 900–910 (1998).
- <sup>6</sup>G. C. Gaunard, "Analysis and comparison of recent resonance scattering formulations by M. S. Choi *et al.* with earlier, traditional RST work," *J. Acoust. Soc. Am.* **104**, 1720–1722 (1998).
- <sup>7</sup>G. C. Gaunard, "Hybrid background coefficients to isolate the resonance spectrogram of submerged shells," *J. Acoust. Soc. Am.* **92**, 1981–1984 (1992).
- <sup>8</sup>M. F. Werby, "The acoustical background for a submerged elastic shell," *J. Acoust. Soc. Am.* **90**, 3279–3287 (1991).
- <sup>9</sup>A. N. Norris and N. Vasudevan, "Acoustic wave scattering from thin shell structures," *J. Acoust. Soc. Am.* **92**, 3320–3336 (1992).
- <sup>10</sup>M.-S. Choi, Y.-S. Joo, and J.-P. Lee, "Evaluation of nuclear fuel rod by ultrasonic resonance scattering," in *New Perspectives on Problems in Classical and Quantum Physics, Part II: Acoustic Propagation and Scattering, Electromagnetic Scattering* (Gordon and Breach, New Delhi, 1998), pp. 101–111.

# Comment on “Effects of aircraft overflights on wilderness recreationists” [J. Acoust. Soc. Am. 100, 2909–2918 (1996)]

Susan L. Staples<sup>a)</sup>

58 Spongia Road, Stone Ridge, New York 12484

(Received 8 April 1997; revised 19 February 1998; accepted 22 May 1998)

A psychologist outside the acoustics community considers the findings of Fidell *et al.* concerning the effects of aircraft overflights on wilderness recreationists [J. Acoust. Soc. Am. 100, 2909–2918 (1996)] in terms of other findings regarding visitor response to aircraft noise in wilderness areas and in light of current decision making about what actions are necessary to protect natural quiet in national parks. The limitations of a one-dimensional dose–response method that relies on annoyance as a global measure of the effect of park noise on visitors are discussed. © 1998 Acoustical Society of America. [S0001-4966(98)01909-2]

PACS numbers: 43.50.Qp [GAD]

I offer comment on the above-referenced article as a psychologist from outside the acoustics community. I am presently researching variables that moderate and mediate the effects of noise as an environmental stressor and am following current policy deliberations concerning aircraft overflights and the protection of natural quiet in national parks. In considering Fidell *et al.*'s findings in conjunction with data from other studies of visitor response to aircraft noise in wilderness settings, I am impressed with a number of puzzling incongruities that lead to questions rather than answers. I note these incongruities and questions below because, from the perspective of my discipline, understanding inconsistencies in the components of individuals' response to noise and identifying intermediate variables is necessary to predict how people react to aircraft noise in wilderness settings.

Fidell and colleagues used on-site opinion surveys to assess outdoor recreationists annoyance with aircraft overflights of three wilderness areas. They found that large majorities of visitors in these wilderness areas were not annoyed by the noise of overflights; fewer than 12% were annoyed to any degree even though the parks were chosen for study because they had periods of relatively high noise exposure. Citing a lack of a significant relationship between the sound of overflights and another measure, the degree to which visitors enjoyed their visit, Fidell *et al.* concluded that there was no evidence that the relatively high levels of overflight noise at many of the parks studied diminished the enjoyment of visits to the parks.

However, a National Park Service (NPS) survey (McDonald *et al.*, 1994) of visitors to 39 national parks across the country found that “enjoying natural quiet” was rated just about as important as “viewing natural scenery” (91% and 93% of visitors, respectively) as a reason for visiting a park. Sound levels measured at 78 locations in 8 national parks indicated that aircraft were audible more than 50% of the time at 34 locations, and most managers of parks with perceived overflight problems rated impacts from aircraft overflights as one of their more important management problems (NPS, 1994). In the context of this information, NPS in its 1994 report to Congress made recommendations for prob-

lem solving with respect to aircraft overflights at the noisier national parks.

The results of the Fidell *et al.* study would appear to be at variance with visitor's stated preference for natural quiet and with the NPS perception of a need for problem solving at the noisier parks. The two sets of findings considered together raise questions about the inconsistency in the various components of visitor response to quiet in national parks. What do these findings imply for federal officials currently debating what actions are necessary to comply with government initiatives to protect natural quiet? How should they account for visitors' self-report that natural quiet is important to the enjoyment of national parks, given the fact that Fidell *et al.* could not quantitatively relate annoyance with noise to enjoyment of a park visit? Referencing Fidell *et al.*'s dose–response data, some may conclude that visitors are not substantially annoyed with present noise levels in park and wilderness areas, and there is not sufficient basis for regulating current levels of commercial traffic. Such a conclusion certainly could be construed as at variance with visitor preferences as assessed by the McDonald *et al.* survey (1994) and with NPS objectives to manage and protect natural quiet as a resource, given projections (NPS, 1994) that no action in parks such as the Grand Canyon will mean the virtual loss of natural quiet by the year 2010. Yet, because of the historical context of dose–response relationships, such implications could follow from a single-minded adherence to the conventional one-size-fits-all dose–response method to the neglect of the larger questions raised by the disparities in individuals' appraisal of environmental noise.

In other work, Fidell and colleagues (1990) elucidate the historical context of the conventional dose–response method that quantitatively relates noise exposure in residential settings surrounding airports to average group response. They differentiate the objectives of that methodology from those needed to respond to the requirements of Public Law 100-91 regarding the protection and management of natural quiet. They explain that the former method has been part of an analysis of ways to make community land use more compatible with airport use; aviation needs were considered primary. Dose–response relationships in conjunction with noise modeling were a convenient and reliable way of establishing a uniform standard of residential noise-exposure that was

<sup>a)</sup>Psychologist, Independent Practice.

considered economically feasible and fair to industry. Annoyance as the measure of human response was useful as a forecaster of public protest and community action that might interfere with airport development. Fidell and his associates maintain that the protection and management of quiet in parklands calls for new assumptions and methods that meet the objective of making aircraft operations more compatible with an existing land use that involves the enjoyment of natural quiet. In this new analysis, preserving land use and park resources becomes primary. Toward this end, Fidell and others have made valuable modifications to conventional dose-response methods by quantifying observer-based audibility of noise, utilizing ambient sound levels and terrain features.

However, examining and questioning the assumptions inherent in the conventional modeling of annoyance as a function of physical noise levels needs to go further. Different procedures of gathering information reflect different questions and fundamentally different conceptions of a satisfactory environment. It is necessary to make certain that decision making regarding natural quiet is structured according to how visitors conceptualize the quality of a wilderness environment and to understand the problems with using annoyance as a summary measure of human response to noise. As early as 1976, Weinstein noted inconsistencies in individuals' appraisal of environmental noise and made several important differentiations that are relevant to the inconsistency in components of visitor response noted above and to the types of questions asked of visitors. For example, asking people what amount of noise they can tolerate in an environment is different than asking them about what type of environment they will regard with favor. Likewise, "annoyance" is a different response with different determinants than "appraised environmental quality." People may say a park area is noisy and yet indicate that they are not annoyed (Jones, 1971). Because annoyance is a measure of an emotional state, it is potentially confounded by a variety of other variables such as the degree to which people acknowledge negative emotions or are willing to express them (Crowne and Marlowe, 1960). The fact that people may not say they are annoyed by noise does not mean that a real deterioration in environmental quality has not occurred. Inconsistency in the different components of a response is common in psychological research; for example, discrepancy between self-report of emotion and physiological indicators of emotional arousal or discrepancy between attitudes and behaviors toward a given object. Understanding has been gained, not by oversimplifying or ignoring inconsistencies, but by mapping out determinants and correlates of different components and elaborating the conceptual base.

If annoyance as a construct is to inform decision making, it will be important to understand what people, under what conditions, are dissatisfied with the loss of natural quiet. In the wilderness study, Fidell *et al.* note that those who valued the absence of the sounds of civilization were more annoyed by aircraft noise. Several psychosocial variables identified in a subsequent survey of response to aircraft overflights over national parks (Anderson *et al.*, 1993) appear to determine visitor dissatisfaction to a degree that ri-

vals noise level. Repeat visitors to a park, small groups of one or two people, visitors who considered natural quiet as a "very" or "extremely" important reason for visiting a site, and people who left their cars for off-the road hikes were more sensitive to aircraft sound than were first time visitors, people in larger groups, visitors who judged quiet as less important, or visitors who did not hike into the park. The degree to which some of these variables determined visitor response is described as equivalent to the effect of a 20-dB increase in loudness of aircraft.

Annoyance may be a better summary measure of human response to noise in residential settings where there is a common set of activities subject to interference (i.e., sleeping, conversation, TV viewing). The Anderson *et al.* data, cited above, suggests that, in national parks, the particular use of the setting is a primary determinant of the likelihood that overflight noise may interfere with activity and be annoying. As a result, the accuracy with which annoyance is predicted may be increased by using a dose-response curve that corresponds to the intended recreational use of the particular area (e.g., backcountry where natural quiet is a basis for use versus frontcountry where it is not primary), as suggested in the National Park Service plan for identifying impacts.

The other measure of human response, "enjoyment of visit", used by Fidell *et al.* is especially problematic. Findings from the recreational literature (Manning, 1985; Williams, 1988) indicate that the extent to which visitors say they enjoy a park visit is not a meaningful indicator of visitor satisfaction because of the lack of variability and specificity in the measure. Most people will say they enjoy their visit even if dissatisfied with several aspects (presumably because of their financial and emotional investment in a vacation). Moreover, because visitor satisfaction, as understood theoretically, consists of multiple dimensions, visitors need to be asked directly about specific aspects of a visit. An example of a measure used in the Anderson *et al.* (1993) survey of park visitors that is more directly related to appraised environmental quality *vis a vis* enjoyment of natural quiet is the degree to which visitors rate aircraft noise as interfering with natural quiet and the sounds of nature. For visitors who decide to leave the noise of road traffic and overlooks for a hike into the park, this measure of activity interference appropriately reflects the effects of overflights on the intended use of the park.

As someone without expertise in acoustics, I can only marvel at the challenge of developing a simple-to-use mathematical model of human response to noise for policy makers. Yet, from the perspective of my discipline, I am also aware of the important unanswered questions raised by the work-to-date on response to noise in wilderness settings: What determines which people, doing what things, in what places, will be annoyed by noise? The answers are necessary if decision makers are to address the multiple uses of the national park setting. My point is that the answers to these questions can be obscured by a single-minded adherence to a methodology that may be oversimplified in important ways. As I see it, using an additional response measure, such as interference with natural quiet, or using different response curves based on the intended use of the setting is a reason-



able and necessary compromise to the simplicity and convenience of the conventional one-dimensional dose-response relationship because it enables the methodology to address relevant components of response to noise.

Anderson, G. S., Horonjeff, R. D., Menge, C. W., Miller, N. P., Robert, W. E., Rossano, C., and Sanchez, G. (1993). "Dose-Response Relationships Derived from Data Collected at Grand Canyon, Haleakala and Hawaii Volcanoes National Parks" (HMMH Report No. 290940.14; NPOA Report No. 93-6) (National Park Service, Denver, CO).

Crowne, D. P., and Marlow, D. A. (1960). "A new scale of social desirability independent of psychopathology," *Journal of Consulting Psychology* **24**, 349-354.

Fidell, S., and Silvati, L. (1990). "Relating the Annoyance of Aircraft Overflights to their Audibility by Outdoor Recreationists," in *Proceedings of Noise-Con 90* (University of Texas, Austin), pp. 339-342.

Jones, G. (1971). "Physiological and Psychological Effects," in *Public Hearing on Noise Abatement and Control*, edited by U.S. Environmental

Protection Agency (U.S. Government Printing Office, Washington, DC), Vol. 7, pp. 280-292.

Manning, R. (1985). *Studies in Outdoor Recreation* (Oregon State U.P., Corvallis, WA).

McDonald, C. C., Baumgartner, R. M., and Iachon, R. (1994). "National Park Service Visitor Survey" (HMMH Report No. 290940.12; NPOA Report No. 94-2) (National Park Service, Denver, CO).

National Park Service (1994). *Report to Congress: Report of Effects of Aircraft Overflights on the National Park Service System* (U.S. Department of Interior National Park Service, Washington, DC).

Weinstein, N. D. (1976). "Human Evaluations of Environmental Noise," in *Perceiving Environmental Quality*, edited by K. H. Craik and E. H. Zube (Plenum, New York), pp. 229-252.

Williams, D. (1988). "Great Expectations and the Limits to Satisfaction: A Review of Recreation and Consumer Satisfaction Research," in *Outdoor Recreation Benchmark: Proceedings of the National Outdoor Recreation Forum* (U.S.D.A. Forest Service General Technical Report SE-52) (U.S.D.A. Forest Service, Washington, DC).

# Response to “Comments on ‘Effects of aircraft overflights on wilderness recreationists’ ” [J. Acoust. Soc. Am. 104, 1726 (1998)]

Sanford Fidell

*BBN Technologies, A Unit of GTE Internetworking, 21128 Vanowen Street, Canoga Park, California 91303*

James Gramann

*Department of Recreation, Park and Tourism Sciences, Texas A&M University, College Station, Texas 77843-2261*

Richard Knopf

*College of Human Services, Arizona State University West, P.O. Box 37100, Phoenix, Arizona 85069-7100*

Karl Pearsons

*BBN Technologies, Canoga Park, California 91303*

(Received 2 April 1998; accepted for publication 22 May 1998)

Dr. Staples' lengthy comments [J. Acoust. Soc. Am. **104**, 1726–1728 (1998)] deal less with the matters of research design or data analysis described by Fidell *et al.* [J. Acoust. Soc. Am. **100**, 2909–2918 (1996)] than with her beliefs about the proper study and interpretation of aircraft noise effects in outdoor recreational settings. Her comments nonetheless raise several interesting issues related to the role of technical expertise in noise-related policy analyses. This response therefore concentrates on those of Staples' comments and arguments that are of general interest, while only secondarily addressing certain inaccuracies and oversimplifications in them. © 1998 Acoustical Society of America. [S0001-4966(98)02009-8]

PACS numbers: 43.50.Qp [GAD]

## I. SUMMARY OF STAPLES' COMMENTS

Staples' substantive comments begin by calling attention to one particular finding of one of the two social surveys described by Fidell *et al.* (Staples, 1998). Staples contrasts this finding with selected findings of several unpublished studies, notes an apparent inconsistency, and inquires rhetorically about the joint implications of the various findings for regulatory policy.

Staples attributes a strawman position (“...single-minded adherence to the conventional one-size-fits-all dose-response method...”) to “some” who may not believe that there is a “sufficient basis for regulating current levels of commercial [air] traffic.” After acknowledging the utility of dosage–response relationships in nonrecreational applications, Staples urges “examination and questioning” of “the assumptions inherent in the conventional modeling of annoyance as a function of physical noise levels.” She then asserts the necessity for structuring policies regarding outdoor recreational noise exposure in accordance with psychological perspectives on the manner in which visitors conceptualize environmental quality.

Several paragraphs are given to distinguishing annoyance from “appraised environmental quality” before Staples notes that properly understood, self-reports of visit enjoyment ought not be interpreted as “a meaningful indicator of visitor satisfaction.” Staples' comments conclude with reiterated warnings against “single-minded adherence” to a “conventional one-dimensional dose–response relationship” that does not adequately address “relevant components of response to noise.”<sup>1</sup>

## II. INCOMPLETE CHARACTERIZATION OF CONCLUSIONS OF FIDELL *et al.* AND COMPARABILITY OF FINDINGS

Staples states that “Fidell *et al.* concluded that there was no evidence that the relatively high levels of overflight noise at many of the parks studied diminished the enjoyment of visits to the park.”<sup>2</sup> Staples then cites information developed in studies of different design as a basis for an argument that “The results of the Fidell *et al.* study would appear to be at variance with visitor's [sic] stated preference for natural quiet and with the NPS perception of a need for problem solving at the noisier parks.”<sup>3</sup>

Staples' characterizations of the conclusions of Fidell *et al.* and her subsequent comparison of findings are incomplete. The full wording of the finding of the *in situ* study is “Little evidence was found that overflights diminished respondents' overall enjoyment of their wilderness visits,<sup>4</sup> nor their intention to return for additional visits.” (Staples is correct, however, that post-visit telephone interviews yielded “No evidence that overflights diminished respondents' enjoyment of their wilderness visits, nor their intention to return for additional visits.”) It is misleading to characterize either statement of findings as a conclusion, since the conclusions that Fidell *et al.* draw deal largely with cautions about generalization of reported findings and recommendations for further study.

It is also misleading to omit mention

- (1) of the supporting evidence that wilderness visitors overwhelmingly intended to revisit, notwithstanding their overflight exposure;

- (2) of the rarity of spontaneous mention of interference with natural quiet as a disfavored aspect of outdoor recreational experiences (cf. Fidell *et al.*, 1996, finding 6) p. 2914, and;
- (3) of the greater dissatisfaction of outdoor recreationists with poor trail maintenance, crowding, insects, and weather than with overflights.

The findings that large majorities of wilderness visitors reported enjoying their visits and intended to revisit overflowed wilderness areas are based on direct and immediate self-reports of actual experiences of individuals engaged in outdoor recreation.<sup>5</sup> The findings that Staples contrasts with these direct self-reports are derived from delayed reports and disparate studies in nonwilderness settings, including interviews posing indirect and hypothetical questions to NPS facility managers about *their* opinions of the opinions of visitors to the facilities under their management (HBRS, 1994a).<sup>6</sup> Staples also omits mention of the findings of an NPS-sponsored study (HBRS, 1994b) documenting recreational benefits enjoyed by air tour passengers.

Staples' mention of the percentage of time that aircraft are audible in national parks is also incomplete. Figure 2.17 of the NPS Report to Congress (National Park Service, 1994) accompanies the audibility time values that Staples cites with additional information in Figure 2.18. Figure 2.18 indicates (in part) that although aircraft noise may be audible 75% of the time at Point Sublime in Grand Canyon National Park, the A-weighted level of the indigenous sound environment that is exceeded 75% of the time at this point is 14 dB—a level two orders of magnitude lower than a whisper heard at 1 m, and five orders of magnitude lower than that of normal conversation.

### III. INACCURATE CHARACTERIZATION OF ROLE OF DOSAGE-RESPONSE RELATIONSHIPS IN POLICY ANALYSES

Staples' comments on the utility of dosage-response relationships are inaccurate in several important respects. For example, the federal perspective on appropriate levels of residential noise exposure was developed prior to widespread acceptance of detailed dosage-response information; Federal Aviation Regulations make it clear that local definitions of land use compatibility take precedence over one-size-fits-all national guidelines; and the prevalence of noise-induced annoyance in a residential area is hardly a useful forecast of "public protest and community action."

It is also inaccurate to characterize annoyance as "a measure of an emotional state." Annoyance is an attitude, not an emotion, with cognitive as well as affective components. As modeled for the last decade (cf. Fidell *et al.*, 1988), noise-induced annoyance is not a unidimensional quantity, but has explicitly recognized acoustic and nonacoustic components. Likewise, the alphabet soup of noise metrics developed following the start of commercial jet transport service is hardly the product of efforts to oversimplify prediction of human response to environmental noise.

### IV. INTERPRETATION OF THE MEANING OF QUESTIONNAIRE RESPONSES

Staples warns against straightforward interpretations of responses to certain questionnaire items on grounds that the responses may be misunderstood.<sup>7</sup> She argues in effect that survey respondents who enjoyed their visits to overflowed areas and intended to return to them for further recreational experiences might have had an even higher quality recreational experience (in the view of others) had it not been for their potential aircraft noise exposure. This is a familiar observation in the recreation management literature.

Simply because visitors say they want to experience natural quiet and that noise interferes with this opportunity does not imply that they expect to experience natural quiet *all the time* or that noise interferes with their enjoyment *all the time*. As both the NPS and USFS studies show, preferences for quiet and sensitivity to noise vary substantially among users. Thus, it is entirely consistent to state a preference for natural quiet as *one* desirable experience during a national park visit (akin to viewing spectacular scenery or unusual wildlife) without implying that it must be experienced throughout the entire visit.

For example, visitors to Yosemite National Park have described themselves as highly satisfied with their overall experience, even though, in response to open-ended questions, they could also identify specific places and times at which they experienced excessive crowding (Gramann, 1992). By clear implication, crowding was not perceived as a problem at many other times and places during their visits. In short, unless aircraft noise intrusions often come to the attention of visitors, *and* natural quiet is important to the visitor, park visitors can still feel very satisfied with the totality of their experience, despite episodes of audible aircraft noise.

One cannot reasonably imply, as Staples does, that because visitors agree with a hypothetical statement that aircraft noise interferes with natural quiet (or with the sounds of nature) that their actual enjoyment is reduced to the extent that extreme mitigation measures are required to preserve a park's attractiveness to future visitors. Research has shown quite convincingly that visitors' conjectures about how they would be affected by hypothetical circumstances (e.g., a certain density of users) can be completely uncorrelated with their actual responses to those conditions (Manning and Ciali, 1980). The hypothetical circumstances focus on conditions that may be only rarely experienced (or noticed in the case of low-level aircraft noise intrusions) in isolation from other favored and disfavored experiences. Reactions to simple hypothetical questions do not necessarily mirror more complex realities. At the very least, the times of occurrence, durations, and places of noise intrusions must be taken into consideration in interpreting such self-reports.

### V. THE ROLE OF TECHNICAL ADVICE IN NOISE-RELATED POLICY ANALYSES

Although the findings reported by Fidell *et al.* can obviously be viewed from varied perspectives, not all perspectives are equally fruitful for all purposes. Staples' comments are made from the perspective of a self-described "psycholo-

gist from outside the acoustics community” who seeks to map out “determinants and correlates of different components [of emotion and physiological indicators of emotional arousal or discrepancy between attitudes and behaviors].” Worthy goals from this perspective include “researching variables that moderate and mediate the effects of noise [as an asserted environmental stressor]” and “elaborating the conceptual base.”

Staples believes that policy and regulatory decision making demand consideration of psychological interpretations of aircraft noise effects on outdoor recreationists. However, it is politics, not science, that is the institution more suited to balancing competing societal values. It is the U.S. Congress—not acousticians, psychologists, sociologists, nor other technocrats—that is responsible for creating federal agencies with conflicting charters with respect to the aircraft noise issues of current interest. It is likewise Congress that sets the legislative priorities that drive federal agencies’ policy-making interests, and Congress that appropriates the funds that sponsor policy analyses. Staples’ concerns about risks of drawing improper policy inferences from the findings reported by Fidell *et al.* are more productively raised in a political rather than in a technical arena.

As it has become increasingly fashionable to represent controversial policy decisions as flowing ineluctably from “scientific” findings, academic and other researchers from a variety of disciplines (acousticians not excepted) have been quick to offer their services to policy makers. Some have confused technical expertise with expertise in policy making. Neither expertise in the measurement and prediction of aircraft noise, nor expertise in any social science subspecialty, automatically confers any particular skill, insight, or privilege in policy-related matters.

None of this implies that aircraft noise intrusions in parks and wildernesses should not be managed. If policy dictates managing for natural quiet, it should be attempted, just as management for other resources—from vegetation to water to wildlife to endangered species to air quality to archeological and historic values and even to visitor enjoyment—occurs because these have been mandated in the political arena. Policymaking is also an exercise in priority setting, however. If technical advice is to inform policy decisions and the setting of priorities, it should provide, as one input into the eventual decision, a complete context of understanding. Staples’ argument ignores impacts on visit enjoyment other than aircraft noise. This does a disservice to a complex issue by distorting the actual context in which visitors make judgments about the quality of their recreational experiences.

## VI. SUBSTANTIVE ISSUES STILL UNRESOLVED

This reply should not be viewed as dismissive of the role of technical analysis in policy making. Indeed, advances in quantifying aircraft overflight noise and its effects in outdoor recreational settings have been useful to both the U.S. Forest Service and the National Park Service in reaching policy decisions. These advances include improvements in characterization of indigenous sound environments, innovative modeling of aircraft noise from an observer- rather than a

source-based perspective, and suggestion of audibility-based rather than absolute noise levels for gauging noise impacts.

Additional improvements in characterizing the interactions of outdoor recreationists with aircraft noise can further inform decision making in this area. It is not self-apparent, however, that identifying multiple intervening variables and “elaborating the conceptual base” are strategies that will necessarily yield a superior reconciliation of competing recreational, economic, national defense, and safety interests. In fact, complexity that does not advance quantitative understanding can be more of a hindrance than a help. Staples’ comments do not describe the manner in which deeper insights into psychological components of reactions to aircraft noise will improve decisions about tolerable numbers, types, times, and levels of aircraft noise intrusions in outdoor recreational settings.

<sup>1</sup>Agencies of at least four U.S. federal departments—Agriculture, Defense, Interior, and Transportation—have complex policy and regulatory interests in matters touched on by Staples. The charters of these agencies, shifting Congressional interests in the issues, and the studies conducted to date on aircraft noise effects in outdoor recreational settings are all more nuanced than might be apparent from Staples’ comments.

<sup>2</sup>It is incorrect to characterize the finding about visit enjoyment as derived from information about visits to parks. As both the title and text of Fidell *et al.* make clear, interviews were conducted only with visitors to U.S. Forest Service-administered wildernesses, rather than with visitors to any parks administered by NPS. The NPS is only one of several federal agencies with responsibilities for managing largely unpopulated, overflown public lands for purposes that sometimes include outdoor recreation.

For example, the administrative goals and practices of the U.S. Forest Service, the Bureau of Land Management, and the Fish and Wildlife Service with respect to outdoor recreation may be inconsistent with those in some NPS-managed parks. Furthermore, basic mandates and policy perspectives are not necessarily consistent over time or within land management agencies. The historic mandate of the National Park Service (NPS) requires the agency to “conserve the scenery and the natural and historic objects and the wildlife therein and to provide for the enjoyment [emphasis added] of same in such manner and by such means as will leave them unimpaired for the enjoyment of future generations” (1916 National Park Service Organic Act). The former requirement inherently conflicts with the latter in many cases, including the one of present interest.

<sup>3</sup>Staples does not indicate why she regards an inconsistency between empirical findings and “NPS perception of a need” as a technical issue. (The comments also gloss over the preliminary and equivocal nature of the findings of both the NPS and USFS Reports to Congress, the limitations of schedule, budget and technology of the studies on which the two reports are based, and the cautions in both reports about limits to generalization of findings.)

<sup>4</sup>It should be noted that visit enjoyment among respondents is usually high in onsite surveys in part because the opinions of dissatisfied former visitors are under-represented among repeat visitors. “Displacement”—a behavioral adjustment to negative experiences on prior visits—of former visitors who no longer return to certain parks or areas within them is well documented (Gramann, 1992; Kuentzel and Heberlein, 1992). Just as some visitors make a behavioral adjustment, others may make a cognitive adjustment by changing their definition of a recreational experience to conform to changing situations rather than becoming dissatisfied with the change. This phenomenon is referred to by Shindler and Shelby (1995) as “product shift.” Whether a park should be managed for the benefit of current or displaced former users is not a technical decision that can be decided on the basis of empirical data alone.

<sup>5</sup>One limitation of the NPS studies is that they did directly not place beliefs about interference with natural quiet in the context of the many other factors that affect visit enjoyment. Nor does Staples, despite her desire to “elaborate the conceptual base” of visitor satisfaction, acknowledge that visit enjoyment may be affected by many factors, of which noise is merely one. The USFS studies emphasize this point.

<sup>6</sup>It is well established that recreation managers’ perceptions may frequently be at odds with visitors’ perceptions (Christensen and Davis, 1984; Weil-

man *et al.*, 1982). Managers' perceptions of visitors' perceptions are often inaccurate with respect to such matters as reasons for visits and judged severity of various problems, including theft, vandalism, litter, rulebreaking, and conflicts among users. To the extent that users and managers share the same "contemplative ideal" of outdoor recreation, their perceptions of other issues are likely to resemble one another's.

Thus, perceptions and preferences of wilderness users and wilderness managers may be more similar than those of users and managers of highly developed campgrounds or frontcountry areas of national parks. While managers of these areas often hold to a contemplative ideal that is at odds with the opportunities they are providing, visitors often do not perceive their experience in the same negative fashion. Aldo Leopold (1949) recognized this disparity as early as 1949, referring to mass recreationists' preference for "fresh air and change of scene." The NPS surveys conducted in Yosemite National Park as early as 1937 documented the same discrepancy (Garrison, 1939). Thus, it has been apparent for more than half a century that, except in very specific circumstances, one cannot reliably infer visitors' perceptions from managers' perceptions.

Understood in this context, Staples' contention that the Forest Service and Park Service studies produced conclusions that were at variance with one another is a considerable oversimplification. The apparent inconsistency between USFS and NPS studies may suggest in part that many visitors have a higher tolerance for low-level aircraft noise intrusions than do managers. "Natural quiet" may not mean the same thing to park visitors—particularly frontcountry visitors—as it means to park managers. Whose standard should prevail in defining and managing natural quiet is not for technical advisers to decide. Good arguments, albeit nontechnical ones, can be made on both sides of the issue.

<sup>7</sup>Staples' comments are inconsistent in rejecting research findings other than those that support her viewpoint (as when she casts doubt on reports of visitors that they enjoyed their visits), while accepting without reservation their opinions that aircraft noise would interfere with natural quiet. Unquestioning acceptance of reports of interference with natural quiet begs a relevant issue in any event: Does such interference (now or in the future) significantly "impair" visit enjoyment? This is an important matter that is not readily resolved in the technical arena. However, failing to acknowledge the nontechnical aspect of this issue gives the appearance of a somewhat facile interpretation of research findings in support of a particular management philosophy.

- Christensen, H. H., and Davis, N. J. (1984). "Evaluating user impacts and management controls: Implications for recreation choice behavior," in *Proceedings—Symposium on Recreation Choice Behavior*, Gen. Tech. Rep. INT-1 84, Ogden, UT: USDA Forest Service Intermountain Research Station, compiled by G. H. Stankey and S. F. McCool, pp. 71–78.
- Fidell, S., Schultz, T. J., and Green, D. M. (1988). "A theoretical interpretation of the prevalence rate of noise-induced annoyance in residential populations," *J. Acoust. Soc. Am.* **84**, 2109–2113.
- Fidell, S., Silvati, L., Howe, R., Pearsons, K. S., Tabachnick, B., Knopf, R. C., Gramann, J., and Buchanan, T. (1996). "Effects of aircraft overflights on wilderness recreationists," *J. Acoust. Soc. Am.* **100**, 2009–2918.
- Garrison, L. A. (1939). "Camper activities in Yosemite Valley, study of 1937–1938," *Yosemite Nature Notes* **18**(6).
- Gramann, J. H. (1992). *Visitors, Alternative Futures, and Recreational Displacement at Yosemite National Park* (National Park Service Western Regional Office, San Francisco, CA).
- HBRS, Inc. (1994a). "Survey of National Park Service Managers Related to Aircraft Overflying National Parks," NPOA Report No. 93-7.
- HBRS, Inc. (1994b). "Air Tow Passengers Survey," NPOA Report No. 94-1.
- Kuentzel, W. F., and Heberlein, T. A. (1992). "Cognitive and behavioral adaptations to perceived crowding: A panel study of coping and displacement," *J. Leisure Res.* **24**, 377–393.
- Leopold, A. (1949). "Conservation esthetic," in *A Sand Country Almanac* (Oxford U.P., London), pp. 165–177.
- Manning, R. E., and Ciali, C. P. (1980). "Recreation density and user satisfaction: A further exploration of the satisfaction model," *J. Leisure Res.* **12**, 329–345.
- National Park Service (1994). "Report to Congress: Report on effects of aircraft overflights on the National Park System," U.S. Department of Interior, Washington, DC.
- Shindler, B., and Shelby, B. (1995). "Product shift in recreation setting: Findings and implications for panel research," *Leisure Sci.* **17**, 91–107.
- Staples, S. (1998). "Comment on 'Effects of aircraft overflights on wilderness recreationists' [*J. Acoust. Soc. Am.* **100**, 2909–2918 (1996)]," *J. Acoust. Soc. Am.* **104**, 1726–1728.
- Weilman, J. D., Dawson, M. S., and Roggenbuck, J. W. (1982). "Park managers' predictions of the motivations of visitors to two National Park Service areas," *J. Leisure Res.* **14**, 1–15.

# Effects of high-frequency amplification on double-vowel identification in listeners with hearing loss

Kathryn Hoberg Arehart

*Department of Speech, Language and Hearing Sciences, University of Colorado at Boulder,  
Campus Box 409, Boulder, Colorado 80309-0409*

(Received 7 August 1997; accepted for publication 9 June 1998)

Arehart *et al.* [J. Speech Lang. Hear. Res. **40**, 1434–1444 (1997)] reported that the ability of listeners with moderate to moderately-severe sensorineural hearing loss to correctly identify two simultaneous vowels was significantly worse than the identification ability of listeners with normal hearing. The present study investigated the effects of amplification on double-vowel identification in six listeners with hearing loss by comparing double-vowel identification with unamplified vowels and amplified vowels. Increasing the sensation level of the second and higher formants by application of high-frequency amplification did not improve the overall ability of listeners with hearing loss to identify double vowels. Spectro-temporal processing deficits not compensated for by increased sensation levels may contribute to the reduced overall performance by listeners with hearing loss on the double-vowel task. © 1998 Acoustical Society of America.  
[S0001-4966(98)05009-7]

PACS numbers: 43.66.Sr, 43.66.Ts, 43.71.Ky [JWH]

## INTRODUCTION

We recently compared the ability of listeners with normal hearing and listeners with moderate to moderately-severe sensorineural hearing loss to use fundamental frequency differences ( $\Delta F_0$ ) in the identification of monotonically presented simultaneous vowels (Arehart *et al.*, 1997). In a double-vowel identification task, both listeners with normal hearing and listeners with hearing loss showed significant  $\Delta F_0$  benefit: Between 0 and 2 semitones, listeners with normal hearing showed an 18.5% average increase in performance; listeners with hearing loss showed a 16.5% increase. However, overall performance by listeners with hearing loss was significantly worse than for listeners with normal hearing. Mean performance by listeners with normal hearing was 68.5% at 0 semitones and 87% at 2 semitones whereas mean performance by listeners with hearing loss was 45.3% at 0 semitones and 61.8% at 2 semitones.

Despite increased presentation levels used in listeners with hearing loss, the double vowels were presented at lower sensation levels to the listeners with hearing loss than to the listeners with normal hearing. The decreased ability of listeners with hearing loss (who have excellent speech recognition scores in quiet) to understand one talker in the presence of a competing talker has been attributed in part to the reduced sensation level of speech in listeners with elevated thresholds (e.g., Zurek and Delhoune, 1987). In a similar way, reduced sensation level of vowel sounds might make identification of concurrent vowels abnormally difficult in listeners with hearing loss despite their excellent recognition of single vowels. Whereas listeners with normal hearing rely on several auditory cues available across the speech spectrum, listeners with hearing loss will not be able to take full advantage of these cues if their elevated thresholds make some cues inaudible.

Besides reduced audibility of speech sounds, deficits in frequency selectivity and in temporal resolution have been

shown to lead to deficits in the ability of listeners with hearing loss to understand one talker in the presence of a competing talker (Baer and Moore, 1994; Festen and Plomp, 1990). Because performance on psychoacoustic tasks is often worse at low sensation levels compared to higher sensation levels (Moore, 1995), low sensation levels of double vowels might exacerbate the effects of spectro-temporal processing deficits in listeners with hearing loss.

Turner and Holte (1987) reported that the ability of some hearing-impaired listeners to discriminate spectral peaks in the second-formant frequency region was worse than the discrimination ability of normal-hearing listeners, even at high presentation levels. The hearing-impaired listeners achieved normal spectral peak discrimination when the second-formant peak was enhanced through high-frequency amplification. Turner and Holte suggested that the improvement observed in the amplified condition was due to increased audibility of the second formant frequency region and to the reduced effects of frequency selectivity deficits. That is, excessive masking of the first formant region on the second formant region was presumably reduced by increasing the amplitude of the second formant region through amplification.

The reduced ability of listeners with hearing loss to identify double vowels in our previous study (Arehart *et al.*, 1997) might be due to reduced sensation level of the higher-frequency formants. Increasing the level of the higher frequency formants would increase their audibility and might also lessen the effects of spectro-temporal processing deficits made worse by low sensation levels. The present study investigated the effects of amplification on double-vowel identification in listeners with hearing loss by comparing double-vowel identification with unamplified vowels and vowels subjected to a high-frequency amplification configuration similar to the one used by Turner and Holte (1987).

TABLE I. Age and audiometric thresholds (in dB HL) of listeners with hearing loss.

Listener	Age	Frequency (Hz)					
		250	500	1000	2000	3000 <sup>a</sup>	4000
11	69	45	55	45	45	65	95
12	66	15	15	10	35	50	60
13	69	40	55	60	55		65
14	53	35	35	40	55	55	60
15	38	25	35	50	60		65
16	67	25	25	30	55	65	70

<sup>a</sup>Thresholds were not available for all listeners at 3000 Hz.

## I. METHOD

### A. Listeners

Participants in this study included six listeners with moderate to moderately-severe sensorineural hearing loss of presumably cochlear origin (age range 36–70 years). Table I provides a summary of the audiometric thresholds of the listeners with hearing loss.

### B. Stimuli

Each double-vowel stimulus was made by adding together two of the following single vowels of American English: /ε/ as in “head,” /a/ as in “hod,” /i/ as in “heed,” /ɜ:/ as in “herd,” /æ/ as in “had.” Steady-state single vowels (820-ms duration; 20-ms rise–fall times) were synthesized using Sensimetrics cascade formant software (Klatt, 1980) with a 20 000-Hz sampling rate and 16-bit quantization. Formant frequencies and bandwidths for the vowels are listed in Arehart *et al.* (1997).

For the double-vowel identification task, each single vowel was paired together with each of the other four vowels, yielding ten double-vowel combinations. (A single vowel was not paired with itself.) Each double-vowel combination resulted in two different stimuli. In one, the first constituent vowel had an  $F_0 = 100$  Hz and the second constituent vowel had an  $F_0 = 100$  Hz +  $\Delta F_0$ , where  $\Delta F_0$  was either 0 or 2 semitones. In the second stimulus, the first constituent vowel had an  $F_0 = 100$  Hz +  $\Delta F_0$  and the second constituent vowel had an  $F_0 = 100$  Hz. Thus for each of the two semitone conditions in the double-vowel task, there were 20 different double-vowel stimuli (10 double-vowel pairs  $\times$  2 fundamental frequency combinations). Double-vowel stimuli were played out in the following way: two constituent single vowels were routed separately through low-pass filters (Tucker Davis Technologies TDT FT5; cutoff frequency = 10 000 Hz), through programmable filters (TDT PF1), and programmable attenuators (TDT PA4), then were combined in a mixer (TDT SM3), and finally delivered to the listener’s ear with a Telephonics TDH-49 earphone.

In the unamplified condition, the programmable filters were bypassed. In the amplified condition, the single vowels were subjected to the high-pass filter shown in Fig. 1. The characteristics of this filter were chosen so as to amplify the second and higher formants by approximately 25 dB. Vowels were played out at 87 dB SPL in the unamplified condition. This level was chosen so as to maximize signal audibility

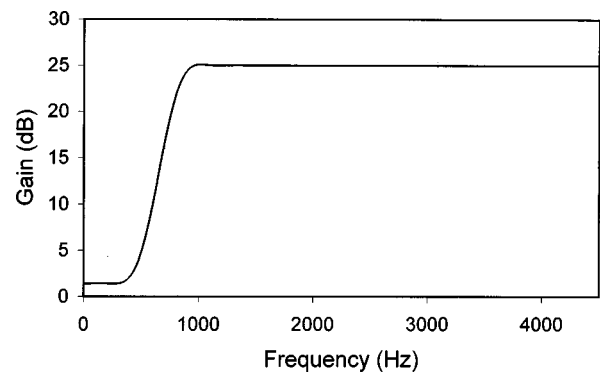


FIG. 1. Gain as a function of frequency of high-frequency amplification applied to vowel sounds.

while not exceeding listeners’ comfortable loudness levels in either the amplified or unamplified conditions. The gain applied to components of the vowels in the amplified condition was determined relative to the level of the components in the unamplified condition. That is, the levels of the low-frequency components in the vowel sounds were the same for both the unamplified and amplified conditions. The levels of the second and higher formants were 25 dB greater in the amplified condition than in the unamplified condition.

### C. Procedure

The listeners’ task was to identify the two vowels contained in the double-vowel signal using a forced-choice paradigm. In a given block, the semitone difference between the constituent vowels was fixed. A listener’s performance was measured by the percentage of trials in which both constituent vowels in the double-vowel stimulus were correctly identified in each of the following four conditions:  $\Delta F_0 = 0$  semitones, vowels unamplified;  $\Delta F_0 = 2$  semitones, vowels unamplified;  $\Delta F_0 = 0$  semitones, vowels amplified;  $\Delta F_0 = 2$  semitones, vowels amplified. Percent correct scores reported here are based on 220 trials for each listener in each condition.<sup>1</sup> Because listeners in this study had all participated previously in Arehart *et al.* (1997), they were well practiced on the double-vowel identification task. All listeners also demonstrated at least 90% accuracy for the single vowels in both the amplified and unamplified conditions.

## II. RESULTS AND DISCUSSION

Table II lists the identification scores (in terms of percentage of trials in which both vowels were correctly identified) for individual listeners in each of the four conditions. A repeated measures analysis of variance (using an arcsine transformation of the percent correct scores) showed a significant main effect of  $\Delta F_0$ ,  $F(1,5) = 10.88$ ,  $p = 0.022$ . No significant effects were found for amplification,  $F(1,5) = 4.78$ ,  $p = 0.08$ , and for the interaction between amplification and  $\Delta F_0$ ,  $F(1,5) = 21.2$ ,  $p = 0.480$ .

Figure 2 shows mean performance of listeners with hearing loss in the unamplified and amplified conditions at  $\Delta F_0 = 0$  semitones and  $\Delta F_0 = 2$  semitones. Mean identifica-

TABLE II. The percentage of trials in which individual listeners identified both vowels correctly is shown for the following conditions:  $\Delta F_0=0$  semitones, vowels unamplified;  $\Delta F_0=2$  semitones, vowels unamplified;  $\Delta F_0=0$  semitones, vowels amplified;  $\Delta F_0=2$  semitones, vowels amplified.

Listener	0 ST	2 ST	0 ST	2 ST
	No Amp	No Amp	Amp	Amp
I1	36	64	35	57
I2	45	76	39	70
I3	30	32	32	30
I4	49	54	32	61
I5	62	69	58	70
I6	62	70	62	72
Mean	47	61	43	60

tion scores for unamplified vowels are also shown for the normal-hearing and hearing-impaired listeners in Arehart *et al.* (1997).

Listeners in the present study benefited from  $\Delta F_0$  cues: between 0 and 2 semitones, listeners demonstrated a 14% improvement on the double-vowel identification task in the unamplified condition and a 17% improvement in the amplified condition. This  $\Delta F_0$  benefit is comparable to the  $\Delta F_0$  benefit for unamplified double-vowel identification for the normal-hearing listeners (18.5%) and hearing-impaired listeners (16.5%) in Arehart *et al.* (1997). However, increasing the sensation level of the higher-frequency formants did not result in improvement in the overall ability of listeners with hearing loss to identify competing vowels. As shown in Fig. 2, mean identification scores of hearing-impaired listeners in both the unamplified and amplified conditions are much worse than the mean identification scores of listeners with normal hearing.

The lack of improvement in overall performance on the double-vowel task due to high-frequency amplification may be due in part to the lack of experience with listening to double vowels in the high-frequency amplification condition. As pointed out by Gatehouse (1989), a period of acclimatization may be required in order to achieve maximum benefit from amplification with a new frequency response. Alternatively, the single amplification scheme used in this study might not incorporate the most appropriate gain characteristic for all of the listeners in this study.

Reduced overall performance by listeners with hearing loss might also be due to spectro-temporal processing deficits that are not compensated for by increasing the sensation level of the higher-frequency formants. Double-vowel perception in normal-hearing listeners is most consistent with models based on a time place analysis (Assman and Summerfield, 1990; Meddis and Hewitt, 1992). These models assume that concurrent vowels are first analyzed by a series of bandpass filters and then subjected to a compressive non-linearity simulating mechanical to neural transduction at an inner hair cell. An autocorrelational analysis then determines the periodicity and their relative strengths in each of the frequency channels. Finally, a pooled autocorrelation function is used to determine which channels show evidence of the periodicity of the first or dominant vowel, the remaining channels are then used to determine the second vowel. In the context of these time-place models, broader auditory filters

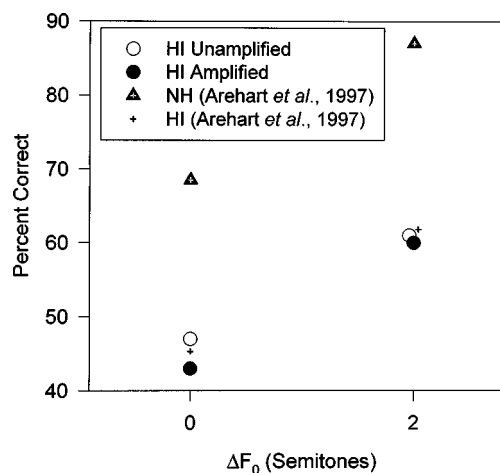


FIG. 2. Mean identification scores (in terms of percentage of trials in which listeners identified both vowels correctly) are shown for the group of listeners with hearing loss for unamplified and amplified vowels for  $\Delta F_0=0$  semitones and  $\Delta F_0=2$  semitones. Also shown are mean percentages for unamplified double-vowel identification for listeners from Arehart *et al.* (1997).

in listeners with hearing loss would increase susceptibility to masking and reduce the extent to which the periodicities of vowels could be separated into different groups of channels. Similarly, deficits in neural synchrony would reduce the precision with which periodicity could be encoded (Moore, 1995; Woolf *et al.*, 1981).

In summary, increasing the level of high-frequency portions of double vowels did not improve the overall ability of listeners with hearing loss to identify double vowels. This finding suggests that spectro-temporal processing deficits *per se* contribute to the degraded ability of listeners with hearing loss to identify correctly two competing vowels.

## ACKNOWLEDGMENTS

This research was supported by a grant from the Deafness Research Foundation. The author extends thanks to Tom Eberhard for technical and programming assistance and to Rebecca Lyders-Gustafson for assistance in data collection.

<sup>1</sup>Due to availability, listener I4 was not able to return for a final visit, so her results are based on 160 trials rather than 220 trials in each condition. Listener I2's results are based on 240 trials rather than 220 trials. Each vowel was tested a proportionately equivalent number of times for each listener in each condition.

Arehart, K. H., King, C. A., and McLean-Mudgett, K. S. (1997). "Role of fundamental frequency differences in the perceptual separation of competing vowel sounds by listeners with normal hearing and listeners with hearing loss," *J. Speech. Lang. Hear. Res.* **40**, 1434–1444.

Assmann, P. F., and Summerfield, Q. (1990). "Modeling the perception of concurrent vowels: Vowels with different fundamental frequencies," *J. Acoust. Soc. Am.* **88**, 680–697.

Baer, T., and Moore, B. C. J. (1994). "Effects of spectral smearing on the intelligibility of sentences in the presence of interfering speech," *J. Acoust. Soc. Am.* **95**, 2270–2280.

Feston, J. M., and Plomp, R. (1990). "Effects of fluctuating noise and interfering speech on the speech-reception threshold for impaired and normal hearing," *J. Acoust. Soc. Am.* **88**, 1725–1736.



- Gatehouse, S. (1989). "Apparent auditory deprivation effects of late onset: The role of presentation level," *J. Acoust. Soc. Am.* **86**, 2103–2106.
- Klatt, D. H. (1980). "Software for a cascade/parallel formant synthesizer," *J. Acoust. Soc. Am.* **67**, 971–995.
- Meddis, R., and Hewitt, M. J. (1992). "Modeling the identification of concurrent vowels with different fundamental frequencies," *J. Acoust. Soc. Am.* **91**, 233–245.
- Moore, B. C. J. (1995). *Perceptual Consequences of Cochlear Damage* (Oxford Medical Publications, New York).
- Turner, C. W., and Holte, L. A. (1987). "Discrimination of spectral-peak amplitude by normal and hearing-impaired subjects," *J. Acoust. Soc. Am.* **81**, 445–451.
- Woolf, N. K., Ryan, A. F., and Bone, R. C. (1981). "Neural phase-locking properties in the absence of outer hair cells," *Hearing Res.* **4**, 335–346.
- Zurek, P. M., and Delhorne, L. A. (1987). "Consonant reception in noise by listeners with mild and moderate sensorineural hearing impairment," *J. Acoust. Soc. Am.* **82**, 1548–1559.

# PROGRAM OF

## The 136th Meeting of the Acoustical Society of America

Norfolk Waterside Marriott Hotel • Norfolk, Virginia • 12–16 October 1998

1a MON. AM

**NOTE:** All Journal articles and Letters to the Editor are peer reviewed before publication. Program abstracts, however, are not reviewed before publication, since we are prohibited by time and schedule.

MONDAY MORNING, 12 OCTOBER 1998

MARRIOTT BALLROOM 3, 8:00 TO 11:45 A.M.

### Session 1aAO

#### Acoustical Oceanography: Shallow Water Geoacoustic Inversions I

Alexandra I. Tolstoy, Cochair

*Integrated Performance Decisions, Inc., 8610 Battailles Court, Annandale, Virginia 22003*

N. Ross Chapman, Cochair

*University of Victoria, School of Earth and Ocean Sciences, P.O. Box 3055, Victoria, British Columbia V8W 3P6, Canada*

Chair's Introduction—8:00

#### *Invited Papers*

8:05

**1aAO1. An overview of the shallow water geoacoustic inversion workshop97.** N. R. Chapman (Univ. of Victoria, P.O. Box 3055, Victoria, BC V8W 3PG, Canada, chapman@uvic.ca) and A. Tolstoy (Integrated Performance Decisions, Inc., Annandale, VA 22003)

In June of 1997 a workshop was held in Vancouver BC with the focus on shallow water geoacoustic inversion methods. The intent was to benchmark a wide variety of inversion methods all applied to common data sets. For that purpose a number of simulated data sets consisting of acoustic fields for vertical and horizontal arrays were prepared and distributed to participants but the values of the geoacoustic parameters were NOT supplied to users. Such parameters included: water depth, sediment layer thickness, sound-speed profile, density, and attenuation, half-space sound-speed, density, and attenuation, and source range and depth. This talk will discuss those test cases and summarize the results obtained by inversion methods based on simulated annealing, genetic algorithms, cw and broadband approaches, neural nets, iterative parameter sequencing, and random searches with gradient descent. Propagation models included normal modes, PE, ray, and full field wave-number integration where cost functions were generally based on the Bartlett MFP but also included high resolution Capon and an approximate maximum likelihood MFP. Most methods were quite successful in estimating sensitive model parameters, but a number of interesting questions remain. These issues and possible future efforts will be discussed. [Work supported by ONR.]

8:25

**1aAO2. Coherent and incoherent shallow water matched field inversion.** Zoi-Heleni Michalopoulou and Michele Picarelli (Dept. of Mathematical Sci., New Jersey Inst. of Technol., Newark, NJ 07102)

Matched field processing (MFP) for geoacoustic inversion has been applied largely in the frequency domain using an incoherent combination of correlations at several frequencies. In source detection and localization problems, similar incoherent broadband MFP techniques have been shown to be inferior to coherent MFP techniques. Coherent MFP exploits source spectrum information when this is available, yielding more robust detection and localization results. This experience suggests that there is potential to improve geoacoustic inversion by MFP using a coherent algorithm. This work assesses that potential through a comparison of inversion results

from incoherent and coherent methods, evaluating performance and cost. Estimates are made of water column depth and sediment geoacoustic properties for both synthetic data and real data from the SWelLEX 96 experiment. The SWelLEX data processed in this work correspond to source transmissions of lfm and hfm pulses, the spectra of which are employed in the coherent processing. [Work supported by ONR, Ocean Acoustics.]

8:45

**1aAO3. Matched-field inversion for geoacoustic uncertainty distributions.** Stan E. Dosso (School of Earth and Ocean Sci., Univ. of Victoria, Victoria, BC V8W 3P6, Canada)

Determining seabed geoacoustic properties from ocean acoustic field measurements represents a nonlinear, nonunique inverse problem with no direct solution. Matched-field inversion methods provide a practical approach to this problem based on searching a multidimensional parameter space for the geoacoustic model that minimizes the mismatch between measured and modeled acoustic fields. Since the parameter space can be large with many local minima, global search algorithms such as simulated annealing or genetic algorithms are typically employed. In addition to determining the single best-fit solution, these search methods have also been applied to compile *a posteriori* distributions of model parameters in an attempt to assess the range of acceptable solutions. However, to date, the definition of what constitutes an acceptable model has been arbitrary with no connection to the uncertainties of the data being inverted. This paper describes an inversion scheme based on sampling the parameter space to compile a distribution of models with mismatch values that are statistically consistent with the noise on the measured acoustic fields. The sampling is carried out using a highly efficient hybrid search algorithm which combines fast simulated annealing and the downhill simplex method.

### Contributed Papers

9:05

**1aAO4. Matched-field bottom property inversion and sensitivity analysis for the SWelLEX series experiments.** Paul A. Baxley and Newell O. Booth (Space and Naval Warfare Systems Ctr., Acoust. Branch D881, 49 575 Gate Rd., Rm. 170, San Diego, CA 92152-6435)

The Shallow Water evaluation cell Experiment (SWelLEX) series, conducted off California between 1993 and 1996, has demonstrated the feasibility of performing matched-field localization in shallow-water (~200 m) environments. A critical issue in these analyses has been the accurate determination of bottom geoacoustic properties. A “best guess” for these parameters resulted in model predictions possessing an excessive number of propagating modes compared to that observed in SWelLEX-1 (August 1993) data. It was hypothesized that the most significant parameters causing this discrepancy were the compressional sound speed and intrinsic attenuation. The values of these properties were then derived via inversions with a single-frequency (70 Hz) SWelLEX-1 source-tow tonal at three stations along a radial track of nearly constant water depth. The use of these optimal parameters greatly enhanced matched-field correlations and localizations at all times along the track, as well as at other frequencies. A sensitivity study performed for an identical track and environment in SWelLEX-3 (July–August 1994) reaffirmed that the geoacoustics properties obtained for SWelLEX-1 are optimal, and suggested that simpler representations of the bottom may be permissible. A similar inversion approach was also performed for the high-slope SWelLEX-4 (March 1995) environment, located off San Clemente Island. [Work supported by ONR/321US.]

9:20

**1aAO5. Predicting the combined effect of model mismatch and noise in matched-field inversion.** Ronald T. Kessel (School of Earth and Ocean Sci., Univ. of Victoria, P.O. Box 3055, Victoria, BC V8W 3P6, Canada)

Matched-field inversion undertakes to match the sound-field of a distant source recorded by a hydrophone array with the predictions of a computer model, the best-match model being the best estimate of the overall propagation scenario (source position and environmental param-

eters). However, the match is never perfect because the model is an ideal (hence mismatched) approximation of the real environment, and because background noise affects the quality of the received signal. Here it is shown how model mismatch and noise together degrade the correlation between the modeled and measured field using the Bartlett processor. Model mismatch is included by analysis of the normal modes of sound propagation, assuming the adiabatic mode approximation for weakly range-dependent media. The result is a fairly simple predictor of the Bartlett correlation expected in practice given estimates of the SNR and model mismatch—the mismatch being cast either in terms of realistic uncertainties for model parameters, or more simply by a single figure of merit quantifying the mean effect of mismatch through its influence on the modes.

9:35

**1aAO6. The behavior of different object functions in a matched-field processing scheme for bottom recognition: A case study.** Michael Taroudakis (Dept. of Mathematics, Univ. of Crete and Foundation for Res. and Technol.-Hellas, P.O. Box 1527, 711 10 Heraklion, Crete, Greece) and Maria Markaki (Foundation for Res. and Technol.-Hellas, Crete, Greece)

Various object functions for broadband inversions of noisy data using matched-field processing for bottom recognition are studied. The study is based on the inversion results obtained by processing synthetic “noisy” data that have been available at a follow-up stage of a benchmark exercise for bottom geoacoustic inversions that was carried out in 1997 (Vancouver, Canada). A genetic algorithm has been used for the implementation of the matched-field processing. The different behavior of the various processors that has already been observed by the authors at the benchmark exercise based on noise-free data is now considered with data that include noise, and their applicability for bottom recognition is analyzed.

9:50

**1aAO7. Geoacoustic inversion using global search.** Peter Gerstoft, Hee Chun Song, William S. Hodgkiss, and William A. Kuperman (Marine Physical Lab., UCSD, La Jolla, CA 92093-0704)

The purpose of an experiment in ocean acoustics is often to estimate a representative set of parameters for a given environmental model and forward propagation model. Global search is a systematic approach to obtain these parameters relative to manual comparisons of the observed and modeled fields. The SAGA-code provides an engine for doing this comparison. The array data type can be transmission loss, complex amplitude, or reverberation. Several choices of state-of-the-art forward models are available as well as several choices of objective functions (least squares, Bartlett, broadband cross correlation, etc.). Finally, the optimization can be carried out either by exhaustive search, genetic algorithms, or simulated annealing. In a Bayesian approach, the result of an inversion is the *a posteriori* probability density for the estimated parameters from which all information such as mean, higher moments, and marginal distributions can be extracted. These distributions are useful in assessing data, environmental model, and obtained estimates. In a recent time reversal mirror experiment [Kuperman *et al.*, J. Acoust. Soc. Am. **103**, 25–40 (1998)], a vertical source array was transmitting to a vertical receive array at range 6.3 km in a 125-m waveguide. It will be investigated how a multisource inversion performs relative to a single source inversion for one way transmission.

10:10–10:25 Break

10:25

**1aAO8. Geoacoustic inversions using light bulb sound sources and measurements of the bottom-reflected acoustic field.** Michael Taroudakis (Dept. of Mathematics, Univ. of Crete and Foundation for Res. and Technol.-Hellas, P.O. Box 1527, 711 10 Heraklion, Crete, Greece), Panagiotis Papadakis (Inst. of Appl. and Computational Mathematics, Crete, Greece), N. Ross Chapman, and Lothar Jaschke (Univ. of Victoria, Victoria, BC V8W 3P6, Canada)

The paper presents results of geoacoustic inversions obtained using a direct inversion scheme based on the calculation of the reflection coefficient of a stratified elastic bottom. The reflection coefficient has been derived from measurements of the acoustic field at a vertical line array of hydrophones moored in the area of the Haro Strait, during the PRIMER sea trial that was carried out in June 1996. Light bulbs have been used as acoustic sources with peak power around 600 Hz. Inversions for the sound speed, the density, and the shear speed of a sediment layer and a semi-infinite substrate and the thickness of the sediment have been performed by separating the various echoes at the receiver and identifying their type through a multiple stage optimization procedure. The results are compared with matched field inversions and a good agreement is demonstrated especially for the parameters of the sediment layer. The applicability of the new method for different experiment setups is also discussed.

### Contributed Papers

10:45

**1aAO9. High resolution geoacoustic inversion using data from a towed broadband source and a bottom moored receiver.** Charles W. Holland and John Osler (SACLANT Undersea Res. Ctr., 19138 La Spezia, Italy)

High resolution geoacoustic models are required for accurate predictions of acoustic propagation and reverberation in shallow water. Our measurement technique employs a towed broadband (400–8000 Hz) source towed near the surface and a moderately deep fixed receiver with source–receiver separations of 0–1000 m. Seafloor reflected data are first processed and inverted in the time domain to get an estimate of interval velocity in each sub-bottom layer. The data are then processed and modeled in the frequency domain to extract sediment layer densities, layer attenuations and velocity gradients. Direct path data are used to calibrate the source. The measurement and inversion technique has been applied at a number of shallow-water sites in the Mediterranean with diverse geoacoustic properties. The frequency domain processing and modeling techniques will be discussed and the geoacoustic inversion results will be shown for several sites. Azimuthal variability of the geoacoustic models will also be discussed.

11:00

**1aAO10. Transmission loss in the Yellow Sea: Data interpretations and model comparisons.** Peter H. Dahl, Christian J. Eggen, Dajun Tang, and Robert C. Spindel (Appl. Phys. Lab., Univ. of Washington, Seattle, WA 98195)

The Yellow Sea represents a natural laboratory for the study of shallow water acoustic propagation as influenced by a strong summer thermocline, energetic internal wave fields, and a seabed considered relatively

range independent. In this paper results of transmission loss measurements obtained in the Yellow Sea, during the joint China-U.S. Yellow Sea '96 experiment, conducted in August 1996 are presented. Explosive sources were deployed at ranges 1–30 km, and acoustic data were recorded on a vertical array that spanned the entire water column depth of ~75 m. The data are in 1/3-octave bands with center frequencies 70 to 700 Hz. A simple geoacoustic model is derived for the seabed that shows consistency with data at ranges of  $O(1)$  km, where raylike properties are exhibited, and of  $O(10)$  km, where modellike properties are exhibited. With summer conditions prevailing, the sound speed profile was described by two isovelocity layers linked by a layer with a linear gradient. Internal tide activity modulated the depth of the linear gradient layer over the course of the experiment, and this effect is also examined using various modeling approaches.

11:15

**1aAO11. Environmental inversion using the singular value decomposition modes of multiple frequency vertical line array data.** Tracianna B. Neilsen and Evan K. Westwood (Appl. Res. Lab., Univ. of Texas, P.O. Box 8029, Austin, TX 78713-8029, neilsen@arlab.utexas.edu)

A method is presented for geoacoustic inversion that uses the depth-dependent normal modes extracted from vertical line array (VLA) data. The normal modes for multiple frequencies are obtained by forming a cross-spectral density matrix (CSDM) for each frequency of VLA data, measured as a source moves outward in range. The singular value decomposition (SVD) of each CSDM yields the depth-dependent normal modes of the ocean environment at the time the signal was recorded [T. B. Neilsen and E. K. Westwood, J. Acoust. Soc. Am. **101**, 3025 (1997)]. The data-extracted mode functions are then used to invert for the environmental parameters. The Levenberg-Marquardt nonlinear optimization method is used to find the best fit between the data-extracted and modeled mode

functions by adjusting the environmental parameters. The algorithm requires computation of the first partial derivatives of the mode functions with respect to the varied parameters, which is achieved using the ORCA normal mode model. The method is useful for determining the sound speed profile and the characteristics of the uppermost bottom layers. Results using simulated data will be presented. [Work supported by U. S. Army Research Office, AASERT Grant number DAAH04-95-1-0486, and ONR.]

11:30

**1aAO12. Broadband geoacoustic inversion using mode traveltime dispersion.** Gopu R. Potty and James H. Miller (Dept. of Ocean Eng., Univ. of Rhode Island, Narragansett, RI 02882)

Inversion of sediment compressional sound speeds using the data from SUS charge explosions acquired during the Shelf Break Primer Experiment in 1996 is presented. A hybrid approach combining a Genetic Algo-

rithm and Levenberg-Marquardt nonlinear least squares method is used for the inversion. This inversion is based on the time-frequency dispersion of the acoustic signal calculated using a wavelet approach. Group speeds for modes 1–7 and for frequencies ranging from 10–200 Hz were obtained from the wavelet scalograms of the acoustic signal. The ocean waveguide depth was approximately 90 m. The minimized objective function is weighted to incorporate the quality of the data at various frequencies and modes. Forward modeling is done using adiabatic normal mode theory assuming a mildly range-dependent environment. Resolution and error of the inversions are expressed in terms of the Hessians and a *posteriori* model standard deviations. Inversion results are compared with compressional speeds based on the data from the nearby AMCOR-6012 site using Biot–Stoll theory. In addition, gravity cores taken at selected locations in the experimental site provide some corroboration of the sediment compressional speeds in the top 4 to 5 m of the sediment. [Work supported by ONR.]

MONDAY AFTERNOON, 12 OCTOBER 1998

MARRIOTT BALLROOM 3, 1:30 TO 4:15 P.M.

### Session 1pAO

## Acoustical Oceanography: Shallow Water Geoacoustic Inversions II

N. Ross Chapman, Cochair

*University of Victoria, School of Earth and Ocean Sciences, P.O. Box 3055, Victoria, British Columbia V8W 3P6, Canada*

Alexandra I. Tolstoy, Cochair

*Integrated Performance Decisions, Inc., 8610 Battailles Court, Annandale, Virginia 22003*

Chair's Introduction—1:30

### Invited Papers

1:35

**1pAO1. Broadband bottom-interacting acoustics in shallow waters.** Mohsen Badiey (Univ. of Delaware, Newark, DE 19716)

Understanding broadband acoustic propagation in shallow-water ocean environments presents a host of challenges for the acoustics community. Insufficient environmental and experimental data make quantitative assessments of predictive models very difficult. On the other hand, due to substantial cost incurred in obtaining the ground truth and high-resolution geoacoustic data, the information is usually limited to a single or at most very few geological cores in a region. For acoustic applications, geological data need to be converted to a set of geoacoustic parameters such as compressional and shear wave speeds, their attenuation profiles, and the bulk density of sediment. In recent years several experiments of broadband acoustic propagation in shallow-water environments have been performed using airgun sources in different water depths. These experiments have been conducted in regions with some geological information. A procedure to convert the measured geological parameters into geoacoustic data in conjunction with the empirical orthogonal functions (EOF) has allowed the creation of statistical and frequency-dependent sediment profiles suitable for propagation modeling. Parabolic equation (PE) and normal mode models have been used to assess the physics of sound propagation in these regions. The results of these investigations are summarized here with regards to the geoacoustic inversion in shallow-water regions.

1:55

**1pAO2. Inversion of broadband ambient noise in shallow water for the geoacoustic parameters of the seabed.** Michael J. Buckingham and Grant B. Deane (Scripps Inst. of Oceanogr., Univ. of California—San Diego, La Jolla, CA 92093-0213, mjb@mpl.ucsd.edu)

Ambient noise propagates through the ocean in much the same way as sound from a man-made source. The noise is a stochastic phenomenon, but some of its statistical measures, for instance, the spatial coherence, may be influenced by the environment in a systematic and stable manner. Such statistical measures may then be inverted to obtain information on the environment. In particular, over the continental shelf, where water depths are less than 200 m, the nature of the seabed has a significant effect on the vertical coherence, or, equivalently, vertical directionality, of the noise in the water column. This suggests that simple measurements of the vertical coherence of the noise, taken with just two hydrophones in the water column, may be inverted to yield the geoacoustic

functions by adjusting the environmental parameters. The algorithm requires computation of the first partial derivatives of the mode functions with respect to the varied parameters, which is achieved using the ORCA normal mode model. The method is useful for determining the sound speed profile and the characteristics of the uppermost bottom layers. Results using simulated data will be presented. [Work supported by U. S. Army Research Office, AASERT Grant number DAAH04-95-1-0486, and ONR.]

11:30

**1aAO12. Broadband geoacoustic inversion using mode traveltime dispersion.** Gopu R. Potty and James H. Miller (Dept. of Ocean Eng., Univ. of Rhode Island, Narragansett, RI 02882)

Inversion of sediment compressional sound speeds using the data from SUS charge explosions acquired during the Shelf Break Primer Experiment in 1996 is presented. A hybrid approach combining a Genetic Algo-

rithm and Levenberg-Marquardt nonlinear least squares method is used for the inversion. This inversion is based on the time-frequency dispersion of the acoustic signal calculated using a wavelet approach. Group speeds for modes 1–7 and for frequencies ranging from 10–200 Hz were obtained from the wavelet scalograms of the acoustic signal. The ocean waveguide depth was approximately 90 m. The minimized objective function is weighted to incorporate the quality of the data at various frequencies and modes. Forward modeling is done using adiabatic normal mode theory assuming a mildly range-dependent environment. Resolution and error of the inversions are expressed in terms of the Hessians and a *posteriori* model standard deviations. Inversion results are compared with compressional speeds based on the data from the nearby AMCOR-6012 site using Biot–Stoll theory. In addition, gravity cores taken at selected locations in the experimental site provide some corroboration of the sediment compressional speeds in the top 4 to 5 m of the sediment. [Work supported by ONR.]

MONDAY AFTERNOON, 12 OCTOBER 1998

MARRIOTT BALLROOM 3, 1:30 TO 4:15 P.M.

### Session 1pAO

## Acoustical Oceanography: Shallow Water Geoacoustic Inversions II

N. Ross Chapman, Cochair

*University of Victoria, School of Earth and Ocean Sciences, P.O. Box 3055, Victoria, British Columbia V8W 3P6, Canada*

Alexandra I. Tolstoy, Cochair

*Integrated Performance Decisions, Inc., 8610 Battailles Court, Annandale, Virginia 22003*

Chair's Introduction—1:30

### Invited Papers

1:35

**1pAO1. Broadband bottom-interacting acoustics in shallow waters.** Mohsen Badiey (Univ. of Delaware, Newark, DE 19716)

Understanding broadband acoustic propagation in shallow-water ocean environments presents a host of challenges for the acoustics community. Insufficient environmental and experimental data make quantitative assessments of predictive models very difficult. On the other hand, due to substantial cost incurred in obtaining the ground truth and high-resolution geoacoustic data, the information is usually limited to a single or at most very few geological cores in a region. For acoustic applications, geological data need to be converted to a set of geoacoustic parameters such as compressional and shear wave speeds, their attenuation profiles, and the bulk density of sediment. In recent years several experiments of broadband acoustic propagation in shallow-water environments have been performed using airgun sources in different water depths. These experiments have been conducted in regions with some geological information. A procedure to convert the measured geological parameters into geoacoustic data in conjunction with the empirical orthogonal functions (EOF) has allowed the creation of statistical and frequency-dependent sediment profiles suitable for propagation modeling. Parabolic equation (PE) and normal mode models have been used to assess the physics of sound propagation in these regions. The results of these investigations are summarized here with regards to the geoacoustic inversion in shallow-water regions.

1:55

**1pAO2. Inversion of broadband ambient noise in shallow water for the geoacoustic parameters of the seabed.** Michael J. Buckingham and Grant B. Deane (Scripps Inst. of Oceanogr., Univ. of California—San Diego, La Jolla, CA 92093-0213, mjb@mpl.ucsd.edu)

Ambient noise propagates through the ocean in much the same way as sound from a man-made source. The noise is a stochastic phenomenon, but some of its statistical measures, for instance, the spatial coherence, may be influenced by the environment in a systematic and stable manner. Such statistical measures may then be inverted to obtain information on the environment. In particular, over the continental shelf, where water depths are less than 200 m, the nature of the seabed has a significant effect on the vertical coherence, or, equivalently, vertical directionality, of the noise in the water column. This suggests that simple measurements of the vertical coherence of the noise, taken with just two hydrophones in the water column, may be inverted to yield the geoacoustic

parameters of the bottom. An essential element of such an inversion procedure is an ambient noise model which includes a geoacoustic model of the sediment. In the presentation, a noise inversion model based on spatial coherence will be described. Examples of inversions for the bottom properties, obtained from real data taken at shallow-water sites in the northern and southern hemispheres, will be presented. [Research supported by ONR.]

2:15

**1pAO3. Shallow-water geoacoustic inversions of seafloor properties in Spencer Gulf.** Grant B. Deane (Marine Physical Lab., Scripps Inst. of Oceanogr., La Jolla, CA 92093-0238, grant@mpl.ucsd.edu), Douglas H. Cato, and Paul Clarke (Maritime Operations Div. Defence Sci. and Technol. Organization, Pyrmont, NSW 2009, Australia)

Preliminary results of an experiment to characterize the geoacoustic properties of the upper few meters of the seafloor in Spencer Gulf, Southwestern Australia, will be presented. The aim of the experiment was to estimate the compressional and shear wave speeds, compressional wave absorption, and sediment density using different inversion techniques and compare the results for consistency. To this end, four measurement methodologies were used, which were: (1) transmission loss measurements, using the support vessel as a moving source, (2) ambient noise coherence measurements, (3) bottom reflectivity measurements, using frequency modulated pings and the sound of imploding light bulbs as sources, and (4) grab bottom samples. The transmission loss measurements show a distinct modal interference structure as a function of source frequency and source–receiver separation, and can be inverted for the average sediment acoustical properties along the source–receiver track. The ambient noise coherence measurements can be inverted for the noise field vertical directional density function, which in turn yields the critical angle of the seafloor averaged over a 5- to 10-km disk. [Work supported by DSTO, Australia, and ONR, USA.]

### Contributed Papers

2:35

**1pAO4. Tomographic inversion of geoacoustic properties in a range-dependent shallow water environment.** Patrick Pignot and Ross Chapman (School of Earth and Ocean Sci., Univ. of Victoria, P.O. Box 3055, Victoria, BC V8W 3P6, Canada)

This paper presents a matched-field tomography method to estimate the geoacoustic properties of the ocean bottom for a range-dependent medium in shallow water. The inversion method has been developed in order to process experimental data recorded during the Haro Strait PRIMER trial. This experiment was carried out in June 1996 and used low-frequency broadband signals that were received on three vertical line arrays. The data inversion is particularly difficult in this experiment because of the complex bathymetry of the experimental site. For this inversion, a range-dependent ray code has first been developed to solve the forward problem allowing an arbitrarily layered bottom environment. The inverse scheme is based on the propagation time and the amplitude of the recorded data and a simple new cost function is proposed. The significant feature of the inversion scheme is the division of the process into a series of layers. Starting with the topmost layer, the range-dependent thickness, sound speed, and density are estimated via a Monte Carlo method. Inversion results are presented on synthetic and experimental data. [Work supported by the Office of Naval Research.]

2:50

**1pAO5. Multiscale estimation of bottom properties.** Subramaniam D. Rajan (Scientific Solutions, Inc., 18 Clinton Dr., Hollis, NH 03049)

In shallow water areas, the ocean bottom plays an important role in the propagation of acoustic energy. It is therefore important to be able to determine the bottom acoustic properties with adequate resolution and accuracy. Further, if the bottom model is to be capable of predicting the

field over a range of frequencies, the model has to be extracted from broadband data. The possibility of obtaining the bottom properties at different scales of resolution is explored. Scaling functions derived from wavelets are used as the basis functions for estimating the bottom properties. Modal inverse method and the multifrequency data acquired during the Hudson Canyon experiment are used for this study.

3:05

**1pAO6. High-resolution geoacoustic inversion from wide-angle seismic reflection measurements.** John C. Osler and Charles W. Holland (SACLANT Undersea Res. Ctr., Viale San Bartolomeo, 400, 19138 La Spezia, Italy, osler@saclantc.nato.int)

Using wide-angle reflections from sub-bottom layers and an analytical inversion, high-resolution geoacoustic models comprised of interval velocities and layer thickness are obtained. The inversion uses the ray-parameter method of Bryan [J. Acoust. Soc. Am. **68**, 1403–1408 (1980)]; the solution for a given layer is independent of the overlying layers and applicable when the water depth is less than the horizontal source–receiver offset. It has been tested using synthetically generated wide angle reflection hyperbolae and found to be robust for water depth/layer thickness ratios as high as 150, including cases with multiple layers and low velocity zones. The experimental geometry consists of a surface-towed impulsive source and a fixed receiver that is moored above the seabed. Experiments have been conducted at several shallow water sites in the Northern Tyrrhenian Sea, Malta Channel, and Gulf of Cadiz. The resulting geoacoustic models form the base from which more complicated models (including velocity gradients, densities, and attenuations) are constructed, for example, by frequency domain modeling of bottom loss data measured with the same experimental geometry. The time domain processing and analysis techniques will be discussed and inversion results will be shown along with seismic reflection profiles.

3:20–3:30 Break

3:30–4:15

Panel Discussion

## Session 1pPA

## Physical Acoustics: Periodic Media and Various Topics

Philip S. Spoor, Chair

*Los Alamos National Laboratory, Division of Material Science and Thermal Physics, MS K764, Los Alamos, New Mexico 87545*

## Contributed Papers

2:00

**1pPA1. An acoustic levitation technique for measuring the rheology of foam.** R. Glynn Holt, Corey C. Clarke, and J. Gregory McDaniel (Dept. of Aerosp. and Mech. Eng., Boston Univ., Boston, MA 02215)

Understanding the rheological behavior of foams is important as a basic problem in fluid physics, and as a practical problem in many industries. Foams are tremendously important in a variety of applications. The most important quality of a foam in many of these applications is its response to imposed strain, or its rheological behavior. However, there exists almost no experimental data on the rheological properties of real 3-D foams. This is due in large part to the earth-based requirements for contact containment, and to the fact that gravity-induced drainage quickly destroys all but the “driest” foams. A unique method to provide noncontact control and manipulation of foam samples, via acoustic levitation is described. The analysis is outlined which will allow determination of a foam’s yield stress, effective bulk modulus, and effective bulk viscosity from the observed response of a foam sample to quasistatic, step function, and periodic acoustic and ambient pressure changes. Preliminary data will also be presented. [Work supported by NASA.]

2:15

**1pPA2. Interaction of a two-phase turbulent/bubbly submerged water jet with a single-phase jet: Measurements of the enhanced hydrodynamic near-field spectrum, part II.** Murray S. Korman, John V. Tobin, and Kathryn M. McMahon (Dept. of Phys., U.S. Naval Acad., Annapolis, MD 21402)

The interaction of mutually perpendicular submerged turbulent water jets is studied from measurements of the hydrodynamic near-field pressure spectrum. One jet is a conventional single-phase, free turbulent shear flow circular jet, while the other jet is a two-phase bubbly jet of similar construction. The overlap region is located at four nozzle diameters ( $4D$ ) away from each orifice. A small hydrophone located outside the overlap region on the symmetry line  $45^\circ$  from each jet axis (and in the far quadrant from each nozzle exit) measures the near-field pressure signature. Spectra are measured at different radial positions from the overlap region (typically  $4D-10D$ ). Very small gas bubbles are generated in the two-phase turbulent jet by pressurized  $N_2$  gas passing through a fritted disk housed in a Buchner funnel located near the nozzle entrance. Spectra are compared for different void fractions and different Reynolds numbers (based on jet diameter). Typically, volume void fractions  $\sim 0.001$  significantly amplify the flow noise coming from jet nozzles ( $D=0.635$  cm) with nozzle exit velocities of 10 m/s. [See earlier work, *J. Acoust. Soc. Am.* **102**, 3184(A) (1997).] [Work supported by the Naval Acad. Res. Council.]

2:30

**1pPA3. Large two-dimensional sonic band gaps.** Francisco Meseguer, Constanza Rubio, Juan Vte. Sanchez-Perez, Rosa Martinez-Sala (Unidad Asociada CSIC-UPV. Dept. Fisica Aplicada, Universidad Politecnica de Valencia, Camino de Vera s/n, 46022 Valencia, Spain, fmese@fis.upv.es), David Caballero, Jose Sanchez-Dehesa, and Jaime Llinares (Universidad Autonoma de Madrid, E-28049 Madrid, Spain)

In this paper it is shown that a two-dimensional honeycomb structure is a good candidate to produce large full band gaps in sonic band gap (SBG) materials. The full gap of the honeycomb lattice can be increased by reducing the symmetry of the cell as it occurs in photonic band gap (PBG) materials. The evolution of the band gap in the honeycomb-triangular transition has been studied. Starting from a honeycomb lattice (with 4 cm diameter cylinders), one can study the transition to a triangular symmetry by placing rods with different diameter (from 0.6 to 4 cm) at the center of the honeycomb lattice. When the diameter cylinder of the center of the unit cell has the same diameter as cylinders of the unit cell (4 cm), the lattice achieves a triangular symmetry. The obtained results are compared with theoretical calculations performed with a variational method.

2:45

**1pPA4. Sound attenuation by a two dimensional array of cylinders.** Francisco Meseguer, Juan Vte. Sanchez-Perez, Constanza Rubio, Rosa Martinez-Sala (Unidad Asociada CSIC-UPV. Dept. Física Aplicada, Universidad Politecnica de Valencia, Camino de Vera s/n, 46022 Valencia, Spain, fmese@fis.upv.es), David Caballero, Jose Sanchez-Dehesa, and Jaime Llinares (Universidad Autonoma de Madrid, E-28049 Madrid, Spain)

Here, it is shown, for the first time, a systematic analysis (experiment and theory) of the acoustic transmission of a two-dimensional periodic array of rigid cylinders with two different configurations: square and triangular. The influence of the filling fractions, ranging from 0.06 up to 0.41, on the appearance of the pseudogaps and full band gaps is studied. Above a certain filling fraction, an overlap is observed between the attenuation peaks measured along the two high symmetry directions of the Brillouin zone. This effect is considered as the fingerprint of the existence of a full acoustic gap. Nevertheless, the comparison with our calculation of band structures shows that the lattice has band states in that frequency range. These bands are called deaf bands (i.e., they cannot be excited by experiments of sound transmission) [Sanchez-Perez *et al.*, *Phys. Rev. Lett.* (to be published)].



**1pPA5. Surface waves attenuation by a two-dimensional elastic band gap crystal.** Francisco Meseguer, Jaime Llinares, Natalia Benaches (Unidad Asociada CSIC-UPV. Dept. Física Aplicada, Universidad Politecnica de Valencia, 46022 Valencia, Spain, fmese@fis.upv.es), Miguel Holgado, Ceferino Lopez (Instituto de Ciencia de Materiales (CSIC), Campus de Cantoblanco, 28049 Madrid, Spain), Jose Sanchez-Dehesa, and David Caballero (Universidad Autonoma, Cantoblanco, 28049 Madrid, Spain)

Experiments on the attenuation of Rayleigh waves in a marble quarry by a periodic array of cylindrical holes, in a honeycomb and in a triangular distribution, are reported. The results are explained in terms of elastic wave crystals, and compared to theoretical calculations performed with scalar waves. The possibility of application to the attenuation of surface waves in seismic movements is also discussed.

3:15

**1pPA6. Acoustic spectral gaps and discrete transmission in slender tubes.** M. S. Kushwaha (Inst. of Phys., UAP, Apdo. Post. J-45, Puebla 72570, Mexico, manvir@sirio.ifuap.buap.mx), A. Akjouj, L. Dobrzynski, B. Djafari-Rouhani, and J. O. Vasseur (LDSMM, U. F. R. de Physique, USTL, 59655 Villeneuve D'Ascq, Cedex, France)

This work reports on the band structure and transmission spectrum for the longitudinal (acoustic) wave propagation in a system made up of  $N'$  dangling side branches (DSB) periodically grafted at each of the  $N$  equidistant sites on a slender tube. A periodic pattern of large stop bands is obtained for the airy DSB on the slender water tube. The emphasis is laid on the interesting result of huge gaps and discrete transmission spectrum due only to the DSB grafted at a *single* site ( $N=1$ ) on the slender tube. Designing the system with open tubes allows achievement of the lowest gap below a threshold frequency and extending up to zero—thereby providing an entirely discrete band structure and transmission spectrum. This should have important consequences for the suppression of low-frequency noise and for designing filters and transducers.

**1pPA7. Sonic stop bands for cubic arrays of rigid inclusions in air.** M. S. Kushwaha (Inst. of Phys., UAP, P.O. Box J-45, Puebla 72570, Mexico, manvir@sirio.ifuap.buap.mx), B. Djafari-Rouhani, L. Dobrzynski, and J. O. Vasseur (LDSMM, U. F. R. de Physique, USTL, 59655 Villeneuve D'Ascq, Cedex, France)

Extensive band structures have been computed for cubic arrays of rigid spheres and cubes in air. Complete stop bands are obtained for face-centered-cubic (fcc) structure; however, there is no gap for the body-centered-cubic (bcc) and simple-cubic (sc) structures. These gaps start opening up for a volume fraction of  $\approx 54\%$  (27%) for spherical (cubic) inclusions and tend to increase with the filling fraction, exhibiting a maximum at the close-packing. A tandem structure that allows us to achieve an ultrawideband filter for environmental or industrial noise in the desired frequency range is proposed. This work is motivated by the recent experimental observation of sound attenuation on the sculpture, by Eusebio Sempere, exhibited at the Juan March foundation in Madrid [Nature **378**, 241 (1995)] and complements the corresponding theoretical work [Appl. Phys. Lett. **70**, 3218 (1997)].

3:45

**1pPA8. A new approach to the analysis of acoustic hole fibers.** Mürvet Üçer and Ergül Akçakaya (Electron. and Commun. Dept., Faculty of Elec.-Electron. Eng., İstanbul Tech. Univ., 80626, Maslak, İstanbul, Turkey)

In this work a new effective analysis method is proposed for the acoustic hole fibers of hexagonal crystal symmetry. Interpreting all quantities appearing in the boundary conditions as the state variables, a first-order differential equations system is obtained to investigate the waves in acoustic hole fibers of hexagonal symmetry. This approach makes it possible to analyze hole fibers by the general transmission-matrix technique. By using this method dispersion relations for all modes are easily obtained. This method can also be applied in the analysis of the multilayered cylindrical fiber for which the individual layers have hexagonal symmetric piezoelectric materials. [Work supported by İTÜ.]

MONDAY AFTERNOON, 12 OCTOBER 1998

HAMPTON ROADS BALLROOM 2, 2:00 TO 4:50 P.M.

### Session 1pSP

## Signal Processing in Acoustics: Time-Frequency Techniques in Acoustic Applications I

James V. Candy, Chair

Lawrence Livermore National Laboratory, P.O. Box 808, L-333, Livermore, California 94550

Chair's Introduction—2:00

### Invited Papers

2:05

**1pSP1. Time-frequency-scale description of signals.** Leon Cohen (Dept. of Phys., City Univ.-Hunter College, 695 Park Ave., New York, NY 10021)

Time-varying spectrum is one of the most primitive sensations we experience since we are surrounded by light of changing color, by sounds of varying pitch, and by many other phenomena whose periodicities change. Hence the need to describe how the spectral content of a signal is changing in time, and to develop the physical and mathematical ideas needed to understand what a time-varying spectrum is. Why this is an elegant and challenging problem, the immense strides that have recently been made, and why new interesting physical quantities must be introduced will all be described. In addition, the immense practical applications over the last few years will be shown in such areas as acoustics, biomedical signals, geophysical signals, fault detection, sonar, etc.

2:50

**1pSP2. Wavelet analysis as a wideband generalization of time-frequency analysis.** Gerald Kaiser (The Virginia Center for Signals and Waves, 1921 Kings Rd., Glen Allen, VA 23060)

The wavelet transform and the windowed Fourier transform are compared. Although these two look quite different in the time domain, they are very similar in the frequency domain. The only difference is that the windowed Fourier transform divides the frequency domain into bands of equal width, whereas the wavelet transform uses frequency bands of constant ratio. This is just how frequency bands occur in practice (in logarithmic rather than linear scale). Since low-frequency bands are narrow while high-frequency bands are wide in this scheme, the Nyquist sampling rates for low-frequency components of the signal are low while those for high-frequency components are high. The sampling rate in wavelet analysis is thus automatically adapted to the frequency range being analyzed. When both the signal and the analyzing wavelet are narrow band, it follows easily that the wavelet transform reduces to the windowed Fourier transform, the analyzing window for the latter being derived from the analyzing wavelet for the former. Therefore wavelet analysis may be viewed as a wideband generalization of ordinary time-frequency analysis, to which it reduces in the narrow-band limit. This view is especially useful in sonar.

3:35–3:50 Break

3:50

**1pSP3. Recursive parameter estimation methods: An adaptive filtering perspective.** Scott Douglas (Dept. of Elec. Eng., Southern Methodist Univ., P.O. Box 750338, Dallas, TX 75275, douglas@seas.smu.edu)

This tutorial provides an overview of recursive parameter estimation methods from the viewpoint of the adaptive filtering field. Specific topics to be discussed include gradient versus least-squares techniques, adaptive infinite-impulse response filters, and bias removal methods. Particular emphasis is placed on the analytical behaviors of the algorithms, their estimation characteristics, and their tracking abilities in mildly nonstationary environments. Applications of the methods to identification problems in acoustics are discussed. [This work has been supported by NSF Grant No. MIP-9501680.]

4:20

**1pSP4. Applications of time-frequency signature analysis to target identification.** G. C. Gaunaud (Naval Surface Warfare Ctr., Carderock Div., Code 684, West Bethesda, MD 20817-5700) and H. C. Strifors (National Defense Res. Establishment, FOA6, Stockholm, S-17290, Sweden)

The overlapping subjects of target identification, inverse scattering, and active classification have many applications that differ depending on specific sensors. Many useful techniques for these relevant subjects have been developed in the frequency and the time domains. A more recent approach views target signatures in the combined or coupled time-frequency (t-f) domain. For either ultra-wideband (UWB) projectors, or UWB processing these joint t-f domain techniques are particularly advantageous. Such analysis requires the use of some of the scores of nonlinear distributions that have been proposed and studied over the years. Basic ones, such as the Wigner distribution [E. Wigner, *Phys. Rev.* **40**, 749 (1932)] and its many relatives, have been shown to belong to the well-studied ‘‘Cohen Class’’ [L. Cohen, *J. Math. Phys.* **7**, 781–786 (1966)]. Half-a-dozen of these distributions will be selected to review applications that the authors have addressed and solved in several areas such as: (a) sonar [Appl. Mech. Rev. **50**, 131–149 (1997)]; (b) mine classification [Ultrasonics J. **33**, 147–153 (1995)]; (c) dolphin biosonar and ID [J. Acoust. Soc. Am. **103**, 1547–1557 (1998)]; and (d) radar [IEEE Proc. **84**, 1231–1248 (1996)]. These examples illustrate how the informative identifying features required for accurate ID are extracted and displayed in this general domain. [Work partially supported by the authors’ institutions and the ONR.]

**NOTE:** Attendance at this Tutorial Lecture requires payment of an additional registration fee.

### Session 1eID

## Interdisciplinary: Tutorial Lecture on Probing the Unknowns of Sonoluminescence

Yves H. Berthelot, Chair

*School of Mechanical Engineering, Georgia Institute of Technology, Atlanta, Georgia 30332*

**Chair's Introduction—7:00**

### *Invited Paper*

**7:00**

**1eID1. Probing the unknowns of sonoluminescence.** Seth Putterman (UCLA, Phys. Dept., Los Angeles, CA 90095)

The passage of sound through a fluid with a trapped bubble leads to the clocklike emission of picosecond flashes of ultraviolet light. In this phenomenon, sonoluminescence (or SL), acoustic energy spontaneously focuses by over 12 orders of magnitude. SL is just one example of energy focusing in bubbly flows. Researchers studying cavitation from a fluid accelerating through a venturi tube in the 1960s observed subnanosecond flashes of light and had in fact at that time discovered the world's fastest manmade source of light. As with many avenues of research on cavitation luminescence, not the least of which is described in Exodus 20:18 [“And all the people saw the sounds”] these wonderful insights were abandoned. SL is extremely sensitive to ambient temperature, strength of the acoustic drive, and doping with noble gases. Despite a plethora of theoretical publications the most basic aspects of SL remain unexplained. Neither the light emitting mechanism nor the size of the bubble nor the range of acoustic drives at which SL can be achieved are understood. It is also a mystery as to why water is the friendliest fluid for SL and it would be most valuable to understand why pure diatomic gas bubbles are very weak, unstable sources of SL. A reasonable picture of the energy concentrating mechanism starts from Rayleigh's 1917 work on the high pressure developed in a collapsing bubble. Femtosecond light scattering from an SL bubble indicates that the collapse is strongly supersonic and suggests the formation of an imploding shock wave that further focuses the acoustic field. Measurements find that the flash of SL is emitted at the minimum radius where the acceleration exceeds  $10^{11}$  g. The flash width is independent of wavelength from the ultraviolet to the infrared suggesting that the light is emitted when the gas is so stressed that it is in a new phase, perhaps a cold dense plasma. Methods of astronomy are being used to beat the diffraction limit and measure the size of the sonoluminescing “hot-spot.” The upper limit of energy focusing that can be achieved with this “star-in-a-jar” has not yet been determined.

**NOTE:** Attendance at this Tutorial Lecture requires payment of an additional registration fee.

### Session 1eID

## Interdisciplinary: Tutorial Lecture on Probing the Unknowns of Sonoluminescence

Yves H. Berthelot, Chair

*School of Mechanical Engineering, Georgia Institute of Technology, Atlanta, Georgia 30332*

**Chair's Introduction—7:00**

### *Invited Paper*

**7:00**

**1eID1. Probing the unknowns of sonoluminescence.** Seth Putterman (UCLA, Phys. Dept., Los Angeles, CA 90095)

The passage of sound through a fluid with a trapped bubble leads to the clocklike emission of picosecond flashes of ultraviolet light. In this phenomenon, sonoluminescence (or SL), acoustic energy spontaneously focuses by over 12 orders of magnitude. SL is just one example of energy focusing in bubbly flows. Researchers studying cavitation from a fluid accelerating through a venturi tube in the 1960s observed subnanosecond flashes of light and had in fact at that time discovered the world's fastest manmade source of light. As with many avenues of research on cavitation luminescence, not the least of which is described in Exodus 20:18 [“And all the people saw the sounds”] these wonderful insights were abandoned. SL is extremely sensitive to ambient temperature, strength of the acoustic drive, and doping with noble gases. Despite a plethora of theoretical publications the most basic aspects of SL remain unexplained. Neither the light emitting mechanism nor the size of the bubble nor the range of acoustic drives at which SL can be achieved are understood. It is also a mystery as to why water is the friendliest fluid for SL and it would be most valuable to understand why pure diatomic gas bubbles are very weak, unstable sources of SL. A reasonable picture of the energy concentrating mechanism starts from Rayleigh's 1917 work on the high pressure developed in a collapsing bubble. Femtosecond light scattering from an SL bubble indicates that the collapse is strongly supersonic and suggests the formation of an imploding shock wave that further focuses the acoustic field. Measurements find that the flash of SL is emitted at the minimum radius where the acceleration exceeds  $10^{11}$  g. The flash width is independent of wavelength from the ultraviolet to the infrared suggesting that the light is emitted when the gas is so stressed that it is in a new phase, perhaps a cold dense plasma. Methods of astronomy are being used to beat the diffraction limit and measure the size of the sonoluminescing “hot-spot.” The upper limit of energy focusing that can be achieved with this “star-in-a-jar” has not yet been determined.

## Session 2aAO

## Acoustical Oceanography and Underwater Acoustics: Acoustics and Ocean Processes

Stanley E. Dosso, Chair

University of Victoria, School of Earth and Ocean Sciences, P.O. Box 1700, Victoria, British Columbia V8W 3P6, Canada

## Contributed Papers

9:00

**2aAO1. Numerical simulation of the transverse current monitoring in the Fram Strait.** Konstantin A. Naugolnykh, Yun-Yu Wang, and E. C. Shang (CIRES, Univ. of Colorado/NOAA/Environ. Technol. Lab., Boulder, CO 80303)

The numerical simulation of transverse current monitoring in the Fram Strait environment is performed using horizontal refraction modal tomography (HRMT). The simplified West Spitsbergen Current profile is constructed in the framework of geostrophic approach and calculation of the modal phase difference between signals arriving along the two paths of acoustical interferometer due to horizontal refraction is made for the sound signal frequencies 100–200 Hz and different sound source depth. It was demonstrated that the measurable modal phase difference in a range of 80–160 can be expected for an averaged current velocity in the strait cross section of 0.3 m/s. At higher frequency of the sound signal the sensitivity of the HRMT increases but the space coherency decreases so the optimal frequency has to be chosen. The strong mode coupling effect presented in such a complex environment was apparently weakened by using the signals propagating along the closed paths.

9:15

**2aAO2. High-frequency forward scatter and propagation experiments in the Delaware Bay.** Wenkai Qin, Mohsen Badiy, Randy Zagar (Univ. of Delaware, Newark, DE 19716, badiy@udel.edu), and Jeff Simmen (Office of Naval Res., Arlington, VA 22217-5000)

In order to assess the temporal and spatial coherence of transmitted broadband acoustic signals (1–20 kHz) in coastal environments, two acoustic experiments were performed in the Delaware Bay during March and September 1997. Accompanied by measurements of the ocean volume (temperature and salinity) and sea surface roughness (0- to 0.5-m wave height), these acoustic experiments included reciprocal acoustic transmissions over a large band of acoustic frequencies and during a variety of sea states. The connection between the stability and coherence of the single surface bounce and the sea surface roughness is studied. In the presence of rough seas (and therefore bubbles), the coherence decreases rapidly between reciprocal receptions as sea state increases, while for calm sea states a high correlation exists between them. Some preliminary modeling results using a high-frequency parabolic equation (PE) model are used to interpret this frequency-dependent behavior.

9:30

**2aAO3. High-frequency reciprocal transmission experiments in the Delaware Bay: Focus on the direct path.** Joe R. Zagar, Mohsen Badiy, Wenkai Qin (Univ. of Delaware, Newark, DE 19716, zagar@udel.edu), and Jeff Simmen (Office of Naval Res., Ocean Acoust. Prog., Arlington, VA 22217-5000)

Broadband reciprocal transmission experiments were performed in the Delaware Bay during March and September of 1997. Also, direct measurements of current, temperature, and salinity profiles as well as winds and surface wave spectra were conducted during the course of both experiments. The purpose of these experiments was to quantitatively assess the impact of different components of environmental variability (such as tides, wind, etc.) on the stability and coherence of broadband acoustic

signals (1–20 kHz) in shallow estuarine environments. In general, the stability and coherence of the received signal will be affected by both surface and volume variabilities, but the impact of volume variability can be most clearly isolated by focusing exclusively on the direct-path component of the received signal. The connection between the stability and coherence of the direct-path arrival is studied under different tidal phases, varying wind conditions, and sea states. A preliminary analysis of the impact of volume variability on the direct-path component of the received signal is discussed. Attempts to reproduce these measurements using a high-frequency parabolic equation (PE) model are also shown.

9:45

**2aAO4. Out-of-plane defocusing in a time reversal mirror.** Hee Chun Song, William A. Kuperman, William S. Hodgkiss, Peter Gerstoft (Scripps Inst. of Oceanogr., Univ. of California, San Diego, La Jolla, CA 92093-0238), T. Akal, C. Ferla (SACLANT Undersea Res. Ctr., 19138 La Spezia, Italy), and D. R. Jackson (Univ. of Washington, Seattle, WA 98105)

Recent time-reversal mirror (TRM) experiments conducted in the Mediterranean Sea in May 1997 extended the range of focus from the earlier results of 6 km to 30 km [Kuperman *et al.*, *J. Acoust. Soc. Am.* **101**, 3088 (1997)]. Ideally, the probe source (PS) should be in the vertical SRA-VRA plane. However, for practical reasons the PS was placed several hundred meters out of this plane. This geometry did not introduce any significant errors at 6 km range in the April 1996 experiment. In the May 1997 experiment, the authors conducted a source tow in which the PS moved along the arc of a circle at a range of 15 km from the SRA and maximum transverse offsets of 1 km from the VRA. The TRM focus appeared robust to the transverse offset of the source from the VRA on one side of the SRA-VRA plane, but defocused on the other side of the plane. Backpropagation simulations reveal that the TRM focusing along this 15-km, mildly range-dependent region is quite sensitive to the geoacoustic properties of the seafloor, e.g., sediment layer thickness and sound speed gradient. This sensitivity is explored to determine the geoacoustic properties of the seafloor.

10:00

**2aAO5. Time reversal mirror as a tool for inversion.** Hee Chun Song, Peter Gerstoft, William A. Kuperman, William S. Hodgkiss (Scripps Inst. of Oceanogr., Univ. of California, San Diego, La Jolla, CA 92093-0238), T. Akal, and C. Ferla (SACLANT Undersea Res. Ctr., 19138 La Spezia, Italy)

Recent time-reversal mirror (TRM) experiments conducted in the Mediterranean Sea in April 1996 showed that TRM can be used for inverting for the ocean environment [Kuperman *et al.*, *J. Acoust. Soc. Am.* **103**, 25–40 (1998)]. The inversion involves comparing the VRA data resulting from time reversal to the SRA data backpropagated to the VRA in simulation. One natural objective function is the Bartlett power. In this paper, both the Bartlett power objective function and an inversion using an objective function based on the compactness of the backpropagated pulse on the VRA are explored. A global inversion genetic algorithm code will be used along with an efficient broadband normal mode forward propagation model.

10:30

**2aAO6. Computed time-reversing array retrofocusing in a dynamic shallow-water sound channel.** Michael R. Dungan and David R. Dowling (Dept. of Mech. Eng. and Appl. Mech., Univ. of Michigan, Ann Arbor, MI 48109, drd@engin.umich.edu)

A time-reversing array (TRA) can retrofocus acoustic energy to the location of its original source even when the acoustic environment is complex and unknown. However, array performance is degraded when the acoustic environment is time dependent. Predictions of array retrofocusing performance require an acoustic propagation model for the environment. The model used in this study is a parabolic equation (PE) code (RAM by M. D. Collins). This study addresses the sensitivity of TRA retrofocusing to time variation in the water column of a shallow-water sound channel. These changes include internal waves and tidal fluctuations. Simulated variations are based on measured oceanic statistics. The influence of waveguide complexity on retrofocusing is also determined by adding range dependence and realistic bottom properties to the computational domain. Results are presented for a variety of ranges and acoustic frequencies. [Work supported by the Office of Naval Research, Ocean Acoustics.]

10:45

**2aAO7. Retro-focusing of a time reversing acoustic array in noisy environments.** Sunny R. Khosla and David R. Dowling (Dept. of Mech. Eng., Univ. of Michigan, Ann Arbor, MI 48109, indu@engin.umich.edu)

The presence of a noise field can significantly alter the focusing properties of a time-reversing array (TRA). A linear, vertical TRA in simple environments containing omni-directional noise is considered. The noise is treated as a Gaussian process and a time reversal formulation incorporating a restriction on the maximum array power output is constructed. Ambient noise present in shallow oceanic environments can lead to a reduction in the retrofocus field signal amplitude because rebroadcast noise consumes array output power. Using the received SNR at the array as the independent parameter, the first and second moments of the time-reversed field are predicted theoretically. Monte-Carlo simulations showing the spatial variation in the field amplitude from realization to realization will also be presented. The results show that the spatial distribution of the rebroadcast mean field is independent of the initial received SNR while the field variance is strongly dependent on it. [Work sponsored by the Office of Naval Research, Ocean Acoustics.]

**2aAO8. Low-frequency acoustic emissions of a plunging water jet.**

**Part I. Experiment.** Thomas K. Berger, Thomas R. Hahn, and Michael J. Buckingham (Scripps Inst. of Oceanogr., Univ. of California—San Diego, 9500 Gilman Dr., La Jolla, CA 92093-0238)

Low-frequency acoustic emissions of bubble clouds entrained by a continuous fresh water jet were experimentally studied. Bubble clouds penetrating 10–20 cm deep into a 160-cm deep pool of fresh water were generated and dispersed by an impinging water stream of 1.6 mm diameter and velocities of up to 10 m/s. The sound field was recorded with small hydrophones at various positions close to the cloud as well as directly in the plume. At frequencies below 1 kHz the power spectral density exhibited a strong resonance structure. The observed resonance frequencies scale with the jet velocity as well as the air volume flux but are largely independent of the details of the air entrainment (e.g., nozzle geometry). Reference measurements in a much larger body of fresh water, a natural lake, are shown to exhibit the same resonances, indicating that wall reflections in the tank do not influence the values of the resonance frequencies. All observations are consistent with an interpretation of the bubble plume as a resonant cavity with a sound speed much smaller than in the surrounding medium.

11:15

**2aAO9. Low-frequency acoustic emissions of a plunging water jet.**

**Part II. Theory.** Thomas R. Hahn, Thomas K. Berger, and Michael J. Buckingham (Scripps Inst. of Oceanogr., Univ. of California—San Diego, 9500 Gilman Dr., La Jolla, CA 92093-0238)

A theory of low-frequency acoustic emissions of a plunging water jet is developed and presented. A plunging liquid jet impinging on a free liquid surface entrains air and produces a bubble cloud with a well-defined geometry. At low frequencies the resulting bubble cloud has a substantially lower sound speed than the surrounding single phase medium. The cloud is modeled as a conical resonant cavity having the apex at the plunging point, with nonuniform sound speed profile and acoustically hard boundaries. Analytical estimates for the eigenfrequencies, based on the wave equation and a simplified void fraction profile, provide insight into the dependence of the resonance frequencies on various system parameters. A more realistic numerical model that includes advection by the surrounding flow and a more appropriate void fraction profile gives remarkable agreement with measured values and scalings for the eigenfrequencies. Further improvements can be made by including turbulent transport and dissolution in the model but at the cost of including additional parameters. Considering the complicated nature of the system, very strong overall agreement of the presented models is found, thus allowing inversions to be performed for important quantities related to the gas transfer, such as the entrainment rate and the void fraction profile.

## Session 2aNSa

## Noise: Community and Transportation Related Noise Issues

Courtney B. Burroughs, Cochair

*Applied Research Laboratory, Pennsylvania State University, P.O. Box 30, State College, Pennsylvania 16801*

Henry Jones, Cochair

*U.S. Army, AFDD/JRPO, AMCOM MS 461, NASA Langley Research Center, Hampton, Virginia 23681*

## Contributed Papers

8:00

**2aNSa1. Noise impact model.** Melissa M. Burn and Kevin A. Bradley (Wyle Labs., 2001 Jefferson Davis Hwy., Ste. 701, Arlington, VA 22202)

A noise impact model (NIM) has been developed that allows the user to examine the impact that quieter aircraft technologies might have on air carrier operating efficiency at major U.S. airports. The analyst selects one of 16 available airports and one of three case years for study, chooses a set of flight tracks, and has the option of reducing the noise of one or more aircraft. Two sets of flight tracks are available for most airports; one that represents actual current conditions, including noise abatement tracks, and a second set that offers more efficient routing. NIM computes the resultant noise impact and the time and distance saved for each operation on the more efficient, alternate tracks. In addition, NIM offers the option of examining the effect that runway use patterns have on capacity and delay for three airports. Noise impact is characterized in three ways; the size of the noise contour footprint, the number of people living within the contours, and the number of homes located in the contours. A World Wide Web implementation of NIM will be available this year through the Aviation System Analysis Capability at [www.asac.lmi.org](http://www.asac.lmi.org).

8:15

**2aNSa2. A theoretical model for parallel noise barriers.** Won-Suk Ohm (Dept. of Mech. Eng., Univ. of Texas, Austin, TX 78712-1063) and B. J. Landsberger (Ctr. for Trans. Res., Univ. of Texas, Austin, TX 78705)

The conventional approach for modeling parallel noise barriers has been mostly based on using the single barrier theory with image sources to model the reflected fields. This approach does not take into account diffraction in the field between the two barriers. The conventional method also tends to predict higher insertion loss degradation than field measurements have shown. A theoretical model is proposed to include diffraction in the part of the field due to single or multiple reflections. For the reflected field between the barriers, a barrier is assumed to act as a baffled sound source whose pressure amplitude and phase are given by that of the reflected wave. The source field and the barrier shape are unrestricted. In this case, only the reflected portion of the incident wave propagates back to the opposite barrier whereas in the image source method the whole incident wave is reflected. The angular spectrum method is used to calculate the field from the various reflections. The new model is compared to various other calculations and published field measurements.

8:30

**2aNSa3. Variability of highway noise barrier insertion loss in the atmosphere.** Scott D. Hansen and Courtney B. Burroughs (Grad. Prog. in Acoust., Penn State Univ., P.O. Box 30, University Park, PA 16802, [chaos@sabine.acs.psu.edu](mailto:chaos@sabine.acs.psu.edu))

Measurements of insertion loss of a model highway noise barrier were performed at the Pennsylvania Transportation Institute test track near State College, PA. An array of microphones was used to provide directionality

to remove arrivals from other than over the top of the barrier. This eliminated arrivals from the ends of the barrier so that the results can be applicable to an infinitely long barrier. Also, the array is used to identify different propagation paths which contribute to the sound field in the shadow zone. Since the insertion loss depends on distances of the source and receiver from the barrier, measurements were made for different source-to-barrier and barrier-to-receiver distances. An analysis of results was used to determine the dependence of insertion loss on key parameters, e.g., ground impedance, wind speed, and barrier height. Numerical models are exercised to explore the dependencies of insertion losses on parameters not easily changed on site, e.g., ground impedance.

8:45

**2aNSa4. Acoustic directivity measurements of the CH-46E, CH-53E, and AH-1A helicopters.** Michael John Lucas (Wyle Labs., 2001 Jefferson Davis Hwy., Ste. 701, Arlington, VA 22202)

Presented in this paper are the results from acoustical measurements made of the CH-46E, CH-53E, and AH-1 helicopters. Results from the test will be used to form a database of sound hemispheres that is currently under development for the rotorcraft noise model. A unique feature of the test was the use of two cranes having a tip height of 180 ft, that suspended two vertical arrays of microphones. Positioned between the two cranes was a third array of microphones located on the ground which completed the shape of a U. The helicopters flew through the center of the array with the plane of the rotor approximately inline with the cranes tips. Carried on board the helicopters was a tracking system which was time synchronized with the acoustic recording equipment. The acoustic data and the tracking data are combined in a computer program that depropagates the sound field to a sound hemisphere which preserves the directivity and frequencies of the acoustic field. A sound hemisphere is constructed for each pass through the acoustic array.

9:00

**2aNSa5. Development of a "quiet by design" approach to reduced-noise gas flow systems for experimental research facilities at NASA Lewis Research Center.** Beth A. Cooper (NASA Lewis Res. Ctr., M.S. 6-4, 21000 Brookpark Rd., Cleveland, OH 44135, [Beth.A.Cooper@lerc.nasa.gov](mailto:Beth.A.Cooper@lerc.nasa.gov)) and David A. Nelson (Hoover & Keith, Inc., Houston, TX 77082)

At the NASA Lewis Research Center, occupational and community noise exposures associated with experimental research in aircraft and space propulsion are managed via a hearing conservation program that prohibits unprotected exposure to A-weighted noise levels above 85 dB. In support of hearing conservation goals, a "buy quiet" program requires project designers and engineers who purchase equipment expected to generate A-weighted noise emission levels above 80 dB to consider noise emissions along with other performance criteria. A *Guide to Specifying Equipment Noise Emission Levels* provides the means to effectively pursue this approach. A recently implemented "quiet by design" initiative complements this program and provides design guidance for new facili-

ties, systems, and equipment designed in-house rather than purchased from an outside vendor. A *Reduced-Noise Gas Flow Systems Design Guide* serves as a companion to the earlier document and covers design practices for reducing noise emission and methods of estimating noise emission from piping and atmospheric vents associated with gas flow sys-

tems. A computer spreadsheet guides the user through the design process from noise emission specification through predictive equations and selection of noise control elements, greatly facilitating the development of noise control strategies for new experimental research facilities and the associated services required for their operation.

TUESDAY MORNING, 13 OCTOBER 1998

HAMPTON ROADS BALLROOM 8, 9:30 TO 11:30 A.M.

### Session 2aNSb

## Noise: Susceptibility to Noise Induced Permanent Threshold Shift (NIPTS) and Age

Larry H. Royster, Cochair

*North Carolina State University, MAE Department, Raleigh, North Carolina 27695-7910*

Julia D. Royster, Cochair

*Environmental Noise Consultants, Inc., P.O. Box 30698, Raleigh, North Carolina 27622-0698*

Chair's Introduction—9:30

### Invited Papers

9:35

**2aNSb1. Does eye color correlate with susceptibility to noise-induced hearing loss?** Julia D. Royster (Environmental Noise Consultants, Inc., P.O. Box 30698, Raleigh, NC 27622-0698, EFFECTIVE\_HCPS@compuserve.com) and Larry H. Royster (North Carolina State Univ., Raleigh, NC 27695-7910)

Several authors over the last 30 years have suggested an association between eye color and susceptibility to both temporary threshold shift (TTS) from noise and noise-induced permanent threshold shift (NIPTS). Pigmentation in the iris is related to the concentration of melanin in the stria vascularis of the cochlea. In earlier research the potential link between susceptibility and pigmentation was not firmly established or explained. More recently, investigators M.-L. Barrenas and P.-A. Hellstrom [Ear Hearing 17, 63–68 (1996)] have suggested possible physiological mechanisms for the effect. This paper summarizes the available literature and provides new data from hearing conservation program audiograms of employees in a large industrial site, compared for groups divided by gender, race, and eye color.

9:55

**2aNSb2. Vascular changes in the inner ear perhaps related to intense sound.** Robert I. Kohut (Dept. of Otolaryngol., Wake Forest Univ. School of Medicine, Winston-Salem, NC 27157-1034, preece@wfubmc.edu)

Vascular disorders of the inner ear have been hypothesized as a cause of hearing loss. Vascular changes of the labyrinth in humans have only been confirmed histopathologically in two instances, an isolated anterior inferior cerebellar artery (AICA) thrombosis and a secondary AICA thrombosis due to basilar artery thrombosis. A third human case is under re-evaluation. The oxygen and carbon dioxide levels in perilymph from humans having sudden hearing loss are consistent with, but not conclusive for, vascular compromise. In animals, recent blood flow studies using Doppler techniques suggest that there can be changes with certain noxious agents, including loud sound. Using other techniques, investigators have demonstrated dynamic vessel changes, blood cell aggregation, offset rebound vasodilation, and A–V shunting in animals in response to loud sound. For systematic vascular disorders, histopathologic studies in humans concerning vascular changes in the inner ear have not been feasible previously. One new collection of human temporal bones at the Department of Otolaryngology at Wake Forest University School of Medicine is unique. Obtained from consecutive autopsies, the collection represents a cross section of society. Studies are underway which should further the understanding of pathogenic mechanisms of abnormalities of hearing and balance, including vascular disorders of the inner ear.

10:15

**2aNSb3. The effects of variability in ear canal geometry and middle ear impedance on noise exposure level.** Robert de Jonge (Dept. of Commun. Disord., Central Missouri State Univ., Warrensburg, MO 64093)

If a group of industrial workers is uniformly exposed to a particular noise level, each person develops a different amount of hearing loss. The reasons for individual differences in susceptibility to noise are not entirely clear, but might relate, in part, to variability in ear canal acoustics and middle ear impedance. This variability alters the sound field to eardrum SPL transformation, effectively changing the magnitude of the exposure, and potentially producing differences in hearing loss. To study these effects, a computer simulation was created from an electrical analog model of the middle ear and a network representation of the ear canal. The model predicts how variation in ear canal geometry (length and diameter) and middle ear load impedance influences the eardrum SPL,



both for individuals wearing hearing protector devices ("leaky" earplugs) and for the unprotected ear. The model also estimates the amount of attenuation offered by the earplug and the amount of conductive hearing loss created by changes in the middle ear. Therefore, it was possible to evaluate whether changes in exposure levels would likely result in hearing loss, given the amount of protection offered by either earplug attenuation or conductive hearing loss.

10:35

**2aNSb4. Susceptibility to hearing loss: Physiological, physical, behavioral and probabilistic factors.** G. Richard Price (U.S. Army Res. Lab., Human Res. and Eng. Directorate, APG, MD 21005-5425, dprice@arl.mil)

The problem of susceptibility to hearing loss is important from both scientific and legal perspectives. In developing and validating a mathematical model of the ear to predict auditory hazard [Price and Kalb, *J. Acoust. Soc. Am.* **100**, 2674 (1996)] it has become critical to identify the sources of variance in hearing loss data. In turn, the model has provided the capacity for insight into processes that are operative. For very intense sounds, losses are virtually instantaneous and both the physical characteristics of the ear and the details of the moment matter. Physiological characteristics such as small ear canals, thick ear drums, active middle ear muscles and narrow annular ligaments promote less loss. Physical details such as the azimuth of the source and the head-related transfer function are also important. Behavioral patterns are critical too—the near-sighted risk-taker may hammer much closer to the unprotected ear than the far-sighted hearing conservationist. And last, the probabilistic details of the impulse itself can be critical. For example, gunfire impulses with the same peak pressures and durations, from the same weapon, may nevertheless differ by a factor of 5 in their predicted effect, due to the details of turbulent flow.

10:55

**2aNSb5. Accounting for possible differences in population susceptibility to noise caused by variations in ear canal geometry.** Larry H. Royster (Dept. of Mech. Eng., North Carolina State Univ., Raleigh, NC 27695-7910) and Julia D. Royster (Environmental Noise Consultants, Inc., Raleigh, NC 27622-0698)

Analysis of large population audiometric data bases, where gender and race have been considered, have consistently yielded significant differences in the indicated hearing thresholds for these subgroups. For whatever reason, females have consistently indicated better hearing than males and blacks have consistently indicated better hearing than whites. White males typically have the worst hearing, white females and black males similar hearing patterns, and black females the most sensitive hearing of all these groups. Therefore, it was deemed appropriate to now try to take into consideration model-predicted eardrum sound pressure level differences (as transferred from the same equivalent diffuse field values) based on known ear canal geometry differences. The findings from this reanalysis of the data bases previously analyzed will be presented.

11:15–11:30

Discussion

TUESDAY MORNING, 13 OCTOBER 1998

HAMPTON ROADS BALLROOM 7, 8:00 TO 9:45 A.M.

### Session 2aPAa

## Physical Acoustics: Propagation and Diffraction

John S. Robertson, Chair

*Georgia College and State University, Department of Mathematics and Computer Science, Milledgeville, Georgia 31061-0490*

### Contributed Papers

8:00

**2aPAa1. Outdoor sound propagation in the U.S. Civil War.** Charles D. Ross (Dept. of Natural Sci., Longwood College, Farmville, VA 23909, cross@longwood.lwc.edu)

In a number of major battles in the U.S. Civil War, unusual atmospheric acoustics played a major role. In this study, the probable causes of the unusual acoustics are given and the resulting effect on military command decisions is described. The causes discussed include sound absorption, wind shear, temperature gradients, and combinations of these. Several cases will also be described in which multiple ground reflections caused sounds of battle to be heard at unusually great distances. The battles studied include Gettysburg, Seven Pines, Perryville, Iuka, Fort Donelson, Gaines Mill, Five Forks, and Chancellorsville.

8:15

**2aPAa2. The effect of mean flow/source motion on sound pressure fields with absorption.** Jeffrey J. Kelly (Virginia Tech Vib. and Acoust. Labs., VCES, 303 Butler Farm Rd., Ste. 101, Hampton, VA 23666)

The sound field for a moving source can be described in either a source-fixed or space-fixed reference frame. Noise source modules for prediction codes are usually formulated in the source frame since this simplifies the boundary conditions associated with the acoustic field. Also, this allows consideration of a distributed source, which is important for Doppler effects. For community noise studies, noise metrics are computed in a ground based coordinate system. In principle, the problem can be formulated and a solution sought in either frame of reference. Once the problem is solved in a particular reference frame, coordinate transformations allow the pressure field to be expressed in different reference frames.

In this study, the problem is formulated in a source-fixed frame. By using Fourier transforms and separation of variables, a solution is determined in the source frame. Directivity patterns are constructed for a cylindrical radiator, which show the influence of Mach number, frequency and displacement pattern on the radiated sound field. The far-field acoustic relations are transformed to emission coordinates that depict what is observed from a space-fixed (ground) reference frame. Effects of mean flow/forward flight on absorption due to viscosity are also presented.

8:30

**2aPAa3. Efficient calculation of scattering into an acoustic shadow zone using empirical orthogonal functions and the Markov approximation.** D. Keith Wilson (U.S. Army Res. Lab., ATTN: AMSRL-IS-EE, 2800 Powder Mill Rd., Adelphi, MD 20783, dkwilson@arl.mil)

In many previous studies, the mean sound level of a signal scattered by turbulence into an atmospheric refractive shadow zone has been calculated using a Monte Carlo procedure. This procedure involves generating many (typically 10 to 100) random realizations of the turbulent field, using a parabolic equation (PE) code to solve for the sound field corresponding to each realization, and then averaging. Unfortunately, this method is computationally intensive because of the large number of PE runs required. In this paper, a different approach, based on combining a distorted-wave Born approximation, a "quasi"-Markov approximation, and decomposition of the turbulence into empirical orthogonal functions, is described. Here "quasi" refers to the fact that the Markov approximation is applied only in the nominal (horizontal) direction of propagation, since the exact direction of propagation is variable. Initial results are promising in that the mean scattered field can be calculated in a small fraction of the time required for a single PE run. However, the new approach underpredicts the Monte Carlo result by 5 to 10 dB. Possible sources of the discrepancy include the Markov approximation, multiple scattering, and inexact treatment of boundary effects.

8:45

**2aPAa4. Sound propagation over a large wedge: A comparison between the geometrical theory of diffraction and the parabolic approximation.** John S. Robertson (Dept. of Mathematics and Computer Sci., Georgia College & State Univ., Milledgeville, GA 31061, jroberts@mail.gac.peachnet.edu)

Low-frequency propagation over wedges, hills, and barriers is an important problem with many applications. Two different propagation models are used to compare the sound field generated by a steady single-frequency source in front of, over, and behind a large, rigid, v-shaped wedge. Predictions along the boundary made with both models at several frequencies are compared and found to be in excellent agreement. The results provide additional evidence that the parabolic approximation is able to account accurately for propagation effects caused by terrain irregularities.

9:00

**2aPAa5. Spatial and temporal characteristics of acoustic Bessel Bullets by modal decomposition.** Peter R. Stepanishen (Dept. of Ocean Eng., Univ. of Rhode Island, Narragansett, RI 02882-1197, stepanishen@oce.uri.edu)

Acoustic Bessel Bullets (BB) are defined to be a class of bandlimited transient localized waves which maintain their spatially dependent shape and time history as they propagate in free space. An analytical approach is presented to investigate the space-time characteristics of such wave fields

which are generated from finite circular planar apertures with radially symmetric space-time noncausal source distributions. The approach is based on a modal decomposition of the space-time planar source distribution which is combined with a generalized space-time impulse response method to determine the field. Numerical results are presented to illustrate the general space-time characteristics of the modal decomposition of the source distributions, the generalized impulse responses and the associated acoustic BB fields.

9:15

**2aPAa6. Influence of viscosity on acoustic diffraction by a half plane.** Allan D. Pierce and Mario Zampolli (Mech. and Aerosp. Eng. Dept., Boston Univ., 110 Cummington St., Boston, MA 02215)

An approximate solution for the diffraction of sound by a half plane in a viscous fluid is given. The solution is derived from the linear equations of fluid dynamics, where the Euler equation is replaced by the Navier-Stokes equation. The resulting equations can be represented as the sum of acoustic and vorticity mode components. The acoustic mode is governed by the acoustic wave equation, while the vorticity mode is governed by a diffusion equation. The two modes each have nonzero velocity at the half plane, but the superposition of the two velocity fields is such that the sum of the tangential components and the sum of the normal components both are zero, in accord with the no-slip condition. Each mode can be approximately represented in terms of Fresnel integrals of complex argument. The solution implies that there is a boundary hemisphere in the vicinity of the edge in which there is no singularity and in which the vorticity mode is of equal importance to the acoustic mode. Outside the boundary hemisphere the acoustic mode dominates and the solution in that region is very nearly the same as originally predicted by Sommerfeld in 1896.

9:30

**2aPAa7. Acoustic measurements in an airport environment and the identification of the sound radiated by aircraft wake vortices.** Neal Fine (Eng. Technol. Ctr., 240 Oral School Rd., Mystic, CT 06355-1208), Frank Rees, and William Von Winkle (Flight Safety Technologies, Inc., New London, CT 06320)

Results are presented of an effort to measure the sound generated by aircraft wake vortices. The objective of the research is to estimate the spectral shape and source levels characteristic of the sound generated by aircraft wakes during approach and landing. Measurements were made at JFK airport in August 1997, for various aircraft, using three Bruel & Kjaer outdoor microphones. The data was recorded to tape and spectrum analysis was performed using a B&K portable spectrum analyzer. The three microphones were placed near the beginning of runways 13L and 22L, arrayed in several configurations parallel to and perpendicular to the runway centerline. Initial spectrum analysis of the data revealed a prominent broadband "hump" in the one-third octave sound-pressure level spectra, centered at approximately 50-60 Hz for a B-747 landing (with a bandwidth of roughly 20-30 Hz). The timing of the hump is consistent with that expected for wake vortex sound and it is hypothesized to be generated by the wake vortices. Cross correlations between microphones arrayed parallel to the runway will test this hypothesis. Additional data, which were recorded in January 1998, will also aid in identifying the wake vortex sound characteristics.

## Session 2aPAb

## Physical Acoustics and Structural Acoustics and Vibration: Scattering

David Feit, Chair

Naval Surface Warfare Center, 9500 MacArthur Boulevard, West Bethesda, Maryland 20817-5000

## Contributed Papers

10:00

**2aPAb1. Visualization of transient acoustic wave scattering from targets with thin shells.** David G. Crighton and Markku J. Vartiainen (Dept. of Appl. Mathematics and Theoretical Phys., Univ. of Cambridge, Silver St., Cambridge CB3 9EW, England, M.J.Vartiainen@damp.cam.ac.uk)

The objective of this work is to gain qualitative and quantitative understanding of acoustic wave scattering from thin shells. Near-field solutions for a pulse excitation are obtained and plotted in a time series. The visualization demonstrates development of transient edge scattering, at close range, of a target that incorporates thin shells and sharp edges. The demonstration is of wide interest and in that, the advantages of the adopted time domain formulation become apparent. Within the calculation technique, pressure difference across the shell has been obtained by the point collocation procedure, based on a boundary integral equation solution for thin shells. The near-field solution is solved from the pressure difference through the classical Helmholtz equation of retarded potentials. The transient scattered field on a plane has then been visualized with a general meshing program. Objects employed include a flat circular disc, a flat rectangular disc, an open cone, and a thin-walled cylinder. Some of the calculations have been verified by comparing the harmonic response, which has been obtained via Fourier deconvolution of the transient far-field transfer function, with existing analytical solutions or experimental results.

10:15

**2aPAb2. Symmetric-wave coincidence-frequency and Rayleigh-wave tunneling backscattering enhancements for plastic shells and solid spheres in water.** Brian T. Hefner and Philip L. Marston (Dept. of Phys., Washington State Univ., Pullman, WA 99164-2814, bhefner@mail.wsu.edu)

Unlike the case of metallic objects, most solid-polymer "plastic" objects have shear and Rayleigh wave phase velocities less than the speed of sound in water. Furthermore, the density contrast with water is relatively small. These differences combine to significantly alter the dominant scattering processes for plastic objects. For example, since the high-frequency limit for the lowest symmetric (or  $s_0$ ) Lamb wave velocity approaches the Rayleigh velocity, reducing the frequency raises the velocity and brings it closer to the speed of sound in water. It is calculated that for shells there is a corresponding rise in radiation damping and that the order of the ray-theoretic coincidence frequency backscattering features is predicted to be reversed in comparison to the order for metallic shells [P. L. Marston and N. H. Sun, *J. Acoust. Soc. Am.* **92**, 3315–3319 (1992)]. The low-frequency supersonic  $s_0$  branch is also greatly affected near the coincidence condition. In addition, backscattering by some solid plastic spheres is predicted to be enhanced in the  $ka=2-10$  region due to tunneling coupling with Rayleigh wave resonances which have been modeled with ray theory. [Work supported by the Office of Naval Research.]

10:30

**2aPAb3. Sound scattering by a stiffened cylindrical shell using elasticity theory.** A. Baillard, J.-M. Conoir, D. Décultot, G. Maze (LAUE URA CNRS 1373, Université du Havre, place R. Schuman, 76610 Le Havre, France), A. Klauson, and J. Metsaveer (Tallinn Tech. Univ., Ehitajate tee 5, EE-0026 Tallinn, Estonia)

Previous articles about stiffened cylindrical shells have described acoustic scattering through theory of thin plates and shells. Considering the dimensions of the studied object, these analyses are limited in frequency range (reduced frequency  $kR < 70$ ). The aim of the present work is to first establish a model using elasticity theory and then to validate it in low frequencies with regard to thin shell theory. As this new model allows us to extend the analysis into high frequencies ( $kR \sim 50-200$ ), numerical and experimental results are compared in this frequency band in order to determine the effects of the internal plate in the acoustic scattering of the shell. The cylindrical shell is made of stainless steel with an internal-to-external radius ratio  $b/a = 0.98$  (medium radius  $R = 25.25$  mm). It is stiffened by a wall (of the same material and thickness) which is soldered along two diametrically opposed generatrix of the shell. In the experimental setup, the air-filled shell is vertically immersed in water and normally insonified by a plane wave. The emitter-receiver transducer turns around the object and records the backscattering spectrum at various angles relative to the wall.

10:45

**2aPAb4. Backscattering enhancement from leaky Rayleigh waves on the flat end of a tilted solid cylinder: Observations and Gaussian beam model.** Karen Gipson and Philip L. Marston (Dept. of Phys., Washington State Univ., Pullman, WA 99164-2814, marston@wsu.edu)

The circular end of a tilted solid cylinder in water was illuminated by high frequency sound. When the angle of incidence was close to the Rayleigh wave coupling angle, a leaky Rayleigh wave was launched which reflects from the rim. The reflected wave passes through a focus which lies on a diameter of the cylinder, and a significantly attenuated leaky wave subsequently reflects back along the diameter from the opposite rim. The radiation from the focused initial reflection was observed to produce a large backscattering enhancement having a far-field amplitude significantly greater than for reflection from a rigid sphere having the same diameter as the cylinder [K. Gipson, Ph.D. thesis, Wash. State Univ. (1998)]. This enhancement was modeled by approximating the leaky wave as a focused Gaussian beam and approximating the initial surface and far-field amplitudes using a variation of a method previously described [P. L. Marston, *J. Acoust. Soc. Am.* **102**, 1628–1638 (1997)]. One of the principal curvatures of the outgoing wavefront vanishes so the enhancement is associated with a far-field caustic. The theory should be applicable to other flat circular targets. [Work supported by the Office of Naval Research.]

11:00

**2aPAb5. Elastic wave scattering from a sphere.** Jean-Pierre Sessarego, Jean Sageloli, Régine Guillermin (CNRS/Laboratoire de Mécanique et d'Acoustique, 13402 Marseille, Cedex 20, France), and Herbert Überall (Catholic Univ., Washington, DC 20064)

Theoretical and experimental studies of the scattering of compressional waves from an elastic sphere imbedded in an isotropic elastic medium have been carried out by the authors; the experiments were performed with impulsive signals. Both monostatic and bistatic scattering amplitudes were obtained. From the calculated resonances exhibited in the individual normal-mode scattering amplitudes, phase-velocity dispersion curves for the circumferential waves excited on the sphere by the scattering process were obtained. The observed scattered pulses exhibit quantitatively the propagation of these circumferential waves and of the radiation shed by them, which becomes very clearly evident in a comparison of (180 deg) monostatic, and of bistatic scattering at 90 deg. Very good agreement is found between the measured pulse shapes, and those obtained by theoretical calculations, but the main result is the verification of the circumferential-wave mechanism of scattering.

11:15

**2aPAb6. Meridional ray amplitudes for high-frequency backscattering from water-filled tilted finite cylindrical shells.** Scot F. Morse and Philip L. Marston (Dept. of Phys., Washington State Univ., Pullman, WA 99164-2814, morse@mail.wsu.edu)

Impulse response measurements have previously shown that the backscattering by moderately thick tilted finite cylindrical shells is enhanced when phase matching to a supersonic meridional leaky wave occurs [Morse *et al.*, *J. Acoust. Soc. Am.* **103**, 785–794 (1998)]. Above the coincidence frequency phase matching to the meridional  $a_0$  leaky Lamb wave occurs for a range of high tilt angles far from broadside incidence and yields large backscattering enhancements. The results of high-frequency tone burst measurements for water-filled shells are presented

and compared with an approximate ray theory. In each case the peak backscattered amplitude for the initial meridional ray is several times larger than the reflection from a rigid sphere having the same radius as the cylinder. Amplitudes for the water-filled shell are generally less than one-half those for the corresponding hollow shell, but can still be understood using ray theory [P. L. Marston, *J. Acoust. Soc. Am.* **102**, 358–369 (1997)]. Multiple internal reflections within the fluid cavity in the meridional plane give rise to regularly spaced enhancements in the time domain, some of which can be several times larger than the signal for the initial meridional ray. [Research sponsored by the Office of Naval Research.]

11:30

**2aPAb7. Calculation of sound scattering from elastic targets using unified FDTD formulas.** Shuozhong Wang (Dept. of Elec. Info. Eng., Shanghai Univ., Shanghai 200072, PROC), Rongqing Wang (760 Res. Inst., Dalian 116013, PROC), and Zhen Fang (Shanghai Univ., Shanghai 200072, PROC)

Underwater sound scattering from objects without shear stress has been treated using the finite-difference method in the time domain [S. Wang, *J. Acoust. Soc. Am.* **99**, 1924–1931 (1996)]. In many realistic targets, however, both longitudinal and transverse waves exist. In order to deal with scattering from such objects, a set of FDTD expressions are established based on Hooke's law. For a 3-D problem, these include six difference equations for stress and three for particle velocity. The expressions reduce to the previously obtained form consisting of four equations (one for sound pressure and three for velocity) if shear wave is absent. On the interface between the water and the solid scatterer, the boundary condition is satisfied by introducing two compliance coefficients which are the averages of compressive compliance and shear compliance of the two media, respectively. Shear compliance is set to infinity both in the water and on the boundary. Thus the FDTD iteration can be done in a unified manner in both media as well as on the boundary. Numerical results for sound fields around and inside an aluminum bar submerged in sea water andinsonified by a plane wave are presented. [Work supported by NNSFC.]

2a TUE. AM

TUESDAY MORNING, 13 OCTOBER 1998

HAMPTON ROADS BALLROOM 1, 8:30 TO 11:25 A.M.

### Session 2aSA

## Structural Acoustics and Vibration: Interior Cabin Noise I

Scott D. Sommerfeldt, Cochair

*Brigham Young University, Department of Physics and Astronomy, P.O. Box 24673, Provo, Utah 84602-4673*

Earl G. Williams, Cochair

*Code 7137, Naval Research Laboratory, Washington, DC 20375*

### Invited Papers

8:30

**2aSA1. Developments in aircraft interior acoustics—Recent progress and directions.** Richard J. Silcox (NASA Langley Res. Ctr., Structural Acoust. Branch, M.S. 463, Hampton, VA 23681-2199)

Aircraft interior noise is a continuing problem for a wide range of aircraft types. High interior noise levels in general aviation aircraft make any communication difficult, significantly impact pilot endurance, and are considered important to the reemergence of this class of aircraft. For passengers in propeller-powered commuter aircraft, conversation is difficult at best and becomes oppressive on the passengers for long periods. It is also regarded as one reason for the replacement of propeller commuter aircraft by the emerging regional jet. In business jets, the passengers are often interested in conducting meetings during flights. This calls for low SPL and SIL for which the aircraft incurs both space and weight penalties. Large commercial aircraft pay a significant weight penalty for current interior noise levels considered acceptable. With the drive for more weight-efficient airframes, the challenge becomes even

more difficult. This paper will overview current efforts to develop both design and noise control techniques. These range from improvements in the quantification of the noise sources, to considerations in the overall structural design, and to the use of both active and passive control tools. In addition, the emerging use of predictive and measurement tools will be discussed and applications to aircraft highlighted.

8:55

**2aSA2. Structural acoustics and active constrained layer damping (ACL D) of an aircraft fuselage section.** Peter C. Herdic<sup>a)</sup> (Naval Res. Lab., Code 7136, Washington, DC 20375), Amr M. Baz (Univ. of Maryland, College Park, MD), Brian H. Houston, and Martin H. Marcus (Naval Res. Lab, Washington, DC)

Active structural acoustic control of an aircraft fuselage section is demonstrated using active constrained layer damping (ACL D), where both interior acoustic levels and surface vibrations are reduced. The uncontrolled response of the fuselage is evaluated under several different physical forcing functions by performing dense spatially sampled broadband (10–1000 Hz) measurements of surface velocity and interior pressure. One of these forcing functions is a point force applied to the stiffener skeletal structure. This response reveals rich structural acoustics, exciting broad wave numbers and local resonances, both of which excite the interior acoustics. This case is further investigated using a finite/infinite element model of the fuselage section and the interior/exterior fluid. Twelve ACL D patches are strategically positioned on the fuselage to target control of the offending modes. Each patch is constructed of a passive viscoelastic layer and an active piezo film; these patches are lightweight and inexpensive, which makes this technique practical in-flight and attractive to commercial industry. Good performance is achieved under a point force disturbance using simple minimization control laws. Reported are the structural acoustics that are observed from these high spatially sampled measurements along with the results of the control experiments. <sup>a)</sup>Also with SFA, Inc., Landover, MD.

9:20

**2aSA3. Turbulent boundary layer noise transmission into an aircraft fuselage—Modeling and analysis.** Gopal P. Mathur and Cliff L. Chin (The Boeing Co., 2401 E. Wardlow Rd., MC 078-0420, Long Beach, CA 90807-4418)

The turbulent boundary layer (TBL) pressure fluctuations on the exterior of an aircraft excite the fuselage structure which in turn radiates noise inside the passenger cabin. In most of the previous analytical and experimental studies of sound transmission loss of structures, only acoustic excitation is considered. It is then assumed that the transmission loss of a structure due to the TBL pressure field will be the same as that for the acoustic field. The main objective of this paper is to examine the effects of the TBL pressure field on the transmission loss of a fuselage structure and compare it with the acoustic transmission loss. The vibration and acoustic response of a circular cylindrical shell due to the TBL excitation is first modeled with a finite-element-based computational approach. The finite-element model of the cylindrical shell panel is validated with the results from classical analytical model. The vibration and acoustic response of an aircraft fuselage due to the TBL pressure field is then calculated using the finite-element model. The incident TBL pressure field is simulated by a cross-spectral formulation of the excitation field. The noise reduction characteristics of the fuselage due to acoustic and TBL pressure fields are compared.

9:45

**2aSA4. Narrow-band and broadband active control in an enclosure using energy density sensors.** John W. Parkins, Jiri Tichy (Penn State Univ., Grad. Prog. in Acoust., Appl. Sci. Bldg., N. Atherton St., State College, PA 16804, jwp6@psu.edu), and Scott D. Sommerfeldt (Brigham Young Univ., Provo, UT 84602)

An active control system has been constructed based on the minimization of the energy density at discrete points within an enclosure. Though most control systems for use in enclosures are based on squared pressure as a cost function, a system based on energy density is more capable of sensing modes contributing to the acoustic field. The enclosure used is lightly damped and measures 1.5×2.4×1.9 m. A measurement system within the enclosure is capable of spatially sampling the pressure field and decomposing the field into complex modal amplitudes, which yield insight into the control phenomena. The control system can use squared pressure as well as energy density as a cost function for comparisons of the two methods. The squared pressure and energy density control are consistent with predictions of active control performance in the case of single-frequency multiple sensor/source configurations. Global control of up to 18 dB is achieved. Broadband control results using a single sensor and control source are also presented.

10:10–10:25 Break

### *Contributed Papers*

10:25

**2aSA5. SEA modeling and analysis of stowage bin noise isolation and reduction.** Jianyong Li and Paul Serati (Boeing Commercial Airplane Group, P.O. Box 3707, M.S. 04-AP, Seattle, WA 98124-2207)

The statistical energy analysis method is applied to the noise prediction and analysis of large passenger airplane stowage bin isolation. The purpose is to reduce the cabin noise generated from the external turbulent boundary layer and transmitted from the stowage bins via their supports. AutoSEATM is adopted for the modeling and analysis of the coupled structural-acoustic problem where the connection between the structural

fuselage and the stowage bins is represented and implemented by a coupling loss factor (CLF). A significant amount of noise level reduction can be achieved by using elastomeric rod ends to replace the metallic rigid connection between the structural fuselage and the stowage bins. It is also possible to obtain a significant amount of weight reduction using the stowage bin isolators instead of the blanket applied to the cabin crown. Some analysis results have shown good agreement with flight test data. This modeling and analysis provides an effective way of reducing cabin noise for large commercial airplanes without any weight penalty. Economic gains will be obtained from both noise reduction and weight saving. [Support for this effort from B. Cimerman of Vibro-Acoustics Sciences, Inc. and Evan B. Davis of Boeing is gratefully acknowledged.]

10:40

**2aSA6. An equivalent source technique for calculating the sound in enclosures.** Marty E. Johnson (Vib. and Acoust. Labs, Virginia Tech., VA 24061-0238), Stephen J. Elliott, Kwang-Hyun Baek, and Juan Garcia-Bonito (Inst. of Sound and Vib. Res., Virginia Tech., VA 24061-0238)

The equivalent source method has previously been used to calculate the exterior sound field radiated or scattered from bodies in the free-field. In this work the method is used to calculate the internal pressure field for an enclosure which can have arbitrary boundary conditions and may include internal scattering objects. The normal velocity on the surfaces of the scattering objects and the enclosure walls is evaluated at a larger number of positions than there are equivalent sources. The sum of the squared difference between this velocity and that expected because of the admittance of the boundary is minimized by adjusting the strengths of the equivalent sources. Example results are presented for the sound field and frequency response inside a damped rectangular enclosure, which compare very well with the conventional modal model. The effect of having rigid spheres inside the enclosure are then investigated, and it is found that the effect is significant even some distance from the spheres and at frequencies for which the size of the sphere is small compared to a wavelength. Finally, the effect of a nonlocally reacting boundary condition is illustrated by assuming that one of the walls of the enclosure is an elastic plate. [Work conducted at the ISVR.]

10:55

**2aSA7. Comparison of the acoustic finite element method and the acoustic boundary element method for interior noise prediction.** Shung H. Sung and Donald J. Nefske (Body Eng. & Integration Dept., General Motors Res. & Development Ctr., Warren, MI 48090-9055)

Comparisons are made of the acoustic finite element method versus the acoustic boundary element method for predicting interior noise in an enclosure. The theoretical formulation of both methods is summarized, and applications are presented of the interior noise prediction in a rectangular

box and in the passenger compartment of an automotive vehicle. The accuracy of the predicted results and the computational performance of the acoustic finite element method versus the acoustic boundary element method are compared. The relative advantages and disadvantages of each method are discussed.

11:10

**2aSA8. Supersonic boundary layer pressure fluctuation and interior noise measurements on the Tupolev 144LL.** Stephen A. Rizzi (Structural Acoust. Branch, NASA Langley Res. Ctr., Hampton, VA 23681-0001, s.a.rizzi@larc.nasa.gov) and Robert G. Rackl (The Boeing Co., Seattle, WA 98124)

A series of six flights were conducted on the Tupolev Tu-144LL "Flying Laboratory" between September 1997 and January 1998 to acquire data for the improvement of a supersonic turbulent boundary layer pressure fluctuation model and near-field jet noise source model, development of an inlet noise source model, and validation of a turbulent boundary layer/structural interaction model. The data set consists of boundary layer pressure fluctuations measured at 25 locations along the length of the fuselage, fuselage sidewall accelerations measured at six locations in the vicinity of the pressure fluctuation measurements, and interior noise measurements at eight locations in the passenger cabin. A total of 17 different conditions were studied over a speed range of 520 km/h to Mach 2.05 and altitude range of 4–17.3 km. The effect of Mach number, boundary layer thickness and air density on the boundary layer pressure autospectra are presented. Boundary layer pressure autospectra are compared with several empirically based models. Coherence between boundary layer pressures and fuselage sidewall vibrations, and fuselage sidewall vibrations and interior noise measurements are also presented.

2a TUE. AM

TUESDAY MORNING, 13 OCTOBER 1998

HAMPTON ROADS BALLROOM 3, 9:00 TO 11:45 A.M.

### Session 2aSC

## Speech Communication: Phonetics, Phonology and Word Perception

Paul A. Luce, Chair

*Department of Psychology, University at Buffalo, 365 Park Hall, Buffalo, New York 14260-4110*

### Contributed Papers

9:00

**2aSC1. Connecting phonetics and phonology: Evidence from Western Arrernte.** Victoria Anderson (Phonet. Lab, 2101 Campbell Hall, Dept. of Linguist., Univ. of California, 405 Hilgard Ave., Los Angeles, CA 90024, victoria@humnet.ucla.edu)

This study investigates two aspects of the relationship between phonetics and phonology. The first section looks for evidence of the influence of phonological patterns on phonetic implementation: specifically, do the number of phonological contrasts along a given phonetic continuum affect the articulatory detail of those contrasts? The second section looks for evidence of the influence of phonetic properties of segments on phonological patterns: in particular, do perceptual characteristics of segments determine distributions of contrasts? To address the two questions in focus here, instrumental articulatory, acoustic, and perceptual evidence was collected from Western Arrernte, a language of Central Australia which provides good test cases for these issues. Results do not indicate evidence for effects of phonological patterns on phonetic implementation, but show

evidence for effects of phonetic characteristics on phonological structure. [This investigation was supported by grants from the National Science Foundation and the Aboriginal and Torres Strait Islander Language Initiatives Program (Australia).]

9:15

**2aSC2. Perception/production asymmetries in the acquisition of phonological categories.** Rachel Hemphill (Dept. of Linguist., Univ. of Chicago, 1010 E. 59th St., Chicago, IL 60637, r-hemphill@uchicago.edu)

One assumption that has driven the development of phonological models is the idea that a single underlying representation (UR) exists in the mind such that talkers draw on it in both producing and perceiving speech. Data from a wide range of linguistic research suggest mismatches in phonetic and phonological abilities between perception and production which would be incompatible with the single UR model. The research reported here was specifically designed to test whether changes in perceptual categorization behavior would influence speech production abilities in a man-

ner consistent with a single UR. Twenty native speakers of English were taught to categorically perceive a three way voicing contrast in synthetic bilabial stop consonants which varied only in VOT [after Pisoni, Alsin, Perey, and Hennessey, JEP: HPP 8(2), 297–314 (1982)]. Perception and production tests were administered following training. Subjects showed the ability, which improved with training, to categorically identify the three-way voicing contrast. Subsequent acoustic and perceptual analyses showed that they were unable to produce the contrast correctly, producing no difference, or manipulating acoustic variables other than VOT (vowel duration, vowel quality, nasalization). These results are explained in terms of separate expressive and receptive representations and the implications for perception/production mappings discussed.

9:30

**2aSC3. Effects of probabilistic phonotactics on the recognition of words in continuous speech.** Daniel E. Gaygen and Paul A. Luce (Dept. of Psych., Univ. at Buffalo, Buffalo, NY 14260, dan@deuro.fss.buffalo.edu)

No invariant or highly probable cue to the borders of words exists in continuous speech. Thus recognizing individual words in speech is not a trivial task. The current study investigates the role of probabilistic phonotactics as a possible source of word border information. Specifically, the trough hypothesis is tested. According to the trough hypothesis, biphones spanning the borders of words should provide cues to those borders if the intraword co-occurrence probability of the biphones is near zero. Lexical decision and word spotting experiments provide evidence for the trough hypothesis only for the beginnings of words. [This research was supported (in part) by research Grant No. 1 R01 DC 0265801-A1 from the National Institute on Deafness and Other Communication Disorders, National Institutes of Health.]

9:45

**2aSC4. Attentional effects of variability in phonetic context.** Howard C. Nusbaum (Dept. of Psych., The Univ. of Chicago, Chicago, IL 60637) and Alexander L. Francis (The Univ. of Chicago, Chicago, IL 60637)

Understanding how listeners cope with variability in the acoustic patterns of phonetic categories is a basic theoretical problem. Our previous research has suggested that talker and speaking rate variation slows phoneme recognition and increases cognitive load whereas amplitude variation does not. The present study examines the effect of varying phonetic context. Previous research has shown that varying phonetic context slows phoneme recognition. Using the same method as in our previous studies, we also found recognition slows when there is variation in phonetic context. In a second study, cognitive load was manipulated using a number recall task with lists varying in length. Consonant recognition performance was measured with a constant vowel context and when vowel context varied. Both conditions were tested with a low cognitive load and a high cognitive load. Our previous experiments demonstrated that talker and rate variability interact with cognitive load to slow phonetic recognition. The results of the present study will be compared with the results of prior work on talker and rate variability. The implications of these findings for the role of attention in theories of speech perception will be discussed.

10:00

**2aSC5. Effects of vowel deletion on lexical access.** Paul C. LoCasto and Cynthia M. Connine (Dept. of Psych., State Univ. of New York, Binghamton, NY)

Vowel elision is a common phonological process whereby an unstressed /ə/ (schwa) vowel is deleted during pronunciation. In three syllable words, the deleted /ə/ occurs in the medial posttonic position (different /dlfr schwant/ → [dlfr schwant]). In two syllable words, the deleted /ə/ occurs in the first syllable (police /polis/ → [plis]). These elided versions (reduced form) are commonly accepted as alternatives to canonical (full form) pronunciations. Two auditory form priming experiments used vowel elision to investigate the effects of phonological variability on lexical access. Subjects were asked to make a lexical decision to either the full

(canonical) or reduced (elided) version of a target word after being primed by either the full or reduced form of the same word or an unrelated control. For both experiments, the results showed that the reduced version was a less effective prime than the full version. Accuracy rates indicated that the two syllable reduced versions were less acceptable variants. The results suggest an asymmetry in the effects of vowel elision in speech recognition and are discussed in terms of similarity mapping and representation of lexical form.

10:15–10:30 Break

10:30

**2aSC6. The emergence of word representation independent of context.** Rory DePaolis (James Madison Univ., Dept. of Commun. Sci. and Disord., Harrisonburg, VA 22807), Marilyn Vihman, and Debbie Morye (Univ. of Wales, Bangor, Gwynedd LL57 2DG, UK)

Eleven-month-old French-learning infants prefer to listen to familiar over unfamiliar words (presented auditorily and independent of context), suggesting that there is a stable (although not necessarily complete) internal representation of word forms by this age [P. A. Halle and B. de Boysson-Bardies, IBAD 17, 463–481 (1994)]. The current study explored word representation by infants learning British English. Infants at 9 and 11 months of age were tested using the headturn preference paradigm as modified by Halle and Boysson-Bardies. Phonetically and phonotactically similar lists of familiar and unfamiliar disyllabic words and phrases were developed and matched for *F0*, amplitude and duration. The lists contained iambic and trochaic patterns in proportions typical for English. While initial results (based on looking times) suggest that the 11-month-old British infants, like the French, preferred the familiar over the unfamiliar list, 9-month-old infants showed no significant preference for either list. The individual infant results suggest that stable representation of word forms begins to emerge at 11 months, mirroring other cognitive advances at this time (e.g., object permanence, problem solving, language specific phonetic attunement). [Work supported by the ESRC.]

10:45

**2aSC7. Phonotactics, phonological neighborhoods, and working memory in spoken word recognition.** M. S. Vitevich (Speech Res. Lab., Dept. of Psych., Univ. of Indiana, Bloomington, IN 47405-1301) and Paul A. Luce (SUNY, Buffalo, NY 14260)

Spoken word recognition has often been described as a competitive process among activated words in memory. Work in this area has demonstrated that words with many similar sounding words (i.e., dense neighborhoods) are recognized more slowly and less accurately than words with few similar sounding words (i.e., sparse neighborhoods). Evidence will be presented from several experiments that suggests that activation at a sublexical level may also play a prominent role in the recognition process. In particular, it is demonstrated that lexical and sublexical activation in spoken word recognition has demonstrably different effects on processing. In particular, it is demonstrated that, when processed at a sublexical level, nonwords composed of phonological segments with high-probability phonotactic patterns are responded to more quickly and accurately than nonwords composed of phonological segments with low-probability phonotactic patterns. However, when processed primarily at the lexical level, nonwords behave much like real words. That is, nonwords having high probability phonotactic sequences and dense neighborhoods are processed more slowly and less accurately than those with low probability phonotactic sequences and sparse neighborhoods. It is also proposed that the differential effects of these two levels of processing may be mediated by short-term verbal memory.

11:00

**2aSC8. Effects of mismatches in talker and emotion on speech perception.** John W. Mullennix, Kelly Mateljan, and Danielle Payne (Dept. of Psych., Univ. of Pittsburgh, Johnstown, PA 15904)

The effects of within-trial mismatches of talker voice and emotional tone of speech on speech perception were examined. Pairs of speech stimuli that matched/mismatched in talker voice and emotional tone of speech were presented to listeners via an AX discrimination paradigm. Results indicated that mismatches in both talker voice and emotional tone produce perceptual interference. However, the interference produced by emotional tone variability was greater under single-talker conditions. The results are discussed within a hierarchical scheme of allocating processing resources to various attributes of the speech signal.

11:15

**2aSC9. The effect of consonant context on vowel goodness rating.** Alice Faber (Haskins Labs., 270 Crown St., New Haven, CT 06511) and Julie M. Brown (Univ. of Connecticut, Storrs, CT 06269)

The effect on within-category discrimination of supposed phonetic prototypes for the sounds of a given language depends on the assumption that the number of prototypes used by speakers of that language is of the same order of magnitude as the number of phonemes in that language. In the present experiment, listeners provided goodness ratings for three sets of synthetic tokens varying in *F2* and *F3*. One set consisted of isolated /i/ tokens while the other two contained appropriate transitions and release bursts for BEEP and GEEK, respectively. Goodness ratings depended not only on a token's position in the grid but also on its phonetic context (zero vs b\_p vs g\_k), reflecting the well-known coarticulatory effects of consonant context on vowel production. The listener judgments thus reflect

the relative appropriateness of a given set of formant values for a consonantal context and not an abstract phonological target underlying all three contexts. [Work supported by NIH Grant No. HD-01994.]

11:30

**2aSC10. Spectral contrast in perception of VCV syllables.** Lori L. Holt (Dept. of Psych., Univ. of Wisconsin, 1202 W. Johnson St., Madison, WI 53706), Andrew J. Lotto (Loyola Univ., 6525 N. Sheridan Rd., Chicago, IL 60625), and Keith R. Kluender (Univ. of Wisconsin, Madison, WI 53706)

The ability of listeners to recover speech information, despite dramatic articulatory and acoustic assimilation between phonetic units, is central to understanding perception of fluent speech. The present studies investigate the effect of preceding acoustic stimuli on identification of a series of synthetic CVs varying acoustically in *F2* onset frequency and perceptually from /ba-da/. Results reveal that naturally produced /i/ and /u/ modulate identification responses to the CV series independent of speaker, suggesting that the effect of preceding V on CV identification is not critically dependent on precise matching of articulatory characteristics between V and CV. Moreover, nonspeech FM glides modeling *F2* transitions of natural Vs shift CV identification in a similar manner, suggesting that quite general auditory mechanisms may contribute to observed shifts in CV identification. Further experiments reveal the effect of preceding V maintains for dichotic presentation and persists, but lessens, with intersyllabic silent intervals increasing to 200 ms. All results can be recast as cases of spectral contrast whereby spectral characteristics of preceding sound modulate perception of CV. These data suggest general auditory processes may play a substantive role in perceptual accommodation of coarticulated speech and provide clues to the nature of the putative auditory mechanisms. [Work supported by NSF.]

2a TUE. AM

TUESDAY MORNING, 13 OCTOBER 1998

HAMPTON ROADS BALLROOM 2, 9:00 A.M. TO 12:00 NOON

**Session 2aSP**

**Signal Processing in Acoustics: Time-Frequency Techniques in Acoustic Applications II**

Edmund J. Sullivan, Chair

*Code 103, Naval Undersea Warfare Center, Newport, Rhode Island 02841*

***Invited Papers***

9:00

**2aSP1. Application of time-frequency techniques to detection of minelike objects in side scan sonar images.** John Impagliazzo and Walter Greene (Naval Undersea Warfare Ctr., Code 8212, Bldg. 679, Newport, RI 02841)

Wavelet analysis techniques were applied to side scan sonar images for the detection of minelike objects. A subwindow of sample images were scanned and compressed using a best level orthogonal wavelet basis. The compressed images were then projected onto a dictionary of target and nontarget examples in wavelet space, using the matching pursuit algorithm of Mallat and Zhang to find the most likely match. With the best level basis, however, signal representations are dependent on their location in space. Because of this, shifted versions of the target examples were included in the dictionary to improve the likelihood of a good numerical match. Shift-invariant wavelet techniques, which provide for target translation while maintaining the same numerical descriptors, were also studied with classifier performance and computational complexity being evaluated. This allowed best bases representations to be applied in the classification algorithm. The overall detection performance was further refined by use of a neural network operating on the set of possible mine detections, which had originated from the matching pursuit classifier.



9:20

**2aSP2. Angle-frequency spectra for broadband pulses.** David Chambers and D. Kent Lewis (Lawrence Livermore Natl. Lab., P.O. Box 808, L-372, Livermore, CA 94551, chambers2@llnl.gov)

Broadband pulses representing localized waves are emitted from an array. A receiver is scanned in angle at a constant distance from the array. The power spectra of the data are displayed as an image with frequency along one dimension and angle along the other. The resulting angle–frequency images are compared with simulations of the array performance. The images show at a glance the changing frequency content of the signal as the angle changes. This method of displaying broadband data greatly assists interpretation of the total beam pattern.

9:40

**2aSP3. Parametric time-frequency estimation of prosthetic heart valve sounds.** D. E. Perkins, G. H. Thomas, and G. A. Clark (Univ. of California, Lawrence Livermore Natl. Lab., P.O. Box 808, Livermore, CA 94551)

Prosthetic heart valves have been responsible for extending the life spans and improving the quality of life of many people with serious heart conditions. Even though the heart valves are extremely reliable, eventually they are susceptible to the long-term fatigue and structural failure effects expected for mechanical devices operating over long periods of time. In this paper the application of parametric time-frequency estimation techniques to acoustic measurement of prosthetic heart valve under test in an anechoic tank is described. The analysis reveals interesting signatures when comparing fractured to normal valve sounds. The emphasis is on the application of recursive parametric techniques to “track” changes in the propagating sounds as it is captured by an omnidirectional hydrophone.

10:00

**2aSP4. Maximum entropy time-frequency analysis.** Patrick J. Loughlin and Berkant Tacer (Dept. of Elec. Eng., Univ. of Pittsburgh, 348 Benedum Hall, Pittsburgh, PA 15261, pat@ee.pitt.edu)

A maximum entropy method for constructing a joint time-frequency density of a signal is presented. The method constructs the density from a set of joint time-frequency moments that are functions of the signal and spectral amplitudes and phases. As such, the moments can be obtained *a priori* from the signal, independent of the density. Unlike the Wigner and other quadratic time-frequency distributions, the maximum entropy density is non-negative and unhindered by cross terms. Also, unlike the spectrogram, it is not limited by a resolution trade-off between time and frequency. Examples are given to demonstrate the method, including maximum entropy densities of speech, bat sonar and acoustic scattering signals. [Supported by ONR.]

10:20

**2aSP5. Acoustic and EM waves for speech processing.** John F. Holzrichter, Greg C. Burnett, Todd A. Gable, and Ng C. Lawrence (Lawrence Livermore Natl. Lab., P.O. Box 808, L-3, Livermore, CA 94550)

The use of low power EM sensors [Holzrichter, Burnett, Ng, and Lea, *J. Acoust. Soc. Am.* **103**, 62 (1998)] enable the determination of several articulator boundary motions, simultaneously—e.g., glottis, jaw, tongue, palate, lips, etc.—leading to new speech processing algorithms. By comparing EM sensor methods of pitch detection to established cepstral and autocorrelation techniques, a tenfold increase in pitch accuracy, a 100-fold reduction in processing time, and robust performance in the presence of high background acoustic noise are obtained. Investigations of the details of the EM sensor signal from the human glottal region indicate that it can be used to provide information on the instant excitation function of voiced speech. Using the ARMA approach, the excitation information is removed from the acoustic signal, yielding well-defined transfer functions, formant locations, and pitch normalized data. In addition, using the glottal timing information, pitch synchronous processing has been employed using ARMA, LPC, Cepstral, and other approximation techniques. The excitation function and the corresponding filter coefficients for each speech unit (e.g., the *a*'s and *b*'s from the ARMA approximation) enable one to reconstruct good quality personalized speech, without the need for residual information.

10:40–10:50 Break

10:50

**2aSP6. Application of wavelet transforms to detection, estimation, modeling, and remote sensing in underwater acoustics.** Leon H. Sibul and Michael J. Roan (Appl. Res. Lab., Penn State Univ., P.O. Box 30, University Park, PA 16804)

It follows from fundamental acoustics that acoustic waves that have been reflected from boundaries or scatterers that are in relative motion in respect to the transmitter/receiver suffer propagation delays and time-scale dilations. Physical and kinematic parameters of distributed, moving scatterers can be estimated using continuous wavelet transforms. For this reason and for the reason that wavelet transform techniques lead to effective modeling of time and space varying media by wideband spreading and scattering functions, continuous wavelet transforms are natural tools for detection and estimation of wideband acoustic signals that have propagated through complex multipath propagation and scattering channels. Wideband spreading functions and scattering functions can be used in model-based environmentally adaptive signal processors. In remote sensing, wavelet transforms are effective for identification, parameter estimation, tracking, and synthesis of distributed acoustic scatterers. Other applications of continuous wavelet transforms include implementation of log-likelihood detectors of distributed scatterers by wideband acoustic signals and acoustic imaging of underwater objects. [This work was supported by The Office of Naval Research, sponsored by Dr. Kam W. Ng, Code ONR 333.]

**2aSP7. Time-frequency analysis of low diffraction beam pulses.** D. Kent Lewis, David H. Chambers (Lawrence Livermore Natl. Lab., 7000 East Ave., M.S. L-372, Livermore, CA 94550), Richard W. Ziolkowski (Univ. of Arizona, Tucson, AZ 95721), Terry L. Henderson, and Ken Krueger (Univ. of Texas, Austin, TX 78713)

Recent work in low diffraction beams has given our group some new sets of wave fields to investigate. Theoretical predictions matched experimental measurements closely, and several comparison techniques were included in the analysis. The field experiments have now been conducted at the NUWC Keyport facility and, most recently, at the University of Texas' Applied Research Laboratory facility in Lake Travis. In cooperation with ARL, a series of low diffraction beam pulses was launched to a wide band width receiver 600 feet distant. Among the comparison methods used was a time-frequency analysis of the received pulse. For each angular position the frequency arrival times via time-frequency analysis are investigated. It is hoped this analysis will shed light on this very interesting phenomena.

### Contributed Papers

11:30

**2aSP8. Time-frequency coding of the line spectrum frequencies.** Davor Petrinovic (Faculty of Elec. Eng. and Computer Sci., Univ. of Zagreb, Unska 3, HR-10000 Zagreb, Croatia, davor.petrinovic@fer.hr)

Line spectrum frequencies (LSF) are one of the most popular representations of the short-time spectrum envelope in speech coding applications. LSF of adjacent speech frames are usually highly correlated, so the bit-rate for spectral envelope coding can be reduced by interframe coding. Several coding methods, such as switched-adaptive interframe vector prediction, vector predictive quantization, segment quantization, and matrix quantization exploit the interframe redundancy. A new method of low bit-rate interframe LSF coding based on the discrete wavelet transform is proposed in this paper. Prior to coding, each of the line spectrum frequencies is transformed to wavelet domain by treating it as a time-varying waveform. By choosing the appropriate mother-wavelet, the higher level approximation coefficient of the wavelet decomposition (residual signal) comprises most of the LSF waveform energy. Since these coefficients, which carry most of the LSF information, are time decimated by a factor of 2 to power of decomposition level, significant bit reduction in coding can be obtained. Several wavelets were investigated, identifying the one with the best energy concentration. Spectral distortion caused by neglecting all of the detail coefficients was also calculated as a function of wavelet type and decomposition level.

11:45

**2aSP9. Space-time signal processing algorithms for a stochastic signal under conditions of 3D antenna motion.** Igor I. Gorban and Sergey P. Volkovetsky (Inst. of Math. Machines and Systems, 42 Ave. Acad. Glushkov, Kiev, Ukraine, 252187, gorban@immsp.kiev.ua)

The paper continues the cycle of earlier works connected with space-time signal processing (STSP) under conditions of a moving antenna [I. I. Gorban, "Optimum space-time signal processing of stochastic signal under conditions of a moving antenna," *Telecommun. Radio Eng.* No. 12, 26–28 (1991); "Estimation of signal parameters when antenna is complicatedly moving in space," *Forum Acusticum*, Antwerp, Belgium, 222 (1996); "Space-time signal processing algorithms for moving antennae," *J. Acoust. Soc. Am.* **100**, 2638 (1996); and others]. It is assumed that the antenna moves in three dimensions with angle rotations around the space axes, the signal is stochastic type with discrete spectrum components, the noise is Gaussian. A maximum likelihood algorithm is developed and a common estimate of space-time signal parameters is researched. It was found that the common estimate of angle and spectrum parameters depends on the level of discrete spectrum components: the estimate becomes worse with decreasing this level. Parameters of antenna motion are essentially influent on the common estimate too. Rising of the constant velocity of the motion leads to decreasing of the common estimate and rising of the variable components of the motion leads to increasing it.

TUESDAY MORNING, 13 OCTOBER 1998

MARRIOTT BALLROOMS 5 AND 6, 9:00 TO 11:20 A.M.

### Session 2aUW

## Underwater Acoustics: Detection and Imaging of Buried Objects I

Nicholas P. Chotiros, Chair

*Applied Research Laboratories, University of Texas, P.O. Box 8029, Austin, Texas 78713-8029*

**Chair's Introduction—9:00**

### Invited Papers

9:05

**2aUW1. Sonar detection and classification of buried targets using broadband dolphin-like signals.** Whitlow W. L. Au (Hawaii Inst. of Marine Biol., P.O. Box 1106, Kailua, HI 96734), Reid H. Shizumura (Orincon Corp., Kailua, HI 96734), Paul E. Nachtigall (Hawaii Inst. of Marine Biol., Kailua, HI), Jerry Moons (Orincon Corp., Kailua, HI), Herbert L. Roitblat (Univ. of Hawaii, Honolulu, HI), and Robert C. Hicks (Orincon Corp., Kailua, HI)

Dolphins have been observed foraging for prey that bury themselves into a sandy bottom. The dolphins swim about 1 to 2 m above the bottom and scan in a circular motion or swim immediately off the bottom, scanning from side to side with their beams pointed approximately normal to the bottom. The dolphin has been emulated by using dolphinlike sonar signals (120-kHz peak frequency, 39-kHz bandwidth, 50- $\mu$ s duration) in order to classify proud and buried targets in real time. The transducer was attached to a bottom-crawling remotely operated vehicle. Target echoes were received via a cable and digitized at 1 MHz. Short-time Fourier

transform and the Morlet wavelet were used to obtain time-frequency representations of the echoes. Echoes were processed in a hierarchical neural network system to perform target classifications. Six targets (cast iron pot, stainless steel sphere, glass jar, concrete tile, and coral rock) were placed either on the ocean bottom or buried into the bottom. Echoes were separated into three target categories: (1) cast iron pot; (2) stainless steel sphere; and (3) remaining four objects. The neural network was able to correctly identify 74%, 97%, and 88% of the category 1, 2, and 3 test echoes.

9:30

**2aUW2. Acoustic propagation across a roughened fluid-fluid interface II.** Joseph L. Lopes, Iris C. Paustian, and Raymond Lim (Coastal Systems Station, NSW Dahlgren Div., Codes R21 and R22, 6703 West Hwy. 98, Panama City, FL 32407-7001)

New data from a laboratory experiment described at a previous meeting of the ASA [J. Acoust. Soc. Am. **102**, 3216 (1997)] are presented. Surface roughness effects on transmission of sound into ocean sediments are studied using a tank containing two immiscible fluids (vegetable oil over glycerin) with polystyrene beads floated at the interface. This allows roughness induced transmission effects to be modeled without interference from effects caused by other sediment properties (e.g., poroelasticity, shear rigidity, etc.). Data analyses indicate significant penetration of acoustic energy at grazing angles below critical as predicted by researchers at APL-UW [e.g., K. L. Williams and D. R. Jackson, J. Acoust. Soc. Am. **100**, 2702 (1996)]. When the data is ensemble averaged over bead distribution and analyzed with incoherent processing methods, this energy is observed to propagate down with an apparent speed about 20% slower than the sound speed of glycerin and at angles about 20°–40° from the interface. However, without ensemble averaging (i.e., pings acquired with a static bead distribution) no consistent propagation angle or speed results, whether using coherent or incoherent processing methods. These results agree qualitatively with simple computer simulations. [Work supported by ONR.]

9:55

**2aUW3. The Helmholtz–Kirchhoff approach to modeling penetration of acoustic waves into rough seabeds.** Eric Pouliquen, Anthony P. Lyons, and Nicholas G. Pace (Saclant Undersea Res. Ctr., Viale S. Bartolomeo, 400 I-19138 La Spezia, Italy)

The Helmholtz–Kirchhoff integral is applied to model the penetration of sound waves into sandy seafloors at grazing angles above and below the critical angle. Although the conditions for the validity of the Kirchhoff approximation can be limiting, this approximation should be valid at high frequency for gently undulating seafloor surfaces even at moderate to low grazing angles, providing that the self-shadowing effect is carefully removed. The analytical development of the method is first presented, followed by numerical examples and comparisons with the experimental data of Maguer *et al.* [SACLANTCEN report, SR-287, April 1998]. The model predicts, in agreement with the 2- to 15-kHz acoustic data, the frequency where the contributions due to roughness effects begin to dominate those due to the evanescent wave. Secondary effects such as Bragg interference patterns and the loss of signal coherence with grazing angle or depth are correctly predicted. The model simulations strongly suggest that roughness of the sediment interface is most likely the cause of anomalous sound penetration into the seabed.

10:20–10:35 Break

### Contributed Papers

10:35

**2aUW4. High-frequency acoustic waves reflection on seafloor.** Claire Drevet (Gesma, BP 42, 29240 Brest Naval, France), Jean-Pierre Sessarego (Lma, 31 Chemin Joseph Aiguier, 13402 Marseille Cedex 20, France), and Marc Brussieux (Gesma, BP 42, 29240 Brest Naval, France)

The purpose of this research is to study the acoustic waves reflection on seafloor in very shallow water in the frequency range 200–700 kHz. Effectively previous operations of detection of proud objects using sonar imagery showed problems in this environmental context caused by a superficially modified sediment structure and an insonification closed to “critical angle.” A study has been done with experimental data collected in a tank (at scale “one”) on calibrated sand. This approach eases control of a lot of acoustical and geophysical parameters. Mono- and bistatic scattering measurements are recorded. Temporal broadband signals are analyzed by Fourier transforms. Results are compared with various theories. It especially emphasizes the Biot propagation model and a composite roughness model. The input sediment structure parameters are debated with discussion about their influence on seafloor reflection. Concerning the nontotal internal reflection below critical angle, the debate is not yet closed and expected additional data experiments on acoustic wave field inside the sediment itself would allow us to understand the mechanism of acoustic waves propagation in very shallow water and extract better models fitting experimental results.

10:50

**2aUW5. Studies on the conversion of near-grazing underwater ultrasonic waves in a sandy seafloor.** Jacques R. Chamuel (Sonoquest Adv. Ultrason. Res., P.O. Box 81153, Wellesley Hills, MA 02181-0001)

Ultrasonic modeling results are presented supporting the hypothesis given by the author [J. R. Chamuel, IEEE Trans. Ultrason. Ferroelectr. Freq. Control, submitted Letter 10 April 1998] explaining the anomalous ultrasonic slow wave observed in water-saturated sand [N. P. Chotiros, J. Acoust. Soc. Am. **97**, 199–214 (1995)] using a layered elastic model. The rapid increase of the shear wave velocity of sand with depth causes the conversion of near-grazing underwater acoustic waves into multiple coupled shear and compressional waves. Physical insight into the physical mechanisms is obtained from the refraction/conversion of broadband transient shear and compressional waves penetrating a layered solid with a low shear wave velocity. Polycarbonate/Plexiglas and wax/polycarbonate layered models were utilized. PP, PS, SP, and SS wave components were detected in the lower solid simulating the multiple features present in the anomalous acoustic sand data. In the effectively layered water/sand model, an underwater acoustic wave incident beyond the compressional wave critical angle is partially converted into a shear wave in the sand which is reconverted into a compressional wave appearing as an anomalous slow wave when detected by a buried receiver. [Work supported by ONR.]

11:05

**2aUW6. Ultrasonic velocity and attenuation in models of dry and wet sands with an embedded object.** Hasson M. Tavossi and Bernhard R. Tittmann (Dept. of Eng. Sci. and Mech., Penn State Univ., University Park, PA 16802-1401)

Propagation of ultrasound in wet and dry sand, up to 6 in. in depth, is investigated. Velocity and attenuation, as a function of mean grain size, water content, and depth, are measured. The results can be used in the detection of the objects embedded in dry and wet sand. Experiments show

that for a dry sand, at frequencies of the order of 500 kHz and above, no through-transmitted signal is detectable. This is due to a very strong attenuation, even for a sample having only a depth of 2 in. However, in a wet sand sample, attenuation is significantly smaller, therefore strong signal is detected at a depth of 6 in. Using low-frequency transducers it is possible to transmit and receive longitudinal ultrasonic pulses in dry sand model medium, for depths of up to several inches. Some application of these results to the detection of objects embedded at a shallow depth of the order of several inches will be discussed.

TUESDAY AFTERNOON, 13 OCTOBER 1998 HAMPTON ROADS BALLROOM 6, 2:30 TO 3:15 P.M.

## Session 2pAAa

### Architectural Acoustics: Reverberation Topics

Richard H. Campbell, Chair

*Bang-Campbell Associates, Box 47, Woods Hole, Massachusetts 02543*

#### Contributed Papers

2:30

**2pAAa1. Archaeological acoustic study of chirped echo from the Mayan pyramid at Chichén Itzá.** David Lubman (14301 Middletown Ln., Westminster, CA 92683)

Handclaps evoke impressive chirped echoes from the unusually narrow limestone staircases of the Mayan pyramid at Chichén Itzá, located in Mexico's northern Yucatan. This highly conspicuous acoustical feature, apparently ignored in the archaeological literature, may provide important clues to Mayan cultural practices of the time. Inspection and ray acoustic modeling provide a simple physical explanation for the chirped echo—the "picket fence effect" due to periodic sound reflections from staircases. The authors argue that chirped echoes were always present, and are not spurious artifacts of reconstruction. It is suggested that the Maya must have noticed and may have exploited his acoustical feature in ceremonies at their sacred site. Is the chirped echo an acoustical design flaw, or intentional acoustical engineering by a perceptive stone age people? The author suggests that the simple acoustical engineering required for intentional design falls well within Mayan capabilities. In seeking a cultural motivation for intentional design, it is speculated that the chirped echo may be intended to imitate the primary call of the Mayan sacred bird, the *resplendent quetzal*. Recorded sound samples show that the two sounds do bear uncanny resemblance. The quetzal hypothesis also provides a credible explanation for the unusually short staircase treads.

2:45

**2pAAa2. Analysis of broadband reverberant fields in terms of time-averaged energy and intensity variables using a boundary element formulation.** Donald B. Bliss and Linda P. Franzoni (Dept. of Mech. Eng. and Mater. Sci., Duke Univ., Durham, NC 27708)

In practice, reverberant sound fields often exhibit significant spatial variation in time-averaged sound pressure level and intensity. In this theory for steady-state, high-frequency, broadband, diffuse sound fields, the enclosure boundaries are replaced by a continuous distribution of broadband uncorrelated sources, each of which provides a constituent field

expressed in terms of time-averaged energy and intensity variables. Superposition of these fields leads to the overall time-averaged acoustic energy and intensity as a function of position. Boundary conditions for radiating and absorbing surfaces are also recast in terms of energy and intensity variables. The use of these averaged variables, which vary slowly in space, allows direct and efficient calculation of important sound field characteristics. The approach is implemented as a boundary element formulation for efficient evaluation of the pressure and intensity fields in enclosures. Application of the method is illustrated by the solution of model problems, which are also solved by classical means for comparison. The approach is much more efficient than a full frequency-dependent calculation, but it also provides more detailed information than is available from other simple theories. An application is the analysis of moderately absorptive enclosures, such as vehicle interiors.

3:00

**2pAAa3. Using iterative regression for estimating reverberation times in two coupled spaces.** Ning Xiang (Natl. Ctr. for Physical Acoust., Univ. of Mississippi, Coliseum Dr., University, MS 38677, nxiang@olemiss.edu) and Mecheal Vorlaender (Institut fuer Technische Akustik, Aachen, Germany)

Sound energy decay in two coupled spaces is, under certain conditions, of a double-slope nature. The present paper deals with identifying two reverberation quantities in these spaces from room impulse responses using Schroeder's backward integration method. Using this method, different decay portions of double-slope decay functions can not always be distinctly recognized since the last part of the decay functions can be strongly deformed by the background noise effect. To overcome this difficulty, a nonlinear, iterative regression approach is proposed to evaluate reverberation quantities in coupled spaces. A multislope decay model is exploited to meet the need of evaluating double-slope decay functions. The present paper reports on the investigation of the approach in terms of simulating decay functions using the decay model. The convergence study on the nonlinear iterative regression conducted in this investigation reveals both the potential feasibility and limitations of the proposed approach.

2p TUE. PM

11:05

**2aUW6. Ultrasonic velocity and attenuation in models of dry and wet sands with an embedded object.** Hasson M. Tavossi and Bernhard R. Tittmann (Dept. of Eng. Sci. and Mech., Penn State Univ., University Park, PA 16802-1401)

Propagation of ultrasound in wet and dry sand, up to 6 in. in depth, is investigated. Velocity and attenuation, as a function of mean grain size, water content, and depth, are measured. The results can be used in the detection of the objects embedded in dry and wet sand. Experiments show

that for a dry sand, at frequencies of the order of 500 kHz and above, no through-transmitted signal is detectable. This is due to a very strong attenuation, even for a sample having only a depth of 2 in. However, in a wet sand sample, attenuation is significantly smaller, therefore strong signal is detected at a depth of 6 in. Using low-frequency transducers it is possible to transmit and receive longitudinal ultrasonic pulses in dry sand model medium, for depths of up to several inches. Some application of these results to the detection of objects embedded at a shallow depth of the order of several inches will be discussed.

TUESDAY AFTERNOON, 13 OCTOBER 1998 HAMPTON ROADS BALLROOM 6, 2:30 TO 3:15 P.M.

## Session 2pAAa

### Architectural Acoustics: Reverberation Topics

Richard H. Campbell, Chair

*Bang-Campbell Associates, Box 47, Woods Hole, Massachusetts 02543*

#### Contributed Papers

2:30

**2pAAa1. Archaeological acoustic study of chirped echo from the Mayan pyramid at Chichén Itzá.** David Lubman (14301 Middletown Ln., Westminster, CA 92683)

Handclaps evoke impressive chirped echoes from the unusually narrow limestone staircases of the Mayan pyramid at Chichén Itzá, located in Mexico's northern Yucatan. This highly conspicuous acoustical feature, apparently ignored in the archaeological literature, may provide important clues to Mayan cultural practices of the time. Inspection and ray acoustic modeling provide a simple physical explanation for the chirped echo—the "picket fence effect" due to periodic sound reflections from staircases. The authors argue that chirped echoes were always present, and are not spurious artifacts of reconstruction. It is suggested that the Maya must have noticed and may have exploited his acoustical feature in ceremonies at their sacred site. Is the chirped echo an acoustical design flaw, or intentional acoustical engineering by a perceptive stone age people? The author suggests that the simple acoustical engineering required for intentional design falls well within Mayan capabilities. In seeking a cultural motivation for intentional design, it is speculated that the chirped echo may be intended to imitate the primary call of the Mayan sacred bird, the *resplendent quetzal*. Recorded sound samples show that the two sounds do bear uncanny resemblance. The quetzal hypothesis also provides a credible explanation for the unusually short staircase treads.

2:45

**2pAAa2. Analysis of broadband reverberant fields in terms of time-averaged energy and intensity variables using a boundary element formulation.** Donald B. Bliss and Linda P. Franzoni (Dept. of Mech. Eng. and Mater. Sci., Duke Univ., Durham, NC 27708)

In practice, reverberant sound fields often exhibit significant spatial variation in time-averaged sound pressure level and intensity. In this theory for steady-state, high-frequency, broadband, diffuse sound fields, the enclosure boundaries are replaced by a continuous distribution of broadband uncorrelated sources, each of which provides a constituent field

expressed in terms of time-averaged energy and intensity variables. Superposition of these fields leads to the overall time-averaged acoustic energy and intensity as a function of position. Boundary conditions for radiating and absorbing surfaces are also recast in terms of energy and intensity variables. The use of these averaged variables, which vary slowly in space, allows direct and efficient calculation of important sound field characteristics. The approach is implemented as a boundary element formulation for efficient evaluation of the pressure and intensity fields in enclosures. Application of the method is illustrated by the solution of model problems, which are also solved by classical means for comparison. The approach is much more efficient than a full frequency-dependent calculation, but it also provides more detailed information than is available from other simple theories. An application is the analysis of moderately absorptive enclosures, such as vehicle interiors.

3:00

**2pAAa3. Using iterative regression for estimating reverberation times in two coupled spaces.** Ning Xiang (Natl. Ctr. for Physical Acoust., Univ. of Mississippi, Coliseum Dr., University, MS 38677, nxiang@olemiss.edu) and Mecheal Vorlaender (Institut fuer Technische Akustik, Aachen, Germany)

Sound energy decay in two coupled spaces is, under certain conditions, of a double-slope nature. The present paper deals with identifying two reverberation quantities in these spaces from room impulse responses using Schroeder's backward integration method. Using this method, different decay portions of double-slope decay functions can not always be distinctly recognized since the last part of the decay functions can be strongly deformed by the background noise effect. To overcome this difficulty, a nonlinear, iterative regression approach is proposed to evaluate reverberation quantities in coupled spaces. A multislope decay model is exploited to meet the need of evaluating double-slope decay functions. The present paper reports on the investigation of the approach in terms of simulating decay functions using the decay model. The convergence study on the nonlinear iterative regression conducted in this investigation reveals both the potential feasibility and limitations of the proposed approach.

2p TUE. PM

**Session 2pAAb**

**Architectural Acoustics: Recording Microphones**

Richard H. Campbell, Chair  
*Bang-Campbell Associates, Box 47, Woods Hole, Massachusetts 02543*

**Chair's Introduction—3:30**

*Invited Papers*

**3:35**

**2pAAb1. Effects of time domain response on sonic characteristics of microphones.** Benjamin D. Findlen, Eric L. Reuter, Richard H. Campbell, and William R. Michalson (Dept. of Elec. and Computer Eng., Worcester Polytechnic Inst., 100 Institute Rd., Worcester, MA 01609, gamera@wpi.edu)

Among practitioners of the recording arts, a correlation is popularly deemed to exist between aspects of a microphone's time domain response and its subjective qualities. This experiment sought to reveal such correlations using appropriate measurement and statistical procedures. Impulse response tests were performed on a set of 12 microphones using both electric spark and maximum length sequence methods. Cumulative spectral decay waterfall plots were then carefully examined for unusual behavior which led to objective feature extraction. Feature-specific quantitative data were then mathematically scaled from both the impulse response and cumulative spectral decay plots to form the objective parameter base. Three musical examples were recorded at each of two proximities with each microphone, and subjective listening tests were performed on these recordings in a controlled environment using expert listeners. The recorded examples included 8 of the 12 microphones and were evaluated for three subjective qualities, namely warmth, brightness, and depth, which provided the subjective parameter base. The data from the objective and subjective tests were statistically analyzed using  $N$ -dimensional replacement [M. H. Moulton, U. of Chicago (1996)]. Complete experimental procedure, results, and implications will be presented.

**4:05**

**2pAAb2. Subjective evaluations of professional microphones.** Lowell Cross (School of Music, The Univ. of Iowa, Iowa City, IA 52242-1793)

Attempts to evaluate microphone performance by listening to individual models via a reproduction chain often reveal subtle, and not-so-subtle, "sonic signatures" which in turn reveal preferences and dislikes among trained listeners. However, there are many factors contributing to the process of evaluation, even if only one microphone type, and only one listener, are involved: (i) monaural versus stereophonic versus ambisonic reproduction; (ii) headphone versus loudspeaker auditioning (again, mono or stereo?); (iii) choice of music, if indeed listening is limited to music; (iv) "direct feed" versus analog versus digital reproduction; (v) personal and environmental factors; (vi) the enhancing or detrimental aspects of microphone "coloration." The foregoing partial list has prompted this listener to treat AB and ABX comparisons of microphones, by individuals or groups, with a certain level of suspicion—in spite of many tests he has conducted involving others. Therefore this presentation will indeed offer subjective views: those of one person with a 35-year history of recording and listening, and with an even longer history of formulating a personal musical taste.

**4:35–5:00**

**Panel Discussion**

## Session 2pAO

## Acoustical Oceanography and Underwater Acoustics: Internal Waves

Ahmad T. Abawi, Chair

SPAWAR Systems Center, 53560 Hull Street, San Diego, California 92152-5001

## Contributed Papers

1:30

**2pAO1. Analysis of acoustic propagation in the region of a shelfbreak front.** Brian J. Sperry, James F. Lynch (Dept. of Appl. Ocean Phys. and Eng., Woods Hole Oceanogr. Inst., Woods Hole, MA 02543), and Ching-Sang Chiu (Naval Postgrad. School, Monterey, CA)

The 1996-97 Shelfbreak Primer Experiments, which involved extensive oceanographic and acoustic measurements, have provided a large dataset with which to investigate the complexities of acoustic propagation in a shelfbreak front region. This paper looks in detail at a subset of the acoustic transmissions extending over a 12-day period during the summer 1996 experiment. Acoustic propagation near the continental shelfbreak is affected by numerous aspects of the oceanography, including but not limited to variable bathymetry, the shelfbreak front, an energetic soliton field, and interactions with occasional Gulf Stream filaments. Because of strong internal wave-induced coupling between the acoustic modes, changes in the large-scale oceanography, such as movement of the front, are difficult to distinguish. The impact of the soliton field on the acoustics is investigated, particularly from the perspective of wanting to invert for the front and other mesoscale features in the presence of this noise. One measure of oceanographic interest is the horizontal wave-number spectrum for the shelfbreak region. The possibility of obtaining this oceanographic quantity from acoustic data is considered. [Work supported by ONR.]

1:45

**2pAO2. Fluctuations in acoustic propagation seen in the SWARM 95 experiment.** Bruce H. Pasewark, Stephen N. Wolf, Marshall H. Orr (Naval Res. Lab., Code 7120, Washington, DC 20375-5350), and James F. Lynch (Woods Hole Oceanogr. Inst., Woods Hole, MA 02542)

Fluctuations in acoustic propagation as seen in data collected during the SWARM 95 experiment are analyzed and related to the oceanographic environment. Acoustic data were collected on a 32 element vertical receiver array which spanned the 88 m water column from depths of 23 to 85 m. The receiver array was located 42 km seaward from two fixed acoustic projectors which transmitted a 224 Hz PRN signal (16 Hz bandwidth) and a 400 Hz PRN signal (100 Hz bandwidth). Intensity statistics, such as scintillation index (SI) and the probability distribution function (PDF), are discussed as a function of depth and time for narrow-band and broadband (replica correlation) processing. Broadband SI is shown to be less than the narrow-band SI which has a typical value of 2. The PDF is shown to be neither a Rayleigh nor a log-normal distribution and evidence is presented that unsaturated scattering processes are involved. [Work supported by the Office of Naval Research.]

2:00

**2pAO3. Coherence of acoustic modes propagating through shallow water internal waves.** Daniel Rouseff (Appl. Phys. Lab., College of Ocean and Fishery Sci., Univ. of Washington, Seattle, WA 98105) and Altan Turgut (Naval Res. Lab., Washington, DC 20375)

The 1995 Shallow Water Acoustics in a Random Medium (SWARM) experiment was conducted off of the New Jersey coast [Apel *et al.*, IEEE J. Ocean. Eng. (1997)]. The experiment featured two well-populated vertical receiving arrays allowing the measured acoustic field to be decomposed into its normal modes. The decomposition was repeated for succes-

sive transmissions allowing the amplitude of each mode to be tracked. The modal amplitudes were observed to decorrelate with time-scales of the order 100 s. In the present work, a theoretical model is proposed explaining the observed decorrelation. Internal solitary wave packets are modeled as mode coupling structures advecting along the acoustic propagation path. Motion of the packets cause the acoustic interference pattern to change. The model is first tested in simple continuous-wave simulations using canonical forms for the internal waves. More detailed time-domain simulations are presented mimicking the situation in SWARM. [Work supported by ONR.]

2:15

**2pAO4. Measurement of modal spectrum of linear internal waves in shallow water and comparison with the Garrett-Munk model.** Kwang Yoo and T. C. Yang (Naval Res. Lab., Washington, DC 20375)

The properties of linear internal waves are well studied in deep ocean and are surprisingly well modeled by the Garrett-Munk model. The properties of linear internal waves in shallow water are not well studied. Experimental measurements may be hindered by the contributions of nonlinear internal waves, the complications caused by range-dependent coastal oceanography, and possible interactions with the bottom boundary layers. There is no reason to expect the Garrett-Munk model to work in shallow water, as some of the assumptions made in the model may be violated. In this paper, the modal spectrum (the modal amplitudes) of the linear internal waves are deduced from approximately 2 h of CTD data collected during the SWARM 95 experiment during a period when nonlinear internal waves are absent or negligible. The method of empirical orthogonal decomposition is applied to the covariance matrix of the sound speed variations assuming that the internal waves modes are uncorrelated. One finds that the eigenvectors of this matrix agree well with the theoretical eigenfunctions of the first five modes of the internal waves. The mode amplitudes are deduced from the eigenvalues and compared with the Garrett-Munk model. The measured mode amplitudes agree with the measurements using a different method which projects the sound speed variations onto the theoretically calculated mode depth functions. [This work is supported by the Office of Naval Research.]

2:30

**2pAO5. Frequency spectrum of linear internal waves in shallow water and a modified Garrett-Munk model.** T. C. Yang and Kwang Yoo (Naval Res. Lab., Washington, DC 20375)

The properties of linear internal waves are well studied in deep ocean and are surprisingly well modeled by the Garrett-Munk model. In the Garrett-Munk model, the internal wave spectrum is the product of the modal spectrum and the wave-number spectrum. The properties of linear internal waves in shallow water are not well studied. In this paper the mode amplitude and frequency spectrum are deduced using the mode decomposition method based on the theoretical mode depth functions. The mode decomposition method is applied to the sound speed variation data as a function of time and depth. Advantages of using sound speed variation data versus the particle displacement data are discussed. The mode amplitude measurements agree with the results using the empirical or-

thogonal decomposition approach. A modified Garrett–Munk model is proposed to explain the deviation of the spectrum slope from the original Garrett–Munk model. [This work is supported by the Office of Naval Research.]

**2:45–3:00 Break**

**3:00**

**2pAO6. Azimuthal coupling computations for transmission loss caused by shelf internal waves.** Roger M. Oba (Naval Res. Lab., Washington, DC 20375-5350)

The amplitude of an acoustic field propagating through a stratified continental shelf water column in the presence of an internal wave packet is azimuthally dependent when referenced to the direction of propagation of the internal wave packet. Internal wave packets propagating across the continental shelf give rise to a highly directional wave-number spectrum of the continental shelf sound velocity field. FOR3D [D. Lee, G. Botseas, and W. L. Siegmann, *J. Acoust. Soc. Am.* **91**, 3192–3202 (1992)], a three dimensional, one-way acoustic propagation model, has been modified to model internal waves in shallow environment on various computational platforms. It allows azimuthal coupling in the propagation, so that horizontal variation of the field may be observed. Results of numerical solutions are presented for propagation through synthesized internal wave packets [D. Tielburger, S. Finette, and S. Wolf, *J. Acoust. Soc. Am.* **101**, 789–808 (1997)] in order to demonstrate the dependence of properties of the acoustic field as a function of range and bearing from the source and internal wave packet. These will also be compared to models that do not take into account azimuthal coupling. [Work supported by the Office of Naval Research.]

**3:15**

**2pAO7. Medium effects on high-frequency propagation: Results from a recent experiment.** Frank S. Henyey, Kevin L. Williams, Stephen A. Reynolds, Daniel Rouseff (Appl. Phys. Lab., College of Ocean and Fishery Sci., Univ. of Washington, Seattle, WA 98105, frank@apl.washington.edu), and Terry E. Ewart (Univ. of Washington, Seattle, WA 98105)

In August 1996, a shallow-water experiment on high-frequency propagation was performed [Williams *et al.*, *J. Acoust. Soc. Am.* **101**, 3159(A) (1997)]. The primary frequency of interest was 75 kHz and the range was 815 m in 70-m-deep water. The focus of the experiment was on the distortion over a 10-m horizontal aperture caused by internal waves and possibly turbulence. Results are presented for two time periods. During the first period, the internal wave energy level was relatively small; nonetheless, constant through cubic terms in a Taylor's series expansion of the acoustic phase can be extracted. These compare well to stochastic model-

ing results. The other period was during a solibore event where a train of high-amplitude, narrow-band internal waves was present. For this situation, the data are compared using deterministic modeling. [Work supported by ONR.]

**3:30**

**2pAO8. A concept for remote acoustic monitoring of solitons generated in straits.** Stanley A. Chin-Bing, David B. King, Alex Warn Varnas, and Robert A. Zingarelli (Naval Res. Lab., Stennis Space Center, MS 39529-5004)

A search algorithm for resonance anomalies (SARA) has been developed to predict possible resonance frequencies of shallow-water soliton packets as they travel through straits. The algorithm relies on characteristics that accompany large losses due to acoustic wave-soliton interactions: (a) acoustic mode conversions; (b) large signal losses within a narrow band of acoustic frequencies; and, (c) large transmission losses due to strong couplings between lower-order propagation modes and higher-order, bottom-interacting modes. The SARA algorithm has been verified using oceanographic data from the Strait of Messina. As a remote acoustic sensor, the SARA algorithm could be used in an "inverse mode" to predict key oceanographic parameters (e.g., predominant horizontal spatial wave numbers and travel speeds) of those soliton packets that produce large acoustic losses. The parameters would initialize a primitive shallow-water soliton model that generates soliton simulations. The SARA algorithm could be used in a forward fashion to validate the soliton simulations. The concept exploits the unique sloping bathymetry of straits, where natural mode stripping can occur around the sills that generate the solitons. Details will be discussed and computer simulations will be presented that illustrate the feasibility of the approach. [Work supported by ONR/NRL and by a High Performance Computing DoD grant.]

**3:45**

**2pAO9. Coupled mode propagation in the presence of internal waves.** Ahmad T. Abawi (SPAWAR Systems Ctr., San Diego, CA 92152-5001) and W. A. Kuperman (Scripps Inst. of Oceanogr., San Diego, CA 92152-6400)

In a previous paper [*J. Acoust. Soc. Am.* **102**, 233–238 (1997)] the effect of mode coupling due to bathymetric variations was studied by means of a new coupled mode parabolic equation model (CMPE). Instead of directly computing the total field, as is done using the conventional parabolic equation method, this model computes the modal coefficients as a function of range and obtains the total field by summing the local modes times the modal coefficients. In the present work, CMPE is used to study mode coupling due to internal waves in a shallow-water environment. The internal wave field is modeled and the spatial and temporal signal coherence across the array caused by interaction with the internal wave field is investigated.



## Session 2pMU

## Musical Acoustics: Analysis of Musical Instruments and the Sounds They Produce

Douglas H. Keefe, Chair

Boys Town National Research Hospital, 555 North 30th Street, Omaha, Nebraska 68131

## Contributed Papers

1:00

**2pMU1. Acoustical studies on steel pans: the role of the skirt.** Uwe J. Hansen<sup>a)</sup> and Thomas D. Rossing (Phys. Dept., Northern Illinois Univ., DeKalb, IL 60115)

Previous studies [Rossing *et al.*, Phys. Today **49**(3), 24–29 (1996)] showed that skirt vibration amplitudes were about 20–40 dB less than amplitudes of the struck note area, and therefore the skirt contributes in a minor way to the total sound level. Nevertheless, the skirt has many resonances of its own and contributes to the timbre of the played instrument, as can be easily heard by damping the skirt. Using electronic TV holography, modes of vibration of steel pan skirts have been recorded when the note area is driven sinusoidally at various frequencies and amplitudes. The modes have varying numbers of nodal meridians and nodal circles, much like those observed in bells and especially in drum shells [Rossing *et al.*, J. Acoust. Soc. Am. **92**, 84–94 (1992)]. Effects of the skirt modes on the sound spectra of the steel pan are discussed. <sup>a)</sup>On leave from Indiana State University, Terre Haute, IN.

1:15

**2pMU2. Normal modes of a triangular aluminum bellplate.** Uwe J. Hansen (Dept. of Phys., Indiana State Univ., Terre Haute, IN 47809)

Triangular aluminum plates have been used as an inexpensive substitute for hand bells [S. Hogg, A. Fisher-Cripps, B. Monsma, and C. Rupil, Proc. 4th Int. Congr. on Sound and Vibr. 2007–2011 (1996)]. The plates are cut from 3-mm aluminum plates with a narrow extension at the right angle apex forming a handle. The corners at the hypotenuse are truncated. The modes of an  $E_5$  plate were observed using electronic holography. Of the nine significant overtones observed, only modes 4, 5, and 8 were relatively close to harmonic. Work reported in the earlier reference suggests indeed that only the fundamental mode contributes significantly to the radiated sound. The modes are compared to the known modes of a standard triangle [E. Watson, D. S. Hampton, and T. D. Rossing, AAPT, Rock Island, 1 Nov. 1986]. The work was performed in the Acoustics Laboratory of the Department of Physics at Northern Illinois University.

1:30

**2pMU3. Arching and rib height in the 2DOF network model of violin cavity resonances.** George Bissinger (Phys. Dept., East Carolina Univ., Greenville, NC 27858)

The 2DOF network model of violin cavity  $A_0$  and  $A_1$  resonances [E. A. G. Shaw, J. Acoust. Soc. Am. **87**, 398–410 (1990)] has been augmented by explicitly incorporating arching and rib height as parameters. Arching was simulated with 26 scaled wedge, block, corner and truncated-corner volumes; rib height was incorporated after accurately determining the cross-sectional area in the plane of the cavity. Optimized  $f$ -hole inertances,  $C$ -bout inertance length, partial volumes, and division parameters [G. Bissinger, J. Acoust. Soc. Am. **101**, 3144 (1997)] were used for all calculations. Calculated  $A_0$  and  $A_1$  mode frequencies and upper bout/lower bout pressure ratios all decrease with increasing rib height or arching with the notable exception of  $A_1$  frequencies, which increase with increased arching.

1:45

**2pMU4. Vibroacoustic properties of a composite harp soundboard.** Curt Preissner and Thomas J. Royston (Univ. of Illinois at Chicago, MC 251, 842 W. Taylor St., Chicago, IL 60607, troyston@uic.edu)

The concert harp has survived through the years much as it was in the 18th century; the construction is still labor intensive, the performance variable, and the durability questionable. These problems can be attributed to the most important part of the harp, the soundboard. Harp soundboards are constructed of spruce wood, which is adversely affected by time, temperature, humidity, and handling. An investigation is underway to replace this fragile sitka spruce soundboard with a more durable material while maintaining acceptable sound quality. The soundboard, a sitka spruce laminate, is already anisotropic; thus, it lends itself to replacement by a carbon fiber reinforced plastic (FRP) laminate. Experimental modal analysis was used to determine vibratory properties of two harp soundboards and uniform spruce beams. Finite element models (FEMs) of the spruce soundboard and beams were developed. The beam FEM aided in the application of laminate theory to determine the lamina stacking sequence to construct a similar composite beam. After experimental verification of the FRP beam, this understanding was applied to construct a FEM of the fiber soundboard. Techniques used to develop and analyze the FRP harp soundboard will be presented.

2:00

**2pMU5. Pianolike tones of multiple strings having stiffness.** William J. Strong (Dept. of Phys. and Astron., Brigham Young Univ., Provo, UT 84602, strongw@acoust.byu.edu)

The strings on a piano have stiffness which gives rise to inharmonic partials that are stretched in frequency relative to harmonic values. In addition, most notes on a piano are strung with more than one string. Even though the multiple strings of a note are tuned to the same nominal frequency, they are never precisely in tune. When the multiple strings are sounded together the resulting tone has partials that increase and decrease in amplitude which results from their in-plane and out-of-phase action on the bridge. In order to illustrate these phenomena, pianolike tones for the note C4 were synthesized in which the parameters of 15 partials were specified for each of three strings. Each of the 45 partials was represented with a decaying sinusoid whose frequency, initial amplitude, and decay rate were specified. The amount of inharmonicity and out-of-tuneness of the strings were varied over a considerable range in order to make their effects apparent. Audio samples were recorded for various combinations of partial parameters.

2:15

**2pMU6. Reed vibration and sound generation in lingual organ pipes.** Thomas D. Rossing,<sup>a)</sup> Judit Angster, and András Miklós (Fraunhofer-Institut für Bauphysik, Stuttgart, Germany)

The reed velocity and the sound pressure inside the shallot have been recorded in lingual organ pipes as the vibrating reed length is varied by means of the tuning wire (Stimmkrücke) (in an  $F_3$  trompette pipe, for example, the sounding frequency was varied from 157 to 325 Hz). Without the resonator, the frequency is a continuous function of the reed vibrating length, but when the conical resonator is added, the pipe frequency

jumps abruptly from below to above each resonance frequency of the sonator. When the natural frequency of the reed (excited by plucking) was varied from 138 to 316 Hz by changing its vibrating length, the pipe frequency changed from 170 to 340 Hz. Reed closure may induce a strong acoustical oscillation in the shallot at a high frequency (approximately 1700 Hz in the  $F_3$  trompette pipe) which strengthens a certain range of harmonics and gives rise to a formant in the pipe sound. The oscillation frequency in the shallot rises rapidly as the reed closes it, and reaches a frequency near the resonance frequency of a tube of comparable length with one closed end. When the resonator is attached, the shallot oscillations are strongly damped. <sup>a)</sup>Permanent address: Physics Dept., Northern Illinois University, DeKalb, IL 60115.

2:30

**2pMU7. Physical modeling of a trombone player's lips.** Daniel O. Ludwigsen and William J. Strong (Dept. of Phys. and Astron., Brigham Young Univ., Provo, UT)

The creation of a physical model is discussed in the context of the lips of a player/trombone system. The lip model is designed to incorporate the salient features of the physical structure of the lips, especially the geometry and material properties. A finite-element model is developed to approximate this structure, while the aerodynamic system is represented by flow equations solved with a finite difference scheme. To drive this model three pressures are applied. The mouth pressure is generated as a constant lung pressure delivered across an airway resistance; the pressure between the lips is dependent on the stream velocity, and the pressure in the mouth-piece is given by the convolution of the volume velocity with the impulse response of the trombone. Together these drive the oscillation of the finite element lip structure, which may be compared with that of previous models and experimental studies.

2:45

**2pMU8. Theoretical consideration on the musical scale of Xoomij singing based on the speech production process.** Yuki Kakita (Dept. of Human Information Sci., Kanazawa Inst. of Tech. (KIT), Ohgigaoka 7-1, Nonoichi-Machi, Kanazawa-Minami 921, Japan)

This paper presents a theoretical consideration on what kind of musical scale can be produced by Xoomij, a type of singing performed in Mongolia and also in some other parts of the Eurasian continent. In Xoomij singing, a tune is produced by selecting appropriate voice harmonics one after another while keeping the fundamental voice pitch constant. The harmonics are selected by changing the shape of the oral cavity which functions as a band-pass filter. Calculations were performed to see what musical scales would be realized when the scale started with one of the 1st to the 30th harmonics of voice, allowing the error of plus/minus a quarter semitone. Some of the findings are: (1) the structure of the scale varies depending on the harmonic that the scale started with, (2) starting the scale with the 5th harmonic produces the widest variety of tunes and the small-

est number of misfitted tones, and (3) a relatively high voice pitch is appropriate for producing an efficient scale, when the cavity resonance suitable for playing music and also the spectral decay of voice source toward the high frequency are considered.

3:00

**2pMU9. Musical instrument identification: A pattern-recognition approach.** Keith D. Martin and Youngmoo E. Kim (MIT Media Lab Machine Listening Group, Rm. E15-401, 20 Ames St., Cambridge, MA 02139)

A statistical pattern-recognition technique was applied to the classification of musical instrument tones within a taxonomic hierarchy. Perceptually salient acoustic features—related to the physical properties of source excitation and resonance structure—were measured from the output of an auditory model (the log-lag correlogram) for 1023 isolated tones over the full pitch ranges of 15 orchestral instruments. The data set included examples from the string (bowed and plucked), woodwind (single, double, and air reed), and brass families. Using 70%/30% splits between training and test data, maximum *a posteriori* classifiers were constructed based on Gaussian models arrived at through Fisher multiple-discriminant analysis. The classifiers distinguished transient from continuant tones with approximately 99% correct performance. Instrument families were identified with approximately 90% performance, and individual instruments were identified with an overall success rate of approximately 70%. These preliminary analyses compare favorably with human performance on the same task and demonstrate the utility of the hierarchical approach to classification.

3:15

**2pMU10. An investigation of different timbral attributes as markers determining metrical structure.** Punita G. Singh (Sound Sense Consultancy Services, 20-A Aurangzeb Rd., New Delhi 110011, India)

Timbre attributes such as spectral locus, spectral density, and temporal envelope slope were studied to determine their relative effectiveness as accent markers defining metrical structure. Complex-tone sequences comprising 12 tones were used as stimuli with points of timbre change at positions implying a triple meter, quadruple meter, compound meter (both triple and quadruple), or unaccented sequences with no timbre changes. Tones at accented positions were made to differ from the rest by using different spectral densities (1, 2, 4, or 8 harmonic components), by changing the locus of components, and by changing the slopes of a two-part temporal amplitude envelope. Listeners were asked to report if the sequence had a triple meter, quadruple meter, ambiguous meter, or no meter. Results thus far indicate that each of the timbre markers used is individually capable of bestowing metrical structure on a sequence. However, when competing cues exist to offer alternative interpretations of meter, more dense spectra appear to dominate over less dense, higher centers of gravity over lower, and sharper attack functions over more gradual rise times.

## Session 2pNS

## Noise: Acoustical Effects of Airbag Deployment

Elliott H. Berger, Chair

*E-A-R/AEARO Company, 7911 Zionsville Road, Indianapolis, Indiana 46268-1657*

## Chair's Introduction—1:00

*Invited Papers*

1:05

**2pNS1. Human auditory response to an air bag inflation noise: Has it been 30 years?** Richard L. McKinley (AFRL/HESN, 2610 Seventh St., WPAFB, OH 45433-7901) and Charles W. Nixon (Veridian, Dayton, OH 45431-1289, cnixon@falcon.al.wpafb.af.mil)

Once upon a time, over 30 years ago, 100 subjects volunteered for exposure to high level impulsive noises generated by the inflation of prototype automobile safety air bags. The government mandated that passive restraint systems, beyond seat belts, be introduced in passenger automobiles within 2 years. The only reasonable candidate was the air bag system, however, none were fully developed for automobile production. One concern was the effect of inflation noise on the auditory systems of vehicle occupants. Ninety-one volunteers qualified for the study; nine were rejected by an otolaryngologist because of head colds, congestion, and upper respiratory infections. Subjects facing forward in the rear seat of a small automobile experienced the noise of simultaneous inflation of a 9-cf passenger air bag and a 2.5-cf driver air bag. The median peak pressure level of the impulsive noises was 168 dB obtained with an overall measurement system ranging from 30 Hz (microphone low frequency cutoff) to 40 000 Hz. The dynamic range was 180 dB. Post-exposure auditory system evaluations included external auditory canals, eardrum membranes, verbal communications-auditory perception, aural discomfort, TTS, and PTS. Results are discussed in terms of the conditions of the exposures, the measurements, and the study population. [Work supported by DOT, National Highway Safety Bureau.]

1:25

**2pNS2. Airbag noise hazard: From theory to validation.** G. Richard Price (U.S. Army Res. Lab, Human Res. and Eng. Directorate, APG, MD 21005-5425, dprice@arl.mil)

Airbag noise is problematic. Peak pressures rise above 170 dB and noise standards declare it hazardous; yet airbags continue to be designed into our automobiles. Scientists agree, however, that the standards may be overconservative and indeed, no epidemic of hearing loss is reported from the highways. A general mathematical model of auditory hazard has been developed [Price and Kalb, *J. Acoust. Soc. Am.* **100**, 2674 (1996)] which addresses such exposures. It predicts and a study shows that the average cat receives a 37 dB PTS from an airbag impulse [Price *et al.*, *J. Acoust. Soc. Am.* **99**, 2464 (1996)]. However, the model suggests the human ear is more robust and predicts the "at risk ear" is one which is not warned, is in a vented compartment (windows open), is facing the noise source and is one which is naturally more fragile [Price, *J. Acoust. Soc. Am.* **102**, 3201 (1997)]. An epidemiological study of airbag noise testing these contentions is just beginning. It will use the Department of Defense hearing conservation database to provide pre- and postexposure audiograms following exposures in automobile accidents. Preliminary data should be available at the time of the meeting.

1:50

**2pNS3. Automobile airbag impulse noise: Otologic symptoms in six patients.** James E. Saunders (Univ. of Oklahoma Health Sci. Ctr., Dept. of Otorhinolaryngology, P.O. Box 26901, WP1360, Oklahoma City, OK 73190), William H. Slattery III, and William M. Luxford (House Ear Clinic, Los Angeles, CA 90057)

Automobile airbag safety systems have successfully reduced the number of occupant injuries from motor vehicle accidents. Unfortunately, airbags are also associated with some inherent risk, including a high-amplitude, short-duration noise from airbag deployment. A review of the available research in the automobile industry indicates that the peak amplitude of this noise may exceed 170 dB sound-pressure level. Despite the increasingly wide application of airbags in automobiles, there have been no previous reports of airbag-related otologic injuries. The authors have encountered six patients with otologic symptoms that appear to be related to airbag impulse noise. Five of these patients have documented hearing loss, one patient reported persistent tinnitus, and two patients have significant dysequilibrium. Although permanent hearing loss from airbag noise appears to be rare, temporary threshold shifts are probably much more common. It is important, therefore, that the clinician be aware of the noise associated with airbag inflation and the possibility of acoustic trauma from these safety devices.

2:10

**2pNS4. Otologic effects of air bag deployment.** Kathleen Yaremchuk (Dept. of Otolaryngol./HNS, Henry Ford Hospital, 2799 W. Grand Blvd., Detroit, MI 48202-2806) and Robert Dobie (Univ. of Texas Health Sci., San Antonio, TX 78284)

The Medical Aspects of Noise Subcommittee of the American Academy of Otolaryngology/Head and Neck Surgery published two requests, in the Academy's monthly journal the *Bulletin*, for information from otolaryngologists on patients that had been exposed to airbag deployment and developed otologic complaints. There were 20 otolaryngologists that replied with reports of 29 patients that had been evaluated for hearing loss, tinnitus, and or vertigo. Seven patients had pre- and post-airbag deployment audiograms that document sensorineural hearing loss. Eighteen patients had asymmetrical sensorineural hearing loss on post airbag deployment audiogram. The most common symptoms after airbag deployment were tinnitus (17) and hearing loss (16). There were two reports of tympanic membrane perforations and one report of a perilymph fistula after exposure to airbag deployment. Two patients complained of vertigo. Two patients complained of recruitment.

2:30

**2pNS5. The auditory effects of a deployment—An individual's experience.** Janet C. Garman (2100 Mulguy Dr., Barrington, IL 60010)

Cases of hyperacusis and tinnitus have been reported after the sudden, loud noise blast and instantaneous air pressure rise of airbag deployment. This presents a serious problem as hyperacusis is a disabling and devastating disorder in which everyday noises are painfully loud. The ears also lose their dynamic range. Hyperacusis drastically alters one's life. It may end careers, place enormous stress on personal relationships, severely limit social and athletic activities and interfere with communication. Hyperacusis sufferers often cannot attend family gatherings, movies, parties, sports events, weddings, and places of worship even using hearing protection. Many cannot use household appliances or power tools. Traveling is difficult. They walk a thin line between overprotection and underprotection. Overprotection causes their hearing to become even more sensitive and underprotection can exacerbate the accompanying tinnitus and worsen the hyperacusis. This paper presents the author's experience with all of the aforementioned issues and how as a result, her life has changed. The question arises whether one should be required by law to place their auditory system in such jeopardy from an airbag which by its own name, supplemental restraint system, concedes it is only an additional safety device with the seat belt being the main form of protection.

2:45–3:15

#### Panel Discussion

TUESDAY AFTERNOON, 13 OCTOBER 1998      HAMPTON ROADS BALLROOM 7, 1:00 TO 4:15 P.M.

### Session 2pPA

#### Physical Acoustics: Bubble Acoustics and Thermoacoustics

R. Glynn Holt, Chair

*Department of Aerospace and Mechanical Engineering, Boston University, 110 Cummington Street, Boston, Massachusetts 02215*

#### Contributed Papers

1:00

**2pPA1. Bubble-based pump for small channels.** H. Yuan and Andrea Prosperetti (Dept. of Mech. Eng., Johns Hopkins Univ., Baltimore, MD 21218)

In the small liquid handling devices that the new silicon manufacturing technologies render possible the problem arises of pumping the liquid through small channels. In this study the possibility of using vapor bubbles generated thermally at suitably spaced time intervals for this purpose is explored theoretically. In the current version of the model the bubbles are one-dimensional "slices" of vapor in which a prescribed law of variation of the internal pressure with time is prescribed. This represents a simplified model of the switching on and off of microheaters embedded in the channel walls. When the thickness of the bubble falls below a certain value, the bubble is removed and that portion of the channel available for flow. It is shown that, with a suitable timing of the application of heat, a net pumping flow can be generated. The effects of liquid viscosity and surface tension are also included in the model and shown to be important

in determining the pumping action. Some initial results in which the bubbles are modeled as spheres will also be presented. [Work supported by the Air Force Office of Scientific Research.]

1:15

**2pPA2. The effects of ambient acceleration on bubble levitation and SBSL.** Sean C. Wyatt, Ronald A. Roy, and R. Glynn Holt (Dept. of Aeronaut. and Mech. Eng., Boston Univ., Boston, MA 02215)

In order to prepare for pending experiments in variable-g environments some of the multiple effects caused by the time-varying acceleration of acoustic resonators used in bubble levitation experiments are considered. The coupled effects of the induced changes in ambient pressure (due to a changing hydrostatic head) and bubble position (due to a change in the buoyant body force) are modeled. Changing the ambient pressure, while holding the acoustic pressure amplitude constant, causes changes in the radial bubble response and diffusive equilibrium requirements. Changing the bubble levitation position causes both the local acoustic pressure

amplitude and gradient to change, which will again impact bubble response. If the bubble must remain in stable diffusive equilibrium, both of these effects will force the bubble equilibrium radius to change. Finally, by using an empirical relation for emitted SL intensity versus bubble response, the variation of emitted light intensity as a function of the changing ambient acceleration is obtained. [Work supported by NASA.]

1:30

**2pPA3. The oscillations of a gas bubble in a tube.** X. Geng, H. Yuan, H. Oğuz, and Andrea Prosperetti (Dept. of Mech. Eng., Johns Hopkins Univ., Baltimore, MD 21218)

In principle, gas bubbles can be effective actuators in small liquid handling devices such as those that the new silicon manufacturing technologies make possible. Their attractiveness for this application stems from an inherently high frequency of vibration, the possibility to power the bubble remotely by ultrasound, and the absence of mechanical moving parts. Among the most fundamental pieces of information that are required to evaluate this application are the natural frequency and damping rate of the volume pulsations of a bubble in the constrained environment of a tube. After a brief review of the pertinent theoretical aspects recently developed by the authors, the paper presents the results of an experiment in which an air bubble in a 1-mm-diam partially filled tube is driven by a thin rod mounted on a loudspeaker. The amplitude of pulsation of the bubble is measured as a function of frequency by phase locking the exposure of a CCD camera with the acoustic wave. A general agreement between theory and experiment is found, although the measured damping rate exceeds the theoretical value. [Work supported by the Air Force Office of Scientific Research.]

1:45

**2pPA4. Effects of shock-excited harmonic modes on bubble levitation, stability, and SL.** Matthias Rueggeberg, Joachim Holzfuss (Inst. of Appl. Phys., Tech. Univ. of Darmstadt, D-64289 Darmstadt, Germany), and R. Glynn Holt (Boston Univ., Boston, MA 02215)

Several experimental groups have commented on a sudden change in position of a levitated bubble very near the threshold for light emission at driving acoustic pressures near 1 atm. Often this leads to an uncontrollable nearly periodic wandering instability of the bubble in the acoustic field. Other groups have observed high-frequency discrete components in the received signal from internally mounted pressure hydrophones, and resonator-wall-mounted piezo-transducers and strain gauges. In order to investigate this effect, a broadband hydrophone was monitored in the water during single bubble levitation at near-SL pressures. Using a signal analyzer, it was ascertained that higher harmonic modes (up to 32 times the fundamental) of the acoustic resonator are excited by the bubble. When there is no bubble levitated, the temporal acoustic field is practically linear. The effects on bubble levitation and bubble dynamics of these shock-excited modes are discussed, and it is shown that many instances of bubble levitation instability can be explained by this effect. How to avoid this behavior in position-sensitive experiments is also discussed. [Work supported by DFG and NASA.]

2:00

**2pPA5. Gas bubble formation in an oscillatory flow.** H. Oğuz (Dept. of Mech. Eng., Johns Hopkins Univ., Baltimore, MD 21218)

Production of bubbles from an underwater orifice is a common process that is often difficult to control. A possible solution is to impose a flow around an underwater orifice so that the size of the detached bubbles can be regulated. A simple way of accomplishing this task is to place a coaxial needle in a short tube. At constant water flow rate, a precise control of the bubble size can be achieved regardless of the orientation of the tube with respect to gravity. Since this arrangement may not be practical in some applications, an oscillatory flow in which the net water flux is zero is a better alternative. A series of experiments in which the flow is actuated by

a rubber membrane driven by a solenoid show that it is possible to phase lock the bubble formation frequency to the forcing frequency under certain conditions. In the inflow phase of the oscillation, the growing bubble that is attached to the needle tip assumes an oblate shape. As a result, when the flow is reversed, the added mass force pushes the bubble away from the needle in a very efficient manner. Axisymmetric boundary integral simulations have been carried out to simulate this process. A very good agreement is found between experiment and the simulations. [Work supported by NASA.]

2:15

**2pPA6. The action of Bjerknes forces on vapor bubbles.** V. Harik, Y. Hao, and A. Prosperetti (Dept. of Mech. Eng., Johns Hopkins Univ., Baltimore, MD 21218)

A considerable fraction of the heat transfer enhancement due to boiling can be ascribed to the buoyant removal of vapor bubbles from the heated surface. Such a mechanism is absent in microgravity where, indeed, transition to film boiling is found to occur at lower heat fluxes than at normal gravity. This problem motivates the present investigation in which the use of acoustic pressure radiation (or Bjerknes) forces for bubble removal is investigated. The paper describes numerical results for the large-amplitude oscillations of a vapor bubble in a liquid accounting for phase change and heat transport both inside and outside the bubble. On the basis of these results, the primary Bjerknes force on the bubble is calculated as a function of the bubble position in the sound field. The secondary Bjerknes force due to a second bubble (simulating a solid wall by the method of images) is also calculated and conditions under which the primary force can overcome the secondary one and dislodge the bubble from the heated surface are determined. [Work supported by NASA.]

2:30–2:45 Break

2:45

**2pPA7. A study of optoacoustics at the vaporization threshold of liquid carbon disulfide.** Stanley A. Cheyne and John M. Long (Dept. of Phys. and Astron., Hampden–Sydney College, Hampden–Sydney, VA 23943)

An optoacoustic technique was used to investigate the vaporization mechanism in liquid carbon disulfide. The amplitude of the acoustic signal varied linearly up to the boiling point where, at that point, the slope of the amplitude versus laser energy curve increased, indicating an increase in optoacoustic conversion efficiency. It was observed that vapor bubbles did not appear until well after the boiling point of the liquid. After achieving the boiling temperature, the propagation time of the acoustic signal increased with a maximum delay of 255 ns. This maximum correlated with the formation of a vapor bubble, suggesting that the delay was possibly due to the acoustic wave propagating in a gaseous medium within the excitation zone where the sound speed was slower.

3:00

**2pPA8. A comparison between two models for bubble dynamics and their predictions for the theory of sonoluminescence of Lohse *et al.*** Y. Hao and Andrea Prosperetti (Dept. of Mech. Eng., Johns Hopkins Univ., Baltimore, MD 21218)

Lohse and co-workers [Hilgenfeldt *et al.*, Phys. Fluids **8**, 2808 (1996)] have formulated a theory of bubble stability in relation to sonoluminescence emission. The theory is based on a simplified model describing the spherical oscillations of a gas bubble. This paper compares the results given by that model with those of a more detailed one in which liquid compressibility and thermal effects in the bubble are accounted for with greater precision. A comparison of the results given by the two models throws some interesting light on the subtle effects of energy dissipation. It is shown that, even though the bubble radius versus time as predicted by

the two models does not differ very much, derived quantities—such as various stability thresholds—are nevertheless substantially affected. In particular, the parametric stability threshold calculated by the new model is in better agreement with experiment. The parameter range where sonoluminescence should be observable according to the new model is enlarged with respect to the original theory of Lohse and co-workers. A study of whether light emission is indeed observable in this extended range should help examine the validity of the theory. [Work supported by the Office of Naval Research and NASA.]

3:15

**2pPA9. Heat transfer measurements on a single stack plate.** Martin Wetzel and Cila Herman (Johns Hopkins Univ., 3400 N. Charles St., Baltimore, MD 21218)

Heat transfer in oscillatory flow with zero mean velocity is different when compared to steady-state flow situations. This is one reason that currently no systematic design methodologies for heat exchangers in such flows exist. For example, instead of the expected heat transfer from a single heated stack plate [Wetzel *et al.*, *J. Acoust. Soc. Am.* **100** (1996)] to the working fluid, the temperature fields visualized with holographic interferometry indicate that heat is transferred from the working fluid into the stack plate at the edge of the plate. To investigate this behavior the local heat fluxes at the edge of the stack plate were measured. These heat fluxes indicate the expected behavior for a low drive ratio. However, as the drive ratio increases, the resulting heat flux vector at the edge of the plate changes its direction and points into the plate, thus confirming the observations made when analyzing the temperature fields. Through an energy balance the magnitudes of the heat fluxes caused by the thermoacoustic effect were determined. The measured data are in good agreement with numerical and analytical predictions. [Work supported by the Office of Naval Research.]

3:30

**2pPA10. Continuous-flow thermoacoustic dehumidifier.** Robert A. Hiller and G. W. Swift (Condensed Matter and Thermal Phys. Group, Los Alamos Natl. Lab., Los Alamos, NM 87545, hiller@lanl.gov)

For applications in gas cooling a thermoacoustic refrigerator may be simplified by using the gas stream itself as the acoustic medium and eliminating the cold heat exchanger by directing the input gas stream through the stack (R. S. Reid *et al.*, "Cyclic Thermodynamics with Open Flow," *Phys. Rev. Lett.* to appear May 25, 1998). This concept may be extended to dehumidification, with the incoming humid air stream being cooled to its dew point and condensing water in the thermoacoustic stack. The water will appear as liquid on the stack surface or as a fog and is removed from the resonator, while the dry air flows out of the system. Design problems

include collecting and removing the condensate from the stack to the outside of the resonator, and optimizing stack design for a working gas in multiple phases. Experimental results and numerical models for a prototype compressed-air dehumidifier will be presented. [Work supported by DOE Office of Basic Energy Sciences.]

3:45

**2pPA11. Mode-locking of acoustic resonators and its application to vibration cancellation in acoustic heat engines.** Philip S. Spoor and Gregory W. Swift (Los Alamos Natl. Lab., Los Alamos, NM 87454)

The problem of two self-maintained acoustic resonators that can "mode-lock" by means of a mutual coupling will be considered; in particular, the effects of varying coupler parameters (such as the diameter of a coupling duct) on the relative phase and amplitude of the oscillations in the two resonators will be explored. Experimental data, numerical simulations, and analytical predictions will be compared. The results will be used to help design a scheme for canceling structural vibrations in a thermoacoustic engine, by rigidly attaching two such engines together and selecting the appropriate coupler, such that the engines are forced to oscillate in antiphase. The interplay between acoustic coupling and "mass coupling" (coupling through the rigid structure) will also be discussed. [Work supported by the Office of Fossil Energy in the US DOE.]

4:00

**2pPA12. Software for thermoacoustic modeling.** Ralph T. Muehleisen (Civil, Environ., and Architectural Eng., Univ. of Colorado, Campus Box 428, Boulder, CO 80309, ralph.muehleisen@colorado.edu)

In modeling thermoacoustic systems, many researchers rely on a freely available software package called DeltaE developed by Bill Ward and Greg Swift at Los Alamos National Lab. While DeltaE is an accurate and useful package, it is only available as a precompiled binary executable. As such, augmentation or modification of the code is impossible. In response to the limitations of DeltaE, a new, freely available software package has been developed. In contrast to the precompiled DeltaE, this new software has been developed as a set of MATLAB subroutines. While certainly not as fast as DeltaE, the MATLAB routines can easily be modified and augmented by researchers using a very wide variety of computing platforms. In addition, the MATLAB software has several new features including the use of complex frequency for determining resonance frequency and quality factors for resonators, and complete access to the spatial pressure, velocity, and temperature profiles throughout the system being modeled. An overview of the features and performance of this software package is presented. [This work was supported by the Office of Naval Research.]

## Session 2pPP

**Psychological and Physiological Acoustics: Issues Related to Binaural Hearing, Temporal and Spectral Processing, and Audiological Testing**

Robert C. Bilger, Chair

*Department of Speech and Hearing Science, University of Illinois at Urbana-Champaign, 901 South 6th Street, Champaign, Illinois 61820***Contributed Papers**

1:30

**2pPP1. Localization of sounds presented over headphones in ambient noise.** Mark A. Ericson (Air Force Res. Lab., 2610 Seventh St., Bldg. 441, Wright-Patterson Air Force Base, OH 45433, mericson@falcon.al.wpafb.af.mil), Robert S. Bolia (Veridian, Dayton, OH), and W. Todd Nelson (Air Force Res. Lab., Wright-Patterson Air Force Base, OH)

Sounds produced in everyday environments often interfere with other sounds. In aerospace and industrial environments the interfering sounds are typically diffuse and mask the desired sound. Relatively few studies have addressed the effects of noisy environments on auditory localization perception. Most localization experiments use stimuli presented in the free field, without maskers or with one directional masker. A few studies [Hirsh, *J. Acoust. Soc. Am.* **22**, 196–200 (1950); Mershon and Lin, *Ergonomics* **30**, 1161–1173 (1987)] have measured auditory localization perception in reverberant environments. However, in these studies both the signal and maskers were produced in the reverberant environment. With virtual audio systems becoming widely available, many applications will likely involve listening to directional sounds over headphones while immersed in a high-intensity diffuse noise field. The current study examines the effect of bandlimiting various frequency regions of a directional noise signal presented over headphones in the presence of ambient noise. The four signal regions include: (1) 0.1 to 1 kHz; (2) 1 to 4 kHz; (3) 4 to 8 kHz; (4) 8 to 16 kHz. Results from this study have implications for the design of directional audio displays in high-noise environments.

1:45

**2pPP2. Inverse filtering of headphones for binaural sound reproduction.** Pauli Minnaar and Henrik Møller (Acoust. Lab., Aalborg Univ., DK-9220 Aalborg, Denmark)

Binaural recordings can be made at a blocked ear canal entrance and can be conveniently played back over headphones. The total transmission is then characterized by a transfer function that includes the responses of the headphone and the microphone as well as the transmission between them. The transfer function can be broken up into a minimum phase and an excess phase component, of which the latter can again be broken up into an all-pass and a linear phase component. In order to make the binaural system acoustically transparent, an equalization filter must be designed as the inverse of the total transfer function. The suitability of various filters for inverting each of the transfer function components is evaluated using data from real ear measurements. The robustness of the equalization is discussed with respect to slight changes in headphone and microphone placement. For the investigation 2892 measurements were made on a range of people wearing various types of headphones and wearing different samples of the same type of headphone.

2:00

**2pPP3. Loudness perception with headphones versus loudspeakers.** Jana Schiffel and Henrik Møller (Acoust. Lab., Aalborg Univ., Fredrik Bajers Vej 7B, DK-9220 Aalborg Ø, Denmark, akustik@kom.auc.dk)

This study examines whether human loudness perception is influenced by the type of sound source, or determined exclusively by the sound pressure received at the eardrum. The literature contains conflicting views on this issue, particularly for the case of listening to earphones compared to, for example, listening to loudspeakers. To begin with, the paper summarizes the controversial results of earlier experiments. Ambiguities and loose ends worth investigating are pointed out; crucial aspects of experimental design are considered, e.g., the test sound material, various ways of binaural versus monaural presentation, and the psychometric method. Following this, new experiments are proposed. They comprise: (1) subjective equal-loudness comparisons (2-AFC) between various types of headphones and loudspeakers at different locations, and (2) probe-microphone measurements of the corresponding sound pressures in the listener's ear canals. Finally, first results are presented. As a practical application, consequences to techniques of headphone calibration are discussed.

2:15

**2pPP4. Sensitivity to quantized variations in the amplitude and interaural phase of a stimulus.** Douglas S. Brungart (Noise and Vib. Branch, Air Force Res. Lab., 2610 Seventh St., WPAFB, OH 45433-7901, and Dept. of Psych., Boston Univ., Boston, MA 02115, brungart@falcon.al.wpafb.af.mil)

The sensitivities of listeners to quantized changes in the amplitude and interaural phase of a stimulus were measured in two-alternative forced-choice experiments. In the amplitude experiment, listeners heard two diotic stimuli (500 Hz tone burst, 5 kHz tone burst, white noise, speech, or musical chord) that varied in amplitude over a 30 dB range either continuously or in discrete (equal dB) steps and were asked to choose the noisier stimulus. In the phase experiment, listeners heard two 500 Hz tone bursts that varied in interaural time delay (ITD) from  $-750 \mu\text{s}$  to  $750 \mu\text{s}$  either continuously or in discrete steps and were asked to choose the noisier stimulus. The amplitude results vary widely across subjects, but indicate that listeners were most sensitive to discrete steps in the amplitude of a sinusoidal signal (threshold step size  $<0.375 \text{ dB}$ ), and least sensitive to discrete steps in the amplitude of white noise (threshold step size  $\approx 2 \text{ dB}$ ). The ITD results indicate that the listeners were sensitive to discrete steps in ITD smaller than  $2.5 \mu\text{s}$ . The results have implications in systems which require instantaneous switching between filters, such as virtual audio displays.

2p TUE. PM

2:45

**2pPP5. A joint time-frequency model of auditory masking.** Jonathan J. O'Donovan and Dermot J. Furlong (Dept. of Electron. and Elec. Eng., Trinity College, Dublin, Ireland)

The perceptual phenomena of temporal and spectral masking (critical band masking) [B. C. J. Moore, *Frequency Selectivity in Hearing* (Academic, New York, 1986)] are related to the ear's limited temporal and spectral resolution. This resolution is known from psychoacoustic experiments but is not typically incorporated in the time-frequency representations used in audio signal processing. A joint time-frequency distribution, modeling both critical band masking and nonsimultaneous (forward and backward) masking, is described here. Applications for such a distribution include audio compression and the modeling of room acoustics. The distribution is developed within the framework of Cohen's class of generalized time-frequency distributions [L. Cohen, "Time-frequency distributions—A review," *Proc. IEEE* **77**, 941–981 (1989)] and is a development from the constant  $Q$  modal distribution [W. J. Pielemier and G. H. Wakefield, "A high resolution time-frequency representation for musical instrument analysis," *J. Acoust. Soc. Am.* **98**, 2382–2396 (1996)]. The design and implementation of this auditory model is detailed.

3:00

**2pPP6. Gap detection thresholds as a function of marker duration in young and old listeners.** Stanley J. Hamstra<sup>a)</sup> and Bruce A. Schneider (Dept. of Psych., Univ. of Toronto at Mississauga, Mississauga, ON L5L 1C6, Canada, s.hamstra@utoronto.ca)

Twenty younger (normal hearing, mean age: 22 years) and twenty older adults (audiometric thresholds <40 dB HL for frequencies between 0.2 and 4 kHz, mean age: 72 years) were asked to discriminate between the presence versus absence of a gap between two equal-duration tonal markers constructed by summing 2-kHz Gaussian-modulated tone pips ( $\sigma = \frac{1}{2}$  ms) spaced  $\frac{1}{2}$  ms apart. The total duration of the two markers was constant within a block of trials but varied between 1 and 1000 ms

across blocks. Gap detection thresholds were determined using a two-interval forced-choice procedure. Notched-noise, centered at 2 kHz, was used to mask on- and off-transients. Gap detection thresholds of older adults were markedly higher than those of younger adults for marker durations less than 150 ms but converged on those of younger adults at 1000 ms. For both age groups, gap detection thresholds were independent of audiometric thresholds. These results indicate that older adults have more difficulty detecting a gap than younger adults when short marker durations (i.e., durations characteristic of speech sounds) are employed. This loss of temporal resolution with age appears to be independent of the ability to detect a tone of this frequency. [Work supported by NSERC.] <sup>a)</sup>Present affiliation: Dept. of Surgery, University of Toronto.

3:15

**2pPP7. Individual differences and instrumental variation in audiological research.** Robert C. Bilger and Ted A. Meyer (Dept. of Speech and Hearing Sci., Univ. of Illinois at Urbana-Champaign, Champaign, IL 61820, r-bilger@uiuc.edu)

Tests used in speech audiometry have traditionally been standardized on young adults with normal hearing. In such cases, the range of test scores has been extended by presenting the materials at different intensity levels or signal-to-noise ratios (S/N). These strategies are essentially attempts to model hearing loss in terms of instrumental changes to a speech test. In the standardization of the Speech Perception In Noise (SPIN) test, we obtained the necessary wide range of test scores by testing a large number of listeners with sensorineural hearing loss. When the variability among SPIN test scores was the result of individual differences, the results were quite different from those in experiments using instrumental differences to extend the range of scores obtained from listeners with normal hearing. The "simulation of hearing loss" fails because instrumental manipulation of signal level or S/N changes the nature of the test not the hearing of the listeners under test. Only when the range in performance is the result of wide individual differences in hearing for speech presented under standard conditions can one evaluate a speech test. Without individual differences, there is no reliability. Predictions of performance derived from experiments driven by instrumental variability have little clinical value. [Work supported by NIH.]

TUESDAY AFTERNOON, 13 OCTOBER 1998 HAMPTON ROADS BALLROOM 1, 1:00 TO 4:30 P.M.

### Session 2pSA

## Structural Acoustics and Vibration: Interior Cabin Noise II

Earl G. Williams, Cochair

*Code 7137, Naval Research Laboratories, Washington, DC 20375*

Scott D. Sommerfeldt, Cochair

*Department Physics and Astronomy, Brigham Young University, N241 ESC P.O. Box 24673, Provo, Utah 84602-4673*

### Invited Papers

1:00

**2pSA1. A comparison of active and adaptive passive noise control systems for the DC-9.** Douglas Swanson, Russell Altieri, and Leslie Fowler (Lord Corp., 110 Lord Dr., Cary, NC 27511)

The aft interior of the DC-9 aircraft is generally considered to be uncomfortably loud (100–110 dBC). This noise is primarily periodic and is caused by imbalances in the fan and turbine of the Pratt Whitney JT8D engine. Lord Corporation has recently developed active and adaptive passive systems to combat this problem. The active system uses four force-generating actuators located on the left and right engine pylons to minimize the response at eight control microphones which are located in the rear of the cabin. The adaptive passive system consists of eight tuned vibration absorbers whose natural frequency is adapted to the engine speed. An overview of each system with theory will be presented as well as experimental results where the tonal noise reduction and engine



speed tracking capabilities of each system were evaluated using an identical engine vibration input on a DC-9 fuselage. These experimental results showed that the active system achieved larger tonal noise reductions and had faster tracking ability than the adaptive passive system.

1:25

**2pSA2. Inverse identification, optimization, and active structural acoustic control of aircraft interior noise using piezoelectric actuators.** Chris R. Fuller, Scott D. Paxton (Vib. and Acoust. Labs., Virginia Tech, Blacksburg, VA 24061), and Gary P. Gibbs (NASA Langley Res. Ctr., Hampton, VA 23681)

This paper discusses an inverse method for identifying the dominant aircraft fuselage normal vibration in terms of interior noise. The identified vibration fields are used in an optimal approach based on a genetic algorithm to locate arrays of piezoelectric actuators. The actuators are used in conjunction with microphone error sensors and an LMS controller to implement an ASAC approach to efficiently reduce the interior noise. The methodology is demonstrated on a business jet fuselage under a variety of excitation types and frequencies. The results demonstrate that the inverse identification method and transducer optimization approach leads to improved control performance in terms of the amount and spatial extent of the noise attenuation. [Work supported by NASA LaRC.]

1:50

**2pSA3. On reconstruction of acoustic pressure fields using the HELS method.** Sean F. Wu (Dept. of Mech. Eng., Wayne State Univ., 5050 Anthony Wayne Dr., Detroit, MI 48202)

The Helmholtz equation-least squares (HELS) method was recently developed by Wang and Wu [J. Acoust. Soc. Am. **102**, 2020–2032 (1997)] to reconstruct the acoustic pressures generated by an arbitrary vibrating structure. In this method the acoustic pressures are expressed in terms of an expansion of “acoustic modes.” The coefficients associated with these acoustic modes are determined by requiring the assumed-form solution to satisfy the pressure boundary condition at measurement points. The errors incurred in this process are minimized by the least-squares method. The advantages of this method are that (1) acoustic pressures can be reconstructed over the entire surface; (2) solutions thus obtained are unique; and (3) efficiency of numerical computation is high, because the number of measurements is determined by that of expansion terms, which is small when a right coordinate system is selected for a particular source geometry under consideration. Such an approach is applicable to both exterior and interior regions. For exterior problems, the reconstructed acoustic pressures can be accurate when the points fall outside the minimum circumscribing spheroidal surface which encloses the vibrating surface, but approximate when they are inside. For interior problems, the accuracy of reconstruction is high because the entire region is inside the minimum circumscribing spheroidal surface. In both cases, the accuracy of reconstruction is limited by excitation frequencies, which is inherent in all expansion theories. [Work supported by NSF.]

2:15–2:30 Break

### Contributed Papers

2:30

**2pSA4. Optimal transducer placement for active control of sound transmission through an aeroelastic plate.** G. Clark Smith and Robert L. Clark (Dept. of Mech. Eng. and Mater. Sci., Duke Univ., Box 90302, Durham, NC 27708-0302, gcs@duke.edu)

The optimal locations of colocated transducers for static and dynamic output feedback control of sound transmission through an aeroelastic plate are investigated. The model of a convected fluid loaded plate coupled to a cavity is presented. The physical dimensions and parameters of the model are chosen to approximate a small commercial aircraft. Development of two optimization approaches is discussed in detail. The first method uses the Sequential Quadratic Programming nonlinear optimization algorithm to minimize the  $H_2$  Norm of the complete system from the disturbance inputs to a weighted sum of cavity acoustic potential energy and feedback control signal energy. The second method utilizes a simple line search routine to maximize a measure of system controllability. Case studies optimizing a control system with one and three sensor/actuator transducers are presented for external flow speeds varying from Mach 0.1 to Mach 1.1. Results show the variation in optimum transducer placement for both the static and dynamic control systems over the range of flow speeds considered. A comparison of the optimal placement determined by each optimization approach is also given. [Work supported by NSF Career Program CMS-9501470.]

2:45

**2pSA5. Global reduction of aircraft interior noise using constant volume velocity actuators.** Steven A. Lane and Robert L. Clark (Dept. of Mech. Eng. and Material Sci., Duke Univ., Durham, NC 27708)

Active noise control of an aircraft interior presents a formidable challenge as a result of the high modal density that is characteristic of such three-dimensional enclosures. In this work, a multiple-input, multiple-

output feedback control strategy using a distributed array of sensors (microphones) and actuators (loudspeakers) was used to achieve global control within the fuselage of a typical business jet aircraft. The transducers were spatially weighted to focus control effort to the dissipation of low frequency acoustic modes of the system. Previous work has shown that global attenuation is indeed possible, but transducer dynamics limited the achievable performance of the controller. In this work, the actuators were compensated using a technique similar to motional feedback in order to approximate a constant volume velocity source over the control bandwidth. This essentially moves the actuator dynamics out of the control bandwidth, enhancing the performance of the active noise controller.

3:00

**2pSA6. Active control of automobile cabin noise with advanced speakers.** Jerome C. Couche, Francois Charette, and Chris R. Fuller (Vib. and Acoust. Labs., Virginia Tech., VA 24061-0238)

The purpose of this presentation is to demonstrate the application of active control of engine noise in the interior cabin of a sport utility vehicle with advanced, compact piezoelectric sound sources. A broadband feed-forward filtered-X LMS algorithm has been used to achieve this goal. Preliminary tests have been conducted using arrangements of up to four commercially available speakers and four microphones. Various reference signals have been studied and these configurations show good results; attenuation of 7 dB at the error sensors has been measured in the 40–500 Hz frequency band and the dimensions of the zone of quiet generated by the control has also been measured. The ultimate goal of the research is the implementation of the active noise control with a new generation of speakers. These speakers use piezoelectric devices to induce the displacement of a speaker membrane, which radiates sound. Their main advantages are weight and dimensions, which are significantly smaller than conventional speakers are. [Work supported by MSI/ONR.]

**2pSA7. A formulation and preliminary validation of an algorithm prescribing the propellers of an aircraft as excitation in an acoustic boundary element analysis.** Nickolas Vlahopoulos (Dept. of Naval Architecture and Marine Eng., Univ. of Michigan, 2600 Draper Rd., Ann Arbor, MI 48109-2145), Karen H. Lyle (U.S. Army Vehicle Technol. Ctr., Hampton, VA), and Casey L. Burley (NASA Langley Res. Ctr., Hampton, VA)

Simulation tools can be utilized in computing and minimizing the interior noise levels in an aircraft subjected to the external acoustic load originating from the propellers. In order to evaluate accurately the interior noise level, and in order to determine the structural changes which will reduce the interior noise, it is important to have an accurate description in terms of magnitude and phase for the external acoustic load exerted on the fuselage. A formulation for modeling the operating propellers of an aircraft as a noise source in a boundary element acoustic analysis was developed, implemented into software, and verified through comparison to test data. It constitutes the initial phase of integrating sophisticated rotorcraft models [D. S. Prichard, D. D. Boyd, and C. L. Burley, "NASA/Langley's CFD-Based BVI Rotor Noise Prediction Systems: (ROTORNET/FPRBVI) An Introduction and User's Guide," NASA Technical Report, TM-109147, November 1994] to a conventional boundary element analysis. The initial validation was performed by comparing numerical results to test data for the external acoustic pressure on the surface of a tilt-rotor aircraft for one flight condition. [Work supported by the NASA, ASEE Faculty Fellowship Program.]

## 3:30

**2pSA8. Effects of pressure loading on the dynamics of a curved piezostucture.** James K. Henry and Robert L. Clark (Dept. of Mech. Eng. and Material Sci., Duke Univ., Box 90302, Durham, NC 27708-0302, jake.henry@duke.edu)

Previous research in active structural acoustic control (ASAC) has focused primarily on flat plates. In order to facilitate the realistic evaluation of the closed loop performance of ASAC systems for aircraft cabin noise reduction, efforts are being made to consider complicating effects in panel dynamics to more accurately reflect the service conditions of aircraft fuselage panels. As part of these efforts, a model of a curved piezostucture was developed and used to determine the effects of curvature on panel dynamics and transducer integration. Curvature was shown to affect transducer coupling and control system bandwidth. The present work considers the effects of internal pressure loading created by aircraft cabin pressurization. Internal pressure loading is shown to affect panel dynamics significantly, raising further issues in control system design and transducer integration for structural acoustic control applications. [Research supported by NASA Langley Research Center under Grant No. NCC 1 250.]

## 3:45

**2pSA9. Characteristics of the Structural Acoustic Loads and Transmission (SALT) facility at NASA Langley Research Center.** Ferdinand W. Grosveld (Lockheed Engineering and Science Co., NASA Langley Res. Ctr., Hampton, VA 23681)

The Structural Acoustic Loads and Transmission (SALT) facility at NASA Langley Research Center consists of a reverberant chamber, an anechoic chamber, and a common window. The 267-m<sup>3</sup> reverberant chamber is structurally isolated from the rest of the building and is the source room in a transmission loss suite configuration. The receiving anechoic chamber is 4.57 m high, 9.63 m long, and 7.65 m wide, measured wedge tip to wedge tip. The window between the two rooms can accommodate

141×141-cm<sup>2</sup> test structures for which sound transmission loss may be measured. Calibration of the transmission loss suite is discussed. The acoustic and structural flanking paths were evaluated by acoustic intensity and cross-spectral accelerometer measurements. Acoustic measurements in the reverberant room are accommodated by covering the window with a stiff, heavy insert. Measured ambient levels, reverberation times, sound field diffusivity, lowest usable frequency, and preferred test object dimensions are discussed. A transportable partition with foam wedges can be placed in front of the covered window in the anechoic chamber to facilitate acoustic free-field measurements. Anechoic room characteristics are presented including acoustic ambient levels, inverse square-law curves, cutoff frequency, and test object versus room size dimensions.

## 4:00

**2pSA10. An experimental evaluation of individual partition segment configurations for the active control of sound transmission.** Timothy W. Leishman<sup>a)</sup> and Jiri Tichy (Grad. Prog. in Acoust., Penn State Univ., 217 Appl. Sci. Bldg., University Park, PA 16802, leishman@sabine.acs.psu.edu)

Lightweight partitions segmented into discretely actuated subsections with mutual interstices and compliant suspensions have been proposed for active sound transmission control (ASTC). In this work, experimental efforts are undertaken to explore important active and passive characteristics of two partition segment models under normal-incidence excitation. The control objective for the configurations is to actively minimize the normal vibration of their transmitting surfaces—instead of an acoustic field quantity in the receiving space. For this functional strategy to be effective, experiments affirm the importance of efficiently and simultaneously controlling vibrations of transmitting subpanels, suspensions, and interstices to achieve high transmission loss. Distinct segment configurations and control schemes allow varying degrees of global transmitting surface vibration control. However, one configuration tested has been theoretically shown to produce efficient control of its various transmitting surfaces using simple control schemes. Measurements confirm that it also provides exceptionally high transmission loss over a broad frequency range—including very low frequencies. <sup>a)</sup>Currently at Crown International, 1718 W. Mishawaka Rd., Elkhart, IN 46515-1000.

## 4:15

**2pSA11. The role of grazing waves in sound transmission through a finite plate.** Valerij A. Masyukov (Inst. for Problems in Mech., Russian Acad. of Sci., prospekt Vernadskogo 101/1, Moscow 117526, Russia, masyuk@ipmmet.ru)

Air sound transmission loss (TL) of a finite elastic plate, placed in an infinite rigid baffle, is computed with regard to, first, a lack of near-grazing waves in incident sound field and, second, diffractive three-dimensional expansion of the sound field radiated by forced bending waves of the finite plate. It is shown that both effects lead to the lack of near-grazing sound waves in transmitted sound field what in turn appreciably increases TL compared with diffuse field and infinite plate. Below coincidence, especially at low frequencies, the second effect usually predominates over the first. At coincidence, in contrast, the first effect always prevails and results in an increase of both TL and limiting frequency. Above coincidence, both effects are always negligible. The computations are compared with numerous measurements of various authors for glass panels of different dimensions and satisfactorily explain the well-known excess of experimental TL values over infinite-plate theory at and below coincidence. Nevertheless the familiar integration formula for infinite plate may be successfully used for finite panels with the only difference that the limiting integration angle of incidence becomes depending on acoustic wave number.

## Session 2pSC

## Speech Communication: Acoustic Cues and Phonetic Perception (Poster Session)

Randy L. Diehl, Chair

Psychology Department, University of Texas, 330 Mezes, Austin, Texas 78712

## Contributed Papers

All posters will be on display from 1:30 p.m. to 4:00 p.m. To allow contributors an opportunity to see other posters, contributors of odd-numbered papers will be at their posters from 1:30 p.m. to 2:45 p.m. and contributors of even-numbered papers will be at their posters from 2:45 p.m. to 4:00 p.m. To allow for extended viewing time, posters will be on display beginning at 10:00 a.m.

**2pSC1. Context and identification of vowels in speech variation.**

Sheila M. Williams and Randy L. Diehl (Dept. of Psych., Univ. of Texas, Austin, TX 78712)

Interpretation of a particular vowel pattern may vary according to the perceived speech patterns of the speaker [P. Ladefoged and D. E. Broadbent, *J. Acoust. Soc. Am.* **29**, 98–104 (1957)]. Formants from a given speaker, using a specific speech style, reflect both anatomical dimensions of the speakers vocal tract and the speakers preferred vocal settings for the context of the utterance. Speech samples of a set of nine vowels in a standard CVC frame [G. E. Peterson and H. L. Barney, *J. Acoust. Soc. Am.* **24**, 175–184 (1952)], recorded from local speakers, were analyzed and resynthesized, manipulating formant values to derive similar formant frequency ratios from different vowel bases. Thus if the listener identifies the vowels according to the formant patterns, the perceived vowel will differ from the base vowel from which it was derived, whereas if the overall formant frequency shift is detected, then the vowel should maintain its identity, differences in quality being attributed to a change of speaker or of speech style. Using listeners from the same speech community, monosyllabic word identification is contrasted with identification of excised vowels to ascertain the effect of word context on distinguishing the relatively long-term formant ratios of the speaker. [Work supported by NIDCD.]

**2pSC2. Perception of stops in naturally produced V[l/r][b/d/g]V tokens: a reassessment of acoustic cues to place of articulation.**

Jeannette M. Denton, Yukari Hirata, Joanna H. Lowenstein, Candace V. Perez, and Karen L. Landahl (Dept. of Linguist., Univ. of Chicago, 1010 E. 59th St., Chicago, IL 60637, kllc@midway.uchicago.edu)

This perceptual experiment reassesses a traditional assumption that the *F3* transition is the primary cue for distinguishing [da] from [ga], evidence of which comes from perceptual experiments using synthetic continua [Mann, *Percept. Psychophys.* **5**, 407–412 (1980); Fowler *et al.*, *ibid.* **48**, 559–570 (1990); Liberman, *Speech* (1996)]. Stimuli were tokens of /alba/, /alda/, /alga/, /arba/, /arda/, /arga/ produced three times by four speakers at three rates (fast, normal, slow), analyzed acoustically by Dainora *et al.* [*J. Acoust. Soc. Am.* **100**, 2601 (1996)] and Hemphill *et al.* [*CLS* **33**, 333–346 (1997)]. Subjects identified tokens in their original carrier sentences using a forced choice paradigm. Stimuli were blocked by speaker and rate; three repetitions of each were randomized within blocks. In five of the 216 tokens, for one or more subjects, the percept of the stop did not match the speaker's intent. Analysis of these tokens showed a mismatch between formant transitions and burst spectra: formant transitions were characteristic of the stop intended by the speaker, while the burst spectra corresponded to the actual percept. These results suggest that when the burst spectra and formant transitions are in conflict, some listeners use the burst as primary for identifying place of articulation.

**2pSC3. The influence of acoustic and semantic information on phoneme categorization in sentences.**

Susan Borsky (San Diego State Univ., San Diego, CA 92182-1518 and Florida Atlantic Univ., Boca Raton, FL 33431, sborsky@mail.sdsu.edu), Lewis P. Shapiro (San Diego State Univ., San Diego, CA 92182-1518), Betty Tuller (Florida Atlantic Univ., Boca Raton, FL 33431), Christina G. Langford, C. Sue Faber, and Kellie A. Wolf (San Diego State Univ., San Diego, CA 92182-1518)

In spoken language, local acoustic information is frequently consistent with more than one phoneme. This study investigates the influence of acoustic and semantic information on phoneme categorization as a sentence unfolds in time. Ten target stimuli forming a Goat-to-Coat continuum were created from natural speech by manipulating the voice onset time of the initial consonant. These stimuli were embedded in biased sentences such as: Goat-biased: The busy dairyman forgot to milk the (Goat/Coat) in the drafty barn. Coat-biased: The careful tailor hurried to press the (Goat/Coat) in the cluttered attic. A cross-modal interference task showed immediate effects of acoustic information; effects of semantic information appeared 450 ms later. A cross-modal identification task showed immediate sentence context effects for ambiguous mid-range stimuli while identifications 450 ms later showed context effects for endpoint stimuli. A word monitoring study showed immediate context effects throughout the acoustic parameter range. These data support an account of auditory sentence comprehension in which semantic information does not immediately and automatically influence phonological analysis of an acoustic signal; contextual influences occur over time or when a task or situation requires explicit judgment about the identity of a stimulus. [Work supported by NIMH, Grant No. MH42900, and NIH, Grant No. DC00494.]

**2pSC4. Burst spectra of word-medial voiced stops: systematicity and variation across speakers and rates.**

Tamra M. Wysocki, Svetlana Soglasnova, Rachel M. Hemphill, M. Catherine Gruber, Sabrina J. Billings, and Karen L. Landahl (Dept. of Linguist., Univ. of Chicago, 1050 E. 59th St., Chicago, IL 60637, t-wysocki@uchicago.edu)

This study extends the investigation of word-medial stop consonants by Hemphill *et al.* [*CLS* **33**(2), 333–346 (1997)]. They found that burst spectra for /d/ and /g/ for one speaker at one rate show invariant properties. In continuation of this work, linear predictive coding and spectrogram analyses were performed on stops, including /b/, in /alba/, /alda/, /alga/, /arba/, /arda/, and /arga/ spoken in a carrier sentence by two male and two female speakers of Midwestern American English across slow, normal, and fast rates. Schematic application of the criteria established by Blumstein and Stevens [*J. Acoust. Soc. Am.* **66**, 1001–1017 (1979)] revealed characteristic spectral features for the burst of /g/ across all speakers and rates: a compact peak in midfrequency range. Spectra of the /b/ tokens displayed considerable variation, although they were generally character-

izable as diffuse-falling or flat. The /d/ tokens displayed even greater variation and failed to show diffuse-rising or any distinctive spectral shape. These findings suggest that while the burst is a relatively more stable correlate for /g/ and /b/, the perception of /d/ may be more dependent upon other cues distributed in the acoustic signal.

**2pSC5. Acoustic characteristics of American English vowels produced by Floridian female speakers.** Katherine C. Bielec (Dept. of Commun. Sci. and Disord., BEH 255, Univ. of South Florida, 4202 E. Fowler Ave., Tampa, FL 33620-8150, kbielec@chuma.cas.usf.edu), Amanda D. Grainger, Winifred Strange, Sonja A. Trent, and Kanae Nishi (Univ. of South Florida, Tampa, FL 33620)

The present study analyzed the temporal, spectral, and dynamic acoustic characteristics of 11 American English (AE) vowels /i, ɪ, e, ε, æ, ʌ, ɑ, ɔ, o, u, ʊ/. The stimuli were produced by 22 monolingual female adult speakers from Florida. The vowels were embedded within the hVd consonantal context in a carrier phrase. Acoustic measurements included vowel duration, fundamental frequency, temporal midpoint and dynamic information. LPC formant contours were measured by the 25%, 50%, and 75% points of the vocalic nuclei. A perceptual vowel identification task was included in the study. Twenty Floridian female adult listeners categorized the 253 vowel stimuli using an interactive, self-paced computer program. Results of acoustic vowel space, spectral movement, discriminant function analysis, and perceptual identification will be presented. [Work supported by NIDCD.]

**2pSC6. Perception of vowel stimuli synthesized with different fundamental frequencies.** Marios Fourakis, Constance Preisel (Dept. of Speech and Hearing Sci., 110 Pressey Hall, 1070 Carmack Rd., Ohio State Univ., Columbus, OH 43210, fourakis.1@osu.edu), and John W. Hawks (Kent State Univ., Kent, OH 44242)

This research examined the perception of 465 vowel stimuli synthesized with both a typically male and a female fundamental frequency ( $F_0$ ) by persons with normal hearing, testing the hypothesis that when people listen to male and female speakers they employ different criteria for each speaker in order to decide which vowel the speaker has produced. The subjects, five male and five female native speakers of Midwestern American English, listened to the 465 vowel tokens synthesized with both  $F_0$ 's. They were asked to decide, for each token, if it was one of eleven possible vowels as in the words: heed, hid, hayed, head, had, hod, hawed, hoed, hood, who'd, hud, or if not, to respond NONE. Next, the token was played again and the subjects indicated their certainty on a scale of 5 (very certain) to 1 (very uncertain). The responses were used to create perceptual maps in which each synthesized point is represented by the vowel code assigned to it by the majority of the subjects. The resulting maps indicate that male and female listeners did not differ in their assignment of vowel categories as a function of  $F_0$ . There were no differences due to the gender of the listener.

**2pSC7. The temporal extent of spectral properties on [voice] judgments.** Michelle R. Molis and Randy L. Diehl (Dept. of Psych., Univ. of Texas, Austin, TX 78712)

Previous results [M. R. Molis and R. L. Diehl, *J. Acoust. Soc. Am.* **99**, 2591(A) (1996)] indicated that, in some instances, changes in spectral properties which extend over the entire length of a consonant-vowel syllable have no effect on the location of stop-consonant [voice] boundaries. Large manipulations in the relative amplitude of the first formant ( $F_1$ ) and the overall spectral tilt produced no changes in subjects' labeling of velar stops. However, in recent experiments, similar spectral manipulations confined to the initial 50 ms following the onset of voicing energy *did* produce significant shifts in [voice] boundaries. Under these conditions, both increased relative  $F_1$  amplitude and increased spectral tilt re-

sulted in an increase in [-voice] responses. Once again, these results are incompatible with the predictions of the "low-frequency hypothesis" [J. Kingston and R. L. Diehl, *Lang.* **70**, 419-454 (1994)]. [Work supported by NIDCD.]

**2pSC8. Processing vowels and lexical tone in Mandarin Chinese.** Yun Ye and Cynthia Connine (Dept. of Psych., SUNY at Binghamton, Binghamton, NY 13902)

Vowel and tone detection tasks were used to investigate the role of tone information in processing Mandarin. In experiment 1, the task required detection of a tone-plus-vowel combination (tone2-/a/). Possible "yes" responses occurred for both word and nonword syllables and showed a lexical advantage. "No" response target stimuli mismatched on either the vowel or the tone and showed faster detections for vowel mismatch stimuli. These results indicate a perceptual advantage for vowel detections. In experiment 2, separate vowel and tone detection tasks were used for target syllables that occurred phrase-finally in a predictive or neutral semantic context. In the neutral context, vowel detections were faster than tone detections. The vowel advantage was neutralized in predictive contexts where tone detections were somewhat faster. The results are discussed in terms of the relationship between the lexical representation of vowels and tones and their temporal availability in running speech.

**2pSC9. Effect of syllable-initial voicing on temporal characteristics of words.** J. Sean Allen and Joanne L. Miller (Dept. of Psych., 125 NI, Northeastern Univ., Boston, MA 02115, jallen@lynx.neu.edu)

As part of an ongoing study of the voicing distinction in syllable-initial stop consonants, we measured segmental durations of consonant-vowel-consonant (CVC) words beginning with voiced stop consonants (e.g., "big," "duck," "gap") and matched CVC words beginning with voiceless stop consonants (e.g., "pig," "tuck," "cap"). Target words were produced in randomized lists together with numerous filler words. Results from the four speakers measured to date revealed a consistent pattern. As expected, initial voiceless stops were associated with a longer vowel-onset-time (VOT) than initial voiced stops. In addition, initial voiceless stops were associated with a shorter vowel duration (measured from the onset of voicing) than initial voiced stops. Thus, the change from voiced to voiceless stop entailed both an increase in VOT and a decrease in vowel duration. However, the magnitude of the decrease in vowel duration was insufficient to compensate fully for the increase in VOT, resulting in a net increase in the duration of the CV portion of words beginning with voiceless as opposed to voided stops. The results are discussed in terms of implications for models of speech production and syllable planning, as well as implications for studies of speech perception. [Work supported by NIH/NIDCD.]

**2pSC10. Initial strengthening and coarticulatory resistance.** Patricia A. Keating (Phonet. Lab, Dept. of Linguist., UCLA, Los Angeles, CA 90095-1543, keating@humnet.ucla.edu)

In previous work, initial strengthening of lingual articulations has been demonstrated in four languages. One possible interpretation of initial strengthening is that it results from increased coarticulatory resistance: consonants in stronger positions resist the weakening that coarticulation would produce. To test this interpretation, a new study examined consonants in CVCs in which the vowel was varied. If initial strengthening is coarticulatory resistance, then there should be less effect of the vowel on the initial consonant than on the final consonant. Test consonants /t d n l/ and vowels /E a u/ were combined with the nontest consonant /b/ in 24 syllables like /tab/ and /bul/; five subjects produced nine repetitions of each in a frame sentence. Maximum linguopalatal contact, measured by electropalatography, was the measure of consonant strengthening and coarticulation. The result was the opposite from the prediction. Initial consonants showed more vowel-dependent variation than did final conso-

nants (in accord with the traditional coarticulation literature). Yet the initial consonants did show more overall contact than final consonants. Thus initial strengthening cannot be attributed to coarticulatory resistance. Additional experiments, including one which looks at initial strengthening in phrase-initial positions, will be reported. [Work supported by NSF.]

**2pSC11. Acoustic correlates of articulatory prosodic strengthening in Korean.** Taehong Cho (Dept. of Linguist., UCLA, Los Angeles, CA 90095)

Recent articulatory studies [e.g., Keating, Cho, Fougeron, and Hsu (1998), forthcoming] using electropalatography have shown that consonants are generally produced with greater linguopalatal contact in domain-initial positions. This effect, known as articulatory prosodic strengthening, is generally cumulative: the higher the prosodic position, the more linguopalatal contact. The goal of this paper is to test for acoustic correlates of any such articulatory variations in Korean consonants /n,t,th,t\*/ in prosodic positions (Utterance-, IP-, AP-, Word- and Syllable-initial), so that eventually the perceptual significance of such correlates can be tested. Results show that the higher domain-initial positions are associated with longer VOTs; longer "total" voiceless duration in closure; lower rms burst energy in stops but with substantial inter-speaker/consonantal variations; lower % of voicing during closure; and lower acoustic energy for nasal /n/. In addition, vowels in domain-initial CV were not found to be necessarily longer in a higher position whereas vowels in domain-final positions were. Linear correlations between each of the acoustic parameters and the articulatory magnitude (linguopalatal contact) will also be discussed. All in all, this study shows that articulatory strengthening in Korean does produce reliable acoustic correlates, which mark off prosodic positions in the speech signal. [Work supported by NSF.]

**2pSC12. Labio-coronal fricatives in Sengwato.** Elizabeth Zsiga (Dept. of Linguist., Georgetown Univ., 37th and O Sts., Washington, DC 20057, zsigael@gusun.georgetown.edu) and One Tlale (Univ. of Botswana, Private Bag 0022, Gabarone, Botswana)

This paper will present evidence for the existence of doubly articulated labio-coronal fricatives in Sengwato (a northern dialect of the Bantu language Setswana). The existence of stops and fricatives that incorporate all two-way combinations of labial, coronal, and dorsal articulations is predicted by phonological feature-geometry models [E. Sagey, MIT dissertation, 1986]. According to Ladefoged and Maddieson [*Sounds of the World's Languages* (1996), p. 331], however, "the world's languages do not use segments that combine two fricative elements." Ladefoged and Maddieson analyzed reported labio-coronal fricatives in Sepedi, a sister language to Setswana, and concluded that the fricative articulations were sequenced. In this presentation, spectrographic analysis and video images from two speakers of Sengwato will be presented, demonstrating that in words like [ɔsa] "to burn," speakers do use two simultaneous fricative articulations. Spectrographic analysis shows a steady-state fricative, not a sequence; and comparison of video images shows that the labial constriction is more extreme than the addition of approximantlike rounding. The data to be presented here will show that, in contrast to Sepedi, Sengwato [ɔs] is a true doubly articulated fricative. This type of sound is indeed represented in the repertoire of human languages.

**2pSC13. Acoustic-perceptual correlates of sentence prominence in Italian questions and statements.** Mariapaola D'Imperio (Dept. of Linguist., OSU, 1712 Neil Ave., Columbus, OH 43210, dimperio@ling.ohio-state.edu)

Recent research on the acoustic correlates of perceived accentual prominence in speech has generally focused on fundamental frequency ( $F_0$ ), while few studies have attempted to shed light on how other parameters, such as duration and intensity, might interact with  $F_0$ . A previous

study on Italian suggests that duration has a major role in signaling lexical stress placement in isolated words [Bertinetto (1980)]. The present work reports on results of an experiment using synthetic speech to test which aspects of the signal, among  $F_0$ , duration, and intensity, are more influential in the extraction of prominence structure at the sentence level and if there are differences between questions and statements. To this scope, a series of LPC-resynthesized stimuli were hybridized following a technique first developed by Nakatani and Aston (1978) and later adopted in Beckman (1986) and Hirschberg and Ward (1993) for English. Specifically, two-word sentences with varying modality (question or statement) and accent structure were manipulated in order to shift the location of perceived prominence from that of nonhybrid stimuli. The stimuli were presented to 21 speakers of the Neapolitan variety of Italian. The results suggest a greater role of duration within question stimuli than within statements.

**2pSC14. The relationship between final alveolar stops and /ai/ offsets in American English.** Erik R. Thomas (Dept. of English, Box 8105, North Carolina State Univ., Raleigh, NC 27695-8105)

Two procedures were conducted to determine the relationship between final /t/ and /d/ and the realization of preceding /ai/ offsets. First, productions of /ai/ offsets in minimal pairs such as *tide/tight* were measured for Anglo sixth-graders and high schoolers from central Ohio, who speak a "General American" dialect, and for Mexican-American junior college students from Laredo, Texas, whose dialect is influenced by Spanish. Both groups tended to produce lower  $F_1$  and higher  $F_2$  before /t/ than before /d/, though the difference was smaller for the Texans than for the Ohioans, which is probably related to the impossibility of tautosyllabic combinations like /taid/ in Spanish. Second, a discrimination test was performed with similar subjects using stimuli representing a continuum of offset formant values, vowel duration, and duration of phonation into closure from most *tide*-like to most *tight*-like. Results showed that offset quality and vowel duration influenced discrimination of /t/ and /d/ by both groups of subjects, though somewhat differentially. The findings reveal that the offset difference exhibits dialectal variation and thus is not simply an artifact of articulatory constraints, and that listeners can access it to differentiate final /t/ and /d/.

**2pSC15. Learning changes in the recognition, repetition, and free recall of pseudowords.** Dragana Barac-Cikoja (NIDCD, NIH, Bethesda, MD), Lyn Goldberg (George Washington Univ., Washington, DC), Kathy Siren (Loyola Univ., Baltimore, MD), and Christy Ludlow (NIDCD, NIH)

Acquisition of a pair of three-syllabic (11-phoneme) pseudowords associated with meaningless ideographs was examined across 15 trials on three tasks. For each word, an ideograph-prompted recall was succeeded by the identification of each constituent syllable among two foils, ending with two repetitions of the recorded pseudoword. The words were alternated throughout the experiment. Subjects verbal productions were phonetically transcribed and scored for segmental and syllabic accuracy. The scores were used to compare changes in performance on: (a) the recall and the repetition tasks, (b) the syllable recognition and the repetition tasks, and (c) between two repetitions. Phonological errors in the three tasks were highly related with intra-syllabic differentiation increasing with learning. [Work supported by NIH Z01 DC 00005-09.]

**Session 2pSPa**

**Signal Processing in Acoustics and Musical Acoustics: Acoustics in Multimedia-Content Issues**

David I. Havelock, Chair

*National Research Council, IMS/ASP, M-36 Montreal Road, Ottawa, Ontario K1A 0R6, Canada*

**Chair's Introduction—1:30**

*Invited Papers*

**1:35**

**2pSPa1. Synchronization of musical sound and visual images: Issues of empirical and practical significance in multimedia development.** Scott D. Lipscomb (Inst. for Music Res., UTSA Div. of Music, 6900 N. Loop 1604 West, San Antonio, TX 78249)

In recent years, there has been a significant number of investigations into the interaction between auditory and visual systems in a multi-modal context, e.g., film, animation, and multimedia software. The author will report results of his own research, confirming a subject preference for alignment of audio-visual (AV) accent structures, i.e., combinations resulting in perceived AV synchronization. A revised version of a model of Film Music Perception [Lipscomb and Kendall (1994)] will be presented, explicating a dynamic relationship between stimulus complexity and significance of AV synchronization in the determination of subject preference ratings. Using these findings as a starting point, the author will illustrate the practical importance of musical sound and its temporal placement within a multimedia context. Multimedia software and technologically enhanced course materials created by the author will provide examples of the effect of combining musical sound and visual images. The presentation will illustrate that the combinatorial effect of such multimedia presentations far surpasses the effect of either auditory or visual stimuli in isolation, resulting in an improved aesthetic experience for the audience and an enhanced learning environment for the student.

**2:05**

**2pSPa2. Music on Image: Compositional strategies for a new art form.** Jean Piche (Universite de Montreal, 200 Vincent d'Indy, Montreal, QC, Canada)

From the author's perspective, the design of video moving pictures, in both narrative and non-narrative forms, share many syntactic traits with music composition, especially electroacoustic composition. Many video art works can be experienced as a raw choreography of emotion where kinetic camera movements, color, and editing build, not a story or even perhaps a theme, but mainly a cortical experience of modernity; this is what much electroacoustic music is about. This talk will expand on key concepts of synchronicity/asynchronicity between musical and pictorial materials. Examples will be drawn from the author's recent development of "paNi IntiyA" in which the video editing/processing was done with a particular musical paradigm in mind, be it granulation, micro-montage, spatialization, cross-fades/morphing or electronic processing. The ultimate goal is to try and imprint onto the image the same generality as the expanded sonic vocabulary of electroacoustic composition. The author calls this form video-music. While this moniker will help to distinguish its intent from the ubiquitous music-video commodity, it more importantly indicates that the gestures, musical and visual, spring forth from the same mind as a single entity, and thus may represent a new form of mediatic expression.

**2:35**

**2pSPa3. Sound source localization in multimedia applications.** Zack Settel (McGill Univ., Music Faculty, 555 rue Sherbrooke West, Montreal, QC H3A 1E3, Canada)

With the arrival of real-time 3-D digital audio processing, techniques for acoustic space modeling and sound source spatialization have become of great interest for implementation in various multimedia applications, ranging from CD-ROM authoring to video conferencing. In surround sound applications, where sound source localization is a primary objective, various digital signal processing (DSP) techniques can be employed to heighten the sense of source localization, often creating a stronger link between sound and image. In several multimedia applications, the degree of live interactivity can play a crucial role in the success of the application. For example, the underlying software in video games, acoustic space simulators, and air traffic monitoring systems (using auditory display) must render audio objects in a real-time acoustically modeled space, based on varying position data supplied to these programs by the user(s). This paper will focus on sound source localization techniques and their use in various multimedia applications, and will examine key issues in implementation.

## Session 2pSPb

## Signal Processing in Acoustics: General Topics in Signal Processing in Acoustics

Karl B. Fisher, Chair

*Applied Research Laboratories, University of Texas, P.O. Box 8029, Austin, Texas 78713-8029*

## Contributed Papers

3:20

**2pSPb1. Use of target characteristics for classification.** Ralph N. Baer and Charles F. Gaumont (Code 7140, Naval Res. Lab., Washington, DC 20375-5350, baer@abyss.nrl.navy.mil)

Scattering from ribbed cylinders exhibits very significant angular dependence. This angular dependence must be accommodated by any active classifier. A numerical technique for incorporating this dependence was previously reported [Charles F. Gaumont, *J. Acoust. Soc. Am.* **101**, 3130 (1997)]. Using a data set simulating both targets and false targets in a shallow water environment, it is demonstrated that the method can be used as a component of an active classifier and produces an improved probability of detection over energy detection. The technique is based upon physics-based wave packets derived from the backscattered signal of a numerical scattering model. There is only one wave packet, originating from the so-called chalice waves, for the particular frequency band in the data set. These wave packets from a numerical model are then used to obtain features from the experimental data. A probabilistic method is then used to combine the features. The resulting performance is determined through the use of ROC curves. [Work supported by ONR.]

3:35

**2pSPb2. Multi-aspect target classification using directionally dependent hidden Markov models.** Paul Runkle and Lawrence Carin (Dept. of Elec. and Computer Eng., Duke Univ., Box 90291, Durham, NC 27708-0291)

Acoustic signals scattered from underwater targets often exhibit characteristics that vary as a function of target-sensor orientation. In this paper, target identification is performed by utilizing physics-based feature extraction in conjunction with discrete hidden Markov model (HMM) classifiers. The signal features are extracted using a matching pursuits algorithm to identify structures that are naturally present in general scattered signals, such as wavefronts and resonances. Although HMMs are traditionally applied to model the temporal variations of features extracted from speech signals, for this research, target-specific HMMs are designed to model the spatial variations of the scattered signal features. In particular, states of the HMM are conceptualized as corresponding to target-sensor orientation intervals. This approach naturally leads to constraints on the model structure that accommodate observations from multiple aspects. Discrimination results are presented for five distinct targets, demonstrating the potential of this classification technique. [Work supported by NRL.]

3:50

**2pSPb3. Active removal of wind noise from outdoor microphones using local velocity measurements.** Michael R. Shust<sup>a)</sup> and James C. Rogers<sup>b)</sup> (Michigan Tech. Univ., Keweenaw Res. Ctr., Houghton, MI 49930, mshust@micro.ti.com)

Wind noise in outdoor microphone measurements can significantly degrade acoustic data. An outdoor active windscreen based upon four local anemometer velocity measurements applied to an unscreened microphone is demonstrated. A simple relationship, developed from the Bernoulli equation, is used to transform hot-film anemometer wind velocity

measurements into microphone wind pressure estimates. Measurements performed outdoors on a horizontally positioned microphone demonstrate that a major part of unscreened microphone wind noise is flow noise caused by interaction between the microphone and adjacent air flow. These measurements also indicate that the dominant source of wind noise in a passively screened microphone are local pressure fluctuations that are *not* correlated with local velocity fluctuations. This important observation indicates that the active windscreen is unlikely to significantly quiet a microphone that has conventional passive screening and that the active windscreen applied to an unscreened microphone is unlikely to surpass the performance of a passive windscreen. Wind energy reduction performance of the active windscreen is shown to be approximately 12 dB for frequencies below 200 Hz and decreases smoothly to approximately 5 dB at 500 Hz. In addition, the active system transfer functions are observed to possess significant stability of over periods of hours. <sup>a)</sup>Currently at Texas Instruments. <sup>b)</sup>Currently at California Maritime Academy.

4:05

**2pSPb4. Auscultation of heart and lung sounds in high-noise environments using adaptive filters.** Jennifer S. Fleeter (Hewlett-Packard, 3404 E. Harmony, Fort Collins, CO 80528, jen@fc.hp.com) and George R. Wodicka (Purdue Univ., West Lafayette, IN 47907)

The clinical utility of a stethoscope in an aircraft is limited by high ambient noise. An adaptive noise-reduction stethoscope was implemented and some of its capabilities evaluated. Noise-corrupted heart and lung sounds, and a noise estimate, were collected using a two-microphone coupler in a simulated aircraft environment with 80–100 dB(SPL) ambient noise. Two adaptive filtering algorithms were compared: least mean square (LMS) and normalized LMS (NLMS). For frequencies between 20 and 800 Hz, the NLMS approach yielded roughly a 25% improvement in the extracted signal-to-noise ratio (SNR), while also providing a reduced adaptation time. Coupler chamber geometry was then examined by comparing two designs, one with a cylindrical microphone chamber and the other conical. There was no observable difference between the extracted signals due to this geometry change. Noise source independence was also investigated through comparison of algorithmic performance for C-130 aircraft and helicopter noise. Helicopter noise yielded an 18% lower SNR than C-130 noise due primarily to its relatively larger low-frequency spectral content. Thus a stethoscope using adaptive filters holds promise to extract heart and lung sounds from high ambient noise environments, with the NLMS providing some performance enhancements under certain conditions.

4:20

**2pSPb5. A comparison of tonal signal extraction methods.** Michael G. Jones (NASA Langley Res. Ctr., 2 N. Dryden St., M.S. 463, Hampton, VA 23681)

The measurement of acoustic pressure signals in the presence of masking noise, often generated by mean flow, is a continual problem in the field of passive liner duct acoustics research. When performing acoustic liner tests in a flow duct facility, the researcher must balance two criteria. The most obvious is to design the acoustic liner such that the maximum

amount of sound absorption is achieved. The other is to obtain a signal-to-noise ratio high enough for quality measurements. For grazing incidence impedance tests, these two criteria are contradictory. As the liner absorptive capacity is increased, the signal-to-noise ratio at the liner trailing edge is decreased. For this reason, measurement methods are needed that are capable of accurately extracting the portion of the measured acoustic pressure which is due to the sound source, even when the desired signal is buried beneath the broadband background noise generated by the presence of mean flow. The results to be presented provide a comparison study of three signal extraction methods for acquiring quality acoustic pressure measurements in the presence of broadband noise (to simulate effects of mean flow). The performance of each method was compared to a baseline measurement of a pure tone acoustic pressure 3 dB above a uniform, broadband noise background.

4:35

**2pSPb6. Performance of passive correlation detectors using autocorrelation and energy spectrum inputs.** Lisa A. Pflug (Naval Res. Lab., Stennis Space Center, MS 39529), George E. Ioup, and Juliette W. Ioup (Univ. of New Orleans, New Orleans, LA 70148, jwiph@uno.edu)

Using the energy spectrum or autocorrelation as a functional input to the cross correlation (energy), bicorrelation, and tricolorrelation detectors for unknown transient signals can result in improved detector performance compared to the correlations of the received signals. Test signals with differing autocorrelation and energy spectrum properties are used in computer simulations with Gaussian noise to compare results using the original received signals, the energy spectra of the received signals, and the autocorrelations of the received signals to form the correlations. Detection

results are presented for the case when only two channels of input data are available to form the correlations, as well as the case when three and four channels of input data are available to form the higher order correlations. In the former case, it is shown that detection performance can be improved for narrow-band signals by using the energy spectrum and autocorrelation functional inputs rather than the original received signal. In the latter case, it is shown that detection performance can be improved by using the autocorrelation input for a broadband signal and the energy spectrum input for a narrow-band signal, and that for the test signals, the tricolorrelation detector performs best. [Research supported by ONR.]

4:50

**2pSPb7. Reduction in computational requirements with matched field processing.** Michael Wazenski (Digital Systems Resources, 12450 Fair Lakes Circle, Ste. 500, Fairfax, VA 22033)

The sensitivity of matched field techniques to source location is a significant benefit from a localization accuracy perspective. Unfortunately, the implementation of matched field techniques in real-time systems is hampered by the computationally demanding hypothesis testing of source location in range and depth. Furthermore, operational requirements of such systems generally do not demand a high degree of accuracy. The Minimum Variance with Environmental Perturbation Constraints (MV-EPC) processor developed by Krolik [J. Acoust. Soc. Am. **92**, 1408–1419 (1992)] has been used to reduce the sensitivity to environmental uncertainty. This same approach can be used to reduce the sensitivity to source location, thereby reducing the number of source location hypotheses. This produces a computational tractable approach to real-time, robust matched field processing. Illustrative simulations and real data results using SWelLEX-96 data are presented.

TUESDAY AFTERNOON, 13 OCTOBER 1998 MARRIOTT BALLROOMS 5 AND 6, 1:30 TO 4:20 P.M.

## Session 2pUW

### Underwater Acoustics: Detection and Imaging of Buried Objects II

Nicholas P. Chotiros, Chair

*Applied Research Laboratories, University of Texas, P.O. Box 8029, Austin, Texas 78713-8029*

#### *Invited Papers*

1:30

**2pUW1. Scattering from buried spheres in a shallow-water laboratory.** Harry J. Simpson (Naval Res. Lab., Code 7136, 4555 Overlook Ave., Washington, DC 20375), Carl K. Frederickson (Univ. of Central Arkansas, Conway, AR 72035), and Brian H. Houston (Naval Res. Lab., Washington, DC 20375)

A series of scattering measurements from buried and proud spheres in the NRL shallow-water laboratory have been conducted in order to understand the scattering of sound from targets at and below the sandy-bottom interface. The water-saturated sandy bottom was a manufactured 212- $\mu\text{m}$  washed and filtered sand. The initial measurements included scattering from two spheres, a solid aluminum sphere with a 15-cm diameter, and a hollow stainless steel sphere with a 60-cm diameter and an  $h/a$  of 0.05. For baseline measurements, free-field and proud measurements of both spheres were made. Buried measurements of the spheres ensconced below the critical angle were conducted with a smoothed interface to quantify contributions from the evanescent wave field. Also investigated is the enhancement due to a roughened sand-water interface. The results of these measurements will be discussed and a preliminary analysis will be presented. [Work supported by ONR.]

1:55

**2pUW2. Detection of buried objects: Tank experiments.** Jean P. Sessarego and Jean Sageloli (CNRS/LMA 31 Chemin Joseph Aiguier, 13402 Marseille Cedex 20, France)

Detection and identification of buried objects in sediments is a wide problem which is far from being solved due to the complexity of the different situations encountered in real life applications (surface roughness, multiple reflections between object and water-sediment interface, complex nature and shape of the target, complex nature of the surrounding medium, porosity, bubbles). In these conditions, it seems hopeless to develop a general method capable of handling all these different situations. One issue for this problem



is to resort to tank experiments and perfectly controlled situations. The aim of this paper is to give some answers to questions which frequently arise in detection problems of buried objects and also to show the limit of the assumptions which are made by most people working in this field. In particular, comments on the influence of the elastic behavior of the surrounding medium on the scattered field will be given; moreover, in the case of a simple shaped object, the shift in the position of resonances which is experimentally observed will be discussed. Finally, an experimental study of the influence of surface roughness will be given in order to show the importance of this effect on target detection.

### Contributed Papers

2:20

**2pUW3. A direct inverse scattering method for imaging obstacles with unknown surface conditions.** Andrew N. Norris (Mech. and Aerosp. Eng., Rutgers Univ., 98 Brett Rd., Piscataway, NJ 08854-8058)

A new technique is described for imaging obstacles using the acoustic far-field response for plane wave incidence. The method requires no *a priori* information about the surface, nor does it depend upon prior knowledge of the surface boundary conditions. The algorithm is straightforward to implement and is illustrated by imaging multiple targets simultaneously for various surface boundary conditions: soft, hard, and impedance. The input data is the full acoustic scattering matrix at a single frequency, from which the eigenvalues and eigenfunctions of the far-field operator are determined. Associated incident wave functions are then used to compute a spatial indicator function which takes on large values in the exterior of the target but is bounded inside the obstacle, or obstacles when there are multiple disconnected surfaces. [Work supported by ONR.]

2:35

**2pUW4. High-resolution velocity images of targets buried in soils.** James Sabatier, Ning Xiang, and Ron Craig (Natl. Ctr. for Physical Acoust., Univ. of Mississippi, University, MS 38677)

Acoustic-to-seismic coupling of airborne sound into the ground is used to detect objects buried in air-filled soils. Target sizes of 0.1–0.25 m are buried in various soils to depths of several centimeters. A sound source suspended in the air above the ground is used to excite vibrations in the poro-elastic soil. Audio frequencies of 1–10 kHz are broadcast. The acoustically induced seismic vibrations are measured using an off-the-shelf scanning laser Doppler vibrometer (LDV). Previous measurements with buried microphones and geophones and modeling show the Biot type II wave carries most of the energy near the soil surface. This wave is locally coupled into the soil, scattered from near-surface buried targets, and then returns to the soil surface. The scattered acoustic velocity field on the surface (summed with the incident and reflected fields) is imaged using the LDV. Using a high spatial resolution scan of 0.003 m, scattered wavefronts from buried targets are observed. These images facilitate visual determination of the target shape. Targets used thus far include solid iron circles, squares, and triangles. [Work supported by CECOM, Night Vision & Electronic Sensor Directorate.]

2:50–3:05 Break

3:05

**2pUW5. Physics of 3-D scattering from rippled seabeds and buried targets in shallow water.** Henrik Schmidt (MIT, Cambridge, MA 02139 and SACLANT Undersea Res. Ctr., La Spezia, Italy), Warren Fox, Alain Maguer, and Edoardo Bovio (SACLANT Undersea Res. Ctr., La Spezia, Italy)

A new wave theory model (OASES-3D) providing consistent modeling of seabed insonification, three-dimensional target scattering, and rough seabed reverberation has been used to investigate the spatial and temporal characteristics of the multistatic scattering and reverberation from rippled, shallow-water seabeds with buried targets. It is shown that the highly polarized spectral characteristics of ripple fields is associated with a reverberation environment which is highly sensitive to both the frequency and insonification aspect relative to the ripples. The theoretical study has suggested that significant gains in subcritical detection performance for buried objects can be achieved by band-limiting the processing to frequencies

below typically 3–5 kHz. The results of 3-D target scattering and reverberation measurements performed by SACLANTCEN in shallow-water environments with rippled, sandy bottoms have confirmed this hypothesis. However, the experiments have consistently shown higher low-frequency reverberation than predicted by the model. Here, OASES-3D has been used to demonstrate that a very small amount of low-wave-number roughness components superimposed on the sand ripples can account for the observed reverberation. This in turn suggests that the use of new low-frequency sonar concepts for buried target detection and classification must be accompanied by adequate environmental assessment incorporating the long-wavelength ( $\lambda > 25$  cm) seabed roughness components. [Work supported in part by SACLANTCEN and ONR, Ocean Acoustics.]

3:20

**2pUW6. Backscattering enhancements for “plastic” scatterers in water and silt: Novel mechanisms and ray models for solids and shells.** Philip L. Marston, Brian T. Hefner, and Florian J. Blonigen (Dept. of Phys., Washington State Univ., Pullman, WA 99164-02814, marston@wsu.edu)

Some “plastic” polymer solids have sufficiently low intrinsic dissipation that they can be approximated as purely elastic for the purpose of understanding the main features of their response to sonar. Unlike metallic objects, the typical plastic object has shear and Rayleigh phase velocities that are less than the speed of sound in water or in silt. In addition, the density contrast with the surroundings is less than for metallic objects. These changes cause major differences in the physical mechanisms for producing backscattering enhancements. For example, partial-wave-series predictions for backscattering by some solid plastic spheres show an enhancement in the  $ka = 2-10$  region due to tunneling coupling to Rayleigh wave resonances. We have modeled this enhancement with ray theory. For plastic shells, since the high-frequency symmetric (or  $s_0$ ) Lamb wave becomes subsonic, there is predicted to be a coincidence enhancement for the  $s_0$  wave. The backscattering by tilted finite-circular plastic solid cylinders [F. J. Blonigen and P. L. Marston, J. Acoust. Soc. Am. **102**, 3088 (1997)] was observed to be enhanced due to the merging of rainbow caustics in the meridional plane. [Work supported by the Office of Naval Research.]

3:35

**2pUW7. High-resolution reconstruction of penetrable obstacles at low frequency.** Luise Couchman, Jeremy A. Warner (Naval Res. Lab., Code 7130, 4555 Overlook Ave., Washington, DC 20735-5350), and Dilip N. Ghosh Roy (SFA, Inc., 1401 McCormick Dr., Landover, MD 20785)

The scattering and inverse scattering of plane acoustic waves from penetrable acoustic targets (including shell-type structures) of arbitrary shapes and compositions are discussed. The scattering problem is solved by combining the technique of shape differentiation of the scattered field with the Padé extrapolation. The solution thus obtained is then used in the inversion recovery of the targets from the far-field data via the Gauss-Newton iterative procedure. Both the shapes and the material parameters of the targets are reconstructed. The advantages of the technique are discussed and numerical results are presented for a number of two-dimensional obstacles. Also presented are some three-dimensional results for Dirichlet objects. As an extension, a random acoustic ambience is considered.

**2pUW8. Experimental results for detection of buried objects at low grazing angles.** Warren L. J. Fox and Alain Maguer (NATO SACLANT Undersea Res. Ctr., Viale San Bartolomeo 400, 19138 La Spezia, Italy)

Extension of buried object detection sonar system concepts to include low grazing angle geometries (i.e., beyond critical angle) would provide useful gains in coverage rate, provided acceptably high detection probabilities can be maintained for sufficiently low probabilities of false alarm. Several experiments have recently been conducted at shallow water sites with sandy seabottoms near Elba Island, Italy, in order to study the acoustic backscattering characteristics of the seabed and buried targets in a range of grazing angles both above and below the nominal critical angle of the seabed. A parametric sonar with significant secondary frequency source levels in the range 2–16 kHz was used (the size of the targets yielded  $ka$  values also in the approximate range 2–16). Modeling results for buried objects have shown that subcritical insonification can produce relatively high monostatic echo levels, especially at lower frequencies where the evanescent field is strongest. Some results of the experiments

are discussed which show promising SNR improvements for subcritical cases when the lowest parts of the frequency band are emphasized, in empirical agreement with the models.

**2pUW9. Performance of a diver-held sub-bottom sonar.** John W. Irza (Sygnus Technology, Inc., 24 Richardson Ave., Arlington, MA 02174, jirza@sygnus.com)

The system design of a hand-held parametric sonar for divers is presented. Operational and technology trades are discussed. Use of an embedded digital signal processing (DSP) device is presented in the context of nonlinear waveform generation and receive signal processing algorithms and data display. Field results from the commercially available diver sonar unit (Sygnus model PDS-120) are presented from various target and bottom experiments. Efficacy of various waveforms with respect to target detection and classification is discussed. Methods for exploiting target resonances excited by the (low-frequency) parametric source are presented.

## Session 3aAA

## Architectural Acoustics: Acoustics for Office Spaces

Kenneth P. Roy, Chair

*Armstrong World Industries, Innovation Center, P.O. Box 3511, Lancaster, Pennsylvania 17604*

Chair's Introduction—8:45

*Invited Papers*

8:50

**3aAA1. Open office acoustics and productivity.** Kenneth P. Roy (Armstrong Innovation Ctr., 2500 Columbia Ave., Lancaster, PA 17604, kproy@armstrong.com)

Since its introduction in the 1960s, open office design has been driven by a need for lower cost, increased flexibility, and enhanced worker productivity. The first two can be easily evaluated, but what about "knowledge worker" productivity? The objective in open office design is to have speech intelligibility within a work space, and speech privacy between adjacent work spaces. This paper presents a first step in evaluating knowledge worker productivity as affected by the acoustic design of the space. Six large companies participated in a study on worker satisfaction and perceived effectiveness both before and after acoustic modifications of their workspace. Even a small increase in worker productivity will warrant incremental investments in acoustic treatments since the productivity payback is relatively short. Accordingly, the facility manager needs to consider the building space as a worker productivity "tool," and not just a space in which to work.

9:15

**3aAA2. Speech privacy in enclosed and open plan: A review and retrospective.** William J. Cavanaugh (Cavanaugh Tocci Associates, Inc., 327F Boston Post Rd., Sudbury, MA 01776)

Research on speech privacy problems in buildings at Bolt Beranek and Newman in the early 1960s showed convincingly that a person's sense of acoustical privacy was directly related to the intelligibility of the intruding speech signal over the continuous ambient sound present [Cavanaugh *et al.*, "Speech privacy in buildings," *J. Acoust. Soc. Am.* **34**, 475–492 (1962)]. Both in laboratory and in real world settings people feel they have "confidential privacy" when the articulation index (AI) of the intruding speech is 0.05 or less. Higher values of AI are acceptable for less demanding tasks, i.e., "normal privacy." The method quantifies each of the significant variables involved and compares a summation of these metrics with response data for prior case histories both to predict, and in the case of existing situations, to evaluate speech privacy conditions in particular cases. R. W. Young reviewed the analysis method and showed that sufficient accuracy was preserved if simple, commonly used A scale sound levels were used in place of more cumbersome frequency based metrics [Young, "Re-vision of the speech privacy calculation," *J. Acoust. Soc. Am.* **38**, 524–533 (1965)]. Later in the 1960s the method was successfully applied to open plan offices which were becoming more prevalent [Hirtle, Watters, and Cavanaugh, "Acoustics of open plane spaces . . . some case histories," *J. Acoust. Soc. Am.* **46**, 91A (1969)]. The lessons learned during the continued development and application of the "Speech privacy calculation" over the years is reviewed and discussed.

9:40

**3aAA3. Comparison between sound transmission measurements made in working offices and in the laboratory.** Steven M. Brown (Steelcase, Inc., CD-5E-16, P.O. Box 1967, Grand Rapids, MI 49501, sbrown@scrbd.com)

Field and laboratory sound transmission measurements on office partitions are compared. The measurements were carried out both in working offices and in a laboratory setting on virtually identical full partition constructions. The effects of various performance-enhancing construction details are examined in both settings. The effects of these details are also compared to expectations based on the architectural acoustics "folklore." Implications are noted for using laboratory sound transmission data in predicting field performance and in guiding the design and specification of partitions intended for use in offices.

10:05

**3aAA4. Field experience in assessing open plan office acoustical privacy.** Lincoln B. Berry and Timothy J. Foulkes (Cavanaugh Tocci Associates, Inc., 327F Boston Post Rd., Sudbury, MA 01776)

Experience continues to show that the significant factors affecting open office plan speech privacy include available masking (background), sound barrier height and absorption, distance between sound source and receiver, ceiling sound absorption, furniture layout, speech effort of occupants, etc. These factors are adequately quantified by currently available metrics, and methods for predicting speech privacy prove to be practical, easy to use, and quite accurate. Case studies of open plan offices will be presented including available systems and approaches for electronic sound masking in both large and small office configurations.

10:30

**3aAA5. Articulation class data: Early returns.** R. Kring Herbert (Ostergaard Acoustical Associates, 200 Executive Dr., West Orange, NJ 07052)

Articulation class (AC) is a single number metric approved by ASTM Committee E-33.02 to characterize the performance of components used in open office environments to provide a degree of acoustical privacy between workstations. The AC values are derived from standardized acoustical laboratory tests using ASTM Standard E-1110. Standard test methods have been developed for ceiling systems (E-1111), furniture panels employed as acoustical barriers (E-1375), and wall finishes and furniture panels in the flanking position (E-1376). Test data are becoming available based on ASTM E-1111 for ceiling assemblies. These data are reviewed for different types of ceiling boards and the merits of the test method are examined with these new data in hand.

10:55

**3aAA6. Speech privacy between closed and open offices.** Kenneth P. Roy (Armstrong Innovation Ctr., 2500 Columbia Ave., Lancaster, PA 17604, kproy@armstrong.com)

Speech privacy between closed and open office spaces is dependent on the noise reduction between the spaces, and the background sound available in the receiving space to mask the intruding speech. System performance was evaluated between both pairs of closed spaces, and closed to open space. Ceilings included both light and air supply devices, and the walls included typical door and utility features. The speech privacy was evaluated based upon both objective and subjective measures of performance. The objective response was calculated based on the articulation index (AI), and the subjective response included both PB word lists and continuous discourse (CD). Proper choice of ceiling and wall materials and system design, in combination with electronic masking sound, will provide adequate speech privacy.

### *Contributed Papers*

11:20

**3aAA7. Transmission of sound through suspended ceilings from HVAC terminal units.** Alf Warnock (Natl. Res. Council Canada, M59 Montreal Rd., Ottawa, ON K1A 0R6, Canada)

An ASHRAE project to investigate factors determining the sound pressure levels in rooms below ceilings concealing air-terminal units has been completed. Four terminal units installed close to the six ceiling types used were the major noise sources. They were supplemented by two simulators powered by loudspeakers. Sound power was measured for each device in the 156 cubic meter test room in its reverberant condition. The levels in the room were measured for each combination of source and ceiling tile. Sound pressure level was measured as a function of distance from two sources in the room below. The main intent of the project was to validate ARI Standard 885 which provides a calculation method for such situations. Differences among ceiling types were less than expected; leakage around the edges of each panel is a dominant transmission path. Ceiling attenuations at low frequencies were found to depend on the area of the lower face of the units. Sound levels in the room were essentially uniform when the source was above the ceiling. The decay of sound with distance from the sources below the ceiling was found to depend on the inverse of the room reverberation time.

11:35

**3aAA8. Airborne and impact sound insulation of joist floor systems: A collection of data.** Alf Warnock (Natl. Res. Council Canada, M59 Montreal Rd., Ottawa, ON K1A 0R6, Canada)

An extensive series of measurements on joist floors of various types was recently completed at the National Research Council. About 190 floors with different joist types, subfloors, ceiling types, ceiling support systems and type and thickness of sound absorber were constructed and measured. The joist types comprised solid wood, wood trusses, I-joists, and steel joists. Three types of sound absorbing material were used: glass, rock and cellulose fiber. The measurements provide an extensive, consistent set for analysis. Measurements of fire resistance made at the same time at NRCC caused changes to be made to the layout of the resilient metal channels used to support the gypsum board. These resulted in reduced sound insulation. For both transmission loss and impact sound, many of the results could be predicted with sufficient accuracy by simple regression analysis using variables such as the mass of the layers, joist depth and spacing, insulation thickness and density and resilient metal channel spacing. The measurements and the more important results will be presented in the paper.

## Session 3aAO

**Acoustical Oceanography: Sediment Geoacoustic Measurements and Models I**

Michael D. Richardson, Chair

*Naval Research Laboratory, Code 7431, Stennis Space Center, Mississippi 39529-5004*

Chair's Introduction—9:00

*Invited Papers*

9:05

**3aAO1. A new approach to seismic wave propagation in unconsolidated and consolidated porous media.** Michael J. Buckingham (Scripps Inst. of Oceanogr., Univ. of California—San Diego, La Jolla, CA 92093-0213, mjb@mpl.ucsd.edu)

Compressional and shear waves in porous media, including saturated marine sediments and dry sedimentary rocks, exhibit an attenuation that scales as the first power of frequency. Biot developed a theory of wave propagation in such materials in which the dissipation was taken to be viscosity of the pore fluid. This, however, yields an attenuation that scales as the square of frequency below some threshold frequency, above which it converts to the square root of frequency. Recently, Buckingham developed an alternative wave theory of porous media in which the dissipation arises from stress relaxation at grain boundaries. Such a mechanism is consistent with the fact that stress and strain in porous media do not follow one another instantaneously. With an appropriate choice for the internal material response function, representing a time-dependent stick-slip process between grains, it turns out that the attenuation scales as the first power of frequency, in accord with observations. Moreover, the dissipation also introduces stiffness into the material, allowing it to support shear, even though the elastic modulus of the medium may be identically zero. These new ideas will be explored in the presentation, and the theoretical predictions will be shown to be consistent with experimental data.

9:25

**3aAO2. Measurements and modeling of sound propagating into unconsolidated water-saturated porous media in a laboratory environment.** Harry J. Simpson, Brian H. Houston, and Luise S. Couchman (Naval Res. Lab., Code 7136, 4555 Overlook Ave., Washington, DC 20375)

Three models of sound propagating into and within a water-saturated sandy bottom are compared to measurements made in the NRL shallow water laboratories. An initial set of measurements was made in a manufactured 212- $\mu\text{m}$  mean diameter sand, which was washed and filtered, to quantify sound penetration as a function of incident angle and interface roughness, as well as to identify the wave types generated within a water-saturated sandy bottom. Measurements have also been made of sound propagation within a water-saturated sandy bottom, which employed a specialized set of transducers to generate and measure compressional waves and a second set of transducers to generate and measure shear waves. Measurements have also been made in a 525- $\mu\text{m}$  mean diameter water-saturated sand. All of the above measurements are compared to a fluid bottom model and a Biot media model, both of which characterize the sound propagating within a water-saturated sandy bottom. In addition, the measurements of sound penetration into the sandy bottom are compared to roughened interface scattering models. [Work supported by NRL and ONR.]

9:45

**3aAO3. Seabed sediment property inversions and verifications.** Tokuo Yamamoto (Geoacoustics Lab., AMP, RSMAS, Univ. of Miami, 4600 Rickenbacker Cswy., Miami, FL 33149, tyamamoto@rsmas.miami.edu)

The acoustic wave propagation model used in inversion is a key to sediment properties inverted from acoustic data. Geoacoustic models (Biot, Squirt Flow, BISQ, Super-k, Gassmann, Wood models) are all reviewed in light of their applicability to seabed sediment inversions. The simplest sediment model is desirable for a given inversion from inverse calculation standpoint. Depending on sediment type and acoustic frequencies, an optimal model is determined. The second key is the acoustic measurement method whose data is used in inversion. The third key to inversions is the availability of reliable ground truth data from established measurement methods. Two examples of shallow-water sediment inversions are shown to demonstrate these points. The first example is imaging the permeability-porosity structure of limestone seabed from cross-well tomography (1–12 kHz) measurements based on the Super-k model as compared with pumping tests, downhole neutron, gamma ray, and acoustic tests, and cores. The second example is inversions of measured (5–15 kHz) acoustic backscatter data for density, sound speed, attenuation, and their spectra based on a Woods sediment model. Crosswell tomography is used to compare with the inversion results. [Work supported by ONR.]

10:05

**3aAO4. Recent *in situ* measurements of sediment geoaoustic properties.** Michael D. Richardson (Marine Geosciences Div., Naval Res. Lab., Stennis Space Center, MS 39529-5004, mike.richardson@nrlssc.navy.mil)

Values of surficial geoaoustic properties have been reported for a variety of siliciclastic and carbonate sediment types in coastal environments using direct *in situ* measurement techniques. Recent measurements in the North Sea have provided detailed profiles of shear wave speed in the upper 30 cm of sediment and increased the meager database of values of shear wave attenuation. These new measurements from North Sea sediments are placed into the context of past measurements and new relationships among sediment physical and geoaoustic properties are presented. Profiles of shear wave speed support theoretical models that predict that the dynamic shear modulus is proportional to the effective stress to the 1/3 power. [Work supported by ONR.]

10:20–10:35 Break

10:35

**3aAO5. Measurement of grain bulk modulus using sound speed measurements through liquid/grain suspensions.** Kevin Briggs, Michael Richardson (Naval Res. Lab., Stennis Space Center, MS 39529-5004), Kevin Williams, and Eric Thorsos (Univ. of Washington, Seattle, WA 98105)

Under certain conditions, Woods equation can be used to predict the speed of sound in liquid/solid grain suspensions when the bulk moduli and densities of the grains and the liquid are known. Alternatively, if the sound speed is measured through a suspension where the bulk modulus of the liquid and the densities of the fluid and grains are known, it is possible to estimate the grain bulk modulus. An experiment was carried out as an initial test of the resolution of measuring grain bulk modulus via this method. Bulk modulus measurements were made of polystyrene beads suspended in water, and of glass beads and sand grains suspended in a high-density liquid. The polystyrene and glass beads had known bulk moduli (4.2e9 and 6.3e10 Nt/m<sup>2</sup>, respectively) and acted as controls. The polystyrene (glass) bead radii were such that the mean  $ka$  was 0.42 (0.25), where  $k$  is the acoustic wave number in the liquid and  $a$  is the bead radius. Corrections to Woods equation are considered as  $ka$  approaches 1. The sand grain modulus results are discussed in the context of porous media sediment models. Planned experimental improvements will be discussed. [Work supported by ONR.]

10:50

**3aAO6. Inversion of sediment properties from chirp sonar data using an extended Biot–Stoll–Gassmann model.** Altan Turgut and Stephen N. Wolf (Naval Res. Lab., Acoust. Div., Washington, DC 20375)

Recently, chirp sonar subbottom profiling systems have been used extensively for subbottom imaging as well as for sediment impedance profile and attenuation estimation [e.g., LeBlanc *et al.*, *J. Acoust. Soc. Am.* **91** (1992)]. Typical mid-frequency (1–20 kHz) chirp sonar signals are highly attenuated in the sediment which makes the usage of a proper pulse propa-

gation and attenuation model in the inversion algorithm necessary. An extended Biot–Stoll–Gassmann model is proposed in accordance with the reported sound speeds and attenuation values for different types of sediments. This model was used in a time-domain inversion algorithm for the estimation of sediment geoaoustic properties (density, sound speeds, and attenuation) as well as mechanical properties such as porosity and permeability. Sensitivity analysis indicated that the new model provides a rapid inversion of porosity profile even in the case of noisy one-dimensional reflection data. In this case, along with the attenuation estimation, other parameters are conveniently calculated using the proposed model. Finally, inversion results with the established confidence intervals are presented for the chirp sonar data collected during the SWARM experiment [Apel *et al.*, *IEEE J. Ocean. Eng.* **22**(3) (1997)]. [Work supported by ONR.]

11:05

**3aAO7. Measurements of acoustic velocity in granular media.** Masao Kimura (Dept. of Ocean Eng., Tokai Univ., 3-20-1 Orido, Shimizu, Shizuoka 424-8610, Japan)

The frame bulk and shear moduli are important in analyzing the acoustic propagation in marine sediments. However, the studies on these moduli are not considered to be sufficient. The frame bulk and shear moduli of marine sediments are related to the longitudinal and shear wave velocities in dry marine sediments. In this paper, the longitudinal and shear wave velocities in dry glass beads with five different grain sizes are measured to investigate the effect of grain size. The grain sizes are 0.05, 0.1, 0.2, 0.4, and 0.8 mm. The longitudinal wave velocities are measured using piezoelectric transducers with the operating frequency of 11.8 kHz. The shear wave velocities are measured using bimorph-type piezoelectric transducers with an operating frequency of 3.5 kHz. The measured results show that the longitudinal wave velocity largely increases and the shear wave velocity slightly increases as the grain size increases.

11:20

**3aAO8. Inversion of seabed porosity and permeability using pore pressure probe data.** Yongke Mu, Mohsen Badiy, Alexander H.-D. Cheng, Zhong Liu (Univ. of Delaware, Newark, DE 19716, badiy@udel.edu), and Richard H. Bennett (Seaprobe Inc., 501 Pine St., Picayune, MS 39466)

In shallow water acoustics two very important physical parameters affecting the acoustic wave dissipation are porosity and permeability. These properties are better obtained *in situ* than in the laboratory. To avoid large-scale acoustic experiment and an inversion that provides only the range averaged properties, the *in situ* pore pressure measurement by probes on and in the surficial sediments could be used. The probe penetrates the seabed and measures the seabed pore pressure response to water waves. To use the data to invert for porosity and permeability, the analytical solution of the forward problem based on the Biot theory of poroelasticity is first constructed. Sensitivity analysis is conducted with respect to the porosity and the degree of saturation. Considering the empirical relationships between physical parameters, a minimum set of data required for predicting the pore pressure is presented. The inversion is applied to the field measured data and the results are compared with the independent measurements of these parameters.

**Session 3aEA****Engineering Acoustics: Nondestructive Evaluation of Materials Using Acoustical Techniques**

P. K. Raju, Chair

*Auburn University, Mechanical Engineering Department, Ross 201, Auburn, Alabama 36849-5341***Chair's Introduction—7:55*****Invited Papers*****8:00****3aEA1. Acoustic condition monitoring.** Robert D. Finch (Dept. of Mech. Eng., Univ. of Houston, Houston, TX 77204-4792)

For a number of years railroad wheels were used as test objects in developing acoustic signature monitoring techniques. This work will be reviewed as well as later laboratory studies using beams to determine the sensitivity of the method. Cracks and other defects can cause shifting and splitting of resonance frequencies, so that these changes can be used to indicate the presence of a defect. The limitation of the vibration monitoring method is that other conditions, such as uncertainties in the geometry of the test object, its surface conditions, and loading can also affect the vibration response, and it is necessary to distinguish the effects due to harmful conditions from those due to harmless ones. The sensitivity of the method is thus determined by the need to make this distinction. The concepts will be illustrated with experimental results from a test fixture for the case of a slotted steel beam, assuming that a slot can be used as a model for a crack. Some experiments with concrete beams will also be viewed.

**8:20****3aEA2. Nondestructive evaluation of textile-reinforced composites based on spacial dependence of ultrasonic scattering.** Patrick H. Johnston (NASA Langley Res. Ctr., M.S. 231, Hampton, VA 23681, p.h.johnston@larc.nasa.gov)

The lateral symmetry of the fiber architecture of standard composite laminates, having unidirectional plies stacked in parallel planes, often allows the propagation of a normally incident compressional wave to be described as a one-dimensional problem. Simple transmission measurements of the amplitude and time of flight of pulsed ultrasound become simply related to the average sound velocity and attenuation of the composite. In recent years, composites have been developed using woven, braided, knitted, and stitched textiles. Propagation of ultrasound in these materials can no longer be adequately described by a one-dimensional model. Although simple transmission ultrasonic measurements can still be made, interpretation of the ultrasonic signals becomes ambiguous. It is believed that improved material characterization can be obtained by increasing the number of degrees of freedom in the measurement through the use of multiple element transducer arrays. In order to demonstrate the feasibility of using arrays to better characterize textile based composites, measurements were made of the angular variation of ultrasonic scattering from several composites. The incident transducer was aligned normal to the surface of the specimens, while a second transducer was used to measure the scattering as a function of azimuthal angle at various nonzero polar angles.

**8:40****3aEA3. Fourier transformation for nondestructive evaluation.** Vinay Dayal (Aerosp. Eng. and Eng. Mech., 304 Town Engineering Bldg., Iowa State Univ., Ames, IA 50011)

Fourier transformation of the time domain signal has been used for a variety of applications in the area of nondestructive evaluation of both isotropic and composite materials. Reflection pulses, which are close together in time domain, can be separated out in the frequency domain. The information from the reflected or refracted pulses was deconvolved and the wave velocity/sample thickness and damping for very thin samples could be measured [V. K. Kinra and V. Dayal, *Exp. Mech.* **28**(3), 288–297 (1988)]. The added advantage of these techniques is that they immediately warn the user of the dispersion in the material. Fourier transform of pulses was applied to the measurement of the wave velocity of Lamb waves. Lamb waves or plate waves are affected by the in-plane material properties and, for platelike structures, this measurement is very useful in making velocity and damping measurements [V. Dayal, *Rev. Prog. QNDE* **13A**, 189–194]. The technique has since been used for the measurements of mechanical properties such as elastic constants of composite materials, automated simultaneous measurement of wave speed and thickness, and measurement of very thin coatings. Various applications will be reviewed.

9:00

**3aEA4. Structural damage identification using free decays.** John Burkhardt (Mech. Eng. Dept., U.S. Naval Acad., Rickover Hall, Annapolis, MD 21402-5042)

A new nondestructive technique is proposed for the identification of structural damage which exploits the unique, nonexponential decay characteristics of locally damaged systems. By statistically modeling both mode shapes and damage characteristics a power-law decay model is derived and advanced as the basis for the newly proposed technique. Theoretical predictions indicate that both the presence and extent of structural damage can be determined by the observation of free structural decays. Numerically simulated structural decays are presented which support the proposed technique.

9:15

**3aEA5. Improvements on the design of the electrodynamic transducer coils used in spectropic determination of acoustic constants of thin bars.** Qiushuang Guo and David A. Brown (Acoust. Res. Lab., Dept. of Elec. and Computer Eng. and Ctr. for Marine Sci. and Technol., UMass—Dartmouth, North Dartmouth, MA 02747)

The resonant bar technique for measuring the acoustic properties of materials is inexpensive, easy to perform, and has the advantage of high signal-to-noise ratio. The design of transducer coils used to selectively excite and detect bar motion is crucial to obtain good data. A new electrodynamic transducer design is presented. The new transducers are small in size and mass and glued at the ends of the bar so that perturbations due to the transducers are small and easy to model. This design is more selective and permits less mechanical cross talk among longitudinal, flexural, and torsional modes. It also has negligible electrical cross talk between transducers. [Work supported by the Ph.D. Program and the Strategic Envirotechnology Partnership (STEP) through the Advanced Technology Center at the University of Massachusetts Dartmouth.]

9:30

**3aEA6. Propagation of transient ultrasound in a thick annulus: Modeling, experiments, and application to crack detection.** Zongbao Li and Yves H. Berthelot (Woodruff School of Mech. Eng., Georgia Inst. of Technol., Atlanta, GA 30332-0405)

Fatigue cracks often develop on the inner surface of annular components such as collars. Ultrasonic guided wave propagation can be used for nondestructive evaluation of such structures. A wave mode expansion solution is formulated for transient excitation of circumferential waves at the outer surface of a thick annulus by a distributed traction source (modeling a piezoelectric source with an angular wedge). The solution provides valuable information on the energy distribution inside the annulus and the modal content of the detected signals. The predicted waveforms are compared with experimental results obtained with a 2.25-MHz transducer for various wedge angles, and for various positions of the receiver on the outer surface. Crack detection in the annulus is investigated with transient circumferential waves. It is shown that a 1-mm machine-made radial crack on the inner surface can be detected. [Work supported by the ONR under a M-URI Center for Integrated Diagnostics.]

9:45

**3aEA7. Diffusion of ultrasound in concrete.** Joseph Turner (Dept. of Eng. Mech., Univ. of Nebraska—Lincoln, W317.4 Nebraska Hall, Lincoln, NE 68588, jat@unlinfo.unl.edu)

The propagation and scattering of ultrasound in concrete is discussed. The heterogeneous composition of concrete causes the ultrasound to scatter considerably. In the limit of many scattering events, the ultrasonic energy density in bars of concrete is shown to evolve in accordance with a one-dimensional diffusion equation. The ultrasonic diffusivity and dissipation are measured experimentally over the frequency range of 100 kHz to 2 MHz. Such frequencies are well above typical frequencies used for concrete inspection. The diffusivity, which is a measure of the microstruc-

ture, is shown to correlate with the strength of the concrete. This technique also allows the true dissipation from viscoelastic effects in the cement to be assessed directly. It is anticipated that the use of these higher frequencies will result in new techniques for characterizing material properties and damage in concrete structures. [Work supported by the Nebraska Research Initiative.]

10:00–10:15 Break

10:15

**3aEA8. Quantitative flaw reconstruction from ultrasonic surface wave fields measured by laser interferometry.** T. Douglas Mast and Grant A. Gordon (Appl. Res. Lab., Penn State Univ., University Park, PA 16802, mast@sabine.acs.psu.edu)

A quantitative imaging method for ultrasonic nondestructive testing of structures is presented. The method employs two-dimensional surface-vibration data that is obtained by laser interferometry methods such as holography and digital phase-stepping shearography. In this method, a surface wave field generated by a narrow-band contacting or noncontacting ultrasonic transducer is Fourier transformed to obtain a spatial-frequency domain representation of the wave field. The appropriate Green's function is then deconvolved from the wave field to obtain quantitative images of effective scattering sources. Since scattering strength is directly proportional to the local contrast of the structure, these images provide a direct map of internal flaws in structures such as plates and shells. The method is valid for strongly scattering inhomogeneities, and can employ scattered evanescent waves to obtain resolution of flaws much smaller than a wavelength. Simulated and experimental results illustrate the efficacy and quality of the imaging method.

10:30

**3aEA9. Backscattering and grain noise in random elastic media, beyond the single scattering model.** Richard L. Weaver (Univ. of Illinois, 216 Talbot Lab., 104 S. Wright St., Urbana, IL 61801)

Specific intensity, or energy per solid angle per area per time, is the appropriate dependent variable for the study of the transport of ultrasonic energy in a random heterogeneous solid. An integro-differential equation (the radiative transfer equation, or RTE) governs its dependence on time and space and propagation direction. The solutions that have been obtained are, however, arguably irrelevant for the experimental configurations in which a phase sensitive transducer of finite aperture is used. Such transducers are not sensitive to specific intensity *per se*. In this work it is shown that the RTE must be modified for the case of a finite aperture piezoelectric transducer. While the RTE governs the propagation of specific intensity between successive scatterings, the propagation from the source to the first scattering, and from the last scattering to the receiver, is governed by a more complicated process. It is found that specific intensity is not the appropriate quantity and that the Wigner distribution (in space and wave number, and in time and frequency) of the source and receiver beam patterns is needed. These modifications are discussed and an example presented in which the backscattered signal in a focused transducer includes both single and multiple scattering.

10:45

**3aEA10. Contact scanning Lamb wave tomography.** Mark Hinders, Eugene Malyarenko, and James McKeon (Appl. Sci. Dept., College of William and Mary, Williamsburg, VA 23187)

Lamb waves are guided ultrasonic waves capable of propagating relatively long distances in platelike structures such as airframe skins, storage tanks, and pressure vessels. Their propagation depends on frequency thickness and material properties, and, because structural flaws present changes in effective thickness and/or material properties, Lamb waves can be employed to assess the integrity of these structures. For structures with large surface areas, a full integrity evaluation can be a time-consuming operation, but with Lamb wave techniques, this evaluation can be performed with waves propagating along one dimension of the inspection



area as the probing transducers are moved in the perpendicular dimension. Such an approach yields information about the presence of flaws within the scanned area. Then, in order to quantitatively characterize the flaws, Lamb wave measurements can be made for a number of projections and an image of the flawed region can be reconstructed tomographically. Contact scanning Lamb wave tomography for metallic and composite structures with flaws is discussed as a practical technique for quantitative nondestructive evaluation.

11:00

**3aEA11. Acoustical characteristics of leak sounds in plastic pipes.** Wing T. Chu and Osama Hunaidi (Inst. for Res. in Construction, Natl. Res. Council of Canada, Ottawa, ON K1A 0R6, Canada, wing.chu@nrc.ca)

As an integral part of the AWWARF/NRC research project on the evaluation of existing methods for pinpointing leaks in plastic pipes, the acoustical characteristics of leak sounds in plastic pipes have been studied at the NRC's PVC pipe experimental leak detection simulator under controlled conditions. Tests have been performed both in the summer and in the winter. Experimental techniques and test results on the frequency content, attenuation rate, and propagation velocity will be presented in this paper.

11:15

**3aEA12. Nondestructive free oscillation method of crack evaluation.** Nadejda I. Bouraou, Anatoliy A. Boyarchuk (Dept. of Orientation and Navigation, Natl. Tech. Univ. of Ukraine, 37, Peremogy pr., Kiev, 252056, Ukraine), and Leonid M. Gelman (Natl. Tech. Univ. of Ukraine, Kiev, 252056, Ukraine)

For nondestructive evaluation of the relative size of a fatigue crack the acoustical free oscillation method is used. The testing object model as a nonlinear oscillator is considered. Object natural frequency shift is used as a testing data. The maximum likelihood equation is solved. New expressions of the relative crack size estimate are received.

11:30

**3aEA13. Nondestructive acoustical forced oscillation method of fatigue cracks.** Leonid M. Gelman and Lyudmila V. Kondratyuk (Dept. of Nondestructive Testing, National Tech. Univ. of Ukraine, 37, Peremogy pr., Kiev, 252056, Ukraine)

For nondestructive testing and evaluation of fatigue cracks the acoustical forced oscillation method with nonstationary excitation is used. The testing object model as a nonlinear oscillator is considered. The nonlinear forced oscillations of the testing object model are investigated. The new decision method ("equivalent frequency" method) of nonlinear differential equations which describe the object forced oscillations is proposed and investigated. Comparison of the proposed method with the classical decision method is given.

11:45

**3aEA14. Nonstationary vibroacoustical excitation for passive-active acoustical nondestructive evaluation of cracks.** Leonid M. Gelman and Nataliya Yu. Ossokina (Dept. of Nondestructive Testing, Natl. Tech. Univ. of Ukraine, 37, Peremogy pr., Kiev, 252056, Ukraine)

For nondestructive evaluation of fatigue cracks the passive-active low-frequency acoustical method of forced oscillations is used. In the case when natural frequencies of tested details are unknown but natural frequency range is known the use of vibroacoustical nonstationary excitation with variable (in natural frequency range) frequency is proposed. The new model of mentioned excitation is proposed and developed. New analytical expressions of current correlation function and spectral density are received and investigated.

3a WED. AM

WEDNESDAY MORNING, 14 OCTOBER 1998

HAMPTON ROADS BALLROOMS 4 AND 5, 9:55 A.M. TO 1:30 P.M.

### Session 3aED

### Education in Acoustics: Demos 2000

Murray S. Korman, Cochair

*Physics Department, U.S. Naval Academy, Annapolis, Maryland 21402*

James M. Sabatier, Cochair

*National Center for Physical Acoustics, University of Mississippi, Coliseum Drive, University, Mississippi 38677*

Chair's Introduction—9:55

### Invited Papers

10:00

**3aED1. Animal bioacoustics in the lab: Some hows and whys of six-legged listeners.** Hamilton Farris (Sec. Neurobiology and Behavior, Mudd Hall, Cornell Univ., Ithaca, NY 14853)

Animal bioacoustics is an interdisciplinary field that may employ concepts from physical acoustics, psychoacoustics, neurobiology, and evolutionary biology to examine the characteristics of sound production and hearing in nonhuman animals. Most of the public's attention to bioacoustics focuses on the acoustic behavior of some of our close mammalian relatives and birds, but equally elaborate acoustic signals have evolved in a wide variety of taxa including many insects. These signals function in such diverse contexts as communication among conspecifics, detecting and avoiding predators, and locating appropriate habitat. For example, as a consequence of the selective pressure from insectivorous bats which echolocate their prey using ultrasound, several insects have

evolved ultrasound sensitivity. When presented with ultrasound, these insects perform evasive behaviors that function in bat avoidance. Demonstrations here will show how the ultrasound-induced startle response is a useful behavioral assay for auditory sensitivity in certain insects (e.g., crickets and beetles). This experimental paradigm can thus be used to teach the laboratory methods required for measuring the characteristics of a sensory system as well as interpreting the evolutionary contexts in which the sensory system has evolved. [Work supported by NIMH.]

10:15

**3aED2. Speech acoustics: Vocal tracts, synthesizers, and talking heads.** Philip Rubin (Haskins Labs. and Yale Univ. School of Medicine, 270 Crown St., New Haven, CT 06511, rubin@haskins.yale.edu)

This presentation provides an introduction to human speech acoustics for a general audience. Acoustic signals are created in humans by a complex sound production system. The nature of this elegant sound-producing device will be shown in a number of ways, including demonstrations of the source-filter model of sound production and an articulatory model that produces sound by attempting to capture what is going on in the vocal tract during speech production. Real listeners do not attend solely to the acoustic signal. Information is available in a number of domains, including visual and tactile. The multimodal nature of speech will be demonstrated by the McGurk effect. Recently there has been considerable interest in the study of audiovisual speech. A portion of the Talking Heads website will be shown illustrating the international excitement in developing aesthetically pleasing and intelligible "talking heads." This approach is of interest to a variety of different groups, including those concerned with language training for the hearing-impaired, the film industry which is interested in increasingly realistic virtual actors and animations, and human-interface developers working on avatars and virtual humans. The presentation will close with a mention of other web resources and teaching tools related to speech acoustics.

10:30

**3aED3. Air column resonance demonstrations.** Uwe J. Hansen (Dept. of Phys., Indiana State Univ., Terre Haute, IN 47809) and Peter Hoekje (Baldwin-Wallace College, Berea, OH 44017)

An impedance head designed and constructed at the Physikalisch Technische Bundesanstalt in Braunschweig, Germany is used to illustrate the pattern of resonances in an air column confined to a cylindrical tube closed on one end and open on the other. This is compared to the pattern observed for a tube closed on both ends. The effect observed when adding a mouthpiece is demonstrated, as is the effect when adding a bell. Finally the resonance patterns associated with a number of brass instruments will be demonstrated.

10:45

**3aED4. Rayleigh to the Internet: Sources for demonstration experiments.** Thomas D. Rossing (Phys. Dept., Northern Illinois Univ., DeKalb, IL 60115)

Ideas for demonstration experiments in musical acoustics come from many sources: books, journals, conferences, even the Internet. The author will share his favorite sources as well as some of his favorite demonstrations.

11:00

**3aED5. Acoustical phase locking.** Robert M. Keolian (Grad. Prog. in Acoust., Penn State Univ., P.O. Box 30, State College, PA 16804-0030, bonzo@sabine.acs.psu.edu)

A self-maintained oscillator, such as a beating heart, influenced by another oscillator, such as a pacemaker, may adjust its frequency so that the phase between the two oscillators is constant, thus making their frequencies identical. In general, the two oscillators will synchronize if the coupling between them is strong enough and their natural frequencies are close enough. This phase locking or entrainment phenomenon is fairly common. Two clocks on the same wall can force each other to tick in unison, the moon shows us only one face because its spin and orbital frequencies are locked, two people walking together often unconsciously adjust their pace until their feet hit the ground simultaneously, and our sleep-wake cycle or the laying of chicken eggs is synchronized with the rotations of the earth. Here, phase locking will be demonstrated with a slide whistle influenced by a nearby loudspeaker.

11:15

**3aED6. An audible demonstration of low-frequency sound propagation in bubbly water.** Ronald A. Roy, Preston S. Wilson (Dept. of Aerosp. and Mech. Eng., Boston Univ., Boston, MA 02215), and William M. Carey (MIT, Cambridge, MA 02139)

Bubbly liquids have long held our attention as a novel medium for acoustic propagation, with nonlinear, dispersive, and attenuative properties that eclipse those present in either the gas or fluid phase alone. For example, when driven at frequencies that are well below the bubble resonance frequency, the material exhibits both high compressibility and high density. This unusual combination results in a mixture sound speed that can range as low as 100 m/s, far less than that of either the air or the water alone. This remarkable effect will be demonstrated by bubbling air through a vertical water-filled tube. The air injection process results in a broadband noise that drives the tube in its fundamental length mode. The frequency of this mode is audible, and scales with the mixture sound speed. By varying the flow rate of air (i.e., the void fraction), it is possible to vary the sound speed and thus control the pitch associated with the tube resonance. Knowledge of this resonance frequency and the length of the tube allows us to determine the mixture sound speed, which can then be compared with theory. [Work supported by ONR.]

11:30

**3aED7. From the speed of light to the speed of sound to chaos: Demos for all occasions..** Murray S. Korman, John V. Tobin, and Kathryn M. McMahon (Dept. of Phys., U.S. Naval Acad., Annapolis, MD 21402, korman@nadn.navy.mil)

In 1676, the Danish astronomer Olaf Roemer discovered variations in the periods of the four known satellites of Jupiter. The periods of these satellites can be determined by means of their eclipses, i.e., the times at which they enter Jupiter's shadow in the sunlight. Roemer found that the periods increased when the earth moved away from Jupiter and decreased when the earth moved towards Jupiter, and he concluded that it must take a finite amount of time for light to traverse the diameter of the earth's orbit. From knowledge of the earth's orbit (at that time), he computed the velocity of light to be 227 000 km/s—the first evidence for a finite speed of light. One can explain the result using the Doppler effect and bring it to life using sound waves. Let the satellite become a stationary source of sound and place a distant microphone on a radius arm that is allowed to rotate (or orbit). Using Doppler shift versus time information, the speed of sound is ultimately determined. We will then shift gears, and present an apparatus which displays a compass needle going from simple harmonic motion to chaotic behavior in a periodically reversing magnetic field.

11:45

**3aED8. Standing waves in an electromagnetically driven conducting wire.** James M. Sabatier and Jessica Drewrey (Natl. Ctr. for Phys. Acoust., Univ. of Mississippi, University, MS 38677)

An elastic cord or slinky is often used to demonstrate various wave phenomena including the nodes and antinodes in standing waves. In this talk the drive force results from the interaction of an electric current in a pretensioned conducting wire and an applied orthogonal magnetic field. If the electric current is sufficiently increased, the wire will glow brightly at the nodes. Due to convective air cooling, the antinodes will be dark. As the wire heats, it elongates, reducing the tension and lowering the resonance frequency. Since this demonstration is typically accomplished using a Variac, the tension in the wire must be adjusted as the wire elongates. Here, a power oscillator will be used to allow for a variable drive frequency.

12:00–12:30 Break

### *Contributed Papers*

12:30

**3aED9. Acoustic levitation of drops in air.** R. Glynn Holt, Corey C. Clarke, and Sean C. Wyatt (Dept. of Aerosp. and Mech. Eng., Boston Univ., Boston, MA 02215)

The nonlinear interaction between an acoustic field and an inclusion possessing acoustic properties that are different from the host medium can, among other effects, yield a net body force on the inclusion. If the vertical component of the field gradient is sufficient (i.e., that of a standing wave) and its amplitude large enough, the force of gravity can be balanced—an effect commonly known as “acoustic levitation.” Acoustic levitation has been used in a wide variety of scientific studies, among them studies of sonoluminescing bubbles and investigations of liquid drop dynamics and surface rheology. A monofrequency air levitator will be demonstrated, and several aspects of drop physics will be illustrated by acoustically manipulating the drops. [Work supported by NASA.]

12:45

**3aED10. A simple apparatus for demonstrating linear and parametrically excited vibrations in strings.** David A. Brown (Acoust. Res. Lab., Dept. of Elec. and Computer Eng. and Ctr. for Marine Sci. & Tech., Univ. of Massachusetts, North Dartmouth, MA 02747) and Bruce Lavoie (Univ. of Massachusetts, Dartmouth, MA)

A simple apparatus for inducing vibrations in strings is presented. The apparatus can be used to excite linear vibrations as well as parametric oscillations in a string under tension. The apparatus consists of an inductive transducer which can be arranged to induce transverse vibrations or to modulate the tension in the string which causes parametrically excited waves. Resonance phenomena in the drive transducer can also be demonstrated.

1:00

**3aED11. Interactive experiences in acoustics.** Lawrence Feth and Martin Gillman (Speech & Hearing Sci., Ohio State Univ., Columbus, OH 43210)

Interactive experiences (IEs) are more than classroom demonstrations because they permit the student to change selected parameters as a means for understanding the acoustical principles being demonstrated. Using the LabView programming language, IEs have been developed to aid in teaching acoustics to nontechnical undergraduates. The IEs run on most Windows 95 PCs. A hands-on demonstration will be given during the presentation. [Work supported by a grant from the Battelle Endowment for Technology and Human Affairs.]

1:15

**3aED12. Low-cost demonstrations in acoustics for high school or liberal arts science courses.** Philip S. Spoor and Robert A. Hiller (Los Alamos Natl. Lab., Los Alamos, NM 87545)

Finding effective demonstrations of physical principles that engage student interest, yet are cheap and easy to carry out, is a constant source of challenge to the high school or college science educator. The authors will share a number of such demonstrations which they have developed by drawing on their pooled knowledge of experimental acoustics. Included will be demonstrations developed for a musical acoustics class taught by one of the authors at Penn State University.

3a WED. AM

## Session 3aNS

### Noise: Product Noise Labeling

Robert D. Hellweg, Jr., Chair

*Digital Equipment Corporation, MS PK02-J/60, 129 Parker Street, Maynard, Massachusetts 01754*

**Chair's Introduction—9:00**

#### *Invited Papers*

**9:05**

**3aNS1. Noise labeling and the acoustical consultant—the importance of standardization.** Bennett M. Brooks (Brooks Acoustics Corp., 27 Hartford Turnpike, Vernon, CT 06066, bbrooks@brooks-acoustics.com)

The acoustical consultant's interest in product noise mirrors that of the general public. He/she may be called upon to provide engineering guidance on product noise to a wide variety of interested parties. These may range from corporate manufacturers to individual users. The issues may range from an improved marketing image for a product to a claimed personal injury. The types of products can include consumer or industrial noise emitters, as well as architectural items such as moveable partitions or residential housing units. Standardized labeling within a general class of products is a useful tool to define the appropriate framework in which to assess the particular noise issues of a given project. Presently, this concept appears more developed in areas other than noise emission. For example, sound transmission class (STC) is an established and generally accepted "label" which precisely defines the acoustical performance of a wall partition. Similar labels for other classes of products would increase the awareness of all concerned of the noise issues involved. Clear communication, effective action, and satisfactory resolution could then be more easily achieved. Consensus standards on noise emission labeling would provide a fair yardstick for comparative product noise assessment.

**9:25**

**3aNS2. The air-conditioning and refrigeration institute sound labeling program—Past, present, and future challenges.** Robert J. Comparin (Copeland Corp., 1673 W. Campbell Rd., Sidney, OH 45365)

In the late 1960s, ARI developed a voluntary sound labeling program for air-cooled condensing units. The program was in response to consumer complaints of excessive noise. A major part of the problem was prominent discrete frequency components. The sound label was based on an overall, A-weighted, sound power level that was adjusted by adding a penalty when prominent discrete frequency components were present. Sound labels were published in an ARI equipment directory and were subject to verification by an independent testing laboratory. Initially, there were a large number of participants in the program and the program resulted in a reduction in overall equipment noise levels including the discrete frequency components. Surprisingly, the introduction of new products with a greater emphasis on lower noise levels has actually led to a reduction in the number of manufacturers participating in the program. This was due to concerns that the discrete frequency penalty adjustment no longer adequately reflected annoyance. ARI is currently working to improving the adjustment for discrete frequency components. The presentation summarizes the history of the ARI sound rating program and examines some of the practical problems associated with the development and maintenance of the program.

**9:45**

**3aNS3. Thirty years experience. . . and 100 million HVI certification labels.** David W. Wolbrink, Gary Crow (Broan Manufacturing Co., Inc., Hartford, WI 53027), John Harper, and Tony Schrank (NuTone, Inc., Cincinnati, OH 45227)

Measuring the sound level of products is fruitful when a practical system for applying sound certification labels to competing products meets with long-term success. A prime example of such success is the sound certification and labeling program of the Home Ventilating Institute (HVI). HVI is the trade association for manufacturers of residential exhaust fans and range hoods. HVI has successfully administered its sound certification program for 30 years, providing a simple, single number, linear rating that consumers can understand. The HVI sound certification and labeling program is today one of the most-used programs of its type (in excess of 100 million labels). Tight control over testing provides certified ratings which enable comparisons even though products are often quite similar. The HVI program measures sound pressure level in 24 one-third octave bands in a third-party semireverberant room and, through the substitution process, establishes sound power. The certified rating is in sones as described by the late Dr. S. S. Stevens of Harvard and published in the *Journal of Acoustic Society of America*.

**10:05**

**3aNS4. European product noise emission labeling and reporting requirements.** Robert D. Hellweg, Jr. (Digital Equipment Corp., MS PK02-1/J60, 129 Parker St., Maynard, MA 01754, robert.hellweg@digital.com)

There are several different types of European requirements on providing product noise information to the purchaser or user of those products. This paper describes and presents details of existing and proposed European product noise labeling and reporting requirements. They may be classified into five general categories: (1) national, European, and International consensus standards; (2)

legal requirements, e.g., European Directives and the consensus standards that have been promulgated in support of them; (3) purchase specifications; (4) manufacturers declaration of conformance standards; and (5) voluntary environmental labels or "Eco-labels" for certain product types which contain acoustical limits and imply the acoustical acceptance of products displaying the Eco-label. Experiences with the European requirements should be considered by the members of ANSI S12 Working Group 38 in the development of an American standard on product noise labeling.

10:25

**3aNS5. Product labeling and sound quality.** Patricia Davies (1077 Ray W. Herrick Labs., Purdue Univ., West Lafayette, IN 47907-1077)

Sound power and dB(A) ratings of commercial products may be deceiving when the consumer is trying to make some judgement as to the pleasantness of the product sound. The quality of the sound is affected by tonal content, tonal relationships, variations in level and spectral balance, in addition to the overall average level of the product sound. Even different level metrics, e.g., A-weighted SPL, and Zwicker Loudness, may give contradictory indications as to which product is quieter. In addition, tuning the product to have a lower metric value may lead to a product that sounds worse, if the key characteristics of that product sound are not taken into consideration in the metric. One approach to rating is to have people rate the product sounds, but if these subjective tests are not carried out in a prescribed and rigorous manner, the results may be meaningless. Ordering effects in sound presentation, inconsistent measurements and the use of nonsound-related product information could lead to poor product sound comparisons. The presentation will be focused on the issues involved in quantifying sound quality for product labeling.

10:45

**3aNS6. Noise labels—Satisfying many users.** J. Pope (Pope Engineering Corp., P.O. Box 236, Newton Center, MA 02459)

In order to be successful, noise labels must provide information that is useable by many different groups (consumers, buyers, manufacturers, etc.). (In this paper, the term "noise label" refers to acoustical information that is provided by a manufacturer or supplier to purchasers or users of products; the information may be presented as a label physically applied to the product, as a "tag" attached to the product, in the products specification sheet, in the products users manual, or possibly in a "catalog" of data on several different products.) The noise label should provide information that permits the purchaser and user to determine the products suitability or compatibility with the environment in which the product will be used. The information in the noise labels for all products should be similar in format and content to enable users both to understand the metrics contained in the label and to make informed decisions based in part upon the information contained in the label. This paper discusses these issues and others that must be resolved in the development of a noise labeling standard by ANSI S12 working group 38 and for its successful implementation.

### *Contributed Paper*

11:05

**3aNS7. Development of a speech-intelligibility-based method of hearing protector selection.** Efreem R. Reeves (Grad. Program in Acoust., Penn State Univ., State College, PA 16802, efreem@sabine.acs.psu.edu) and Kevin Michael (Michael & Assoc., 246 Woodland Dr., State College, PA 16803)

Commonly, attenuation and comfort are the major criteria used in selecting a hearing protective device (HPD) for a given noise environment. The objective of this study was to develop a method of HPD selection in which speech intelligibility is introduced as an additional selection parameter. Subjects with normal hearing, mild hearing loss due to noise

exposure, and severe hearing loss due to noise exposure listened to speech presented in a background of noise. Both the speech and noise were filtered to emulate the transfer function of either an average plug type or an average muff type HPD, and the resulting signal was presented to the listener via headphones. Three noises with spectra of high-, middle-, and low-frequency energy concentration, respectively, were used, making for a total of six tested conditions. For each condition, six presentation levels were tested, simulating various degrees of HPD attenuation. A HPD selection criteria was developed based on the word recognition scores for each condition. This criteria was tested using actual hearing protectors in a free-field environment, and a comparison with the results from the simulation was made.

11:20–11:50

### **Panel Discussion**

**Session 3aPA****Physical Acoustics: Ultrasonic Sensors, Motors and Other Devices**

George Mozurkewich, Cochair

*Ford Motor Company Research Laboratory, Mail Drop 3028, P.O. Box 2053, Dearborn, Michigan 48121-2053*

Yves H. Berthelot, Cochair

*School of Mechanical Engineering, Georgia Institute of Technology, Atlanta, Georgia 30332-0405***Invited Papers****8:30****3aPA1. Physical and chemical sensing applications of acoustic devices.** Stephen J. Martin (Microsensor R&D Dept., Sandia Natl. Labs., Albuquerque, NM 87185-1425)

Acoustic devices are finding a number of applications as physical and chemical sensors. Thickness-shear mode resonators, for example, can be operated in a fluid to measure properties such as density and viscosity. These devices are being developed for *in situ* monitoring applications, including engine oil for condition-based maintenance. The surface acoustic wave (SAW) device serves as a versatile platform for constructing gas-phase chemical sensors. These devices serve as extremely sensitive gravimetric detectors with chemical selectivity conferred by depositing a chemically sensitive film onto the device surface. Selectivity can be further enhanced by using arrays of chemical sensors combined with a pattern recognition algorithm. Flexural plate wave (FPW) devices, consisting of a self-supporting membrane in which acoustic waves are excited, can be used in a number of sensing applications. These devices are sensitive to either mass accumulation or a change in membrane tension. Chemical sensors can be constructed by depositing a chemically sensitive film onto the membrane surface; species absorption leads to a change in the membrane's areal mass density. Alternatively, sensors for pressure and acceleration can be constructed which rely on the device's sensitivity to membrane tension. Sensor systems using these various sensor platforms will be described.

**9:00****3aPA2. Piezoelectric sensors.** Ryszard M. Lec (Dept. of Elec. and Computer Eng., 109 Barrows Hall, Univ. of Maine, Orono, ME 04469, lec@eece.maine.edu)

A piezoelectric medium provides an attractive technology for realizing a variety of sensors that exhibit high sensitivity, small size and portability, fast responses, ruggedness and robustness, excellent aging characteristics, high accuracy, and the capability to measure multiple quantities in a single sensor package. Sensors based on this technology can be produced using standard photolithography and, hence, are inexpensive. Piezoelectric sensors are fabricated from materials in which the electromechanical transduction takes place within the material. This material-based transduction process very positively influences the performance of acoustic sensors in terms of their reliability, size, and cost. Piezoelectric sensors are versatile and can measure, in principle, any type of measurand. Usually, piezoelectric sensing is accompanied by both mechanical displacement and electrical field. Thus, both the electrical and mechanical properties of the environment can be monitored directly by piezoelectric sensors. One may increase the number of measurands detected by the acoustic sensor by attaching or connecting a specific sensing element to a piezoelectric transducer/substrate. In this paper, piezoelectric sensing mechanisms and a wide range of bulk piezoelectric waves used in the sensor development are described. Applications of piezoelectric sensors in the chemical, environmental, medical, automotive, and aeronautic industries are also provided.

**9:30****3aPA3. Designing piezoceramic actuators and motors.** Ephraim Garcia (Ctr. for Intelligent Mechatronics, Vanderbilt Univ., Box 1592, Station B, Nashville, TN 37235, garciae@ctrvax.Vanderbilt.edu)

Piezoelectric actuators have high energy densities and are capable of producing high force, high bandwidth output. However, they lack the stroke required by many practical applications. Solid-state mechanisms have been designed that utilize flexure hinges to efficiently amplify the stroke of a piezoelectric stack element up to five times. The designs avoid the losses encountered in traditional hinge joints, which are primarily due to tolerance problems, and they minimize losses due to material strain. The mechanisms have been successfully employed in micropositioners for several different applications, including mirror positioners for wavefront compensation and proof mass actuators for vibration suppression. Piezoceramic actuators have also been employed in very high stroke mechanisms: linear and rotary motors. These motors fall into two classes, the ultrasonic motors and the quasistatic type motors. The ultrasonic motors, such as the traveling wave motor, must run at very high frequencies, usually at the resonance frequency of the stator. The quasistatic type motors, such as the inchworm motors, are able to run at low frequencies, but also can be operated at resonance to achieve higher speeds. Both inchworm motors and ultrasonic motors have been successfully demonstrated as prototype devices.

**10:00–10:15 Break**

10:15

**3aPA4. Stabilization of a capillary bridge in air beyond the Rayleigh–Plateau limit in low gravity using acoustic radiation pressure.** Mark J. Marr-Lyon, David B. Thiessen, and Philip L. Marston (Dept. of Phys., Washington State Univ., Pullman, WA 99164-2814, o9938156@mail.wsu.edu)

In the absence of gravity, cylindrical capillary bridges consisting of liquid between two circular supports naturally become unstable and break when the length of the bridge exceeds its circumference. This limit is known as the Rayleigh–Plateau limit. The stability of liquid bridges is important to various technologies even in normal gravity. In experiments performed aboard NASA's low gravity KC-135 aircraft, it was found that acoustic radiation pressure can be used to stabilize capillary bridges against breakup. Capillary bridges composed of a mixture of water and glycerol were deployed in a 21 kHz ultrasonic standing wave in air. The bridges were extended to a length about 11% beyond the natural limit, and the extended bridges broke immediately when the ultrasound was turned off. In contrast with previous work [M. J. Marr-Lyon *et al.*, *J. Fluid Mech.* **351**, 345–357 (1997)], this stabilization method does not use active feedback; the stabilization is a passive effect of the sound field. The acoustic wavelength is chosen such that the radiation pressure due to the sound field is a function of the local bridge radius, such that areas of larger radius are squeezed, and areas of smaller radius are expanded. [Work supported by NASA.]

10:30

**3aPA5. Fiber optic interferometric sensor for ultrasound.** Brad Beadle and Jacek Jarzynski (Georgia Inst. of Technol., School of Mech. Eng., Atlanta, GA 30332)

A fiber optic interferometric sensor, designed to detect tangential surface strains in the frequency range  $\sim 200$  kHz to 1 MHz, is described. The sensor is configured with a large number of segments of the fiber bonded to a thin plastic or metal base plate. The base plate can then be attached with a shear wave couplant to the solid sample of interest and the fiber sensor can be used to detect, in this sample, ultrasonic waves with a tangential surface displacement component. The sensor forms one arm of a Mach–Zehnder interferometer and the sensor sensitivity is proportional to the number of fiber segments bonded to the base plate. The fiber segments bonded to the base plate are of equal length and the maximum response of the sensor is at the frequency for which the bonded segment length is one-half of the tangential component of ultrasonic wavelength. The sensor is directional, with maximum response in the direction broadside to the bonded segment array. Measurements of the sensor performance are presented and compared with a theoretical model. [This work is supported by the ONR M-URI program.]

10:45

**3aPA6. Application of resonant ultrasound spectroscopy to geomaterials.** Alexander L. Matveyev, Alexander M. Sutin, Andrey I. Potapov (Inst. of Appl. Phys., 46 Ulyanov St., Nizhny Novgorod, 603600, Russia), and Paul A. Johnson (Los Alamos Natl. Lab., Los Alamos, NM 87545)

Our objective is to apply resonant ultrasound spectroscopy (RUS) for obtaining the full elastic tensor of geomaterials. To our knowledge, RUS has never been successfully applied to complex materials such as rock: materials that are anisotropic and often inhomogeneous, and that contain grain-to-grain contacts, microcracks, etc. The fundamental problem with applying RUS to rock is high dissipation in the material, and the problem of coupling into all possible modes. The high dissipation limits the frequency band, and coupling into all modes controls the outcome of whether or not the full elastic tensor can be obtained. Our current experiment is operable in the frequency band of 3–30 kHz. Numerous sensor positions were tested in order to excite and detect different resonant modes. To date, the method has been applied to a rectangular brick sample. The comparison with theoretical calculation demonstrates that all modes (eigenfre-

quencies) of the sample were detected with high accuracy. Preliminary testing on cylindrical sandstone samples was also carried out. Duplicating the result from the brick in the rock sample is in progress. [This work is supported by the United States Industry Coalition, with the US DOE Contract W-7405-ENG-36, through the University of California.]

11:00

**3aPA7. Acoustic resonance spectroscopy for the water pollution detection.** Tetsuro Oishi (Acoust. Res. Lab., Dept. of Elec. and Computer Eng. and Ctr. for Marine Sci. and Technol., UMass—Dartmouth, North Dartmouth, MA 02747, toishi@umassd.edu)

A resonator is investigated using acoustic resonance spectroscopy for use in sensing pollutants in water. This work was partially funded and supported by the STRategic Envirotechnology Partnership (STEP) through the Advanced Technology Center at the University of Massachusetts—Dartmouth. The transmitter and receiver are coupled externally to the wall of the cavity. The transmitter generates the sound using a swept frequency source. The receiver on the opposite side of the wall of the cavity can detect the transmitted signal. The acoustic properties of liquids such as velocity and attenuation can be calculated from the observed spectrum signal. A small amount of chemicals in water can change those acoustic properties of water. Experiments using several different kinds of chemicals are described to demonstrate the possibilities of this technique for the water pollution detection.

11:15

**3aPA8. Direct and inverse problems of linear resonant ultrasound spectroscopy.** Andrey V. Lebedev, Irina A. Soustova (Inst. of Appl. Phys., Russ. Acad. of Sci., Nizhny Novgorod, Russia), Lev A. Ostrovsky (Univ. of Colorado, Boulder, CO), and Paul A. Johnson (Los Alamos Natl. Lab., Los Alamos, NM)

The model approach of linear resonance ultrasound spectroscopy (LRUS) is described: obtaining the elastic moduli and Q values from resonance spectral measurements at frequencies ranging from several kHz to tens of kHz on complex solids such as rock. In the direct (forward) problem, LRUS is based on the variational principle, that of determining the eigenvalues from resonance spectral peaks of samples (complex in the general case). By minimizing the difference between the measured and calculated resonant modes for a given geometry of the sample, the linear properties of the sample (inverse problem) can be determined. The method was tested by comparing theoretical and experimental results obtained by Demarest [H. Demarest, *J. Acoust. Soc. Am.* **49**, 768–775 (1971)] and data obtained from experiments carried out in IAP RAS on rectangular bricks at audio frequencies. Comparison of measured and calculated data showed that the difference may be as low as 0.6%. [This work is supported by the United States Industry Coalition, with the U.S. DOE, Contract No. W-7405-ENG-36, through the University of California.]

11:30

**3aPA9. Historical sketches I. The acoustical contributions of Karl Rudolph Koenig.** Robert T. Beyer (Dept. of Phys., Brown Univ., Providence, RI 02912)

While the acoustical contributions of Helmholtz, Rayleigh, and Bell are remembered, many of the secondary lights of acoustics in the nineteenth century have faded away. This is the first of what is hoped to be a series of recollections of a number of them. One such leader was Karl Rudolph Koenig. Born and educated in Koenigsberg, Germany (now Kaliningrad, Russia), he spent his adult life in Paris, where he established a laboratory for making acoustical instruments, including tuning forks, resonators, and devices for the visualization of sound and for obtaining ultrasonic frequencies. Details of some of his instruments and discoveries will be presented and his role assessed.

## Session 3aPP

**Psychological and Physiological Acoustics: Spatial Hearing, Temporal and Spectral Processing, Emissions, and Tinnitus (Poster Session)**

John H. Grose, Chair

*Division of Otolaryngology, University of North Carolina, 610 Burnett-Womack Building, Chapel Hill, North Carolina 27599-7070***Contributed Papers**

All posters will be on display from 9:00 a.m. to 11:30 a.m. To allow contributors an opportunity to see other posters, contributors of odd-numbered papers will be at their posters from 9:00 a.m. to 10:15 a.m. and contributors of even-numbered papers will be at their posters from 10:15 a.m. to 11:30 a.m. To allow for extended viewing time, posters will remain on display until 4:00 p.m.

**3aPP1. Sound movement: The dynamics of interaural amplitude and phase modulation processing are different.** Caroline Witton, Adrian Rees, B. Vishwanatha Rao, Timothy D. Griffiths, and Gary G. R. Green (Dept. of Physiological Sci., Univ. of Newcastle upon Tyne, Newcastle upon Tyne, NE2 4HH, UK)

Listeners use two binaural cues when detecting motion of a sound in the horizontal plane; interaural amplitude and phase modulation (IAM and IPM). It has been suggested that IAM is converted into the same neural code as IPM, in which case the dynamics of IAM and IPM processing should be the same. To test this hypothesis, three subjects participated in 2-AFC psychophysical experiments. Thresholds were measured for detection and modulation-direction discrimination of linear IAM and IPM of a 500 Hz tone, for ramp durations between 20 and 1000 ms. At durations between 200 and 1000 ms detection thresholds for both cues remained constant. IAM sensitivity decreased in a biphasic manner at durations below 200 ms, whereas IPM sensitivity remained constant until much shorter durations (60 ms). This suggests that IAM detection has a longer integration period than IPM detection. Discrimination thresholds for IAM were 3 to 4 times smaller than detection thresholds (mean ratio 0.29, s.d.=0.04,  $n=3$ ). IPM discrimination thresholds were similar to IPM detection thresholds (mean ratio 0.81, s.d.=0.05,  $n=3$ ). These results demonstrate that the dynamics of IAM and IPM processing are not the same, and the hypothesis is rejected.

**3aPP2. How well does natural motion induce auditory motion aftereffects?** Michael F. Neelon and Rick L. Jenison (Dept. of Psych., Univ. of Wisconsin, 1202 W. Johnson St., Madison, WI 53706)

There is evidence that a repeatedly traversing sound source induces motion aftereffects in listeners [D. W. Grantham, *Percept. Psychophys.* **45**, 129–136 (1989)]. Other work has found aftereffects for acoustic attributes often involved in motion, e.g., for level or frequency changes [Reinhardt–Rutland, *Percept. Psychophys.* **28**, 569–571 (1980); Shu *et al.*, *Nature* **364**, 721–723 (1993)]. Few studies, however, have investigated adaptation in the presence of more ecologically valid motion. Normally, stimuli in adaptation paradigms include changes in spectral cues and interaural differences but not the changes in amplitude or frequency that occur with motion under more natural spatial trajectories, e.g., linear approach. The questions arise whether such aftereffects are due to fatiguing neurons mostly sensitive to arbitrary interaural modulations, or are units truly responsive to lawful, natural motion? If integrated motion detectors exist, then including amplitude and frequency changes in adapting stimuli should enhance aftereffects. Subjects will be adapted to three types of stimuli: those with interaural changes only, with amplitude and frequency

changes only, or with interaural, amplitude and frequency changes following lawful motion. Greater magnitude aftereffects for latter stimuli or aftereffects induced by middle stimuli may reveal which acoustic attributes hypothesized motion detectors are responsive to. [Work supported by NSF.]

**3aPP3. Visual influences on auditory distance perception.** Julie M. Brown (Dept. of Psych., Univ. of Connecticut, 406 Babbidge Rd., Box U-20, Storrs, CT 06269 and Haskins Labs., jmb94006@uconnvm.uconn.edu), Krista L. Anderson, Carol A. Fowler, and Claudia Carello (Univ. of Connecticut, Storrs, CT 06269)

Much of the work on sound localization has focused on sound sources in the horizontal plane. This study looks at the auditory perception of distance using a reaching task [L. D. Rosenblum, A. P. Wuestefeld, and K. L. Anderson, *Ecological Psych.* **8**, 1–24 (1996)]. In this task, blindfolded participants judged the reachability of a rattle based on a straight right arm reach. In order to investigate visual influences on auditory distance perception, in another condition, participants judged the reachability of an “auditory” rattle while simultaneously viewing a “visual” rattle that did not produce sound. The “visual” rattle was placed 8 cm in front of the “auditory” rattle or 8 cm behind it. Compared to an auditory alone condition, participants were more likely to judge that the rattle was within reach when the visual stimulus was closer to the participant than the auditory stimulus. These results show that vision influences the perception of sound source distance.

**3aPP4. Interhemispheric transfer time of audiomotor information.** Robert S. Bolia (Veridian, 5200 Springfield St., Dayton, OH 45431, rbolia@falcon.al.wpafb.af.mil), Mark A. Ericson (Wright–Patterson Air Force Base, OH), and Brian D. Simpson (Wright State Univ., Dayton, OH)

Since the crossed–uncrossed difference technique was first described by Poffenberger [*Arch. Psychol.* **23**, 1–73 (1912)], it has been used numerous times to measure interhemispheric transfer time (IHTT) of visuo-motor information via the commissural system [see Marzi, Bisiacchi, and Nicoletti, *Neuropsychologia* **29**, 1163–1177 (1991), for a review]. In spite of its widespread use by vision researchers, this technique has never been used to measure IHTT of audiomotor information. In the present study, audiologically normal dextral listeners made a simple reaction time re-



sponse to brief spatialized bursts of broadband noise presented dichotically over insert earphones. For each listener, one block of 120 trials was completed with each hand. Half of the stimuli in each of the response conditions (right/left hand) were presented in the right hemifield, the remaining half in the left hemifield. Crossed–uncrossed differences were computed for each listener. Results will be discussed in terms of IHTT for audiomotor information and the possibility of cerebral lateralization of auditory localization processing.

**3aPP5. Effect of audiometric test room noise on monaural and binaural thresholds.** Jennifer B. Tufts and Tom Frank (Penn State Univ., University Park, PA 16802)

This study determined if the maximum permissible ambient noise levels (MPANLs) for audiometry specified in the revision of ANSI S3.1-199x provided the same amount of threshold shift for monaural and binaural listening. Sound-field monaural and binaural warble-tone thresholds (125–8000 Hz) were obtained on 24 normal-hearing subjects in quiet (ambient) and in two background noise conditions. One noise condition approximated the ANSI S3.1-199x ears not covered MPANLs (ANSI noise). The other noise condition was 20 dB higher than the ANSI MPANLs (ANSI noise + 20). Monaural thresholds were about 2 dB higher than binaural thresholds in quiet and in each noise condition. The difference between the monaural minus the binaural threshold shifts in each noise condition (ANSI noise + 20 minus ambient; ANSI noise minus ambient) averaged over frequency was typically less than 1 dB. Thus the MPANLs in the revision of ANSI S3.1-199x are appropriate for both monaural and binaural testing.

**3aPP6. The first pitch-shift effect as a Doppler effect. A simple physical explanation to a complex perceptual phenomenon.** Pantelis N. Vassilakis (UCLA, Systematic Musicology, Box 951 616, Los Angeles, CA 90095, pantelis@ucla.edu)

The first pitch-shift effect describes the relationship between pitch and center frequency of complex stimuli with equally spaced components and fixed frequency spacing:  $f_0$ . It is described mathematically by a saw-tooth function in a model introduced by de Boer [Doctoral dissertation, University of Amsterdam (1956)]. Researchers usually favor a more ambiguous frequency-shift/pitch-shift relationship that better justifies the generally accepted explanation (perceptual detection of a wave signal's time-fine-structure). Pilot experiments, however, indicate that: (a) the patterned pitch ambiguities reported by previous studies may be artifacts of experimental design, not challenging de Boer's model, and (b) no model accounts for the present study's reported pitch for frequency shifts:  $f_0/2$ . The explanation introduced presently argues that (a) modulations resulting from wave superposition are waves themselves, with velocity ( $V_{\text{Group}}$ ) that is independent from the velocity of their constituent components ( $V_{\text{Phase}}$ ), and (b) uniform frequency shifts of a complex wave's components change the relationship between  $V_{\text{Group}}$  and  $V_{\text{Phase}}$ , changing the effective frequency of the emerging modulations relative to a fixed point in the medium of propagation. These relative speed/frequency changes predict pitch shifts that agree with observation (including the case of frequency-shifts:  $f_0/2$ ), making the first pitch-shift effect a version of the Doppler effect.

**3aPP7. Discrimination of the fundamental frequency of unresolved harmonics.** Joseph W. Hall III, Emily Buss, and John H. Grose (Univ. of North Carolina School of Medicine, Div. of Otolaryngol., CB 7070, Chapel Hill, NC 27599-7070)

Listeners were presented with five consecutive harmonics centered on the twentieth harmonic of either 50, 100, 150, 200, or 250 Hz. The phase relation among harmonics was either cosine, Schröder, or random. For each standard fundamental frequency, the smallest discriminable change

in fundamental frequency was determined. In general, discrimination performance was better for cosine phase than for the other phase relations, particularly for large standard fundamental frequencies. Results will be considered in terms of the hypothesis that the pitch of unresolved harmonics is based upon both envelope and fine structure cues, with fine structure cues becoming less of a factor in frequency regions where phase locking to fine structure diminishes.

**3aPP8. High-frequency (8–20 kHz) reference thresholds for audiometry.** Tom Frank, Erinn Bruno, Anthony Fowler, and Elise Uhring (Dept. of Commun. Disord., Penn State Univ., 110 Moore Bldg., University Park, PA 16802)

ANSI (S3.6-1996) and ISO (CD 389-5, 1996) have reported interim high-frequency (8–16 kHz) reference equivalent threshold sound pressure levels (RETSPLs). Since the interim RETSPLs were derived using very limited data, there is a need to increase the data base for specifying high-frequency RETSPLs. Thus, this study determined high-frequency (8–20 kHz) thresholds for 50 young adults having normal low-frequency (0.25–8 kHz) hearing across four test sessions, separated by at least one day, using Sennheiser HDA 200 and Koss HV/Pro earphones. The mean thresholds increased as frequency increased, especially at 16 kHz and above, and were similar to the ANSI and ISO interim RETSPLs. However, the standard deviations were very high and the range scores were very wide for each earphone at each frequency. This would indicate that specifying high-frequency RETSPLs may not be feasible due to very high intersubject threshold variability. On the other hand, the intrasubject threshold differences across each possible test session comparison were found to be very repeatable and within a clinically acceptable range. This would indicate the usefulness of high-frequency audiometry for monitoring patients having or suspected of having otopathology. [Work supported by the Pennsylvania Lions Hearing Research Foundation.]

**3aPP9. Discrimination of degraded conspecific song in zebra finches (*Taeniopygia guttata*).** Bernard Lohr, Robert J. Dooling (Dept. of Psych., Univ. of Maryland, College Park, MD 20742, blohr@bss3.umd.edu), Frederic Theunissen (Univ. of California, Berkeley, CA), and Alison Doupe (Univ. of California, San Francisco, CA)

Thresholds for detecting degraded conspecific songs in zebra finches were measured using operant conditioning. A parametric representation of song obtained by decomposing natural songs using a bank of frequency filters served as a model for synthetic songs. Degraded songs were produced by progressively changing the instantaneous relative phase across adjoining frequency bands. Control songs preserving original phase relationships have generated neural responses in the avian forebrain nucleus HVC that are indistinguishable from responses to natural versions of the bird's own song (BOS). Our thresholds showed that birds were very sensitive to modifications in BOS, giving results very similar to those obtained from neural recordings in HVC. Moreover, our bird thresholds were similar to those obtained for humans tested with the same task. Unlike electrophysiological results, however, behavioral thresholds for discriminating changes in song were not selective for an individual's own song, nor for the song played forwards or backwards. These results suggest that

precise temporal information present in the relative phase of any complex sound is preserved in both high level general auditory areas as well as in areas specialized for detecting particular songs. [Work supported by NIH.]

**3aPP10. Across-frequency gap duration discrimination.** John H. Grose, Joseph W. Hall III, and Emily Buss (Div. Otolaryngol./Head and Neck Surgery, Univ. of North Carolina, Chapel Hill, NC 27599-7070)

Gap detection performance declines as the two markers defining the gap are shifted apart in frequency. The purpose of this study was to determine whether this frequency dependence is also seen for gap duration discrimination, where an increase in the duration of a base silent interval is discriminated. Two standard gap durations were employed: 35 and 250 ms. The two markers defining the gap were either isofrequency (1035 Hz) or were separated by 3 or 6 ERBs above and below 1035 Hz (1519/685 Hz, 2188/432 Hz). In another condition the marker frequencies were randomly chosen. The nominal duration of the second marker was always 300 ms but the nominal duration of the first marker was either 12.5, 50, or 300 ms. Irrespective of nominal duration, the actual duration of each marker was randomized over a range of  $\pm 20\%$  on each interval of a trial to prevent overall duration of the stimulus complex serving as a viable cue. Results from listeners with normal hearing indicated that gap duration discrimination generally declined when the markers were separated in frequency. The effect of varying the duration of the first marker was not constant across listeners. [Work supported by NIH NIDCD R01-DC01507.]

**3aPP11. Relation of backward masking and frequency discrimination to reading and language among 5- to 12-year-old children.** Gabrielle H. Saunders, Athanassios Protopapas, Gaston R. Cangiano, Talya Salz, and Lin F. Cerles (Scientific Learning Corp., 1995 University Ave., Ste. 400, Berkeley, CA 94704, gaby@scilearn.com)

Psychoacoustic adaptive threshold estimation procedures were implemented as "computer games" to measure, with no experimenter intervention, backward detection masking and frequency discrimination in 54 children aged 5–12 years. Assessments of the subjects' pure-tone hearing thresholds (52 normal), language abilities (CELF-3; 2 below average), and reading skills (Woodcock Reading Mastery; none below average) were also made. Thresholds were successfully obtained for detection of a 20-ms 1-kHz tone followed immediately by a 300-ms bandpass (600–1400 Hz) noise masker (46 children); for frequency discrimination of 250-ms tones in the 800- to 1200-Hz range (41 children); and for discrimination of 20-ms tones at 900 and 1100 Hz, each followed by a 300-ms bandpass noise masker at an adaptively varied ISI (27 children). Success at obtaining a valid threshold was not related to the child's age, although the frequency discrimination thresholds were. Receptive language ability was significantly correlated with backward masking; reading skills were sig-

nificantly correlated with frequency discrimination. Related findings have been reported for adult poor readers [Protopapas *et al.*, *J. Acoust. Soc. Am.* **102**, 3188 (1997)] and specifically language impaired children [Wright *et al.*, *Nature* **387**, 176–178 (1997)], consistent with an auditory processing deficit hypothesis in reading and language impairments.

**3aPP12. The effect of middle ear resonant frequency, ear canal resonance, and ear canal volume on TEOAE.** Tina Jupiter and Shannon Giacomazza (Dept. of Speech, Commun. Sci., and Theatre, St. John's Univ., 8000 Utopia Pkwy., Jamaica, NY 11439)

It is well known that there is a large inter-individual variability in the size of the TEOAE. Quantifying the sources of variability can help to determine the influences of some of the factors that can affect test results. The difference found in TEOAE may be due to the difference in size and shape of the ear rather than cochlear mechanics. The effect of ear canal volume between the probe and the tympanic membrane influences the intensity and spectrum of the stimulus as well as the characteristics of the response. A small ear canal volume should result in a higher stimulus sound-pressure level. This can determine both the effectiveness of the evoking stimulus as well as the response that is measured. We will report results of the study of the relation between ear canal volume, ear canal resonant frequency, and resonant frequency of the middle ear on TEOAE for 20 normal hearing young adults. The purpose is to determine if the characteristics associated with TEOAE are influenced by middle ear resonance and ear canal resonance and volume. By quantifying some of the variables that can effect TEOAE the test interpretation may be clarified.

**3aPP13. Multidimensional scaling of judgments on tinnitus and imitation tinnitus.** Tao Zhang and Merrilynn J. Penner (Dept. of Psych., Univ. of Maryland, College Park, MD 20742, p-tzhang@bss3.umd.edu)

Sixteen normal subjects were asked to judge the dissimilarity between any pair of stimuli chosen from 13 imitation tinnitus. Six tinnitus subjects were asked to perform the same task on 13 imitation tinnitus plus their own tinnitus. Multidimensional scaling was used to analyze the dissimilarity data and to provide a geometric representation. For 13 imitation tinnitus, there was no significant difference between the judgments by normal subjects and tinnitus subjects. All subjects distinguished imitation tinnitus mainly based on the overall sensation level. The frequency at the center of gravity of the stimulus spectrum played a secondary role in the judgments. Each tinnitus subject perceived their own tinnitus and its imitation in a similar way. With respect to the current stimulus set, imitation tinnitus was a good, but not the best, simulation of the corresponding tinnitus. [Work supported by NIH.]

## Session 3aSAa

## Structural Acoustics and Vibration: Flow Excitation

Dean E. Capone, Cochair

*Applied Research Laboratory, Pennsylvania State University, P.O. Box 30, State College, Pennsylvania 16804*

Lisa Grega, Cochair

*Carderock Division, Naval Surface Warfare Center, 9500 MacArthur Boulevard, Bethesda, Maryland 20817-5000*

## Contributed Papers

8:00

**3aSAa1. Prediction of flow-induced structural vibration and sound radiation using energy flow analysis.** F. Han, R. J. Bernhard, and L. Mongeau (Ray W. Herrick Labs., School of Mech. Eng., Purdue Univ., West Lafayette, IN 47907)

The energy flow analysis method (EFA) was used to predict the vibration response and the associated radiated sound power of a plate excited by turbulent boundary layer flows and separated–reattached flows. The power input from the turbulent flow into the structure was calculated using the mechanical impedance of the structure and the cross-power spectral density or the wave-number-frequency spectral density of the wall pressure field. The Smol'yakov–Tkachenko model was used to describe the pressure field under the turbulent boundary layer, and the Corcos model was used to describe the wall pressure field beneath the separated–reattached flow. Experiments were performed using a clamped aluminum plate mounted flush with the floor of a low-speed, closed test section wind tunnel. A fence was used to trip the flow upstream of the plate. The wall pressure fluctuations, the plate velocity, and the acoustic pressure radiated from the plate on its quiescent side were measured using flush-mounted microphones, a scanning laser vibrometer, and a microphone located in a soundproofed enclosure located beneath the test section floor, respectively. Frequency-averaged EFA predictions compared favorably with the measured data in the frequency range where the plate modal density was sufficiently high.

8:15

**3aSAa2. Nonlinear response and acoustic radiation from a curved panel structure.** Lucio Maestrello (NASA Langley Res. Ctr., Fluid Mech. & Acoust. Div., M.S. 463, Hampton, VA 23681-2199, l.maestrello@larc.nasa.gov)

Periodic and chaotic responses on a fuselage type of structure are observed when forced by high intensity tonal sound at normal and oblique incidence angles. The experiment is conducted with an aluminum curved aircraft-type fuselage structure panel subdivided by a tear stopper mounted in a rigid baffle. A sound power level of 130 dB is used to produce periodic responses with two tonal components and 137 dB power is used to produce chaotic responses. The fundamental tone distributes energy to other components, and the response becomes temporally and spatially complex, an indication of nonlinear pattern formation in which temporal and then spatio-temporal chaos begins. At oblique incidence the panels response is bifurcated; as such, the waves lose their spatial homogeneity and chaotic patches form. Results for various input loads, structural response, and sound pressure transmission are discussed.

8:30

**3aSAa3. Nonaxisymmetric disturbances in a jet and their effect on structural loading.** Alvin Bayliss (Northwestern Univ., Evanston, IL 60208) and Lucio Maestrello (NASA Langley Res. Ctr., Hampton, VA 23681-2199)

A model of sound generated in a high subsonic (Mach 0.9) circular jet is solved numerically in cylindrical coordinates for nonaxisymmetric disturbances. The jet is excited by transient mass injection by a finite duration pulse via a rotating ring source. The flow field near-field and far-field pressure disturbances corresponding to these sources are described. In particular, the resulting pressure field which would serve to excite nearby panels is illustrated together with results on the excitation of thin slices of nearby panels. Considered are both the short-time behavior of the jet and the long-time behavior, after the initial excitation pulse has exited the computational domain.

8:45

**3aSAa4. Estimation of flow-induced vibration parameters of marine risers.** Catherine Stamoulis and J. Kim Vandiver (Dept. of Ocean Eng., MIT, Cambridge, MA 02139)

Flow-induced vibration of marine risers may be characterized by modal frequencies, mode shapes, and participation factors. These parameters cannot always be estimated accurately using methods that require *a priori* knowledge of the mode shape matrix. Therefore a combined system and subspace identification method was developed to estimate the risers' modal parameters in the presence of unknown input, i.e., fluid forces. Data were analyzed, from an experiment involving a model riser under uniform and shear flow. ARMA models were used to describe the data dependence in state space. Subspace identification was used to reduce computational time. Modal parameters including structural damping were estimated from the state matrix of the system. Contrary to previous studies, it was found that mode shapes are complex, i.e., the system's damping is nonproportional. The estimated damping ratios were in the range 0.03–0.07. The deviation of the results from those obtained using conventional methods, which assume that mode shapes are real and may be described approximately by sine functions, was significant when the structure was subjected to shear flow. Thus such *a priori* assumptions are inaccurate in these cases. In contrast, system identification methods which use only the available data are appropriate.

9:00

**3aSAa5. Vibration of a cavitating elastic wing in a periodically perturbed flow: Excitation of subharmonics.** Svetlana I. Kovinskaya and Eduard L. Amromin (Beltran, Inc., 1133 East 35 St., Brooklyn, NY 11210, amromin@aol.com)

Vibration of an elastic cavitating wing in periodically perturbed flows is analyzed. Because cavity thickness and length are perturbed, too, an excitation with a fixed frequency leads to a parametric vibration of the

wing, and this vibration spectra's amplitudes have nonlinear dependencies on amplitudes of the perturbations. Numerical analysis was carried out for two-dimensional flow of an ideal fluid. Wing vibration was described by the equation for a beam in bending motions. As a result, two frequency bands of an essential vibration increase are found. A high-frequency band is mainly associated with an elastic resonance of the wing, and a cavity

can do certain damping there. A low-frequency band is associated with cavity volume oscillations. The governing parameter for the low-frequency vibration is the Strouhal number (Sh) based on the cavity length. The most significant vibration in the low-frequency band corresponds to approximately constant values of Sh and has the most extensive subharmonics.

WEDNESDAY MORNING, 14 OCTOBER 1998 HAMPTON ROADS BALLROOM 1, 9:30 TO 11:30 A.M.

### Session 3aSAb

## Structural Acoustics and Vibration: Radiation

Richard Szwerc, Chair

*Carderock Division, Naval Surface Warfare Center, 9500 MacArthur Boulevard, Bethesda, Maryland 20817-5700*

### Contributed Papers

9:30

**3aSAb1. Condensing structural finite-element meshes into coarser acoustic element meshes.** John Fahnlne (Appl. Res. Lab., 16 Appl. Sci. Bldg., University Park, PA 16804)

One method for computing the sound power radiated by a structure is to perform a finite-element analysis of the structural vibrations and a boundary element analysis of the radiated acoustic field. Both analyses are valid in the low- to mid-frequency range and standard implementations require six elements per wavelength. In many cases of practical interest, the structural wavelengths are much smaller than the acoustic, and, thus, using the same mesh for both analyses results in an overly refined acoustic mesh. The extra refinement results in considerable computational expense in the acoustic analysis because the time required to solve the fully populated, complex matrix system depends on the number of unknowns cubed. Here, it is shown that the efficiency of the acoustic analysis can be significantly increased by constructing the acoustic element mesh from conglomerations of structural elements. Two methods are suggested for deriving the basis functions for the acoustic field, and the accuracies of both methods are assessed. A simple analysis of the computation times is given, and the predicted reductions in the times are verified through several example problems. Overall, the results demonstrate that the condensation can dramatically reduce the computation times without significantly altering the solution accuracies.

9:45

**3aSAb2. Homogenization of fluid-loaded plates over the full frequency range for efficient calculation of structural acoustic behavior.** Donald B. Bliss and Linda P. Franzoni (Dept. of Mech. Eng. and Mater. Sci., Duke Univ., Durham, NC 27708)

A homogenization method for complex structures, applicable over the entire frequency range, has been developed. This approach has application to naval structures, e.g., ribbed shells, and to aerospace structures, e.g., panel-frame fuselages. The homogenization method utilizes a local/global decomposition facilitated by adding and subtracting canceling smooth forces. The global problem has an infinite-order structural operator, and periodic discontinuities are replaced by an equivalent distributed suspension with slowly varying properties. The global problem can be solved very efficiently since all rapidly varying scales have been removed. The local problem, which provides transfer function information for the global problem, is solved separately and independently, except for amplitude information from the global problem. Once formulated for a specific structure, the self-contained global problem is solved first, and the local solution can be reconstructed afterwards. The application of this approach to structural waves on fluid-loaded plates is described. The analytical reformulation embodied in this homogenization method allows the global prob-

lem to be solved at lower resolution than the length of flexural waves on the original structure. Furthermore, the effects of fluid radiation can be transferred to the global problem. [Work sponsored by ONR.]

10:00

**3aSAb3. Estimation of far-field acoustic power radiation from vibrating plates.** Khalilur Rahman (Dept. of Mech. Eng., BUET, Dhaka, Bangladesh), Nirmal Kumar Mandal (Inst. of Noise and Vib., Univ. of Technol., Jalan Semarak, Malaysia, <dfkj0001@utmkl.utm.my>), and Wahhaj Uddin (Tuskegee Univ., Tuskegee, AL 36088)

The total average acoustic power radiation from one side of a rectangular flat plate, vibrating in its natural modes under a mixed boundary condition of one end simply supported, while the other three are fixed, has been estimated. The radiation efficiency of the plate with same end conditions has also been found for verifying the method of the present study by comparison with those established in literature. Numerical results on the acoustic power radiation by the plate have been obtained for various mode orders, aspect ratios, and thickness ratios. The characteristic beam functions developed by Warburton have been used for representing the vibration modes of the rectangular flat plate. At low mode orders, the power radiation from the plate is observed to increase with the increase of mode orders. But at the higher-mode orders, the acoustic power radiation is observed to fluctuate, maintaining nearly the same average magnitude. With further increased mode orders, the waviness is reduced gradually. The variation of acoustic power radiation for two different materials has been studied. It is observed that at low mode orders, a steel plate radiates more acoustic power than that of the plastic plate but at high mode, the reverse is true.

10:15

**3aSAb4. Numerical prediction of noise radiated from a panel subjected to boundary layer excitation.** Michael J. Allen and Nickolas Vlahopoulos (Dept. of Naval Architecture and Marine Eng., Univ. of Michigan, 2600 Draper Rd., Ann Arbor, MI 48109-2145)

In this work an algorithm is developed for combining finite element and boundary element techniques for computing the noise radiated from a panel subjected to boundary layer pressure loading. The excitation is presented in terms of the auto and cross power spectral densities [F. Han, "Measurement of pressure fluctuations under turbulent boundary layer," Ray W. Herrick Laboratories, Report-213, HL 97-14, Purdue University]. The structural finite element model for the panel is divided into a number of sections. A uniform pressure is applied as excitation on each section separately. The corresponding vibration is computed, and is utilized as excitation for an acoustic boundary element analysis. The acoustic response is computed at any data recovery point of interest. The relation-

ships between the acoustic response and the pressure excitation applied at each particular section of the panel constitute a set of transfer functions. They are combined with the spectral densities of the excitation for computing the noise generated from the vibration of the panel subjected to the boundary layer excitation. This development has the potential of computing wind noise in automotive applications, or boundary layer noise in aircraft applications. [Work supported by Rackham School of Graduate Studies, Univ. of Michigan, and Ford Motor Co.]

10:30

**3aSAb5. Radiation efficiency of convected fluid-loaded plates.** Kenneth D. Frampton (Dept. of Mech. Eng., Duke Univ., Box 90 300, Durham, NC 27708)

The radiation of sound from geometrically simple vibrating structures into stationary fluids is well understood. However, to date, very few investigations have considered the effects that a convected fluid has on structural acoustic radiation. The purpose of this investigation is to quantify the effects of various structural and fluid parameters on the sound radiated from a vibrating elastic plate into a convected fluid medium. The discussion will include a description of modeling an elastic plate imbedded in an infinite baffle and coupled to a semi-infinite convected fluid field. Furthermore, the importance of a coupled model approach (where the fluid pressures generated by the plate motion in turn force the plate response) will be discussed. The influence of several system parameters on the plate radiation efficiency will be discussed. Included in these parameters are the fluid velocity, plate aspect ratio, fluid-to-plate mass ratio, and others. It will be demonstrated that the effects of convected fluid loading on sound radiation can be very significant.

10:45

**3aSAb6. Transient boundary integral solution for arbitrarily shaped thin shells.** Markku J. Vartiainen (Dept. of Appl. Mathematics and Theoretical Phys., Univ. of Cambridge, Silver St., Cambridge CB3 9EW, England, M.J.Vartiainen@damtp.cam.ac.uk)

The transient acoustic wave from thin, arbitrarily shaped three-dimensional surfaces is computed using the boundary integral equation method. Helmholtz' equation of retarded potentials is discretized by spatial and temporal, quadratically varying, conforming elements. When the body interior collapses into a thin shell, the resulting equation set from the ordinary integral equation becomes underdetermined. Therefore, the normal derivative has been taken, which, due to the hard body boundary condition, cancels the self term and leads to an equation of the Fredholm second kind. In this, the potential difference between the two sides of the surface is a variable instead of the potential itself. In the presentation a collocation solution method for the equation is shown, and a numerical computation algorithm reviewed. By comparing solutions with those ob-

tained from the ordinary retarded potential equation, the approach is shown to have good accuracy when applied to closed bodies such as a sphere and a cone-sphere. The method for thin shells is verified with frequency domain solutions for certain shapes where exact far-field solutions are available. The solutions in the frequency domain have been extracted from the transient ones by Fourier deconvolution.

11:00

**3aSAb7. Acoustic harmonic radiation from long thin bodies of revolution via generalized internal source density method.** Peter R. Stepanishen (Dept. of Ocean Eng., Univ. of Rhode Island, Narragansett, RI 02882-1197, stepanishen@oce.uri.edu)

A previously developed generalized internal source density method [P. R. Stepanishen, *J. Acoust. Soc. Am.* **102**, 1955–1963 (1997)] is used to investigate acoustic harmonic radiation from circular cylinders with hemispherical end caps and normal velocity distributions corresponding to the lowest nonaxisymmetric ( $n=1$ ) circumferential modes. A classical least squares approach leads to an inhomogeneous integral equation for the internal dipole line source distributions. Singular value decomposition methods are then used to determine the source distributions for the velocities of interest. The pressure and velocity fields in the fluid are readily obtained from line integrals of the dipole line source distribution. Numerical results are presented to illustrate the general characteristics of the source distributions and the near and far field radiation as a function of  $L/a$  (length/radius) and  $ka$  (normalized frequency) for various velocity distributions of interest.

11:15

**3aSAb8. Dissipation and the resolution of nonuniqueness in structural dynamics.** John J. McCoy (The Catholic Univ. of America, School of Eng., Washington, DC 20064)

The inverse problem of determining the causative forces acting at multiple point-ports of a structural element, based on motion data at these same ports, is nonuniquely posed at isolated critical frequencies for which the determinant of the mobility matrix vanishes. This nonuniqueness is resolved in the presence of a dissipation that removes the critical frequencies from the axis of real numbers. Demonstrated is that the resolution is achieved at the price of a prediction that is unduly sensitive to any uncertainty in the description of the dissipation mechanism. The demonstration is provided through a small parameter, asymptotic representation of the solution of the inverse problem, which obtains in the presence of a weak dissipation. This representation, which is achieved via a rescaling of the inverse problem solution, shows a unique description of the limit point result, provided the limit process is specified. The nonuniqueness that applies to the idealized formulation that one obtains for dissipation free systems is thus seen to reflect a physics of different limit processes resulting in different predictions at the limit point.

3a WED. AM

Session 3aSC

Speech Communication: Physical Models for Speech Production and Automatic Speech Recognition

Maureen L. Stone, Chair

Otolaryngology, Room 525, University of Maryland Medical School, 16 South Eutaw Street, Frenkil Building, Baltimore, Maryland 21201-1593

Contributed Papers

9:00

**3aSC1. A sparse ultrasound data set for reconstructing tongue surfaces.** Andrew J. Lundberg (Dept. of Computer Sci., Johns Hopkins Univ., 3400 N. Charles St., NEB 224, Baltimore, MD 21218) and Maureen Stone (Univ. of Maryland Med. School, Baltimore, MD 21201)

This work presents a method for reconstructing time-motion sequences of 3-D tongue surfaces during speech from ultrasound data. Earlier work [Stone and Lundberg, *J. Acoust. Soc. Am.* **99**, 3728–3737 (1996)] produced 3-D reconstructions of steady-state tongue surfaces from 60 coronal slices. For motion sequences, collecting 60 coronal slices would be impractical, and possibly unnecessary. Therefore, this study used the steady-state reconstructions as a model for planning data collection and reconstruction from a sparse data set. Six coronal tongue contours were used to reconstruct 3-D surfaces. Selection of contours was globally optimized using simulated annealing. Sparse and dense reconstructions were compared using worst error, average error, and percentage of surface coverage. For all speech sounds, worst error was 2 mm, average error was 0.4 mm, and average reconstruction coverage was 83%. To generalize the method across subjects' optimal slice locations were estimated in a simpler way. Six midsagittal points were optimized to reconstruct the midsagittal contour. Corresponding coronal slices were then used to reconstruct 3-D surfaces. Errors and reconstruction coverage were comparable to the 3-D optimized sparse set. This method is adequate for calculating a sparse data set, and for collecting time motion data and reconstructing 3-D surface motion. [Work supported by NIH Grant No. DC01758.]

9:15

**3aSC2. Direct numerical simulations of impulsively started jets with application to speech production.** L. Mongeau, S. H. Frankel (School of Mech. Eng., Purdue Univ., West Lafayette, IN 47907), and R. C. Scherer (Bowling Green State Univ., Bowling Green, OH 43403)

Many aspects of the conversion of the air flow through the larynx into sound are still insufficiently understood for the purposes of making precise diagnostic decisions in the voice clinic, targeting optimal intervention strategies for voice problems and voice training, and achieving high-quality articulatory speech synthesis. In a previous study, experiments performed using a dynamic physical model of the larynx revealed the presence of a transient pulse occurring immediately after the instant of vocal fold separation, prior to the formation of a quasisteady developing jet [Mongeau *et al.*, *J. Acoust. Soc. Am.* **102**, 1121–1133 (1997)]. The purpose of the present study was to investigate this phenomenon numerically using direct and large eddy simulations of an impulsively started free planar jet. The compressible Navier–Stokes equations were integrated using a two–four compact finite-difference scheme. A nonuniform Cartesian grid was used with Navier–Stokes characteristic boundary conditions. Preliminary results confirmed the presence of an acoustic pulse immediately following the imposition of a pressure gradient across the orifice. The feasibility of extending this conclusion for the case of three-dimensional confined jets will be discussed. [Work supported by NIH.]

9:30

**3aSC3. Determination of the stochasticity of the excitation function of speech.** Chuang He and George Zweig (Los Alamos Natl. Lab, T-division, M/S B276, Los Alamos, NM 87545)

The frequency above which the excitation function of a voiced vowel becomes essentially stochastic is determined. It varies with speaker and stress. Knowledge of this transition frequency can be used to develop better spectral subtraction denoising algorithms, where different methods of spectral estimation are used above and below this frequency. In addition, whenever speech is (1) unvoiced, or voiced with constant pitch, and (2) the convolution of an excitation function with another function, a normalized variance of the spectral estimate of speech can be defined which equals the normalized variance of the spectral estimate of the excitation function. This normalized variance measures the frequency dependence of the relative strengths of the stochastic and deterministic components present in the excitation function. As expected, for voiced vowels the normalized variance is small at low frequencies, confirming that the excitation function is largely deterministic. At high frequencies the normalized variance is large and the excitation function is primarily stochastic. Therefore, voiced vowels are whispered at high frequencies. [Work supported by DOE applied mathematics program and DARPA information technology office.]

9:45

**3aSC4. The coarticulation of coronal stops: A modeling study.** Christine Ericsson, Björn Lindblom, Johan Stark (Dept. of Linguist., Stockholm Univ., S-10691 Stockholm, Sweden, ericsson@ling.su.se), and Johan Sundberg (Royal Inst. of Technol., S-10044 Stockholm, Sweden)

Articulatory data were obtained from x-ray films [P. Branderud *et al.*, *Fonetik* **98**, 168–171 (1998) and [www.ling.su.se/fon/publications/](http://www.ling.su.se/fon/publications/)] and analyzed by finding the best-matching profiles generated by APEX, an eight-parameter speech production model developed at SU and KTH [J. Stark *et al.*, *Fonetik* **98**, 184–187 (1998)]. APEX was calibrated to reflect the vocal tract characteristics of individual subjects and the vowel-dependent movements associated with dental and retroflex Swedish stops were depicted as trajectories in the APEX parameter space. The mapping of x-ray observations onto APEX parameters provides an opportunity to reexamine traditional issues arising in the context of coarticulation. The results will be compared with quantitative predictions derived from Döhman's "uniform coarticulation" formula [*J. Acoust. Soc. Am.* **41**, 310–320 (1967)] and from alternative hypotheses based on APEX parameter optimization. [Work supported by the HSRF and RJ research councils of Sweden.]

10:00

**3aSC5. Effect of vocal tract inertance on phonation threshold pressure: theory and measurements.** Roger W. Chan and Ingo R. Titze (Natl. Ctr. for Voice and Speech, Dept. of Speech Pathol. and Audiol., The Univ. of Iowa, Iowa City, IA 52242, chan@alto.shc.uiowa.edu)

In a previous analytical study [Titze, *J. Acoust. Soc. Am.* **83**, 1536–1552 (1988)], it was shown that vocal fold oscillation is facilitated by the presence of a vocal tract, i.e., phonation threshold pressure is lowered by an inertive acoustic impedance of the vocal tract. Results of a recent

simulation study [Titze and Story, *J. Acoust. Soc. Am.* **101**, 2234–2243 (1997)] support the theory and show that a narrow “epilarynx tube” (area  $<1.0 \text{ cm}^2$ ) in the lower vocal tract provides impedance-matching and gives the biggest facilitative effect. This small-amplitude oscillation theory was revised in the present study to simultaneously account for vocal fold mucosal wave propagation and vocal tract inductance, as energy transfer mechanisms for flow-induced oscillation. Analytical expressions of phonation threshold pressure were derived showing the relative contributions of the two mechanisms. Empirical data on the effect of vocal tract on phonation threshold pressure were also obtained in a physical model of the vocal fold mucosa [Titze *et al.*, *J. Acoust. Soc. Am.* **97**, 3080–3084 (1995)]. Both analytical and experimental results show that the facilitative effects of vocal tract on the “ease” of phonation are the most prominent under specific glottal geometry and biomechanical conditions. [Supported by NIH Grant No. P60-DC00976.]

**10:15–10:30 Break**

**10:30**

**3aSC6. Open-phase integrated sound pressure as a tool for analyzing factors that affect glottic source wave.** S. A. Elder (Phys. Dept., U.S. Naval Acad., 572 Holloway Rd., Annapolis, MD 21402, elder@arctic.nadn.navy.mil) and P. F. Castellanos (Univ. of Maryland School of Medicine, Baltimore, MD 21201)

For experimental situations such as Sondhi tube and low-voice anechoic chamber measurements, where head resonance and room reflection contamination of the glottic source wave are small, the open-phase single glottic pulse of integrated sound pressure is a useful tool for assessing conditions of sound generation in the larynx. In some cases this parameter becomes a surrogate glottic area function, while in others it mimics the DEGG, suggesting a second sound source associated with the switching on and off of the glottic jet at the beginning and ending of open phase. Like the EGG, integrated sound pressure (ISP) has the advantage of being noninvasive and could be useful for screening pathological laryngeal conditions. Examples are presented for both *in vitro* and *in vivo* phonation of single glottic pulses (SGP).

**10:45**

**3aSC7. Contributions of vocal tract shape to voice quality.** Brad H. Story (Wilbur James Gould Voice Research Center, Denver Center for the Performing Arts, 1245 Champa St., Denver, CO 80204), Ingo R. Titze (Univ. of Iowa, Iowa City, IA 52242), and Eric A. Hoffman (Univ. of Iowa College of Medicine, Iowa City, IA 52242)

Three-dimensional vocal tract shapes and consequent area functions representing the vowels [i a u] have been acquired from one male and one female subject using MRI. The two subjects were highly trained professional singers, and both were adept at manipulation of vocal tract shape to alter voice quality. Each vowel was performed four times, each with one of the four voice qualities: typical speech, yawny, twangy, and high pitched classical singing. The purpose of the study was to determine how the vocal tract shape can be manipulated to alter vocal quality while retaining a desired phonetic quality. Relative to typical speech, the resulting area functions show, in general, that the lower pharynx is widened for both the yawny and classical singing productions and narrowed for the twangy voice type. Additionally, the yawny and classical singing qualities have widened oral cavities while the twangy quality shows decreased oral cavity area. This contrasts, however, with the lip opening where the twangy quality shows larger area than any of the other three qualities.

**11:00**

**3aSC8. Detecting hesitations in the automatic recognition of spontaneous speech.** Douglas O’Shaughnessy, Clark Z. Lee, Hesham Tolba, Rachid El Meliani, Weiyang Li, and Zhong-Hua Wang (INRS-Telecommunications, 16 Pl. du Commerce, Nuns Island, QC H3E 1H6, Canada)

Practical speech recognizers must accept normal conversational voice input (including hesitations). However, most automatic speech recognition work has concentrated on read speech, whose acoustic aspects differ significantly from speech found in actual dialogues. Hesitations, filled pauses,

and restarts (after aborted utterances) are common in natural speech, yet few recognition systems handle such disfluencies with any degree of success. Among other problems, filled pauses (e.g., “uhh,” “umm”), unlike silences, resemble phones as part of words in continuous speech. The work reported here further develops techniques to allow identification of filled pauses. The problem of finding and correcting restarts is also examined, i.e., not just determining where the speech interruption occurs, but also estimating which words are undesired. The Switchboard database (of natural telephone conversations, yielding relatively poor recognition rates to date) provided data for the study. While most automatic recognition methods rely entirely on spectral envelope (e.g., low-order cepstral coefficients), identifying hesitation phenomena requires using a combination of spectra, fundamental frequency and duration.

**11:15**

**3aSC9. Fundamental frequency synchronous spectral analysis for vowel classification.** Bingjun Dai and Stephen A. Zahorian (Dept. of Elec. and Computer Eng., Old Dominion Univ., Norfolk, VA 23529, zahorian@ece.odu.edu)

A method is described and tested for spectral analysis of vowels using window lengths that are integer multiples of the pitch period for voiced signals. For segments of vowels selected from steady-state vowels, the average fundamental frequency is first determined using “standard” autocorrelation methods. The acoustic signal is then analyzed again to determine fundamental frequency on a cycle-by-cycle basis. The signal is resampled at a higher rate so that each pitch period has the same number of samples. Spectral analysis is implemented such that harmonics of the fundamental coincide with FFT samples. Cepstral analysis is then performed on this spectrum with and without fundamental-frequency-dependent frequency shifting as a speaker normalization. This processing method was tested using a database of 150 speakers (50 children, 50 women, and 50 men) for ten monophthong vowels produced in isolation. As a control, spectral analysis was also performed on Hamming-windowed speech segments without regard to fundamental frequency. Neural network classification tests indicated only minor changes in classification rates with the fundamental-synchronous method versus the conventional method. The implication of this work is that spectral smearing due to window effects is a minor effect for vowel spectral analysis. [Funded by NSF, Grant No. NSF-BES-9411607.]

**11:30**

**3aSC10. Articulatory speech recognition using hierarchical, interpolating hidden Markov models.** Daniel C. Fain and Alan H. Barr (Computation and Neural Systems, California Inst. of Technol., Pasadena, CA 91125, {fain,barr}@gg.caltech.edu)

Articulatory speech recognizers infer the configuration and movement of a speaker’s vocal apparatus as an intermediate representation between acoustics and phonetics. Articulatory modeling makes coarticulation processes explicit, as opposed to the conventional triphone technique of elaborating all coarticulation combinations. In the present study, hierarchical, interpolating hidden Markov models (HMMs) transform acoustics into articulation and articulation into phonetics. Articulatory and acoustic data with transcriptions are used for both training and testing. The articulatory data, collected by the University of Wisconsin, consist of synchronized recordings during speech of x-ray microbeam positions, throat vibration, and acoustics. State variables of the Markov model represent articulator configurations. These variables change continuously between targets to represent coarticulation. In this model, their state changes are driven by a top-level state variable which changes from phone to phone. The model emits both articulator positions and acoustic analysis coefficients, when viewed as a generator (in recognition, these emissions are the inputs). Variational techniques make the training problem tractable. The latest phonetic-recognition results of the model will be contrasted with baseline HMM systems trained on acoustic and articulatory data. [Work supported in part by NIMH, the NSF/DARPA STC for Computer Graphics and Scientific Visualization, and Hewlett-Packard.]

**Session 3aSP**

**Signal Processing in Acoustics, Structural Acoustics and Vibration and Engineering Acoustics:  
Performance of Active Noise Control Systems in Real-World Applications**

Anthony J. Brammer, Cochair

*National Research Council, Institute of Microstructural Sciences, Montreal Road, Ottawa, Ontario K1A 0R6, Canada*

Stephen C. Thompson, Cochair

*Knowles Electronics, Inc., 1151 Maplewood Drive, Itasca, Illinois 60143*

**Chair's Introduction—8:30**

***Invited Papers***

**8:35**

**3aSP1. Practical implementation of active noise control.** George J. Pan and Anthony J. Brammer (Inst. for Microstructural Sci., Natl. Res. Council of Canada, Montreal Rd., Ottawa, ON K1A 0R6, Canada, george.pan@nrc.ca)

Effective application of active noise control requires an understanding of acoustics, control theory, signal processing, and electronics. The physical mechanism of control may involve localized cancellation, modifying the impedance of an unwanted source, or the absorption or reflection of energy. Successful implementation relies on realistic modeling and robust design of the active noise control system. It also depends on precise realization of the control algorithms. Analog controllers offer the attraction of simplicity and speed, but cannot adapt to changes in the acoustic system. Nonparametric identification of the electroacoustic system, such as formed by the secondary source and error sensor, is essential. The causality condition for adaptive feedforward control of broadband noise introduces another challenge for applications to small acoustic devices, such as hearing protectors. Performance of localized active control also depends on the coherence between the signal that will be chosen to drive the controller and the noise at the cancellation point. This coherence function reflects the nature of the sound field and the passive acoustic system. The influence of these factors on active reduction will be discussed with reference to the performance of a digital ANR hearing protector.

**9:00**

**3aSP2. Real-world performance of headset active noise reduction systems.** R. B. Crabtree (Defence and Civil Institute of Environmental Medicine, 1133 Sheppard Ave. West, P.O. Box 2000, Toronto, ON M4G 1C4, Canada)

Active noise reduction (ANR) in headsets promotes the electro-acoustic cancellation of sound within the ear cups of a hearing protector. Operating at frequencies below 1000 Hz, ANR augments attenuation where passive protection is minimal. Personal ANR can reduce the potential for hazardous noise exposure and can facilitate auditory communications. ANR system performance has been characterized to assist purchasing departments in making informed decisions about commercial devices suitable for use in high-noise environments such as helicopters and tracked vehicles. Test methods were developed to assess: (a) active attenuation properties, (b) issues of fitting integrity, (c) speech discrimination performance, (d) saturation or overload threshold limit, and (e) general suitability for long-term use. When properly designed and applied, personal ANR can enhance the listening environment for the user. Nonetheless, performance limitations have been identified in certain devices. Some tended to overload easily or to cease operating under adverse conditions, and others became unstable when the seal around the ear was broken. Proper fitting is pivotal to satisfactory ANR operation, particularly in units with low overload tolerance. Ultimately, the function of any ANR system must be understood in relation to its intended operating environment.

**9:25**

**3aSP3. Active noise reduction for cellular and PCS handsets.** Michael A. Zuniga (Lucent Technologies-Bell Labs, 1919 S. Eads St., Ste. 300, Arlington, VA 22202)

The effectiveness of active noise reduction (ANR) technology in Prototype cellular and PCS handsets has been investigated by developing prototype terminals with both feedback and feedforward control approaches. In contrast to ANR headsets, which present a relatively stable and favorable earpiece (i.e., receiver-error-microphone) transfer function (TF) to the ANR control system, an even greater challenge is faced in applying ANR to cellular/PCS handsets where the corresponding TF varies with positioning of the earpiece about the ear. As a first step in the investigation, a practical cellular/PCS handset earpiece, suitable for ANR, but with reduced position variability in the earpiece TF, has been developed using a lumped parameter, equivalent circuit model of the earpiece-ear system. Experimental results are presented for the new earpiece design tested against different users' ears and against several acoustic load impedances. As the next step in the investigation, both feedback and fixed feedforward ANR control algorithms were implemented on a low-latency programmable ASIC developed specifically for ANR applications. The ANR performance results are presented for both feedback and feedforward designs tested against a range of users and also as measured against a B&K 4195 "leaky" coupler.



10:05

**3aSP4. Considerations in the design of ANR communication headsets.** Daniel M. Gauger and Roman S. Sapiejewski (Bose Corp., M.S. 271, The Mountain, Framingham, MA 01701)

Active noise reduction integrated into communication headphones or headsets began to see use in high-noise military and commercial environments in the late 1980s. In a few applications ANR headphones have been quite successful; however, the technology has not seen the widespread use that was originally promised. Based on this experience, engineering challenges facing the designer as well as factors contributing to the success or failure of the technology in various applications to date will be discussed. Opportunities for improvement in new designs will also be examined.

10:30

**3aSP5. Commercial active noise control solutions for aircraft—A variety of approaches.** Lane Miller, Mark Norris, and Dino Rossetti (Thomas Lord Research Ctr., 405 Gregson Dr., Cary, NC 27511)

Today's aerospace market is placing increasing emphasis on reducing noise and vibration to enhance passenger comfort. Lord offers high-performance active solutions for aircraft noise problems with its NVX active systems. There are currently over 50 Lord NVX™ Active Systems flying on a variety of aircraft around the world. These systems include active isolations systems for the Cessna Citation X business jet, a pylon active structural control system for DC9 aircraft, and speaker-based active noise control systems for corporate turboprops. While the systems share many commonalities, they represent a variety of different approaches to the individual noise problems of these aircraft. Each of these problems requires a solution optimally designed for the application. During the presentation, the system components and general operation will be discussed. The benefits and limitations of these approaches will also be covered. How each system was optimized for its specific application will also be discussed. Numerous noise and vibration performance measurements will be presented. Further, the robustness and reliability of the various systems will be addressed.

10:55

**3aSP6. A brief social history of active noise control in ducts.** L. J. Eriksson (6105 Fairfax Ln., Madison, WI 53718)

Considerable progress has been made in the application of active noise control in ducts since the pioneering work by Lueg over 60 years ago. These developments will be briefly reviewed with special emphasis on three remaining technical challenges including inadequate transducer output power and signal coherence at frequencies below about 50–100 Hz and high modal content at frequencies above about 500–1000 Hz. Although the potential for improvement remains significant, some problems may be approaching fundamental physical limits. However, widespread application may be more restricted by various social and commercial issues. Among these are the relatively low value that is often placed on noise control and energy savings, the lack of an adequate infrastructure to supply and maintain active noise control systems, and the cultural and business changes required to apply a technology that requires system design, easily demonstrates its performance, and often reveals the noise level of the source. Technological similarities between ANC systems and electronic security systems will be discussed. Social-cultural similarities between these systems and a weapon of warfare, the machine gun, will also be considered [John Ellis, *The Social History of the Machine Gun* (The Johns Hopkins University Press, Baltimore, 1975)].

### Contributed Papers

11:20

**3aSP7. Performance and maintenance requirements of active control systems.** Cary D. Bremigan (Digisonix, LLC, 908 Stewart St., Madison, WI 53713, cbremigan@digisonix.com)

Vehicle designers are continually looking for methods to improve in-cabin noise vibration and harshness (NVH). Active control systems offer a variety of techniques for low-frequency NVH control. Active systems allow the designer to trade between the factors of NVH performance, weight, package space, and cost. Examples of systems are active interior sound control and active-mounts/active-vibration control. The performance of these systems directly impacts the sound and vibration field, to which the operator and passengers are exposed. The system stability and robustness must be monitored and maintained at all times. The focus of this paper will be on active interior systems, highlighting performance and diagnostics. The closed loop control functions found in most active systems present unique opportunities for system maintenance and diagnostics. Several methods for component diagnostics will be discussed. Also, the diagnostic advantages of stand-alone and integrated active systems will be considered.

11:35

**3aSP8. A comparison of ANR headset performance for loopshaping and  $H_\infty$  control system design.** Michael A. Vaudrey (Adaptive Technologies, Inc., Blacksburg, VA 24060, mvaudrey@vt.edu), Daniel G. Cole, and William R. Saunders (Virginia Tech, Blacksburg, VA 24060)

Active noise reduction (ANR) has been widely accepted as a critical component in circumaural hearing protectors and communication headsets for many commercial and military applications. That is because ANR headsets provide the end-user with at-ear noise suppression that is more effective than passive configurations alone can offer. In the past few years, there have been significant advances in this technology area. These are largely related to attempts to transition from traditional analog control hardware to digital implementations. One benefit of digital controller design is the ease of constructing optimal and robust compensators. The traditional approach in designing feedback ANR headsets is usually "loopshaping," which is a somewhat heuristic design method. The desire for further improvements in feedback ANR headset performance is leading engineers toward more analytical approaches for controller design, including the robust techniques of  $H_\infty$ . This presentation compares and

contrasts loopshaping and optimal controller design for the single-input, single-output disturbance rejection problem. A controls engineer experienced in loopshaping design techniques and a controls engineer experienced in optimal controller design techniques compare results for an ANR

headset design. Constraints are placed on bandwidth, actuator force, and system design. It is shown that the loopshaping design can perform as good as or better than the optimal control solution for the given constraints.

WEDNESDAY MORNING, 14 OCTOBER 1998

MARRIOTT BALLROOM 2, 9:00 TO 11:45 A.M.

### Session 3aUW

## Underwater Acoustics: Computational and Theoretical Underwater Acoustics

Michael D. Collins, Chair

Naval Research Laboratory, Code 7140, Washington, DC 20375-5350

### Contributed Papers

9:00

**3aUW1. New and improved parabolic equation models.** Michael D. Collins (Naval Res. Lab., Washington, DC 20375, collins@ram.nrl.navy.mil)

The stability of the self starter and the accuracy of the elastic parabolic equation have been improved. The self starter is an initial condition that is generated by applying an operator to the source term [IEEE J. Ocean. Eng. **22**, 102–109 (1997)]. Although the self starter is continuous, numerical difficulties can arise for problems involving relatively deep water and/or low bottom attenuation and/or high frequency. This problem has been eliminated by placing the pole of the smoothing operator far from the eigenvalues of the depth separated wave equation. The improved self starter has been incorporated into Version 1.1 of RAM (range-dependent acoustic model), which is available by anonymous ftp from ram.nrl.navy.mil. The elastic parabolic equation accounts for compressional and shear waves in the sediment. Handling a sloping ocean bottom is complicated by the change in the number of dependent variables across the interface. Gradual slopes can be handled accurately by applying a coordinate translation to flatten the ocean bottom interface. Energy is conserved and the adiabatic mode solution is invariant under this mapping. This approach has been incorporated into Version 1.0 of RAMS, which is also available by ftp. [Work supported by ONR.]

9:15

**3aUW2. A new method for calculating temporal intensity correlations in partially saturated scattering.** James S. Gerber (Phys. Dept., Univ. of California—Santa Cruz, Santa Cruz, CA 95064, jamie@pacific.ucsc.edu)

Intensity correlations in time for acoustic scattering from internal waves are investigated using path integral methods. A new perturbative procedure for calculating the temporal intensity autocorrelation  $\langle I(x,0)I(x,t) \rangle$ , valid in the partially saturated scattering regime, is introduced. Partial saturation describes a situation in which smaller scales of the scatterer cause the geometrical raypath to fracture into myriad microrays but where the larger scales lead to correlation between these micromultipaths. This situation is of particular relevance in acoustic propagation through internal waves due to the wide range of vertical scales as well as the separability of the internal wave power spectrum. It is shown that the perturbative method being introduced has greater accuracy as well as a wider range of applicability than the standard method [Flatté *et al.*, J. Acoust. Soc. Am. **77**, 1723–1731 (1985)]. A computer simulation of acoustic propagation through an evolving internal wave field has been implemented to provide a basis for comparison with the theory. Application to calculation of higher moments of intensity will be discussed. [Work supported by ONR.]

9:30

**3aUW3. Benchmark models for propagation and scattering in Biot media.** Ralph A. Stephen (Woods Hole Oceanogr. Inst., Woods Hole, MA 02543-1542)

Benchmark models have proved useful in comparing algorithms for studying acoustic wave propagation and scattering [for example, Jensen and Ferla, J. Acoust. Soc. Am. **97**, 1499–1510 (1990); or Stephen, J. Acoust. Soc. Am. **100**, 2070–2078 (1996)]. By addressing the same problem various investigators can focus on the strengths and weaknesses of various codes as objectively as possible. Ideally benchmark models should address a physically realistic experiment. Often the real experiment is so complex, however, that a sequence of models of increasing complexity is necessary to study the effects of one variable at a time. Some effort is required by the community to agree on a set of problems that is relevant but also amenable to solution by a number of methods. The necessity to accurately predict seafloor scattering strengths from high-porosity muds and sediments, often including gas bubbles in the subbottom, has prompted a renewed interest in Biot theory. For saturated, porous media there is some debate on the relevance of Biot theory to field observations which makes a series of benchmark problems even more important. Some candidate benchmark models for Biot media, for which reference solutions are available, are proposed. [Work funded by ONR.]

9:45

**3aUW4. Simulated wave propagation in elastic environmental flat and sloping waveguides by a finite length ping time-dependent ray trace model.** Elmer White (130 Moonraker Dr., Slidell, LA 70458)

A finite length ping ray trace program (FLPRT) has been extended that is now capable of simulating time-dependent wave motion in a complicated elastic bathymetric waveguide. From the original concept of sound waves being generated from an infinite set of point sources, FLPRT expands a finite set into following ray theory including shear and compression logic in a half space. Wave propagation is demonstrated in a constant velocity shallow ocean environment for both flat and sloping bathymetries. Not only is the objective to compare the model-generated transmission loss calculations against those computed by EFEPE, an elastic parabolic equation model by M. Collins of ARL, but also to show the time-generated path of the acoustic waves in both cases. Narrow angle generated pings show different nonmodal characteristics than those generated by wide angle pulses which exhibit fluctuating waves predicted by normal-mode theory. As in all cases, adiabaticity is assumed within each very small incremental time step. A 3–5 min VCR(TV) presentation will be shown demonstrating wave motion in the presence of a flat and wedge half-space exhibiting both shear and compressional waves on the half-space.

**3aUW5. Calculations of acoustic scattering from an elastic ocean bottom.** Daniel Wurmser, Robert F. Gragg, and Roger Gauss (Code 7144, Naval Res. Lab., Washington, DC 20375-5350, wurmser@abyss.nrl.navy.mil)

The problem of acoustic scattering from the rough interface between the ocean and an elastic bottom is examined. A recently developed reciprocal scattering formalism [D. Wurmser, *J. Math. Phys.* **37**, 4434–4479 (1996)] allows existing numerical and operator expansion methods to be used to calculate scattering from rougher and/or higher-dimensional surfaces than would otherwise be possible. Here, the method is used to generate new physically intuitive versions of perturbation theory and the small slope approximation for the bottom scattering problem. The results are compared to those for the analogous two-fluid theory. The relative merits of the various approximations are discussed. Finally, the significance of the work to low-angle scattering is discussed. [Work supported by ONR.]

10:15–10:30 Break

10:30

**3aUW6. Nonuniform acoustic localization: Decay of the incoherent impulse response.** Eric Smith (Appl. Res. Labs., Univ. of Texas, Austin, TX 78731-8029)

Acoustic localization in random-scattering media is a consequence of backscatter enhancement in the regime of strong scattering. In statistically uniform, conservative media, idealized localization is predicted to lead, above a critical frequency, to eternal trapping of wave energy within the bulk, and decoupling of interior, strongly scattered wave solutions from any propagating spectrum exterior to the strong-scattering region. Small-size correlations show a diffusive transient approach to the later, stationary noise spectrum. It is shown here that strong but nonuniform scattering leads to “almost-localization,” producing scattered solutions that are weakly coupled to a propagating spectrum in the manner of resonances. Such states produce an exponential, rather than diffusive, decay tail in the incoherent late-time impulse response, with a time constant predicted to exhibit universal scaling with frequency for smooth nonuniformity. The predicted relation agrees well with a long-known scaling regime in earthquake-seismic coda, which has been attributed to multiple scatter. Preliminary evidence is presented for similar exponential decay in impulse reflections from saturated sand, suggesting a similar multiple-scattering origin. [Work supported by the Office of Naval Research, Code 3210A.]

10:45

**3aUW7. Mode coupling in the presence of random sediments and shallow water variability.** Roger M. Oba (Naval Res. Lab., Washington, DC 20375-5350)

The continental shelf west of Florida has a relatively flat bottom over a range of tens of kilometers, and the bottom and water column have fairly well characterized acoustic parameters. Parabolic equation models are used for acoustic propagation in both elastic and purely acoustic cases. The calculated effect of shear contribution is comparatively small. The variation in mode coupling over a frequency range of about 100–400 Hz is evaluated. Even in this flat-bottom case, modal coupling due to the environment occurs, especially at lower frequencies. The water column tends to be downward refracting (especially the bottom half), so that the variation in the penetrability of the sediment leads to strongly changing amounts of mode coupling. In the case of softer bottoms, this can lead to very significant coupling. [Work supported by the Office of Naval Research.]

**3aUW8. Optimal performance bounds for the classification of acoustic sources by depth in an oceanic waveguide.** Stacy L. Tantum, Loren W. Nolte (Dept. of Elec. Eng., Duke Univ., Box 90291, Durham, NC 27708-0291), and Michael T. Wazenski (Digital System Resources, Inc., Fairfax, VA 22033)

The classification of acoustic sources by depth is an application of matched-field processing which is important for both civilian and military surveillance operations, where the emphasis is placed on the correct classification of surface and submerged sources rather than the accurate estimation of the source's depth. This classification task can be posed as a composite hypothesis decision problem and approached using signal detection theory. The strength of this approach is that it is robust to uncertainties in the propagation environment and the specific source position. The likelihood ratio for this detection problem has been derived and used to determine through simulation the performance bounds for this problem under varying degrees of uncertainty regarding the acoustic environment. Results are presented in the form of receiver operating characteristic (ROC) curves for a shallow water channel with various levels of *a priori* knowledge concerning the source position. [Research supported by SPAWAR.]

11:15

**3aUW9. The surprising relationship between the atomic Lamb shift and acoustics.** Daniel Wurmser (Code 7144, Naval Res. Lab., Washington, DC 20375-5350, wurmser@abyss.nrl.navy.mil)

An analogy with a well-known quantum effect provides insight into the low grazing angle interaction of an acoustic field with a rough surface. The Lamb shift in the hydrogen atom is produced by random fluctuations that ultimately arise from second quantization. These can be introduced phenomenologically into the old quantum theory. Since the Coulomb potential is the Green's function for 3-D space, a contact potential affecting the first moment of the field survives stochastic averaging, and produces the Lamb shift. [For example, C. Cohn-Tanoudji, J. Dupont-Roc, and G. Grynberg, *Atom-Photon Interactions: Basic Processes and Applications* (Wiley, New York, 1992), p. 317.] For a classical acoustic field in the low grazing angle limit (described by the parabolic equation), a rough surface along an interface or a cusp generates a similar contact potential. This leads to a modified range-independent propagation equation for the first moment of the stochastic acoustic field. New boundary conditions at the interface lead to roughness-induced modifications to Snell's Law. [Work supported by ONR.]

11:30

**3aUW10. A hybrid ray and parabolic equation simulator.** Kourosh Kalantar Zadeh (Dept. of Elec. Eng., Tarbiat Modarres Univ., Tehran/Iran), Payman Shahsavari, and Khodabakhsh Amindehghan (J. Eng. Res. Ctr.)

The model used here is a hybrid model. It consists of two basic parts. Standard ray theory method [A. Zielinski and X. Gen, *IEEE Oceans'94*, III, 184–189] used in high frequencies and finite difference parabolic equations [D. Huang, *J. Acoust. Soc. Am.* **84**, 1405–1413 (1988)] used in lower frequencies for the shallow water cases. In both high frequency and low frequency cases the acoustic wave propagation simulator can be used for range-dependent environments. The simulator is highly user friendly. Thus a nonprofessional user is able to work with it easily. For the user, inputs are speed and bottom profiles, source level, beam pattern, and depth and environmental data. Outputs are pressure phase and amplitude in each point of underwater and bottom media. For checking correctness of the results, they were compared with various available benchmarks and they seemed to be quite acceptable. The implementation is to run on PCs under DOS operating systems.

**Meeting of Accredited Standards Committee (ASC) S2 on Mechanical Vibration and Shock**

to be held jointly with the

**U.S. Technical Advisory Group (TAG) Meeting for ISO/TC 108 Mechanical Vibration and Shock (and subcommittees ISO/TC 108/SC1, SC2, SC3, SC5, and SC6)**

D. J. Evans, Chair S2 and Chair of the U.S. Technical Advisory Group (TAG) for ISO/TC 108,  
Mechanical Vibration and Shock

*National Institute of Standards and Technology (NIST), Acoustics, Mass and Vibrations Group, Building 233, Room A147,  
Gaithersburg, Maryland 20899*

**Accredited Standards Committee S2 on Mechanical Vibration and Shock.** Working group chairs will present reports of their recent progress on writing and processing various shock and vibration standards. There will be a report on the interface of S2 activities with those of ISO/TC 108 (the Technical Advisory Group for ISO/TC 108 consists of members of S2, S3, and other persons not necessarily members of those Committees), including plans for future meetings of ISO/TC 108 and/or its Subcommittees.

**Scope of S2:** Standards, specifications, methods of measurement and test, and terminology in the fields of mechanical vibration and shock, and condition monitoring and diagnostics of machines, but excluding those aspects which pertain to biological safety, tolerance and comfort.

WEDNESDAY AFTERNOON, 14 OCTOBER 1998

MARRIOTT BALLROOM 7, 12:50 TO 2:45 P.M.

**Session 3pAB****Animal Bioacoustics: Terrestrial Animal Bioacoustics**

Peter M. Scheifele, Chair

*National Undersea Research Center, University of Connecticut, Avery Point, Groton, Connecticut 06340-6097*

**Chair's Introduction—12:50*****Invited Papers*****12:55**

**3pAB1. Long range seismic characteristics of Asian elephant (*Elephas maximus*) vocalizations and locomotion** Byron T. Arnason (Tezar, Inc., P.O. Box 26235, Austin, TX 78755-0235), Caitlin E. O'Connell, and Lynette A. Hart (Univ. of California, Davis, CA 95616)

Seismic components of Asian elephant (*Elephas maximus*) vocalizations and locomotion were recorded at a range of distances. To study the properties of sound attenuation in the ground, a string of four geophones was placed at approximately 30 m intervals from the elephants, up to 120 m from the signal source. Precise distances between sensors was measured with a differential GPS. Some trials were also conducted using microphone/geophone pairs at 30- and 120-m distances to compare attenuation in the air in relation to attenuation in the ground. Recordings were made with a four channel data acquisition system, processing signals simultaneously from the geophone string and the microphone/geophone pairs at the near and remote locations. Previous studies indicated that elephant vocalizations and locomotion produce Rayleigh waves, a type of ground surface wave. In this study, the long-range seismic characteristics of the signal sources is described. The propagation of elephant vocalizations in the air and ground is quantified at a range of distances up to 120 m and the rates of signal attenuation within each of the two media are compared.

**1:20**

**3pAB2. Effects of simulated aircraft noise on the behavior and egg production of white leghorn chickens.** Ann Bowles, Erik Berg, and Natalie Abraham (Hubbs-Sea World Res. Inst., 2595 Ingraham St., San Diego, CA 92109, annb1@san.rr.com)

White leghorn chicken poults (3 weeks and 8 weeks of age) and laying pullets (48 weeks of age) were exposed to a series of simulated jet aircraft overflights. Poultry were exposed in small groups (~35 birds/pen) in barns equipped with a U. S. Air Force-designed simulation system. For poult experiments, 72 pens were exposed four to six times per day for 4 days. For experiments with laying hens, 60 pens were exposed four times per day for two 5-day blocks over a 2-week period. Level of exposure ranged from 105 dB ASEL down to the ambient noise floor in the barns. Ambient noise was dominated by poultry vocalizations and fan noise (70–85 dBA). Behavior, food and water consumption, mortality, weights (poults), and laying success (hens) were measured for each pen

**Meeting of Accredited Standards Committee (ASC) S2 on Mechanical Vibration and Shock**

to be held jointly with the

**U.S. Technical Advisory Group (TAG) Meeting for ISO/TC 108 Mechanical Vibration and Shock (and subcommittees ISO/TC 108/SC1, SC2, SC3, SC5, and SC6)**

D. J. Evans, Chair S2 and Chair of the U.S. Technical Advisory Group (TAG) for ISO/TC 108,  
Mechanical Vibration and Shock

*National Institute of Standards and Technology (NIST), Acoustics, Mass and Vibrations Group, Building 233, Room A147,  
Gaithersburg, Maryland 20899*

**Accredited Standards Committee S2 on Mechanical Vibration and Shock.** Working group chairs will present reports of their recent progress on writing and processing various shock and vibration standards. There will be a report on the interface of S2 activities with those of ISO/TC 108 (the Technical Advisory Group for ISO/TC 108 consists of members of S2, S3, and other persons not necessarily members of those Committees), including plans for future meetings of ISO/TC 108 and/or its Subcommittees.

**Scope of S2:** Standards, specifications, methods of measurement and test, and terminology in the fields of mechanical vibration and shock, and condition monitoring and diagnostics of machines, but excluding those aspects which pertain to biological safety, tolerance and comfort.

WEDNESDAY AFTERNOON, 14 OCTOBER 1998

MARRIOTT BALLROOM 7, 12:50 TO 2:45 P.M.

**Session 3pAB****Animal Bioacoustics: Terrestrial Animal Bioacoustics**

Peter M. Scheifele, Chair

*National Undersea Research Center, University of Connecticut, Avery Point, Groton, Connecticut 06340-6097*

Chair's Introduction—12:50

***Invited Papers***

12:55

**3pAB1. Long range seismic characteristics of Asian elephant (*Elephus maximus*) vocalizations and locomotion** Byron T. Arnason (Tezar, Inc., P.O. Box 26235, Austin, TX 78755-0235), Caitlin E. O'Connell, and Lynette A. Hart (Univ. of California, Davis, CA 95616)

Seismic components of Asian elephant (*Elephus maximus*) vocalizations and locomotion were recorded at a range of distances. To study the properties of sound attenuation in the ground, a string of four geophones was placed at approximately 30 m intervals from the elephants, up to 120 m from the signal source. Precise distances between sensors was measured with a differential GPS. Some trials were also conducted using microphone/geophone pairs at 30- and 120-m distances to compare attenuation in the air in relation to attenuation in the ground. Recordings were made with a four channel data acquisition system, processing signals simultaneously from the geophone string and the microphone/geophone pairs at the near and remote locations. Previous studies indicated that elephant vocalizations and locomotion produce Rayleigh waves, a type of ground surface wave. In this study, the long-range seismic characteristics of the signal sources is described. The propagation of elephant vocalizations in the air and ground is quantified at a range of distances up to 120 m and the rates of signal attenuation within each of the two media are compared.

1:20

**3pAB2. Effects of simulated aircraft noise on the behavior and egg production of white leghorn chickens.** Ann Bowles, Erik Berg, and Natalie Abraham (Hubbs-Sea World Res. Inst., 2595 Ingraham St., San Diego, CA 92109, annb1@san.rr.com)

White leghorn chicken poults (3 weeks and 8 weeks of age) and laying pullets (48 weeks of age) were exposed to a series of simulated jet aircraft overflights. Poultry were exposed in small groups (~35 birds/pen) in barns equipped with a U. S. Air Force-designed simulation system. For poult experiments, 72 pens were exposed four to six times per day for 4 days. For experiments with laying hens, 60 pens were exposed four times per day for two 5-day blocks over a 2-week period. Level of exposure ranged from 105 dB ASEL down to the ambient noise floor in the barns. Ambient noise was dominated by poultry vocalizations and fan noise (70–85 dBA). Behavior, food and water consumption, mortality, weights (poults), and laying success (hens) were measured for each pen

throughout the experiment. Neither poults nor hens responded to simulated overflights with panic flight, piling, or any other hazardous behavior, regardless of exposure level. However, 8-week-old poults picked at one another more often in the most highly exposed pens. Hens exhibited brief, small decreases in laying rate after initial exposure. Over the experimental period, the decrease was not significant. [Work supported by the U.S. Air Force, AL/OEBN, Wright-Patterson Air Force Base (F41624-95-C-6014 DO-C9).]

### Contributed Papers

1:45

**3pAB3. Vocal tract dynamics during calling in nonhuman mammals.** W. Tecumseh Fitch (Harvard/MIT Speech & Hearing Sci., 33 Kirkland St., #1036, Cambridge, MA 02138)

Nonhuman vocal tract anatomy has traditionally been described in static terms, typically based on postmortem dissections. However, cineradiographic studies of chewing and swallowing have revealed that animals are capable of a considerable range of articulatory movements, and video analyses have indicated correlations between lip articulation and call acoustics in nonhuman primates. These observations suggest that our understanding of animal production acoustics could be enhanced by considering dynamic movements of vocal tract articulators: the lips, jaw, tongue, velum and larynx. We present results of a cineradiographic analysis of vocal tract dynamics during calling by several terrestrial mammal species. A substantial decensus of the larynx was observed during calling, which enables animals which normally breathe through the nose to vocalize orally. Further data demonstrate considerably greater attenuation of sound passing through the nasal passages than of orally emitted sound, suggesting that facultative lowering of the larynx into the oral cavity would allow the animal to produce louder calls. These data suggest that vocal tract dynamics may play a more significant role in animal vocalization than has been previously recognized.

2:00

**3pAB4. Measurement of several types of “deer whistles” for motor vehicles: Frequencies, levels, and animal threshold responses.** Peter M. Scheifele (Natl. Undersea Res. Ctr., Univ. of Connecticut—Avery Point, Groton, CT 06340-6097, scheifele@uconnvm.uconn.edu), David G. Browning (Univ. of Rhode Island, Kingston, RI 02881), and Lesa M. Scheifele (The Lost Ark, Inc., Norwich, CT 06360)

Small plastic whistles, commonly called “deer whistles,” which are attached, usually in pairs, to the front bumper of motor vehicles are sold to assist in preventing vehicle–deer collisions, an increasingly common road hazard. At vehicle speeds greater than 30 mph (15 m/s) the air forced through these whistles supposedly produces one or more tones which alert a deer or other wild animal of the vehicles approach in time to, hopefully, avoid a damaging collision. Some whistles are advertised to be in the ultrasonic range (typically 18–20 kHz), while others only mention “high” frequencies. Several have a high-frequency (open ended) and low-frequency (close ended) pair. Measurements of frequency and levels for several different whistles are presented. The possible affect on deer and other animals (such as a dog in the vehicle), based on hearing thresholds and ambient noise conditions, is discussed.

2:15

**3pAB5. Masking of tones by harmonic complexes in the budgerigar (*Melopsittacus undulatus*).** Micheal L. Dent, Robert J. Dooling (Dept. of Psych., Univ. of Maryland, College Park, MD 20742, p-mdent@bss3.umd.edu), Marjorie R. Leek, and Van Summers (Army Audiol. and Speech Ctr., Walter Reed Army Medical Ctr., Washington, DC 20307)

Birds frequently show psychoacoustic abilities remarkably similar to those of humans in spite of considerable differences in auditory structure and function. Harmonic complexes constructed in positive and negative Schröder phase are differentially effective as maskers in humans, even though they have essentially identical temporal envelopes and long-term spectra [V. Summers and M. R. Leek, *Hear. Res.* **118**, 139–150 (1998)]. Because these masking differences are believed to be closely tied to cochlear mechanisms in mammals, investigations of Schroeder-phase masking in birds might reveal the contributions of particular auditory structures to complex sound processing in both species. To this end, three budgerigars were trained by operant conditioning and tested using the method of constant stimuli to detect pure tones masked by Schroeder waveforms. In parallel testing, two human listeners showed more masking by the negative than by the positive Schroeder waveforms. However, none of the birds showed greater masking by the negative than the positive waves, and in some cases the positive waveform was the more effective masker. These results may reflect structural differences underlying the traveling wave in these two species, as well as a difference in active processing in avian versus mammalian cochleas. [Work supported by NIH DC00198.]

2:30

**3pAB6. On the possibility of the time-reversal method use in animal echolocation.** Daniel R. Raichel (Dept. of Mech. Eng., Steinman Hall, The City College of The City Univ. of New York, New York, NY 10031)

A number of theories have been advanced on the concept of echo evaluation in the auditory systems of bats and cetaceans. K. L. Beuter suggested that bats use neurological processes to evaluate echoes, and Berkowitz and Suga (1989) found different neural mechanisms in two species of bats. Raichel expressed his belief that cetaceans as well as bats are capable of spectral evaluation of signals to obtain information on their surroundings. Palakal and his co-workers developed a cortical model of the neural processing of acoustic patterns entailing temporal pattern recognition (1995). In an application of the phase conjugation method of nonlinear optics, M. Fink developed the acoustic concept of time reversal mirrors in the 1980s and applied it to evaluate materials. Kuperman, Hodgkiss, and Song (1998) demonstrated via experiment that the time-reversal mirror can be used in the ocean to refocus an incident acoustic field back to its origin. Combining the elements of the above cited theories, it is conceivable that cetaceans (and bats) can apply the time-reversal principal to evaluate the reflections of the signals they emit in the course of echolocation.

3p WED. PM

**Session 3pAO****Acoustical Oceanography: Sediment Geoacoustic Measurements and Models II**

Dajun Tang, Chair

*Applied Physics Laboratory, University of Washington, 1013 NE 40th Street, Seattle, Washington 98105***Chair's Introduction—1:00*****Invited Papers*****1:05****3pAO1. Spatial heterogeneity of acoustic bottom backscattering model parameters and predicted results.** Kevin B. Briggs (Seafloor Sci. Branch, Naval Res. Lab., Stennis Space Center, MS 39529, kevin.briggs@nrlssc.navy.mil)

Sediment geoacoustic and roughness measurements were made during a mine burial experiment in the North Sea in November 1997. The experiment site was a sand ridge (20.5–32-m water depth) influenced by strong tidal currents and wave action. Stereo photographs indicated that the sediment roughness was characterized by cross-rippled fine sand that transitioned to straight- and sinuous-rippled mixtures of fine quartz sand and mollusk shell fragments. Box core samples were subsampled with core tubes from which measurements of sediment compressional wave velocity and attenuation, density, and grain size distribution were made. Values for sediment velocity ratio, density ratio, slope of the roughness power spectrum, roughness spectral strength, and other measured and calculated parameters were used as input parameters for the composite roughness model to predict bottom backscattering strengths from various regions within the experiment site. Horizontal and vertical variability in sediment properties is high relative to other shallow sites under the influence of strong hydrodynamic forcing. There is a marked interdependence among sediment geoacoustic properties, water depth and bottom roughness features. The influence of hydrodynamic conditions and sediment type on the acoustic model predictions is demonstrated by the spatial variability in predicted scattering of high-frequency sound from the site.

**1:25****3pAO2. Two- and three-dimensional heterogeneity in carbonate sediments using resistivity imaging.** Peter D. Jackson, Robert C. Flint (BGS, Keyworth, Nottingham NG12 5GG, UK, p.jackson@bgs.ac.uk), and Kevin B. Briggs (Naval Res. Lab., Stennis Space Center, MS 39529)

Improving the characterization of buried inhomogeneities will lead to better models for predicting bottom acoustic backscattering. Sediment volume heterogeneity has been investigated using fine scale electrical resistivity data which is sensitive to porosity and sediment structure, both macro and micro. 3D electrical resistivity experiments are described where a 2D network of resistivity electrodes was used on the surface of freshly collected box cores from the Dry Tortugas, Key West. The resulting 3D resistivity data provides a unique insight into the spatial variability of sediment porosity and structure at the cm scale. Complementary X-radiograph cores provided 2D datasets of resistivity and porosity, at higher resolution. They have been used to establish the porosity-resistivity-microstructure relationships for these carbonate sediments, with microstructure being described in terms of tortuosity. These relationships have been used to extend our interpretation in terms of porosity and tortuosity to the corresponding 3D box core resistivity datasets. Sediment tortuosity has been investigated by numerically modeling the flow of electrical currents through a range of pore morphologies in three dimensions. The results show particular sensitivity to the connectivity of intra-particle porosity, particle shape and the relative sizes of pores and throats.

**1:45****3pAO3. The impact of anisotropic roughness on acoustic interaction with the seafloor.** Anthony P. Lyons, Eric Pouliquen, Warren L. J. Fox (SACLANT Undersea Res. Ctr., APO AE 09613, lyons@saclantc.nato.int), and Patricia A. G. Thomson (Defence Evaluation and Res. Agency, Dorset, UK)

Accurate description of small scale sediment roughness and its dynamics plays an essential role in the understanding of high-frequency acoustic interaction with the seafloor. The influence of surface waves can be very strong in shallow water, commonly producing relatively large, oriented, and quasi-periodic sediment features, i.e., ripple fields. One-dimensional analysis, which can be limiting in the study of anisotropic seafloors, has traditionally been used to describe sediment roughness spectra. Due to the windowing and averaging operations used to reduce bias at higher spatial frequencies, these studies have usually missed the small bandwidth components that exist. This talk will focus on seafloor roughness and acoustic measurements taken recently on rippled seafloors near Elba Island, Italy. Results of high-resolution two-dimensional roughness measurements obtained with a fully digital close-range photogrammetry system will be presented and compared with previous descriptions of roughness spectra. Acoustic backscatter and penetration measurements, which show a definite sensitivity to the anisotropic nature of the seafloor, will be compared to models that incorporate the measured ripple structure.

**3pAO4. Scattering due to bioturbation in marine sediments.** Christopher D. Jones and Darrell R. Jackson (Appl. Phys. Lab., Univ. of Washington, Seattle, WA 98105, cjohnes@apl.washington.edu, drj@apl.washington.edu)

Biologically active sediments are continually modified by epifauna (organisms that live on the sediment surface) and infauna (organisms living within the sediment). The collective mixing effect of these organisms is termed bioturbation. Bioturbation is pervasive and significantly affects the acoustic scattering characteristics of the seafloor. Epifaunal activity, such as locomotion and home building, creates roughness at the sediment-water interface. Infaunal activity, such as tube building, is responsible for the vertical and horizontal redistribution of solid material within the volume of the sediment, creating spatial and temporal inhomogeneities in sediment bulk properties (density, porosity, and compressibility). Classical diagenetic models describe bioturbational mixing as an idealized mass balance between adjacent layers of sediment. A proposed extension is to describe mixing as a stochastic forced diffusion process. The temporal and spatial spectrum of fluctuations in the sediment density and interface roughness are then found by modeling the biological forcing as a filtered Poisson process. By coupling the bioturbation model with scattering models, the effects of biological activity on acoustic scattering from the sea-floor can be studied. Applications include the remote sensing of benthic biology and the time evolution of targets on the seafloor. [Work supported by ONR.]

### Contributed Paper

2:25

**3pAO5. Geoacoustic parameters for high-frequency bottom scattering.** Dajun Tang (Appl. Phys. Lab., Univ. of Washington, Seattle, WA 98105)

In order to model scattering of high-frequency sound owing to sediment volume inhomogeneities, several geoacoustic parameters are needed. If the sediment is modeled as a fluid medium, which is believed appropriate for most sediment types, in addition to mean sound-speed profile,

mean density profile, and attenuation coefficient as a function of frequency, one needs a set of parameters controlling the stochastic nature of the scatterers. For the minimum, one needs the spatial autocorrelation functions of sound speed and density, and cross-correlation function between sound speed and density. In this presentation, first numerical simulations of volume scattering will be given to highlight the needs of the geoacoustic parameters. Then, *in situ* and laboratory measurements as well as modeling of the stochastic geoacoustic parameters will be discussed.

WEDNESDAY AFTERNOON, 14 OCTOBER 1998

HAMPTON ROADS BALLROOM 3, 1:00 TO 2:30 P.M.

### Session 3pEA

#### Engineering Acoustics and Noise: Flow and Aerodynamic Noise

Gregory L. Wojcik, Cochair

*Weidlinger Associates, Inc., 4410 El Camino Real, Suite 110, Los Altos, California 94022-1049*

George S. K. Wong, Cochair

*National Research Council, Institute for National Measurement Standards, Montreal Road, Ottawa, Ontario K1A 0R6, Canada*

### Contributed Papers

1:00

**3pEA1. On the statistical characteristics of a flow noise field inside a flexible liquid-filled cylindrical array.** Boris Aronov (Acoust. Res. Lab., Dept. of Elec. and Computer Eng. and Ctr. for Marine Sci. and Technol., UMass—Dartmouth, North Dartmouth, MA 02747) and David A. Brown (UMass—Dartmouth, North Dartmouth, MA 02747)

The statistical characteristics of the flow noise field inside a flexible liquid-filled axially streamlined array are considered. General expressions are obtained for the flow noise cross-spectral density and coherence function. The coherence function and the gain in signal-to-noise cross-spectral density and coherence versus hydrophone separation installed inside the tube are calculated.

1:15

**3pEA2. Validation of a method for educing liner impedance in the presence of grazing flow.** Maureen B. Tracy (NASA Langley Res. Ctr., M.S. 461, Hampton, VA 23681-0001, M.B.Tracy@larc.nasa.gov) and Willie R. Watson (NASA Langley Res. Ctr., Hampton, VA 23681-0001)

A method for extracting the normal-incidence acoustic impedance of a test liner installed in the lower wall of a duct carrying a uniform flow was previously reported [W. R. Watson, M. G. Jones, and T. L. Parrott, AIAA paper No. 98-2279 (1998)]. This method has been extended to include the effects of shear flow and has been applied to data obtained for two dissimilar liners in the presence of grazing flow. The normal incidence impedance spectrum of the first liner was known to be flow independent while that of the second liner was expected to be flow dependent. A total



pressure survey of the flow-impedance tube was performed to obtain an accurate description of the mean flow field in the vicinity of the liners. Acoustic data was obtained for a frequency range of 0.5–3.0 kHz and flow Mach numbers up to 0.5. Impedance spectra deduced without flow for both liners reproduced that obtained experimentally in a normal-incidence impedance tube. As expected, when the grazing flow was turned on, the deduced impedance spectra for the first liner showed no sensitivity to the grazing flow while that of the second liner was flow dependent.

1:30

**3pEA3. Exhaust mixing noise computed from time-accurate simulation of compressible free jet turbulence.** David B. Schein (Northrop Grumman Corp., 9H11/GK, 8900 E. Washington Blvd., Pico Rivera, CA 90660 and Dept. of Mech. and Aerosp. Eng., UCLA) and William C. Meecham (UCLA, Los Angeles, CA, meechem@seas.ucla.edu)

A computational fluid dynamics model for free, heated jet flow and resultant far-field sound has been developed which uses large-eddy simulation (LES) and Lighthill's acoustic analogy. A subgrid scale model for small-scale compressible turbulence is employed incorporating a combination of the popular Smagorinsky model and a deductive model. The model has been tested using published experimental mean flow field and rms fluctuation data [W. R. Quinn and J. Militzer, *Phys. Fluids* **31**(5) (1988)] for a turbulent free square jet. The ultimate objective is to address large Reynolds number, high subsonic (compressible) flow with realistic geometries more representative of aircraft engine exhausts than typically considered using direct numerical simulation (DNS). The far-field sound and directivity is computed using the time-derivative form of Lighthill's source-integral result formulated in terms of quadrupole sources from the simulated flow field, which is integrated in time and contains the fluctuations set up by the time-varying stress tensor. Simulation for a WR 19-4 turbofan engine exhaust ( $Re \approx 2 \times 10^6$  based on exit velocity and diameter) was performed, and propagated jet noise results compared with experimental acoustics data.

1:45

**3pEA4. Advanced methods for jet noise suppression.** Vladimir M. Kouznetsov, Rudolf K. Karavosov (Central Aerohydrodynamics Inst. (TsAGI), Acoust. Div., Radio str., 17, 107005 Moscow, Russia), and Mikhail M. Gilinsky (NASA Langley Res. Ctr., M.S. 166, Hampton, VA 23681-0001)

Investigations of noise reduction possibilities for singular annular and coaxial jets at the expense of varying issue conditions are carried out. The measurements were made in an anechoic chamber; microphones were set both in the near acoustic field along the external boundary of the jet mixing zone and in the far acoustic field on an arc of the circle with 2.5-m radius. The investigation results of aeroacoustic characteristics of jets issuing from an annular nozzle with central plug are presented. The effect of the central plug shape and of its axial position on the aeroacoustic characteristics of issuing jets are studied over a wide range of subsonic and supersonic pressure ratios at the nozzle exit plane. No considerable variation of thrust losses at varying the central plug shape and position were observed. Variations of issue conditions of coaxial jets were realized at the expense of both variations of external and internal contour flow parameters and organization of flow mixing in the common mixing chamber.

The spectral noise component character was observed to be varying as well as the acoustic power level of the issuing jets to be decreasing. Quite a definite correspondence between the results of measuring aerodynamic and acoustic characteristics is found. [The investigations were partly realized with support of CRDF according to award RE2-136.]

2:00

**3pEA5. Effect of issue conditions and jet nozzle shape on jet noise.** Vladimir M. Kouznetsov, Anatoli G. Munin, Sergey Yu. Makashov, and Evgeny V. Vlasov (Central Aerohydrodynamics Inst. (TsAGI), Acoust. Div., Radio str., 17, 107005 Moscow, Russia)

The results of experimental and predicted investigations on aeroacoustic characteristics of jets issuing from ejector noise-suppressor nozzles designed for power plants of supersonic passenger aircraft of the second generation are presented. Different versions of rectangular nozzles with ejector are investigated, the design of which and position relative to the nozzle exit plane vary. Jet noise level reduction by the value of 4 to 5 dB was achieved without substantial variation of thrust characteristics. In the case of jet issue from a rectangular nozzle with the exit section of special form, the discrete noise components at supercritical pressure ratios in the nozzle were completely suppressed. When a multi-element corrugated ejector nozzle was used, jet noise level reduction over a wide frequency range was observed in comparison with the case of jet issue from an annular nozzle of identical exit section area. In the frequency range corresponding to the component of the so-called "mixing noise," the jet noise level reduction achieved the value of 14 dB. Predicted evaluation of the efficiency of applying a multi-element ejector nozzle on the basis of evaluating the components of "mixing noise" and "lobe noise" was realized. The investigation results for noise of jets issuing from singular corrugated elements showed that jet noise level reduction by the value of 3–4 dB could be achieved at the expense of varying corrugation cross-section shape. [The investigations were partly realized with support of International Scientific-Technical Center (ISTC) according to Project ISTC-TsAGI #200-95.]

2:15

**3pEA6. Directivity of noise radiated by a vortex ring.** Victor F. Kopiev, Mikhail Yu. Zaitsev, and Sergey A. Chernyshev (Central Aerohydrodynamics Inst. (TsAGI), Acoust. Div., Radio str., 17, 107005 Moscow, Russia)

It is shown theoretically that the vortex ring noise is to consist of three quadrupoles with axis along the ring velocity vector. These are axisymmetrical modes and two-mode families with dependency on the azimuthal angle "fi" of  $\exp(i*fi)$  and  $\exp(2i*fi)$  kind. Each family consists of an infinite number of closely disposed modes with an identical accumulation point. This fact does not allow the separation of the quadrupoles from the spectrum analysis since all the modes are disposed in a coinciding narrow frequency interval. To reveal the noise directivity, the noise generated by a freely flying vortex ring in the anechoic chamber is measured with the use of an array of six microphones set around the movement axis. A special analysis of six measured signals which account simultaneously for azimuthal and transversal directivity of acoustic signals has allowed the separation of each quadrupole component and has proven that the vortex ring noise really consists of three equally excited quadrupoles perceived in the far field as narrow-band random noise. [The investigations were partly realized with support of CRDF according to award RE2-134.]

## Session 3pPA

## Physical Acoustics: Nonlinear Acoustics

Robin O. Cleveland, Chair

Aerospace and Mechanical Engineering, Boston University, 110 Cummington Street, Boston, Massachusetts 02215

## Contributed Papers

1:00

**3pPA1. Dependence of surface wave nonlinearity on propagation direction in crystalline silicon.** R. E. Kumon, M. F. Hamilton (Dept. of Mech. Eng., Univ. of Texas, Austin, TX 78712-1063), Yu. A. Il'inskii, and E. A. Zabolotskaya (MacroSonix Corp., Richmond, VA 23228)

The nonlinearity matrix elements  $R_{lm}$  (corresponding to generation of harmonic  $l+m$ ) for a surface wave in a crystal depend on both the plane of propagation and the direction of propagation in that plane [Hamilton *et al.*, *Nonlinear Acoustics in Perspective*, edited by R. J. Wei (Nanjing U.P., Nanjing, 1996), pp. 64–69]. Propagation at angle  $\theta$  with respect to the  $\langle 100 \rangle$  direction in the (001) plane of crystalline silicon was considered. Because of symmetry it is sufficient to investigate  $R_{lm}(\theta)$  for  $0^\circ \leq \theta \leq 45^\circ$ . Consider first  $R_{11}$ , which corresponds to second-harmonic generation. The sign of  $R_{11}$  indicates whether finite-amplitude effects cause a waveform to steepen forward or backward.  $R_{11} < 0$  for  $0^\circ \leq \theta < 21^\circ$  and  $32^\circ < \theta \leq 45^\circ$  is obtained, with  $R_{11} > 0$  for  $21^\circ < \theta < 32^\circ$ . Moreover, it appears that all elements  $R_{lm}(\theta)$  have the same sign dependence and zero crossings ( $\theta \approx 21^\circ$  and  $\theta \approx 32^\circ$ ). Numerical simulations reveal that for  $0^\circ \leq \theta < 21^\circ$  and  $32^\circ < \theta \leq 45^\circ$  positive segments of the longitudinal particle velocity waveform steepen backward in space (i.e., opposite what a sound wave does in air), they propagate almost linearly at  $\theta \approx 21^\circ$  and  $\theta \approx 32^\circ$ , and between these angles they steepen forward. Nonlinearity thus varies far more strongly than small-signal sound speed as a function of propagation direction. [Work supported by ONR.]

1:15

**3pPA2. Energy losses in a boundary layer of an acoustical resonator.** Yurii A. Ilinskii, Bart Lipkens, and Evgenia A. Zabolotskaya (MacroSonix, 1570 East Parham Rd., Richmond, VA 23228)

A one-dimensional model of nonlinear standing waves in an oscillating closed cavity has been developed and was presented at previous meetings. The present study focuses on an investigation of energy losses in the boundary layer and on the effect of the boundary layer on the acoustic field in the resonator. The boundary layer dissipation is much greater than the dissipation caused by volume attenuation. The fluid motion in the boundary layer is considered in a linear approximation. The boundary layer model is coupled with the one-dimensional model for the acoustics in the volume of the resonator. An interaction term which represents the flow from the boundary layer to the volume of the resonator is added to the mass conservation equation. A new modified one-dimensional equation that takes into account the flow from the boundary layer is obtained. Waveforms and harmonic amplitudes of pressure and velocity are calculated along the resonator axis with the modified model. The dissipation in the boundary layer and  $Q$ -factor of the resonator are also calculated. Results are presented for three geometries, i.e., a cone, a horn-cone, and a bulb.

1:30

**3pPA3. Localization of cracks using vibromodulation detection technique.** Alexander M. Sutin and Dmitry D. Donskoy (Davidson Lab., Stevens Inst. of Tech., 711 Hudson St., Hoboken, NJ 07030)

The vibroacoustic modulation technique has been recently introduced as a new tool for nondestructive inspection and evaluation of fatigued, defective, or fractured materials. This technique employs the nonlinear interaction of ultrasound and vibration in the presence of defects. Vibration changes the contact area within a defect effectively modulating an ultrasonic signal passing through this varying contact interface. This paper presents further development of the modulation technique enabling it to determine the location of a defect. The authors have developed and tested various algorithms to find crack location. There are time domain and frequency domain based algorithms. One of the time domain approaches utilizes the correlation between the location of the crack and the arrival time of the modulated portion of the probe ultrasonic signal. This time is determined by the relative distance between locations of the crack and the impact. Another time domain-based approach uses modulation as a "mark" to distinguish the high-frequency tone-burst probe signal reflected from the crack and from all other structural and material inhomogeneities. The frequency domain algorithm analyzes spectral shape which depends on relative position of an impact and a crack. All of these algorithms have been experimentally tested and verified. [Work supported by Gas Research Institute.]

1:45

**3pPA4. Some characteristics of the self-induced sound-producing instabilities of under-expanded supersonic jets: Screech feedback.** Alan Powell (Dept. of Mech. Eng., Univ. of Houston, Houston, TX 77204-4792)

The screech feedback loop differs from that of classical edgetones mainly in that: (a) the feedback is acoustic (vice hydrodynamic); (b) the source region (periodic stream disturbances interacting with the quasiperiodic spatial cell structure of the jet) is usually extensive, represented by a phased array of monopoles (vice a point dipole) with its "centroid" at  $h$ ; (c) the feedback path length  $h$  between nozzle and effective source point, always crucial to the frequency, is strongly amplitude-dependent (vice given nozzle-edge distance) and presently inestimable; (d) the postulate of maximum amplitude in the nonlinear limit cycle implies self-adjustment, jointly, of amplitude and  $h$ , with the phased array emitting preferentially towards the nozzle, that emission tending to maximize and so yielding a good frequency estimate not based on  $h$ ; (e) for round jets, the jet instability may be varicose, sinuous, or helical (vice just sinuous); for the helical jet instability (f) the acoustic feedback field must be correspondingly helical [Am. Inst. Aero. Astro. Paper 90-3980 (1990)], (g) the assumption of acoustic cutoff yields its cessation frequency, approximately; and (h) while the source mechanism remains controversial (vice an unambiguous force-dipole), a limiting amplitude is postulated for rectangular jets that also yields useful results.

2:00

**3pPA5. Acoustic radiation pressure angular distributions and dependence on radius for the stabilization of liquid bridges in air and in immiscible liquids.** Philip L. Marston, David B. Thiessen, and Mark J. Marr-Lyon (Dept. of Phys., Washington State Univ., Pullman, WA 99164-2814, marston@wsu.edu)

Long liquid bridges are naturally unstable to the growth of an axisymmetric capillary mode. The active control of the axial distribution of the radiation pressure on density-matched oil bridges surrounded by water has been used to stabilize long bridges [M. J. Marr-Lyon *et al.*, *J. Fluid Mech.* **351**, 345–357 (1997)]. Bridges in air have been passively stabilized in low gravity [M. J. Marr-Lyon *et al.*, submitted to this meeting] without active control by using the radial dependence of the angular average of the pressure [P. L. Marston, *J. Acoust. Soc. Am.* **97**, 3377 (1995)]. The angular distribution of the radiation pressure affects the bridge response and was calculated and interpreted for cases of interest using the partial-wave series for circular cylinders. The tendency of bridges in air to flatten affects the choice of acoustic frequency for active control while the viscous dissipation of capillary modes is important for extending the integration time of the feedback. While ultrasound in the liquid bath was actively adjusted

to expand the slender end of the bridge, calculations indicate that in air the fat end should be squeezed in order to reduce complications from flattening the bridge. [Work supported by NASA.]

2:15

**3pPA6. Self-action of the acoustical wave in glass with cracks.** Veniamin N. Nazarov, Irina A. Soustova, and Alexander M. Sutin (Inst. of Appl. Phys., 46 Ulyanov St., Nizhny Novgorod, 603600, Russia)

The recently developed nonlinear acoustic method for nondestructive testing uses the modulation of sound by vibrations. However, there are many other nonlinear acoustic effects that could also be used for nondestructive testing. These effects include: amplitude-dependent internal friction, high-amplitude vibration shifting the resonance frequency, generation of higher harmonics, and others. These effects were observed in a glass rod that was fractured by an intensive laser beam, while a similar unfractured glass rod did not exhibit them. The resonance acoustical field in the glass rod was excited on the frequency about 4 kHz and the strain in this field was up to  $10^{-5}$ . Some of the observed effects varied in time, which suggests a change in the crack contact surfaces due to the acoustical field. A theoretical model of acoustic propagation in cracked media to explain the observed nonlinear behaviors is discussed. [This work is supported by the United States Industry Coalition, with the US DOE Contract W-7405-ENG-36, through the University of California.]

WEDNESDAY AFTERNOON, 14 OCTOBER 1998

HAMPTON ROADS BALLROOM 1, 12:20 TO 2:45 P.M.

### Session 3pSA

## Structural Acoustics and Vibration: Machinery Silencing R&D at Annapolis—An Historical Perspective

Louis A. Herstein III, Cochair  
2722 Hanson Avenue, Baltimore, Maryland 21209-3911

Joseph W. Dickey, Cochair  
Johns Hopkins University, 3400 North Charles Street, Baltimore, Maryland 21218-2689

Chair's Introduction—12:20

### Invited Papers

12:25

**3pSA1. Annapolis Laboratory contribution to reduction and isolation of shipboard noise.** James R. Denham (2844 Fort Scott Dr., Arlington, VA 22202)

The Annapolis Laboratory of the Carderock Division of the Naval Surface Weapons Center has continually been in the forefront in development of hardware and criteria for reducing and isolation of shipboard noise. The laboratory has achieved major reductions in noise generated by pumps, fans, and valves. Their efforts have also resulted in improved damping treatments for piping and foundations.

12:50

**3pSA2. Annapolis Laboratory contribution to structureborne noise measurement and analysis.** Louis A. Herstein III (2722 Hanson Ave., Baltimore, MD 21209-3911)

The Annapolis Laboratory of the Carderock Division of the Naval Surface Weapons Center has continually been in the forefront of the development of instrumentation and standards for the measurement and analysis of the structureborne noise generated by shipboard machinery. This effort included but was not limited to sensor mounting and calibration techniques, equipment mounting fixtures, analysis instrumentation, and criteria for permissible shipboard machinery noise levels. The Laboratory also established the Machinery Acoustic Data Information Center (MADIC), which provided the Navy's only central source of such information for ship design and operational requirements. One of the results of this effort was MIL-STD-740, the military standard for machinery noise measurement procedures and criteria. An ASA/ANSI standard S2.16-1997, which was based upon MIL-STD-740, has recently been issued.

**3pSA3. Fully and partially constrained elastic–viscoelastic–elastic laminates.** B. E. Douglas (NSWC/Carderock Div., 9500 MacArthur Blvd., West Bethesda, MD 20817-5700)

This paper addresses the history and philosophy of designing constrained layer damping in heavy structures. It follows research pioneered at the Annapolis Laboratory of the Carderock Division of the Naval Surface Warfare Center from the 1960s to the present, emphasizing the various inherent damping mechanisms embedded in elastic–viscoelastic laminates. The basic damping mechanisms embedded in the elastic–viscoelastic–elastic laminates include shear damping, where plane sections remain plane through the cross section of the laminate, compression Voigt damping, where the face layers move out-of-phase to control resonance response of flexural waves, and shear Voigt damping where the face layers are designed to move out of phase manner to convert in-plane mechanical vibratory energy to heat. Closed-form expressions for the complex wave number of these three mechanisms are presented and discussed. The shear damper is found to be useful for light extended structures requiring broadband damping, e.g., fatigue problems in aerospace applications. The compression Voigt and shear Voigt dampers are found useful for heavy structures requiring narrow-band damping, typically a few octaves. The role of constraining layer discontinuity is discussed in terms of nondispersive and dispersive.

**3pSA4. A practical method for predicting ship machinery noise.** Ronald Darby (RAD Eng., Ltd., 44-401 Kaneohe Bay Dr., Kaneohe, HI 96744)

The development of a ship's noise prediction method at Annapolis from 1960 to 1967 is reviewed. In 1960, the Noise Transmission Branch was exploring mechanical impedance measurement concepts. Numerous structureborne and waterborne tests were made on machines, foundations, flexible couplings and conduits in the laboratory as well as on the SS427. The effort was complicated because of the large number of matrix elements describing even a simple machine foundation and the problems in obtaining meaningful measurements using the state-of-the-art instrumentation. The team's ivy tower collapsed by urgent requests to predict radiated noise from a whole ship to assist BUSHIPS in decision making. A prediction model was developed using the force transfer factor concept by Wright and Akey. Based on in-house measurements and estimates from available literature, each transmission path component was categorized as a single spectrum. Vibration levels for each machine type were fed into representations of its transmission path components: isolation mounts, foundation, flanking paths (piping, conduits, etc.), and the hull. The team ended up with a practical prediction scheme to aid in the preliminary design stages of new ships and in guiding priorities for future research in ship silencing.

**3pSA5. Supplementarity of damping and isolation and the invasion of humane aliens.** G. Maidanik (CDNSWC (DTMB), 9500 MacArthur Blvd., West Bethesda, MD 20817)

The principle of supplementarity of damping and isolation states: When the inherent damping is increased in a driven structure that is coupled to a passive structure, the noise control benefit to the passive structure may not be as high as one may primitively predict. The coupling, in this case, may be in charge of the prevailing damping. On the other hand, when the driven and passive structures are merely isolated, this noise control effort may also not be effective. The increase in reverberation in the driven structure compensates, in part, for the increased isolation—reduced coupling. However, when both isolation and damping are instituted, the reverberation in the driven structure is controlled by the increase in damping and, then, the noise control in the passive structure is effective. The principle of supplementarity of damping and isolation is, thereby, explained. The relevance of this principle to the invasion of Earth by Humane Aliens will be narrated the way it was related, many years ago, to my colleagues at the Annapolis Lab.

### *Contributed Paper*

**3pSA6. Boundary condition sensitivity for hybrid SEA/FEA modeling.** Brian H. Tracey and Jerome E. Manning (Cambridge Collaborative, Inc., 689 Concord Ave., Cambridge, MA 02138-1002, btracey@ccinc.com)

Hybrid SEA/FEA techniques offer the promise of improved noise and vibration predictions for midfrequency problems. One of the outstanding issues in hybrid modeling is how best to use FEA estimates of midfrequency response. Perturbation theory and Monte Carlo simulations of simple plates are used to study the sensitivity of FEA estimates to uncer-

tainty in boundary conditions. For low modal overlap, the main effect of random boundary conditions is to cause shifts in mode frequencies. Sensitivity to these perturbations can be reduced through appropriate frequency averaging. For intermediate or high modal overlap, perturbations of mode shapes are shown to have a more significant effect on prediction accuracy. Mode shape perturbations cause phase errors to accumulate away from the drive point, leading to high sensitivity for FEA transfer acceleration predictions. Numerical results also indicate a decay of the coherent response similar to that predicted by Rybak for inhomogeneous plates.

## Session 3pSC

**Speech Communication: Speaking Rate Effects, Automatic Speech Recognition, and Physical Models of Speech Production (Poster Session)**

Douglas D. O'Shaughnessy, Chair

*INRS-Telecommunications, 16 Place du Commerce, Nuns Island, Quebec H3E 1H6, Canada**Contributed Papers*

All posters will be on display from 1:00 p.m. to 2:45 p.m. To allow contributors an opportunity to see other posters, contributors of odd-numbered papers will be at their posters from 1:00 p.m. to 2:00 p.m. and contributors of even-numbered papers will be at their posters from 2:00 p.m. to 2:45 p.m. To allow for extended viewing time, posters will remain on display until 11:00 a.m. on Thursday, 15 October.

**3pSC1. The effect of intrasentence pause on the articulation rate of prepausal and postpausal utterances.** Kuniko Kakita (Dept. of Liberal Arts, Toyama Prefectural Univ., Kosugi-machi, Imizu-gun, Toyama 939-03, Japan, kakita@pu-toyama.ac.jp)

This study examined the effect of intrasentence pause on the temporal organization of the utterances both preceding and following the pause. Japanese sentences, consisting of six phrases ("bunsetsu") with a possible pause location after the third phrase, were produced (1) without any intrasentence pause (NoP condition), (2) with a short pause (ShP condition), and (3) with a normal-length pause (NrP condition). The articulation rate (mora/s) for each phrase in the ShP and NrP conditions was normalized with respect to the articulation rate for the corresponding phrase in the NoP condition for the purpose of comparison. For the ShP and NrP conditions, the phrase immediately preceding the intrasentence pause showed a notable decrease in articulation rate compared with the NoP condition (approx. 10%), while the sentence initial and final phrases showed slight increase in articulation rate (approx. 5%), suggesting that pause insertion is not a localized speech event but that it involves the temporal reorganization of the utterance as a whole. The difference in pause conditions was reflected consistently in the amount of articulation rate decrease in the prepausal phrase, the normal-length pause accompanying a greater articulation rate decrease than the short pause.

**3pSC2. The effect of speaking rate on lingual behavior for a transconsonantal vocalic gesture: An x-ray microbeam study.** Kate Bunton and Gary Weismer (Univ. of Wisconsin-Madison)

The purpose of the present study was to further explore the relationship between speaking rate and articulatory movements. A good deal of evidence suggests that speaking rate variation is accompanied by changes in the extent of overlap for successive articulatory gestures, however, previous work has shown that a simple model of gestural sliding is inadequate to explain changes in acoustic measures across speaking rates [Weismer *et al.* (in submission)]. Therefore, a more descriptive study of movement may be one step toward developing an acoustic model of changes in articulatory processes across speaking rate. Exploration of lingual movement across speaking rate was carried out using data from the x-ray microbeam data base. Ten speakers produced multiple tokens of the sentence "The other one is too big" at different speaking rates. Plots of the changing tongue contour through the VCV sequence /ubl/ from "too big" were examined to determine if the pattern of tongue movement was similar across speaking rates but with more or less overlap, or if the behaviors

looked qualitatively different. Preliminary results show at least two different variations in lingual movement underlying changes in speaking rate. [Work supported by DC00820 and DC00319.]

**3pSC3. Segmental and prosodic effects on coda glottalization.** Marie K. Huffman (Dept. of Linguist., SUNY at Stony Brook, Stony Brook, NY 11794-4376)

Glottalization is a common property of coda t's in American English. Previous work [J. Pierrehumbert, Proc. CLS 2, 232-256 (1994)] found coda glottalization to be affected by following segmental context. This paper examines segmental and prosodic contextual factors as they condition the occurrence of glottalization on "voiceless" stops [p] and [t] in English. Following Pierrehumbert's methodology, audio recordings were made of discourse fragments containing open-ended lists, which minimize phonation changes associated with low pitch. To test the effect of segmental context, various sounds were placed in the onset of the second member of compounds such as "kite maker" and "suit fitter." To test the effect of prosodic context, these list items were compared with single word list items, as in "color, height, make, . . ." with a phrase boundary after the coda consonant. For coda [t], glottalization is more common before sonorants, and is affected little by a following phrase boundary. In contrast, coda [p] is less frequently glottalized, and is more sensitive to context. Glottalization is more frequent before sonorants, without an intervening phrase boundary. Thus, the strength of segmental and phrasal context effects in determining the occurrence of glottalization depends on the target segment. [Work supported by NSF.]

**3pSC4. Experimental study of the target undershoot model using acoustic and "articulatory" data.** Michel Pitermann (Dept. of Psych., Queen's Univ., Kingston, K7L 3N6, Canada, mpiter@portia.psyc.queensu.ca) and Sorin Ciocea (Lab. of Exp. Phonet., Free Univ. of Brussels, CP 110, 50 Ave. F.-d. Roosevelt, B-1050 Brussels, Belgium)

In a previous study [M. Pitermann and J. Schoentgen, 1st ESCA Tutorial and Research Workshop on Speech Production Modeling, 17-20 (1996)], the influence of speaking rate and emphatic stress on formant frequencies and corresponding target estimates were analyzed for the vowels [a] and [ε] in an [i-i] context. Unreached targets were estimated by means of two dynamic and two kinetic models of formant transitions. The results showed that both formant frequencies and target estimates varied with speaking rate and emphatic stress. In the present survey, we analyzed "articulatory" targets for the same corpus in the framework of a vocal

tract model. The “articulatory” trajectories were analytically calculated by means of an acoustic-to-articulatory inversion carried out on a six-tube Kelly-Lochbaum model of the vocal tract [S. Ciocea, “Semi-analytic formant-to-area mapping,” Ph.D. thesis (1997)]. Targets were then estimated by means of asymptotes or steady-state solutions of transition models fitted to trajectories of the palatal region. The results suggest that “articulatory” target estimates did not depend on speaking rate, emphatic stress and speaker for a subset of speaking rate and stress pairs. The results will be discussed with respect to possible inversion artifacts and the possibility of target invariance.

**3pSC5. The structure of repetition strings in the Switchboard corpus.** Cynthia Girand, Alan Bell, Dan Jurafsky (Dept. of Linguist., Univ. of Colorado, Boulder, CO 80309), and Eric Fosler-Lussier (Int’l Computer Sci. Inst. and the Univ. of California, Berkeley, CA)

An investigation of reduction in the ten most frequent English function words in Switchboard, to be presented at ICSLP’98, found that repetition or following silence or filled pause, which were taken as symptoms of planning problems, were strongly associated with longer durations and lack of reduction, extending earlier results for the definite article [J. E. Foxtree and H. H. Clark, *Cog.* **62**, 151–167 (1997)]. As a followup to this study, the structure of unplanned repetition strings is examined more closely. The study is based on an analysis of the lexical transcriptions of the repetitions of words and short phrases from over 100 h of recorded conversations from the Switchboard corpus. Detailed information about the phonetic form and contexts of repetitions is taken from a phonetically transcribed sample of 4 h of conversation [S. Greenberg *et al.*, ICSLP 96 Proc. (1996)]. Repetitions are overwhelmingly unplanned; are overwhelmingly function words; and are mostly single repetitions of words, although complex strings with multiple repetitions of words, and short phrases combined with silences and filled pauses are not uncommon. The form of repetition strings, including internal and overall durations, are related to variables of rate and context.

**3pSC6. Speech recognition in a reverberant environment using matched filter array processing and linguistic-tree maximum likelihood linear regression adaptation.** Prabhu Raghavan, Richard J. Renomeron,<sup>a)</sup> ChiWei Che, Samir Chenoukh, Dong-Suk Yuk, and James L. Flanagan (CAIP Ctr., Rutgers Univ., 96 Frelinghuysen Rd., Piscataway, NJ 08854)

Performance of automatic speech recognition systems trained on close-talking data suffers when the systems are used in a distant-talking environment due to the mismatch in training and testing conditions. Microphone array sound capture can remove some of the mismatch by removing ambient noise and reverberation, resulting in an approximation to a clean speech signal. However, this often does not improve the performance sufficiently. But, using array signal capture in conjunction with Hidden Markov Model (HMM) adaptation on the clean-speech models can result in high recognition accuracy. This paper describes an experiment in which the output of an eight-element microphone array system using MFA processing is used for speech recognition with LT-MLLR adaptation. The recognition is done in two passes. In the first pass, an HMM trained on clean data is used to recognize the speech. Using the results of this pass, the HMM model is adapted to the environment using the LT-MLLR algorithm. This adapted model is then used to recognize the speech. It is shown that the use of MFA and LT-MLLR results in high-accuracy recognition. [Work supported by DARPA Contract DABT63-93-C-0037.]

<sup>a)</sup> Currently at Raytheon Systems Company, Falls Church, VA.

**3pSC7. *N*-best breadth search for large vocabulary continuous speech recognition using a long span language model.** DongSuk Yuk (Dept. of Computer Sci., Rutgers Univ., New Brunswick, NJ 08903, yuk@caip.rutgers.edu), ChiWei Che, Prabhu Raghavan, Samir Chenoukh, and James Flanagan (Rutgers Univ., Piscataway, NJ 08855)

In a large vocabulary continuous speech recognition system, high-level linguistic knowledge can enhance performance. However, integration of high-level linguistic knowledge and complex acoustic models under an efficient search scheme is still problematic. Higher-order *n*-grams are so computationally expensive, especially when the size of vocabulary is large, that real time processing is not possible yet. In this report, the *n*-best breadth search algorithm is proposed under the framework of the *state space search*, which can handle higher order *n*-grams and complex sub-word acoustic models such as the *cross-word triphones*. The *n*-best breadth search is a combination of the *best first search* and the *breadth first search*. The proposed algorithm can be extended to handle other types of language models such as the stochastic context-free grammar, and different types of acoustic models including the neural networks. Compared with the conventional beam-search method, this pilot experiment shows that the proposed algorithm decreases execution time with little effect on performance. [This research was supported by ARPA Contract No. DABT63-93-C-0037.]

**3pSC8. Modeling the subglottal space for American English /r/. Carol Y. Espy-Wilson (Dept. of Elec. and Computer Eng., Boston Univ., 44 Cummington St., Boston, MA 02115), Suzanne E. Boyce (Univ. of Cincinnati, Cincinnati, OH 45221), Michel T. T. Jackson (Sensimetrics Corp., Cambridge, MA 02139), Abeer Alwan, and Shrikanth Narayanan (UCLA, Los Angeles, CA 90024)**

One challenge in modeling the acoustics of American English /r/ is the fact that *F3* may vary from 1300–2000 Hz in different contexts, even in the same speaker. Previous models have accounted for *F3* lowering to the upper portion of this range, but have not accounted for the lower *F3* range. In previous work, acoustical models of /r/ were tested utilizing the Maeda computer model (Maeda, 1982) and vocal tract dimensions for /r/ derived from MRI studies of two American English speakers. It was concluded that the *F3* range exhibited by the speakers could be modeled successfully only by including the sublingual space. In the study presented here, two methods were examined for incorporating the sublingual space, (i) as an extra cavity resonator, and (ii) as an increment to the length and volume of the front 190 cavity. Using a recently developed adaptation of the Maeda model that incorporates a side branch from the front cavity, theoretical projections were compared against model results with and without the sublingual space resonator. It was concluded that an adequately low *F3* can be generated using either method of incorporation, as long as certain conditions apply.

**3pSC9. Functions of the muscles of the tongue during speech.** Masanobu Kumada (Haskins Labs., New Haven, CT 06511, Yale Univ. School of Medicine, Univ. of Tokyo, Natl. Defense Medical College, kumada@haskins.yale.edu), Robert T. Todd (Yale Univ. School of Medicine, New Haven, CT), Fredericka Bell-Berti (St. John’s Univ., Jamaica, NY), Mamoru Niitsu (Univ. of Tsukuba, Ibaraki, Japan), Hajime Hirose (Kitasato Univ., Kanagawa, Japan), and Seiji Niimi (Univ. of Tokyo, Tokyo, Japan)

To investigate the functions of tongue muscles during speech, three methods were combined: conventional MRI, to identify the musculature; tagging snapshot MRI, to visualize the displacement of tissues and measure contractions of muscles; and electromyography (EMG), to observe muscle activities. Five Tokyo-dialect speakers produced sustained phonations of five Japanese vowels. (Sessions of five English speakers are also planned to observe English vowels and consonants.) Muscle contractions of four regions of genioglossus (GG1-4, anterior to posterior), styloglossus (SG), vertical (V), superior and inferior longitudinal (SL, IL) were measured. The functional units of GG seemed to be overlapped with each

other: GG3-4 to make the highest point of the tongue higher, working against V; GG2-4 to move the most posterior point anteriorly; and GG1-3 to move the highest point anteriorly, working against SG. SL contributed to groove formation. IL contributed to "landslide" formation in /o/ by keeping the lower half of the tongue forward against the posterior pull on the upper half by SG. EMG potentials from GG were higher in the supine than in the upright position, suggesting that there may be a system to generate different neural command patterns in relation to the direction of gravity. [Work supported by NIH DC-00865 to Haskins Laboratories, by St. John's University, and by a Grant-in-Aid for Scientific Research (No. 01440071) from the Japanese Ministry of Education, Science, and Culture to the Department of Speech Physiology, Faculty of Medicine, University of Tokyo.]

**3pSC10. MRI vocal tract measurements of African American and White American boys.** Richard J. Morris (Dept. of Commun. Disord., Florida State Univ., Tallahassee, FL 32306-1200, rmorris@mailers.fsu.edu) and Jeffrey R. Fitzsimmons (Univ. of Florida, Gainesville, FL 32610)

The purpose of this project was to use magnetic resonance imaging (MRI) procedures to reveal any developmental differences between White American and Black American boys. Four boys completed the task, one 10-year-old and one 14-year-old of each racial group. Each boy was positioned on a gurney inside a General Electric 3 Tesla MRI unit. A neck coil was used to obtain all images using a gradient-echo, spin density weighted sequence with an excitation time no longer than 2 ms and a relaxation no longer than 4.9 ms; the total acquisition time per image was no longer than 327 ms. Images were taken during productions of the vowels /i/, /a/, and /u/ and the words "bottle," "pot," "dot," "tot," "got," and "cot." Software was used to determine the oral, pharyngeal and laryngeal boundaries from the images. These boundaries were used to

determine the glottal area, vocal fold length, and vocal fold thickness; the height, depth, width and volume of the pharynx; and the height, length, width and volume of the oral cavity. These data were compared with acoustic and aerodynamic data from the same subjects to provide evidence of any vocal tract differences that might underlie perceived speech differences.

**3pSC11. The APEX model: From articulatory positions to sound.** Johan Stark, Christine Ericsson, Björn Lindblom (Dept. of Linguist., Stockholm Univ., S-10691 Stockholm, Sweden, stark@ling.su.se), and Johan Sundberg (Royal Inst. of Technol., S-10044 Stockholm, Sweden)

From input specifications for lips, tongue tip, tongue body, jaw opening and larynx height, APEX constructs an articulatory profile which is used to derive an estimate of the associated area function and the formant frequencies. The geometry of the APEX vocal tract is customized according to x-ray data from an individual speaker [P. Branderud *et al.*, *Fonetik* **98**, 168–171 (1998) and [www.ling.su.se/fon/publications/](http://www.ling.su.se/fon/publications/)]. The input measurements are contours sampled as *x/y* points for the shape of fixed structures such as the mandible, hard palate, and posterior pharyngeal wall, and certain selectively chosen configurations of articulators whose shape and position vary (e.g., lips, tongue tip, tongue body). Observed tongue contours of /i/, /u/ and /a/, and "rest" are used to provide reference contours for the rules of APEX. The general philosophy behind the procedure is to have APEX represent certain key configurations as faithfully as possible and then derive intermediate articulations by a set of physiologically motivated interpolation rules [B. Lindblom and J. Sundberg, *J. Acoust. Soc. Am.* **50**, 1166–1179 (1979)]. An evaluation of the articulatory and acoustic performance of APEX will be presented. [Work supported by the HSFR and RJ research councils of Sweden.]

WEDNESDAY AFTERNOON, 14 OCTOBER 1998

MARRIOTT BALLROOM 2, 1:00 TO 2:15 P.M.

### Session 3pUW

## Underwater Acoustics: Reverberation and Scattering

William M. Carey, Chair  
*NUWC, Old Lyme, Connecticut 06374*

### Contributed Papers

1:00

**3pUW1. A Lloyd-mirror model to estimate the scattering strength of fish near rough ocean boundaries.** Roger C. Gauss (Naval Res. Lab., Washington, DC 20375-5350, gauss@abyss.nrl.navy.mil), Redwood W. Nero (Naval Res. Lab., Stennis Space Center, MS 39529-5004), and Daniel Wurmser (Naval Res. Lab., Washington, DC 20375-5350)

It is well known that a point scatterer located near the sea surface creates an acoustic dipole and that one near the ocean bottom is in general described by a series of higher-order moments (e.g., a double monopole in the simplest case of a hard, flat bottom). This Lloyd-mirror effect has been coupled with a resonant fish scattering model of Love [R. H. Love, "Resonant acoustic scattering by swimbladder-bearing fish," *J. Acoust. Soc. Am.* **64**, 571–580 (1978)] to develop a simple model which predicts the backscattering strengths of a variety of fish species known to occur (during at least part of a diurnal cycle) in near-boundary layers. The model is applied to and compared with measurement results from Critical Sea Test 7 (CST-7 Phase 2) to demonstrate that fish can be significant contributors to low-grazing-angle scattering. The general implications of the model are that observed enhancements in backscattering strength over

levels predicted by first-order rough-surface scattering theories may, in some cases, be primarily due to backscatter from near-surface fish (rather than from bubbles or the sediment volume). [Work supported by ONR.]

1:15

**3pUW2. The influence of large-scale seafloor slope and bottom velocity on low-grazing-angle monostatic acoustic reverberation.** Robert J. Greaves (MIT/WHOI Joint Prog. in Marine Geology and Geophys., Woods Hole Oceanogr. Inst., Woods Hole, MA 02543, greaves@erl.mit.edu) and Ralph A. Stephen (Woods Hole Oceanogr. Inst., Woods Hole, MA 02543)

Analysis of low-grazing-angle monostatic reverberation data acquired at Site A on the Acoustic Reverberation Special Research Program 1993 Acoustics Cruise suggests that scattered signals cannot be quantitatively explained in terms of large-scale slope alone, even though a strong correspondence between high intensity backscatter and seafloor ridges is observed. Numerical modeling using a finite-difference solution to the elastic wave equation shows that large-scale seafloor slope and subsurface aver-

age velocity influence the backscattered intensity levels but that the source of scattering is wavelength-scale heterogeneity. The results of the modeling suggest that the influence of large-scale seafloor slope is strongest at small grazing angles. For example, for a rough seafloor and a source wave field incident at  $15^\circ$  relative to the horizontal, a change in the seafloor slope from  $0^\circ$  to  $15^\circ$  yields a 5-dB change in backscatter intensity, while a change from  $15^\circ$  to  $30^\circ$  in seafloor slope yields only a 1-dB change in backscatter intensity. The influence of average subseafloor velocity is shown to be a bimodal effect. Homogeneous soft bottoms, e.g., sediment, generate dramatically less backscatter than homogeneous hard bottoms, such as basalt.

1:30

**3pUW3. Low-grazing-angle monostatic acoustic reverberation from rough seafloors.** Robert J. Greaves (MIT/WHOI Joint Prog. in Marine Geology and Geophys., Woods Hole Oceanogr. Inst., Woods Hole, MA 02543, greaves@erl.mit.edu) and Ralph A. Stephen (Woods Hole Oceanogr. Inst., Woods Hole, MA 02543)

The objective of this research is to interpret matched-filtered, beam-formed monostatic acoustic reverberation data acquired when the seafloor is insonified by a bandlimited, low-grazing-angle acoustic pulse. This paper addresses the hypothesis that observed backscatter signals are produced by a combination of seafloor (interface) and subseafloor (volume) scattering from structure having variations at scale lengths comparable to the wavelength of the insonifying acoustic field. Numerical modeling, using a finite-difference solution to the elastic wave equation, is performed to quantitatively predict the monostatic acoustic reverberation signals from rough seafloor, with and without subseafloor volume heterogeneity. Wavelength-scale seafloor roughness and subseafloor volume heterogeneity are defined using stochastic distributions with Gaussian autocorrelations. Modeling results show that scattering from rough, basaltic bottoms is dominated by interface scattering. Subseafloor volume heterogeneity is shown to be capable of producing scattered signals comparable to rough seafloor scattering when the bottom is smooth and/or has a low velocity.

1:45

**3pUW4. Environmental factors for site-to-site differences in low-frequency surface scatter.** Jeffrey L. Hanson (Johns Hopkins Univ., Appl. Phys. Lab., Laurel, MD 20723)

Acoustic reverberation experiments conducted during the extensive Critical Sea Test (CST) Program have indicated that near-surface microbubble clouds are the primary source of low-frequency (0–1000 Hz) acoustic surface scatter during elevated winds. A crucial issue remaining

from CST, however, is the explanation of large (greater than 15 dB) site-to-site differences in surface scattering strength. Using the extensive CST environmental observation set, as well as satellite remote sensing products available over the World Wide Web, we have investigated the hypothesis that site-to-site differences are controlled by processes related to the supply, mixing, and removal of near-surface bubbles in the ocean. It is found that much of the variability can be empirically explained by considering the mean ocean temperature, biological productivity, and wave conditions at each site. These results provide important clues as to the controlling factors for surface scatter in shallow water areas, where biological productivity is highest. The implications for improving an operational surface scattering prediction capability, using readily available (e.g., satellite observations) environmental inputs, will be discussed. [Work supported by the Office of Naval Research/Ocean Acoustics.]

2:00

**3pUW5. Sound propagation in bubbly liquids, a review and research issues.** W. M. Carey (NUWC, Old Lyme, CT 06371), R. A. Roy (Dept. of Aerosp. and Mech. Eng., Boston Univ., Boston, MA 02215), and K. W. Commander (Coastal Systems Station, Panama City, FL 32407, w.carey@ieee.org)

Sound propagation in bubbly liquids has been studied since the work of Wood (1932). He showed the sonic speed at low frequencies could be calculated for an air bubble–water mixture by use of the mixture density and compressibility. Experimental and theoretical investigations prior to 1985 confirmed his work and provided a basis for the understanding of the sonic speed variation from a low-frequency subsonic region, through a supersonic region, and ultimately to a sonic region at higher frequencies. Renewed interest in the properties of bubbly liquids has resulted from sound scattering from the sea surface, ship's wakes, and the bubble-related production of underwater sound. Papers have been written on the sound speed variation with frequency, most notably by Commander and Prosperetti (1989), which summarize the dispersive characteristic and methods for the calculation of this characteristic as a function of the bubble size number density spectrum and the acoustic frequency. However, many recently published papers are not consistent with these classical results. It is the purpose of this paper to place contemporary work in perspective by providing a concise theoretical overview. Furthermore, this paper will discuss unresolved research issues of frequency-dependent attenuation factors and dissolution effects. [Work supported by ONR.]

3p WED. PM



**Session 4aAA****Architectural Acoustics: Acoustics of Organ Performance Spaces I**

Dan Clayton, Chair

*128A Greenacres Avenue, White Plains, New York 10606-3121***Chair's Introduction—8:00*****Invited Papers*****8:05****4aAA1. Evolution of the secular organ performance space: An historical overview.** Dan Clayton (Consultant, 128A Greenacres Ave., White Plains, NY 10606-3121, DanClayton@compuserve.com)

The earliest organ was the 3rd century (BC) Greek "hydraulis," a machine of wind-blown pipes which evolved through Roman and Byzantine eras into a musical instrument, by the 13th century becoming the exclusive domain of the church. The organ remained largely in the church through the 17th century, by which time it had matured into the sophisticated instrument we know today. By the 18th century the organ was being used outside the church, first in royal salons and music rooms. The Hanover Square rooms, complete with a small pipe organ, opened in 1775 and for the next century was London's principal concert hall. The English "town hall" tradition of organ and choral music began in the mid-19th century, spreading rapidly throughout Britain, and eventually to other countries, most notably Australia and the U.S. Most of the "great" concert halls of the late 19th and early 20th centuries (Amsterdam, Boston, Leipzig, Vienna, etc.) included significant organs. The 20th century has seen the widest variety of organ styles and rooms, including sumptuous private residences, massive outdoor exhibition amphitheatres, and extravagant theatre organs. Expansion of higher education beginning in the 1950s brought many important university installations, most recently culminating in highly specialized "pure" organ performance rooms.

**8:25****4aAA2. Design criteria for organ performance halls and concert halls with organs.** Dana L. Kirkegaard (Kirkegaard Acoust., 4927 Wallbank Ave., Downers Grove, IL 60515)

While it is generally understood that reverberation time is an important criterion in designing an organ performance hall, little has been written on the importance of the organ's transient response or its unique distribution in space. Whereas an orchestra is generally confined to a stage platform, the organ pipe chests may rise to different levels at heights 15–40 ft or more above the stage. As a result, EDT, C50, C80, IACC and other parameters sensitive to placement of the source may vary significantly between the stage platform and various divisions in the organ. This spatial differentiation is an important element in the design of an organ performance hall. Integration of an organ in the design of either a concert hall or recital hall presents several design challenges. The physical height of the organ is often in conflict with the need to provide early reflections for ensemble support. Optimal criteria for RT, G, C50, C80, and other acoustical parameters may also be at odds, particularly in a University recital hall. The spatial distribution of the organ may play an important role in meeting these design challenges.

**8:45****4aAA3. Spaces designed exclusively for pipe organs.** Robert Mahoney (Robert F Mahoney & Associates, 2333 Mapleton Ave., Boulder, CO 80304-3753)

Rarely are spaces designed exclusively for the needs of pipe organs; most often other musical instruments or ensembles must be accommodated in the same room the organ occupies and as a result the overall acoustical design goals are not those that would most complement the organ's sound. Rarer still is the design leadership in such projects entrusted to the acoustician. Two such rarities will be presented: the Krapf Organ Studio at the University of Iowa (a remodeling and consolidation of two existing spaces), and the Bales Recital Hall at the University of Kansas at Lawrence (an entirely new space). The development of design goals and the architectural realization of them are discussed. Measurements of several room acoustical attributes were made during the course of construction of the Bales Recital Hall using a variety of techniques which reveal the influence of the introduction of audience seating and the completed organ.

**9:05****4aAA4. Three organs, three recital halls, three acoustic spaces: Designing the right organ for each project.** Hellmuth Wolff (Wolff & Associés Ltée, 1260, Rue Tellier, Laval, QC H7C 2H2, Canada, HellmuthWolff@compuserve.com)

Building organs for concert halls or churches is almost always an exercise in adapting an instrument to a space which was not designed for an organ, neither physically nor acoustically. The author has designed and built four organs in university recital halls and will discuss three of these, one of which is a rare exception: (1) Redpath Hall at McGill University in Montréal—a former lecture hall turned recital hall, due in large part to the addition of a new French-baroque style organ in 1981. Besides a new hardwood floor and

air conditioning, no acoustical changes were made to the hall. (2) Stetson Chapel at Kalamazoo College in Kalamazoo, Michigan—a 1930s chapel rebuilt and restored in 1986 and now mainly used as the college’s recital hall. Significant improvements to the room’s acoustics were made, and a three-manual eclectic-design organ installed in 1987. (3) Bales Organ Recital Hall at the University of Kansas in Lawrence, Kansas—a new space built in 1996 exclusively for use of the organ faculty and for organ recitals. A large three-manual French-romantic organ is the centerpiece of this spectacular hall.

9:25

**4aAA5. Flexible acoustics for two purpose-built organ recital halls.** David Kahn (Acoustic Dimensions, Inc., 2 East Ave., Larchmont, NY 10538)

It is rare today for any purpose-built music performance spaces to be commissioned, be they opera houses, concert halls, organ recital halls, etc. In order for any performance venue to be truly successful today, it must have flexibility included in its design, allowing the space to function well for the wide range of performance types that will inevitably be scheduled. The same can be said for purpose-built pipe-organ recital halls. While the highest design priority might be organ music, all but the most esoteric of these rooms will also be required to support far more than pipe-organ music. This paper will discuss two “purpose-built” pipe-organ recital halls with flexible acoustics devices which allow these spaces to function well for uses other than pipe-organ recitals. North Hall at the Peabody Conservatory at Johns Hopkins University in Baltimore, MD, is now used primarily as a pipe-organ recital hall for a new Holtkamp tracker organ. This hall also continues to function as a rehearsal room for large ensembles. The University of Northern Iowa is building a multi-purpose 125-seat organ recital hall and choral rehearsal room. This hybrid space uses additional partially coupled volumes to better support a new Hellmuth Wolff tracker organ.

9:45

**4aAA6. Design problems of a concert hall with an organ.** Minoru Nagata (Nagata Acoustics, Inc., 8F, 5-23-13, Sendagaya, Shibuya-ku, Tokyo, 151-0051, Japan)

Organ music is not common in Japan, which has a poor church-music tradition. Almost all organ concerts are performed in concert halls. This is a major difference from the situation in North America and European countries. Concert halls in Japan are therefore generally expected to also serve as organ recital halls. In order to fulfill the requirements of both concert halls for classical music in general, and organ recital halls in particular, several ideas and devices have been developed and introduced such as movable reflectors, ceilings, partitions, and a reverberation enhancing system using digital signal processing (DSP). The presentation will explain these measures and their effects on the listening experience and discuss the problems involved in carrying out such design work.

10:05–10:20 Break

10:20

**4aAA7. The making of Spivey Hall.** Rein Pirn (Acentech, Inc., 33 Moulton St., Cambridge, MA 02138)

Since its opening in the winter of 1991, Spivey Hall on the campus of Clayton College and State University in Morrow, Georgia has gained a fine reputation among both performing artists and concert goers. That reputation acquired a new dimension with the dedication, in the spring of 1992, of the Albert Schweitzer Memorial Organ, which from the very beginning had been the *raison d’être* for the hall’s design. This paper provides an overview of the acoustical design process, presents the hall in words and pictures, examines the numerical results (RT, EDT, TS, C80, G, LEF, IACC), draws comparisons with other similar halls, and concludes with a brief excerpt from a recording made on the Spivey Hall organ.

10:40

**4aAA8. Considering the pipe organ from a scientific and engineering perspective.** Fritz Noack (Noack Organ Co., Inc., Main and School Sts., Georgetown, MA 01833, noackorgan@aol.com)

Acoustics of the pipe organ as a *musical instrument* will be discussed, both with and without the effects of the surrounding architecture (i.e., in and out of the acoustical context of a performance space). For the theoretical condition of the organ removed from its acoustic environment, the paper will examine key elements which contribute to, or otherwise affect, sound produced by the pipes. These include key action, windchest design and pipe-interval layout, wind pressure(s), scaling and voicing decisions, arrangement of divisions, casework or enclosure (fully encased or unencased, open or behind a facade, solid or resonant case panels), facade pipe and pipe shade details, etc. This theory will be contrasted with the real-world condition of the organ directly affected by its acoustic environment, including location in the room, free-standing case or fully/partially chambered installation, etc. The author will conclude with general guidelines for planning a new organ in a variety of architectural spaces and acoustic conditions (existing and known, or on paper and merely predicted), including location, layout of manual and pedal divisions, tonal design, pipe scaling, and voicing.

11:00

**4aAA9. Merrill Auditorium/Portland City Hall Auditorium renovation.** Edward Dugger (Kirkegaard & Associates, 4910 Main St., Downers Grove, IL 60515)

The Portland City Hall Auditorium, Portland, Maine, built in 1912, was specifically constructed for pipe organ recitals and lectures. Over the years, the hall had gone through several renovations and adjustments to further increase its functional use while keeping the Kotzmar Organ as a key feature of the hall. This paper will discuss the changes in the acoustic character of the hall as it went through the various renovations leading to its final version as a multipurpose venue. Comparisons of the original hall’s acoustic characteristics and measurements will also be used to verify the acoustician’s design criteria to the recently completed project. Additional insights into architectural, structural, mechanical and electrical system design for pipe organ rooms will also be offered.

11:20

**4aAA10. From reverberation chamber to movable ceiling: Organ builder meets acoustician and architect through artistic and scientific cooperation in concert-hall organ projects.** Philipp Klais (Johannes Klais Orgelbau, Kölnstrasse 148, D-53111 Bonn, Germany, Orgelbau\_Klais@public.kuttig.com)

A successful concert-hall organ holds a commanding musical presence. As a solo instrument the organ must be flexible and comprehensive, and when playing with full symphony orchestra the organ's great power and impact allow it to stand in stark tonal and dynamic contrast to the orchestra. Every concert-hall organ project poses a different set of design challenges and requires a unique solution—the most successful of these are when the organ builder is involved from the early project design stages. Klais Orgelbau has designed and built pipe organs for many international concert halls including those in Kyoto, Japan; Athens, Greece; Krakau, Poland; Munich, Germany; and Cologne, Germany. Five current and upcoming major projects include concert hall instruments in Kuala Lumpur, Malaysia; Bochum, Germany; Birmingham, UK; Halle, Germany; and Singapore. The considerable experience gained from this wide variety of projects will be reviewed. Project examples include such special acoustic features as stage canopies and reverberation chambers (Birmingham and Singapore) and a movable ceiling (Kuala Lumpur). The author will discuss the results of collaborations with acousticians and architects as well as those projects where the organ builder could only respond and react to planning and design decisions already in place.

11:40

**4aAA11. Organ acoustics and the concert hall.** Paul H. Scarbrough, J. Christopher Jaffe (Jaffe Holden Scarbrough Acoustics, Inc., 114A Washington St., Norwalk, CT 06854, pscarbrough@jhsacoustics.com), and Jack Bethards (Schoenstein & Co., San Francisco, CA 94110)

Providing an optimal acoustical environment for a pipe organ requires close collaboration between organ builder and acoustical consultant throughout the design process. Each brings unique and complementary perspectives to this subject. The organ builder offers not only a knowledge of the instrument but often a wealth of practical acoustical experience from a multitude of specific organ installations. The acoustical consultant offers extensive knowledge of acoustical principles as well as an understanding of how these must be interpreted and applied in architectural design. The authors discuss the nature of their design collaboration on recent projects and in the process examine a broad range of issues including: preferred reverberation and frequency response characteristics for organ, the essential balance between reverberation and clarity, ideal placement of the organ within the concert room, differences between spaces dedicated to organ and those that also accommodate instrumental and choral ensembles, and the importance of proper sound isolation and quiet ambient environments. The authors cite relevant aspects of their projects including the Kennedy Center Concert Hall, Severance Hall, the Weidner Center at the University of Wisconsin at Green Bay, and Holzclaw Hall at the University of Arizona.

THURSDAY MORNING, 15 OCTOBER 1998

MARRIOTT BALLROOM 7, 8:30 TO 11:20 A.M.

### Session 4aAB

## Animal Bioacoustics: Shallow-Water Bioacoustics I

Whitlow W. L. Au, Cochair

*Hawaii Institute of Marine Biology, P.O. Box 1106, Kailua, Hawaii 96734*

Peter M. Scheifele, Cochair

*National Undersea Research Center, University of Connecticut, Avery Point, Groton, Connecticut 06340-6097*

Chair's Introduction—8:30

### Invited Papers

8:35

**4aAB1. Shallow-water ambient noise from snapping shrimp and dolphins.** Whitlow W. L. Au (Hawaii Inst. of Marine Biol., P.O. Box 1106, Kailua, HI 96734), Marc O. Lammers (Univ. of Hawaii, Honolulu, HI 96822), and Kiara Banks (Texas A&M Univ., College Station, TX 77843)

Snapping shrimp are among the major sources of biological noise in shallow bays, harbors, and inlets, in temperate and tropical waters. Snapping shrimp sounds can severely limit the use of underwater acoustics since their snaps are very broadband with energy from several hundred Hertz to 200 kHz. Snapping shrimp noise is always present having little diurnal and seasonal variations. Peak-to-peak source levels can be as high as 189 dB *re*:1  $\mu$ Pa. Dolphin emissions are another common source of biological noise. Dolphin sound emissions can be categorized as whistles, burst pulses, and echolocation clicks. Whistles usually contain energy in the 5–20-kHz range, although higher-order harmonics can extend beyond 100 kHz. Burst pulse signals and echolocation clicks are

broadband, short duration signals with frequency components beyond 150 kHz. Peak-to-peak source levels of echolocation signals can be as high as 220–225 dB *re*: 1  $\mu$ Pa. Burst pulses are similar in shape to echolocation clicks but with about 6–10-dB lower amplitude. Inter-click intervals for burst pulses are about 2 to 3 ms or less and about 20–30 ms for echolocation signals. Dolphins often swim through an area and then leave, whereas snapping shrimps are forever.

9:00

**4aAB2. Exploring the form and function of biological sounds in shallow water from the perspective of a systems designer.** William T. Ellison (Marine Acoust., Inc., P.O. Box 340, Litchfield, CT 06759, wemai@aol.com) and Christopher W. Clark (Cornell Univ., Ithaca, NY 14850)

The potential utility of biological sounds is examined from a sonar system perspective. Evaluation of the temporal, spatial, and spectral properties of these sounds from a system designer's view can provide significant insight as to their possible function. The broadband sonar equations for both passive and active operations are used to evaluate this functionality with special attention paid to issues of shallow water propagation as well as those sound properties that most affect signal processing; time-bandwidth product, spatial and temporal resolving characteristics, and signal repetition rate. Specific examples are used to illustrate these findings, including blue and fin whale calls recorded off the coast of Southern California, bowhead whale calls from the spring migration off the coast of Barrow, Alaska, and humpback whale sounds recorded off the island of Hawaii. The use of a systems approach to evaluating biological sounds can also provide insight into several related areas of recent interest: (1) the effects biological sounds may have on man-made systems, (2) the effect man-made sounds may have on the ability of animals to communicate as well as acoustically sense their environment, and (3) designing underwater experiments to evaluate these issues.

9:25

**4aAB3. Bowhead whale call detection rates versus distance from airguns operating in the Alaskan Beaufort Sea during fall migration, 1996.** Charles R. Greene, Jr. (Greeneridge Sci., Inc., 4512 Via Huerto, Santa Barbara, CA 93110, cgreene@greeneridge.com), W. John Richardson (LGL Ltd., Environmental Res. Assoc., King City, ON L7B 1A6, Canada), and Naomi S. Altman (Cornell Univ., Ithaca, NY 14853)

Four autonomous seafloor recorders stored sounds continuously for 15–22 days in September 1996 off Prudhoe Bay. Three recorders were 31, 44, and 62 km offshore (water depths 25 to 44 m), transecting the normal fall westward migration path of bowhead whales. The fourth recorder was 45 km southeast ("upstream") of the other three and 72 km east of the airguns. Each record was transcribed to note times whale calls and airgun pulses were heard. Call detection rates at the four recorders were compared for times with and without airgun pulses at the recorder nearest to the airguns. At the recorder closest to the airguns, call detection rates were lower ( $P < 0.02$ ) at times with pulses than without them. At the recorder farthest offshore, call detection rates were higher when airgun pulses were evident close to shore than without pulses. These results imply that either some whales swam an indeterminate distance farther offshore, or changed their calling behavior, or both when the airguns were operating close to shore. [Work supported by BP Exploration (Alaska), Inc., Anchorage, AK.]

9:50–10:05 Break

10:05

**4aAB4. Biological high-frequency ambient noise.** Michael C. Macaulay (Appl. Phys. Lab., Univ. of Washington, 1013 NE 40th St., Seattle, WA 98105)

Biological sources of ambient noise have long been known to be produced by many invertebrates, fish, and marine mammals. Investigations have identified, specifically, many causative organisms that produce noise levels well in excess of those produced by purely physical phenomena (e.g., wind, wave activity, rain, etc.). The noise level produced by many of these sources can be as intense as many electronic systems (i.e., greater than 200 dB at 1 m // 1  $\mu$ Pa). In other cases, it interferes with our ability to utilize high-frequency acoustic signals for detection of objects or for measuring environmental sources of noise. This presentation will examine some of the known sources of biological ambient noise in relation to noise levels of nonbiological origin, whether known sources can be used as representative less well-known sources, and possible sources of error in the determination of signal characteristics. The primary purpose of this presentation is to place boundary conditions on the extent of our present knowledge, suggest guidelines for improving our understanding of their possible impact, and to point out where our information may be deficient.

10:30

**4aAB5. Sound production by fishes.** David A. Mann (Tucker-Davis Technologies, 4550 NW 6th St., Gainesville, FL 32609 and Mote Marine Lab., Sarasota, FL, david@tdt-quick.com)

Many fishes produce sounds associated with aggression, courtship, and mating. These sounds are typically low frequency (<1000 Hz), and generally either tonal or broadband pulsed sounds. Sounds are typically produced by vibrating the swimbladder directly with muscles, or through stridulation of bones or pharyngeal jaws. The loudest sounds are produced by fishes that have drumming muscles located on their swimbladder, such as the toadfish (140 dB *re*: 1  $\mu$ Pa). Some fishes like croakers and drums form large spawning aggregations, which can produce loud, sustained sound. Temporal patterns of sound production often follow patterns of courtship and mating, and in many species show an increase in activity at dusk and dawn. While a few fishes have been intensively studied, there is a need for more data on the diversity of fishes that produce sounds. For example, of 59 species of toadfishes, only 4 have been recorded, and of 209 species of cusk eels, only 1 has been recorded. Furthermore, more quantitative data on SPLs and sound propagation are needed to understand the role of the environment on fish sound production. [Work supported by NIH, ONR, and TDT.]

10:55

**4aAB6. Environmental constraints on sound transmission by humpback whales.** Eduardo Mercado III (Dept. of Psych., Univ. of Hawaii at Manoa, Honolulu, HI 96822) and L. Neil Frazer (Univ. of Hawaii at Manoa, Honolulu, HI 96822)

Singing humpback whales in Hawaii produce a variety of sounds at high source levels (ca. 185 dB *re*: 1  $\mu$ Pa), in water 15–500 m deep. The utility of these sounds is limited by their detectability and discriminability (which is a function of their acoustic features and the channel through which they are transmitted). To investigate how shallow water propagation might constrain humpback whales use of sound, simulations were run to calculate optimum frequencies for environments frequented by singers [here optimum frequency is the  $f$  that maximizes  $\max_{z_r} I(z_r, f)$ , where  $I$  is intensity, and  $z_r$  is receiver depth]. Simulations were performed using ORCA, an acoustic propagation model for multilayered acousto-elastic ocean environments based on normal mode theory [Westwood *et al.*, J. Acoust. Soc. Am. **100**, 3631–3645 (1996)]. The frequency band tested was 20–4000 Hz; the sub-bottom was taken to be a 50-m-thick sandy/silty layer with gradient, above a basalt half-space. Water depth, source depth and thermocline axis depth were varied across simulations. Source depth was found to be a major determinant of which frequencies propagated the farthest. Optimal frequencies decreased as source depth increased; they were typically above 500 Hz for source depths of 30 m or less. Humpbacks could affect transmission range (by factors of 2 to 3) by adjusting their position and sounds in response to environmental factors.

THURSDAY MORNING, 15 OCTOBER 1998 HAMPTON ROADS BALLROOM 3, 9:00 TO 11:25 A.M.

### Session 4aEA

### Engineering Acoustics: In-Air Actuators

Thomas R. Howarth, Chair

*Naval Research Laboratory, Code 7135, 4555 Overlook Avenue, SW, Washington, DC 20375-5350*

Chair's Introduction—9:00

#### *Invited Papers*

9:05

**4aEA1. The effect of load conditions on the design and performance of actuators.** Marty E. Johnson and Chris R. Fuller (Vib. and Acoust. Lab., Virginia Tech, Blacksburg, VA 24061-0238)

This paper demonstrates the effect of dynamic load conditions on the design and performance of actuators. Actuators have both active and passive properties that determine their overall performance. The interaction between the active and passive components of an actuator, and hence the performance, will depend on both the objective (i.e., the actuator used in a control system or as a source) and the dynamics of the structure to which the actuator is attached. It is shown that it is mainly the active properties of an actuator which are affected by the load conditions of the structure. Changes in the active properties due to varying load conditions are demonstrated for various actuator types. By altering the passive properties of an actuator (i.e., mass and stiffness) it is possible to enhance the performance of the actuator used in a particular application. It is shown that the optimal actuator design depends on both the dynamics of the structure to which the actuator is attached and the performance objective. It will be demonstrated that actively changing the passive properties of an actuator allows significant enhancement of performance.

9:25

**4aEA2. Determination of the driving signal parameters to maximize the performance of a piezoceramic inchworm actuator.** Jeremy E. Frank, Gary H. Koopmann, George A. Lesieutre, and Weiching Chen (Ctr. for Acoust. and Vib., Penn State Univ., 157 Hammond Bldg., University Park, PA 16802)

A series of linear piezoceramic inchworm actuators with various applications have been developed. There are three active piezoceramic elements within the inchworm: two “clamps” and one “pusher,” each of which is driven independently with a voltage of up to 120 V. Large displacements are achieved by repetitively advancing and clamping the pushing element, with each small step on the order of 10  $\mu$ m. A program using LABVIEW software is used to generate the driving signals to the clamps and pusher. With this program, experiments are performed to study the dynamics of the system, and in particular to identify the conditions for maximum force and velocity as well as the onset of resonance within the clamp and pusher elements. The maximum frequency, force, and velocity for the inchworm are shown to depend on the end loading condition, the type of load (mass or spring), as well as the input signal parameters, which are the frequency, phasing amplitude, and shape of the waveforms. The result of the experimentation is a set of waveform parameters that optimizes the inchworm performance for a specific loading condition.

4a THU. AM

**4aEA3. Thin, low-frequency, high-displacement actuator panels.** James F. Tressler, Thomas R. Howarth, and Joseph A. Bucaro (Naval Res. Lab., Washington, DC 20375-5350, tressler@acoustics.nrl.navy.mil)

The Naval Research Laboratory has recently developed a thin, lightweight, high-displacement, low-frequency actuator panel. The 4-in. × 4-in. × 0.25-in.-thick panels consist of cymbal-type flexensional actuator subelements placed mechanically and electrically in parallel between two stiff cover plates. Two different panel designs have been considered: one to operate in the frequency band of 100 Hz to 1 kHz, the other to operate between 1 and 10 kHz. Each of the panels was evaluated for its normal displacement using laser Doppler vibrometry (LDV) techniques over both decade bands. For the low-frequency cymbal panel driven at its resonance frequency of 444 Hz, a displacement of 2.5- $\mu$ m for a 1-V drive has been observed. At this frequency, the cymbal drivers can be driven at higher drive levels for larger displacements if desired. An advanced, higher displacement design utilizes copper-electroplated, graphite-epoxy cover plates. Preliminary data indicate that even higher displacements can be achieved with this design. Applications to both acoustic source generation and structural control technologies will be discussed. [This research is supported by the Office of Naval Research, Code 321SS.]

#### 10:05–10:15 Break

#### 10:15

**4aEA4. High displacement, high force piezoelectric actuator and sensor.** Richard Bishop and Karla Mossi (Face International Corp., 427 W. 35th St., Norfolk, VA 23508, dick@faceco.com)

A piezoelectric actuator and sensor which develops unusually high forces and displacements, and which is very rugged and durable, was invented by NASA at the Langley Research Center, Hampton, Virginia. Face International Corporation, under license from NASA Langley, has furthered the development of this actuator/sensor technology, and has successfully brought it to commercial production. Trade-named THUNDER, the device derives its improved performance from two unique features. First, THUNDER is composed of a piezoelectric ceramic core which is enclosed in a sandwich having metal foil faces. The metal faces are bonded with a very strong hot-melt adhesive which enables the actuator, operating as a unimorph, to develop large displacements and support heavy loads without failure. Second, through unique design features, the ceramic core of THUNDER is subjected to thermal expansion during manufacture. The thermal effects place the faces of the ceramic in compression so that it can undergo severe bending without cracking. The combination of the described design features of THUNDER permit its operation as a sensitive motion sensor and voltage generator as well as making it a superior solid state actuator.

#### 10:35

**4aEA5. Unimorph and bimorph actuators.** Shoko Yoshikawa, Erik Saarmaa, Nicholas Kottenstette, and Robert Jacques (Active Control eXperts, 215 First St., Cambridge, MA 02142)

Although piezoelectric ceramic unimorph and bimorph actuators have been around for several decades, detailed scientific understanding and design limitations have not yet been clarified. This study compares unimorph and bimorph actuators and the effects of thermally induced stress on the ceramics. The experimental results and analytical models show that there are optimum thickness and modulus ratios of piezoelectric and non-piezoelectric (substrate) layers for each application, depending on the need for either free stroke or blocked force. Bimorph actuators were found to be significantly more energy efficient than unimorph actuators. The stress effect of the piezoelectric ceramic layer caused by thermal mismatch to the actuator performance was not significant compared with the experimental data and modeled values. However, in soft piezoelectric ceramics, reduction of capacitance due to stress was significant and influenced actuator energy input. Asymmetric thermal stress also caused bowing of thin piezoelectric ceramic samples. The effect of this shape was modeled and compared to the experimental results.

### Contributed Papers

#### 10:55

**4aEA6. Surface pressure fluctuations induced by oscillated spoilers in a flow.** S. Chang and L. Mongeau (School of Mech. Eng., Purdue Univ., West Lafayette, IN 47907)

Recent studies have shown the feasibility of controlling the flow-induced resonance of closed pipes or cavities exposed to a grazing flow using oscillated leading edge spoilers [Kook *et al.*, Proc. 4th AIAA/CEAS Aero. Conf., paper 98-2349, Toulouse (June, 1998)]. Oscillated spoilers can be driven to regulate the phase of the discrete vortices shed near the separation point at the upstream edge of the cavity. Significant reductions in cavity pressure levels were achieved using these actuators, in conjunction with robust feedback control methods and a microphone within the resonant cavity acting as the error sensor. In the present study, the vortex shedding process associated with the actuated spoiler was investigated. Flow visualization was performed to provide a qualitative description of the flow field. The surface pressure downstream of an oscillated spoiler hinged on a flat, rigid plane installed in a wind tunnel was measured for a range of free stream velocities, spoiler angles, oscillation amplitudes, and frequencies. The results were compared with predictions from an analytical model based on vortex sound theory.

#### 11:10

**4aEA7. Optimal performance of thermoacoustic coolers with spring-mass and electrodynamic driver resonator configurations.** B. L. Minner, C. Savran, L. Mongeau, and J. E. Braun (School of Mech. Eng., Purdue Univ., West Lafayette, IN 47907)

Acoustic resonators are often used on the cold side of thermoacoustic coolers in order to maintain the proper phasing between fluid particle displacement, pressure, and temperature within the stack. These devices tend to occupy a large volume, which is a potential disadvantage for applications where space is at a premium. In the present study, two alternative cold side resonator configurations were evaluated: (1) a spring-mass system; and (2) an electrodynamic driver. The inverse problem of determining the system parameters required in order to operate the system at resonance for given compression ratios, complex pressure phase gradients, operating frequency, and load impedance was solved. The optimal efficiency of the alternative resonator systems was calculated and compared with that of a system with an acoustical resonator configuration. For this, previously reported robust optimal design methodologies were used [Minner *et al.*, J. Acoust. Soc. Am. **98**, 2961 (1995)]. The benefits and disadvantages of each resonator configuration will be discussed.

**Session 4aID****Interdisciplinary—Women in Acoustics: Diversity in Science and Engineering**

Barbara J. Sotirin, Chair

*Cold Regions Research and Engineering Laboratory, 72 Lyme Road, Hanover, New Hampshire 03755-1290***Chair's Introduction—9:30**

9:35

**4aID1. Science and Engineering Outlook: The People (and What They Do).** Mary Golladay (Program Director for Education and Human Resources Program, Div. of Sci. Resources Studies, National Science Foundation, 4201 Wilson Blvd., Ste. 965, Arlington, VA 22230)

10:05

**4aID2. Science and Engineering Outlook: The Dollars (and Who Spends Them).** Mary Golladay (Program Director for Education and Human Resources Program, Div. of Sci. Resources Studies, National Science Foundation, 4201 Wilson Blvd., Ste. 965, Arlington, VA 22230)

10:35

**4aID3. NIDCD Research and Training Support.** Amy Donahue (Chief, Hearing and Balance/Vestibular Sciences Branch, National Institute on Deafness and Other Communication Disorders, National Institutes of Health, EPS, Rm. 400-C-10, 6120 Executive Blvd., MSC 7180, Bethesda, MD 20892-7180)

11:05

**4aID4. Tips for Small Fish in the Big Funding Sea.** Mardi Hastings (Dept. of Mech. Eng., Ohio State Univ., 206 W. 18 Ave., Columbus, OH 43210-1107)

THURSDAY MORNING, 15 OCTOBER 1998

HAMPTON ROADS BALLROOM 2, 8:00 A.M. TO 12:55 P.M.

**Session 4aPA****Physical Acoustics and Noise: Sonic Boom Symposium I—Theoretical Studies**

Christine M. Darden, Chair

*NASA Langley Research Center, Mail Stop 119, Hampton, Virginia 23681-0001***Invited Papers**

8:00

**4aPA1. Rise profiles of initial shocks in sonic boom waveforms.** Allan D. Pierce (Dept. of Aerosp. and Mech. Eng., Boston Univ., 110 Cummington St., Boston, MA 02115, adp@enga.bu.edu)

The pressure versus time in a sonic boom waveform received at the ground usually begins with a sudden rise in pressure which has a duration of the order of 1 to 10 ms. The explanation of the detailed shape of this portion, termed the rise phase, of the waveform has been a challenging research topic for several decades. It is now well established that there are two dominant causes of the finite duration of this phase: vibrational relaxation of the diatomic molecules in the air and atmospheric turbulence. In the present paper, the author attempts to give an account of some of the theoretical issues that one confronts in the search for a quantitative practicable theory that incorporates these causes into predictive models for the rise phase. An assessment is also given of the simpler theories (those not requiring detailed numerical simulation) that have been proposed in recent years. It is argued that, for many purposes, an acceptable estimate of the dominant features of the rise phase can be made with only a limited knowledge of the state of the atmosphere. [Work supported by NASA-LRC.]

**4aPA2. Modification of sonic boom waveforms during propagation from the source to the ground.** Henry E. Bass, Richard Raspet, James P. Chambers, and Mark Kelly (National Ctr. for Physical Acoust., Univ. of Mississippi, University, MS 38677)

A number of physical processes work to modify the shape of sonic boom waveforms as the waveform propagates from the aircraft to a receiver on the ground. These include frequency-dependent absorption, nonlinear steepening, and scattering by atmospheric turbulence. Reflections from the ground can also affect the waveform received by a listener above the surface. In the past two decades, each of these effects has been introduced into numerical prediction algorithms and results compared to experimental measurements. There is still some disagreement between measurements and prediction, but those differences are now in the range of tens of percent. The processes seem to be understood. The present understanding of sonic boom evolution will be presented along with experimental justification.

**4aPA3. Sonic boom propagation through turbulence: A geometric acoustics and a KZK approach.** Bart Lipkens (MacroSonic, 1570 East Parham Rd., Richmond, VA 23228), Philippe Blanc-Benon, Laurent Dallois (Laboratoire de Mécanique des Fluides et d'Acoustique, UMR CNRS 5509, Ecole Centrale de Lyon, BP 163 69131 Ecully Cedex, France), Mark Hamilton, and David T. Blackstock (Univ. of Texas, Austin, TX 78712-1063)

Sonic boom propagation is strongly affected by atmospheric turbulence. It has been shown that turbulence affects the perceived loudness of sonic booms, mainly by changing its peak pressure and rise time. The models reported here describe the nonlinear propagation of sound through turbulence. The turbulence is modeled as a set of individual realizations of a random temperature or velocity field. In the first model, linear geometric acoustics is used to trace rays through each realization of the turbulent field. A nonlinear transport equation is then derived along each eigenray connecting the source and receiver. The transport equation is solved by a Pestorius algorithm. In the second model, the KZK equation is modified to account for the effect of a random temperature field and it is then solved numerically. Results show that, on average, turbulence decreases the mean peak pressure and increases the rise time. Nonlinear distortion is less when turbulence is present than without it. The geometric acoustics results indicated that the effects of random vectorial fields are stronger than those of random temperature fields. The location of the caustics and the deformation of the wavefront are also presented. [Work supported by a grant from NASA.]

**4aPA4. A nonlinear geometrical theory of diffraction for predicting sonic boom in the shadow zone.** François Coulouvrat (Lab. de Modélisation en Mécan.—UPMC&CNRS, case 162, 4 pl Jussieu, F75252 Paris cedex 05 France)

Inside the geometrical shadow zone, it is well-known that the sound field emanates from rays diffracted by creeping waves propagating along the ground. A nonlinear, time-domain formulation of the geometrical theory of diffraction is proposed. Nonlinear effects are shown to be small, except for small sound speed gradients. In the linear case, the matching with geometrical acoustics leads to an analytical expression for the pressure field in the shadow zone, that takes into account all creeping waves and finite ground impedance. Numerical simulations indicate the ground impedance influences the sonic boom amplitude and rise time mostly close to the carpet edge. Comparisons with Concorde sonic boom measurements are favorable. In the nonlinear case, a generalized Burgers equation is proposed for modeling the sound field in the shadow zone over a rigid ground. The classical viscous term is replaced by a "diffraction operator" that describes the way sound diffracts along the ground. This operator takes into account the sound absorption and dispersion associated to all creeping waves. [Work supported by Aérospatiale Aéronautique, Toulouse, France.]

**4aPA5. State of the art of sonic boom modeling.** Kenneth J. Plotkin (Wyle Labs., 2001 Jefferson Davis Hwy., Ste. 701, Arlington, VA 22202)

The fundamentals of sonic boom theory were established and validated in the 1950s and early 1960s. By the early 1970s, these were implemented into practical models. Over the past decade, there have been requirements for design tools for an advanced supersonic transport and environmental assessment of launch vehicles and military aircraft operations. This has resulted in a number of advances in the understanding of sonic boom shock rise times, propagation through turbulence, use of computational fluid dynamics in sonic boom modeling, and analysis of launch vehicle sonic boom including the effect of large underexpanded rocket plumes. This paper reviews the early established theory, the recent advances in theory, and the application of these advances to practical models.

**4aPA6. Atmospheric turbulence conditions leading to focused and folded sonic boom wavefronts.** Andrew A. Piacsek (Central Washington Univ., Ellensburg, WA 98926)

A model proposed by Pierce [A. S. Pierce and D. J. Maglieri, *J. Acoust. Soc. Am.* **51**, 702–721 (1971)] to explain the variability of rise times in sonic booms invokes the process of wavefront focusing and folding. Although nonlinear theory applied to a propagating discontinuity predicts that a curved wavefront will always tend to straighten, the finite rise time of a sonic boom permits wavefront folding when the wavefront curvature is sufficiently small [A. A. Piacsek, *J. Acoust. Soc. Am.* **99**, 2539 (1996)]. In the present work, the effect of turbulence is modeled as a rippling of the sonic boom wavefront; two important length scales of this rippling are correlated, via numerical experiments, with wavefront folding. This permits the computation of length and energy scales of atmospheric turbulence associated with the ripple scales of interest and, thus, with folded wavefronts. Additionally, numerical results are shown of the propagation of the positive phase of an N-wave whose wavefront comprises multiple ripples of different length scales. The simulated shock profiles at several propagation distances are compared with representative sonic boom profiles recorded during test flights.



10:45

**4aPA7. Parametric study of supersonic aircraft shape for reduced boom.** Victor V. Kovalenko, Leonid L. Teperin, and Yuri L. Zhilin (Central Aerohydrodynamic Inst. (TsAGI), Moscow, Russia)

For future supersonic commercial aircraft it is important to know the strength of their sonic booms and to search for ways to reduce levels. This paper discusses: (1) the method of sonic boom calculation, (2) the effect of aircraft parameters on sonic boom magnitude, and (3) the design of an aircraft shape to reduce sonic boom. The pressure field near an aircraft is calculated using a finite-difference marching procedure in conjunction with a linear-theory panel method. With use of Zhilin's integral, the near field is transformed to a Whitham  $F$ -function, which is the initial data for the wave propagation. The problem of wave propagation in the nonuniform stratified atmosphere is solved by a system of nonlinear equations to obtain the sonic boom signature at the ground. A global parametric study was conducted to include the influence of approximately 16 aircraft parameters, such as dihedral and sweep angle, wing location, canard, etc. Also, for a given wing and fuselage volume distribution, the sonic boom level was minimized by adjusting the wing mean camber surface. This solution was obtained by the inverse aerodynamic method based on linear (panel method) and nonlinear (Euler equation) algorithms.

11:10

**4aPA8. On matching sonic boom near-field and far-field solutions.** Victor V. Kovalenko and Yuri L. Zhilin (Central Aerohydrodynamic Inst. (TsAGI), Moscow, Russia)

An improved method for matching three-dimensional flow near an airplane and its corresponding far-field solution is presented. It is based on an integral formulation of linear theory. An asymptotic solution is calculated as an integral of velocity disturbances in close vicinity to the body.

11:35

**4aPA9. Review and status of sonic boom noise penetration into the ocean.** Victor W. Sparrow (Grad. Prog. in Acoust., Penn State Univ., 157 Hammond Bldg., University Park, PA 16802, sparrow@helmholtz.acs.psu.edu)

Since the 1970 Sonic Boom Symposium, held at the ASA's 80th meeting in Houston, TX, substantial progress has been made in understanding the penetration of sonic boom noise into the ocean. The state of the art at that time was documented by J. C. Cook, T. Goforth, and R. K. Cook [J. Acoust. Soc. Am. **51**, 729–741 (1972)]. Since then, additional experiments have been performed which corroborate R. K. Cook's and K. Sawyers' theory for sonic boom penetration into a flat ocean surface. In addition, computational simulations have validated that theory and extended the work to include arbitrarily shaped waveforms penetrating flat ocean surfaces. Further numerical studies have investigated realistic ocean surfaces including both large-scale ocean swell and small-scale surface roughness. Research has also been performed on the effects of ocean inhomogeneities due to bubble plumes. This paper will provide a brief overview of these developments.

12:00

**4aPA10. Sonic boom noise penetration under a wavy ocean.** H. K. Cheng and C. J. Lee (Univ. of Southern California & HKCX Res., Los Angeles, CA 90089-1191)

Interaction of incident sonic boom waves with a wavy ocean can profoundly influence their underwater noise propagation and affect the perceived sound-pressure level far more significantly than anticipated from the flat-ocean (Sawyer) model. The theory assumes a small departure (in surface slope) from a flat ocean; the study takes into consideration the extremely high water-to-air density ratio, and the sound speed being higher in water than in air. The analysis treats the time-dependent interaction with a sinusoidal surface wave train, addressing primarily the case in which the wave-field Mach number is subsonic underwater. Two distinct wave components, identifiable via the stationary-phase principle, emerge in the sound field far below the surface. The reinforcing mechanism implicit in the stationary phase leads to a greatly reduced signal attenuation rate, and renders the waviness influence an effect of the first-order importance at large depth. Dominant frequencies and sound-pressure levels computed at various depths for the model of a fully developed sea state are compared to available data of underwater sound characteristics pertaining to baleen whales. Pronounced sea-floor effects and the significant differences between space launch and aircraft sonic boom noise underwater are noted.

### Contributed Papers

12:25

**4aPA11. Modeling of surface wave and bubble effects on sonic boom underwater penetration.** Brian H. Tracey (Cambridge Collaborative, Inc., 689 Concord Ave., Cambridge, MA 02138-1002)

Standard theories of sonic boom penetration into the ocean assume the ocean is a homogeneous halfspace. Recently, efforts have been made to allow for a more realistic model of the ocean, including the effects of surface waves and near-surface bubble plumes. Studies of these effects have been carried out using BEM techniques [Rochat and Sparrow, J.

Acoust. Soc. Am. **102**, 3159(A) (1997)]. As an alternative approach, scattering and propagation codes developed for underwater acoustics problems can be adapted to calculate boom penetration. Both rough surface and volume scattering theories have previously been integrated into ocean acoustics propagation codes. These implementations can be used to study propagation of scattered sound in the ocean, and have given results which compare favorably with data. The applicability of existing underwater acoustics approaches to sonic boom penetration is discussed. Several adaptations of these approaches are identified which could lead to more efficient calculation of sonic boom penetration.

12:40

**4aPA12. Propagation of sonic booms through a water fog.** Y. Xu (Dialogic Corp., 1515 Rte. 10, Parsippany, NJ 07054)

Sonic boom propagation in a quiet, water-fog atmosphere is investigated. An evolutionary equation that governs the development of sonic boom is derived. The interaction between sonic boom shock and droplet spectrum in fog (due to vaporization and liquefaction) is considered. The

effect of nonlinearity, attenuation, and dispersion due to multiple relaxation and viscosity are also taken into account. A computer code is developed to solve the evolutionary equation. From the numerical solutions of the equation, it is found that not only the relaxation and heat conduction increase the nonlinear distortion, but the droplet spectrum in fog greatly influences the development of sonic boom. The change of droplet spectrum affects the rise time of N wave and even causes sonic boom shock to degenerate to a series of waves.

THURSDAY MORNING, 15 OCTOBER 1998 HAMPTON ROADS BALLROOM 1, 8:30 TO 11:50 A.M.

### Session 4aSA

#### Structural Acoustics and Vibration: Structureborne Noise

Gerard P. Carroll, Cochair

*Carderock Division, Code 7250, Naval Surface Warfare Center, West Bethesda, Maryland 20817-5000*

Joseph M. Cuschieri, Cochair

*Department of Ocean Engineering, Florida Atlantic University, Center for Acoustics and Vibration, Boca Raton, Florida 33431*

#### Invited Papers

8:30

**4aSA1. Update on the structureborne noise standard structures.** Gerard Carroll (Naval Surface Warfare Ctr., Carderock Div., Bethesda, MD 20817-5000), Joseph M. Cuschieri (Florida Atlantic Univ., Boca Raton, FL 33431), and Courtney B. Burroughs (Penn State Univ., State College, PA 16804)

In 1994 the authors, along with a number of interested parties, established a set of structures of increasing complexity intended to be used as standards for investigating structureborne noise prediction techniques. The structures are: a T-beam, a ribbed panel and an acoustic enclosure. This activity was jointly sponsored by Technical Committees of the Institute of Noise Control Engineers (Prediction and Modeling) and the Acoustical Society of America (Structural Acoustics and Vibration). With the assistance of funding from the Structural Acoustics Branch of the NASA Langley Research Center, these structures have been built and experimentally characterized by various interested parties with the intention of providing a baseline check for the various analytical methods. This paper will introduce the structures and present the results which have been obtained thus far in this investigation, thereby creating the framework for viewing the more recent work to be presented by other authors within this session.

8:55

**4aSA2. Reporting on the work of the French commission for vibroacoustic software validation.** L. Gagliardini and C. Valor (PSA Peugeot-Citroen, 18, rue des Fauvelles F92250, La Garenne Colombes, France)

Between 1993 and 1996, a French group gathering most of the national laboratories and companies involved in vibroacoustics modeling, as well as major European vibroacoustic software producers, worked at producing reference results for elementary vibroacoustics problems. Four calculation cases and one experimental case were examined. These cases mainly consist of plates, coupled with finite or infinite fluid media, and submitted to point force loading. Calculations or measurements were carried out in the overall frequency range of 20 Hz to 20 kHz using analytic, when possible, numerical, and energetical methods. Results consist of narrow-band and third octave plots of averaged quantities such as mean squared velocity or radiated power. The spread in between results provided by various members of the group is shown. Individual results are justified by scientific references that were not discussed.

9:20

**4aSA3. Experimental characterization and finite-element modeling of a Lexan ribbed panel.** Dean E. Capone and Steve A. Hambric (Appl. Res. Lab., Penn State Univ., P.O. Box 30, State College, PA 16804)

In 1994 an in-depth investigation was proposed to characterize the structure-borne noise characteristics of a set of standard test systems [C. B. Burroughs, J. M. Cuschieri, and J. M. Carroll, Proc. Noise-Con **94**, 541-544 (1994)]. The studies would serve to validate the experimental, analytical, and numerical techniques used in the analysis of the systems. As a part of this effort, the response of a Lexan ribbed panel was investigated both experimentally and numerically. The drive point admittance and operating deflection shapes of the panel were used to characterize the vibration response. The operating deflection shapes were measured using a scanning laser Doppler system. The presence of the ribs on the panel results in both global and local modes within the panel. The experimental results compare favorably to the results from a finite element model of the panel. Comparisons to an aluminum ribbed panel with the same dimensions of the Lexan panel are also presented. The shift in panel resonance frequencies due to material properties is illustrated in the experimental results, and correctly predicted in the finite-element results.

**4aSA4. Laser vibrometer dynamics testing of a lexan ribbed panel test structure.** Robert L. West, William R. Saunders, and Ricardo A. Burdisso (Mech. Eng. Dept., Virginia Tech, Blacksburg, VA 24061-0238)

The lexan ribbed panel test structure is one of three “standard” test structures used within a round-robin test/analysis study. The objective for the overall study is characterization of both vibration and structure-borne acoustics of these test structures. Furthermore, the study seeks to establish a baseline for the evaluation of various experimental and analytical techniques and their applicability for characterizing these structures. This paper describes the experimental setup, the acquired data as well as the resulting dynamics characterization of the ribbed panel machined from lexan. The panel is  $1.52 \times 0.91 \times 0.006$  m overall with four equally spaced ribs 0.4 m apart. The panel is suspended by shock cord to simulate a free-free boundary condition and is excited by an electromagnetic shaker resulting in primarily out-of-plane motion. In this study, the vibration characterization is derived from mobility FRFs from accelerometer data. The mobility FRFs are also used to establish ten frequencies for multisine testing using a scanning laser Doppler vibrometer. A new technique is used to extract a spatially continuous, three-dimensional dynamic response field at all ten frequencies. Acoustic characterization of the panel is accomplished through sound pressure level measurements at a few spatial locations at the same ten frequencies.

10:10

**4aSA5. SEA analysis of the T-beam and acoustic cavity using alternative SEA approaches.** Joe Cuschieri (Ctr. for Acoust. and Vib., Ocean Eng. Dept., Florida Atlantic Univ., Boca Raton, FL 33431)

SEA results have been generated for the T-beam structure using two different approaches—a home grown SEA solution and a solution generated using a commercial SEA package. The results generated from these two approaches, while both generally matching the experimental mean results, are different. In this paper, possible reasons for the differences in the results are explored by analyzing the determined coupling loss factors, other components in the solution and the solution in general. The same type of analysis is performed for the acoustic cavity structure. In this case as well, SEA results are generated using the alternative SEA approaches. From a comparison of the full and intermediate SEA results obtained from the different approaches, the possible reasons for the differences are investigated. The two main conclusions of this study are that, (a) when using SEA as a predictive tool, very much depends on the input model and the basis of the solution; (b) the predictive results have to be treated with some caution. [Work sponsored by NASA Langley.]

### Contributed Papers

10:35

**4aSA6. Finite-element predictions and experimental measurements of aircraft fuselage panel dynamic response.** Ralph D. Buehrlé (NASA Langley Res. Ctr., Structural Acoust. Branch, M.S. 463, Hampton, VA 23681-2199) and Gary A. Fleming (NASA Langley Res. Ctr., Hampton, VA 23681-2199)

Results from an analytical and experimental study of the dynamic response of an aircraft fuselage panel are presented. The ability to predict the dynamic response of a complex stiffened panel into the kilohertz region using finite-element methods is examined. Beam and plate element models of the stiffeners are evaluated with numerous mechanisms for attaching the stiffeners to the plate elements representing the panel skin. The analytical models are validated with an extensive database of Scanning Laser Doppler Vibrometer (SLDV) data acquired by the Naval Research Laboratory and Electro-Optic Holography (EOH) measurements. For both measurement techniques, forced response data were acquired with soft springs supporting the panel to simulate free-free boundary conditions. The analytical results were obtained from a normal mode analysis of the various panel finite element models with free-free boundary conditions. The finite element models are described and comparisons between the analytical and experimental results are presented.

10:50

**4aSA7. Dispersion relations for waves on doubly periodic beams.** Dimitar P. Gueorguiev, J. Gregory McDaniel, and Pierre E. Dupont (Dept. of Aerosp. and Mech. Eng., Boston Univ., 110 Cummington St., Boston, MA 02215)

Waves in periodic structures are highly dispersive, experiencing either small or large spatial decays depending on whether the frequency lies in a pass or stop band. For ribbed plates, these dispersion relations have been analytically derived by Rumerman [M. L. Rumerman, *J. Acoust. Soc. Am.* **57**, 370–373 (1975)]. This presentation concerns the dispersion of waves in doubly periodic structures, which have received considerably less attention in the literature. The problem analyzed here consists of an infinitely long beam or plate which is attached to two types of substructures. Each

type of substructure is characterized in the frequency domain by a complex impedance and is attached to the beam at evenly spaced positions. The presentation will describe the extent to which singly periodic physics prevail and the possibility of creating very wide stop or pass bands by adjusting the parameters of the doubly periodic structure. Ultimately, this work is intended to aid in the design of structures which either confine or release energy near drive-points over very wide frequency bands. [Work supported by NSF.]

11:05

**4aSA8. Numerical implementation and marine applications of an energy finite element formulation.** Nickolas Vlahopoulos, Luis Octavio Garza-Rios (Dept. of Naval Architecture and Marine Eng., Univ. of Michigan, 2600 Draper Rd., Ann Arbor, MI 48109-2145), and Christopher Mollo (Automated Analysis Corp.)

The statistical energy analysis (SEA) is an established numerical technique appropriate to high-frequency vibro-acoustic analysis [R. Lyon, *Statistical Energy Analysis of Dynamical Systems: Theory and Applications* (MIT, Cambridge, MA, 1975)]. The energy finite element analysis (EFEA) constitutes a recent theoretical development [O. M. Bouthier and R. J. Bernhard, “Models of space averaged energetics of plates,” *AIAA J.* **30**(3) (March 1992)]. In this work a numerical implementation of the EFEA is utilized for analyzing two marine structures, and numerical results are compared to SEA solutions from VAPEPS. First, a plate assembly representing the engine foundation of a frigate ship is analyzed. Previous SEA results and test data are available in the literature and they are included in the comparison [R. Lyon, “In-plane contribution to structural noise transmission,” *Noise Control Eng. J.* **26**, 22–27 (1986)]. In the second application the structure of a fishing boat is modeled by both methods. The results are compared, and the EFEA is further utilized for identifying design modifications. [Work supported by the Michigan Sea Grant.]

**4aSA9. An approach for modeling spot-welded joints in an energy finite element formulation.** Xi Zhao, Nickolas Vlahopoulos (Dept. of Naval Architecture and Marine Eng., Univ. of Michigan, 2600 Draper Rd., Ann Arbor, MI 48109-2145), and Thomas Allen (Ford Motor Co., Dearborn, MI)

An emerging simulation technology is the energy finite element analysis (EFEA) [P. Cho, "Energy Flow Analysis of Coupled Structures," Ph.D. dissertation, Purdue University, 1993; O. M. Bouthier and R. J. Bernhard, "Models of space averaged energetics of plates," *AIAA J.* **30**(3) (March 1992)]. In order for this method to be applicable to automotive structures it is important that it be suitable for modeling spot-welded joints. This work presents a development effort in computing the energy transmitted through spot-welded joints, and utilizing the information in an EFEA formulation. It is based on principles utilized for deriving coupling loss factors for statistical energy analysis (SEA) from conventional finite element models [C. Simmons, "Structure-borne sound transmission through plate junctions and estimates of SEA coupling loss factors using the finite element method," *J. Sound Vib.* **144**(2), 215–227 (1991)]. There are two components to the new development: (i) Deriving numerically information about the energy ratio between spot-welded members. (ii) Incorporating information for the energy transferred between members in the EFEA analysis. Technical information and comparison of numerical results to test data will be presented. [Work supported by Automated Analysis Corp. and Ford Motor Co.]

**4aSA10. Analytical/numerical matching applied to a finite beam with multiple nonperiodically spaced constraints.** Linda P. Franzoni and Christopher D. Park (Dept. of Mech. Eng. and Mater. Sci, Duke Univ., Durham, NC 27708)

Analytical/numerical matching (ANM) is used to solve for structural vibrations of a finite beam constrained by multiple, nonperiodic supports. The ANM solution decomposes the stated problem into global, local, and matching problems. The global problem addresses large scale effects, with structural discontinuities replaced by smooth distributed forces. The local problem models the rapidly changing region around a structural discontinuity. These constituent problems are solved independently by the most efficient method available. Here, the local problem is solved numerically using finite element analysis (FEA) and the matching problem is solved analytically. The global problem is modeled using FEA with third-order Bernoulli–Euler beam elements. However, the solution procedure of the FEA model must be modified, in order to be compatible with ANM. Two-dimensional plane elements are required only in the local solution, to resolve the discontinuity. This finite-element order reduction provides significant savings in computation time. Comparison with traditional solution methods shows that the ANM approach accurately solves for local effects at each support, in addition to the overall response of the vibrating structure. The framework of applying ANM to more complex problems is also presented. [Work sponsored by ONR.]

THURSDAY MORNING, 15 OCTOBER 1998 MARRIOTT BALLROOMS 5 AND 6, 9:00 TO 11:45 A.M.

### Session 4aSC

## Speech Communication: Language, Learning and Sinusoidal Models for Speech Processing

James M. Hillenbrand, Chair

*Department of Speech Pathology and Audiology, Western Michigan University, Kalamazoo, Michigan 49008*

### Contributed Papers

9:00

**4aSC1. Effects of speaking fundamental frequency on the normalization of Cantonese level tones.** Patrick C. M. Wong and Randy L. Diehl (Dept. of Psych., Univ. of Texas, Austin, TX 78712, pcmwong@ccwf.cc.utexas.edu)

Four experiments were designed to look at how Cantonese level tones are perceived. In all the experiments, subjects were asked to identify the Cantonese syllable /si/, which could be perceived as three different words depending on the associated tone. The first two experiments, in which tokens were either mixed or blocked by speakers, showed that Cantonese tones are difficult to identify in isolation. Performance was greatly improved when a phonetic context was provided in the third experiment. In this experiment, Cantonese speakers were asked to produce a semantically neutral Cantonese sentence ending with the target syllable /si3/ (/si/ with Tone 3, the mid-level tone). The fundamental frequency ( $F_0$ ) of the context (i.e., the nontarget portion of the sentence) was raised or lowered via resynthesis. When the  $F_0$  of the context was raised (lowered), subjects perceived the target syllable as a lower (higher) tone. In the fourth experiment, an English context was used instead. The results did not differ significantly from the third experiment, which may suggest that, in judging tonal value, Cantonese listeners rely on speaking  $F_0$  of the context. [Work supported by NIDCD.]

9:15

**4aSC2. Perceptual assimilation of Japanese vowels by American English listeners: effects of speaking style.** Kanae Nishi (Dept. of Psych., Univ. of South Florida, 4202 E. Fowler Ave. Tampa, FL 33620, knishi@luna.cas.usf.edu), Winifred Strange (Dept. of Commun. Sci. and Disord., Univ. of South Florida, Tampa, FL 33620), Reiko Akahane-Yamada (ATR Human Information Processing Res. Labs., Kyoto 619-02, Japan), Sonja A. Trent, and David H. Thornton (Univ. of South Florida, Tampa, FL 33620)

Our previous research on perceptual assimilation of non-native vowels to native categories showed that patterns of spectral and temporal assimilation vary with speaking style (citation vs sentence) and consonantal context. Japanese (J) listeners' perceptual assimilation of American English (AE) long and short vowels to long (2-mora) and short (1-mora) categories was more consistent when the target syllables were presented in sentences (Strange, *et al.* ATR Technical Report, TR-H-218, 1997). In the present study, AE listeners categorized 4 speakers' tokens of 10 J vowels /ii, i, ee, e, aa, a, oo, o, uu, u/ into 11 native AE categories and rated their goodness-of-fit on a 7-point scale (7 = native). Results indicated that patterns of temporal assimilation of the J short vowels /e, a, u/ differed with speaking style. Assimilation of /e/ to mid or high front spectral AE categories also varied with context and individual speakers. Goodness-of-fit ratings suggested that all 10 J vowels were considered relatively "good" instances of AE categories (medians = 5 to 7). In comparison

with J listeners' perception of AE vowels, AE listeners judged cross-language similarities between J and AE vowels more on the basis of their spectral characteristics than on their temporal characteristics.

9:30

**4aSC3. The role of preceding closure interval and voice onset time in the perception of voicing: A comparison of English versus Spanish-English bilinguals.** Kerry P. Green (Dept. of Psych., Univ. of Arizona, Tucson, AZ 85721, kgreen@u.arizona.edu), Mary L. Zampini (Univ. of Arizona, Tucson, AZ 85721), and Connie Clarke (Univ. of Arizona, Tucson, AZ 85721)

Green *et al.* [J. Acoust. Soc. Am. **102**, 3136 (1997)] showed that Spanish speakers (monolingual and bilingual) use preceding closure interval (CI) to help distinguish the voicing characteristics of word-initial stops during production, while native English (NE) speakers do not. The current study compared NE and Spanish-English bilinguals with respect to the role of CI in the perception of voicing in word-initial stops. Members from a /bada-pada/ continuum, varying in voice onset time (VOT) from pre-voiced to long lag values, were presented in an English and a Spanish sentence context using three different preceding CIs: 25, 75 and 125 ms. NE listeners were presented with either the English sentence tokens or the Spanish sentence tokens. One group of Bilinguals (in English mode) was presented with the English sentences while a second group (in Spanish mode) was presented with the Spanish sentences. Each subject was presented with the continuum in isolation after presentation of the sentences. The results show that although the bilinguals have similar VOT boundaries to monolinguals when the tokens are presented in isolation, they exhibit greater sensitivity to CI in the sentence context, as evidenced by larger shifts in VOT boundaries as a function of preceding CI.

9:45

**4aSC4. Children's perceptual weighting strategies for speech are not as flexible as adults.** Susan Nittrouer, Marnie E. Miller, Court S. Crowther, and Mary Jane Manhart (Boys Town Natl. Res. Hospital, 555 North 30th St., Omaha, NE 68131)

Mann and Soli (1991) showed that adults modify their perceptual weighting strategies for the same phonetic decision based on the order of segments within syllables. The authors examined whether children similarly modify their perceptual weighting strategies. Fricative-vowel (FV) and vowel-fricative (VF) syllables were constructed with synthetic fricative noises varying from /ʃ/ to /s/, and natural /a/ and /u/ portions with transitions appropriate for a preceding or a following /ʃ/ or /s/. Spectrograms revealed that the acoustic information about fricative identity provided by the vocalic portion was impoverished for VF compared to FV syllables. These stimuli were played in their original order to adults and children (ages 7 and 5) in experiment 1, and in reverse order in experiment 2. Results for adults and, to a lesser extent, for 7-year-olds replicated earlier results showing that the perceptual weights assigned to acoustic properties within the vocalic portion differ depending on segmental order. In contrast, results for 5-year-olds suggested that these listeners applied the same strategies during fricative labeling, regardless of segmental order. Thus the flexibility to modify perceptual weighting strategies for speech according to segmental order apparently emerges with experience.

10:00

**4aSC5. Ability to perceive non-native contrasts with natural and synthetic speech stimuli.** Peter C. Gordon, Lisa Keyes, and Yiu-Fai Yung (Dept. of Psych., Univ. of North Carolina, Chapel Hill, NC 27599-3270, pcg@email.unc.edu)

The perception of the distinction between /r/ and /l/ by native speakers of American English and of Japanese was studied using natural and synthetic speech. The American subjects were all nearly perfect at recognizing the natural speech sounds while there was substantial variation among the Japanese subjects in their accuracy of recognizing naturally produced /r/ and /l/. A logit model, which additively combined the acoustic information conveyed by *F1*-transition duration and by *F3*-onset frequency,

provided a good fit to the perception of synthetic /r/ and /l/ by the American subjects. There was substantial variation among the Japanese subjects in whether the *F1* and *F3* cues had a significant effect on their classifications of the synthetic speech; greater use of the *F1* and *F3* cues in classifying the synthetic speech sounds was positively related to accuracy in recognizing natural /r/ and /l/. These results show that tests using natural and synthetic speech tap into the same variation of ability in perceiving the non-native /r/-/l/ contrast by Japanese speakers. The relation between performance on natural and synthetic speech also provides external validation of the logit model by showing that it predicts performance beyond the data to which it was fit.

10:15–10:30 Break

10:30

**4aSC6. Perceptual learning of synthetic speech.** Alexander L. Francis (Dept. of Psych. and Dept. of Linguist., The Univ. of Chicago, Chicago, IL 60637) and Howard C. Nusbaum (The Univ. of Chicago, Chicago, IL 60637)

Over the course of a lifetime, listeners are likely to encounter many unfamiliar talkers speaking the listeners' native language. Despite the fact that talkers may differ radically in the way they sound, listeners normally learn to understand the novel speech patterns of unfamiliar talkers without difficulty. Part of learning to understand an unfamiliar talker speaking a familiar language is learning to relate novel acoustic patterns in the unfamiliar speech to existing mental representations of familiar phonetic categories. This process has frequently been described in terms of modifying an existing psychological "space" of mental representations by shifting the focus or weight of attention to linguistically useful aspects of the speech signal. In the experiment reported here, native English listeners were trained to better understand an unfamiliar talker—a computer speech synthesizer. Training to recognize and transcribe English words resulted in a significant increase in listeners' abilities to understand words and to identify consonants. Training also strongly influenced the distribution of attention to particular features of the speech signal, as indicated by changes in listeners' judgments of the similarity of consonants after training. Implications for theories of perceptual learning and phonetic categorization will be discussed.

10:45

**4aSC7. A damped sinewave vocoder.** James M. Hillenbrand (Speech Pathol. and Audiol., Western Michigan Univ., Kalamazoo, MI 49008) and Robert A. Houde (RIT Research Corp., Rochester, NY 14623)

A speech analysis-synthesis system is described that operates by summing exponentially damped sinusoids at frequencies corresponding to spectral peaks derived from speech signal. The analysis begins with the calculation of a smoothed Fourier spectrum. A running average of spectral amplitudes is then computed for each frame over an 800-Hz window. The running average is subtracted from the smoothed spectrum to produce a "masked" spectrum. The signal is resynthesized by summing exponentially damped sinusoids at frequencies corresponding to peaks in the masked spectra. If an autocorrelation-derived periodicity measure indicates that a given analysis frame is voiced, the damped sinusoids are pulsed at a rate corresponding to the measured fundamental period. For unvoiced intervals, the damped sinusoids are pulsed on and off at random intervals. Results of a perceptual evaluation of the vocoder will be reported.

11:00

**4aSC8. Audio signal noise reduction using multiresolution sinusoidal modeling.** David V. Anderson and Mark A. Clements (Ctr. for Signal and Image Processing, Georgia Inst. of Technol., Atlanta, GA 30332-0250, dva@eedsp.gatech.edu)

The multiresolution sinusoidal transform (MRST) provides a sparse representation for speech signals by utilizing several psychoacoustic phenomena. It is well suited to applications in signal enhancement because the

signal is represented in a parametric manner that is easy to manipulate. The MRST has the additional advantage that it is both particularly well suited to typical speech signals and well matched to the human auditory system. The currently reported work removes noise from a speech signal corrupted by additive noise by applying an adaptive Wiener filter to the MRST parameters and then conditioning the parameters to reduce "musical noise." In informal tests, MRST based noise reduction was found to provide significant reduction in background noise for moderate SNRs while virtually eliminating the "musical noise" often associated with spectral subtraction or adaptive Wiener filtering.

11:15

**4aSC9. Perception of English vowels by native speakers of Japanese.** Takeshi Nozawa (Dept. of English, Kansai Univ. of International Studies, 1-18 Aoyama, Shijimi-cho Miki-shi, Hyoto 673-0521, Japan)

Japanese children and adults living in the United States took the English Vowel Perception Test. Fourteen vowel contrasts were chosen. All the subjects heard the digitized stimuli through headphones, which were tokens of English vowels spoken by multiple talkers. American children and adults also took part in this experiment as control groups. A' scores were computed for each vowel contrast. A' scores for Japanese subjects were significantly lower in all contrasts but one (/i/ vs /ε/), and for Japanese subjects significant difference in A' scores among vowel contrasts were found. It was expected that Japanese children would do it better than adults, but their A' scores were no better than adult Japanese. Since American children did as well as American adults, the poor performance of those Japanese children was not attributed to the experiment design. To see if and how the exposure to English changed those Japanese subjects' perception of English vowels, Japanese teenagers who had never lived out

of Japan were brought in. Though some subjects were exceptionally good, no significant difference was observed in A' scores between Japanese living in the United States and those who study English in Japan.

11:30

**4aSC10. Prosodic boundaries and syntactic branching in Japanese and English.** John C. Ingram (Dept. of English, Univ. of Queensland, Brisbane, 4072 Australia, jingram@lingua.cltr.uq.edu.au)

This paper explores communalities and differences in prosodic boundary marking in English and Japanese. Kubozono (1989) observed an interesting asymmetry in Japanese: that the onset of a right branching syntactic constituent is characterized by sudden pitch rise, not observed at the onset of a left-branching constituent, which he attributed to the phonetic realization rule of a metrical boost. Left-branching constitutes the unmarked direction of embedding in Japanese phrase structure. English is overwhelmingly right branching in its syntactic structures. The metrical boost proposed by Kubozono is similar to the mechanism of *f0* baseline resetting often proposed to explain juncture marking at major phrase boundaries. English has a prosodic asymmetry, parallel to the Japanese case, whereby prosodic boundary marking is required, at the boundary of certain left-branching constituents. The paper seeks to replicate Kubozono's observations and to compare the phonetic realization of juncture in Japanese and English from pairs of syntactically ambiguous left- and right-branching phrasal constructions. A perceptual experiment was conducted to ascertain that Japanese listeners reliably employed prosody to disambiguate the utterances. Acoustic measurements of fundamental frequency and segment duration were made to assess Kubozono's theory of a metrical boost.

THURSDAY MORNING, 15 OCTOBER 1998

MARRIOTT BALLROOM 2, 8:45 TO 11:45 A.M.

### Session 4aUW

## Underwater Acoustics: Shallow Water Noise and General Topics

Timothy H. Ruppel, Chair

Naval Research Laboratory, Stennis Space Center, Mississippi 39529-5004

### Contributed Papers

8:45

**4aUW1. Comparison of transmission loss for underwater sound pulses measured using matched filters and integrated received power.** Daniel Hutt and James Theriault (Defence Res. Establishment Atlantic, 9 Grove St., Dartmouth, NS B2Y 3Z7, Canada, daniel.hutt@drea.dnd.ca)

Transmission loss (TL) may be found from the amplitude of a matched filter correlation applied to a pulsed acoustical signal. Use of matched filters to determine TL is advantageous because the technique can be applied continuously in real time without previously determining the pulse arrival time. However, distortion of the transmitted waveform by scattering, multiple path propagation, and Doppler frequency shift reduces the amplitude of the matched filter output thus increasing the TL determined in this way. The conventional TL calculation involves filtering the signal and integrating the received power for the duration of the pulse which yields a TL based on total received energy. This method must be applied after data is collected because the time of arrival of the pulses must first be determined. TL measurements derived using both methods were compared for data gathered during two trials in the Gulf of Mexico in both shallow and deep water environments. The transmitted waveforms were linear frequency-modulated pulses with a frequency range of 10 Hz, centered at 1055, 1225, and 1395 Hz. Results of the comparison will be presented.

9:00

**4aUW2. Model-data comparisons for Rapid Response 98 TL experiments.** B. Edward McDonald, John Osler, Melchiorre Ferla, and Jurgen Sellschopp (Saclant Undersea Res. Ctr., Viale San Bartolomeo 400, 19138 La Spezia, Italy)

In February 1998 a set of acoustic transmission loss (TL) experiments were carried out in the Gulf of Cadiz as part of the Rapid Response 98 exercise. TL experiments have the potential for improving bottom parameterization through inverse modeling. Concurrent ocean measurements revealing a variety of range dependences in the acoustic environment will be discussed. During the TL experiments, Sus charges were deployed along two approximately orthogonal tracks, with a vertical hydrophone array at their intersection. One Sus deployment track resulted in strongly range dependent propagation from deep to shallow water, while the other track resulted in weakly range dependent propagation in shallow water. TL data from the vertical array were compared with results from three models: Astral (invoking adiabatic modes), Grab (Gaussian ray bundles), and Ram (Pade approximant parabolic equation). The weakly range dependent track yields satisfactory agreement among models and data. The range dependent track, however, reveals occasional failures of the adiabatic mode

model to explain the data. The other two models, however, did yield satisfactory agreement with data. Implications for the adequacy of existing bottom parametrization will be discussed.

9:15

**4aUW3. Environmental factors governing shallow-water active sonar.**

Peter G. Cable (GTE BBN Technologies, Union Station, New London, CT 06320-6147, pcable@bbn.com) and William M. Carey (Old Lyme, CT 06371)

Recent experiments have measured the broadband sound transmission, coherency, reverberation and bottom backscattering strength in a variety of shallow-water environments with sand-silt bottoms. Ancillary range and time-dependent conductivity and temperature versus depth along with bathymetry were also obtained. The measurements were performed with especially designed impulsive sources, and vertical and horizontal receiving arrays. This paper presents key results on the spatial coherency of the received signals, the frequency dependence of the effective attenuation factors and the frequency dependent backscatter strength coefficient. The broadband coherency measurements, although variable from site to site, were found to be consistent with lengths of 30–35 wavelengths at 400 Hz at 40-km range. The frequency-dependent effective attenuation factor varied as frequency to a fractional power ranging between 0.15–0.25 dB/km at 100 Hz and 0.4–0.55 dB/km at 1 kHz. Bottom backscattering strengths at grazing angles on the order of 10 deg were found 10–15 dB lower at 200 Hz as compared to 1 kHz. The results are shown to be consistent with those of other investigators and are shown to place realistic limits on shallow-water sonar parameters. [Work supported by DARPA.]

9:30

**4aUW4. Mode scintillation and surface/submerged discrimination in SwellEx-96.** Vincent E. Premus (MIT Lincoln Lab., 244 Wood St., Lexington, MA 02173-9185)

It has been proposed that the short time-scale scintillation of normal mode amplitudes may be an effective discriminant for passive surface/submerged acoustic source classification in a shallow waveguide [V. Premus, *J. Acoust. Soc. Am.* (submitted)]. The approach is based on a two part hypothesis which states: (1) platform motion in the vertical due to surface or internal wave action induces observable temporal fluctuations in normal mode amplitudes, and (2) the probability densities of mode amplitude scintillation for surface and submerged sources are well separated under modest depth fluctuation conditions. In this work, results from the application of the mode scintillation classifier to narrow-band vertical array data collected during SwellEx-96 Event S5 are reviewed. Classifier output in the form of a thresholded mode scintillation interest image provides empirical evidence to support the classification hypothesis for the lowest order resolvable modes. Limitations imposed by the non-fully spanning nature of the vertical aperture will be discussed. [Work sponsored in part by SPAWAR, under Air Force Contract No. F19628-95-C-0002. Opinions, interpretations, conclusions, and recommendations are those of the authors and are not necessarily endorsed by the U.S. Air Force.]

9:45

**4aUW5. Reverberation limitations in the active detection and localization of objects submerged in shallow water.** Nicholas C. Makris, Yi-San Lai, and Purnima Ratilal (MIT, 77 Massachusetts Ave., Cambridge, MA 02139)

A common problem in the active detection and localization of an object submerged in shallow water arises when acoustic returns from the object become indistinguishable from seafloor returns. Given a horizontal receiving array, the intensity of match-filtered and beamformed echo-returns can be plotted as a function of range and azimuth. Difficulties in detecting the presence of a submerged object in such an image arise in two ways. The first is unique to range and azimuth dependent waveguides.

Even if the object produces the dominant return in its range-azimuth resolution cell and stands above background reverberation in adjacent cells, it may be camouflaged by prominent returns from neighboring cells that clutter the image. The second occurs when seafloor reverberation from the resolution cell of the object is so intense that the object's presence is not statistically significant in that cell. The extent to which seafloor reverberation limits the detection and localization of submerged objects in these ways is quantitatively investigated. A model for full-field scattering from a submerged object is combined with a model for reverberation in a shallow-water waveguide. These are used to simulate range-azimuth images of the acoustic returns received by a bistatic system in a range-dependent waveguide.

10:00

**4aUW6. Mode coupling produced by a cylindrical structure in a shallow water environment.** Angie Sarkissian (Naval Res. Lab., Washington, DC 20375-5350, angie@aquanrl.navy.mil)

A structure placed in a shallow water environment between a source and a receiver produces mode coupling with strength that depends on various parameters: the depth of the structure, its orientation, the sound speed profile at the location of the structure, the frequency as well as the mode number of the incident field. The mode coupling produced by a cylindrical shell with hemispherical end-caps is examined by varying the parameters. [Work supported by ONR.]

10:15–10:30 Break

10:30

**4aUW7. Ping-to-ping variations in the underwater environment and synthetic aperture sonar performance.** Timothy H. Ruppel (Naval Res. Lab., Stennis Space Center, MS 39529-5004)

In synthetic aperture sonar (SAS), a target is rapidly and repeatedly pinged from a moving acoustic array platform, with the resulting received data combined to achieve a high-resolution acoustic image. SAS technology has demonstrated some real promise in the field of mine hunting, and may have other applications as well. However, if the underwater environment changes between pings, then the individual receiving elements will have random phase errors and the SAS image may be substantially degraded. This paper will quantify the performance losses with simple simulations for a range of frequencies and environmental variabilities, concentrating on those which are consistent with experimental observation for the real ocean. The effect of motion compensation on these errors will also be discussed. [This work was funded by the Office of Naval Research.]

10:45

**4aUW8. Feature localization and classification from echolocation constraints with navigation uncertainty.** John J. Leonard and Hans Jacob S. Feder (MIT, Dept. of Ocean Eng., Cambridge, MA 02139)

This talk will describe techniques for the classification and localization of simple geometric features from sonar data in the presence of navigation uncertainty. The goal is to recover the geometry of one or more unknown objects, the location of the object(s) in the global reference frame, and the trajectory of the sensor via combination of echolocation constraints obtained from multiple positions. The sonar is assumed to be a single transducer with a wide beam, which yields accurate range information but provides only weak angle constraints. Previous research has considered this problem without navigation uncertainty or using multi-element sonar array configurations [J. Leonard, *J. Acoust. Soc. Am.* **93**, 2340(A) (1993); L. Kleeman and R. Kuc, *Int. J. Robotics Res.* **14**(4) (1995)]. Echolocation constraints serve as input to a concurrent mapping and localization algorithm that performs both discrete (number and type of features) and con-

tinuous (location of features and sensor) estimation. Experimental results will be presented using a 675-kHz underwater mechanically scanned profiling sonar mounted on a large workspace robotic positioning system in a testing tank at MIT.

11:00

**4aUW9. Long time-base measurements of surf noise.** Grant B. Deane (Marine Physical Lab., Scripps Inst. of Oceanogr., La Jolla, CA 92093-0238, grant@mpl.ucsd.edu)

Preliminary results from an experiment conducted over a year to measure surf noise will be presented. In July of 1997 a surf-monitoring sensor array comprised of four broadband hydrophones and a pressure sensor were deployed in 7 m of water, 200 m southwest of Scripps Pier and roughly 200 m from the surf line. Underwater ambient noise over the frequency range of 50 Hz to 22.5 kHz and wave height data from the pressure sensor has been acquired for 9 min every hour almost continuously since deployment. The resulting data set is in excess of 20 000 9-min samples, providing data through a wide range of incident wave fields and weather conditions, including several winter storms. Surf noise predominates on the frequency band of a few hundred Hertz up to 1 kHz. Variations in the surf noise levels can be seen on time scales of seconds, due to individual breaking waves; hours, due to tidal variations; and days, due to variations in the incident wave field amplitude. A preliminary analysis of the correlation between surf noise spectral levels and environmental factors, such as wave height and tidal variations, will be presented. [Work supported by ONR.]

11:15

**4aUW10. Fine delay estimation in sonar echoes using frequency Prony method.** Mathew J. Palakal and Min Liang (Dept. of Computer Sci., Indiana Univ.-Purdue Univ., 723 W. Michigan St., SL 280, Indianapolis, IN 46202)

Wideband sonar target recognition is becoming important due to the fact that the echo reflected from a target contains more information about the target signatures. In a wide bandwidth sonar system, the echo consists of a sequence of the weighted transmitted signals emanating from the

different scattering centers on the target. When a transmitted sonar waveform  $u(t)$  is reflected from a stationary or slow moving target, the received echo  $e(t)$  is the convolution of the transmitted signal  $u(t)$  and the target impulse response  $h(t)$ , i.e.,  $e(t) = \int_{-\infty}^{\infty} u(\tau) \cdot h(t - \tau) = \sum_{i=1}^M a_i \cdot u(t - \tau_i)$ , where  $a_i$  is the reflection strength of the  $i$ th scatterer on the target,  $\tau_i$  is the two-way propagation time delay between the  $i$ th scatterer and the transmitter/receiver, and  $M$  is the total number of point scatterers on target. The estimates of the parameters  $\{a_i\}_{i=1}^M$  are normally chosen as target feature for classification and the difficulty is in estimating these parameters. In this work, the relative differences between time delays  $\{\tau_i\}_{i=1}^M$ , i.e., fine delays  $\{\Delta\tau_i = \tau_{i+1} - \tau_i\}_{i=1}^{M-1}$ , and the normalized reflection strengths  $\{\alpha_i = a_i / \min(a_i)\}_{i=1}^M$  are selected as sonar target features. The Prony method is used in frequency domain to estimate parameters  $\{a_i\}_{i=1}^M$  and  $\{\tau_i\}_{i=1}^M$  and hence the target features. The methodology used for deriving the frequency Prony method (FPM) and the results of target feature extraction in noiseless case will be presented. [Work supported in part by NSF.]

11:30

**4aUW11. Investigation of underwater acoustic noise for three different areas.** Dariush Esmaeili (J. Eng. Res. Ctr.), Abdolrahim Javaherian (Tehran Inst. of Geophys.), and Kourosh Kalantar Zadeh (Tarbiat Modarres Univ.)

The results of underwater acoustic noise measurements at different sites in the Persian Gulf, Karadj Dam lake and at a small lake west of Tehran are investigated on the basis of time series and relative power spectra. Several possible sources such as shipping, wind, surf, industrial activities on shore, thermal agitation etc. are distinguished to determine the most probable origins of the observed noise. The ambient noise of the Persian Gulf is found to be a composite of at least three overlapping components: turbulent-pressure fluctuations, noise due to shipping with a maximum relative power around 50–60 Hz, and that due to wind with a maximum around 800 Hz. Spectrum characteristics of each component and of the composite are shown. The radiated noise of some different classes of ships and boats measured in the Persian Gulf and Karadj Dam lake are also discussed. Additional sources, including those of intermittent and local effects, such as bubbles, rain, snow, flying aircraft, etc., are also investigated in the small lake. Finally the Gaussianity and stationarity of the recorded data are studied through appropriate tests.



## Meeting of the Standards Committee Plenary Group

### ORGANIZATION OF STANDARDS COMMITTEE PLENARY GROUP MEETING

S1 Acoustics—U.S. Technical Advisory Group (TAG) for IEC/TC 29 Electroacoustics and ISO/TC 43 Acoustics

S3 Bioacoustics—U.S. Technical Advisory Group (TAG) for ISO/TC 43 Acoustics, IEC/TC 29 Electroacoustics, and ISO/TC 108/SC4 Human Exposure to Mechanical Vibration and Shock

S12 Noise—U.S. Technical Advisory Group (TAG) for ISO/TC 43/SC1 Noise and ISO/TC 94/SC12 Hearing Protection

The meeting of the Standards Committee Plenary Group will precede the meetings of the Accredited Standards Committees S1, S3, and S12, to take place in the following sequence on the same day: S12—9:30 to 11:30 a.m., Hampton Roads Ballroom 8; S1— 2:00 to 3:15 p.m., Hampton Roads Ballroom 8; S3—3:30 to 4:45 p.m., Hampton Roads Ballroom 8.

Discussion at the Standards Committee Plenary Group meeting will consist of national items relevant to all S Committees, plus a review of the international standardization (U.S. TAG) activities including reports on recent meetings and planning for forthcoming meetings.

Members of S2 on Mechanical Vibration and Shock (and U.S. TAG for ISO/TC 108 and five of its Subcommittees, SC1, SC2, SC5, and SC6) are also encouraged to attend the Standards Committee Plenary Group meeting, even though the S2 meeting will take place one day earlier, on Wednesday, 14 October 1998 at 9:00 a.m.

The U. S. Technical Advisory Group (TAG) Chairs for the various international Technical Committees and Subcommittees under ISO and IEC, which are parallel to S1, S2, S3, and S12 are as follows:

<u>U.S. TAG Chair/Vice Chair</u>	<u>TC or SC</u>	<u>U.S. TAG</u>
<b>ISO</b>		
P. D. Schomer, Chair, H. E. von Gierke, Vice Chair	ISO/TC 43 Acoustics	S1 and S3
P. D. Schomer, Chair H. E. von Gierke, Vice Chair	ISO/TC 43/SC1 Noise	S12
E. H. Berger, Chair	ISO/TC 94/SC12 Hearing Protection	S12
D. Reynolds, Chair H. E. von Gierke, Vice Chair	ISO/TC 108/SC4 Human Exposure to Mechanical Vibration and Shock	S3
D. J. Evans, Chair	ISO/TC 108 Mechanical Vibration and Shock	S2
R. H. Mehta, Chair K. Won, Vice Chair	ISO/TC 108/SC1 Balancing, including Balancing Machines	S2
A. F. Kilcullen, Chair	ISO/TC 108/SC2 Measurement and Evaluation of Mechanical Vibration and Shock as Applied to Machines, Vehicles and Structures	S2
B. E. Douglas, Chair	ISO/TC 108/SC3 Use and Calibration of Vibration and Shock Measuring Instruments	S2
D. J. Vendittis, Chair	ISO/TC 108/SC5 Condition Monitoring and Diagnostics of Machines	S2
G. Booth, Chair	ISO/TC 108/SC6 Vibration and Shock Generating Systems	S2
<b>IEC</b>		
V. Nedzelitsky, U.S. TA	IEC/TC 29 Electroacoustics	S1 and S3

**4a THU. AM**

**Meeting of Accredited Standards Committee (ASC) S12 on Noise**

P. D. Schomer, Chair S12, and Chair U.S. Technical Advisory Group (TAG) for ISO/TC 43/SC1, Noise  
*U.S. CERL, P.O. Box 9005, Champaign, Illinois 61826-9005*

B. M. Brooks, Vice Chair, S12  
*Brooks Acoustics Corporation, P.O. Box 3322, Vernon, Connecticut 06066*

H. E. von Gierke, Vice Chair, U.S. Technical Advisory Group (TAG) for ISO/TC 43/SC1, Noise  
*1325 Meadow Lane, Yellow Springs, Ohio 45387*

E. H. Berger, Chair, U. S. Technical Advisory Group (TAG) for ISO/TC 94/SC12, Hearing Protection  
*E-A-R/Aearo Company, 7911 Zionsville Road, Indianapolis, Indiana 46268-1657*

**Accredited Standards Committee S12 on Noise.** Working group chairs will report on their progress for the production of noise standards.

**Scope of S12:** Standards, specifications and terminology in the field of acoustical noise pertaining to methods of measurement, evaluation and control; including biological safety, tolerance and comfort and physical acoustics as related to environmental and occupational noise.

**Session 4pAA**

**Architectural Acoustics: Acoustics of Organ Performance Spaces II**

Dan Clayton, Chair  
*128A Greenacres Avenue, White Plains, New York 10606-3121*

*Invited Papers*

1:30

**4pAA1. The Göteborg Organ Art Center: An international research center for organ history, organ building, teaching, and performance practice.** Mendel Kleiner (Chalmers Univ. of Technol., Dept. of Appl. Acoust., S-41296 Göteborg, Sweden, mk@ta.chalmers.se)

The multidisciplinary Göteborg Organ Art Center (GoArt) project focuses on historical instruments as primary-source documents for performance practice research. Models of instruments are studied to fully document the design and quality of building materials and historical building procedures to explore and reconstruct the aesthetic and practical process of assembly, thereby recovering craft knowledge lost during 20th century industrialization. The project strives to achieve a level of quality in tone-production and craftsmanship not attained since the historical period, providing future organ-builders with functional knowledge of historical craft techniques and the extremely high-quality standards of historical instrument models. Research studies are made in collaboration with the Chalmers University of Technology on antique and contemporary pipe materials, development of new materials with the same properties as the old ones, studies of airflow systems and their effects on tone production in organ pipes, collection and analysis of information about the scaling, dimensions, and design of organ pipes, studies of tone production in organ pipes, and the relationship between organ and room acoustics. This presentation will focus on interaction between organ and church acoustics, studies on subjective perception of organ tone, and flue pipe modeling.

1:50

**4pAA2. Organic Rice—Designing a recital hall for the king of instruments.** Joseph W. A. Myers (Kirkegaard & Associates, 3910 Main St., Downers Grove, IL 60515)

The Edythe Bates Old Recital Hall at Rice University's Shepherd School of Music is a purpose-built organ performance hall, seating approximately 200. It houses a 75-stop French-style organ built by C. B. Fisk from tonal design by Manuel Rosales. The bare room was completed in 1991; a wood floor, loose chairs, and retractable acoustic banner system were added in 1995; the organ itself was installed in 1996; and diffusive elements were added to the rear wall in 1997 as voicing was completed. At each of these intermediate conditions reverberation times were measured and the acoustics of the room subjectively evaluated. The gradual fit-up of

**Meeting of Accredited Standards Committee (ASC) S12 on Noise**

P. D. Schomer, Chair S12, and Chair U.S. Technical Advisory Group (TAG) for ISO/TC 43/SC1, Noise  
*U.S. CERL, P.O. Box 9005, Champaign, Illinois 61826-9005*

B. M. Brooks, Vice Chair, S12  
*Brooks Acoustics Corporation, P.O. Box 3322, Vernon, Connecticut 06066*

H. E. von Gierke, Vice Chair, U.S. Technical Advisory Group (TAG) for ISO/TC 43/SC1, Noise  
*1325 Meadow Lane, Yellow Springs, Ohio 45387*

E. H. Berger, Chair, U. S. Technical Advisory Group (TAG) for ISO/TC 94/SC12, Hearing Protection  
*E-A-R/Aearo Company, 7911 Zionsville Road, Indianapolis, Indiana 46268-1657*

**Accredited Standards Committee S12 on Noise.** Working group chairs will report on their progress for the production of noise standards.

**Scope of S12:** Standards, specifications and terminology in the field of acoustical noise pertaining to methods of measurement, evaluation and control; including biological safety, tolerance and comfort and physical acoustics as related to environmental and occupational noise.

**Session 4pAA**

**Architectural Acoustics: Acoustics of Organ Performance Spaces II**

Dan Clayton, Chair  
*128A Greenacres Avenue, White Plains, New York 10606-3121*

*Invited Papers*

1:30

**4pAA1. The Göteborg Organ Art Center: An international research center for organ history, organ building, teaching, and performance practice.** Mendel Kleiner (Chalmers Univ. of Technol., Dept. of Appl. Acoust., S-41296 Göteborg, Sweden, mk@ta.chalmers.se)

The multidisciplinary Göteborg Organ Art Center (GoArt) project focuses on historical instruments as primary-source documents for performance practice research. Models of instruments are studied to fully document the design and quality of building materials and historical building procedures to explore and reconstruct the aesthetic and practical process of assembly, thereby recovering craft knowledge lost during 20th century industrialization. The project strives to achieve a level of quality in tone-production and craftsmanship not attained since the historical period, providing future organ-builders with functional knowledge of historical craft techniques and the extremely high-quality standards of historical instrument models. Research studies are made in collaboration with the Chalmers University of Technology on antique and contemporary pipe materials, development of new materials with the same properties as the old ones, studies of airflow systems and their effects on tone production in organ pipes, collection and analysis of information about the scaling, dimensions, and design of organ pipes, studies of tone production in organ pipes, and the relationship between organ and room acoustics. This presentation will focus on interaction between organ and church acoustics, studies on subjective perception of organ tone, and flue pipe modeling.

1:50

**4pAA2. Organic Rice—Designing a recital hall for the king of instruments.** Joseph W. A. Myers (Kirkegaard & Associates, 3910 Main St., Downers Grove, IL 60515)

The Edythe Bates Old Recital Hall at Rice University's Shepherd School of Music is a purpose-built organ performance hall, seating approximately 200. It houses a 75-stop French-style organ built by C. B. Fisk from tonal design by Manuel Rosales. The bare room was completed in 1991; a wood floor, loose chairs, and retractable acoustic banner system were added in 1995; the organ itself was installed in 1996; and diffusive elements were added to the rear wall in 1997 as voicing was completed. At each of these intermediate conditions reverberation times were measured and the acoustics of the room subjectively evaluated. The gradual fit-up of

the room provides an interesting look at the incremental effect of each modification. The extensive adjustable acoustic banner system also provides a dramatic degree of variability in the room's acoustic environment. This paper compares the acousticians' design intent for the room to the completed room and presents data and observations about the effects on the recital hall of the architectural modifications and acoustic banners.

2:10

**4pAA3. New organs in new spaces: A discussion of acoustical considerations from the organ builder's perspective.** David C. Pike (C. B. Fisk, Inc., 18 Kondelin Rd., Gloucester, MA 01930, cbfisk@cove.com)

Thoughtful planning for new pipe organs in different architectural environments and in a variety of acoustical conditions is a crucial part of organ design. Organs, perhaps more than any other musical instrument, rely on their surroundings for their ultimate success or failure. The organ builder must take into account many factors, some of which are not under his or her direct control, in formulating optimum organ placement, case design, facade arrangement, interior layout, tonal design, pipe scaling and construction techniques, and voicing. Meaningful dialogue with an acoustician at an early stage in a project can have tremendous ramifications for the completed room and organ. C. B. Fisk, Inc., has much recent experience with large concert and recital hall instruments. The Fisk organs installed during this decade at the Meyerson Symphony Center in Dallas, Texas, Minato Mirai Hall in Yokohama, Japan, and in particular, Edythe Bates Old Recital Hall at Rice University in Houston, Texas, provide valuable case histories for both organ builder and acoustician. Each features the work of a different acoustical consultant. In all three cases the final result reflects the degree to which the acoustics were specifically optimized for the pipe organ.

2:30

**4pAA4. Acoustical design for organs in educational facilities.** Russell Cooper (Jaffe Holden Scarbrough Acoustics, Inc., 114A Washington St., Norwalk, CT 06854)

The organ as an instructional as well as recital instrument poses many acoustical challenges for the design team. Among those are the surfaces near the organist by which he can hear him/herself, overall volume for proper loudness, and the size of the organ relative to the size of the space. The design team must usually plan the space for an instrument that arrives long after opening night. This involves careful planning, experience in organ requirements, and a good relationship and coordination with the organ builder and faculty. Projects cited are The University of South Carolina, The University of North Carolina, The University of Georgia, Cleveland State University, and the University of North Texas.

2:50

**4pAA5. Objective and subjective evaluations of pipe organ sound.** Vladimir Chaloupka (Phys. Dept. and School of Music, Univ. of Washington 35-1560, Seattle, WA 98195-1560, vladi@u.washington.edu)

Study of correlations between the perceptual and the physical attributes of musical sound is an important part of musical acoustics. This paper will review the status of this field, with particular attention to the pipe organ sound. The pipe organ is an ideal subject for such studies: the sound is simple enough for a study to be feasible, yet complex enough for the study to be interesting. A procedure for systematic measurements and evaluation of many aspects of the organ sound will be described. An interactive, PC-based system enables an efficient yet precise measurement of the fundamental frequencies, spectra of the partials, as well as of the nonharmonic component of all the pipes in an organ, and the transient behavior of selected pipes. Results are presented in a compact and easily understandable form: a "fingerprint" of the instrument. The main room acoustics measurements are also made. The emphasis is on the old but still intriguing question: what imperfections are necessary for achieving the perception of perfection (e.g., small but desirable irregularities in tuning, and in the scaling behavior). If the planned organ concert indeed takes place, measurements of the organ(s) will be made, and the results will be available.

3:10–3:25 Break

### *Contributed Papers*

3:25

**4pAA6. Optimum organ acoustics reconciled with other hall uses.** David Lloyd ben Yaacov Yehuda Klepper (Arzei HaBeira 50-40, Jerusalem 97356, Israel)

Providing optimum acoustics for a large musical instrument, the organ, to insure good sound distribution and proper times of arrival for performer and audience is a formidable task, involving consideration of reverberation times over the frequency range, initial time delay gaps, early to reverberant ratios, and energy frequency balance. To coordinate these parameters for the organ and also maintain them near optimum for chamber groups, orchestras, and choruses, adds further complications. Some guidelines in architectural design are presented, and examples drawn from buildings built over a period of 36 years are shown, with the important role of adjustability, in suspended sound-reflecting panels, stage-enclosure elements, stage floors on elevators, and even the organ itself, emphasized.

One important example using electronics for music is shown, and provision of high-speech intelligibility through sound systems is also summarized for each example. The case studies are from work performed by the acoustical consulting firms of Bolt Beranek and Newman, and Klepper Marshall King, although the author has moved to independent practice in Jerusalem. George Izenour was Theatre Consultant for several projects shown.

3:40

**4pAA7. Quality reverberation fields for organ music.** Bertram Kinzey, Jr., Gary Siebein, and Martin Gold (Univ. of Florida, Dept. of Architecture, P.O. Box 115702, Gainesville, FL 32611-5702)

Organists and organ builders commonly specify a long reverberation time for a room for an organ. This simple quantitative statement ignores consideration of a larger specification required to insure appropriate qual-

ity of the reverberant field to insure that music heard has acceptable clarity, intimacy, diffusion, and other attributes required for excellent completion of the musical sound. Measurements other than reverberation time are examined to establish the role they should play in an adequate specifica-

tion for a reverberant field for organ music. The acoustics of several rooms with large organs will be compared to illustrate the importance of these newer measures of acoustic quality in a more complete description of the rooms.

3:55–4:00 Break

4:00–5:00

Panel Discussion

THURSDAY AFTERNOON, 15 OCTOBER 1998

MARRIOTT BALLROOM 7, 1:00 TO 1:45 P.M.

### Session 4pAB

#### Animal Bioacoustics: Shallow-Water Bioacoustics II

Whitlow W. L. Au, Cochair

*Hawaii Institute of Marine Biology, P.O. Box 1106, Kailua, Hawaii 96734*

Peter M. Scheifele, Cochair

*National Undersea Research Center, University of Connecticut, Avery Point, Groton, Connecticut 06340-6097*

#### Contributed Papers

1:00

**4pAB1. Monitoring airgun sound levels with an array of hydrophones in an ocean bottom cable.** Charles R. Greene, Jr. and Robert G. Norman (Greeneridge Sciences, Inc., 4512 Via Huerto, Santa Barbara, CA 93110)

In shallow water, three-dimensional seismic surveys for oil and gas sometimes use a large array of hydrophones on the bottom as receivers for sound pulses originating from an array of airguns. There is concern that intense airgun pulses may disturb or (at close range) injure protected marine mammals like seals and whales. Permits to conduct the surveys often require that the pulse levels at various distances be measured to determine or verify safety zone radii. Protected animals observed within the safety zone may be cause to interrupt the survey. However, the sound field around the airgun array depends on aspect and local propagation conditions as well as distance. These details have been difficult to study with conventional methods. An array of 600 hydrophones in the ocean bottom cables was deployed by the seismic contractor during a survey in the Alaskan Beaufort Sea. Each pulse was received and recorded simultaneously at all hydrophones while the airgun source moved across the receiving array. This method can provide detailed empirical data on the sound field at relatively low cost. [Work supported by BP Exploration (Alaska), Inc., Anchorage, AK, hydrophone data provided by Northern Geophysical of America.]

1:15

**4pAB2. Stochastic dynamical modeling of marine mammal vocalization waveforms.** Thomas J. Hayward (Naval Res. Lab., Washington, DC 20375-5350)

Stochastic models have been developed for approximating acoustic waveforms of marine animal sounds. The models provide a general method for replicating the time-frequency features and variations of vocalization waveforms based on limited databases of recorded samples. For each sample waveform, a linear-system model is constructed, and the system parameters are determined so that the impulse response of the system optimally fits the sampled waveform. Then, the statistical variability of the

system parameters within the ensemble of recorded samples is characterized, and procedures for generating new waveforms based on those statistical distributions are defined. The linear-system models generate waveforms that are similar to the recorded samples and interpolate among the feature variations of those samples. In addition, the models suggest possible physical mechanisms of sound generation by marine animals. The approach is then extended to provide for representation and simulation of extended time series consisting of patterned repetitions of marine animal sounds, e.g., click bursts and codas of dolphins and whales. Applications to modeling of underwater noise generated by marine animals are presented. [Work supported by the Office of Naval Research.]

1:30

**4pAB3. Adaptive classification of ensonified underwater objects.** David A. Helweg and Patrick W. B. Moore (SPAWARSYSCEN San Diego, Code D351, 49620 Beluga Rd., San Diego, CA 92152-6506)

The biological sonar system of bottlenose dolphins is adapted for cluttered, high noise, and extremely reverberant shallow-water environments such as bays, estuaries, and near-shore waterways. Echolocation behavior and signals are plastic, modified in-stride during encounters with novel targets and in novel surroundings. Moreover, biosonar target discrimination performance provides an existence proof for biological sonar-based recognition of various kinds of targets. For the dolphin this is accomplished in part by auditory neural computations that are not yet fully understood. A model of adaptive target classification processes was developed using heuristics based on dolphin psychophysics and echolocation behavior. Echoes were recorded while a dolphin ensonified several aspect-dependent targets during a target discrimination task. A computational model of dolphin ear filters was adapted to include filter gain recursively scaled to acoustical characteristics of local ambient noise and reverberation. Stochastic noise was attenuated by multi-ping fusion within an Integrator Gateway processing scheme. Output from the spectral filters served as inputs for a neural net target classifier. The system accommodated changes in local ambient noise and produced classification significantly better than did traditional classifiers that lacked adaptive filtering processes. [Work funded by ONR 321US.]

**Session 4pBB****Biomedical Ultrasound/Bioresponse to Vibration: Models for Tissue-Ultrasound Interaction**

T. Douglas Mast, Cochair

*Applied Research Laboratory, Pennsylvania State University, University Park, Pennsylvania 16801*

E. Carr Everbach, Cochair

*Department of Engineering, Swarthmore College, 500 College Avenue, Swarthmore, Pennsylvania 19081-1397***Chair's Introduction—1:25*****Invited Papers*****1:30****4pBB1. Microcalcifications and high-performance breast ultrasound.** Martin E. Anderson, Gregg E. Trahey (Dept. of Biomed. Eng., Duke Univ., Durham, NC 27708), and Mary S. C. Soo (Duke Univ. Medical Ctr., Durham, NC 27710)

Breast microcalcifications (MCs) are small crystals of calcium phosphate which are in some cases the only evidence of malignancy. Thus MCs serve as important diagnostic indicators, despite the fact that mammography has a low specificity in cases where MCs are the only suspicious feature. The overall sensitivity and specificity of mammography is also reduced in the radiographically dense breast. While the adjunctive use of breast ultrasound continues to expand with advances in the state of the art, ultrasound is currently not considered a reliable means to visualize MCs. Their improved visualization under ultrasound would be of significant clinical benefit, particularly in the dense breast. The findings to date of ongoing studies of the *in vivo* acoustic properties of MCs and breast tissues are reviewed. These include investigations of the scattering properties of MCs and breast tissue as well as direct measurements of *in vivo* phase aberrators and mean tissue sound speed using MCs as *in vivo* point scatterers. These studies suggest that MCs have elastic acoustic properties, and that gross sound speed error and tissue backscatter are the most significant factors limiting the visualization performance of ultrasound, among those studied. [This work is supported by NIH Grant Nos. RO1-CA43334-01 and RO1-CA76059-01.]

**2:00****4pBB2. A model for elastic wave propagation in tissue.** Thomas L. Szabo (Hewlett-Packard, M.S. 095, 3000 Minuteman Rd., Andover, MA 01810, tom\_szabo@hp.com)

Data for attenuation in tissue fit a power law form: frequency raised to an exponent  $y$  which is typically between 1 and 2. A new self-consistent comprehensive causal model for elastic wave propagation in tissues with this type of loss has been derived based on the assumption that the loss per wavelength is small. The model agrees well with data and has the following features: (1) This model is in the form of a time domain wave equation with convolution operators for loss and phase velocity that depend on the value of  $y$ . (2) The frequency domain solution is expressed as a material transfer function that includes a velocity dispersion term which is maximum for  $y=1$  and zero for  $y=0$  or  $y=2$ . (3) The time domain solution is a material impulse response which can be used to predict broadband pulse propagation in tissues.

**2:30****4pBB3. Large-scale modeling of ultrasound transducer pulses in lossy, nonlinear tissue.** Greg Wojcik, John Mould, Laura Carcione (Weidlinger Assoc., 4410 El Camino Real, Ste. 110, Los Altos, CA 94022, greg@ca.wai.com), Bengt Fornberg (Univ. of Colorado, Boulder, CO 80309), Robert Waag (Univ. of Rochester, Rochester, NY 14627), and Sevig Ayter (Acuson Corp., Mountain View, CA 94039)

Broadband finite-element modeling codes have proven effective in the hands of medical ultrasound transducer designers. Similar modeling advantages have not yet been realized by image processing engineers concerned with aberrating media. Their principal difficulty is the much larger physical scale of bioacoustic models for imaging, e.g., a 20-cm round trip at 5 MHz is 600 wavelengths. Conventional (low order) finite-element/finite-difference wave solvers are inadequate at this scale because of cumulative numerical errors and computer limits. The solution is more accurate algorithms, based on spectral methods or high-order finite differences, in conjunction with parallel processing. The modeling problem is described, starting from a detailed transducer section, coupled to the heterogeneous abdominal wall and deeper tissue, to the scattering object(s) and back. Computed examples illustrate fundamental modeling and phenomenological issues. Solving the bioacoustic equations in the time domain is essential, and comprehensive models include both frequency-dependent absorption and second-order nonlinearity ( $B/A$  parameter). Algorithmic issues involve balanced, high-order space and time differential operators, treatment of discontinuities, radiation boundary conditions, and parallelization. The key is maintaining consistent, high-order accuracy throughout the analysis. An overall capability is demonstrated. [Work supported by DARPA, ONR, NSF, and NIH.]

## Contributed Papers

3:15

**4pBB4. Simulation of ultrasonic propagation, scattering, and attenuation in the human chest wall.** T. Douglas Mast (Appl. Res. Lab., Penn State Univ., University Park, PA 16802, mast@sabine.acs.psu.edu), Laura M. Hinkelman (Penn State Univ., University Park, PA 16802), and Robert C. Waag (Univ. of Rochester, Rochester, NY 14627)

A finite-difference time-domain model for ultrasonic pulse propagation through soft tissue [Mast *et al.*, J. Acoust. Soc. Am. **102**, 1177–1190 (1997)] has been extended to incorporate absorption effects as well as longitudinal-wave propagation in cartilage and bone. This extended method has been used to simulate ultrasonic propagation through anatomically detailed chest wall models. The inhomogeneous chest wall structure is represented by two-dimensional tissue maps determined by staining chest wall cross sections to identify connective tissue, muscle, fat, cartilage, and bone, scanning the stained cross sections at 300 dpi, and processing the scanned images to assign a tissue type to each pixel. Each pixel of the tissue map is then assigned a sound speed, density, and absorption value determined from published measurements to be representative of the local tissue type. Computational results for wavefront distortion including amplitude fluctuations, arrival time fluctuations, and waveform distortion show qualitative agreement with measurements performed on the same specimens [Hinkelman *et al.*, J. Acoust. Soc. Am. **101**, 2365–2373 (1997)]. Visualization of simulated tissue-ultrasound interactions in the chest wall shows possible mechanisms for image aberration in echocardiography, including effects due to reflection and diffraction from rib structures.

3:30

**4pBB5. Coupled thermal-acoustic simulation results with temperature-dependent tissue parameters for therapeutic ultrasound.** Ibrahim M. Hallaj (Appl. Phys. Lab., Univ. of Washington), Robin O. Cleveland, Ronald A. Roy, and R. Glynn Holt (Boston Univ., Boston, MA)

Recently the authors used direct simulations of the transient acoustic pressure field to calculate heat energy deposition and, thus, temperature fields in two-dimensional tissue like media [J. Acoust. Soc. Am. **102**, 3172(A) (1997)]. It is known that acoustic-induced temperature rises will alter the properties of the medium in hyperthermia situations. In this presentation the simulations are extended to simultaneously solve the wave propagation and tissue heating problems so that the effect of temperature-dependent tissue parameters can be accounted for directly. In other words, there is a continuous feedback of temperature on the sound propagation parameters, which in turn affects the thermal energy deposition. The simulations are second order accurate in time, fourth order in space full wave calculations using the finite-difference time-domain technique, and allow for finite-amplitude wave propagation in an inhomogeneous, thermoviscous fluid. The model allows for spatially and temporally varying sound speed, density, attenuation coefficient, and nonlinearity parameter, as well as variable thermal properties and perfusion. Acoustic pressure, thermal dose, and tissue temperature are calculated, and conclusions are made regarding qualitative and quantitative aspects of focusing behavior contrasted to the case where the propagation and thermal parameters are kept constant. [Work sponsored by ONR and DARPA.]

3:45

**4pBB6. Bubble-mediated hyperthermia in an instrumented tissue phantom.** Patrick Edson, R. Glynn Holt, and Ronald A. Roy (Dept. of Aersp. and Mech. Eng., Boston Univ., Boston, MA 02215)

The coagulation of blood by ultrasound, a procedure termed acoustic hemostasis by us, involves the contributions of several physical and biophysical effects. To investigate these effects, experiments have been un-

dertaken involving rapid hyperthermia in an instrumented tissue phantom. Previously, the authors have reported a sharp increase in the rate of heating with increasing peak negative insonation pressure [J. Acoust. Soc. Am. **103**(A) (1998)]. This increase occurs at a well-defined pressure, a threshold effect not unlike that observed at the onset of inertial acoustic cavitation. It was postulated that this effect may be the result of such cavitation activity leading to bubble-enhanced heating. The results of experiments in which the temperature rise and cavitation activity are monitored simultaneously are reported. The results will be interpreted in the light of the aforementioned cavitation effect, as well as competing explanations such as the excess absorption associated with the formation of nonlinearity in the pressure profile. [Work supported by DARPA.]

4:00

**4pBB7. Ultrasonic periodontal probe.** Mark Hinders, Alan Guan, and John Companion (Appl. Sci. Dept., College of William and Mary, Williamsburg, VA 23187)

This talk discusses proof of concept *in vitro* testing of an ultrasonic probe for imaging periodontal structures. This technique allows accurate measurements of disease activity for patient risk assessment and treatment outcome evaluation without the need for ionizing radiography or manual periodontal probing. This technique promises reduced variability and improved ease of use, in comparison to conventional manual periodontal probing. The work discussed here is the first step to establish the ultrasound periodontal probe as a clinically valuable tool for patient assessment and the first noninvasive measure of periodontal disease activity. Data from cadaver samples using a prototype intraoral ultrasound instrument is compared to conventional manual probing subsequently performed on the annotated cadaver samples. The results discussed here are being used to refine the technique, improve the analysis of scan signals, and develop the framework of the software that will be used during a subsequent *in vitro* testing program.

4:15

**4pBB8. An estimation technique of the vector component of blood flow from Doppler information on a plane.** Shigeo Ohtsuki (Precision and Intelligence Lab., Tokyo Inst. of Technol., Midori-ku Nagatsuta 4259, Yokohama, 226-8503 Japan)

The information of the ultrasonic Doppler effect is the velocity component of ultrasonic scatters in the direction of the ultrasonic beam in fluid. Scanning the ultrasonic beam, a colored Doppler image can be obtained on a plane. Using this data, the velocity component perpendicular to the ultrasonic beam is estimated. In this case, the observation plane is in three-dimensional flow. Considering sources of fluid in the plane, the flow function method [S. Ohtsuki and M. Tanaka, J. Visual. Soc. Jpn. **1869**, 40–44 (1998)] is applied. This flow function method was developed for streamlines on a medical ultrasonic colored Doppler image of blood flow in the heart. The flow function without sources is expressed as a single-valued function. The flow function of sources is a multi-valued function named a laminar function. The flow function on an observation plane is the combination of these two functions. The gradient of the flow function on the plane is a flow vector component. The estimation technique introduced here is an application of the flow function method.

## Session 4pEA

## Engineering Acoustics: Transducers and Transducer Materials

Harold C. Robinson, Cochair

*Naval Undersea Warfare Center, Code 2131, 1176 Howell Street, Newport, Rhode Island 02841-1708*

James F. Tressler, Cochair

*Naval Research Laboratory, Code 7130, 4555 Overlook Avenue, SW, Washington, DC 20375-5350*

## Contributed Papers

1:00

**4pEA1. Large-signal characterization of prestressed PMN-PT-Ba and PMN-PT-Sr at various temperatures.** Elizabeth A. McLaughlin, Robert S. Janus, Kim D. Gittings, and Lynn Ewart (NUWC, Code 2131, 1176 Howell St., Newport, RI 02841)

Quasistatic (10-Hz) electromechanical measurements were made of two relaxor ferroelectrics, PMN-PT-Ba (90 mol% lead-magnesium-niobate, 10 mol% lead-titanate, doped with 3% barium) and PMN-PT-Sr (88 mol% lead-magnesium-niobate, 10 mol% lead-titanate, 2 mol% strontium, w/2500 ppm iron oxide) under high electric fields (0–1.5 MV/m) and high mechanical prestresses (0–41.4 MPa) over a temperature range (–5–40 °C). The measured quantities—the piezoelectric constant,  $d_{33}$ , the permittivity,  $\epsilon_{33}^T$ , the Young's modulus,  $Y_{33}^E$ , the electromechanical coupling factor,  $k_{33}$ , and the energy density,  $U$ —are found for both small and large ac signal conditions. These measurement conditions and material properties are of great interest for applications in high-power Navy sonar transducers to material manufacturers. Material property trends with increasing prestress, temperature, and electric field are identified. The PMN-PT-Sr is shown to have better properties for sonar transducers than the PMN-PT-Ba. Compared to Navy type-III PZT piezoelectric ceramic, the energy density of PMN-PT-Sr at 5 °C and 41.4 MPa is nearly 11 dB higher and the coupling 23% lower.

1:15

**4pEA2. The energy analysis of the piezoceramic bodies under nonuniform deformations.** Boris Aronov (Acoust. Res. Lab., Dept. of Elec. and Computer Eng. and Ctr. for Marine Sci. and Technol., UMass—Dartmouth, North Dartmouth, MA 02747) and David A. Brown (UMass—Dartmouth, North Dartmouth, MA 02747)

One of the most powerful and clear methods of solving electromechanical transducer problems is an energy method based on the use of Lagrange equations. To apply this method to piezoceramic transducers one needs to have an expression for internal energy of a piezoceramic body in a convenient form. Such a general expression for energy under arbitrary nonuniform deformations is developed and discussed. It is shown that under certain conditions the electrical and mechanical variables in the expression for internal energy of a piezoceramic body can be separated. The underlying physics for this condition is illustrated with an example of piezoceramic rods with transverse and axial polarization. In the case of electrical and mechanical variables that are not separated, the contribution of mutual terms in the total internal energy is expressed analytically and can be easily treated.

1:30

**4pEA3. On the optimizing of the effective electromechanical coupling coefficients of piezoceramic bodies.** Boris Aronov (Acoust. Res. Lab., Dept. of Elec. and Computer Eng. and Ctr. for Marine Sci. and Technol., UMass—Dartmouth, North Dartmouth, MA 02747) and David A. Brown (UMass Dartmouth, N. Dartmouth, MA 02747)

The effective electromechanical coupling coefficients are defined based on the expression for internal energy of a piezoceramic body. By means of this definition, conditions are obtained under which an effective coupling coefficient for any given deformation distribution can be maximized and shown to be equal to a corresponding coupling coefficient of the piezoceramic material. A simple practical way to optimize the effective coupling coefficients of transducers by changing its electrode shape is discussed. Examples of transducers vibrating in longitudinal and flexural modes are considered.

1:45

**4pEA4. Simultaneous measurements of bulk and shear moduli of voided polymers in the 0.5- to 2.5-kHz range.** R. Lance Willis, Lei Wu, and Yves H. Berthelot (Woodruff School of Mech. Eng., Georgia Inst. of Technol., Atlanta, GA 30332-0405)

The complex, frequency-dependent, bulk and shear moduli of polymers containing microscopic inclusions can be measured simultaneously [see *J. Acoust. Soc. Am.* **102**, 3549–3555 (1997)]. The method consists in measuring the surface dynamics of the sample under harmonic test by noncontact laser Doppler interferometry and by matching the experimental results with numerical predictions in which the two complex moduli are the adjustable parameters. Results obtained with a sample of known properties (lucite) confirm the validity of the method. Improvements to the system will be discussed. It is more compact and it uses only two miniature fiberoptic probe heads which can be scanned along the surface of the sample. Automated data acquisition with a lock-in amplifier greatly improves the speed of the experiment and enables good frequency resolution (less than 1 Hz) between 0.5 and 2.5 kHz. The measurement errors associated with this technique will be discussed in detail. In particular, measurements made on several samples taken from the same panel will be presented to quantify manufacturing variability. [Work supported by ONR, code 334.]

2:00

**4pEA5. Calibration of high-intensity pulsed pressure fields.** Sameer I. Madanshetty and Jogesh B. Chandran (Mech. and Nuclear Eng., 339 Durland Hall, Kansas State Univ., Manhattan, KS 66506-5106)

Meaningful studies in acoustic cavitation require a thorough knowledge of the imposed acoustic fields. Besides knowing the field pattern one needs to know the pressure amplitudes imposed by the transducer. As an alternative to risking a fragile reference transducer like the GEC-Marconi bilaminar PVDF membrane hydrophone to high-intensity pressure fields, a



robust method of absolute calibration involving a reflection type, pendulating radiation force balance is presented. In the process of characterizing such radiation force targets, the experiments indicate that the radiation force determined is not independent of the size of the target and one needs to account for an induced mass effect in seeking the radiation force balance. Additionally, using another modified design of the target to allow complete transmission of the sound beam one might be able to resolve the effect of streaming induced deflection and hence measure both the radiation force and the streaming force associated with long duty cycle pressure pulses. At low duty cycles of 1% no streaming force is observed. The fully reflecting radiation force balance for the calibration of high-intensity, low-megahertz frequency, focused acoustic fields has been found satisfactory for general purpose laboratory work.

2:15

**4pEA6. Development of a passive sonar system for localization of an underground sound origin.** Soon Suck Jarng (Dept. of Control and Instrumentation, Chosun Univ., 375 Seoseok-Dong, Dong-Ku, Kwang-Ju, 501-759, South Korea)

The aim of the work described in this paper is to develop a complex underground acoustic system which detects and localizes the origin of an underground hammering sound using an array of hydrophones located about 100 m underground. Three different methods for the sound localization will be presented, a time-delay method, a power-attenuation method and a hybrid method. In the time-delay method, the cross correlation of the signals received from the array of sensors is used to calculate the time delays between those signals. In the power-attenuation method, the powers of the received signals provide a measure of the distances of the source from the sensors. A new hybrid method has been developed for estimating the origin of the underground acoustic source by coupling both methods. The Nelder-Mead simplex search algorithm is then used to numerically estimate the position of the source in those methods. For each method the sound localization is carried out in three dimensions underground. The distance between the true and estimated origins of the source is in some cases less than 6 m for a search area of radius 250 m.

2:30–2:45 Break

2:45

**4pEA7. Development of transducers to measure the velocity reduction of materials at flexural wave numbers.** Patrick J. Klippel, D. H. Trivett (Naval Undersea Warfare Ctr., Div. Newport, Code 2131, 1176 Howell St., Newport, RI 02841, klippelpj@code20nl.npt.nuwc.navy.mil), and A. Mark Young (Florida Atlantic Univ., Boca Raton, FL 33431)

A major noise source for velocity sensors in a hull array configuration is back plane (i.e., hull flexural vibration) noise. The level of back plane noise is a function of frequency and wave number, and depends upon the velocity reduction properties provided by a pressure release decoupling baffle. The Naval Undersea Warfare Center, Division Newport, has designed, constructed, and tested two Flexural Wavenumber Transducers capable of measuring the velocity reduction of materials. One is designed to characterize materials along the flexural branch, *in vacuo*, of a thin steel plate supporting quarter-scale experiments and the other along the flexural of a thick steel plate supporting full-scale evaluations. Both transducers operate within an environmentally controlled pressure vessel allowing velocity reduction measurements to be made over a wide range of temperatures and hydrostatic pressures. Both the design and experimental results will be presented. [Work supported by PEO(USW)/ASTO, Code D3 and ONR, Code 334.]

3:00

**4pEA8. Directivity of a continuous, uniform strength, circular arc source, phased to its diameter-sensitivity to phasing errors.** William Thompson, Jr. (Appl. Res. Lab. and Dept. of Eng. Sci. and Mech., Penn State Univ., University Park, PA 16802)

An expression is presented for the in-plane directivity function of a continuous, uniform strength, circular arc source (or receiver) wherein the output of each element of the arc is phase shifted by a fixed fraction of the wavelength distance from that element to the diameter of the circle which is parallel to the chord joining the end points of the arc. Normally one chooses that fraction to be unity in order to simulate a straight line source, thereby achieving a narrow beamwidth. Some numerical results for various size arcs, for the case where the arc radius measures many wavelengths, are presented to illustrate how the beam pattern deteriorates (the beamwidth broadens and the side lobes increase in level) as that phase shift fraction is varied from the value unity. [Work supported by M. Dembrak, ASTO, through the Naval Sea Systems Command under contract No. N00039-D-0042, delivery order No. 53.]

3:15

**4pEA9. Optimization of fiber optic acoustic transduction for neutrally buoyant accelerometers.** David A. Brown, Boris Arinov, Lawrence Reinhart (Acoust. Res. Lab., Dept. of Elect. and Computer Eng. and the Ctr. for Marine Sci. and Technol., Univ. of Massachusetts, Dartmouth), Lan Cheng, and Hardiman Jim (Univ. of Massachusetts, Dartmouth)

It is desirable to maximize both the sensitivity and bandwidth of fiber optic accelerometers used for acoustic motion, accelerometer, and pressure-gradient sensor applications. Designs and figures-of-merit for centrally and peripherally supported flexural disks and compressional type accelerometers will be presented and compared. The optimization of optical fiber coils, coating diameter, materials properties, and packaging will also be discussed. [Work supported by ONR, NUWC, and the UMass Dartmouth Ph.D. Program.]

3:30

**4pEA10. Computational and experimental comparison of acoustic radiation of micro-loudspeakers.** Jennifer A. Shaw and Courtney B. Burroughs (Grad. Prog. in Acoust., 217 Appl. Sci. Bldg., Penn State Univ., University Park, PA 16802, jshaw@sabine.acs.psu.edu)

Experimental and computational methods were used to evaluate the acoustic performance of micro-loudspeakers which are utilized by portable communication devices. Experimental microphone measurements were taken in an anechoic chamber to determine the acoustic radiation as a function of frequency. Computational predictions were based on diaphragm surface velocity measurements obtained with a scanning laser doppler vibrometer. The velocity measurements were imported into SYSNOISE, and BEM analysis was used to calculate the acoustic radiation. Directivity patterns plotted in SYSNOISE were compared to those obtained by experimental methods. [Work supported by Motorola, Inc.]

3:45

**4pEA11. Acoustic gas concentration analyzer.** Jennifer P. Florance, Sherwood T. Hoadley, and Allan J. Zuckerwar (NASA Langley Res. Ctr., Hampton, VA 23681)

A free-field acoustical gas purity analyzer/speed-of-sound measurement device has been developed as part of a calibration effort for the NASA Langley Transonic Dynamics Tunnel, an aeroelastic research facility which utilizes either an air or heavy gas testing medium. The device consists of a 40-kHz transmitter, two receivers, and a thermocouple, all housed within a portable anechoic chamber. The transmitter diameter/acoustic wavelength ratio is such that ultrasonic transmission takes place without sidelobes within a narrow illumination zone, precluding the need to correct for boundary layer losses. The time difference between the two received signals and the known distance between the receivers are used to obtain the sound speed. Sound speed, local temperature, and properties of

the known pure gases are then used to calculate the gas purity. In wind-off conditions (where temperature corrections due to flow are avoided), the analyzer has achieved sound speed accuracies within approximately 0.11% in air and 0.05% in R134a. Gas purity values (which do not require tunnel-flow-condition matching) within 0.2% average uncertainty, compared to a calibrated infrared purity gauge, have been obtained both wind-on and off.

4:00

**4pEA12. Matched field processing photoacoustic signals to localize small gas leaks.** Serdar H. Yönak and David R. Dowling (Dept. of Mech. Eng. and Appl. Mech., Univ. of Michigan, Ann Arbor, MI 48109-2121)

Leaks from devices that are filled with pressurized gases and liquids are not only costly to consumers and manufacturers but may also be harmful to the environment. Detecting these leaks and determining their location is a critical process. Previous results have shown that a gas leak small enough to fill a thimble in 5 days could be detected and localized by using photoacoustic signals, two microphones, and Bartlett matched field processing. The present work considers the impact of using the broadband characteristics of the photoacoustic source, adaptive matched field processors, and four microphones. Photoacoustic sound is generated by rapidly scanning a carbon dioxide laser tuned to  $10.6 \mu$  over the suspected leak area. Sulfur hexafluoride is the tracer gas. A comparison is made between two-microphone and four-microphone results. Advantages and disadvantages of the adaptive matched field processors when compared to the Bar-

tlett processor for the problem at hand are discussed. Leak location uncertainty due to microphone directivity and microphone placement error is also discussed. Experimental results are presented. [Sponsored by Ford Motor Company.]

4:15

**4pEA13. Time-domain analysis of nonlinear transducer networks.** Daniel M. Warren (Knowles Electronics, Inc., 1151 Maplewood Dr., Itasca, IL 60143, daniel.warren@knowlesinc.com)

The existence of computer methods for the construction of network system equations from a netlist description and numerical methods for the solution of initial-value problems in mixed differential-algebraic equations (DAE's) allow the time-domain analysis of networks containing nonlinear elements. This paper will demonstrate these techniques in application to electromechanical transduction systems exhibiting small- and large-signal nonlinear behavior. Nonlinear constitutive equations defining electromechanical elements in transducer networks will be developed in the proper form for inclusion in a modified nodal formulation. It will be shown that consistent sets of initial conditions can be determined from a modified netlist under limited circumstances, but these limitations do not significantly constrain the utility of method in this application. In fact, this approach opens the method up to elements with static behavior, such as permanent magnets or electrets. Time-domain behavior of the system is numerically derived from the descriptor equations by a backward difference formula (BDF) DAE integrator appropriate for stiff systems.

THURSDAY AFTERNOON, 15 OCTOBER 1998 HAMPTON ROADS BALLROOM 8, 1:00 TO 2:00 P.M.

### Session 4pNS

## Architectural Acoustics and Noise: Progress Report on ASA's Role in Noise and Its Control

Bennett M. Brooks, Chair

*Brooks Acoustics Corp., 27 Hartford Turnpike, Vernon, Connecticut 06066*

This meeting is to review current progress and to invite further discussions to increase awareness of ASA in noise control and related architectural issues.

THURSDAY AFTERNOON, 15 OCTOBER 1998 HAMPTON ROADS BALLROOM 2, 2:00 TO 5:35 P.M.

### Session 4pPA

## Physical Acoustics and Noise: Sonic Boom Symposium II—Experiments and Analysis

Kenneth J. Plotkin, Chair

*Wyle Laboratories, 2001 Jefferson Davis Highway, Suite 701, Arlington, Virginia 22202*

### Invited Papers

2:00

**4pPA1. Thirteen sonic booms of space shuttles approaching Edwards Air Force Base, 1988–1993.** Robert W. Young (1696 Los Altos Rd., San Diego, CA 92109-1321)

Thirteen sonic booms of space shuttles approaching Edwards Air Force Base, 1988–1993, were measured at a site 10 miles west of EAFB with Brüel & Kjaer 2230 Precision Integrating sound level meter #1082228; CEL-493/2 Precision Integrating Impulse sound level meter #198107; CEL-238A Secondary Processor #151020; GenRad 1982 Precision sound level meter #0169; Rion NL-11

Precision Integrating sound level meter #1140255; RACAL 4D7680-3 tape recorder #11224. On 30 Jan 1992 sound-pressure levels were peak *flaT* 133 dB; peak *Awt* 127 dB; max fast *Cwt* 113dB; max fast *Awt* 98 dB. Sound exposure levels *flaT* 126 dB; *Cwt* 108 dB; *Awt* 90 dB. On 16 May 1992 sound-pressure levels *PKT* 131 dB; *MXFC* 112 dB; *MXFA* 95 dB. Sound exposure levels *CSEL* 107 dB and *ASEL* 91 dB. Some 8 min before a space shuttle landing the latitude, longitude, altitude, and Mach number at 1-s intervals were supplied by AEROPAC. By Carlson theory, W. J. Galloway calculated for 30 Jan 1992 slant distance of 89 kft to sound-measurement site from origin of the sonic boom where Discovery was flying Mach 1.6, altitude 68 kft above mean sea level. On 16 May 1992 the slant distance was 88 kft from origin where Endeavor was flying Mach 1.6, altitude 72 kft.

## 2:25

**4pPA2. Research on a sonic boom evaluation and low-boom and low-drag design.** Kenjiro Inagaki, Ayano Yamamoto, Hirokage Ogoshi, Kenji Hayama, and Kenji Sakai (1.Kawasaki-Cho, Kakamigahara City, Gifu-Pref. 504-8710, Japan, inagaki\_k@giw.khi.co.jp)

Kawasaki Heavy Industries, Ltd. has been researching on a sonic boom since 1990 toward the development of the next-generation SST (super sonic transport). A small chamber where a similar-sonic-boom could be created was made in 1993, and over 200 tests were carried out to see the reaction of people inside the chamber. As the result, it was found that A-weighted sound-pressure level (ASEL) and Stevens' Mark VII perceived level (PL) were good metrics for boom evaluation, and the intolerable levels of ASEL and PL were studied. At the same time, an aerodynamic design technique was developed, which was produced by combining the low-boom theory of Darden (NASA) with the low-drag design method of super sonic aircraft. The validity of the design technique was verified by computational fluid dynamics (CFD) and wind tunnel testing. The effect of trim characteristics on a sonic boom has also been studied for more practical investigations. A boom propagation has also been calculated recently by using Hayes' program for more understanding. The effects of weight, altitude, and Mach number on a propagating boom were investigated by parametric studies using the next-generation SST configurations in Japan.

## 2:50

**4pPA3. Underwater measurements and modeling of a sonic boom.** Francine Desharnais and David M. F. Chapman (Defence Res. Establishment Atlantic, P.O. Box 1012, Dartmouth, NS B2Y 3Z7, Canada, desharnais@drea.dnd.ca)

During a sea trial on the Scotian Shelf, acoustic signals from a sonic boom were recorded on several hydrophones of a vertical array. The array spanned the lower 50 m of the water column above a sand bank at 75-m water depth. The source of the sonic boom was deduced to be a Concorde supersonic airliner traveling at about Mach 2. The water-borne waveform was observed to decay as an evanescent wave below the sea surface, as expected. The very calm weather resulted in low ambient noise and low self-noise at the hydrophones, resulting in good signal-to-noise ratio on the upper hydrophones; however, the decreased signal amplitude is more difficult to detect towards the lower part of the water column. The period of the observed waveform is of the order 0.25 s, corresponding to a peak frequency of about 4 Hz. The shape of the measured waveform differs slightly from the theoretical N-shape waveform predicted with Sawyers theory [J. Acoust. Soc. Am. **44**, 523–524 (1968)]. A simple shallow ocean geoacoustic model suggests that this effect may be caused by seismo-acoustic interaction of the infrasonic waves with the elastic sediments that form the seabed.

## 3:15–3:30 Break

## 3:30

**4pPA4. SR-71 sonic boom propagation experiment.** Edward A. Haering, Jr., L. J. Ehernberger, and James E. Murray (NASA Dryden Flight Res. Ctr., MS D-2027, P.O. Box 273, Edwards, CA 93523-0273, ed.haering@dfrc.nasa.gov)

SR-71 sonic boom signatures were measured to validate sonic boom propagation prediction codes in support of the High Speed Research Program. An SR-71 aircraft generated sonic booms from Mach 1.25 to Mach 1.6, at altitudes of 31 000–48 000 ft, and at various gross weights. An F-16XL aircraft measured the SR-71 near-field shock waves from close to the aircraft to more than 8000 ft below, gathering 105 signatures. A YO-3A aircraft measured the SR-71 sonic booms from 21 000–38 000 ft below, recording 17 passes, including booms reflected off the ground. Three types of ground sensors were deployed to three station locations near the aircraft ground track, recording 172 signatures. Signatures of the F-16XL were also gathered. Atmospheric data were recorded for each flight. These results show that shock wave patterns and coalescence vary with SR-71 gross weight, Mach number, and altitude. This paper describes the design and execution of the flight research experiment, including instrumentation and flight maneuvers of the three aircraft. A guide to the entire digital database of sonic boom signatures, flight conditions, and atmospheric properties is included.

## 3:55

**4pPA5. Prediction of SR-71 sonic booms by THOR and Thomas codes.** Gerry L. McAninch (Fluid Mech. and Acoust. Div., NASA Langley Res. Ctr., Hampton, VA 23681-0001)

A major concern of recent sonic boom work has been accounting for the effects of molecular relaxation on sonic boom waveforms. Several new codes accounting for these effects have been developed since sonic boom research was reinitiated. In order to validate these codes, sonic boom signatures generated by an SR-71 aircraft have been measured near the aircraft and at several altitudes below the aircraft and on the ground. In the current study, two computer codes, the Thomas code and a highly modified version of THOR, have been used to propagate some of the sonic boom waveforms measured near the SR-71 aircraft to the ground, and to altitudes at which the waveforms have been measured. The results of this study will be presented. The results from the Thomas code provide two

things. First, they provide an indication of the prediction capability available when the current sonic boom research began. Second, they provide an indication of the validity of the results provided by THOR, by providing reasonable estimates of overall signal length and amplitude. The results from THOR provide an indication of the capability provided by the research supported in the last few years.

#### 4:20

**4pPA6. Validation of sonic boom propagation codes using SR-71 flight test data.** Lyudmila G. Ivanteeva, Victor V. Kovalenko, Evgeny V. Pavlyukov, and Leonid L. Teperin (Central Aerohydrodynamic Inst. (TsAGI), Moscow, Russia)

Two propagation codes are compared with SR-71 flight test data from 1995. Code ZEPHYRUS (NASA) was developed for level flight in a stratified atmosphere with horizontal winds. Signal propagation marches along ray paths determined by geometrical acoustics, alternating between time and frequency domains. Atmospheric absorption effects are applied in the frequency domain. Propagation continues through caustics (ray focusing). Code BOOM (TsAGI) is based on the Whitham  $F$ -function method, without accounting for atmospheric absorption. Ray tracing includes effects of vehicle acceleration and three-component winds. Experimental data include pressure signatures measured by a chase plane (30 to 80 bodylengths away) and a low-flying observation plane (200–300 bodylengths). The observation plane recorded both direct and reflected waves. At distances of about 30 body lengths, predictions show only negligible differences between the codes. Small differences appear in predicted far-field signatures due to atmospheric absorption. Comparison of computed and measured results shows good agreement with peak pressure, duration, and wave shape, thus validating computational codes. [Work supported by the Boeing Company.]

#### 4:45

**4pPA7. Sonic boom environmental impact prediction methods and issues.** Joel Garrelick, Kyle Martini (Cambridge Acoustical Associates/ETC, Analysis and Technology, Inc., 84 Sherman St., Cambridge, MA 02140), and Carina Ting (Vision R. E., Ashland, MA)

Concerns over the environmental impact of sonic booms include their effect on humans, other animals, and fabricated structures. Over the past few years, CAA has been involved in a number of projects focusing on the latter two concerns. Specifically, working with Hubbs Sea World to supplement previous empirical studies, an analytical model was developed for estimating the sonic boom induced response of fertilized tern eggs and evaluated the potential for damage. Working with Wyle Laboratories, Inc., both direct and reciprocal structural-acoustic testing techniques were developed for simulating structural responses in order to assess damage. These methods were validated by comparison with data from actual flyovers. Currently, with Marine Acoustics, Inc., the authors are involved in a project to assess testing and other issues associated with predicting the subsea penetration of sonic booms for assessing marine mammal impacts. Here at issue are those physical processes that may transform from second to first order in light of the evanescent attenuation of the typically subsonic, “primary” acoustic wave that penetrates to depth. These three projects are reviewed in this talk. Particular attention is given to idealizations in the prediction process, the associated uncertainties, and their effects on the overall impact evaluation process. [Work supported by The Armstrong Laboratory of The U.S. Air Force.]

#### 5:10

**4pPA8. Generation and measurement of laboratory scale focused sonic booms.** Richard P. Welle and Munson A. Kwok (Mech. and Propulsion Dept., The Aerospace Corp., P.O. Box 92957, M5-753, Los Angeles, CA 90009-2957, welle@aero.org)

Development of an accurate modeling code for rocket-generated, focused sonic booms requires experimental verification. Opportunities to make field measurements of shock waves from rocket launches are rare and unpredictable because of launch delays and last minute trajectory modifications. Laboratory simulations of accelerated supersonic trajectories have been hampered by the difficulty of accelerating laboratory scale projectiles in supersonic flight. This difficulty can be overcome by using acoustic reflectors with constant speed projectiles to create virtual projectiles with accelerated trajectories. A supersonic projectile, such as a bullet, moving past a curved acoustic reflector will generate shock waves which, after reflection, will appear to be coming from a bullet following a curved, accelerating trajectory. A simply curved reflector can shape the virtual trajectory of a  $M = 1.2$  projectile to closely simulate the portion of a typical rocket launch trajectory which generates a focused sonic boom incident on the surface. For proper scaling to full size vehicles, laboratory scale measurements require microphones with well-characterized frequency responses up to at least 1 MHz. The results obtained with a custom fabricated device based on an earlier design [E. P. Cornet, ARL-TR-72-40, Applied Research Laboratories, University of Texas (1972)] will be reported.

## Session 4pSA

**Structural Acoustics and Vibration: Active Control: Applications and Patent Overview**

Sabih I. Hayek, Chair

*Department of Engineering Mechanics, Pennsylvania State University, 227 Hammond Building, State College, Pennsylvania 16802***Invited Paper**

1:15

**4pSA1. Patents and noise cancellation.** James W. Hiney (Technology Law Offices of Virginia, P.O. Box 818, Middleburg, VA 20118)

This presentation will initially center on a brief overview of the Patent Law as it now exists after the 1995 and subsequent changes including patent term, Patent Cooperation Treaty enlarged membership, changes in prosecution, trends in the courts interpretation of patents, and proposed changes. A discussion of the patentability of algorithms in acoustic software will be made with illustrations. The presentation will then deal with some developments in acoustics and recently awarded patents which may prove to be of significance. To illustrate the importance of patents to growth of companies within the acoustics field, the current status of patents in the field of noise cancellation or sound attenuation will be addressed and examples shown of various positions of companies within the field and their focus. Specifically, the patent holdings of several companies within the field will be analyzed and the pattern of concentration of each company illustrated. To conclude, an analyses of expiring patents in the noise cancellation field will be presented to show opportunities for companies to expand into new areas now open for competition.

**Contributed Papers**

1:45

**4pSA2. Simulation results of loudness-based active noise control.** Scott D. Sommerfeldt and Timothy O. Samuels (Dept. of Phys., Brigham Young Univ., Provo, UT 84602, s\_sommerfeldt@byu.edu)

For many active noise control applications, the desired result is to reduce the noise perceived by a human listener. Typical active noise control systems operate in a manner that reduces the sound pressure level at the location of one or more error sensors. However, it has been shown that decreasing the sound pressure level at a location does not guarantee a similar decrease in the perceived loudness at that location. In fact, in some cases it is possible to reduce the overall sound pressure level of a signal, but have the perceived loudness increase. In this work, the filtered-x algorithm that is commonly used for active noise control has been modified to incorporate the approximate response of the human auditory system. This was done to see if improved subjective results could be obtained when minimizing a signal that approximates the loudness rather than the sound pressure level. It has been found that the effectiveness of this technique is largely dependent upon the nature of the input noise signal, as well as on the number of coefficients used in the controller. Simulation results will be presented to illustrate where this technique may be useful.

2:00

**4pSA3. Advanced modeling of active control of fan noise for turbofan engines.** Florence V. Hutcheson, Chris R. Fuller, Ricardo A. Burdisso (Vib. and Acoust. Labs., Dept. of Mech. Eng., Virginia Tech, Blacksburg, VA 24061-0238), and Mark H. Dunn (Old Dominion Univ., Norfolk, VA 23529)

An advanced model of active control of fan noise for turbofan engines is being developed using the ducted fan noise prediction code TBIEM3D [M. H. Dunn, NASA/CR-97-206232, Sept. 1997]. An engine fan surrounded by a duct of finite length and cylindrical profile, translating in its axial direction with a uniform speed, is considered. A collection of spinning line sources located inside the duct are used to simulate the fan noise. Control sources modeled by point monopoles are placed along the duct inner wall to generate the secondary field that destructively interferes with the fan noise. A feedforward active noise control algorithm is simulated.

Test cases were performed to demonstrate the feasibility of the model to perform active noise control studies. First- and fourth-order circumferential modes generated at a blade passage frequency of 1000 Hz were generated and targeted for control using far-field and inlet error sensors combined with a rigid or lined duct inner wall. Interference between inlet and outlet radiation, as well as the reflection from the duct openings and near-field effects were included. This model was found to be accurate, fast, and versatile. [Work supported by NASA Langley Research Center.]

2:15

**4pSA4. Active control design for acoustic radiation using mixed-norm optimization.** David E. Cox (NASA Langley Res. Ctr., Hampton, VA 23681, d.e.cox@larc.nasa.gov), James K. Henry, and Robert L. Clark (Duke Univ., Durham, NC 27708)

The interpretation of system norms is important in the design of optimal control laws. The infinity-norm allows for stability analysis even when the design model contains errors or uncertainties.  $H_\infty$  robust control design makes use of this property. In many physical situations the two-norm can be related to system energy and is a more meaningful measure of performance. This is the basis of control designs such as LQR/LQG. Traditionally, optimal control laws are designed with respect to one of these norms. New methods in solving linear matrix inequalities (LMIs), however, make it possible to directly solve optimization problems whose cost functions involve a mixture of norms. In this work linear matrix inequalities are used to design controllers which suppress acoustic radiation from a driven plate. Specifically, a rectangular aluminum plate is instrumented with four piezoelectric sensor/actuators which provide both sensing and actuation. A laser Doppler velocimeter is used to measure velocity of the plate over a grid of points. Radiation filters predict far field acoustic power from the velocity measurements and are used for the design of optimal control laws. Both experimental and simulated results are presented which show the benefit of mixed norm control design made possible using LMIs.

**4pSA5. Active control of a mechanical interface by use of power-flow control laws.** Brian H. Houston, Larry A. Kraus,<sup>a)</sup> Peter C. Herdic,<sup>a)</sup> Douglas M. Photiadis (Naval Res. Lab., Code 7136, 4555 Overlook Ave., SW, Washington, DC 20375), and Robert D. Corsaro (Naval Res. Lab., Code 7135)

The active control of dynamic mechanical impedance is of general interest due to a variety of potential defense and civilian applications. These include control systems to minimize aircraft and aerospace vehicle interior acoustic levels. Control of impedance or mechanical power flow at a boundary is one of the most challenging in active control due to the requirement for the collocation of sensors and actuators. In addition to the challenge of developing the devices, some of the technical issues include the selection of the appropriate physical control law, the degree of interconnectivity (local versus global control), device linearity, component and processor delays, system identification, and performance versus robustness tradeoffs. Recently, single node experiments were carried out at NRL's Laboratory for Structural Acoustics with an integrated passive/active device that minimizes mechanical power flow. The results of these experiments will be discussed with a focus on the application of different control approaches and the physics involved. <sup>a)</sup>Also with SFA, Inc., Lanover, MD20785.

**4pSA6. Active control of mechanical impedance for characterizing actuator performance.** Jean-Marc F. Bras, Marty E. Johnson, and Chris R. Fuller (Vib. and Acoust. Labs., Virginia Tech., VA 24061-0238)

The performance of an actuator is often difficult to predict under realistic loads and it is therefore important to characterize actuators using a more sophisticated range of tests than the standard blocked force and free displacement tests. This presentation describes the development of a test apparatus used to conduct such a range of tests. It principally focuses on a method of altering the mechanical impedance seen by the test actuator to be characterized, using an active control system with a control actuator. The mechanical impedance in the test rig can be varied over a range of mechanical conditions experienced in real applications. The test actuator and the control actuator are placed in series and clamped in a rigid structure that has high impedance. The force output ( $F$ ) and the velocity output ( $V$ ) of the test actuator can be monitored using a force gauge and an accelerometer. While driving the test actuator with a test signal, an adaptive controller, using the filtered-X LMS algorithm, drives the control actuator such that the measured impedance ( $Z=F/V$ ) matches the desired load impedance. By including a second control actuator, impedance on both sides of the test actuator can be varied simultaneously. [Work supported by MSI/DARPA.]

**4pSA7. An active-passive distributed absorber for vibration and sound radiation control.** Pierre E. Cambou (Dept. of Mech. Eng., Virginia Tech., Randolph Hall, Blacksburg, VA 24061, pcambou@vt.edu) and Chris R. Fuller (Virginia Tech., Blacksburg, VA 24061)

A new device has been developed to reduce structural vibrations and their associated radiated sound. The work is a contribution to the research of efficient and low cost devices that implement simultaneously the advantages of active and passive noise control techniques. A theoretical model was developed to investigate the potential of a new "active-passive distributed vibration absorber." From this knowledge, prototypes have been designed and their potential experimentally investigated. The device subsequently developed can be described as a skin that can be mechanically and electrically tuned to reduce unwanted vibration and/or sound in a distributed manner. Preliminary results show that the new distributed treatment out-performs state-of-the-art point active-passive absorbers. The compact design and its efficiency make it suitable for many applications especially in the transportation industry. [Work supported by the ONR.]

**4pSA8. Active control of transmission of turbulent boundary layer noise using smart foam elements.** Jason R. Griffin, Marty E. Johnson, and Chris R. Fuller (Vib. and Acoust. Lab., Virginia Tech., VA 24061-0238)

Results concerning the active control of transmission of turbulent boundary layer noise using smart foam elements will be presented. Smart foam consists of a cylindrical shaped PVDF film embedded within partially reticulated polyurethane acoustic foam. A smart foam element is an active-passive control device utilizing the passive absorption characteristics of the foam (effective at high frequencies) and the electrically driven PVDF film as the active element (effective at lower frequencies). This lightweight, compact arrangement lends itself well to the control of aircraft cabin noise resulting from an exterior turbulent boundary layer. Six smart foam elements (each 2 in. thick  $\times$  4 in.  $\times$  5 in.) are used to control the sound transmission through a 0.05 in. thick  $\times$  10 in.  $\times$  20 in. aluminum plate mounted in a wind tunnel. The sound transmission is monitored by measuring the pressure inside an externally mounted anechoic box that encloses the plate. Various control strategies are tested and results compared.

**4pSA9. Active control of structural intensity in an infinite elastic plate.** Sabih I. Hayek, Jungyun Won (Active Vib. Control Lab., Dept. of Eng. Sci. and Mech., Penn State Univ., University Park, PA 16802), and Gimhan Kim<sup>a)</sup> (Kumoh Natl. Univ. of Technol., Kumi, Kyungbuk, 730-701, Korea)

In this study, the active control of active vibrational structural intensity (SI) in an infinite elastic plate is discussed. The plate is excited by mechanical noise sources, which generate a vector active SI field in the plate. A set of control actuators made up of point forces and point moments are located judiciously on the plate. The vibrational active SI-vector components are quadratic functions of the mechanical noise sources and control actuators magnitudes and phases. Thus the magnitude-squared active vector-SI at a sensor point is an expression with up to fourth power in the sources and actuators magnitudes and phases. An algorithm is developed to minimize the active SI using steepest descent on the gradient of the magnitude-squared total SI to obtain optimum values for magnitudes and phases of the control point actuators. Test cases are discussed to exhibit the influence of excitation structural wavelength, relative location of the control actuators to the mechanical noise source region, the orientation of the point moments, and the optimum combination of point forces and moments to minimize the total intensity in the near and far field. An attempt is made to explore actuators configurations that result in efficient local or global control. <sup>a)</sup>Currently Visiting Scholar at Penn State.

**4pSA10. A feedback approach to adapting solid state tuned vibration absorbers for control of sound radiation and structural vibration.** R. I. Wright, F. Charette, M. Johnson, and C. R. Fuller (Vib. and Acoust. Lab., Virginia Tech., VA 24061-0238)

To further explore the complementary nature of active-passive systems, a multi-channel feedback approach to adapting tuned vibration absorbers (ATVAs) has been developed. The vibration absorbers consist of lumped mass-spring systems whose resonance behavior can be varied electronically through a feedback loop. The feedback controller consists of a two coefficient FIR filter, implemented on a DSP, where the input is the acceleration of the ATVA mass and the output is a force acting in parallel with the stiffness of the absorber. By separating the feedback signal into the principle real and imaginary components, the effective natural frequency and damping of the ATVA can be altered independently. This approach gives control of the resonance frequency while also allowing simultaneous removal of damping from the ATVA, thus increasing effectiveness. A multiple-channel genetic algorithm is used to adapt the resonant characteristics of each absorber (i.e., detune them) to minimize the structural sound radiated to the far field. Theoretical development of the local feedback tuning laws as well as the global strategy for minimizing

the radiated sound will be addressed. Experimental results comparing the globally detuned configuration versus all ATVAs tuned to resonate at the disturbance frequency will be presented for a simply supported plate. By utilizing the passive advantages of this compact system, very good attenuation of structural born sound is seen while requiring only a fraction of the power of a fully active system.

4:00

**4pSA11. Reduction of total powerflow in a fluid filled pipe using an active/passive approach.** Satish C. Kartha, Marty E. Johnson, and Chris R. Fuller (Vib. and Acoust. Lab., Virginia Tech., VA 24061-0238)

This presentation describes the implementation of active/passive approaches for the reduction of total acoustic power flow in fluid filled pipes. Active/passive systems are essentially passive devices whose properties can be altered using a control system. For example, a Helmholtz resonator has been fitted with a variable neck aperture allowing the resonant frequency of the device to be altered. Other passive devices such as a delay line and a quarter wavelength tube have been used as active/passive devices. These active/passive devices have been designed to gain maximum performance (trade-off between flexibility of application and control authority). Various sensing approaches using PVDF (polyvinylidene fluoride) cables/films and an array of microphones have been tested and are compared. The various active/passive approaches developed have been compared to totally active approaches in terms of flexibility and control authority. [Work supported by University of Karlskrona/Ronneby.]

4:15

**4pSA12. Improved performance of output active structural acoustic control using collocated strain-based transducers.** Jeffrey S. Viperman (Dept. of Mech. Eng., Univ. of Maine, 5711 Boardman Hall, Orono, ME 04469-5711, jsv@umeme.maine.edu) and Robert L. Clark, Jr. (Duke Univ., Durham, NC 27708)

A simple method of greatly improving performance of direct rate feedback (DRFB) control of piezostructures is presented. Piezostructures are not generally amenable to application of DRFB control since the compliance of the piezostructure generally increases with increasing frequency due to the structural differentiation performed by the transducers. Some improvement can be gained through selecting the width and position of the piezoceramic patch such that certain groups of modes will cancel from the response. However, a more drastic improvement is gained by increasing the size of the rectangular aperture to cover at least 50% of the structural dimension(s). It is shown that the rectangular aperture of the piezoceramic acts as a low-pass filter with corner frequency inversely proportional to the transducer aperture size. Using a large aperture results in better coupling into lower-frequency modes targeted by the control system as well as decreased control effort. Analytical open and closed loop results for an acoustically radiating simply supported plate piezostructure are presented.

4:30

**4pSA13. Electroelastic nonlinearities in piezoelectric transducers and their effect on vibratory energy transmission, transduction, and dissipation in structural systems.** Thomas J. Royston and Soon-Hong Lee (Univ. of Illinois at Chicago, MC 251, 842 W. Taylor St., Chicago, IL 60607, troyston@uic.edu)

Though all structural dynamic systems are inherently nonlinear, the majority of analyses are typically based on the assumption of linearity. While vibration of passive systems is often reasonably described by linear system theory, particularly in the audio and ultrasonic frequency ranges, the vibrations of systems employing integrated actuators fabricated from smart materials often are not, whether they be based on piezoelectric, electrostrictive, or magnetostrictive technologies, etc. Nonlinearities can affect the system performance through a loss of actuation authority, stability, and/or system functionality. Recognizing this, some researchers have included nonlinearities in their formulations for the constitutive equations of the smart material. Typical nonlinear operators are either in the form of higher-order polynomial expressions or various hysteresis operators involving the electrical (magnetic), elastic and/or electroelastic (magnetoelastic) relations. An important fundamental issue is how the different types of nonlinearities affect the smart material in its role as source, conduit, transformer and/or receiver/dissipator of vibroacoustic energy in a smart structure. This is the principle focus of this study in which a generic active vibration isolation application is considered. The effect of different types of nonlinearities with respect to how vibratory energy flows throughout the smart structural system is investigated. [Work supported by NSF.]

4:45

**4pSA14. Noise control of structures with dipole acoustic cell devices, an analytical study.** Zachary T. Kitts and Ricardo A. Burdissio (Mech. Eng. Dept., Virginia Tech, 131 NEB, Blacksburg, VA 24060-0238, rburdiss@vt.edu)

A new passive surface treatment has been developed to attenuate low frequency radiated noise from large structural surfaces. The acoustic treatment consists of an array of weak radiating cells that covers the structure's surface. Each cell is a mechanical device that has two surfaces. The cells are driven by the motion of the structure and designed such that the two surfaces operate nearly out-of-phase, effectively creating dipole acoustic sources. Preliminary experimental results for nine cells applied to a simply supported plate driven by a white noise input show a 10 dB of sound power reduction over a frequency range of 100–1600 Hz. An analytical model is used to gain physical insight on noise control properties of the cells-plate system. Interaction effects of the system such as mass loading, damping, and dynamic coupling of the cells and plate are also investigated. The model is also utilized in design optimization studies of the weak radiating cells for beam and plate structures subjected to broadband inputs.

## Session 4pSC

## Speech Communication: Speech Pathologies and Auditory/Visual Feedback for Speech Production (Poster Session)

Stephen A. Zahorian, Chair

*Department of Electrical and Computer Engineering, Old Dominion University, Norfolk, Virginia 23529*

### Contributed Papers

All posters will be on display from 1:30 p.m. to 4:00 p.m. To allow contributors an opportunity to see other posters, contributors of odd-numbered papers will be at their posters from 1:30 p.m. to 2:45 p.m. and contributors of even-numbered papers will be at their posters from 2:45 p.m. to 4:00 p.m. To allow for extended viewing time, posters will be on display starting at 11:00 a.m.

**4pSC1. Adaptation to altered feedback in speech.** Jeffery A. Jones, K. G. Munhall (Dept. of Psych., Queen's Univ., Kingston, ON K7L 3N6, Canada, jones@psyc.queensu.ca), and E. Vatikiotis-Bateson (ATR Human Information Processing Res. Labs., Kyoto, Japan)

This study focuses on how the control of fundamental frequency ( $F_0$ ) of the voice is influenced by modulations of auditory feedback. A methodology analogous to one used in visual perturbation studies of limb movements was used. In these studies, optical feedback is distorted and subjects adapt to the transformed conditions by relearning the spatial coordinates used in visuomotor control. It was investigated whether  $F_0$  control would exhibit an analogous adaptation response to altered auditory feedback conditions. Subjects were exposed to pitch-shifted auditory feedback through headphones while producing (a) sustained vowels and (b) sentence material. The  $F_0$  feedback was increased in 2 cent steps that were not noticed by the talkers. Both aural- and bone-conducted masking noise were used to minimize feedback from the true  $F_0$ . During the transformed feedback condition, subjects decreased their pitch in response to the increasing pitch feedback. However, preliminary analyses did not reveal evidence of adaptation to the auditory transformations. This was examined by unexpectedly introducing normal feedback trials to test for "aftereffects." Results will be discussed in terms of sensorimotor learning and the role of internal models of sensory feedback in speech motor control. [Work supported by NIH NIDCD Grant No. DC-00594 and NSERC.]

**4pSC2. Phonological disorders and spatio-temporal precision of stop consonant gestures.** Jan Edwards, Marios Fourakis (Dept. of Speech and Hearing Sci., Ohio State Univ., Columbus, OH 43210, edwards.212@osu.edu), Mary Beckman, Pauline Welby, and Ying Xu (Ohio State Univ., Columbus, OH 43210)

In previous work, we have explored methods for assessing the production of the velar-alveolar contrast in word-initial stops [Edwards *et al.*, JSHR (in press)]. We found that children with phonological disorders had steeper second formant slopes than their age peers for lingual consonant-vowel transitions, suggesting more ballistic movement patterns for the children with phonological disorders. They also appeared to be initiating the vocalic movement later in the consonant-vowel sequence. Both patterns could contribute to the appearance of less precise spatial targets for lingual closures. These patterns suggested that at least part of the knowledge deficit that constitutes "phonological disorder" is a poor cognitive representation of the motor control structures necessary for producing lingual gestures and coordinating these gestures with each other. In this paper, we continue to examine spatiotemporal precision of stop consonant gestures in preschool children with phonological disorders, age peers, and adults. We have measured both  $F_2$  and  $F_3$  as well as point velocity over time. Preliminary analyses suggest that the less precise articulations of

children with phonological disorders will be observed in measures such as higher and more variably timed  $F_2$  peak velocities. [Work supported by NIDCD Grant No. DC02932.]

**4pSC3. A study of vowel production in persons with dysphagia.** Joanne L. DiMaggio and Fredericka Bell-Berti (Dept. of Speech, Commun. Sci., and Disord., St. John's Univ., 8000 Utopia Pkwy., Jamaica, NY 11439)

Dysphagia refers to disorders of any stage(s) of swallowing (oral preparatory, oral, pharyngeal, and esophageal). Dysfunctions in any of the first three stages result from problems in the use of the oral and/or pharyngeal musculature, which is also the musculature of speech articulation. Thus one would expect a correlation between dysphagia and dysarthria. However, clinical observation have led to the impression that it is possible to have dysphagia without obvious dysarthria. Thus in this study, formant frequency measures of the vowels of three groups of subjects: persons with dysphagia and mild dysarthria; persons with dysphagia and moderate-to-severe dysarthria; and age matched normal subjects are examined. The speech sample contains the hVd items used by G. E. Peterson and H. L. Barney [J. Acoust. Soc. Am. **24**, 175-184 (1952)], as well as additional CVCs in which the initial and final consonants are varied, to examine their effects on vowel productions by these subjects. [Work supported by St. John's University.]

**4pSC4. An interactive user interface for selecting optimal listening conditions.** Christine M. Rankovic (Dept. of Speech-Lang. Pathol. and Audiol., Northeastern Univ., 360 Huntington Ave., Boston, MA 02115)

An audio-visual interface was developed to allow listeners to hear a range of different conditions and convey their preferences. Feasibility for selecting optimal listening conditions was assessed for eight normal-hearing listeners. The visual display was a 4-by-4 matrix with the  $x$  and  $y$  axes representing two different manipulations of the frequency-gain characteristic. For a speech-in-noise condition, the axes represented low-frequency gain and broadband gain. For a filtered-speech condition, the axes represented high-pass cutoff frequency and bandwidth. Subjects altered the amount of processing applied to the ongoing speech (or speech in noise) by moving a screen pointer from cell to cell. Selections were compared to percent-correct scores for lists constructed from the same speech items (nonsense syllables), and to articulation indices (AIs). It took approximately 2 min to select, and selected conditions typically had AIs within 0.10 of the highest AI in the matrix. A potential application is determining settings for nonlinear hearing aids. [Work supported by NIDCD.]



**4pSC5. An auditory-feedback-based model of speech production in the developing child.** Daniel E. Callan, Raymond D. Kent, Hourii K. Vorperian (Dept. of Communicative Disord., Univ. of Wisconsin, Waisman Ctr., 1500 Highland Ave., Rm. 437, Madison, WI 53706, decallan@students.wisc.edu), and Frank H. Guenther (Dept. of Cognit. and Neural Systems, Boston Univ., Boston, MA 02215)

The purpose of this project is to demonstrate that self-produced auditory feedback is sufficient to train a mapping between auditory target space and articulatory reference space under conditions in which the structures of speech production are undergoing considerable developmental restructuring. One challenge for competing theories that propose invariant constriction targets is that it is unclear what teaching signal could specify constriction location and degree so that a mapping between constriction target space and articulatory reference space can be learned. It is predicted that a model trained by auditory feedback will accomplish speech goals, in auditory target space, by continuously learning to use different articulatory configurations to adapt to the changing acoustical properties of the vocal tract during development. The Maeda articulatory synthesis part of the DIVA neural network model [Guenther *et al.*, Psych. Rev. (in press)] was modified to reflect the development of the vocal tract by using measurements taken from MR images of children. The model accurately produced English vowels during development using various auditory target spaces. Stable constriction patterns were maintained throughout development using differing articulatory configurations to accomplish the same speech goals demonstrating that auditory feedback is sufficient to accommodate speech production development. [Work supported by NIHCD.]

**4pSC6. The integration of discriminative and maximum likelihood distance measures for a vowel articulation training aid.** A. Matthew Zimmer and Stephen A. Zahorian (Dept. of Elec. and Computer Eng., Old Dominion Univ., Norfolk, VA 23529, azimm001@odu.edu)

Improvements to the vowel articulation training aid described in a previous paper [Zimmer, Zahorian, and Auberg, J. Acoust. Soc. Am. **101**, 3199(A) (1997)] have been made. The system uses a standard Windows 95/NT compatible sound card on a multimedia PC to provide continuous feedback about articulation for ten American English monophthong vowels in two modes: an  $F1/F2$  style "ellipse" display and a vowel bargraph display. Neural network discriminative classifiers are used to produce the display outputs based on 12 features. Though testing showed that the system provided useful output for most voiced speech sounds, the network would classify some out-of-category sounds (e.g., nonvowel sounds, ambient noise) as belonging to one of the ten vowel categories. Experimental tests indicate that the inclusion of a generalized Euclidean distance measure to compare the feature values of an utterance with the average feature values for the vowel category specified by the neural network output help to greatly reduce the number of out-of-category sounds improperly classified as "correct" responses. The paper will describe the processing in more detail and summarize experimental results from vowel classification tests. [Funded by NSF, Grant No. NSF-BES-9411607.]

**4pSC7. The effect of perceptual training on the identification of a non-native phoneme contrast and its relationship to the MMN auditory evoked potential.** Janet W. Stack and Susan D. Dalebout (Commun. Disord. Prog., Univ. of Virginia, Charlottesville, VA 22903)

The mismatch negativity (MMN) auditory evoked potential reflects the detection of minimal stimulus differences at a pre-attentive level. It has been reported that the MMN reflects acoustic, rather than phonetic processing of speech stimuli. The purpose of the present study was to examine the effects of perceptual training on (1) the behavioral ability of native speakers of American English to label a pair of Hindi stop consonants, and (2) the presence or absence of the MMN. Hindi voiceless unaspirated stop consonants contrasted by dental and retroflexplace of articulation ([t̪] versus [t̪ʳ]) were used. Prior to training, the MMN was present in 4 of 12 listeners and labeling ability was poor. Ten perceptual training sessions resulted in significant improvement in labeling ability. There was some

generalization to a different voicing contrast (voiced unaspirated Hindi stop consonants [d̪] versus [d̪ʳ]). There was also a significant increase in the number of listeners demonstrating an MMN in response to both contrasts after training. The group of listeners who had MMN responses after training also had significantly higher change scores from pre-test to post-test on the behavioral task. These results suggest that the MMN may have utility as an objective indicator of learning.

**4pSC8. Spectral properties of fricatives in Parkinson's Disease.** Paul McRae (Dept. of Communicative Disord., San Diego State Univ., 5500 Campanile Dr., San Diego, CA 92182-1518) and Kris Tjaden (SUNY, 113 Park Hall, Buffalo, NY 14260)

Consonant imprecision is one of the most prominent speech characteristics of Parkinson's Disease (PD). Few studies have characterized the nature of the imprecision for sound classes other than stop consonants, however. Research further suggests that consonant imprecision may improve with slowed speaking rate, perhaps as a result of increased articulatory displacements [M. P. Caligiuri, Brain Lang. **35**, 493–502 (1989)]. In the current study, nine speakers with PD and nine age and gender matched neurologically healthy speakers read the Farm Passage at habitual and slow reading rates. Spectral moments were used to describe /s/ and /ʃ/ fricatives occurring in the word initial position of the reading passage. For both the habitual and slow rate conditions, moment coefficients for speakers with PD were compared to moment coefficients for the healthy speakers to characterize between group differences in fricative productions. Within each speaker group, moment coefficients for the habitual rate condition were compared to moment coefficients for the slow rate condition to evaluate the effects of slowed speaking rate on fricative productions.

**4pSC9. Visual influences on the perception of alveolar/velar place discrimination.** Michelle Hampson, Frank Guenther, and Michael Cohen (Dept. of Cognit. and Neural Systems, Boston Univ., Boston, MA 02215)

Using ten acoustic stimuli ranging along a /ga/–/da/ continuum, visual influences on the psychophysical boundary between the auditory percepts of /ga/ and /da/ were investigated. A significant shift in the perceptual boundary was found depending on whether syllables were dubbed onto a video of a speaker uttering /da/, or whether they were dubbed onto a video of the same speaker uttering /ga/. The tongue of the speaker was not visible in either video clip, so only subtle cues were available to distinguish place of articulation in the two conditions. The shift in auditory perception was in a direction consistent with the visual information, and indicates that even the subtle visual cues available to discriminate velar stop consonants from alveolar stop consonants can play a role in speech perception. The possibility that other (nonarticulatory) visual cues could be conditioned to play a similar role in speech perception is raised.

**4pSC10. Perception of synthetic vowels by cochlear implant recipients.** John W. Hawks (School of Speech Path. & Audiol., Kent State Univ., Kent, OH 44242) and Marios S. Fourakis (The Ohio State Univ., 1070 Carmack Rd., Columbus, OH 43210)

Adult recipients of cochlear implants (Nucleus and Clarion) provided identifications and confidence ratings for two sets of 465 vowel-like tokens which were synthesized with two fundamental frequency ( $F_0$ ) contours representative of a typical male voice and female voice. Formant combinations used for the stimulus sets sampled a large range encompassing all nonretroflex vowels of American English. Subjects assigned each token to one of ten American English vowel qualities or to a category indicating it was not one of the ten, and rated their confidence of identification on a five-point scale. Various perceptual maps were constructed from these responses based on number of agreements per token, most often used ID category per token, and average ratings. These maps will be

compared with similar maps derived from normal hearing subjects. Comparison and discussion will address general differences in perceptual vowel spaces and rating patterns between the subject groups, as well as specific differences related to the two different  $F_0$  contours. Within the implanted subject group, the effects of implant processor type and electrode mapping differences on perception will be explored.

**4pSC11. Voice  $F_0$  responds to auditory feedback pitch shifts during both steady and dynamic vocal behaviors.** Theresa Burnett and Charles Larson (Dept. of Commun. Sci. and Disord., Northwestern Univ., 2299 North Campus Dr., Evanston, IL 60202)

When trying to hold steady voice fundamental frequency ( $F_0$ ), subjects vocally oppose experimentally introduced small upward or downward shifts in auditory feedback pitch. These voice  $F_0$  responses have a latency of 100–150 ms, and occur despite efforts by subjects to ignore the feedback pitch shifts. The consistent and involuntary nature of these responses provides evidence of closed-loop fine control of voice  $F_0$ . Studies of oculomotor and limb movement systems have revealed different control strategies for static versus dynamic behaviors. It is not clear whether the fine control voice  $F_0$  likewise differs. For this reason, a study was undertaken to determine if the voice  $F_0$  response to pitch-shifted auditory feedback was affected by task dynamics. Specifically, a comparison was made between responses to pitch shifts introduced during voice  $F_0$  hold and ramp tasks. Results indicate a similar role of the voice  $F_0$  response across both vocal behaviors, namely, to facilitate production of an intended target, be it static or dynamic.

**4pSC12. Auditory lexical decision in young and older adults: Effects of lexicality and similarity neighborhood structure on spoken word recognition.** Mara B. Goodman and Paul A. Luce (Lang. Percept. Lab., Dept. of Psych. and Ctr. for Cognit. Sci., Univ. at Buffalo, Buffalo, NY 14260)

Younger and older (70+ yrs) adults made verbal lexicality judgments for words and nonwords presented in the clear. Stimuli included mono- and bi-syllabic items with high and low frequency-weighted similarity neighborhoods. Items were presented auditorily and subjects were asked to

respond yes for word and no for nonword as quickly and accurately as possible. Subjects response times were measured from the onset of the auditory stimulus to the onset of the verbal response. Young and older subjects showed markedly different effects of lexicality on accuracy and reaction time. Moreover, differential age effects for similarity neighborhood structure on processing time were observed (independent of the frequency of the target word). Implications of present results for recognition strategies of older adults will be discussed. [This research was supported (in part) by research Grant No. 1 R01 DC 0265801-A1 from the National Institute on Deafness and Other Communication Disorders, National Institutes of Health.]

**4pSC13. Modified LPC resynthesis for controlling speech stimulus discriminability.** Athanassios Protopapas (Scientific Learning Corp., 1995 University Ave., Ste. 400, Berkeley, CA 94704, protopap@scilearn.com)

Phonetically ambiguous speech stimuli are needed in many experimental situations, and various editing and splicing methods have been devised to construct them, sometimes with results of questionable naturalness. A resynthesis procedure based on Linear Predictive Coding (LPC) is presented here whereby interpolation of vocal tract equivalent model parameters (log area ratio coefficients) ensures vocal tract compatible, perceptually ambiguous results. An important extension of this method is also presented: Extrapolation along the same line, defined by the points corresponding to a minimal pair, leads to “exaggerated” speech stimuli that differ from each other more than the original (natural) recordings and, acoustically, in much the same way; e.g., critical formant transition differences are automatically enhanced by increased frequency range and peak amplitude. Such stimuli are potentially very useful in perceptual training of language-learning impaired children and of second-language learners who cannot discriminate certain non-native contrasts. Examples of ambiguous and exaggerated stimuli are shown along with perceptual (categorization and discrimination) performance of English and Japanese speakers for stimuli synthesized along (and beyond) an /r/-/l/ continuum. Preliminary training results indicate that such exaggerated stimuli are useful in making second language contrasts distinctive.

**Meeting of Accredited Standards Committee (ASC) S1 on Acoustics**

J. P. Seiler, Chair S1

*U. S. Department of Labor, Cochran Mill Road, P.O. Box 18233, Building 038, Pittsburgh, Pennsylvania 15236*

G. S. K. Wong, Vice Chair S1

*Institute for National Measurement Standards, National Research Council, Ottawa, Ontario K1A 0R6, Canada*

P. D. Schomer, Chair, U. S. Technical Advisory Group (TAG) for ISO/TC 43, Acoustics  
*U.S. CERL, P.O. Box 9005, Champaign, Illinois 61826-9005*

H. E. von Gierke, Vice Chair, U. S. Technical Advisory Group (TAG) for ISO/TC 43, Acoustics  
*1325 Meadow Lane, Yellow Springs, Ohio 45387*

V. Nedzelnitsky, U. S. Technical Advisor (TA) for IEC/TC 29, Electroacoustics  
*National Institute of Standards and Technology (NIST), Building 233, Room A149, Gaithersburg, Maryland 20899*

**Accredited Standards Committee S1 on Acoustics.** Working group chairs will report on their preparation of standards on methods of measurement and testing, and terminology, in physical acoustics, electroacoustics, sonics, ultrasonics, and underwater sound. Work in progress includes measurement of noise sources, noise dosimeters, integrating sound-level meters, and revision and extension of sound level meter specifications. Open discussion of committee reports is encouraged.

**Scope of S1:** Standards, specifications, methods of measurement and test and terminology in the field of physical acoustics including architectural acoustics, electroacoustics, sonics and ultrasonics, and underwater sound, but excluding those aspects which pertain to biological safety, tolerance and comfort.

**Meeting of Accredited Standards Committee (ASC) S3 on Bioacoustics**

L. S. Finegold, Chair S3

*USAF Armstrong Lab., Noise Effects Branch AL/OEBN, 2610 Seventh Street, Wright Patterson Air Force Base,  
Ohio 43433-7901*

R. F. Burkard, Vice Chair S3

*Hearing Research Laboratory, State University of New York at Buffalo, 215 Parker Hall, Buffalo, New York 14214*

P. D. Schomer, Chair, U. S. Technical Advisory Group (TAG) for ISO/TC 43, Acoustics  
*U.S. CERL, P.O. Box 9005, Champaign, Illinois 61826-9005*

D. Reynolds, Chair, U. S. Technical Advisory Group (TAG) for ISO/TC 108/SC4, Human Exposure to Mechanical Vibration  
and Shock  
*3939 Briar Crest Court, Las Vegas, Nevada 89120*

H. E. von Gierke, Vice Chair, U. S. Technical Advisory Group (TAG) for ISO/TC 43, Acoustics and ISO/TC 108/SC4,  
Human Exposure to Mechanical Vibration and Shock  
*1325 Meadow Lane, Yellow Springs, Ohio 45387*

**Accredited Standards Committee S3 on Bioacoustics.** The current status of standards under preparation will be discussed. In addition to those topics of interest, including hearing conservation, noise, dosimeters, hearing aids, etc., consideration will be given to new standards which might be needed over the next few years. Open discussion of committee reports is encouraged.

**Scope of S3:** Standards, specifications, methods of measurement and test, and terminology in the fields of mechanical shock and physiological acoustics, including aspects of general acoustics, shock, and vibration which pertain to biological safety, tolerance, and comfort.

**Session 5aAA****Architectural Acoustics: Characteristics of Scattering**

Peter D'Antonio, Chair

*RPG Diffusor Systems, Inc., 651 Commerce Drive, #C, Upper Marlboro, Maryland 20772-8782***Chair's Introduction—9:00*****Invited Papers*****9:05****5aAA1. A review of diffusor design over the past two decades.** Peter D'Antonio (RPG Diffusor Systems, Inc., Upper Marlboro, MD 20774) and Trevor J. Cox (Univ. of Salford, Salford M5 4WT, UK)

In the later 1970s Manfred Schroeder suggested using number theory sequences to approximate uniform angular scattering. Today tens of thousands of these diffusors are in use in almost every type of architectural acoustic application. Schroeder's work has been a catalyst, enabling the design of numerous new diffusor types. D'Antonio employed additive modulation, in the form of a self-similar fractal diffusor to minimize the lobing associated with periodic arraying and to extend the frequency bandwidth. Angus suggested multiplicative spread spectrum modulation and orthogonal modulation to minimize lobing. Angus has suggested binary reflection-absorption amplitude gratings, which D'Antonio has used for 2-D planar binary amplitude diffusors. Cox used numerical optimization and boundary element prediction techniques to optimize the performance of number-theory diffusors, stepped diffusors, curved and fractal shapes. Cox and D'Antonio are developing optimized aperiodic shapes to form aesthetically pleasing diffusing acoustical sculpture. Shape optimization has significantly expanded the choice of available diffusors. Today, diffusors can be designed for a specific appearance, specified scattering coverage, given source and receiver positions and a desired frequency bandwidth. All of these surfaces developed over the past two decades comprise an expanded palette of scattering surfaces. These complement contemporary architecture in the way that statuary and relief ornamentation blended with classical architecture.

**9:30****5aAA2. Practical prediction techniques for sound diffusors.** Trevor J. Cox (Dept. of Acoust. and Audio Eng., Univ. of Salford, Salford M5 4WT, UK, t.j.cox@acoustics.salford.ac.uk)

In recent decades accurate methods for predicting the diffraction and scattering from diffusing surfaces have been developed. This paper will review the methods that are available based on the Helmholtz–Kirchhoff integral equation. The application of various accurate boundary element methods to a variety of diffusing surfaces such as Schroeder diffusors and simple reflectors will be presented. In addition, a review of more approximate, but faster, techniques will be given. Many modern diffusors, such as Schroeder diffusors and some optimized surfaces, rely on these approximate prediction methods in their design. The implications of using approximate methods to diffuser design and application will be discussed.

**9:55****5aAA3. Experimental measurement and characterization of scattering surfaces.** Peter D'Antonio (RPG Diffusor Systems, Inc., Upper Marlboro, MD 20774), Trevor J. Cox, Tristan Hargreaves, and Y. W. Lam (Univ. of Salford, Salford M5 4WT, UK)

As the centennial of Sabine's research, which founded modern architectural acoustics, is celebrated, the need for an experimental measurement standard to characterize scattering surfaces is becoming acute. These data are needed to characterize and rank potential diffusing surfaces and to improve the accuracy of geometrical room modeling programs. Two approaches are currently being studied. One measures the 2-D or 3-D directional distribution of scattered sound for a given angle of incidence and frequency. This is used to determine the diffusion parameter, which characterizes the uniformity of the angular response. The other determines the ratio of nonspecular scattered energy to total scattered energy, for directional or randomly incident sound. This yields the scattering coefficient, which contains no diffusivity information, but can be used in geometrical modeling programs. A goal of this research is to determine both diffusivity and scattered energy ratios from a single method, which is also theoretically predictable.

**10:20****5aAA4. Diffuser assessment using surface spherical harmonics.** James A. S. Angus (Dept. of Electron., Univ. of York, York, England)

The problem of deriving a diffusion figure of merit may be alleviated by forming a continuous, functional representation of its polar pattern, expressing the polar patterns mathematically, as a continuous function of direction. This paper develops a form of continuous, orthogonal representation by expressing a diffusors polar pattern as a weighted sum of surface spherical harmonics (a hierarchical set of basis functions which are orthogonal upon the surface of a sphere). The surface spherical harmonic weights can be calculated from a limited set of experimental measurements by means of a discrete Fourier analysis. The resulting spherical harmonic representation is continuous, yielding a modeled polar pattern for any arbitrary direction. It is also hierarchical, in that the more harmonics that are included the greater the accuracy of the model, and has a meaningful spatial structure, with particular surface

spherical harmonic weights expressing particular patterns of directional variation in the polar pattern. The paper first explains surface spherical harmonics and a means of efficiently deriving them from measured or calculated data. The implication and applications to diffuser assessment are then discussed and finally some results of the analysis applied to diffuser assessment are presented.

10:45

**5aAA5. Diffusion coefficients.** Tristan J. Hargreaves, Trevor J. Cox, Y. W. Lam (Dept. of Acoust. and Audio Eng., Univ. of Salford, Salford M5 4WT, UK, t.j.cox@acoustics.salford.ac.uk), and Peter D'Antonio (RPG Diffusor Systems, Inc., Upper Marlboro, MD 20772)

For nearly a century, the absorption coefficient has been used as a measure for the amount of energy lost when sound reflects from a surface. There is now a need for a diffusion coefficient which measures the angular distribution of the reflected energy. Diffusion coefficients enable the worth of diffusing surfaces to be evaluated and in the future could help improve the accuracy of geometric room acoustic modeling. A current investigation is looking at forming a diffusion coefficient that is clearly defined, has physical rigor, is usable in a variety of real life applications, and is easy to measure. The problems associated with finding a single parameter to meet all the above criteria will be discussed. A variety of measures for monitoring the diffusion from un baffled surfaces will be presented, as well as possible solutions for baffled and large surfaces.

### Contributed Paper

11:10

**5aAA6. An analytical decomposition of the Biot–Tolstoy edge diffraction model.** U. Peter Svensson, Roger Andersson (Dept. of Appl. Acoust., Chalmers Univ. of Technol., S-41296 Gothenburg, Sweden, peter@ta.chalmers.se), and John Vanderkooy (Univ. of Waterloo, Waterloo, ON N2L 3G1, Canada)

The sound field for a rigid, infinite wedge which is irradiated from a point source has an explicit impulse response solution which has been given by Biot and Tolstoy. This solution has been the basis for methods to calculate sound fields by summing up all specular reflections from finite surfaces and edge diffraction components from finite edge segments.

However, these methods have usually relied on assumptions about the solution for finite edges. In this paper an edge diffraction model is presented which uses directional edge sources and analytical expressions for the directivities are derived to give exactly the Biot–Tolstoy solution for an infinite wedge. Unlike other models, with this new model explicit expressions can be found for certain geometries, such as the on-axis scattering from a rigid circular disc, for which both the first-order and the second-order edge diffraction can be derived. Furthermore, this model can be used to incorporate low-order edge diffraction into room acoustics prediction programs, which should improve them significantly at low frequencies.

FRIDAY MORNING, 16 OCTOBER 1998

HAMPTON ROADS BALLROOM 8, 8:30 TO 11:00 A.M.

### Session 5aNS

#### Noise: Measurement Errors, Calibration Precision and Accuracy

Robert A. Putnam, Cochair

*Westinghouse GSD, MC 590, 4400 Alafaya Trail, Orlando, Florida 32826*

Felix Z. Sachs, Cochair

*U.S. Army, CHPPM, 5158 Blackhawk Road, Aberdeen Proving Ground, Maryland 21010-5422*

Chair's Introduction—8:30

### Invited Papers

8:35

**5aNS1. Improved precision in field measurements of sound from large ID fans.** Wayne E. Bradley (Stone and Webster Engineering Corp., 245 Summer St., Boston, MA 02210)

An electric utility was receiving complaints about noise from their power plant from residences nearly 2 miles away. An onsite and off-site noise survey confirmed the neighbors complaints, and indicated that the sound was coming from the plant ID fans via the stack. Most of the complaints occurred when the plant went to low load at night. A study was therefore undertaken to determine how the fan sound level varied with plant load. A simple, reliable, and inexpensive means was sought to make repeatable fan sound pressure level measurements without penetrating the stack. Both narrow-band and  $\frac{1}{3}$ -oct band measurements were taken from fixed and scanned microphone locations at the fans, in the stack annulus, and on the boiler roof during boiler ramp ups and ramp downs. A sampling methodology was developed with a high degree of precision allowing reliable measurements of ID fan blade pass frequency tone level versus plant load. Subsequent noise measurements evaluated modifications to the fan inlet, cutoff, blade tips, and fan speed with a relatively high degree of precision.

9:00

**5aNS2. Precision and accuracy estimation based on round robin field testing—A case history.** Felix Z. Sachs (U.S. Army Ctr. for Health Promotion and Preventive Medicine, 5158 Blackhawk Rd., Aberdeen Proving Ground, MD 21010-5422)

A standard method for field measurement of *in-situ* noise lacked precision and accuracy information. A relatively straightforward round robin test organizes to provide data brought to light several problems and considerations. The initial test objective was to select experienced participants, hand them the written standard measurement procedure and collate the results. Problems arose in noise source and background noise variation, procedure interpretation among participants, instrumentation usage, and in the procedure itself. After a retest the standard deviation among participants was 0.7 dB for A-weighted and 1.8–4.1 dB for individual octave bands. Considerations and lessons learned will be discussed including instrumentation (one set for all participants or separate sets), noise source monitoring for uniformity, reported statistical quantity, approaches for adjustments to variables held constant, data recording, and logistics. [The opinions or assertions contained herein are the views of the author and are not to be construed as official or as reflecting the views of the Department of the Army or the Department of Defense.]

9:25

**5aNS3. Perspectives on uncertainty, tolerance, and precision in outdoor sound measurements.** Robert Putnam (Westinghouse MC590, 4400 Alafaya Trail, Orlando, FL 32826)

Outdoor acoustical surveys typically involve greater variations in sound levels than indoor or laboratory measurements, whether the object is the determination of ambient statistical information, or the characterization of outdoor noise sources, such as for regulatory compliance purposes. Historical usage of each of the terms uncertainty, tolerance, and precision has been inconsistent and often vague, which leads to misunderstanding among all parties concerned with the definition of sound levels. The value we have come to refer to as uncertainty in outdoor sound measurements usually includes tolerance and precision. The field of acoustics is making progress in standardizing the definitions and uses of these, often misused, terms. This paper will discuss the perspectives of ISO, ANSI, ASME, and ASTM toward these terms, especially in light of recent standardization efforts. The use of the term tolerance, it will be recommended, should properly be a narrow one, as it is presently given in ASME Performance Test Codes. This paper will summarize concise definitions and recommendations for standard usage, together with classification of the constituent elements of each term, in order to promote consistency within the acoustical community, thereby helping to insure improved clarity on the subject among all concerned parties.

9:50–10:05 Break

### Contributed Papers

10:05

**5aNS4. Uncertainty of acoustic calibrations performed at different ambient pressures.** Erling Frederiksen (Brüel & Kjaer, 2850 Naerum, Denmark, erlingfred@bk.dk)

The sensitivity of measurement microphones and the sound pressure produced by acoustic calibrators can be highly influenced by the ambient static pressure. Therefore such transducers should ideally be calibrated at a static pressure which is essentially equal to that existing at the site where the sound measurement is performed. However, in general, this is not possible and not necessary. Most often it is sufficient to know the typical pressure coefficients valid for the applied type of microphone and calibrator and to use those either for correction of the measurement results or just for estimation of the uncertainty. For few applications, like noise approvals of aircraft, it might be worth the costs and efforts to calibrate the transducers at the measurement conditions. This paper describes how the Brüel & Kjaer Reciprocity Calibration System Type 9699 which includes a pressure chamber was used for accurate and quite fast determination of pressure influence on laboratory and working standard microphones and on sound level calibrators. Calibration results and estimated uncertainties will be presented for some frequently applied types of microphone and calibrator.

10:20

**5aNS5. Reverberation room qualification using the m-sequence as multitone signals.** Wing T. Chu (Inst. for Res. in Construction, Natl. Res. Council Canada, Ottawa, ON K1A 0R6, Canada, wing.chu@nrc.ca)

There is a revised interest in replacing the time-consuming and burdensome methods in the current ANSI and ISO standards for qualifying reverberation rooms for sound power measurements of discrete frequency sources. With the advent of digital signal processing, a combination of a deterministic multitone test signal and an FFT routine could be used to perform a fairly quick qualification test. A more elegant method using the

m-sequence as the deterministic multitone signal has been tested in the IRC/NRC laboratory. This method has the advantage that it is relatively immune to external background noise so that the near field response of the test loudspeaker could be determined outdoors without using an anechoic room. In addition, all the required frequency components in the different one-third octave bands can be obtained in one single measurement. A detailed description of the procedure and results obtained will be presented.

10:35

**5aNS6. Precision grade sound power measurement using the sound intensity scanning technique: Comparison of methods for accuracy estimation.** Stephen E. Keith, Vincent Chiu, and Stephen H. P. Bly (Radiation Protection Bureau, Health Canada, 775 Brookfield Rd., 6301B, Ottawa, ON K1A 1C1, Canada, skeith@hpb.hwc.ca)

To assist the development of a precision scanning intensity standard for sound power determinations, this study investigated two accuracy estimation methods proposed by ISO Working Group 25. One method used the F4 sampling criterion from the precision grade discrete point intensity standard [ISO 9614-1:1993], adapted for the scanning intensity technique. The other method assumed that measurement accuracy was related to the difference between measurements using two different scanning paths. This method was a variation of the repeatability test from the engineering grade scanning intensity standard [ISO 9614-2:1996]. The study compared the estimated accuracy from each of the two methods to a third accuracy estimate, the difference between a sound power determination using the scanning intensity technique and a precision grade measurement using sound pressure [ISO 3745:1977]. All measurements were made under hemi-anechoic conditions and all intensity scanning was done manually. Results were obtained for the following three sound sources: a Brüel & Kjaer reference source, a vacuum cleaner, and a loudspeaker. The results suggested that both of the proposed methods can be of use in achieving precision grade accuracy.

5a FRI. AM

10:50–11:00

Discussion

FRIDAY MORNING, 16 OCTOBER 1998

HAMPTON ROADS BALLROOM 2, 8:10 TO 11:30 A.M.

**Session 5aPA**

**Physical Acoustics, Noise and Animal Bioacoustics: Sonic Boom Symposium III—Human and Animal Acceptability Studies and Panel Discussion**

Daryl Boness, Chair

*Department of Zoological Research, National Zoological Park, Smithsonian Institution, Washington, DC 20008*

***Invited Papers***

8:10

**5aPA1. Summary of USAF sonic boom research.** Micah Downing (QAT Testing, Inc., 680 Northland Blvd., Ste. 106, Cincinnati, OH 45240) and Brenda Cook (Langley Air Force Base, Hampton, VA)

This presentation summarizes the sonic boom research performed and sponsored by the U.S. Air Force during the 80s and 90s. The U.S. Air Force has funded research for sonic boom measurements and computer modeling as well as its effects on humans, animals, and structures. The primary motivation has been to better understand the potential impacts that supersonic operations have on the environment so that any adverse impact can be minimized while maintaining operational readiness. The developments and the findings from the projects will be highlighted along with a discussion about future research goals.

8:35

**5aPA2. Sonic boom acceptability studies at NASA Langley Research Center.** Brenda M. Sullivan and Kevin P. Shepherd (Fluid Mech. and Acoust. Div., NASA Langley Res. Ctr., M/S 463, Hampton, VA 23681, b.m.sullivan@larc.nasa.gov)

As part of the High Speed Research Program at NASA, Langley Research Center conducted a series of studies during the period 1990–1995 to evaluate human responses to sonic boom impact. This work, in combination with aircraft configuration design efforts, was aimed at determining the feasibility of overland supersonic flight. NASA conducted a three part program, comprising laboratory studies, in-home field experiments and community surveys. The laboratory studies used a sonic boom simulator and were designed to quantify relative loudness and annoyance response to a wide range of shaped boom signatures that might be produced by advanced aircraft configurations. The primary conclusion was that several common noise metrics were able to reliably predict judged loudness/annoyance. Field experiments were conducted in people's homes using a noise simulation system. A controlled sound environment of booms of known level and number was introduced into a realistic home setting and human responses to a variety of boom exposures were assessed. It was found that the "equal energy" hypothesis was applicable to these boom exposures. Community surveys were conducted in two areas routinely impacted by sonic booms from military aircraft. Relationships between boom exposure and residents annoyance were developed for the two survey areas.

9:00

**5aPA3. Influence of low-frequency content on rate of growth of annoyance of high-energy impulsive sounds.** Sanford Fidell, Laura Silvati, Karl S. Pearsons, Richard R. Howe, and Stephen J. Lind (BBN Technologies, Canoga Park, CA 91303)

Various "corrections" have been suggested to measures of high-energy impulsive sounds to account for their seemingly anomalous annoyance, some on the basis of the findings of studies that may not have accurately reproduced the low-frequency content of high-energy impulses. The present study measured rates of growth of annoyance of impulsive and nonimpulsive sounds by adaptive paired comparisons of the annoyance of five variable level signals and 29 impulsive and nonimpulsive fixed level signals. All test sounds were presented for judgment in a specially designed low-frequency test facility. When the annoyance of an aircraft flyover was compared to that of a low-frequency band of noise and of sonic booms accompanied by rattle, the relative rates of growth of annoyance were not much different from 1:1. When the annoyance of sonic booms that were *not* accompanied by rattle was compared with that of sounds containing more higher-frequency energy (an aircraft flyover and an octave band of noise centered at 1 kHz), the relative rates of growth of annoyance were nearly 2:1. These differences in relative rates of growth of annoyance of impulsive and nonimpulsive sounds are as plausibly attributed to their relative low-frequency content, as to impulsiveness *per se*.

9:25

**5aPA4. A study of sonic boom effects on seals breeding on Sable Island, Canada.** Elizabeth A. Perry, Daryl J. Boness, and Stephen J. Insley (Dept. of Zoological Res., Natl. Zoological Park, Washington, DC 20008)

Researchers were on Sable Island, Canada (440°N, 600°W), for the 1997 grey seal (*Halichoerus grypus*) breeding season to study the affects of sonic booms on seal behavior. The physical parameters of 36 sonic booms associated with the Concorde's trans-Atlantic flights were recorded. The average minimum overpressure was -0.568 PSF and mean maximum overpressure was 0.935 PSF. Data were collected on frequency of aggression, movements, and distances moved in 10-min periods before and after booms to detect changes in general agitation of pups and adults. The number of mother-pup pairs nursing and number of nursing bouts interrupted during the minute of sonic booms were compared to those in randomly chosen minutes to measure immediate startle responses of seals. There was no difference in the behavior of adults nor pups between 10-min periods before and after booms, nor did their behavior differ in the minute of booms when compared to randomly chosen control minutes. Female heart rates did not vary before, during and after booms but pup heart rates were variable. A similar study on Sable Island harbour seals (*Phoca vitulina*) is being conducted for comparison.

9:50

**5aPA5. Effects of simulated N-waves on the auditory brainstem response of three species of pinnipeds.** Ann E. Bowles, Larry Wolski, and Erik Berg (Hubbs-Sea World Res. Inst., 2595 Ingraham St., San Diego, CA 92109, annb1@san.rr.com)

Pinnipeds (seals and sea lions) on breeding beaches and hauling areas can be exposed to sonic booms from existing and planned civilian supersonic aircraft. Although carpet booms do not produce detectable threshold shifts in humans, the available anatomical information is not adequate to extrapolate models for humans to pinnipeds. Therefore, rehabilitated stranded California sea lions (*Zalophus californianus*), harbor seals (*Phoca vitulina*), and elephant seals (*Mirounga angustirostris*) were exposed to simulated N-waves with levels up to 6 psf and rise times as low as 0.4 ms. The auditory brainstem response (ABR) was used to estimate auditory sensitivity before and after exposure. The test signals were broadband clicks, and tone pips at 2 and 8 kHz. Level of the least detectable ABR waveform was used to estimate best sensitivity, while latencies to the major peaks of the waveform were used to monitor recovery rates. Latency shifts (2 ms) that recovered over the course of a 2-h post-exposure monitoring period were found in some individuals, but these did not correspond to a change in least detectable ABR for any animal. [Work supported by NASA Contract NAS1-20101.]

10:15–10:30 Break

10:30–11:30

Panel Discussion

Past, Present, and Future of Sonic Boom Research

**Moderator:**

Victor Sparrow, The Pennsylvania State University, University Park, PA

**Panelists:**

Henry E. Bass, Director, National Center for Physical Acoustics, University, MS

J. Micah Downing, QAT Testing, Inc., Cincinnati, OH

Domenic Maglieri, Eagle Aeronautics, Inc., Newport News, VA

John Morgenstern, Lockheed Martin Skunkworks, Palmdale, CA

Kevin P. Shepherd, NASA Langley Research Center, Hampton, VA

5a FRI. AM